

THE PRIMARY MAGMATIC CONCENTRATION AND SECONDARY REMOBILISATION OF PLATINUM-GROUP ELEMENTS IN NI-CU SULPHIDE ORES

Robert David Knight

Submitted in partial fulfilment of the requirements for the degree of Ph.D.

May 2014

DECLARATION

This work has not been submitted in substance for any other degree or award at this or any other university or place of learning, nor is being submitted concurrently in candidature for any degree or other award.
Signed …… (candidate) Date ……

STATEMENT 1

This thesis is being submitted in partial fulfillment of the requirements for the degree of PhD

Signed …… (candidate) Date ……

STATEMENT 2

This thesis is the result of my own independent work/investigation, except where otherwise stated.

Other sources are acknowledged by explicit references. The views expressed are my own.

Signed …… (candidate) Date ……

STATEMENT 3

I hereby give consent for my thesis, if accepted, to be available for photocopying and for inter-library loan, and for the title and summary to be made available to outside organisations.

Signed …… (candidate) Date ……

Acknowledgements

Studying for my PhD has been, quite simply, an extremely trying and testing time accompanied by a rollercoaster of emotions. I cannot express in words the sheer amount of joy and accomplishment I feel having finally completed the thing! Something that would not have been possible without the following people, to whom I owe an immeasurable debt of gratitude;

- My supervisors Dr. Hazel Prichard and Dr. Iain McDonald whose expertise and knowledge has guided me through this project from start to finish.
- Professor Cesar Ferreira Filho, who liaised with Mirabela Mineração, both allowing me to complete and assisting me in fieldwork conducted at the Mirabela mine site in Brazil.
- Dr. Christina Yan Wang, Professor Mingjie Zhang, and Qingyan Tang in both arranging and assisting me with fieldwork at the Jinchuan mine site in China.
- Cardiff University technical staff, in particular Pete Fisher for all of his SEM expertise, and Tony Oldroyd who I pestered with many other questions relating to laboratory and rock preparation work.
- Many other members of academic staff at Cardiff University for both scientific and thoroughly entertaining non-scientific conversation.
- Postgraduate PhD students at Cardiff University who have been essential for beer, banter, and for the comfort that you aren't the only one banging your head against the wall at times...
- Last, but not least, my friends and family for their unconditional and continued support.

Abstract

The PGE mineralisation in the Fazenda Mirabela ultramafic-mafic and Jinchuan ultramafic intrusions has been characterised by determining the platinum-group mineralogy of each complex and the concentration of PGE in solid solution in the base metal sulphides (BMS).

The Mirabela intrusion is largely unaltered and hosts two PGE occurrences from which 128 Au- and Ag-bearing minerals and 716 PGM have been identified; predominantly Pt-Pd-Ni tellurides in the Santa Rita sulphide ore deposit and to a lesser extent in the underlying sulphur-poor dunite. A localised Pd-Cu±Pb alloy assemblage is identified in the dunite in the central zone of the intrusion. The PGM assemblages at the edges of the intrusion are relatively As-rich containing sperrylite ($PtAs_2$); arsenic may have been introduced through crustal assimilation.

Two orebodies (#1 and #24) have been studied from the Jinchuan intrusion which has undergone extensive greenschist facies alteration. A total of 64 Au- and Ag-bearing minerals and semimetal alloys, and 93 PGM have been identified including michenerite (PdTeBi), froodite ($PdBi_2$), members of the hollingworthite-irarsite-platarsite solid solution series ([RhIrPt]AsS), sperrylite and maslovite ($Pt[BiTe]_2$) in decreasing order of abundance. The PGM vary across these two orebodies as a result of sulphide fractionation, with the Ni/MSS-rich orebody #1 hosting early crystallising sulpharsenides and As-bearing PGM whereas the relatively Cu/ISS-rich orebody #24 hosts more Pd-bearing PGM with Pd partitioning into the Cu-rich sulphide liquid during MSS crystallisation.

These studies show that Bi- and Te-bearing PGM ($[PtPdNi]Te_2$, $PdBi_2$, PdBiTe) may exsolve from the BMS during sub-solidus cooling after these elements have partitioned into the BMS at high temperatures whereas As-bearing PGM ($PtAs_2$, [RhIrPt]AsS) and sulpharsenides (gersdorffite-cobaltite [NiAsS-CoAsS]) may crystallise early directly from an As-bearing immiscible sulphide melt.

In the Mirabela intrusion, the IPGE and Rh have partitioned into MSS, from which pentlandite, pyrrhotite and pyrite have exsolved. Osmium and Ir preferentially partitioned into pyrite (with Co) whereas Ru and Rh partitioned equally between pentlandite and pyrite. In the Jinchuan intrusion, Ir, Rh and Pt have preferentially partitioned into early crystallising sulpharsenides (from which [RhIrPt]AsS PGM exsolve) depleting MSS in these elements. Palladium is identified in pentlandite in both complexes studied and may have diffused from ISS/chalcopyrite or partitioned into MSS at an earlier magmatic stage. Platinum does not usually partition into BMS (excluding sulpharsenides) and instead forms PGM. However, Pt does partition into pentlandite in the Mirabela sulphur-poor dunite where semimetal concentrations are very low and Pt-bearing PGM form only in low quantities, if at all.

Minor localised serpentinisation of the Mirabela intrusion does not remobilise the PGE with the primary magmatic distribution of PGE and PGM preserved; the latter are predominantly associated with interstitial BMS and occur in sulphide stringers shown to be of magmatic origin. Pervasive greenschist facies hydrothermal alteration at Jinchuan altered and oxidised the BMS during a process of sulphur loss, resulting in the formation of secondary magnetite and the liberation of Pd, Bi and Te which coalesce to form secondary froodite and michenerite in situ at the edges of these replacement oxides; however, the PGE are not extensively remobilised. Both complexes show that the semimetal content of the ore-forming magma is critical in controlling the distribution of PGE into BMS and/or PGM.

Contents

1. Introduction

1.1 Introduction 1

1.2 Thesis Aims 2

1.3 Thesis Structure 3

2. Literature Review

2.1 Introduction 4

2.2 The Importance and Rarity of Platinum-Group Elements 4

2.3 Introduction to Magmatic Sulphide Ore Deposits 7

2.4 Genesis of Magmatic Sulphide Ore Deposits 9

2.4.1 The effect of pressure on sulphide solubility 10

2.4.2 The effect of temperature on sulphide solubility 10

2.4.3 The effect of magma composition on sulphide solubility 11

2.4.4 The effect of oxygen and sulphur fugacity on sulphur solubility 12

2.4.5 The requirement of external sulphur 13

2.4.6 Metal concentrations of the sulphide liquid 14

2.5 Sulphide Fractionation and Partitioning of PGE 17

2.6 Combined PGE and PGM Studies 19

2.6.1 Bushveld Igneous Complex, South Africa 19

2.6.1.1 The Platreef 20

2.6.1.2 Merensky Reef 22

2.6.2 Noril'sk, Siberia 25

2.6.3 Sudbury, Canada 27

2.6.4 Stillwater Complex, Montana 29

2.6.5 Penikat, Finland 32

2.6.6 Aguablanca Ni-Cu Deposit, Southwest Spain 33

2.7 Other Studies of PGM and PGE Remobilisation 34

2.7.1 Bacuri Complex, Brazil 35

2.7.2 Jinbaoshan Pd-Pt Deposit, China 35

2.7.3 Shetland Ophiolite, Shetland Islands, Northeast Scotland 36

2.7.4 Raglan, Cape Smith, Quebec, Canada 37

2.7.5 Experimental studies of Pt and Pd mobility 38

2.8 Discussion and Summary of PGE Behaviour 39

2.9 Thesis Study Areas 44

3. Analytical Methods

3.1 Introduction 45

3.2 Major and Trace Element Geochemistry 45

3.3 Whole-Rock PGE Analysis 45

3.4 Mineralogical Analysis 46

3.5 Laser Ablation-ICP-MS 47

4. Ni-Cu-PGE Sulphide Mineralisation of the Fazenda Mirabela Intrusion, Brazil

4.1 Introduction 49

4.2 Regional and Local Geology of the Mirabela Intrusion 49

4.3 Sampling and Analytical Methods 54

4.4 Stratigraphy 55

4.5 Borehole Profiles 58

4.5.1 Santa Rita ore zone 58

4.5.2 Basal PGE anomaly 66

4.6 Geochemistry 68

4.6.1 Major element geochemistry 68

4.6.2 Chondrite normalised REE profiles 78

4.6.3 Trace element bivariate plots 80

4.6.4 Whole-rock PGE data and chondrite normalised profiles 84

4.6.5 Semimetal Analyses 88

4.7 Platinum-Group Mineralogy 90

4.7.1 PGM assemblages 90

4.7.2 Assemblage (i) PGE tellurides 96

4.7.3 Assemblage (ii) PGE tellurides and sperrylite 97

4.7.4 BMS stringers and associated PGM 99

4.7.5 Assemblage (iii) Pd alloys 103

4.7.6 PGM abundance and size distribution 103

4.8 Laser Ablation-ICP-MS 105

4.8.1 Santa Rita ore zone 106

4.8.2 Sulphur-poor dunite 109

4.9 Discussion 112

4.9.1 Major and trace element geochemistry 112

4.9.2 Pt-Pd tellurides in layered complexes 113

4.9.3 Formation of Pt-Pd-Ni-Fe tellurides 114

4.9.4 Formation of sperrylite and irarsite 116

4.9.5 PGM-bearing BMS stringers 118

4.9.6 Variation in PGM abundance 121

4.9.7 Formation of the Pd-alloy assemblage 124

4.9.8 Variation in Pd/Pt ratio 127

4.9.9 IPGE and cobalt in pyrite 128

4.10 Model and Summary 131

5. Platinum-Group Mineralogy and PGE Mineralisation of the Jinchuan Intrusion, China

5.1 Introduction 135

5.2 Geology of the Jinchuan Intrusion 135

5.3 Sampling 141

5.4 Analytical methods 142

5.5 Silicate and Sulphide Petrography 144

5.6 Major Element Geochemistry 148

5.6.1 Major element Harker diagrams 148

5.6.2 Trace element bivariate plots 150

5.7 Whole-Rock PGE Data and Chondrite Normalised Profiles 153

5.8 Platinum-Group Mineralogy 156

5.8.1 Variation in PGM from orebodies #1 and #24 163

5.9 Laser Ablation-ICP-MS 165

5.10 Discussion 168

5.10.1 Formation of PGM 168

5.10.2 The role of sulpharsenides as collectors of PGE 172

5.10.3 Platinum nugget effect 175

5.10.4 Variation of PGM and whole-rock PGE concentrations 176

5.11 Conclusions 183

6. Discussion and Conclusions

6.1 Comparing the PGE Mineralisation of the Mirabela and Jinchuan Intrusions 185

6.2 The Partitioning Behaviour of PGE 189

6.3 The Primary Magmatic Formation of PGM 192

6.4 The Secondary Remobilisation of PGE 195

6.5 Conclusions 198

References 200

Appendices

Appendix A:	Mirabela Sample List	219
Appendix B:	Mirabela Borehole Mine Assay Data	221
Appendix C:	Mirabela Major Element Data (ActLabs)	261
Appendix D:	Mirabela Trace REE Data (Cardiff University)	264
Appendix E:	Mirabela PGE Whole-Rock Data (ActLabs)	265
Appendix F:	Mirabela Semimetal Data (ActLabs)	267
Appendix G:	Mirabela Full PGM Mineralogical Data	269
Appendix H:	Mirabela PGM, Labelled Images	290
Appendix I:	Mirabela Full LA-ICP-MS Data (Cardiff University)	1018
Appendix J:	Jinchuan Sample List	1026
Appendix K:	Jinchuan Major Element Data (Cardiff University)	1028
Appendix L:	Jinchuan PGE Whole-Rock Data (Cardiff University)	1029
Appendix M:	Jinchuan Full PGM Mineralogical Data	1031
Appendix N:	Jinchuan PGM, Labelled Images	1036
Appendix O:	Jinchuan Full LA-ICP-MS Data (Cardiff University)	1138

List of Figures

Figure 1.1: Sketch showing sources and locations of Pt and Pd (Prichard, 2007). 2

Figure 2.1: Plot of ore grade (Ni wt. %) versus production and reserves of ore (Mt) for major Ni and PGE sulphide deposits of the world (after Naldrett, 2011). 7

Figure 2.2: Results of mantle melting modelling showing how the concentrations of Cu, Ni, Pt and Pd vary in a developing partial melt (modified from Naldrett, 2011). 15

Figure 2.3: Geological map showing the geology of the Bushveld Complex and expanded view of the Northern Limb with the Platreef (modified from Hutchinson and McDonald, 2008 [modified from van der Merwe, 1978 and Ashwal *et al.*, 2005]). 21

Figure 2.4: Geological map of the western lobe of the Bushveld Complex, South Africa; (a) simplified geological map (Godel *et al.*, 2007 [modified after Von Gruenewaldt, 1986; 1989]) and (b) generalised stratigraphy of the Bushveld Complex (Godel *et al.*, 2007 [modified after Eales and Cawthorn, 1996]). 24

Figure 2.5: Location (inset) and geological maps of the Sudbury Igneous Complex and its Ni-Cu-PGE deposits (modified from Dare *et al.*, 2010b [modified from Barnes and Lightfoot, 2005 after Souch *et al.*, 1969]). 28

Figure 2.6: Geological map (modified from Godel and Barnes, 2008a [modified after Mc Callum *et al.*, 1980; Zientek *et al.*, 2002]) and stratigraphic column (modified from Godel and Barnes, 2008a [modified after Zientek *et al.*, 2002]) of the Stillwater Complex. 31

Figure 4.1: Maps showing the location of the Mirabela intrusion and simplified geology of the south-southeast Bahia granulite region (Barnes et al., 2011 [after Barbosa et al., 2003]) and regional terrane boundaries (Barnes et al., 2011 [after Barbosa and Sabaté, 2004]). 50

Figure 4.2: Geological map of the Fazenda Mirabela intrusion (modified after Barnes et *al.*, 2011; Inwood et *al.*, 2011) showing the location of the boreholes sampled; MBS209 and MBS158 from the northern zone, MBS604 and MBS605 from the central zone and MBS565 and MBS569 from the southern zone. 52

Figure 4.3: Reflected and transmitted light photomicrographs showing the silicate and sulphide petrography of the Mirabela intrusion. 57

Figure 4.4: Geochemical profiles of the boreholes studied. 60

Figure 4.5: Back-scattered electron images of BMS in the sulphur-poor dunite. 67

Figure 4.6: Harker diagrams plotted against MgO using mine assay data (one metre composite intervals of diamond drill core were analysed by multi-element ICP-MS). 70

Figure 4.7: Harker diagrams plotted against MgO using sample only data (ActLabs completed on only samples selected (PTSR01-72) from the six boreholes studied). 71

Figure 4.8: Major element geochemical profiles of the boreholes studied. 72

Figure 4.9: Chondrite normalised REE diagrams a) selected representative samples from the central zone boreholes MBS604 with an additional dunite sample from MBS605 (PTSR25) and b) selected representative samples from the northern zone borehole MBS158. 79

Figure 4.10: A series of trace element bivariate plots constructed to determine the role of magma mixing and crustal contamination in the genesis of the Mirabela intrusion and Santa Rita ore zone 81

Figure 4.11: The change in La/Sm ratios with depth displayed for three boreholes from the northern, central and southern zone for comparison. 83

Figure 4.12a): Chondrite normalised PGE diagrams showing pattern 1) positive Pd anomaly in the sulphur-poor dunite hosting the basal PGE anomaly (profiles split by borehole number). 85

Figure 4.12b): Chondrite normalised PGE diagrams showing pattern 2) positive Pt anomaly in the Santa Rita ore zone (profiles split by borehole number). 86

Figure 4.12c): Chondrite normalised PGE diagrams showing pattern 3) straight profiles with no Pt or Pd anomaly in the 'transition zone' between the Santa Rita ore zone and the underlying sulphur-poor dunite (profiles split by borehole number). 87

Figure 4.12d): Schematic diagram showing where the three PGE patterns described above occur within the Mirabela straigraphy. 88

Figure 4.13: Semimetals (As and Te in ppm) plotted with sulphur (S in wt. %) against depth for a) borehole MBS209 (northern zone), b) borehole MBS158 (northern zone), c) borehole MBS565 (southern zone), d) borehole MBS569 (southern zone); *dashed line marks the top of the dunite in each borehole for reference. 89

Figure 4.14: Schematic diagram showing the location of the different PGM assemblages identified: (i) PGE tellurides, (ii) PGE tellurides with sperrylite and (iii) the localised Pd alloy assemblage. 91

Figure 4.15: Pie charts showing the proportion of different PGM types in different zones of the intrusion. 95

Figure 4.16: Back-scattered electron images of the typical PGM observed from assemblage (i) and (ii). 100

Figure 4.17: Back-scattered electron images of BMS and magnetite stringers and their associated PGM. 101

Figure 4.18: Back-scattered electron images of the typical PGM observed from Pd alloy assemblage (iii) in the sulphur-poor dunite zone (MBS604 - central zone only). 102

Figure 4.19: PGM size distribution graphs showing; a) the proportion of PGM per interval size (μm^2) calculated by the number of PGM per interval size and b) the proportion of PGM per interval size (μm^2) calculated by the total area of PGM per interval size. 104

Figure 4.20: PGM size distribution graphs showing; a) the proportion of PGM per interval size (μm^2) calculated by the number of PGM per interval size for the Santa Rita ore zone and b) the proportion of PGM per interval size (μm^2) calculated by the number of PGM per interval size for the sulphur-poor dunite zone. 105

Figure 4.21: Histograms showing the concentrations of PGE and Co (where significant) in pentlandite, pyrrhotite and pyrite from the Santa Rita ore zone against the number of analyses completed. 110

Figure 4.22: Time (s) versus counts (per second) spectra for laser ablation ICP-MS analyses of the Mirabela BMS. 111

Figure 4.23: Diagram demonstrating the formation of BMS stringers and associated PGM. 119

Figure 4.24: Formation of PGM and micro-symplectite textures in BMS in the sulphur-poor dunite. 126

Figure 4.25: Diagram summarising processes controlling PGM formation in the Mirabela intrusion. 132

Figure 5.1: Location and geological map of the Jinchuan intrusion (modified from Chai and Naldrett, 1992; Lehmann *et al.*, 2007; Song *et al.*, 2012). Schematic locations of the boreholes sampled are marked. 136

Figure 5.2: Diagram showing the location and depths of the samples studied from the Jinchuan intrusion within their respective boreholes. 143

Figure 5.3: Scans of the Jinchuan core sampled showing the different types of sulphide mineralisation identified. 145

Figure 5.4: Reflected light photomicrographs showing the sulphide petrography of the Jinchuan intrusion. 146

Figure 5.5: Transmitted light photomicrographs showing the silicate petrography of the Jinchuan intrusion. 147

Figure 5.6: Major element Harker diagrams plotted against MgO for selective representative samples showing two distinct groups; 1 and 2. 149

Figure 5.7: A series of trace element bivariate plots constructed to determine the difference in the genesis between orebody #1 and orebody #24 in the Jinchuan intrusion. 152

Figure 5.8: Chondrite normalised PGE diagrams showing a) samples from borehole ZKS-09, orebody #24, segment I to the west and b-d) samples from DZK09-01, DZK12-06 and DZK14-02 respectively, orebody #1, segment II to the east. 154

Figure 5.9: Chondrite normalised PGE diagrams showing original and duplicate analyses used to check for analytical drift in isolation. a-d) Significant variation in Pt and occasionally Rh (b) can be observed. 155

Figure 5.10: Back-scattered electron images of the typical PGM observed in samples from the Jinchuan intrusion. 160

Figure 5.11: Back-scattered electron images of the small zoned euhedral gersdorffite-cobaltite (Gers-Cob) phases hosting irarsite with minor Pt ([Ir,Pt]AsS) in their cores. 161

Figure 5.12: PGM size distribution graphs showing a) the proportion of PGM per interval size (μm^2) calculated by the number of PGM per interval size and b) the proportion of PGM per interval size (μm^2) calculated by the total area of PGM per interval size. 162

Figure 5.13: Pie charts showing the proportion of different PGM types in the two different orebodies studied; a) by the total area of PGM identified in orebody #1, segment II, and b) by the total area of PGM identified in orebody #24, segment I. 164

Figure 5.14: Histograms showing the concentrations of Pd in pentlandite from the Jinchuan intrusion (orebodies #1 and #24). 166

Figure 5.15: Diagram showing the formation of primary secondary Pd-PGM during post-magmatic alteration. 169

Figure 5.16: Chondrite normalised PGE diagrams with samples separated according to sulphide ore type. 178

Figure 5.17: Chondrite normalised PGE diagrams with samples separated according to lithology. 179

Figure 5.18: Summary of PGM formation and PGE behaviour in the Jinchuan intrusion. 182

List of Tables

Table 2.1: Table showing the important metallurgical properties of the PGE and Au (Gunn *et al.*, 2009). 5

Table 2.2 Relative abundances of PGE in the Earth's crust. 5

Table 2.3: The average prices of the PGE for 2013 at the time of writing in USD/oz. 5

Table 2.4: Table showing average sulphide compositions of different classes of Ni deposits and the differences in base metal and PGE ratios (after Naldrett, 2004). 8

Table 2.5: Table displaying the distribution of the PGE in BMS (pyrrhotite, pentlandite, pyrite, chalcopyrite) and PGM for the major PGE deposits reviewed in this chapter. 41

Table 2.6: Table displaying average PGE concentrations in orebodies #24, #1 and #2 from the Jinchuan intrusion (after Chai and Naldrett, 1992b). 47

Table 3.1: Compositions of quenched sulphide standards used for LA-ICP-MS. Dashes indicate that the element was not added to the standard. 48

Table 4.1: Depth, dip and azimuth information for the boreholes sampled. 54

Table 4.2: Abundance of different PGM types in all PGM-bearing samples analysed. 92

Table 4.3: Selective representative quantitative analyses (wt. %) of PGM with derived empirical formulae. 94

Table 4.4: Laser ablation ICP-MS results for chalcopyrite, pentlandite, pyrrhotite and pyrite from the Santa Rita ore zone. 107

Table 4.5: Laser ablation ICP-MS results for chalcopyrite, pentlandite, pyrite and BMS mixes from the sulphur-poor dunite. 108

Table 5.1: Table displaying average PGE concentrations in orebodies #24, #1 and #2 from the Jinchuan intrusion (after Chai and Naldrett, 1992b). 137

Table 5.2: Numbers and types of PGM observed in the samples studied from orebodies #1 and #24 from segments II and I respectively of the Jinchuan intrusion. 157

Table 5.3: Selective representative quantitative analyses (wt. %) of PGM with derived empirical formulae. 159

Table 5.4: Laser ablation ICP-MS results for chalcopyrite, pentlandite, pyrrhotite and pyrite from the Jinchuan intrusion. 167

Table 6.1: Comparison of average whole-rock PGE concentrations for individual and combined boreholes of the Mirabela and Jinchuan intrusions. *n.a. = not analysed, sulphur-poor samples from the Jinchuan intrusion and Mirabela Santa Rita ore zone have been ignored in order to obtain relevant average PGE values. 186

Table 6.2: Comparison of the PGM and average PGE concentrations in solid solution in BMS of the Mirabela and Jinchuan intrusions. 187

1. Introduction

1.1 Introduction

This thesis presents and discusses the results of a study on the behaviour of the platinum-group elements (PGE) during primary magmatic crystallisation and subsequent metamorphism and alteration. Two PGE-bearing Ni-Cu sulphide deposits hosted in the Fazenda Mirabela ultramafic-mafic intrusion, Brazil, and the Jinchuan ultramafic intrusion, China, have been examined. The Mirabela intrusion is almost completely unaltered retaining primary magmatic minerals and textures except for minor localised serpentinisation whereas the Jinchuan intrusion has been extensively altered by regional greenschist facies metamorphism. Together they provide settings in which to investigate the PGE from their initial magmatic concentration to their remobilisation during late-stage magmatic processes and secondary low temperature alteration.

Recent advances in laser ablation-inductively coupled plasma-mass spectrometry (LA-ICP-MS) now allows traces of PGE to be identified in base metal sulphides (BMS) at concentrations of parts per billion (ppb). Thus, the study of PGE in BMS combined with the identification of platinum-group minerals (PGM) allows the total distribution of PGE to be established in any given sample and compared with whole-rock PGE analyses. This combined approach has been utilised in this thesis which expands upon the ever increasing body of data and literature on the distribution of PGE between PGM and BMS. This distribution is complex and controlled by a number of different factors that have been determined for the two intrusions considered here.

The world's major economic PGE deposits are hosted by giant mafic-ultramafic magmatic systems including PGE-rich reefs and chromitites in the Bushveld Igneous Complex, and the Noril'sk-Talnakh deposits in feeder sills/intrusions to the Siberian flood basalts; however, many smaller mafic-ultramafic intrusions also host significant concentrations of PGE. These all represent a part of the natural world distribution of PGE (Fig. 1.1) whereby these elements are extracted from the Earth's mantle during partial melting and are concentrated by magmatic processes. Placer deposits may form during the erosion of these magmatic occurrences. Increasingly, the PGE are being reintroduced into the environment by anthropogenic pollution (e.g., Prichard, 2007).

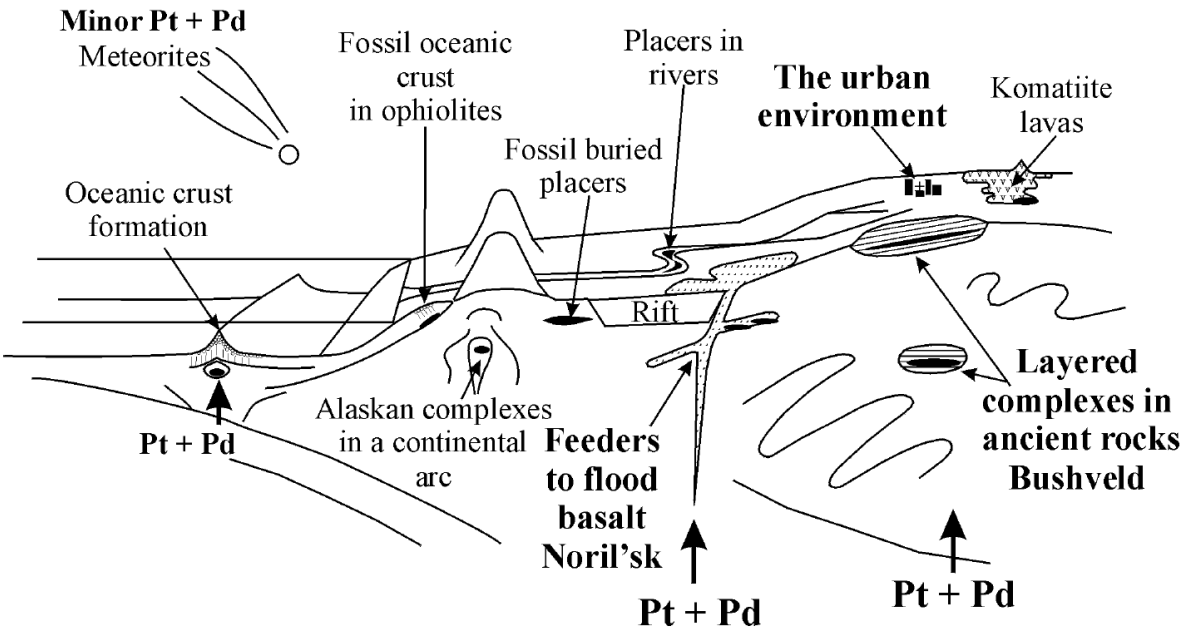


Figure 1.1: Sketch showing sources and concentrations of Pt and Pd (Prichard, 2007).

1.2 Thesis Aims

The aims of this thesis are to:

1) Further the understanding of the magmatic partitioning behaviour of PGE into the crystallisation products of immiscible sulphide melts (typically monosulphide solid solution [MSS], intermediate solid solution [ISS] and their exsolution products pentlandite, pyrrhotite and chalcopyrite) by identifying the PGE as trace elements in solid solution in BMS.
2) Further the understanding of the formation of PGM using mineralogical studies (PGM crystal forms, sizes, mineral associations and chemistries) to make deductions regarding both the timing and processes of PGM formation.
3) Analyse the behaviour of the PGE, both in solid solution in the BMS and as PGM during different types of post-magmatic hydrothermal alteration (e.g., minor localised serpentinisation - Mirabela intrusion, Brazil and regional greenschist facies metamorphism - Jinchuan intrusion, China) and assess the potential for PGE remobilisation during these events.
4) Compare and contrast the results presented here with those of other natural and experimental studies as described in the following literature review (chapter 2).

1.3 Thesis Structure

This thesis is comprised of six chapters including this introduction. Chapter 2 comprises a literature review focussed on an introduction to magmatic sulphide deposits and both the primary magmatic and secondary behaviour of PGE as determined by various experimental and natural studies. Chapter 3 documents the analytical procedures used in collecting various types of geochemical and mineralogical data at Cardiff University.

Chapters 4 and 5 detail the study of PGE mineralisation in the Fazenda Mirabela intrusion, Brazil and the Jinchuan intrusion, China, respectively. These chapters occur in an expanded paper format containing their own separate discussion sections. Finally, Chapter 6 compares the PGE mineralisation of both the Mirabela and Jinchuan intrusions directly, as well as with the expected behaviour of the PGE as determined from the following literature review.

2. Literature Review

2.1 Introduction

This chapter introduces magmatic sulphide ore deposits, assesses the controls on their genesis and reviews experimental studies on the partitioning of PGE into different BMS phases as they form during sulphide melt fractionation. Further natural studies of magmatic sulphide ore deposits are also reviewed. The work presented in this thesis is the result of the combined use of a scanning electron microscope (SEM) to identify and analyse PGM, and LA-ICP-MS to determine PGE concentrations in solid solution in BMS. As such, the following literature review of natural sulphide ore deposits has been restricted to deposits where authors have either completed similar combined studies in single publications, or where separate studies of both the PGM and the PGE in BMS are available for the same deposit. This allows for the full behaviour of the PGE to be examined and compared to the work presented here. Additional studies investigating the post-magmatic remobilisation of PGE have also been included where deemed significant to this thesis, including some experimental studies of Pt and Pd mobility.

2.2 The Importance and Rarity of Platinum-Group Elements

The PGE consist of six metals; osmium (Os), iridium (Ir), ruthenium (Ru), rhodium (Rh), platinum (Pt) and palladium (Pd). Their unique physical properties (Table 2.1) including high melting points, chemical inertness, low coefficient of thermal expansion, ability to catalyse chemical reactions and high resistance to corrosion make them highly important in various industrial applications (Gunn *et al.*, 2009 - BGS Commodity Report; Platinum Today, 2013; Cowley, 2013 [Johnson Matthey Platinum Review]).

Platinum and Pd are of major commercial significance and can be utilised with Rh as catalysts in catalytic converters, used to convert the toxic by-products of combustion in the automotive industry. A significant amount of Pt is also used in the manufacture of jewellery. Platinum and Pd are used in electrical and chemical applications, dentistry and the manufacture of glass as well as in many other industrial applications around the world. Iridium and Ru are mainly used in electronic and chemical applications whereas Pt is also used in medical applications such as chemotherapy (Gunn *et al.*, 2009 - BGS Commodity Report; Platinum Today 2013; Cowley, 2013 [Johnson Matthey Platinum Review]).

Element	Pt	Pd	Rh	Ir	Ru	Os	Au
Atomic weight	195.08	106.42	102.91	192.22	101.07	190.23	196.97
Atomic number	78	46	45	77	44	76	79
Density (gcm^{-3})	21.45	12.02	12.41	22.65	12.45	22.61	19.3
Melting point (^oC)	1769	1554	1960	2443	2310	3050	1064
Electrical resistivity (Micro-ohm cm at 0^oC)	9.85	9.93	4.33	4.71	6.8	8.12	2.15
Hardness (Mohs)	4-4.5	4.75	5.5	6.5	6.5	7	2.5-3

Table 2.1: Table showing the important metallurgical properties of the PGE and Au (Gunn *et al.*, 2009 - BGS Commodity Report).

The demand for Pt (and possibly Pd) is only expected to rise as 'clean' fuel cell technology is developed with an increasing number of countries adopting tighter carbon emission policies. Fuel cells are electrochemical devices that use a PGE alloy (predominantly platinum) catalyst to convert fuel (hydrogen and an oxidant [oxygen or air]) into electricity with heat as a by-product and are therefore a much cleaner alternative to current non-renewable energy sources.

Study/Reference	Calculated Concentrations of PGE in the Earth's Crust (ppb)					
	Os	Ir	Ru	Rh	Pt	Pd
Rudnick and Gao, 2003	0.03	0.02	0.34	n.d.	0.50	0.52
Wedepohl, 1995	0.05	0.05	0.1	0.06	0.40	0.40
Ehrenbrink and Jahn, 2001	0.03	0.02	0.21	n.d.	0.51	0.52

Table 2.2 Relative abundances of PGE in the Earth's crust, n.d. = not determined.

Average prices of the PGE for 2013 at the time of writing in USD/oz					
Os*	Ir	Ru	Rh	Pt	Pd
~380	963.07	83.53	1111.36	1526.22	728.66

Table 2.3: The average prices of the PGE for 2013 at the time of writing in USD/oz (http://www.platinum.matthey.com/prices), *(http://taxfreegold.co.uk/osmiumpricesusdollars.html).

Despite the growing importance of PGE in industrial applications, they are extremely rare in the Earth's crust, more so than the rare earth elements (REE) with their calculated abundances given in Table 2.2. The rarity of the PGE coupled with their unique metallurgical properties critical for industrial applications makes these metals highly valuable (Table 2.3).

The rarity of PGE in the Earth's crust stems from the formation of the Earth and the processes that affected it during its early history. No more than 100 Ma after its accretion (4.5 Ga), it is theorised that the interior of the Earth was partially molten allowing for elements to reorganise themselves (Lunine, 1999). Based on their valence structure and the effects of the size of atoms, elements are divided into lithophiles ("rock-loving" silicate phases), siderophiles ("iron-loving" metal phases) and chalcophiles ("ore-loving" forming sulphur-bearing or sulphide phases). During this time, dense iron sulphide and oxide melts sank into the centre of the planet (Kleine, 2011). The gravitational energy released from this process was similar to the total energy emitted during Earth's accretion, causing further melting of the Earth's interior and upper layers resulting in the formation a differentiated planet (core, mantle and crust) (Lunine, 1999). As the PGE are both siderophile and chalcophile elements as well as dense, it is not surprising that at this point, the majority of the Earth's PGE budget is hypothesised to have partitioned into the dense iron core of the planet leaving the mantle depleted in these metals.

However, mantle concentrations of siderophile elements are much higher than predicted from metal-silicate partition experiments at variable temperatures and pressures (e.g., Ringwood, 1966; Ringwood and Kesson, 1977; Holzheid *et al.*, 2000; Ertel *et al.*, 2006; Walker, 2009; Mann *et al.*, 2012). The difference could be accounted for by the addition of 0.5-1% of primitive meteoritic material after core formation had completed (Kimura *et al.*, 1974). It is theorised that the mantle was effectively re-fertilised in PGE as well as other dense metallic elements during a period of meteorite impacts known as the "Late Heavy Bombardment" to account of this discrepancy (e.g., Chou, 1978; Morgan *et al.*, 1981; Becker *et al.*, 2006; Brenan and McDonough, 2009) which occurred after the formation of a differentiated Earth given the failure of this material to equilibrate with the core (Kimura *et al.*, 1974). Lunar evidence suggests that these impacts occurred or peaked at ~3.9 Ga (e.g., Tera *et al.*, 1974), however, more recent models suggest that there may not have been an impact peak at ~3.9 Ga and argue that a broader period of impacts may have occurred instead ~4.0-3.4 Ga tailing off gradually (e.g., Hartmann *et al.*, 2007). It is now thought that less than 1% of the Earth's total PGE budget is in the mantle, and even less in the crust.

In the crust, the PGE may bond together as PGE alloys or with base metals (e.g., Ni and Cu) and semimetals (As, Bi, Sb, Se, and Te) forming PGM. Alternatively, PGE may occur as trace elements in solid solution in BMS. Regardless of which, the majority of economic PGE occurrences are associated with magmatic sulphide ore deposits (Naldrett, 2004).

2.3 Introduction to Magmatic Sulphide Ore Deposits

Magmatic sulphide deposits can be broadly divided into two classes; those that are Ni-Cu-rich with relatively low PGE and high whole-rock sulphide content (20-90%) and those that are PGE-rich with low sulphide content (0.5-5%) (Naldrett, 2004). These two classes are further subdivided based on the petrographic framework of the ore host with Ni-Cu occurrences subdivided into NC-1 to NC-7 and PGE occurrences subdivided into PGE-1 to PGE-6 (Naldrett, 2004).

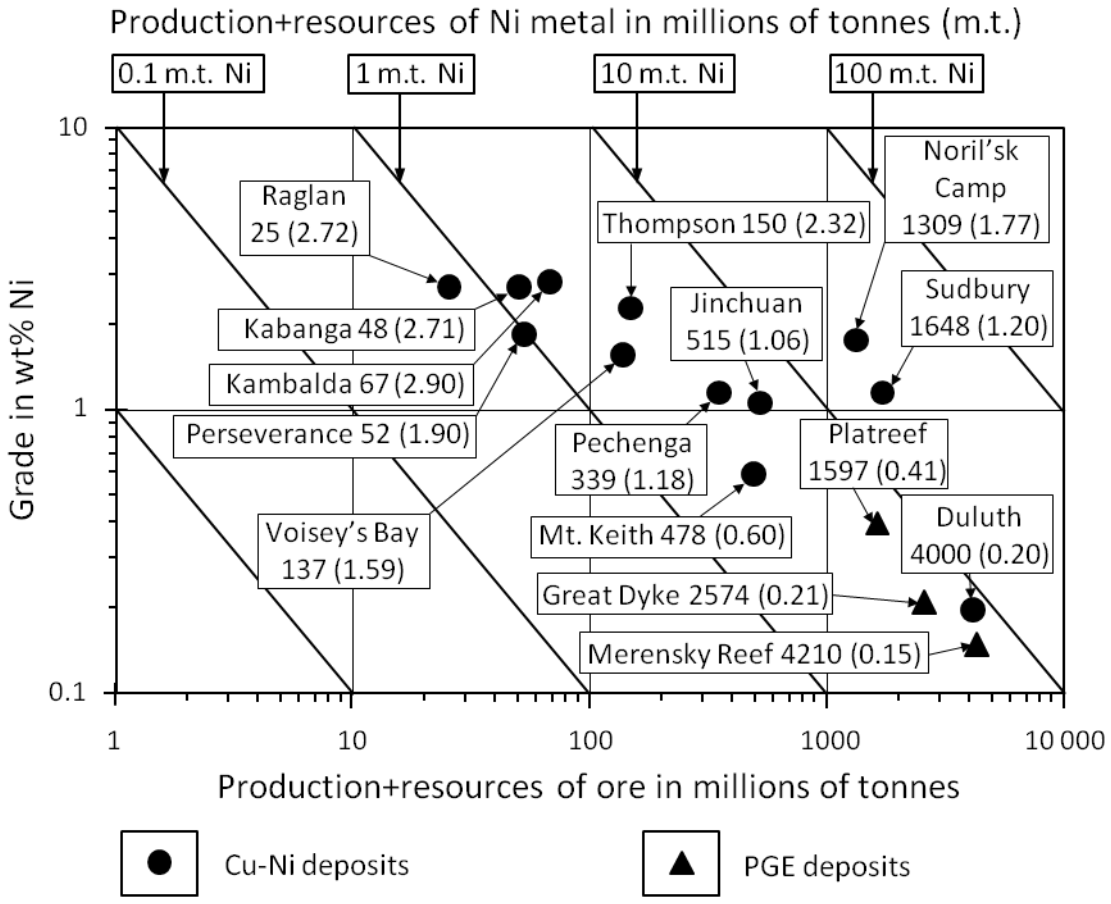


Figure 2.1: Plot of ore grade (Ni wt. %) versus production and reserves of ore (Mt) for major Ni and PGE sulphide deposits of the world (after Naldrett, 2011).

	Wt% Ni in 100% Sulphide		Ni/Cu	Ni/Co	Pd/Pt	Pd/Ir	(Pt+Pd)/ (Ni+Cu)
	Range	Average					
Archaean komatiite-related deposits							
Western Australia							
Kambalda	9-19	14.20	13.50	0.07	1.39	8.87	0.23
Zimbabwe (massive ore)							
Trojan		10.80	7.71		0.49	7.14	0.27
Epoch		23.60	58.00		0.49	0.95	0.09
Shangani		13.33	13.50		0.30	8.58	0.18
Canada							
Langmuir		12.33	25.08		1.88	5.88	0.14
Alexo		6.42	15.07		2.62	77.27	0.59
Proterozoic komatiite-related deposits							
Cape Smith Belt							
Raglan	10.4-15.3	12.8	3.88	0.02	2.84	38.06	0.78
Thompson Nickel Belt							
Pipe-2		3.95	24.68	22.00	2.26	2.15	0.04
Thompson		8.46	14.32	50.00	4.46	13.40	0.24
Bucko Lake		20.85	3.88		2.87	21.19	0.32
Flood basalt-related deposits							
Noril'sk		6.25	0.58	58.00	3.43	217.34	4.48
Duluth		4.09	0.33	10.50	3.35	184.17	1.70
Great Lakes Nickel		5.19	0.52		4.02	303.56	1.70
Insizwa		5.88	0.91		2.40	18.12	0.73
Anorthosite-related deposits							
Voisey's Bay	3.64-4.61	4.07	1.87	18.00	1.29	59.98	0.08
Other deposits							
Pechenga	2.7-13.7	10.49	1.86	26.00	1.33	9.74	0.16
Jinchuan	9.4-11.0	10.69	1.76	56.00	1.00	14.37	0.36
Sudbury	2.5-8.0	5.5	1.11	32.00	1.26	30.65	0.18

Table 2.4: Table showing average sulphide compositions of different classes of Ni deposits and the differences in base metal and PGE ratios (after Naldrett, 2004).

The three most important deposits in the world in terms of Ni content are Noril'sk in Russia, Sudbury in Canada and Jinchuan in China (Naldrett, 2011). Important reserves of Ni also occur in the PGE reefs of the Bushveld Igneous Complex as well as in the sulphide zones of the Great Dyke in Zimbabwe, however, the grades are low (0.04-0.41%); therefore Ni is only produced as a by-product of mining. The most economically important PGE deposits in the world are hosted by the Bushveld Igneous Complex which includes the Platreef, Merensky Reef and UG2 chromitite deposits. Noril'sk and the Main Sulphide Zone of the Great Dyke are also of considerable importance. A plot of grade versus tonnage for these and other economically important deposits is given in Figure 2.1 after Naldrett (2011).

Different types of Ni-Cu-PGE sulphide deposits are commonly identified by observing variations in metal tenor (metal in 100% sulphides) and the ratios of particular element pairs. For example, Archaean komatiite deposits typically exhibit high Ni tenor as well as high Ni/Cu ratios; a result of the high Ni content of their source magmas. Eckstrand (1975) indirectly explained that the Mt Keith and Epoch deposits hosted in Archaean komatiites have particularly high Ni/Cu ratios as they were subjected to post-magmatic talc-carbonate alteration which liberated Ni from the silicates which subsequently partitioned into the adjacent sulphides.

Pd/Ir ratios are used to quantify the steepness of mantle or chondrite normalised PGE profiles. Archaean komatiite deposits exhibit relatively low Pd/Ir ratios which increase progressively with deposits that are related to less mafic magmas; deposits related to flood basalts exhibit the highest Pd/Ir ratios (Naldrett, 2004). Different classes of deposit also have characteristic proportions of PGE measured using the ratio of (Pt+Pd)/(Ni+Cu), with the PGE measured in parts per million (ppm) and Ni and Cu measured in wt. %. The difference in these ratios is displayed in Table 2.4 which generally shows that Ni-Cu sulphide deposits have ratios of <0.5, except in the case of those related to flood basalts which have ratios of 0.5-5 whereas PGE deposits yield ratios of typically 10-30, but can be well over 100.

2.4 Genesis of Magmatic Sulphide Ore Deposits

Several key aspects must be considered with a view to the genesis of PGE-bearing magmatic sulphide deposits; i) how sulphide saturation is achieved in the host magma leading to the formation and separation of an immiscible sulphide liquid into which the chalcophile elements partition, ii) how the sulphides react with a sufficient degree of fresh magma in order to scavenge and concentrate an economic quantity of chalcophile elements (Ni, Cu, Co and PGE) and iii) how the sulphides are subsequently concentrated or spatially restricted to occur in a quantity that constitutes an ore deposit.

The pressure, temperature, composition and oxidation state of the magma are all important factors which control the solubility of Fe-sulphide in magmas and therefore potentially affecting the point at which sulphide saturation is achieved. The sulphur content required for sulphide saturation, known as SCSS (the sulphur content of the silicate magma in equilibrium

with sulphide-rich liquid at the point of sulphur saturation) can therefore vary according to changes in the factors mentioned above.

2.4.1 The effect of pressure on sulphur solubility

Mavrogenes and O'Neill (1999) studied the SCSS of a basaltic and a picritic melt as a function of pressure and temperature from 5-90 kb and 1400-1800°C, respectively. The SCSS of both melts was shown to decrease exponentially with increasing pressure. Huang and Williams (1980) studied portions of the Fe-Si-S-O system at 32 kb and reported that the miscibility gap between sulphide and silicate liquids expands with increasing pressure. Wendlandt (1982) studied the solubility of sulphur in silicate melts coexisting with iron sulphide melt as a function of pressure and temperature for three silicate compositions: Mt. Hood andesite, Grande Ronde basalt and Goose Island basalt (FeOt = 5.4%, 11.1% and 17.0%, respectively). Experimental pressures varied from 12.5-30 kb and temperatures from 1300-1460^{o}C. In agreement with the studies above, the results of their experiments also show that sulphur solubility decreases with increasing pressure and they suggest that the miscibility gap between natural silicate and sulphide melts expands with increasing pressure. Consequently, a magma generated in equilibrium with residual sulphide in the mantle becomes sulphide undersaturated during adiabatic ascent and sulphide saturation should occur only after a significant amount of silicate crystallisation in a closed-system. These data also suggest that if a magma leaves the mantle unsaturated in sulphide, it will be even more so as that magma rises and pressure decreases. Therefore, in order to invoke sulphide saturation, other factors/processes are required to both cancel out the effect of pressure and to continue to lower the SCSS to the point at which sulphide saturation can be achieved.

2.4.2 The effect of temperature on sulphur solubility

Studies have shown that SCSS increases with increasing temperature; however, there is little data on the details of this subject. Haughton *et al.* (1974) studied the effects of temperature and fugacities of the gaseous species O_2 and S_2 on the solubility of sulphur in mafic magmas using experiments conducted at one atmosphere total pressure and with fO_2 and fS_2 controlled by the mixing of SO_2, CO_2 and CO. They found that SCSS increases with temperature and were able to quantify that a temperature increase of 100^{o}C magnifies the capacity of a magma

to dissolve sulphur by a factor of five to seven times, assuming a constant ratio of fO_2 and fS_2. Wendlandt (1982) also showed that sulphur solubility increases with increasing temperature while Naldrett (2004) further suggested that the SCSS of a magma at 1450^{o}C may be three to five times the SCSS of the same magma at 1200^{o}C. Liu *et al.* (2007) studied the sulphur concentration in a range of silicate melts (basaltic to rhyolitic) with varying water contents (0 to ~9 wt. %) at sulphide saturation (SCSS) experimentally under a temperature range of 1150-1450^{o}C and a pressure range of 500 MPa to 1 GPa in a piston-cylinder apparatus. In their experiments, temperature was confirmed to have a positive effect on the SCSS. The experiments of Mavrogenes and O'Neill (1999) show that both the basaltic and picritic compositions studied are rather insensitive to temperature suggesting that temperature is not an important factor in the control of sulphide solubility. Therefore, if there is no other change in the magma composition, a sulphide unsaturated magma at depth will remain so as it rises and cools due to the dominant effect of pressure. Silicates will crystallise before any sulphide liquid separates and those sulphides that develop subsequently will be mixed with the silicate cumulates.

2.4.3 The effect of magma composition on sulphur solubility

FeO and TiO_2 concentrations affect sulphur solubility and variation in these elements occurs during magma crystallisation and fractionation, and is not something that is easily altered by processes external to the magma chamber Naldrett (2004). The experiments of Wendlandt (1982) found that sulphur solubility increases with increasing FeOt content of the silicate melt.

Mathez (1976) studied a suite of fresh basalt glasses containing sulphide globules composed of finely intergrown pyrrhotite, Cu-Fe sulphide, and frequently pentlandite from the Juan de Fuca Ridge and 17 localities elsewhere in the Atlantic and Pacific basins. He suggested that fractional crystallisation of olivine should cause sulphide liquids to exsolve from the magma whereas plagioclase fractionation should drive the liquid further from sulphide saturation. However, he further suggested that fractional crystallisation may not result in the separation of large quantities of sulphide liquid when taking into account more typical fractionation models involving plagioclase and olivine separation in a ratio of ~10:3, where liquid compositions are driven approximately parallel to a sulphide saturation plane if constant temperature is assumed.

Czamanske and Moore (1977) studied the bulk composition of immiscible sulphide globules in fresh submarine basalt samples from the Mid-Atlantic Ridge and found that the sulphur content of the host glasses shows a strong correlation with FeO content, increasing from 840 ppm to 1,370 ppm as FeO content increases from 8.0 to 12.6 wt. %. This positive relationship of FeO with SCSS is in line with the studies of Mathez (1976) and Wendlandt (1982) above, and Czamanske and Moore (1977) consider fractional crystallisation the dominant factor in keeping the differentiating melt at sulphide saturation.

Irvine (1975) found that if a mafic magma with sufficient Cr becomes extensively contaminated with felsic melt, the resulting increase in silica and alkalis in the hybrid can cause periods of isolated chromite crystallisation resulting in the formation of chromitite layers. He suggested that the same type of contamination mechanism may lead to concentrated deposits of magnetite, and of relevance to this study, immiscible sulphide liquid.

Ripley and Li (2013) suggest that the sulphur content required to induce sulphide liquid saturation can be reduced by typically 200 to 700 ppm when contaminating mantle-derived magmas with siliceous country rocks or their partial melts; alternatively, magma mixing may also lower the sulphur content needed to attain sulphide saturation by similar amounts. However, magma mixing can only trigger sulphide saturation if both end-members are close to sulphide saturation (Naldrett, 2011).

2.4.4 The effect of oxygen and sulphur fugacity on sulphur solubility

Buchanan and Nolan (1979) studied three synthetic tholeiitic melts experimentally at 1200^{o}C under controlled oxygen and sulphur fugacities at one atmosphere total pressure. They found that in sulphide-undersaturated silicate melts, the amount of dissolved sulphur increases with increasing sulphur fugacity and decreasing oxygen fugacity. Haughton *et al.* (1974) also showed that increases in fO_2 and fS_2 cause decreases and increases in sulphur solubility, respectively, while Liu *et al.* (2007) noted the same regarding fO_2.

Oxidation of a magma may therefore result in sulphide saturation and crucially, without necessarily causing any significant silicate crystallisation (Naldrett, 2004). This may have been important in the genesis of the Platreef which is a sulphide-poor PGE-rich deposit. Buchanan and Rouse (1984) suggest that oxidation and sulphide saturation occurred as a result of the assimilation of limestone. However, S isotope work by Holwell *et al.* (2007) and

Penniston-Dorland *et al.* (2008) shows that the Platreef sulphides have a predominantly magmatic signature and suggest that only localised contamination of the Platreef magma with the country rocks has occurred. Holwell *et al.* (2007) instead suggest that sulphide saturation was achieved in a deep seated staging chamber prior to the emplacement of the Platreef. However, it has also been noted that an exponential increase in the SCSS may occur with increasing fO_2 due to the contribution of sulphate species in the melt (Jugo, 2009).

2.4.5 The requirement of external sulphur

There are several lines of evidence that suggest the formation of Ni-Cu sulphide deposits is reliant on the input of external sources of sulphur close to the final emplacement of the deposit. The first of which is the detection of non-mantle sulphur isotope ratios, for instance, at Noril'sk and Duluth (e.g., Ripley, 1981; Ripley and Aljassar, 1987; Li *et al.*, 2003). Sulphur isotope fractionation is normally expressed as the ratio of $^{34}S/^{32}S$ relative to troilite (FeS) from the Diablo Iron meteorite (with zero recognised as the value for primitive mantle) by the equation given below,

$$\delta^{34}S\ ‰ = \left[\frac{^{34}S/^{32}S\ (sample) - {}^{34}S/^{32}S\ (standard)}{^{34}S/^{32}S\ (standard)} \right] x\ 1000$$

The variation in sulphur isotopes is represented as $\delta^{34}S$ and values of between -0.2 and +0.2 are considered to be magmatic. A shift in $\delta^{34}S$ towards negative or positive values typically suggests that the assimilation of crustal sulphide or sulphate, respectively, has occurred; however, some crustal sulphide can be unusually enriched in ^{34}S (e.g., Sælen *et al.*, 1993). A second line of evidence is the association of magmatic sulphides with xenoliths observed at Voisey's Bay and Duluth (e.g., Ripley and Alawi, 1986; Mariga *et al.*, 2006) as well as the association of sulphide ores with evaporites at Noril'sk (e.g., Naldrett *et al.*, 1992). Finally, the prominent effect of pressure on the solubility of Fe-sulphide in the magma (e.g., Huang and Williams, 1980; Wendlandt, 1982; Mavrogenes and O'Neill, 1999) suggests that a magma will not naturally achieve sulphide saturation during its assent through the crust. Therefore, either a change in magma composition is required through magma mixing or through the input of external sulphur for sulphide saturation to be achieved. The former may only achieve sulphide saturation if both end-member magmas are already close to sulphide saturation themselves (Ripley and Li, 2013).

Ripley and Li (2013) suggest that if sulphide saturation is achieved by fractional crystallisation alone, it does so only after Ni has been depleted by olivine crystallisation. Any sulphide that subsequently forms in the late stages of closed system crystallisation would be Cu- and PGE-rich, but this is unlikely to form an economic deposit unless the collection of the cotectic proportion of immiscible sulphide is extremely efficient. Ripley and Li (2013) further suggest that although contamination and magma mixing may result in sulphide saturation without the addition of crustal sulphur, Ni-rich sulphide deposits can form in such cases only from large-volume, open systems, where the efficiency of sulphide collection is high.

Moreover, Keays and Lightfoot (2010) demonstrate that the geochemical signatures of two formations from the southern Deccan province (the Bushe and Poladpur Formations) are indicative of a wide degree of crustal contamination, with the Bushe Formation exhibiting a stronger crustal contamination signature than the most contaminated Siberian Trap basalt formations. Despite this, Keays and Lightfoot (2010) show that the contaminated Deccan Trap lavas did not achieve sulphide saturation as both the Bushe and Poladpur basalts are undepleted in Ni, Cu and PGE. They therefore suggest that a S-rich crustal contaminant is required for the genesis of magmatic Ni-Cu-PGE sulphide deposits.

2.4.6 Metal concentrations of the sulphide liquid

For a magmatic sulphide occurrence to be economic, one must also consider the composition of the sulphide liquid itself which depends on the partition coefficients of the chalcophile elements into the sulphide liquid, the composition of the silicate magma, and the ratio of silicate magma to sulphide liquid involved in the reaction. The composition of the silicate magma depends on the amount of partial melting that occurs in the mantle. Based on calculations made by Ghiorso *et al.* (2002) using the program pMELTS, Figure 2 (after Naldrett, 2011) shows how a portion of the Hart and Zindler (1986) mantle melts (0-100%) in terms of how the concentrations of Cu, Ni, Pt and Pd vary in the developing partial melt. Accepting the common assumption that the mantle contains 200 ppm S and therefore ~500 ppm sulphide (Palme and O'Neill, 2004), modelling using the equation of Li and Ripley (2009) indicates that by 13.5% melting, the sulphide in the mantle source is completely dissolved in the partial melt. The PGE, Au, Ni and Cu all have high partition coefficients into the sulphide oxide liquid (e.g., Stone *et al.*, 1990; Fleet and Stone, 1991; Bezmen *et al.*, 1994;

Fleet *et al.*, 1996; Crocket *et al.*, 1997). Figure 2.2 shows that the Ni content of the partial melt increases with increased melting. Copper, Pt and Pd show limited increase in the partial melt during the early stages of melting until all of the sulphide in the source mantle has been dissolved. Platinum and Pd partition into the sulphide liquid more strongly than Cu and so are held back in the residue for longer until the very last few percent of sulphides are dissolved. Thus, partial melts that have not dissolved all of the sulphide in the source mantle will be Cu-PGE depleted and have higher Cu/Pd ratios than those that have dissolved all of the sulphide in the source mantle (Naldrett, 2011). At the point where all of the sulphide has been dissolved (13.5% melting), Cu, Pt and Pd concentrations in the partial melt are at their maximum. Further melting introduces more silicate melt without additional Cu, Pt and Pd and therefore dilutes these metal concentrations in the partial melt.

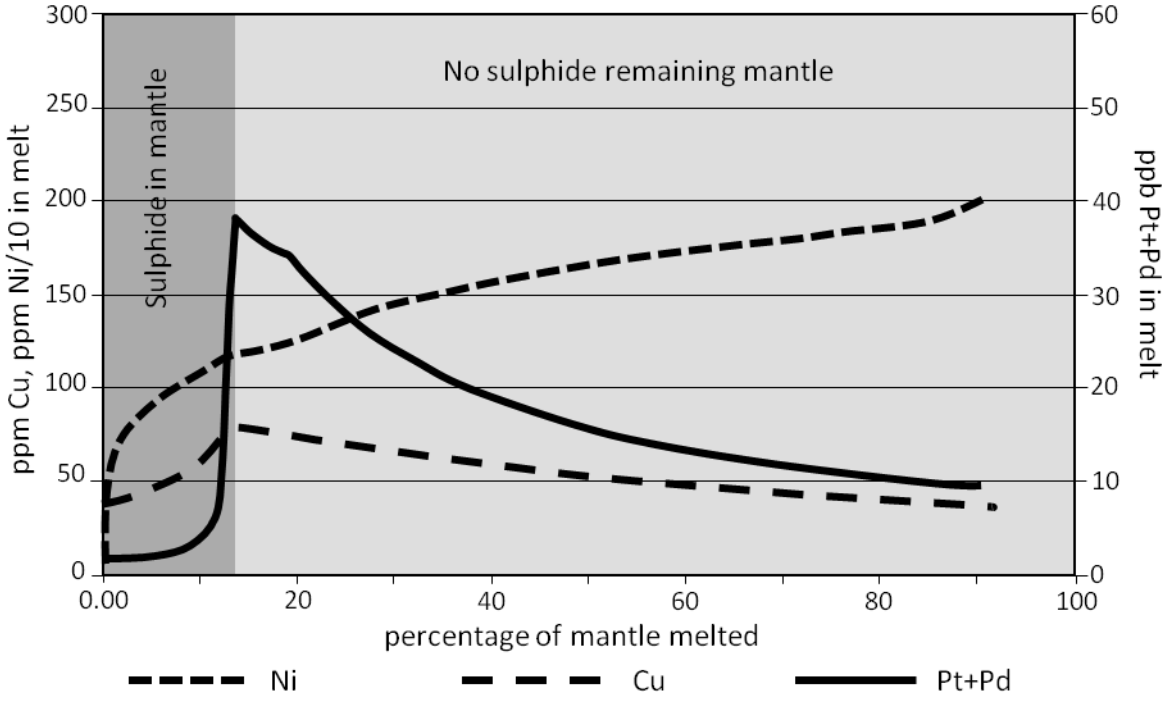


Figure 2.2: Results of mantle melting modelling showing how the concentrations of Cu, Ni, Pt and Pd vary in a developing partial melt (full details are given in text, modified from Naldrett, 2011).

Mungall and Brenan (2014) have measured and used new experimental partition coefficients of the PGE in order to develop a fully constrained model of PGE behaviour during mantle melting. They too find that residual mantle retains PGE until the sulphide has been completely dissolved; however, they also find that residual alloys or PGM in the residue have a strong control on PGE fractionation. Once all of the sulphide has been dissolved during melting at low pressure, the residual mantle develops high Pt/Pd and low Pd/Ir ratios due to the formation of Pt and Ir alloys in the restite. However, at high pressures (given the effect of

pressure on fO_2 and fS_2), there is an increase in alloy solubility with Pt alloy becoming soluble resulting in the formation of only Ir alloy in the residual mantle. The IPGE and Rh are compatible in olivine and large amounts of (or higher temperature) mantle melting is required to produce high concentrations of these metals in the magma (Mungall and Brenan, 2014).

The ratio of the mass of the silicate magma to the mass of the sulphide liquid has a significant effect on the metal content of the sulphides and can be measured using two methods; the R factor and the N factor. The R factor is defined as the ratio of the mass of the silicate magma over that of the sulphide liquid (Campbell and Naldrett, 1979) and assumes that the sulphide liquid equilibrated in bulk with the magma and was then removed. Essentially, low R-factors result in relatively low metal tenors in sulphide whereas high R-factors result in relatively high metal tenors. The PGE are particularly affected by variations in R, more so than the base metals, due to their high partition coefficients into sulphide liquids.

The N factor assumes that the sulphide liquid is interacting dynamically with the silicate magma (Naldrett, 2004). Examples of this interaction include the formation of sulphide droplets at the top of a magma chamber that then slowly settle through the chamber (Brugmann *et al.*, 1993). Alternatively, sulphides may be confined in a hydrodynamic trap within magma conduits, along which fresh magma continues to flow and interact with the trapped sulphides (e.g., at Noril'sk, Naldrett *et al.*, 1992; 1995). During this interaction, the sulphide liquid progressively increases its metal content as it removes chalcophile elements from the continued supply of fresh magma. The main difference between the R and N factors is that a change in N affects the metal content of the sulphide liquid more rapidly than a change in R.

Kerr and Leitch (2005) suggest that some high-grade magmatic Ni-Cu(±PGE) deposits and many magmatic PGE(±Ni-Cu) deposits require very high magma/sulphide ratios or R factors that appear improbable given physical and kinetic constraints. Quantitative modelling of sulphide upgrading through open-system processes whereby an early-formed sulphide liquid reacts with multiple later batches of silicate magma (suggested for example at Noril'sk, Naldrett *et al.*, 1995) demonstrates that this is more efficient than a closed system. Kerr and Leitch (2005) suggest that the majority of these later magmas will be sulphur under-saturated and will therefore partly re-dissolve pre-existing sulphide liquids, further increasing metal concentrations in the remaining sulphide liquids as a result of the high partition coefficients of the base metals and PGE into the sulphide liquid. Quantitative models of this combined

process termed "multistage-dissolution upgrading" show that it could reduce the required mass of silicate magma to the sulphide liquid by up to two orders of magnitude (Kerr and Leitch, 2005).

2.5 Sulphide Fractionation and Partitioning of PGE

It has long been known that sulphide liquids differentiate as they cool (e.g., Hawley, 1965; Keays and Crocket, 1970; Naldrett *et al.*, 1982). The first phase to crystallise from the sulphide liquid is monosulphide solid solution (MSS) which occurs at ~1000^{o}C, leaving a Cu-rich residual liquid which crystallises to form intermediate solid solution (ISS) at ~900^{o}C. As temperatures fall below 650^{o}C, MSS re-crystallises to form pyrrhotite and pentlandite whereas ISS re-crystallises to chalcopyrite (Yund and Kullerud, 1966; Barnes *et al.*, 1997; Ballhaus *et al.*, 2001; Mungall *et al.*, 2005; Holwell and McDonald, 2010). Early forming MSS cumulates and the resulting residual Cu-rich sulphide liquid may therefore separate from each other forming an intrusion where zones of Ni-Fe-sulphide mineralisation occur away from Cu-Fe-sulphide mineralisation (Ebel and Naldrett, 1997; Naldrett *et al.*, 1997). Due to this sulphide fractionation, it is important not only to study the partition coefficients of the PGE into the sulphide liquid, but also into the different crystallisation products of the sulphide liquid.

Fleet *et al.* (1993) used experiments to determine how PGE and Au behave in terms of partitioning between MSS and a sulphide liquid consisting of Fe-Ni-Cu at temperatures of between 1000-1040^{o}C. Bulk compositions and PGE concentrations of typical magmatic sulphides associated with mafic and ultramafic systems were used. They found that Au, Pt and Pd were incompatible with MSS and would therefore remain in the sulphide liquid during MSS crystallisation whereas Os, Ir, Ru (the IPGE) and Rh are compatible with MSS. Ballhaus *et al.* (2001) showed that Pt and Pd are incompatible with MSS having partition coefficients of less than 0.1 (MSS/sulphide liquid) whereas Ir, Ru and Rh are compatible with MSS having partition coefficients of between 3 and ~10.

Further experiments by Li *et al.* (1996) produced similar results with Pt, Pd and Cu shown to be incompatible with MSS whereas Ir and Rh were shown to be compatible with MSS. Os and Ru were not studied in these experiments. Mungall *et al.* (2005) showed in similar experiments that Cu, Pt, Pd and Au are all strongly incompatible with MSS whereas Ir and

Rh are strongly compatible and Ru moderately to strongly compatible. The incompatibility of Cu in MSS explains why after the crystallisation of MSS, the residual sulphide liquid is Cu-rich and why chalcopyrite is the sulphide phase to re-crystallise from ISS. Nickel partitions into MSS, but is not strongly compatible having a partition coefficient of ~1 (Barnes *et al.*, 1997), and during exsolution at lower temperatures forms pentlandite with Fe and S.

At this stage of research it appears that the variation in precious metals and PGE in different sulphide phases may be due purely to the fractionation of the sulphide liquid containing these elements. However, natural occurrences of PGE appear far more complex than this research could account for. Further studies by Peregoedova (1998) showed experimentally that Pt and Pd are not only incompatible with MSS, but also incompatible with ISS. This suggests that these elements are in fact concentrated into a late stage immiscible semimetal-rich melt during the crystallisation of ISS (e.g., Holwell and McDonald, 2007).

Furthermore, Helmy *et al.* (2007) studied the effects of Te on the partition coefficients of Pt and Pd (MSS/sulphide liquid) and found that as the concentrations of Te are increased, the partition coefficients of Pt and Pd into MSS decrease. This is due to Te forming complexes with Pt and Pd and effectively stabilising them in the melt without the need for the PGE to partition into any sulphide phase. They also found that Pt had a greater affinity to bond with semimetals to form PGM than Pd. Therefore, with limited semimetals available, excess Pd would be accommodated by pentlandite rather than competing with Pt to form PGM with the semimetals.

Helmy *et al.* (2010) have determined the partition coefficients for Se, Te, As, Sb, and Bi between MSS and sulphide melt experimentally at 950^{o}C and show that Bi, Sb and Te are highly incompatible with MSS and will preferentially partition into the fractionated sulphide liquid. They argue that this rules out the possibility of these elements forming PGM with PGE via exsolution from the MSS (or MSS crystallisation products pyrrhotite and pentlandite) during sub-solidus cooling and instead agree with Holwell and McDonald (2007) and Helmy *et al.* (2007) who argue that many discrete Sb-Te-Bi-PGE minerals have crystallised or exsolved from droplets of late-stage fractionated immiscible Sb-Te-Bi-enriched melts. Helmy *et al.* (2010) find that the behaviour of As is more complex and dependant on the proportions of Pt and Pd that are present. If Pt is dominant, sperrylite ($PtAs_2$) may crystallise, whereas if Pd is dominant, an immiscible Pd-As-liquid may separate from the sulphide melt; both of these processes occur early before the crystallisation of MSS.

2.6 Combined PGE and PGM Studies

The following section reviews available literature on Ni-Cu-PGE sulphide deposits, including many of the world's most economically important deposits, where studies of both the platinum-group mineralogy and the concentrations of PGE in solid solution in the BMS are available. The full distribution of the PGE in these systems is therefore understood and allows the overall behaviour of the PGE, both primary and secondary, to be analysed.

2.6.1 Bushveld Igneous Complex, South Africa

The Bushveld Complex in South Africa is the largest known layered intrusion on Earth, comprised of a 7-9 km thick sequence of mafic and ultramafic lithologies with an outcrop/subcrop area of ~65,000 km^2 (Eales and Cawthorn, 1996). The complex lies almost entirely within the bounds of the Transvaal sedimentary basin (Eriksson *et al.*, 1991) and contains a significant proportion of the world's PGE resources in three main deposits; the UG2 chromitite, the Merensky Reef and the Platreef (Morrissey, 1998; Cowley, 2013 [Johnson Matthey Platinum Review]).

The Bushveld Complex has been dated by Scoates and Friedman (2008) who used single crystal chemical abrasion ID-TIMS U-Pb dating of zircon from a sample of pegmatitic feldspathic orthopyroxenite from the Merensky Reef (West mine, Townlands shaft, Rustenburg section) yielding a crystallisation age of 2054.4±1.3 Ma. Further U-Pb SHRIMP dating of zircon crystals from a number of chromitite layers located near the top of the Critical Zone by Yudovskaya *et al.* (2013) yield similar ages of 2051±9 Ma and 2056±5 Ma.

The Bushveld Complex intruded the Transvaal Supergroup; a supracrustal volcano-sedimentary sequence, the age of which is poorly constrained between 2550-2060 Ma (Nelson *et al.*, 1999; Buick *et al.*, 2001). The Bushveld Complex consists primarily of the Rustenburg Layered Suite (South African Committee for Stratigraphy, 1980) which is an approximately 8 km thick succession of layered ultramafic and mafic units which are exposed in five major limbs of the complex; most notably the eastern, western and northern limbs. The Rustenburg Layered Suite is sub-divided into five zones which are, from the base upwards, the Marginal Zone, Lower Zone, Critical Zone, Main Zone and the Upper Zone (Hall, 1932).

2.6.1.1 The Platreef

The Platreef is a 10-300m thick unit comprised of pyroxenitic and gabbroic lithologies containing PGE and BMS mineralisation forming the basal sequence of the northern limb of the Bushveld Complex (Fig. 2.3) (Gain and Mostert, 1982; McDonald *et al.*, 2005). The Platreef extends from the town of Mokopane northwards for approximately 40 km and is overlain by norites and gabbronorites generally assigned to the Main Zone of the Rustenburg Layered Suite (e.g., van der Merwe, 1976; Ashwal *et al.*, 2005; McDonald *et al.*, 2005). The footwall to the Platreef transitions from the south to the north of the northern limb into progressively older sedimentary units consisting of Archaean to early Proterozoic Transvaal Supergroup units and then into igneous Archaean basement (Wagner, 1929).

The main sulphides in the Platreef are pentlandite, pyrrhotite and chalcopyrite which occur as millimetre sized fractionated blebs as well as interstitially; however, massive sulphides also occur near the footwall contact and are chalcopyrite-rich (Hutchinson and Kinnaird, 2005). PGM occur as Pd-bearing tellurides, antimonides, bismuthides, bismuth-antimonides, and bismuthotellurides as well as Pt-bearing arsenides and antimonides, all of which are identified in secondary silicates and adjacent to or along the margins of composite sulphides; however, they rarely occur within or enclosed by sulphides (Hutchinson and Kinnaird, 2005). In addition to these PGM, Holwell and McDonald (2007) have identified Pt-Pd sulphides, PGE sulpharsenides and Pt-Pd alloys with Fe, Cu, Sn and Pb. Armitage *et al.* (2002) also note the presence of high temperature Pt-Fe and Pt-Sn alloys.

A model of formation by Hutchinson and Kinnaird (2005) for these observed PGM requires that sulphide droplets scavenged the PGE from a relatively large volume of melt. The sulphides are then altered by the addition of sulphur and semimetals from the de-volatilisation of the floor rocks and xenoliths. Finally, late stage fluids altered and remobilised the PGE resulting in the formation of secondary PGM that are disseminated in tremolite, talc and serpentine, explaining the decoupling of PGE and BMS (Cu and Ni) observed. It is proposed by Armitage *et al.* (2002) that later hydrothermal alteration and serpentinisation has affected parts of the reef resulting in the redistribution of PGE into the footwall. The PGE are redistributed as low temperature PGM assemblages that are devoid of sulphur.

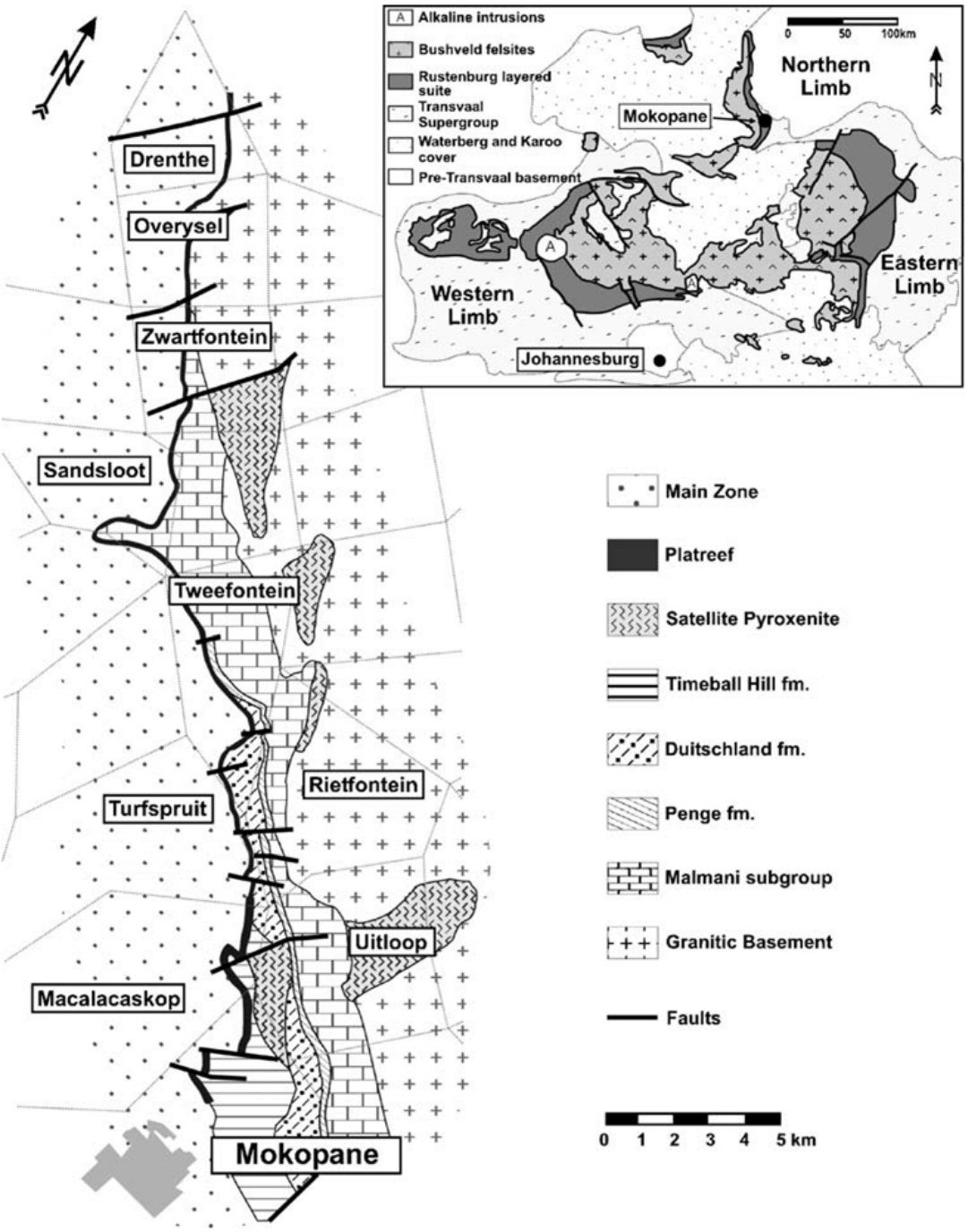


Figure 2.3: Geological map showing the geology of the Bushveld Complex and expanded view of the Northern Limb with the Platreef (modified from Hutchinson and McDonald, 2008 [modified from van der Merwe, 1978 and Ashwal *et al.*, 2005]).

At Overysel (Fig. 2.3), the footwall of the Platreef consists of anhydrous Archaean gneiss rather than the Transvaal Supergroup. Not only do the PGE and BMS contents continue from the Platreef into the footwall gneiss, the PGM assemblages in both the Platreef and gneiss are identical. These features coupled with the lack of any hydrothermal overprinting suggests that the anhydrous gneiss has protected the Platreef from hydrothermal alteration, therefore preserving the most primary style of PGE mineralisation (Holwell and McDonald, 2006).

Iridium, Ru and Rh are depleted at depth compared to Pt, Pd and Au which reflects the fractionation of the original sulphide liquid where MSS has crystallised at depth in the Platreef concentrating the IPGE and Rh. Hutchinson and McDonald (2008) add that the top of the Platreef shows little contamination and redistribution of PGM, however, towards the footwall, felsic melts have contaminated the Platreef and remobilised the Pt- and Pd-bearing PGM. The remaining residual Cu-rich sulphide liquid has then percolated through into the underlying Archaean gneiss through interconnected melt networks, a result of the intrusion of the Platreef and evidenced by quartz and felsic contamination of the Platreef near its footwall contact (Holwell and McDonald, 2006).

A laser ablation-ICP-MS study of the Platreef BMS by Holwell and McDonald (2007) shows that the PGE and semimetals are collected by the sulphide liquid with the IPGE and Rh partitioning into MSS. The IPGE remain in solid solution after the exsolution of pyrrhotite and pentlandite in equal proportions whereas Rh preferentially partitions into pentlandite at this stage. Platinum, Pd and Au are incompatible with MSS and so are concentrated into the residual Cu-rich sulphide liquid. They are further concentrated into a late stage liquid with the semimetals during the crystallisation of ISS. This late stage Pt-Pd-bearing semimetal-rich liquid is then expelled to sulphide grain boundaries, forming Pt and Pd tellurides and electrum. Drops of this semimetal-rich liquid were also trapped in crystallising MSS and ISS resulting in micro inclusions of Pt bismuthotellurides identified in all phases. Excess Pd has been accommodated by pentlandite via diffusion (Holwell and McDonald, 2007).

2.6.1.2 Merensky Reef

The Merensky Reef is a sulphide-bearing, PGE-rich horizon that occurs towards the top of the Critical Zone (Fig. 2.4) (Campbell *et al.*, 1983; Ballhaus and Stumpfl, 1986; Naldrett *et al.*, 1986). The Merenksy Reef varies between 0.3-1 metres thick (Kinloch, 1982; Kinloch and Peyerl, 1990), occurs at the base of the Merensky cyclic unit and consists of mineralised pegmatitic bronzitite, norite and anorthosite orthocumulates (Campbell *et al.*, 1983; Ballhaus and Stumpfl, 1986; Naldrett *et al.*, 1986).

Studies by Kinloch (1982) and Kinloch and Peyerl (1990) detailed the PGM identified in different types of Merensky Reef across the Bushveld Complex. These studies identified several different types of Merensky Reef; normal reef (30-35 cm thick), wide reef (similar to

normal reef but up to 1.5m thick), contact reef (where the reef narrows to a thin chomitite stringer) and pothole reef (occurring as depressions in both the Merensky Reef and UG2 chomitite). These studies show that normal reef contains 89% Pt-Pd sulphides by volume (Kinloch, 1982), predominantly braggite ([PtPd]S) and cooperite (PtS) (Kinloch and Peyerl, 1990). Wide reef contains a variety of Pt-Pd tellurides, predominantly moncheite ($PtTe_2$), merenskyite ($PdTe_2$) and kotulskite (PdTe) (Kinloch and Peyerl, 1990). Contact reef contains 87% laurite (RuS_2) by volume given its association with chromite and 11% Pt-Pd sulphides (Kinloch, 1982). Pothole reef contains 92% Pt-Fe alloy with an As-rich front characterised by sperrylite occurring between pothole and normal reef (Kinloch, 1982). In a subsequent study, Kinloch and Peyerl (1990) found that Pt-Fe alloy occurs in the centre of these potholes with Pt-Pd telluides occurring at the edges. Both studies suggest that potholes have formed during volatile release from underlying monomineralic anorthosite giving rise to the variation in platinum-group mineralogy observed.

Godel *et al.* (2007) studied normal 'narrow' Merensky Reef from Frank Shaft, Rustenburg Platinum Mine and show that 65-85% of the PGE are hosted in PGM comprised of Pt-Fe alloys, Pt-Pd sulphides and Pt-Pd bismuthotellurides with the remaining balance of PGE hosted in solid solution in BMS. Prichard *et al.* (2004a) identified the predominant PGM in 'normal' Merensky Reef samples from the Impala Platinum mine, Reinkoyalskraal farm, situated in the western lobe of the Bushveld Complex as moncheite, merenskyite, cooperite, braggite and laurite, with these minerals located at the contacts between the BMS and silicates and/or oxides or hosted within the BMS themselves.

Godel *et al.* (2007) found that pentlandite is the principal host of PGE and is preferentially enriched in Pd, Rh and Co. Pyrrhotite hosts the IPGE and Rh but not Pt or Pd whereas chalcopyrite hosts only extremely small concentrations of PGE although it does contain Ag and Cd in solid solution. Platinum and Au do not partition into any BMS and instead form PGM and electrum, respectively.

A laser ablation-ICP-MS study by Ballhaus and Sylvester (2000) shows that the IPGE partition equally into pyrrhotite and pentlandite whereas Rh and some Pd partition into pentlandite. Platinum, Au, Re and some Pd do not partition into any BMS and instead form discrete phases (PGM). Olivine and chromite which were often suspected of hosting Os, Ir and Rh were found to be below the detection limit of the analyses. All phases studied contain PGM micro inclusions. In the sulphides these consist of Os-Ir-Pt and Pt-Pd-Au whereas in

olivine and chromite they consist of Pt±Au-Pd. These PGM are unlikely to have formed via exsolution as evidenced by micro inclusions being identified in olivine and chromite, for which solid solution analyses of PGE are below the limit of detection. Therefore, Ballhaus and Sylvester (2000) suggest that the layer of melt that preceded the Merensky Reef was oversaturated in PGE, resulting in the direct crystallisation of PGM from an immiscible sulphide melt during the crystallisation of olivine and chromite. In this case, the sulphides did not play a role in concentrating the PGE, they simply immobilised the PGE within the melt layer.

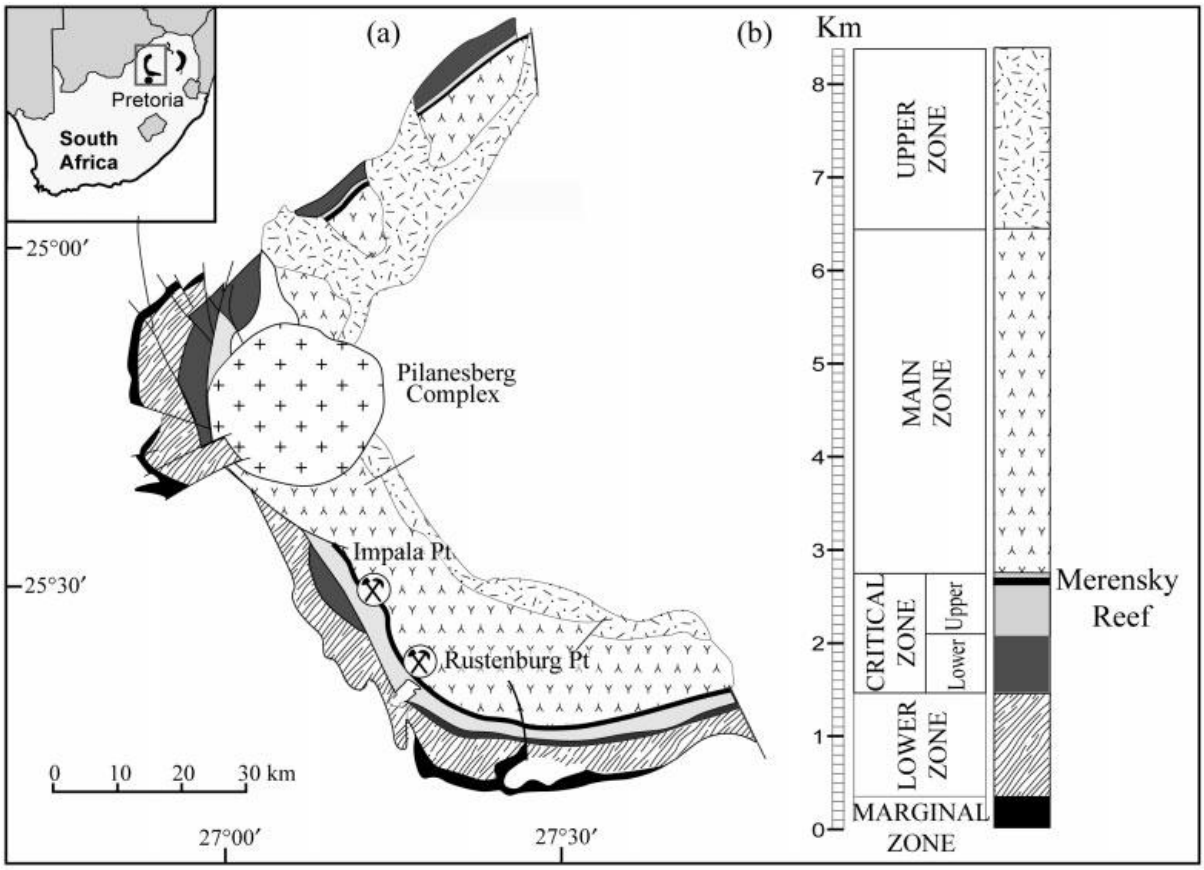


Figure 2.4: Geological map of the western lobe of the Bushveld Complex, South Africa; (a) simplified geological map (Godel *et al.*, 2007 [modified after Von Gruenewaldt, 1986; 1989]) and (b) generalised stratigraphy of the Bushveld Complex (Godel *et al.*, 2007 [modified after Eales and Cawthorn, 1996]).

Osbahr *et al.* (2013) conducted LA-ICP-MS analyses on the BMS of samples from four Merensky Reef intersections from both the eastern and western lobes of the Bushveld Complex. They found that pentlandite is the principal host of Pd and Rh (with concentrations of up to 1750 ppm and 1000 ppm, respectively). Low but significant concentrations of Os, Ir and Ru occur in pyrrhotite with chalcopyrite being virtually barren. Pyrrhotite and chalcopyrite combined usually account for <10% of the whole-rock PGE content whereas

pentlandite can account for up to 100% of the whole-rock Pd and Rh as well as smaller amounts (10-40%) of Os, Ir and Ru with the remainder (including up to 100% of the whole-rock Pt) occurring in discrete PGM.

Godel *et al.* (2007) also focus on a chromitite layer within the reef which is enriched in PGE by a factor of five in comparison to the silicate section of the reef; however, the BMS are only enriched by a factor of two in comparison with the BMS found within the silicates. They conclude that the balance must be contributed by PGM which would have co-crystallised from the magma with chromite before sulphide saturation was achieved; alternatively, the BMS and PGM may have been concentrated together during cumulate sorting (Maier *et al.*, 2013). After sulphide saturation, the immiscible sulphide liquid would have sunk down into the chromitite layer enriching the PGE content further. Barnes and Maier (2002) agree that the co-crystallisation of PGM and chromite directly from the magma is a possibility; they also note that this process is poorly understood. Alternatively, they argue that a trapped sulphide liquid within the chromitite layer could have produced the balance of PGM by the removal of Fe and sulphur, provoking the crystallisation of PGM.

2.6.2 Noril'sk, Siberia

The Noril'sk-Talnakh region, Siberia, hosts one of the largest known concentrations of Ni, Cu and PGE in the world (Naldrett *et al.*, 1992; Naldrett, 2004). These disseminated and massive Ni-Cu-PGE sulphide deposits are associated with the Permo-Triassic Siberian Traps and are hosted within differentiated ultramafic-mafic bodies that have intruded the sedimentary sequence that immediately underlies the Siberian flood basalts (Hawkesworth *et al.*, 1995; Arndt, 2011). High PGE concentrations are found in the deposits hosted by the Noril'sk, Talnakh, and Kharaelakh intrusions with tenors of 30-50 ppm total PGE in undifferentiated sulphides, ~10 ppm in pyrrhotite-rich massive sulphide and up to 120 ppm in Cu-rich sulphide ores (Naldrett *et al.*, 1996; Naldrett, 2004). These host intrusions appear to be co-magmatic with parts of the flood basalt stratigraphy and have formed along sills that appear to have fed these extrusive volcanics (Naldrett *et al.*, 1992; Hawkesworth *et al.*, 1995).

The relationship between the ore-bearing intrusions and the Siberian trap flood basalts (e.g., Naldrett *et al.*, 1992; 1995; Hawkesworth *et al.*, 1995) has been the subject of controversy

(e.g., Latypov, 2002; Arndt *et al.*, 2003; Li *et al.*, 2003; Ripley and Li, 2003; Ripley *et al.*, 2003), mainly as a result of geochemical variation between the intrusions and the related flood basalts. As such, several differing models have been suggested for the formation of these Ni-Cu-PGE deposits. The majority of these proposed models (e.g., Naldrett, 1992; 2004; Arndt *et al.*, 1998; Li *et al.*, 2009; Arndt, 2011) suggest that sulphides formed as a result of the assimilation of sulphur-rich evaporites occurring in the country rock adjacent to the feeder sills of the Siberian Traps. The sulphide tenor was then very effectively upgraded during the prolonged interaction of a continuous flow of fresh magma with sulphides that became trapped in these feeder zones. The exact timings of sulphur saturation and the nature of the magmas involved are subject to ongoing debate.

Cabri *et al.* (2002) studied the distribution of Pd, Rh and Ru in three small samples of disseminated ore from the layered Medevezhiy Ruchei Ni-Cu-PGE mine using micro-PIXE analyses. They found that Pd is preferentially concentrated in pentlandite (up to ~67% in the samples studied). About two thirds of the whole-rock Rh is found in pyrrhotite with significant concentrations identified in pentlandite. About one third of the whole-rock Ru is hosted by pentlandite with the remainder distributed variably between pyrrhotite, chalcopyrite and pyrite.

Barnes *et al.* (2006) completed a study of PGM combined with LA-ICP-MS analyses in order to establish the behaviour of the PGE and test the fractionation model of sulphide liquids at Noril'sk. They studied zoned sulphide droplets from the Noril'sk 1 Medvezky Creek Mine. They found that Ni, Cu, Ag, Re, Os, Ir, Ru, Rh and Pd are largely concentrated in solid solution in BMS whereas less than 25% of the Au, Cd, Pt and Zn are hosted in BMS. The IPGE, Rh and Re preferentially partition into MSS and equally between pyrrhotite and pentlandite during the exsolution of these phases; pentlandite also concentrates Pd and Co. These results support the sulphide fractionation model as the IPGE and Rh are compatible with MSS which exsolves to pyrrhotite and pentlandite. Barnes *et al.* (2006) found that chalcopyrite and cubanite concentrate Ag, Cd and Zn which also supports the sulphide fractionation model as these elements are compatible with ISS which subsequently exsolves to form these Cu-sulphides. Gold and Pt do not partition into the BMS and instead form tellurides, bismuthides and alloys. Textures suggest that Pd has not only diffused from within MSS into pentlandite during the exsolution of pyrrhotite and pentlandite, but has also diffused into pentlandite from the Cu-rich portion of the sulphide blebs (Barnes *et al.*, 2006).

Barnes *et al.* (2008) argue that sulphide droplets in the sub-volcanic sills were rapidly cooled preventing the exsolution of PGM from the sulphides. Where cooling rates are slower (e.g., in layered intrusions), more time is available allowing the exsolution of PGE from the BMS resulting in the formation of PGM within the sulphides. They suggest that either Pt entered the BMS at high temperatures and exsolved during cooling, or alternatively, that Pt was not incorporated into the BMS at all and was instead concentrated into a late stage immiscible melt which cooled and crystallised to form PGM directly.

2.6.3 Sudbury Igneous Complex, Canada

The Sudbury Igneous Complex is a meteorite impact structure which formed at ~1.85 Ga (Fig. 2.5) (Krogh *et al.*, 1984; Davis, 2008) and is a layered intrusion predominantly comprised of quartz norite (~56% SiO_2) at the base through to a thin Transition Zone of quartz gabbro which is overlain by granophyre (~70% SiO_2) (Zieg and Marsh, 2005). The complex is host to one of the largest Ni-Cu-PGE mining districts in the world and third in world PGE production behind the Bushveld Complex and Noril'sk-Talnakh (Farrow and Lightfoot, 2002; Ames and Farrow, 2007). It is commonly accepted that the Ni-Cu-PGE mineralisation is magmatic and is zoned as a result of sulphide fractionation (e.g., Hawley, 1965; Keays and Crocket, 1970; Li and Naldrett, 1993; Naldrett *et al.*, 1999; Ames and Farrow, 2007; Dare *et al.*, 2010a; 2011) into pyrrhotite-rich (Fe-Ni-rich, Pt-Pd-poor) and chalcopyrite-rich (Cu-Pt-Pd-Au-Ag-rich) sulphide zones (e.g., Naldrett *et al.*, 1982; 1999; Li *et al.*, 1992; Li and Naldrett, 1993; Farrow and Lightfoot, 2002; Ames and Farrow, 2007). The country rocks which were subjected to flash melting consisted of Archaean Levack granite gneiss in the North Range and Palaeoproterozoic meta-volcanic and meta-sedimentary rocks of the Huronian Supergroup in the South Range (Dare *et al.*, 2010a).

Dare *et al.* (2010a; 2010b) studied both the platinum-group mineralogy and the distribution of PGE in BMS in samples from the western branch (402 Trough) of the Creighton Ni-Cu-PGE sulphide deposit situated in the South Range of the Sudbury Igneous Complex. The majority of the mineralisation at Creighton is distributed throughout a number of orebodies hosted in a branching trough comprising several embayments; the Main Embayment and the 402 Trough, of which the 402 Trough plunges NE and forms the western branch of the Creighton deposit (Dare *et al.*, 2010a).

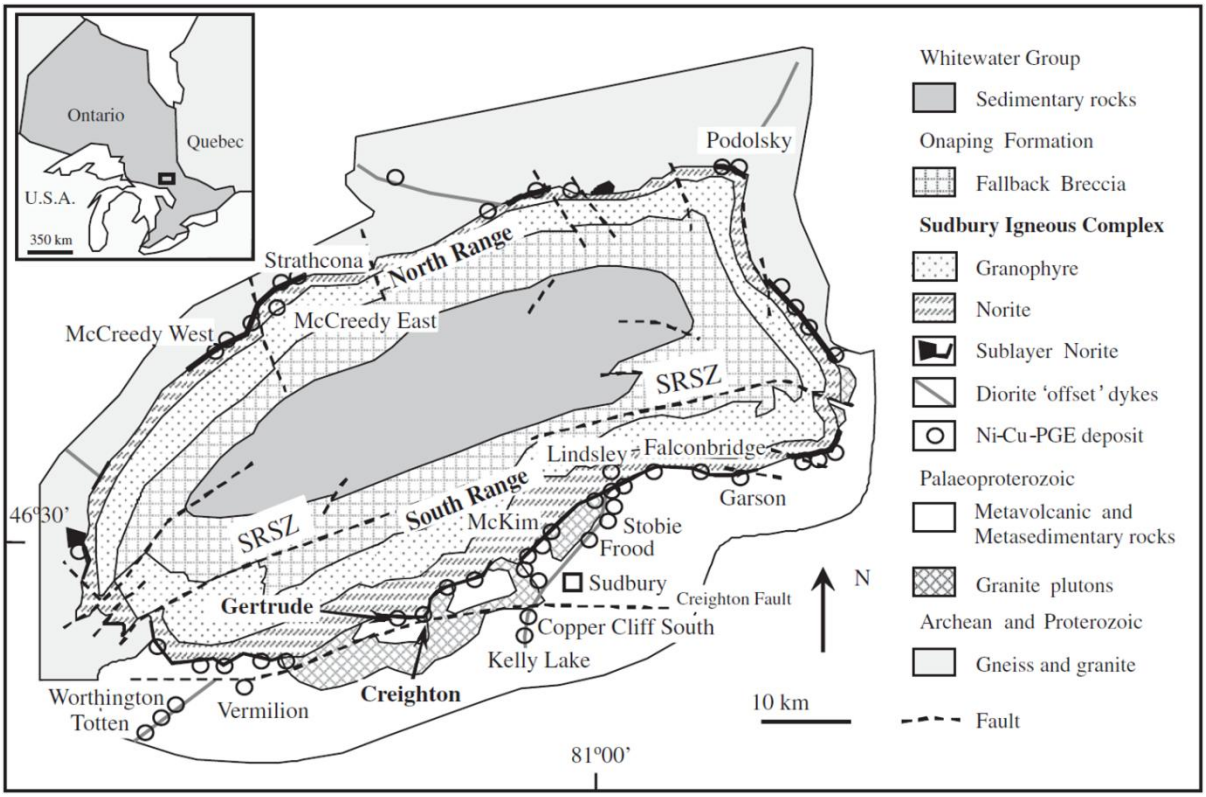


Figure 2.5: Location (inset) and geological maps of the Sudbury Igneous Complex and its Ni-Cu-PGE deposits (modified from Dare *et al.*, 2010b [modified from Barnes and Lightfoot, 2005 after Souch *et al.*, 1969]).

Dare *et al.* (2010a) found that 40-90% of the Os, Pd, Ru, Cd, Sn, and Zn are in solid solution in BMS whereas less than 35% of the Ag, Au, Bi, Ir, Mo, Pb, Pt, Rh Re, Sb and Te are in solid solution in BMS. They identified that Os and Ru are concentrated in equal proportions in pyrrhotite, pentlandite and pyrite; Co and Pd are concentrated in pentlandite, and Ag, Cd, Sn, Zn and in rare cases Au and Te are concentrated in chalcopyrite. Selenium is distributed equally between pyrrhotite, pentlandite and chalcopyrite. The presence of euhedrally zoned irarsite (IrAsS), hollingworthite (RhAsS), sperrylite ($PtAs_2$) and PGE-Ni-rich cobaltite and the lack of Ir and Rh in BMS suggests that these PGM crystallised early from the immiscible sulphide liquid depleting later crystallising MSS in these PGE. The PGM likely crystallised at temperatures of between 900-1200^{o}C and were subsequently surrounded by MSS cumulates (Dare *et al.*, 2010b). It is suggested again that Pd diffuses from chalcopyrite into pentlandite during the exsolution of pentlandite from MSS (Dare *et al.*, 2010a). Late-stage magmatic or hydrothermal fluids then remobilised some Pd at temperatures of less than 540^{o}C to form michenerite (PdBiTe) which is located in, or juxtaposed against silicate phases.

Szentpeteri *et al.* (2002) recognise the same PGM assemblages in the 100 and 120 orebodies of the offset sub-layer as well as in the Lady Violet deposit of the contact sub-layer in the

Copper Cliff North area. However, they propose, that these zoned PGM have formed via the exsolution of PGE from MSS at temperatures of between 550-600^{o}C. Late stage crystallisation and hydrothermal fluids have resulted in the observed hydrous silicate phases and remobilisation of PGM.

Huminicki *et al.* (2005) have studied both the PGM and PGE in solid solution in sulphides and sulpharsenides using laser ablation microprobe-ICP-MS in samples from the Kelly Lake Ni-Cu-PGE sulphide deposit in the Copper Cliff offset. They found that the majority of the Pt (98%), Rh (97%), and Ir (86-91%), and lesser but still significant proportions of Pd (77-87%) and Ru (67-71%) occur in discrete PGM, with the reminder occurring in solid solution in gersdorffite (1,700 ppm ΣPGE), pentlandite (1.35 ppm), chalcopyrite (0.5 ppm) and pyrrhotite (0.3 ppm).

Dare *et al.* (2011) discovered PGE concentrations in pyrite when studying the McCreedy East deposit in the North Range of Sudbury. Along with more than 18 other deposits including Strathcona, Fraser, Coleman, McCreedy West, and Craig, the McCreedy East deposit is situated in the Onaping-Levack embayment which is a shallow, 8 km long embayment found along the North Range of the Sudbury structure (Dare *et al.*, 2011). In the South Range, the footwall rocks are As-rich metasediments which introduced As into the system resulting in the early crystallisation of As-bearing PGM. They suggest that in the North Range however, the footwall rocks are As-poor granites and the lack of semimetals in the system preserves the concentration of PGE in BMS. They find that the IPGE, Rh and Re preferentially partition into pyrrhotite, pentlandite and pyrite whereas Pt forms PGM; Pd is again concentrated in pentlandite. Two forms of pyrite are present; i) primary zoned pyrite which has exsolved from MSS and is enriched in IPGE and As±Pt and ii) secondary pyrite, formed by the alteration of MSS cumulates by late magmatic or hydrothermal fluids. This pyrite is un-zoned and contains low concentrations of IPGE and Re inherited from the pyrrhotite and pentlandite it has replaced (Dare *et al.*, 2011).

2.6.4 Stillwater Complex, Montana

The Stillwater Complex is an ultramafic-mafic layered body situated in Montana, USA, that has intruded into middle to late Archaean meta-sedimentary rocks (Fig. 2.6). The intrusion has been dated at 2705±4 Ma using U-Pb zircon-baddeleyite age dating by Premo *et al.*

(1990). The Stillwater Complex is host to several layers of PGE enrichment including the Picket Pin deposit and most importantly, the J-M Reef (Godel and Barnes, 2008b). The J-M Reef is a 1-3m thick PGE-enriched layer (average Pt+Pd at ~18 ppm) containing disseminated sulphides that is associated with an olivine-bearing cumulate (OB-1; olivine gabbronorite and troctolite) of the Lower Banded Series (Barnes and Naldrett, 1986; Lee, 1996; Zientek *et al.*, 2002). The complex has been subjected to several metamorphic and/or hydrothermal processes resulting in the alteration of both the silicates and BMS (Page, 1976; Czamanske and Loferski, 1996; Polovina *et al.*, 2004).

Godel and Barnes (2008a; 2008b) studied the PGE mineralisation of the J-M reef at the East Boulder mine. Godel and Barnes (2008a) identified a variety of PGM consisting of Pd±Pt sulphides, Pt-Fe alloy (isoferroplatinum), Pd±Pt tellurides and Pd-Cu alloy (skaergaardite) with minor native Pd, laurite and palladian electrum (Au-Pd-Ag alloy). They suggested that these PGM formed via exsolution from the sulphides given that the majority of them are closely associated with the BMS (either identified enclosed within the BMS or situated at the edge of the BMS and in contact with an adjacent sulphide, silicate or oxide phase). These PGM account for all of the Pt, half the Pd, Ru, and Ir, and a smaller proportion of the Os identified by whole-rock PGE analyses with the balance being accounted for in situ in the BMS.

Godel and Barnes (2008b) found that the sulphur, Ni and Cu are coupled with the PGE indicating that the BMS are the principle hosts of the PGE. Palladium is the dominant PGE present (followed by Pt, with Pd/Pt ratios of 3.3) and accounts for 95% of PGE identified in solid solution in BMS. Pentlandite contains the highest weight fraction of PGE compared to other BMS. Conversely, they found that Pt occurs almost exclusively as PGM and does not partition into BMS. S/Se ratios and the presence of secondary magnetite indicate that 20-50% of the sulphur has been lost from the original magmatic composition. The highest PGE concentrations are within areas most enriched in secondary magnetite although these areas do not contain the least sulphur, suggesting that desulphurisation and the formation of secondary magnetite are the result of two independent processes (Godel and Barnes, 2008b).

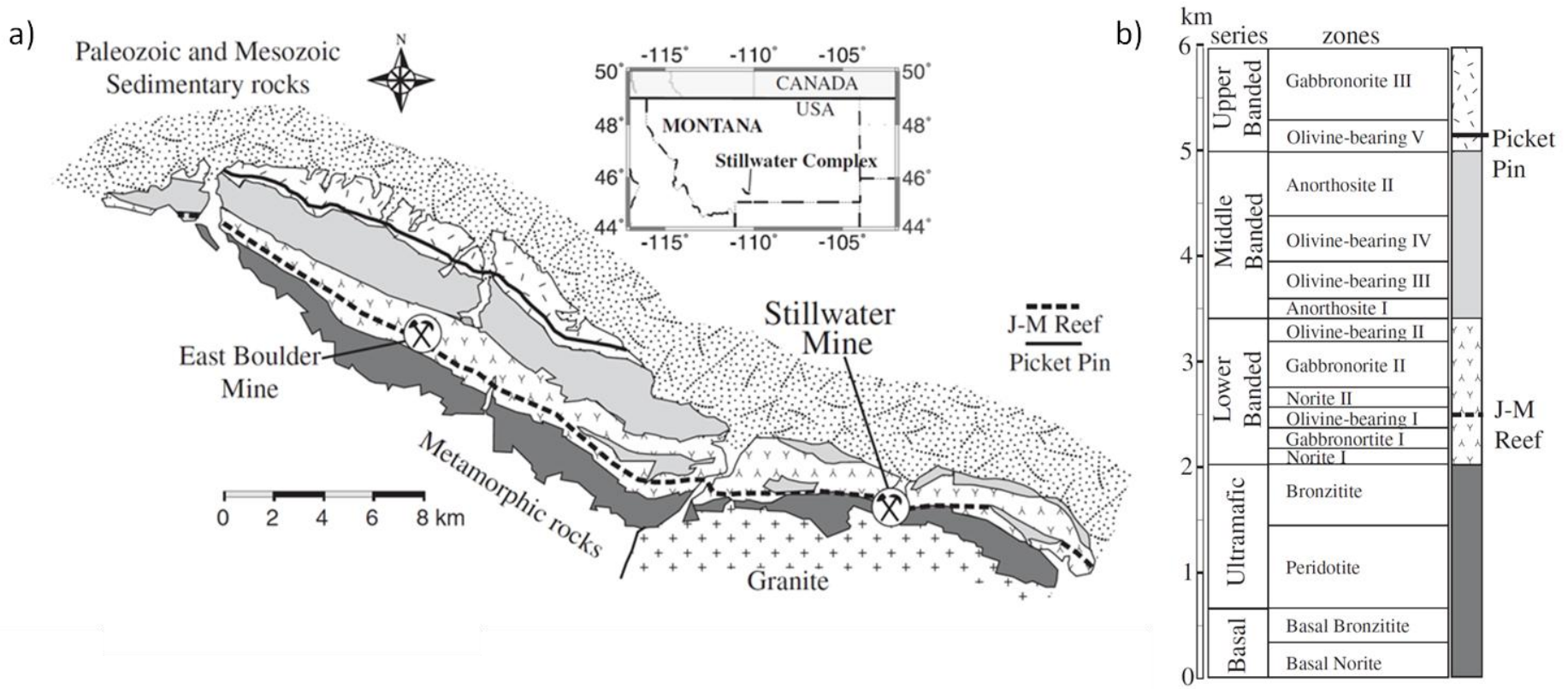


Figure 2.6: Geological map (modified from Godel and Barnes, 2008a [modified after Mc Callum *et al.*, 1980; Zientek *et al.*, 2002]) and stratigraphic column (modified from Godel and Barnes, 2008a [modified after Zientek *et al.*, 2002]) of the Stillwater Complex.

Godel and Barnes (2008b) conclude that an immiscible sulphide liquid interacted with a large volume of melt which then percolated downwards in the magma as far as porosity would allow. During magma cooling, instabilities triggered partial desulphurisation of the sulphides. Fluids then altered the BMS to secondary magnetite and deposited Pd (possibly sourced from the footwall of the reef) which precipitated as Pd alloys while excess Pd diffused into pentlandite.

2.6.5 Penikat, Finland

The Penikat intrusion in northern Finland is a Palaeoproterozoic ultramafic-mafic layered intrusion that hosts three layers enriched in PGE; the SJ, AP and PV reefs. Barnes *et al.* (2008) studied both the PGM and PGE in BMS in samples from the AP and PV reefs with the SJ reef ignored due to its low sulphur content. These reefs occur as narrow layers (AP 20-40 cm thick; PV ~1m thick) that are enriched in PGE and contain 1-4 vol. % BMS hosted within gabbronorites (Halkoaho *et al.*, 2005).

In the AP reef, Barnes *et al.* (2008) found that the most common PGM are Pd-bearing (Pd-bismuthotellurides and Pd-arsenides) with Rh-(Ir-Pt)-sulpharsenides and Pt-arsenides occurring less commonly with approximately half of these PGM occurring with the BMS and half with the silicates. Halkoaho (1993) reports a similar PGM assemblage for the AP reef comprised of approximately 44% Pd-Pt-bismuthotellurides, 20% sperrylite, 23% Pd-arsenoantimonides or tellurides, 6% Pd-Pt-sulphides, 4% hollingworthite-irarsite (RhAsS-IrAsS) and 4% electrum (AuAg).

In the PV reef, Barnes *et al.* (2008) identified predominantly sperrylite as well as Pd-bismuthotellurides with the majority of the PGM (96%) identified in the BMS or at the contacts between BMS and adjacent silicates. This agrees with an earlier study by Huhtelin *et al.* (1990) who reported sperrylite, Pd-bismuthotellurides, Au-Ag phases and Pd-arsenoantimonides. However, they report that 50% of these are associated with silicate phases rather than the BMS.

Barnes *et al.* (2008) found that the PGE content in BMS varies widely across the PGE reefs at Penikat from 8-70%. There are many PGM present and the BMS have undergone extensive re-crystallisation during greenschist facies metamorphism (Alapieti and Lahtinen, 1986). The majority of the PGM observed are associated with BMS, however, a significant amount are

not. There are three possible explanations proposed by Barnes *et al.* (2008) to account for this; i) originally, PGM exsolved from the BMS during sub-solidus cooling, however, the BMS have since been remobilised leaving behind insoluble PGM, ii) fluids with a suitable chemistry have remobilised the PGM away from the BMS, or iii) Pd and to a lesser extent Pt have been introduced by hydrothermal fluids from which PGM have crystallised directly.

2.6.6 Aguablanca Ni-Cu Deposit, Southwest Spain

Several studies of the Aguablanca Ni-Cu-PGE deposit in southwest Spain have been undertaken in order to understand both the primary magmatic distribution and the secondary remobilisation of the PGE. The deposit is hosted in the Aguablanca Stock which is related to calc-alkaline arc plutonism, and is essentially comprised of a dioritic unit (hornblende-biotite and quartz diorite) and a gabbronorite unit (massive gabbronorite, pyroxene gabbro and norite) (Tornos *et al.*, 2006). Three types of ore have been identified; i) massive to semi-massive sulphide mineralisation occurring in chaotic magmatic breccias, ii) disseminated ore surrounding these mineralised magmatic breccias and iii) irregular discontinuous zones of sulphides within the magmatic breccias and in distal parts of the deposit (Rio Narcea Recursos, 2009).

A mineralogical study by Piña *et al.* (2008) identified a variety of Pt-Pd bismuthotellurides including merenskyite, melonite ($NiTe_2$), michenerite, moncheite as well as sperrylite. The mineral associations of these Pd-bearing PGM (commonly enclosed within sulphides) (Piña *et al.*, 2008) and their textures (usually rounded grains and laths) together with the inferred temperature of crystallisation of <500°C suggests that Pd and Pt initially partitioned into the BMS before exsolving with Bi, Te and As to form the PGM observed (Piña *et al.*, 2011). Piña *et al.* (2008) also suggest that post-magmatic hydrothermal fluids have partially remobilised Pt, Au and Cu evidenced by textural observations (such as sperrylite losing its euhedral shape when in contact with altered minerals) in order to account for negative Pt and Au anomalies in mantle-normalised chalcophile element profiles and the lack of Cu-S correlation.

Suárez *et al.* (2010) show how these PGM are progressively altered and dispersed into iron oxides that form the overlying gossan of the deposit. They studied both the upper (more altered) and lower (less altered) sections of the gossan to determine the effects of weathering

on the PGE/PGM. They concluded that a systematic breakdown and remobilisation of the PGM had occurred in the gossan due to the effects of weathering. The breakdown of pre-formed PGM, Pt arsenides and Pt-Pd bismuthotellurides occurs first with the Pt PGM breaking down more slowly as they are more stable. During this breakdown, the formation of partially oxidised PGM takes place until a wide range of oxidised Pt and Pd phases have formed. These oxide phases then evolve further into Fe-PGE-oxides and PGE-hydroxides. It is noted that the dispersion of Pd throughout Fe-oxides is greater than that of the other PGE. In this weathering, oxidising environment, oxides rather than alloys have formed during the progressive surface alteration of magmatic PGM.

A LA-ICP-MS study of the Aguablanca BMS by Piña *et al.* (2011) shows that the majority of the IPGE and Rh occur in solid solution in pyrrhotite and pentlandite whereas only ~30% of the Pd is taken up in pentlandite. Platinum and the remainder of the Pd occur as constituents in the aforementioned PGM. They suggest that the presence of Pd in pentlandite is likely due to the effect of limited sulphide fractionation (with some Pd remaining in MSS) combined with Pd diffusion into pentlandite from both the MSS and Cu-rich sulphides during sub-solidus cooling. Piña *et al.* (2011) have also identified PGE in solid solution in two types of pyrite. Large idiomorphic pyrite which may be an exsolution product of MSS or the alteration product of pyrrhotite, hosts the IPGE, Rh (4-31 ppm) and Pt (up to 15 ppm) whereas secondary ribbon-like pyrite hosts only the IPGE and Rh in similar concentrations to the pyrrhotite that it has replaced.

2.7 Other Studies of PGM and PGE Remobilisation

This section reviews literature that is focussed on identifying and recording post-magmatic remobilisation of PGE and/or PGM in altered deposits and occurrences. It is difficult to understand the full distribution of PGE in these deposits as such studies are predominantly mineralogically based given the difficulties in determining in situ PGE concentrations of highly altered and deformed BMS. Nonetheless, these mineralogical studies provide valuable insight into the post-magmatic mobility behaviour of PGE and/or PGM and have therefore been reviewed below. A section briefly noting some experimental work on the mobilisation of the PGE is also included.

2.7.1 Bacuri Complex, Brazil

The Bacuri Complex is an ultramafic-mafic layered intrusion situated in Amapa State in the Amazon region of Brazil and was emplaced between 2940-1920 Ma (Rb/Sr dating of host country rocks, Montalvão and Tassinari, 1984). The complex occupies an area of at least 55 km^2, however, the limits of the intrusion are not well known due to lack of exposure and lateritic cover (Prichard *et al.*, 2001). The original lithologies of the complex consisted of peridotite including pyroxenite, chromitite, gabbro and mafic anorthosite (Matos *et al.*, 1992 cited by Prichard *et al.*, 2001), however, the complex has since been intensely faulted, folded and subjected to extensive serpentinisation, predominantly resulting in secondary serpentine and tremolite-talc schists.

Prichard *et al.* (2001) evaluated the mobility of Pd in areas of serpentinisation and laterisation in the Bacuri Complex. In serpentinised samples that have not undergone laterisation, Pd bismuthides occur with chalcopyrite within chlorite filled veins cross cutting serpentine and chromite. It is thought that these veins occur only a few micrometres from the original magmatic source of PGE indicating limited mobility of Pd during serpentinisation.

Low Pt/Pd ratios of <1 indicate primary magmatic PGE values, however, in the serpentinised areas values of up to four are recorded, controlled by the partial removal of Pd during serpentinisation. Pt/Pd ratios of up to 26 occur in laterised samples, in which the Pd has been almost completely removed while the Pt remains (Prichard *et al.*, 2001).

2.7.2 Jinbaoshan Pd-Pt Deposit, China

Wang *et al.* (2008) studied the effects of post-magmatic hydrothermal alteration on PGM from the Jinbaoshan Pd-Pt deposit. The Jinbaoshan Pd-Pt deposit in Southwest China is one of five variably sized orebodies hosted by a large sill-like ultramafic intrusion approximately 4,760m long, 760-1,240m wide, and 8-170m thick and composed predominately of wehrlite (Wang *et al.*, 2008). SHRIMP U-Pb zircon dating gives an age of ~260 Ma and the intrusion is therefore contemporaneous with the Emeishan continental flood basalts (Tao *et al.*, 2009). The Jinbaoshan Pd-Pt deposit is defined by rocks with concentrations of >0.5 ppm Pt+Pd. Post-magmatic hydrothermal activity has extensively altered the host intrusion of the deposit with primary olivine, clinopyroxene and chromite having been variably altered to serpentine, actinolite-tremolite, biotite, and magnetite (Wang *et al.*, 2008).

The PGM identified here are Te-, Sn- and As-bearing. Wang *et al.* (2008) show that primary euhedral chromite is enclosed within or interstitial to olivine. Interstitial chromite is partially-totally altered to magnetite. The BMS are interstitial to olivine and the PGM are associated with these sulphides or occur within altered clinopyroxene and chromite.

Wang *et al.* (2008) summarise that moncheite was initially formed during the alteration of clinopyroxene. Moncheite was then altered to Pt-Fe alloy where it was in contact with serpentine. Furthermore, sudburyite (PdSb) is found in late stage veins indicating that late stage Pd remobilisation occurred. The remobilised or secondary PGM remain in close proximity to the BMS, indicating that the PGE have only been mobile over short distances.

2.7.3 Shetland Ophiolite, Shetland Islands, Northeast Scotland

The Shetland Islands which lie off the northeast coast of the Scottish mainland are host to the Shetland Ophiolite which is exposed on the most north easterly islands of Unst and Fetlar. The complex is comprised of a typical ophiolite sequence of mantle harzburgite overlain by cumulate dunite, wehrlite, pyroxenite and gabbro (Flinn, 1985; Prichard, 1985); the uppermost part of which is intruded by dykes, the geochemistry of which indicate a supra-subduction zone setting (Prichard and Lord, 1988).

Prichard *et al.* (1994) studied the mobility of PGE during hydrothermal alteration and weathering of a variety of PGE-bearing chromite-rich lithologies from the Shetland Ophiolite. Primary magmatic PGE are preserved in the form of laurite which resides within chromite. There are also Pt- and Pd-rich inclusions in clinopyroxene which represent droplets of PGE-enriched immiscible sulphide liquid. Pt and Pd PGM are associated with BMS which are identified within serpentine and chlorite. Prichard *et al.* (1994) suggest that during silicate alteration, the PGE were liberated from the BMS resulting in the formation of PGM. PGM are also identified away from the BMS, being completely enclosed in altered silicates. In these cases, the PGM are semimetal-bearing (As, Sb and Te) which are thought to have been introduced with the altering hydrothermal fluids (Prichard *et al.*, 1994). Subsequent removal of the semimetals has left residual Pt and Pd alloys. Late stage weathering processes have produced Pt and Pd ochres. The alteration documented here demonstrates only short range (micrometre-scale) mobility of the PGE (Pt and Pd), however, Pt and Rh identified in alloclase-gersdorffite in solid solution near the basal contact of the ophiolite at Cliff

demonstrates how PGE can be mobile up to at least a few hundred metres from the original magmatic source (Prichard *et al.*, 1994).

2.7.4 Raglan, Cape Smith Belt, Quebec, Canada

The Raglan Ni-Cu-(PGE) sulphide deposits are located in the eastern section of the Cape Smith Belt, northern Quebec, Canada. The deposits lie near the base of the Chukotat Group basalt and picrite with orebodies forming lenses composed of massive and disseminated sulphide in mesocumulate peridotite, olivine oikocrystic pyroxenite and pyroxenite of the Raglan Formation (Lesher and Charland, 1999; Naldrett, 2004). Primary igneous features have been variably affected by shearing with deformed ores displaying aligned intergrowths of sulphide and tremolite-actinolite laths and needles with patches of chlorite and serpentine (Seabrook *et al.*, 2004). Dillon-Leitch *et al.* (1986) have previously suggested that the PGE grade is related to sulphide content and that Pt and Pd have been remobilised and redistributed as a result of their transport in hydrothermal fluids during regional greenschist facies metamorphism.

Seabrook *et al.* (2004) studied the platinum-group mineralogy of two orebodies at Raglan, the Katiniq and Zone 2 orebodies in order to better understand the genesis of the deposits. They found that the majority of PGM occur within or at the edge of sulphides juxtaposed against silicates. A third of the PGM are represented by sperrylite with the remaining PGM comprised of sudburyite and merenskyite. Sperrylite is the most abundant PGM at Katiniq with merenskyite the most abundant PGM in Zone 2.

Seabrook *et al.* (2004) found that Pt PGM are associated with pyrrhotite and pentlandite in MSS ores. Chalcopyrite-rich ores also contain Pt-bearing PGM with Pd PGM occurring in secondary veins. PGE, especially Pd, have been remobilised by extensive low temperature alteration of the ultramafic protolith under greenschist facies conditions. Shearing has also affected the deposit and sudburyite (and rarely sperrylite) occur in secondary carbonate veins in these shear zones. Sperrylite loses its typical euhedral form where it is in contact with altered silicates.

2.7.5 Experimental studies of Pt and Pd mobility

A thorough review of experimental research of Pt and Pd mobility has been undertaken by Wood (2002) and the main conclusions of this study relevant to this thesis are given here. Experimental data for Pt and Pd has been determined up to ~300^{o}C, however, data is poor for Pt and Pd at temperatures over 300^{o}C and for the other PGE in general. At geologically relevant fO_2, the predicted oxidation states for all PGE in solution are 2^+ (Wood, 2002; Hanley, 2005) and it is generally understood that oxidising and/or acidic solutions are required to transport Pt and Pd, irrespective of salinity (Wood, 2002).

Given the oxidation states of Pt and Pd, they are expected to bond with soft ligands (e.g., HS^-, Cl^-) whereas complexes with hard ligands are not expected with the exception of carboxylates, NH_3 and OH^- (Wood, 2002). Hanley (2005) argues that at low temperatures (<500ºC), PGE ions will behave as soft Lewis acids and will form the strongest complexes with soft Lewis bases such as bisulphide (HS^-) whereas chloride complexes are more likely to form at higher temperatures (>500^{o}C).

Low temperature hydrothermal solutions (<500ºC) in equilibrium with pyrite and/or pyrrhotite and Cl-rich hydroxysilicate alteration minerals such as chlorite, albite, epidote, and calcite are incapable of dissolving large volumes Pt and Pd (Wood, 2002; Hanley, 2005). Under these conditions the PGE are more likely to form bisulphide complexes rather than chloride complexes (Hanley, 2005). Bisulphide complexes are incapable of redistributing significant amounts of PGE unless fluid:rock ratios are very high with very effective depositional mechanisms (Hanley, 2005). Furthermore, in the event of PGE chloride complexes forming, experiments by Wood and Normand (2008) demonstrate that unrealistically large amounts of oxidising and acidic fluids are required to react with a given mass of basalt in order to overcome the acid- and redox-buffering capacity of the rock and to mobilise palladium as a chloride complex. This has implications for both ultramafic and mafic lithologies.

Although experimental data for the PGE at high temperatures is poor, the solubility of Pt may be very high (at ppm-level) in high temperature (800-900ºC) high salinity brines and may be controlled by HCl complexing, hydroxide complexing, or the formation of heterogeneously distributed colloidal particles (Hanley, 2005).

Wood (2002) notes that elements such as As, Bi, Sb, Se and Te (the semimetals) form very insoluble compounds with the PGE and as such, the precipitation of these PGM can occur from PGE-bearing fluids that inherit a critical concentration of semimetals. However, it is unclear how soluble PGE sulphides, oxides and alloys are under various hydrothermal conditions.

2.8 Discussion and Summary of PGE Behaviour

It is clear from these studies that not only do the individual PGE behave differently, their behaviour changes as a consequence of different magma compositions, cooling rates and post-magmatic alteration. General patterns have emerged from this review of the studies above regarding the behaviour of the PGE during magmatic conditions (summarised in Table 2.5) which indicate that in a magmatic system without an abundance of semimetals, the IPGE (Os, Ir and Ru) as well as Rh will partition into MSS as it crystallises from an immiscible sulphide liquid. Osmium, Ir and Ru then partition equally between pyrrhotite and pentlandite during the sub-solidus exsolution of these phases (e.g., Fleet *et al.*, 1993; Li *et al.*, 1996; Ballhaus and Sylvester, 2000; Mungall *et al.*, 2005; Barnes *et al.*, 2006; Godel *et al.*, 2007; Holwell and McDonald, 2007). Rhodium, however, has a preference for pentlandite at this stage (e.g., Ballhaus and Sylvester, 2000; Godel *et al.*, 2007; Holwell and McDonald, 2007). The IPGE and Rh have also been identified in pyrite where it occurs as an exsolution product of MSS (e.g., at Sudbury, Dare *et al.*, 2011).

Platinum, Pd and Au are incompatible with both MSS and ISS and instead partition into a late stage immiscible sulphide liquid which may also contain semimetals (Peregoedova, 1998; Holwell and McDonald, 2007; 2010). This late stage melt is expelled to sulphide grain boundaries and upon cooling forms PGM. It is shown that Pt has a greater preference for forming PGM with semimetals than Pd (Helmy *et al.*, 2007), therefore, when a limited amount of semimetals are available, Pt will form PGM whereas excess Pd will diffuse into pentlandite (e.g., Holwell and McDonald, 2007; Godel and Barnes, 2008a).

Barnes *et al.* (2006) demonstrated that Pd will partition into a Cu-rich liquid; either ISS or a late stage immiscible sulphide melt; Pd appears to partition into the latter when semimetal content is relatively high. The affinity of Pd with Cu-rich sulphide liquid is evidenced by its presence as Pd-bearing PGM in chalcopyrite portions of BMS blebs from a dyke in Uruguay

(Prichard *et al.*, 2004b). Palladium has also been shown to exsolve from Cu-rich portions of sulphide blebs at Noril'sk by Barnes *et al.* (2006) in the form of Pd-bearing PGM.

However, this experimental and observed behaviour of Pd does not explain why it is often identified in solid solution in pentlandite, and in many cases in high concentrations. Dare *et al.* (2010a) proposed that Pd may diffuse into pentlandite from adjacent chalcopyrite during sub-solidus exchange. Piña *et al.* (2011) suggest that the presence of Pd in pentlandite is the result of limited sulphide fractionation with some Pd remaining in MSS (which subsequently diffuses into pentlandite during its exsolution from MSS) combined with the diffusion of Pd from Cu-rich sulphides during sub-solidus cooling. Osbahr *et al.* (2013) suggest that where high concentrations of Pd are identified in pentlandite where it is isolated in silicates in the Merensky Reef, Pd may have diffused from an evolved sulphide liquid as it migrated through solidified silicates along their grain boundaries as suggested by Mungall and Su (2005). Alternatively, Osbahr *et al.* (2013) suggest that significant concentrations of Pd may have partitioned into MSS at an earlier magmatic stage, eliminating the need for Pd diffusion from fractionated Cu-rich sulphides.

The timing of PGM formation versus the incorporation of PGE into BMS appears to vary in different deposits and even within a single deposit. There is growing evidence that the presence of semimetals has an influence on the partitioning of PGE into the BMS. Dare *et al.* (2010b) suggested for Sudbury that when volatile elements, especially arsenic, were introduced into the magma from the surrounding basement during melting, Os, Ir, Ru and Rh crystallised into PGM-bearing sulpharsenides at high temperatures, directly from the sulphide liquid and prior to the formation of MSS. Another example demonstrating the effect of As in the melt changing the behaviour of the PGE is documented in ultramafic intrusive complexes in the Andriamena region of Madagascar. McDonald (2008) showed that in this case, high As concentrations have resulted in the early crystallisation of Pt-Ir-Rh arsenides and sulpharsenides. This is evidenced by the dissociation of these PGM with BMS and their incorporation as inclusions in subsequently crystallising olivine. It appears that as the concentrations of semimetals in the melt increases, the solubility of PGE in the sulphide liquid decreases (Helmy *et al.*, 2007). Thus the presence of different semimetals changes how different PGE behave and directly affects the types of PGM that may form. Hutchinson and McDonald (2008) suggested that the assimilation of As and Sb into the sulphide melt from the surrounding country rocks of the Platreef in the Bushveld Complex may cause Pt-bearing PGM to crystallise early rather than Pt remaining in the sulphide melt. Holwell and

Deposit/Occurrence	MSS			ISS	PGM	References
	Pyrrhotite	Pentlandite	Pyrite	Chalcopyrite		
Platreef	IPGE	IPGE, Rh, Pd	N/A	Barren	Pd-Te, Pd-Bi, Pd-Sb, Pd-Bi-Sb, Pt-As, Pt-Sb	Holwell and McDonald, 2007; Hutchinson and Kinnaird, 2005
Merensky Reef	IPGE, minor Rh	IPGE, Rh, Pd	N/A	Barren	Pt-Fe, Pt-Pd-S, Pt-Pd-Bi-Te	Godel *et al.*, 2007; Ballhaus and Sylvester, 2000
Noril'sk	IPGE, Rh	IPGE, Rh, Pd	N/A	Barren	Pt-Te, Pt-Bi, Pt alloy	Barnes *et al.*, 2006
Sudbury	Os, Ru	Os, Ru	Os, Ru	Barren	IrAsS, RhAsS, PGE-Ni-Cobaltite, PdBiTe	Dare *et al.*, 2010a; 2010b; Szentpeteri *et al.*, 2002
Stillwater J-M Reef	Low Concentrations	IPGE, Rh, Pd	N/A	Barren	(Pd±Pt)-S, Pt-Fe, (Pd±Pt)-Te, Pd-Cu, Pd,Ru(Ir,Os)S_2, Au-Pd-Ag	Godel and Barnes, 2008a; 2008b
Penikat AP-Reef	All PGE (minor)	All PGE (Pd, Rh)*	N/A	Barren	Pd-Bi-Te, Pd-As-Sb, Rh-(Ir-Pt)-As-S, Pt-As Pd-Pt-S, Pd-As,	Halkaoho 1993 Barnes *et al.*, 2008
Penikat PV-Reef	Ru	Pd, Ru	N/A	Pd	Pt-As, Pd-Bi-Te, Pd-As-Sb	Huhtelin *et al.*, 1990 Barnes *et al.*, 2008

Deposit/Occurrence	MSS			ISS	PGM	References
	Pyrrhotite	Pentlandite	Pyrite	Chalcopyrite		
Aguablanca	IPGE, Rh	IPGE, Rh, Pd	Idiomorphic IPGE, Rh, Pt Ribbon-replacement IPGE, Rh	Barren	Pt-As, Pt-Pd-Bi-Te, Fe-PGE-oxides PGE-hydroxides	Piña *et al.*, 2008 Piña *et al.*, 2011 Suárez *et al.*, 2010

Table 2.5: Table displaying the distribution of the PGE in BMS (pyrrhotite, pentlandite, pyrite, chalcopyrite) and PGM for the major PGE deposits reviewed in this chapter.
* = predominantly Pd and Rh

McDonald (2007) have shown that when Bi and Te are present, Os, Ir, Ru and Rh will partition into MSS, however, Pt, Au and some Pd will partition into a late stage semimetal-rich melt that is expelled to sulphide grain boundaries during ISS crystallisation forming PGM on cooling.

Further research is required regarding the post-magmatic remobilisation of PGE in order to characterise their behaviour during different types of alteration. It is clear from this review that post-magmatic alteration is a significant process in both concentrating and redistributing the PGE, controlling their final position within their magmatic host.

There is little research into the remobilisation of Os, Ir, Ru and Rh with the majority of research focused on Pt and Pd. If PGE are present in solid solution in BMS, hydrothermal fluids may liberate PGE from their BMS hosts resulting in the formation of PGM within and at the edges of these sulphides (e.g., Li *et al.*, 2004; Hutchinson and Kinnaird, 2005; Hutchinson and McDonald, 2008). However, at low temperatures (<500^{o}C), it is more likely that sulphur will be remobilised while the PGE remain relatively immobile (Wood, 2002; Hanley, 2005). Indeed, it has been argued and demonstrated that hydrothermal fluids typically only mobilise the PGE very short distances (micrometres) (e.g., Prichard *et al.*, 1994; 2001; Wang *et al.*, 2008), however, Pd mobility of up to several hundreds of metres has been documented (e.g., Prichard *et al.*, 1994). Natural and experimental studies both suggest that Pd is far more mobile than Pt during secondary alteration (e.g., Fuchs and Rose, 1974; Prichard *et al.*, 1994; 2001; Seabrook *et al.*, 2004; Barnes *et al.*, 2008; Wang *et al.*, 2008; Suárez *et al.*, 2010) with Pt only considered to be mobile in high temperature (800-900ºC) high salinity brines (Hanley, 2005). Weathering again shows that Pd is far more mobile than Pt (e.g., Fuchs and Rose, 1974; Prichard *et al.*, 2001). The remobilisation of PGE during weathering is briefly noted in the above review, however, further literature on the effects of supergene alteration on the PGE is not further considered as it is not relevant to this thesis.

The magmatic concentration of PGE appears to be relatively well understood in comparison to the post-magmatic remobilisation of PGE. The presence of PGE in pyrite must be explored further and the continued testing of this typical PGE behaviour in magmatic processes should be conducted. The remobilisation of PGE requires much further research, particularly studying deposits that have been subjected to different types/degrees of alteration to understand how this secondary alteration affects the behaviour of individual PGE and PGM.

2.9 Thesis Study Areas

The following section briefly introduces the study areas of this thesis, the Mirabela intrusion, Brazil and the Jinchuan intrusion, China. More detailed reviews of these intrusions are given in their respective chapters.

The Fazenda Mirabela complex is an ultramafic-mafic layered intrusion situated in Bahia State, north-eastern Brazil and hosts the stratiform Santa Rita Ni-Cu-(PGE) sulphide ore deposit (Inwood *et al.*, 2011; Barnes *et al.*, 2011). The intrusion is almost completely unaltered and preserves magmatic minerals and textures, despite being ~2 Ga (Silva *et al.*, 1996), making it an ideal natural laboratory to study the primary magmatic concentration of PGE in the absence of any significant secondary processes.

The ~800 Ma Jinchuan ultramafic igneous intrusion (Li *et al.*, 2005; Yan *et al.*, 2005; Tian *et al.*, 2007; Zhang *et al.*, 2010) is situated in Northwest China and is the third largest Ni-Cu-(PGE) deposit in the world after Noril'sk and Sudbury (Naldrett, 2011). The intrusion hosts net-textured sulphide mineralisation as well as disseminated and rare massive ores. The intrusion has been variably affected by greenschist facies metamorphism resulting in the presence of variably altered ores ranging from areas that are completely serpentinised to areas that display unaltered magmatic minerals and textures (Chai and Naldrett, 1992b; Zhou *et al.*, 2002; Li *et al.*, 2004; Naldrett, 2004; Ripley *et al*, 2005; Yang *et al.*, 2006). This intrusion is therefore an ideal natural laboratory to study both the magmatic concentration and secondary remobilisation of PGE during post-magmatic hydrothermal alteration.

3. Analytical Methods

3.1 Introduction

The following section details the methods used in the preparation and analysis of samples at Cardiff University. Details of the methodologies used in the preparation and analysis of samples undertaken externally are given where appropriate in chapter 4.

3.2 Major and Trace Element Geochemistry

Samples were initially jaw crushed for their preliminary disaggregation before undergoing fine grinding in a TEMA agate ball mill. The resulting powders then underwent a loss on ignition (LOI) procedure. One to two grams of material (accurately recorded) is weighed in a crucible ('wet' weight) before being placed in a furnace at 900^{o}C for two hours. The powder and crucible are then re-weighed ('dry' weight) and the LOI calculated gravimetrically.

A mixture of 0.100±0.002g of the ignited powder and 0.600±0.005g of lithium borate flux (50% metaborate, 50% tetraborate) is mixed and transferred to a platinum crucible, to which two to three drops of lithium iodine wetting agent is added. The samples are then fused using a Claisse Fluxy automated fusion system with the resulting melts added to solutions of 20 ml of 10% nitric acid plus 30 ml of deionised water (18 Mohm-cm). The solutions are heated on a hotplate to 70-80^{o}C and actively mixed until the glass (resulting from the melt) is dissolved. The solutions are then spiked with 1 ml of 100 ppm Rh stock solution and made up to a volume of 100 ml with deionised water before being analysed for major and trace elements using a JY Horiba Ultima 2 inductively coupled plasma-optical commission ICP-OES and a Thermo X7 series inductively coupled plasma-mass spectrometer (ICP-MS). Further details of the analytical methodology are given in McDonald and Viljoen (2006).

3.3 Whole-Rock PGE Analysis

A mixture of 6g Na_2CO_3, 12g borax, 0.9g sulphur, 1.08g nickel, and 1g silica (all within 10% error) is added to 15g of sample. In order to check the quality of the analyses and to check for analytical drift, two standards (WMG-1 and TDB-1), two blanks (mixtures that contain no sample material and 10g of silica) and duplicate samples (one duplicate for every ten samples) are run. The mixtures are added to clay crucibles which are placed in a furnace at 1050^{o}C for 90 minutes.

For particularly sulphur-rich samples, the amount of sample added to the mixtures was reduced to 10g in order to avoid too large a volume of sulphide melt forming during the furnace stage which would then failed to separate properly from the silicate melt. For these sulphur-rich samples, the above LOI procedure was also employed, although the time the sample spent in the furnace was reduced from two to one hour in order to drive off some of the sulphur.

Sulphide buttons are retrieved from the crucibles once they have cooled and are weighed. These sulphide buttons are transferred to beakers containing hydrochloric acid which are heated on hotplates until the buttons are completely dissolved; more acid is added if required. Once the buttons have been completely dissolved, deionised water is added to the solutions. Noble metals that had been dissolved in these solutions are then co-precipitated with Te (0.2 ml of 10,000 ppm solution) using 2-3 ml of $SnCl_2$ and boiling for one hour.

Once cool, the solutions are filtered under vacuum and placed in Teflon containers. Once dry, the samples are spiked with 0.2 ml of 2500 ppb Tl solution to correct for any analytical drift. A solution of 4 ml of hydrochloric acid and 3 ml of nitric acid is then added to each of the Teflon containers which are placed on a hot plate for 2-3 hours in order to dissolve the filter papers and metal contents. Once the solutions have cooled, deionised water is added to produce 50 ml solutions which are then analysed for all six PGE and Au on a Thermo X7 series ICP-MS. The determined PGE concentrations are corrected for the amount of sample used in the Ni-fire assay mixtures and for LOI procedures if performed.

3.4 Mineralogical Analysis

Thin sections of the samples were examined using conventional optical transmitted and reflected light microscopy. PGM and their associated sulphide and silicate minerals were identified and analysed using a Cambridge Instruments (now Carl Zeiss NTS) S360 scanning electron microscope (SEM). Polished blocks and thin sections were searched systematically for PGM using the SEM set at a magnification of x100. Quantitative analyses of the larger PGM (>0.4x0.4 µm) were obtained using an Oxford Instruments INCA Energy EDX analyser attached to the SEM. Operating conditions for the quantitative analyses were 20 kV, with a specimen calibration current of ~1 nA and a working distance of 25 mm. A cobalt reference standard was regularly analysed in order to check for any drift in the analytical conditions. A comprehensive set of standards obtained from MicroAnalysis Consultants Ltd. (St Ives,

Cambridgeshire) was used to calibrate the EDX analyser. Images were obtained using a four-quadrant back-scattered detector operating at 20 kV, a beam current of ~500 pA, and a working distance of 13 mm, under which conditions, magnifications of up to x15000 are possible.

3.5 Laser Ablation-ICP-MS

Analyses were carried out using a New Wave Research UP213 UV laser system coupled to a Thermo X Series ICP-MS. Details of the procedures for the laser analysis follow those given in Holwell and McDonald (2007). PGE and other elements were determined in time-resolved analysis mode (time slices of 350 ms) as the laser beam followed a line designed to sample different sulphide phases. The beam diameter employed was 30 μm, with a frequency of 10 Hz and the sample was moved at 6 μm/s relative to the laser. Acquisitions lasted between 80 and 400s, and a gas blank was measured for 30-40s prior to the start of the analysis. Sulphur concentrations were measured prior to LA-ICP-MS using the SEM and ^{33}S was used as an internal standard. Subtraction of gas blanks and internal standard corrections were performed using Thermo Plasmalab software.

Calibration was performed using a series of synthetic Ni-Fe-S standards prepared from quenched sulphides produced by Iain McDonald at Cardiff University. The standards incorporate S, Ni, Fe and Cu as major elements and Co, Zn, As, Se, Ru, Rh, Pd, Ag, Cd, Sb, Te, Re, Os, Ir, Pt, Au and Bi as trace elements. The compositions of the five sulphide standards are given in Table 3.1. Major elements were determined by SEM and trace elements by solution ICP-MS after dissolution of between 2 and 5 individual sulphide spherules from each class of standard. Sulphide spherules were mounted in resin and polished to produce the laser standards. Sulphide homogeneity was checked using the SEM; this revealed complete homogeneity in Fe-Ni-S standards 1, 2 and 5 and only minor separation of blebs of Cu-rich sulphide (1-2 microns across) in standards 2 and 3 that contain Cu as a major element. The standards produce five point calibration curves for S, Ni and Fe. Standards 1, 4 and 5 produce three point calibration curves for PGE, Ag, Cd, Re, Au and semimetals. Standards 1, 2 and 3 produce three point calibration curves for Cu, Co and Zn and matrix-matched corrections for argide species (59Co40Ar, 61Ni40Ar, 63Cu40Ar, 65Cu40Ar, 66Zn40Ar) that interfere with light PGE isotopes.

Element		Standards				
		Std-1	Std-2	Std-3	Std-4	Std-5
S	wt. %	29.50	30.1	28.60	31.60	30.1
Fe	wt. %	5.18	7.3	4.15	9.47	10.6
Ni	wt. %	62.37	51.7	46.90	59.03	58.3
Cu	wt. %	-	11.0	19.81	-	-
Co	ppm	36.00	4850.0	15000.00	-	-
Zn	ppm	100.00	3000.0	4600.00	-	-
As	ppm	-	-	-	57.00	108.0
Se	ppm	-	-	-	140.00	264.0
Ru	ppm	-	-	-	51.00	160.0
Rh	ppm	-	-	-	51.00	160.0
Pd	ppm	-	-	-	50.00	120.0
Ag	ppm	-	-	-	147.00	152.0
Cd	ppm	143.00	-	-	-	-
Sb	ppm	-	-	-	52.00	108.0
Te	ppm	-	-	-	210.00	644.0
Re	ppm	-	-	-	61.00	127.0
Os	ppm	-	-	-	50.00	160.0
Ir	ppm	-	-	-	55.00	160.0
Pt	ppm	-	-	-	50.00	125.0
Au	ppm	-	-	-	44.00	125.0
Bi	ppm	6.00	6.5	5.00	146.00	263.0

Table 3.1: Compositions of quenched sulphide standards used for LA-ICP-MS. Dashes indicate that the element was not added to the standard.

Corrections for 106Cd on 106Pd and 108Cd on 108Pd were determined using Standard 1. Argide and isobaric-corrected data are indicated by asterisks beside 99Ru, 103Rh, 106Pd and 108Pd in Table 4.4, Table 4.5 and Table 5.3. Where independent corrections have been applied to different isotopes of the same element (e.g., 66Zn40Ar on 106Pd and 108Cd on 108Pd) the independently corrected values vary by less than 20% (and commonly <5%) indicating that the corrections are robust. The accuracy of the LA-ICP-MS procedure for PGE was checked by the analysis of the Laflamme-Po724 standard, run as an unknown against the Cardiff University sulphide standards.

4. Ni-Cu-PGE Sulphide Mineralisation in the Fazenda Mirabela Intrusion, Brazil

4.1 Introduction

The Fazenda Mirabela complex is an ultramafic-mafic layered intrusion situated in Bahia State, north-eastern Brazil (Fig. 4.1) and hosts the Santa Rita sulphide ore deposit (Inwood *et al.*, 2011; Barnes *et al.*, 2011). A Ni-Cu-sulphide ore zone that varies in thickness up to 200m. This ore zone is also PGE-bearing with Pt+Pd concentrations of typically between 0.1-0.5 ppm. The orebody is hosted in the lower ultramafic portion of the Mirabela intrusion but lies close to the boundary to the overlying mafic sequence.

This study systematically documents the full distribution of and variation in PGE across the Mirabela intrusion. The platinum-group mineralogy, whole-rock PGE data, and the PGE concentrations in solid solution in BMS have been determined for samples collected from six boreholes across the intrusion; two from the northern zone, two from the southern zone and two from the central zone. Major and trace element geochemistry allows the mineralisation observed in the Mirabela intrusion to be placed in context within the igneous stratigraphy.

4.2 Regional and Local Geology of the Mirabela Intrusion

The Mirabela Fazenda ultramafic-mafic body was intruded into the southern portion of the Archaean-Palaeoproterozoic Itabuna-Salvador-Curaça belt, close to the Archaean Jequié block in the west (Fig. 4.1). The Itabuna-Salvador-Curaça belt is comprised predominantly of a low-K calc-alkaline plutonic suite and was formed during the collision of several Archaean blocks during the Palaeoproterozoic Transamazonian orogeny (2.15-2.05 Ga) (Barbosa and Sabaté, 2004). The immediate country rocks to the intrusion consist of a previously deformed sequence of granulite facies charnockite and enderbite orthogneisses, as well as a supracrustal sequence consisting primarily of gneisses, meta-gabbronorite sills, banded iron formations and rare serpentinites (Barbosa and Sabaté, 2004). Silva *et al.* (1996) dated the Mirabela intrusion using the Sm-Nd method at 2.2 Ga, however, this age contradicts the observation that the intrusion postdates the peak granulite facies metamorphism of the region which occurred at ~2.1 Ga (Barnes *et al.*, 2011). The age of the intrusion is therefore thought to be ~2.0 Ga.

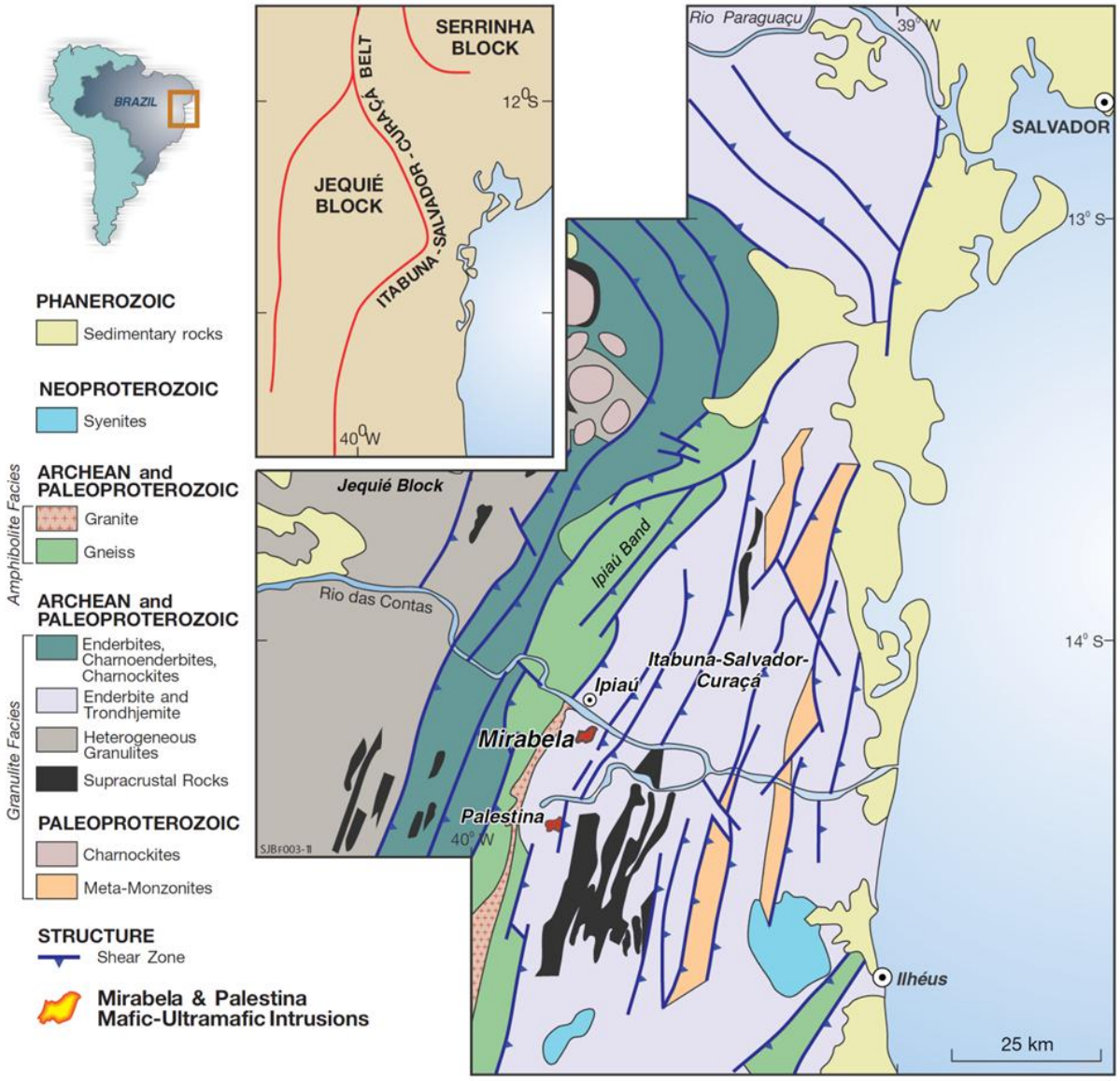


Figure 4.1: Maps showing the location of the Mirabela intrusion and simplified geology of the south-southeast Bahia granulite region (Barnes *et al.*, 2011 [after Barbosa *et al.*, 2003]) and regional terrane boundaries (Barnes *et al.*, 2011 [after Barbosa and Sabaté, 2004]).

The intrusion can be broadly divided into two northeast-dipping sequences (Fig. 4.2); a lower sequence exposed in the western part of the intrusion comprised of ultramafic lithologies and an upper sequence exposed in the eastern part of the intrusion comprised of mafic lithologies. The surface expression of the intrusion is approximately 2.5x4.2 km covering an area of ~7 km^2 (Barnes *et al.*, 2011). The stratigraphic base of the Mirabela intrusion is a reversely differentiated sequence comprising ~90m of gabbronorite overlain by ~130m of orthopyroxenite. These units are overlain by the ultramafic sequence that is typically ~730m thick and consists of ~600m dunite, ~50m harzburgite, ~25m olivine orthopyroxenite and

~50m orthopyroxenite. The ultramafic sequence is capped by a websterite unit only a few metres thick. This is overlain by the mafic sequence (~1000m thick) comprised of gabbronorite, leuco-gabbronorite and augite norite (Barnes *et al.*, 2011). The intrusion has been cross-cut by later minor dolerite and felsic pegmatitic dykes; however, it shows no evidence of the high level of alteration and deformation that has affected the surrounding country rocks, although significant laterisation has occurred at the surface of the intrusion, particularly over the lower or western ultramafic sequence (Inwood *et al.*, 2011).

The Santa Rita ore deposit consists of a stratiform zone up to 200m thick of disseminated sulphides which is thicker than other stratiform sulphide zones in layered intrusions (e.g., individual sulphide zones in the Great Dyke [<10m], Wilson *et al.*, 1989; Munni Munni [~20m thick], Barnes *et al.*, 1992; as well as the Merensky Reef in the Bushveld Complex and the J-M Reef in the Stillwater Complex which are only a metre or so thick, e.g., Maier, 2005; Naldrett *et al.*, 2009).

The Santa Rita Ni-Cu-(PGE) sulphide orebody is a semi-continuous stratiform zone of disseminated sulphides situated within the upper ~100m of the ultramafic sequence, predominantly in the orthopyroxenite unit (excluding the uppermost part of this lithology) down into the upper part of the harzburgite (Barnes *et al.*, 2011). The orebody varies in thickness and in its exact position within the igneous stratigraphy from the north to the south of the intrusion. The ore zone occurs as a single well defined layer ~50m thick in the northern part of the intrusion; however, it transitions into a thick (up to ~200m) discontinuous zone at the southern margin of the intrusion while transgressing upwards through the ultramafic stratigraphy (Barnes *et al.*, 2011). The ore zone consists of between 0.5-5 wt. % disseminated sulphides and is PGE bearing with Pt+Pd concentrations typically between 0.1-0.5 ppm. The BMS assemblage is dominated by pentlandite (52%) which is accompanied by violarite (7%), chalcopyrite (14%), pyrite (14%) and pyrrhotite (9%) (Inwood *et al.*, 2011).

A zone of sulphur-poor (<0.1 wt. % S) PGE mineralisation has been identified in the upper portion of the dunite which underlies the Santa Rita ore zone. Barnes *et al.* (2011) demonstrated that the Pt and Pd tenors for this zone were significantly higher than those observed in the relatively BMS-rich Santa Rita ore zone and referred to this interval as the "basal PGE anomaly". The combined proven and probable reserves of the Santa Rita deposit as of January 2011 stood at 159 million metric tonnes at 0.52 wt. % Ni, 0.13 wt. % Cu, 0.015 wt. % Co, and 86 ppb Pt (Mirabela Nickel Ltd., Annual Report 31 Dec. 2010).

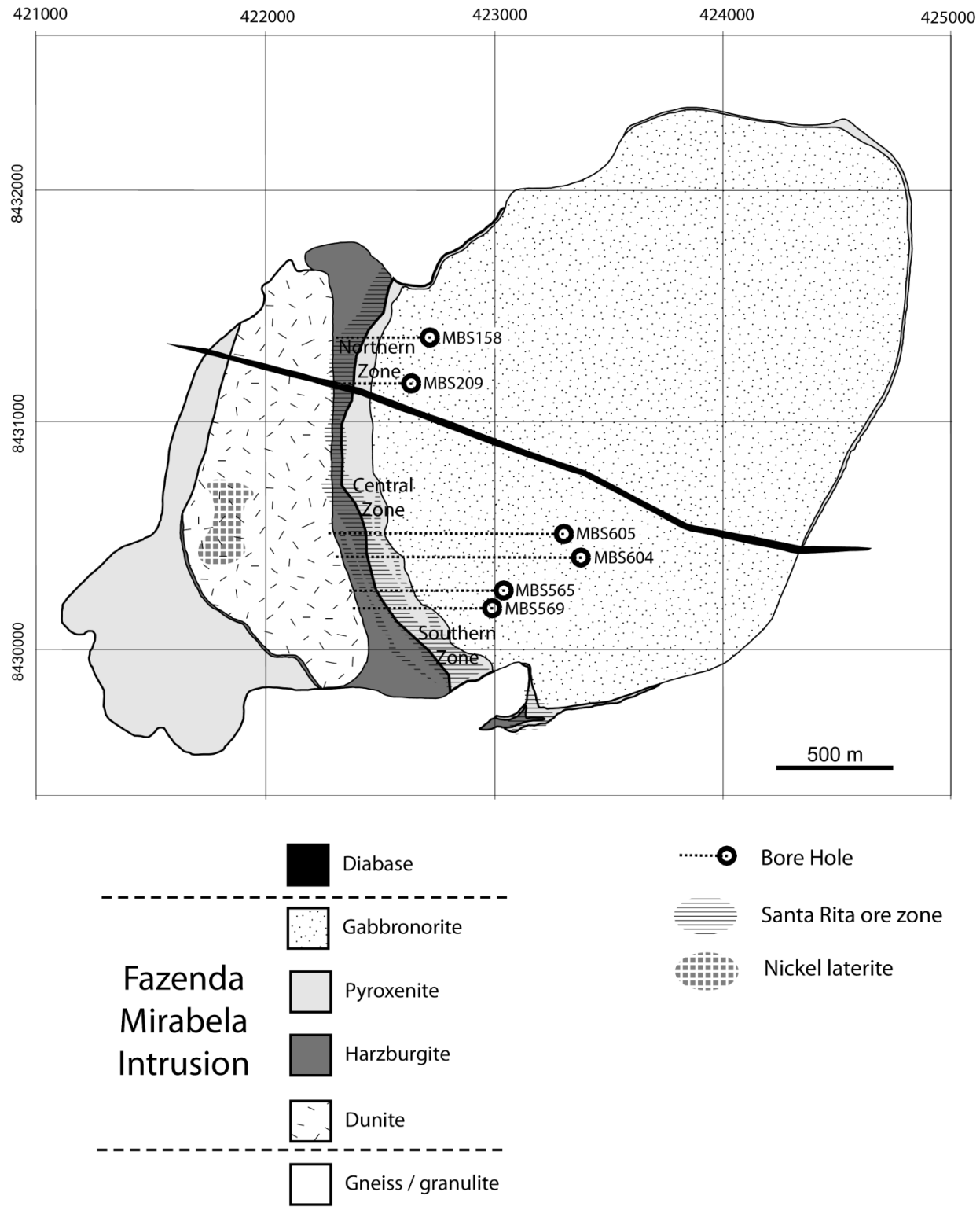


Figure 4.2: Geological map of the Fazenda Mirabela intrusion (modified after Barnes et *al.*, 2011; Inwood et *al.*, 2011) showing the location of the boreholes sampled; MBS209 and MBS158 from the northern zone, MBS604 and MBS605 from the central zone and MBS565 and MBS569 from the southern zone.

The Mirabela intrusion is also host to another zone of mineralisation. The Peri Peri Prospect has been identified at the contact between the intrusion and the country rocks at the northeastern edge of the intrusion (Inwood *et al.*, 2011). Disseminated sulphide mineralisation with a maximum width of 60m has been identified in the steeply south-southwest dipping contact zone (primarily composed of ultramafic rocks), however; the mineralisation does locally transgress into the basement granulite country rock (Inwood *et al.*, 2011).

The stratiform Santa Rita orebody may represent one or a series of magmatic pulses entraining metal-rich sulphides. The source of these magmatic pulses may be from a deeper staging chamber where early sulphide saturation allowed the sulphide liquid to scavenge the metals from the ascending magma forming the bulk of the Fazenda Mirabela intrusion (Inwood *et al.*, 2011). Barnes *et al.* (2011) characterised the Santa Rita orebody as having very high Ni tenors while being generally PGE-poor. They attributed the formation of the Santa Rita ore zone and the Ni-rich nature of the sulphide ore to the prolonged mixing of an initially magnesian moderately Ni-enriched resident "M-type magma" close to sulphide saturation with a relatively Ni-PGE-depleted and cooler replenishing "G-type magma" charged with suspended sulphide liquid droplets. Barnes *et al.* (2011) suggest that the initial mixing of a small proportion of G-type magma with a large volume of resident M-type magma caused the re-dissolution of suspended sulphide liquid droplets. Continued mixing of larger proportions of the G-type magma caused the hybrid magma to reach sulphide saturation causing the re-precipitation of sulphide liquid. This results in the formation of the basal PGE anomaly, a thin zone consisting of high R, PGE-enriched sulphides that have predominantly equilibrated with a PGE-undepleted M-type-rich hybrid magma. Continued mixing results in the chamber becoming progressively dominated by PGE-poor G-type magma which results in higher rates of sulphide accumulation forming the Santa Rita ore zone hosting lower PGE tenors. Barnes *et al.* (2011) note that a contributing factor in forming high Ni tenors may be the reaction between the sulphide liquid and coexisting olivine in an environment where both phases equilibrate with a large reservoir of silicate magma. Furthermore, higher Ni content in sulphide gives rise to an increased tendency for Ni to partition into sulphide from adjacent olivine, forming a positive feedback mechanism (Barnes *et al.*, 2011).

4.3 Sampling and Analytical Methods

The Mirabela intrusion has been divided into three zones for mining purposes; southern, central and northern. For this study, drill core from six boreholes was sampled (Fig. 4.2); two boreholes from the central zone (MBS604 and MBS605; samples PTSR01-25), two from the northern zone (MBS209 and MBS158; samples PTSR26-49) and two from the southern zone (MBS565 and MBS569; samples PTSR50-72) (Appendix A). Further borehole information is given in Table 4.1. Sampling was completed with the aid of mine assay data (Appendix B) in order to collect samples with both the highest PGE contents from each lithology as well as variable Pd/Pt ratios. The sampling was also extended ~100m above and below the defined economic limits of the Santa Rita ore zone in order to sample all lithologies present in the intrusion and all anomalous Pt and Pd occurrences (i.e., "the basal PGE anomaly").

A total of 72 samples were collected; 12 from each borehole sampled, except in the case of MBS604 where 13 samples were collected and MBS565 where only 11 samples were collected as a sample of gabbronorite could not be obtained from this hole. The silicate and sulphide mineralogy of all of the samples collected was characterised using transmitted and reflected light microscopy of thin sections and polished blocks (PTSR01-25), and polished thin sections (PTSR26-72). Of the 72 samples collected, 63 were selected for detailed mineralogical analysis while PGE-poor gabbronorite and websterite samples were not studied for PGM. PGM and their associated sulphide and silicate minerals were identified and analysed using a Cambridge Instruments (now Carl Zeiss NTS) S360 scanning electron microscope, the details of which and method used are given in section 3.4.

Borehole	Depth (m)	Dip	Azimuth
MBS604	1072	68	270
MBS605	1067	69	270
MBS209	356	60	270
MBS158	368	60	270
MBS565	630	61	270
MBS569	761	60	270

Table 4.1: Depth, dip and azimuth information for the boreholes sampled.

The commercial mine assay data available for all boreholes studied were determined from one metre composite intervals of diamond drill core by ALS Chemex Ltd., Vancouver, Canada. This ALS Chemex data was collected by Ni-fire assay, used to determine Au, Pt, and Pd by ICP-MS finish with multi-element ICP-MS used to obtain data for the other elements reported here. Further major and trace element geochemistry data of all of the samples

collected (PTSR01-72) were determined by Actlabs. Semimetal concentrations (As, Bi, Sb, Se, Te) were determined by Actlabs for samples PTSR26-72 (northern and southern zones). Additional trace element analyses were run at Cardiff University (ICP-MS) for selective representative samples from the central and northern zones to obtain values for the REE that were below the limit of detection when analysed by Actlabs. Whole-rock PGE (excluding Os) and Au data were obtained from Actlabs by Ni-fire assay for all samples studied.

A total of 31 samples from all six boreholes studied (northern, central and southern zones) including samples from both the Santa Rita ore zone and underlying sulphur-poor dunite were selected for LA-ICP-MS.

4.4 Stratigraphy

The boreholes studied intersect all of the major lithologies present in the Mirabela intrusion. These are, from the bottom of each borehole to the top; dunite, harzburgite, orthopyroxenite, websterite and gabbronorite. Magnesium and Cr contents both progressively decrease upwards from the dunite to the gabbronorite (Fig. 4.4a-f). The igneous rocks in the central zone of the intrusion are all adcumulates with a maximum of five modal percent intercumulus silicates (typically plagioclase, clinopyroxene and phlogopite) whereas in the northern and southern zones, the rocks typically become mesocumulates with ~10 modal percent intercumulus silicates.

The deepest part of the intrusion intersected by the boreholes studied comprises the uppermost part of the dunite unit. This unit is predominantly comprised of typical subhedral olivine crystals ~2-4 mm in size (Fig. 4.3D). Orthopyroxene oikocrysts are present in this dunite giving rise to whole-rock Mg contents lower than that expected of a typical dunite (e.g., ~35% MgO) (Fig. 4.3E). These oikocrysts can reach up to ~1.5 cm in size. This unit is overlain by harzburgite where orthopyroxene and olivine are present in equal proportions with both minerals commonly 1-2 mm in size (Fig. 4.3F).

Gradational progression into olivine orthopyroxenite and orthopyroxenite then occurs as a result of fractional crystallisation. The orthopyroxenite layer is the thickest lithology encountered in the boreholes studied. The olivine orthopyroxenite is predominantly comprised of orthopyroxene (~75-80 modal percent) with olivine comprising the remainder of the rock (~15-20 modal percent). Orthopyroxene crystals are commonly 1-2 mm in size

and are typically brown in colour in plane polarised light due to fine-scale exsolution of clinopyroxene. Commonly, the edges of these crystals are clear and exsolution free (Fig. 4.3F); in other crystals, exsolution can still be observed at the crystal edges but to a lesser extent than is present in the centre. This exsolution texture is also observed in orthopyroxene crystals in harzburgite (Fig. 4.3F). The olivine crystals are subhedral and can be either cumulate crystals, similar in shape and size to the orthopyroxene, or present as much smaller crystals (<0.5 mm) forming chadacrysts with chromite within orthopyroxene oikocrysts. Where olivine forms as 'normal' cumulate crystals similar to orthopyroxene, its distribution is heterogeneous forming olivine-rich and olivine-poor patches. The orthopyroxenite unit is predominately comprised of subhedral-euhedral crystals of orthopyroxene commonly 1-2 mm in size which exhibit the same fine exsolution features noted above.

The websterite above these units acts as a cap rock for the ultramafic sequence and is a thin layer (~10-15m) comprised of orthopyroxene and clinopyroxene in equal proportions (Fig. 4.3G). Orthopyroxene crystals (and occasionally clinopyroxene) occur as relatively large (1-2 mm) subhedral crystals that sit within a much finer matrix of clinopyroxene crystals (0.2-0.5 mm) which are also more anhedral. The websterite unit is overlain by gabbronorite which forms part of the upper mafic sequence. However, only the lowermost part of the gabbronorite is intersected by the boreholes studied. This unit is comprised of fairly uniform sized euhedral-subhedral crystals of clinopyroxene and plagioclase which are commonly 1-2 mm across; however, many crystals are smaller in size at ~0.5 mm (Fig. 4.3H).

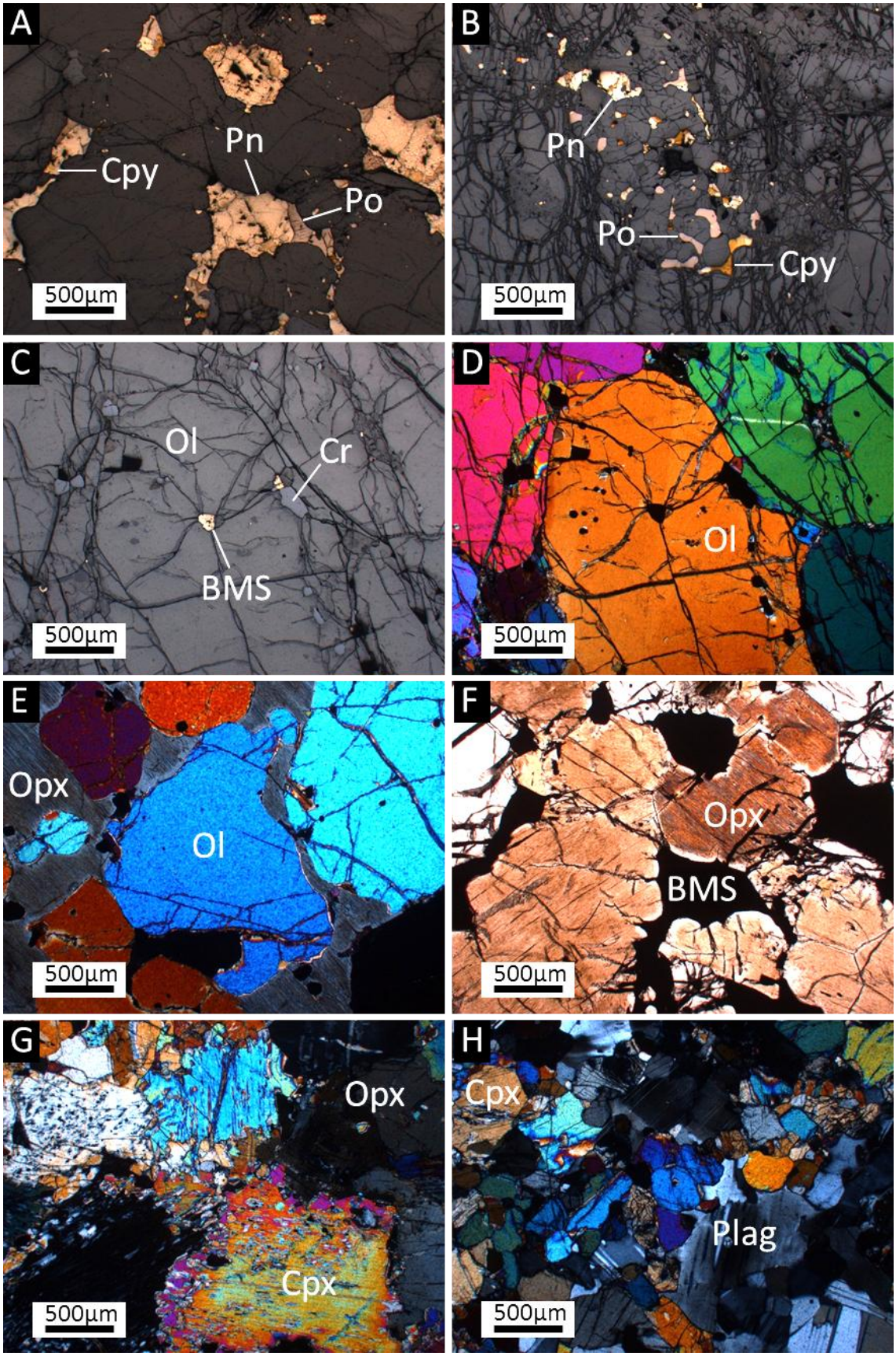


Figure 4.3: Reflected and transmitted light photomicrographs showing the silicate and sulphide petrography of the Mirabela intrusion. A) BMS occurring interstitially to olivine and orthopyroxene crystals in harzburgite. B) Small fine grained sulphides which are intergrown with fine grained intercumulus silicates (plagioclase, clinopyroxene and phlogopite). C) Minor pentlandite and chalcopyrite with chromite in the sulphur-poor dunite. D) Unaltered dunite showing adcumulate texture. E) Orthopyroxene oikocryst in dunite. F) Harzburgite with orthopyroxene exhibiting fine exsolution of clinopyroxene. G) Websterite. H) Gabbronorite.

4.5 Borehole Profiles

Borehole profiles have been constructed for all six holes studied (Fig. 4.4a-f) which display Mg (wt. %), Cr (wt. %), S (wt. %), Pt (ppm), Pd (ppm), as well as Pd/Pt and Cu/Pd ratio data (mine assay data, Appendix B). The tops of these boreholes typically intersect the lowermost gabbronorite and terminate at depth where they intersect the upper portion of the dunite. Platinum and Pd contents above the Santa Rita ore zone are extremely low, being close to or at the detection limit (Pd 0.5 ppb, Pt 0.3 ppb). As a result, Pd/Pt ratios above the Santa Rita ore zone are anomalous given the large error in these low level analyses and should be ignored. Sample numbers are marked as dashed horizontal lines located at their respective depths in each profile, thus showing how the sampling was extended below the economic limits defining the Santa Rita ore zone into the sulphur-poor dunite hosting the basal PGE anomaly.

4.5.1 Santa Rita ore zone

The Santa Rita sulphide ore zone occurs within the ultramafic sequence, predominantly in the orthopyroxenite layer (excluding the upper part of this lithology) as well as in the uppermost part of the underlying harzburgite which includes the upward gradational transition from harzburgite to olivine orthopyroxenite (Fig. 4.4a-f). The Santa Rita ore zone is clearly defined in all boreholes by increased sulphur characterising a thick layer of disseminated sulphides (predominantly pentlandite with chalcopyrite, pyrrhotite and minor pyrite). This zone is accompanied by an increase predominantly in Ni, but also Cu. The unusual Ni-rich nature of this deposit is also noted by Barnes *et al.* (2011) who calculated Ni tenors of 20% in this zone. Using microscopy, minor amounts of pyrite are observed to be intergrown with pentlandite. Pentlandite (±intergrown pyrite) tends to form the cores of interstitial sulphide crystals (typically ~1 mm across) with chalcopyrite and pyrrhotite restricted to the crystal edges. Much smaller chalcopyrite and pyrrhotite crystals do occur separately from these larger composite BMS.

Two main types of sulphide morphology are recognised; i) BMS occurring interstitially to olivine and orthopyroxene crystals (Fig. 4.3A) and ii) small fine grained sulphides (Fig. 4.3B) which are intergrown with fine grained intercumulus silicate phases (plagioclase, clinopyroxene and phlogopite). The interstitial sulphides exhibit low dihedral angles but more

commonly have rounded terminations that were previously noted by Barnes *et al.* (2011). Very small sulphide blebs have also been identified within the cleavage planes of orthopyroxene crystals. The intrusion is remarkably unaltered with magmatic minerals and textures preserved. Only minor chalcocite, millerite and native copper have been identified as secondary phases.

Sulphides also occur as stringers that are often only a few microns wide. These appear to be primary based on their composition (pentlandite, chalcopyrite and pyrrhotite) and originate from interstitial sulphides. These stringers are commonly aligned giving rise to a pseudo-fabric within the rock in some cases. Minor localised patches and veins of post-magmatic serpentinisation are observed in the Santa Rita ore zone and in some cases these are associated with the BMS stringers noted above.

This sulphide mineralisation is also accompanied by elevated PGE concentrations. Platinum+Pd contents vary from the northern to the southern zones. In the northern zone, Pt+Pd concentrations in the Santa Rita orebody vary up to 1.2 ppm with an average of ~0.3 ppm. In the central zone, Pt+Pd concentrations in the Santa Rita ore zone vary up to 1.6 ppm in MBS604 and only up to 0.6 ppm in MBS605 with an average of ~0.2 ppm over both boreholes. Finally, in the southern zone, Pt+Pd concentrations in the Santa Rita ore zone vary up to 0.5 ppm with an average of ~0.1 ppm. These PGE concentrations closely follow the sulphur content of the Santa Rita ore zone with peaks and troughs in sulphur content correlating to peaks and troughs in Pt and Pd content.

A unique chromite-rich seam (>10 wt. % chromite) is present midway through the Santa Rita ore zone in MBS604 (Fig. 4.4a). This thin (~2m thick) seam is hosted within the orthopyroxenite layer, however, the silicate minerals associated with the chromite-rich seam include both orthopyroxene and olivine cumulates. Whole-rock PGE contents associated with this chromite-rich seam are the highest identified in the investigated core with Pd >0.5 ppm and Pt particularly elevated at >1 ppm (mine assay data capped at 1 ppm). Palladium/Pt ratios are typically <1 over the entire Santa Rita ore zone even within the chromite-rich seam although this ratio does vary and correlates with changes in sulphur content.

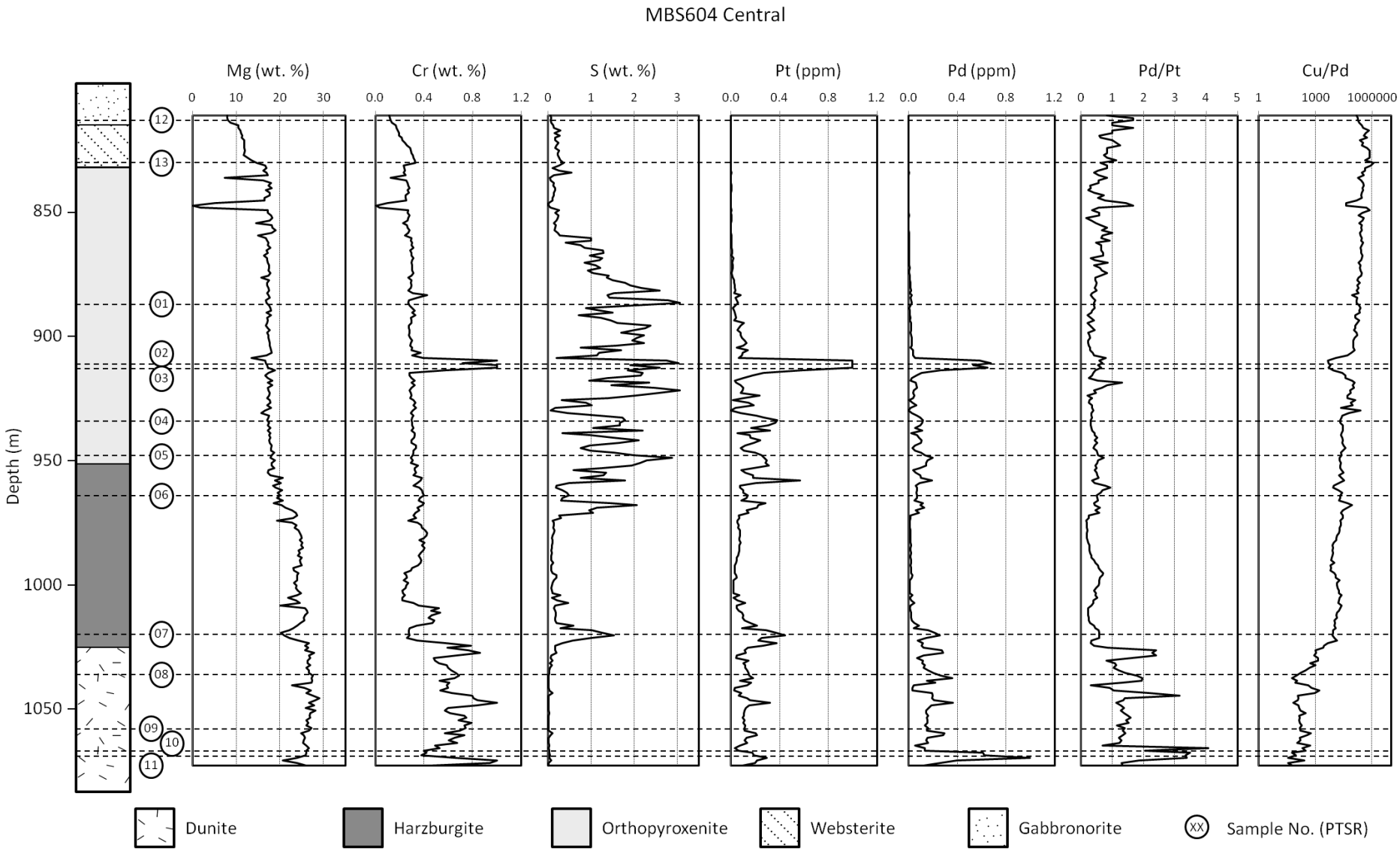


Figure 4.4a): Geochemical profile of borehole MBS604 (central zone) showing the depth at which samples (numbered) were collected.

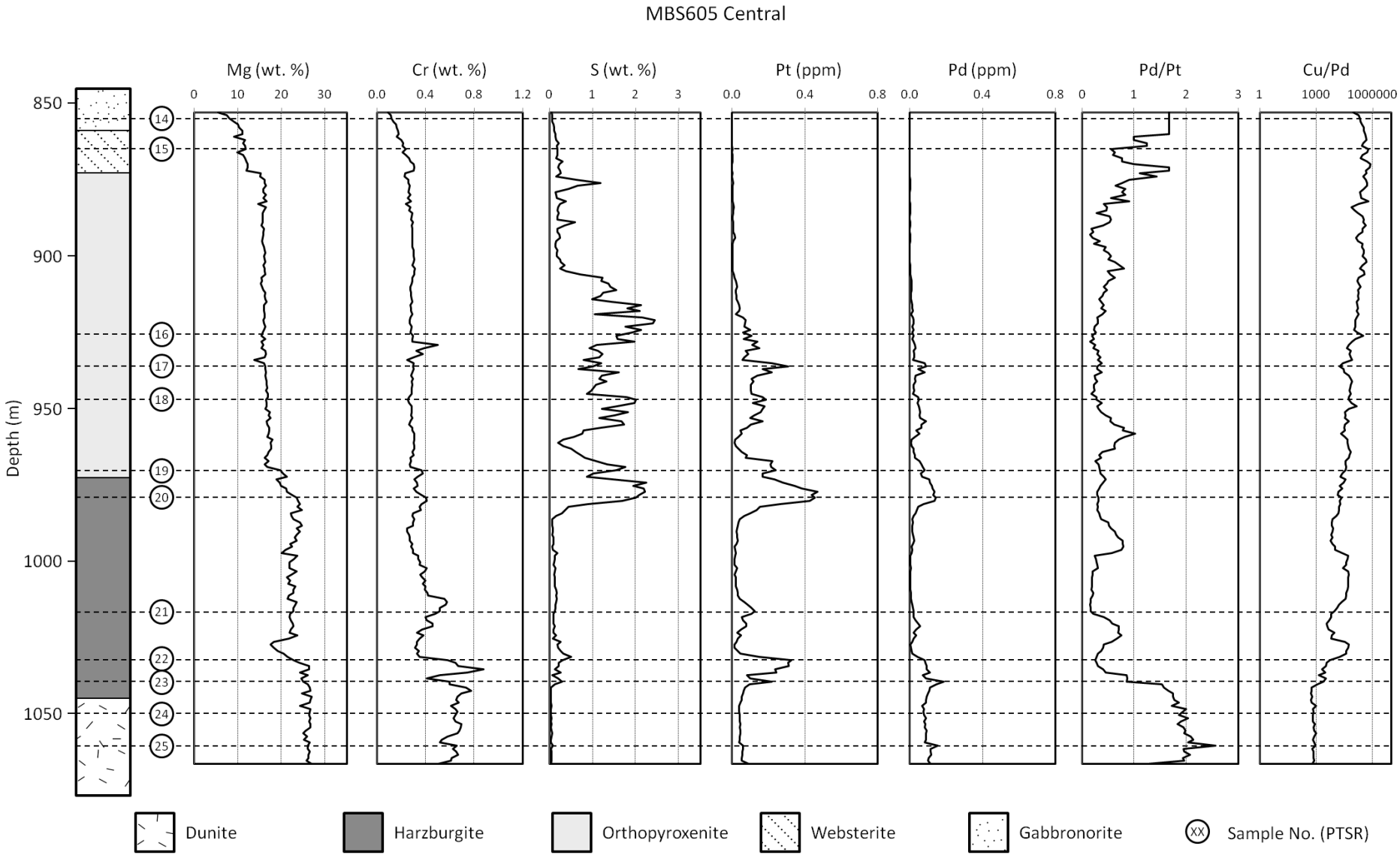


Figure 4.4b): Geochemical profile of borehole MBS605 (central zone) showing the depth at which samples (numbered) were collected.

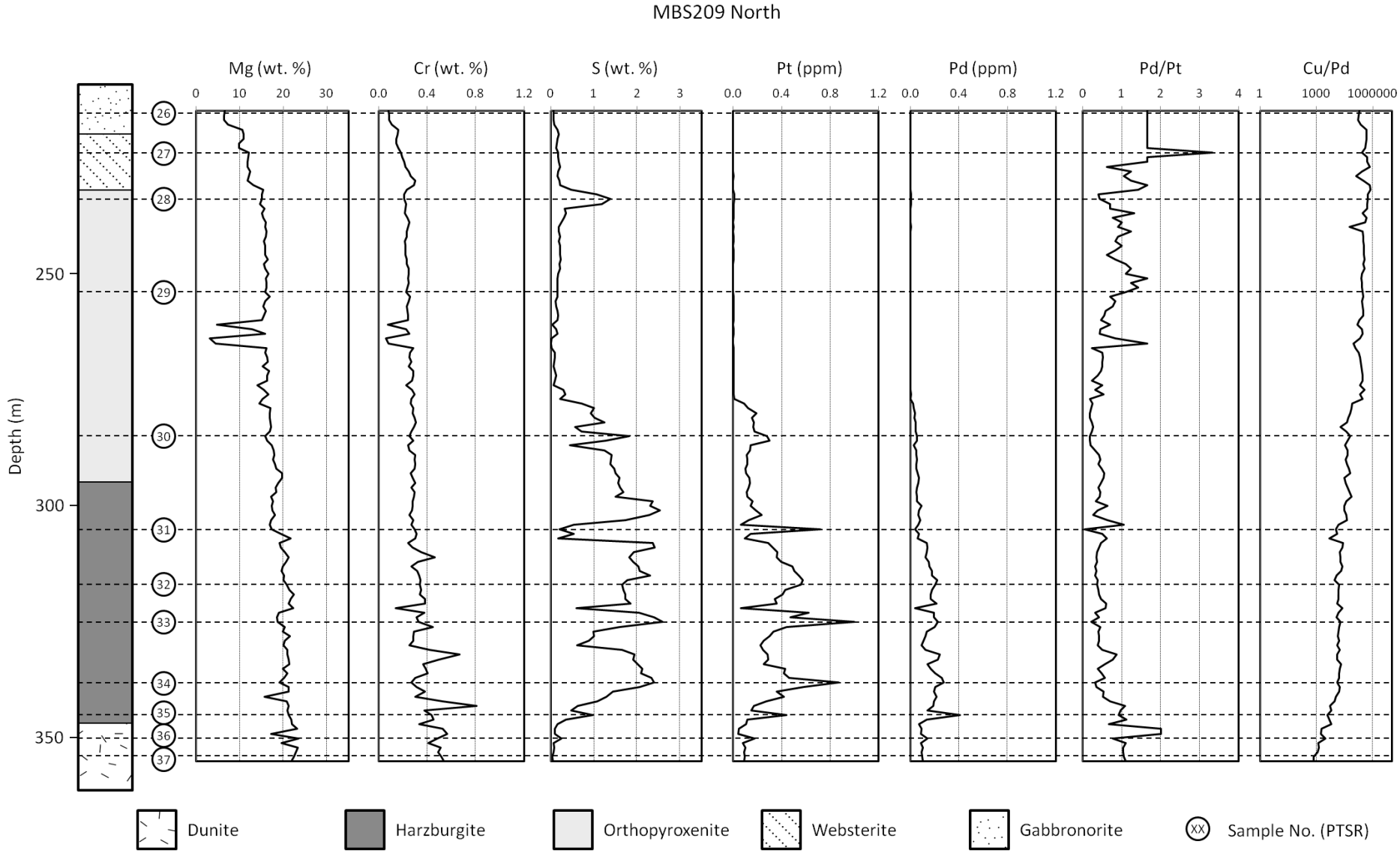


Figure 4.4c): Geochemical profile of borehole MBS209 (northern zone) showing the depth at which samples (numbered) were collected.

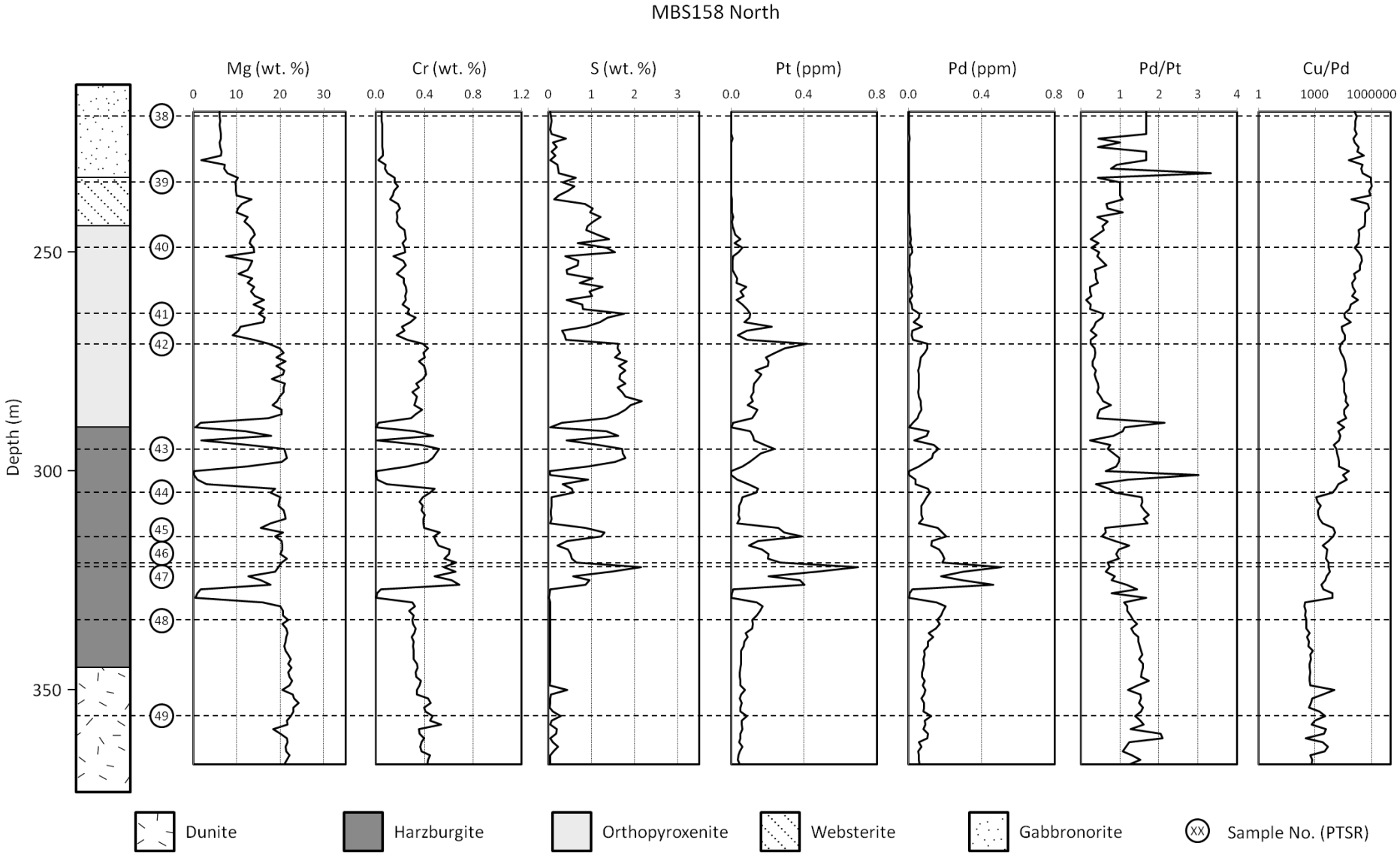


Figure 4.4d): Geochemical profile of borehole MBS158 (northern zone) showing the depth at which samples (numbered) were collected.

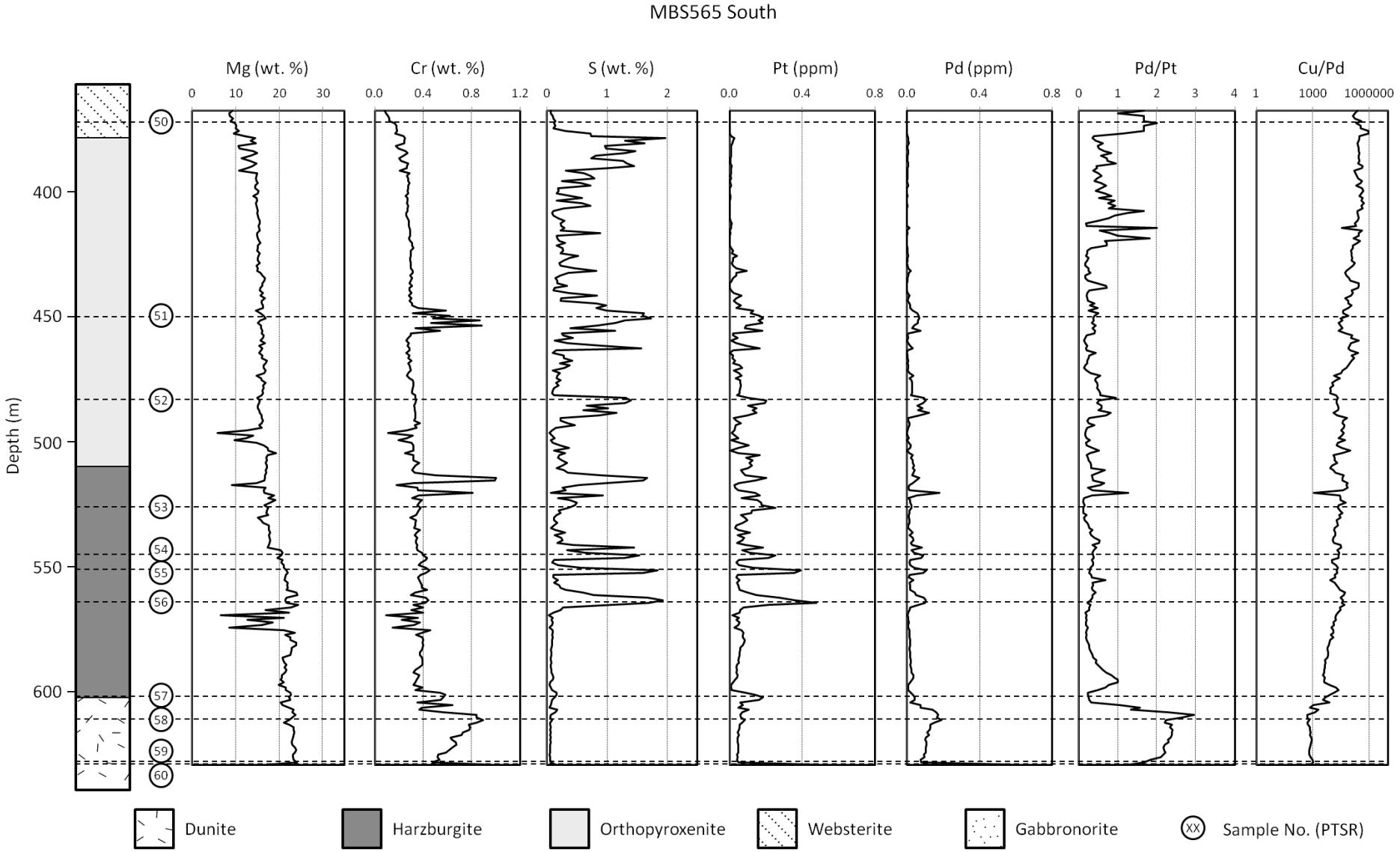


Figure 4.4e): Geochemical profile of borehole MBS565 (southern zone) showing the depth at which samples (numbered) were collected.

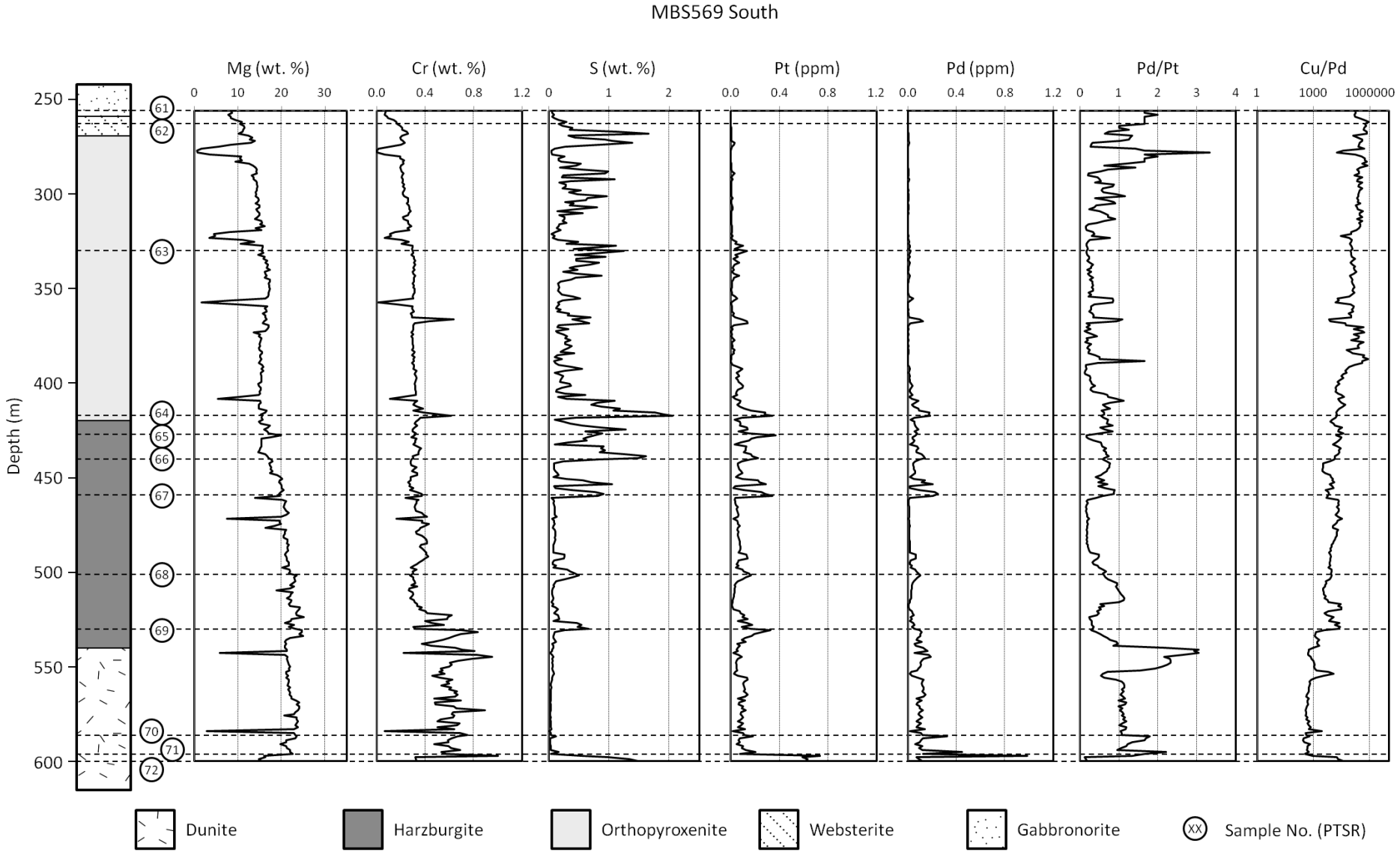


Figure 4.4f): Geochemical profile of borehole MBS569 (southern zone) showing the depth at which samples (numbered) were collected.

4.5.2 Basal PGE anomaly

Further PGE mineralisation, identified by Barnes *et al.* (2011) as the "basal PGE anomaly", occurs in the upper part of the dunite which acts as the footwall to the overlying Santa Rita ore zone and harzburgite. This zone of PGE mineralisation typically occurs 50-75m below the base of the Santa Rita ore zone is observed in the central zone and southern zone borehole profiles (Fig. 4.4a-b and Fig. 4.4e-f, respectively). However, this zone of PGE mineralisation is not observed in the northern zone due to the restricted depth of these particular boreholes. It is hypothesised that the basal PGE anomaly also occurs in the northern zone of the intrusion; however, a deeper borehole is required to confirm this. The host dunite has extremely low sulphur concentrations (typically <0.1 wt. %) with no sulphides visible in hand specimen; however, sulphides may be observed using microscopy (Fig. 4.3C). Pentlandite is the dominant sulphide phase present accompanied by minor chalcopyrite and in contrast to the Santa Rita ore zone, pyrite and pyrrhotite are both almost entirely absent from this sulphur-poor dunite zone. The BMS are extremely disseminated throughout the dunite forming very small (<150 µm across) interstitial crystals.

Sulphide-silicate mixtures exhibiting micro-scale textures that resemble symplectites are observed (Fig. 4.5A-F). These and other sulphides are often located adjacent to phlogopite (Fig. 4.5A-B and G). These sulphides may also exhibit micro-scale patches and veinlets of magnetite within them (Fig. 4.5E-F). In one case a magnetite rim is observed partially enclosing a patch of silicate material which also includes a small bleb of pentlandite adjacent to a larger crystal of pentlandite (Fig. 4.5H). As in the Santa Rita ore zone, localised areas and veins of serpentinisation are observed.

The dunite therefore displays a decoupling between S and the PGE (Fig. 4.4a-b and Fig. 4.4e-f). Platinum+Pd concentrations of the basal PGE anomaly typically average ~0.2 ppm over the four boreholes in the central and southern zones where it is intercepted. In this sulphur-poor dunite zone, Pt+Pd concentrations are also highly variable with concentrations of up to 1717 ppb recorded in MBS569, 1297 ppb in MBS605, 1161 ppb in MBS565 and 406 ppb in MBS605. These high concentrations usually occur over 1-2 metres near to or at the base of the boreholes suggesting that the PGE concentrations may continue to increase at depth. However, this is speculative and at the time of writing, deeper boreholes are planned to determine whether this PGE mineralisation continues at depth but have not yet been drilled.

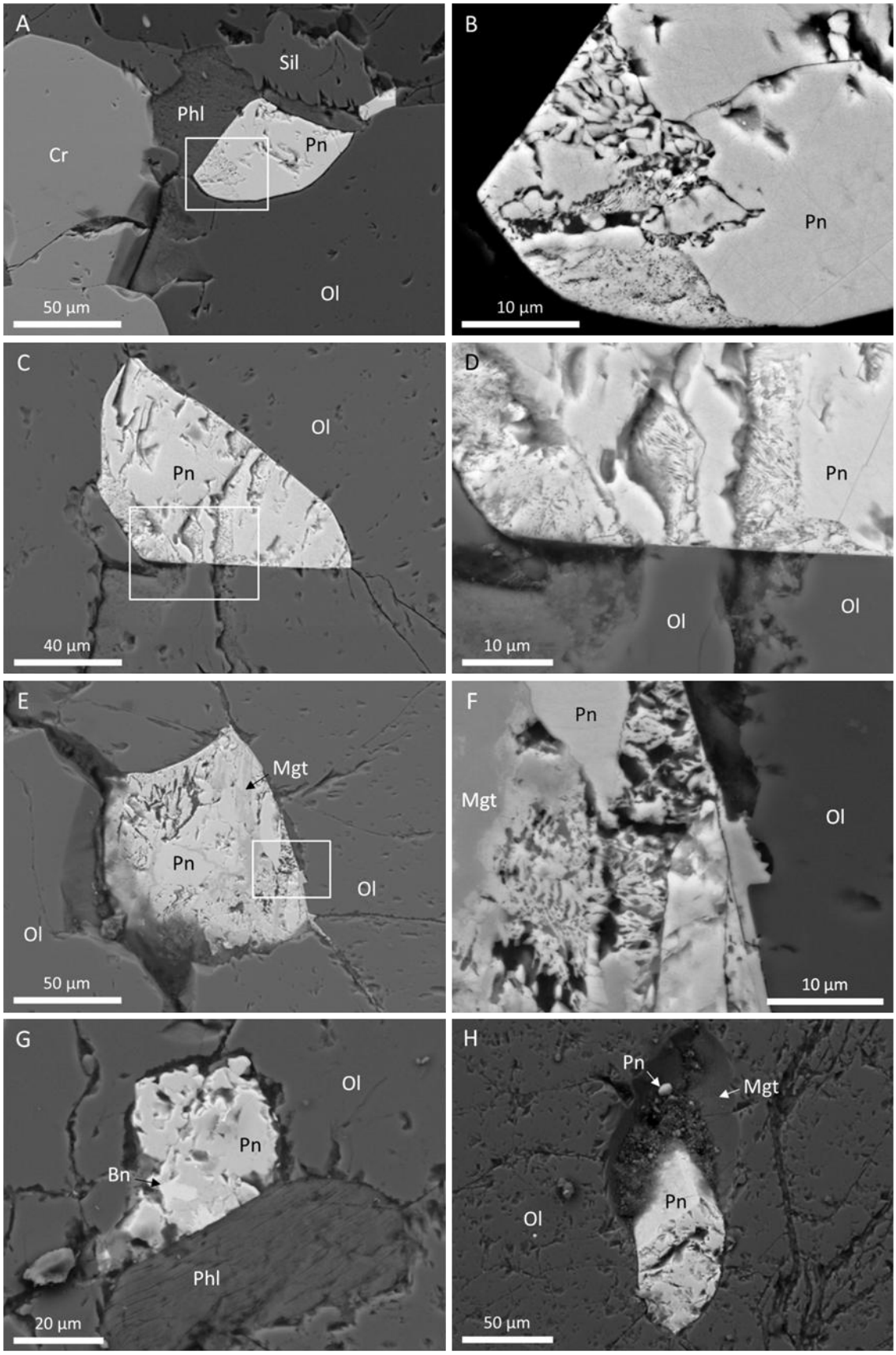


Figure 4.5: Back-scattered electron images of BMS in the sulphur-poor dunite. A and inset B) micro-symplectite textures in pentlandite (Pn). C and inset D) micro-symplectite textures in Pn with alteration extending into surrounding olivine (Ol). E and inset F) micro-symplectite textures in Pn with accompanying magnetite (Mgt). G) Pn and bornite (Bn) occurring adjacent to phlogopite (Phl). H) Example of possible sulphur loss marked by a preserved droplet of Pn in a patch of varying silicate chemistry partially rimmed by Mgt.

In obvious contrast to the Santa Rita ore zone, Pd/Pt ratios in this zone are typically >1. In MBS605 and MBS565 Pd/Pt ratios are slightly higher (~2) (Fig. 4.4b and Fig. 4.4e) than those in MBS604 and MBS569 (~1-1.5) (Fig. 4.4a and Fig. 4.4f) where this ratio is also more variable. In one northern borehole, MBS158, a change in Pd/Pt ratio is also observed at the base of the Santa Rita ore zone (Fig. 4.4d). However, this is not thought to be related to the presence of the basal PGE anomaly as there is no accompanying increase in the overall PGE concentrations as noted in the central and southern boreholes. The transition from high Pd/Pt ratios in the dunite to low ratios in the Santa Rita ore zone is sharp and occurs near the upper boundary of the dunite in all boreholes where the basal PGE anomaly is intersected. Thus, the dunite is relatively more Pd-enriched whereas the Santa Rita ore zone is more Pt-enriched.

4.6 Geochemistry

The major and trace element geochemistry of the Mirabela complex has been studied to better understand the genesis of the intrusion and therefore the context of the Ni-Cu-PGE sulphide mineralisation examined. Whole-rock PGE and semimetal analyses were undertaken in order to match these with the platinum-group mineralogy to understand any elemental controls on the types of PGM being formed within the different zones of mineralisation observed.

4.6.1 Major element geochemistry

Two data sets have been used to analyse the major element geochemistry. The first of which is the mine assay data for which one metre composite intervals of diamond drill core were analysed by multi-element ICP-MS (Appendix B). This data is available on a metre scale for all boreholes studied. The second data set consists of analyses by Actlabs completed on samples selected (PTSR01-72) from the six boreholes examined as opposed to every metre of each borehole (Appendix C).

Harker diagrams have been produced using both data sets with TiO_2, Al_2O_3, Fe_2O_3 (T), Na_2O, CaO and MnO plotted against MgO given the ultramafic nature of the intrusion (Fig. 4.6; Fig 4.7). Plots of K_2O and P_2O_5 against MgO have been omitted due to their low concentrations. Both data sets show negative correlations between MgO versus TiO_2, Al_2O_3, Na_2O and CaO

whereas a positive correlation is observed between MgO and Fe_2O_3 (T). Although there is some scatter in these diagrams, these relationships are clear.

The negative correlation observed between CaO and MgO is only semi-continuous as there are no samples with CaO contents of between ~6-10 wt. %. MnO versus MgO shows a unique pattern where a positive correlation is observed until MnO content appears to peak at around ~26-27 wt. % MgO; relatively constant MnO contents (~0.15-0.18 wt. %) are observed with further increases in MgO. Plots of Al_2O_3 and CaO against MgO show anomalies in the mine assay data only (Fig. 4.6), as some samples exhibit anomalously low MgO but retain concentrations of CaO (~2-4 wt. %) and Al_2O_3 (~10-12 wt. %). These samples break away to the left of the more prominent negative correlations identified above.

Major element borehole profiles have also been constructed for all six holes studied (Fig. 4.8a-f) using mine assay data which display MgO (wt. %), Fe_2O_3 (T) (wt. %), MnO (wt. %), Al_2O_3 (wt. %), Na_2O (wt. %), CaO (wt. %) and TiO_2 (wt. %). MgO contents are at their maximum at the base of the boreholes and decrease both gradually and in steps moving upwards through the Mirabela stratigraphy; Fe_2O_3 broadly follows the same pattern. This MgO decrease is accompanied by step increases in Al_2O_3, Na_2O and CaO. These step increases may be responsible for the semi-continuous nature of some Harker diagram trends, particularly that of CaO against MgO. TiO_2 shows both step and gradual increases in content in a similar manner to the pattern of decreasing MgO. MnO displays a gradual increase in content with decreasing MgO until near the top of the boreholes where it peaks just before CaO increases from ~5-15%. From this point upward, MnO decreases following the trends of MgO and Fe_2O_3. TiO_2 contents follow a similar pattern to MnO in some boreholes; however, it is not as prominent.

There are several sharp zones in some of the boreholes which are defined by low MgO, Fe_2O_3, MnO and high Al_2O_3, NaO_2 with variable CaO and TiO_2 content. These relatively thin zones (~5m) are very distinct and separate from the general patterns described above. These zones are reflected in the Harker diagrams as the samples stated previously that exhibit anomalously low MgO but retain concentrations of CaO (~2-4 wt. %) and Al_2O_3 (~10-12 wt. %).

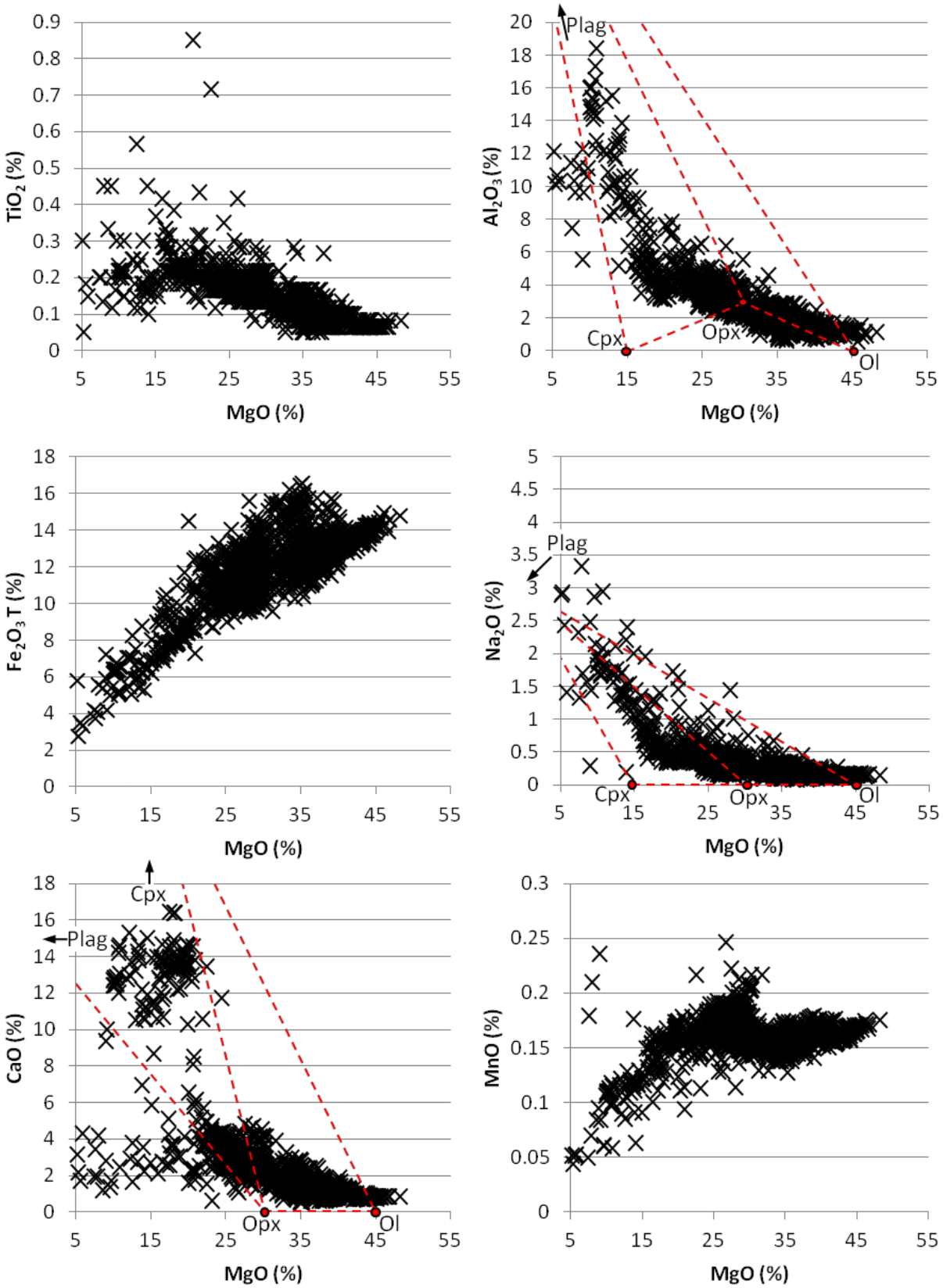


Figure 4.6: Harker diagrams plotted against MgO using mine assay data (one metre composite intervals of diamond drill core were analysed by multi-element ICP-MS). Mineral compositions of olivine (Ol), orthopyroxene (Opx), clinopyroxene (Cpx) and plagioclase (Plag) are plotted in order to show the minerals crystallising in different fields of the Harker diagrams. Ol and Opx compositions have been determined from SEM analyses; Cpx and Plag compositions have been determined from the best fitting mixtures of diopside-hedenbergite and albite-anorthite end-members, respectively.

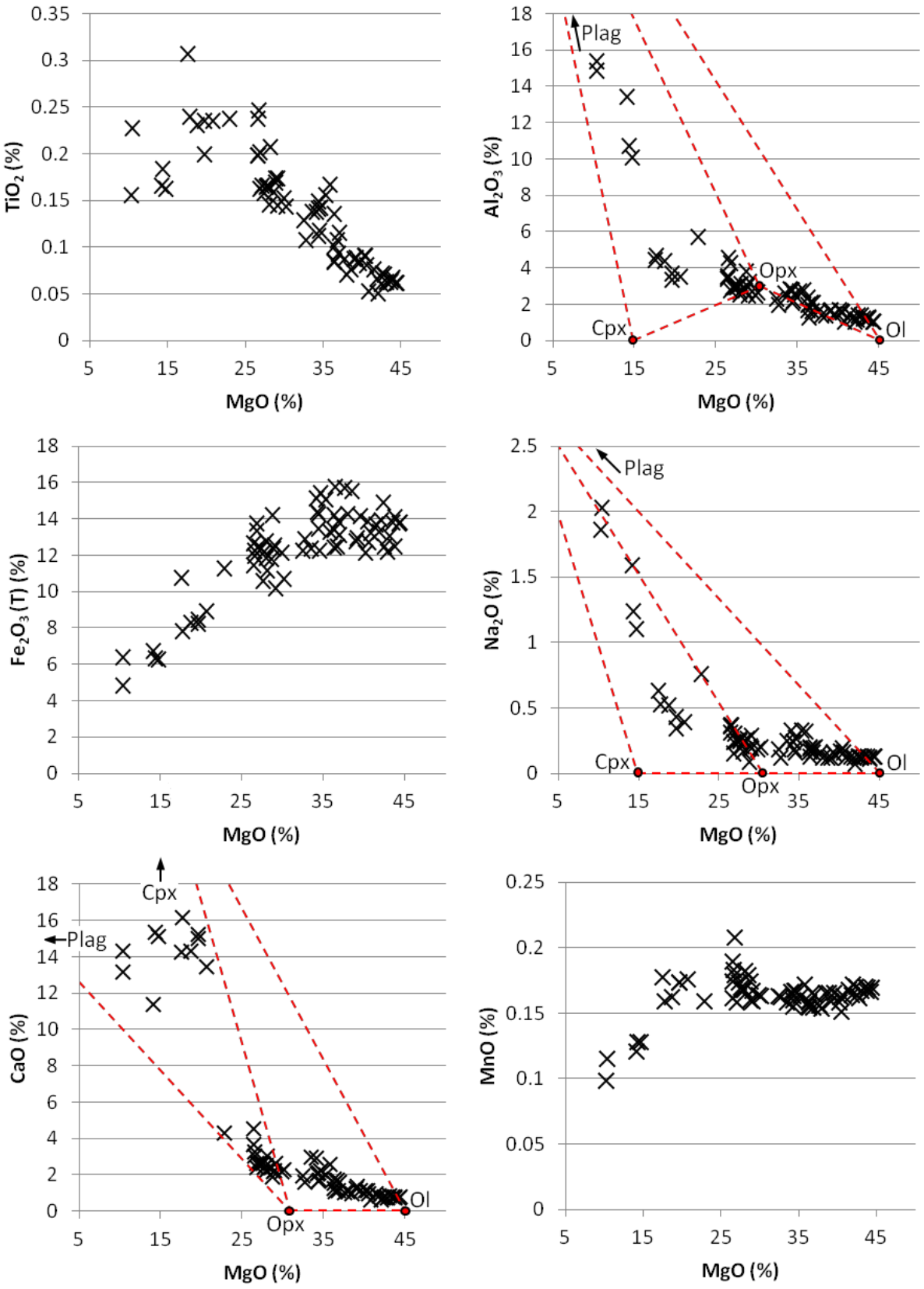


Figure 4.7: Harker diagrams plotted against MgO using sample only data (Actlabs completed on selected samples [PTSR01-72] from the six boreholes studied). Mineral compositions of olivine (Ol), orthopyroxene (Opx), clinopyroxene (Cpx) and plagioclase (Plag) are plotted in order to show the minerals crystallising in different fields of the Harker diagrams. Ol and Opx compositions have been determined from SEM analyses; Cpx and Plag compositions have been determined from the best fitting mixtures of diopside-hedenbergite and albite-anorthite end-members, respectively.

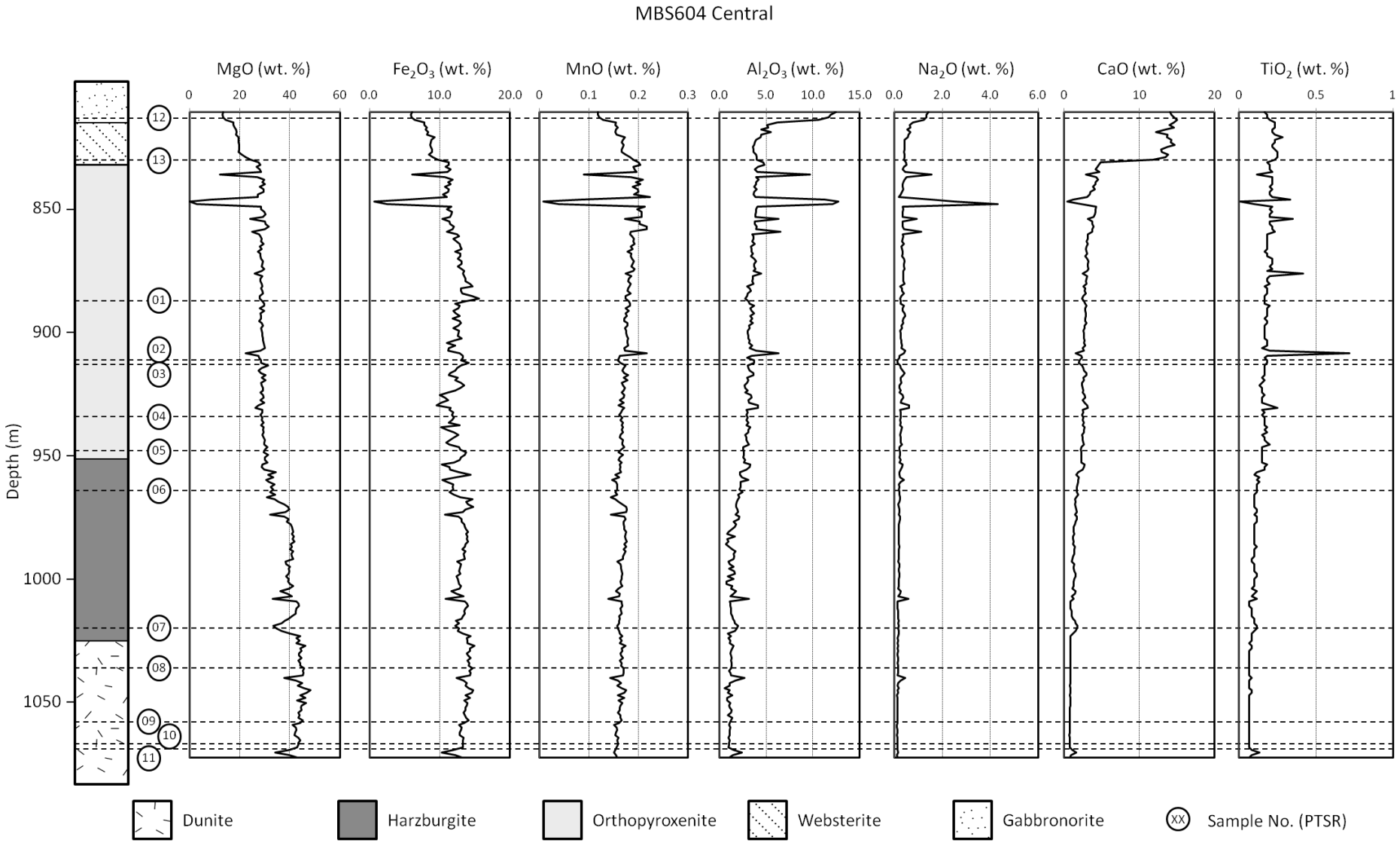


Figure 4.8a): Major element geochemical profile of borehole MBS604 (central zone) showing the depth at which samples (numbered) were collected.

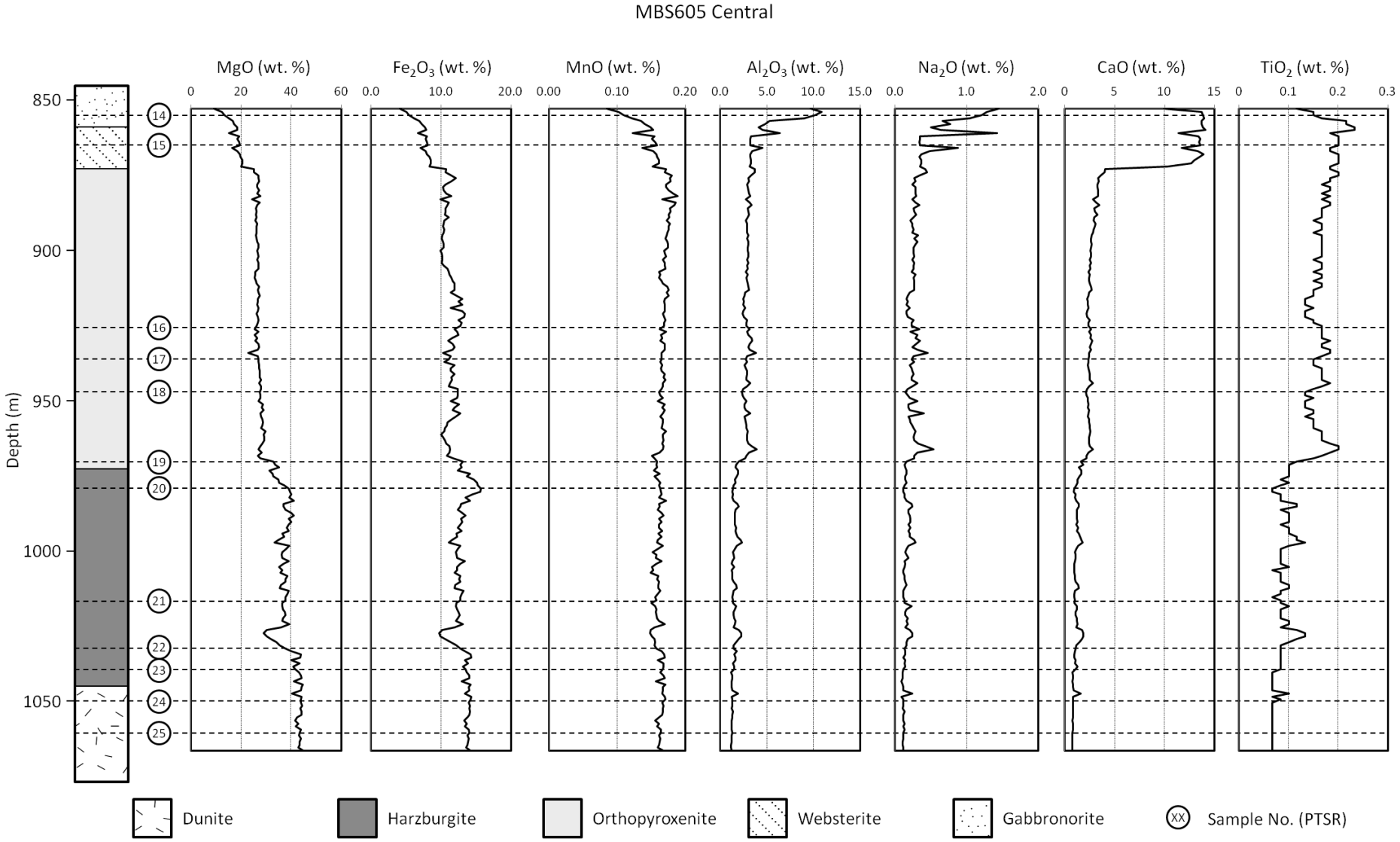


Figure 4.8b): Major element geochemical profile of borehole MBS605 (central zone) showing the depth at which samples (numbered) were collected.

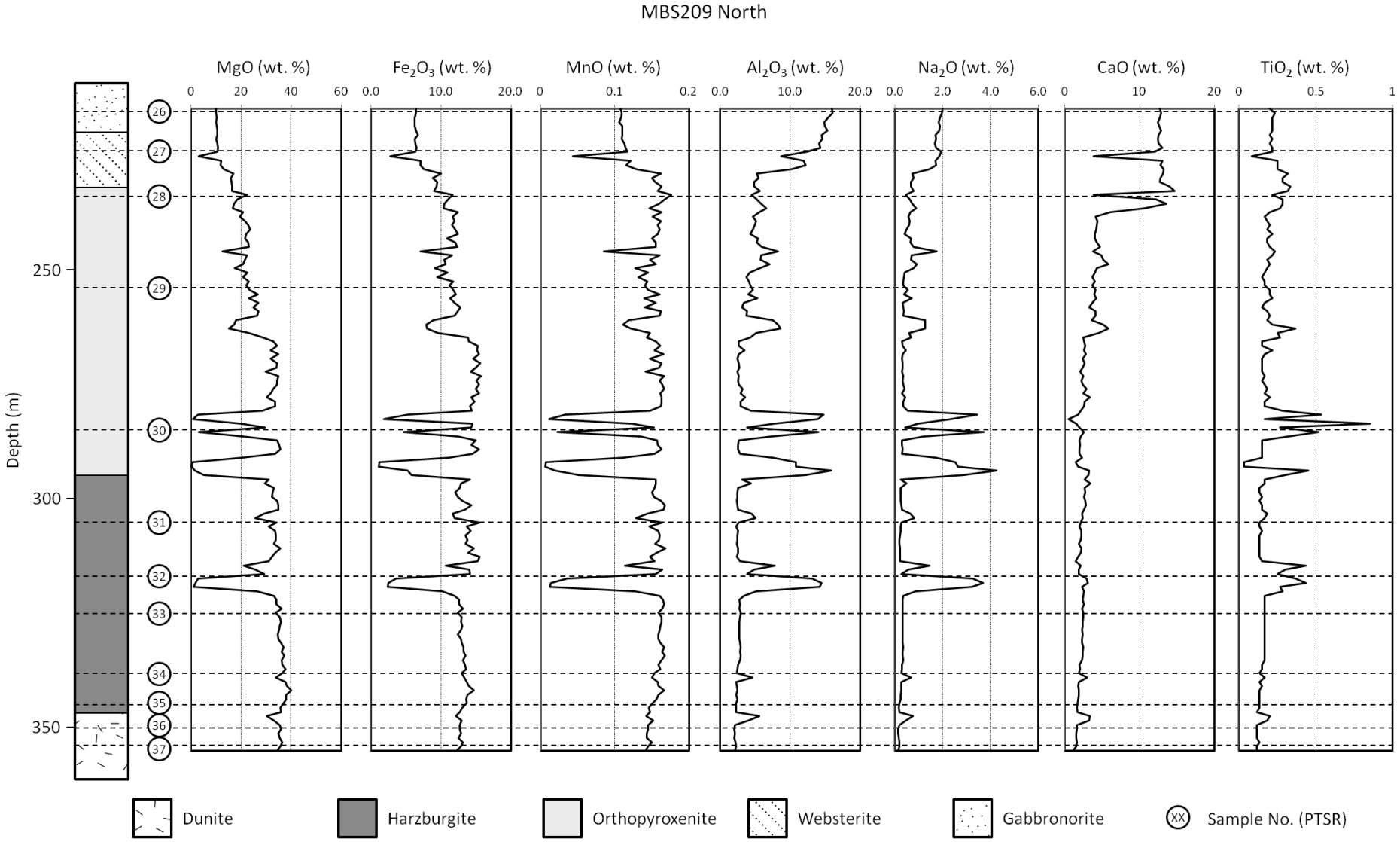


Figure 4.8c): Major element geochemical profile of borehole MBS209 (northern zone) showing the depth at which samples (numbered) were collected.

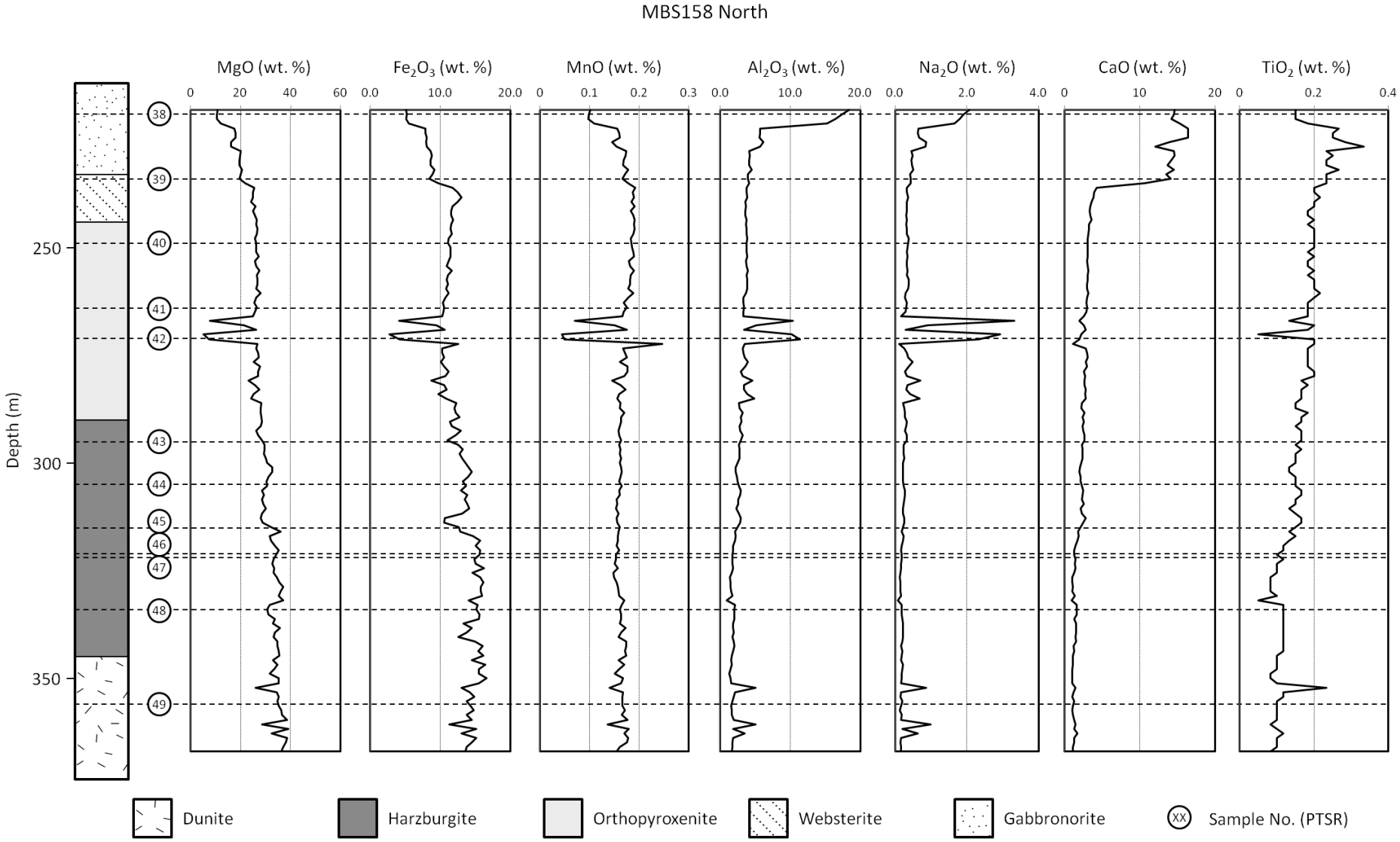


Figure 4.8d): Major element geochemical profile of borehole MBS158 (northern zone) showing the depth at which samples (numbered) were collected.

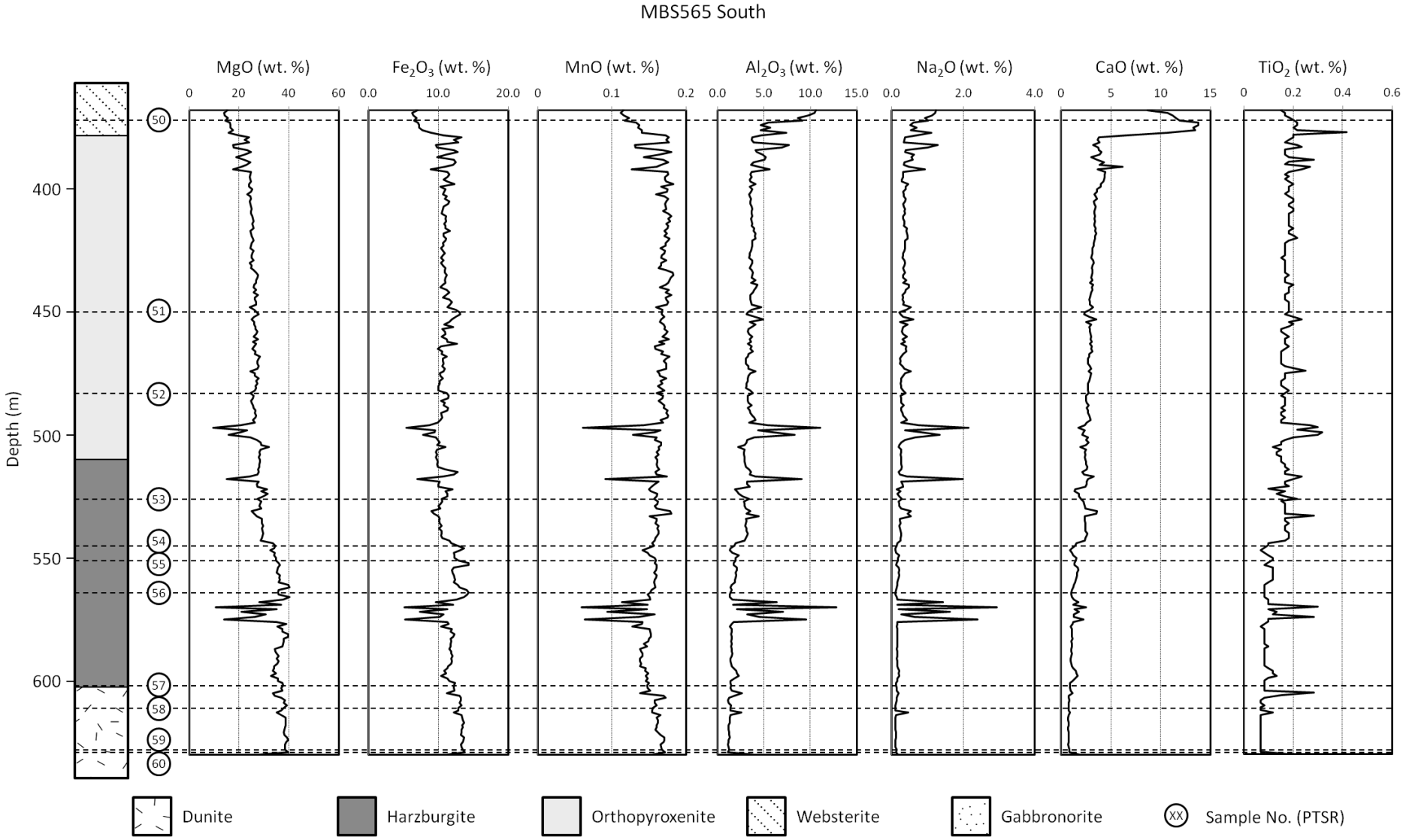


Figure 4.8e): Major element geochemical profile of borehole MBS565 (southern zone) showing the depth at which samples (numbered) were collected.

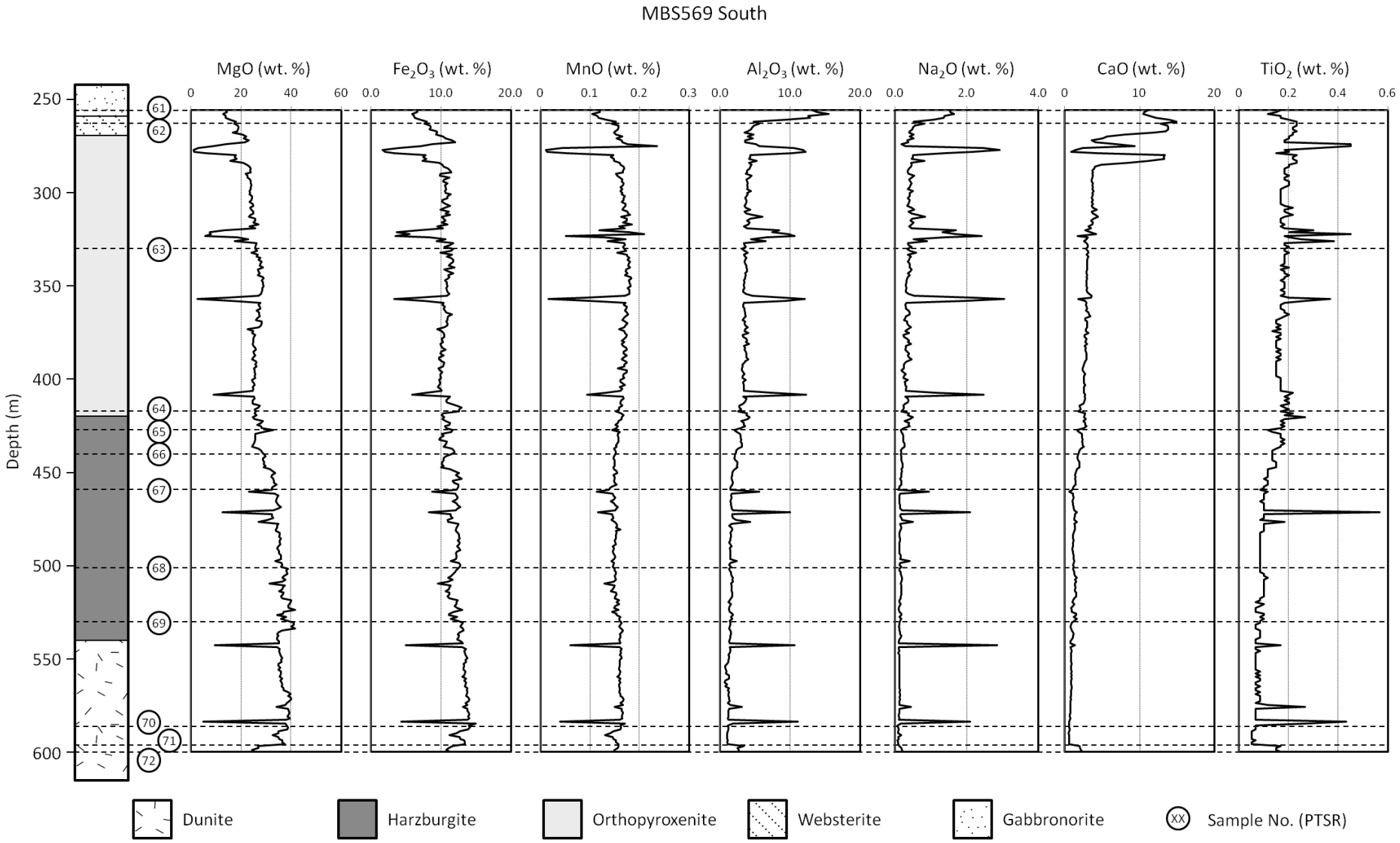


Figure 4.8f): Major element geochemical profile of borehole MBS569 (southern zone) showing the depth at which samples (numbered) were collected.

4.6.2 Chondrite normalised REE profiles

Representative samples from the central and northern zones of the Mirabela intrusion have been analysed at Cardiff University for REE (Appendix D). Chondrite normalised REE profiles have been constructed using the values given in McDonough and Sun (1995). The samples analysed include one of each lithology from boreholes MBS604 (central zone; Fig. 4.9a) and MBS158 (northern zone; Fig. 4.9b). The lowermost dunite from MBS605 (central zone) has also been analysed (Fig. 4.9a) given the unique platinum-group mineralogy of the MBS604 dunite (documented below in section 4.7.5). In general, the northern zone samples are slightly more enriched in REE than the central zone samples.

In the central zone, the gabbronorite and websterite samples exhibit similar flat profiles whereas the northern zone equivalents display slight LREE enrichment with slightly negative slopes. No Eu anomaly is observed in either of the gabbronorite samples. Orthopyroxenite and olivine orthopyroxenite samples have been grouped together and in the central zone show relatively flat profiles with some very minor enrichment in La and Ce. In the northern zone samples, these orthopyroxenites exhibit LREE enrichment which is much more noticeable than the slight enrichment noted in the overlying websterite and gabbronorite. Sample PTSR41, an olivine orthopyroxenite from the northern zone displays a slight negative Eu anomaly.

REE data of harzburgite sample PTSR07 from the central zone produces a slightly positive slope indicating LREE depletion; however, there is some enrichment in La and Ce giving rise to a rather strange profile. In the northern zone, the harzburgite displays a pattern of very slight LREE enrichment, parallel with the pattern for that of the gabbronorite and websterite although hosting less REE.

All three dunite samples analysed from the two central zone boreholes (MBS604 and MBS605) and from one northern zone borehole (MBS158) are comparable with each other. All show LREE enrichment, more so than the overlying harzburgites with steeper profiles. In the northern zone, this profile is comparable to those displayed by the orthopyroxenite and olivine orthopyroxenite samples. In the central zone, the dunite patterns of LREE enrichment are the steepest and most prominent, with the overlying samples displaying relatively flat profiles.

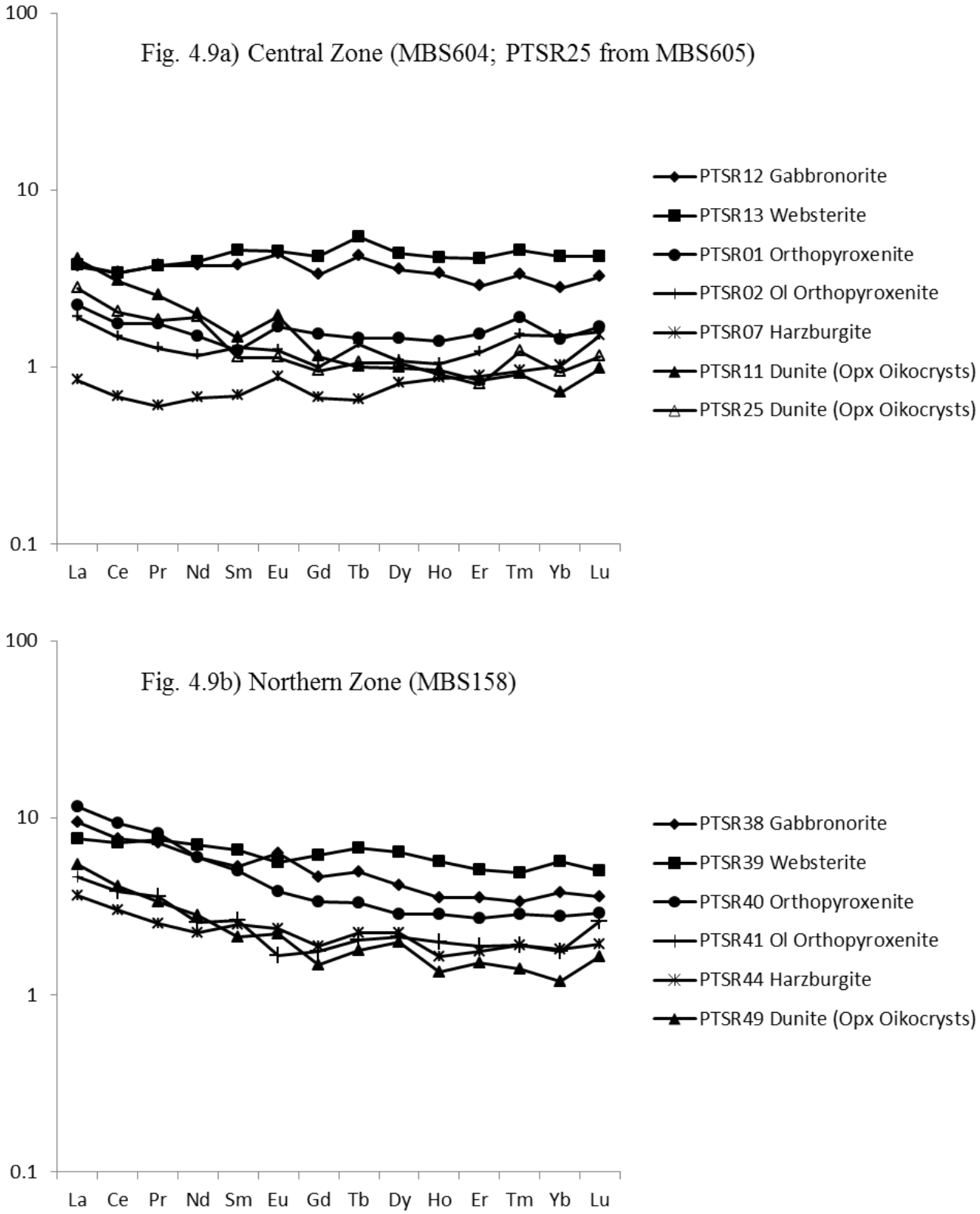


Figure 4.9: Chondrite normalised (using the values given in McDonough and Sun, 1995) REE diagrams, a) selected representative samples from the central zone borehole MBS604 with an additional dunite sample from MBS605 (PTSR25), and b) selected representative samples from the northern zone borehole MBS158.

4.6.3 Trace element bivariate plots

Trace element data collected by ActLabs has been used to determine the role of magma mixing and crustal contamination in the genesis of the Mirabela intrusion and the Santa Rita sulphide ore zone.

REE ratio bivariate plots of La/Sm-Sm and Ce/Yb-Ce (Fig. 4.10a-b) have been produced in an attempt to determine whether magma mixing has occurred. Plots showing the variation of La/Sm ratios with depth within the boreholes studied (Fig. 4.11) have also been constructed for the same purpose. These bivariate plots show that all of the lithologies from the different boreholes studied are closely grouped. Fractional crystallisation trends are observed in both plots as linear trends, however, websterite samples are observed at the end of these trends as opposed to gabbronorite. This is likely a result of the partition coefficients of these elements into the mineral species present in these different lithologies. Similarly, on the Rb/Sr-Sr plot (Fig. 4.10c), gabbronorite samples are isolated from the main Mirabela group due to increased Sr content, accounted for by the presence of plagioclase. Deviations are observed in La/Sm ratios plotted with depth in their respective boreholes (Fig. 4.11), however, these are not consistent across the intrusion. Furthermore, there are no step changes in La/Sm ratios associated with changes in lithology.

To determine the role of crustal contamination, geochemical data of the country rock Itabuna-Salvador-Curaça belt TTG suites (Pinho *et al.*, 2011) have been plotted with the Mirabela intrusives on a series of trace element bivariate plots including Rb/Sr-Sr, Sm/Nd-Nd and P_2O_5-Zr (the latter plotted due to the nature of the country rocks) (Fig. 4.10c-d, f). A plot of Ti-Zr has also been constructed (Fig. 4.10e) (a basalt discrimination diagram) to check for any trends that might not otherwise be displayed in more traditional plots. The Mirabela samples and the country rocks form two distinct groups and the Mirabela samples do not migrate towards the country rocks on these plots as they evolve (i.e., from dunite to gabbronorite). In some cases, this dissociation of the two groups is further pronounced by each data set exhibiting minor individual trends (fractional crystallisation for the Mirabela data) which run parallel to each other (e.g., Ce/Yb-Yb and Ti-Zr) (Fig. 4.10b, e). It should be noted that it is not clear if the TTG suite analysed by Pinho *et al.* (2011) is representative of the immediate country rocks to the Mirabela intrusion. Data for Nb is poor, with most analyses being below the limit of detection, therefore Th/Nb ratios cannot be used to infer crustal contamination.

Fig. 4.10a)

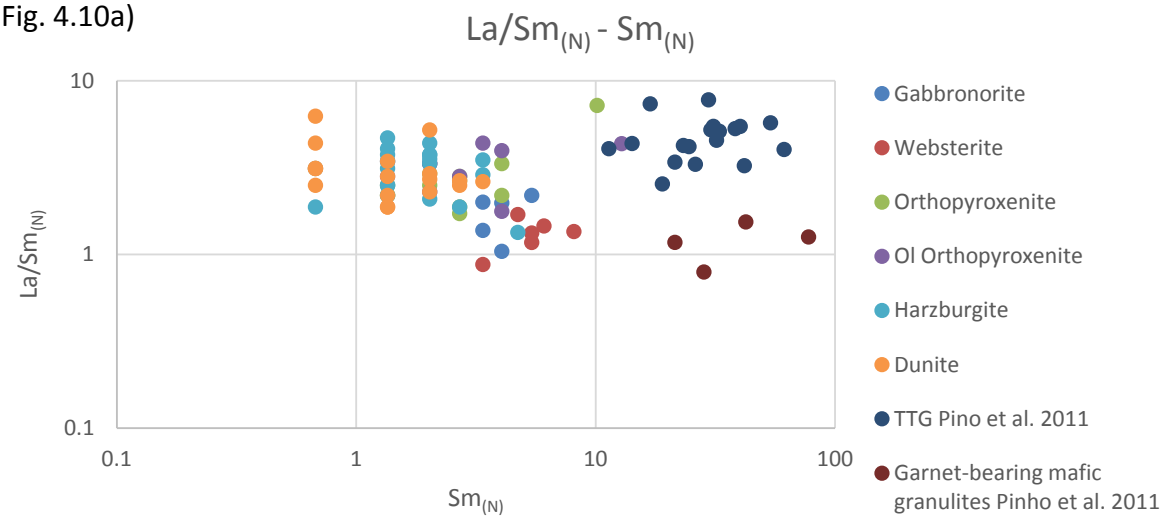


Fig. 4.10b)

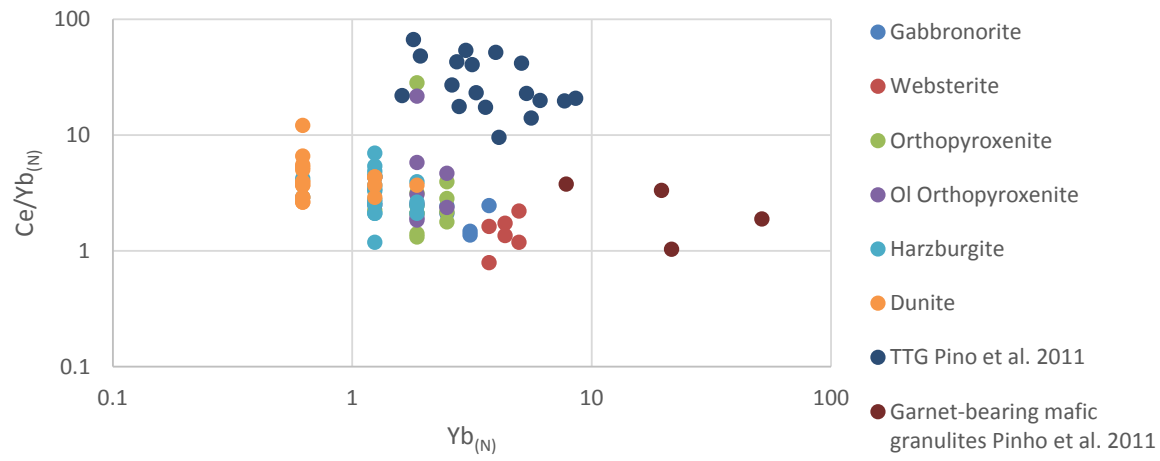


Fig. 4.10c)

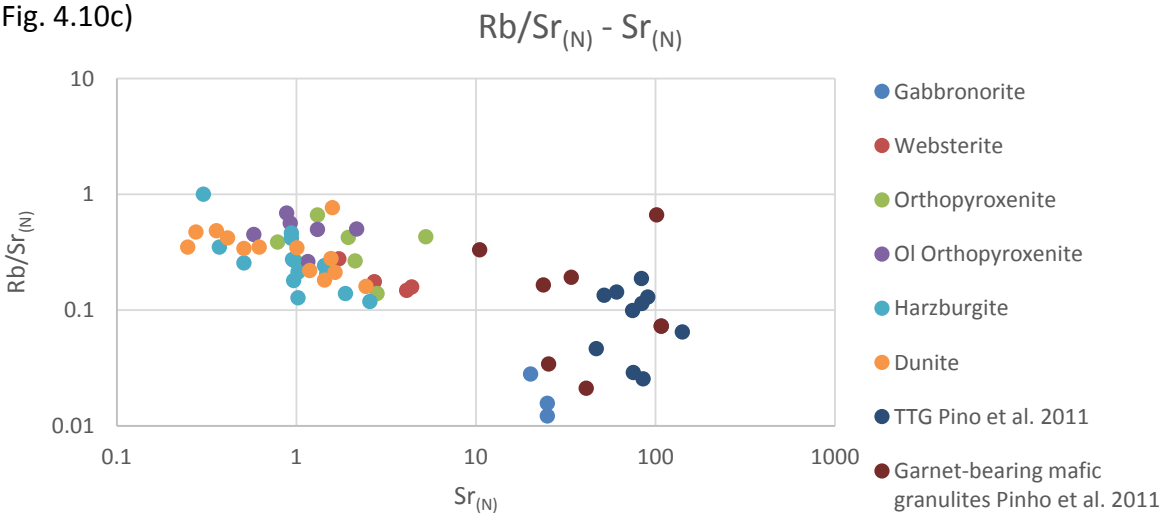


Fig. 4.10d)

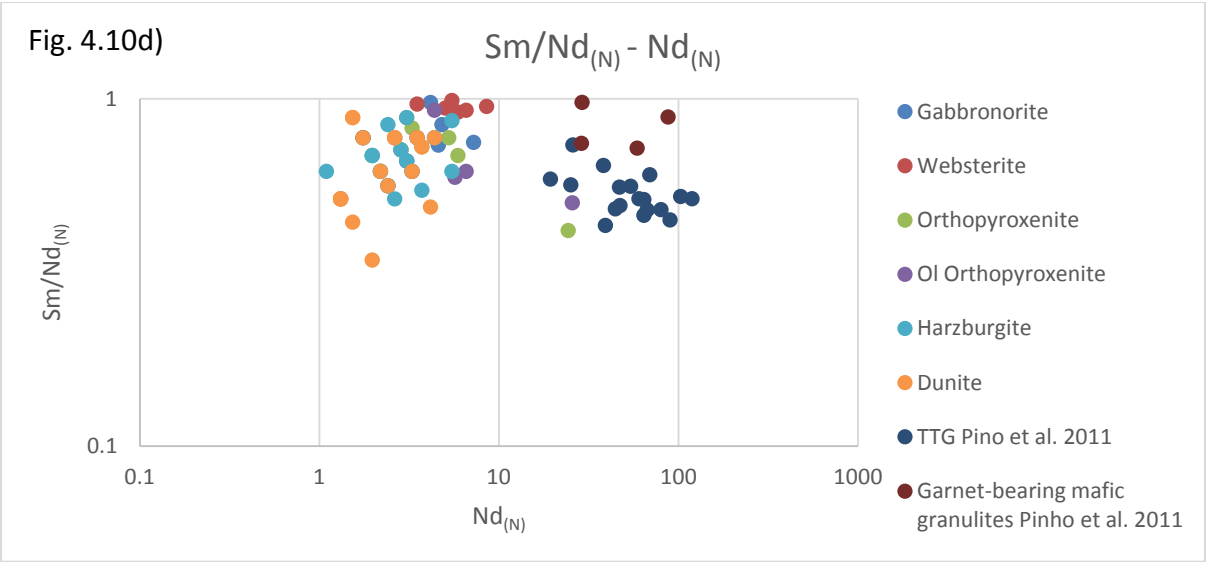


Fig. 4.10e)

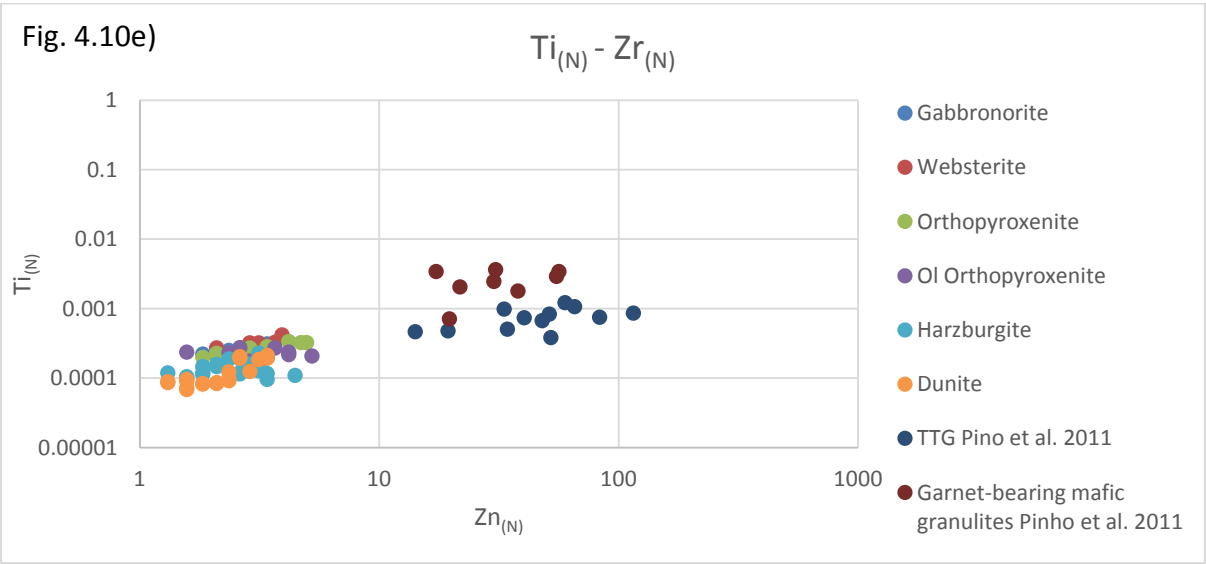


Fig. 4.10f)

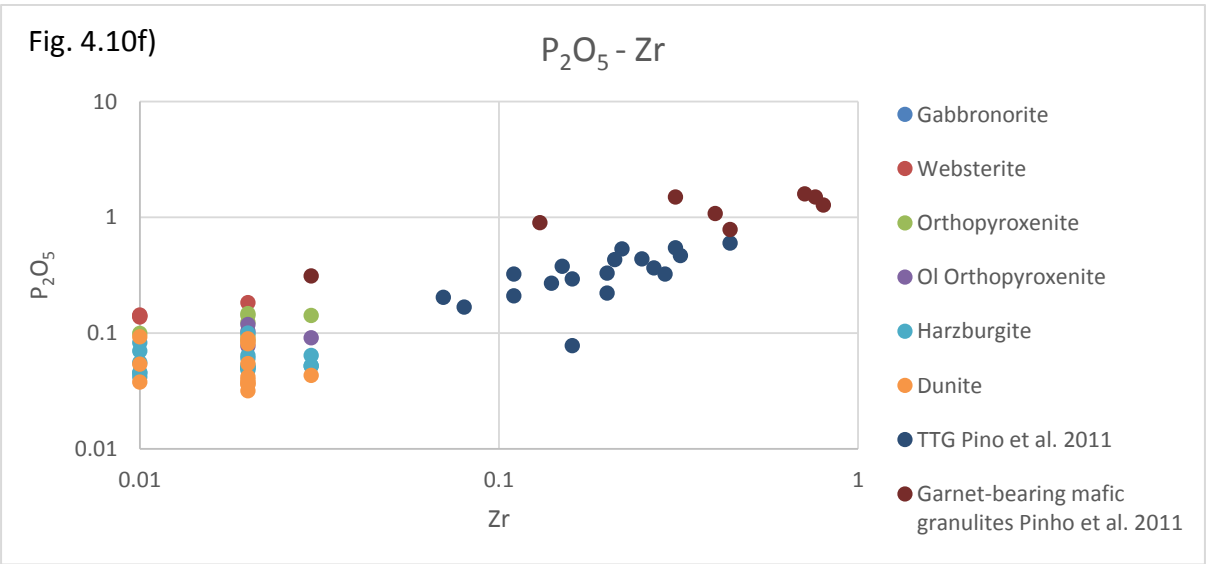


Figure 4.10a-f): A series of trace element bivariate plots constructed to determine the role of magma mixing and crustal contamination in the genesis of the Mirabela intrusion and Santa Rita ore zone. (N) = chondrite normalised using the values given in McDonough and Sun (1995).

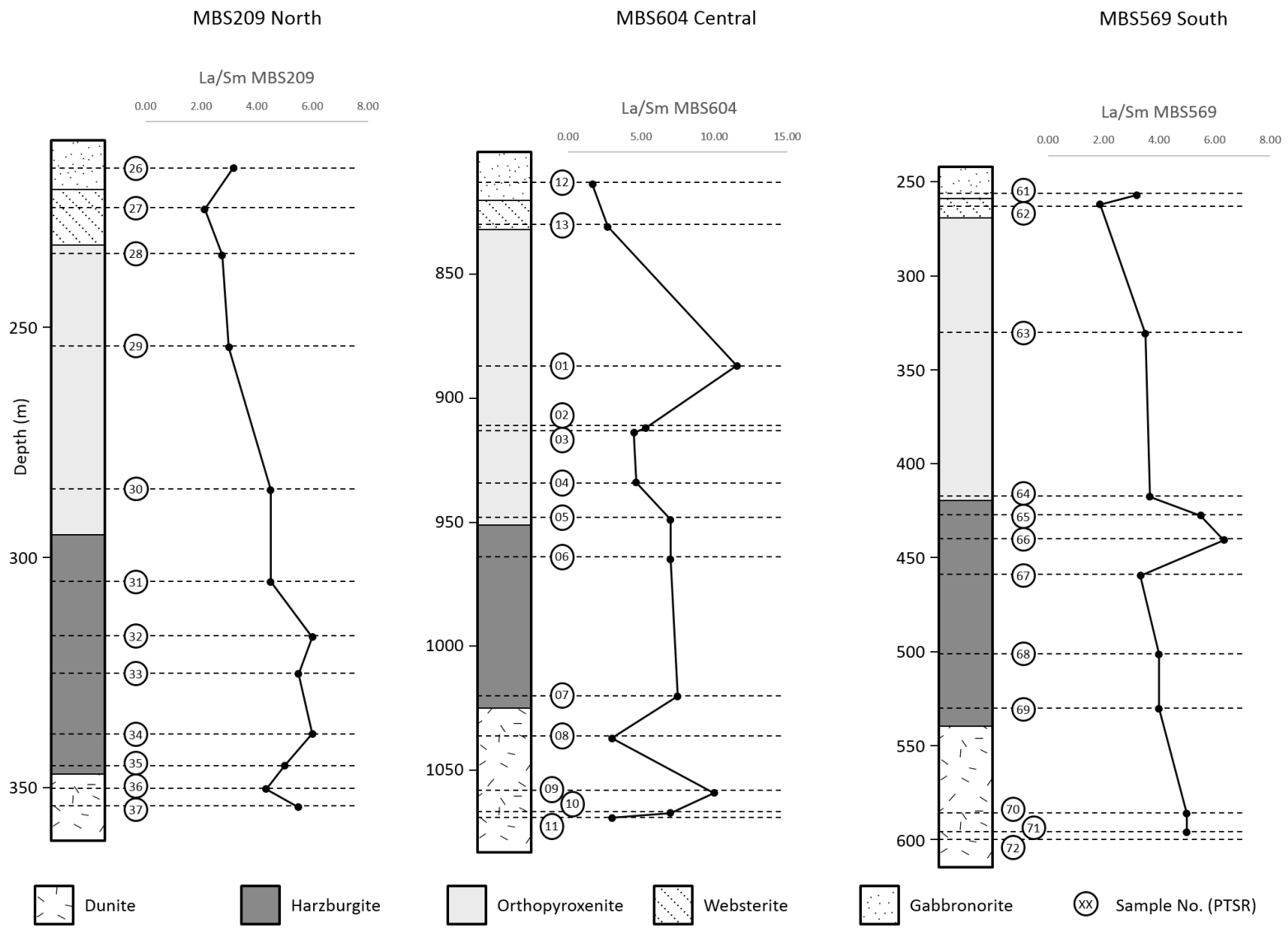


Figure 4.11: The change in La/Sm ratios with depth displayed for three boreholes from the northern, central and southern zone for comparison.

4.6.4 Whole-rock PGE data and chondrite normalised profiles

The PGE whole-rock data is provided by Actlabs by Ni-fire assay and includes Au but excludes Os (Appendix E). Chondrite normalised plots used to analyse whole-rock PGE data have been constructed using the values given in Lodders (2003) and three distinct patterns are identified. These patterns all show general positive trends but demonstrate varying Pd/Pt ratios.

The first pattern (1) observed displays a positive Pd anomaly (Fig. 4.12a) and occurs in the deepest samples analysed from each borehole which consist predominantly of sulphur-poor dunite but is also observed in two harzburgite samples (PTSR48 and PTSR44). This positive Pd anomaly appears to be the result of higher Pd concentrations in respect to the other PGE; however, the effect is enhanced in some samples by the depletion of Pt.

The second pattern (2) observed displays a positive Pt anomaly (Fig. 4.12b) and occurs in orthopyroxenite, olivine orthopyroxenite and harzburgite samples. Only in one case does this pattern occur in a dunite (PTSR45). All of the samples that exhibit this second pattern (positive Pt anomaly) are stratigraphically higher than all of the samples that exhibit the first pattern (positive Pd anomaly) within their respective boreholes.

The third pattern (3) observed displays general positive slopes without any significant Pt or Pd anomaly (Fig. 4.12c) and occurs in harzburgite and dunite samples, except in one case where one olivine orthopyroxenite exhibits this pattern (PTSR66). Stratigraphically, these samples typically occur at an 'intermediate' level between those samples that host the Pd anomaly (1) at depth and those that host the Pt anomaly (2) at a more shallow level in their respective boreholes. In some cases, samples that are considered to be stratigraphically related to those samples hosting the positive Pt anomaly (2) at shallower levels instead exhibit the third PGE pattern (3) showing no Pt or Pd anomaly (PTSR33 and PTSR43). This behaviour is also shown in a more extreme way by PTSR44 which is related stratigraphically to those samples hosting the Pt anomaly (2), however, this particular sample exhibits a positive Pd anomaly (1) usually associated with deeper and predominantly dunite samples. The location of the samples in the Mirabela stratigraphy displaying these different PGE profile patterns is shown schematically in Figure 4.12d.

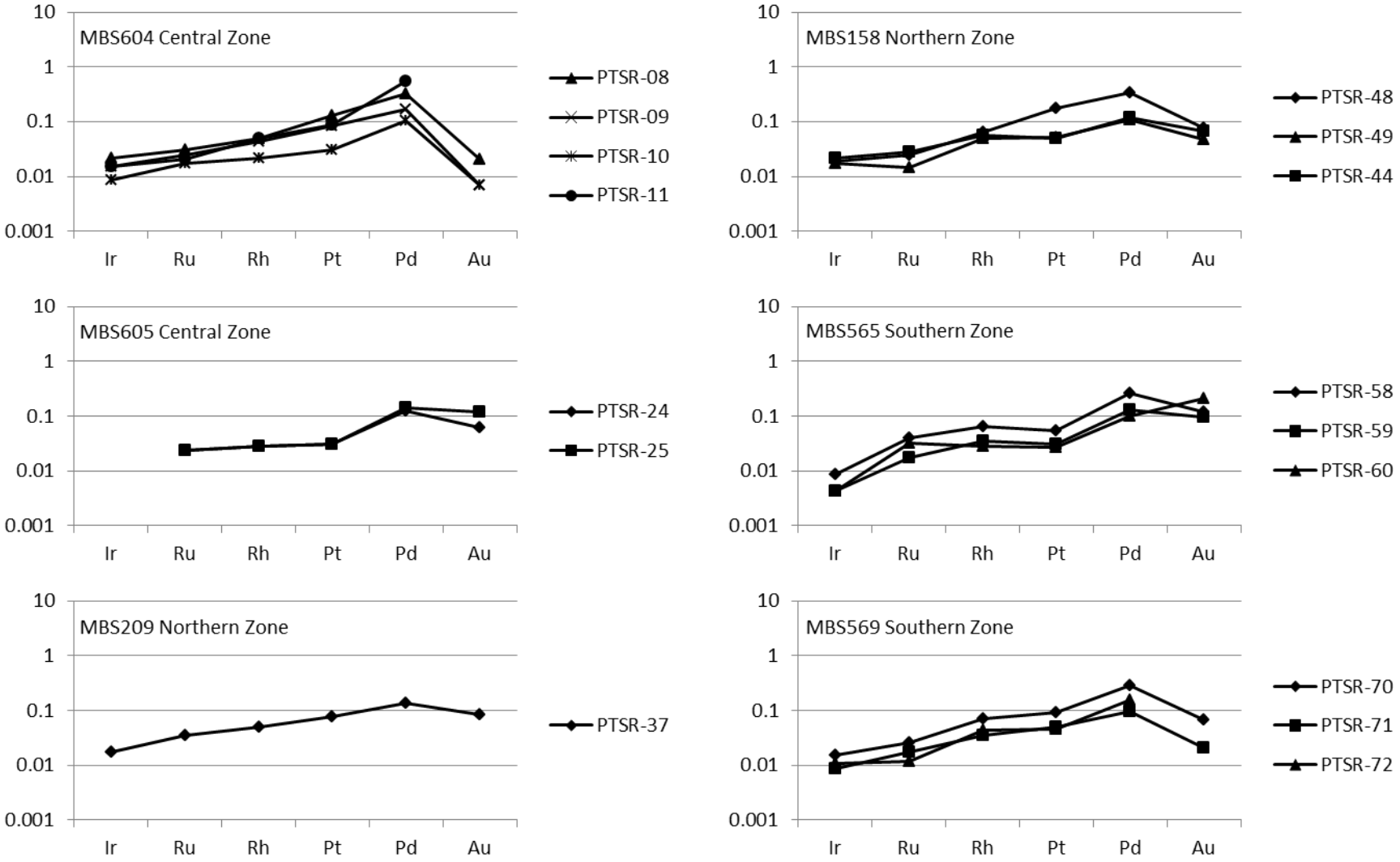


Figure 4.12a): Chondrite normalised (using the values given in Lodders, 2003) PGE diagrams showing pattern 1) positive Pd anomaly in the sulphur-poor dunite hosting the basal PGE anomaly (profiles split by borehole number).

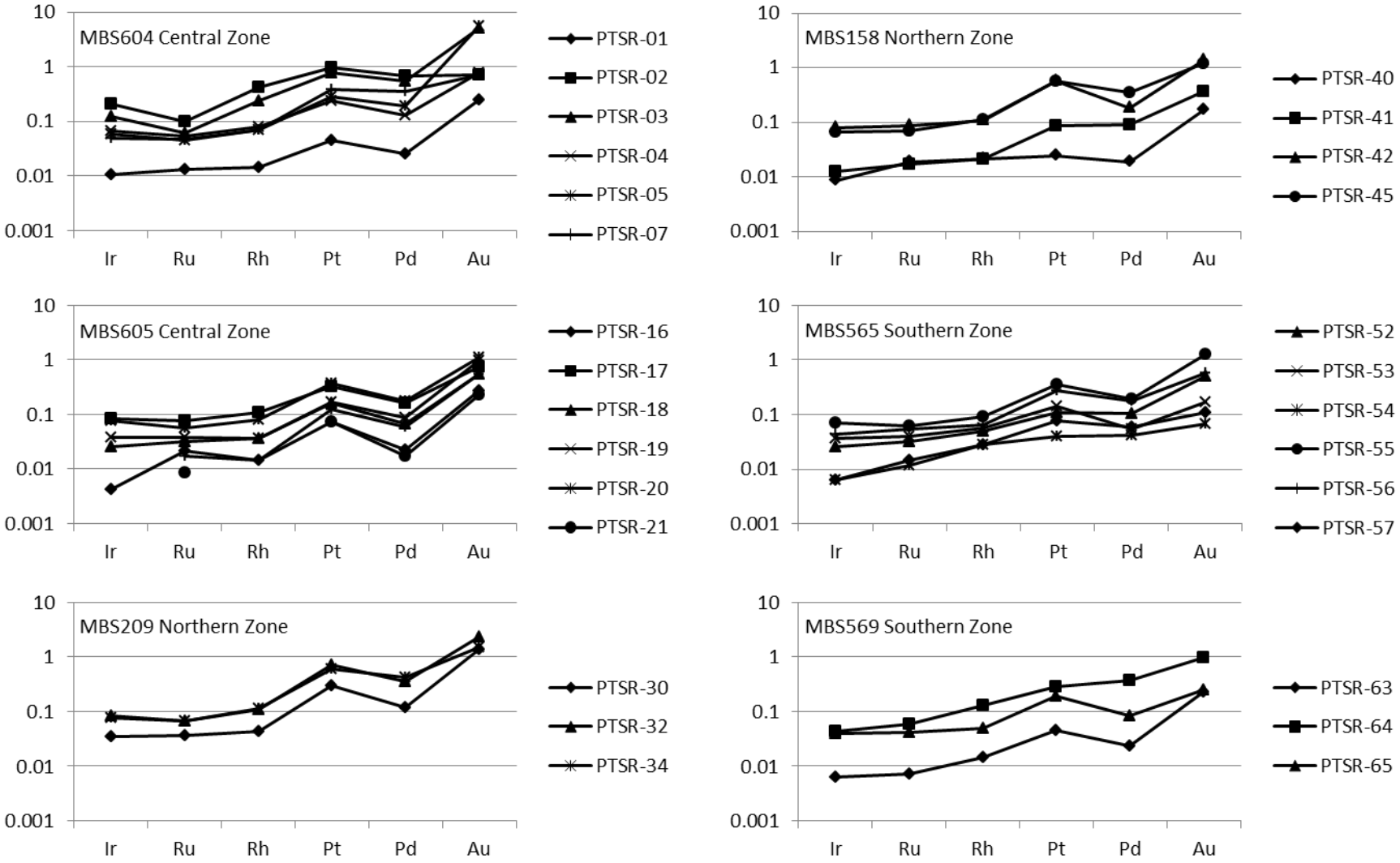


Figure 4.12b): Chondrite normalised (using the values given in Lodders, 2003) PGE diagrams showing pattern 2) positive Pt anomaly in the Santa Rita ore zone (profiles split by borehole number).

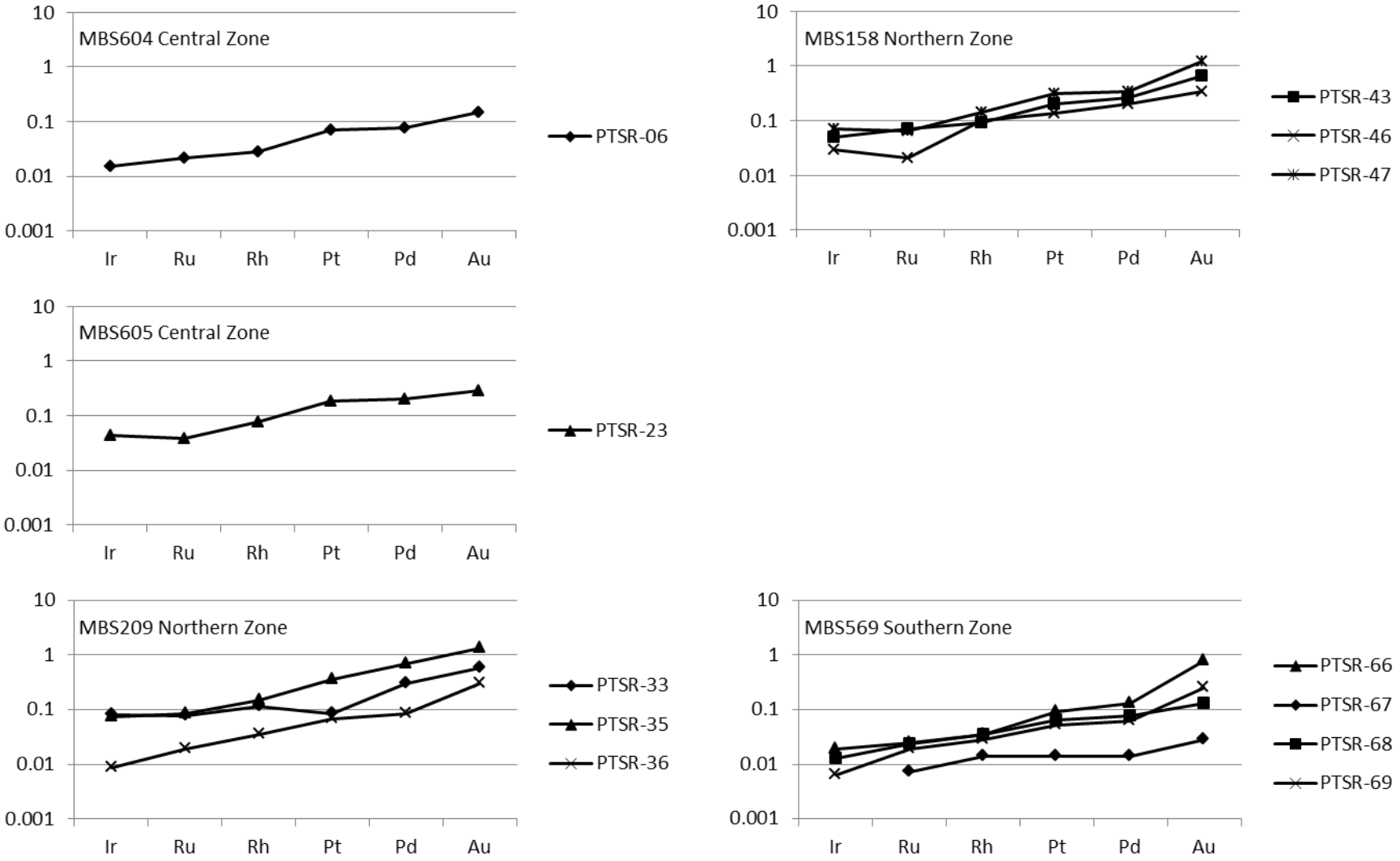


Figure 4.12c): Chondrite normalised (using the values given in Lodders, 2003) PGE diagrams showing pattern 3) straight profiles with no Pt or Pd anomaly in the 'transition zone' between the Santa Rita ore zone and the underlying sulphur-poor dunite (profiles split by borehole number).

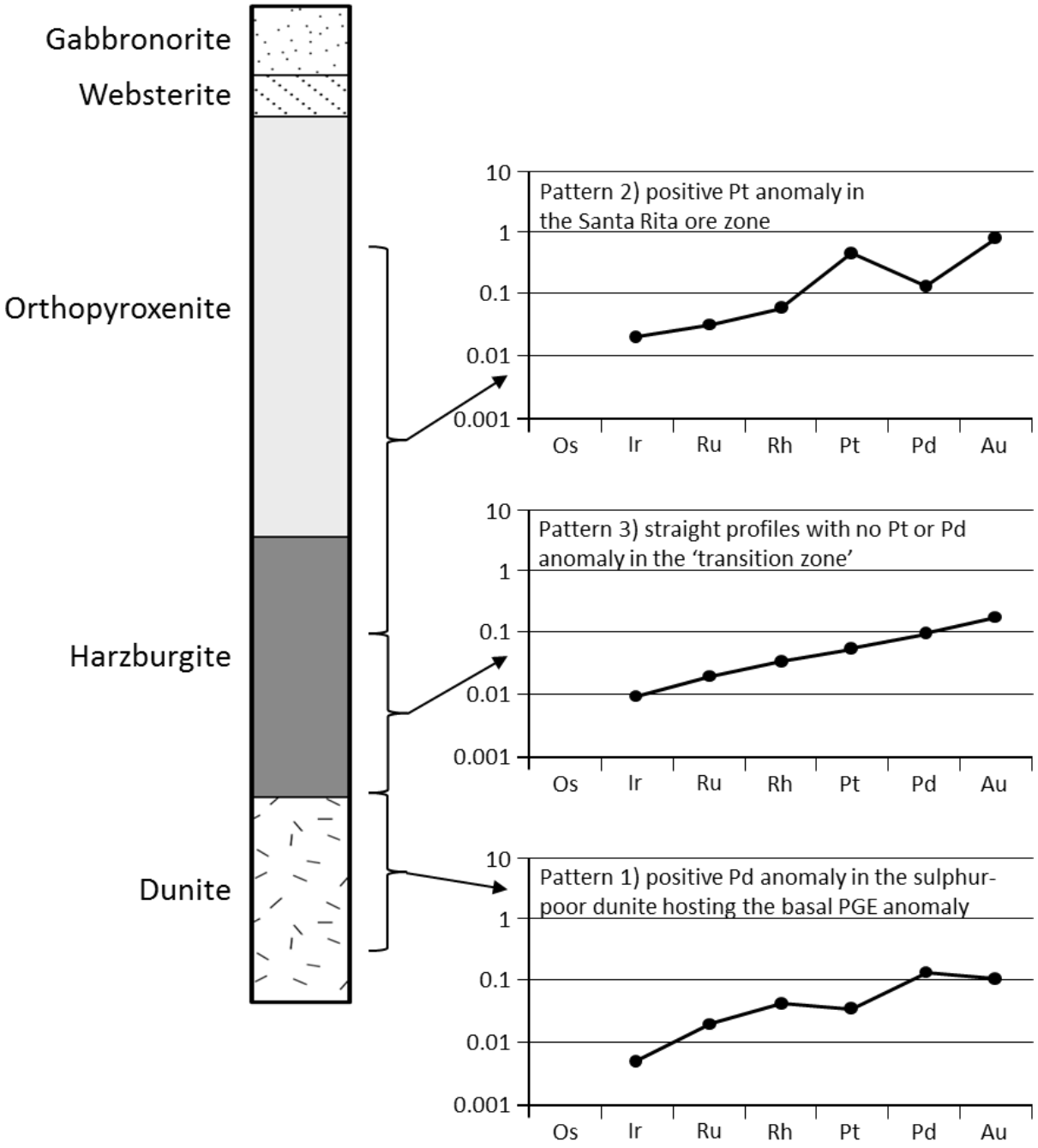


Figure 4.12d): Schematic diagram showing where the three PGE patterns described above occur within the Mirabela straigraphy.

4.6.4 Semimetal Analyses

The semimetals As, Bi, Sb, Se and Te were selected for specific analyses due to their role in forming minerals with the PGE. It is therefore crucial to understand their abundance and distribution throughout the studied boreholes. Semimetal analyses by Actlabs for all the samples studied from the northern and southern boreholes (MBS209, MBS 158, MBS565 and MBS569) are displayed as borehole profiles with sulphur (Fig. 4.13a-d) (Appendix F).

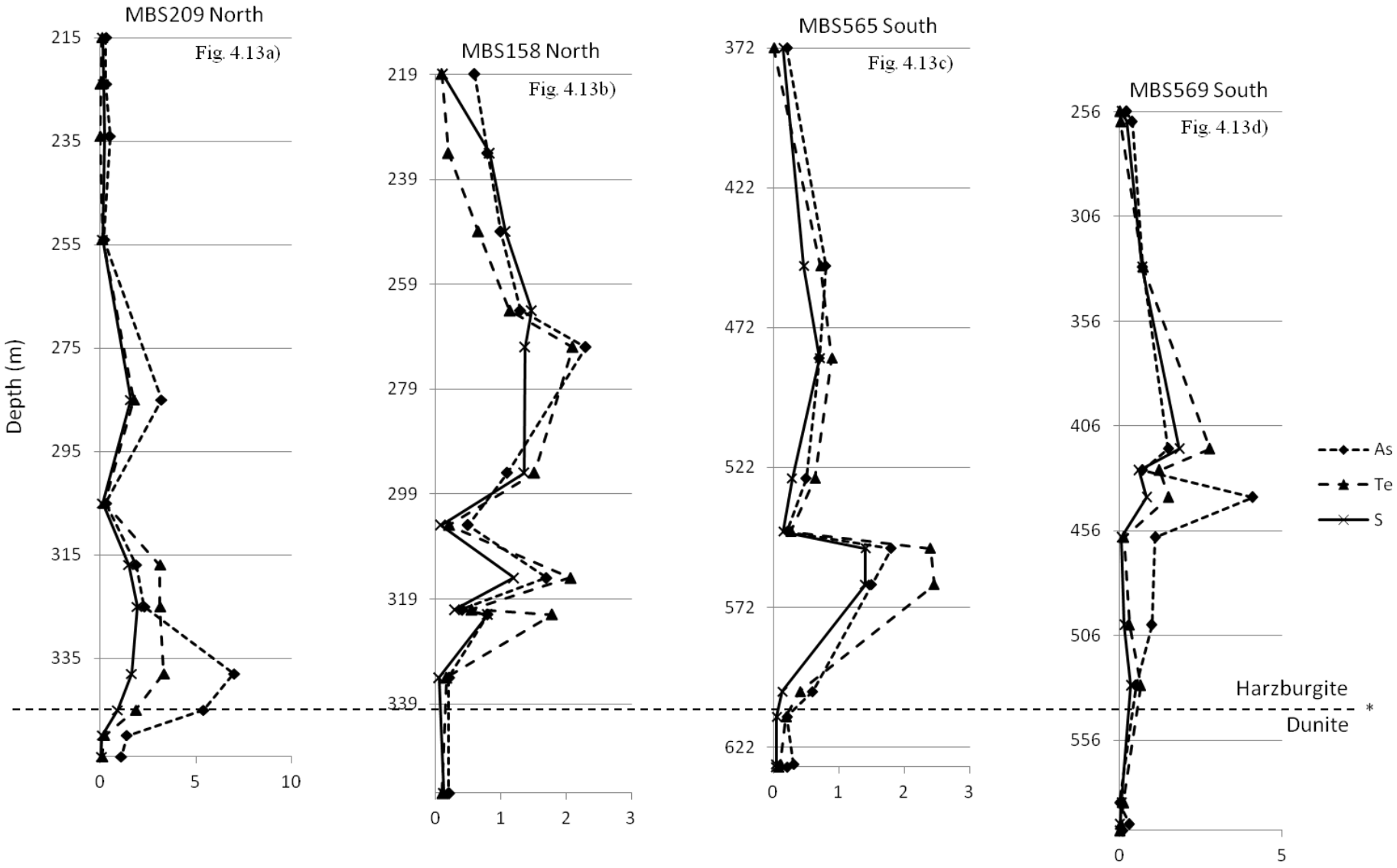


Figure 4.13: Semimetals (As and Te in ppm) plotted with sulphur (S in wt. %) against depth for a) borehole MBS209 (northern zone), b) borehole MBS158 (northern zone), c) borehole MBS565 (southern zone), d) borehole MBS569 (southern zone); *dashed line marks the top of the dunite in each borehole for reference.

These analyses show that Bi, Sb and Se have extremely low concentrations in the majority of the samples and can be considered virtually absent and are therefore not plotted on the borehole profiles for simplicity. The only semimetals of significance appear to be As and Te which, for the most part, correlate with and follow the distribution of sulphur.

4.7 Platinum-Group Mineralogy

4.7.1 PGM assemblages

This study has revealed the presence of three distinct PGM assemblages; (i) predominantly Pt-Pd-Ni-Fe tellurides with accessory Ag telluride, rare electrum and native Au grains, (ii) Pt-Pd-Ni-Cu-Fe tellurides and abundant sperrylite ($PtAs_2$) with accessory Ag telluride, rare electrum and native Au grains, and (iii) Pd alloys with minor PGE-bearing arsenides and sulphides. The types and abundance of PGM identified per sample studied are given in Table 4.2. Full PGM mineralogical data and labelled PGM images are given in Appendix G and Appendix H, respectively.

These three assemblages occupy different positions in the Mirabela intrusion (Fig. 4.14). PGE telluride assemblage (i) is observed in the central zone of the intrusion within the Santa Rita ore zone in both boreholes studied (MBS604 and MBS605). This assemblage is also identified in the sulphur-poor dunite in MBS605 only. PGE telluride and arsenide assemblage (ii) is located in the northern and southern zones of the intrusion and occurs in both the Santa Rita ore zone and the sulphur-poor dunite. Finally, the Pd alloy assemblage (iii) is localised and identified in the central zone of the intrusion in the sulphur-poor dunite in borehole MBS604 only. Where both assemblage (i) and (ii) are identified in the sulphur-poor dunite, the types of PGM observed are consistent with their counterparts identified in the Santa Rita ore zone (excluding the localised Pd alloy assemblage [iii]). However, the PGM in this dunite zone are consistently much smaller and have a much lower abundance than their Santa Rita ore zone counterparts (Table 4.2). In addition to Table 4.2, the proportions of the different PGM types identified are displayed as pie charts (divided into the central zone and northern-southern zones given the location of the different PGM assemblages [i] and [ii]), calculated using both the numbers of PGM identified for each PGM type as well as the total area of PGM identified for each PGM type (Fig. 4.15a-d).

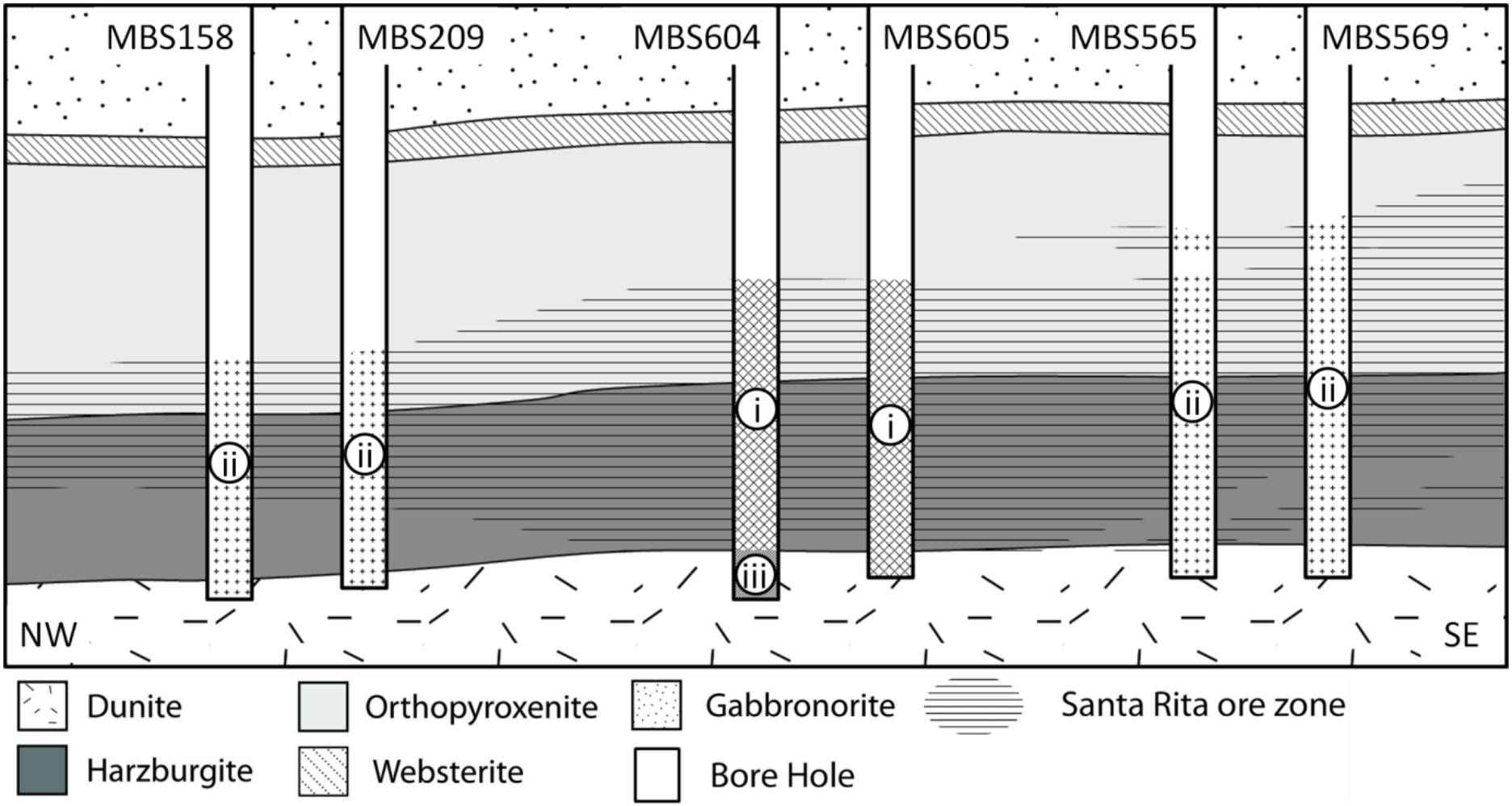


Figure 4.14: Schematic diagram showing the location of the different PGM assemblages identified: (i) PGE tellurides, (ii) PGE tellurides with sperrylite and (iii) the localised Pd alloy assemblage.

Zone	Borehole	Sample No.	Platinum-Group Mineral Types									
			$(Ni,Cu,Pt,Pd)(Bi,Te)_2$	Ag-Pd-Te	Ag_2Te	$(Pt,Fe,Rh)As_2$	Au-(Ag,Cu,Fe)	Pd-(Cu,Pb)	(Ir,Pt,Rh)AsS	Other	Undif.	Total
Central	MBS604	PTSR-01	2	-	9	-	-	-	-	-	-	11
		PTSR-02	15	-	-	-	-	-	-	-	-	15
		PTSR-03	15	-	-	-	2	-	-	-	4	21
		PTSR-04	5	-	2	-	1	-	-	1	1	10
		PTSR-05	20	-	8	-	-	-	-	2	3	33
		PTSR-07	15	-	-	-	-	-	-	-	-	15
		PTSR-08	1	-	-	2	-	8	1	1	1	14
		PTSR-09	1	-	-	-	-	1	1	1	1	5
		PTSR-11	-	-	-	-	-	6	-	4	-	10
	MBS605	PTSR-16	3	-	2	-	-	-	-	-	-	5
		PTSR-17	13	-	2	-	-	-	-	-	-	15
		PTSR-18	5	-	1	-	1	-	-	-	-	7
		PTSR-19	6	-	2	2	1	-	1	-	3	15
		PTSR-20	15	-	3	-	-	-	-	2	2	22
		PTSR-21	7	-	-	-	-	-	-	-	-	7
		PTSR-22	18	-	-	-	1	-	-	-	2	21
		PTSR-23	9	-	-	-	2	-	-	1	-	12
		PTSR-24	5	-	-	-	-	-	-	-	1	6
		PTSR-25	3	-	-	-	-	-	-	-	-	3
Northern	MBS209	PTSR-30	7	-	6	1	-	-	1	1	3	19
		PTSR-32	17	4	5	2	-	-	1	1	5	35
		PTSR-33	9	1	3	4	-	-	-	2	2	21
		PTSR-34	18	2	-	10	-	-	2	-	-	32
		PTSR-35	29	7	4	19	1	-	1	3	6	70
		PTSR-36	2	-	-	-	-	-	-	-	-	2
		PTSR-37	3	-	-	-	-	-	2	-	-	5
	MBS159	PTSR-40	9	-	10	-	-	-	-	-	-	19

Zone	Borehole	Sample No.	Platinum-Group Mineral Types									
			$(Ni,Cu,Pt,Pd)(Bi,Te)_2$	Ag-Pd-Te	Ag_2Te	$(Pt,Fe,Rh)As_2$	Au-(Ag,Cu,Fe)	Pd-(Cu,Pb)	(Ir,Pt,Rh)AsS	Other	Undif.	Total
Northern	MBS159	PTSR-41	8	-	5	1	-	-	-	-	1	15
		PTSR-42	16	1	4	7	1	-	-	3	1	33
		PTSR-43	18	1	4	-	-	-	-	-	3	26
		PTSR-44	1	-	-	-	-	-	-	3	-	4
		PTSR-45	21	-	-	3	3	-	1	-	1	29
		PTSR-46	7	-	-	-	4	-	2	-	2	15
		PTSR-47	17	-	-	-	-	-	-	1	2	20
		PTSR-48	1	-	-	2	-	-	1	1	-	5
Southern	MBS565	PTSR-51	7	-	-	-	1	-	1	-	1	10
		PTSR-52	6	-	3	4	1	-	1	-	4	19
		PTSR-53	4	-	-	3	-	-	1	-	-	8
		PTSR-54	2	1	-	1	-	-	-	-	4	8
		PTSR-55	30	1	-	-	1	-	-	1	1	34
		PTSR-56	15	2	2	-	4	-	-	-	2	25
		PTSR-57	4	-	-	-	2	-	-	-	1	7
		PTSR-58	6	-	-	4	-	1	2	1	1	15
		PTSR-59	3	-	-	-	2	-	-	-	-	5
		PTSR-60	4	-	-	-	-	-	-	-	-	4
	MBS569	PTSR-63	10	-	5	-	-	-	1	-	4	20
		PTSR-64	18	-	13	4	2	-	1	-	7	45
		PTSR-65	11	-	1	-	-	-	-	1	1	14
		PTSR-66	8	-	3	-	-	-	-	-	3	14
		PTSR-67	2	-	-	-	-	-	-	-	-	2
		PTSR-68	4	-	-	4	-	-	-	-	1	9
		PTSR-69	1	1	-	-	1	-	-	-	-	3
		PTSR-70	4	-	-	-	-	-	-	-	-	4
		PTSR-71	-	-	-	-	-	-	-	1	-	1
Total			480	21	97	73	31	16	21	31	74	844

Table 4.2: Abundance of different PGM types in all PGM-bearing samples analysed. Undif = undifferentiated.

Borehole	Sample	PGM No.	Quantitative Analyses (wt. %)										PGM Composition
			Fe	Ni	Cu	As	Pd	Ag	Te	Pt	Bi	Total	
MBS158	PTSR-40	A1	-	18.97	-	-	0.41	-	80.52	-	-	99.90	$(Ni_{1.01}Pd_{0.01})_{1.02}Te_{1.98}$
MBS158	PTSR-40	H1	-	8.89	-	-	0.85	-	69.40	21.16	-	100.30	$(Ni_{0.56}Pt_{0.40}Pd_{0.03})_{0.99}Te_{2.01}$
MBS604	PTSR-07	K1	0.65	14.51	-	-	2.75	-	73.79	5.79	-	97.49	$(Ni_{0.83}Pt_{0.10}Pd_{0.09})_{1.02}(Te_{1.94}Fe_{0.04})_{1.98}$
MBS605	PTSR-22	G1	2.68	14.89	-	-	2.15	-	75.40	3.67	-	98.79	$(Ni_{0.82}Pd_{0.06}Pt_{0.06})_{0.94}(Te_{1.90}Fe_{0.16})_{2.06}$
MBS605	PTSR-22	B1	2.09	12.38	-	-	4.09	-	70.07	11.34	-	99.97	$(Ni_{0.71}Pt_{0.19}Pd_{0.13})_{1.03}(Te_{1.84}Fe_{0.13})_{1.97}$
MBS605	PTSR-20	F1	1.03	9.10	-	-	1.97	-	68.54	18.05	-	98.69	$(Ni_{0.56}Pt_{0.34}Pd_{0.07})_{0.97}(Te_{1.96}Fe_{0.07})_{2.03}$
MBS604	PTSR-07	F1	2.57	6.28		-	10.80	-	66.36	13.21	-	99.22	$(Ni_{0.38}Pd_{0.36}Pt_{0.24})_{0.98}(Te_{1.85}Fe_{0.17})_{2.02}$
MBS604	PTSR-03	C1	0.54	5.67	-	-	8.77	-	67.86	16.40	-	99.24	$(Ni_{0.36}Pt_{0.31}Pd_{0.31})_{0.98}(Te_{1.98}Fe_{0.04})_{2.02}$
MBS158	PTSR-46	H1	0.96	5.42			9.55		68.51	15.69	-	100.13	$(Ni_{0.34}Pd_{0.33}Pt_{0.30})_{0.97}(Te_{1.97}Fe_{0.06})_{2.03}$
MBS158	PTSR-40	K1	1.35	19.72	-	-	-	-	79.74	-	-	100.81	$Ni_{1.02}(Te_{1.90}Fe_{0.08})_{1.98}$
MBS158	PTSR-40	I1	1.64	18.65	-	-	-	-	76.99	-	2.71	99.99	$Ni_{0.99}(Te_{1.88}Fe_{0.09}Bi_{0.04})_{2.01}$
MBS604	PTSR-07	C1	-	5.89	-	-	3.40	-	65.23	25.11	-	99.63	$(Pt_{0.50}Ni_{0.39}Pd_{0.12})_{1.01}Te_{1.99}$
MBS158	PTSR-46	F1	-	4.41	-	-	6.13	-	65.68	24.25	-	100.47	$(Pt_{0.48}Ni_{0.29}Pd_{0.23})_{1.00}Te_{2.00}$
MBS158	PTSR-40	E1	-	-	-	-	-	62.02	37.91	-	-	99.93	$Ag_{1.98}Te_{1.02}$
MBS158	PTSR-40	M1	-	-	-	-	-	61.02	38.31	-	-	99.33	$Ag_{1.96}Te_{1.04}$
MBS565	PTSR-58	A1	-	-	-	42.60	-	-	-	57.12	-	99.72	$Pt_{1.02}As_{1.98}$
MBS569	PTSR-68	F1	-	-	-	44.27				56.67	-	100.94	$Pt_{0.99}As_{2.01}$
MBS569	PTSR-68	G1	-	-	34.62	-	-	-	65.93	-	-	100.55	$Cu_{1.03}Te_{0.97}$

Table 4.3: Selective representative quantitative analyses (wt. %) of PGM with derived empirical formulae.

Fig: 4.15a) Central zone PGM by number

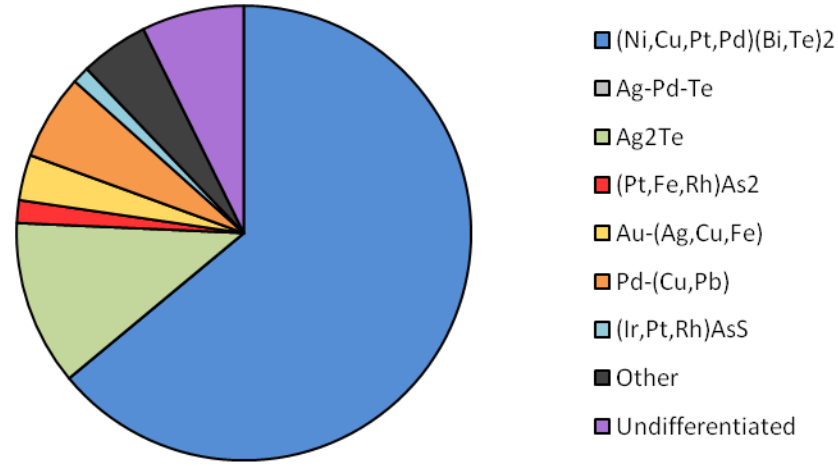


Fig: 4.15b) Northern and southern zone PGM by number

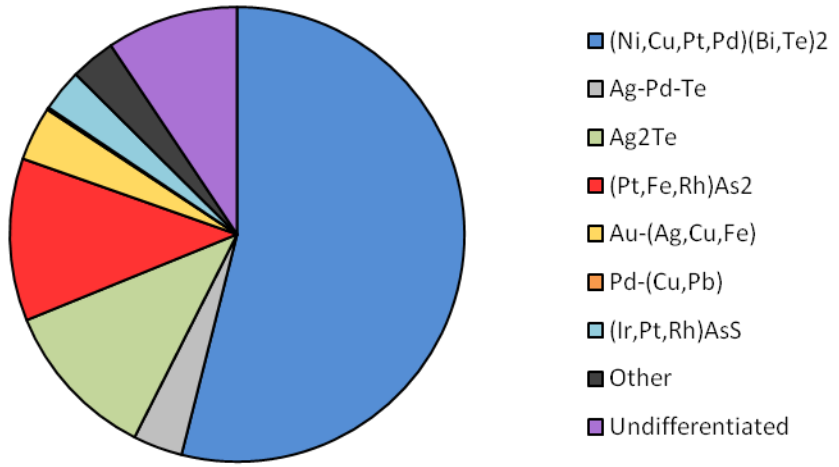


Fig: 4.15c) Central zone PGM by area

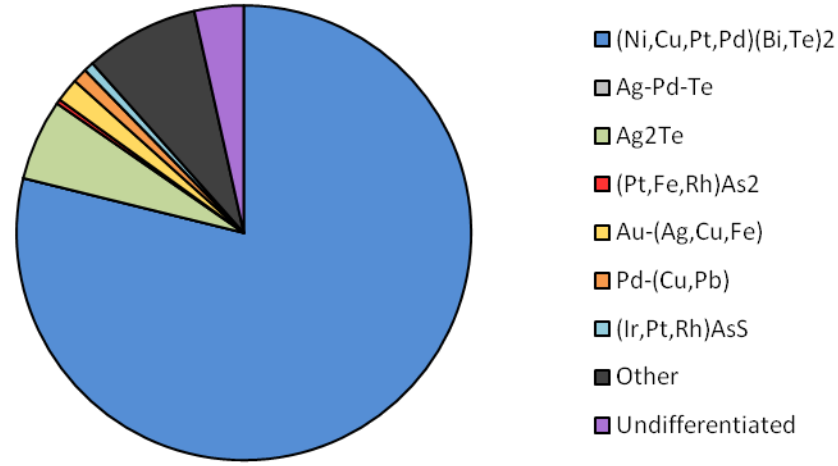


Fig: 4.15d) Northern and southern zone PGM by area

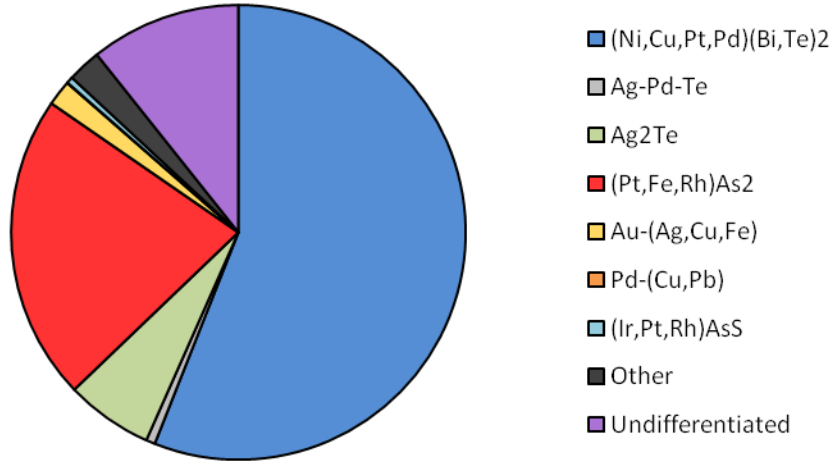


Figure 4.15: Pie charts showing the proportion of different PGM types in different zones of the intrusion; a) by the number of different PGM identified in the central zone, b) by the number of different PGM identified in the northern and southern zones, c) by the total area of PGM identified in the central zone, d) by the total area of PGM identified in the northern and southern zones.

4.7.2 Assemblage (i) PGE tellurides

Assemblage (i) comprising predominantly Pt-Pd-Ni-Fe tellurides with accessory Ag telluride, rare electrum and native Au, occurs in the central zone of the Mirabela intrusion within the Santa Rita ore zone in both boreholes studied (MBS604 and MBS605) and also within the sulphur-poor dunite in borehole MBS605 only (Fig. 4.14). This assemblage is present in samples PTSR01-07 (MBS604) and PTSR16-25 (MBS605).

Pt-Pd-Ni-Fe tellurides are predominantly associated with the BMS either appearing to be fully enclosed by the sulphides (Fig. 4.16A-C) or at the edge of the sulphides where they are also in contact with either a silicate, oxide or other sulphide phase (Fig. 4.16D-E). The PGM are associated with all of the sulphide phases present in the Santa Rita ore zone; pentlandite, chalcopyrite, pyrrhotite and pyrite. None of these PGM are spatially associated with chromite crystals, even in samples from the chromite-rich seam that is located midway through the Santa Rita ore zone in MBS604 which hosts both PGM assemblage (i) and the highest PGE contents in the investigated core (Pd >0.5 ppm, Pt >1 ppm) (Fig. 4.4a). These PGE tellurides display a variety of crystal forms including laths and tabular crystals (Fig. 4.16A, D-E) as well as rounded blebs (Fig. 4.16B). Where these tellurides occur within but near the edges of the BMS, they tend to be much more anhedral, with part of the PGM simply aligned along the edge of its host sulphide.

The chemistry of these Pt-Pd-Ni-Fe tellurides varies with Pt, Pd and Ni substituting for each other while minor amounts of Fe may substitute for Te (Table 4.3). As these elements readily substitute for each other in these PGM, Pt-Te, Pd-Te and Ni-Te phases and combinations thereof are all observed. Where present, Fe typically comprises <5 wt. % of these PGM. Quantitative analyses of these PGE tellurides show they have the empirical formula $(PtPdNi)(TeFe)_2$ (Table 4.3).

In the Santa Rita ore zone, the PGE tellurides associated with the BMS cover a wide range of sizes, although the vast majority of crystals have areas of between 1-16 μm^2. The largest telluride identified is 690 μm^2 while the smallest is <0.1 μm^2.

Silver tellurides are also identified with the PGE tellurides within the Santa Rita ore zone. These Ag tellurides are again associated with all of the types of BMS present. They tend to be more anhedral in shape than the PGE tellurides. A minority of the Ag tellurides observed

form thin veneers partially enveloping the PGE tellurides. The Ag tellurides are similar in size to the PGE tellurides with the majority of grains having areas of between 1-16 μm^2.

Other phases in assemblage (i) include electrum. The majority of these electrum grains have subhedral forms and fall within the same 1-16 μm^2 size range as the PGE and Ag tellurides. One electrum grain identified appears to be contained in olivine whereas the other six observed are associated with the BMS. One native Au grain and one Au-Cu alloy are also identified; both occurring within orthopyroxene.

4.7.3 Assemblage (ii) PGE tellurides and sperrylite

Assemblage (ii) comprising predominantly Pt-Pd-Ni-Cu-Fe tellurides and sperrylite with accessory Ag telluride, rare electrum and native Au grains, occurs in the northern and southern zones of the Mirabela intrusion within both the Santa Rita ore zone and the sulphur-poor dunite (Fig. 4.14). This assemblage is present in samples PTSR28-37 (MBS209) and PTSR40-49 (MBS158) in the northern zone as well as PTSR51-60 (MBS565) and PTSR63-72 (MBS569) in the southern zone.

The most common PGM identified within these samples are Pt-Pd-Ni-Fe tellurides. These tellurides are identical to those identified within assemblage (i) noted above and so their mineral associations and chemistry are not discussed further here. Pt-Te±Fe grains, unlike the other PGE tellurides, all consistently exhibit euhedral lath crystal forms (Fig. 4.16E).

In the Santa Rita ore zone, the size range that these tellurides encompass is large with sizes from 0.5-100 μm^2 consistently recorded, however, the vast majority fall between 1-16 μm^2. Only 18 PGM are larger than 100 μm^2 with the largest identified at ~640 μm^2.

Copper tellurides are also observed in the northern and southern zones of the intrusion. Copper may also substitute for Ni, Pt and Pd in the tellurides noted above, however, only one Cu-bearing telluride has been analysed quantitatively giving a formula of CuTe as opposed to $CuTe_2$ and so appears to be a unique mineral different from the other Pt-Pd-Ni tellurides observed. Where present, Cu-bearing telluride PGM (or pure CuTe) have similar characteristics in terms of crystal form and mineral associations to the Pt-Pd-Ni tellurides.

Sperrylite ($PtAs_2$, determined by quantitative analyses; Table 4.3) crystals are relatively abundant and typically range in size from ~1-450 μm^2 with smaller crystals much more

common than larger ones. The largest sperrylite identified falls outside of this range and is 1.5 mm^2. The majority of these grains are anhedral or subhedral with few euhedral sperrylite crystals identified. They are predominantly situated within or closely associated with the BMS (Fig. 4.16F-G). Conversely, sperrylite is very rarely identified within silicate and oxide phases.

PGM that belong to the hollingworthite-irarsite-platarsite solid solution series ([RhIrPt]AsS) have also been identified (Fig. 4.16H). Ten are Ir-dominant, all of which are Pt-bearing. Five are Pt-dominant, four of which are Ir-bearing and one is Rh-bearing. The remaining three are Rh-dominant and are slightly more complex with the presence of more than two PGE and the addition of Os (Rh-Ir-Pt-As-S, Rh-Pt-Os-As-S, Rh-Pt-Os-Ir-As-S). The size range of these PGM is relatively restricted at ~0.5-7.5 μm^2 with only one grain larger than his range identified at 14 μm^2. These Ir-Rh-Pt-bearing PGM exhibit a variety of crystal forms from anhedral to subhedral with some even exhibiting distinct tabular forms. The majority of these PGM are located within the BMS with only four identified in silicates; two of which retain a close association with sulphides.

Five Pt-S minerals have been identified which are extremely variable in size from ~4-110 μm^2. They exhibit subhedral to euhedral crystal forms including three which are lath shaped. Three are located in BMS while the remaining two are found in a silicate and oxide phase, respectively. Rare PGE-bearing alloys have also been identified which include one of each of the following; Pd-Cu, Ru-Os, Pt-Fe and Pt-Ir. These PGE-alloys are relatively small (<6 μm^2) and are all identified within BMS.

Accessory Ag and Au phases are again common in the northern and southern zones of the Mirabela intrusion. Two types of silver tellurides occur, Ag-Te and Ag-Pd-Te. The majority of the pure Ag-Te crystals identified range in size from ~1-20 μm^2. The larger sized grains are much rarer with only nine crystals larger than 20 μm^2 observed with the largest at ~250 μm^2. These tellurides tend to be anhedral with a minority exhibiting lath shapes or some subhedral form. They are predominantly observed in BMS and more rarely in silicates. Out of the 16 Ag-Te crystals identified within silicate phases, half retain an association and contact with BMS. Quantitative analyses of these Ag tellurides show they have the empirical formula Ag_2Te (hessite) (Table 4.3).

The Ag-Pd-Te grains exhibit the same behaviour and crystal forms as the pure silver tellurides although they are fewer in number. They are also slightly smaller with the majority of the Ag-Pd-Te minerals falling between ~1-10 μm^2. Some larger grains do occur up to ~30 μm^2 with the largest observed at ~70 μm^2 which is considerably isolated from the rest of the size range.

The Au-bearing alloys identified consist of native Au, electrum, Au-Cu, Au-Ag-Cu, and Au-Ag-Fe. These Au-bearing alloys have a general size range of ~1-10 μm^2. Some larger crystals do occur up to ~126 μm^2. The majority of these alloys are anhedral although a few can be considered subhedral. These alloys predominantly occur within the BMS and very rarely in silicates and oxides where they maintain some association and contact with the BMS.

4.7.4 BMS stringers and associated PGM

In the Santa Rita ore zone, BMS (and rarely magnetite) stringers may host both Pt-Pd-Ni tellurides and more surprisingly sperrylite, although the latter are only observed in the northern and southern zones which host PGM assemblage (ii). These PGM may occur near interstitial composite sulphides which act as the source of these sulphide stringers (Fig. 4.17A, E). In these cases, the PGM have a direct or close association with the interstitial composite sulphide. Alternatively, PGM are also identified in stringers where they are very distal from the interstitial sulphide source (Fig. 4.17B-C, F). Rarely, these PGM are also identified within magnetite stringers (Fig. 4.17D) which often retain some connection to the sulphides.

On occasion, PGM may only exhibit a tentative association with their host sulphide stringer (Fig. 4.17G). In a small number of cases, these sulphide stringers appear stretched out in such a way that small sections of sulphide can be observed in a boudinage-type texture leaving short (~ 5 μm) veinlet shaped PGM within the silicates with only a tentative association with BMS observed in two dimensions (Fig. 4.17H).

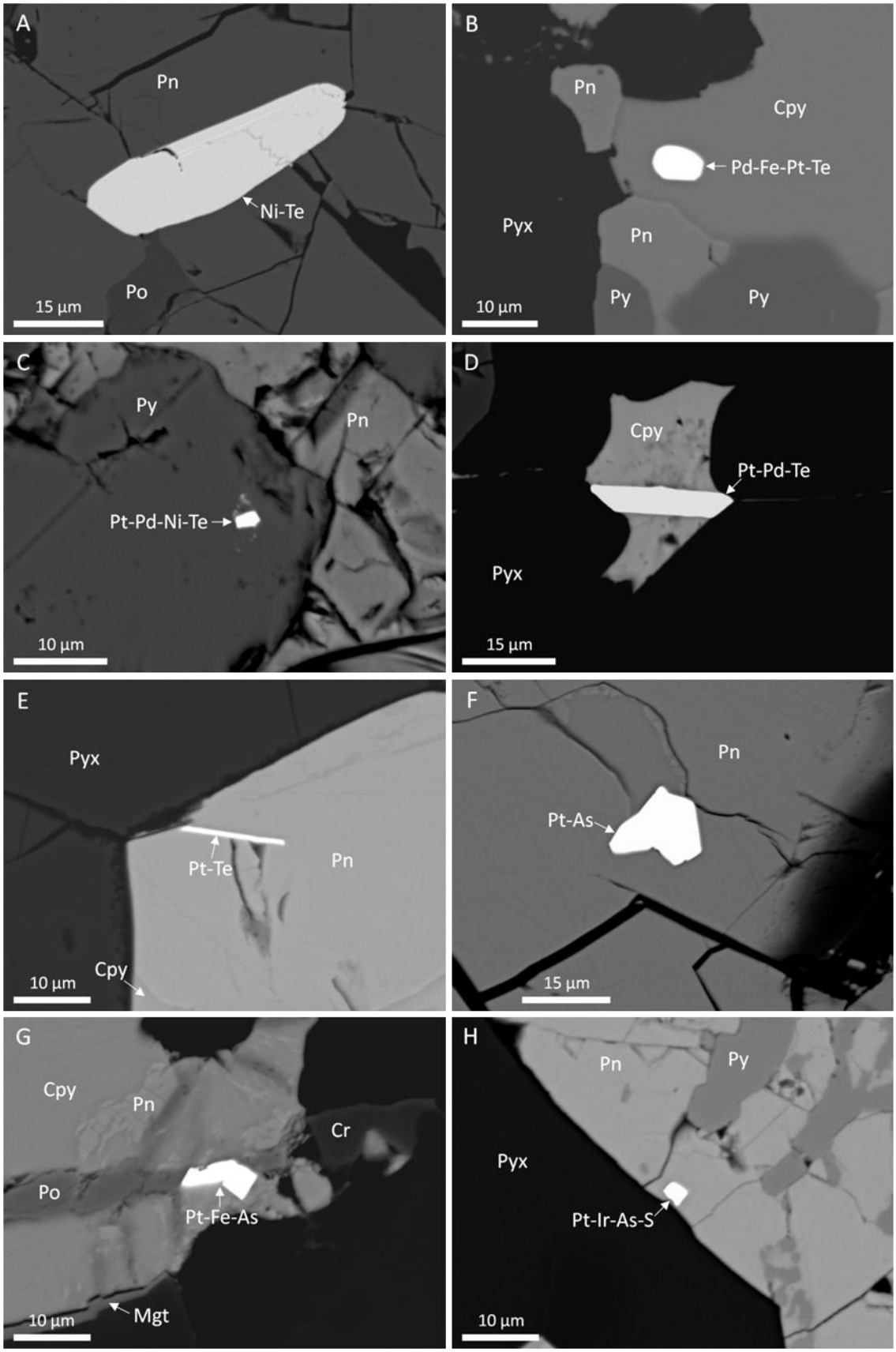


Figure 4.16: Back-scattered electron images of the typical PGM observed from assemblage (i) and (ii). A) Partially rounded Ni-Te lath in pentlandite (Pn) with associated pyrrhotite (Po). B) Rounded Pd-Fe-Pt-Te in chalcopyrite (Cpy) with associated pyrite (Py) and Pn. C) Pt-Pd-Ni-Te in Py. D) Pt-Pd-Te lath in Cpy. E) Thin Pt-Te lath in Pn. F) Sperrylite ($PtAs_2$) in Pn. G) Sperrylite+Fe in BMS mix. H) Platarsite+Ir in Pn.

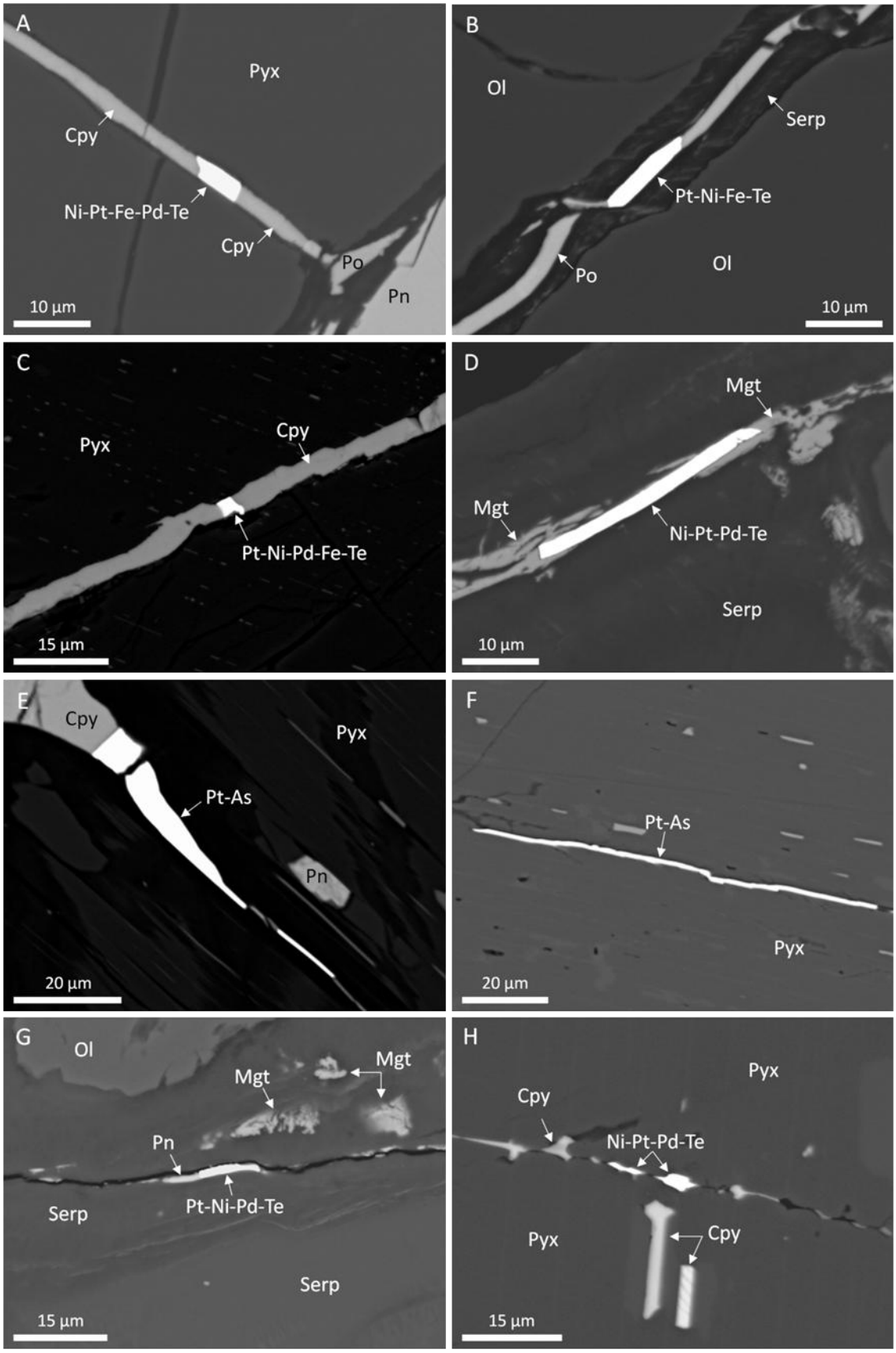


Figure 4.17: Back-scattered electron images of BMS and magnetite stringers and their associated PGM. A) Ni-Pt-Fe-Pd-Te within a chalcopyrite (Cpy) stringer originating from an interstitial composite BMS. B) Pt-Ni-Fe-Te within a pyrrhotite (Po) stringer enveloped by serpentine (Serp). C) Pt-Ni-Pd-Fe-Te within a distal Cpy stringer. D) Ni-Pt-Pd-Te within a magnetite (Mgt) stringer. E) Sperrylite ($PtAs_2$) within a Cpy stringer originating from interstitial composite BMS. F) Sperrylite within a distal Cpy stringer. G) Pt-Ni-Pd-Te displaying a tentative association with BMS. H) Cpy stringer and associated PGM displaying boudinage-type texture.

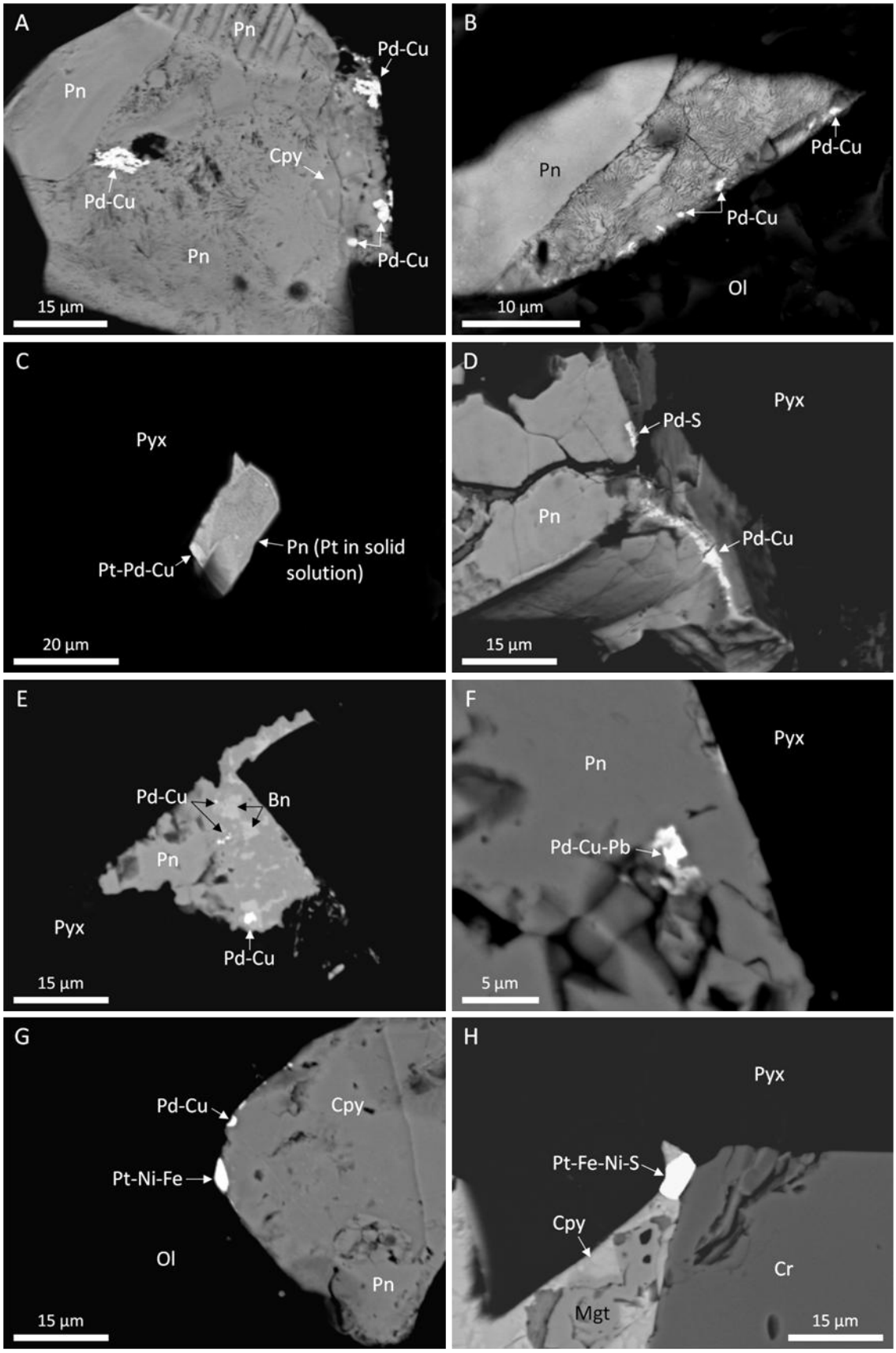


Figure 4.18: Back-scattered electron images of the typical PGM observed from Pd alloy assemblage (iii) in the sulphur-poor dunite zone (MBS604 - central zone only). A) Pd-Cu alloys within pentlandite (Pn) and minor chalcopyrite (Cpy) displaying micro symplectite-like textures. B) Pd-Cu alloys within Pn micro symplectite-like texture. C) Pt-Pd-Cu within Pn which has high concentrations of Pt in solid solution. D) Pd-Cu and Pd-S within Pn. E) Pd-Cu alloys within Pn with associated bornite (Bn). F) Pd-Cu-Pb alloy within Pn. G) Pd-Cu and Pt-Ni-Fe alloys within Cpy. H) Pt-Fe-Ni-S within Cpy with associated magnetite (Mgt).

4.7.5 Assemblage (iii) Pd alloys

Assemblage (iii), comprising predominantly Pd alloys with minor PGE-bearing arsenides and sulphides occurs in the central zone of the Mirabela intrusion in the sulphur-poor dunite in one borehole only (Fig. 4.14) in samples PTSR08-PTSR11 (MBS604). In this assemblage, Pd alloys are the most common PGM identified and are predominantly Pd-Cu±Pb alloys (Fig. 4.18A-G). Other alloy phases include one Pd-Pb-Ag-Cu alloy and one Pt-Fe-Ni alloy (Fig. 4.18G).

Other minor PGE-bearing minerals observed include two sperrylites and one Pt-Pd-Te-As grain, although the latter may be the result of two small PGM being analysed as a composite crystal. PGE-bearing sulphides are also identified including several Pd-Cu-Fe sulphides and one Pd sulphide. One unusual (Ir-Os-Pt-Ru-Cu)-As-S crystal is also observed. Where these Pd alloys are present, telluride minerals are rare (Table 4.2). Given the 29 PGM identified in these samples, only two are tellurides (Ag-Pd-Te, Pt-Pd-Te).

These PGM are associated only with pentlandite and chalcopyrite as these are the only two sulphide phases present in this dunite zone. PGM are found in both within what appear to be unaltered fresh magmatic sulphides (Fig. 4.18D-H) and sulphides exhibiting micro-scale symplectite-like textures intergrown with silicate material (Fig. 4.18A-B). Where present in these sulphides showing symplectite-like textures, the PGM are situated at the crystal edges and exhibit anhedral crystal forms. In contrast, PGM situated within unaltered sulphides usually have more subhedral crystal forms.

4.7.6 PGM abundance and size distribution

The size distribution of all the PGM identified in the Mirabela intrusion has been calculated and plotted as bar charts using different interval sizes (μm^2). Figure 4.19a) displays the proportion of PGM per size interval calculated by the number of PGM identified in each size interval whereas Figure 4.19b) displays the proportion of PGM per size interval calculated by the total area of PGM identified in each size interval. These graphs do not differentiate between the different types of PGM observed. However, they do show that despite the fact that the majority of PGM calculated by number (>70%) fall between the size range of 1-15.9 μm^2 (Fig. 4.19a), they account only for ~42 % of the total PGM area observed (Fig. 4.19b). Conversely, almost 60% of the total PGM area observed is accounted for by PGM larger than

15.9 μm^2 (Fig. 4.19b). They also show that while PGM in the size range >324 μm^2 are rare (Fig. 4.19a), they account for a significant proportion (~9%) of the total area of PGM observed (Fig. 4.19b).

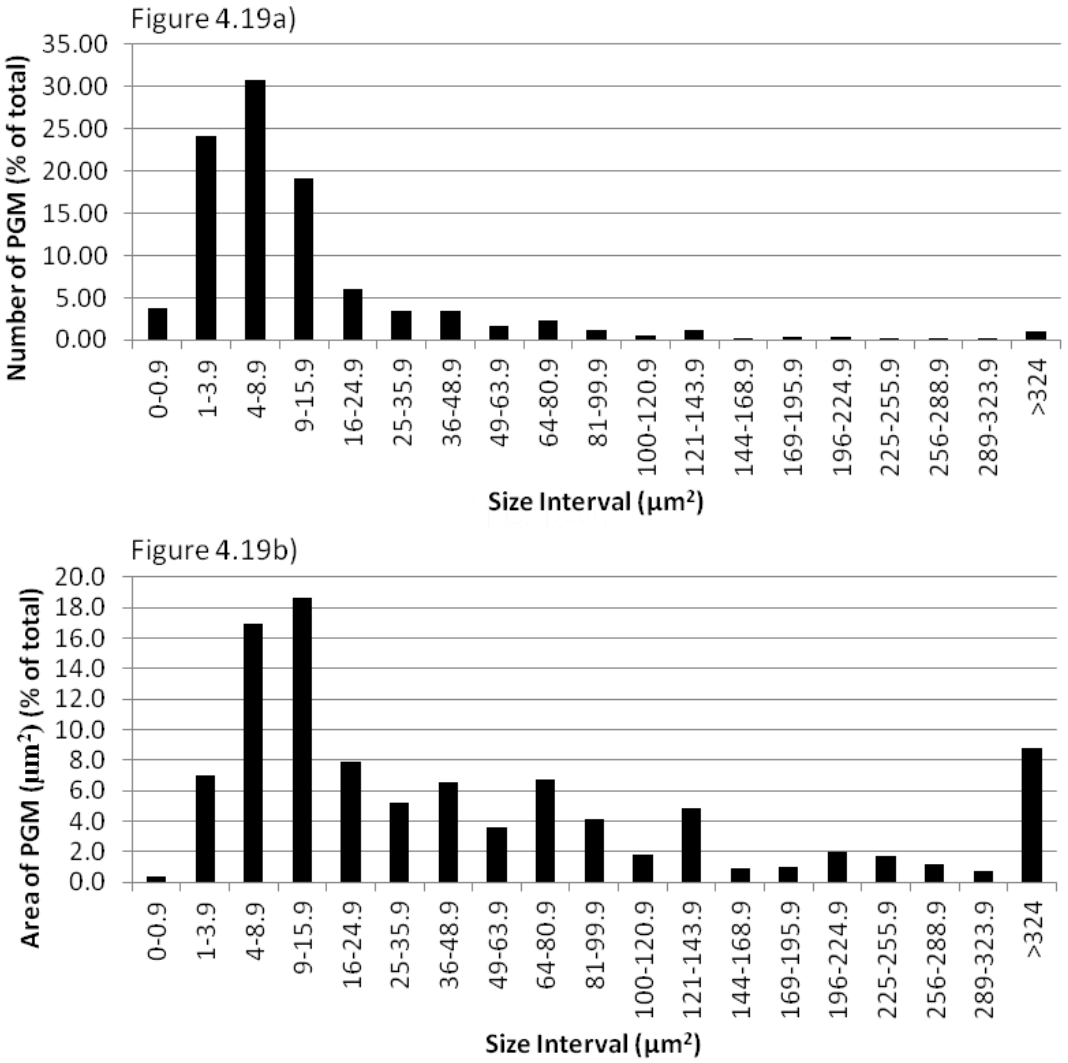


Figure 4.19: PGM size distribution graphs showing; a) the proportion of PGM per interval size (μm^2) calculated by the number of PGM per interval size and b) the proportion of PGM per interval size (μm^2) calculated by the total area of PGM per interval size.

There is a difference in both the abundance and size of PGM in the Santa Rita ore zone compared to those observed in the underlying sulphur-poor dunite regardless of which PGM assemblage is present. In the Santa Rita ore zone, PGM tend to be larger, typically falling within the size range of 1-15.9 μm^2 and are more abundant with ~17 PGM identified per sample (thin section) studied (calculated from Table 4.2) (Fig. 4.20). In the underlying sulphur-poor dunite however, the PGM are much smaller, typically <8.9 μm^2 and less abundant with only ~5 PGM identified per sample studied (calculated from Table 4.2) (Fig. 4.20).

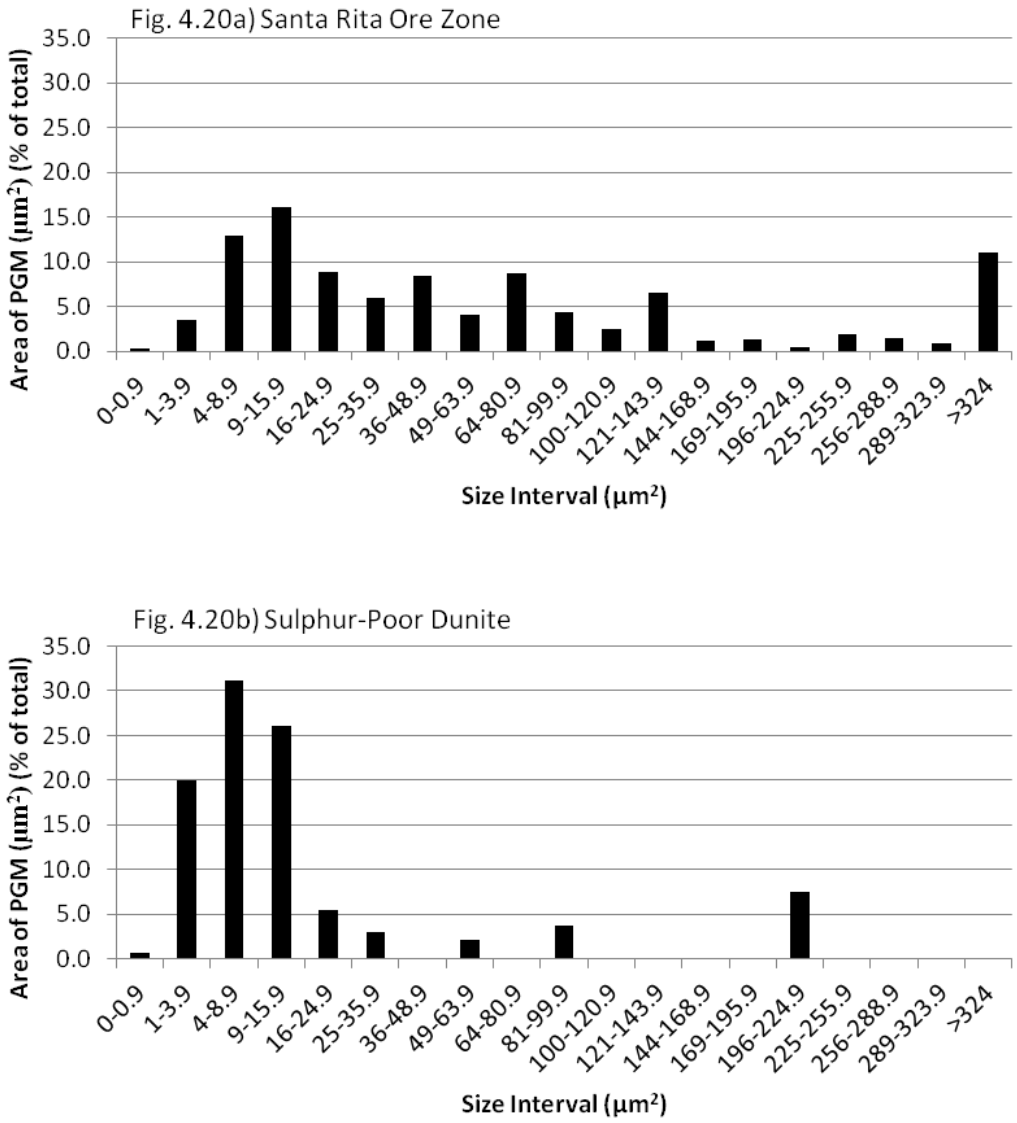


Fig. 4.20: PGM size distribution graphs showing; a) the proportion of PGM per interval size (μm^2) calculated by the total area of PGM per interval size for the Santa Rita ore zone and b) the proportion of PGM per interval size (μm^2) calculated by the total area of PGM per interval size for the sulphur-poor dunite zone.

4.8 Laser Ablation-ICP-MS

PGE and semimetal contents in solid solution in BMS have been determined using LA-ICP-MS (Table 4.4 - Santa Rita ore zone, Table 4.5 - sulphur-poor dunite zone; full data in Appendix I). Two consistent and distinct patterns have been identified which consist of PGE-poor BMS in the Santa Rita sulphide ore zone and very PGE-rich BMS in the underlying sulphur-poor dunite footwall. In the Santa Rita zone, all of the BMS phases identified have been analysed including dominant pentlandite as well as pyrrhotite, pyrite and chalcopyrite. However, in the sulphur-poor dunite, predominantly pentlandite and chalcopyrite have been identified and therefore analysed although two pyrite crystals have also been successfully

analysed. In many cases, only composite sulphides can be analysed in this zone given the low sulphur content of the dunite and the small size of the individual sulphides. Therefore it is sometimes impossible to split one sulphide phase from another. In these cases the analyses are reported as BMS mixes (most commonly a mix of pentlandite and chalcopyrite, e.g., Pn-Cpy; Table 4.5). These composite sulphides have been ignored in the Santa Rita ore zone for clarity, but have been included for the sulphur-poor dunite samples given their significant PGE content and the rarity of relatively large mono-phase sulphides in this zone. In order to show that these analyses represent true solid solution of PGE, analyses which indicated higher than average Te or As concentrations coupled with anomalously high PGE have been discounted from the data set as it is likely that PGM (predominantly Pt-Pd-Ni-Cu-Fe-Te or Pt-As) have been intercepted by the laser trace in these cases. Likewise, analyses where the time resolved spectra (TRA) have clearly indicated the presence of PGM or PGM micro-inclusions have also been discounted.

4.8.1 Santa Rita ore zone

In the Santa Rita ore zone, the BMS host very low concentrations of PGE in solid solution. Histograms showing the concentrations of PGE and Co (where these are significant) in pentlandite, pyrrhotite and pyrite from the Santa Rita ore zone against the number of analyses completed are given in Figure 4.21. These graphs display the range of PGE concentrations observed and should be used in conjunction with the average PGE concentrations in Table 4.4. In both chalcopyrite and pyrrhotite, the average concentrations of all 6 PGE individually are <1 ppm. The highest Rh and Pt concentrations recorded in any sulphide phase are 1.1 ppm and 1.6 ppm, respectively. Although several relatively high concentrations of Os do occur in some of the BMS analysed (up to 4.5 ppm), these concentrations do not occur regularly enough to influence the low average of <1 ppm. Pentlandite is the principal host of the PGE with Pd concentrations of up to 13 ppm observed and an average value of 2.3 ppm; pentlandite also hosts low but significant concentrations of Os and Ru (Fig. 4.21a-c and Fig. 4.22a-b). More unusual is the identification of Os and Ru in pyrite with concentrations of up to 2.2 ppm Os and 3.7 ppm Ru recorded, with average values 0.6 ppm and 0.8 ppm, respectively (Fig. 4.21h-i and Fig. 4.22a). Furthermore, pyrite also consistently hosts significant concentrations of cobalt (0.8-3.2 wt. %) (Fig. 4.21g).

Mineral Analysed		Element	^{59}Co	^{61}Ni	^{65}Cu	^{189}Os	^{193}Ir	^{99}Ru	^{103}Rh	^{195}Pt	^{105}Pd	^{197}Au	^{75}As	^{209}Bi	^{121}Sb	^{125}Te
			ppm	wt. %	wt. %	ppm	ppm	ppm*	ppm*	ppm	ppm	ppm	ppm	ppm	ppm	ppm
Sulphides from the Santa Rita ore zone																
Cpy	*n=48*	Ave	201.22	1.83	26.78	0.03	<0.02	0.14	<0.10	0.05	0.27	0.02	28.30	0.21	0.09	2.22
		Min	0.09	0.00	15.69	<0.02	<0.02	<0.05	<0.10	<0.02	<0.20	<0.02	11.09	0.01	<0.01	<0.05
		Max	1887.00	10.37	34.08	0.80	0.03	0.63	0.10	0.58	1.58	0.14	50.22	1.64	0.32	18.50
Pn	*n=95*	Ave	3026.20	26.76	0.37	0.52	0.09	0.91	0.11	0.03	2.31	0.02	17.71	1.23	0.15	14.08
		Min	670.00	18.03	0.00	<0.02	<0.02	<0.05	<0.10	<0.02	<0.20	<0.02	4.89	0.00	<0.01	0.27
		Max	7313.00	41.92	2.71	4.49	0.91	6.36	1.13	0.73	12.97	0.26	35.59	25.51	2.20	58.28
Po	*n=36*	Ave	65.57	0.63	0.08	0.55	0.11	0.58	0.04	0.07	0.01	0.02	14.26	0.27	0.07	1.31
		Min	1.29	0.00	0.00	0.00	<0.02	<0.05	<0.10	<0.02	<0.20	<0.02	0.30	0.05	<0.01	<0.05
		Max	615.20	2.89	2.26	3.80	0.90	5.73	1.03	1.58	0.52	0.32	25.33	1.40	0.16	5.21
Py	*n=38*	Ave	16671.29	1.06	0.33	0.61	0.18	0.78	0.14	0.03	0.12	0.03	8.49	5.05	0.10	4.47
		Min	8569.00	0.02	0.00	<0.02	<0.02	<0.05	<0.10	<0.02	<0.20	<0.02	1.11	0.09	0.02	0.06
		Max	32030.00	8.38	2.45	2.16	1.00	3.68	0.77	0.14	1.52	0.17	22.41	18.24	0.90	27.16

Table 4.4: Laser ablation ICP-MS results for chalcopyrite, pentlandite, pyrrhotite and pyrite from the Santa Rita ore zone.

Cpy = chalcopyrite, Pn = pentlandite, Po = pyrrhotite, Py = pyrite, *n* = number of minerals analysed, Ave = mean, Min = minimum value, Max = maximum value.

Mineral Analysed		Element	^{59}Co	^{61}Ni	^{65}Cu	^{189}Os	^{193}Ir	^{99}Ru	^{103}Rh	^{195}Pt	^{105}Pd	^{197}Au	^{75}As	^{209}Bi	^{121}Sb	^{125}Te
			ppm	wt. %	wt. %	ppm	ppm	ppm*	ppm*	ppm	ppm	ppm	ppm	ppm	ppm	ppm
Sulphides from the sulphur-poor dunite zone																
Cpy	*n=36*	Ave	515.71	2.52	25.27	<0.02	0.07	0.06	<0.10	0.08	8.81	0.13	28.70	0.02	0.08	0.40
		Min	18.84	0.28	19.73	0.00	<0.02	<0.05	<0.10	<0.02	0.52	0.03	25.40	0.01	0.03	<0.05
		Max	1346.00	6.08	32.60	0.00	0.12	0.12	<0.10	0.24	15.90	0.24	31.71	0.02	0.11	0.60
Pn	*n=27*	Ave	5913.33	24.60	0.73	4.22	1.74	6.28	4.33	4.33	42.47	0.14	17.29	0.78	0.23	3.26
		Min	2416.00	15.84	0.01	<0.02	<0.02	<0.05	<0.10	<0.02	3.88	<0.02	1.79	0.03	0.02	<0.05
		Max	9761.00	31.82	2.54	38.25	28.69	59.13	36.15	28.89	254.30	1.61	44.85	5.10	2.77	20.90
Pn-Cpy Mix	*n=8*	Ave	5561.50	22.92	6.95	1.16	0.57	3.33	2.21	2.57	42.42	0.14	15.43	1.67	0.17	2.87
		Min	1367.00	8.25	1.19	<0.02	<0.02	<0.05	<0.10	<0.02	0.80	<0.02	1.26	0.02	0.04	0.16
		Max	8910.00	33.95	18.45	5.18	2.61	11.48	8.82	14.70	124.89	0.37	24.07	5.83	0.58	11.13
Py	*n=2*	Ave	10915.00	0.43	0.65	3.52	1.57	2.80	<0.10	<0.02	0.37	<0.02	8.79	2.23	0.08	1.31
		Min	9920.00	0.19	0.39	0.96	0.67	<0.05	<0.10	<0.02	0.26	<0.02	4.76	1.89	0.08	0.58
		Max	11910.00	0.66	0.92	6.08	2.48	5.61	<0.10	<0.02	0.49	<0.02	12.81	2.57	0.09	2.05
Pn-Py Mix	*n=1*	n/a	5750.00	22.55	0.38	0.30	27.87	1.37	0.68	12.50	570.40	0.05	32.24	2.32	0.04	<0.05
Pn-Py-Cpy Mix	*n=1*	n/a	3245.00	13.70	8.96	0.04	18.68	1.63	<0.10	6.20	371.70	0.20	48.18	0.54	0.04	0.13

Table 4.5: Laser ablation ICP-MS results for chalcopyrite, pentlandite, pyrite and BMS mixes from the sulphur-poor dunite.

Cpy = chalcopyrite, Pn = pentlandite, Py = pyrite, *n* = number of minerals analysed, Ave = mean, Min = minimum value, Max = maximum value.

4.8.2 Sulphur-poor dunite

The BMS analysed in the sulphur-poor dunite samples host very high concentrations of PGE. In this zone, chalcopyrite is the least PGE-enriched sulphide considering that pyrrhotite is absent in these samples and has therefore not been analysed. Only three pure chalcopyrite and two pyrite crystals have been analysed due to their small size and rarity (the latter refers to pyrite only), therefore, a possible sampling effect should be considered when interpreting the following results. Chalcopyrite contains low average concentrations (<1 ppm) of Os, Ir, Ru, Rh and Pt, but significant average concentrations of Pd 8.8 ppm.

One of the pyrite crystals also contains significant concentrations of PGE; 6 ppm Os, 2.5 ppm Ir and 5.6 ppm Ru while being poor in Rh, Pt and Pd. It should be noted that the other pyrite crystal analysed is PGE-poor with individual PGE concentrations all <1 ppm.

Pentlandite is the most PGE-enriched sulphide in these samples exhibiting high average concentrations of all six PGE; 4.2 ppm Os, 1.7 ppm Ir, 6.3 ppm Ru, 4.3 ppm Rh, 4.3 ppm Pt and 42.5 ppm Pd (Fig. 4.22c-d). As in the Santa Rita ore zone, Pd is the most enriched PGE in these sulphides with concentrations of up to 254 ppm identified in pentlandite. The highest concentrations identified for the other PGE are as follows; 38.3 ppm Os, 28.7 ppm Ir, 59.1 ppm Ru and 36.1 ppm Rh. The most spectacular result of these laser analyses is the identification of Pt in BMS in a non-PGE reef setting, with concentrations of up to 28.9 ppm identified (Fig. 4.22d).

Average concentrations of PGE in Pn-Cpy BMS mixes are also relatively high with 1.2 ppm Os, 3.3 ppm Ru, 2.2 ppm Rh, 2.6 ppm Pt and 42.4 ppm Pd with ranges given in Table 4.5. However, these sulphides are Ir-poor with an average concentration of only 0.6 ppm. The highest Pd concentrations identified overall are 371 ppm and 570 ppm occurring in two other BMS mixes consisting of pentlandite-pyrite and pentlandite-pyrite-chalcopyrite, respectively. Although not every sulphide analysed from the S-poor dunite zone contains high levels of PGE in solid solution, the average results and the consistency as well as abundance of high PGE concentrations in the sulphides suggests that these results are not simply anomalous or an artefact of sampling.

There does not appear to be any variation laterally from the north to the south of the intrusion in terms of PGE in solid solution in the BMS. The main variation appears to be purely vertically and associated with the change from the Santa Rita sulphide ore zone into the underlying sulphur-poor dunite.

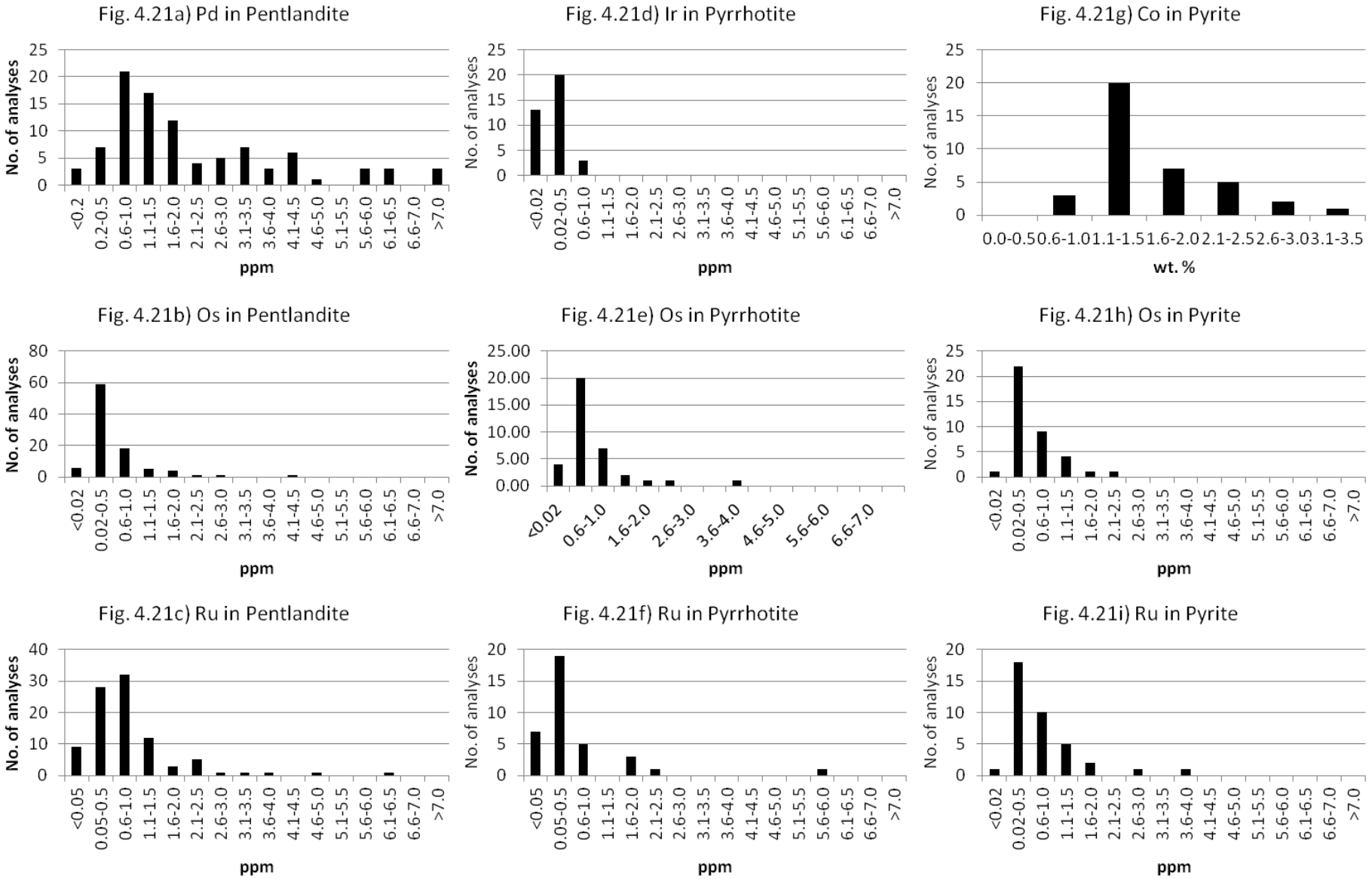


Figure 4.21: Histograms showing the concentrations of PGE and Co (where significant) in pentlandite, pyrrhotite and pyrite from the Santa Rita ore zone against the number of analyses completed.

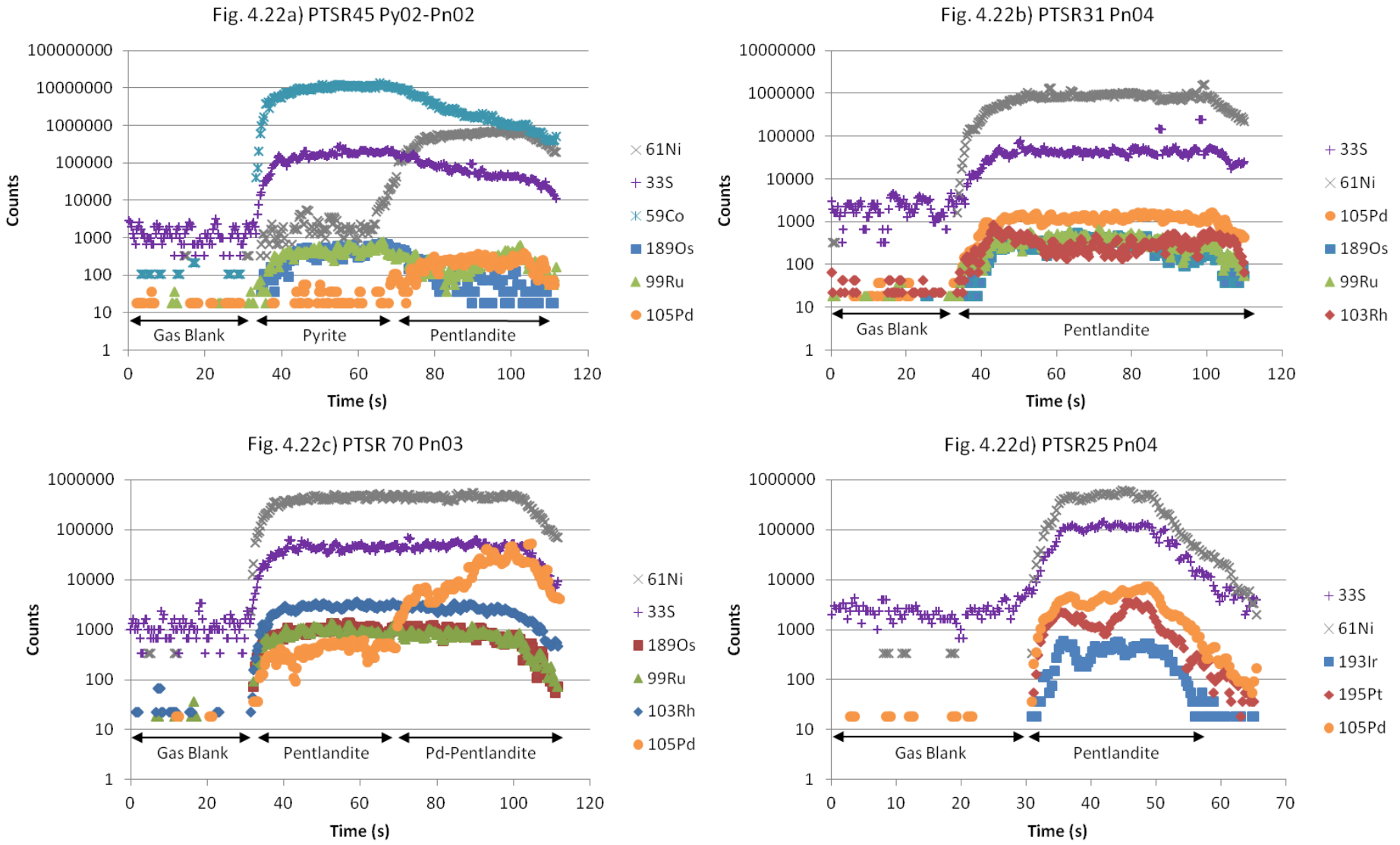


Figure 4.22: Time (s) versus counts (per second) spectra for laser ablation ICP-MS analyses of the Mirabela BMS; a) pyrite-pentlandite (Py-Pn) from the Santa Rita ore zone with pyrite hosting significant Co, Os and Ru, b) Pn from the Santa Rita ore zone hosting significant Os, Ru, Rh and Pd, c) Pn from the sulphur-poor dunite hosting high concentrations of Os, Ru, Rh and Pd, and d) Pn from the sulphur-poor dunite hosting high concentrations of Ir, Pt and Pd.

4.9 Discussion

4.9.1 Major and trace element geochemistry

Major element Harker diagrams (Fig. 4.6; Fig. 4.7) combined with the igneous stratigraphy of the Mirabela intrusion suggest that the main controlling factor on the formation of the complex is fractional crystallisation. However, variations in the geochemical borehole profiles (Fig. 4.4a-f) suggest that this is not a closed system. Fluctuating chromite concentrations suggest that further magmatic pulses occurred or conditions within the magma chamber were changing in a way that brought chromite onto the liquidus.

REE patterns (Fig. 4.9a-b) also suggest that pulses of magma may have been introduced at different stages during fractional crystallisation with fluctuations in the amount of LREE enrichment observed (although the general change in REE content with depth is controlled by the presence/absence of olivine). The lowermost dunites sampled display LREE enrichment, however, the overlying harzburgite samples exhibit relatively flat profiles. Above the harzburgite, orthopyroxenite and olivine orthopyroxenite samples once again show LREE enrichment similar to those patterns displayed by the dunite below. These are then overlain by websterite and gabbronorite which show relatively flat profiles. This change in LREE enrichment may be suggesting that at least two major pulses of magmatism were involved in the formation of the Mirabela intrusion, each accompanied by an increase in LREE.

The sharp zones in some of the major element borehole profiles (Fig. 4.8a-f) also observed in the Harker diagrams (Fig. 4.6) defined by samples exhibiting low MgO, Fe_2O_3, MnO and high Al_2O_3 and NaO_2 with variable CaO and TiO_2 content can be explained by the interception in these boreholes of later cross-cutting felsic pegmatitic and dolerite dykes which are also observed in the drill core studied.

Rare earth and trace element data collected by ActLabs has been used to determine the role of magma mixing and crustal contamination in the genesis of the Mirabela intrusion and the Santa Rita sulphide ore zone. The role of magma mixing as suggested by Barnes *et al.* 2011 for the genesis of the Mirabela intrusion and the associated Santa Rita ore zone must be assessed. The close grouping of the Mirabela intrusives displayed on REE ratio diagrams (Fig. 4.10a-b) demonstrates that there are no significant changes in La/Sm or Ce/Yb ratios over the different lithologies analysed. Furthermore, there are no step changes in La/Sm ratios plotted against depth associated with changes in lithology (Fig. 4.11). These

observations suggest the Mirabela intrusion is the result of the fractional crystallisation of one magma. However, using this data it would be difficult to determine if magma mixing has occurred between two compositionally similar magmas.

As noted in Barnes *et al.* (2011), there are no reliable chilled margins preserved at Mirabela and therefore no compositions for the two proposed end-member magmas. As a result, studying the mixing between these proposed magmas is impossible using whole-rock chemistry and any minor change in chemistry due to magma mixing cannot be distinguished from fractional crystallisation trends. There is, however, very little textural evidence for magma mixing with only very minor resorption textures and post-cumulus mineral growth present. Microprobe analyses of these overgrowths and determination of rim-core trace element ratios for the cumulus minerals may provide further insight into the genesis of the intrusion regarding magma mixing, however, these analyses were beyond the scope of this thesis. Although Barnes *et al.* (2011) provide compelling arguments that the Santa Rita ore zone could not have formed by closed system fractionation (also evidenced by the reoccurrence of cumulus chromite and olivine in the harzburgite and orthopyroxenite units and Fig. 4.9a-b), no consideration is given to open system fractionation utilising only one magma source, possibly from a deep seated staging chamber.

If crustal contamination has occurred, one would expect that the as the Mirabela sequence evolved from dunite to gabbronorite, their chemical signatures should migrate towards that of the country rocks represented by the TTG suites analysed by Pinho *et al.* (2013). However, this migration is not observed on plots of Rb/Sr-Sr, Sm/Nd-Nd, Ti-Zr, and P_2O_5-Zr (Fig. 4.10 c-f). Instead, the two data sets form two separate groups and in some cases, the individual data sets appear to trend parallel to each other, indicating that no crustal contamination has occurred. There is also no difference in these plots when comparing the intrusion margins (northern and southern zone boreholes) to the central zone, which might be expected if the intrusion margins have preferentially experience a degree of crustal contamination.

4.9.2 Pt-Pd tellurides in layered complexes

The most abundant PGM observed in this study are Pt-Pd-Ni-Fe tellurides. Pt-Pd-Bi tellurides are commonly described from other layered intrusions. For example, michenerite (PdBiTe) is the most common Pd-bearing PGM in Sudbury and moncheite ($PtTe_2$) is the most

common Pt-bearing PGM in the As-poor North Range at Sudbury (Farrow and Lightfoot, 2002). Amongst the great variety of the PGM recorded from the Bushveld Complex, Pt-Pd tellurides are commonly recorded (e.g., Kinloch, 1982) comprising 6.5% to 33.5% of the PGM in the Merensky reef (Cawthorn *et al.*, 2002). Analysis of Pt-Pd tellurides (moncheite) from Lac des Iles and Stillwater show that they have a low Ni content, generally less than 0.25 wt. % while Pd content is also very low (0.08 wt. % and not determined, respectively) (Cabri, 2002). Pt-Pd tellurides that host high Ni contents appear to be much rarer with these types of PGM only identified recently in the Sakatti Ni-Cu-PGE deposit, Finland (Brownscombe *et al.*, 2013) and in the Mirabela intrusion as demonstrated by this study.

4.9.3 Formation of Pt-Pd-Ni-Fe tellurides

Pt-Pd-Ni-Fe tellurides are predominantly associated with the BMS, either appearing to be fully enclosed by the sulphide (Fig. 4.16A-C) or occurring at the edge of the sulphide where they are also in contact with silicates, oxides or other sulphide phases (Fig. 4.16D-E). This close association indicates that these PGM have likely formed via a process of exsolution from their host sulphides during sub-solidus cooling. Conversely, if these PGM were found mostly within silicates and oxides, one could speculate that these PGM had crystallised early, directly from an immiscible sulphide liquid and have subsequently become enclosed within these later crystallising silicates and oxides. Furthermore, the lath-like and rounded shapes of these PGM (Fig. 4.16A-E) are also typical of exsolution (Peregoedova *et al.*, 2004). It is noted, however, that when these PGM are identified towards and in contact with the edge of their host BMS, the sulphide crystal shape limits the formation of the PGM. As such, in these cases it appears that the PGM deviate from their preferred exsolution forms (rounded and lath shaped) and are forced to follow the same shape or boundary outline of their host sulphides as they exsolve.

For these PGM to form via exsolution, an immiscible sulphide melt would have initially collected the chalcophile elements; particularly the PGE, Ni, Cu and semimetals (especially Te). During fractional crystallisation of the sulphide liquid, monosulphide solid solution (MSS) crystallises leaving a Cu-rich sulphide liquid from which intermediate solid solution (ISS) crystallises (e.g., Holwell and McDonald, 2010). Pentlandite, pyrrhotite and chalcopyrite exsolve from MSS and ISS during sub-solidus cooling. Further cooling may result in the exsolution of PGE and semimetals from these BMS as they become unstable in

these sulphides at lower temperatures forming PGM (Barnes *et al.*, 2008). Barnes *et al.* (2008) also suggest that the rate of cooling affects the quantities of PGM formed. Slow cooling allows the PGE to exsolve forming PGM whereas rapid cooling does not allow the exsolution of PGE so they remain trapped in the sulphides in solid solution. Therefore, it appears that the Mirabela intrusion has cooled sufficiently slowly to allow for the exsolution of PGE to form abundant PGM.

Tellurium may be one of the most important factors in controlling the formation of these PGM due to its effect on the solubility of PGE, particular of Pt and Pd in an immiscible sulphide melt. Experimental studies suggest that Pt, Pd and the semimetals are extremely incompatible with regard to MSS (Fleet *et al.*, 1993; Li *et al.*, 1996; Ballhaus *et al.*, 2001; Mungall *et al.*, 2005; Helmy *et al.*, 2007; 2010). The incompatibility of Pt, Pd and Au with ISS is also noted (Peregoedova, 1998). Studies of natural deposits support these experimental results suggesting that Pt and Pd remain in a late-stage semimetal-rich liquid during the crystallisation of both MSS and ISS. This experimental research indicates that elevated semimetal content, can reduce the solubility of PGE in the BMS making the production of a late-stage PGE-bearing semimetal-rich melt more likely in a semimetal- or Te-rich system (e.g., Helmy *et al.*, 2007; Hutchinson and McDonald, 2008; Helmy *et al.*, 2010; Holwell and McDonald, 2010).

Several examples of the formation of late-stage PGE- and semimetal-rich melts are observed in natural studies of PGE mineralisation. One such example is the identification of Pt tellurides in the central high-grade sector of the Platreef (Holwell *et al.*, 2006; Holwell and McDonald, 2007) where the most "primary" style of that mineralisation is developed. These tellurides are thought to have crystallised from a late-stage semimetal-rich melt. Experiments by Tomkins (2010) suggest that where an immiscible As-sulphosalt has formed, it may percolate through MSS, particularly at triple points collecting semimetals and PGE that are incompatible with the MSS leaving a PGE- and semimetal-rich melt from which PGM may crystallise. Cabri and Laflamme (1976) attributed the formation of discrete PGM in Cu-Ni deposits in Sudbury to the concentration of semimetals and PGE, first into a Cu-rich sulphide liquid during the crystallisation of MSS and then into a Pd-Pt-Te-Bi-Sb-(As?)-rich liquid during the crystallisation of ISS. PGM then formed from this late-stage PGE- and semimetal-rich liquid as predicted by some experimental studies. Prichard *et al.* (2004b) also demonstrated that PGE collected in a late-stage volatile-rich melt during the fractionation of an immiscible sulphide bleb in a dyke from Uruguay.

It appears that the Mirabela Pt-Pd-Ni-Fe tellurides have not formed from a late-stage semimetal-rich melt as they do not exhibit the characteristics of other PGM that have formed via this method from the studies mentioned above (i.e., they are not consistently identified at the edges of the sulphides or associated with the products of a late-stage sulphide melt or Cu-sulphides). However, it is suggested here that the presence of Te within the BMS has aided the exsolution of Pt, Pd and Ni from the BMS leaving little PGE in solid solution in the Santa Rita ore zone (Table 4.4). In order to account for the association of these Pt-Pd-Ni-Fe tellurides with all of the sulphide phases present (pentlandite, pyrrhotite, pyrite and chalcopyrite), it appears that the Pt, Pd and Te have entered into both MSS and ISS during their crystallisation from the sulphide liquid and into all the subsequently exsolving sulphides as opposed to forming a late-stage semimetal-rich liquid, before exsolving to form PGM on further cooling.

The only PGM observed within the chromite-rich seam intersected in MBS604 (Fig. 4.4a) are Pt-Pd-Ni tellurides and these are not associated with the chromite crystals themselves. The presence of the chromite-rich seam indicates a reversal in the overall continuous fractionation path of the Mirabela intrusion and it is significant therefore that it contains the most anomalous PGE grades. Precipitation of PGE from a fresh input of more primitive magma may have resulted in elevated PGE concentrations, however, density settling of cumulates during slumping could also account for these features (Maier *et al.*, 2013).

4.9.4 Formation of sperrylite and irarsite

Irarsite is rare and occurs in all zones of the intrusion. Sperrylite, however, is relatively abundant but only occurs within the northern and southern zones of the intrusion, being almost totally absent from the central zone (Fig. 4.14 and Fig. 4.15). These types of As-bearing PGM when found completely enclosed by silicates and oxides are often interpreted to have crystallised early, directly from an immiscible sulphide melt and subsequently become trapped in later crystallising silicate and oxide phases.

Dare *et al.* (2010b) suggested that for Sudbury, when volatile elements, especially arsenic were introduced into the magma from the surrounding basement, the IPGE and Rh crystallised into early PGM-bearing sulpharsenides at high temperatures directly from the sulphide liquid before the formation of MSS and ISS. Another example is documented in

ultramafic intrusive complexes in the Andriamena region of Madagascar. McDonald (2008) showed that in this case, high As contents have resulted in the early crystallisation of Pt-Ir-Rh arsenides and sulpharsenides. This is evidenced by their dissociation with the BMS and incorporation as inclusions in olivine. Furthermore, Hutchinson and McDonald (2008) suggested that the assimilation of As, Sb, Bi, and Te into the sulphide melt from the surrounding country rock of the Platreef in the Bushveld Complex may have caused Pt-bearing PGM to crystallise early rather than being incorporated into solid solution in BMS.

In the Mirabela intrusion, however, the majority of these sperrylite and irarsite grains remain associated with the BMS (Fig. 4.16F-H). It is therefore unclear whether these PGM have crystallised early directly from the sulphide melt as in the cases noted above, or whether these PGM have exsolved from the BMS during sub-solidus cooling in a manner similar to that described for the PGE-tellurides.

These PGM could maintain an association with the BMS even if they have crystallised early directly from the sulphide liquid in the event that they do not cleanly separate from the sulphide liquid. This may result in these As-bearing PGM appearing completely enclosed by the BMS or being associated with minor BMS where the PGM have partially separated the sulphide liquid. The latter may explain why some sperrylite grains are much larger than their host sulphides. In these cases, it is unlikely that exsolution could account for their formation. However, these observations of PGM and BMS size are limited to two-dimensions and may not be accurate.

The spatial variation in sperrylite across the intrusion whereby these As-bearing PGM are restricted to the northern and southern margins may be explained by the possible addition of As from the surrounding country rocks through crustal assimilation. This assimilated As-bearing crustal material was poorly mixed within the magma chamber to leave the spatial variation observed with sperrylite (and therefore relatively As-rich material) observed only in the northern and southern zones or margins of the intrusion. In this case, the northern and southern zones which are in contact with the country rocks would inherit this assimilated As leaving the central zone with its original magmatic As budget which appears to be very low given the lack of any appreciable As-bearing minerals observed in this zone. However, trace element bivariate plots suggest that the Mirabela intrusives have not been contaminated by the ingestion of TTG country rocks of the Itabuna-Salvador-Curaça belt (Fig. 4.10). If crustal contamination has occurred, particularly at the intrusion margins, one would expect a

variation in these trace elements between the central zone of the intrusion and the intrusion margins (northern and southern zones) which is not observed with the Mirabela intrusives tightly grouped together. This indicates that another process, not yet identified, may be responsible for the zonation of As across the intrusion.

4.9.5 PGM-bearing BMS stringers

In the Santa Rita ore zone, BMS (and rarely magnetite) stringers with associated PGM are present. These stringers are often roughly aligned producing a pseudo-fabric in some of the samples studied. The types of PGM associated with these stringers are variable and include both Pt-Pd-Ni-Cu-Fe tellurides and sperrylite. The BMS stringers themselves emanate from interstitial sulphides at junctions between the sulphides and silicates and/or oxides, and may extend for several millimetres. The associated PGM can occur at any point along these stringers including at their origin where the PGM are still associated with 'normal' interstitial BMS up to the termination of the stringer where the PGM may appear to be almost enclosed within silicates while retaining only a minor association to the sulphide stringer.

These sulphide stringers and associated PGM may be the result of either post-magmatic hydrothermal remobilisation of the BMS and PGM, or the migration of late-stage fractionated sulphide liquids. It is well known that hydrothermal fluids can remobilise sulphides and PGE. The remobilisation of Pd bismuthides with chalcopyrite within chlorite filled veins is observed by Prichard *et al.* (2001) in the Bacuri complex in Brazil. Furthermore, in the Jinbaoshan Pd-Pt deposit in Southwest China, sudburyite ([PdNi]Sb) is found in late-stage veins proximal to high temperature occurrences of BMS hosted PGM. This demonstrates the small millimetre scale mobility of Pd during post-magmatic hydrothermal alteration (Wang *et al.*, 2008). However, PGM-bearing veinlets have also been observed in the Stillwater Complex (Zientek, 2002) and emanating from an immiscible sulphide bleb from a dyke in Uruguay (Prichard *et al.*, 2004b). In both cases, it was proposed that these BMS and PGM filled veinlets were the product of the last stages of crystallisation of an evolved volatile-rich sulphide melt. Whether of late magmatic or post-magmatic origin, it appears that both the BMS and PGE/PGM have been redistributed at the same time into these stringers evidenced by their close association (Fig. 4.17A-H).

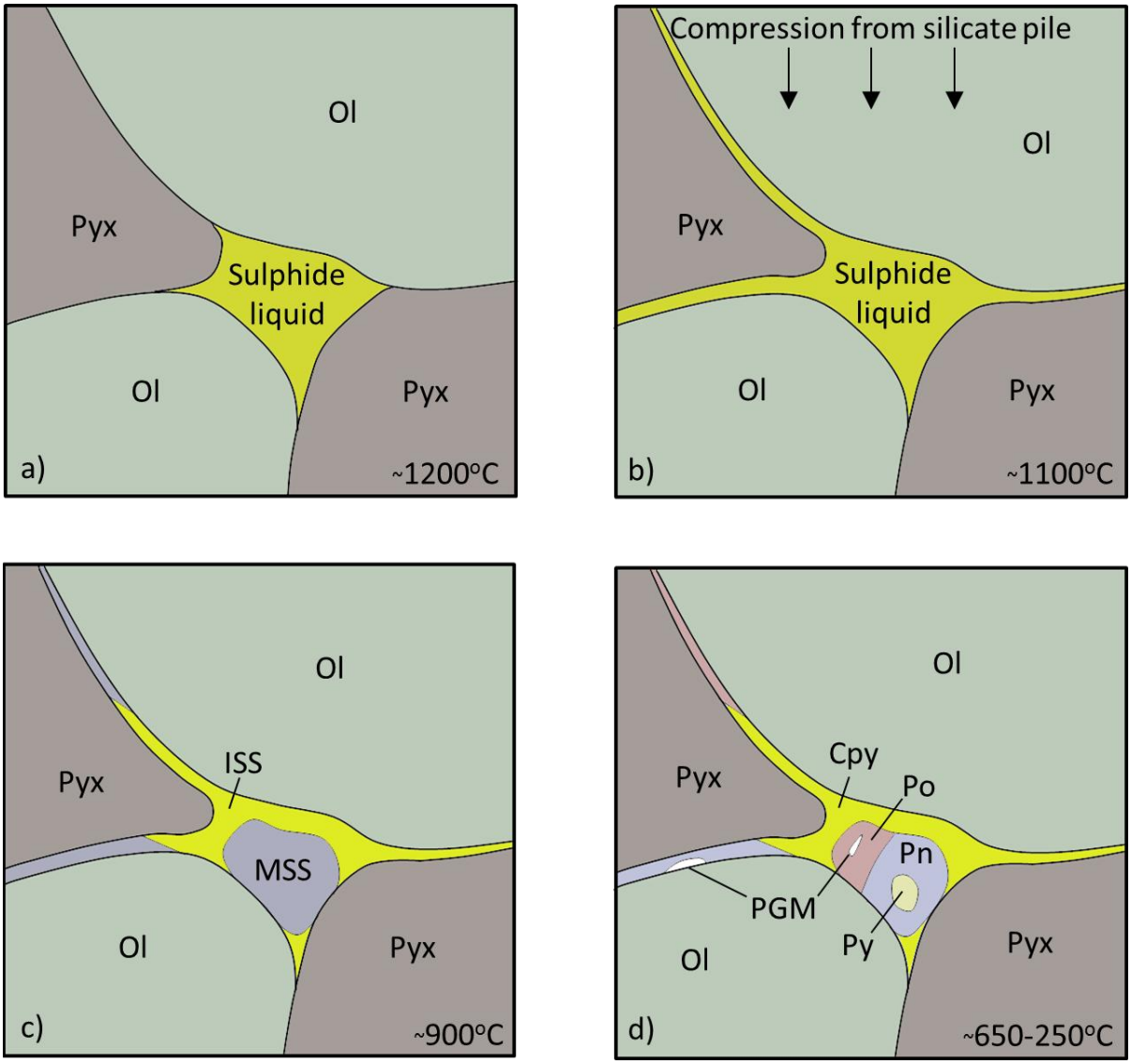


Figure 4.23: Diagram demonstrating the formation of BMS stringers and associated PGM; a) sulphide liquid coalesces as interstitial blebs to olivine (Ol) and pyroxene (Pyx), b) compression from the growing silicate crystal pile forces sulphide liquid into stringers along silicate grain boundaries in the direction of least resistance, c) the sulphide liquid crystallises to MSS and ISS, d) which subsequently re-crystallise to pentlandite (Pn), pyrrhotite (Po), pyrite (Py) and chalcopyrite (Cpy) during sub-solidus cooling. PGM exsolve from interstitial sulphides and BMS stringers during further cooling.

There is some evidence for the hydrothermal remobilisation of these BMS stringers and their associated PGM. Hydrothermal alteration with fluids travelling in a preferred direction would account for the alignment of the sulphide stringers. It is true that many of these BMS stringers are associated with serpentine (Fig. 4.17D, G) indicating post-magmatic hydrothermal interaction is responsible for their formation; however, these later serpentinising fluids may simply be travelling along planes of weakness in the rock including pre-existing BMS stringers. There is also little to suggest that the BMS have been affected or altered by any hydrothermal fluid as might be expected if the sulphides were remobilised and redistributed (i.e., there is a lack of secondary sulphides to support this argument).

Furthermore, the studies above suggest that Pd is far more mobile than Pt, thus one might expect to have more Pd dominant PGM associated with these sulphide stringers, but this is not the case as sperrylite is often observed (Fig. 4.17E-F). Platinum mobility has been recorded in quartz veins in the Waterberg deposit, South Africa. These veins show many features typical of low pressure epithermal quartz veins (Armitage *et al.*, 2007) and Pt appears to have been mobile in low temperature (200-300^{o}C), highly oxidising, low salinity fluids (McDonald *et al.*, 1999). However, this system represents a fluid-rock ratio for which there is no evidence of in the Mirabela intrusion where magmatic minerals and textures are largely preserved. Pt solubility may also be very high (at ppm-level) in high temperature (800-900ºC), high salinity brines (Hanley, 2005), whereas the minor alteration observed in the Santa Rita ore zone is associated with low temperature fluids and the formation of serpentine. It therefore appears unlikely that the PGE have been remobilised and redistributed with the BMS by hydrothermal processes to form sulphide stringers and their associated PGM, including sperrylite. Furthermore, Wood (2002) notes that As, Bi, Sb, Se and Te form very insoluble compounds with the PGE. This suggests that these vein associated PGM have formed in situ by magmatic processes such as crystallisation from the immiscible sulphide liquid or exsolution from the BMS during sub-solidus cooling.

A more reasonable explanation of these BMS stringers and their associated PGM is that they are the result of the migration and crystallisation of late-stage PGE-bearing sulphide liquids. However, if this was the case, one would expect that these stringers would be mostly comprised of chalcopyrite or another late-stage Cu-sulphide phase given the known sulphide fractionation of MSS, ISS and late-stage sulphide melts. However, chalcopyrite, pentlandite and pyrrhotite stringers are all commonly observed (Fig. 4.17B and G). Furthermore, the chemistry of the PGM also remains constant. In a fractionating system one would expect the nature of these PGM to change as certain elements become depleted. Finally, this explanation cannot account for the alignment of the sulphide stringers noted. Late-stage sulphide liquid off-shoots from interstitial crystals would arguably travel in all orientations randomly.

It is therefore argued here that these BMS stringers and their associated PGM are the result of a mechanical process, most likely compressional forces derived from gravity settling and compacting of crystals in the magma chamber before the sulphide liquid had crystallised. This compression forced a portion of the sulphide liquid, which at this point was coalescing as interstitial blebs (Fig. 4.23a-b), outwards through the crystal pile in the direction of least resistance along the boundaries of olivine and pyroxene crystals (either replacing any

interstitial silicate melt or migrating through solidified silicates along their grain boundaries as suggested by Mungall and Su [2005]) giving rise to the alignment of these sulphide stringers observed. This unfractionated sulphide liquid then cooled and crystallised to form both MSS and ISS (Fig. 4.23c) which explains the varying composition (pentlandite, pyrrhotite, chalcopyrite and pyrite) of the BMS stringers currently observed and the consistent chemistry of the associated PGM which re-crystallised and exsolved during further cooling, respectively (Fig. 4.23d).

4.9.6 Variation in PGM abundance

In the sulphur-poor dunite below the Santa Rita ore zone, the types of PGM observed remain the same as those identified within the Santa Rita ore zone apart from in one borehole, MBS604 in the central zone which hosts a localised and distinct Pd-alloy assemblage as discussed below (section 4.9.7). Disregarding this localised Pd-alloy assemblage, the main difference between the PGM in the sulphur-poor dunite and the Santa Rita ore zone is their abundance. PGM are much more abundant in the Santa Rita ore zone at ~17 PGM per sample (thin section) studied compared to ~5 PGM per sample (thin section) studied identified in the sulphur-poor dunite. Whole-rock PGE concentrations remain relatively constant throughout both zones. Therefore, PGE content is not controlling the difference in the PGM abundance observed over these two zones with the balance of PGE taken up in solid solution in the BMS. This is demonstrated by the Santa Rita ore zone hosting relatively PGE-poor BMS (Table 4.4) and the dunite hosting PGE-rich BMS (Table 4.5). The concentration of sulphur, however, varies drastically between the two zones with the Santa Rita ore zone being relatively S-rich at an average of 0.97 wt. % S and the dunite zone being extremely poor in sulphur at an average of 0.04 wt. % S. Although sulphur does not comprise an elemental component in the PGM observed, it does closely correlate with semimetal content (Fig. 4.13a-d), specifically As and Te; conversely Bi and Sb concentrations are extremely low and are not considered here. Incidentally, this correlates with the PGM data as no Sb-bearing PGM are observed and Bi-bearing PGM comprise an extremely low proportion of the total numbers of PGM identified. Therefore, in the Santa Rita ore zone, sulphur and therefore As and Te are readily available for the PGE to bond with forming abundant PGM whereas in the dunite zone below, sulphur and therefore As and Te contents are extremely low, resulting in a limit being imposed on the numbers of semimetal-bearing PGM that can readily form.

One must now consider the origin of both the low concentrations of sulphur and semimetals within the dunite zone. In this zone, micro-scale sulphide-silicate graphic textures, very high PGE tenors, an unusual BMS assemblage (pentlandite with minor chalcopyrite) and Pd-Cu alloys (identified in borehole MBS604) cannot be explained by normal magmatic processes, particularly when compared to the Santa Rita ore zone. In this dunite, it appears that a continuum of late-stage processes has occurred in order to produce the resulting sulphide and platinum-group mineralogy. The sulphides present, which are typically <150 µm, are predominantly pentlandite with chalcopyrite (Fig. 4.5A-F) (ignoring very minor pyrite observed in central zone borehole MBS605). Many of these sulphides show symplectite-like textures on a micro-scale appearing intergrown with olivine and occasionally orthopyroxene, particularly where the sulphide is in contact with phlogopite mica (Fig. 4.5A-B, G).

These sulphides may not, however, be true symplectites. There are only a few examples of sulphide-silicate symplectites in the literature. A troilite symplectite in orthopyroxene from the Acapulco meteorite is noted by El Goresy *et al.* (2005) which they ascribe to the simultaneous crystallisation of troilite and orthopyroxene from a silicate-sulphide melt. Marma (2002) also identifies a symplectite of chalcopyrite and orthopyroxene in the Birch Lake Cu-Ni-PGE deposit in the South Kawishiwi intrusion in the Duluth Complex although this texture is not explained. These examples are much coarser than the micro-scale textures observed in the Mirabela intrusion. In both of these cases it also appears that the sulphide liquid was incorporated into the crystallising silicates. However, in the Mirabela dunite zone it appears that sulphides are being partially replaced by silicate material indicating that sulphur loss may have occurred. A process of sulphur loss could also account for the high PGE tenors observed and the unusual of BMS assemblage of pentlandite with minor chalcopyrite with iron-sulphides almost completely absent.

To account for sulphur loss during the formation of the Platinova Reef in the Skaergaard intrusion, Andersen (2006) states that oxidation would attack the sulphides mobilising the S as H_2S or SO_2. Pyrrhotite would consequently be converted to Fe-oxides while chalcopyrite would be converted to Fe-oxides as well as bornite, digenite, chalcocite, and under extreme circumstances, native Cu. Another possible example of this process of sulphur loss is documented in the Jinchuan intrusion, northwestern China, where the BMS have been altered to magnetite during post magmatic hydrothermal alteration (Ripley *et al.*, 2005; Prichard *et al.*, 2013).

In the Mirabela intrusion, the presence of phlogopite, commonly observed in contact with these micro-scale symplectite-like textures identified in many sulphides (Fig. 4.5A-B, G), supports the presence of, or interaction with, a high temperature melt or fluid. Therefore, these symplectite-like textures may have formed by a process of sulphur loss via the partial dissolution of the BMS by a late-stage melt or high temperature hydrothermal fluid. It is possible that this liquid was forced upwards through the olivine crystal mush as it was compacted.

A similar model is suggested for the formation of Pt-Pd reefs by Boudreau and McCallum (1992) who use the J-M reef in the Stillwater Complex as a case study. They suggest that the footwall cumulates to the J-M reef were originally sulphide saturated given their high Pd and Pt concentrations and that these cumulates have lost sulphur to a fluid phase exsolving from intercumulus liquid. PGE and sulphur were essentially leached from the footwall cumulates and transported upwards to the position of the reef. Boudreau and McCallum (1992) note that unrealistically large amounts of fluid are required to transport high concentrations of Pt and Pd (hence the remaining concentration of these PGE in the footwall cumulates), however, relatively small amounts of liquid can remobilise sulphur.

Watkinson *et al.* (2002) have also noted the importance of deuteric fluids that exsolve from the magma during crystallisation in forming and modifying or upgrading PGE occurrences and deposits. In the Lac des Ilse Complex, Ontario, Watkinson *et al.* (2002) suggest that both PGE and sulphur were remobilised and deposited together by high temperature deuteric fluids, however, the continued exsolution of this fluid during cooling resulted in the dissociation of PGE and sulphur due to continued sulphur remobilisation. They also suggest that at the Salt Chuck Mine, Alaska, the magmatic concentration of PGE was modified by a late-stage hydrothermal deuteric overprint. In this case they note that the PGE were remobilised into veins, although it is not clear if fluids enhanced or decreased the PGE tenor of the magmatic ore. This upgrading or modification has resulted in zones that contain very little sulphide content but up to 0.5 ppm Pd (Watkinson *et al.*, 2002); similar to the concentrations identified in the sulphur-poor dunite in the Mirabela intrusion.

A process of sulphur loss by small amounts of late stage high temperature deuteric fluid (or melt) may therefore have occurred in the dunite zone of the Mirabela intrusion and is evidenced by the presence of magnetite (Fig. 4.5E-F), the partial replacement of BMS forming the micro-scale symplectite-like textures observed (Fig. 4.5A-F) and the partial

replacement/removal of BMS, predominantly pyrite and pyrrhotite which are virtually absent from the Mirabela dunite. Furthermore, the partial replacement of pentlandite rimmed by magnetite is also observed (Fig. 4.5H), as is minor bornite (e.g., Fig. 4.5G) which can be a product of sulphur loss from chalcopyrite as noted by Andersen (2006).

As the semimetals correlate strongly with sulphur, it appears that as sulphur was removed from the dunite zone, so were the associated semimetals. To account for the loss of semimetals, this process of sulphur loss must have occurred while the sulphides were only partially crystallised (MSS only). The semimetals and Pt would have preferentially partitioned into a Cu-rich fractionated sulphide liquid (e.g., Hanley *et al.*, 2010; Pattern *et al.*, 2013) (Fig. 4.24a), the majority of which could have then been removed by a late-stage melt or high temperature deuteric fluid while continued fluid/melt-MSS interaction dissolved FeS from the MSS forming micro symplectite-like sulphides (Fig. 4.24bii). This process explains the low volumes of chalcopyrite observed in this zone. As a result, only low concentrations of Te and As remain which may form low quantities of PGM with only a small portion of the PGE budget with the balance of PGE identified in the high tenor BMS (Fig. 4.24cii). This concentration of PGE into the sulphides in solid solution is twofold when compared to that of the Santa Rita ore zone. Firstly, the Santa Rita ore zone has a much greater quantity of PGM than the dunite zone, so already the concentration of PGE in the BMS is diluted when compared to the dunite sulphides. Secondly, the PGE in the BMS are diluted further by the fact that there is much more sulphur in the Santa Rita ore zone and therefore a much larger volume of sulphides in which to host the remaining PGE, whereas in the dunite zone, very few sulphides must host almost the entire whole-rock PGE budget in solid solution.

4.9.7 Formation of the Pd-alloy assemblage

Borehole MBS604 in the central zone of the Mirabela intrusion hosts a localised Pd-alloy assemblage (iii) that is identified in the sulphur-poor dunite (Fig. 4.14). This zone contains predominantly Pd-Cu±Pb alloys and Pd-S grains with minor additional alloy phases also noted (Fig. 4.18 A-H). Pd-Cu alloys are unusual PGM and have been observed most commonly in placer deposits or lateritic soils where sulphur or semimetals have been lost from precursor PGM by oxidation (Salpéteur *et al.* 1995; McDonald *et al.* 1999). Many Pd-Cu minerals have also been identified in the Freetown Layered Complex, Sierra Leone, where they are associated with chalcopyrite, bornite and Fe-oxides (Bowles *et al.*, 2013).

Many Pd-Cu minerals are observed in the Platinova Reef in the Skaergaard intrusion where sulphur loss has also occurred (Anderson, 2006).

Some literature demonstrates that PGE alloys may form as a result of sulphur loss. Kinloch (1982) suggests that in the Bushveld Complex, the interaction of volatiles related to feeder zones with sulphides results in the formation of Pt-Fe alloys. An analogy of converter matte produced from sulphide concentrates of Bushveld ore minerals suggests that volatiles with a high oxygen fugacity (f_{O_2}) may oxidise Fe to Fe_3O_4 while removing S as SO_2 (Kinloch, 1982). In this case, Pt does not readily form oxides, but instead alloys with Fe to form isoferroplatinum (Pt_3Fe).

It is suggested that a process of sulphur loss involving a high temperature deuteric fluid or melt with a high f_{O_2} accounts for the formation of micro-scale symplectite like textures in the BMS, the loss of Cu-rich sulphide liquid and associated semimetals and Pt, the complete loss of pure Fe-sulphides combined with formation of secondary magnetite and high PGE tenors is also responsible for the formation of the Pd alloy assemblage (iii) in the Mirabela intrusion. The localised zone hosting these predominantly Pd-Cu alloys intercepted in borehole MBS604 has apparently been affected by this late-stage melt or high temperature deuteric fluid more intensely than it has other areas of the dunite zone. As a result, in this localised area, the entire volume of any remaining Cu-rich sulphide liquid carrying the semimetals was removed while the crystallised MSS underwent a greater degree of dissolution resulting in the absence of any telluride or arsenide PGE phases which could not form (Fig. 4.24bi). The majority of the PGE therefore remained in solid solution; however, some PGE exsolved forming PGE alloys and/or PGE sulphides instead of Te- or As-bearing PGM that would have formed preferentially as observed in the Santa Rita ore zone in the presence of semimetals. As PGE saturation in the sulphides analysed has not been reached (given the high concentrations of PGE that can occur in BMS in reef type settings, e.g., the J-M reef, Godel and Barnes, 2008), the exsolution of these alloys may have been encouraged by the process of sulphur loss (Fig. 4.24ci). In at least one example it is clear that sulphur loss and the formation of symplectite-like sulphide textures has encouraged the formation of Pd-Cu alloys. In Figure 4.18B, a pentlandite crystal can be observed, half of which is unaltered, and half of which exhibits a complex micro-scale symplectite-like texture. Only the altered portion of this pentlandite crystal hosts Pd-Cu alloys (Fig. 4.24di). This suggests that as the sulphide was dissolved/removed, the PGE were expelled from solid solution within the sulphide resulting in the formation of the Pd-Cu alloys observed.

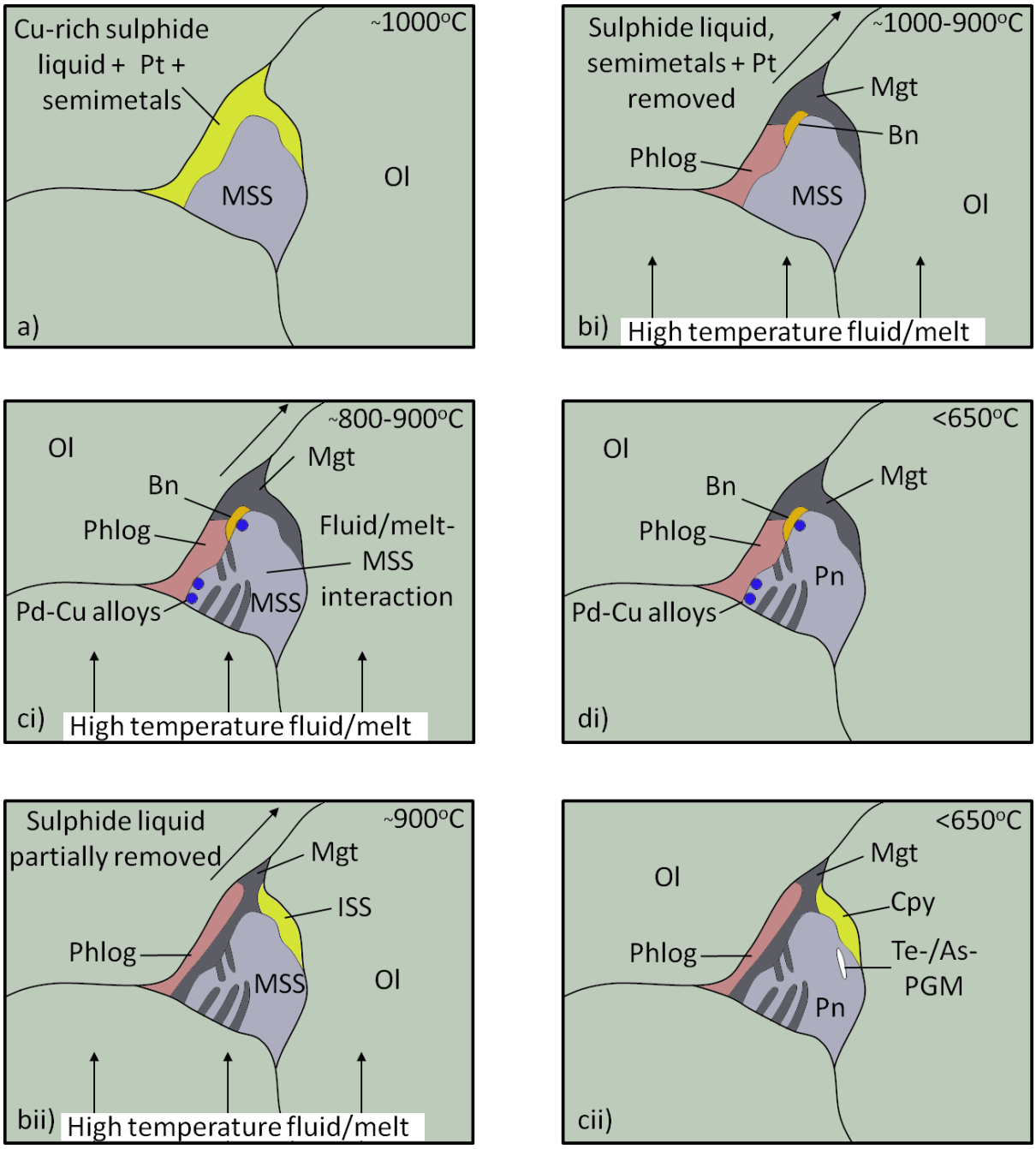


Figure 4.24: Formation of PGM and micro-symplectite textures in BMS in the sulphur-poor dunite; a) MSS crystallises from interstitial sulphide liquid leaving a Cu-rich sulphide liquid into which Pt and the semimetals partition, bi) in MBS604, a high temperature deuteric fluid/melt with a high oxygen fugacity removes all of this Cu-rich liquid and associated metals, replacing it with phlogopite mica (Phlog), minor bornite (Bn) and magnetite (Mgt), c) continued fluid/MSS interaction results in the formation of micro-symplectite textures in the MSS where FeS is partially/totally replaced by Mgt forcing PGE, primarily Pd to exsolve forming Pd-Cu alloys, d) pentlandite (Pn) exsolves from Ni-rich MSS; bii) in the other boreholes studied, the high temperature fluid/melt only partially removes the Cu-rich sulphide liquid, the remainder of which crystallises to form minor ISS, cii) some semimetals are retained resulting in the exsolution of PGE-tellurides or arsenides (As-bearing PGM at intrusion margins only) during sub-solidus cooling.

4.9.8 Variation in Pd/Pt ratio

Three types of PGE profiles have been recognised in the Mirabela intrusion. The first pattern (1) exhibits a positive Pd anomaly and occurs typically in the sulphur-poor dunite zone, the second pattern (2) exhibits a positive Pt anomaly and typically occurs in orthopyroxenite-harzburgite samples marking the Santa Rita ore zone, and the third pattern (3) exhibits straight positive slopes without any significant Pt or Pd anomaly and occurs typically in lower harzburgite and upper dunite samples (a zone marking the transition between the Santa Rita ore zone and the sulphur-poor dunite; these samples are effectively grouped together with Santa Rita ore zone samples for the purpose of this study given their sulphur content and quantities of PGM hosted) (Fig. 4.12a-d).

These three patterns relate not only to the abundance of PGM observed in each zone but also the associated sulphur and therefore semimetal content. Pattern 1 is effectively identified in the dunite zone and relates to an average of ~5 PGM per sample (thin section) studied with an average sulphur content of 0.04 wt. % per sample. Pattern 2 is effectively identified in the Santa Rita ore zone and relates to an average of ~17 PGM per sample (thin section) studied with an average sulphur content of 1.10 wt. % per sample. Finally, pattern 3 is effectively identified in samples that bridge the transition from the Santa Rita ore zone (and from a high PGM to low PGM zone/high S to low S zone) and relates to an average of ~16 PGM per sample (thin section) studied with an average sulphur content of 0.61 wt. % per sample. It should be noted that samples that exhibit pattern 3 are effectively recognised as Santa Rita ore zone samples for this study. As such, the combination of pattern 1 and 3 yields an average of ~17 PGM per sample (thin section) studied with an average sulphur content of 0.97 wt. % per sample.

In the dunite zone, the PGE profile pattern 1 reflects high Pd/Pt ratios which then transition into relatively low Pd/Pt ratios upwards into the Santa Rita ore zone (Fig. 4.4a-f) with this transition marked by samples exhibiting PGE profile pattern 3 (Fig. 4.12c). This variation in PGE profile and Pd/Pt ratios appears to be controlled by the concentrations of Pd in solid solution in the BMS. In the dunite zone, the Pd content of the BMS, particularly in pentlandite is extremely high, especially in relation to Pt. As there are very few PGM in this zone, there are few opportunities for Pt to become stable. Therefore, it is possible that during the process of sulphur loss in this zone described above, the majority of Pt which does not preferentially partition into MSS partitioned into a Cu-rich sulphide liquid which was then

removed by a late-stage melt or high temperature deuteric fluid with sulphur and semimetals resulting high Pd/Pt ratios.

In the recently discovered Offset Zone of the Mine Block Intrusion of the Lac des Iles Complex, Boudreau *et al.* (2014) have identified Pd mineralisation with unusually high Pd/Pt ratios in rocks that range from relatively unaltered norite to amphibolites and chlorite-actinolite-talc schist. They found that in the most altered rocks Pt content decreases by 65% and Pd increases modestly by 5%, however, they also suggested that the initial Pd content in the most altered rocks was higher than in other lithologies and that Pd was also lost in part during alteration. It is known that Pt solubility may be very high (at ppm-level) in high temperature (800–900ºC), high salinity fluids (Hanley, 2005). Therefore, it is also possible that this process of sulphur loss in the Mirabela dunite may have also mobilised a portion of the Pt that was initially in solid solution in pentlandite, however, the chemistry of this proposed deuteric fluid is not known.

Other variations in the Pd/Pt ratio observed in the borehole profiles (Fig. 4.4a-f) are likely the result of drastically varying sulphur content. This correlates to PGE content which can be very low close to the detection limits giving rise to erroneous values and unpredictable variations in Pd/Pt ratios.

4.9.9 IPGE and cobalt in pyrite

Pyrite is rarely analysed for PGE and other metals, however, it is demonstrated in this study that pyrite is a host for the IPGE (Os and Ru) (Table 4.4). In the Santa Rita ore zone, the average Os and Ru content of pyrite is 0.6 ppm and 0.8 ppm, respectively. Although these concentrations may not appear to be particularly high, they are certainly significant when compared to the average concentrations of PPGE (Pt, Pd and Rh) in pyrite which are all individually ≤0.1 ppm. Furthermore, the average concentration of Pd detected in pentlandite in the Santa Rita ore zone is only 2.3 ppm. The whole-rock PGE analyses show that there is much more Pd available than Ru and Os, therefore these PGE are much more effectively concentrated in pyrite than Pd is in pentlandite, however, this does not take into account the abundance of Pd-bearing PGM and absence of Ru-Os-bearing PGM. In the dunite zone of the intrusion, only two pyrite crystals have been analysed for PGE in solid solution. One pyrite contains PGE in substantially higher concentrations in solid solution than pyrite in the Santa

Rita ore zone; however, the other pyrite crystal analysed contains extremely low concentrations of PGE (Table 4.5). This may be an artefact of sampling and therefore these results are not being taken into consideration here.

Cobalt is also concentrated in pyrite with concentrations varying from 0.8 to 3.2 wt. % which is very high when compared to the Co concentrations measured in the other BMS (pentlandite, pyrrhotite and chalcopyrite). It should be noted that the Co content of pyrite in the dunite is not higher than that of the pyrite in the Santa Rita ore zone.

The discovery of both PGE and Co in pyrite has only come to prominence relatively recently with Ru identified in pyrite in the Imandra Layered Complex in northerwestern Russia (Barkov *et al.*, 1997), Pd identified in pyrite in the Keivitsansarvi Ni-Cu-PGE deposit in northern Finland (Gervilla and Kojonen, 2002) and Ru and Pt identified in pyrite in the Main Sulphide Zone of the Great Dyke in Zimbabwe (Oberthür *et al.*, 1997).

PGE have also been identified in pyrite by Dare *et al.* (2010a) at the Creighton Ni-Cu-PGE sulphide deposit at Sudbury. They observed that Os and Ru were found in equal proportions in pentlandite, pyrrhotite and pyrite and that Co and Ni have a greater preference for pyrite than pyrrhotite. The origin of the pyrite in their study is far from certain and the fact that the Os and Ru occur in equal proportions in the pyrite, pentlandite and pyrrhotite suggest that pyrite may have formed either as an exsolution product from MSS or is secondary and has simply inherited PGE from the sulphides it has replaced. Given that the Co and Ni have a greater preference for pyrite, this may indicate that it has formed via exsolution from MSS or that these elements have diffused into the pyrite from the surrounding pyrrhotite (Dare *et al.*, 2010a). A study of the Aguablanca Ni-Cu-PGE deposit in Spain by Piña *et al.* (2011) has revealed the presence of two types of pyrite; large idiomorphic pyrite which hosts elevated Pt and Rh concentrations and what is proposed to be secondary ribbon-like pyrite which hosts IPGE and Rh concentrations similar to those of the pyrrhotite it has replaced. Again, by the author's own admission, the origin of the idiomorphic pyrite is uncertain and may be either an exsolution product of MSS or the alteration product of pyrrhotite. Smith *et al.* (2014) have also identified appreciable quantities of IPGE, Pd and Rh in pyrite in samples from the Grasvally Norite-Pyroxenite-Anorthosite (GNPA) member within the northern limb of the Bushveld Complex. In this case, secondary pyrite and millerite replace primary pentlandite and pyrrhotite and inherit their PGE contents. However, Pd concentrations are lower than the

primary sulphides, suggesting that hydrothermal fluids have remobilised small concentrations of Pd (Smith *et al.*, 2014).

Dare *et al.* (2011) identified two types of pyrite from the McCreedy East deposit at Sudbury. The first is oscillatory zoned and hosts elevated IPGE concentrations compared to that of pyrrhotite and pentlandite while being Pt-Pd-poor and the second is unzoned with low concentrations of IPGE. They proposed that this accessory oscillatory zoned pyrite exsolved from MSS given its high IPGE content relative to pyrrhotite and pentlandite and that the oscillatory zoning formed during its growth. They also suggested that the unzoned pyrite identified was secondary and has simply inherited the low concentrations of IPGE from the pyrrhotite and pentlandite it has replaced.

Lorand and Alard (2010) recently identified pyrite enriched in IPGE compared to pyrrhotite and pentlandite from a Pyrenean peridotite mantle massif. They also ascribed the origin of pyrite to exsolution from a sulphur-rich MSS citing the experiments of Naldrett *et al.* (1967) which show that small amounts of pyrite can exsolve from sulphur-rich MSS at temperatures below ~700^{o}C.

Several lines of evidence suggest that the pyrite in the Mirabela intrusion is primary and has also exsolved from MSS. Firstly, the intrusion is almost completely unaltered with no real textural or chemical evidence for secondary sulphide remobilisation or alteration in the Santa Rita ore zone. Secondly, pyrite hosts individual IPGE in greater concentrations than both pyrrhotite and pentlandite (excluding Ru in pentlandite which has an average of 0.9 ppm compared to 0.8 ppm in pyrite) suggesting that it has not simply replaced these sulphides and inherited their PGE content. This is also supported by the Pd-poor nature of pyrite. If pyrite had replaced pentlandite (commonly found intergrown with pyrite), one might expect pyrite to host Pd in solid solution in similar concentrations to that of pentlandite. Therefore the pyrite in the Mirabela intrusion appears to be primary and small amounts volumetrically have exsolved from MSS. This is also further supported by the presence of Pt-Pd-Ni-Te grains being present within pyrite (Fig. 4.16C).

It is still uncertain whether these IPGE and Co have immediately partitioned into exsolving pyrite controlled perhaps by high partition coefficients for pyrite or whether the IPGE and Co have subsequently diffused into pyrite from the adjacent BMS. Nonetheless, this study suggests that primary pyrite should be seriously considered as a potential host for the IPGE

and other important metals such as cobalt, particularly in a system with high PGE tenor (e.g., a PGE reef type setting).

4.10 Model and Summary

The following describes a possible sequence of crystallisation of the PGE and sulphides in the Mirabela intrusion based on the observations described above:

1. Sulphur saturation was achieved in the magma chamber, possibly through magma mixing as suggested by Barnes *et al.* (2011). They attributed the formation of the Santa Rita ore zone and the Ni-rich nature of the sulphide ore to the mixing of an initially S-undersaturated, moderately Ni-enriched resident magma with a relatively low Ni, PGE-depleted, and significantly lower temperature replenishing magma charged with suspended sulphide liquid droplets. However, trace element data suggests that the Mirabela intrusion has only one source magma, unless the two magmas proposed by Barnes *et al.* (2011) are compositionally similar. In which case, the lack of chilled margins means that patterns pertaining to magma mixing are impossible to discriminate from patterns of fractional crystallisation. The PGE, semimetals and other chalcophile elements partitioned into the forming immiscible sulphide melt. At this point the PGE and semimetal budget (primarily Te) of the magma was evenly distributed throughout the immiscible sulphide liquid.

2. Assimilation of country rocks may have occurred at the margins of the intrusion including the northern and southern zones of what becomes the Santa Rita ore zone (Fig. 4.25 1a). Crustal As added to the magma partitioned into the nearest available sulphide liquid locally at the margins with only minor magma mixing occurring laterally with 3D tomography studies undertaken by Barnes *et al.* (2011) demonstrating that the sulphides have poor interconnectivity. Therefore, the sulphide liquid is unlikely to have mixed dynamically leaving the relatively As-enriched sulphide liquid segregated to the margins (northern and southern zones) of the intrusion. However, no discernible crustal contamination is observed from rare earth and trace element data plots, therefore, the addition of As via crustal assimilation remains speculative and another process may be responsible for its zoning across the intrusion.

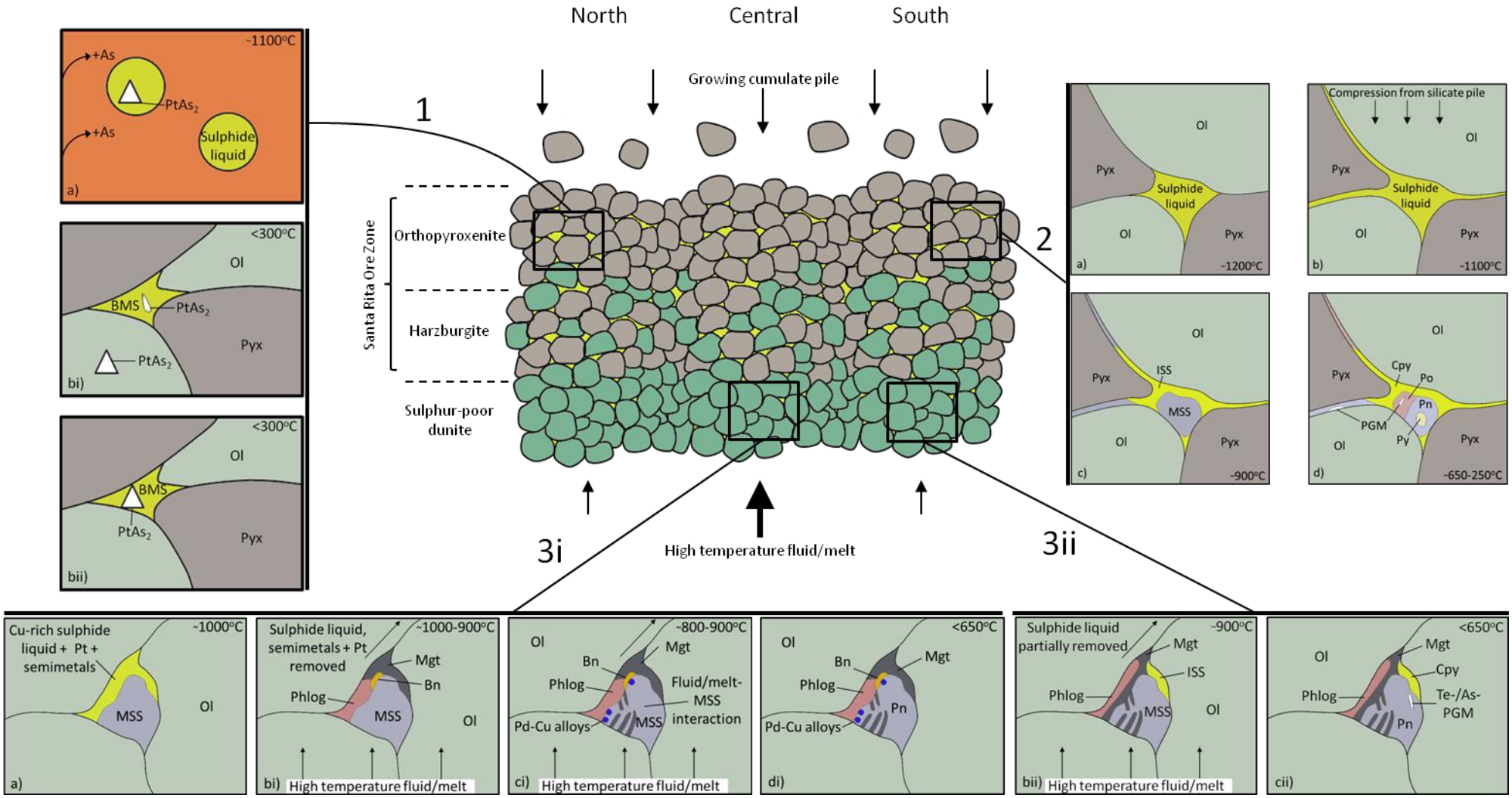


Figure 4.25: Diagram summarising processes controlling PGM formation in the Mirabela intrusion. 1) Formation of sperrylite ($PtAs_2$) at the margins of the intrusion; a) As is zoned and may have been introduced from country rocks via crustal assimilation at the intrusion margins. Sperrylite may crystallise early directly from As-bearing sulphide liquid, bi) this sperrylite may become trapped in subsequently crystallising silicates, alternatively, sperrylite may exsolve from the BMS during sub-solidus cooling, bii) early crystallising sperrylite may remain associated with later crystallising BMS if it does not separate from the sulphide liquid. 2) Formation of BMS stringers and primary PGM - full explanation given in Fig. 4.23. 3i and 3ii) Formation of micro-scale sulphide symplectites and their associated PGM in the sulphur-poor dunite zone - full explanation given in Fig. 4.24.

3. Sperrylite and irarsite may have crystallised early directly from the immiscible sulphide melt as some of these PGM are identified in unaltered silicate phases (Fig. 4.25 1a-b). In this case, the majority of these PGM have not cleanly separated from the sulphide liquid leaving these PGM with both minor and major associations with the BMS as observed (Fig. 4.25 1c). Alternatively, some of these PGM may have exsolved from the BMS during sub-solidus cooling (Fig. 4.25 1b).

4. As the cumulate pile in the magma chamber grew and compacted, sulphide liquid coalescing interstitially to the silicates in the Santa Rita ore zone was compressed and forced out away from these pools of interstitial sulphide liquid into cross cutting veins aligned in the direction of least compressive force producing BMS stringers carrying PGE (Fig. 4.24 2a-b).

5. Sulphide crystallisation began.

6. After partial sulphide crystallisation (MSS only), a melt high temperature deuteric fluid which exsolved from the magma with a high f_{O_2} interacted with both the crystallised BMS and remaining sulphide liquid (Cu-rich fractionated sulphide liquid hosting the majority of the Pt and semimetals) in the dunite zone (Fig. 4.24 3a-bi). This interaction resulted in the dissolution of Fe-sulphide from crystallised MSS and the removal of the remaining sulphide liquid containing Cu, semimetals, and Pt (Fig. 4.24 3bii-ci). This interaction affected the dunite with varying intensity. The dunite intersected in borehole MBS604 was apparently most intensely affected given the presence of Pd-Cu alloys. In this case, all of the remaining Cu-rich fractionated sulphide liquid was removed with the semimetals and the fluid/melt-sulphide interaction prompted the exsolution of PGE from MSS as micro-scale symplectite textures developed, forming PGE alloys and sulphides in the absence of Te and As (Fig. 4.24 3bi-ci). Predominantly Pd and other PGE (including minor Pt) were retained in the remaining crystallised sulphide. However, as already noted, the majority of the Pt was lost with the uncrystallised fractionated sulphide liquid due to its preference against partitioning into MSS. This explains the high Pd/Pt ratios in this zone compared to the low ratios in the overlying rocks.

7. As the sulphide liquid crystallised forming MSS and ISS in the Santa Rita ore zone, the IPGE and Rh partitioned into MSS (Fig. 4.24 2c). As pentlandite, pyrrhotite, and pyrite re-crystallised from MSS during sub-solidus cooling, Os and Ir preferentially partitioned into pyrite (with Co) whereas Ru and Rh partitioned equally into pentlandite and pyrite. Chalcopyrite exsolved from ISS. Platinum and Pd have apparently partitioned equally into

the different BMS present or diffused into these phases before exsolving as Pt-Pd-Ni-Fe tellurides during further sub-solidus cooling to account for their presence in all of the BMS phases observed (Fig. 4.24 2d). The incorporation of Ni into these PGE tellurides which is rarely observed, may be due to the high Ni tenor of the sulphide ores as noted by Barnes *et al.* (2011).

8. In the dunite zone (excluding in borehole MBS604 which is discussed in point 6), pentlandite exsolved from small volumes of MSS (Fig. 4.24 3di-cii) relative to the Santa Rita ore zone while even less chalcopyrite exsolved from limited ISS with the majority of the Cu- and Fe-sulphide component having been preferentially dissolved/removed during the process of sulphur loss noted above (Fig. 4.24 3cii). At this stage, the majority of the PGE partitioned into pentlandite with only relatively small concentrations of Pd remaining in chalcopyrite. With only small concentrations of Te and As remaining in the sulphides (the latter at the intrusion margins only), only small quantities of PGE tellurides and arsenides exsolved from the BMS during sub-solidus cooling (Fig. 4.24 3cii). The balance of PGE was retained in the BMS resulting in the formation of high PGE tenor sulphides.

9. The PGE and PGM have not been affected or remobilised by minor post-magmatic serpentinisation.

5. Platinum-Group Mineralogy and PGE Mineralisation of the Jinchuan Intrusion, China

5.1 Introduction

The Jinchuan ultramafic igneous intrusion, situated in Northwest China (Fig. 5.1), is the third largest Ni-Cu-(PGE) deposit in the world after Noril'sk and Sudbury (Naldrett, 2011). It has ore reserves of >500 million metric tons at Ni and Cu grades of 1.1 wt. % and 0.7 wt. % respectively (Tang *et al.*, 2009). The deposit was discovered in the 1950s and has been primarily mined for Ni and Cu since 1966 (Tang and Li, 1995). PGE are mined as an increasingly important by-product with ~95% of the total production of Pt and Pd in China now sourced from Jinchuan (Tang *et al.*, 2009).

The aims of this study are to characterise the PGE mineralisation within two orebodies from the Jinchuan intrusion by analysing both the platinum-group mineralogy and PGE content in solid solution in the BMS. One borehole from orebody #24, segment I and 3 boreholes from orebody #1, segment II have been sampled, allowing the variation in PGE mineralisation both laterally across the intrusion and with depth through the Jinchuan stratigraphy to be documented. The magmatic and hydrothermal processes responsible for the current distribution of the PGE in the intrusion have been separated and investigated.

5.2 Geology of the Jinchuan Intrusion

The Jinchuan complex is situated at the northern margin of the fault bounded Longshoushan Belt which occurs along the south western margin of the North China Craton (Fig. 5.1). The intrusion has been emplaced into the marbles and gneisses of the Baijiazuizi complex. The Baijiazuizi complex overlies the schists and banded marbles of the Tamazigou complex and both complexes have been intruded by multiple generations of later granitic and mafic dykes. These formations are unconformably overlain by less metamorphosed strata consisting of Denzigou conglomerates, quartzites, metabasalts, shales, and limestones and younger Hanmushan sericite-quartz schists, calcareous schists and limestone breccias (Chai and Naldrett, 1992a; Zhou *et al.*, 2002; Li *et al.*, 2004).

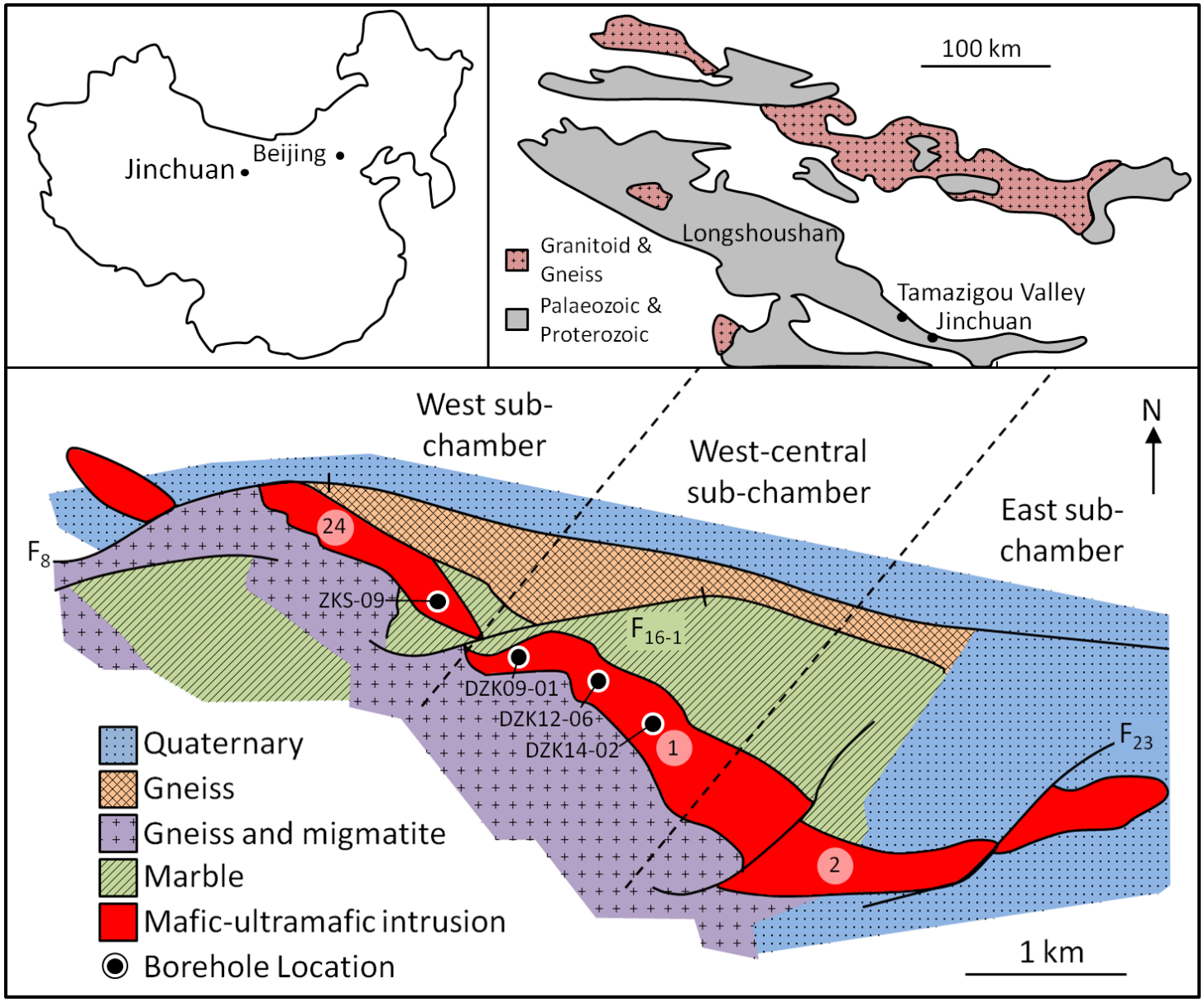


Figure 5.1: Location and geological map of the Jinchuan intrusion (modified from Chai and Naldrett, 1992; Lehmann *et al.*, 2007; Song *et al.*, 2012). Schematic locations of the boreholes sampled are marked.

The Jinchuan intrusion is approximately 6500m long, 500m wide and more than 1100m deep in its central part and exhibits a dyke-like form striking roughly northwest-southeast, parallel to the regional structural trend. The intrusion is cut by a series of northeast trending strike slip faults dividing it into sections. Originally, the complex was divided into Mining Areas III, I, II, and IV by the Sixth Geological Unit of the Geological Survey of Gansu Province (S.G.U., 1984). However, based on the geometry and distribution of rock types, Chai and Naldrett (1992b) divided the intrusion into three magma sub-chambers; the west, west-central and east sub-chambers which host orebodies #24, #1 and #2, respectively. Average whole-rock PGE concentrations for the different orebodies calculated from analyses given in Chai and Naldrett (1992b) are given in Table 5.1.

Orebody No.	No. of Samples	Average Whole-Rock PGE (ppb)					
		Os	Ir	Ru	Rh	Pt	Pd
Orebody #24	14	14.2	15.3	16.9	7.2	313.8	166.3
Orebody #1	35	32.3	32.9	36.3	18.9	1185.2	266.9
Orebody #2	20	11.6	12.6	12.7	8.6	72.5	92.3

Table 5.1: Table displaying average PGE concentrations in orebodies #24, #1 and #2 from the Jinchuan intrusion (after Chai and Naldrett, 1992b).

The intrusion is essentially comprised of five rock major lithologies, which are, in decreasing order of abundance; lherzolite, dunite, plagioclase lherzolite, olivine websterite, and websterite (Chai and Naldrett, 1992a; Zhou *et al.*, 2002; Yang *et al.*, 2006). Rare gabbro also occurs at the margins of the intrusion in a few places (Li and Ripley, 2011). The crystallisation sequence of the primary igneous minerals is chromite, olivine, orthopyroxene, clinopyroxene and plagioclase (Yang *et al.*, 2006).

The mineralisation in the Jinchuan intrusion occurs predominantly as net-textured as well as minor disseminated and rare massive Ni-Cu-(PGE) sulphide ores. Net-textured sulphide ore is associated with dunites where sulphides occur interstitially to olivine cumulates, generally located towards the base of the intrusion. The sulphides are composed principally of primary pyrrhotite, pentlandite, and chalcopyrite as well as secondary violarite and cubanite (Chai and

Naldrett, 1992b; Yang *et al.*, 2006). Orebody #1 is the largest in the Jinchuan intrusion occurring ~300m below the surface, orebody #2 is the second largest occurring ~400m below the surface and orebody #24 is the third largest and is exposed at the surface as a result of uplift and erosion (Li and Ripley, 2011).

The Jinchuan intrusion and its surrounding country rocks have undergone regional post-magmatic greenschist facies hydrothermal alteration and shear deformation evidenced by the presence of schist fabrics and typical greenschist facies hydrothermal minerals (Chai and Naldrett, 1992b; Zhou *et al.*, 2002; Li *et al.*, 2004; Naldrett, 2004; Yang *et al.*, 2006). A detailed study of the alteration within the intrusion has been conducted by Ripley *et al.* (2005). They found that olivine has been altered to mixtures of serpentine and fine grained magnetite whereas interstitial pyroxene and minor plagioclase have been altered to mixtures of chlorite, amphibole, epidote, clinozoisite, Na-rich feldspar, and lesser amounts of calcite. The intrusion has been variably affected by this hydrothermal alteration resulting in mix of both totally and partially altered ultramafic rocks being preserved. In contrast, some parts of the intrusion are unaltered and retain their primary magmatic minerals and textures (Zhou *et al.*, 2002; Li *et al.*, 2004). The Jinchuan sulphide ores have also been affected by this regional post-magmatic alteration and as such, up to 30% of the BMS have been replaced by magnetite, serpentine and chlorite (Ripley *et al.*, 2005). As a result, a degree of the metals and sulphur in the BMS have been removed and re-deposited on a centimetre scale in fine ribbons and veins within secondary alteration minerals (Ripley *et al.*, 2005).

The age of the Jinchuan intrusion is somewhat controversial and ages calculated from various studies have produced a large range of dates. Sm-Nd dating of the intrusion has yielded ages of 1508±31 Ma (Tang *et al.*, 1992) and 970±310 Ma (Zhang *et al.*, 2004). Re-Os isochron dating of the sulphide ores has yielded ages of 833±35 Ma (Yang *et al.*, 2005) and Re-Os isochron dating of disseminated ores, sulphides from the disseminated ores and massive ores have given ages of 1117±67 Ma, 1074±120 Ma and 867±75 Ma, respectively (Yang *et al.*, 2008). However, the methods used above are unreliable given the degree of post-magmatic alteration to which the Jinchuan intrusion has been subjected. Dating methods less susceptible to alteration have yielded ages that are much more closely grouped. Li *et al.* (2005) undertook SHRIMP U-Pb analyses of zircon and baddeleyite reporting ages of 827±8 Ma and 812±26 Ma respectively. A similar study was also undertaken by Yan *et al.* (2005); however, they interpreted the resulting age of ~837 Ma as the metamorphic age of the intrusion. Tian *et al.* (2007) reported ages of 807 Ma determined by U-Pb isotope

measurements using LA-ICP-MS for magmatic zircon crystals. The most recent study dating the Jinchuan intrusion is by Zhang *et al.* (2010), who reported a U-Pb ID-TIMS zircon age of 831.8±0.6 Ma.

There are few published studies on the distribution of both the concentration of PGE in solid solution in the BMS and the types and abundance of PGM observed in the Jinchuan ores. In addition, many studies do not cite specific sample locations, relying on grab samples from ore stockpiles or underground samples for which specific localities are not given. Padmaite (PdBiSe), sperrylite ($PtAs_2$) and irarsite (IrAsS) have been described by Prichard *et al.* (2005). Sperrylite, froodite ($PdBi_2$), and michenerite (PdTeBi) have also been reported in a brief study by Su *et al.* (2008) with Yang *et al.* (2006) identifying moncheite ($PtTe_2$), merenskyite ($PdTe_2$), kotulskite (PdTe), and Ag-Pd-Te-Bi compounds in addition to those already reported.

Yang *et al.* (2006) identified three different types of PGE mineralisation and concluded that this variation was the result of post-magmatic hydrothermal remobilisation, transport and re-deposition of the PGE. Su *et al.* (2008) also suggested that the PGE are subject to post-magmatic hydrothermal alteration which has affected both the silicates and the sulphides to account for the significant decoupling between Pt and Pd and also between Ru, Rh and Ir observed in their analyses.

Chai *et al.* (1993) used accelerator mass spectrometry (AMS) to measure PGE and Au in situ in pentlandite, pyrrhotite and chalcopyrite. They found that pentlandite is the main carrier of the PGE and can regularly account for up to 46% of the Os, Ru and Rh in the sulphide ores. The abundances of these elements in pentlandite increase with that of the whole-rock PGE content. Pentlandite is particularly enriched in Pd (up to 20 times whole-rock concentrations). They suggested that Pd, Os, Ru and Rh tend to partition into MSS whereas the Pt, Au and Ir which have relatively poor concentrations in the sulphides analysed, partitioned into a late stage liquid during the sulphide melt fractionation and crystallisation.

The Jinchuan primary magma is thought to have had an MgO content of ~12 wt. % and it is likely that the Jinchuan igneous body is the ultramafic cumulate of a high-Mg basaltic magma related to continental rifting (Chai and Naldrett, 1992a). Large negative εNd(T) values (-8.9 to -12.0) that decrease with increasing La/Sm suggest that the parental magmas were derived from a long-term enriched lithospheric mantle and experienced crustal contamination (Li *et*

al., 2005); the latter is also evidenced by the relative enrichment of incompatible trace elements coupled with negative U-Th and Nb-Ta anomalies (Lehmann *et al.*, 2007).

The west-central subchamber of the intrusion is narrow and deep exhibiting concentric enrichments of cumulus olivine crystals and interstitial sulphides in the core varying laterally through lherzolite and olivine pyroxenite toward the margins (Chai and Naldrett, 1992a; Li *et al.*, 2004). It has been suggested that this sub-concentric zonation is the result of flow differentiation during continued magma flow through the central subchamber (Chai and Naldrett, 1992; DeWaal *et al.*, 2004; Li *et al.*, 2004). The eastern subchamber is shallow and wide and shows vertical stratification, grading from dunite at the base upward into lherzolite and plagioclase lherzolite, then back to lherzolite at the top (Chai and Naldrett, 1992a). The eastern and western subchambers probably represent a higher level of the magma chamber, where crystallisation was marked by convection and periodic replenishment (Chai and Naldrett, 1992a) resulting in complex lithological banding and interfingering (DeWaal *et al.*, 2004). Sulphide enrichment toward the lower contact in the eastern and western segments may have, in part, resulted from gravitational settling during magma ascent (Li *et al.*, 2004).

The intrusion is thought to have formed as a result of the emplacement of various crystal mushes from a deep seated staging chamber (DeWaal *et al.*, 2004; Song *et al.*, 2006; 2009) between 4-9 km depth given the observed sequence of crystallisation (DeWaal *et al.*, 2004) and the high concentrations of olivine crystals (mostly >50 modal %) and sulphide (averaging ~5 wt. %) in the rocks (Li *et al.*, 2004). Features that are consistent with the interpretation that the Jinchuan deposit was formed by olivine- and sulphide-laden magma (Li *et al.*, 2004). Geological field mapping by Lehmann *et al.* (2007) led them to conclude that the intrusion was emplaced as a sill and not a sub-vertical dyke as previously thought.

Sulphide mineralisation is the consequence of the segregation of immiscible sulphide liquids from the Jinchuan silicate magmas (Chai and Naldrett, 1992b), with sulphides concentrated at the expense of intercumulus silicates in all segments of the intrusion (Li *et al.*, 2004). Chai and Naldrett (1992b) suggest that the Jinchuan magma contained small olivine crystals and immiscible sulphide liquid droplets which were subsequently concentrated by the process of flow differentiation and gravitational settling in funnel shaped feeders to the intrusion. The continued flow of magma through the concentrated olivine and sulphide liquid portion then upgraded the metal tenor of the sulphides before the system cooled and crystallised (Naldrett, 2004). It is suggested that in this model, the process of fractional crystallisation would have played a major role in triggering sulphide saturation (Li and Ripley, 2011).

An alternative model is that crystal mushes forming in a staging chamber resulted in the pre-concentration of sulphide liquid by liquid stratification (DeWaal *et al.*, 2004). Supporters of this model argue that the compositional heterogeneity of the disseminated sulphides observed in the intrusion cannot be accounted for by in situ differentiation or fractional crystallisation (Li *et al.*, 2004; Song *et al.*, 2006, respectively), but is consistent with differentiation and segregation of immiscible sulphide liquid from a basaltic magma in a staging chamber (Li *et al.*, 2004; Song *et al.*, 2006). Alternatively, Lehmann *et al.* (2007) suggest that the contamination of the ore forming magma via the assimilation of carbonate-rich fluids (country rock marble) increased the oxygen fugacity of the magma and led to the segregation of metal-rich sulphides.

5.3 Sampling

Four boreholes from two orebodies within the Jinchuan intrusion were sampled on site at Jinchuan. Three boreholes from the relatively MSS-rich orebody #1 in segment II were selected; borehole DZK12-06 (samples RK01-15), borehole DZK14-2 (samples RK16-26) and borehole DZK09-01 (RK27-34). These boreholes traverse orebody #1 from east to west. A further borehole, ZKS-09 (samples RK39-49), was sampled from the more Cu-rich orebody #24, segment I. The location of these boreholes is shown schematically in Figure 5.1. Furthermore, borehole information and the location and depths of each sample in their respective boreholes are shown in Figure 5.2.

As no geochemical data were available during this sampling, the decision was made to sample different types of sulphide mineralisation exhibiting different degrees of secondary hydrothermal alteration (documented in section 5.5). This sampling strategy has allowed the assessment of how the PGE mineralisation varies in different types of sulphide mineralisation and in samples displaying different degrees/intensities of hydrothermal alteration. This sampling was also designed to examine changes in the PGE mineralisation across the intrusion laterally (from the west, orebody #24 to the east, orebody #1) and with depth in the individual boreholes vertically through the Jinchuan stratigraphy. Correlation of the stratigraphy across the different boreholes has not been attempted due to the lack of downhole geochemical information.

5.4 Analytical Methods

Whole-rock PGE and Au analyses were performed on 42 samples from the 45 collected at Cardiff University using the Ni-fire assay procedure given in section 3.3. Two marble samples were not analysed for PGE (RK15 and RK26) and an insufficient amount material for sample RK14 meant that it too could not be analysed. Whole-rock major and trace element analyses were performed on 15 samples thought to be representative of the typical lithologies observed and sampled (five from borehole DZK12-06 orebody #1, four from DZK09-01 orebody #1 and six from ZKS-09 orebody #24) using the procedure given in section 3.2.

A total of 41 polished thin sections were produced. A polished thin section for sample RK26 (marble) was not produced and thin sections for samples RK22, RK28, RK32 and RK47 failed given the poor competency of these samples; however, two sections were made from sample RK24. All of these polished thin sections except RK15 (marble) were studied mineralogically using conventional transmitted and reflected light microscopy. PGM and their associated sulphide and silicate minerals were identified and analysed using a Cambridge Instruments (now Carl Zeiss NTS) S360 scanning electron microscope, the details of which and method used are given in section 3.4. A total of 10 thin sections from orebody #24 and 30 from orebody #1 were analysed.

Fourteen samples from the four boreholes studied with relatively high whole-rock PGE concentrations displaying different types of sulphide mineralisation and hosting different numbers of PGM were selected for LA-ICP-MS analyses in order to determine PGE concentrations in solid solution in the BMS present, the procedure for which is given in section 3.5.

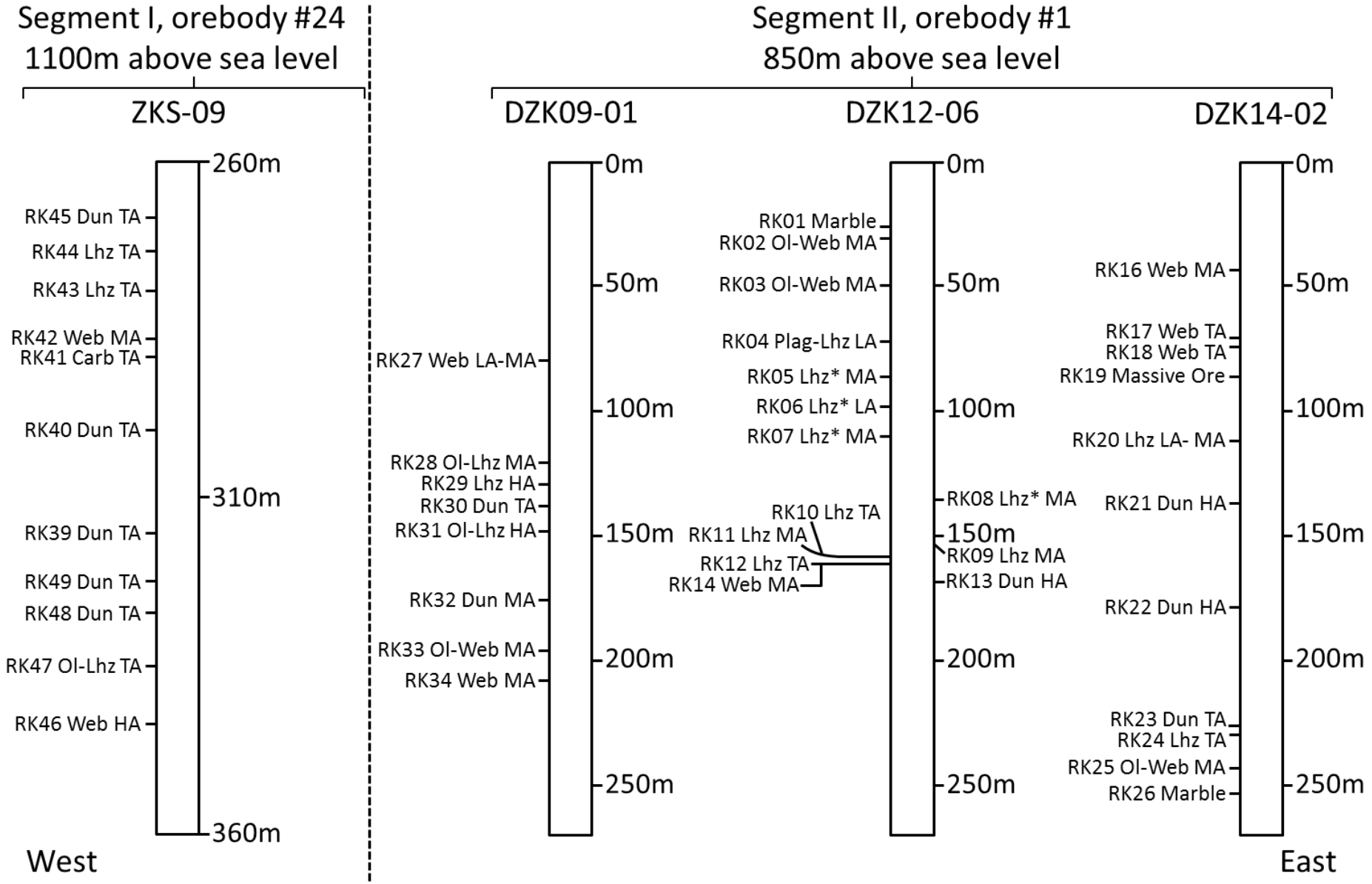


Figure 5.2: Diagram showing the location and depths of the samples studied from the Jinchuan intrusion within their respective boreholes. Dun = Dunite, Lhz = Lherzolite, Lhz* = Lherzolite with orthopyroxene oikocrysts, Web = Websterite, Carb = Carbonate, Ol = Olivine, Plag = Plagioclase; LA = Lightly Altered (5-35%), MA = Moderately Altered (35-65%), Heavily Altered (65-95%), TA = Totally Altered (95-100%).

5.5 Silicate and Sulphide Petrography

The selected samples from all four boreholes exhibit various types of sulphide mineralisation. Net-textured sulphide ore is common and is predominantly associated with dunite (Fig. 5.3A). Alternatively, 'patchy' net-textured ore may occur where the interstitial space between the olivine crystals is occupied by 'patches' of both sulphides and silicates (which are now altered) in varying proportions (Fig. 5.3B). Disseminated sulphides are also observed, commonly in lherzolite samples (plagioclase lherzolite; Fig. 5.3C). Massive ore is rare and may incorporate minor silicate and carbonate material (Fig. 5.3D). The ores sampled also exhibit evidence of secondary BMS remobilisation. Both small scale remobilisation of the BMS can occur with sulphides being transported by and subsequently crystallising in veins of variable composition (Fig. 5.3E) and larger scale remobilisation of massive sulphide, again incorporating both silicate and carbonate material (Fig. 5.3F).

The use of reflected light microscopy reveals further details of the sulphide petrography. The dominant sulphide phases present are pentlandite, pyrrhotite and chalcopyrite which are observed in net-textured (Fig. 5.4A-B), disseminated (Fig. 5.4C) and massive sulphide ores (Fig. 5.4D). Minor gersdorffite-cobaltite (NiAsS-CoAsS) and nickeline (NiAs) are also observed. The primary BMS are commonly veined, enveloped and replaced by secondary magnetite (e.g., Fig. 5.4B). The partial oxidation of pentlandite and pyrrhotite is also observed. Rare secondary violarite and cubanite are also identified; however, the most common secondary sulphide is pyrite which occurs in/as veins with other remobilised BMS cross-cutting the primary magmatic sulphide and silicate mineralogy (Fig. 5.3E and 5.4F).

The secondary alteration of the sulphides observed in the samples studied is in agreement with Ripley *et al.* (2005) who state that up to 30% of the BMS have been replaced by magnetite, serpentine and chlorite resulting in a proportion of the metals and sulphur in the BMS having been removed and re-deposited on a centimetre scale in fine ribbons and veins within secondary alteration minerals.

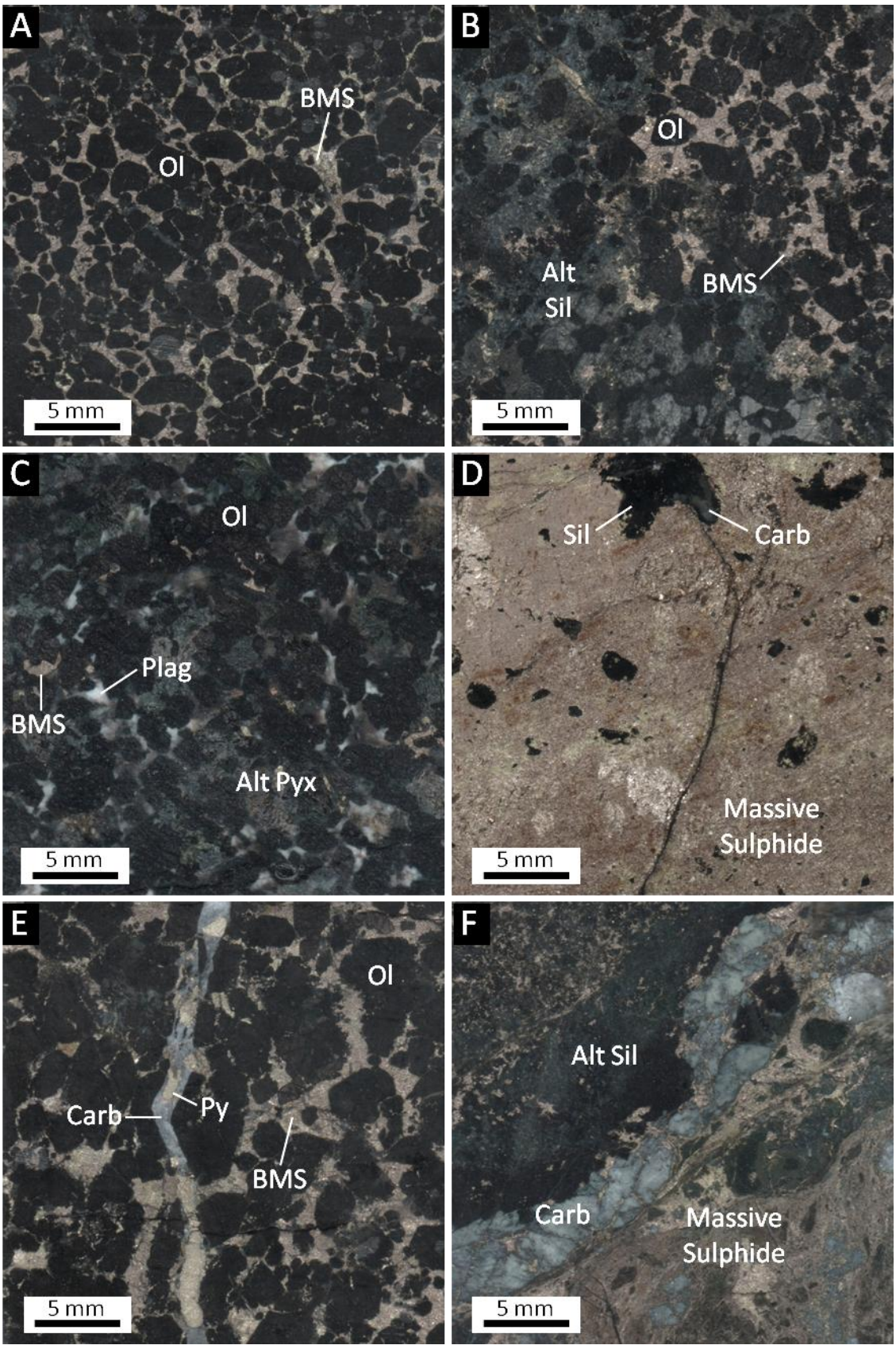


Figure 5.3: Scans of the Jinchuan core sampled showing the different types of sulphide mineralisation identified. A) Net-textured sulphide ore in dunite, Ol - olivine. B) 'Patchy' net-textured sulphide ore with interstitial sites to Ol variably filled by sulphides (BMS) and altered silicates (Alt Sil). C) Disseminated sulphides in plagioclase (Plag) lherzolite. D) Massive sulphide ore incorporating minor silicate and carbonate (Carb) material. E) Small scale sulphide (pyrite - Py) remobilisation in a carbonate vein. F) Massive sulphide remobilisation incorporating silicate and carbonate material.

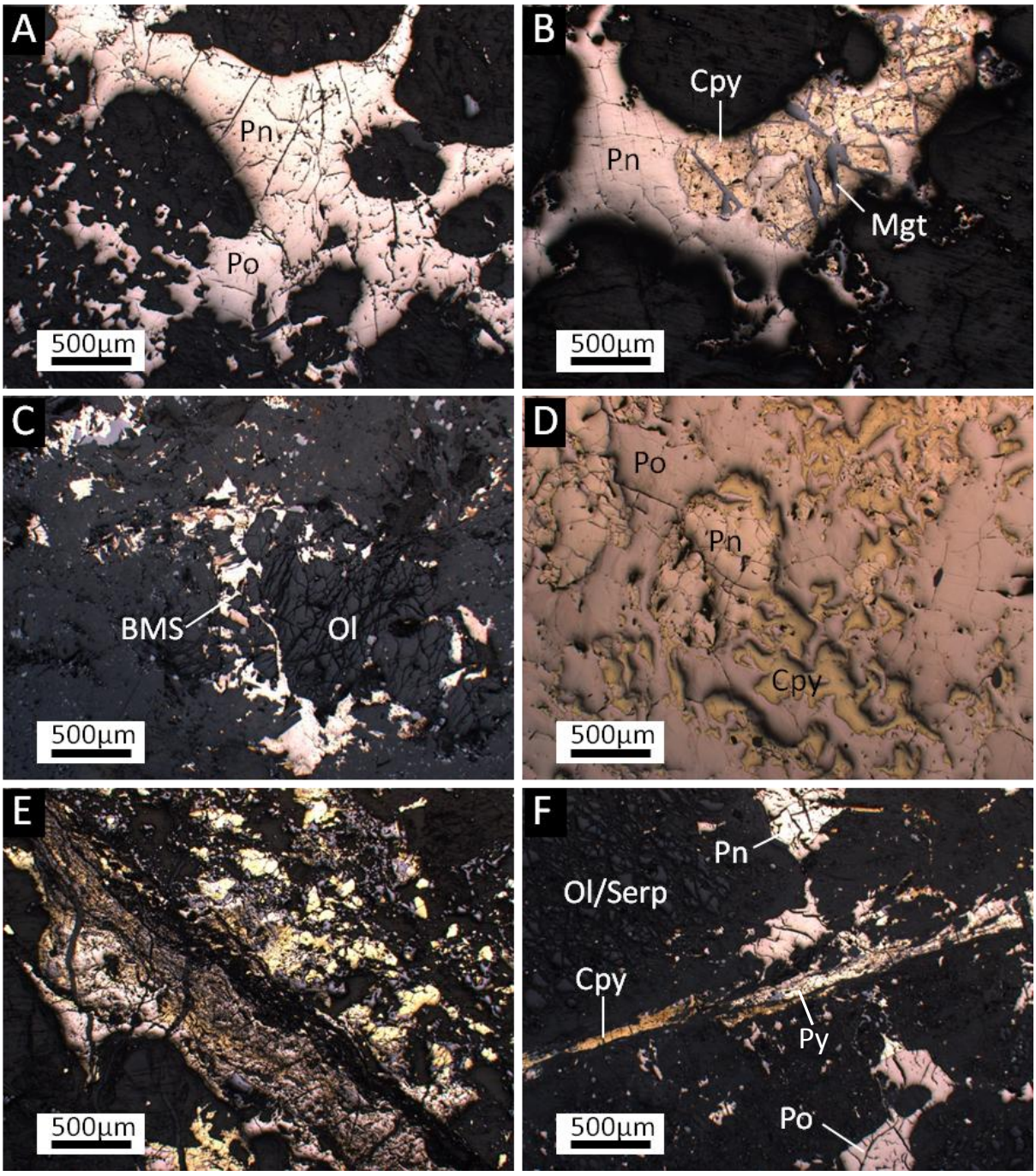


Figure 5.4: Reflected light photomicrographs showing the sulphide petrography of the Jinchuan intrusion. A) Net-textured BMS (pentlandite - Pn and pyrrhotite - Po) in dunite. B) Net-textured BMS (Pn and chalcopyrite - Cpy) with secondary magnetite (Mgt) veining predominantly in Cpy. C) Disseminated BMS with secondary Mgt surrounding olivine (Ol). D) Massive BMS (Pn, Po and Cpy). E-F) Examples of BMS remobilisation into veins with magnetite cross-cutting magmatic BMS and silicates (Serp - serpentine).

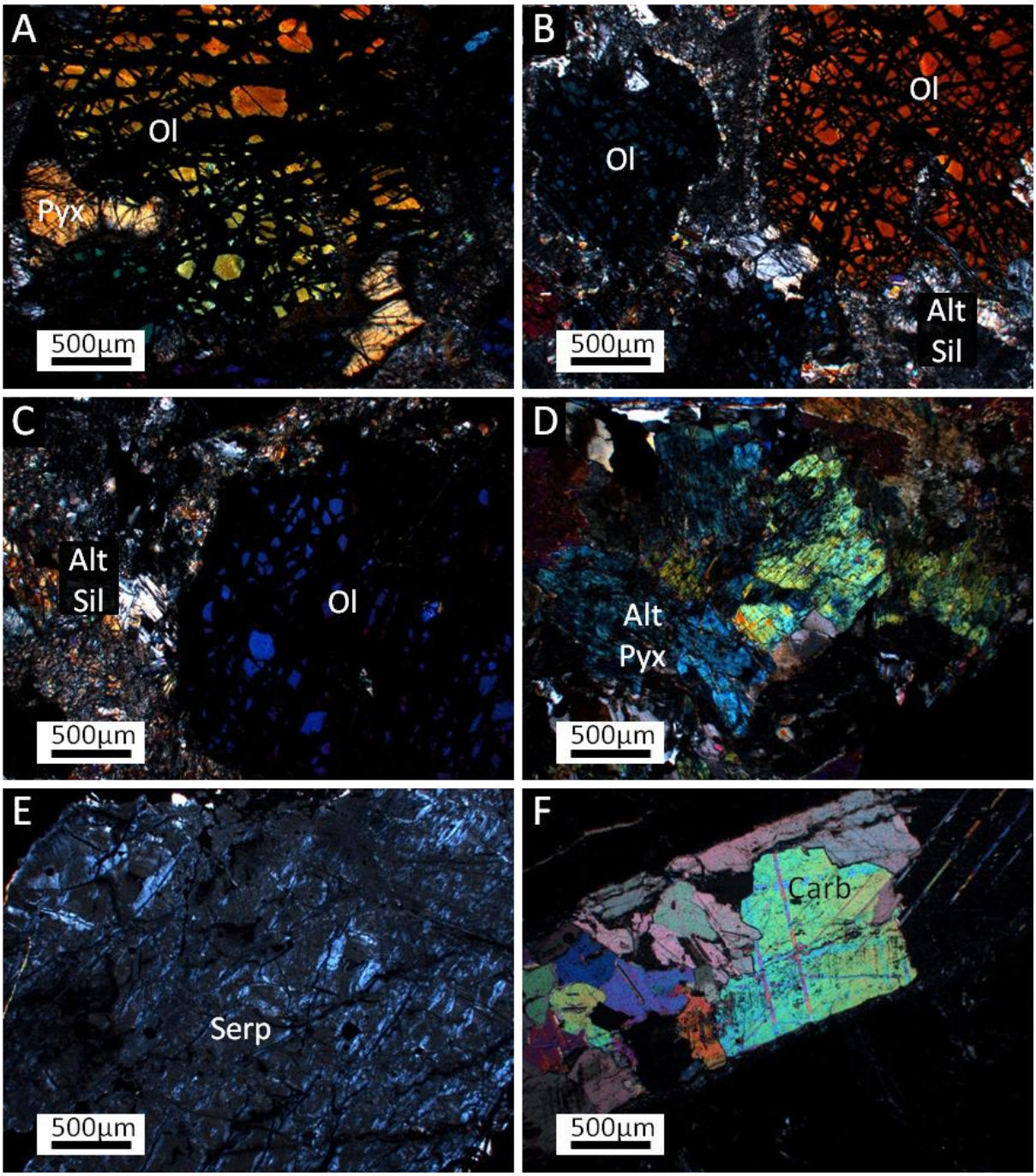


Figure 5.5: Transmitted light photomicrographs showing the silicate petrography of the Jinchuan intrusion. A) Altered relict olivine (Ol) with minor orthopyroxene (Pyx) preserved. B-C) Altered relict olivine with partially altered interstitial silicates (Alt Sil; primarily pyroxene altered to actinolite and tremolite) in lherzolite. D) Partially altered websterite. E) Completely serpentinised olivine (Serp) in dunite. F) Addition of secondary carbonate (Carb).

The lithologies hosting this mineralisation consist of dunite, websterite±olivine and lherzolite±minor plagioclase. These samples have undergone varying degrees of greenschist facies alteration. Cumulus olivine and pyroxene crystals are typically 0.5-2 cm in size and are enclosed by a fine grained altered silicate groundmass or interstitial sulphides. Olivine is always altered to some extent, occurring as relict olivine veined and enclosed by secondary serpentine and magnetite (Fig. 5.5A-C). Olivine is commonly observed having been completely altered to serpentine and magnetite (Fig. 5.5E), particularly in dunite samples hosting net-textured sulphides. Interstitial pyroxene and minor plagioclase (where present) have been altered to mixtures of fined grained chlorite, tremolite and actinolite (Fig. 5.5B-C) in lherzolite samples. In some websterite samples, orthopyroxene is partially preserved with the remainder altered to chlorite and amphibole (Fig. 5.5D). In many cases there are secondary veins of carbonate cross-cutting the greenschist facies alteration minerals (Fig. 5.5F) which most likely originate from the marbles into which the Jinchuan complex has intruded.

5.6 Major and Trace Element Geochemistry

5.6.1 Major element Harker diagrams

Major element Harker diagrams plotted against MgO for the 15 representative samples analysed from three different boreholes show two distinct groups of samples; group 1 and group 2. Two samples, a marble and a carbonatised websterite are shown to be independent of these two groups. Both of these samples have much lower MgO at ~15 wt. % and much higher CaO (~15 wt. % for the carbonatised websterite and ~40 wt. % for the marble) than the two main groups.

Group 1 consists predominantly of websterite, olivine websterite and lherzolite with orthopyroxene oikocrysts whereas group 2 consists of lherzolite, olivine-rich lherzolite and dunite. Both group 1 and 2 exhibit similar MgO concentrations at ~25-30 wt. %, however, group 1 samples have higher TiO_2 (~0.3-0.5 wt. %), Al_2O_3 (~3.0-6.5 wt. %), and Na_2O (~3.0-7.0 wt. %) concentrations than group 2 (~0.5-0.2 wt. %, ~0.0-2.2 wt. %, and ~0.0-1.0 wt. %, respectively) whereas group 2 samples have higher Fe_2O_3 (~30-35 wt. %) than group 1 (~15-25 wt. %). Both groups have similar CaO (~0.0-5.0 wt. %) and MnO (~0.15-0.20 wt. %) concentrations.

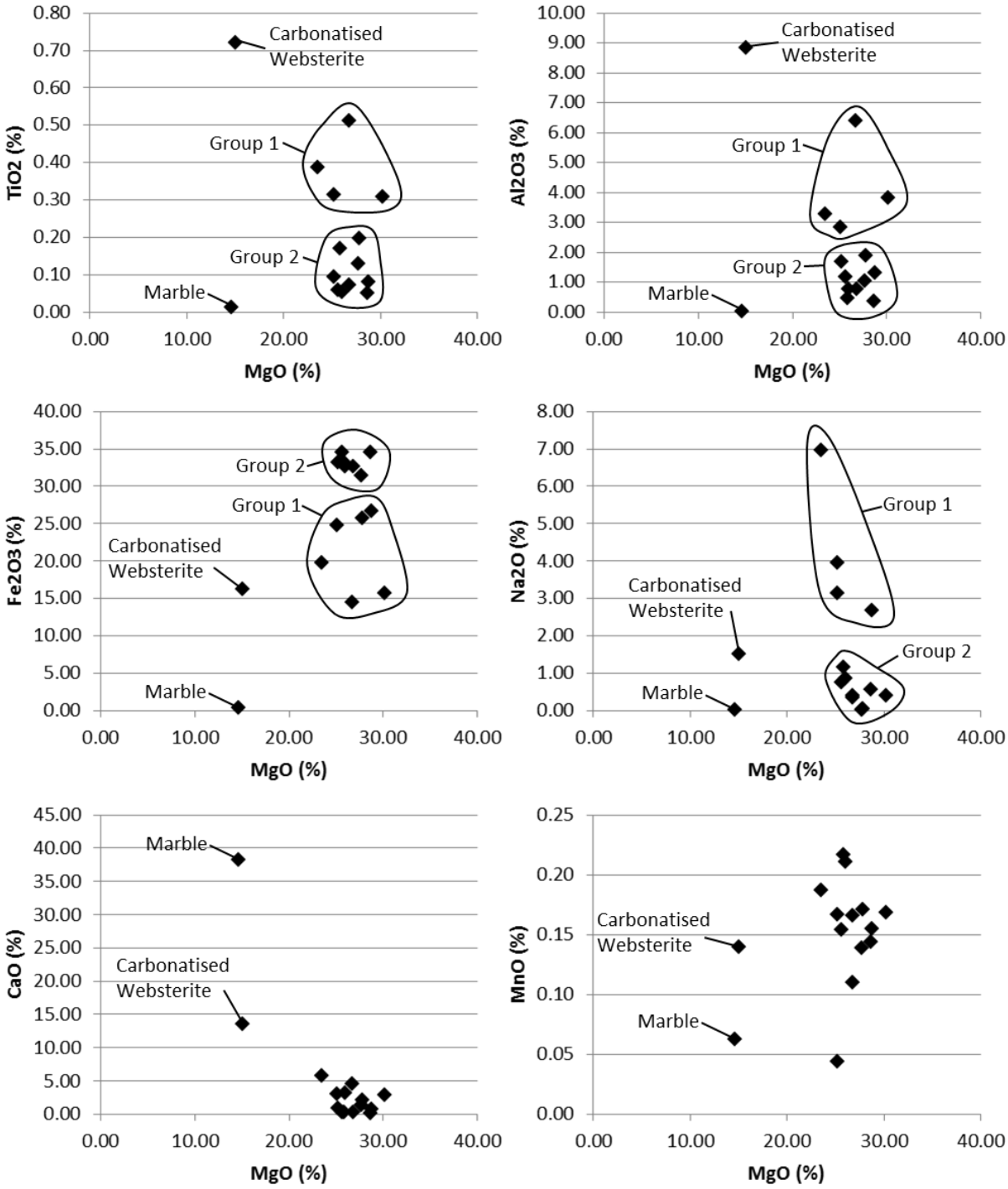


Figure 5.6: Major element Harker diagrams plotted against MgO for selective representative samples showing two distinct groups; 1 and 2.

5.6.2 Trace element bivariate plots

Trace element bivariate plots have been constructed in an effort to determine any differences in the genesis of the two orebodies studied. Plots of La/Sm-Sm and Sm/Nd-Nd (Fig. 5.7a-b) show that the chemistry of the different lithologies of the Jinchuan intrusion over the different orebodies overlap (i.e., there is no discernible difference between the chemistry of the orebody #1 and orebody #24 rocks). This same pattern is observed on basalt discrimination diagrams of Zr/Y-Ti/Y, V-Ti, and Y-Nb (Fig. 5.7d-f).

An overall pattern is observed, however, particularly in the plots of La/Sm-Sm and Sm/Nd-Nd (Fig. 5.7a-b) showing a trend of the evolution of dunite to websterite. The dunite and lherzolite samples are relatively closely grouped whereas websterite samples are somewhat isolated. This may represent typical fractional crystallisation or that two different magmas are involved in the formation of dunite/lherzolite and websterite, respectively. If the latter is true, the development of these two magmas has been consistent across both orebodies producing the overlap in orebody #1 and orebody #24 dunite, lherzolite and websterite samples, respectively.

High Th/Nb ratios (0.16-0.63) indicate that the Jinchuan magma has undergone variable degrees of crustal contamination. The plot of U/Th-Th (Fig. 5.7c) shows that the lithologies show similar degrees of crustal contamination which have been slightly modified as a product of fractional crystallisation. Lehmann *et al.* (2007) state that this relative enrichment of incompatible trace elements coupled with negative U-Th and Nb-Ta anomalies in all samples from the intrusion provide evidence that the parental magma assimilated granitoid rocks in the lower crust. In situ crustal contamination is also clearly shown by carbonate material in the ultramafics including the presence of decarbonitised marble xenoliths.

Fig. 5.7a)

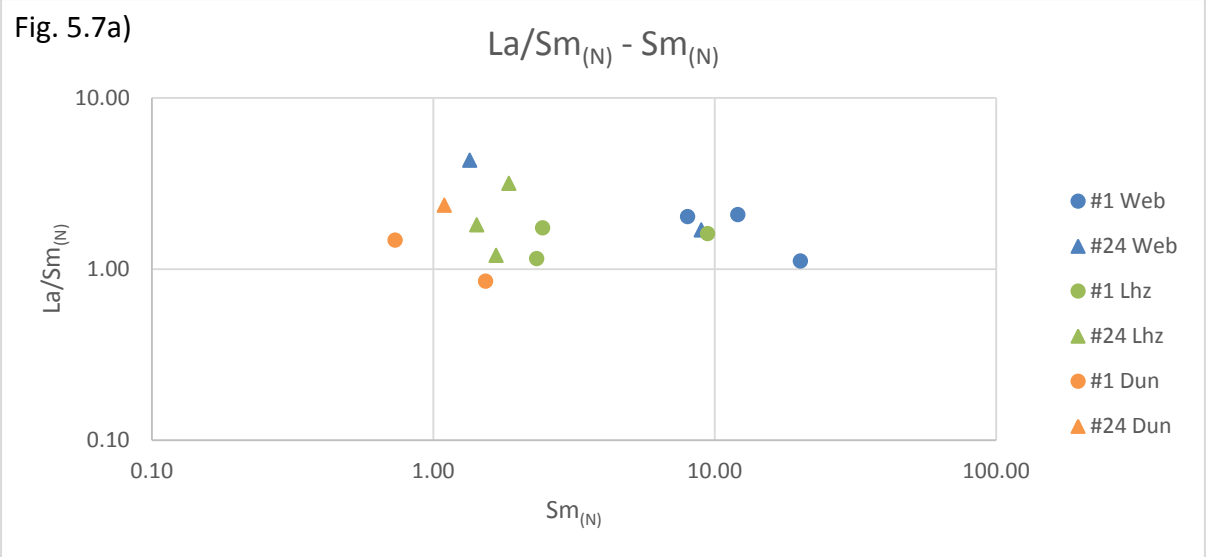


Fig. 5.7b)

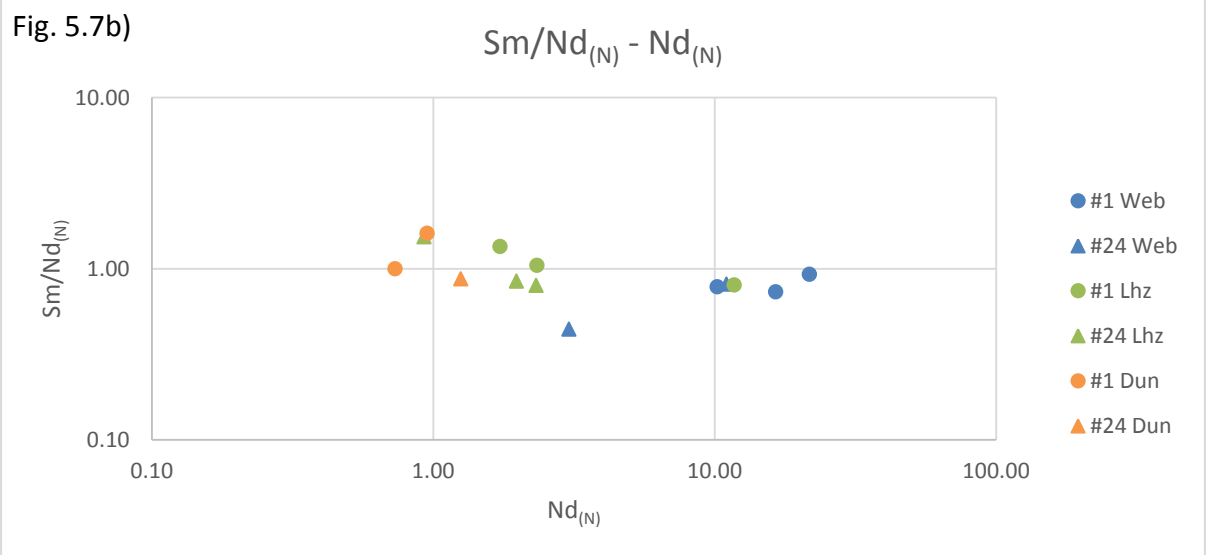


Fig. 5.7c)

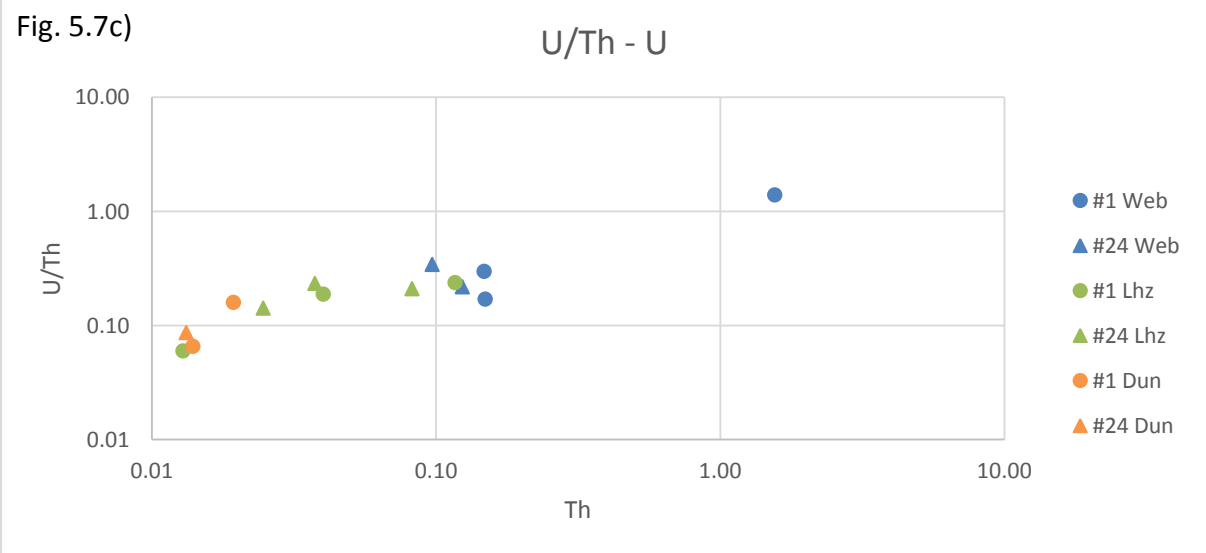


Fig. 5.7d)

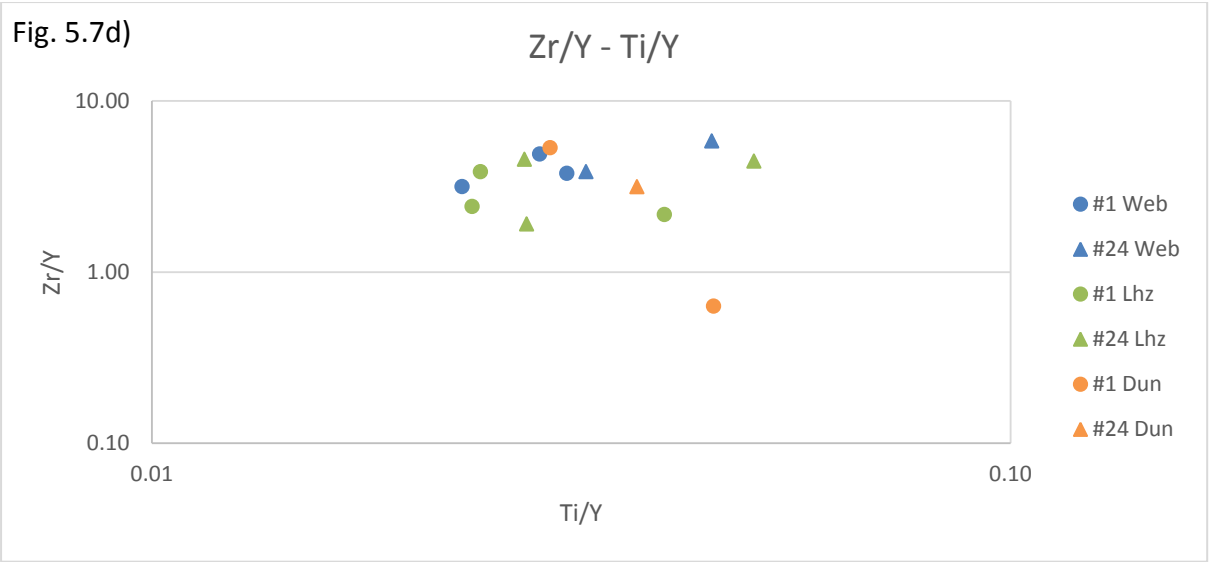


Fig. 5.7e)

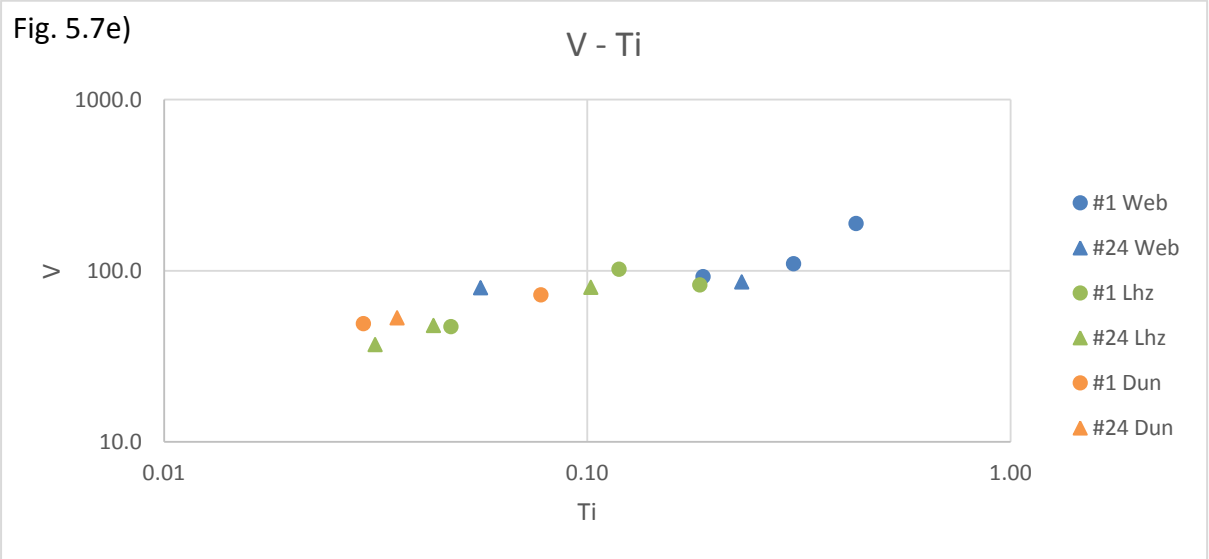


Fig. 5.7f)

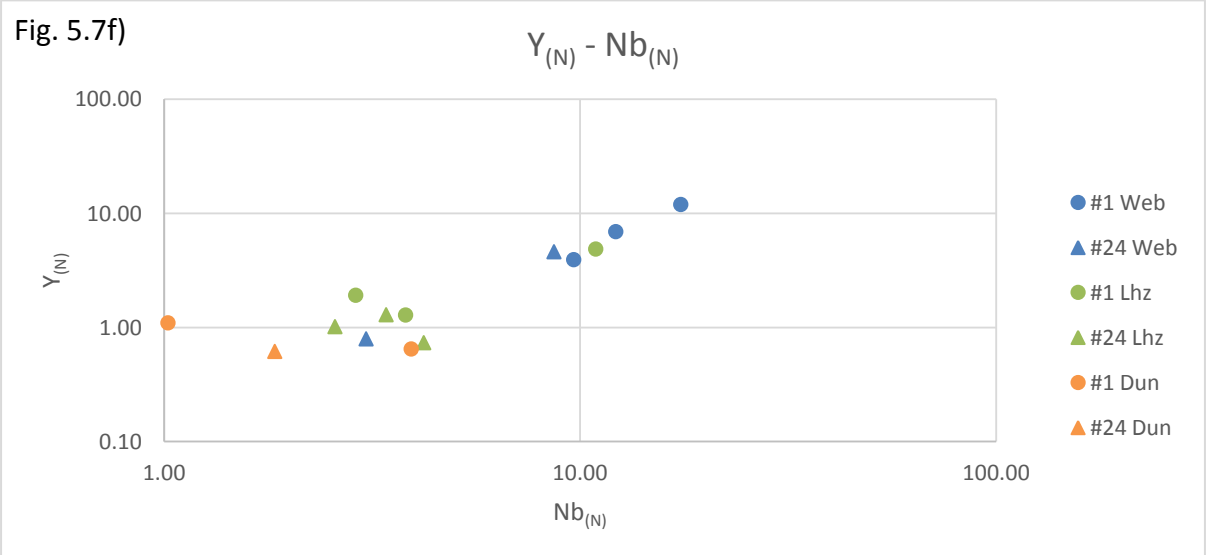


Figure 5.7a-f): A series of trace element bivariate plots constructed to determine the difference in the genesis between orebody #1 and orebody #24 in the Jinchuan intrusion. (N) = chondrite normalised using the values given in McDonough and Sun (1995).

5.7 Whole-Rock PGE Data and Chondrite Normalised Profiles

Chondrite normalised plots used to display and interpret whole-rock PGE data have been constructed using the values given in Lodders (2003). The data have been divided into four separate graphs relating to the four different boreholes sampled. The chondrite normalised patterns all have positive slopes but they show significant variation in elevation.

The most westerly borehole, ZKS-09 in orebody #24, segment I, displays what appear to be relatively elevated PGE profiles that are quite closely spaced (Fig. 5.8a). However, progressively towards the east into orebody #1, segment II (boreholes DZK09-01, DZK12-06 and DZK14-02 in order from west to east within orebody #1), PGE concentrations generally decrease (Fig. 5.8b-d). Furthermore, the PGE profiles for individual samples in each borehole become progressively further apart representing differing concentrations of total PGE, although the positive slopes remain relatively constant.

Whole-rock Pt concentrations vary greatly with anomalously high and low values displayed. Negative Pt anomalies are particularly prominent in orebody #24 (Fig. 5.8a) whereas in the other three boreholes from orebody #1, both positive and negative Pt anomalies are observed (Fig. 5.8 b-d). These Pt anomalies become even more apparent when studying original and duplicate samples used in the Ni-fire assay procedure in order to check for any analytical drift in isolation (Fig. 5.9). The majority of the PGE match closely with each other, however, Au, Pt and to some extent Rh (RK18) show variation in the duplicated sample runs.

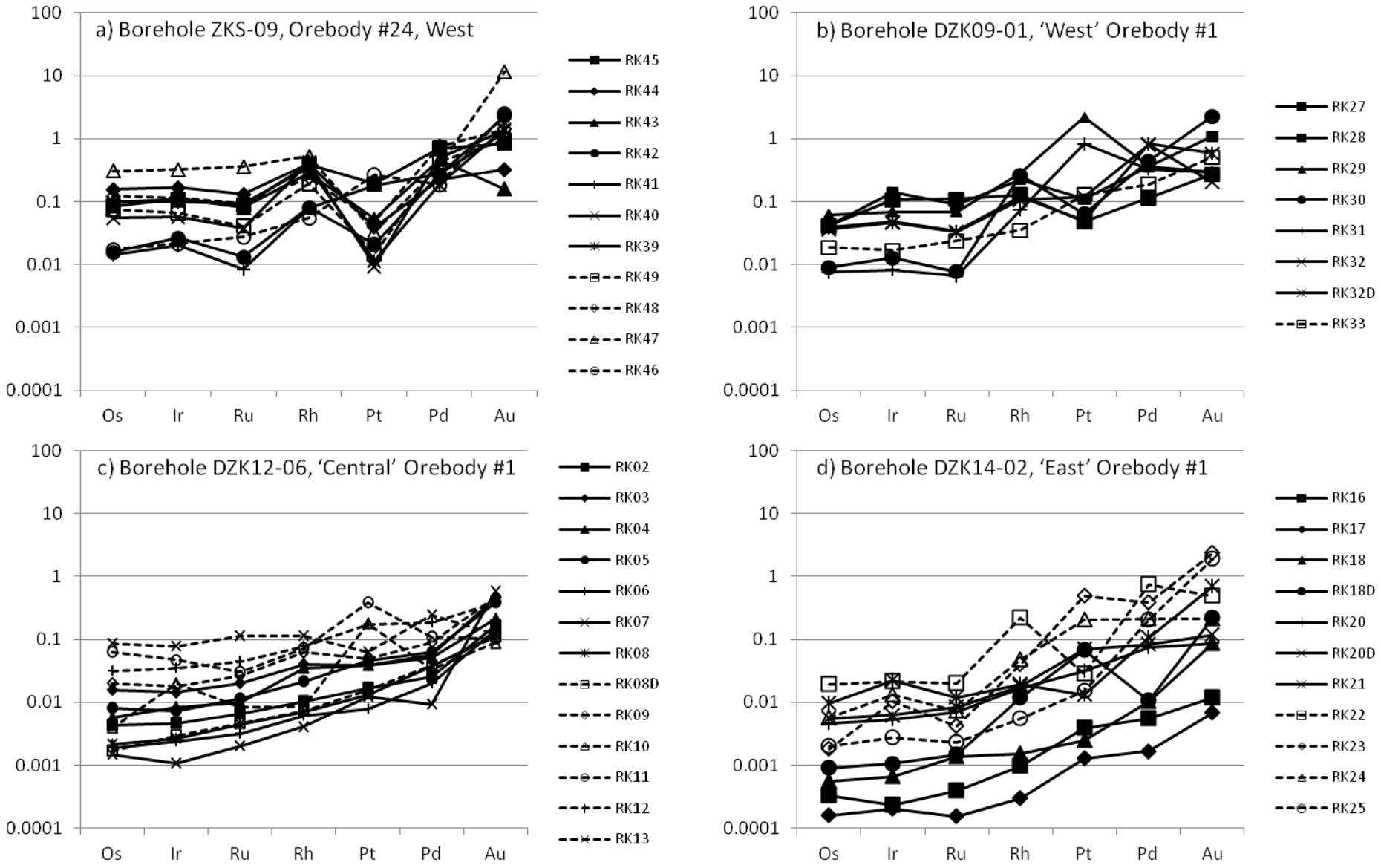


Figure 5.8: Chondrite normalised (using the values given in Lodders, 2003) PGE diagrams showing a) samples from borehole ZKS-09, orebody #24, segment I to the west and b-d) samples from DZK09-01, DZK12-06 and DZK14-02, respectively, orebody #1, segment II to the east.

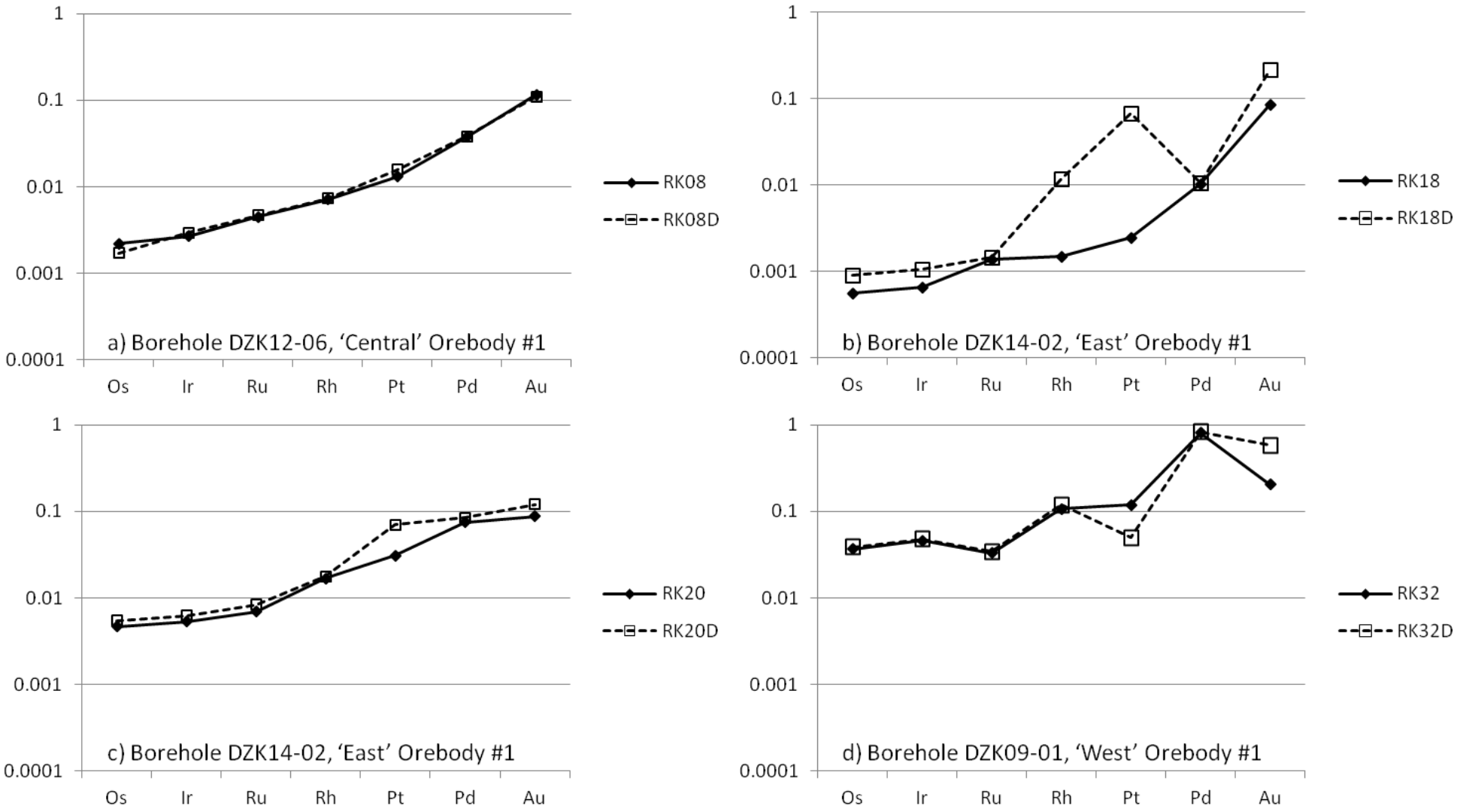


Figure 5.9: Chondrite normalised (using the values given in Lodders, 2003) PGE diagrams showing original and duplicate analyses used to check for analytical drift in isolation. a-d) Significant variation in Pt and occasionally Rh (b) can be observed.

5.8 Platinum-Group Mineralogy

A total of 93 PGM have been identified. These fall into the following five categories; froodite ($PdBi_2$±Fe), michenerite (PdBiTe±Fe-Pb), maslovite ($Pt[Bi,Te]_2$), members of the hollingworthite-irarsite-platarsite solid solution series ([RhIrPt]AsS) and sperrylite ($PtAs_2$). Rare additional PGM falling outside of these categories are grouped together as "other" PGM. A further 64 associated accessory minerals identified include Au-Ag-Fe, Ag-Te and semimetal-rich Pb-bearing phases. The types and numbers of PGM and associated accessory minerals observed in the samples studied are given in Table 5.2. Selective representative quantitative analyses and PGM formulae are given in Table 5.3.

Palladium-bearing PGM, froodite and michenerite which have been identified quantitatively, typically occur as subhedral grains exhibiting either lath or sub-rounded crystal forms although anhedral forms are noted occasionally. The majority of these PGM are associated with the BMS occurring either apparently enclosed by these sulphide phases (Fig. 5.10A) or at their edges where the PGM are also in contact with a silicate, oxide or another sulphide phase. In some cases, these Pd-bearing PGM are associated with magnetite (Fig. 5.10B) or partially oxidised pentlandite or pyrrhotite. They are also often associated with PGE-barren semimetal- and Pb-bearing minerals. These Pd-bearing PGM are relatively small averaging 5.5 μm^2 and have quite a restricted size range from 0.4-24.4 μm^2. Quantitative analyses have also revealed one Pd-bearing PGM with the formula $(PdNi)(TeBi)_2$.

Another Bi- and Te-bearing PGM, maslovite has been identified quantitatively. Only three of these minerals have been observed. These PGM display similar subhedral crystal forms to froodite and michenerite, however, they exhibit three different mineral associations with one identified within BMS (Fig. 5.10C), one occurring in a zone of BMS veining and one within serpentine (Fig. 5.10D). The size of these three maslovites is extremely variable with sizes of 2.3 μm^2, 7.8 μm^2 and 47.4 μm^2 recorded.

Sperrylite is predominately identified within silicates (Fig. 5.10E) and is less commonly observed with the BMS. It generally occurs as euhedral-subhedral crystals, however, one sperrylite appears sheared and heavily fractured (Fig. 5.10F). Sperrylite occurs as rare but much larger crystals (compared to the Pd-bearing PGM) ranging in size from 10.3-172.5 μm^2 with an average size of 62.3 μm^2.

Orebody	Borehole	Sample No.	Platinum-Group Mineral Types									
			Au-Ag-Fe	Ag-Te	Semimetal Alloy	$PdBi_2$±Fe	PdBiTe± Fe-Pb	$Pt(BiTe)_2$	(RhIrPt)AsS	$PtAs_2$	Other	Total
#1	DZK12-06	RK01	-	-	-	-	-	-	-	-	-	-
#1	DZK12-06	RK02	1	-	-	2	-	-	-	1	-	4
#1	DZK12-06	RK03	-	1	2	2	-	-	-	-	2	7
#1	DZK12-06	RK04	-	-	5	-	-	2	-	-	2	9
#1	DZK12-06	RK05	-	5	1	-	-	-	1	-	1	8
#1	DZK12-06	RK06	-	1	1	-	-	-	-	-	-	2
#1	DZK12-06	RK07	-	-	2	1	-	-	-	-	-	3
#1	DZK12-06	RK08	-	-	-	-	-	-	-	-	-	-
#1	DZK12-06	RK09	-	-	-	-	-	-	1	-	-	1
#1	DZK12-06	RK10	1	7	-	-	-	-	1	1	-	10
#1	DZK12-06	RK11	-	-	-	-	-	-	-	-	-	-
#1	DZK12-06	RK12	-	-	-	-	-	-	1	-	-	1
#1	DZK12-06	RK13	-	-	-	-	-	-	1	-	-	1
#1	DZK12-06	RK14	-	-	-	-	-	-	2	-	1	3
Orebody #1 - DZK12-06 Total			2	14	11	5	0	2	7	2	6	49
#1	DZK14-02	RK16	-	-	-	-	-	-	-	-	-	-
#1	DZK14-02	RK17	-	-	-	-	-	-	-	-	-	-
#1	DZK14-02	RK18	-	-	-	-	-	-	-	-	-	-
#1	DZK14-02	RK19	-	-	-	-	-	-	3	-	-	3
#1	DZK14-02	RK20	-	1	-	2	1	-	1	-	-	5
#1	DZK14-02	RK21	-	-	-	-	1	-	-	-	3	4
#1	DZK14-02	RK23	-	-	-	-	-	-	-	-	-	-
#1	DZK14-02	RK24A	1	-	-	-	-	-	-	1	-	2
#1	DZK14-02	RK24B	1	4	3	-	1	-	-	-	4	13
#1	DZK14-02	RK25	4	-	1	-	-	-	-	-	-	5
Orebody #1 - DZK14-02 Total			6	5	4	2	3	0	4	1	7	32

Orebody	Borehole	Sample No.	Platinum-Group Mineral Types									
			Au-Ag-Fe	Ag-Te	Semimetal Alloys	$PdBi_2$±Fe	PdBiTe± Fe-Pb	$Pt(BiTe)_2$	(RhIrPt)AsS	$PtAs_2$	Other	Total
#1	DZK09-01	RK27	-	-	-	-	-	-	-	1	5	6
#1	DZK09-01	RK29	-	-	1	-	-	-	1	-	-	2
#1	DZK09-01	RK30	1	-	-	2	-	-	-	-	1	4
#1	DZK09-01	RK31	-	-	-	-	-	-	-	1	-	1
#1	DZK09-01	RK33	1	3	1	-	4	-	-	1	2	12
#1	DZK09-01	RK34	2	-	-	-	-	-	-	-	-	2
Orebody #1 - DZK09-01 Total			4	3	2	2	4	0	1	3	8	27
Orebody #1 - All Boreholes Total			12	22	17	9	7	2	12	6	21	108
#24	ZKS-09	RK39	-	-	-	1	1	-	-	-	-	2
#24	ZKS-09	RK40	-	-	4	6	3	-	-	-	-	13
#24	ZKS-09	RK41	-	-	-	-	-	-	-	-	-	-
#24	ZKS-09	RK42	8	-	-	-	-	-	1	-	-	9
#24	ZKS-09	RK43	-	1	-	-	1	-	1	-	1	4
#24	ZKS-09	RK44	-	-	-	1	-	-	-	-	-	1
#24	ZKS-09	RK45	-	-	-	3	7	1	-	-	-	11
#24	ZKS-09	RK46	-	-	-	-	-	-	-	-	-	-
#24	ZKS-09	RK48	-	-	-	3	5	-	-	-	1	9
#24	ZKS-09	RK49	-	-	-	-	-	-	-	-	-	-
Orebody #24 - ZKS-09 Total			8	1	4	14	17	1	2	0	2	49

Table 5.2: Numbers and types of PGM observed in the samples studied from orebodies #1 and #24 from segments II and I, respectively, of the Jinchuan intrusion.

Borehole	Sample	PGM No.	Quantitative Analyses (wt. %)													PGM Composition
			S	Fe	Co	Ni	Cu	As	Pd	Te	Os	Ir	Rh	Pt	Bi	Total	
DZK12-06	RK14	NA1	19.85	4.65	23.15	8.92	-	43.97	-	-	-	-	-	-	-	100.54	Gersdorffite-Cobaltite
DZK09-01	RK29	NA2	19.64	5.82	21.01	9.92	-	42.89	-	-	-	-	-	-	-	99.28	Gersdorffite-Cobaltite
DZK14-02	RK21	C1	20.15	6.59	17.27	11.01	-	42.07	-	-	-	-	2.75	-	-	99.84	Gersdorffite-Cobaltite + Rh
DZK14-02	RK21	D1	20.08	5.80	18.04	11.67	1.00	42.83	-	-	-	-	0.57	-	-	99.99	Gersdorffite-Cobaltite + Rh
DZK12-06	RK10	G1	-	-	-	-	-	43.86	-	-	-	-	-	56.30	-	100.16	$Pt_{0.99}As_{2.01}$
DZK14-02	RK24A	B1	-	-	-	-	-	41.27	-	-	-	-	-	58.94	-	100.21	$Pt_{1.06}As_{1.94}$
ZKS-09	RK42	F1	11.08	-	-	-	-	26.81	-	-	4.35	43.59	-	13.19	-	99.02	$(Ir_{0.67}Pt_{0.20}Os_{0.07})_{0.94}As_{1.05}S_{1.01}$
ZKS-09	RK40	F1	-	-	-	-	-	-	20.57	-	-	-	-	-	79.63	100.20	$Pd_{1.01}Bi_{1.99}$
ZKS-09	RK48	F1	-	-	-	-	-	-	21.40	-	-	-	-	-	78.84	100.24	$Pd_{1.04}Bi_{1.96}$
ZKS-09	RK43	B1	-	-	-	-	-	-	24.43	29.53	-	-	-	-	47.07	101.03	$Pd_{1.00}Bi_{0.99}Te_{1.01}$
ZKS-09	RK48	G1	-	-	-	-	-	-	22.89	29.43	-	-	-	-	48.12	100.44	$Pd_{0.96}Bi_{1.02}Te_{1.02}$
DZK14-02	RK24B	E1	-	-	-	5.61	-	-	17.71	53.27	-	-	-	-	24.30	100.89	$(Pd_{0.63}Ni_{0.36})_{0.99}(Te_{1.57}Bi_{0.44})_{2.01}$
ZKS-09	RK45	F1	-	-	-	-	-	-	-	44.57	-	-	-	37.96	16.79	99.32	$Pt_{0.94}(Bi_{0.38}Te_{1.68})_{2.06}$

Table 5.3: Selective representative quantitative analyses (wt. %) of PGM with derived empirical formulae.

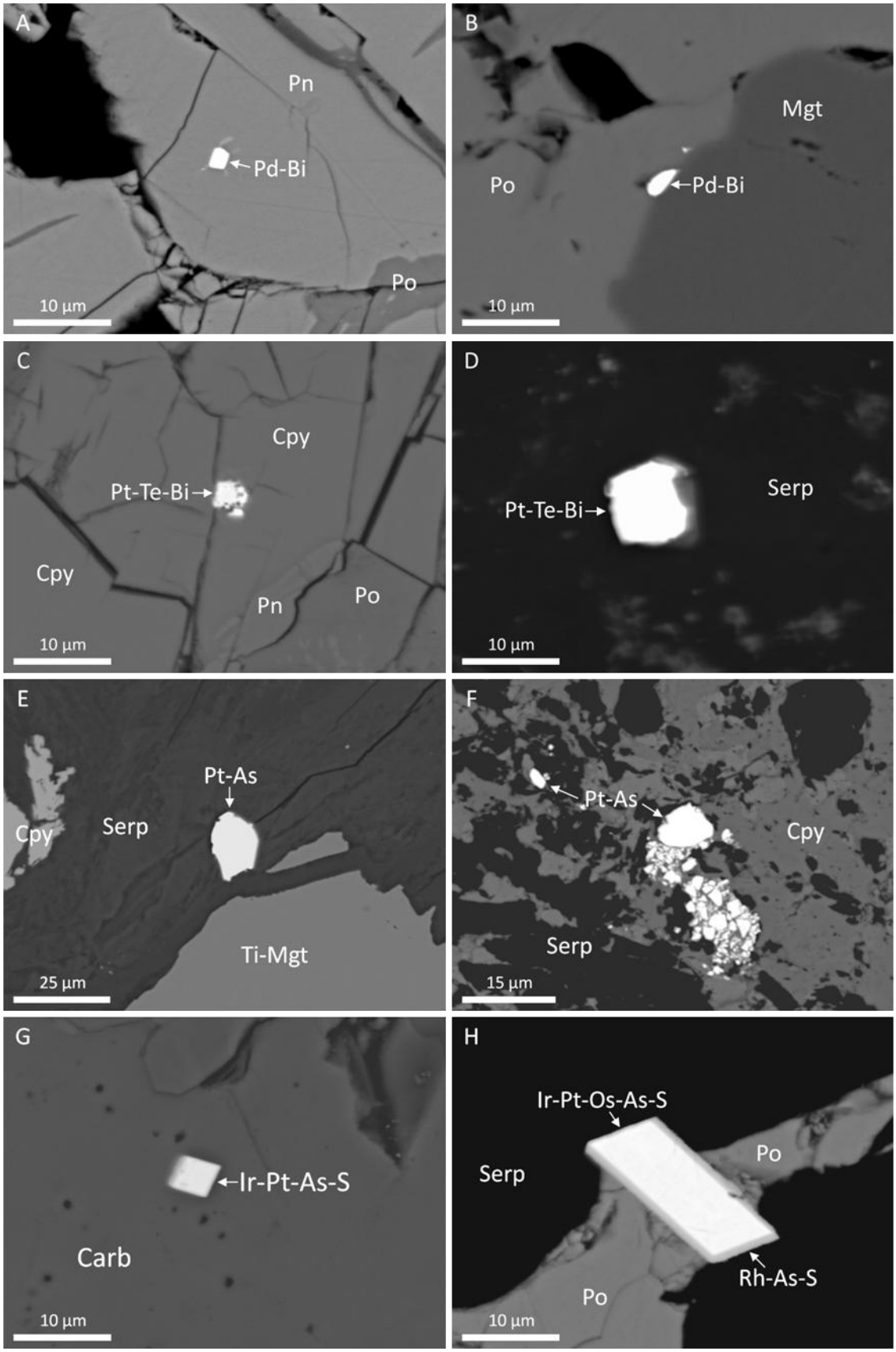


Figure 5.10: Back-scattered electron images of the typical PGM observed in samples from the Jinchuan intrusion. A) Tabular or lath shaped froodite ($PdBi_2$) within pentlandite (Pn) associated with pyrrhotite (Po). B) Froodite occurring within Po and associated with magnetite (Mgt). C) Maslovite ($Pt[BiTe]_2$) within chalcopyrite (Cpy) associated with Pn and Po. D) Maslovite within serpentine (Serp). E) Sperrylite ($PtAs_2$) within Serp. F) Sheared sperrylite within altered Cpy with Serp. G) Euhedral tabular irarsite with Pt in carbonate (Carb). H) Irarsite (IrAsS) with minor Pt and Os rimmed by hollingworthite (RhAsS) associated with Po.

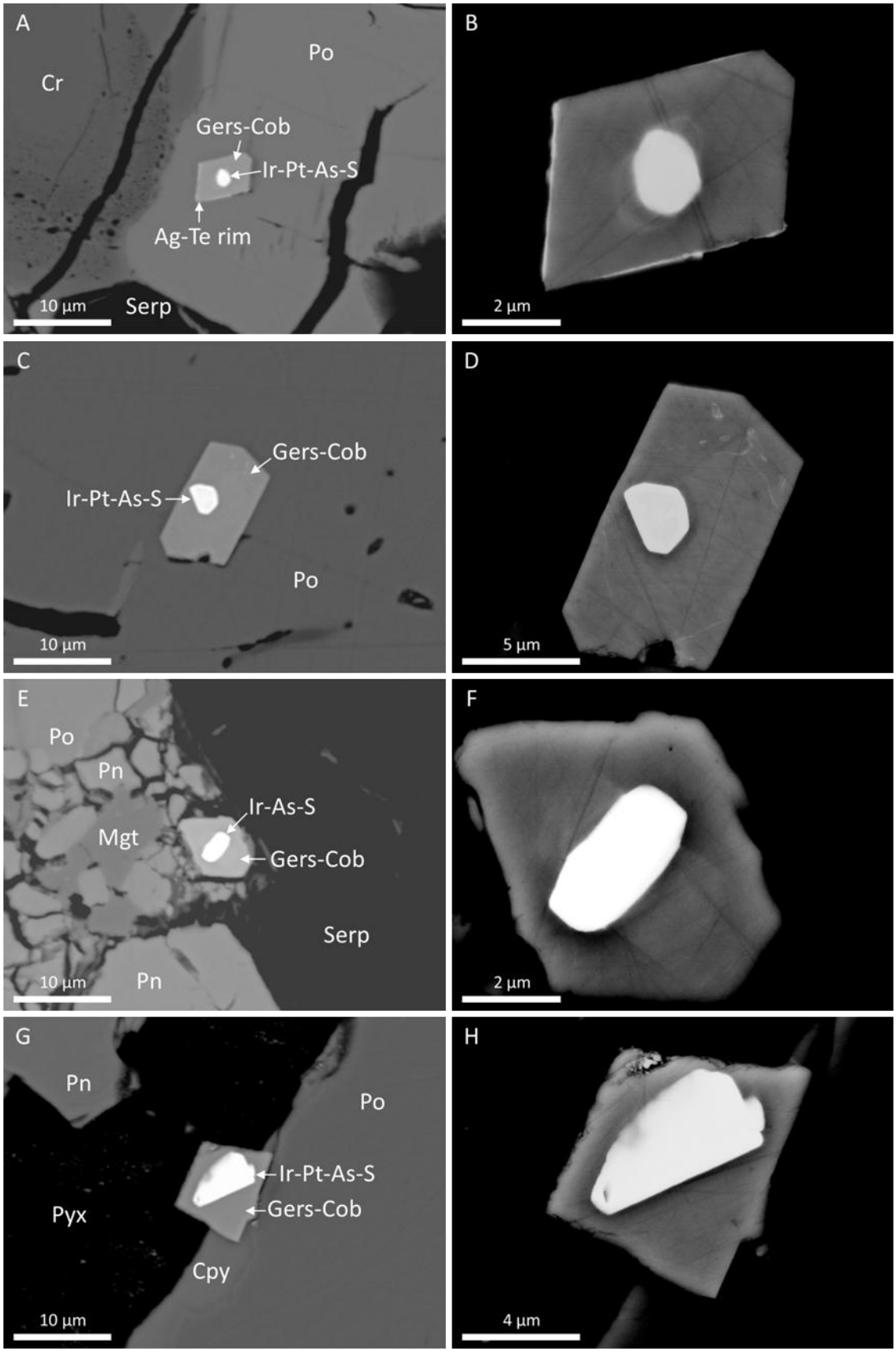


Figure 5.11: Back-scattered electron images of small zoned euhedral gersdorffite-cobaltite (Gers-Cob) hosting irarsite with minor Pt ([Ir,Pt]AsS) in their cores. These may exhibit partial halos of PGE-rich material (A, F) and minor anhedral patches of Ir-Rh exsolution (D). Zoning is also indicated by dense (bright) material occurring at the edges of the Gers-Cob (F, H). Cpy - chalcopyrite, Cr - chromite Mgt - magnetite Pn - pentlandite, Po - pyrrhotite, Pyx - pyroxene.

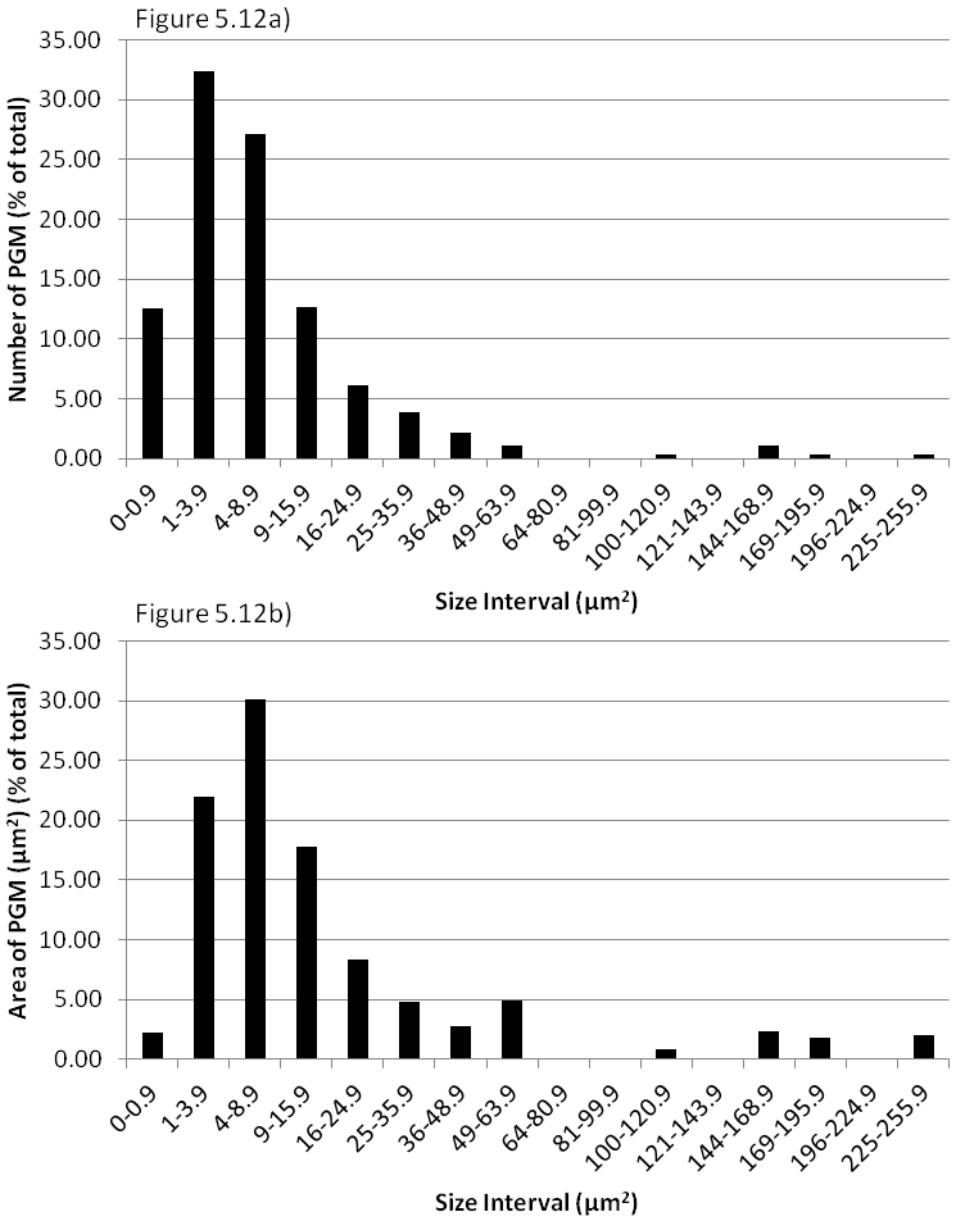


Figure 5.12: PGM size distribution graphs showing a) the proportion of PGM per interval size (μm^2) calculated by the number of PGM per interval size and b) the proportion of PGM per interval size (μm^2) calculated by the total area of PGM per interval size.

A characteristic feature of these ores is the overwhelming association of members of the hollingworthite-irarsite-platarsite solid solution series (typically irarsite with minor Pt and Rh) occurring within gersdorffite-cobaltite (Fig. 5.11A-H). Despite the rarity of gersdorffite-cobaltite crystals in the Jinchuan ores, particularly in comparison to the other sulphides present, euhedral irarsite (Fig. 5.11A-D), typically 5-20 μm^2, is consistently identified within small gersdorffite-cobaltite crystals, usually <0.5 mm^2. Rhodium and sometimes Ir are identified in solid solution in some of these gersdorffite-cobaltite crystals. In several cases, Rh concentrations are high enough (up to 2.75 wt. %) to produce slightly brighter anhedral

patches within the gersdorffite-cobaltite in backscattered electron images (Fig. 5.11B, F). Furthermore, these gersdorffite-cobaltite crystals appear slightly zoned with denser (brighter) material concentrated towards the edges of the crystals.

A separate group of irarsites are observed that are not associated with gersdorffite-cobaltite and are identified predominantly within silicates but may also be associated with the BMS. These irarsites typically exhibit tabular euhedral crystal forms (Fig. 5.10G) and may be wholly or partially enveloped by hollingworthite (RhAsS; Fig. 5.10H). They are also slightly larger than those identified within gersdorffite-cobaltite ranging in size from 1.3-106 μm^2 and averaging 21 μm^2.

Accessory electrum, Ag-Te and semimetal (mixtures of Bi, Te, Se as well as Pb) minerals also occur in many of the samples studied and vary in abundance depending on the sample type. Silver telluride and semimetal minerals often accompany PGM and are therefore mostly associated with the BMS. Electrum occurs as both rare large isolated crystals (up to 250 μm^2) or as smaller grains (averaging 7 μm^2) in clusters (Fig. 5F) and is again mostly associated with the sulphides but is also identified within oxides and silicates.

PGM size distribution graphs (Fig. 5.12) show ~70% of the PGM fall within the size interval 1-15.9 μm^2 and that PGM of this size account for ~70% of the total PGM area observed in the Jinchuan intrusion. These graphs also show that PGM <1 μm^2 in size are frequent but are relatively insignificant in accounting for the total area of PGM observed.

5.8.1 Variation in PGM between orebodies #1 and #24

There is a dramatic difference in the platinum-group mineralogy between the more MSS-rich orebody #1, segment II and the more Cu-rich orebody #24, segment I. Orebody #1 hosts the vast majority of the irarsite and all of the sperrylite identified whereas orebody #24 hosts a much larger number of Pd-bearing phases (predominantly froodite and michenerite).

A total of 30 samples from orebody #1 were analysed for PGM and only ten samples from orebody #24. However, despite this, only 16 Pd-bearing PGM are identified in orebody #1 compared with 26 in orebody #24. In contrast, 12 irarsites and six sperrylites are identified in orebody #1 with only two irarsites identified in orebody #24 and sperrylite absent. Even when estimating the effect of the different number of samples (effectively multiplying the PGM numbers of orebody #24 by a factor of three), the variation in As-bearing PGM is still significant and the variation in Pd-bearing phases becomes enhanced.

Fig. 5.13a) Orebody #1, Segment II PGM proportions by total area

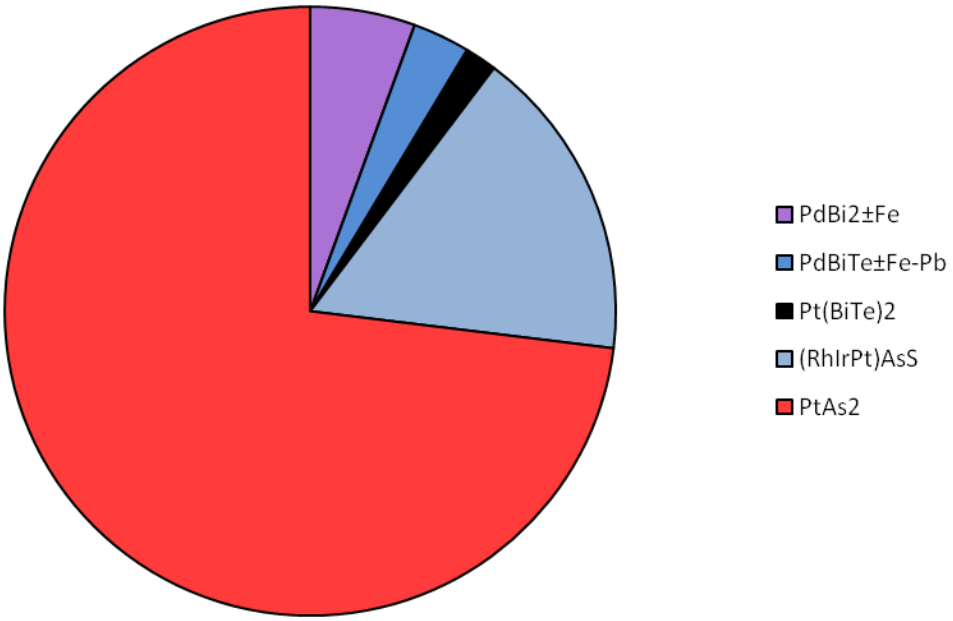


Fig. 5.13b) Orebody #24, Segment I PGM proportions by total area

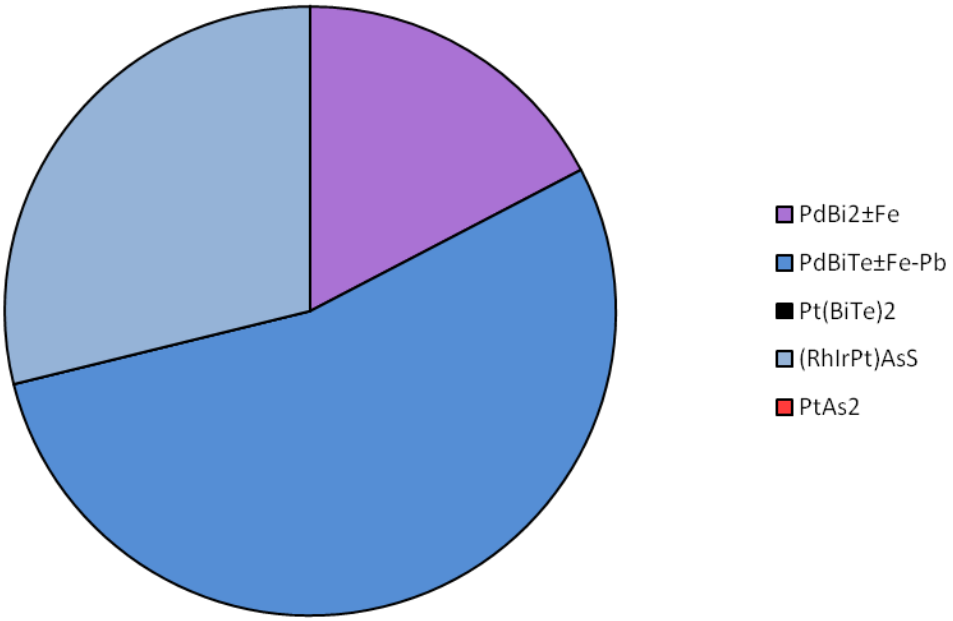


Figure 5.13: Pie charts showing the proportion of different PGM types in the two different orebodies studied; a) by the total area of PGM identified in orebody #1, segment II, and b) by the total area of PGM identified in orebody #24, segment I.

Pie charts displaying the proportions of the total areas for each type of PGM identified for orebodies #1 and #24 are shown in Figure 5.13. These show that although only six sperrylite grains are identified in orebody #1, they are sufficiently large to account for almost three quarters of the total PGM area calculated. The majority of the remaining quarter is accounted for by irarsite with the Pd-bearing phases, despite being greater in number, accounting for very little of the total PGE distribution given their small size. In contrast, in orebody #24 three quarters of the total PGM area calculated is accounted for by Pd-bearing PGM. Although only two irarsites are identified in orebody #24, they are sufficiently large to account for the remaining PGM area.

These charts effectively show that As-bearing phases are much less common than Pd-bearing phases, however, they are also much larger and are more significant in controlling the total distribution of PGE in any given sample. These charts also show the stark contrast in the types and numbers of PGM observed in the different orebodies studied (#1 and #24 from segments II and I, respectively).

5.9 Laser Ablation-ICP-MS

PGE and semimetal contents in solid solution in BMS have been determined using LA-ICP-MS (Table 5.4). Samples with relatively high whole-rock PGE concentrations that also display varying types of sulphide mineralisation, varying degrees of greenschist facies alteration and different numbers of PGM were selected for analysis. The principle primary BMS identified (pentlandite, pyrrhotite and chalcopyrite) as well as secondary pyrite where present were analysed predominantly for PGE and semimetals (As, Bi, Sb, Se and Te). The PGE content of gersdorffite-cobaltite crystals could not be analysed due to their small size and the fact that they often host PGM.

In order to show that these analyses represent true solid solution of PGE, analyses which indicate higher than average semimetal concentrations coupled with anomalously high PGE have been discounted from the data set as it is likely that PGM have been intercepted by the laser trace in these cases. Likewise, analyses where the time resolved spectra have clearly indicated the presence of PGM or PGM micro-inclusions have also been discounted.

The concentration of PGE in solid solution in all the BMS phases analysed is very low. With the exception of Pd in pentlandite, the average concentration of any individual PGE in any

sulphide analysed is <0.2 ppm. Pyrite where analysed is particularly PGE-poor with all of the PGE below their respective detection limits. Pentlandite is the only BMS to host any

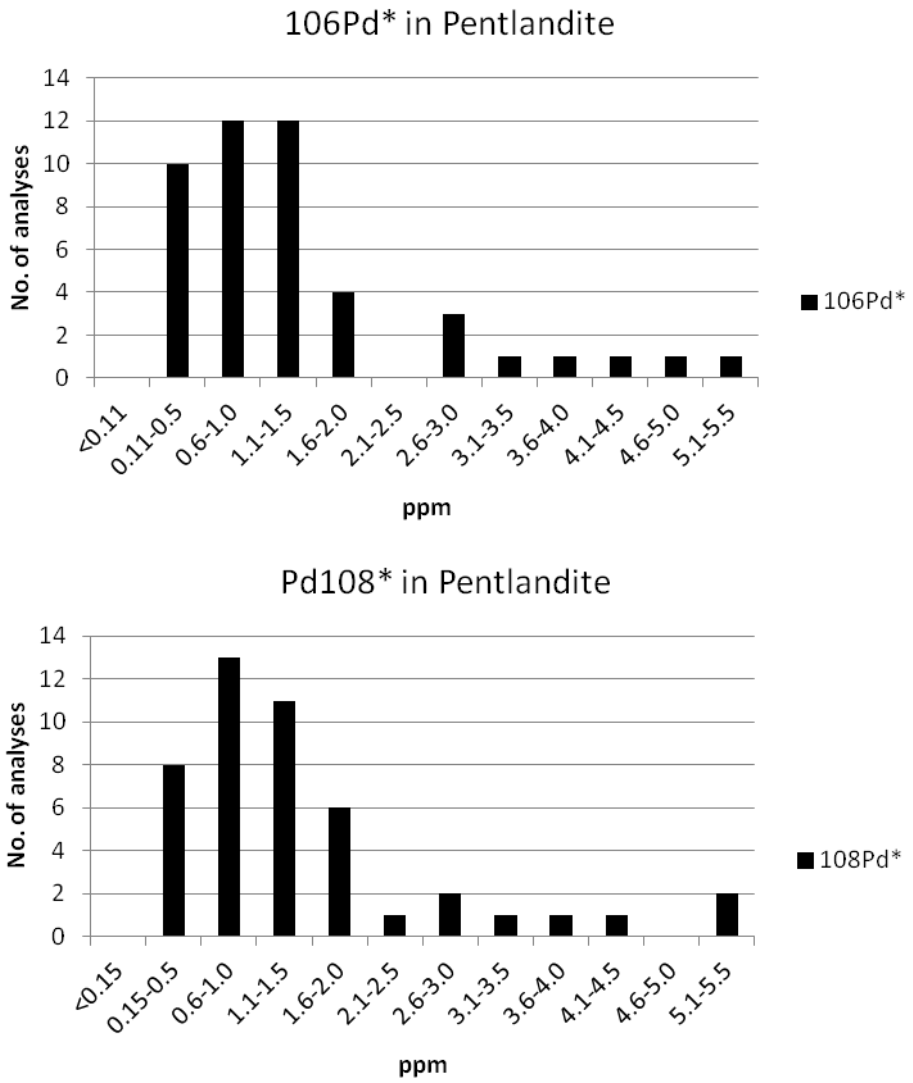


Figure 5.14: Histograms showing the concentrations of Pd in pentlandite from the Jinchuan intrusion (orebodies #1 and #24).

PGE of significance with average Pd concentrations of 1.5 ppm. Commonly, concentrations of Pd in pentlandite are shown to be slightly lower at 0.6-1.5 ppm (Fig. 5.14) with the total average brought up by higher but less common concentrations of up to ~5 ppm.

There does not appear to be any correlation between the concentration of PGE in solid solution in BMS with (i) the type of sulphide mineralisation observed, (ii) the degree of greenschist facies alteration, or (iii) the numbers of PGM observed in the analysed sample.

Mineral		Element	57Fe	59Co	61Ni	65Cu	189Os	193Ir	101Ru	103Rh	195Pt	106Pd	108Pd	197Au	109Ag	75As	209Bi	121Sb	82Se	125Te	111Cd	185Re
Analysed			wt. %	ppm	wt. %	wt. %	ppm	ppm	ppm*	ppm*	ppm	ppm*	ppm*	ppm	ppm	ppm	ppm	ppm	ppm	ppm	ppm	ppm
Sulphides from the Jinchuan intrusion																						
Cpy	*n=20*	Ave	30.88	78.20	0.41	27.39	0.07	<0.02	0.07	<0.10	<0.02	0.07	0.09	0.07	9.13	<5.00	3.83	<0.75	111.88	3.01	8.42	0.20
		Min	24.81	<5.00	<0.05	21.90	<0.02	0.00	<0.05	<0.10	<0.02	<0.11	<0.15	<0.01	1.52	<5.00	0.23	<0.75	86.58	<0.80	<0.80	<0.02
		Max	41.96	245.90	1.33	32.61	1.25	0.09	0.49	<0.10	<0.02	0.44	0.47	0.27	47.83	<5.00	16.84	<0.75	170.50	11.51	42.90	0.71
Pn	*n=46*	Ave	38.22	5480.81	28.25	0.40	0.16	0.01	0.16	0.04	<0.02	1.47	1.50	0.04	13.02	4.88	1.82	0.02	128.99	9.99	0.12	0.27
		Min	26.68	84.26	0.48	<0.03	0.00	<0.02	<0.05	<0.10	<0.02	0.19	0.16	<0.01	0.67	<5.00	0.09	<0.75	89.24	<0.80	<0.80	<0.02
		Max	63.59	7512.00	34.80	5.06	0.80	0.21	2.59	0.78	0.03	5.17	5.27	0.21	65.62	42.10	10.26	0.86	184.60	53.63	4.57	1.05
Po	*n=43*	Ave	61.74	271.88	1.47	0.11	0.12	0.01	0.09	0.01	<0.02	0.12	0.11	0.01	10.50	<5.00	1.67	<0.75	123.57	7.42	0.02	0.22
		Min	42.40	<5.00	0.06	0.08	0.00	<0.02	<0.05	<0.10	<0.02	<0.11	<0.15	<0.01	0.46	<5.00	0.07	<0.75	79.56	<0.80	<0.80	<0.02
		Max	72.75	5932.00	29.31	1.31	0.74	0.12	0.59	0.20	0.03	2.43	2.19	0.15	283.60	<5.00	9.14	<0.75	168.30	270.00	0.99	1.30
Py	*n=3*	Ave	52.30	<5.00	<0.05	<0.03	<0.02	<0.02	<0.05	<0.10	<0.02	<0.11	<0.15	0.20	1.34	7.11	0.03	0.28	204.43	1.93	<0.80	<0.02
		Min	49.93	<5.00	<0.05	<0.03	<0.02	<0.02	<0.05	<0.10	<0.02	<0.11	<0.15	0.07	0.17	<5.00	<0.05	<0.75	119.78	1.41	<0.80	<0.02
		Max	53.77	<5.00	<0.05	<0.03	<0.02	<0.02	<0.05	<0.10	<0.02	<0.11	<0.15	0.37	3.31	21.33	0.08	0.85	352.40	2.40	<0.80	<0.02

Table 5.4: Laser ablation ICP-MS results for chalcopyrite, pentlandite, pyrrhotite and pyrite from the Jinchuan intrusion.

Cpy = chalcopyrite, Pn = pentlandite, Po = pyrrhotite, Py = pyrite, *n* = number of minerals analysed, Ave = mean, Min = minimum value, Max = maximum value.

5.10 Discussion

5.10.1 Formation of PGM

Evidence discussed below suggests that the Pd-bearing PGM along with the accessory semimetal-rich Pb-bearing minerals have most likely formed by a process of exsolution from the BMS during sub-solidus cooling. However, As-bearing phases such as sperrylite and members of the hollingworthite-irarsite-platarsite solid solution series (the latter where not observed in gersdorffite-cobaltite) appear to have crystallised early, directly from an immiscible sulphide liquid. The formation of members of the hollingworthite-irarsite-platarsite solid solution series, where they occur within gersdorffite-cobabltite, is discussed separately in section 5.9.2 below.

Froodite and michenerite are predominantly identified within the BMS (e.g., Fig. 5.10A) and are commonly observed associated with semimetal and Pb-bearing minerals. These Pd-bearing PGM commonly exhibit lath and rounded forms which are both typical of exsolution textures (Peregoedova *et al.*, 2004). In some cases, both these Pd-bearing PGM and semimetal minerals are associated with secondary alteration or magnetite veining. This has also been noted for Jinchuan by Prichard *et al.* (2013) who suggested that different stages of secondary alteration were responsible firstly for the formation of froodite, and secondly for the alteration of froodite to padmaite (PdBiSe) along these BMS-magnetite junctions. They proposed that during the first stage of alteration, PGE (Pd) and semimetals (Bi and Te) were liberated from the BMS as they were altered to magnetite during sulphur loss while Se was mobilised from the BMS during a second stage of alteration. The same processes may be occurring in the samples analysed in this study, however, there is no overwhelming correlation of froodite or michenerite being associated with magnetite either within or at the junctions of magnetite adjacent to BMS, although these textural features are frequently observed (e.g., Fig. 5.10B).

It therefore appears that Pd-bearing PGM, where observed within the BMS without any association with secondary magnetite, have formed via exsolution from the sulphides during magmatic sub-solidus cooling without the need for secondary alteration processes (Fig. 5.15a-b). However, where Pd-bearing PGM are observed at the edges of secondary magnetite, it appears that post-magmatic hydrothermal alteration of the BMS to magnetite via a process of sulphur loss has liberated the PGE and semimetals from the sulphide(s) being replaced (Fig. 5.15.c). The PGE and semimetals then coalesce at the edge of the secondary

magnetite to form PGM. In this case, Pd and the associated semimetals that form these PGM are demonstrating small scale mobility over the distance of the individual sulphide crystal being replaced. Furthermore, Dare *et al.* (2010b) have shown that late-stage magmatic or hydrothermal fluids can remobilise PGE at temperatures of less than 540°C forming michenerite at the Creighton Ni-Cu-PGE deposit, Sudbury. The temperature of the hydrothermal fluids responsible for the alteration of the Jinchuan intrusion are estimated at 300-400°C from oxygen isotope work by Ripley *et al.* (2005) indicating that the same process could have occurred in forming secondary PGM (froodite and michenerite) at Jinchuan.

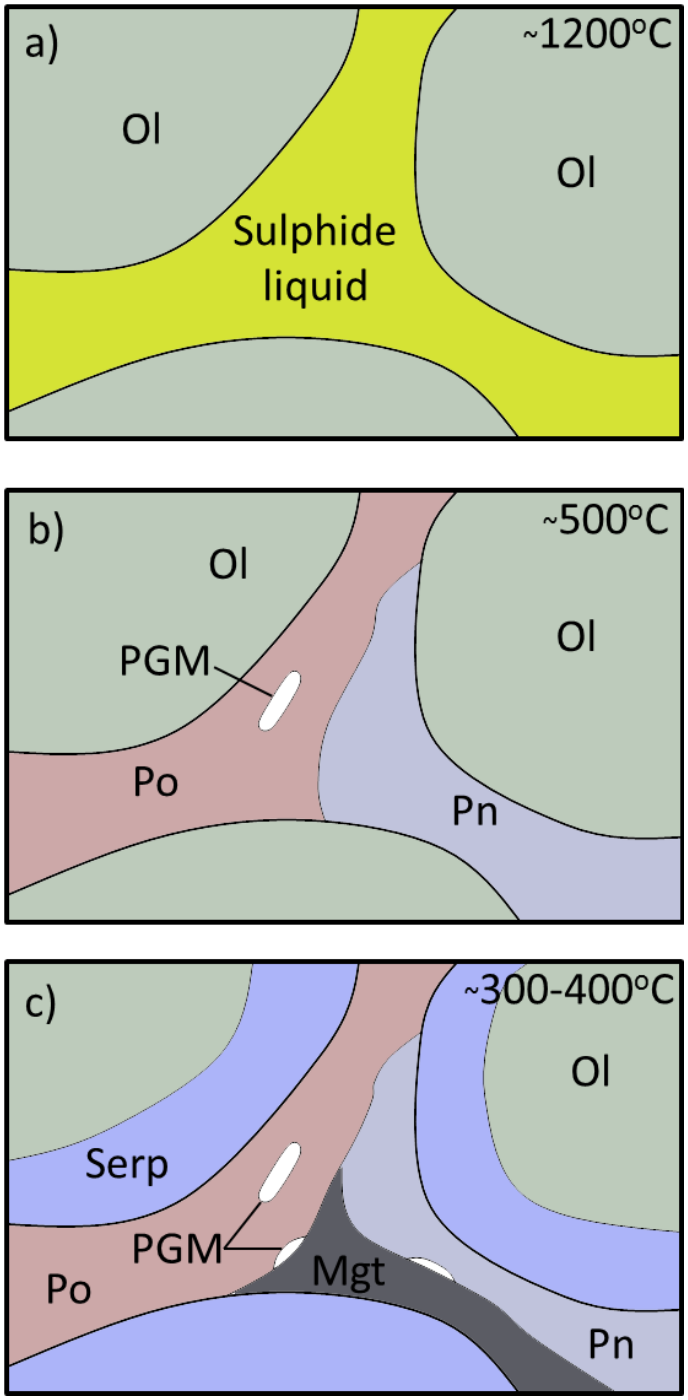


Figure 5.15: Diagram showing the formation of primary and secondary Pd-PGM; a) example of sulphide liquid interstitial to olivine (Ol) at high temperature, b) the sulphide liquid cools and crystallises to MSS and ISS. MSS shown in this example subsequently re-crystallises to pyrrhotite (Po) and pentlandite (Pn). Primary Pd-PGM may form via PGE exsolution during sub-solidus cooling, and c) post-magmatic greenschist facies hydrothermal alteration results in Po and Pn being replaced by magnetite (Mgt) during sulphur loss and serpentinisation (Serp) of olivine. Pd, Bi and Te are remobilised from these oxidised and replaced sulphides to the edges of the secondary Mgt where they exsolve to form Pd-PGM.

It has been shown that if PGE are present in solid solution in BMS, hydrothermal fluids may liberate PGE from their BMS hosts resulting in the formation of PGM within and at the edges of the BMS. However, it is rare that the PGE are extensively remobilised and they are usually only transported very short distances (micrometres) in most cases (e.g., Prichard *et al.*, 1994; 2001; Wang *et al.*, 2008). Wood and Normand (2008) demonstrated experimentally that unrealistically large volumes of oxidising and acidic fluids are required to react with a given mass of basalt (analogous to the Jinchuan mafic-ultramafic lithologies) in order to overcome the acid- and redox-buffering capacity of the rock and to mobilise Pd as a chloride complex. Conversely, they found that Pd-chloride complexes can be easily transported through a rock with minimal acid- and redox-buffering capacity, such as clean quartz sandstone.

Sa *et al.* (2005) studied the distribution of base metals and PGE in magnetitite and its host rocks in the Rio Jacaré Intrusion, Northeastern Brazil. They suggested that sulphur (along with Cu and Au given their geochemical correlation) was remobilised by either late magmatic fluid or post-magmatic metamorphic events, however, the PGE have not been extensively remobilised evidenced by the association of Pd-bearing PGM with the BMS and the small variation in the Pt/Pd ratios (~1.4) observed. Wood (2002) also notes that hydrothermal solutions in equilibrium with alteration minerals such as chlorite, albite, epidote and calcite, such as those responsible for the hydrothermal alteration of the Jinchuan intrusion, are incapable of dissolving large amounts of Pt and Pd. Hanley (2005) suggests that in low temperature hydrothermal environments associated with the occurrence of Cl-rich hydroxysilicate minerals, the PGE are unlikely to be mobilised as chloride complexes, but rather as bisulphide complexes. He suggests that significant transport of the PGE as bisulphide complexes is unlikely although chloride may still be significant in redistributing sulphur as well as base (e.g., Cu, Fe) and precious (e.g., Ag) metals.

Therefore, in the Jinchuan intrusion, although sulphur has been lost during hydrothermal alteration associated with greenschist facies metamorphism, the PGE have remained largely immobile. During BMS alteration and sulphur loss, PGE are forcibly exsolved to form PGM, thus explaining the association of froodite with secondary magnetite.

There is no evidence that pre-existing, magmatically formed PGM have been remobilised under greenschist facies conditions given their highly insoluble nature as the PGE have formed compounds with the semimetals (Wood, 2002). However, the formation of padmaite as discussed in Prichard *et al.* (2013) suggests that existing PGM (froodite) can be modified; in this case by the addition of Se at the expense of Bi. Padmaite is not observed in the

samples analysed for this study so there is not enough evidence here to further the ideas put forward in Prichard *et al.* (2013) regarding the remobilisation of Se from the BMS to form these unusual PGM during a second stage of alteration.

In contrast to the Pd-bearing phases, it appears highly likely that both sperrylite and members of the hollingworthite-irarsite-platarsite solid solution series, where they occur outside of gersdorffite-cobaltite, have crystallised early, directly from an immiscible sulphide liquid. Indicators for this include the fact that these PGM exhibit unimpeded euhedral crystal forms and that they are commonly observed enclosed within silicate phases although they are also found to a lesser extent associated with the BMS (Fig. 5.10E-H). If they had formed as a result of exsolution from the sulphides, one would expect that they would have a strong association with the BMS, unless extensive sulphur loss has occurred. Although there is evidence for sulphur loss in the Jinchuan intrusion (e.g., Ripley *et al.*, 2005; Prichard *et al.*, 2013), these sulphides are usually replaced by secondary minerals, either sulphides (e.g., cubanite or violarlite) or magnetite, neither of which are especially associated with sperrylite or irarsite.

Many studies have shown that the presence of As in the immiscible sulphide melt may lead to the early crystallisation of As-bearing PGM, predominantly sperrylite and irarsite. McDonald (2008) showed that in ultramafic intrusive complexes in the Andriamena region of Madagascar, high As concentrations have resulted in the early crystallisation of Pt-Ir-Rh arsenides and sulpharsenides which subsequently become trapped in later crystallising silicates, including olivine. Coghill and Wilson (1993) suggest similar processes have occurred in the Great Dyke, Zimbabwe. They suggest that sperrylite was part of a high temperature PGM assemblage that crystallised before the formation of MSS; these PGM are then enclosed in silicates which crystallise at lower temperatures. Hutchinson and McDonald (2008) have also suggested that the assimilation of As, Sb, Bi and Te into the sulphide melt from the country rock to the Platreef in the Bushveld Complex may have caused Pt-bearing PGM to crystallise early rather than being incorporated into solid solution in BMS.

Some of the sperrylite and irarsite grains may have a small amount of undifferentiated sulphide material associated with them. It is likely that as the early As-bearing PGM crystallised, a small amount of sulphide liquid remained attached to the newly formed PGM as it separated from the bulk of the sulphide liquid. These PGM in particular could not have formed via exsolution as the small volume of sulphide material present could not host enough

PGE in solid solution to exsolve a PGM larger in size than the host sulphide, although these observations are restricted to two-dimensions under the SEM.

The few maslovite crystals identified may have formed either via exsolution from the BMS or as a result of early crystallisation from the sulphide liquid. One maslovite is identified within BMS (Fig. 5.10C), one occurs in a zone of BMS veining and one is identified within serpentine (Fig. 5.10D). All of these examples exhibit subhedral crystal forms. It is not prudent to suggest one method of formation over another based on such a small sample set of three crystals, especially when they exhibit such different mineral associations and sizes.

Gold in the intrusion may have two different origins. If the Au is primary (i.e., magmatic) and has partitioned into the immiscible sulphide liquid, it is unlikely to have partitioned into any sulphide phase as predicated by many experimental studies and would have instead continuously fractionated into late-stage melts before crystallising as Au or electrum associated with the BMS (e.g., Fleet *et al.*, 1993; Peregoedova, 1998; Mungall *et al.*, 2005). As the majority of the Au and electrum grains observed are associated with the BMS, it appears likely that these precious metal minerals have crystallised directly from a late-stage fractionated sulphide melt. However, Au is also mobile, particularly complexed with sulphur (Zhu *et al.*, 2011); therefore Au could have been relatively easily redistributed within (Vikentyev *et al.*, 2004), or introduced into, the Jinchuan intrusion during post-magmatic alteration. However, this model appears unlikely as Au and electrum are not commonly observed associated with secondary alteration silicates as would be expected if this was the case.

5.10.2 The role of sulpharsenides as collectors of PGE

The awareness of an affinity of PGE with sulpharsenides is fast growing, as evidenced by recent literature (e.g., Dare *et al.*, 2010b; Godel *et al.*, 2012; Prichard *et al.*, 2013). The consistent identification of irarsite within small zoned euhedral gersdorffite-cobaltite as well as the identification of Ir and Rh in solid solution in these sulpharsenides in this study (Fig. 5.11A-H) again highlights the importance of sulpharsenides as collectors of PGE.

Piña *et al.* (2013) have demonstrated the affinity of PGE with As by showing that the PGE will preferentially partition into arsenide/sulpharsenide phases over sulphide phases by analysing coexisting arsenide and sulphide minerals from the Amasined Cr-Ni mineralisation in the Beni Bousera lherzolite massif, North Morocco, using LA-ICP-MS. Maucherite

($Ni_{11}As_8$) coexists in equilibrium with pyrrhotite, pentlandite, and chalcopyrite with these arsenide and sulphide minerals accounting for the bulk of the PGE (except Pt) and chalcophile elements. Laser ablation analyses show that maucherite is strongly enriched in all chalcophile elements, apart from Se, relative to sulphide minerals.

It has been determined by the experiments of Fleet *et al.* (1993) that if the As content of a sulphide liquid is ~0.1 wt. %, an arsenide melt may form and separate from the immiscible sulphide liquid. This separation may occur both early, before the crystallisation of MSS or late, after the crystallisation of MSS. If an arsenide melt forms early before the crystallisation of MSS, the PGE should partition into this arsenide melt leaving the MSS which crystallises subsequently depleted in PGE (Wood, 2003 cited by Dare *et al.*, 2010b). Conversely, if an arsenide melt forms after the crystallisation of MSS, it should be depleted in the IPGE and Rh which preferentially partition into MSS (Fleet *et al.*, 1993), e.g., at the Las Aguilas Ni-Cu-PGE deposit (Gervilla *et al.*, 1997). The presence of an arsenide melt is typically evidenced by its crystallisation products, commonly a nickeline-maucherite-gersdorffite assemblage (e.g., Serranía de Ronda and Beni Bousera - Gervilla *et al.*, 1997; Talnotry intrusion, Scotland - Power *et al.*, 2004; Dundonald Beach South komatiite, Canada - Hanley, 2007). Therefore, an arsenide melt may have formed and separated from the immiscible sulphide liquid in the Jinchuan intrusion from which minor gersdorffite-cobaltite and nickeline crystallised.

However, it has also been suggested that gersdorffite-cobaltite and nickeline may crystallise directly from the magma before sulphide saturation is achieved or directly from an As-bearing immiscible sulphide liquid without requiring the formation of a separate arsenide melt. Merkle (1992) has suggested that PGM and As-rich phases identified as inclusions in chromite and orthopyroxene indicate that these minerals have crystallised before the formation of an immiscible sulphide melt in the middle group of chromitite layers at Marikana, western Bushveld Complex. Hanley (2007) suggested that the PGE-rich sulpharsenides (gersdorffite-nickeline) observed in the Dundonald Beach South Ni-Cu occurrence, Canada, could represent sulpharsenide crystals that separated either from a silicate magma or an immiscible sulphide liquid.

Other studies keep the details of the genesis of these sulpharsenides vague. Mondal *et al.* (2001) identified euhedral gersdorrfite-cobaltite crystals with irarsite-hollingworthite PGM in their cores in the Nuasahi ultramafic-mafic complex, Orissa, India. They suggested that these sulpharsenides crystallised prior to the formation of interstitial chalcopyrite, pyrrhotite and

pyrite. Song *et al.* (2004) also identified small zoned euhedral cobaltite-gersdorffite crystals with Rh-Pt-Ni-rich cores containing up to 6.4 wt. % Rh and 0.5 wt. % Pt as well as having a Co-rich margin in the Yangliuping Ni-Cu(-PGE) sulphide deposit in China**.** They suggested that these minerals crystallised before the exsolution of pentlandite from MSS above temperatures of 600^{o}C.

The small zoned PGE- and/or PGM-bearing euhedral gersdorffite-cobaltite identified in the present study of the Jinchuan intrusion most closely match those observed by Dare *et al.* (2010b) in the Creighton deposit, Sudbury, who also give the most detail into the genesis of these sulpharsenides. They identified euhedral zoned gersdorffites that host irarsite in their cores which themselves are often enveloped by hollingworthite. They argued that these sulpharsenides crystallised from an As-bearing immiscible sulphide melt and did not require the formation of a separate arsenide melt. Dare *et al.* (2010b) explain that if these gersdorffites crystallised from an arsenide melt that formed early, they should show enrichment in Pd which would have preferentially partitioned into an arsenide melt at this stage (Helmy *et al.*, 2010). If these gersdorffites crystallised from an arsenide melt that formed late, as proposed by Gervilla *et al.* (1997) for the Las Aguilas deposit, Argentina, they would be depleted in the IPGE which would have preferentially partitioned into MSS. Furthermore, Dare *et al.* (2010b) argue that the lack of any rock-forming proportions of a nickeline-maucherite-gersdorffite assemblage having been identified at Sudbury also indicate that no separate arsenide melt was ever formed. The gersdorffites in the Creighton deposit, Sudbury, do not show either enrichment in Pd or depletion in the IPGE and Dare *et al.* (2010b) instead propose that small amounts of zoned PGE-rich sulpharsenides and sperrylite crystallised at high temperatures (~1200-900^{o}C) from the immiscible sulphide melt which subsequently became trapped in the later crystallising MSS cumulates which were consequently depleted in these PGE (Ir, Rh and Pt).

The gersdorffite-cobaltite crystals in the Jinchuan intrusion closely match the mineralogy and chemistry of those described by Dare *et al.* (2010b) at Creighton being Ir-, Rh- and Pt-rich and Pd-poor. As such, it appears that they too have crystallised early from an As-bearing immiscible sulphide melt at high temperatures before the crystallisation of MSS in a similar manner as described by Dare *et al.* (2010b) without a separate arsenide melt having formed which is also evidenced by the lack of rock-forming proportions of a nickeline-maucherite-gersdorffite assemblage observed in the Jinchuan intrusion.

5.10.3 Platinum nugget effect

Whole-rock PGE data from Jinchuan has often shown a large variation in Pt concentrations (e.g., Chai and Naldrett, 1992; Song *et al.*, 2006) leading to both positive and negative Pt anomalies observed on chondrite normalised plots which have not yet been satisfactorily explained. This study shows similar erratic Pt anomalies (Fig. 5.8 and Fig. 5.9). Song *et al.* (2009) have suggested that the Pt anomalies displayed by massive sulphide ores and some of the net-textured sulphide ores cannot be explained by sulphide segregation under variable R factors. Instead, they suggest that the sulphide melts that formed the massive ores have previously crystallised Pt-Fe alloys directly from the immiscible sulphide liquid. However, there is no direct evidence for the existence of these Pt-Fe alloys from any PGM study of the Jinchuan ores. Song *et al.* (2009) also suggest an alternative explanation for the negative Pt anomalies in the massive sulphide ores at Jinchuan claiming that the Pt might have been selectively leached by hydrothermal fluids during the remobilisation of the sulphide melts that produced the massive sulphides that occur in cross-cutting veins. Su *et al.* (2008) also suggest that the significant decoupling between Pt and Pd is the result of post-magmatic hydrothermal alteration. This also seems unlikely as it is readily accepted that Pd is much more mobile than Pt under various conditions (e.g., Prichard *et al.*, 1994; 2001; Wood, 2002; Seabrook *et al.*, 2004; Barnes *et al.*, 2008; Wang *et al.*, 2008; Suárez *et al.*, 2010) whereas Pt only appears to be mobile in high temperature (800–900ºC), high salinity brines (Hanley, 2005) or under unusual circumstances, e.g., the formation of the Waterberg Pt deposit in South Africa (McDonald *et al.*, 1999; Armitage *et al.*, 2007). As a result, Pd anomalies as opposed to Pt anomalies would be observed if this processes of leaching occurred. Finally, it is shown here and in other studies that Pt anomalies are both positive and negative and occur in all of the sulphide ore types observed and therefore cannot be controlled by the processes put forward by Song *et al.* (2009) regarding massive sulphide ores only. Chen *et al.* (2013) attributed the negative Pt anomalies of the net-textured and massive sulphide ores to the preferential extraction of Pt into Cu-rich residual melts due to the presence of As, Te, and Bi. However, textural relationships show that Pt-bearing PGM (and sulpharsenides) appear to have crystallised early, directly from the sulphide melt before the segregation of a Cu-rich melt.

It appears that all of the Pt in the intrusion is in the form of PGM as Pt concentrations in solid solution in the BMS are consistently below the detection limit of 0.02 ppm with only two analyses above this detection limit at 0.03 ppm (Table 5.4). Therefore, it is suggested here

that these Pt anomalies may well be explained by a platinum nugget effect resulting from the presence of large, rare and heterogeneously distributed sperrylite. Irarsite only contains minor concentrations of Pt and the other Pt-bearing PGM maslovite is both much smaller than the sperrylite observed and much rarer. These positive and negative Pt anomalies can also be noted in the numerical whole-rock PGE data which shows that within the samples analysed, the average Pt concentration is 143 ppb. However, the standard deviation of these samples is very large at 348, a result of both anomalously high (e.g., RK23 - 488 ppb, RK31 - 830 ppb, RK29 - 2.2 ppm) and low Pt concentrations (e.g., RK40 - 9ppb, RK21 - 13ppb; all concentrations cited from net-textured sulphide ores for true comparison).

The average size of the sperrylites identified is greater than that of any other PGM type at 62.3 μm^2. Furthermore, the size range of these sperrylite crystals extends up to 172.5 μm^2 making some of these PGM extremely large. Only six sperrylites have been observed in the samples studied (Table 5.2), however, the size of these grains as noted above means that they account for almost three quarters of the total area of PGM observed in orebody #1 (Fig. 5.13a) making them critically important in controlling the total distribution of Pt in the intrusion.

Platinum anomalies are emphasised further by their presence in PGE profiles where only the original sample and its duplicate analysis are displayed together in isolation (Fig. 5.9). In these examples, all of the PGE contents are consistent across the original and duplicate run apart from Pt and to some extent Rh (sample RK18). These profiles demonstrate how Pt anomalies can occur even in two batches of powder weighing 15g sourced from a homogenised powder of 0.3-0.5 kg. This is difficult to explain unless one considers that large heterogeneous sperrylite crystals may be responsible.

The study of PGM is inherently problematic in attempting to identify all the different types of PGM that may be present in any one sample given the limited two-dimensional surface being viewed. It is possible the larger sperrylite crystals exist that have not yet been identified and may be responsible for particularly high whole-rock Pt concentrations, such as in RK29 which has 2.2 ppm Pt.

5.10.4 Variation of PGM and whole-rock PGE concentrations

There is a difference in both the types and quantities of PGM observed in the two orebodies studied. Although both irarsite and Pd-bearing PGM are observed in both orebodies, As-

bearing PGM are predominantly identified in orebody #1, segment II, to the east, whereas Pd-bearing PGM are much more abundant in orebody #24, segment I, to the west. Furthermore, in orebody #24, As-bearing PGM are much rarer with only two irarsites identified and sperrylite absent (Table 5.2).

Whole-rock PGE content also appears to change over the four boreholes studied from west to east (orebody #24 to orebody #1) becoming more variable due to lower PGE content (Fig. 5.8). However, this change can be attributed to a variation in the sample types (lithologies and sulphide ores) collected from each borehole. Net-textured sulphide ores are predominantly hosted in dunite, olivine-rich lherzolite and some lherzolite samples whereas patchy net-textured ore occurs primarily in lherzolite while disseminated ore is observed in lherzolite with orthopyroxene oikocrysts and websterite±olivine. The degree of post-magmatic hydrothermal alteration that these samples have experienced also appears to be related to these different lithologies hosting different sulphide ore types. Samples hosting net-textured ore display higher degrees of alteration characterised by group 2 samples in the major element Harker diagrams (Fig. 5.6). These samples are more olivine-rich and have been largely serpentinised. The presence of net-textured sulphides may aid the movement of post-magmatic hydrothermal fluids leading to more pervasive alteration. Alternatively, more evolved samples with pyroxene which host disseminated ore or patchy net-textured ore may restrict fluid movement and reduce the degree of alteration experienced by these samples.

These lithologies and sulphide ore types are related to the whole-rock PGE contents displayed in the chondrite normalised PGE diagrams (Fig. 5.16 and Fig. 5.17). The majority of samples from orebody #24 are relatively coarse grained dunites hosting net-textured sulphide ores. This explains not only the tightly spaced nature of the samples in the chondrite normalised PGE diagrams (Fig. 5.8a) but also why the PGE content of these samples is typically higher (with higher sulphide content relating to higher PGE concentrations) than in dunites from other boreholes where these lithologies hosting net-textured sulphides are slightly finer grained. In the other boreholes studied, a greater variety of ore types have been sampled, ranging from net-textured, patchy net-textured and disseminated ores in a wider range of lithologies. The greatest diversity in samples were taken from borehole DZK12-02 in the eastern part of orebody #1 including some of the most disseminated ores with the lowest whole-rock PGE contents resulting in widely spaced PGE profiles (Fig. 5.8d). As a result of the PGE correlation with sulphide ore type and lithology noted above, the PGE contents of the samples/boreholes do not vary with depth as there is no clear correlation with

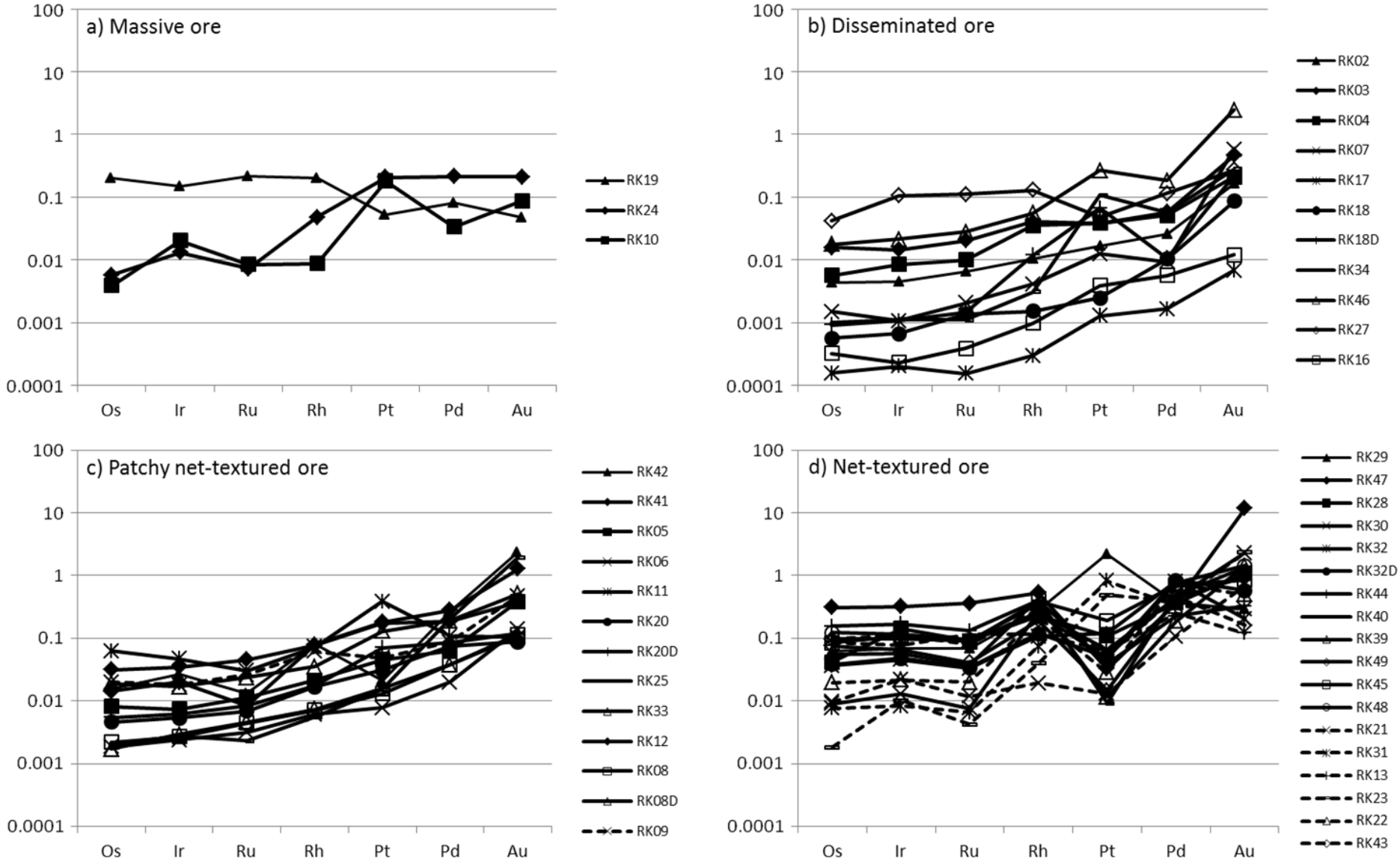


Figure 5.16: Chondrite normalised (using the values given in Lodders, 2003) PGE diagrams with samples separated according to sulphide ore type.

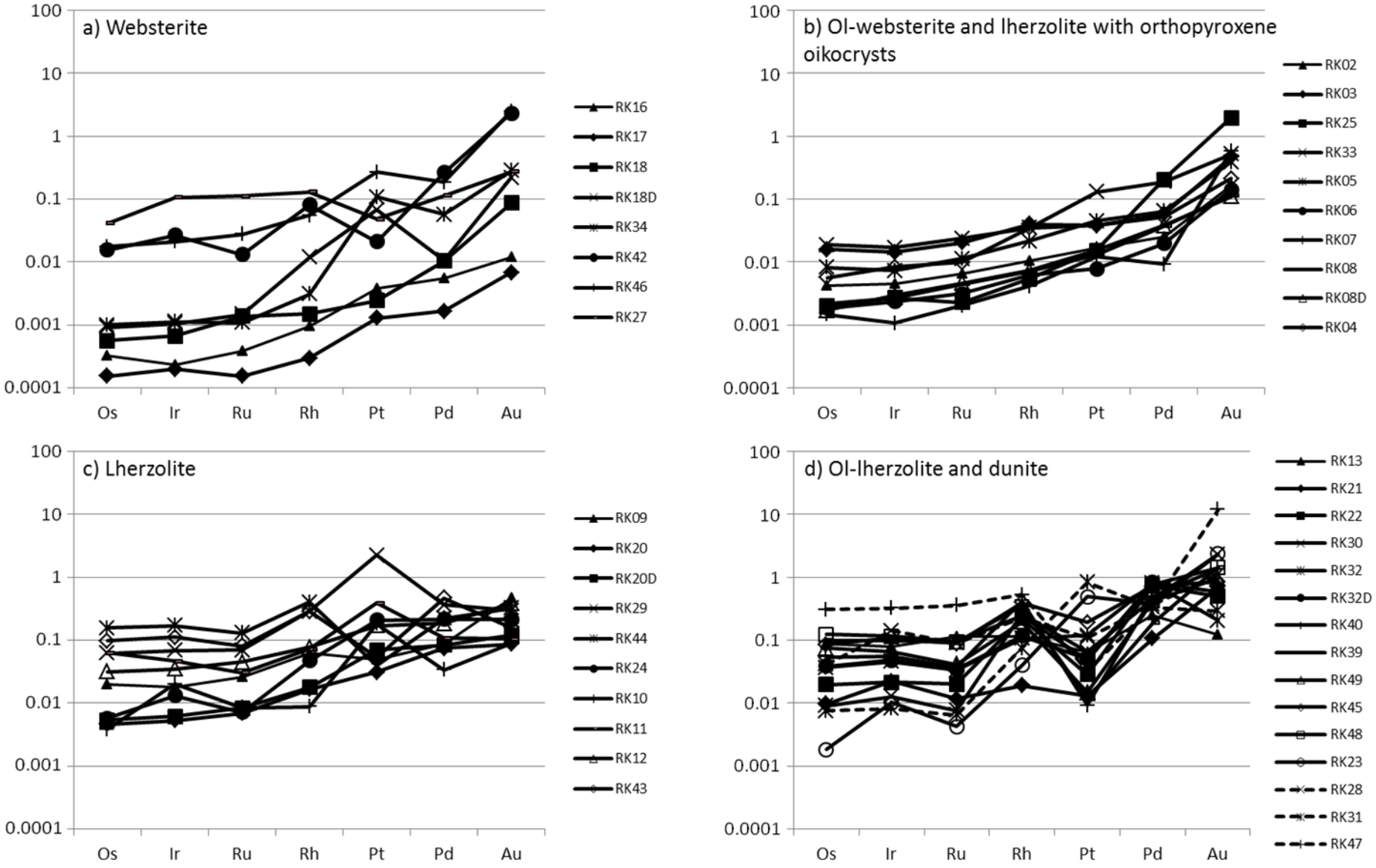


Figure 5.17: Chondrite normalised (using the values given in Lodders, 2003) PGE diagrams with samples separated according to lithology.

lithology (and therefore sulphide ore type) with depth (Fig. 5.2). The chondrite normalised PGE profiles suggest that there has been no significant PGE fractionation between samples and boreholes as the slopes of these profiles are relatively constant. This is supported by Pd/Ir ratios, the ranges of which do not change significantly between boreholes.

The variation in the PGM observed may be due to a variation in the whole-rock concentration of As between these two orebodies with higher As concentrations in orebody #1 giving rise to more As-bearing PGM (sperrylite and irarsite) and sulpharsenides (gersdorffite-cobaltite). Conversely, orebody #24 is relatively As-poor resulting in the formation of very few As-bearing PGM. This is further supported by the fact that no sulpharsenides have been identified in orebody #24. This difference in As content cannot be secondary given the apparent early crystallisation of these As-bearing PGM and sulpharsenides and therefore must be related to the magmatic genesis of the orebodies. One explanation for this difference in As content may be related to the difference in crustal material assimilated. However, the immediate country rocks to both orebodies #1 and #24 are similar (gneiss and marble) and therefore these intrusions would have undergone a similar magmatic genesis.

Song *et al.* (2012) however, suggest that the eastern and western parts of the Jinchuan intrusion, separated by the fault $F_{16\text{-}1}$ (Fig. 5.1), are in fact two different intrusions that have been juxtaposed by this fault. They demonstrate that these two intrusions have different stratigraphic sequences with the western part of segment II marked by a sulphide dunite core (orebody #1) enveloped by lherzolite (Song *et al.*, 2009) whereas segment I (including orebody #24) consists of Upper and Lower units (interpreted as magmatic mega cycles with regular variations in lithology and chemistry) which are distinguishable by both the lithological sequences present, compositional variations and also by the grain sizes of olivine crystals.

Furthermore, the fault $F_{16\text{-}1}$ shares its strike with faults F_8 and F_{23} (Fig. 5.1) and all three are left lateral strike-slip faults that formed during the Mesozoic and Cenozoic and are still active. The amount of movement on faults F_8 and F_{23} is ~800m and ~300m, respectively (Sixth Geological Unit, 1984). Song *et al.* (2012) suggest that the amount of left lateral movement on the fault $F_{16\text{-}1}$ is ~500m given the distribution Palaeoproterozoic marble on the two sides of the fault. Therefore, if segments I and II were originally an individual intrusion, fault $F_{16\text{-}1}$ should have offset these segments by several hundreds of metres, however, this is not the case. Instead it appears that segment I and II were originally separate individual intrusions that have been juxtaposed by the post-magmatic movement along fault $F_{16\text{-}1}$.

This interpretation of segment I and II developing as separate intrusions allows for their genesis to differ, potentially leading to a difference in As content. The immediate country rocks to the two intrusions would have been similar, so As concentrations derived from crustal assimilation at this level in the crust would not have differed greatly. However, it is possible that different As-bearing lithologies exist at depth affecting the ore-forming magma that crystallised in segment I differently to that which crystallised in segment II, especially if these two magmas also followed different pathways to the surface. This difference in genesis may also explain the difference in the sulphide chemistries of the orebodies (Cu- or Ni-rich). However, trace element bivariate plots of U/Th-Th (Fig. 5.7c) show that both orebodies #1 and #24 have been subjected to a similar amount of crustal contamination by similar granitoid material in the lower crust (Lehmann *et al.*, 2007). There is also no direct evidence for As-bearing crustal rocks at depth. As the chemistry of the dunites, lherzolites and websterites in both orebodies all overlap, respectively, it is sensible to conclude that one magma has formed both of these orebodies; or if websterite has crystallised from a separate magma, it has also affected both orebodies in the same manner (Fig. 5.7a-f). Furthermore, this model by Song *et al.* (2012) is contrary to genetic models of the Jinchuan intrusion where it is interpreted as a conduit to high-Mg basalts which have since been eroded fed from a single source or staging chamber (e.g., Chai and Naldrett, 1992a; DeWaal *et al.*, 2004; Li *et al.*, 2004; Song *et al.*, 2006; Lehmann *et al.*, 2007).

Alternatively, this variation in the different types and abundances of PGM present in the two orebodies may have formed as the result of sulphide liquid fractionation. The crystallisation of early forming As-bearing PGM (sperrylite and members of the hollingworthite-irarsite-platarsite solid solution series) and sulpharsenides initially occurred in orebody #1 (Fig. 5.18). The remaining sulphide liquid may have then started migrate from the east (orebody #1) to the west (orebody #24). During this migration, MSS crystallisation continued with the sulphide liquid progressively fractionating as it migrated. This has resulted in a relatively MSS-rich, Cu-poor orebody #1 hosting sulpharsenides and early forming As-bearing PGM. At this point the majority of the Pd would have partitioned into the fractionated Cu-rich sulphide liquid which then cooled and crystallised forming the Cu-rich, MSS-poor orebody #24. Palladium-bearing PGM then exsolved from this ore during sub-solidus cooling while Pt-Ir-Rh-bearing PGM are rare/absent with these elements having been depleted by the early crystallisation of sperrylite, irarsite and sulpharsenides in oreobdy #1.

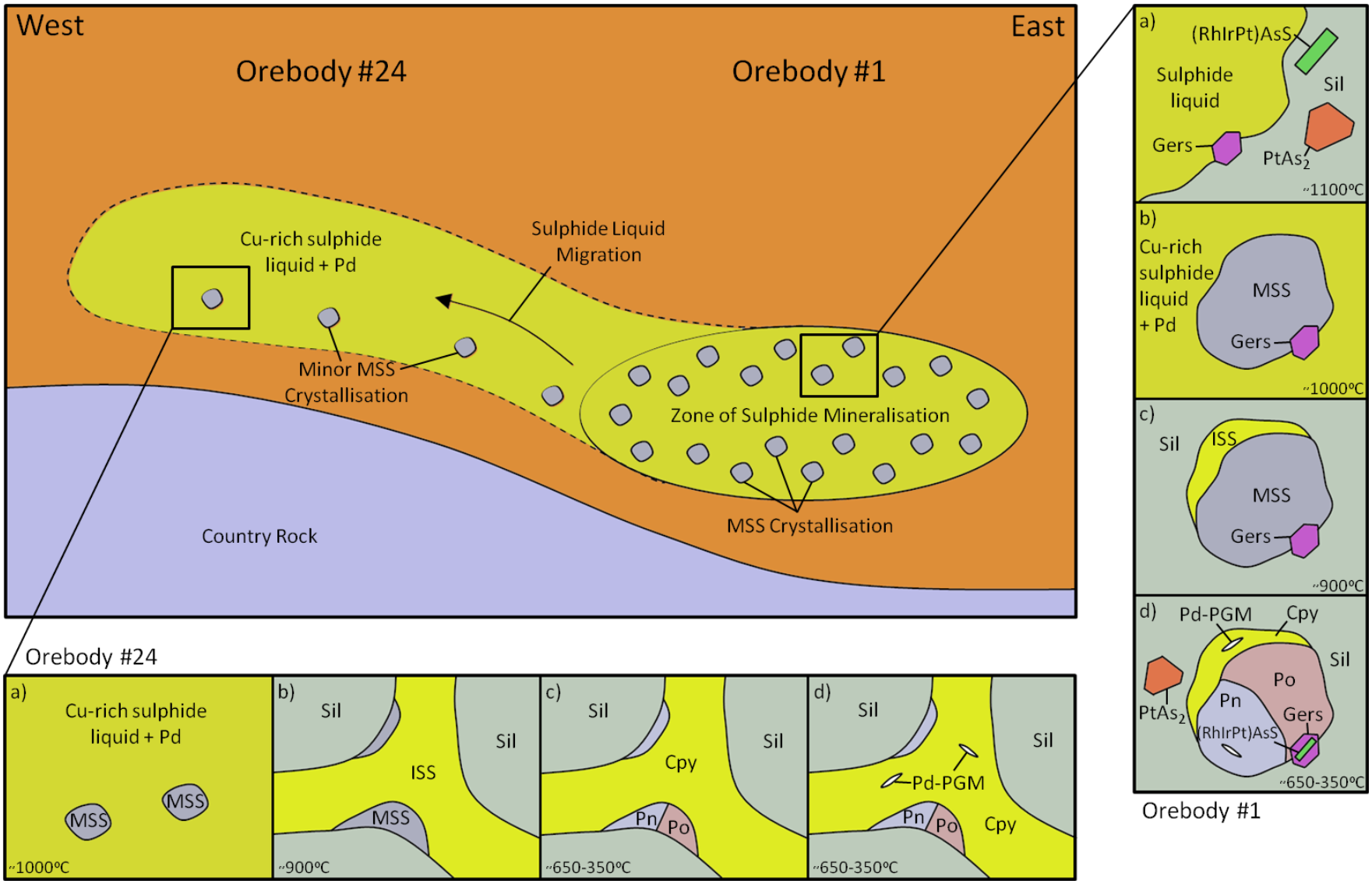


Figure 5.18: Summary of PGM formation and PGE behaviour in the Jinchuan intrusion. Orebody #1; a) Sperrylite ($PtAs_2$), members of the hollingworthite-irarsite-platarsite solid solution series ([RhItPt]AsS) and gersdorffite-cobaltite (Gers; into which Pt, Ir and Rh partition) crystallise early, directly from an As-bearing sulphide liquid from which they may separate, b) MSS begins to crystallise and some Pd partitions into the resulting Cu-rich sulphide liquid which starts to migrate to the west forming orebody #24, c) the remaining Cu-rich sulphide liquid crystallises to ISS and d) minor Pd-bearing PGM exsolve from the re-crystallised BMS (Cpy - chalcopyrite, Pn - pentlandite, Po - pyrrhotite) and (RhIrPt)AsS exsolves from Gers during sub-solidus cooling. Orebody #24 a) minor MSS crystallises from the migrating Cu-rich sulphide liquid into which some Pd has partitioned, b) ISS crystallises, c) Cpy, Pn and Po re-crystallise from ISS and MSS, respectively and d) relatively large quantities of Pd-PGM exsolve from these BMS, particularly from Cpy during sub-solidus cooling.

The separation of MSS and ISS in this manner would require sulphide crystallisation to occur in a dynamic environment allowing for the significant movement of the differentiated sulphide crystals and liquids. This method of fractionation could also explain the particularly prominent negative Pt anomalies observed in the samples of orebody #24 (Fig 5.8a) with Pt mostly removed by the early crystallisation of sperrylite, members of the hollingworthite-irarsite-platarsite solid solution series and by the partitioning of Pt into early crystallising sulpharsenides leaving the resulting Cu-rich sulphide liquid which migrated to form orebody #24 strongly depleted in Pt. Alternatively, samples in orebody #1 show both positive and negative Pt anomalies (Fig. 5.8b-d); a result of the Pt nugget effect described above (section 5.9.3).

5.11 Conclusions

Two distinct platinum-group mineral assemblages are observed in two different orebodies in the Jinchuan intrusion. The more MSS-rich orebody #1, segment II, to the east, hosts the vast majority of the irarsite and all of the sperrylite identified whereas the more Cu-rich orebody #24, segment I, to the west, hosts a much larger quantity of Pd-bearing PGM (predominantly froodite and michenerite).

Sperrylite, members of the hollingworthite-irarsite-platarsite solid solution series and sulpharsenides (gersdorffite-cobaltite) appear to have crystallised early, directly from an As-bearing immiscible sulphide liquid. Platinum, Ir and Rh have partitioned into small early forming euhedral gersdorffite-cobaltite crystals depleting MSS in these PGE and subsequently exsolving from these sulpharsenides to form members of the hollingworthite-irarsite-platarsite solid solution series at their cores.

Primary magmatic froodite and michenerite appear to have formed via exsolution from the BMS. However, secondary froodite and michenerite may have also formed during post-magmatic hydrothermal greenschist facies alteration which has both partially oxidised pentlandite and pyrrhotite and replaced them with magnetite during sulphur loss. Palladium, Bi and Te have been liberated from these partially oxidised or replaced BMS before coalescing and exsolving to form Pd-PGM at the edges of these secondary phases.

A process of dynamic sulphide liquid fractionation may account for the difference in PGM types between orebody #1 and orebody #24. The early crystallisation of As-bearing PGM (sperrylite and members of the hollingworthite-irarsite-platarsite solid solution series) and

sulpharsenides into which Pt, Rh and Ir have partitioned occurred in orebody #1 depleting any subsequently crystallising sulphides in these PGE. The crystallisation of MSS began and continued while the fractionating Cu-rich sulphide liquid (into which the majority of Pd has partitioned) migrated towards the west to form orebody #24. ISS crystallised and chalcopyrite, pentlandite and pyrrhotite re-crystallised from both ISS and MSS respectively during sub-solidus cooling. Pd-bearing PGM then exsolved from the BMS, predominantly in the more Cu-rich orebody #24 on further cooling.

6. Discussion and Conclusions

6.1 Comparing the PGE Mineralisation of the Mirabela and Jinchuan Intrusions

The PGE mineralisation in the Mirabela and Jinchuan intrusions varies in terms of whole-rock PGE concentrations (Table 6.1), the PGE concentrations in solid solution in the BMS and the PGM that have been identified from each intrusion (Table 6.2). The intrusions have also been subjected to different degrees of post-magmatic hydrothermal alteration affecting the PGE differently.

In the Jinchuan intrusion, many Bi-bearing and Bi-Te-bearing PGM are observed (predominantly froodite [$PdBi_2$] and michenerite [PdBitTe]), however, in the Mirabela intrusion, Bi-bearing PGM are extremely rare with the majority of PGM identified as tellurides ([PtPdNi][FeTe]). This variation in PGM is due to the variation in the semimetal content of the sulphides. The Jinchuan intrusion hosts concentrations of both Bi and Te, although it is probably more Bi-rich given the observation of pure Bi-bearing PGM (froodite). Conversely, the Mirabela intrusion hosts concentrations of Te, but is relatively Bi-poor.

Sperrylite ($PtAs_2$) is identified in both the Jinchuan and Mirabela intrusions; however, in both of these complexes the position of sperrylite is restricted. In the Jinchuan intrusion, sperrylite is confined to orebody #1, segment II and is absent in orebody #24, segment I. This is most likely the result of the early crystallisation of sperrylite from an immiscible sulphide liquid combined with dynamic sulphide liquid fractionation, although this could also be explained by the two orebodies (orebody #1 and orebody #24) having developed separately as individual intrusions with ore-forming magmas inheriting different As concentrations during their genesis. In the Mirabela intrusion, sperrylite is restricted to northern and southern margins of the intrusions and is absent in the central part of the intrusion. This suggests that As has been introduced from the country rocks through crustal assimilation leading to the zonation of As and consequently sperrylite in the intrusion. However, trace element data does not show any evidence of crustal contamination, therefore, As zoning may have been achieved by another as of yet unknown process.

Intrusion/Deposit	Zone	Segment	Borehole	Os (ppb)	Ir (ppb)	Ru (ppb)	Rh (ppb)	Pt (ppb)	Pd (ppb)	Au (ppb)
Mirabela	Central	NA	MBS604	n.a.	25	27	14	284	169	175
	Central	NA	MBS605	n.a.	13	23	6	154	62	71
	Northern	NA	MBS209	n.a.	23	35	11	282	158	139
	Northern	NA	MBS158	n.a.	18	29	11	217	119	81
	Southern	NA	MBS565	n.a.	10	23	7	110	68	46
	Southern	NA	MBS569	n.a.	8	16	6	94	76	39
			Mirabela Total Average	n.a.	16	26	9	190	109	92
Jinchuan	Orebody #1	II	DZK14-02 (East)	12	11	19	8	98	112	91
	Orebody #1	II	DZK12-06 (Central)	9	9	15	5	80	44	38
	Orebody #1	II	DZK09-01 (West)	14	23	29	19	410	229	95
	Orebody #24	I	ZKS-09	46	48	61	39	80	232	323
			Jinchuan Total Average	20	23	31	18	167	154	136

Table 6.1: Comparison of average whole-rock PGE concentrations for individual and combined boreholes from the Mirabela and Jinchuan intrusions. *n.a. = not analysed, sulphur-poor samples from the Jinchuan intrusion and Mirabela Santa Rita ore zone have been ignored in order to obtain relevant average PGE values.

Intrusion/Deposit	Sulphide	189Os (ppm)	193Ir (ppm)	101Ru* (ppm)	103Rh* (ppm)	195Pt (ppm)	105Pd (ppm)	106Pd* (ppm)	108Pd* (ppm)	Significant PGM
Mirabela Santa Rita Ore Zone	Cpy	0.03	<0.02	0.14	<0.10	0.05	0.27	-	-	
	Pn	0.52	0.09	0.91	0.11	0.03	2.31	-	-	Pt-Pd-Ni-Fe tellurides
	Po	0.55	0.11	0.58	0.04	0.07	0.01	-	-	Sperrylite (PtAs2)
	Py	0.61	0.18	0.78	0.14	0.03	0.12	-	-	
Mirabela Dunite Zone	Cpy	<0.02	0.07	0.06	<0.10	0.08	8.81	-	-	Pd-Cu±Pb
	Pn	4.22	1.74	6.28	4.33	4.33	42.47	-	-	
Jinchuan	Cpy	0.07	<0.02	0.07	<0.10	<0.02	-	0.07	0.09	Froodite (PdBi2)
	Pn	0.16	0.01	0.16	0.04	<0.02	-	1.47	1.50	Michenerite (PdBiTe)
	Po	0.12	0.01	0.09	0.01	<0.02	-	0.12	0.11	Sperrylite (PtAs2)
	Py	<0.02	<0.02	<0.05	<0.10	<0.02	-	<0.11	<0.15	Irarsite ([RhIrPt]AsS)

Table 6.2: Comparison of the PGM and average PGE concentrations in solid solution in BMS in the Mirabela and Jinchuan intrusions.

There is a greater proportion of hollingworthite-irarsite-platarsite ([RhIrPt]AsS) PGM in the Jinchuan intrusion (accounting for 8.8% of the PGM identified) compared to the Mirabela intrusion (accounting for only 2.5% of the PGM identified). This is reflected in the variation in the whole-rock PGE concentrations of the two intrusions. The concentrations of both the IPGE and Rh are higher in the Jinchuan intrusion than in the Mirabela intrusion (Table 6.1), potentially explaining the greater quantities of irarsite-type PGM.

Despite the difference in the IPGE and Rh, whole-rock Pt and Pd concentrations of the two intrusions are similar, although Pt concentrations in the Jinchuan intrusion are much more erratic due to the presence of large, rare and heterogeneously distributed sperrylite. One possible explanation for the lower concentrations of IPGE and Rh relative to Pt and Pd in the Mirabela intrusion is that the sulphide liquid that formed the Ni-Cu-(PGE) mineralisation may have undergone a degree of fractionation early in its history before its final emplacement. The IPGE and Rh would have partitioned into MSS, a proportion of which may have separated from the sulphide liquid leaving it depleted in these PGE relative to Pt and Pd.

The sulphide assemblages of each intrusion are also different. Primary pyrite that has exsolved from MSS in small volumes is observed in the Mirabela intrusion whereas only secondary pyrite is observed at Jinchuan which occurs as veins cross-cutting primary magmatic BMS and silicates; the result of post-magmatic sulphide remobilisation. However, sulpharsenides (gersdorffite-cobaltite) are only observed in the Jinchuan intrusion and not at Mirabela. These differences are likely due to the sulphide melts having different compositions (sulphur and metal contents, particularly As when considering the formation of sulpharsenides). Both pyrite and gersdorffite-cobaltite are extremely important in their respective intrusions in concentrating and controlling the distribution of PGE.

The BMS in Santa Rita ore zone of the Mirabela intrusion host higher concentrations of all PGE in solid solution than the Jinchuan BMS (excluding Pt) (Table 6.2). This is due to both the early crystallisation of As-bearing PGM and sulpharsenides at Jinchuan into which Pt, Ir and Rh have partitioned leaving the subsequently crystallising sulphides depleted in these PGE. Furthermore, post-magmatic greenschist facies alteration of the Jinchuan sulphides resulted in the liberation of Pd and semimetals (Bi and Te) from the BMS, thus forming more PGM than would have otherwise formed via exsolution during normal magmatic sub-solidus cooling. This is evidenced by michenerite and froodite forming at the edges of secondary magnetite. Conversely, no evidence of PGE or PGM remobilisation is evident in the Mirabela

intrusion which has only been subjected to minor low temperature serpentinisation compared to Jinchuan which has been subjected to regional greenschist facies metamorphism at temperatures of 300-400^{o}C (Ripley *et al.*, 2005). The BMS in the dunite zone of the Mirabela intrusion are particularly enriched in PGE. This zone is both sulphur- and semimetal-poor leaving little for the PGE to bond with to form PGM. As a result, the PGE have partitioned into solid solution in the minor BMS available. Minor Pd-Cu alloys have formed in the absence of semimetal-bearing PGM.

6.2 The Partitioning Behaviour of PGE

Most studies of the partitioning behaviour of the PGE have concentrated on the experimental partitioning of PGE into MSS, ISS and their main exsolution products; pentlandite, pyrrhotite and chalcopyrite. However, several difficulties come into effect when applying the findings of this research to natural magmatic systems. One of which is the presence of early forming PGM into which certain PGE may preferentially partition leaving the immiscible sulphide liquid depleted in these PGE. Late forming PGM or those that form via exsolution from the BMS will also reduce the concentration of certain PGE in the BMS that would otherwise be expected to remain in solid solution, thus making the testing of these experimental studies difficult. Lastly, pentlandite, pyrrhotite and chalcopyrite are not the only primary magmatic sulphides that form via exsolution from MSS and ISS. As observed in both the literature and the studies presented here, primary pyrite may also exsolve from MSS. Furthermore, sulpharsenides may crystallise early, directly from an As-bearing immiscible sulphide liquid or from a separate arsenide melt which may form and separate from an As-bearing immiscible sulphide liquid at an early or late-stage (i.e., prior to, or after the crystallisation of MSS).

Experimental and natural studies of the partitioning of PGE have generally shown that the IPGE and Rh consistently partition into MSS as it crystallises from an immiscible sulphide liquid. Osmium, Ir and Ru then partition equally between pyrrhotite and pentlandite during their exsolution from MSS during sub-solidus cooling (e.g., Fleet *et al.*, 1993; Li *et al.*, 1996; Ballhaus and Sylvester, 2000; Mungall *et al.*, 2005; Barnes *et al.*, 2006; Godel *et al.*, 2007; Holwell and McDonald, 2007) whereas Rh has been shown to preferentially partition into pentlandite (e.g., Ballhaus and Sylvester, 2000; Godel *et al.*, 2007; Holwell and McDonald, 2007).

In contrast Pt, Pd and Au are incompatible with both MSS and ISS (e.g., Peregoedova, 1998; Ballhaus and Sylvester, 2000; Mungall *et al.*, 2005; Barnes *et al.*, 2006; Godel *et al.*, 2007; Holwell and McDonald, 2007; Hutchinson and McDonald, 2008) and instead of partitioning into any BMS phase, these metals are concentrated into a fractionated late-stage (after MSS and ISS crystallisation) immiscible sulphide melt that often contains semimetals (Holwell and McDonald, 2007; 2010). This late-stage melt may then be expelled to sulphide grain boundaries, crystallising to form PGM on cooling.

For the study of the PGE mineralisation in the Jinchuan intrusion documented in this thesis, the main difficulty in assessing the partitioning behaviour of the PGE into the different BMS is the very low concentrations of PGE in solid solution in the BMS analysed. Despite this, significant concentrations of Pd have been identified in pentlandite. The study of the PGE mineralisation in the Mirabela intrusion presented here also demonstrates that Pd has a particular preference for pentlandite over the other sulphide phases. This has also been documented in many other natural studies. However, calculated partition coefficients show that Pd should partition into a Cu-rich liquid; not only into a late-stage fractionated immiscible sulphide melt but also into ISS (Barnes *et al.*, 2006). Palladium has been shown to exsolve from Cu-rich portions of blebs at Noril'sk by Barnes *et al.* (2006) while the presence of Pd-bearing PGM in late-stage Cu-rich sulphides in BMS blebs from Uruguay (Prichard *et al.*, 2004b) apparently confirms that Pd may well partition into either ISS or a late-stage Cu-rich liquid.

Helmy *et al.* (2007) have shown experimentally that Pt has a greater preference for forming PGM with semimetals than Pd does. Therefore, if Pt and Pd are concentrated into a late-stage immiscible sulphide melt that contains a limited amount of semimetals, Pt will preferentially form PGM with these available semimetals while excess Pd will subsequently be accommodated by pentlandite by a process of diffusion (Holwell and McDonald, 2007; Godel and Barnes, 2008a,). Dare *et al.* (2010a) has also proposed that the Pd may diffuse into pentlandite from adjacent chalcopyrite during sub-solidus exchange. In the Jinchuan intrusion, Pd-bearing PGM are more prominent in the more Cu-rich orebody #24 compared to the more MSS-rich orebody #1, however, greater concentrations are identified in pentlandite in solid solution than in chalcopyrite. This again provides evidence that Pd will preferentially partition into ISS or a late-stage Cu-rich melt before diffusing into adjacent pentlandite and/or exsolving from the Cu-sulphides as PGM. Alternatively, Osbahr *et al.* (2013) also suggest that significant concentrations of Pd may partition into MSS at an earlier magmatic

stage eliminating the need for Pd diffusion from fractionated Cu-rich sulphides. Although this model opposes the results of many experimental studies, it does account for the concentrations of Pd observed in pentlandite when MSS (pentlandite and pyrrhotite) and ISS (chalcopyrite) are removed from each other due to the fractional crystallisation of the sulphide liquid, rendering diffusion an irrelevant process (e.g., Jinchuan - the separation of orebodies #1 and #24, Mirabela - chalcopyrite-poor, sulphur-poor dunite).

The results of LA-ICP-MS analyses of the BMS from the Santa Rita ore zone in the Mirabela intrusion provide important data on the partitioning of PGE into different BMS phases despite the majority of the PGE having formed large quantities of PGM. This study has found that the IPGE and Rh partition into MSS in agreement with many experimental and natural studies (e.g., Fleet *et al.*, 1993; Li *et al.*, 1996; Ballhaus and Sylvester, 2000; Mungall *et al.*, 2005; Barnes *et al.*, 2006; Godel *et al.*, 2007; Holwell and McDonald, 2007). However, the partitioning of these PGE during the formation of sub-solidus exsolution products from MSS is complicated by the presence of pyrite, believed to have formed in small amounts via exsolution from MSS. This study therefore documents how these PGE partition between pyrrhotite, pentlandite and pyrite during their exsolution from MSS, something which has not been examined in detail previously. This study has found that Rh will preferentially partition into pentlandite and pyrite. Ruthenium is present in all three phases; however, it also shows a preference for pentlandite and pyrite. Os and Ir partition into all three phases, however, concentrations of these PGE are higher in pyrite compared to both pyrrhotite and pentlandite, into which lower concentrations of these PGE have partitioned equally. In summary, out of these three exsolution products, pyrite is the primary host of the IPGE and Rh. Pentlandite, however, hosts the highest concentrations of total PGE overall given its significant Pd concentrations.

Data from Dare *et al.* (2011), Pina *et al.* (2011) and Lorand and Alard (2010) who have also observed significant concentrations of PGE in pyrite, combined with the study of the Mirabela BMS, show that when pyrite exsolves from MSS, the IPGE will preferentially partition into pyrite over pentlandite and pyrrhotite, whereas Rh will preferentially partition into both pyrite and pentlandite equally. Conversely, where pyrite is secondary, it may simply inherit the PGE residing in the sulphides it has replaced. However, pyrite is not a guaranteed host of PGE. Secondary pyrite in the Jinchuan intrusion forming veins or stringers cross-cutting magmatic silicates and sulphides is barren in terms of PGE content in solid solution. In this case, it has not replaced any existing sulphide phase so has not inherited any pre-

existing PGE content. It is clear that primary pyrite where it has exsolved from MSS may be an important economic host of PGE and should not be disregarded as a gangue mineral during processing. New experimental studies are required to determine the partition coefficients of the IPGE and Rh into pyrite over pentlandite and pyrrhotite.

The presence of gersdorffite-cobaltite in the Jinchuan intrusion has also further complicated the process of analysing the partitioning behaviour of the PGE. It is demonstrated here that at least Ir, Rh and Pt preferentially partition into these sulpharsenides where they crystallise early, directly from an As-bearing immiscible sulphide melt at high temperatures. These small euhedral zoned gersdorffite-cobaltite crystals with PGM (members of the hollingworthite-irarsite-platarsite solid solution series) identified in their cores have also been identified in the Spotted Quoll nickel ore deposit in the Forrestania greenstone belt, Western Australia (Prichard *et al.*, 2013) and in the Creighton Ni-Cu-PGE sulphide deposit, Sudbury, Canada (Dare *et al.*, 2010b). LA-ICP-MS analyses have not been undertaken on these sulpharsenides due to their small size; however, Ir and Rh have been detected in solid solution in gersdorffite-cobaltite in the Jinchuan intrusion under the SEM at concentrations of up to several wt. %. This again shows that future experimental studies must also take into account the partition coefficients of PGE into sulpharsenides over the immiscible sulphide liquid, MSS and ISS.

In the Mirabela intrusion, the sulphur-poor PGE-bearing dunite footwall to the Santa Rita ore zone offers an almost unique opportunity to examine the partitioning behaviour of the PGE without the influence of semimetals or an abundance of PGM, making this zone an ideal natural laboratory. However, this zone in the intrusion is not without its own problems. The BMS are extremely small and difficult to analyse, furthermore, pyrrhotite is absent and pyrite very rare. The LA-ICP-MS results show that under these conditions pentlandite can host all six PGE in significant concentrations including Pt, but is predominantly enriched in Pd in extremely very concentrations compared with pentlandite in the Santa Rita ore zone (Table 6.2) and in many other layered intrusions. Chalcopyrite hosts significant concentrations of Pd only, although not to the same extent as pentlandite.

6.3 The Primary Magmatic Formation of PGM

The three most common methods of PGM formation are the early crystallisation of PGM directly from an immiscible sulphide melt at high temperatures, the concentration of PGE and

semimetals into a late-stage fractionated sulphide melt from which PGM crystallise, or via the partitioning into at high temperatures and subsequent exsolution of PGE from BMS during sub-solidus cooling. The semimetals (As, Bi, Sb, Se and Te) are critically important in controlling which methods of PGM formation occur in any given complex and as a result, greatly influence the partition coefficients of PGE into the BMS as calculated in many experimental studies as noted above.

It has been well documented in the literature and confirmed in the studies presented here that if As is present in the immiscible sulphide melt, PGM, commonly sperrylite and members of the hollingworthite-irarsite-platarsite solid solution series, may crystallise early directly from this melt and subsequently become trapped in later crystallising silicate, oxide and sulphide phases (e.g., Coghill and Wilson, 1993; McDonald. 2008; Hutchinson and McDonald, 2008). Both sperrylite and irarsite are consistently identified within silicate phases in the Jinchuan intrusion suggesting that they did indeed crystallise early directly from the immiscible sulphide melt. Sperrylite crystals associated with very minor BMS are identified in both the Jinchuan and Mirabela intrusions may also have crystallised early. In these cases however, a small amount of sulphide liquid has remained with the PGM as they have crystallised and segregated from the bulk of the sulphide melt. An alternative explanation for the presence of these PGM is that they have formed via exsolution from the sulphides; however, subsequent sulphur loss has occurred remobilising the sulphides (partially or totally) away from the PGM. This is unlikely to have occurred in the Santa Rita ore zone of the Mirabela intrusion given the lack of evidence for secondary sulphur loss or remobilisation. In the Jinchuan intrusion, post-magmatic sulphur loss is documented by the formation of secondary sulphide minerals (e.g., cubanite, violarite) and magnetite; however, these minerals are not associated with sperrylite.

It is clear from the partitioning behaviour implied above that at least Pt, Ir, and Rh have a strong affinity with As given their preference for sulpharsenides over the immiscible sulphide liquid. After partitioning into early forming gersdorffite-cobaltite in the Jinchuan intrusion, these PGE have exsolved during sub-solidus cooling to form members of the hollingworthite-irarsite-platarsite solid solution series in the cores of these sulpharsenides.

Helmy *et al.* (2007) have suggested that as the concentration of semimetals in the melt increases, the solubility of the PGE in the sulphide liquid decreases as they will preferentially form PGM with these semimetals. Furthermore, Holwell and McDonald (2007) have shown that when Bi and Te are present, the IPGE and Rh will behave as normal partitioning into

MSS, however, Pt, Au and some Pd will preferentially partition into a late-stage semimetal-rich melt that is expelled to grain boundaries during the crystallisation of ISS forming discrete PGM phases during cooling. Barnes *et al.* (2008) have also suggested that at Noril'sk, Pt may not have been incorporated into BMS at all and was instead concentrated into a late-stage immiscible melt which cooled and crystallised PGM directly in a similar manner as described above. In the studies of the PGE mineralisation of the Mirabela and Jinchuan intrusions, no evidence of the formation of a late-stage semimetal-rich sulphide melt has been observed as PGM are not consistently found expelled to the edges of sulphide crystals in a manner suggested by Holwell and McDonald (2007).

Instead, Bi- and Te-bearing PGM identified in the Mirabela and Jinchuan intrusions are predominantly identified in the BMS either occurring completely enclosed by these sulphide phases or occurring within and at the edges of these sulphides. These PGM commonly exhibit rounded-lath crystal forms which typically result from exsolution processes (Peregoedova *et al.*, 2004). Both the crystal forms and mineral associations of these PGM suggest that they have formed as a result of the exsolution of PGE and semimetals (Bi and Te) from the BMS during sub-solidus cooling.

Using evidence from Noril'sk, Barnes *et al.* (2008) have argued that if sub-solidus cooling is rapid, the PGE are not given sufficient time to exsolve and therefore remain in solid solution in the BMS. However, where cooling is slow, such as in the case of layered intrusions, more time is available allowing the exsolution of PGE from the BMS forming PGM within these sulphides. Based on this theory, the layered Mirabela and Jinchuan intrusions have both cooled relatively slowly based on the abundant PGM observed in both complexes.

It is curious that despite the obvious presence of Bi and Te in these complexes evidenced by abundant Bi- and Te-bearing PGM that have formed via exsolution from the BMS, no fractionated late-stage semimetal-rich sulphide melt has formed. In the Jinchuan intrusion it appears that although Pd partitioned into the resulting Cu-rich sulphide liquid during the crystallisation of MSS, it did not further segregate into a fractionated late-stage semimetal-rich sulphide melt during the crystallisation of ISS evidenced by the lack of Pd-bearing phases identified at the edges of Cu-rich BMS. Instead Pd has seemingly partitioned into ISS with semimetals and during sub-solidus cooling has formed PGM within chalcopyrite. It is speculated here that a critical amount of semimetals and possibly PGE may be required before a fractionated late-stage semimetal-rich melt may form; however, it is unclear quantitatively what concentrations are may be required.

6.4 The Secondary Remobilisation of PGE

Post-magmatic processes may result in the remobilisation and dispersion or concentration of PGE. The research presented here shows that under temperatures of ~400^{o}C, magmatic PGM (i.e., those formed via exsolution from the BMS during sub-solidus cooling or early crystallisation directly from an immiscible sulphide melt) are not remobilised. The vast majority of the PGM observed in these studies are those where PGE form very insoluble compounds with the semimetals As, Bi, and Te (Wood, 2002). It is not clear from this research how PGE sulphides or oxides (the latter most commonly observed in supergene environments) might behave during post-magmatic alteration. In the Mirabela intrusion, sulphide stringers with associated PGM appear, at first observation, that they may have formed by hydrothermal processes and would therefore represent the hydrothermal remobilisation of magmatic PGM, with chemistries of magmatic PGM and 'hydrothermal' PGM matching. However, these stringers and associated PGM have been shown in this thesis to be primary magmatic features. It has been demonstrated that although magmatic PGM are unlikely to be remobilised at these temperatures (≤400^{o}C), they can be altered. Prichard *et al.* (2013) showed that in the Jinchuan intrusion, froodite ($PdBi_2$) can be altered to padmaite (PdBiSe) by the addition of Se from hydrothermal fluids at the expense of Bi.

Therefore, remobilisation of the PGE is relatively restricted to the liberation and redistribution of PGE from solid solution in the BMS. In the complexes studied in this thesis, there are two potential sources of PGE remobilisation, high temperature deuteric fluids (800-900^{o}C) which exsolve from the magma during fractional crystallisation, and post-magmatic low temperature (≤400^{o}C) metamorphic fluids. In the Mirabela intrusion, the sulphur-poor dunite hosts sulphides with very high PGE concentrations, a zone described by Barnes *et al.* (2011) as the basal PGE anomaly. The PGE content of these sulphides has been effectively upgraded by a process of sulphur loss caused by the interaction of these sulphides with high temperature deuteric fluids (or a late stage melt). Under these high temperature conditions, Pt can be soluble if these fluids are also saline (Hanley, 2005). It is not clear whether Pt loss from solid solution in pentlandite has contributed to the high Pd/Pt ratios in this zone. Pd/Pt ratios are elevated by the retention of Pd in pentlandite and formation of Pd-bearing PGM coupled with the loss of Pt with uncrystallised Cu-rich sulphide liquid and the presence of very few Pt-bearing PGM.

Watkinson *et al.* (2002) suggest that PGE mineralisation at Lac des Ilse, Ontario, is the result of high temperature deuteric fluids and that the sulphur poor nature of this mineralisation has

resulted from sulphur loss during continued fluid flow at lower temperatures. They also suggest that at the Salt Chuck Mine, Alaska, the primary magmatic concentration of PGE has been modified by late-stage hydrothermal deuteric fluids with the PGE remobilised into veins. However, in this case, it is not clear whether this remobilisation has enhanced or decreased the PGE tenor of the magmatic ore.

However, the processes occurring in the Mirabela dunite more closely match those described by Boudreau and McCallum (1992). They suggest that in the formation of the J-M reef, predominantly sulphur and some portion of the Pt and Pd have been leached from the footwall cumulates and transported upwards to the position of the reef by deuteric fluids exsolving from intercumulus melt. They also note that an unrealistically large amount of fluid is required to transport high concentrations of Pt and Pd, however, relatively small amounts of fluid can remobilise sulphur. Therefore, in the Mirabela intrusion, only small amounts of deuteric fluid have interacted with the dunite hosted sulphides, whereas at Lac des Ilse and the Salt Chuck Mine, comparatively large amounts of fluid are responsible for the mobilisation of PGE.

The effect of low temperature alteration in the Mirabela intrusion is extremely limited. Only very minor serpentinisation is observed which has no discernible effect on the PGE. In contrast, the Jinchuan intrusion has been subjected to extensive low temperature greenschist facies metamorphism. Under these conditions sulphur loss is observed, however, the PGE themselves have not been remobilised. Palladium-bearing PGM are often identified associated with unaltered magmatic BMS, however, they are also associated with secondary magnetite which replaces the sulphides during sulphur loss and oxidation. In these cases, during sulphur loss, the PGE and semimetals that were initially hosted in solid solution in the affected sulphides are liberated from solid solution and expelled to the edges of the newly formed magnetite where they crystallise as PGM. The crystallisation of PGM in this case does not necessarily show small scale mobility of the PGE; rather the diffusion and exsolution of PGE which are clearly insoluble relative to sulphur under these conditions. It is unclear whether minor amounts of PGE are dissolved in the hydrothermal fluids; however, there is no evidence of their re-precipitation, in secondary pyrite for example, if they were partially dissolved in the first place.

Hanley (2005) suggests that in low temperature hydrothermal environments associated with the occurrence of Cl-rich hydroxysilicate minerals, the PGE are unlikely to be mobilised as chloride complexes, but rather as bisulphide complexes. He suggests that significant

transport of the PGE as bisulphide complexes is unlikely, although chloride may still be significant in redistributing sulphur as well as base (e.g., Cu, Fe) and precious (e.g., Ag) metals. Wood (2002) also notes that hydrothermal solutions in equilibrium with alteration minerals such as chlorite, albite, epidote and calcite, such as those responsible for the hydrothermal alteration of the Jinchuan intrusion, are incapable of dissolving large amounts of Pt and Pd.

Wood and Normand (2008) demonstrated experimentally that unrealistically large amounts of oxidising and acidic fluids are required to react with a given mass of basalt in order to overcome the acid- and redox-buffering capacity of the rock and to mobilise palladium as a chloride complex. Conversely, they found that Pd-chloride complexes can be easily transported through a rock with minimal acid- and redox-buffering capacity, such as clean quartz sandstone. This experimental data may explain the solubility of Pt and high concentrations of Pt-Pd-Au in quartz veins formed by low temperature (200-300^{o}C), highly oxidising, low salinity fluids comprising the Waterberg deposit in South Africa (McDonald *et al.* 1999; Armitage *et al.*, 2007).

Hydrothermal processes can affect the PGE in several ways. Firstly, the PGE can be completely remobilised and redistributed, in some cases forming an economic hydrothermal PGE deposit (e.g., the Waterberg Pt deposit). More commonly, the PGE are affected by hydrothermal processes that result in sulphur remobilisation (as well as base metals such as Fe and Cu, and precious metals including Ag) rather than PGE remobilisation. Sulphur loss can result in the upgrading of PGE tenor whereby PGE are further concentrated into the remaining sulphide. This concentration of PGE is likely the result of their high partition coefficients into the BMS and PGE diffusion in manner slightly analogous to the sulphide upgrading model of Kerr and Leitch (2005). Alternatively, sulphur loss can result in the formation of abundant PGM as the PGE and semimetals are forcibly expelled from altered sulphides and combine to form PGM. Whether PGE tenor is increased of whether PGM are formed may depend on the temperature of the sulphides at the point at which they are altered. At high temperatures, PGE diffusion will be relatively rapid allowing PGE to migrate from altering sulphide into unaltered BMS and vice versa at low temperatures. The rate at which sulphur loss occurs may also determine the behaviour of the PGE in a similar manner. Finally, in the event that all of the sulphur is lost from a relatively low temperature system, magmatically formed PGM and those that are the result of sulphur loss, will both become isolated in altered silicates as well as in secondary magnetite and oxides given their relative

insolubility. Therefore, the type and degree of both late magmatic and post-magmatic metamorphic alteration of PGE-bearing BMS has significant implications for the economic recovery of PGE.

6.5 Conclusions

The major findings of this thesis are list below:

- Semimetal content is critical in controlling the types and quantity of PGM that form as well as the process and timing of their formation. For instance, the presence of As in the immiscible sulphide melt may lead to the early crystallisation of sperrylite. Alternatively, PGE may either concentrate into the BMS and exsolve as PGM during sub-solidus cooling or concentrate into a late-stage semimetal-rich liquid depending on the concentration of semimetals in the sulphide liquid.
- PGM types and abundances may vary within intrusions through; i) the possible addition of semimetals via assimilation of crustal material leading to the zonation of semimetal concentrations and the semimetal-bearing PGM that form subsequently (alternatively, As zoning in the Mirabela intrusion may have been achieved by another, as of yet unknown, process), ii) sulphide fractionation in a dynamic environment leading to MSS- and ISS-rich ores separating and hosting different types of PGM given the partitioning behaviour of PGE into MSS and ISS and iii) the interaction of late-stage magmatic melts or deuteric fluids with PGE-bearing BMS and/or PGM.
- Primary pyrite that exsolves from MSS may contain significant IPGE, Rh and Co concentrations and should not be disregarded as a gangue mineral. As such, the processing of sulphide ores by floatation to remove pyrite should be reconsidered.
- Platinum, Ir and Rh will preferentially partition into As-bearing PGM and sulpharsenides where they crystallise early, directly from an As-bearing immiscible sulphide liquid as opposed to remaining in the sulphide melt. Although As is considered a penalty element in mining, its presence is much more important in concentrating the PGE than sulphide.
- In the absence of semimetals, the majority of the PGE will partition into the available BMS in high concentrations; minor PGE alloys may form.

- Magmatically formed PGM containing semimetals are very insoluble and are not remobilised during low temperature alteration ($\leq 400^{o}C$). Minor amounts of PGE may be mobilised under these conditions, however, sulphur loss more readily occurs resulting in the forced liberation and exsolution of PGE forming PGM which become enclosed in secondary magnetite or secondary/altered silicates as observed in the Jinchuan intrusion.
- High temperature deuteric fluids are more likely to remobilise the PGE, however, large volumes of fluid are required (e.g., Boudreau and McCallum, 1992; Watkinson *et al.*, 2002). Small amounts of this fluid will result primarily in sulphur loss as observed in the Mirabela sulphur-poor dunite.

References

Alapieti T.T., and Lahtinen, J.J., 1986. Stratigraphy, petrology, and platinum-group element mineralization of the early Protorozoic Penikat layered intrusion, Northern Finland. *Economic Geology*, 81, 1126–1136.

Ames D.E., and Farrow C.E.G., 2007. Metallogeny of the Sudbury mining camp, Ontario. *In* Mineral Deposits of Canada: A Synthesis of Major Deposit-Types, District Metallogeny, the Evolution of Geological Provinces, and Exploration Methods (ed WD Goodfellow), Geological Association of Canada, Mineral Deposits Division, Special Publication No. 5, pp. 329-350.

Andersen J.C.Ø., 2006. Postmagmatic sulphur loss in the Skaergaard Intrusion: Implications for the formation of the Platinova Reef. *Lithos*, 92, 198-221.

Armitage P.E.B., McDonald I., Edwards S.J., and Manby G.M., 2002. Platinum-group element mineralization in the Platreef and calc-silicate footwall at Sandsloot, Potgietersrus District, South Africa. *Applied Earth Science (Transactions of the Institute of Mining and Metallurgy B)*, 111(1), 36-45.

Armitage P.E.B., McDonald I., and Tredoux M., 2007. A geological investigation of the Waterberg hydrothermal platinum deposit, Mookgophong, Limpopo Province, South Africa. *Applied Earth Science (Transactions of the Institute of Mining and Metallurgy B)*, 116, 113-129.

Arndt N.T., 2011. Insights into the Geologic Setting and Origin of the Ni-Cu-PGE Sulfide Deposits of the Noril'sk Talnakh Region, Siberia. Reviews in Economic Geology, 17, 199-216.

Arndt N.T, Chauvel C., Czamanske G.K., and Fedorenko V.A., 1998. Two mantle sources, two plumbing systems: tholeiitic and alkaline magmatism of the Maymecha River basin, Siberian flood volcanic province. *Contributions to Mineralogy and Petrology*, 133, 297-313.

Arndt N.T., Czamanske G.K., Waker R.J., Chauvel C., and Fedorenko V.A., 2003. Geochemistry and origin of the intrusive hosts of the Noril'sk-Talnakh Cu-Ni-PGE sulfide deposits. *Economic Geology*, 98(3), 495-515.

Ashwal L.D., Webb S.J., and Knoper M.W., 2005. Magmatic stratigraphy in the Bushveld Northern Lobe: continuous geophysical and mineralogical data from the 2950 m Bellevue drillcore. *South African Journal of Geology*, 108(2), 199-232.

Ballhaus C.G., and Stumpfl E.F., 1986. Sulfide and platinum mineralization in the Merensky Reef: evidence from hydrous silicates and fluid inclusions. *Contributions to Mineralogy and Petrology*, 94, 193-204.

Ballhaus C., and Sylvester P., 2000. Noble Metal Enrichment Processes in the Merensky Reef, Bushveld Complex. *Journal of Petrology*, 41(4), 545-561.

Ballhaus C., Tredoux M., and Späth A., 2001. Phase relations in the Fe-Ni-Cu-PGE-S system at magmatic temperature and application to massive sulphide ores of the Sudbury Igneous Complex. *Journal of Petrology*, 42, 1911-1926.

Barbosa J.S.F., and Sabaté P., 2004. Archean and Paleoproterozoic crust of the São Francisco Craton, Bahia, Brazil: geodynamic features. *Precambrian Research*, 133, 1-27.

Barkov A.Y., Halkoaho T.A.A., Laajoki K.V.O., Alapeiti T.T., and Peura R.A., 1997. Ruthenian pyrite and nickeloan malanite from the Imandra Layered Complex, Northwestern Russia. *The Canadian Mineralogist*, 38, 887-897.

Barnes S.J., and Naldrett A.J., 1986. Geochemistry of the J-M Reef of the Stillwater Complex, Minneapolis Adit Area II. Silicate Mineral Chemistry and Petrogenesis. *Journal of Petrology*, 27(4), 791-825.

Barnes S.J., Hoatson D.M., and Keays R.R., 1992. Distribution of sulfides and PGE within the mineralized porphyritic Websterite zone of the Munni Munni Complex, Western Australia. *Australian Journal of Earth Sciences*, 39, 289-302.

Barnes S.J., Osborne G.A., Cook D., Barnes L., Maier W.D., and Godel B., 2011. The Santa Rita Nickel Sulfide Deposit in the Fazenda Mirabela Intrusion, Bahia, Brazil: Geology, Sulfide Geochemistry, and Genesis. *Economic Geology*, 106, 1083-1110.

Barnes S-J., and Maier W.D., 2002. Platinum-group elements and microstructures of normal Merensky Reef from Impala Mines, Bushveld Complex. *Journal of Petrology*, 43(1), 103-128.

Barnes S-J., Cox R.A., and Zientek M.L., 2006. Platinum-group element, Gold, Silver and Base Metal distribution in compositionally zoned sulphide droplets from the Medvezky Creek Mine, Noril'sk, Russia. *Contributions to Mineralogy and Petrology*, 152, 187-200.

Barnes S.-J., Makovicky E., Makovicky M., Rose-Hansen J., and Karup-Moller S., 1997. Partition coefficients for Ni, Cu, Pd, Pt, Rh, and Ir between monosulfide solid solution and sulphide liquid and the formation of compositionally zoned Ni - Cu sulfide bodies by fractional crystallization of sulfide liquid. *Canadian Journal of Earth Sciences*, 34, 366-374.

Barnes S-J., Prichard H.M., Cox R.A., Fisher P.C., and Godel B., 2008. The location of the chalcophile and siderophile elements in platinum-group element ore deposits (a textural, microbeam and whole rock geochemical study): Implications for the formation of the deposits. *Chemical Geology*, 248, 295-317.

Becker H., Horan M.F., Walker R.J., Gao S., Lorand J-P., and Rudnick R.L., 2006. Highly siderophile element composition of the Earth's primitive upper mantle: Constraints from new data on peridotite massifs and xenoliths. *Geochimica et Cosmochimica Acta*, 70, 4528-4550.

Bezman N.I., Asif M., Brügmann G.E., Romanenko I.M., and Naldrett A.J., 1994. Distribution of Pd, Rh, Ru, Ir, Os and Au between sulphide and silicate melts. *Geochimica et Cosmochimica Acta*, 58(4), 1251-1260.

Boudreau A.E., and McCallum I.S., 1992. Concentration of Platinum-Group Elements by Magmatic Fluids in Layered Intrusions. *Economic Geology*, 87, 1830-1848.

Boudreau A.E., Djon L., Tchalikian A., and Corkery J., 2014. The Lac Des Iles Palladium Deposit, Ontario, Canada part I. The effect of variable alteration on the Offset Zone. *Mineralium Deposita*, 49, 625-654.

Brenan J.M., and McDonough W.F., 2009. Core formation and metal–silicate fractionation of osmium and iridium from gold. *Nature Geoscience*, DOI: 10.1038/NGEO658.

Brownscombe W., Herrington R.J., Wilinson J.J., Beery A.J., Coppard J., Ihlenfeld C., Klatt S., Hartshorne C., Boyce A.J., and Taylor R.N., 2013. Geochemistry of the Sakatti magmatic Cu-Ni-PGE deposit, northern Finland. *In* 12th SGA Biennial Meeting 2013 Proceedings, 3, 956-959.

Brügmann G.E., Naldrett A.J., Asif M., Lightfoot P.C., Gorbachev N.S., and Fedorenko V.A., 1993. Siderophile and chalcophile metals as tracers of the evolution of the Siberian Trap in the Noril'sk region, Russia. *Geochimica et Cosmochimica Acta*, 57, 2001-2018.

Buchanan D.L., and Nolan J., 1979. Solubility of sulphur and sulphide immiscibility in synthetic tholeiite melts and their relevance to Bushveld-Complex rocks. *The Canadian Mineralogist*, 17, 483-494.

Buchanan D.L., and Rouse J.E., 1984. Role of contamination in the precipitation of sulphides in the Platreef of the Bushveld Complex. *In* Sulphide Deposits in Mafic and Ultramafic Rocks (eds DL Buchanana and MJ Jones). Special Publication Institute of Mining and Metallurgy, pp. 141-146.

Buick I.S., Maas R., and Gibson R., 2001. Precise U-Pb titanite age constraints on the emplacement of the Bushveld Complex, South Africa. *Journal of the Geological Society*, 158, 3-6.

Cabri L.J., 2002. The platinum-group minerals. *In* The Geology, Geochemistry, Mineralogy and Mineral Beneficiation of the Platinum-group elements (ed LJ Cabri) Canadian Institute of Mining, Metallurgy and Petroleum, Montreal, Special Volume 54, pp. 13-131.

Cabri L.J., and Laflamme J.H.G., 1976. The Mineralogy of the Platinum-Group Elements from Some Copper-Nickel Deposits of the Sudbury Area, Ontario. *Economic Geology*, 71, 1159-1195.

Carbi L.J., Wilson J.M.D., Distler V.V., Kingslon D., Nejedly Z. and Sluzheniken S.F., 2002. Mineralogical distribution of trace platinum-group elements in the disseminated sulphide ores of Noril'sk 1 layered intrusion. *Applied Earth Science (Transactions of the Institute of Mining and Metallurgy B)*, 111, B15-B22.

Campbell I.H., and Naldrett A.J., 1979. The influence of silicate:sulfide ratios on the geochemistry of magmatic sulphides. *Economic Geology*, 74(6), 1305-1506.

Campbell I.H., Naldrett A.J., and Barnes S.J., 1983. A Model for the Origin of the Platinum-Rich Sulfide Horizons in the Bushveld and Stillwater Complexes. *Journal of Petrology*, 24, 133-165.

Cawthorn R.G., Merkle R.K.W., and Viljoen M.J., 2002. Platinum-group element deposits in the Bushveld Complex, South Africa. *In* The Geology, Geochemistry, Mineralogy and Mineral Beneficiation of the Platinum-group elements (ed LJ Cabri) Canadian Institute of Mining, Metallurgy and Petroleum, Montreal, Special Volume 54, pp. 389-429.

Chai G., and Naldrett A.J., 1992a. Characteristics of Ni-Cu-PGE mineralization and genesis of the Jinchuan Deposit, Northwest China. *Economic Geology*, 87, 1475-1495.

Chai G., and Naldrett A.J., 1992b. The Jinchuan ultramafic intrusion: Cumulate of a high-Mg basaltic Magma. *Journal of Petrology*, 33(2), 277-303.

Chai G., Naldrett A.J., and Rucklidge J.C., 1993. In situ quantitative analyses for PGE and Au in sulfide minerals of the Jinchuan Ni-Cu deposit by accelerator mass spectrometry. *The Canadian Mineralogist*, 33, 277-303.

Chen L-M., Song X-Y., Keays R.R., Tian Y-L., Wang Y-S., Deng Y-F., and Xiao J-F., 2013. Segregation and Fractionation of Magmatic Ni-Cu-PGE Sulfides in the Western Jinchuan Intrusion, Northwestern China: Insights from Platinum Group Element Geochemistry. *Economic Geology*, 108, 1793-1811.

Chou C-L., 1978. Fraction of siderophile elements in the Earth's upper mantle. *Proceedings of the 9th Lunar Planetary Science Conference*, 219-230.

Cowley A., 2013. PLATINUM 2013, Interim Review, Johnson Matthey. www.platinum.matthey.com/media/1614079/platinum_2013.pdf.

Crocket J.H., Fleet M.E., and Stone W.E., 1997. Implications of composition for experimental partitioning of platinum-group elements and gold between sulfide liquid and basalt melt: The significance of nickel content *Geochimica et Cosmochimica Acta*, 61(19), 4139-4149.

Czamanske G.K., and Loferski P.J., 1996. Cryptic trace-element alteration of anorthosite, Stillwater Complex, Montana. *Canadian Mineralogist*, 34, 559-576.

Czamanaske G.K., and Moore J.G., 1977. Composition and phase chemistry of sulfide globules in basalt from the Mid-Atlantic Ridge rift valley near 37°N lat. *Geological Society of America Bulletin*, 88(4), 587-599.

Dare S.A.S., Barnes S-J., and Prichard H.M., 2010a. The distribution of platinum group elements (PGE) and other chalcophile elements among sulphides from the Creighton Ni–Cu–PGE sulphide deposit, Sudbury, Canada, and the origin of palladium in pentlandite. *Mineralium Deposita*, 45(8), 765-793.

Dare S.A.S., Barnes S-J., Prichard H.M., and Fisher P.C., 2010b. The timing and formation of platinum-group minerals from the Creighton Ni-Cu-platinum-group element sulphide rich deposit, Sudbury, Canada: Early crystallisation of PGE-rich sulpharsenides. *Economic Geology*, 105, 1071-1096.

Dare S.A.S., Barnes S-J., Prichard H.M., and Fisher P.C., 2011. Chalcophile and platinum-group element (PGE) concentrations in the sulphide minerals from the McCreedy East deposit, Sudbury, Canada, and the origin of PGE in pyrite. *Mineralium Deposita*, 46, 381-407.

Davis D.W., 2008. Sub-million-year age resolution of Precambrian igneous events by thermal extraction–thermal ionization mass spectrometer Pb dating of zircon: Application to crystallization of the Sudbury impact melt sheet. *Geology*, 36, 383-386.

De Waal S.A., Xu Z., Li C., and Mouri H., 2004. Emplacement of viscous mushes in the Jinchuan ultramafic intrusion, western China. *The Canadian Mineralogist*, 42, 371-392.

Dillon-Leitch H.C.H., Watkinson D.H. and Coats C.J.A., 1986. Distribution of platinum-group elements in the Donaldson West deposit, Cape Smith belt, Quebec. *Economic Geology*, 81, 1147-1158.

Eales H.V., and Cawthorn R.G., 1996. The Bushveld Complex. *In* Layered Intrusions (ed RG Cawthorn), Elsevier, Amsterdam, pp. 181-229.

Ebel D.S., and Naldrett A.J., 1997. Crystallization of sulfide liquids and the interpretation of ore composition. *In* Proceedings of IGCP Project 336 conference "Intraplate Magmatism and related Mineralisation". *Canadian Journal of Earth Sciences*, 34(4), 352-365.

Eckstrand O.R., 1975. The Dumont Serpentinite: A Model for Control of Nickeliferous Opaque Mineral Assemblages by Alteration Reactions in Ultramafic Rocks. *Economic Geology*, 70, 183-201.

El Goresy A., Zinner E., Pellas P., and Caillet C., 2005. A menagerie of graphite morphologies in the Acapulco meteorite with diverse carbon and nitrogen isotopic signatures: implications for the evolution history of acapulcoite meteorites. *Geochimica et Cosmochimica Acta*, 69, 4535-4556.

Eriksson P.G., Schreiber U.M., and van der Neut M., 1991. A review of the sedimentology of the Early Proterozoic Pretoria Group, Trasvaal Sequence, South Africa: implications for tectonic setting. *Journal of African Earth Sciences*, 13(1), 107-119.

Ertel W., Walter M.J., Drake M.J., and Sylvester P.J., 2006. Experimental study of platinum solubility in silicate melt to 14 GPa and 2273 K: Implications for accretion and core formation in Earth. *Geochimica et Cosmochimica Acta*, 70, 2591-2602.

Farrow C.E.G., and Lightfoot P.C., 2002. Sudbury PGE revisited: Towards an integrated model. *In* The Geology, Geochemistry, Mineralogy and Mineral Beneficiation of the Platinum-group elements (ed LJ Cabri) Canadian Institute of Mining, Metallurgy and Petroleum, Montreal, Special Volume 54, pp. 273-297.

Fleet M.E., and Stone W.E., 1991. Partitioning of platinum-group elements in the Fe-Ni-S system and their fractionation in nature. *Geochimica et Cosmochimica Acta*, 55, 245-253.

Fleet M.E., Chryssoulis S.L., Stone W.E., and Weisener C.G., 1993. Partitioning of platinum-group elements and Au in the Fe - Ni - Cu - S system: experiments on the fractional crystallization of sulphide melt. *Contributions to Mineralogy and Petrology*, 115, 36-44.

Fleet M.E., Crocket J.H., and Stone W.E., 1996. Partitioning of platinum-group elements (Os, Ir, Ru, Pt, Pd) and gold between sulphide liquid and basalt melt. *Geochimica et Cosmochimica Acta*, 60(13), 2397-2412.

Flinn D., 1985. The Caledonides of Shetland. *In* The Caledonide Orogen: Scandinavia and Related Areas, 2 (eds DG Gee and BA Sturt). Wiley, London, 1159-1172.

Fuchs W.A., and Rose A.W., 1974. The geochemical behaviour of platinum and palladium in the weathering cycle in the Stillwater Complex, Montana. *Economic Geology*, 69, 332-346.

Gain S.B., and Mostert A.B., 1982. The Geological Setting of the Platinoid and Base Metal Sulfide Mineralization in the Platreef of the Bushveld Complex in Drenthe, North of Potgietersrus. *Economic Geology*, 77, 1395-1404.

Gervilla F., and Kojonen K., 2002. The platinum-group minerals in the upper section of the Keivitsansarvi Ni-Cu-PGE deposit, Northern Finland. *The Canadian Mineralogist*, 40, 377-394.

Gervilla F., Anguita A.S., Acevedo R.D., and Hach-Ali P.F., 1997. Platinum group element sulfoarsenides and bismuthtellurides in the metamorphosed Ni-Cu deposits at Las Aguilas (Province of San Luis, Argentina). *Mineralogical Magazine*, 61, 861-877.

Ghiorso M.S., Hirschmann M.M., Reiners P.W., and Kress V.C., III, 2002. The pMELTS: A revision of MELTS for improved calculation of phase relations and major element partitioning related to partial melting of the mantle to 3 GPa. *Geochemistry, Geophysics, Geosystems*, 3(5), doi: 10.1029/2001GC000217.

Godel B., and Barnes S-J., 2008a. Image analysis and composition of platinum-group minerals in the J-M Reef, Stillwater Complex. *Economic Geology*, 103, 637-651.

Godel B., and Barnes S-J., 2008b. Platinum-group elements in sulphide minerals and the whole rocks of the J-M Reef (Stillwater Complex): Implication for the formation of the reef. *Chemical Geology*, 248, 272-294.

Godel B., Barnes S-J., and Maier W.D., 2007. Platinum-Group Elements in Sulphide Minerals, Platinum-Group Minerals, and Whole-Rocks of the Merensky Reef (Bushveld Complex, South Africa): Implications for the Formation of the Reef. *Journal of Petrology*, 48(8), 1569-1604.

Godel B., González-Álvarez I., Barnes S.J., Barnes S-J., Parker P., and Day J., 2012. Sulfides and Sulfarsenides from the Rosie Nickel Prospect, Duketon Greenstone Belt, Western Australia. *Economic Geology*, 107, 275-294.

Gunn G., and Benham A., 2009. Platinum Commodity Profile. British Geological Survey, pp. 32

Halkoaho T., 1993. The Sompujarvi and Ala-Penikka PGE reefs in the Penikat layered intrusion, northern Finland: implications for PGE reef-forming processes. Acta University Ouluensis, 249, 1-122.

Halkoaho T., Alapieti T.T., and Huhtelin T., 2005. The Somujarvi, Ala-Penikka and Paasivaara PGE reef in the Penikat layered intrusion, northern Finland. Geological Survey Finland, Guide 51a, 33-76.

Hall A.L., 1932. The Bushveld Igneous Complex in the central Transvaal. Geological Society, South Africa, Memoir, 28, pp. 544.

Hanley J.J., 2005. The Aqueous Geochemistry of the Platinum Group Elements (PGE) in Surficial, Low-T Hydrothermal and High-T Magmatic-Hydrothermal Environments. *In* Exploration for platinum-group element deposits. Mineralogical Association of Canada Short Course Series 35 (ed JE Mungall), Oulu, Finland, pp. 35-56.

Hanley J.J., 2007. The role of arsenic-rich melts and mineral phases in the development of high-grade Pt-Pd mineralization within komatiite-associated magmatic Ni-Cu sulfide horizons at Dundonald Beach south, Abitibi subprovince, Ontario, Canada. *Economic Geology*, 102, 305-317.

Hart S.R., and Zindler A., 1986. In search of a bulk-Earth composition. *Chemical Geology*, 57, 247-267.

Hartmann W.K., Quantin C., and Mangold N., 2007. Possible long-term decline in impact rates 2. Lunar impact-melt data regarding impact history. *Icarus*, 186, 11-23.

Haughton D.R., Roeder P.L., and Skinner B.J., 1974. Solubility of Sulfur in Mafic Magmas. *Economic Geology*, 69, 451-467.

Hawkesworth C.J., Lightfoot P.C., Fedorenko V.A., Blake S., Naldrett A.J., Doherty W., and Gorachev N.S., 1995. Magma differentiation and mineralisation in the Siberian continental flood basalts. *Lithos*, 34, 61-88.

Hawley J.E., 1965. Upside-down zoning at Frood, Sudbury, Ontario. *Economic Geology*, 60, 529-575.

Helmy H.A., Ballhaus C., Berndt J., Bockrath C., and Wohlgemuth-Ueberwassar C., 2007. Formation of Pt, Pd and Ni tellurides: experiments in sulphide-telluride systems. *Contributions to Mineralogy and Petrology*, 153, 577-591.

Helmy H.A., Ballhaus C., Wohlgemuth-Ueberwassar C., Fonseca R.O.C., and Laurenz V., 2010. Partitioning of Se, As, Sb, Te and Bi between monosulfide solid solution and sulfide melt - Application to magmatic sulfide deposits. *Geochimica et Cosmochimica Acta*, 74, 6174-6179.

Holwell D.A., and McDonald I., 2006. Petrology, geochemistry and the mechanisms determining the distribution of platinum-group element and base metal sulphide mineralisation in the Platreef at Overysel, northern Bushveld Complex, South Africa. *Mineralium Deposita*, 41, 575-598.

Holwell D.A., and McDonald I., 2007. Distribution of platinum-group elements in the Platreef at Overysel, northern Bushveld Complex: a combined PGM and LA-ICP-MS study. *Contributions to Mineralogy and Petrology*, 154, 171-190.

Holwell D.A., and McDonald I,. 2010. A review of the behaviour of platinum-group elements within natural magmatic sulphide ore systems: The importance of semimetals in governing partitioning behaviour. *Platinum Metals Review*, 54, 26-36.

Holwell D.A., McDonald I., and Armitage P.E.B., 2006. Platinum-group mineral assemblages in the Platreef at the South Central Pit, Sandsloot Mine, northern Bushveld Complex, South Africa. *Mineralogical Magazine*, 70, 83-101.

Holzheid H., Sylvester P., O'Neill H.St.C., Rubie D.C., and Palme H., 2000; Evidence for a late chondritic veneer in the Earth's mantle from high-pressure partitioning of palladium and platinum. *Nature*, 406, 396-399.

Huang, W-L., and Williams R.J., 1980. Melting relations of portion of the system Fe-S-Si-O to 32 kb with implication to the nature of the mantle-core boundary. (abstract) Lunar and Planetary Science XI, Lunar and Planetary Institute, Houston, 486-488

Huhtelin T.A., Alapieti T.T., and Lahtinen J.J., 1990. The Paasivaara PGE Reef in the Penikat Layered Intrusion, Northern Finland. *Contributions to Mineralogy and Petrology*, 42(1-4), 57-70.

Hutchinson D., and Kinnaird J.A., 2005. Complex multistage genesis for the Ni–Cu–PGE mineralisation in the southern region of the Platreef, Bushveld Complex, South Africa. *Applied Earth Science (Transactions of the Institute of Mining and Metallurgy B)*, 114(4), 208-224.

Hutchinson D., and McDonald I., 2008. Laser ablation ICP-MS study of platinum-group elements in sulfides from the Platreef at Turfspruit, northern limb of the Bushveld Complex, South Africa. *Mineralium Deposita*, 43, 695-711.

Inwood N., Smith R., and Guzman C., 2011. Santa Rita Project Technical Report, Mirabela Nickel Ltd.

Irvine T.N., 1975. Crystallization sequences in the Muskox intrusion and other layered intrusions-II. Origin of chromitite layers and similar deposits of other magmatic ores. *Geochimica et Cosmochimica Acta*, 39, 991-1020.

Jugo P.J., 2009. Sulfur content at sulfide saturation in oxidized magmas. *Geology*, 37, 415-418.

Keays R.R., and Crocket J.H., 1970. A Study of Precious Metals in the Sudbury Nickel Irruptive Ores. *Economic Geology*, 65, 438-450.

Keays R.R., and Lightfoot P.C., 2010. Crustal sulfur is required to form magmatic Ni-Cu sulfide deposits: evidence from chalcophile element signatures of Siberian and Deccan Trap basalts. *Mineralium Deposita*, 45, 241-257.

Kerr A., and Leitch A.M., 2005. Self-Destructive Sulfide Segregation Systems and the Formation of High-Grade Magmatic Ore Deposits. *Economic Geology*, 100, 311-332.

Kimura K., Lewis R.S., and Anders E., 1974. Distribution of gold and rhenium between nickel-iron and silicate melts: implications for the abundance of siderophile elements on the Earth and Moon. *Geochimica et Cosmochimica Acta*, 88, 683-701.

Kinloch E.D., 1982. Regional Trends in the Platinum-Group Mineralogy of the Critical Zone of the Bushveld Complex, South Africa. *Economic Geology*, 77, 1328-1347.

Kinloch E.D., and Peyerl W., 1990. Platinum-Group Minerals in Various Rock Types of the Merensky Reef: Genetic Implications. *Economic Geology*, 85, 537-555.

Kleine T., 2011. Earth's patchy late veneer. *Nature*, 477, 168-169.

Krogh TE., Davis D.W., and Corfu F., 1984. Precise U-Pb zircon and baddeleyite ages for the Sudbury area. *In* The Geology and Ore Deposits of the Sudbury Structure (Eds EG Pye, AJ Naldrett and PE Gilbin), Ontario Geological Survey Special Volume, 1, 431-446.

Latypov R.M., 2000. Phase equilibria constraints on relations of ore-bearing intrusions with flood basalts in the Noril'sk region, Russia. *Contributions to Mineralogy and Petrology*, 143, 438-449.

Lee C.A., 1996. A Review of Mineralization in the Bushveld Complex and some other Layered Mafic Intrusions. *In* Layered Intrusions (ed RG Cawthorn), Elsevier, Amsterdam, pp. 103-146.

Lehmann J., Arndt N., Windley B., Zhou M-F., Wang C.Y., and Harris C., 2007. Field relationships and geochemical constraints on the emplacement of the Jinchuan intrusion and its Ni-Cu-PGE sulphide deposit, Gansu, China. *Economic Geology*, 102, 75-94.

Lesher C.M., and Charland A., 1999. Geology of the Katiniq area. *In* Komatiitic-Peridotite-Hosted Ni-Cu-(PGE) Deposits of the Raglan Area, Cape Smith Belt, New Quebec (ed CM Lesher). Mineral Exploration Research Centre, Laurentian University, Sudbury, Guidebook, 2, 91-106.

Li C., and Naldrett A.J., 1993. Sulfide capacity of magma: A quantitative model and its application to the formation of sulphide ores at Sudbury, Ontario. *Economic Geology*, 88, 1253-1260.

Li C., and Ripley E.M., 2009. Sulfur Contents at Sulfide-Liquid or Anhydrite Saturation in Silicate Melts: Empirical Equations and Example Applications. *Economic Geology*, 104(3), 405-412.

Li C., and Ripley E.M., 2011. The Giant Jinchuan Ni-Cu-(PGE) Deposit: Tectonic Setting, Magma Evolution, Ore Genesis and Exploration Implications. Reviews in Economic Geology, 17, 163-180.

Li C., Naldrett A.J., Coats C.J.A., and Johannessen P., 1992 Platinum, palladium, gold, and copper-rich stringers at the Strathcona mine, Sudbury - their enrichment by fractionation of a sulfide liquid. *Economic Geology*, 87(6), 1584-1598.

Li C., Barnes S-J., Makovicky E., Rose-Hansen J., and Makovicky M., 1996. Partitioning of nickel, copper, iridium, rhenium, platinum, and palladium between monosulfide solid solution and sulphide liquid: Effects of composition and temperature. *Geochimica et Cosmochimica Acta*, 60(7), 1231-1238.

Li C., Ripley E.M., and Naldrett A.J., 2003. Compositional variations of olivine and sulfur isotopes in the Noril'sk and Talnakh intrusions, Siberia: Implications for ore-forming processes in dynamic magma conduits. *Economic Geology*, 98(1), 69-86.

Li C., Xu Z., de Waal S.A., Ripley E.M., and Maier W.D., 2004. Compositional variations of olivine from the Jinchuan Ni–Cu sulphide deposit, western China: implications for ore genesis. *Mineralium Deposita*, 39, 159-172.

Li C., Ripley E.M., and Naldrett A.J., 2009. A new genetic model for the giant Ni-Cu-PGE sulfide deposits associated with the Siberian flood basalts. *Economic Geology*, 104(2), 291-301.

Li X.H., Su L., Chung S-L., Li Z.X., Liu Y., Song B., and Liu D.Y., 2005. Formation of the Jinchuan ultramafic intrusion and the world's third largest Ni-Cu sulphide deposit: Associated with the ~825 Ma south China mantle plume? *Geochemistry, Geophysics, Geosystems*, 6(11):Q11004, doi:10.1029/2005GC001006.

Liu Y., Samaha N-T., and Baker D.R., 2007. Sulfur concentration at sulfide saturation (SCSS) in magmatic silicate melts. *Geochimica et Cosmochimica Acta*, 71, 1783-1799.

Lodders K., 2003. Solar system abundances and condensation temperatures of the elements. *Astrophysical Journal*, 591, 1220–1247.

Lorand J-P., and Alard O., 2010. Pyrite tracks assimilation of crustal sulfur in Pyrenean peridotites. *Contributions to Mineralogy and Petrology*, 101, 151-128.

Lunine J.I., 1999. Earth, Evolution of a Habitable World. Cambridge University Press, pp. 319.

Maier W.D., 2005. Platinum-group element (PGE) deposits and occurrences: Mineralization styles, genetic concepts, and exploration criteria. Invited presidential review. *Journal of African Earth Sciences*, 41, 165–191.

Maier W.D., Barnes S.-J., and Groves D.I., 2013. The Bushveld Complex, South Africa: formation of platinum-palladium, chrome- and vanadium-rich layers via hydrodynamic sorting of a mobilized cumulate slurry in a large, relatively slowly cooling, subsiding magma chamber. *Mineralium Deposita*, 48, 1-56.

Mann U., Frost D.J., Rubie D.C., Becker H., and Audétat A., 2012. Partitioning of Ru, Rh, Pd, Re, Ir and Pt between liquid metal and silicate at high pressures and high temperatures - Implications for the origin of highly siderophile element concentrations in the Earth's mantle. *Geochimica et Cosmochimica Acta*, 84, 593-613.

Mariga J., Ripley E.M., and Li C., 2006. Petrologic evolution of gneissic xenoliths in the Voisey's Bay Intrusion, Labrador, Canada: Mineralogy, reactions, partial melting, and mechanisms of mass transfer. *Geochemistry, Geophysics, Geosystems*, 7, doi: 10.1029/2005GC001184.

Marma J.C., 2002. Magmatic and hydrothermal PGE mineralization of the Birch Lake Cu-Ni-PGE deposit in the South Kawishiwi Intrusion, Duluth Complec, Northeast Minnesota. Unpublished, M.Sc thesis, University of Wisconsin, pp. 101.

Mathez E.A., 1976. Sulfur Solubility and Magmatic Sulfides in Submarine Basalt Glass. *Jounral of Geophysical Research*, 81(23), 4269-4276.

Mavrogenes J.A., and O'Neill H.St.C., 1999. The relative effects of pressure, temperature and oxygen fugacity on the solubility of sulphide in mafic magmas. *Geochimica et Cosmochimica Acta*, 63(7-8), 1173-1180.

McDonald I., 2008. Platinum-group element and sulphide mineralogy in ultramafic complexes at western Andriamena, Madagascar: *Applied Earth Science (Transactions of the Institute of Mining and Metallurgy B)*, 117, 1-10.

McDonald I., and Viljoen K.S. 2006. Platinum-group element geochemistry of mantle eclogites: a reconnaissance study of xenoliths from the Orapa kimberlite, Botswana. *Applied Earth Science (Transactions of the Institute of Mining and Metallurgy B)*, 115, B81-93.

McDonald I., Ohnenstetter D., Ohnenstetter M., and Vaughan D.J., 1999. Palladium oxides in ultramafic complexes near Lavatrafo, Western Andriamena, Madagascar. *Mineralogical Magazine*, 63, 345-352.

McDonald I., Ohnenstetter D., Rowe J.P., Tredoux M., Pattrick R.A.D., and Vaughan D.J., 1999. Platinum precipitation in the Waterberg deposit, Naboomspruit, South Africa. *South African Journal of Geology*, 102, 184-191.

McDonald I., Holwell D.A., and Armitage P.E.B., 2005. Geochemistry and mineralogy of the Platreef and "Critical Zone" of the northern lobe of the bushveld Complex, South Africa: implications for Bushveld stratigraphy and the development of PGE mineralisation. *Mineralium Deposita*, 40, 526-549.

McDonough W.F., and Sun S.S., 1995. The composition of the Earth. *Chemical Geology*, 120(3-4), 223-253.

Merkle R.K.W., 1992. Platinum-group minerals in the middle group of chromitite layers at Marikana, Western Bushveld Complex - indications for collection mechanisms and postmagmatic modification. *The Canadian Mineralogist*, 29, 209-221.

Mondal S.K., Baidya T.K., Gururaja Rao K.N., and Glascock M.D., 2001. PGE and Ag mineralization in a breccia zone of the Precambrian Nuasahi ultramafic-mafic complex, Orissa, India. *The Canadian Mineralogist*, 39, 979-996.

Montalvao R.M.G., and Tassinari C.C.G., 1984. Geocronologia precambriana do Território Federal do Amapá (Brasil). *In* Symposium Amazônico, 2, Manaus, *Anais*, 53-57.

Morgan J.W., Wandless G.A., Petrie R.K., and Irving A.J., 1981. Composition of the Earth's upper mantle - I. Siderophile trace elements in ultramafic nodules. Tectonophysics, 75, 47-67.

Morrissey C.J., 1998. Exploration for Platinum: A Contemporary Viewpoint. *In* Geo-Platinum 87 (eds HM Prichard, PJ Potts, JFW Bowles and SJ Cribb), Elsevier, London, pp. 1-12.

Mungall J.E., and Brenan J.M., 2014. Partitioning of platinum-group elements and Au between sulfide liquid and basalt and the origins of mantle-crust fractionation of the chalcophile elements. *Geochimica et Cosmochimica Acta*, 125, 265-289.

Mungall J.E., Andrews D.R.A., Cabri L.J., Sylvester P.J., and Tubrett M., 2005. Partitioning of Cu, Ni, Au, and platinum-group elements between monosulfide solid solution and sulphide melt under controlled oxygen and sulphur fugacities. *Geochimica et Cosmochimica Acta*, 69, 4349-4360.

Naldrett A.J., 2004. Magmatic Sulphide Deposits: Geology, Geochemistry and Exploration, Springer Verlaag, pp. 728.

Naldrett A.J., 2011. Fundamentals of magmatic sulphide deposits. *In* Magmatic Ni-Cu and PGE deposits: Geology, geochemistry, and genesis. Reviews in Economic Geology, 17, 1-50.

Naldrett A.J., Craig J.R., and Kullerud G., 1967. The central portion of the Fe-Ni-S system and its bearing on pentlandite exsolution in iron-nickel sulfides ores. *Economic Geology*, 62, 826-847.

Naldrett A.J., Gasparrini E.C., and Barnes S.J., 1986. The Upper Critical Zone of the Bushveld Complex and the Origin of Merensky-type Ores. *Economic Geology*, 81, 1105-1117.

Naldrett A.J., Innes D.G., Sowa J., and Gorton M.P., 1982. Compositional variations within and between 5 Sudbury ore-deposits. *Economic Geology*, 77, 1519-1534.

Naldrett A.J., Lightfoot P.C., Fedorenko V.A., Doherty W., and Gorbachev N.S., 1992. Geology and geochemistry of intrusions and flood basalts of the Norilsk region, USSR, with implications for the origin of the Ni-Cu ores. *Economic Geology*, 87(4), 975-1004.

Naldrett A.J., Fedorenko V.A., Lightfoot P.C., Junilov V.I., Gorbachev N.S., Doherty W., and Johan Z., 1995. Ni-Cu-PGE deposits of Norilsk region, Siberia - their formation in conduits for flood-basalt volcanism. *Applied Earth Science (Transactions of the Institute of Mining and Metallurgy B)*, 104, B18-B36.

Naldrett A.J., Fedorenko V.A., Asif M., Shushen L., Kunilov V.E., Stekhin A.I., Lightfoot P.C., and Gorbachev N.S., 1996. Controls on the composition of Ni-Cu sulfide deposits as illustrated by those at Noril'sk, Siberia. *Economic Geology*, 91(4), 751-773.

Naldrett A.J., Ebel D.S., Asif M., Morrison G., and Moore C.M., 1997. Fractional crystallisation of sulfide melts as illustrated at Noril'sk and Sudbury. *European Journal of Mineralogy*, 9(2), 365-377.

Naldrett A.J., Asif M., Schandl E., Searcy T., Morrison G.G., Binney W.P., and Moore C., 1999. Platinum-group elements in the sudbury ores: Significance with respect to the origin of different ore zones and to the exploration for footwall orebodies. *Economic Geology*, 94(2), 185-120.

Naldrett A.J., Wilson A., Kinnaird J.A., and Chunnett G., 2009. PGE tenor and metal ratios within and below the Merensky Reef, Bushveld Complex: implications for its genesis. *Journal of Petrology*, 50, 625-659.

Nelson D.R., Trendall A.F., and Altermann W., 1999. Chronological correlations between the Pilbara and Kaapvaal cratons. *Precambrian Research*, 97, 165-189.

Oberthür T., Cabri L.J., Weiser T.W., McMahon G., and Müller P., 1997. Pt, Pd and other trace elements in sulfides of the Main Sulfide Zone, Great Dke, Zimbabwe: A reconnaissance study. *The Canadian Mineralogist*, 35, 597-609.

Osbahr I., Klemd R., Oberthür T., Brätz H., and Schouwstra R., 2013. Platinum-group element distribution in base-metal sulphides of the Merensky Reef from the eastern and western Bushveld Complex, South Africa. *Mineralium Deposita*, 48, 211-232.

Page N.J., 1976. Serpentinization and alteration in an olivine cumulate from the Stillwater Complex, Southwestern Montana. *Contributions to Mineralogy and Petrology*, 54(2), 127-137.

Palme H., and O'Neill H.St.C., 2004. Cosmochemical Estimates of Mantle Composition. *In* Treatise on Geochemistry (ed RW Carlson), pp 1-38.

Peregoedova A.V., 1998. The experimental study of the Pt–Pd partitioning behaviour between monosulfide solid solution and Cu–Ni–sulfide melt at 900–840°C. 8th International Platinum Symposium Abstracts. Geological Society of South Africa and South African Institute of Mining and Metallurgy Symposium Series S18, 325-327.

Peregoedova A.V., Barnes S-J., and Baker D.R., 2004. The formation of Pt-Ir alloys and Cu-Pd-rich sulfide melts by partial desulfurization of Fe-Ni-Cu sulfides: results of experiments and implications for natural systems. *Chemical Geology*, 208, 247-264.

Peucker-Ehrenbrink B., and Jahn B-M., 2001. Rhenium-osmium isotope systematics and platinum group element concentrations: Loess and the upper continental crust. *Geochemistry, Geophysics, Geosystems*, 2, doi: 2001GC000172.

Piña R., Gervilla F., Ortega L. and Lunar R., 2008. Mineralogy and geochemistry of platinumgroup elements in the Aguablanca Ni-Cu deposit (SW Spain). *Mineralogy and Petrology*, 92, 259-282.

Piña R., Gervilla F., Barnes S-J., Ortega L. and Lunar R., 2011 Distribution of platinum-group and chalcophile elements in the Aguablanca Ni-Cu sulfide deposit (SW Spain): Evidence from a LA-ICP-MS study. *Chemical Geology*, 302–303, 61–75.

Piña R., Gervilla F., Barnes S-J., Ortega L. and Lunar R., 2013. Partition Coefficients of Platinum Group and Chalcophile Elements Between Arsenide and Sulfide Phases as Determined in the Beni Bousera Cr-Ni Mineralization (North Morocco). *Economic Geology*, 108, 935-951.

Pinho I.C.A., Barbosa J.S.F., Leal A.B.M., Martin H., and Peucat J-J., 2011. Geochemical modelling of the tonalitic and trondhjemitic granulites from the Itabuna-Salvador-Curaçá Block, Bahia, Brazil. *Journal of South American Earth Sciences*, 31, 312-323.

Platinum Today, 2013. Platinum Today, 2013 Applications. Available at http://www.platinum.matthey.com/about-pgm/applications

Polovina J.S., Hudson D.M., and Jones R.E., 2004. Petrographic and geochemical characteristics of postmagmatic hydrothermal alteration and mineralization in the J-M Reef, Stillwater Complex, Montana. *Canadian Mineralogist*, 42, 261-277.

Power M.R., Pirrie D., Jedwab J., and Stanley C.J., 2004. Platinum-group element mineralization in an As-rich magmatic sulfide system, Talnotry, southwest Scotland. *Mineralogical Magazine*, 68, 395-411.

Premo W.R., Helz R.T., Zientek M.L., and Langston R.B., 1990. U-Pb and Sm-Nd ages for the Stillwater Complex and its associated sills and dikes, Beartooth Mountains, Montana: Identification of a parent magma? *Geology*, 18, 1065-1068.

Prichard H.M., 1985. The Shetland Ophiolite. *In* The Caledonide Orogen: Scandinavia and Related Areas, 2 (eds DG Gee and BA Sturt). Wiley, London, 1173-1184.

Prichard H.M., 2007. Natural and artificial platinum and palladium occurrences worldwide. *In* Advances in Science: Earth Science; From Earthquakes to Global Warming (Eds. PR Sammonds and JMT Thompson). Royal Society Series on Advances in Science, Vol. 2, Imperial College Press, Ch 13, pp. 273-291.

Prichard H.M., and Lord R.A., 1988. The Shetland ophiolite: evidence for a supra-subductio zone origin and implications for platinum-group-element mineralization. *In* Mineral Deposits within the European Community (eds J Boissonnas and P Omenetto). Springer-Verlag, Berlin, Germany, 289-302.

Prichard H.M., Ixer R.A., Lord R.A., Maynard J., and Williams N., 1994. Assemblages of platinum-group minerals and sulphides in silicate lithologies and chromite-rich rocks within the Shetland Ophiolite. *The Canadian Mineralogist*, 32, 271-294.

Prichard H.M., Sá J.H.S., and Fisher P.C., 2001. Platinum-group mineral assemblages and chromite composition in the altered and deformed Bacuri Complex, Amapa, Northeastern Brazil. *The Canadian Mineralogist*, 39, 377-396.

Prichard H.M., Barnes S-J., Maier W.D. and Fisher P.C., 2004a. Variations in the nature of the platinum-group minerals in a cross-section through the Merensky Reef at Impala Platinum: Implications for the mode of formation of the reef. *The Canadian Mineralogist*, 42, 423-437.

Prichard H.M., Hutchinson D., and Fisher P.C., 2004b. Petrology and crystallisation history of multiphase sulphide droplets in a mafic dike from Uruguay: Implications for the origin of Cu-Ni-PGE-sulphide deposits. *Economic Geology*, 99, 365-376.

Prichard H.M., Fisher P.C., McDonald I., Zhou M-F., and Wang C.Y., 2005. Platinum-group minerals in the Jinchuan complex, China. In Platinum-group elements - from genesis to beneficiation and environmental impact (eds TO Törmänen and TT Alapieti). 10th International Pt Symposium Finland - Extended Abstracts Vol. 219-222.

Prichard H.M., Fisher P.C., McDonald I., Knight R.D., Black A.P., Sharp D.R., and Williams J.P., 2013. The Distribution of PGE and the Role of Arsenic as a Collector of PGE in the Spotted Quoll Nickel Ore Deposit in the Forrestania Greenstone Belt, Western Australia. *Economic Geology*, 108(8), 1903-1921.

Prichard H.M., Knight R.D., Fisher P.C., McDonald I., Zhou M-F., and Wang C.Y., 2013. Distribution of platinum-group elements in magmatic and altered ores in the Jinchuan intrusion, China: an example of selenium remobilization by postmagmatic fluids. Mineralium Deposita, 48(6), 767-786.

Ringwood A.E., 1966. Chemical evolution of the terrestrial planets. *Geochimica et Cosmochimica Acta*, 30, 41-104.

Ringwood A.E., and Kesson S.E., 1977. Basaltic magmatism and the bulk composition of the Moon II. Siderophile and volatile elements in Moon, Earth and chondrites: implications for lunar origin. *Moon*, 16, 425-464.

Rio Narcea Recursos S.A., 2009. Technical report on the Aguablanca Ni-Cu Deposit, Extremadura Region, Spain. Lunding Mining Corporation, Report Number 08511150292.

Ripley E.M., 1981. Sulfur Isotopic Studies of the Dunka Road Cu-Ni Deposit, Duluth Complex, Minnesota. *Economic Geology*, 76, 610-620.

Ripley E.M., and Alawi J.A., 1986. Sulfide mineralogy and chemical evolution of the Babbitt Cu-Ni deposit, Duluth Complex, Minnesota, *The Canadian Mineralogist*, 24, 347-368.

Ripley E.M., and Aljassar T.J., 1987. Sulfur and oxygen isotope studies of melt-country rock interaction, Babbitt Cu-Ni deposit, Duluth Complex, Minnesota. *Economic Geology*, 82(1), 87-107.

Ripley E.M., and Li C., 2003. Sulfur isotope exchange and metal enrichment in the formation of magmatic Cu-Ni-(PGE) deposits. *Economic Geology*, 98(3), 635-641.

Ripley E.M., and Li C., 2013. Sulfide Saturation in Mafic Magmas: Is External Sulfur Required for Magmatic Ni-Cu-(PGE) Ore Genesis? *Economic Geology*, 108, 45-58.

Ripley E.M., Lightfoot P.C., Li C., and Elswick E.R., 2003. Sulfur isotopic studies of continental flood basalts in the Noril'sk region: Implications for the association between lavas and ore-bearing intrusions. *Geochimica et Cosmochimica Acta*, 67(15), 2805-2817.

Ripley E.M., Sarkar A., and Li C., 2005. Mineralogic and Stable Isotope Studies of Hydrothermal Alteration at the Jinchuan Ni-Cu Deposit, China. *Economic Geology*, 100, 1349-1361.

Rudnick R.L., and Gao S., 2003. Composition of the continental crust. *In* Treatise on Geochemistry (ed RL Rudnick), Vol. 3. Oxford, Elsevier, pp. 1-56.

Sá J.H.S., Barnes S.-J., Prichard H.P., and Fisher P.C., 2005. The Distribution of Base Metals and Platinum-Group Elements in Magnetitite and Its Host Rocks in the Rio Jacaré Intrusion, Northeastern Brazil. *Economic Geology*, 100, 333-348.

SACS (South African Committee on Stratigraphy), 1980. Stratigraphy of South Africa. Geological Survey of South Africa, Handbook, 8, pp. 690.

Sælen G., Raiswell R., Talbot R.J., Skei J.M., and Bottrell S.H., 1993. Heavy sedimentary sulfur isotopes as indicators of super-anoxic bottom-water conditions. Geology, 21, 1091-1094.

Salpéteur I., Martel-Jantin B., and Rakotomanana D., 1995. Pt and Pd mobility in ferralitic soils of the West Andriamena area (Madagascar); evidence of a supergene origin of some Pt and Pd minerals. *Chronique de la Recherche Minière*, 520, 27-45.

Scoates J.S., and Friedman R.M., 2008. Precise age of the platiniferous Merensky Reef, Bushveld Complex, South Africa, by the U-Pb zircon chemical abrasion ID-TIMS technique. *Economic Geology*, 103(3), 465-471.

Seabrook C.L., Prichard H.M., and Fisher P.C., 2004. Platinum-group minerals in the Raglan Ni-Cu-(PGE) sulphide deposit, Cape Smith, Quebec, Canada. *The Canadian Mineralogist*, 42, 485-497.

S.G.U. (The Sixth Geological Unit of Gansu Geological Survey, China), 1984. Geology of Baijiazuezhi Cu-Ni Deposit (in Chinese). Beijing: Geological Publication Bureau, China, pp. 325.

Silva M.G. da, Martin H., and Abram M.B., 1996. Datação do corpo máfico-ultramáfico da Fazenda Mirabela (Ipiaú-BA.) pelo método Sm, Nd: Implicações petrogenéticas e geotectônicas. *Congresso Brasileiro De Geológia*, 39, 217-220.

Smith J.W., Holwell D.A., and McDonald I., 2014. Precious and base metal geochemistry and mineralogy of the Grasvally Norite-Pyroxenite-Anorthosite (GNPA) member, northern Bushveld Complex, South Africa: implications for a multistage emplacement. *Mineralium Deposita*, DOI 10.1007/s00126-014-0515-6.

Song X-Y., Zhou M-F., and Cao Z-M., 2004. Genetic relationships between base-metal sulfides and platinum-group minerals in the Yangliuping Ni-Cu-(PGE) sulfide deposit, Southwestern China. *The Canadian Mineralogist*, 42, 469-483.

Song X-Y Zhou M-F., Wang C.Y., Qi L., and Zhang C-J., 2006. Role of Crustal Contamination in Formation of the Jinchuan Intrusion and Its World-Class Ni-Cu-(PGE) Sulfide Deposit, Northwest China. *International Geology Review*, 48, 1113-1132.

Song X-Y., Keays R.R., Zhou M-F., Qi L., Ihlenfeld C., and Xiao J-F., 2009. Siderophile and chalcophile elemental constraints on the origin of the Jinchuan Ni-Cu-(PGE) sulfide deposit, NW China. *Geochimica et Cosmochimica Acta*, 73, 404-424.

Song X-Y., Danyushevsky L.V., Keays R.R., Chen L-M., Wang Y-S., Tian Y-L., and Xiao J-F., 2012. Structural, lithological, and geochemical constraints on the dynamic magma plumbing system of the Jinchuan Ni-Cu sulfide deposit, NW China. *Mineralium Deposita*, 47, 277-297.

Stone W.E., Crocket J.H., and Fleet M.E., 1990. Partitioning of palladium, iridium, platinum, and gold between sulphide liquid and basalt melt at 1200^{o}C. *Geochimica et Cosmochimica Acta*, 54, 2341-2344.

Su S., Li C., Zhou M-F., and Ripley E.M., 2008. Controls on variations of platinum-group element concentrations in the sulphide ores of the Jinchuan Ni-Cu deposit, western China. *Mineralium Deposita*, 43, 609-622.

Suárez S., Prichard H.M., Velasco F., Fisher P.C., and McDonald I., 2010. Alteration of platinum-group minerals and dispersion of platinum-group elements during progressive weathering of the Aguablanca Ni-Cu deposit, SW Spain. *Mineralium Deposita*, 45, 331-350.

Szentpetéri K., Watkinson, D.H., Molnár F., and Jones P.C., 2002. Platinum-group elements-Co-Ni-Fe sulpharsenides and mineral paragenesis in Cu-Ni-platinum-group element deposits, Copper Cliff North Area, Sudbury, Canada. *Economic Geology*, 97, 1459-1470.

Tang Z.L. and Li W.Y., 1995. Genesis Model and Geological Contrast of the Jinchuan (Pt-bearing) Cu-Ni Sulfide Deposit. Beijing Geological Publishing House, pp. 209 (in Chinese).

Tang Z.L., Yang J., and Xu S., 1992. Sm-Nd dating of the Jinchuan ultramafic rock body, Gansu, China. *Chinese Science Bulletin*, 37, 1988-1990 (in Chinese).

Tang Z.L., Song X-Y., and Su S., 2009. Ni-Cu deposits related to high Mg basaltic magma, Jinchuan, western China. *In* New developments in magmatic Ni-Cu and PGE deposits (eds C Li and EM Ripley). Beijing, Geological Publishing House, pp. 121-140.

Tao Y., Li C., Hu R., Ripley E.M., Du A., and Zhong H., 2007. Petrogenesis of the Pt–Pd mineralized Jinbaoshan ultramafic intrusion in the Permian Emeishan Large Igneous Province, SW China. *Contributions to Mineralogy and Petrology*, 153, 321-337.

Tera, F., Papanastassiou D.A., and Wasserburg G.J., 1974. Isotopic evidence for a terminal lunar cataclysm. *Earth and Planetary Science Letters*, 22, 1-21.

Tian Y-L., Wu S-J., Meng R., Wang Y-S., Lin C-L., and Xiao L-Z., 2007. LA-ICPMS zircon U-Pb age of the Jinchuan ultramafic intrusion. *Acta Mineralogica Sinica*, 27, 211-217 (in Chinese with English abstract).

Tomkins A.G., 2010. Wetting facilitates late-stage segregation of precious metal-enriched sulfosalt melt in magmatic sulfide systems. *Geology*, 38, 951-954.

Tornos F., Galindo C., Casquet C,. Rodríguez Pevida L., Martínez C., Martínez E., Velasco F., and Iriondo A., 2006. The Aguablanca Ni-(Cu) sulfide deposit, SW Spain: geologic and geochemical controls and the relationship with a midcrustal layered mafic complex. *Mineralium Deposita*, 41, 737-769.

van der Merwe M.J., 1976. Layered sequence of Potgietersrus limb of Bushveld Complex. *Economic Geology*, 71(7), 1337-1351.

Vikentyev I.V., Yudovskaya M.A., Mokhov A.V., Kerzin A.L., and Tsepin A.I., 2004. Gold and PGE in massive sulfide ore of the Uzelginsk deposit, southern Urals, Russia. *The Canadian Mineralogist*, 42, 651-665.

Wagner P.A., 1929. The platinum deposits and mines of South Africa. Oliver and Boyd, Edinburgh, pp. 326.

Walker R.J., 2009. Highly siderophile elements in the Earth, Moon and Mars: Update and implications for planetary accretion and differentiation. *Chemie der Erde*, 69, 101–125.

Wang C.Y., Prichard H.M., Zhou M-F., and Fisher P.C., 2008. Platinum-group minerals from the Jinbaoshan Pd-Pt deposit, SW China: evidence for magmatic origin and hydrothermal alteration. *Mineralium Deposita*, 43, 791-803.

Watkinson D.H., Lavigne M.J., and Fox P.E., 2002. Magmatic-Hydrothermal Cu- and Pd-rich Deposits in Gabbroic Rocks from North America. *In* The Geology, Geochemistry, Mineralogy and Mineral Beneficiation of the Platinum-group elements (ed LJ Cabri) Canadian Institute of Mining, Metallurgy and Petroleum, Montreal, Special Volume 54, pp. 299-319.

Wedepohl K.H., 1995. The composition of the continental crust. *Geochimica et Cosmochimica Acta*, 59, 1217-1232.

Wendlant R.F., 1982. Sulfide saturation of basalt and andesite melts at high pressures and temperatures. *American Mineralogist*, 67, 877-885.

Wilson A.H., Naldrett A.J., and Tredoux M., 1989. Distribution and controls of platinum-group element and base element mineralization in the Darwendale subchamber of the Great Dyke, Zimbabwe. *Geology*, 17, 649-652.

Wood M., 2003. Arsenic in igneous systems: An experimental investigation. Unpublished B.A.Sc. thesis, University of Toronto, Canada, pp. 32.

Wood S.A., 2002. The aqueous geochemistry of the platinum-group elements with applications to ore deposits *In* The Geology, Geochemistry, Mineralogy and Mineral Beneficiation of the Platinum-group elements (ed LJ Cabri) Canadian Institute of Mining, Metallurgy and Petroleum, Montreal, Special Volume 54, pp. 211-249.

Wood S.A., and Normand C., 2008. Mobility of palladium chloride complexes in mafic rocks: insights from a flow-through experiment at 25 ^{o}C using air-saturated, acidic, and Cl-rich solutions. *Mineralogy and Petrology*, 92, 81-97.

Yan H.Q., Su S.G., Jiao J.G., and Tang H., 2005. Metallogenetic epoch of Jinchuan Cu-Ni (PGE) magmatic sulfide deposit. *Earth Science Frontiers*, 12, 309-315 (in Chinese with English abstract).

Yang G., Du A.D., Lu J.R., Qu W.J., and Chen J.F., 2005. Re-Os (ICP-MS) dating of the massive sulfide ores from the Jinchuan Ni-Cu-PGE deposit. *Science in China Series D*, 48, 1372-1677.

Yang S., Qu W., Tian Y., Chen J., Yang G., and Du A., 2008. Origin of the inconsistent apparent Re-Os ages of the Jinchuan Ni-Cu sulfide ore deposit, China: Post-segregation diffusion of Os. *Chemical Geology*, 247, 401-418.

Yang X-Z., Ishihara S., and Zhao D-H., 2006. Genesis of the Jinchuan PGE deposit, China: evidence from fluid inclusions, mineralogy and geochemistry of precious elements. *Mineralogy and Petrology*, 86, 109-128.

Yudoskaya M., Kinnaird J., Naldrett A.J., Rodionov N., Antonov A., Simakin S., and Kuzmin D., 2013. Trace-element study and age dating of zircon from chromitites of the Bushveld Complex (South Africa). *Mineralogy and Petrology*, 107, 915-942.

Yund R.A., and Kullerud G., 1966. Thermal Stability of Assemblages in the Cu-Fe-S System. *Journal of Petrology*, 7, 454-488.

Zhang M., Kamo S.L., Li C., Hu P., and Ripley E.M., 2010. Precise U-Pb zircon-baddeleyite age of the Jinchuan sulfide ore-bearing ultramafic intrusion, western China. *Mineralium Deposita*, 45, 3-9.

Zhang Z., Du A., Tan S., Lu J., Wang J., and Yang G., 2004. Age of the Jinchuan copper-nickel deposit and isotopic geochemical feature of its source. *Acta Mineralogica Sinica*, 78, 359-365.

Zhou M-F., Yang Z-X., Song X-Y., Keays R.R., and Lesher C.M., 2002. Magmatic Ni-Cu-(PGE) sulphide deposits in China. *In* The Geology, Geochemistry, Mineralogy and Mineral Beneficiation of the Platinum-group elements (ed LJ Cabri) Canadian Institute of Mining, Metallurgy and Petroleum, Montreal, Special Volume 54, pp. 619-636.

Zhu Y., An F., Tan J., 2011. Geochemistry of hydrothermal gold deposits: A review. *Geoscience Frontiers*, 2, 367-374.

Zieg M.J., and Marsh B.D., 2005. The Sudbury Igneous Complex: Viscous emulsion differentiation of a superheated impact melt sheet. *Geological Society of America Bulletin*, 117(11-12), 1427-1450.

Zientek M.J., Cooper R.W., Corson S.R., and Geraghty E.P., 2002. PGE mineralisation in the Stillwater Complex, Montana. *In* The Geology, Geochemistry, Mineralogy and Mineral Beneficiation of the Platinum-group elements (ed LJ Cabri) Canadian Institute of Mining, Metallurgy and Petroleum, Montreal, Special Volume 54, pp. 459-481.

Appendix A: Mirabela Sample List (C = Central Zone, N = Northern Zone, S= Southern Zone)

Zone-Hole	Sample No.	Metre From	Metre To	Sample Description
C MBS604	PTSR12	813	814	Gabbronorite
C MBS604	PTSR13	830	831	Websterite
C MBS604	PTSR01	886	887	Orthopyroxenite
C MBS604	PTSR02	911	912	Olivine orthopyroxenite
C MBS604	PTSR03	913	914	Olivine orthopyroxenite
C MBS604	PTSR04	933	934	Orthopyroxenite
C MBS604	PTSR05	948	949	Olivine Orthopyroxenite
C MBS604	PTSR06	964	965	Harzburgite
C MBS604	PTSR07	1019	1020	Harzburgite
C MBS604	PTSR08	1036	1037	Dunite (orthopyroxene oikocrysts)
C MBS604	PTSR09	1058	1059	Dunite (orthopyroxene oikocrysts)
C MBS604	PTSR10	1066	1067	Dunite (orthopyroxene oikocrysts)
C MBS604	PTSR11	1068	1069	Dunite (orthopyroxene oikocrysts)
C MBS605	PTSR14	855	856	Gabbronorite
C MBS605	PTSR15	865	866	Websterite
C MBS605	PTSR16	924	925	Orthopyroxenite
C MBS605	PTSR17	935	936	Orthopyroxenite
C MBS605	PTSR18	946	947	Orthopyroxenite
C MBS605	PTSR19	969	970	Olivine Orthopyroxenite
C MBS605	PTSR20	979	980	Harzburgite
C MBS605	PTSR21	1015	1016	Harzburgite
C MBS605	PTSR22	1031	1032	Harzburgite
C MBS605	PTSR23	1039	1040	Harzburgite
C MBS605	PTSR24	1050	1051	Dunite (orthopyroxene oikocrysts)
C MBS605	PTSR25	1060	1061	Dunite (orthopyroxene oikocrysts)
N MBS209	PTSR26	215	216	Gabbronorite
N MBS209	PTSR27	224	225	Websterite
N MBS209	PTSR28	234	235	Orthopyroxenite
N MBS209	PTSR29	254	255	Orthopyroxenite
N MBS209	PTSR30	285	286	Orthopyroxenite
N MBS209	PTSR31	305	306	Olivine Orthopyroxenite
N MBS209	PTSR32	317	318	Harzburgite
N MBS209	PTSR33	325	326	Harzburgite
N MBS209	PTSR34	338	339	Harzburgite
N MBS209	PTSR35	345	346	Harzburgite
N MBS209	PTSR36	350	351	Dunite
N MBS209	PTSR37	354	355	Dunite
N MBS158	PTSR38	219	220	Gabbronorite
N MBS158	PTSR39	234	235	Websterite
N MBS158	PTSR40	249	250	Orthopyroxenite
N MBS158	PTSR41	264	265	Olivine Orthopyroxenite
N MBS158	PTSR42	271	272	Harzburgite
N MBS158	PTSR43	295	296	Dunite (orthopyroxene oikocrysts)
N MBS158	PTSR44	305	306	Harzburgite
N MBS158	PTSR45	315	316	Dunite (orthopyroxene oikocrysts)
N MBS158	PTSR46	321	322	Dunite (orthopyroxene oikocrysts)
N MBS158	PTSR47	322	323	Dunite (orthopyroxene oikocrysts; sulphide veins)
N MBS158	PTSR48	334	335	Harzburgite

Zone-Hole	Sample No.	Metre From	Metre To	Sample Description
N MBS158	PTSR49	356	357	Dunite (orthopyroxene oikocrysts)
S MBS565	PTSR50	372	373	Websterite
S MBS565	PTSR51	450	451	Orthopyroxenite
S MBS565	PTSR52	483	484	Orthopyroxenite
S MBS565	PTSR53	526	527	Olivine Orthopyroxenite
S MBS565	PTSR54	545	546	Harzburgite
S MBS565	PTSR55	551	552	Harzburgite
S MBS565	PTSR56	564	565	Harzburgite
S MBS565	PTSR57	602	603	Harzburgite
S MBS565	PTSR58	611	612	Dunite (orthopyroxene oikocrysts)
S MBS565	PTSR59	628	629	Dunite (orthopyroxene oikocrysts)
S MBS565	PTSR60	629	630	Dunite (orthopyroxene oikocrysts)
S MBS569	PTSR61	256	257	Gabbronorite
S MBS569	PTSR62	261	262	Websterite
S MBS569	PTSR63	330	331	Orthopyroxenite
S MBS569	PTSR64	417	418	Olivine Orthopyroxenite
S MBS569	PTSR65	427	428	Olivine Orthopyroxenite
S MBS569	PTSR66	440	441	Olivine Orthopyroxenite
S MBS569	PTSR67	459	460	Harzburgite
S MBS569	PTSR68	501	502	Harzburgite
S MBS569	PTSR69	530	531	Harzburgite
S MBS569	PTSR70	586	587	Dunite
S MBS569	PTSR71	596	597	Dunite (altered, venulated)
S MBS569	PTSR72	599	600	Dunite

Appendix B: Mirabela Borehole Mine Assay Data

Hole_ID	m From	m To	S (wt. %)	Ni (wt. %)	Cu (wt. %)	Pd (ppb)	Pt (ppb)	Pd/Pt	Cu/Pd	MgO (wt. %)	Fe_2O_3 (wt. %)	MnO (wt. %)	Al_2O_3 (wt. %)	Na_2O (wt. %)	CaO (wt. %)	TiO_2 (wt. %)
MBS-565	367	368	0.06	0.048	0.012	0.5	0.3	1.7	232000	15.31	6.93	0.12	10.58	1.23	8.69	0.15
MBS-565	368	369	0.06	0.042	0.009	0.5	0.5	1	174000	13.93	6.28	0.11	10.43	1.21	10.66	0.17
MBS-565	369	370	0.09	0.051	0.013	1	0.6	1.7	131000	14.33	6.45	0.12	9.73	1.12	11.19	0.17
MBS-565	370	371	0.11	0.062	0.017	1	0.6	1.7	172000	15.52	6.88	0.12	8.62	0.93	11.49	0.18
MBS-565	371	372	0.14	0.062	0.019	0.5	0.3	1.7	378000	14.43	6.55	0.12	9.11	1.02	11.89	0.2
MBS-565	372	373	0.12	0.068	0.02	1	0.5	2	202000	16.32	7.02	0.13	5.48	0.61	13.75	0.22
MBS-565	373	374	0.14	0.071	0.018	0.5	0.3	1.7	366000	16.66	7.21	0.14	4.67	0.51	13.73	0.22
MBS-565	374	375	0.11	0.062	0.018	0.5	0.3	1.7	352000	16.48	7.23	0.13	5.71	0.7	13.25	0.2
MBS-565	375	376	0.3	0.109	0.045	0.5	0.3	1.7	904000	17.66	7.69	0.14	4.67	0.54	13.42	0.22
MBS-565	376	377	0.72	0.228	0.092	1	0.9	1.1	923000	15.82	8.99	0.14	7.39	1.11	10.58	0.42
MBS-565	377	378	0.73	0.306	0.117	4	10.4	0.4	291250	19.98	10.75	0.17	4.72	0.7	6.52	0.2
MBS-565	378	379	1.97	0.7	0.267	9	26.3	0.3	296667	23.96	13.31	0.18	3.76	0.36	3.81	0.2
MBS-565	379	380	1.3	0.569	0.214	8	18.5	0.4	267500	22.3	12.17	0.17	3.7	0.35	3.64	0.18
MBS-565	380	381	1.62	0.589	0.246	10	16.4	0.6	246000	24.13	12.82	0.18	3.91	0.34	3.86	0.17
MBS-565	381	382	0.96	0.387	0.13	5	10.4	0.5	259000	17.49	9.62	0.13	7.67	1.29	3.23	0.22
MBS-565	382	383	0.98	0.396	0.114	4	7.9	0.5	285000	17.91	9.85	0.13	6.92	1	3.71	0.23
MBS-565	383	384	1.47	0.573	0.171	6	9.2	0.7	285000	23.21	12.18	0.17	4.12	0.39	3.76	0.17
MBS-565	384	385	1.29	0.519	0.175	6	7.3	0.8	291667	24.71	12.8	0.18	4.23	0.38	4.04	0.17
MBS-565	385	386	0.81	0.34	0.108	4	7.2	0.6	268750	22.3	11.14	0.16	4.84	0.62	3.86	0.17
MBS-565	386	387	0.73	0.336	0.115	4	5.6	0.7	287500	18.82	9.85	0.14	5.22	0.55	3.02	0.18
MBS-565	387	388	1.26	0.498	0.154	5	6.9	0.7	308000	22.05	12.25	0.17	5.03	0.58	3.6	0.28
MBS-565	388	389	1.33	0.539	0.156	6	6.3	1	260000	24.54	12.52	0.18	3.87	0.35	4.32	0.18
MBS-565	389	390	1.45	0.53	0.267	6	13.4	0.4	445000	22.88	12.14	0.17	3.63	0.34	3.86	0.17
MBS-565	390	391	1.03	0.397	0.161	4	8.5	0.5	401250	21.06	10.97	0.16	4.44	0.47	6.17	0.27
MBS-565	391	392	0.31	0.167	0.048	3	8.3	0.4	160333	17.66	8.86	0.13	5.63	0.93	3.65	0.23
MBS-565	392	393	0.61	0.292	0.092	5	10.2	0.5	184000	24.71	11.34	0.17	3.67	0.32	4.41	0.18
MBS-565	393	394	0.72	0.298	0.085	4	6.9	0.6	213250	24.46	11.57	0.18	3.57	0.31	4.37	0.17
MBS-565	394	395	0.79	0.314	0.102	4	8.7	0.5	253750	24.29	11.29	0.17	3.65	0.31	4.34	0.18
MBS-565	395	396	0.25	0.161	0.042	1	2.5	0.4	419000	24.46	10.71	0.17	3.46	0.28	4.3	0.17
MBS-565	396	397	0.56	0.253	0.108	3	5.4	0.6	360000	24.87	11.27	0.17	3.51	0.28	4.24	0.18
MBS-565	397	398	0.72	0.353	0.12	6	8.7	0.7	199167	23.96	12.32	0.18	4.12	0.46	4	0.2
MBS-565	398	399	0.18	0.16	0.041	1	1.8	0.6	408000	23.96	10.31	0.17	3.48	0.39	3.99	0.18
MBS-565	399	400	0.19	0.188	0.048	1	2.3	0.4	480000	25.2	11.05	0.17	3.72	0.39	3.57	0.18
MBS-565	400	401	0.16	0.164	0.039	1	1.5	0.7	389000	24.87	10.81	0.17	3.59	0.32	3.57	0.18

Hole_ID	m From	m To	S (wt. %)	Ni (wt. %)	Cu (wt. %)	Pd (ppb)	Pt (ppb)	Pd/Pt	Cu/Pd	MgO (wt. %)	Fe_2O_3 (wt. %)	MnO (wt. %)	Al_2O_3 (wt. %)	Na_2O (wt. %)	CaO (wt. %)	TiO_2 (wt. %)
MBS-565	401	402	0.4	0.255	0.089	3	3.6	0.8	295667	23.3	10.69	0.16	3.38	0.34	3.34	0.17
MBS-565	402	403	0.58	0.28	0.089	2	3.9	0.5	447000	24.54	11.22	0.17	3.48	0.34	3.48	0.18
MBS-565	403	404	0.16	0.146	0.038	1	1.1	0.9	379000	24.79	10.97	0.18	3.63	0.39	3.6	0.2
MBS-565	404	405	0.58	0.283	0.103	2	2.7	0.7	515000	24.21	11.54	0.17	3.57	0.38	3.27	0.2
MBS-565	405	406	0.72	0.326	0.115	3	3.2	0.9	381667	24.54	11.35	0.17	3.57	0.31	3.36	0.18
MBS-565	406	407	0.28	0.177	0.046	1	1.3	0.8	456000	24.71	10.78	0.17	3.67	0.34	3.43	0.18
MBS-565	407	408	0.11	0.131	0.024	1	0.6	1.7	237000	24.96	10.62	0.17	3.78	0.36	3.41	0.2
MBS-565	408	409	0.08	0.133	0.024	1	0.8	1.3	244000	24.71	10.52	0.17	3.67	0.35	3.33	0.2
MBS-565	409	410	0.11	0.136	0.025	1	1.1	0.9	253000	24.87	10.51	0.18	3.68	0.36	3.34	0.18
MBS-565	410	411	0.18	0.151	0.028	1	1.3	0.8	275000	25.29	11.11	0.18	3.74	0.32	3.39	0.18
MBS-565	411	412	0.29	0.212	0.046	2	4.1	0.5	230500	25.62	11.02	0.18	3.63	0.32	3.36	0.18
MBS-565	412	413	0.22	0.172	0.035	2	11.5	0.2	174500	25.7	11.07	0.18	3.68	0.35	3.37	0.18
MBS-565	413	414	0.24	0.184	0.041	2	10	0.2	207000	25.29	10.81	0.17	3.72	0.35	3.34	0.18
MBS-565	414	415	0.29	0.207	0.051	15	7.5	2	34133	25.54	10.99	0.18	3.67	0.34	3.3	0.18
MBS-565	415	416	0.23	0.184	0.04	1	1.9	0.5	403000	25.7	10.99	0.17	3.95	0.42	3.44	0.2
MBS-565	416	417	0.88	0.457	0.136	5	6.3	0.8	271000	24.62	11.64	0.17	3.91	0.4	3.41	0.18
MBS-565	417	418	0.16	0.15	0.027	1	1	1	269000	24.71	10.72	0.17	4.08	0.42	3.53	0.18
MBS-565	418	419	0.17	0.155	0.029	2	1.1	1.8	143500	25.04	10.75	0.17	4.02	0.44	3.39	0.2
MBS-565	419	420	0.2	0.166	0.033	1	1.5	0.7	332000	25.54	11.12	0.18	4.06	0.44	3.41	0.22
MBS-565	420	421	0.3	0.208	0.047	2	2.8	0.7	236500	25.95	11.02	0.18	3.76	0.36	3.32	0.18
MBS-565	421	422	0.16	0.16	0.028	2	2.8	0.7	138000	25.04	10.64	0.17	3.74	0.36	3.25	0.17
MBS-565	422	423	0.26	0.195	0.042	3	9.7	0.3	139333	24.87	10.75	0.17	3.78	0.36	3.26	0.17
MBS-565	423	424	0.27	0.197	0.043	4	18.5	0.2	107750	24.62	10.41	0.17	3.65	0.38	3.13	0.17
MBS-565	424	425	0.22	0.182	0.036	3	13.7	0.2	120000	25.7	10.61	0.17	3.61	0.35	3.15	0.17
MBS-565	425	426	0.52	0.31	0.079	7	41.2	0.2	112286	25.29	10.97	0.17	3.5	0.32	3.11	0.17
MBS-565	426	427	0.38	0.253	0.062	5	20.6	0.2	123600	24.96	10.62	0.17	3.5	0.32	3.08	0.17
MBS-565	427	428	0.28	0.204	0.046	4	18.4	0.2	116000	25.04	10.37	0.17	3.4	0.3	3.04	0.15
MBS-565	428	429	0.2	0.173	0.035	2	12	0.2	176000	25.7	10.77	0.17	3.72	0.35	3.23	0.17
MBS-565	429	430	0.23	0.185	0.041	3	18.3	0.2	137333	24.38	10.41	0.17	3.76	0.38	3.25	0.17
MBS-565	430	431	0.46	0.286	0.079	9	37.7	0.2	87667	25.04	10.68	0.17	3.61	0.35	3.15	0.17
MBS-565	431	432	0.82	0.445	0.14	23	94.7	0.2	60870	24.71	11.02	0.16	3.48	0.32	3.05	0.17
MBS-565	432	433	0.35	0.235	0.059	11	37.7	0.3	53364	25.95	10.91	0.17	3.65	0.34	3.16	0.17
MBS-565	433	434	0.22	0.183	0.037	6	36.7	0.2	61333	26.78	10.95	0.18	3.82	0.38	3.11	0.17
MBS-565	434	435	0.14	0.152	0.025	3	19.1	0.2	82000	27.69	11.22	0.18	3.72	0.31	3.05	0.18
MBS-565	435	436	0.17	0.164	0.029	3	13.5	0.2	95333	27.36	10.99	0.18	3.65	0.31	2.99	0.17

Hole_ID	m From	m To	S (wt. %)	Ni (wt. %)	Cu (wt. %)	Pd (ppb)	Pt (ppb)	Pd/Pt	Cu/Pd	MgO (wt. %)	Fe_2O_3 (wt. %)	MnO (wt. %)	Al_2O_3 (wt. %)	Na_2O (wt. %)	CaO (wt. %)	TiO_2 (wt. %)
MBS-565	436	437	0.17	0.162	0.029	1	2.2	0.5	286000	26.78	10.97	0.18	4.06	0.4	3.13	0.17
MBS-565	437	438	0.33	0.235	0.057	2	2.9	0.7	283500	26.78	11.04	0.18	3.63	0.32	2.9	0.17
MBS-565	438	439	0.13	0.153	0.026	1	1.4	0.7	257000	26.03	10.65	0.17	4.29	0.49	3.19	0.2
MBS-565	439	440	0.11	0.139	0.024	2	7.5	0.3	120000	25.7	10.25	0.16	4.18	0.49	3.06	0.18
MBS-565	440	441	0.36	0.254	0.069	5	24	0.2	138800	26.86	11.17	0.18	3.99	0.39	3.13	0.18
MBS-565	441	442	0.83	0.46	0.143	13	65.6	0.2	109615	25.95	11.54	0.17	3.84	0.38	3.02	0.18
MBS-565	442	443	0.24	0.2	0.043	8	37.7	0.2	53875	27.61	11.12	0.18	3.55	0.3	2.92	0.17
MBS-565	443	444	0.22	0.19	0.04	5	21.5	0.2	79000	26.37	10.67	0.17	3.57	0.32	2.85	0.17
MBS-565	444	445	0.82	0.482	0.121	16	41	0.4	75625	26.37	11.52	0.17	3.51	0.3	2.83	0.17
MBS-565	445	446	0.98	0.521	0.21	18	63.3	0.3	116667	26.86	11.94	0.18	3.63	0.34	2.85	0.18
MBS-565	446	447	0.82	0.469	0.141	18	37.5	0.5	78333	26.86	11.65	0.17	3.65	0.32	2.88	0.18
MBS-565	447	448	0.99	0.561	0.136	32	129	0.2	42344	24.21	11.25	0.16	4.69	0.54	3.18	0.18
MBS-565	448	449	1.61	0.84	0.245	58	117	0.5	42241	26.03	12.45	0.17	3.7	0.4	2.85	0.18
MBS-565	449	450	1.59	0.69	0.524	65	166	0.4	80615	27.19	13.02	0.17	3.23	0.22	2.34	0.18
MBS-565	450	451	1.73	0.99	0.198	68	184	0.4	29044	27.86	13.15	0.17	3.12	0.24	2.31	0.17
MBS-565	451	452	1.3	0.68	0.232	60	158	0.4	38667	26.03	12.47	0.17	4.04	0.31	2.8	0.2
MBS-565	452	453	1.13	0.61	0.14	61	182	0.3	22951	24.96	11.9	0.17	4.91	0.61	3.53	0.23
MBS-565	453	454	0.83	0.499	0.118	40	92.2	0.4	29375	26.12	11.59	0.16	3.5	0.23	2.5	0.18
MBS-565	454	455	0.39	0.237	0.107	29	85.7	0.3	36897	26.12	10.81	0.17	4.08	0.44	2.99	0.2
MBS-565	455	456	1.13	0.6	0.173	74	182	0.4	23311	26.61	12.11	0.17	3.7	0.31	2.81	0.18
MBS-565	456	457	0.25	0.195	0.044	8	19.9	0.4	54375	26.53	10.59	0.17	3.33	0.3	2.91	0.15
MBS-565	457	458	0.27	0.209	0.05	4	20.8	0.2	124000	27.28	10.92	0.17	3.29	0.28	2.88	0.15
MBS-565	458	459	0.43	0.286	0.073	7	45	0.2	104571	26.86	10.99	0.17	3.38	0.31	2.94	0.17
MBS-565	459	460	0.13	0.145	0.028	1	7.4	0.1	280000	25.95	10.48	0.17	3.76	0.42	2.99	0.18
MBS-565	460	461	0.34	0.239	0.064	6	37.9	0.2	106667	27.61	11.18	0.18	3.46	0.3	2.97	0.17
MBS-565	461	462	0.92	0.517	0.173	19	90.3	0.2	90789	25.54	11.25	0.16	3.63	0.38	3.05	0.17
MBS-565	462	463	1.57	0.84	0.235	31	167	0.2	75806	26.78	12.65	0.17	3.25	0.27	2.87	0.17
MBS-565	463	464	0.15	0.166	0.04	4	20.8	0.2	100750	26.2	10.38	0.16	3.67	0.4	3.06	0.18
MBS-565	464	465	0.09	0.139	0.025	1	2.3	0.4	252000	25.37	9.94	0.16	3.55	0.39	2.99	0.17
MBS-565	465	466	0.28	0.225	0.058	5	19.2	0.3	115600	26.61	10.58	0.17	3.8	0.4	3.13	0.15
MBS-565	466	467	0.28	0.208	0.064	4	16.1	0.2	160000	26.37	10.47	0.17	3.31	0.32	2.83	0.15
MBS-565	467	468	0.42	0.282	0.079	7	31.9	0.2	113286	28.52	11.19	0.18	3.27	0.27	2.83	0.15
MBS-565	468	469	0.21	0.182	0.037	4	19.1	0.2	91500	27.86	10.68	0.17	3.06	0.23	2.71	0.15
MBS-565	469	470	0.38	0.264	0.067	9	56.9	0.2	74778	27.28	10.68	0.17	3.08	0.24	2.7	0.15
MBS-565	470	471	0.29	0.225	0.054	9	71.1	0.1	60000	27.28	10.77	0.17	3.08	0.23	2.71	0.15

Hole_ID	m From	m To	S (wt. %)	Ni (wt. %)	Cu (wt. %)	Pd (ppb)	Pt (ppb)	Pd/Pt	Cu/Pd	MgO (wt. %)	Fe_2O_3 (wt. %)	MnO (wt. %)	Al_2O_3 (wt. %)	Na_2O (wt. %)	CaO (wt. %)	TiO_2 (wt. %)
MBS-565	471	472	0.09	0.132	0.019	5	24.7	0.2	37800	27.86	10.57	0.17	3.31	0.3	2.91	0.17
MBS-565	472	473	0.21	0.214	0.054	16	53.1	0.3	33438	27.44	10.88	0.17	3.34	0.35	2.98	0.2
MBS-565	473	474	0.17	0.222	0.049	36	65.3	0.6	13667	24.54	10.75	0.16	4.12	0.54	2.78	0.25
MBS-565	474	475	0.16	0.182	0.039	14	32.8	0.4	27571	26.28	10.21	0.16	3.51	0.36	2.98	0.17
MBS-565	475	476	0.23	0.192	0.042	24	58.3	0.4	17542	26.45	10.27	0.16	3.34	0.31	2.92	0.17
MBS-565	476	477	0.15	0.166	0.03	28	60.4	0.5	10536	27.94	10.64	0.17	3.29	0.27	2.85	0.17
MBS-565	477	478	0.19	0.178	0.037	29	61.6	0.5	12862	26.95	10.18	0.17	3.25	0.27	2.8	0.15
MBS-565	478	479	0.12	0.142	0.023	28	59.9	0.5	8179	27.28	10.19	0.17	3.14	0.24	2.71	0.15
MBS-565	479	480	0.09	0.145	0.025	28	54.2	0.5	8786	26.61	9.97	0.16	3.12	0.26	2.67	0.15
MBS-565	480	481	0.08	0.147	0.025	30	55.7	0.5	8433	26.95	10.04	0.17	3.08	0.27	2.66	0.17
MBS-565	481	482	0.12	0.162	0.039	22	39.8	0.6	17500	26.45	9.99	0.17	3.55	0.31	2.7	0.18
MBS-565	482	483	1.31	0.73	0.204	95	101	0.9	21474	24.62	11.18	0.16	3.8	0.39	2.74	0.17
MBS-565	483	484	1.39	0.77	0.188	103	202	0.5	18252	25.79	11.47	0.17	3.25	0.24	2.52	0.15
MBS-565	484	485	1.3	0.68	0.172	91	194	0.5	18901	25.45	11.42	0.17	3.23	0.26	2.49	0.17
MBS-565	485	486	0.66	0.406	0.129	59	103	0.6	21864	24.87	10.37	0.16	3.25	0.27	2.49	0.17
MBS-565	486	487	1.01	0.558	0.201	87	150	0.6	23103	24.96	10.95	0.17	3.31	0.27	2.56	0.17
MBS-565	487	488	0.6	0.381	0.136	62	126	0.5	21935	25.54	10.75	0.17	3.65	0.34	2.74	0.17
MBS-565	488	489	1.15	0.69	0.153	121	149	0.8	12645	25.79	11.37	0.17	3.29	0.26	2.53	0.15
MBS-565	489	490	0.86	0.518	0.141	69	100	0.7	20435	26.53	11.27	0.17	3.44	0.27	2.7	0.17
MBS-565	490	491	0.23	0.205	0.041	6	23.6	0.3	68167	26.45	10.34	0.17	3.55	0.3	2.7	0.15
MBS-565	491	492	0.22	0.192	0.033	8	39.1	0.2	41250	26.86	10.45	0.18	3.74	0.32	2.8	0.15
MBS-565	492	493	0.34	0.252	0.057	15	62.1	0.2	37667	26.53	10.59	0.17	3.95	0.38	2.88	0.17
MBS-565	493	494	0.46	0.311	0.062	13	32.6	0.4	47615	25.54	10.24	0.17	4.06	0.43	2.95	0.15
MBS-565	494	495	0.15	0.165	0.026	6	29.5	0.2	43833	26.37	9.95	0.17	3.4	0.27	2.57	0.15
MBS-565	495	496	0.08	0.123	0.016	5	28.3	0.2	32200	20.73	8.68	0.14	5.42	0.75	2.34	0.27
MBS-565	496	497	0.04	0.06	0.009	2	11.9	0.2	45500	9.63	5.42	0.06	11.09	2.14	1.74	0.3
MBS-565	497	498	0.08	0.13	0.017	5	30.4	0.2	34000	23.3	9.56	0.17	4.38	0.38	2.38	0.22
MBS-565	498	499	0.13	0.156	0.024	10	49.7	0.2	24000	20.56	9.46	0.16	5.97	0.82	2.22	0.32
MBS-565	499	500	0.06	0.088	0.011	2	7.2	0.3	54000	15.9	7.76	0.13	8.29	1.33	2.13	0.3
MBS-565	500	501	0.09	0.153	0.021	10	54.5	0.2	21400	24.46	9.64	0.16	3.93	0.66	2.66	0.2
MBS-565	501	502	0.21	0.195	0.038	21	107	0.2	18095	27.11	9.89	0.16	3.17	0.36	2.48	0.17
MBS-565	502	503	0.36	0.266	0.061	17	49.1	0.3	35765	28.6	10.17	0.17	3.14	0.27	2.76	0.15
MBS-565	503	504	0.12	0.144	0.02	2	3.9	0.5	99500	28.85	9.82	0.17	2.93	0.22	2.52	0.15
MBS-565	504	505	0.3	0.278	0.048	14	49.3	0.3	34429	31.92	11.05	0.16	2.25	0.19	1.92	0.12
MBS-565	505	506	0.2	0.182	0.042	33	168	0.2	12788	28.6	9.86	0.16	2.93	0.26	2.48	0.15

Hole_ID	m From	m To	S (wt. %)	Ni (wt. %)	Cu (wt. %)	Pd (ppb)	Pt (ppb)	Pd/Pt	Cu/Pd	MgO (wt. %)	Fe_2O_3 (wt. %)	MnO (wt. %)	Al_2O_3 (wt. %)	Na_2O (wt. %)	CaO (wt. %)	TiO_2 (wt. %)
MBS-565	506	507	0.18	0.171	0.03	21	89.6	0.2	14333	28.19	9.59	0.16	2.87	0.26	2.38	0.13
MBS-565	507	508	0.25	0.211	0.044	31	127	0.2	14097	28.52	9.81	0.16	2.85	0.24	2.41	0.13
MBS-565	508	509	0.33	0.228	0.065	33	109	0.3	19576	27.86	9.66	0.16	2.93	0.26	2.39	0.15
MBS-565	509	510	0.26	0.213	0.042	39	122	0.3	10872	28.36	9.81	0.16	2.91	0.26	2.46	0.15
MBS-565	510	511	0.16	0.168	0.027	32	102	0.3	8531	28.36	9.91	0.16	2.95	0.26	2.48	0.15
MBS-565	511	512	0.28	0.231	0.052	42	63.4	0.7	12381	28.02	9.79	0.16	2.97	0.26	2.49	0.17
MBS-565	512	513	0.34	0.264	0.057	36	73.8	0.5	15694	28.11	9.92	0.16	3.04	0.28	2.64	0.17
MBS-565	513	514	0.89	0.49	0.127	28	86.4	0.3	45357	27.61	11.02	0.16	3.4	0.27	2.59	0.18
MBS-565	514	515	1.66	0.86	0.268	70	201	0.3	38286	27.77	12.75	0.16	3.59	0.19	2.1	0.17
MBS-565	515	516	1.6	0.83	0.191	51	141	0.4	37451	27.44	12.25	0.16	3.5	0.23	2.28	0.17
MBS-565	516	517	0.98	0.572	0.234	33	51.1	0.6	70909	24.38	10.69	0.17	4.1	0.43	3.29	0.23
MBS-565	517	518	0.53	0.304	0.09	15	27.1	0.6	60067	14.92	6.93	0.09	9.03	2	2.7	0.2
MBS-565	518	519	0.26	0.244	0.05	7	29.6	0.2	71857	27.94	10.22	0.16	3.21	0.27	2.53	0.17
MBS-565	519	520	0.31	0.314	0.068	16	47.2	0.3	42250	27.11	9.99	0.16	3.21	0.3	2.56	0.17
MBS-565	520	521	0.06	0.17	0.02	178	140	1.3	1096	27.44	10.01	0.15	3.44	0.32	2.41	0.18
MBS-565	521	522	0.93	0.61	0.15	54	167	0.3	27778	31.17	12.05	0.15	1.91	0.13	1.37	0.1
MBS-565	522	523	0.18	0.295	0.028	9	66.5	0.1	30667	29.02	10.99	0.15	2.12	0.24	1.32	0.17
MBS-565	523	524	0.38	0.394	0.054	18	151	0.1	30222	31.59	11.29	0.16	2.32	0.16	1.8	0.13
MBS-565	524	525	0.5	0.429	0.104	19	172	0.1	54737	29.68	11.25	0.16	2.74	0.22	1.78	0.17
MBS-565	525	526	0.46	0.381	0.063	27	177	0.2	23222	27.44	10.47	0.16	3.4	0.28	1.97	0.22
MBS-565	526	527	0.35	0.327	0.059	27	253	0.1	21889	29.02	10.58	0.16	2.87	0.19	2.25	0.15
MBS-565	527	528	0.19	0.221	0.038	14	122	0.1	26929	28.44	10.29	0.16	2.93	0.22	2.32	0.17
MBS-565	528	529	0.22	0.216	0.05	13	121	0.1	38462	28.11	10.02	0.16	2.93	0.22	2.34	0.17
MBS-565	529	530	0.16	0.203	0.03	12	62.8	0.2	24583	28.94	10.31	0.16	3.08	0.26	2.43	0.17
MBS-565	530	531	0.12	0.169	0.034	11	83.6	0.1	30727	25.04	8.99	0.18	3.57	0.53	3.61	0.17
MBS-565	531	532	0.12	0.185	0.025	14	97.3	0.1	18000	26.12	9.32	0.18	3.1	0.44	3.51	0.17
MBS-565	532	533	0.17	0.195	0.03	15	72.7	0.2	20067	27.03	10.02	0.15	4.42	0.53	2.35	0.28
MBS-565	533	534	0.12	0.172	0.019	9	36.4	0.2	21556	29.27	10.18	0.16	3.08	0.23	2.38	0.17
MBS-565	534	535	0.06	0.157	0.012	8	29.8	0.3	14375	29.1	10.14	0.16	3.1	0.23	2.36	0.17
MBS-565	535	536	0.14	0.195	0.023	17	49.5	0.3	13706	29.18	10.18	0.16	3.04	0.24	2.41	0.18
MBS-565	536	537	0.3	0.256	0.049	32	113	0.3	15156	29.68	10.47	0.16	3.02	0.22	2.45	0.17
MBS-565	537	538	0.13	0.174	0.023	14	45.7	0.3	16071	29.27	10.11	0.16	3.1	0.23	2.45	0.17
MBS-565	538	539	0.24	0.231	0.04	31	78.9	0.4	12871	29.43	10.49	0.16	3.1	0.24	2.45	0.17
MBS-565	539	540	0.26	0.243	0.042	36	68.6	0.5	11778	29.6	10.49	0.16	3.25	0.27	2.6	0.18
MBS-565	540	541	0.17	0.203	0.028	21	41	0.5	13333	29.43	10.34	0.16	3.19	0.27	2.55	0.18

Hole_ID	m From	m To	S (wt. %)	Ni (wt. %)	Cu (wt. %)	Pd (ppb)	Pt (ppb)	Pd/Pt	Cu/Pd	MgO (wt. %)	Fe_2O_3 (wt. %)	MnO (wt. %)	Al_2O_3 (wt. %)	Na_2O (wt. %)	CaO (wt. %)	TiO_2 (wt. %)
MBS-565	541	542	0.43	0.367	0.091	30	86.6	0.3	30433	29.27	10.58	0.16	3.08	0.24	2.46	0.18
MBS-565	542	543	1.45	0.81	0.275	83	186	0.4	33133	28.77	11.52	0.16	2.95	0.24	2.39	0.17
MBS-565	543	544	0.33	0.437	0.056	27	70	0.4	20667	33.66	11.84	0.15	1.97	0.16	1.54	0.1
MBS-565	544	545	0.64	0.53	0.101	40	114	0.4	25250	34.49	12.72	0.16	1.81	0.13	1.4	0.1
MBS-565	545	546	1.53	0.96	0.215	91	251	0.4	23626	33.99	13.71	0.15	1.38	0.09	1.06	0.08
MBS-565	546	547	1.28	0.89	0.187	81	213	0.4	23086	32.5	13.14	0.14	1.32	0.09	0.91	0.07
MBS-565	547	548	0.12	0.371	0.019	18	53.6	0.3	10500	34.32	12.22	0.15	1.61	0.12	1.11	0.08
MBS-565	548	549	0.08	0.351	0.014	14	38.4	0.4	10286	33.99	12.27	0.15	2.27	0.2	1.19	0.1
MBS-565	549	550	0.18	0.393	0.033	19	52.7	0.4	17263	34.82	12.3	0.16	1.95	0.18	1.55	0.12
MBS-565	550	551	0.56	0.5	0.087	39	129	0.3	22179	34.82	12.9	0.16	1.97	0.18	1.5	0.12
MBS-565	551	552	1.83	1.07	0.199	109	393	0.3	18257	35.82	14.37	0.16	1.76	0.13	1.33	0.1
MBS-565	552	553	1.6	1	0.183	91	358	0.3	20110	36.31	14.28	0.16	1.76	0.12	1.33	0.08
MBS-565	553	554	0.11	0.313	0.021	14	45.9	0.3	14857	35.65	12.24	0.16	2.06	0.19	1.64	0.12
MBS-565	554	555	0.11	0.315	0.02	12	36.6	0.3	16250	35.32	11.94	0.16	2.08	0.2	1.69	0.12
MBS-565	555	556	0.18	0.375	0.031	37	53.8	0.7	8459	35.15	12.07	0.16	1.98	0.19	1.6	0.12
MBS-565	556	557	0.12	0.348	0.021	14	40.2	0.3	15071	36.48	12.22	0.16	2.04	0.2	1.61	0.12
MBS-565	557	558	0.2	0.402	0.034	18	49.4	0.4	19056	36.15	12.28	0.16	1.97	0.19	1.51	0.12
MBS-565	558	559	0.23	0.428	0.041	17	51	0.3	24235	36.31	12.35	0.16	1.85	0.18	1.44	0.12
MBS-565	559	560	0.31	0.466	0.054	19	55.3	0.3	28526	35.82	12.22	0.16	1.85	0.16	1.37	0.1
MBS-565	560	561	0.59	0.52	0.228	43	100	0.4	53023	39.63	12.75	0.16	1.55	0.15	1.29	0.08
MBS-565	561	562	0.78	0.64	0.227	50	147	0.3	45400	40.13	13	0.16	1.42	0.13	1.23	0.08
MBS-565	562	563	1.67	1.13	0.269	93	274	0.3	28925	35.82	14.01	0.15	1.51	0.12	1.09	0.08
MBS-565	563	564	1.92	1.22	0.423	106	359	0.3	39906	35.49	14.37	0.15	1.42	0.11	1.04	0.08
MBS-565	564	565	1.69	1.1	0.36	99	479	0.2	36364	35.98	14.11	0.15	1.34	0.11	1.01	0.08
MBS-565	565	566	1.08	0.77	0.298	64	216	0.3	46563	40.29	13.71	0.15	1.32	0.13	1.09	0.08
MBS-565	566	567	0.27	0.487	0.053	20	76.3	0.3	26500	37.64	12.55	0.15	1.64	0.15	1.26	0.1
MBS-565	567	568	0.22	0.364	0.043	15	58.4	0.3	28800	28.02	9.61	0.11	6.39	1.43	1.69	0.1
MBS-565	568	569	0.11	0.384	0.019	9	54.3	0.2	20889	36.81	12.15	0.15	1.68	0.16	1.22	0.1
MBS-565	569	570	0.03	0.093	0.005	3	15.7	0.2	17000	10.73	5.18	0.06	12.75	2.94	2.48	0.3
MBS-565	570	571	0.1	0.286	0.015	9	50.8	0.2	16111	34.99	11.29	0.15	2.08	0.19	1.32	0.1
MBS-565	571	572	0.07	0.17	0.012	7	37.4	0.2	17143	20.89	7.31	0.09	7.07	1.63	1.79	0.13
MBS-565	572	573	0.09	0.26	0.013	10	56.2	0.2	12500	30.76	10.77	0.16	3.17	0.26	1.25	0.12
MBS-565	573	574	0.08	0.216	0.012	9	49.5	0.2	13111	26.45	10.22	0.14	4.52	0.65	1.25	0.28
MBS-565	574	575	0.04	0.109	0.006	6	25.4	0.2	9500	14.06	5.26	0.06	9.54	2.4	2.24	0.1
MBS-565	575	576	0.1	0.3	0.016	13	67.6	0.2	12615	34.99	11.27	0.14	1.76	0.16	1.19	0.1

Hole_ID	m From	m To	S (wt. %)	Ni (wt. %)	Cu (wt. %)	Pd (ppb)	Pt (ppb)	Pd/Pt	Cu/Pd	MgO (wt. %)	Fe_2O_3 (wt. %)	MnO (wt. %)	Al_2O_3 (wt. %)	Na_2O (wt. %)	CaO (wt. %)	TiO_2 (wt. %)
MBS-565	576	577	0.1	0.308	0.017	14	78.1	0.2	12214	38.97	11.51	0.14	1.51	0.16	1.12	0.08
MBS-565	577	578	0.08	0.278	0.013	14	75	0.2	9357	35.32	10.41	0.13	1.34	0.13	0.97	0.07
MBS-565	578	579	0.09	0.336	0.017	14	75.2	0.2	11929	37.48	11.9	0.15	1.53	0.15	1.09	0.08
MBS-565	579	580	0.08	0.334	0.014	17	84.4	0.2	8294	37.48	11.75	0.15	1.55	0.15	1.06	0.08
MBS-565	580	581	0.08	0.344	0.014	19	80.8	0.2	7421	39.63	12.34	0.15	1.49	0.15	1.05	0.08
MBS-565	581	582	0.08	0.346	0.014	20	74.7	0.3	7100	39.63	12.11	0.15	1.57	0.16	1.08	0.08
MBS-565	582	583	0.07	0.32	0.01	16	60.6	0.3	5938	37.81	11.75	0.15	1.53	0.16	1.12	0.08
MBS-565	583	584	0.06	0.332	0.01	16	57.3	0.3	6250	37.81	11.84	0.15	1.47	0.15	1.04	0.08
MBS-565	584	585	0.07	0.319	0.011	17	55.8	0.3	6706	37.64	11.78	0.14	1.55	0.15	1.08	0.08
MBS-565	585	586	0.07	0.326	0.012	19	56	0.3	6474	37.48	11.77	0.15	1.49	0.15	1.11	0.1
MBS-565	586	587	0.06	0.296	0.011	18	50.7	0.4	5944	34.32	11.57	0.14	1.51	0.13	0.99	0.08
MBS-565	587	588	0.06	0.302	0.01	22	49.1	0.4	4545	34.66	11.81	0.14	1.57	0.15	1.04	0.08
MBS-565	588	589	0.07	0.312	0.011	22	50.7	0.4	4909	35.15	11.87	0.14	1.59	0.15	1.06	0.08
MBS-565	589	590	0.06	0.317	0.009	20	41.5	0.5	4450	35.82	12.05	0.14	1.51	0.15	1.02	0.08
MBS-565	590	591	0.06	0.321	0.009	21	38.2	0.5	4476	35.15	11.88	0.14	1.42	0.13	0.94	0.08
MBS-565	591	592	0.07	0.328	0.01	24	39.5	0.6	4125	35.82	11.92	0.14	1.38	0.15	0.92	0.08
MBS-565	592	593	0.07	0.317	0.011	27	39	0.7	4000	35.32	11.82	0.14	1.45	0.16	1.02	0.08
MBS-565	593	594	0.09	0.315	0.013	37	44.7	0.8	3486	34.16	11.41	0.14	1.55	0.15	1.06	0.08
MBS-565	594	595	0.11	0.319	0.015	36	39.7	0.9	4250	34.16	11.27	0.15	1.78	0.18	1.19	0.1
MBS-565	595	596	0.09	0.29	0.012	29	28.9	1	4138	33.66	10.87	0.14	2	0.2	1.46	0.12
MBS-565	596	597	0.05	0.282	0.008	19	19	1	4105	34.82	11.09	0.15	2.06	0.19	1.53	0.12
MBS-565	597	598	0.04	0.244	0.006	8	10.5	0.8	7750	32.83	10.41	0.15	2.29	0.22	1.65	0.13
MBS-565	598	599	0.06	0.305	0.01	6	8.9	0.7	17000	35.65	11.27	0.15	1.8	0.16	1.41	0.1
MBS-565	599	600	0.08	0.353	0.014	6	12.7	0.5	23667	35.65	11.57	0.15	1.44	0.15	1.15	0.08
MBS-565	600	601	0.16	0.426	0.029	21	89.1	0.2	13619	37.48	12.44	0.15	1.4	0.12	0.91	0.08
MBS-565	601	602	0.16	0.421	0.026	32	138	0.2	8156	37.64	12.2	0.15	1.47	0.12	0.9	0.08
MBS-565	602	603	0.13	0.41	0.02	44	183	0.2	4591	36.81	12.25	0.15	1.42	0.13	0.88	0.08
MBS-565	603	604	0.08	0.375	0.014	42	163	0.3	3405	37.31	12.27	0.15	1.51	0.13	0.95	0.08
MBS-565	604	605	0.07	0.3	0.015	19	59.6	0.3	7632	33.66	11.22	0.14	2.65	0.19	1.15	0.28
MBS-565	605	606	0.06	0.332	0.008	75	71.9	1	1027	34.32	13.07	0.17	1.8	0.15	0.77	0.15
MBS-565	606	607	0.04	0.353	0.005	75	48.1	1.6	693	36.98	13.24	0.17	1.28	0.13	0.76	0.08
MBS-565	607	608	0.17	0.439	0.027	139	104	1.3	1914	38.47	13.2	0.16	1.1	0.13	0.8	0.07
MBS-565	608	609	0.14	0.415	0.021	163	71.4	2.3	1307	37.97	13.08	0.16	1.21	0.12	0.76	0.07
MBS-565	609	610	0.06	0.368	0.009	171	58	2.9	520	39.3	13.28	0.16	1.47	0.11	0.76	0.08
MBS-565	610	611	0.05	0.374	0.009	164	61.7	2.7	518	37.97	12.85	0.16	1.38	0.11	0.76	0.07

Hole_ID	m From	m To	S (wt. %)	Ni (wt. %)	Cu (wt. %)	Pd (ppb)	Pt (ppb)	Pd/Pt	Cu/Pd	MgO (wt. %)	Fe_2O_3 (wt. %)	MnO (wt. %)	Al_2O_3 (wt. %)	Na_2O (wt. %)	CaO (wt. %)	TiO_2 (wt. %)
MBS-565	611	612	0.08	0.375	0.013	191	85.6	2.2	654	36.98	12.82	0.15	1.4	0.11	0.74	0.07
MBS-565	612	613	0.05	0.336	0.008	152	69.3	2.2	513	34.99	12.17	0.15	2.59	0.46	0.91	0.12
MBS-565	613	614	0.05	0.364	0.007	131	55.1	2.4	550	36.98	13.32	0.17	1.38	0.12	0.76	0.07
MBS-565	614	615	0.06	0.386	0.009	129	55.4	2.3	690	38.64	13.45	0.16	1.32	0.11	0.71	0.07
MBS-565	615	616	0.05	0.383	0.009	124	51.6	2.4	694	38.64	13.51	0.16	1.32	0.09	0.71	0.07
MBS-565	616	617	0.06	0.376	0.009	110	46.1	2.4	773	38.8	13.65	0.16	1.34	0.11	0.73	0.07
MBS-565	617	618	0.05	0.383	0.009	122	51.3	2.4	713	38.64	13.42	0.16	1.21	0.09	0.73	0.07
MBS-565	618	619	0.06	0.367	0.009	105	44.8	2.3	838	38.3	13.48	0.16	1.23	0.09	0.71	0.07
MBS-565	619	620	0.05	0.372	0.009	101	44.3	2.3	861	38.14	13.31	0.16	1.17	0.11	0.7	0.07
MBS-565	620	621	0.06	0.372	0.009	107	46.4	2.3	832	37.81	13.28	0.16	1.25	0.12	0.73	0.07
MBS-565	621	622	0.05	0.376	0.008	109	49.5	2.2	771	38.14	13.25	0.17	1.25	0.12	0.76	0.07
MBS-565	622	623	0.05	0.387	0.007	104	47.8	2.2	692	39.13	13.7	0.17	1.32	0.12	0.77	0.07
MBS-565	623	624	0.05	0.396	0.007	103	47.1	2.2	670	39.63	13.61	0.17	1.23	0.11	0.76	0.07
MBS-565	624	625	0.05	0.389	0.007	106	47.9	2.2	642	38.97	13.54	0.17	1.19	0.11	0.77	0.07
MBS-565	625	626	0.04	0.385	0.006	92	42.4	2.2	652	38.3	13.27	0.17	1.13	0.09	0.69	0.07
MBS-565	626	627	0.05	0.389	0.008	98	46.5	2.1	786	38.3	13.35	0.17	1.19	0.11	0.76	0.07
MBS-565	627	628	0.05	0.395	0.007	76	41.3	1.8	974	38.47	13.5	0.17	1.27	0.13	0.8	0.07
MBS-565	628	629	0.06	0.399	0.008	78	46.7	1.7	1077	39.8	13.75	0.17	1.13	0.12	0.81	0.07
MBS-565	629	630	0.16	0.288	0.05	640	521	1.2	780	27.11	10.99	0.15	4.08	0.18	1.94	0.18
MBS-569	256	257	0.06	0.041	0.008	0.5	0.3	1.7	164000	13.91	6.59	0.12	13.11	1.52	11.12	0.17
MBS-569	257	258	0.06	0.042	0.009	0.5	0.3	1.7	172000	14.26	6.63	0.12	13.87	1.54	10.61	0.15
MBS-569	258	259	0.09	0.049	0.015	1	0.5	2	145000	12.87	5.93	0.1	15.51	1.64	10.49	0.12
MBS-569	259	260	0.06	0.042	0.008	0.5	0.3	1.7	162000	13.75	6.19	0.12	12.57	1.39	11.36	0.17
MBS-569	260	261	0.09	0.05	0.013	0.5	0.3	1.7	260000	13.76	6.28	0.12	12.83	1.36	12.22	0.17
MBS-569	261	262	0.16	0.071	0.024	0.5	0.3	1.7	484000	15.69	7.06	0.13	9.3	1.05	13.99	0.2
MBS-569	262	263	0.29	0.106	0.043	0.5	0.3	1.7	856000	17.99	8.03	0.15	4.76	0.53	14.9	0.23
MBS-569	263	264	0.17	0.077	0.027	0.5	0.3	1.7	540000	17.25	7.63	0.14	5.57	0.82	12.73	0.23
MBS-569	264	265	0.23	0.09	0.032	0.5	0.5	1	638000	18.74	8.44	0.16	4.86	0.55	13.7	0.23
MBS-569	265	266	0.39	0.123	0.051	1	1	1	510000	19.07	8.56	0.16	4.57	0.5	13.8	0.22
MBS-569	266	267	0.35	0.111	0.047	1	0.8	1.3	470000	18.65	8.34	0.16	4.38	0.49	13.8	0.22
MBS-569	267	268	1.13	0.254	0.134	2	2.7	0.7	670000	18.32	9.39	0.15	3.95	0.42	13.47	0.23
MBS-569	268	269	1.66	0.382	0.203	3	4.7	0.6	676667	16.75	9.49	0.15	3.48	0.39	11.82	0.22
MBS-569	269	270	0.33	0.142	0.049	4	3	1.3	123500	20.56	9.34	0.15	4.74	0.53	8.09	0.22
MBS-569	270	271	0.44	0.192	0.091	4	3.1	1.3	226250	22.05	10.31	0.17	3.97	0.42	5.68	0.2
MBS-569	271	272	0.93	0.398	0.188	5	4	1.3	376000	21.06	10.64	0.15	4.67	0.51	5.07	0.2

Hole_ID	m From	m To	S (wt. %)	Ni (wt. %)	Cu (wt. %)	Pd (ppb)	Pt (ppb)	Pd/Pt	Cu/Pd	MgO (wt. %)	Fe_2O_3 (wt. %)	MnO (wt. %)	Al_2O_3 (wt. %)	Na_2O (wt. %)	CaO (wt. %)	TiO_2 (wt. %)
MBS-569	272	273	1.05	0.513	0.19	5	4.8	1	380000	22.97	11.62	0.16	3.51	0.34	3.65	0.18
MBS-569	273	274	1.39	0.73	0.281	10	31.7	0.3	281000	21.56	12.08	0.17	3.59	0.38	4.1	0.18
MBS-569	274	275	0.85	0.437	0.178	7	24.9	0.3	254286	13.83	8.78	0.18	5.14	0.19	6.94	0.45
MBS-569	275	276	0.27	0.129	0.048	2	7.3	0.3	239500	9	7.22	0.24	5.54	0.28	9.39	0.45
MBS-569	276	277	0.1	0.019	0.05	1	0.7	1.4	497000	2.77	3.93	0.04	10.58	2.47	2.41	0.32
MBS-569	277	278	0.05	0.007	0.002	0.5	0.3	1.7	38000	0.9	1.67	0.01	11.79	2.93	1.47	0.18
MBS-569	278	279	0.05	0.007	0.002	1	0.3	3.3	18000	1.24	2.04	0.01	12.17	2.16	0.88	0.2
MBS-569	279	280	0.06	0.025	0.008	0.5	0.3	1.7	160000	5.8	3.33	0.05	10.28	1.4	4.32	0.15
MBS-569	280	281	0.26	0.093	0.037	1	0.5	2	368000	17.83	7.86	0.15	4.33	0.5	13.35	0.23
MBS-569	281	282	0.17	0.074	0.026	0.5	0.3	1.7	526000	17.33	7.49	0.14	4.27	0.5	13.17	0.22
MBS-569	282	283	0.16	0.079	0.027	0.5	0.3	1.7	530000	18.07	7.88	0.15	4.1	0.47	13.29	0.22
MBS-569	283	284	0.21	0.087	0.034	0.5	0.3	1.7	686000	15.55	7.36	0.15	5.18	0.82	11.26	0.23
MBS-569	284	285	0.53	0.2	0.079	2	1.7	1.2	392500	20.73	9.79	0.16	4.08	0.44	8.52	0.23
MBS-569	285	286	0.46	0.228	0.075	1	1.6	0.6	754000	22.22	10.25	0.16	4.52	0.47	4.93	0.2
MBS-569	286	287	0.19	0.139	0.032	1	0.7	1.4	318000	23.3	10.35	0.17	4.29	0.44	4.09	0.2
MBS-569	287	288	0.54	0.281	0.084	4	5.6	0.7	209000	23.8	11.02	0.17	4.18	0.39	3.96	0.18
MBS-569	288	289	0.99	0.444	0.133	5	9.6	0.5	266000	23.55	11.35	0.17	3.85	0.35	3.68	0.18
MBS-569	289	290	0.93	0.424	0.152	6	28.4	0.2	253333	23.71	11.49	0.17	3.85	0.36	3.79	0.18
MBS-569	290	291	0.24	0.168	0.045	3	14.5	0.2	150333	21.81	9.91	0.15	3.67	0.38	3.67	0.18
MBS-569	291	292	0.22	0.157	0.038	1	2.2	0.5	378000	22.47	9.81	0.15	4.48	0.54	3.75	0.2
MBS-569	292	293	1.1	0.521	0.173	8	15.9	0.5	216250	22.55	11.27	0.16	4.16	0.46	3.68	0.18
MBS-569	293	294	0.36	0.205	0.062	3	5.6	0.5	206333	23.46	10.45	0.17	3.72	0.39	3.6	0.18
MBS-569	294	295	0.18	0.156	0.039	1	2.6	0.4	390000	23.88	10.28	0.16	3.82	0.43	3.6	0.2
MBS-569	295	296	0.28	0.199	0.054	2	2.3	0.9	269000	23.71	10.91	0.17	3.91	0.46	3.75	0.2
MBS-569	296	297	0.28	0.191	0.05	2	2.4	0.8	250000	24.04	10.61	0.17	3.87	0.43	3.69	0.2
MBS-569	297	298	0.23	0.168	0.039	1	1.7	0.6	392000	23.71	10.64	0.16	3.97	0.42	3.81	0.18
MBS-569	298	299	0.53	0.273	0.085	3	5.5	0.5	284333	23.88	10.74	0.17	3.84	0.36	3.71	0.17
MBS-569	299	300	0.34	0.204	0.051	2	3.3	0.6	255500	23.38	10.61	0.16	4.35	0.5	3.86	0.17
MBS-569	300	301	0.48	0.257	0.074	3	3.2	0.9	245000	23.63	10.71	0.17	3.85	0.4	3.71	0.17
MBS-569	301	302	0.97	0.463	0.143	6	5.2	1.2	238333	23.21	11.42	0.16	3.93	0.4	3.81	0.17
MBS-569	302	303	0.64	0.335	0.104	5	13.1	0.4	208000	24.29	10.94	0.17	3.76	0.4	3.71	0.17
MBS-569	303	304	0.62	0.331	0.094	4	5.8	0.7	234000	24.46	10.91	0.17	3.59	0.35	3.65	0.17
MBS-569	304	305	0.27	0.185	0.044	2	2.3	0.9	220500	24.04	10.18	0.17	3.78	0.4	3.82	0.17
MBS-569	305	306	0.41	0.237	0.063	2	2.2	0.9	312500	23.3	10.19	0.16	3.7	0.39	3.64	0.17
MBS-569	306	307	0.35	0.221	0.052	3	7.1	0.4	174333	24.71	10.64	0.17	3.65	0.38	3.81	0.17

Hole_ID	m From	m To	S (wt. %)	Ni (wt. %)	Cu (wt. %)	Pd (ppb)	Pt (ppb)	Pd/Pt	Cu/Pd	MgO (wt. %)	Fe_2O_3 (wt. %)	MnO (wt. %)	Al_2O_3 (wt. %)	Na_2O (wt. %)	CaO (wt. %)	TiO_2 (wt. %)
MBS-569	307	308	0.8	0.375	0.124	6	16.2	0.4	206667	24.79	11.29	0.17	3.44	0.34	3.62	0.18
MBS-569	308	309	0.45	0.241	0.068	3	12.8	0.2	228000	23.63	10.57	0.17	3.65	0.46	3.81	0.22
MBS-569	309	310	0.14	0.123	0.021	0.5	1	0.5	424000	24.04	9.89	0.17	4.29	0.54	4.28	0.18
MBS-569	310	311	0.56	0.298	0.085	3	4.8	0.6	282333	24.79	11.14	0.18	3.44	0.38	3.58	0.18
MBS-569	311	312	0.18	0.14	0.029	1	1.4	0.7	287000	24.87	10.67	0.18	3.78	0.46	3.78	0.2
MBS-569	312	313	0.26	0.159	0.04	1	1.4	0.7	395000	23.96	11.29	0.18	4.57	0.63	4.17	0.22
MBS-569	313	314	0.26	0.161	0.042	2	2.2	0.9	207500	22.97	10.11	0.16	6.07	0.84	4.46	0.18
MBS-569	314	315	0.23	0.166	0.039	1	1.6	0.6	394000	25.62	10.44	0.17	4.29	0.49	3.85	0.17
MBS-569	315	316	0.3	0.195	0.052	2	4.6	0.4	261500	25.7	10.65	0.17	3.87	0.43	3.54	0.17
MBS-569	316	317	0.18	0.149	0.031	1	4.7	0.2	312000	24.96	10.12	0.17	4.23	0.53	3.81	0.17
MBS-569	317	318	0.16	0.155	0.031	1	6.7	0.1	306000	26.86	10.95	0.18	3.99	0.46	3.68	0.18
MBS-569	318	319	0.13	0.131	0.027	1	6.7	0.1	266000	23.21	9.45	0.16	3.42	0.39	3.16	0.17
MBS-569	319	320	0.2	0.163	0.038	2	11.3	0.2	188500	25.54	10.27	0.17	3.85	0.46	3.53	0.18
MBS-569	320	321	0.11	0.105	0.021	2	6.1	0.3	103000	13.22	6.81	0.12	8.43	1.71	2.74	0.3
MBS-569	321	322	0.05	0.051	0.01	1	2.7	0.4	100000	7.48	3.72	0.18	7.44	1.32	3.41	0.2
MBS-569	322	323	0.1	0.071	0.012	4	13.5	0.3	28750	7.91	5.55	0.21	9.67	1.7	4.21	0.45
MBS-569	323	324	0.07	0.034	0.008	1	1.3	0.8	80000	5.52	3.53	0.05	10.66	2.43	1.71	0.18
MBS-569	324	325	0.15	0.148	0.033	3	12	0.3	111333	18.41	8.39	0.13	6.63	1.39	3.06	0.2
MBS-569	325	326	0.49	0.328	0.092	9	45.2	0.2	101667	22.88	10.69	0.17	4.38	0.53	2.94	0.25
MBS-569	326	327	0.29	0.2	0.05	6	36.1	0.2	83667	17.49	9.35	0.13	6.48	0.89	2.6	0.38
MBS-569	327	328	1.12	0.595	0.18	18	102	0.2	100000	26.03	11.75	0.17	3.38	0.36	2.97	0.18
MBS-569	328	329	0.86	0.454	0.146	13	69.9	0.2	112308	25.95	11.29	0.17	3.48	0.38	3.06	0.18
MBS-569	329	330	0.41	0.256	0.074	6	30.8	0.2	122833	25.7	10.45	0.17	3.67	0.47	3.11	0.2
MBS-569	330	331	1.25	0.66	0.21	22	135	0.2	95455	25.54	11.8	0.17	3.14	0.34	2.88	0.18
MBS-569	331	332	0.87	0.478	0.148	15	85.9	0.2	98667	26.28	11.45	0.17	3.48	0.4	3.11	0.18
MBS-569	332	333	0.44	0.277	0.073	7	36.4	0.2	103714	24.21	9.92	0.15	3.91	0.59	3.18	0.2
MBS-569	333	334	0.94	0.512	0.152	14	57.7	0.2	108571	26.7	11.61	0.17	3.34	0.36	2.94	0.18
MBS-569	334	335	0.46	0.288	0.079	5	21.5	0.2	158800	26.2	10.84	0.18	3.59	0.44	3.18	0.18
MBS-569	335	336	0.46	0.301	0.082	7	38.9	0.2	116429	27.77	11.37	0.18	3.72	0.4	3.12	0.18
MBS-569	336	337	0.84	0.463	0.158	17	69.6	0.2	92647	26.95	11.74	0.18	3.55	0.39	2.99	0.18
MBS-569	337	338	0.68	0.377	0.12	10	30.3	0.3	120000	28.11	11.74	0.18	3.48	0.36	3.01	0.18
MBS-569	338	339	0.44	0.298	0.081	5	17.3	0.3	162800	27.69	11.38	0.18	3.53	0.4	2.98	0.18
MBS-569	339	340	0.35	0.237	0.056	4	14.1	0.3	140500	27.44	11.14	0.18	3.74	0.42	3.01	0.17
MBS-569	340	341	0.48	0.295	0.076	5	26.4	0.2	152800	28.77	11.95	0.18	3.74	0.42	3.04	0.2
MBS-569	341	342	0.24	0.182	0.037	2	6.9	0.3	184000	26.7	10.51	0.17	3.82	0.47	3.02	0.17

Hole_ID	m From	m To	S (wt. %)	Ni (wt. %)	Cu (wt. %)	Pd (ppb)	Pt (ppb)	Pd/Pt	Cu/Pd	MgO (wt. %)	Fe_2O_3 (wt. %)	MnO (wt. %)	Al_2O_3 (wt. %)	Na_2O (wt. %)	CaO (wt. %)	TiO_2 (wt. %)
MBS-569	342	343	0.48	0.29	0.067	5	25.3	0.2	134800	26.95	11.05	0.17	3.82	0.43	2.92	0.18
MBS-569	343	344	0.88	0.482	0.141	17	68.6	0.2	82941	27.53	11.8	0.18	3.55	0.36	2.9	0.18
MBS-569	344	345	0.45	0.297	0.081	8	24.1	0.3	100625	26.7	11.04	0.17	3.65	0.42	2.98	0.2
MBS-569	345	346	0.37	0.238	0.059	5	20.3	0.2	118600	28.69	11.27	0.18	3.53	0.35	2.97	0.18
MBS-569	346	347	0.2	0.169	0.033	3	9.2	0.3	109000	28.85	11.07	0.18	3.53	0.34	3.02	0.18
MBS-569	347	348	0.15	0.147	0.024	2	6.2	0.3	122000	28.27	10.62	0.18	3.4	0.32	2.92	0.17
MBS-569	348	349	0.16	0.157	0.028	2	6.1	0.3	138000	28.6	10.82	0.18	3.44	0.32	2.97	0.18
MBS-569	349	350	0.18	0.16	0.029	2	6.5	0.3	144500	28.6	10.82	0.18	3.4	0.31	2.94	0.18
MBS-569	350	351	0.16	0.155	0.025	2	5.9	0.3	126000	28.85	10.91	0.18	3.36	0.31	2.94	0.18
MBS-569	351	352	0.15	0.153	0.024	2	5.9	0.3	118500	28.52	10.79	0.18	3.44	0.32	2.98	0.18
MBS-569	352	353	0.19	0.168	0.03	2	8.9	0.2	150000	28.36	10.89	0.18	3.33	0.31	2.94	0.17
MBS-569	353	354	0.22	0.175	0.034	3	10.7	0.3	113000	28.27	10.97	0.18	3.29	0.31	3.05	0.18
MBS-569	354	355	0.4	0.247	0.064	8	37.9	0.2	80125	27.94	11.21	0.18	3.61	0.38	3.29	0.18
MBS-569	355	356	0.52	0.299	0.081	43	51.5	0.8	18791	26.95	10.89	0.17	4.59	0.54	3.61	0.17
MBS-569	356	357	0.23	0.167	0.044	20	23.4	0.9	22000	13.91	6.61	0.09	9.3	2.2	3.53	0.2
MBS-569	357	358	0.15	0.011	0.002	1	1.2	0.8	15000	2.55	3.29	0.02	12.06	3.05	1.8	0.37
MBS-569	358	359	0.18	0.101	0.019	2	5.4	0.4	94000	16.42	7.62	0.1	9.28	1.95	2.76	0.27
MBS-569	359	360	0.14	0.157	0.027	2	7.2	0.3	136000	27.77	10.44	0.17	3.42	0.32	2.91	0.18
MBS-569	360	361	0.12	0.155	0.027	2	7.2	0.3	133000	26.86	10.22	0.17	3.25	0.3	2.87	0.17
MBS-569	361	362	0.2	0.174	0.033	3	10.7	0.3	110667	27.36	10.55	0.17	3.25	0.31	2.92	0.17
MBS-569	362	363	0.14	0.157	0.026	2	8.2	0.2	128000	27.61	10.38	0.17	3.46	0.31	2.98	0.17
MBS-569	363	364	0.34	0.232	0.053	7	22.2	0.3	75857	26.12	10.58	0.17	3.46	0.38	2.87	0.18
MBS-569	364	365	0.32	0.225	0.051	5	14.1	0.4	102800	27.11	10.77	0.17	3.59	0.4	3.18	0.18
MBS-569	365	366	0.7	0.389	0.112	11	33.1	0.3	101818	27.11	11.55	0.18	3.57	0.4	3.23	0.2
MBS-569	366	367	0.39	0.262	0.061	95	87.6	1.1	6453	27.53	11.04	0.17	3.61	0.31	3.43	0.18
MBS-569	367	368	0.55	0.33	0.093	121	130	0.9	7686	26.53	10.95	0.17	3.4	0.3	2.8	0.17
MBS-569	368	369	0.67	0.376	0.112	22	137	0.2	50909	25.95	10.97	0.17	3.19	0.26	2.73	0.15
MBS-569	369	370	0.17	0.167	0.032	6	23.7	0.3	53167	28.19	10.75	0.17	3.59	0.34	2.98	0.15
MBS-569	370	371	0.14	0.143	0.023	0.5	2.9	0.2	454000	28.19	10.91	0.18	3.48	0.34	2.99	0.15
MBS-569	371	372	0.33	0.24	0.057	4	14.7	0.3	143250	27.86	10.95	0.17	3.53	0.38	2.98	0.17
MBS-569	372	373	0.12	0.132	0.02	0.5	4.3	0.1	404000	27.11	10.47	0.17	3.93	0.44	3.05	0.15
MBS-569	373	374	0.14	0.136	0.025	0.5	2.7	0.2	492000	22.63	9.49	0.16	3.51	0.35	2.87	0.17
MBS-569	374	375	0.24	0.189	0.041	3	9.4	0.3	137000	24.96	10.11	0.17	3.5	0.3	2.83	0.13
MBS-569	375	376	0.31	0.212	0.053	2	4.5	0.4	263500	24.46	10.39	0.17	4.01	0.39	3.15	0.17
MBS-569	376	377	0.27	0.209	0.049	2	11.5	0.2	242500	25.54	10.45	0.17	3.21	0.24	2.66	0.17

Hole_ID	m From	m To	S (wt. %)	Ni (wt. %)	Cu (wt. %)	Pd (ppb)	Pt (ppb)	Pd/Pt	Cu/Pd	MgO (wt. %)	Fe_2O_3 (wt. %)	MnO (wt. %)	Al_2O_3 (wt. %)	Na_2O (wt. %)	CaO (wt. %)	TiO_2 (wt. %)
MBS-569	377	378	0.36	0.241	0.062	6	30.1	0.2	102667	25.2	10.48	0.17	3.33	0.26	2.69	0.15
MBS-569	378	379	0.27	0.202	0.046	1	7.3	0.1	463000	24.96	10.11	0.17	3.74	0.34	2.94	0.17
MBS-569	379	380	0.27	0.218	0.051	2	7.1	0.3	255000	24.79	10.25	0.16	3.85	0.39	2.84	0.15
MBS-569	380	381	0.38	0.257	0.067	3	13.3	0.2	222333	24.96	10.28	0.17	3.65	0.36	2.8	0.15
MBS-569	381	382	0.33	0.218	0.053	2	10.6	0.2	262500	24.54	9.95	0.16	4.08	0.44	3.01	0.15
MBS-569	382	383	0.25	0.188	0.042	7	27.7	0.3	59286	24.79	10.07	0.17	3.38	0.31	2.64	0.15
MBS-569	383	384	0.2	0.185	0.036	4	18.7	0.2	91000	25.7	10.25	0.17	3.51	0.31	2.81	0.15
MBS-569	384	385	0.42	0.273	0.069	6	27.1	0.2	115000	25.87	10.69	0.17	3.46	0.3	2.78	0.17
MBS-569	385	386	0.14	0.149	0.024	0.5	1.3	0.4	478000	24.96	10.02	0.17	3.65	0.34	2.88	0.15
MBS-569	386	387	0.1	0.141	0.021	0.5	1	0.5	418000	25.12	9.97	0.17	3.74	0.39	2.9	0.17
MBS-569	387	388	0.22	0.194	0.039	0.5	1	0.5	774000	25.62	10.37	0.17	3.72	0.35	2.94	0.17
MBS-569	388	389	0.09	0.139	0.02	0.5	0.3	1.7	396000	24.96	9.78	0.17	3.78	0.39	2.92	0.15
MBS-569	389	390	0.11	0.135	0.02	0.5	1.1	0.5	398000	24.46	9.71	0.16	4.06	0.47	2.97	0.17
MBS-569	390	391	0.16	0.164	0.029	2	13.2	0.2	146000	25.87	10.08	0.17	3.59	0.34	2.78	0.15
MBS-569	391	392	0.38	0.265	0.065	8	54.7	0.1	81750	26.2	10.49	0.17	3.48	0.3	2.7	0.15
MBS-569	392	393	0.55	0.348	0.097	16	92	0.2	60750	25.54	10.44	0.17	3.23	0.26	2.6	0.15
MBS-569	393	394	0.26	0.227	0.049	10	73.5	0.1	49400	26.2	10.31	0.17	3.23	0.26	2.52	0.15
MBS-569	394	395	0.1	0.168	0.03	5	44.2	0.1	59400	25.2	9.62	0.16	3.1	0.26	2.41	0.15
MBS-569	395	396	0.17	0.187	0.031	8	59.6	0.1	39125	25.37	9.86	0.17	3.08	0.19	2.41	0.15
MBS-569	396	397	0.24	0.224	0.053	17	68.4	0.2	30882	25.45	10.17	0.17	3.27	0.24	2.55	0.15
MBS-569	397	398	0.22	0.202	0.041	11	40.5	0.3	37364	25.54	9.98	0.17	3.5	0.31	2.78	0.15
MBS-569	398	399	0.2	0.196	0.038	15	58.8	0.3	25533	25.45	9.95	0.17	3.23	0.26	2.57	0.15
MBS-569	399	400	0.19	0.18	0.034	18	62.6	0.3	19111	25.62	9.99	0.17	3.17	0.24	2.56	0.17
MBS-569	400	401	0.35	0.25	0.061	26	84.6	0.3	23615	24.29	9.76	0.16	3.61	0.35	2.56	0.17
MBS-569	401	402	0.37	0.27	0.068	38	98.1	0.4	17868	24.62	9.81	0.16	3.25	0.27	2.56	0.17
MBS-569	402	403	0.22	0.194	0.039	27	97	0.3	14370	25.2	9.89	0.17	3.31	0.28	2.6	0.17
MBS-569	403	404	0.13	0.153	0.024	15	57.3	0.3	16067	25.37	9.78	0.17	3.36	0.3	2.76	0.17
MBS-569	404	405	0.12	0.15	0.024	16	47.1	0.3	15000	24.71	9.52	0.16	3.42	0.32	2.6	0.17
MBS-569	405	406	0.27	0.217	0.051	24	39.3	0.6	21083	24.96	9.91	0.17	3.36	0.31	2.63	0.17
MBS-569	406	407	0.61	0.382	0.11	35	49.6	0.7	31286	24.62	10.15	0.16	3.34	0.31	2.63	0.17
MBS-569	407	408	0.15	0.138	0.038	9	12.5	0.7	42333	17.08	7.88	0.13	7.39	1.15	2.57	0.22
MBS-569	408	409	0.29	0.17	0.065	31	33.1	0.9	20935	8.92	5.93	0.09	12.26	2.48	2.8	0.2
MBS-569	409	410	1.1	0.62	0.213	86	76.1	1.1	24767	25.12	11.34	0.17	3.33	0.3	2.66	0.18
MBS-569	410	411	0.8	0.475	0.168	57	74.3	0.8	29474	25.37	11.08	0.17	3.72	0.36	2.73	0.2
MBS-569	411	412	0.71	0.434	0.148	30	51.5	0.6	49333	24.54	10.72	0.16	3.65	0.38	2.71	0.18

Hole_ID	m From	m To	S (wt. %)	Ni (wt. %)	Cu (wt. %)	Pd (ppb)	Pt (ppb)	Pd/Pt	Cu/Pd	MgO (wt. %)	Fe_2O_3 (wt. %)	MnO (wt. %)	Al_2O_3 (wt. %)	Na_2O (wt. %)	CaO (wt. %)	TiO_2 (wt. %)
MBS-569	412	413	0.88	0.54	0.174	47	71.3	0.7	37021	24.62	10.82	0.16	3.48	0.35	2.62	0.2
MBS-569	413	414	1.18	0.74	0.211	86	112	0.8	24535	24.54	11.39	0.16	3.33	0.3	2.5	0.2
MBS-569	414	415	1.07	0.68	0.168	91	163	0.6	18407	27.53	12.2	0.17	2.74	0.24	2.03	0.17
MBS-569	415	416	1.77	1.07	0.283	177	285	0.6	15989	26.95	13.01	0.16	2.76	0.26	2.07	0.18
MBS-569	416	417	1.92	1.08	0.305	171	277	0.6	17836	25.37	12.61	0.16	3.02	0.23	2.14	0.2
MBS-569	417	418	2.06	1.21	0.33	184	341	0.5	17935	25.87	12.57	0.15	2.59	0.18	1.85	0.17
MBS-569	418	419	0.45	0.303	0.08	53	87	0.6	15075	25.45	10.34	0.16	3.87	0.39	2.73	0.22
MBS-569	419	420	0.1	0.148	0.021	21	28.9	0.7	10190	26.03	10.08	0.17	3.76	0.36	2.66	0.18
MBS-569	420	421	0.24	0.216	0.042	52	73.8	0.7	8058	24.54	10.51	0.16	4.16	0.5	2.55	0.27
MBS-569	421	422	0.36	0.268	0.066	54	78.5	0.7	12148	25.37	10.18	0.16	3.95	0.42	2.81	0.18
MBS-569	422	423	0.55	0.371	0.08	61	73.2	0.8	13180	28.69	10.67	0.16	2.97	0.27	2.46	0.17
MBS-569	423	424	0.87	0.482	0.231	70	135	0.5	33000	28.02	11.28	0.16	3.4	0.39	2.77	0.18
MBS-569	424	425	1.28	0.75	0.197	88	138	0.6	22330	26.45	11.25	0.15	3.36	0.38	2.76	0.17
MBS-569	425	426	0.61	0.402	0.104	52	62	0.8	19904	27.86	10.59	0.16	3.55	0.42	2.91	0.18
MBS-569	426	427	0.89	0.473	0.292	75	151	0.5	38933	28.27	10.74	0.15	2.93	0.26	2.55	0.17
MBS-569	427	428	0.76	0.565	0.106	64	368	0.2	16484	32.83	11.67	0.15	1.97	0.16	1.62	0.12
MBS-569	428	429	0.64	0.477	0.109	37	212	0.2	29459	29.1	11.51	0.16	2.32	0.19	1.89	0.13
MBS-569	429	430	0.58	0.396	0.104	36	168	0.2	28889	25.62	10.14	0.16	2.85	0.22	2.29	0.17
MBS-569	430	431	0.63	0.43	0.11	51	147	0.3	21569	25.62	10.35	0.16	2.87	0.23	2.32	0.17
MBS-569	431	432	0.32	0.257	0.068	42	77.6	0.5	16143	25.62	9.97	0.16	2.87	0.23	2.34	0.17
MBS-569	432	433	0.1	0.152	0.018	16	29	0.6	11000	25.62	9.72	0.16	3.04	0.24	2.42	0.18
MBS-569	433	434	0.91	0.64	0.135	73	128	0.6	18425	25.45	10.87	0.16	2.91	0.23	2.34	0.17
MBS-569	434	435	0.87	0.535	0.227	83	124	0.7	27349	25.04	10.75	0.15	3.06	0.27	2.43	0.18
MBS-569	435	436	0.93	0.593	0.163	71	119	0.6	22958	24.71	10.61	0.15	3.12	0.27	2.41	0.17
MBS-569	436	437	0.85	0.544	0.164	71	105	0.7	23099	24.38	10.42	0.15	3.1	0.27	2.56	0.17
MBS-569	437	438	1.27	0.84	0.225	111	164	0.7	20270	26.95	11.55	0.15	2.55	0.2	2.15	0.15
MBS-569	438	439	1.61	1.04	0.177	130	175	0.7	13615	27.86	11.88	0.15	2.31	0.16	1.96	0.13
MBS-569	439	440	1.49	0.95	0.192	139	223	0.6	13777	28.36	11.98	0.15	2.27	0.18	1.94	0.13
MBS-569	440	441	0.83	0.564	0.121	94	161	0.6	12819	29.27	11.38	0.15	2.06	0.16	1.8	0.13
MBS-569	441	442	0.24	0.264	0.043	60	86.7	0.7	7233	29.76	10.71	0.15	2.1	0.19	1.75	0.13
MBS-569	442	443	0.09	0.195	0.015	45	57.8	0.8	3244	28.6	10.41	0.15	2.04	0.18	1.69	0.13
MBS-569	443	444	0.09	0.186	0.014	45	59.4	0.8	3200	28.77	10.39	0.15	2.19	0.19	1.85	0.13
MBS-569	444	445	0.09	0.19	0.016	48	63.9	0.8	3250	29.18	10.22	0.15	2.42	0.2	1.99	0.15
MBS-569	445	446	0.09	0.184	0.015	49	70	0.7	3122	28.94	10.14	0.15	2.48	0.22	2.03	0.15
MBS-569	446	447	0.11	0.205	0.018	59	85	0.7	3119	29.76	10.35	0.15	2.32	0.22	1.97	0.15

Hole_ID	m From	m To	S (wt. %)	Ni (wt. %)	Cu (wt. %)	Pd (ppb)	Pt (ppb)	Pd/Pt	Cu/Pd	MgO (wt. %)	Fe_2O_3 (wt. %)	MnO (wt. %)	Al_2O_3 (wt. %)	Na_2O (wt. %)	CaO (wt. %)	TiO_2 (wt. %)
MBS-569	447	448	0.14	0.212	0.024	57	94.3	0.6	4140	28.85	10.05	0.15	2.44	0.22	2.01	0.15
MBS-569	448	449	0.16	0.266	0.027	35	64.3	0.5	7600	31.42	11.29	0.15	2.06	0.18	1.62	0.12
MBS-569	449	450	0.08	0.259	0.013	16	39.5	0.4	8188	32.58	12	0.15	1.8	0.2	1.53	0.12
MBS-569	450	451	0.3	0.375	0.055	50	94.6	0.5	11020	33.5	12.6	0.16	1.76	0.19	1.47	0.12
MBS-569	451	452	0.57	0.478	0.139	140	224	0.6	9929	32.33	12.15	0.15	1.7	0.18	1.4	0.12
MBS-569	452	453	0.71	0.545	0.142	112	235	0.5	12679	32.09	12.51	0.15	1.66	0.18	1.46	0.12
MBS-569	453	454	1.05	0.77	0.143	203	286	0.7	7044	32.83	12.98	0.15	1.61	0.15	1.37	0.1
MBS-569	454	455	0.09	0.262	0.016	16	34	0.5	9875	33.16	11.67	0.15	1.72	0.19	1.47	0.12
MBS-569	455	456	0.11	0.273	0.015	13	20.2	0.6	11538	33.16	11.84	0.15	1.8	0.18	1.48	0.12
MBS-569	456	457	0.38	0.433	0.041	92	104	0.9	4467	33.99	12.52	0.15	1.7	0.18	1.44	0.12
MBS-569	457	458	0.77	0.593	0.14	219	251	0.9	6370	32.83	12.48	0.14	1.55	0.13	1.25	0.1
MBS-569	458	459	0.91	0.7	0.169	247	285	0.9	6842	32.25	12.42	0.14	1.49	0.12	1.16	0.1
MBS-569	459	460	0.81	0.68	0.114	203	343	0.6	5591	32.42	12.25	0.14	1.49	0.09	1.01	0.08
MBS-569	460	461	0.05	0.181	0.007	15	35.3	0.4	4733	23.13	8.74	0.11	5.56	0.94	0.64	0.12
MBS-569	461	462	0.08	0.276	0.012	6	28.6	0.2	20667	33.33	12.04	0.15	1.62	0.15	1.15	0.1
MBS-569	462	463	0.09	0.286	0.014	6	34.4	0.2	22833	34.99	12.2	0.15	1.53	0.13	1.16	0.1
MBS-569	463	464	0.08	0.291	0.015	7	35.9	0.2	20857	34.49	12.45	0.15	1.59	0.13	1.19	0.1
MBS-569	464	465	0.09	0.286	0.015	7	40.2	0.2	21857	34.16	12.24	0.15	1.55	0.13	1.18	0.1
MBS-569	465	466	0.1	0.283	0.016	9	57	0.2	18111	33.83	11.72	0.14	1.44	0.13	1.08	0.08
MBS-569	466	467	0.1	0.296	0.017	8	46.8	0.2	21625	34.32	12.25	0.15	1.51	0.13	1.16	0.1
MBS-569	467	468	0.1	0.302	0.018	8	50.9	0.2	22250	34.82	12.45	0.15	1.51	0.15	1.15	0.1
MBS-569	468	469	0.1	0.309	0.018	10	57.4	0.2	18200	35.82	12.75	0.16	1.59	0.15	1.26	0.1
MBS-569	469	470	0.1	0.299	0.016	11	61	0.2	14909	34.82	12.44	0.15	1.66	0.15	1.26	0.1
MBS-569	470	471	0.13	0.287	0.02	10	55.6	0.2	20000	32.92	12.17	0.15	1.85	0.2	1.34	0.1
MBS-569	471	472	0.06	0.102	0.017	5	20.6	0.2	33200	12.44	8.25	0.12	10	2.1	1.65	0.57
MBS-569	472	473	0.09	0.271	0.017	9	49.7	0.2	18778	32.42	11.39	0.15	1.76	0.16	1.37	0.1
MBS-569	473	474	0.09	0.267	0.017	10	55.4	0.2	17100	32.42	11.39	0.15	1.74	0.15	1.41	0.1
MBS-569	474	475	0.1	0.273	0.017	11	55.3	0.2	15000	32.83	11.65	0.15	1.81	0.18	1.33	0.1
MBS-569	475	476	0.08	0.256	0.014	13	71.1	0.2	10615	30.43	10.91	0.14	2.27	0.2	1.32	0.08
MBS-569	476	477	0.07	0.232	0.011	10	54.9	0.2	10900	26.95	11.02	0.15	4.29	0.5	1.65	0.18
MBS-569	477	478	0.1	0.302	0.018	9	51.5	0.2	19778	34.99	12.51	0.15	1.61	0.15	1.3	0.1
MBS-569	478	479	0.11	0.295	0.019	11	60.1	0.2	17091	34.32	12.4	0.15	1.23	0.16	1.39	0.1
MBS-569	479	480	0.11	0.295	0.018	10	55.5	0.2	18100	34.49	12.2	0.15	1.66	0.18	1.39	0.1
MBS-569	480	481	0.11	0.281	0.018	10	57.7	0.2	17700	33.83	12.11	0.16	1.72	0.16	1.41	0.1
MBS-569	481	482	0.1	0.288	0.016	11	61	0.2	14909	33.83	12.14	0.15	1.66	0.15	1.34	0.1

Hole_ID	m From	m To	S (wt. %)	Ni (wt. %)	Cu (wt. %)	Pd (ppb)	Pt (ppb)	Pd/Pt	Cu/Pd	MgO (wt. %)	Fe_2O_3 (wt. %)	MnO (wt. %)	Al_2O_3 (wt. %)	Na_2O (wt. %)	CaO (wt. %)	TiO_2 (wt. %)
MBS-569	482	483	0.11	0.305	0.017	12	69.4	0.2	14167	35.32	12.44	0.15	1.49	0.13	1.23	0.08
MBS-569	483	484	0.1	0.31	0.017	14	73.7	0.2	11929	35.32	12.55	0.15	1.55	0.13	1.16	0.08
MBS-569	484	485	0.09	0.3	0.014	13	74.2	0.2	11077	35.15	12.57	0.15	1.53	0.13	1.15	0.08
MBS-569	485	486	0.08	0.297	0.013	15	73.3	0.2	8933	35.82	12.65	0.15	1.45	0.15	1.16	0.08
MBS-569	486	487	0.08	0.296	0.014	16	79	0.2	9000	35.32	12.41	0.15	1.44	0.15	1.22	0.08
MBS-569	487	488	0.08	0.3	0.014	17	78.8	0.2	7941	35.49	12.67	0.15	1.28	0.13	1.11	0.08
MBS-569	488	489	0.08	0.298	0.015	18	73.9	0.2	8167	35.65	12.62	0.15	1.42	0.13	1.16	0.08
MBS-569	489	490	0.08	0.29	0.012	17	61.5	0.3	6765	34.82	12.35	0.15	1.64	0.12	1.16	0.08
MBS-569	490	491	0.26	0.405	0.049	62	129	0.5	7935	34.49	12.62	0.15	1.4	0.12	1.01	0.08
MBS-569	491	492	0.26	0.419	0.052	63	130	0.5	8286	34.82	12.8	0.15	1.44	0.13	1.08	0.08
MBS-569	492	493	0.25	0.398	0.048	62	139	0.4	7710	35.15	12.34	0.15	1.42	0.13	1.15	0.08
MBS-569	493	494	0.09	0.3	0.017	22	60.7	0.4	7545	35.15	12.12	0.15	1.47	0.13	1.15	0.08
MBS-569	494	495	0.07	0.295	0.012	17	54.4	0.3	7294	35.82	12.27	0.15	1.47	0.16	1.19	0.08
MBS-569	495	496	0.07	0.292	0.012	17	47.9	0.4	7294	35.82	12.25	0.15	1.47	0.16	1.25	0.08
MBS-569	496	497	0.12	0.322	0.023	29	63.9	0.5	7931	35.98	12.18	0.15	1.45	0.15	1.23	0.08
MBS-569	497	498	0.08	0.278	0.013	21	43.5	0.5	6286	33.5	11.38	0.14	2.36	0.4	1.3	0.08
MBS-569	498	499	0.31	0.427	0.053	56	95.8	0.6	9482	36.15	12.62	0.15	1.42	0.15	1.19	0.08
MBS-569	499	500	0.36	0.452	0.062	70	105	0.7	8900	36.48	12.77	0.15	1.27	0.12	1.16	0.08
MBS-569	500	501	0.44	0.495	0.077	88	149	0.6	8761	35.98	12.71	0.15	1.53	0.19	1.22	0.08
MBS-569	501	502	0.5	0.545	0.094	104	166	0.6	9010	38.8	12.42	0.15	1.25	0.13	1.18	0.08
MBS-569	502	503	0.39	0.477	0.068	80	122	0.7	8525	37.97	12.11	0.15	1.34	0.13	1.19	0.08
MBS-569	503	504	0.26	0.41	0.049	66	92.2	0.7	7409	38.14	12.01	0.15	1.51	0.16	1.32	0.08
MBS-569	504	505	0.12	0.335	0.02	46	55.3	0.8	4348	38.47	11.77	0.15	1.53	0.16	1.33	0.1
MBS-569	505	506	0.1	0.304	0.018	37	38.9	1	4892	37.31	11.45	0.15	1.66	0.18	1.39	0.1
MBS-569	506	507	0.08	0.272	0.012	29	30.4	1	4276	36.31	11.07	0.15	1.83	0.2	1.65	0.12
MBS-569	507	508	0.09	0.305	0.014	34	36.7	0.9	4206	37.81	11.67	0.15	1.7	0.2	1.41	0.1
MBS-569	508	509	0.07	0.252	0.01	31	32.2	1	3355	36.48	11.04	0.15	1.78	0.19	1.57	0.1
MBS-569	509	510	0.06	0.239	0.009	28	28.3	1	3250	31.26	9.58	0.13	1.57	0.16	1.39	0.1
MBS-569	510	511	0.06	0.287	0.01	28	27.5	1	3536	37.48	11.42	0.15	1.62	0.18	1.43	0.1
MBS-569	511	512	0.06	0.281	0.01	26	24.6	1.1	3654	36.65	11.22	0.15	1.64	0.18	1.48	0.1
MBS-569	512	513	0.07	0.281	0.011	25	22.5	1.1	4400	36.48	11.12	0.15	1.64	0.18	1.4	0.1
MBS-569	513	514	0.08	0.267	0.009	25	22	1.1	3720	35.15	10.69	0.14	1.62	0.18	1.41	0.1
MBS-569	514	515	0.07	0.273	0.009	17	15.2	1.1	5529	36.98	11.22	0.15	1.74	0.18	1.57	0.1
MBS-569	515	516	0.05	0.266	0.009	14	14	1	6214	36.65	11.21	0.15	1.76	0.18	1.55	0.1
MBS-569	516	517	0.08	0.278	0.014	5	9.7	0.5	27800	35.98	10.97	0.15	1.68	0.16	1.54	0.1

Hole_ID	m From	m To	S (wt. %)	Ni (wt. %)	Cu (wt. %)	Pd (ppb)	Pt (ppb)	Pd/Pt	Cu/Pd	MgO (wt. %)	Fe_2O_3 (wt. %)	MnO (wt. %)	Al_2O_3 (wt. %)	Na_2O (wt. %)	CaO (wt. %)	TiO_2 (wt. %)
MBS-569	517	518	0.06	0.275	0.01	5	8	0.6	20600	36.31	11.21	0.15	1.55	0.16	1.32	0.08
MBS-569	518	519	0.11	0.34	0.018	6	12.3	0.5	29667	40.13	12.38	0.16	1.32	0.13	1.18	0.08
MBS-569	519	520	0.15	0.364	0.027	9	16.8	0.5	30000	39.8	12.24	0.15	1.17	0.12	1.05	0.07
MBS-569	520	521	0.12	0.334	0.019	31	72.1	0.4	6226	39.13	12.2	0.16	1.55	0.16	1.34	0.1
MBS-569	521	522	0.09	0.332	0.015	39	81.1	0.5	3795	38.64	12	0.15	1.36	0.13	1.15	0.08
MBS-569	522	523	0.15	0.382	0.026	48	112	0.4	5313	38.97	12.37	0.15	1.28	0.11	0.88	0.07
MBS-569	523	524	0.16	0.398	0.027	23	96.5	0.2	11783	41.62	13.08	0.16	1.28	0.11	0.95	0.07
MBS-569	524	525	0.18	0.369	0.028	34	138	0.2	8324	36.81	11.82	0.14	1.4	0.12	0.99	0.07
MBS-569	525	526	0.08	0.28	0.012	18	59.3	0.3	6556	36.65	11.19	0.15	1.76	0.18	1.57	0.1
MBS-569	526	527	0.47	0.457	0.098	40	134	0.3	24550	34.49	11.12	0.15	1.81	0.18	1.55	0.1
MBS-569	527	528	0.54	0.565	0.074	53	176	0.3	13962	37.97	12.32	0.16	1.55	0.12	1.25	0.08
MBS-569	528	529	0.48	0.472	0.083	31	87.9	0.4	26613	35.98	11.38	0.16	1.76	0.18	1.62	0.1
MBS-569	529	530	0.66	0.65	0.104	51	162	0.3	20392	38.47	12.38	0.16	1.4	0.15	1.27	0.08
MBS-569	530	531	0.26	0.419	0.038	96	327	0.3	3938	40.96	13.11	0.16	1.47	0.12	0.99	0.08
MBS-569	531	532	0.1	0.343	0.015	110	257	0.4	1318	40.96	12.97	0.16	1.44	0.12	0.88	0.07
MBS-569	532	533	0.09	0.325	0.012	100	194	0.5	1230	39.96	12.82	0.16	1.32	0.11	0.81	0.07
MBS-569	533	534	0.08	0.332	0.012	102	171	0.6	1157	41.46	13.12	0.16	1.3	0.13	0.85	0.07
MBS-569	534	535	0.08	0.35	0.012	81	116	0.7	1457	36.48	13.24	0.17	1.45	0.13	0.95	0.08
MBS-569	535	536	0.1	0.338	0.015	71	91.4	0.8	2056	34.99	12.67	0.16	1.53	0.15	1.11	0.08
MBS-569	536	537	0.12	0.337	0.018	114	121	0.9	1553	34.32	12.42	0.16	1.53	0.15	1.2	0.08
MBS-569	537	538	0.06	0.316	0.009	52	53.2	1	1635	34.82	12.55	0.16	1.47	0.18	1.16	0.08
MBS-569	538	539	0.08	0.329	0.013	64	74.2	0.9	2063	34.49	12.54	0.16	1.45	0.16	1.12	0.08
MBS-569	539	540	0.08	0.339	0.012	125	58.5	2.1	968	34.32	12.3	0.16	1.38	0.12	0.98	0.07
MBS-569	540	541	0.06	0.339	0.008	147	48.2	3	558	35.15	12.87	0.16	1.28	0.11	0.81	0.07
MBS-569	541	542	0.06	0.34	0.009	162	55.2	2.9	549	35.15	13.11	0.16	1.38	0.11	0.8	0.07
MBS-569	542	543	0.02	0.085	0.003	52	17.1	3	500	9.55	5.02	0.06	10.6	2.86	1.39	0.17
MBS-569	543	544	0.06	0.33	0.009	169	64.3	2.6	538	34.49	13.05	0.16	1.4	0.11	0.76	0.07
MBS-569	544	545	0.08	0.342	0.014	189	87.3	2.2	725	35.32	13.63	0.16	1.49	0.11	0.87	0.07
MBS-569	545	546	0.06	0.326	0.01	131	56.8	2.3	748	35.15	13.35	0.16	1.49	0.12	0.98	0.08
MBS-569	546	547	0.07	0.324	0.011	111	47.7	2.3	982	35.32	13.42	0.16	1.32	0.09	0.9	0.07
MBS-569	547	548	0.06	0.334	0.011	99	42.6	2.3	1061	35.65	13.51	0.16	1.21	0.12	0.84	0.07
MBS-569	548	549	0.07	0.333	0.013	105	46.8	2.2	1190	35.98	13.64	0.16	1.28	0.12	0.88	0.07
MBS-569	549	550	0.07	0.342	0.011	101	48	2.1	1079	36.48	13.81	0.16	1.27	0.12	0.9	0.07
MBS-569	550	551	0.06	0.341	0.01	84	43.6	1.9	1167	35.98	13.54	0.16	1.15	0.12	0.84	0.07
MBS-569	551	552	0.07	0.348	0.012	76	49.5	1.5	1513	36.15	13.63	0.16	1.15	0.13	0.88	0.07

Hole_ID	m From	m To	S (wt. %)	Ni (wt. %)	Cu (wt. %)	Pd (ppb)	Pt (ppb)	Pd/Pt	Cu/Pd	MgO (wt. %)	Fe_2O_3 (wt. %)	MnO (wt. %)	Al_2O_3 (wt. %)	Na_2O (wt. %)	CaO (wt. %)	TiO_2 (wt. %)
MBS-569	552	553	0.08	0.347	0.015	24	34.1	0.7	6042	34.82	13.2	0.16	1	0.13	0.95	0.07
MBS-569	553	554	0.09	0.361	0.015	13	22.1	0.6	11692	34.99	13.3	0.16	0.68	0.12	0.88	0.07
MBS-569	554	555	0.07	0.341	0.011	31	56.9	0.5	3419	35.65	13.25	0.16	0.72	0.13	0.87	0.07
MBS-569	555	556	0.06	0.347	0.011	81	131	0.6	1309	34.99	13.21	0.16	0.83	0.12	0.85	0.07
MBS-569	556	557	0.06	0.346	0.01	126	137	0.9	802	35.82	13.54	0.16	0.91	0.13	0.94	0.08
MBS-569	557	558	0.05	0.338	0.007	117	109	1.1	632	35.98	13.45	0.16	0.81	0.13	0.91	0.07
MBS-569	558	559	0.04	0.331	0.007	110	98.2	1.1	636	35.65	13.34	0.16	1.25	0.13	0.92	0.08
MBS-569	559	560	0.04	0.329	0.007	117	103	1.1	607	35.32	13.04	0.15	1.23	0.13	0.9	0.07
MBS-569	560	561	0.05	0.336	0.007	126	111	1.1	571	36.48	13.58	0.16	1.3	0.13	0.92	0.08
MBS-569	561	562	0.04	0.335	0.007	126	118	1.1	548	35.65	13.32	0.16	0.74	0.13	0.9	0.08
MBS-569	562	563	0.04	0.343	0.007	120	107	1.1	542	36.15	13.61	0.16	0.6	0.13	0.88	0.07
MBS-569	563	564	0.04	0.337	0.007	129	119	1.1	535	36.31	13.51	0.16	1	0.13	0.9	0.07
MBS-569	564	565	0.04	0.341	0.007	146	140	1	445	36.15	13.42	0.16	0.74	0.13	0.92	0.08
MBS-569	565	566	0.04	0.339	0.005	129	116	1.1	419	36.81	13.8	0.16	1.25	0.13	0.92	0.07
MBS-569	566	567	0.03	0.331	0.004	67	58.2	1.2	567	36.98	13.65	0.16	1.08	0.15	0.9	0.07
MBS-569	567	568	0.04	0.33	0.005	113	114	1	478	38.64	13.77	0.16	1.3	0.13	0.84	0.08
MBS-569	568	569	0.02	0.328	0.004	78	65.6	1.2	462	39.8	13.74	0.16	1.17	0.15	0.84	0.07
MBS-569	569	570	0.03	0.326	0.004	71	61.4	1.2	521	38.8	13.64	0.16	1.19	0.15	0.84	0.08
MBS-569	570	571	0.03	0.335	0.004	98	99	1	439	39.8	13.91	0.17	1.25	0.13	0.81	0.08
MBS-569	571	572	0.03	0.334	0.004	96	88.3	1.1	417	39.96	14.1	0.17	1.3	0.15	0.84	0.08
MBS-569	572	573	0.03	0.335	0.005	125	123	1	376	39.3	14	0.17	1.4	0.12	0.8	0.08
MBS-569	573	574	0.02	0.321	0.004	94	86.5	1.1	426	38.3	13.51	0.16	1.1	0.12	0.78	0.07
MBS-569	574	575	0.02	0.318	0.004	88	78.2	1.1	420	37.81	13.81	0.17	1.42	0.13	0.83	0.12
MBS-569	575	576	0.02	0.279	0.004	96	88.9	1.1	375	34.16	13.14	0.15	3.08	0.44	0.78	0.27
MBS-569	576	577	0.04	0.338	0.006	117	101	1.2	496	38.8	13.81	0.16	1.23	0.12	0.77	0.07
MBS-569	577	578	0.02	0.327	0.004	92	83.8	1.1	413	38.97	13.78	0.16	1.13	0.12	0.76	0.07
MBS-569	578	579	0.03	0.329	0.004	70	59	1.2	586	39.3	14	0.17	1.15	0.13	0.76	0.07
MBS-569	579	580	0.03	0.33	0.005	108	98.4	1.1	463	38.97	14.03	0.17	1.17	0.11	0.71	0.07
MBS-569	580	581	0.03	0.325	0.005	86	86.1	1	570	38.47	13.88	0.16	1.17	0.11	0.73	0.07
MBS-569	581	582	0.03	0.329	0.005	68	56.8	1.2	721	39.47	14.11	0.17	1.1	0.12	0.77	0.07
MBS-569	582	583	0.05	0.326	0.008	138	117	1.2	580	37.97	13.75	0.16	1.15	0.11	0.7	0.07
MBS-569	583	584	0.01	0.038	0.004	13	12.5	1	2769	4.71	4.37	0.04	11.07	2.1	0.64	0.43
MBS-569	584	585	0.03	0.318	0.004	106	98.3	1.1	377	37.81	15.01	0.17	1.78	0.16	0.62	0.27
MBS-569	585	586	0.03	0.334	0.005	118	110	1.1	407	38.3	13.95	0.16	1.11	0.08	0.6	0.07
MBS-569	586	587	0.12	0.373	0.02	322	180	1.8	621	38.8	14.17	0.16	1.13	0.09	0.66	0.07

Hole_ID	m From	m To	S (wt. %)	Ni (wt. %)	Cu (wt. %)	Pd (ppb)	Pt (ppb)	Pd/Pt	Cu/Pd	MgO (wt. %)	Fe_2O_3 (wt. %)	MnO (wt. %)	Al_2O_3 (wt. %)	Na_2O (wt. %)	CaO (wt. %)	TiO_2 (wt. %)
MBS-569	587	588	0.02	0.319	0.004	125	74.2	1.7	288	38.47	13.93	0.16	1.13	0.11	0.69	0.07
MBS-569	588	589	0.02	0.292	0.003	108	64.8	1.7	278	34.99	12.72	0.15	1.04	0.09	0.63	0.05
MBS-569	589	590	0.02	0.285	0.003	97	72.7	1.3	330	34.82	12.21	0.14	0.98	0.09	0.57	0.05
MBS-569	590	591	0.02	0.267	0.004	58	47.6	1.2	638	32.58	11.27	0.13	0.96	0.18	0.66	0.05
MBS-569	591	592	0.03	0.304	0.006	119	100	1.2	479	34.99	12.7	0.15	1	0.09	0.59	0.05
MBS-569	592	593	0.03	0.303	0.004	93	88.4	1.1	473	35.15	12.82	0.15	1.02	0.11	0.59	0.05
MBS-569	593	594	0.03	0.316	0.005	118	123	1	441	36.48	13.35	0.15	1.08	0.08	0.6	0.07
MBS-569	594	595	0.16	0.378	0.025	446	202	2.2	552	36.31	13.44	0.15	1.02	0.09	0.63	0.05
MBS-569	595	596	0.03	0.304	0.004	122	73.3	1.7	344	37.48	13.42	0.16	1.04	0.09	0.64	0.05
MBS-569	596	597	0.55	0.38	0.086	984	733	1.3	875	26.61	11.71	0.16	3.4	0.13	1.99	0.17
MBS-569	597	598	0.99	0.66	0.126	71	590	0.1	17676	26.95	11.17	0.16	2.48	0.19	2.06	0.15
MBS-569	598	599	1.34	0.87	0.192	92	630	0.1	20870	24.46	10.79	0.15	2.66	0.2	2.18	0.15
MBS-569	599	600	1.49	0.83	0.463	118	618	0.2	39237	25.45	11.29	0.15	2.78	0.22	2.41	0.17
MBS-604	812	813	0.06	0.039	0.008	0.5	0.6	0.8	154000	13.3	6.03	0.12	12.43	1.42	14.06	0.17
MBS-604	813	814	0.07	0.039	0.009	0.5	0.3	1.7	178000	13.18	5.89	0.12	11.88	1.35	14.27	0.18
MBS-604	814	815	0.06	0.039	0.009	0.5	0.3	1.7	170000	13.38	6.02	0.12	11.7	1.35	14.62	0.18
MBS-604	815	816	0.07	0.044	0.01	0.5	0.5	1	198000	14.49	6.45	0.13	10.58	1.23	15.04	0.2
MBS-604	816	817	0.12	0.06	0.014	0.5	0.5	1	280000	17.41	7.81	0.15	6.16	0.78	14.55	0.23
MBS-604	817	818	0.14	0.06	0.017	0.5	0.3	1.7	332000	17.41	7.79	0.15	5.08	0.63	13.99	0.23
MBS-604	818	819	0.28	0.091	0.033	0.5	0.5	1	652000	18.07	8.22	0.16	5.2	0.66	14.62	0.23
MBS-604	819	820	0.15	0.073	0.023	0.5	0.5	1	450000	18.41	7.99	0.15	4.46	0.53	13.46	0.22
MBS-604	820	821	0.27	0.093	0.036	1	1.7	0.6	359000	18.82	8.35	0.15	5.48	0.66	12.23	0.22
MBS-604	821	822	0.17	0.076	0.027	0.5	0.8	0.6	534000	18.57	8.21	0.16	4.48	0.58	13.75	0.23
MBS-604	822	823	0.17	0.076	0.023	1	1	1	230000	19.57	9.26	0.17	4.42	0.57	13.66	0.28
MBS-604	823	824	0.24	0.092	0.033	1	0.9	1.1	333000	19.57	8.78	0.17	3.89	0.43	14.2	0.23
MBS-604	824	825	0.19	0.083	0.028	1	0.8	1.3	278000	19.57	8.71	0.17	3.76	0.42	14.13	0.23
MBS-604	825	826	0.17	0.083	0.027	0.5	0.6	0.8	542000	19.73	8.68	0.17	3.74	0.42	14.69	0.22
MBS-604	826	827	0.25	0.102	0.038	0.5	0.6	0.8	750000	19.9	8.74	0.17	3.61	0.43	13.7	0.22
MBS-604	827	828	0.23	0.1	0.036	0.5	0.6	0.8	724000	19.73	8.91	0.17	3.67	0.43	12.91	0.23
MBS-604	828	829	0.22	0.103	0.036	0.5	0.7	0.7	718000	19.48	8.92	0.17	3.65	0.4	12.97	0.25
MBS-604	829	830	0.26	0.102	0.037	0.5	0.6	0.8	732000	20.81	8.46	0.17	3.89	0.42	13.78	0.25
MBS-604	830	831	0.29	0.118	0.042	1	0.9	1.1	424000	22.47	8.96	0.18	3.99	0.43	13.43	0.25
MBS-604	831	832	0.37	0.16	0.058	0.5	0.8	0.6	1166000	24.38	9.71	0.19	3.99	0.4	11.74	0.23
MBS-604	832	833	0.25	0.145	0.043	0.5	0.6	0.8	856000	27.53	11.34	0.2	4.69	0.49	4.84	0.18
MBS-604	833	834	0.11	0.111	0.022	0.5	0.6	0.8	434000	28.19	11.31	0.2	4.8	0.5	4.6	0.2

Hole_ID	m From	m To	S (wt. %)	Ni (wt. %)	Cu (wt. %)	Pd (ppb)	Pt (ppb)	Pd/Pt	Cu/Pd	MgO (wt. %)	Fe_2O_3 (wt. %)	MnO (wt. %)	Al_2O_3 (wt. %)	Na_2O (wt. %)	CaO (wt. %)	TiO_2 (wt. %)
MBS-604	834	835	0.25	0.167	0.043	1	1.9	0.5	432000	26.78	10.84	0.19	4.14	0.4	4.41	0.2
MBS-604	835	836	0.55	0.271	0.084	3	7.2	0.4	281333	28.11	11.55	0.19	3.8	0.34	4.16	0.2
MBS-604	836	837	0.13	0.156	0.035	1	1.8	0.6	352000	28.6	11.12	0.2	4.02	0.46	4.72	0.22
MBS-604	837	838	0.04	0.077	0.017	1	1.2	0.8	172000	12.14	6.08	0.09	9.69	1.56	2.91	0.12
MBS-604	838	839	0.06	0.144	0.026	1	1.8	0.6	258000	26.86	10.78	0.18	3.91	0.51	4.24	0.22
MBS-604	839	840	0.14	0.153	0.032	1	1.8	0.6	323000	29.76	11.82	0.21	4.18	0.43	4.52	0.22
MBS-604	840	841	0.12	0.158	0.035	1	3.5	0.3	349000	28.94	11.19	0.19	3.91	0.38	4.17	0.22
MBS-604	841	842	0.16	0.148	0.032	1	3.3	0.3	315000	30.01	11.55	0.2	3.95	0.35	4.14	0.22
MBS-604	842	843	0.16	0.152	0.034	1	4.5	0.2	335000	27.94	10.77	0.19	3.68	0.34	3.81	0.2
MBS-604	843	844	0.14	0.142	0.029	1	2.4	0.4	287000	29.43	11.25	0.2	3.97	0.38	4.11	0.22
MBS-604	844	845	0.14	0.139	0.026	1	1.4	0.7	260000	29.43	11.19	0.2	3.74	0.32	3.51	0.2
MBS-604	845	846	0.11	0.136	0.029	1	1.9	0.5	292000	27.36	10.45	0.19	3.63	0.27	3.43	0.2
MBS-604	846	847	0.11	0.132	0.015	1	1.3	0.8	150000	27.36	11.01	0.22	3.85	0.18	3.01	0.22
MBS-604	847	848	0.01	0.056	0.004	1	0.7	1.4	43000	8.57	5.42	0.08	11.24	1.56	1.19	0.33
MBS-604	848	849	0.01	0.001	0.002	0.5	0.3	1.7	40000	0.1	0.64	0.01	12.72	2.52	0.41	0.01
MBS-604	849	850	0.06	0.049	0.024	0.5	0.9	0.6	478000	3.02	2.53	0.04	12.07	4.33	2.29	0.1
MBS-604	850	851	0.26	0.236	0.071	1	2.8	0.4	714000	28.52	11.69	0.21	4.02	0.35	4.24	0.22
MBS-604	851	852	0.17	0.146	0.031	1	1.7	0.6	309000	28.52	11.07	0.2	3.89	0.36	4.13	0.2
MBS-604	852	853	0.24	0.172	0.038	2	3.4	0.6	190000	29.93	11.78	0.21	3.89	0.35	4.18	0.22
MBS-604	853	854	0.22	0.161	0.035	1	6.2	0.2	347000	30.35	11.64	0.21	3.85	0.34	4.11	0.2
MBS-604	854	855	0.19	0.146	0.03	1	3.1	0.3	295000	29.35	11.44	0.21	3.82	0.34	3.88	0.2
MBS-604	855	856	0.13	0.126	0.021	1	2.1	0.5	213000	24.21	10.34	0.17	6.35	0.93	3.13	0.35
MBS-604	856	857	0.18	0.145	0.028	1	1.6	0.6	278000	30.01	11.41	0.2	3.8	0.34	3.69	0.2
MBS-604	857	858	0.17	0.145	0.026	1	1.2	0.8	264000	30.26	11.44	0.2	3.78	0.34	3.71	0.2
MBS-604	858	859	0.15	0.158	0.028	1	1.5	0.7	279000	31.67	12.07	0.22	3.99	0.35	3.88	0.22
MBS-604	859	860	0.22	0.193	0.044	2	2	1	218500	30.18	11.85	0.22	3.95	0.4	3.72	0.22
MBS-604	860	861	0.27	0.259	0.07	3	4.4	0.7	234333	24.87	11.05	0.18	6.54	1.13	3.74	0.23
MBS-604	861	862	1	0.474	0.145	5	7.7	0.6	290000	27.77	12.45	0.18	3.51	0.35	3.12	0.18
MBS-604	862	863	1	0.474	0.152	6	6.6	0.9	253333	28.36	12.72	0.19	3.67	0.38	3.16	0.18
MBS-604	863	864	0.41	0.25	0.066	2	4.2	0.5	329000	28.77	11.94	0.19	3.63	0.35	3.11	0.18
MBS-604	864	865	0.75	0.385	0.115	4	6.2	0.6	287500	28.6	12.37	0.19	3.5	0.32	2.98	0.18
MBS-604	865	866	0.84	0.428	0.12	5	7.8	0.6	239000	29.52	12.87	0.19	3.8	0.39	3.16	0.18
MBS-604	866	867	1.27	0.593	0.183	7	11	0.6	260714	28.11	12.97	0.18	3.34	0.3	2.95	0.18
MBS-604	867	868	1.29	0.597	0.181	7	10	0.7	258571	28.69	13.17	0.19	3.42	0.31	2.9	0.18
MBS-604	868	869	0.97	0.467	0.152	5	7.2	0.7	304000	27.19	12.18	0.18	3.46	0.35	2.92	0.17

Hole_ID	m From	m To	S (wt. %)	Ni (wt. %)	Cu (wt. %)	Pd (ppb)	Pt (ppb)	Pd/Pt	Cu/Pd	MgO (wt. %)	Fe_2O_3 (wt. %)	MnO (wt. %)	Al_2O_3 (wt. %)	Na_2O (wt. %)	CaO (wt. %)	TiO_2 (wt. %)
MBS-604	869	870	1.26	0.593	0.171	6	19.9	0.3	284167	28.27	12.92	0.19	3.57	0.35	3.04	0.18
MBS-604	870	871	1.2	0.581	0.181	7	16.2	0.4	257857	28.36	12.91	0.18	3.4	0.31	2.83	0.18
MBS-604	871	872	0.84	0.433	0.128	7	8.3	0.8	182143	28.6	12.54	0.19	3.74	0.4	3.08	0.22
MBS-604	872	873	1.1	0.538	0.172	7	16.9	0.4	245714	29.18	13.1	0.19	3.89	0.42	3.2	0.22
MBS-604	873	874	1.21	0.599	0.18	8	13.5	0.6	225000	29.02	13.17	0.19	3.7	0.39	3.12	0.22
MBS-604	874	875	0.93	0.474	0.144	6	9	0.7	240000	28.85	12.58	0.19	3.72	0.39	3.12	0.2
MBS-604	875	876	1.05	0.527	0.17	6	7.2	0.8	282500	29.68	13.1	0.19	3.87	0.42	3.23	0.22
MBS-604	876	877	1.41	0.74	0.206	8	13	0.6	257500	28.85	13.5	0.19	3.67	0.38	3.01	0.18
MBS-604	877	878	1.36	0.77	0.148	8	17.9	0.4	185000	26.03	13.32	0.17	4.5	0.36	2.43	0.42
MBS-604	878	879	1.5	0.8	0.182	11	24.6	0.4	165455	29.02	13.48	0.19	3.59	0.36	3.02	0.2
MBS-604	879	880	1.79	0.9	0.317	14	28.2	0.5	226429	28.27	13.65	0.18	3.55	0.36	2.99	0.18
MBS-604	880	881	1.9	1.01	0.229	14	29.7	0.5	163571	28.27	13.67	0.18	3.51	0.36	2.84	0.18
MBS-604	881	882	2.17	1.09	0.253	13	30.1	0.4	194615	28.85	14.3	0.18	3.65	0.42	2.95	0.2
MBS-604	882	883	2.59	1.39	0.292	19	38.7	0.5	153684	29.1	14.73	0.18	2.93	0.24	2.57	0.17
MBS-604	883	884	1.53	0.85	0.195	10	28.2	0.4	194500	28.44	13.07	0.18	3.23	0.31	2.76	0.18
MBS-604	884	885	1.38	0.73	0.208	25	82	0.3	83200	28.94	13	0.18	3.4	0.32	2.7	0.18
MBS-604	885	886	1.42	0.73	0.214	13	35.2	0.4	164615	29.27	13.24	0.18	3.04	0.39	2.87	0.18
MBS-604	886	887	2.78	1.52	0.331	22	49.1	0.4	150455	27.94	14.58	0.17	2.95	0.28	2.5	0.17
MBS-604	887	888	3.05	1.74	0.356	24	58.2	0.4	148333	28.11	15.58	0.17	2.78	0.24	2.39	0.17
MBS-604	888	889	1.98	1	0.317	16	38.6	0.4	198125	29.1	13.8	0.18	3.12	0.27	2.66	0.17
MBS-604	889	890	0.88	0.468	0.14	6	13.9	0.4	233333	29.68	12.22	0.18	3.23	0.27	2.8	0.17
MBS-604	890	891	1.22	0.67	0.208	10	28.6	0.3	208000	29.93	12.84	0.18	3.7	0.4	2.97	0.2
MBS-604	891	892	1.49	0.81	0.252	11	33.9	0.3	229091	28.02	12.71	0.17	3.33	0.35	2.76	0.18
MBS-604	892	893	0.71	0.439	0.102	8	38.1	0.2	126875	29.76	11.95	0.18	3.46	0.35	2.77	0.18
MBS-604	893	894	1.22	0.69	0.167	13	43.5	0.3	128462	28.36	12.34	0.17	3.72	0.43	2.91	0.18
MBS-604	894	895	1.45	0.8	0.218	11	26.4	0.4	198182	28.6	12.9	0.18	3.31	0.44	2.85	0.18
MBS-604	895	896	1.61	0.76	0.332	21	108	0.2	158095	28.44	11.81	0.17	3.51	0.36	2.81	0.17
MBS-604	896	897	2.38	1.24	0.303	23	81	0.3	131739	27.77	12.84	0.17	3.31	0.34	2.8	0.18
MBS-604	897	898	2.26	1.1	0.29	23	62.7	0.4	126087	28.69	13.07	0.18	3.55	0.38	2.94	0.18
MBS-604	898	899	2	1.03	0.23	22	51.3	0.4	104545	29.35	12.68	0.18	3.19	0.28	2.67	0.17
MBS-604	899	900	1.7	0.84	0.262	18	77.8	0.2	145556	28.44	11.95	0.17	3.23	0.32	2.67	0.17
MBS-604	900	901	2.23	1.06	0.368	22	81.1	0.3	167273	28.77	12.8	0.18	3	0.24	2.56	0.17
MBS-604	901	902	2.06	1	0.305	27	93.6	0.3	112963	28.94	12.7	0.18	3.02	0.26	2.62	0.17
MBS-604	902	903	1.95	0.97	0.255	26	113	0.2	98077	29.1	12.61	0.18	3.08	0.26	2.62	0.17
MBS-604	903	904	2.23	1.1	0.291	28	127	0.2	103929	29.27	13.1	0.18	3.1	0.26	2.6	0.17

Hole_ID	m From	m To	S (wt. %)	Ni (wt. %)	Cu (wt. %)	Pd (ppb)	Pt (ppb)	Pd/Pt	Cu/Pd	MgO (wt. %)	Fe_2O_3 (wt. %)	MnO (wt. %)	Al_2O_3 (wt. %)	Na_2O (wt. %)	CaO (wt. %)	TiO_2 (wt. %)
MBS-604	904	905	1.57	0.78	0.25	25	101	0.2	100000	29.35	12.11	0.18	3.21	0.28	2.67	0.18
MBS-604	905	906	0.76	0.423	0.13	13	46.9	0.3	100000	29.6	11.04	0.18	3.19	0.28	2.66	0.18
MBS-604	906	907	1.69	0.72	0.444	39	137	0.3	113846	29.93	12.21	0.18	3.48	0.32	2.8	0.18
MBS-604	907	908	1.18	0.574	0.282	36	95.5	0.4	78333	30.18	11.32	0.17	3.23	0.3	2.46	0.15
MBS-604	908	909	1.14	0.63	0.183	38	93.6	0.4	48158	28.19	11.21	0.17	3.91	0.44	2.62	0.2
MBS-604	909	910	0.2	0.211	0.062	52	65.7	0.8	11923	22.47	12.85	0.22	6.33	0.39	1.53	0.72
MBS-604	910	911	2.75	1.5	0.265	583	1000	0.6	4545	27.53	13.28	0.16	3.44	0.2	2.24	0.18
MBS-604	911	912	3.02	1.58	0.319	676	1000	0.7	4719	27.77	13.34	0.16	2.97	0.22	2.36	0.17
MBS-604	912	913	1.91	1.03	0.335	531	1000	0.5	6309	28.44	13.08	0.16	3.72	0.13	1.99	0.18
MBS-604	913	914	2.59	1.32	0.325	650	1000	0.7	5000	28.6	14.17	0.16	3.68	0.13	1.97	0.18
MBS-604	914	915	1.84	0.97	0.231	263	586	0.4	8783	31.34	13.02	0.17	3	0.24	2.35	0.17
MBS-604	915	916	2.19	1.13	0.282	105	271	0.4	26857	28.77	12.52	0.17	3.06	0.27	2.57	0.17
MBS-604	916	917	2.15	1.16	0.238	63	176	0.4	37778	27.61	12.24	0.17	3.23	0.34	2.64	0.17
MBS-604	917	918	1.38	0.79	0.102	26	104	0.3	39231	28.6	11.44	0.17	3.67	0.42	2.95	0.17
MBS-604	918	919	0.95	0.523	0.148	17	31.5	0.5	87059	30.35	11.32	0.18	3.63	0.38	2.94	0.17
MBS-604	919	920	2.34	0.96	0.635	56	43.1	1.3	113393	28.69	12.61	0.17	2.99	0.26	2.52	0.15
MBS-604	920	921	1.47	0.6	0.631	66	78.9	0.8	95606	30.35	12.22	0.18	3.12	0.26	2.59	0.17
MBS-604	921	922	2.47	1.06	0.716	68	104	0.7	105294	28.6	13.04	0.17	2.93	0.28	2.38	0.15
MBS-604	922	923	3.06	1.55	0.279	41	97.8	0.4	68049	28.85	13.45	0.17	2.7	0.22	2.38	0.13
MBS-604	923	924	2.56	1.23	0.29	39	82.4	0.5	74359	29.35	12.92	0.17	2.78	0.22	2.49	0.15
MBS-604	924	925	2.03	1.07	0.22	45	234	0.2	48889	29.18	12.25	0.17	3	0.26	2.56	0.15
MBS-604	925	926	1.39	0.75	0.179	37	104	0.4	48378	28.36	11.17	0.17	2.78	0.2	2.42	0.15
MBS-604	926	927	0.32	0.239	0.052	4	14.8	0.3	129250	29.35	10.01	0.17	3.38	0.34	2.73	0.17
MBS-604	927	928	0.88	0.471	0.244	34	143	0.2	71765	29.52	10.78	0.17	3.44	0.36	2.8	0.15
MBS-604	928	929	1.02	0.365	0.599	65	187	0.3	92154	28.36	11.18	0.16	3.12	0.3	2.49	0.15
MBS-604	929	930	0.17	0.17	0.032	14	39.8	0.4	22714	29.85	10.17	0.17	3.14	0.26	2.69	0.15
MBS-604	930	931	0.06	0.132	0.024	1	2.5	0.4	239000	27.53	9.55	0.16	4.16	0.61	3.06	0.2
MBS-604	931	932	0.46	0.305	0.149	26	78.9	0.3	57308	26.12	11.57	0.17	4.14	0.62	3.15	0.25
MBS-604	932	933	1.2	0.7	0.179	70	209	0.3	25500	29.1	11.41	0.17	2.91	0.23	2.48	0.15
MBS-604	933	934	1.72	0.92	0.234	96	274	0.4	24375	28.94	11.97	0.16	3.02	0.27	2.52	0.17
MBS-604	934	935	1.78	0.99	0.231	117	382	0.3	19744	28.27	11.8	0.16	2.87	0.26	2.41	0.15
MBS-604	935	936	1.67	0.9	0.233	111	365	0.3	20991	29.1	12.02	0.17	3.02	0.26	2.55	0.17
MBS-604	936	937	1.66	0.86	0.258	95	305	0.3	27158	28.69	11.78	0.16	2.89	0.23	2.43	0.17
MBS-604	937	938	1.05	0.565	0.159	55	165	0.3	28909	29.6	11.25	0.17	3.06	0.26	2.62	0.17
MBS-604	938	939	2.19	1.14	0.317	111	324	0.3	28559	28.6	12.81	0.17	2.91	0.24	2.46	0.17

Hole_ID	m From	m To	S (wt. %)	Ni (wt. %)	Cu (wt. %)	Pd (ppb)	Pt (ppb)	Pd/Pt	Cu/Pd	MgO (wt. %)	Fe_2O_3 (wt. %)	MnO (wt. %)	Al_2O_3 (wt. %)	Na_2O (wt. %)	CaO (wt. %)	TiO_2 (wt. %)
MBS-604	939	940	0.33	0.242	0.055	23	53.8	0.4	23913	29.6	10.24	0.17	3.27	0.32	2.71	0.18
MBS-604	940	941	0.98	0.544	0.147	67	154	0.4	21866	29.18	11.02	0.17	3.12	0.28	2.62	0.17
MBS-604	941	942	1.52	0.82	0.213	84	163	0.5	25357	29.6	12.02	0.17	3.08	0.27	2.62	0.18
MBS-604	942	943	2.1	1.1	0.297	104	240	0.4	28558	29.1	12.68	0.16	2.78	0.24	2.39	0.15
MBS-604	943	944	1.65	0.88	0.25	99	190	0.5	25253	29.43	12.01	0.16	2.89	0.26	2.42	0.17
MBS-604	944	945	0.97	0.555	0.158	51	120	0.4	30980	30.1	11.48	0.17	2.87	0.26	2.49	0.17
MBS-604	945	946	0.75	0.443	0.118	31	79.7	0.4	38065	29.93	10.91	0.17	3	0.27	2.56	0.18
MBS-604	946	947	0.98	0.546	0.146	53	107	0.5	27547	29.93	11.35	0.17	3.14	0.31	2.64	0.2
MBS-604	947	948	1.53	0.83	0.211	99	196	0.5	21313	31.01	12.78	0.17	2.57	0.2	2.27	0.15
MBS-604	948	949	1.98	1.02	0.314	136	251	0.5	23088	30.1	12.97	0.17	2.55	0.2	2.2	0.15
MBS-604	949	950	2.88	1.59	0.364	197	273	0.7	18477	29.52	13.74	0.16	2.59	0.24	2.28	0.15
MBS-604	950	951	2.29	1.25	0.305	157	296	0.5	19427	31.34	13.57	0.17	2.63	0.23	2.32	0.15
MBS-604	951	952	2.13	1.16	0.309	145	282	0.5	21310	30.18	13.05	0.16	2.55	0.22	2.25	0.15
MBS-604	952	953	1.93	1.08	0.284	143	313	0.5	19860	30.18	12.81	0.16	2.74	0.27	2.29	0.15
MBS-604	953	954	1.24	0.72	0.185	90	184	0.5	20500	31.01	12	0.17	2.65	0.2	2.29	0.15
MBS-604	954	955	0.59	0.382	0.089	39	88.3	0.4	22923	28.94	10.31	0.16	3.33	0.35	2.71	0.18
MBS-604	955	956	1.34	0.77	0.179	59	120	0.5	30254	28.69	11.35	0.16	3.21	0.31	2.59	0.17
MBS-604	956	957	1.28	0.81	0.17	95	184	0.5	17895	29.68	11.48	0.16	2.87	0.27	2.43	0.17
MBS-604	957	958	0.75	0.5	0.247	100	181	0.6	24700	34.32	12.72	0.16	2.21	0.2	1.82	0.12
MBS-604	958	959	1.79	1.12	0.636	195	568	0.3	32615	31.42	14.44	0.15	2.23	0.2	1.57	0.1
MBS-604	959	960	0.48	0.437	0.159	88	202	0.4	18011	33.5	12.27	0.16	2.4	0.23	1.9	0.13
MBS-604	960	961	0.19	0.253	0.052	57	74.5	0.8	9053	30.59	10.42	0.15	3.08	0.39	1.83	0.12
MBS-604	961	962	0.18	0.254	0.059	68	72.6	0.9	8632	31.51	11.01	0.15	2.25	0.26	1.85	0.13
MBS-604	962	963	0.33	0.35	0.111	68	101	0.7	16250	33.99	11.91	0.16	2.29	0.19	1.74	0.12
MBS-604	963	964	0.44	0.375	0.174	65	104	0.6	26769	32.33	11.84	0.16	2.27	0.2	1.71	0.12
MBS-604	964	965	0.49	0.451	0.149	71	141	0.5	20986	33.33	11.95	0.16	2.14	0.18	1.67	0.12
MBS-604	965	966	0.33	0.346	0.141	67	128	0.5	20970	32.17	11.39	0.15	2.48	0.22	1.67	0.12
MBS-604	966	967	0.31	0.359	0.075	45	84.4	0.5	16733	34.16	12	0.16	1.98	0.2	1.86	0.1
MBS-604	967	968	1.45	0.9	0.546	116	286	0.4	47069	30.84	12.92	0.14	2.12	0.23	1.6	0.1
MBS-604	968	969	2.06	0.83	0.815	96	227	0.4	84896	33.83	14.73	0.15	2.02	0.23	1.46	0.1
MBS-604	969	970	1.14	0.71	0.615	129	215	0.6	47674	35.32	13.78	0.16	1.83	0.22	1.54	0.1
MBS-604	970	971	0.96	0.71	0.166	58	128	0.5	28621	37.81	14.07	0.17	1.76	0.16	1.41	0.1
MBS-604	971	972	1.04	0.74	0.179	83	144	0.6	21506	39.3	14.8	0.18	1.81	0.18	1.55	0.1
MBS-604	972	973	0.25	0.36	0.044	16	65.7	0.2	27188	39.8	13.68	0.18	1.91	0.2	1.6	0.12
MBS-604	973	974	0.31	0.371	0.051	18	71.4	0.3	28389	38.3	13.35	0.17	2.02	0.2	1.72	0.12

Hole_ID	m From	m To	S (wt. %)	Ni (wt. %)	Cu (wt. %)	Pd (ppb)	Pt (ppb)	Pd/Pt	Cu/Pd	MgO (wt. %)	Fe_2O_3 (wt. %)	MnO (wt. %)	Al_2O_3 (wt. %)	Na_2O (wt. %)	CaO (wt. %)	TiO_2 (wt. %)
MBS-604	974	975	0.11	0.238	0.019	9	55.9	0.2	21111	32	10.74	0.14	1.72	0.19	1.41	0.1
MBS-604	975	976	0.13	0.281	0.022	10	54.1	0.2	22100	37.81	12.71	0.17	2.12	0.24	1.72	0.12
MBS-604	976	977	0.14	0.3	0.025	11	62.8	0.2	22636	39.47	13.14	0.17	2.1	0.24	1.65	0.12
MBS-604	977	978	0.12	0.296	0.021	11	59.6	0.2	19000	38.8	13.11	0.17	1.51	0.2	1.51	0.12
MBS-604	978	979	0.15	0.328	0.028	15	75.4	0.2	18333	40.29	13.48	0.17	1.8	0.19	1.41	0.1
MBS-604	979	980	0.13	0.325	0.023	13	74.4	0.2	17308	40.79	13.63	0.17	1.68	0.18	1.29	0.1
MBS-604	980	981	0.1	0.321	0.017	13	73.7	0.2	13231	41.12	13.8	0.17	1.28	0.18	1.22	0.1
MBS-604	981	982	0.09	0.315	0.016	13	69.3	0.2	12154	41.46	14.04	0.18	0.98	0.18	1.25	0.1
MBS-604	982	983	0.1	0.309	0.018	14	69.8	0.2	12643	40.79	13.74	0.17	0.79	0.19	1.36	0.1
MBS-604	983	984	0.1	0.319	0.017	18	78.2	0.2	9389	41.62	13.95	0.17	1.64	0.18	1.18	0.1
MBS-604	984	985	0.09	0.317	0.015	19	71.7	0.3	8105	41.12	13.85	0.17	0.79	0.18	1.19	0.1
MBS-604	985	986	0.09	0.313	0.015	18	67.4	0.3	8556	41.95	14.01	0.18	0.94	0.18	1.23	0.1
MBS-604	986	987	0.08	0.308	0.014	18	67.4	0.3	7889	40.29	13.68	0.17	0.72	0.18	1.18	0.1
MBS-604	987	988	0.09	0.307	0.016	19	66.2	0.3	8526	40.79	13.61	0.17	1	0.2	1.4	0.12
MBS-604	988	989	0.08	0.298	0.014	18	56.6	0.3	7778	39.96	13.21	0.17	1.34	0.19	1.34	0.1
MBS-604	989	990	0.07	0.302	0.012	16	49.5	0.3	7250	41.46	13.67	0.17	1.74	0.19	1.33	0.1
MBS-604	990	991	0.08	0.303	0.013	19	46.3	0.4	6789	40.63	13.37	0.17	1.53	0.19	1.3	0.1
MBS-604	991	992	0.12	0.341	0.019	20	44.9	0.4	9650	40.96	13.48	0.17	1.59	0.18	1.18	0.1
MBS-604	992	993	0.07	0.32	0.011	18	33.5	0.5	6222	41.46	13.55	0.17	1.51	0.18	1.08	0.08
MBS-604	993	994	0.07	0.299	0.012	19	33.9	0.6	6526	38.3	12.52	0.16	0.94	0.16	1.02	0.08
MBS-604	994	995	0.07	0.301	0.013	20	32.2	0.6	6400	38.47	13.02	0.16	1.13	0.2	1.36	0.1
MBS-604	995	996	0.11	0.306	0.022	22	31.7	0.7	9864	40.13	12.92	0.16	1.49	0.2	1.27	0.1
MBS-604	996	997	0.2	0.346	0.034	30	44.5	0.7	11200	39.63	12.81	0.17	1	0.18	1.27	0.1
MBS-604	997	998	0.2	0.347	0.033	28	46.2	0.6	11643	39.8	12.75	0.17	1.55	0.19	1.34	0.1
MBS-604	998	999	0.13	0.298	0.023	12	20.8	0.6	19250	39.63	12.91	0.17	1.62	0.22	1.47	0.12
MBS-604	999	1000	0.1	0.288	0.016	12	21	0.6	13500	38.47	12.38	0.17	0.89	0.2	1.48	0.12
MBS-604	1000	1001	0.09	0.294	0.015	11	19.6	0.6	13818	39.47	12.6	0.17	1.51	0.19	1.36	0.1
MBS-604	1001	1002	0.08	0.308	0.013	9	19.4	0.5	14444	39.3	12.62	0.16	0.77	0.19	1.22	0.1
MBS-604	1002	1003	0.09	0.312	0.015	9	22	0.4	17000	39.96	12.8	0.16	0.76	0.19	1.22	0.1
MBS-604	1003	1004	0.1	0.313	0.017	10	21.5	0.5	16700	41.29	13.02	0.17	1.36	0.19	1.23	0.1
MBS-604	1004	1005	0.29	0.443	0.074	32	71.3	0.4	23031	39.8	12.9	0.16	1.27	0.16	1.08	0.08
MBS-604	1005	1006	0.09	0.267	0.023	12	23.3	0.5	18833	36.15	11.68	0.15	1.76	0.26	1.53	0.12
MBS-604	1006	1007	0.21	0.372	0.038	22	56.1	0.4	17182	39.13	12.4	0.16	1.51	0.23	1.41	0.1
MBS-604	1007	1008	0.47	0.537	0.07	45	117	0.4	15533	40.79	13.38	0.16	1.19	0.15	1.04	0.08
MBS-604	1008	1009	0.17	0.326	0.039	16	47.6	0.3	24625	33.16	10.84	0.14	3.19	0.59	1.22	0.12

Hole_ID	m From	m To	S (wt. %)	Ni (wt. %)	Cu (wt. %)	Pd (ppb)	Pt (ppb)	Pd/Pt	Cu/Pd	MgO (wt. %)	Fe_2O_3 (wt. %)	MnO (wt. %)	Al_2O_3 (wt. %)	Na_2O (wt. %)	CaO (wt. %)	TiO_2 (wt. %)
MBS-604	1009	1010	0.14	0.367	0.022	11	47.4	0.2	20182	42.62	13.55	0.17	1.1	0.12	0.87	0.07
MBS-604	1010	1011	0.16	0.389	0.027	15	64.8	0.2	17933	43.44	13.83	0.17	1.15	0.12	0.84	0.07
MBS-604	1011	1012	0.18	0.393	0.029	21	93.8	0.2	14000	43.78	14.05	0.17	1.17	0.12	0.83	0.07
MBS-604	1012	1013	0.18	0.38	0.03	23	103	0.2	12870	42.62	13.64	0.16	1.21	0.13	0.87	0.08
MBS-604	1013	1014	0.17	0.378	0.03	23	98.3	0.2	13130	42.28	13.47	0.16	1.23	0.15	0.97	0.08
MBS-604	1014	1015	0.16	0.37	0.026	27	111	0.2	9704	42.45	13.57	0.17	1.25	0.15	0.99	0.08
MBS-604	1015	1016	0.2	0.39	0.05	47	163	0.3	10574	40.96	13.28	0.16	1.38	0.15	1.01	0.08
MBS-604	1016	1017	0.59	0.57	0.084	87	212	0.4	9701	39.63	13.17	0.16	1.44	0.15	1.18	0.1
MBS-604	1017	1018	0.28	0.369	0.048	41	91.1	0.5	11683	38.14	12.32	0.16	1.57	0.18	1.4	0.1
MBS-604	1018	1019	1.01	0.72	0.133	160	289	0.6	8281	36.65	12.74	0.16	1.68	0.16	1.5	0.1
MBS-604	1019	1020	1.26	0.93	0.185	213	373	0.6	8685	33.5	12.2	0.16	1.97	0.19	1.79	0.12
MBS-604	1020	1021	1.53	0.94	0.206	258	448	0.6	7984	34.66	12.78	0.16	1.87	0.16	1.68	0.12
MBS-604	1021	1022	1	0.77	0.146	146	251	0.6	10000	36.65	12.57	0.16	1.64	0.18	1.51	0.1
MBS-604	1022	1023	0.58	0.554	0.102	74	228	0.3	13784	40.13	13.32	0.16	0.89	0.18	1.15	0.08
MBS-604	1023	1024	0.34	0.464	0.053	117	378	0.3	4496	44.11	14.44	0.17	1.25	0.15	0.85	0.08
MBS-604	1024	1025	0.16	0.375	0.029	105	262	0.4	2790	42.62	13.83	0.16	0.98	0.13	0.85	0.08
MBS-604	1025	1026	0.17	0.389	0.03	121	142	0.9	2471	43.94	13.94	0.17	1.15	0.15	0.87	0.08
MBS-604	1026	1027	0.17	0.372	0.028	272	114	2.4	1022	42.62	13.95	0.16	1.08	0.12	0.83	0.07
MBS-604	1027	1028	0.2	0.405	0.03	285	126	2.3	1060	46.1	14.94	0.17	1.49	0.15	0.85	0.08
MBS-604	1028	1029	0.07	0.325	0.01	121	50.6	2.4	843	44.27	14.28	0.17	1.34	0.13	0.83	0.08
MBS-604	1029	1030	0.06	0.324	0.01	71	44.6	1.6	1380	44.61	14.3	0.17	1.21	0.16	0.85	0.07
MBS-604	1030	1031	0.11	0.34	0.016	117	145	0.8	1333	43.78	13.88	0.16	1.17	0.13	0.8	0.07
MBS-604	1031	1032	0.04	0.315	0.006	113	104	1.1	513	43.61	14.07	0.17	1.21	0.13	0.84	0.07
MBS-604	1032	1033	0.09	0.353	0.013	135	120	1.1	993	44.77	14.37	0.17	1.32	0.15	0.81	0.07
MBS-604	1033	1034	0.04	0.316	0.006	124	119	1	484	43.28	13.91	0.16	1.25	0.15	0.81	0.07
MBS-604	1034	1035	0.03	0.317	0.005	163	135	1.2	288	44.27	14.24	0.17	1.28	0.13	0.83	0.07
MBS-604	1035	1036	0.03	0.311	0.003	205	144	1.4	156	44.11	14.11	0.16	1.3	0.15	0.81	0.07
MBS-604	1036	1037	0.02	0.321	0.003	264	150	1.8	95	45.6	14.65	0.17	1.21	0.15	0.84	0.07
MBS-604	1037	1038	0.01	0.315	0.002	361	185	2	55	45.1	14.21	0.17	1.06	0.15	0.85	0.07
MBS-604	1038	1039	0.01	0.319	0.002	149	76.9	1.9	107	45.43	14.44	0.17	1.19	0.15	0.84	0.07
MBS-604	1039	1040	0.01	0.317	0.002	219	166	1.3	82	45.27	14.3	0.17	1.27	0.13	0.84	0.07
MBS-604	1040	1041	0.01	0.288	0.002	40	132	0.3	400	37.81	12.37	0.14	2.68	0.44	0.8	0.08
MBS-604	1041	1042	0.02	0.33	0.002	30	33.2	0.9	633	42.45	13.4	0.16	1.72	0.27	0.81	0.07
MBS-604	1042	1043	0.03	0.338	0.005	29	27.8	1	1552	44.94	13.85	0.17	1.1	0.16	0.84	0.07
MBS-604	1043	1044	0.11	0.366	0.017	191	87.3	2.2	911	43.11	13.67	0.16	1.08	0.13	0.77	0.07

Hole_ID	m From	m To	S (wt. %)	Ni (wt. %)	Cu (wt. %)	Pd (ppb)	Pt (ppb)	Pd/Pt	Cu/Pd	MgO (wt. %)	Fe_2O_3 (wt. %)	MnO (wt. %)	Al_2O_3 (wt. %)	Na_2O (wt. %)	CaO (wt. %)	TiO_2 (wt. %)
MBS-604	1044	1045	0.01	0.318	0.002	197	62.5	3.2	112	45.6	14.13	0.17	0.53	0.18	0.8	0.07
MBS-604	1045	1046	0.01	0.335	0.002	190	136	1.4	121	48.25	14.8	0.17	1.11	0.13	0.84	0.08
MBS-604	1046	1047	0.01	0.328	0.002	208	154	1.4	111	46.76	14.58	0.17	0.93	0.15	0.84	0.08
MBS-604	1047	1048	0.01	0.306	0.002	363	324	1.1	63	44.11	13.71	0.16	1.34	0.09	0.76	0.07
MBS-604	1048	1049	0.02	0.331	0.002	188	149	1.3	128	46.26	14.3	0.17	0.85	0.12	0.84	0.07
MBS-604	1049	1050	0.01	0.314	0.002	167	122	1.4	138	42.95	13.45	0.16	0.85	0.13	0.8	0.07
MBS-604	1050	1051	0.02	0.318	0.002	144	114	1.3	153	46.6	13.93	0.17	1.15	0.13	0.83	0.07
MBS-604	1051	1052	0.03	0.318	0.004	146	106	1.4	288	44.61	13.88	0.16	1.06	0.13	0.8	0.07
MBS-604	1052	1053	0.02	0.307	0.002	163	109	1.5	135	44.44	13.68	0.16	1.1	0.13	0.78	0.07
MBS-604	1053	1054	0.01	0.305	0.002	151	95.5	1.6	146	44.61	13.68	0.16	1.28	0.13	0.78	0.07
MBS-604	1054	1055	0.01	0.294	0.002	157	110	1.4	134	43.28	13.42	0.16	1.25	0.12	0.74	0.07
MBS-604	1055	1056	0.02	0.302	0.002	154	101	1.5	149	43.94	13.57	0.16	0.87	0.13	0.76	0.07
MBS-604	1056	1057	0.02	0.302	0.003	134	117	1.1	187	43.28	13.78	0.16	1.34	0.13	0.74	0.07
MBS-604	1057	1058	0.02	0.305	0.002	159	115	1.4	145	45.1	14.1	0.17	1.23	0.13	0.76	0.07
MBS-604	1058	1059	0.02	0.298	0.002	148	111	1.3	155	44.11	13.52	0.16	1.13	0.12	0.74	0.07
MBS-604	1059	1060	0.11	0.343	0.016	293	206	1.4	556	41.12	12.77	0.15	1.06	0.11	0.71	0.07
MBS-604	1060	1061	0.06	0.329	0.01	286	215	1.3	353	42.28	13.11	0.16	1.19	0.11	0.73	0.07
MBS-604	1061	1062	0.02	0.302	0.002	156	129	1.2	141	42.62	13.02	0.16	1.08	0.12	0.74	0.07
MBS-604	1062	1063	0.02	0.294	0.002	145	112	1.3	152	42.12	12.82	0.15	1.11	0.12	0.74	0.07
MBS-604	1063	1064	0.01	0.307	0.002	162	132	1.2	105	41.95	12.9	0.15	1.11	0.11	0.7	0.07
MBS-604	1064	1065	0.03	0.311	0.003	53	77.2	0.7	509	43.28	13.44	0.16	0.96	0.13	0.77	0.07
MBS-604	1065	1066	0.02	0.311	0.003	136	33.5	4.1	199	44.11	13.27	0.16	1.08	0.12	0.74	0.07
MBS-604	1066	1067	0.03	0.305	0.004	131	63.9	2.1	305	43.28	13.31	0.16	1.02	0.13	0.76	0.07
MBS-604	1067	1068	0.03	0.295	0.003	609	175	3.5	56	43.28	13.34	0.16	1.02	0.12	0.73	0.07
MBS-604	1068	1069	0.04	0.3	0.005	622	186	3.3	87	42.95	13.28	0.16	0.96	0.13	0.74	0.07
MBS-604	1069	1070	0.03	0.238	0.004	1000	297	3.4	35	39.8	11.94	0.15	1.51	0.13	1.08	0.08
MBS-604	1070	1071	0.07	0.181	0.01	399	216	1.8	253	34.16	10.25	0.15	2.42	0.16	1.64	0.13
MBS-604	1071	1072	0.01	0.244	0.001	257	198	1.3	35	39.8	12.25	0.15	1.44	0.09	0.9	0.08
MBS-604	1072	1072.8	0.01	0.284	0.001	120	90.9	1.3	58	43.11	13.21	0.16	1.02	0.13	0.73	0.07
MBS-605	853	854	0.05	0.028	0.005	0.5	0.3	1.7	96000	9.1	4.17	0.08	9.67	1.44	9.99	0.12
MBS-605	854	855	0.06	0.038	0.009	0.5	0.3	1.7	182000	12.32	5.03	0.1	10.88	1.28	13.67	0.15
MBS-605	855	856	0.06	0.04	0.01	0.5	0.3	1.7	202000	13.38	5.42	0.11	10.2	1.21	13.8	0.15
MBS-605	856	857	0.07	0.044	0.011	0.5	0.3	1.7	224000	14.99	6.19	0.12	8.99	1.04	13.92	0.17
MBS-605	857	858	0.09	0.053	0.014	0.5	0.3	1.7	272000	16.58	6.86	0.13	5.29	0.66	13.67	0.22
MBS-605	858	859	0.11	0.06	0.017	0.5	0.3	1.7	338000	17.08	7.23	0.14	4.8	0.77	13.67	0.22

Hole_ID	m From	m To	S (wt. %)	Ni (wt. %)	Cu (wt. %)	Pd (ppb)	Pt (ppb)	Pd/Pt	Cu/Pd	MgO (wt. %)	Fe_2O_3 (wt. %)	MnO (wt. %)	Al_2O_3 (wt. %)	Na_2O (wt. %)	CaO (wt. %)	TiO_2 (wt. %)
MBS-605	859	860	0.11	0.06	0.017	0.5	0.3	1.7	338000	18.32	7.73	0.15	4.14	0.5	13.84	0.23
MBS-605	860	861	0.14	0.068	0.019	0.5	0.3	1.7	384000	18.32	7.91	0.15	4.53	0.63	14.06	0.23
MBS-605	861	862	0.14	0.062	0.021	0.5	0.5	1	416000	15.11	6.71	0.12	6.39	1.43	11.35	0.18
MBS-605	862	863	0.15	0.073	0.023	0.5	0.5	1	468000	19.32	8.03	0.15	3.31	0.35	13.36	0.2
MBS-605	863	864	0.21	0.084	0.032	1	0.8	1.3	319000	18.57	7.86	0.15	3.23	0.35	13.54	0.2
MBS-605	864	865	0.17	0.074	0.026	1	0.8	1.3	258000	19.32	8.02	0.16	3.19	0.34	13.42	0.2
MBS-605	865	866	0.19	0.081	0.03	0.5	0.9	0.6	596000	19.48	8.13	0.16	3.21	0.35	13.59	0.2
MBS-605	866	867	0.18	0.073	0.026	0.5	0.8	0.6	520000	16.47	7.08	0.14	4.5	0.88	11.7	0.18
MBS-605	867	868	0.19	0.078	0.029	1	1.7	0.6	290000	18.49	7.78	0.15	3.46	0.49	13.29	0.18
MBS-605	868	869	0.15	0.07	0.023	1	1.3	0.8	227000	19.4	7.96	0.16	3.23	0.36	13.91	0.2
MBS-605	869	870	0.31	0.113	0.049	1	1.3	0.8	485000	19.82	8.38	0.16	3.19	0.34	13.47	0.2
MBS-605	870	871	0.23	0.102	0.038	0.5	0.5	1	758000	20.4	8.54	0.16	3.31	0.36	12.97	0.2
MBS-605	871	872	0.2	0.101	0.036	0.5	0.3	1.7	718000	20.4	8.56	0.16	3.31	0.36	12.68	0.2
MBS-605	872	873	0.25	0.118	0.044	1	0.6	1.7	436000	19.9	8.41	0.15	3.12	0.35	10.27	0.18
MBS-605	873	874	0.26	0.138	0.046	1	0.9	1.1	464000	25.2	10.75	0.17	3.72	0.42	4.09	0.18
MBS-605	874	875	0.16	0.114	0.031	1	0.7	1.4	310000	25.12	10.64	0.17	3.7	0.44	4.02	0.2
MBS-605	875	876	0.62	0.263	0.089	2	2.2	0.9	444000	26.86	11.51	0.18	3.27	0.34	3.64	0.2
MBS-605	876	877	1.19	0.426	0.207	4	5.2	0.8	517500	26.86	12.12	0.18	3.04	0.27	3.37	0.18
MBS-605	877	878	0.66	0.28	0.1	2	3.1	0.6	499500	27.28	11.47	0.18	3.08	0.28	3.4	0.18
MBS-605	878	879	0.45	0.213	0.07	2	2.4	0.8	349500	26.37	10.68	0.17	2.87	0.24	3.27	0.17
MBS-605	879	880	0.14	0.111	0.021	1	1.3	0.8	207000	26.28	10.31	0.17	2.95	0.28	3.32	0.18
MBS-605	880	881	0.15	0.118	0.022	1	1.2	0.8	224000	27.19	10.41	0.17	3	0.28	3.33	0.18
MBS-605	881	882	0.17	0.132	0.025	1	1.8	0.6	253000	26.37	10.72	0.18	3.06	0.28	3.34	0.17
MBS-605	882	883	0.38	0.214	0.058	1	1.1	0.9	577000	27.61	11.51	0.19	3.23	0.3	3.37	0.18
MBS-605	883	884	0.25	0.158	0.037	2	4.8	0.4	184500	24.29	9.97	0.17	2.76	0.24	2.85	0.17
MBS-605	884	885	0.2	0.148	0.03	4	8.3	0.5	74000	27.36	11.11	0.19	3.16	0.28	3.16	0.18
MBS-605	885	886	0.19	0.139	0.032	3	6.5	0.5	107667	26.45	10.95	0.18	3.36	0.34	3.51	0.18
MBS-605	886	887	0.22	0.149	0.033	2	7.1	0.3	166000	25.95	10.64	0.18	2.93	0.26	2.98	0.17
MBS-605	887	888	0.19	0.138	0.028	1	1.9	0.5	280000	26.03	10.64	0.18	3	0.27	3.04	0.17
MBS-605	888	889	0.19	0.151	0.034	1	1.8	0.6	343000	25.95	10.57	0.18	3.06	0.3	3.29	0.17
MBS-605	889	890	0.59	0.304	0.093	3	5.6	0.5	311333	26.12	11.12	0.18	2.93	0.26	2.99	0.17
MBS-605	890	891	0.35	0.18	0.085	2	4.9	0.4	423500	25.62	10.45	0.17	2.76	0.22	2.88	0.15
MBS-605	891	892	0.18	0.142	0.028	1	5.5	0.2	284000	26.53	10.44	0.18	2.91	0.24	3.08	0.17
MBS-605	892	893	0.18	0.14	0.028	1	4.7	0.2	278000	26.2	10.34	0.17	2.89	0.24	3.02	0.17
MBS-605	893	894	0.23	0.156	0.036	2	12.9	0.2	178000	26.2	10.47	0.17	2.91	0.26	2.91	0.17

Hole_ID	m From	m To	S (wt. %)	Ni (wt. %)	Cu (wt. %)	Pd (ppb)	Pt (ppb)	Pd/Pt	Cu/Pd	MgO (wt. %)	Fe_2O_3 (wt. %)	MnO (wt. %)	Al_2O_3 (wt. %)	Na_2O (wt. %)	CaO (wt. %)	TiO_2 (wt. %)
MBS-605	894	895	0.25	0.165	0.039	3	15.2	0.2	130667	26.12	10.44	0.17	2.87	0.24	2.81	0.15
MBS-605	895	896	0.16	0.149	0.032	2	5.8	0.3	161000	25.87	10.22	0.17	3.04	0.32	2.74	0.17
MBS-605	896	897	0.14	0.138	0.028	1	4.3	0.2	282000	26.03	10.12	0.17	2.89	0.27	2.63	0.17
MBS-605	897	898	0.14	0.135	0.027	1	2.2	0.5	266000	26.53	10.27	0.17	3.04	0.31	2.63	0.17
MBS-605	898	899	0.18	0.154	0.033	1	2.4	0.4	331000	26.86	10.38	0.17	3	0.28	2.69	0.17
MBS-605	899	900	0.17	0.154	0.033	1	2	0.5	330000	26.95	10.35	0.17	2.95	0.26	2.64	0.17
MBS-605	900	901	0.17	0.146	0.029	1	1.8	0.6	294000	26.45	9.97	0.17	2.93	0.26	2.6	0.17
MBS-605	901	902	0.25	0.18	0.042	1	2	0.5	419000	26.78	10.12	0.17	2.99	0.26	2.63	0.17
MBS-605	902	903	0.27	0.188	0.045	1	1.6	0.6	447000	26.95	10.25	0.17	3	0.27	2.67	0.17
MBS-605	903	904	0.36	0.223	0.059	2	2.8	0.7	293500	26.37	10.19	0.17	2.85	0.24	2.52	0.15
MBS-605	904	905	0.25	0.184	0.041	2	2.5	0.8	204500	26.86	10.14	0.17	2.99	0.27	2.63	0.17
MBS-605	905	906	0.39	0.24	0.067	2	4.1	0.5	333500	26.86	10.37	0.17	2.87	0.26	2.55	0.17
MBS-605	906	907	0.72	0.35	0.178	5	9.2	0.5	356000	27.03	10.97	0.17	2.93	0.26	2.56	0.17
MBS-605	907	908	1.23	0.589	0.155	9	14.4	0.6	172222	25.54	11.12	0.16	2.74	0.23	2.41	0.15
MBS-605	908	909	1.2	0.591	0.151	10	19.9	0.5	151000	25.7	11.27	0.16	2.95	0.28	2.52	0.17
MBS-605	909	910	1.37	0.69	0.212	12	25.1	0.5	176667	25.37	11.48	0.16	2.8	0.26	2.43	0.17
MBS-605	910	911	1.41	0.67	0.247	11	26.6	0.4	224545	25.79	11.68	0.16	2.91	0.27	2.48	0.15
MBS-605	911	912	1.55	0.79	0.165	10	21.1	0.5	164500	26.2	12	0.17	2.95	0.27	2.52	0.17
MBS-605	912	913	1.25	0.581	0.157	9	21.3	0.4	174444	27.11	11.91	0.17	3.02	0.27	2.62	0.17
MBS-605	913	914	1.18	0.549	0.15	9	22.7	0.4	166667	26.7	11.95	0.17	3.06	0.27	2.69	0.15
MBS-605	914	915	0.99	0.485	0.138	8	24.2	0.3	171875	27.03	11.44	0.17	2.66	0.2	2.45	0.15
MBS-605	915	916	1.45	0.71	0.174	12	32.9	0.4	145000	27.53	12.27	0.17	2.59	0.18	2.39	0.15
MBS-605	916	917	2.13	1.07	0.239	16	38.3	0.4	149375	26.61	13.02	0.17	2.48	0.16	2.28	0.13
MBS-605	917	918	1.81	0.89	0.252	15	41.6	0.4	168000	26.61	12.47	0.17	2.55	0.18	2.34	0.13
MBS-605	918	919	2.09	1.1	0.23	17	37.4	0.5	135294	26.53	13.04	0.17	2.48	0.16	2.31	0.13
MBS-605	919	920	1.05	0.513	0.142	8	20.7	0.4	176875	26.86	11.38	0.17	2.66	0.2	2.41	0.15
MBS-605	920	921	2.15	1.13	0.243	18	60.5	0.3	135000	26.7	13.05	0.17	2.46	0.16	2.25	0.13
MBS-605	921	922	2.45	1.29	0.271	22	72.7	0.3	123182	26.2	13.41	0.17	2.42	0.16	2.21	0.13
MBS-605	922	923	2.4	1.24	0.252	21	70.2	0.3	120000	26.61	13.3	0.17	2.51	0.18	2.27	0.13
MBS-605	923	924	1.76	0.9	0.191	16	66.1	0.2	119063	26.95	12.51	0.17	2.91	0.26	2.5	0.15
MBS-605	924	925	2.12	1.17	0.233	23	101	0.2	101304	26.61	12.98	0.17	2.78	0.23	2.42	0.15
MBS-605	925	926	1.91	0.98	0.242	16	61.4	0.3	151250	26.12	12.77	0.17	2.82	0.23	2.36	0.17
MBS-605	926	927	1.55	0.564	0.602	20	108	0.2	301000	25.45	11.98	0.16	3.12	0.34	2.67	0.17
MBS-605	927	928	1.58	0.88	0.174	14	62.5	0.2	123929	27.03	12.35	0.17	2.87	0.22	2.45	0.17
MBS-605	928	929	1.98	1.15	0.182	22	138	0.2	82500	25.45	12.51	0.16	3.04	0.31	2.64	0.17

Hole_ID	m From	m To	S (wt. %)	Ni (wt. %)	Cu (wt. %)	Pd (ppb)	Pt (ppb)	Pd/Pt	Cu/Pd	MgO (wt. %)	Fe_2O_3 (wt. %)	MnO (wt. %)	Al_2O_3 (wt. %)	Na_2O (wt. %)	CaO (wt. %)	TiO_2 (wt. %)
MBS-605	929	930	1.09	0.568	0.151	27	109	0.2	55741	26.28	11.58	0.17	3.33	0.28	2.6	0.17
MBS-605	930	931	0.93	0.49	0.138	33	150	0.2	41667	25.54	11.08	0.16	3.4	0.35	2.76	0.18
MBS-605	931	932	1.13	0.597	0.155	23	72.7	0.3	67174	26.95	11.64	0.17	3.14	0.3	2.63	0.17
MBS-605	932	933	1.24	0.67	0.157	26	88.7	0.3	60192	27.28	11.98	0.17	3.04	0.24	2.49	0.17
MBS-605	933	934	1.15	0.582	0.161	24	68	0.4	66875	26.7	11.69	0.17	3.16	0.31	2.62	0.18
MBS-605	934	935	0.8	0.442	0.137	17	56.5	0.3	80588	22.8	10.28	0.16	3.82	0.46	2.45	0.18
MBS-605	935	936	1.2	0.587	0.22	82	217	0.4	26829	26.61	11.39	0.17	2.85	0.26	2.48	0.17
MBS-605	936	937	1.01	0.527	0.161	90	307	0.3	17889	26.95	11.15	0.17	2.76	0.23	2.42	0.15
MBS-605	937	938	0.67	0.38	0.138	48	168	0.3	28646	26.95	10.52	0.16	2.87	0.27	2.42	0.15
MBS-605	938	939	1.61	0.81	0.26	84	219	0.4	30952	27.19	12	0.17	2.63	0.2	2.34	0.15
MBS-605	939	940	1.21	0.596	0.188	34	140	0.2	55147	27.11	11.37	0.16	2.76	0.23	2.39	0.17
MBS-605	940	941	1.16	0.59	0.19	27	106	0.3	70370	27.36	11.38	0.16	2.87	0.24	2.46	0.17
MBS-605	941	942	1.33	0.66	0.279	34	116	0.3	82059	27.44	11.91	0.17	2.87	0.26	2.5	0.17
MBS-605	942	943	1.08	0.541	0.163	23	102	0.2	70652	27.44	11.48	0.17	2.83	0.23	2.52	0.17
MBS-605	943	944	1.02	0.518	0.147	23	103	0.2	63696	27.86	11.62	0.17	2.8	0.23	2.5	0.17
MBS-605	944	945	0.97	0.483	0.149	25	102	0.2	59600	27.19	11.34	0.17	3.19	0.31	2.81	0.18
MBS-605	945	946	0.87	0.466	0.128	19	108	0.2	67368	28.02	11.11	0.17	2.87	0.24	2.46	0.17
MBS-605	946	947	1.8	0.96	0.242	46	168	0.3	52609	27.94	12.38	0.17	2.46	0.18	2.24	0.15
MBS-605	947	948	2.01	1.1	0.275	52	184	0.3	52885	27.36	12.44	0.16	2.31	0.15	2.14	0.13
MBS-605	948	949	1.97	1.08	0.328	43	115	0.4	76279	27.61	12.38	0.16	2.4	0.18	2.18	0.13
MBS-605	949	950	1.56	0.548	0.755	52	177	0.3	145192	27.61	12.31	0.17	2.55	0.2	2.34	0.15
MBS-605	950	951	1.22	0.66	0.275	53	169	0.3	51887	27.03	11.39	0.16	2.8	0.31	2.35	0.13
MBS-605	951	952	1.82	0.98	0.189	57	158	0.4	33158	28.77	12.58	0.17	2.61	0.19	2.36	0.13
MBS-605	952	953	1.51	0.8	0.196	55	120	0.5	35545	28.19	11.95	0.17	2.57	0.19	2.31	0.13
MBS-605	953	954	1.16	0.581	0.187	56	100	0.6	33304	29.1	11.68	0.17	2.72	0.2	2.45	0.15
MBS-605	954	955	1.67	0.71	0.5	91	169	0.5	54945	27.61	12.74	0.17	3.23	0.4	2.39	0.15
MBS-605	955	956	1.74	0.93	0.217	64	104	0.6	33906	27.86	12.12	0.16	2.59	0.19	2.31	0.13
MBS-605	956	957	1.19	0.599	0.195	65	80.7	0.8	29923	28.44	11.57	0.17	2.68	0.2	2.43	0.15
MBS-605	957	958	0.79	0.43	0.122	37	47	0.8	32838	28.6	10.98	0.17	2.76	0.22	2.48	0.15
MBS-605	958	959	0.76	0.412	0.108	54	52.9	1	20000	28.36	10.85	0.17	2.8	0.24	2.52	0.15
MBS-605	959	960	0.56	0.351	0.103	30	36.5	0.8	34333	27.86	10.59	0.17	2.8	0.26	2.52	0.15
MBS-605	960	961	0.32	0.242	0.057	12	17	0.7	47250	29.76	10.51	0.17	2.95	0.28	2.6	0.17
MBS-605	961	962	0.2	0.185	0.037	8	12.6	0.6	46000	29.02	10.05	0.17	2.91	0.27	2.53	0.17
MBS-605	962	963	0.33	0.236	0.057	12	19.5	0.6	47833	29.18	10.28	0.17	2.89	0.26	2.46	0.17
MBS-605	963	964	0.51	0.355	0.11	21	33.2	0.6	52143	29.27	10.61	0.17	2.91	0.27	2.48	0.17

Hole_ID	m From	m To	S (wt. %)	Ni (wt. %)	Cu (wt. %)	Pd (ppb)	Pt (ppb)	Pd/Pt	Cu/Pd	MgO (wt. %)	Fe_2O_3 (wt. %)	MnO (wt. %)	Al_2O_3 (wt. %)	Na_2O (wt. %)	CaO (wt. %)	TiO_2 (wt. %)
MBS-605	964	965	0.61	0.429	0.142	21	53.7	0.4	67619	28.36	10.75	0.17	3.02	0.32	2.46	0.18
MBS-605	965	966	0.74	0.484	0.162	27	82.4	0.3	60000	27.69	11.25	0.17	3.34	0.42	2.5	0.2
MBS-605	966	967	0.83	0.496	0.144	27	72.9	0.4	53333	26.86	11.29	0.17	3.89	0.54	2.85	0.2
MBS-605	967	968	1.08	0.63	0.206	55	220	0.3	37455	28.19	11.19	0.16	3.06	0.31	2.39	0.18
MBS-605	968	969	1.34	0.79	0.232	65	209	0.3	35692	26.7	10.81	0.15	2.78	0.27	2.2	0.17
MBS-605	969	970	1.77	0.97	0.283	71	213	0.3	39859	27.77	11.78	0.15	2.68	0.27	2.18	0.15
MBS-605	970	971	1.55	0.89	0.296	82	241	0.3	36098	32.83	13.15	0.16	1.98	0.16	1.65	0.12
MBS-605	971	972	1.02	0.68	0.143	60	168	0.4	23833	33.66	12.75	0.16	1.72	0.13	1.87	0.1
MBS-605	972	973	0.87	0.63	0.13	69	166	0.4	18841	35.15	12.92	0.16	1.64	0.15	1.4	0.1
MBS-605	973	974	1.47	0.82	0.382	106	232	0.5	36038	31.34	12.38	0.15	1.89	0.16	1.67	0.1
MBS-605	974	975	2.25	1.24	0.322	112	278	0.4	28750	32.58	14.15	0.16	1.93	0.16	1.68	0.1
MBS-605	975	976	1.95	1.2	0.219	122	344	0.4	17951	32.92	13.68	0.15	1.8	0.15	1.51	0.1
MBS-605	976	977	2.19	1.3	0.314	125	383	0.3	25120	34.99	14.73	0.16	1.57	0.15	1.32	0.08
MBS-605	977	978	2.22	1.38	0.204	135	470	0.3	15111	35.15	15.15	0.16	1.66	0.16	1.3	0.1
MBS-605	978	979	2.08	1.32	0.183	128	437	0.3	14297	37.14	15.23	0.16	1.45	0.13	1.15	0.08
MBS-605	979	980	2.01	1.18	0.318	142	454	0.3	22394	38.97	15.73	0.16	1.34	0.12	0.98	0.07
MBS-605	980	981	1.68	1.07	0.233	135	427	0.3	17259	39.47	15.58	0.16	1.28	0.12	0.92	0.07
MBS-605	981	982	0.88	0.67	0.143	75	260	0.3	19067	40.13	14.51	0.17	1.34	0.13	1.08	0.08
MBS-605	982	983	0.44	0.479	0.075	47	154	0.3	15936	39.13	13.52	0.16	1.32	0.13	1.06	0.08
MBS-605	983	984	0.37	0.455	0.063	40	135	0.3	15700	40.96	14.15	0.17	1.44	0.16	1.16	0.08
MBS-605	984	985	0.29	0.381	0.051	33	101	0.3	15303	36.81	12.85	0.16	1.83	0.23	1.46	0.12
MBS-605	985	986	0.15	0.315	0.028	23	68.4	0.3	12000	36.98	12.74	0.16	2	0.24	1.43	0.12
MBS-605	986	987	0.06	0.281	0.011	15	41.5	0.4	7200	37.81	12.42	0.16	1.62	0.19	1.23	0.08
MBS-605	987	988	0.07	0.306	0.012	17	33.8	0.5	6824	40.13	13.08	0.16	1.55	0.19	1.26	0.1
MBS-605	988	989	0.07	0.312	0.01	16	31.3	0.5	6500	40.96	13.52	0.17	1.55	0.2	1.23	0.1
MBS-605	989	990	0.08	0.307	0.012	16	28.9	0.6	7750	38.97	12.85	0.16	1.59	0.22	1.25	0.1
MBS-605	990	991	0.08	0.302	0.012	16	25.5	0.6	7500	40.13	13.08	0.17	1.59	0.22	1.27	0.1
MBS-605	991	992	0.07	0.297	0.012	19	28.9	0.7	6421	38.97	12.78	0.16	1.55	0.19	1.19	0.08
MBS-605	992	993	0.09	0.294	0.015	20	28.7	0.7	7250	38.14	12.45	0.16	1.68	0.22	1.37	0.1
MBS-605	993	994	0.09	0.292	0.014	25	32	0.8	5560	38.97	12.92	0.17	1.61	0.19	1.23	0.1
MBS-605	994	995	0.09	0.272	0.014	19	24.5	0.8	7263	36.48	12.21	0.16	1.74	0.2	1.4	0.1
MBS-605	995	996	0.07	0.254	0.01	10	12.6	0.8	10300	37.31	12.3	0.17	1.83	0.2	1.57	0.12
MBS-605	996	997	0.08	0.243	0.014	14	18.6	0.8	9714	34.82	11.55	0.16	2.17	0.27	1.68	0.12
MBS-605	997	998	0.18	0.277	0.029	12	21.2	0.6	24167	33.33	11.15	0.16	2.31	0.28	1.8	0.13
MBS-605	998	999	0.13	0.316	0.02	4	16.7	0.2	49750	39.13	12.74	0.17	1.8	0.19	1.37	0.1

Hole_ID	m From	m To	S (wt. %)	Ni (wt. %)	Cu (wt. %)	Pd (ppb)	Pt (ppb)	Pd/Pt	Cu/Pd	MgO (wt. %)	Fe_2O_3 (wt. %)	MnO (wt. %)	Al_2O_3 (wt. %)	Na_2O (wt. %)	CaO (wt. %)	TiO_2 (wt. %)
MBS-605	999	1000	0.12	0.307	0.018	4	14.7	0.3	44500	37.97	12.42	0.16	1.57	0.16	1.19	0.08
MBS-605	1000	1001	0.11	0.311	0.016	4	14.6	0.3	39750	36.31	12.15	0.15	1.34	0.15	1.06	0.08
MBS-605	1001	1002	0.1	0.295	0.016	4	14	0.3	39500	36.15	12.22	0.16	1.45	0.16	1.12	0.08
MBS-605	1002	1003	0.14	0.327	0.021	8	26.7	0.3	26625	36.31	12.34	0.16	1.53	0.19	1.12	0.08
MBS-605	1003	1004	0.13	0.343	0.02	4	20.1	0.2	48750	38.97	13.38	0.16	1.32	0.13	1.02	0.08
MBS-605	1004	1005	0.11	0.314	0.016	3	15	0.2	51667	36.98	12.77	0.16	1.25	0.15	0.99	0.08
MBS-605	1005	1006	0.13	0.31	0.02	4	21	0.2	49750	35.15	12.34	0.15	1.51	0.13	0.97	0.1
MBS-605	1006	1007	0.13	0.329	0.02	4	21.4	0.2	50250	36.48	12.34	0.15	1.25	0.12	0.98	0.07
MBS-605	1007	1008	0.13	0.323	0.021	4	21.5	0.2	51250	35.65	11.95	0.15	1.28	0.12	0.98	0.08
MBS-605	1008	1009	0.13	0.341	0.02	4	21.1	0.2	48750	38.47	12.81	0.16	1.3	0.13	1.06	0.08
MBS-605	1009	1010	0.15	0.343	0.024	5	27.6	0.2	47200	37.81	12.61	0.16	1.32	0.13	1.06	0.08
MBS-605	1010	1011	0.17	0.351	0.026	7	32	0.2	37714	37.81	12.8	0.16	1.42	0.15	1.12	0.08
MBS-605	1011	1012	0.16	0.313	0.024	6	30.1	0.2	40000	35.98	12.04	0.16	1.68	0.16	1.39	0.1
MBS-605	1012	1013	0.17	0.314	0.026	7	43.8	0.2	37286	35.49	12	0.16	1.78	0.13	1.43	0.1
MBS-605	1013	1014	0.16	0.364	0.025	11	68.8	0.2	22909	38.97	13.22	0.16	1.4	0.12	1.04	0.08
MBS-605	1014	1015	0.14	0.345	0.022	13	84.9	0.2	16769	38.47	12.97	0.16	1.38	0.12	0.99	0.08
MBS-605	1015	1016	0.14	0.347	0.023	17	106	0.2	13294	37.81	12.74	0.16	1.27	0.12	0.95	0.07
MBS-605	1016	1017	0.12	0.324	0.019	21	126	0.2	9000	37.81	12.82	0.16	1.38	0.13	1.04	0.08
MBS-605	1017	1018	0.09	0.303	0.015	23	107	0.2	6348	36.48	12.2	0.15	1.34	0.13	0.97	0.08
MBS-605	1018	1019	0.09	0.283	0.014	22	52.4	0.4	6227	36.31	12.11	0.16	1.74	0.23	1.2	0.1
MBS-605	1019	1020	0.1	0.291	0.016	32	60.8	0.5	4938	36.65	12.34	0.16	1.55	0.16	1.2	0.08
MBS-605	1020	1021	0.1	0.303	0.016	46	79.5	0.6	3500	37.48	12.48	0.16	1.45	0.15	1.12	0.08
MBS-605	1021	1022	0.13	0.322	0.021	56	78.7	0.7	3732	37.64	12.7	0.16	1.4	0.15	1.09	0.08
MBS-605	1022	1023	0.1	0.291	0.016	35	49.2	0.7	4629	36.65	12.38	0.16	1.53	0.18	1.23	0.08
MBS-605	1023	1024	0.1	0.286	0.018	20	28.8	0.7	9100	36.31	12.17	0.16	1.64	0.16	1.22	0.1
MBS-605	1024	1025	0.15	0.332	0.025	36	48	0.8	6917	39.13	13.14	0.17	1.57	0.18	1.33	0.1
MBS-605	1025	1026	0.08	0.273	0.013	21	31.4	0.7	6143	35.98	11.95	0.15	1.4	0.15	1.19	0.08
MBS-605	1026	1027	0.26	0.283	0.046	14	24.9	0.6	33071	30.35	10.17	0.15	1.98	0.2	1.76	0.12
MBS-605	1027	1028	0.18	0.227	0.027	5	11.9	0.4	54400	29.1	9.72	0.15	2.29	0.24	1.85	0.13
MBS-605	1028	1029	0.2	0.244	0.031	6	15	0.4	51167	30.18	9.95	0.15	2.29	0.24	1.87	0.13
MBS-605	1029	1030	0.26	0.301	0.043	11	30.4	0.4	39273	31.75	10.59	0.15	1.97	0.18	1.78	0.12
MBS-605	1030	1031	0.33	0.364	0.053	14	46.4	0.3	37857	33.99	11.41	0.16	1.68	0.16	1.51	0.1
MBS-605	1031	1032	0.51	0.482	0.076	42	149	0.3	18024	35.49	12.22	0.15	1.44	0.16	1.18	0.08
MBS-605	1032	1033	0.31	0.42	0.045	83	326	0.3	5386	37.64	12.74	0.16	1.45	0.13	1.11	0.08
MBS-605	1033	1034	0.21	0.364	0.031	87	307	0.3	3506	39.96	13.45	0.16	1.76	0.15	1.04	0.08

Hole_ID	m From	m To	S (wt. %)	Ni (wt. %)	Cu (wt. %)	Pd (ppb)	Pt (ppb)	Pd/Pt	Cu/Pd	MgO (wt. %)	Fe_2O_3 (wt. %)	MnO (wt. %)	Al_2O_3 (wt. %)	Na_2O (wt. %)	CaO (wt. %)	TiO_2 (wt. %)
MBS-605	1034	1035	0.21	0.399	0.03	94	310	0.3	3181	43.78	14.27	0.17	1.49	0.15	1.01	0.08
MBS-605	1035	1036	0.13	0.364	0.02	95	235	0.4	2116	43.61	14.3	0.17	1.64	0.12	1.01	0.08
MBS-605	1036	1037	0.26	0.385	0.033	110	244	0.5	3036	40.13	13.38	0.16	1.61	0.15	1.09	0.08
MBS-605	1037	1038	0.07	0.325	0.01	71	82.7	0.9	1338	43.28	13.88	0.17	1.34	0.13	1.04	0.08
MBS-605	1038	1039	0.2	0.349	0.028	88	101	0.9	3170	40.79	13.14	0.17	1.53	0.15	1.32	0.08
MBS-605	1039	1040	0.3	0.416	0.045	188	218	0.9	2388	41.46	13.54	0.17	1.51	0.12	1.13	0.08
MBS-605	1040	1041	0.12	0.359	0.018	146	95.1	1.5	1199	43.11	13.67	0.16	1.15	0.11	0.81	0.07
MBS-605	1041	1042	0.04	0.317	0.006	110	69.9	1.6	555	43.94	14.03	0.17	1.28	0.11	0.84	0.07
MBS-605	1042	1043	0.04	0.325	0.006	107	64.7	1.7	551	44.11	14.08	0.17	1.32	0.11	0.83	0.07
MBS-605	1043	1044	0.04	0.3	0.005	102	58.2	1.8	510	40.96	13.01	0.16	1.19	0.09	0.76	0.07
MBS-605	1044	1045	0.04	0.327	0.006	92	52.5	1.8	598	44.61	14.24	0.17	1.23	0.11	0.83	0.07
MBS-605	1045	1046	0.04	0.32	0.005	91	51.5	1.8	527	44.11	13.95	0.17	1.25	0.12	0.85	0.07
MBS-605	1046	1047	0.04	0.318	0.005	88	47.4	1.9	557	43.94	14.1	0.17	1.27	0.12	0.9	0.07
MBS-605	1047	1048	0.05	0.282	0.007	69	40	1.7	971	40.29	13.4	0.17	1.89	0.24	1.64	0.1
MBS-605	1048	1049	0.04	0.316	0.005	79	39.4	2	671	44.11	14.37	0.17	1.25	0.09	0.85	0.07
MBS-605	1049	1050	0.04	0.323	0.005	75	38.7	1.9	720	43.94	14.28	0.17	1.32	0.12	0.88	0.08
MBS-605	1050	1051	0.04	0.31	0.005	80	43	1.9	650	43.78	13.94	0.17	1.27	0.12	0.85	0.07
MBS-605	1051	1052	0.05	0.324	0.006	89	43.6	2	685	44.27	14.14	0.17	1.28	0.12	0.88	0.07
MBS-605	1052	1053	0.04	0.318	0.005	78	41.1	1.9	692	43.61	14.05	0.17	1.25	0.11	0.84	0.07
MBS-605	1053	1054	0.05	0.332	0.007	87	47.4	1.8	839	44.11	14.2	0.17	1.36	0.13	0.87	0.07
MBS-605	1054	1055	0.04	0.315	0.006	84	43	2	714	44.11	14.1	0.17	1.3	0.12	0.85	0.07
MBS-605	1055	1056	0.05	0.303	0.008	94	47.2	2	809	42.45	13.75	0.16	1.27	0.12	0.83	0.07
MBS-605	1056	1057	0.06	0.311	0.009	90	46	2	978	41.46	13.31	0.16	1.23	0.12	0.8	0.07
MBS-605	1057	1058	0.05	0.314	0.007	91	43.5	2.1	769	42.95	13.7	0.16	1.19	0.13	0.85	0.07
MBS-605	1058	1059	0.04	0.31	0.006	90	42	2.1	644	41.79	13.42	0.16	1.19	0.12	0.84	0.07
MBS-605	1059	1060	0.04	0.324	0.006	81	39.8	2	753	43.94	14	0.16	1.23	0.13	0.85	0.07
MBS-605	1060	1061	0.08	0.348	0.014	156	60.9	2.6	904	43.28	14.05	0.16	1.27	0.12	0.8	0.07
MBS-605	1061	1062	0.04	0.324	0.007	115	59.1	1.9	617	43.11	13.78	0.16	1.21	0.12	0.78	0.07
MBS-605	1062	1063	0.05	0.323	0.008	113	57.8	2	699	43.94	13.97	0.16	1.21	0.12	0.8	0.07
MBS-605	1063	1064	0.05	0.327	0.009	120	57.9	2.1	708	43.44	13.88	0.16	1.19	0.11	0.77	0.07
MBS-605	1064	1065	0.05	0.32	0.008	105	54.1	1.9	743	43.44	13.81	0.16	1.15	0.11	0.78	0.07
MBS-605	1065	1066	0.05	0.314	0.008	101	51.6	2	772	42.78	13.63	0.16	1.17	0.12	0.78	0.07
MBS-605	1066	1067	0.04	0.336	0.007	116	93.4	1.2	638	44.77	14.27	0.17	1.19	0.12	0.78	0.07
MBS-158	218	219	0.05	0.025	0.006	0.5	0.3	1.7	122000	9.98	6.41	0.11	15.97	1.98	12.69	0.2
MBS-158	219	220	0.06	0.027	0.008	0.5	0.3	1.7	158000	10.03	6.41	0.11	16.04	1.97	12.84	0.23

Hole_ID	m From	m To	S (wt. %)	Ni (wt. %)	Cu (wt. %)	Pd (ppb)	Pt (ppb)	Pd/Pt	Cu/Pd	MgO (wt. %)	Fe_2O_3 (wt. %)	MnO (wt. %)	Al_2O_3 (wt. %)	Na_2O (wt. %)	CaO (wt. %)	TiO_2 (wt. %)
MBS-158	220	221	0.07	0.026	0.007	0.5	0.3	1.7	136000	10.18	6.28	0.11	15.42	1.89	12.65	0.22
MBS-158	221	222	0.06	0.027	0.007	0.5	0.3	1.7	134000	9.95	6.22	0.11	14.85	1.82	12.4	0.22
MBS-158	222	223	0.05	0.026	0.006	0.5	0.3	1.7	124000	10.28	6.26	0.11	14.91	1.89	12.58	0.22
MBS-158	223	224	0.07	0.028	0.008	0.5	0.3	1.7	152000	10.4	6.42	0.11	15.3	1.86	12.9	0.22
MBS-158	224	225	0.4	0.118	0.041	4	8.9	0.4	101750	10.43	6.75	0.11	14.45	1.69	12.54	0.2
MBS-158	225	226	0.11	0.037	0.012	1	1	1	120000	10.03	6.28	0.11	14.59	1.71	12.44	0.22
MBS-158	226	227	0.19	0.048	0.02	1	2.3	0.4	195000	10.38	6.33	0.11	14.13	1.66	12.49	0.2
MBS-158	227	228	0.08	0.033	0.009	0.5	0.3	1.7	170000	10.83	6.53	0.11	14.34	1.71	13.04	0.22
MBS-158	228	229	0.17	0.046	0.018	0.5	0.3	1.7	368000	10.58	6.36	0.12	12.34	1.93	12.01	0.22
MBS-158	229	230	0.05	0.012	0.003	0.5	0.3	1.7	62000	2.94	2.82	0.04	8.67	1.86	3.85	0.08
MBS-158	230	231	0.21	0.061	0.032	1	1.1	0.9	320000	12.01	7.05	0.12	11.94	1.69	13	0.25
MBS-158	231	232	0.23	0.061	0.028	1	1.3	0.8	277000	11.79	7.08	0.12	12.19	1.73	12.75	0.25
MBS-158	232	233	0.24	0.066	0.032	1	0.3	3.3	322000	12.93	7.53	0.13	10.24	1.46	13.21	0.25
MBS-158	233	234	0.63	0.158	0.088	1	2.3	0.4	880000	16.91	9.99	0.16	5.23	0.73	13.14	0.32
MBS-158	234	235	0.33	0.099	0.047	0.5	0.5	1	930000	15.97	8.81	0.15	5.48	0.78	12.8	0.28
MBS-158	235	236	0.6	0.175	0.096	1	1	1	962000	16.22	9.45	0.15	4.86	0.66	12.69	0.28
MBS-158	236	237	0.45	0.122	0.069	1	1	1	694000	16.32	9.41	0.16	4.86	0.67	13.95	0.33
MBS-158	237	238	0.24	0.081	0.041	0.5	0.5	1	826000	16.48	9.05	0.16	5.67	0.78	14.69	0.32
MBS-158	238	239	0.14	0.097	0.025	3	2.8	1.1	82333	22.3	11.67	0.18	4.46	0.47	3.83	0.22
MBS-158	239	240	0.85	0.257	0.124	2	3.1	0.6	617500	18.41	11.02	0.17	5.25	0.62	12.19	0.28
MBS-158	240	241	1.03	0.285	0.145	2	2.9	0.7	725000	17.08	10.48	0.16	5.82	0.71	13.54	0.28
MBS-158	241	242	0.97	0.287	0.139	3	2.8	1.1	463333	16.58	10.35	0.15	6.63	0.89	10.68	0.27
MBS-158	242	243	1.21	0.399	0.182	4	9.8	0.4	455000	20.73	12.41	0.16	5.56	0.63	6.06	0.2
MBS-158	243	244	1.04	0.373	0.184	4	5.9	0.7	460000	19.4	11.68	0.15	4.67	0.57	4.14	0.17
MBS-158	244	245	0.91	0.377	0.164	4	7.2	0.6	408750	21.47	11.95	0.16	5.12	0.61	4.39	0.18
MBS-158	245	246	0.87	0.456	0.157	8	13.9	0.6	195625	22.8	11.59	0.16	4.89	0.59	4.31	0.2
MBS-158	246	247	1.14	0.578	0.189	9	21.8	0.4	209444	23.46	12.05	0.16	4.67	0.49	4.24	0.18
MBS-158	247	248	1.4	0.79	0.252	13	52	0.3	193846	21.97	12.41	0.16	4.33	0.42	4.04	0.22
MBS-158	248	249	0.68	0.392	0.157	8	17.8	0.4	195625	21.47	10.82	0.15	5.37	0.67	4.09	0.18
MBS-158	249	250	1.34	0.75	0.2	16	61.2	0.3	124688	22.88	12.02	0.15	5.25	0.63	4.28	0.18
MBS-158	250	251	1.54	0.69	0.351	18	39.2	0.5	195000	23.13	12.28	0.15	5.93	0.77	4.72	0.2
MBS-158	251	252	0.39	0.259	0.138	5	12	0.4	276000	12.55	7.05	0.09	8.26	1.75	3.76	0.23
MBS-158	252	253	0.69	0.381	0.147	5	9.4	0.5	294000	22.39	11.57	0.16	5.82	0.7	4.94	0.22
MBS-158	253	254	0.68	0.366	0.117	5	7.8	0.6	234000	21.64	10.48	0.15	5.76	0.67	5.19	0.18
MBS-158	254	255	0.42	0.235	0.071	3	8.6	0.3	236333	20.64	10.65	0.15	7.03	0.92	5.82	0.2

Hole_ID	m From	m To	S (wt. %)	Ni (wt. %)	Cu (wt. %)	Pd (ppb)	Pt (ppb)	Pd/Pt	Cu/Pd	MgO (wt. %)	Fe_2O_3 (wt. %)	MnO (wt. %)	Al_2O_3 (wt. %)	Na_2O (wt. %)	CaO (wt. %)	TiO_2 (wt. %)
MBS-158	255	256	0.44	0.256	0.078	7	18.7	0.4	110714	17.33	9.06	0.13	5.71	0.77	4.27	0.18
MBS-158	256	257	1.03	0.552	0.181	13	34.6	0.4	139231	22.47	10.97	0.14	4.18	0.4	4.02	0.17
MBS-158	257	258	0.72	0.408	0.105	12	28	0.4	87083	20.64	9.48	0.13	3.78	0.38	3.74	0.15
MBS-158	258	259	1.26	0.73	0.181	19	82.7	0.2	95263	23.13	11.77	0.14	4.12	0.35	4.04	0.17
MBS-158	259	260	0.95	0.519	0.163	12	51.2	0.2	135417	21.97	11.22	0.14	4.25	0.35	3.71	0.17
MBS-158	260	261	1.02	0.523	0.164	18	69.3	0.3	91111	23.3	11.8	0.14	4.63	0.53	4.13	0.2
MBS-158	261	262	0.42	0.313	0.073	4	30.1	0.1	182250	26.78	12.17	0.16	4.04	0.39	3.97	0.2
MBS-158	262	263	0.78	0.455	0.126	16	63.3	0.3	78750	22.97	11.29	0.14	5.31	0.69	4.21	0.22
MBS-158	263	264	0.8	0.459	0.125	19	85.8	0.2	65526	26.95	11.97	0.16	3.4	0.32	3.67	0.17
MBS-158	264	265	1.76	1.05	0.21	59	104.5	0.6	35593	24.79	12.77	0.14	3.08	0.35	3.29	0.15
MBS-158	265	266	1.37	0.67	0.211	56	102.5	0.5	37679	27.03	12.4	0.16	3.82	0.38	4.13	0.18
MBS-158	266	267	1.19	0.572	0.223	28	73.3	0.4	79643	26.53	11.95	0.16	3.76	0.35	4.16	0.2
MBS-158	267	268	0.87	0.458	0.175	72	222	0.3	24236	17.91	8.95	0.12	7.48	1.27	3.64	0.18
MBS-158	268	269	0.32	0.21	0.057	21	87.7	0.2	27048	17.25	7.89	0.11	8.26	1.27	5.12	0.22
MBS-158	269	270	0.38	0.195	0.056	15	38.2	0.4	37267	14.99	8.02	0.12	8.62	1.27	5.86	0.37
MBS-158	270	271	0.4	0.261	0.082	22	88.3	0.2	37455	22.97	9.58	0.15	5.12	0.59	4.52	0.25
MBS-158	271	272	1.62	1	0.24	101	417	0.2	23762	28.69	13.91	0.14	4.33	0.66	2.48	0.27
MBS-158	272	273	1.61	0.96	0.207	102	296	0.3	20294	32.75	13.98	0.15	2.66	0.31	2.55	0.15
MBS-158	273	274	1.67	0.95	0.202	89	241	0.4	22697	34.32	15.3	0.16	2.63	0.32	2.73	0.15
MBS-158	274	275	1.54	0.86	0.2	65	191	0.3	30769	31.67	15.15	0.15	3.46	0.46	2.63	0.22
MBS-158	275	276	1.81	0.93	0.234	62	204	0.3	37742	34.99	15.44	0.17	2.65	0.34	2.81	0.17
MBS-158	276	277	1.63	0.94	0.24	59	201	0.3	40678	31.67	14.65	0.15	2.46	0.31	2.45	0.15
MBS-158	277	278	1.79	0.88	0.232	51	133.5	0.4	45490	34.49	15.58	0.16	2.68	0.34	2.71	0.15
MBS-158	278	279	1.66	0.9	0.212	57	164	0.3	37193	33.99	14.94	0.16	2.7	0.34	2.45	0.15
MBS-158	279	280	1.65	0.94	0.168	56	148.5	0.4	30000	29.85	14.21	0.14	2.46	0.31	2.07	0.15
MBS-158	280	281	1.79	0.9	0.183	54	128	0.4	33796	34.82	15.73	0.17	2.63	0.35	2.53	0.17
MBS-158	281	282	1.61	0.86	0.195	55	121	0.5	35364	34.32	15.08	0.16	2.53	0.34	2.27	0.15
MBS-158	282	283	1.71	0.89	0.18	52	124.5	0.4	34519	34.32	15.44	0.16	2.66	0.35	2.43	0.17
MBS-158	283	284	1.78	0.85	0.247	54	108.5	0.5	45741	32.92	14.94	0.17	3.17	0.4	2.92	0.18
MBS-158	284	285	2.16	1.09	0.265	67	120.5	0.6	39552	31.84	15.44	0.16	2.93	0.31	2.48	0.17
MBS-158	285	286	1.91	0.86	0.366	68	89.2	0.8	53824	30.18	14.37	0.16	3.53	0.43	3.39	0.2
MBS-158	286	287	1.78	0.89	0.243	71	145.5	0.5	34225	33.5	14.8	0.16	2.89	0.36	2.7	0.17
MBS-158	287	288	1.61	0.87	0.186	55	128.5	0.4	33727	33.5	14.14	0.16	2.95	0.36	2.62	0.17
MBS-158	288	289	1.35	0.89	0.214	49	116.5	0.4	43673	28.52	14.44	0.15	4.38	0.53	2.14	0.28
MBS-158	289	290	0.32	0.161	0.038	24	11.2	2.1	15875	2.87	5.28	0.03	14.78	3.45	1.83	0.53

Hole_ID	m From	m To	S (wt. %)	Ni (wt. %)	Cu (wt. %)	Pd (ppb)	Pt (ppb)	Pd/Pt	Cu/Pd	MgO (wt. %)	Fe_2O_3 (wt. %)	MnO (wt. %)	Al_2O_3 (wt. %)	Na_2O (wt. %)	CaO (wt. %)	TiO_2 (wt. %)
MBS-158	290	291	0.04	0.021	0.007	2	1.8	1.1	35500	0.75	1.83	0.01	13.94	2.33	0.57	0.17
MBS-158	291	292	1.34	0.64	0.192	110	103.5	1.1	17455	20.06	14.51	0.12	7.65	0.96	1.58	0.85
MBS-158	292	293	1.62	0.84	0.208	99	120	0.8	21010	29.6	14.37	0.15	3.87	0.43	1.99	0.27
MBS-158	293	294	0.42	0.204	0.051	29	125.5	0.2	17690	3.13	4.69	0.02	14.06	3.71	2.55	0.52
MBS-158	294	295	1.17	0.7	0.13	138	183	0.8	9420	21.06	12.5	0.14	7.22	1.19	2.15	0.32
MBS-158	295	296	1.71	0.96	0.212	163	239	0.7	13006	34.49	15.01	0.16	2.63	0.3	2.01	0.15
MBS-158	296	297	1.73	0.89	0.195	136	162.5	0.8	14338	35.15	14.37	0.16	2.57	0.31	2.04	0.15
MBS-158	297	298	1.78	0.85	0.217	129	131.5	1	16822	35.65	15.44	0.16	2.55	0.32	2.03	0.15
MBS-158	298	299	1.54	0.8	0.172	96	99.7	1	17865	33.5	14.51	0.15	2.85	0.31	2.01	0.15
MBS-158	299	300	0.9	0.482	0.101	56	62.6	0.9	17946	20.23	11.09	0.11	7.48	1.73	2.29	0.15
MBS-158	300	301	0.03	0.01	0.006	1	1.6	0.6	63000	0.4	1.19	0.01	10.85	2.52	1.46	0.03
MBS-158	301	302	0.04	0.008	0.009	3	1	3	30667	0.23	1.16	0.01	10.77	2.63	1.8	0.03
MBS-158	302	303	0.92	0.143	0.187	39	31.9	1.2	47821	1.48	5.28	0.02	15.89	4.25	3.25	0.45
MBS-158	303	304	0.33	0.229	0.061	36	95	0.4	16861	5.12	5.78	0.05	12.17	2.88	3.16	0.3
MBS-158	304	305	0.55	0.497	0.126	106	149	0.7	11840	31.01	14.2	0.15	3.1	0.26	2.64	0.17
MBS-158	305	306	0.58	0.461	0.097	118	136	0.9	8178	29.43	12.9	0.15	4.38	0.5	3.46	0.17
MBS-158	306	307	0.07	0.233	0.011	97	62.3	1.6	1082	33.08	12.65	0.15	2.57	0.24	2.67	0.13
MBS-158	307	308	0.07	0.223	0.011	85	54.3	1.6	1306	32.5	12.01	0.15	2.42	0.24	2.8	0.13
MBS-158	308	309	0.07	0.236	0.013	69	44.8	1.5	1899	32.25	12.44	0.15	2.49	0.24	2.57	0.15
MBS-158	309	310	0.06	0.245	0.01	71	44	1.6	1408	34.32	13.04	0.16	2.38	0.26	2.8	0.13
MBS-158	310	311	0.06	0.252	0.01	69	39.8	1.7	1435	34.82	14.3	0.17	2.46	0.28	2.87	0.15
MBS-158	311	312	0.08	0.258	0.013	78	48.9	1.6	1615	34.99	13.47	0.17	2.53	0.3	2.57	0.15
MBS-158	312	313	0.04	0.204	0.014	55	32.4	1.7	2455	29.35	11.72	0.14	4.46	0.63	2.32	0.18
MBS-158	313	314	0.86	0.66	0.138	160	258	0.6	8594	25.7	11.95	0.13	5.01	0.81	2.45	0.17
MBS-158	314	315	1.3	0.91	0.202	185	293	0.6	10919	33.99	15.51	0.16	2.63	0.27	2.2	0.13
MBS-158	315	316	1.23	0.87	0.185	207	387	0.5	8937	31.01	13.74	0.15	2.27	0.24	2.01	0.13
MBS-158	316	317	0.43	0.445	0.067	129	149	0.9	5225	33.5	14.23	0.16	2.53	0.26	2.22	0.15
MBS-158	317	318	0.21	0.304	0.031	122	98.9	1.2	2541	33.83	13.52	0.16	2.49	0.22	2.21	0.13
MBS-158	318	319	0.45	0.422	0.071	166	171	1	4301	33.83	13.78	0.16	2.42	0.2	2.13	0.13
MBS-158	319	320	0.51	0.471	0.075	184	205	0.9	4098	33.16	13.5	0.15	2.34	0.2	1.94	0.13
MBS-158	320	321	0.55	0.458	0.074	194	201	1	3794	35.65	14.73	0.17	2.51	0.23	2.22	0.13
MBS-158	321	322	0.65	0.514	0.097	186	270	0.7	5188	33.5	13.85	0.16	2.53	0.23	2.14	0.13
MBS-158	322	323	2.15	1.36	0.253	508	695	0.7	4980	32.25	15.51	0.15	2.38	0.23	1.8	0.13
MBS-158	323	324	1.45	0.94	0.175	299	471	0.6	5836	31.01	15.3	0.15	2.83	0.22	1.5	0.15
MBS-158	324	325	0.57	0.382	0.073	176	205	0.9	4142	20.89	10.71	0.11	7.82	1.46	2.15	0.43

Hole_ID	m From	m To	S (wt. %)	Ni (wt. %)	Cu (wt. %)	Pd (ppb)	Pt (ppb)	Pd/Pt	Cu/Pd	MgO (wt. %)	Fe_2O_3 (wt. %)	MnO (wt. %)	Al_2O_3 (wt. %)	Na_2O (wt. %)	CaO (wt. %)	TiO_2 (wt. %)
MBS-158	325	326	0.95	0.69	0.102	292	377	0.8	3493	25.62	14.07	0.16	4.86	0.55	1.93	0.3
MBS-158	326	327	0.86	0.64	0.095	465	401	1.2	2052	29.27	14.2	0.16	3.82	0.27	1.86	0.25
MBS-158	327	328	0.05	0.037	0.005	19	13.2	1.4	2632	2.74	3.59	0.04	13.15	3.26	2.91	0.37
MBS-158	328	329	0.03	0.016	0.003	4	5.1	0.8	8500	1.64	2.52	0.01	14.49	3.69	3.12	0.43
MBS-158	329	330	0.02	0.007	0.002	2	1.2	1.7	8500	0.9	2.43	0.01	14.25	3.24	2.29	0.27
MBS-158	330	331	0.05	0.157	0.004	154	140.5	1.1	286	26.28	10.18	0.13	5.08	0.86	2.55	0.28
MBS-158	331	332	0.05	0.186	0.005	203	172.5	1.2	256	33.08	12	0.16	3.42	0.35	2.46	0.17
MBS-158	332	333	0.05	0.205	0.006	188	159	1.2	303	33.99	12.58	0.16	2.72	0.32	2.45	0.17
MBS-158	333	334	0.04	0.199	0.005	177	139.5	1.3	282	34.16	12.64	0.17	2.85	0.34	2.56	0.17
MBS-158	334	335	0.04	0.223	0.005	156	117	1.3	333	36.15	13.11	0.16	2.72	0.32	2.35	0.17
MBS-158	335	336	0.05	0.199	0.006	172	119.5	1.4	349	33.83	12.4	0.16	2.91	0.34	2.5	0.17
MBS-158	336	337	0.04	0.216	0.005	149	116	1.3	349	35.32	12.95	0.16	2.83	0.34	2.46	0.17
MBS-158	337	338	0.04	0.222	0.006	108	79.8	1.4	519	35.82	12.91	0.16	2.78	0.34	2.38	0.17
MBS-158	338	339	0.04	0.219	0.005	134	91.7	1.5	373	35.32	13.07	0.16	2.7	0.32	2.39	0.17
MBS-158	339	340	0.04	0.215	0.005	107	72.6	1.5	458	35.15	12.9	0.16	2.74	0.32	2.34	0.17
MBS-158	340	341	0.04	0.207	0.005	105	69.8	1.5	438	34.66	12.44	0.16	2.72	0.32	2.39	0.17
MBS-158	341	342	0.05	0.218	0.007	86	56.2	1.5	756	34.99	12.87	0.16	2.72	0.32	2.35	0.17
MBS-158	342	343	0.04	0.223	0.005	87	55.6	1.6	552	35.98	12.98	0.16	2.8	0.32	2.32	0.17
MBS-158	343	344	0.04	0.226	0.005	80	53.7	1.5	575	36.98	13.25	0.17	2.87	0.35	2.49	0.17
MBS-158	344	345	0.04	0.223	0.004	86	54.5	1.6	512	36.15	13.24	0.16	2.83	0.32	2.39	0.17
MBS-158	345	346	0.04	0.225	0.004	79	49.9	1.6	506	37.31	13.54	0.17	2.89	0.34	2.42	0.17
MBS-158	346	347	0.04	0.228	0.004	74	47.5	1.6	568	36.15	13.14	0.16	2.83	0.35	2.35	0.17
MBS-158	347	348	0.04	0.238	0.004	75	49	1.5	520	36.48	13.4	0.16	2.53	0.3	2.03	0.15
MBS-158	348	349	0.04	0.251	0.005	88	50.5	1.7	511	37.64	13.64	0.16	2.49	0.3	2.07	0.15
MBS-158	349	350	0.03	0.248	0.004	76	52.4	1.5	553	36.48	13	0.15	2.34	0.28	1.87	0.13
MBS-158	350	351	0.44	0.388	0.097	90	75.3	1.2	10778	33.83	13.3	0.15	4.59	0.66	2.99	0.17
MBS-158	351	352	0.06	0.273	0.021	84	55.1	1.5	2536	37.81	13.65	0.16	2.31	0.27	1.93	0.13
MBS-158	352	353	0.04	0.278	0.005	71	46.4	1.5	704	38.3	13.97	0.16	2.4	0.27	1.82	0.15
MBS-158	353	354	0.04	0.271	0.005	85	57.1	1.5	576	40.13	14.73	0.17	2.49	0.27	1.9	0.13
MBS-158	354	355	0.03	0.261	0.004	83	52.4	1.6	458	37.97	13.75	0.16	2.27	0.26	1.86	0.13
MBS-158	355	356	0.1	0.29	0.014	79	51.6	1.5	1709	37.97	13.58	0.16	2.42	0.26	1.79	0.13
MBS-158	356	357	0.29	0.371	0.043	122	88.2	1.4	3516	36.98	13.67	0.15	2.25	0.2	1.72	0.13
MBS-158	357	358	0.07	0.268	0.008	87	57	1.5	943	35.65	13.1	0.15	2.31	0.18	1.67	0.13
MBS-158	358	359	0.05	0.25	0.006	91	56.6	1.6	637	35.82	12.67	0.15	2.23	0.2	1.75	0.12
MBS-158	359	360	0.2	0.269	0.029	79	62	1.3	3608	30.35	12.1	0.14	5.56	0.74	3.4	0.2

Hole_ID	m From	m To	S (wt. %)	Ni (wt. %)	Cu (wt. %)	Pd (ppb)	Pt (ppb)	Pd/Pt	Cu/Pd	MgO (wt. %)	Fe_2O_3 (wt. %)	MnO (wt. %)	Al_2O_3 (wt. %)	Na_2O (wt. %)	CaO (wt. %)	TiO_2 (wt. %)
MBS-158	360	361	0.18	0.266	0.031	106	52	2	2896	33.08	12.95	0.15	4.06	0.47	3.26	0.18
MBS-158	361	362	0.04	0.242	0.003	104	49.9	2.1	317	35.49	12.68	0.14	2.12	0.19	1.65	0.12
MBS-158	362	363	0.1	0.276	0.013	54	43.5	1.2	2444	35.82	12.71	0.14	2.04	0.15	1.61	0.12
MBS-158	363	364	0.22	0.326	0.034	70	61.3	1.1	4786	34.99	12.9	0.14	2.06	0.15	1.55	0.12
MBS-158	364	365	0.12	0.291	0.017	51	47.6	1.1	3235	35.32	12.54	0.14	2	0.18	1.57	0.12
MBS-158	365	366	0.04	0.254	0.003	54	41.4	1.3	556	36.48	13.18	0.15	2.21	0.19	1.68	0.13
MBS-158	366	367	0.04	0.251	0.004	55	36.4	1.5	673	35.65	12.9	0.14	2.23	0.2	1.6	0.12
MBS-158	367	368	0.04	0.248	0.004	59	47.5	1.2	644	34.49	12.22	0.14	2.1	0.15	1.12	0.12
MBS-209	215	216	0.07	0.034	0.009	0.5	0.3	1.7	188000	10.76	5.13	0.1	18.4	2.08	14.62	0.15
MBS-209	216	217	0.06	0.034	0.009	0.5	0.3	1.7	172000	10.63	5.23	0.1	17.33	1.91	14.48	0.15
MBS-209	217	218	0.06	0.035	0.008	0.5	0.3	1.7	162000	10.71	5.08	0.1	16.46	1.79	14.2	0.15
MBS-209	218	219	0.08	0.042	0.011	0.5	0.3	1.7	218000	12.1	5.48	0.11	15.23	1.66	15.32	0.18
MBS-209	219	220	0.15	0.072	0.023	0.5	0.3	1.7	458000	17.49	7.85	0.15	5.74	0.66	16.44	0.27
MBS-209	220	221	0.18	0.071	0.024	0.5	0.3	1.7	476000	17.99	7.89	0.16	5.67	0.63	16.37	0.25
MBS-209	221	222	0.16	0.07	0.023	0.5	0.3	1.7	466000	18.16	8.01	0.16	5.65	0.67	16.37	0.25
MBS-209	222	223	0.14	0.067	0.021	0.5	0.3	1.7	416000	16.35	7.96	0.14	6.14	0.86	13.94	0.28
MBS-209	223	224	0.13	0.067	0.02	0.5	0.3	1.7	392000	16.3	8.08	0.15	5.67	0.85	12.01	0.33
MBS-209	224	225	0.17	0.078	0.026	1	0.3	3.3	258000	19.98	8.64	0.17	4.16	0.46	14.55	0.23
MBS-209	225	226	0.17	0.079	0.026	0.5	0.3	1.7	518000	19.9	8.75	0.17	4.19	0.49	14.62	0.25
MBS-209	226	227	0.18	0.079	0.026	0.5	0.3	1.7	514000	19.65	8.62	0.17	4.14	0.46	14.2	0.23
MBS-209	227	228	0.21	0.095	0.034	0.5	0.8	0.6	674000	19.57	8.56	0.17	4.14	0.47	13.68	0.23
MBS-209	228	229	0.17	0.092	0.026	1	0.8	1.3	262000	20.56	9.18	0.18	4.48	0.51	14.55	0.27
MBS-209	229	230	0.16	0.098	0.025	2	1.9	1.1	125500	19.98	8.91	0.17	3.93	0.42	13.46	0.23
MBS-209	230	231	0.2	0.103	0.032	1	0.8	1.3	315000	19.57	8.44	0.17	4.01	0.43	14.06	0.23
MBS-209	231	232	0.21	0.112	0.033	0.5	0.3	1.7	664000	21.89	9.71	0.18	4.16	0.44	10.59	0.23
MBS-209	232	233	0.47	0.192	0.072	1	0.7	1.4	720000	25.45	11.69	0.19	3.76	0.32	4.28	0.2
MBS-209	233	234	1.06	0.42	0.164	3	7.3	0.4	546667	24.96	12.45	0.19	3.76	0.34	3.89	0.2
MBS-209	234	235	1.39	0.521	0.211	4	9.1	0.4	527500	25.04	12.98	0.19	3.87	0.36	3.83	0.22
MBS-209	235	236	1.18	0.448	0.147	3	4.3	0.7	490000	24.29	12.47	0.18	3.61	0.32	3.6	0.2
MBS-209	236	237	0.32	0.178	0.05	1	1.4	0.7	503000	26.03	11.75	0.19	3.72	0.34	3.39	0.2
MBS-209	237	238	0.36	0.187	0.056	2	1.5	1.3	278500	24.96	11.49	0.18	3.59	0.32	3.29	0.18
MBS-209	238	239	0.31	0.173	0.047	1	1.3	0.8	474000	25.62	11.57	0.19	3.59	0.31	3.41	0.18
MBS-209	239	240	0.25	0.155	0.039	1	1	1	394000	26.45	11.8	0.19	3.74	0.32	3.53	0.2
MBS-209	240	241	0.19	0.135	0.03	5	5.5	0.9	59400	26.2	11.52	0.19	3.67	0.31	3.26	0.18
MBS-209	241	242	0.19	0.137	0.03	1	0.8	1.3	296000	26.7	11.47	0.19	3.8	0.34	3.23	0.2

Hole_ID	m From	m To	S (wt. %)	Ni (wt. %)	Cu (wt. %)	Pd (ppb)	Pt (ppb)	Pd/Pt	Cu/Pd	MgO (wt. %)	Fe_2O_3 (wt. %)	MnO (wt. %)	Al_2O_3 (wt. %)	Na_2O (wt. %)	CaO (wt. %)	TiO_2 (wt. %)
MBS-209	242	243	0.21	0.147	0.031	1	1.1	0.9	314000	26.53	11.62	0.19	3.76	0.32	3.11	0.2
MBS-209	243	244	0.19	0.138	0.031	1	1.2	0.8	306000	25.7	11.12	0.18	3.87	0.38	3.06	0.2
MBS-209	244	245	0.21	0.143	0.034	1	1	1	340000	26.2	11.07	0.18	3.8	0.36	3.05	0.2
MBS-209	245	246	0.21	0.148	0.034	1	1.2	0.8	342000	26.37	11.39	0.19	3.78	0.35	3.04	0.2
MBS-209	246	247	0.22	0.147	0.034	1	1.6	0.6	341000	26.37	11.39	0.19	3.78	0.34	3.05	0.18
MBS-209	247	248	0.23	0.156	0.036	1	1.2	0.8	357000	27.28	11.47	0.19	3.87	0.35	3.09	0.2
MBS-209	248	249	0.2	0.144	0.032	1	0.9	1.1	318000	25.79	11.19	0.18	3.67	0.34	2.95	0.18
MBS-209	249	250	0.21	0.156	0.035	1	0.8	1.3	354000	26.37	10.92	0.18	3.78	0.34	3.02	0.18
MBS-209	250	251	0.17	0.138	0.028	1	0.9	1.1	275000	27.61	11.64	0.19	3.97	0.35	3.15	0.2
MBS-209	251	252	0.16	0.13	0.025	1	0.6	1.7	251000	26.45	11.09	0.18	3.78	0.34	3.01	0.18
MBS-209	252	253	0.15	0.133	0.026	1	0.8	1.3	259000	26.86	10.85	0.18	3.91	0.38	3.05	0.2
MBS-209	253	254	0.15	0.136	0.026	1	0.7	1.4	261000	26.86	11.04	0.18	3.84	0.38	2.99	0.2
MBS-209	254	255	0.15	0.137	0.03	1	0.9	1.1	295000	26.2	10.82	0.18	3.87	0.36	2.98	0.2
MBS-209	255	256	0.15	0.15	0.032	1	1.4	0.7	316000	27.94	11.19	0.19	3.68	0.3	3.12	0.22
MBS-209	256	257	0.11	0.141	0.026	1	1.2	0.8	255000	26.37	10.72	0.18	3.29	0.28	2.94	0.2
MBS-209	257	258	0.13	0.137	0.029	1	1.3	0.8	285000	25.45	10.31	0.17	3.33	0.32	2.84	0.18
MBS-209	258	259	0.15	0.143	0.03	1	1.7	0.6	304000	26.53	10.52	0.17	3.46	0.31	2.99	0.18
MBS-209	259	260	0.17	0.143	0.032	1	1.8	0.6	316000	25.79	10.44	0.17	3.36	0.3	2.9	0.18
MBS-209	260	261	0.16	0.144	0.019	1	2.1	0.5	190000	24.96	10.27	0.17	3.33	0.18	2.52	0.18
MBS-209	261	262	0.04	0.049	0.008	0.5	0.7	0.7	154000	7.86	4.06	0.07	10.37	3.32	1.94	0.13
MBS-209	262	263	0.13	0.123	0.027	1	2.2	0.5	273000	21.39	9.42	0.15	5.2	0.9	2.53	0.2
MBS-209	263	264	0.15	0.135	0.028	1	2.3	0.4	283000	26.37	10.64	0.17	3.42	0.3	2.78	0.18
MBS-209	264	265	0.02	0.028	0.01	0.5	0.6	0.8	206000	5.24	2.73	0.04	10.17	2.93	2.18	0.05
MBS-209	265	266	0.01	0.045	0.005	0.5	0.3	1.7	92000	7.38	4.17	0.05	11.41	2.32	1.96	0.2
MBS-209	266	267	0.02	0.127	0.006	0.5	2.1	0.2	118000	26.7	12.57	0.25	3.51	0.12	1.09	0.2
MBS-209	267	268	0.09	0.129	0.018	1	2	0.5	176000	26.28	10.25	0.17	3.21	0.26	2.77	0.18
MBS-209	268	269	0.09	0.131	0.022	1	1.9	0.5	216000	26.95	10.24	0.17	3.36	0.32	2.94	0.18
MBS-209	269	270	0.08	0.135	0.023	1	2	0.5	228000	27.28	10.52	0.17	3.53	0.36	3.01	0.18
MBS-209	270	271	0.07	0.13	0.025	1	2	0.5	251000	25.29	10.04	0.16	4.01	0.5	2.77	0.18
MBS-209	271	272	0.09	0.138	0.027	1	2.1	0.5	267000	27.86	10.48	0.18	3.59	0.39	2.98	0.18
MBS-209	272	273	0.12	0.144	0.029	1	2.6	0.4	285000	26.95	11.15	0.18	2.99	0.27	2.53	0.2
MBS-209	273	274	0.1	0.14	0.028	1	4.3	0.2	284000	27.03	10.72	0.17	3.23	0.34	2.69	0.2
MBS-209	274	275	0.06	0.112	0.021	1	2	0.5	206000	23.3	8.72	0.15	4.59	0.7	2.62	0.17
MBS-209	275	276	0.3	0.257	0.071	2	6.1	0.3	353000	25.79	10.52	0.16	3.46	0.35	2.66	0.18
MBS-209	276	277	0.34	0.261	0.063	3	5.5	0.5	209667	27.61	10.88	0.17	3.44	0.31	2.8	0.17

Hole_ID	m From	m To	S (wt. %)	Ni (wt. %)	Cu (wt. %)	Pd (ppb)	Pt (ppb)	Pd/Pt	Cu/Pd	MgO (wt. %)	Fe_2O_3 (wt. %)	MnO (wt. %)	Al_2O_3 (wt. %)	Na_2O (wt. %)	CaO (wt. %)	TiO_2 (wt. %)
MBS-209	277	278	0.21	0.198	0.059	2	10.6	0.2	292500	25.29	9.66	0.16	3.89	0.42	2.71	0.17
MBS-209	278	279	0.71	0.593	0.184	23	89.9	0.3	79783	24.13	10.82	0.15	4.84	0.69	2.77	0.17
MBS-209	279	280	1	0.64	0.201	27	123	0.2	74444	28.19	12.22	0.16	2.66	0.23	2.31	0.15
MBS-209	280	281	0.93	0.65	0.219	36	194	0.2	60833	28.11	12.02	0.16	2.76	0.26	2.22	0.15
MBS-209	281	282	1.02	0.66	0.146	30	157	0.2	48667	28.11	12.21	0.17	3.25	0.27	2.6	0.18
MBS-209	282	283	1.25	0.84	0.172	41	171	0.2	41951	28.27	12.74	0.16	2.91	0.28	2.38	0.17
MBS-209	283	284	0.56	0.427	0.083	45	164	0.3	18467	28.52	11.37	0.16	3.06	0.32	2.52	0.17
MBS-209	284	285	0.71	0.493	0.161	41	177	0.2	39268	27.94	11.62	0.16	2.8	0.31	2.39	0.15
MBS-209	285	286	1.83	1.16	0.326	53	278	0.2	61509	26.37	12.95	0.16	2.83	0.28	2.43	0.17
MBS-209	286	287	1.27	0.81	0.247	56	302	0.2	44107	27.11	12.17	0.16	3.19	0.32	2.59	0.17
MBS-209	287	288	0.45	0.355	0.094	29	144	0.2	32310	28.69	10.99	0.16	2.99	0.32	2.59	0.17
MBS-209	288	289	1.25	0.8	0.205	46	140	0.3	44565	29.52	12.57	0.16	2.65	0.24	2.29	0.15
MBS-209	289	290	1.41	0.82	0.216	47	113	0.4	45957	29.68	13.17	0.16	2.78	0.24	2.41	0.17
MBS-209	290	291	1.4	0.86	0.191	54	118	0.5	35370	29.27	12.71	0.16	2.76	0.24	2.36	0.15
MBS-209	291	292	1.38	0.79	0.193	46	116	0.4	41957	30.1	13.07	0.16	2.74	0.26	2.35	0.15
MBS-209	292	293	1.47	0.82	0.258	50	102	0.5	51600	30.51	13.51	0.16	2.53	0.23	2.17	0.15
MBS-209	293	294	1.5	0.82	0.352	58	104	0.6	60690	32.75	14.05	0.16	2.19	0.22	2	0.13
MBS-209	294	295	1.6	0.94	0.217	71	133	0.5	30563	32.75	14.51	0.17	2.21	0.22	1.96	0.13
MBS-209	295	296	1.57	0.92	0.226	65	138	0.5	34769	31.17	13.9	0.16	2.44	0.23	2.13	0.15
MBS-209	296	297	1.61	0.99	0.242	52	128	0.4	46538	30.26	13.22	0.16	2.48	0.23	2.14	0.15
MBS-209	297	298	1.69	0.97	0.289	49	109	0.4	58980	30.51	13.68	0.17	2.65	0.24	2.28	0.15
MBS-209	298	299	1.5	0.79	0.363	51	117	0.4	71176	28.6	12.88	0.16	2.91	0.27	2.45	0.17
MBS-209	299	300	2.37	1.42	0.214	54	158	0.3	39630	29.35	13.85	0.16	2.83	0.27	2.35	0.17
MBS-209	300	301	2.31	1.36	0.291	94	146	0.6	30957	28.69	13.48	0.15	2.63	0.26	2.27	0.15
MBS-209	301	302	2.53	1.42	0.217	70	184	0.4	31000	29.02	13.83	0.15	2.59	0.24	2.53	0.15
MBS-209	302	303	2.29	1.43	0.246	62	233	0.3	39677	30.01	14.13	0.15	2.31	0.23	2.07	0.13
MBS-209	303	304	1.73	1	0.33	81	127	0.6	40741	28.6	13.1	0.16	2.66	0.23	2.25	0.15
MBS-209	304	305	0.53	0.34	0.102	67	63	1.1	15224	27.94	10.65	0.15	2.91	0.26	2.76	0.17
MBS-209	305	306	0.2	0.202	0.042	38	717	0.1	11132	28.85	10.49	0.15	2.87	0.26	2.46	0.17
MBS-209	306	307	0.53	0.398	0.094	72	144	0.5	13097	32.25	12.6	0.16	2.53	0.23	2.14	0.15
MBS-209	307	308	0.17	0.295	0.028	57	92.6	0.6	4912	35.98	12.81	0.16	2.14	0.19	1.75	0.13
MBS-209	308	309	2.37	1.38	0.362	136	291	0.5	26618	31.67	14.65	0.16	2.25	0.24	1.85	0.15
MBS-209	309	310	2.42	1.38	0.349	139	328	0.4	25108	32.25	15.66	0.16	2.15	0.22	1.71	0.13
MBS-209	310	311	1.93	1.25	0.225	133	366	0.4	16917	33.83	15.01	0.15	1.89	0.19	1.44	0.12
MBS-209	311	312	1.82	1.16	0.241	126	360	0.4	19127	35.15	15.66	0.16	1.87	0.16	1.27	0.12

Hole_ID	m From	m To	S (wt. %)	Ni (wt. %)	Cu (wt. %)	Pd (ppb)	Pt (ppb)	Pd/Pt	Cu/Pd	MgO (wt. %)	Fe_2O_3 (wt. %)	MnO (wt. %)	Al_2O_3 (wt. %)	Na_2O (wt. %)	CaO (wt. %)	TiO_2 (wt. %)
MBS-209	312	313	1.92	1.23	0.283	148	399	0.4	19122	34.16	15.58	0.15	1.76	0.19	1.27	0.1
MBS-209	313	314	2.04	1.21	0.37	156	487	0.3	23718	33.08	14.87	0.15	1.76	0.19	1.44	0.12
MBS-209	314	315	2.07	1.31	0.353	178	505	0.4	19831	32.58	15.01	0.15	1.72	0.16	1.33	0.1
MBS-209	315	316	2.31	1.51	0.209	178	544	0.3	11742	33.5	16.23	0.16	1.83	0.16	1.39	0.1
MBS-209	316	317	1.78	1.23	0.203	223	576	0.4	9103	33.16	14.58	0.15	1.66	0.15	1.25	0.1
MBS-209	317	318	1.65	1.09	0.332	205	557	0.4	16195	34.49	15.66	0.15	1.44	0.13	0.98	0.08
MBS-209	318	319	1.68	1.14	0.252	175	429	0.4	14400	35.49	16.16	0.15	1.51	0.15	1.02	0.08
MBS-209	319	320	1.73	1.16	0.253	168	405	0.4	15060	37.14	15.8	0.16	1.45	0.15	1.06	0.08
MBS-209	320	321	1.73	1.17	0.245	164	342	0.5	14939	35.98	15.8	0.16	1.53	0.15	1.04	0.08
MBS-209	321	322	1.86	1.18	0.275	214	358	0.6	12850	35.32	15.94	0.16	1.8	0.18	1.33	0.1
MBS-209	322	323	0.6	0.568	0.098	39	65.4	0.6	25026	36.98	13.98	0.17	0.96	0.08	0.88	0.05
MBS-209	323	324	2.05	1.26	0.299	195	622	0.3	15333	31.59	15.3	0.17	2.15	0.19	1.64	0.12
MBS-209	324	325	2.4	1.61	0.237	194	469	0.4	12216	30.68	15.08	0.16	2.02	0.19	1.6	0.12
MBS-209	325	326	2.59	1.6	0.431	224	1000	0.2	19241	31.01	15.58	0.16	2.08	0.19	1.6	0.12
MBS-209	326	327	1.59	1.06	0.33	197	437	0.5	16751	33.83	15.44	0.16	2	0.2	1.29	0.12
MBS-209	327	328	0.99	0.75	0.203	136	334	0.4	14926	33	13.28	0.16	1.87	0.22	1.53	0.12
MBS-209	328	329	1	0.74	0.169	123	297	0.4	13699	35.82	14.44	0.17	1.89	0.23	1.51	0.12
MBS-209	329	330	0.88	0.71	0.172	105	250	0.4	16381	33.83	13.75	0.16	1.95	0.23	1.51	0.12
MBS-209	330	331	0.61	0.569	0.117	89	225	0.4	13090	33.16	12.55	0.16	1.76	0.22	1.43	0.12
MBS-209	331	332	1.65	1.05	0.217	124	246	0.5	17500	34.66	14.94	0.17	1.98	0.2	1.51	0.12
MBS-209	332	333	1.94	1.22	0.306	244	281	0.9	12541	34.66	16.01	0.17	2	0.18	1.18	0.12
MBS-209	333	334	1.91	1.25	0.293	225	290	0.8	13022	35.32	15.37	0.17	1.83	0.2	1.22	0.12
MBS-209	334	335	2.02	1.27	0.301	142	249	0.6	21197	35.49	16.16	0.17	1.62	0.19	1.06	0.1
MBS-209	335	336	2.12	1.4	0.291	164	426	0.4	17744	32.92	14.51	0.16	1.59	0.18	1.08	0.1
MBS-209	336	337	2.09	1.35	0.324	206	417	0.5	15728	34.82	16.44	0.17	1.66	0.22	1.08	0.1
MBS-209	337	338	2.34	1.45	0.42	259	459	0.6	16216	33.5	15.44	0.16	1.49	0.2	1.04	0.1
MBS-209	338	339	2.4	1.62	0.34	272	867	0.3	12500	31.75	15.51	0.15	1.3	0.19	1.02	0.08
MBS-209	339	340	2.07	1.35	0.355	202	580	0.3	17574	35.15	16.58	0.17	1.45	0.19	0.98	0.08
MBS-209	340	341	1.44	0.95	0.303	194	358	0.5	15619	35.15	15.51	0.16	1.53	0.18	0.99	0.1
MBS-209	341	342	1.3	0.84	0.234	216	419	0.5	10833	26.12	13.01	0.14	5.06	0.88	1.39	0.23
MBS-209	342	343	1.08	0.8	0.18	192	271	0.7	9375	34.49	14.24	0.17	2.1	0.18	1.2	0.12
MBS-209	343	344	0.62	0.593	0.104	190	173	1.1	5447	35.15	14.87	0.17	1.98	0.15	1.04	0.12
MBS-209	344	345	0.47	0.509	0.087	142	147	1	6134	34.82	13.71	0.17	1.8	0.2	1.25	0.1
MBS-209	345	346	0.97	0.78	0.152	407	440	0.9	3722	35.15	14.25	0.17	1.61	0.16	1.09	0.1
MBS-209	346	347	0.35	0.441	0.066	133	118	1.1	4992	36.31	14.73	0.17	1.62	0.13	0.98	0.1

Hole_ID	m From	m To	S (wt. %)	Ni (wt. %)	Cu (wt. %)	Pd (ppb)	Pt (ppb)	Pd/Pt	Cu/Pd	MgO (wt. %)	Fe_2O_3 (wt. %)	MnO (wt. %)	Al_2O_3 (wt. %)	Na_2O (wt. %)	CaO (wt. %)	TiO_2 (wt. %)
MBS-209	347	348	0.16	0.327	0.045	72	106	0.7	6278	36.48	13.71	0.17	1.66	0.19	1.11	0.1
MBS-209	348	349	0.09	0.321	0.017	90	44.7	2	1889	38.47	14.44	0.18	1.91	0.18	1.26	0.1
MBS-209	349	350	0.1	0.257	0.015	86	42.7	2	1709	28.44	11.25	0.14	5.04	1	1.46	0.08
MBS-209	350	351	0.24	0.38	0.043	138	177	0.8	3123	38.97	15.08	0.18	1.89	0.2	1.22	0.1
MBS-209	351	352	0.06	0.261	0.011	86	77.8	1.1	1267	32.42	13	0.17	3.5	0.63	1.68	0.12
MBS-209	352	353	0.08	0.298	0.013	102	98.8	1	1314	38.64	15.15	0.18	1.87	0.18	1.23	0.1
MBS-209	353	354	0.06	0.299	0.011	93	89	1	1183	37.97	14.44	0.18	1.8	0.15	1.22	0.1
MBS-209	354	355	0.04	0.309	0.007	99	93.9	1.1	727	37.14	13.7	0.16	1.72	0.18	1.12	0.1
MBS-209	355	356	0.05	0.297	0.007	101	90.5	1.1	693	36.15	13.52	0.15	1.7	0.18	1.09	0.08

Appendix C: Mirabela Major Element Data (ActaLabs; *denotes detection limit, C = Central Zone, N = Northern Zone, S= Southern Zone)

Zone-Hole	Sample No.	SiO2 (wt. %) *0.01	Al2O3 (wt. %) *0.01	Fe2O3(T) (wt. %) *0.01	MnO (wt. %) *0.001	MgO (wt. %) *0.01	CaO (wt. %) *0.01	Na2O (wt. %) *0.01	K2O (wt. %) *0.01	TiO2 (wt. %) *0.001	P2O5 (wt. %) *0.01	LOI	Total
C MBS604	PTSR0012	52.54	10.71	6.34	0.13	14.31	15.36	1.24	0.08	0.18	< 0.01	0.07	101.00
C MBS604	PTSR0013	53.00	3.49	8.92	0.18	20.69	13.45	0.39	0.05	0.24	< 0.01	0.16	100.60
C MBS604	PTSR0001	50.51	2.78	13.36	0.21	26.79	2.63	0.24	0.08	0.16	< 0.01	1.10	97.86
C MBS604	PTSR0002	47.00	4.23	13.75	0.18	26.82	2.41	0.15	0.02	0.20	< 0.01	0.07	94.84
C MBS604	PTSR0003	45.22	3.81	14.23	0.17	28.76	1.88	0.09	< 0.01	0.17	< 0.01	0.20	94.54
C MBS604	PTSR0004	53.34	2.99	12.19	0.17	27.69	2.44	0.26	0.04	0.17	< 0.01	0.29	99.57
C MBS604	PTSR0005	49.89	2.49	12.56	0.17	29.03	2.22	0.19	0.03	0.14	< 0.01	0.43	97.13
C MBS604	PTSR0006	47.15	2.19	12.25	0.17	34.49	1.74	0.16	0.06	0.12	0.01	0.49	98.84
C MBS604	PTSR0007	48.59	1.94	12.90	0.16	32.66	1.61	0.12	0.02	0.11	0.03	-0.53	97.61
C MBS604	PTSR0008	38.88	1.26	13.27	0.16	41.88	0.83	0.12	0.02	0.07	0.02	0.68	97.19
C MBS604	PTSR0009	40.12	1.27	12.46	0.17	43.75	0.75	0.11	0.02	0.07	< 0.01	-0.66	98.08
C MBS604	PTSR0010	40.81	1.05	13.83	0.17	44.43	0.78	0.13	0.02	0.06	< 0.01	-1.00	100.30
C MBS604	PTSR0011	40.50	1.05	13.75	0.17	44.28	0.73	0.13	0.02	0.06	0.02	-0.85	99.88
C MBS605	PTSR0014	51.99	10.06	6.24	0.13	14.70	15.11	1.10	0.05	0.16	< 0.01	0.09	99.64
C MBS605	PTSR0015	52.89	3.32	8.47	0.17	19.67	15.26	0.34	0.01	0.20	< 0.01	-0.13	100.20
C MBS605	PTSR0016	52.08	2.91	12.35	0.17	27.29	2.64	0.25	0.04	0.16	0.02	0.41	98.32
C MBS605	PTSR0017	51.69	2.71	11.84	0.17	27.92	2.55	0.21	0.03	0.17	< 0.01	0.12	97.40
C MBS605	PTSR0018	52.52	2.53	12.79	0.17	28.00	2.23	0.17	0.03	0.15	0.02	-0.32	98.27
C MBS605	PTSR0019	50.97	2.75	11.78	0.18	28.55	2.39	0.26	0.06	0.16	< 0.01	0.74	97.86
C MBS605	PTSR0020	40.36	1.38	15.53	0.17	38.54	0.97	0.12	0.02	0.08	0.01	-0.10	97.08
C MBS605	PTSR0021	41.20	1.42	13.68	0.17	41.41	1.00	0.13	0.02	0.08	0.01	-0.73	98.37
C MBS605	PTSR0022	43.45	1.43	14.18	0.17	39.50	1.13	0.14	0.03	0.08	0.02	-0.25	99.89
C MBS605	PTSR0023	43.94	1.62	12.75	0.17	38.95	1.27	0.12	0.02	0.09	0.03	-0.67	98.28
C MBS605	PTSR0024	39.41	1.37	12.47	0.16	42.51	0.80	0.13	0.03	0.07	0.03	-0.94	96.04
C MBS605	PTSR0025	40.77	1.22	14.11	0.17	43.80	0.81	0.12	0.02	0.07	< 0.01	-1.08	100.00
N MBS209	PTSR0026	51.62	15.38	4.82	0.10	10.31	14.33	1.86	0.13	0.16	< 0.01	0.29	99.00
N MBS209	PTSR0027	53.26	3.70	8.25	0.17	19.63	15.02	0.43	0.05	0.24	0.01	-0.01	100.70
N MBS209	PTSR0028	53.97	3.48	11.46	0.19	26.47	3.66	0.36	0.06	0.20	< 0.01	-0.08	99.76
N MBS209	PTSR0029	54.08	3.13	11.14	0.18	28.14	3.05	0.25	0.07	0.21	0.02	-0.06	100.20

Zone-Hole	Sample No.	SiO2 (wt. %) *0.01	Al2O3 (wt. %) *0.01	Fe2O3(T) (wt. %) *0.01	MnO (wt. %) *0.001	MgO (wt. %) *0.01	CaO (wt. %) *0.01	Na2O (wt. %) *0.01	K2O (wt. %) *0.01	TiO2 (wt. %) *0.001	P2O5 (wt. %) *0.01	LOI	Total
N MBS209	PTSR0030	50.42	2.92	12.51	0.16	27.00	2.66	0.30	0.08	0.17	0.01	1.34	97.57
N MBS209	PTSR0031	52.33	3.21	10.17	0.16	29.09	2.64	0.29	0.06	0.17	0.02	-0.01	98.13
N MBS209	PTSR0032	38.05	1.59	15.73	0.16	37.64	1.05	0.16	0.04	0.09	0.03	3.50	98.05
N MBS209	PTSR0033	43.57	2.07	14.26	0.16	34.38	1.66	0.18	0.03	0.11	< 0.01	1.64	98.07
N MBS209	PTSR0034	36.16	1.27	15.79	0.15	36.39	1.07	0.20	0.04	0.09	0.02	6.25	97.43
N MBS209	PTSR0035	39.48	1.60	13.84	0.15	36.81	1.15	0.16	0.03	0.09	0.01	3.77	97.12
N MBS209	PTSR0036	39.75	1.60	13.84	0.16	40.42	1.13	0.19	0.05	0.09	0.02	2.16	99.41
N MBS209	PTSR0037	38.58	1.66	12.15	0.16	40.20	1.17	0.17	0.04	0.09	0.01	2.59	96.83
N MBS158	PTSR0038	52.05	14.87	6.36	0.12	10.42	13.16	2.03	0.18	0.23	< 0.01	0.20	99.60
N MBS158	PTSR0039	50.24	4.45	10.75	0.18	17.50	14.27	0.63	0.20	0.31	0.02	1.21	99.74
N MBS158	PTSR0040	52.31	5.71	11.28	0.16	22.86	4.31	0.76	0.19	0.24	0.03	0.64	98.50
N MBS158	PTSR0041	48.55	3.38	12.68	0.16	26.48	4.55	0.37	0.10	0.20	0.02	0.70	97.19
N MBS158	PTSR0042	41.09	2.80	15.15	0.17	34.07	2.91	0.33	0.06	0.14	< 0.01	2.15	98.86
N MBS158	PTSR0043	39.23	2.71	15.09	0.16	35.29	2.03	0.33	0.07	0.16	0.01	3.15	98.24
N MBS158	PTSR0044	39.64	2.57	12.34	0.16	33.54	3.01	0.25	0.04	0.14	0.01	6.52	98.22
N MBS158	PTSR0045	39.29	2.52	15.42	0.17	34.58	2.26	0.27	0.08	0.14	< 0.01	3.68	98.43
N MBS158	PTSR0046	38.58	2.73	13.45	0.16	34.34	2.15	0.24	0.04	0.15	0.02	5.71	97.58
N MBS158	PTSR0047	37.75	2.76	14.37	0.16	34.31	2.08	0.24	0.04	0.14	0.02	6.79	98.66
N MBS158	PTSR0048	45.21	2.76	13.31	0.17	35.80	2.61	0.32	0.05	0.17	0.02	-0.12	100.30
N MBS158	PTSR0049	37.94	2.36	13.38	0.16	36.37	1.80	0.19	0.05	0.14	0.02	6.03	98.42
S MBS565	PTSR0050	52.84	4.68	7.83	0.16	17.72	16.16	0.53	0.05	0.24	0.01	0.19	100.40
S MBS565	PTSR0051	50.20	4.54	11.98	0.17	26.49	3.06	0.31	0.03	0.24	0.02	-0.36	96.68
S MBS565	PTSR0052	52.61	2.94	10.59	0.17	27.58	2.62	0.25	0.06	0.16	< 0.01	0.22	97.21
S MBS565	PTSR0053	52.09	2.64	10.72	0.16	30.17	2.28	0.20	0.03	0.14	< 0.01	-0.17	98.26
S MBS565	PTSR0054	45.24	1.95	12.43	0.16	36.30	1.55	0.17	0.04	0.10	0.02	1.82	99.78
S MBS565	PTSR0055	43.56	1.67	14.22	0.16	36.32	1.27	0.13	0.02	0.08	0.02	0.16	97.63
S MBS565	PTSR0056	40.38	1.40	14.27	0.15	37.94	1.08	0.12	0.02	0.07	0.01	1.32	96.76
S MBS565	PTSR0057	40.20	1.55	12.72	0.15	40.53	1.00	0.16	0.04	0.08	0.02	1.18	97.65
S MBS565	PTSR0058	39.40	1.36	12.19	0.16	42.81	0.73	0.12	0.03	0.07	0.02	-0.36	96.53
S MBS565	PTSR0059	39.00	1.18	13.05	0.17	43.10	0.83	0.13	0.02	0.06	0.01	-0.68	96.87

Zone-Hole	Sample No.	SiO2 (wt. %) *0.01	Al2O3 (wt. %) *0.01	Fe2O3(T) (wt. %) *0.01	MnO (wt. %) *0.001	MgO (wt. %) *0.01	CaO (wt. %) *0.01	Na2O (wt. %) *0.01	K2O (wt. %) *0.01	TiO2 (wt. %) *0.001	P2O5 (wt. %) *0.01	LOI	Total
S MBS565	PTSR0060	39.45	1.18	13.80	0.17	43.53	0.79	0.13	0.02	0.06	0.02	-0.97	98.18
S MBS569	PTSR0061	52.94	13.43	6.72	0.12	14.14	11.40	1.59	0.13	0.17	< 0.01	-0.03	100.60
S MBS569	PTSR0062	52.37	4.38	8.27	0.16	18.78	14.33	0.52	0.05	0.23	0.01	0.08	99.18
S MBS569	PTSR0063	53.12	3.53	12.25	0.18	26.61	3.28	0.37	0.09	0.25	0.02	0.05	99.75
S MBS569	PTSR0064	48.51	3.00	12.38	0.16	28.87	2.20	0.21	0.04	0.17	< 0.01	1.22	96.77
S MBS569	PTSR0065	48.41	2.32	12.25	0.16	32.40	1.93	0.18	0.05	0.13	0.02	1.62	99.46
S MBS569	PTSR0066	49.89	2.48	12.15	0.16	29.88	2.17	0.18	0.05	0.15	0.03	0.24	97.39
S MBS569	PTSR0067	44.52	2.09	13.10	0.16	36.97	1.63	0.20	0.06	0.12	< 0.01	1.21	100.10
S MBS569	PTSR0068	41.64	1.67	12.96	0.16	39.18	1.38	0.16	0.03	0.09	0.02	1.65	98.94
S MBS569	PTSR0069	46.65	2.07	12.51	0.17	36.71	1.72	0.19	0.04	0.11	0.02	-0.26	99.92
S MBS569	PTSR0070	38.66	1.14	14.92	0.17	42.34	0.76	0.13	0.03	0.06	0.02	0.20	98.43
S MBS569	PTSR0071	37.03	1.03	13.22	0.16	40.78	0.65	0.12	0.02	0.05	0.02	4.12	97.22
S MBS569	PTSR0072	40.21	1.04	13.91	0.17	42.03	0.64	0.07	0.01	0.05	< 0.01	-0.53	97.62

Appendix D: Mirabela Trace REE Data (Cardiff University C = Central Zone, N = Northern Zone, S= Southern Zone)

Zone-Hole	Sample No.	139La (ppm)	140Ce (ppm)	141Pr (ppm)	146Nd (ppm)	147Sm (ppm)	153Eu (ppm)	157Gd (ppm)	159Tb (ppm)	163Dy (ppm)	165Ho (ppm)	166Er (ppm)	169Tm (ppm)	172Yb (ppm)	175Lu (ppm)
C MBS-604	PTSR-012	0.87	2.09	0.35	1.71	0.56	0.24	0.66	0.15	0.87	0.18	0.46	0.08	0.45	0.08
C MBS-604	PTSR-013	0.89	2.10	0.35	1.82	0.67	0.26	0.84	0.20	1.08	0.23	0.65	0.11	0.68	0.10
C MBS-604	PTSR-01	0.53	1.07	0.16	0.68	0.18	0.10	0.31	0.05	0.36	0.08	0.25	0.05	0.23	0.04
C MBS-604	PTSR-02	0.45	0.91	0.12	0.53	0.19	0.07	0.20	0.05	0.27	0.06	0.19	0.04	0.24	0.04
C MBS-604	PTSR-07	0.20	0.42	0.06	0.31	0.10	0.05	0.13	0.02	0.20	0.05	0.14	0.02	0.16	0.04
C MBS-604	PTSR-11	0.97	1.88	0.24	0.90	0.22	0.11	0.23	0.04	0.24	0.05	0.13	0.02	0.12	0.02
C MBS-605	PTSR-25	0.66	1.25	0.17	0.87	0.17	0.06	0.19	0.04	0.26	0.05	0.13	0.03	0.15	0.03
N MBS-158	PTSR-38	2.23	4.67	0.67	2.75	0.79	0.36	0.92	0.18	1.02	0.19	0.57	0.08	0.61	0.09
N MBS-158	PTSR-39	1.80	4.44	0.69	3.23	0.98	0.32	1.23	0.24	1.57	0.31	0.82	0.12	0.91	0.12
N MBS-158	PTSR-40	2.76	5.70	0.76	2.74	0.74	0.22	0.67	0.12	0.70	0.16	0.43	0.07	0.45	0.07
N MBS-158	PTSR-41	1.11	2.36	0.33	1.17	0.39	0.09	0.35	0.07	0.53	0.11	0.30	0.05	0.28	0.06
N MBS-158	PTSR-44	0.87	1.85	0.23	1.03	0.37	0.13	0.37	0.08	0.55	0.09	0.28	0.05	0.29	0.05
N MBS-158	PTSR-49	1.29	2.50	0.31	1.30	0.32	0.12	0.29	0.06	0.49	0.07	0.24	0.03	0.19	0.04

Appendix E: Mirabela PGE Whole-Rock Data (ActaLabs; *denotes detection limit, C = Central Zone, N = Northern Zone, S= Southern Zone)

Zone-Hole	Sample No.	Ir (ppb) *1	Ru (ppb) *1	Rh (ppb) *1	Pt (ppb) *1	Pd (ppb) *1	Au (ppb) *1
C MBS604	PTSR0012	< 1	5	< 1	< 1	< 1	< 1
C MBS604	PTSR0013	< 1	6	< 1	< 1	< 1	< 1
C MBS604	PTSR0001	5	9	2	46	15	36
C MBS604	PTSR0002	100	70	60	991	409	103
C MBS604	PTSR0003	59	43	34	770	325	733
C MBS604	PTSR0004	31	37	11	238	76	114
C MBS604	PTSR0005	27	31	10	285	114	802
C MBS604	PTSR0006	7	15	4	70	45	22
C MBS604	PTSR0007	23	32	10	390	209	106
C MBS604	PTSR0008	10	21	7	132	188	3
C MBS604	PTSR0009	7	17	6	84	99	1
C MBS604	PTSR0010	4	12	3	31	60	1
C MBS604	PTSR0011	7	14	7	89	317	< 1
C MBS605	PTSR0014	< 1	5	< 1	< 1	< 1	< 1
C MBS605	PTSR0015	< 1	6	< 1	< 1	< 1	< 1
C MBS605	PTSR0016	2	15	2	74	13	39
C MBS605	PTSR0017	39	53	15	321	96	109
C MBS605	PTSR0018	12	22	5	159	39	80
C MBS605	PTSR0019	18	26	5	169	51	143
C MBS605	PTSR0020	36	39	11	378	105	161
C MBS605	PTSR0021	< 1	6	< 1	73	10	33
C MBS605	PTSR0022	< 1	12	2	122	35	81
C MBS605	PTSR0023	20	26	11	186	116	41
C MBS605	PTSR0024	< 1	16	4	31	74	9
C MBS605	PTSR0025	< 1	16	4	30	84	17
N MBS209	PTSR0026	< 1	6	< 1	< 1	< 1	6
N MBS209	PTSR0027	< 1	3	1	< 1	< 1	< 1
N MBS209	PTSR0028	< 1	6	< 1	< 1	< 1	15
N MBS209	PTSR0029	< 1	5	1	1	< 1	20
N MBS209	PTSR0030	16	25	6	292	68	196
N MBS209	PTSR0031	4	14	4	65	32	24
N MBS209	PTSR0032	39	46	15	709	210	338
N MBS209	PTSR0033	38	52	16	84	173	85
N MBS209	PTSR0034	36	46	16	609	247	220
N MBS209	PTSR0035	35	57	21	355	403	189
N MBS209	PTSR0036	4	13	5	66	49	44
N MBS209	PTSR0037	8	24	7	77	81	12
N MBS158	PTSR0038	< 1	< 1	< 1	1	2	< 1
N MBS158	PTSR0039	< 1	8	1	2	2	14
N MBS158	PTSR0040	4	13	3	25	11	24
N MBS158	PTSR0041	6	12	3	86	53	55
N MBS158	PTSR0042	38	59	15	564	107	202
N MBS158	PTSR0043	23	49	13	199	155	95
N MBS158	PTSR0044	10	19	8	50	70	10
N MBS158	PTSR0045	32	49	16	565	212	178

Zone-Hole	Sample No.	Ir (ppb) *1	Ru (ppb) *1	Rh (ppb) *1	Pt (ppb) *1	Pd (ppb) *1	Au (ppb) *1
N MBS158	PTSR0046	14	14	14	138	119	49
N MBS158	PTSR0047	33	45	20	313	202	178
N MBS158	PTSR0048	9	17	9	177	201	11
N MBS158	PTSR0049	8	10	7	51	64	7
S MBS565	PTSR0050	7	1	7	< 1	< 1	< 1
S MBS565	PTSR0051	< 1	24	11	7	25	7
S MBS565	PTSR0052	12	22	7	110	60	73
S MBS565	PTSR0053	17	27	8	141	32	25
S MBS565	PTSR0054	3	8	4	40	24	10
S MBS565	PTSR0055	33	43	13	349	112	183
S MBS565	PTSR0056	20	37	9	268	102	83
S MBS565	PTSR0057	3	10	4	77	34	16
S MBS565	PTSR0058	4	28	9	54	155	17
S MBS565	PTSR0059	2	12	5	31	77	14
S MBS565	PTSR0060	2	22	4	27	58	30
S MBS569	PTSR0061	< 1	5	< 1	1	1	< 1
S MBS569	PTSR0062	< 1	10	< 1	< 1	3	< 1
S MBS569	PTSR0063	3	5	2	46	14	33
S MBS569	PTSR0064	20	41	18	287	216	139
S MBS569	PTSR0065	19	28	7	194	48	36
S MBS569	PTSR0066	9	17	5	92	75	113
S MBS569	PTSR0067	< 1	5	2	14	8	4
S MBS569	PTSR0068	6	16	5	65	45	19
S MBS569	PTSR0069	3	13	4	52	36	36
S MBS569	PTSR0070	7	18	10	91	168	10
S MBS569	PTSR0071	4	12	5	50	57	3
S MBS569	PTSR0072	5	8	6	45	90	< 1

Appendix F: Mirabela Semimetal Data (ActaLabs; *denotes detection limit,
C = Central Zone, N = Northern Zone, S= Southern Zone)

Zone-Hole	Sample No.	As (ppm) *0.1	Bi (ppm) *0.02	Sb (ppm) *0.02	Se (ppm) *0.1	Te (ppm) *0.02	S (wt. %) *0.001
N MBS209	PTSR0026	0.30	0.03	0.03	0.40	0.10	0.12
N MBS209	PTSR0027	0.30	< 0.02	0.03	0.50	0.04	0.19
N MBS209	PTSR0028	0.50	0.05	0.05	1.20	< 0.02	0.24
N MBS209	PTSR0029	0.20	0.02	0.03	0.90	0.11	0.12
N MBS209	PTSR0030	3.20	0.33	0.04	11.80	1.77	1.61
N MBS209	PTSR0031	0.30	< 0.02	0.03	0.60	0.22	0.11
N MBS209	PTSR0032	1.90	0.19	0.02	12.00	3.14	1.51
N MBS209	PTSR0033	2.30	0.20	< 0.02	14.50	3.13	1.92
N MBS209	PTSR0034	7.00	0.24	< 0.02	13.80	3.33	1.66
N MBS209	PTSR0035	5.40	0.11	0.02	7.10	1.86	0.90
N MBS209	PTSR0036	1.40	< 0.02	< 0.02	1.00	0.22	0.10
N MBS209	PTSR0037	1.10	< 0.02	< 0.02	0.50	0.10	0.05
N MBS158	PTSR0038	0.60	< 0.02	0.02	0.50	0.09	0.11
N MBS158	PTSR0039	0.80	0.05	< 0.02	2.70	0.19	0.83
N MBS158	PTSR0040	1.00	0.11	< 0.02	6.10	0.65	1.07
N MBS158	PTSR0041	1.30	0.15	< 0.02	8.40	1.13	1.47
N MBS158	PTSR0042	2.30	0.14	< 0.02	10.20	2.09	1.36
N MBS158	PTSR0043	1.10	0.15	< 0.02	9.50	1.51	1.35
N MBS158	PTSR0044	0.50	< 0.02	< 0.02	0.70	0.20	0.08
N MBS158	PTSR0045	1.70	0.13	0.03	9.20	2.06	1.20
N MBS158	PTSR0046	0.40	0.02	< 0.02	2.00	0.55	0.29
N MBS158	PTSR0047	0.80	0.08	< 0.02	5.90	1.78	0.79
N MBS158	PTSR0048	0.20	< 0.02	< 0.02	0.20	0.17	0.05
N MBS158	PTSR0049	0.20	0.06	< 0.02	0.70	0.10	0.12
S MBS565	PTSR0050	0.20	< 0.02	< 0.02	0.50	< 0.02	0.15
S MBS565	PTSR0051	0.80	0.05	< 0.02	2.40	0.72	0.47
S MBS565	PTSR0052	0.70	0.07	0.03	4.10	0.89	0.70
S MBS565	PTSR0053	0.50	0.03	0.02	2.00	0.63	0.28
S MBS565	PTSR0054	0.20	< 0.02	0.08	0.80	0.26	0.14
S MBS565	PTSR0055	1.80	0.14	< 0.02	8.50	2.40	1.41
S MBS565	PTSR0056	1.50	0.15	0.03	10.50	2.46	1.40
S MBS565	PTSR0057	0.60	< 0.02	1.10	1.00	0.40	0.14
S MBS565	PTSR0058	0.20	< 0.02	0.03	0.10	0.19	0.05
S MBS565	PTSR0059	0.30	< 0.02	< 0.02	0.30	0.10	0.04
S MBS565	PTSR0060	0.20	< 0.02	0.02	0.10	0.08	0.04
S MBS569	PTSR0061	0.20	< 0.02	0.04	< 0.1	0.02	0.08
S MBS569	PTSR0062	0.40	< 0.02	0.05	0.90	0.03	0.23
S MBS569	PTSR0063	0.70	0.06	0.02	4.00	0.72	0.70
S MBS569	PTSR0064	1.50	0.21	0.06	11.40	2.77	1.84
S MBS569	PTSR0065	0.70	0.06	0.02	4.60	1.23	0.60
S MBS569	PTSR0066	4.10	0.13	0.08	5.60	1.52	0.84
S MBS569	PTSR0067	1.10	< 0.02	< 0.02	0.50	0.13	0.06
S MBS569	PTSR0068	1.00	< 0.02	< 0.02	1.10	0.30	0.15
S MBS569	PTSR0069	0.50	0.02	< 0.02	2.00	0.65	0.34
S MBS569	PTSR0070	< 0.1	< 0.02	< 0.02	0.40	0.12	0.06

Zone-Hole	Sample No.	As (ppm) *0.1	Bi (ppm) *0.02	Sb (ppm) *0.02	Se (ppm) *0.1	Te (ppm) *0.02	S (wt. %) *0.001
S MBS569	PTSR0071	0.30	< 0.02	< 0.02	0.10	0.04	0.02
S MBS569	PTSR0072	0.10	< 0.02	< 0.02	0.20	0.02	0.02

Appendix G: Mirabela Full PGM Mineralogical Data (BMS = Base metal sulphides, Cpy = Chalcopyrite, Cr = Chromite,Mgt = Magnetite, Ol = Olivine, Pn = Pentlandite, Po = Pyrrhotite, Py = Pyrite, Pyx = Pyroxene, Serp = Serpentine, Sil = Unknown Silicate)

Drill Hole	Sample No.	PGM No.	PGM Composition	Size (µm)			Area (µm^2)	Association
MBS604	PTSR-01	A1	Ag-Te	1.4	x	3.3	4.62	Within BMS, within Pn and in contact at edge with Po
		A2	Ag-Te	1.0	x	3.4	3.4	Within BMS, within Pn (Pn associated with Po)
		A3	Ag-Te	0.8	x	1.3	1.04	Within BMS, within Pn (Note, 1-3 goes left to right on image)
		B1	Ni-Pt-Te	1.9	x	3.7	7.03	Within BMS, within Py (Py associated with Pn)
		B2	Ni-Pt-Te	1.8	x	1.8	3.24	Within BMS, within Py (Note, B2 observed in B1 Loc 1 Image)
		C1	Ag-Te	0.8	x	3.1	2.48	Within/edge BMS, within/edge Py (Py associated with Pn) and in contact with Pyx
		C2	Ag-Te	4.7	x	5.3	24.91	Within/edge BMS, within/edge Pn (mostly within Pn) and in contact with Pyx
		C3	Ag-Te	0.8	x	10.6	8.48	Within/edge BMS, within/edge Pn and in contact with Pyx (Note, 1-3 goes left to right on image)
		D1	Ag-Te	2.7	x	4.1	11.07	Within BMS, within Pn (Pn associated with Py). Note: size = size of largest fragment of PGM grain
		E1	Ag-Te	1.9	x	11.6	22.04	Within/edge BMS, within/edge Pn and in contact with Pyx
		F1	Ag-Te	1.7	x	2.3	3.91	Within BMS, within Po (Po associated with Pn)
MBS604	PTSR-02	A1	Pt-Pd-Te	1.1	x	1.6	1.76	Within/edge BMS, within edge Pn/Cpy and in contact with Pyx (Pn/Cpy associated with Py)
		B1	Pt-Pd-Ni-Fe-Te	2.3	x	4.6	10.58	Within BMS, within Pn (Pn associated with Cr)
		C1	Pt-Ni-Pd-Te	2.5	x	4.1	10.25	Within silicate, within Pyx
		D1	Pt-Ni-Pd-Te	2.4	x	5.4	12.96	Within/edge BMS, within edge Pn/Cpy and in contact with Pyx
		E1	Ni-Pt-Te	1.4	x	4.2	5.88	Within/edge BMS, within/edge Cpy and in contact with Pyx
		F1	Pt-Pd-Te	0.5	x	5.2	2.6	Within BMS, within Pn
		G1	Pt-Pd-Ni-Te	1.1	x	7.2	7.92	Within BMS, within Pn
		H1	Pt-Pd-Ni-Te	2.3	x	6.4	14.72	Within/edge BMS, within/edge Pn (Pn associated with Mgt and Cpy) and in contact with Pyx
		I1	Pt-Te	2.4	x	10.0	24	Within/edge BMS, within/edge Pn (Pn associated with Py) petruding from BMS into Pyx
		I2	Pt-Te	2.2	x	24.9	54.78	Within/edge BMS, within/edge Pn (Pn associated with Py) petruding from BMS into Pyx
		J1	Pt-Ni-Pd-Te	4.3	x	9.9	42.57	Within BMS, within Pn
		K1	Pt-Ni-Te	3.1	x	5.6	17.36	Within Pyx and in contact with sulphide stringer oxidised Po (associated with Po crystal?)
		K!	Second Part of K1	2.1	x	5.4	11.34	As above, smaller part of PGM divided by thin 'string' of PGM
		L1	Pt-Ni-Pd-Te	2.9	x	8.3	24.07	Brightest top section only, the remaining bright patch is oxidised Cu-Ni-Fe-bearing, little Te and no PGE detected. In contact with Pyx and Cpy, unknown if the PGM lies within either of these phases
		M1	Pt-Pd-Ni-Te	3.3	x	7.6	25.08	Within/edge BMS, within/edge Pn/Py and in contact with Pyx
		N1	Ni-Fe-Pt-Te	0.8	x	1.7	1.36	Within/edge BMS, within edge Pn/Py and in contact with Pyx
MBS604	PTSR-03	A1	Pt-Pd-Te	1.3	x	2.5	3.25	Within BMS, within Pn (Pn associated with Po)
		B1	Pt-Te	1.9	x	4.1	7.79	Within BMS, within Pn
		C1	Ni-Pt-Pd-Te	7.7	x	16.3	125.51	Within/edge BMS, within/edge Cpy/Pn and in contact with Pyx
		D1	Pt-Ni-Te/Ag-Te	0.7	x	13.1	9.17	Within/edge BMS, within/edge Cpy stringer and in contact with Pyx
		D2	Pd-Te	1.0	x	4.3	4.3	Within/edge BMS, within/edge Cpy stringer and in contact with Pyx
		D3	Ni-Pt-Pd-Te/Ag-Te	1.7	x	5.8	9.86	Within/edge BMS, within/edge Cpy stringer and in contact with Pyx
		E1	Pd-Pt-Ni-Fe-Te	15.6	x	18.6	290.16	Within/edge BMS, within/edge Cpy/Py and in contact with Serp
		F1	Pt-Te	3.7	x	19.6	72.52	Within Serp and in contact with Pn
		G1	Pt-Ni-Pd-Te/Ag-Te	0.7	x	22.1	15.47	Potentially associated with Pn/Mgt stringer within fracture/vein within Ol/Serp

Drill Hole	Sample No.	PGM No.	PGM Composition	Size (µm)			Area (µm^2)	Association
MBS604	PTSR-03	G2	Pt-Ni-Pd-Te/Ag-Te	0.4	x	6.8	2.72	Potentially associated with Pn/Mgt stringer within fracture/vein within Ol/Serp
		H1	Pt-Ni-Pd-Te	1.8	x	29.6	53.28	Potentially associated with Po stringer aligned along fracture/vein in Pyx
		H2	Au	1.5	x	5.3	7.95	Within Pyx
		I1	Pt-Ni-Pd-Te	1.2	x	9.3	11.16	Associated with Pn stringer aligned along fracture/vein in Serp
		J1	Pt-Pd-Ni-Te	2.0	x	9.6	19.2	Within BMS, within Pn (Pn associated with Py)
		K1	Pt-Pd-Fe-Te	1.6	x	2.0	3.2	Within BMS, within Pn (Pn associated with Mgt and Cr)
		L1	Pt-Pd-Ni-Te	1.7	x	1.7	2.89	Within BMS, within Cpy
		L2	Pt-Pd-Ni-Te	1.5	x	2.1	3.15	Within BMS, within Cpy
		M1	Pt-Ni-Pd-Te	1.3	x	2.9	3.77	Within/edge BMS, within/edge Po and in contact with Pyx
		N1	Pt-Pd-Te±Ni	1.0	x	8.9	8.9	PGM cluster with only the largest measured for size. Associated with Cpy stringer aligned along fracture/vein in Serp
		O1	Au-Ag	2.4	x	3.1	7.44	Within/edge BMS, within/edge Cpy and in contact with Pyx
		P1	Pt-Te	8.3	x	11.6	96.28	Within/edge BMS, within/edge Pn (Pn associated with Py) and in contact with Pyx
MBS604	PTSR-04	A1	Au-Ag	4.4	x	4.7	20.68	Within BMS, within Cpy
		B1	Pb-Ag-Se-Te	1.9	x	2.7	5.13	Within/edge BMS, within/edge Cpy and in contact with Pyx
		B2	Ag-Te (darker)	2.1	x	5.4	11.34	Within/edge BMS, within/edge Cpy and in contact with Pyx
			Pb-Fe-Te (lighter)	3.6	x	4.3	15.48	Within/edge BMS, within/edge Cpy and in contact with Pyx
	Light Pic	B3	Pt-Bi-Te (lighter)	2.3	x	5.0	11.5	Within BMS, within Cpy
			Ag-Te (darker)	2.4	x	3.2	7.68	Within BMS, within Cpy
		C1	Ni-Pt-Pd-Te	6.6	x	6.8	44.88	Within BMS, within Pn
		D1	Ag-Te/Pt-Ni-Te	4.5	x	11.8	53.1	Within/edge BMS, within/edge Pn (Pn associated with Py) and in contact with Pyx
		E1	Ni-Pt-Pd-Te	2.1	x	2.5	5.25	Rimmed on one side by Pd-Te-O, size measured does not include rim (1.5x2.4). Edge BMS, edge Pn and in contact with Pyx. Unknown if hosted in BMS or silicates
		F1	Pt-Ni-Te	3.8	x	4.0	15.2	Associated with BMS (Po or Py) stringer along fracture/vein/crystal boundary in/of Pyx
		G1	Ni-Pt-Pd-Te	1.9	x	5.4	10.26	Within/edge BMS, within/edge Pn (Pn associated with Po) and in contact with Pyx
MBS604	PTSR-05	A1	Ni-Pt-Fe-Pd-Te	2.8	x	7.4	20.72	Within BMS, within Cpy
		B1	Ni-Pb-Bi-Te	0.6	x	1.9	1.14	Within/edge BMS, within/edge Cpy and in contact with Pyx
		B2	Pb-Ni	0.2	x	1.2	0.24	Within BMS, within Cpy
		C1	Ni-Pd-Pt-Te	3.3	x	5.8	19.14	Within BMS, within Cpy (Cpy associated with Py)
		D1	Ni-Pt-Pd-Te/Ag-Te	1.3	x	2.8	3.64	Within/edge BMS, within/edge Pn (Pn associated with Po) and in contact with Pyx
		E1	Ni-Pt-Te	5.0	x	13.2	66	Within/edge BMS, within/edge Po and in contact with Pyx
		F1	Fe-Pb-Ni-Te-Bi	1.0	x	3.6	3.6	Within/edge BMS, within/edge Cpy (Cpy associated with Cr) and in contact with Pyx
		G1	Ag-Te	0.6	x	6.3	3.78	Within Pyx and associated with BMS (Cpy?) stringer
		G2	Ni-Pt-Te/Ag-Te	0.5	x	1.6	0.8	Within/edge BMS, within/edge Cpy and in contact with Pyx
		G3	Ni-Pt-Te	2.0	x	4.1	8.2	Within/edge BMS, within/edge Cpy and in contact with Pyx
		H1	Ni-Pt-Pd-Fe-Te/Ag-Te	2.3	x	4.6	10.58	Within/edge BMS, within/edge Pn (Pn associated with Po) and in contact with Pyx
		H2	Ag-Te	1.3	x	2.0	2.6	Within Pyx associated with Pn stringer connected to H1
		H3	Ni-Pt-Pd-Te	0.4	x	7.1	2.84	Within/edge BMS, within/edge Po/Pn and in contact with Pyx
		I1	Ni-Ag-Te	0.8	x	4.6	3.68	Within BMS, within/edge Po and Cpy (Po and Cpy associated with Pn)
		J1	Pt-Pd-Ni-Ir-Te	2.0	x	4.4	8.8	Within/edge BMS, within/edge Pn/Po mix and in contact with Pyx
			Ag-Te	1.8	x	3.4	6.12	Rims half of the above PGM (J1) (largest size taken)
		J2	Ag-Te	<1.0	x	<1.0	<1.0	Various small (<1µm) scattered crystals within/edge BMS, within/edge Po/Pn mix and in contact with Pyx

Drill Hole	Sample No.	PGM No.	PGM Composition	Size (µm)			Area (µm^2)	Association
MBS604	PTSR-05	K1	Ag-Te	2.0	x	2.2	4.4	Within BMS, within Cpy
		L1	Ni-Pt-Fe-Pd-Te	6.0	x	11.3	67.8	Within/edge BMS, within/edge Cpy and in contact with Pyx
		M1	Ni-Pt-Te	1.0	x	11.2	11.2	Within/edge BMS, within/edge Po and in contact with Pyx
		N1	Ni-Pd-Pt-Fe-Te	2.0	x	2.7	5.4	Within/edge BMS, within/edge Cpy (Cpy associated with Po) and in contact with Serp
		O1	Ni-Pt-Pd-Te	1.3	x	5.1	6.63	Within BMS, within Pn (Pn associated with Po)
		P1	Pt-Ni-Pd-Te	4.3	x	19.1	81.366	Within/edge BMS, within/edge Po (Po associated with Cpy) and in contact with Serp
		Q1	Ag-Te	1.2	x	3.3	3.96	Within/edge BMS, within/edge Cpy and in contact with Pyx
		R1	Ni-Pt-Pd-Te	1.5	x	5.8	8.7	Within BMS, within Po
		S1	Ni-Pt-Pd-Te	1.6	x	4.7	7.52	Within/edge BMS, within/edge Pn and in contact with Cr
		T1	Ni-Pt-Pd-Te	1.1	x	2.2	2.42	Within/edge BMS, within/edge Pn (Pn associated with Po) and in contact with Pyx
		U1	Ag-Te	2.0	x	3.6	7.2	Within/edge BMS, within/edge Pn and in contact with Serp
		V1	Ni-Pd-Te	1.2	x	2.3	2.76	Within BMS, within Cpy
		W1	Ag-Te	3.4	x	4.5	15.3	Within/edge BMS, within/edge Pn and in contact with Pyx
		X1	Ni-Pt-Pd-Te	1.3	x	4.2	5.46	Within BMS, within Cpy
		Y1	Ni-Pt-Te	3.2	x	10.8	34.56	Within/edge(?) Pn/Po and in contact with Pyx (relationship not clear)
		Z1	Ni-Pt-Te	1.9	x	2.2	4.18	Within BMS, within Pn
MBS604	PTSR-06		No PGM observed					No PGM observed
MBS604	PTSR-07	A1	Ni-Pt-Pd-Te	5.8	x	13.5	78.3	Within/edge BMS, within/edge Cpy/(Py or Po mix) and in contact with Pyx
		B1	Ni-Pd-Te	1.8	x	3.8	6.84	Within BMS, within/edge Py and in contact with Pn at top edge
		C1	Pt-Ni-Pd-Te	5.5	x	31.7	174.35	Aligned within silicate (Serp?) vein cutting Ol, little sulphide present. PGM fragmented, total size measured
		D1	Pt-Ni-Pd-Fe-Te	1.9	x	2.1	3.99	Within/edge BMS, within/edge Cpy vein and in contact with Pyx
		E1	Ni-Pt-Pd-Te	0.5	x	67.5	33.75	Within/edge BMS, alinged with Cpy stringer and in contact with Ol
		F1	Ni-Pd-Pt-Te	3.7	x	4.2	15.54	Within/edge BMS, within Pn (Pn associated with Po) and in contact with Pyx
		G1	Ni-Pt-Pd-Fe-Te	1.6	x	8.7	13.92	Within/edge BMS, within/edge Cpy and in contact with Pyx
		H1	Pt-Pd-Te	0.6	x	20.0	12	Within BMS, within Pn with one tip of the PGM in contact with Pyx
		I1	Ni-Pt-Pd-Te	1.9	x	7.8	14.82	Within/edge BMS, within/edge Pn/Py mix and in contact with Pyx
		J1	Ni-Pt-Pd-Te	0.9	x	2.1	1.89	Within BMS, within/edge Cpy/Pn (Cpy and Pn associated with Po and Cr)
		K1	Ni-Pt-Pd-Te	12.8	x	20.2	258.56	Within BMS, within Pn
		L1	Ni-Pd-Te	0.7	x	2.3	1.61	Within/edge BMS, within/edge Cpy (Cpy associated with Pn) and in slight contact with Cr at one tip
		M1	Ni-Pd-Te	0.5	x	3.8	1.9	Within BMS, within Po (Po associated with Pn)
		N1	Ni-Pd-Pt-Te	4.2	x	8.7	36.54	Within Pyx and associated with fragmented end of Cpy
		O1	Ni-Pt-Pd-Fe-Te	1.6	x	3.0	4.8	Within/edge BMS, within/edge Cpy (Cpy associated with Pn) and in contact with Pyx
MBS604	PTSR-08	A1	Pt-As	0.3	x	0.7	0.21	Within/edge BMS, within/edge Pn and in contact with Ol
		A2	Pt-As	0.8	x	1.9	1.52	Within/edge BMS, within/edge Pn and in contact with Ol
		A3	Pd-Pb	0.8	x	0.8	0.64	Within BMS, within Pn
		B1	Pd-Cu-Pb	1.2	x	1.9	2.28	Within BMS, within Pn
		C1	Pd-S	1.3	x	14.0	18.2	Within BMS, within Pn, diffuse margins
		C2	Pd-Cu	0.6	x	3.3	1.98	Within BMS, within/edge Pn and in contact with Fe-Ni(-O?)
		D1	Pt-Ni-Fe	1.7	x	4.5	7.65	Within/edge BMS, within/edge Cpy (Cpy associated with Pn) and in contact with Ol
		D2	Pd-Cu	0.6	x	1.3	0.78	Within/edge BMS, within/edge Cpy (Cpy associated with Pn) and in contact with Ol (other small PGM here not measured due to small size)

Drill Hole	Sample No.	PGM No.	PGM Composition	Size (µm)			Area (µm^2)	Association
MBS604	PTSR-08	D3	Pd-Cu	0.9	x	0.9	0.81	Within/edge BMS, within/edge Pn (Pn associated with Cpy) and in contact with Ol
		E1	Pd-Ag-Pb-Cu	0.9	x	1.1	0.99	Within/edge BMS, within/edge Cpy/Pn
		E2	Pd-Pb	0.3	x	0.3	0.09	Within/edge BMS, within/edge Cpy and in contact with Pyx
		F1	Ir-Ru-Os-Cu-Pt-As-S	0.9	x	1.0	0.9	Within/edge BMS, within/edge Pn and in contact with Cr
		G1+	Pd-Cu	1.0	x	1.5	1.5	Within BMS, within Pn and Cu-sulphide mix (smaller PGM = Pd-Cu, not measured due to small size)
		H1	Pd-Fe-Te/Pt-As	2.0	x	2.9	5.8	Within/edge BMS, within Pn (Pn associated with Cpy) and in contact with Ol
MBS604	PTSR-09	A1	Pd-Fe-Te/Ag-Te	1.0	x	4.4	4.4	Within BMS, wtihin Pn/Cpy mix
		A2	Pd-Pt-Te	1.0	x	4.3	4.3	Within BMS, wtihin Pn/Cpy mix
		B1	Pt-Cu-Ir-S	4.5	x	1.7	7.65	Within BMS, within Pn (Pn associated with Cr)
		C1a	Pt-Pd-Cu (bottom left)	1.3	x	4.6	5.98	Within Pt-bearing Pn and Pyx
		C1b	Pt-bearing Pn (central)	10.8	x	20.4	220.32	Within Pyx
MBS604	PTSR-10		No PGM observed					No PGM observed
MBS604	PTSR-11	A1	Pt-Fe-Ni-S	3.7	x	7.0	25.9	Within/edge BMS, within/edge Cpy (Cpy associated with Mgt) and in contact with Cr and Pyx
		B1	Cu-Pd-Fe-S	1.0	x	2.1	2.1	Within BMS, within Pn
		B2	Cu-Pd-Fe-S	1.0	x	2.0	2	Within BMS, within Pn
		B3	Cu-Pd-Fe-S	1.2	x	4.4	5.28	Within/edge BMS, within/edge Pn and in contact with Pyx
		C1	Pd-Cu	2.6	x	6.6	17.16	Within BMS, within Pn
		C2	Pd-Cu	3.0	x	3.9	11.7	Within/edge BMS, within/edge Pn/Cpy mix and in contact with silicate
		C3	Pd-Cu	1.3	x	2.6	3.38	Within/edge BMS, within/edge Pn/Cpy mix and in contact with silicate
		C4	Pd-Cu	0.7	x	0.9	0.63	Within BMS, within Pn/Cpy mix
		D1	Pd-Cu	0.8	x	4.1	3.28	Within Ol but associated with Pn
		E1	Pd-Cu	0.5	x	2.0	1	Within/edge BMS, within/edge Pn and in contact with Mgt
MBS605	PTSR-16	A1	Ni-Pt-Te	1.6	x	2.5	4	Within BMS, within Po (Po associated with Cpy)
		B1	Ni-Fe-Te	4.9	x	14.3	70.07	Within/edge BMS, within/edge Cpy and in contact with Pyx
		C1	Ag-Fe-Te Various	2.7	x	3.2	8.64	Approximately 5 grains within BMS, within/edge Py/Cpy/Pn
		D1	Ag-Te Various	3.3	x	11.7	38.61	Within/edge Mgt and in contact with Py and Pyx (Py associated with Pn and Po)
		E1	Ni-Pt-Fe-Te	2.9	x	6.9	20.01	Within BMS, within Pn
MBS605	PTSR-17	A1	Ni-Pt-Pd-Te	3.7	x	10.4	38.48	Within/edge BMS, within/edge Cpy/Po and in contact with Pyx
		B1	Ni-Pt-Pd-Te	0.5	x	0.5	0.25	Within BMS, within Cpy (Cpy associated with Py and Pn)
		C1	Ni-Pd-Pt-Te	1.9	x	4.2	7.98	Within BMS, within Pn/Po mix
		D1	Ni-Pt-Pd-Te	1.8	x	2.8	5.04	Within/edge BMS, within/edge Po and in contact with Pyx
		E1	Ni-Pt-Pd-Te	0.2	x	4.5	0.9	Associated with Cpy along a fracture/vein within Pyx
		E2	Ni-Pt-Fe-Pd-Te	1.8	x	4.3	7.74	Associated with Cpy along a fracture/vein within Pyx
		F1	Ni-Pt-Fe-Pd-Te	2.2	x	4.2	9.24	Within BMS, within Po (Po associated with Cpy)
		G1	Ag-Te (/Pt-Te)	2.0	x	3.2	6.4	Within/edge BMS, within/edge Cpy and in contact with Pyx
		H1	Ni-Pt-Pd-Te	0.9	x	9.4	8.46	Associated with Py/Po stringer aligned along fracture/vein in Pyx
		J1	Ni-Pt-Pd-Fe-Te	2.6	x	3.2	8.32	Within BMS, within Py (Py associated with Pn)
		K1	Pt-Ni-Te	1.5	x	3.0	4.5	Within BMS, within Pn
		L1	Ni-Pt-Te	0.4	x	1.5	0.6	Within BMS, within Po (Po associated with Cpy)
		M1	Ni-Pd-Pt-Te	0.3	x	0.9	0.27	Within BMS, within Cpy
		N1	Ag-Te	3.5	x	13.5	47.25	Within BMS, within/edge Py and in contact with Pn along crystal boundary
		O1	Ni-Pt-Fe-Pd-Te	4.7		8.1	38.07	Within/edge BMS, within/edge Cpy and in contact with Pyx

Drill Hole	Sample No.	PGM No.	PGM Composition	Size (µm)	Area (µm^2)	Association
MBS605	PTSR-18	A1	Ni-Pt-Te	1.2 x 1.7	2.04	Within BMS, within Po
		B1	Ni-Pt-Pd-Te	1.2 x 4.5	5.4	Within BMS, within Cpy
		C1	Au-Ag	1.3 x 4.0	5.2	Within BMS, within Cpy
		D1	Ni-Pt-Te	2.1 x 2.6	5.46	Within BMS, within Pn
		E1	Ni-Pt-Pd-Te	1.7 x 4.3	7.31	Within BMS, within Pn (Pn associated with Py)
		F1	Ag-Te	3.0 x 6.6	19.8	Within/edge BMS, within/edge Pn and in contact with Cr
		G1	Ni-Pt-Fe-Te	2.0 x 7.1	14.2	Within/edge BMS, within/edge Po and in contact with Pyx
MBS605	PTSR-19	A1	Ni-Pd-Te	2.0 x 3.4	6.8	Within BMS, within/edge Pn/Po
		B1	Au-Ag-Fe	1.5 x 2.0	3	Within/edge BMS, within/edge small crystal of Cpy (1.0 x 2.8) and in contact with Pyx
		C1a	Ni-Pd-Pt-Te/Ag-Te	0.7 x 4.5	3.15	Within/edge BMS, within/edge Pn (Pn associated with Po) and in contact with Pyx
		D1	Ag-Te	3.7 x 4.3	15.91	Within BMS, within Pn (Pn associated with Py)
		E1-2	Ag-Te/Ni-Pd-Pt-Te	1.8 x 13.6	24.48	Within BMS, PGM surrouding Py crystal within Pn (Py also present in Cpy in same image)
		F1	Ni-Pd-Pt-Te	1.7 x 3.8	6.46	Within/edge BMS, within/edge Cpy and in contact with Pyx
		G1	Ir-Pt-As-S	5.1 x 5.3	27.03	Associated with sulphides (Cpy) within silicate mix (ring/doughnut shaped PGM)
		H1	Pt-Fe-As	2.5 x 3.8	9.5	Associated with minor BMS stringer from Pn/Py/Cpy composite crystal within Pyx
		I1	Ni-Pt-Te	1.5 x 5.0	7.5	Within BMS, within/edge Cpy and Po (Cpy and Po associated with Py and Pn)
		J1	Ni-Fe-Pd-Pt-Te	1.4 x 2.2	3.08	Within BMS, within/edge Cpy and Py (Cpy and Py associated with Pn)
		K1	Ni-Pt-Pd-Te	1.5 x 2.3	3.45	Within BMS, within Pn
		L1	Pt-As	1.7 x 3.0	5.1	Within/edge BMS, within/edge Cpy and in contact with Pyx
		M1	Ni-Pd-Pt-Te/Ag-Te	1.0 x 5.8	5.8	Within/edge BMS, within/edge Pn (Pn associated with Po) and in contact with Pyx
		N1	Ag-Te	1.9 x 2.6	4.94	Within/edge BMS, within/edge Cpy/Pn mix and in contact with Pyx
		O1	Ni-Fe-Te	2.3 x 5.9	13.57	Within/edge BMS, within/edge Pn and in contact with Pyx
MBS605	PTSR-20	A1	Pt-Ni-Te	1.6 x 15.3	24.48	Associated with Py/Po? Stringer within Ol
		B1	Pb-Ag-Te	0.4 x 1.3	0.52	Within BMS, within Cpy
		B2	Ag-Te	1.3 x 1.8	2.34	Within BMS, within Cpy
		B3	Pd-Pt-Ni-Te	1.1 x 1.5	1.65	Within BMS, within Cpy
		C1	Ni-Pt-Fe-Pd-Te	2.8 x 14.3	40.04	Within BMS, within Po (Po associated with Py)
		C+	Re-Cu-S	0.3 x 1.7	0.51	Within BMS, within Po with one crystal in contact with Py (four crystals in total, average size measured)
		D1	Pt-Ni-Te	1.0 x 102.0	102	Associated with Py/Po stringer aligned along fracture/vein within Pyx
		D2	Ni-Te	1.0 x 2.6	2.6	Within/edge BMS, within/edge Py/Po and in contact with Pyx/Serp
		D3	Fe-Te	0.8 x 8.8	7.04	Within/edge BMS, within/edge Py/Po and in contact with Pyx/Serp
		E1	Ni-Pt-Pd-Te	2.5 x 3.0	7.5	Within BMS, within Pn/Cpy mix
		F1	Ni-Pt-Pd-Te	9.6 x 72.1	692.16	Within/edge BMS, within/edge Cpy/Po and in contact with Pyx at one edge
		G1	Ni-Pt-Fe-Te	9.7 x 18.1	175.57	Within/edge Cr/Mgt mix (Cr/Mgt associated with Cpy)
		H1	Pt-Ni-Fe-Te/Ag-Te	0.9 x 2.6	2.34	Edge BMS, edge Pn and in contact or within Pyx
		H2	Ag-Te	0.2 x 0.7	0.14	Edge BMS, edge Pn and in contact or within Pyx
		H3	Ag-Te	0.2 x 0.8	0.16	Edge BMS, edge Pn and in contact or within Pyx
		I1	Ni-Pt-Fe-Te	1.9 x 3.3	6.27	Within/edge BMS, within Pn/Po and in contact with Ol
		I2	Ni-Fe-Te	2.0 x 6.2	12.4	Within/edge BMS, within Pn/Po and in contact with Ol
		J1	Ni-Pt-Pd-Te	1.1 x 2.1	2.31	Within/edge BMS, within/edge Pn (Pn associated with Py) and in contact with Pyx
		K1	Ni-Pt-Pd-Te	2.8 x 2.8	7.84	Within BMS, within Pn,
		L1	Ni-Pd-Pt-Fe-Te	2.7 x 3.9	10.53	Within BMS, within Py (Py associated with Pn)

Drill Hole	Sample No.	PGM No.	PGM Composition	Size (μm)			Area (μm^2)	Association
MBS605	PTSR-20	M1	Ni-Fe-Pt-Pd-Te	2.6	x	13.1	34.06	Within BMS, within Py (Py associated with Cpy)
		N1	Ni-Pt-Te/Ag-Te	2.1	x	3.6	7.56	Within BMS, within Pn
MBS605	PTSR-21	A1	Pt-Pd-Te	0.9	x	1.5	1.35	Within BMS, within Pn (Pn associated with Py)
		B1	Pt-Te	0.2	x	2.9	0.58	Within BMS, within/edge Py/Cpy
		B2	Pt-Te	0.2	x	8.4	1.68	Within BMS, within/edge Py/Cpy
		C1	Pt-Te	0.9	x	1.6	1.44	Within/edge BMS, within/edge Pn and in contact with Ol
		D1	Pt-Te	1.6	x	4.1	6.56	Within/edge BMS, within/edge Pn and in contact with Pyx
		E1	Pt-Fe-Ni-Te	1.8	x	5.3	9.54	Within/edge BMS, within/edge Pn and in contact with Pyx
		F1	Ni-Bi	0.5	x	1.8	0.9	Within BMS, within Cpy (Cpy associated with Pn)
MBS605	PTSR-22	A1	Ni-Pt-Pd-Te	2.7	x	8.5	22.95	Within/edge BMS, within/edge Cpy and in contact with Pyx
		B1	Ni-Pt-Pd-Fe-Te	4.6	x	9.4	43.24	Within/edge BMS, within/edge Pn/Py and in contact with silicate?
		C1	Ni-Pt-Pd-Fe-Te	0.7	x	5.8	4.06	Within/edge BMS, within/edge Pn (Pn associated with Py) and in contact with Ol/Serp
		D1	Ni-Pt-Pd-Fe-Te	1.7	x	3.1	5.27	Within/edge BMS, within/edge Pn and in contact with Pyx
		E1	Ni-Fe-Te	0.6	x	1.6	0.96	Within BMS, within Cpy (Cpy associated with Pn)
		F1	Au-Ag	1.9	x	5.6	10.64	Within/edge Cpy/Pyx mix (skimmed surface of minerals, techincally within Cpy)
		G1	Ni-Fe-Pt-Pd-Te	3.8	x	5.5	20.9	Within BMS, within Pn/Po mix
		H1	Ni-Pt-Pd-Te	0.8	x	3.2	2.56	Within BMS, within Cpy (Cpy associated with Pn)
		I1	Ni-Pt-Pd-Te	1.3	x	2.0	2.6	Within/edge BMS, within/edge Po and in contact with Pyx
		J1	Ni-Pt-Pd-Te	0.7	x	1.9	1.33	Within BMS, within Py (Py associated with Cpy)
		K1	Ni-Pt-Pd-Te	3.5	x	4.7	16.45	Within/edge BMS, within/edge Cpy (Cpy associated with Pn) and in contact with Pyx
		L1	Ni-Pt-Fe-Te/Ag-Te	2.5	x	2.7	6.75	Within/edge BMS, within/edge Cpy and in contact with Ol
		M1	Ni-Fe-Pt-Pd-Te	2.6	x	3.4	8.84	Within/edge BMS, within/edge Pn and in contact with Ol
		N1	Ni-Pt-Pd-Te	0.5	x	28.3	14.15	Within/edge BMS, within/edge Cpy vein (associated with Mgt) and in contact with Ol
		O1	Ni-Pt-Pd-Te	2.0	x	2.7	5.4	Within BMS, within Pn
		P1	Ni-Pt-Pd-Te	3.2	x	4.5	14.4	Within BMS, within Pn
		Q1	Ni-Pt-Pd-Te	1.5	x	2.2	3.3	Within/edge BMS, within/edge Cpy and in contact with Ol
		R1	Ni-Pt-Pd-Te	1.7	x	2.4	4.08	Within BMS, within Pn
		S1	Pt-Ni-Pd-Te	0.7	x	3.2	2.24	Within Ol and associated (spatially) with Cpy (Cpy associated with Py)
		T1	Ni-Pt-Te	1.0	x	7.7	7.7	Within BMS, within Pn
		U1	Ni-Pt-Te/Ag-Te	0.8	x	8.9	7.12	Within BMS, within/edge Cpy/Pn
MBS605	PTSR-23	A1	Pt-Pd-Te	1.0	x	5.7	5.7	Within BMS, within Cpy
		B1	Au-Cu-Ag-Pd	9.6	x	12.6	120.96	Within/edge BMS, within/edge Cpy/Mgt and in contact with Pyx
		C1	Pt-Pd-Ni-Te	1.3	x	2.4	3.12	Within BMS, within Py (Py associated with Pn)
		D1	Au-Ag	2.6	x	3.7	9.62	Associated with termination of fracture/vein (no BMS content) within Ol
		E1	Pt-Pd-Ni-Te	2.2	x	9.8	21.56	Within Ol
		F1	Pt-Pd-Te	4.1	x	22.2	91.02	Within/edge BMS, within/edge Cpy and in contact with Pyx
		G1	Pt-Pd-Ni-Te	4.4	x	7.5	33	Within/edge BMS, within edge Cpy/Pyx
		G2	Pt-Pd-Te	1.0	x	1.4	1.4	Within/edge BMS, within edge Cpy/Pyx
		H1	Au-Cu	2.6	x	7.6	19.76	Within Pyx
		I1	Pt-Te	1.1	x	5.5	6.05	Within BMS, within Pn (Pn associated with Cpy)
		J1	Cu-Pt-Te	2.3	x	4.8	11.04	Within/edge BMS, within/edge Pn and in contact with Ol and Pyx
		K1	Pd-Ni-Pt-Te	1.1	x	1.8	1.98	Within BMS, within Pn/Py mix
MBS605	PTSR-24	A1	Pt-Pd-Te	1.4	x	8.2	11.48	Within/edge BMS, within Pn and in contact with Pyx

Drill Hole	Sample No.	PGM No.	PGM Composition	Size (μm)			Area (μm^2)	Association
MBS605	PTSR-24	B1	Pd-Pt-Te/Ag-Te	1.3	x	2.0	2.6	Within/edge BMS, within/edge Cpy and in contact with Ol
		C1	Pd-Pt-Fe-Te	1.5	x	2.2	3.3	Within/edge BMS, within/edge Cpy and in contact with Ol
		D1	Pt-Ni-Pd-Te	0.8	x	2.5	2	Within BMS, within Cpy
		E1	Pt-Te	1.5	x	2.0	3	Within BMS, within Pn (Pn associated with Cr)
		F1	Pt-Te	1.1	x	3.8	4.18	Within/edge BMS, within/edge Cpy (Cpy associated with Pn) and in slight contact with Ol
MBS605	PTSR-25	C1	Pt-Ni	1.3	x	1.5	1.95	Within Cpy which occurs within Cr
		D1	Pt-Te	0.6	x	1.6	0.96	Within/edge BMS, within/edge Pn and in contact with Pyx
		E1	Pt-Pd-Te	1.7	x	3.5	5.95	Within/edge BMS, within/edgen Cpy (Cpy associated with Pn and Cr) and in contact with Pyx
MBS209	PTSR-28		No PGM Observed					No PGM observed
MBS209	PTSR-29		No PGM Observed					No PGM observed
MBS209	PTSR-30	A1	Pt-Ir-As-S	1.9	x	2.5	4.75	Within BMS, within Pn (associated with Py)
		B1	Ni-Pd-Pt-Te/Ag-Te	1.4	x	1.9	2.66	Within BMS, within Pn (Pn associated with Cpy and Cr)
		C1	Ag-Te	1.7	x	3.2	5.44	Within/edge BMS, within/edge Po/Pn mix and in contact with Cr and Pyx
		D1	Pt-As	1.8	x	2.2	3.96	Within/edge BMS, within/edge Cpy and in contact with Pyx
		E1	Pt-As/Ni-Te	1.4	x	2.8	3.92	Within/edge BMS, within/edge Cpy and in contact with Pyx
		F1	Ni-Pd-Te	2.1	x	2.5	5.25	Within/edge BMS, within/edge Pn/Py mix and in contact with Pyx
		G1	Ni-Pd-Fe-Te	5.0	x	5.1	25.5	Within BMS, within Pn
		H1	Ag-Ni-Te	2.0	x	2.6	5.2	Within/edge BMS, within/edge Pn (Pn associated with Py) and in contact with Pyx (partially associated with BMS stringer)
		I1	Ag-Te	1.6	x	2.8	4.48	Within/edge BMS, within/edge Po (Po associated with Pn) and in contact with Pyx
		J1	Ag-Te	3.6	x	7.4	26.64	Within BMS, within Pn
		J2	Ag-Te	0.9	x	1.9	1.71	Within/edge BMS, within/edge Pn and in contact with Pyx
		K1	Ni-Te	1.7	x	2.5	4.25	Within BMS, within Po
		L1	Ni-Pd-Te	2.2	x	2.6	5.72	Within BMS, within Pn
		M1	Ag-Te	3.5	x	4.3	15.05	Within BMS, within Pn (Pn associated/intergrown with Py)
		N1	Ag-Te	4.1	x	11.7	47.97	Within BMS, within Cpy (Cpy associated with Pn and Py)
		O1	Ni-Te	1.0	x	3.6	3.6	Within BMS, within Cpy/Pn
		P1	Ni-Te/Ag-Te	1.6	x	4.9	7.84	Within/edge BMS, within/edge Cpy/Pn and in contact with Pyx
		Q1	Ni-Te	1.8	x	2.7	4.86	Within BMS, within Pn (Pn associated with Cpy)
		R1	Ni-Fe-Pd-Te	2.2	x	3.4	7.48	Within/edge BMS, within/edge Pn and in contact with Pyx
MBS209	PTSR-31		No PGM Observed					No PGM observed
MBS209	PTSR-32	A1	Pt-As	4.0	x	10.0	40	In contact with A2/A3 and Serp
		A2	Ni-Fe-Te	3.1	x	7.4	22.94	In contact with A1/A3
		A3	Ag-Pd-Te	0.5	x	9.3	4.65	Rims A2 and is specifically in contact with Mgt (Mgt associated with Pn and Py)
		B1	Ni-Fe-Te/Ag-Te	6.7	x	11.7	78.39	Within BMS, within Pn (Ag-Te occurs in lighter streak in Ni-Fe-Te)
		C1	Re-Cu-Pb-Os-S	2.4	x	4.8	11.52	Associated with BMS stringer with Serp cutting Pyx
		D1	Ni-Fe-Te	4.0	x	4.5	18	Within BMS, within Pn (Pn associated with Py)
		D2	Ag-Te	2.2	x	4.2	9.24	Within BMS, within Pn (Pn associated with Py) (top part of PGM)
		D3	Ag-Pd-Te	0.7	x	6.8	4.76	Within BMS, within Pn (Pn associated with Py) (left edge of PGM)
		E1	Pd-Ni-Pt-Fe-Te/Ag-Te	3.8	x	5.7	21.66	Within/edge BMS, within/edge Py and in contact with Ca-oxide and Serp
		F1	Ni-Fe-Te	2.9	x	5.3	15.37	Within/edge BMS, within/edge Py/Po and in contact with Serp/Pyx
		F2	Ir-Pt-As-S	0.7	x	2.2	1.54	Within/edge BMS, within/edge Py/Po and in contact with Serp/Pyx (bottom left of PGM)
		F3	Ag-Te	1.5	x	1.6	2.4	Within/edge BMS, within/edge Py/Po and in contact with Serp/Pyx (bottom right of PGM)

Drill Hole	Sample No.	PGM No.	PGM Composition	Size (µm)			Area (µm^2)	Association
MBS209	PTSR-32	G1	Ag-Te	1.6	x	4.7	7.52	Within BMS, within Py (Py associated with Pn and minor Cpy)
		H1	Ni-Fe-Te	3.6	x	14.3	51.48	Within Mgt (Mgt associated with Pn, Py and Serp)
		I1	Ni-Pd-Te/Pt-As	1.7	x	2.3	3.91	Within BMS, within Pn (Pn associated with Cr)
		J1	Ni-Fe-Te	4.2	x	5.9	24.78	Within/edge BMS, within/edge Pn and in contact with Pyx
		J2	Ni-Te	3.0	x	3.0	9	Within/edge BMS, within/edge Pn and in contact with Pyx
		J3	Ag-Te	0.6	x	2.7	1.62	Within/edge BMS, within/edge Pn and in contact with Pyx
		J4	Ag-Pd-Te	1.0	x	6.0	6	Within/edge BMS, within/edge Pn and in contact with Pyx
		K1	Pt-Fe-As	3.0	x	8.0	24	Within BMS, within/edge Po/Pn (Po/Pn associated with Cpy and Mgt)
		L1	Ni-Fe-Te	7.2	x	10.6	76.32	Within BMS, within Pn
		L2	Ag-Pd-Te	0.6	x	7.0	4.2	Within BMS, within Pn
		M1	Ni-Pt-Pd-Te	1.9	x	3.2	6.08	Within/edge BMS, within/edge Cpy and in contact Ol/Serp
		N1	Pt-Fe-As	1.6	x	2.6	4.16	Witihin Serp (possible association with Po?)
		O1	Ni-Fe-Te	1.0	x	4.8	4.8	Within/edge BMS, within/edge Pn/Cpy mix (associated with Mgt) and in contact with silicate (relationship unclear)
		P1	Ni-Fe-Te	7.0	x	10.1	70.7	Within/edge BMS, within/edge Pn and associated with/in contact with silicate vein cutting Pn
		P2	Ni-Fe-Te	1.5	x	3.6	5.4	Within/edge BMS, within/edge Pn and associated with/in contact with silicate vein cutting Pn
		P3	Ni-Fe-Te	1.6	x	1.6	2.56	Within/edge BMS, within/edge Pn and associated with/in contact with silicate vein cutting Pn
		Q1	Ni-Pt-Pd-Te	2.5	x	4.5	11.25	Within/edge BMS/Mgt mix and in contact with Ol/Serp
		Q2	Ni-Pt-Pd-Te	0.8	x	4.9	3.92	Within/edge BMS/Mgt mix and in contact with Ol/Serp
		Q3	Fe-Ni-Pd-Te/Ag-Te	1.2	x	1.6	1.92	Within/edge BMS/Mgt mix and in contact with Ol/Serp
		R1	No Data				NA	No Data
		S1	Ni-Te	2.2	x	5.9	12.98	Within/edge BMS, within/edge Pn (Pn associated with Py) and in contact with Ol/Serp
		T1	Ni-Pd-Te	1.6	x	4.6	7.36	Within BMS, within Pn
		U1	Ni-Fe-Pd-Te	2.3	x	6.3	14.49	Within/edge BMS, within/edge Pn and in contact with Serp
		V1	Ni-Pd-Te/Ag-Te	13.8	x	18.3	252.54	Within/edge BMS, within/edge Pn/Cpy with minor contact with silicate
MBS209	PTSR-33	A1	Pt-Fe-As	2.6	x	4.0	10.4	Associated with fracture/vein (Serp?) within Pyx
		B1	Ag-Te	3.5	x	7.9	27.65	Within/edge BMS, within/edge Pn/Py
		C1	Ni-Fe-Te	4.4	x	8.8	38.72	Within/edge BMS, within/edge Cpy (Cpy associated with Cr) and in contact with Pyx
		D1	Ni-Fe-Te	6.3	x	7.7	48.51	Within/edge BMS, within/edge Pn and in contact with Pyx/Serp
		E1	Ni-Fe-Te	6.4	x	13.3	85.12	Within/edge BMS, within/edge Pn (Pn associated with Po) and in contact with Serp
		F1	Pt-As (fragmented)	11.3	x	41.0	463.3	Within?/edge Pn/Po (Pn/Po associated with Cpy) and in contact with Pyx, Serp and Cr
		G1	Ni-Fe-Te	7.3	x	20.6	150.38	Within BMS, within Pn (Pn associated with Py and Cpy)
		G2	Ag-Pd-Te	1.6	x	6.0	9.6	Within BMS, within Pn (Pn associated with Py and Cpy)
		H1	Ni-Fe-Te	3.7	x	11.4	42.18	Within/edge BMS, within/edge Cpy and in contact with Serp vein and possibly Cr
		H2	Ag-Te	2.6	x	5.3	13.78	Within/edge BMS, within/edge Cpy and in contact with Serp vein and possibly Cr
		I1	Ni-Fe-Te	4.0	x	7.5	30	Within/edge BMS, within/edge Cpy (Cpy associated with Po) and in contact with Pyx
		J1	Ni-Fe-Te	2.7	x	4.0	10.8	Within/edge BMS, within/edge Pn and in contact with Serp/Ol
		K1	Ni-Te (/Ag-Te)	2.4	x	3.3	7.92	Within/edge BMS, within/edge Pn and in contact with Pyx
		L1	Ni-Te	4.0	x	4.1	16.4	Within BMS, within Pn
		M1	Ni-Fe-Te	3.6	x	6.2	22.32	Within/edge BMS, within/edge Cpy and in contact with Pyx
		N1	Ag-Te/Au	1.4	x	3.1	4.34	Within BMS, within Cpy (Cpy associated with Pn and Cr)
		O1	Ag-Te	1.4	x	3.3	4.62	Within BMS, within Pn (Pn associated/enclosed by Cpy)

Drill Hole	Sample No.	PGM No.	PGM Composition	Size (µm)	Area (µm^2)	Association
MBS209	PTSR-33	P1	Re-Cu-S	8.7 x 10.3	89.61	Within/edge BMS, within/edge Pn and in contact with Cr
		Q1	Pt-As	11.5 x 14.7	169.05	Within BMS, within Pn
		R1	Pt-As	14.9 x 17.9	266.71	Within/edge BMS, within/edge Pn (Pn associated with Cr) and in contact with Pyx
		S1	Native Pt - Genuine?	1.9 x 6.0	11.4	Within Pyx
MBS209	PTSR-34	A1	Pt-As	1.3 x 2.9	3.77	Within BMS, within Cpy
		B1	Ni-Pd-Te (cut by vein/fracture)	9.5 x 13.4	127.3	Within BMS, within Pn
		C1	Ni-Fe-Pd-Te	2.1 x 2.3	4.83	Within BMS, within Pn (Pn associated with Cr)
		D1	Ni-Pd-Pt-Te	0.8 x 3.2	2.56	Within /edge BMS, within/edge Pn (Pn associated with Po) and in contact with Pyx
		E1	Pt-As	0.8 x 3.8	3.04	Within BMS, within Cpy (Cpy associated with Pn)
		F1	Ni-Te	4.6 x 15.1	69.46	Within/edge BMS, within/edge Po (Po closely associated with Pn) and in contact with Serp
		G1	Ni-Te	3.5 x 4.0	14	Within/edge BMS, within Cpy/Pn and in contact with Pyx
		H1	Pt-As (cut by vein, fragmented end)	22.7 x 65.1	1477.77	Within/edge BMS, within/edge Pn/Po mix (Pn/Po associated with Mgt) PGM partially rimmed by Mgt and possible contact with Serp/Ol
		I1	Pt-Fe-As	3.7 x 5.1	18.87	Wtihin/edge BMS, within/edge Po (Po associated with Pn) and in contact with Serp
		J1	Pt-As	3.3 x 4.2	13.86	Within Pyx
		K1	Ni-Te	1.5 x 3.0	4.5	Within BMS, within Po (Po associated with Pn)
		L1	Ni-Pd-Te	23.1 x 23.5	542.85	Within BMS, within Pn
		M1	Pt-As	8.5 x 12.6	107.1	Within Serp
		N1	Ni-Fe-Pd-Te	3.4 x 3.8	12.92	Within BMS, within Pn
		O1	Pt-As rimmed by Ni-Te	2.4 x 3.4	8.16	Within/edge BMS, within/edge Cpy (Cpy associated with Po) and in contact with Pyx/Serp?
		P1	Ni-Pd-Te	1.0 x 2.5	2.5	Within/edge BMS, within/edge Pn (Pn associated with Po and Cpy) and in contact with silicate
		Q1	Ni-Fe-Te	6.2 x 7.0	43.4	Within BMS, within Pn
		R1	Ni-Pd-Fe-Te	3.2 x 3.4	10.88	Within BMS, within Pn
		S1	Ir-Pt-Rh-As-S	1.6 x 3.1	4.96	Within BMS, within Po (Po associated with Pn)
		S2	Rh-Ir-Pt-As-S	1.4 x 3.5	4.9	Within/edge BMS, within/edge Po (Po associated with Pn) and in contact with Ol/Serp
		T1	Ni-Fe-Te	5.7 x 10.1	57.57	Within BMS, within Pn
		U1	Ni-Fe-Te	5.0 x 7.4	37	Within BMS, within Pn
		V1	Ni-Fe-Te (cut by vein/fracture)	4.1 x 13.3	54.53	Within BMS, within Pn
		W1	Pt-Fe-As	3.2 x 5.3	16.96	Within Serp (possibly associated with Po)
		X1	Ni-Te	1.8 x 3.7	6.66	Within/edge BMS, within/edge Pn and in contact with Serp
		Y1	Pt-Fe-As	1.9 x 2.2	4.18	(Within/)edge Mgt (Mgt associated with Pn) and in contact with Pyx
		Z1	Pd-Ni-Te	0.8 x 1.8	1.44	Within BMS, within Po/Pn mix
		AA1	Ni-Fe-Te	1.4 x 3.4	4.76	Within BMS, within Pn (associated with Po and Mgt)
		AA2	Ag-Pd-Te	1.7 x 2.1	3.57	Within BMS, within Pn (associated with Po and Mgt)
		AB1	Ni-Fe-Te	1.6 x 1.9	3.04	Within Mgt
		AC1	Ag-Pd-Te	2.9 x 5.1	14.79	Within/edge BMS, within/edge Pn and in contact with Pyx
		AD1	Pt-As	1.7 x 2.3	3.91	Wtihin/edge BMS, within/edge Cpy and in contact with Pyx
MBS209	PTSR-35	A1	Ni-Fe-Pd-Te	2.5 x 5.0	12.5	Associated with Pn and Pn/BMS stringer within Pyx
		A2	Ni-Fe-Pd-Te	0.4 x 32.3	12.92	Associated with Pn and Pn/BMS stringer within Pyx
		B1	Pd-Pt-Ni-Te	2.3 x 3.0	6.9	Within BMS, within Pn (Pn associated with Po)
		B2	Pt-As	1.3 x 1.4	1.82	Within BMS, within Pn (Pn associated with Po)
		C1	Pt-As rimmed by Pd-Pt-Te	3.9 x 6.5	25.35	Within/edge BMS Pn (Pn associated with Cpy) and in contact with Serp
		C2	Pd-Pt-Te	2.1 x 5.6	11.76	Within/edge BMS Pn (Pn associated with Cpy) and in contact with Serp

Drill Hole	Sample No.	PGM No.	PGM Composition	Size (μm)			Area (μm^2)	Association
MBS209	PTSR-35	D1	Pt-Fe-As	1.8	x	3.2	5.76	Within/edge BMS, within/edge Pn/Po mix and possible contact with Pyx
		E1	Ni-Pd-Te/Ag-Te	1.4	x	2.0	2.8	Within Mgt vein cutting Cr/Ol/Serp
		E2	Ni-Pd-Te	1.0	x	4.4	4.4	Within Mgt vein cutting Cr/Ol/Serp
		F1	Pt-Te	1.0	x	1.7	1.7	Within/edge BMS, within/edge Pn and in contact with Pyx
		G1	Pt-As	1.0	x	1.0	1	Within Pyx
		G2	Pt-S	8.5	x	8.6	73.1	Within Pyx
		G3	Pt-As	4.8	x	5.4	25.92	Within Pyx
		H1	Pd-Ni-Te	1.2	x	3.0	3.6	Within/edge Pn stringer and in contact with Pyx
		H2	Pd-Ag-Te	1.6	x	2.9	4.64	Within/edge Pn stringer and in contact with Pyx
		I1	Ag-Pd-Te	1.1	x	5.2	5.72	Within/edge BMS, within/edge Pn and in contact with Pyx/Serp
		I2	Pd-Ag-Ni-Te	1.0	x	2.0	2	Associated with minor/stringer BMS within Serp/Pyx
		I3	Ag-Pd-Te	0.7	x	1.7	1.19	Associated with minor/stringer BMS within Serp/Pyx
		I4	Ag-Te	0.7	x	3.4	2.38	Associated with minor/stringer BMS within Serp/Pyx
		J1	Pd-Ni-Fe-Te	2.3	x	4.2	9.66	Within/edge BMS, within/edge Pn (Pn associated with Po) and in contact with Serp
		J2	Pt-Rh-As	1.5	x	1.5	2.25	Within/edge BMS, within/edge Pn (Pn associated with Po) and in contact with Serp
		J3	Pt-Fe-As	1.5	x	1.7	2.55	Within/edge BMS, within/edge Pn (Pn associated with Po) and in contact with Serp
		K1	Pd-Ni-Te/Ag-Te	1.4	x	8.4	11.76	Within/edge with BMS stringer and in contact with Serp
		K2	Ni-Pd-Pt-Te	1.1	x	2.5	2.75	Within/edge with BMS stringer and in contact with Serp
		L1	Ni-Pd-Fe-Te	4.7	x	6.1	28.67	Within/edge BMS, within/edge Pn/Po mix and in contact with Serp
		M1	Ni-Pd-Fe-Te	3.0	x	3.8	11.4	Within BMS, within Pn
		N1	Pt-As	2.0	x	5.6	11.2	Within BMS, within/edge Pn/Po/Cpy (BMS associated with Cr)
		N2	Pt-Rh-As	1.3	x	1.8	2.34	Within BMS, within/edge Pn/Po/Cpy (BMS associated with Cr)
		O1	Pt-As/Pt-Pd-Te	1.3	x	1.8	2.34	Within/edge BMS, within/edge Pn (Pn associated with Po) and in contact with Serp/Pyx
		P1	Ag-Te	1.7	x	5.1	8.67	Within/edge BMS, within/edge Pn/Po mix and in contact with Serp
		P2	Ag-Te	1.0	x	2.0	2	Within BMS, within Pn/Po mix
		P3	Ag-Te	1.4	x	1.4	1.96	Within/edge BMS, within/edge Pn/Po mix and in contact with Serp
		P4	Ag-Pd-Te	1.4	x	3.1	4.34	Within/edge BMS, within/edge Pn/Po mix and in contact with Serp
		P5	Ag-Pd-Te	1.4	x	2.4	3.36	Within Serp, possible contact with Cr
		P6	Ag-Pd-Te	1.4	x	0.7	0.98	Within BMS, within Pn/Po mix
		Q1	Pt-As	2.0	x	3.4	6.8	Within Pyx
		R1	Pd-Te	1.9	x	2.9	5.51	Within/edge BMS, within/edge Cpy (Cpy associated with Pn) and in contact with Serp
		S1	Ni-Pd-Pt-Te	0.6	x	9.9	5.94	Associated with Po stringer and in contact with Serp
		S2	Ni-Pd-Pt-Te	1.0	x	2.6	2.6	Associated with Po stringer and in contact with Serp
		T1	Ni-Pd-Pt-Te	0.6	x	12.2	7.32	Tentative association with BMS veins/stringers cutting Serp/Ol
		T2	Ni-Pd-Te	1.0	x	1.2	1.2	Tentative association with BMS veins/stringers cutting Serp/Ol
		U1	Pd-Ni-Te	2.0	x	3.0	6	Within/edge BMS, within/edge Pn and in contact with Serp
		V1	Pt-As	1.8	x	2.7	4.86	Within/edge BMS, within/edge Pn/Po mix and in contact with Pyx
		W1	Ni-Pd-Pt-Te	1.9	x	2.5	4.75	Wtihin BMS, within Pn/Po mix
		X1	Ni-Pd-Te/Ag-Te	6.8	x	12.9	87.72	Within/edge BMS, within/edge Cpy and in contact with Serp
		Y1	Ni-Pd-Pt-Te	1.6	x	17.0	27.2	Within Pyx
		Y2	Ni-Pd-Pt-Te	1.6	x	8.2	13.12	Within Pyx
		Y3	Ni-Cu-Pd-Te	1.6	x	3.3	5.28	Within Pyx
		Y4	Ni-Cu-Pd-Te	1.6	x	2.7	4.32	Within Pyx

Drill Hole	Sample No.	PGM No.	PGM Composition	Size (μm)			Area (μm^2)	Association
MBS209	PTSR-35	Y5	Ni-Cu-Pd-Te	1.1	x	4.9	5.39	Within Pyx
		Z1	Ni-Te/Ag-Te	2.5	x	5.4	13.5	Associated with Pn/Po stringer (associated with Cr) and in contact with Pyx
		AA1	Pt-Fe-As	2.2	x	4.3	9.46	Within/edge BMS, within/edge Cpy (Cpy associated with Mgt) and in contact with Pyx
		AA2	Pd-Ni-Fe-Te	2.9	x	9.0	26.1	Within/edge BMS, within/edge Cpy (Cpy associated with Mgt) and in contact with Pyx
		AB1	Ni-Pd-Te	1.0	x	7.1	7.1	Associated with Po stringer within Serp, in contact with Serp
		AB2	Au-Ag	0.5	x	1.4	0.7	Associated with Po stringer within Serp, in contact with Serp
		AC1	Pd-Ni-Te	1.8	x	2.3	4.14	Within BMS, within Pn
		AD1	Pt-Fe-S	9.7	x	11.3	109.61	Within/edge Po and in contact with Cr and Pyx
		AD2	Pt-Fe-Cu-As	4.9	x	8.1	39.69	Within Serp/Pyx
		AE1	Ni-Pd-Te/Ag-Te	2.7	x	3.3	8.91	Within/edge BMS, within/edge Po (Po associated with Pn) and in contact with Pyx
		AF1	Pd-Ag-Te	0.5	x	7.5	3.75	Possible association with BMS stringer(s) related to Cpy crystal within Pyx
		AF2	Pt-As	0.6	x	1.4	0.84	Possible association with BMS stringer(s) related to Cpy crystal within Pyx
		AF3	Pt-Rh-As	1.1	x	2.7	2.97	Possible association with BMS stringer(s) related to Cpy crystal within Pyx
		AF4	Pd-Te	1.0	x	1.6	1.6	Possible association with BMS stringer(s) related to Cpy crystal within Pyx
		AG1	Pt-As	6.4	x	6.6	42.24	Within/edge BMS, within/edge Cpy and in contact with Pyx
		AG2	Pt-As	4.3	x	31.9	137.17	Within/edge BMS, within/edge Cpy/Pn and in contact with Pyx
		AG3	Pt-As	0.5	x	13.1	6.55	Within/edge BMS, within/edge Cpy/Pn and in contact with Pyx
		AH1	Ni-Pd-Te	1.8	x	4.1	7.38	Within BMS, within Po/Pn mix
		AI1	Pt-Fe-As	0.6	x	4.5	2.7	Within/edge Po stringer cutting through Cr and in contact with Cr and Serp vein
		AJ1	Pd-Ni-Te	1.3	x	2.3	2.99	Within BMS, within Pn/Po mix
		AK1	Rh-Pt-Os-As-S	2.3	x	2.5	5.75	Within/edge BMS, within/edge Cpy and in contact with Pyx/Serp
MBS209	PTSR-36	A1	Pt-Ni-Pd-Fe-Te	2.7	x	3.4	9.18	Within Pyx, possible association with BMS mix
		B1	Pt-Pd-Ni-Te	0.7	x	2.4	1.68	Within/edge BMS, within/edge Pn/Cpy and in contact with Pyx
MBS209	PTSR-37	A1	Pt-Cu-Te	2.0	x	3.8	7.6	Within/edge BMS, within/edge Pn and in contact with Serp
		B1	Pt-Cu-Te	1.2	x	2.2	2.64	Within/edge BMS, within/edge Pn (Pn associated with native Cu) and in contact with Pyx
		C1	Ir-Pt-As-S	1.2	x	4.1	4.92	Within/edge BMS, within/edge Pn and in contact with Serp
		D1	Pt-Cu-Te	1.3	x	1.9	2.47	Within BMS, within Pn/Cpy(?) BMS mix
		E1	Pt-Ir-As-S	3.8	x	3.8	14.44	Within/edge BMS, within/edge Pn and in contact with Pyx
MBS158	PTSR-40	A1	Ni-Fe-Te	6.9	x	8.6	59.34	Within BMS, within Pn
		B1	Ag-Te	1.1	x	3.7	4.07	Within/edge BMS, within/edge BMS (Cpy?) stringer and in contact with Pyx
		C1	Ni-Te	1.4	x	3.0	4.2	Within BMS, within Po
		D1	Ni-Te	0.9	x	1.4	1.26	Within BMS, within Py/Pn mix
		E1	Ag-Te	4.5	x	15.9	71.55	Within/edge BMS, within/edge Pn and in contact with Pyx
		E+	Ag-Te					Various small phases within Pyx or within/edge Pn and in contact with Pyx
		F1	Ni-Fe-Te	1.4	x	3.0	4.2	Within BMS, within Pn (Pn associated with Po and Mgt)
		F2	Ag-Te	1.0	x	8.2	8.2	Within BMS, within Pn (Pn associated with Po and Mgt)
		G1	Ni-Pt-Te	0.7	x	1.6	1.12	Within BMS, within Cpy (Cpy associated with Pn)
		H1	Ni-Pt-Te	8.7	x	9.2	80.04	Within/edge BMS, within/edge Cpy and in contact with Pyx/Serp
		I1	Ni-Fe-Te	3.2	x	4.2	13.44	Within/edge BMS, within/edge Pn (Pn associated with Po) and in contact with Pyx
		J1	Ni-Fe-Te	1.6	x	6.4	10.24	Within/edge BMS, within/edge Pn/Cpy and in contact with Pyx
		K1	Ni-Te	6.4	x	11.0	70.4	Within BMS, within Pn
		L1	Ag-Te	1.9	x	9.3	17.67	Within/edge BMS, within/edge Cpy and in contact with Pyx
		L2	Ag-Te	4.4	x	5.2	22.88	Within/edge Pyx and Serp

Drill Hole	Sample No.	PGM No.	PGM Composition	Size (µm)	Area (µm^2)	Association
MBS158	PTSR-40	L3	Ag-Te	2.2 x 4.4	9.68	Within/edge Pyx and Serp
		L4	Ag-Te	2.2 x 2.2	4.84	Within/edge Pyx and Serp
		L+	Ag-Te			Various small phases mostly within Pyx
		M1	Ag-Te	5.0 x 7.6	38	Within BMS, within Pn
MBS158	PTSR-41	A1	Ni-Pt-Te	0.5 x 4.7	2.35	Within/edge BMS, within/edge BMS (Cpy?) stringer and in contact with Pyx
		B1	Ni-Te	2.5 x 4.5	11.25	Within BMS, within Po
		C1	Ni-Te (/Pt-As)	1.3 x 3.3	4.29	Within/edge BMS, within/edge Pn/Py mix and in contact with Pyx
		D1	Pt-As	0.4 x 6.1	2.44	Within Pyx
		E1	Ni-Pt-Te	1.5 x 6.6	9.9	Associated with Cpy stringer within Pyx
		F1	Ag-Te	2.1 x 3.6	7.56	Within/edge Po (Po associated with Cpy and Pn) and in contact with Pyx
		G1	Ni-Te	2.2 x 3.0	6.6	Within BMS, within Po
		H1	Ni-Pt-Te	2.0 x 4.8	9.6	Within BMS, within Pn
		I1	Ag-Te	1.9 x 2.8	5.32	Within/edge BMS, within/edge Cpy and in contact with Pyx
		J1	Ag-Te	2.4 x 4.5	10.8	Within BMS, within Cpy (Cpy associated with Pn)
		J2	Ag-Te	0.8 x 1.8	1.44	Within/edge Cpy (Cpy associated with Pn) and partially in contact with Pyx
		K1	Pt-Ni-Pd-Te/Ag-Te	1.7 x 9.9	16.83	Within/edge BMS, within/edge Cpy and in contact with Pyx/Ol/Serp
		L1	Ni-Pt-Te	0.7 x 6.0	4.2	Edge Pn within Calc-silicate, possible association with Pn stringer from Pn crystal
		L2	Ni-Pt-Te	0.8 x 3.7	2.96	Possible association with Cpy/Pn stringer within calc-silicate
		L3	Ag-Te	0.5 x 8.6	4.3	Possible association with Cpy stringer within calc-silicate
MBS158	PTSR-42	A1	Pt-As	0.9 x 3.1	2.79	Within/edge BMS, within/edge Cpy/Pn and in contact with Serp/Ol
		A2	Ag-Pd-Te	0.5 x 1.4	0.7	Within/edge BMS, within/edge Cpy/Pn and in contact with Serp/Ol
		B1	Ni-Pt-Pd-Te	1.0 x 3.7	3.7	Within/edge BMS, within/edge Pn (Pn associated with Cr) and in contact with Pyx
		C1	Ni-Te	1.0 x 1.3	1.3	Within/edge BMS, within/edge Cpy (Cpy associated with Po,Pn and Cr) and in contact with Pyx
		D1	Pt-As	2.5 x 11.5	28.75	Within BMS, within Cpy
		E1	Ni-Pd-Te	1.3 x 2.4	3.12	Within/edge BMS, within/edge Pn/Fe2S and in contact with Cr
		F1	Ni-Pd-Pt-Te	1.2 x 5.9	7.08	Within BMS, within Cpy (Cpy associated with Pn)
		G1	Ni-Te	4.5 x 10.4	46.8	Within BMS, within Pn
		H1	Ag-Te	2.4 x 6.0	14.4	Within/edge BMS, within/edge Pn and in contact with Serp
		H2	Ag-Te	1.3 x 2.2	2.86	Within/edge BMS, within/edge Pn and in contact with Serp
		H3	Ag-Te	1.3 x 3.9	5.07	Within/edge BMS, within/edge Pn and in contact with Serp
		I1	Ni-Fe-Te	5.9 x 7.6	44.84	Within/edge BMS, within/edge Pn and in contact with Serp/Pyx
		J1	Ag-Au	2.7 x 2.9	7.83	Within/edge BMS, within/edge Cpy/Pn (Cpy/Pn associated with Cu-Fe-sulphide) and in contact with Pyx
		K1	Ni-Te	0.6 x 5.0	3	Within/edge BMS, within/edge Cpy stringer within Pyx
		L1	Ni-Te	0.6 x 3.3	1.98	Within/edge BMS, within/edge Pn and in contact with Pyx
		M1	Ni-Te/Ag-Te	1.9 x 3.8	7.22	Within/edge BMS, within/edge Po and in contact with Serp/Pyx
		N1	Ni-Pd-Te	1.0 x 1.8	1.8	Within BMS, within Po (associated with Pn)
		O1	Ni-Pd-Te	0.8 x 1.6	1.28	Within BMS, within Pn (associated with Po)
		P1	Ni-Pd-Te	0.8 x 4.3	3.44	Within/edge BMS, within/edge Pn and in contact with Serp
		Q1	Pt-Fe-As	3.8 x 14.2	53.96	Within Pyx/Serp
		R1	Pt-Fe-S	2.6 x 7.2	18.72	Within/edge BMS, within/edge Po (Po associated with Pn) and in contact with Ol
		S1	Pt-Fe-S	1.3 x 3.0	3.9	Within/edge BMS, within/edge Po/Pn mix and in contact with Ol
		T1	Pt-Fe-S	2.0 x 3.9	7.8	Within/edge BMS, within/edge Cpy and in contact with Ol

Drill Hole	Sample No.	PGM No.	PGM Composition	Size (μm)			Area (μm^2)	Association
MBS158	PTSR-42	U1	Ni-Pd-Te	1.5	x	2.0	3	Within BMS, within Pn (Pn associated with Cpy)
		V1	Pt-As	0.8	x	2.3	1.84	Within BMS, within Cpy (associated with Pn)
		V2	Ni-Pd-Te	0.8	x	2.9	2.32	Within BMS, within Cpy (associated with Pn)
		W1	Ag-Te	0.3	x	58.8	17.64	Within BMS, within Pn
		X1	Ni-Pt-Te	6.2	x	10.0	62	Within/edge BMS, within/edge Po and in contact with Pyx
		X2	Ni-Te	0.3	x	15.5	4.65	Associated with thin BMS stringer within Pyx
		Y1	Pt-Pd-Te	0.7	x	2.3	1.61	Within/edge BMS, within/edge Cpy (Cpy associated with Pn) and in contact with Cr
		Z1	Pt-As	5.3	x	6.3	33.39	Within BMS, within Cpy/Po mix (BMS associated with Mgt and Cr)
		AA1	Pt-As	2.2	x	3.6	7.92	Within BMS, within Cpy
		AB1	Pt-As	1.1	x	2.4	2.64	Within BMS, within Pn/Po mix
MBS158	PTSR-43	A1	Ni-Pd-Pt-Fe-Te	1.7	x	5.9	10.03	Within BMS, within Po
		B1	Ni-Fe-Pt-Pd-Te	1.9	x	9.6	18.24	Within/edge BMS, within Po and in contact with Pyx
		C1	Ni-Pd-Fe-Pt-Te	4.8	x	5.4	25.92	Within BMS, within Pn
		D1	Ni-Pd-Pt-Te	1.7	x	2.8	4.76	Within/edge BMS, within/edge Po (Po associated with Pn) and in contact with Pyx
		E1	Ni-Te	1.8	x	4.8	8.64	Within/edge BMS, within/edge Po and in contact with Pyx
		F1	Pd-Ni-Pt-Fe-Te/Ag-Te	6.4	x	11.3	72.32	Within silicate phase(?) between Cpy and Pyx
		F2	Ni-Pd-Pt-Te/Ag-Te	1.6	x	51.1	81.76	Within/edge Pyx
		G1	Ni-Fe-Pt-Pd-Te	2.4	x	7.6	18.24	Within BMS, within Pn (Pn associated with Po)
		H1	Ni-Pt-Pd-Te	1.0	x	6.9	6.9	Associated with Po stringers within Serp
		H2	Ni-Pt-Pd-Te	1.0	x	11.9	11.9	Associated with Po stringer within Serp
		I1	Ni-Pt-Pd-Te	1.1	x	1.5	1.65	Within/edge BMS, within/edge Pn (Pn associated with Po) and in contact with Pyx
		J1	Ni-Pt-Pd-Te	0.7	x	2.5	1.75	Within/edge BMS, within/edge Pn and in contact with Mgt
		K1	Ag-Te	0.5	x	61.7	30.85	Associated with BMS stringer within Pyx
		L1	Ni-Pt-Pd-Te	2.5	x	3.7	9.25	Within BMS, within Py (Py associated with Cpy)
		M1	Ni-Pt-Te	1.7	x	6.2	10.54	Within BMS, within Pn
		N1	Ni-Fe-Te	22.6	x	28.3	639.58	Within Pyx and in contact with Cr
		O1	Pt-Pd-Ni-Te	0.6	x	3.1	1.86	Within BMS, within Pn (Pn associated with Cpy)
		P1	Ni-Pt-Pd-Te	2.1	x	30.0	63	Within/edge BMS, within/edge Po/Mgt and in contact with Serp
		Q1	Ni-Pt-Fe-Pd-Te	1.6	x	7.0	11.2	Within BMS, within Cpy/Po mix
		R1	Ni-Pt-Te rimmed by Ag-Te	12.8	x	16.9	216.32	Within BMS, within Pn (Pn associated with Po)
		R2	Ag-Te	1.2	x	5.0	6	Within/edge BMS, within/edge Pn (Pn associated with Po) and in contact with silicate vein
		S1	Ni-Pd-Pt-Fe-Te/Ag-Te	4.7	x	5.8	27.26	Within/edge BMS, within/edge Pn/Cpy and in contact with Serp
		S2	Ag-Te	1.2	x	4.1	4.92	Within Serp (possible association with BMS stringer)
		T1	Ni-Fe-Pd-Te	2.7	x	5.3	14.31	Within BMS, within Po
		U1	Ag-Te	2.4	x	2.9	6.96	Within/edge Fe-suphide/Mgt and in contact with Pyx/Serp
		U2	Ag-Te	2.0	x	5.2	10.4	Within/edge BMS, within/edge Fe2S/Cpy and in contact with Serp
MBS158	PTSR-44	A1	Ag-Cu-Zn	1.6	x	9.8	15.68	Within Serp (hole in slide?)
		B1	Cu-Au-Pd	2.5	x	4.2	10.5	Associated with Pn/Cpy/Cr composite crystal and BMS stringers within Pyx
		C1	Pt-Te-Bi	2.0	x	6.6	13.2	Within Serp/Ol and in contact with BMS mix
		C2	Pd-Ag-Pt-Fe-Te	1.7	x	7.2	12.24	Within Serp/Ol and in contact with BMS mix
MBS158	PTSR-45	A1	Au-Ag-Fe	4.4	x	5.0	22	Within/edge BMS, within/edge Cpy (Cpy associated with Cr) and in contact with Pyx
		B1	Ni-Pd-Pt-Te	1.5	x	3.2	4.8	Within BMS, within Po (Po associated with Pn)
		B2	Pt-As	1.0	x	1.9	1.9	Within BMS, within Po (Po associated with Pn)

Drill Hole	Sample No.	PGM No.	PGM Composition	Size (μm)			Area (μm^2)	Association
MBS158	PTSR-45	C1	Ni-Fe-Te rimmed by Pt-Pd-Te	7.6	x	13.7	104.12	Within BMS, within Pn
		D1	Au	2.6	x	2.9	7.54	Within Serp
		E1	Pd-Ni-Pt-Te/Pt-As	1.2	x	5.1	6.12	Within/edge BMS, within/edge Pn and in contact with Pyx
		F1	Ni-Fe-Pd-Te	3.6	x	8.5	30.6	Within/edge BMS, within/edge Po (Po associated with Pn) and in contact with Cr and Serp
		G1	Ni-Pd-Te	1.4	x	2.5	3.5	Within BMS, within Cpy (Cpy associated with Po and Pn)
		H1	Ni-Pd-Pt-Te	1.1	x	2.6	2.86	Within/edge BMS, within/edge Po (Po associated with Pn) and in contact with Pyx
		I1	Ag-Au	2.2	x	2.9	6.38	Within BMS, within Cpy (Cpy associated with Cu-rich sulphide exsolution phases)
		J1	Ni-Pd-Te	1.7	x	4.4	7.48	Within/edge BMS, within/edge Cpy/Pn mix and in contact with Serp/Pyx
		K1	Ni-Pd-Pt-Te	0.9	x	2.2	1.98	Within BMS, within/edge Pn
		L1	Pt-As	5.9	x	8.2	48.38	Within/edge Cr (Cr associated with Cpy and Pn) and in contact with Serp
		M1	Pd-Ni-Pt-Fe-Te	3.8	x	6.2	23.56	Within/edge BMS, within/edge Pn/Cpy mix and in contact with Serp
		M2	Ir-Pt-As-S	1.8	x	1.9	3.42	Within/edge BMS, within/edge Pn/Cpy mix and in contact with Serp
		N1	Ni-Pt-Te	3.8	x	5.5	20.9	Within/edge BMS, witin/edge Cpy and in contact with Pyx
		O1	Pt-As	1.1	x	6.1	6.71	Within/edge BMS, within/edge Po and in contact with Serp
		P1	Ni-Te	2.7	x	4.4	11.88	Within BMS, within Po (Po associated with Pn)
		Q1	Ni-Fe-Pd-Te	4.5	x	6.1	27.45	Within BMS, within Po/BMS mix
		R1	Ni-Fe-Pt-Te	5.6	x	8.5	47.6	Within BMS, within Pn
		S1	Pd-Ni-Pt-Te x2	1.7	x	5.1	8.67	Within/edge BMS, within/edge Pn and in contact with Serp
		T1	Ni-Pd-Te	0.8	x	1.7	1.36	Within BMS, within Cpy (Cpy associated with Pn exsolution features)
		U1	Ni-Pd-Te	2.1	x	2.4	5.04	Within BMS, within Pn
		V1	Ni-Fe-Te	3.4	x	5.2	17.68	Within/edge BMS, within/edge Po and in contact with Serp/Pyx
		W1	Ni-Pd-Te	0.5	x	7.6	3.8	Within BMS, within Po (Po associated with Pn)
		X1	Ni-Pd-Fe-Pt-Te	2.2	x	2.9	6.38	Within BMS, within Cpy/Po mix
		Y1	Ni-Fe-Te	3.2	x	4.0	12.8	Within BMS, within Pn/Po mix
		Z1	Ni-Fe-Pd-Pt-Te	11.0	x	15.2	167.2	Within BMS, within Pn
		AA1	Ni-Pd-Fe-Te	4.2	x	6.1	25.62	Within BMS, within Pn
MBS158	PTSR-46	A1	Ni-Pt-Pd-Te				58.5	Within/edge BMS, within/edge Pn/Cpy mix and in contact with Pyx/Serp
		B1	Ni-Pd-Te/Pt-As	2.7	x	5.0	13.5	Within/edge BMS, within/edge Po and in contact with Pyx
		C1	Au-Cu-Fe	3.4	x	3.5	11.9	Within/edge BMS, within/edge Pn (Pn associated with Po and Cr) and in contact with Pyx
		D1	Au-Cu-Ag-Fe	1.8	x	4.0	7.2	Within/edge BMS, within/edge Cpy and in contact with Pyx
		D2	Au-Cu-Ag-Fe	0.2	x	4.4	0.88	Within/edge BMS, within/edge Cpy and in contact with Pyx
		E1	Ni-Pd-Fe-Pt-Te	4.0	x	11.1	44.4	Within BMS, within Pn (possible contact with silicate?)
		F1	Pt-Ni-Pd-Te/Ag-Te	15.4	x	29.7	457.38	Within Serp (possible association with Po/BMS mix/Cr; relationship unclear)
		G1	Pd-Ni-Pt-Te	2.1	x	2.4	5.04	Within BMS, within Pn/Po mix
		H1	Pt-Pd-Ni-Fe-Te	13.4	x	31.1	416.74	Within/edge BMS, within/edge Pn/Po (Pn/Po associated with Mgt) mix and in contact with Cpy
		I1	Ni-Pd-Pt-Te	1.0	x	1.0	1	Within BMS, within Po (Po associated with Mgt and Cr)
		J1	Ag-Au-Cu-Fe	1.4	x	3.5	4.9	Within BMS, within Pn/Cu-rich sulphide mix
		K1	Ni-Pt-Te	0.8	x	1.2	0.96	Within/edge BMS, within/edge Pn and in contact with Serp
		L1	Pd-Pt-Te	2.0	x	4.0	8	Within BMS, within Cpy
		M1	Pt-Ir-As-S	0.5	x	1.1	0.55	Within BMS, within Pn
		M2	Pt-Ir-As-S	0.7	x	0.8	0.56	Within BMS, within Pn
MBS158	PTSR-47	A1	Ni-Pt-Pd-Te	1.9	x	31.4	59.66	Within/edge Mgt stringer within Serp
		B1	Ni-Pt-Pd-Fe-Te	5.3	x	6.9	36.57	Within BMS, within Pn

Drill Hole	Sample No.	PGM No.	PGM Composition	Size (µm)			Area (µm^2)	Association
MBS158	PTSR-47	C1	Pb-Ag-Au-Se	0.9	x	3.2	2.88	Within/edge BMS, within/edge Cpy and in contact with Pyx
		D1	Pt-Pd-Ni-Fe-Te	4.5	x	4.8	21.6	Within BMS, within Cpy (Cpy associated with Cu-rich sulphide exsolution features and Cr)
		E1	Ni-Pt-Pd-Fe-Te	2.2	x	4.4	9.68	Within/edge BMS, within/edge Pn and in contact with Serp
		F1	Ni-Pt-Pd-Te	9.6	x	12.2	117.12	Within BMS, within/edge Po/Cpy
		G1	Ni-Pd-Pt-Te	1.4	x	3.6	5.04	Within BMS, within Pn (Pn associated with Po)
		H1	Ni-Pt-Pd-Te	1.4	x	10.5	14.7	Within Mgt (Mgt associated with Pn/Po)
		I1	Ni-Pd-Pt-Fe-Te	3.5	x	5.1	17.85	Within BMS, within Po/Pn mix
		J1	Ni-Pt-Pd-Fe-Te	1.9	x	2.2	4.18	Within/edge BMS, within/edge Pn (Pn associated with Po) and in contact with Serp
		K1	Ni-Pt-Pd-Fe-Te/Pb-Te	1.7	x	5.1	8.67	Associated with Po within Serp/Pyx
		K2	Ni-Pt-Pd-Te/Pb-Te	1.1	x	3.6	3.96	Associated with Po within Serp/Pyx
		L1	Ni-Pt-Pd-Te	1.5	x	3.5	5.25	Within/edge BMS, within/edge Po stringer and in contact with Pyx/Serp
		L2	Ni-Pt-Te	1.5	x	3.5	5.25	Within/edge BMS, within/edge Po stringer and in contact with Pyx/Serp
		M1	Ni-Pt-Pd-Te	12.8	x	38.9	497.92	Within/edge BMS, within/edge Py/Pn and in contact with Serp
		M2	Ni-Pt-Pd-Te	8.2	x	8.2	67.24	Within/edge BMS, within/edge Py/Pn and in contact with Serp
		M3	Ni-Pt-Pd-Te	4.2	x	4.2	17.64	Within/edge BMS, within/edge Py/Pn and in contact with Serp
		M+	Various Ni-Pt-Pd-Te					Various small grains within/edge Pn and in contact with Serp
		N1	Ni-Pt-Pd-Te	6.5	x	7.0	45.5	Within Pyx and in contact with Mgt
		O1	Ni-Pd-Pt-Te	1.9	x	3.2	6.08	Within/edge BMS, within/edge Po and in contact with Serp
MBS158	PTSR-48	A1	Cu-Pt-Pd	1.6	x	5.2	8.32	Within BMS, within Pn/BMS mix
		B1	Pt-As	0.6	x	1.6	0.96	Within/edge BMS, within/edge Cpy/BMS mix (associated with Pn) and in contact with Ol/Serp
		B2	Cu-Pd-Pt-Te	3.1	x	3.2	9.92	Within/edge BMS, within/edge Cpy/BMS mix (associated with Pn) and in contact with Ol/Serp
		C1	Os-Ru-Pt-As-S	1.6	x	3.2	5.12	Within /edge BMS, within/edge Pn/Cpy mix and in contact with Pyx
		D1	Pt-As	2.0	x	2.4	4.8	Within/edge BMS, within Pn (Pn associated with Pn/Cpy mix) and in contact with Ol
MBS158	PTSR-49		No PGM Observed					
MBS565	PTSR-51	A1	Ni-Pd-Fe-Te/Ag-Te	4.6	x	7.1	32.66	Within/edge BMS, within Py (Py associated with Cpy) and in contact with Pyx
		B1	Ir-Pt-As-S	0.9	x	4.2	3.78	Within Pyx
		C1	Ni-Fe-Te	3.2	x	4.1	13.12	Within/edge BMS, within/edge Cpy and in contact with Pyx
		D1	Ni-Te (+Ag in brighter streaks)	11.9	x	45.8	545.02	Within BMS, within Pn (and minor Po)
		E1	Ni-Fe-Te	2.4	x	3.2	7.68	Within BMS, within Po (Po associated with Cr)
		F1	Ni-Te	1.6	x	4.0	6.4	Within BMS, within Po
		G1	Ni-Fe-Te	2.0	x	14.6	29.2	Within BMS, within Po
		H1	Ni-Pt-Te	4.3	x	32.5	139.75	Within BMS, within Pn/Py
		I1	Ni-Pt-Fe-Te	1.3	x	8.0	10.4	Within BMS, within Po
		J1	Au-Ni-Cu	3.0	x	10.2	30.6	Within Pyx
MBS565	PTSR-52	A1	Ir-Pt-Rh-Os-As-S	1.1	x	5.2	5.72	Within BMS, within Pn (Pn associated with Py)
		B1	Ni-Pt-Fe-Te/Ag-Te	2.9	x	12.6	36.54	Within/edge BMS, within/edge Pn (associated with Py) and in contact with Mgt (rims composite sulphide crystal) and Pyx
		C1	Pt-As	5.6	x	12.8	71.68	Within/edge BMS, within/edge Cpy and in contact with Pyx
		D1	Ni-Pd-Te/Ag-Te	1.5	x	4.0	6	Within BMS, within Pn
		E1	Ag-Te (/Ni-Pt-Te)	2.4	x	3.1	7.44	Within/edge BMS, within/edge Po (Po associated with Pn) and in contact with Pyx
		F1	Ni-Pt-Te	3.1	x	5.8	17.98	Within/edge BMS, within/edge Pn and in contact with Pyx
		F2	Ni-Pt-Te	0.7	x	2.4	1.68	Within/edge BMS, within/edge Pn and in contact with Pyx
		G1	Pt-As	1.0	x	91.9	91.9	Associated with BMS stringer within Pyx

Drill Hole	Sample No.	PGM No.	PGM Composition	Size (µm)			Area (µm^2)	Association
MBS565	PTSR-52	H1	Pd-Fe-Pt-Te	4.0	x	6.1	24.4	Within BMS, within Cpy (Cpy associated with Pn and Py)
		I1	Pt-Fe-As	1.7	x	7.6	12.92	Associated with Cpy stringer within Pyx
		I2	Pt-As(-Ir)	0.6	x	21.8	13.08	Within Pyx
		J1	Ni-Fe-Te	1.6	x	2.0	3.2	Within/edge BMS, within/edge Py/Mgt (Py/Mgt associated with Po)
		J2	Ag-Te	0.5	x	1.8	0.9	Within/edge BMS, within/edge Py/Mgt (Py/Mgt associated with Po)
		K1	Pd-Pt-Fe-Te	2.4	x	3.1	7.44	Within/edge BMS, within/edge Pn/Mgt (Pn/Mgt associated with Py)
		L1	Au-Ag-Fe	3.8	x	5.0	19	Within/edge BMS, within/edge Pn (Pn associated with Cpy) and in contact with Pyx
		M1	Ni-Fe-Pt-Pd-Te	4.1	x	6.4	26.24	Within BMS, within Pn (Pn associated with Cpy and Py)
		N1	Ni-Pt-Pd-Te/Ag-Te	2.2	x	2.7	5.94	Within/edge BMS, within/edge Cpy (Cpy associated with Py) and in contact with Pyx
		O1	Ag-Te/Pd-Ni-Te	1.7	x	4.5	7.65	Within BMS, within Pn (Pn associated with Cpy and Py)
		O2	Ag-Te	1.8	x	2.1	3.78	Within BMS, within/edge Pn/Cpy (Pn/Cpy associated with Py)
MBS565	PTSR-53	A1	Pt-As	1.4	x	1.8	2.52	Within BMS, within Pn
		B1	Pt-Te	0.6	x	5.9	3.54	Within/edge BMS, within/edge Pn (Pn associated with Py) and in contact with Pyx
		C1	Pt-Fe-Te	3.5	x	9.1	31.85	Within/edge BMS, within/edge Pn (Pn associated with Py and Po) and in contact with Pyx
		D1	Ru-Pt-Os-As-S?	1.0	x	3.2	3.2	Within/edge BMS, within/edge Py/Cpy and in contact with Pyx
		E1	Pt-Te	0.6	x	12.9	7.74	Within BMS, within Pn (Pn associated with Cpy)
		F1	Pt-Fe-As	1.7	x	5.8	9.86	Associated with Cpy stringer within Pyx
		G1	Pt-As	2.0	x	3.0	6	Within/edge BMS, within/edge Py (Py associated with Pn and Cr) and in contact with Pyx
		H1	Pt-Te	1.2	x	3.9	4.68	Within BMS, within Cpy (Cpy associated with Py)
MBS565	PTSR-54	A1	Pt-As	8.1	x	15.1	122.31	Within/edge BMS, within/edge Cpy and in contact with Pyx/Serp
		B1	Ag-Pd-Te/Cu-Te	3.9	x	4.0	15.6	Within BMS, within Pn
		C1	Ni-Te	6.9	x	9.8	67.62	Within/edge BMS, within/edge Pn/Py and in contact with Pyx/Serp
		C2	Ag-Pd-Te	0.9	x	1.4	1.26	Associated with BMS stringer and C1 from Pn/Py crystal and in contact witht Pyx/Serp
		D1	Ni-Pt-Te/Ag-Te	5.8	x	10.9	63.22	Within BMS, within Pn
		D2	Ag-Te/Cu-Te	1.6	x	4.0	6.4	Within BMS, within Pn
		D3	Ag-Te/Cu-Te	0.7	x	11.9	8.33	Within/edge BMS, within/edge Pn and in contact with Pyx
		E1	Ni-Pt-Pd-Te	1.9	x	2.7	5.13	Within BMS, within Cpy (Cpy associated with Pn and Cr)
MBS565	PTSR-55	A1	Au-Ag	3.0	x	3.1	9.3	Within/edge BMS, within/edge Cpy and in contact with Pyx
		B1	Pt-Ni-Te	4.8	x	4.9	23.52	Associated with possible BMS stringer within Pyx
		C1	Pt-Ni-Te	1.1	x	2.3	2.53	Possible association with BMS (Cpy) stringer within Pyx
		C2	Cu-Te	1.7	x	3.4	5.78	Possible association with BMS (Cpy) stringer within Pyx
		C3	Pb-Te	3.4	x	8.0	27.2	Possible association with BMS (Cpy) stringer within Pyx
		C4	Pb-Te	0.9	x	4.6	4.14	Possible association with BMS (Cpy) stringer within Pyx
		D1	Ni-Pt-Fe-Te	2.5	x	13.5	33.75	Within BMS, within Pn
		D2	Pb-Pd-Te	0.7	x	24.4	17.08	Within BMS, within Pn
		E1	Ni-Pt-Pd-Te	2.4	x	4.3	10.32	Within BMS, within Po (Po associated Pn) and in contact with Pyx
		F1	Ni-Pt-Fe-Pd-Te	2.9	x	6.4	18.56	Within/edge BMS, within/edge Cpy stringer (Cpy stringer associated with Pn and Po composite sulphide) and in contact with Pyx
		G1	Ni-Fe-Pt-Pd-Te	1.3	x	6.5	8.45	Within/edge BMS, within/edge Po (Po associated with Pn) and in contact with Cr
		H1	Ni-Pt-Fe-Pd-Te	2.8	x	3.7	10.36	Within BMS, within Pn
		I1	Pt-Ni-Fe-Te	1.9	x	11.9	22.61	Within/edge BMS, within/edge Po stringer and in contact with Serp (Po stringer hosted by Serp vein within Ol
		J1	Ni-Pt-Pd-Te	2.1	x	2.4	5.04	Within BMS, within Po (associated with Pn)

Drill Hole	Sample No.	PGM No.	PGM Composition	Size (μm)			Area (μm^2)	Association
MBS565	PTSR-55	J2	Ni-Pt-Pd-Te	2.1	x	1.9	3.99	Within BMS, within Po (associated with Pn)
		J3	Ni-Pt-Fe-Pd-Te	2.1	x	2.6	5.46	Within Pyx
		K1	Ni-Pt-Pd-Te	2.0	x	6.8	13.6	Associated with Pn/Po stringer within Pyx
		L1	Ni-Pt-Pd-Fe-Te	2.1	x	3.2	6.72	Within/edge BMS, within/edge Po (Po associated with Pn) and possibly in contact with Pyx
		M1	Ag-Pb-Te	0.7	x	25.0	17.5	Associated with Cpy stringer within Pyx
		M2	Pt-Ni-Te	0.9	x	1.4	1.26	Associated with Cpy stringer within Pyx
		N1	Ni-Pt-Fe-Pd-Te	8.1	x	9.4	76.14	Within BMS, within/edge Cpy/Po (Cpy/Po associated with Pn)
		O1	Ni-Pt-Te	1.9	x	2.4	4.56	Within BMS, within Py (Py associated with Pn)
		P1	Ni-Pt-Pd-Te	1.4	x	1.8	2.52	Within BMS, within Pn (Pn associated with Po)
		Q1	Ni-Pt-Fe-Pd-Te	3.0	x	4.1	12.3	Within/edge BMS, within/edge Cpy/Pn (Cpy/Pn associated with Py) and in contact with Pyx
		Q2	Ni-Pt-Te/Ag-Te	0.5	x	1.7	0.85	Within/edge BMS, within/edge Py (Py associated with Pn and Cpy) and in contact with Pyx
		R1	Pt-Ir-Ni-Te rimmed by Ni-Pt-Pd-Te (/Ag-Te)	3.4	x	7.6	25.84	Within/edge BMS, within/edge Cpy (Cpy associated with Py) and in contact with Serp
		S1	Ni-Pt-Te	2.7	x	4.6	12.42	Within BMS, within Pn
		T1	Ni-Pt-Fe-Te	1.5	x	6.7	10.05	Within/edge BMS, within/edge Cpy and in contact with Pyx
		U1	Pt-Ni-Te	7.7	x	14.1	108.57	Within/edge BMS, within/edge Pn and in contact with Serp
		V1	Ni-Pt-Fe-Pd-Te	3.5	x	4.3	15.05	Within BMS, within/edge Cpy/Py
		W1	Ni-Pt-Fe-Pd-Te	3.0	x	27.5	82.5	Within BMS, within/edge Cpy/Py
		X1	Ni-Pt-Fe-Te	2.7	x	16.4	44.28	Within/edge BMS, within/edge Py/Pn and in contact with Pyx
		X2	Ni-Pt-Fe-Te	1.9	x	24.0	45.6	Within BMS, within/edge Py/Pn
		X3	Ni-Pt-Fe-Pd-Te	2.4	x	7.5	18	Within BMS, within/edge Py/Pn
		X4	Ni-Pt-Fe-Te	1.2	x	6.7	8.04	Within/edge BMS, within/edge Pn (Pn associated with Py) and in contact with Pyx
		Y1	Ni-Pt-Fe-Pd-Te	5.0	x	5.7	28.5	Within BMS, within Pn
MBS565	PTSR-56	A1	Ni-Pd-Te	9.0	x	12.9	116.1	Within BMS, within Pn
		B1	Ni-Pt-Te	1.3	x	8.1	10.53	Within/edge BMS, within/edge Po/Pn and in contact with Ol/Serp
		C1	Ni-Fe-Pd-Te	4.9	x	7.3	35.77	Within BMS, within Po
		D1	Ag-Te	1.4	x	12.1	16.94	Within/edge BMS, within/edge Cpy/Po and in contact with Ol
		D2	Au-Ag-Fe-Cu	2.4	x	4.6	11.04	Within/edge BMS, within Cpy/Po and in contact with Pyx
		E1	Ag-Au	1.4	x	3.1	4.34	Within/edge BMS, within/edge Cpy/Pn and in contact with Serp/Mgt
		F1	Ni-Pt-Te	0.5	x	16.2	8.1	Associated with BMS stringer within Pyx
		G1	Ni-Pt-Te	1.1	x	8.8	9.68	Associated with Pn/Po stringer within Ol
		G2	Ni-Pt-Te	0.5	x	5.2	2.6	Associated with Pn/Po stringer within Ol
		H1	Ni-Fe-Te	2.4	x	5.0	12	Within/edge BMS, within/edge Po (Po associated with Pn) and in contact with Cr
		I1	Au-Cu-Ag-Fe	2.3	x	2.3	5.29	Within BMS, within Cpy
		J1	Ag-Te	2.5	x	5.3	13.25	Within/edge BMS, within Po and in contact with Cr and Serp
		K1	Ni-Fe-Te	1.9	x	5.8	11.02	Within/edge BMS, within Cpy and in contact with Serp
		K2	Cu-Ni-Te	0.7	x	0.7	0.49	Within/edge BMS, within Cpy and in contact with Serp
		K3	Ag-Pd-Te	1.7	x	2.6	4.42	Within/edge BMS, within Cpy and in contact with Serp
		L1	Ni-Pt-Fe-Te	7.5	x	10.0	75	Within BMS, within Pn
		M1	Ni-Fe-Pt-Pd-Te	3.4	x	4.2	14.28	Within BMS, within Pn (Pn associated with Cpy and Cr)
		N1	Ni-Pt-Te	1.7	x	3.1	5.27	Within BMS, within Py (Py associated with Pn a#nd Cpy)
		O1	Ni-Te	1.6	x	3.2	5.12	Within BMS, within Pn
		P1	Ag-Au/Ag-Te	2.4	x	4.5	10.8	Within BMS, within Cpy

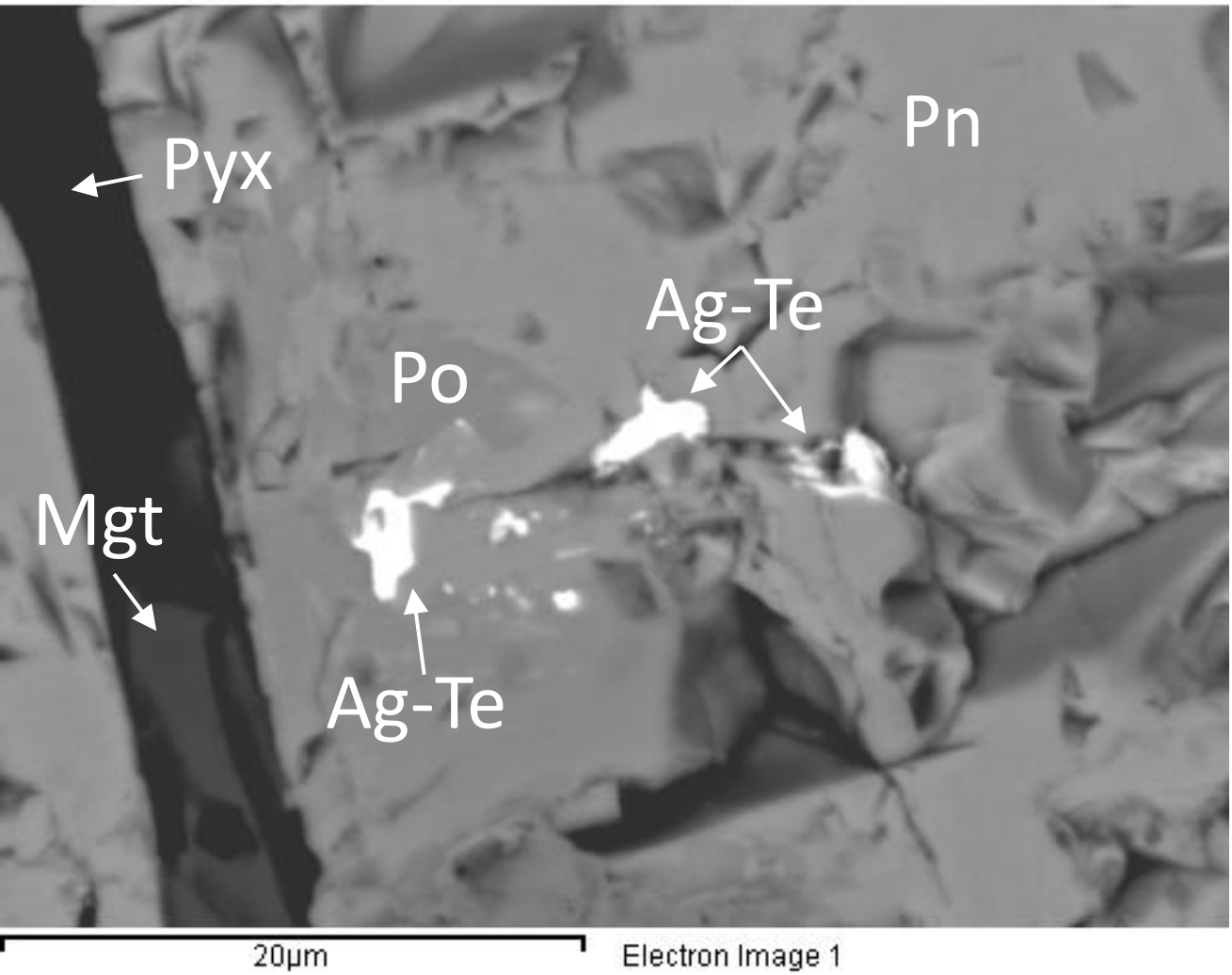
Drill Hole	Sample No.	PGM No.	PGM Composition	Size (μm)			Area (μm^2)	Association
MBS565	PTSR-56	P2	Ag-Cu/Pb-Te	0.9	x	3.3	2.97	Within BMS, within Cpy
		Q1	Ni-Te	4.3	x	7.7	33.11	Within BMS, within Pn
		Q2	Ag-Pd-Te	1.4	x	1.4	1.96	Within BMS, within Pn
		R1	Au-Ag-Cu-Fe	3.8	x	4.0	15.2	Within/edge BMS, within/edge Cpy and in contact with Ol/Serp
		S1	Ni-Te	5.5	x	13.6	74.8	Within/edge BMS, within Pn and in contact with Cr and Sil/Serp
MBS565	PTSR-57	A1	Cu-Pt-Te	2.9	x	3.3	9.57	Within silicate between Cpy and Cr
		B1	Ag-Au	5.3	x	23.9	126.67	Within Ol
		C1	Cu-Pt-Te	2.1	x	4.3	9.03	Within BMS, within Pn
		D1	Cu-Au-Fe	1.7	x	3.6	6.12	Within/edge BMS, within/edge Cpy/Cr
		E1	Pt-Cu-Ni-Fe-Pd-Te	1.4	x	4.8	6.72	Within/edge BMS, within/edge Pn and in contact with Pyx/Ol
		E2	Cu-Pt-Te	0.8	x	4.8	3.84	Within/edge BMS, within/edge Pn and in contact with Pyx/Ol
		F1	Cu-Te/Pt-As	1.4	x	7.7	10.78	Within/edge BMS, within/edge Pn (Pn associated with Mgt) and in contact with Ol
MBS565	PTSR-58	A1	Pt-As	6.1	x	9.2	56.12	Within/edge BMS, within/edge Pn and in contact with Serp/Ol
		A2	Ir-Pt-As-S	1.7	x	1.8	3.06	Within/edge BMS, within/edge Pn and in contact with Serp/Ol
		A3	Cu-Pd-Te	9.1	x	10.9	99.19	Within/edge BMS, within/edge Pn and in contact with Serp/Ol
		B1	Rh-Pt-Os-Ir-As-S	1.3	x	2.5	3.25	Within/edge BMS, within/edge Pn/Gers-Cob and in contact with Pyx/Serp
		B2	Co-Ni-As-S Gersdorffite-Cobaltite	1.5		2.8	4.2	Within/edge Pn and in contact with Pyx/Serp
		C1	Pd-Pt-Ni-Fe-Te	1.3	x	2.7	3.51	Within BMS, within Pn
		D1	Pd-Te	0.8	x	3.1	2.48	Within/edge BMS, within Pn(+Cu) and possibly in contact with Ol
		E1	Pd-Te/Pt-As	1.7	x	2.7	4.59	Within/edge BMS, within Pn/Cpy mix and in contact with Pyx
		F1	Cu-Te (/Ag-Te)	1.9	x	5.2	9.88	Within/edge BMS, within/edge Pn and in contact with Pyx
		F2	Cu-Pd	0.6	x	7.9	4.74	Within/edge BMS, within/edge Pn and in contact with Pyx
		G1	Pt-Ni-Pd-Fe-Te	1.8	x	2.5	4.5	Within BMS, within Pn
		H1	Pd-Te	2.1	x	4.9	10.29	Within/edge BMS, wtihin Pn/Cpy mix (edge of slide, association unclear)
		H2	Pt-As	0.2	x	4.0	0.8	Within/edge BMS, wtihin Pn/Cpy mix (edge of slide, association unclear)
		I1	Pt-As	1.6	x	5.2	8.32	Within BMS, within Pn/Cpy mix
		I2	Ru-Os	0.7	x	3.8	2.66	Within BMS, within Pn/Cpy mix
		J1	Pt-As	1.2	x	1.6	1.92	Within BMS, wtihin Pn
MBS565	PTSR-59	A1	Cu-Au-Fe	1.3	x	3.2	4.16	Within/edge BMS, within/edge BMS mix and possibly in contact with Ol/Pyx
		B1	Cu-Au	0.8	x	3.2	2.56	Within Pyx
		C1	Pt-Te	1.0	x	1.5	1.5	Within/edge BMS, within/edge Pn and in contact with Cr
		D1	Pt-Fe-Te	2.0	x	2.6	5.2	Within/edge BMS, within/edge Pn and in contact with Pyx
		E1	Pt-Fe	1.6	x	1.7	2.72	Within/edge BMS, within/edge Cpy (or other Cu sulphide) and in contact with Ol
MBS565	PTSR-60	A1	Pt-Ni-Cu-Pd-Te	0.5	x	3.0	1.5	Within BMS, within Pn
		B1	Pt-Pd-Cu-Te	2.8	x	3.6	10.08	Within/edge BMS, within/edge Cpy and in contact with Ol
		C1	Pd-Ni-Pt-Cu-Te	2.2	x	5.7	12.54	Within BMS, within/edge Pn/Cpy mix
		D1	Pt-Fe-Te	1.3	x	3.0	3.9	Within/edge BMS, within/edge Cpy (or other Cu Sulphide)/Cr and in contact with Pyx
MBS569	PTSR-63	A1	Ni-Fe-Pt-Te	1.5	x	3.1	4.65	Within/edge BMS, within/edge Po/Mgt (Po associated with Pn)
		B1	Ni-Te	1.3	x	3.5	4.55	Within BMS, within Pn/Po (Pn/Po associated with Py)
		C1	Ag-Te	1.0	x	1.2	1.2	Within/edge BMS, within/edge Py (Py associated with Cpy) and in contact with Pyx
		C2	Pt-Fe-Ni-Te	0.4	x	1.9	0.76	Within/edge BMS, within/edge Py (Py associated with Cpy) and in contact with Pyx
		D1	Ni-Pt-Te	7.3	x	11.1	81.03	Within BMS, within Pn (associated with Py)
		D2	Ni-Fe-Pt-Te	3.6	x	4.6	16.56	Within BMS, within Pn (associated with Py)

Drill Hole	Sample No.	PGM No.	PGM Composition	Size (μm)			Area (μm^2)	Association
MBS569	PTSR-63	E1	Pt-Ni-Fe-Te/Ag-Te	3.5	x	13.0	45.5	Within BMS, within Pn
		E2	Ni-Pd-Te	3.0	x	3.9	11.7	Within BMS, within Pn
		F1	Ni-Pd-Pt-Te	0.9	x	2.9	2.61	Within BMS, within Cpy (Cpy associated with Pn and Po)
		G1	Ni-Pt-Fe-Pd-Te	1.5	x	7.9	11.85	Within BMS, within Pn (Pn associated with Py)
		G2	Ag-Te	2.2	x	8.6	18.92	Within BMS, within Pn (Pn associated with Py)
		G3	Ag-Te	1.0	x	9.4	9.4	Within/edge BMS, within/edge Pn (Pn associated with Py) and in contact with Pyx
		H1	Ni-Pt-Fe-Te	2.8	x	3.5	9.8	Within BMS, within Py (Py associated with Pn and Cr)
		H2	Ir-Pt-As-S	1.2	x	2.3	2.76	Within BMS, within Py (Py associated with Pn and Cr)
		I1	Pt-Te	0.3	x	2.6	0.78	Within BMS, within Pn
		J1	Pt-Ni-Fe-Te/Ag-Te	1.5	x	12.6	18.9	Unknown
		J	Ag-Te	12.2	x	20.4	248.88	Unknown (approximate total size)
		K1	Ni-Pt-Fe-Te/Ag-Te	3.0	x	4.8	14.4	Within BMS, within Pn
		L1	Ni-Fe-Pt-Te/Ag-Te	3.0	x	8.2	24.6	Within BMS, within Py (Py associated with Cpy and Mgt)
		L2	Ag-Te	2.5	x	3.1	7.75	Within/edge BMS, within/edge Py/Mgt (Py/Mgt associated with Cpy)
MBS569	PTSR-64	A1	Pt-Cu-Te	0.6	x	5.6	3.36	Within/edge BMS, within/edge Py/Cpy (Pn/Cpy associated with Pn and Cr) and in contact with Pyx
		B1	Ni-Pd-Te	11.9	x	12.7	151.13	Within BMS, within Pn
		C1	Ni-Te	1.1	x	1.6	1.76	Within BMS, within Py (Py associated with Pn)
		D1	Ag-Te/Ni-Te	0.7	x	2.8	1.96	Unknown
		D2	Ni-Pd-Te	2.3	x	4.6	10.58	Unknown
		E1	Ni-Pd-Pt-Te	21.7	x	24.4	529.48	Within/edge BMS, within Pn and in contact with Pyx
		E2	Ag-Te	1.8	x	1.8	3.24	Within silicate vein cross cutting Pn and in contact with Pn
		E3	Pt-As	4.5	x	24.4	109.8	Within/edge BMS, within Pn and in contact with Pyx
		E4	Pt-Fe-As	2.0	x	3.1	6.2	Within Pyx
		F1	Ni-Pd-Pt-Fe-Te/Ag-Te	7.3	x	8.4	61.32	Within BMS, within Pn
		G1	Ag-Te	0.7	x	4.3	3.01	Within/edge BMS, within/edge Cpy (Cpy associated with Py) and in contact with Pyx
		G2	Ag-Te	0.4	x	0.7	0.28	Within/edge BMS, within/edge Py (Py associated with Cpy) and in contact with Pyx
		H1	Ni-Pd-Pt-Fe-Te	2.1	x	2.9	6.09	Within/edge BMS, within/edge Cpy (Cpy associated with Py and Pn) and in contact with Cr
		H2	Pt-As	0.5	x	3.2	1.6	Within/edge BMS, within/edge Cpy (Cpy associated with Py and Pn) and in contact with Cr
		I1	Pd-Pt-Te	2.9	x	4.2	12.18	Within BMS, within Cpy
		J1	Ni-Te	1.6	x	3.5	5.6	Within BMS, within Py (Py associated with Cpy)
		K1	Au-Ag-Fe	1.2	x	2.1	2.52	Within BMS, within/edge Cpy/Py
		L1	Ni-Pd-Fe-Pt-Te	4.9	x	5.2	25.48	Within BMS, within Pn
		M1	Ni-Pd-Te/Ag-Te	6.6	x	7.3	48.18	Within/edge BMS, within/edge Pn/Cpy/Py and in contact with Pyx
		M2	Ni-Pd-Fe-Te	5.5	x	5.8	31.9	Within BMS, within Py
		M3	Ag-Te	0.9	x	4.0	3.6	Within Pyx
		M4	Ag-Te	1.0	x	4.0	4	Within Pyx
		N1	Ni-Pd-Fe-Pt-Te	2.9	x	6.1	17.69	Within BMS, within Cpy (Cpy associated with Pn)
		O1	Ni-Pd-Te	7.3	x	12.6	91.98	Within BMS, within Pn
		O2	Ag-Te	1.2	x	6.4	7.68	Within BMS, within Pn
		O3	Ag-Te	1.4	x	2.5	3.5	Within BMS, within/edge Cpy/Pn
		P1	Ni-Pd-Fe-Te	2.4	x	4.7	11.28	Within BMS, within Pn
		Q1	Au-Ag	0.6	x	1.6	0.96	Within BMS, within/edge Py/Pn

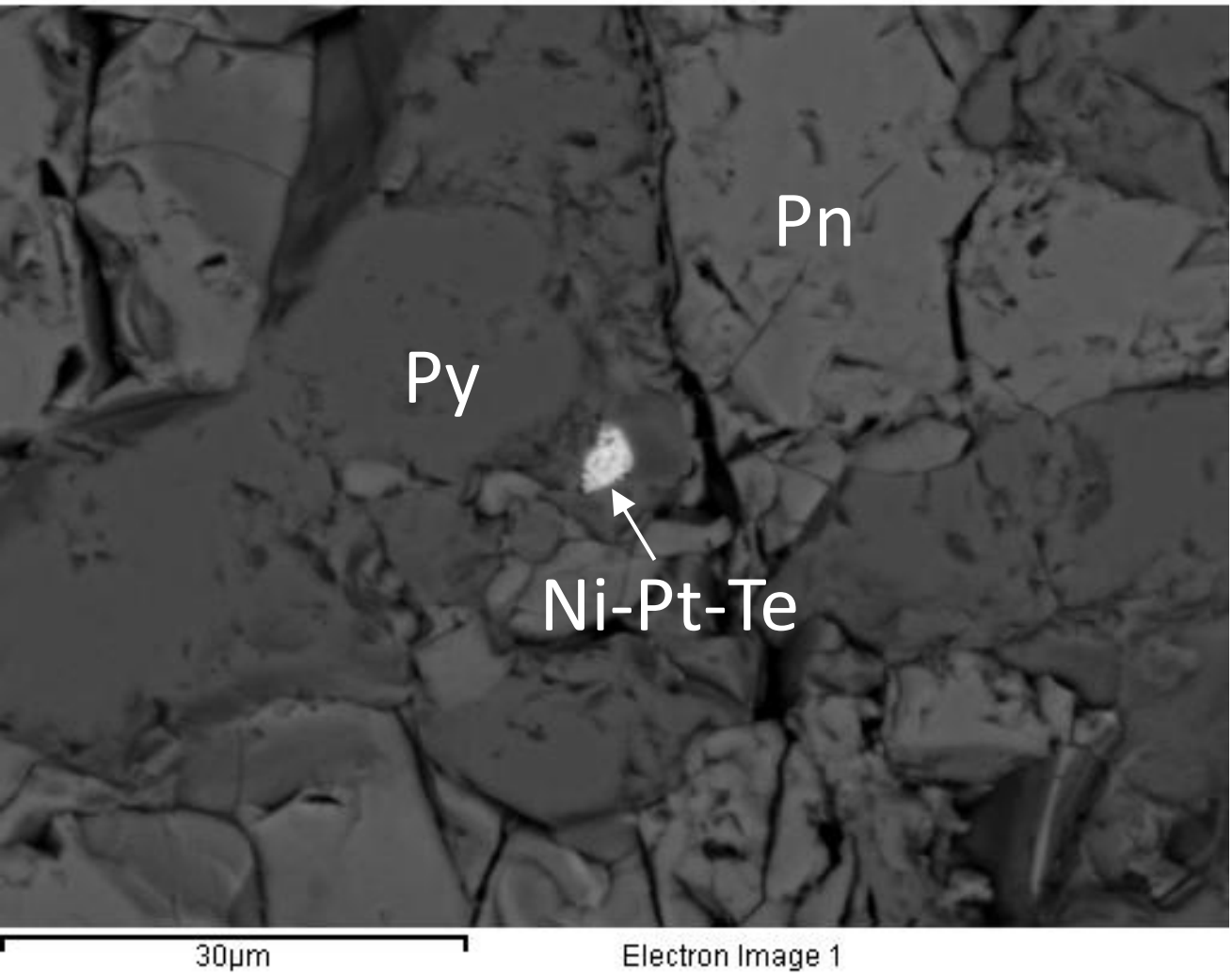
Drill Hole	Sample No.	PGM No.	PGM Composition	Size (µm)			Area (µm^2)	Association
MBS569	PTSR-64	R1	Cu-Pd-Pt-Te	1.3	x	1.8	2.34	Within BMS, within Pn (Pn associated with Py)
		S1	Ni-Pd-Pt-Te	1.5	x	1.7	2.55	Within BMS, within Pn
		T1	Ni-Pd-Fe-Pt-Te	3.3	x	3.7	12.21	Within BMS, within Cpy (Cpy associated with Pn and Py)
		U1	Ag-Te	7.7	x	9.0	69.3	Within BMS, within Pn
		U2	Ag-Te	1.7	x	2.1	3.57	Within BMS, within Pn
		U3	Ag-Te/Cu-Te	0.9	x	3.9	3.51	Within BMS, within Pn
		U4	Ag-Te	1.4	x	2.7	3.78	Within BMS, within Pn
		V1	Ni-Pt-Pd-Te/Pt-As	2.3	x	2.7	6.21	Within/edge BMS, within/edge Cpy and in contact with Pyx
		W1	Ir-Pt-As-S	1.5	x	5.1	7.65	Within Pyx, associated with Cpy
		X1	Ni-Pd-Te/Ag-Te	7.4	x	18.3	135.42	Edge Py and in contact with Serp/Pyx
		X2	Ag-Te	5.5	x	11.7	64.35	Edge Py and in contact with Serp/Pyx
		X3	Ag-Te	4.3	x	6.6	28.38	Edge Py and in contact with Serp/Pyx
		X4	Ag-Te	1.0	x	11.7	11.7	Within/between Pn/Py, possible contact with Pyx/Serp
		Y1	Pt-As	1.9	x	3.6	6.84	Within BMS, within Cpy
		Z1	Ni-Pd-Te	1.7	x	3.3	5.61	Within BMS, within Pn
		AA1	Pt-As/Ni-Pd-Pt-Te	1.5	x	3.2	4.8	Within BMS, within Pn (associated with Po)
		AB1	Ni-Te	3.6	x	5.0	18	Within/edge BMS, within/edge Cpy/Pn (Cpy/Pn associated with Po) and in contact with Pyx
MBS569	PTSR-65	A1	Ni-Pt-Fe-Pd-Te	1.9	x	8.6	16.34	Within/edge BMS, within/edge Po (Po associated with Pn) and in contact with Serp/Pyx
		B1	NA					
		C1	Ni-Fe-Pt-Te	2.0	x	3.5	7	Within Mgt (Mgt associated with Pn)
		C2	Ni-Fe-Pt-Te	1.7	x	2.8	4.76	Within/edge BMS, within/edge Pn/Mgt
		D1	Ni-Pt-Te	4.3	x	15.9	68.37	Within/edge BMS within/edge Pn/Po mix and in contact with Serp
		E1	Pt-Ni-Fe-Te/Ag-Te	0.9	x	11.9	10.71	Within Pyx and associated with Po
		F1	Pt-Ni-Pd-Te	0.7	x	2.1	1.47	Within/edge BMS, within/edge Cpy and in contact with Serp/Pyx
		G1	Ni-Pt-Fe-Te	2.9	x	8.6	24.94	Within/edge BMS, within/edge Po and in contact with Pyx
		H1	Pt-Ni-Fe-Te	2.0	x	4.3	8.6	Assocated with Cpy stringer within Pyx
		H2	Ag-Te	0.8	x	3.8	3.04	Assocated with Cpy stringer within Pyx
		I1	Re-Cu-Ti-Pb-Os-S?	0.9	x	1.6	1.44	Within BMS, within Pn
		J1	Ni-Pt-Pd-Fe-Te	3.1	x	6.1	18.91	Within BMS, within Pn
		K1	Pt-Ni-Pd-Fe-Te	1.0	x	2.7	2.7	Within/edge BMS, within/edge Pn (Pn associated with Po) and in contact with Serp
		L1	Pt-Ni-Te	1.8	x	7.3	13.14	Within/edge BMS, within/edge Po and in contact with Pyx
		M1	Pt-Ni-Te	0.8	x	13.8	11.04	Associated with Cpy/Pn stringer with Serp veins within Pyx
MBS569	PTSR66	A1	Ag-Te (/Pt-Te)	1.1	x	5.0	5.5	Within/edge BMS, within/edge Cpy (Cpy associated with Pn) and in contact with Pyx
		A2	Ag-Te	0.5	x	0.5	0.25	Within/edge BMS, within/edge Cpy/Pn and in contact with Pyx
		B1	Ni-Pt-Te	6.2	x	7.6	47.12	Within BMS, within Pn
		C1	Ni-Pt-Te	1.6	x	2.1	3.36	Within BMS, within Cpy
		C2	Pt-Ni-Pd-Te	1.6	x	2.7	4.32	Within BMS, within Cpy (Cpy associated with Pn)
		D1	Pt-Ni-Fe-Te/Ag-Te	3.9	x	9.7	37.83	Within/edge BMS, within/edge Pn and in contact with Pyx
		E1	Ni-Pt-Fe-Pd-Te	3.2	x	16.6	53.12	Within BMS, within Pn (Pn associated with Py)
		E2	Ag-Te	0.6	x	2.1	1.26	Within/edge BMS, within/edge Pn (Pn associated with Py) and in contact with Pyx
		F1	Pt-Ni-Fe-Te/Ag-Te	1.8	x	4.0	7.2	Within/edge BMS, within/edge Pn (Pn associated with Py) and in contact with Pyx
		G1	Ni-Pt-Pd-Fe-Te	4.0	x	6.4	25.6	Within BMS, within/edge Pn/Cpy (Pn/Cpy associated with Po and Py)
		H1	Ni-Pt-Te	5.9	x	13.0	76.7	Within BMS, within Pn (Pn associated with Py)

Drill Hole	Sample No.	PGM No.	PGM Composition	Size (µm)			Area (µm^2)	Association
MBS569	PTSR66	I1	Pd-Pt-Ni-Te/Ag-Te	3.6	x	3.6	12.96	Within BMS, within/edge Pn/Cpy
		J1	Ni-Pt-Fe-Pd-Te	5.8	x	6.9	40.02	Within/edge BMS, within/edge Pn (Pn associated with Po) and in contact with Pyx
		K1	Pt-Ni-Pd-Te	1.4	x	4.1	5.74	Within/edge BMS, within/edge Cpy and in contact with Pyx
MBS569	PTSR67	A1	Pt-Ni-Pd-Te	1.2	x	3.5	4.2	Within BMS, within Pn
		B1	Cu-Te	2.7	x	4.5	12.15	Within/edge BMS, within/edge Pn and in contact with Serp/Ol
MBS569	PTSR68	A1	Pt-Ni-Te/Pt-As	1.8	x	2.2	3.96	Within/edge BMS, within/edge Cpy/Pn (and Cpy/Pn mix) and in contact with Pyx
		B1	Cu-Te	1.5	x	1.9	2.85	Within/edge BMS, within/edge Pn and in contact with Pyx
		B2	Pt-As (/Ni-Te)	0.5	x	1.5	0.75	Within/edge BMS, within/edge Pn and in contact with Pyx
		C1	Pt-As	1.5	x	5.1	7.65	Within/edge BMS, within/edge Pn and in contact with Serp
		D1	Ni-Cu-Pd-Fe-Te	1.7	x	4.0	6.8	Within/edge BMS, within/edge Pn (Pn associated with Ni2S) and in contact with Pyx
		E1	Cu-Pt-Pd-Te	1.9	x	3.2	6.08	Within/edge BMS, within/edge Pn and in contact with Ol
		F1	Pt-As	4.3	x	19.1	82.13	Within/edge Cpy stringer/vein and in contact with Pyx/Serp
		G1	Cu-Fe-Te	10.5	x	12.4	130.2	Associated with BMS within Serp/Ol
			Bight patches Pd-Cu-Te					
		H1	Pt-Fe-As	1.4	x	4.8	6.72	Within Ol/Serp and in contact with Cr
MBS569	PTSR-69	A1	Ag-Pd-Te	2.7	x	3.3	8.91	Within BMS, within/edge Py/Pn
		B1	Pt-Te	1.3	x	9.2	11.96	Within/edge BMS, within/edge Cpy/Pn and in contact with Pyx
		C1	Au-Ag	2.2	x	2.4	5.28	Within/edge BMS, within/edge Cpy and in contact with Pyx
MBS569	PTSR-70	A1	Pt-Cu-Fe-Te	2.6	x	2.9	7.54	Within /edge BMS, within/edge BMS mix and in contact with Mgt rim?
		B1	Pt-Te	0.5	x	1.9	0.95	Within BMS, within Cpy
		C1	Pt-Te	1.4	x	2.5	3.5	Within/edge BMS stringer within Ol and in contact with Ol
		D1	Cu-Pt-Ni-Pd-Te	2.0	x	2.1	4.2	Within/edge BMS, within/edge Pn and in contact with Ol
MBS569	PTSR-71	A1	Pt-Fe-S	2.4	x	2.6	6.24	Within BMS, within Pn
MBS569	PTSR-72		No PGM Observed					No PGM Observed

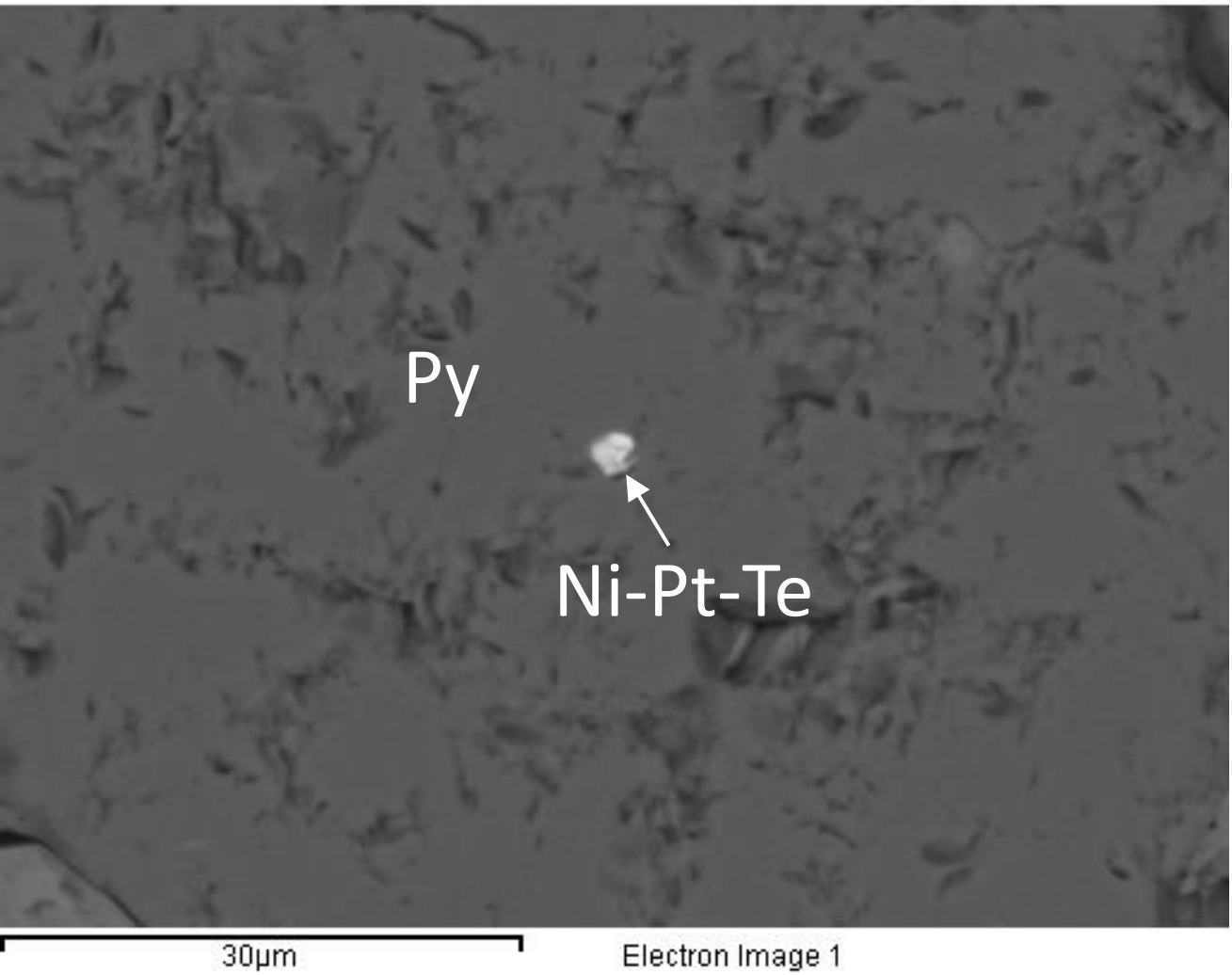
PTR01 A 1-3



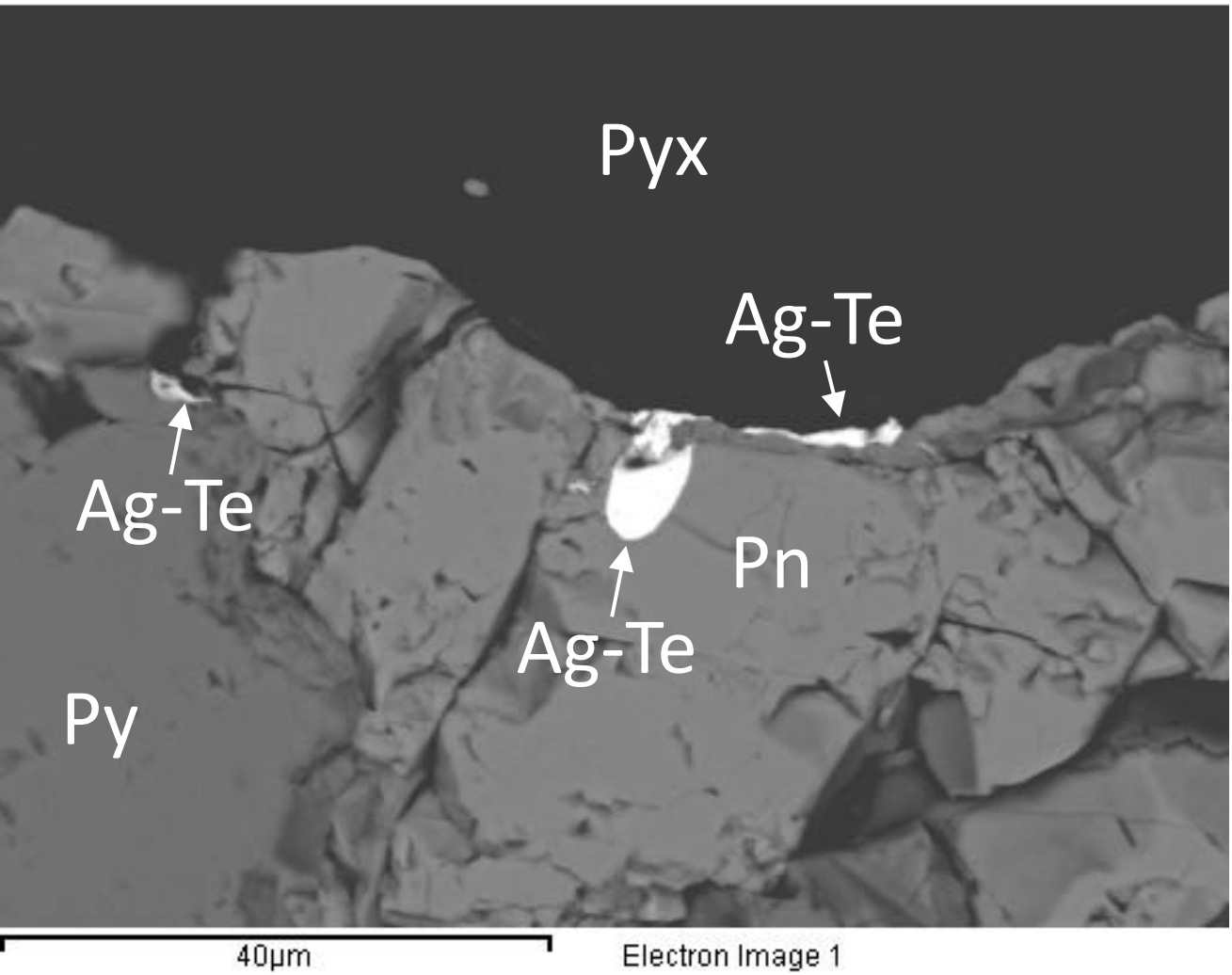
PTR01 B 1



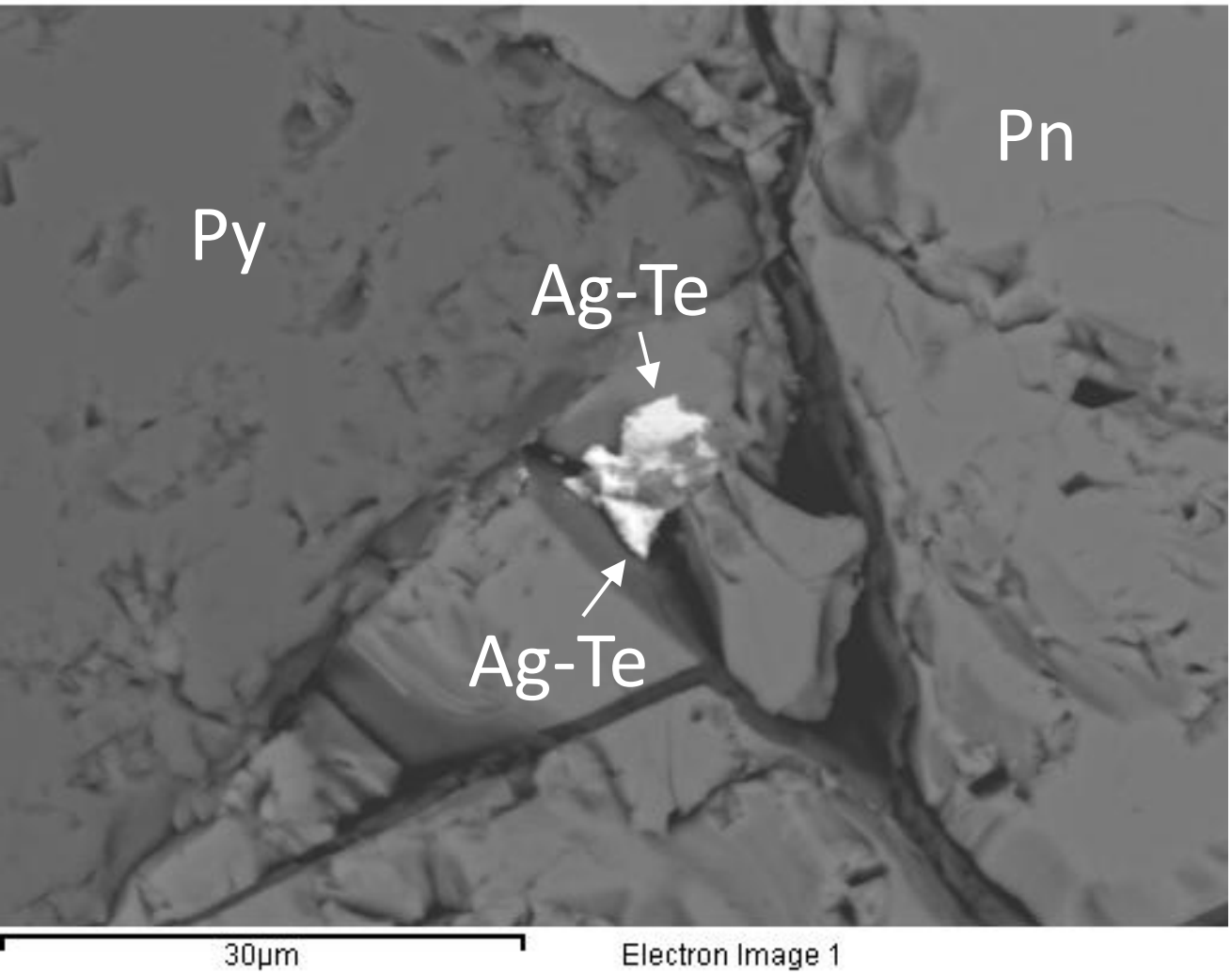
PTR01 B2



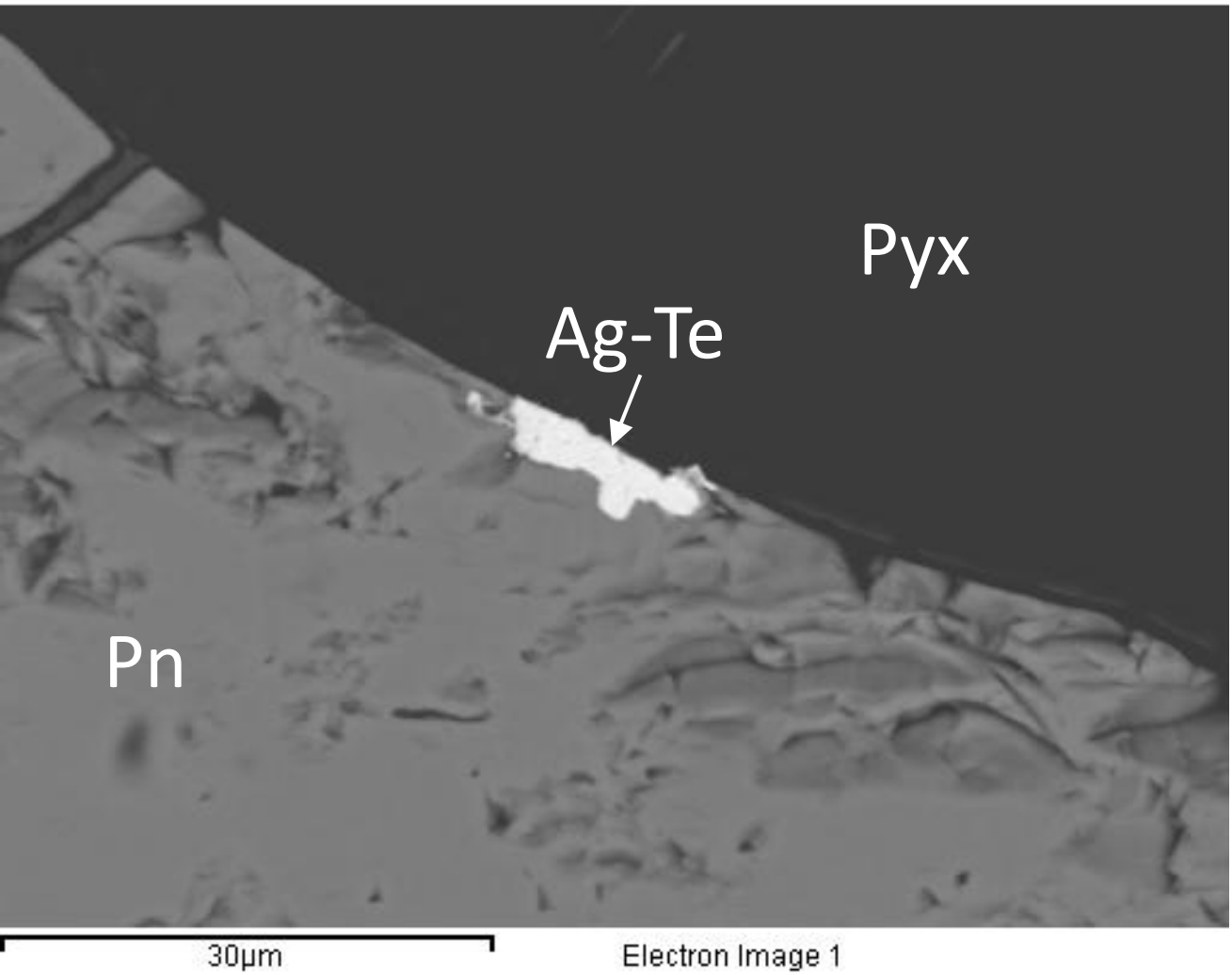
PTR01 C 1-3



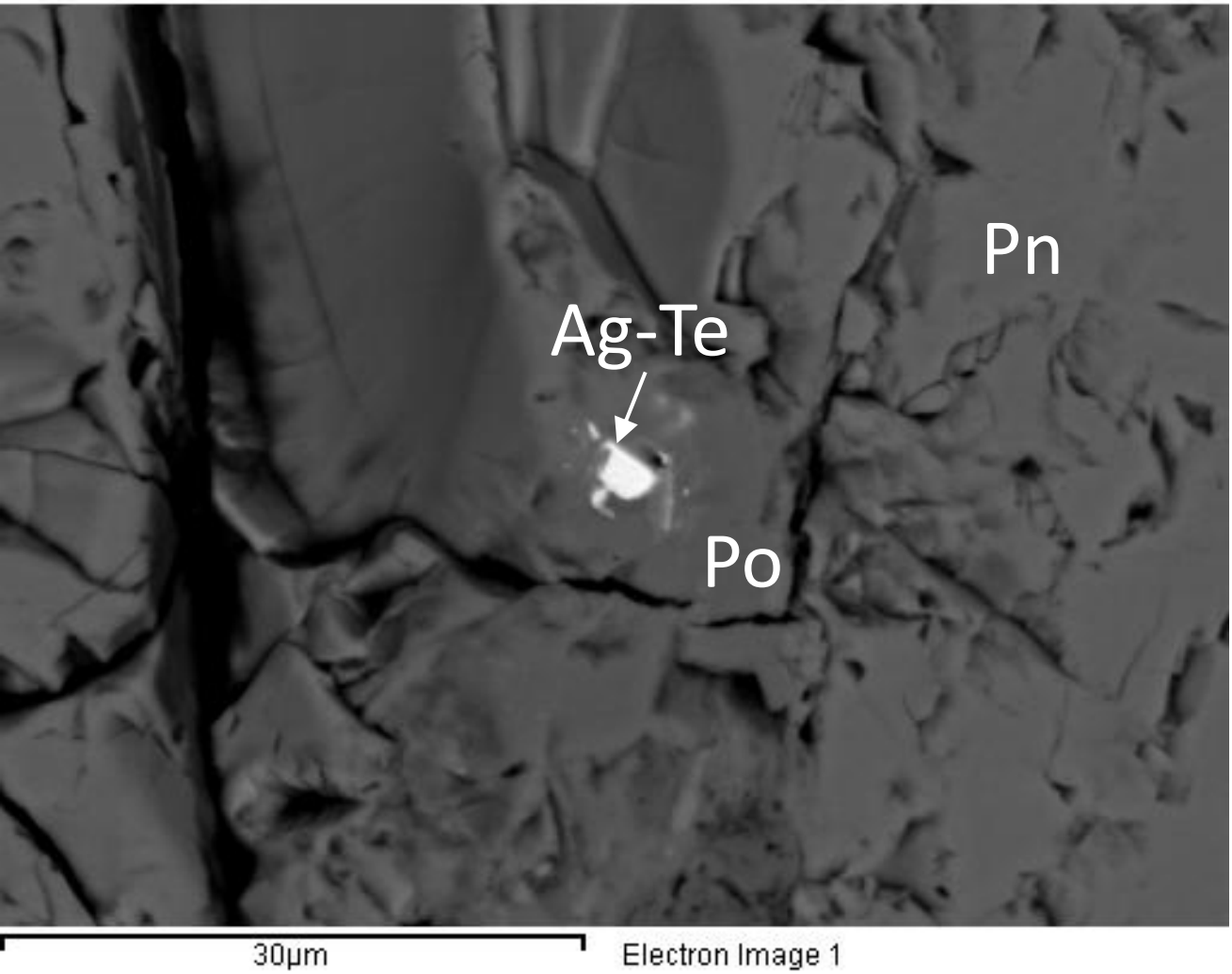
PTR01 D 1



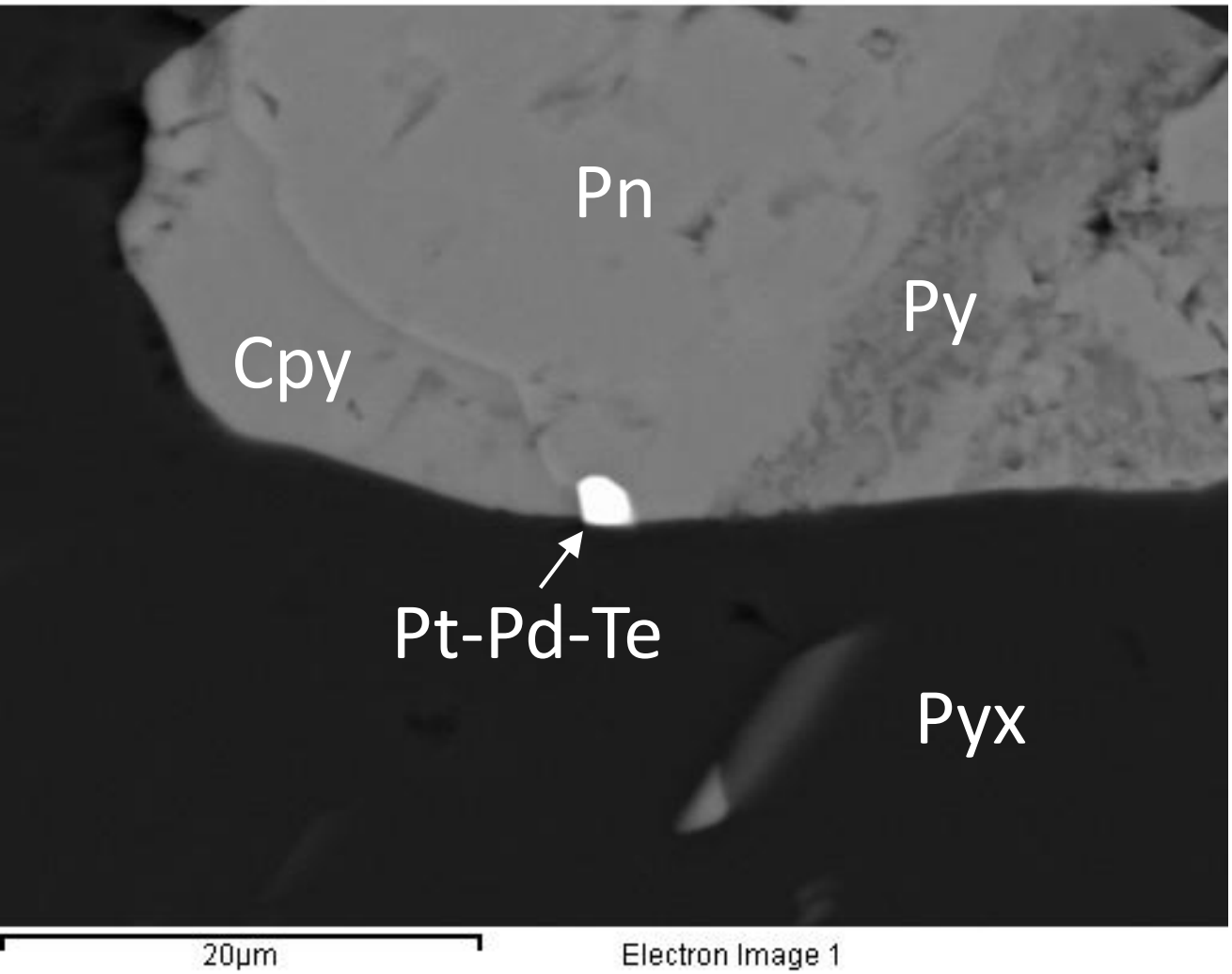
PTR01 E 1



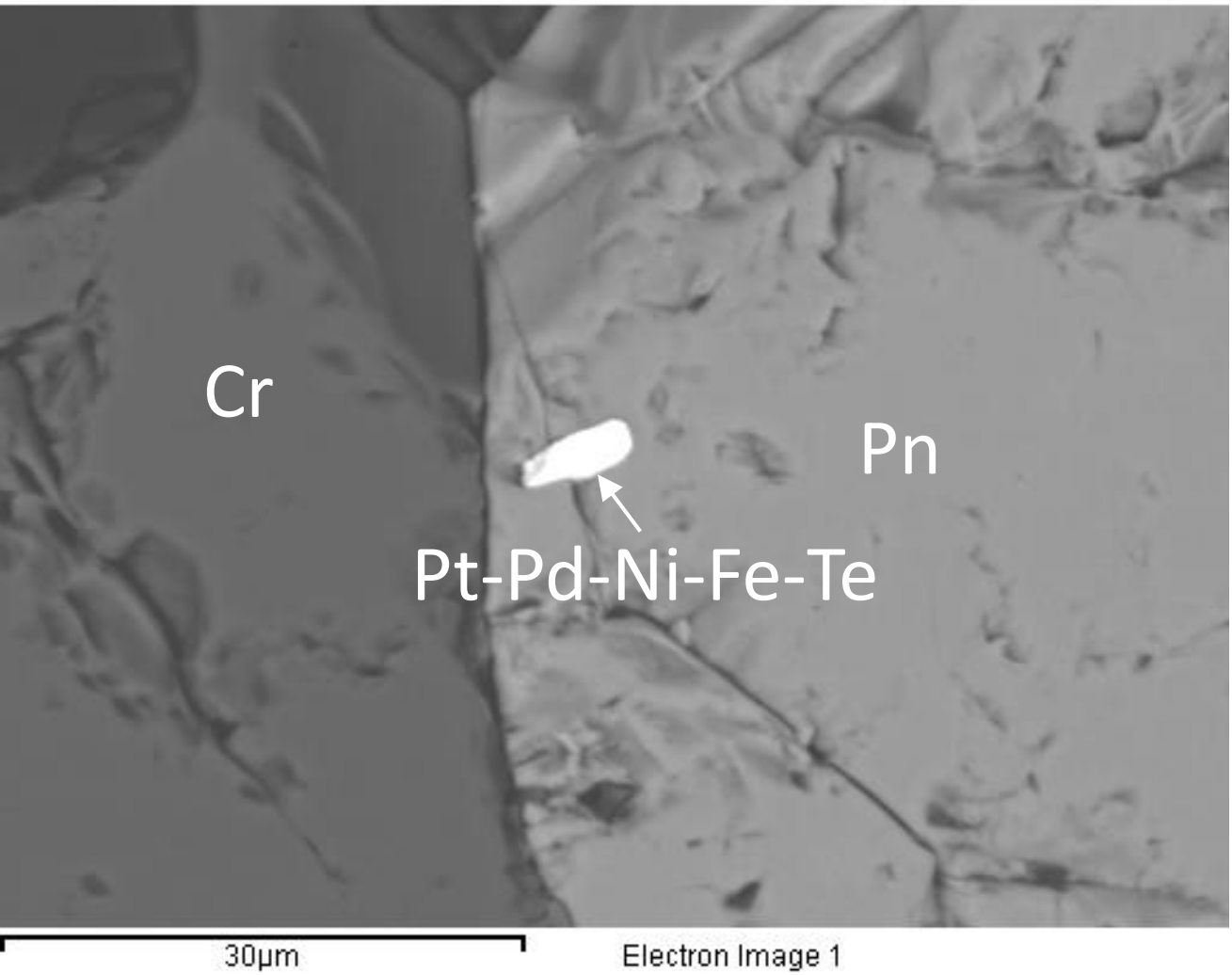
PTR01 F 1



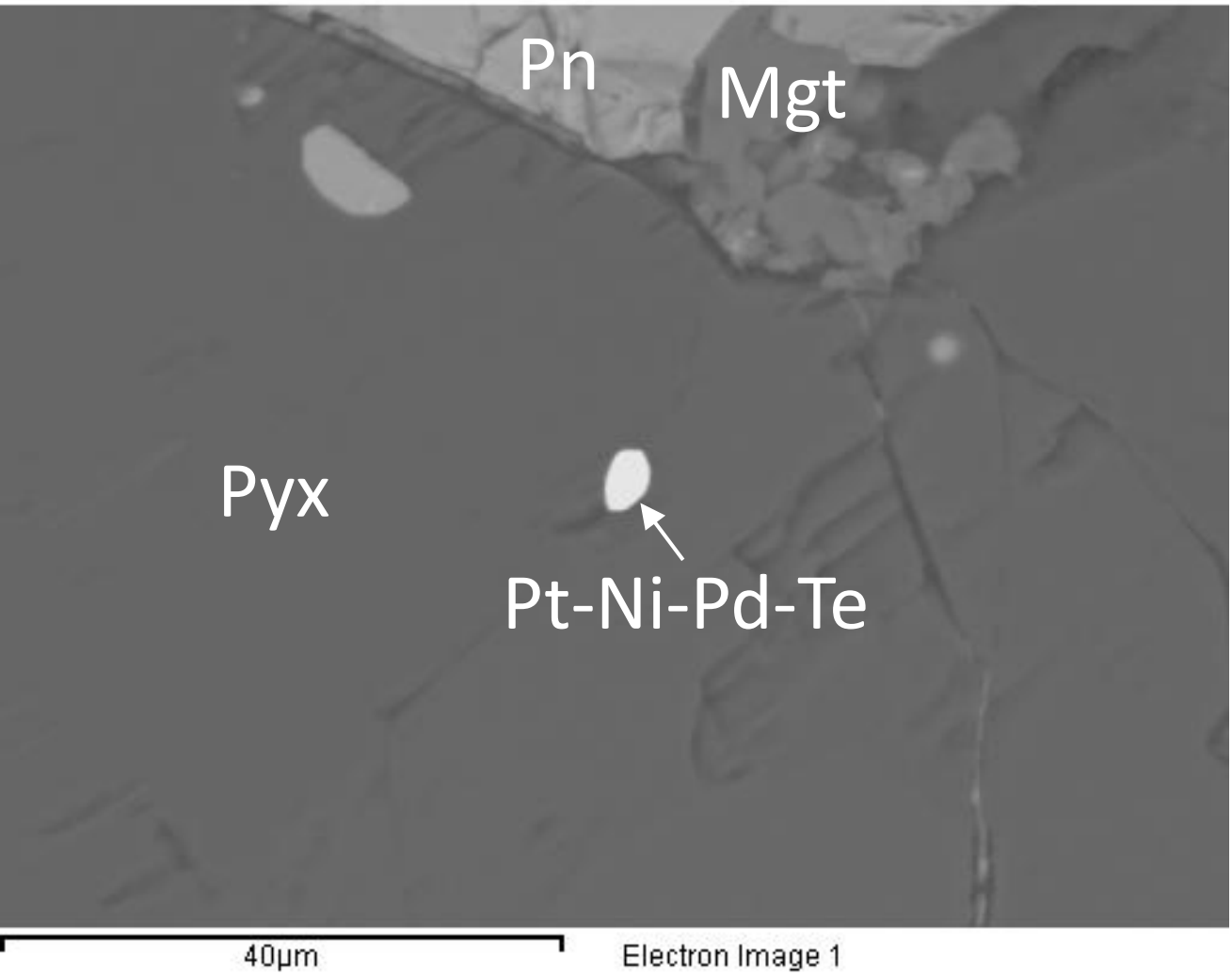
PTR02 A 1



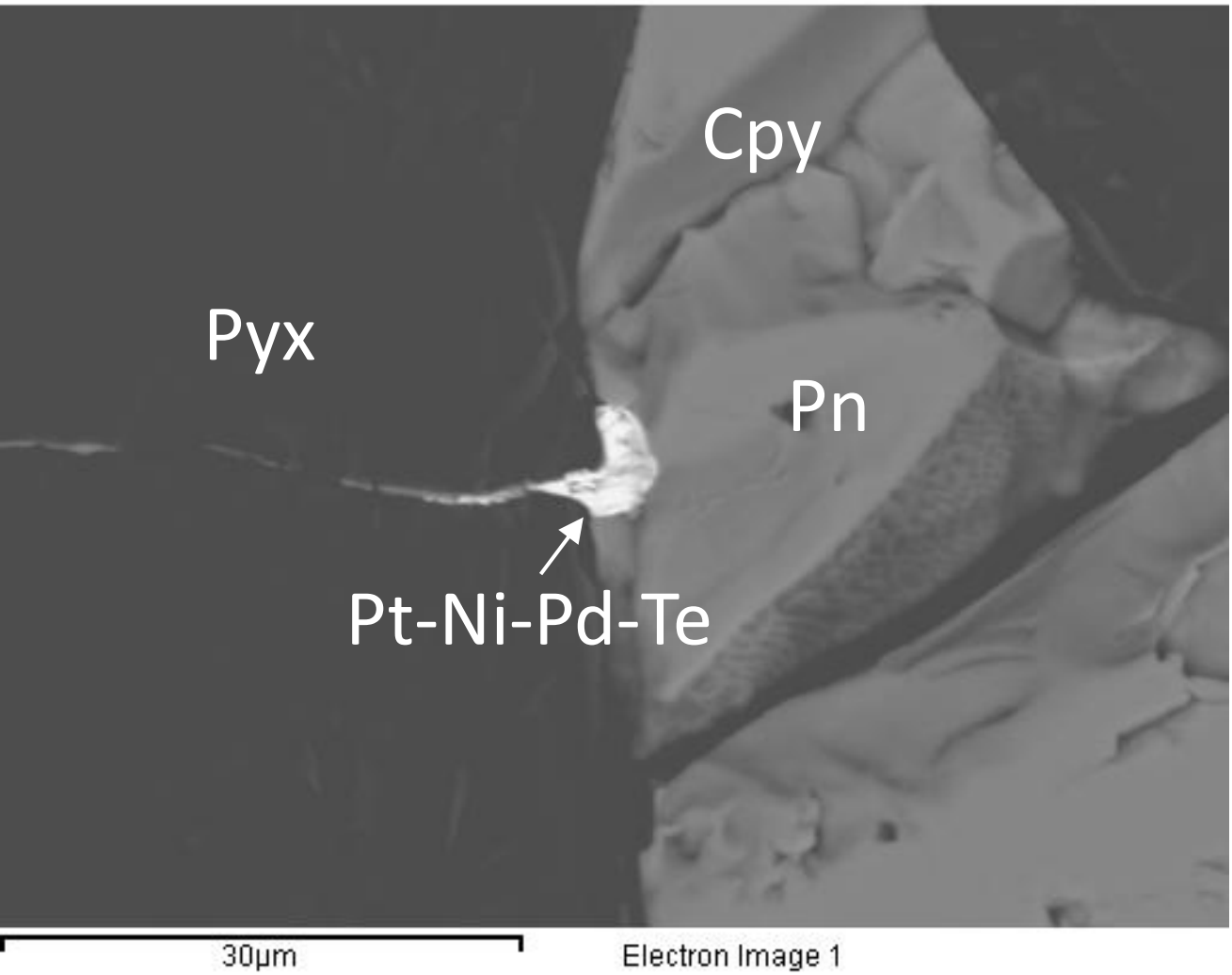
PTR02 B 1



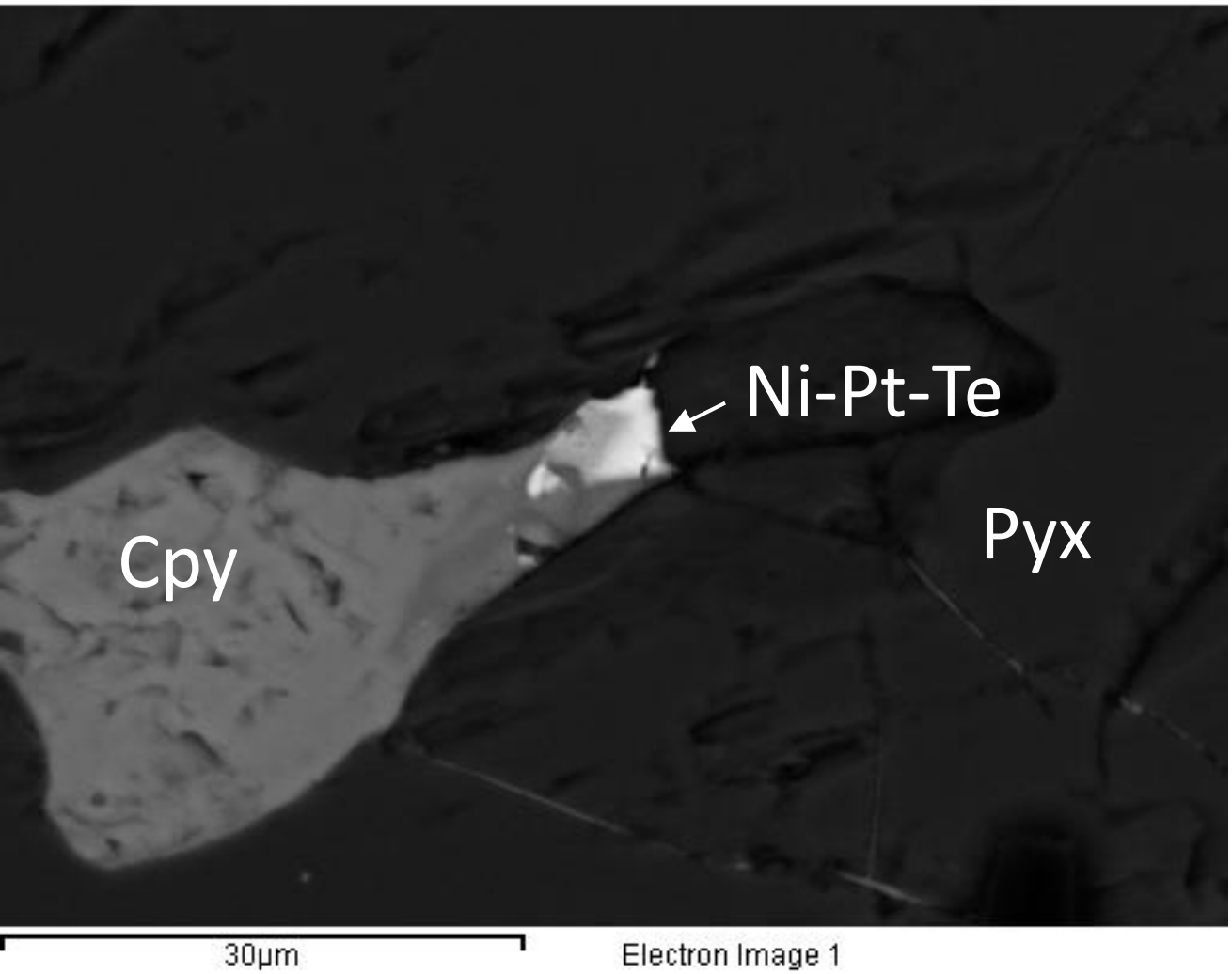
PTR02 C 1



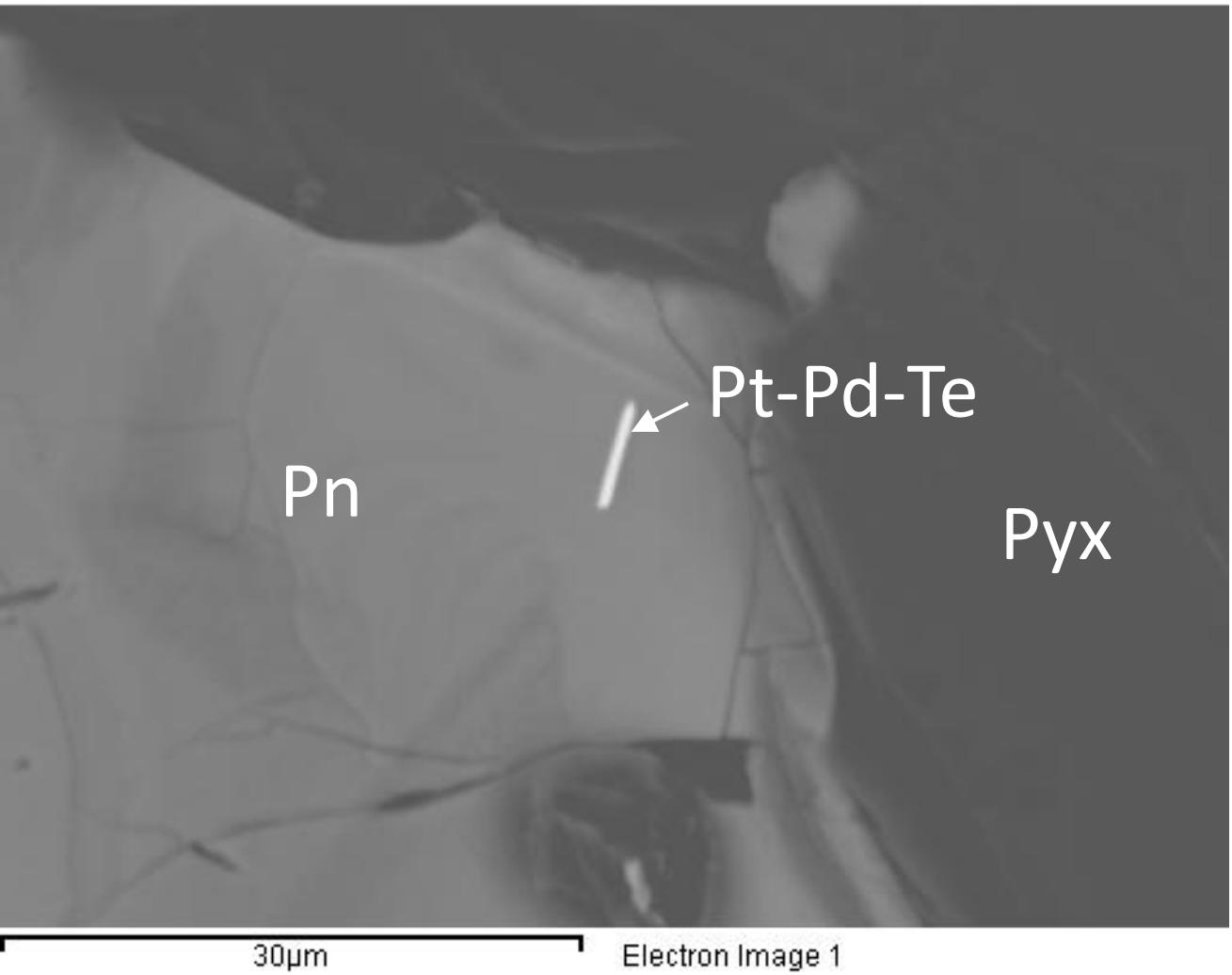
PTR02 D 1



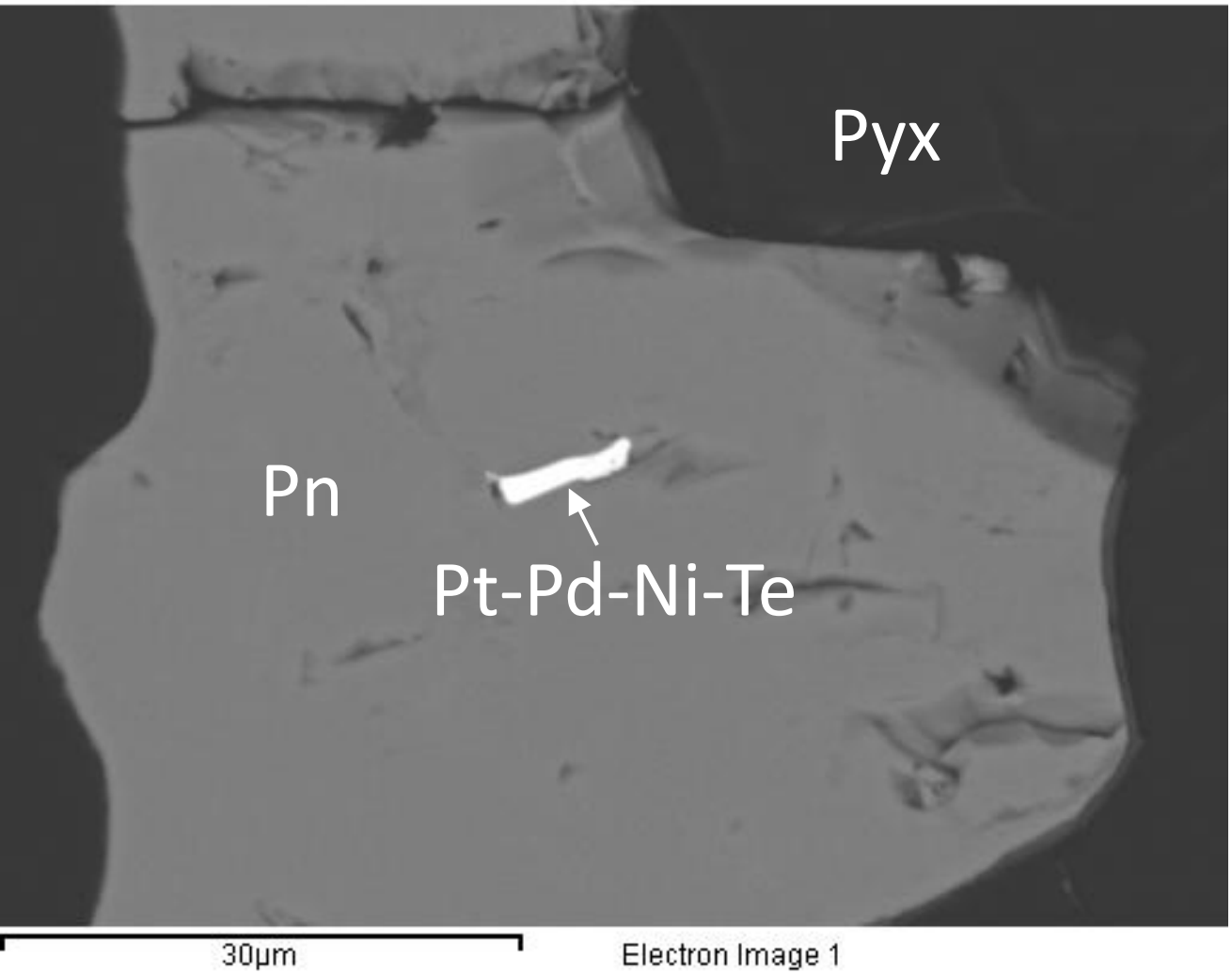
PTR02 E 1



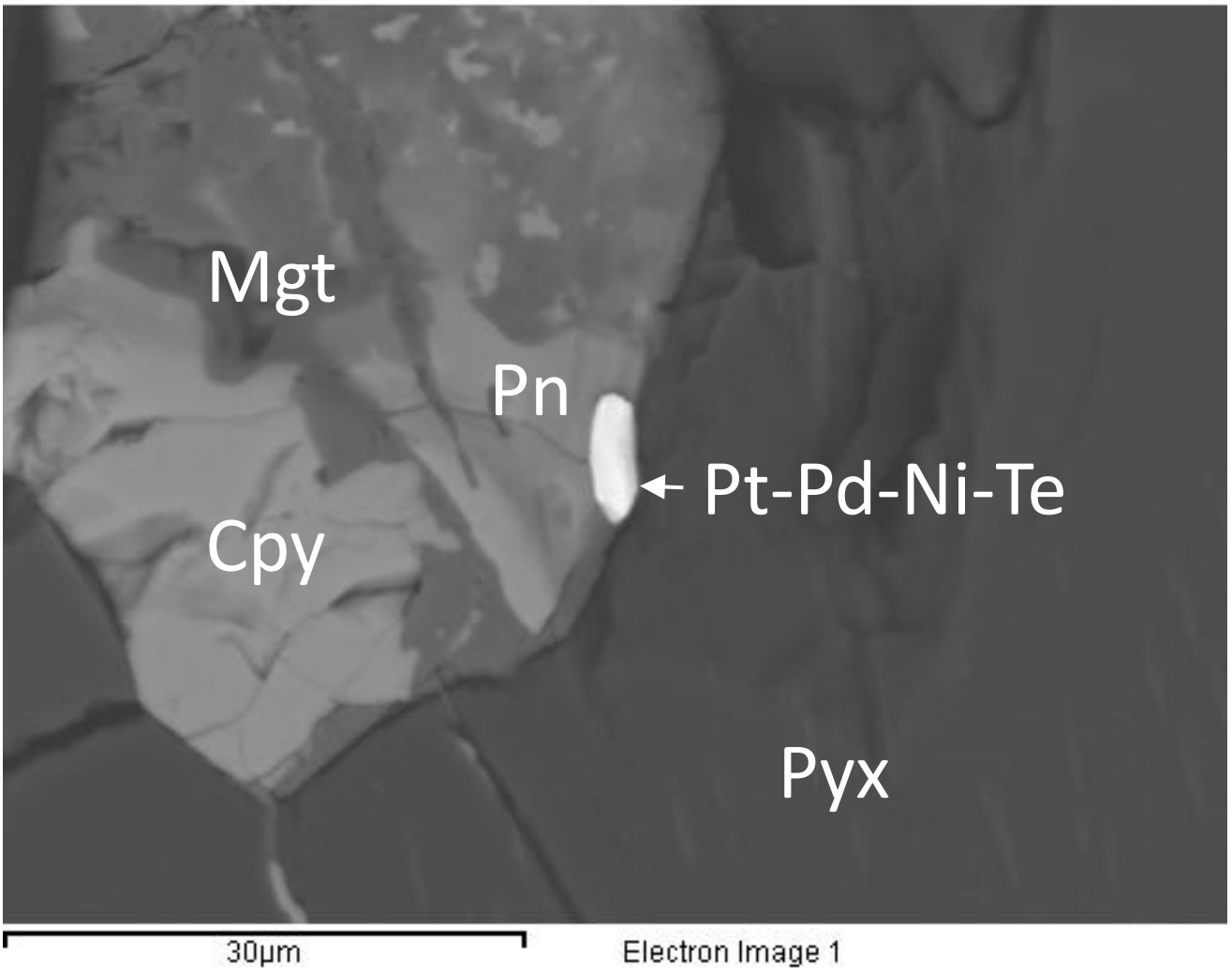
PTR02 F 1



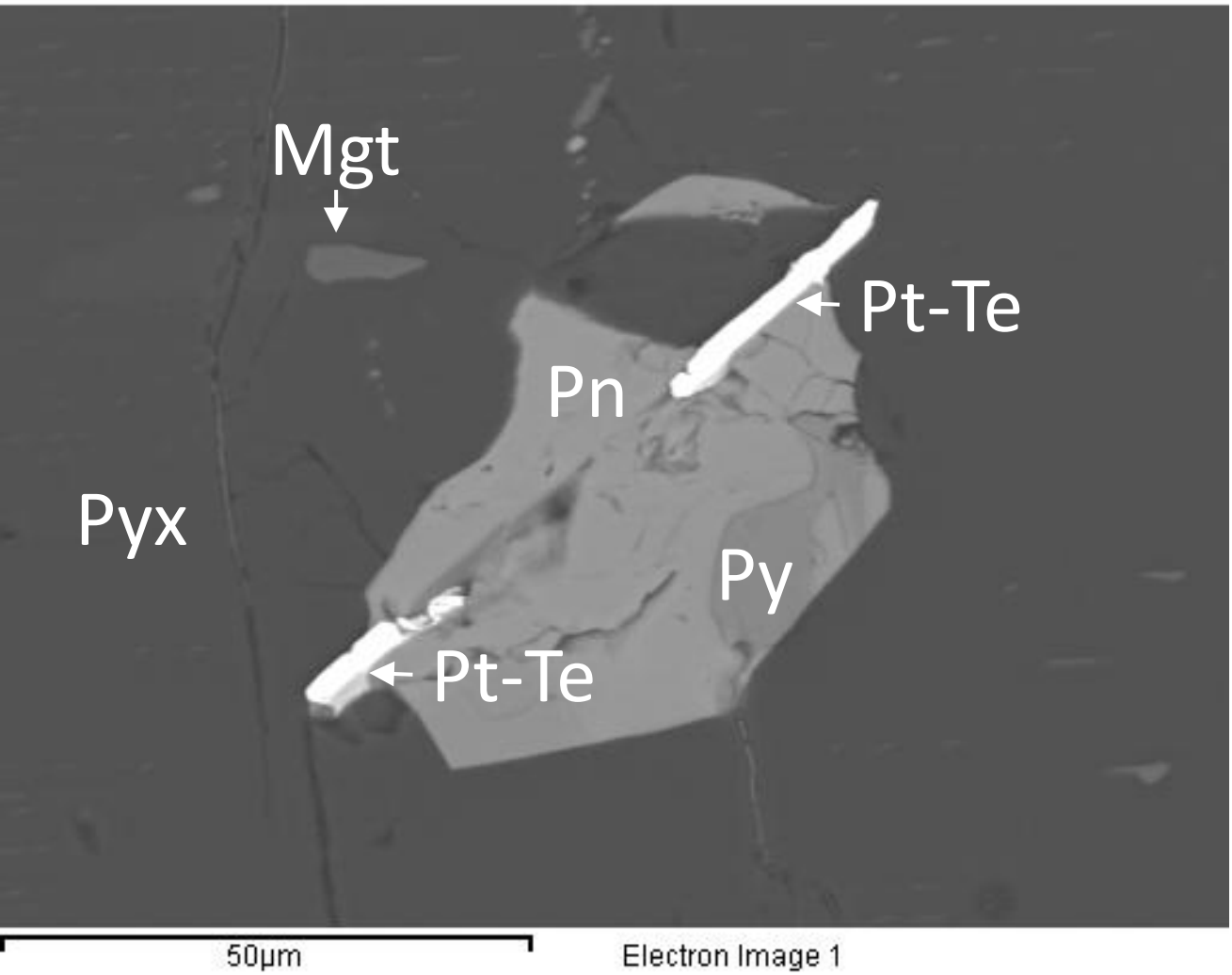
PTR02 G 1



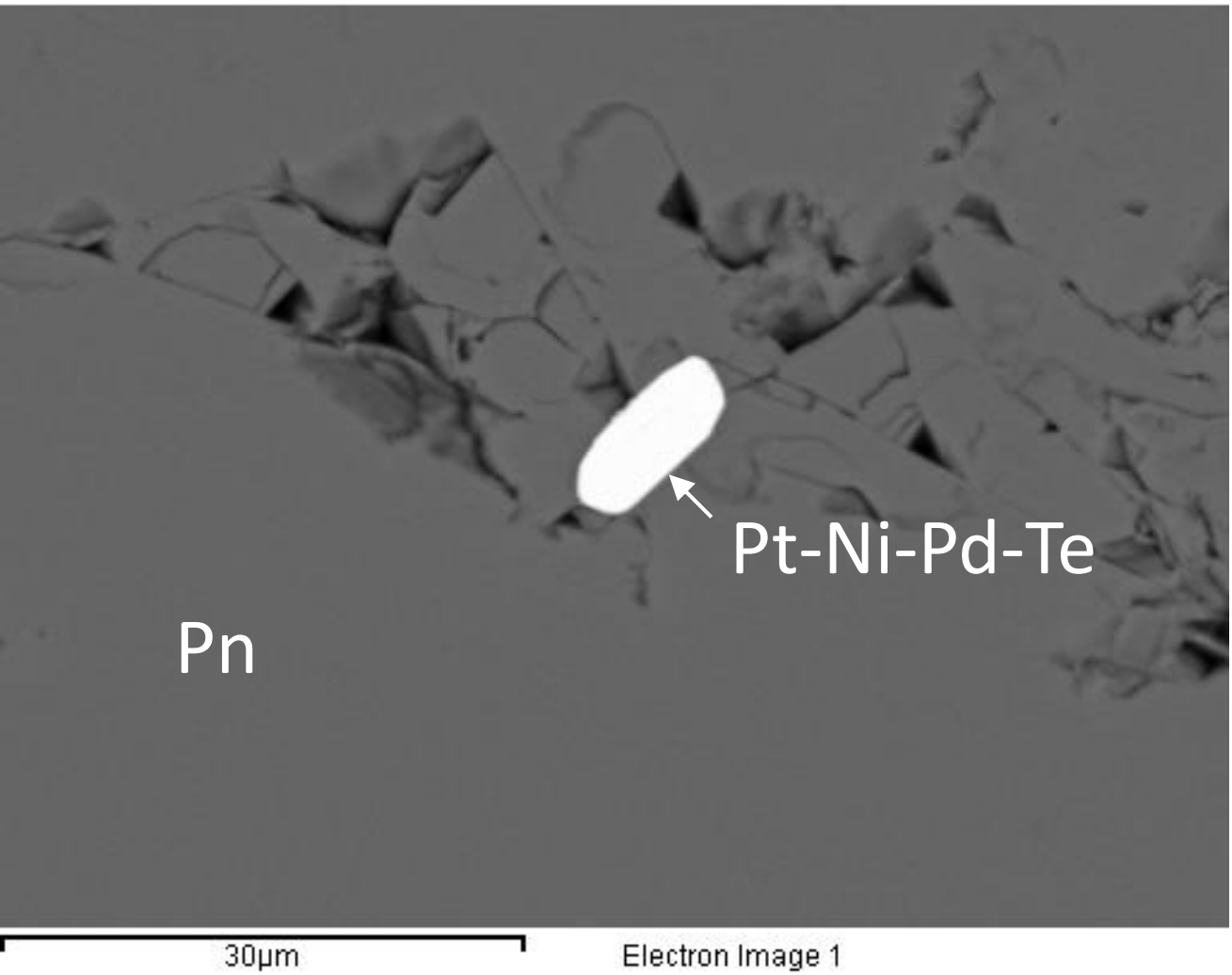
PTR02 H 1



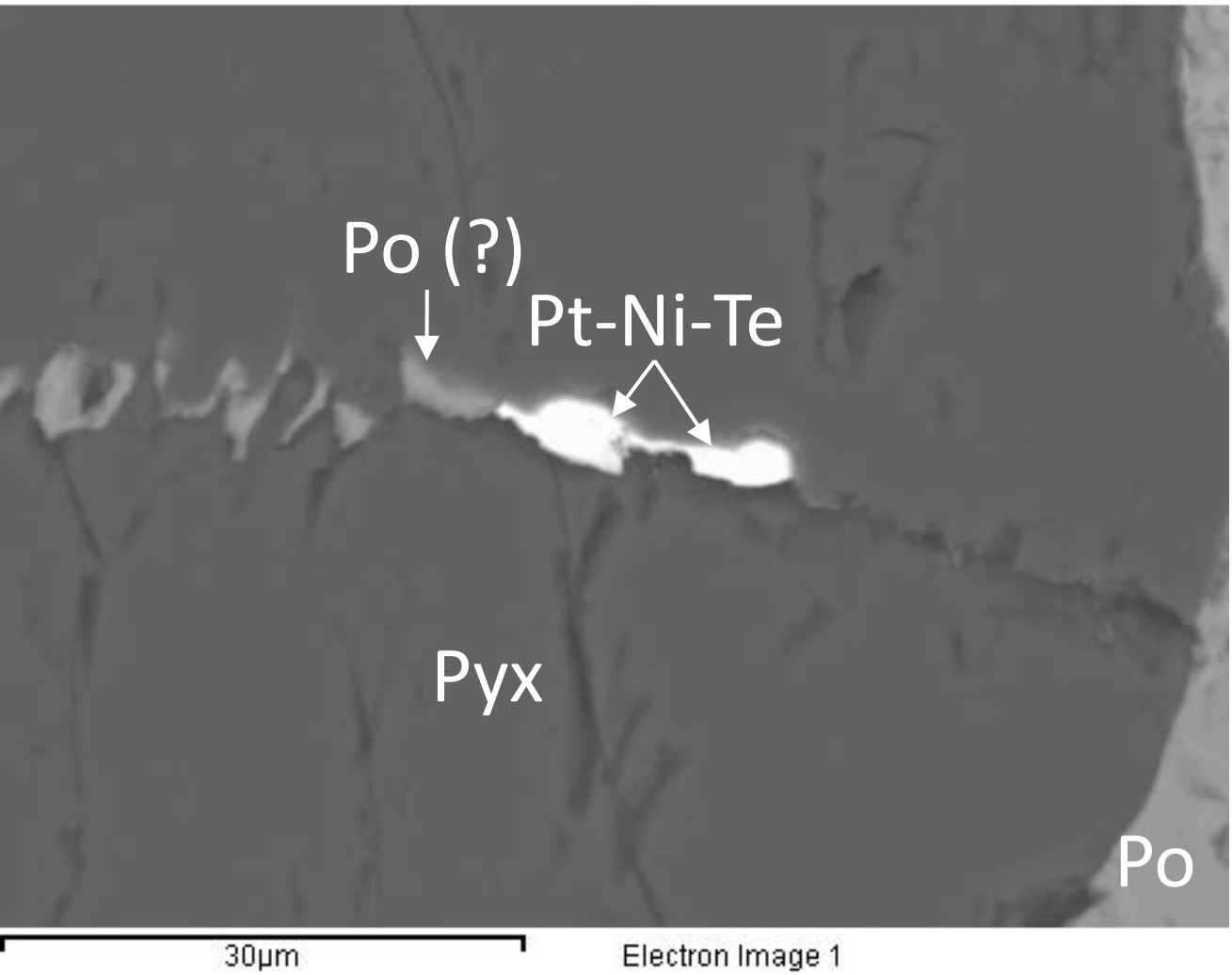
PTR02 I 1-2



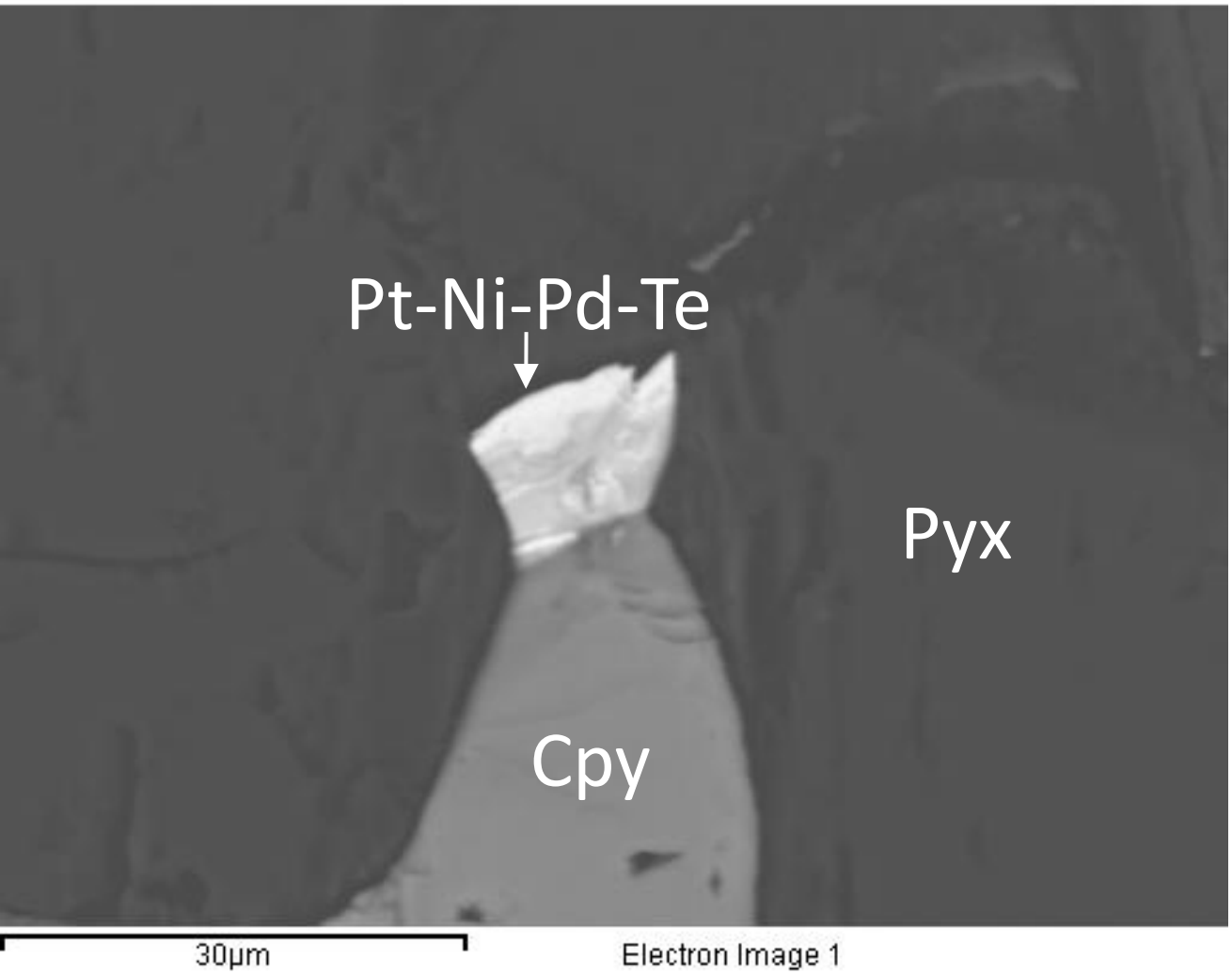
PTR02 J 1



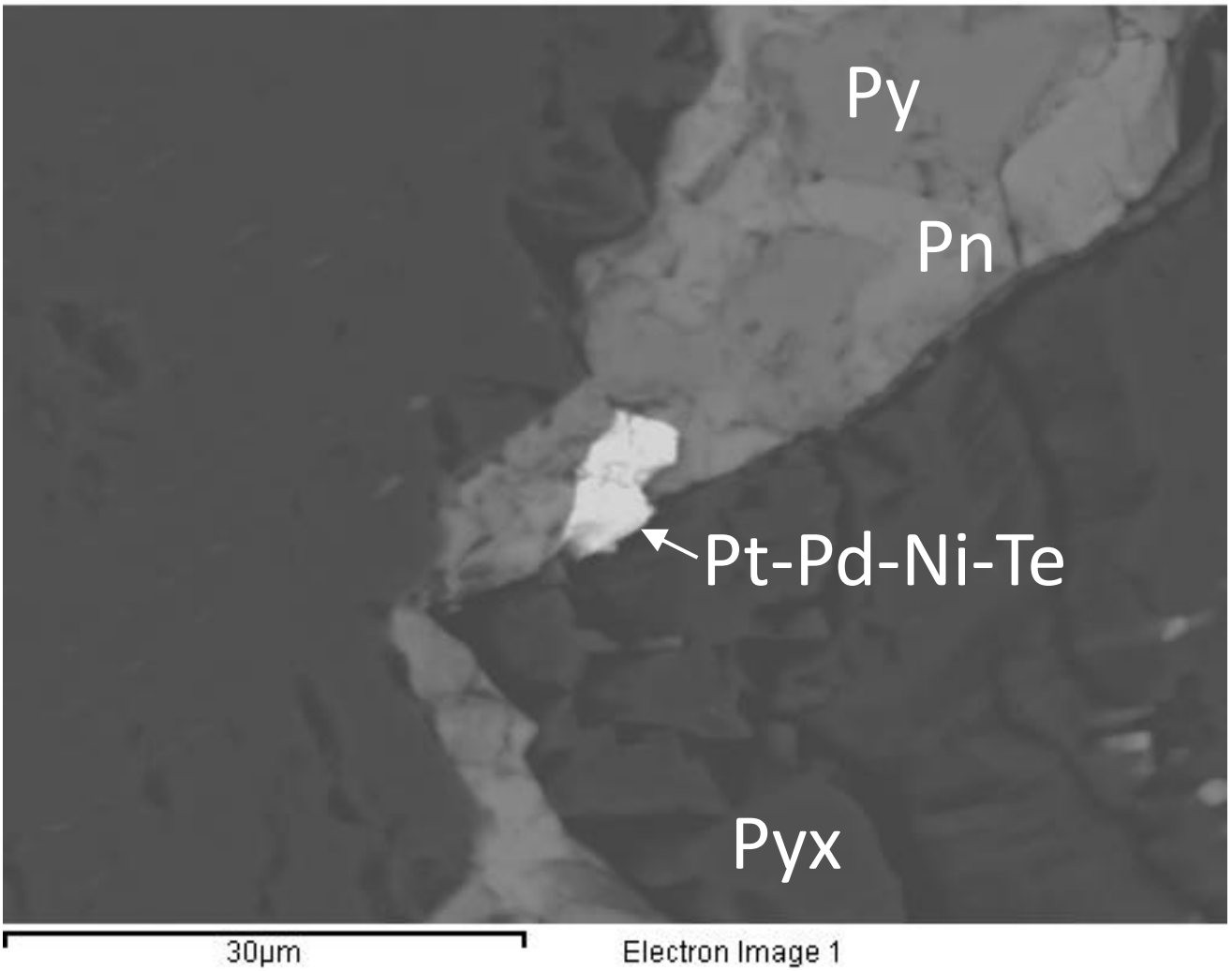
PTR02 K 1



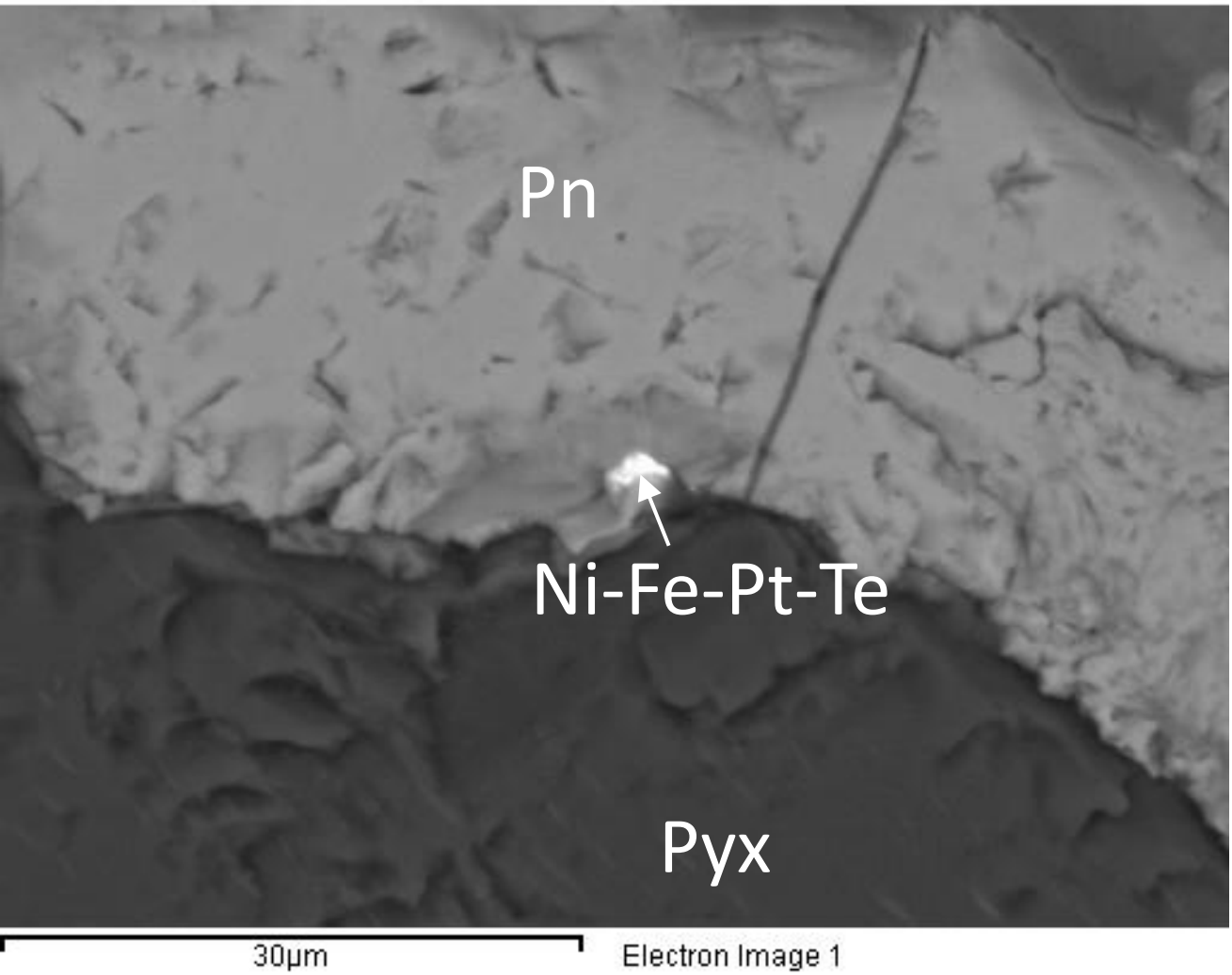
PTR02 L 1



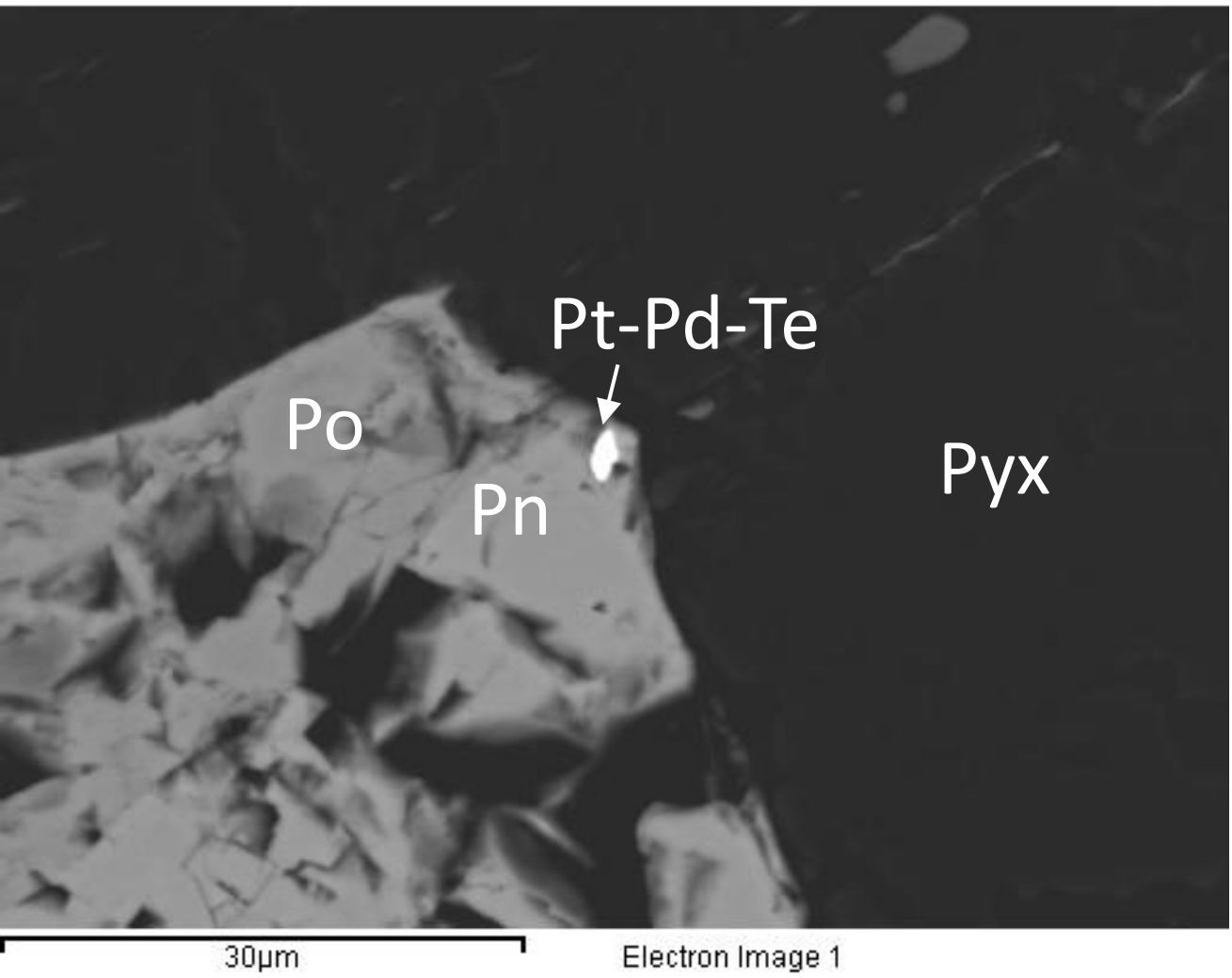
PTR02 M 1



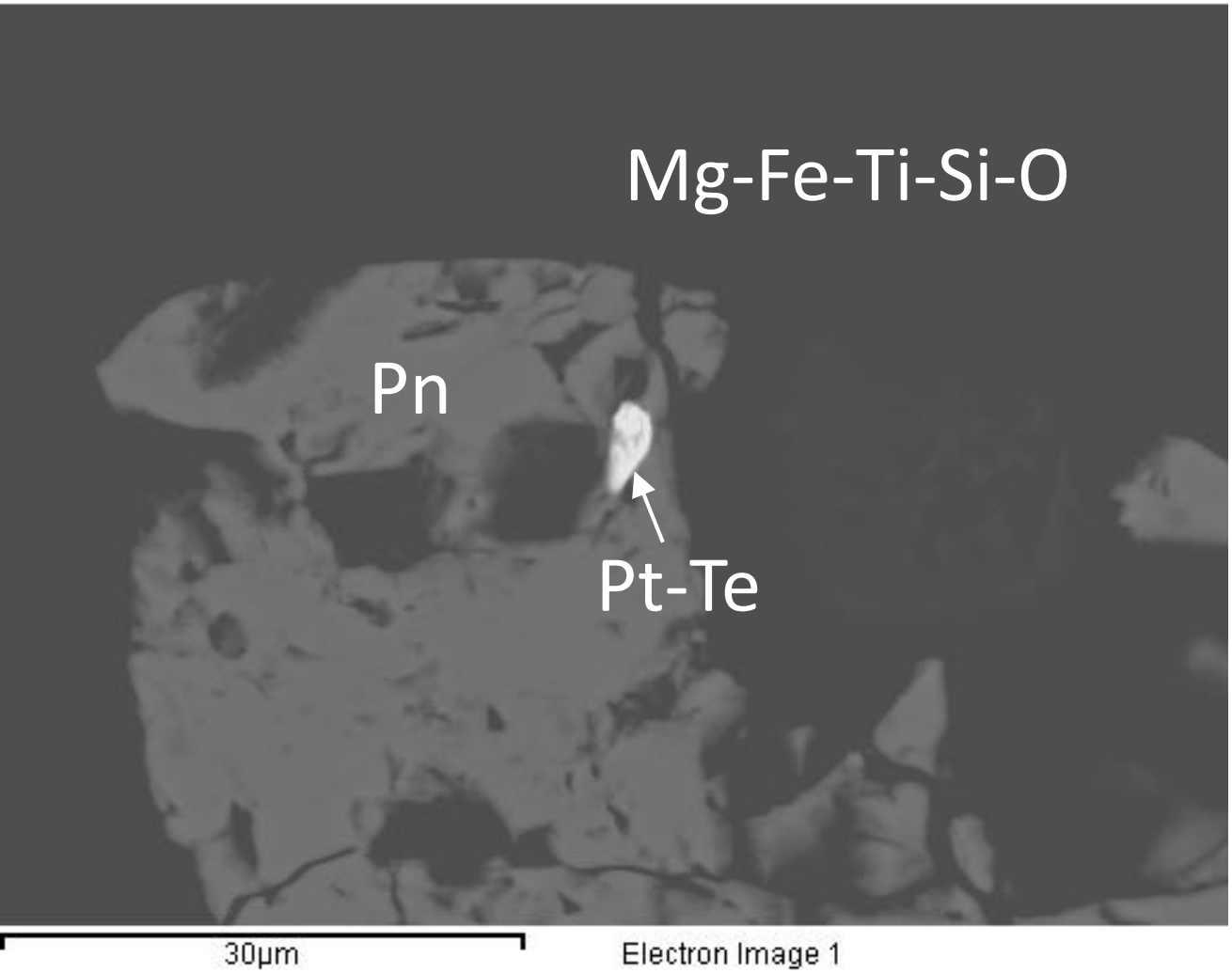
PTR02 N 1



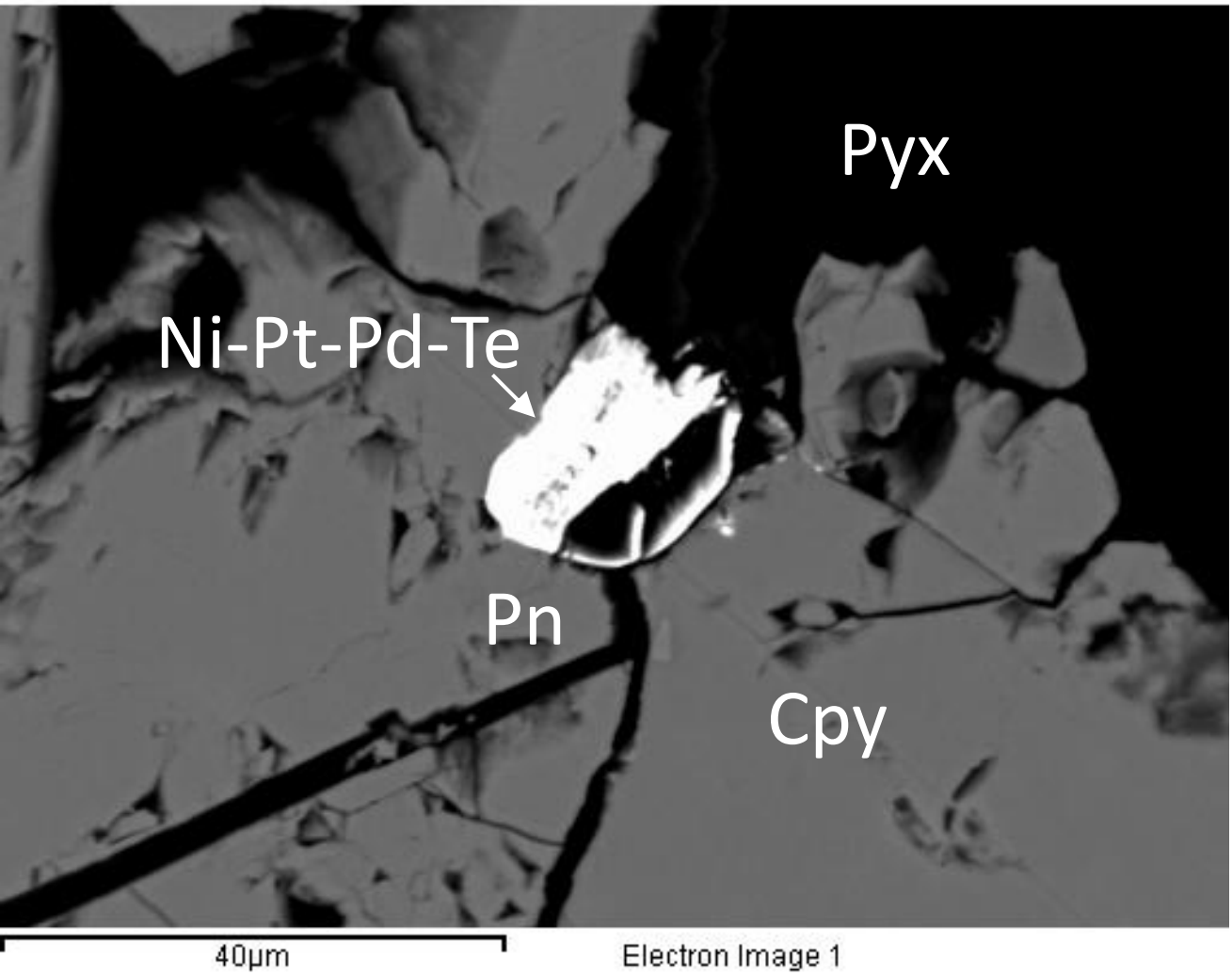
PTR03 A 1



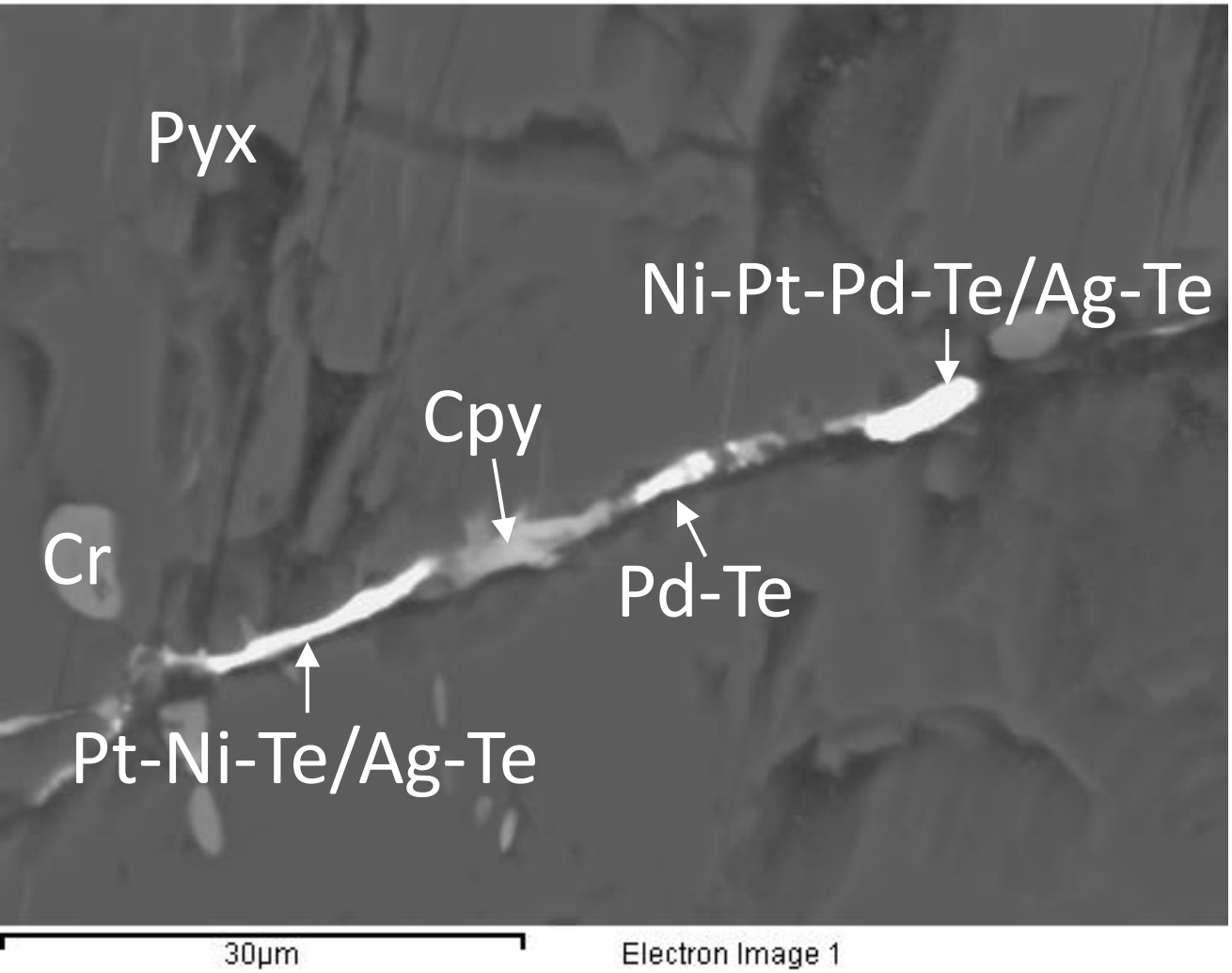
PTR03 B 1



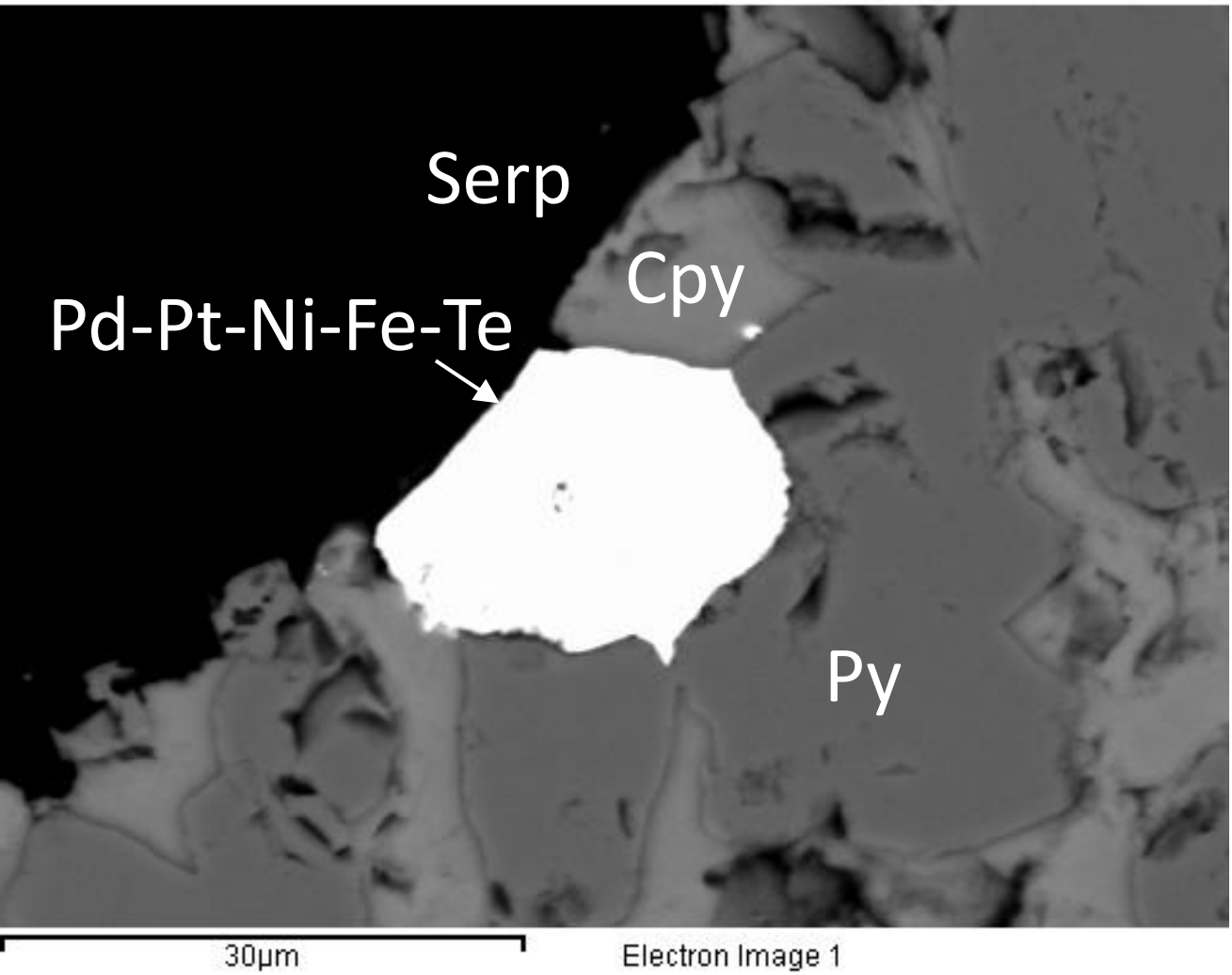
PTR03 C 1



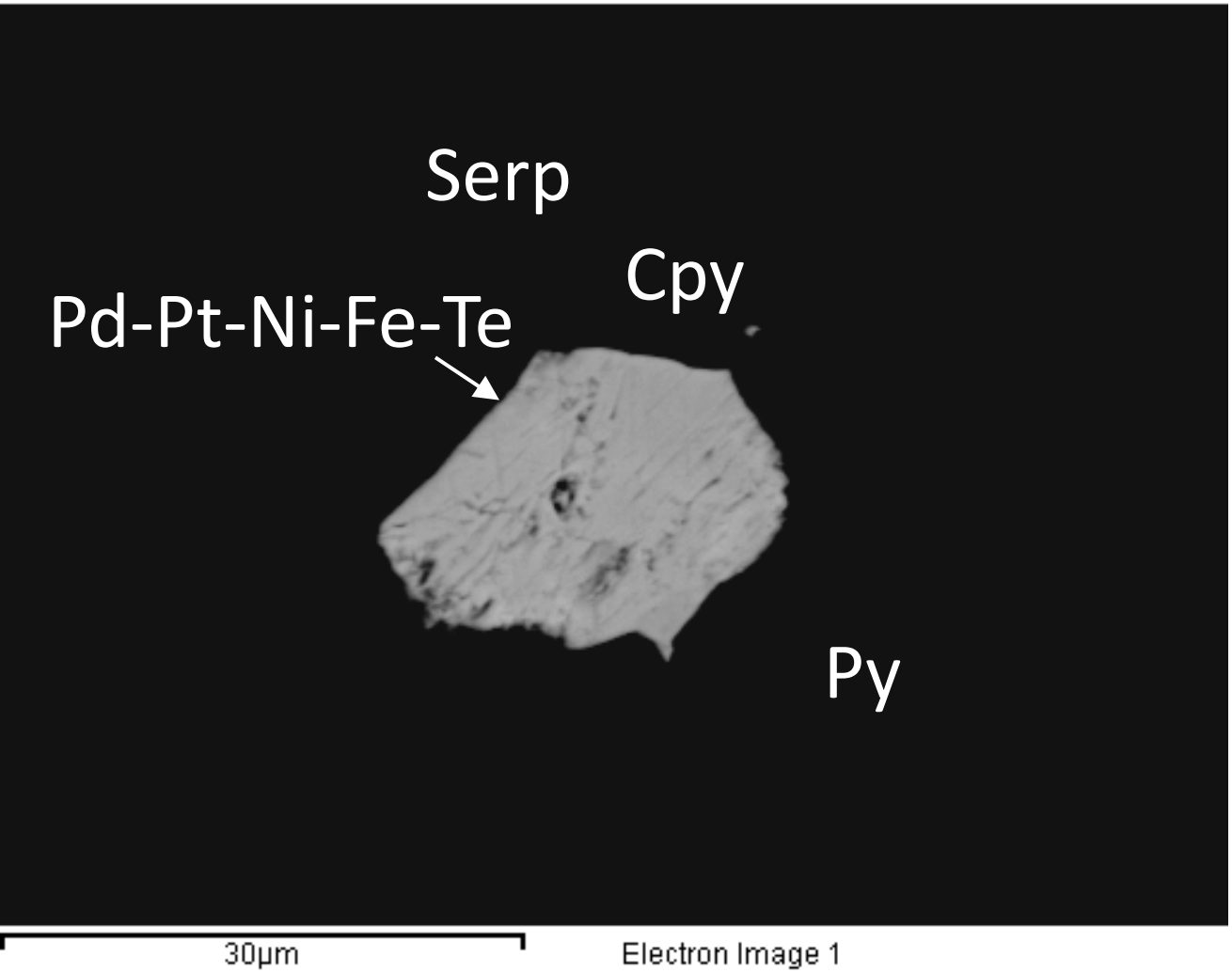
PTR03 D 1-3


Pyx
Ni-Pt-Pd-Te/Ag-Te
Cpy
Cr
Pd-Te
Pt-Ni-Te/Ag-Te
30µm
Electron Image 1

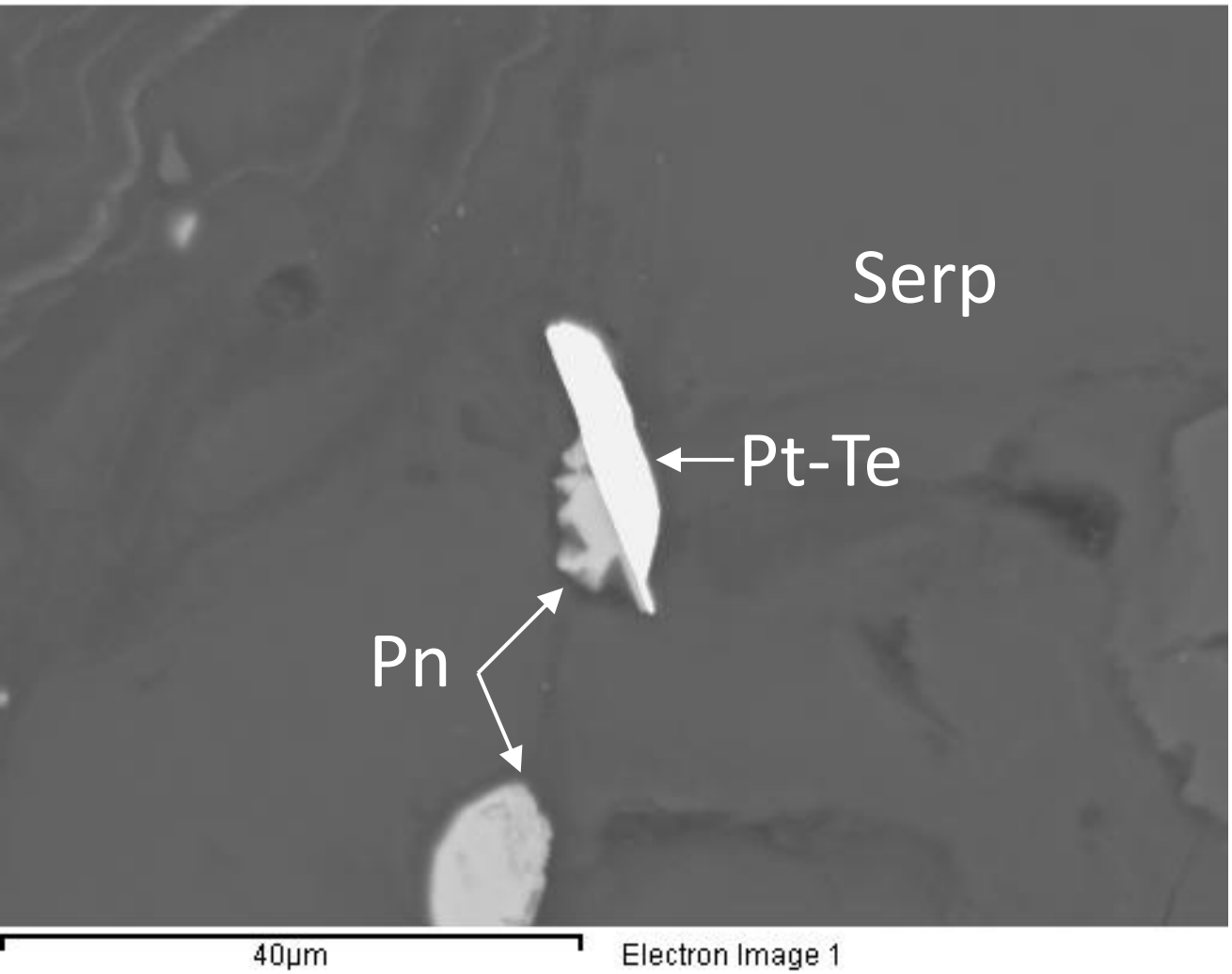
PTR03 E 1



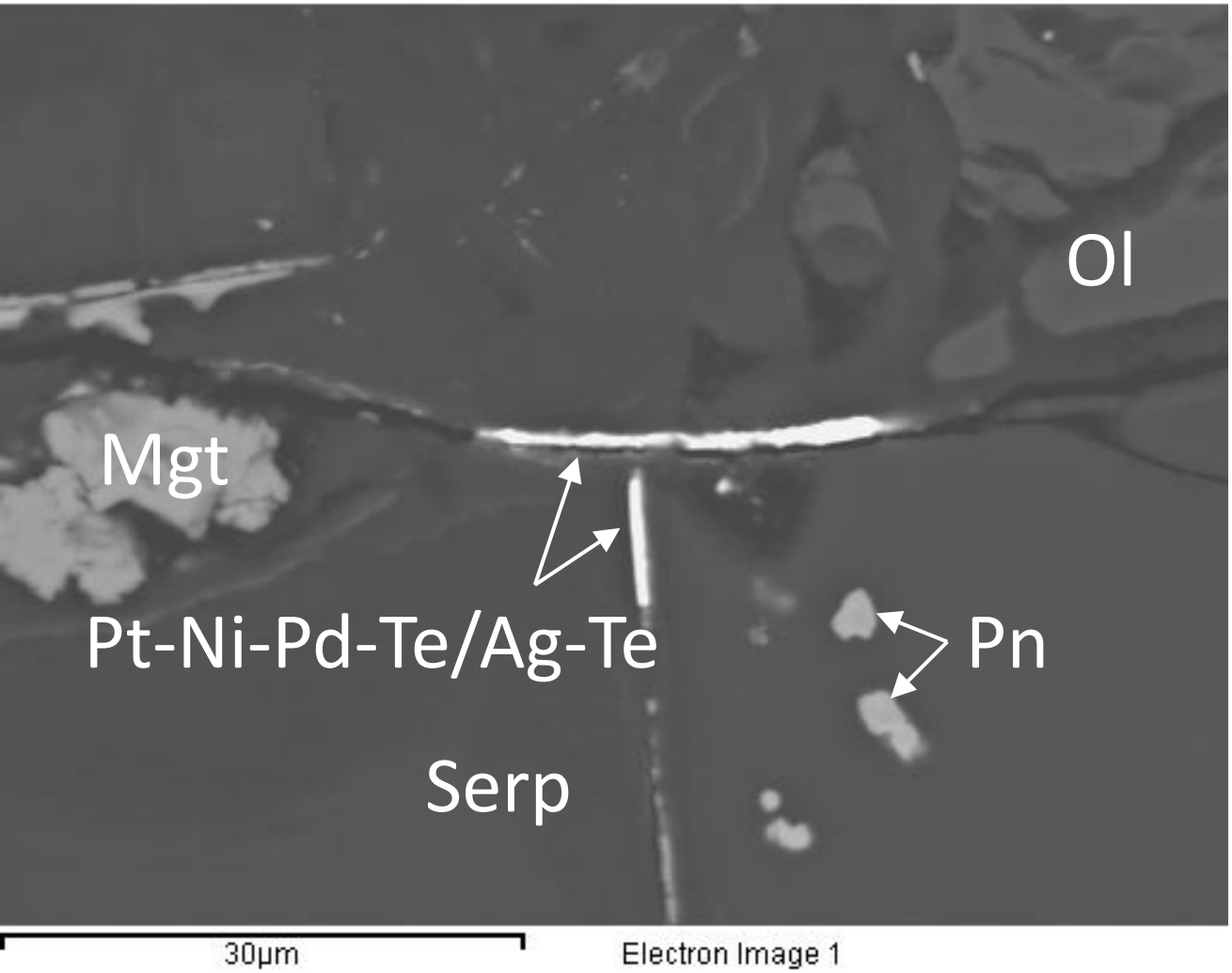
PTR03 E 1



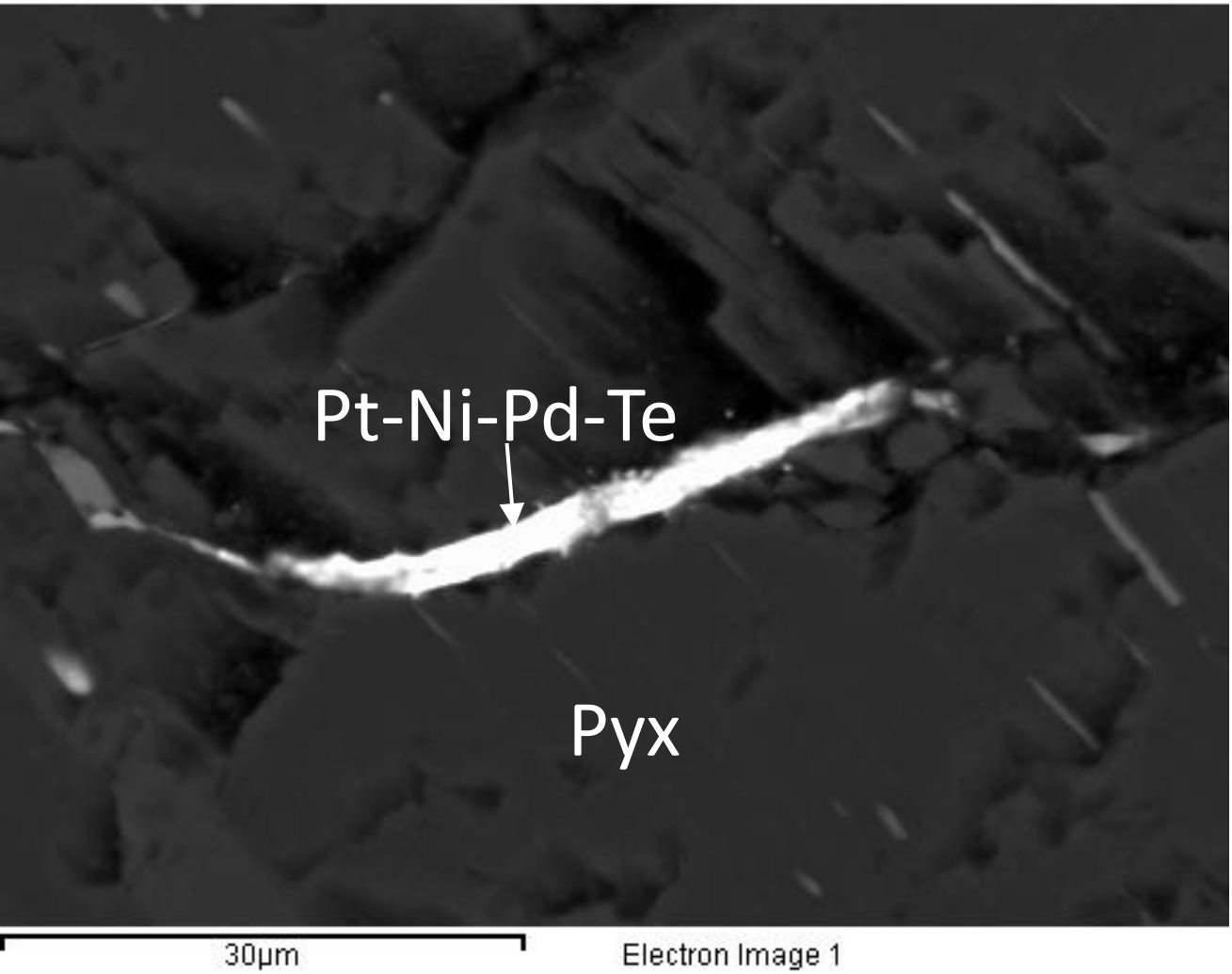
PTR03 F 1



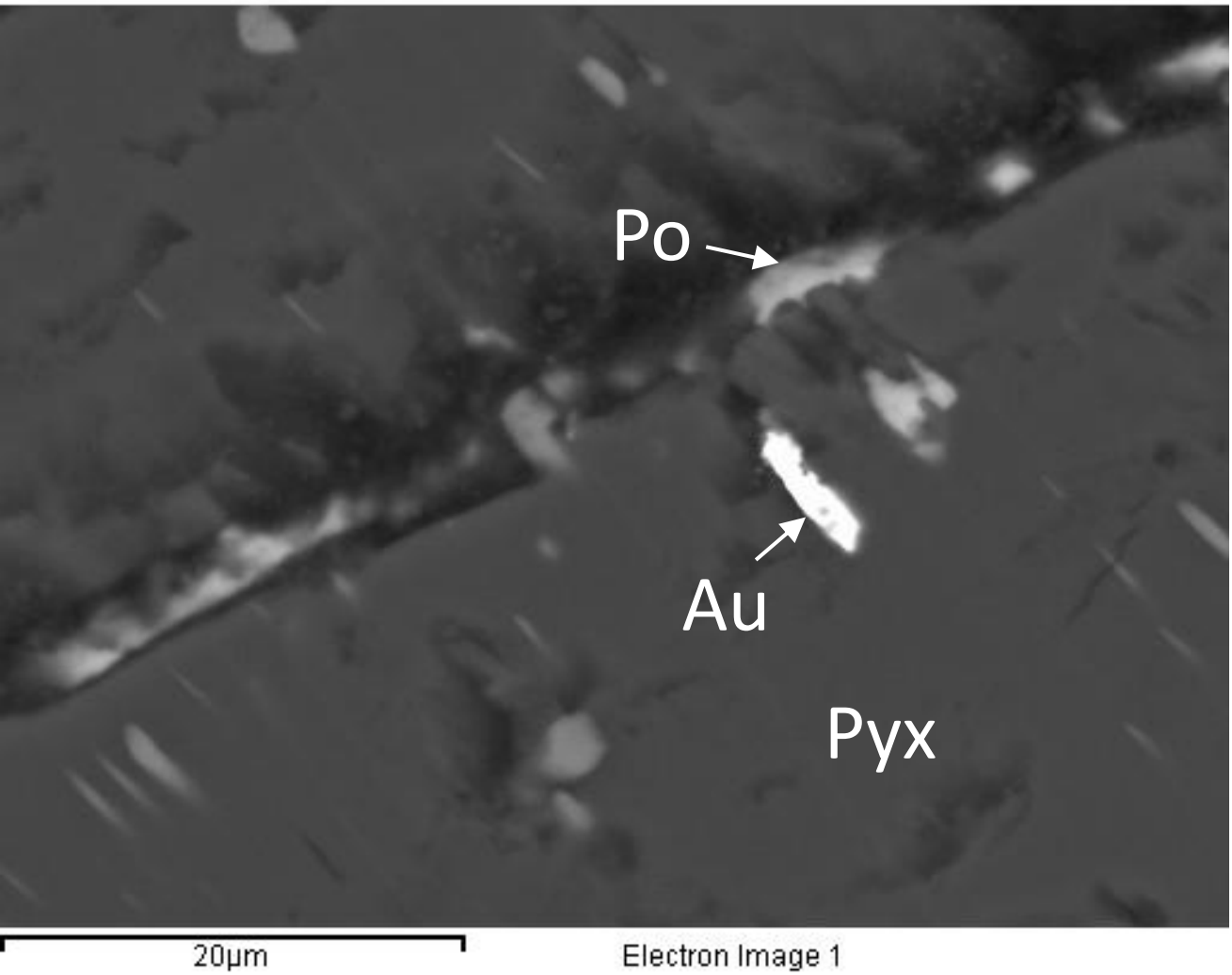
PTR03 G 1-2



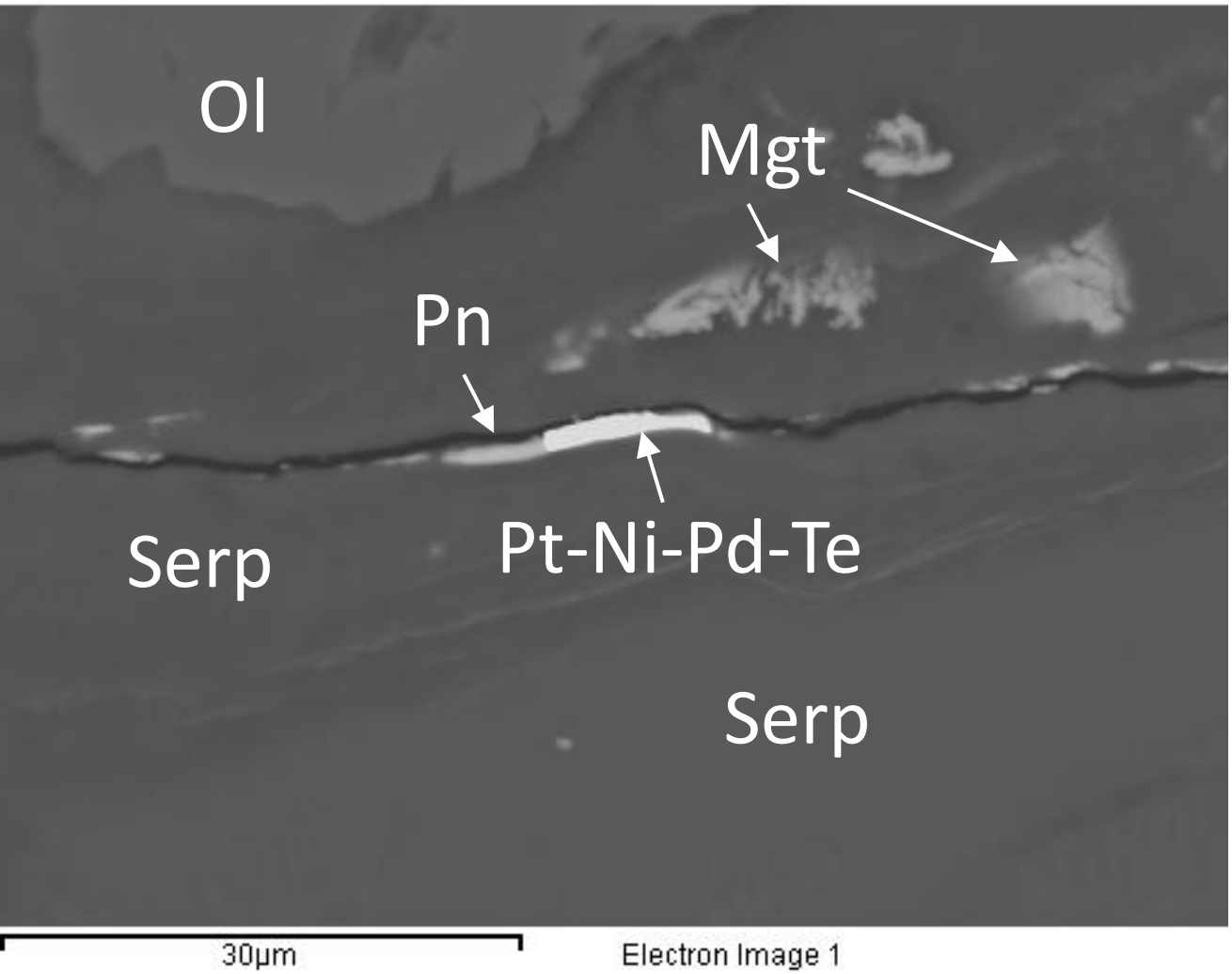
PTR03 H 1



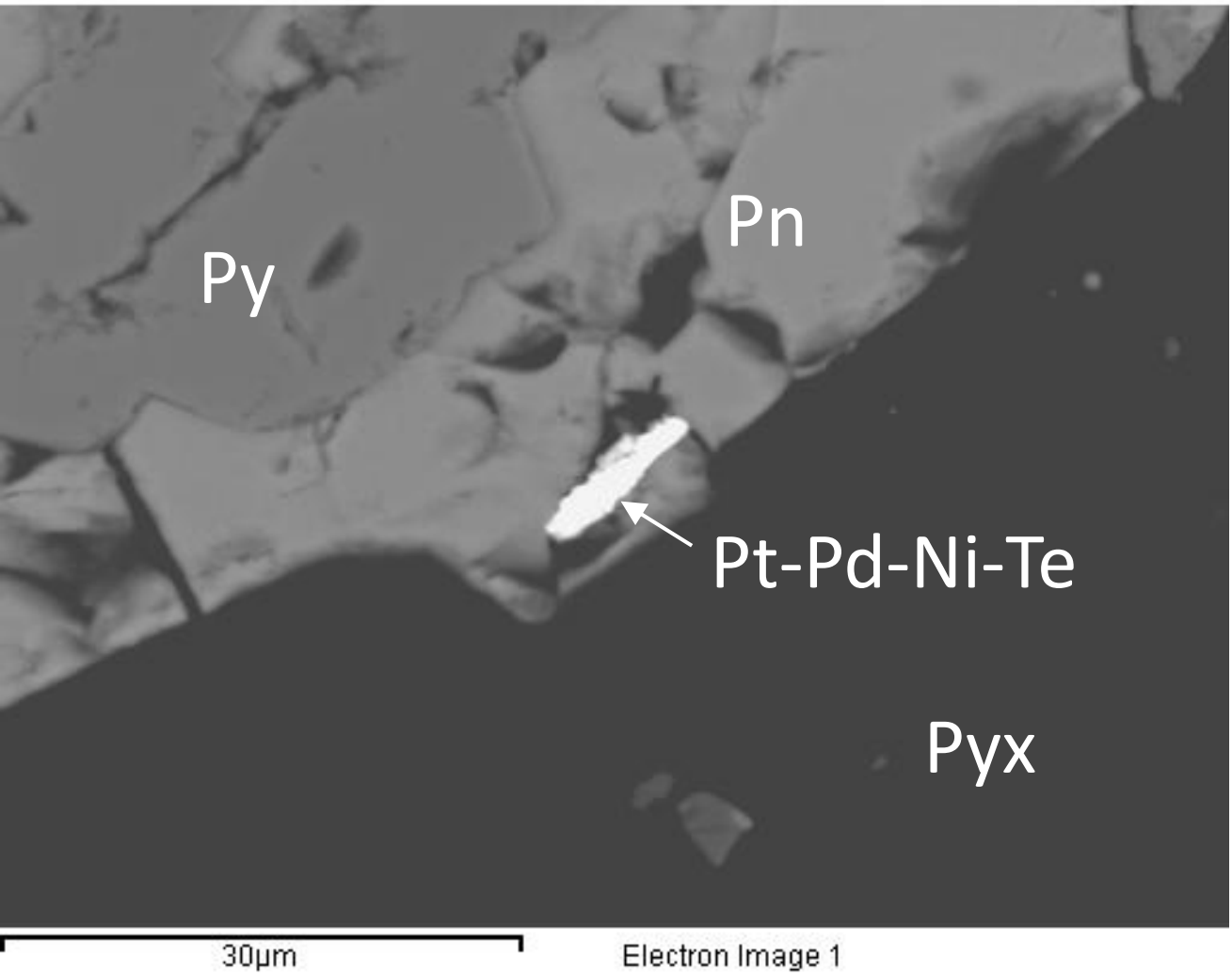
PTR03 H 2



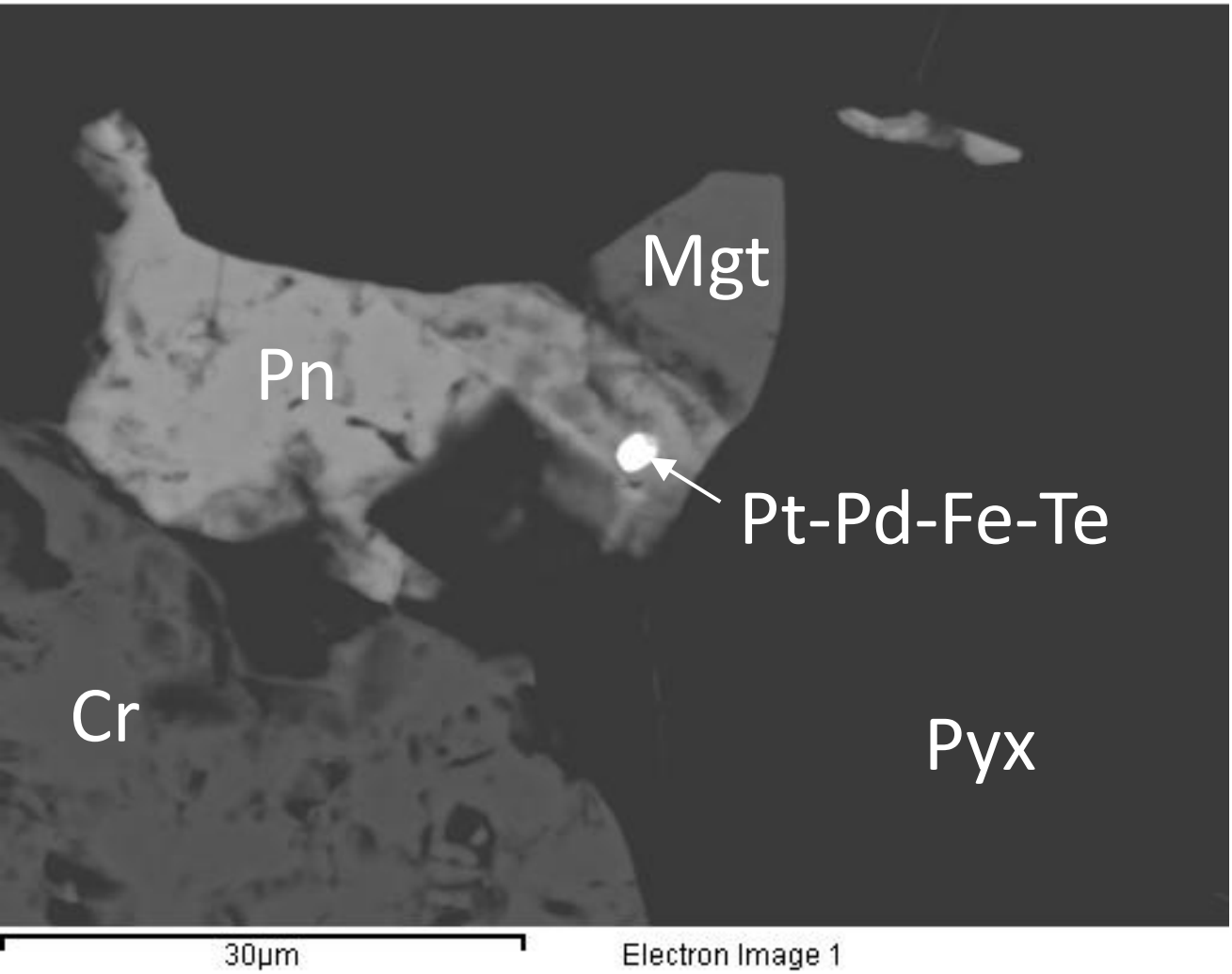
PTR03 I 1



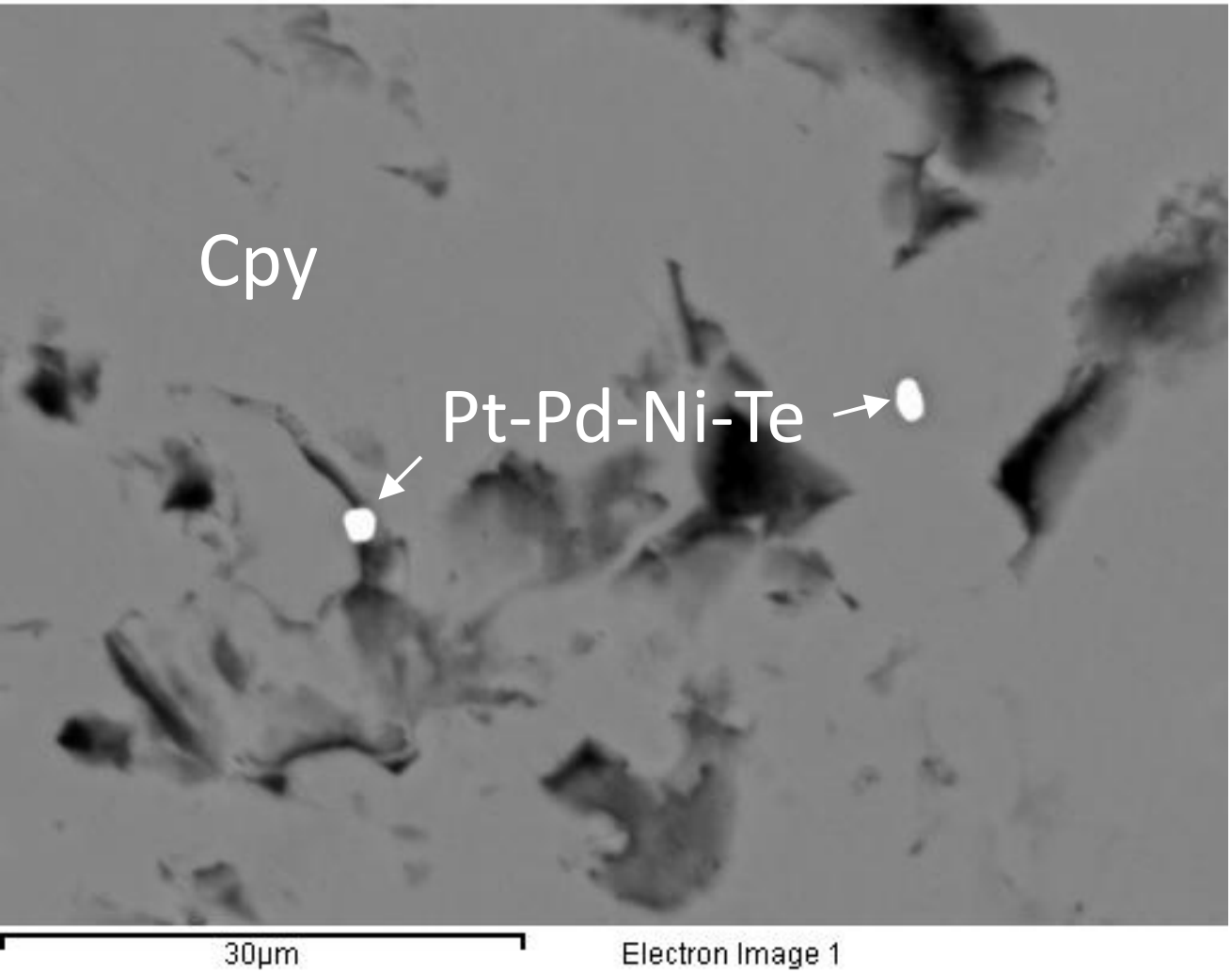
PTR03 J 1



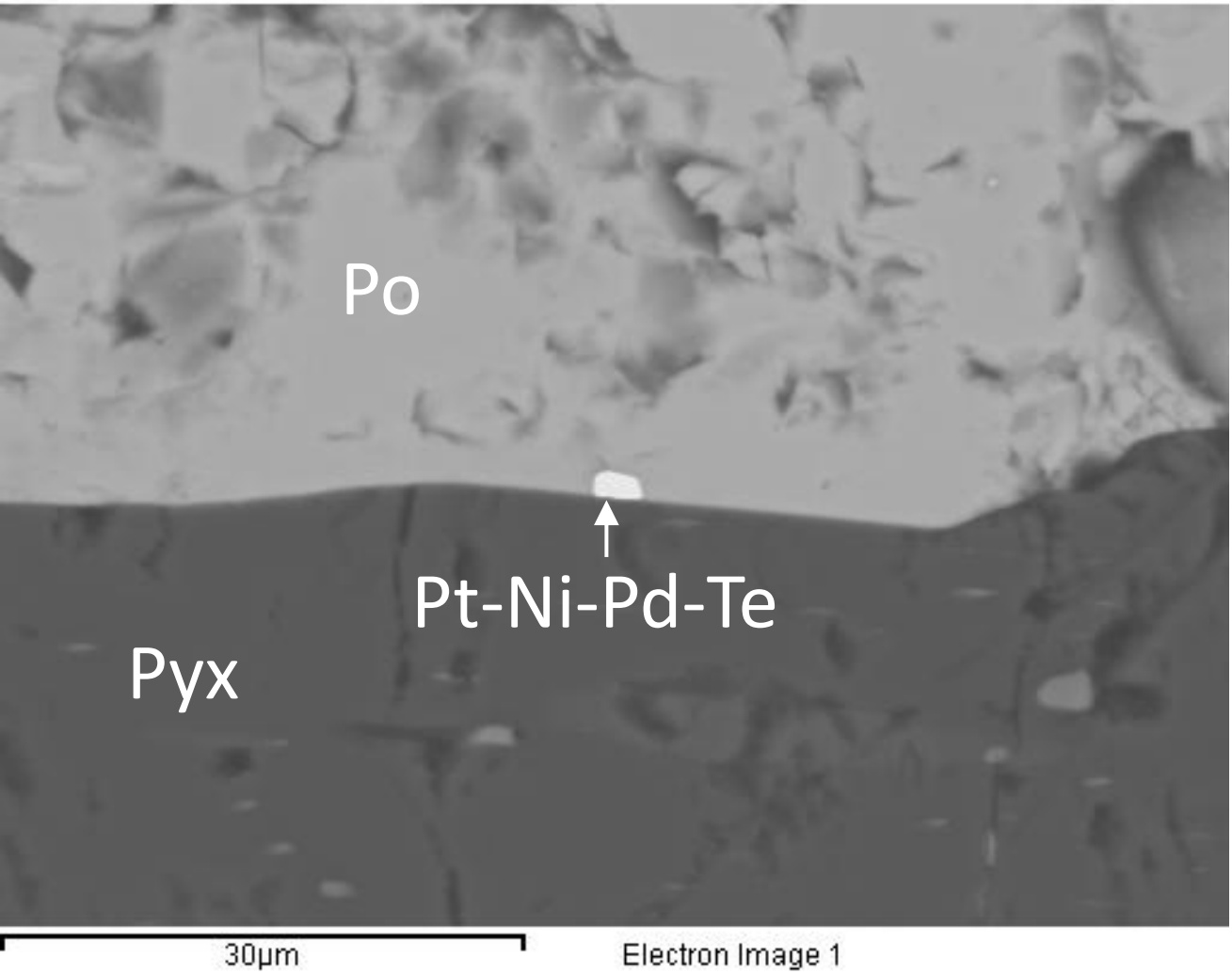
PTR03 K 1



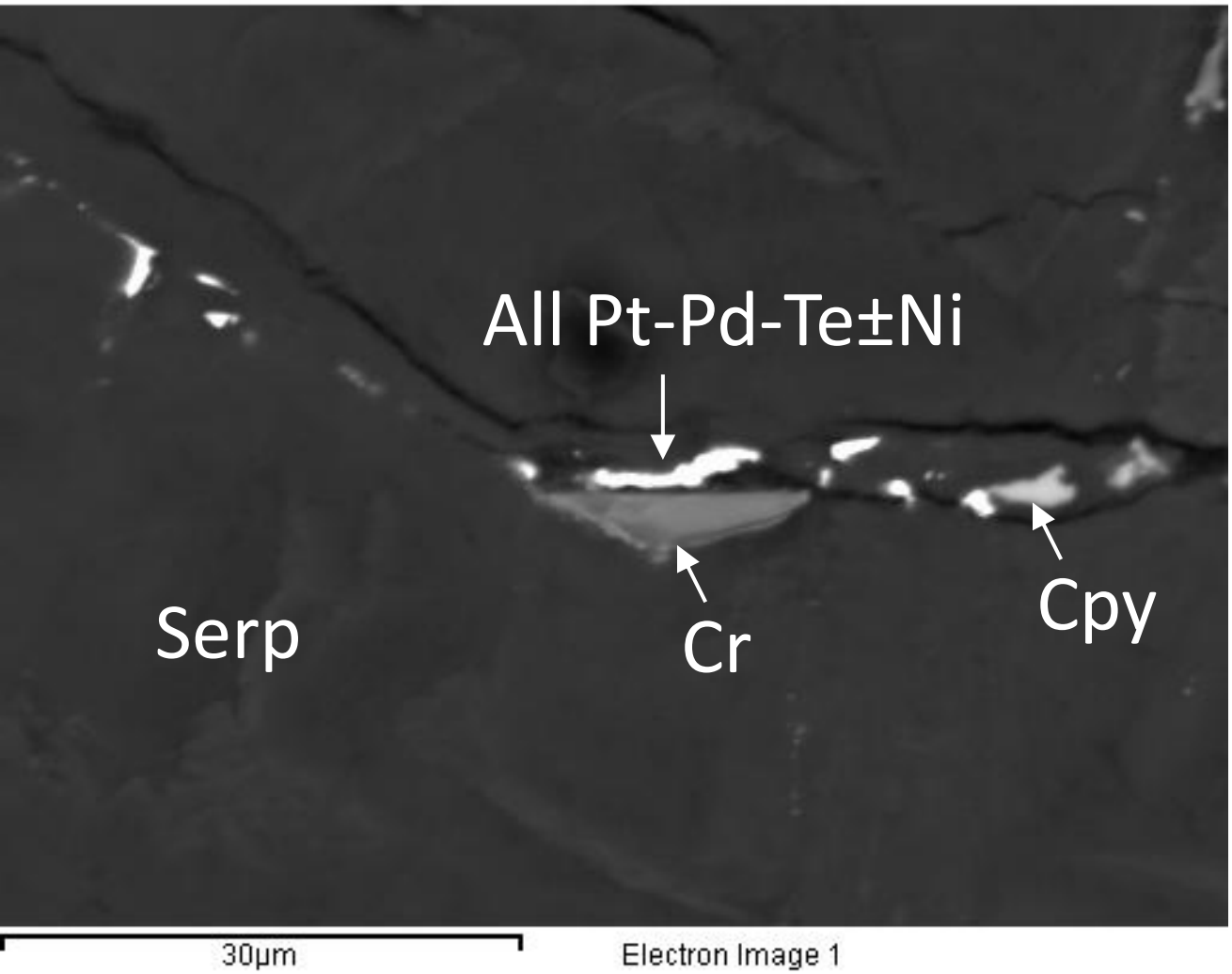
PTR03 L 1-2



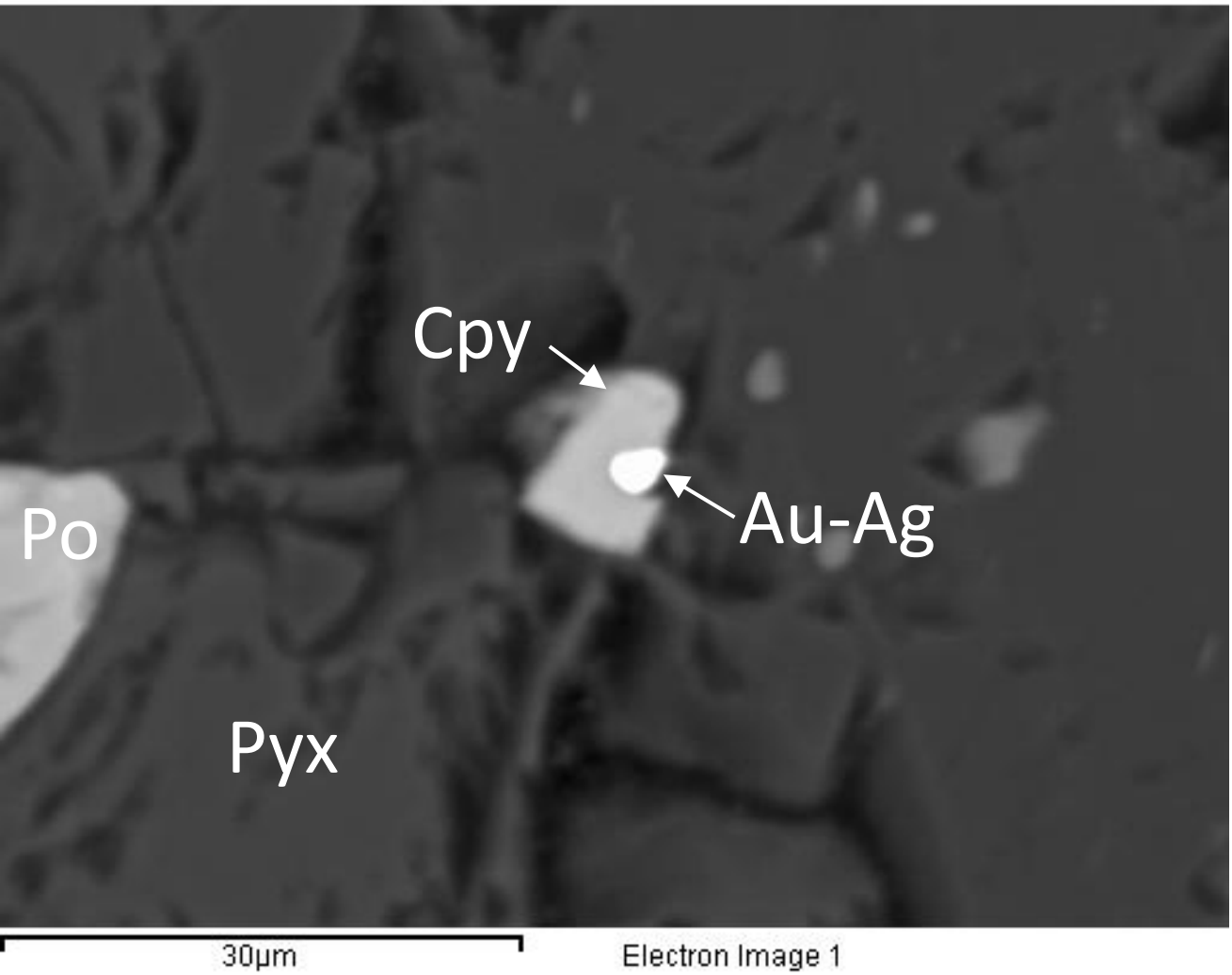
PTR03 M 1



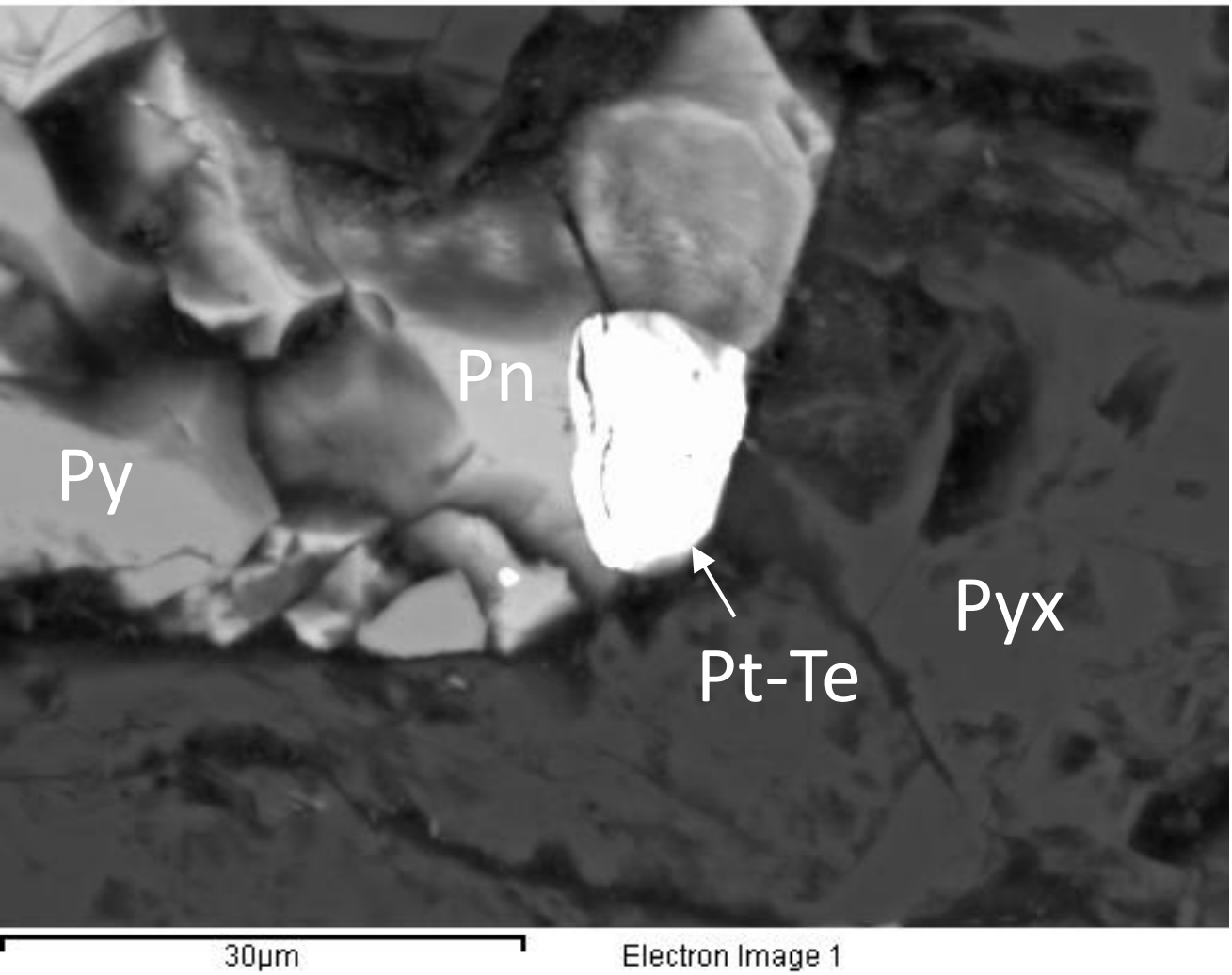
PTR03 N Cluster



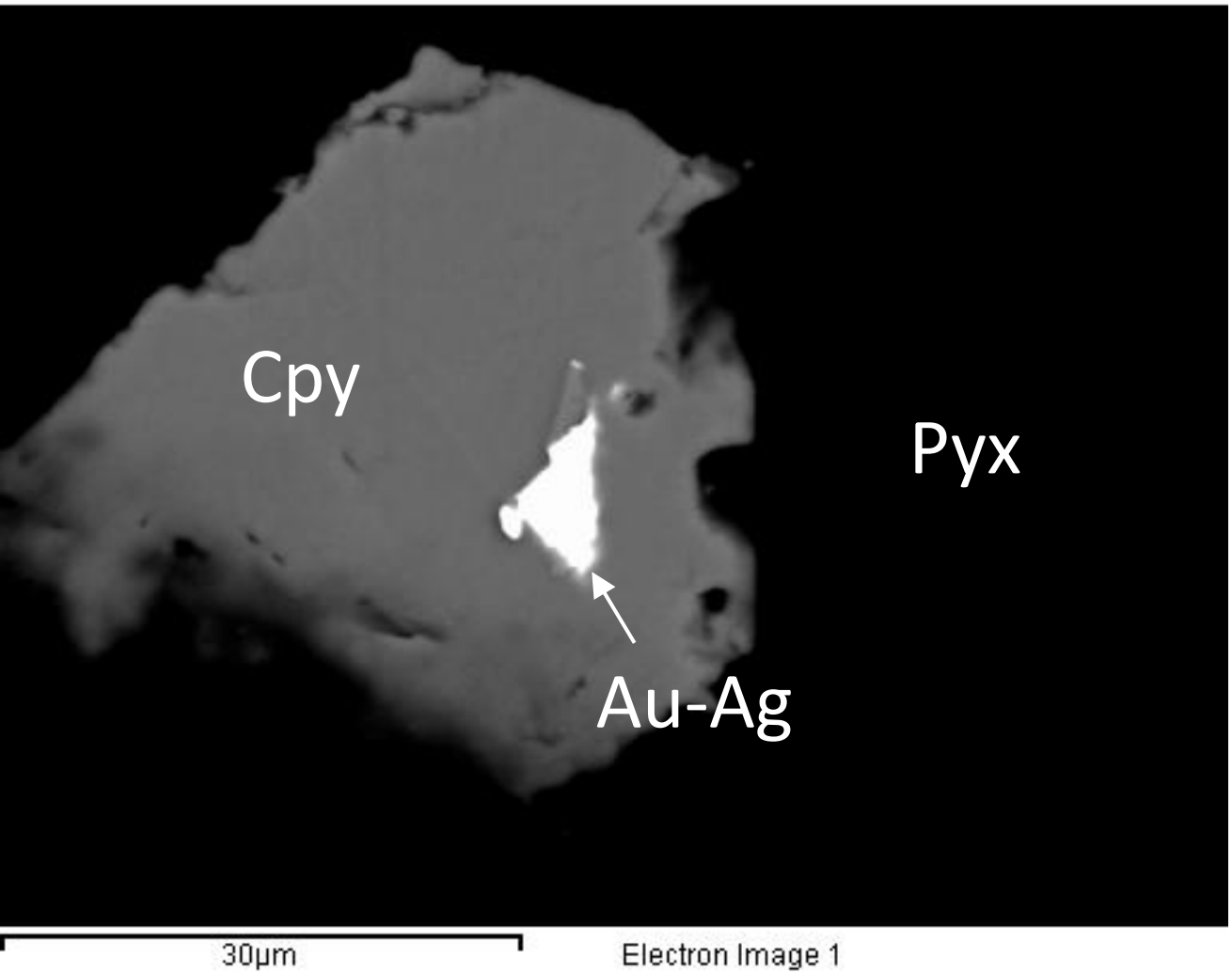
PTR03 O 1



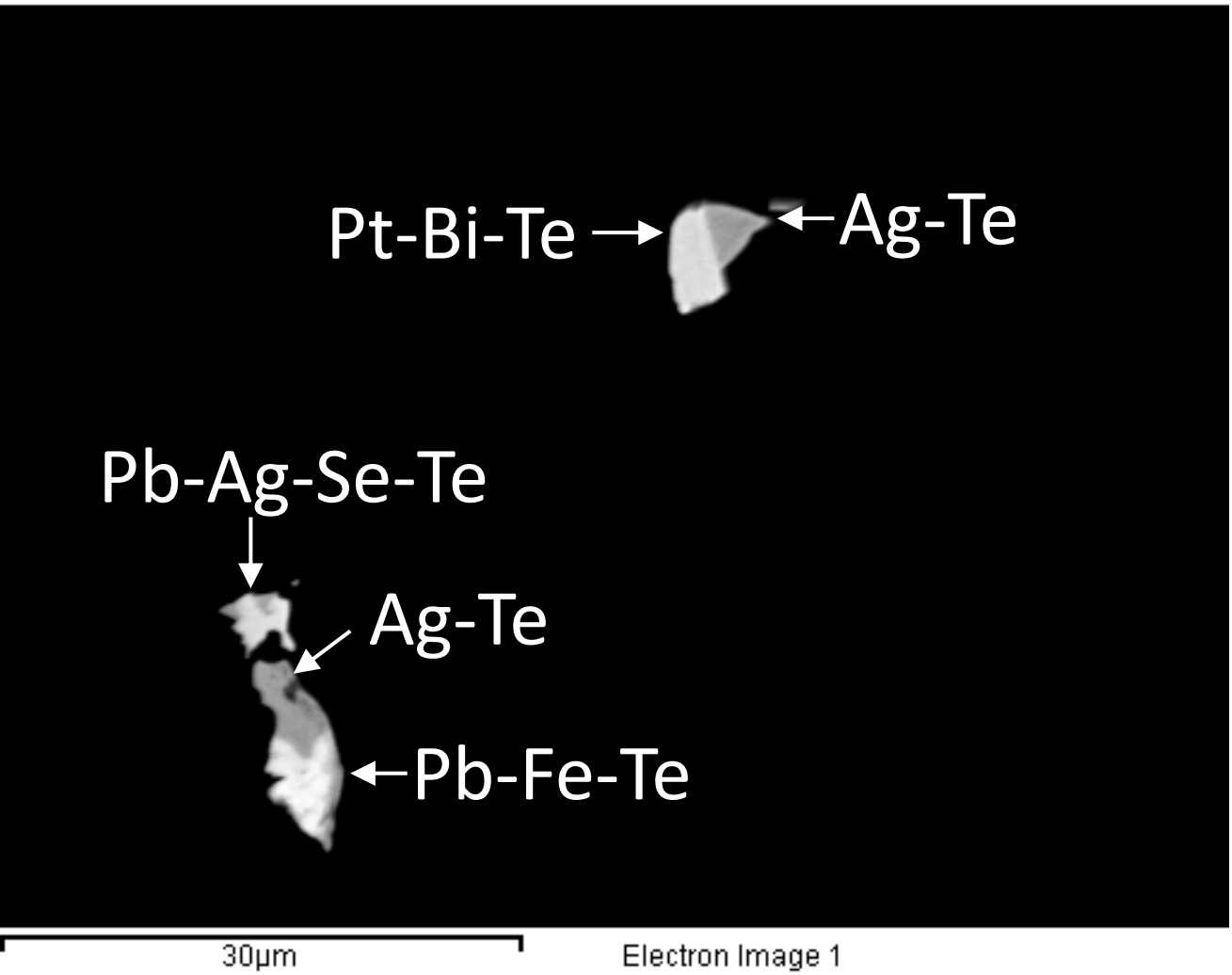
PTR03 P 1



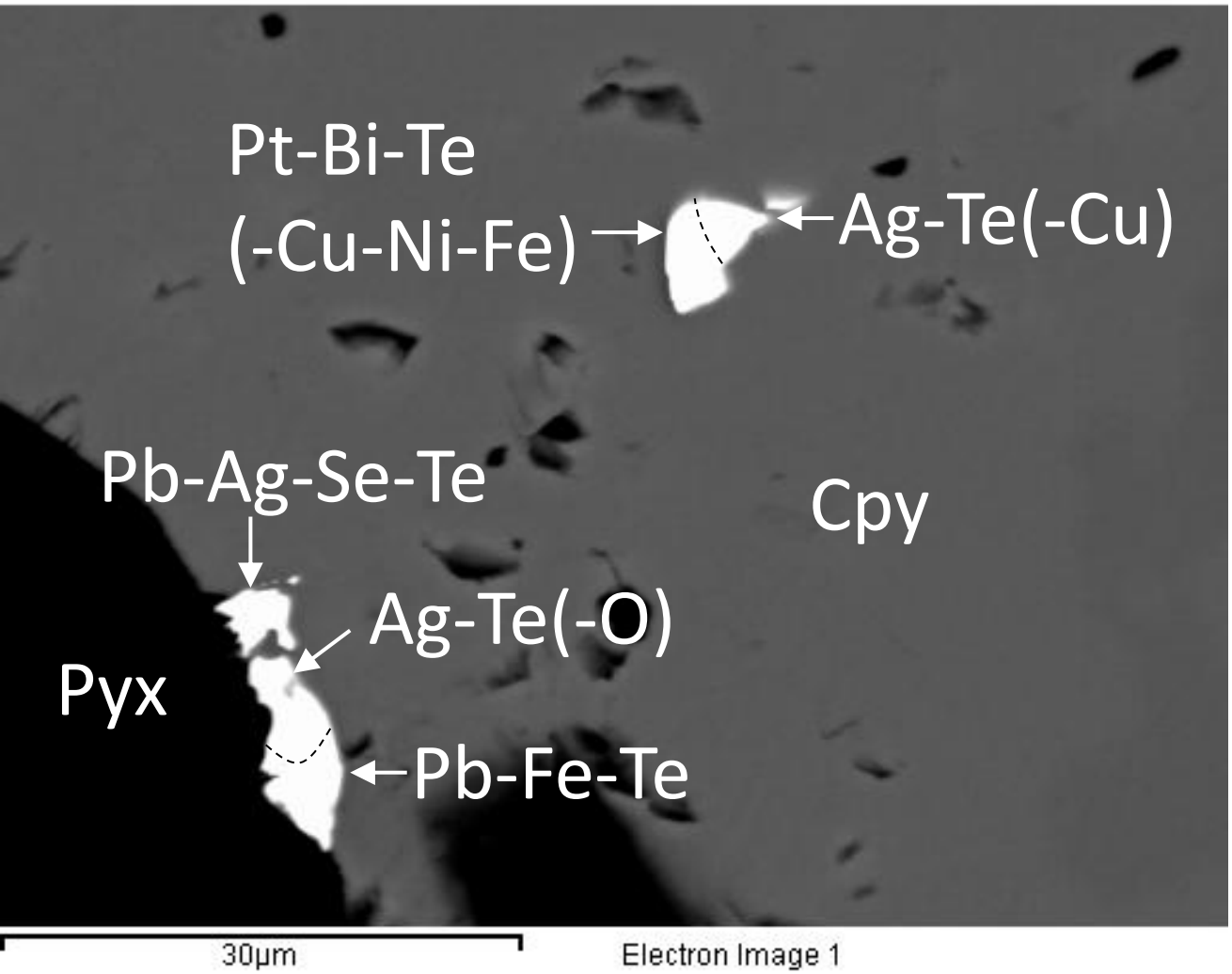
PTR04 A 1



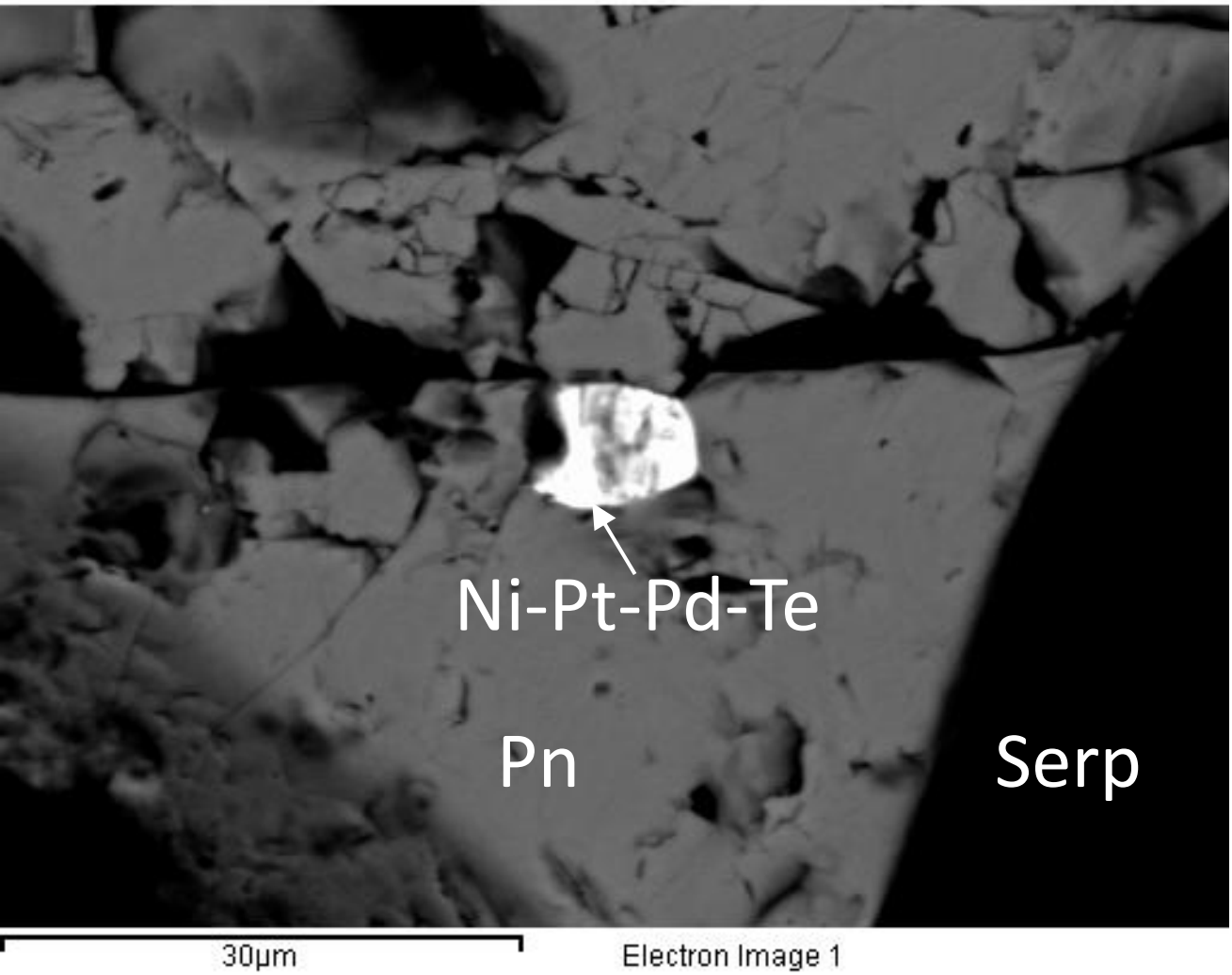
PTR04 B 1-3 Dark



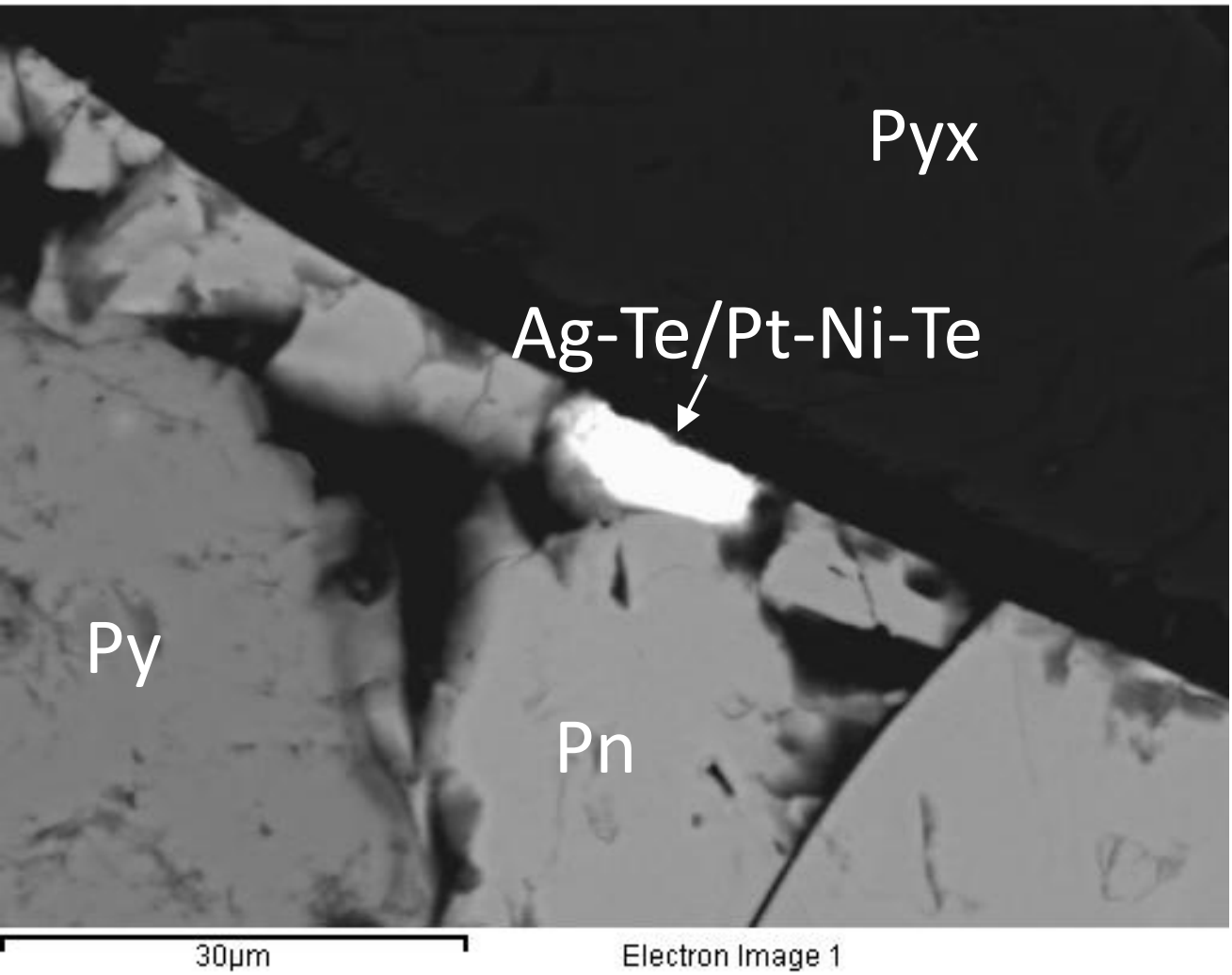
PTR04 B 1-3 Light



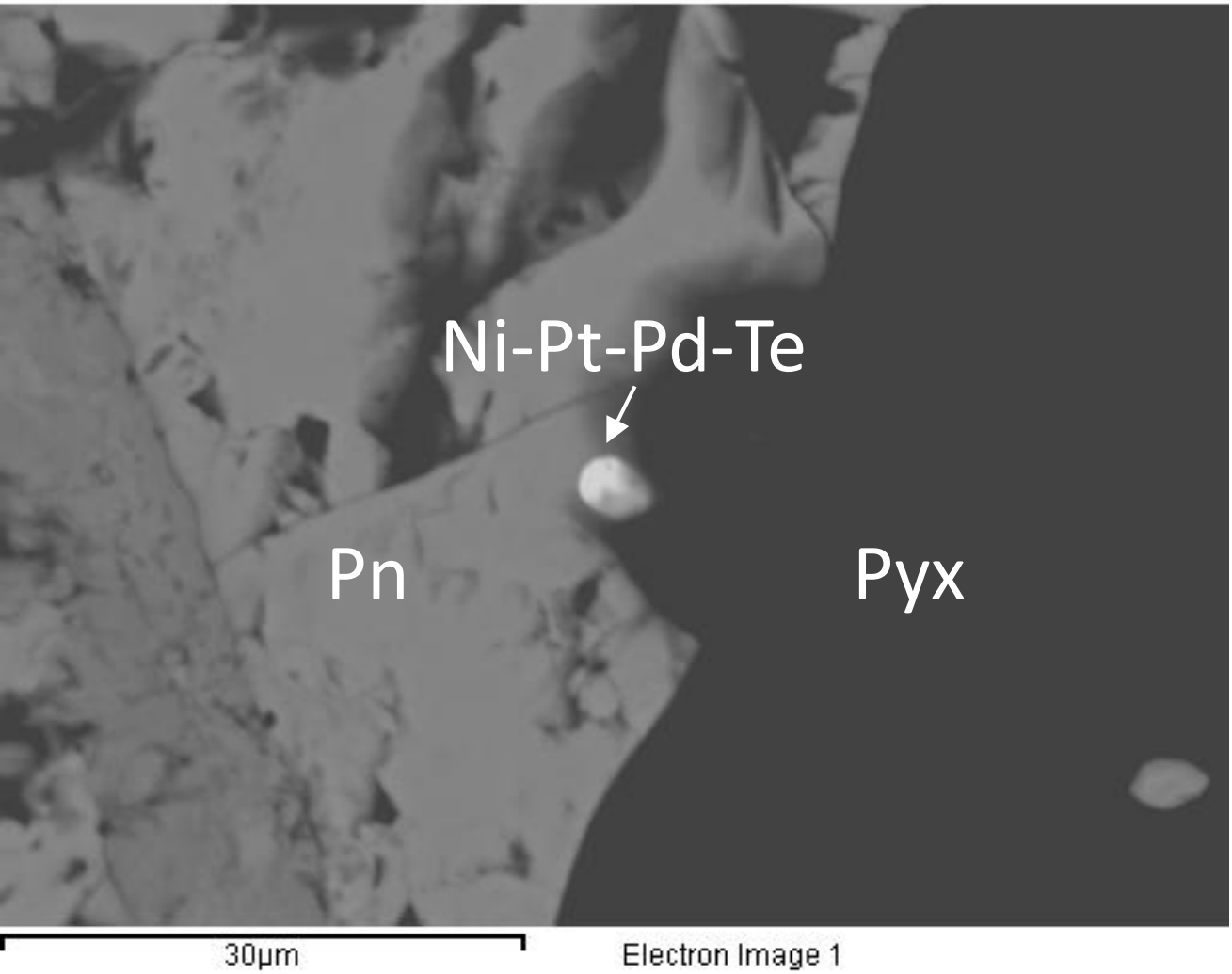
PTR04 C 1



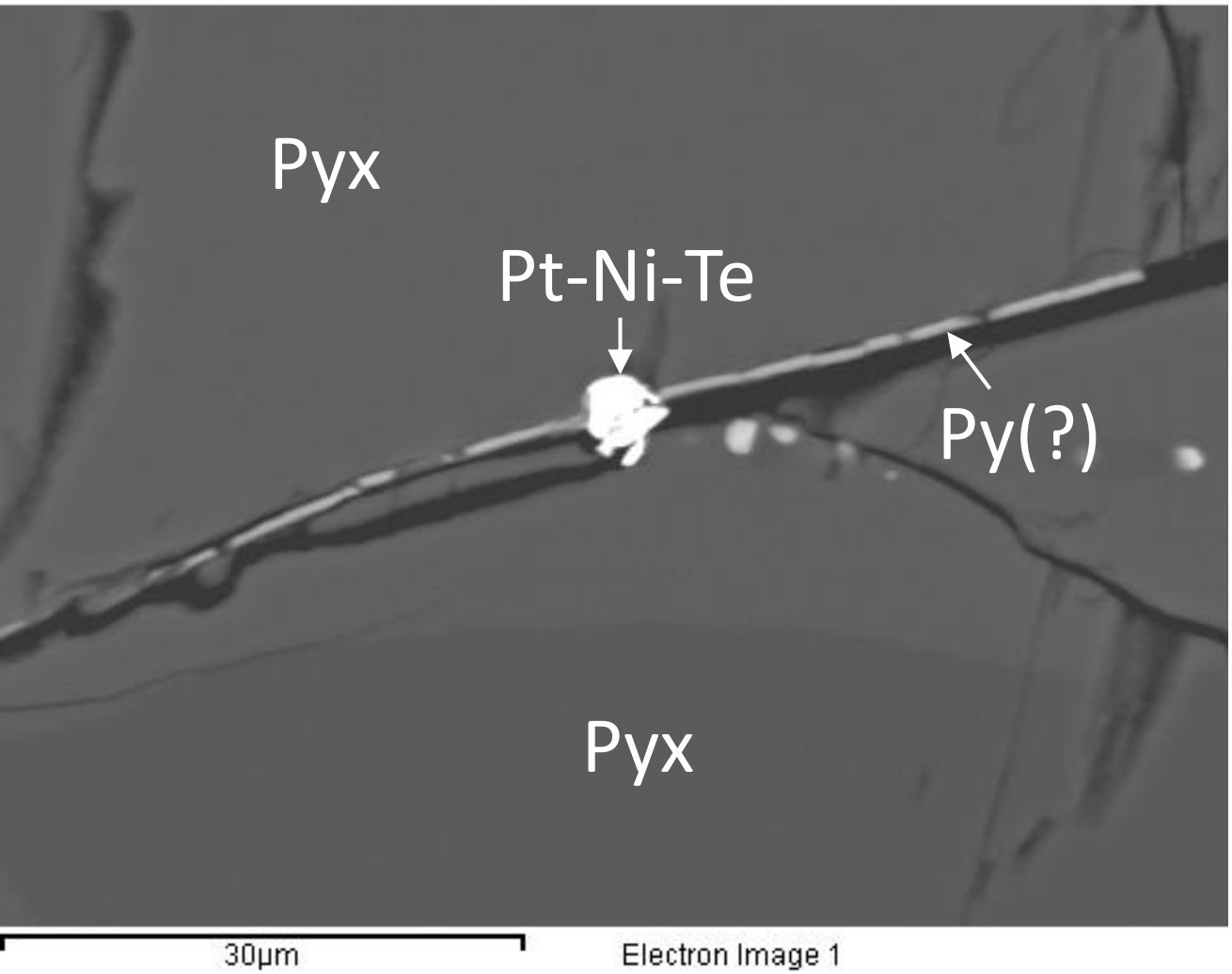
PTR04 D 1



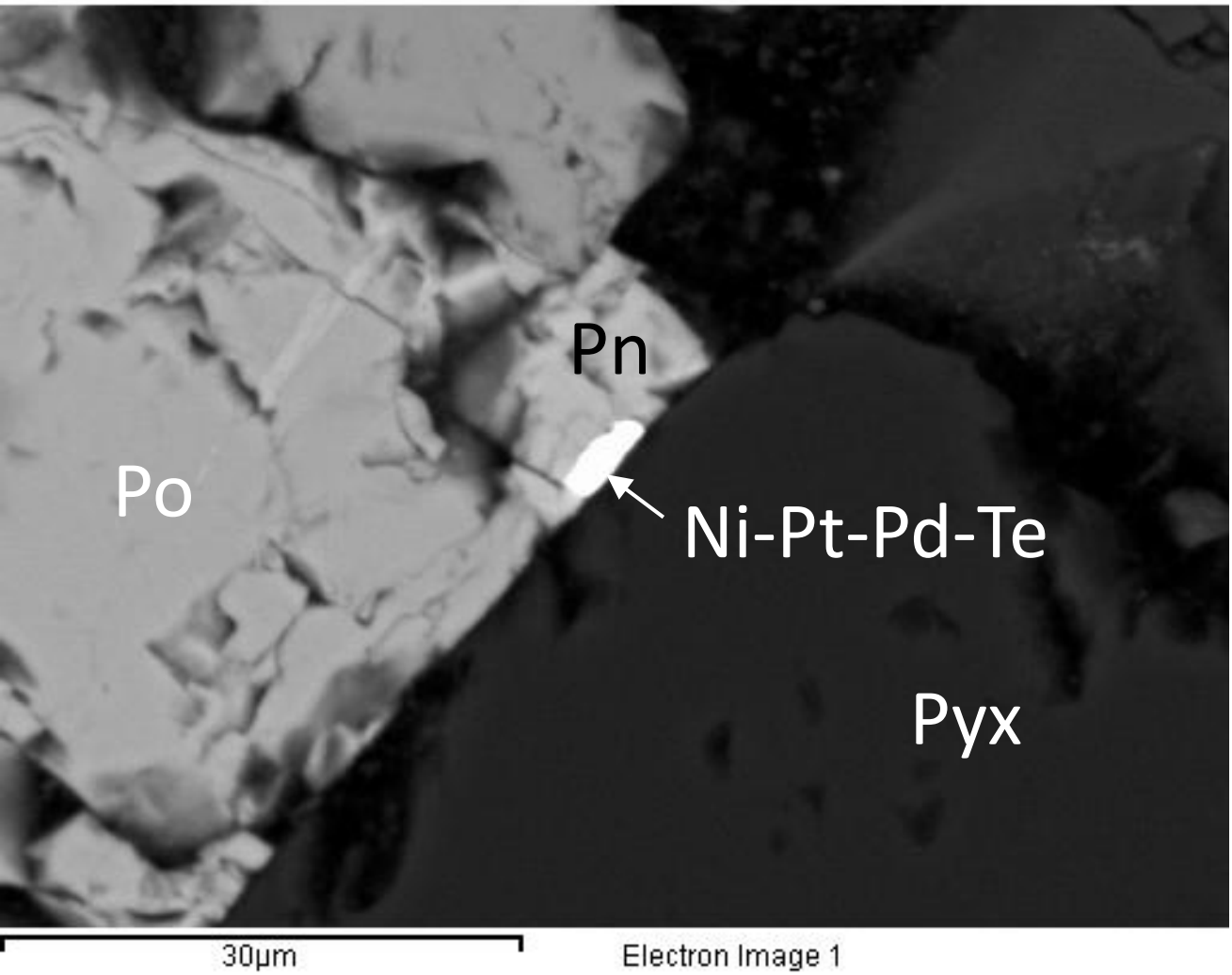
PTR04 E 1



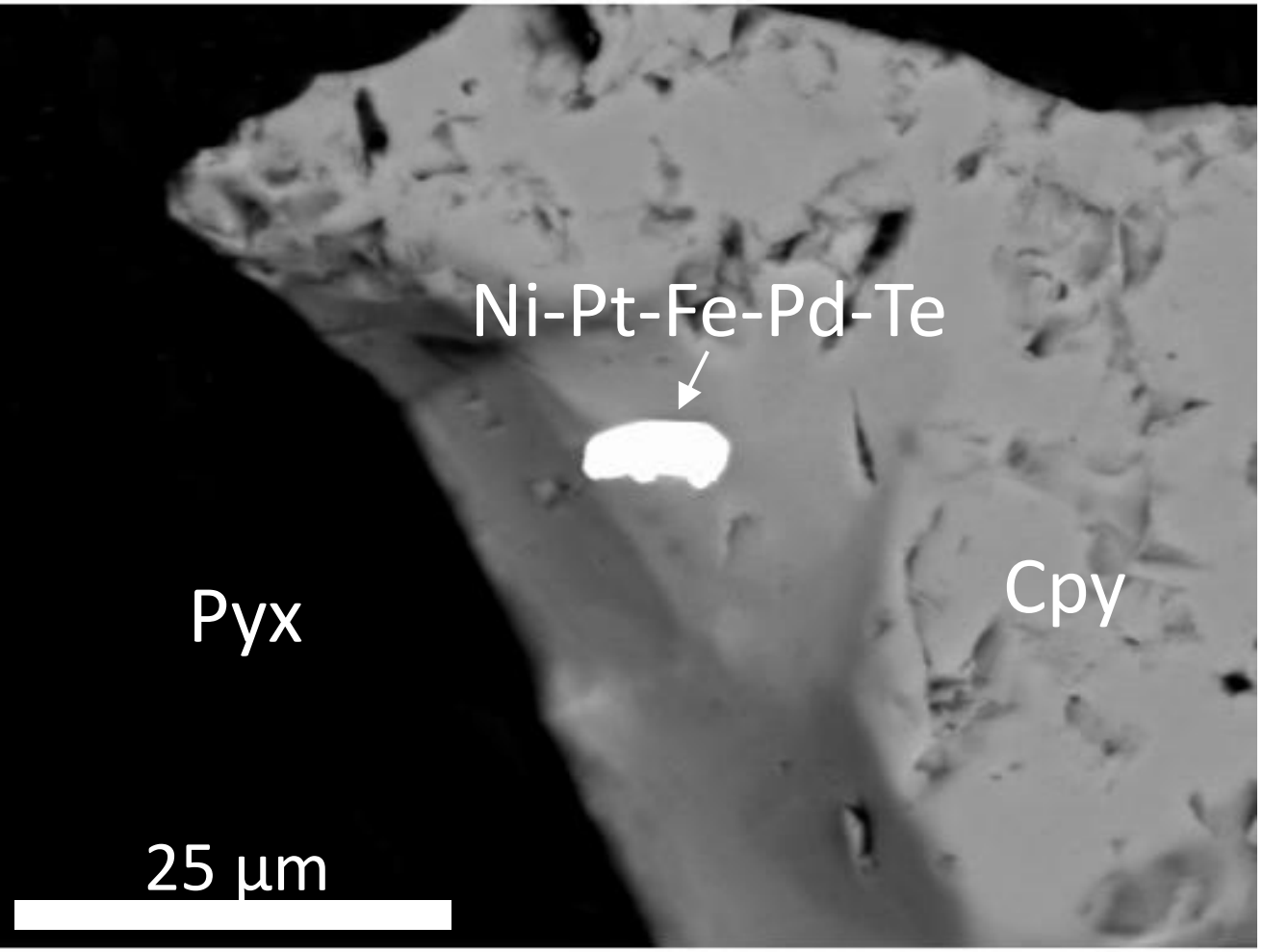
PTR04 F 1



PTR04 G 1

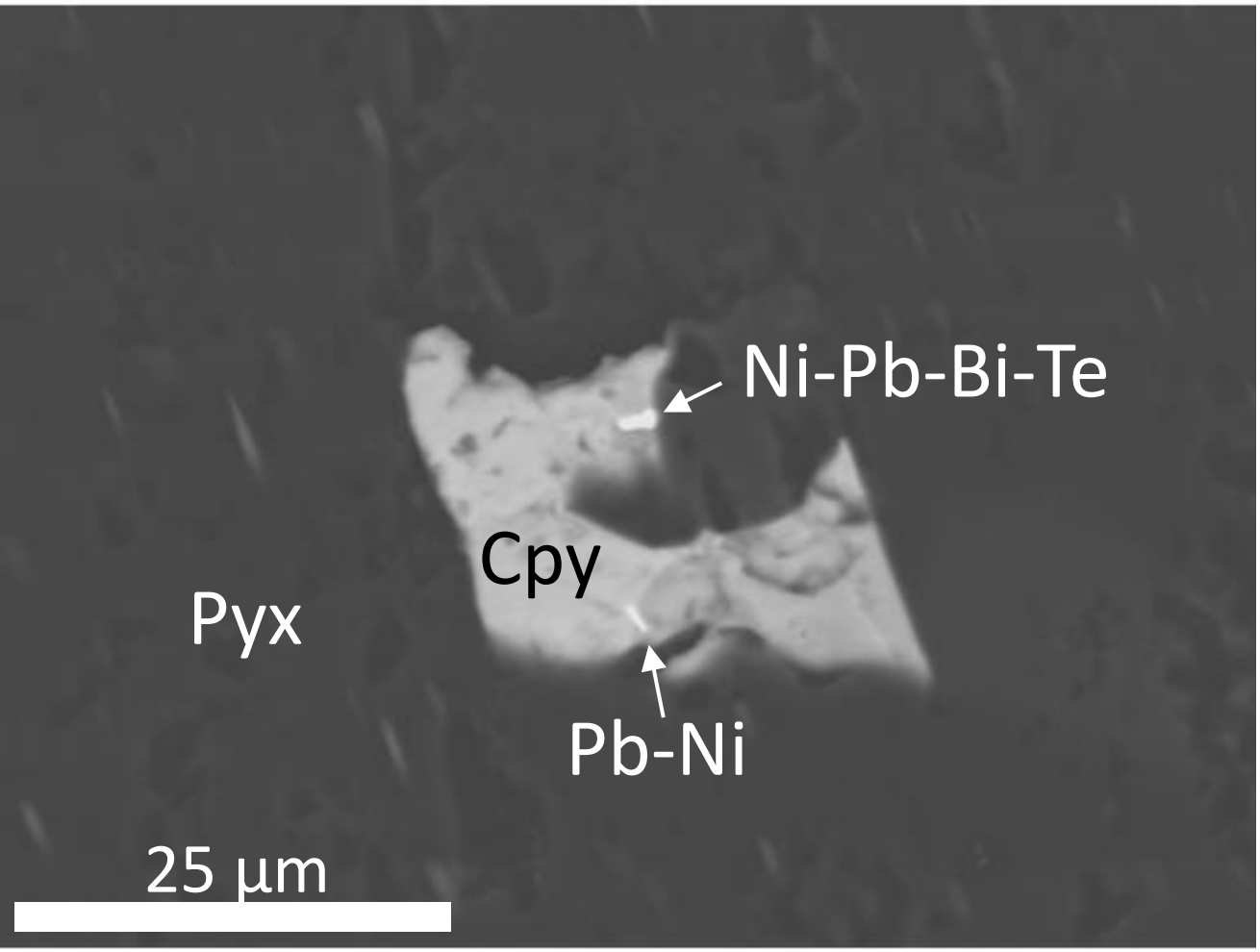


PTR05 A 1



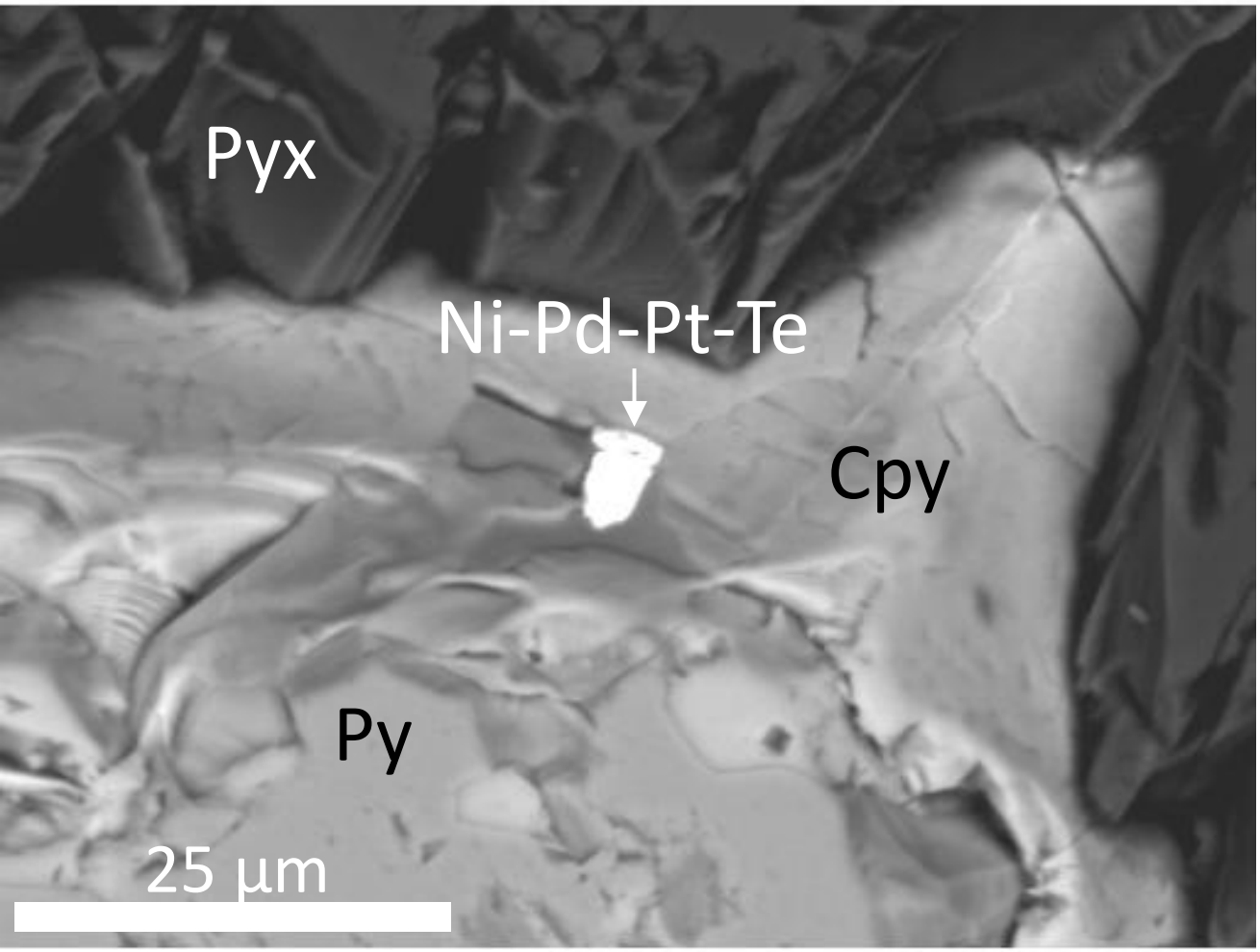
Electron Image 1

PTR05 B 1-2



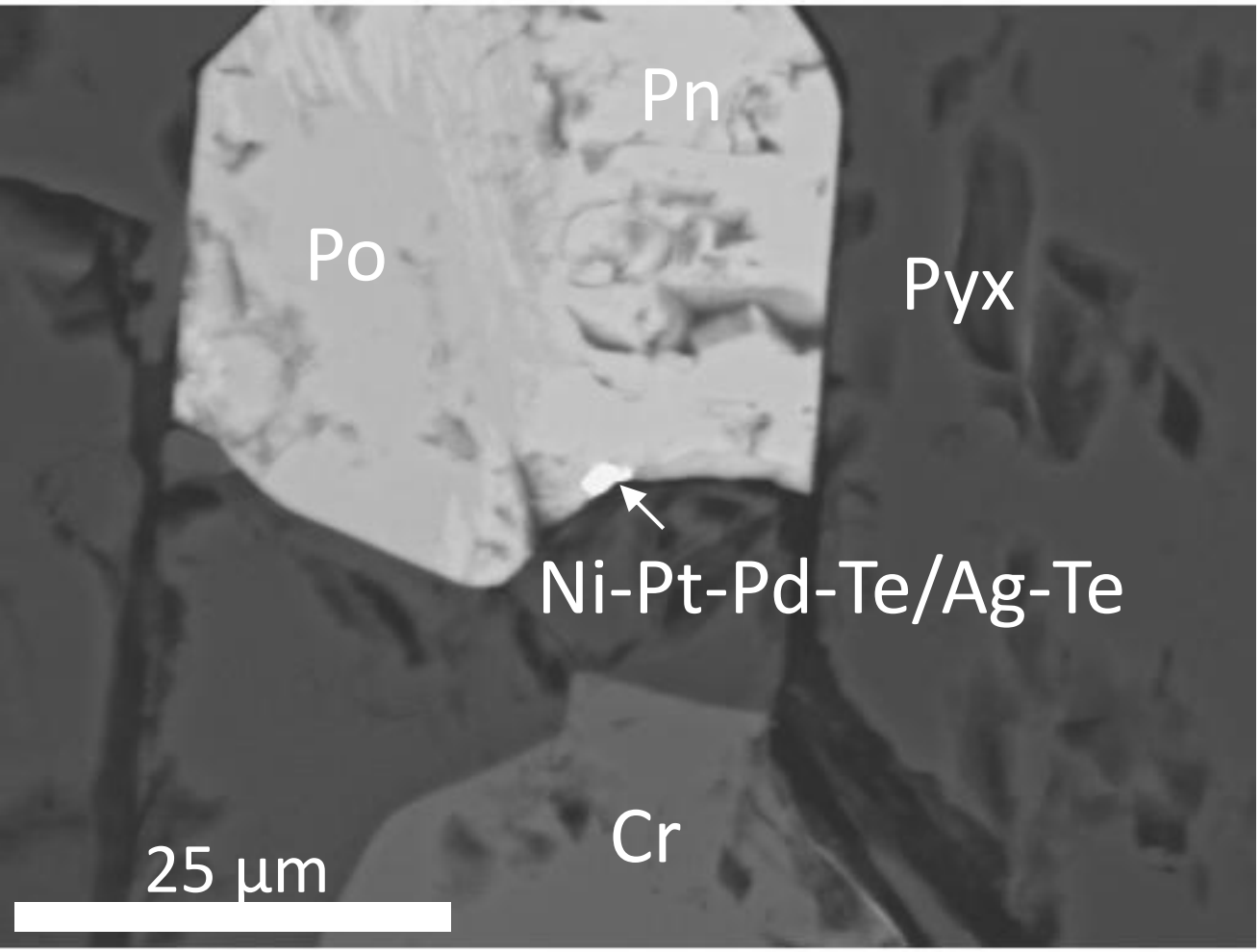
Electron Image 1

PTR05 C 1



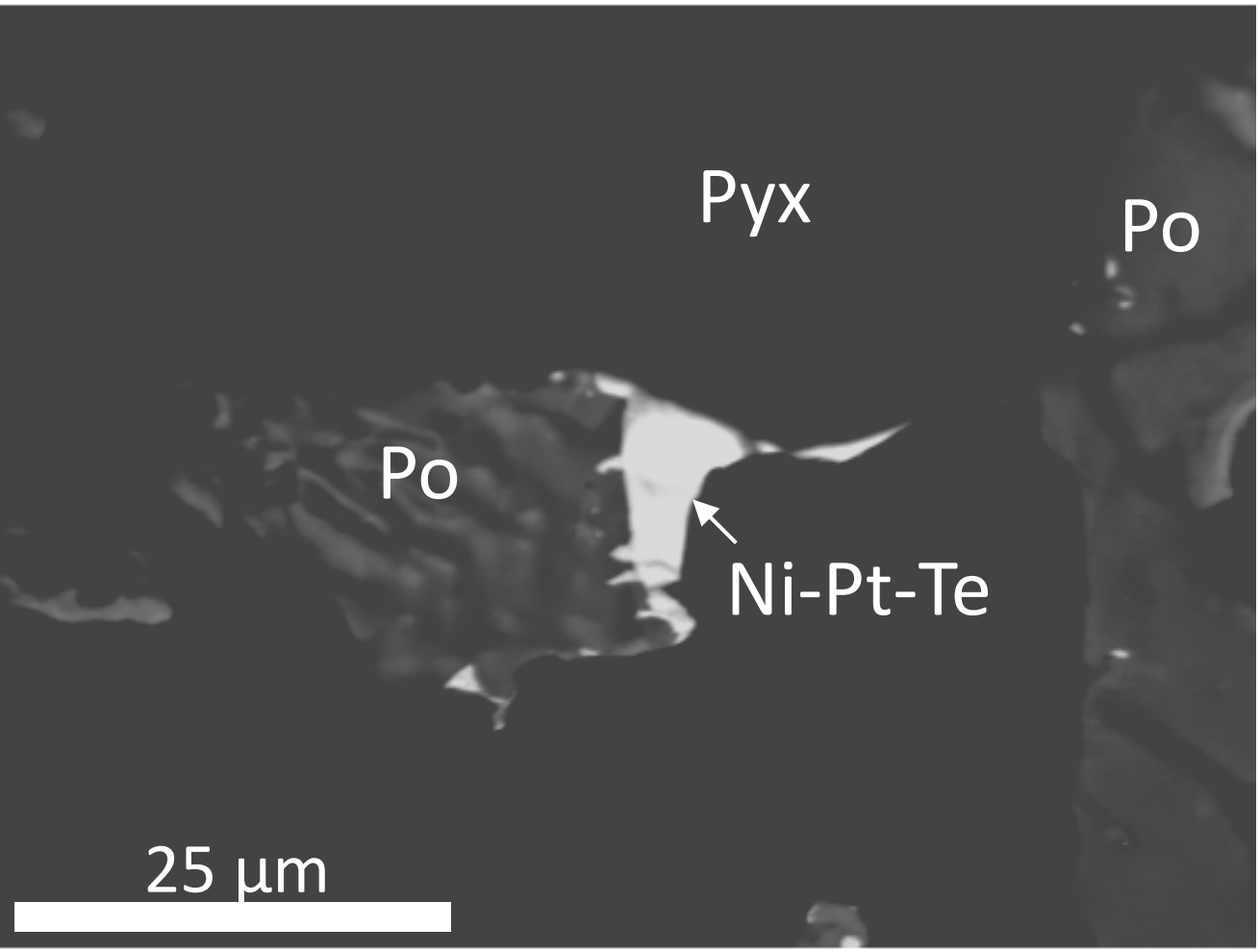
Electron Image 1

PTR05 D 1



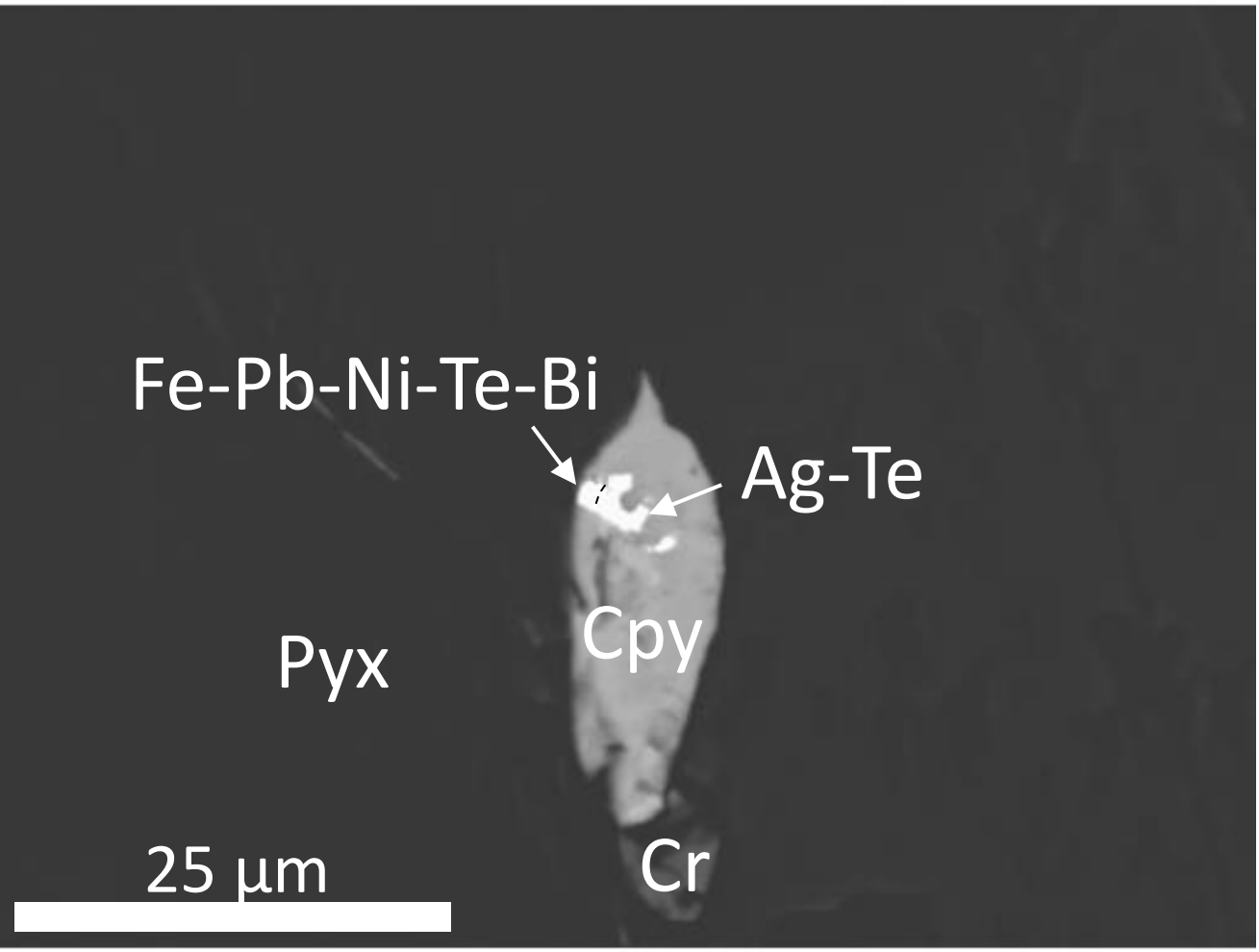
Electron Image 1

PTR05 E 1



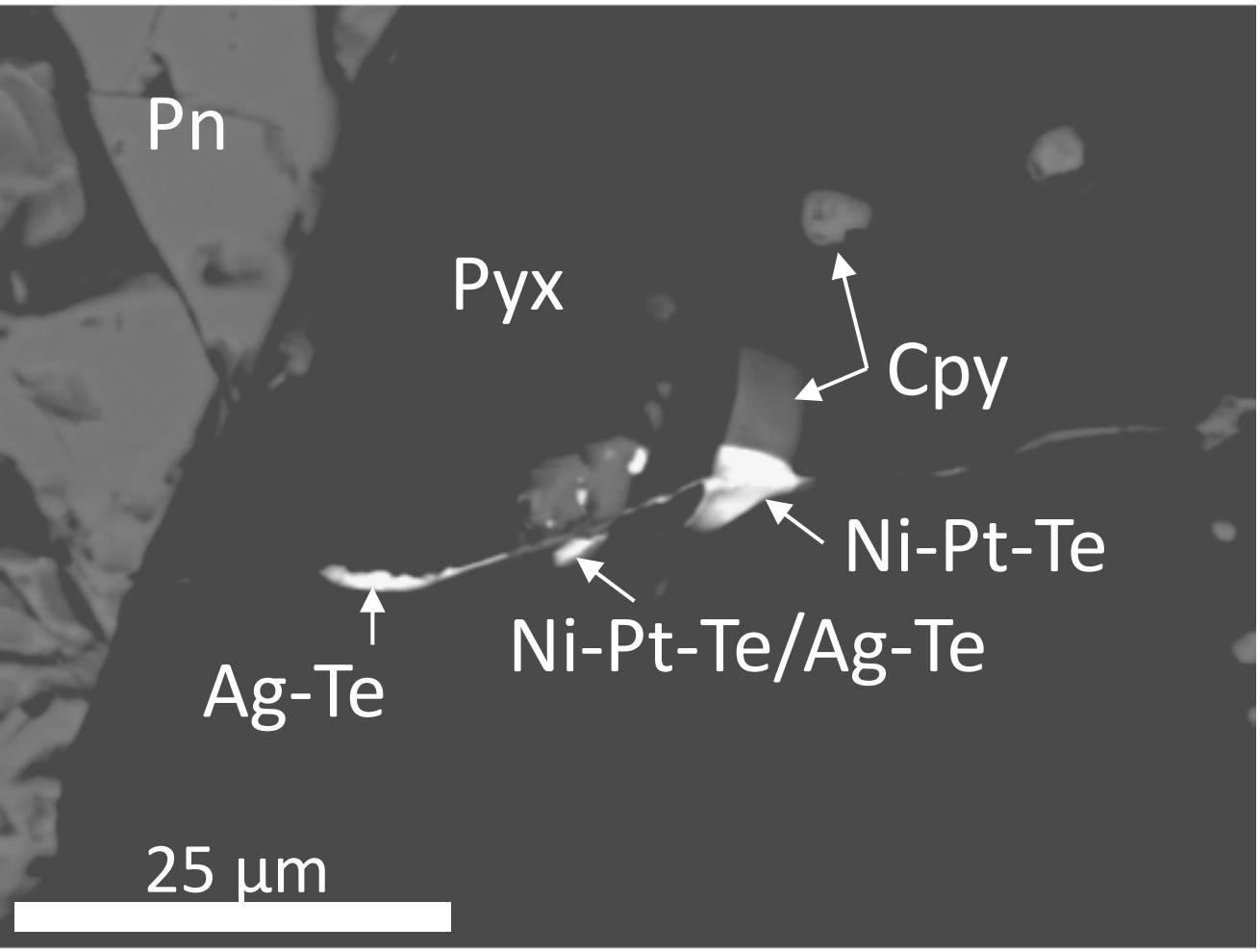
Electron Image 1

PTR05 F 1



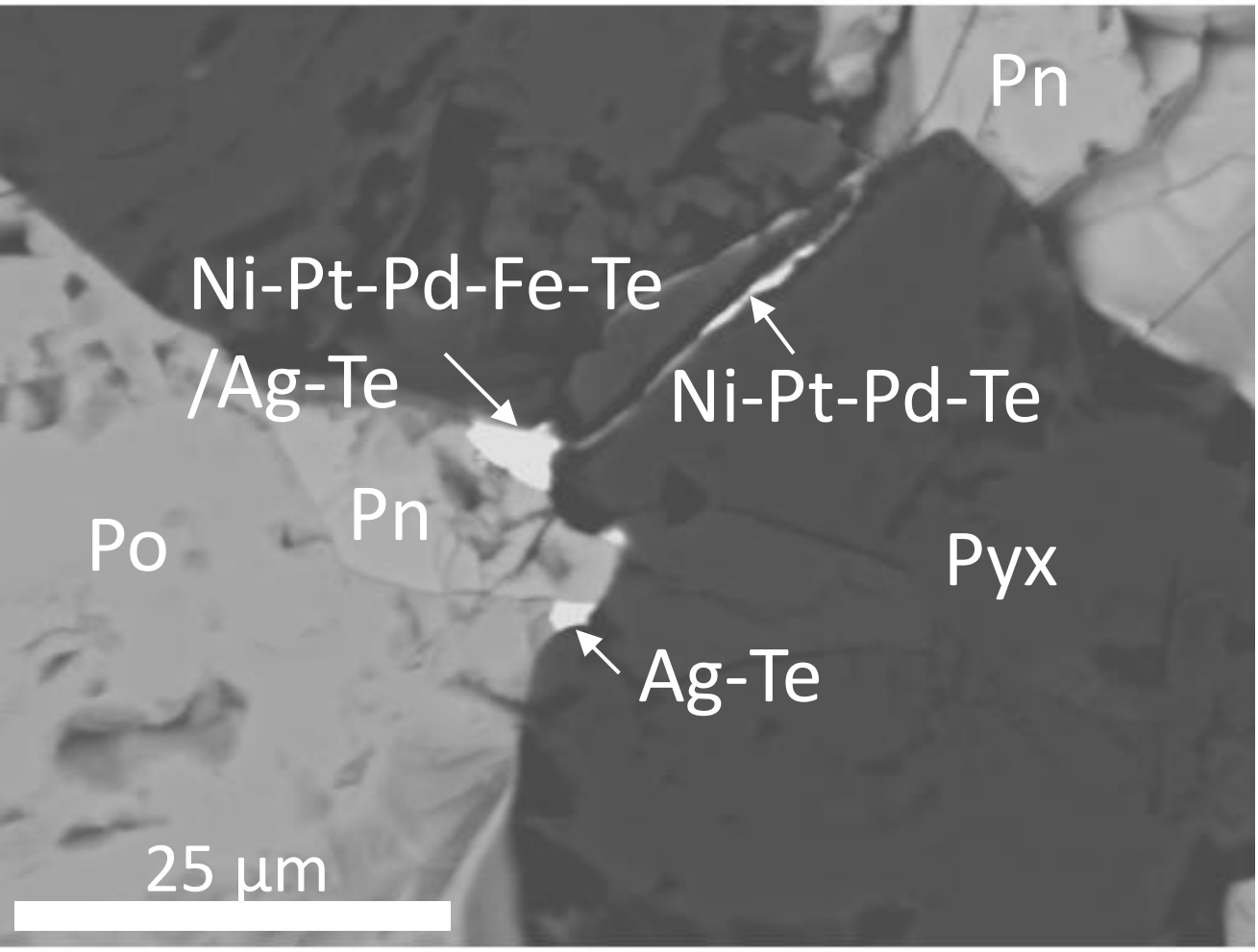
Electron Image 1

PTR05 G 1-3



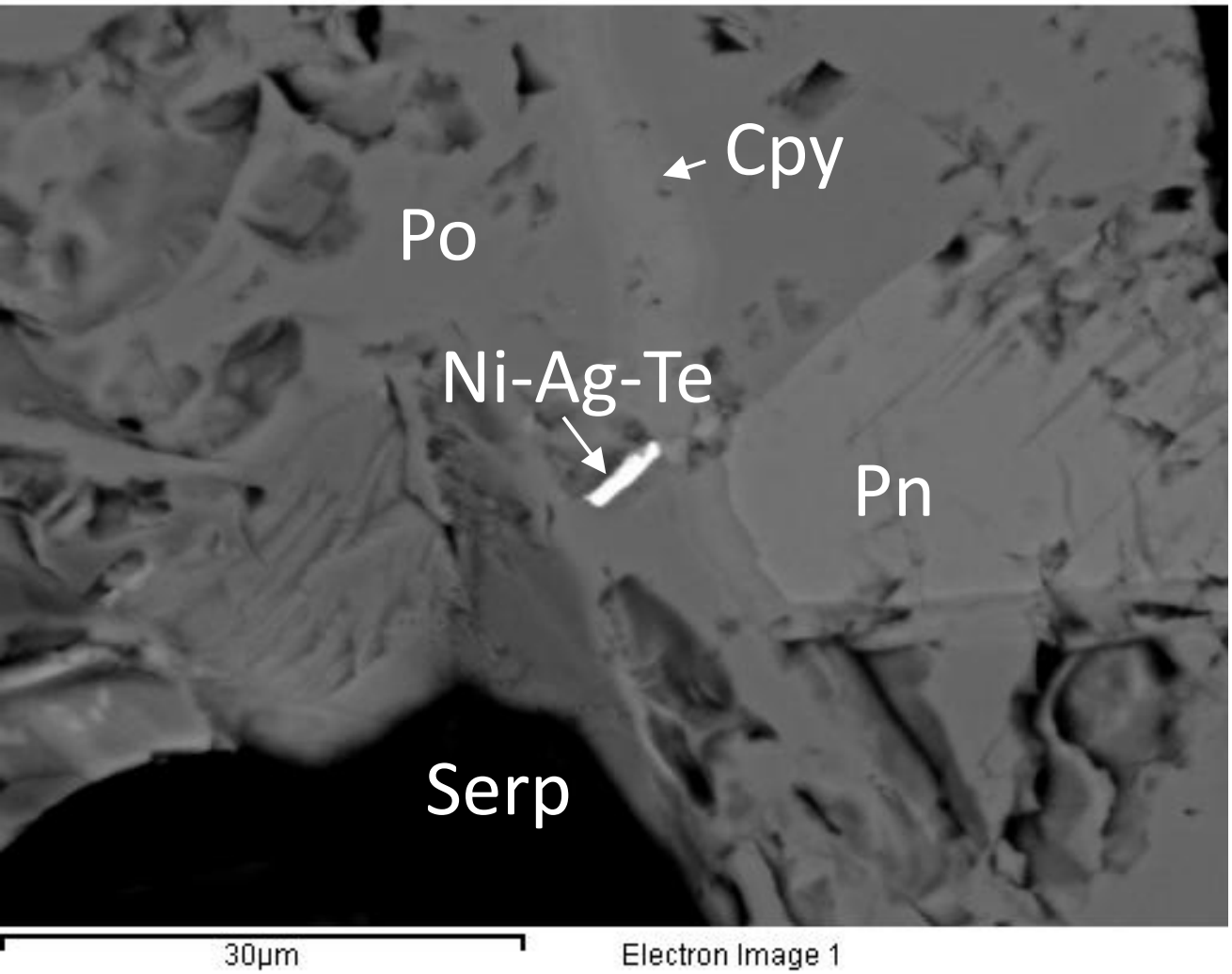
Electron Image 1

PTR05 H 1-3

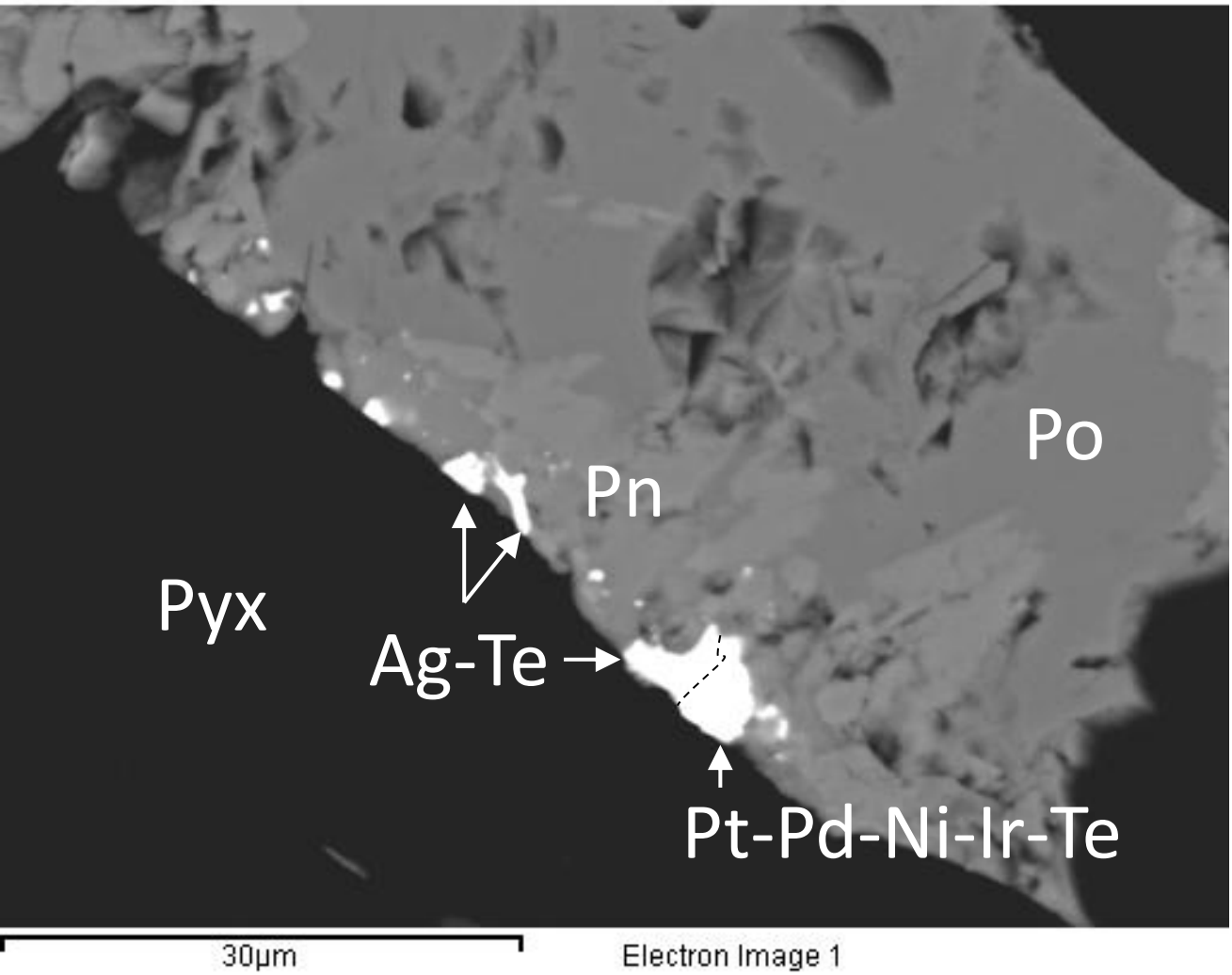


Electron Image 1

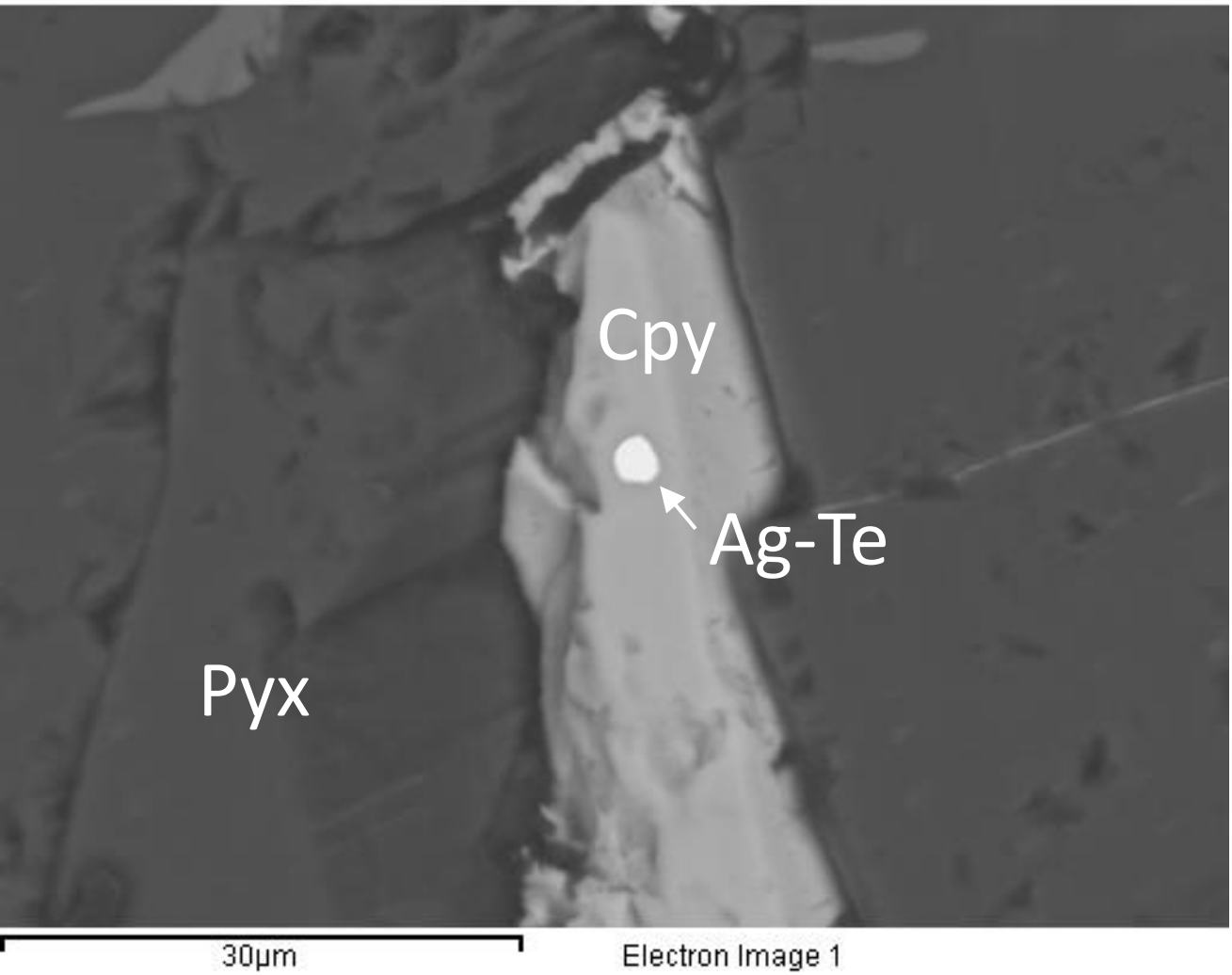
PTR05 I 1



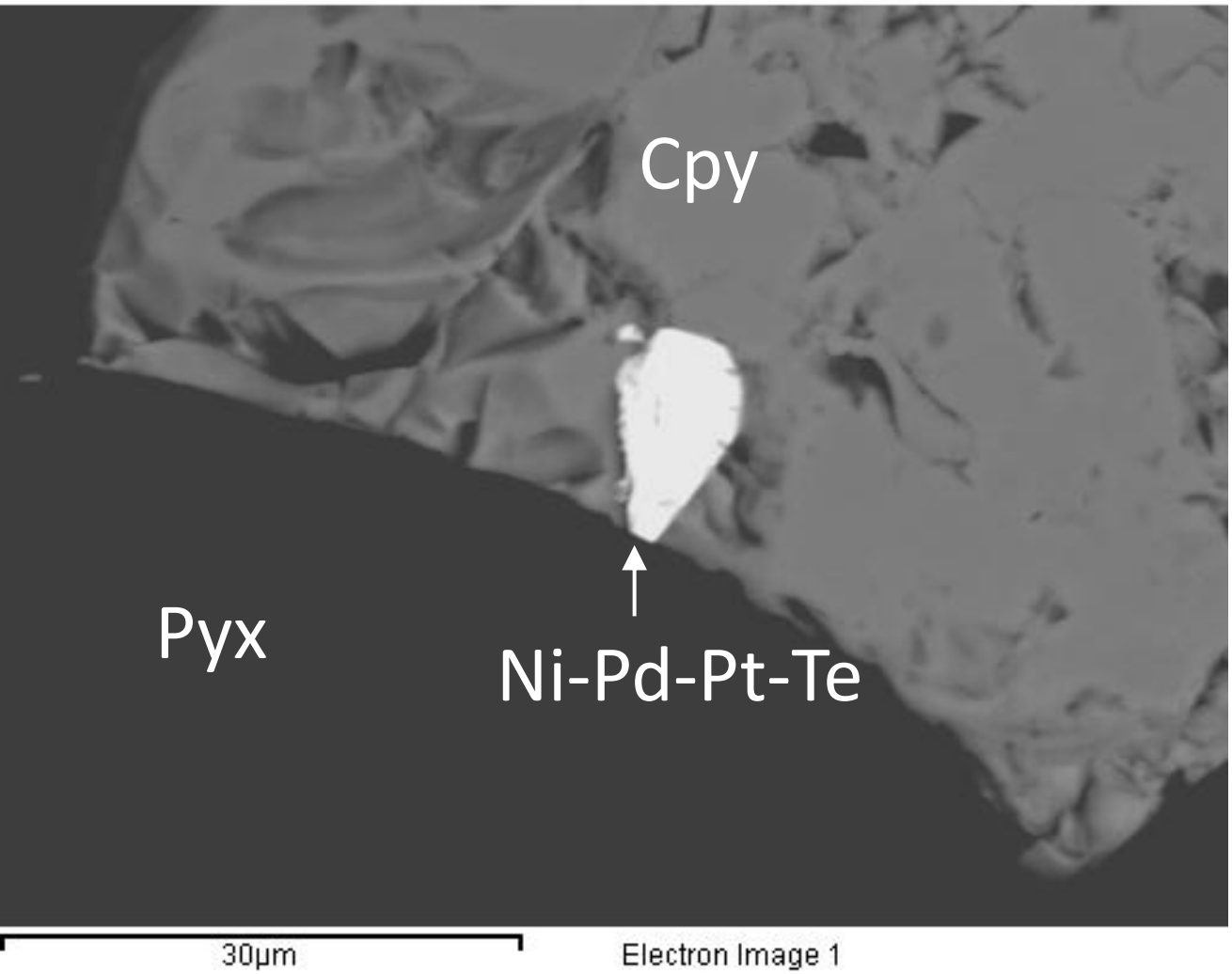
PTR05 J 1-2



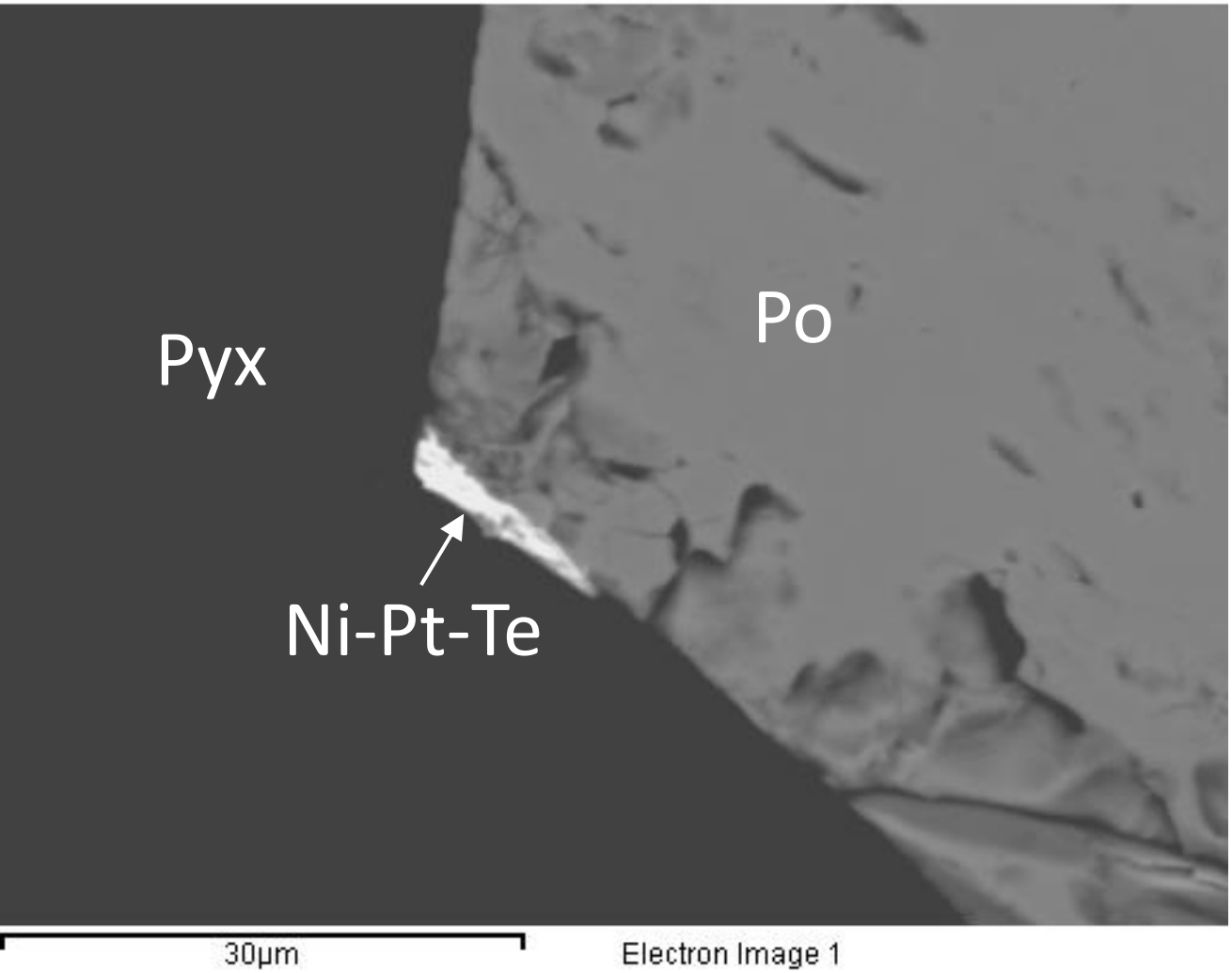
PTR05 K 1



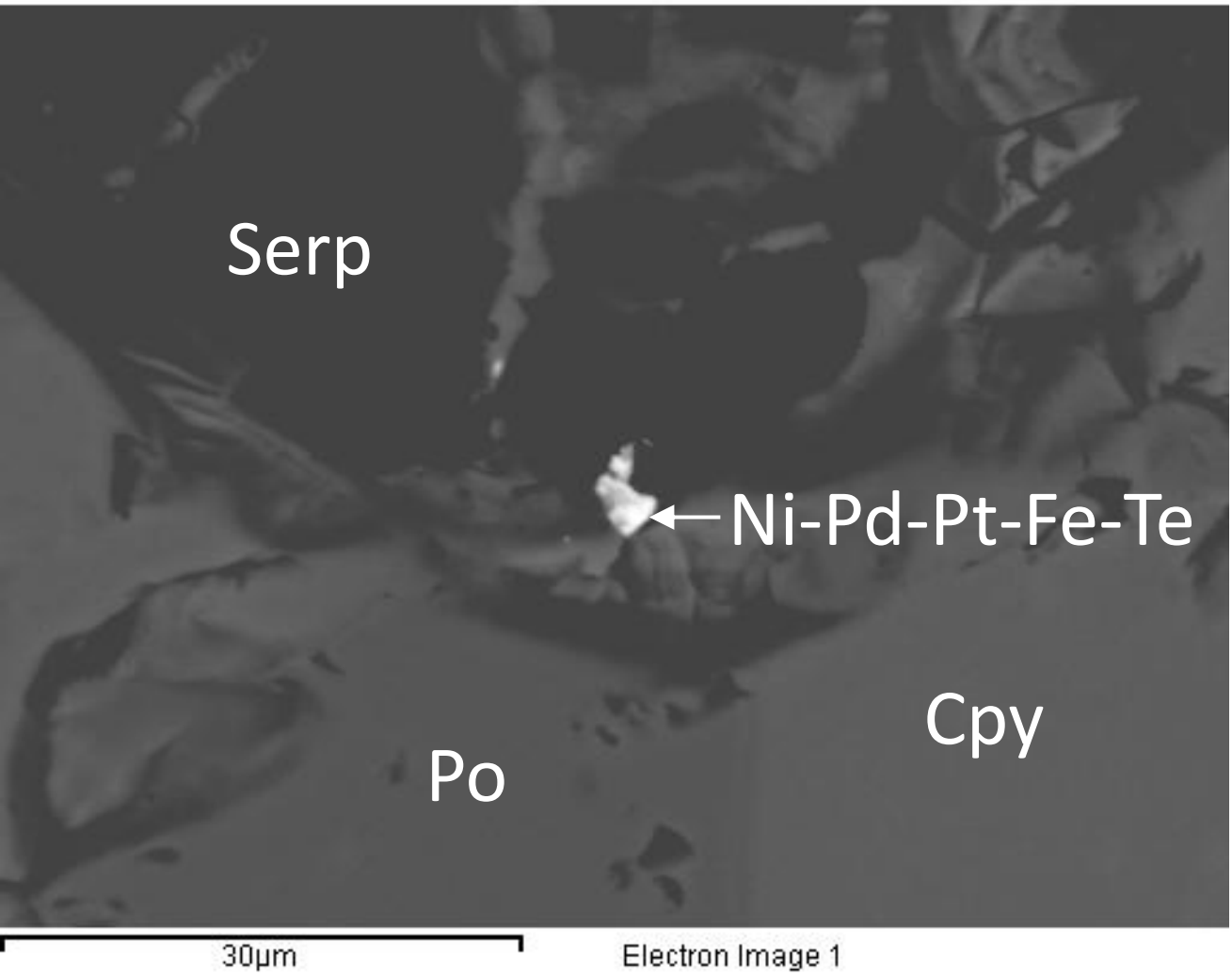
PTR05 L 1



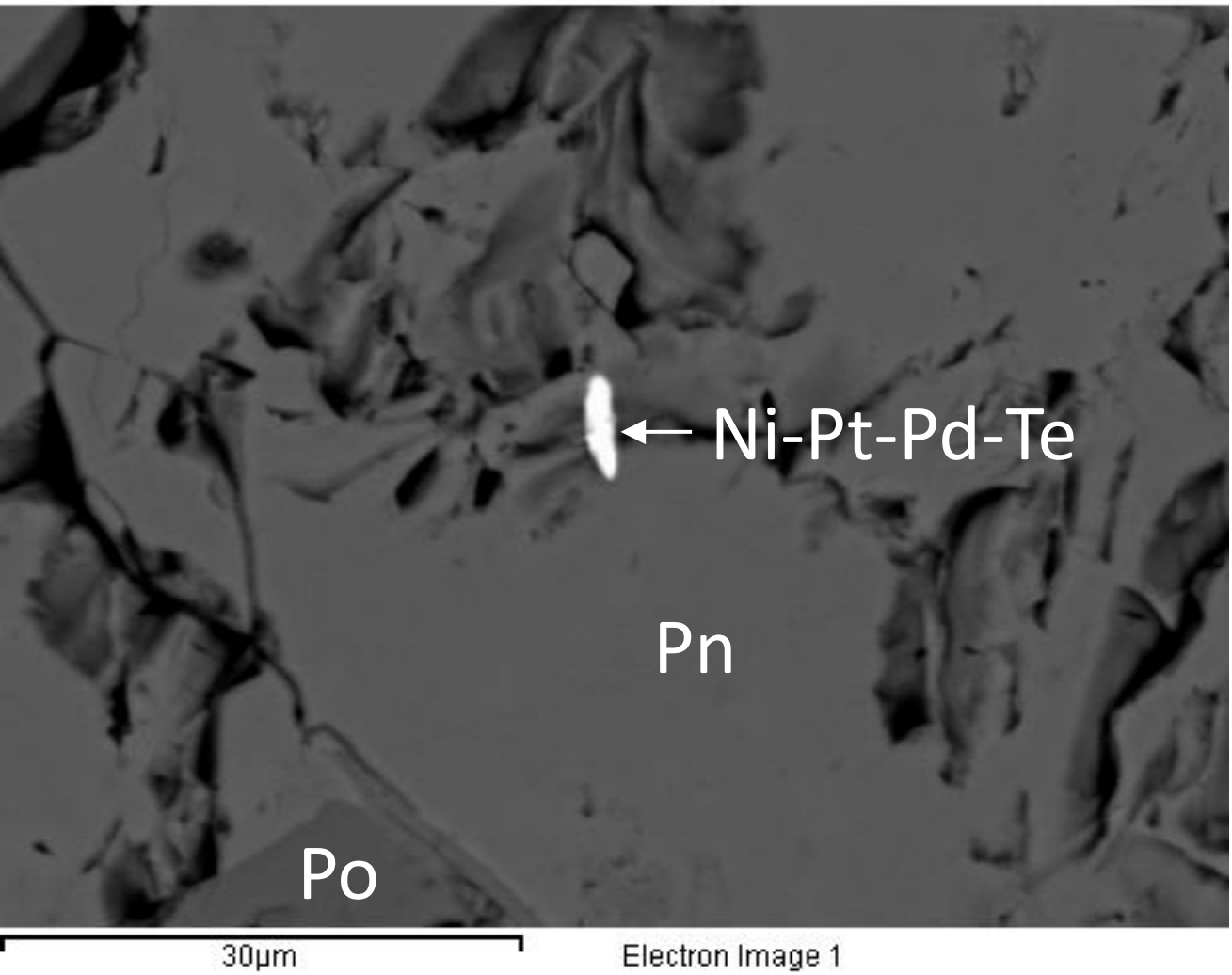
PTR05 M 1



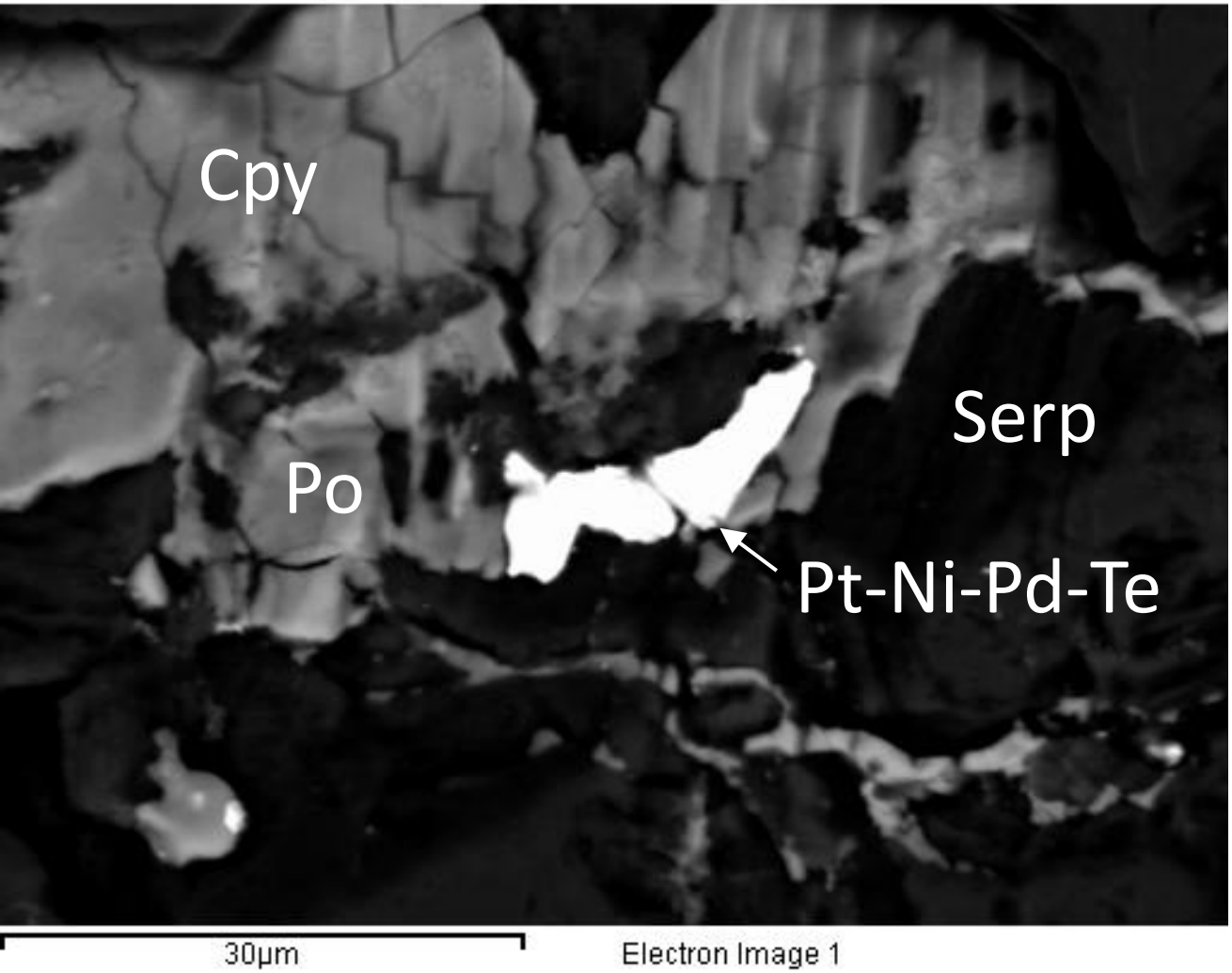
PTR05 N 1



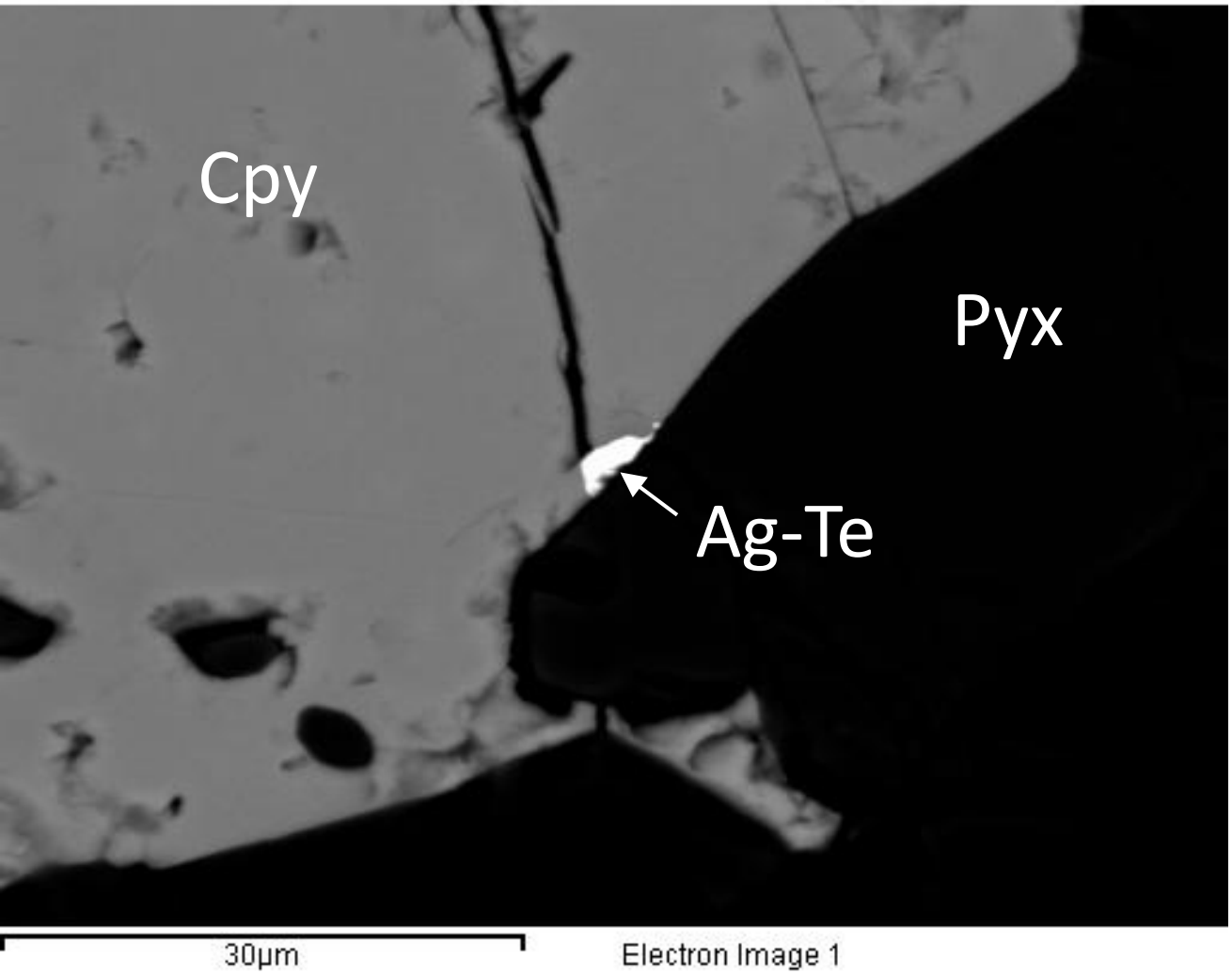
PTR05 O 1



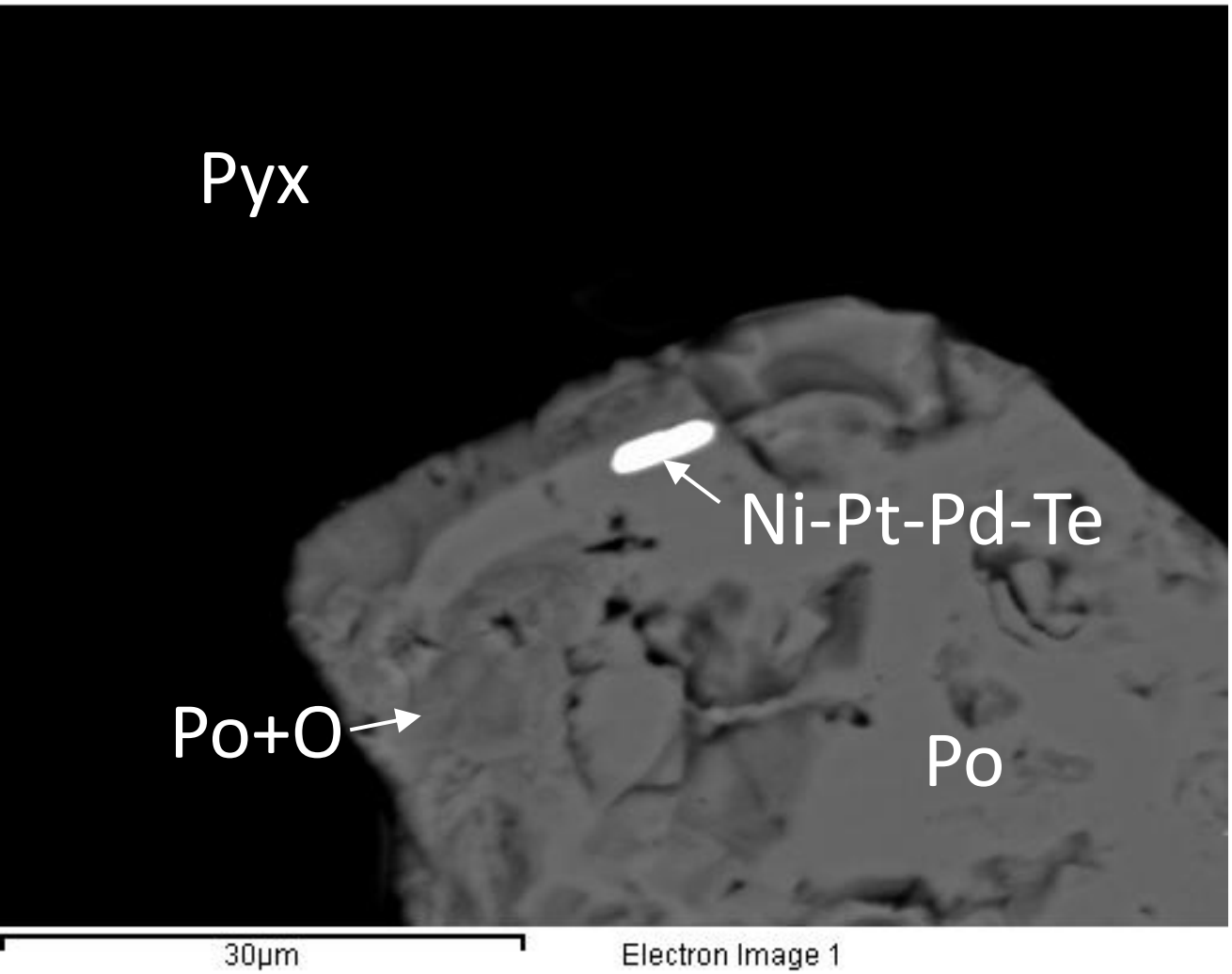
PTR05 P 1



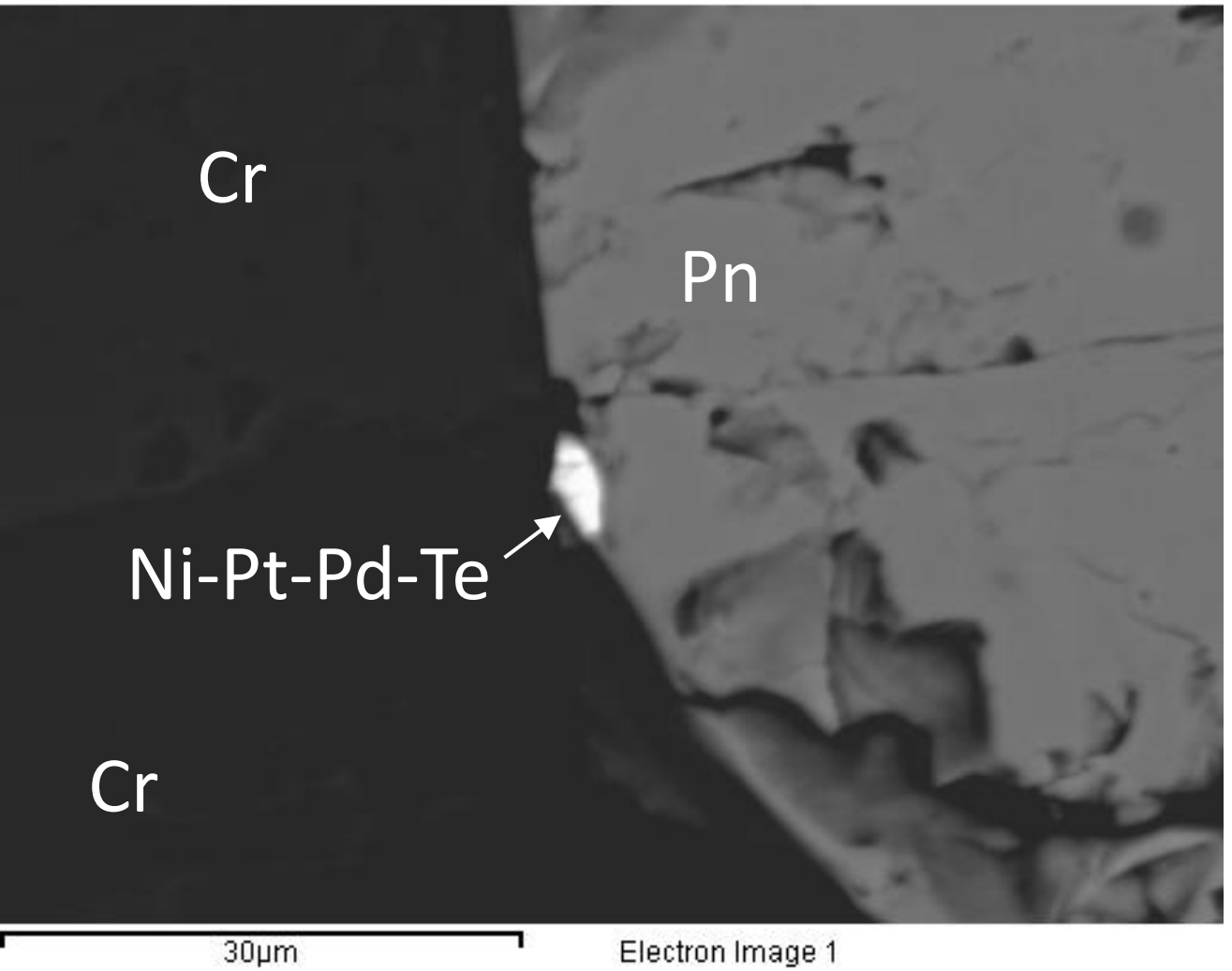
PTR05 Q 1



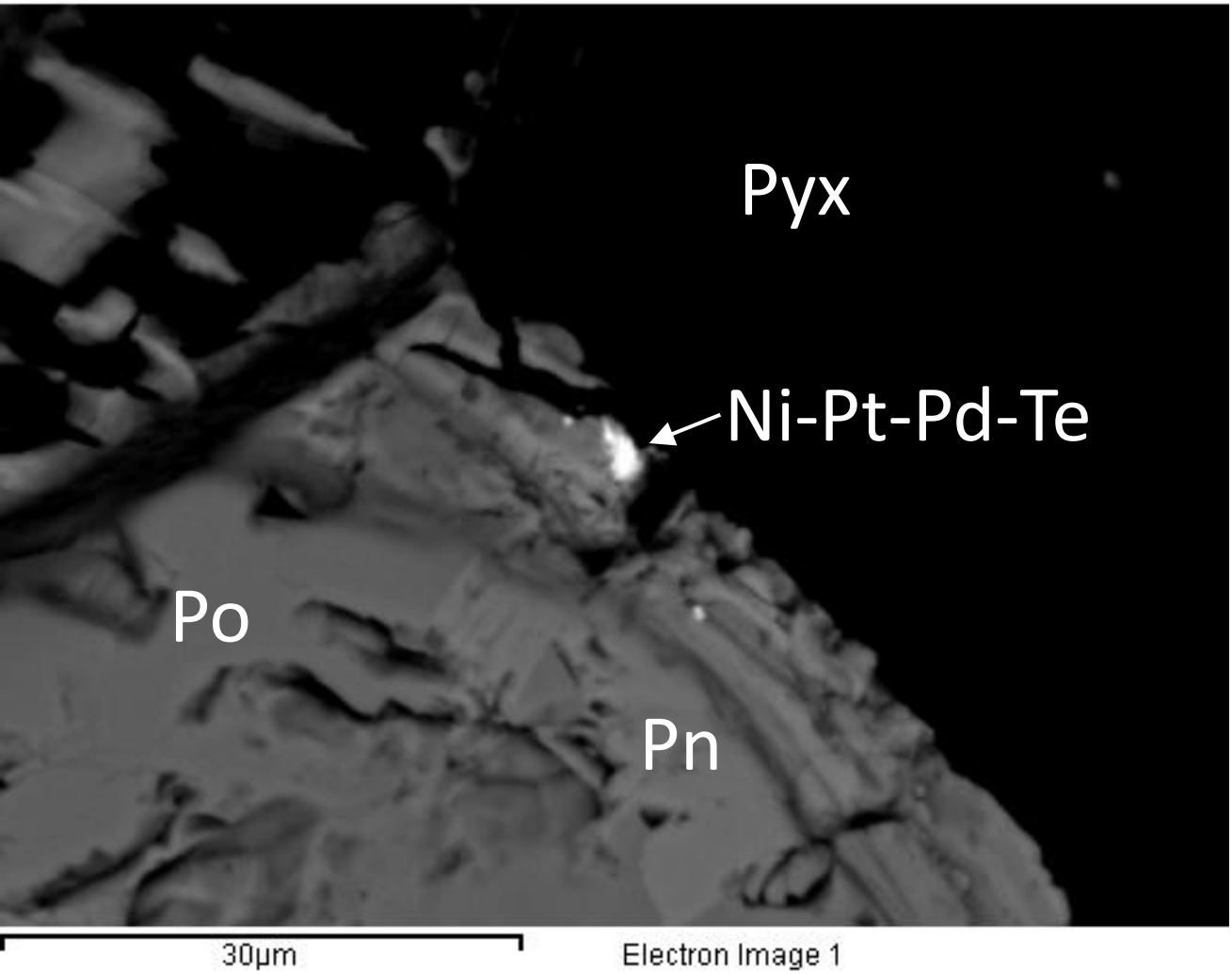
PTR05 R 1



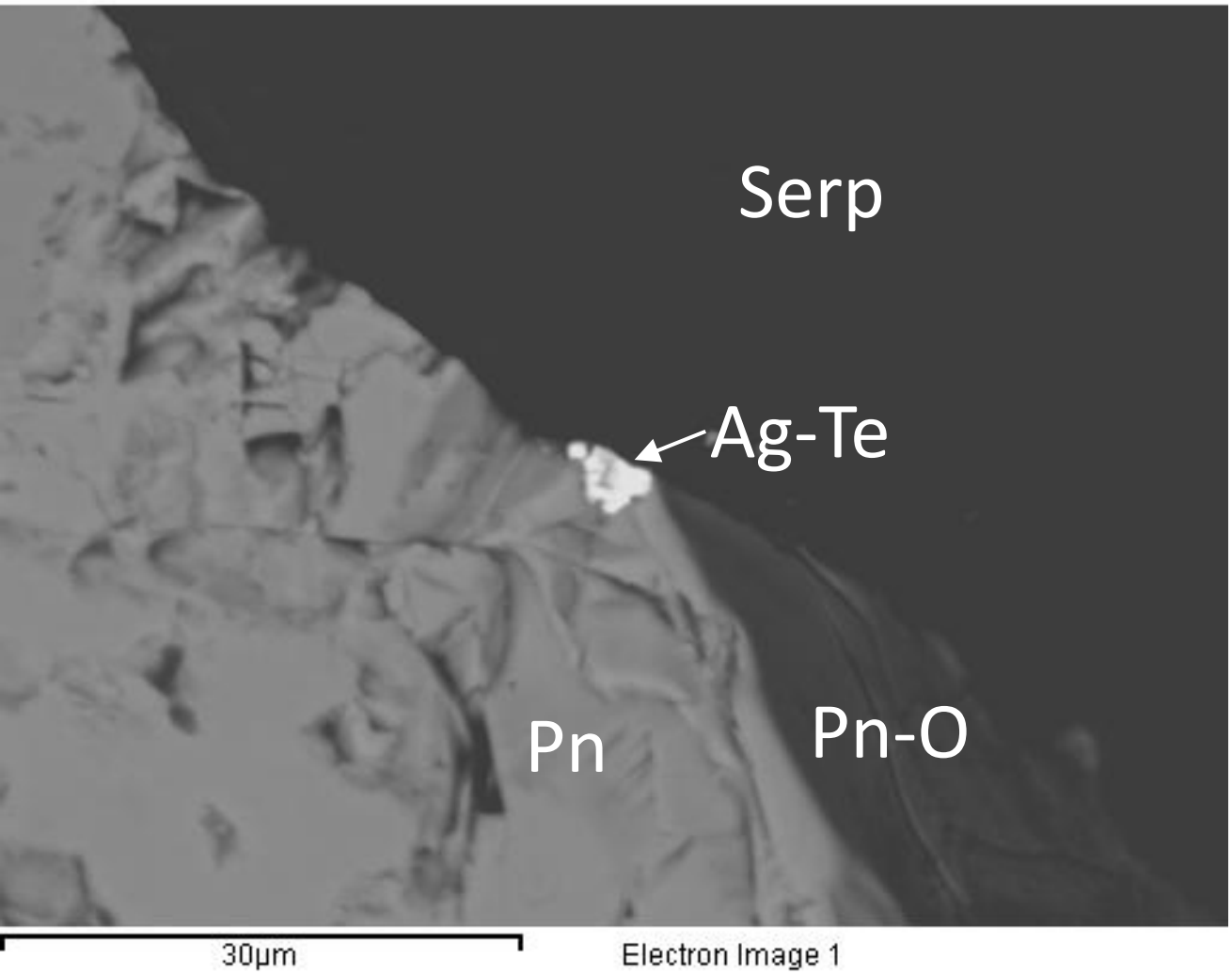
PTR05 S 1



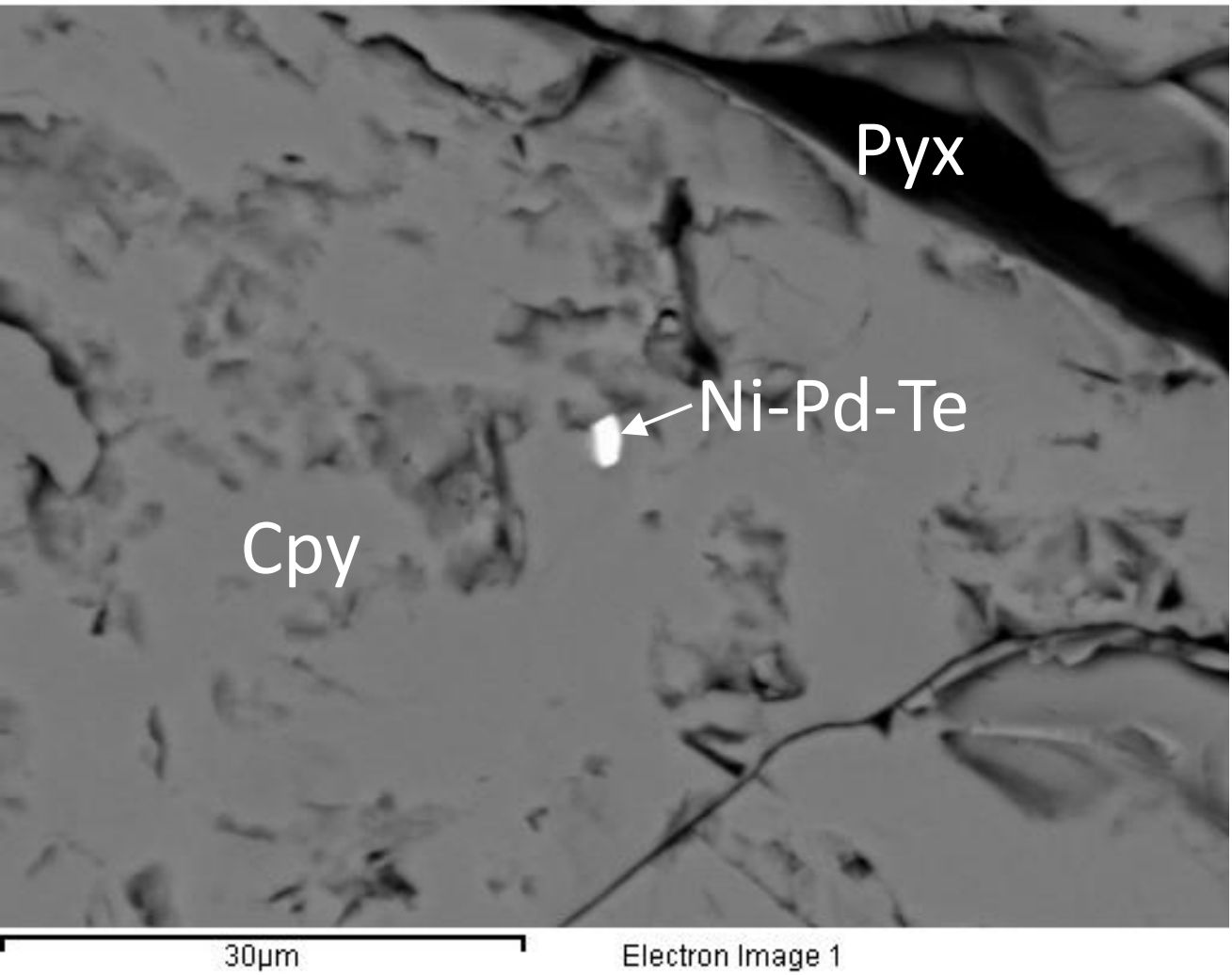
PTR05 T 1



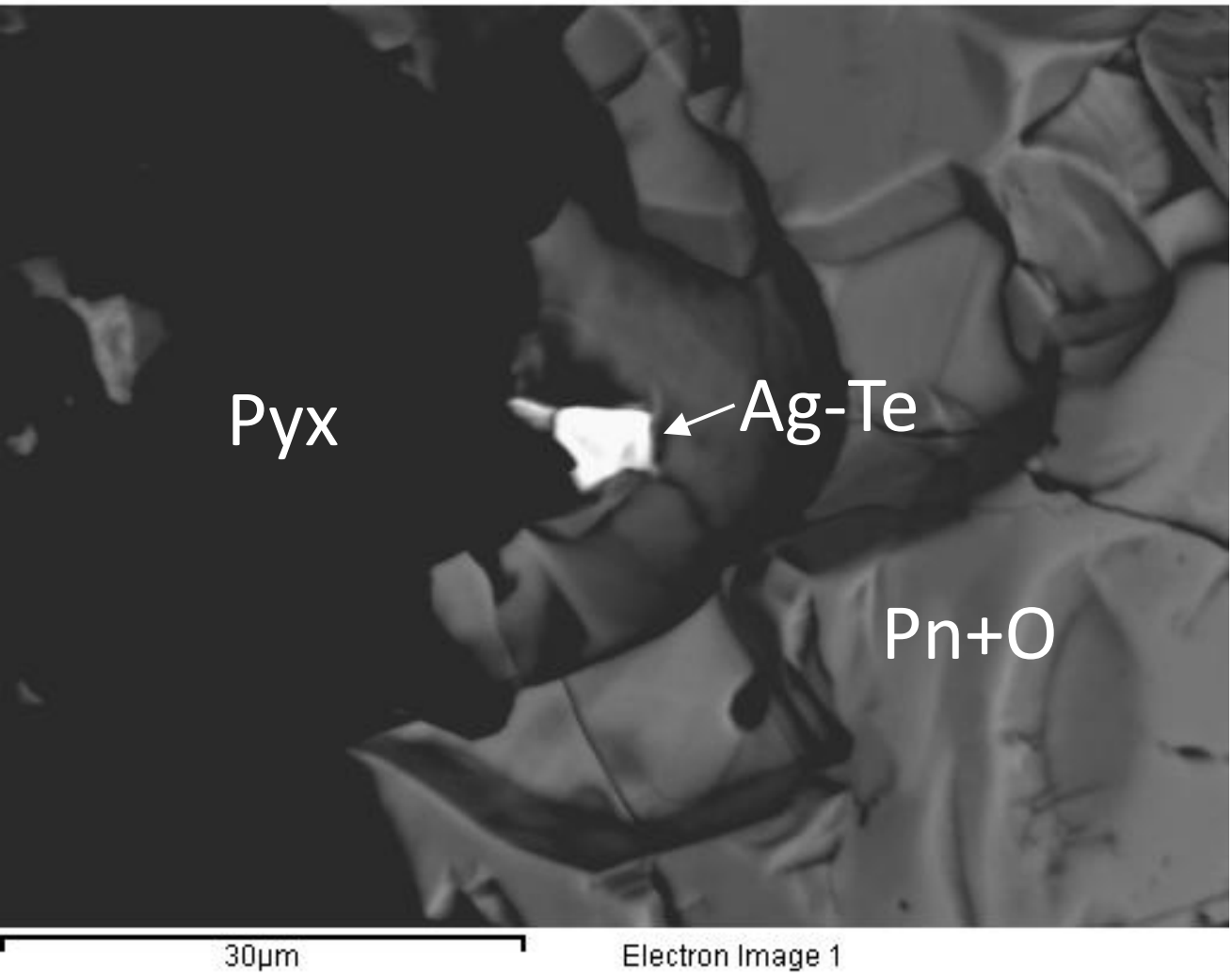
PTR05 U 1



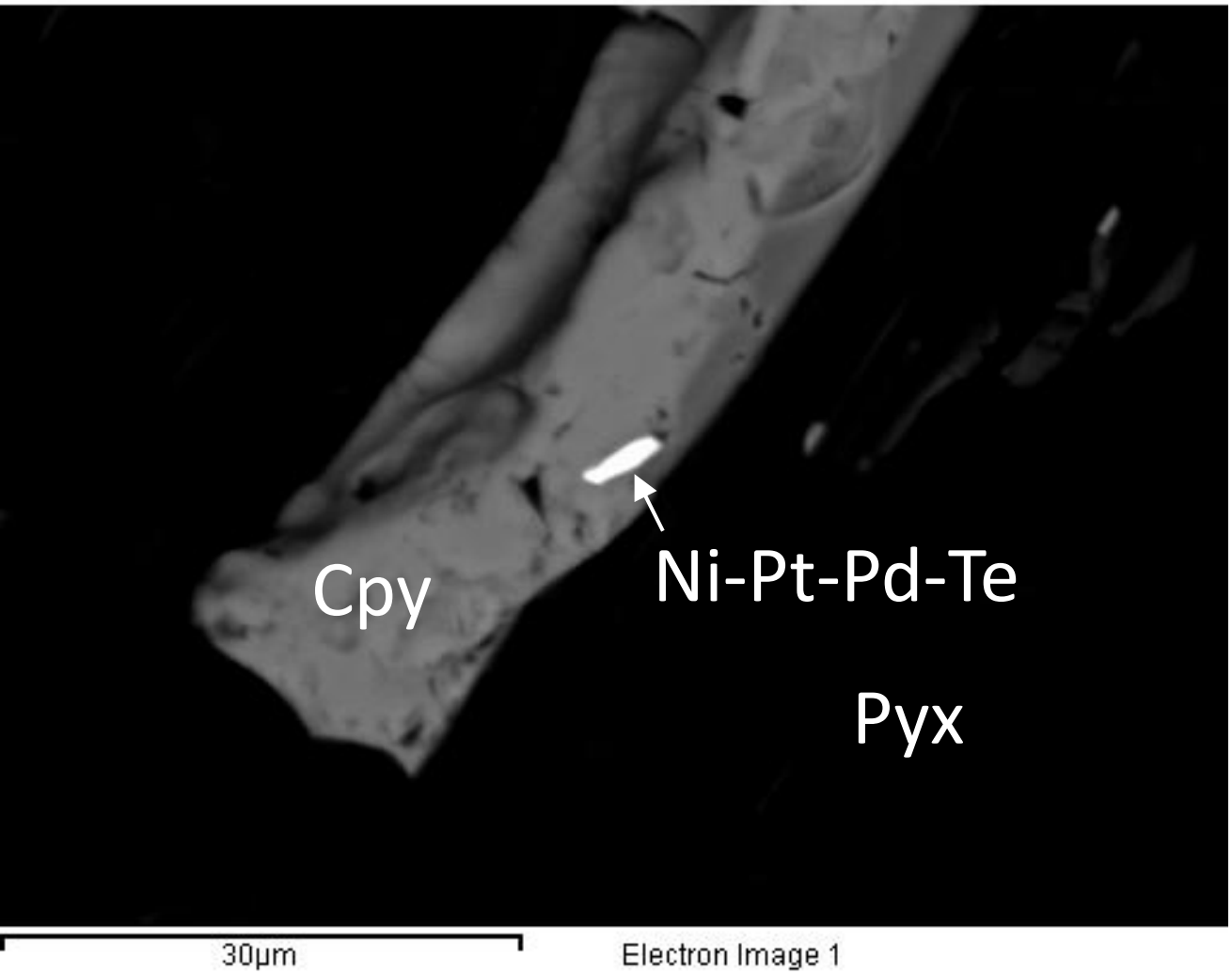
PTR05 V 1



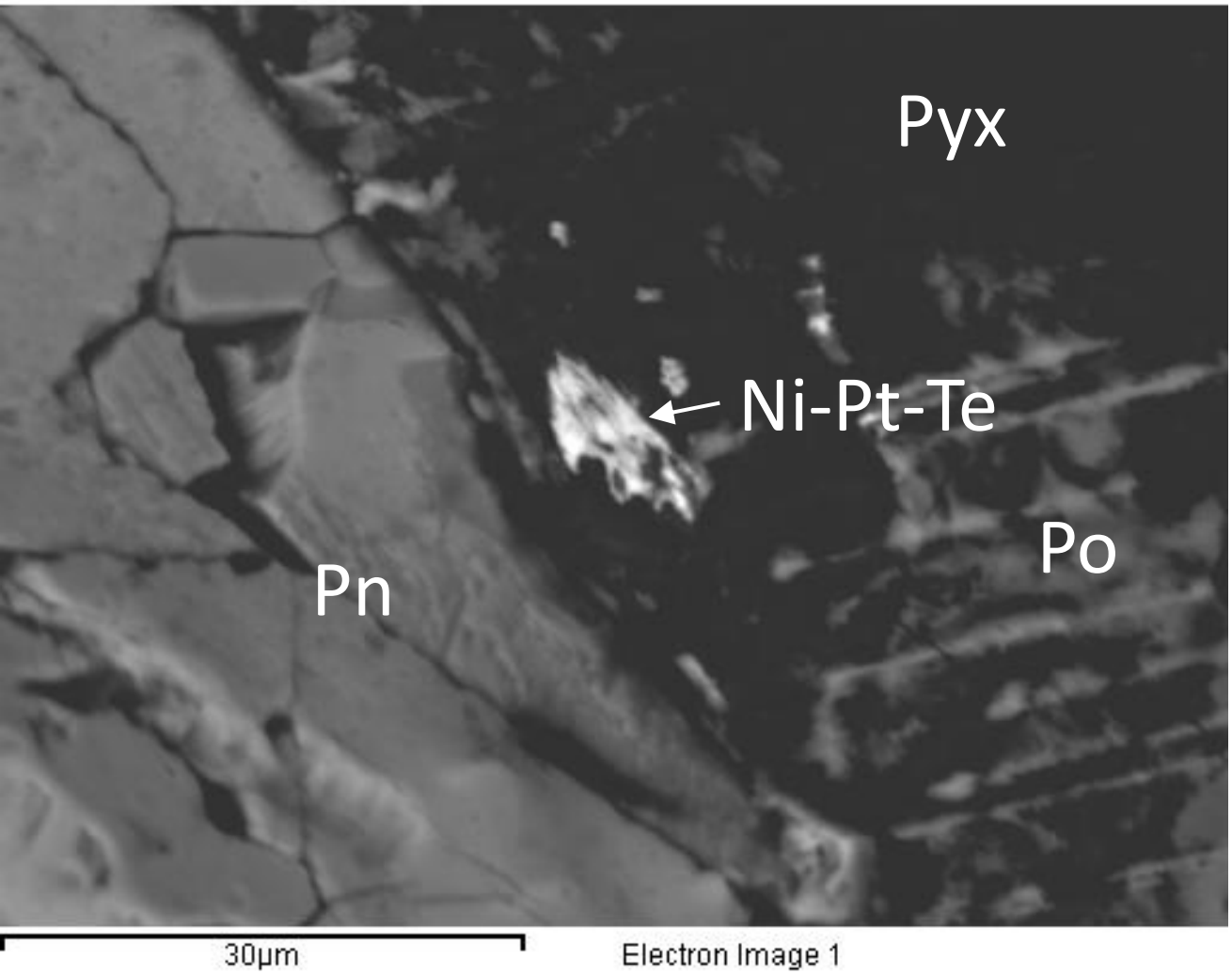
PTR05 W 1



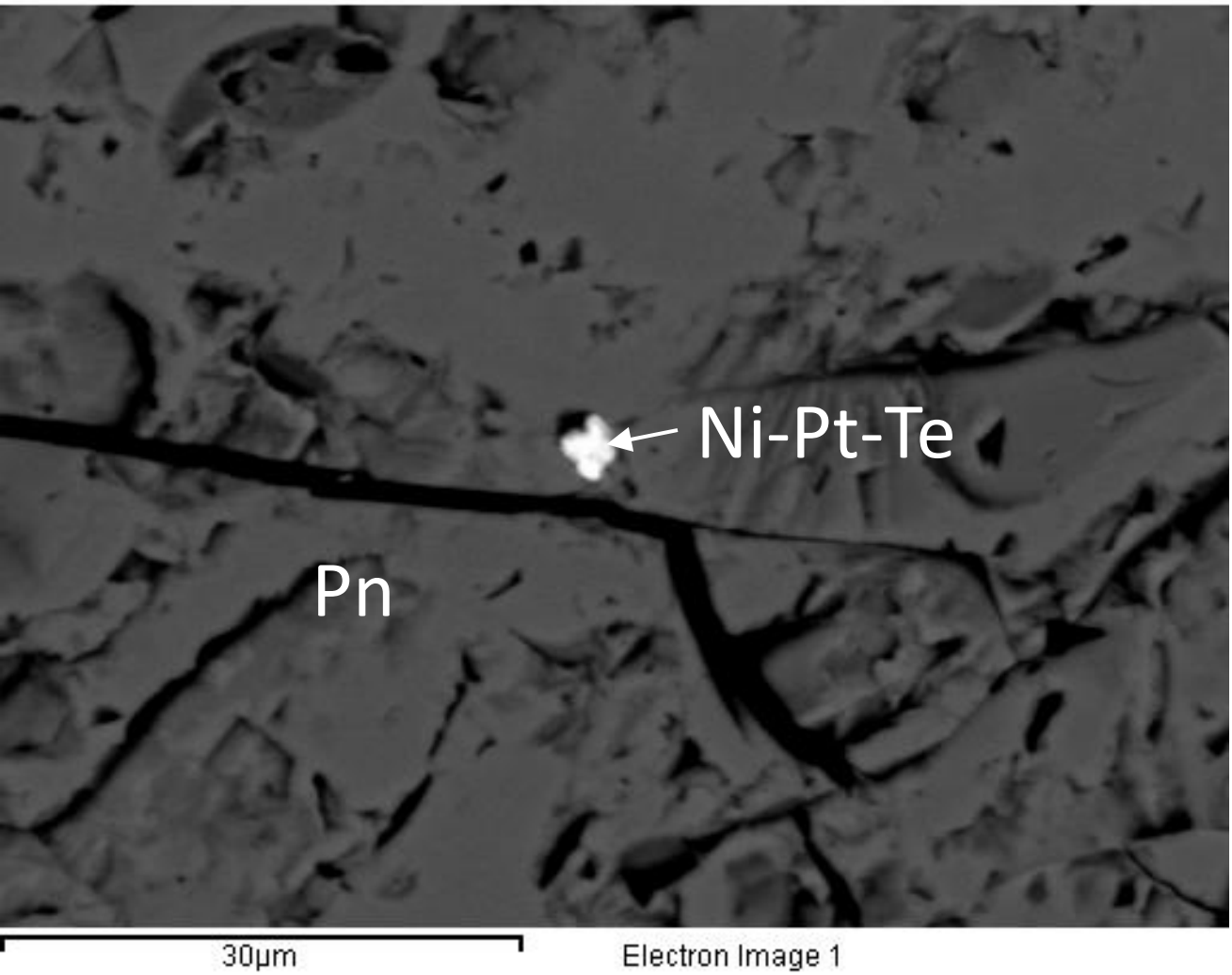
PTR05 X 1



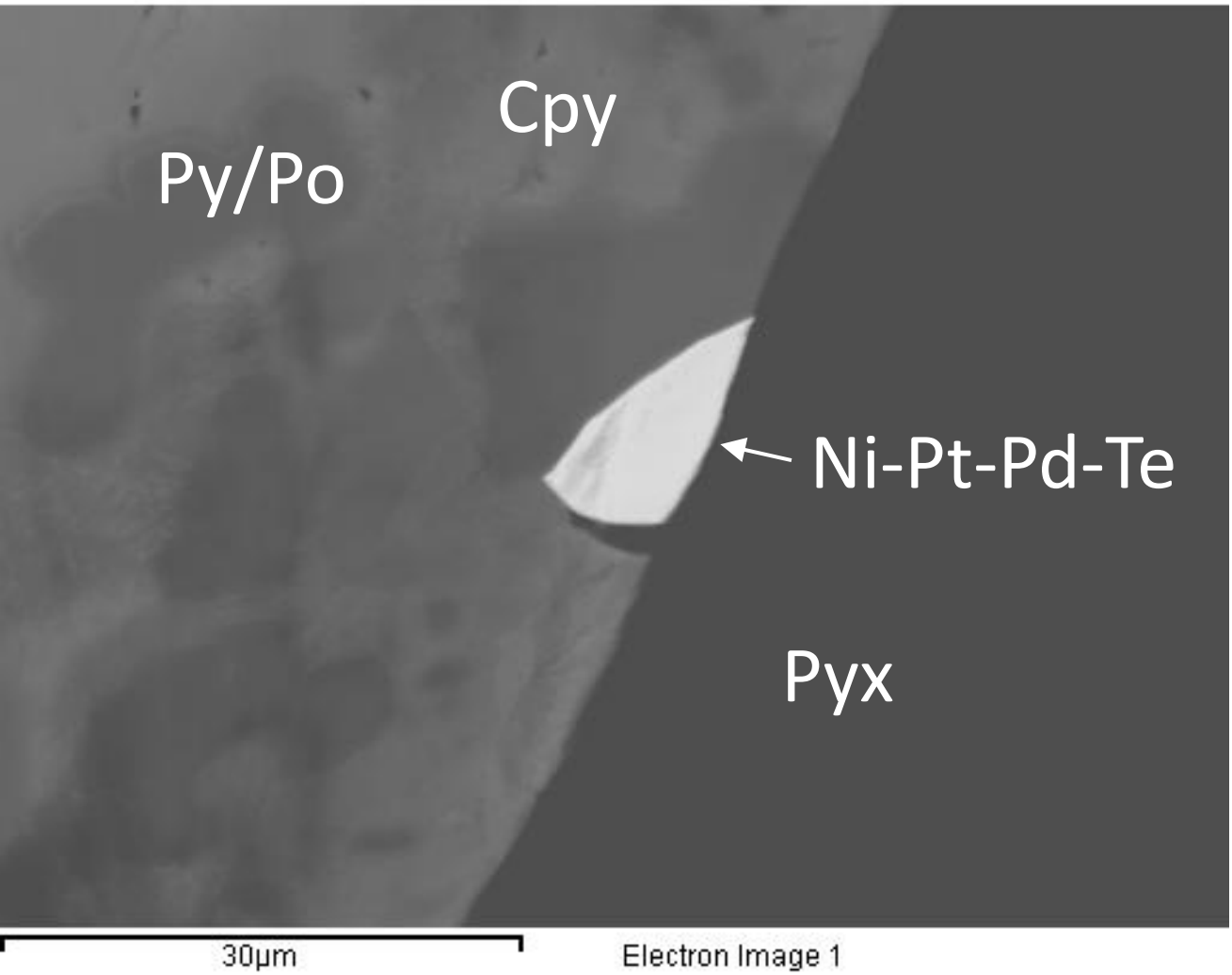
PTR05 Y 1



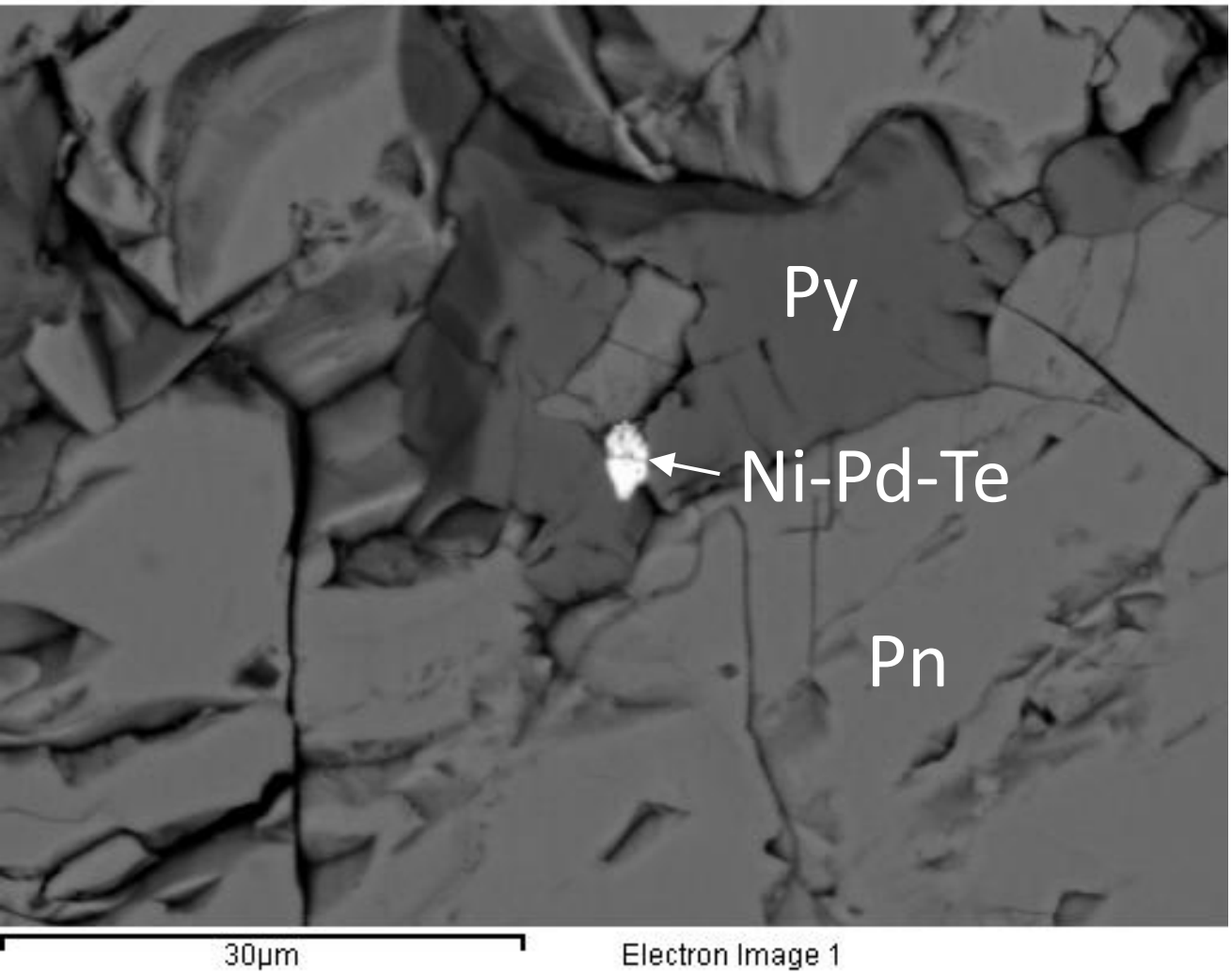
PTR05 Z 1



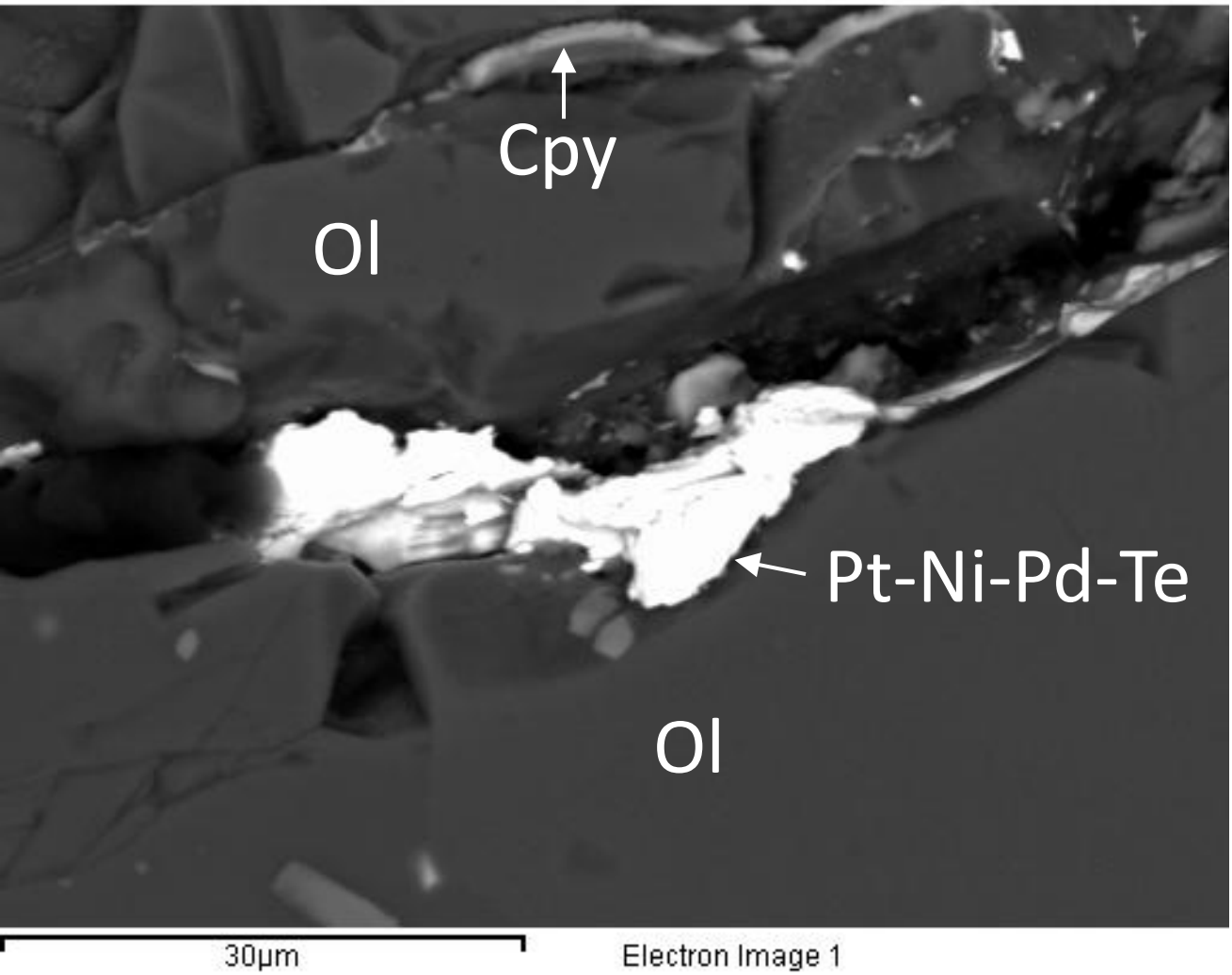
PTR07 A 1



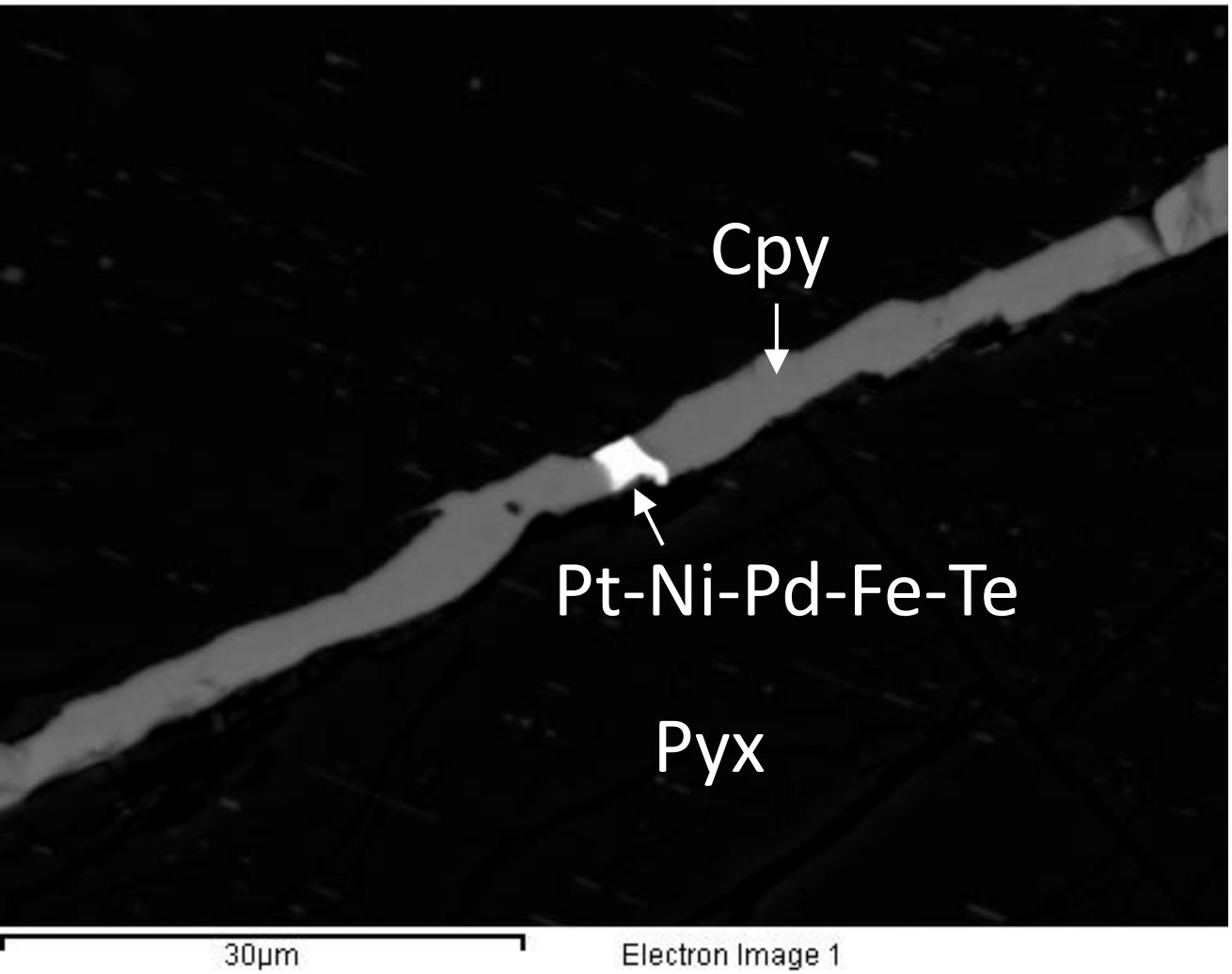
PTR07 B 1



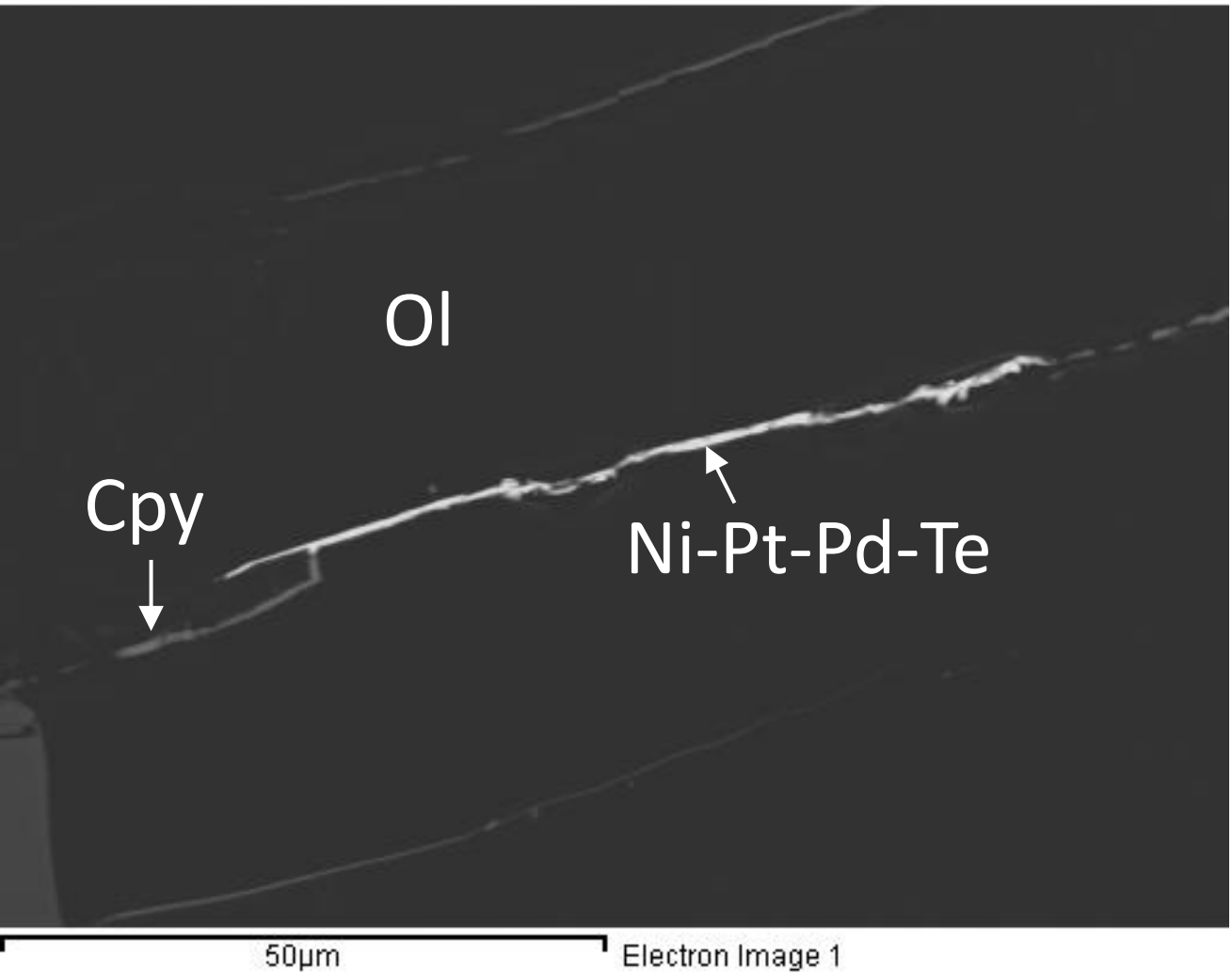
PTR07 C 1



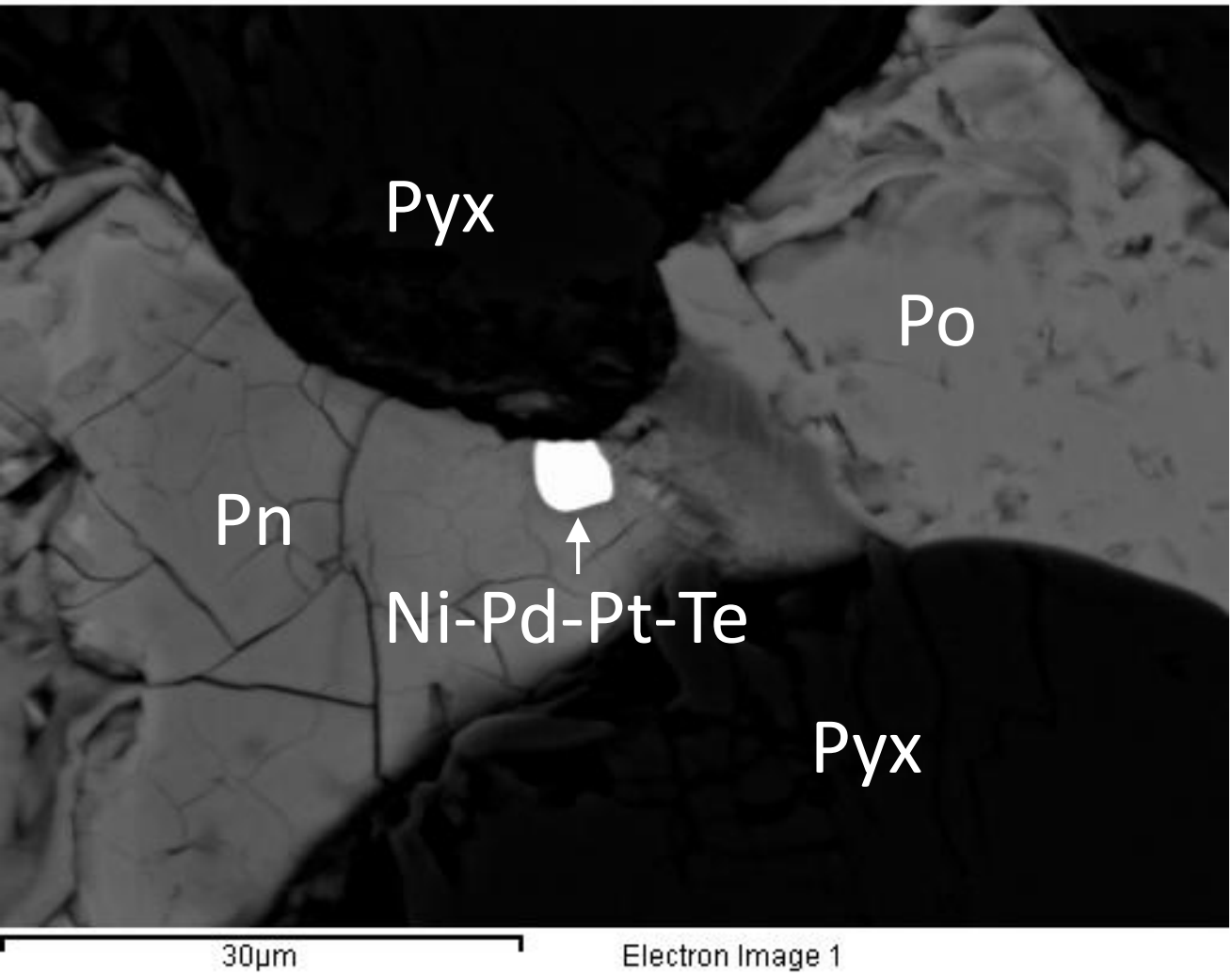
PTR07 D 1



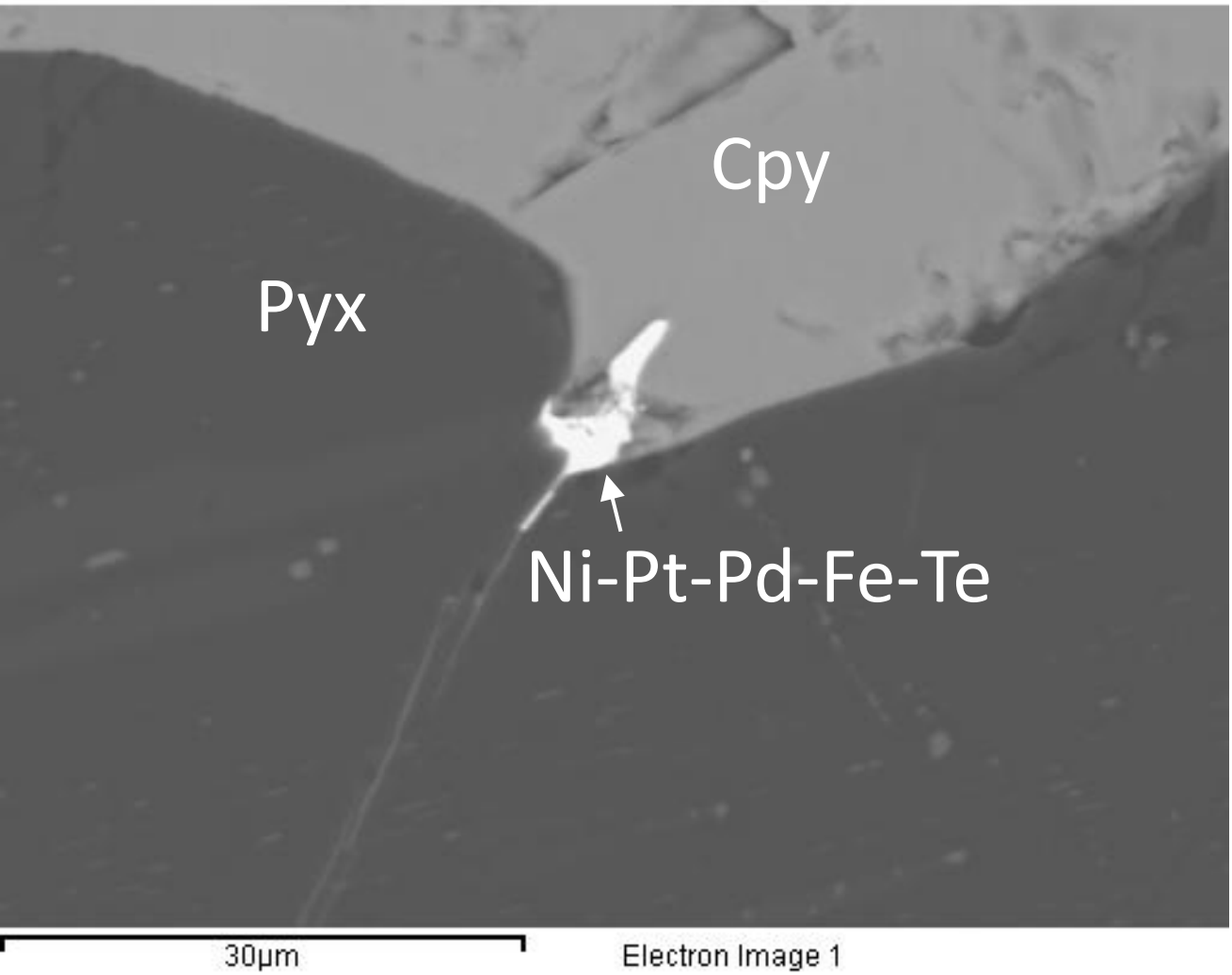
PTR07 E 1



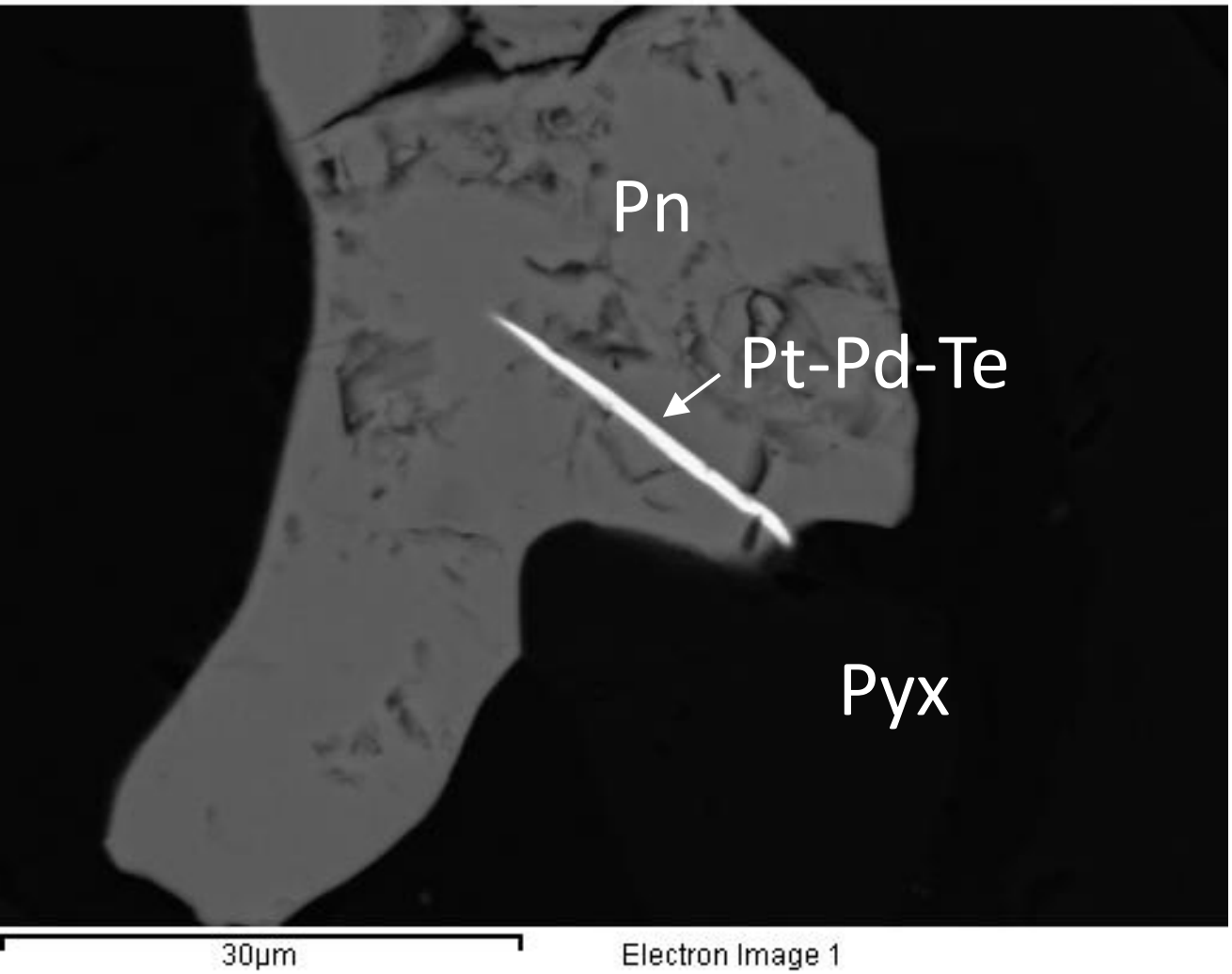
PTR07 F 1



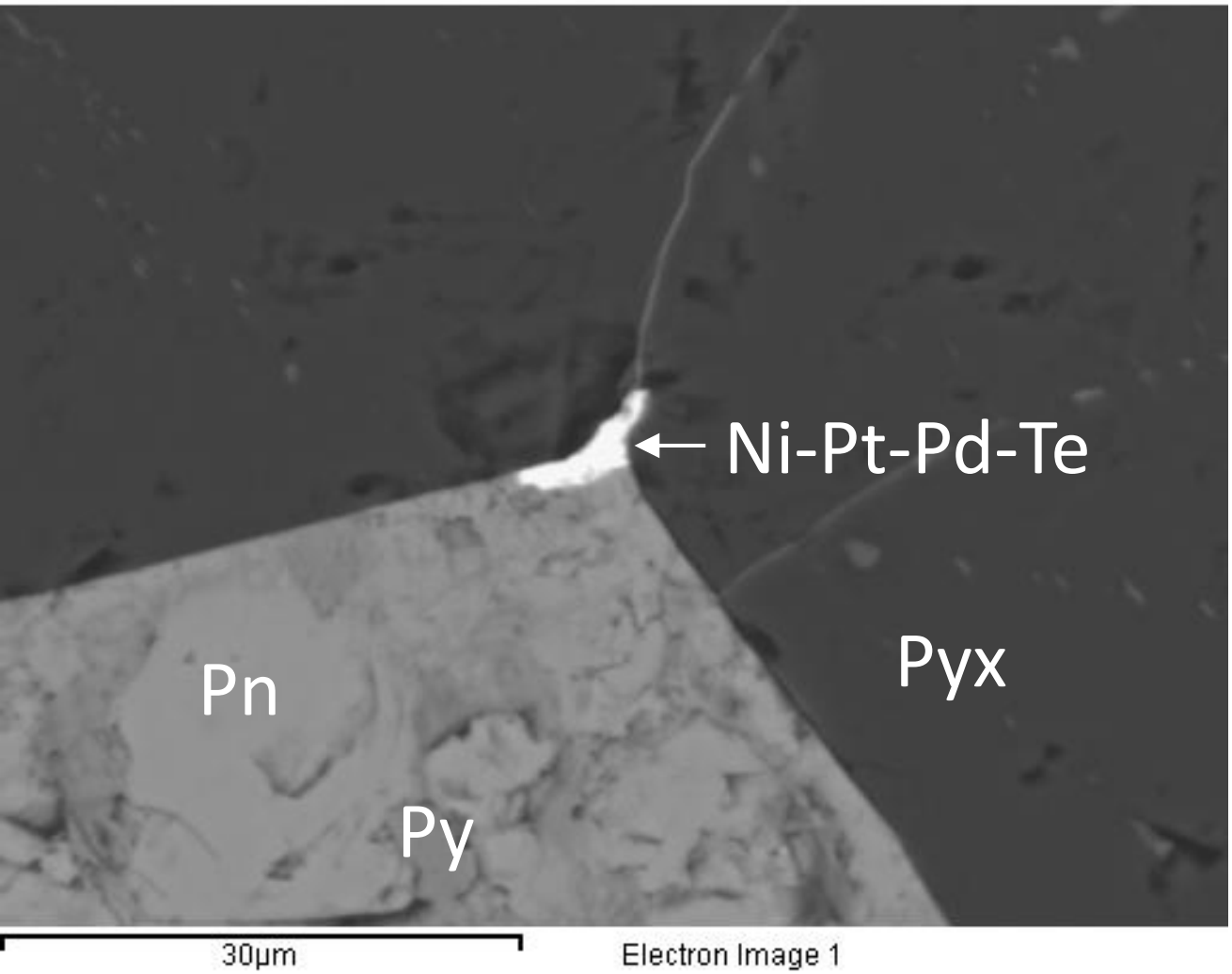
PTR07 G 1



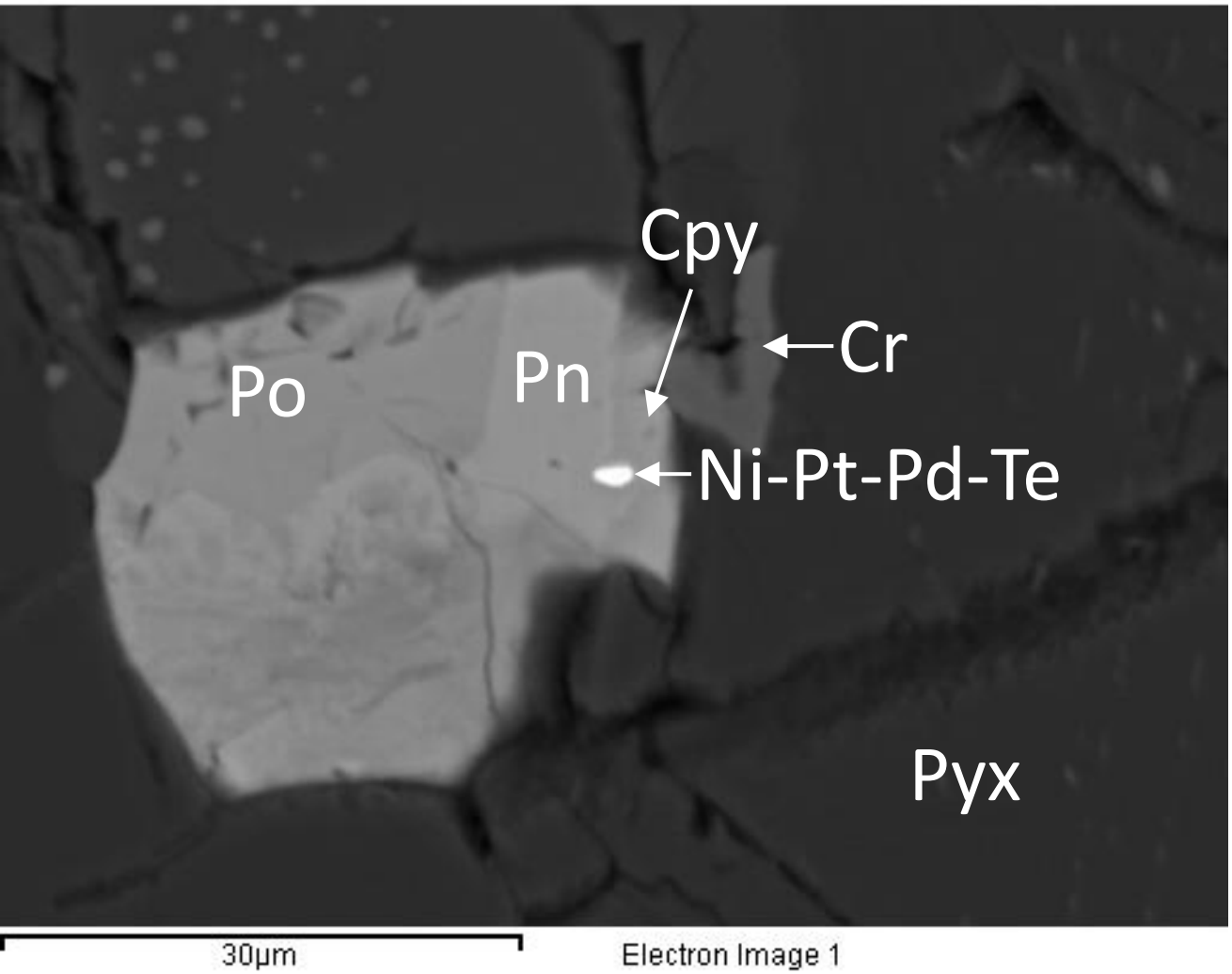
PTR07 H 1



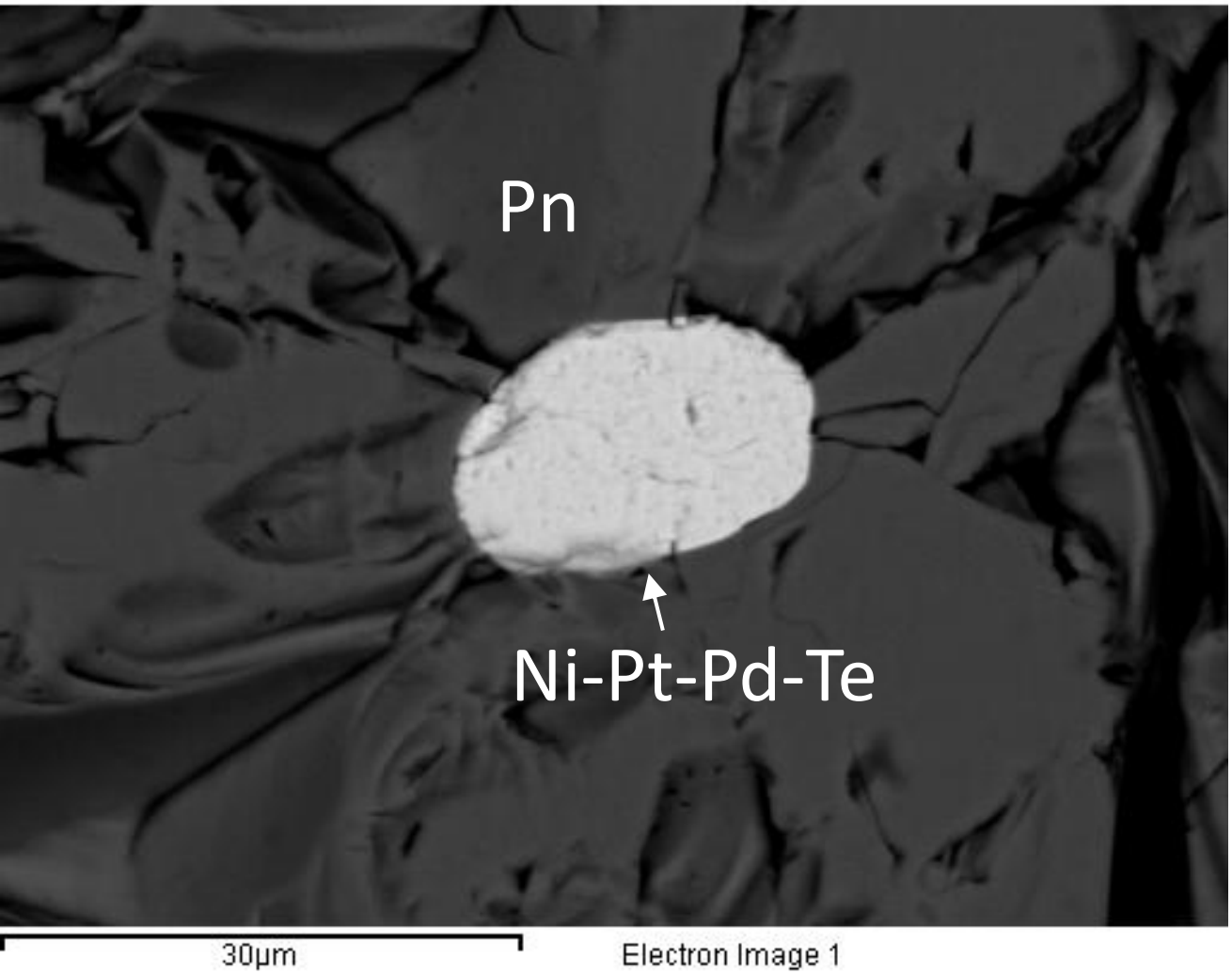
PTR07 I 1



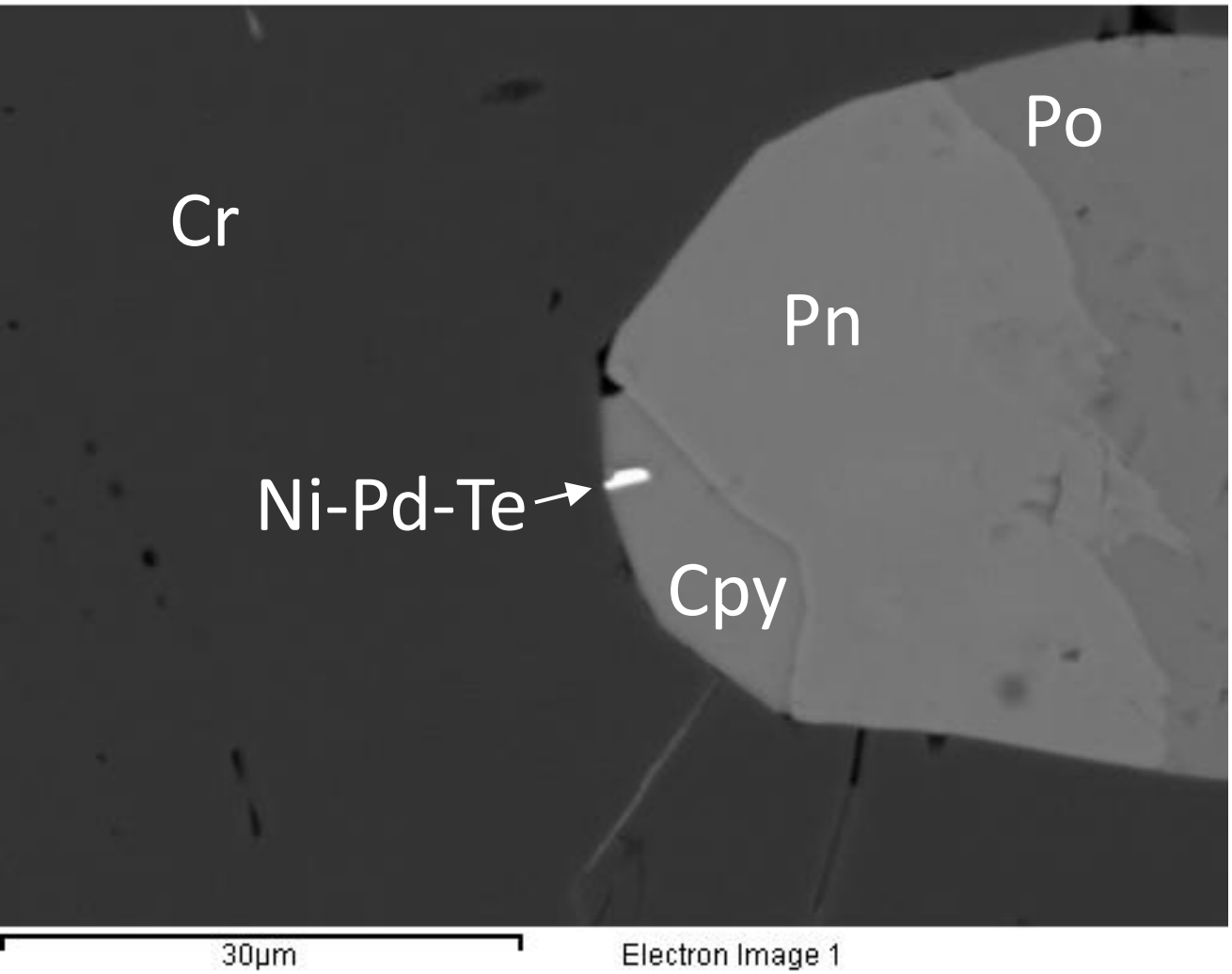
PTR07 J 1



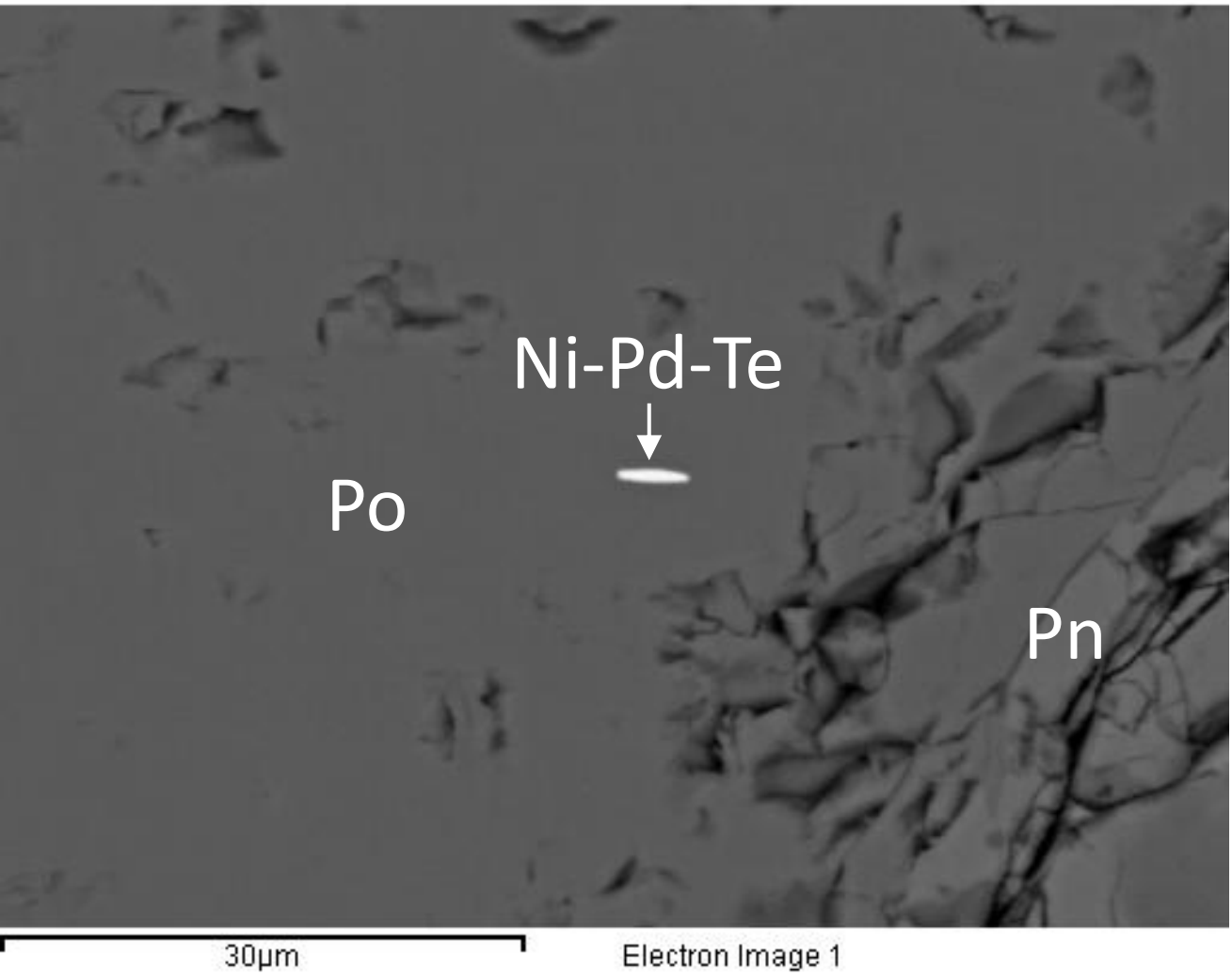
PTR07 K 1



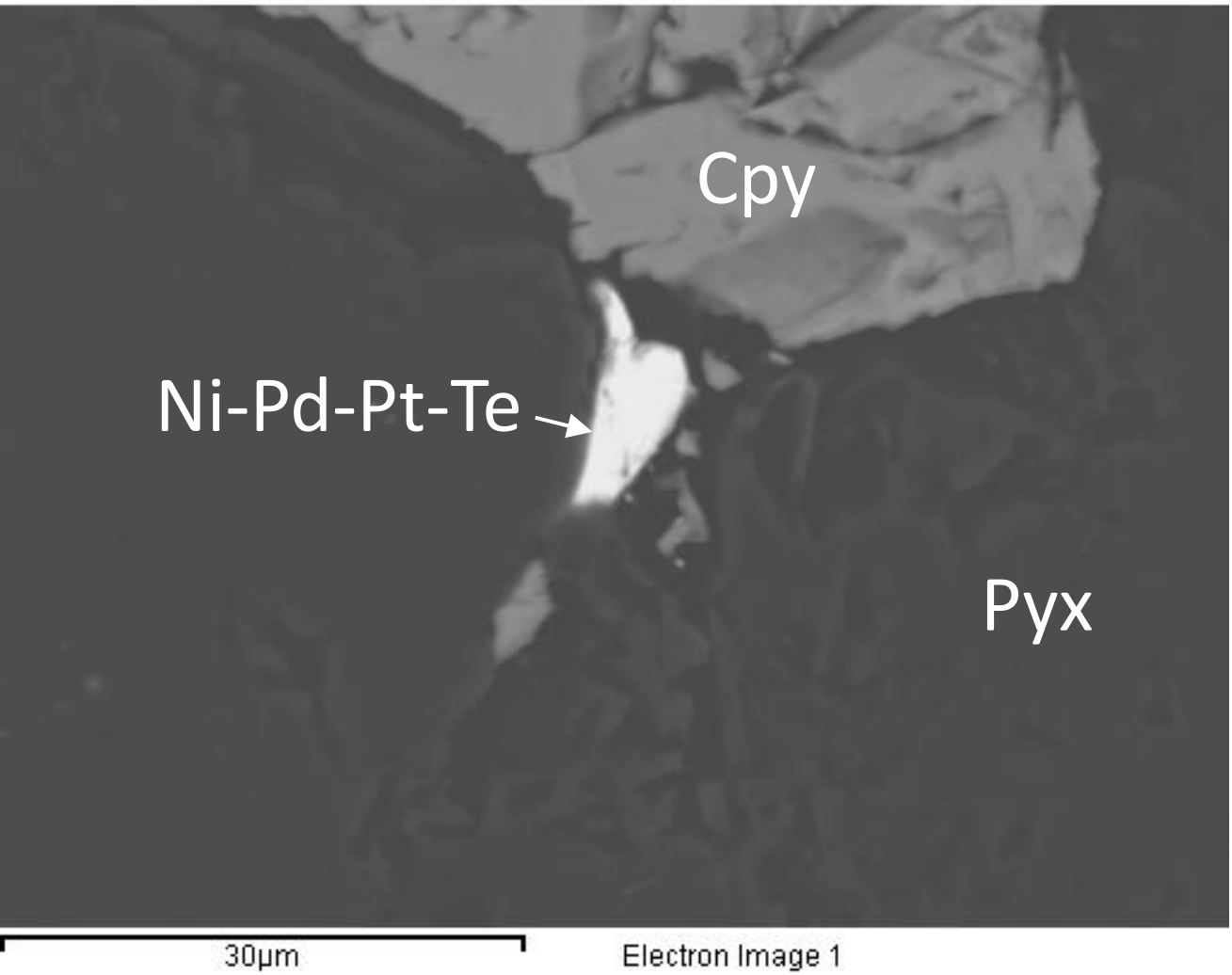
PTR07 L 1



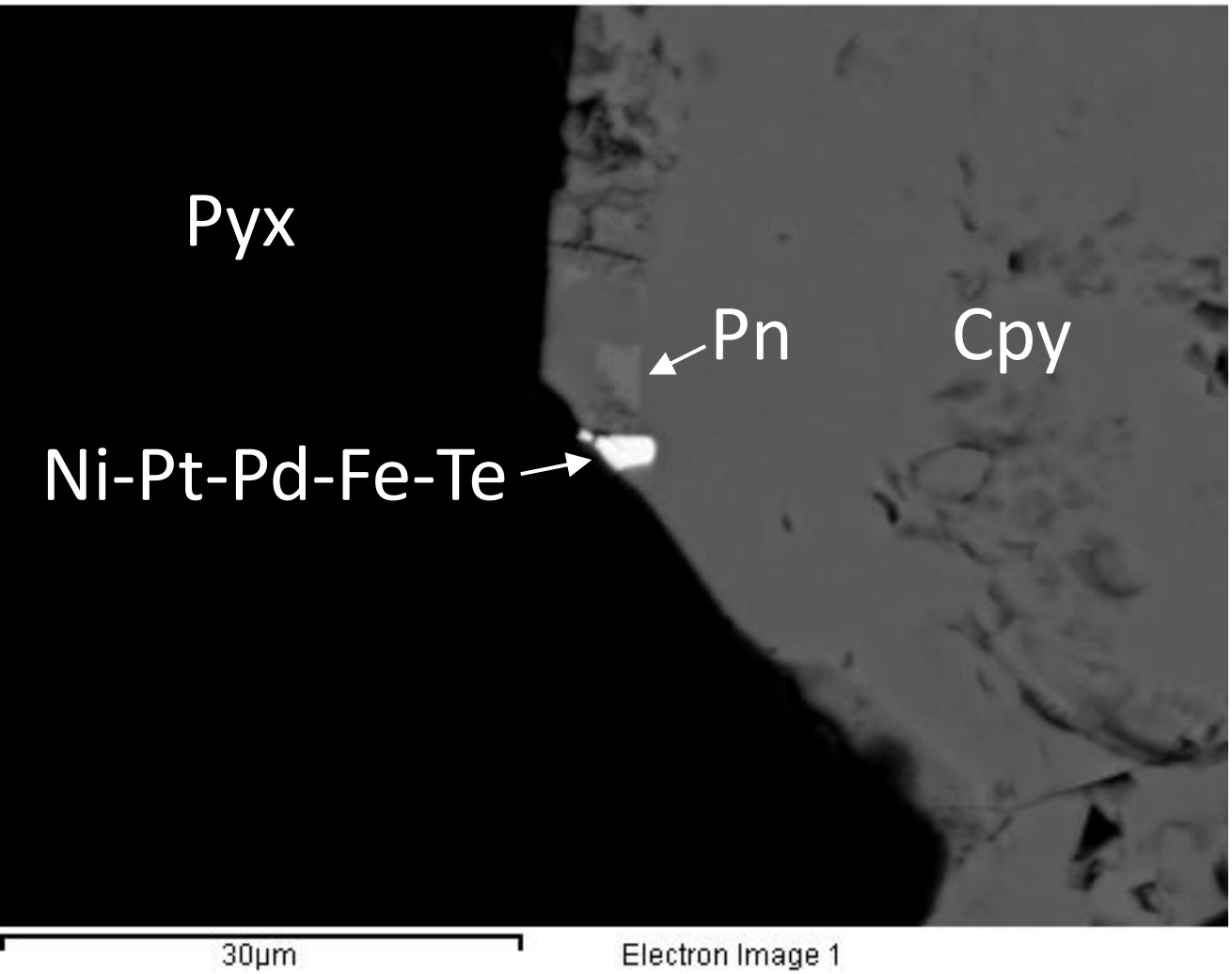
PTR07 M 1



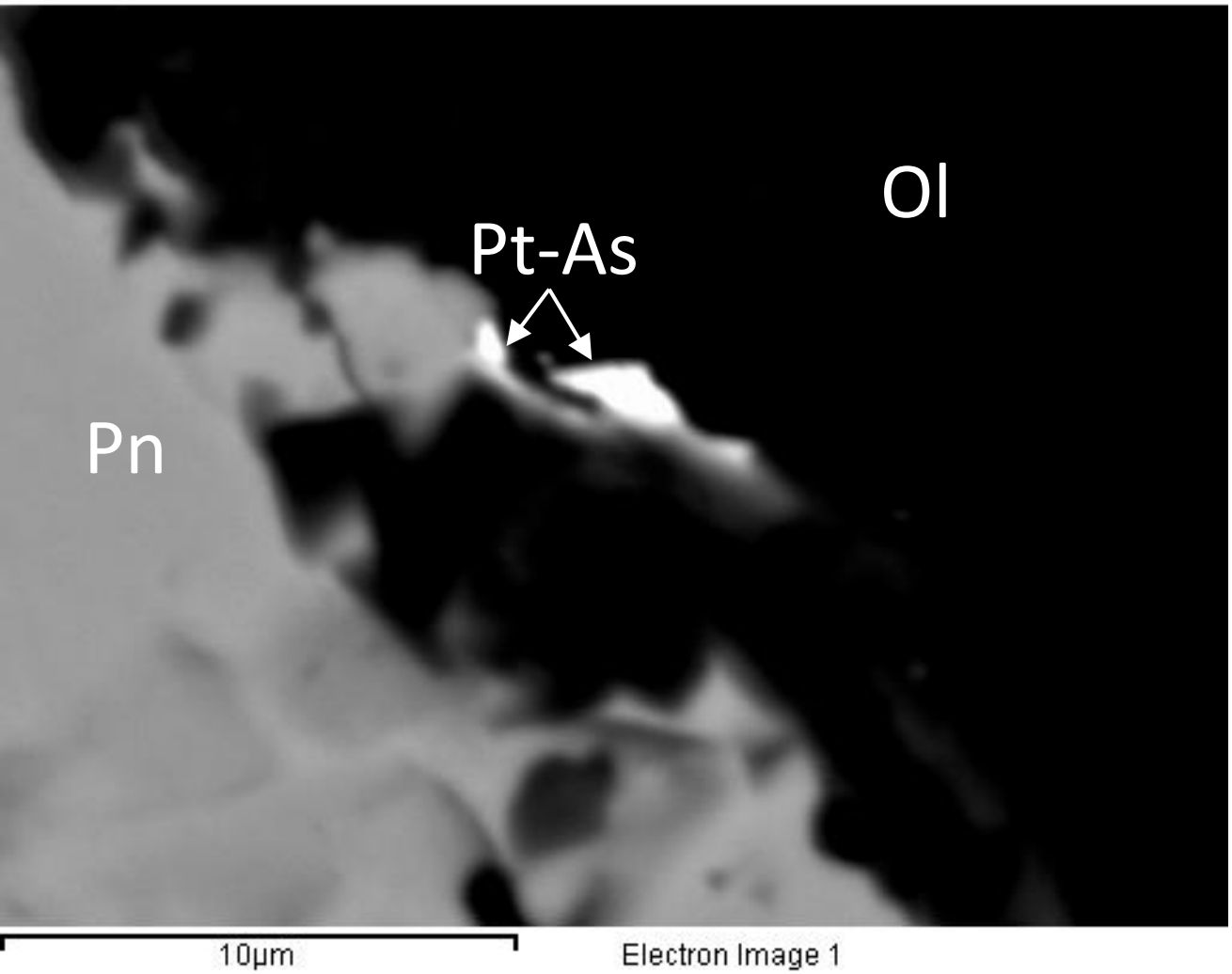
PTR07 N 1



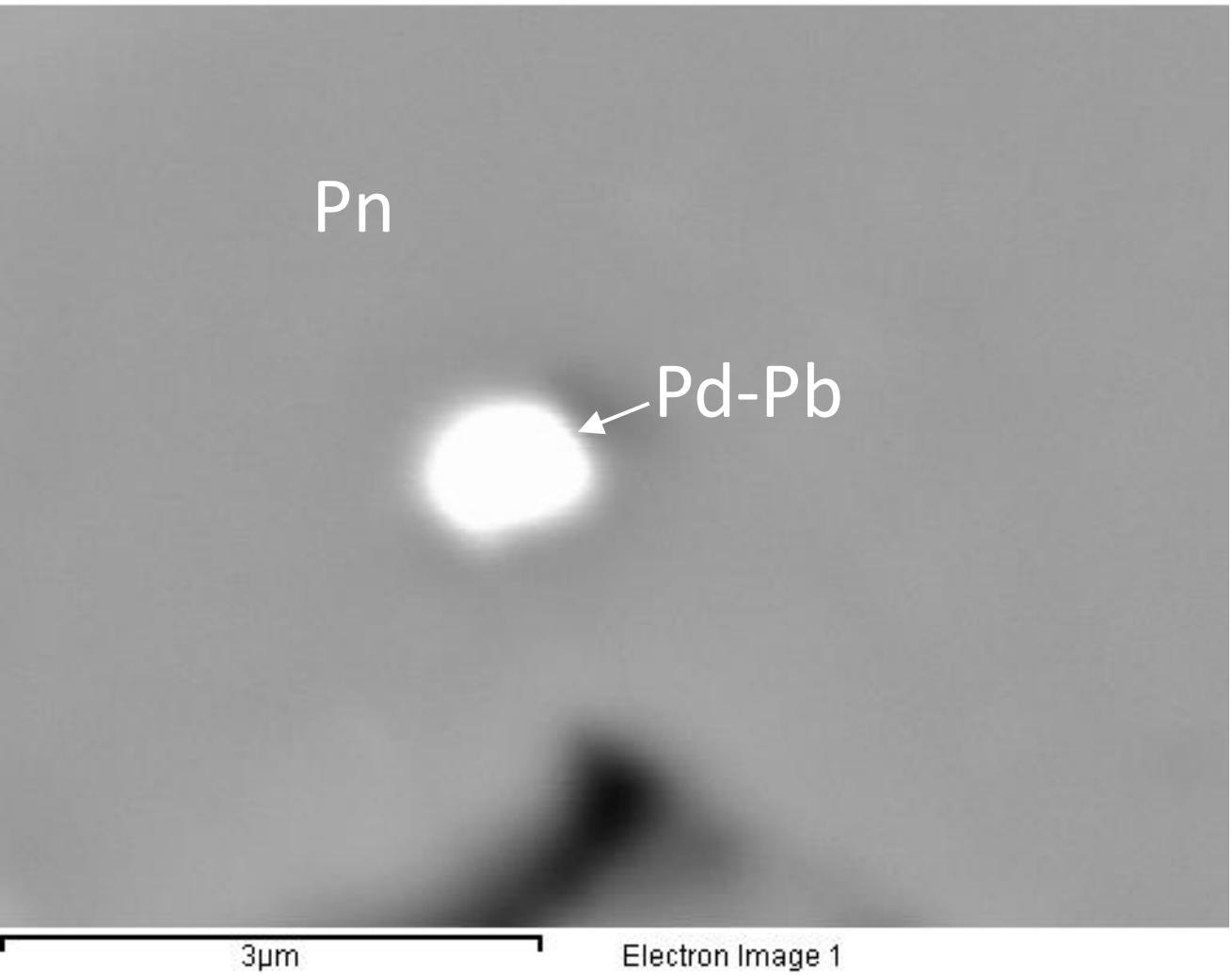
PTR07 O 1



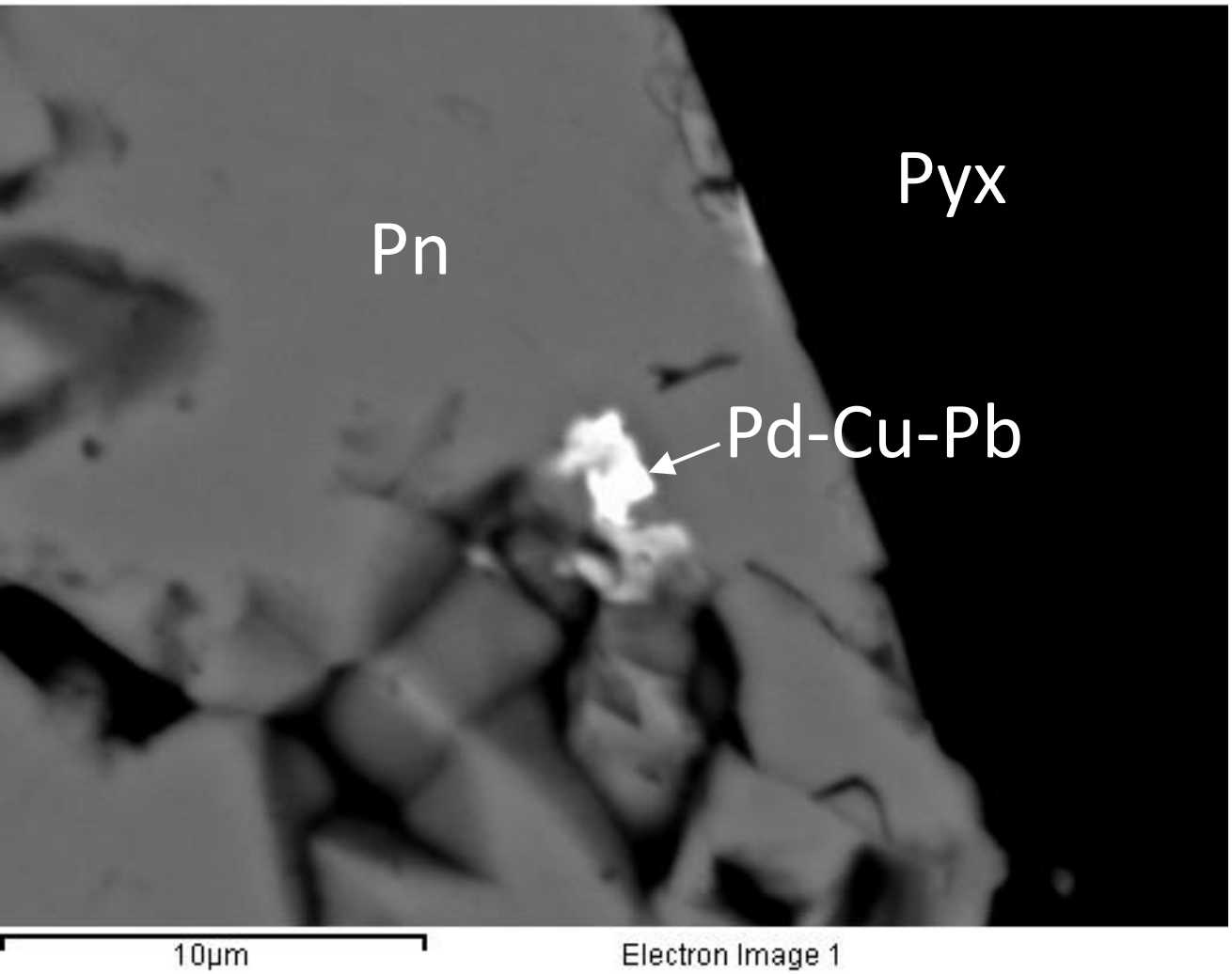
PTR08 A 1-2



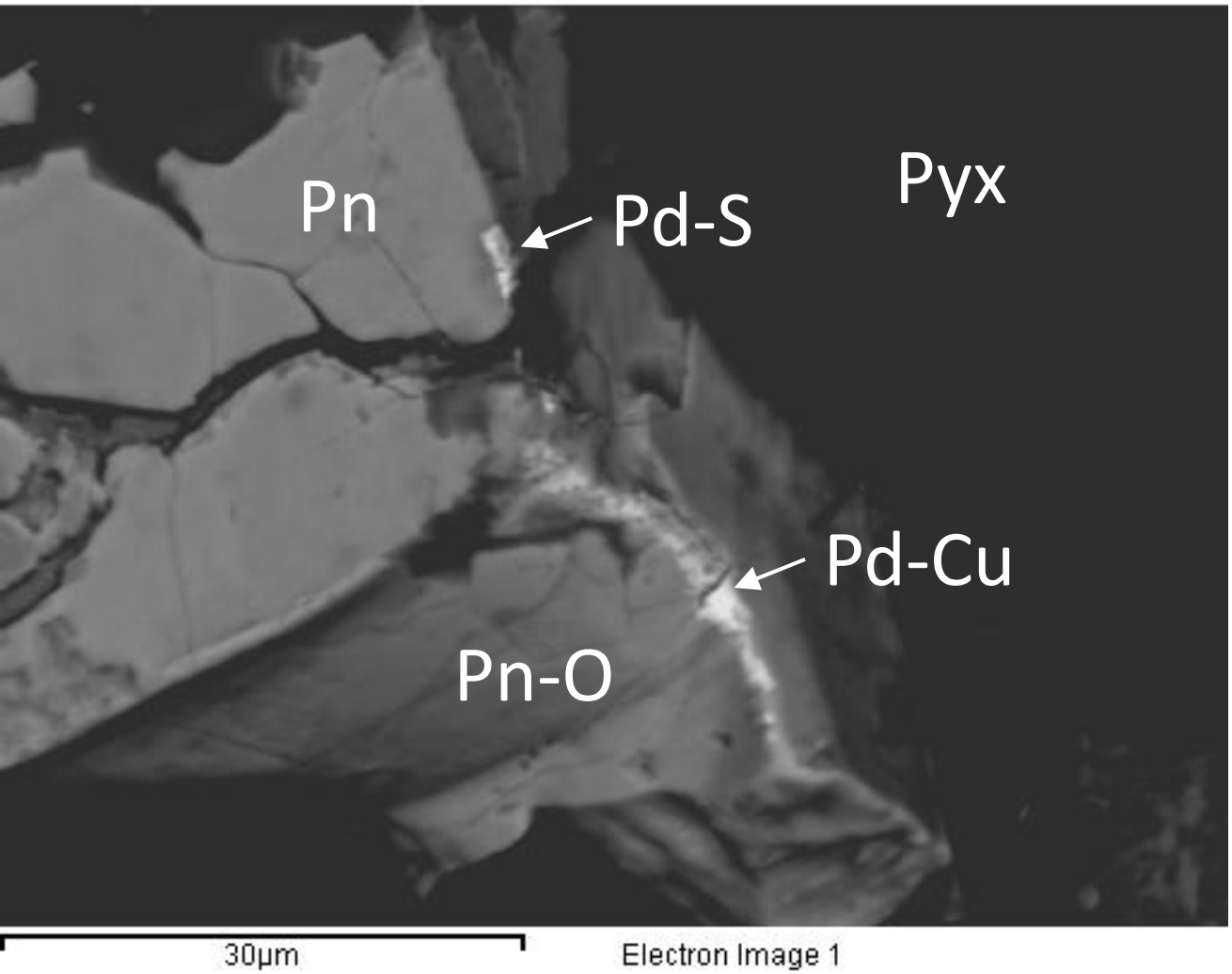
PTR08 A 3



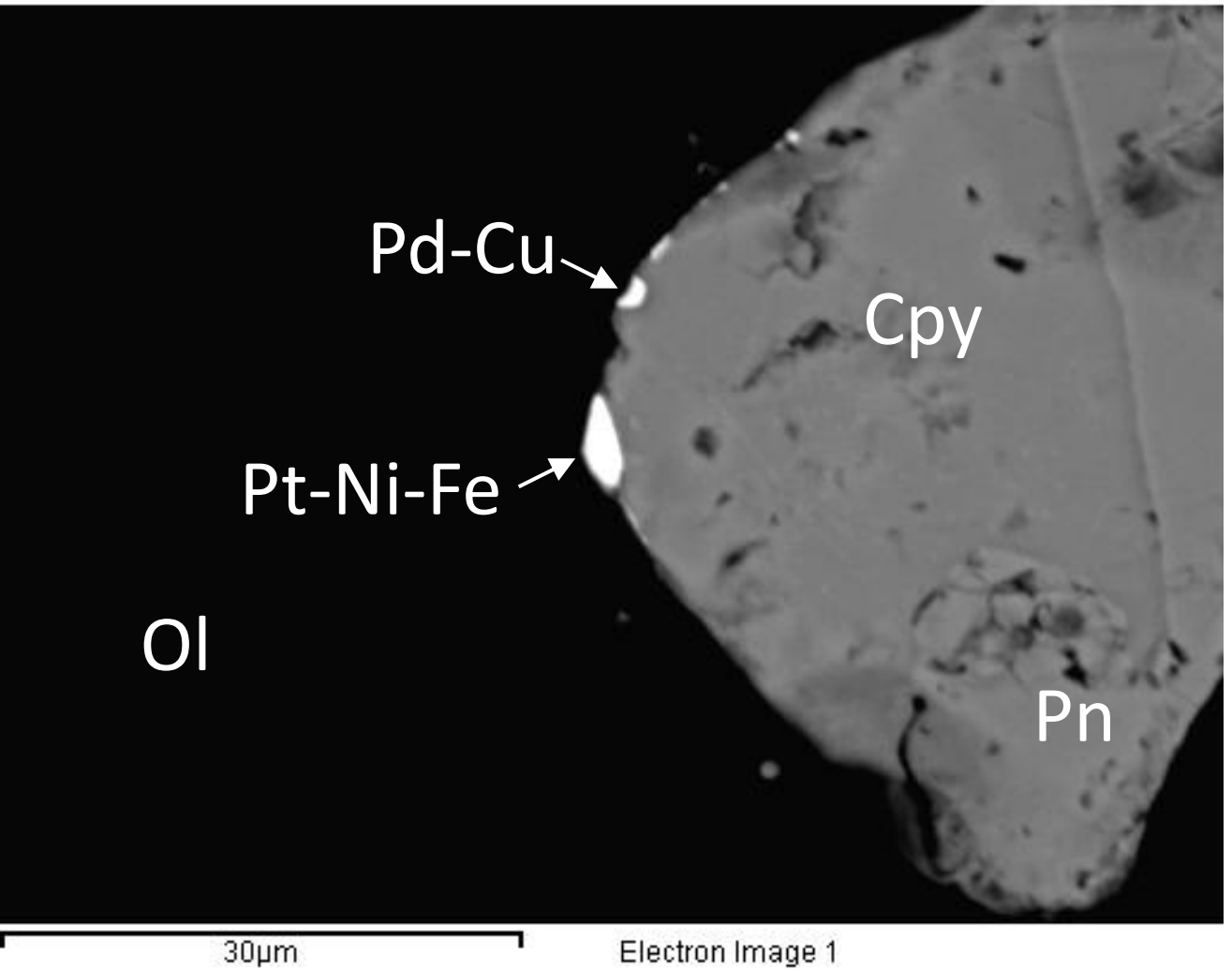
PTR08 B 1



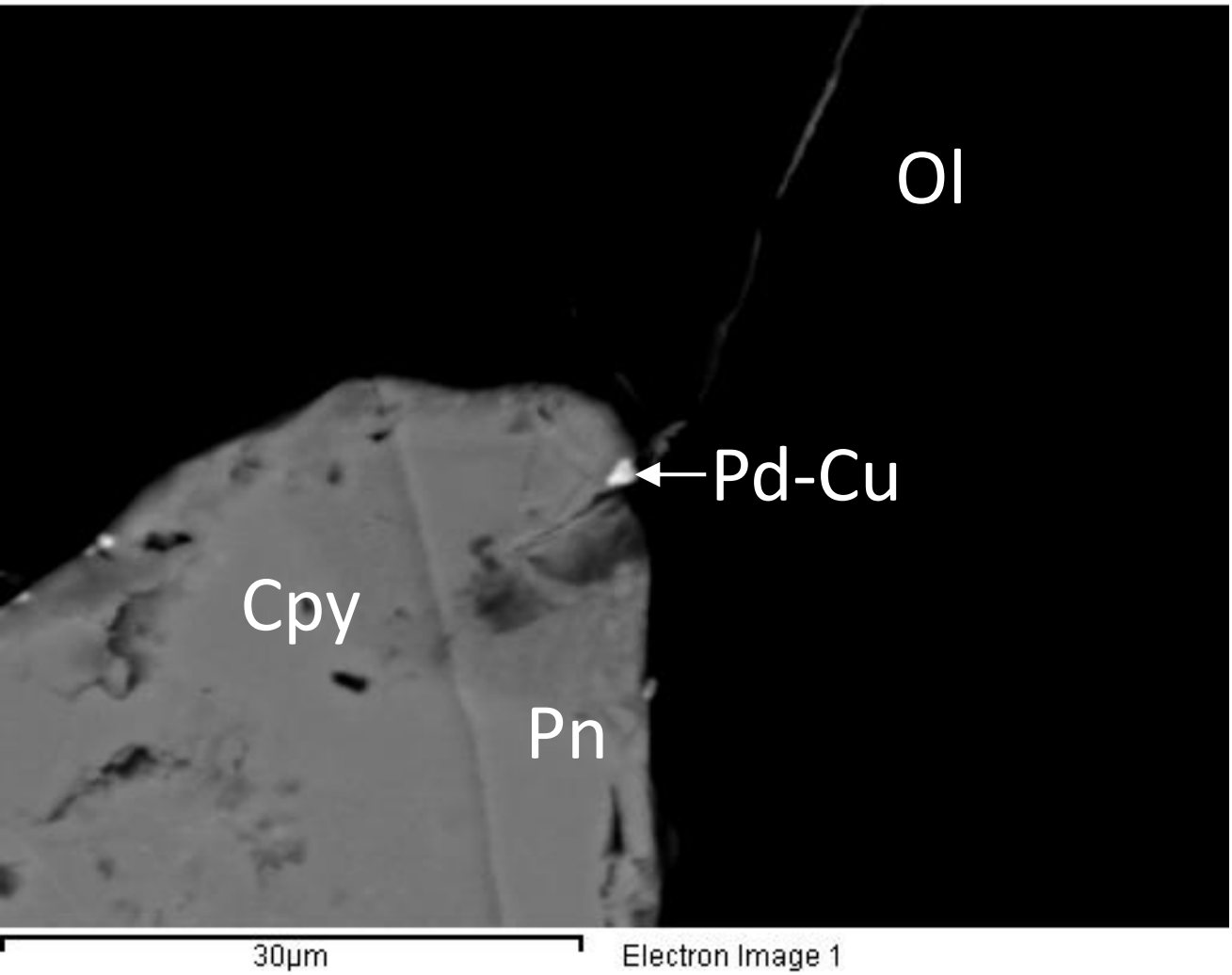
PTR08 C 1-2



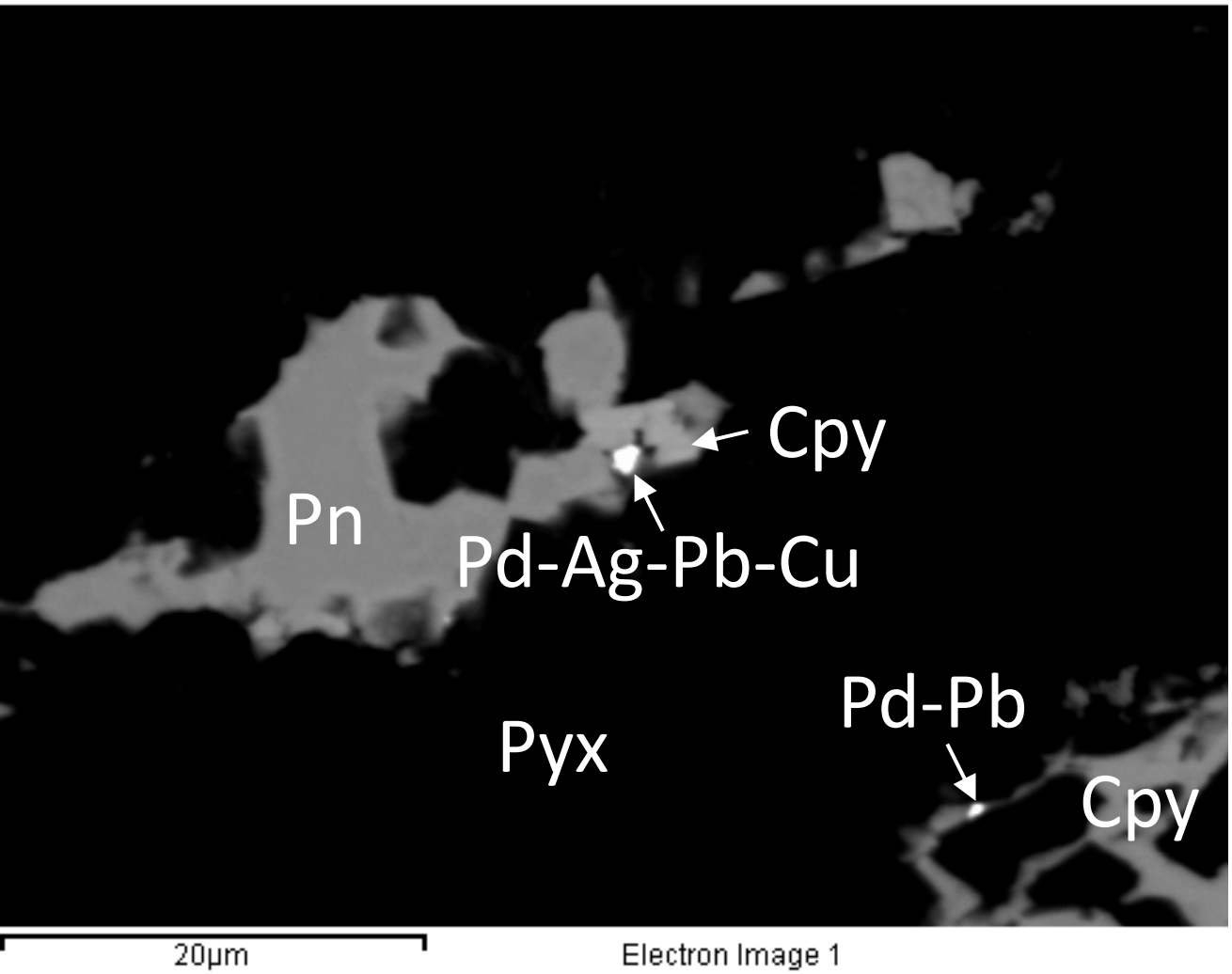
PTR08 D 1-2



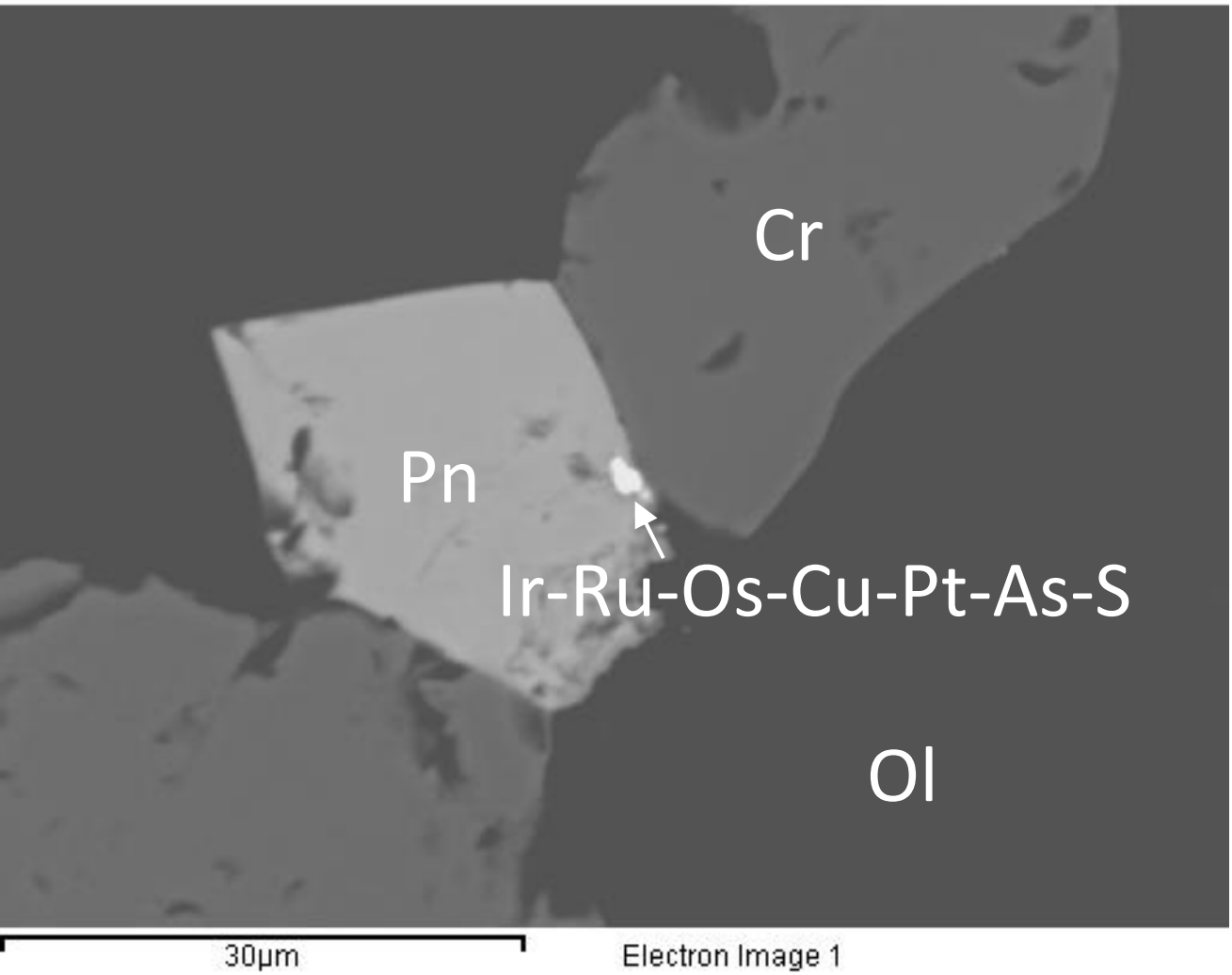
PTR08 D 3



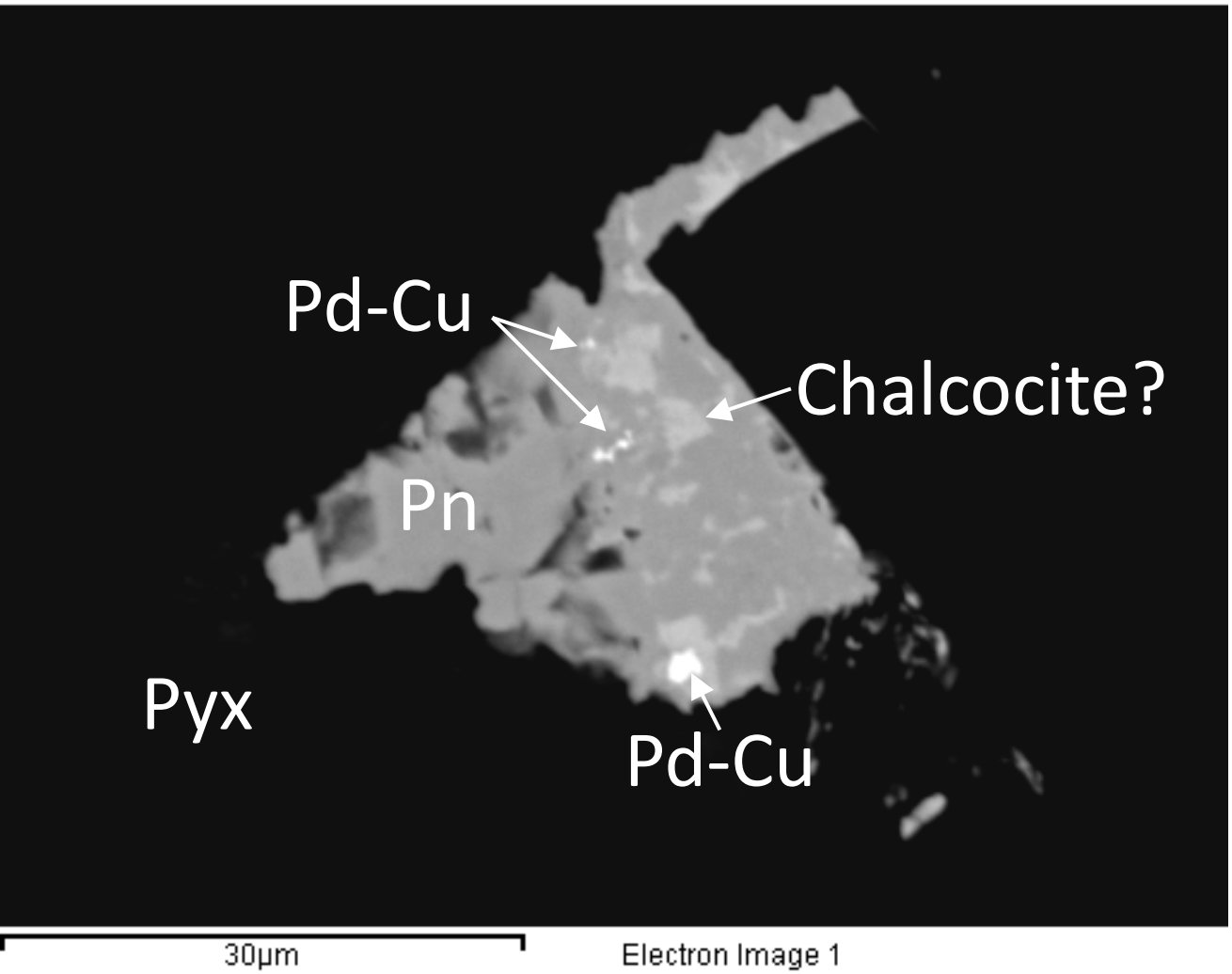
PTR08 E 1-2



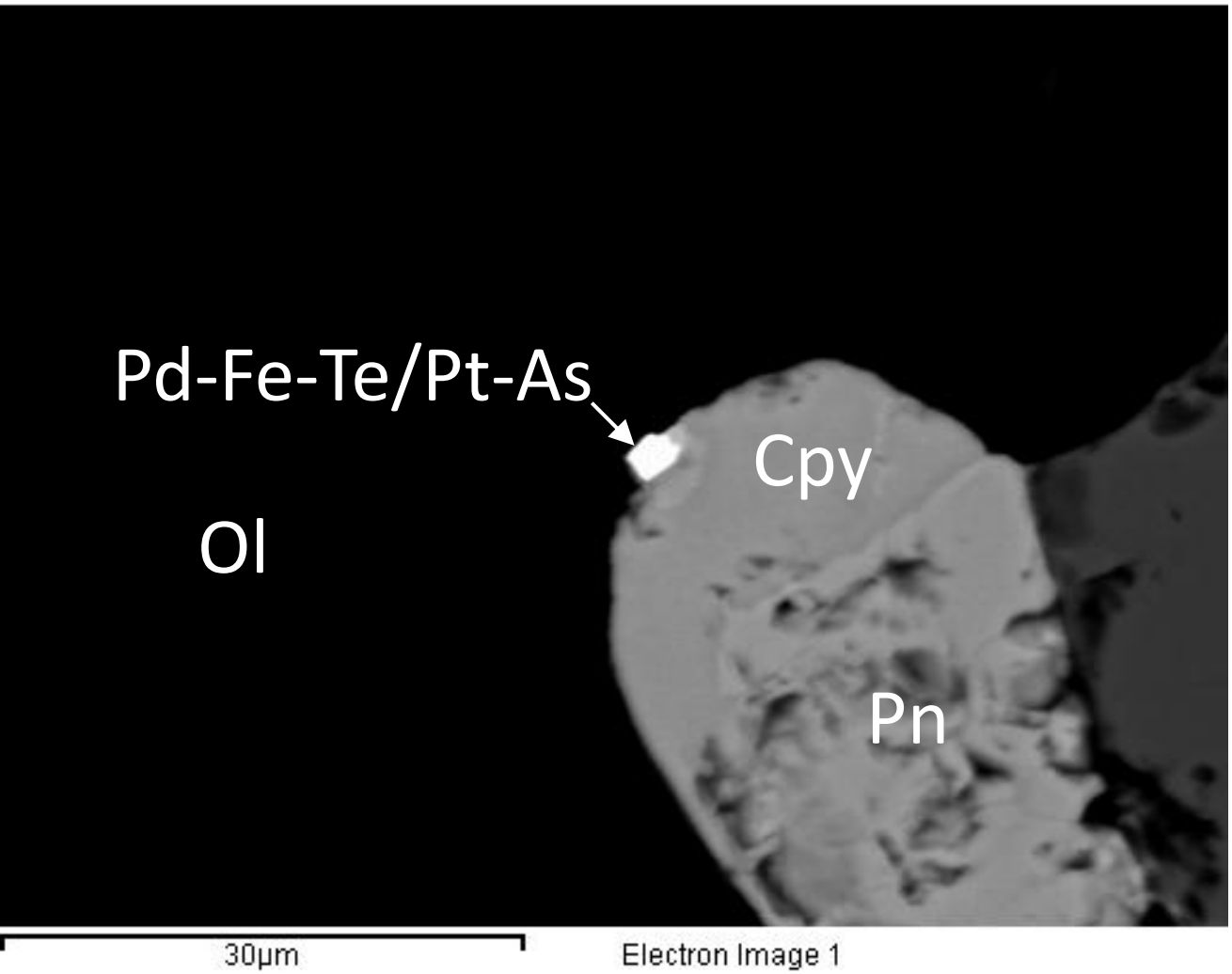
PTR08 F 1



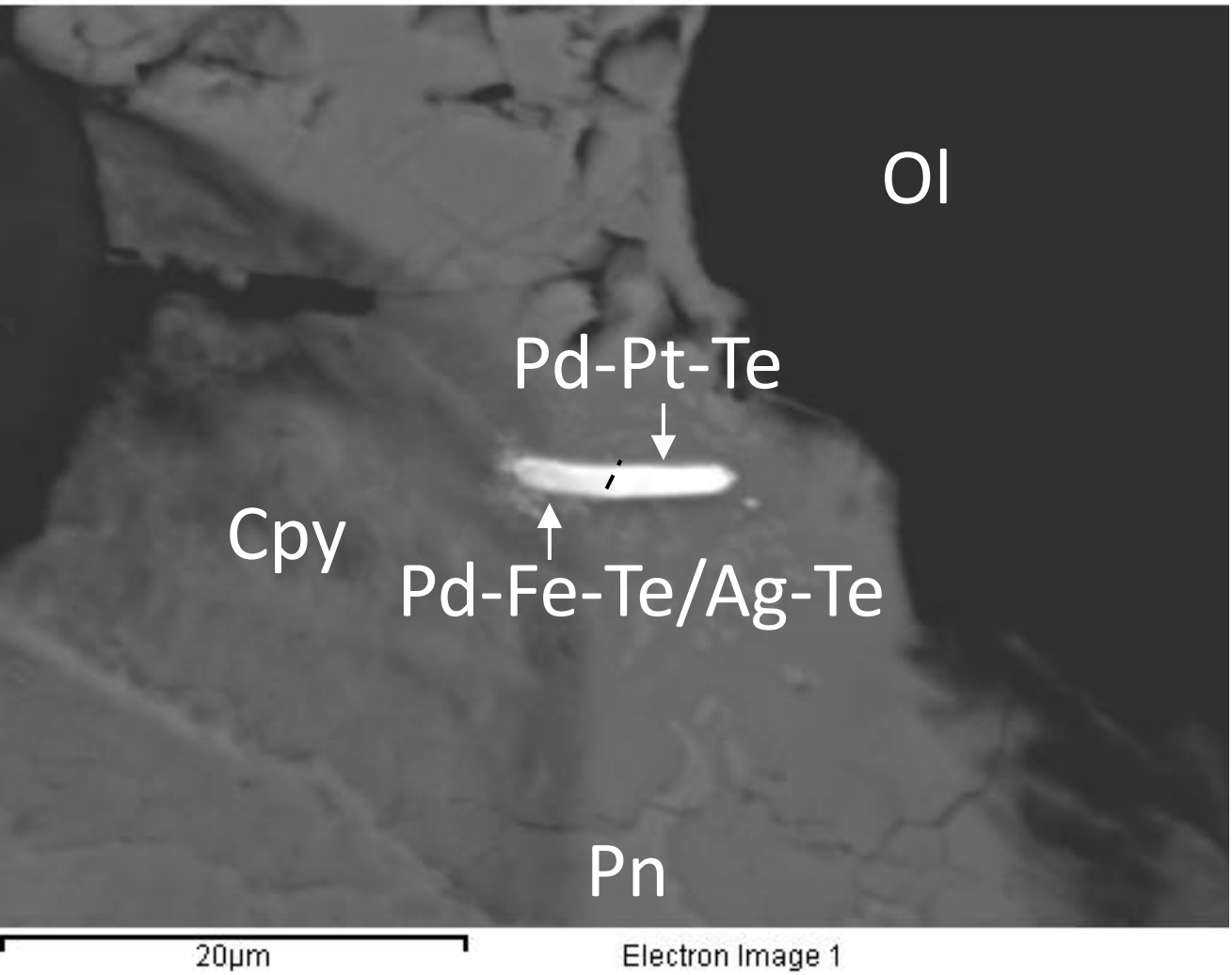
PTR08 G 1+



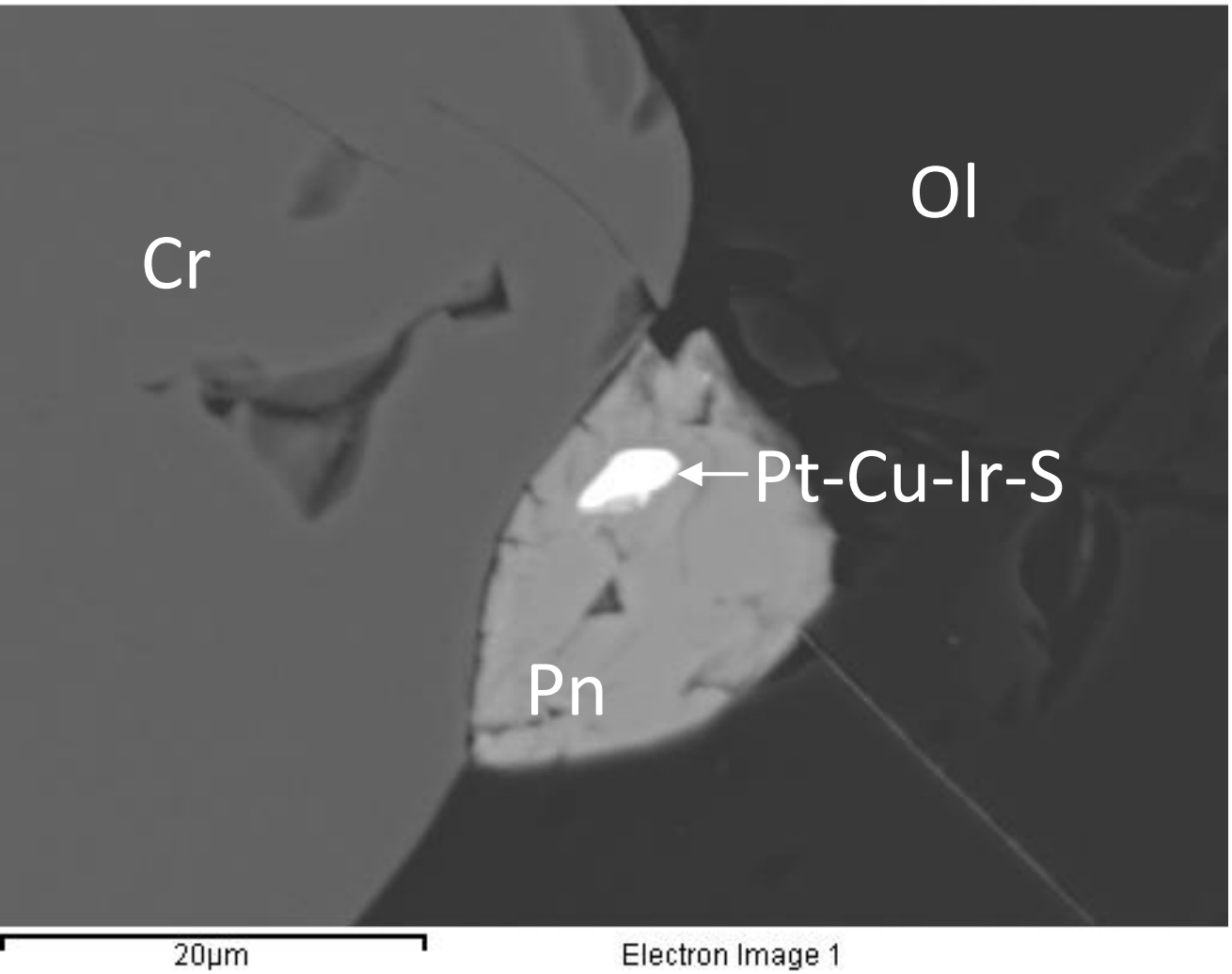
PTR08 H 1



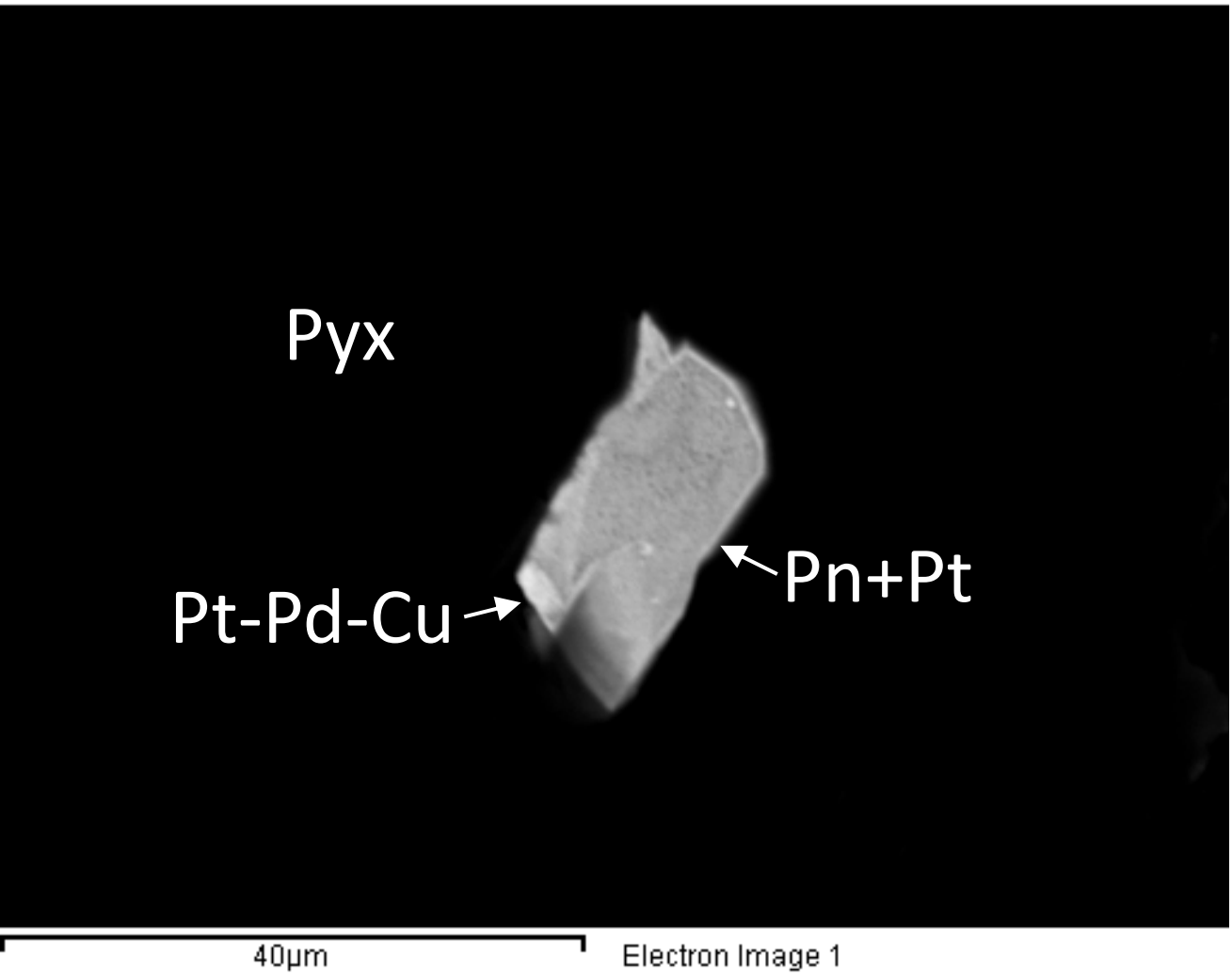
PTR09 A 1-2



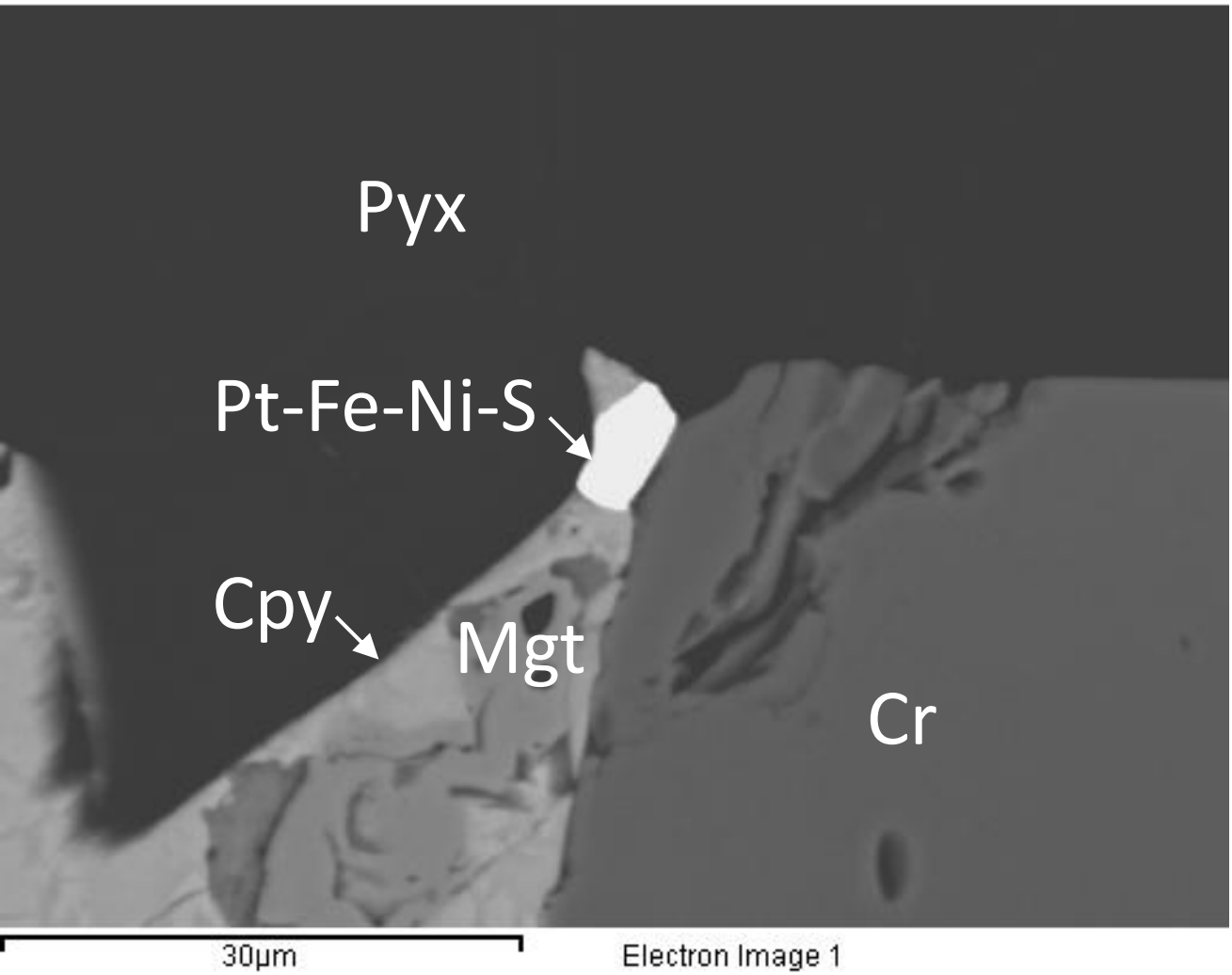
PTR09 B 1



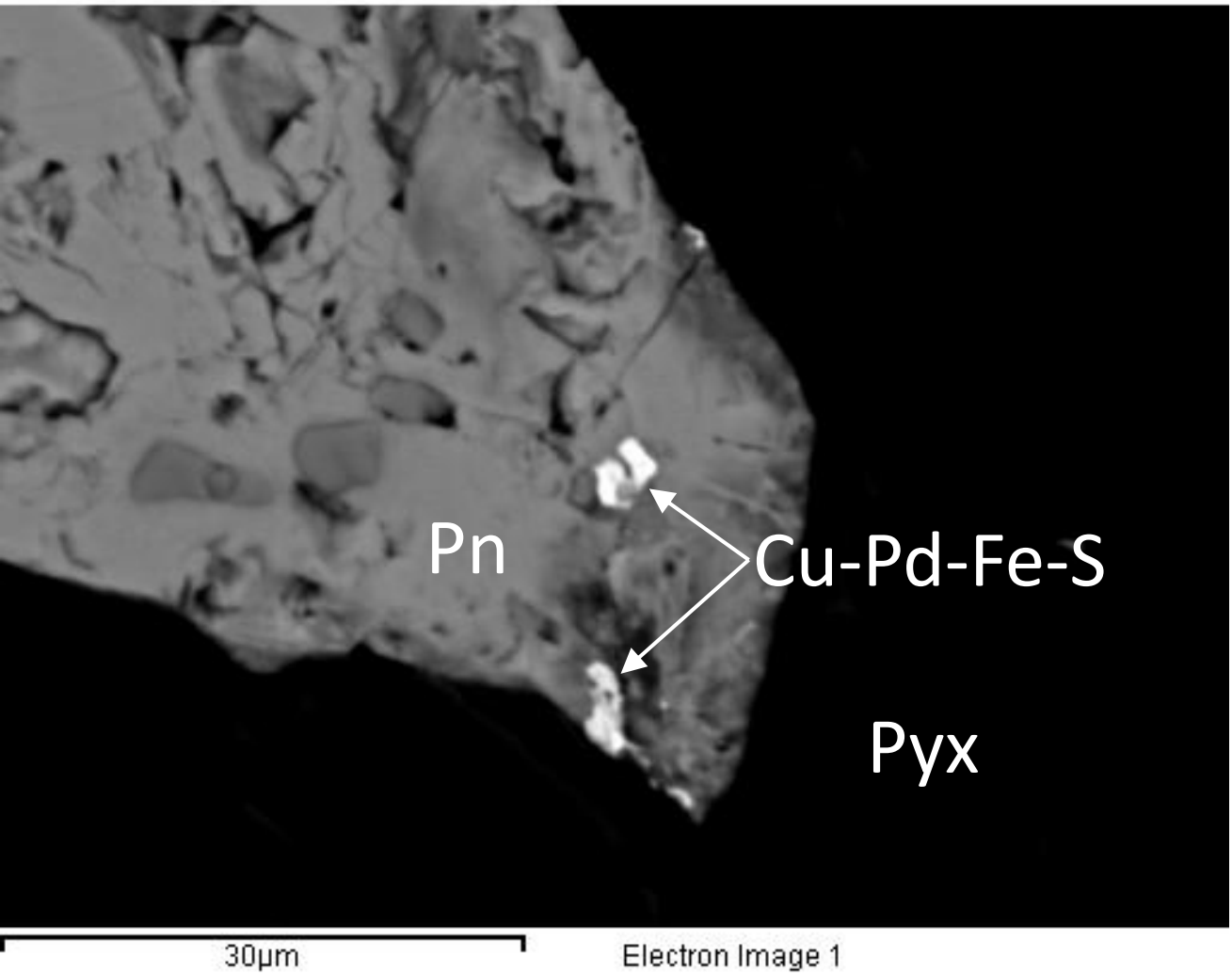
PTR09 C 1



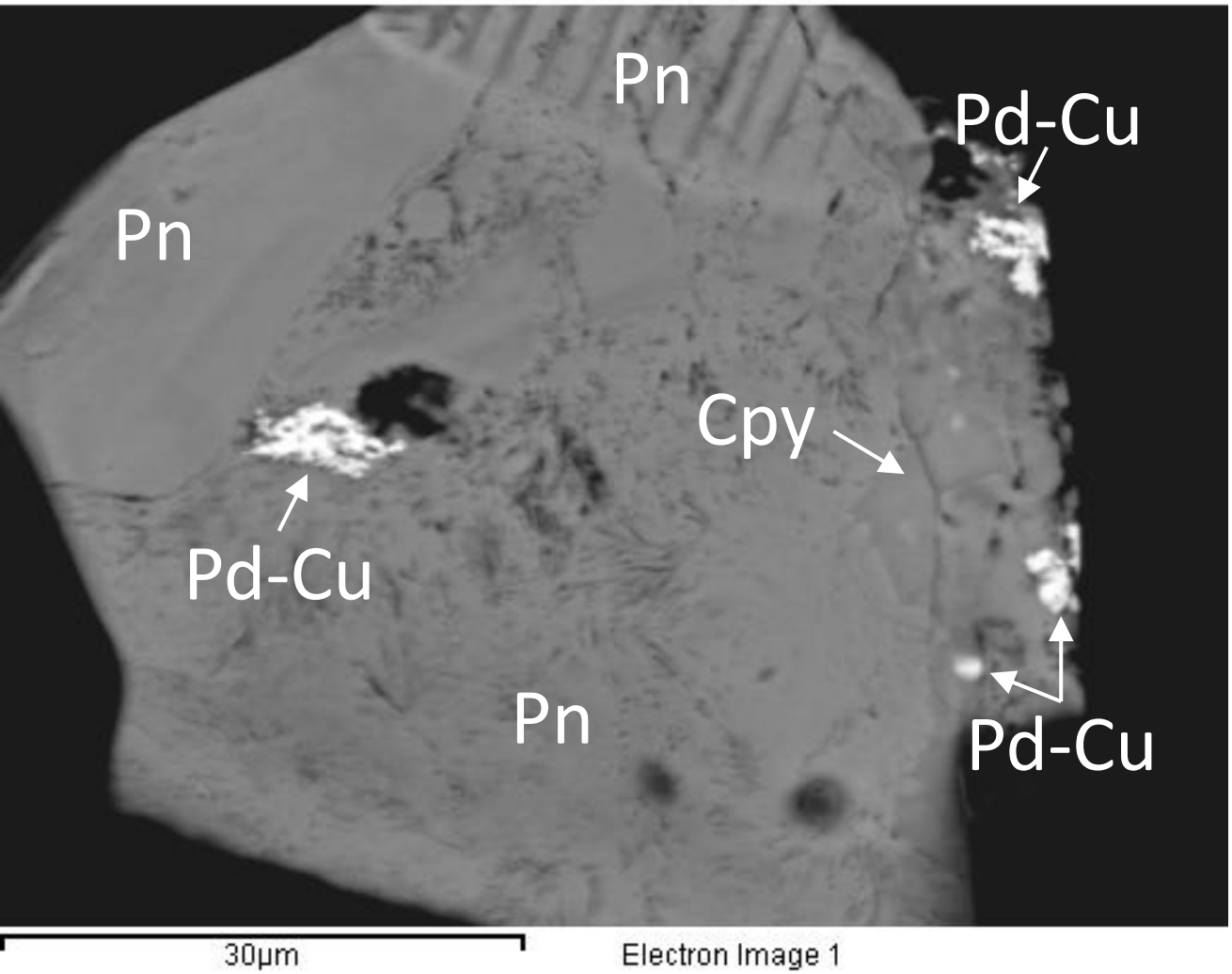
PTR11 A 1



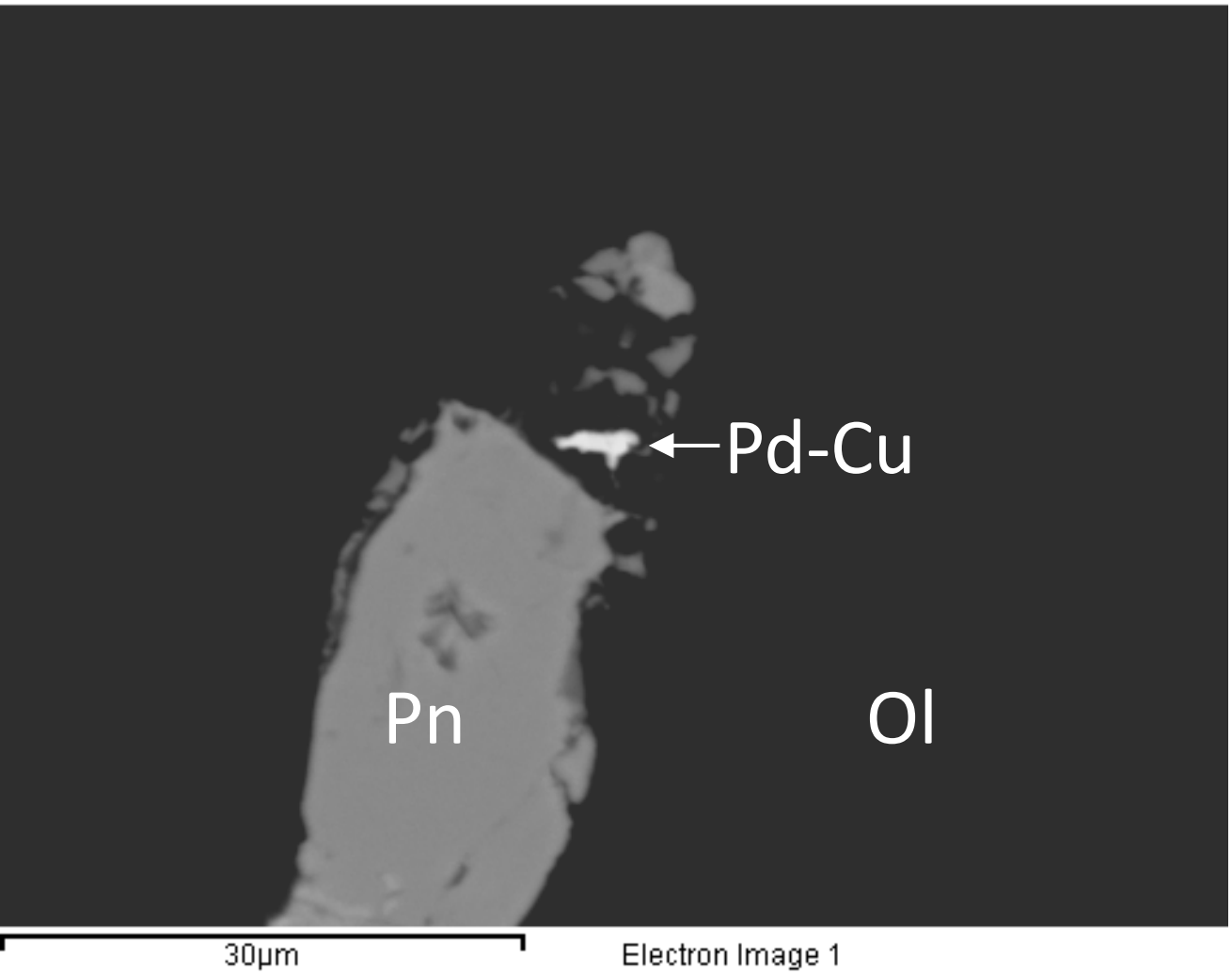
PTR11 B 1-3



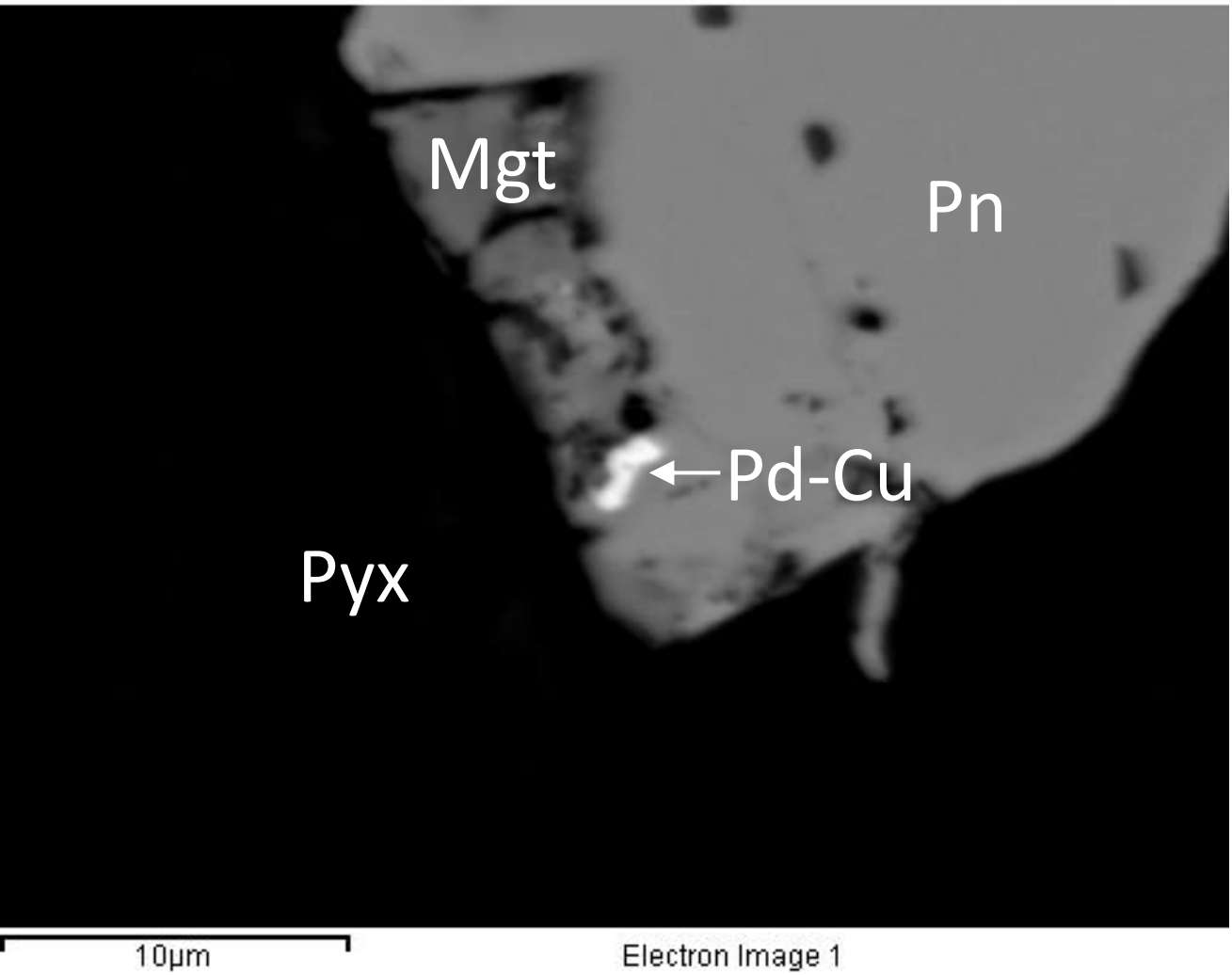
PTR11 C 1-4



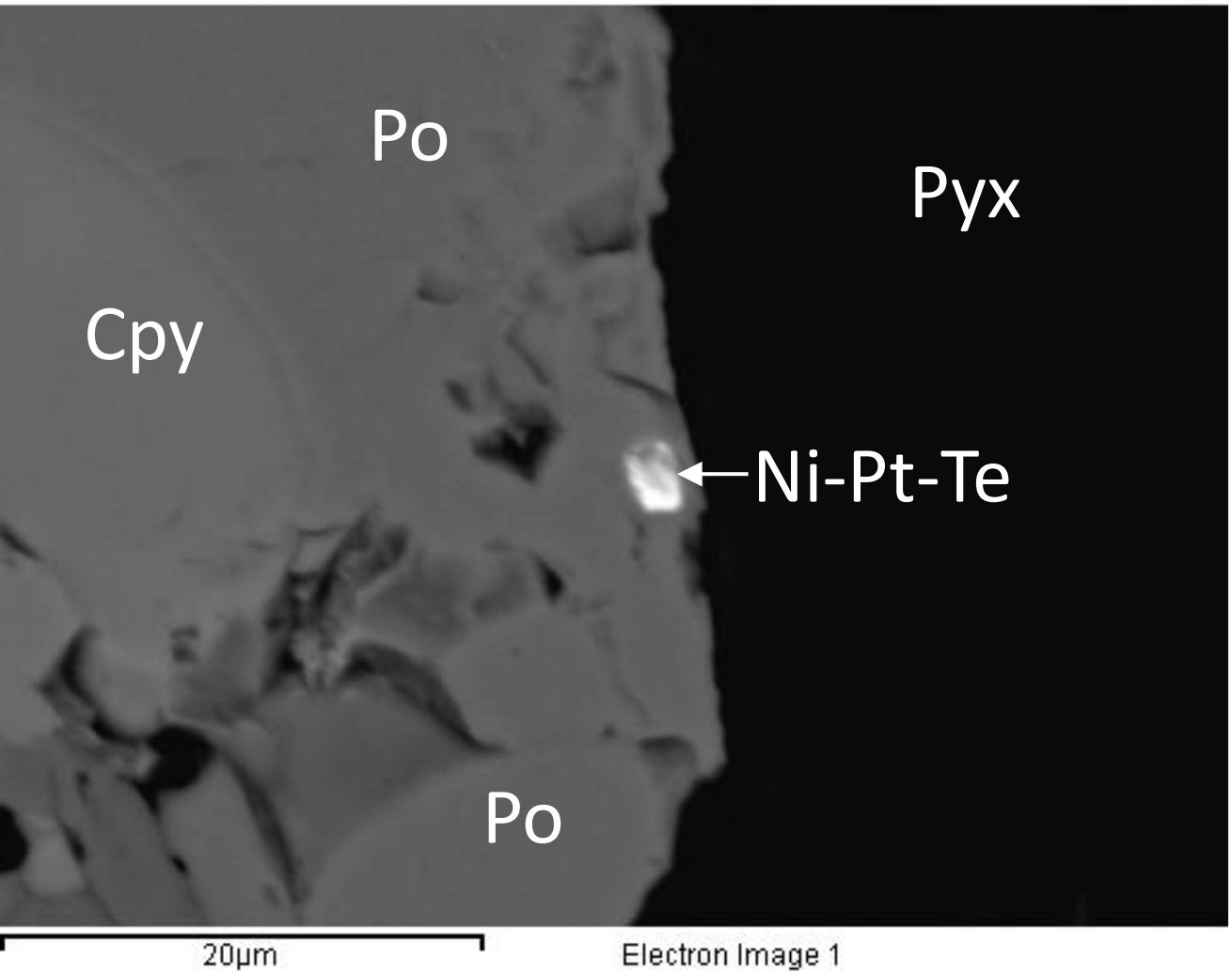
PTR11 D 1



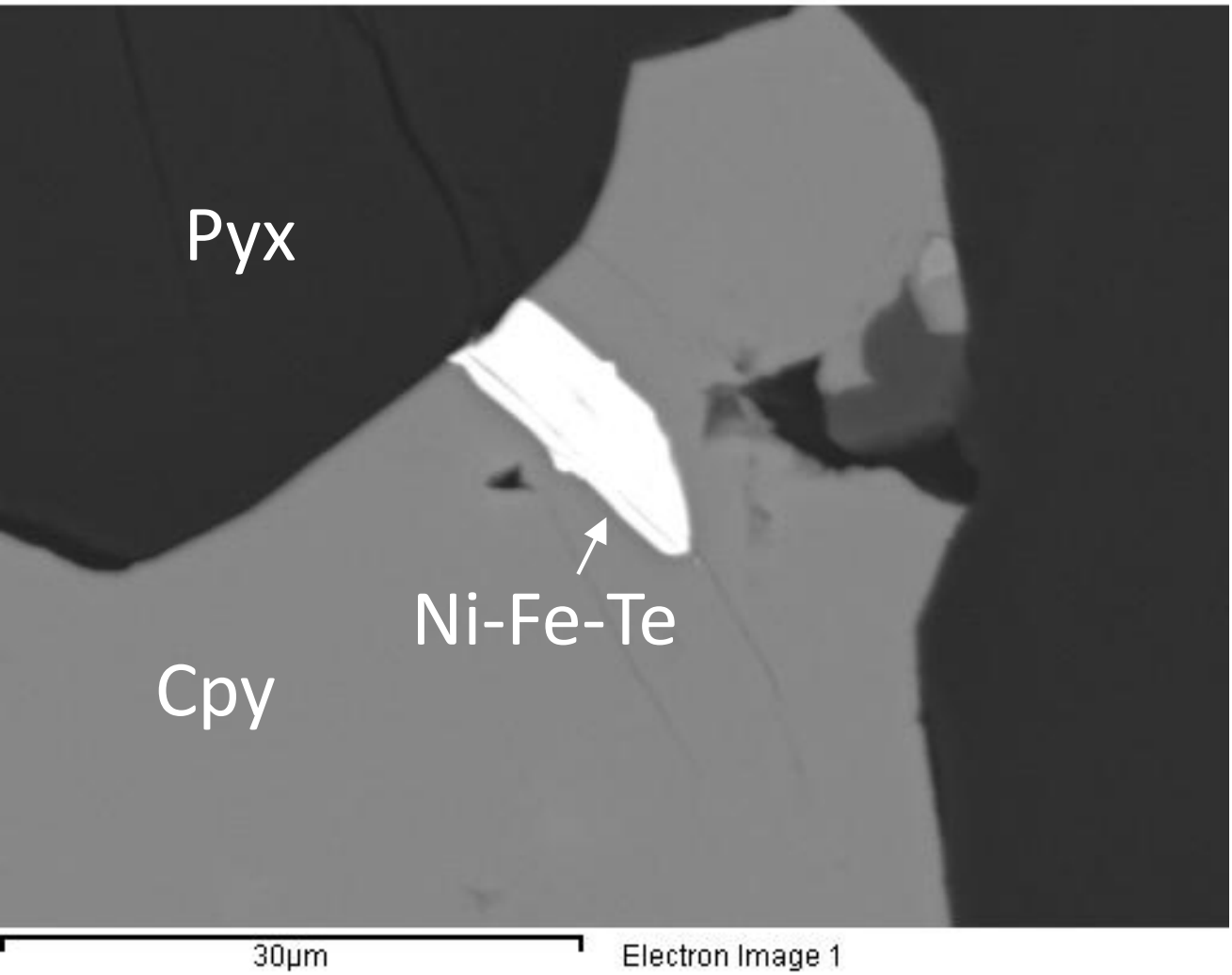
PTR11 E 1



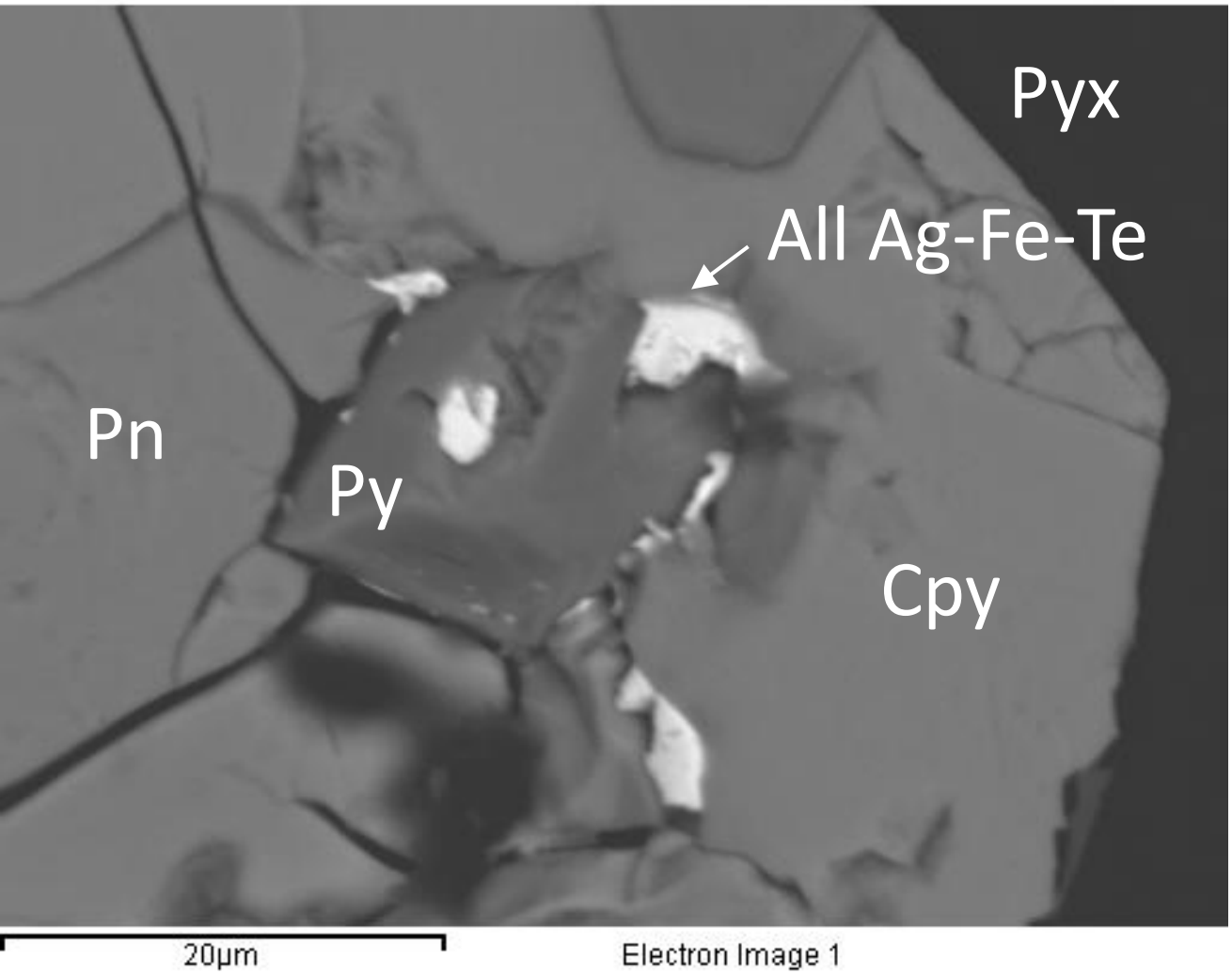
PTR16 A 1



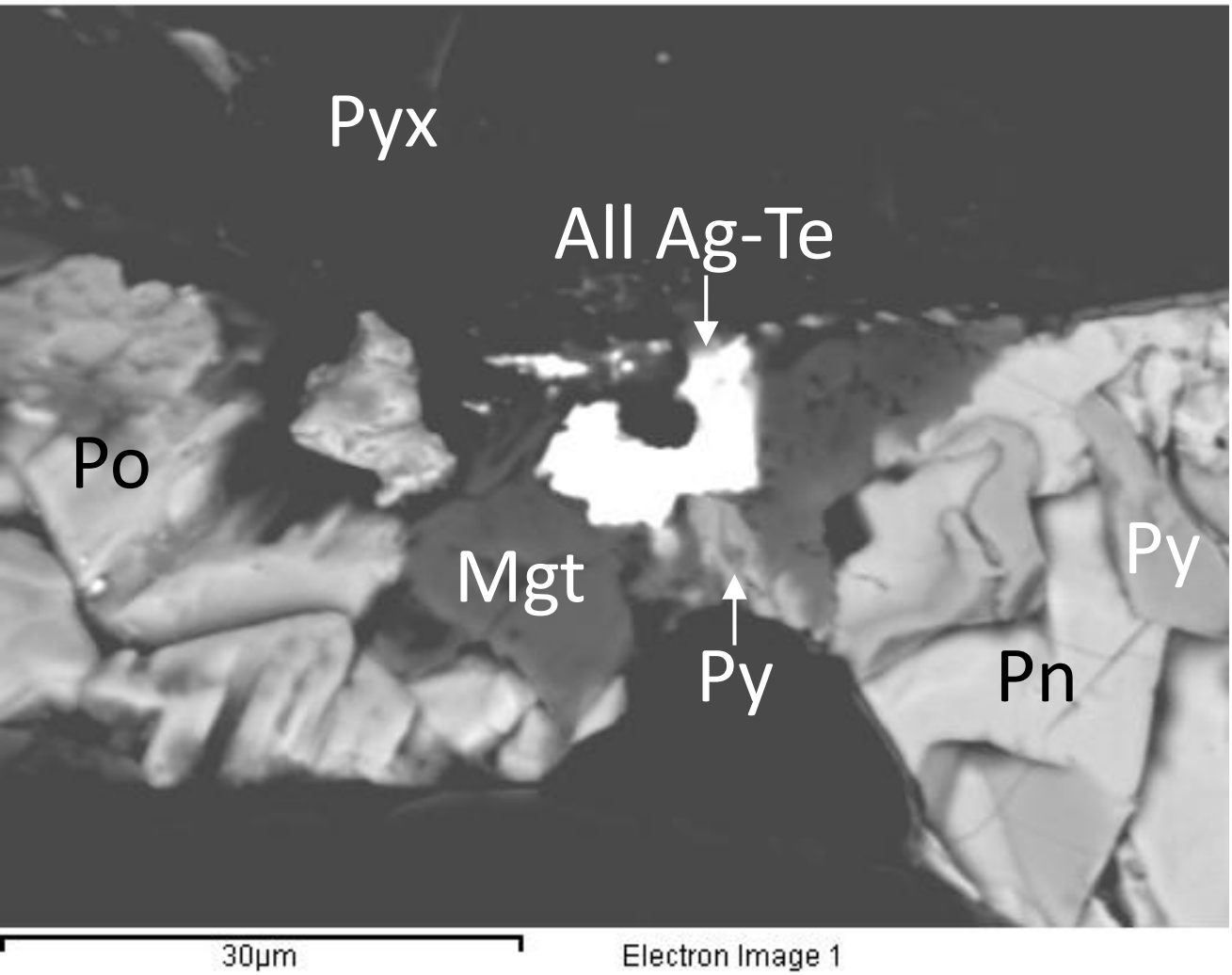
PTR16 B 1



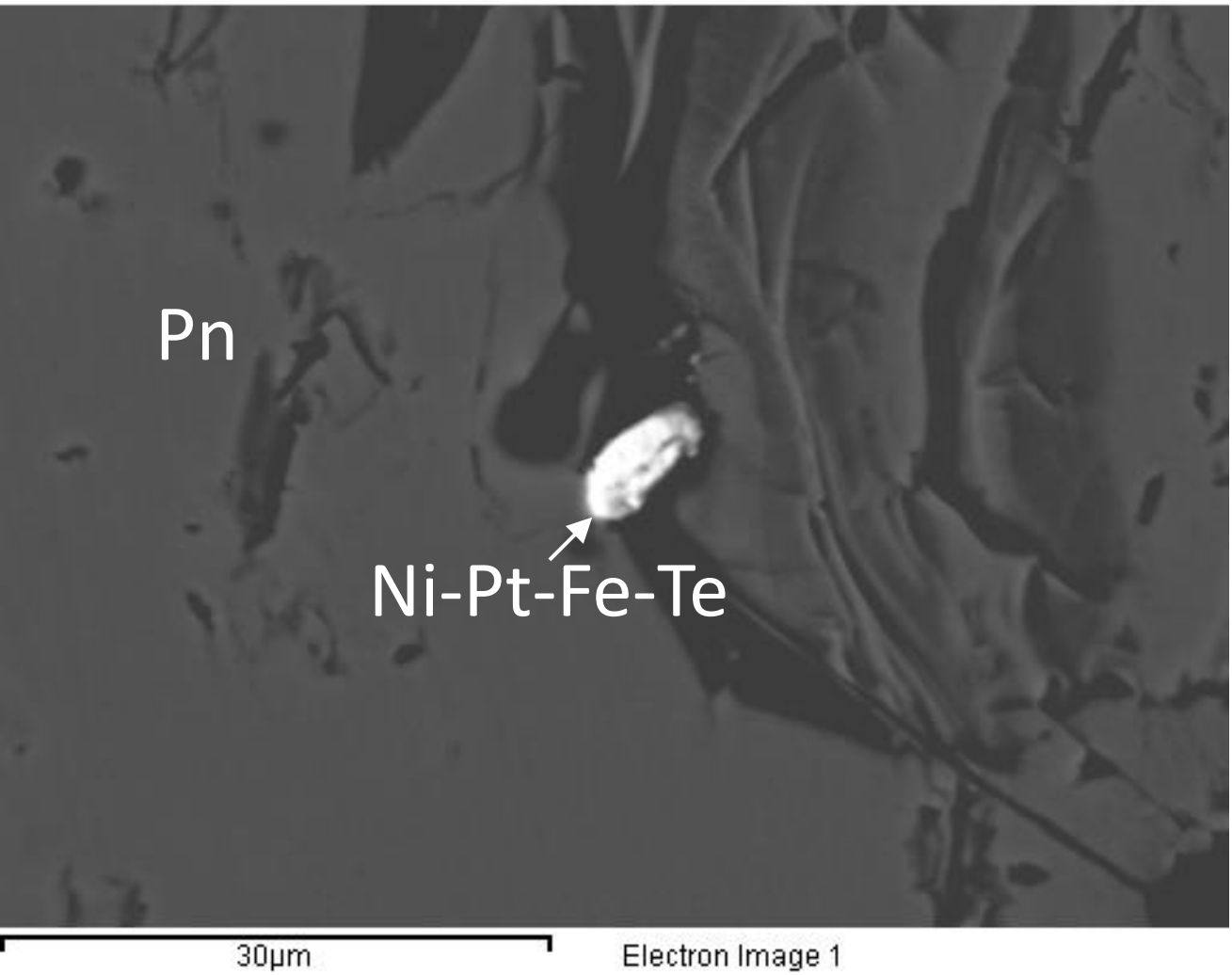
PTR16 C 1



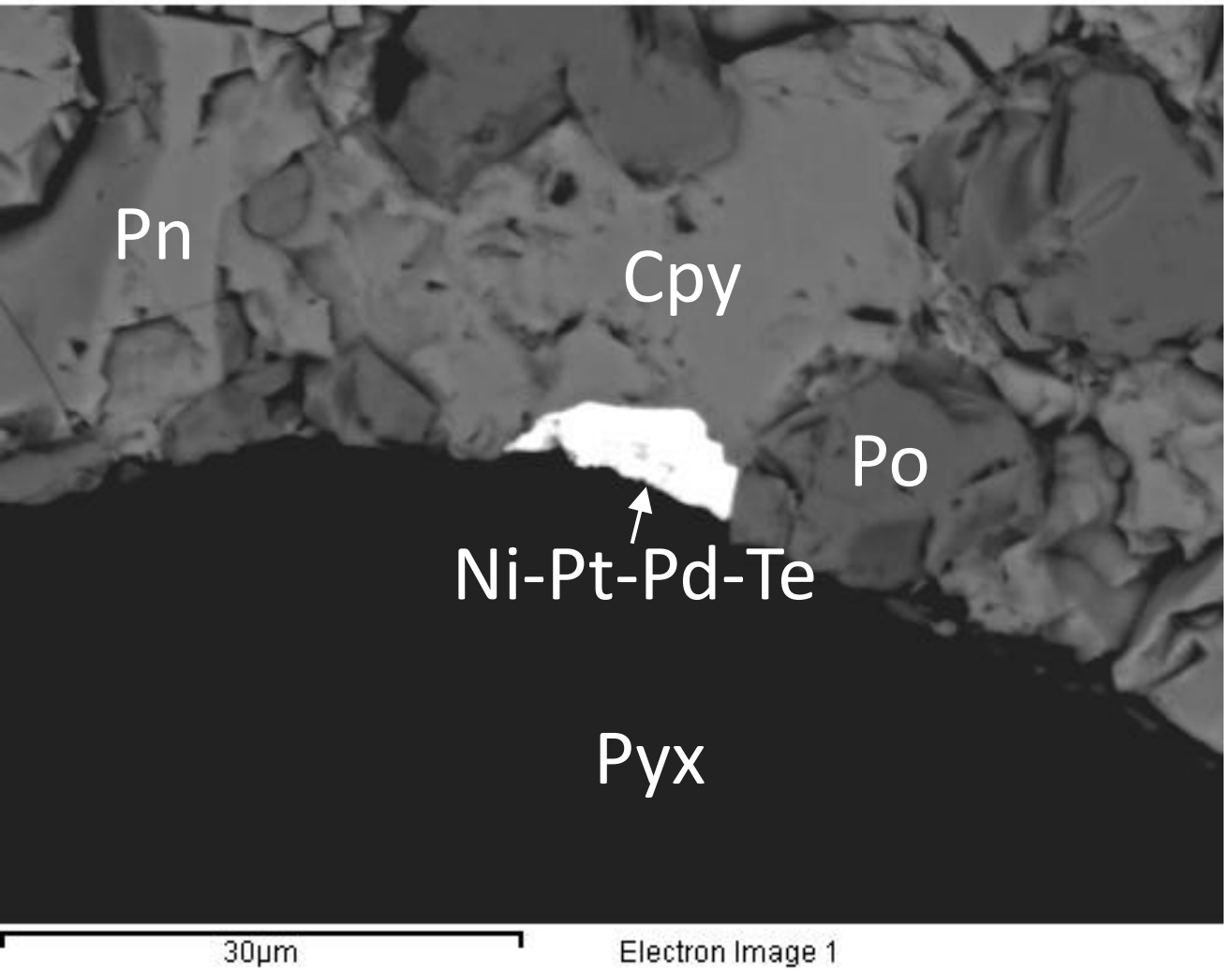
PTR16 D 1



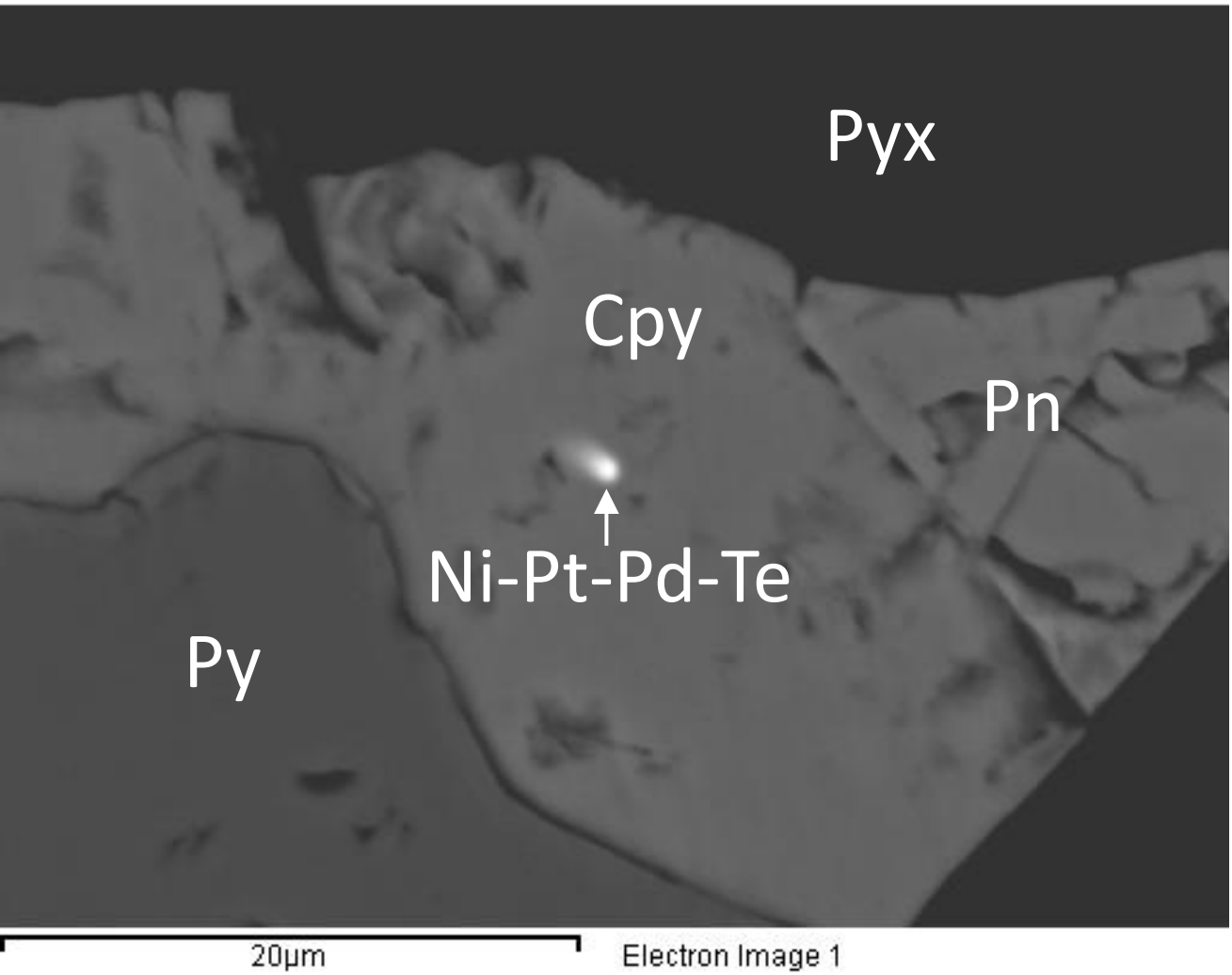
PTR16 E 1



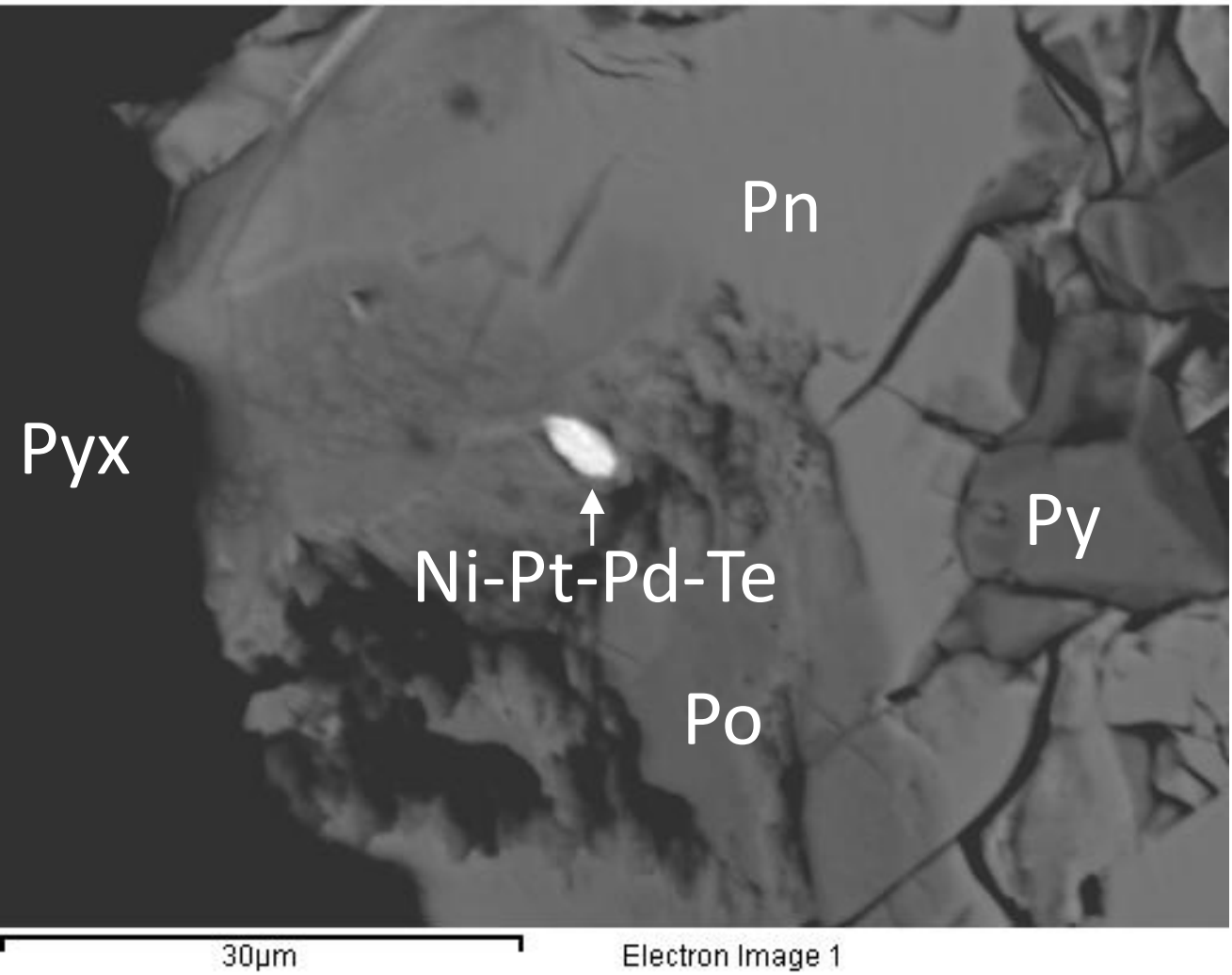
PTR17 A 1



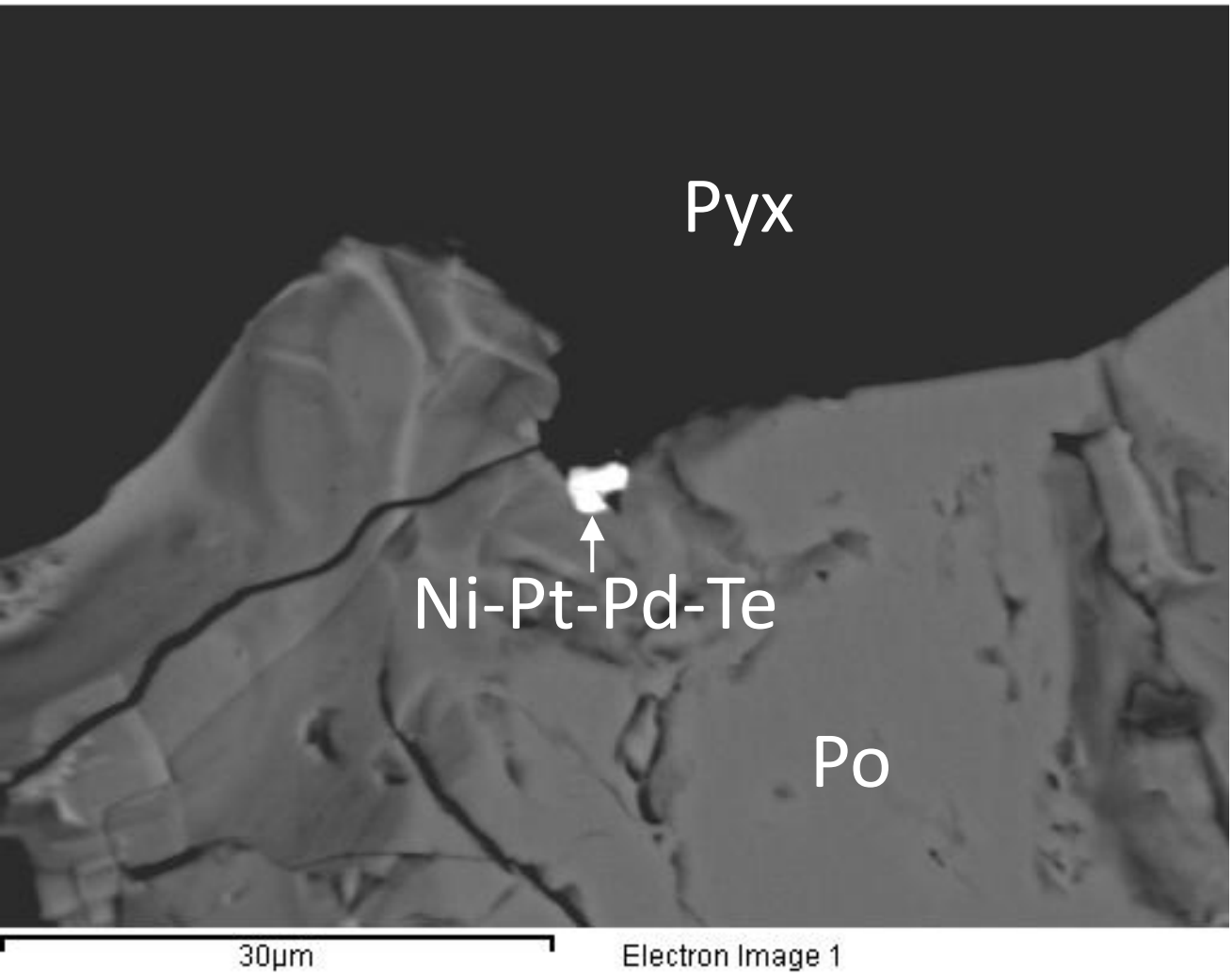
PTR17 B 1



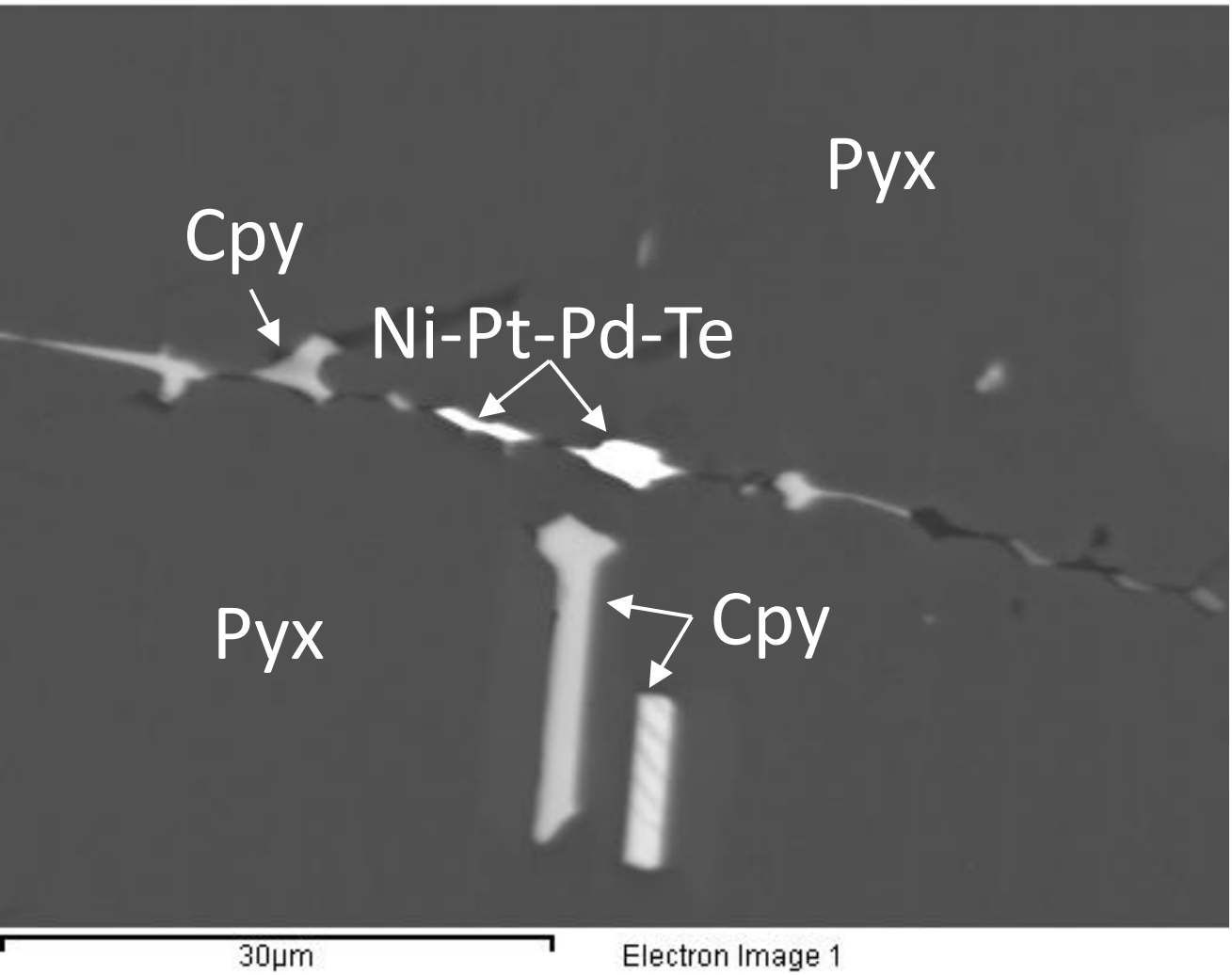
PTR17 C 1



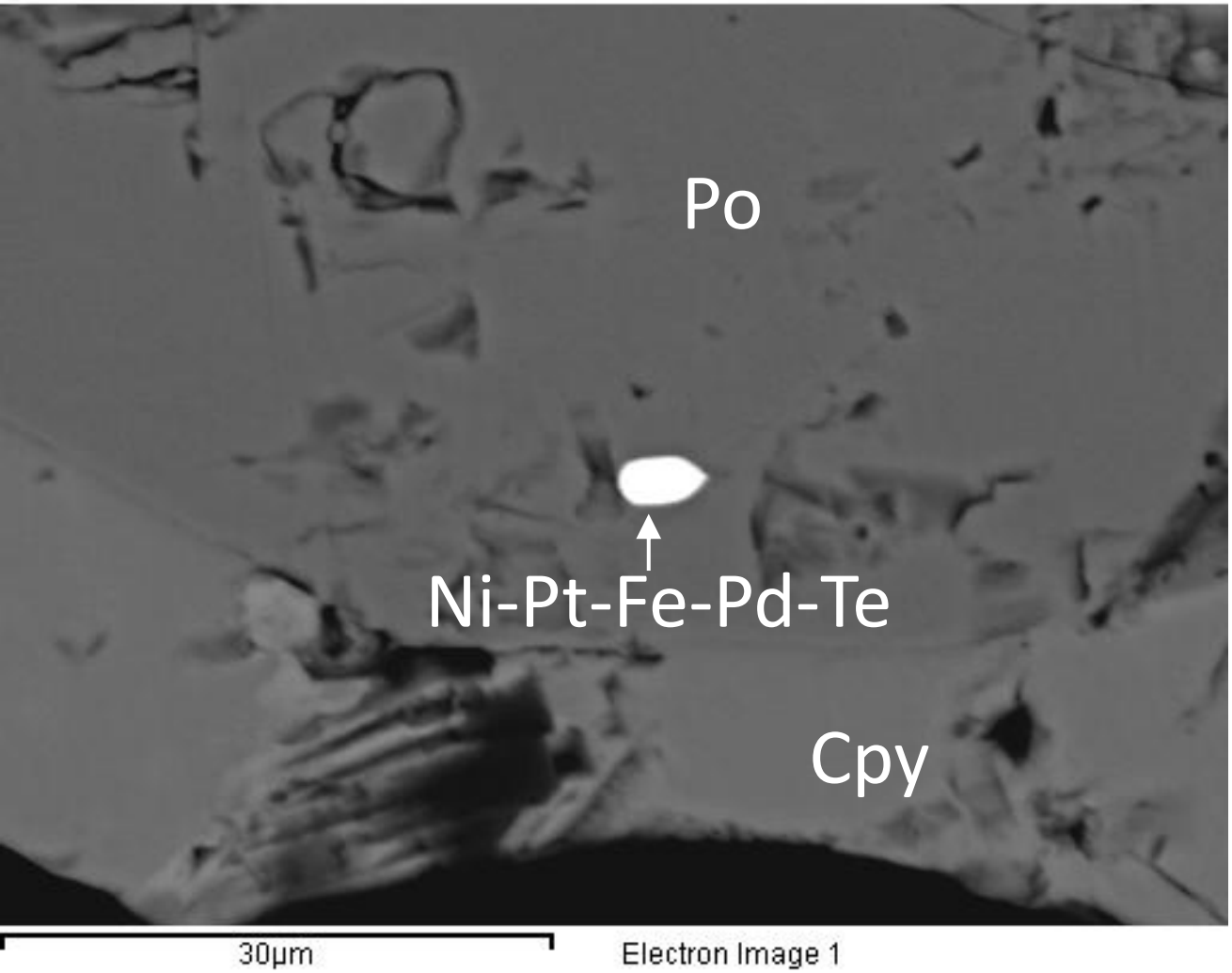
PTR17 D 1



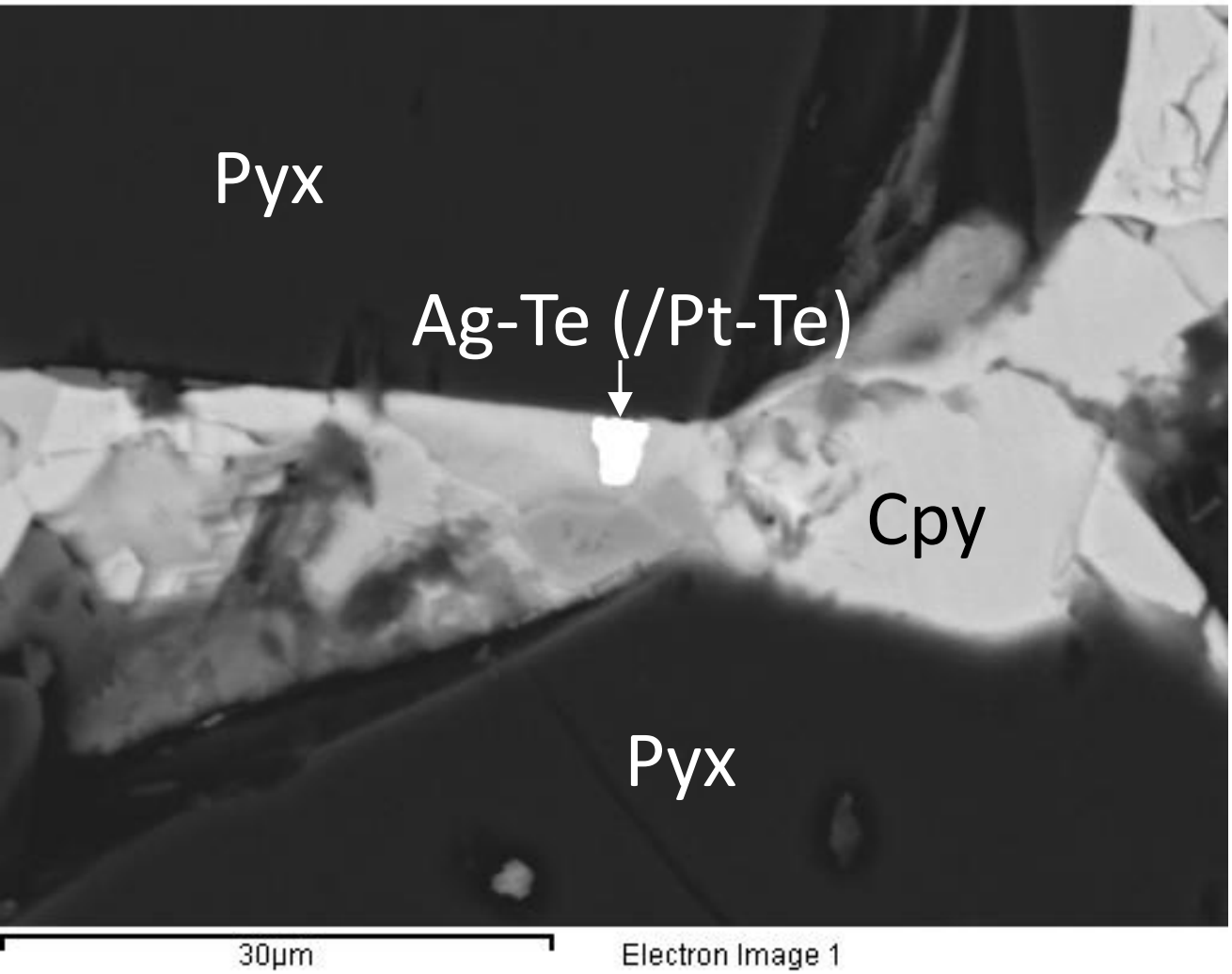
PTR17 E 1-2



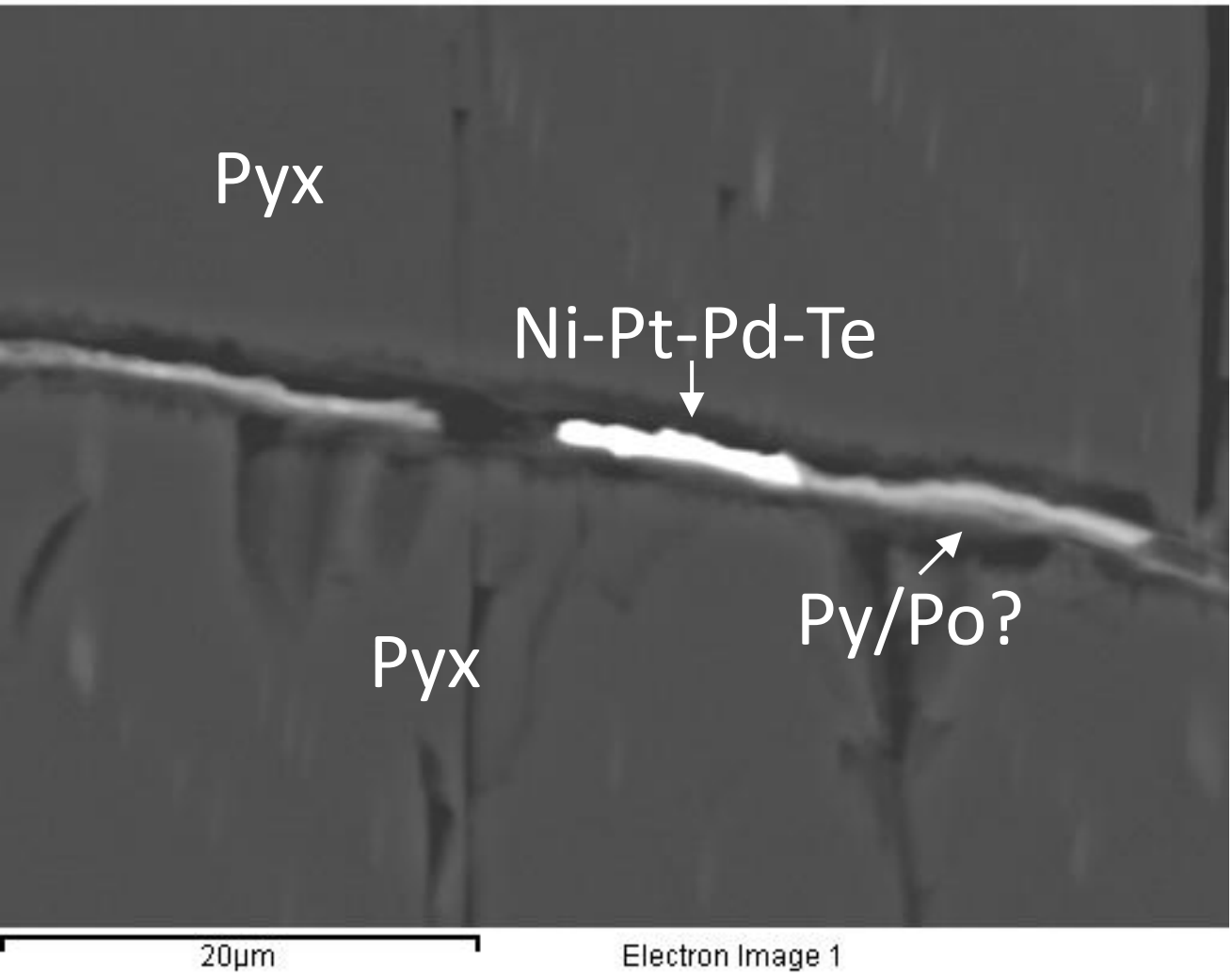
PTR17 F 1



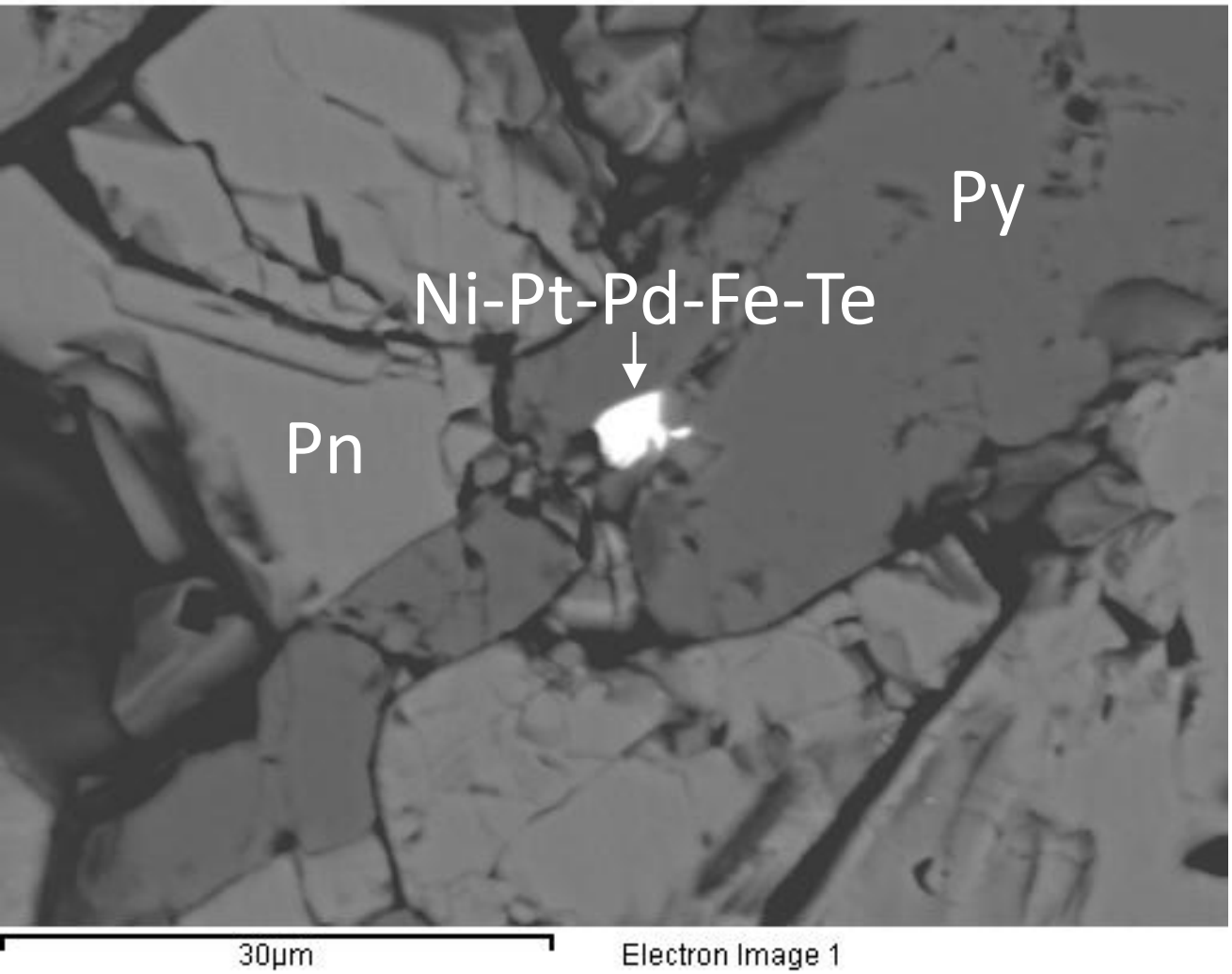
PTR17 G 1



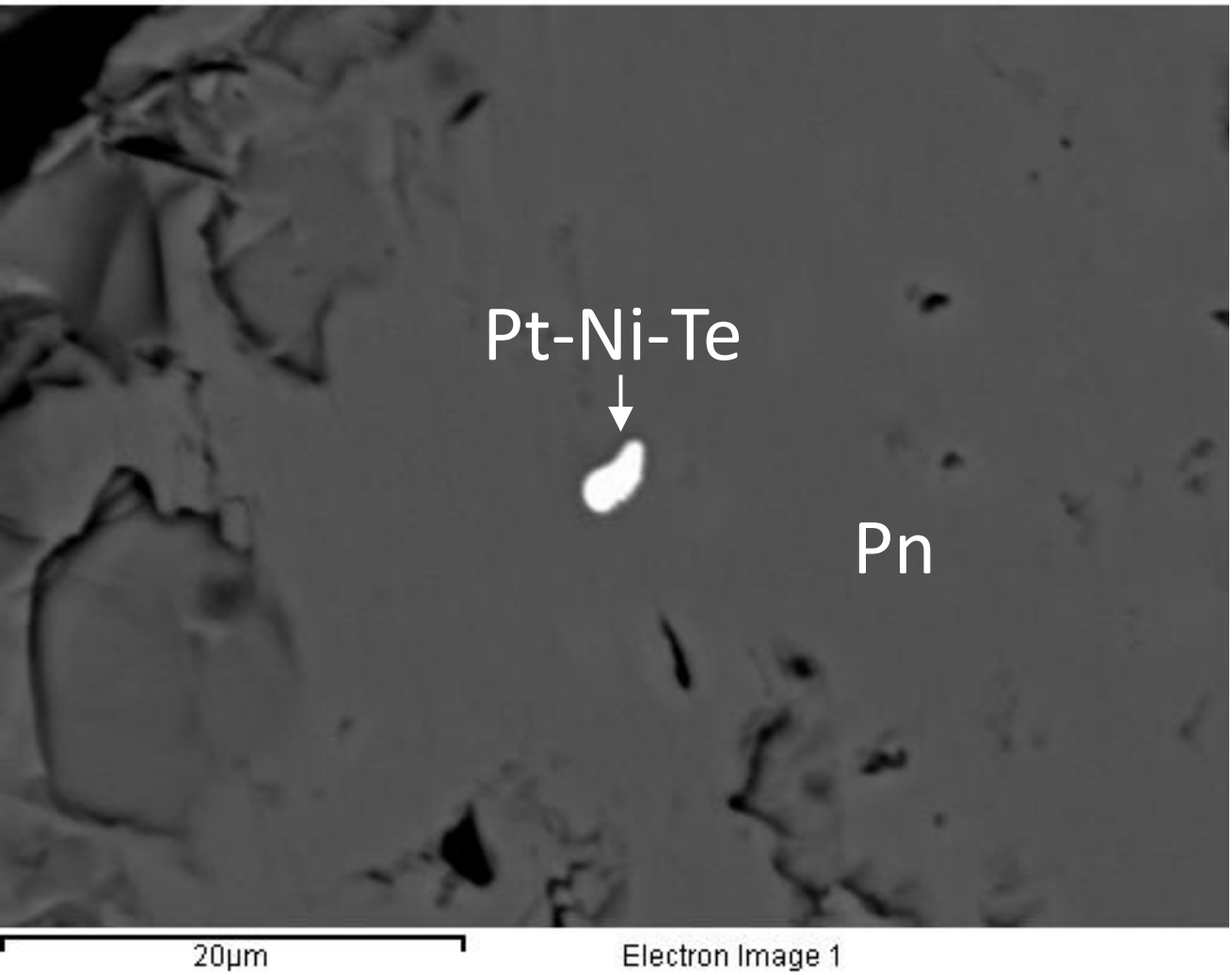
PTR17 H 1



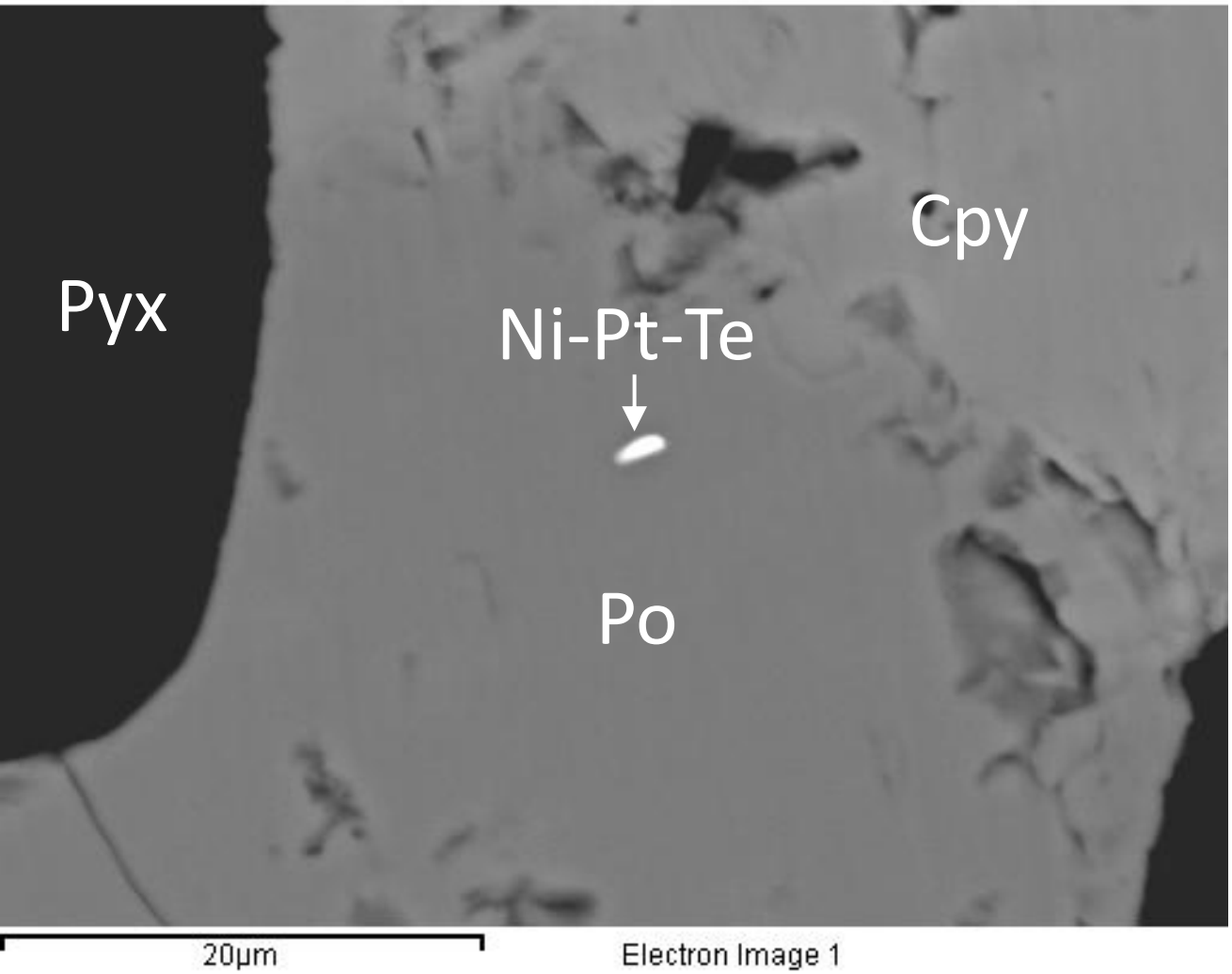
PTR17 J 1



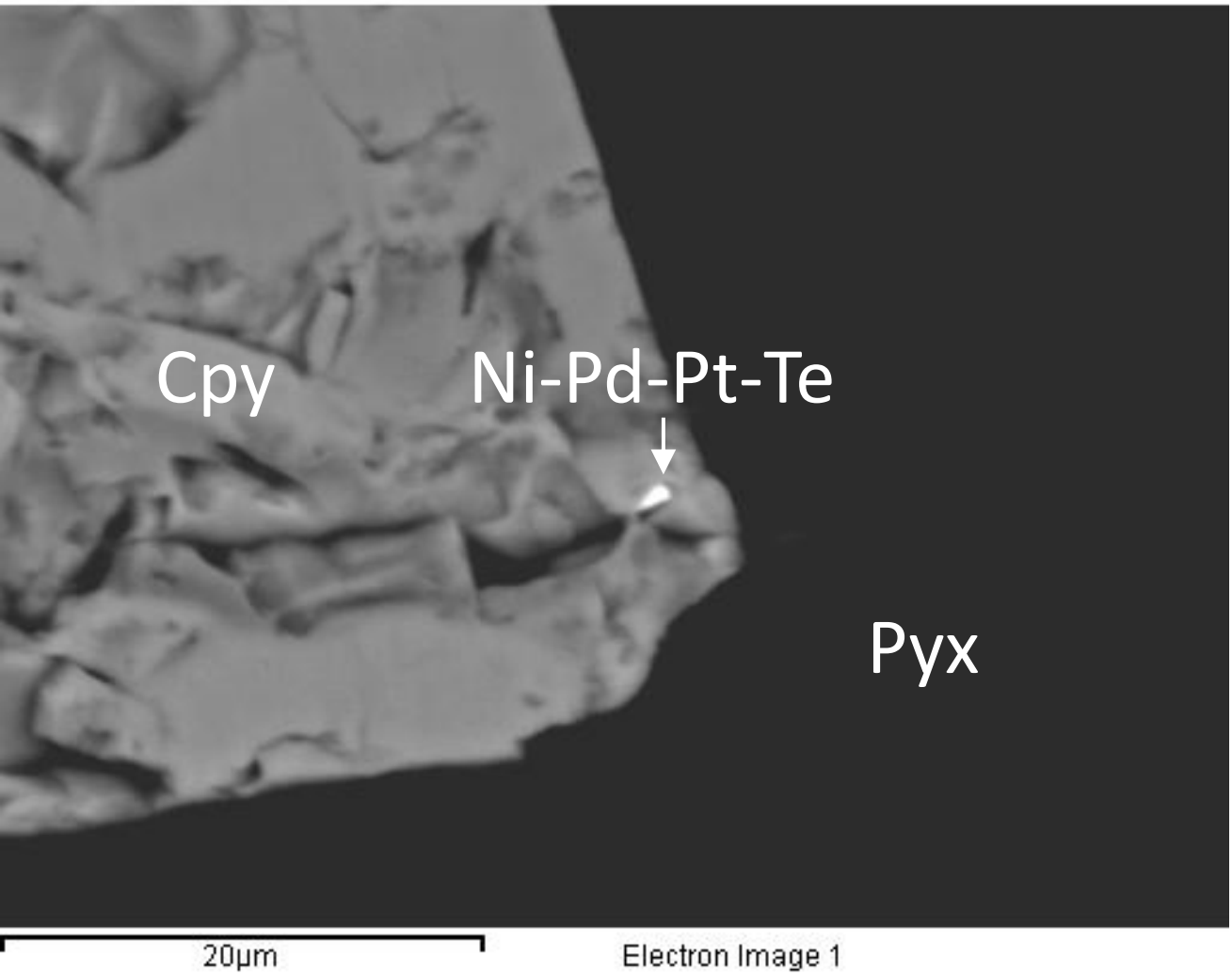
PTR17 K 1



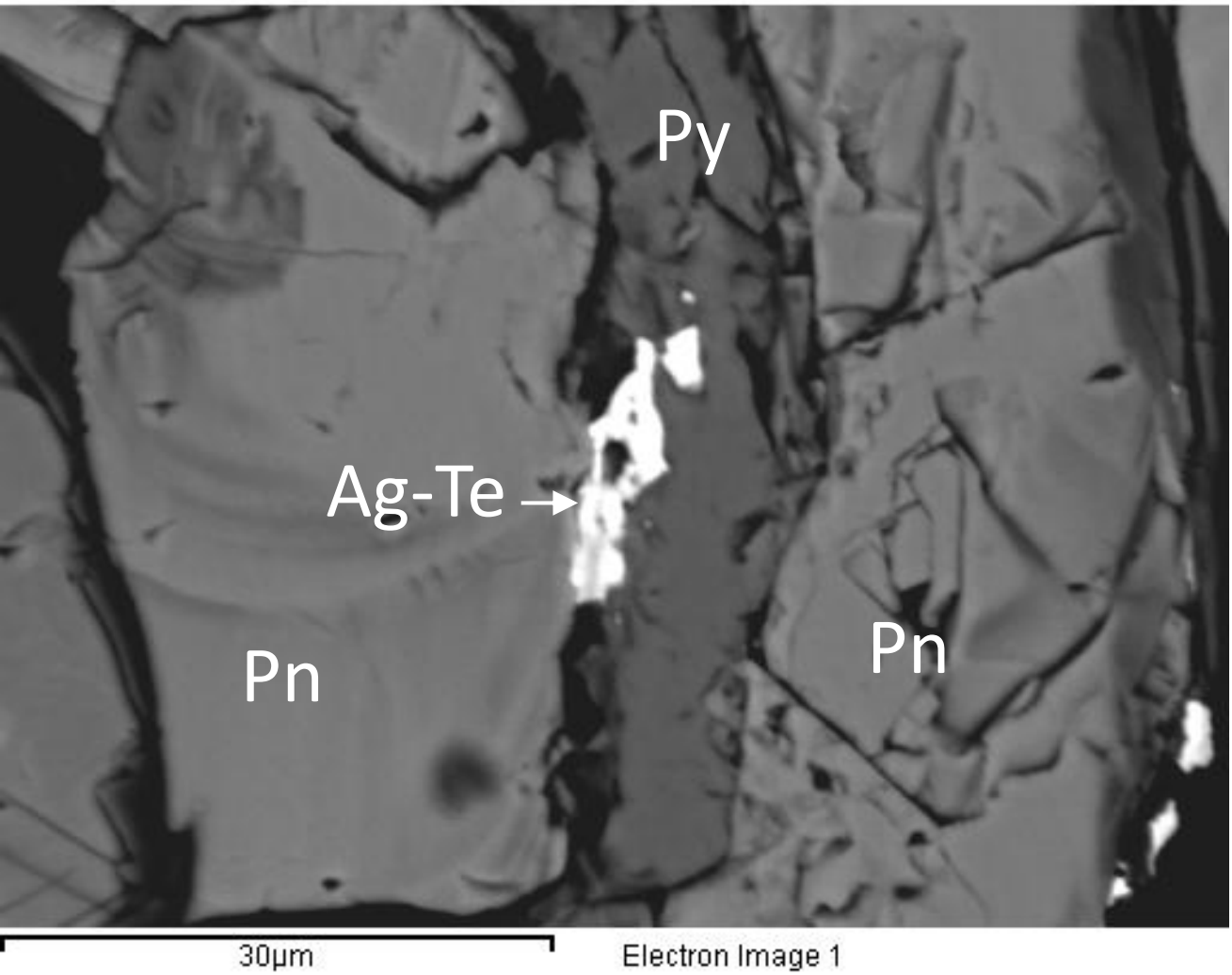
PTR17 L 1



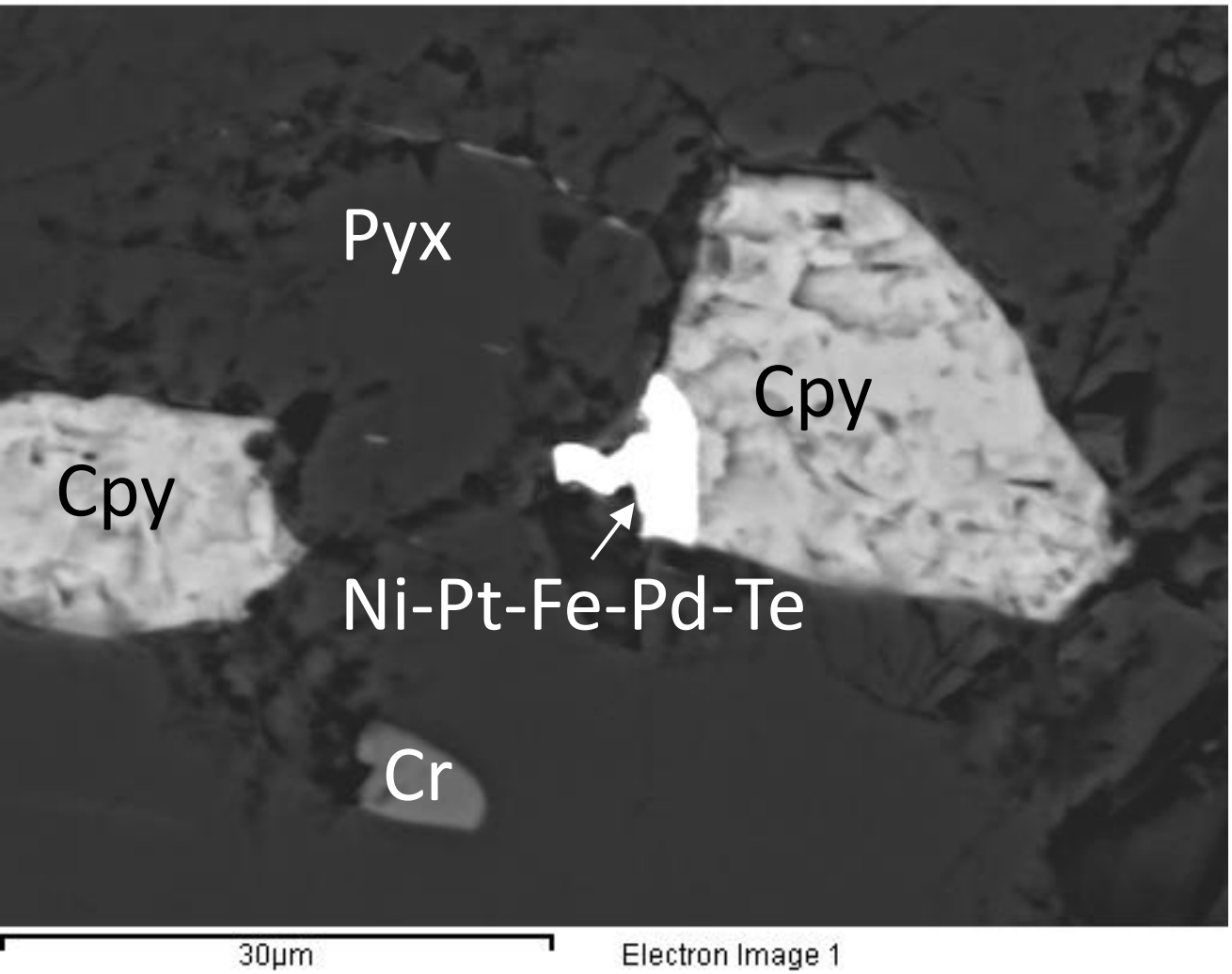
PTR17 M 1



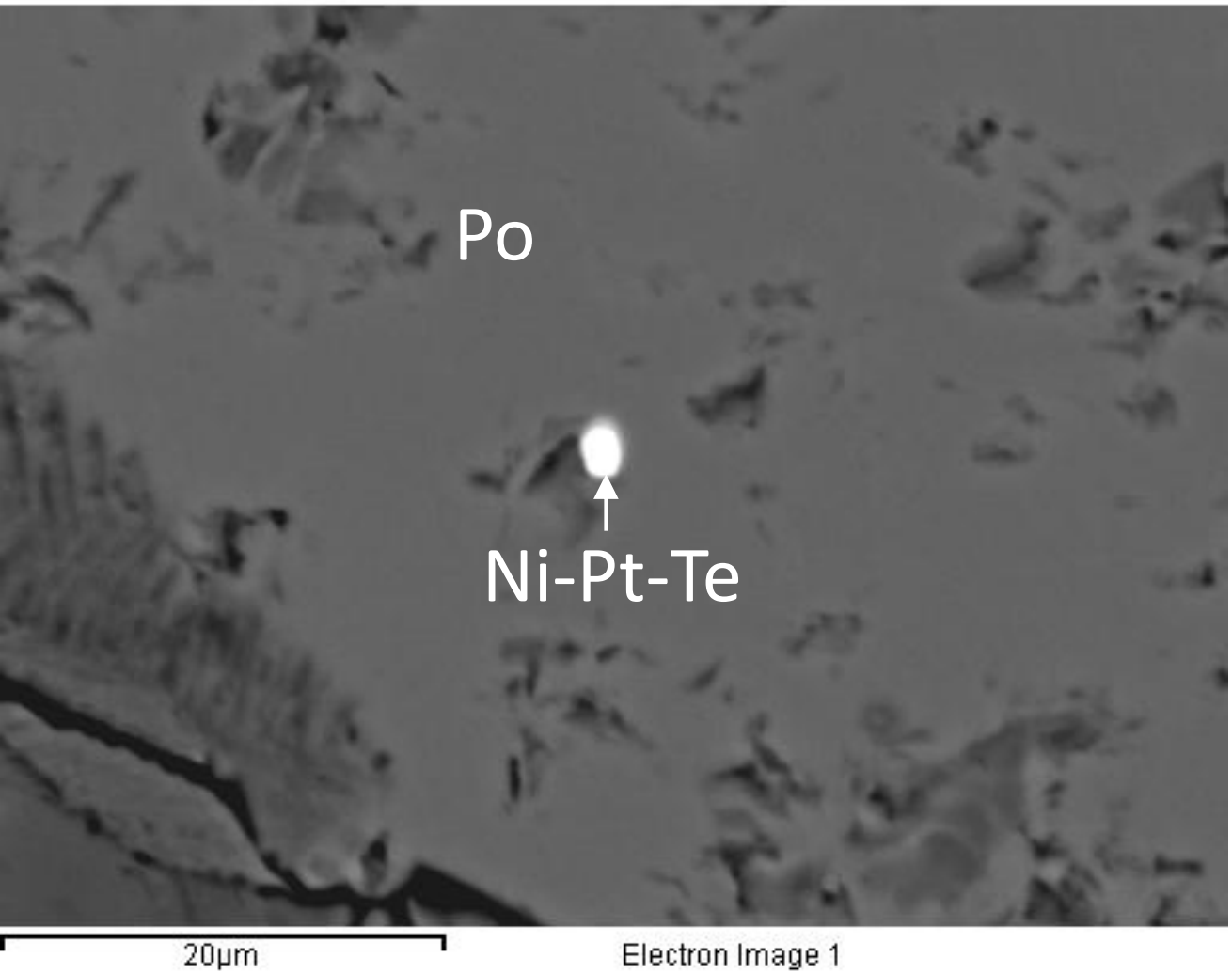
PTR17 N 1



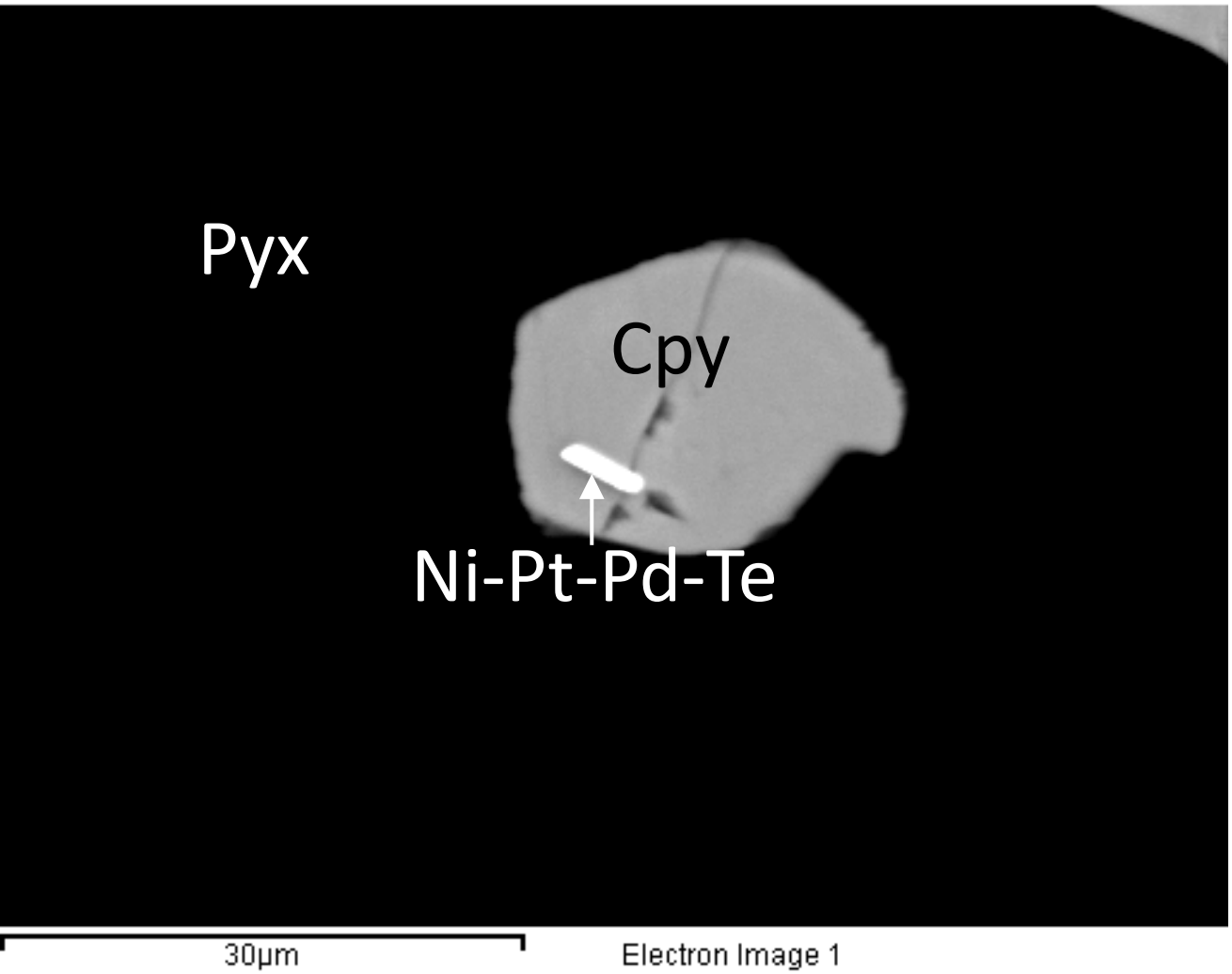
PTR17 O 1



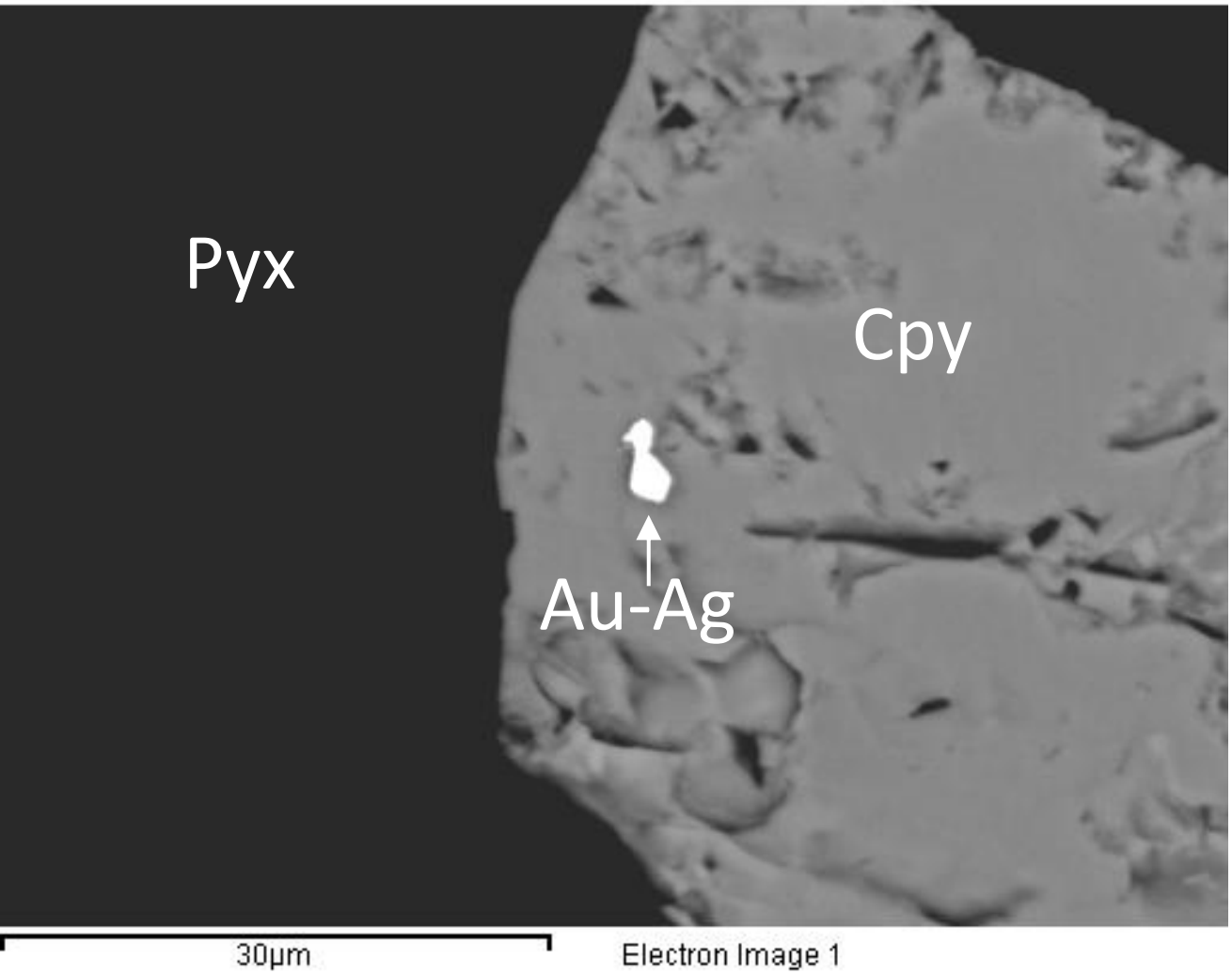
PTR18 A 1



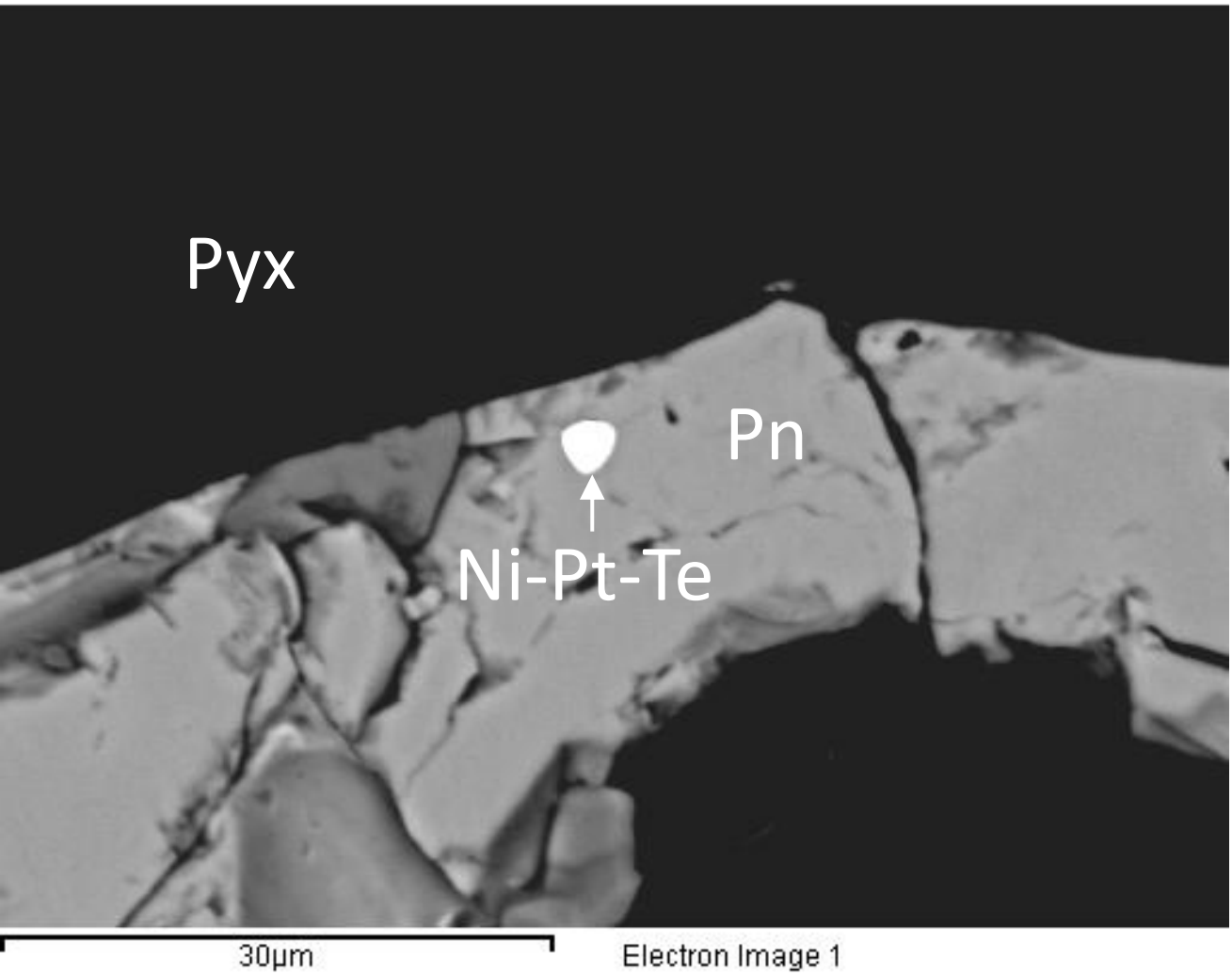
PTR18 B 1



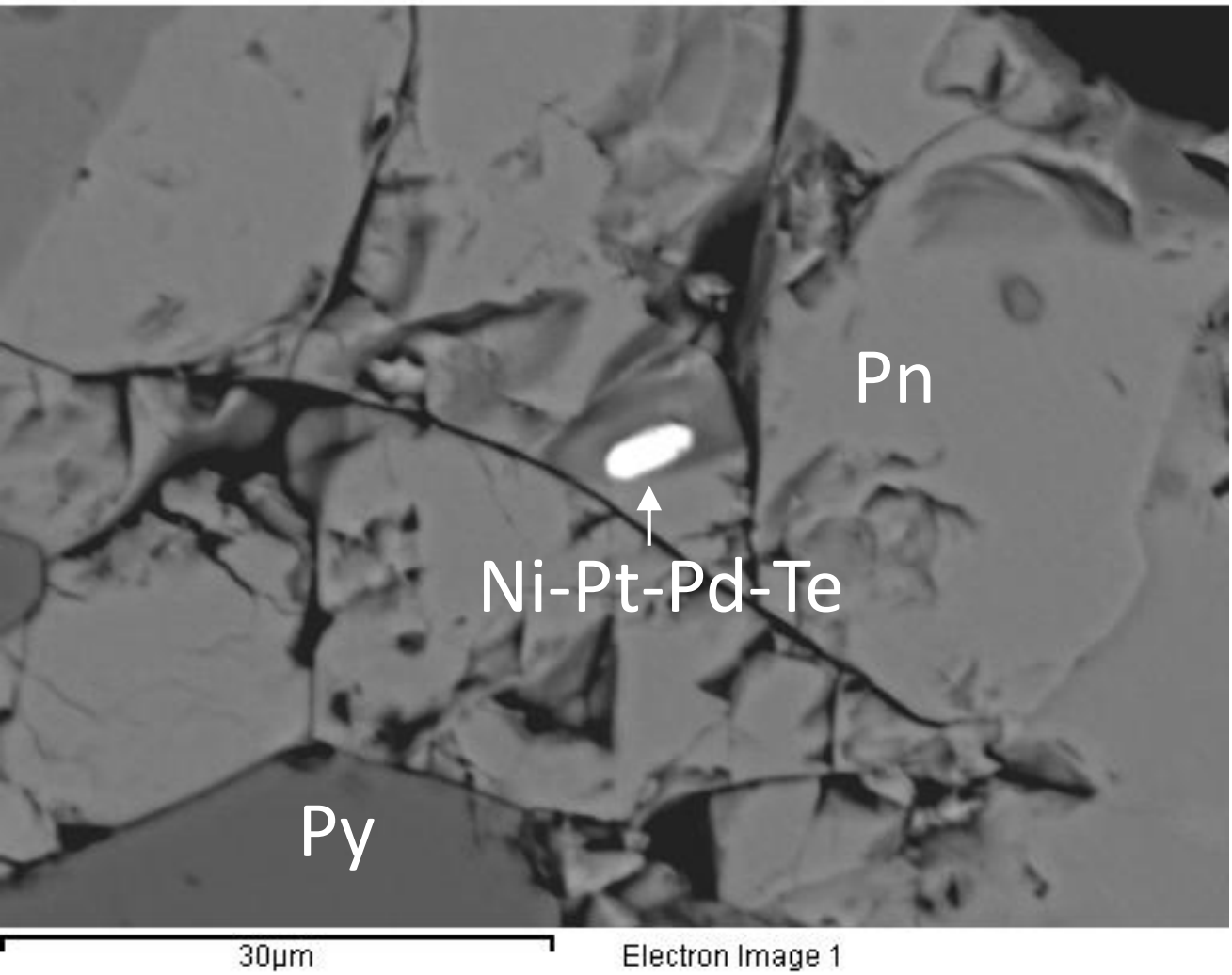
PTR18 C 1



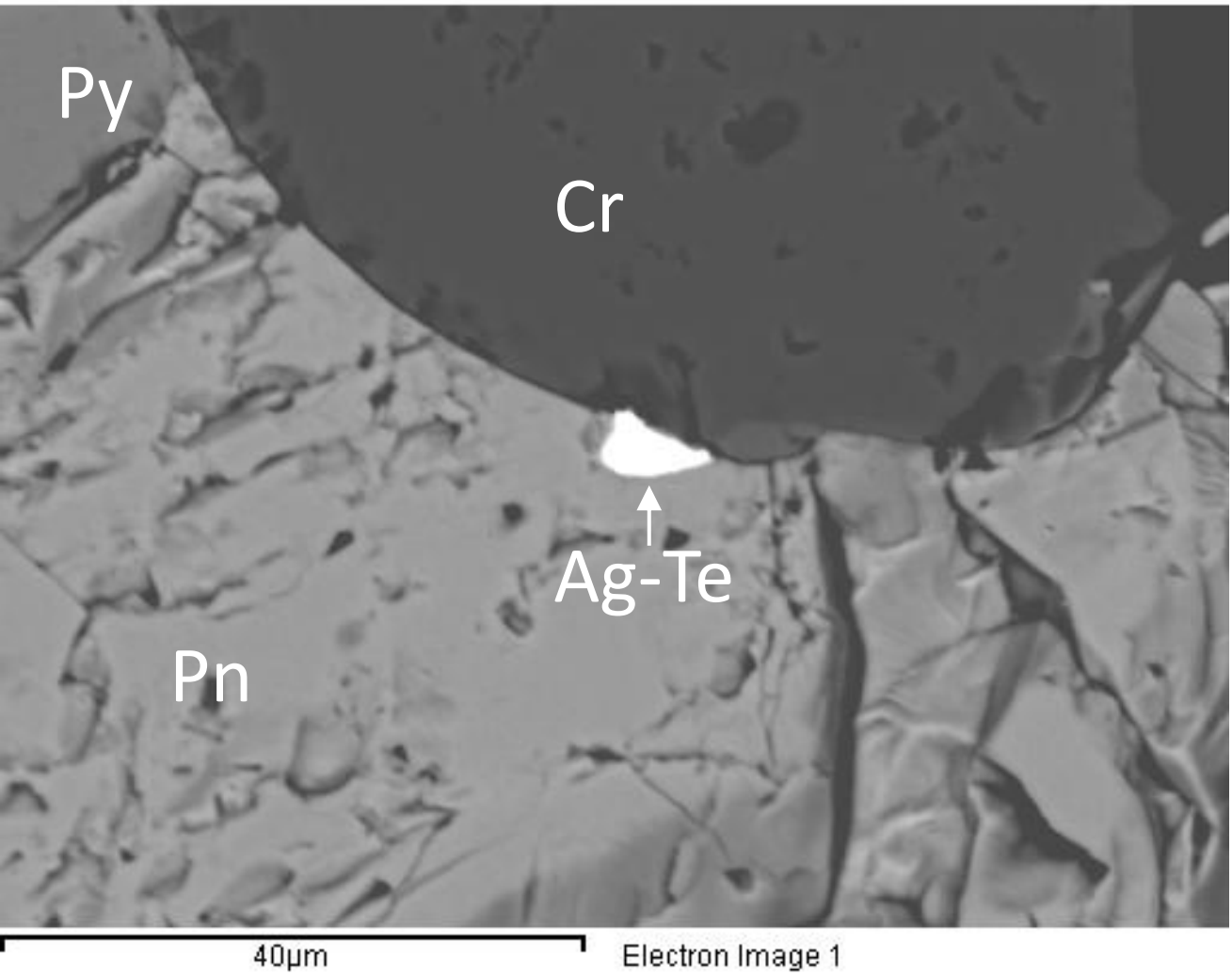
PTR18 D 1



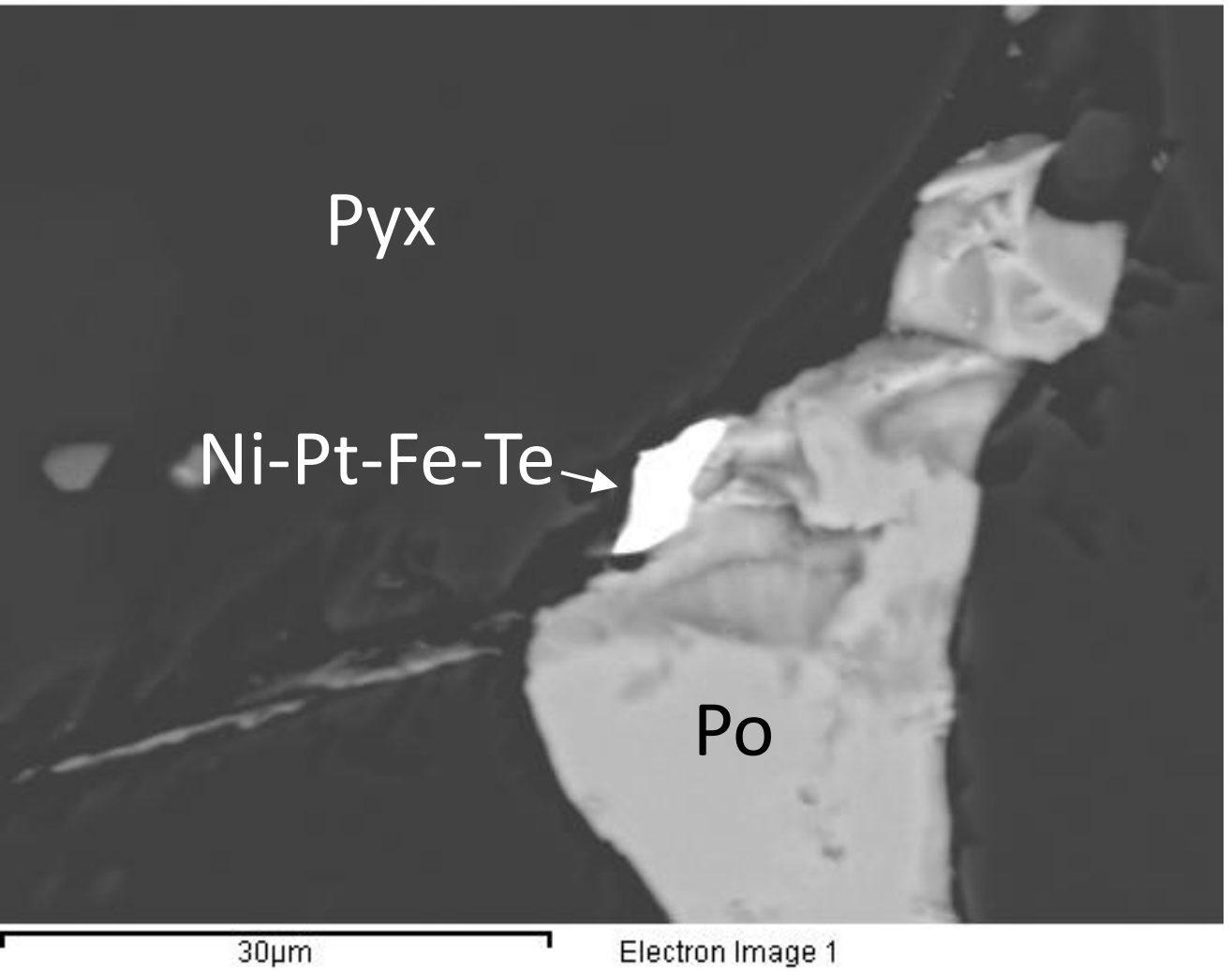
PTR18 E 1



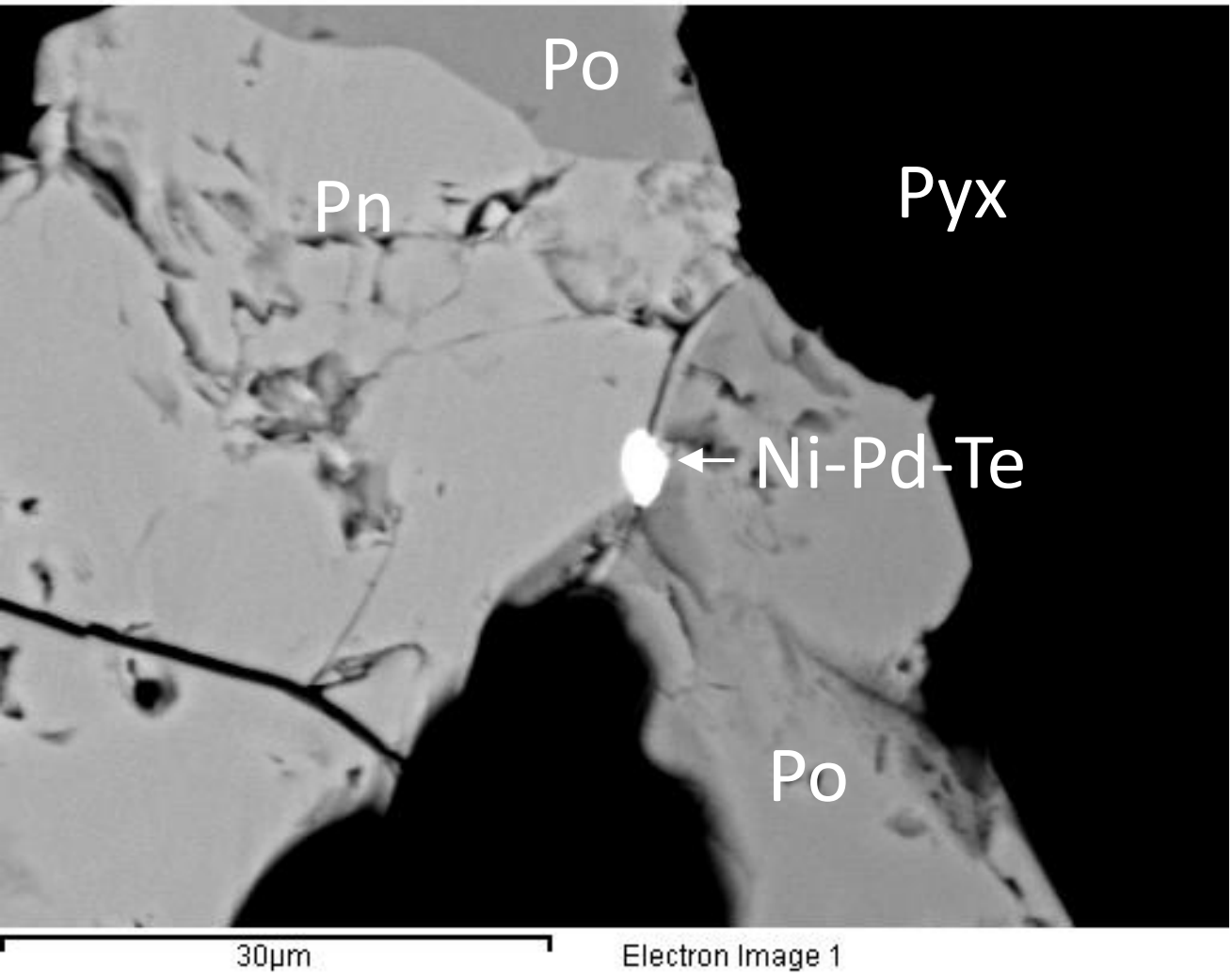
PTR18 F 1



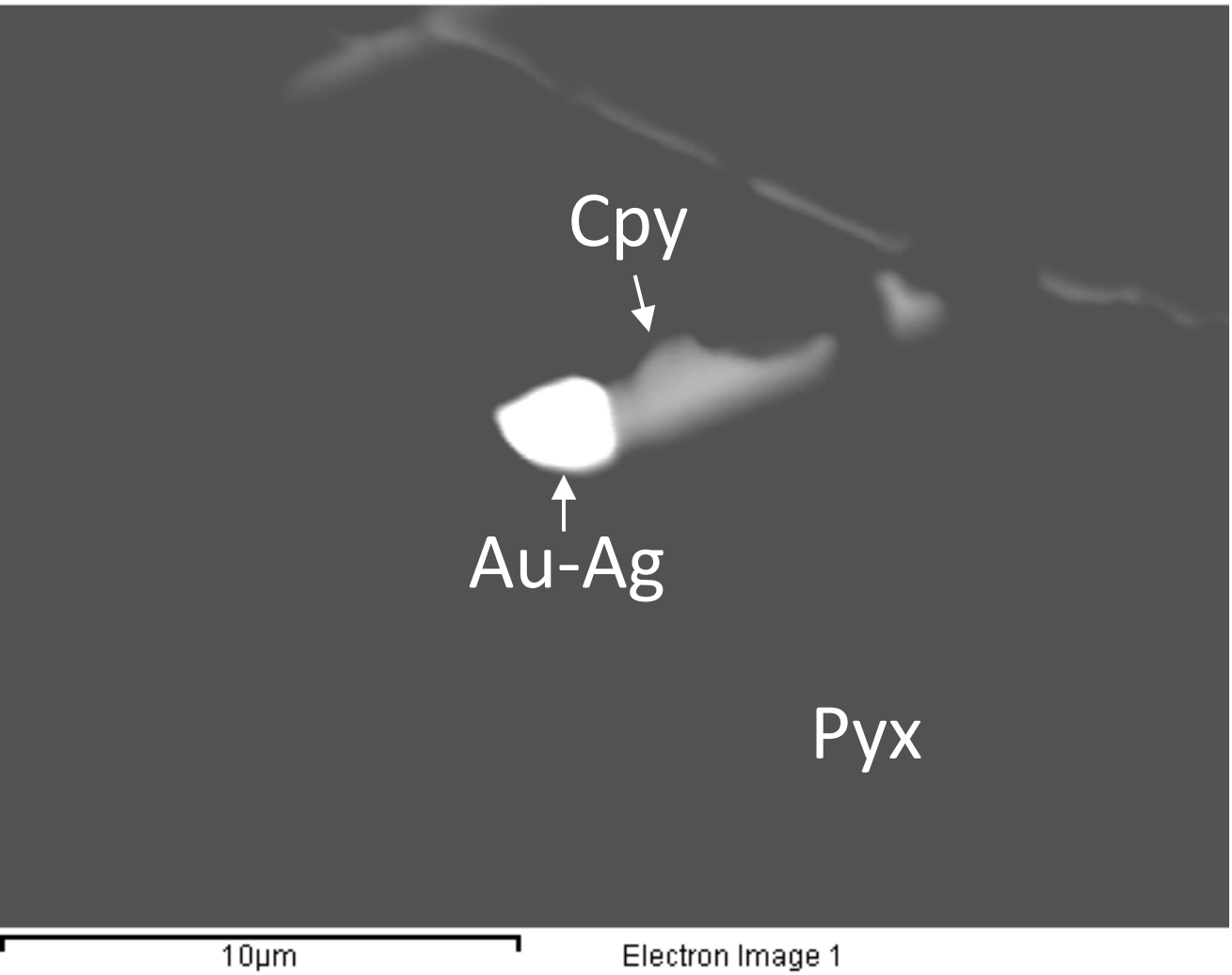
PTR18 G 1



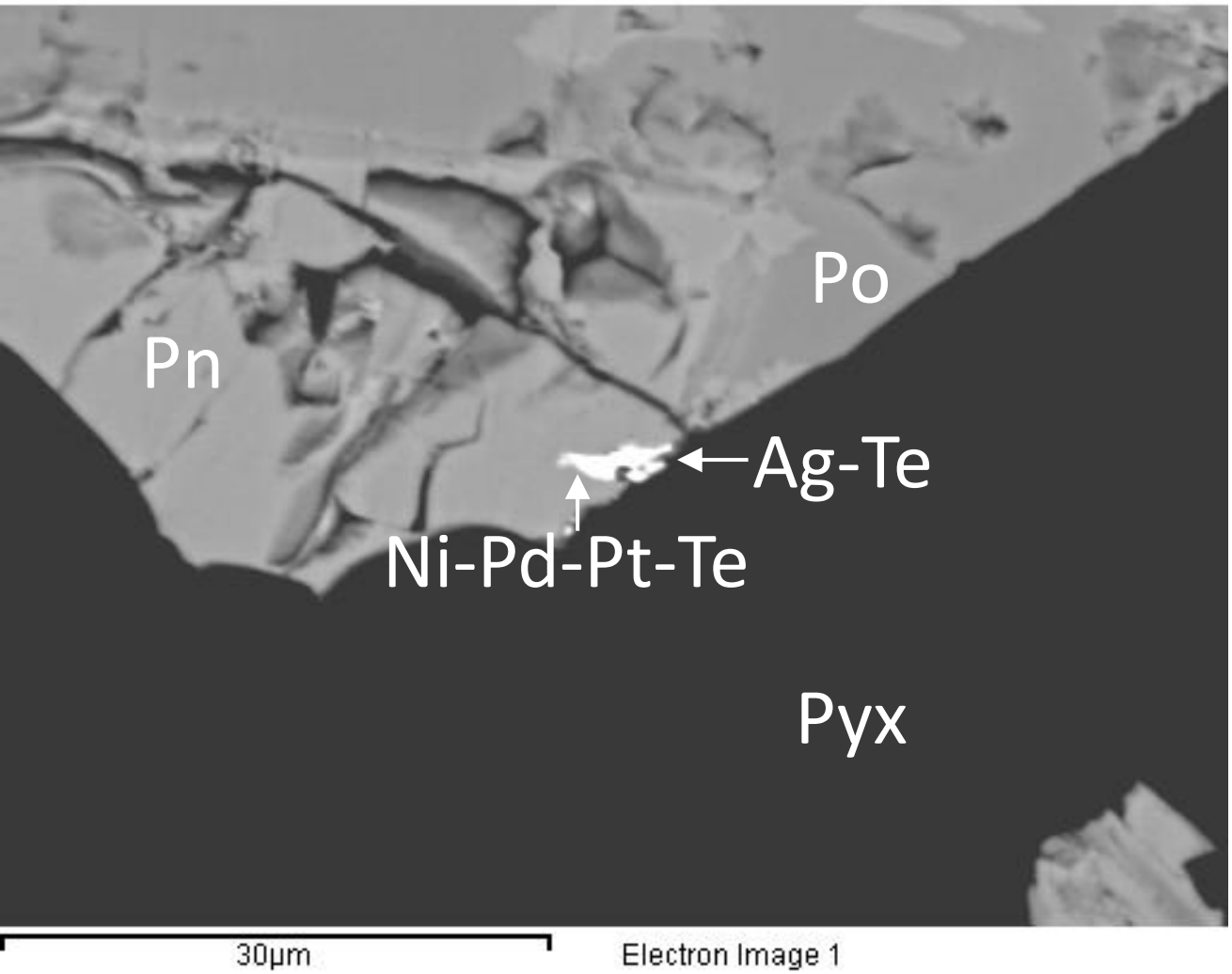
PTR19 A 1



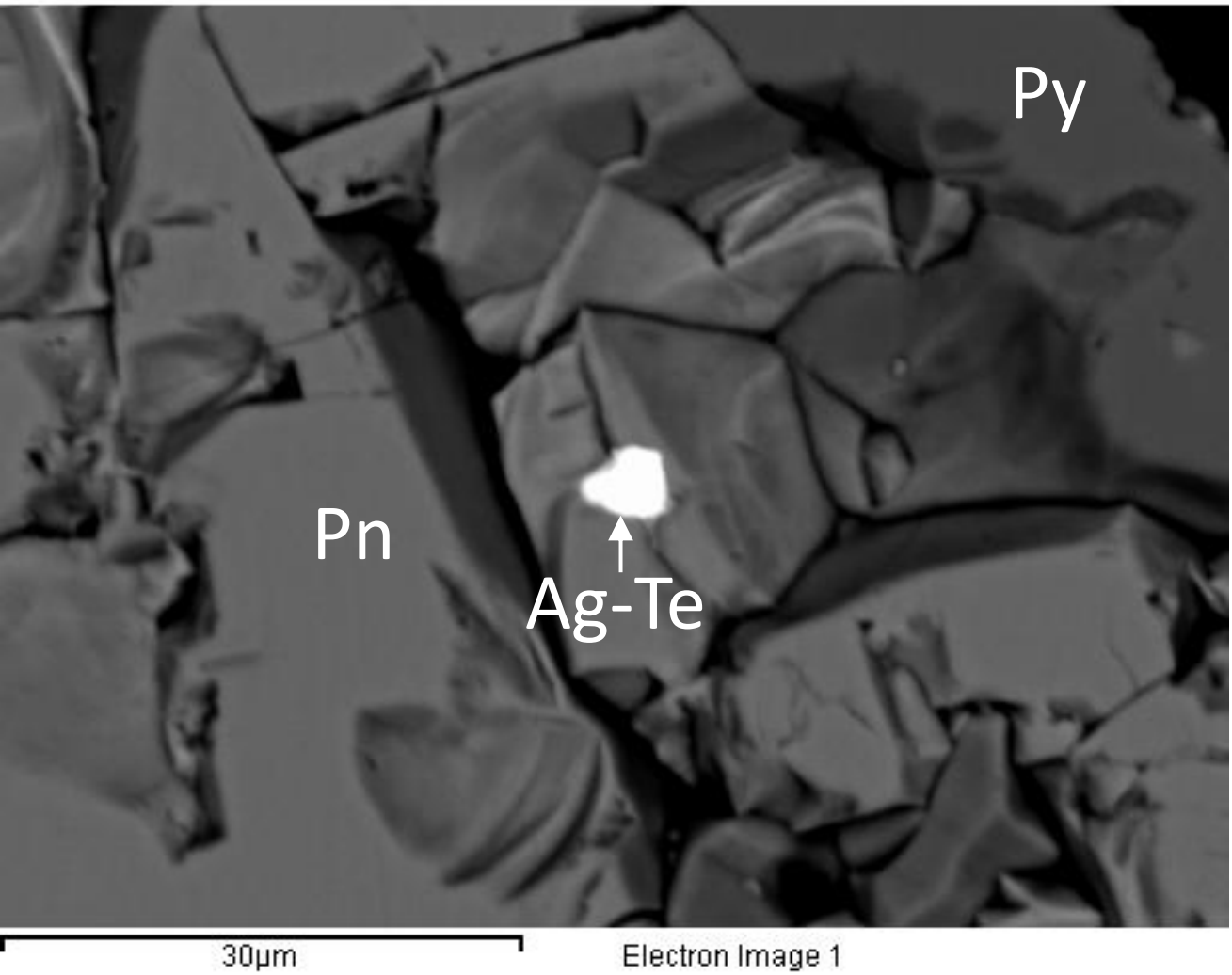
PTR19 B 1



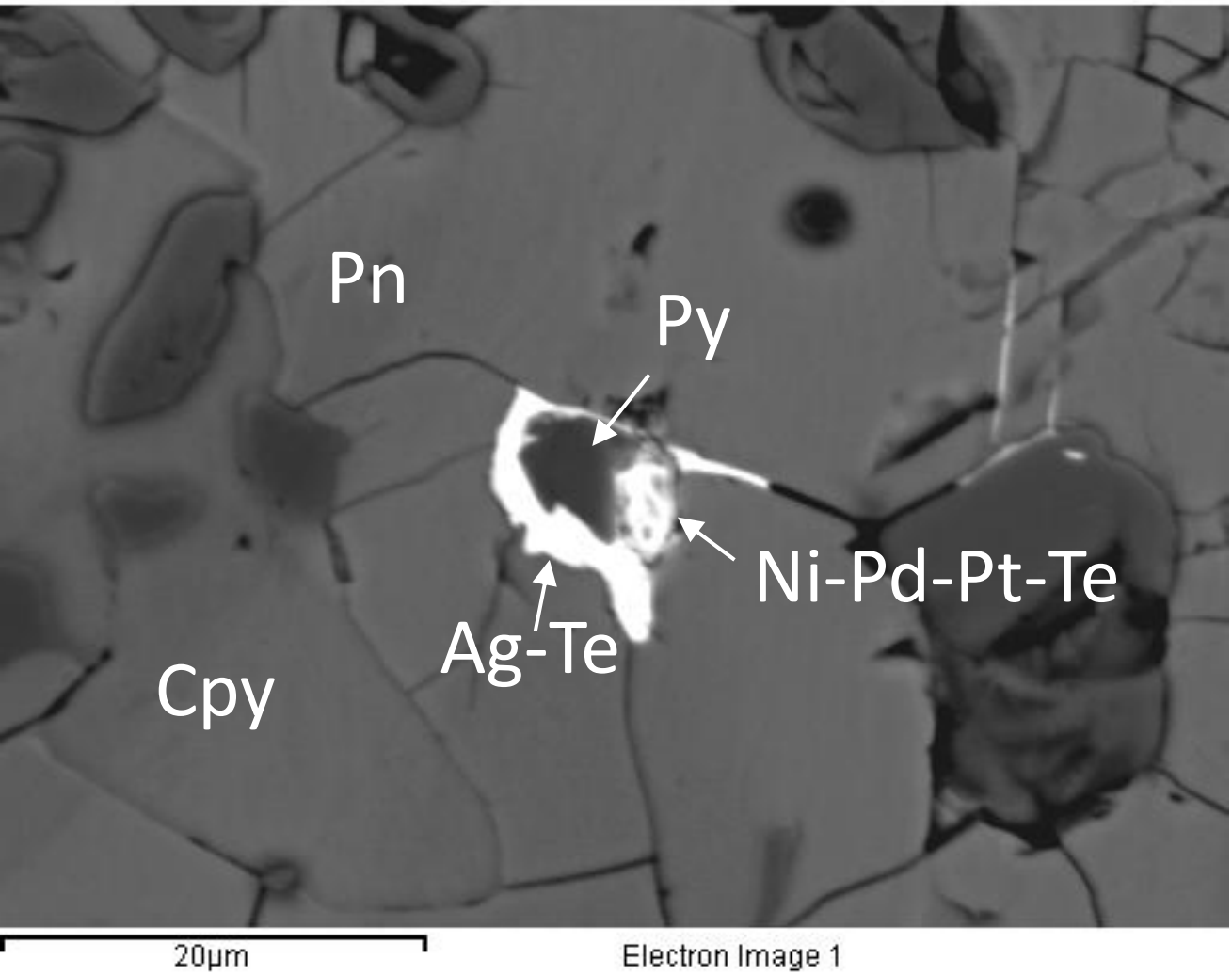
PTR19 C 1-2



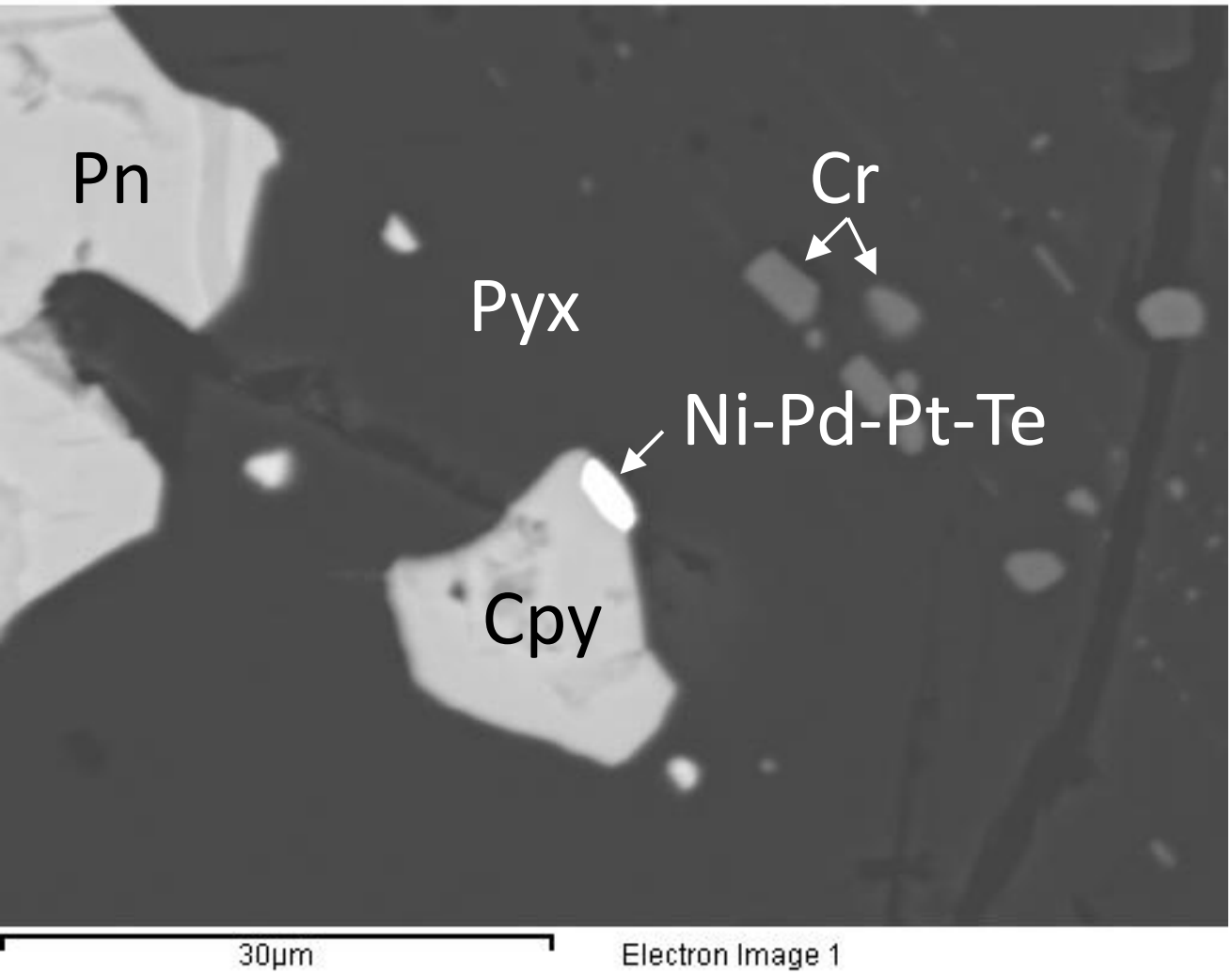
PTR19 D 1



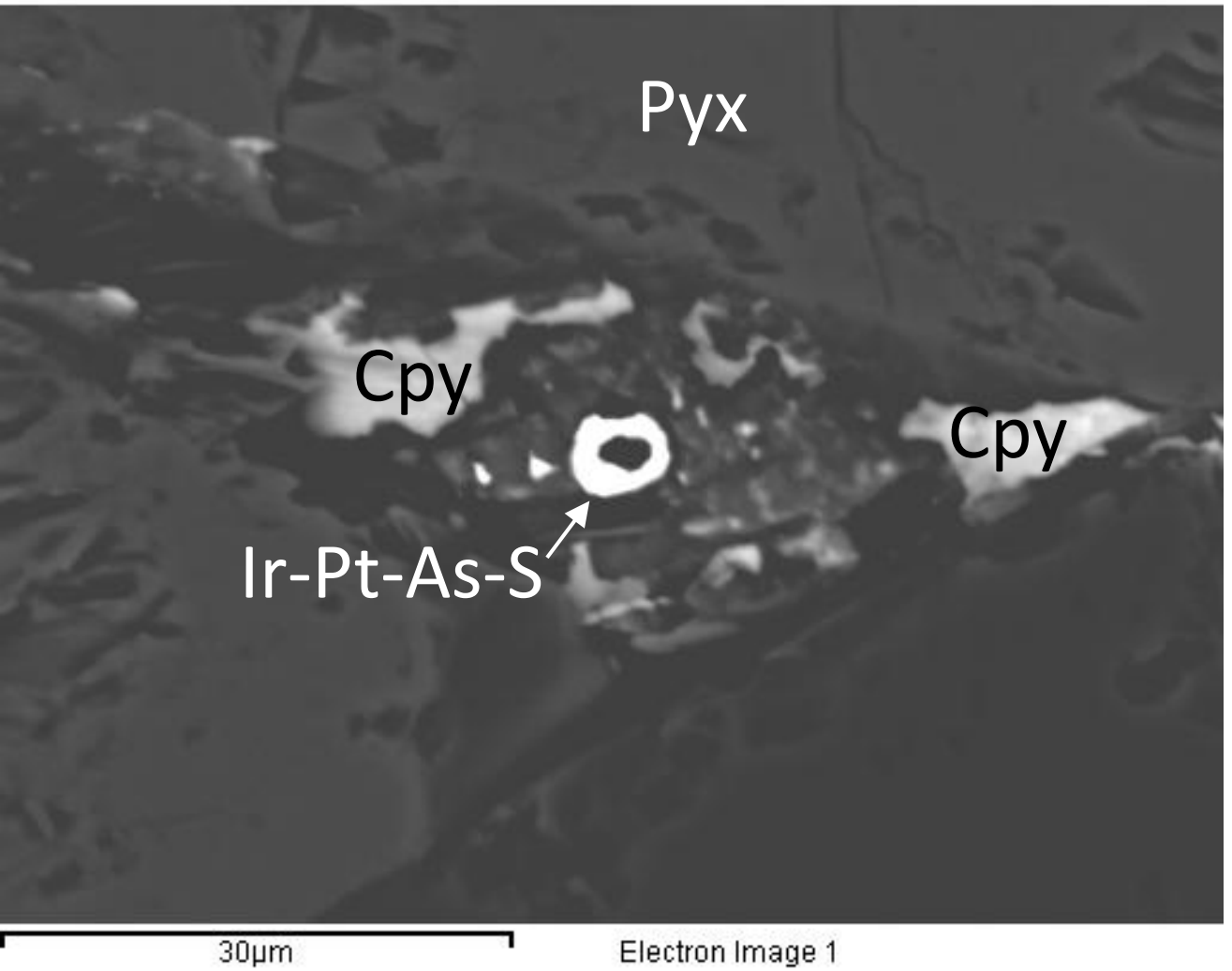
PTR19 E 1-2



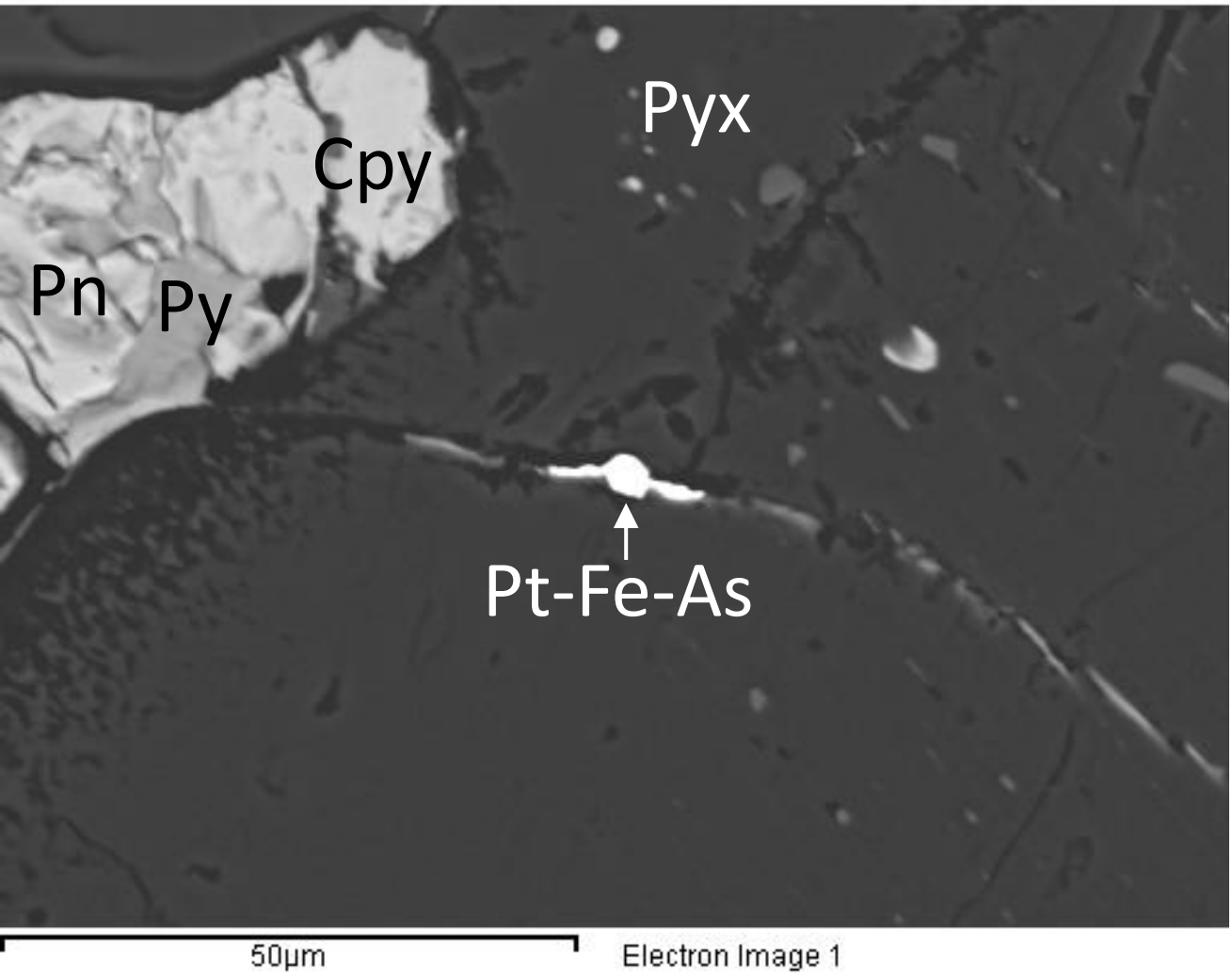
PTR19 F 1



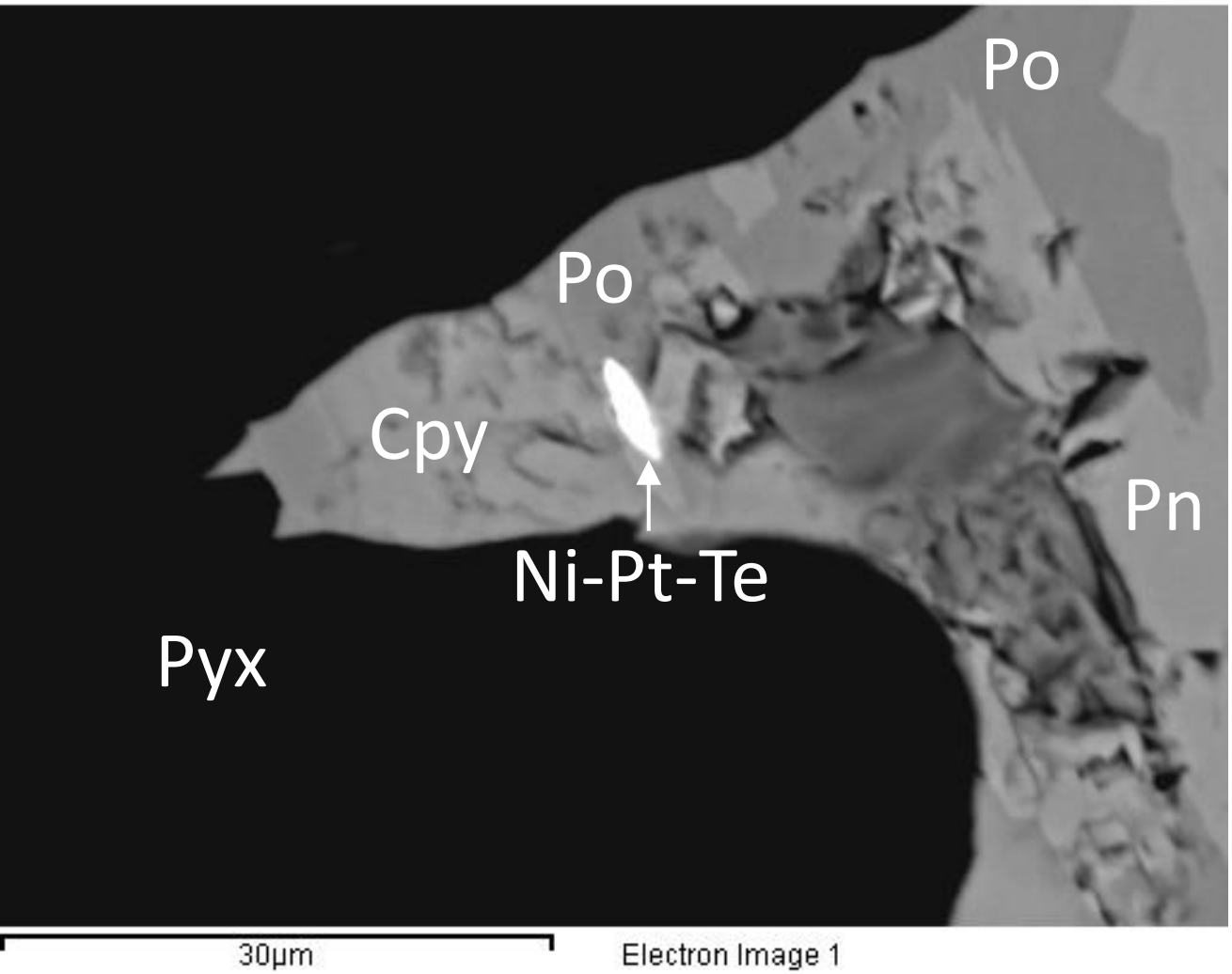
PTR19 G 1



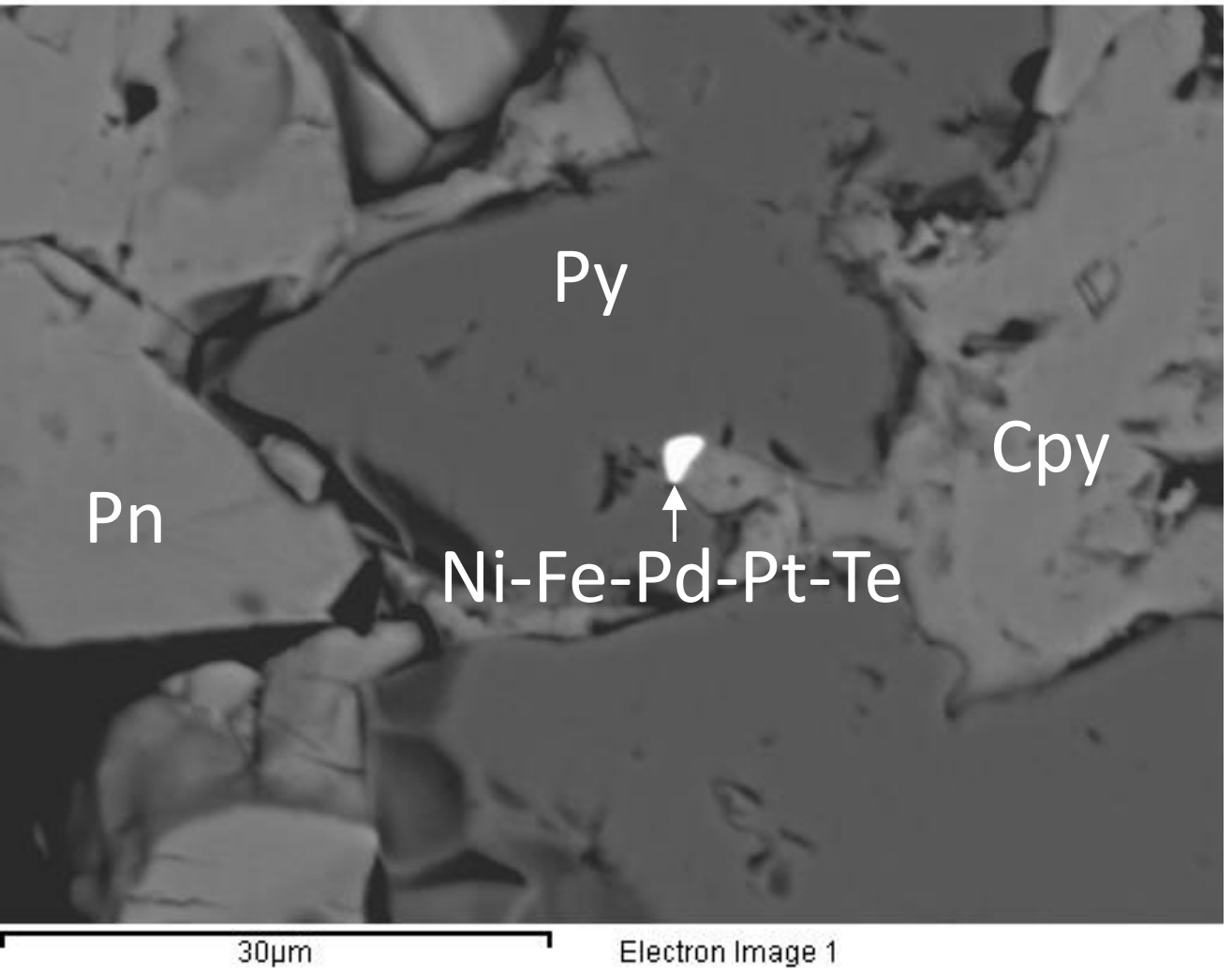
PTR19 H 1



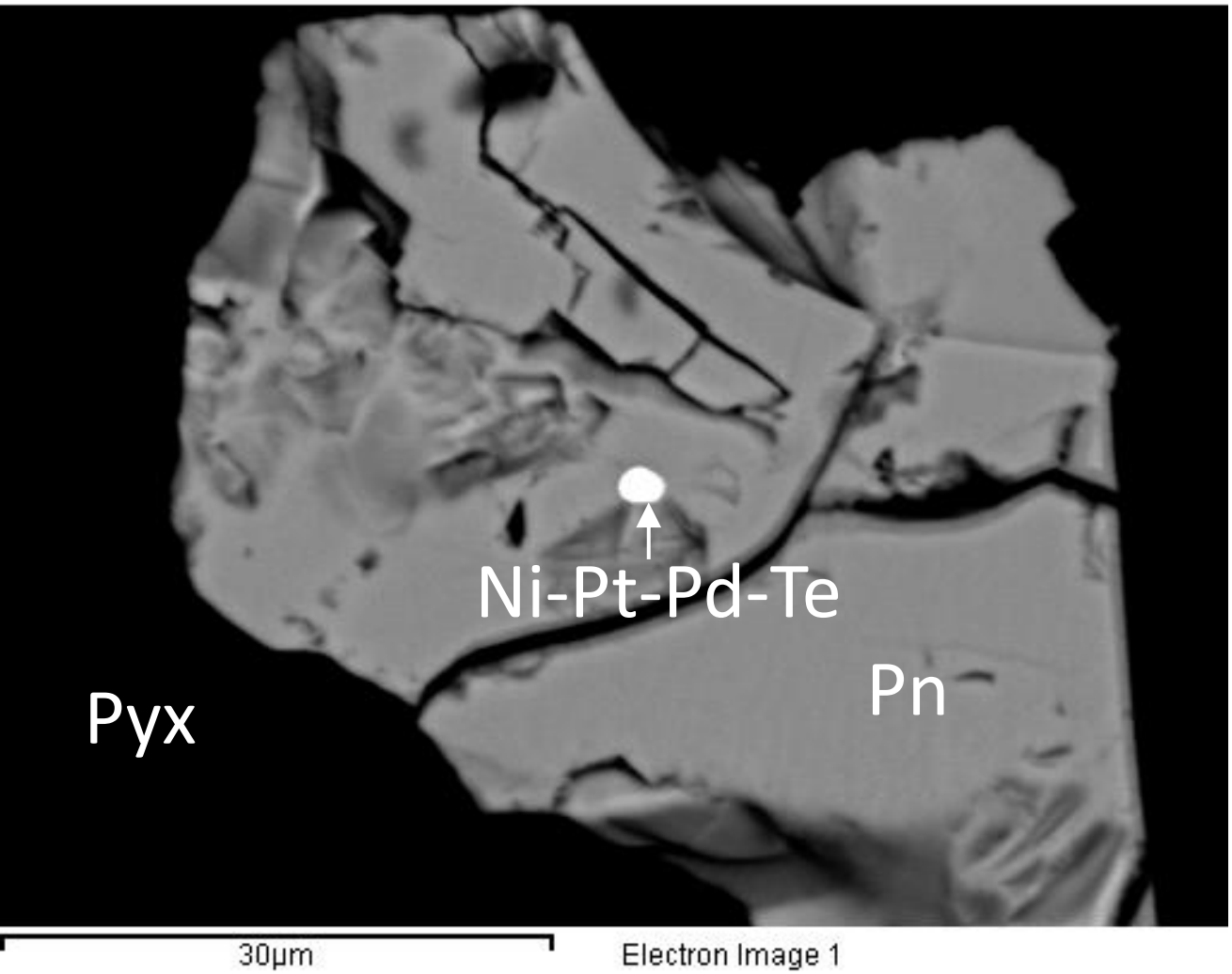
PTR19 I 1



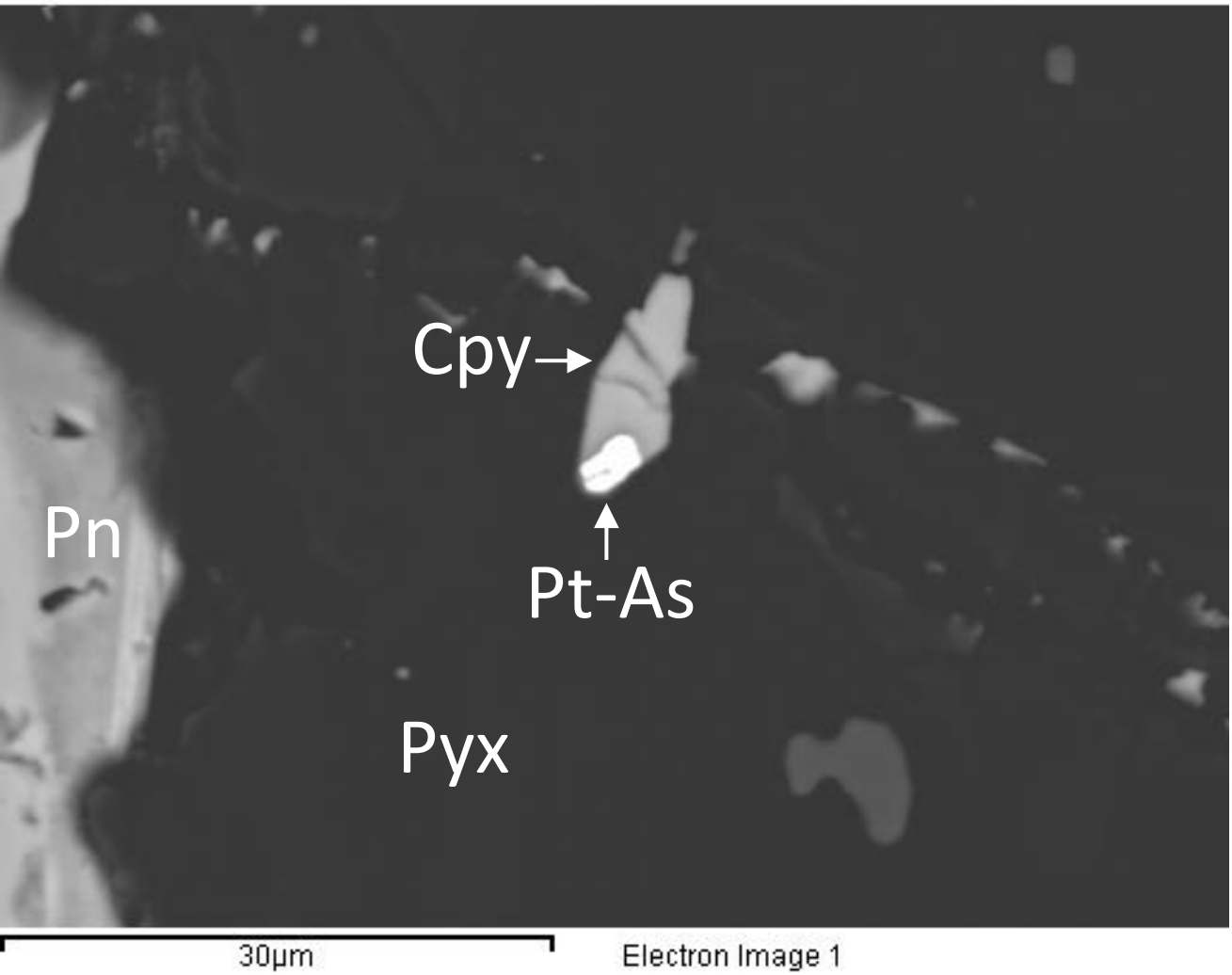
PTR19 J 1



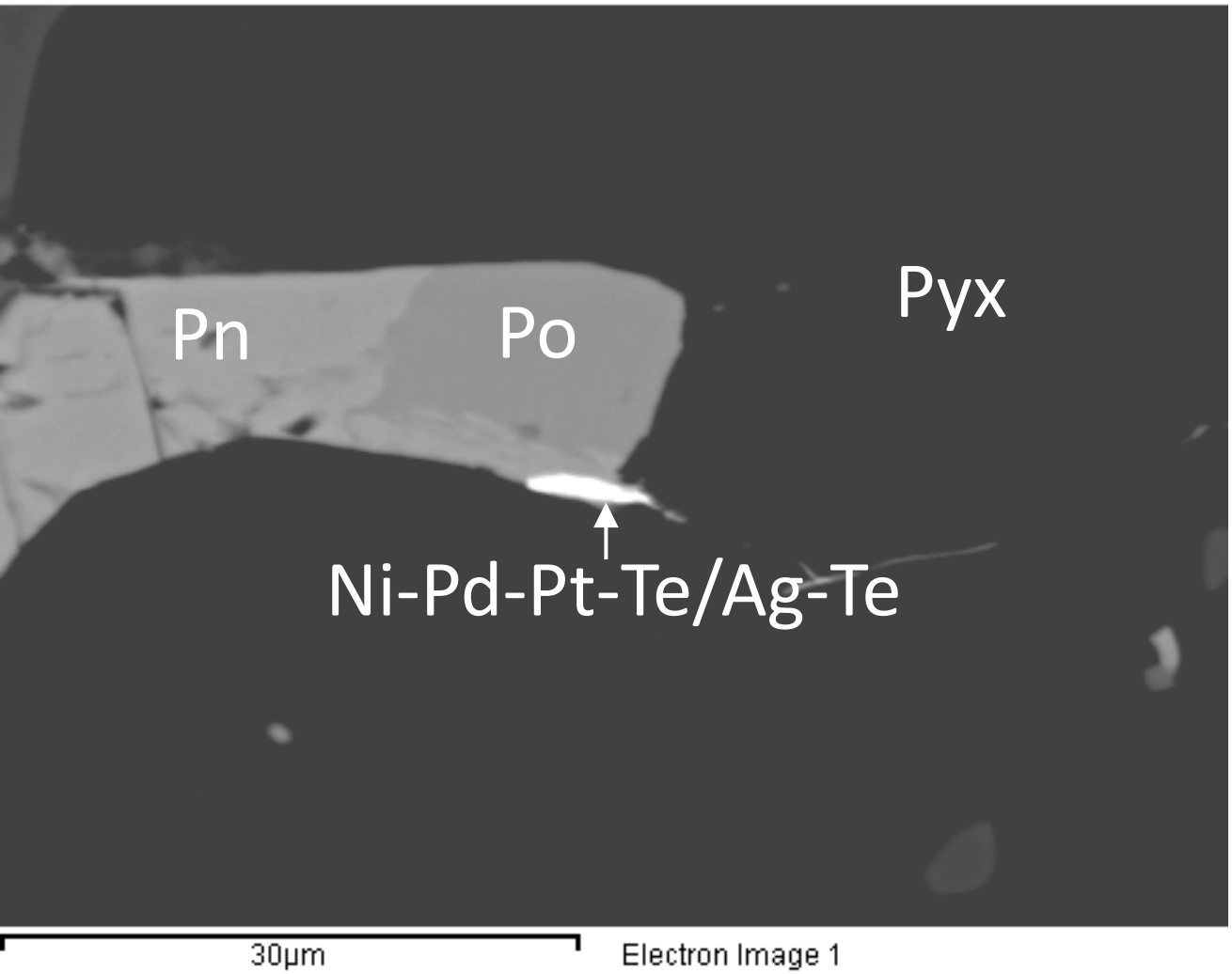
PTR19 K 1



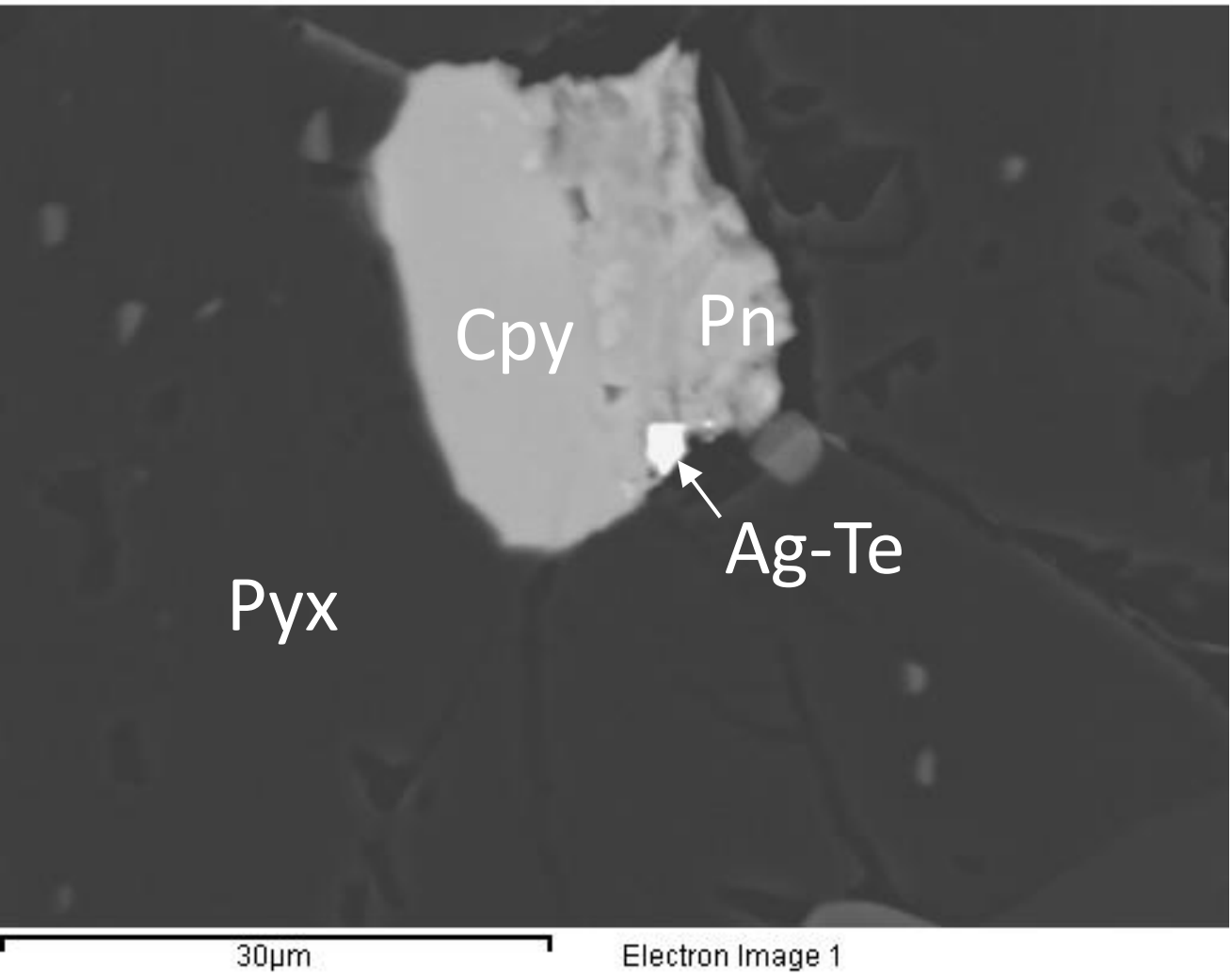
PTR19 L 1



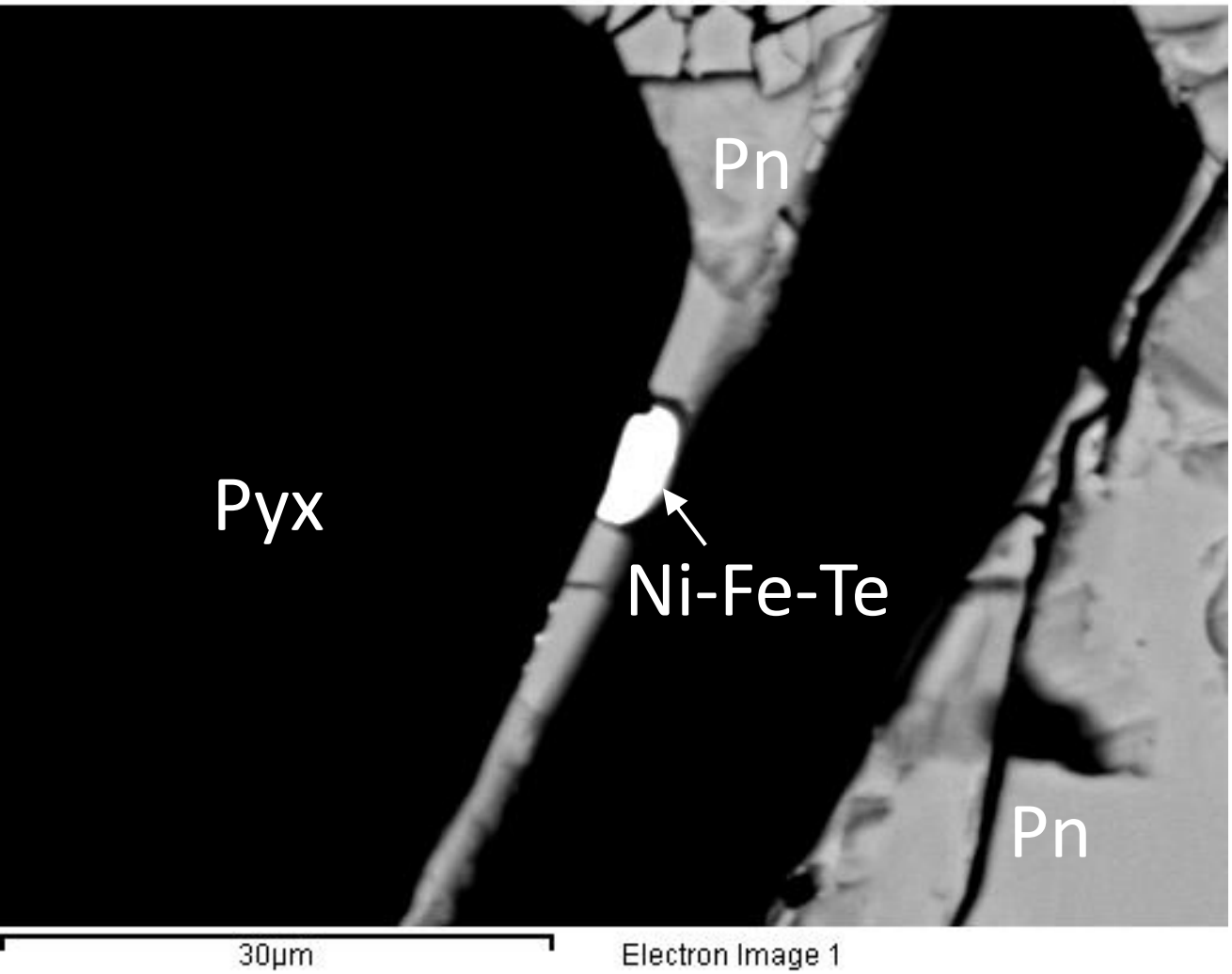
PTR19 M 1



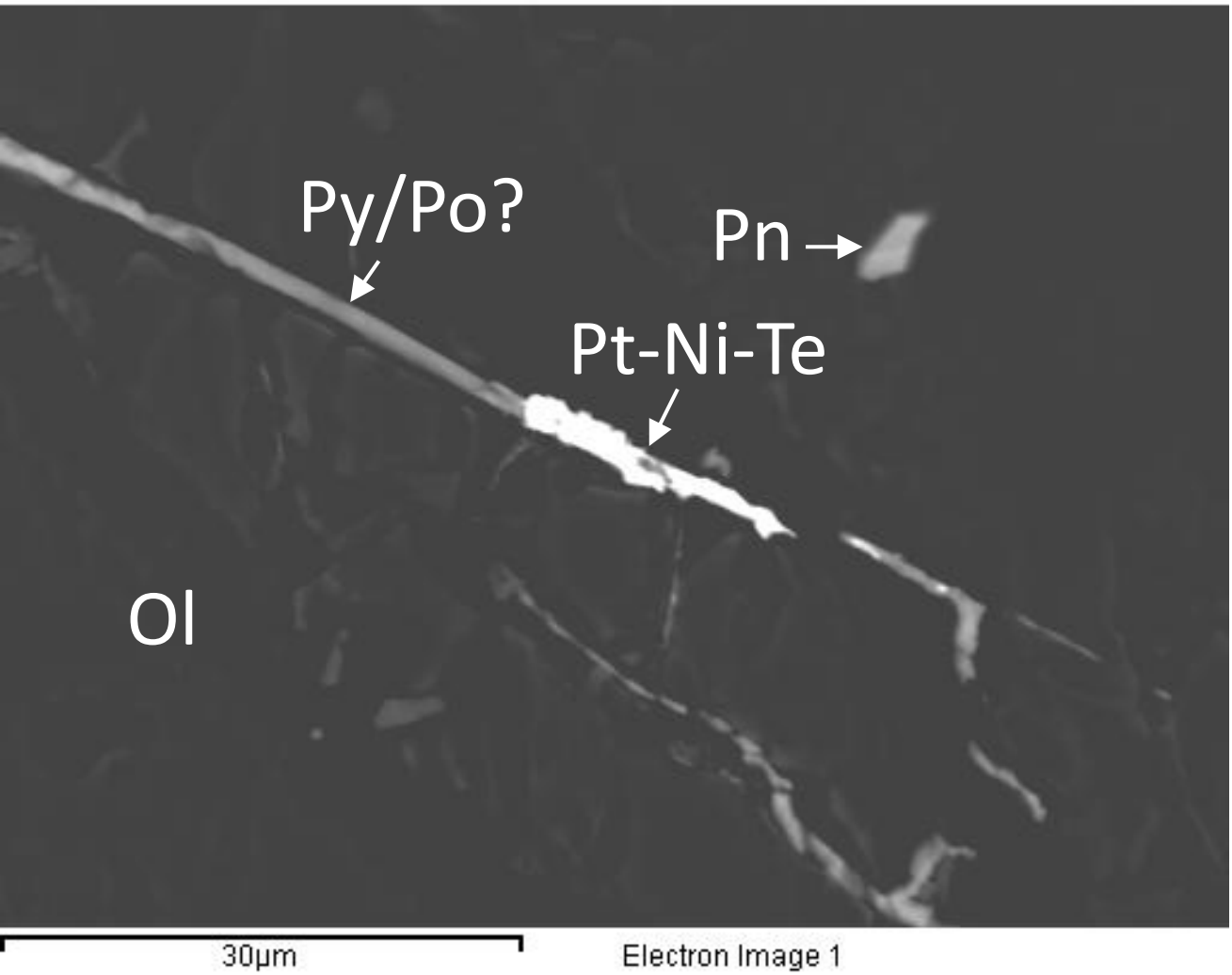
PTR19 N 1



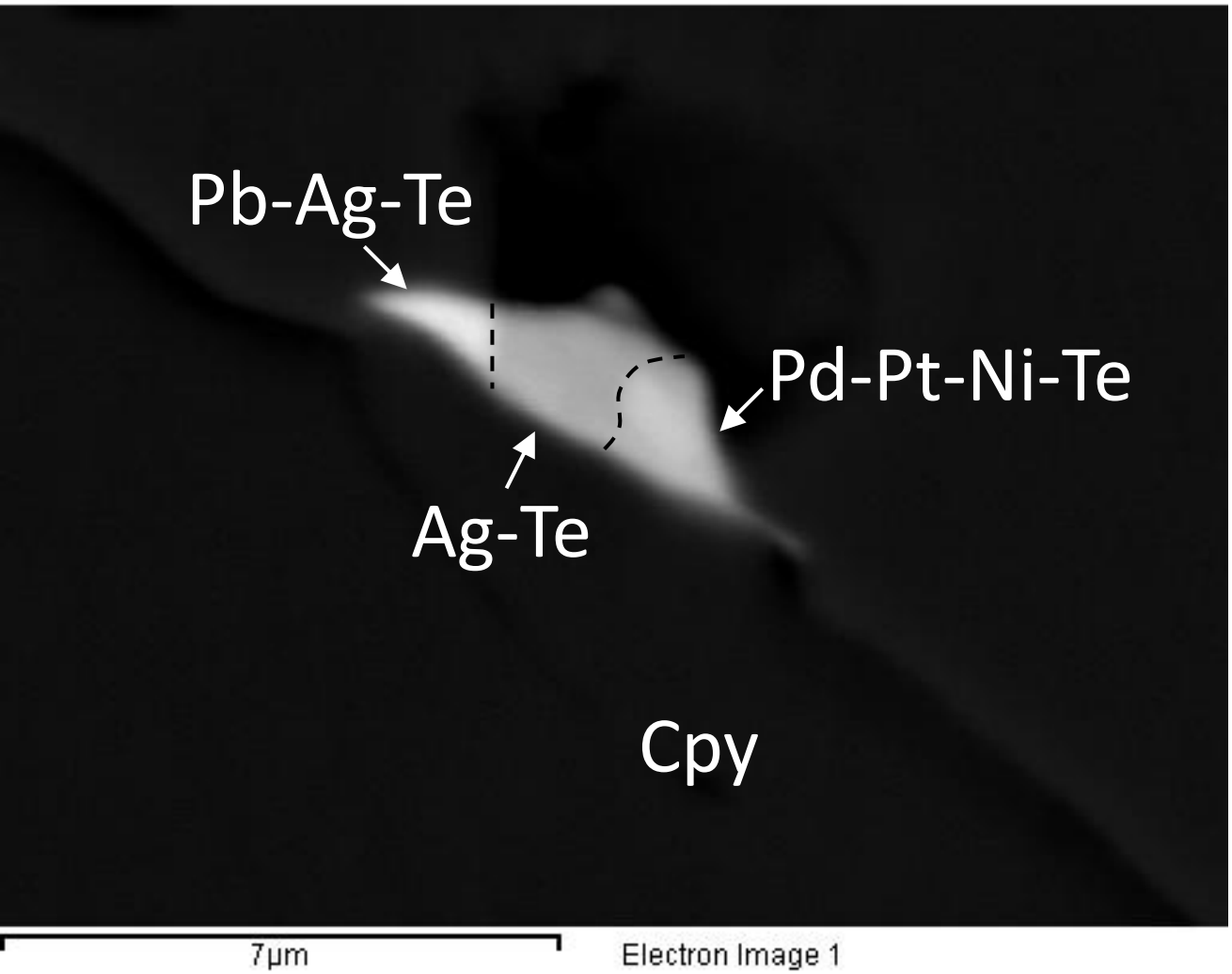
PTR19 O 1



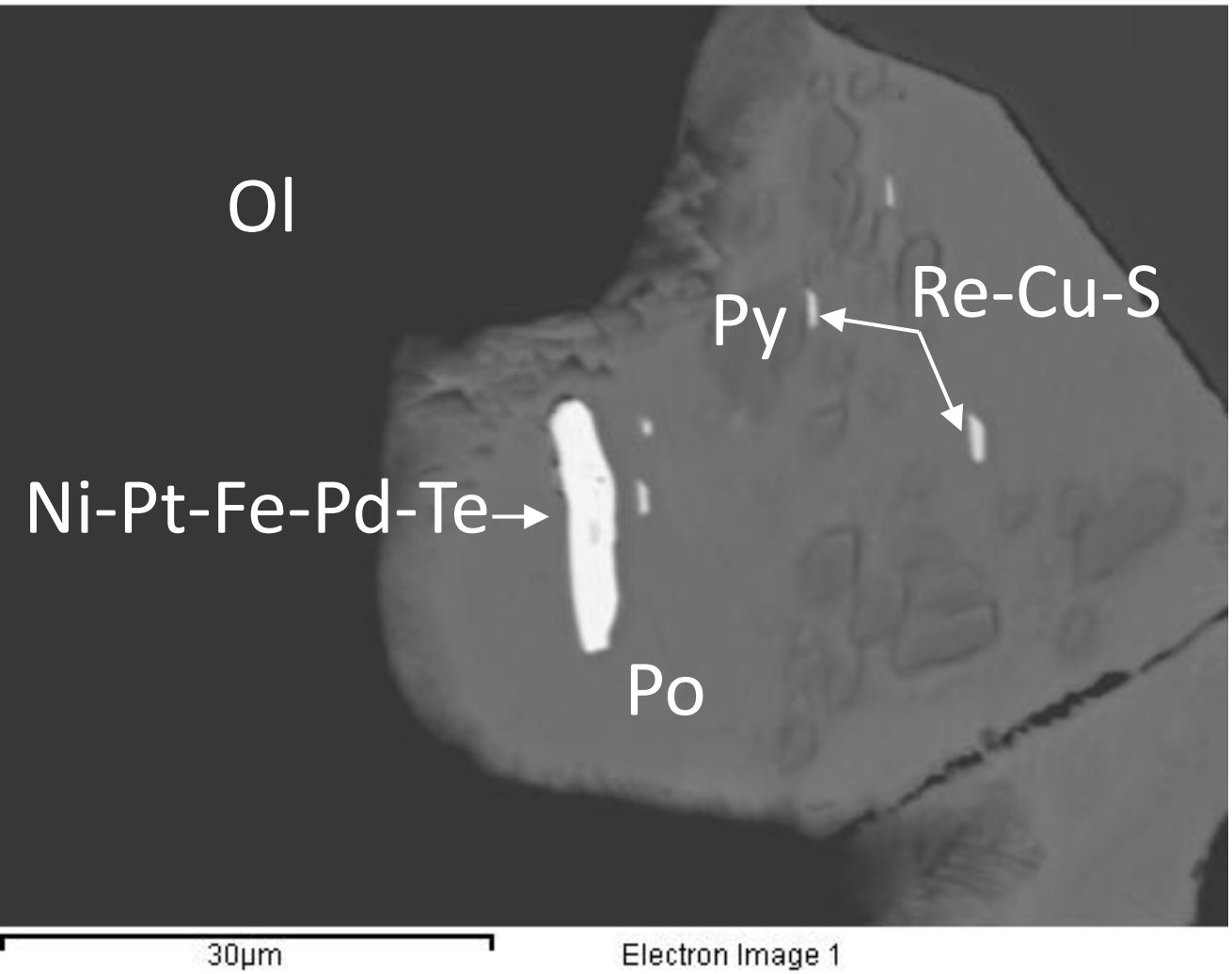
PTR20 A 1



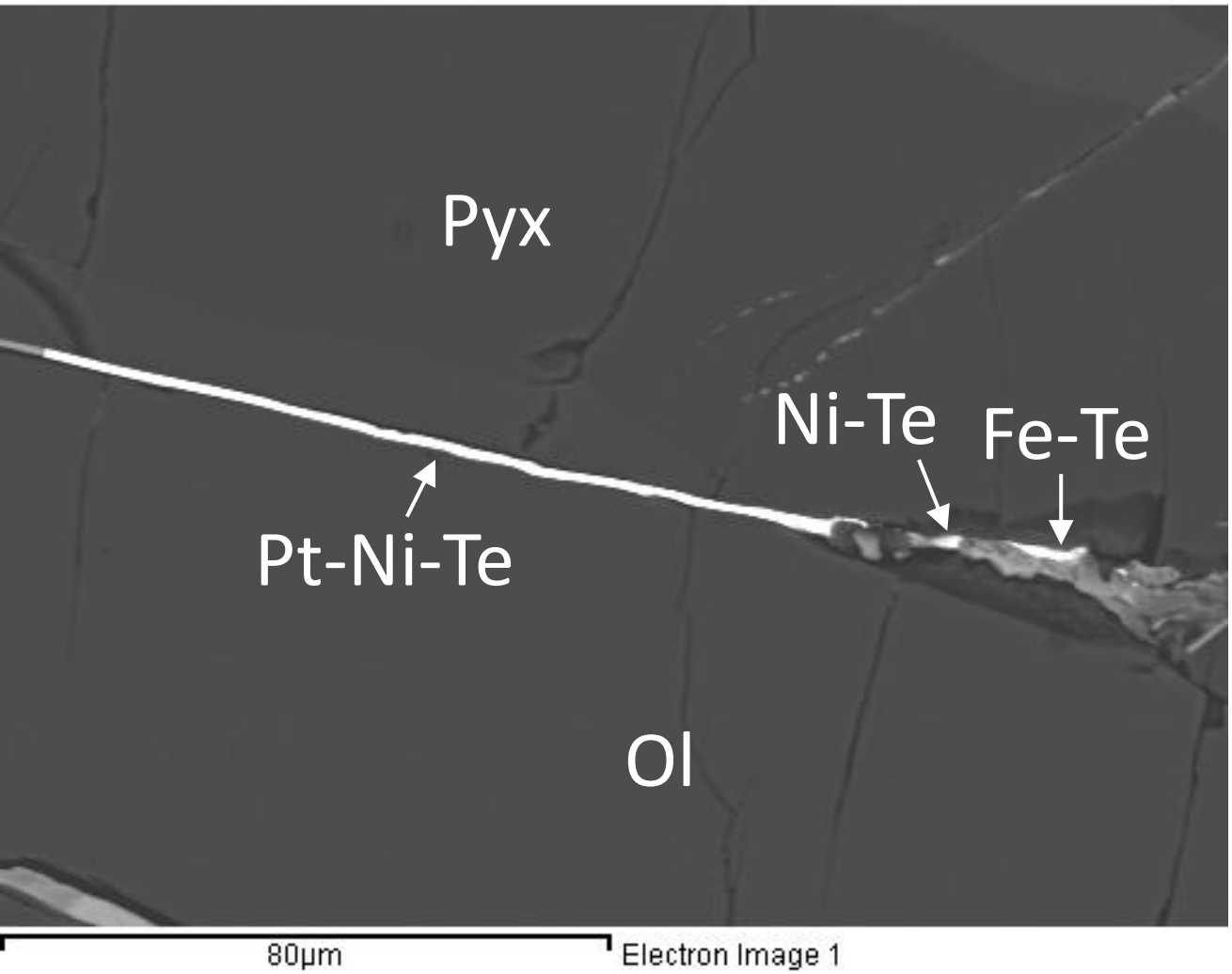
PTR20 B 1-3



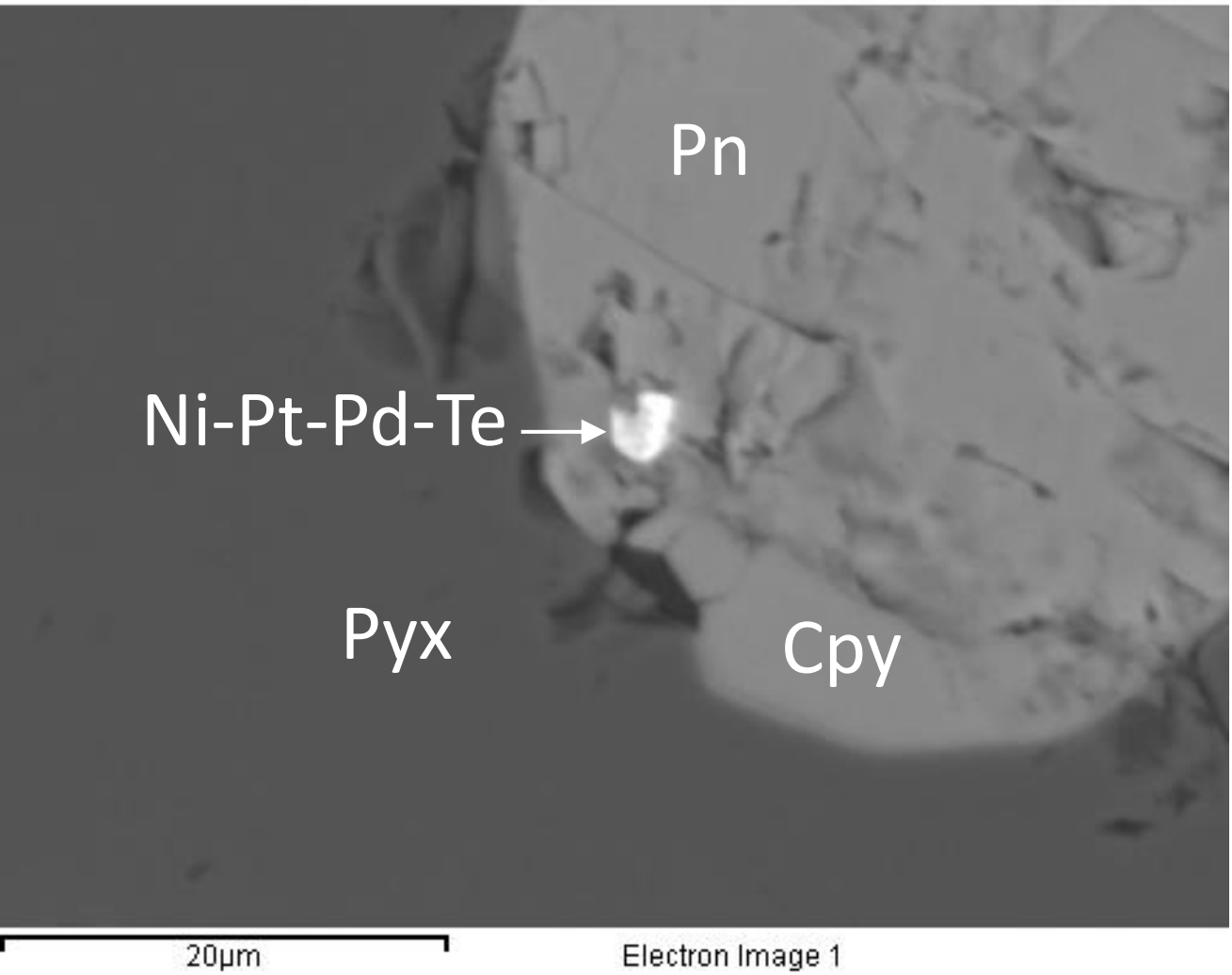
PTR20 C 1+



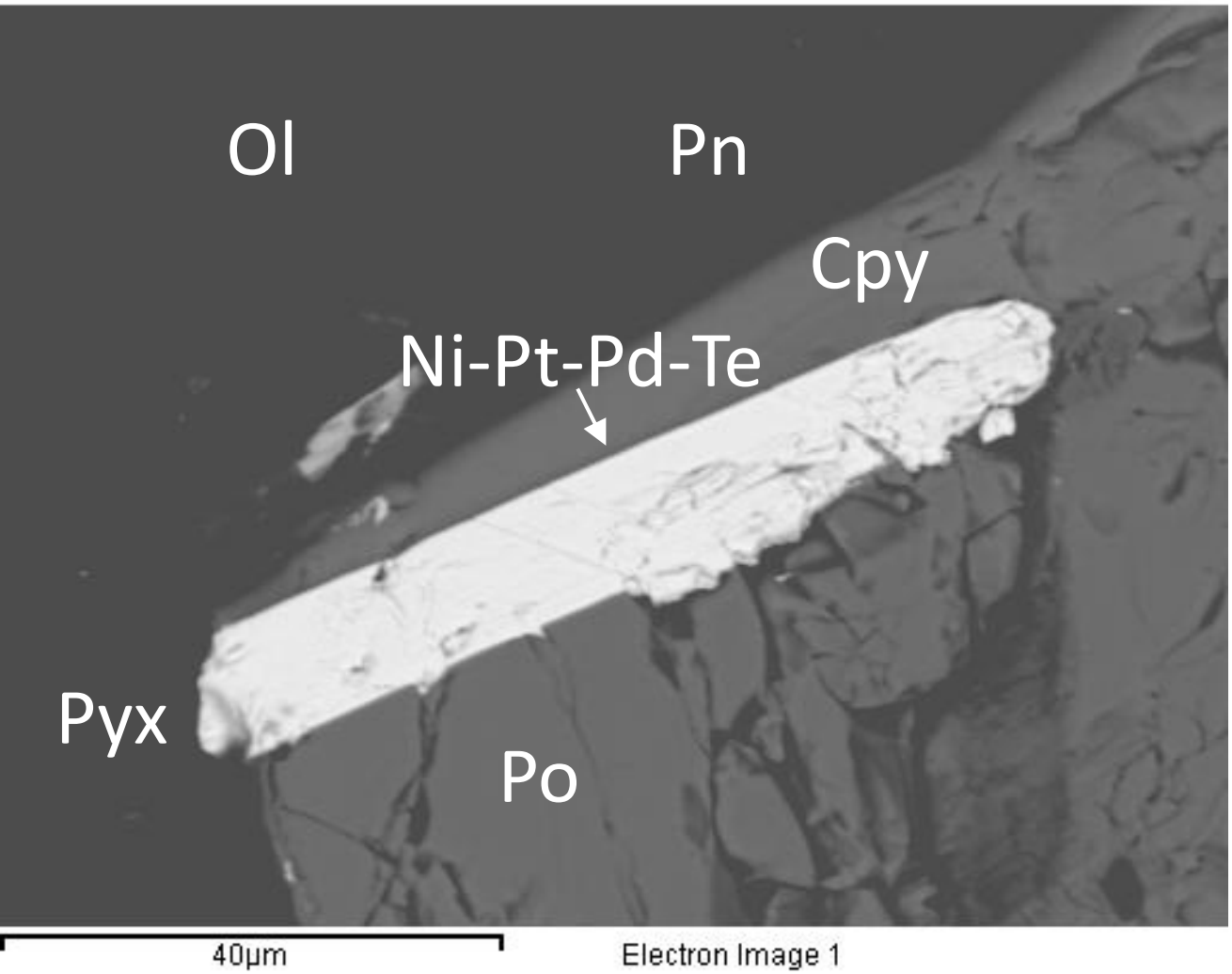
PTR20 D 1-3



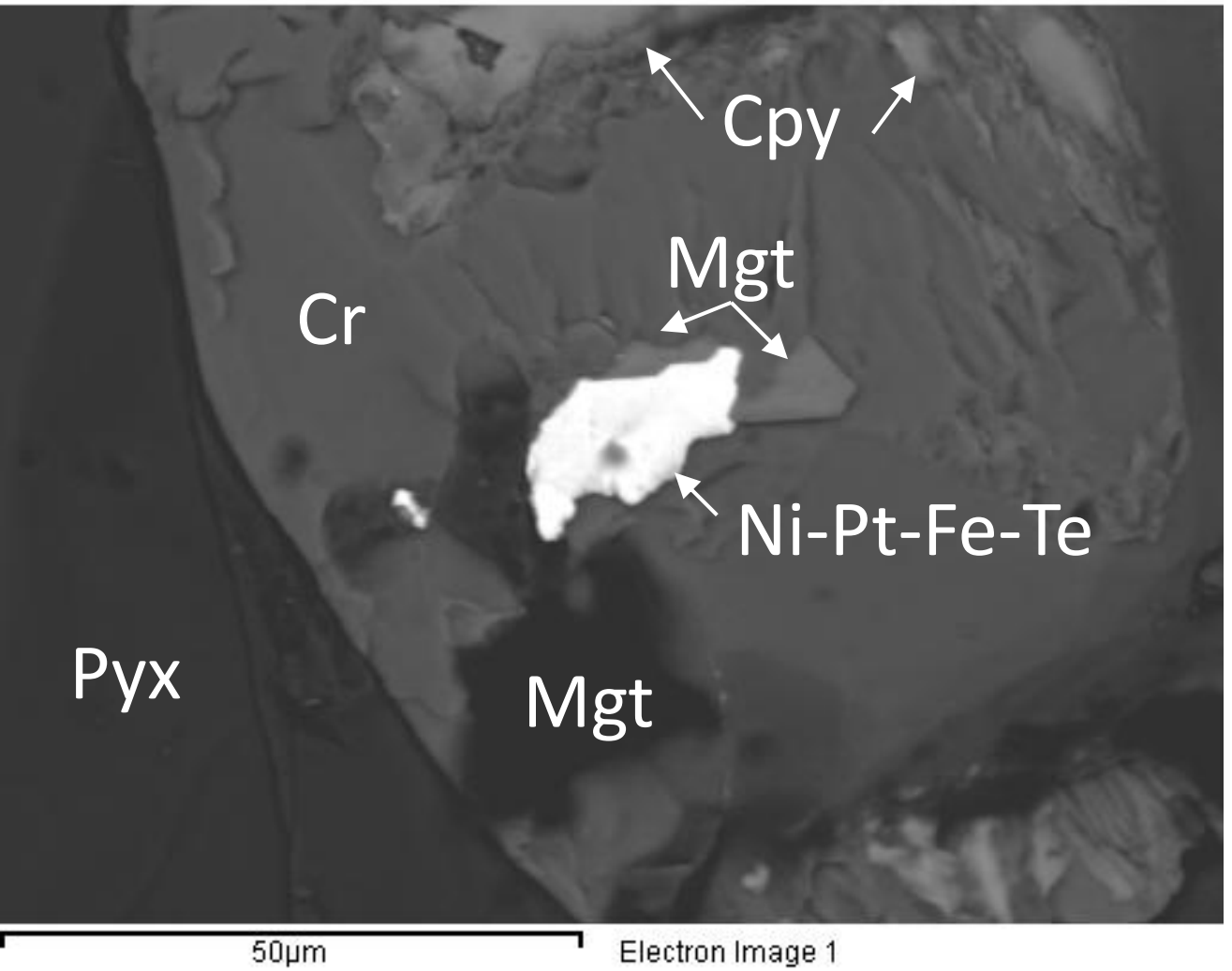
PTR20 E 1



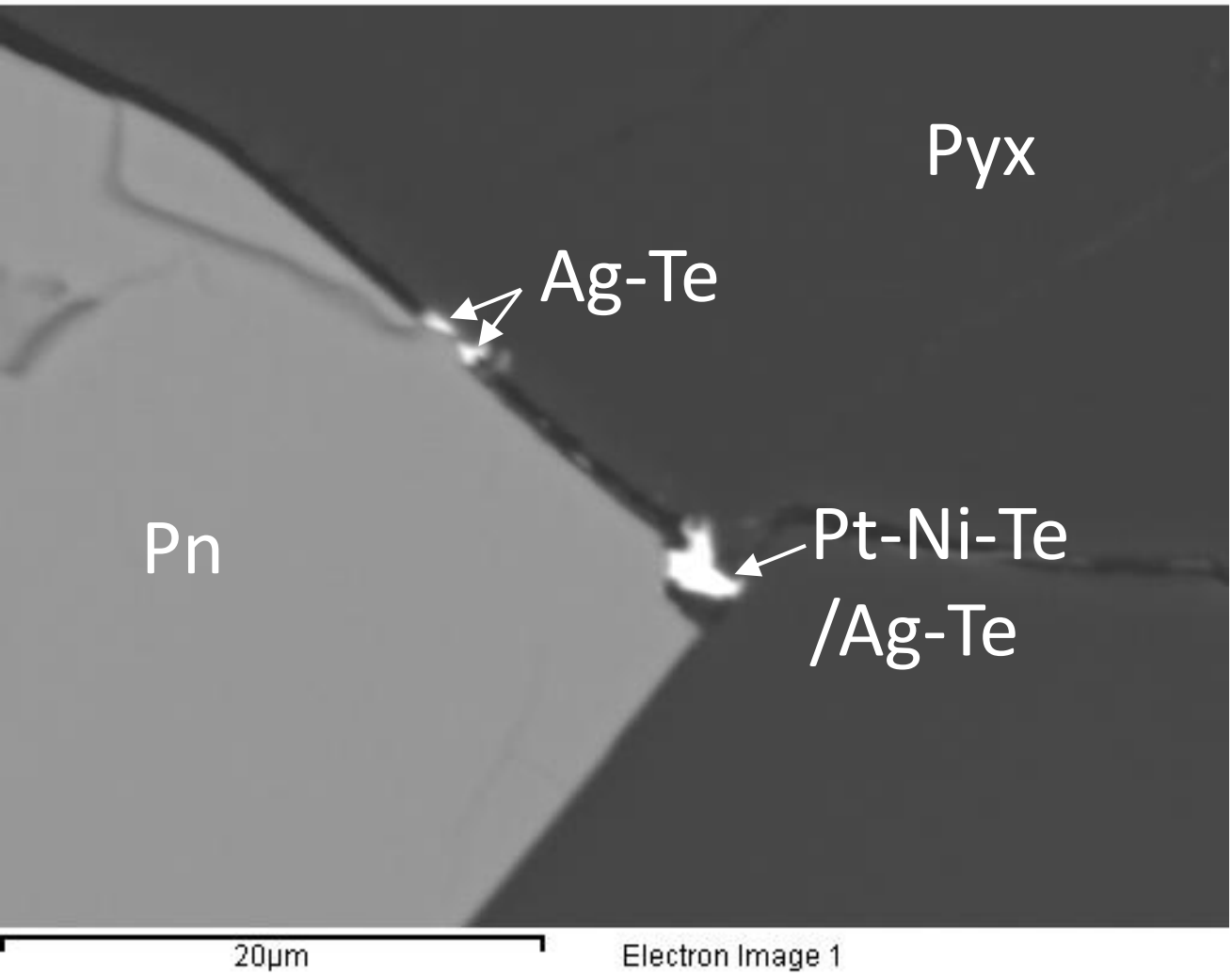
PTR20 F 1



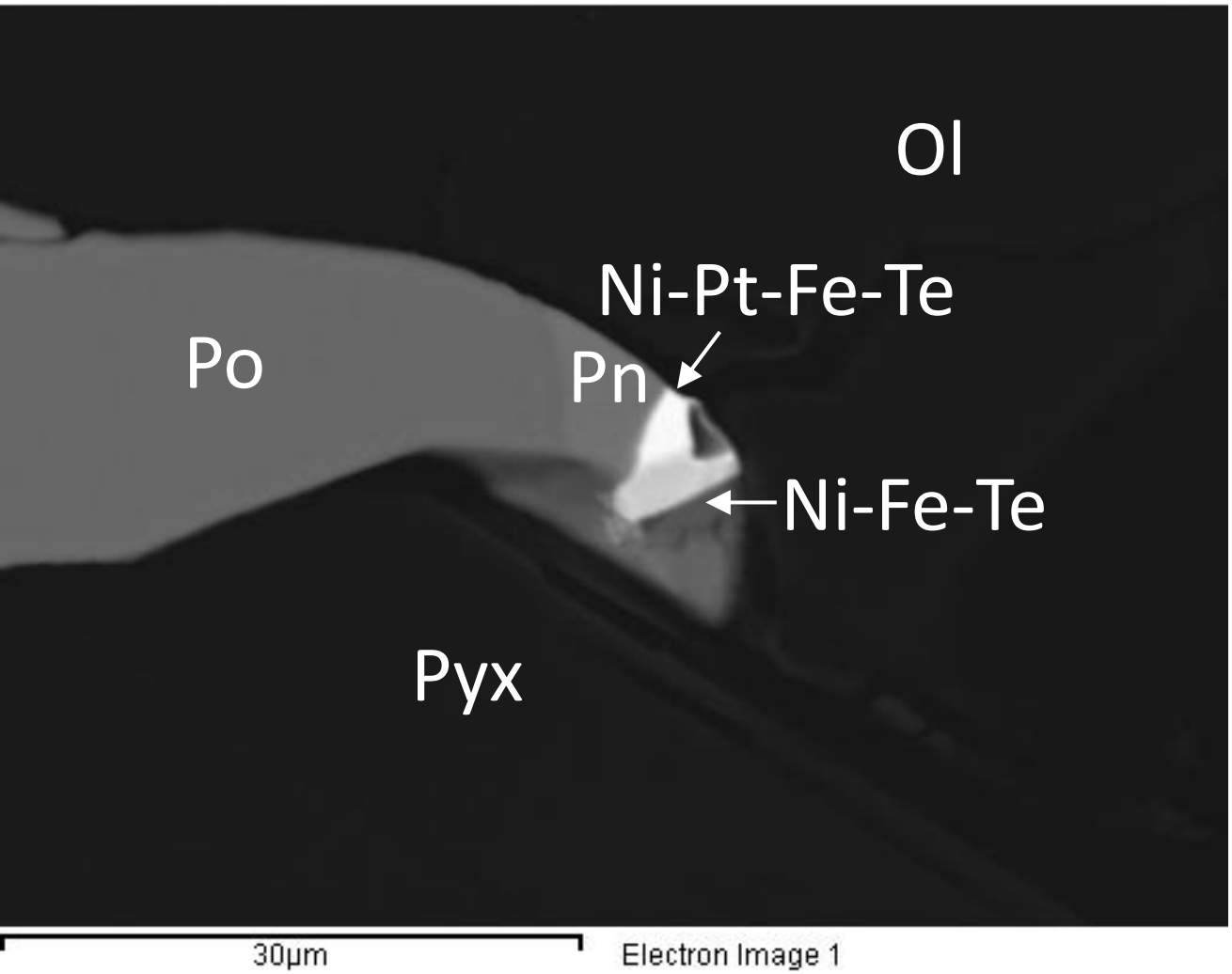
PTR20 G 1



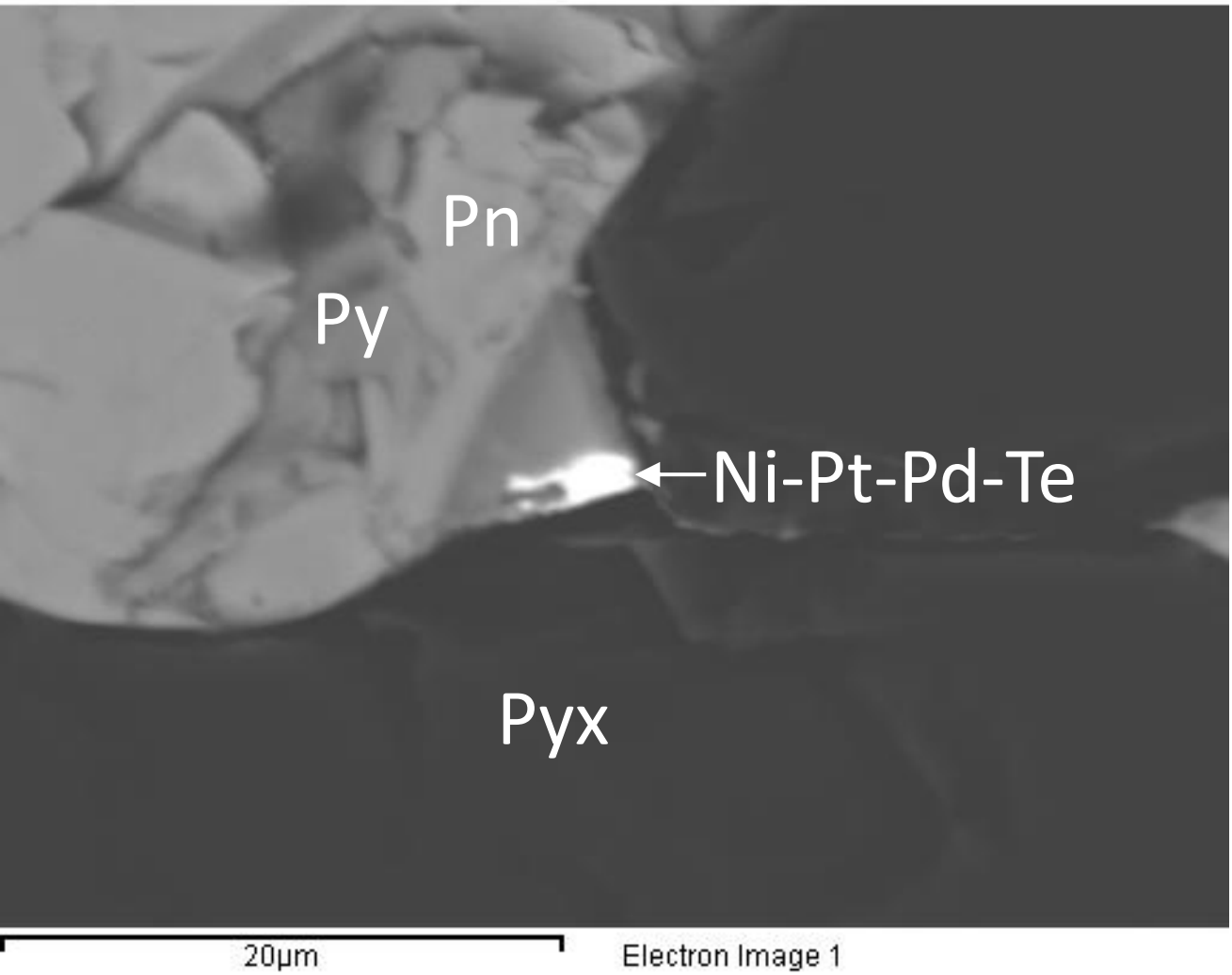
PTR20 H 1-3



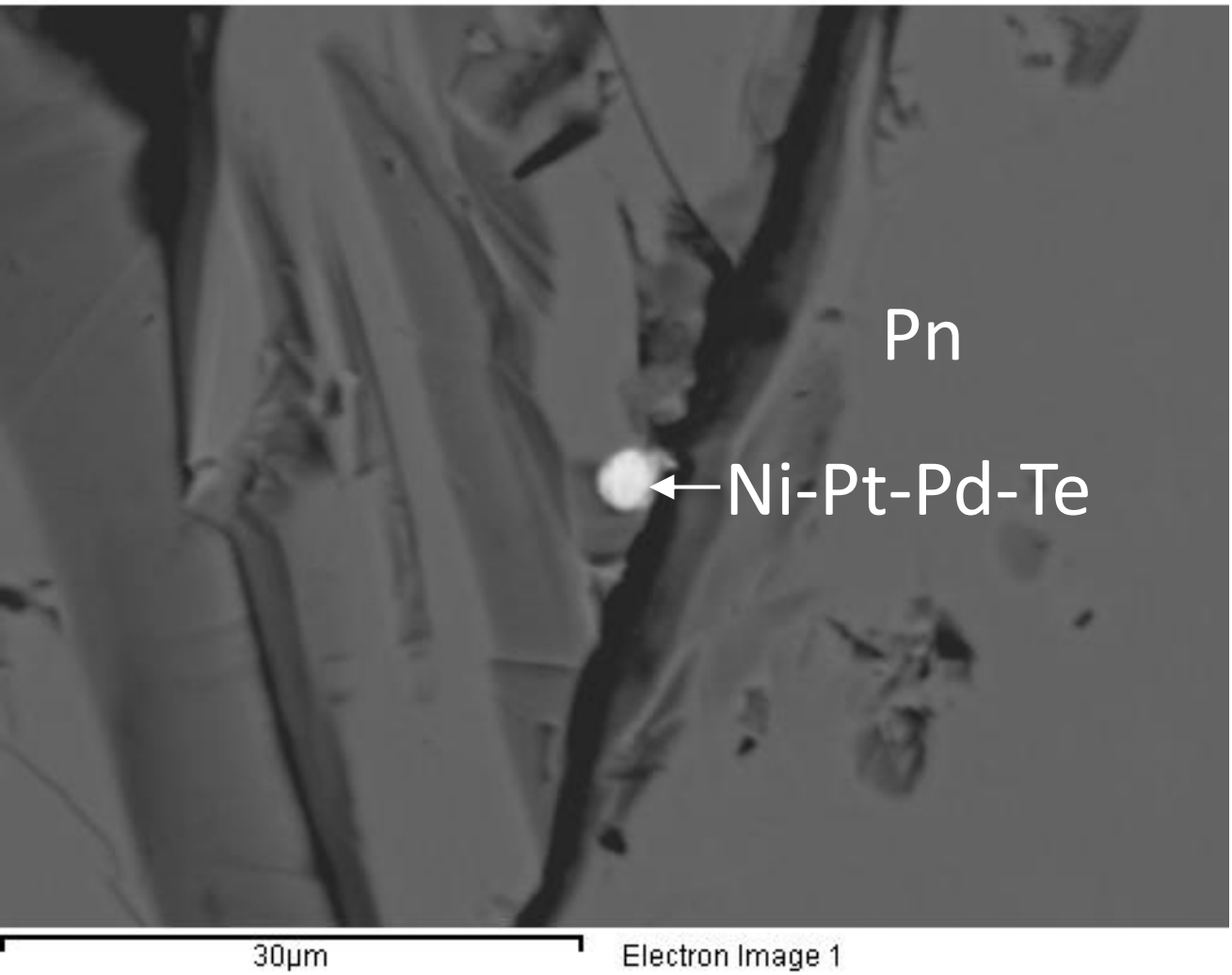
PTR20 I 1-2



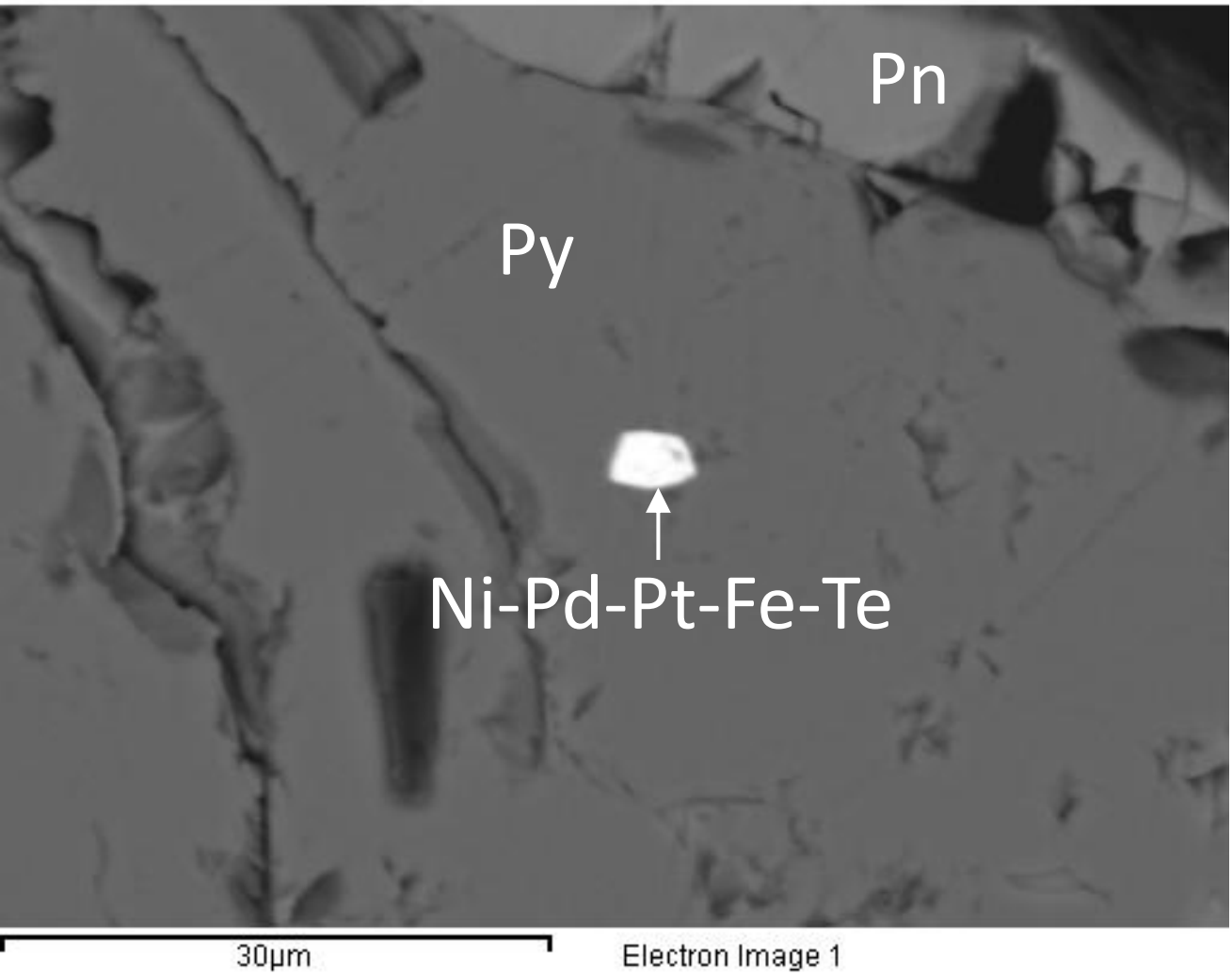
PTR20 J 1



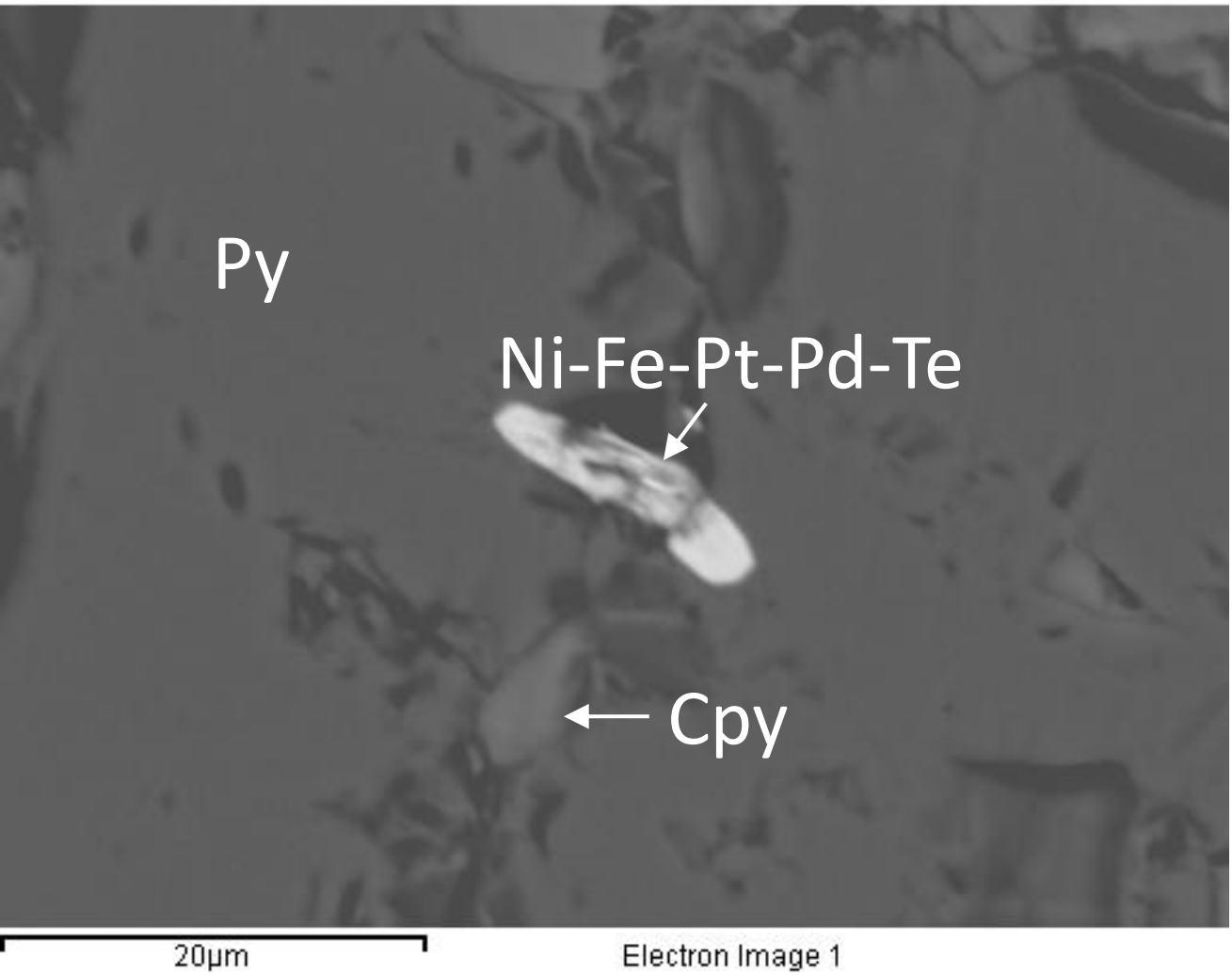
PTR20 K 1



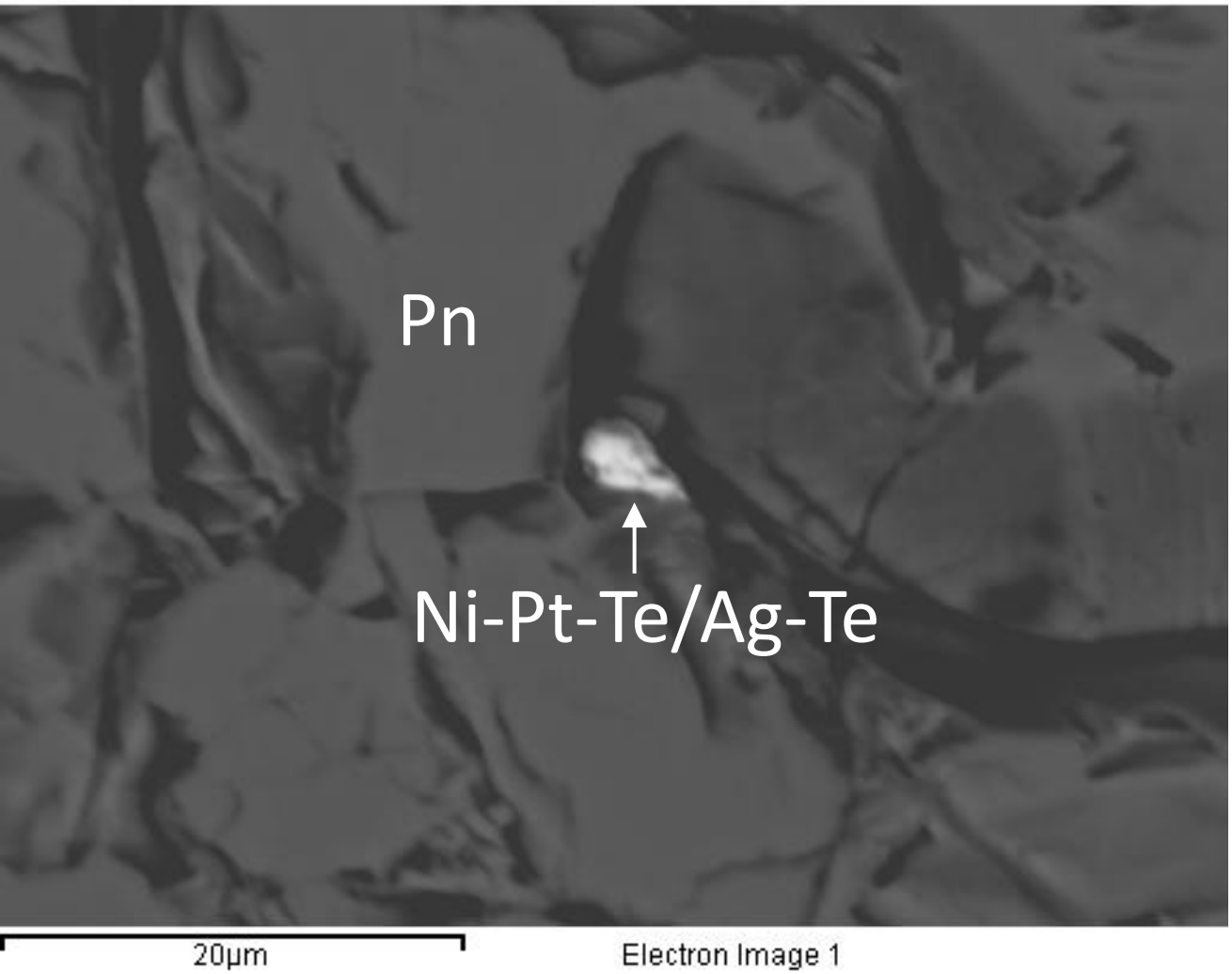
PTR20 L 1



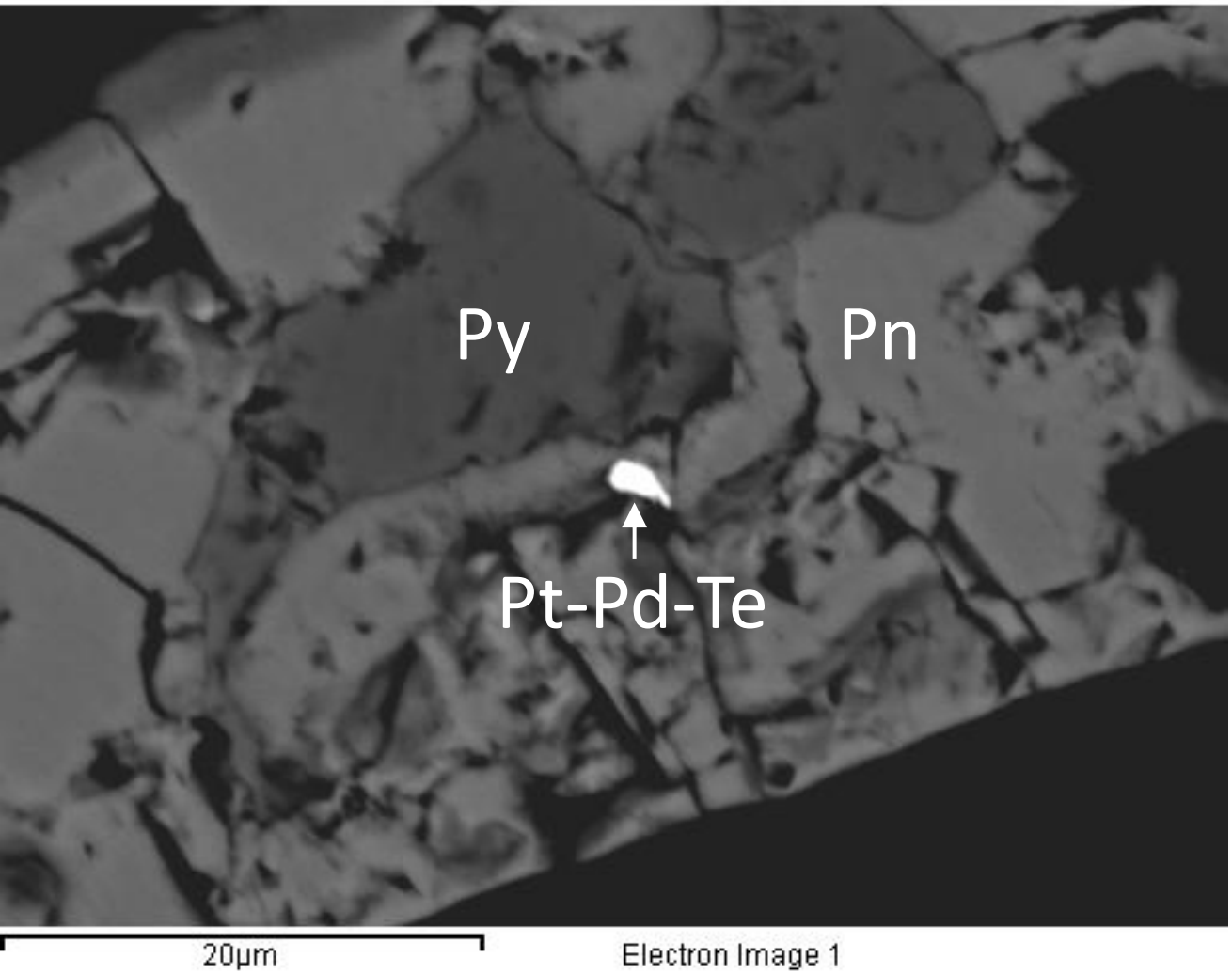
PTR20 M 1



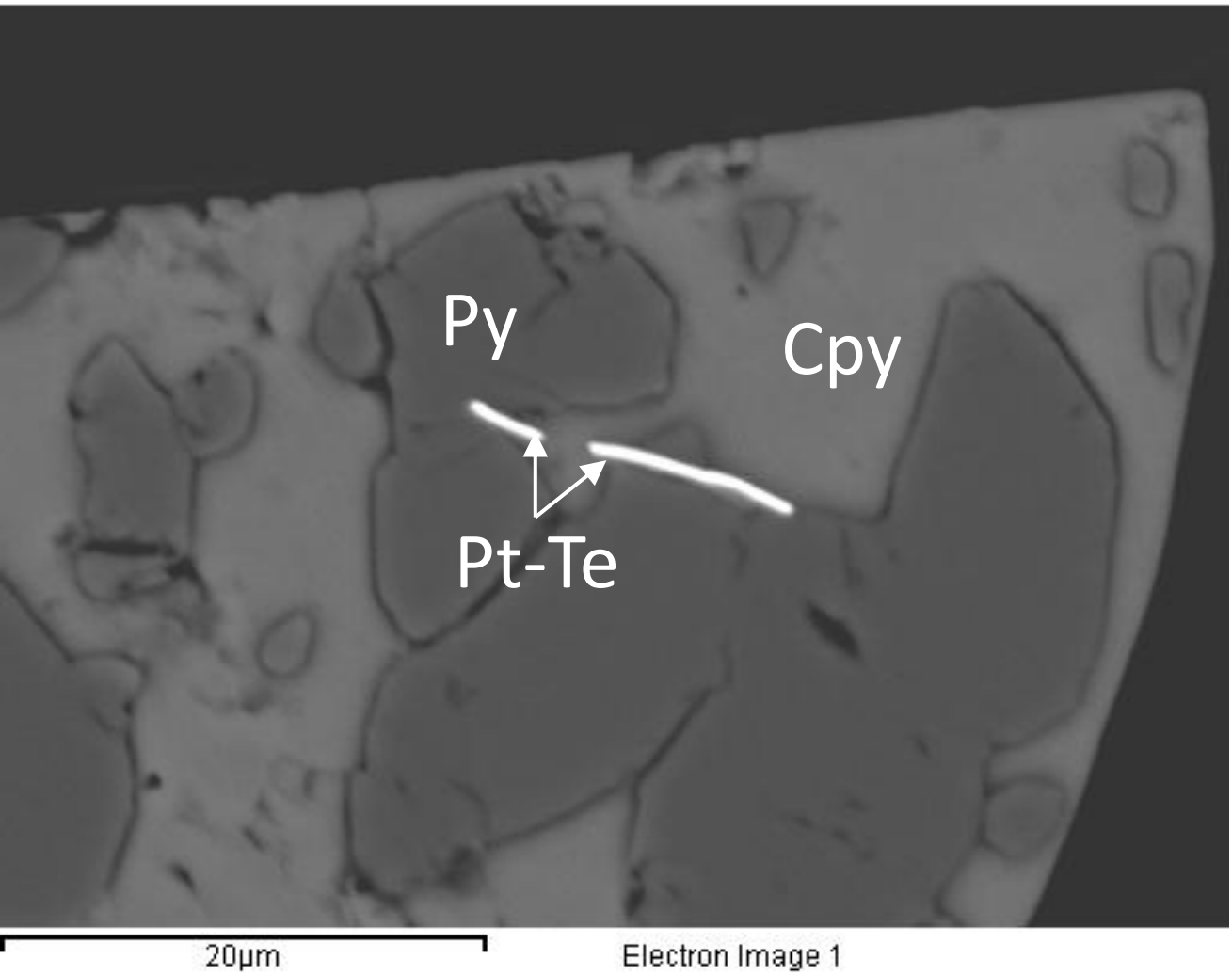
PTR20 N 1



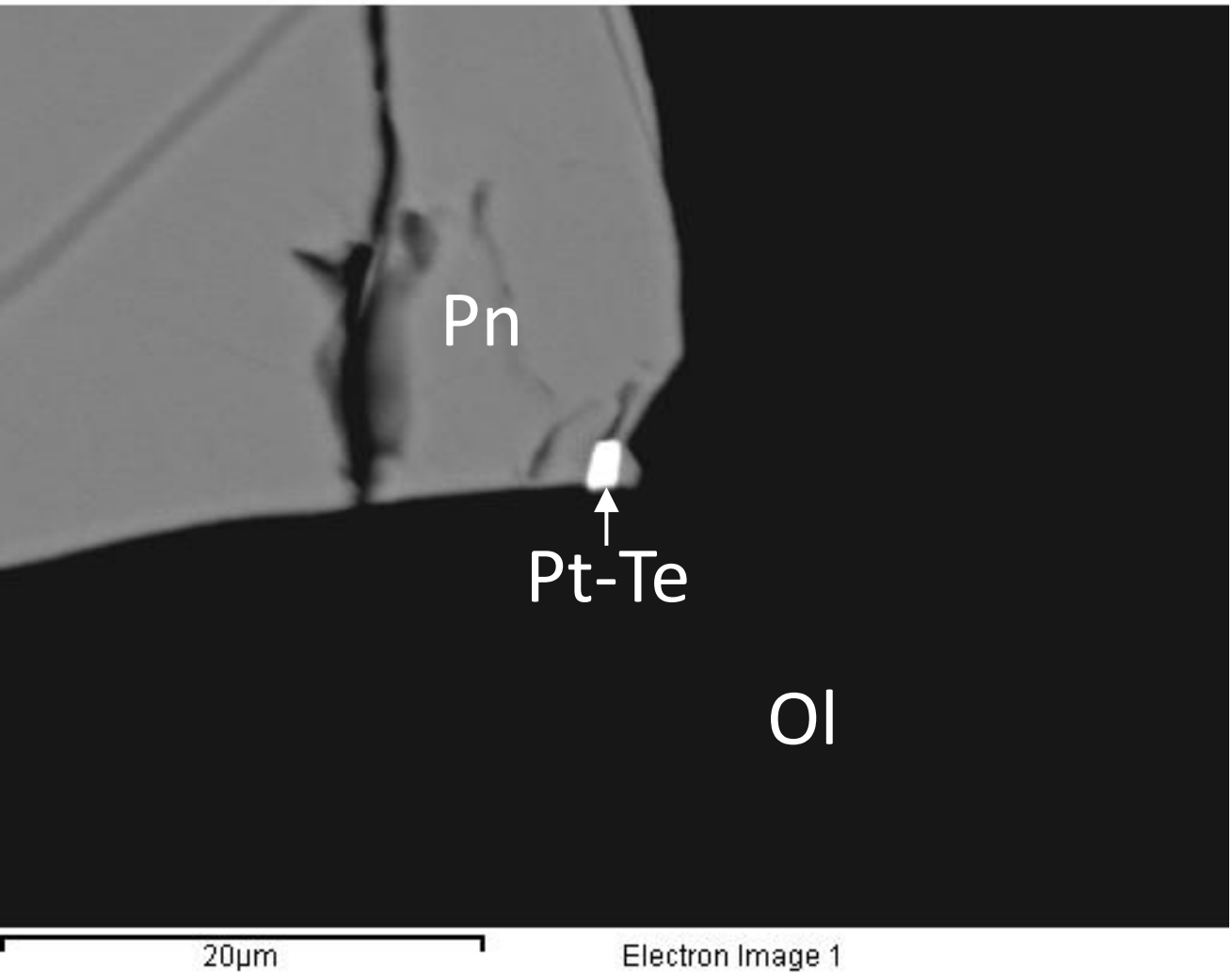
PTR21 A 1



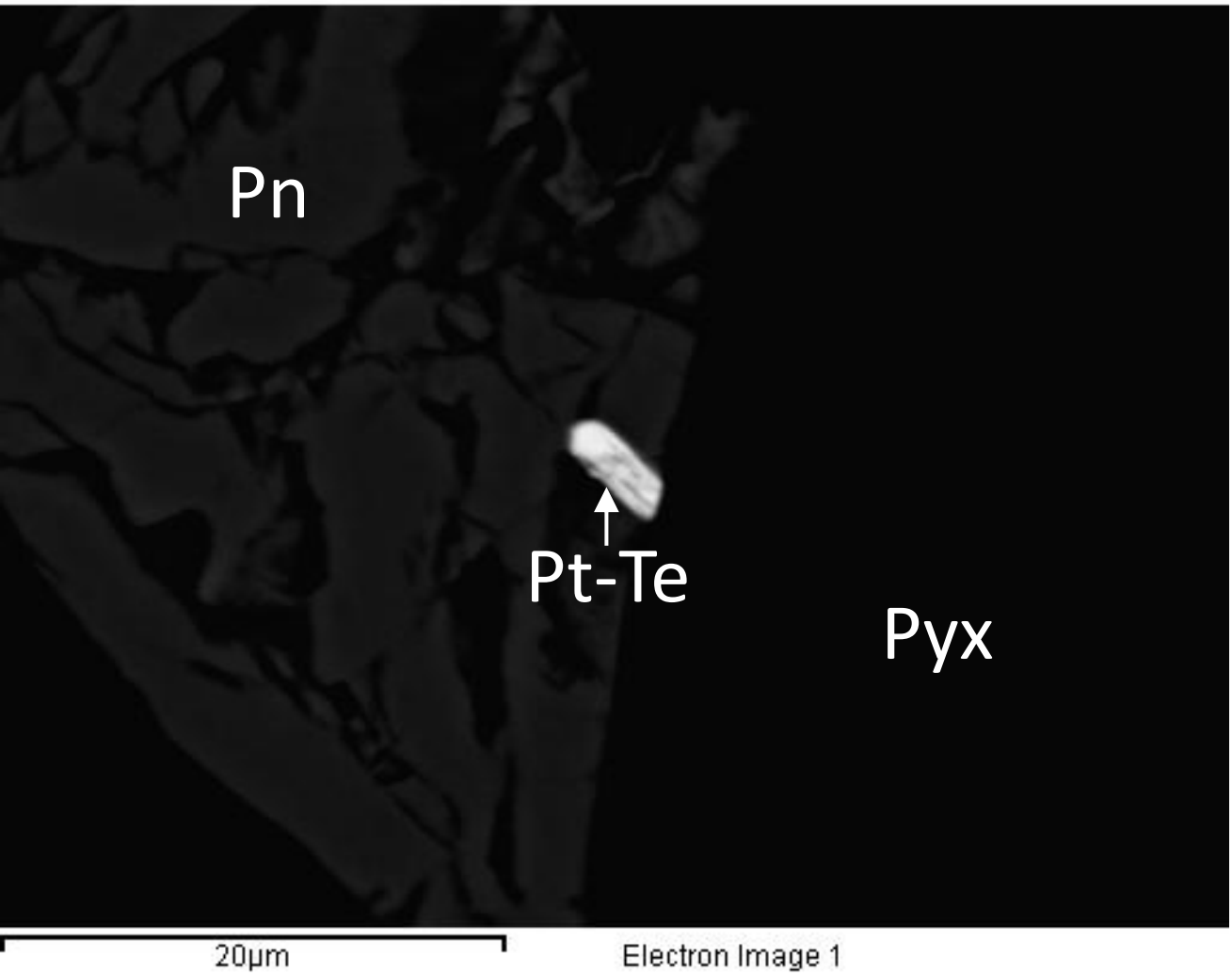
PTR21 B 1-2



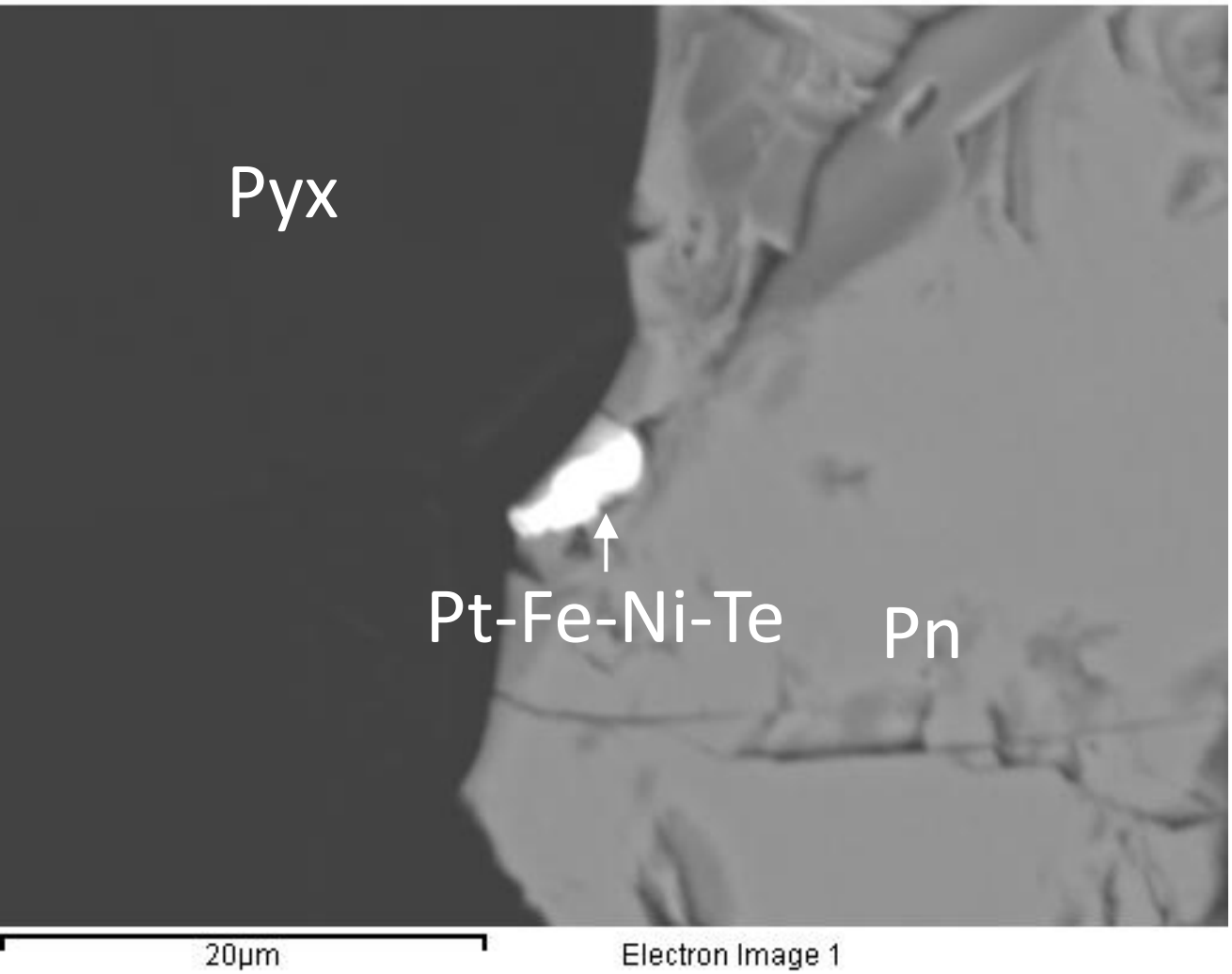
PTR21 C 1



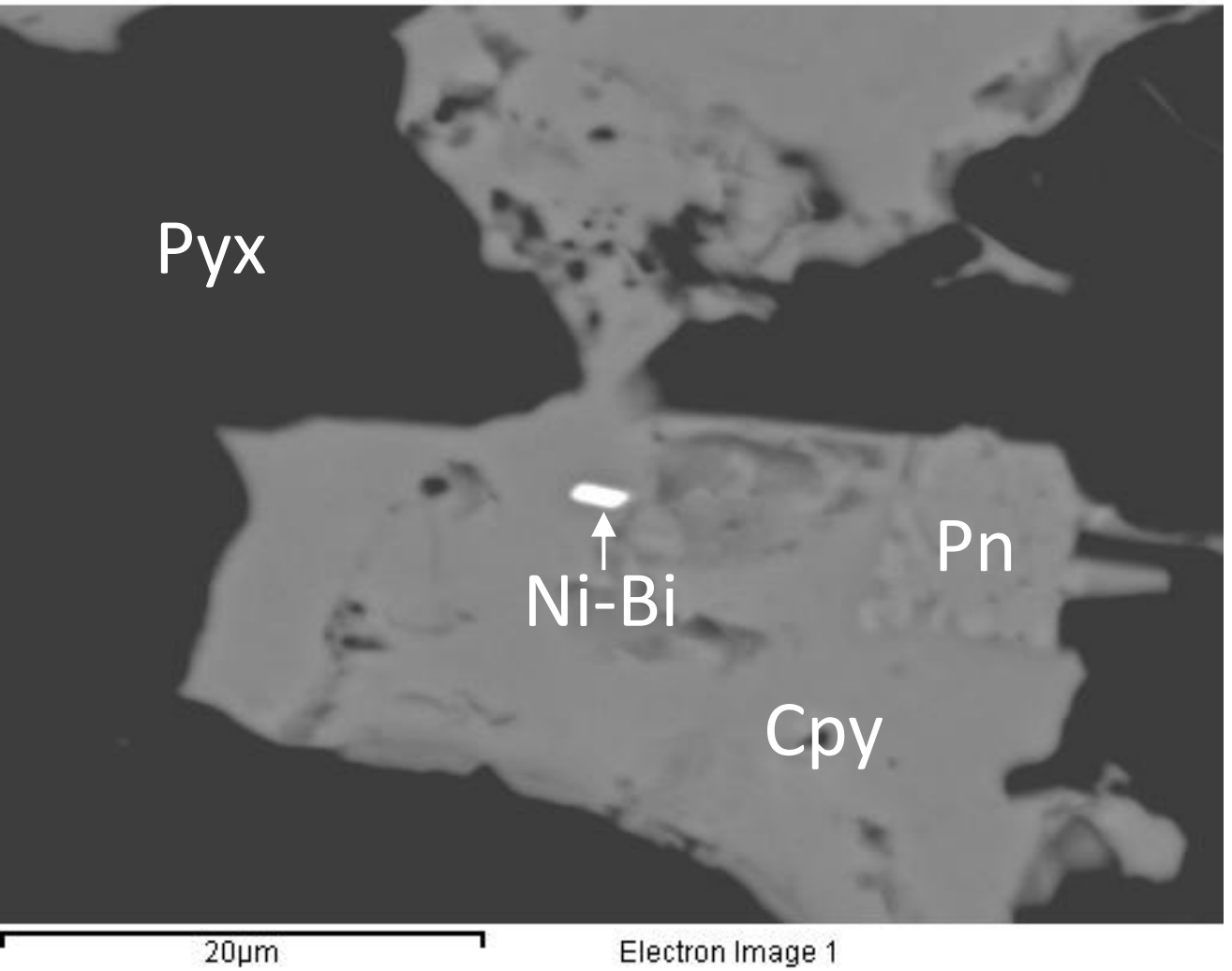
PTR21 D 1



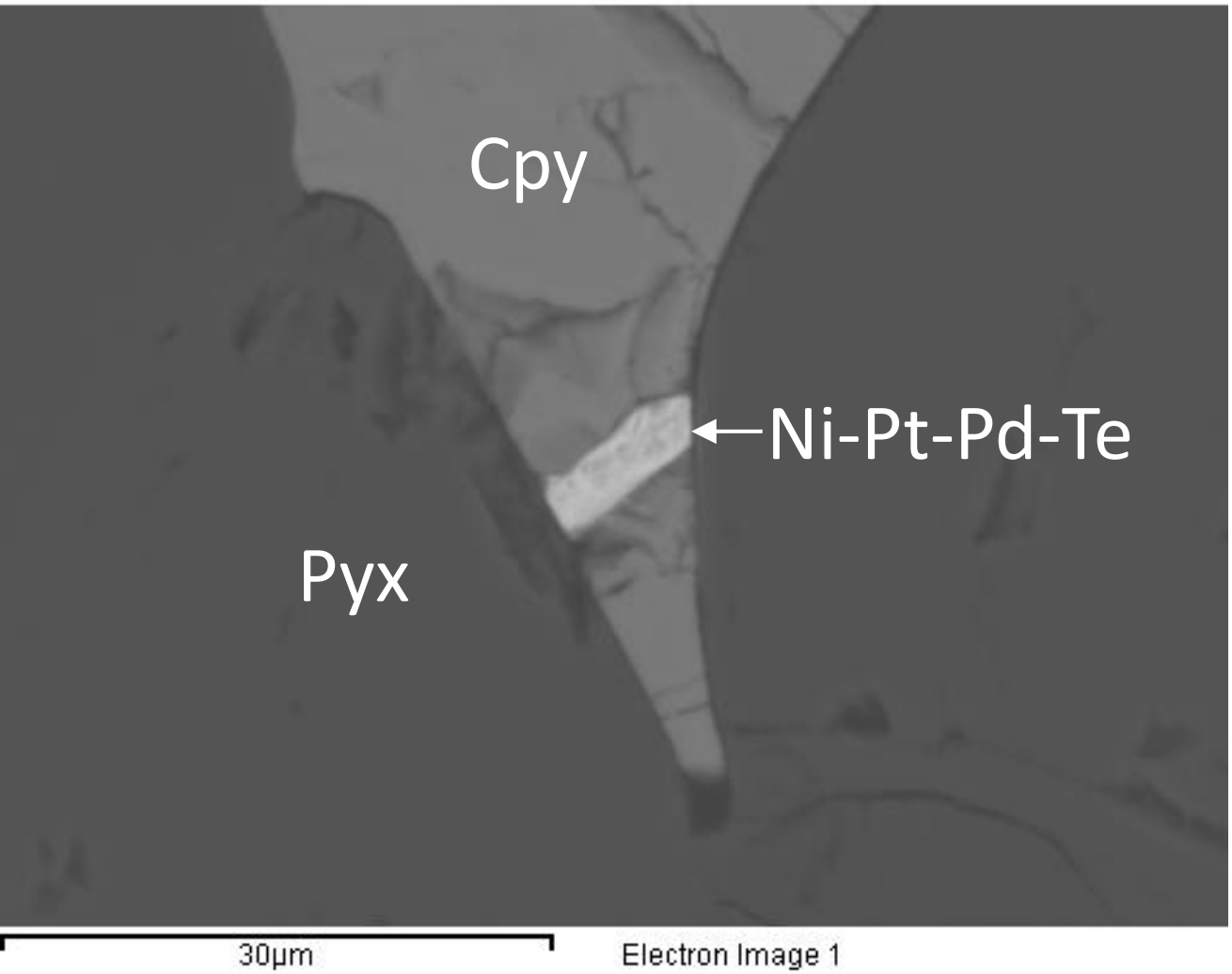
PTR21 E 1



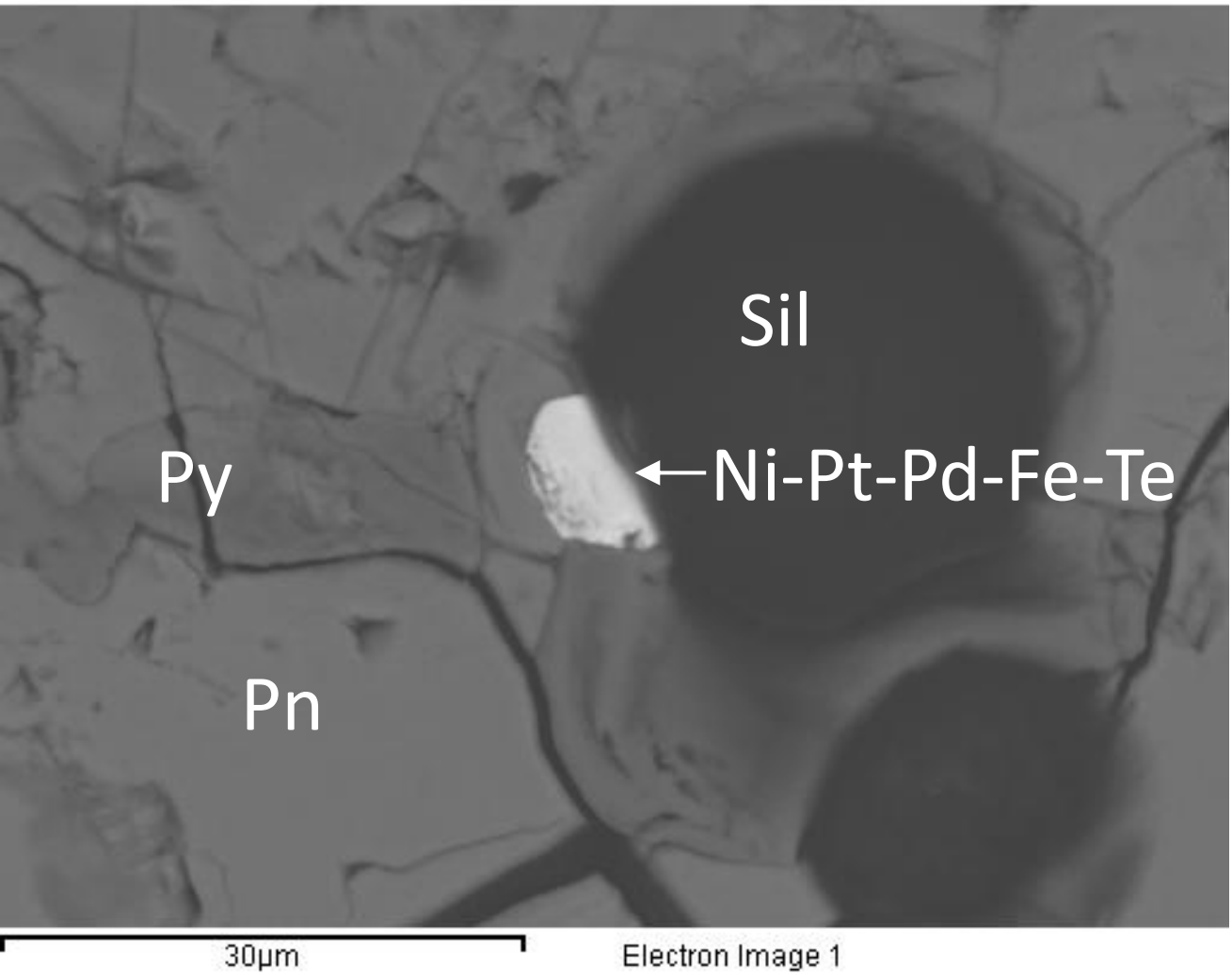
PTR21 F 1



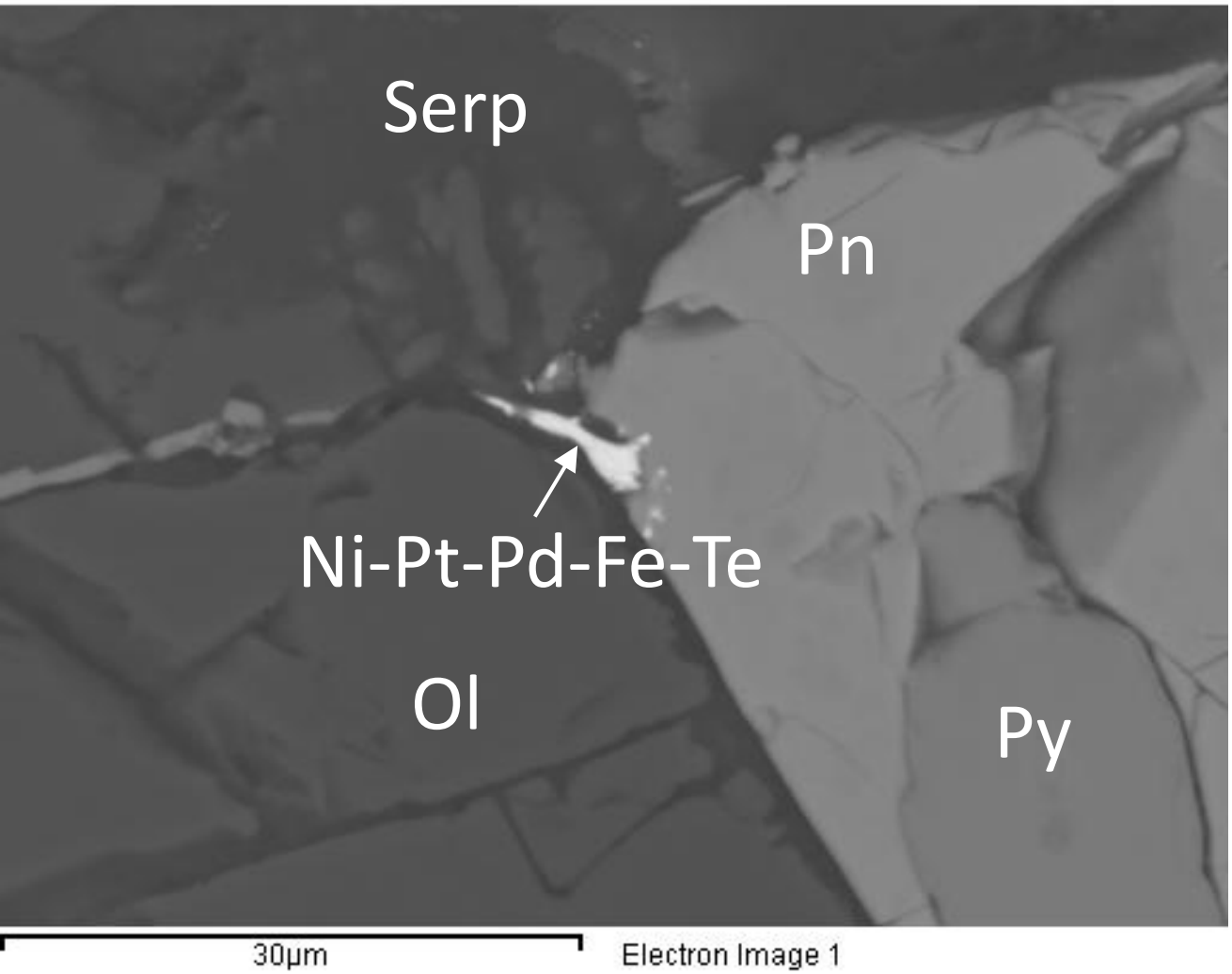
PTR22 A 1



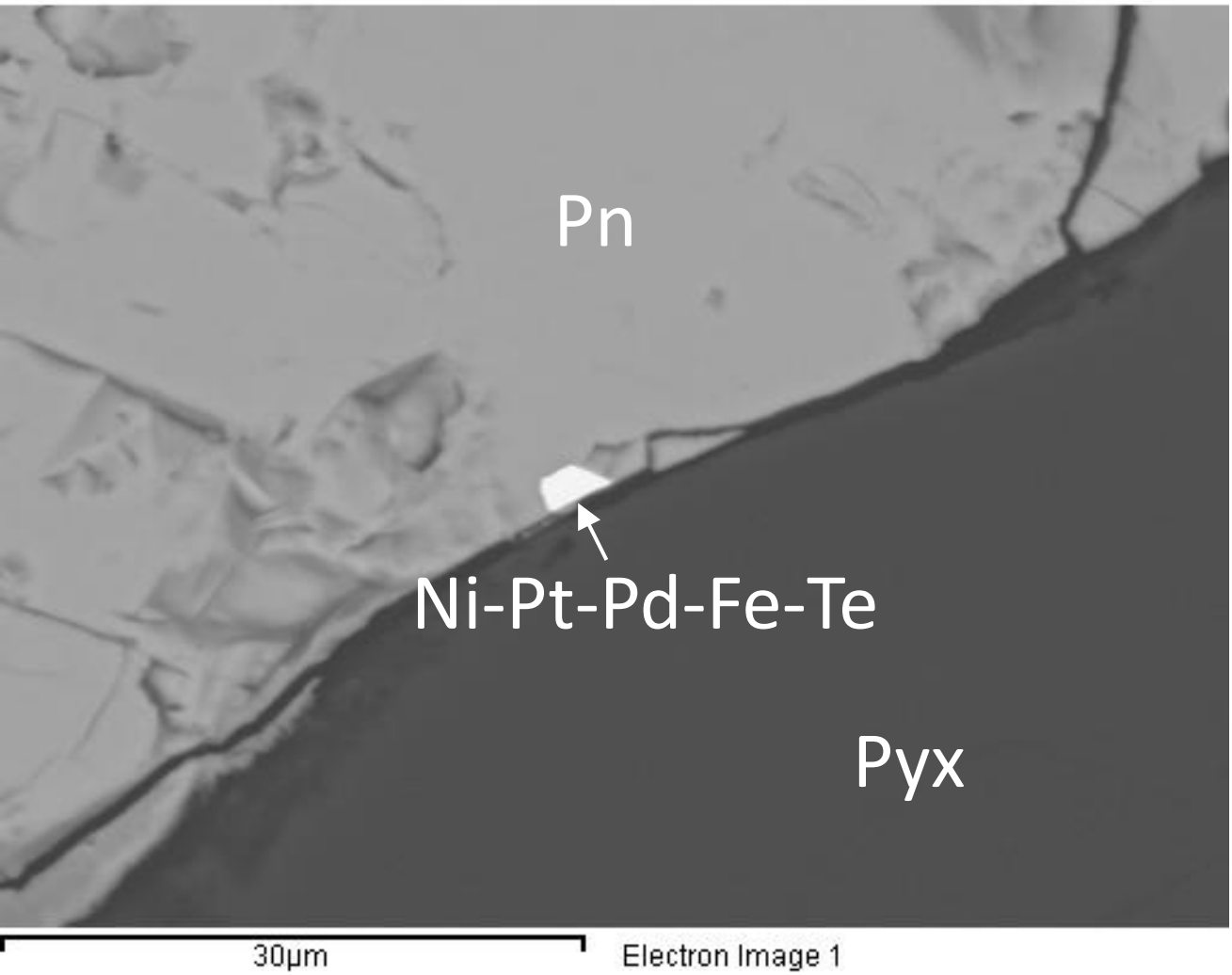
PTR22 B 1



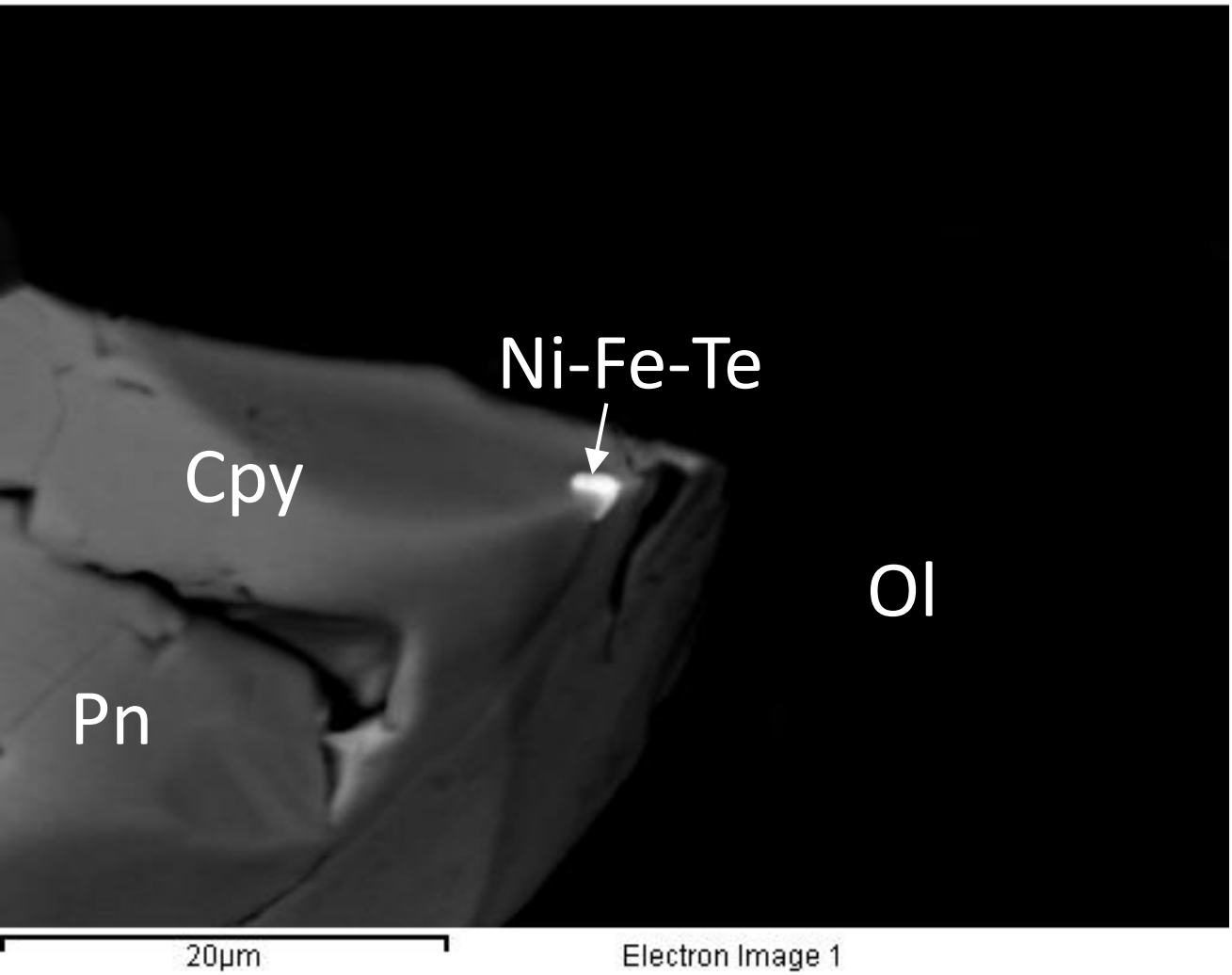
PTR22 C 1



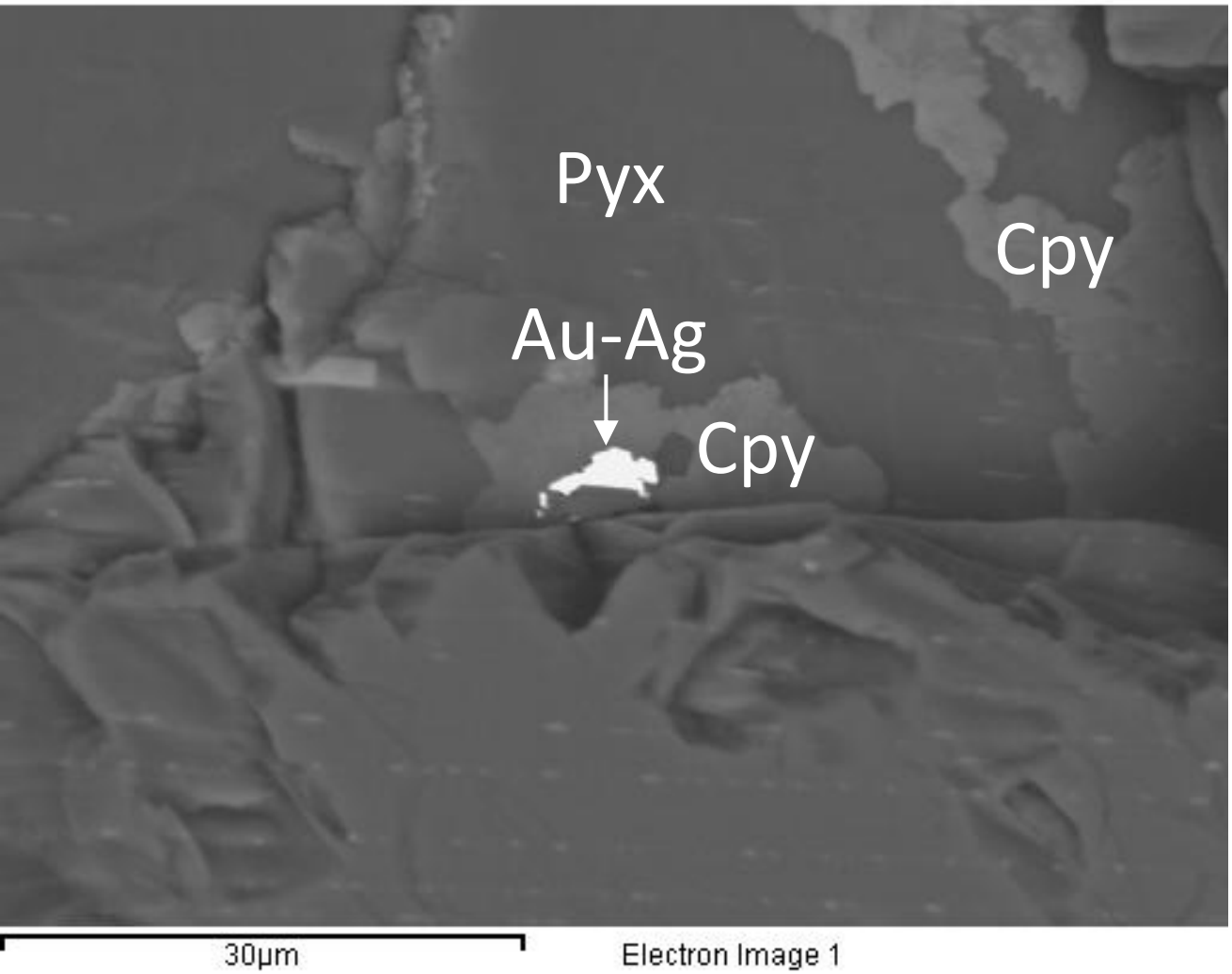
PTR22 D 1



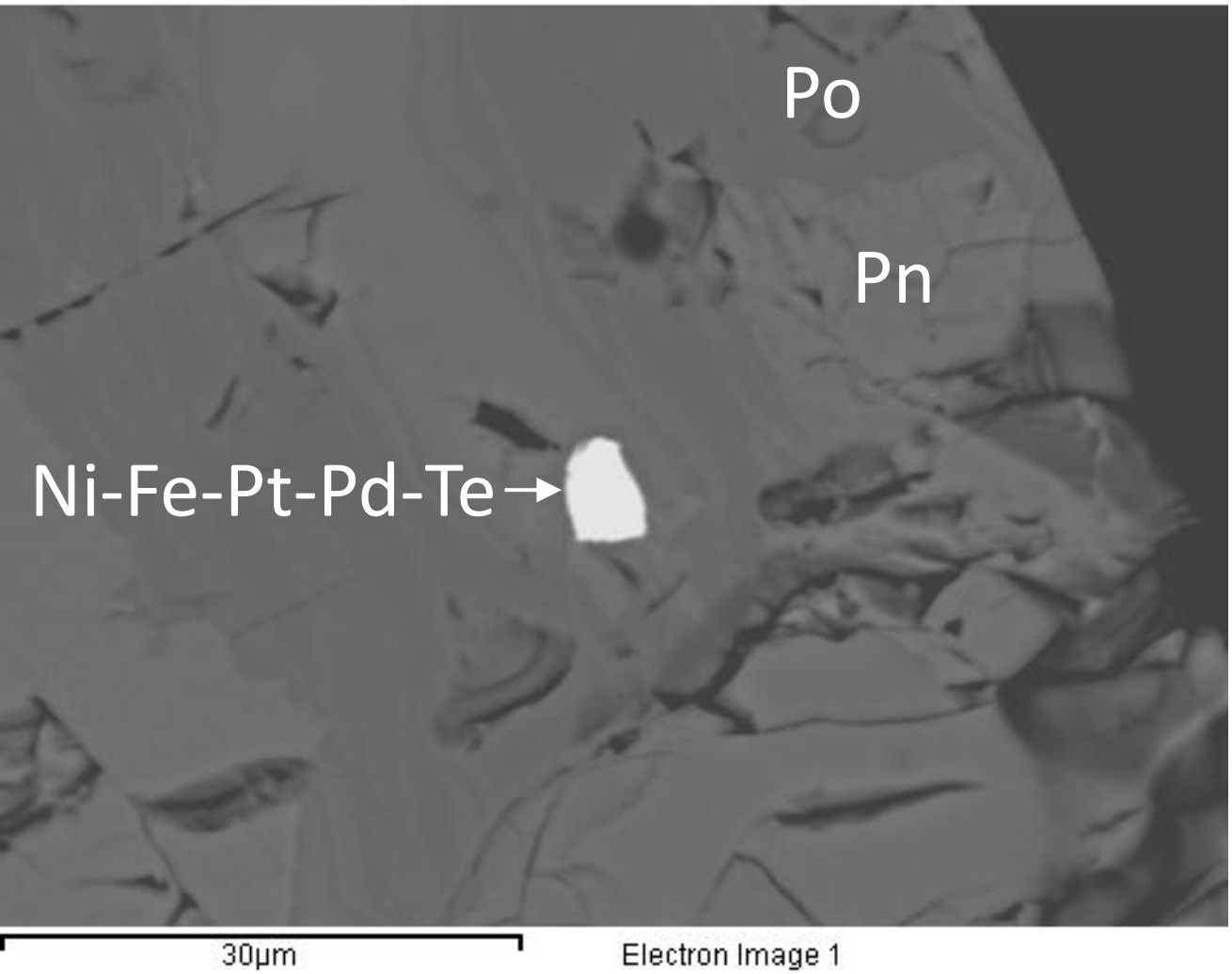
PTR22 E 1



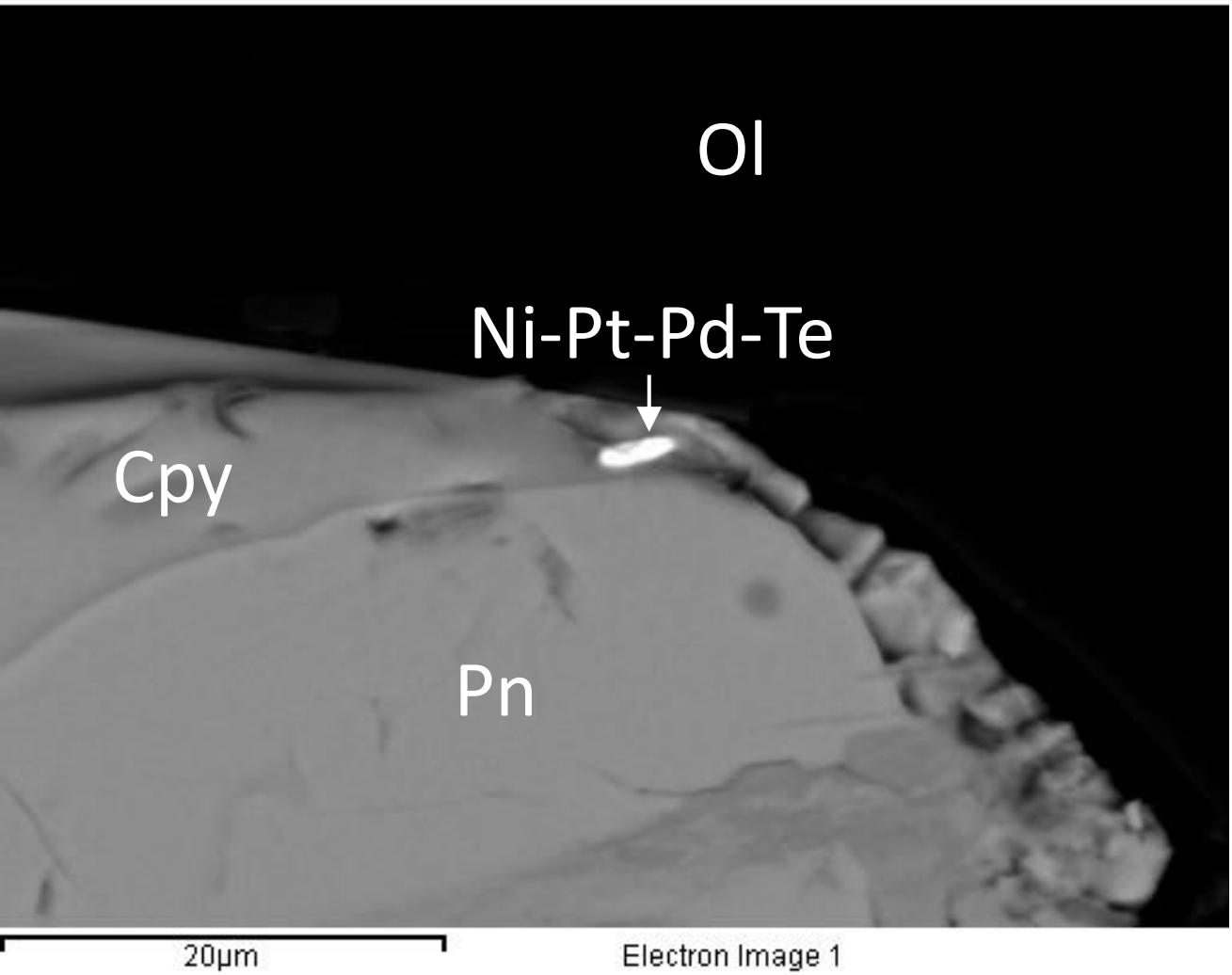
PTR22 F 1



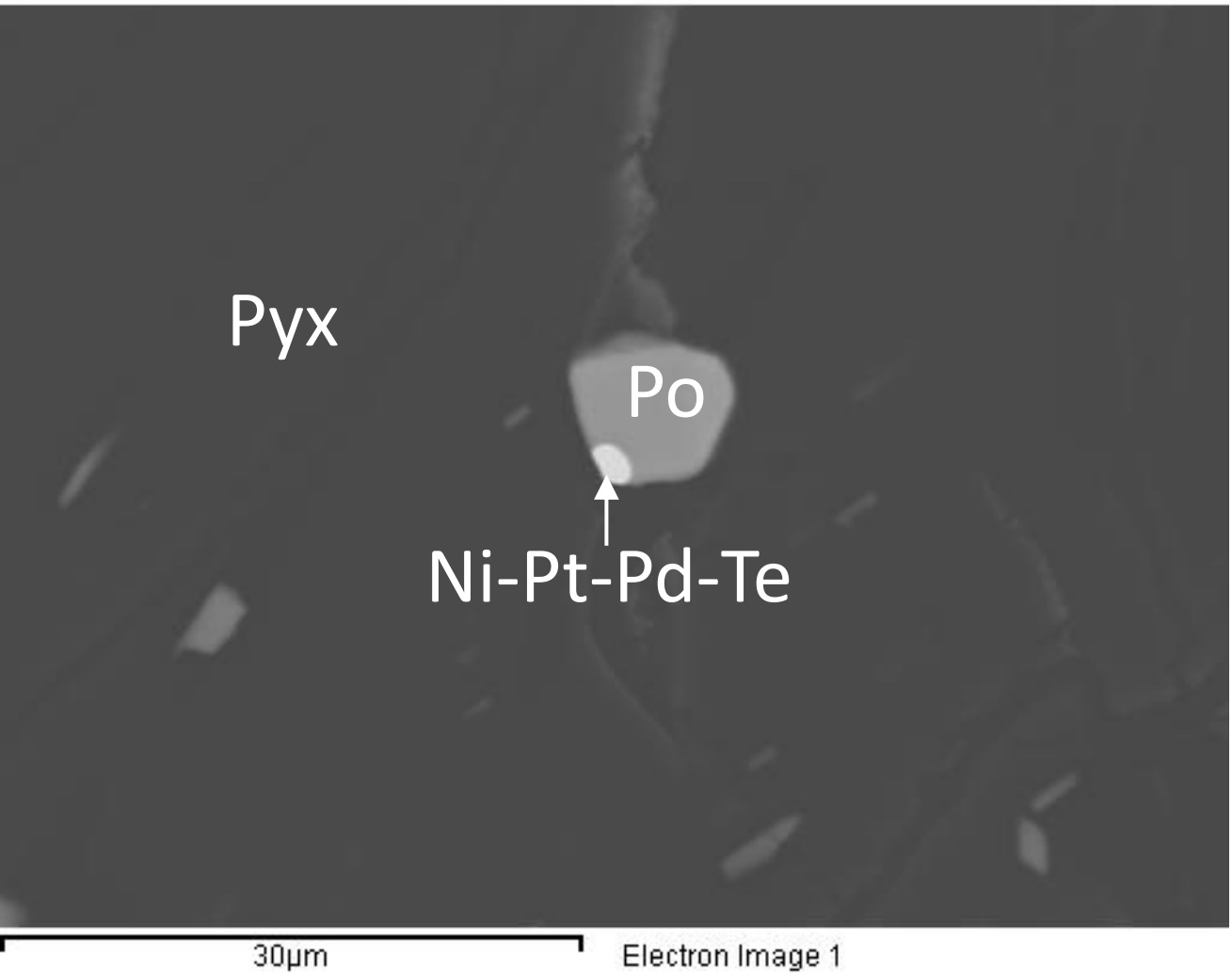
PTR22 G 1



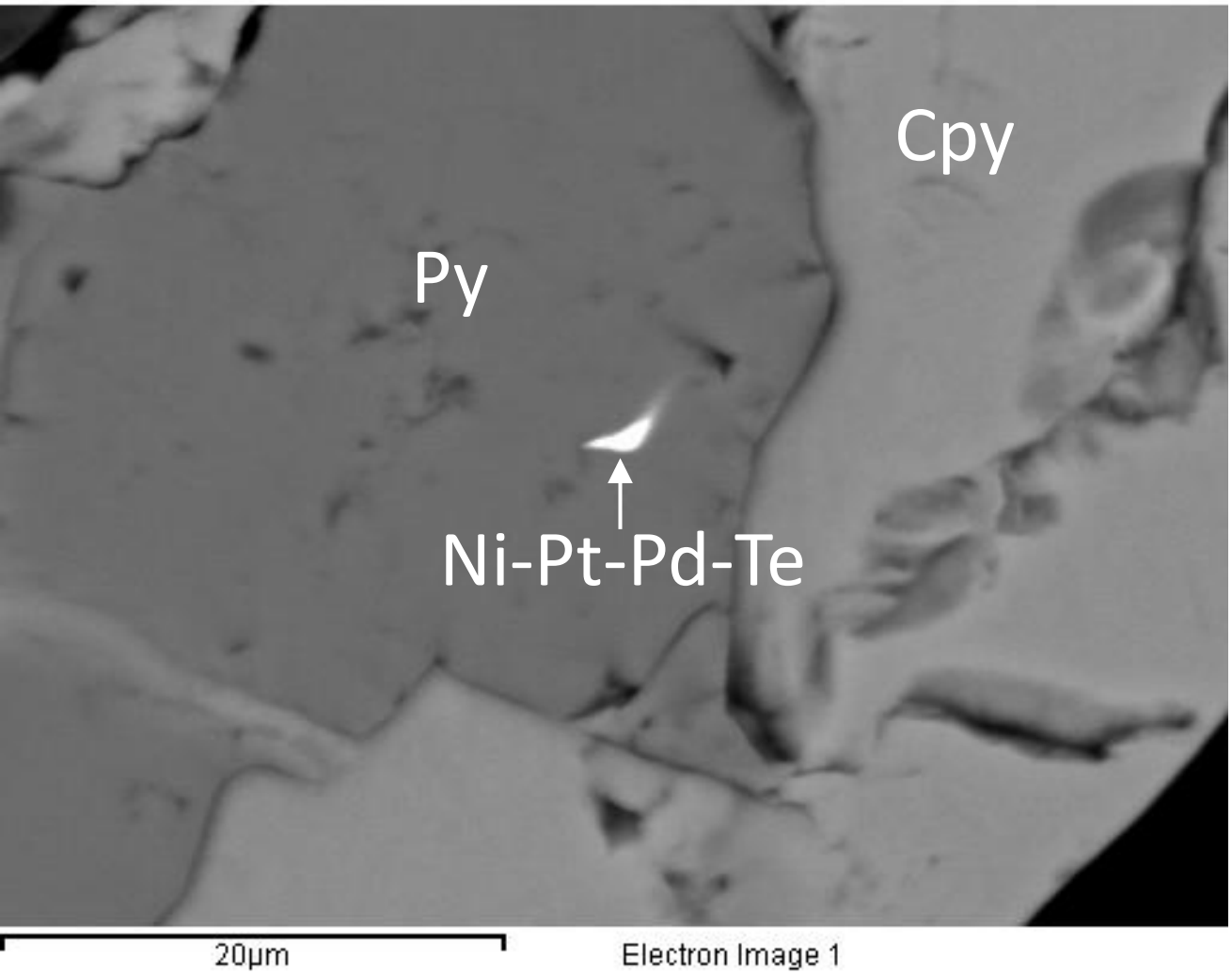
PTR22 H 1



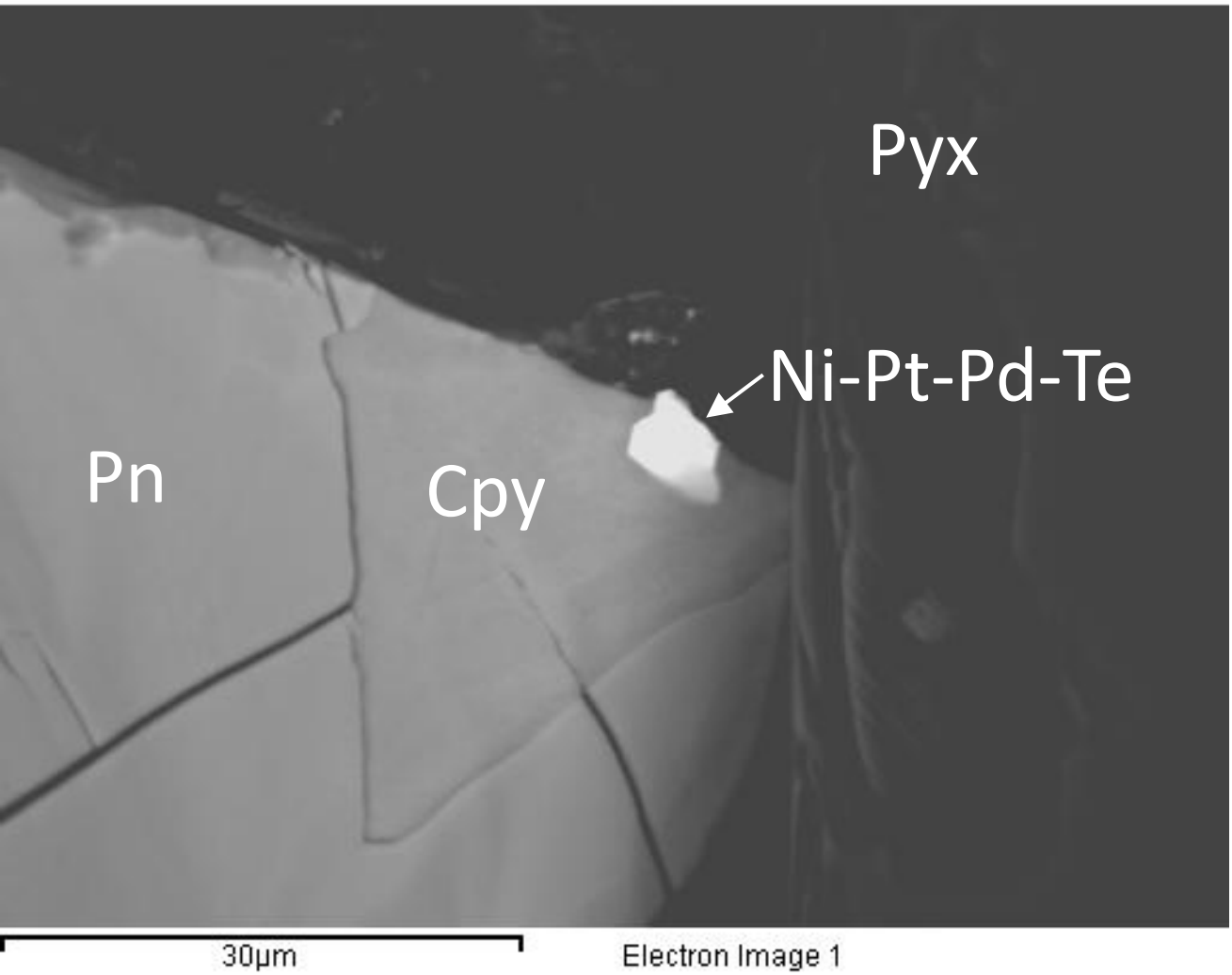
PTR22 I 1



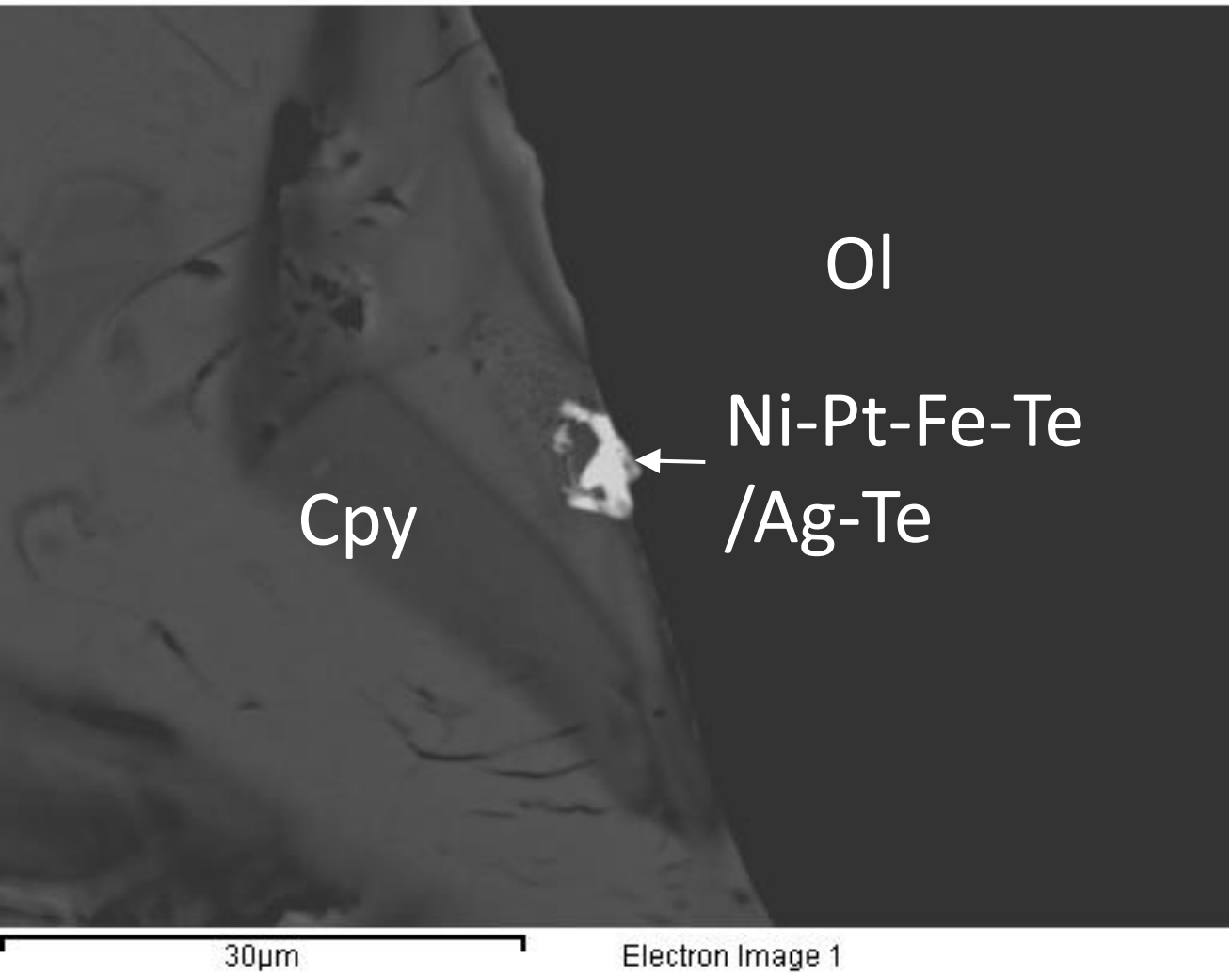
PTR22 J 1



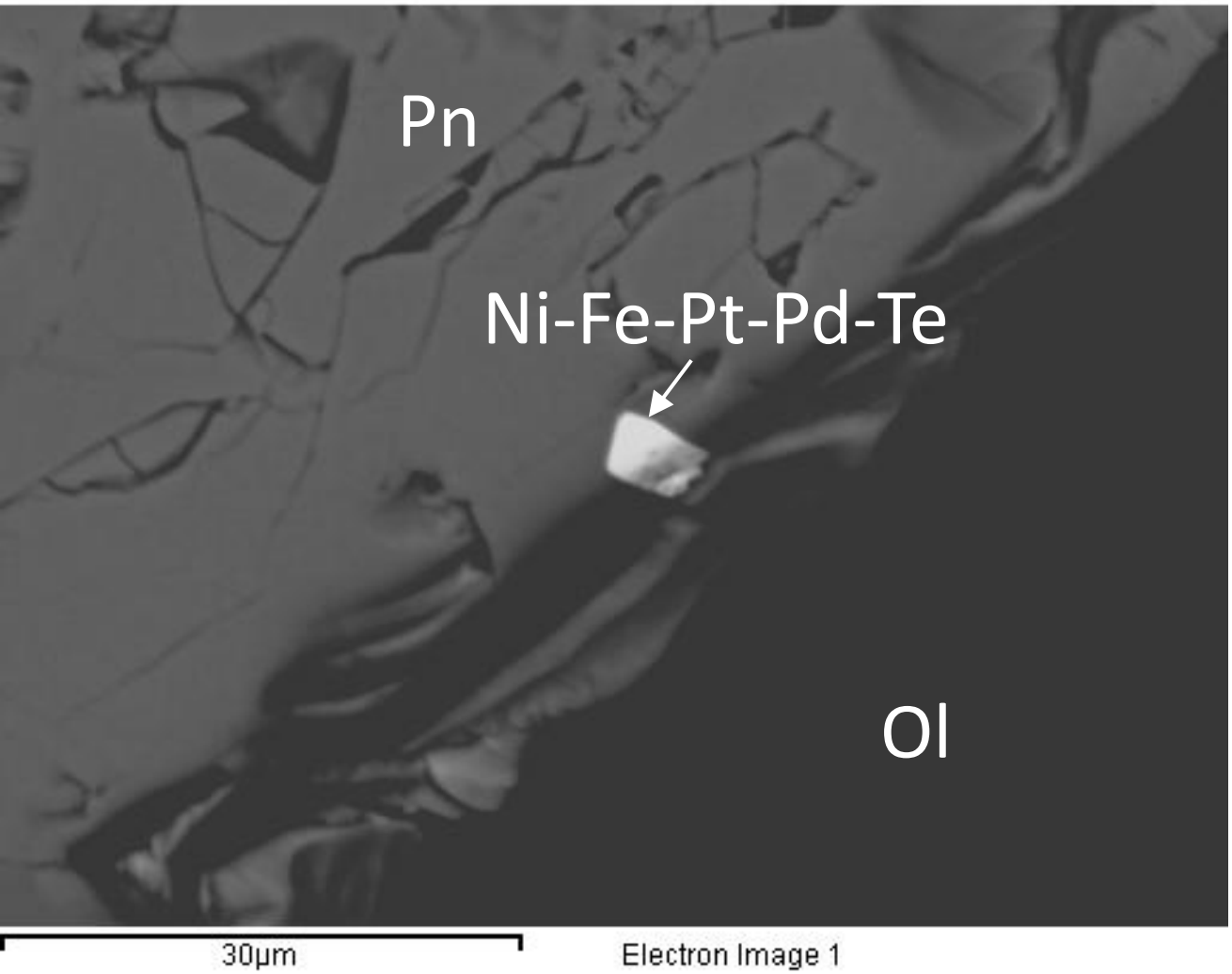
PTR22 K 1



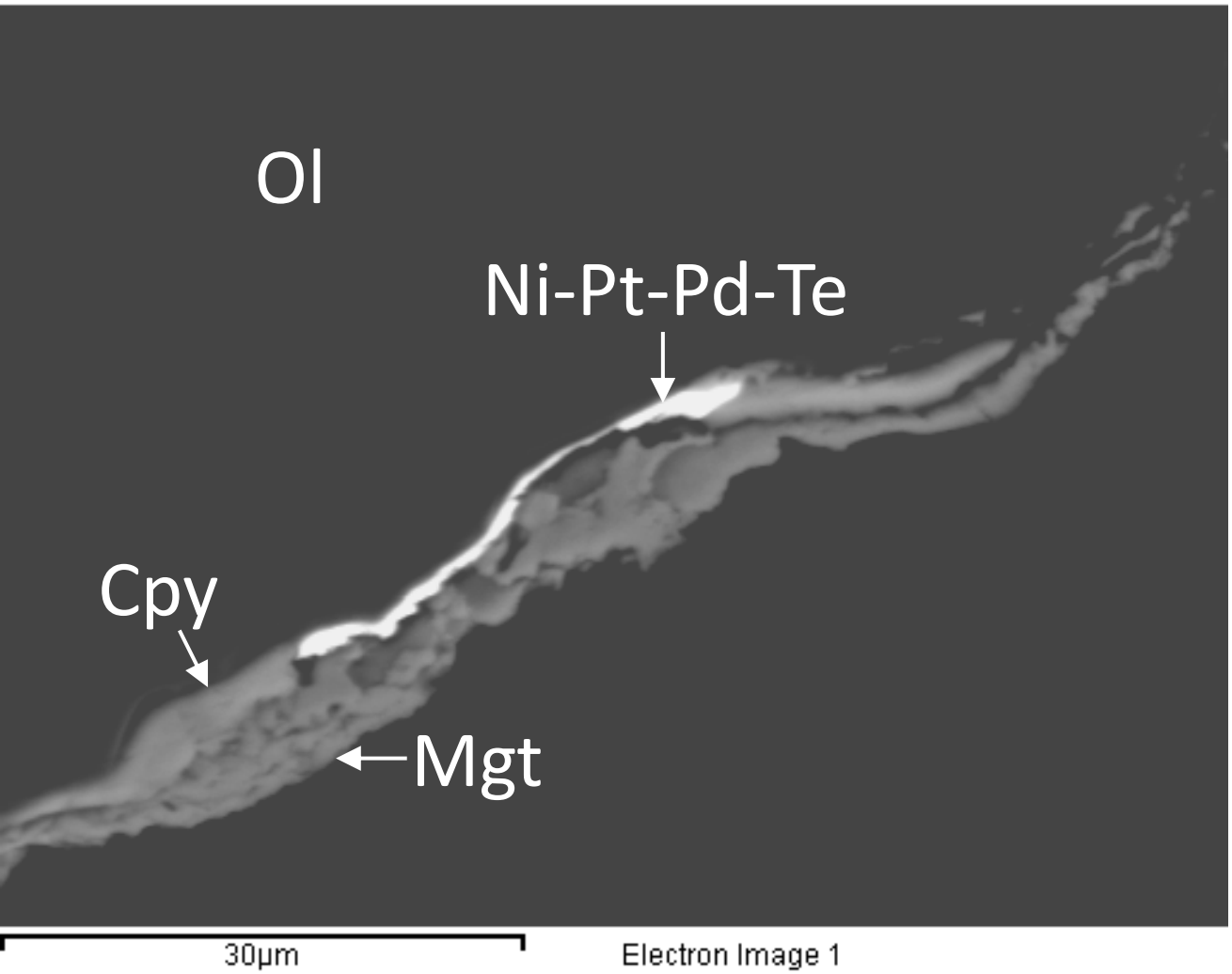
PTR22 L 1



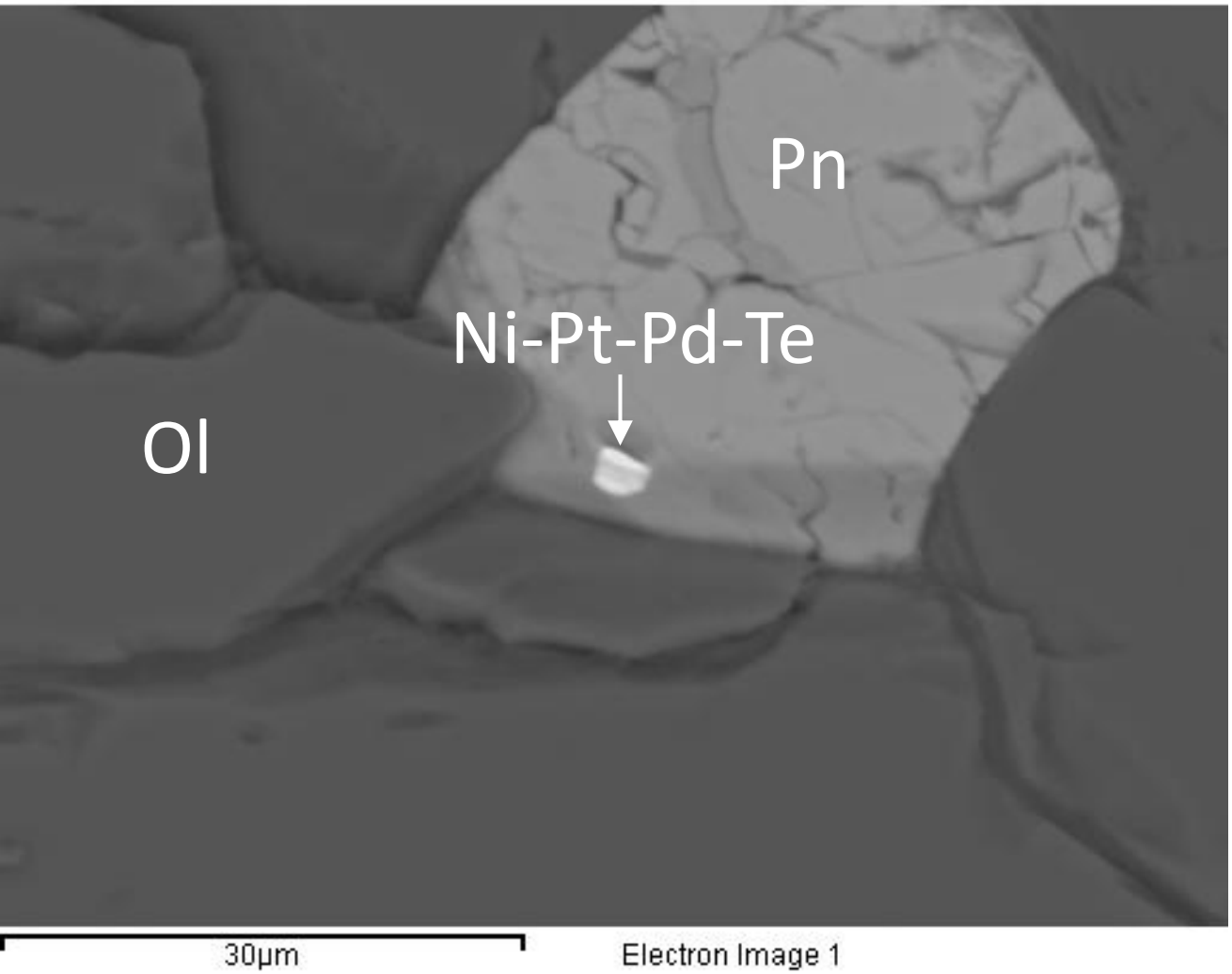
PTR22 M 1



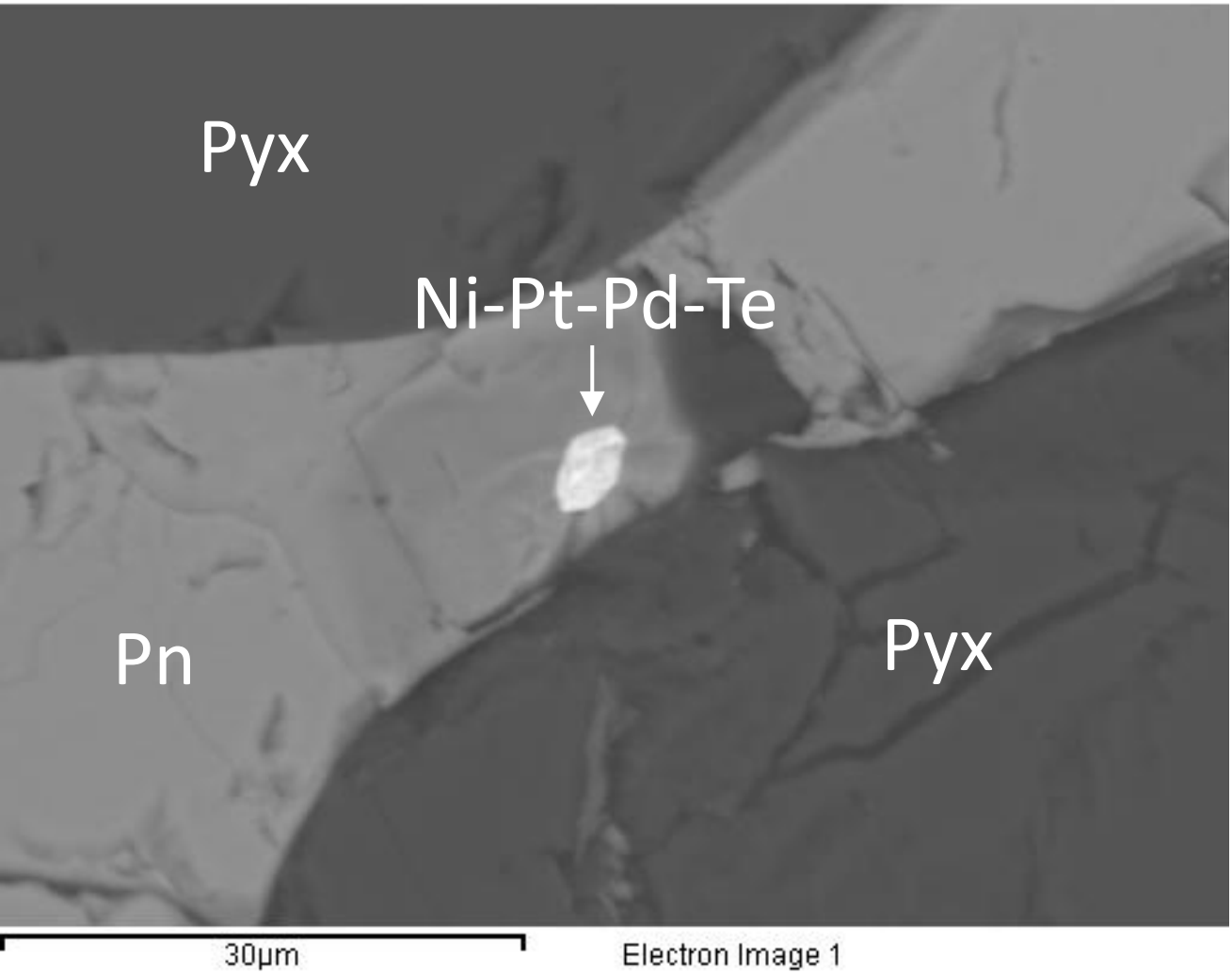
PTR22 N 1



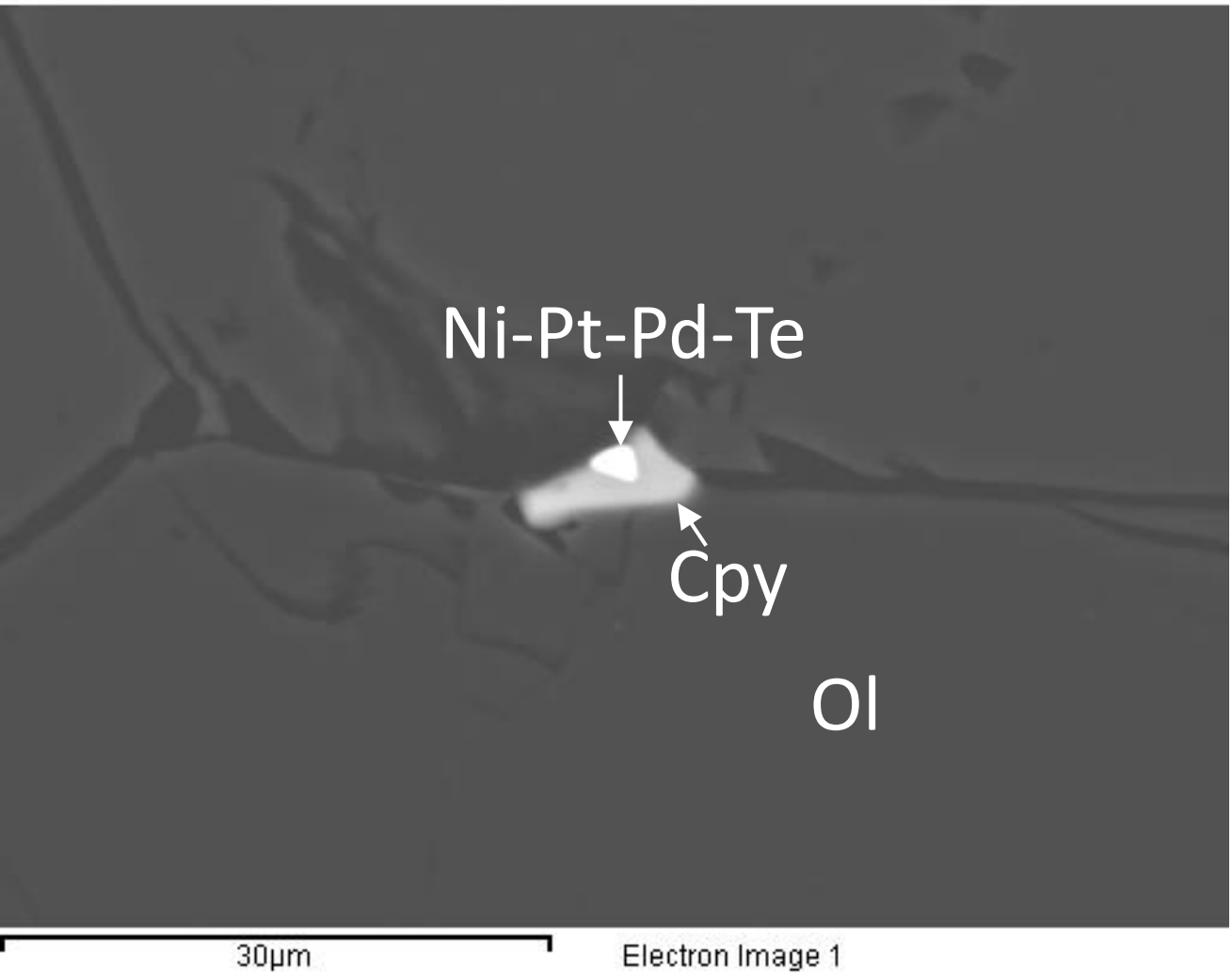
PTR22 O 1



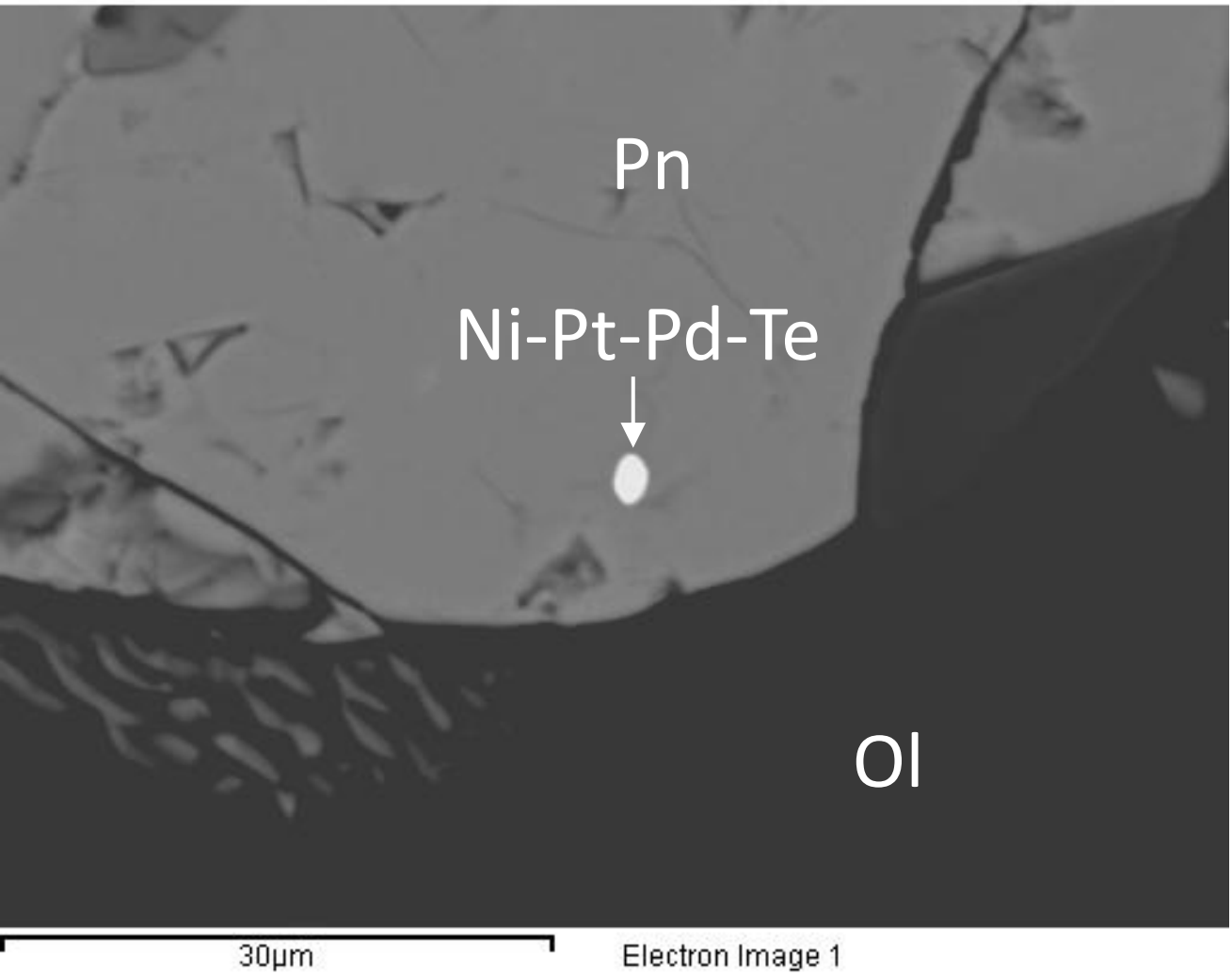
PTR22 P 1



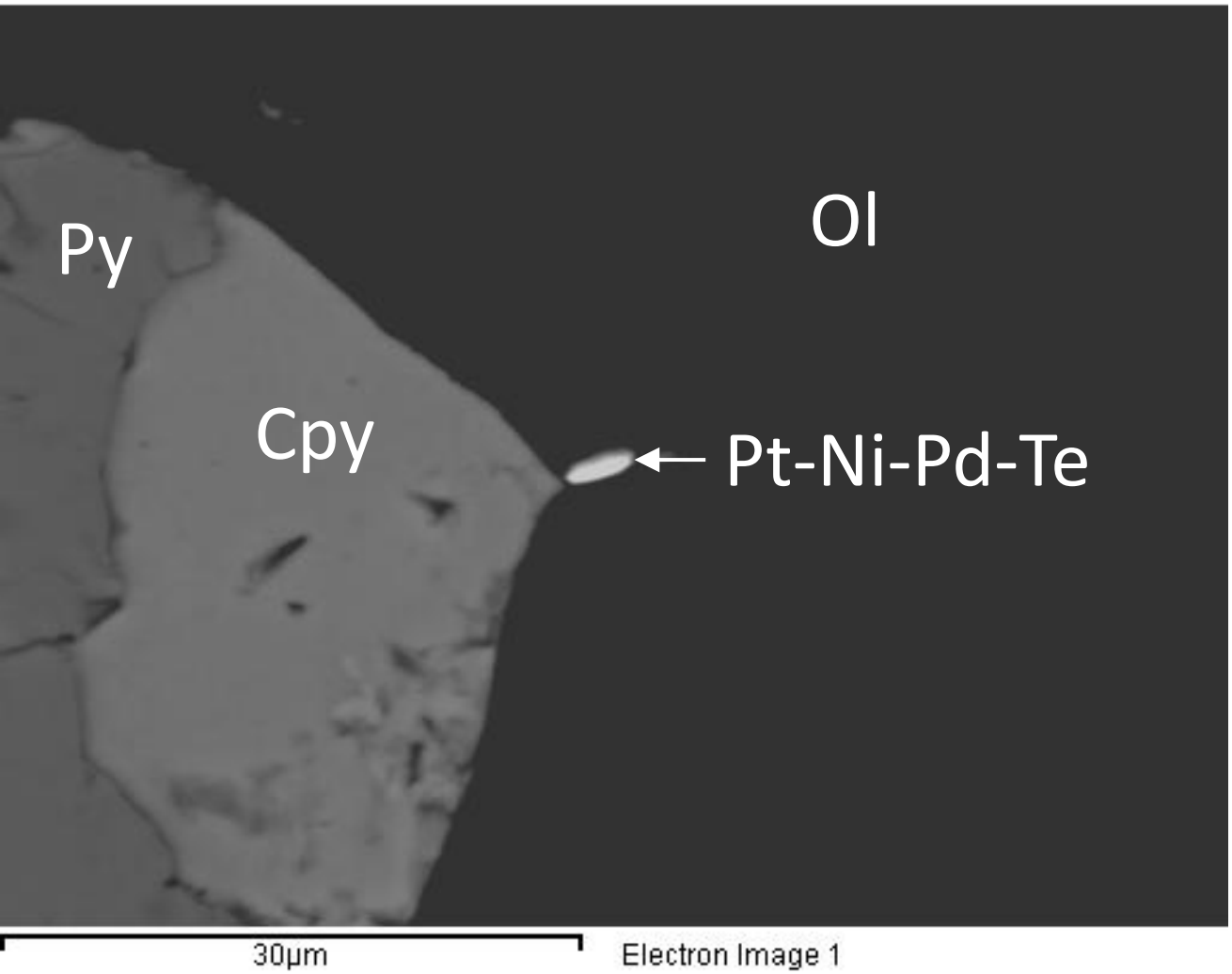
PTR22 Q 1



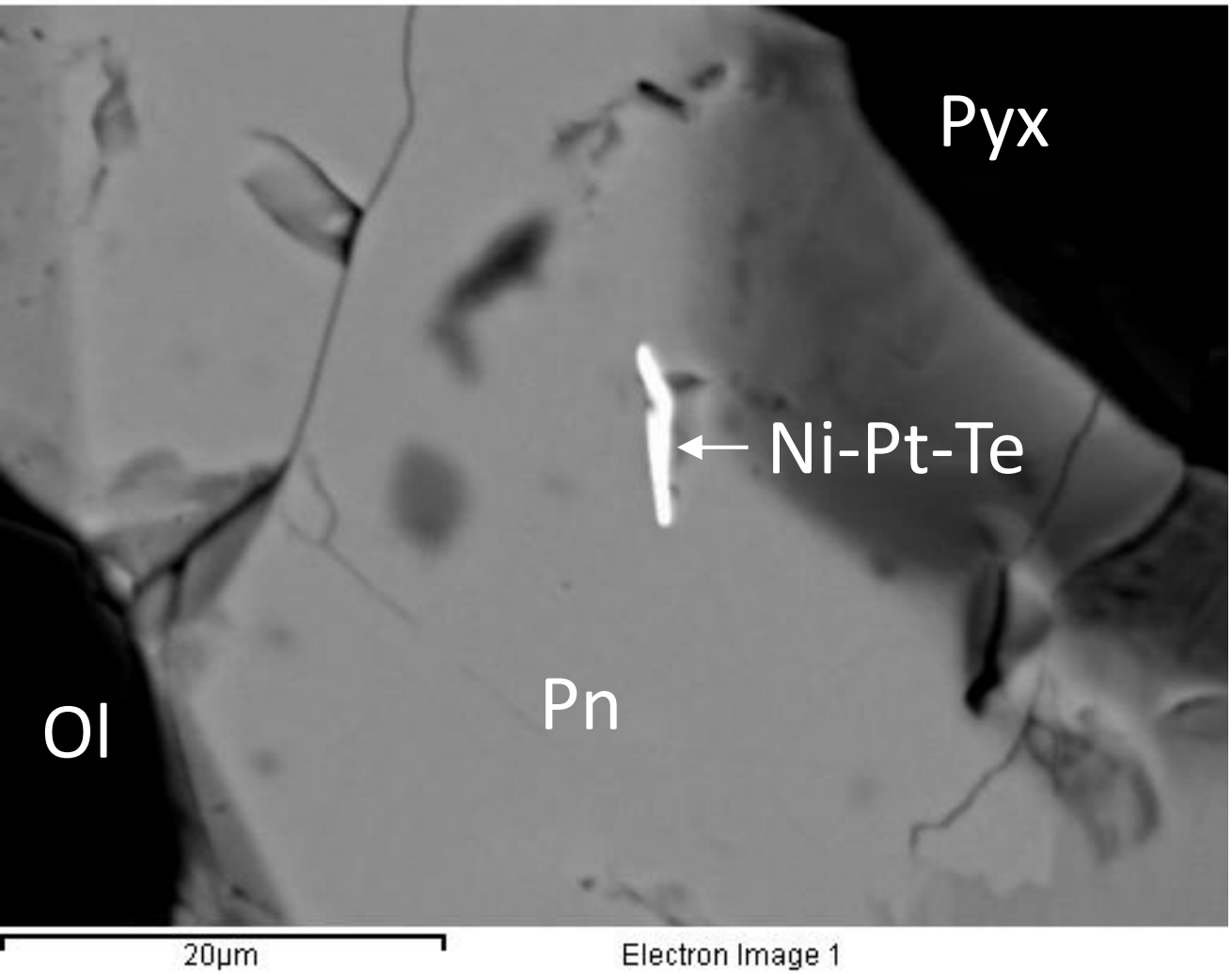
PTR22 R 1



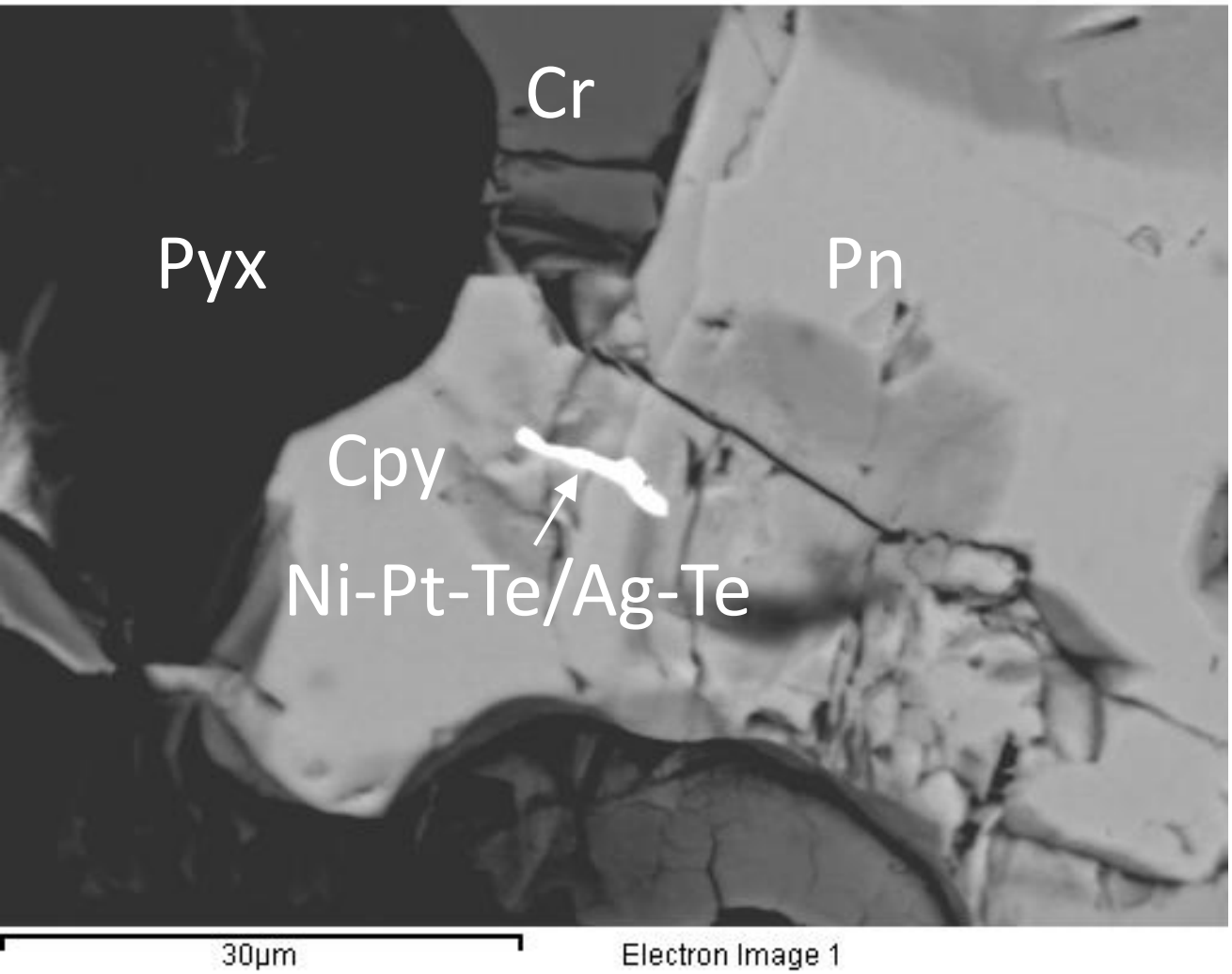
PTR22 S 1



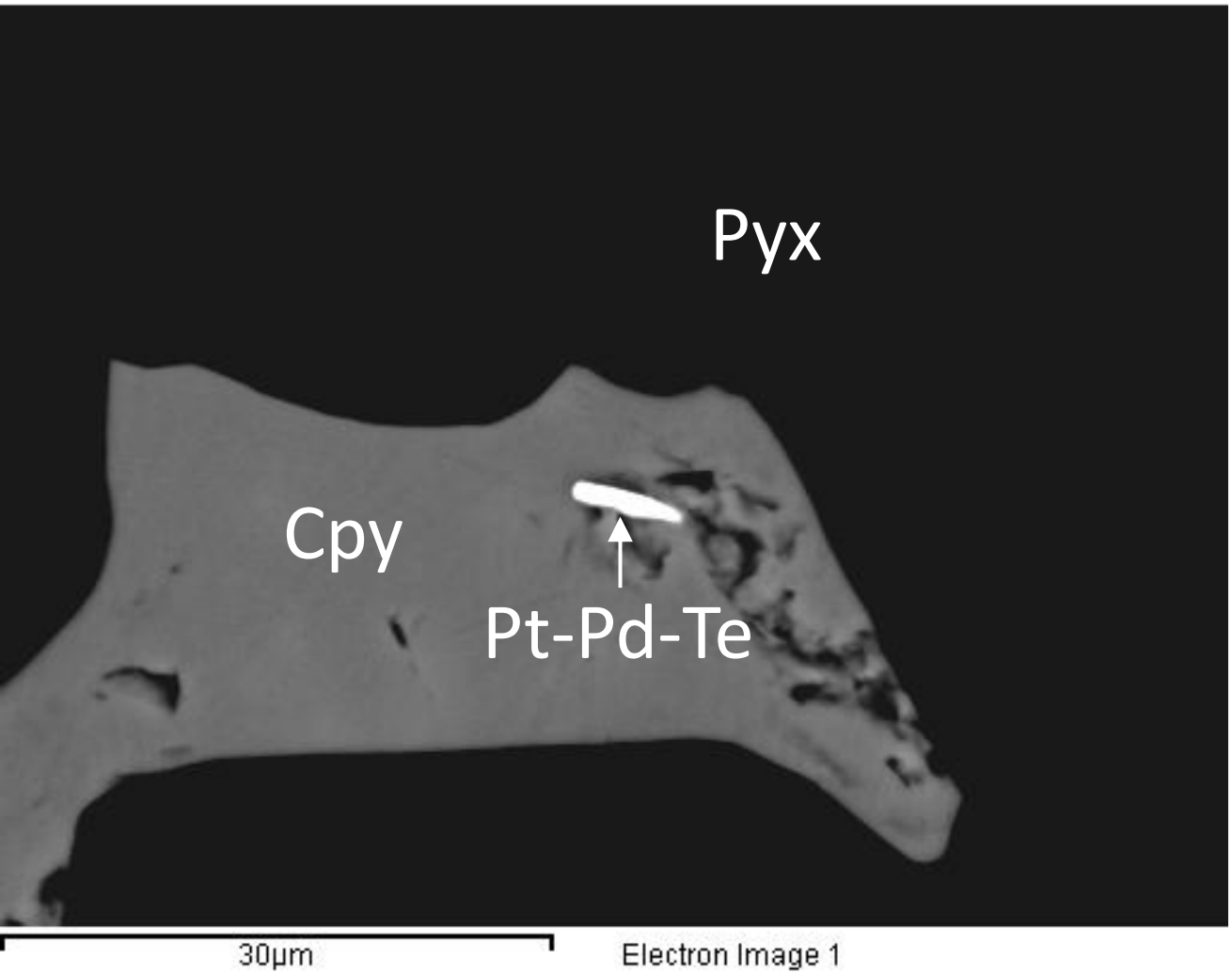
PTR22 T 1



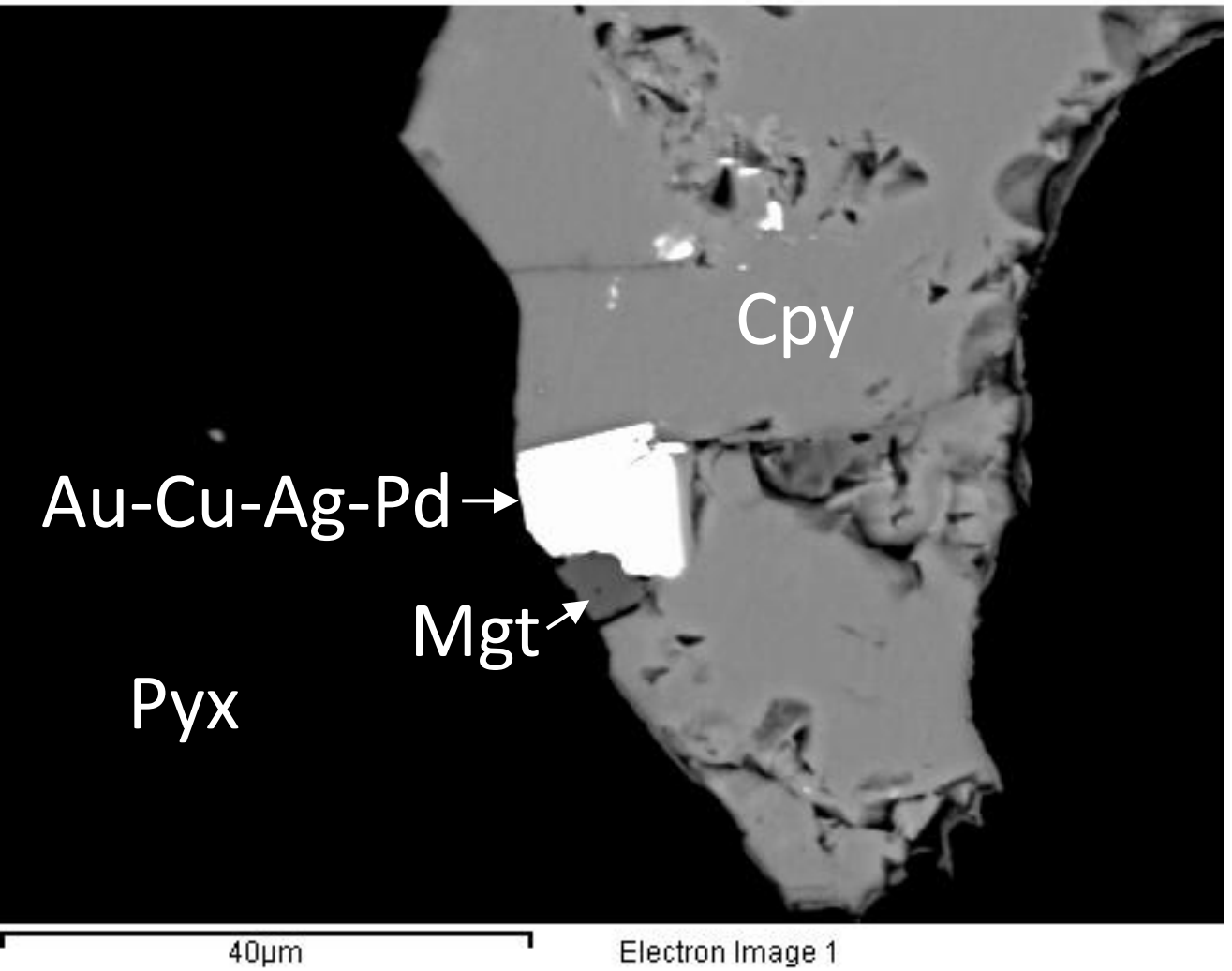
PTR22 U 1



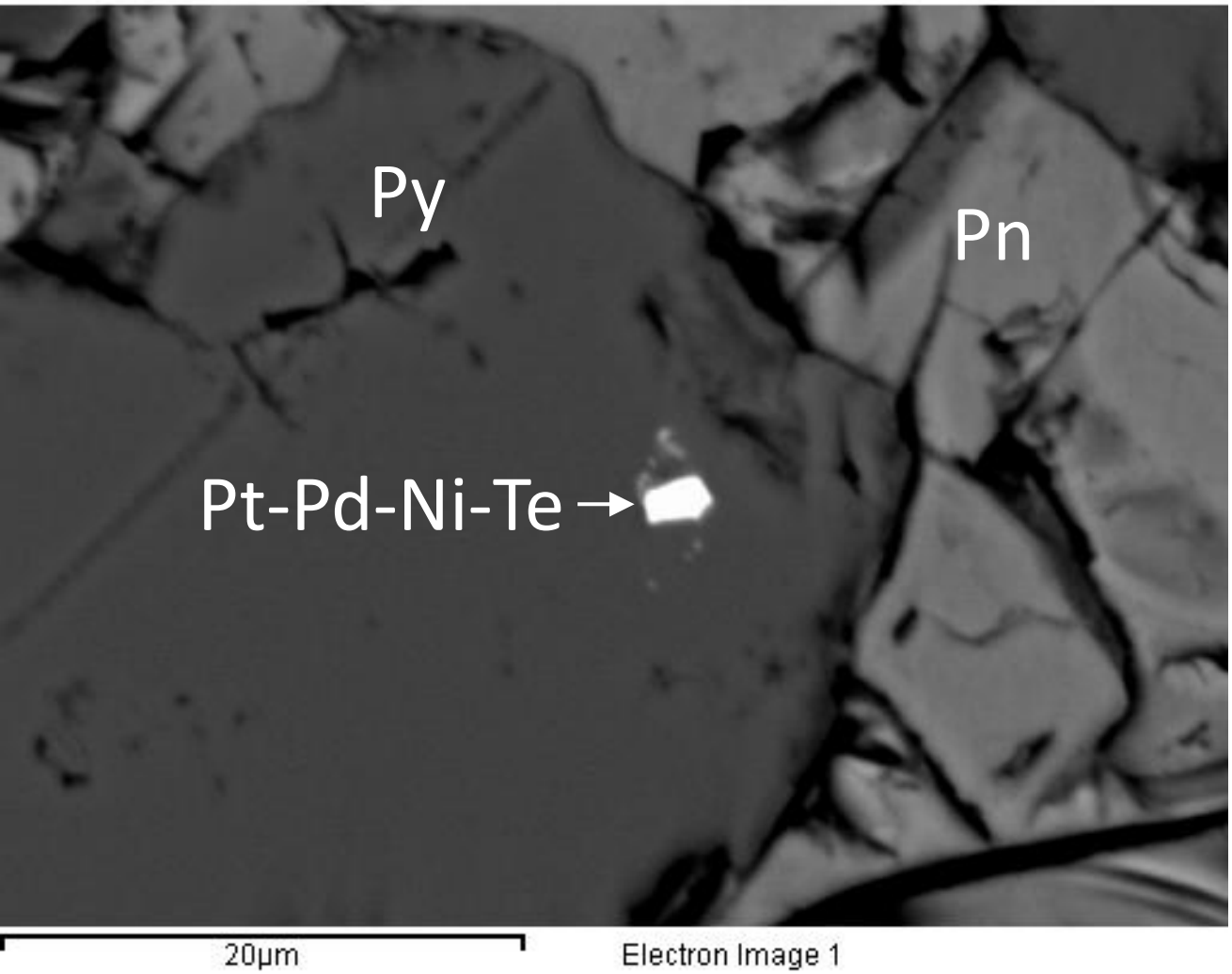
PTR23 A 1



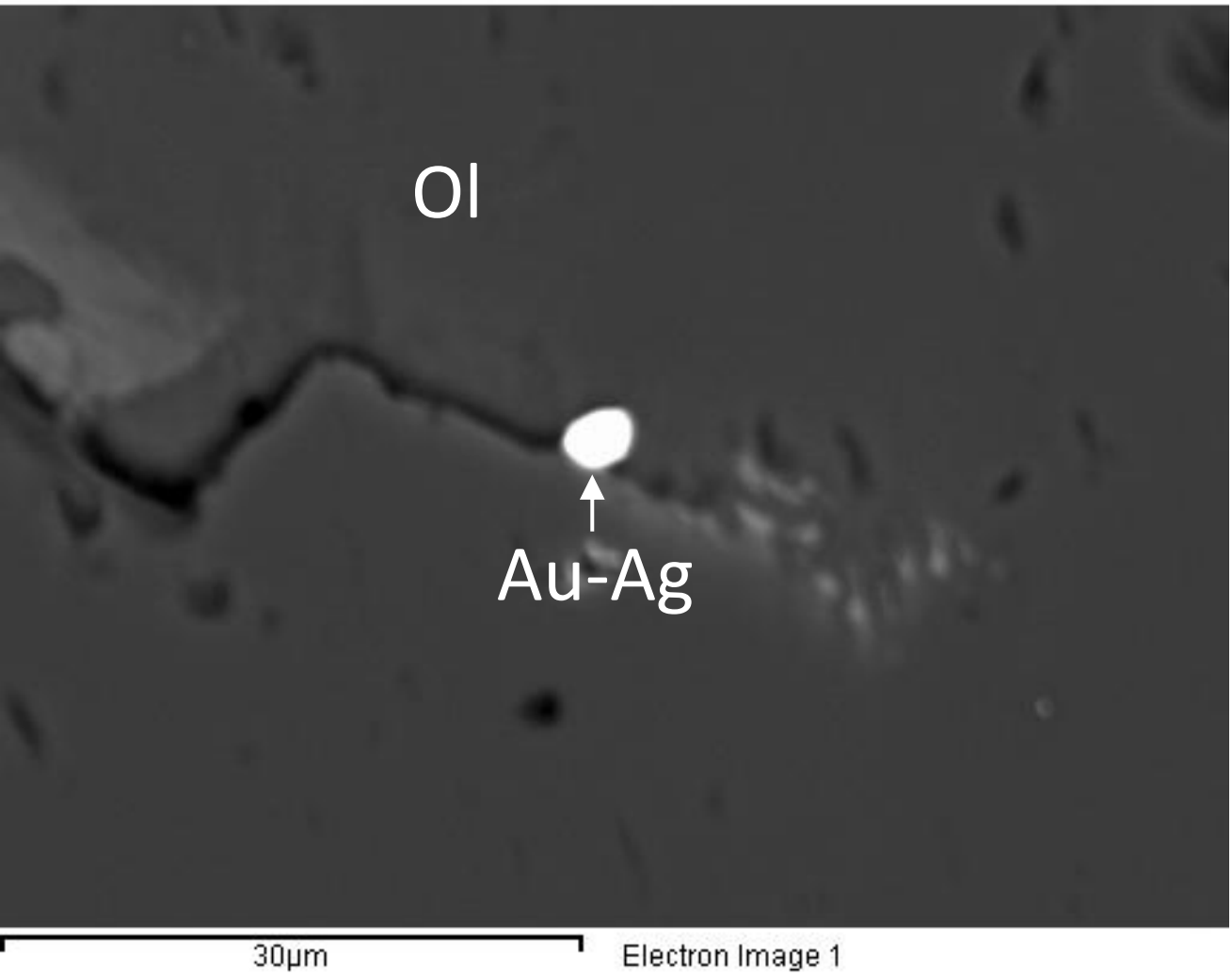
PTR23 B 1



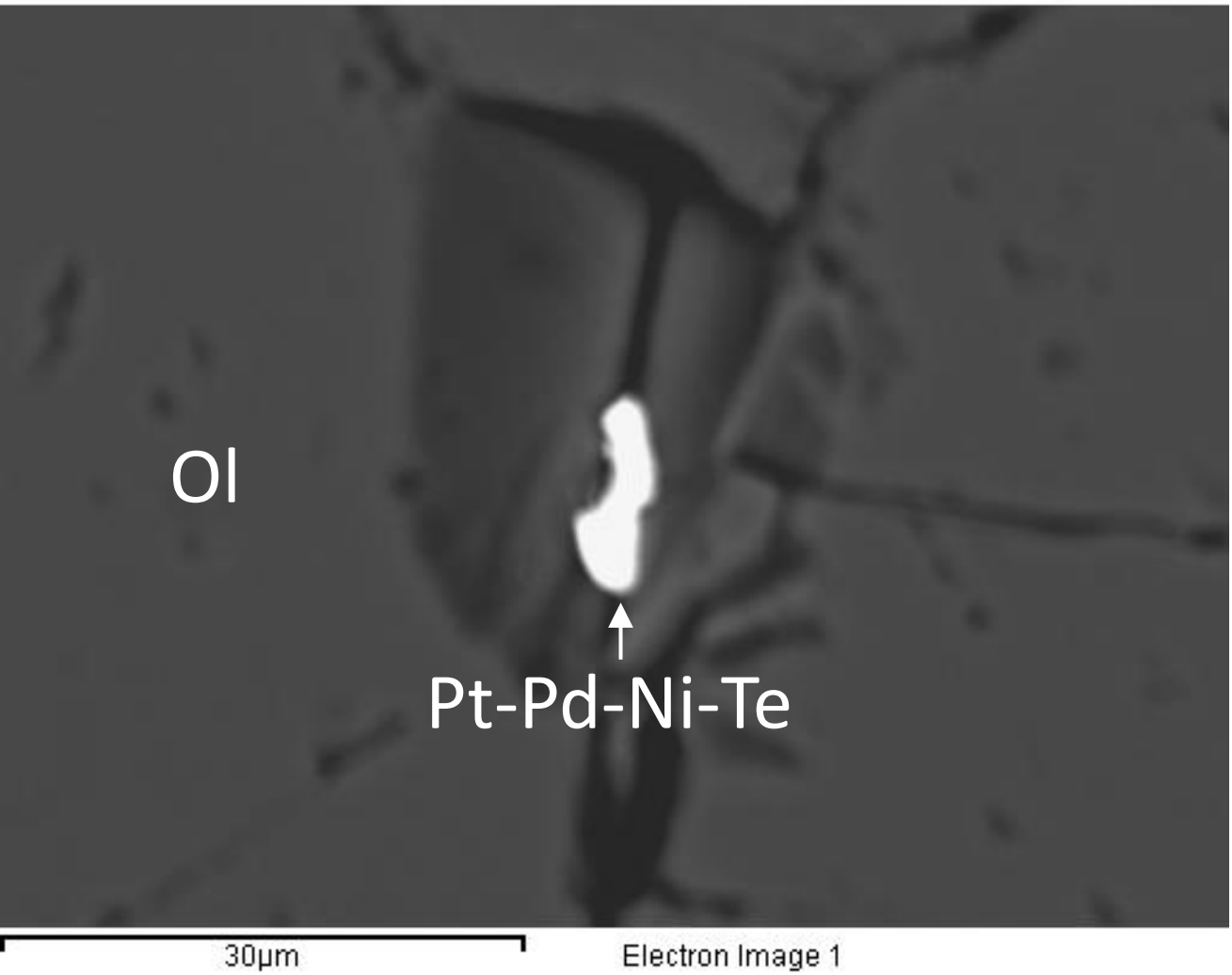
PTR23 C 1



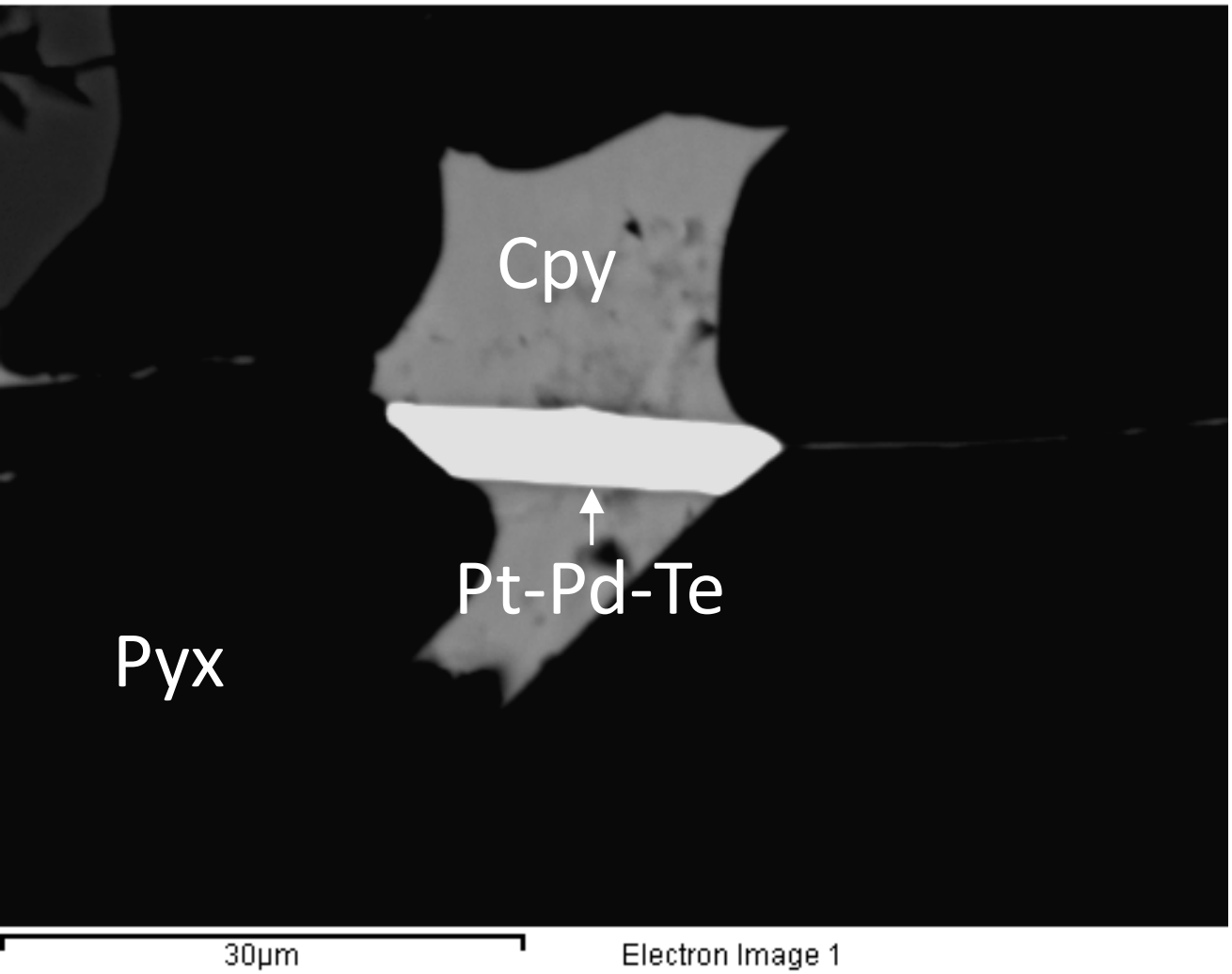
PTR23 D 1



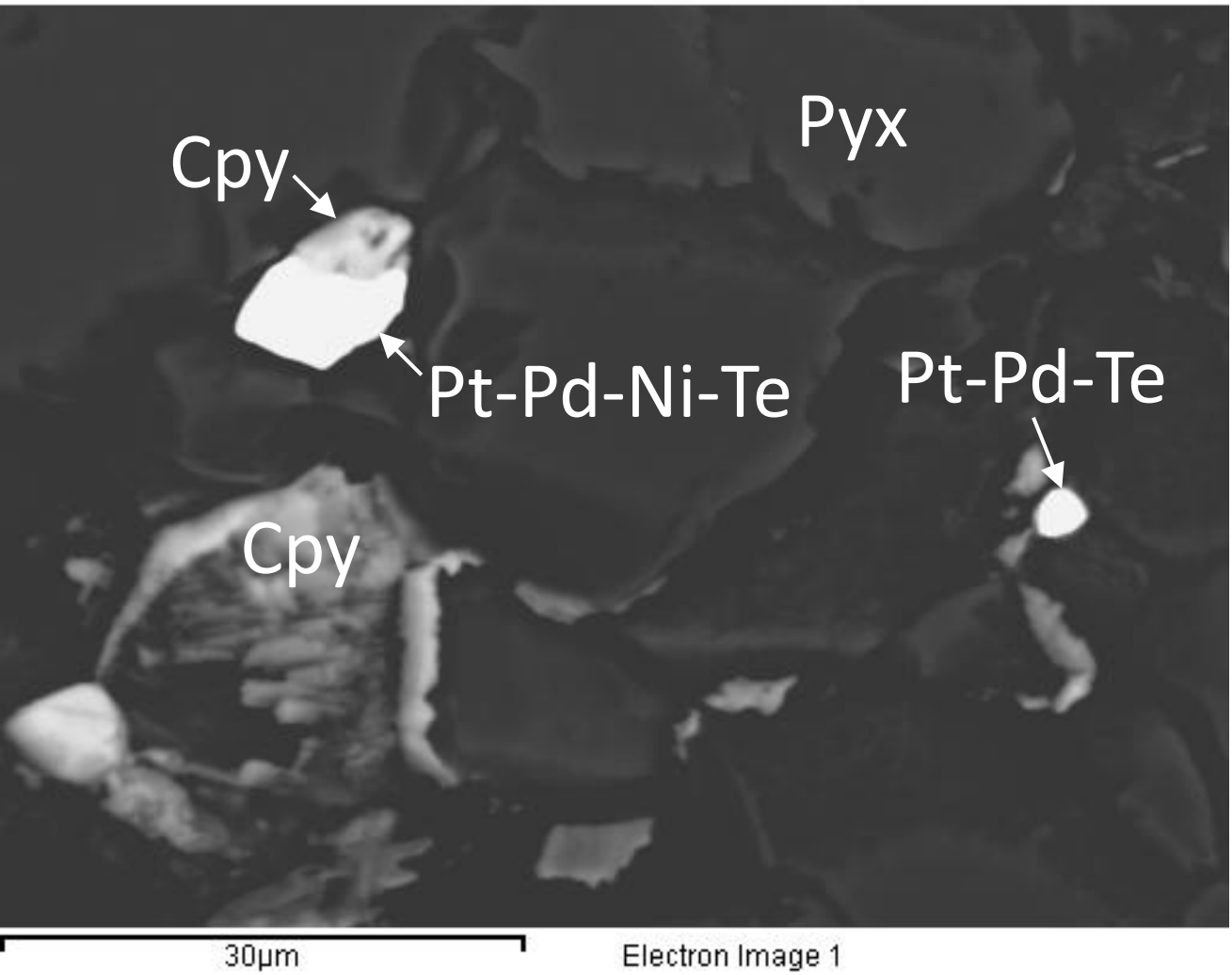
PTR23 E 1



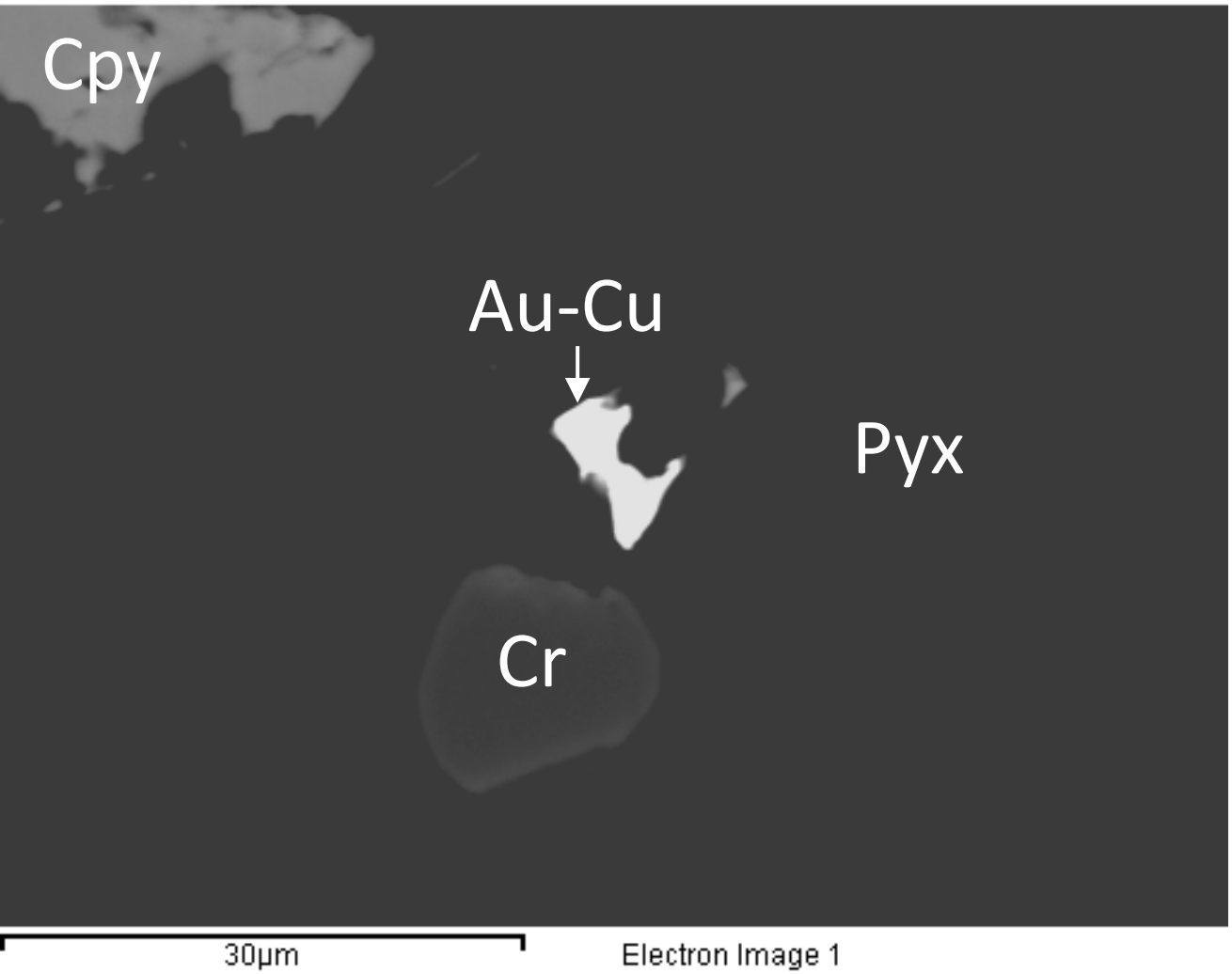
PTR23 F 1



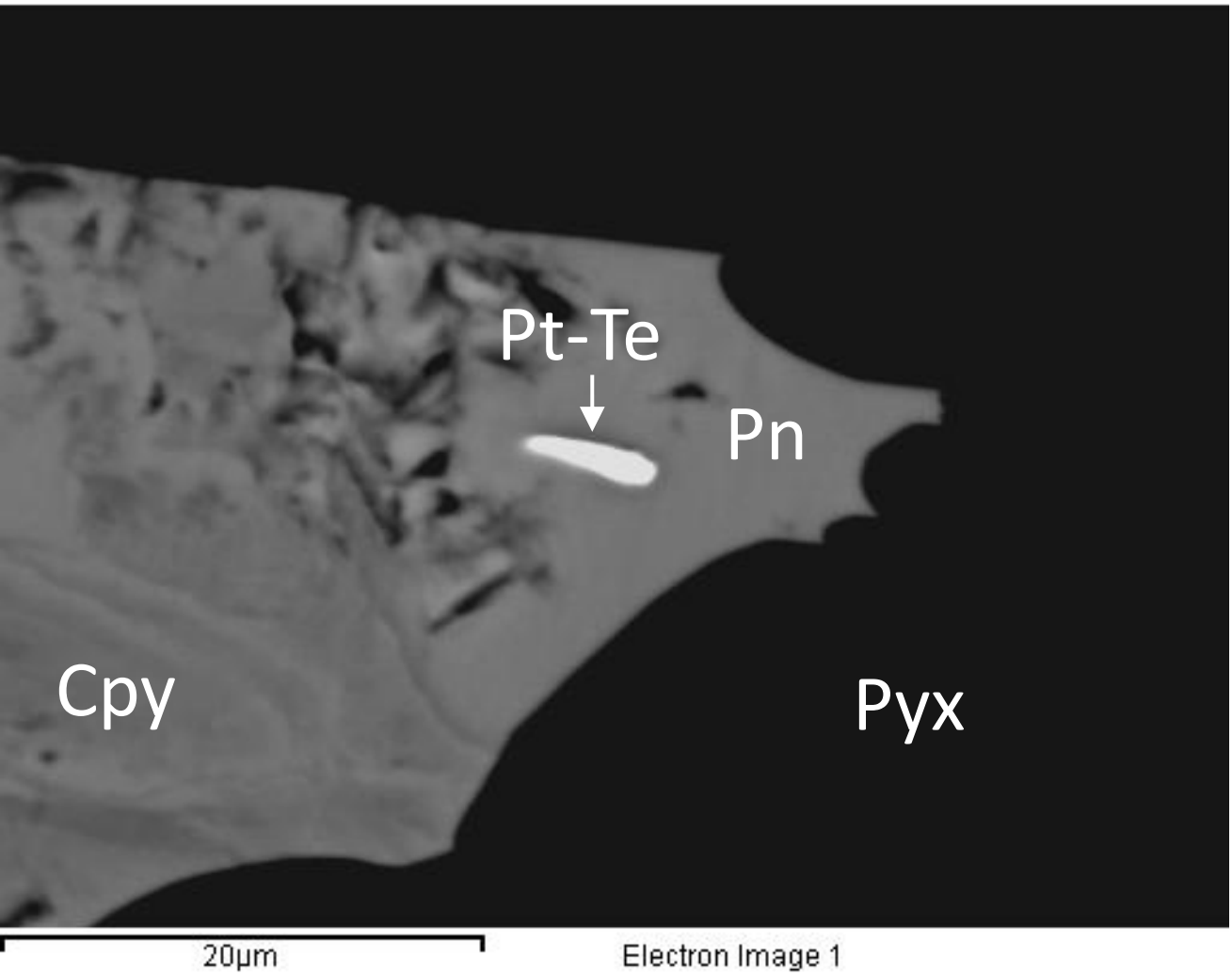
PTR23 G 1-2



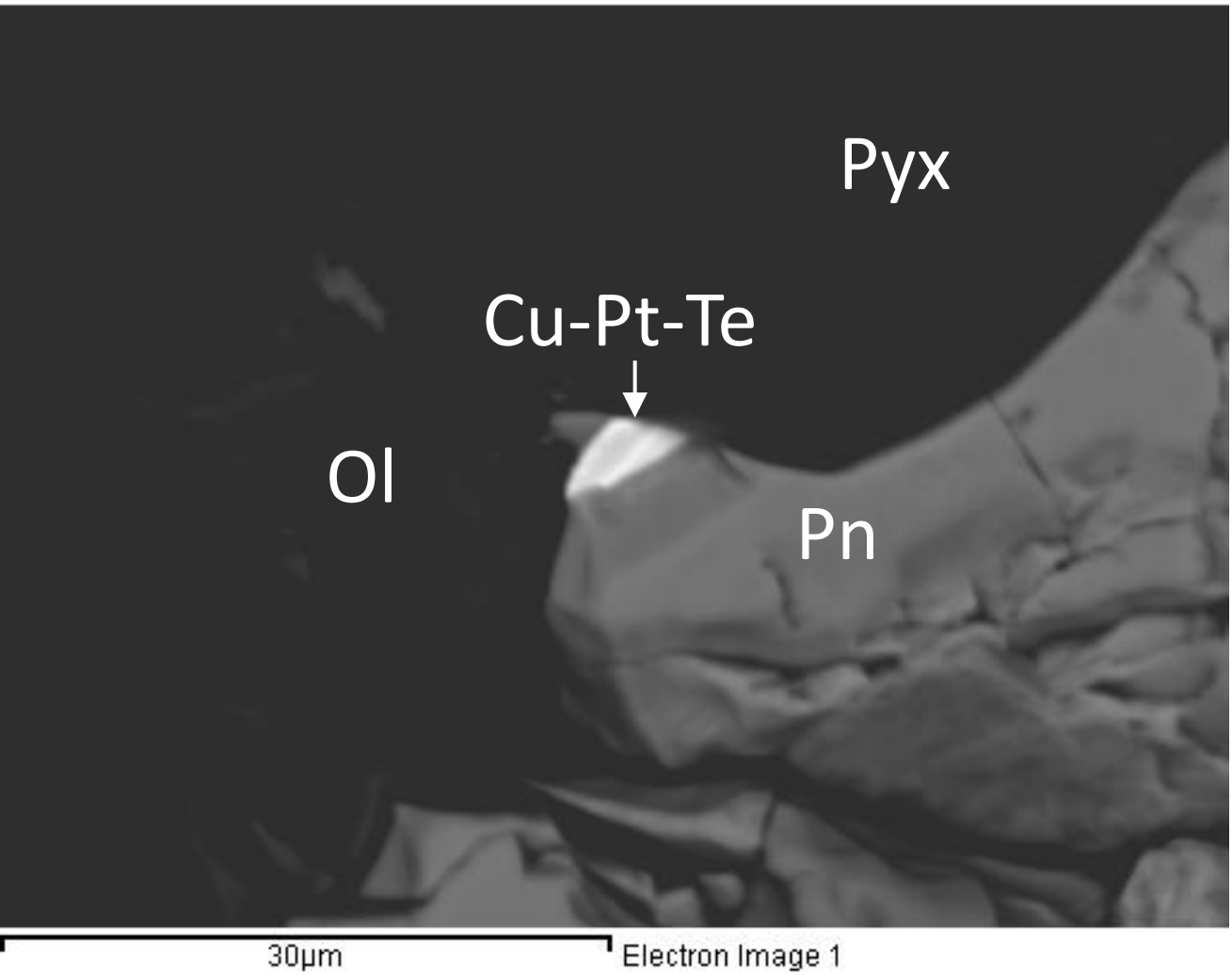
PTR23 H 1



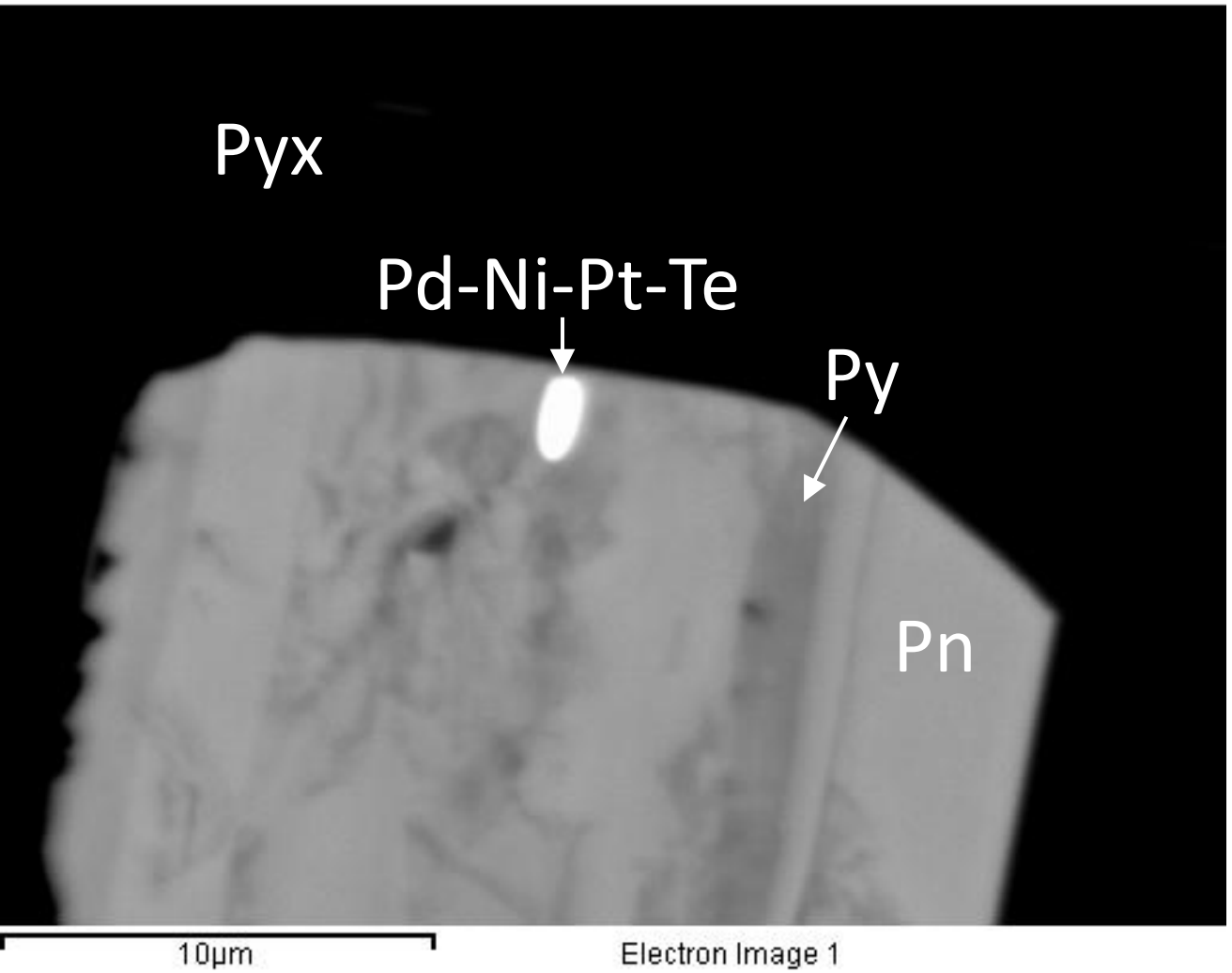
PTR23 I 1



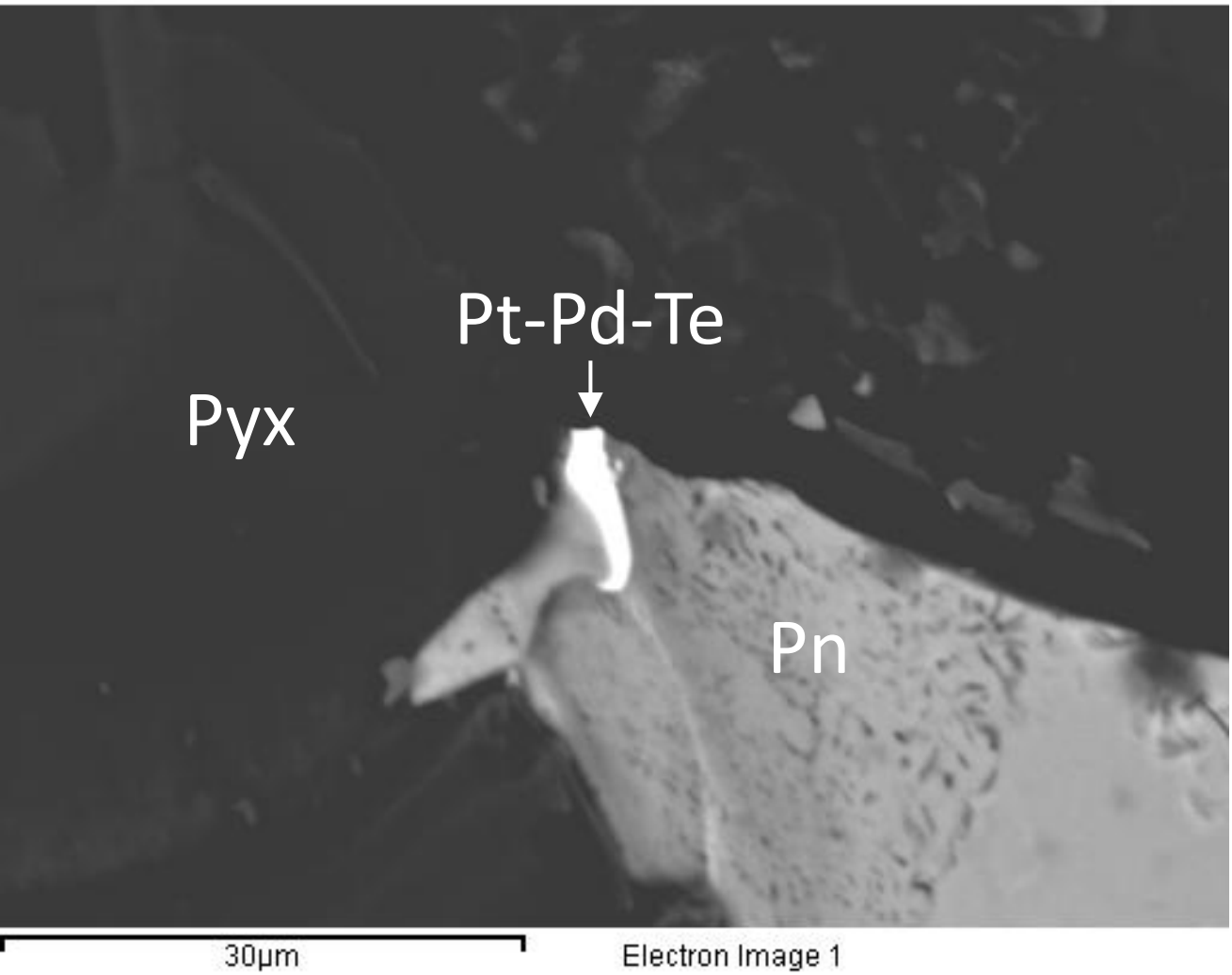
PTR23 J 1



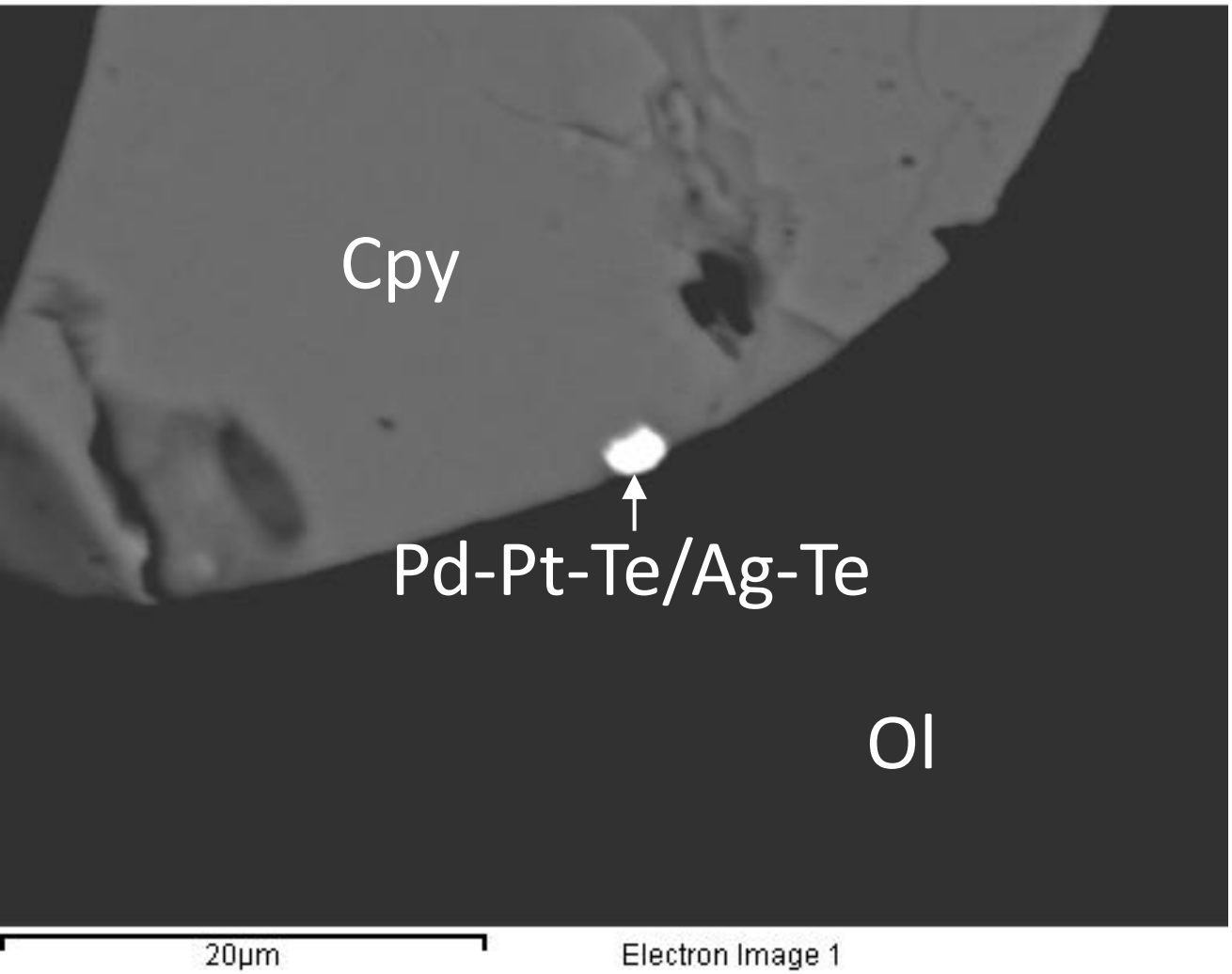
PTR23 K 1



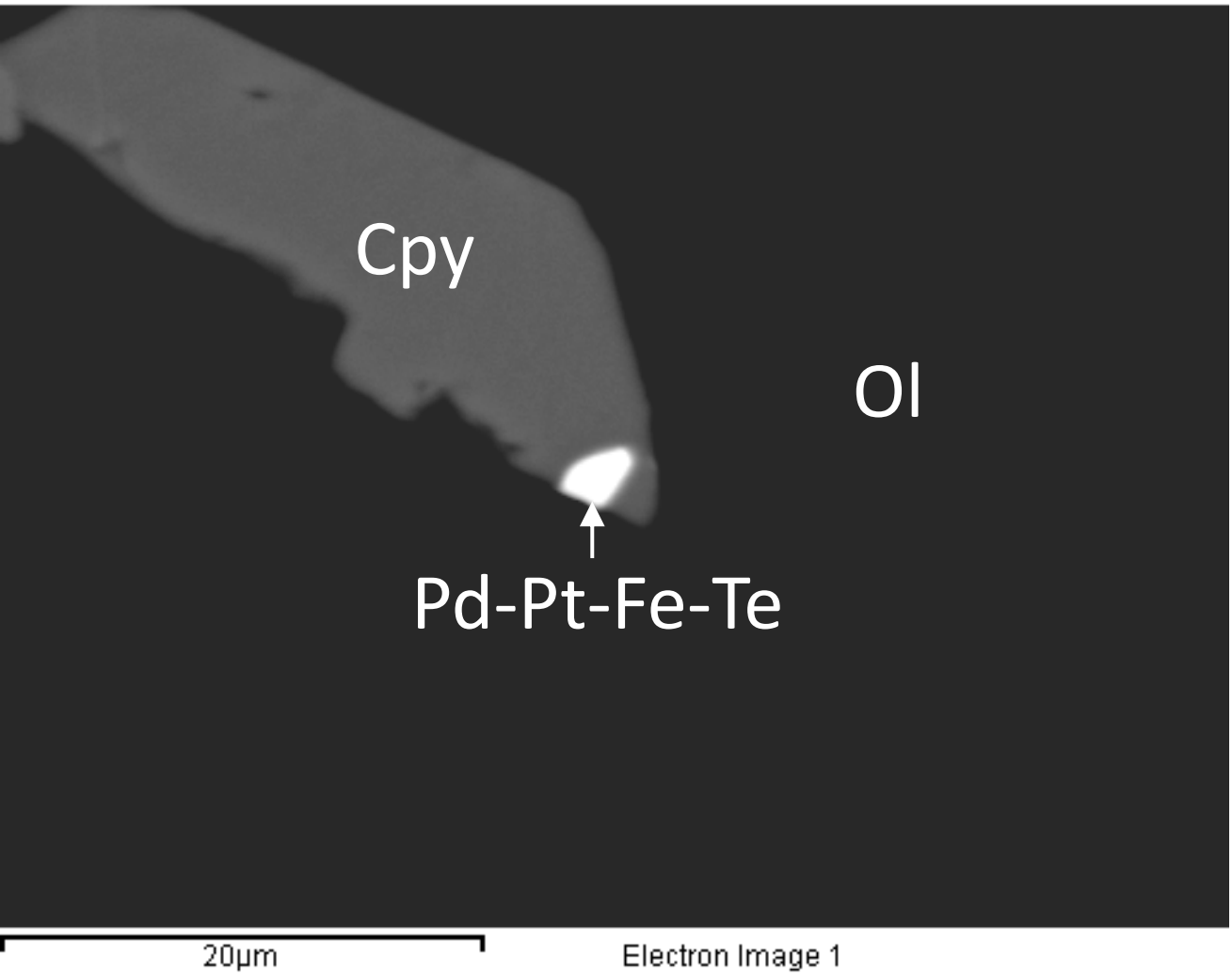
PTR24 A 1



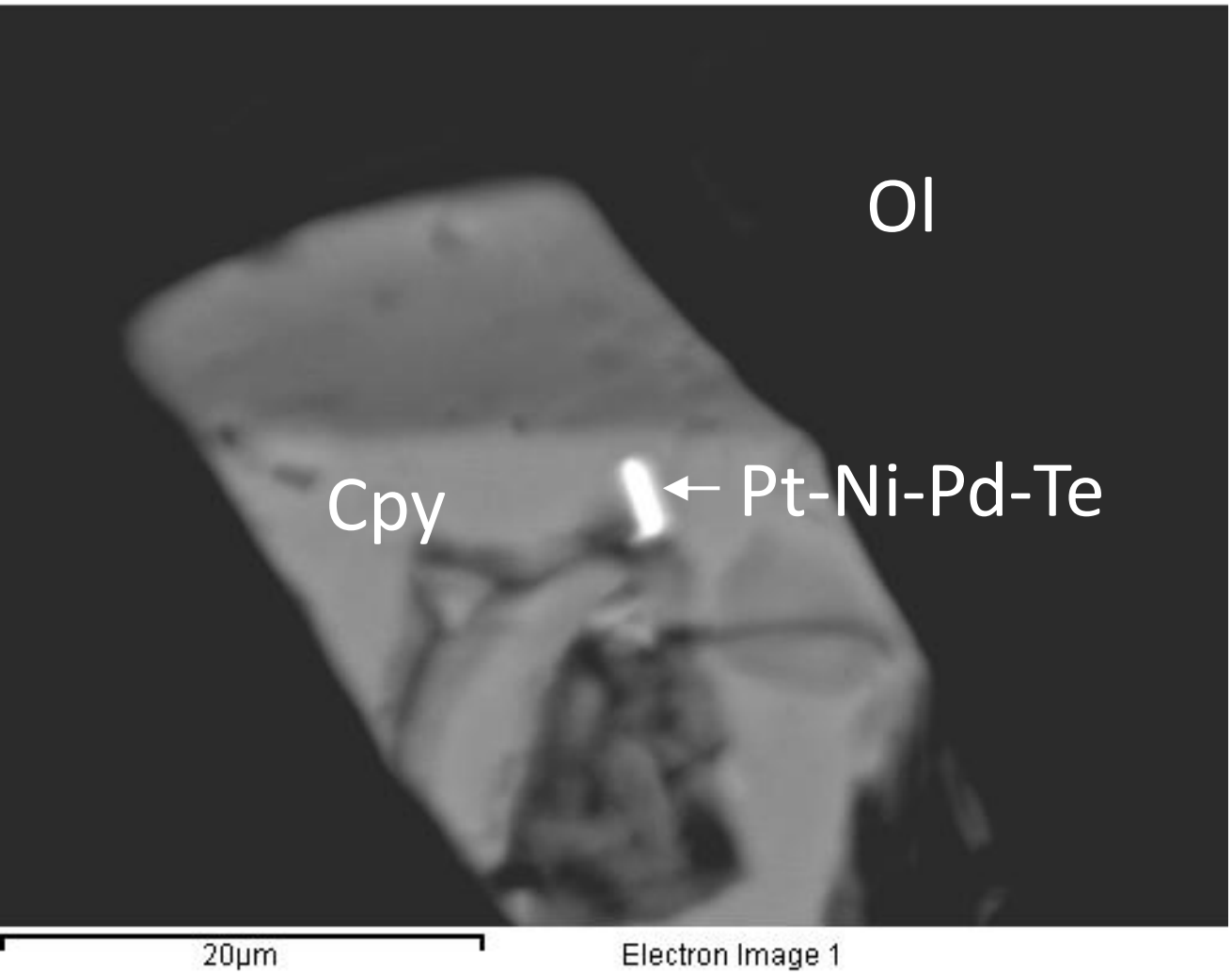
PTR24 B 1



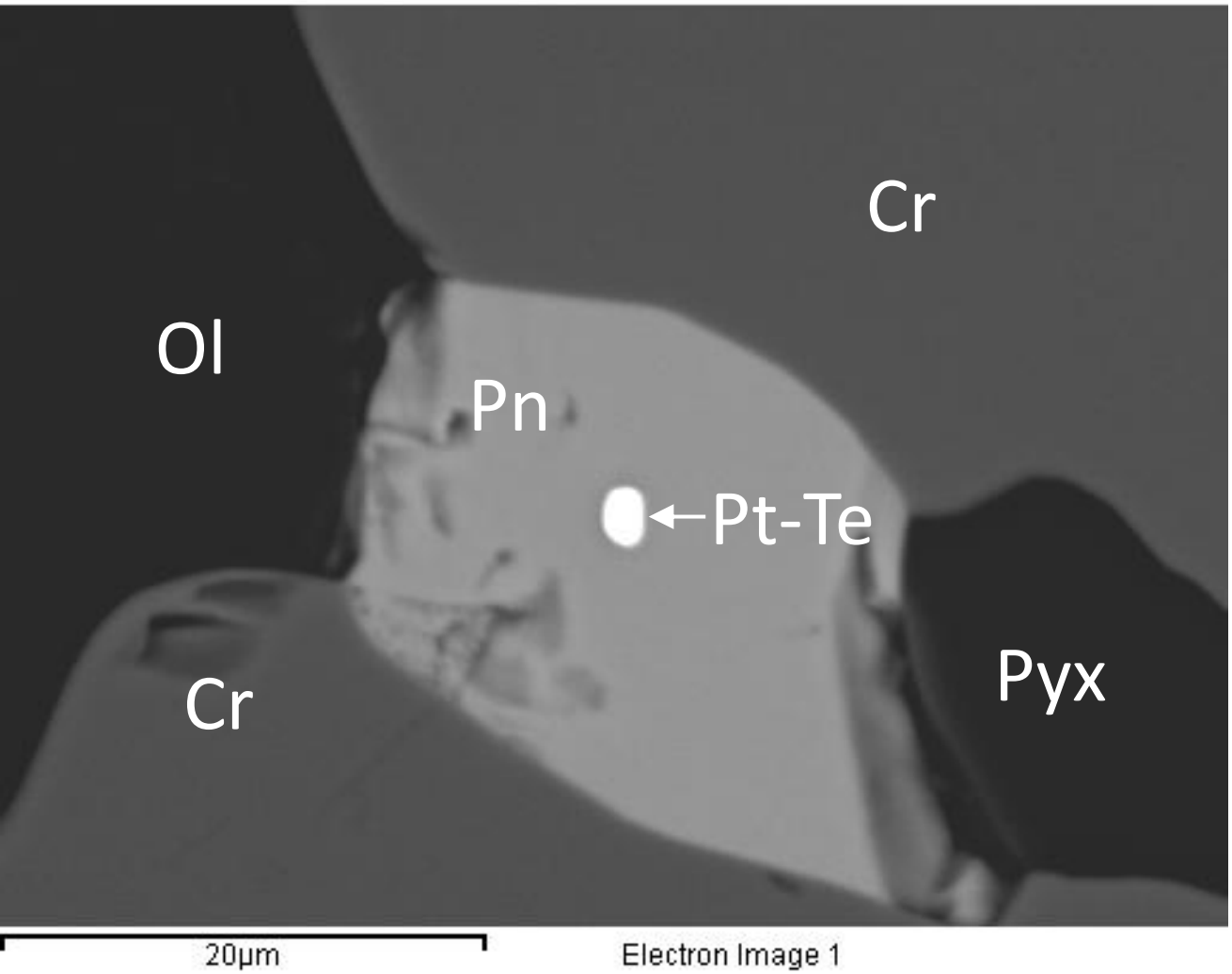
PTR24 C 1



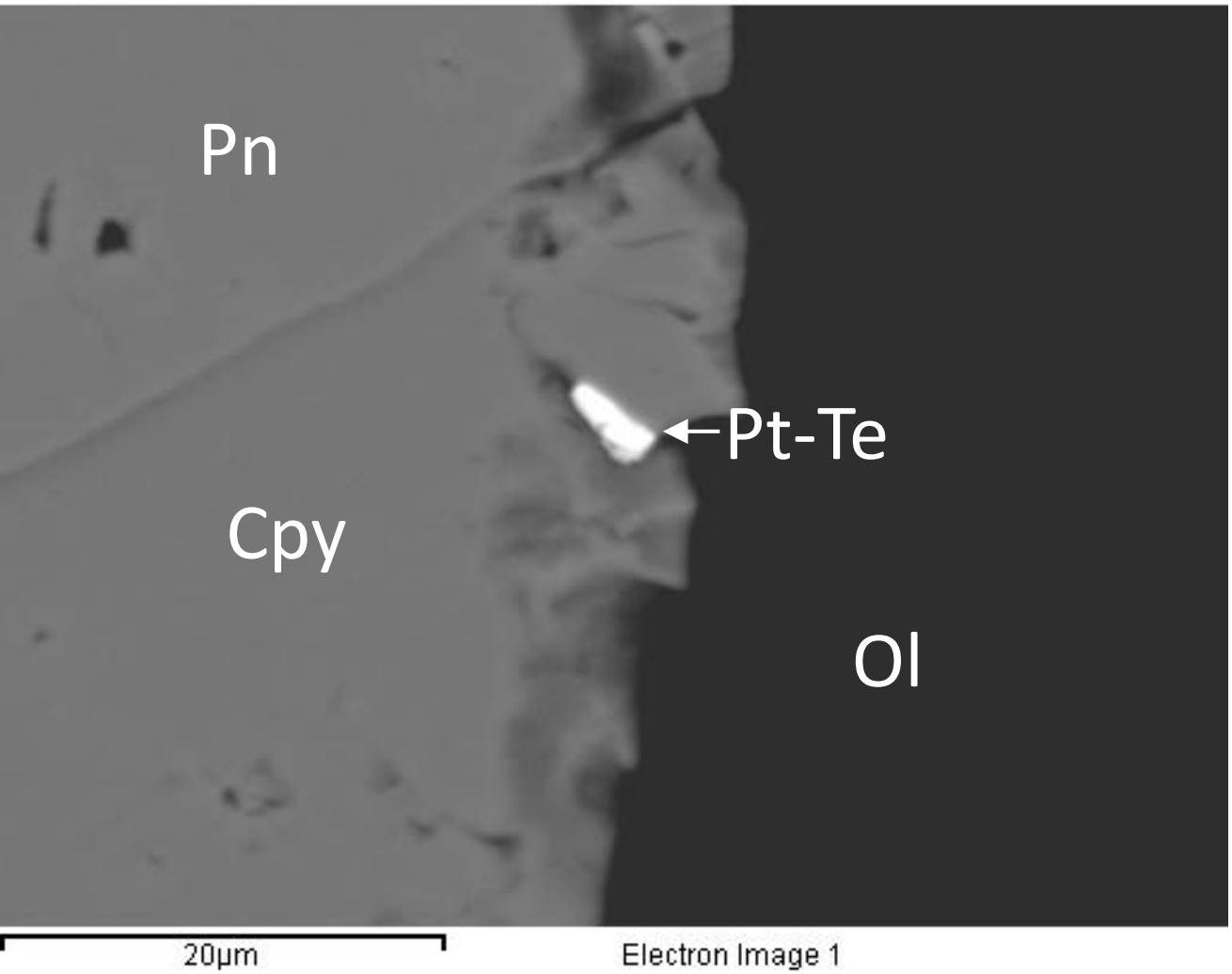
PTR24 D 1



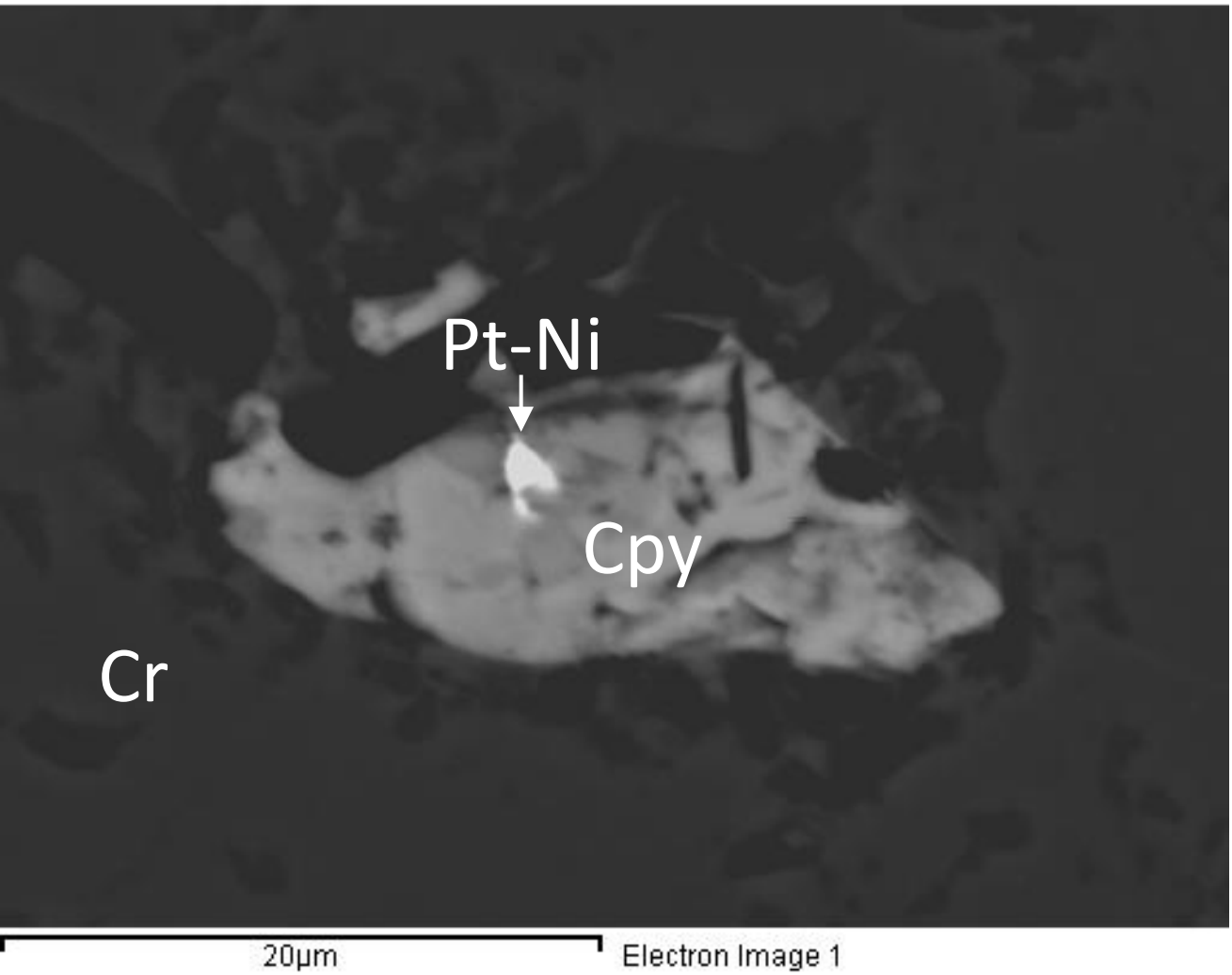
PTR24 E 1



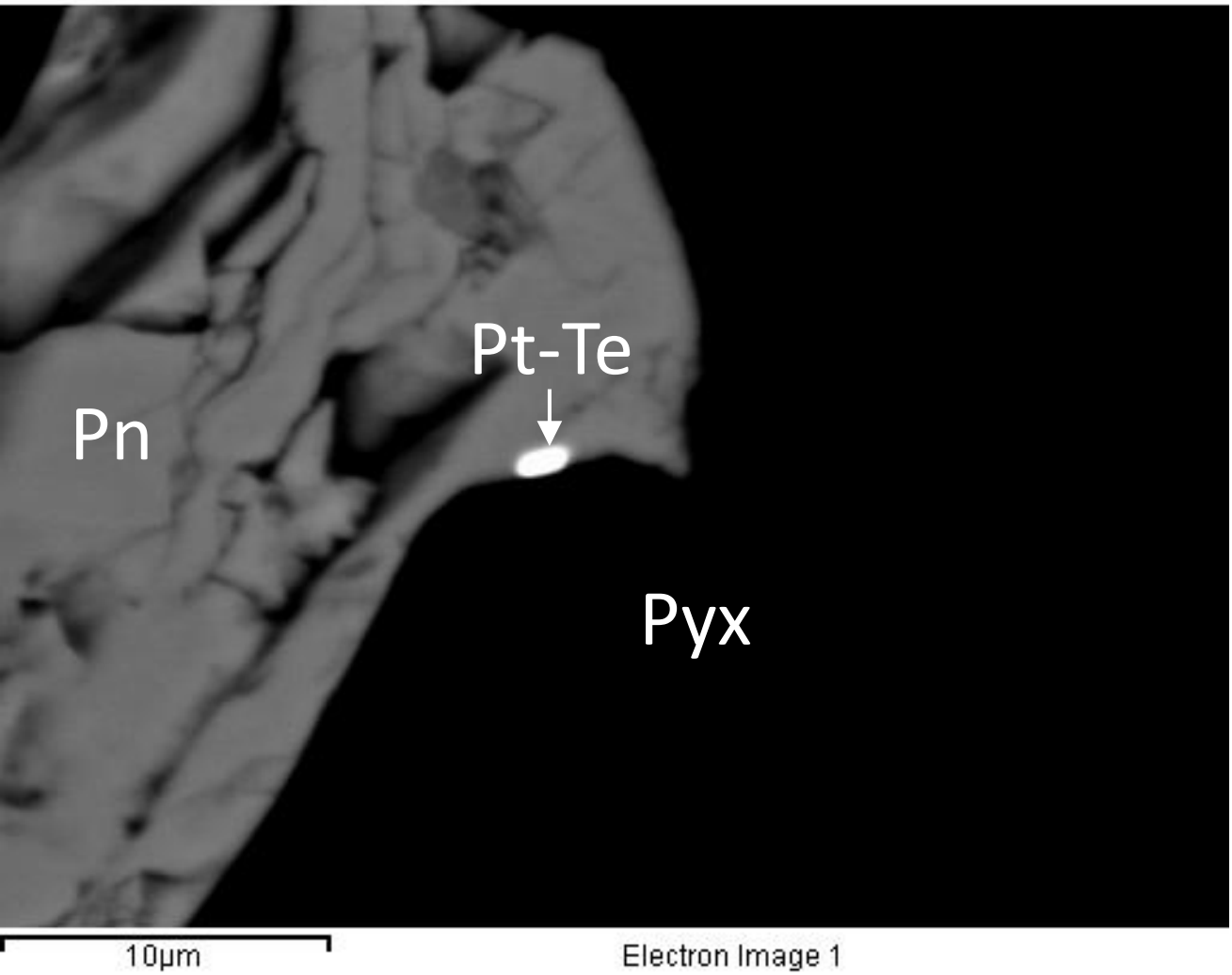
PTR24 F 1



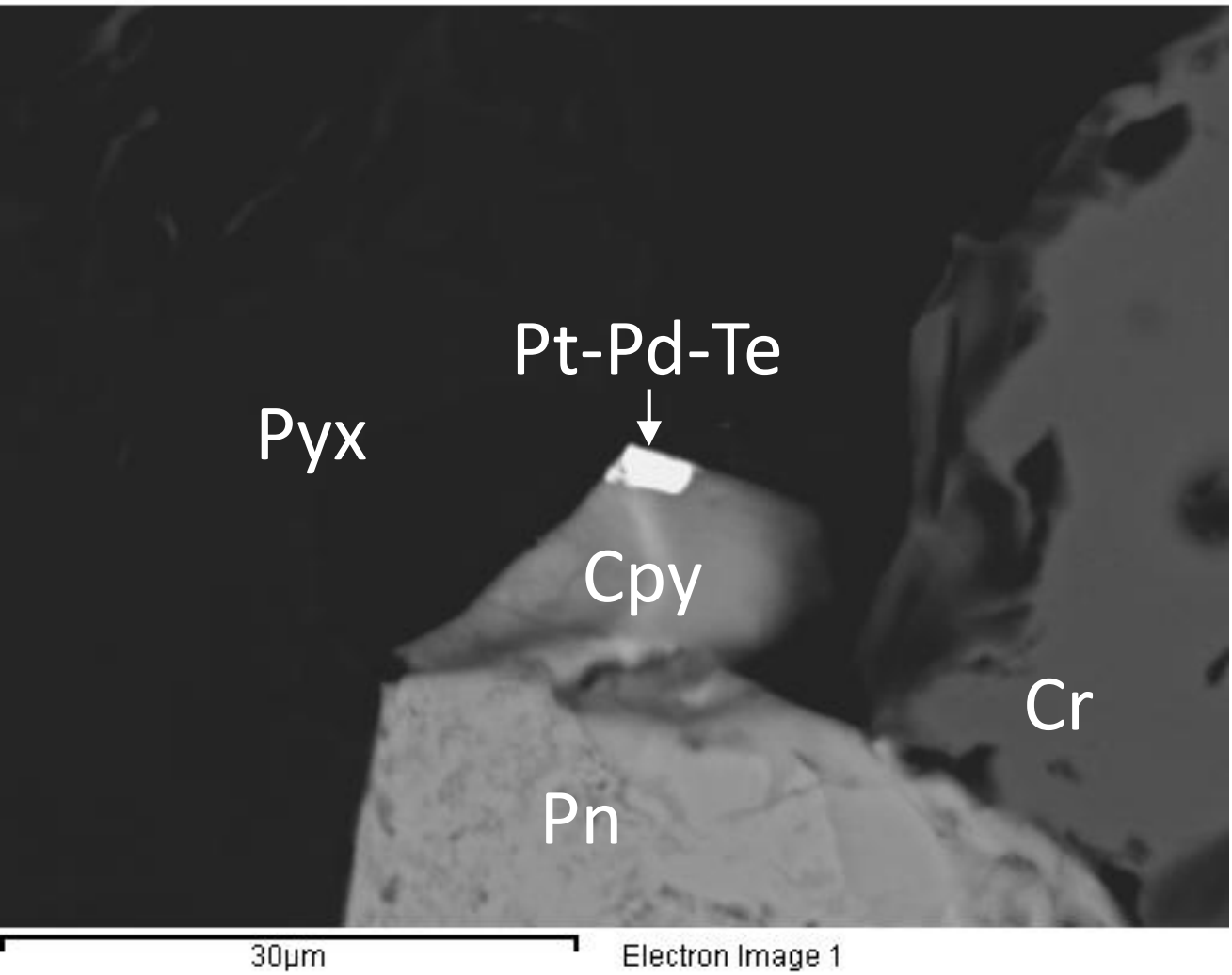
PTR25 C 1



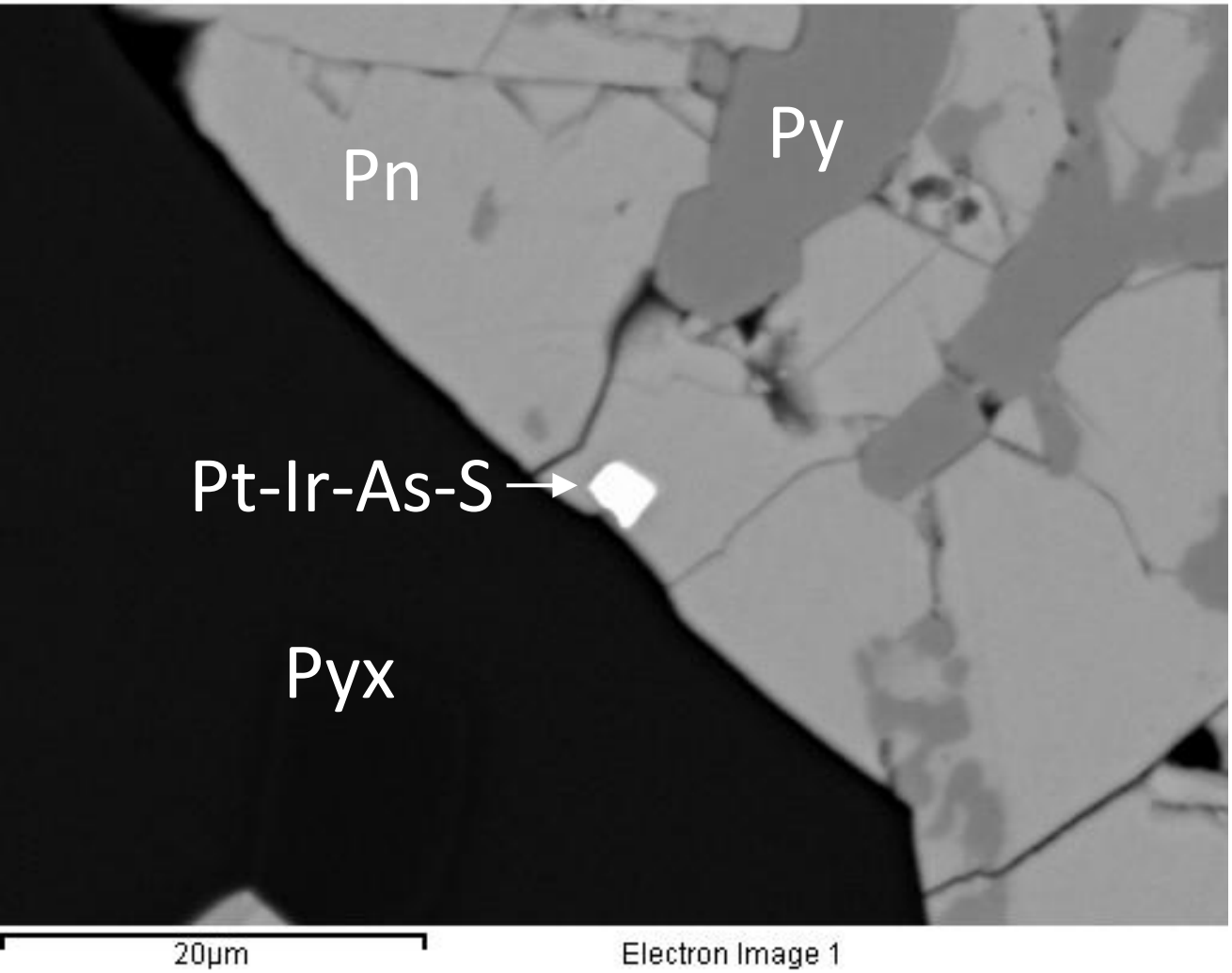
PTR25 D 1



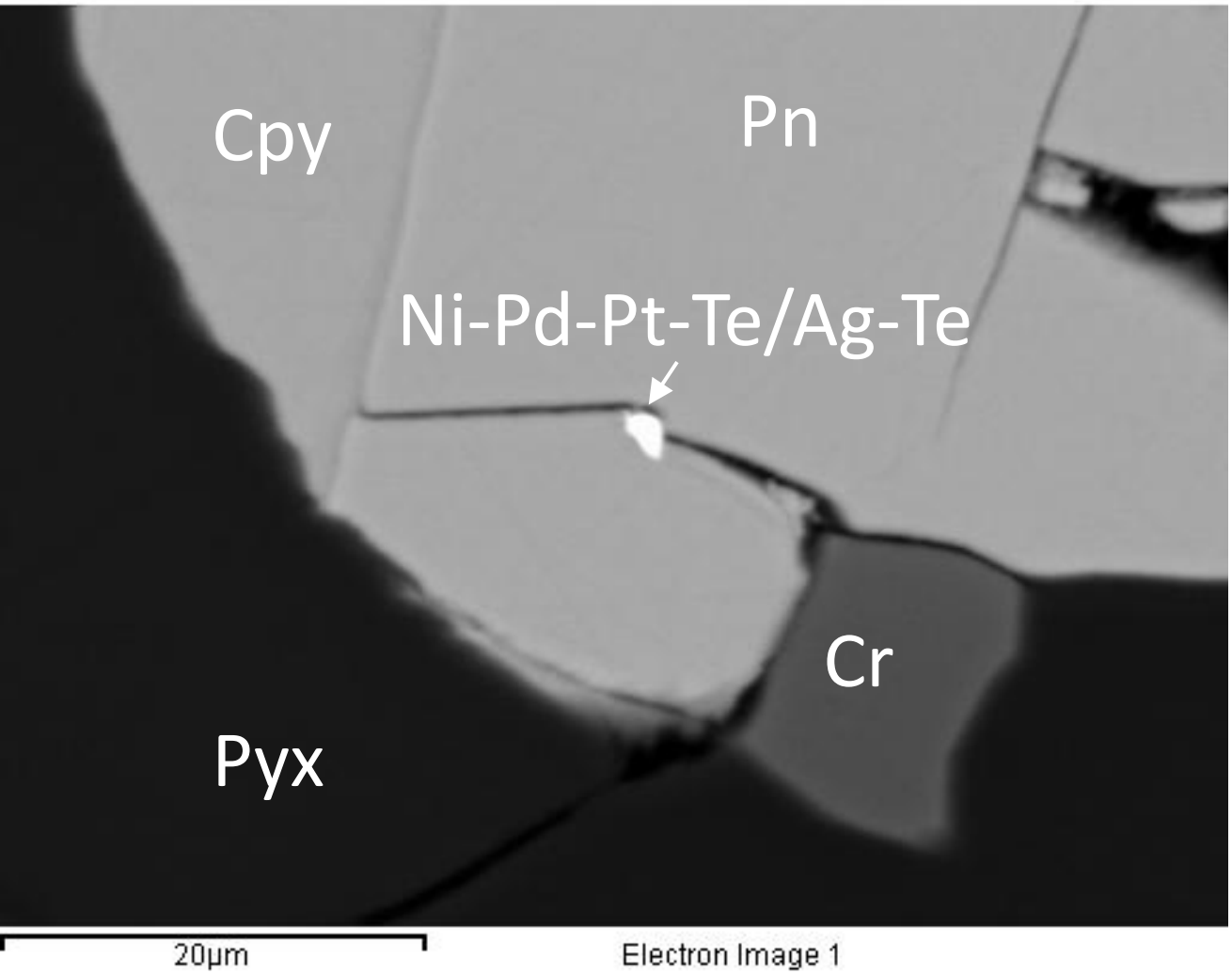
PTR25 E 1



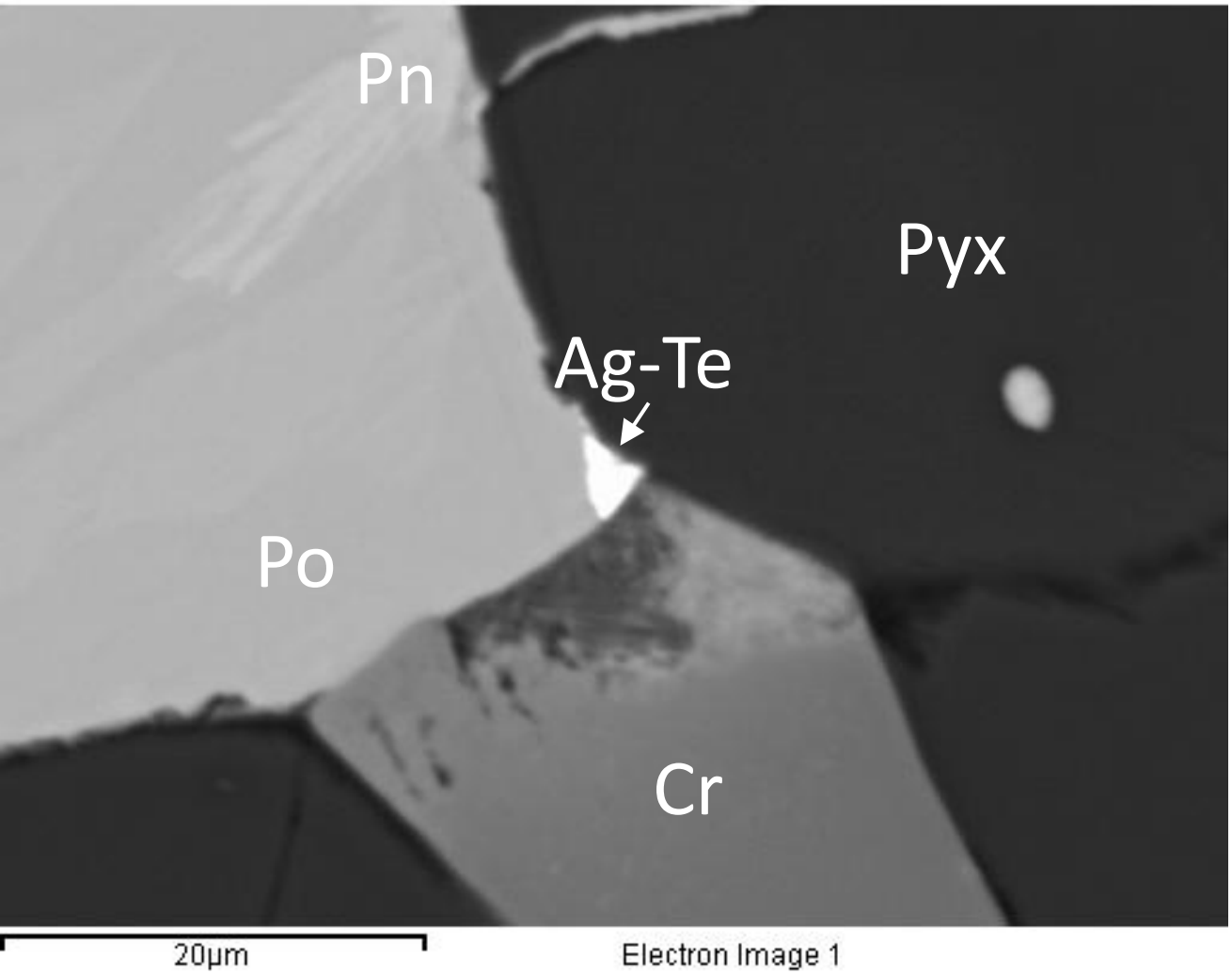
PTSR-30 A 1



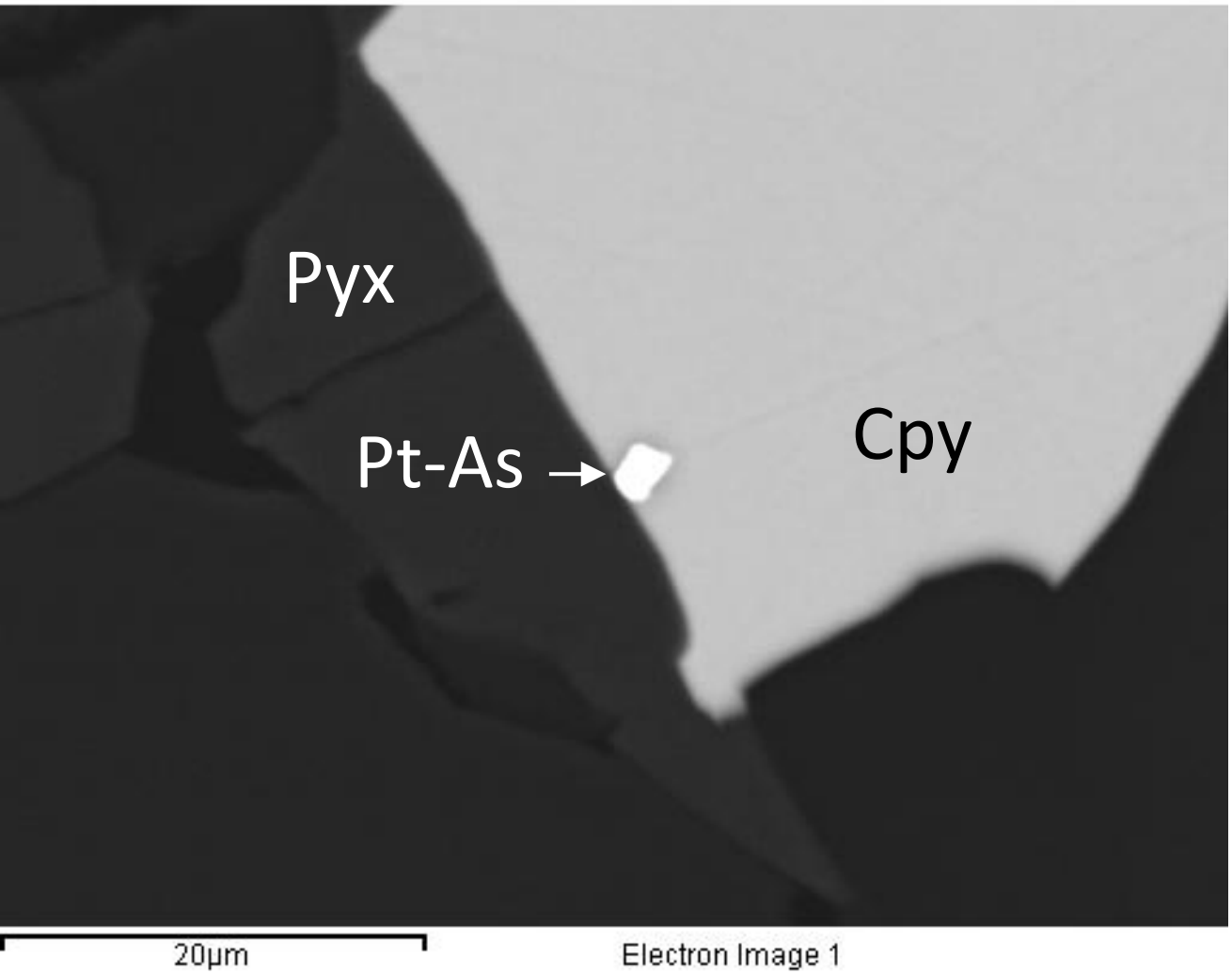
PTSR-30 B 1



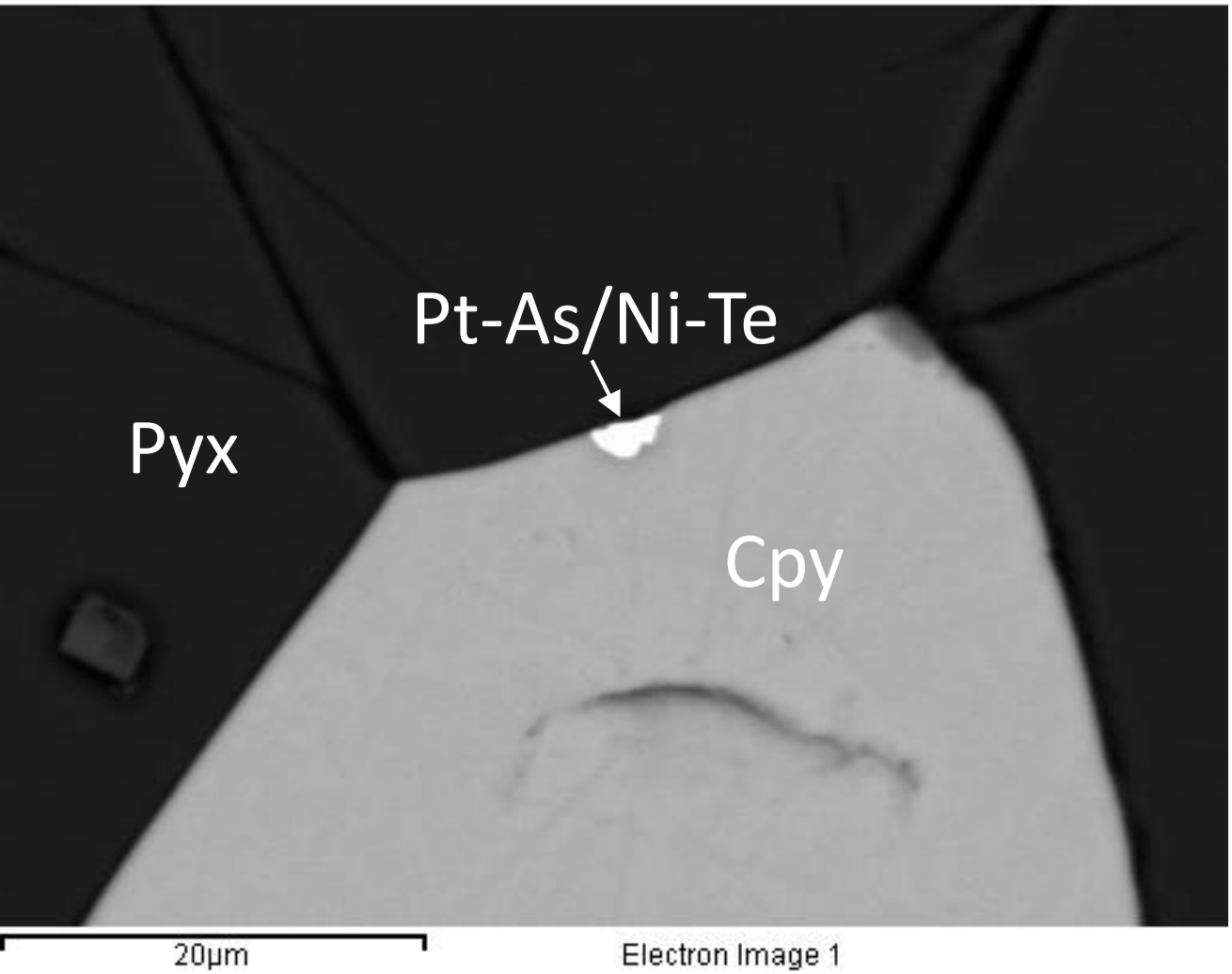
PTSR-30 C 1



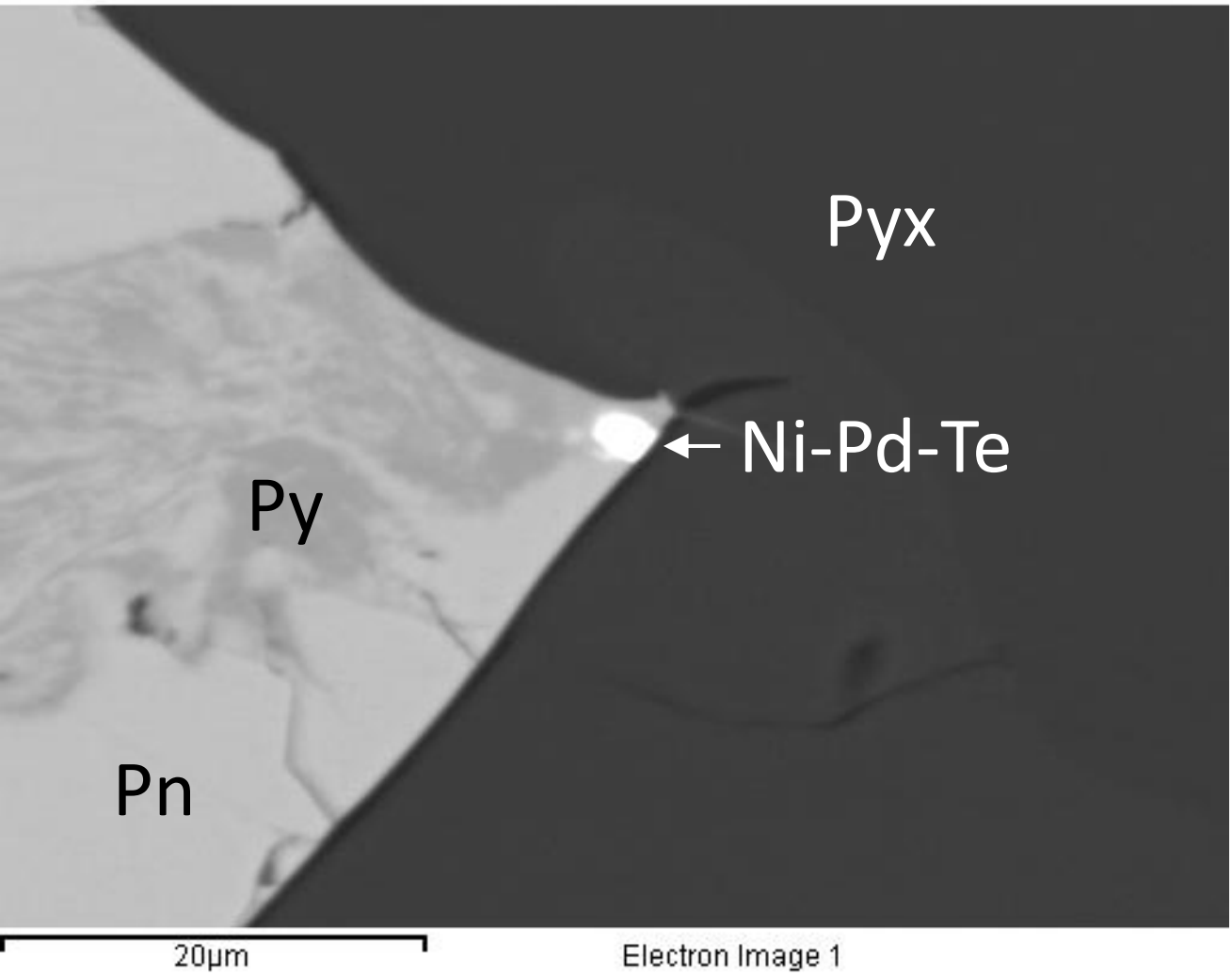
PTSR-30 D 1



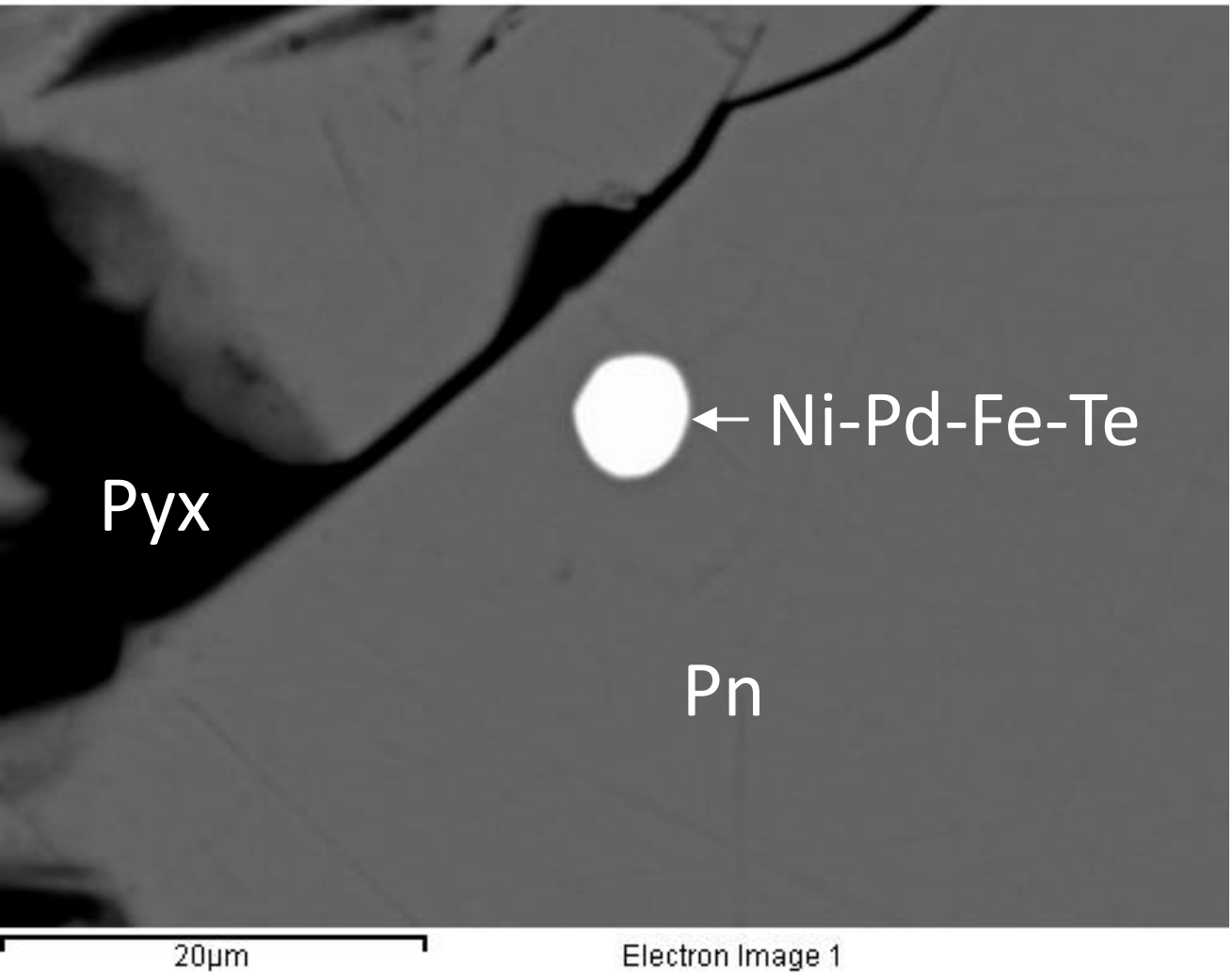
PTSR-30 E 1



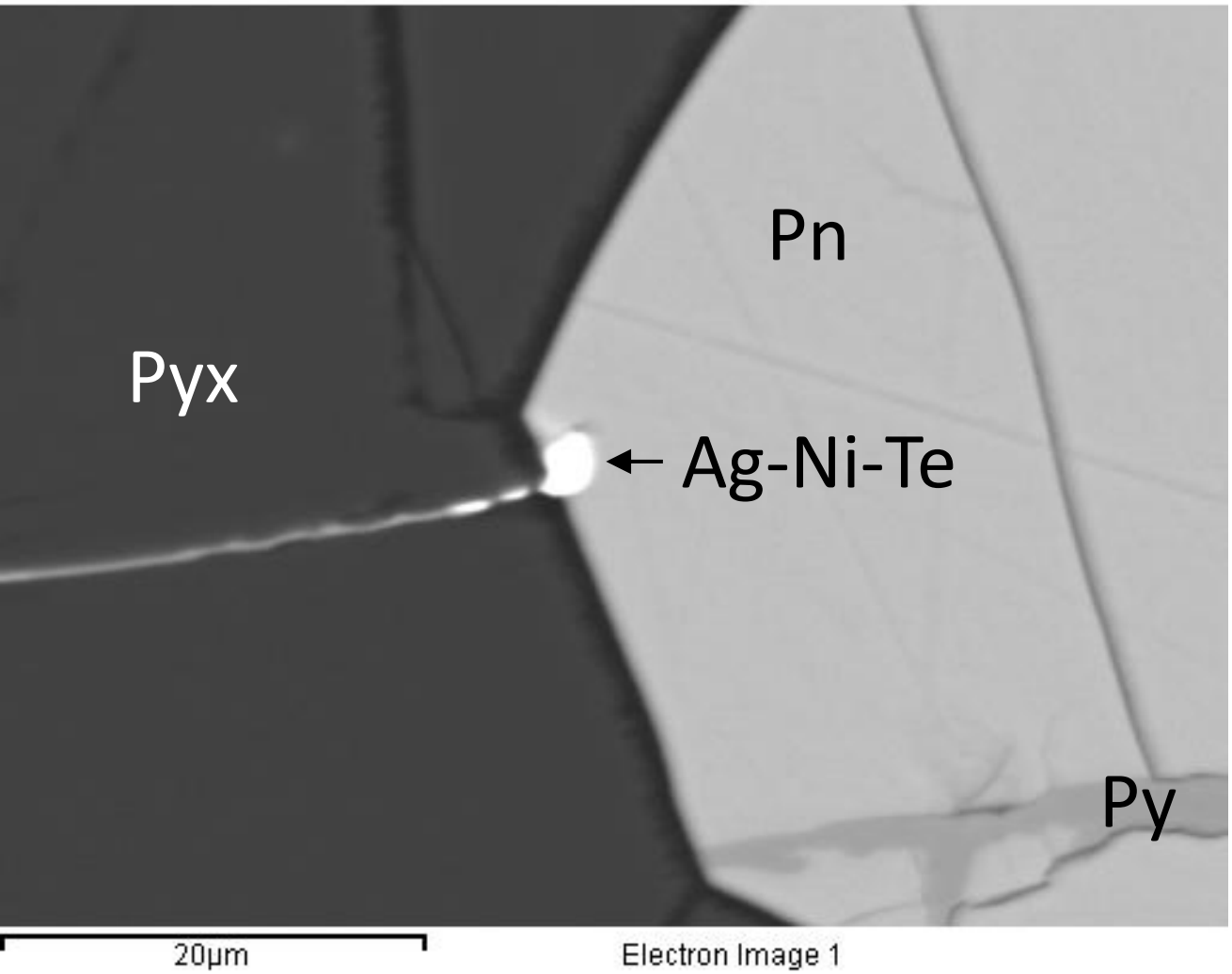
PTSR-30 F 1



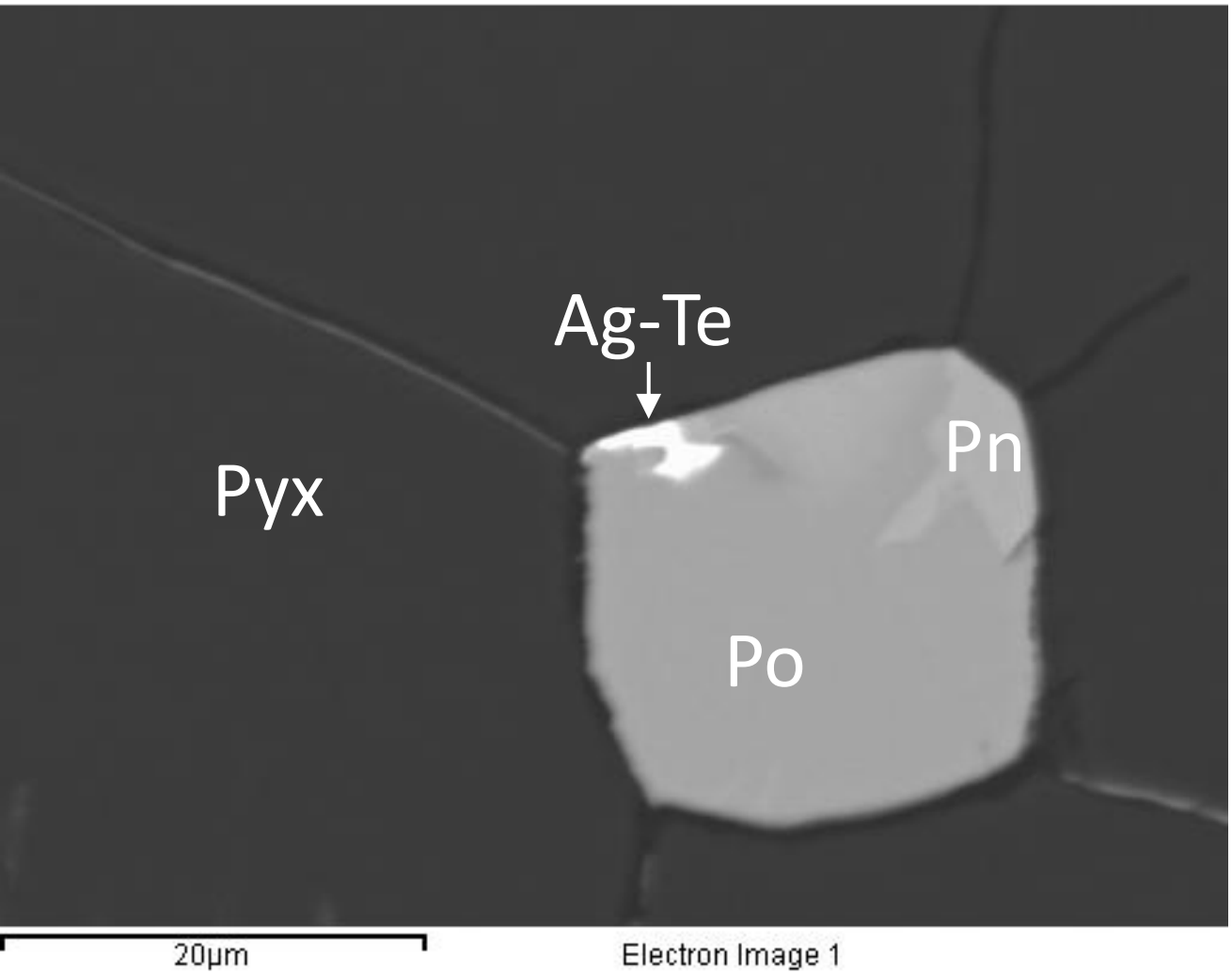
PTSR-30 G 1



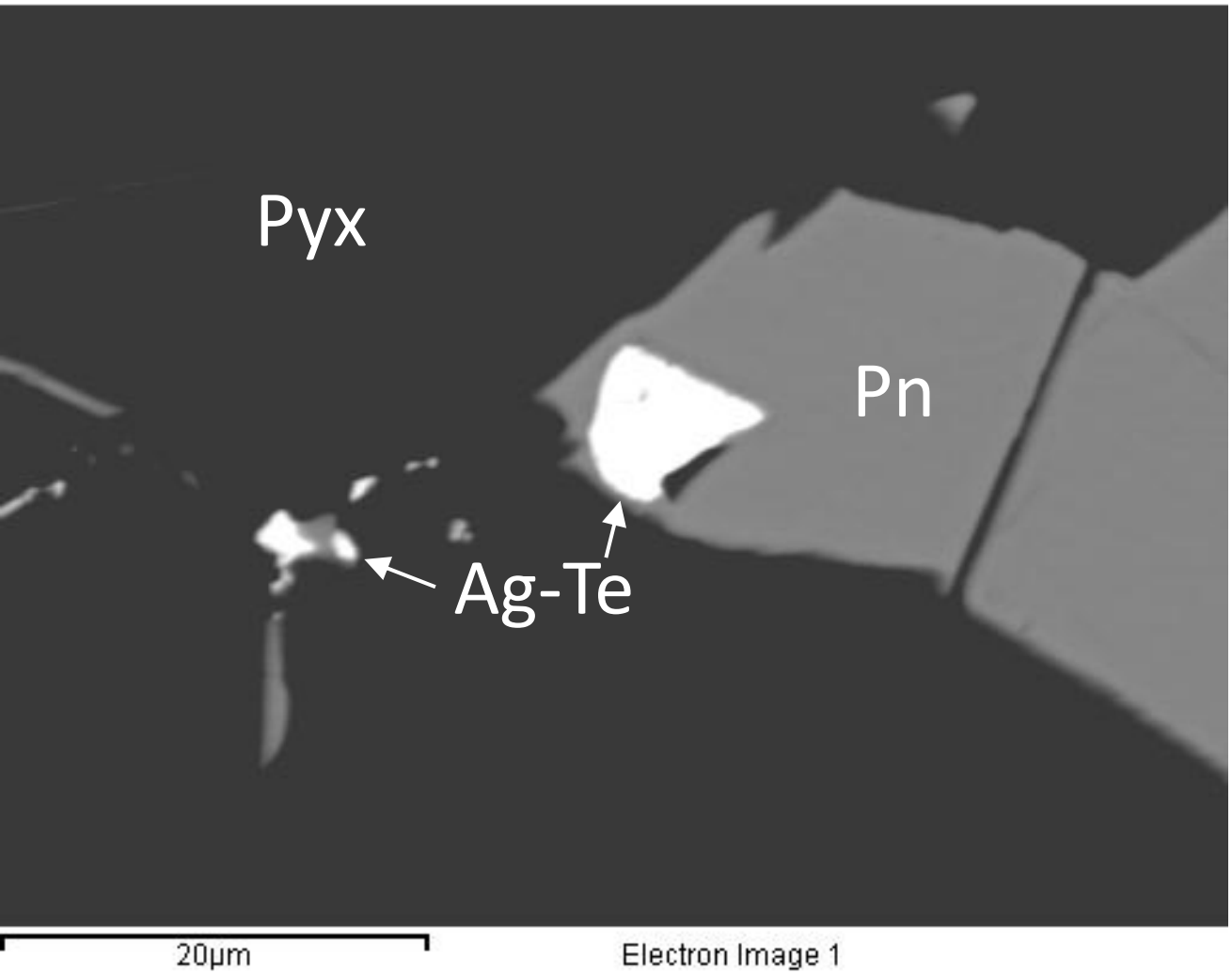
PTSR-30 H 1



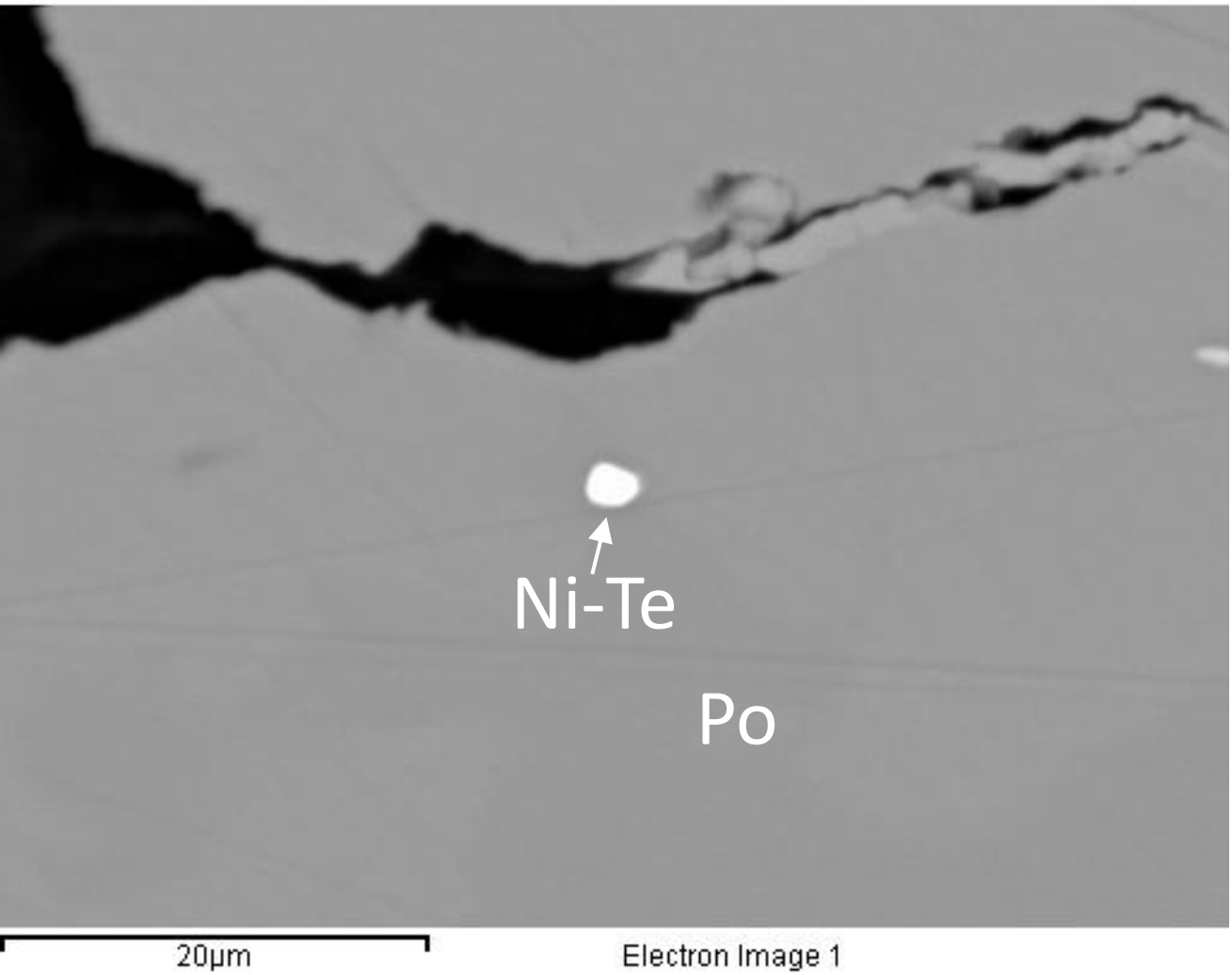
PTSR-30 I 1



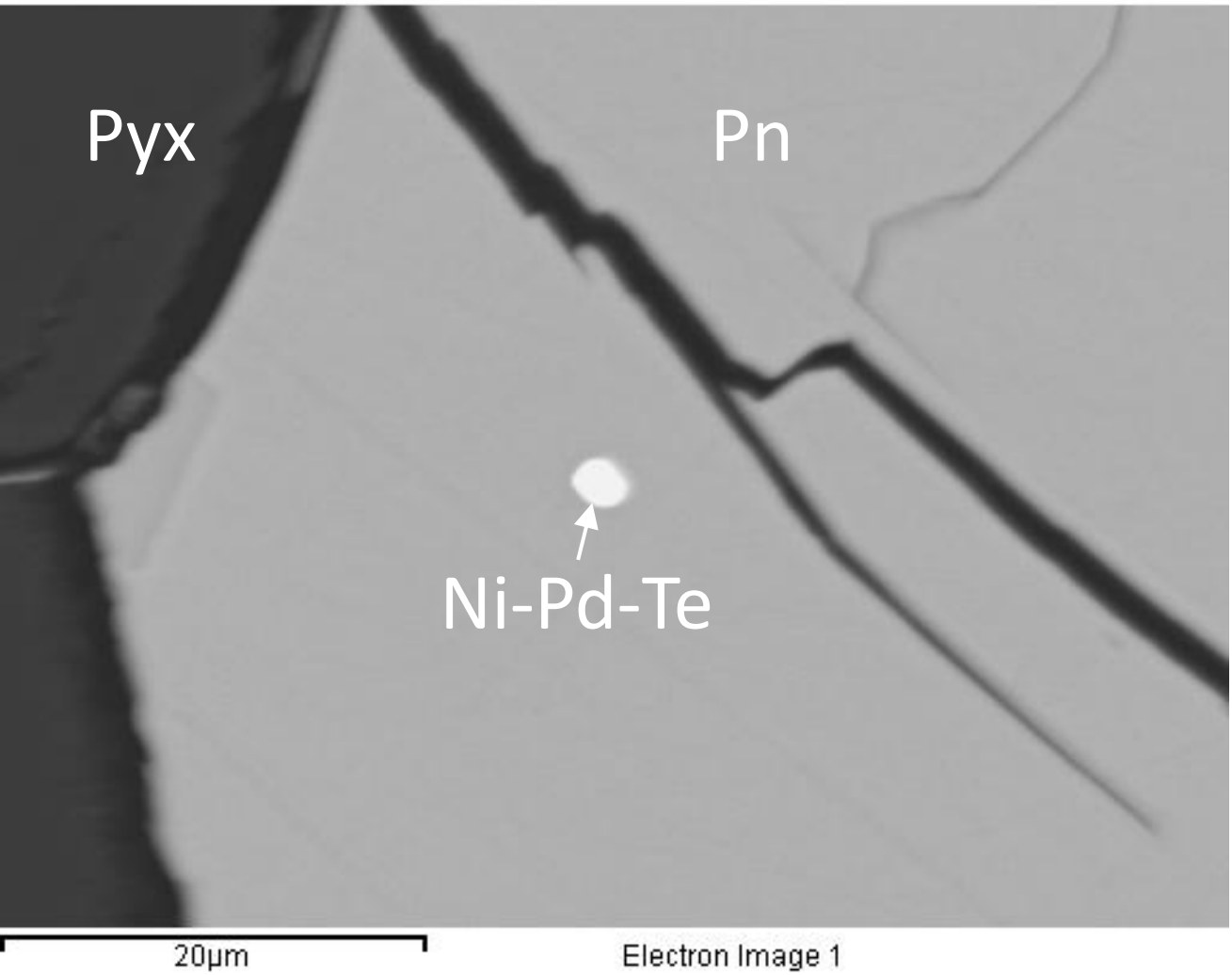
PTSR-30 J 1-2



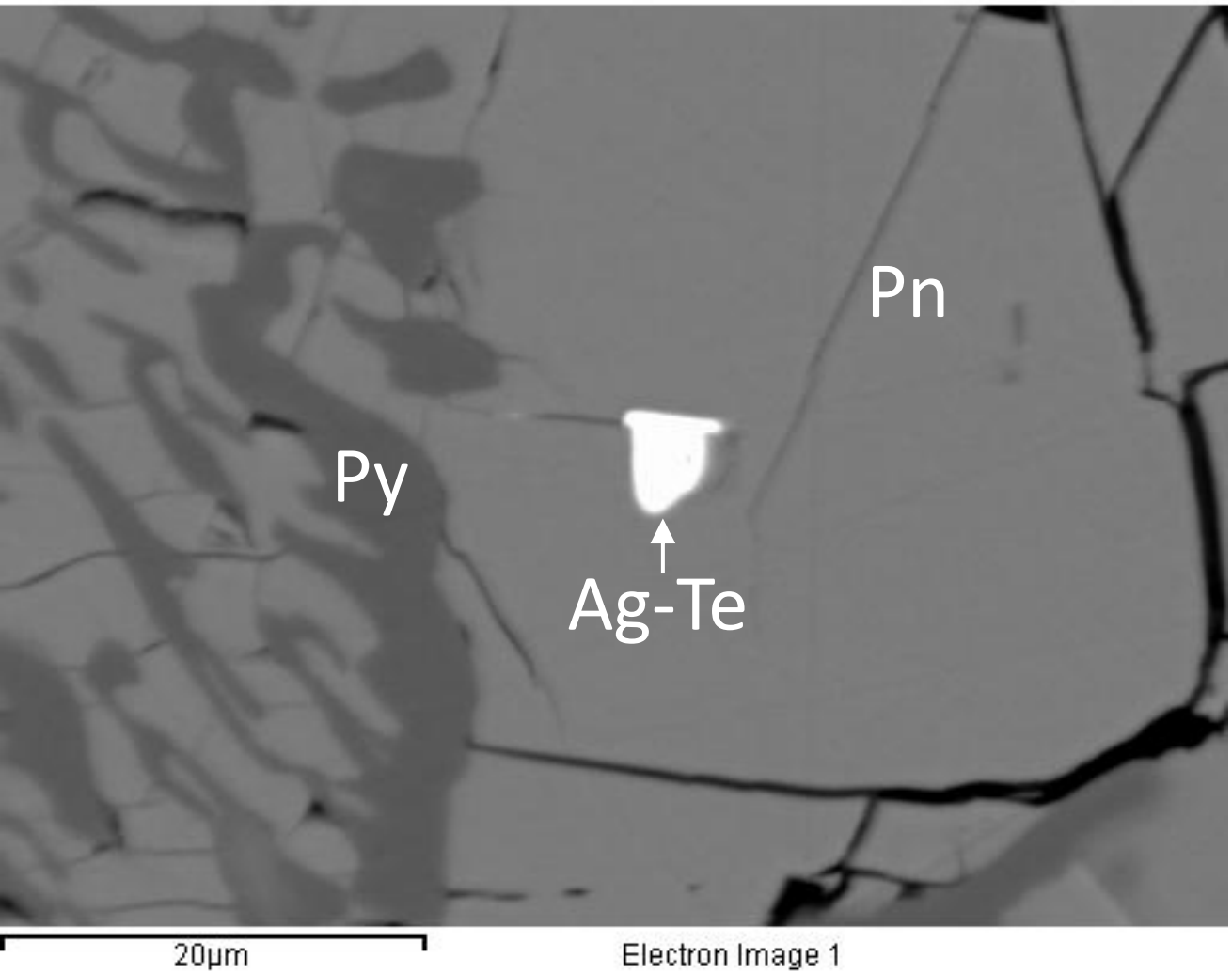
PTSR-30 K 1



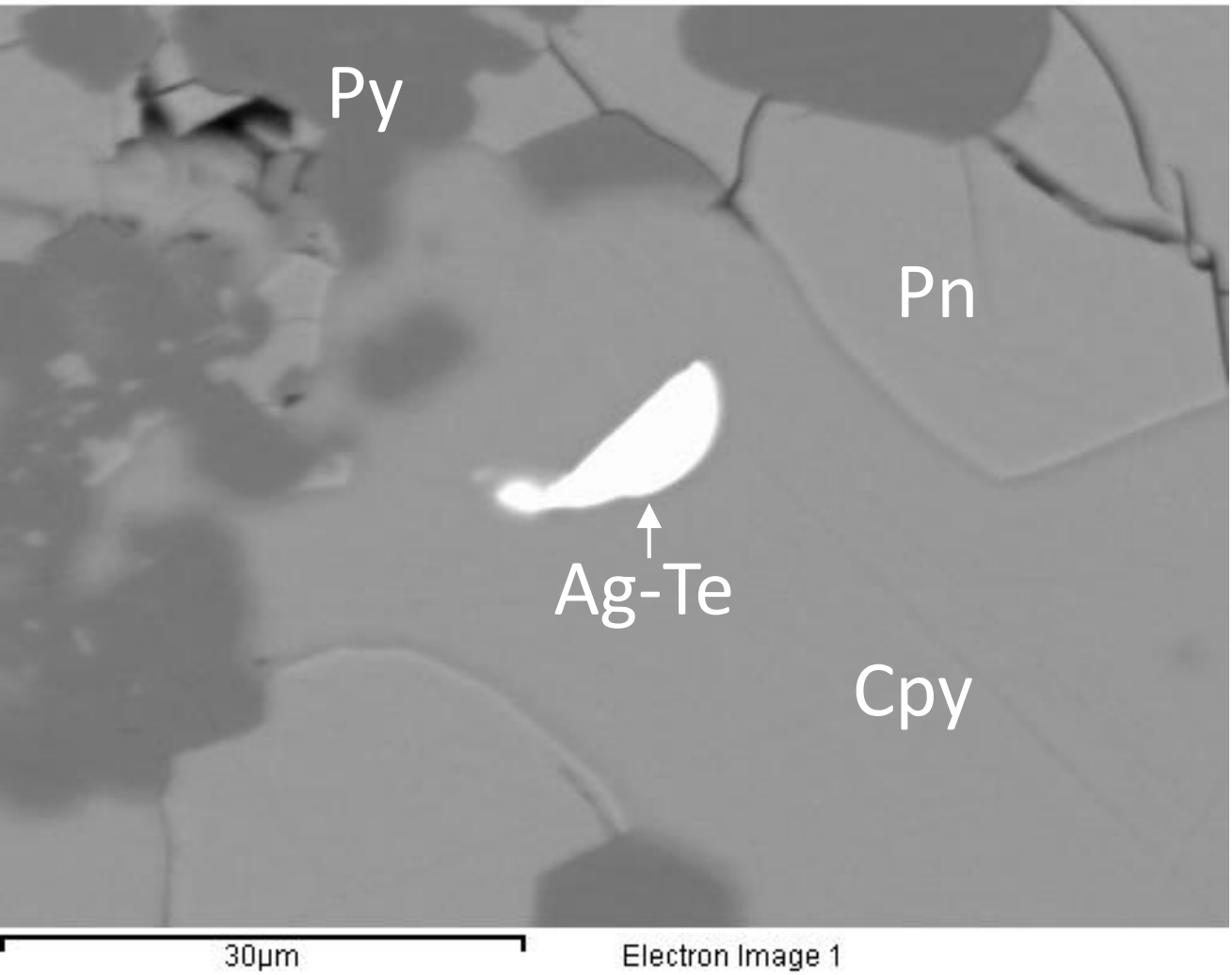
PTSR-30 L 1



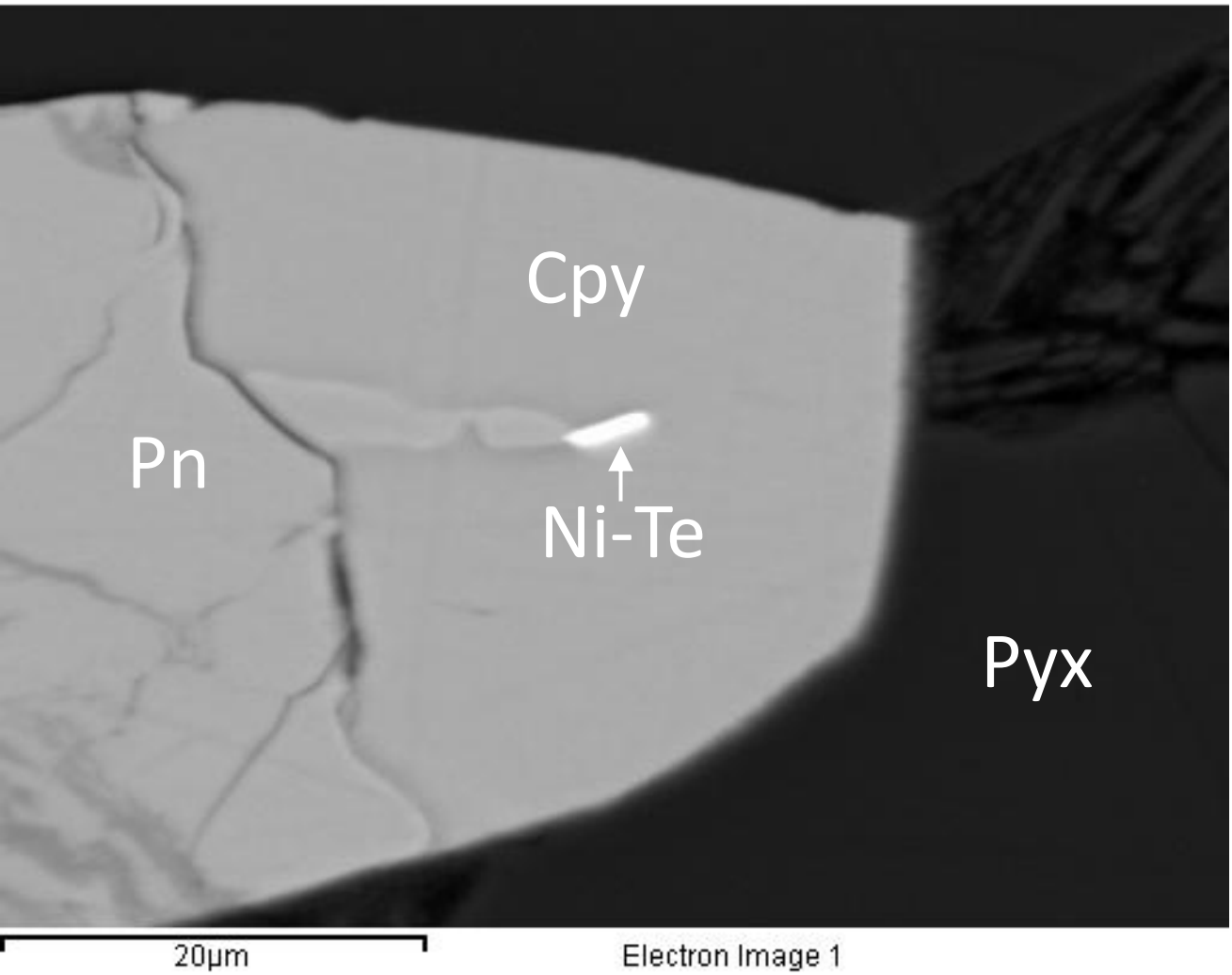
PTSR-30 M 1



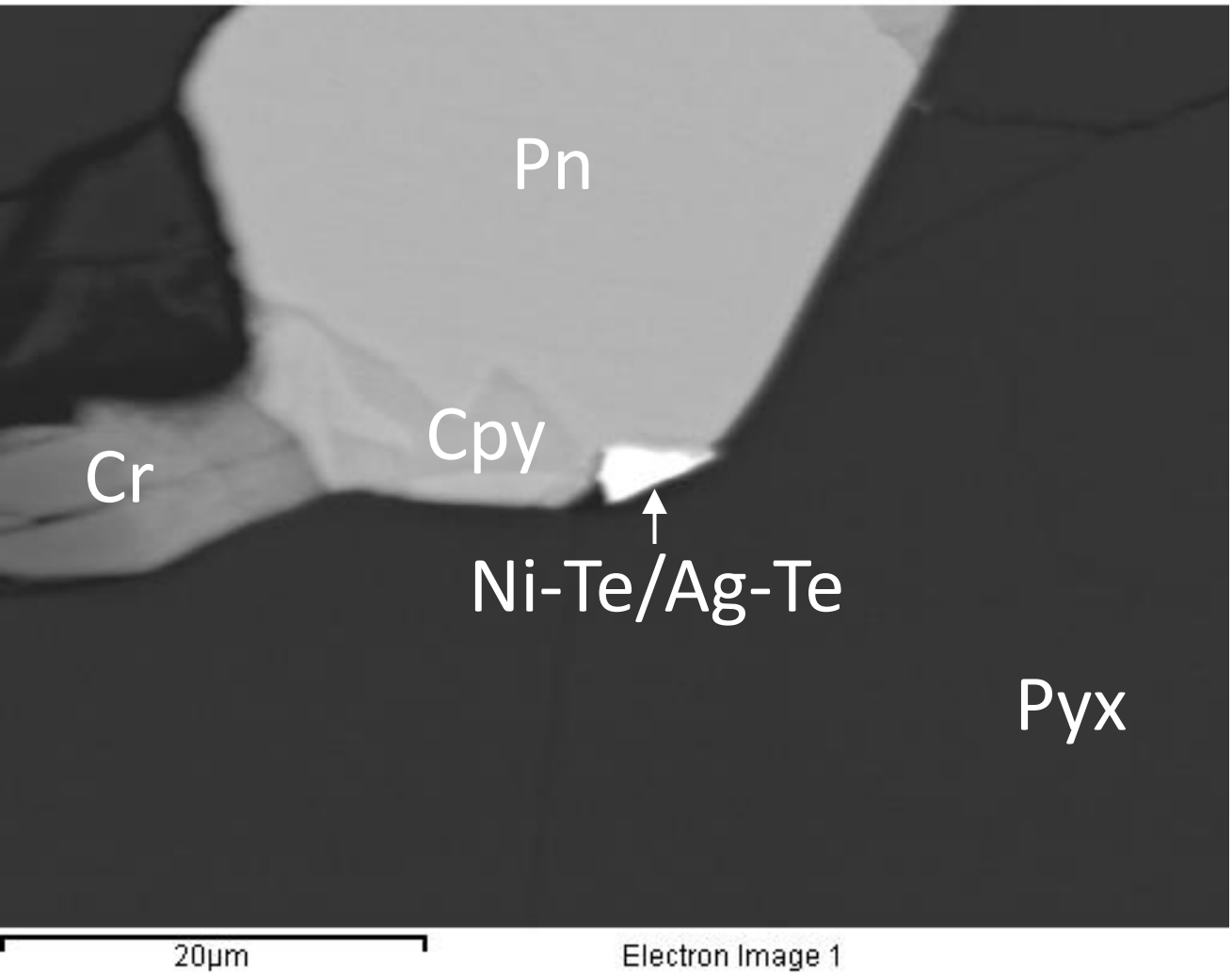
PTSR-30 N 1



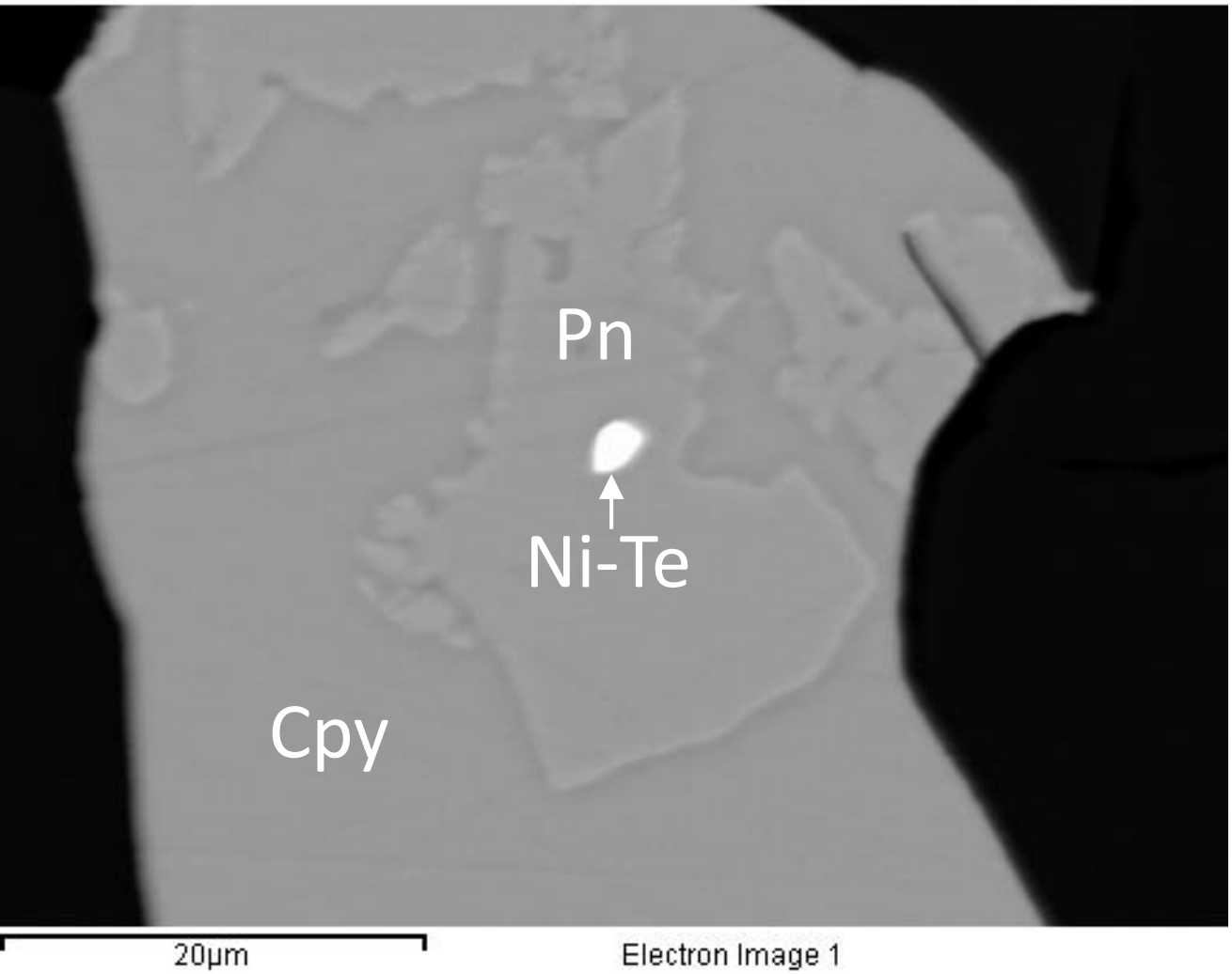
PTSR-30 O 1



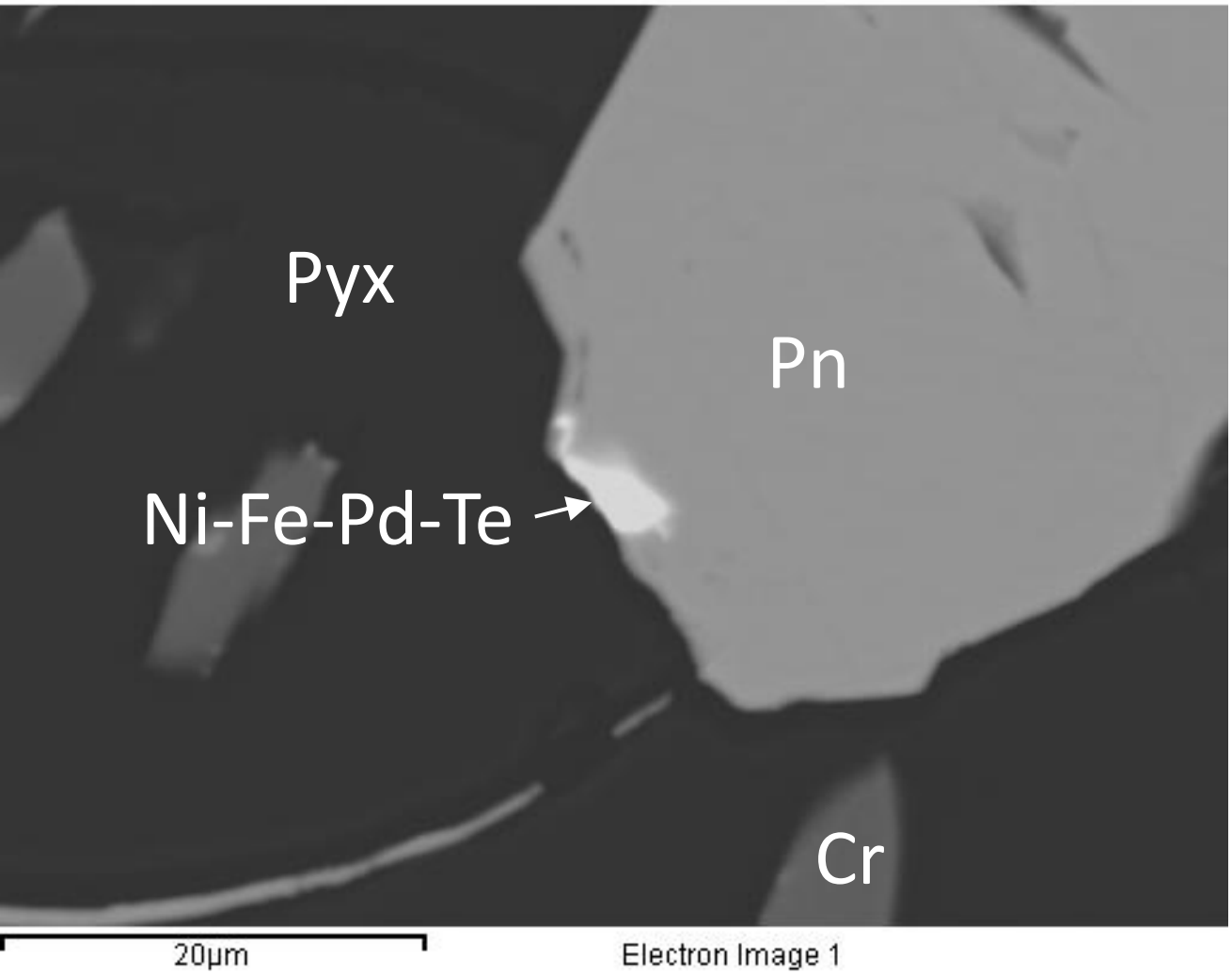
PTSR-30 P 1



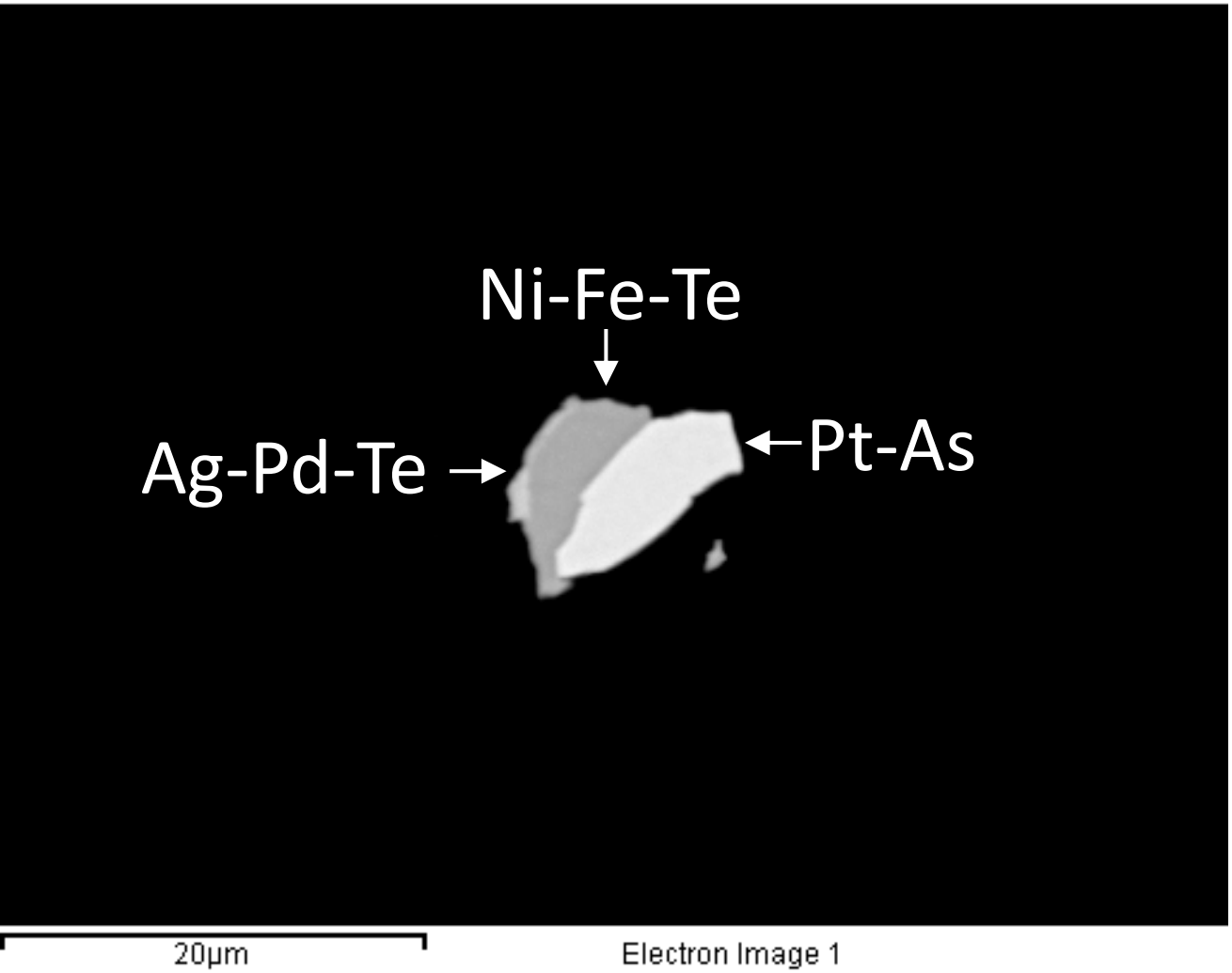
PTSR-30 Q 1



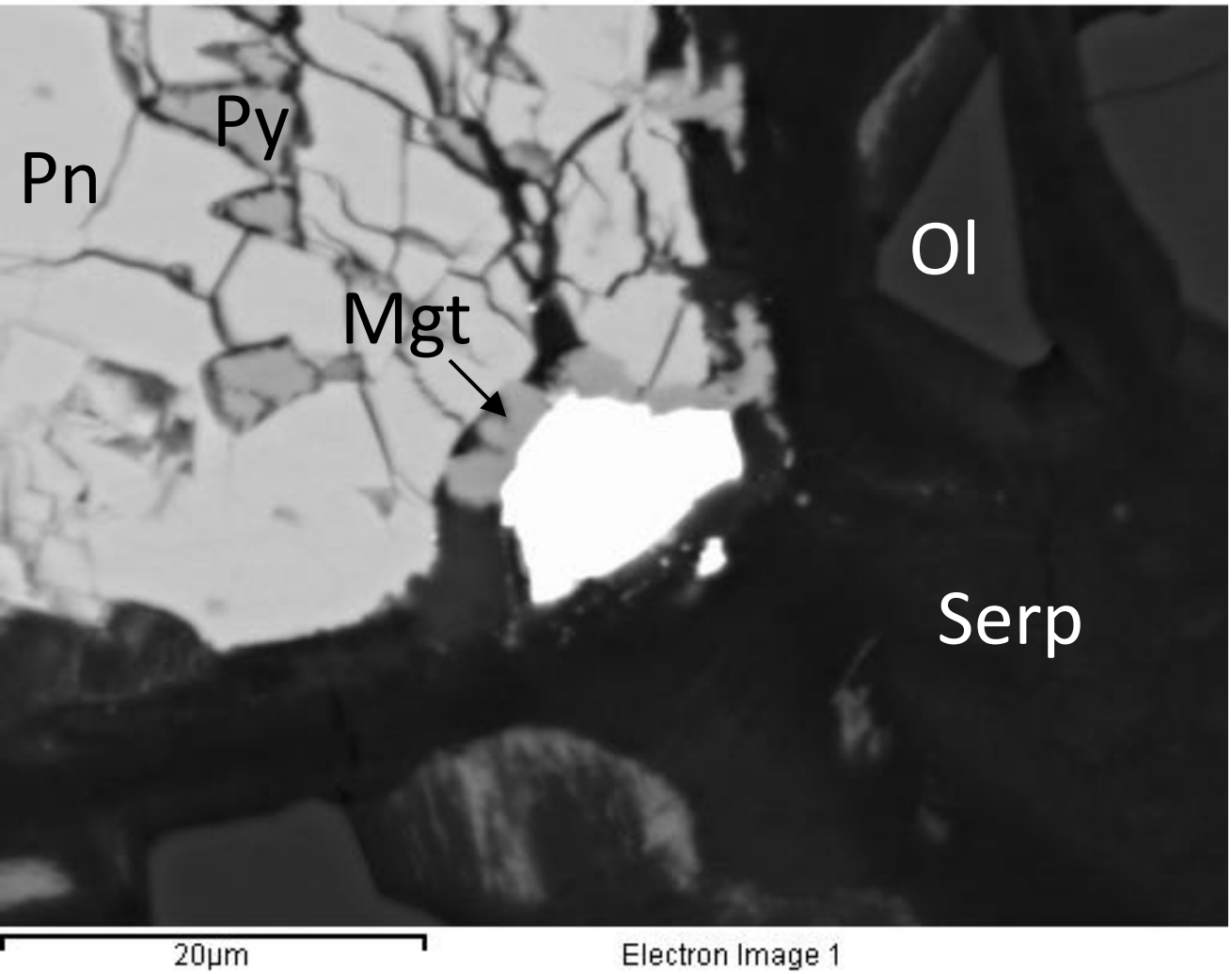
PTSR-30 R 1



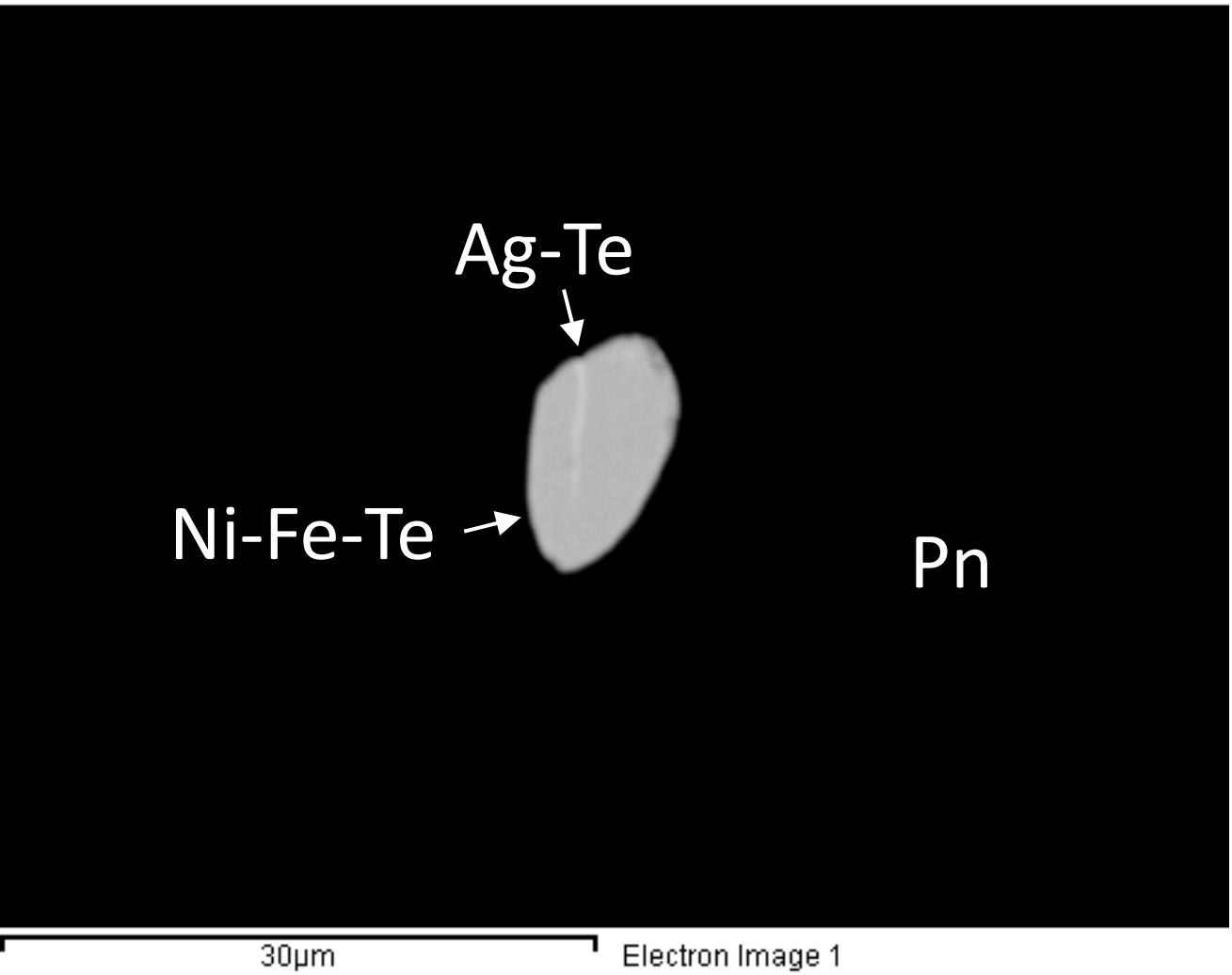
PTSR-32 A 1-3



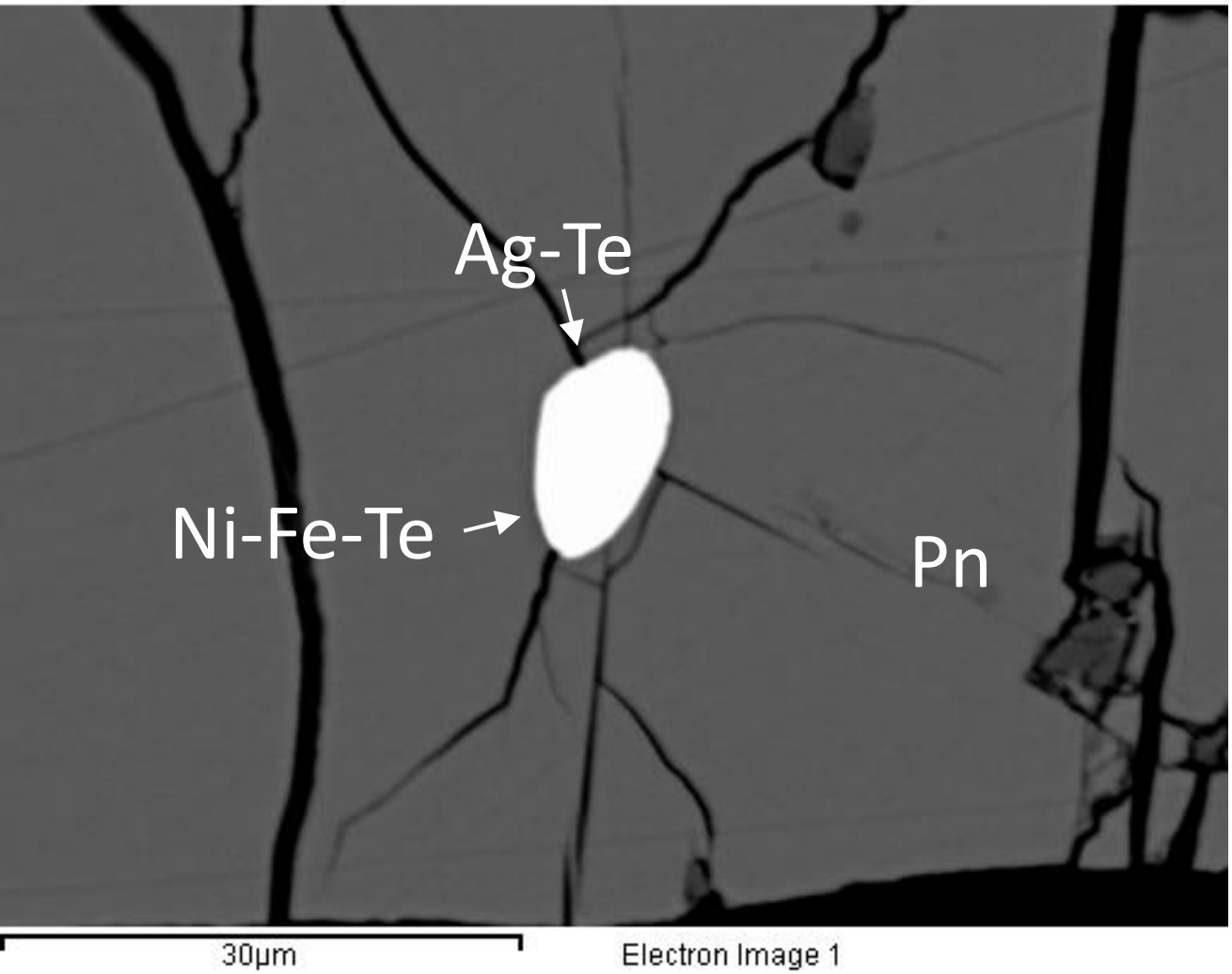
PTSR-32 A 1-3 Light



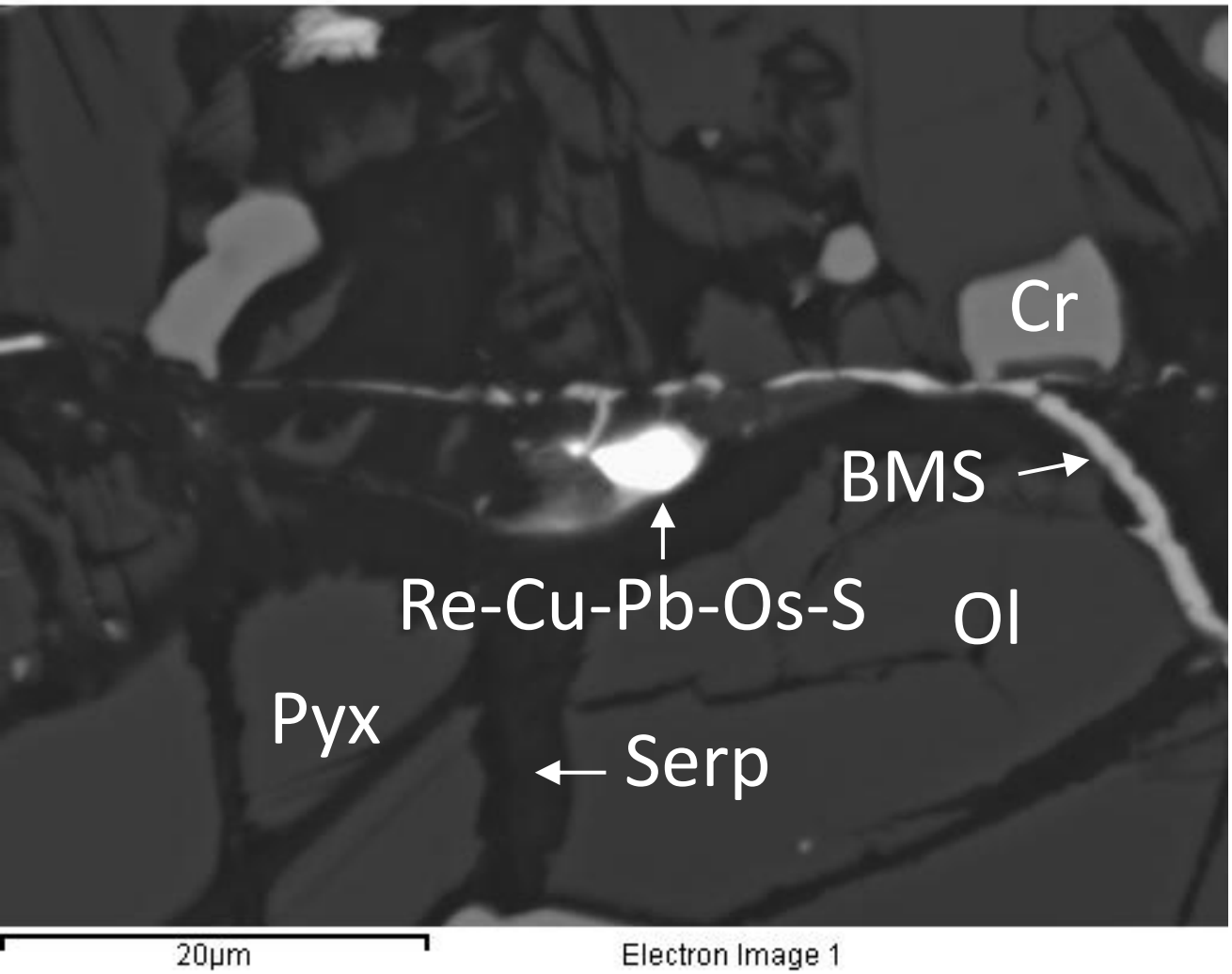
PTSR-32 B 1



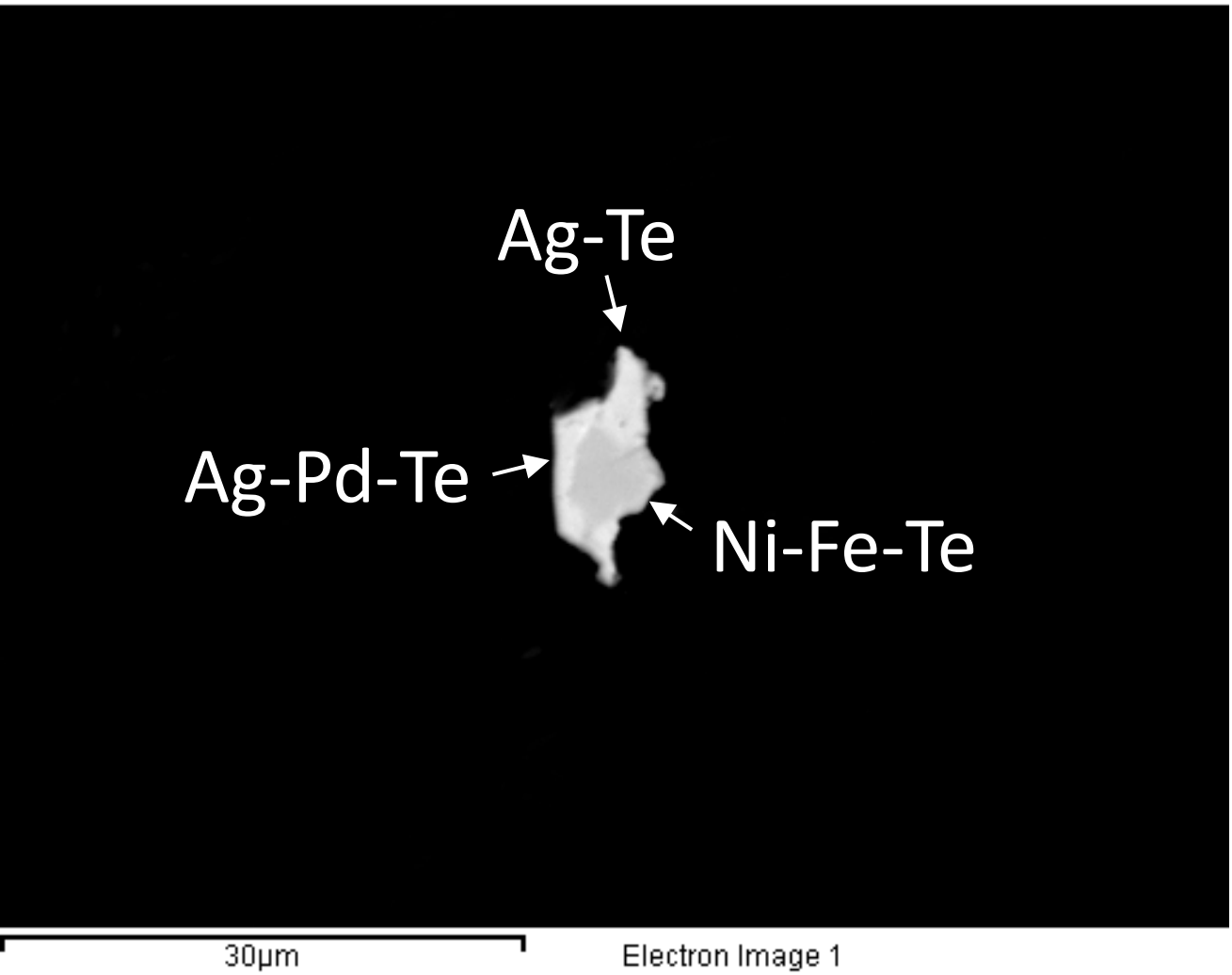
PTSR-32 B 1 Light



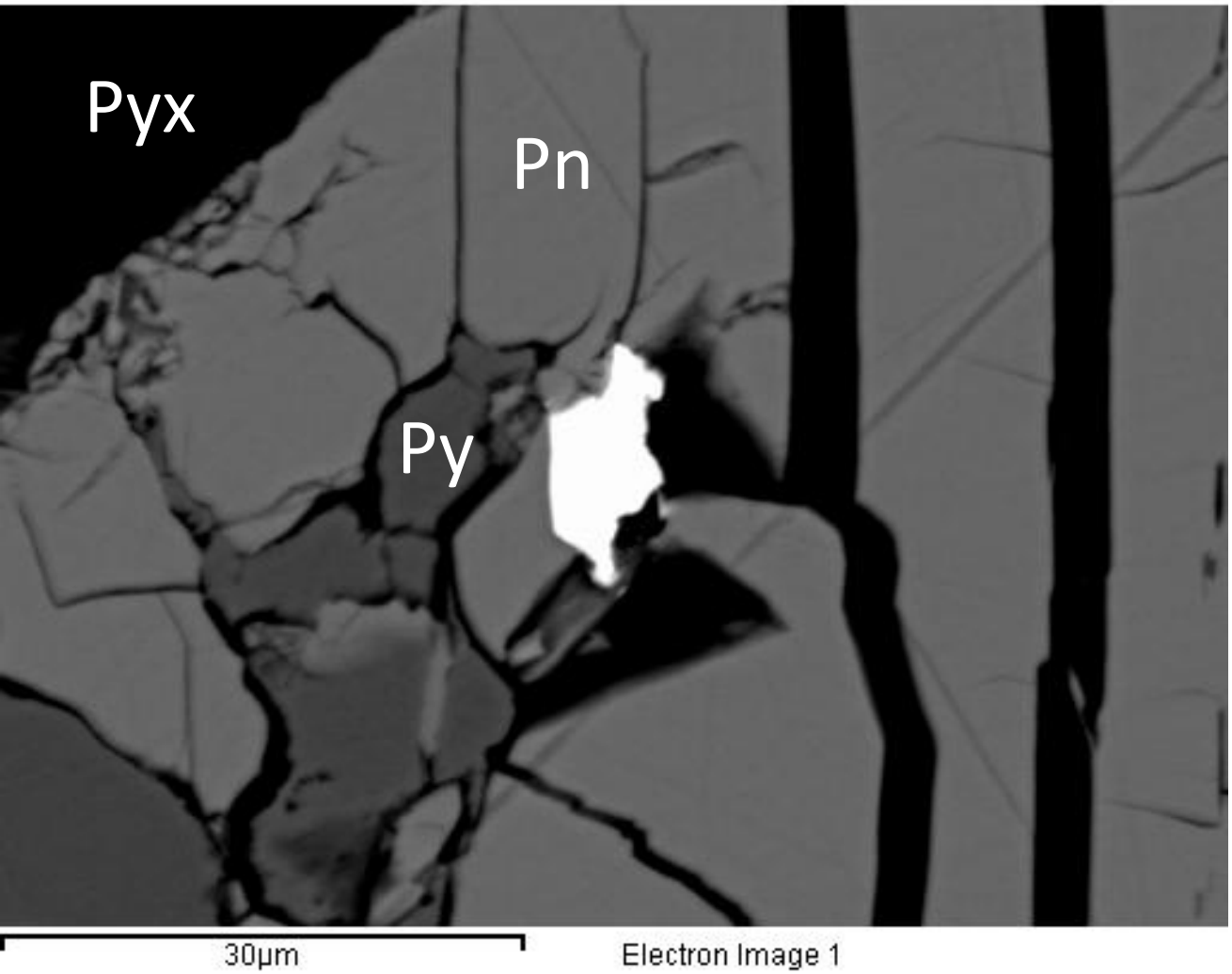
PTSR-32 C 1



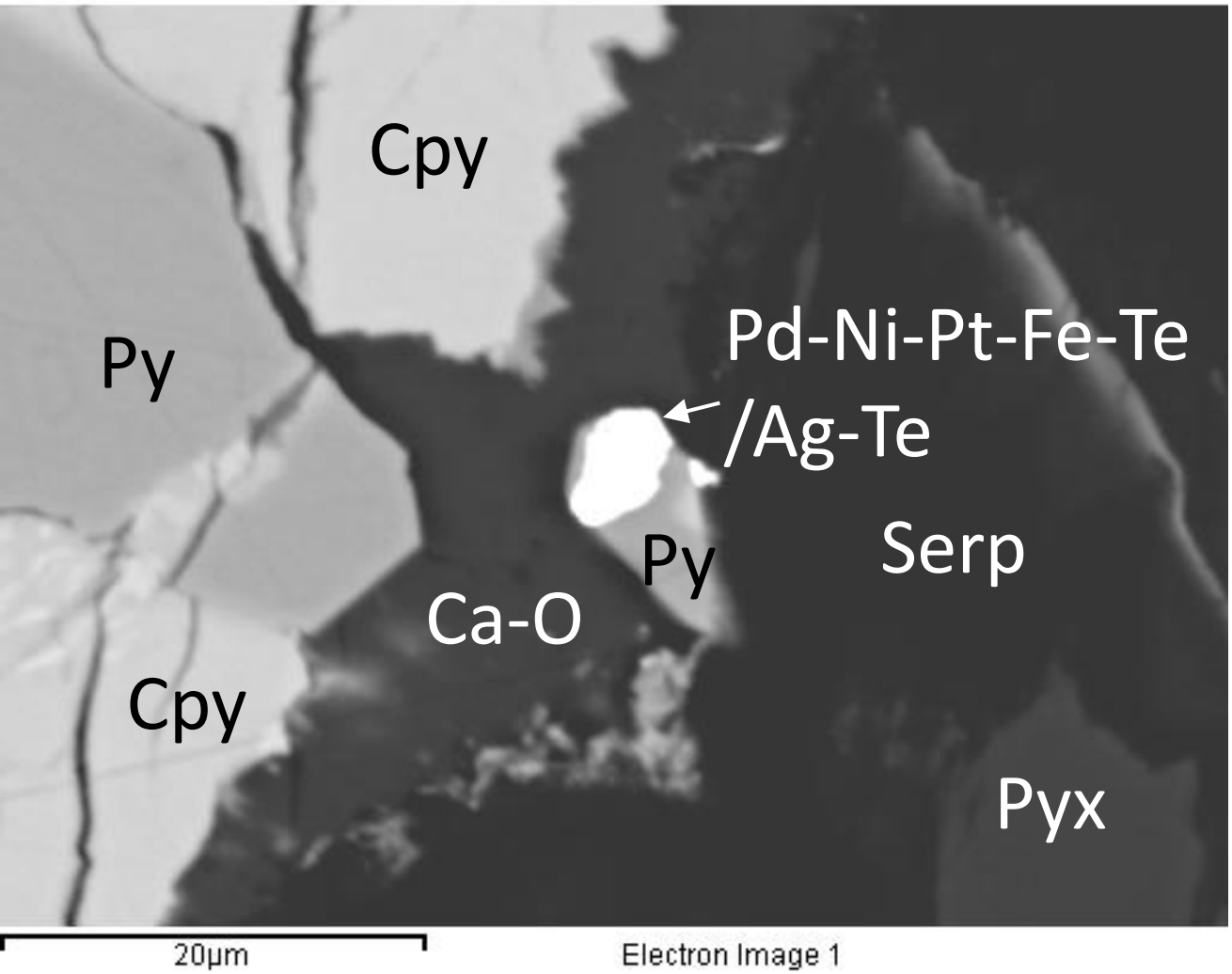
PTSR-32 D 1-3



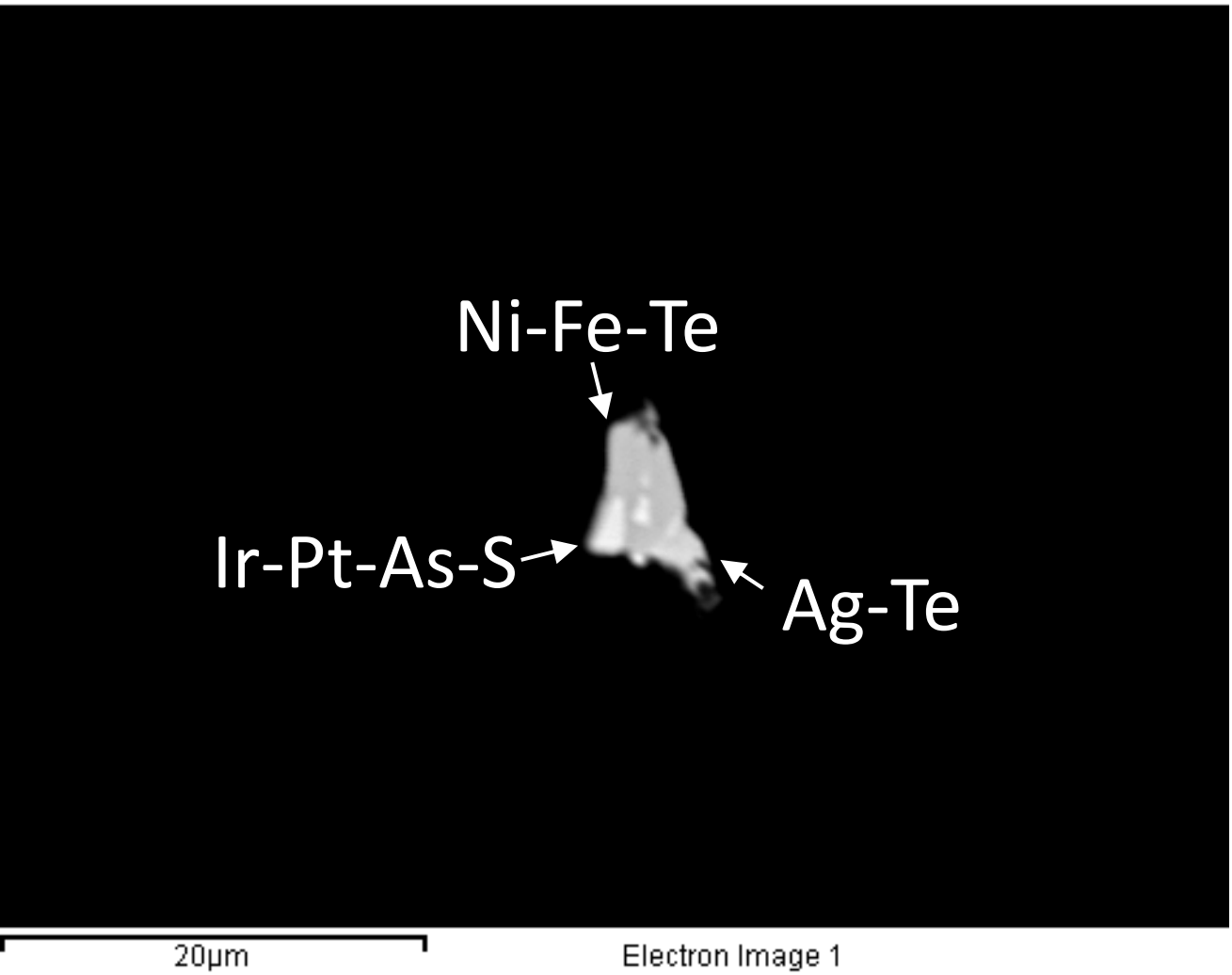
PTSR-32 D 1-3 Light



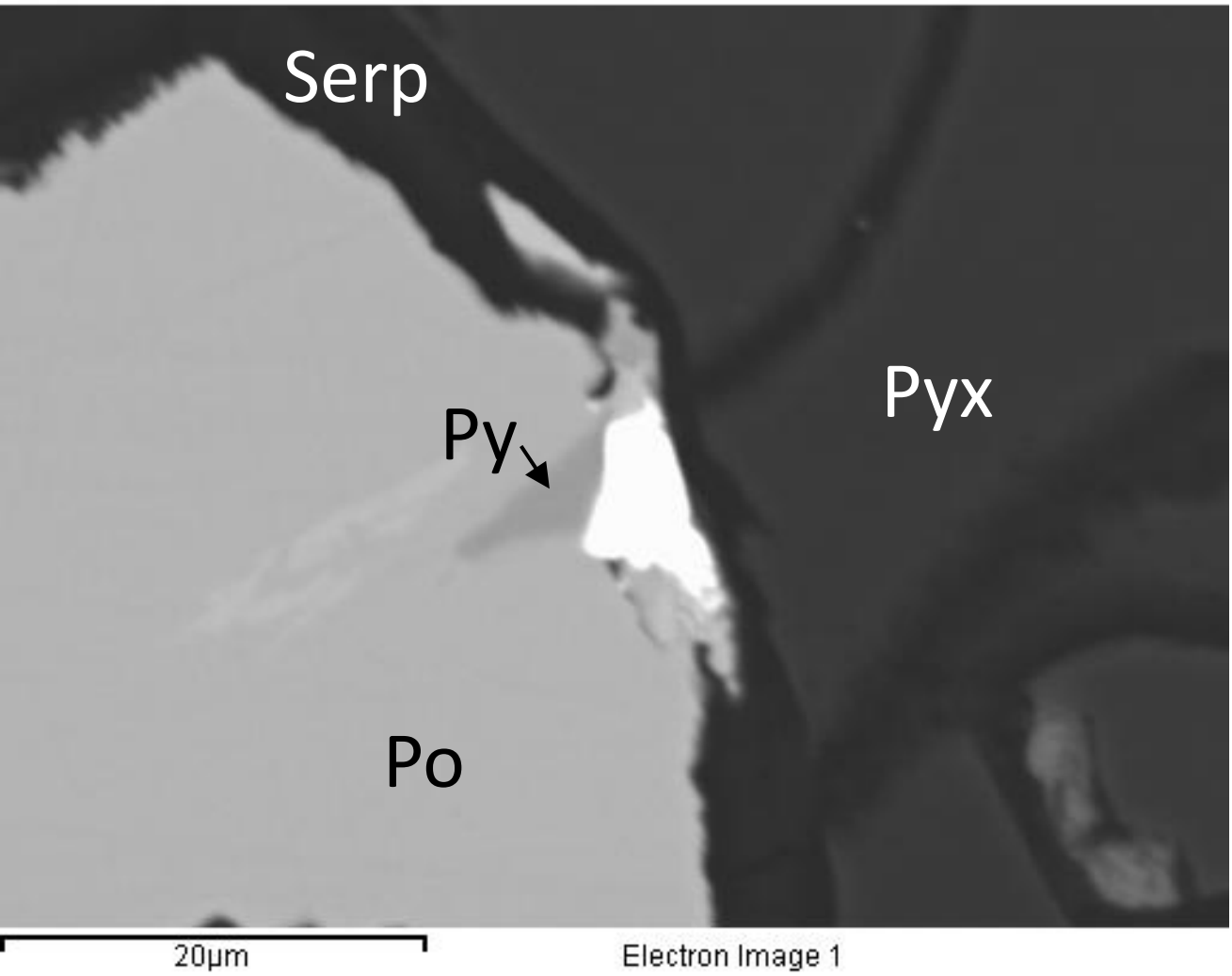
PTSR-32 E 1


Cpy
Py
Pd-Ni-Pt-Fe-Te
/Ag-Te
Py
Serp
Ca-O
Cpy
Pyx
20µm
Electron Image 1

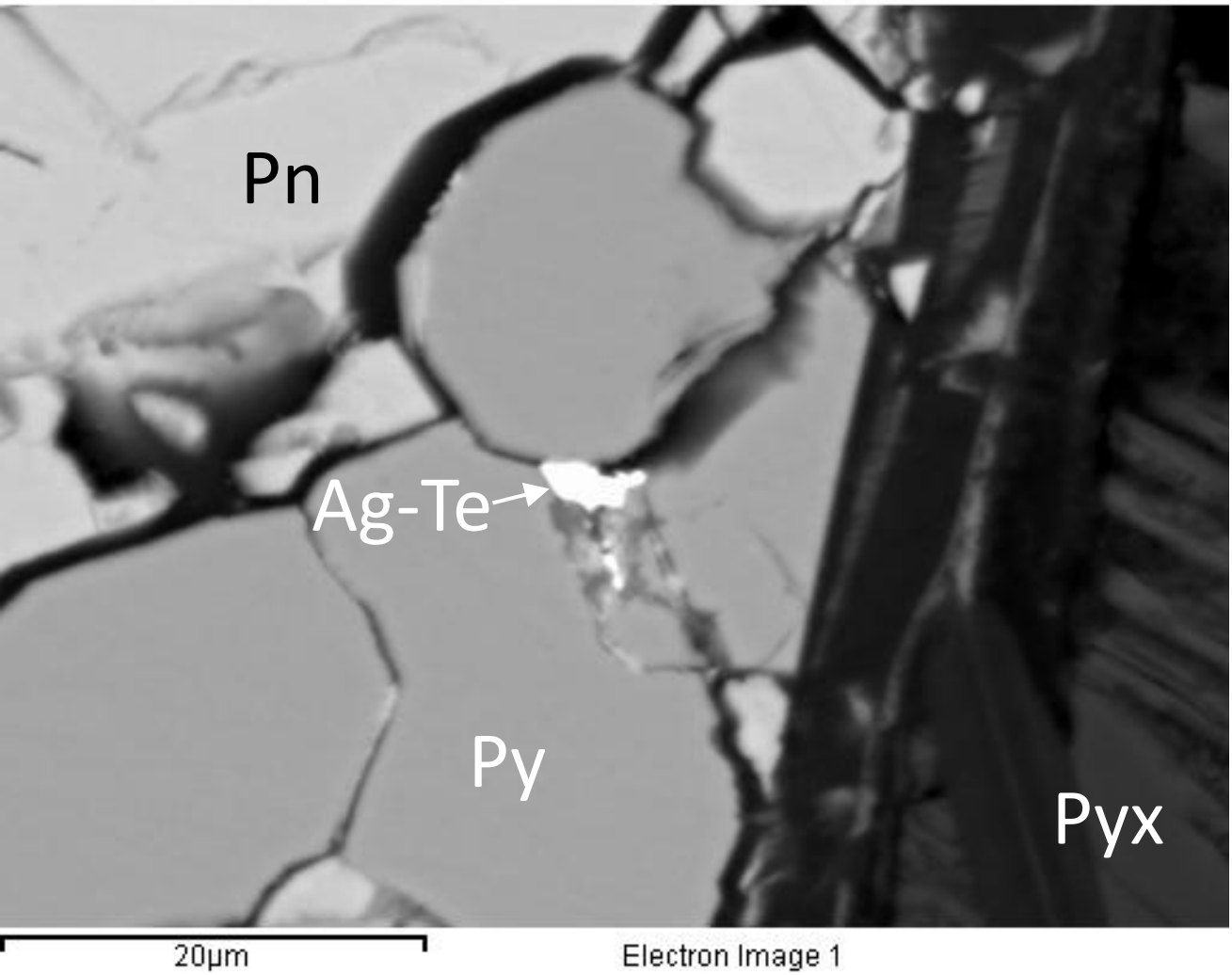
PTSR-32 F 1-3



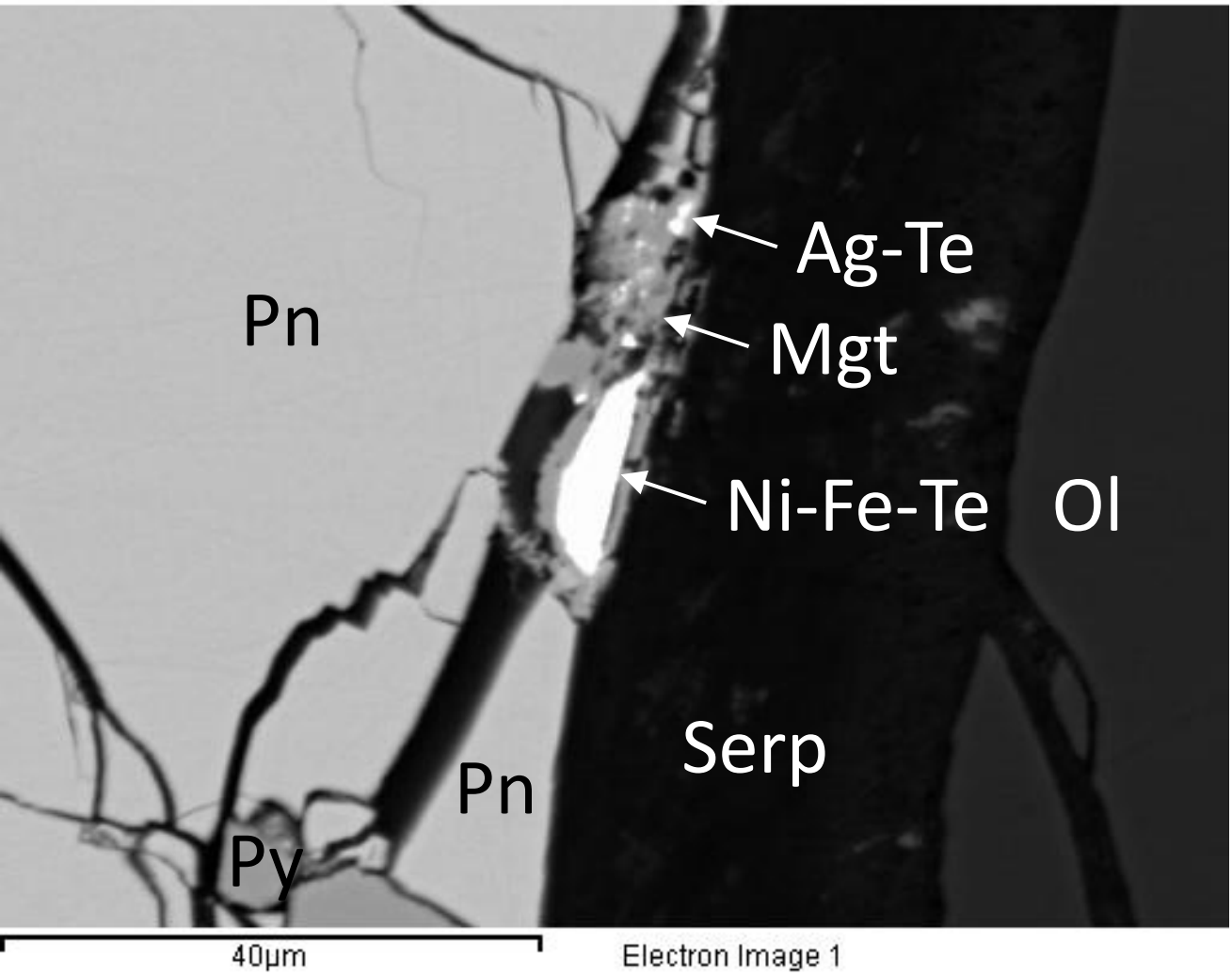
PTSR-32 F 1-3 Light



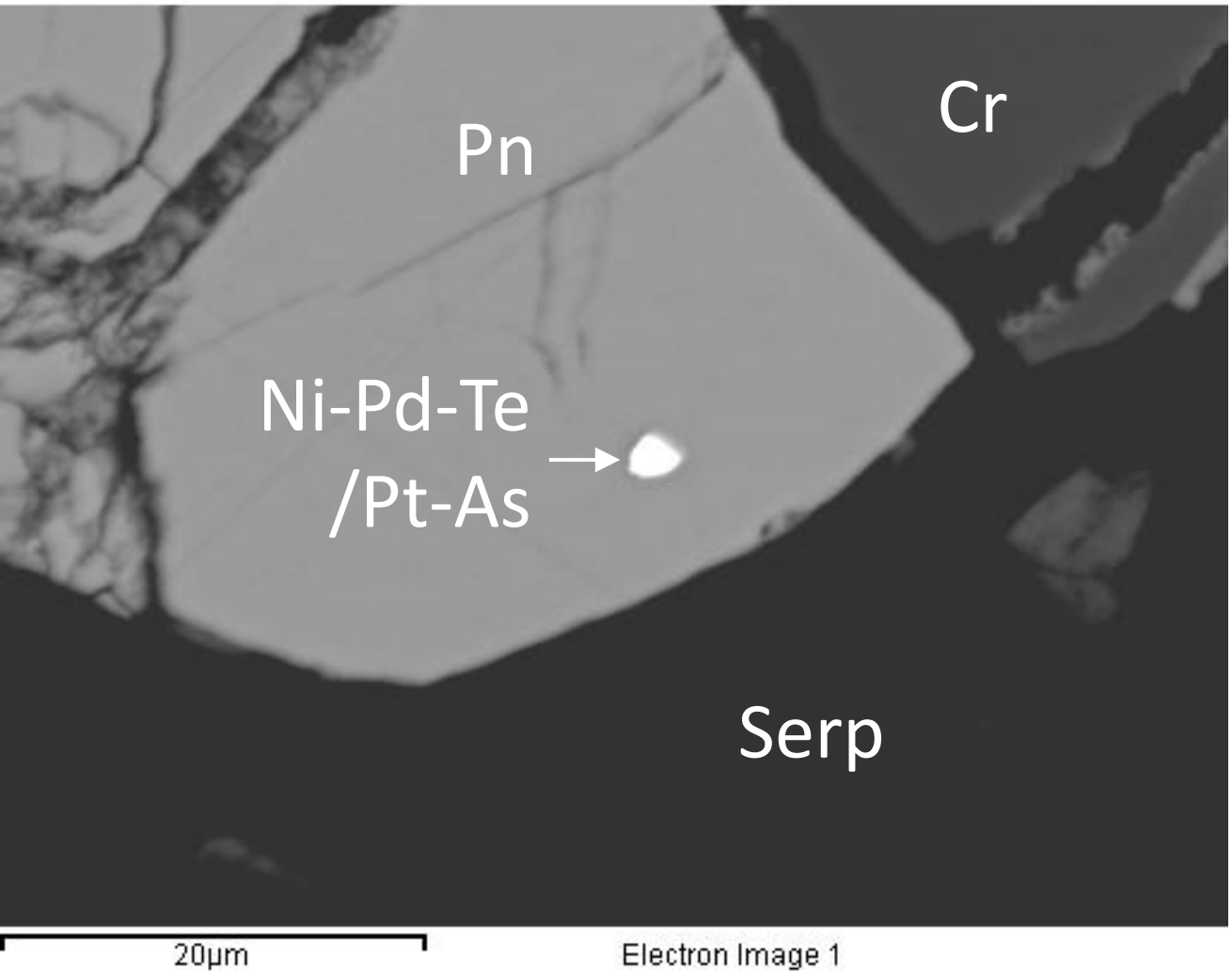
PTSR-32 G 1



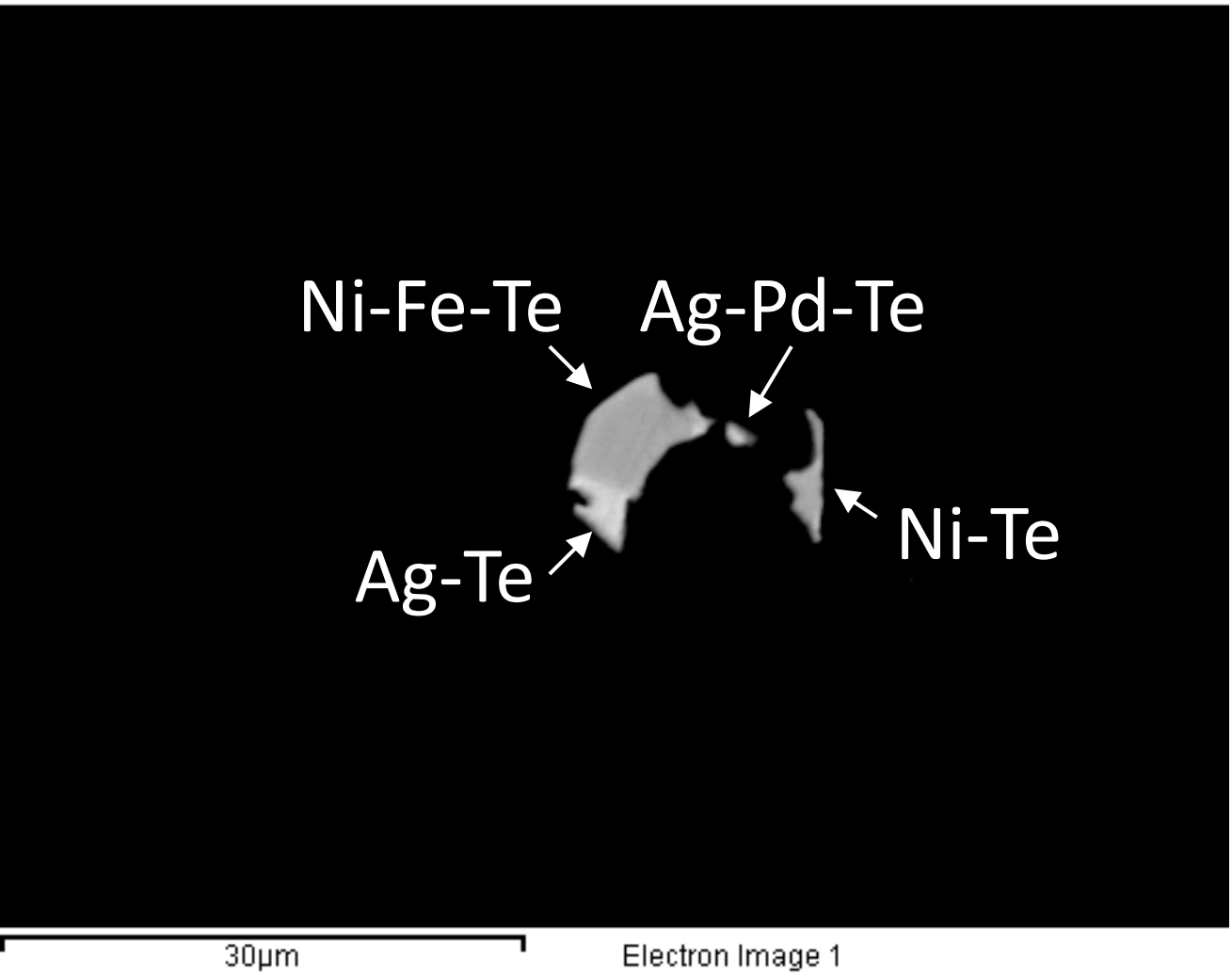
PTSR-32 H 1



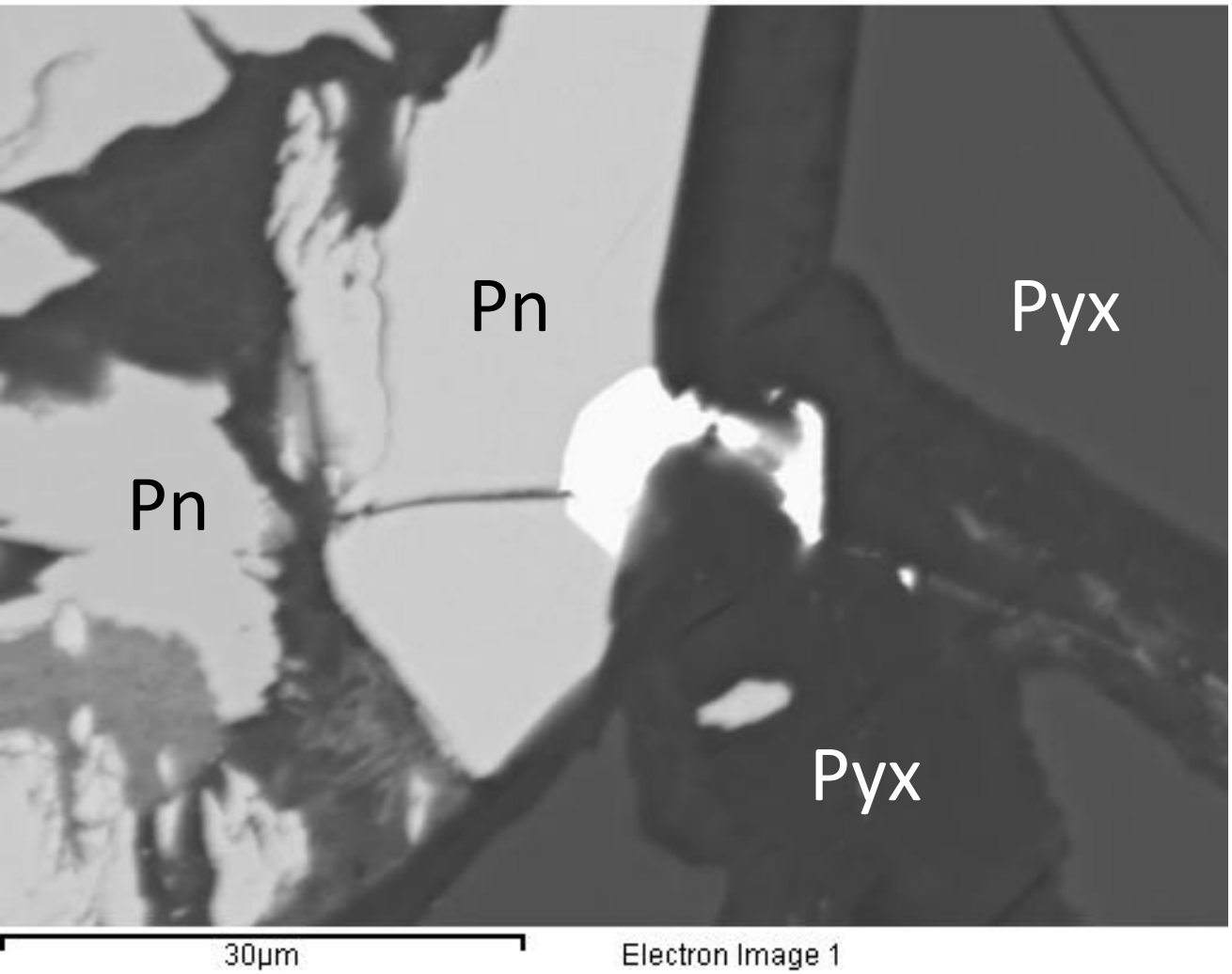
PTSR-32 I 1



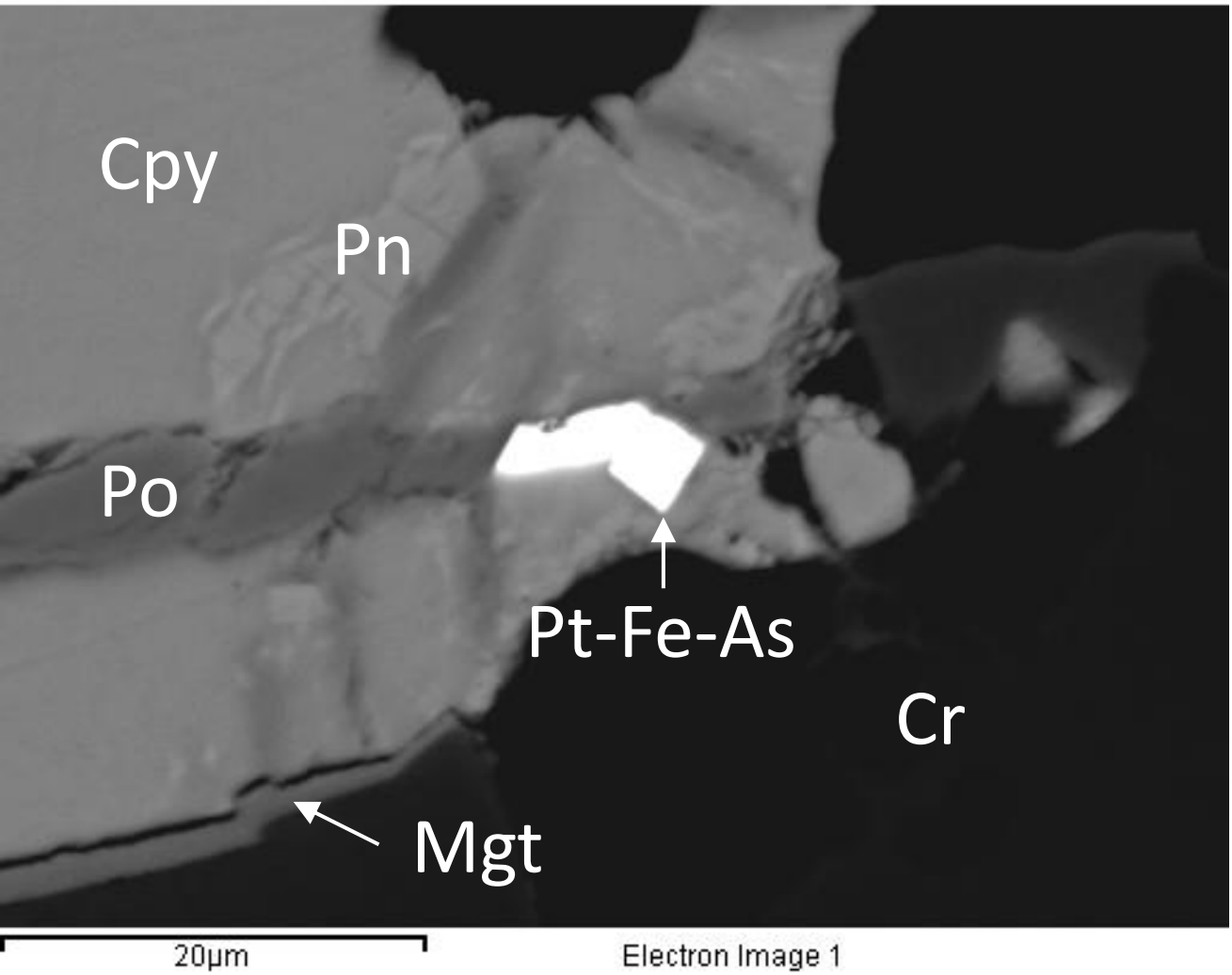
PTSR-32 J 1-4



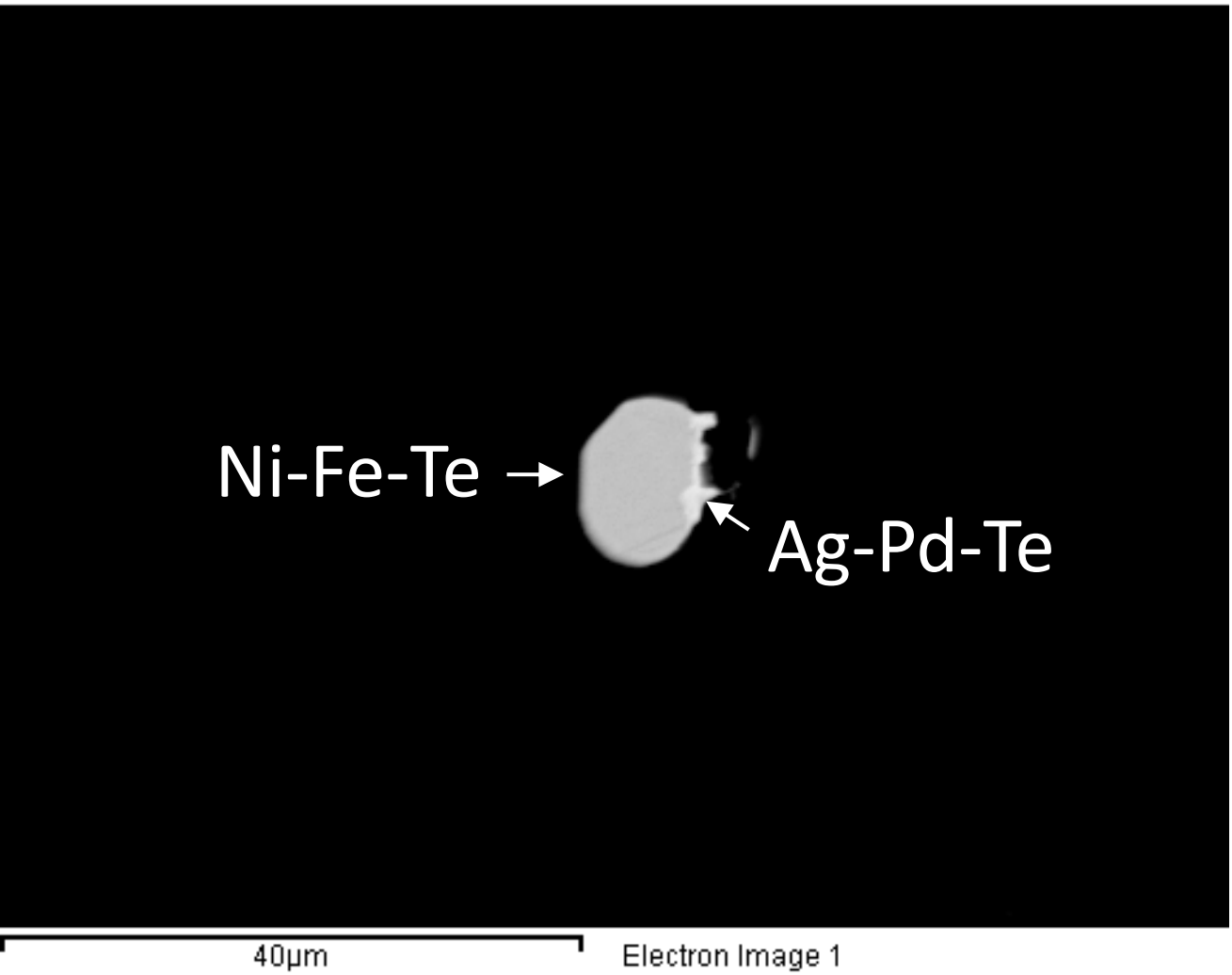
PTSR-32 J 1-4 Light



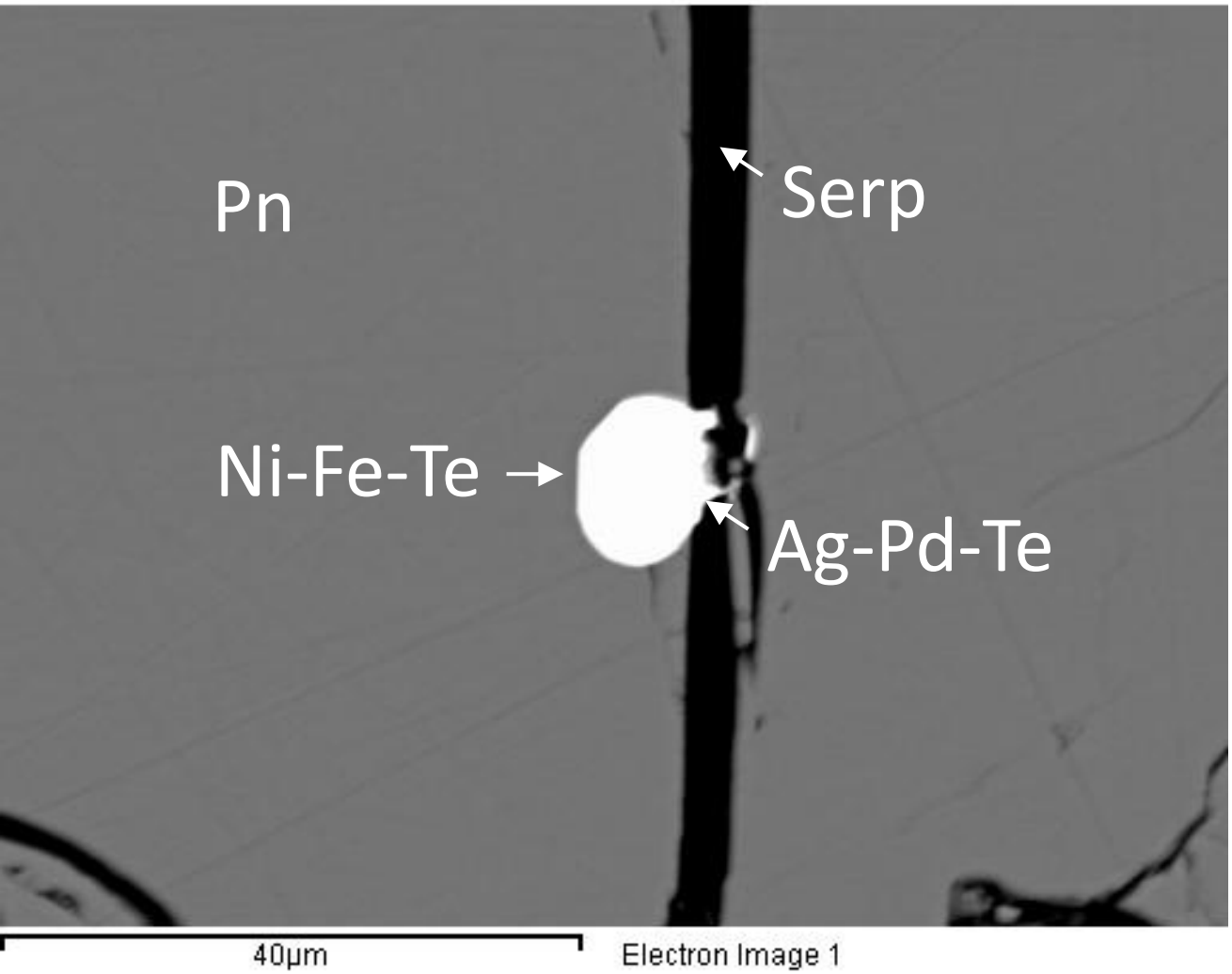
PTSR-32 K 1



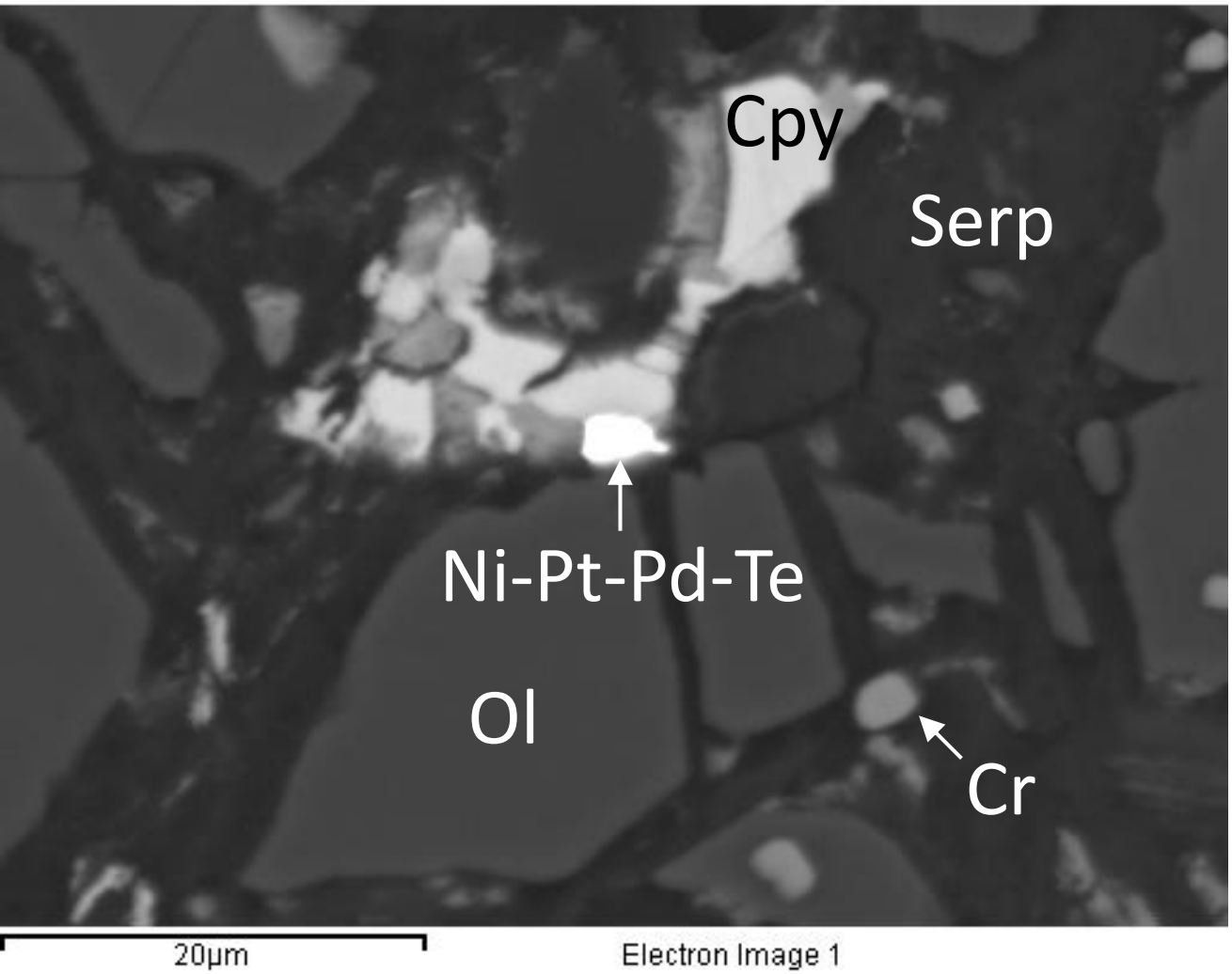
PTSR-32 L 1-2



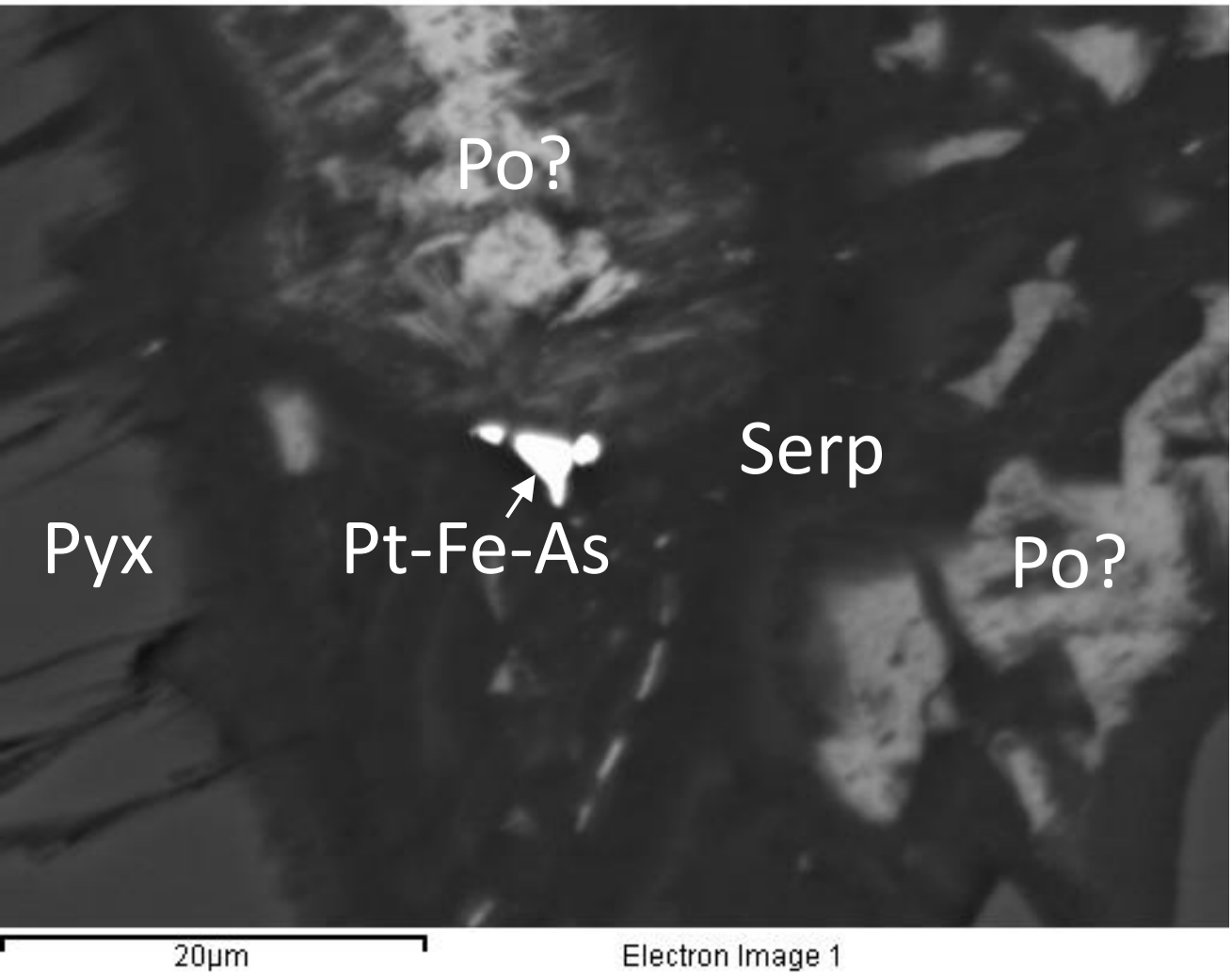
PTSR-32 L 1-2 Light



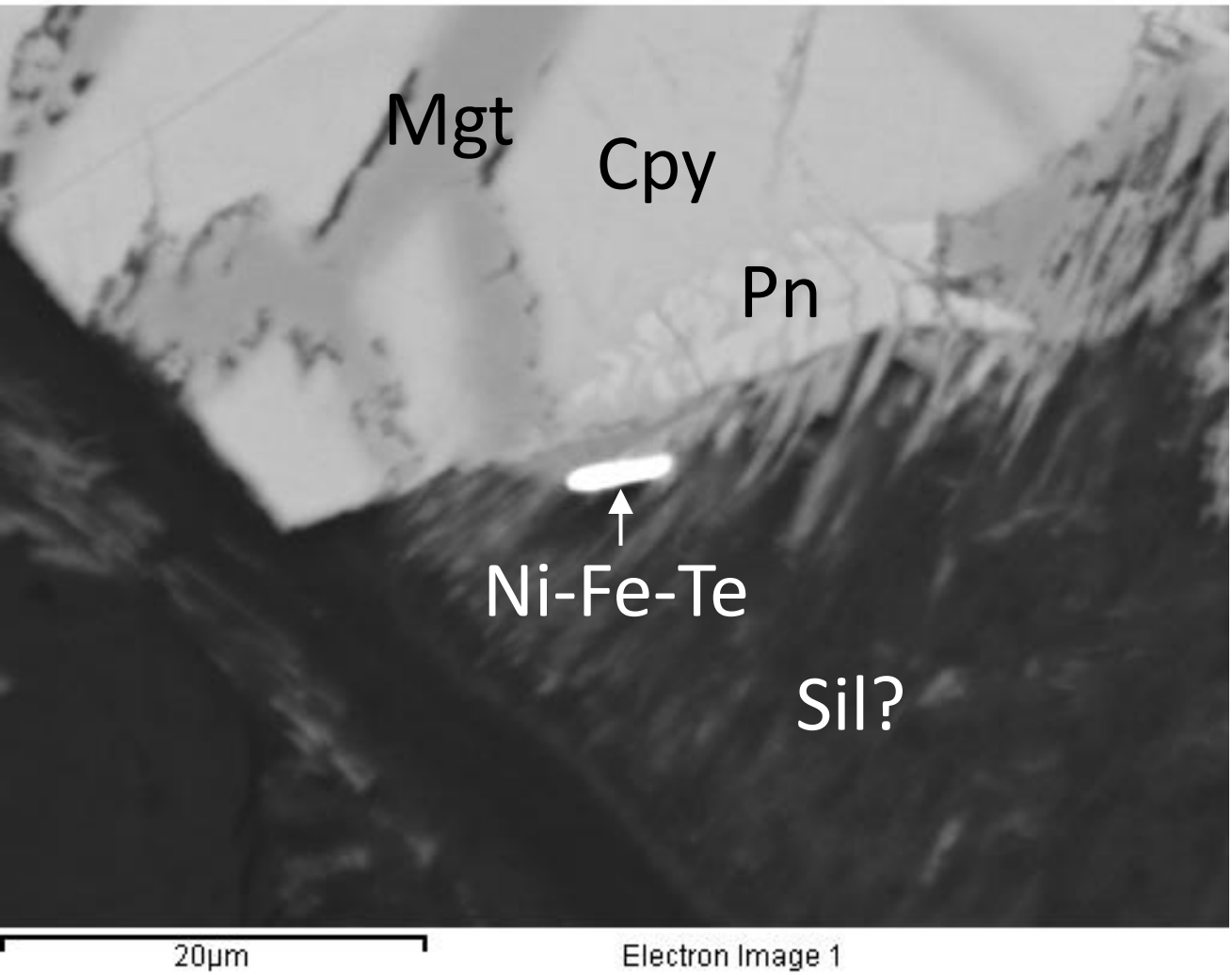
PTSR-32 M 1



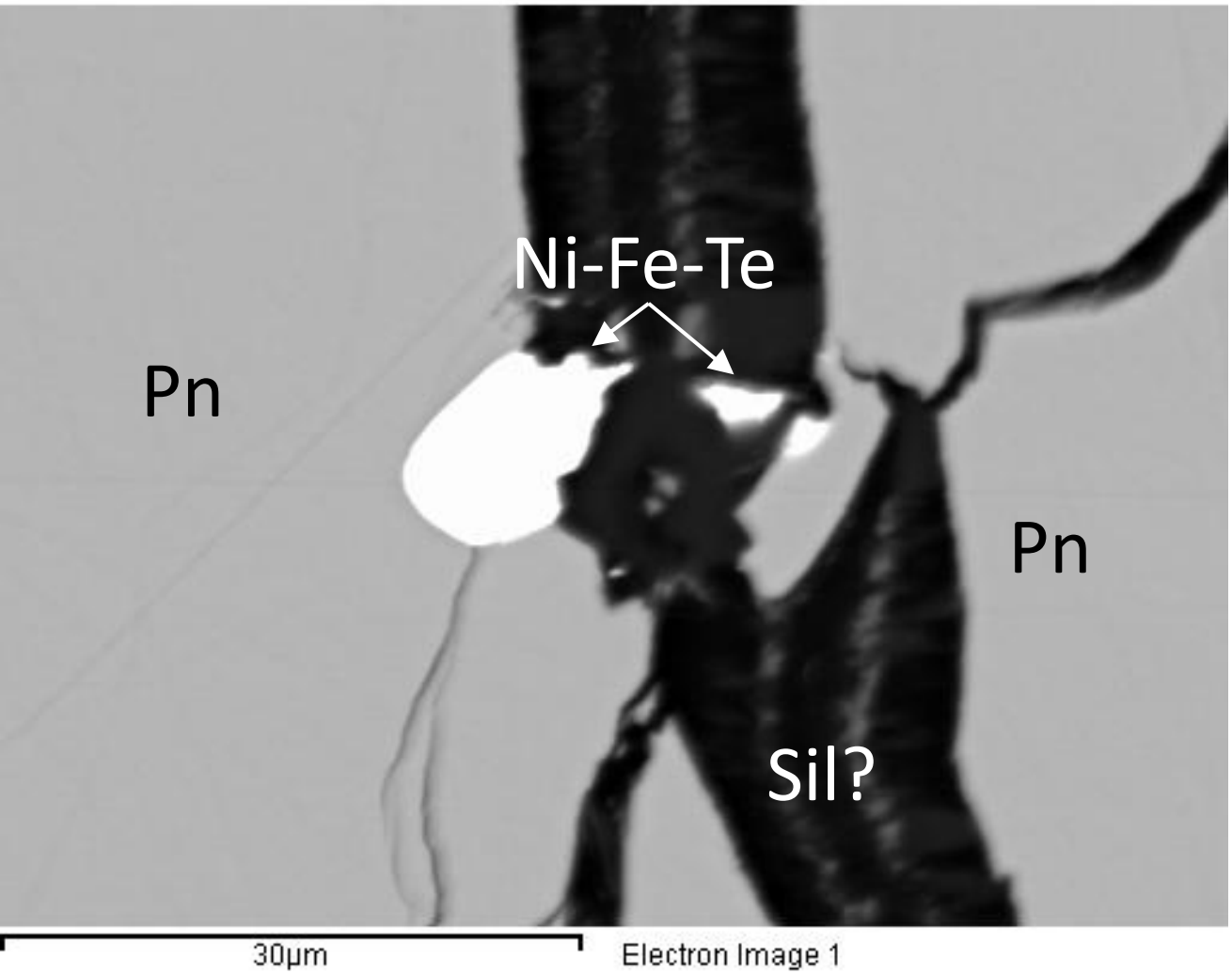
PTSR-32 N 1



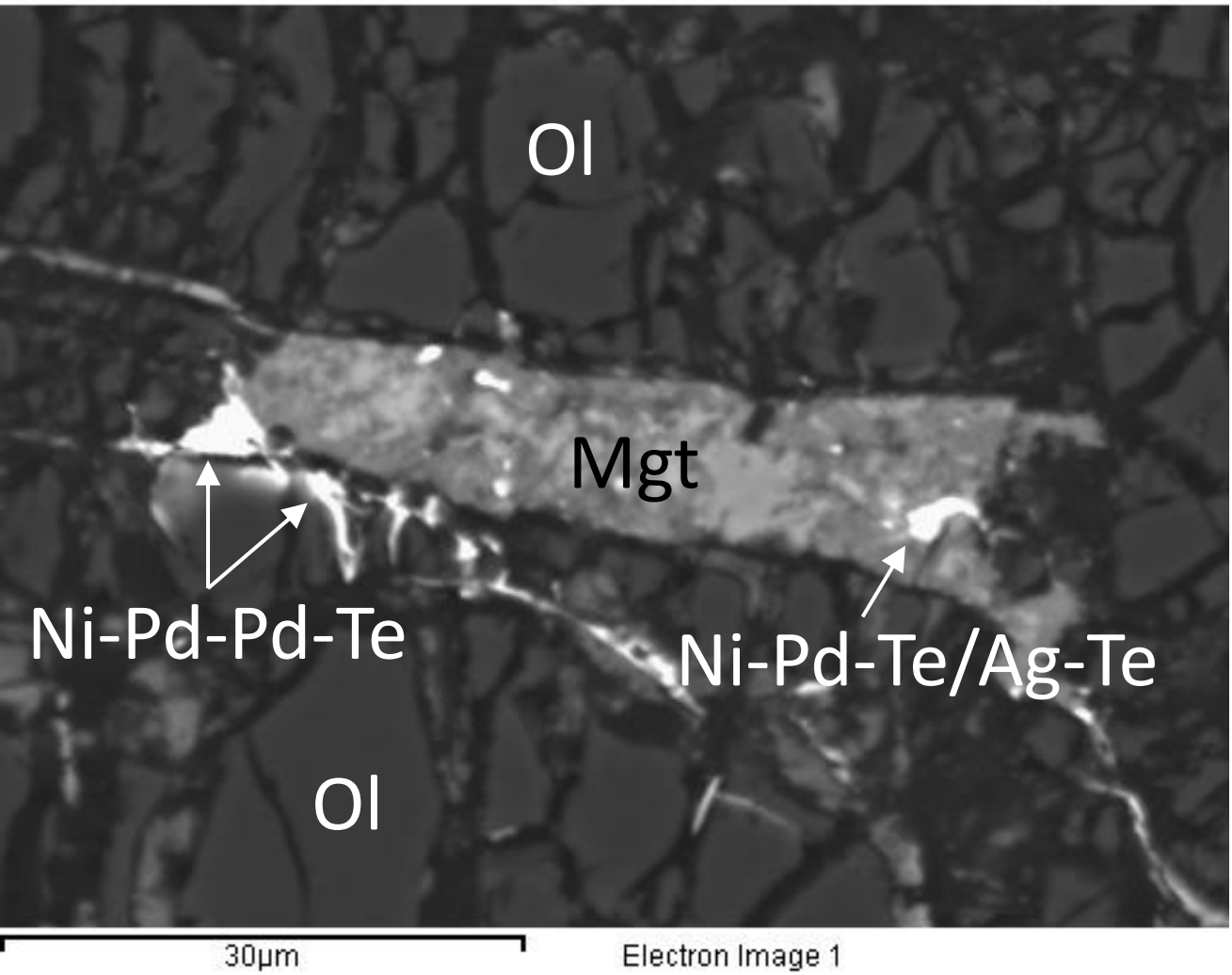
PTSR-32 O 1



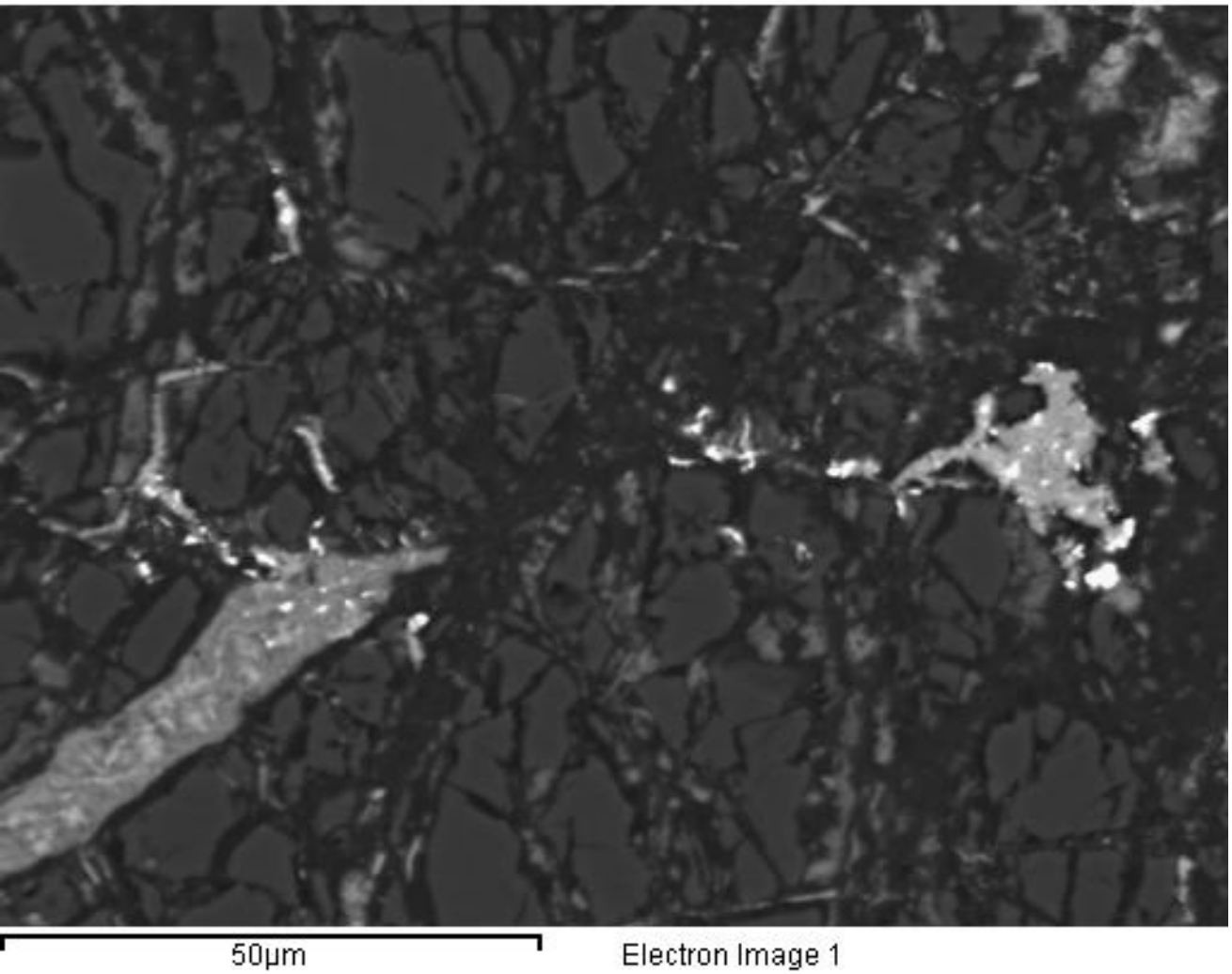
PTSR-32 P 1-3



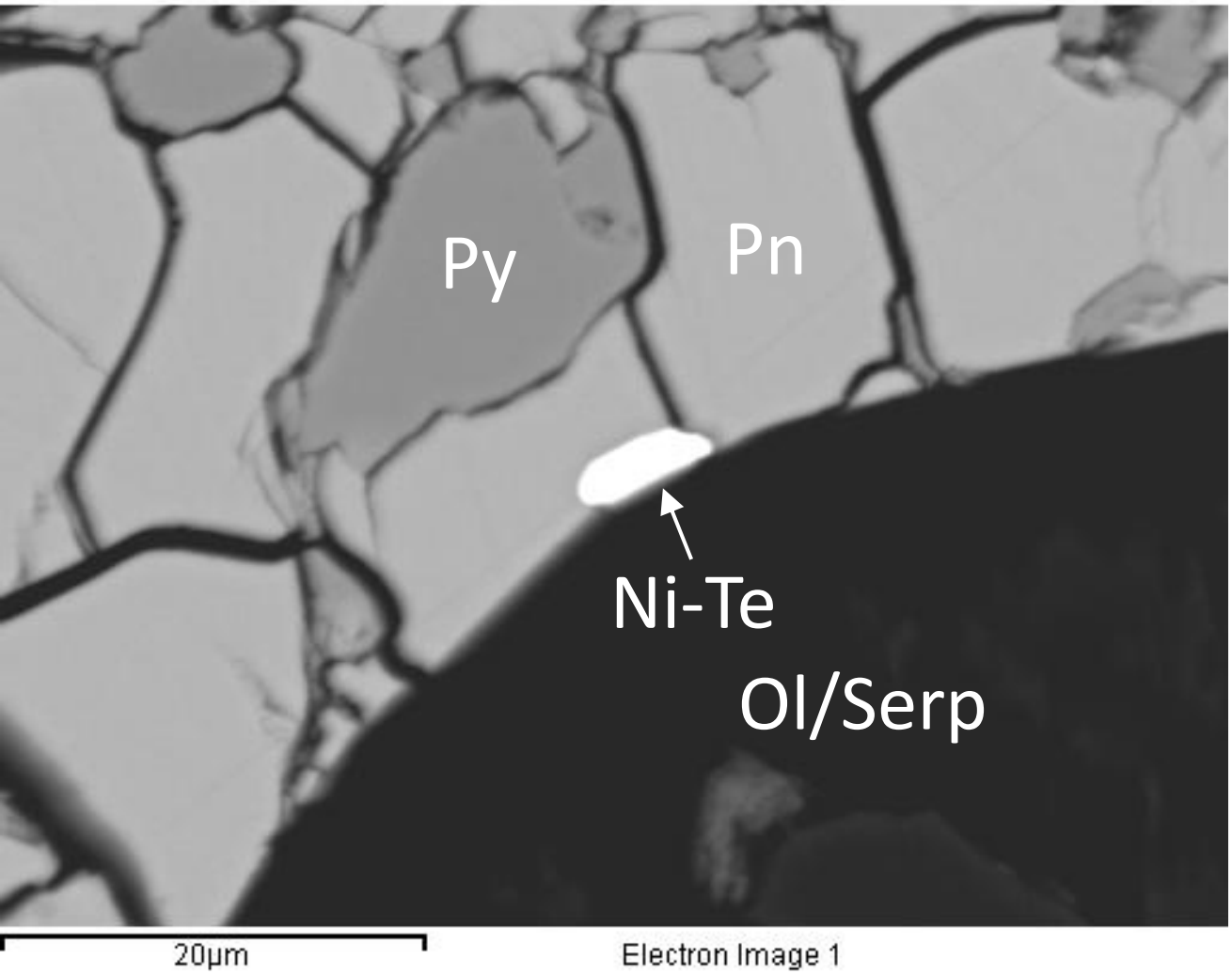
PTSR-32 Q 1-3



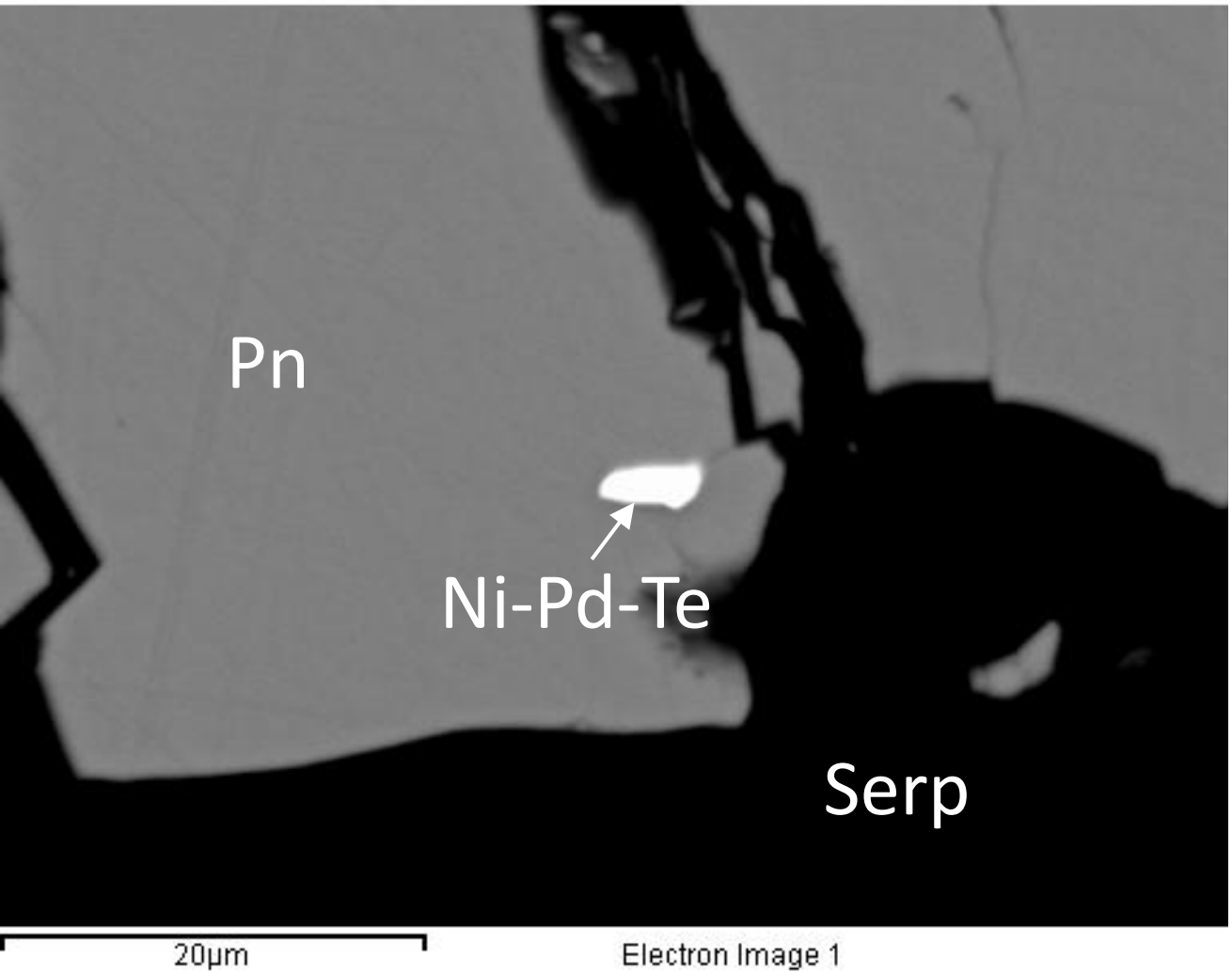
PTSR-32 R 1 No Data



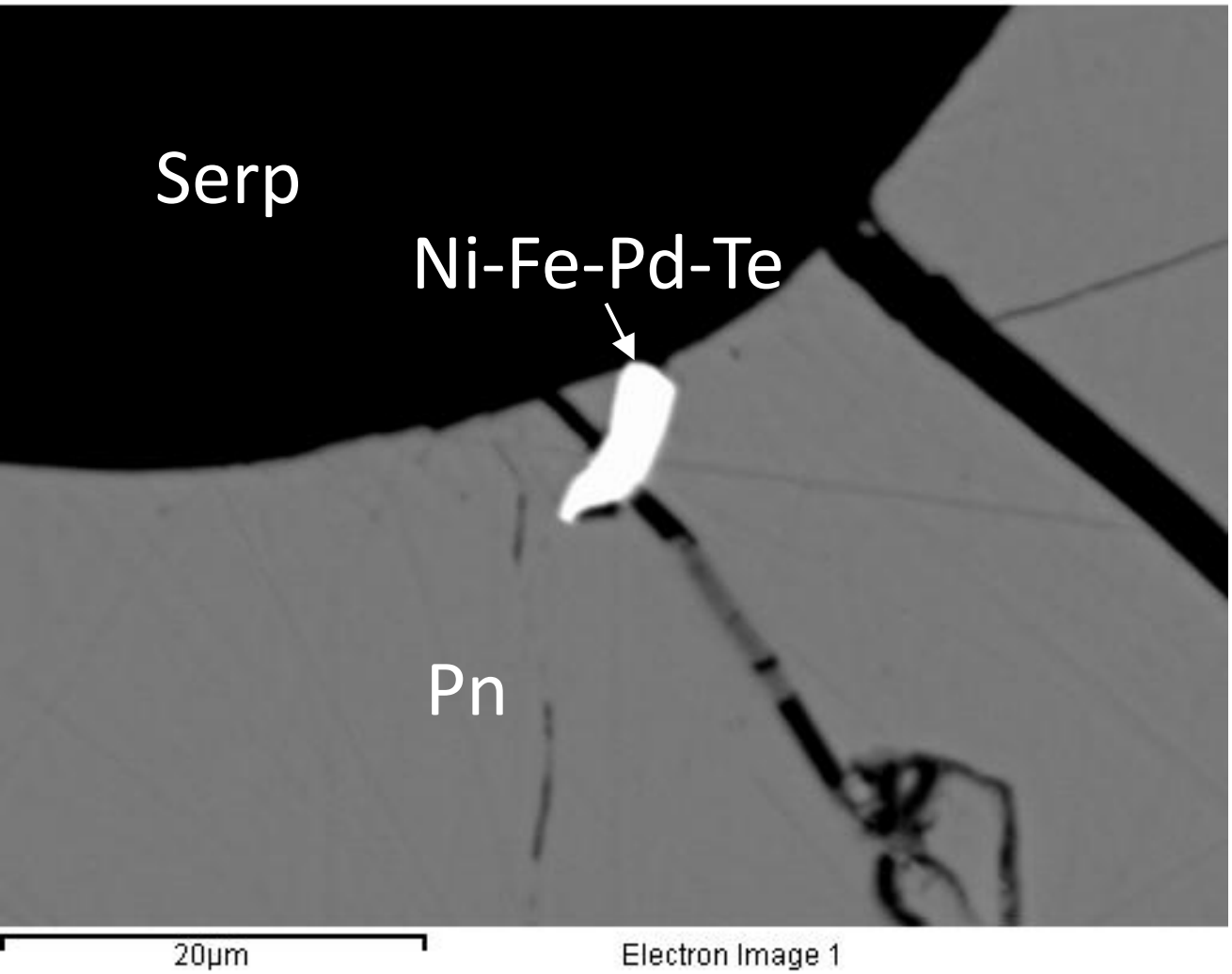
PTSR-32 S 1



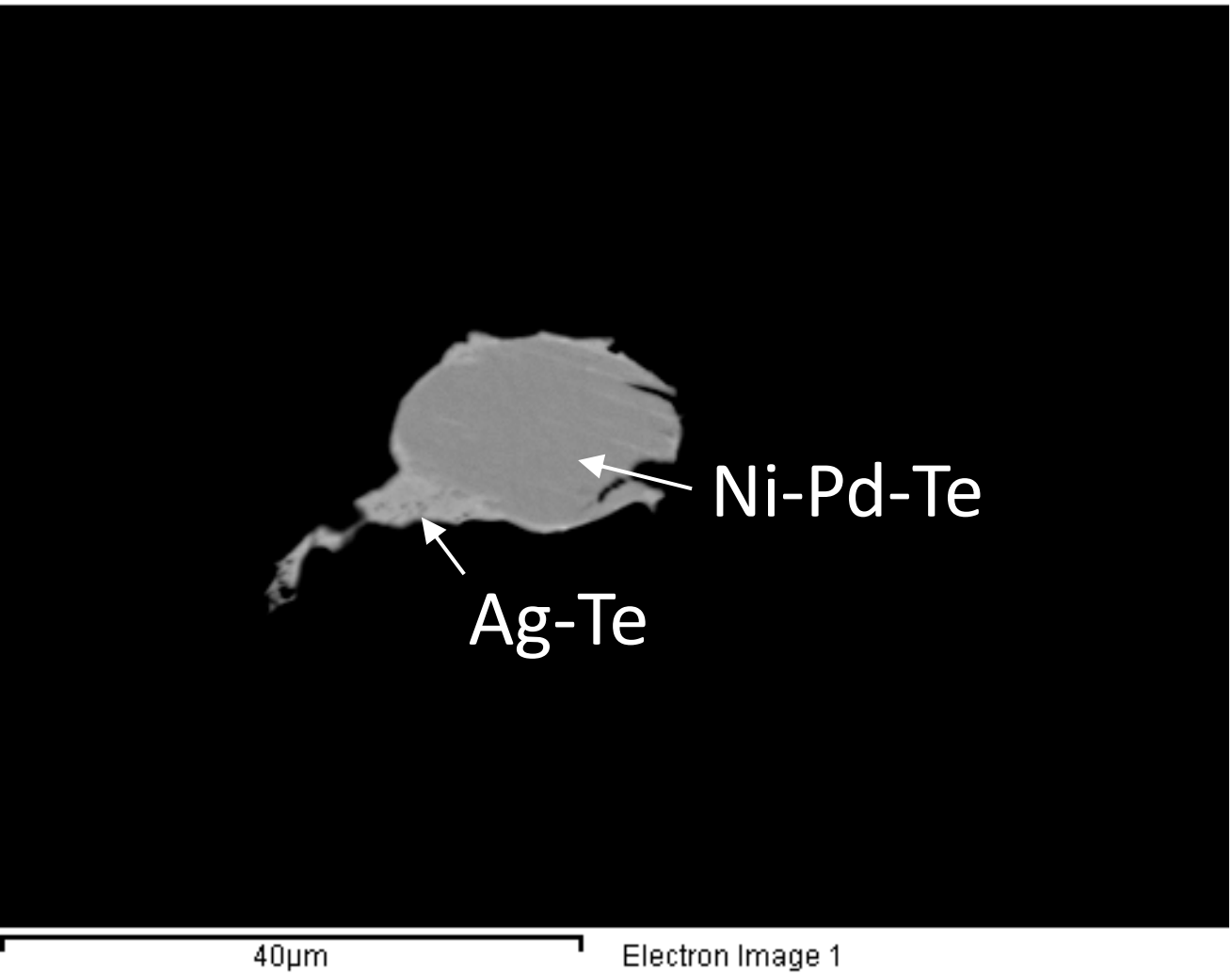
PTSR-32 T 1



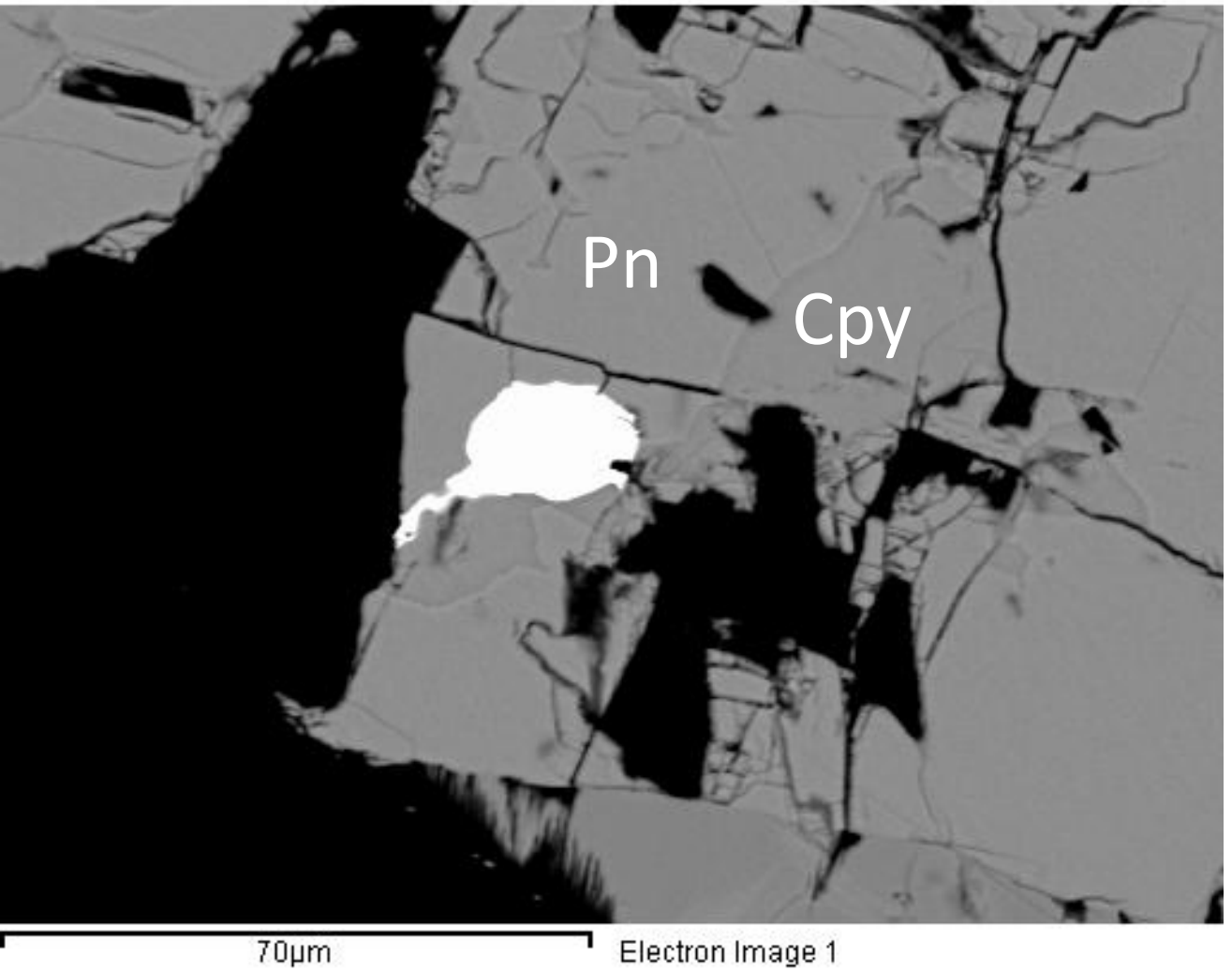
PTSR-32 U 1



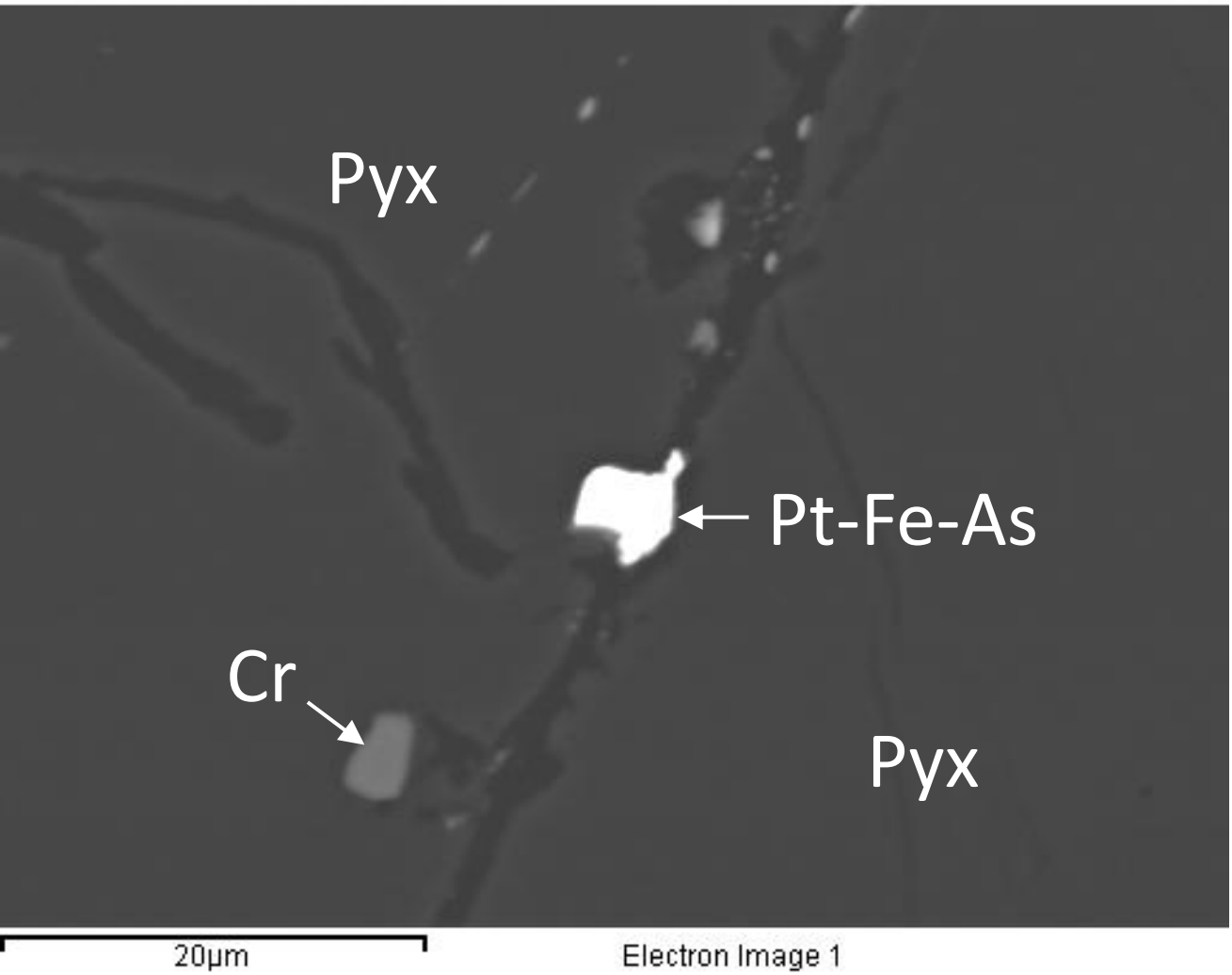
PTSR-32 V 1



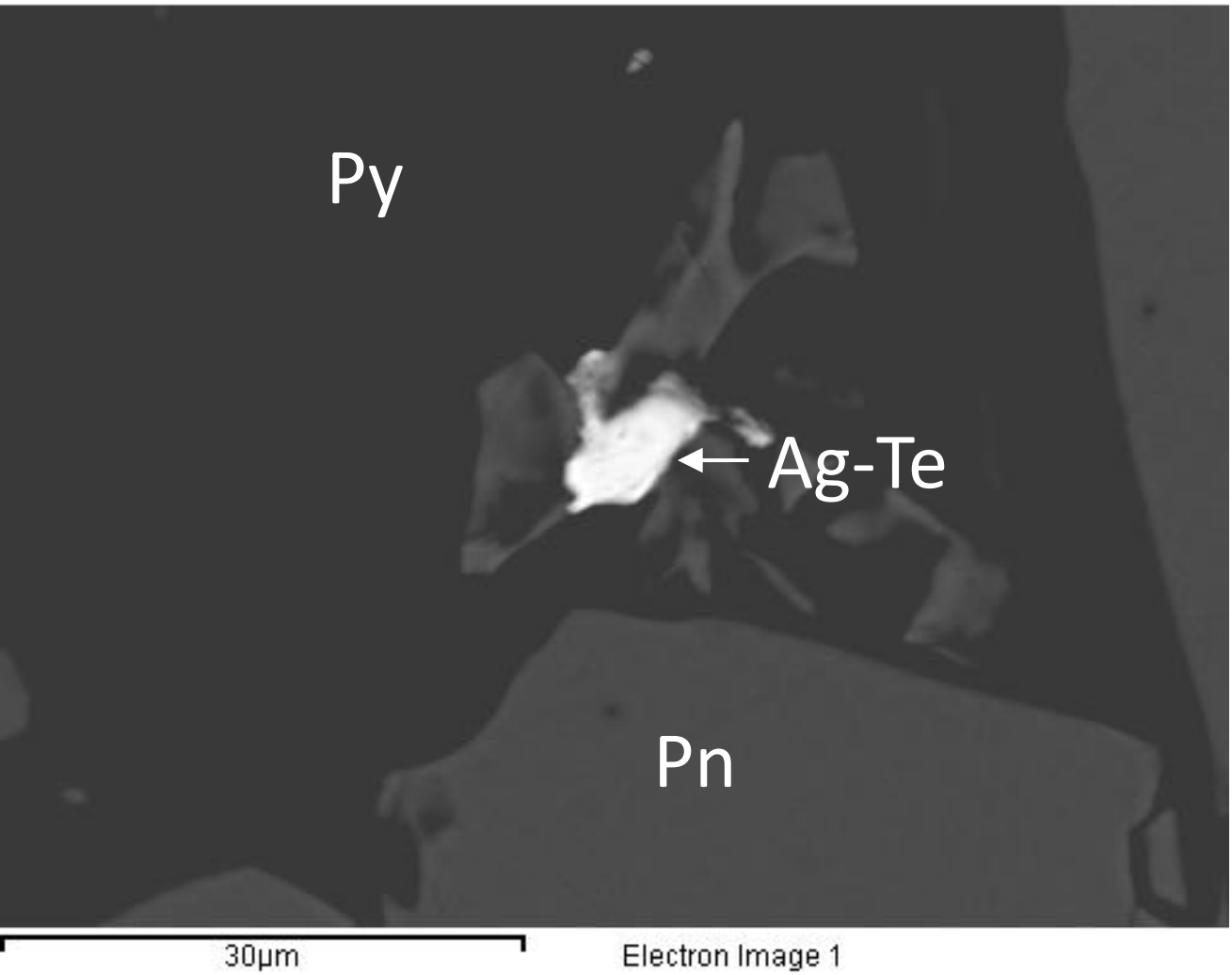
PTSR-32 V 1 Light



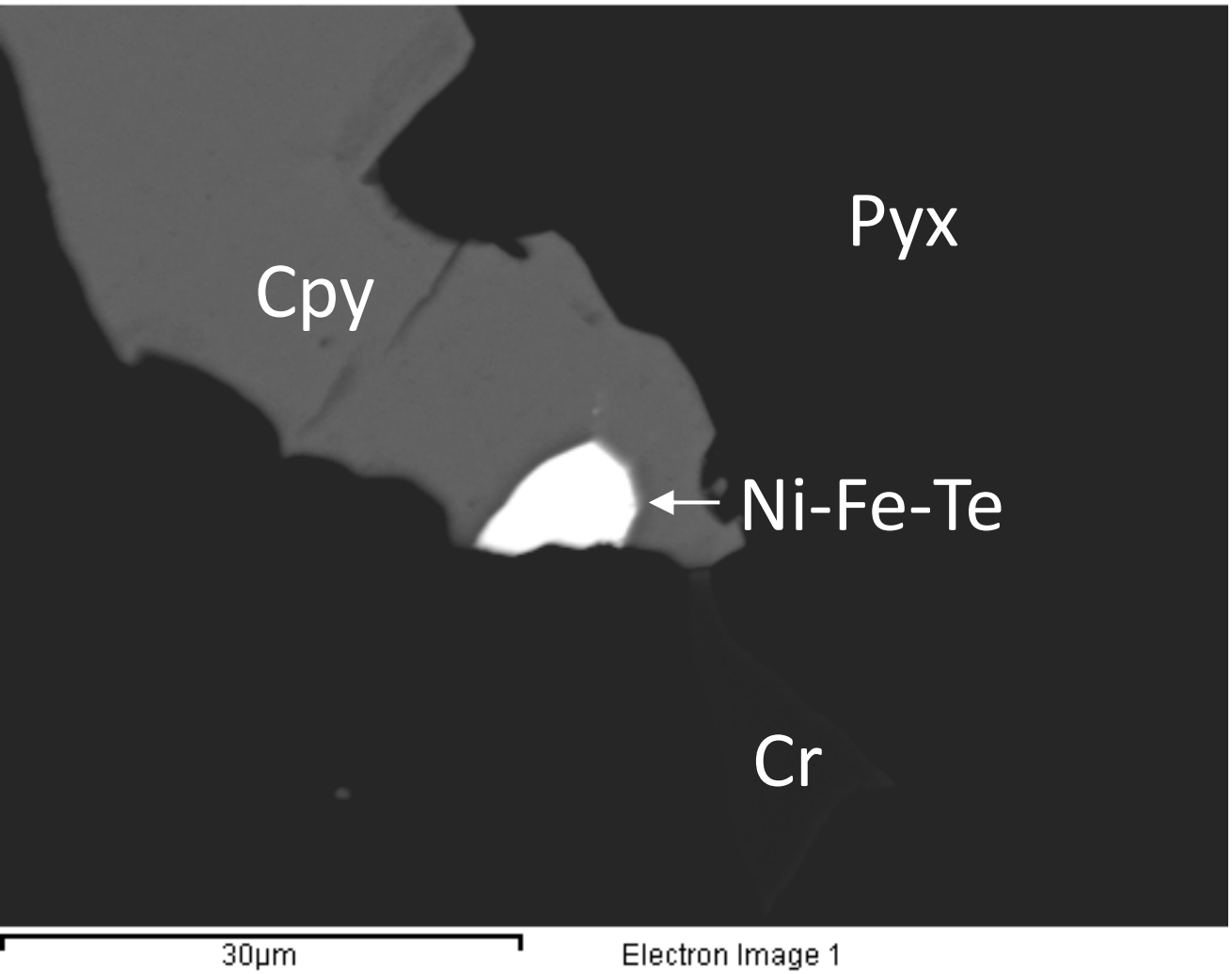
PTSR-33 A 1



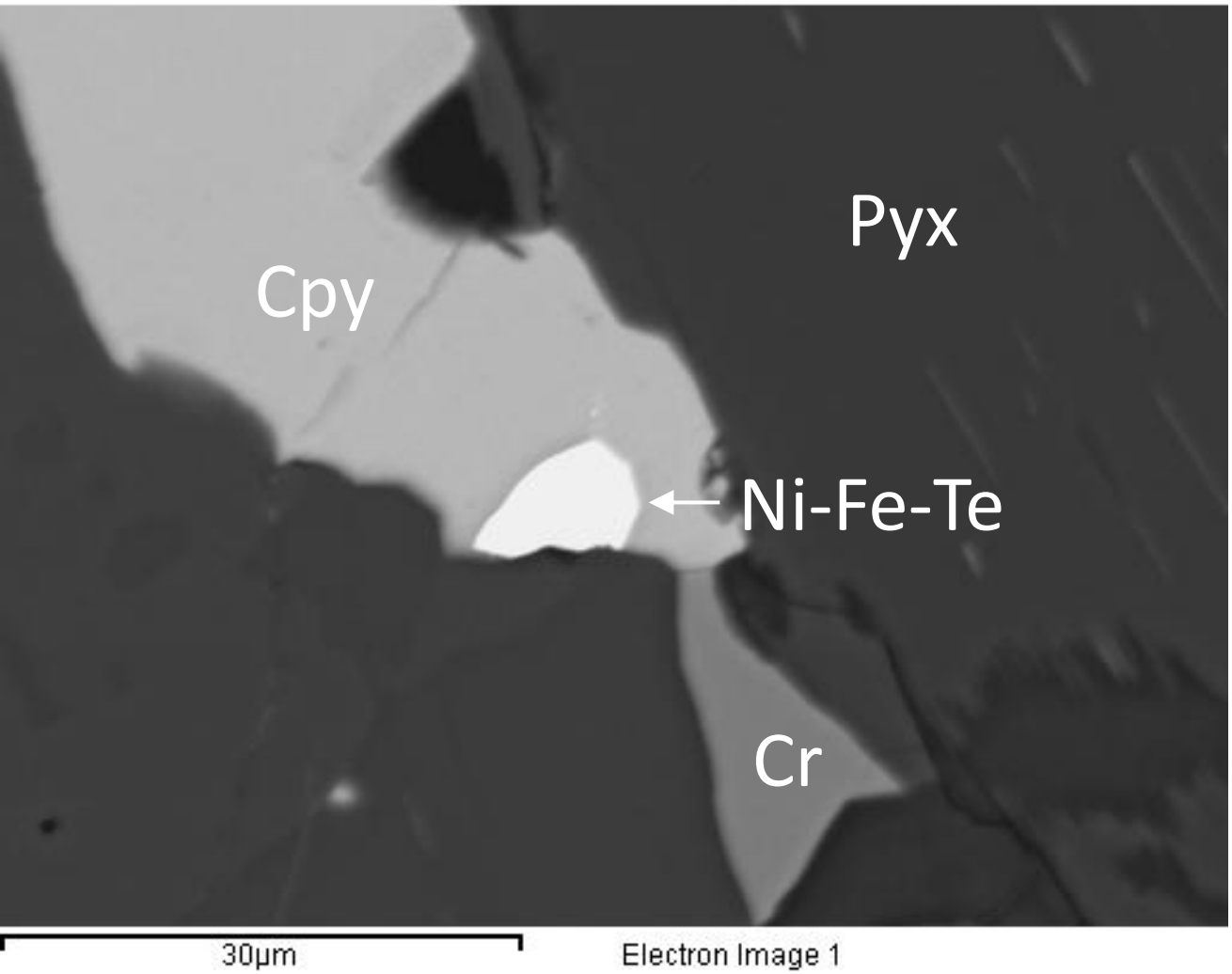
PTSR-33 B 1



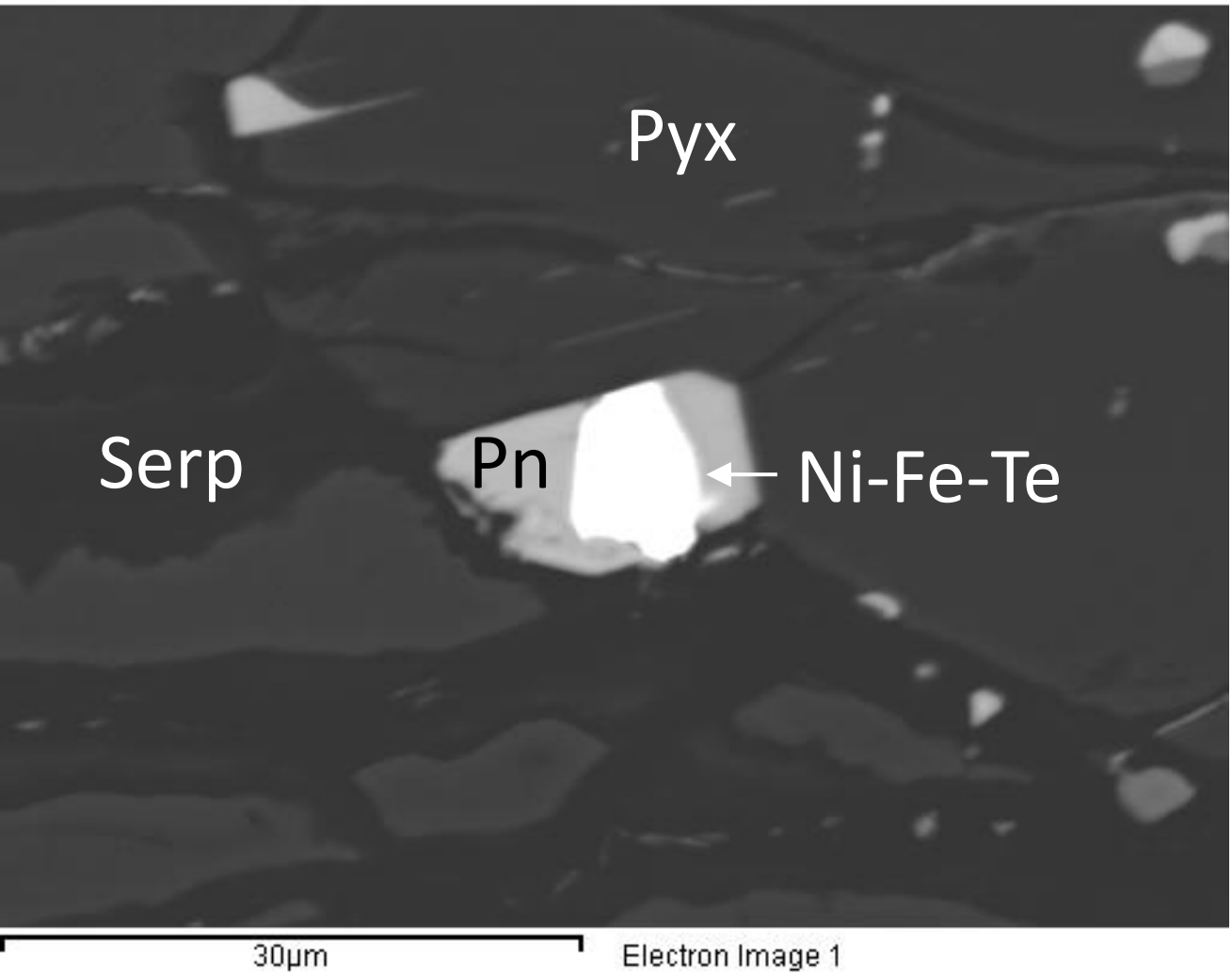
PTSR-33 C 1



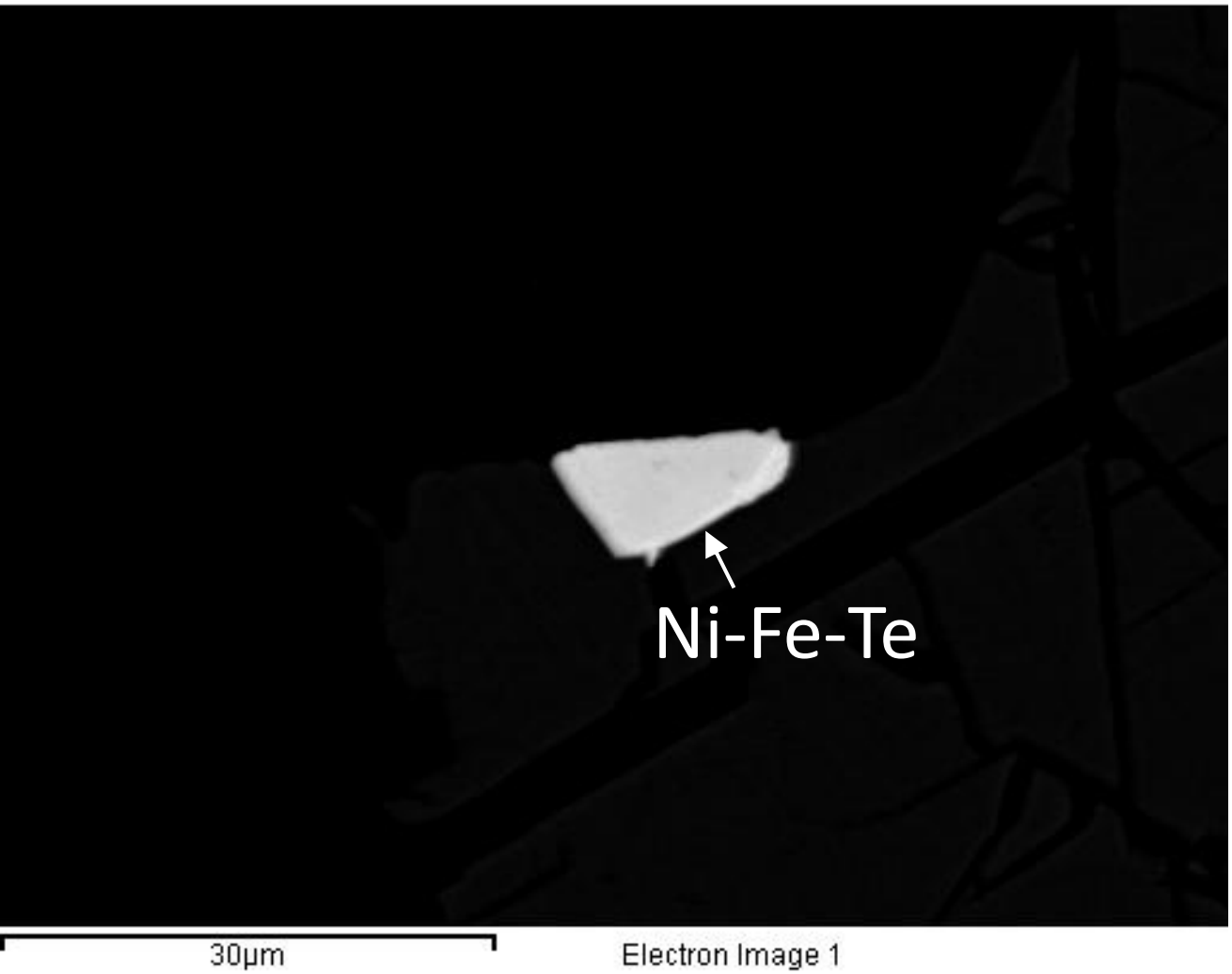
PTSR-33 C 1 Light



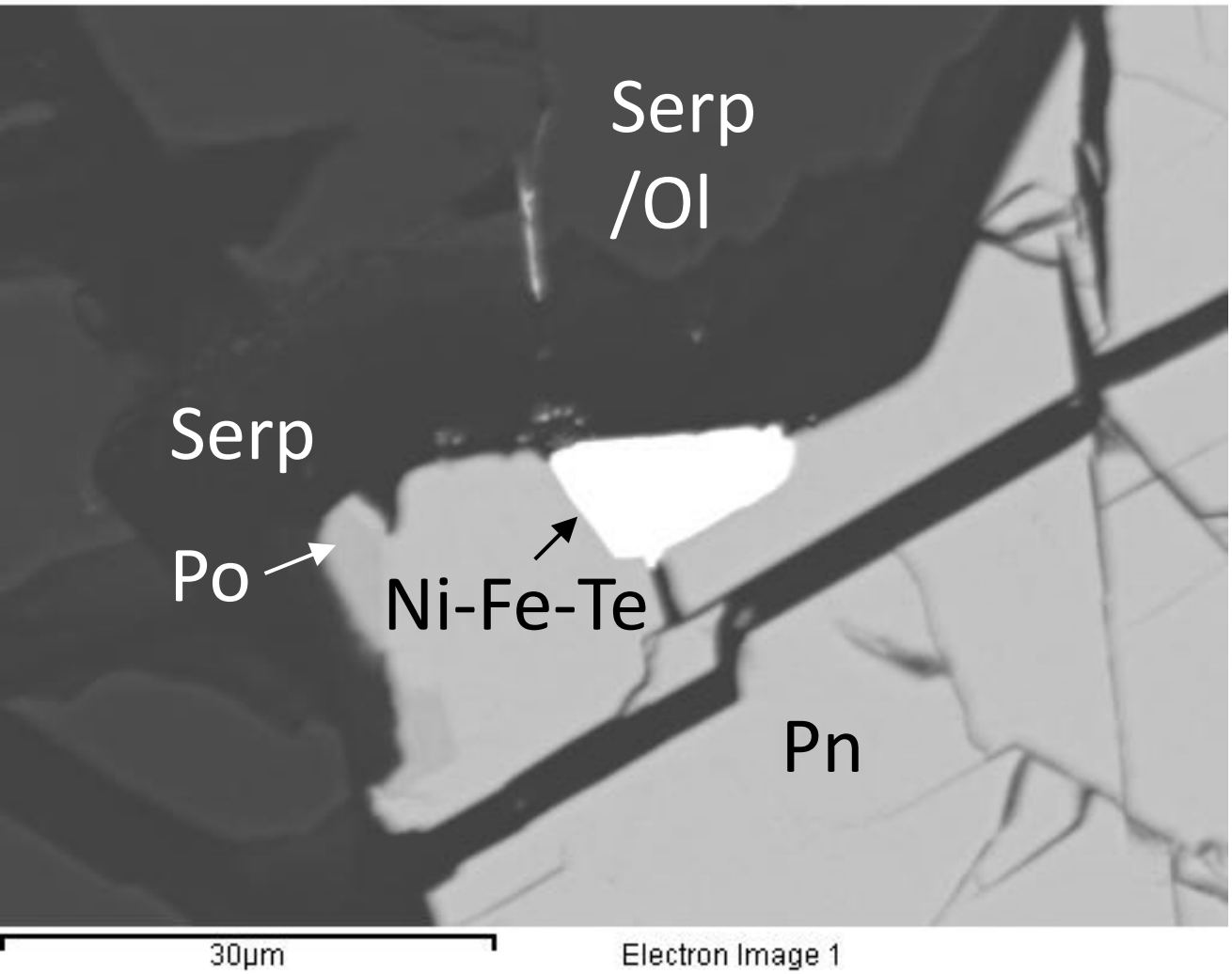
PTSR-33 D 1



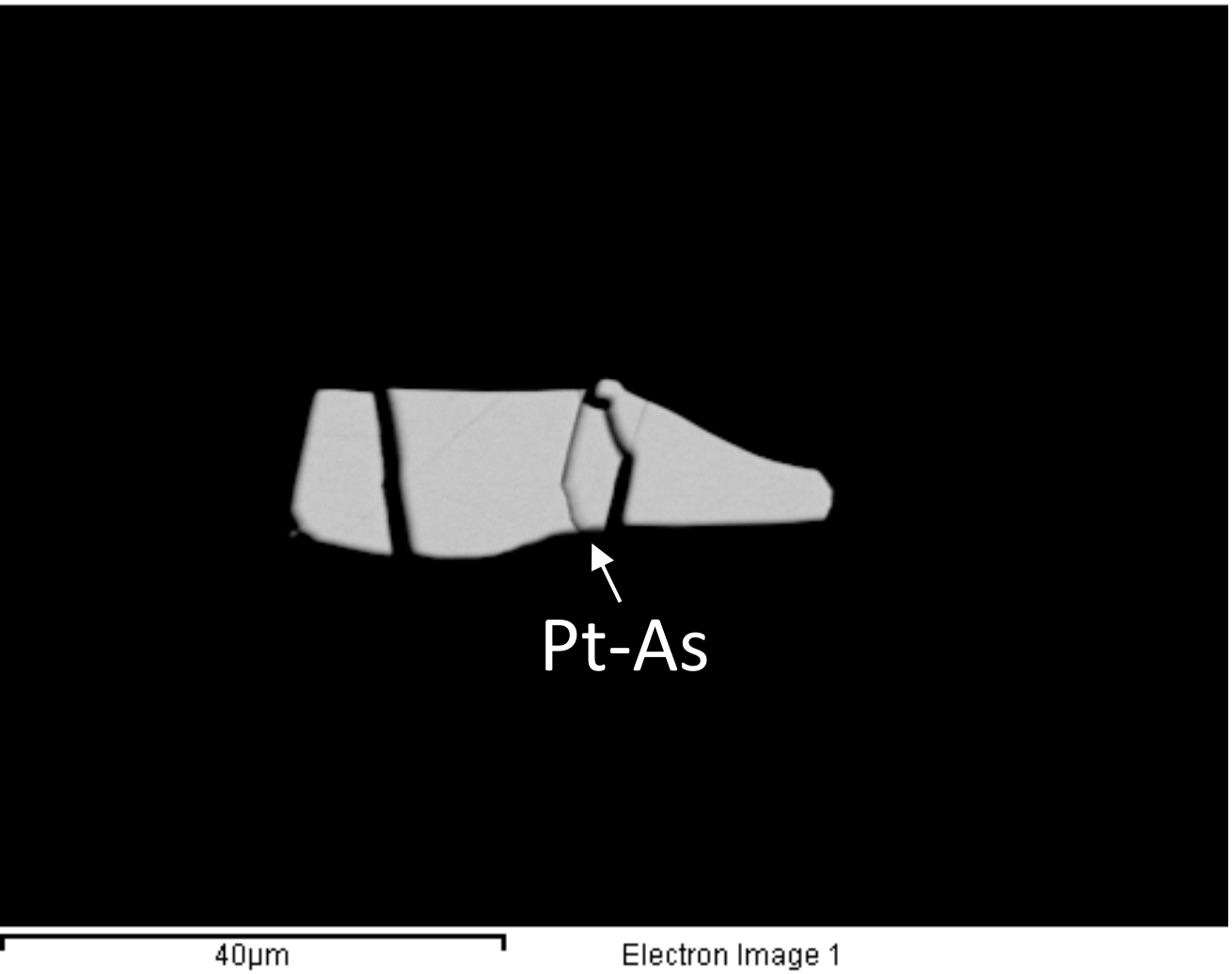
PTSR-33 E 1



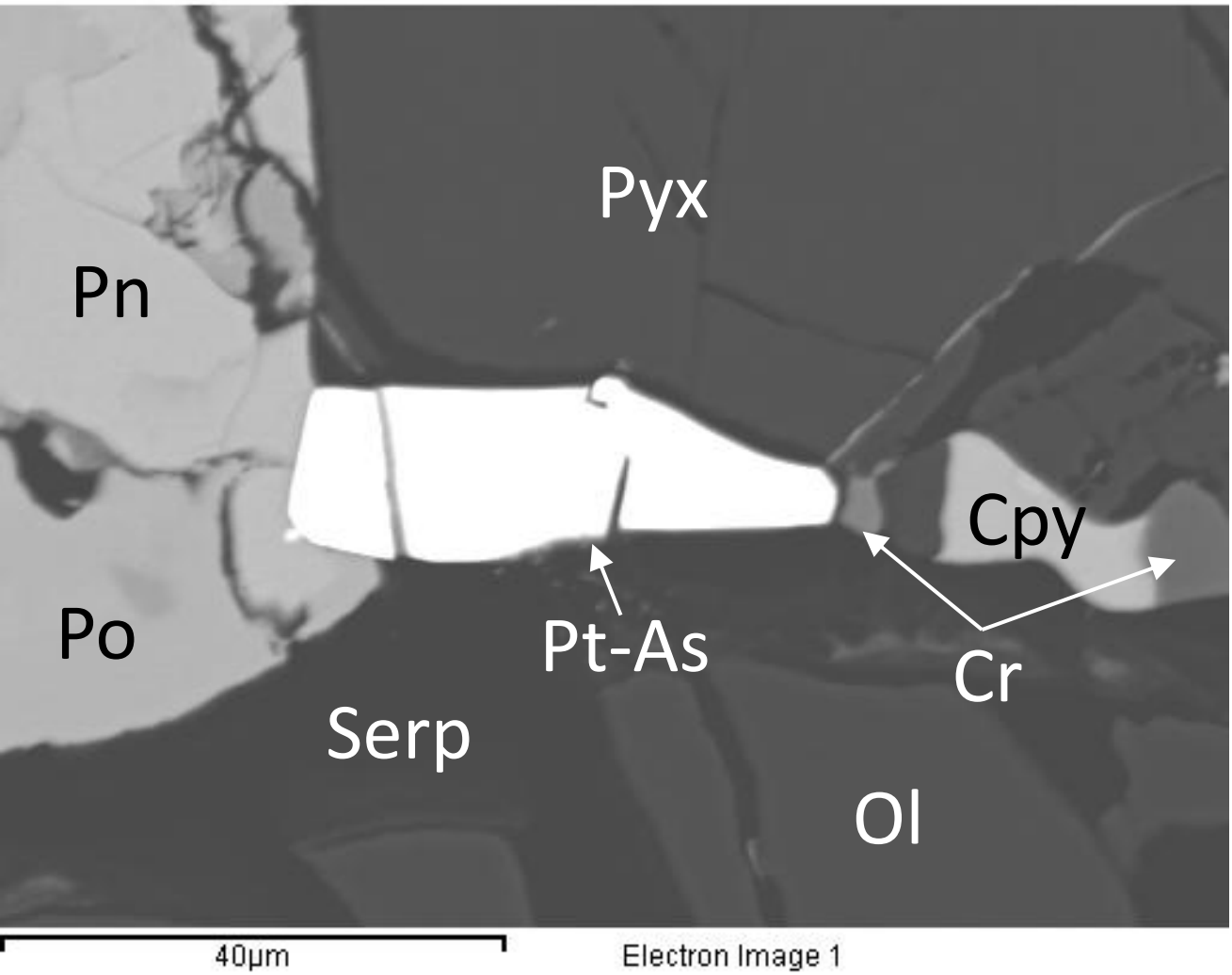
PTSR-33 E 1 Light



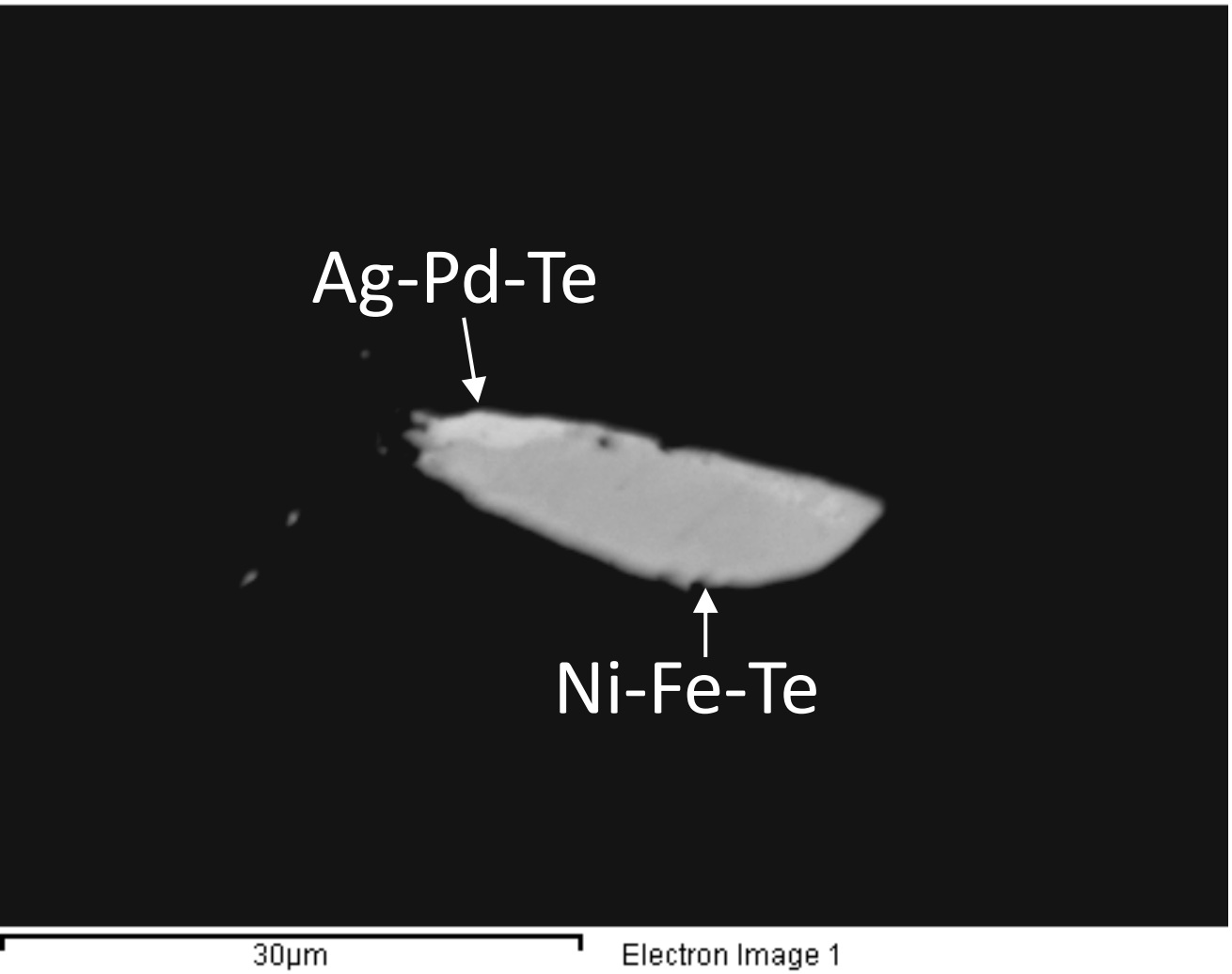
PTSR-33 F 1



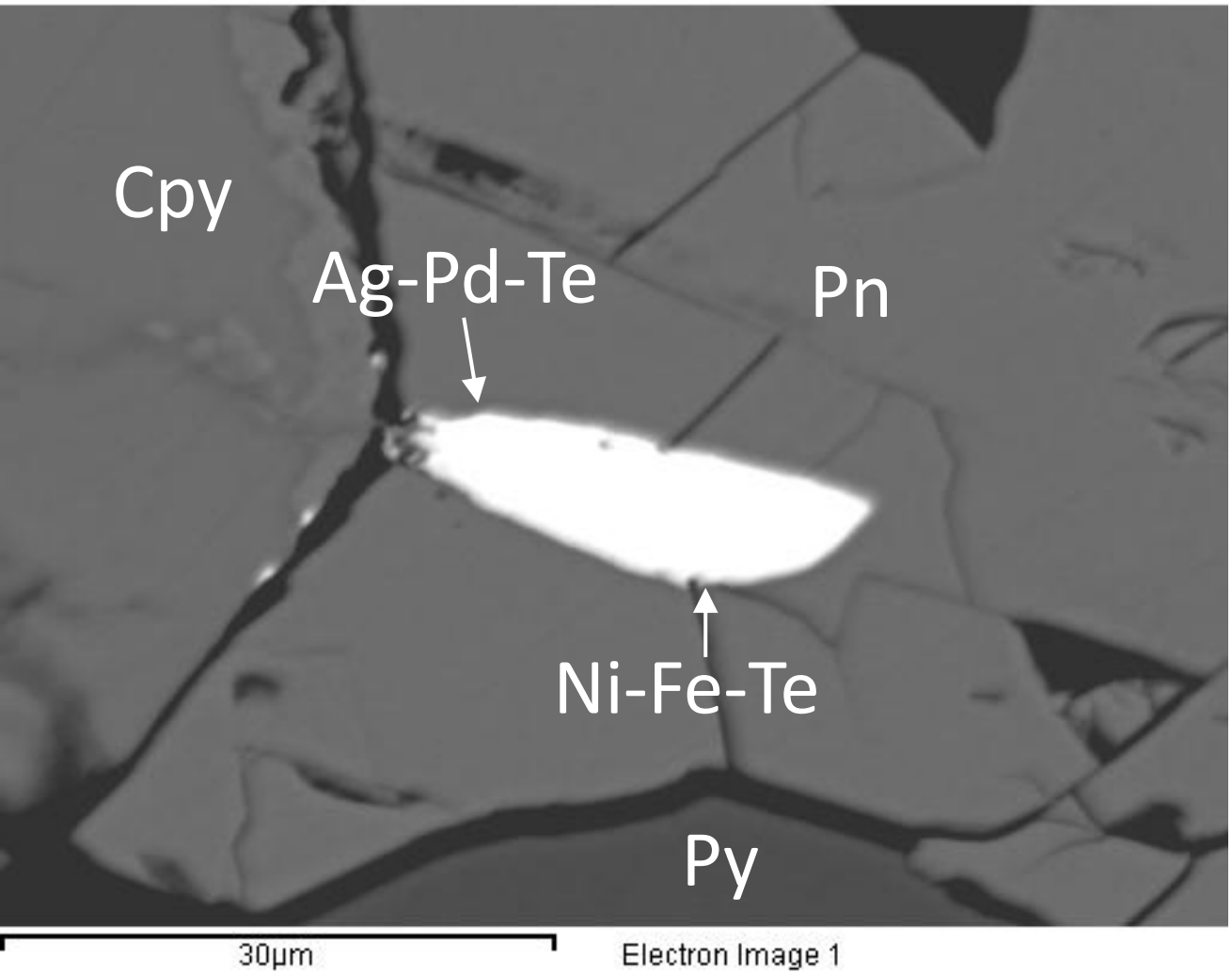
PTSR-33 F 1 Light



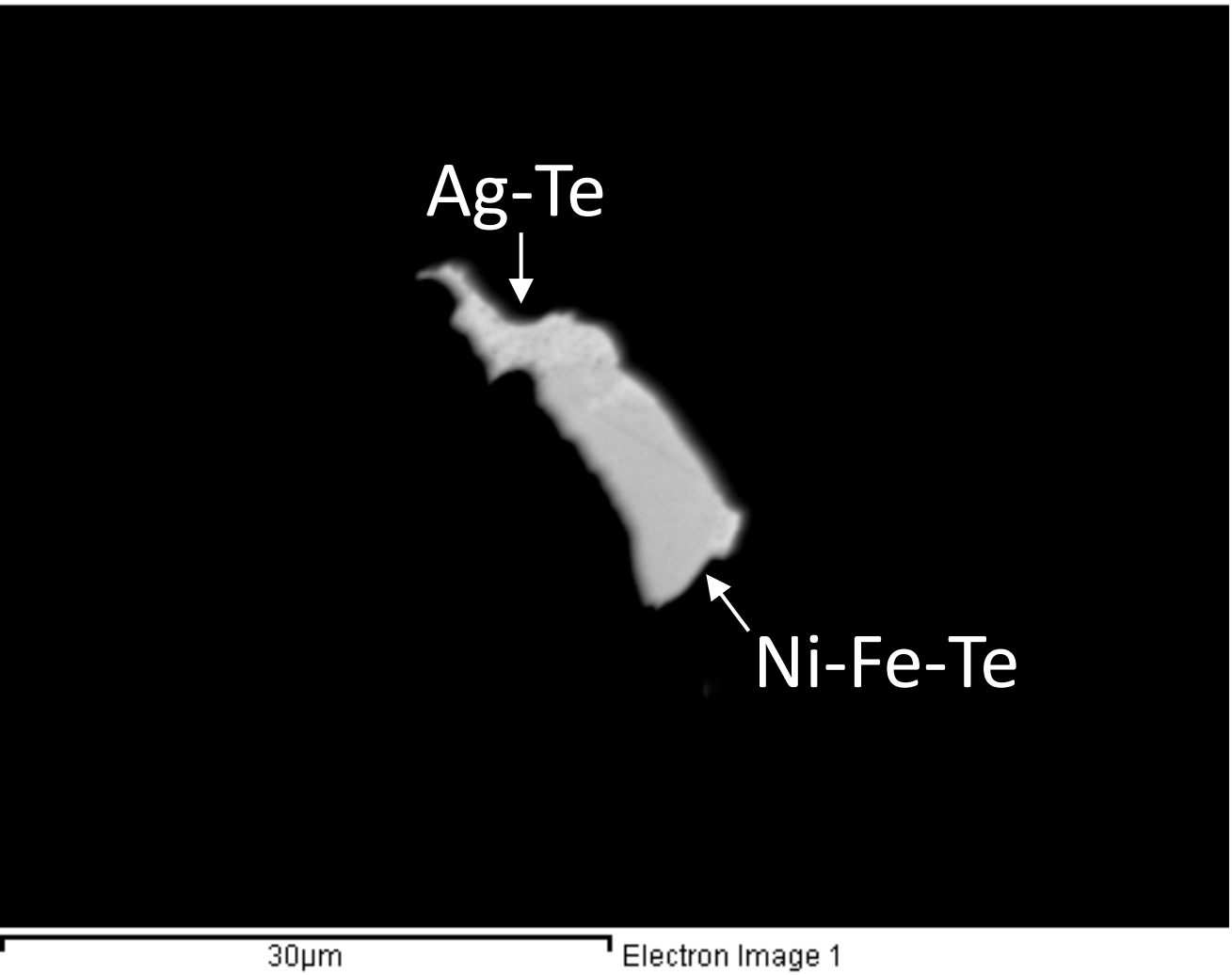
PTSR-33 G 1-2



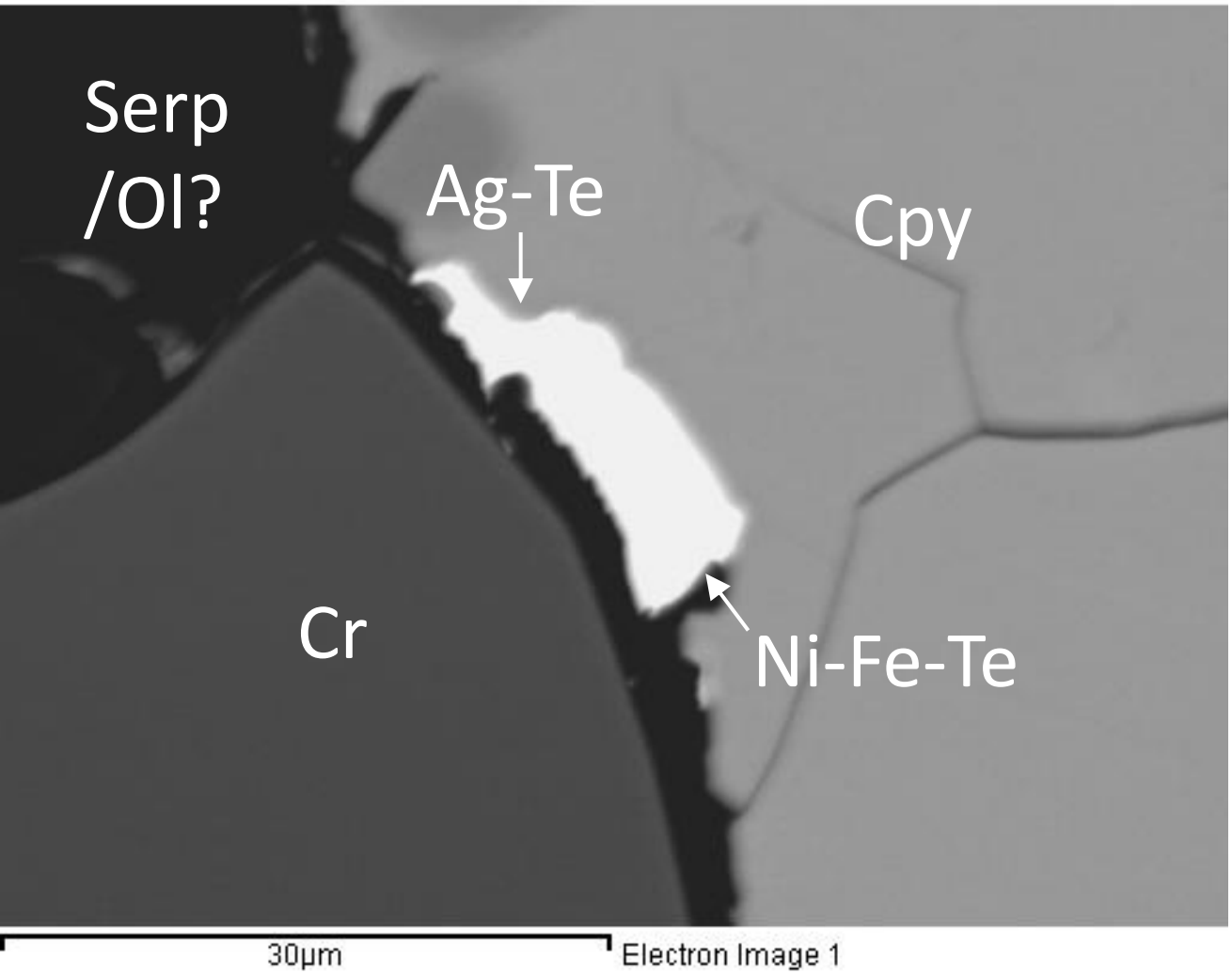
PTSR-33 G 1-2 Light



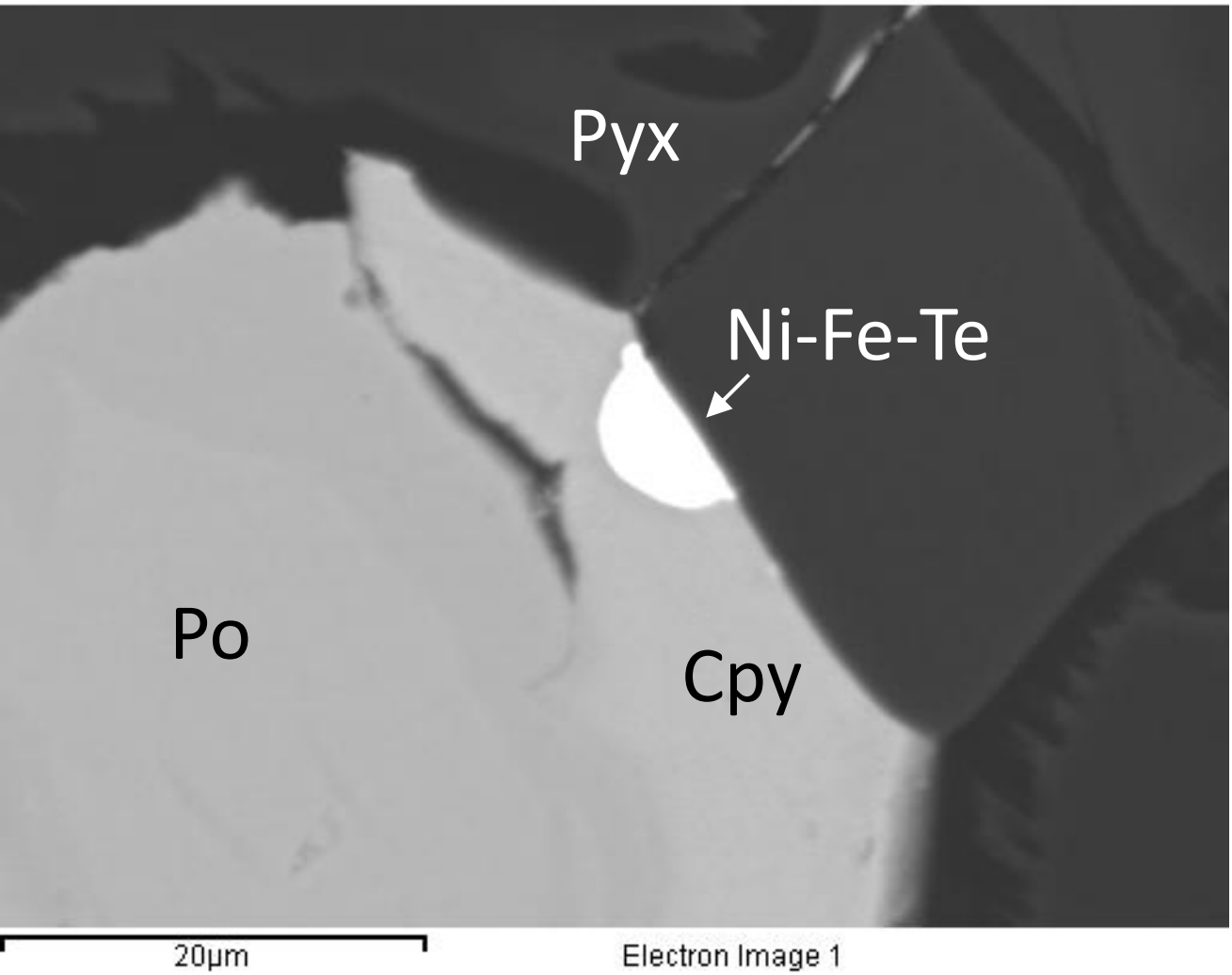
PTSR-33 H 1-2



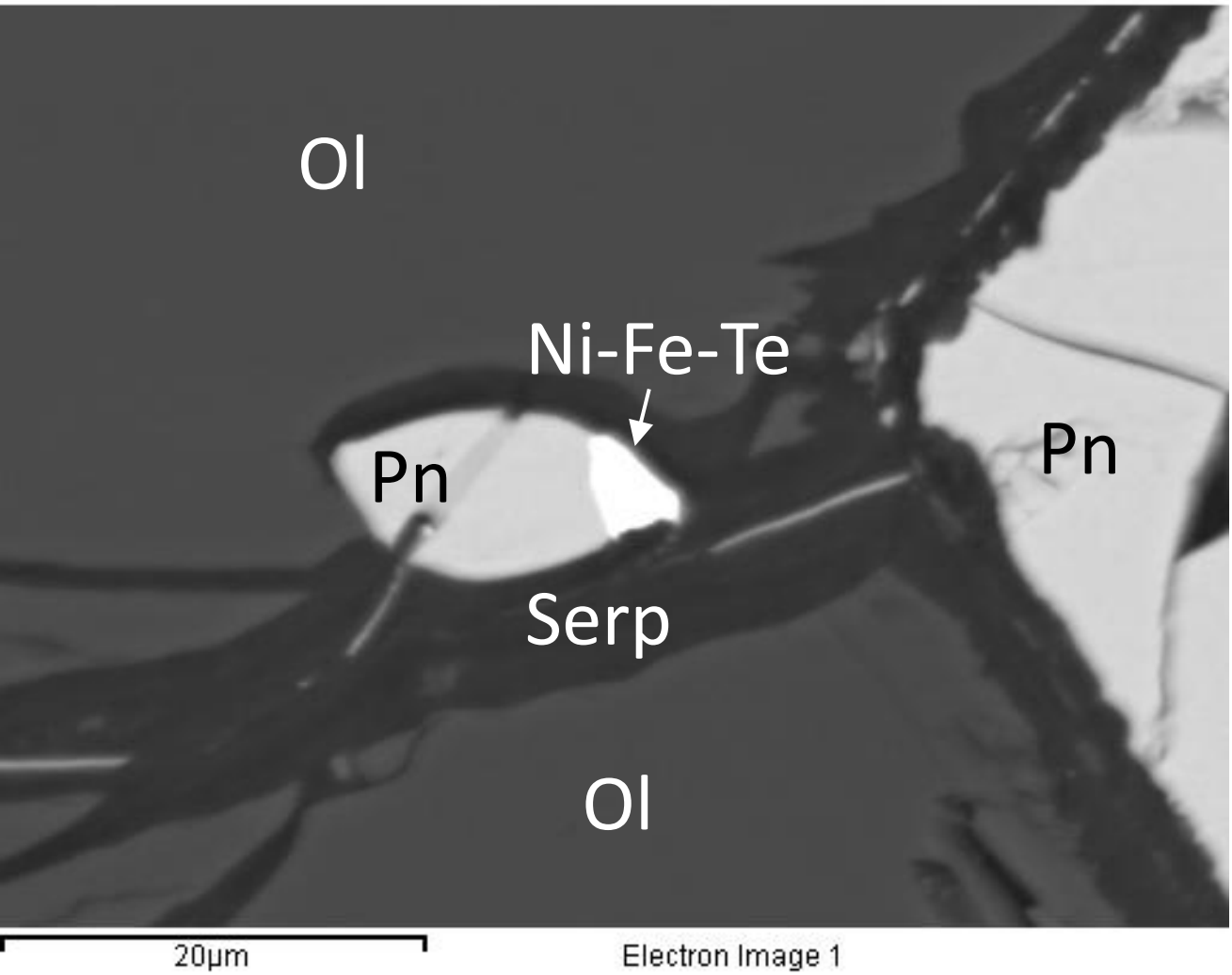
PTSR-33 H 1-2 Light



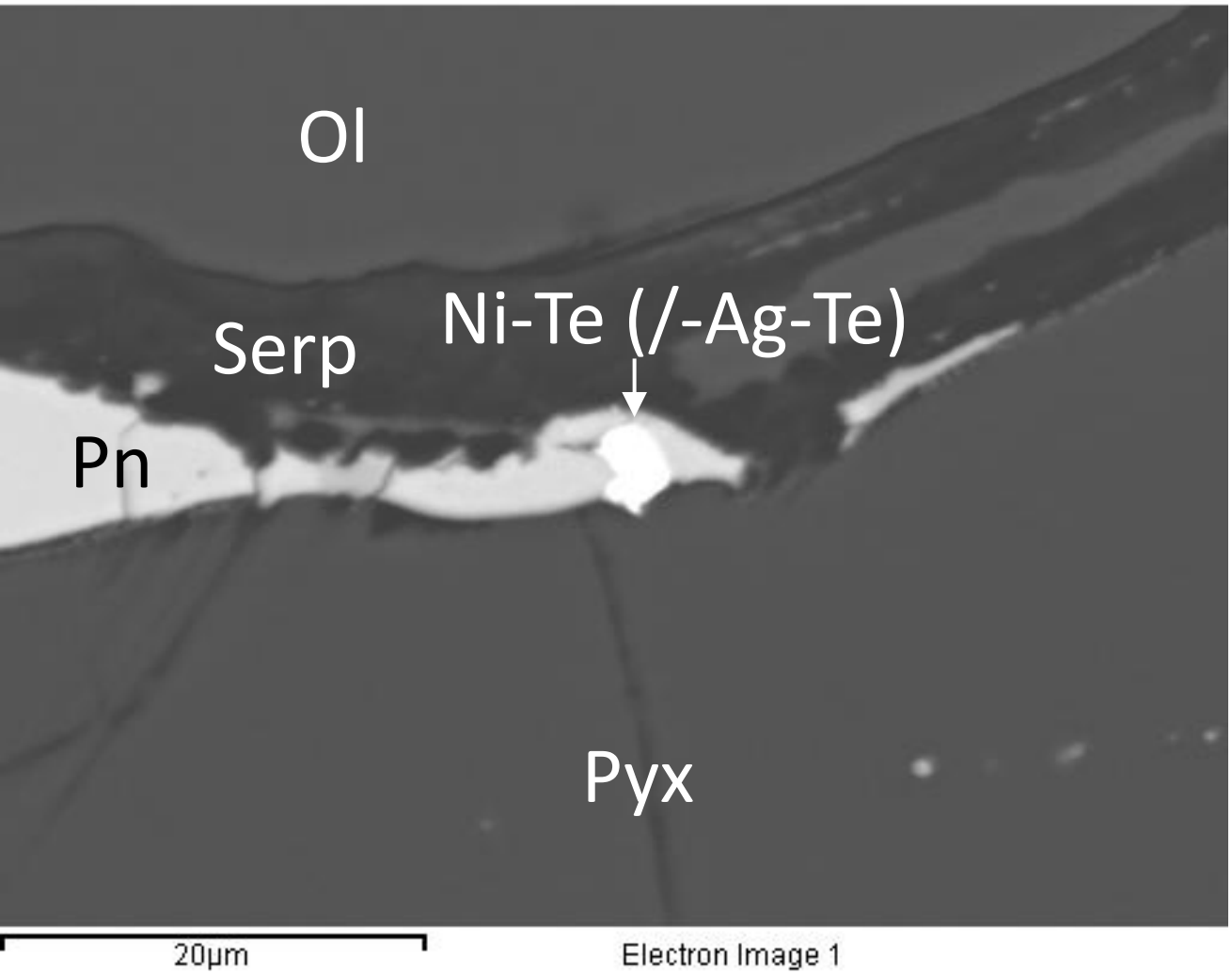
PTSR-33 I 1



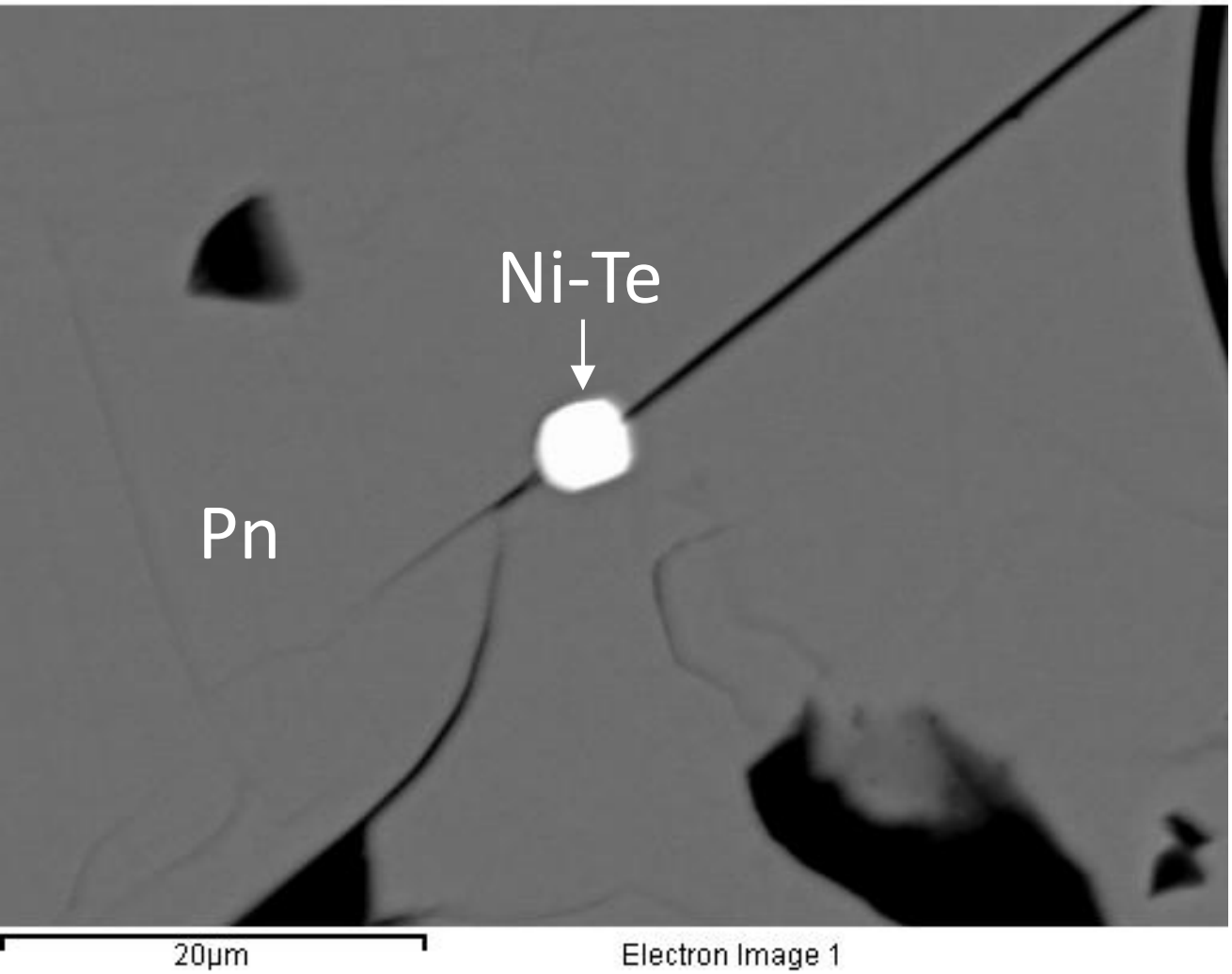
PTSR-33 J 1



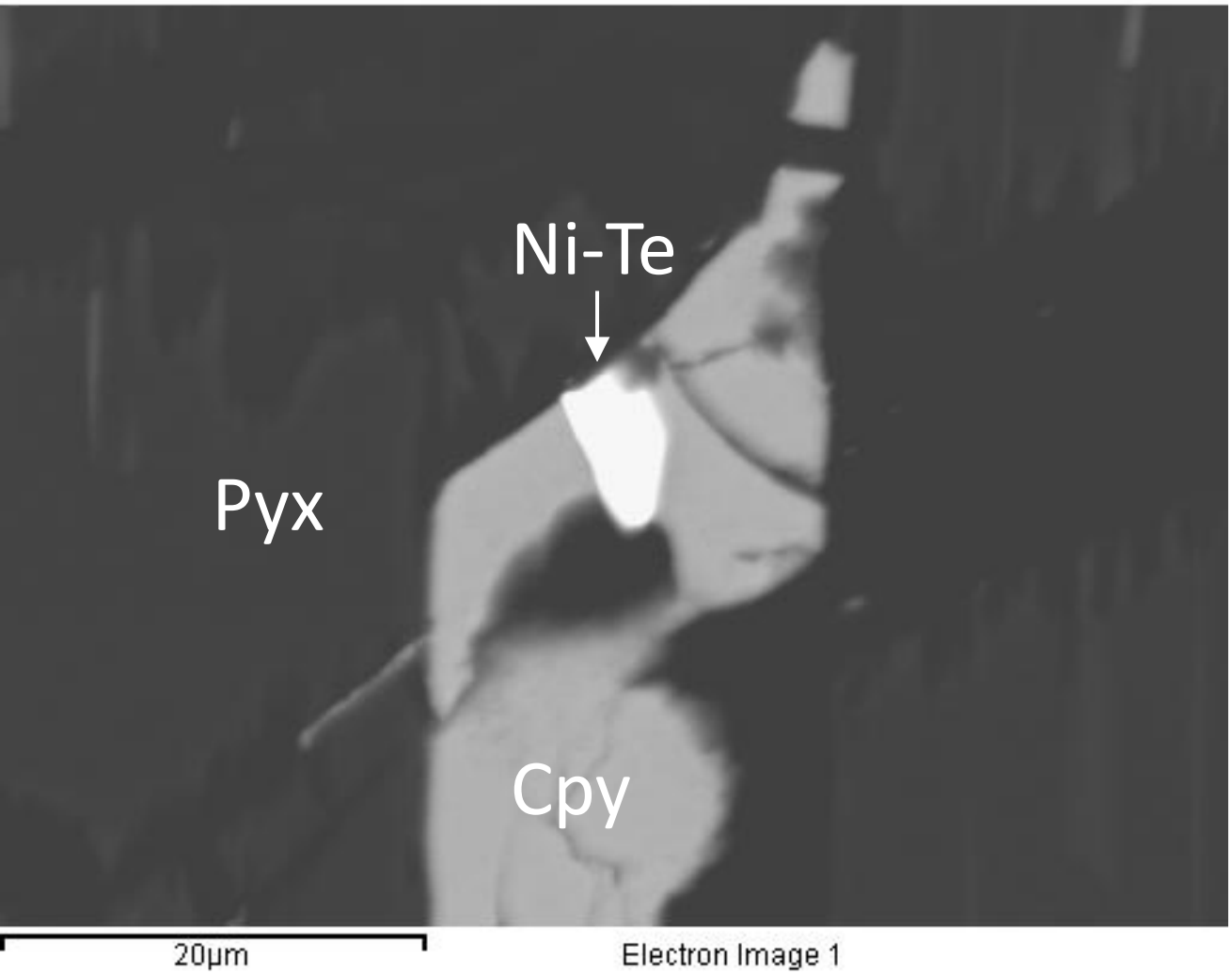
PTSR-33 K 1



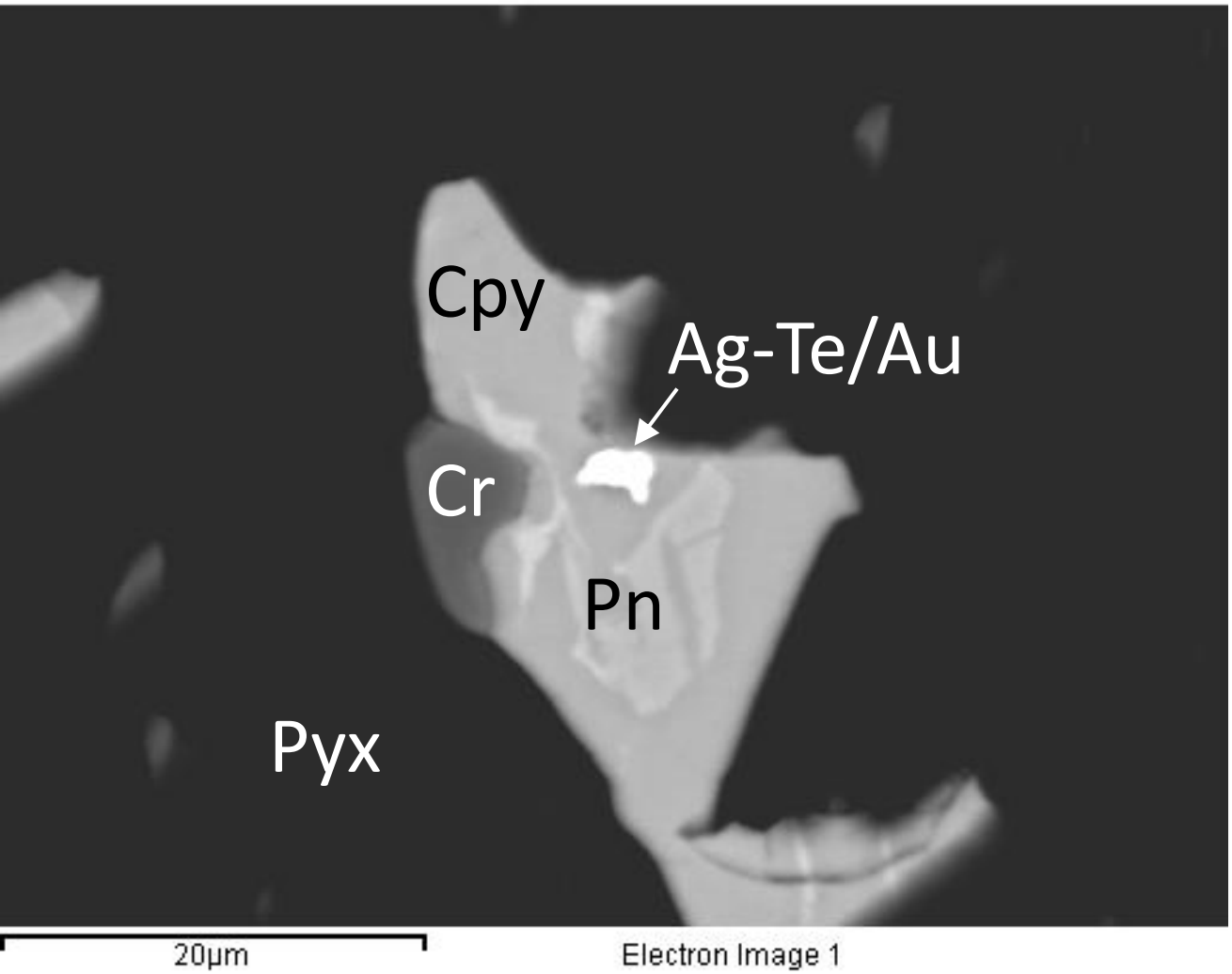
PTSR-33 L 1



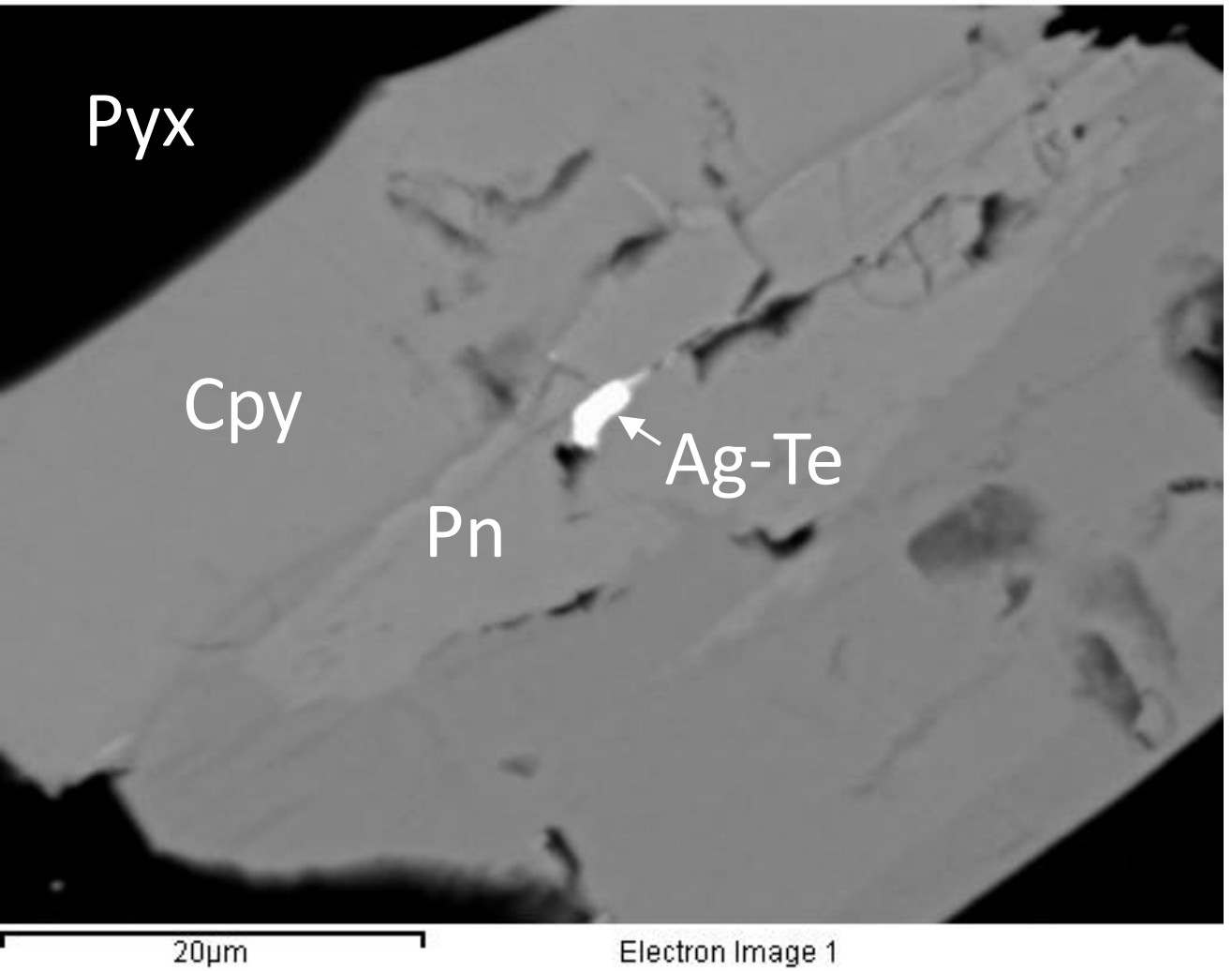
PTSR-33 M 1



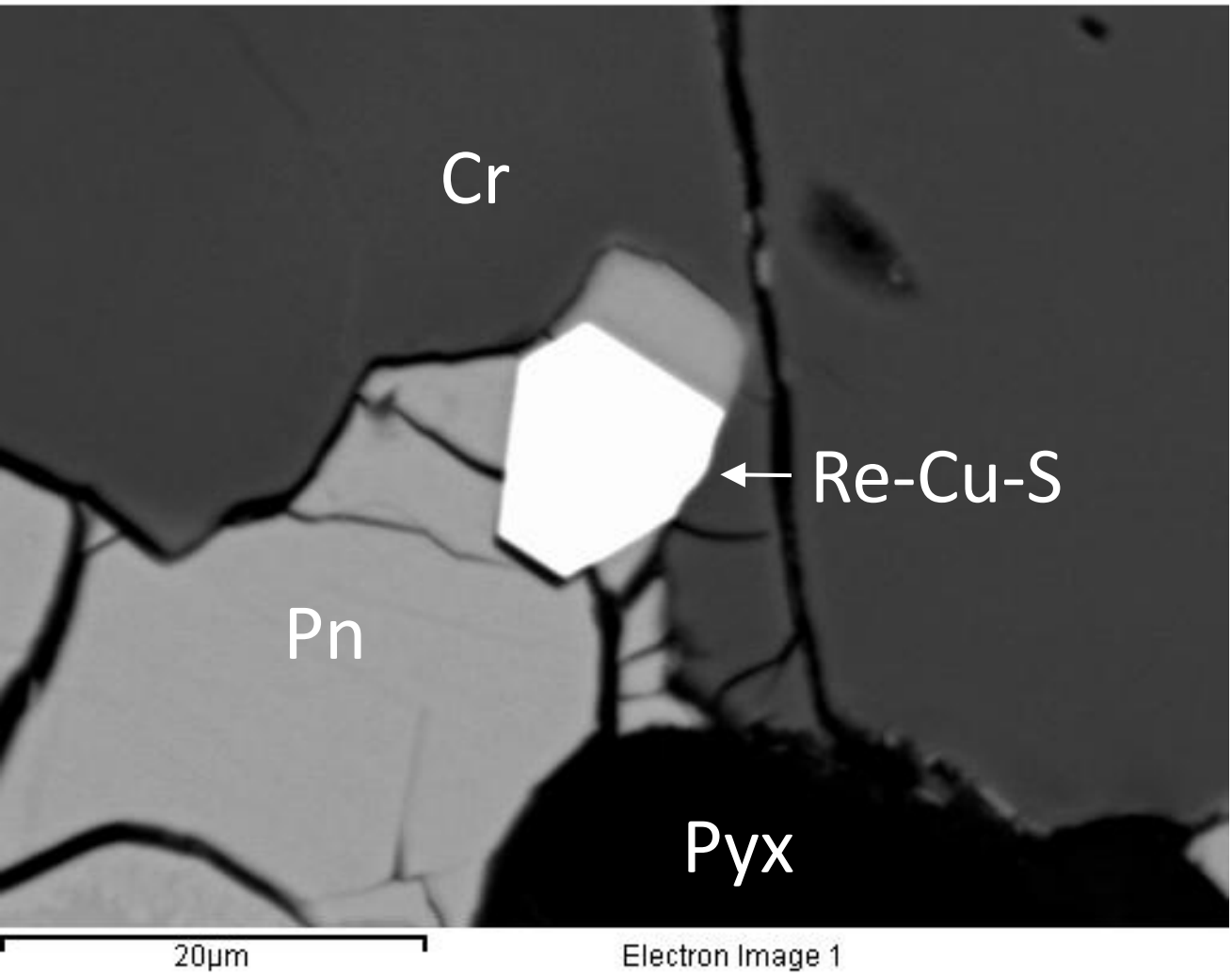
PTSR-33 N 1



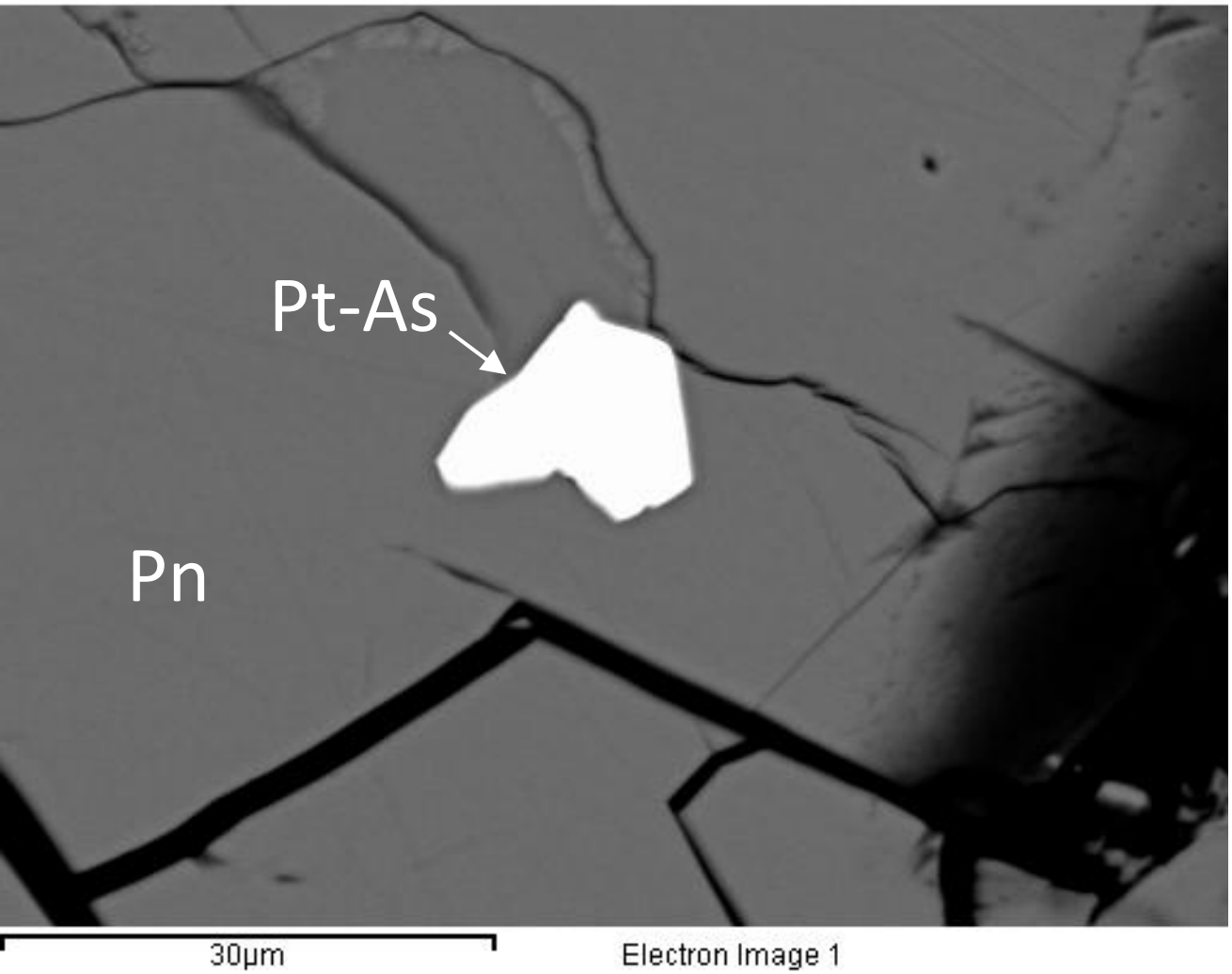
PTSR-33 O 1



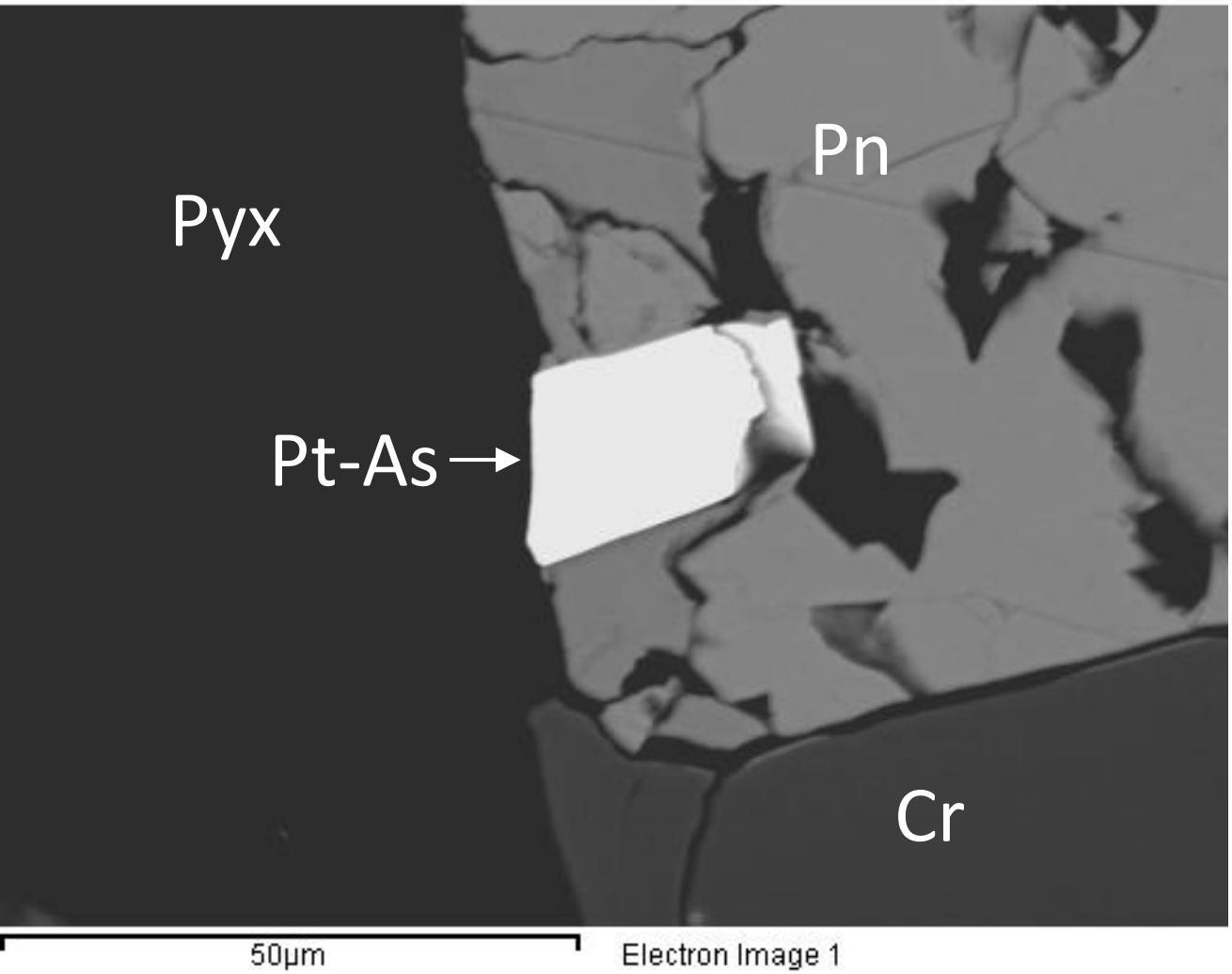
PTSR-33 P 1



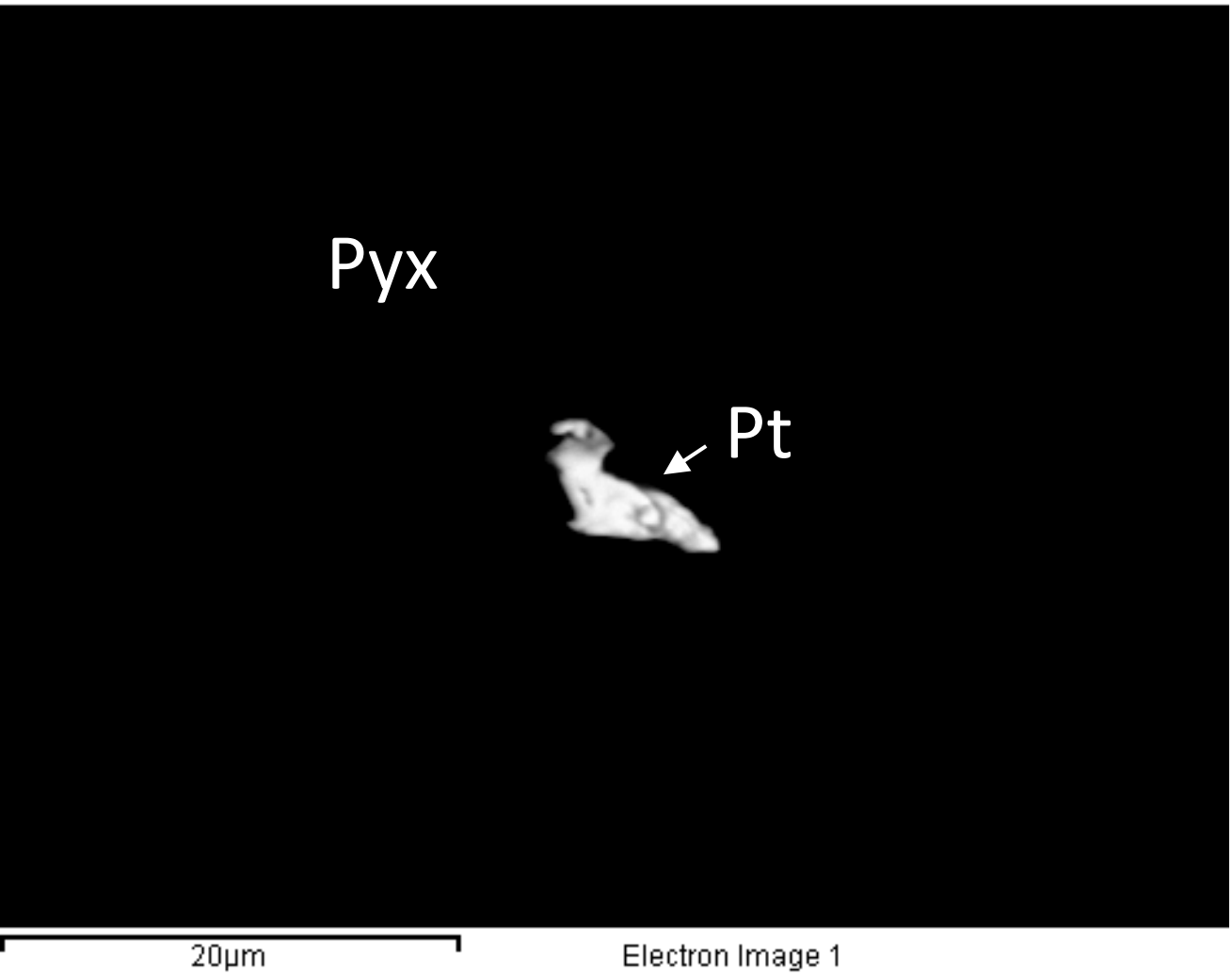
PTSR-33 Q 1



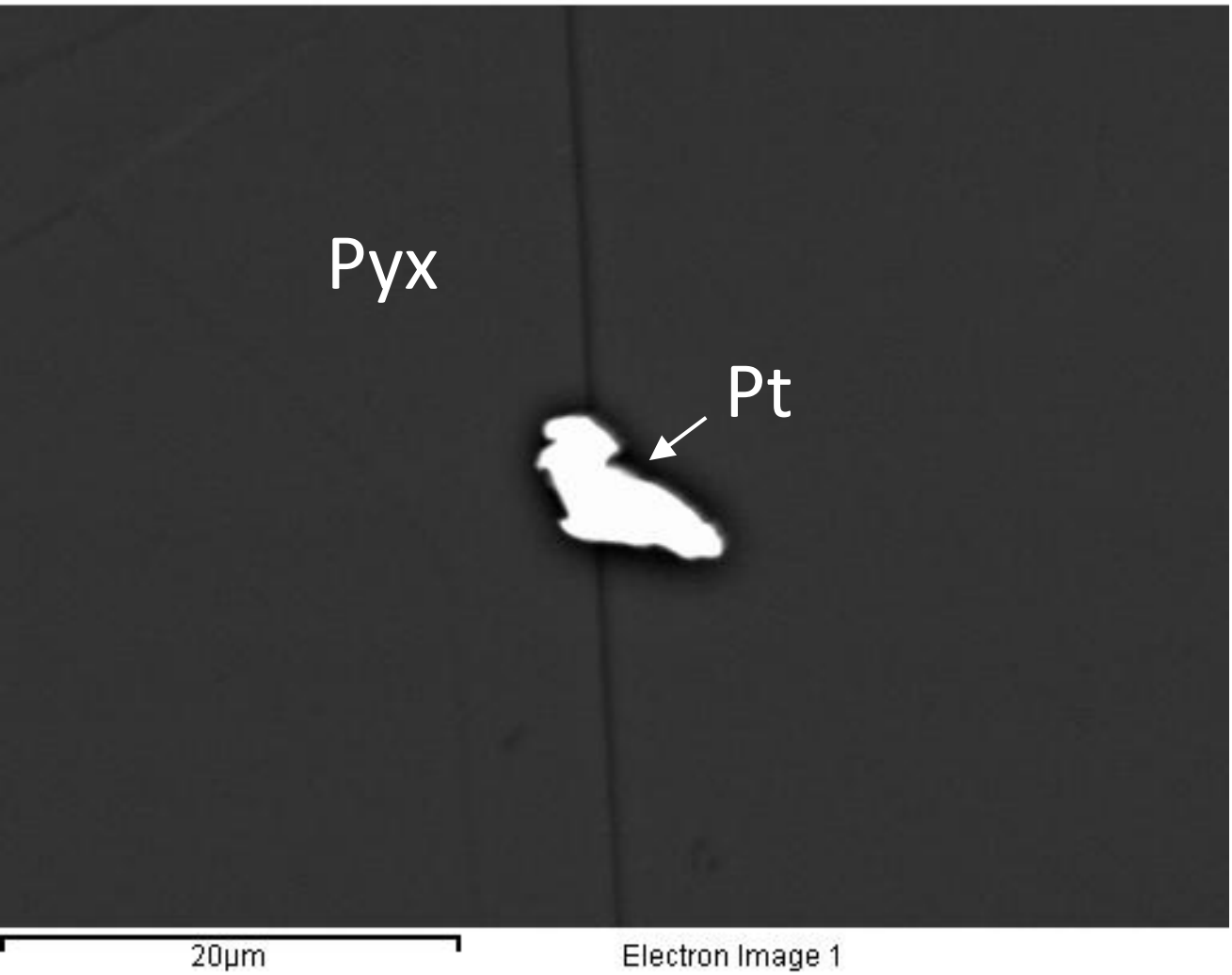
PTSR-33 R 1



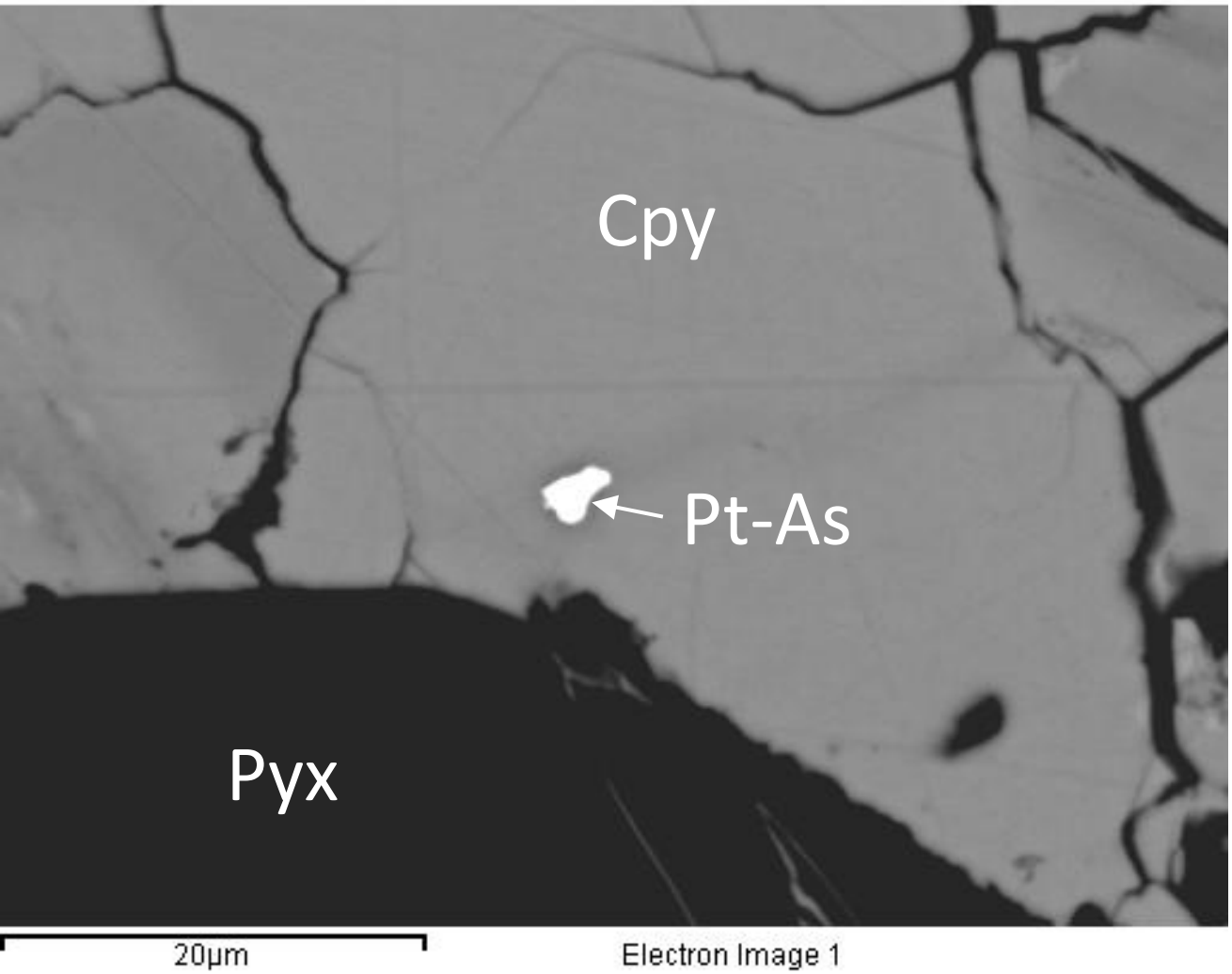
PTSR-33 S 1



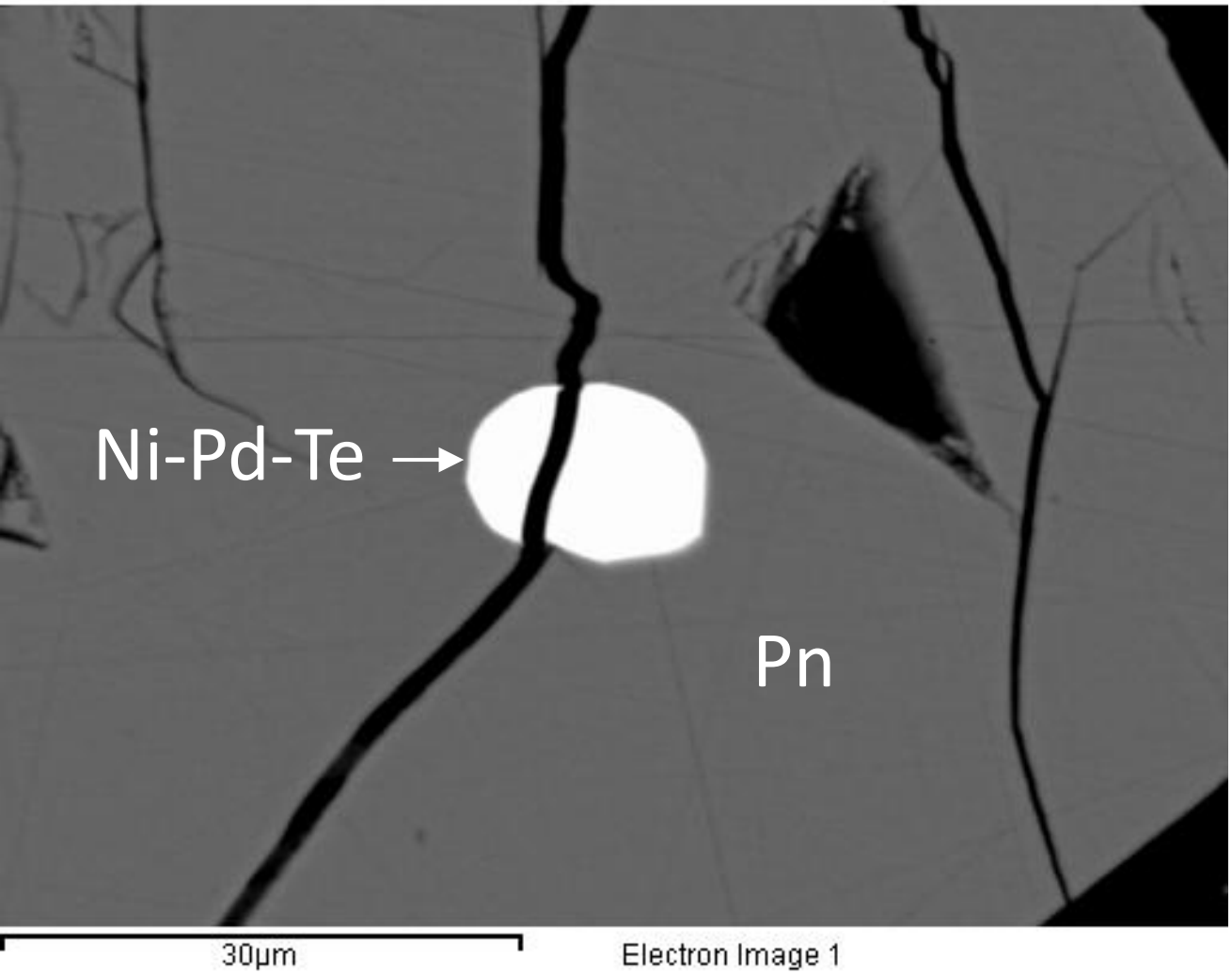
PTSR-33 S 1 Light



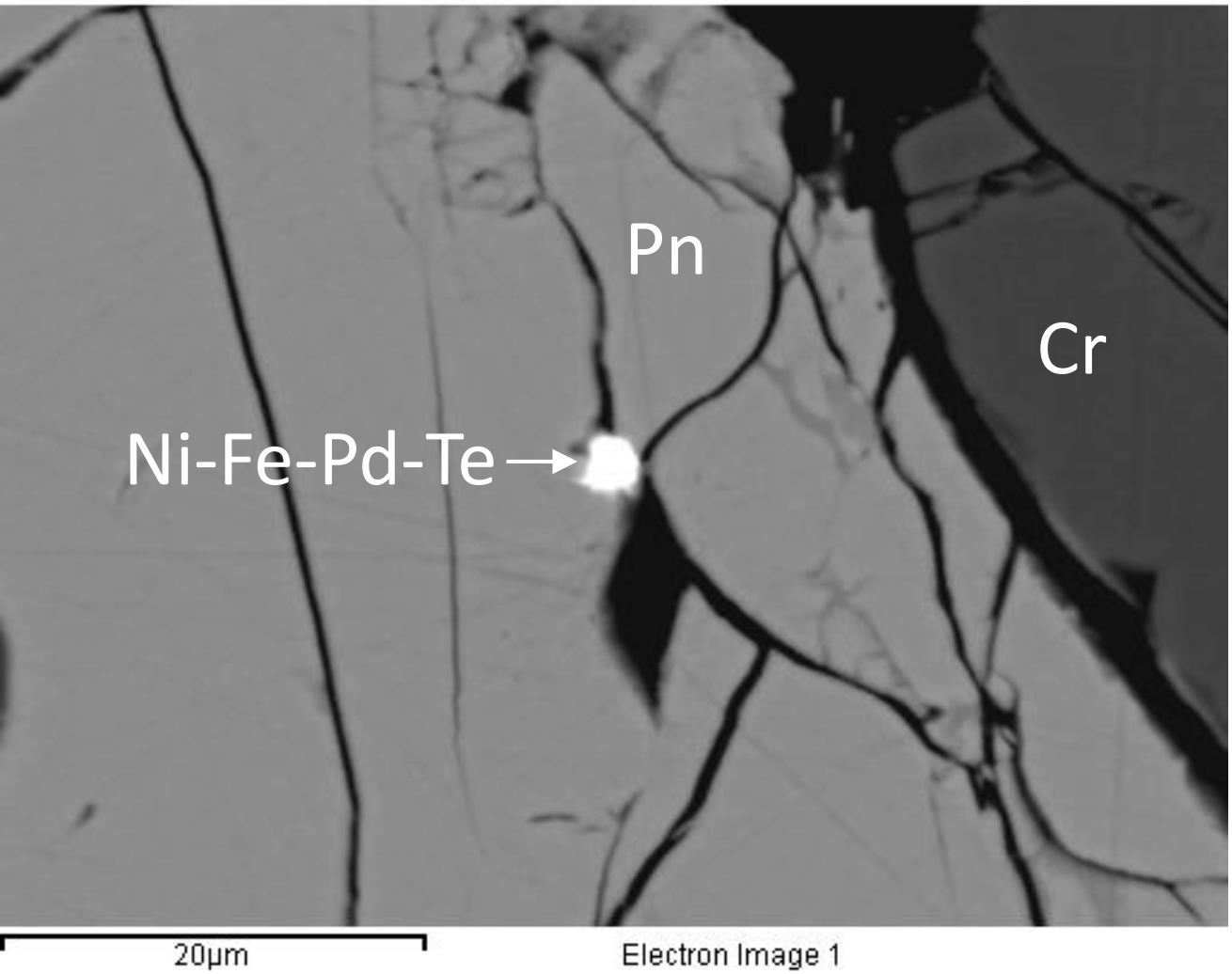
PTSR-34 A 1



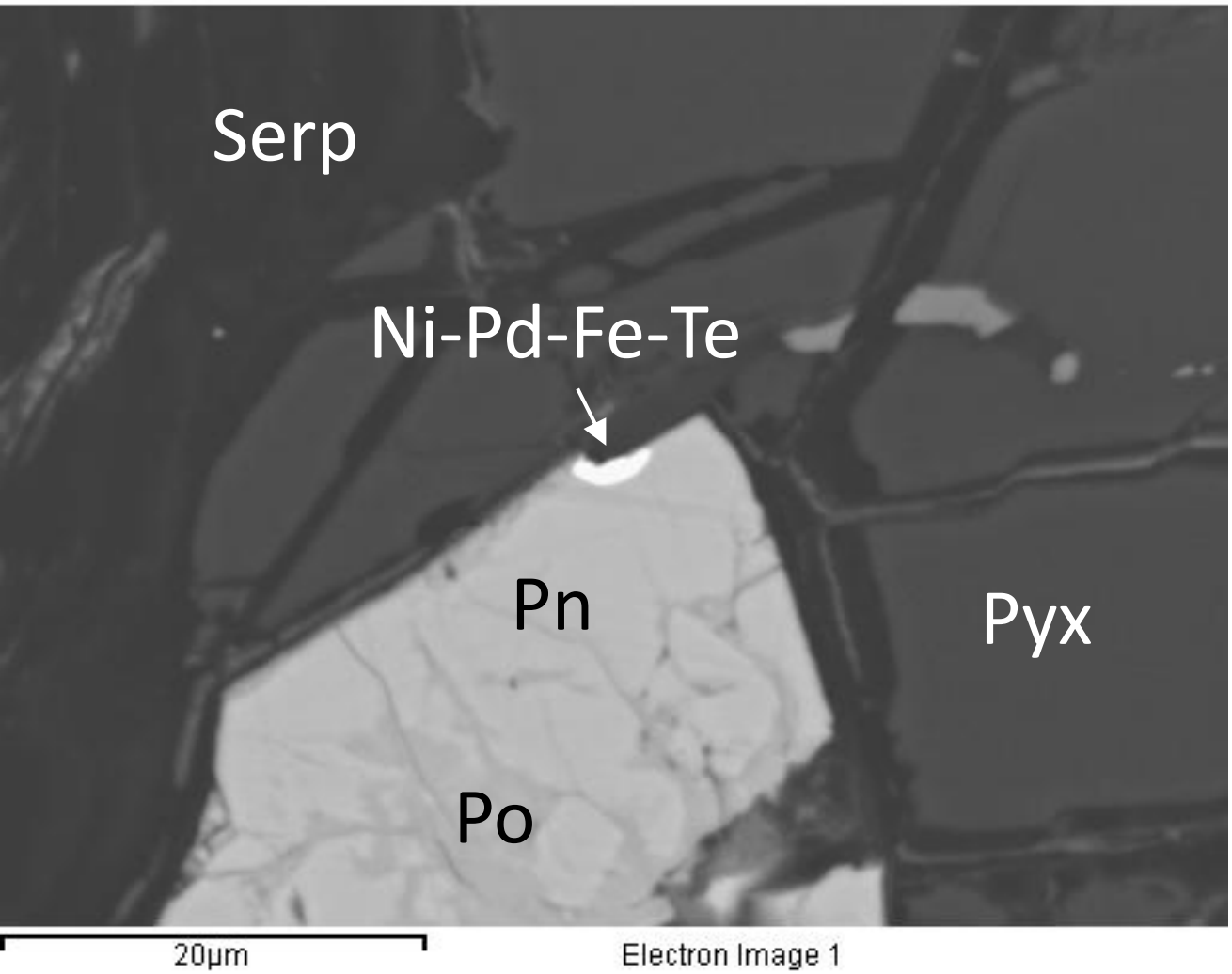
PTSR-34 B 1



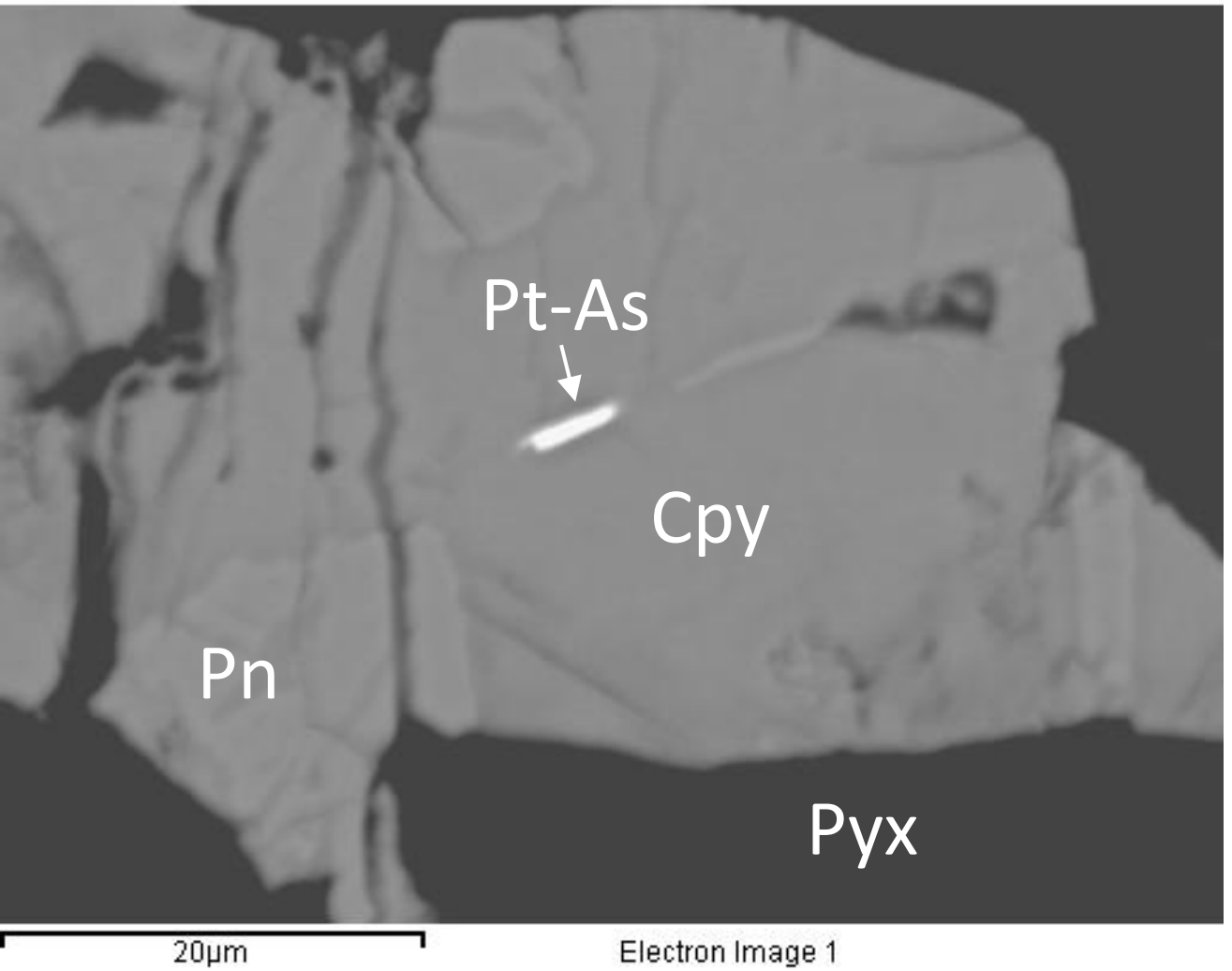
PTSR-34 C 1



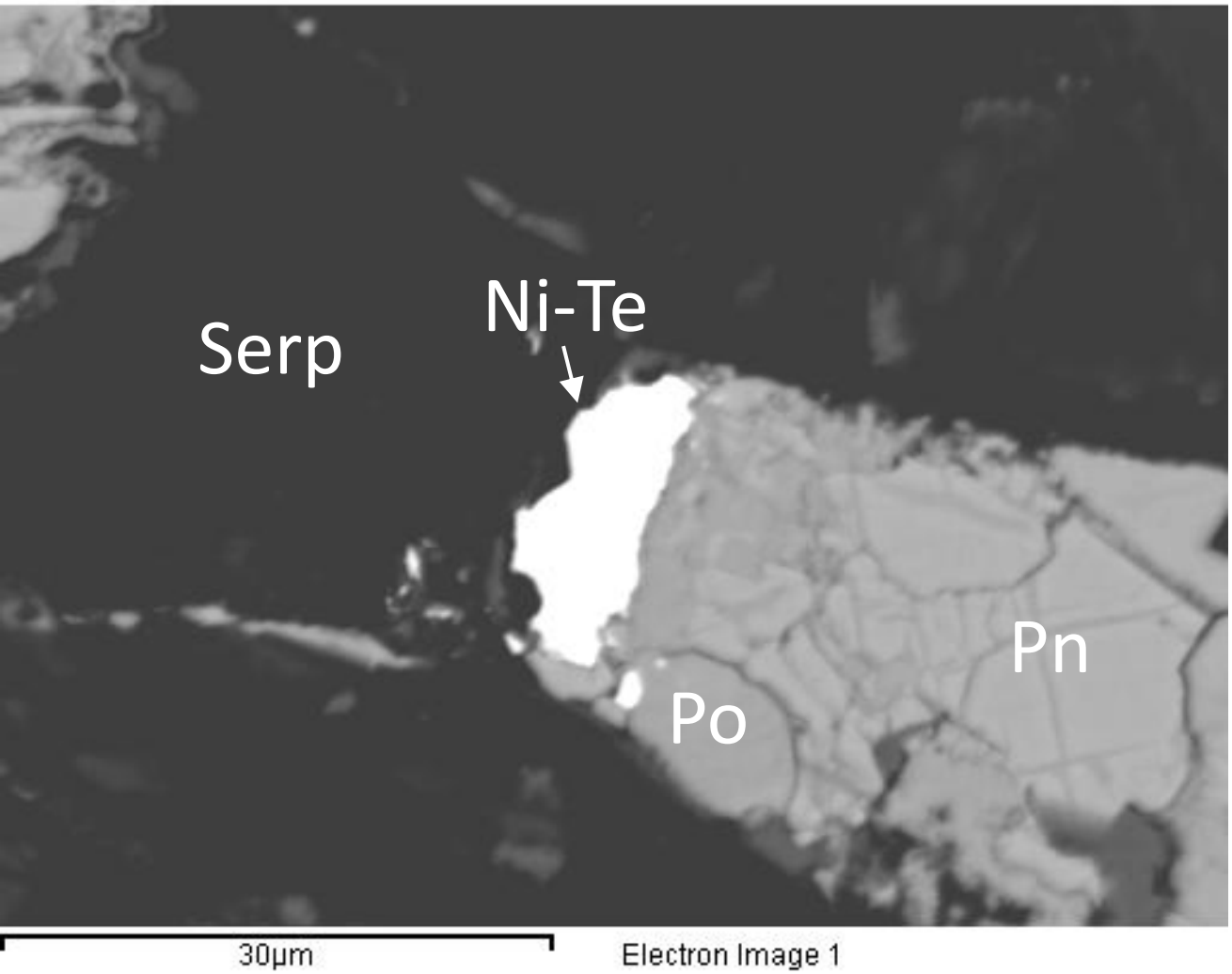
PTSR-34 D 1



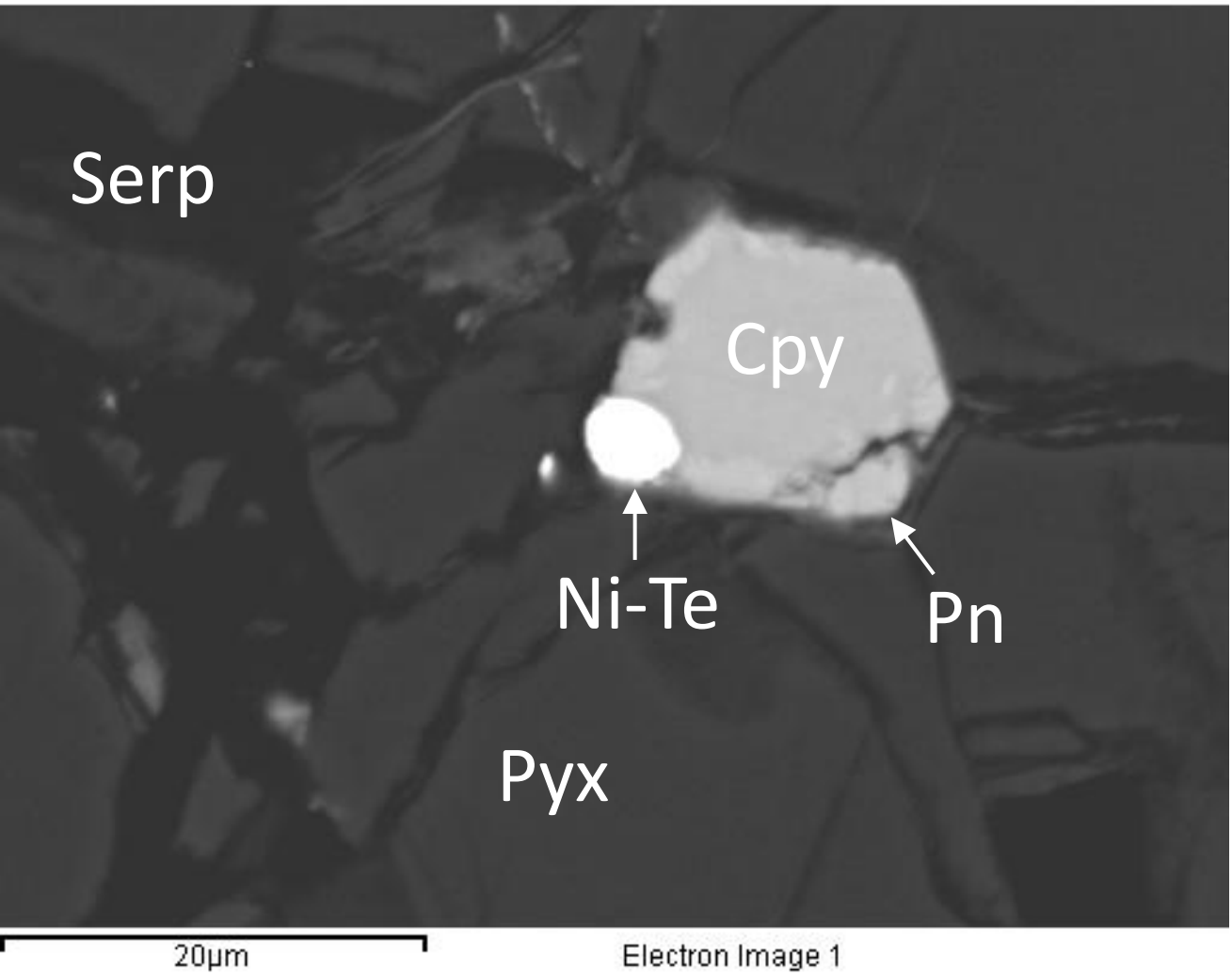
PTSR-34 E 1



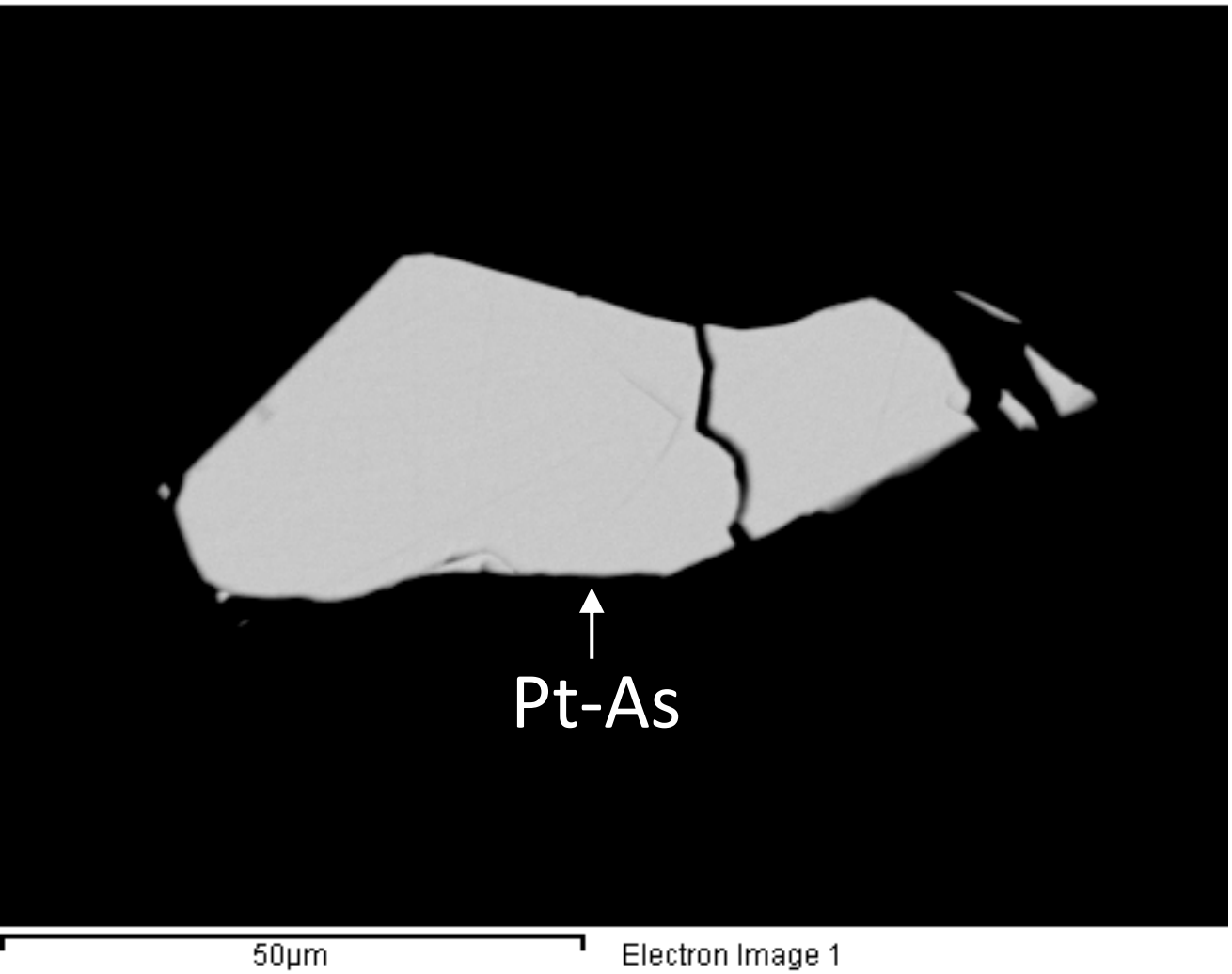
PTSR-34 F 1



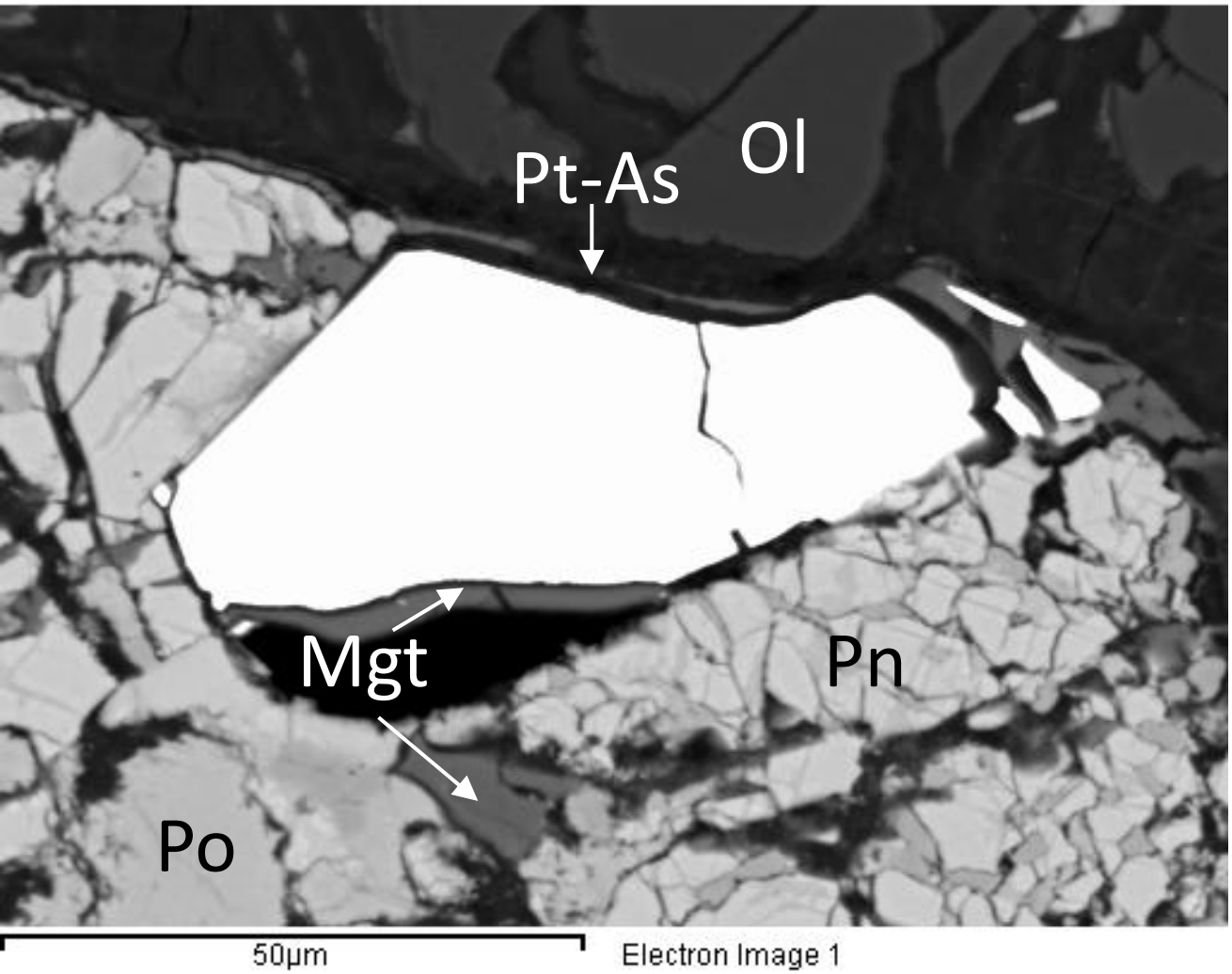
PTSR-34 G 1



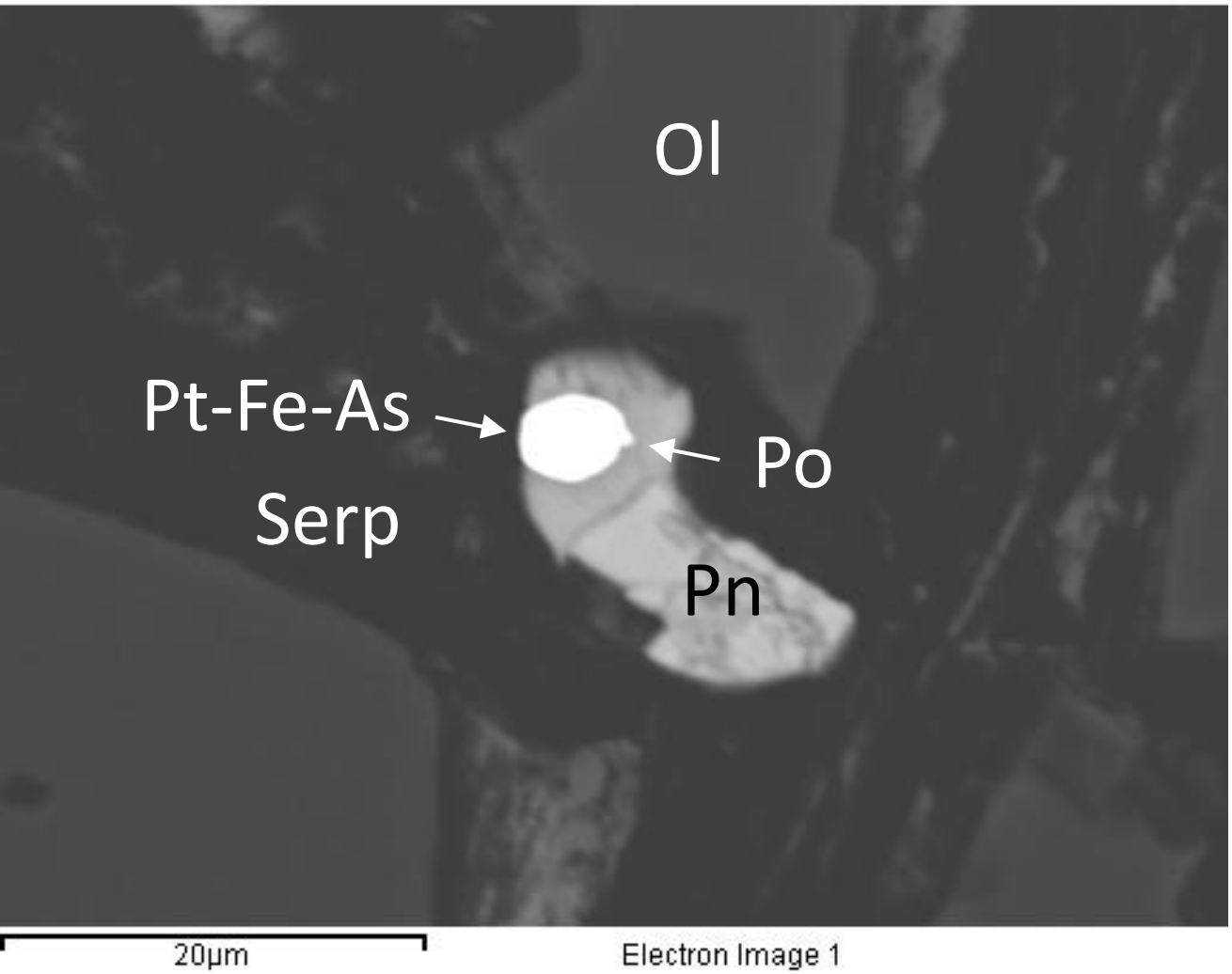
PTSR-34 H 1



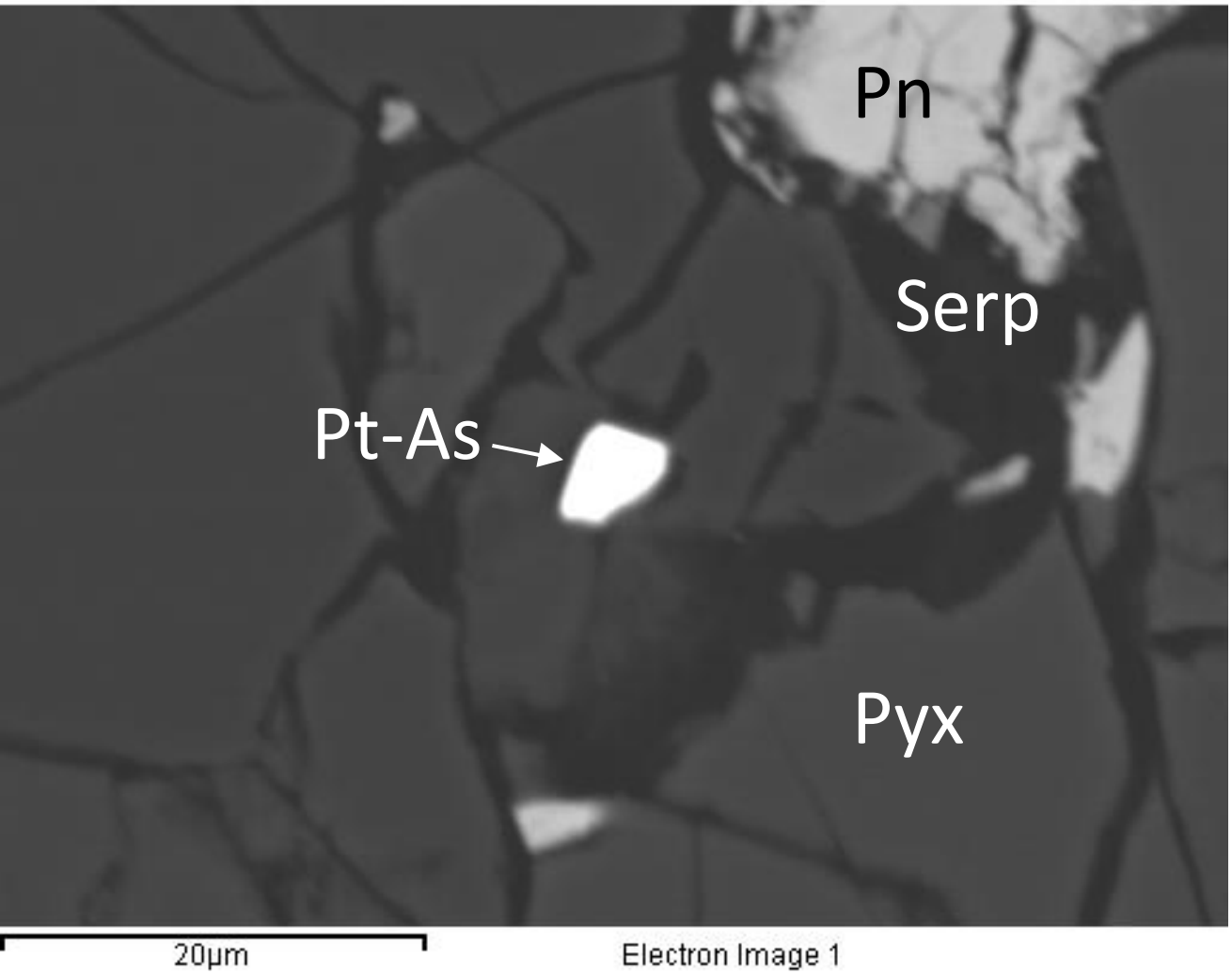
PTSR-34 H 1 Light



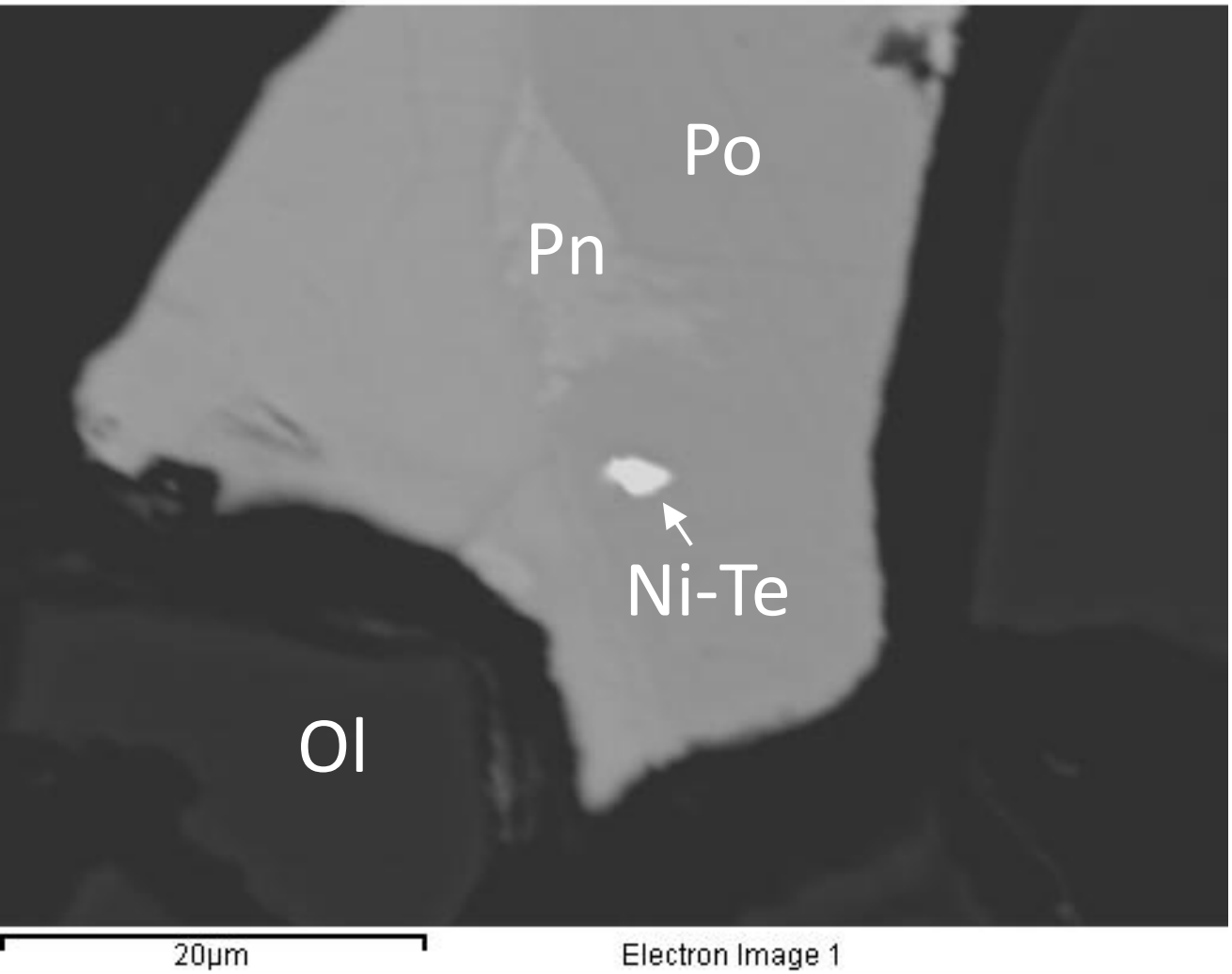
PTSR-34 I 1



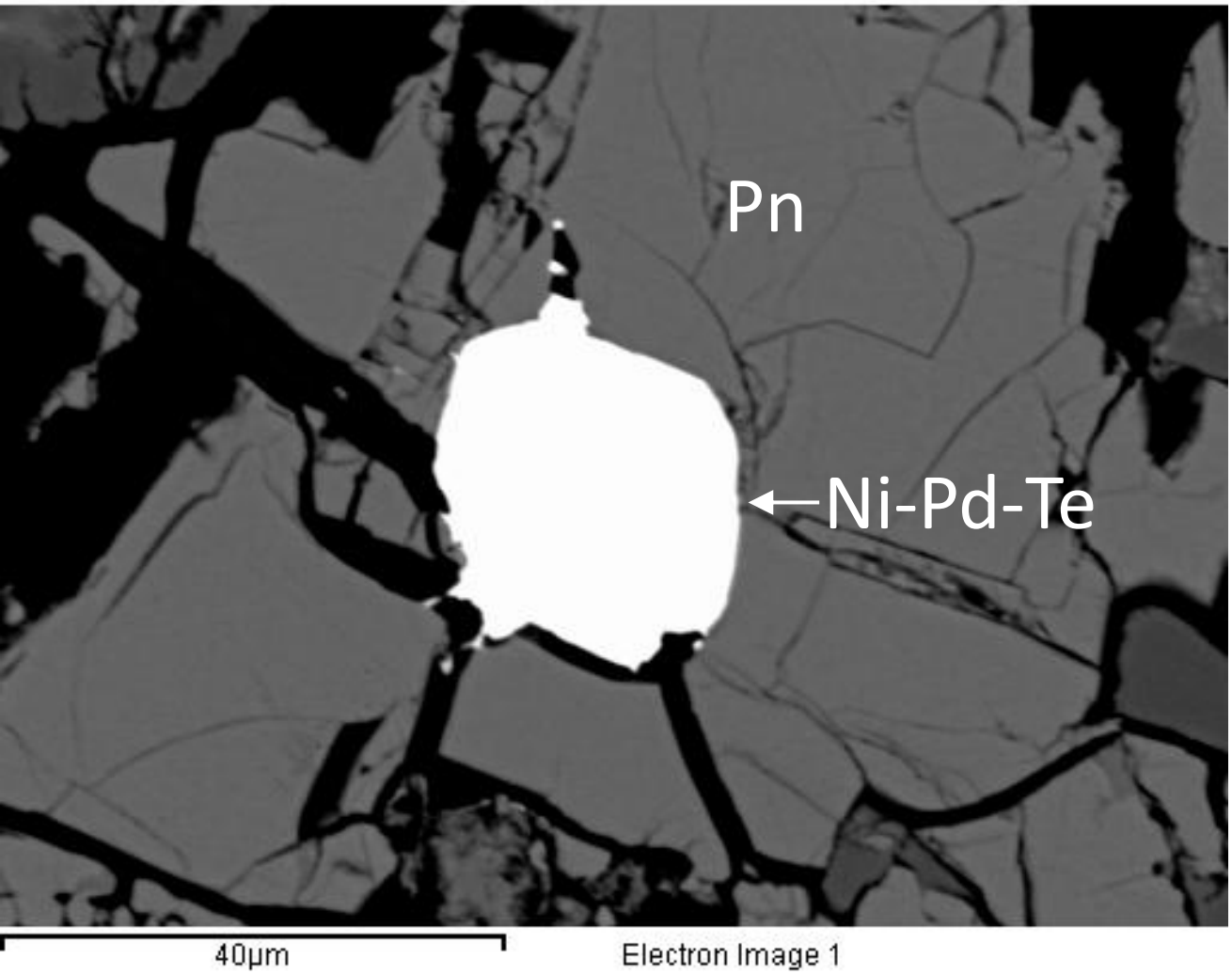
PTSR-34 J 1



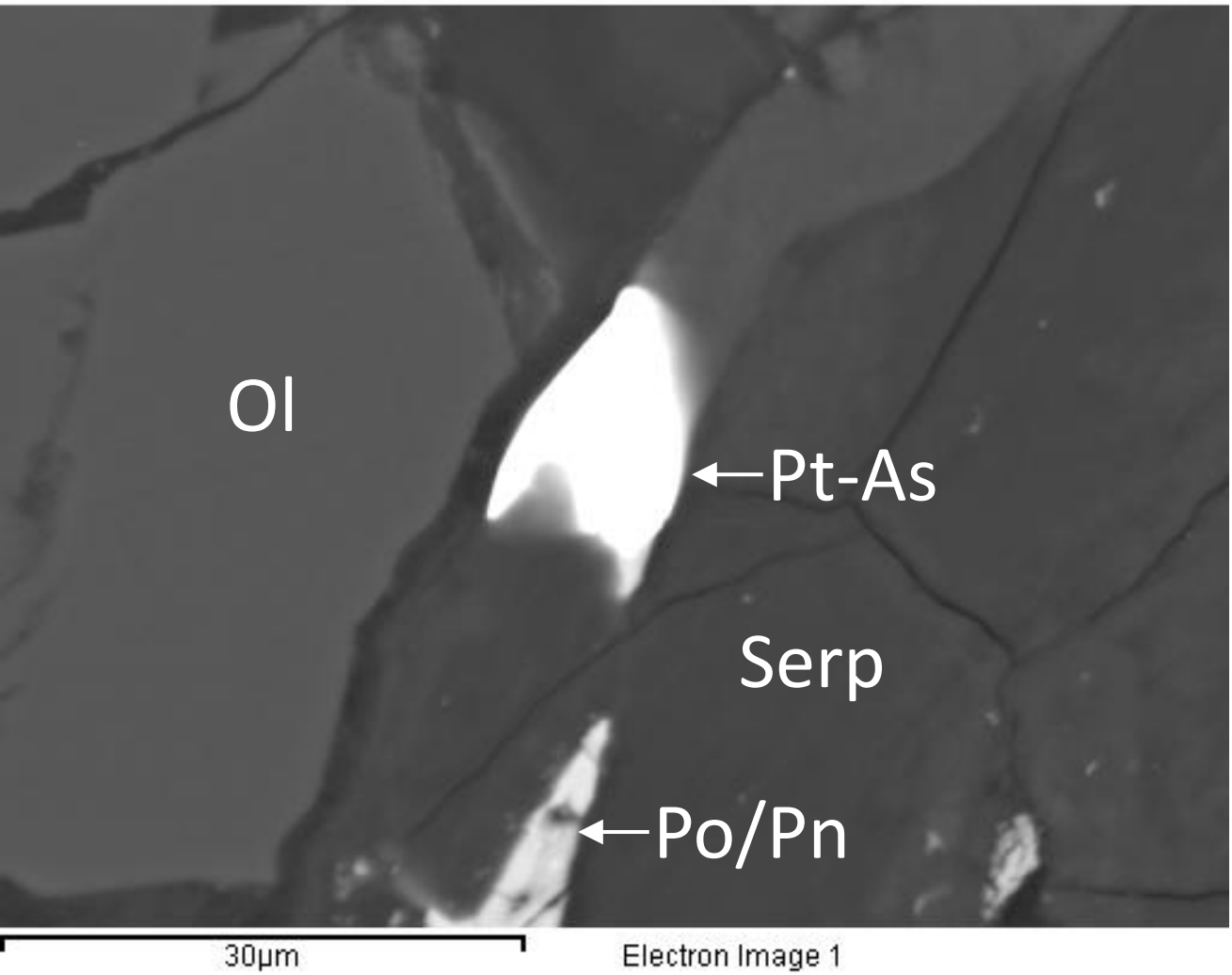
PTSR-34 K 1



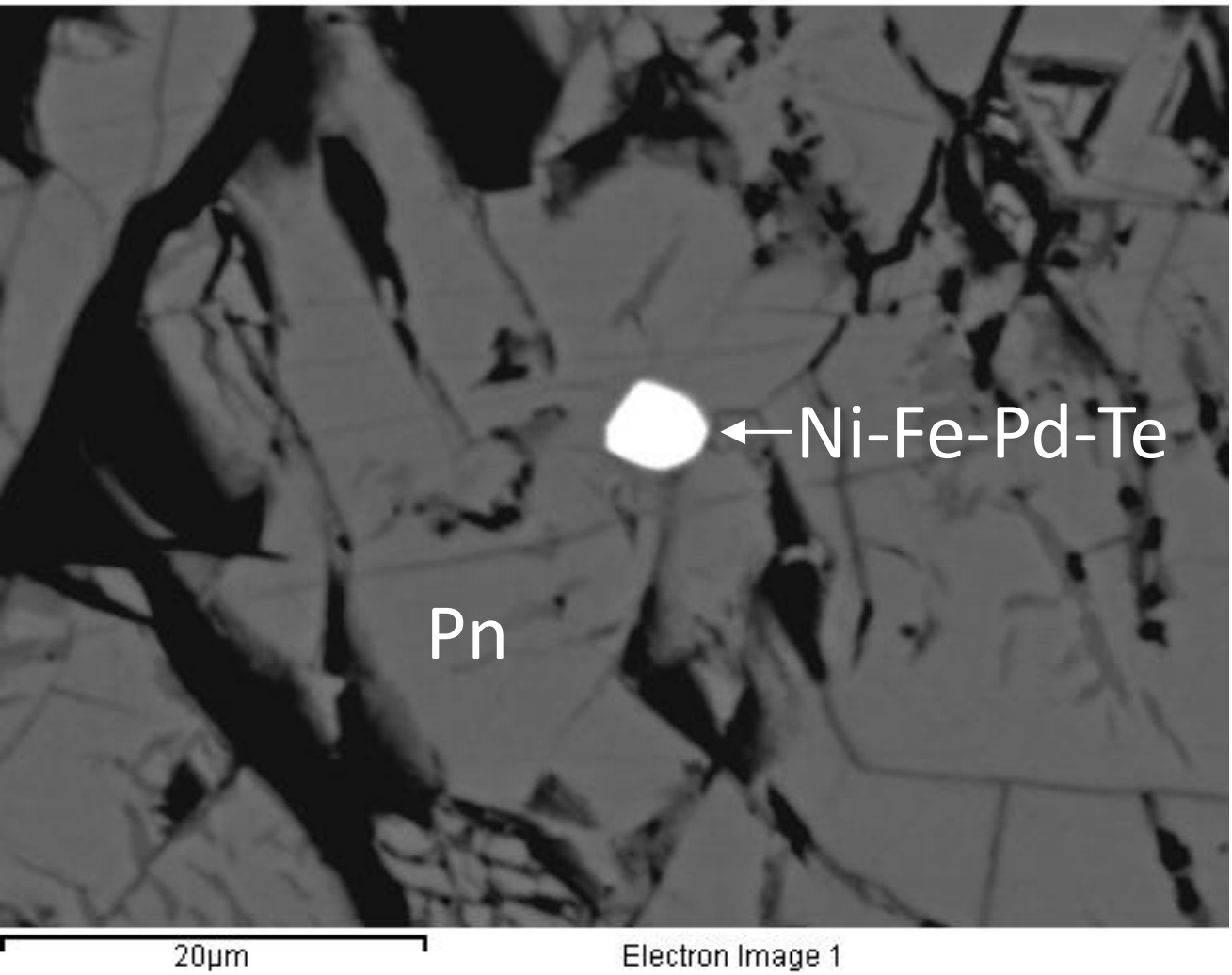
PTSR-34 L 1



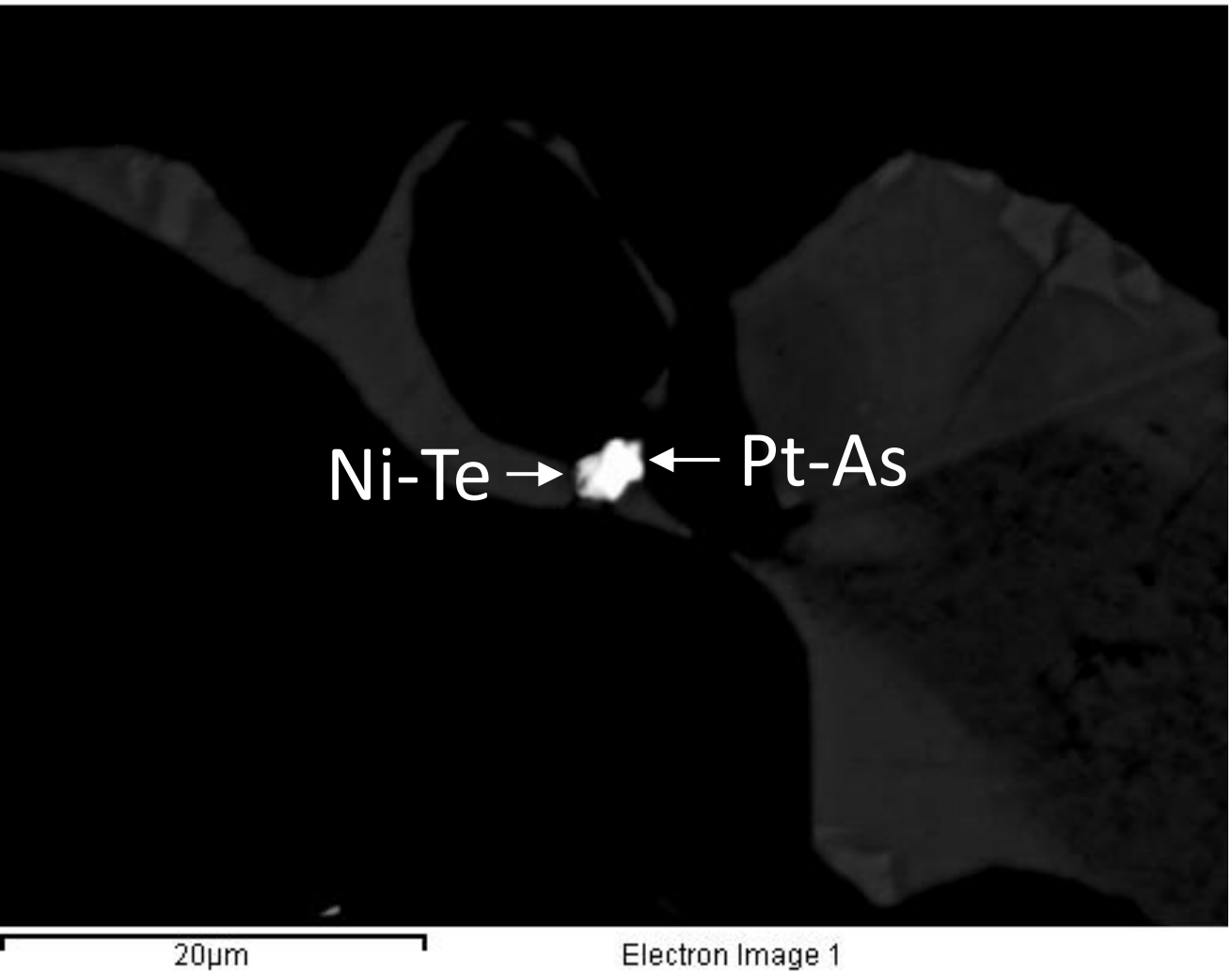
PTSR-34 M 1



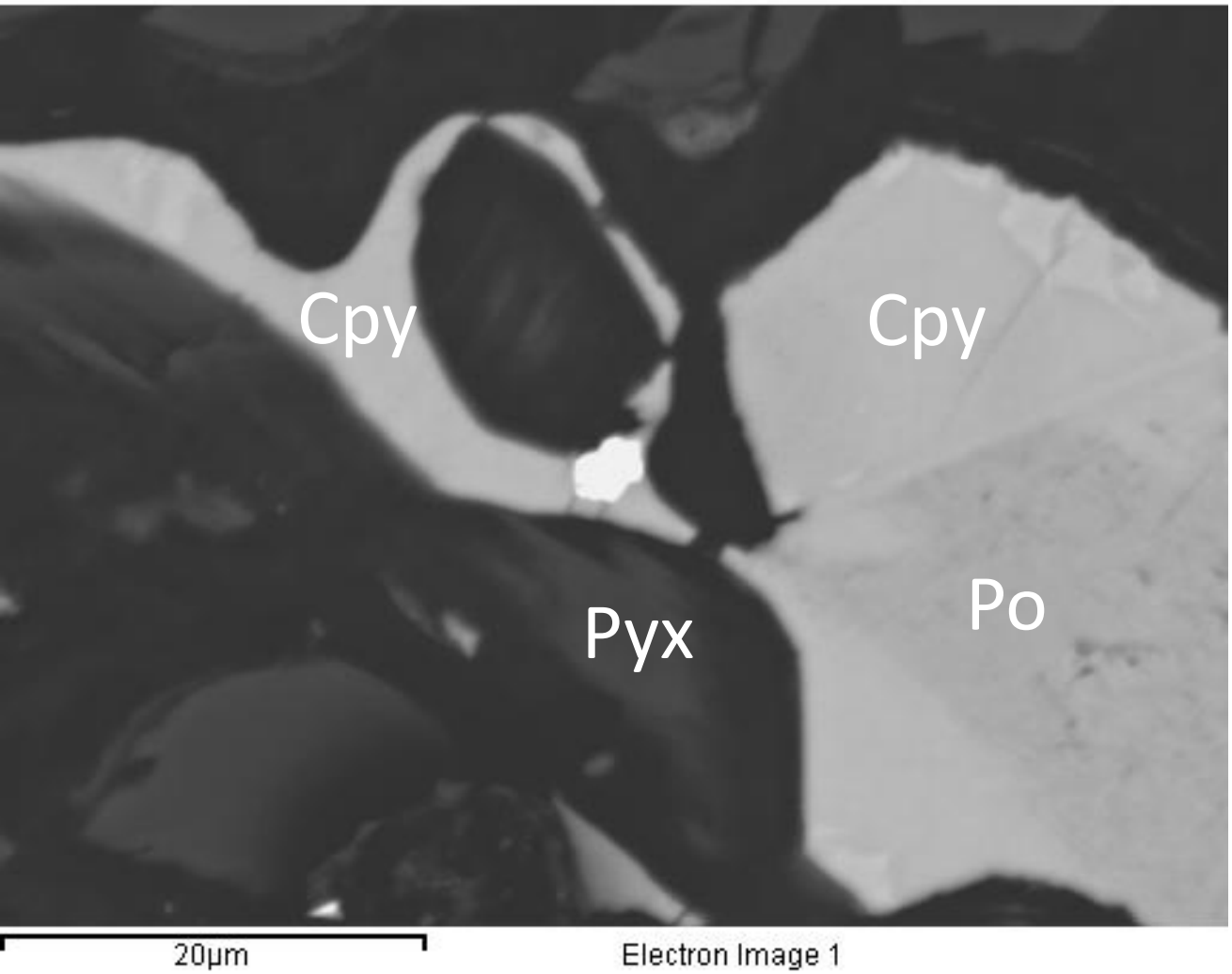
PTSR-34 N 1



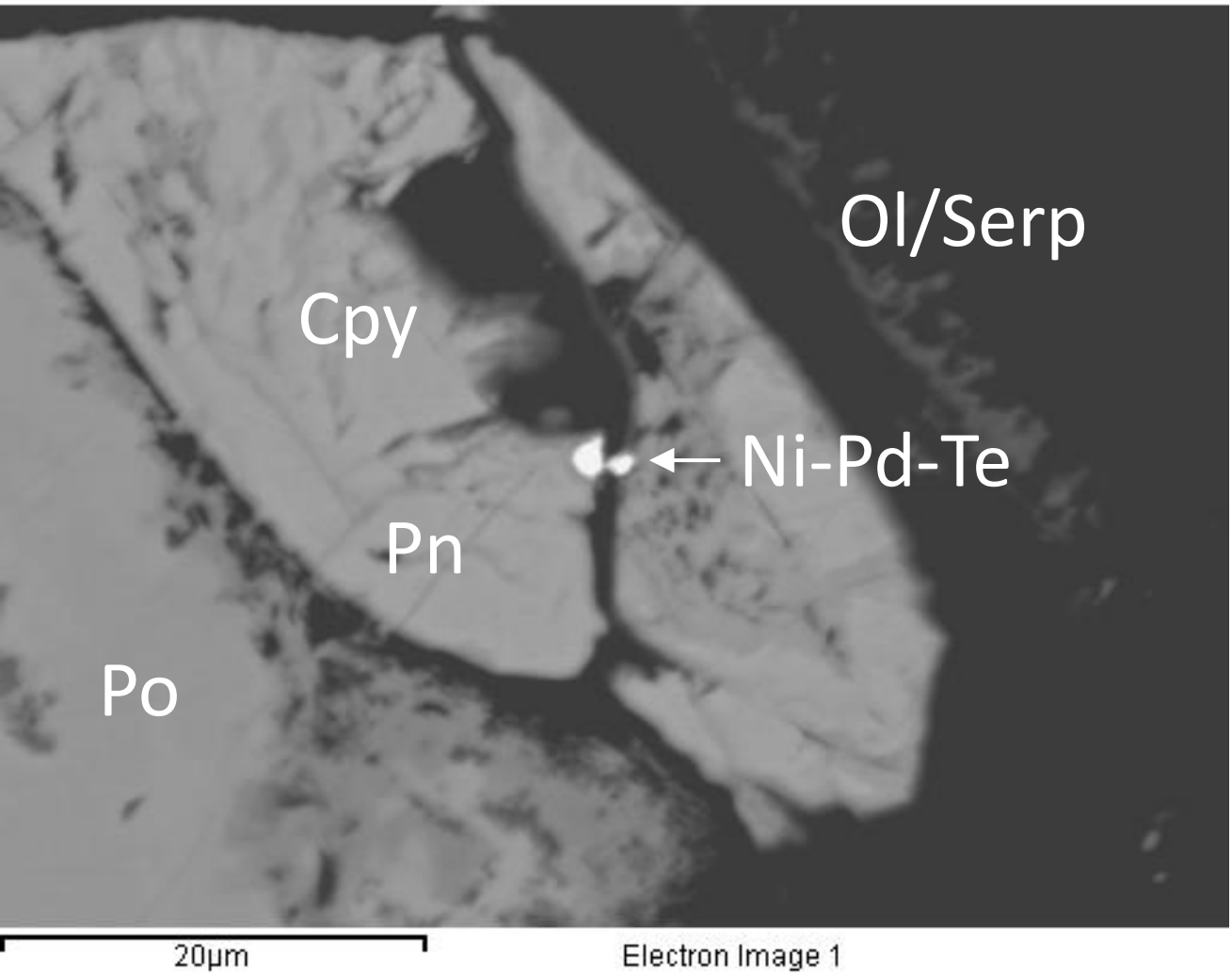
PTSR-34 O 1



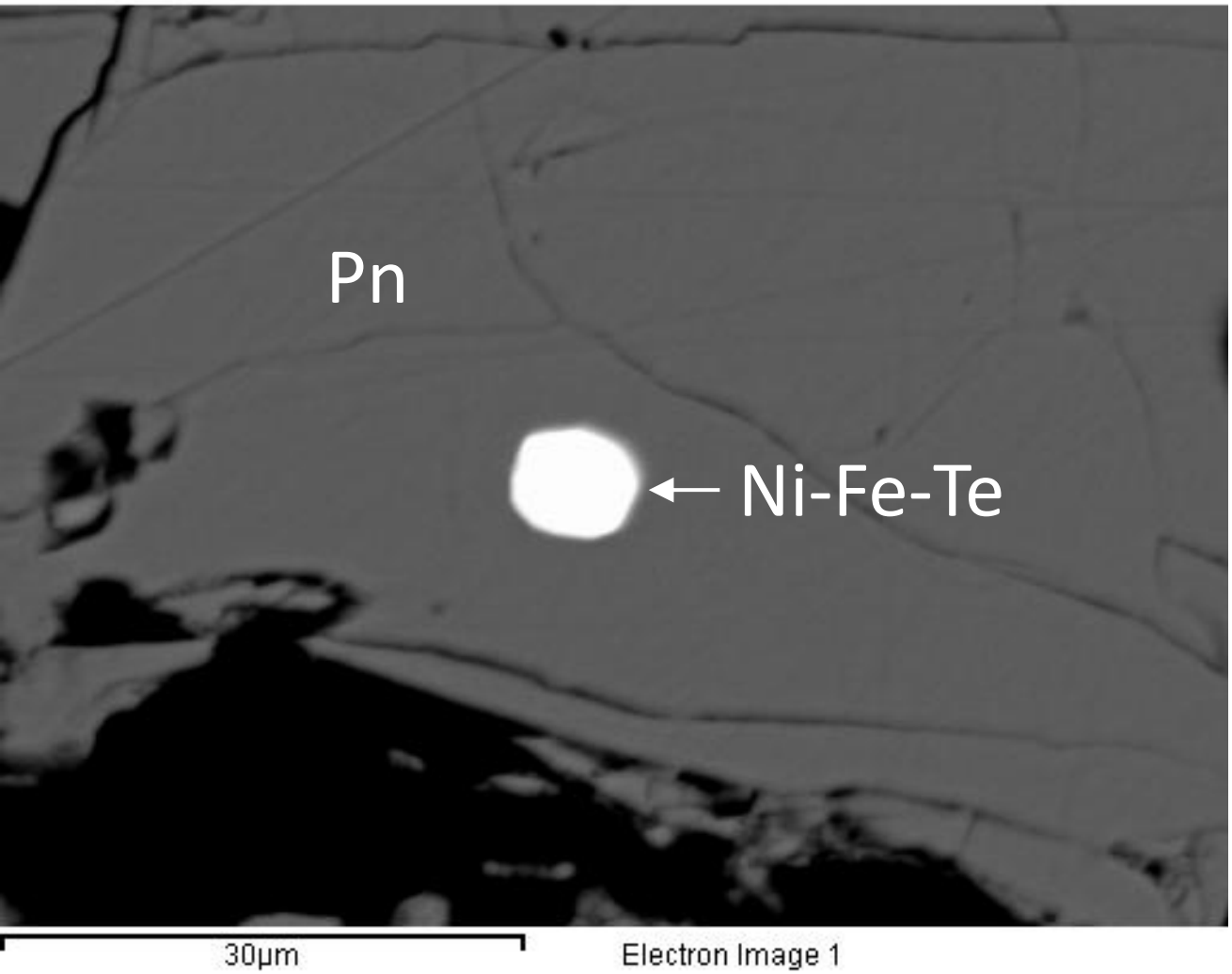
PTSR-34 O 1 Light



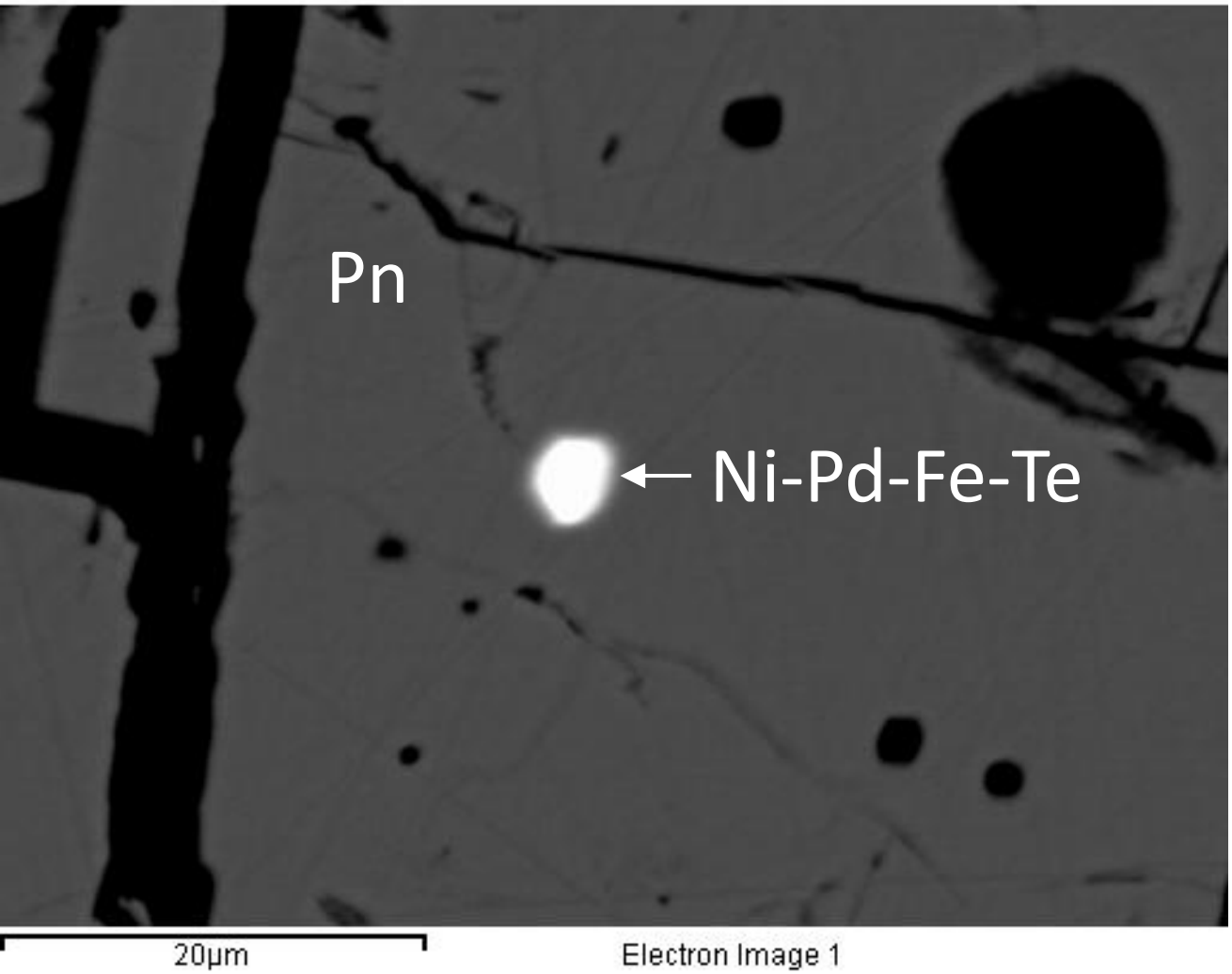
PTSR-34 P 1



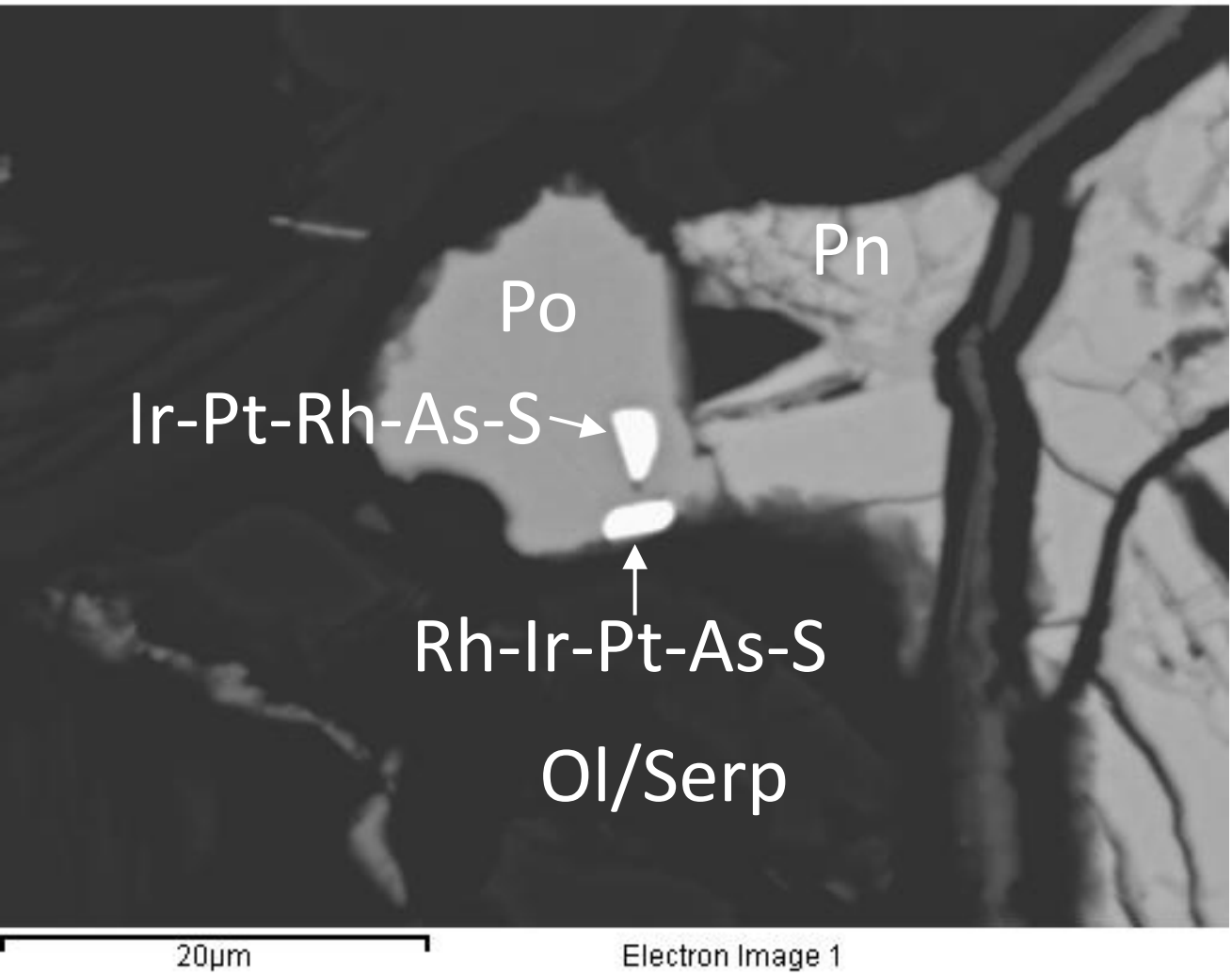
PTSR-34 Q 1



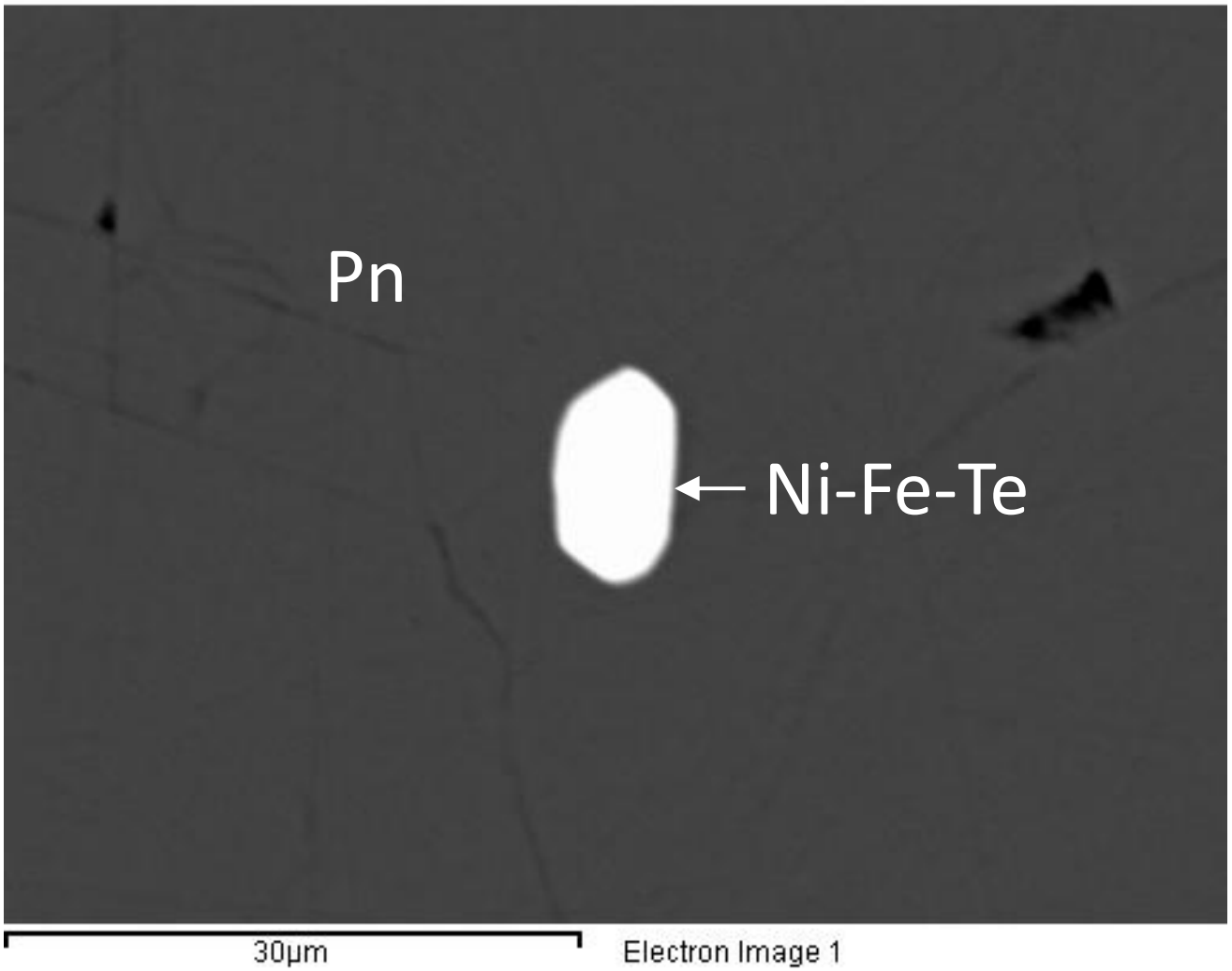
PTSR-34 R 1



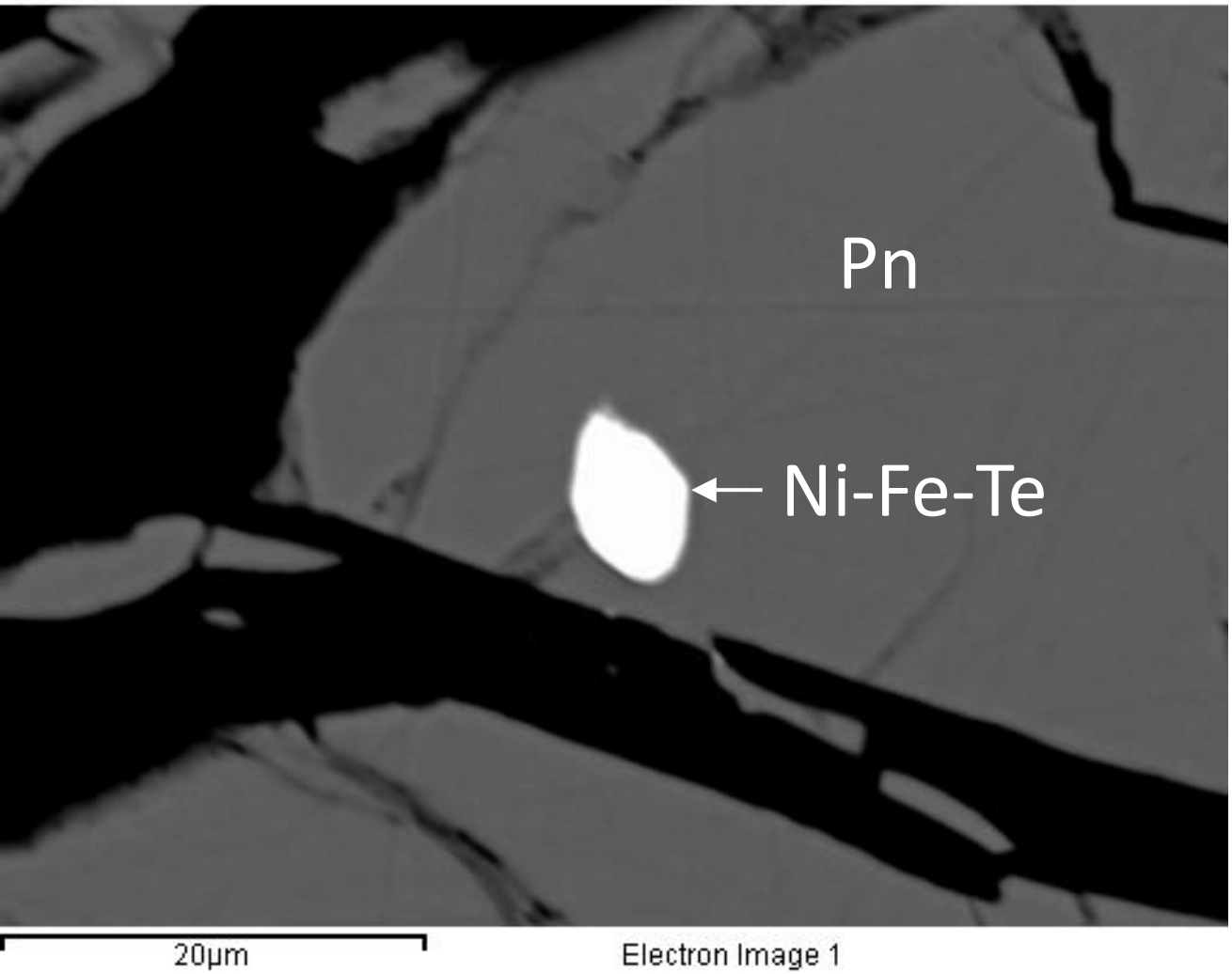
PTSR-34 S 1-2



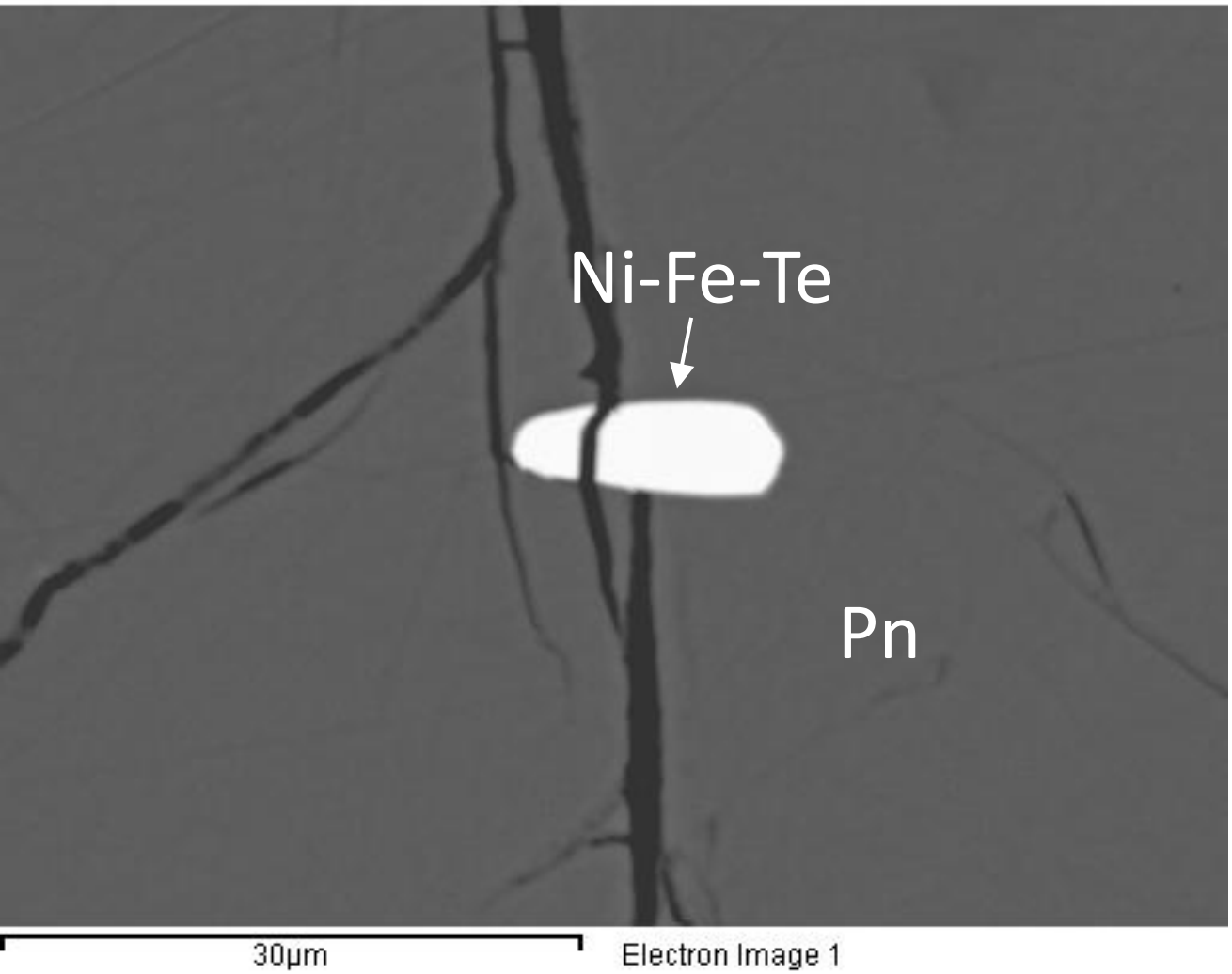
PTSR-34 T 1



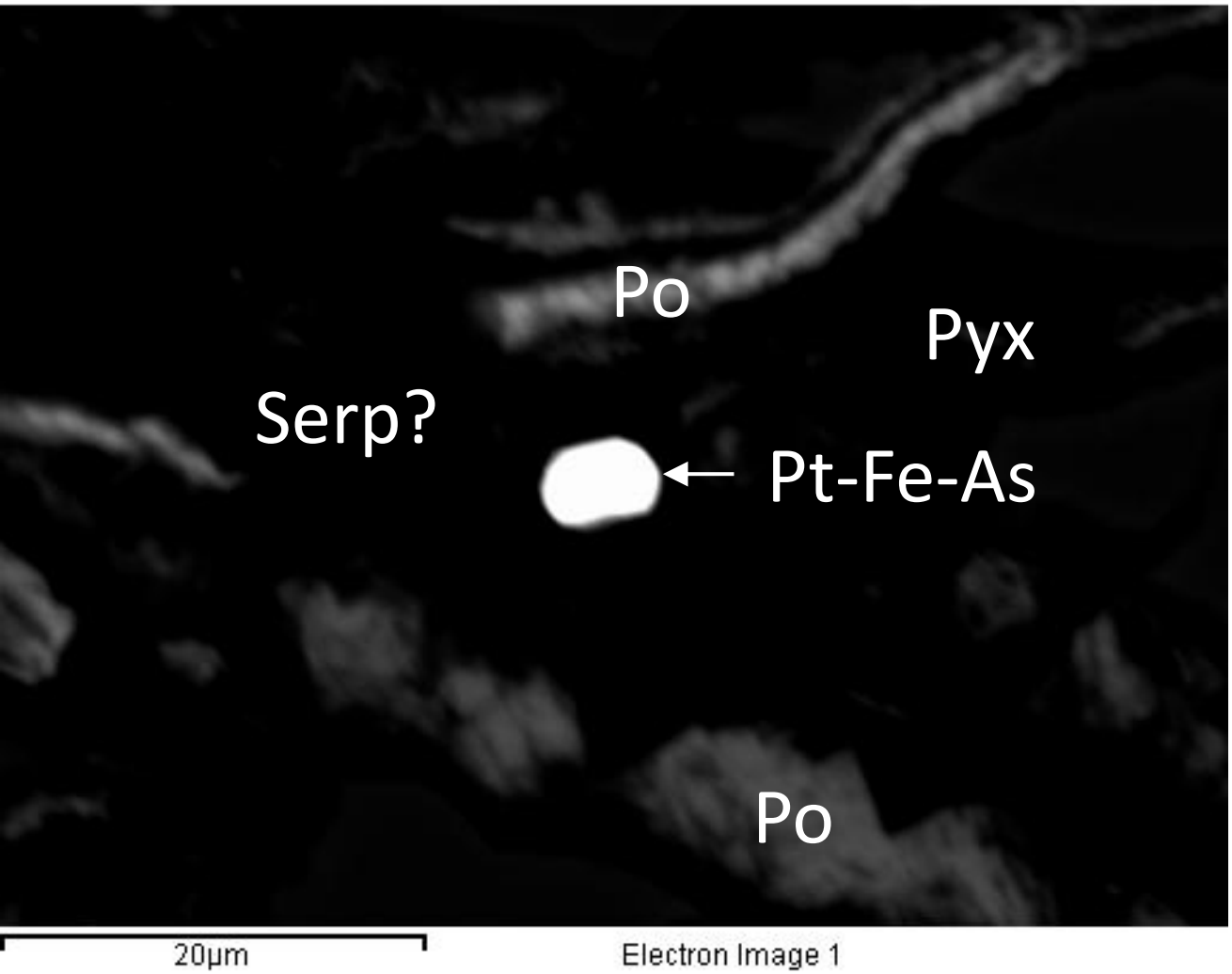
PTSR-34 U 1



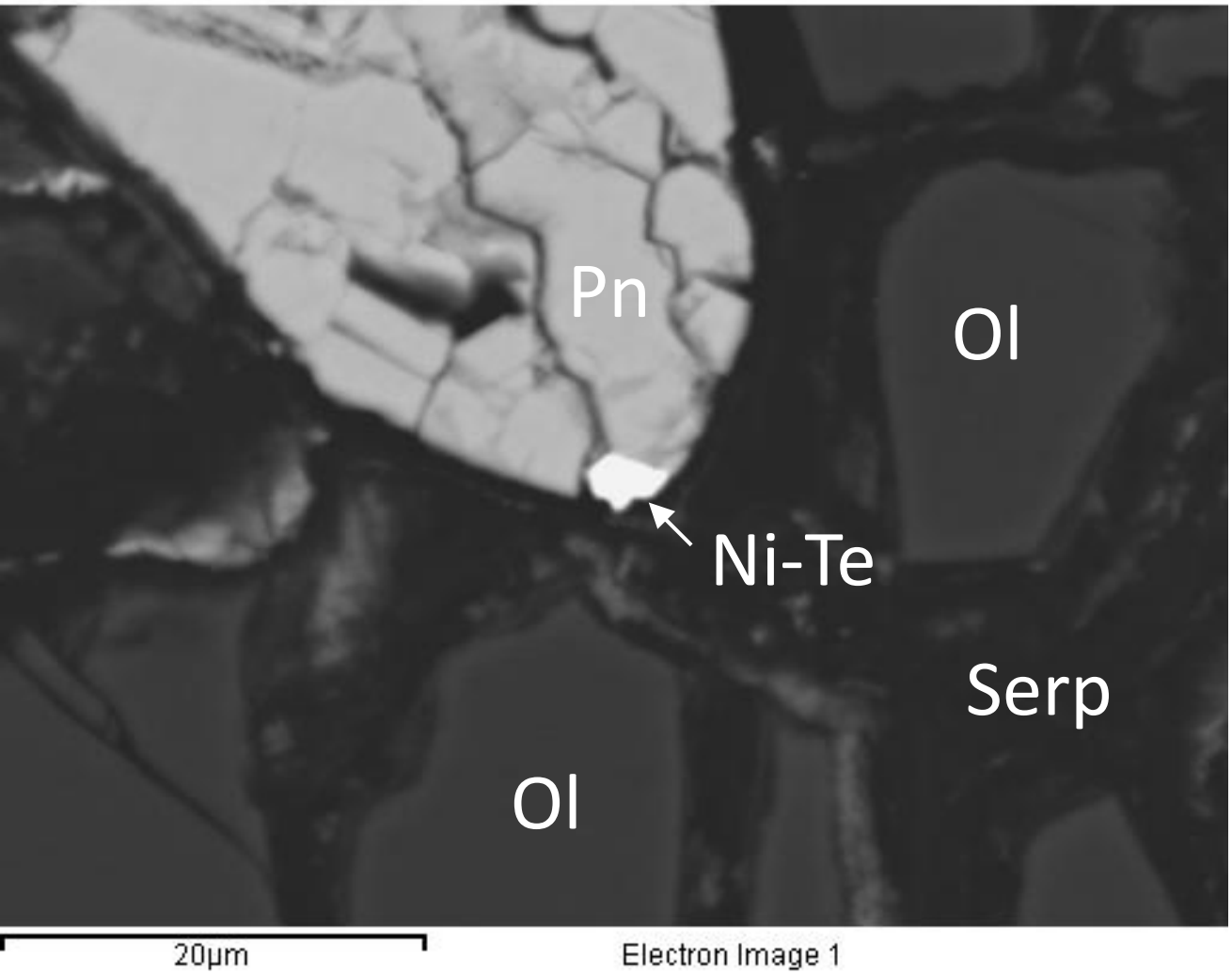
PTSR-34 V 1



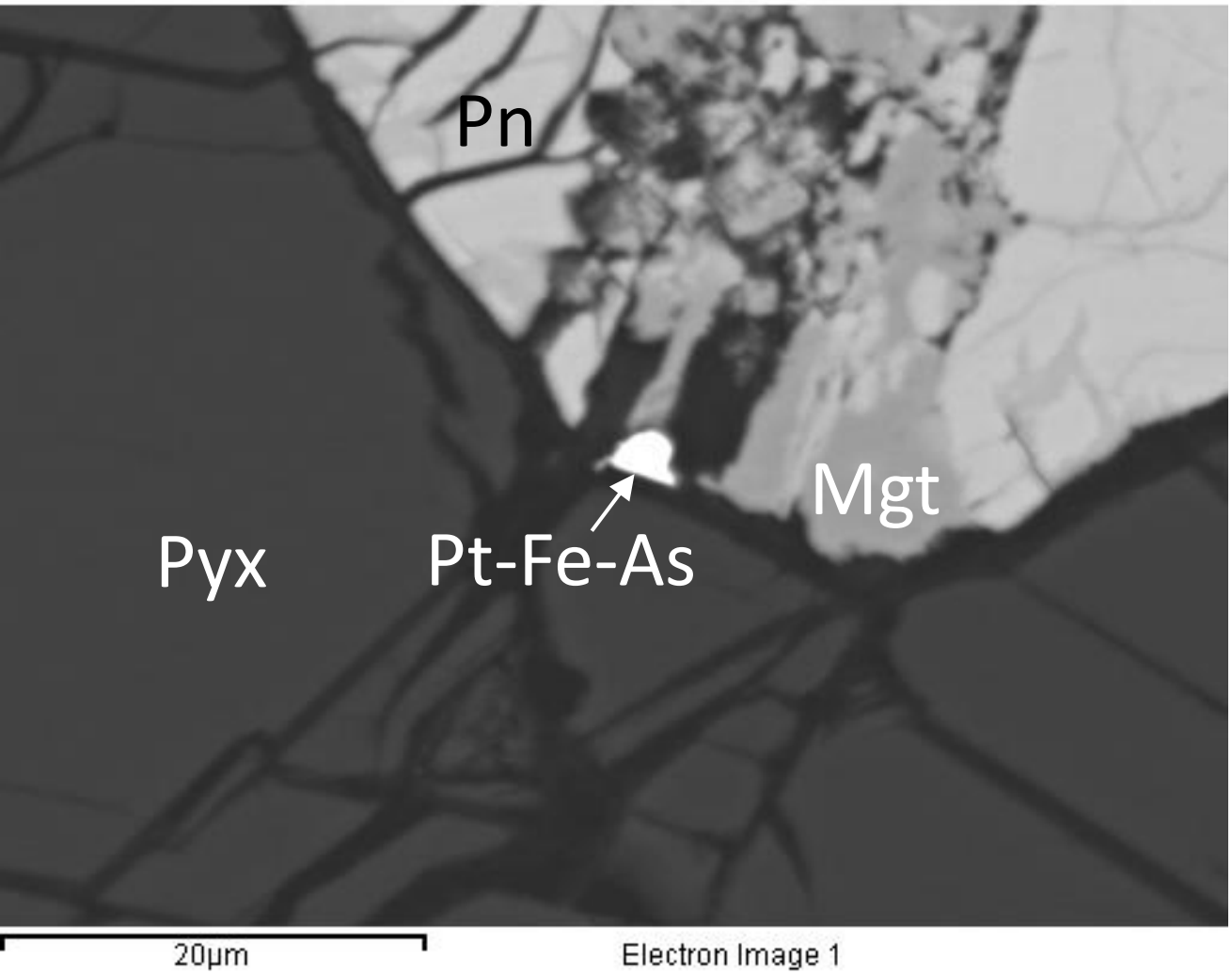
PTSR-34 W 1



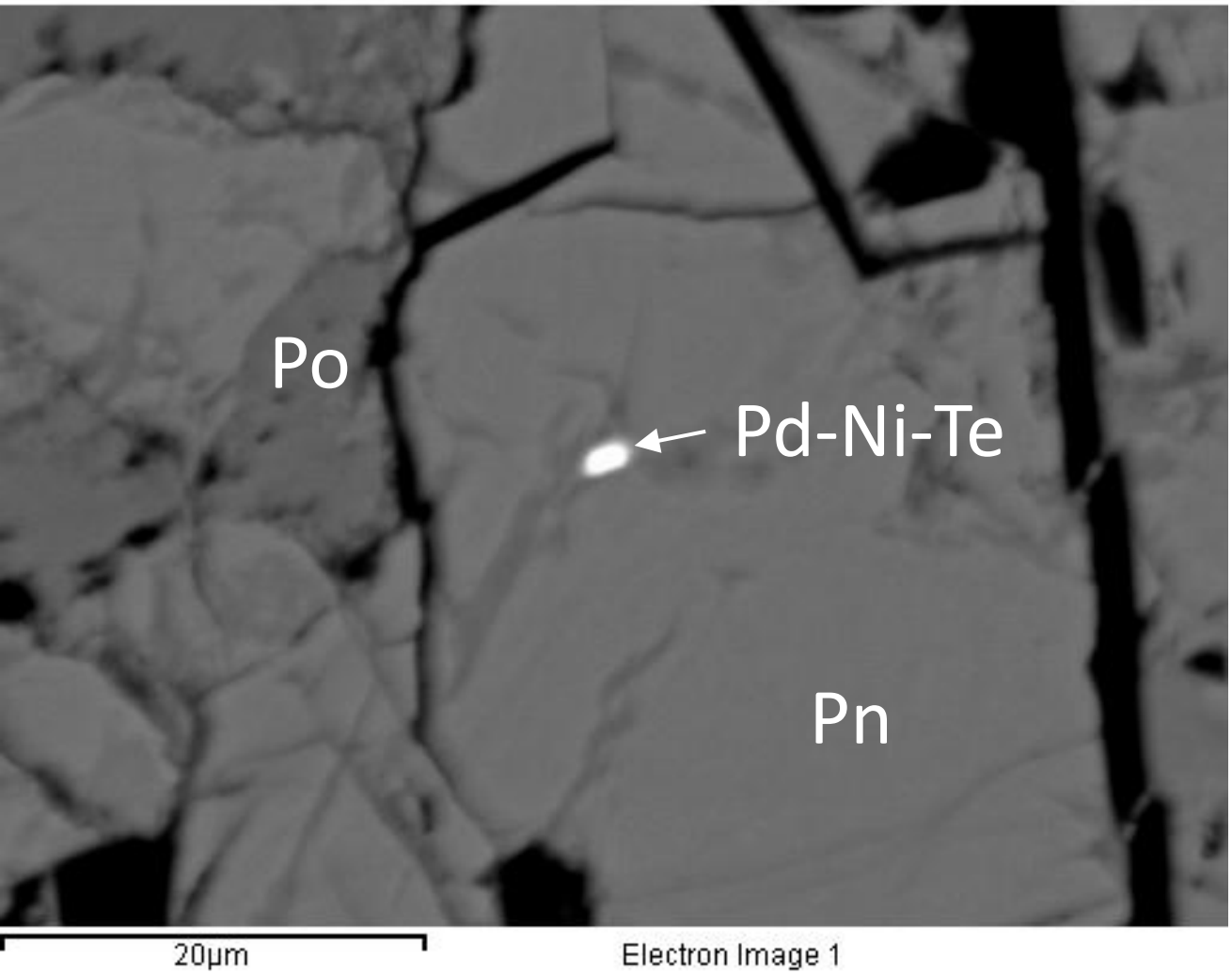
PTSR-34 X 1



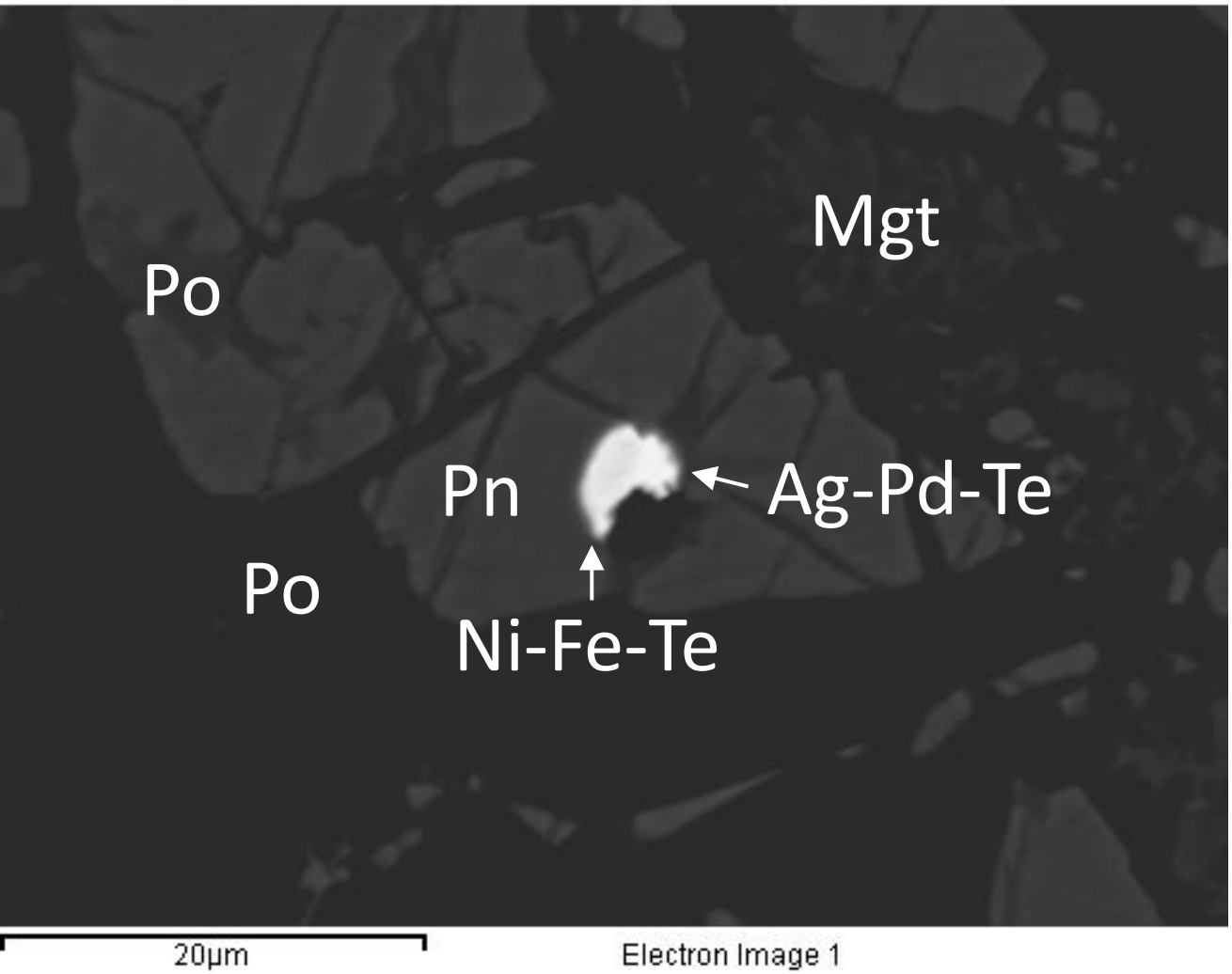
PTSR-34 Y 1



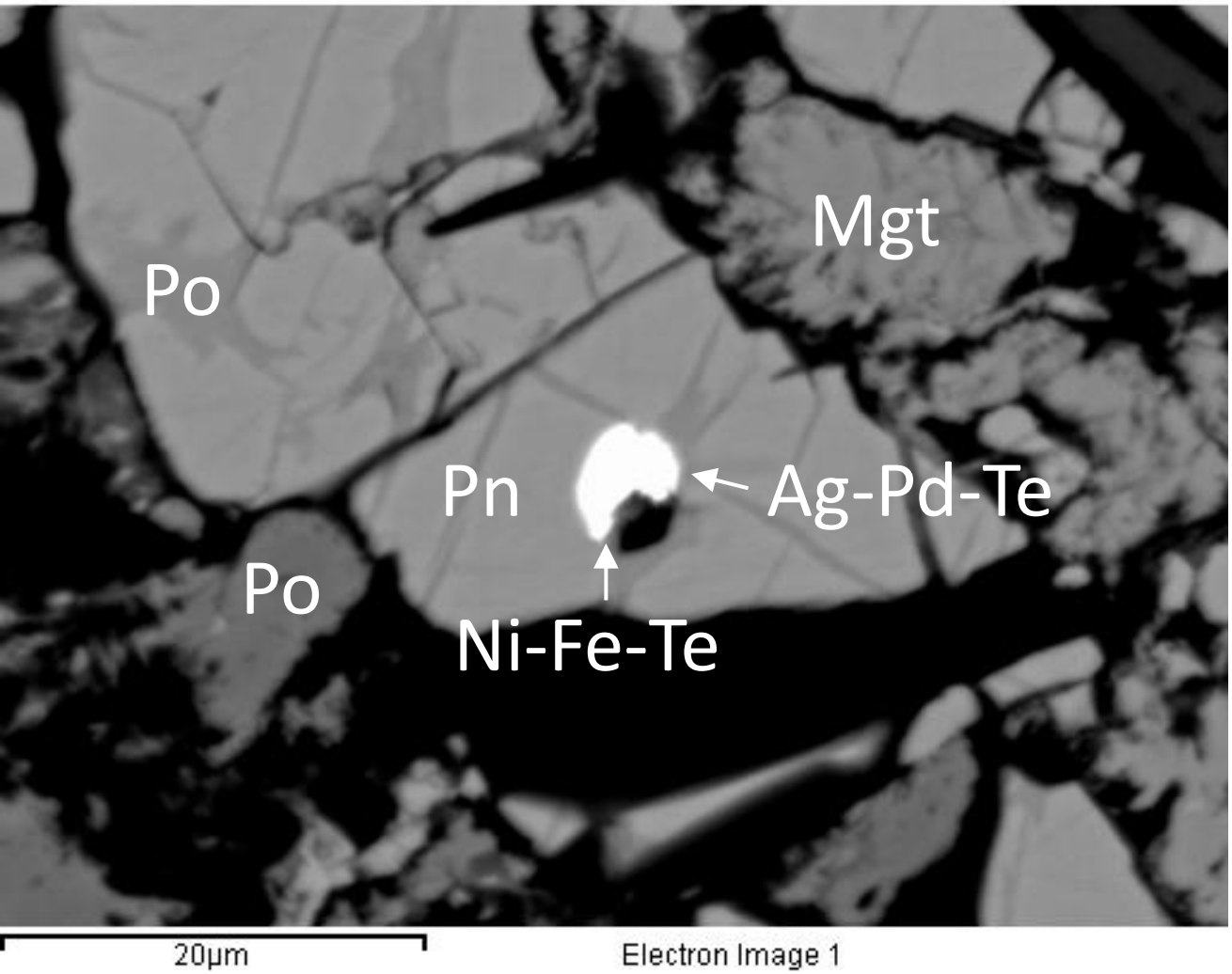
PTSR-34 Z 1



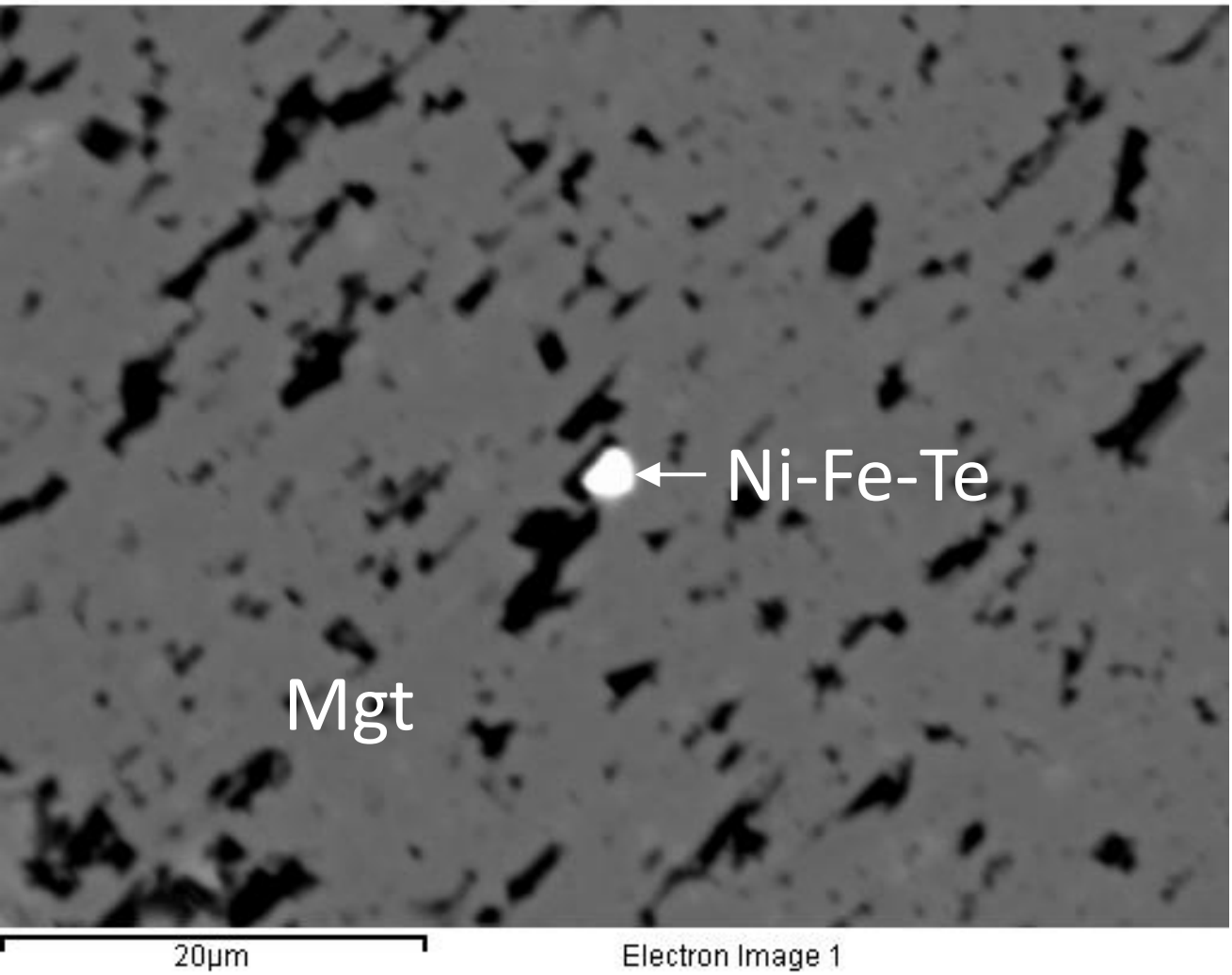
PTSR-34 AA 1-2



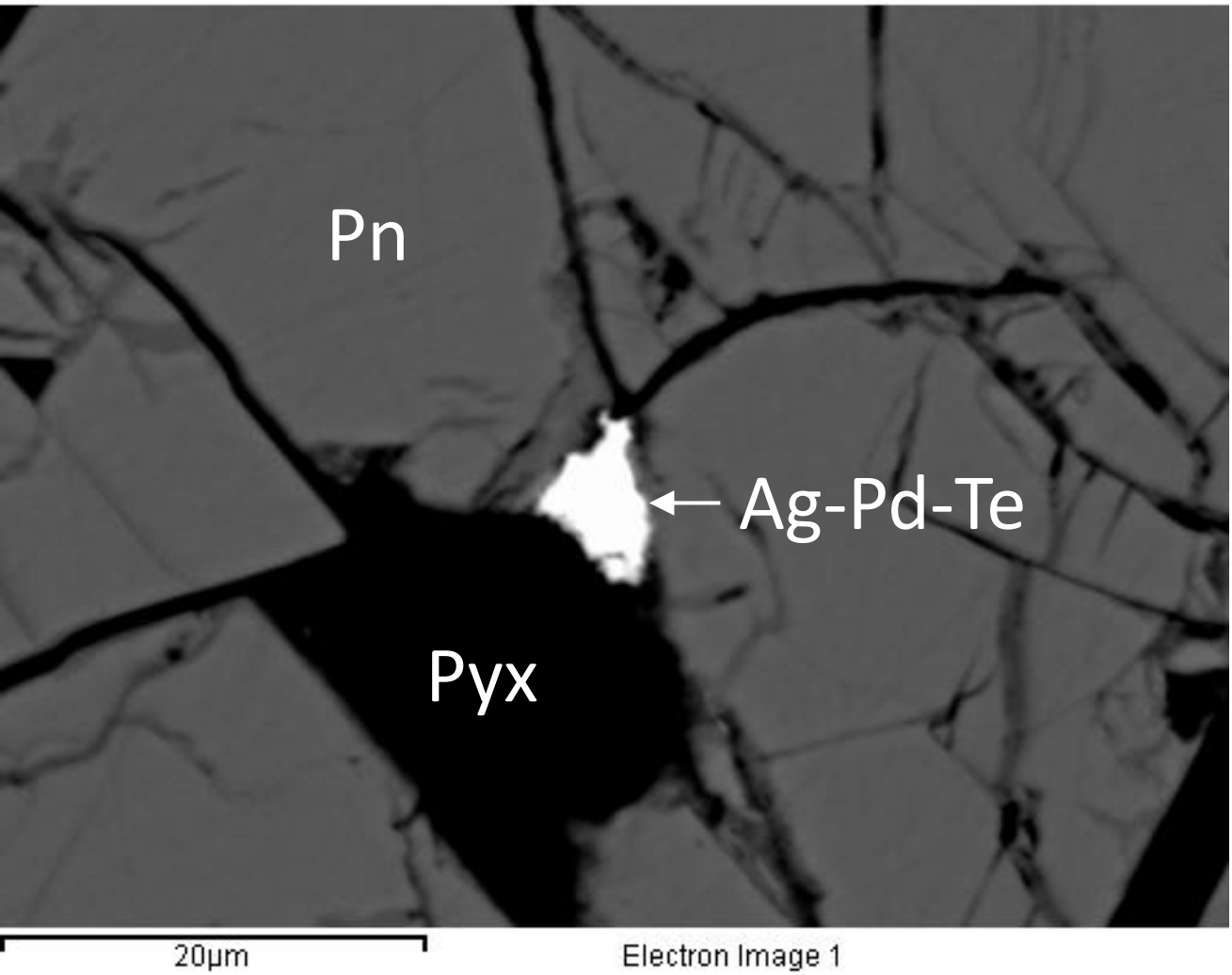
PTSR-34 AA 1-2 Light



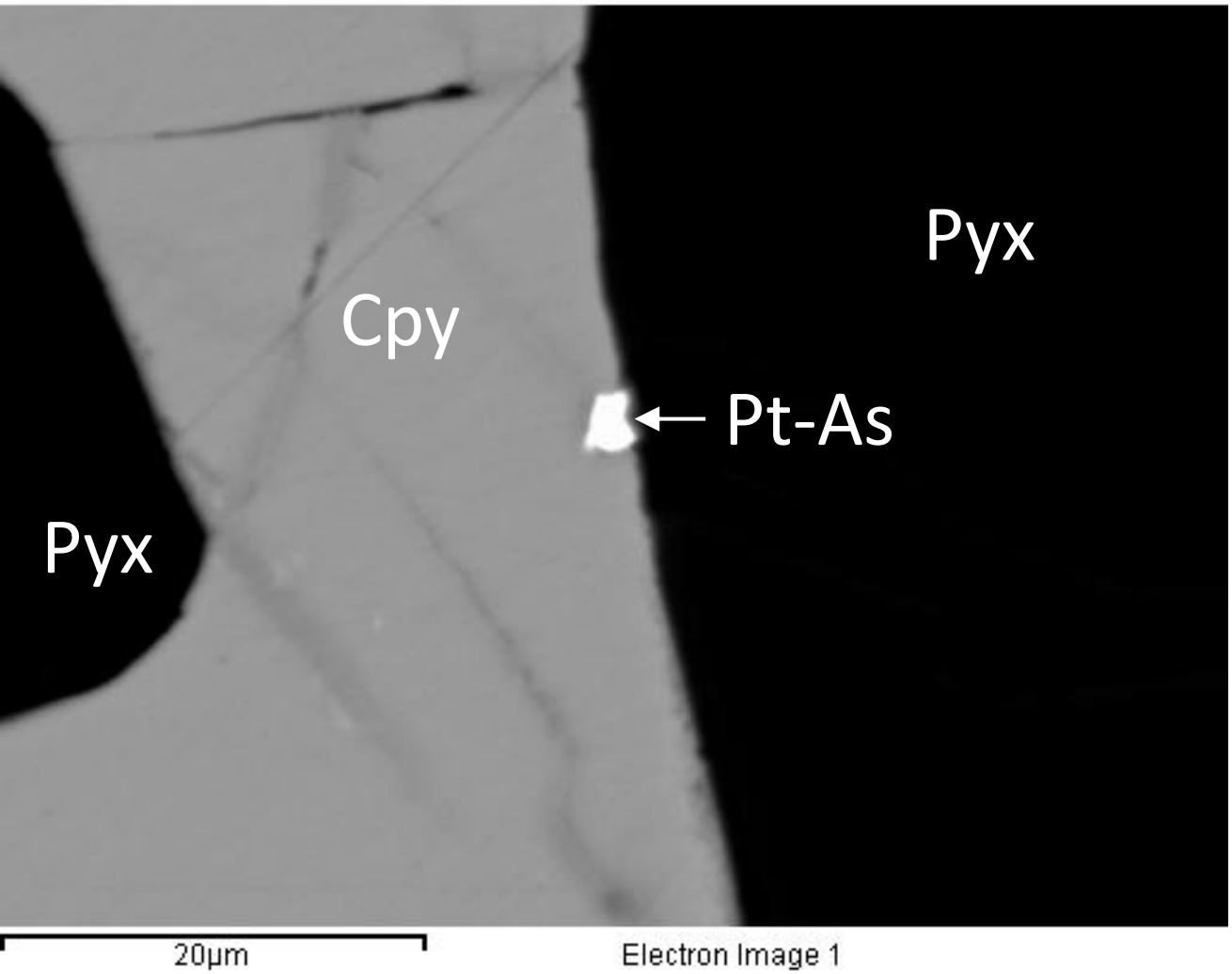
PTSR-34 AB 1



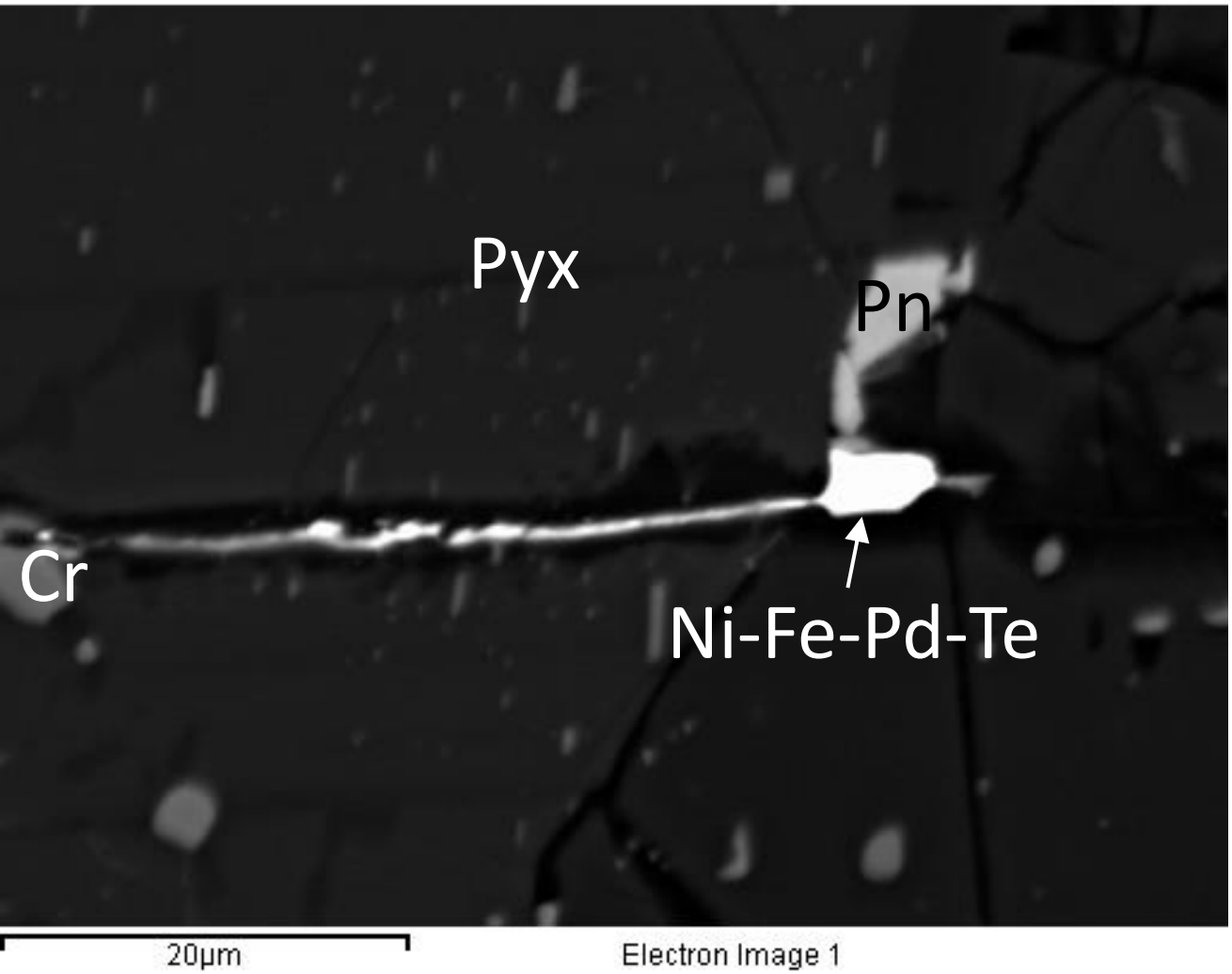
PTSR-34 AC 1



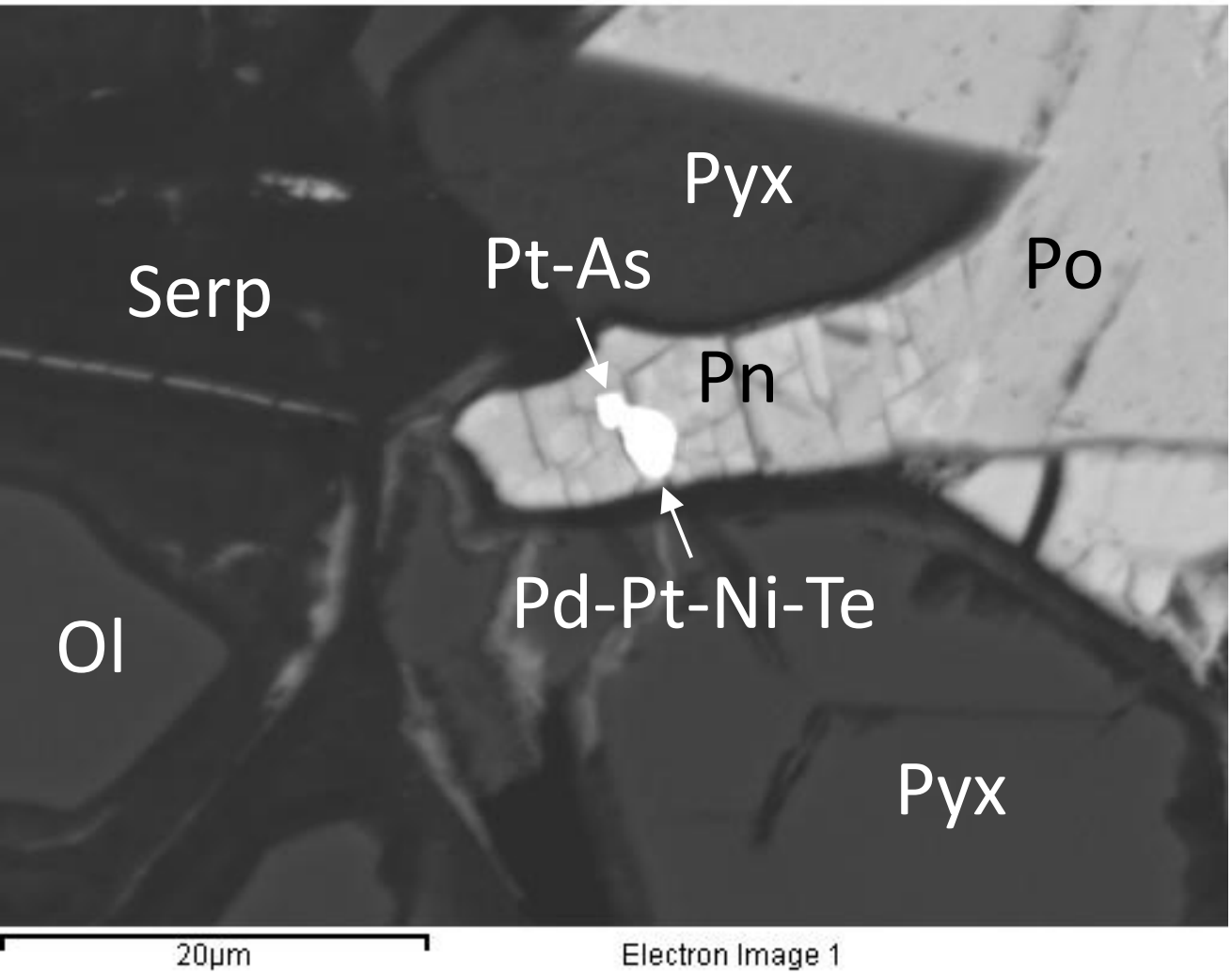
PTSR-34 AD 1



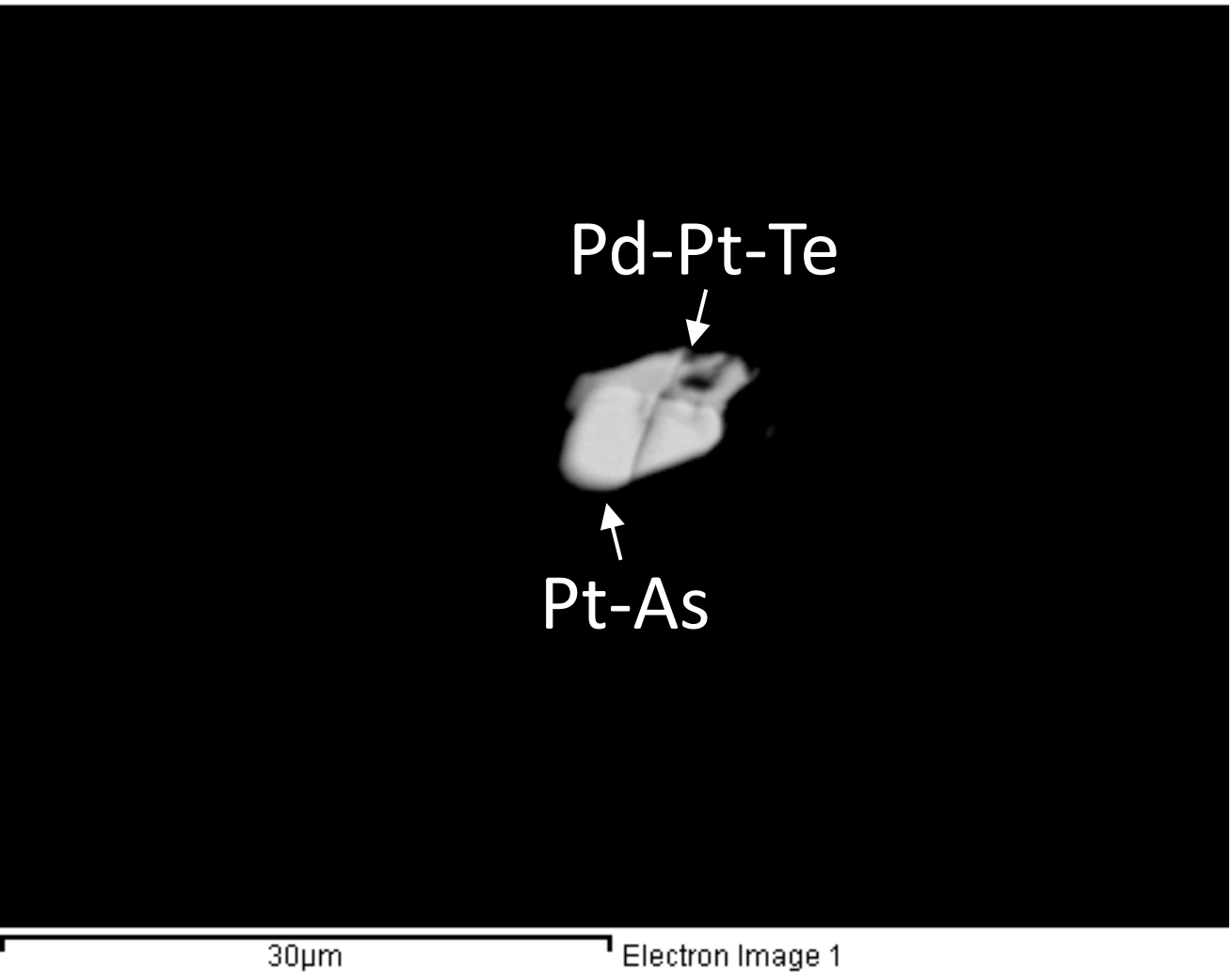
PTSR-35 A 1-2



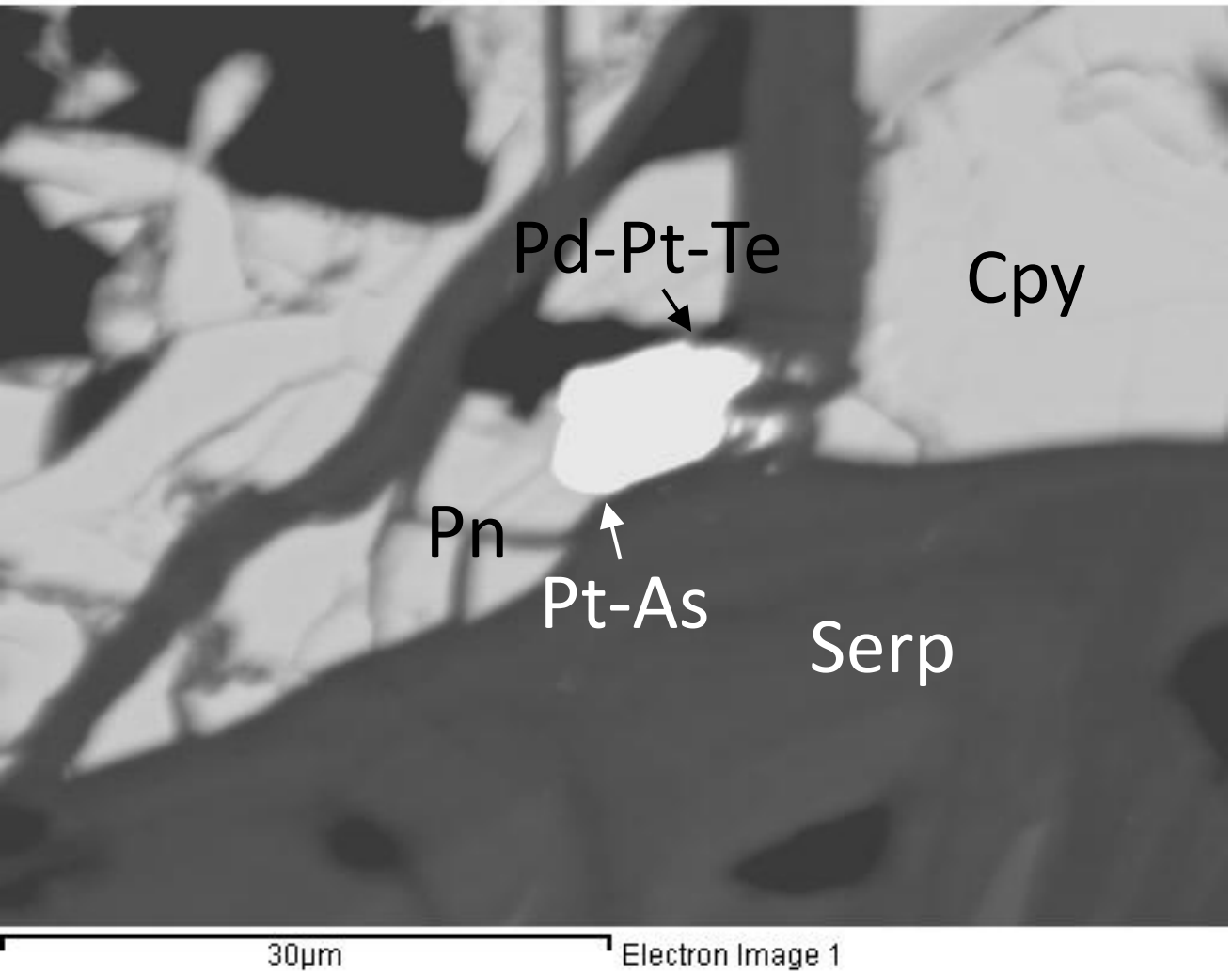
PTSR-35 B 1-2



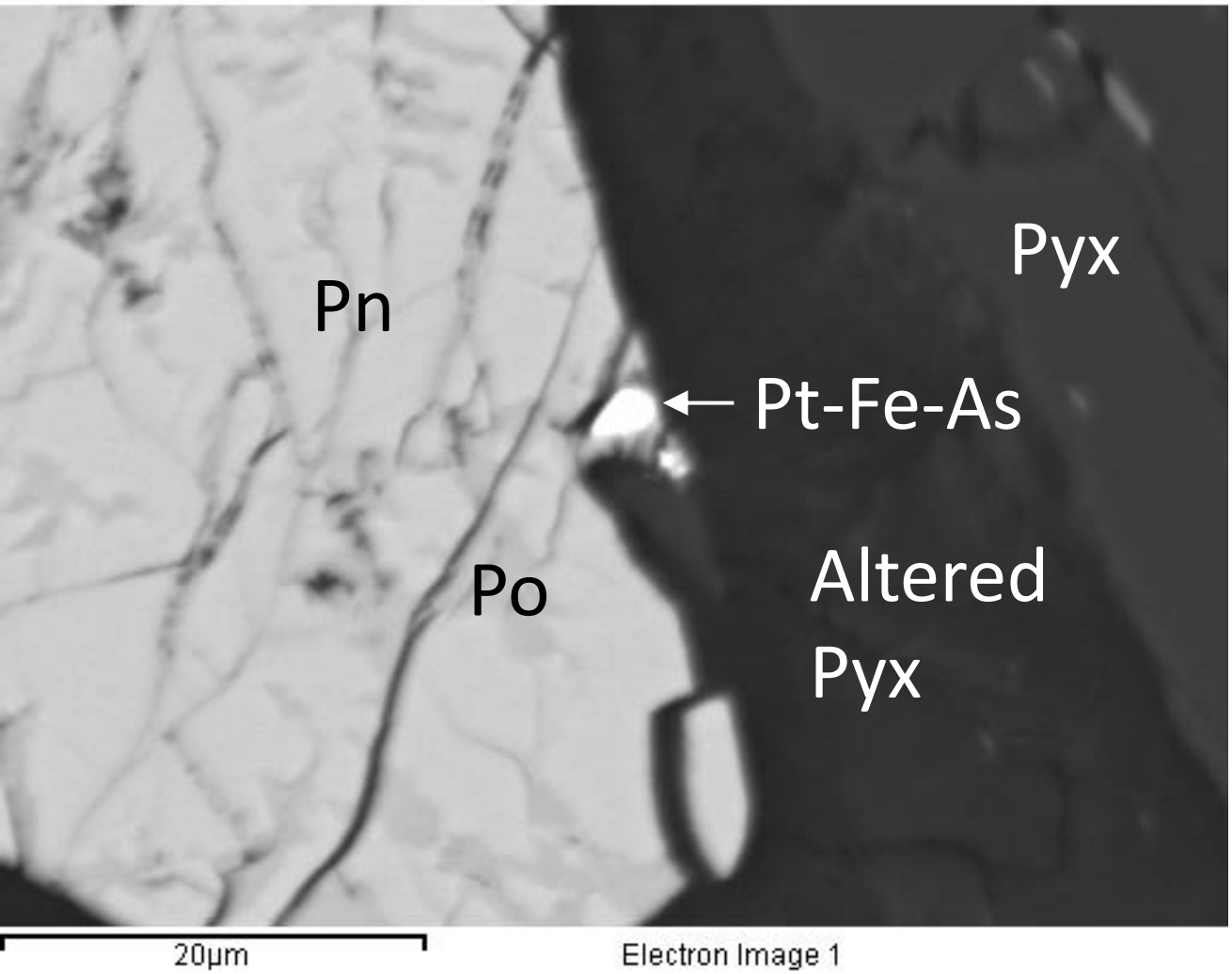
PTSR-35 C 1-2



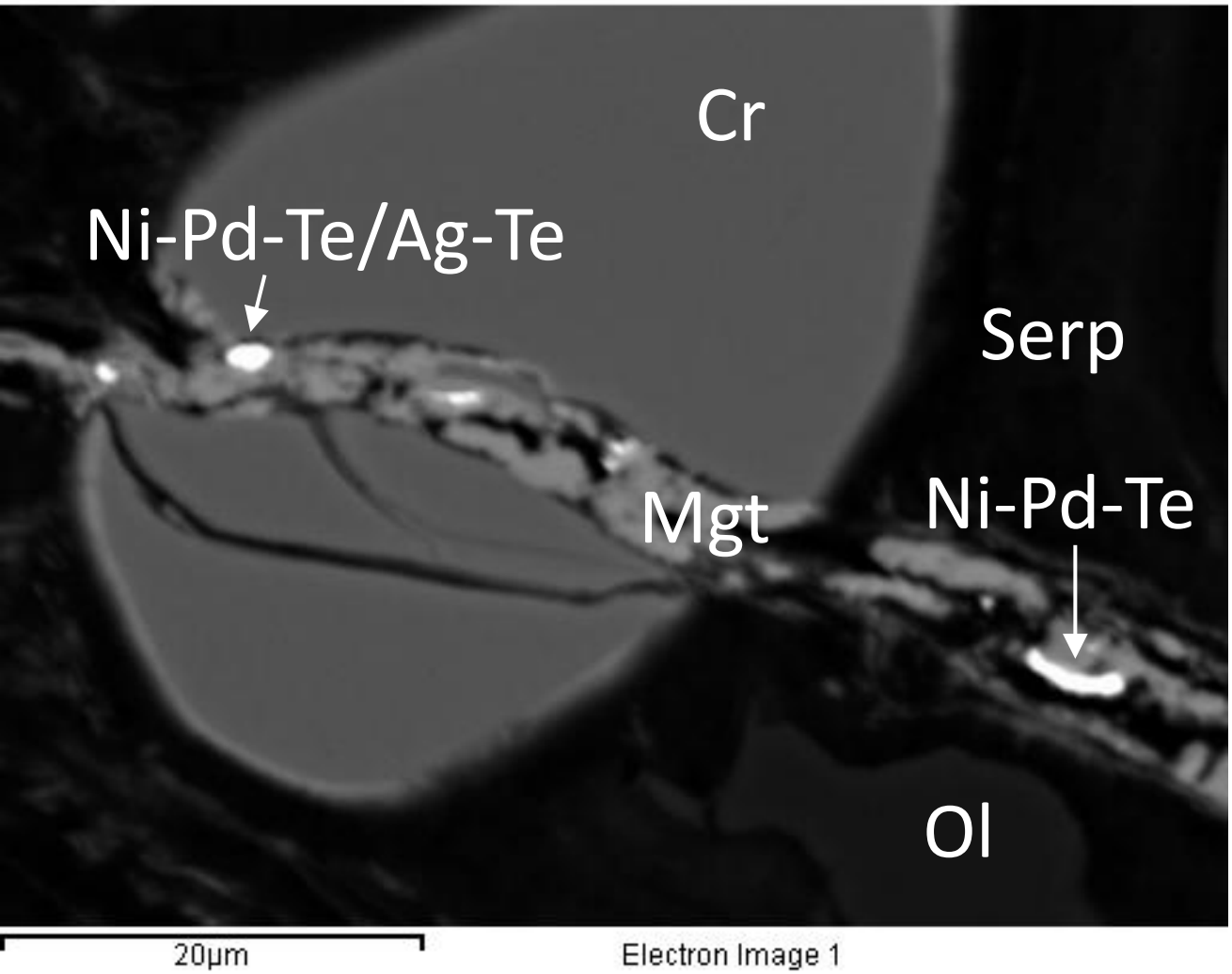
PTSR-35 C 1-2 Light



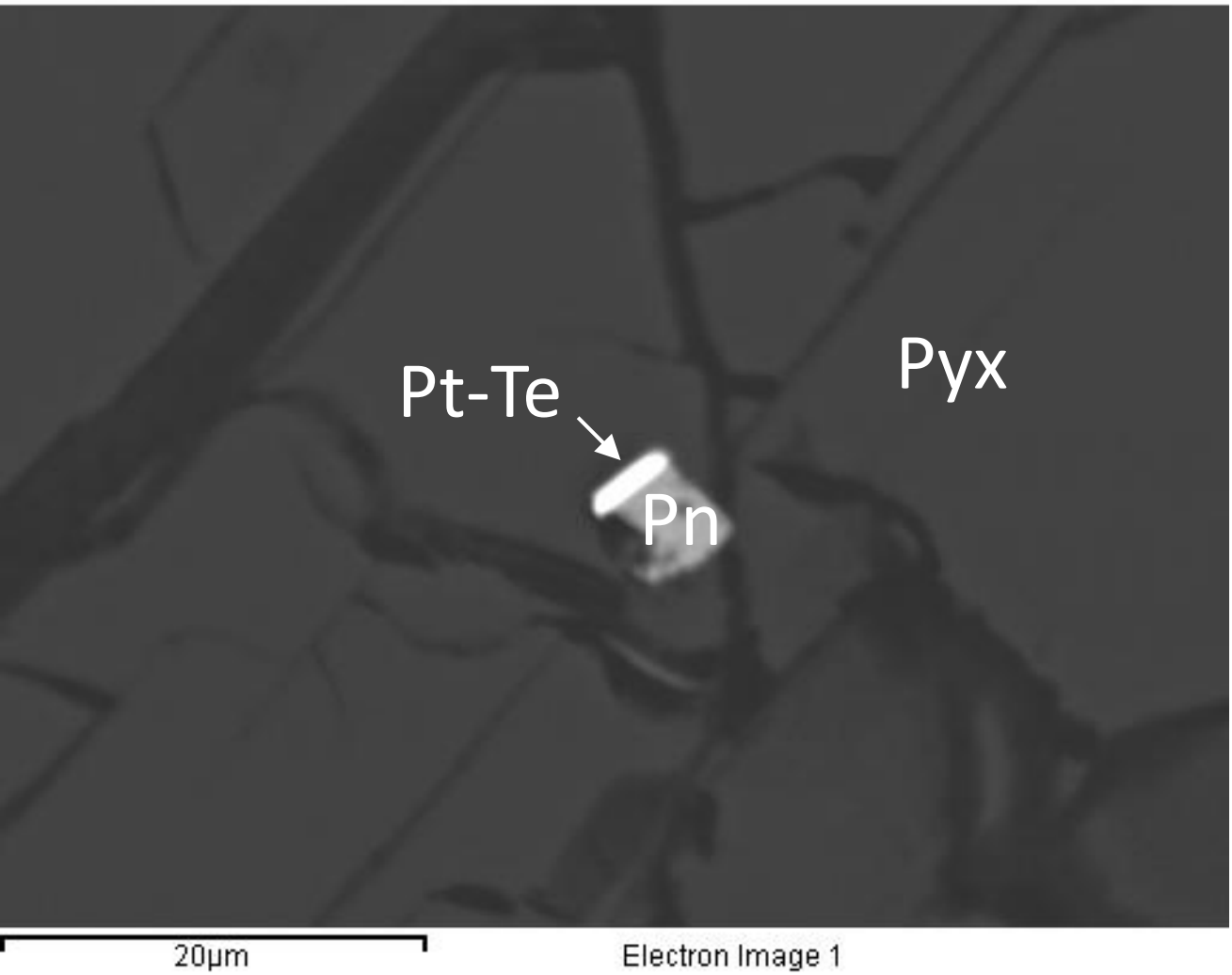
PTSR-35 D 1



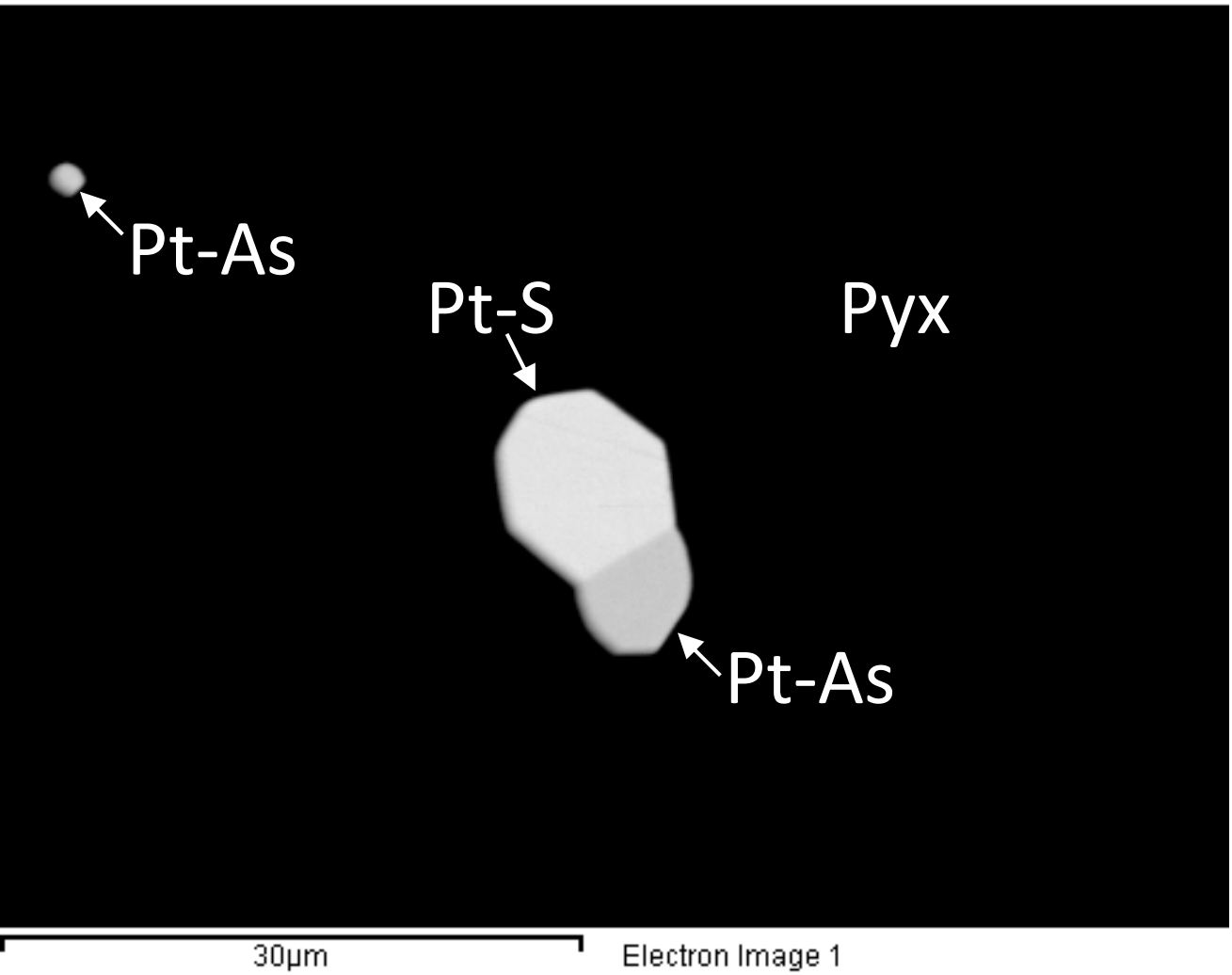
PTSR-35 E 1-2



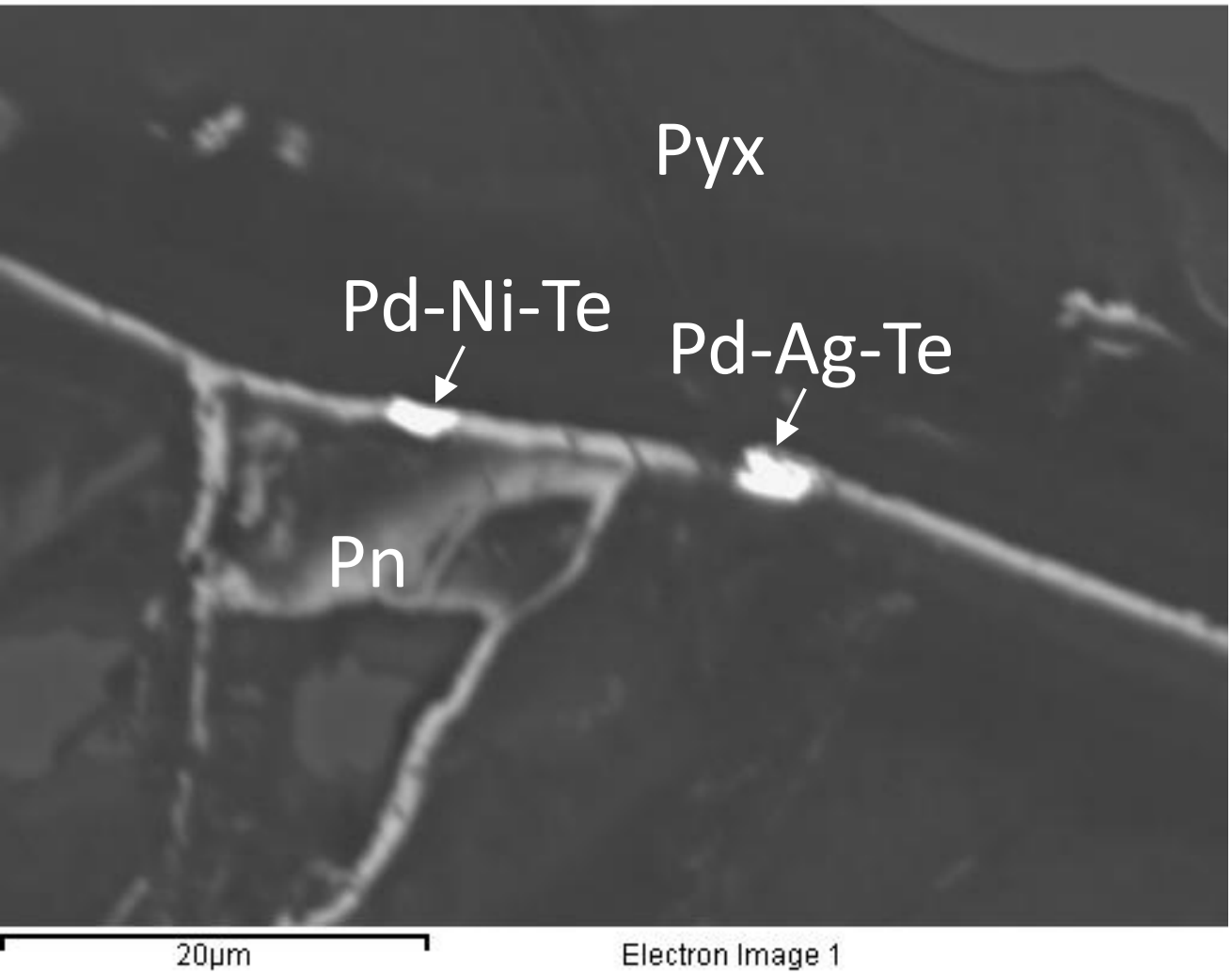
PTSR-35 F 1



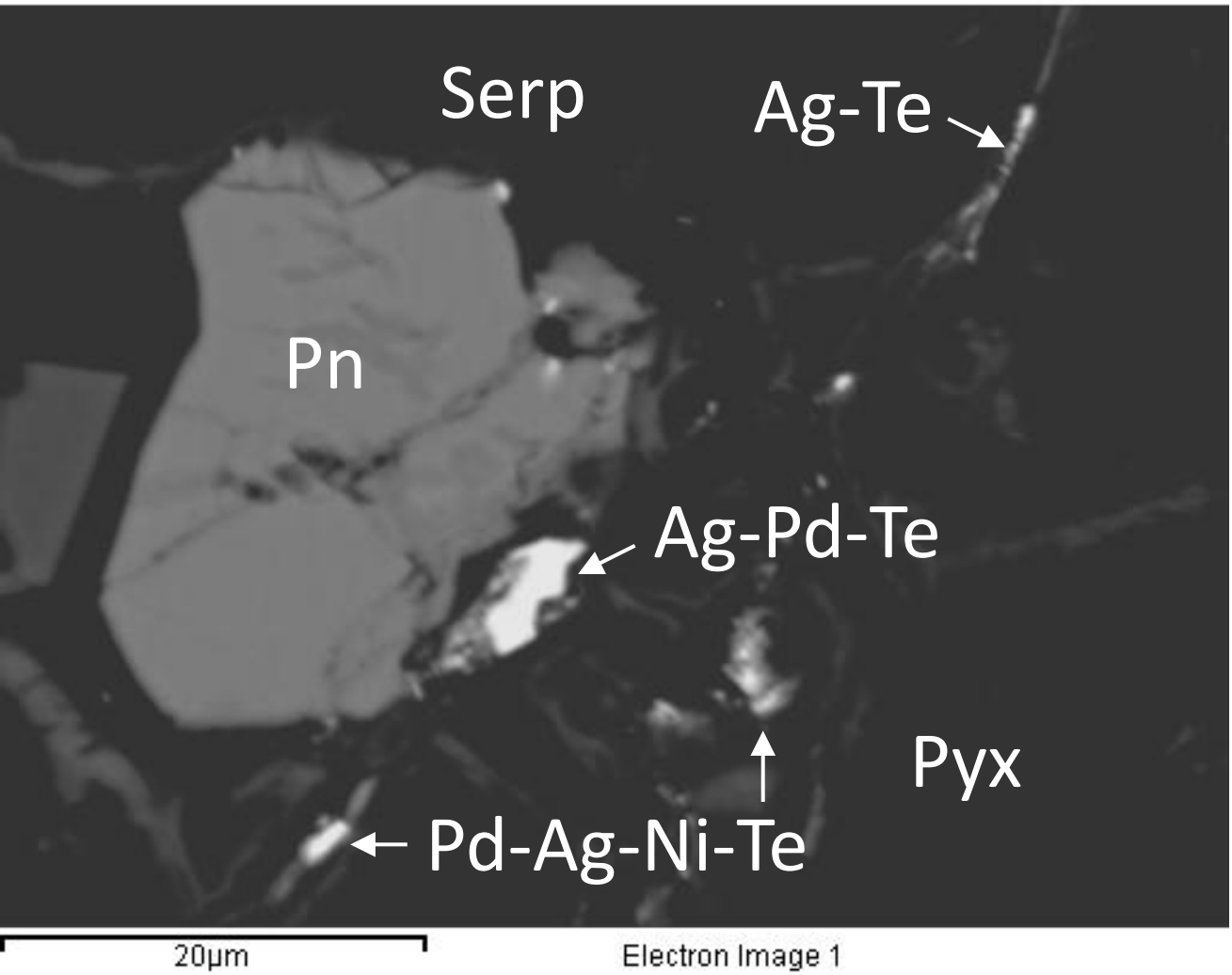
PTSR-35 G 1-3



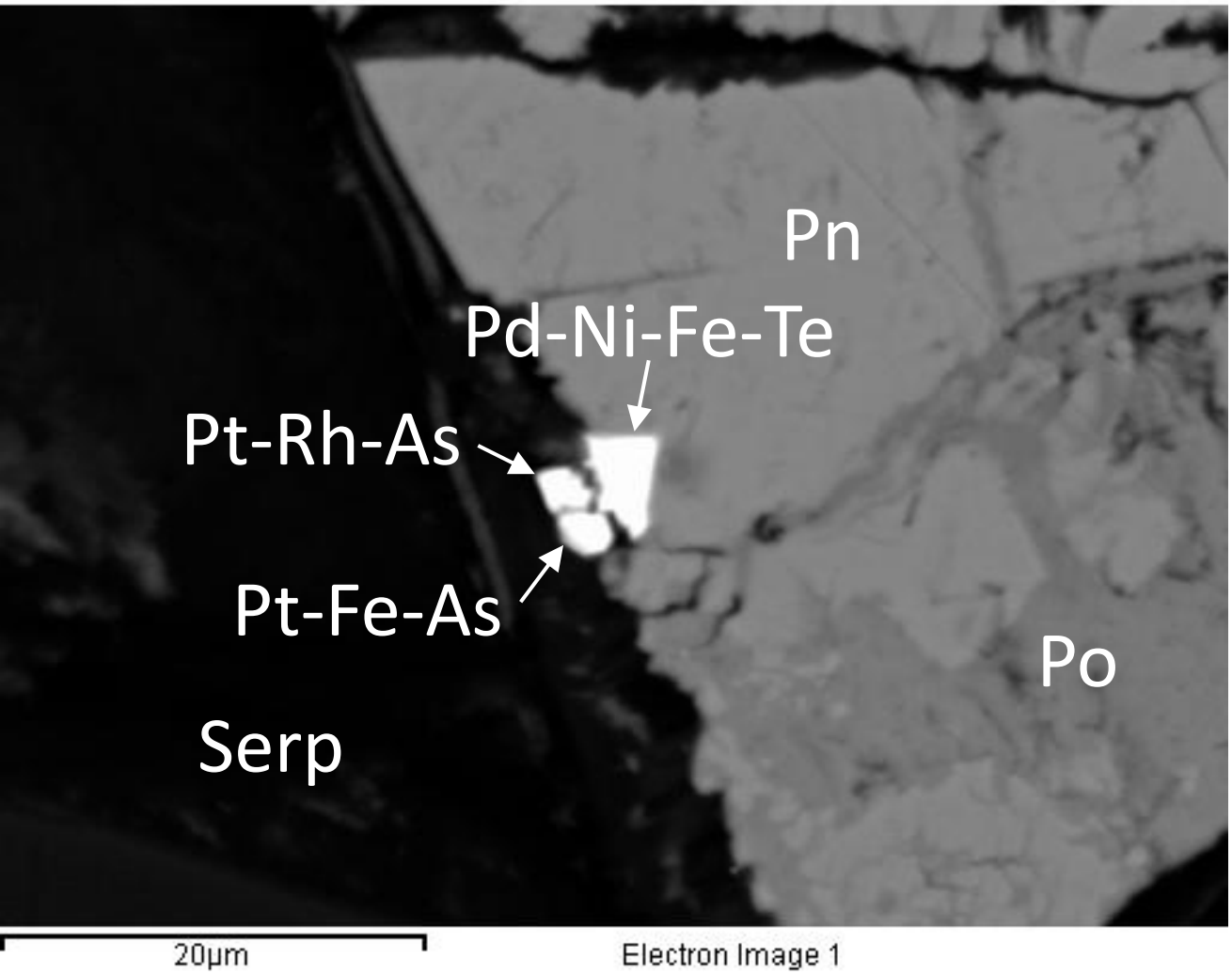
PTSR-35 H 1-2



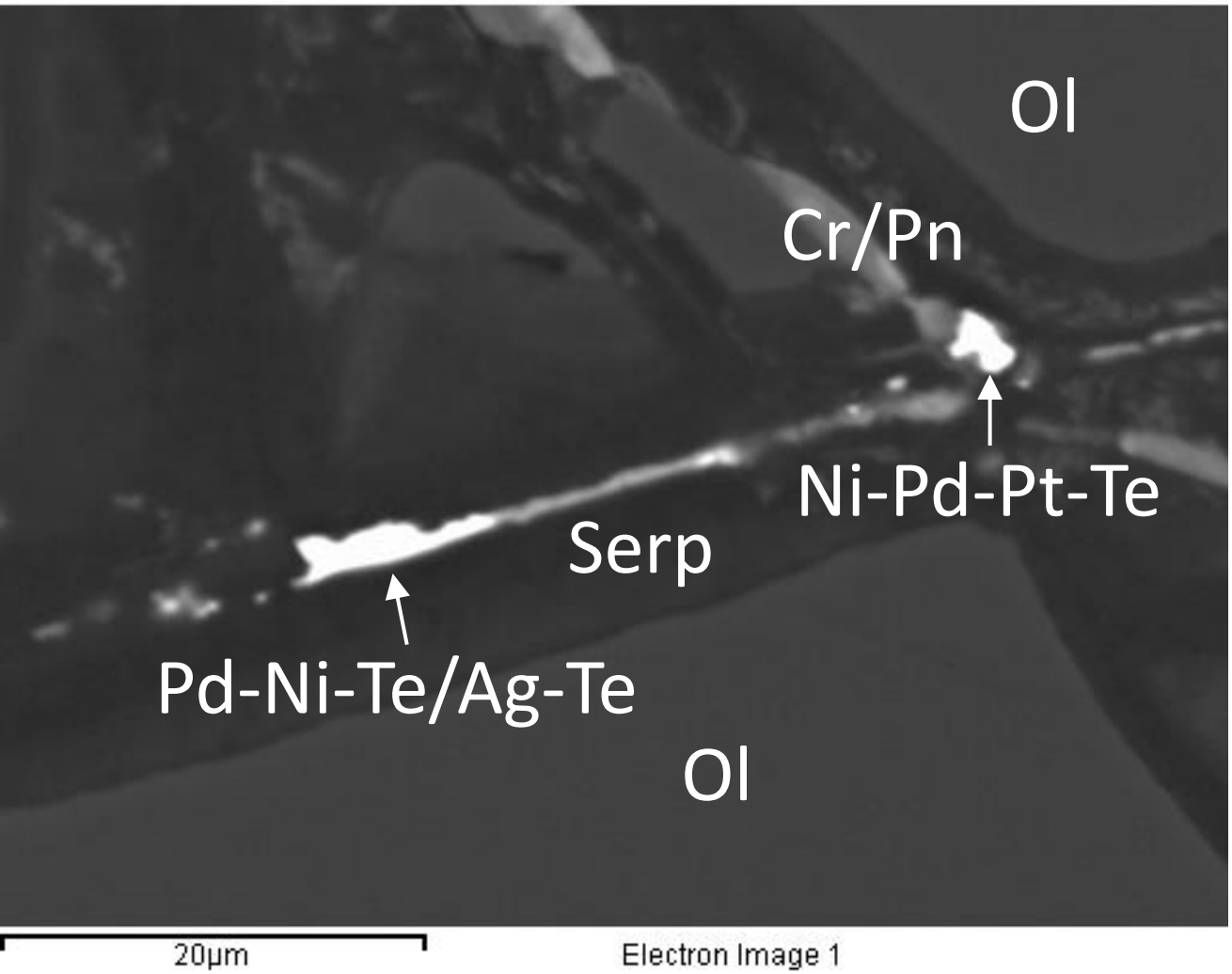
PTSR-35 I 1-4



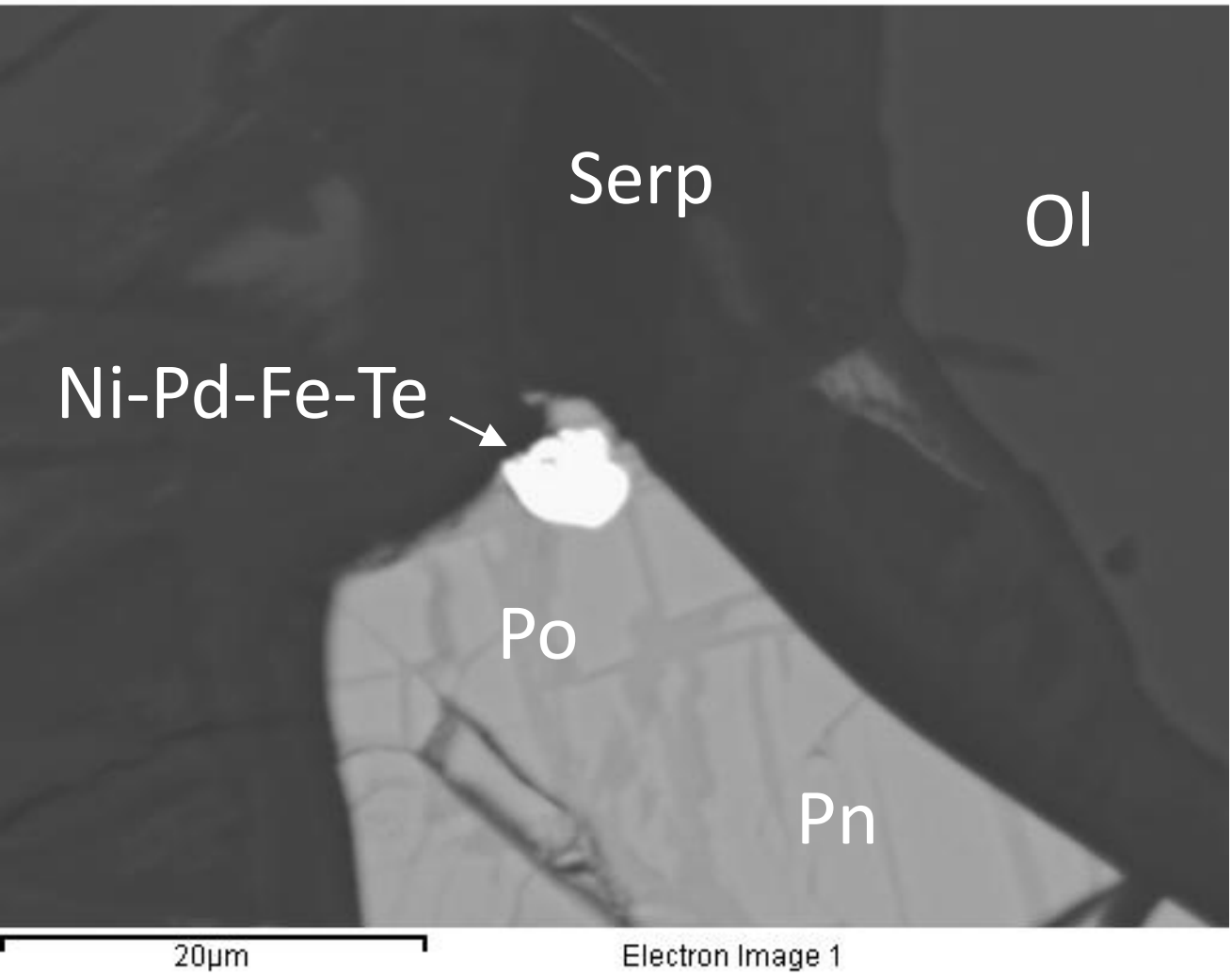
PTSR-35 J 1-3



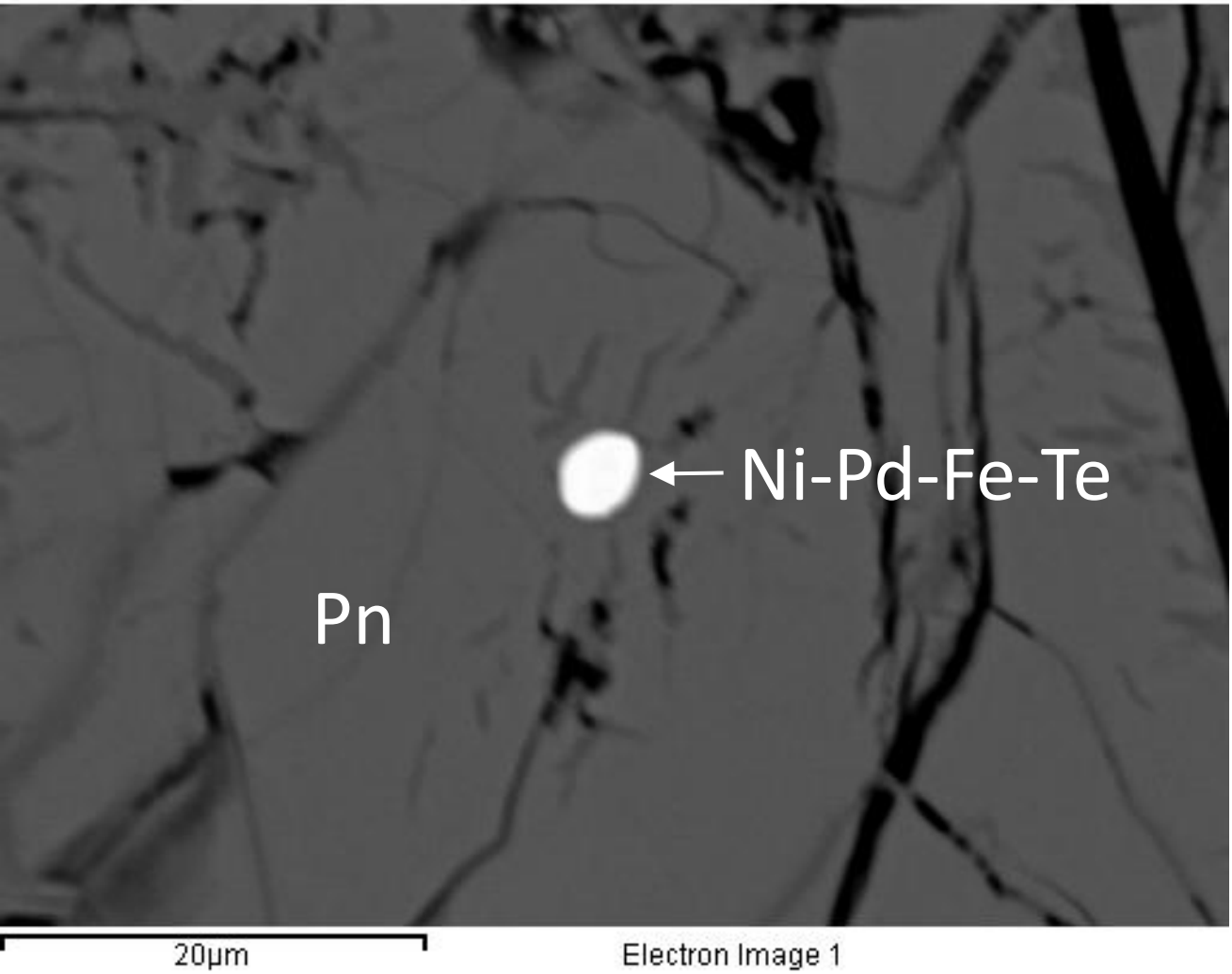
PTSR-35 K 1-2



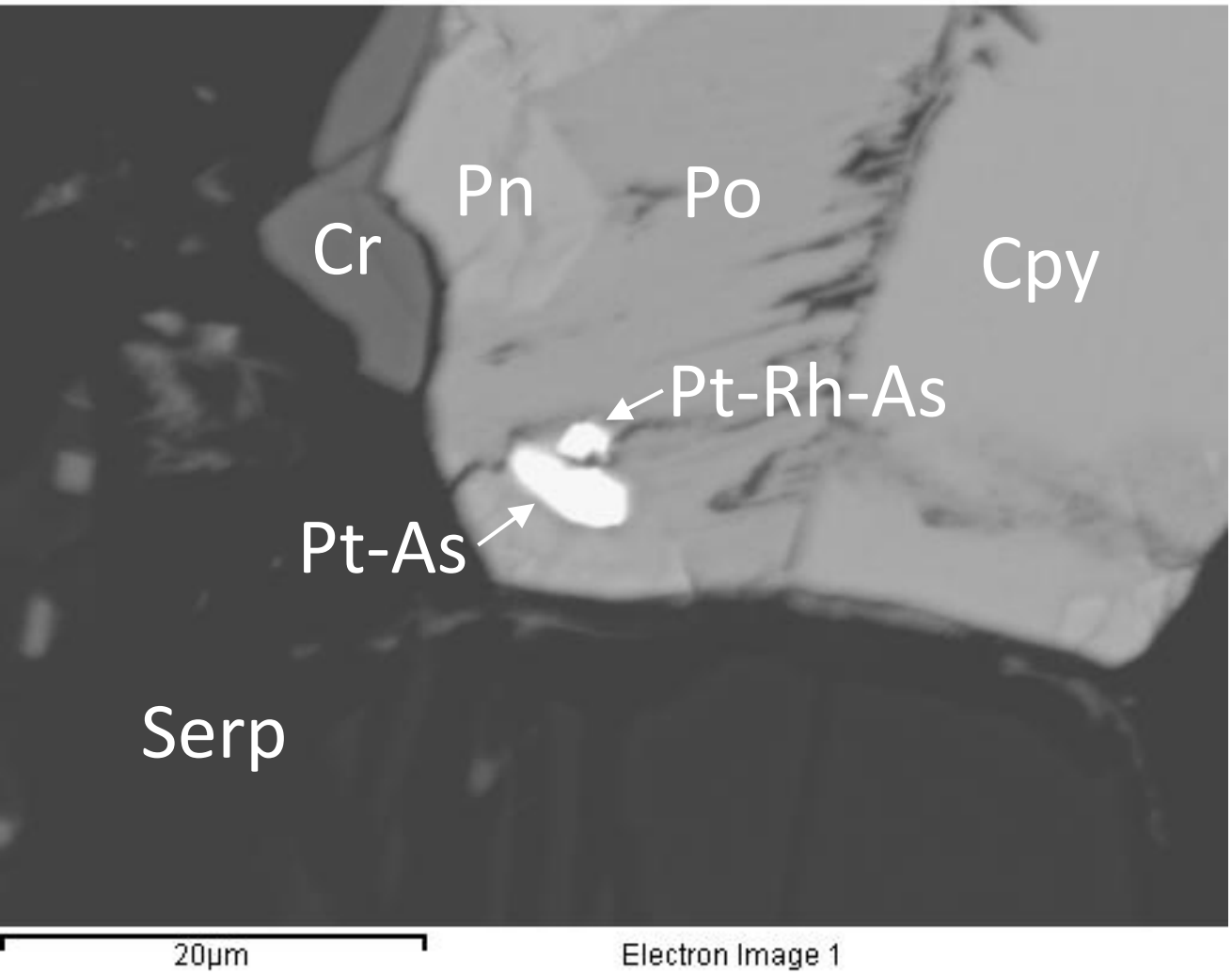
PTSR-35 L 1



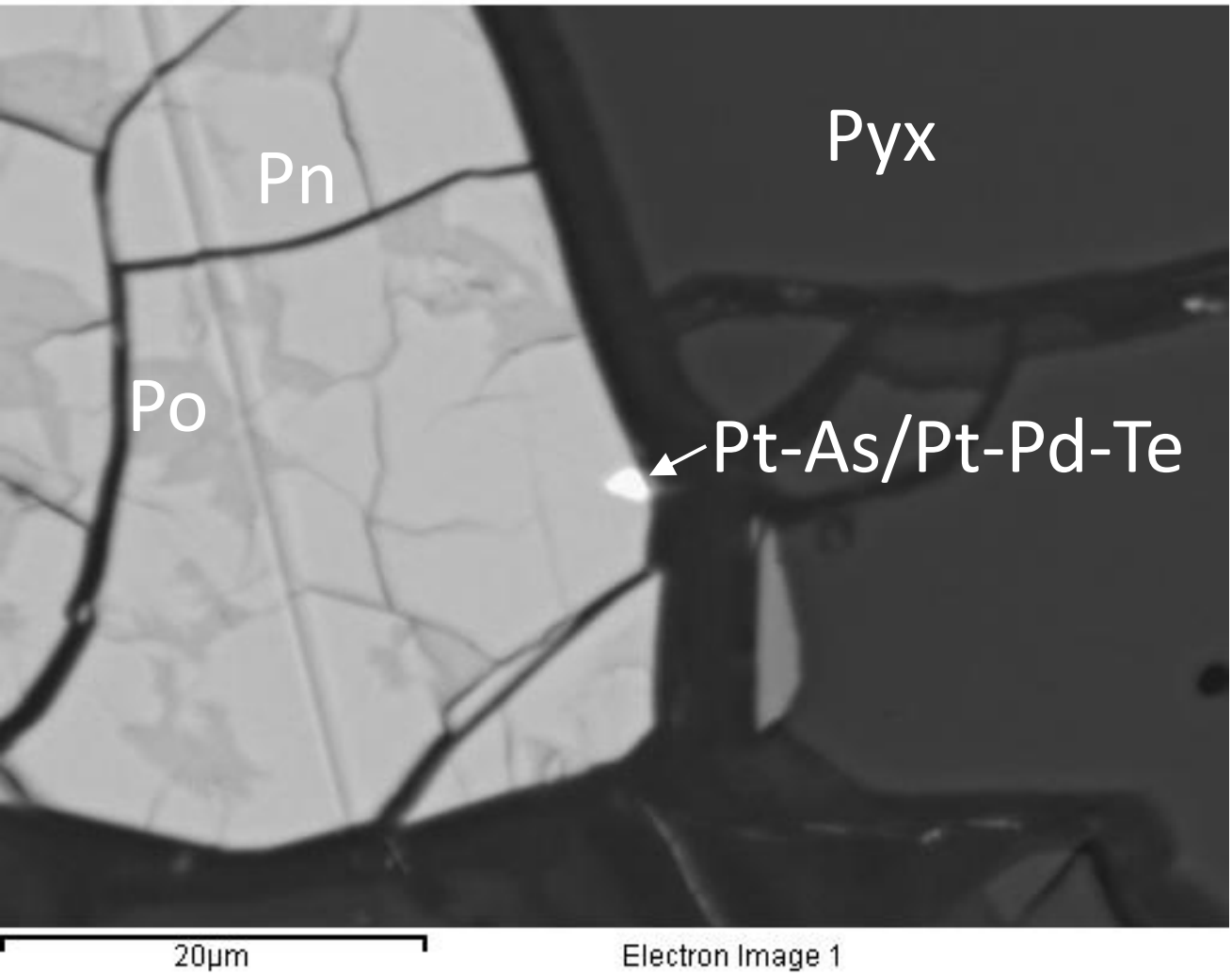
PTSR-35 M 1



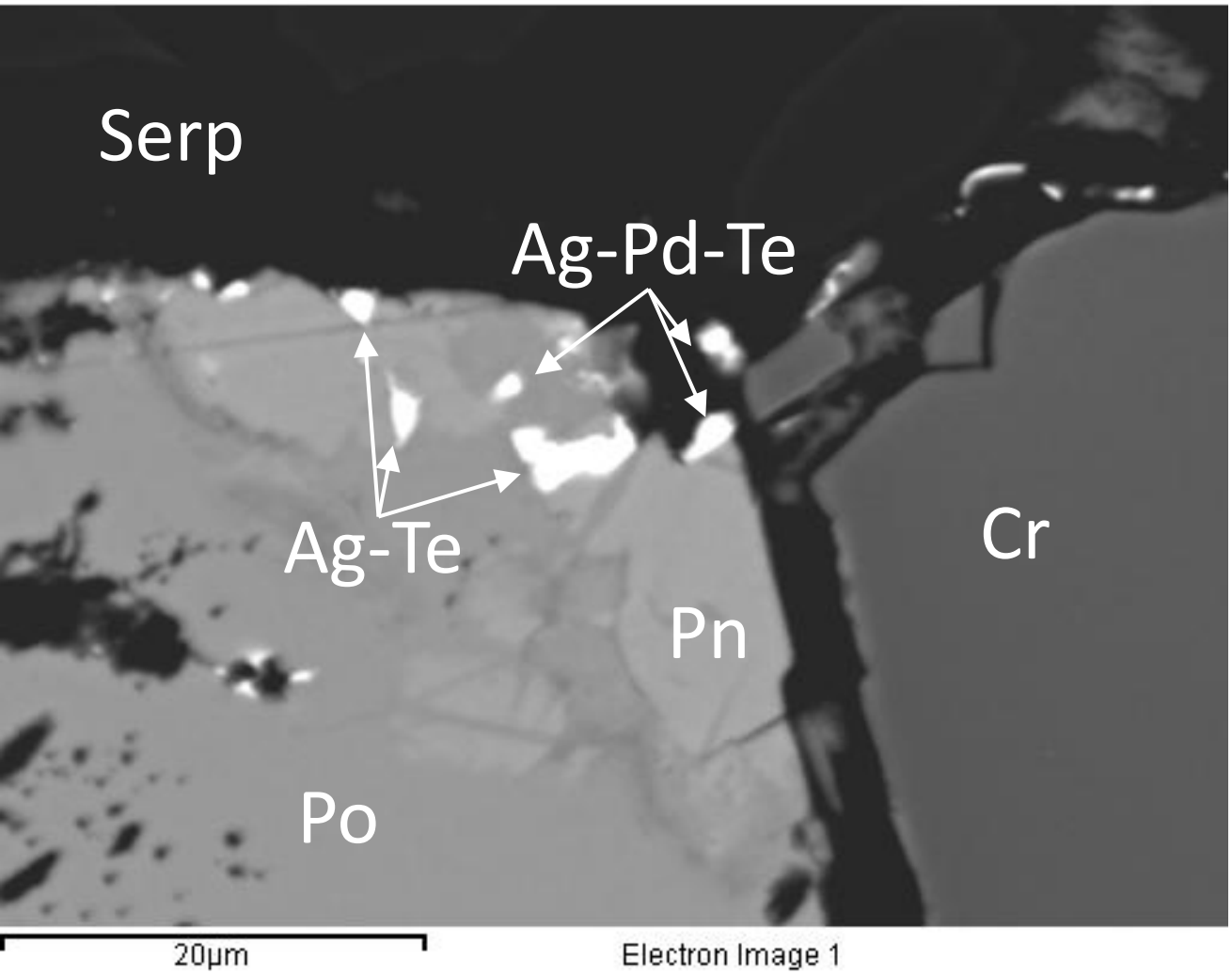
PTSR-35 N 1-2



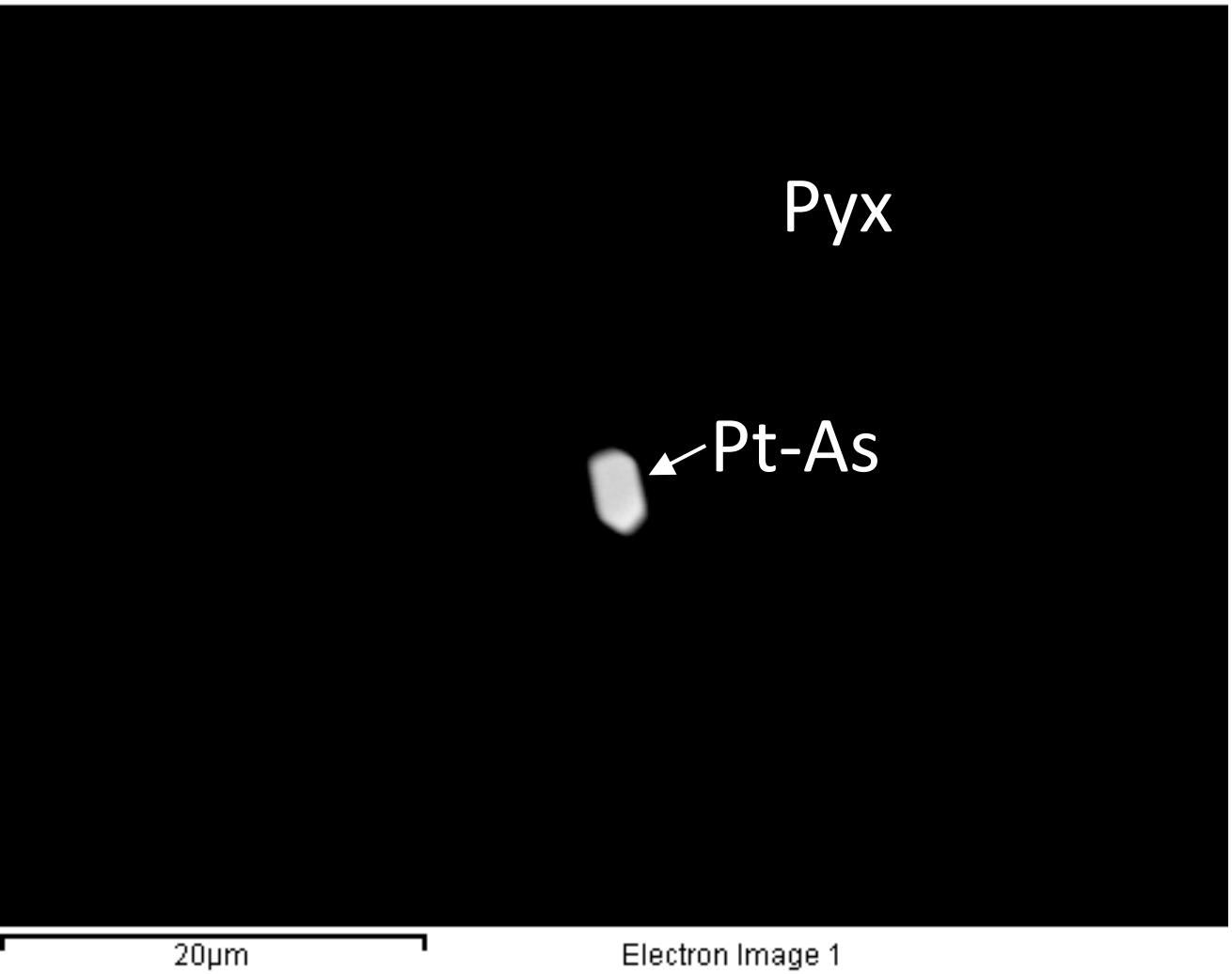
PTSR-35 O 1



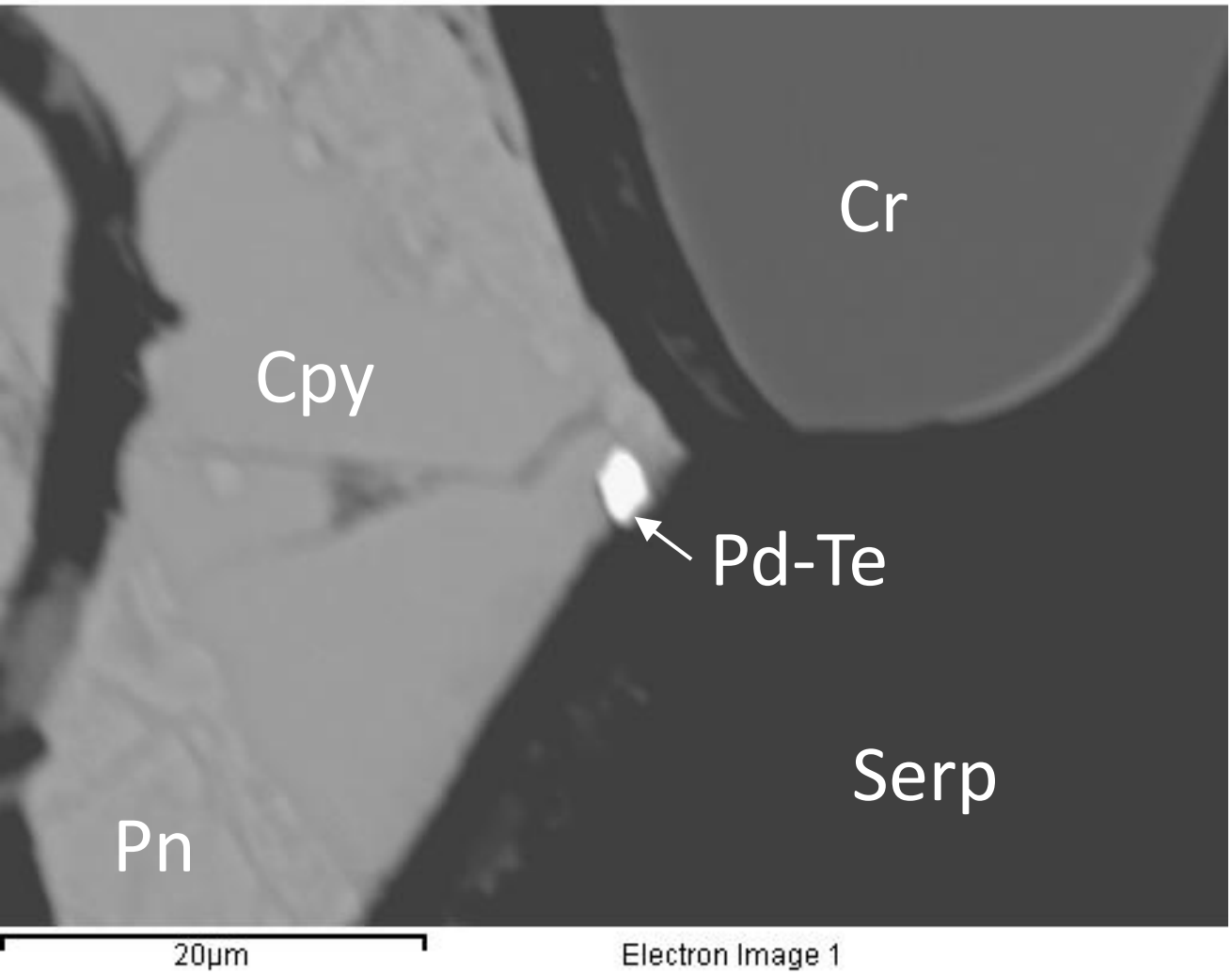
PTSR-35 P 1-6



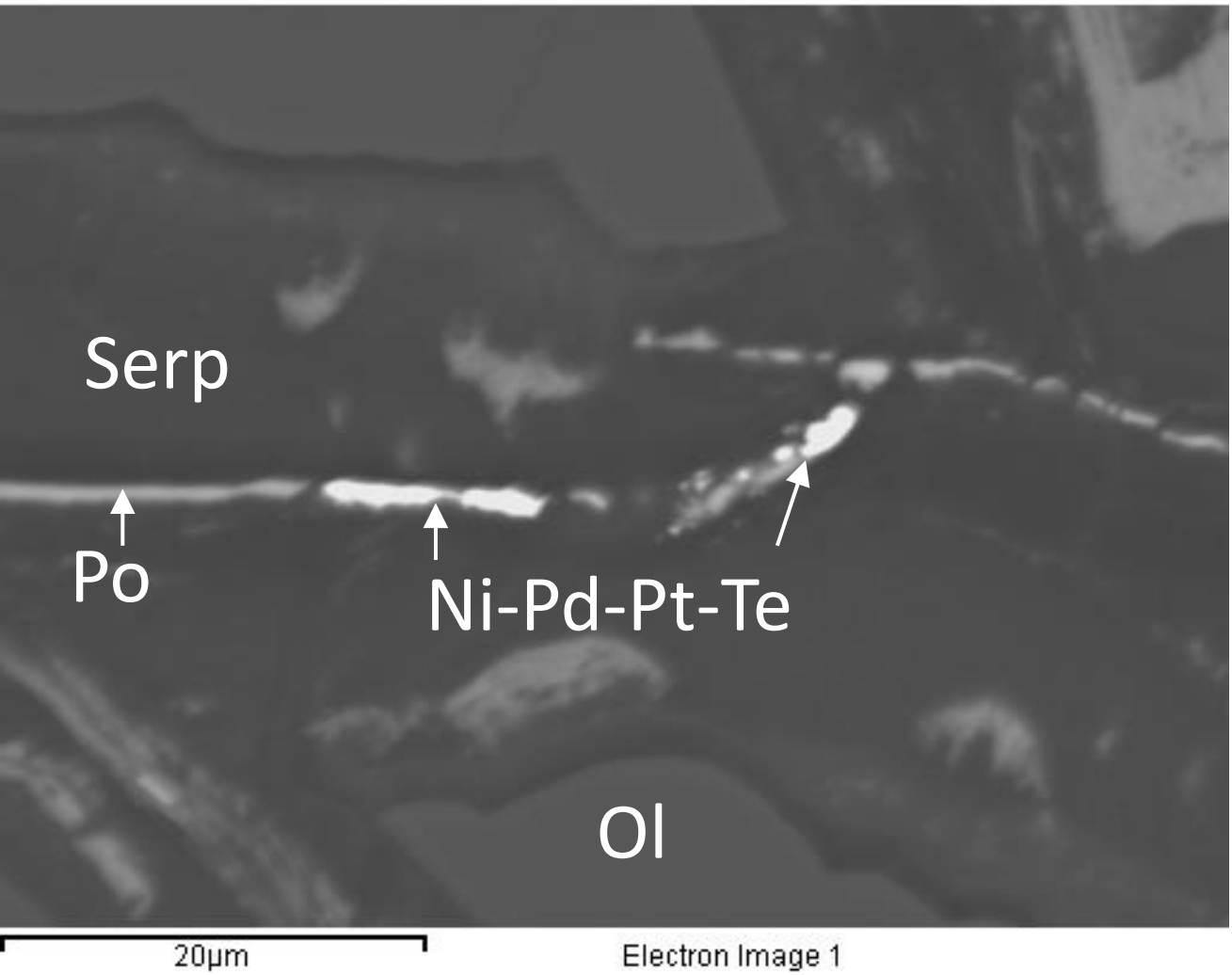
PTSR-35 Q 1



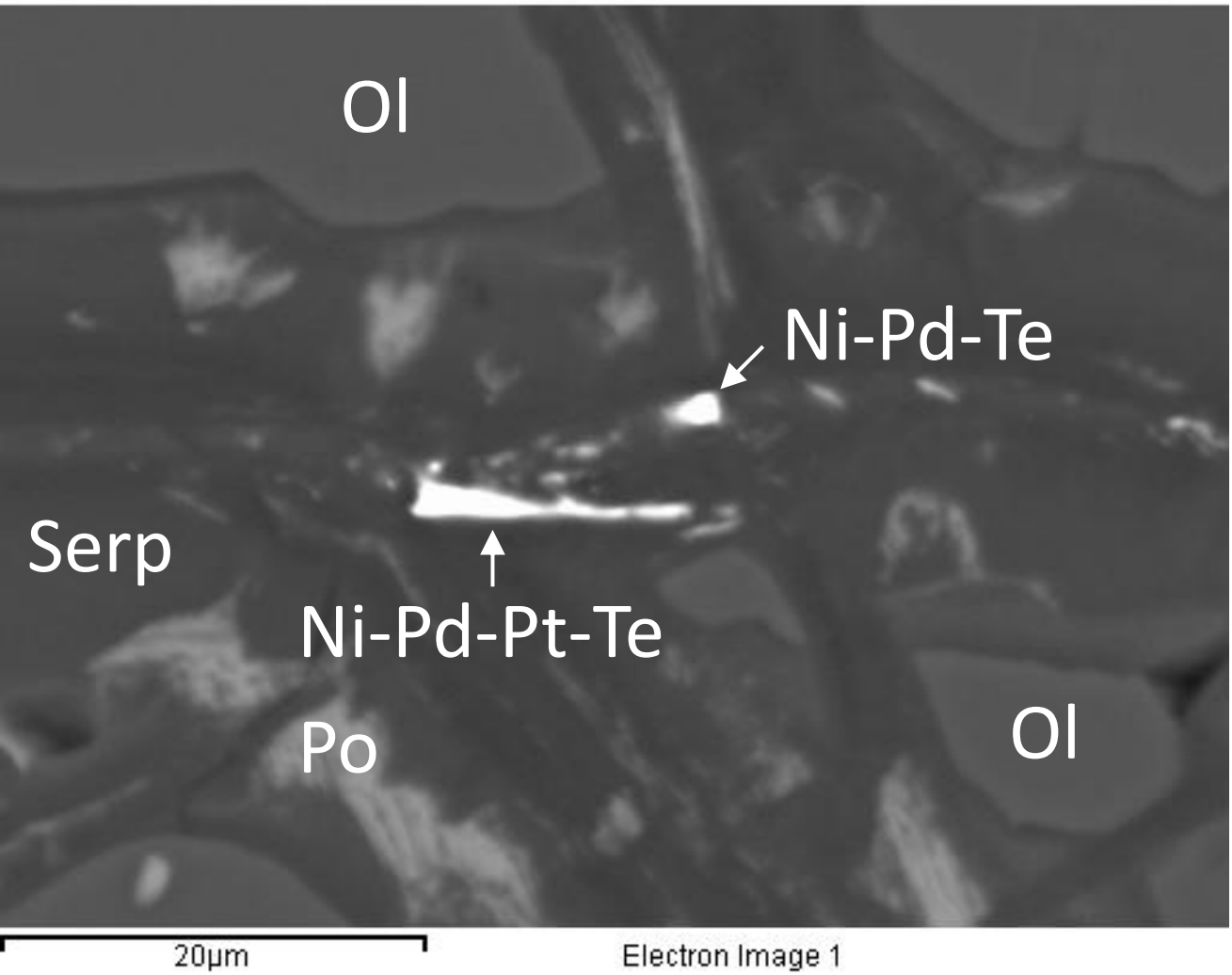
PTSR-35 R 1



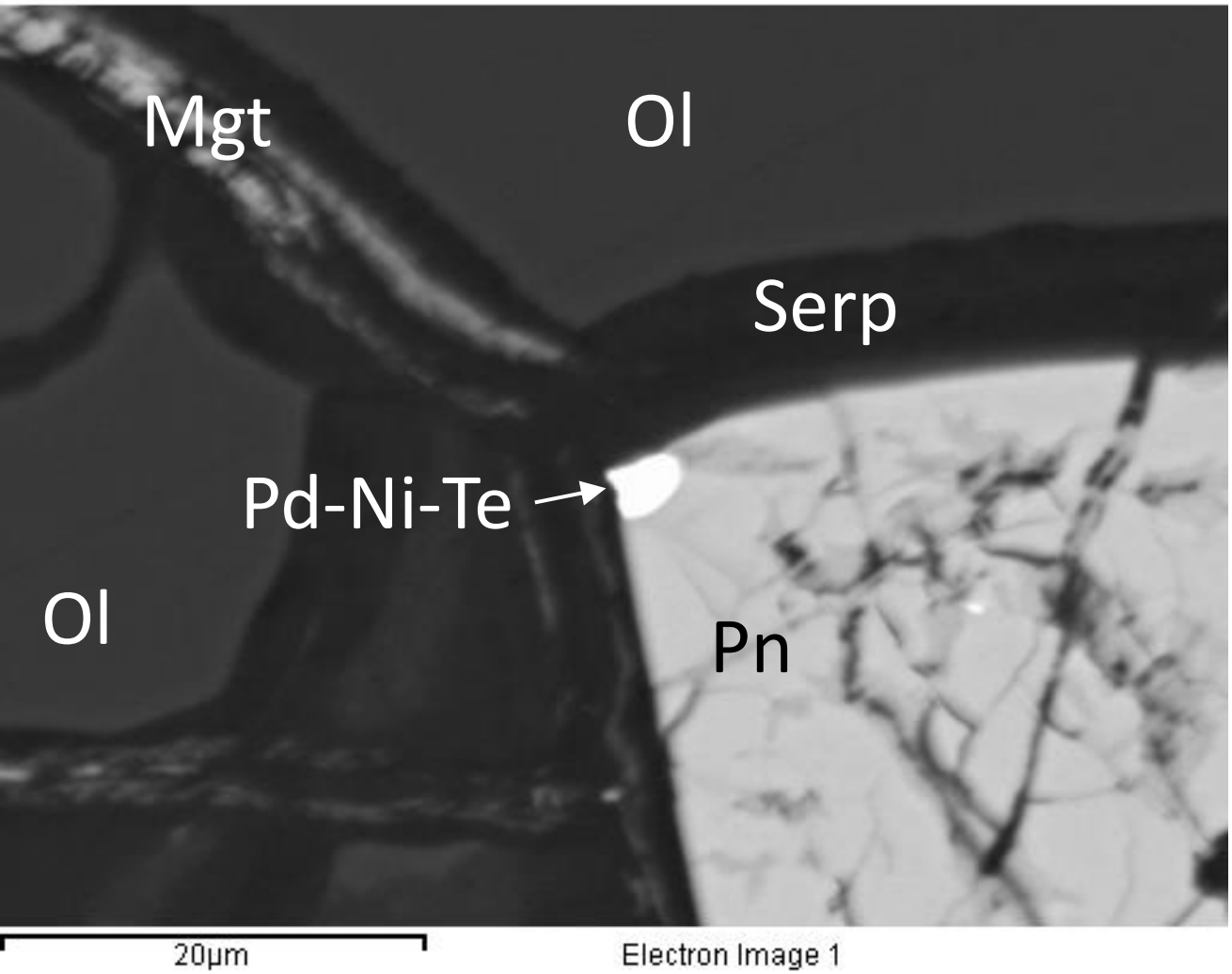
PTSR-35 S 1



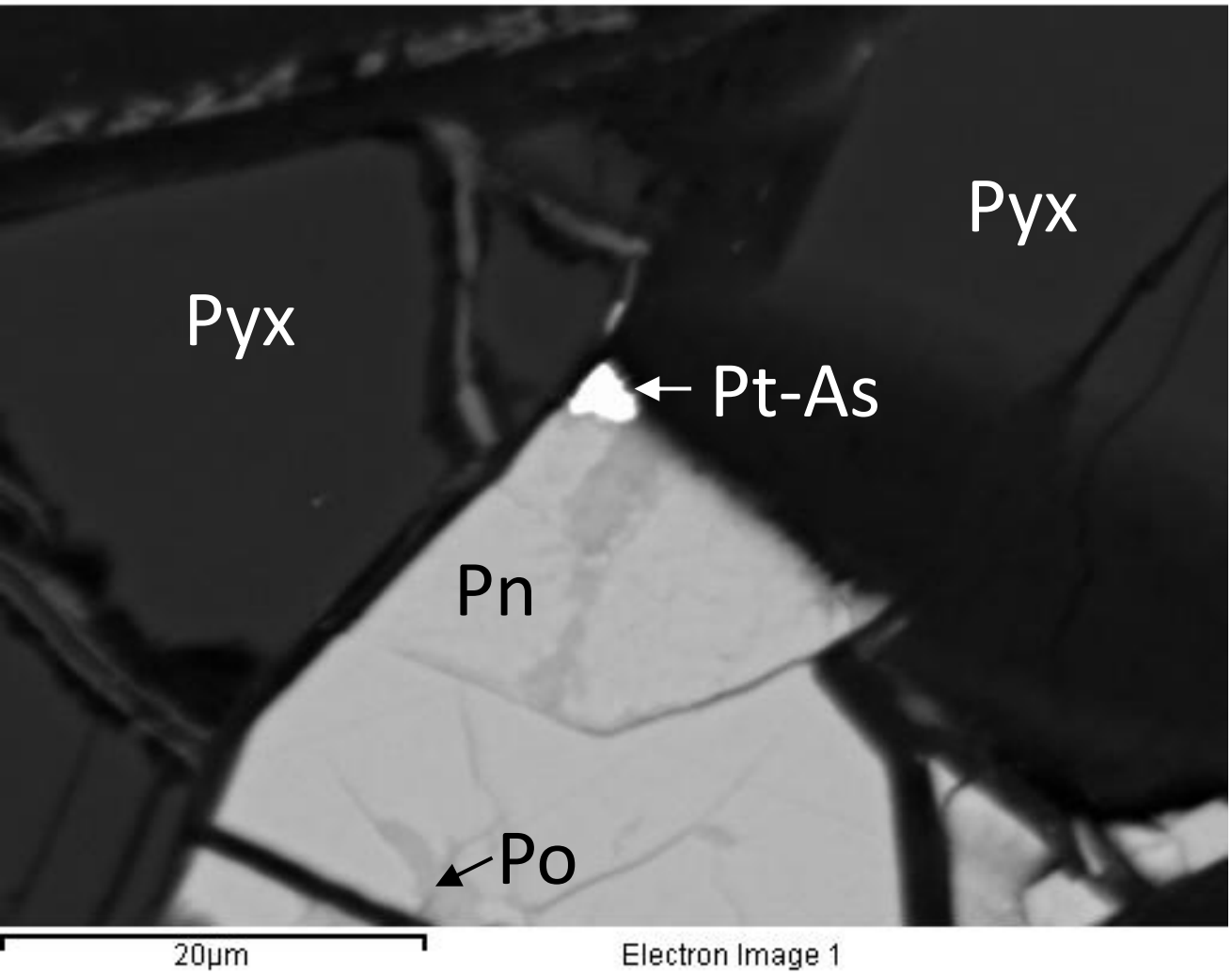
PTSR-35 T 1-2



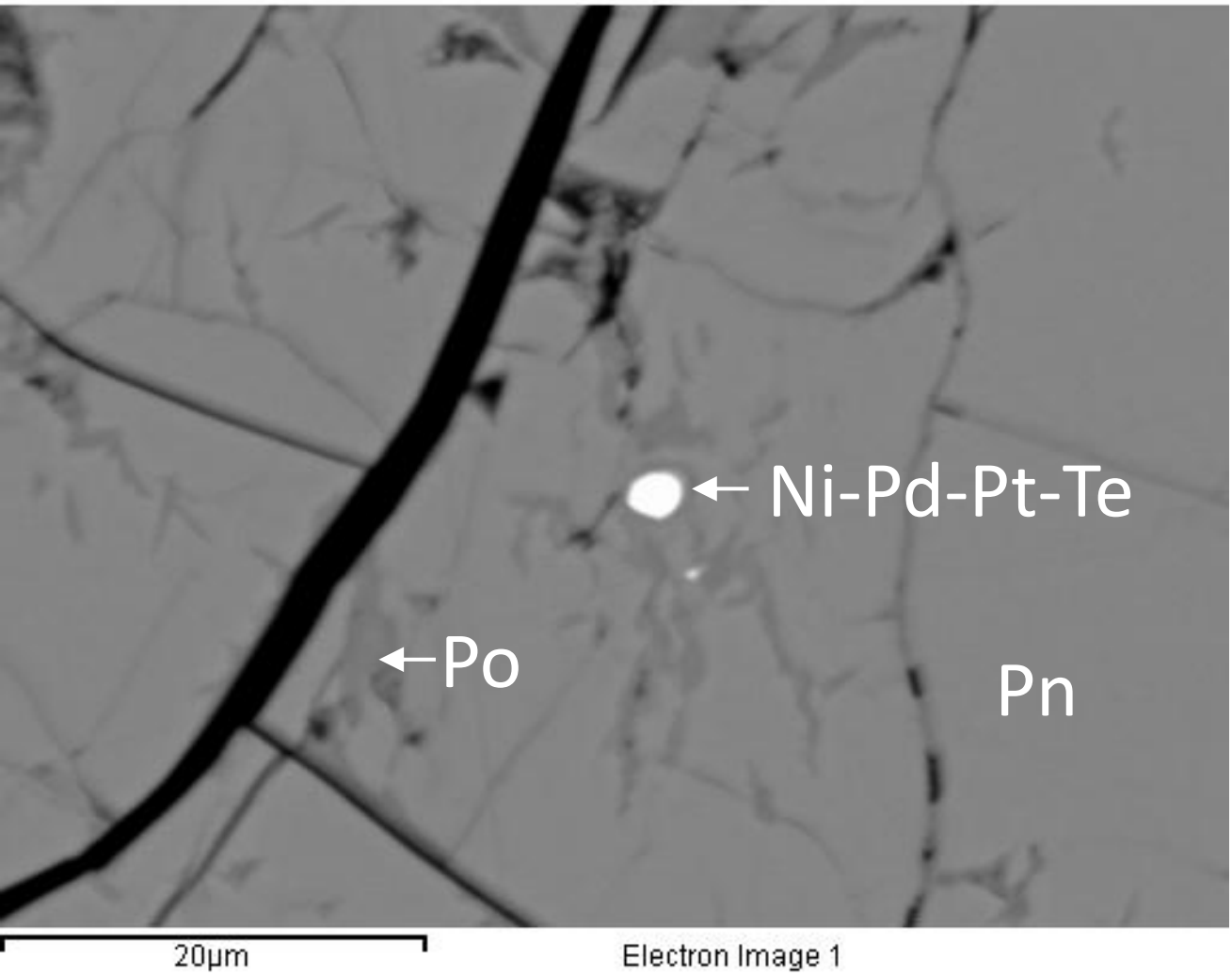
PTSR-35 U 1



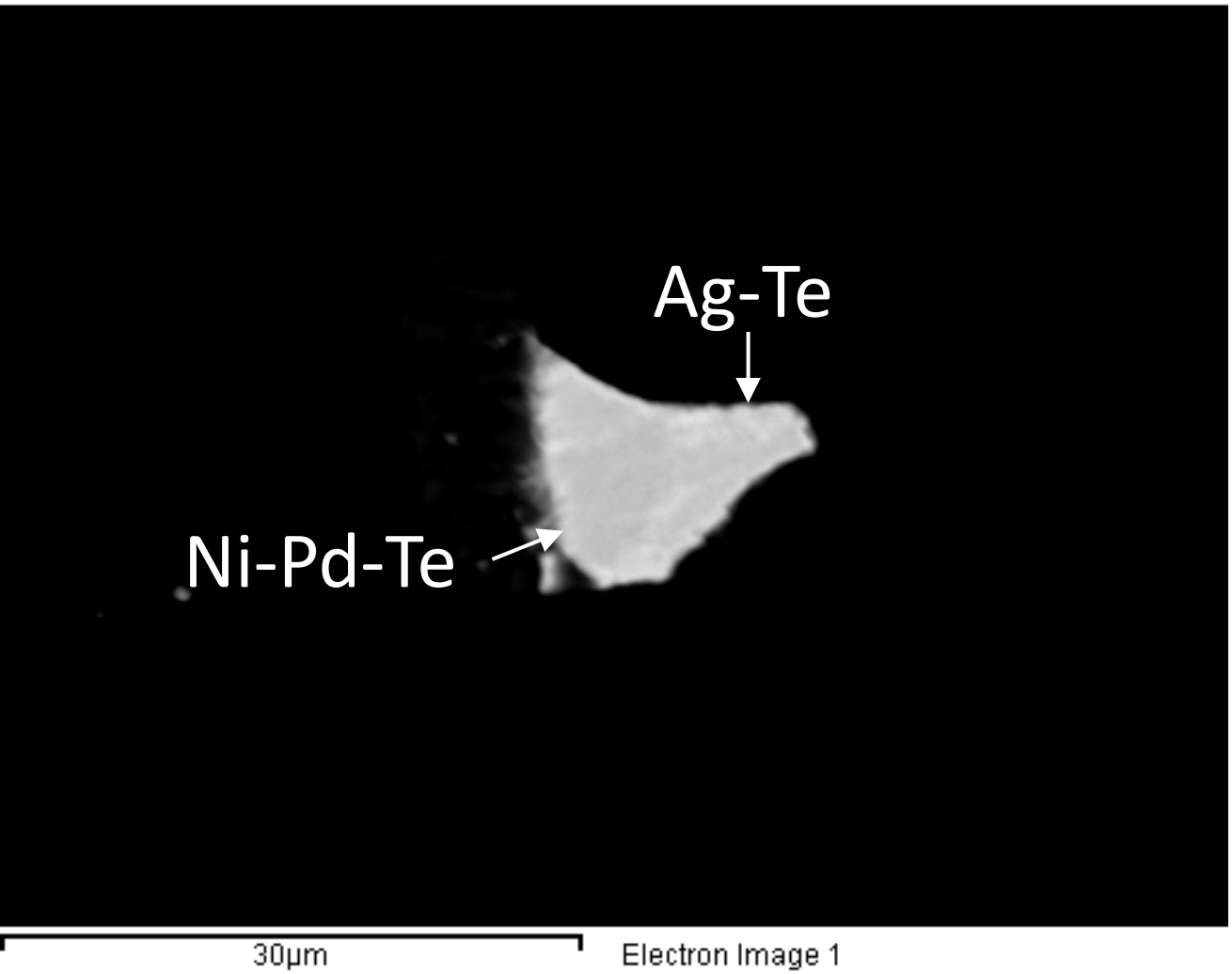
PTSR-35 V 1



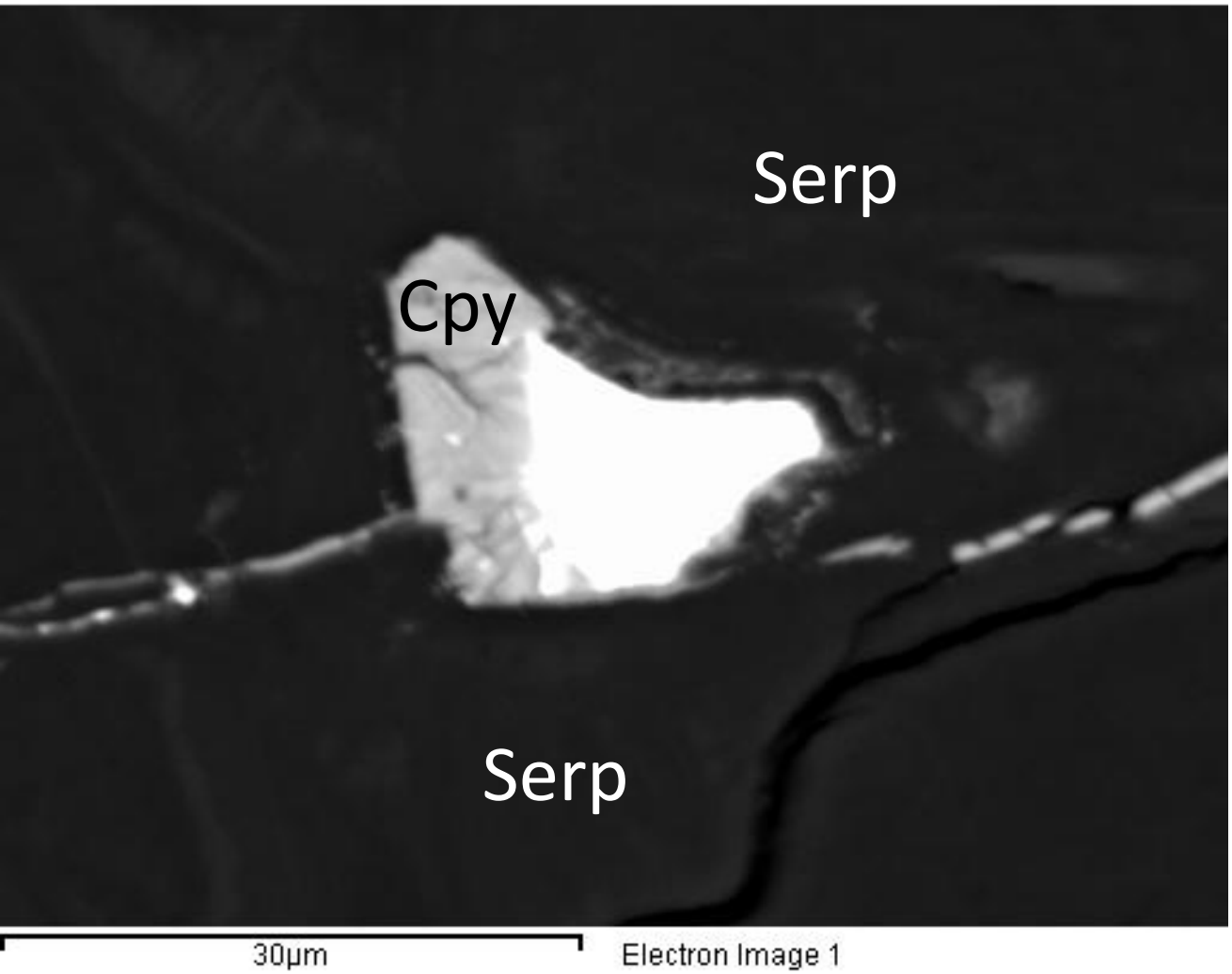
PTSR-35 W 1



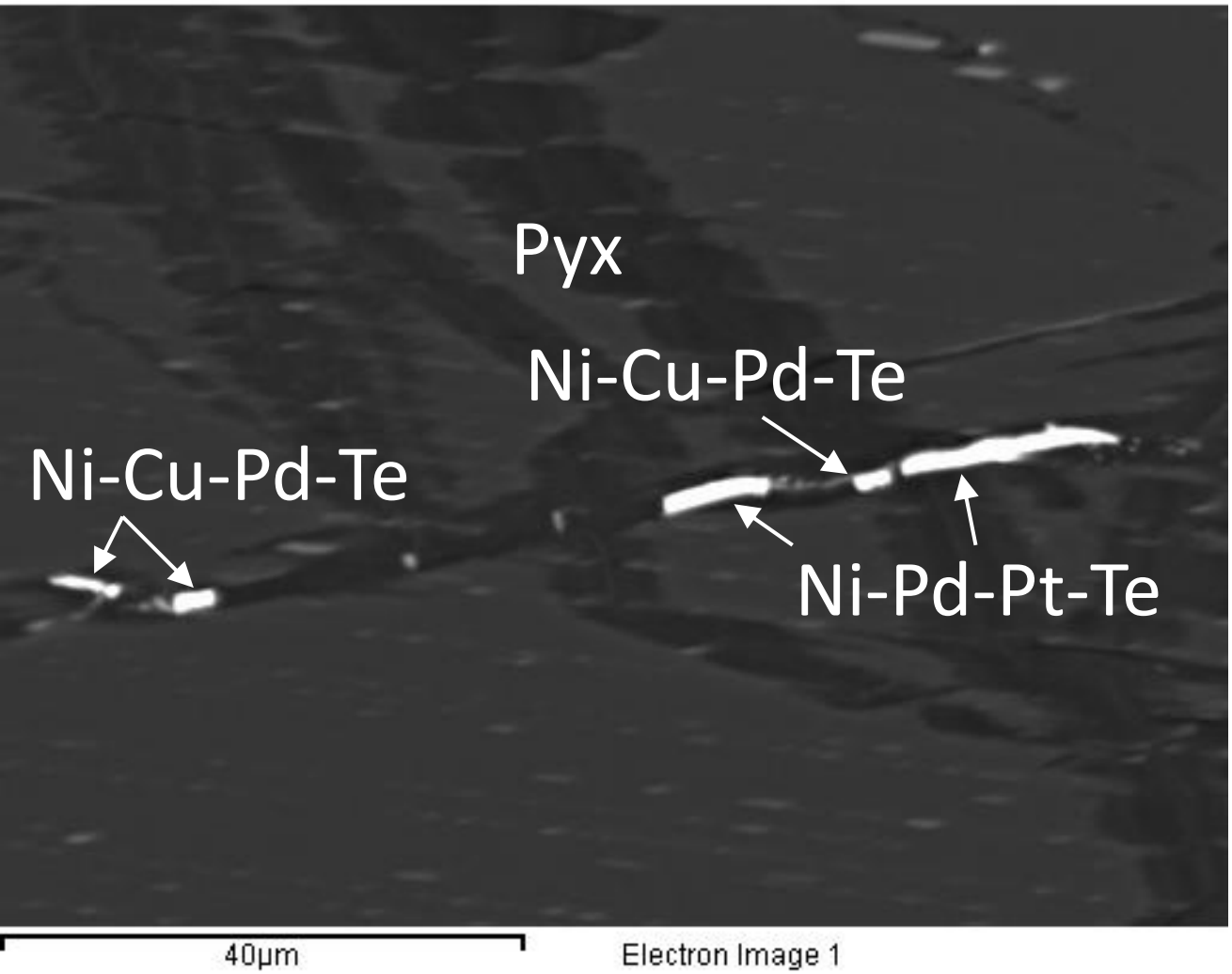
PTSR-35 X 1



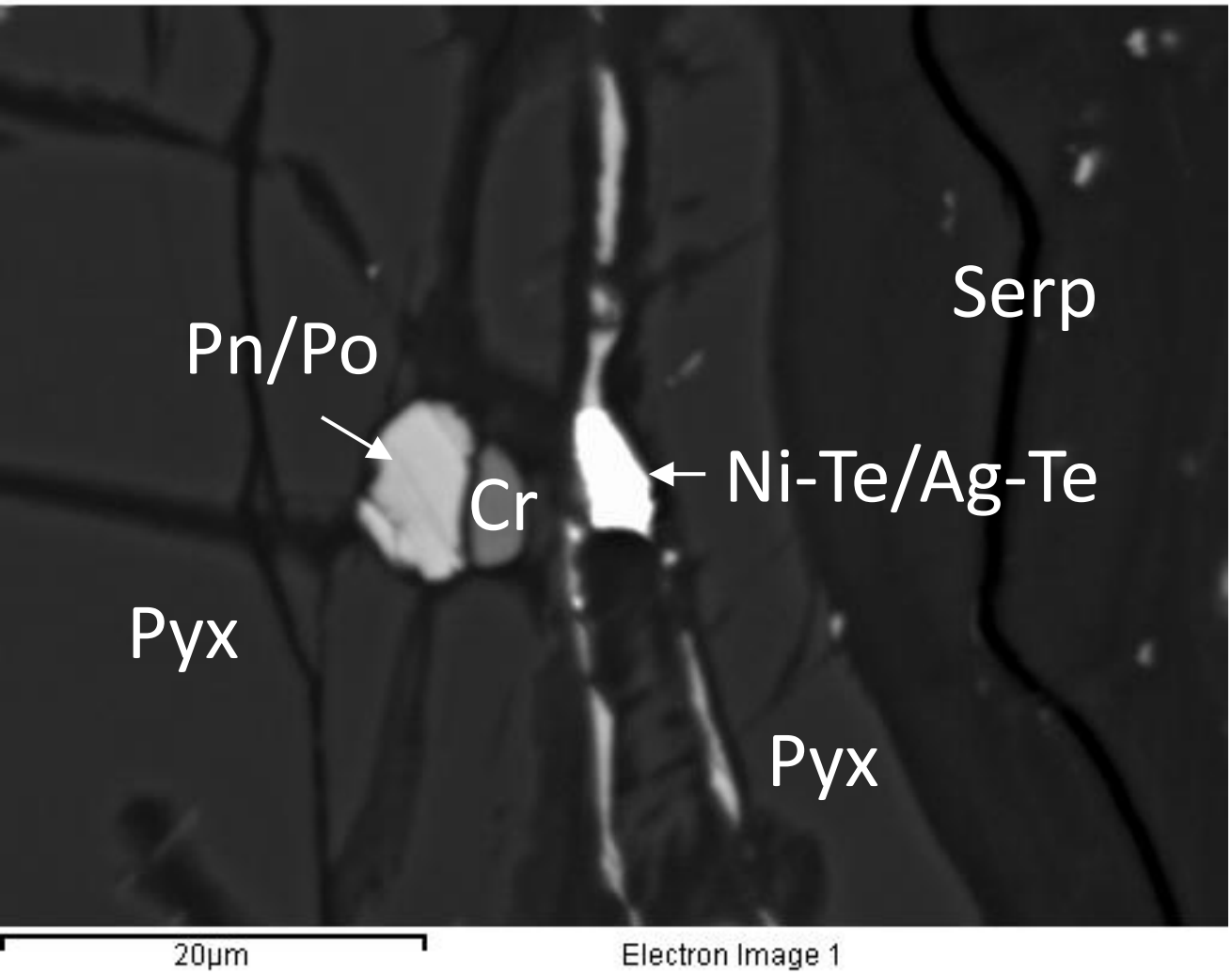
PTSR-35 X 1 Light



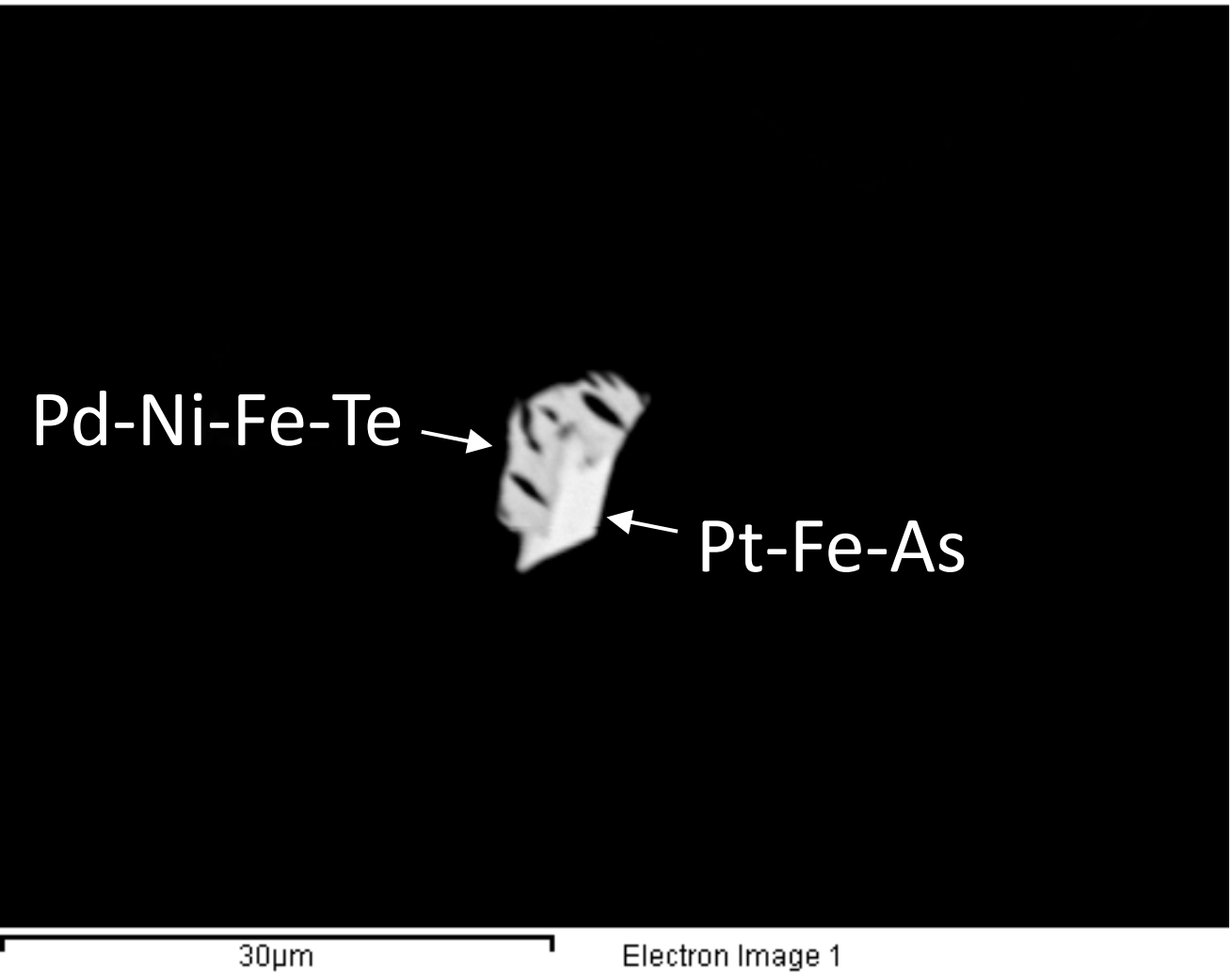
PTSR-35 Y 1-5



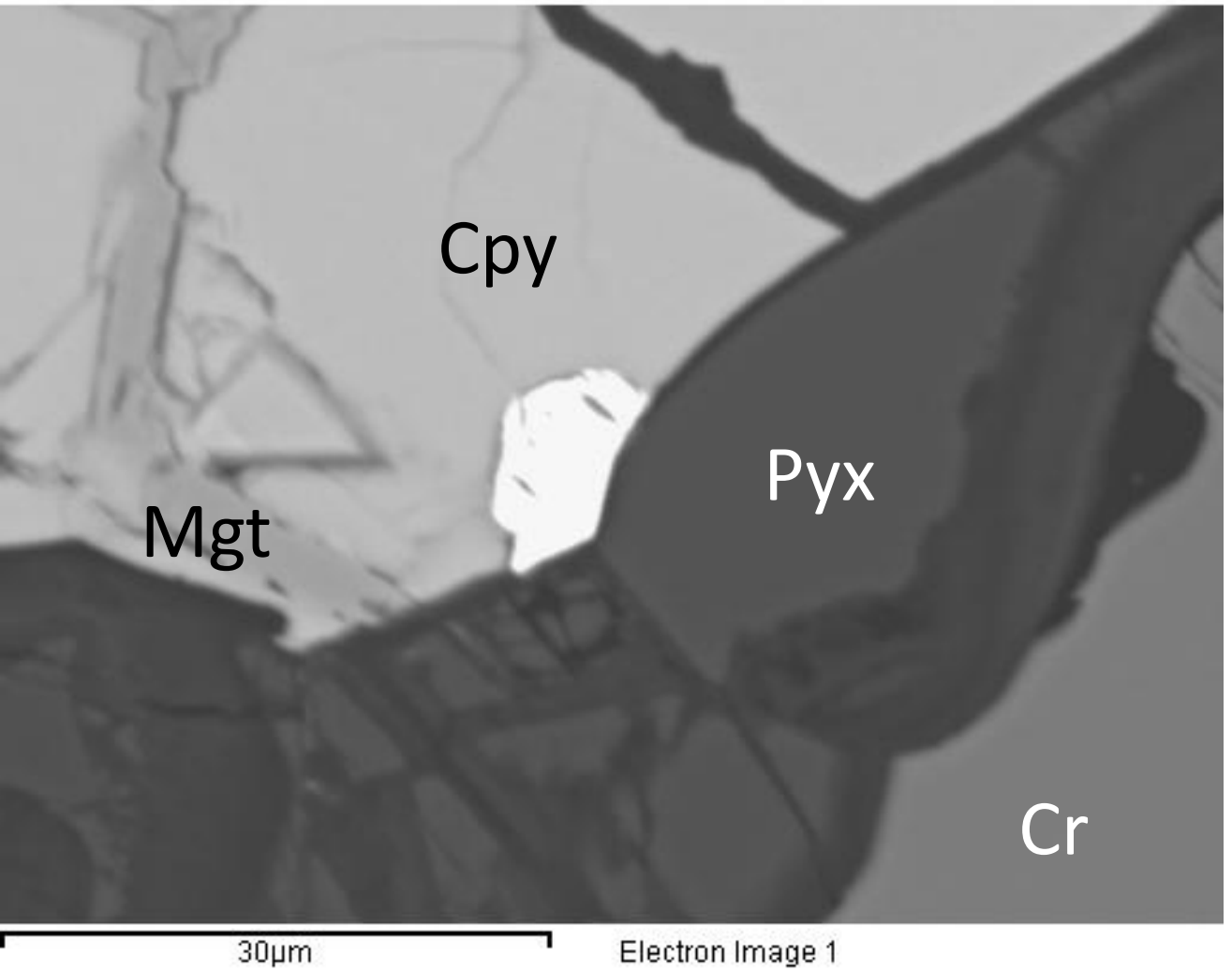
PTSR-35 Z 1



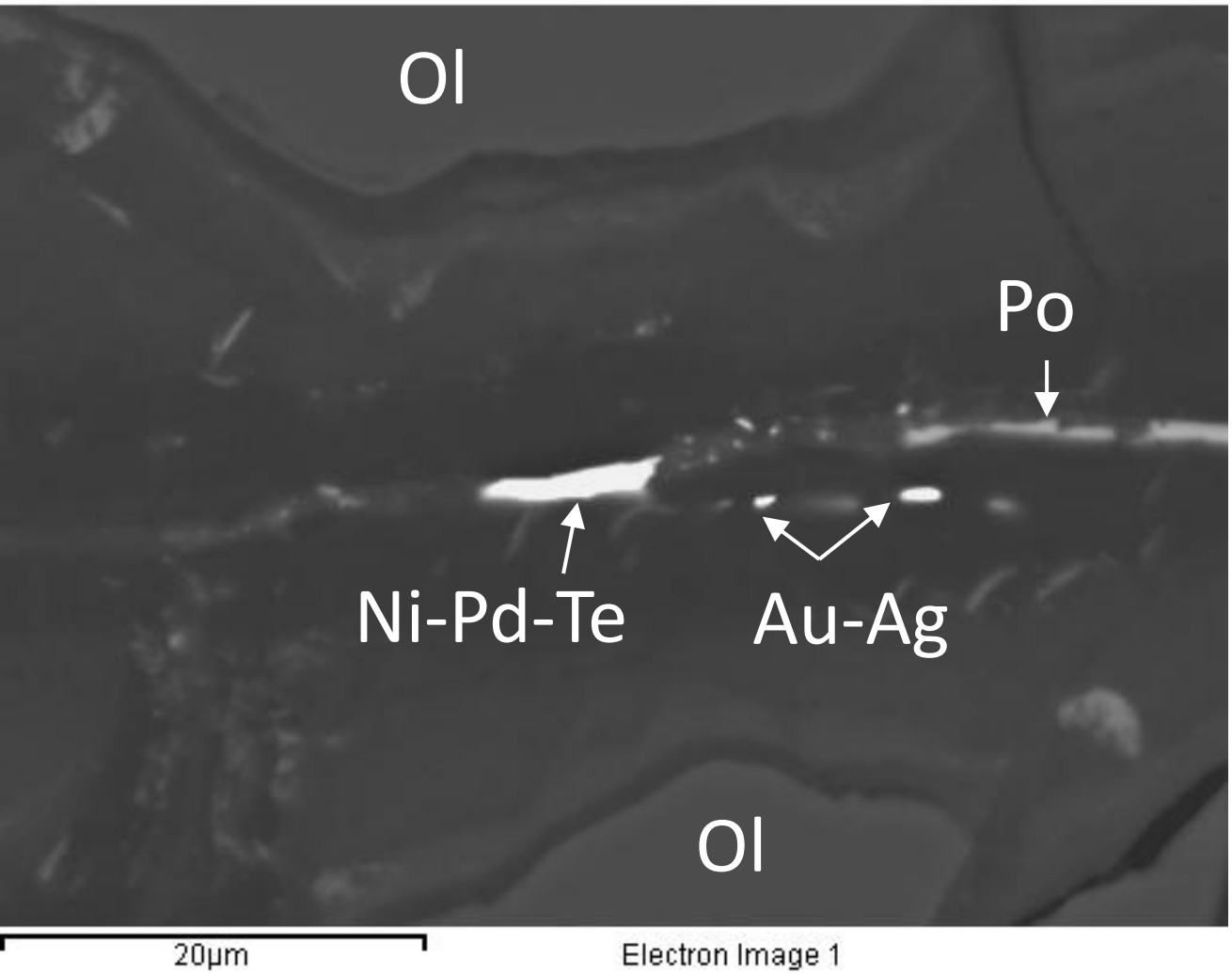
PTSR-35 AA 1-2



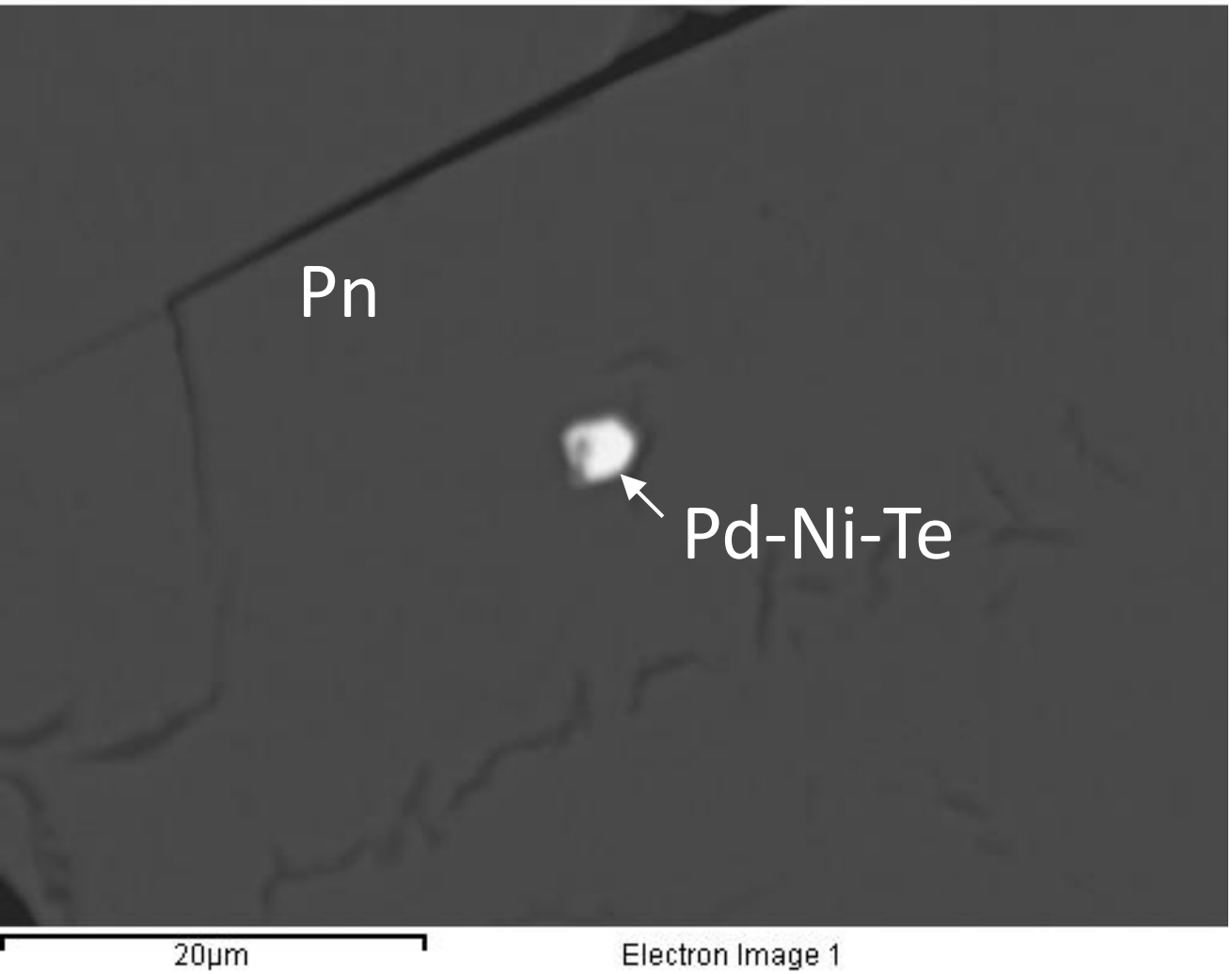
PTSR-35 AA 1-2 Light



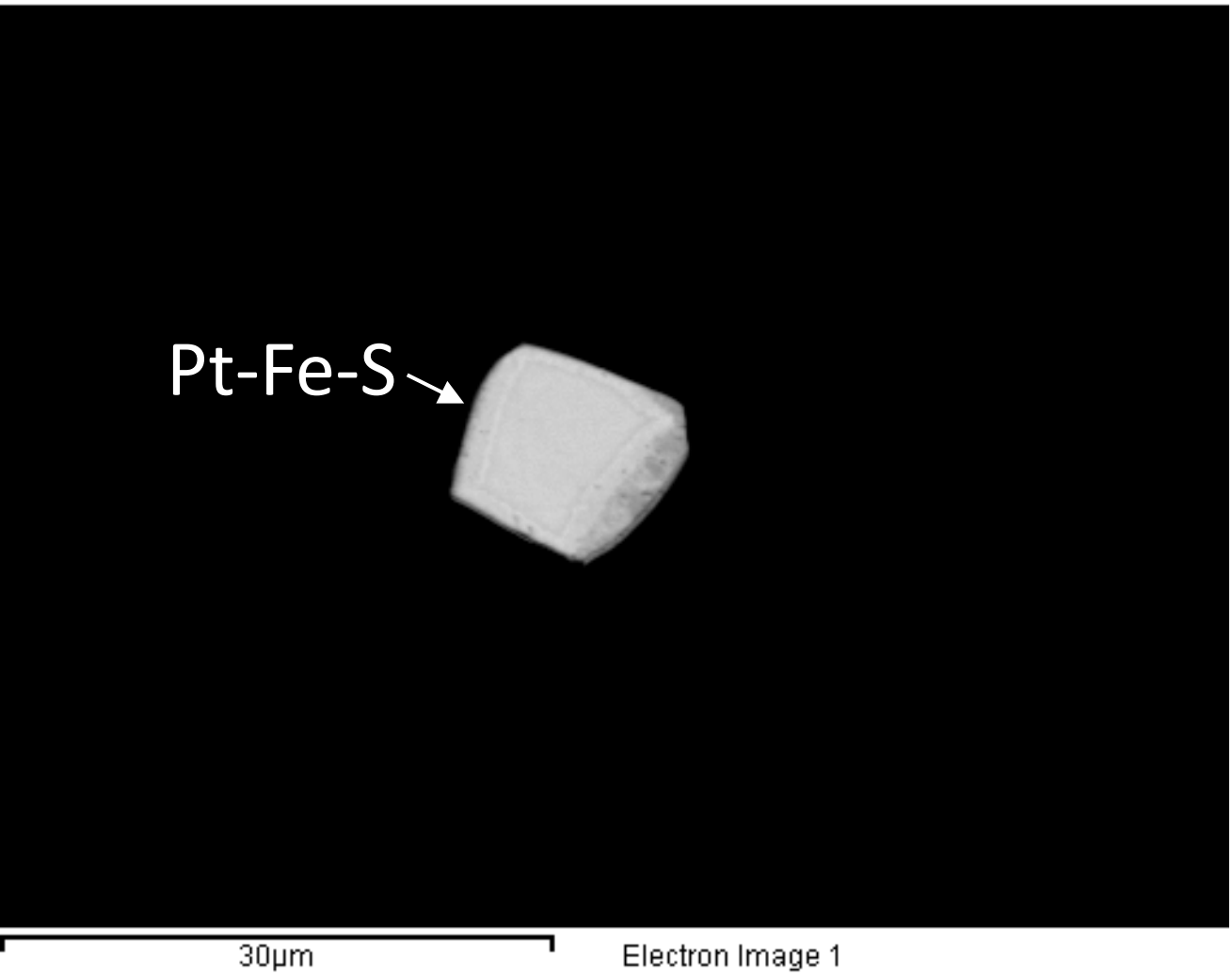
PTSR-35 AB 1-2



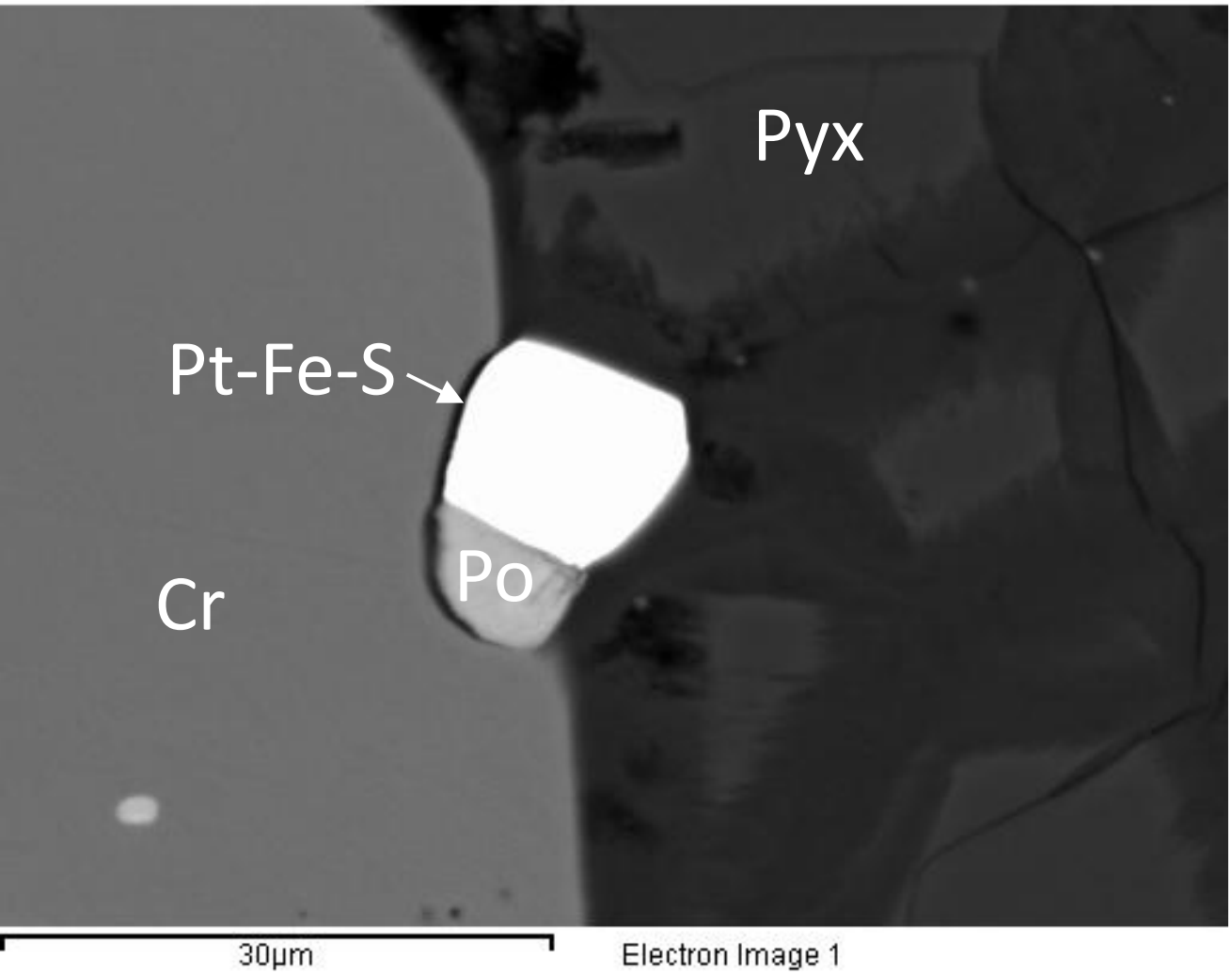
PTSR-35 AC 1



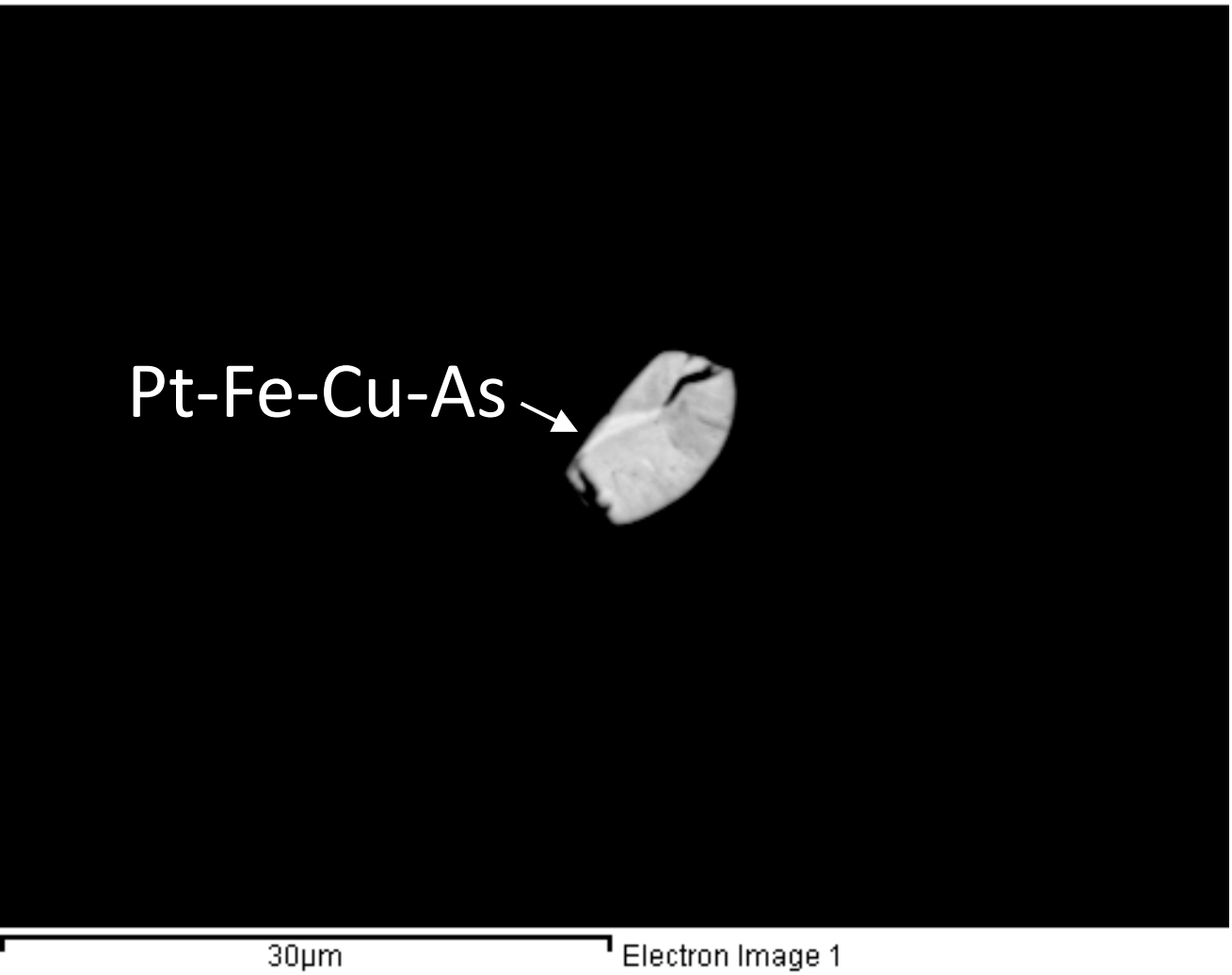
PTSR-35 AD 1



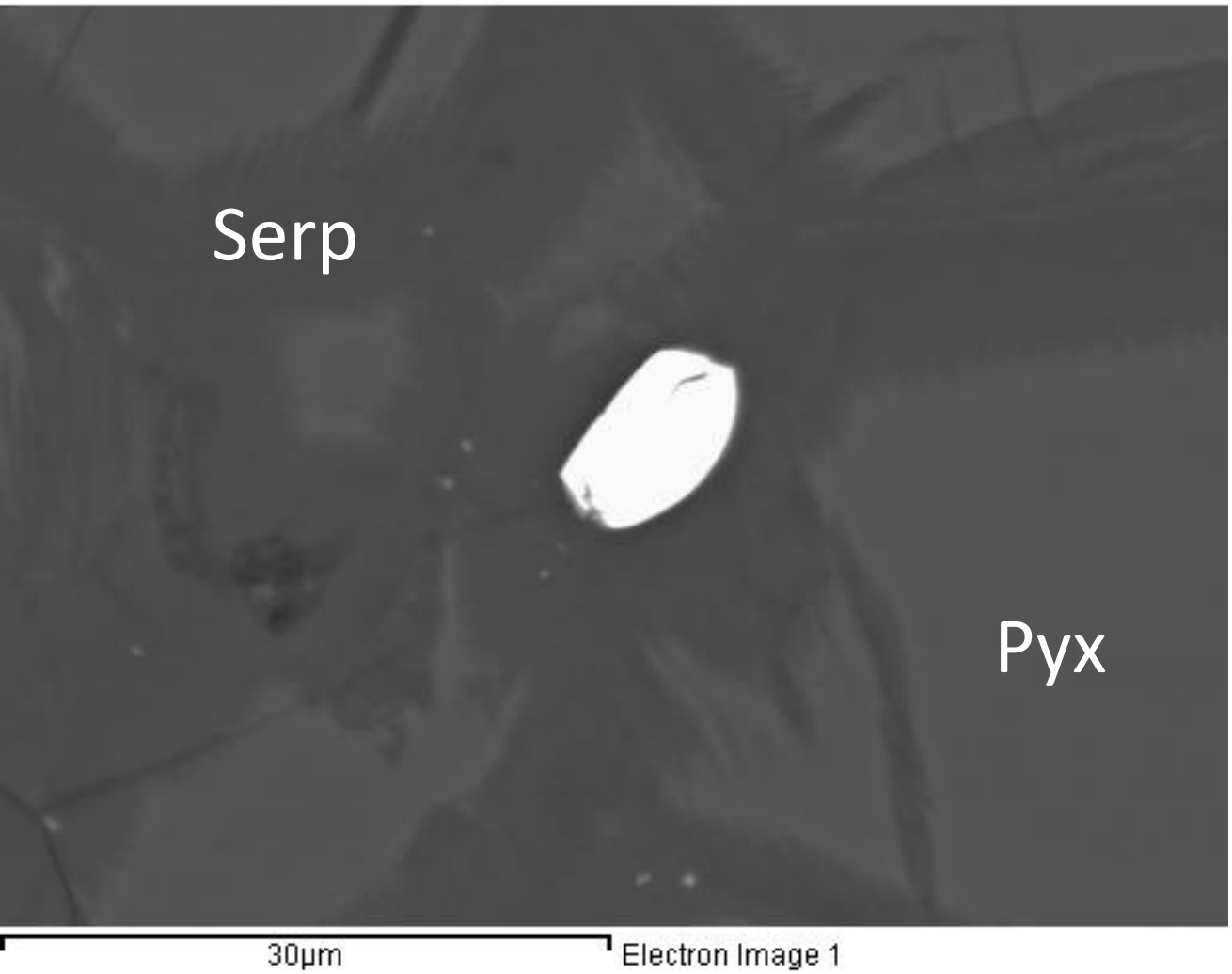
PTSR-35 AD 1 Light



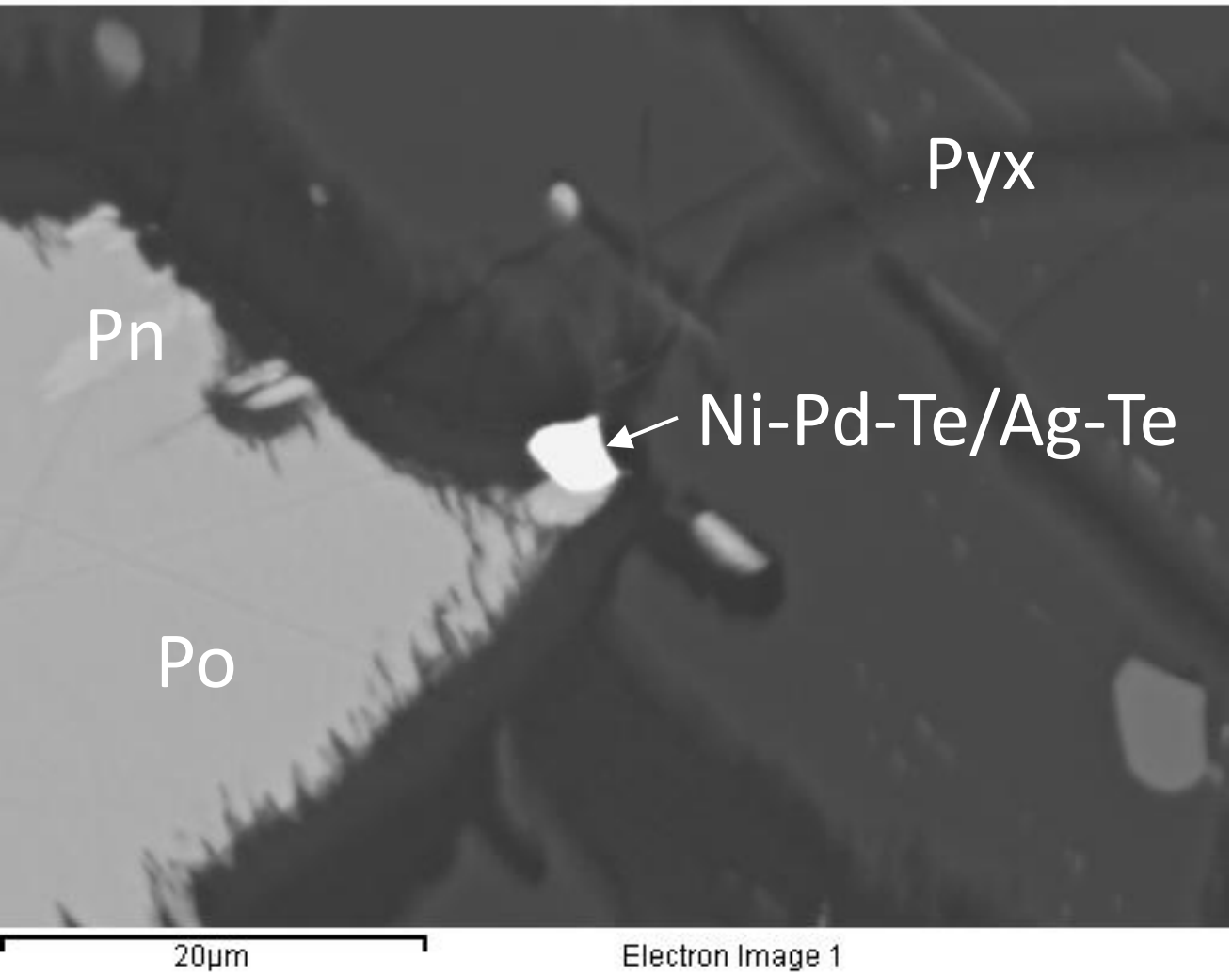
PTSR-35 AD 2



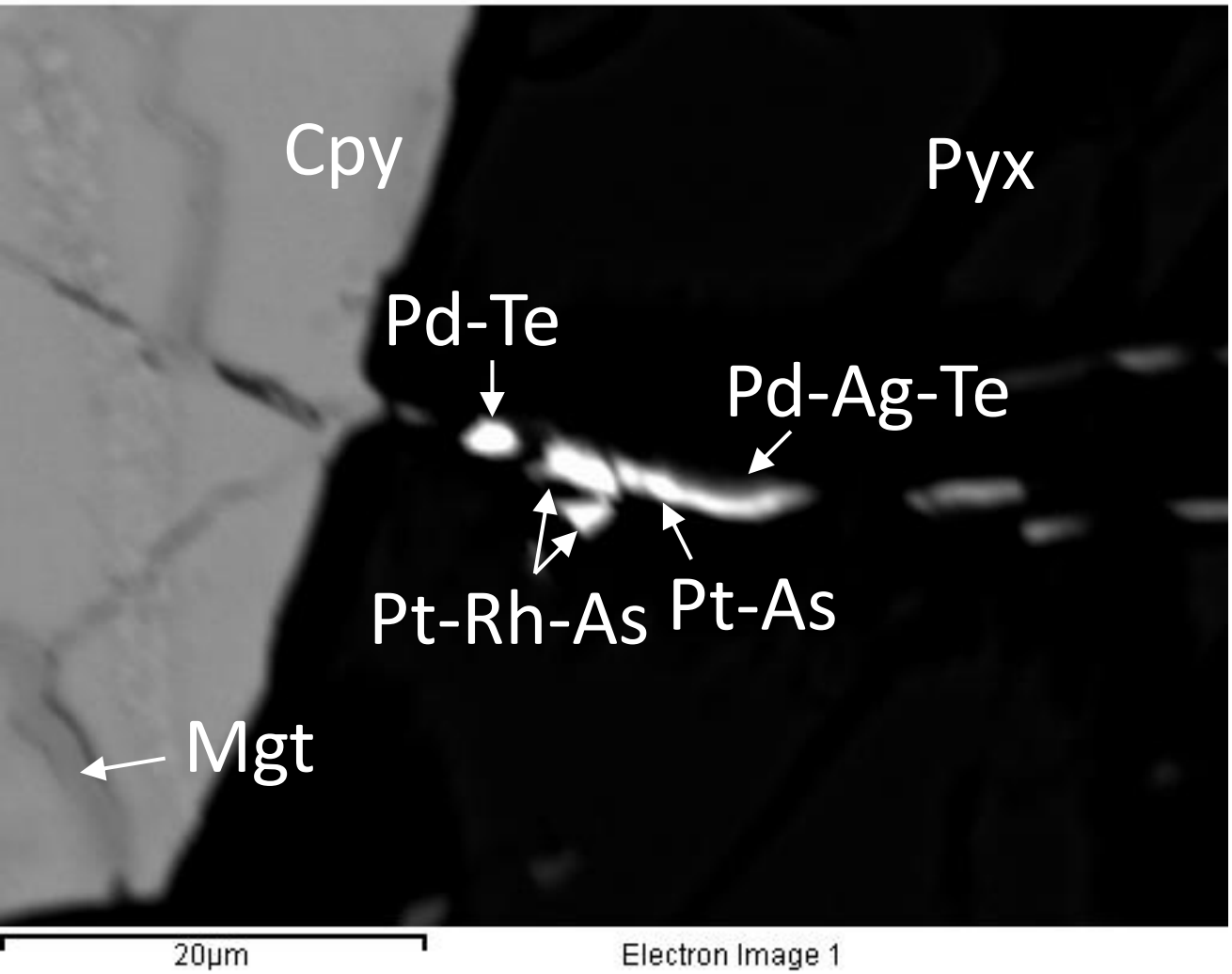
PTSR-35 AD 2 Light



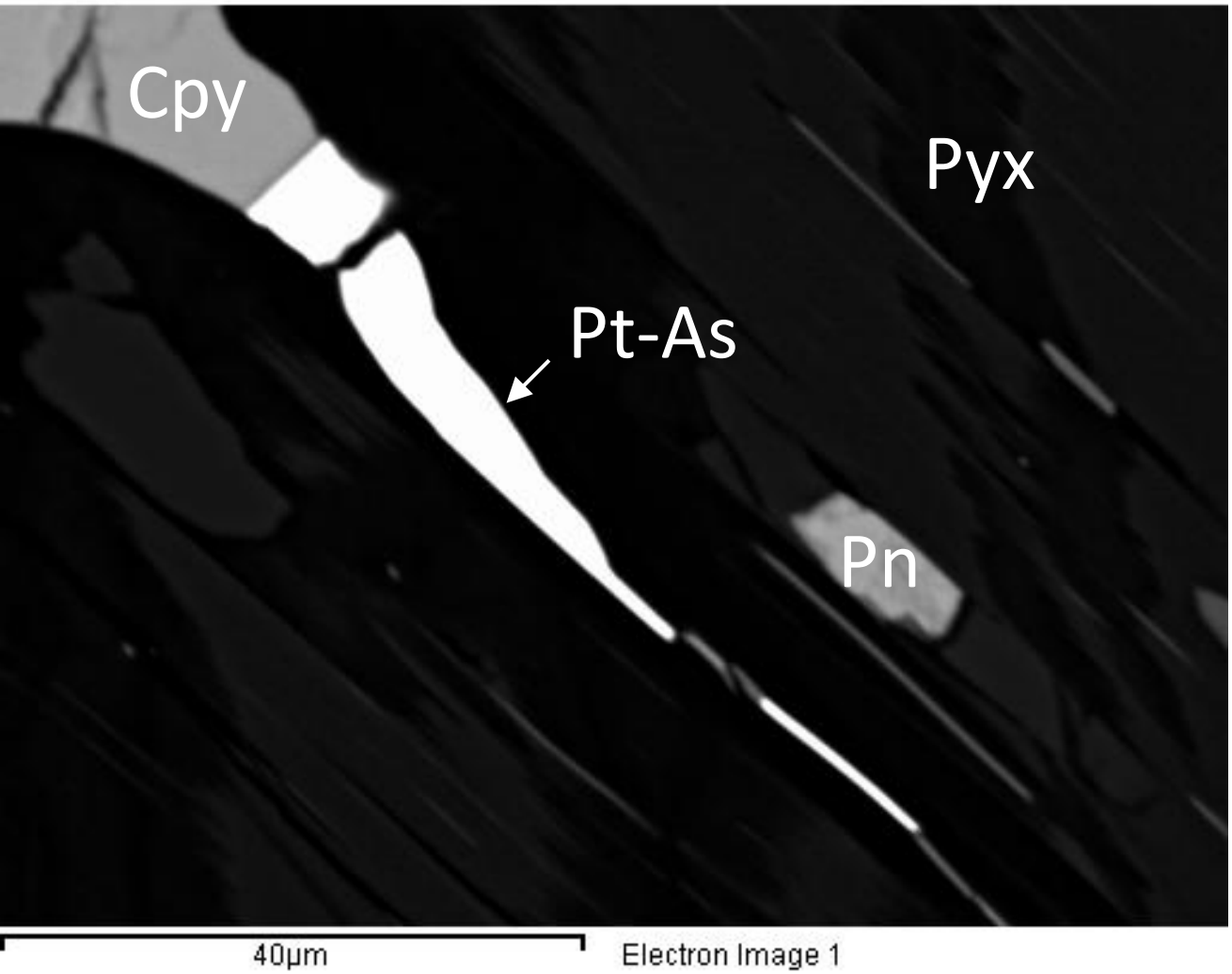
PTSR-35 AE 1



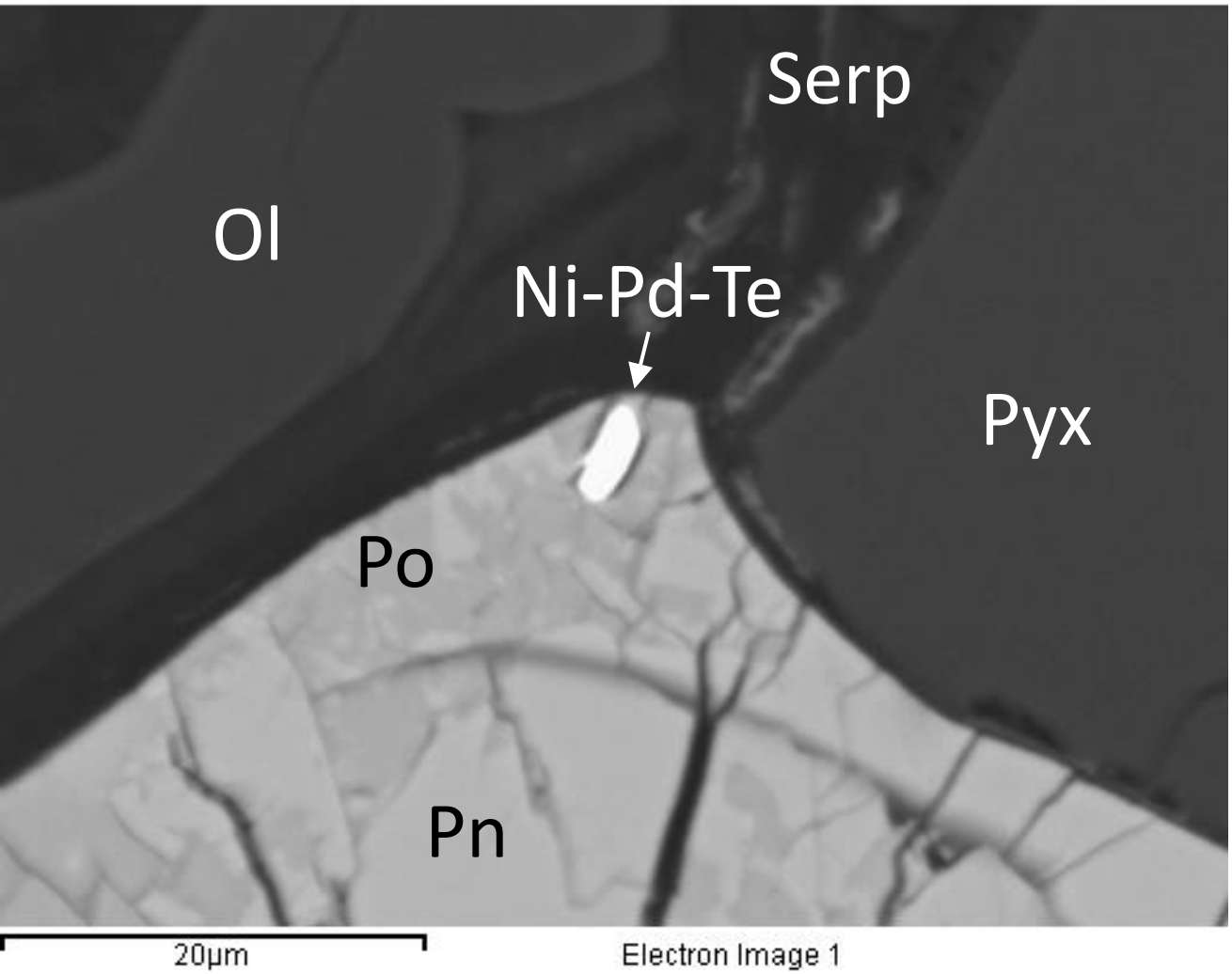
PTSR-35 AF 1-4



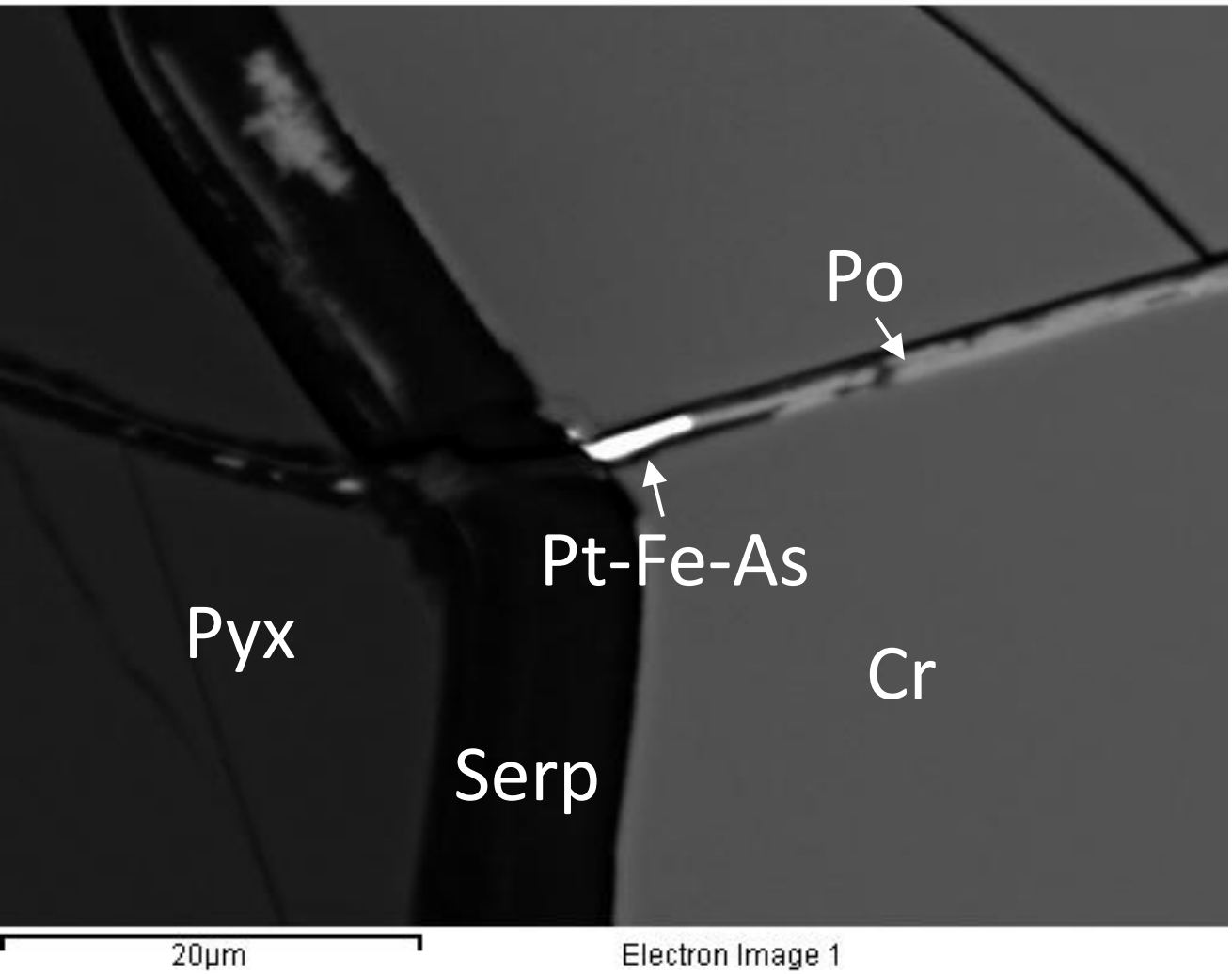
PTSR-35 AG 1-3



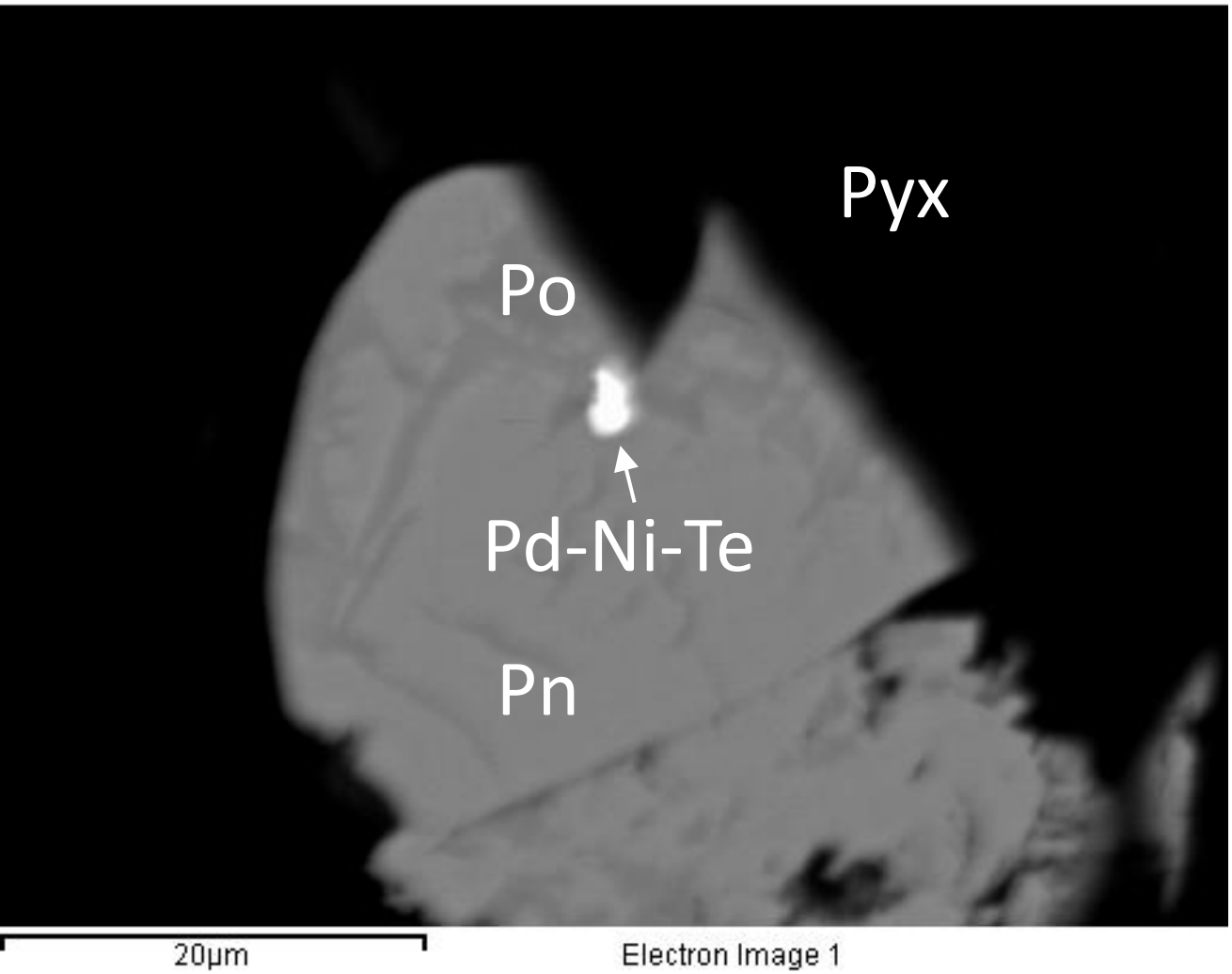
PTSR-35 AH 1



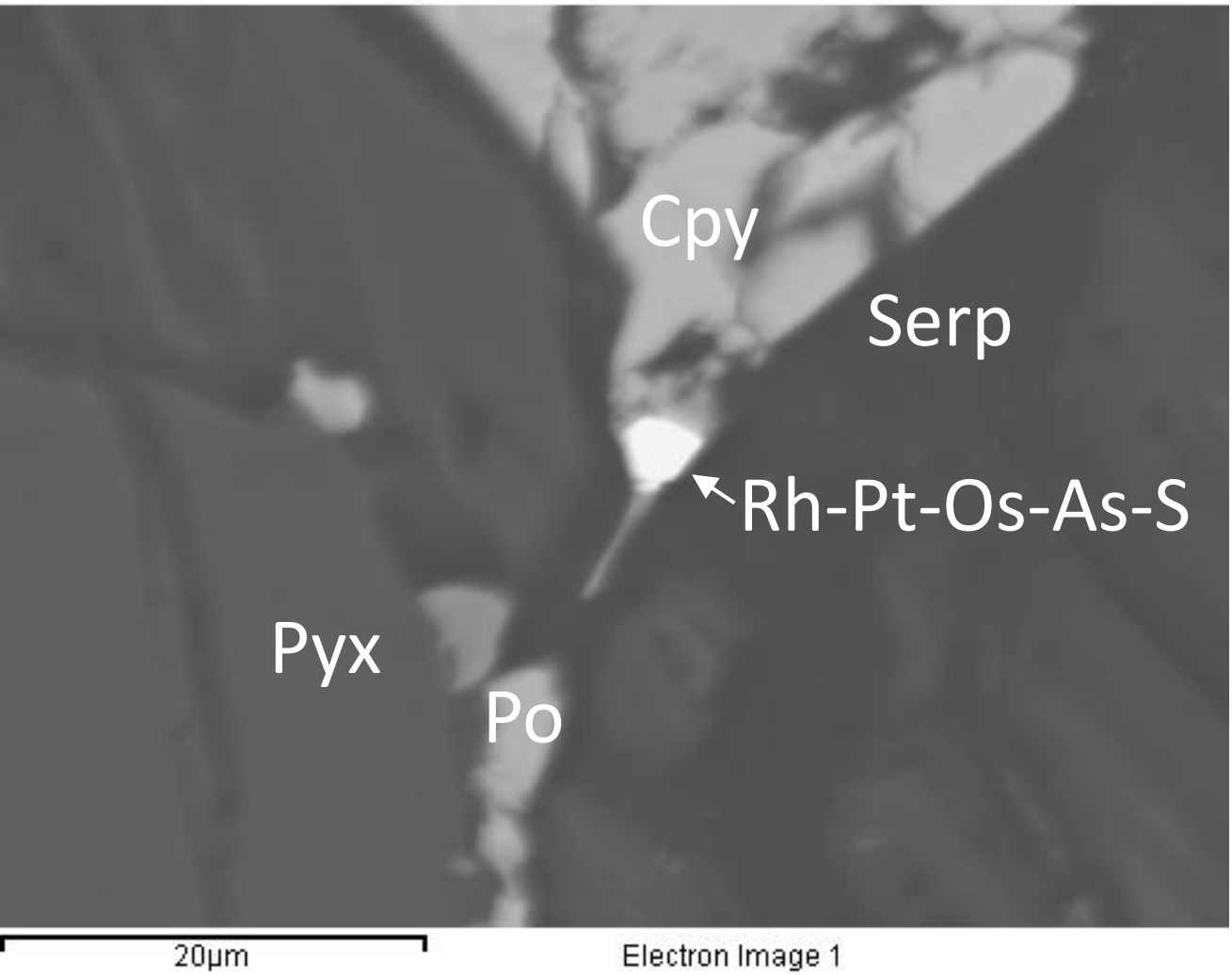
PTSR-35 AI 1



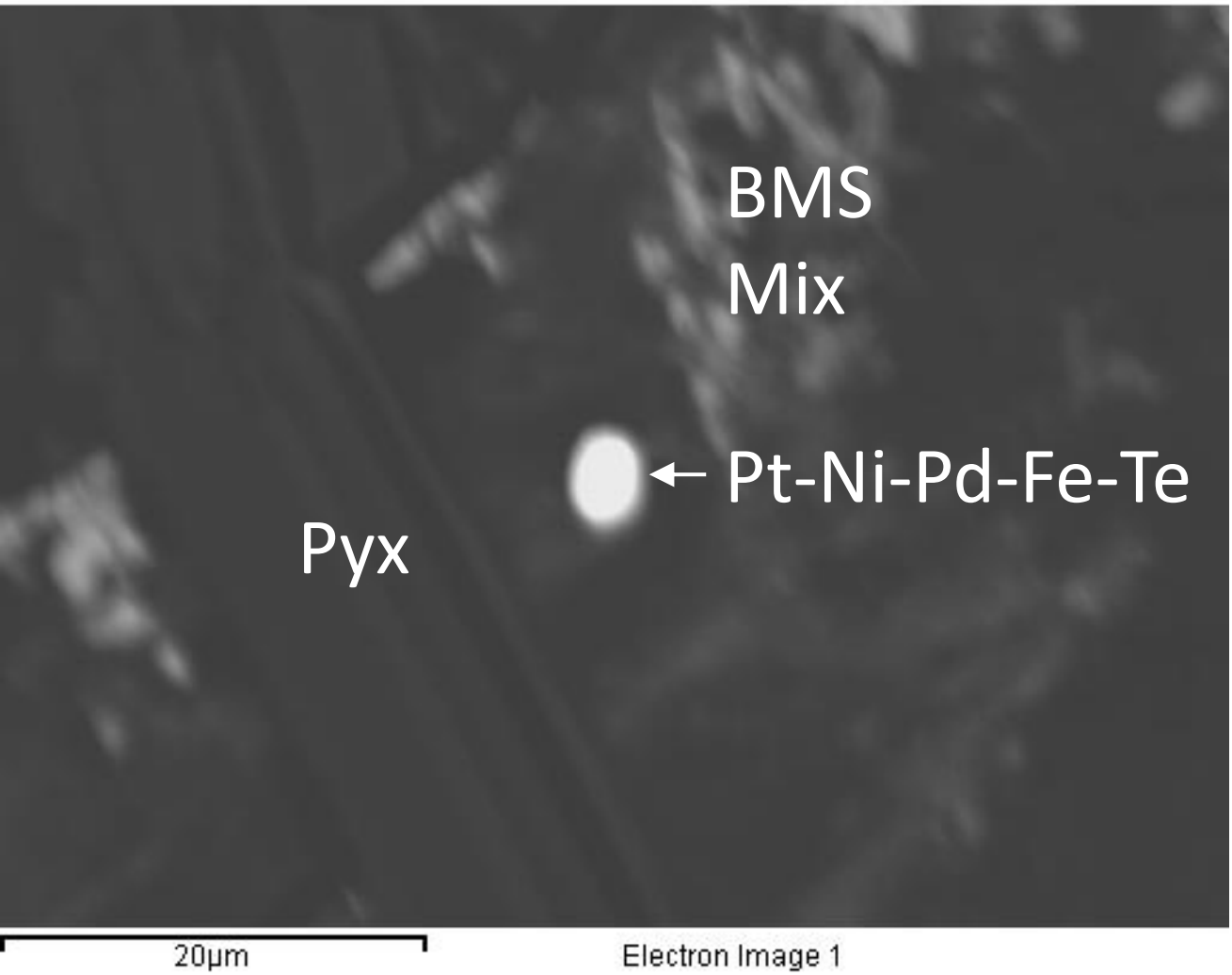
PTSR-35 AJ 1



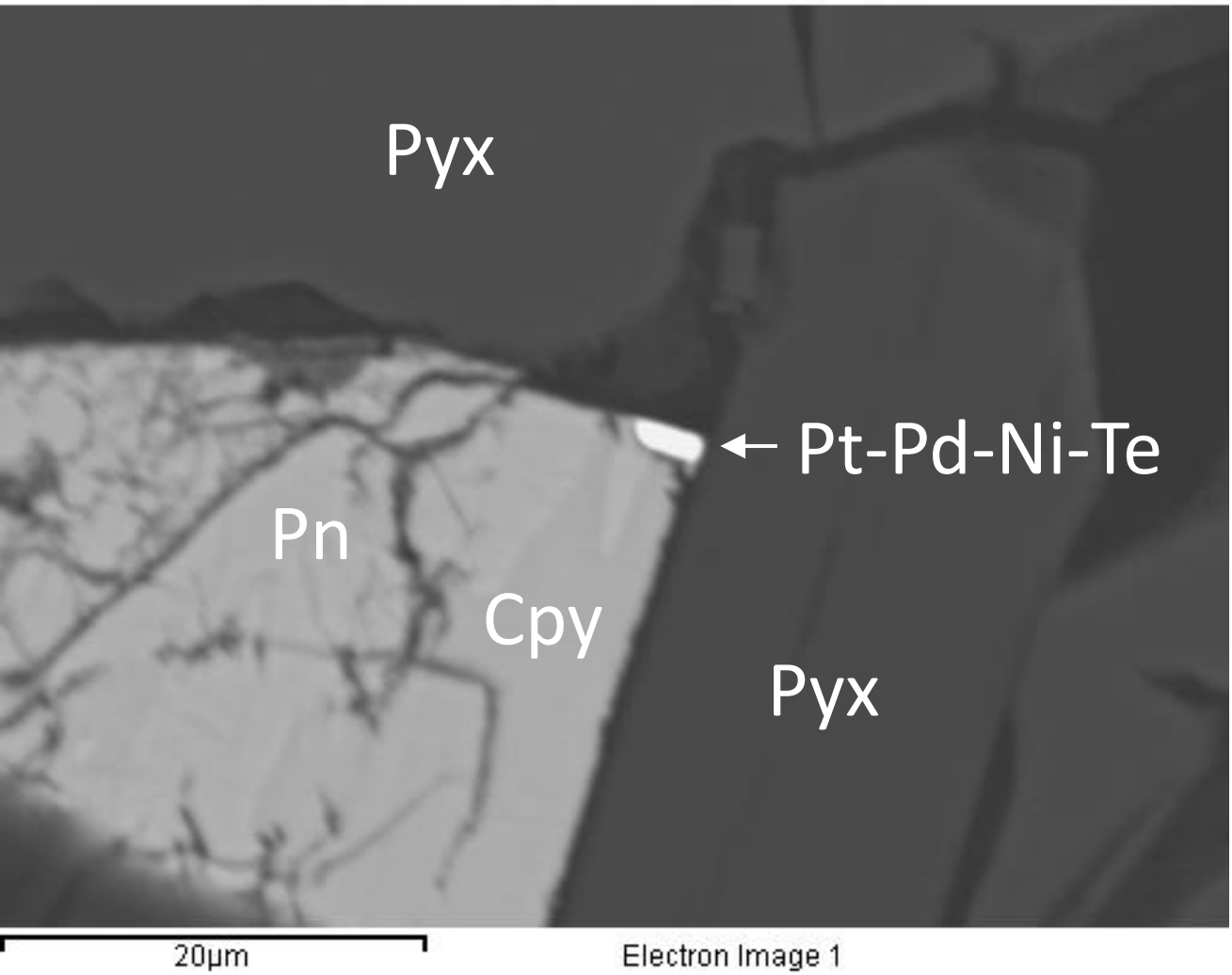
PTSR-35 AK 1



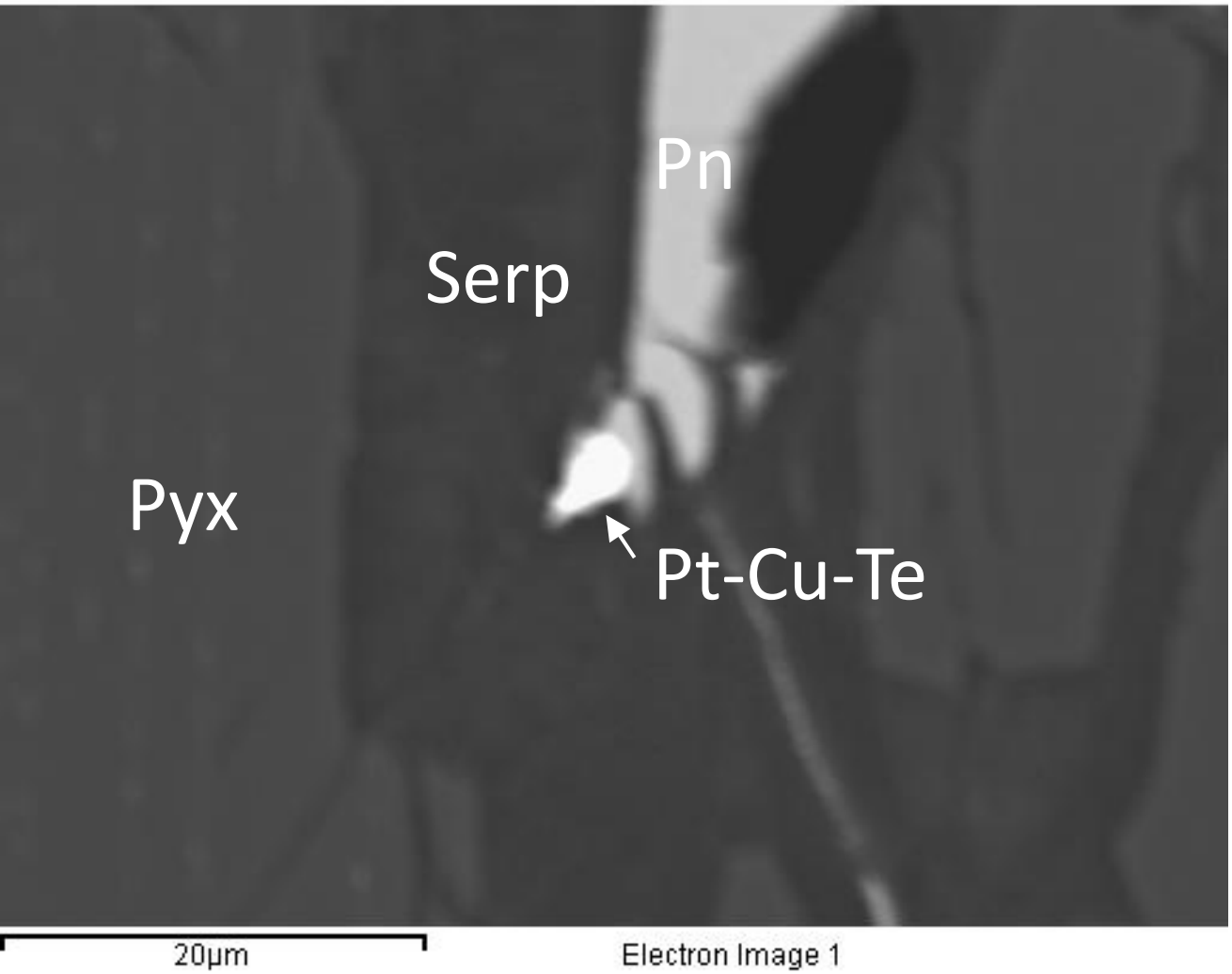
PTSR-36 A 1



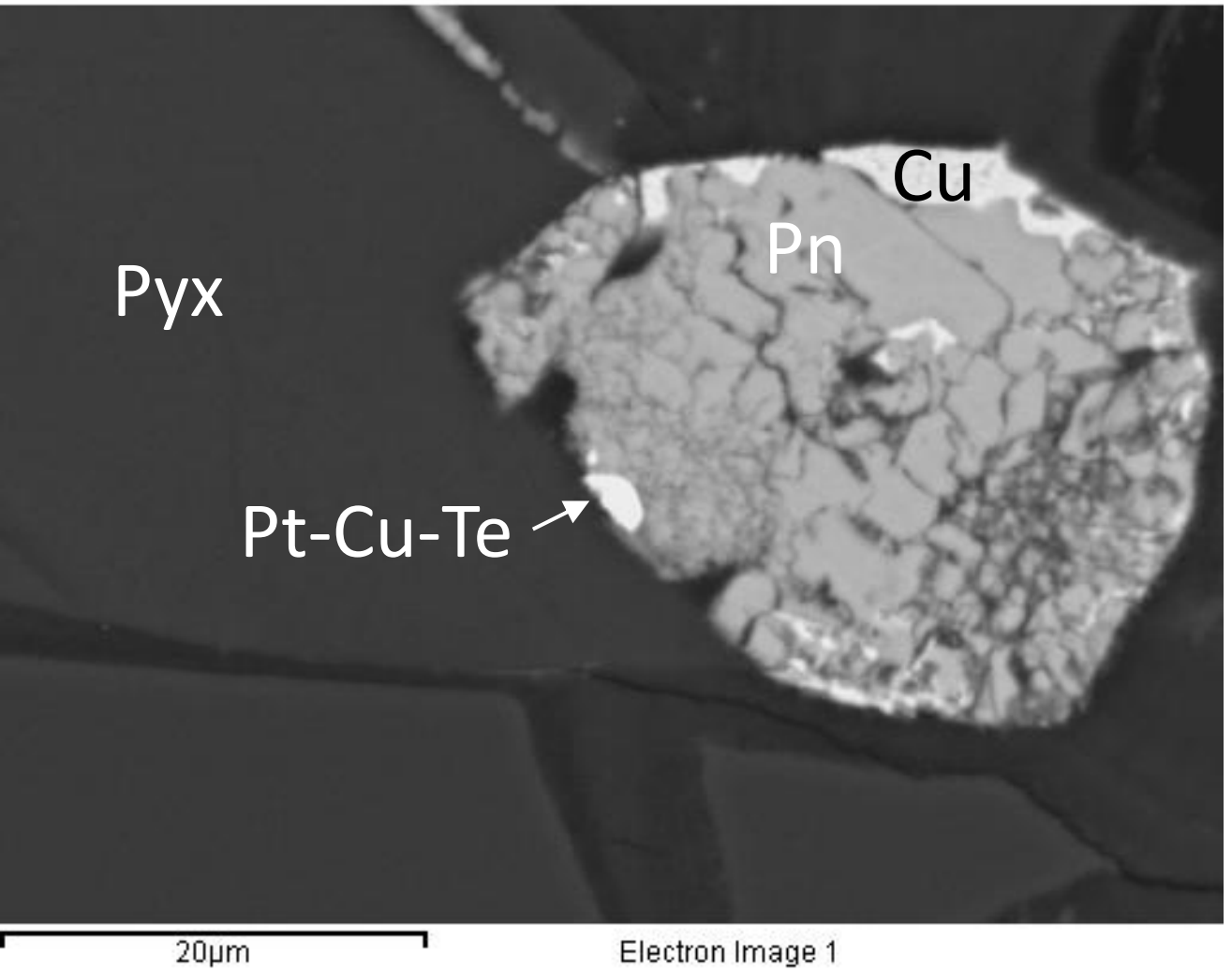
PTSR-36 B 1



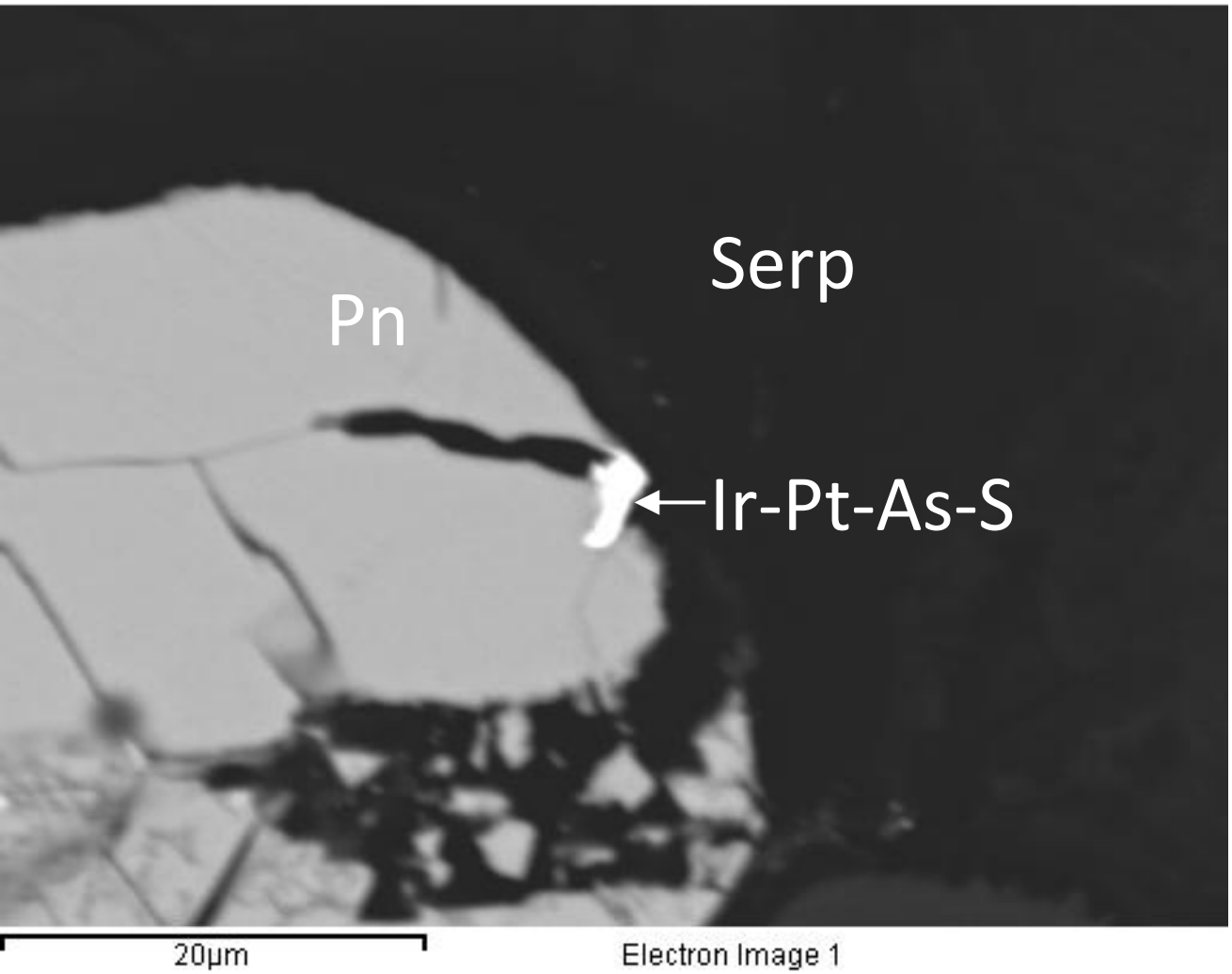
PTSR-37 A 1



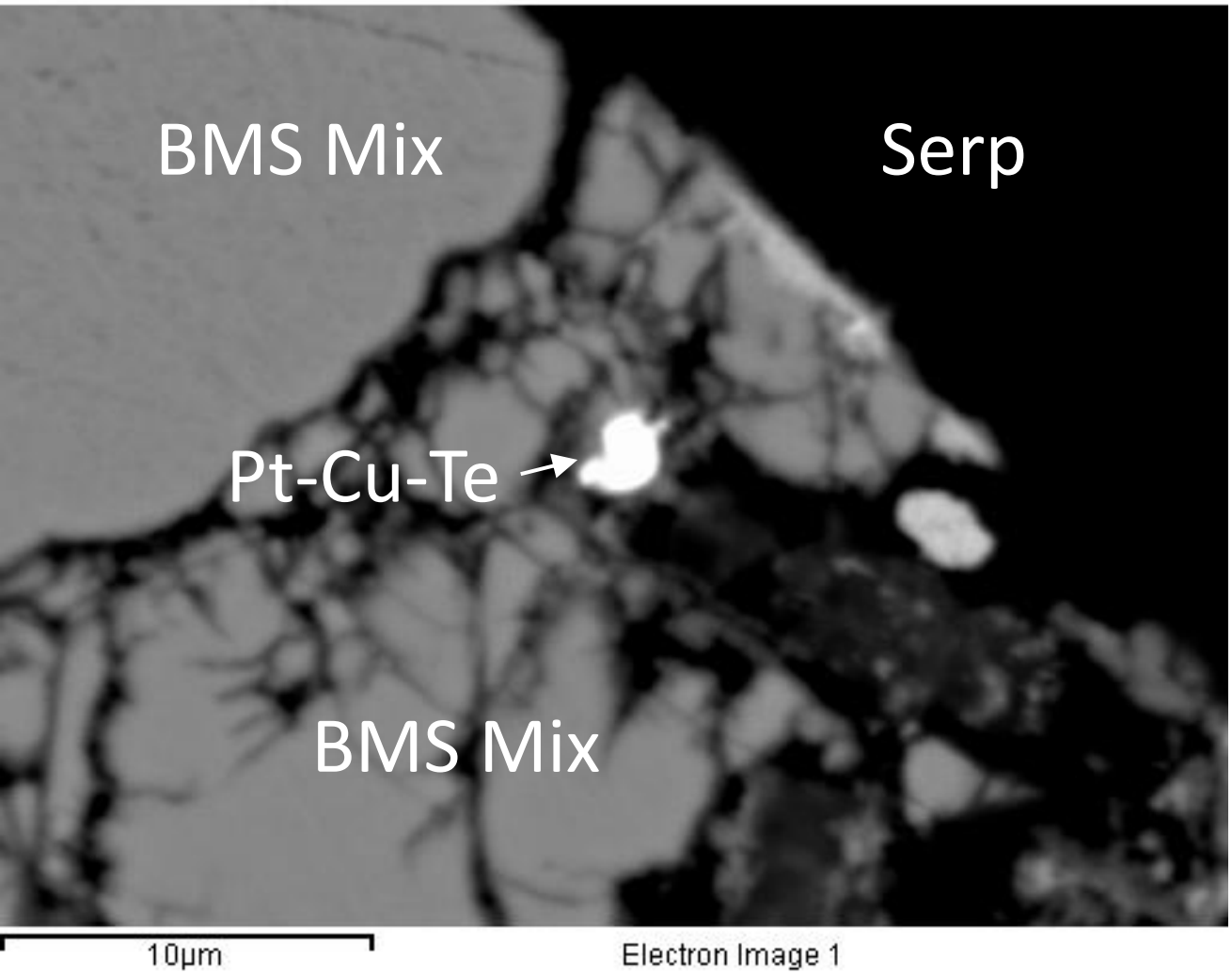
PTSR-37 B 1



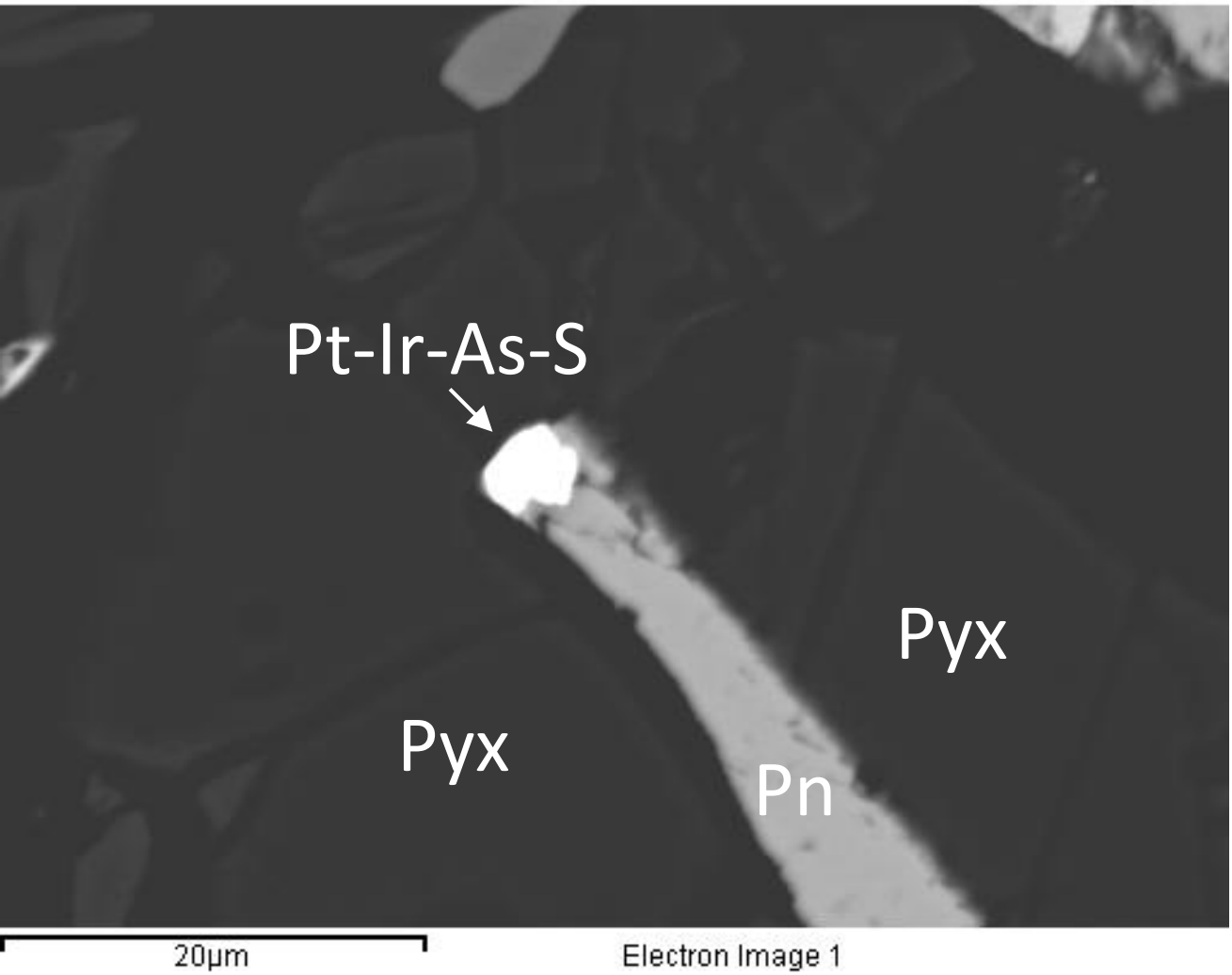
PTSR-37 C 1



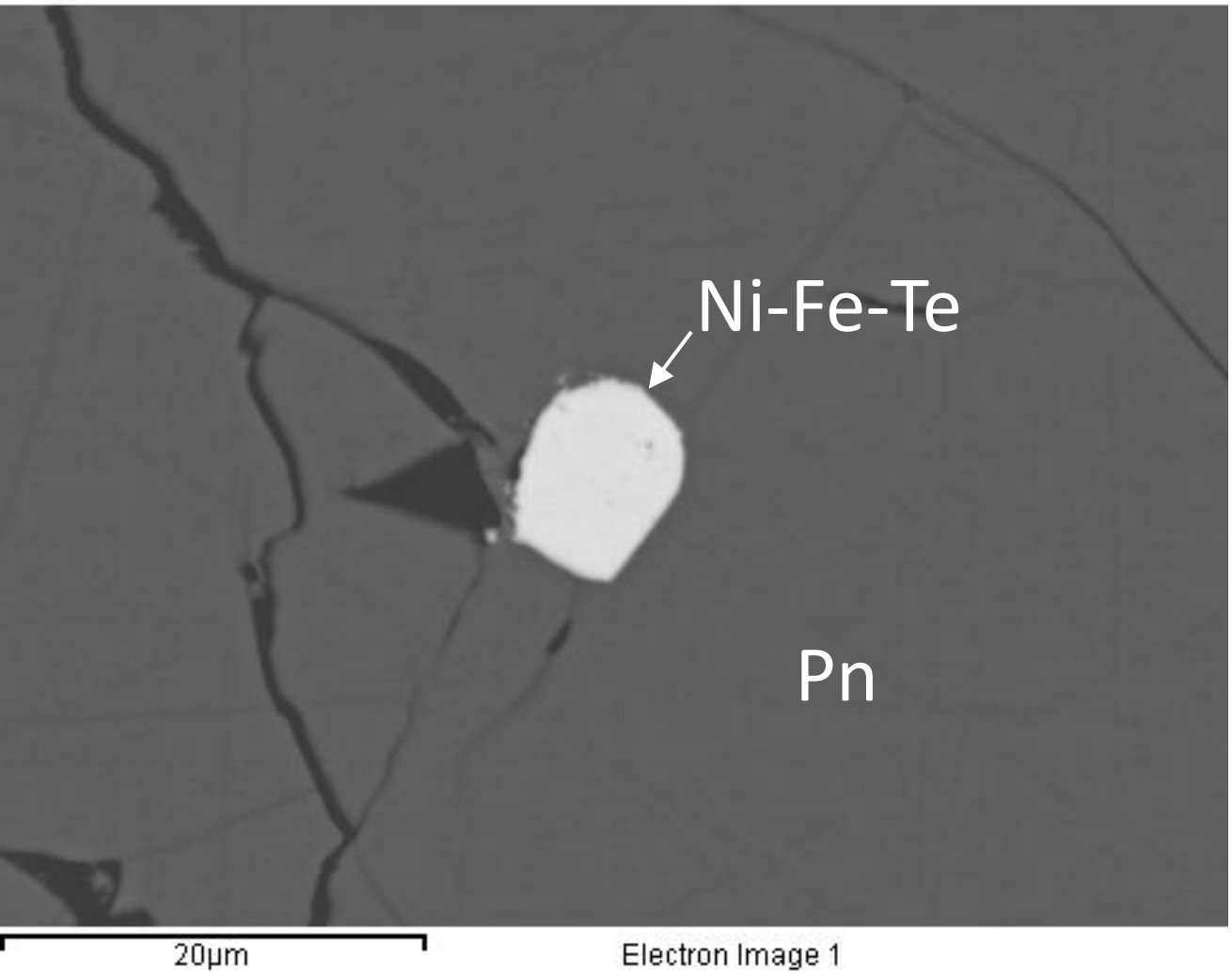
PTSR-37 D 1



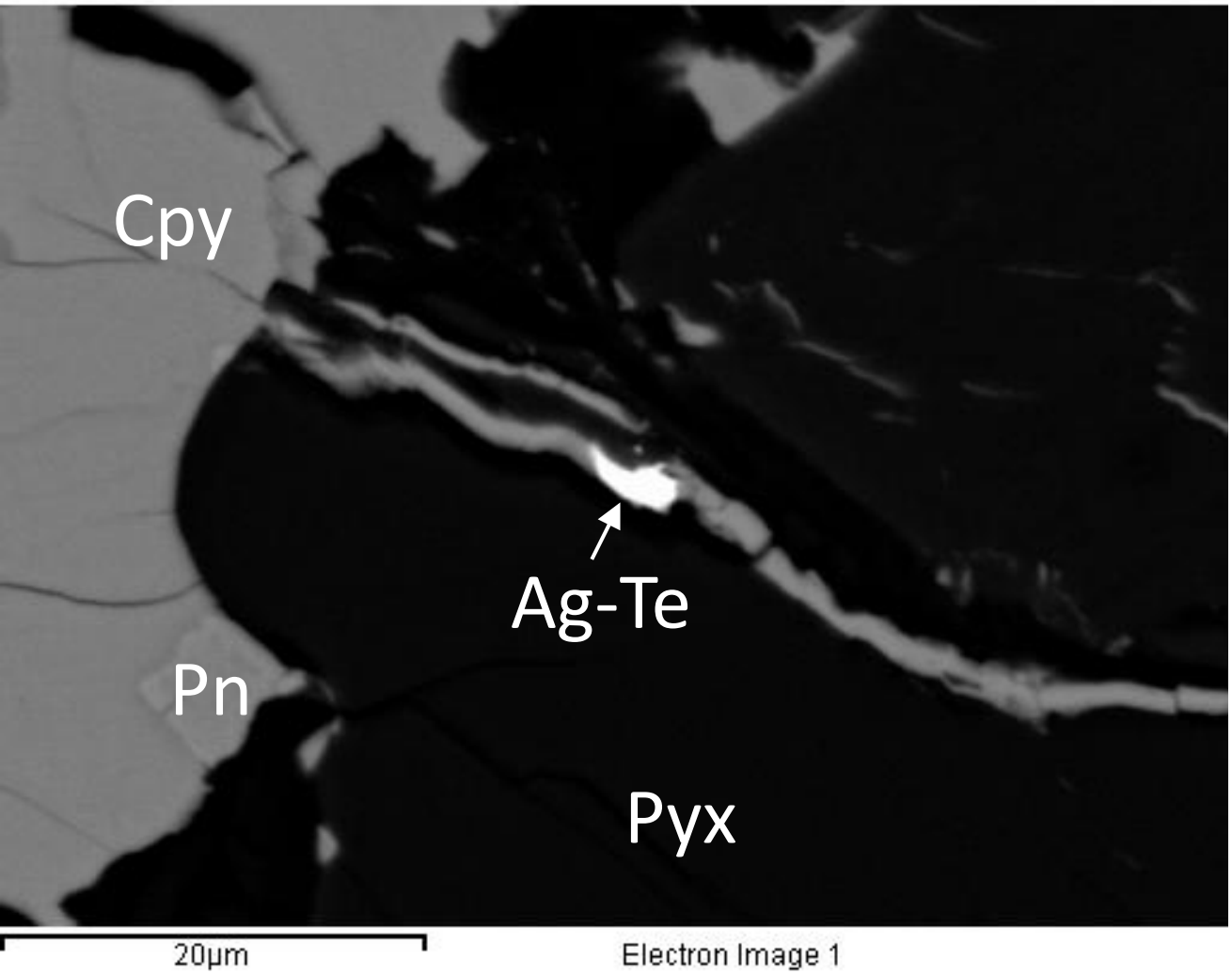
PTSR-37 E 1



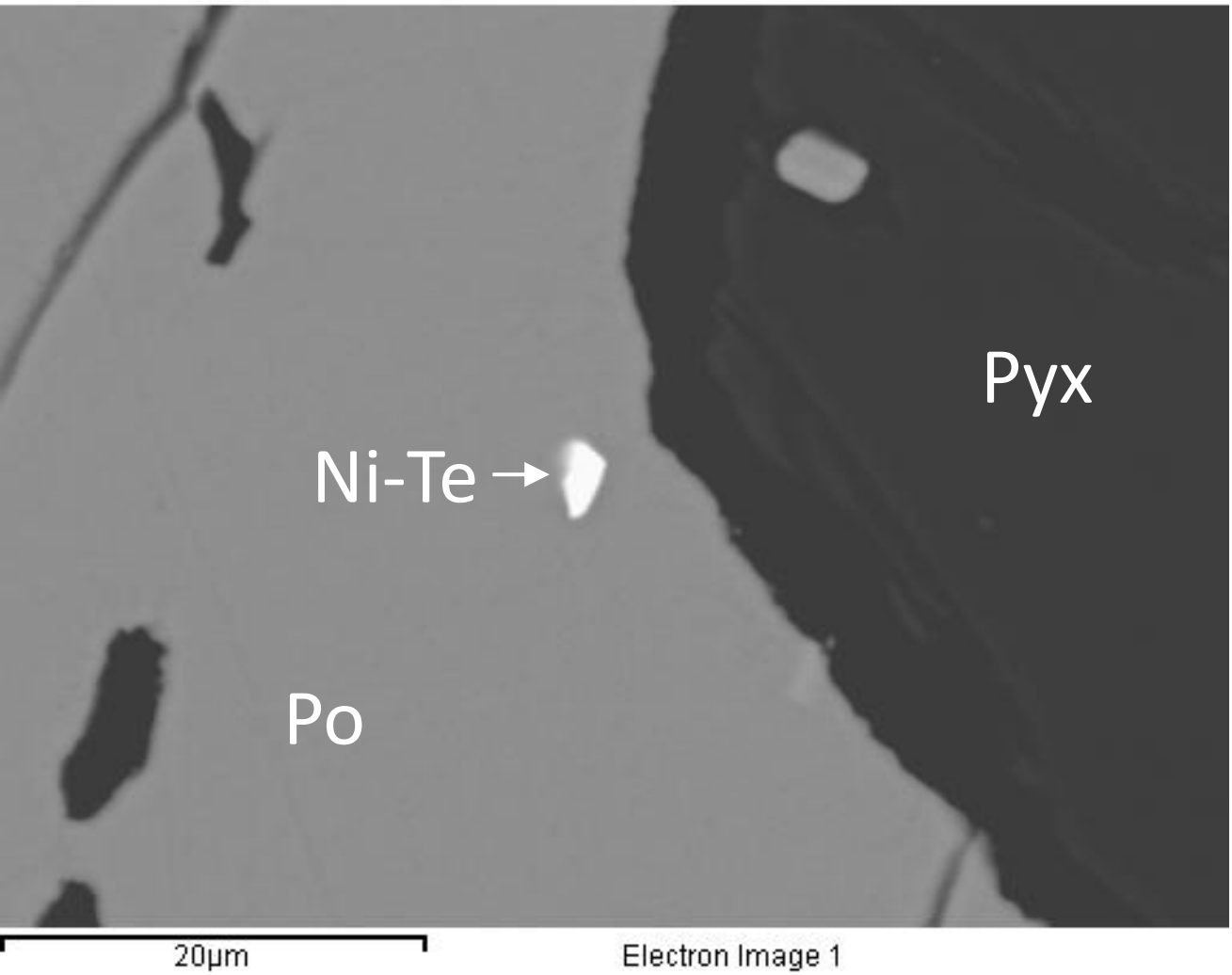
PTSR-40 A 1



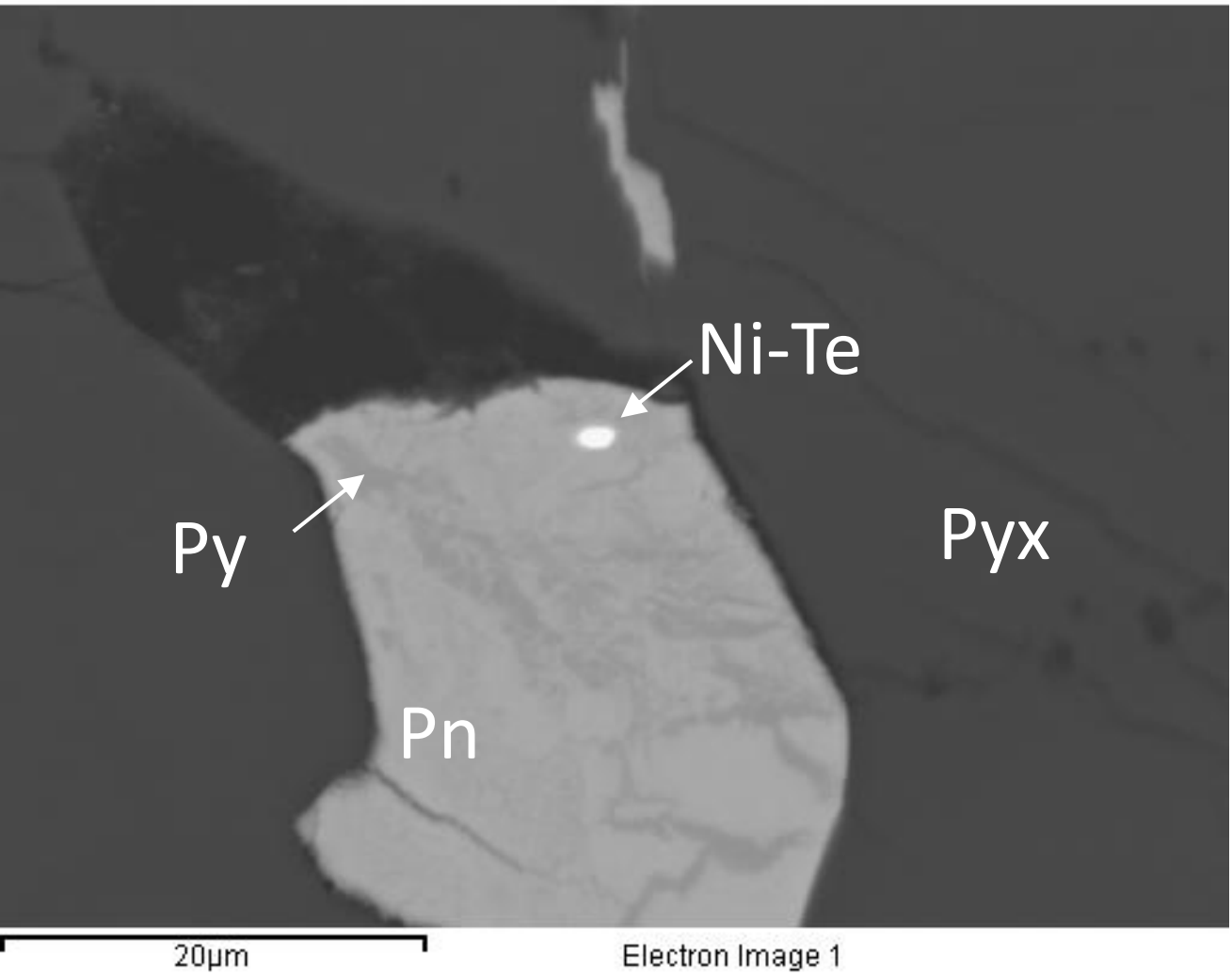
PTSR-40 B 1



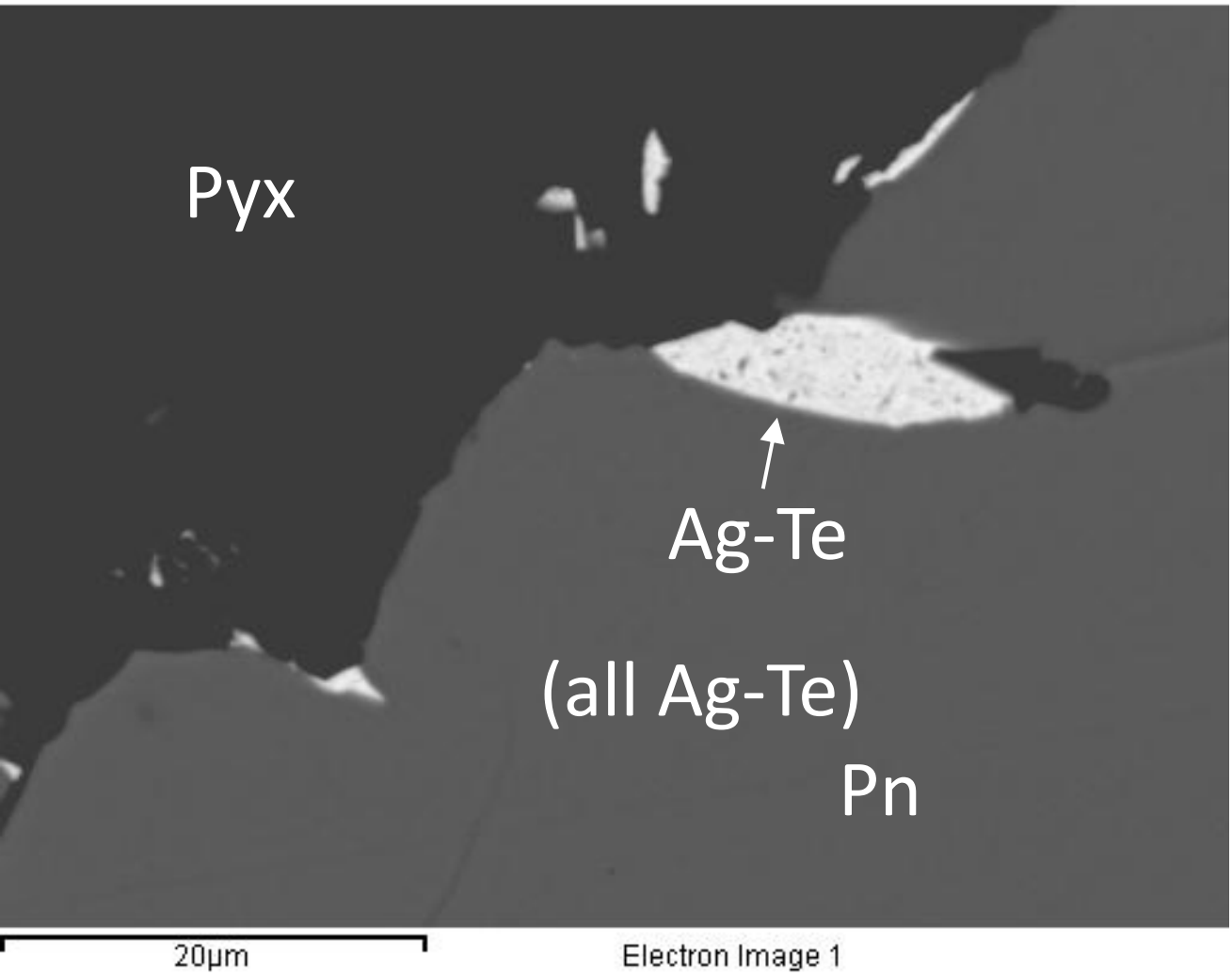
PTSR-40 C 1



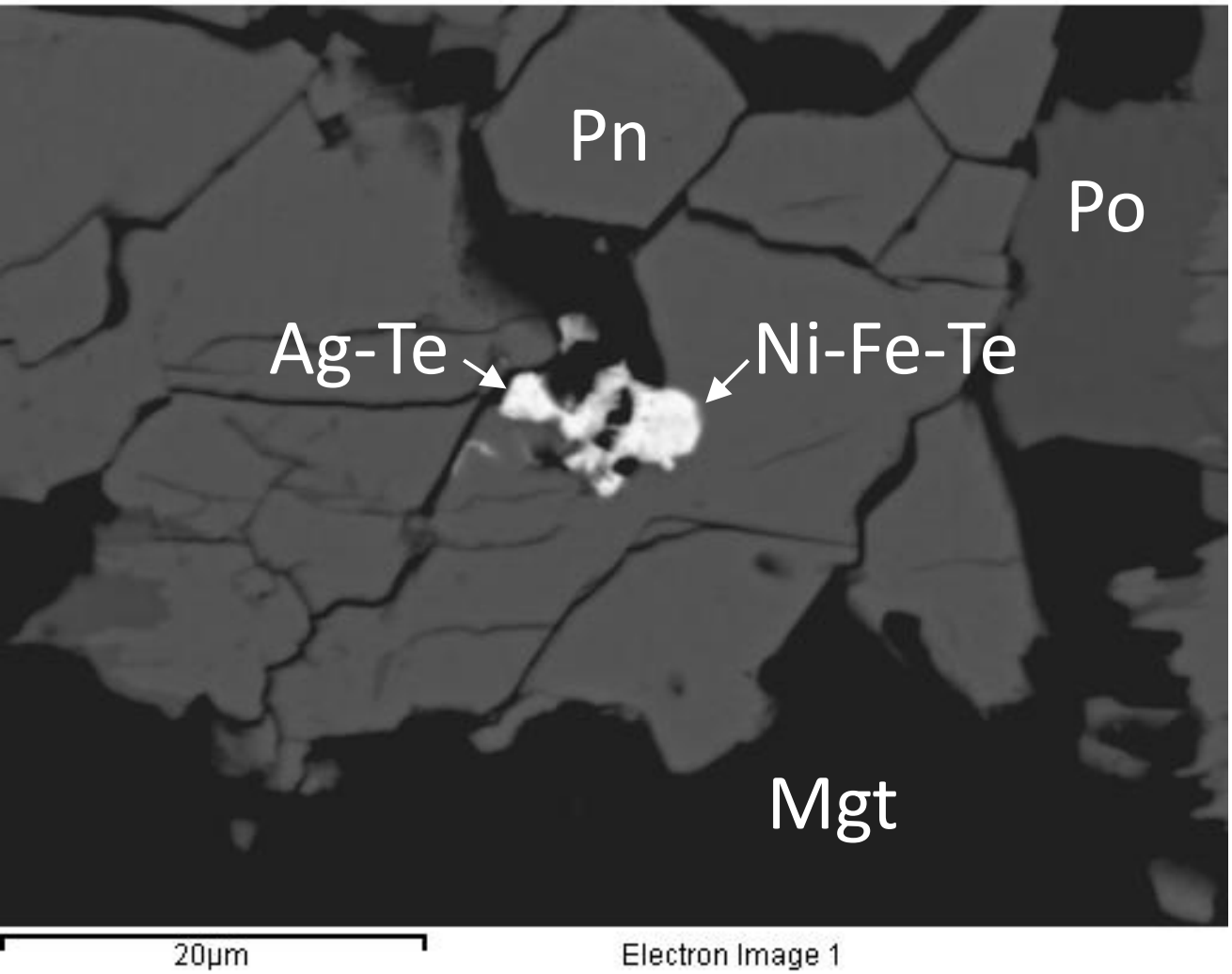
PTSR-40 D 1



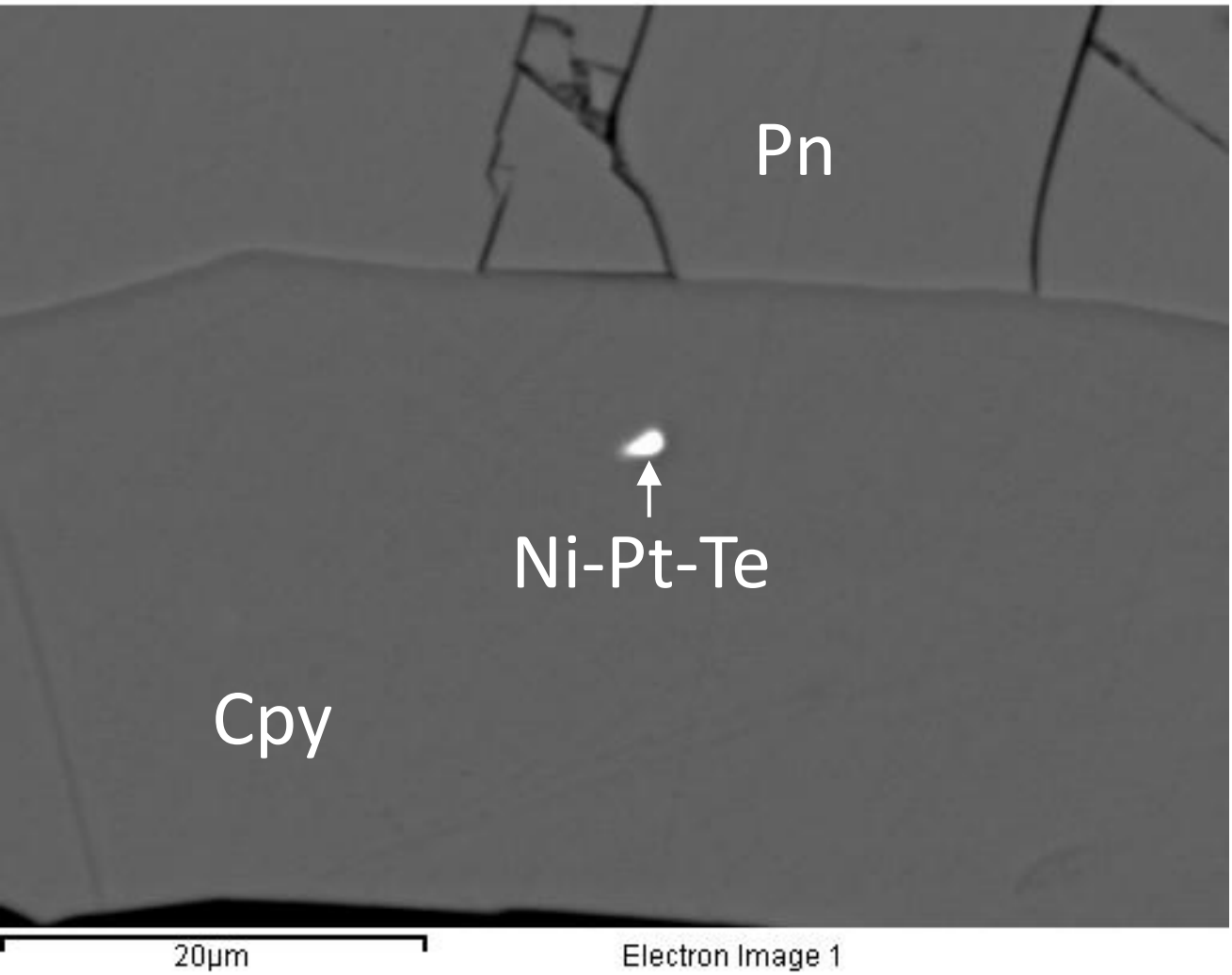
PTSR-40 E 1+



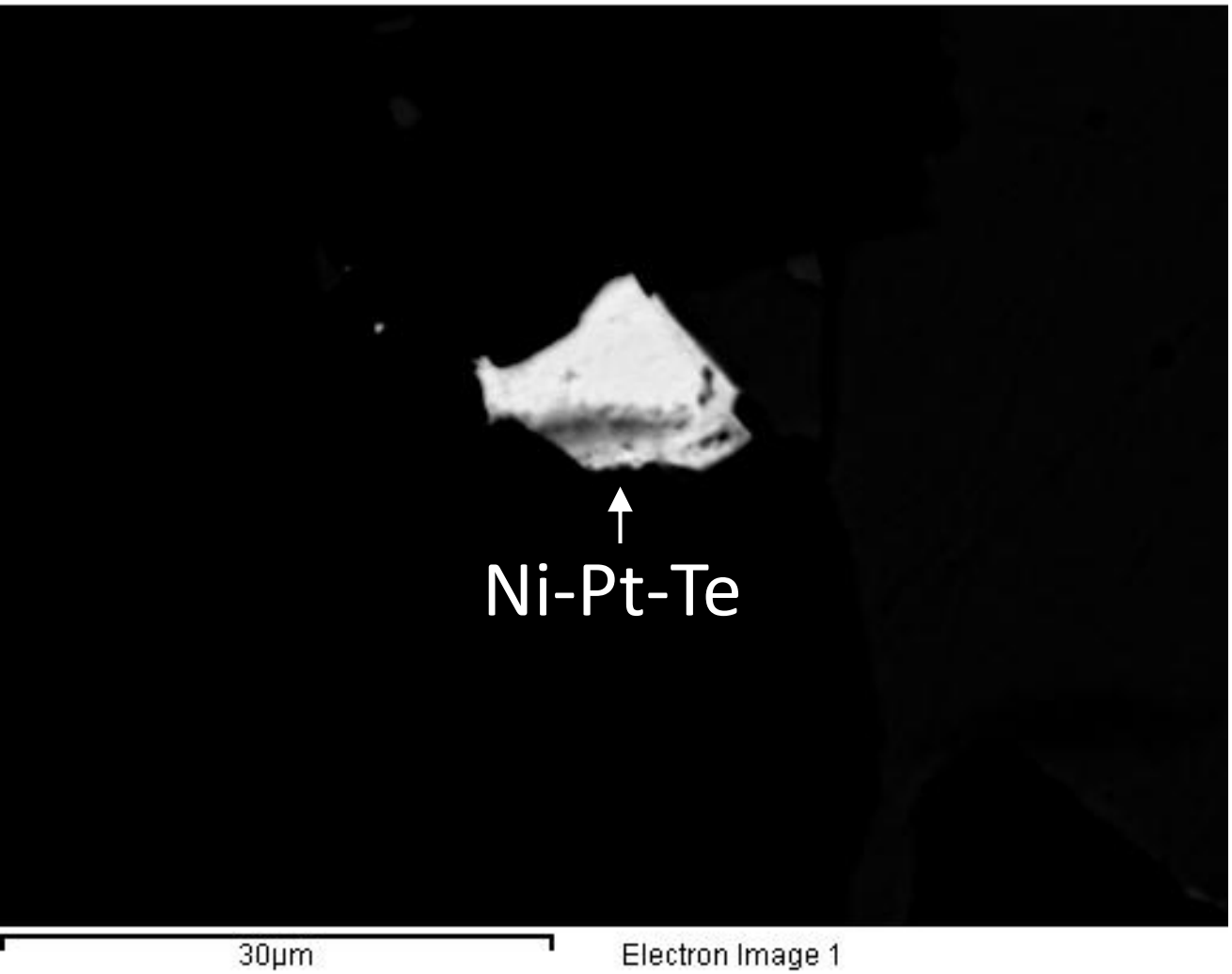
PTSR-40 F 1-2



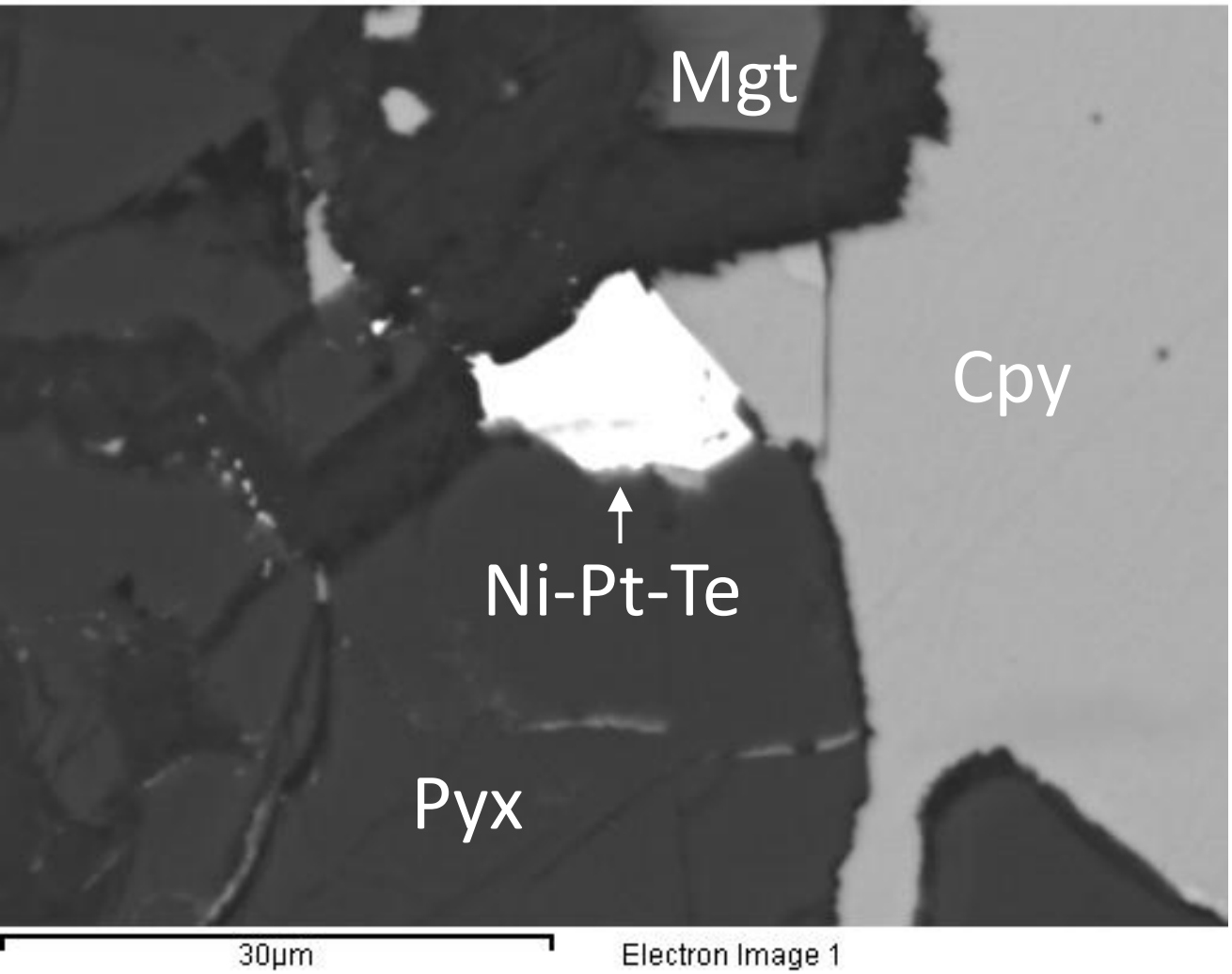
PTSR-40 G 1



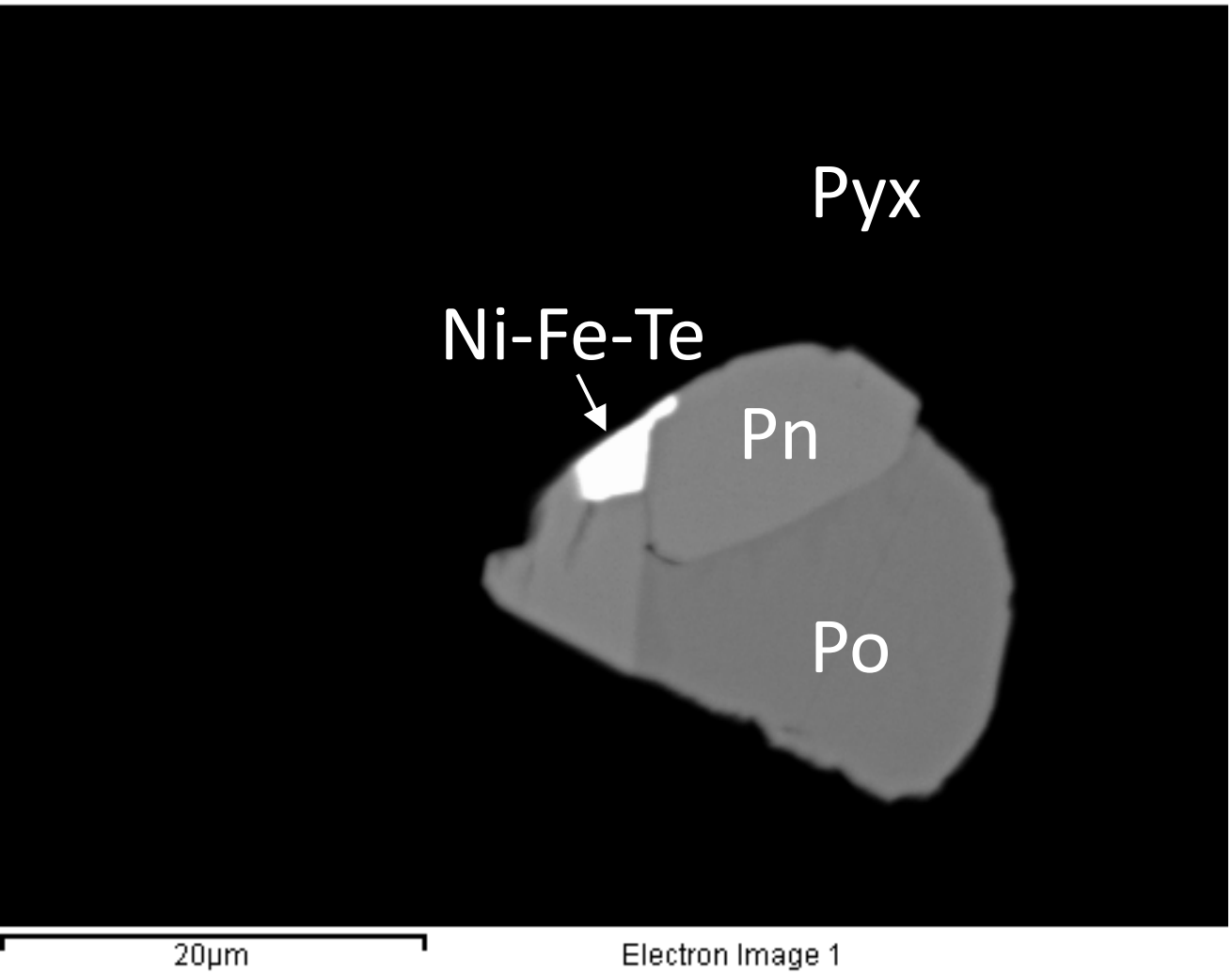
PTSR-40 H 1



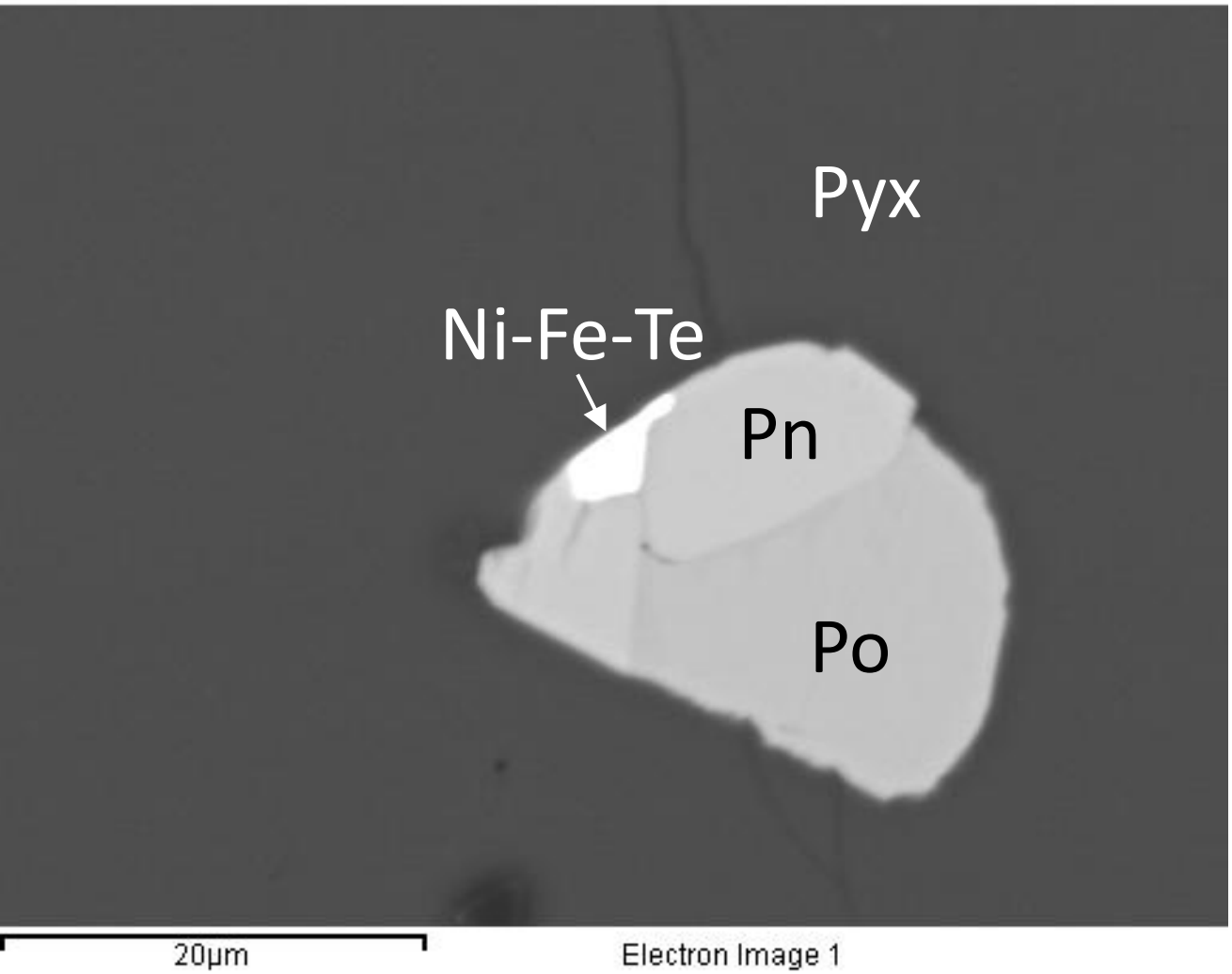
PTSR-40 H 1 Light



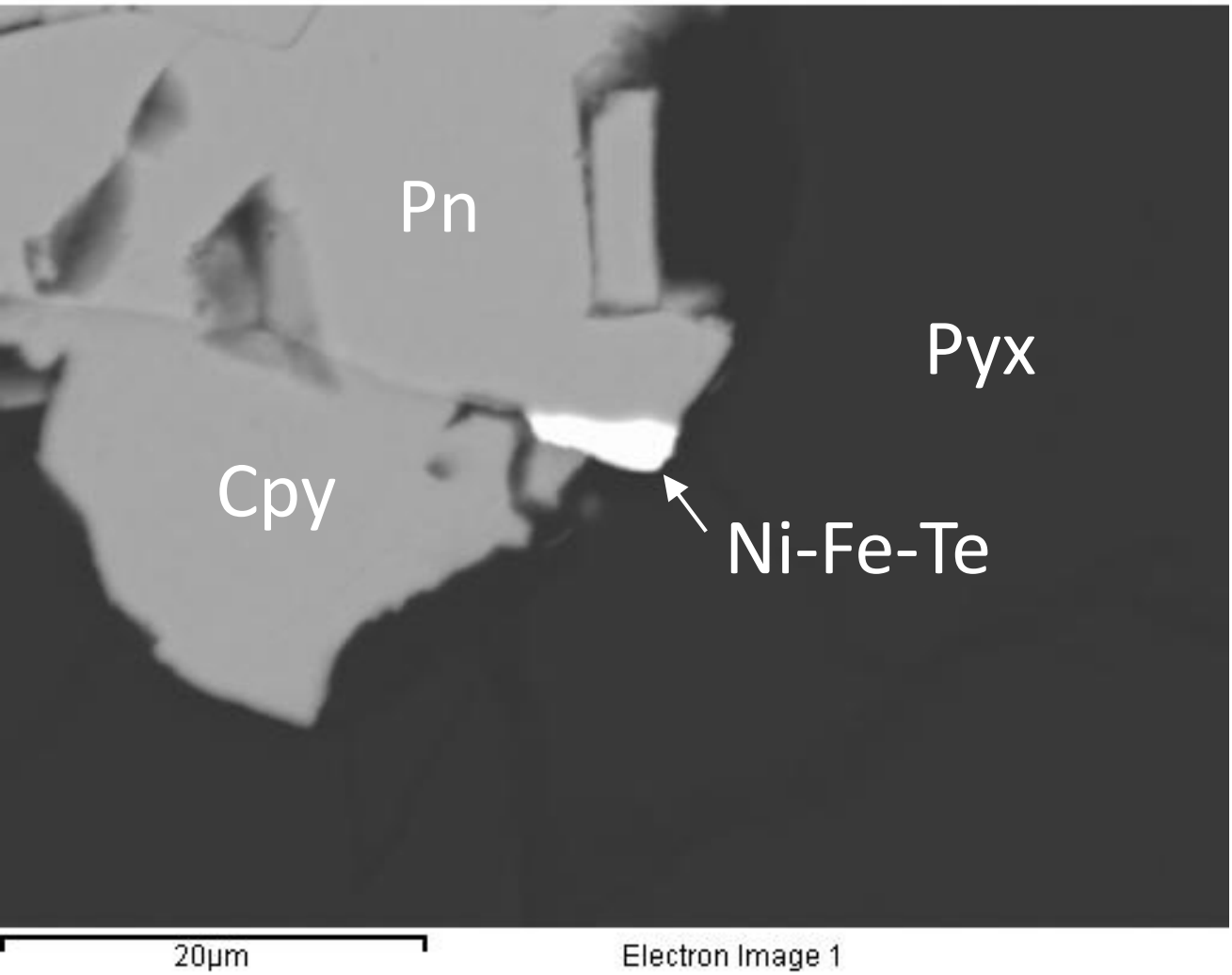
PTSR-40 I 1



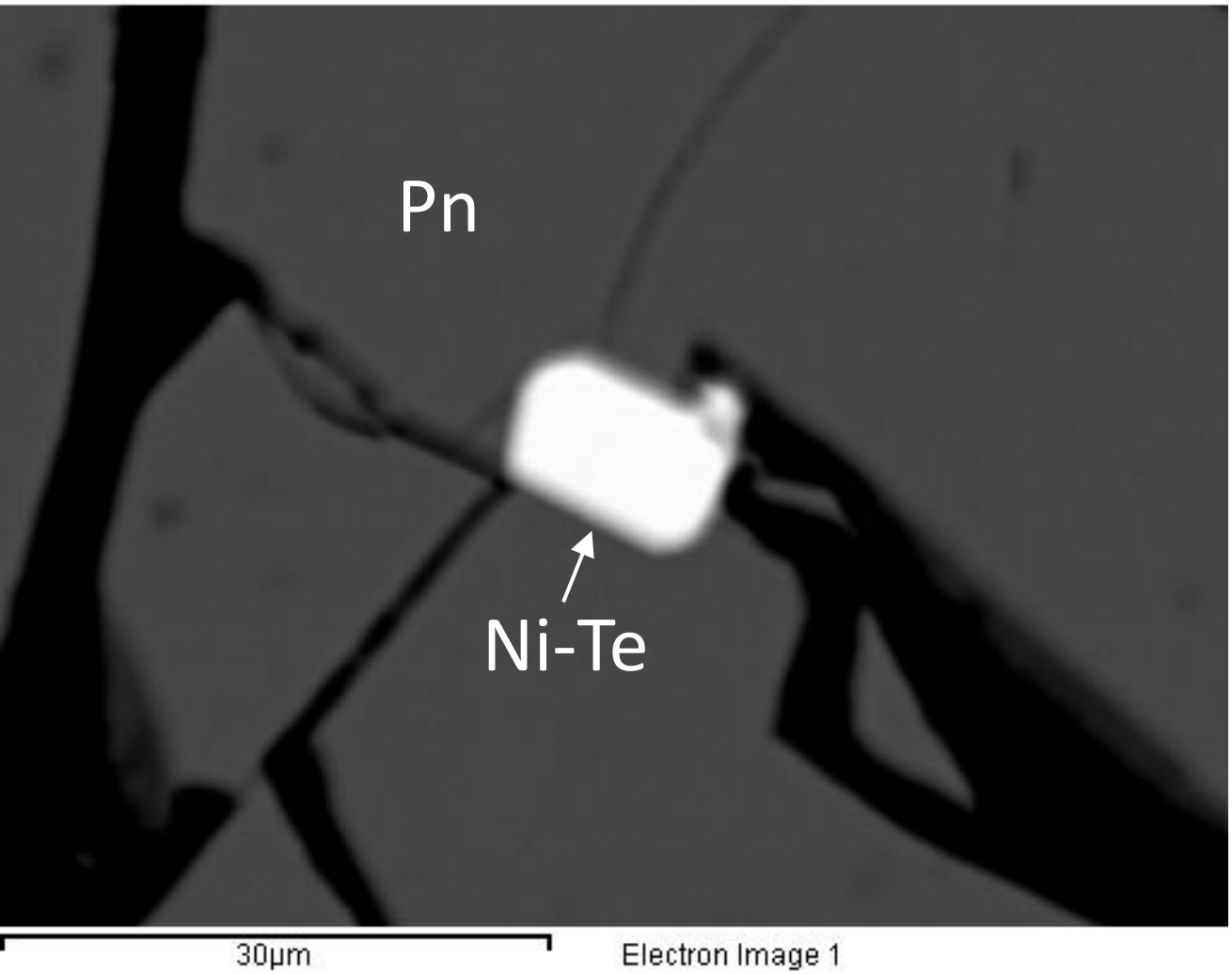
PTSR-40 I 1 Light



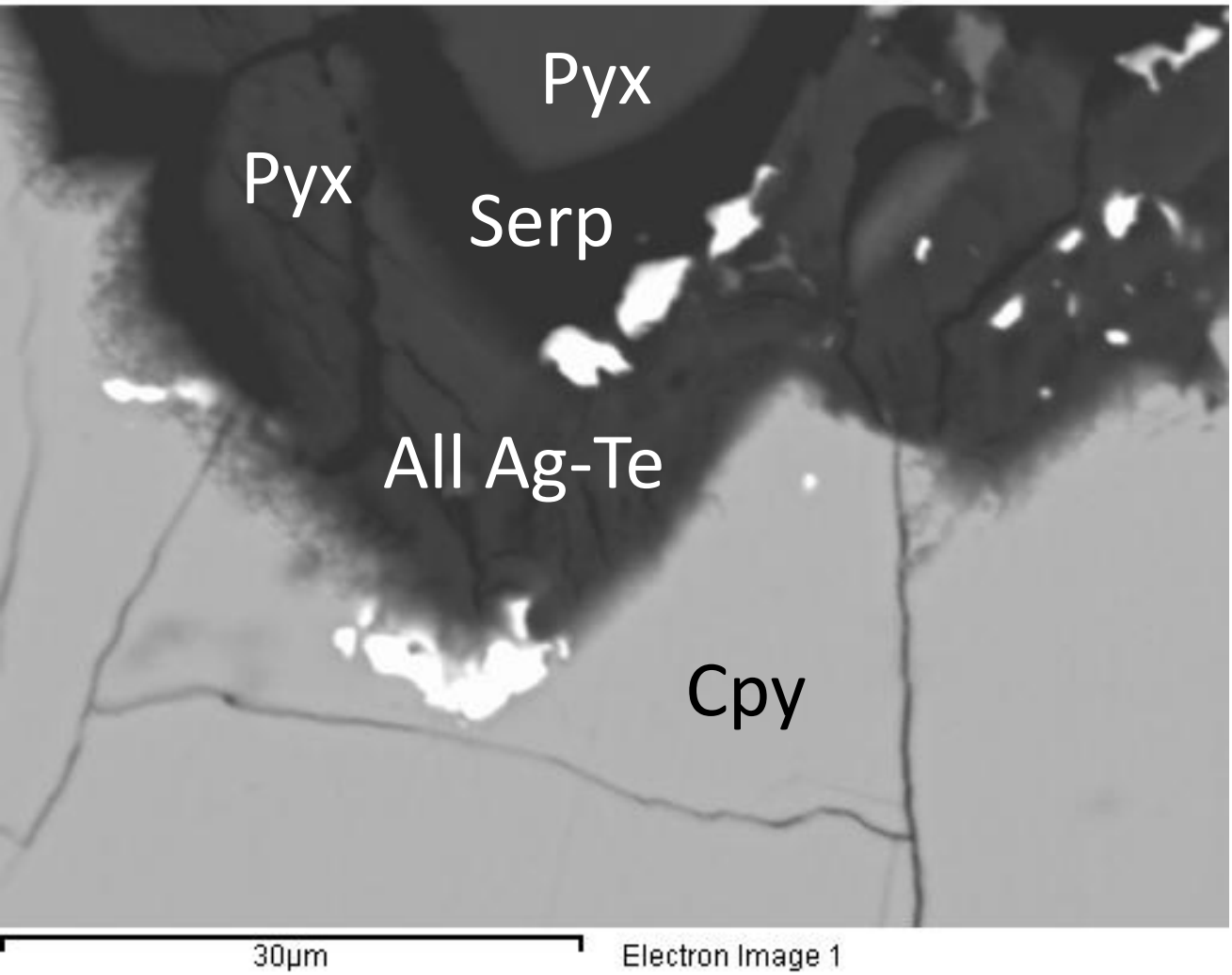
PTSR-40 J 1



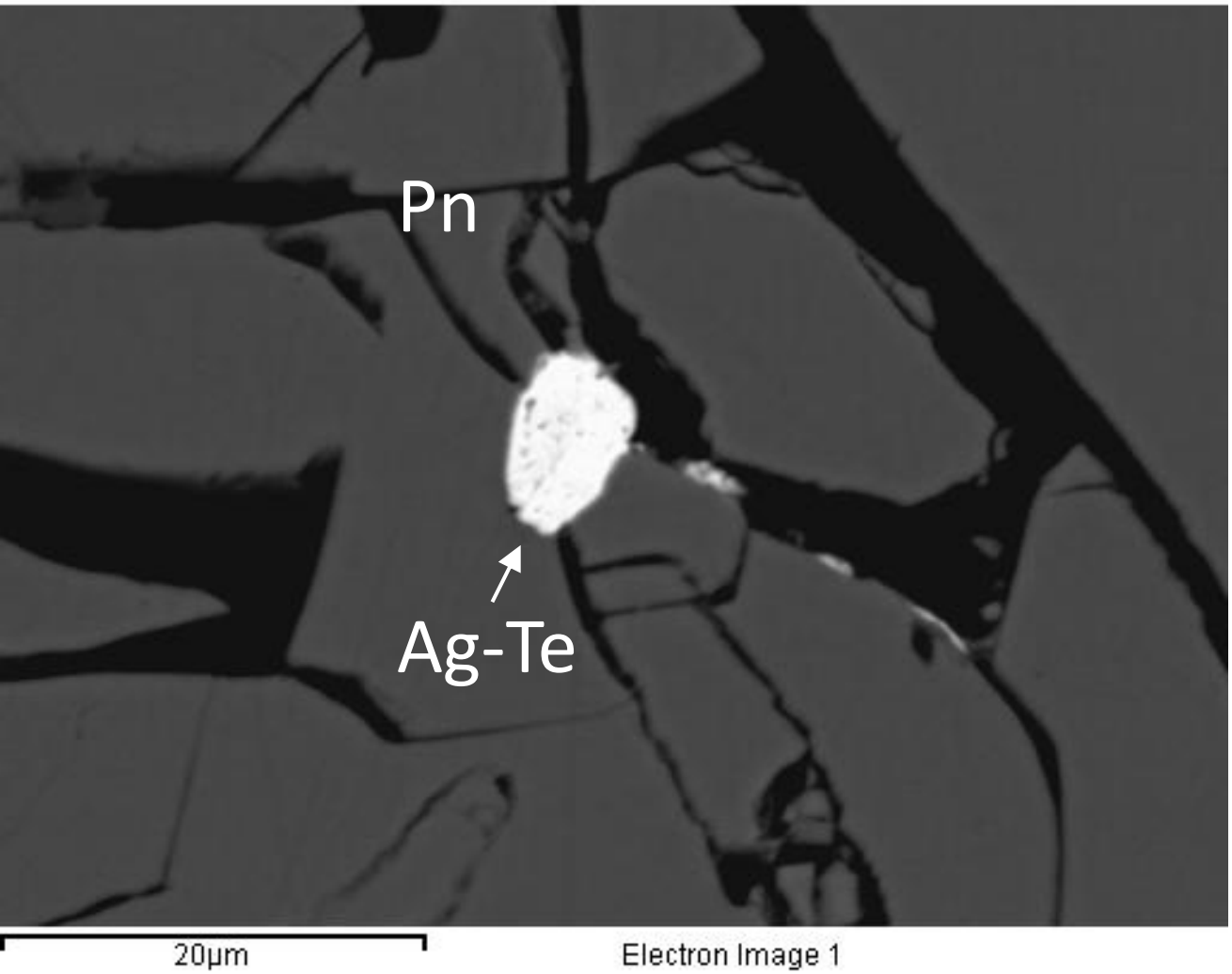
PTSR-40 K 1



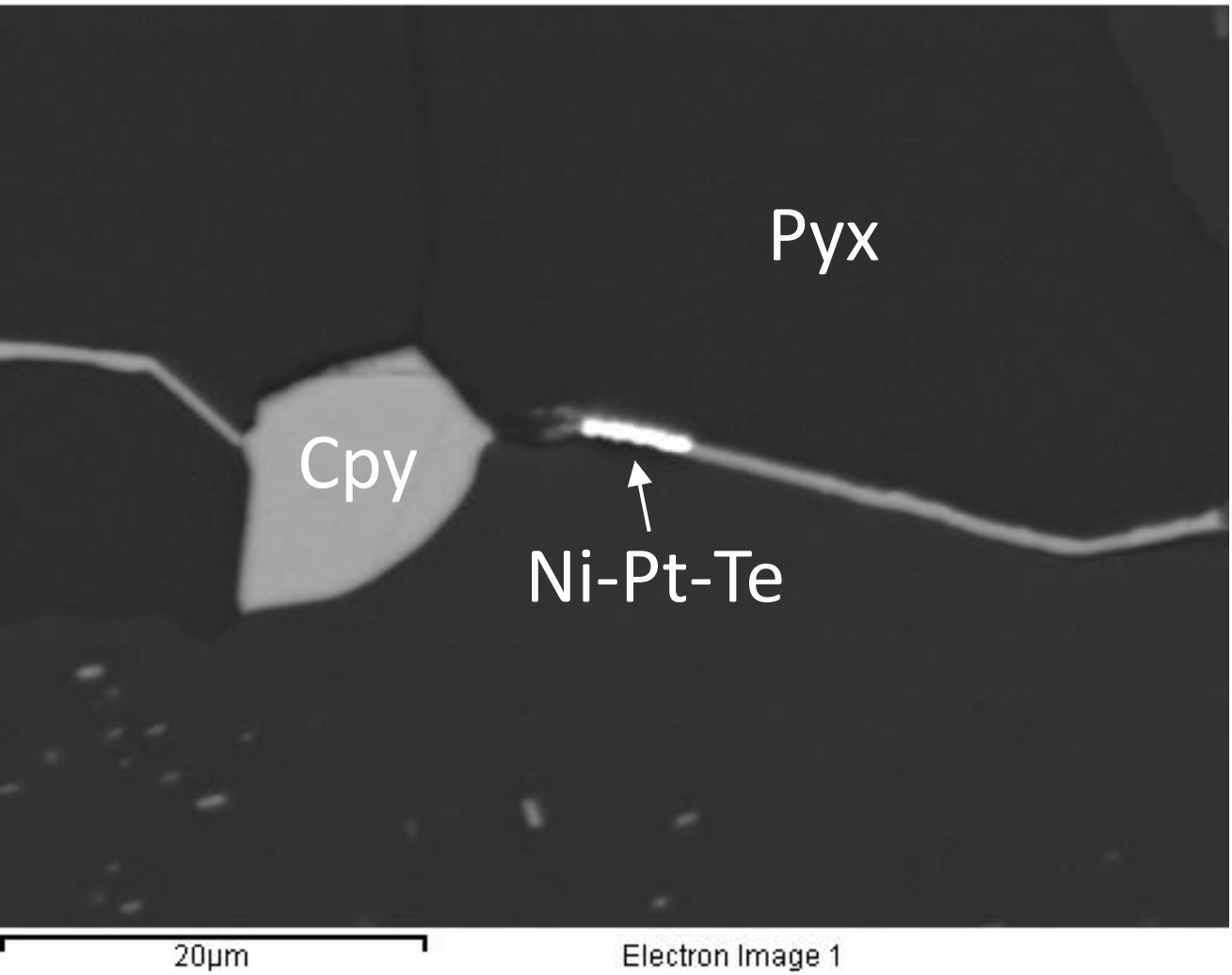
PTSR-40 L 1-4+



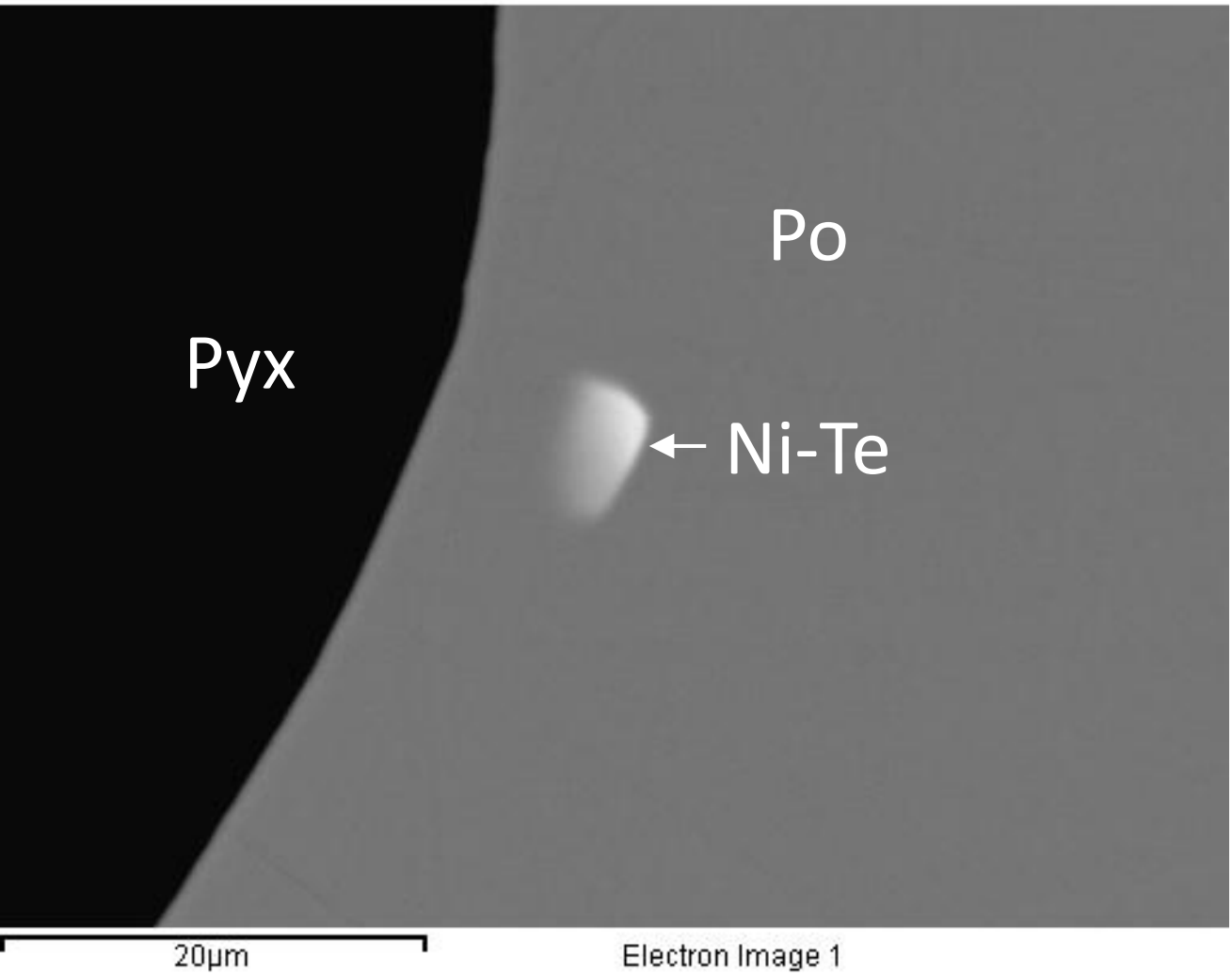
PTSR-40 M 1



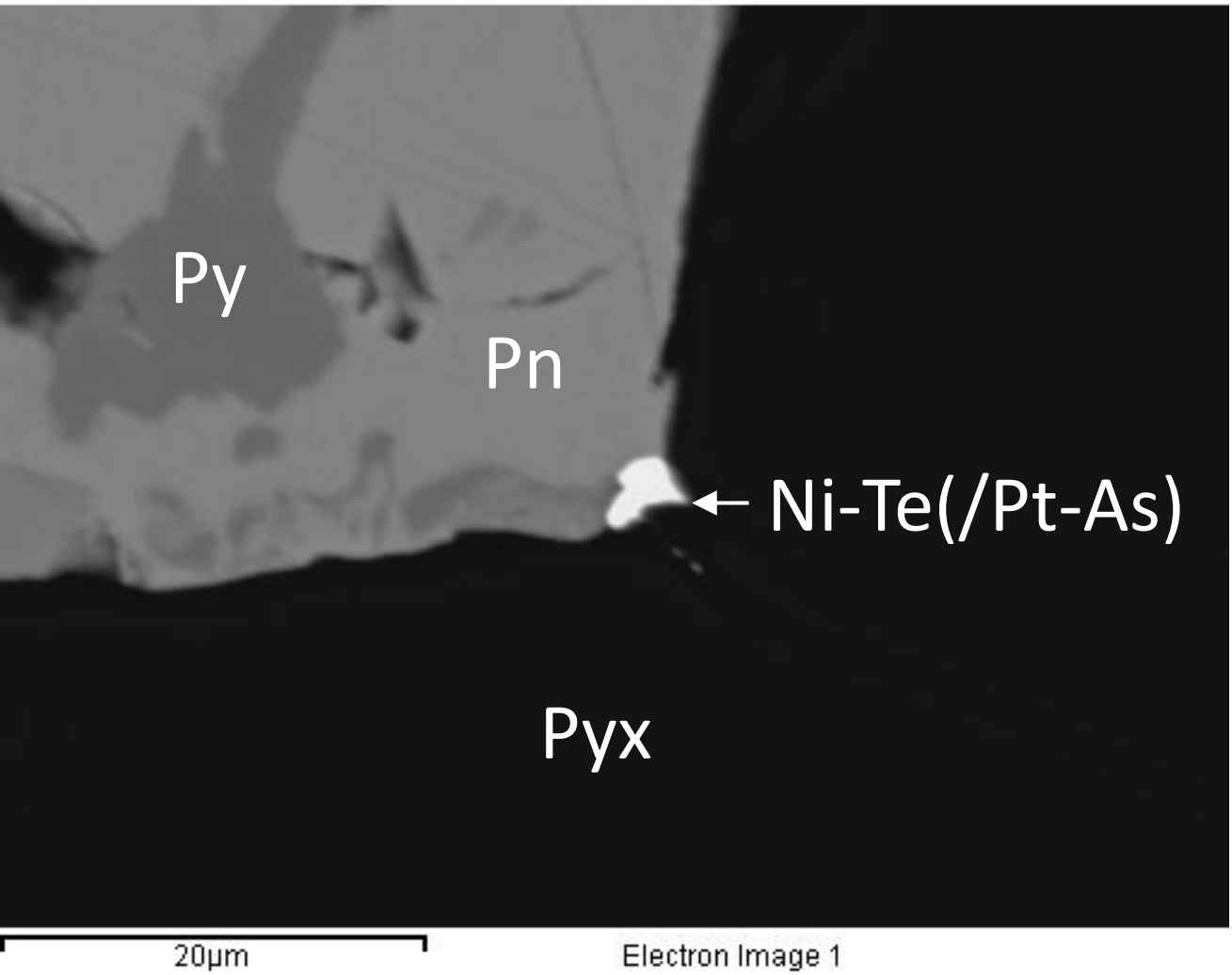
PTSR-41 A 1



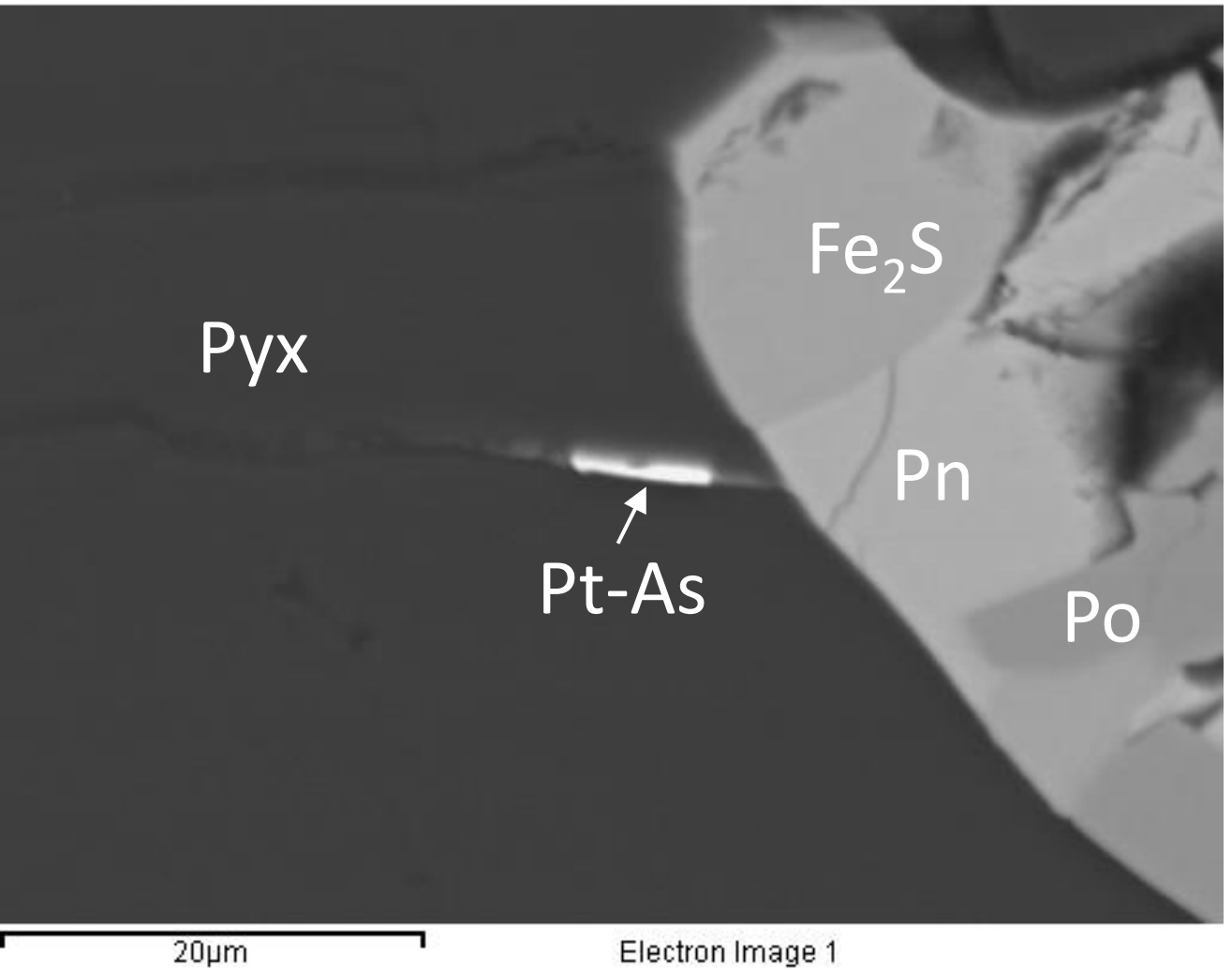
PTSR-41 B 1



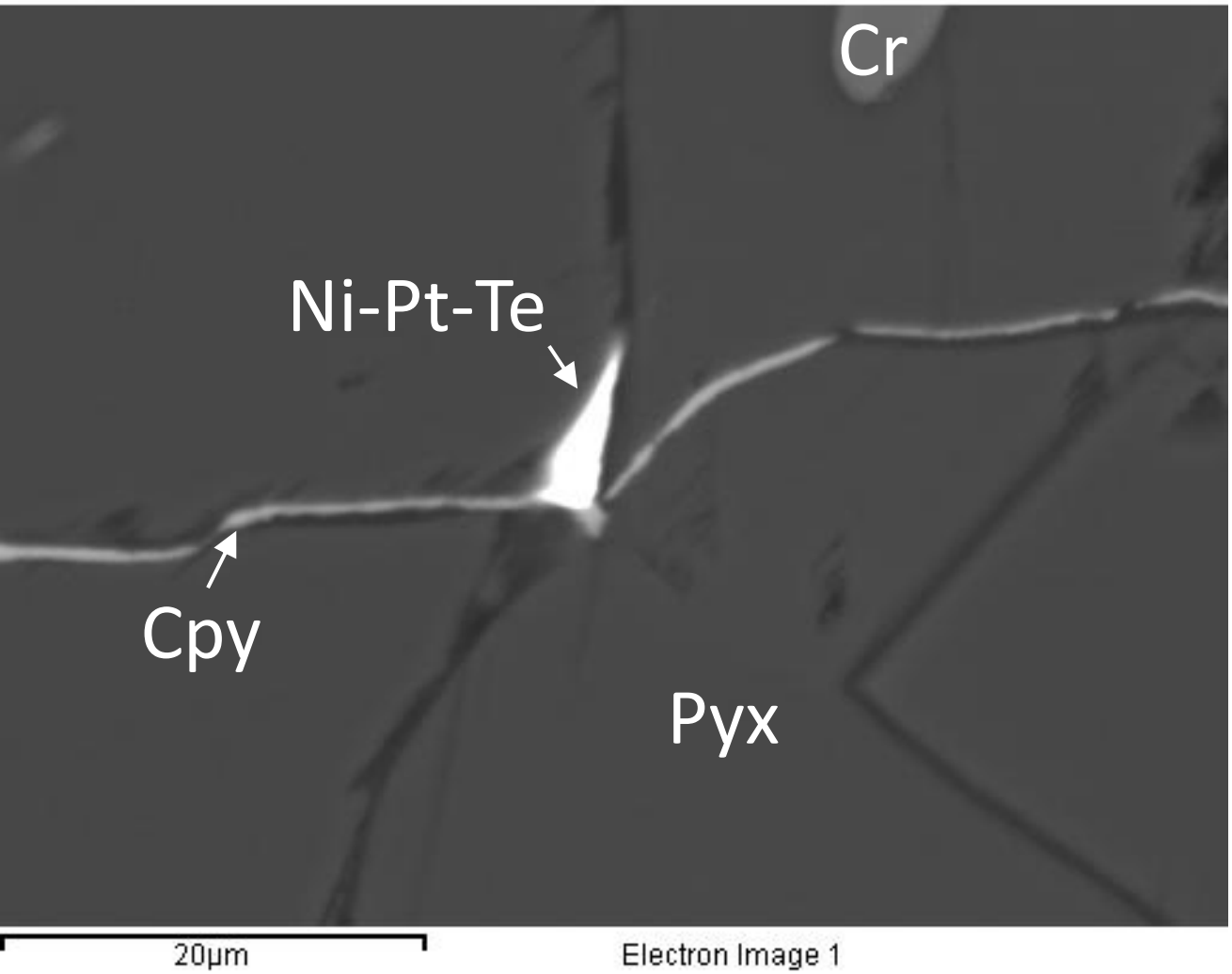
PTSR-41 C 1



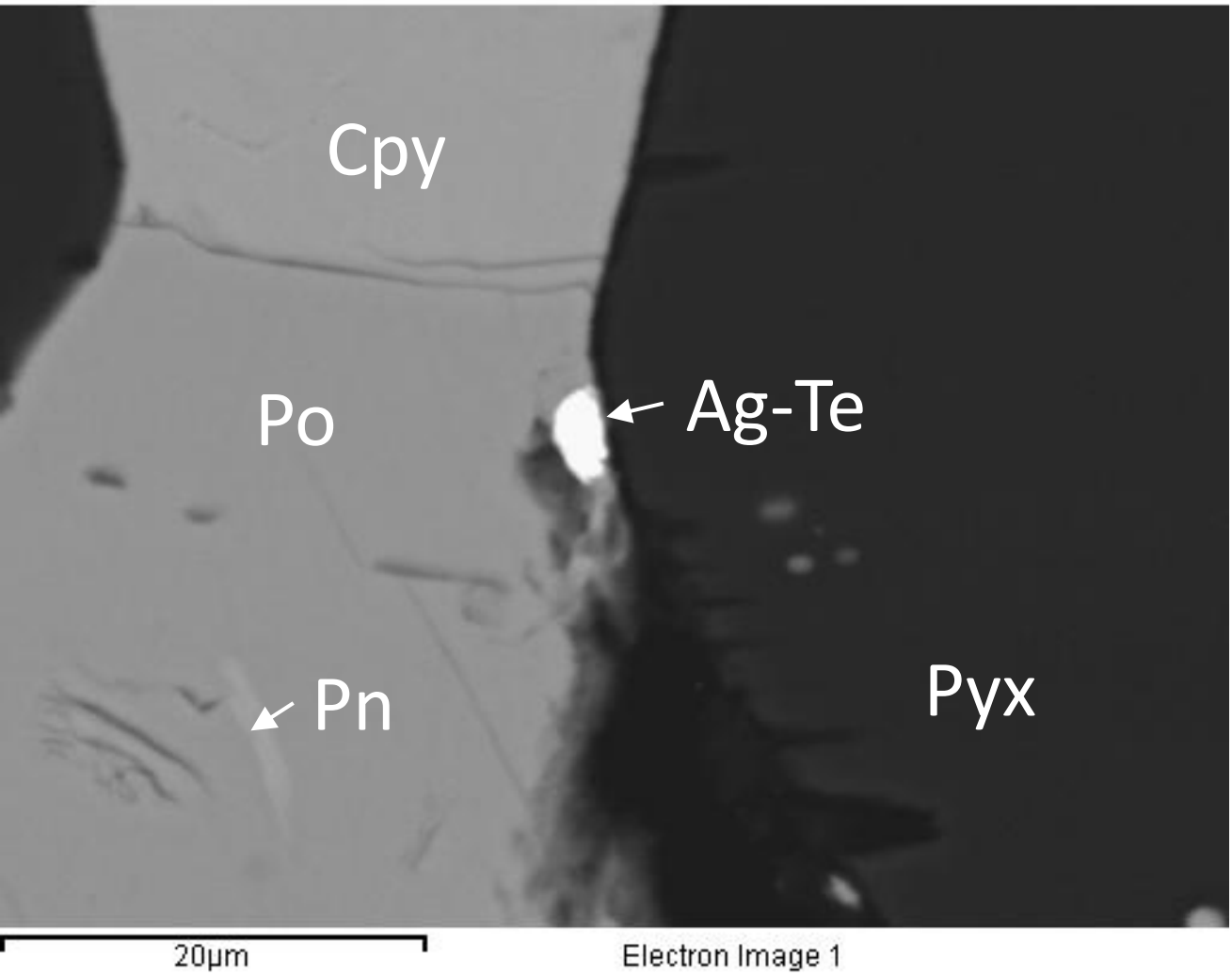
PTSR-41 D 1



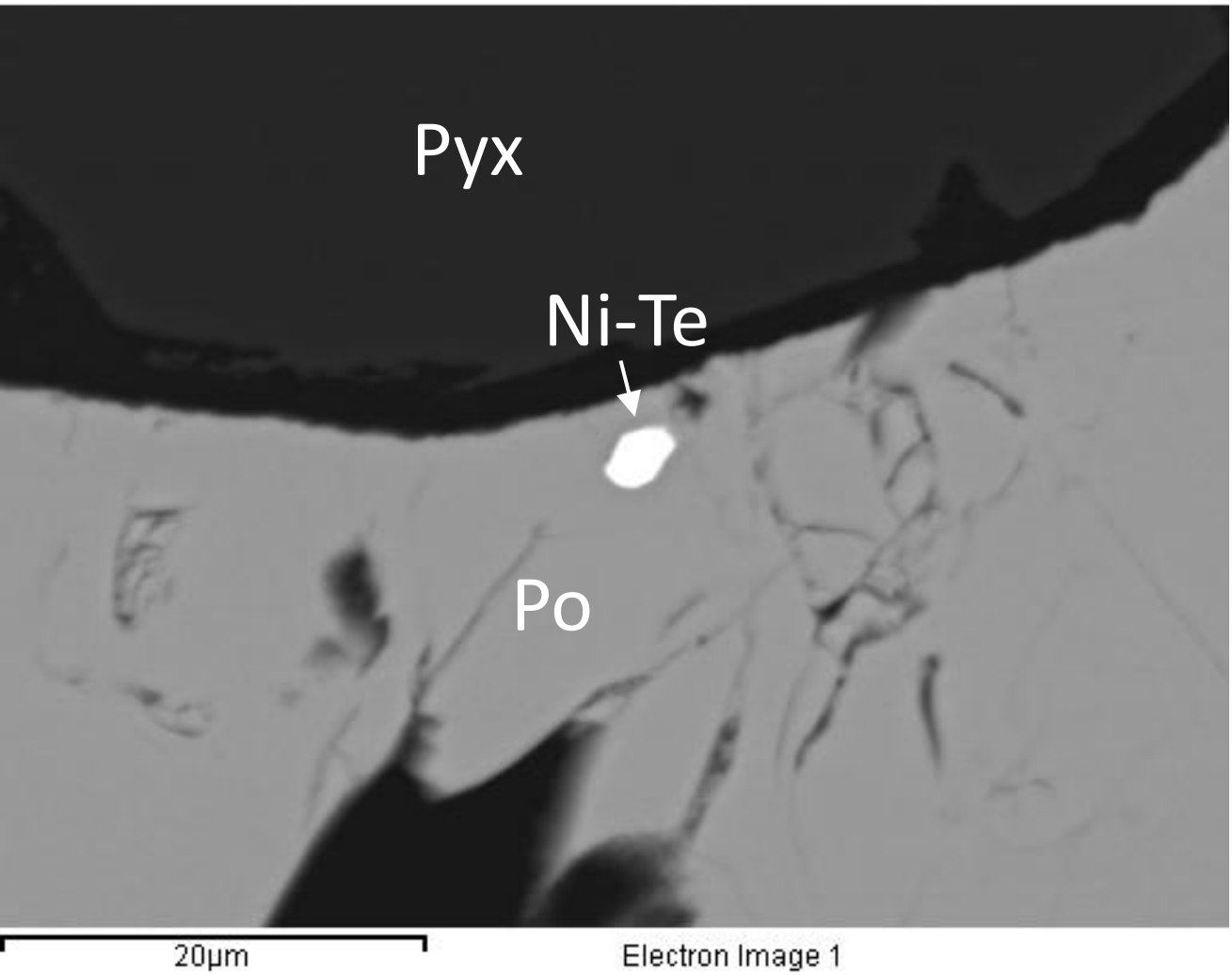
PTSR-41 E 1



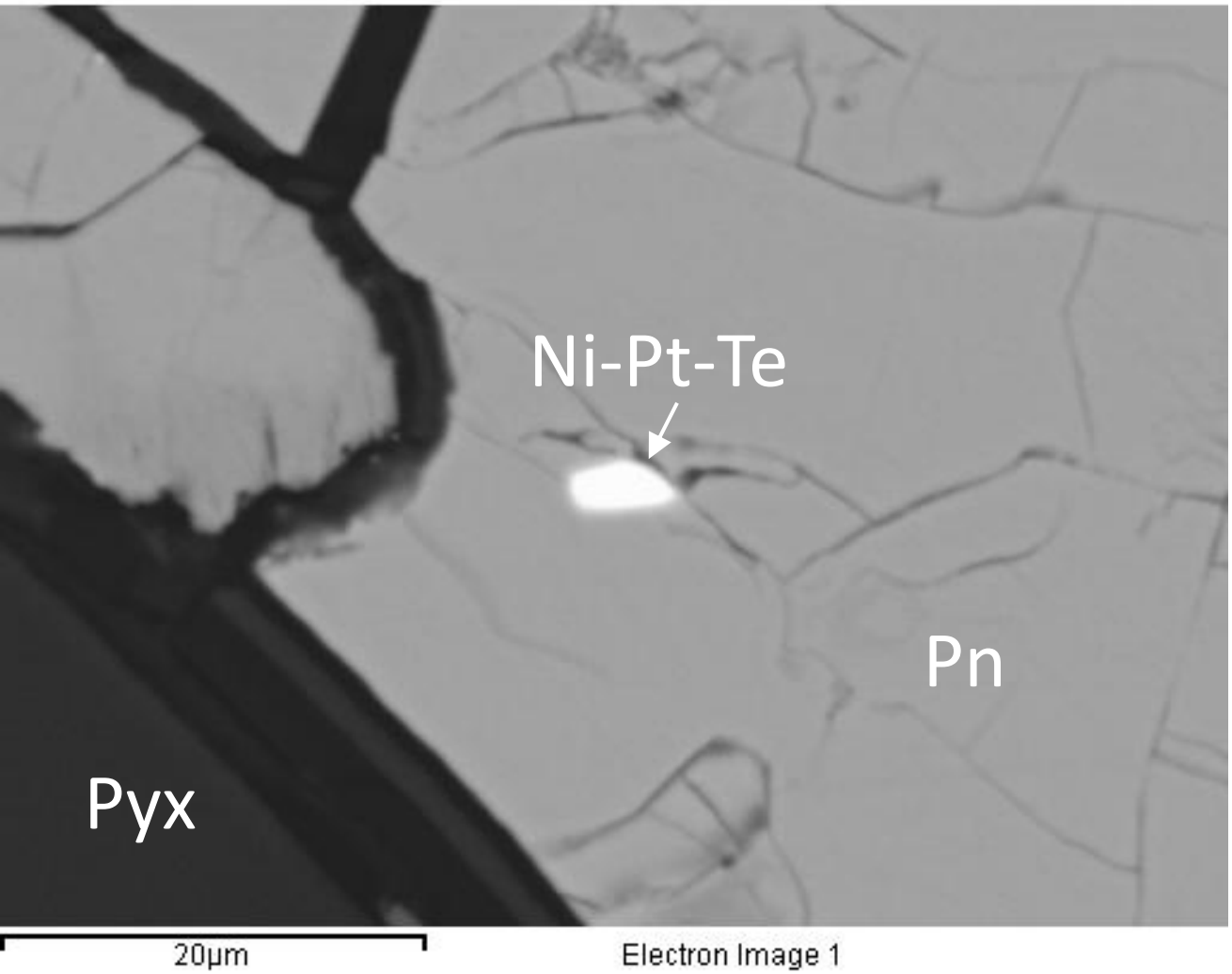
PTSR-41 F 1



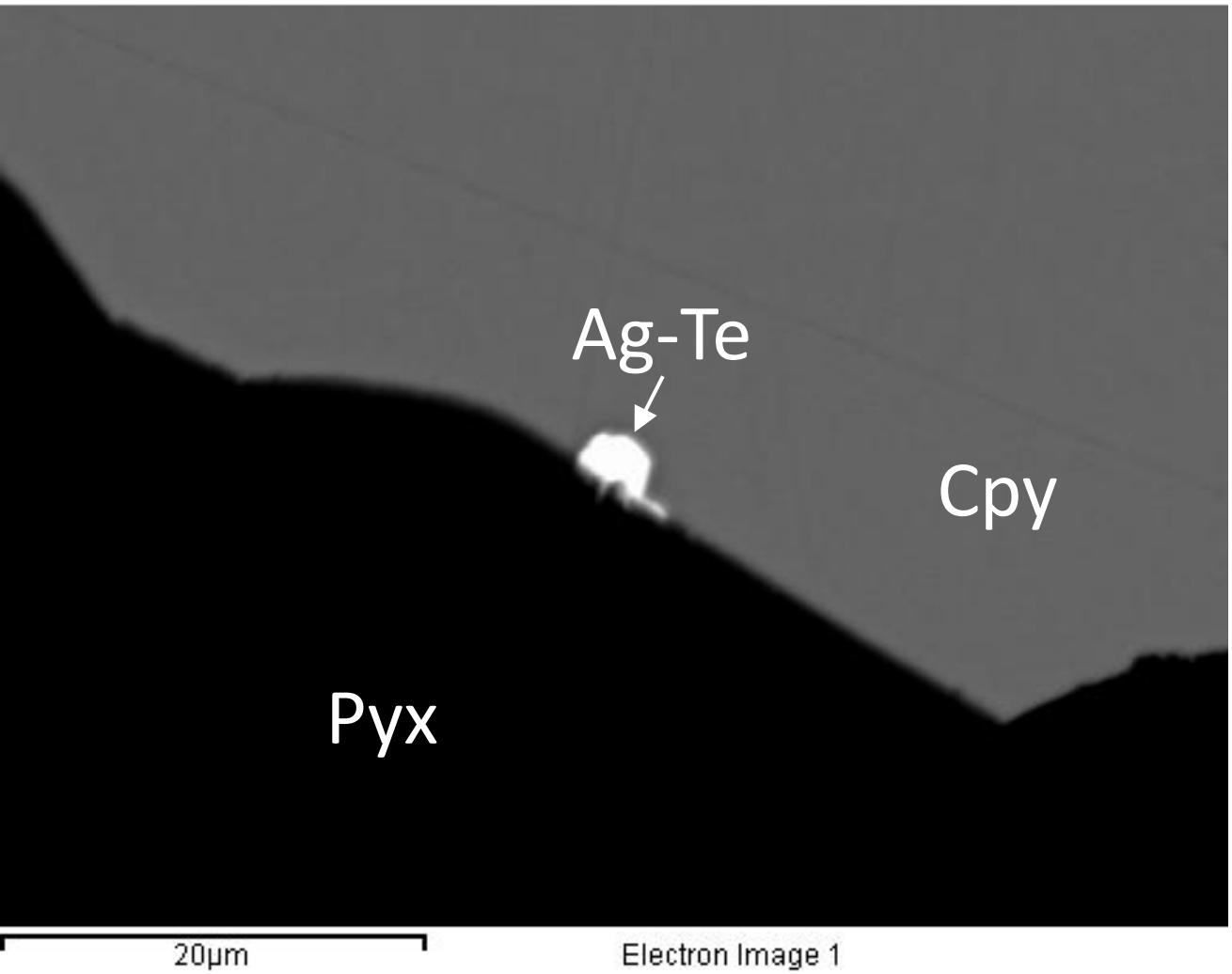
PTSR-41 G 1



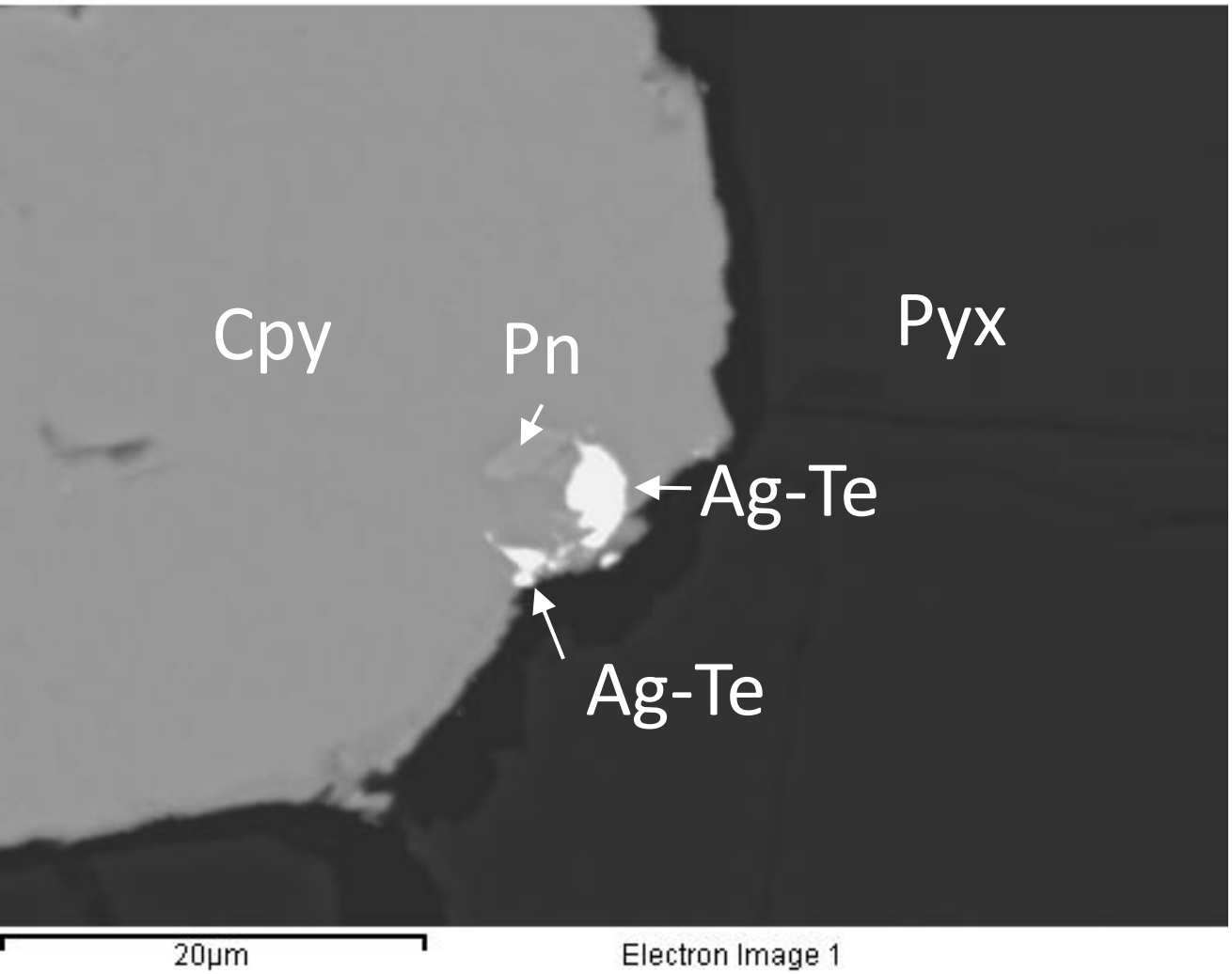
PTSR-41 H 1



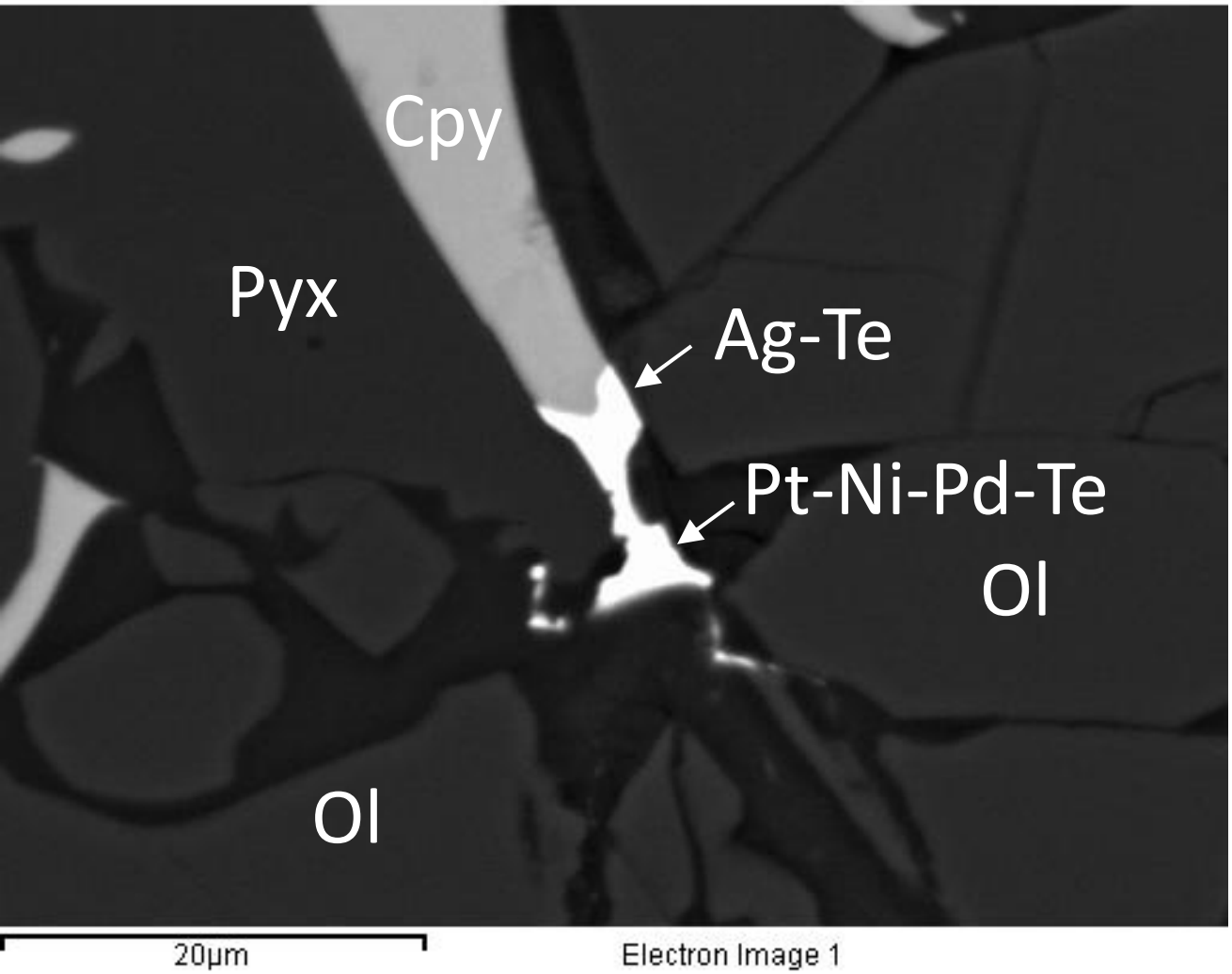
PTSR-41 I 1



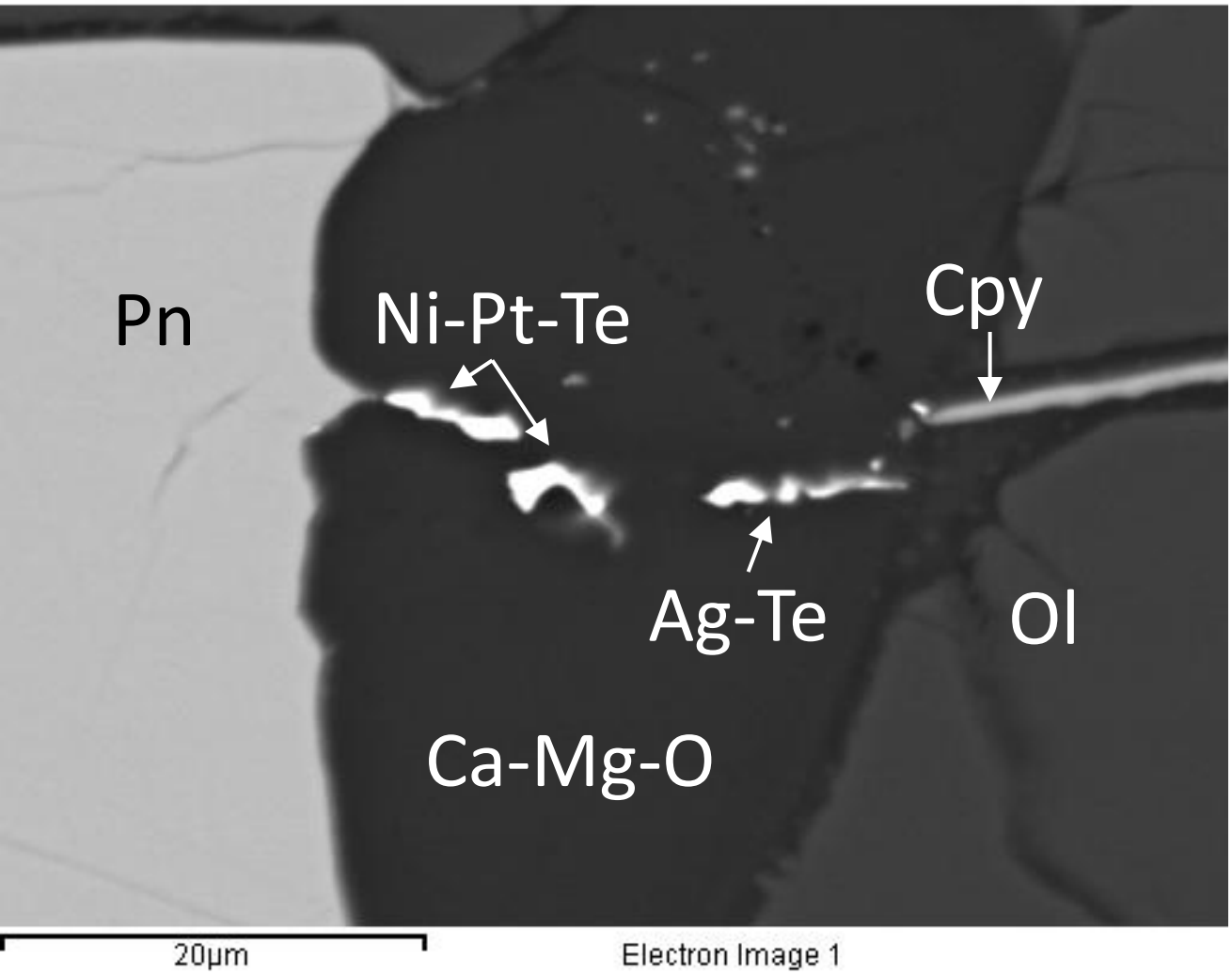
PTSR-41 J 1-2



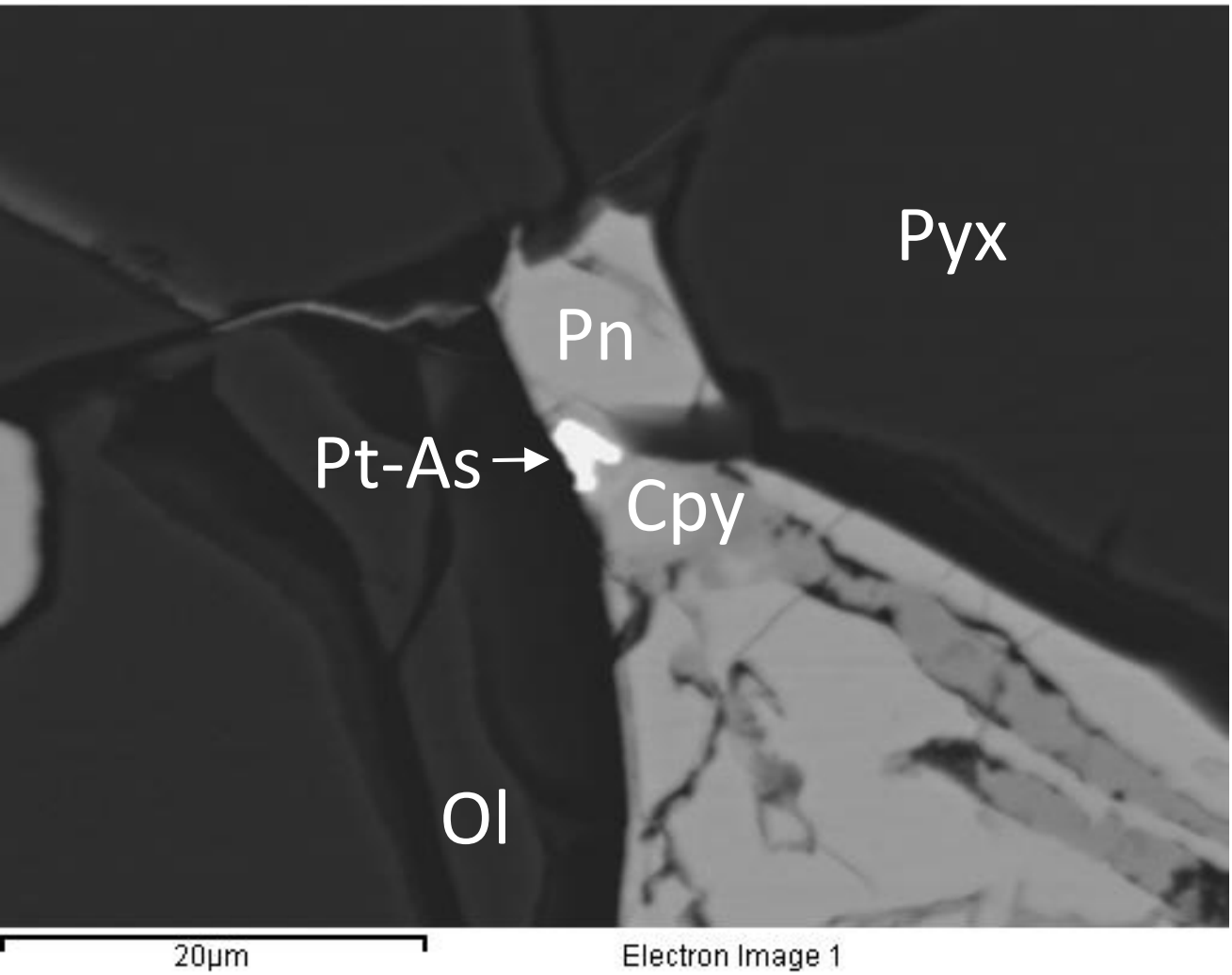
PTSR-41 K 1



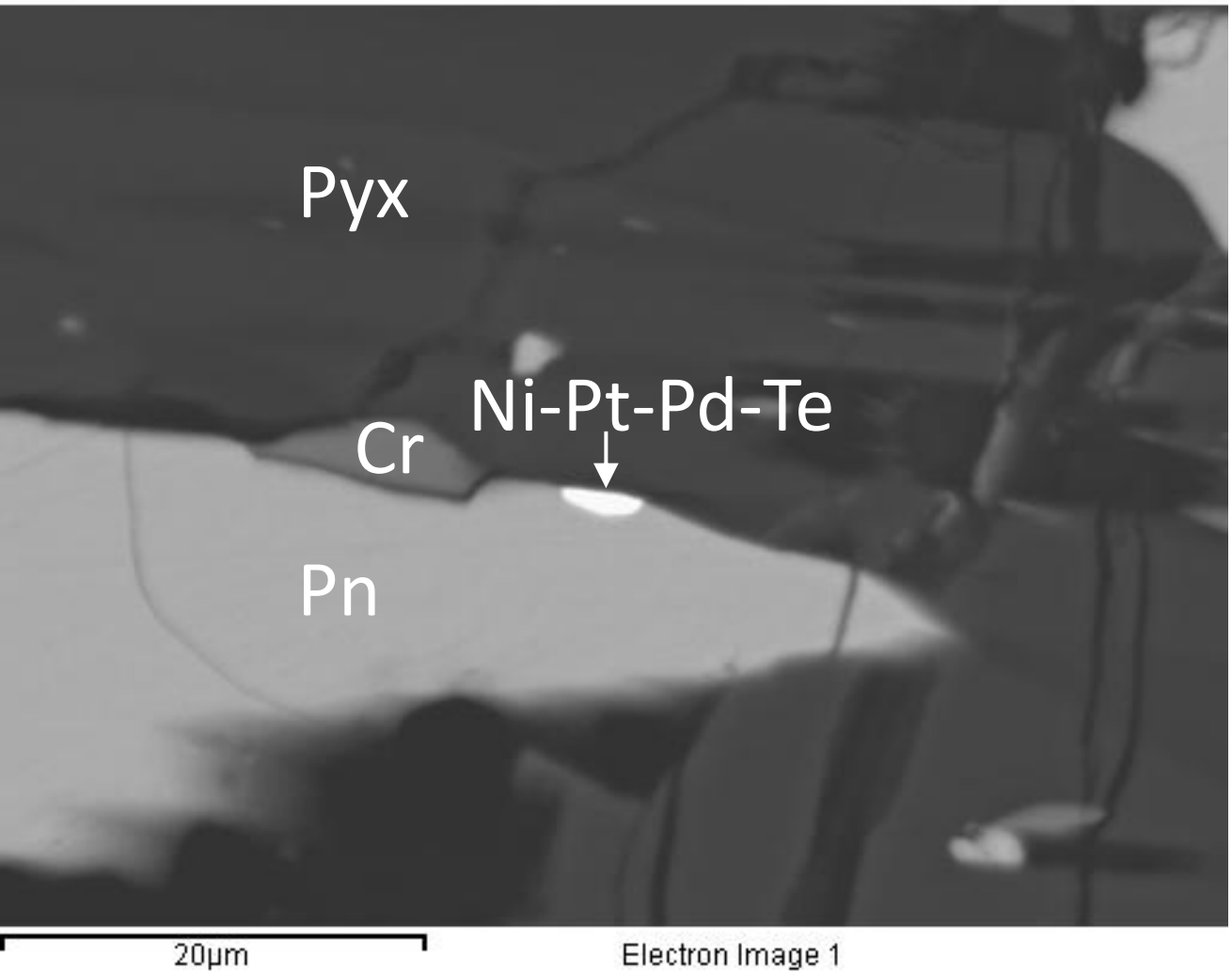
PTSR-41 L 1-3



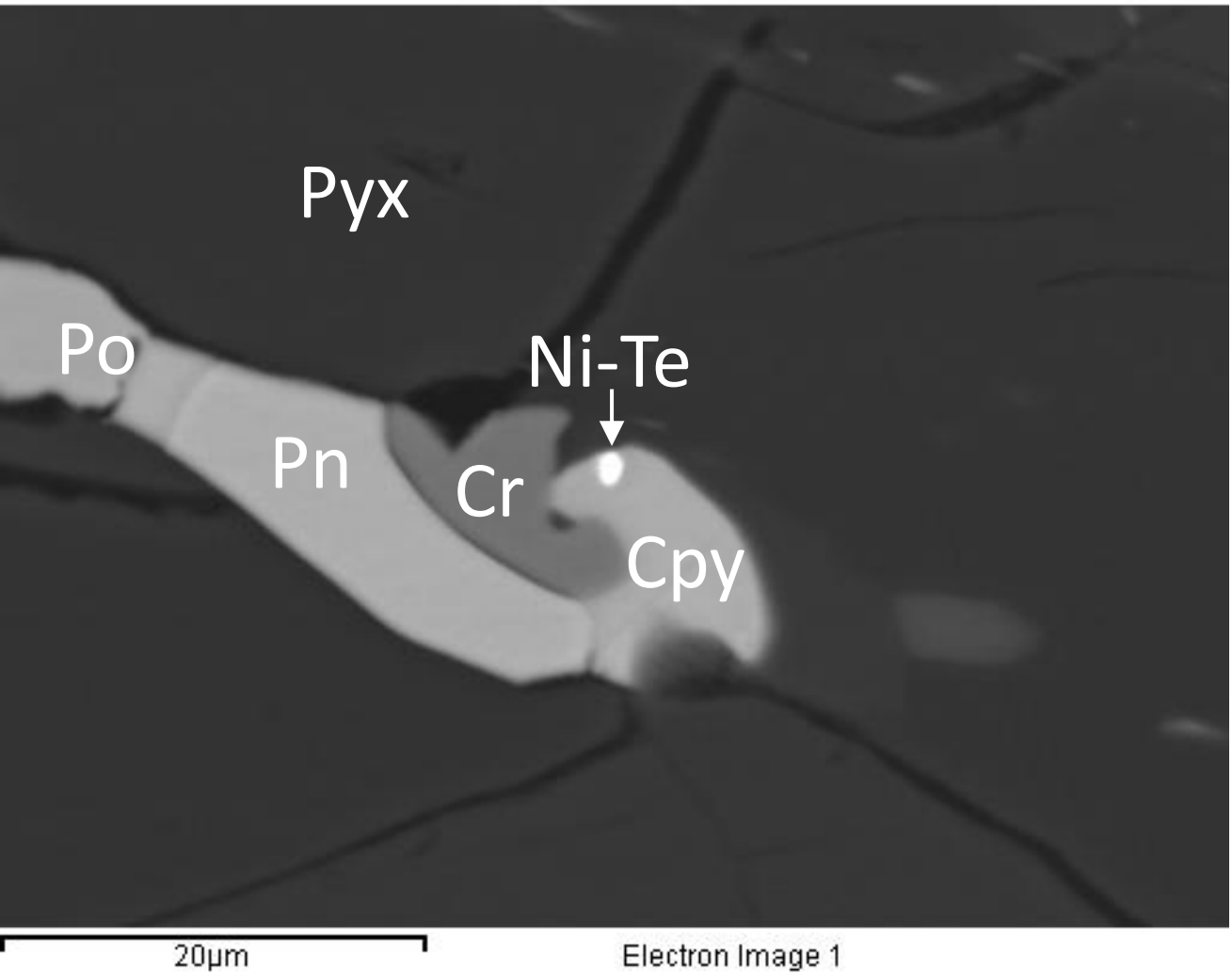
PTSR-42 A 1



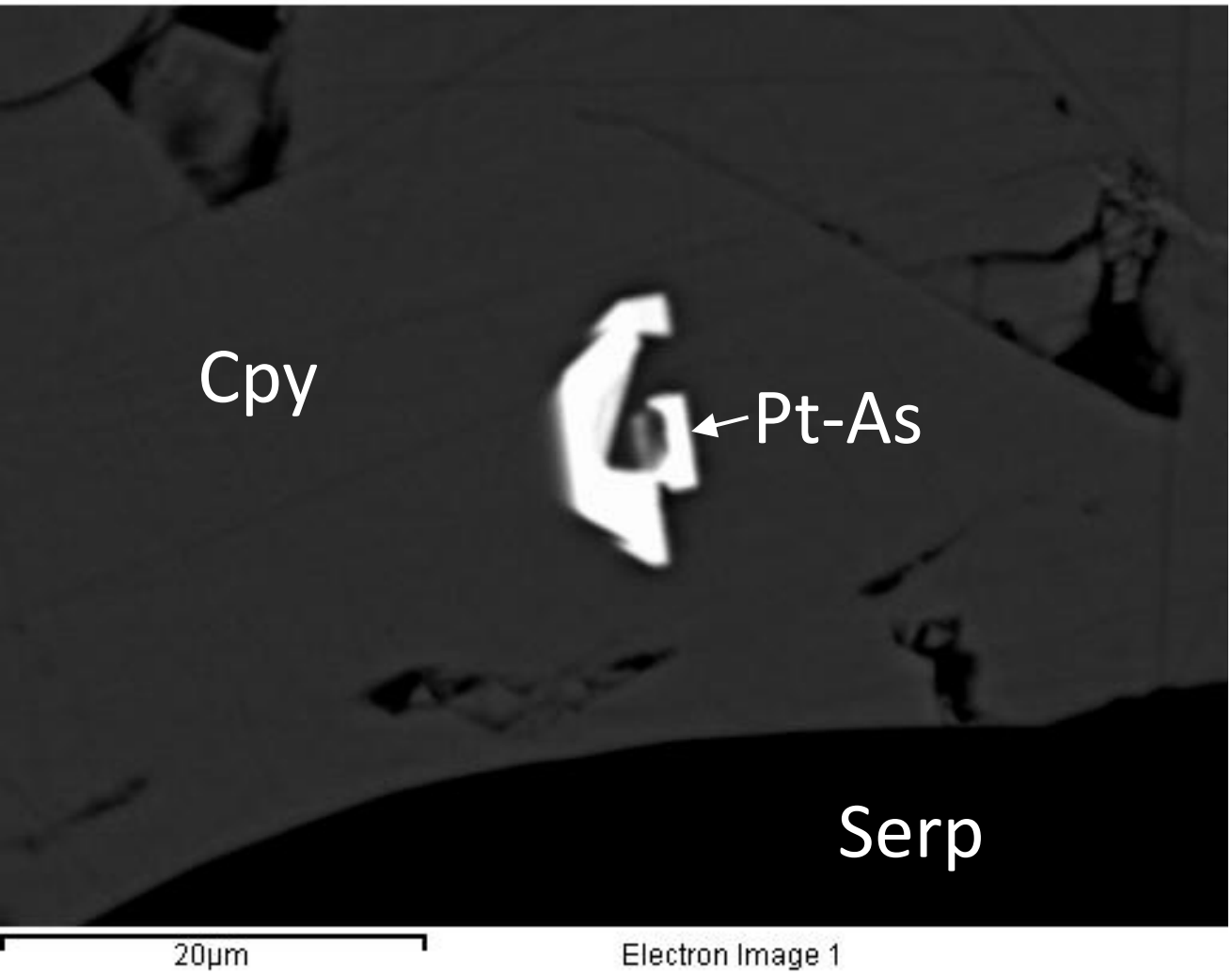
PTSR-42 B 1



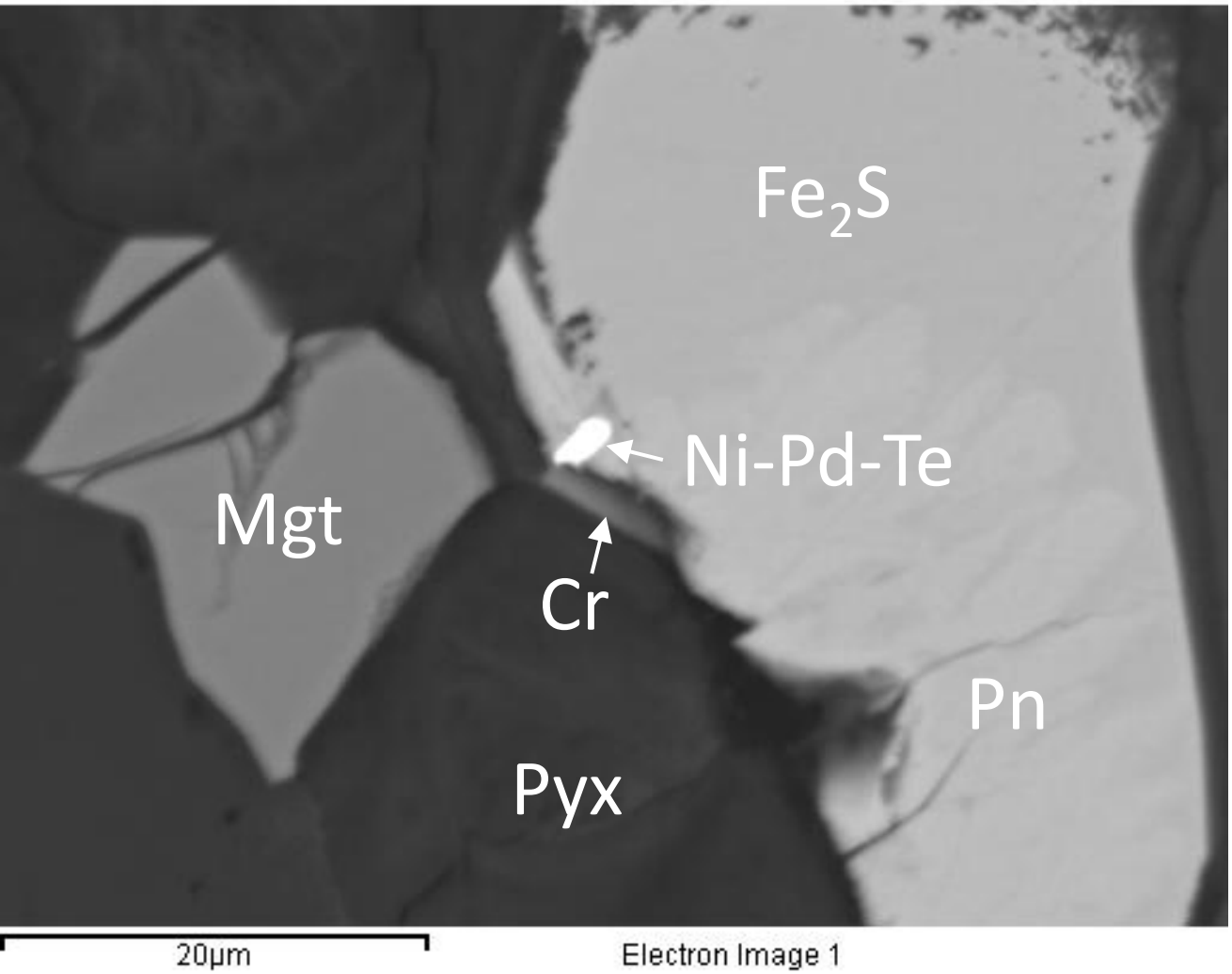
PTSR-42 C 1



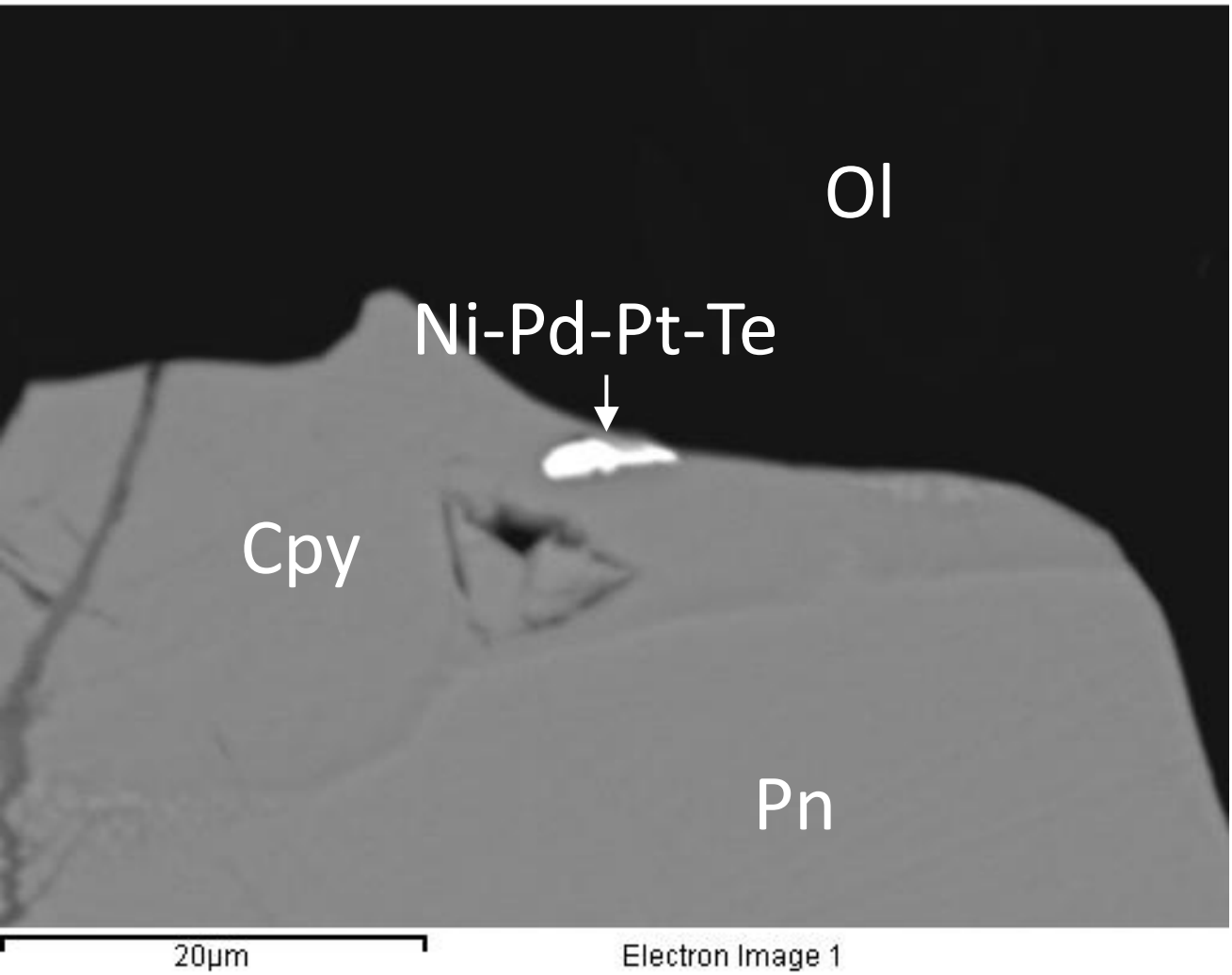
PTSR-42 D 1



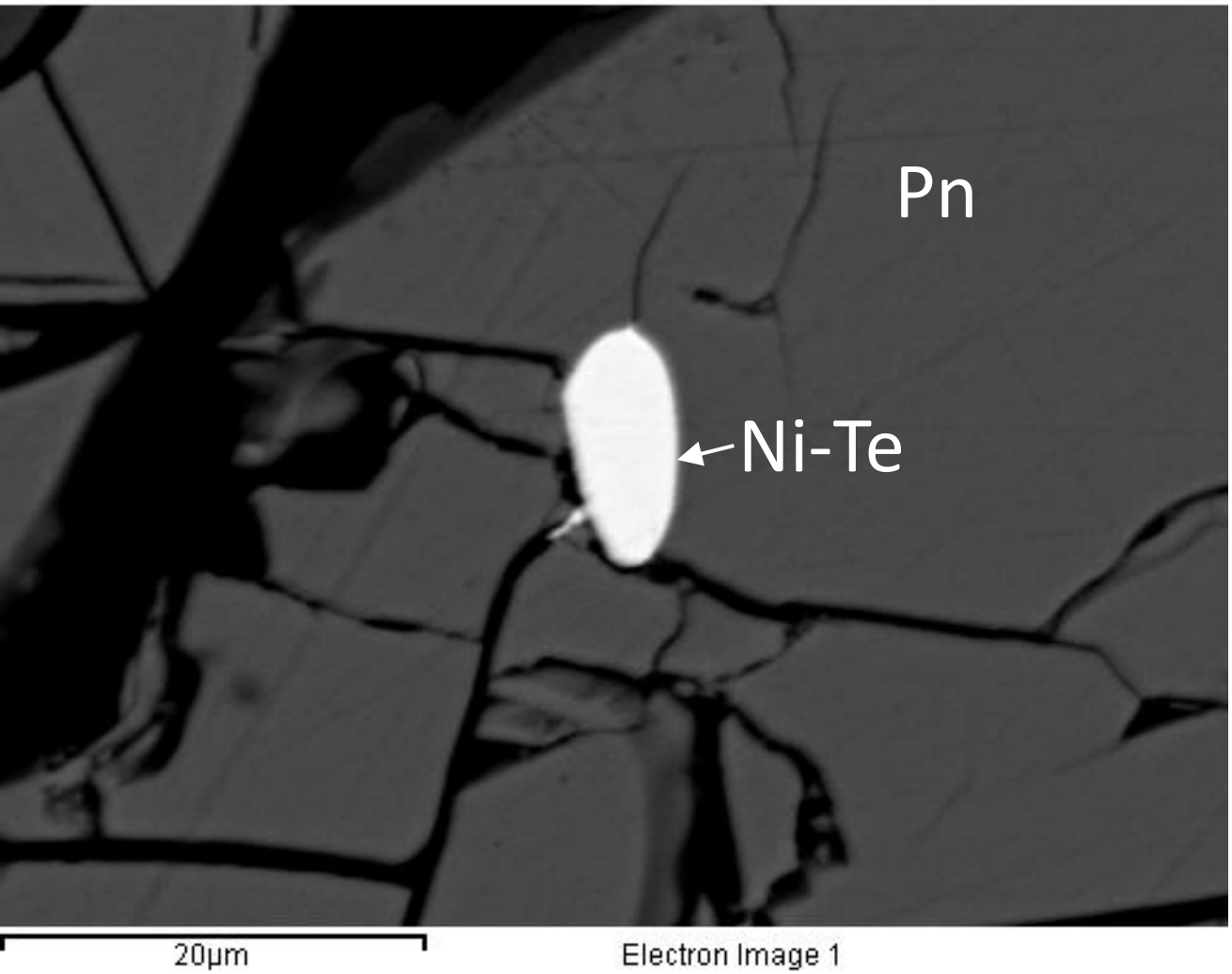
PTSR-42 E 1



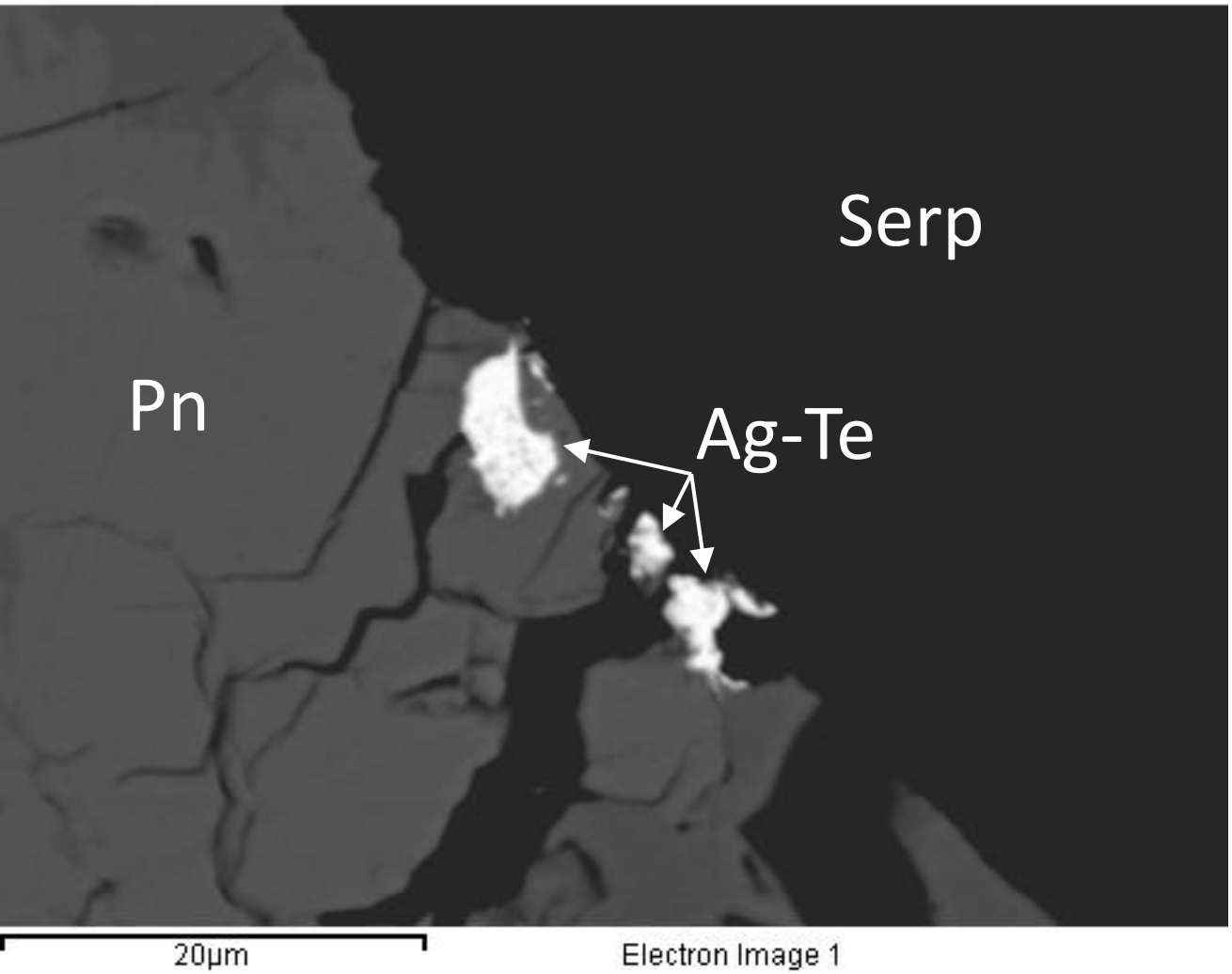
PTSR-42 F 1



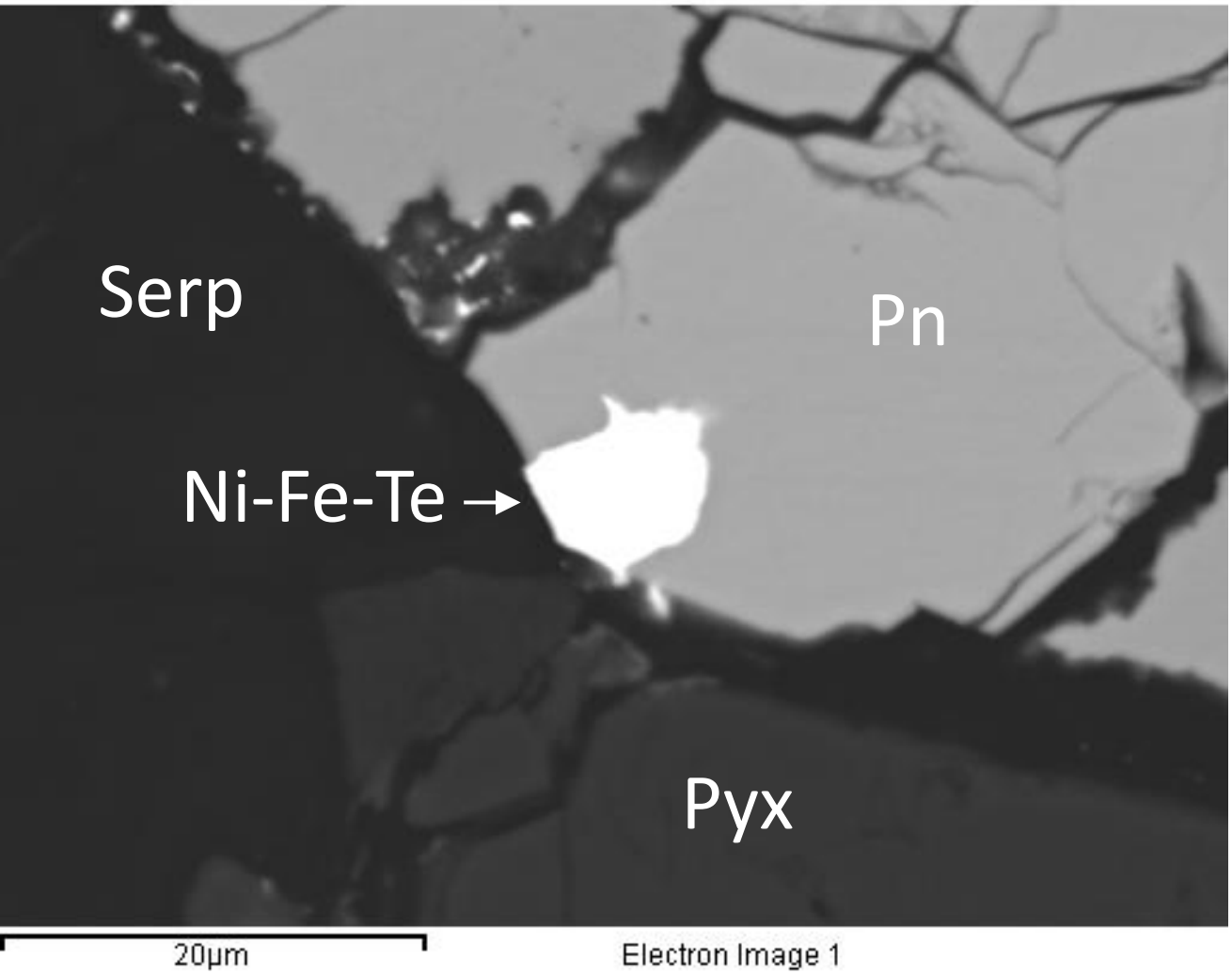
PTSR-42 G 1



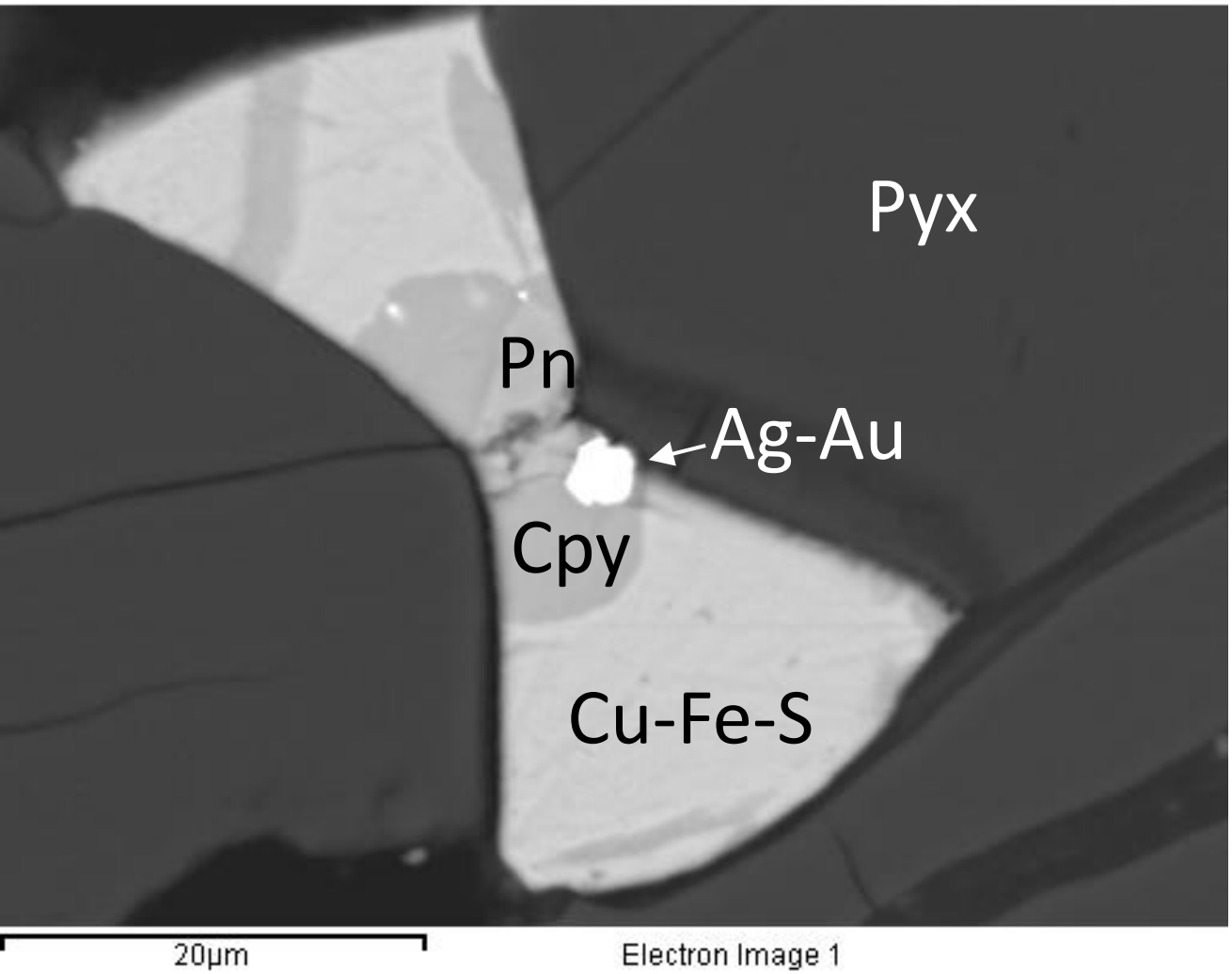
PTSR-42 H 1-3



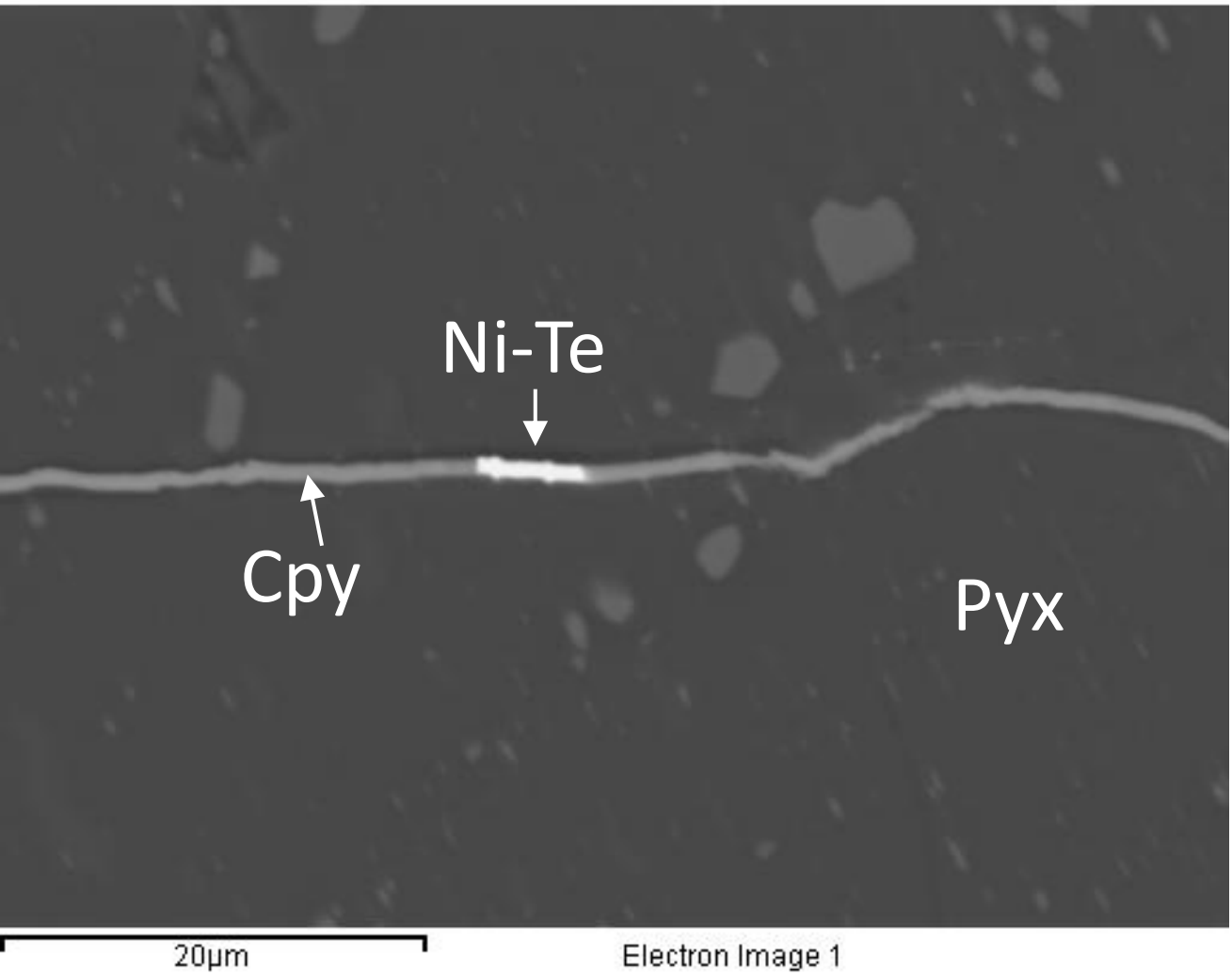
PTSR-42 I 1



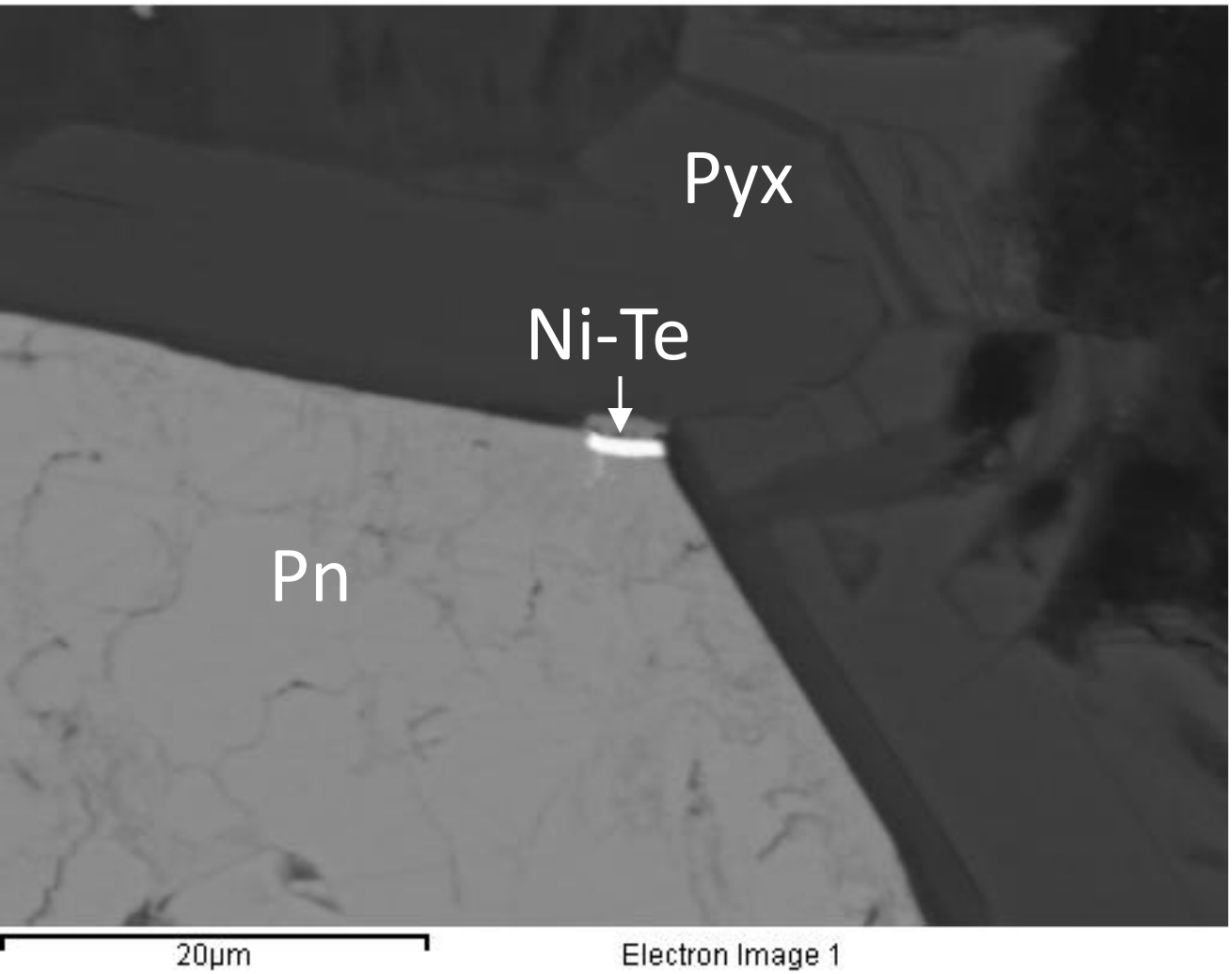
PTSR-42 J 1



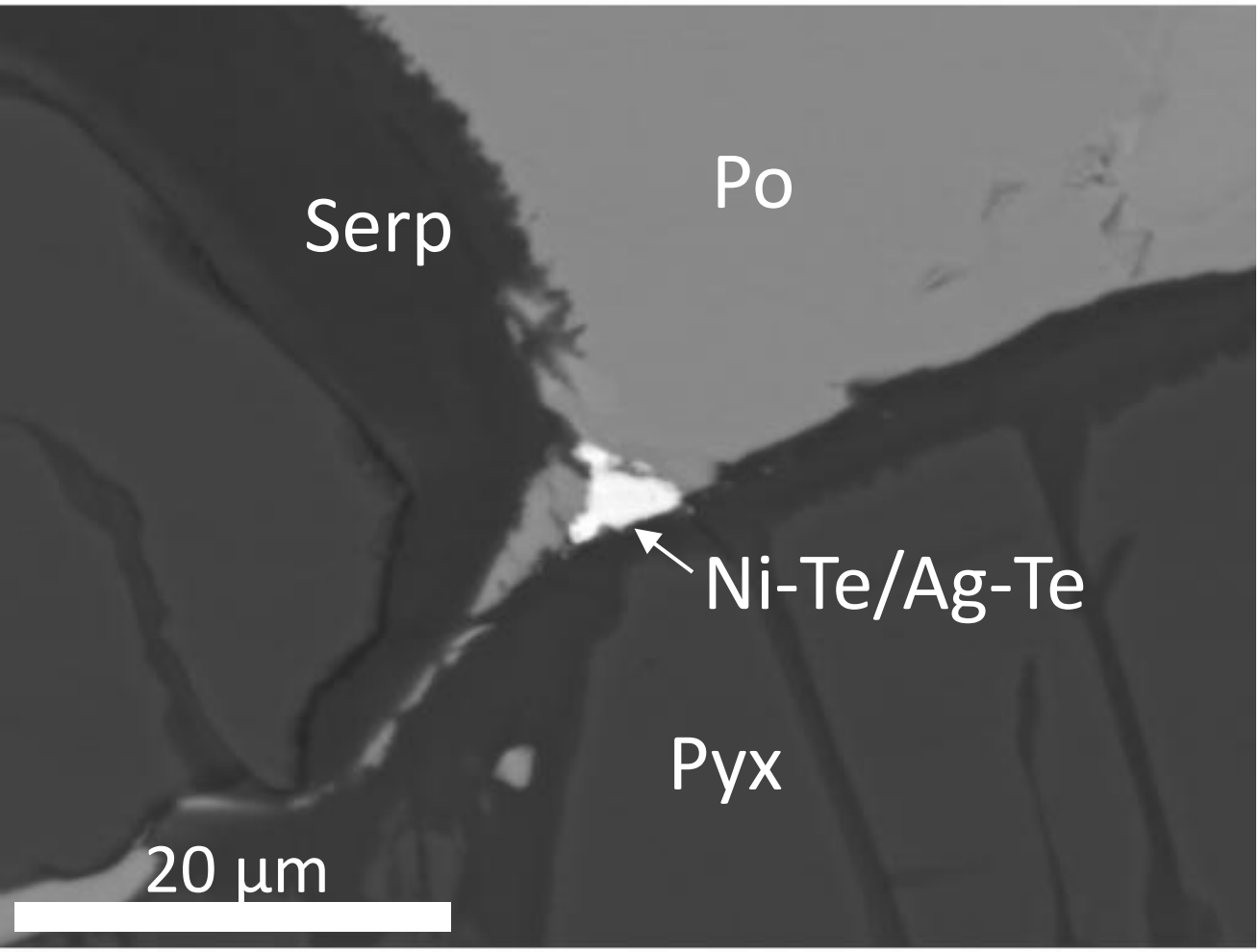
PTSR-42 K 1



PTSR-42 L 1

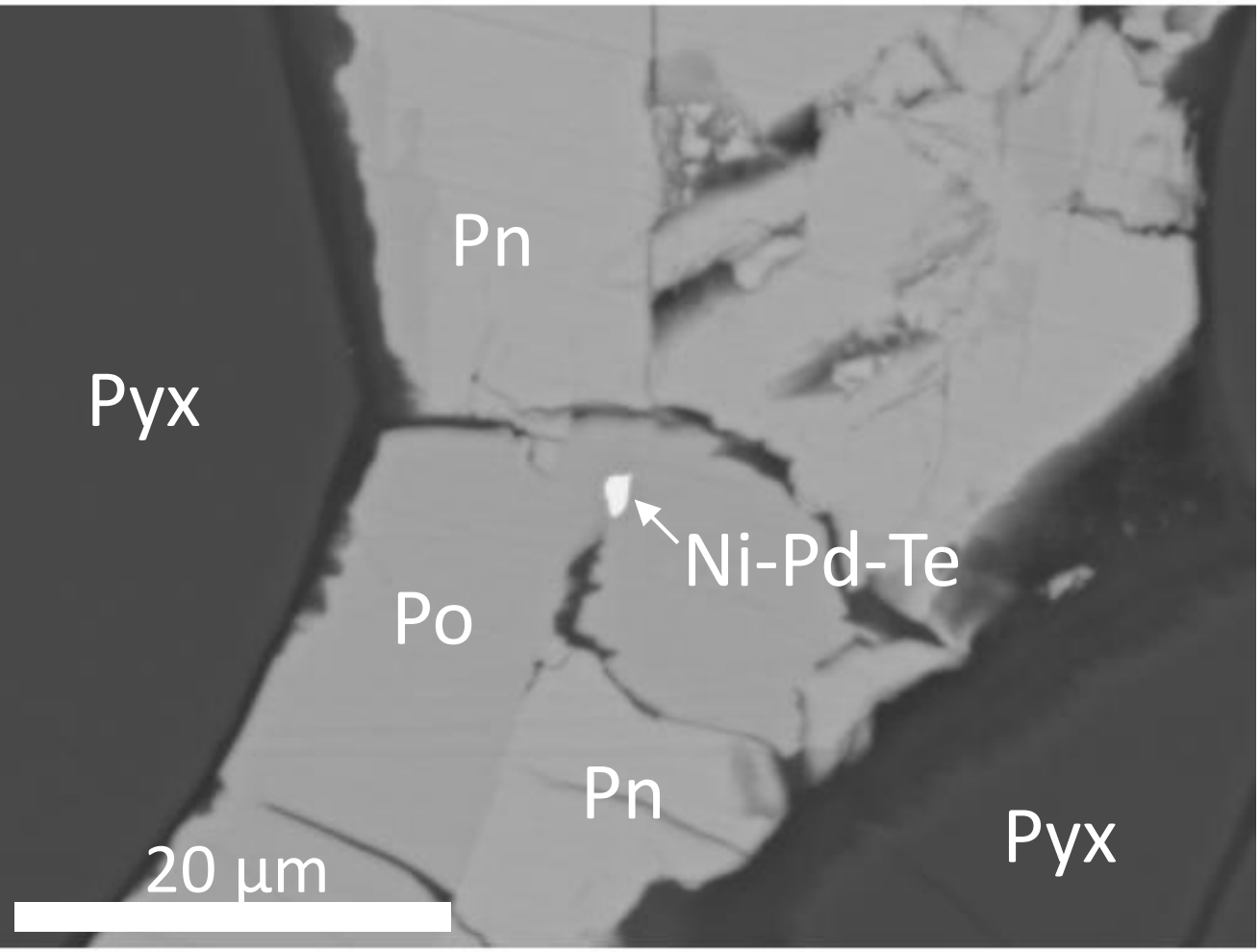


PTSR-42 M 1



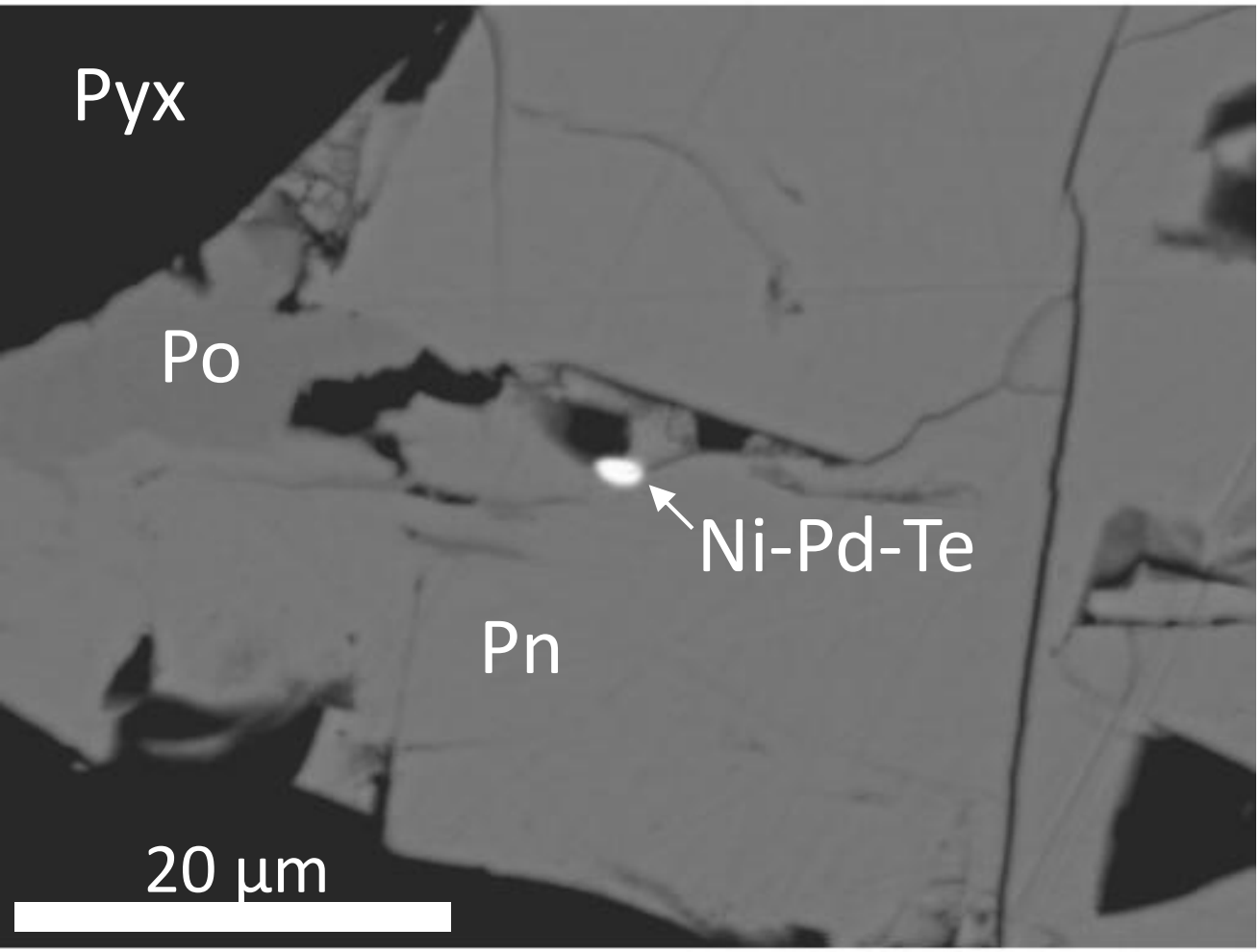
Electron Image 1

PTSR-42 N 1



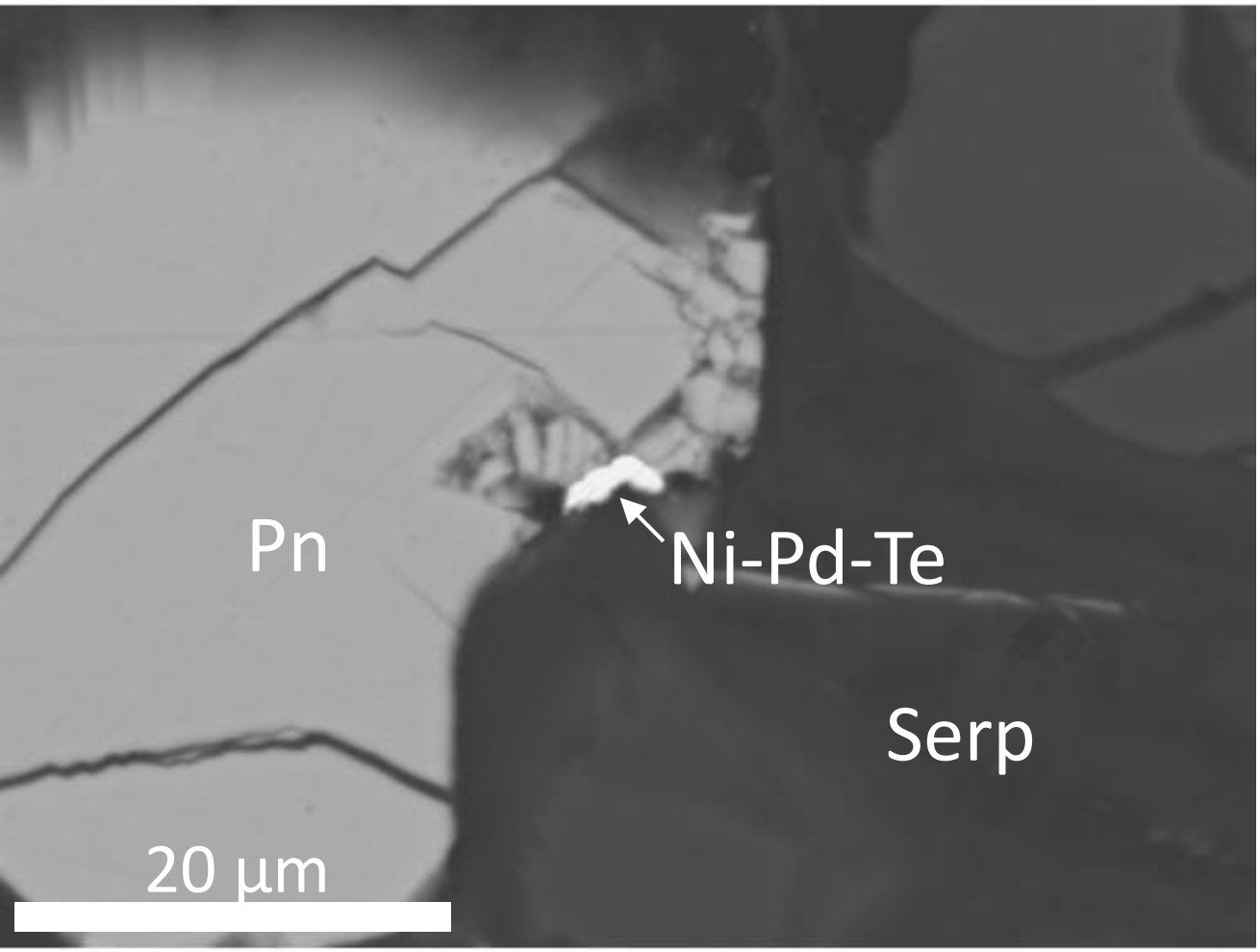
Electron Image 1

PTSR-42 O 1



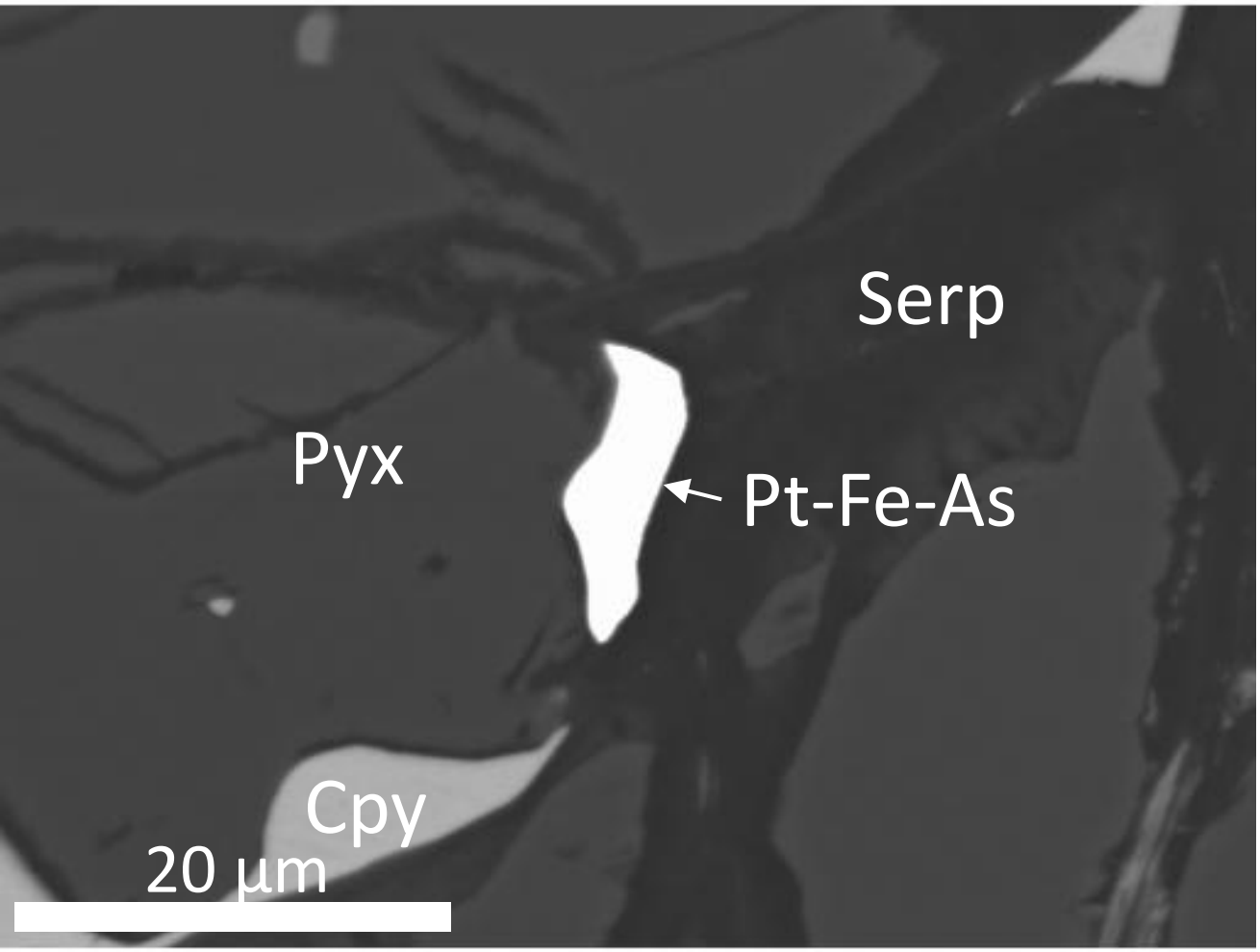
Electron Image 1

PTSR-42 P 1



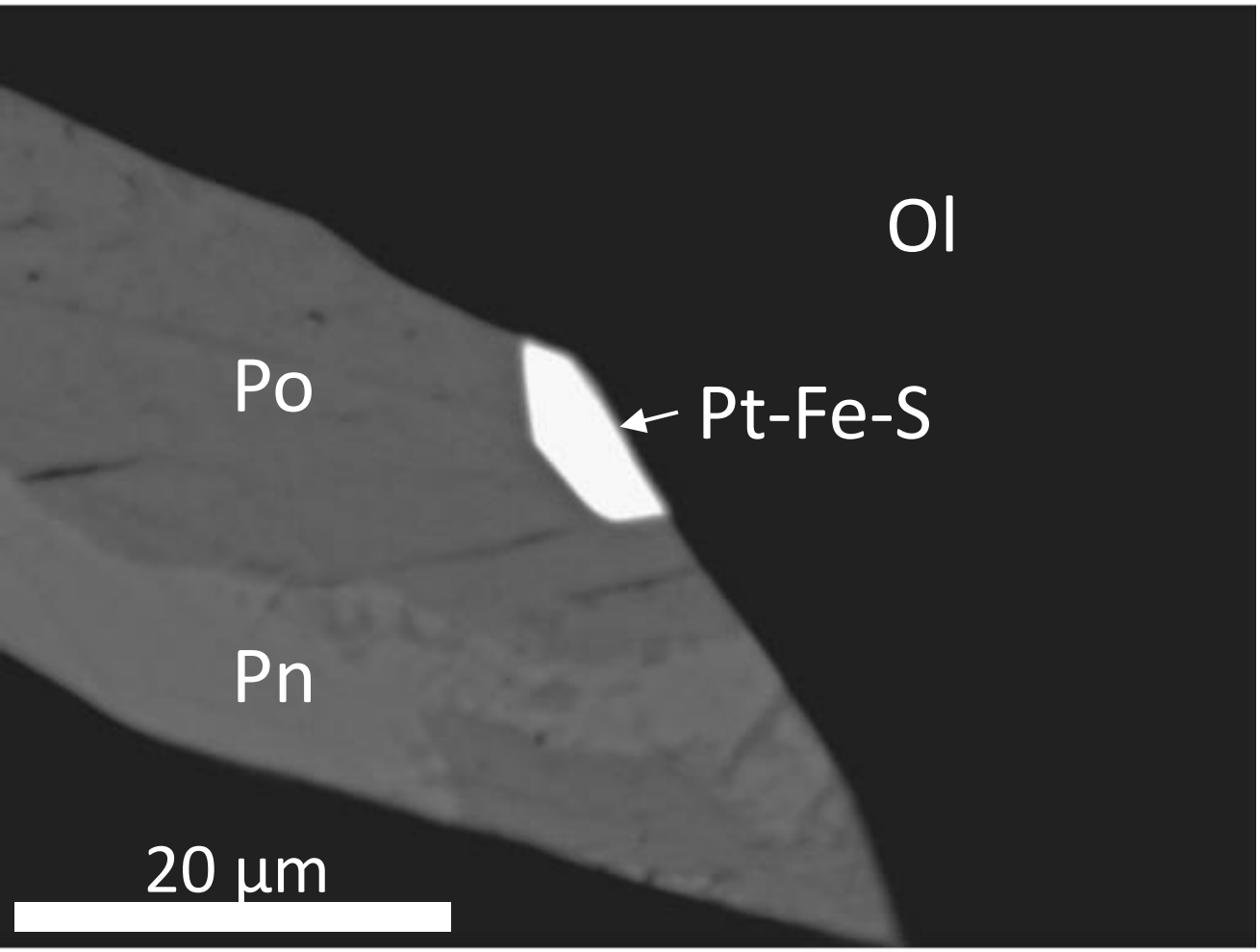
Electron Image 1

PTSR-42 Q 1



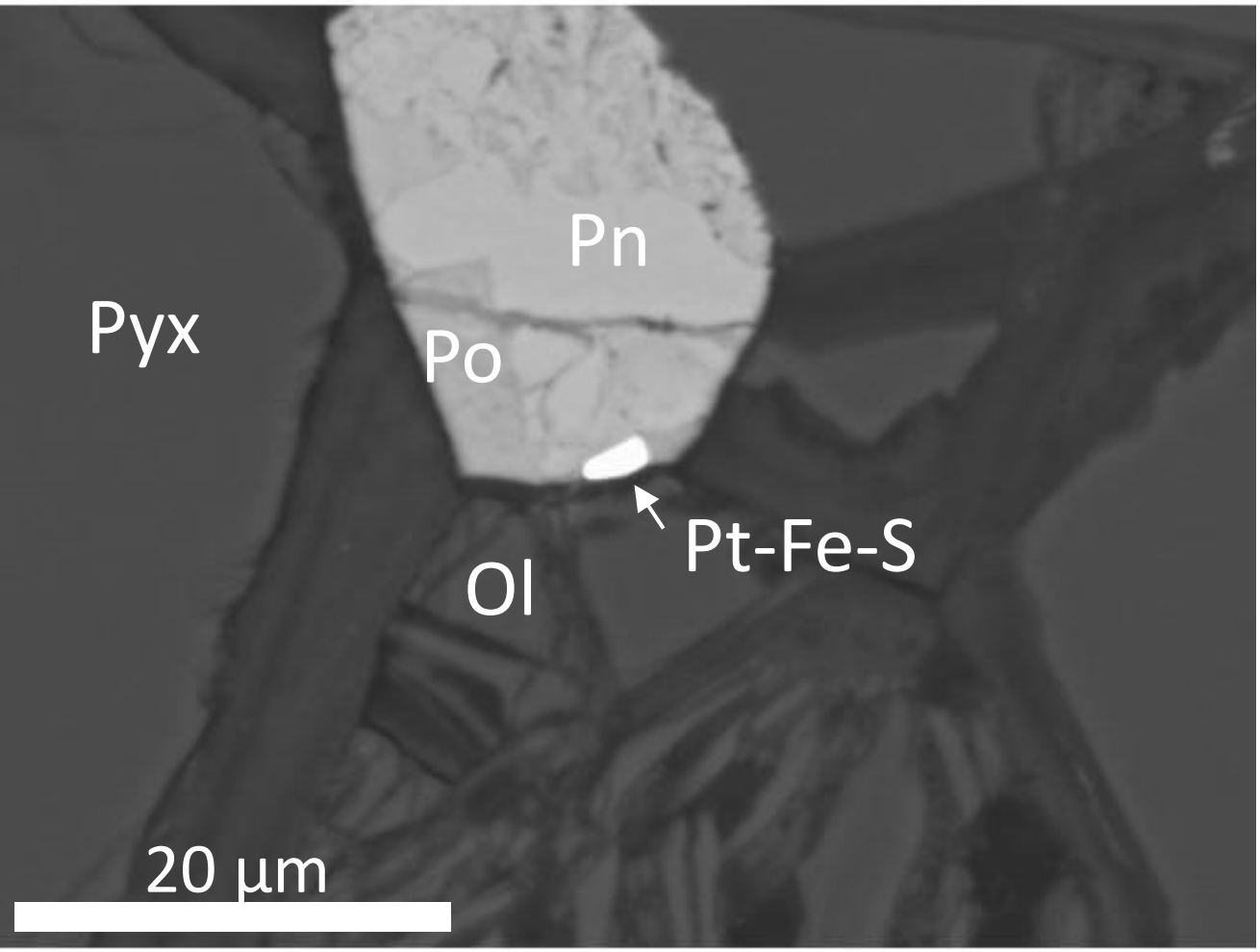
Electron Image 1

PTSR-42 R 1



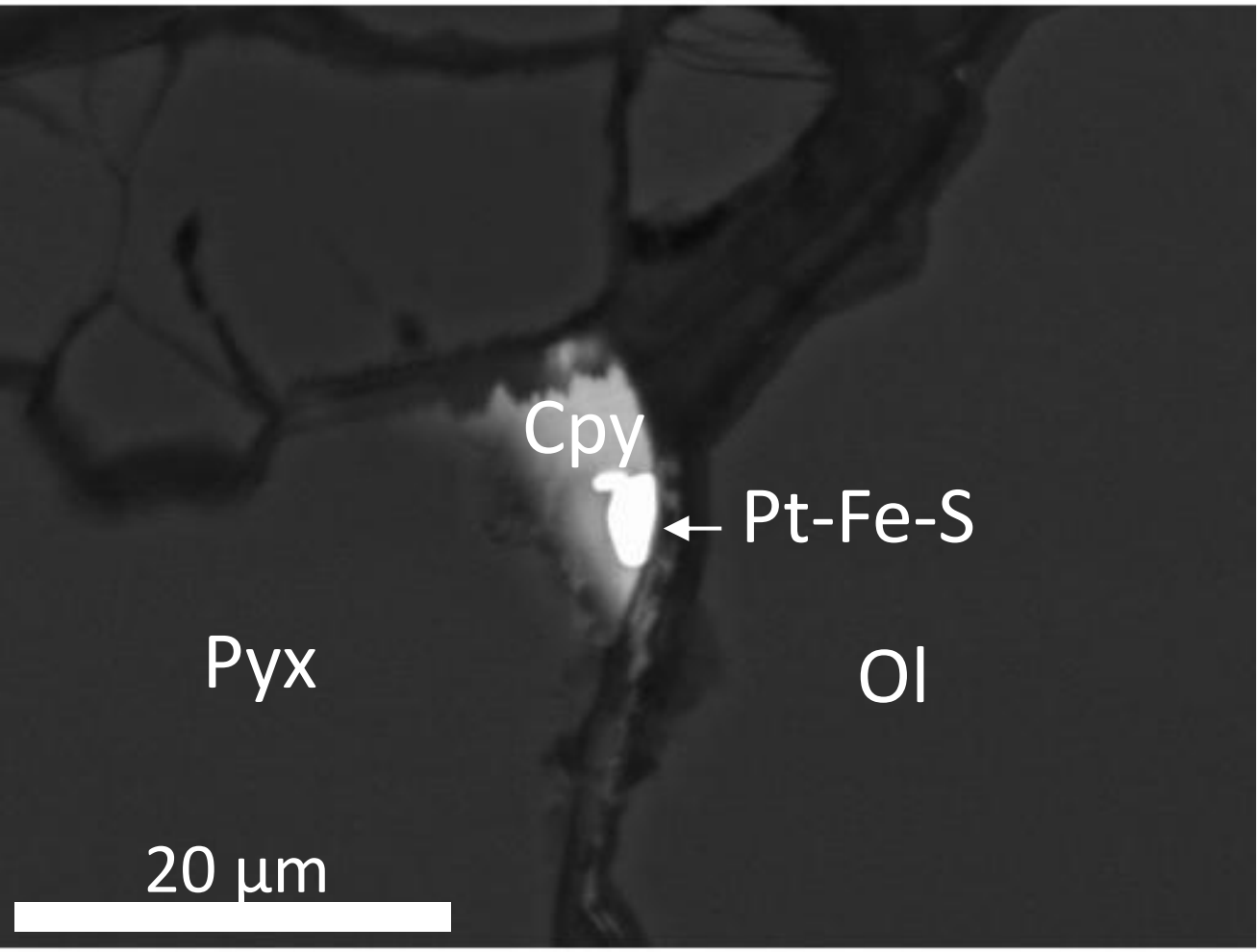
Electron Image 1

PTSR-42 S 1



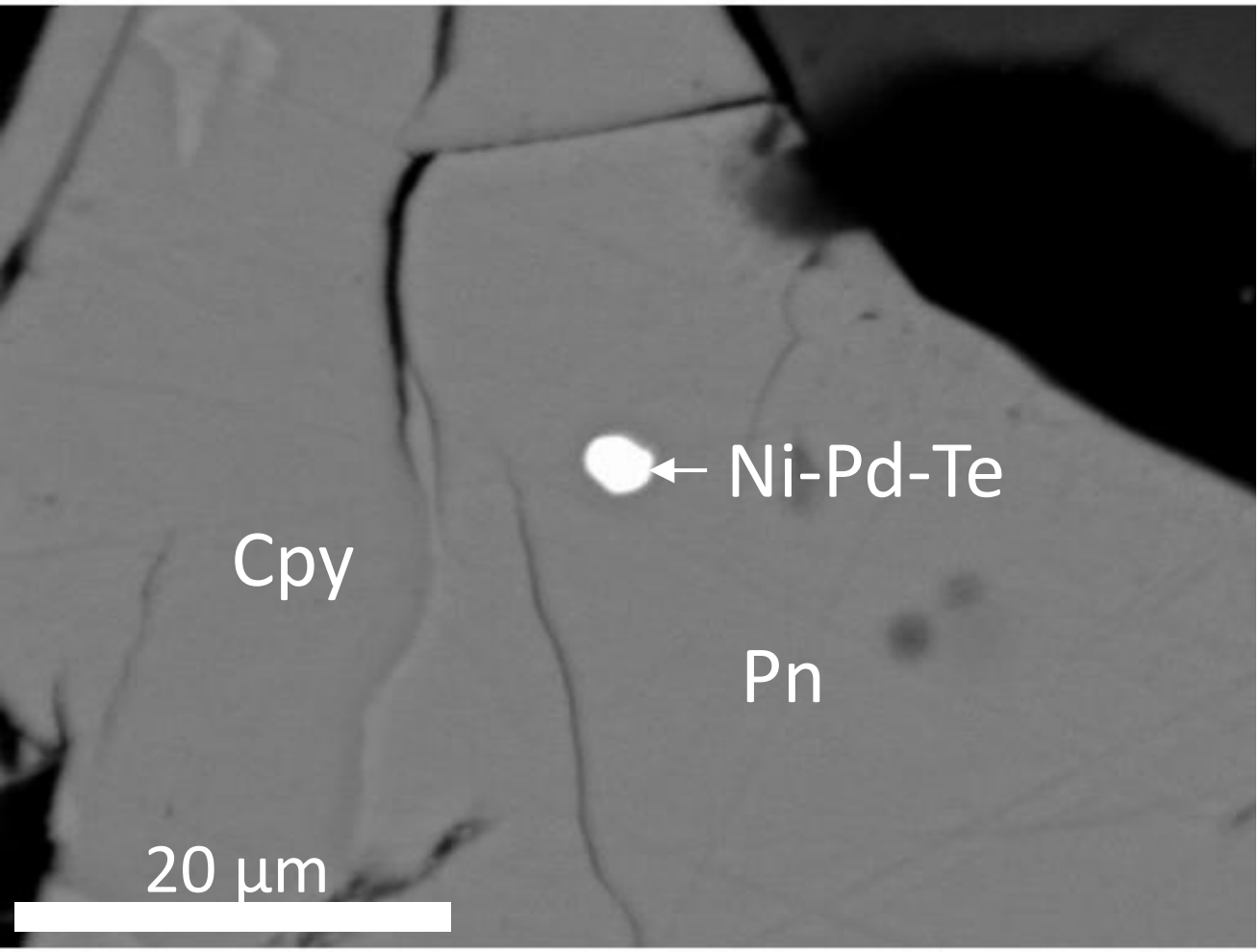
Electron Image 1

PTSR-42 T 1



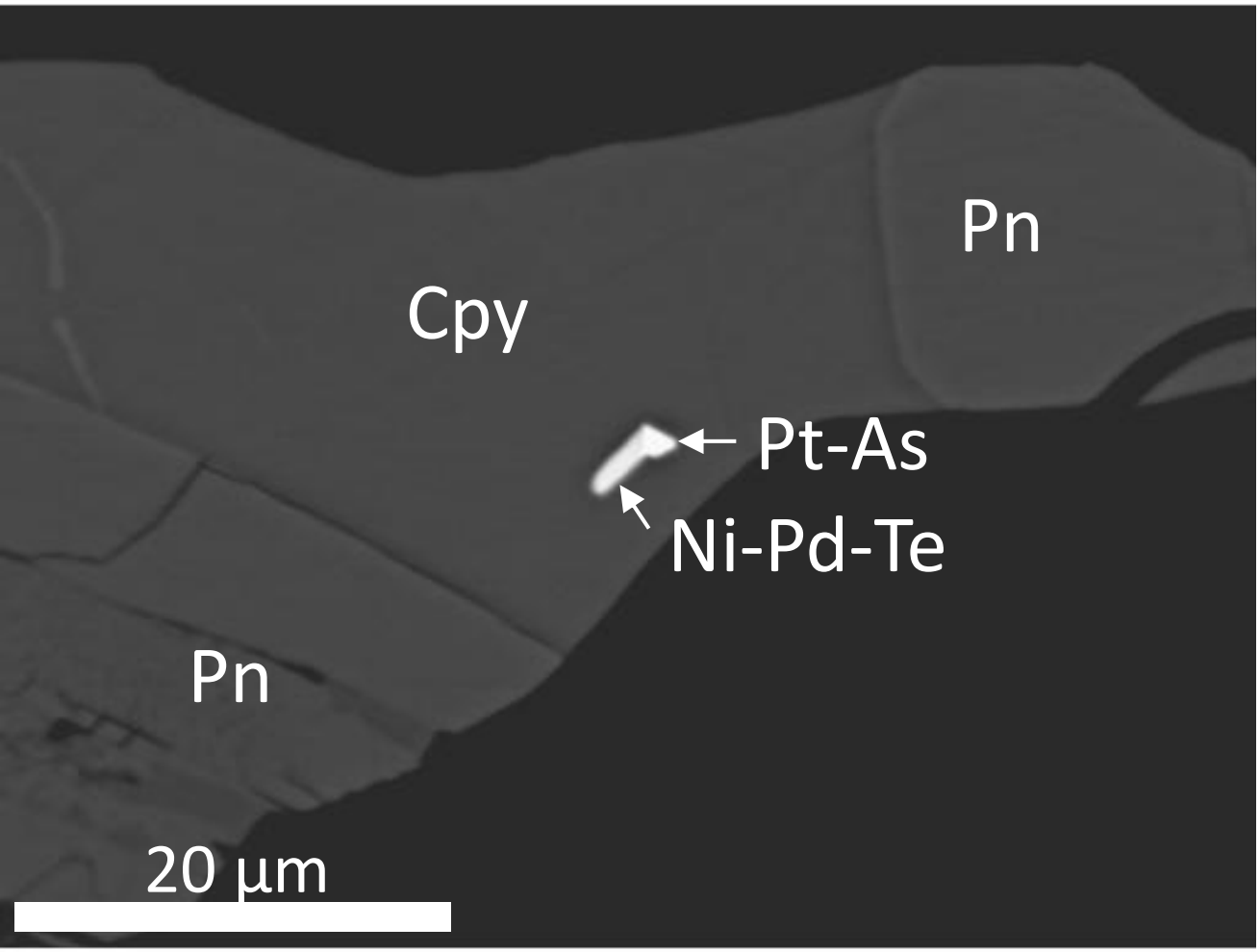
Electron Image 1

PTSR-42 U 1



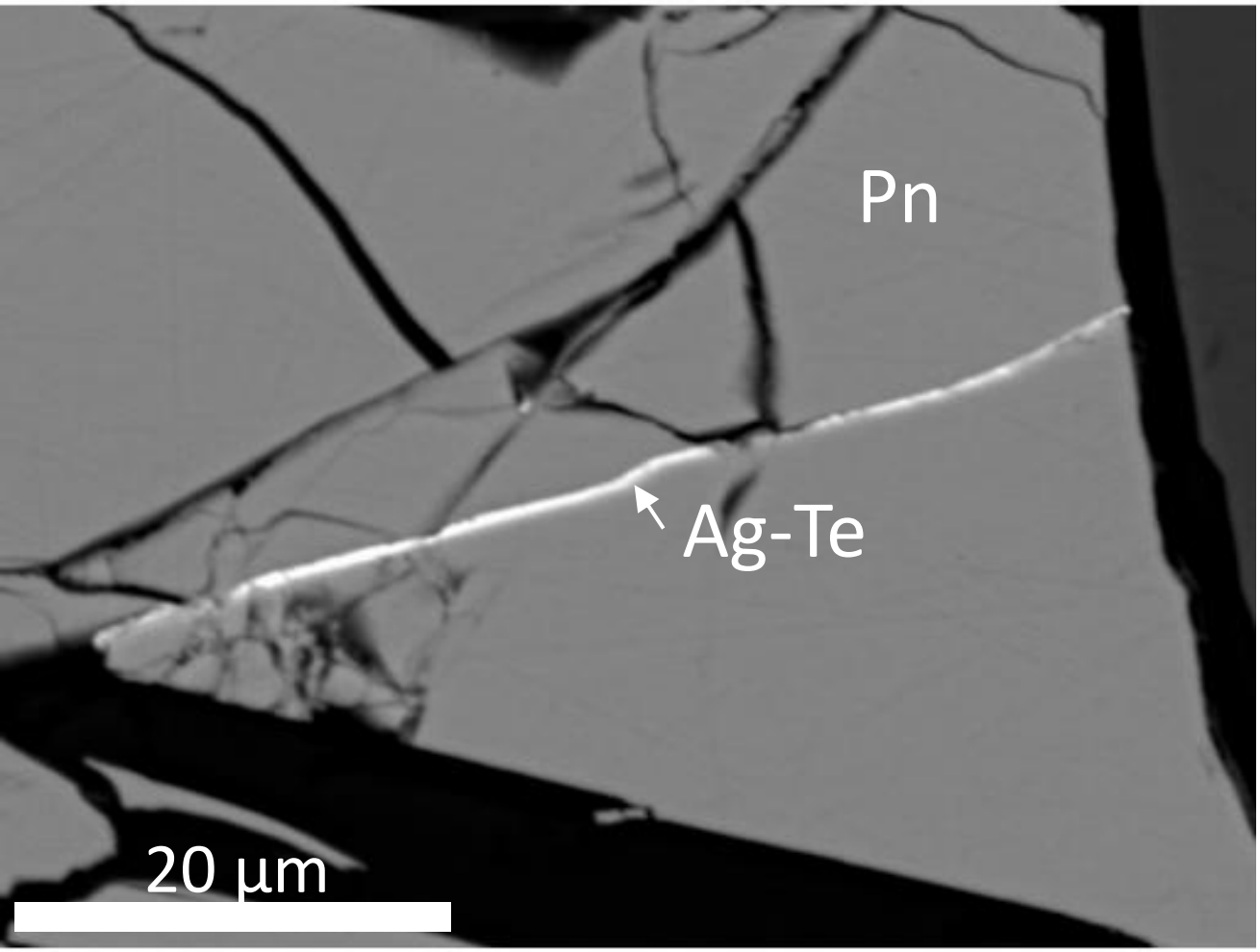
Electron Image 1

PTSR-42 V 1-2



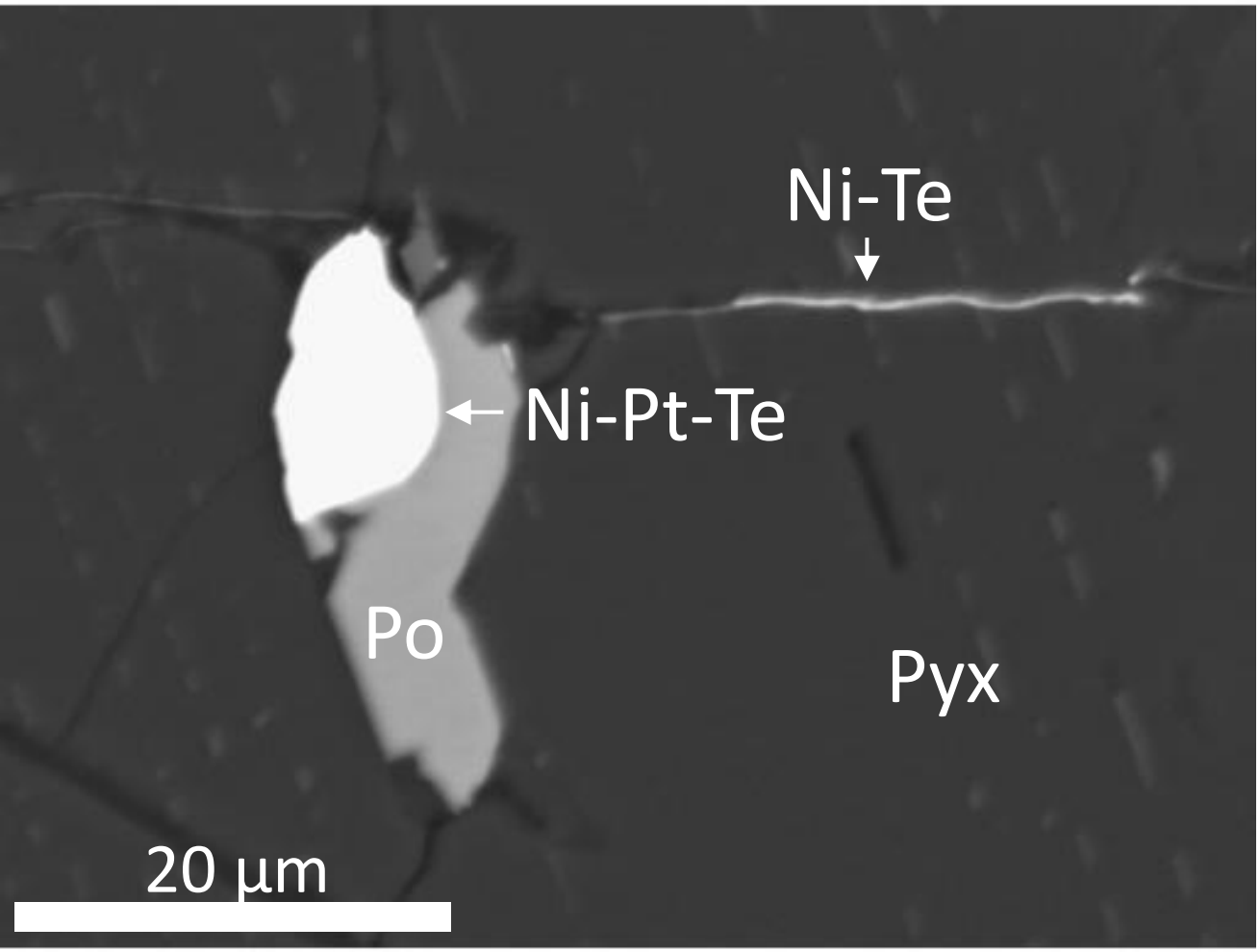
Electron Image 1

PTSR-42 W 1



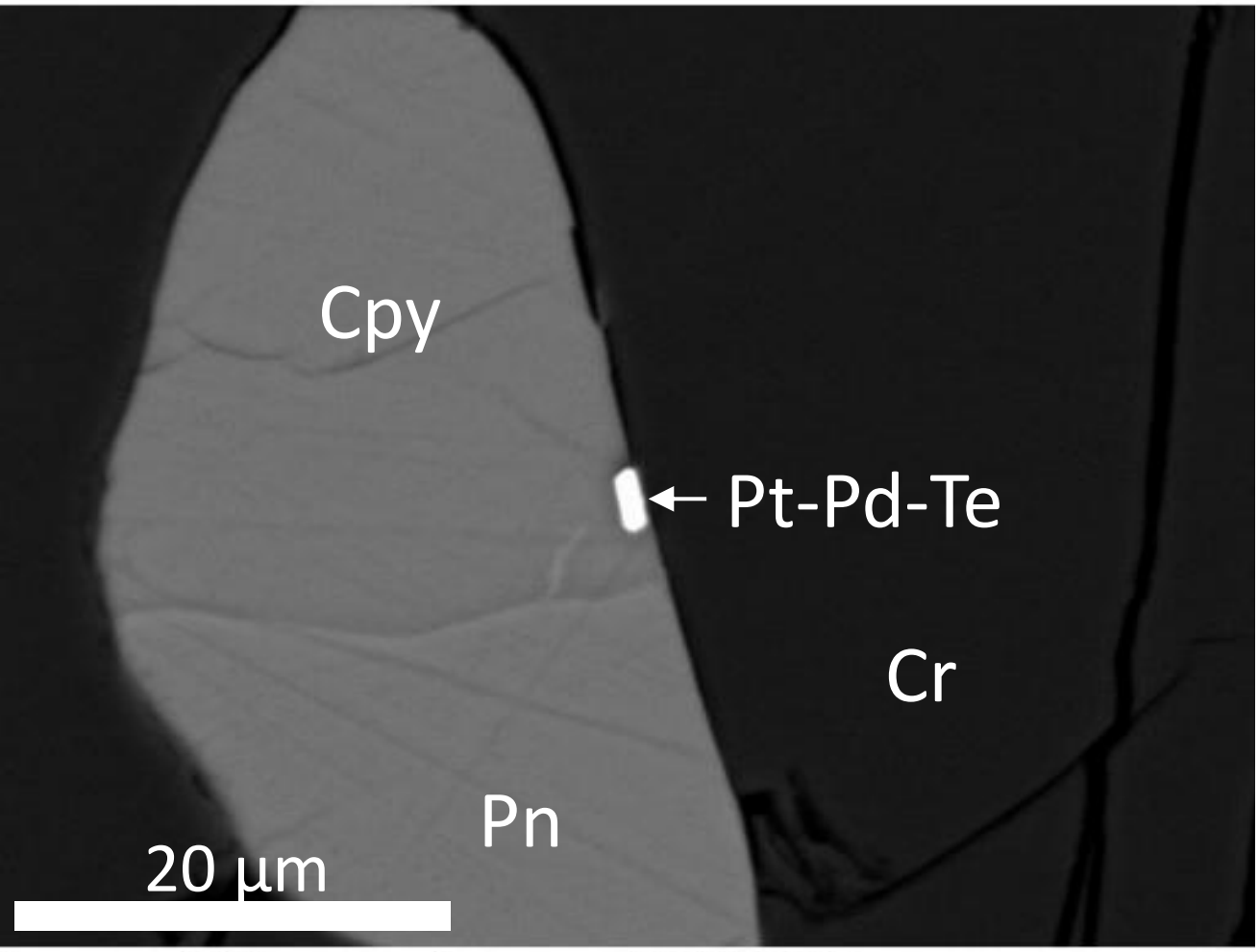
Electron Image 1

PTSR-42 X 1-2



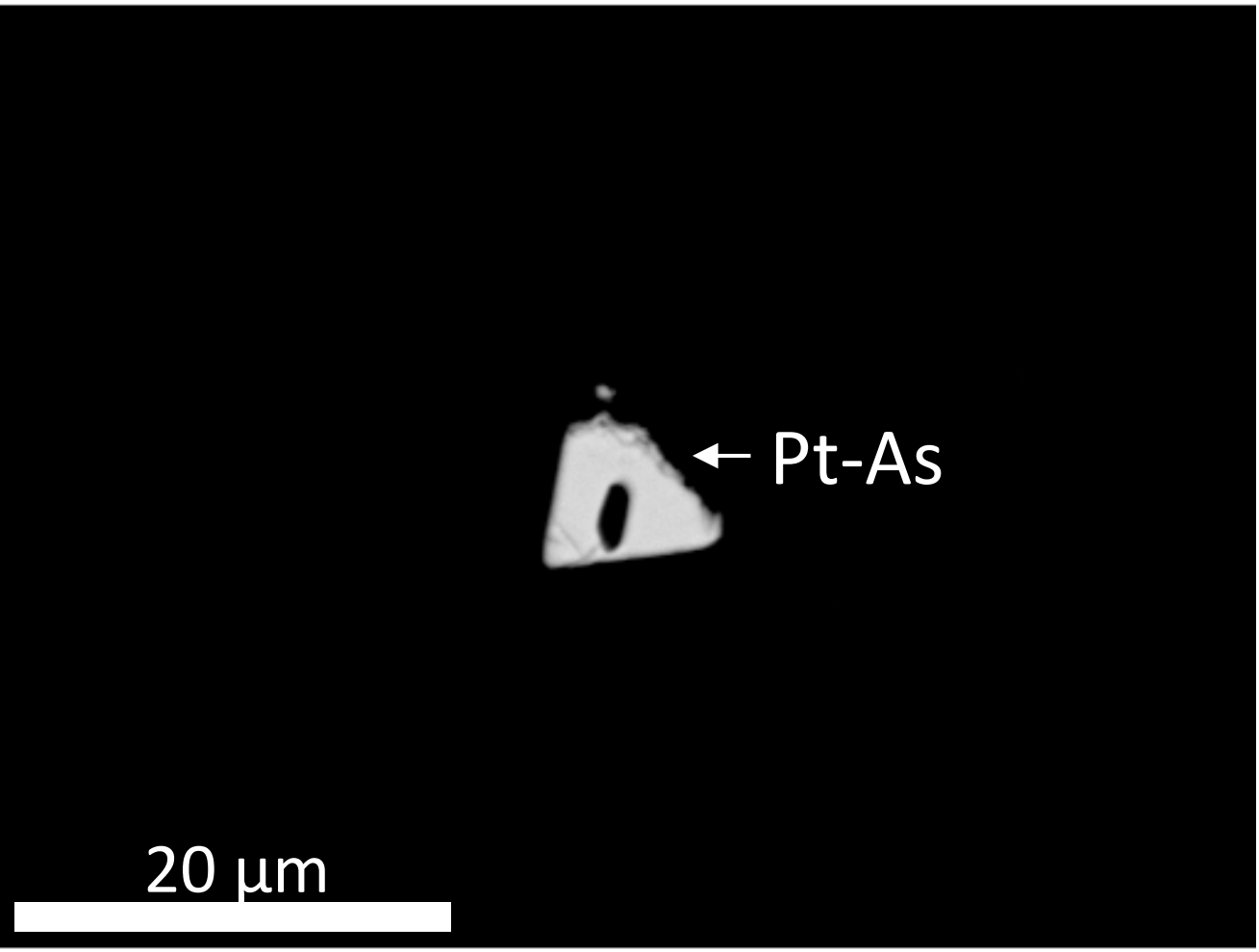
Electron Image 1

PTSR-42 Y 1



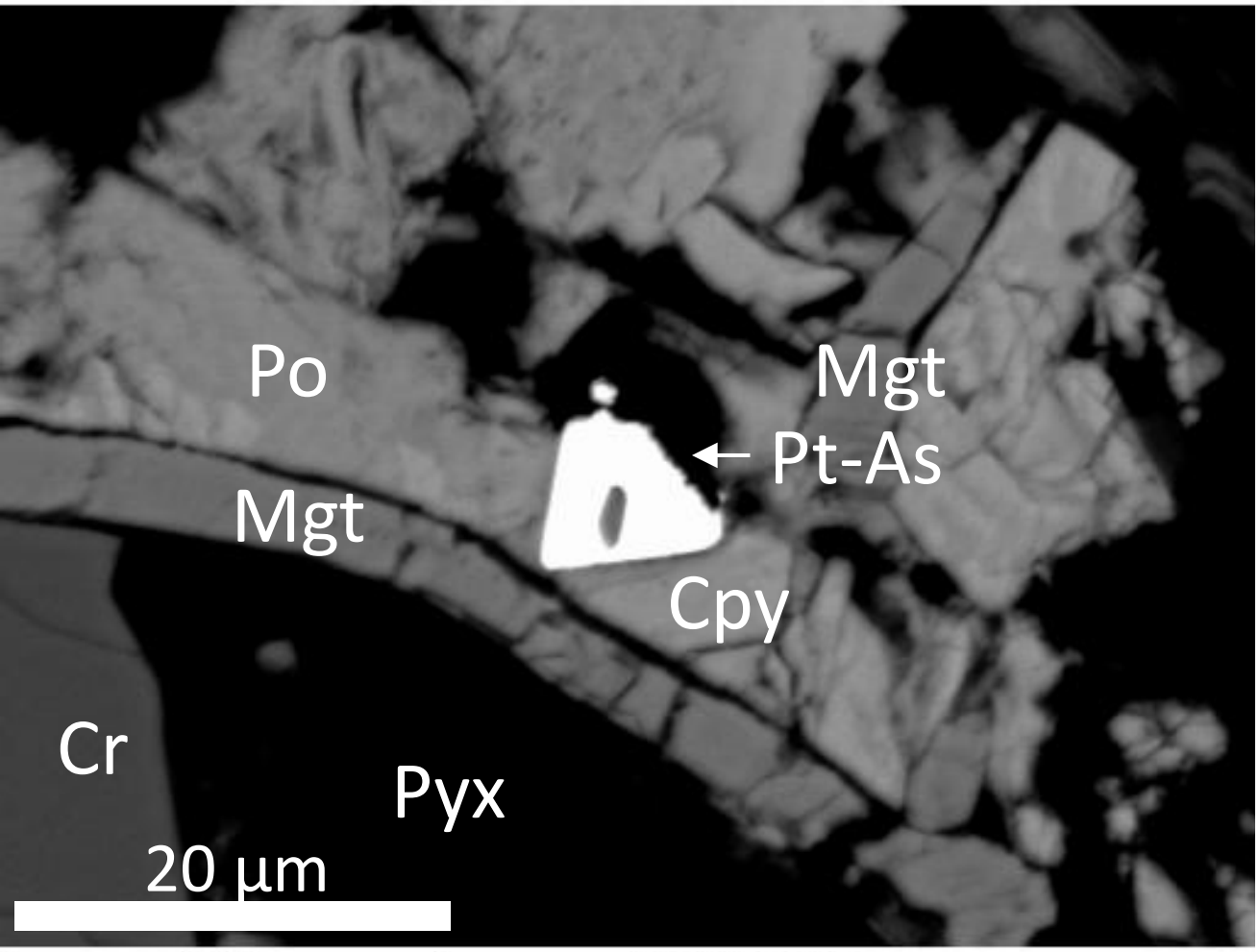
Electron Image 1

PTSR-42 Z 1



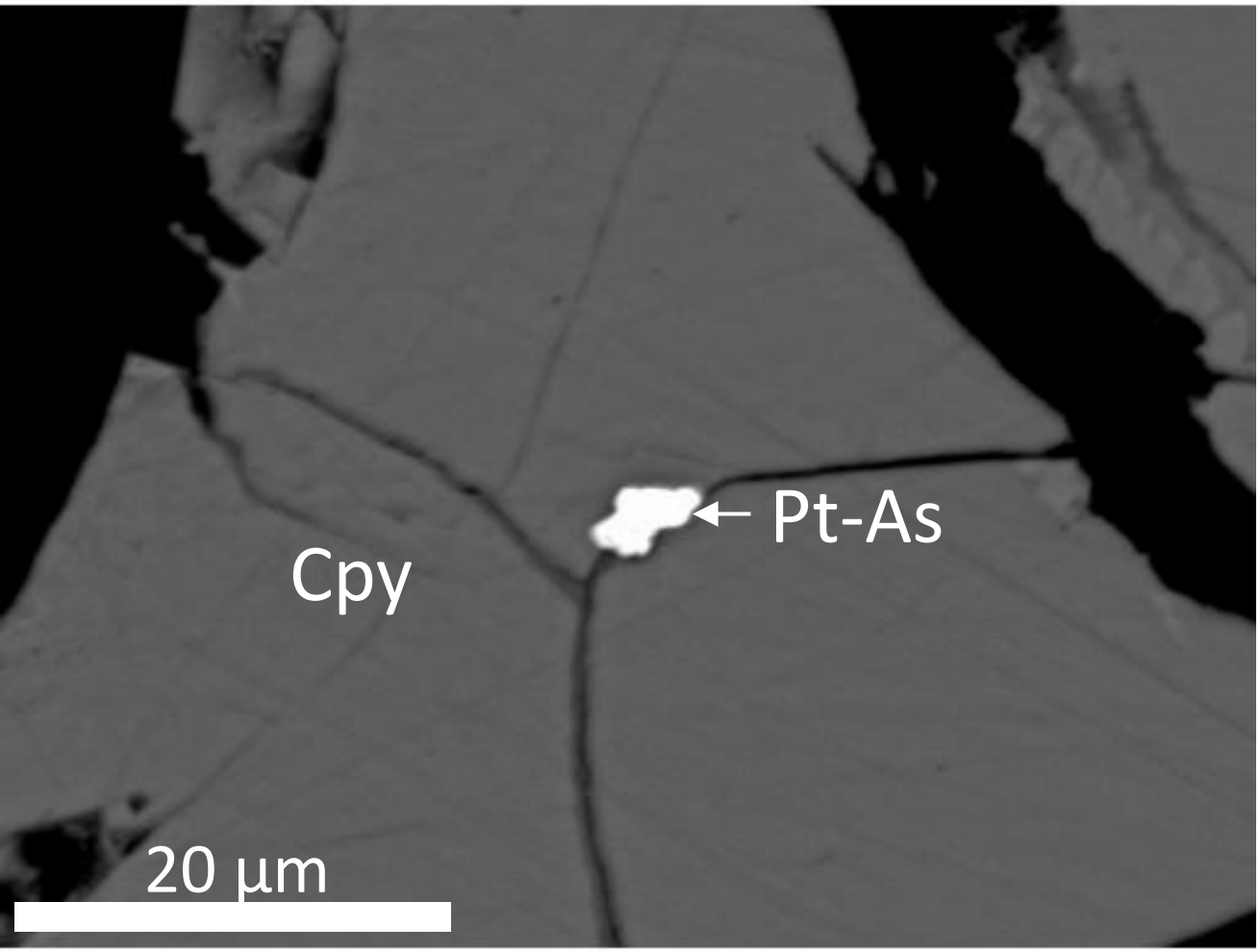
Electron Image 1

PTSR-42 Z 1 Light



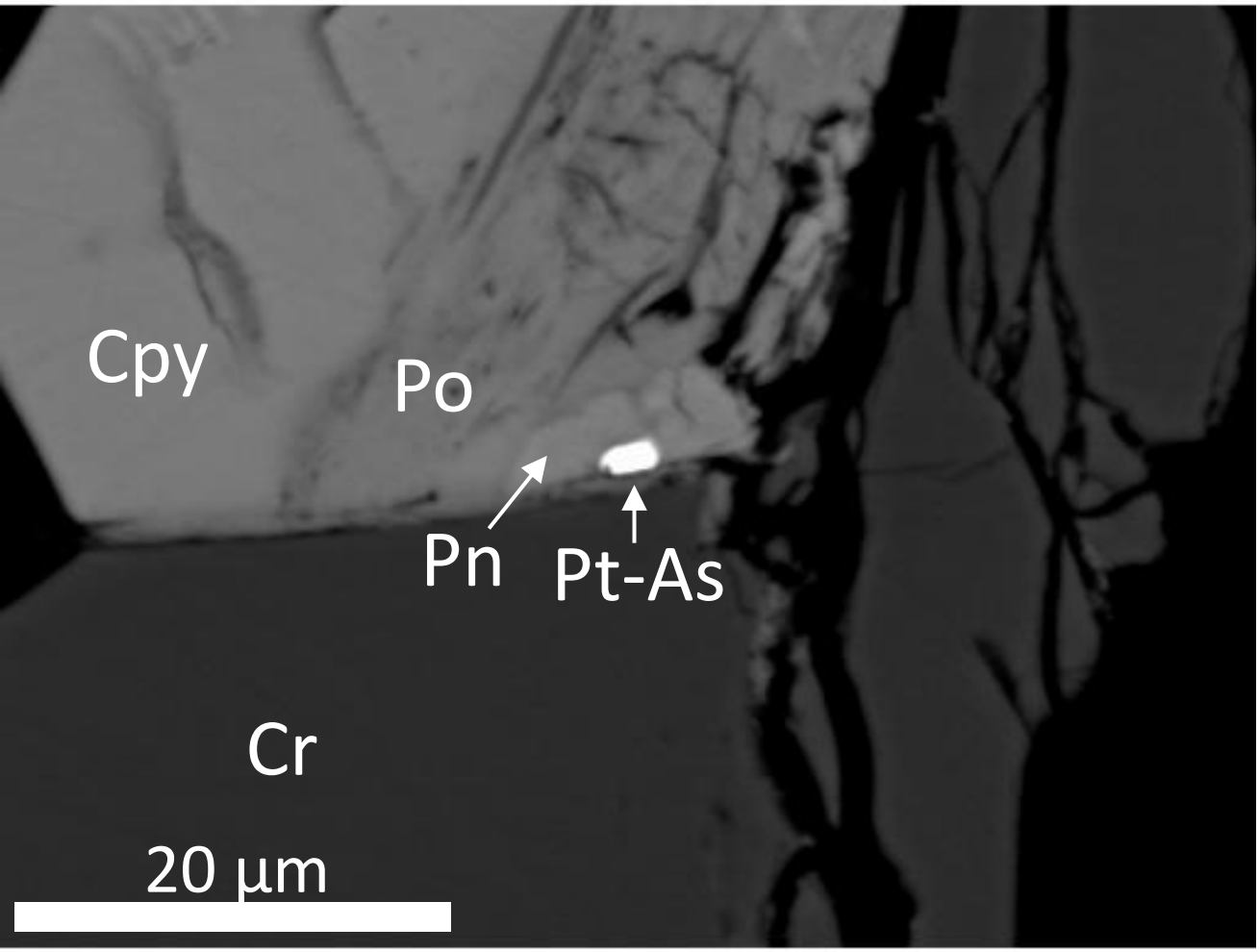
Electron Image 1

PTSR-42 AA 1



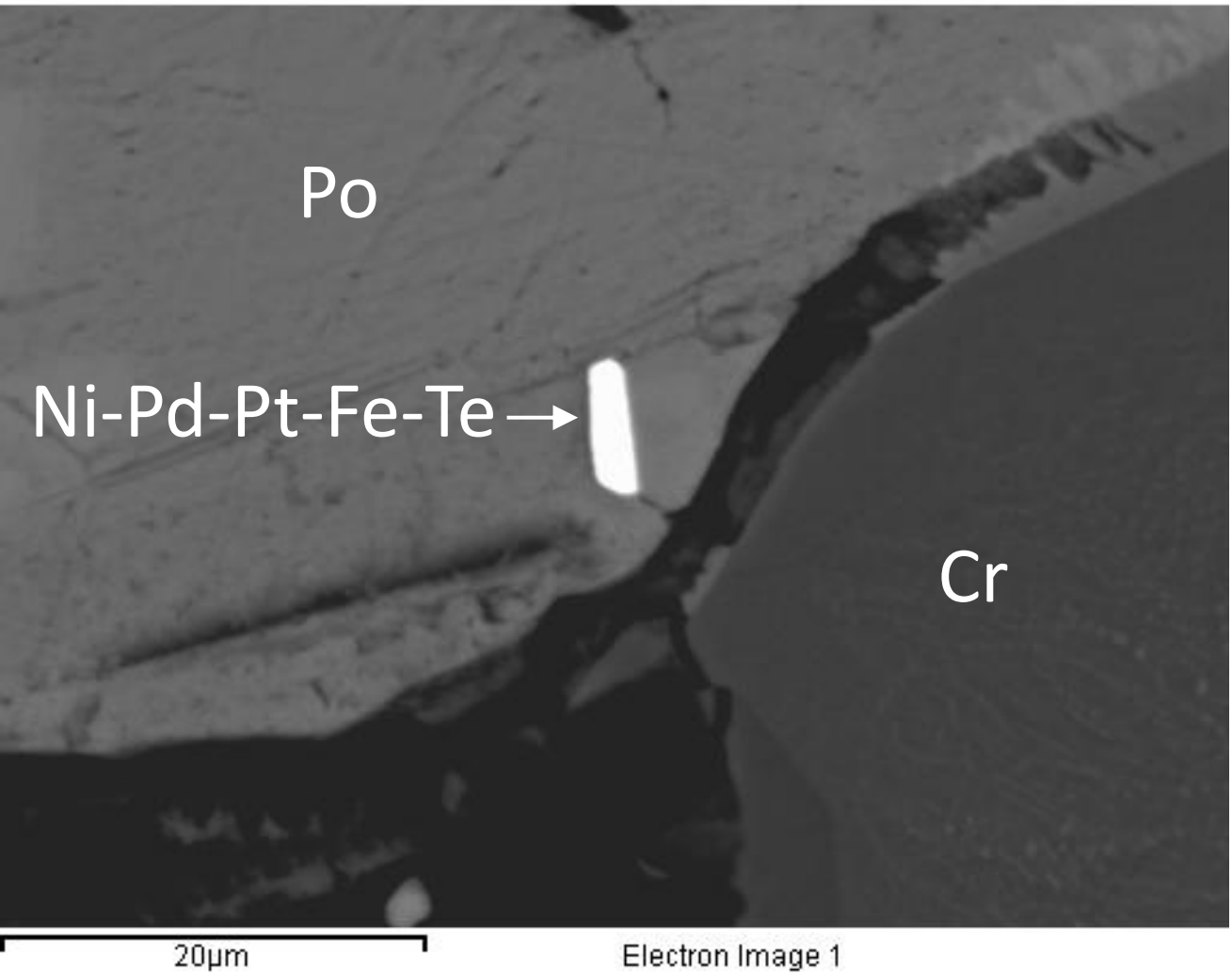
Electron Image 1

PTSR-42 AB 1

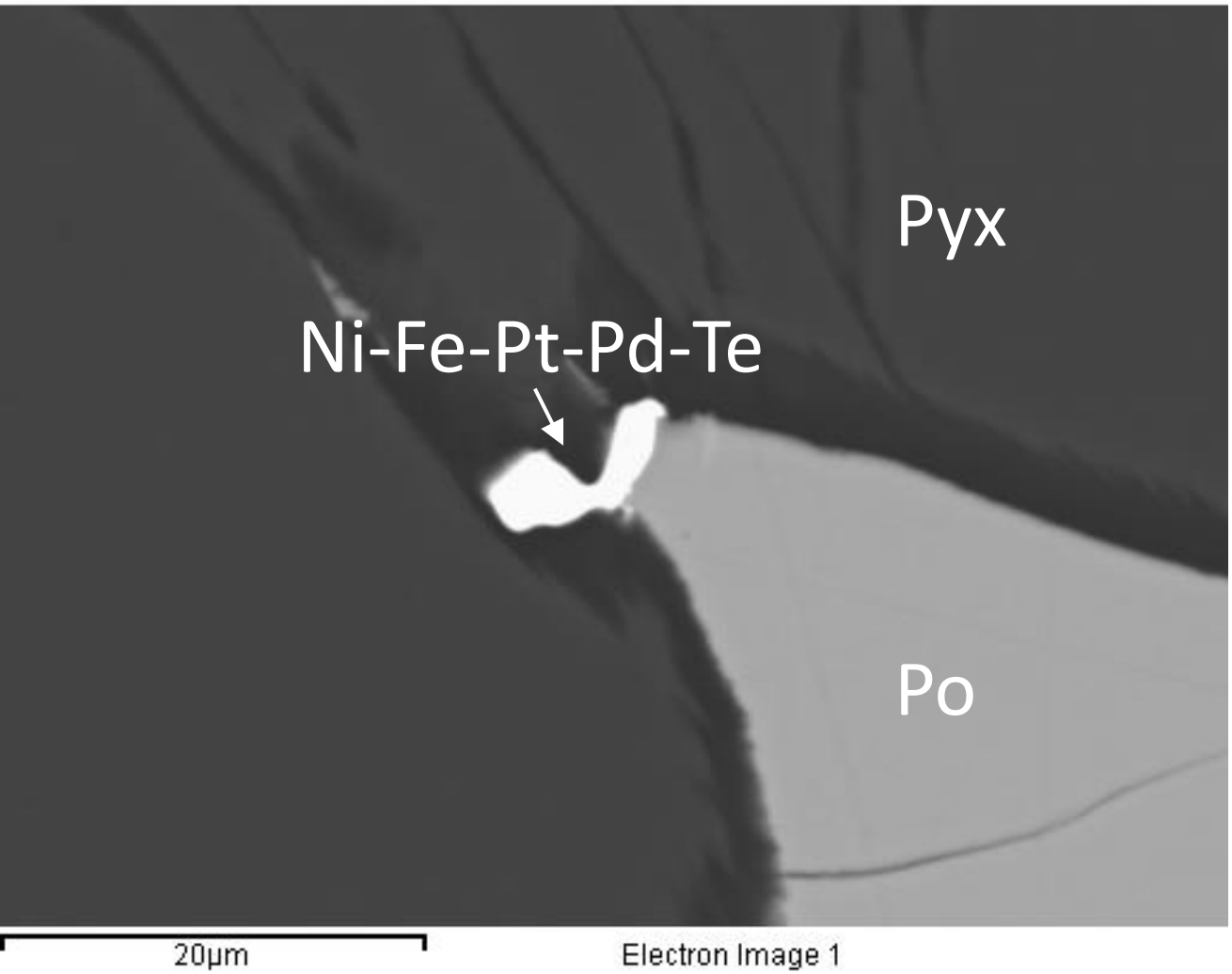


Electron Image 1

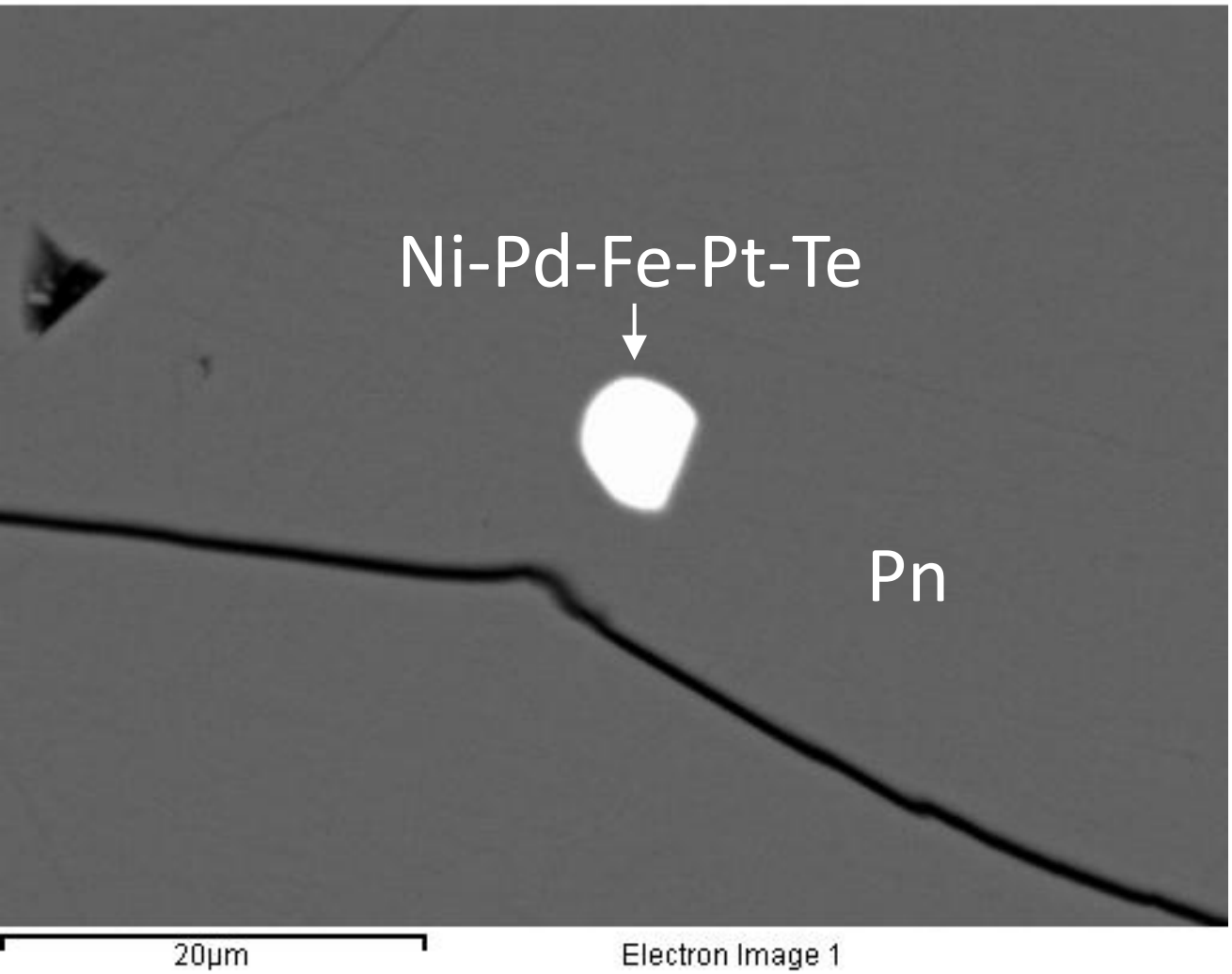
PTSR-43 A 1



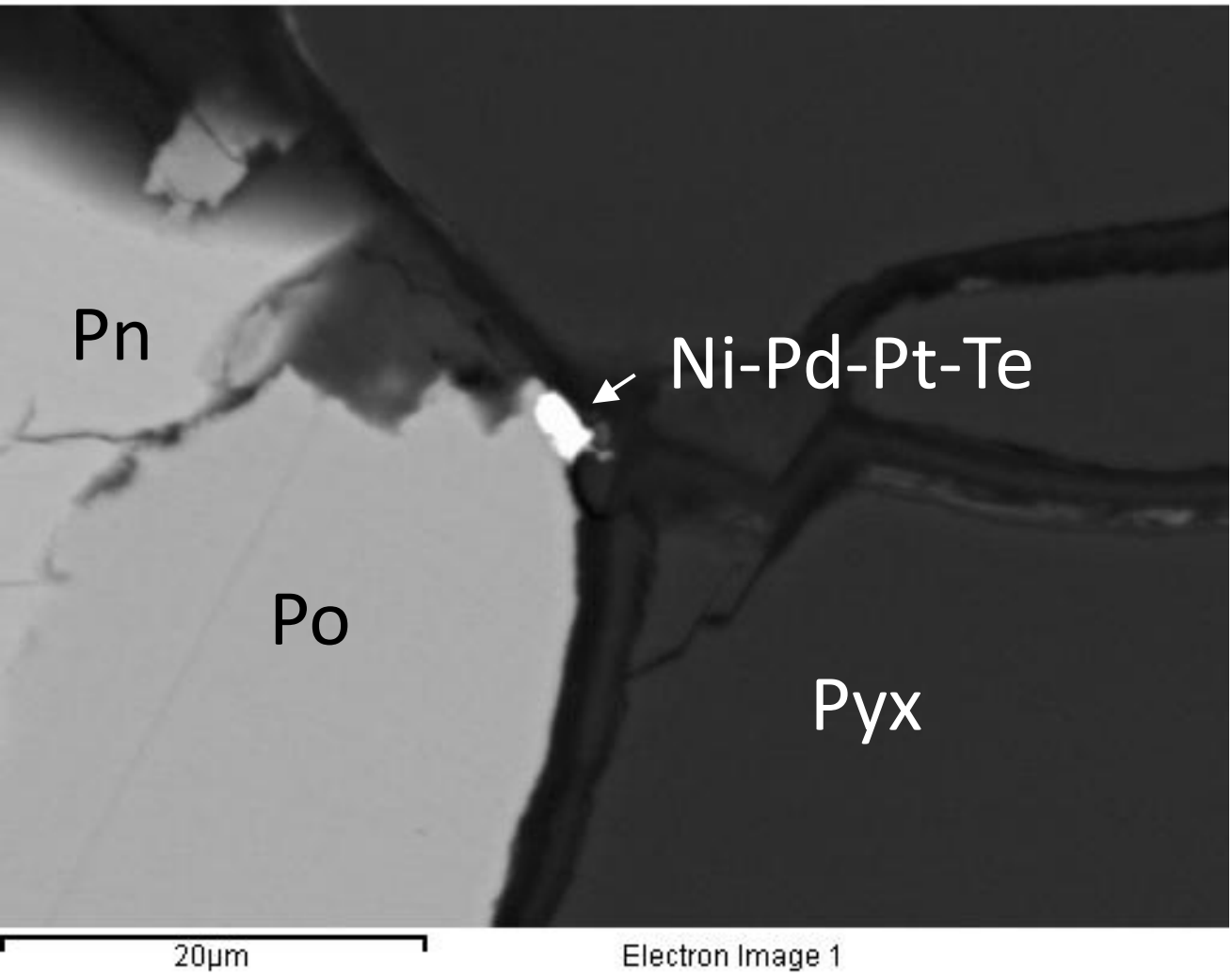
PTSR-43 B 1



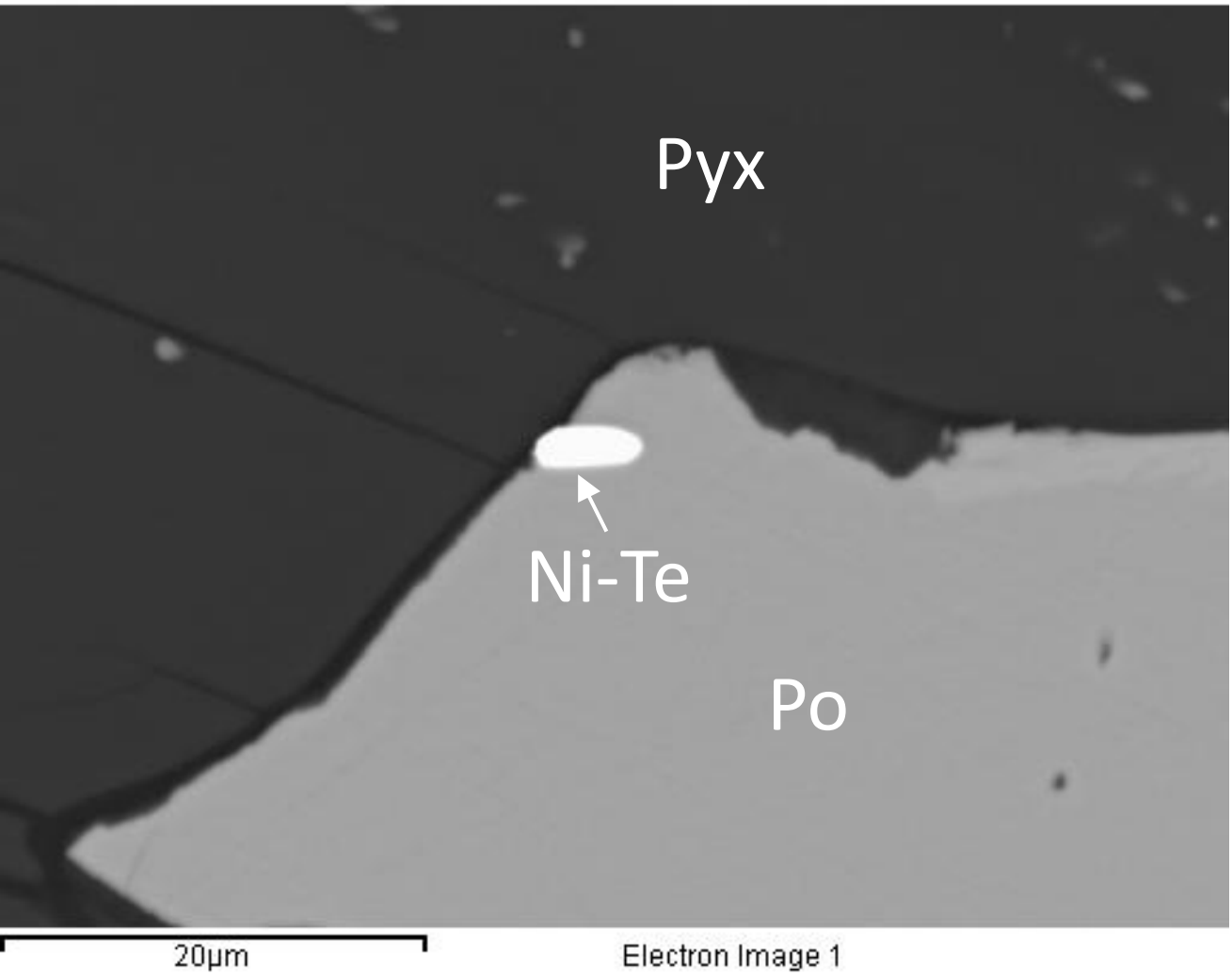
PTSR-43 C 1



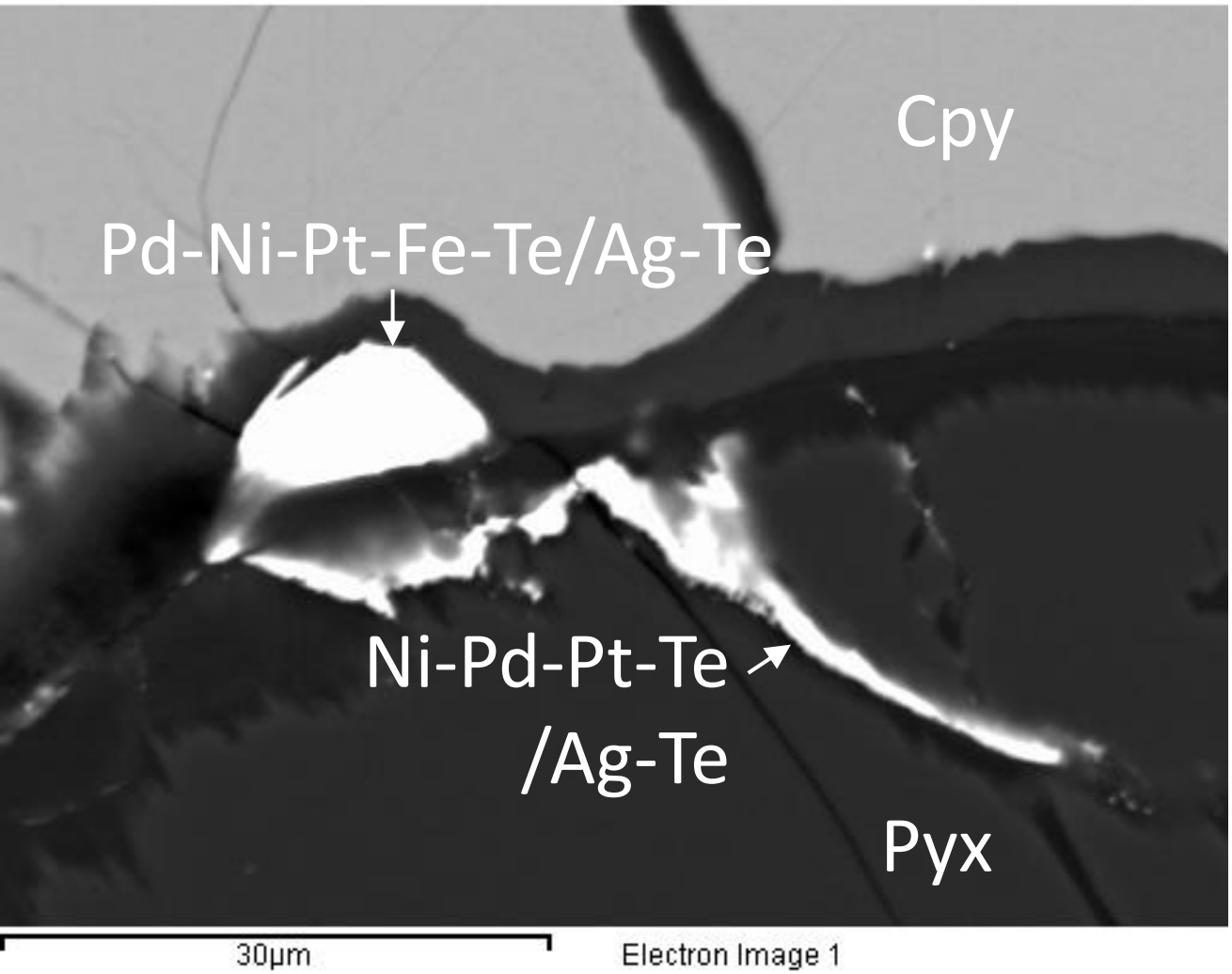
PTSR-43 D 1



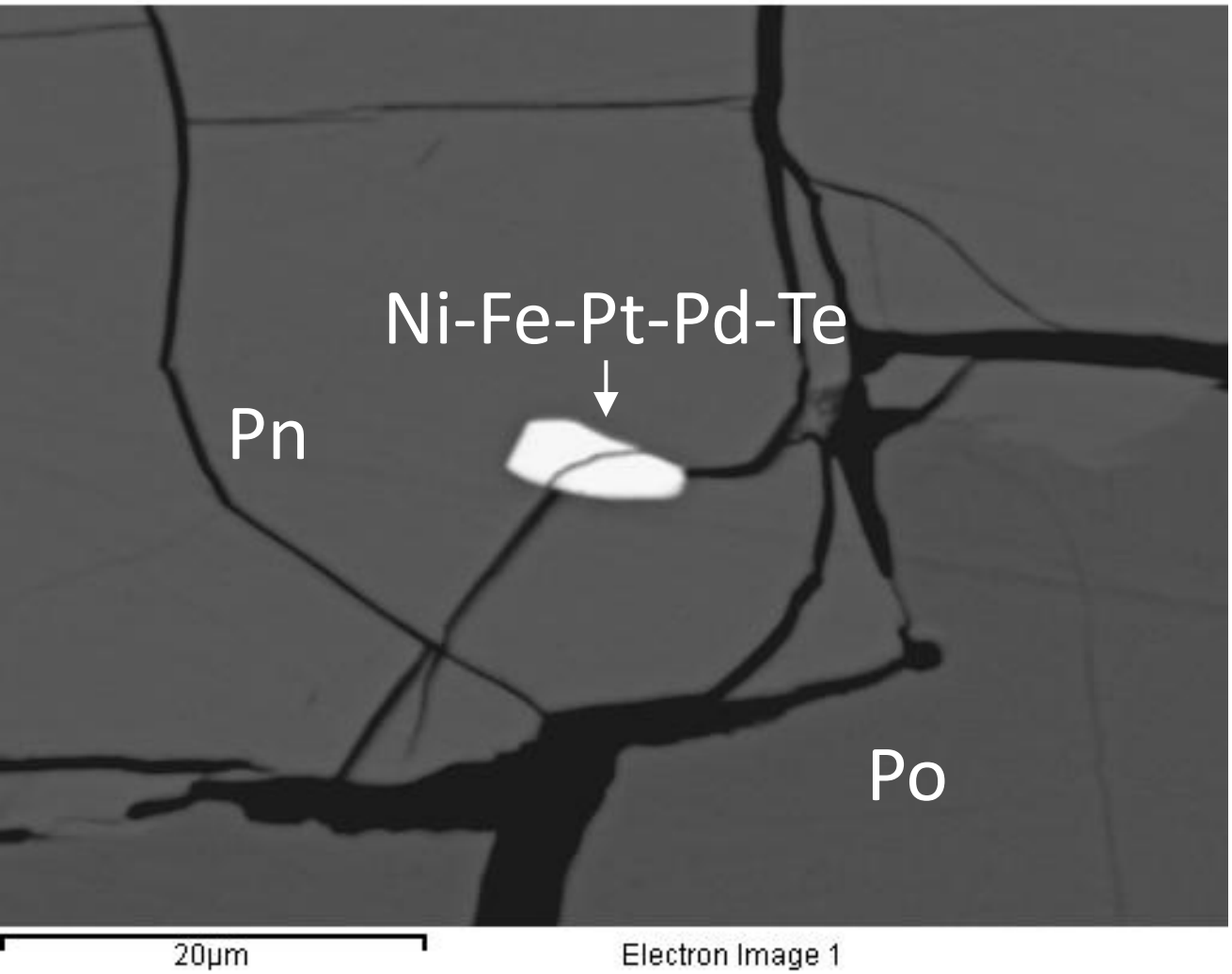
PTSR-43 E 1



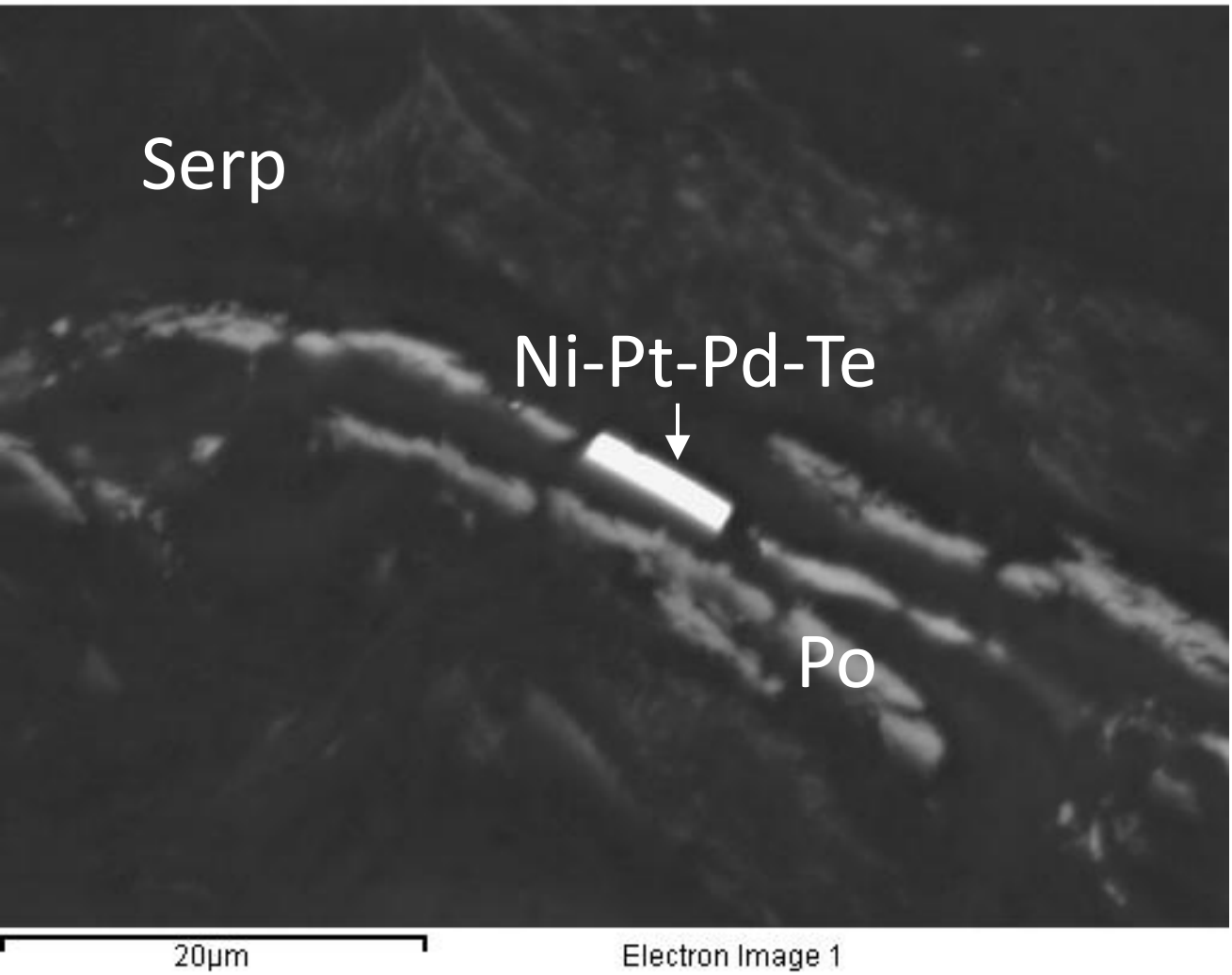
PTSR-43 F 1-2


Cpy
Pd-Ni-Pt-Fe-Te/Ag-Te
Ni-Pd-Pt-Te
/Ag-Te
Pyx
30µm
Electron Image 1

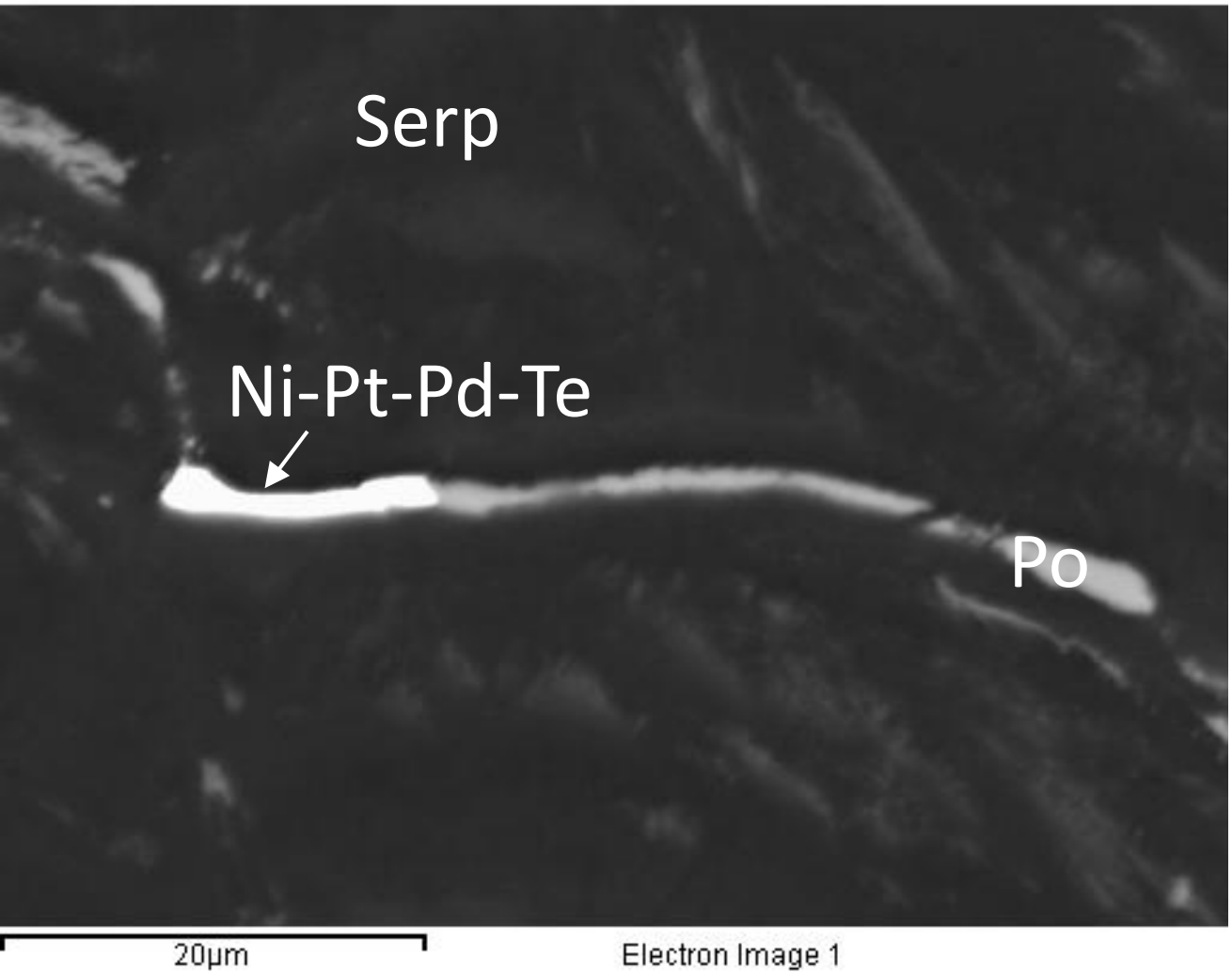
PTSR-43 G 1



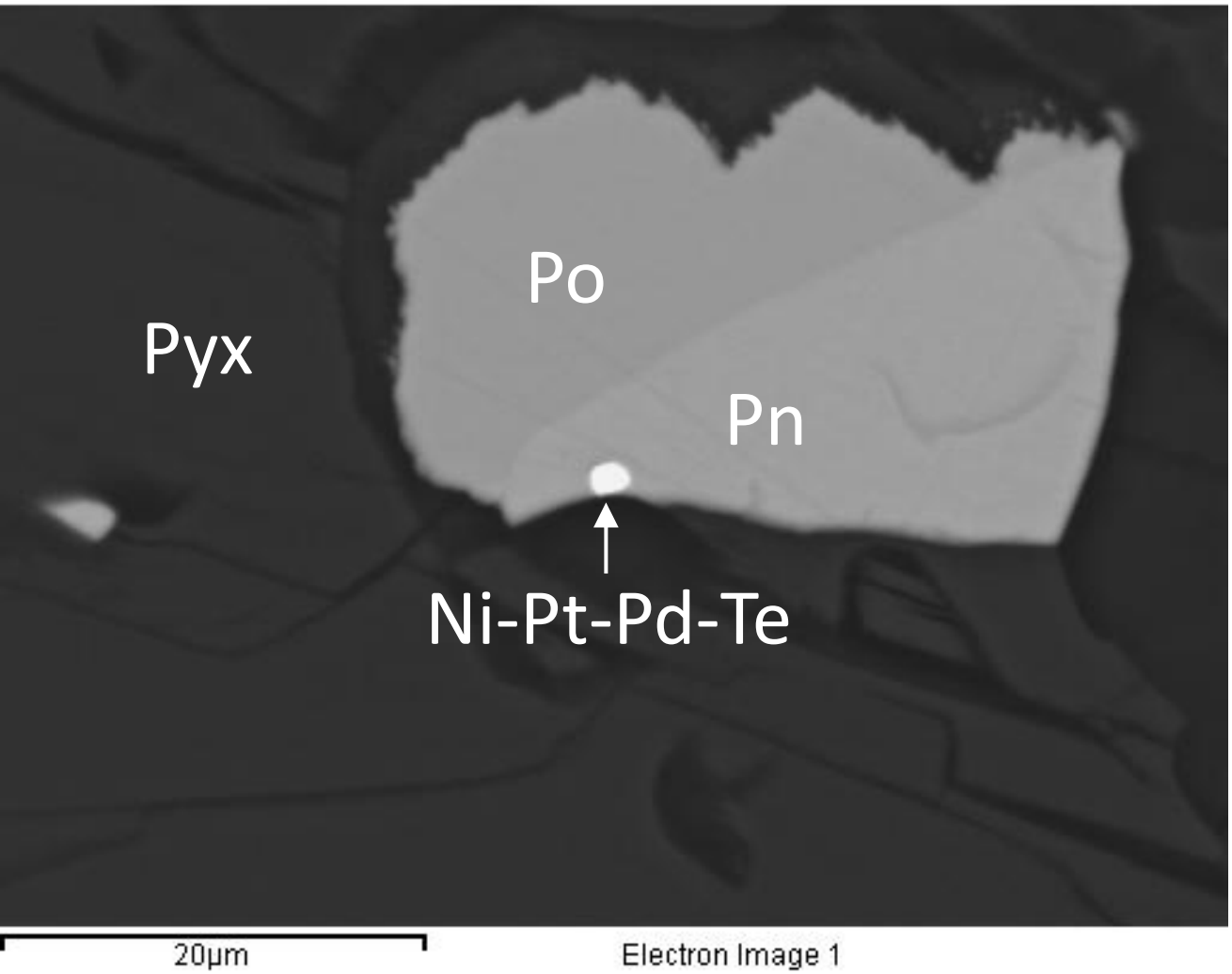
PTSR-43 H 1



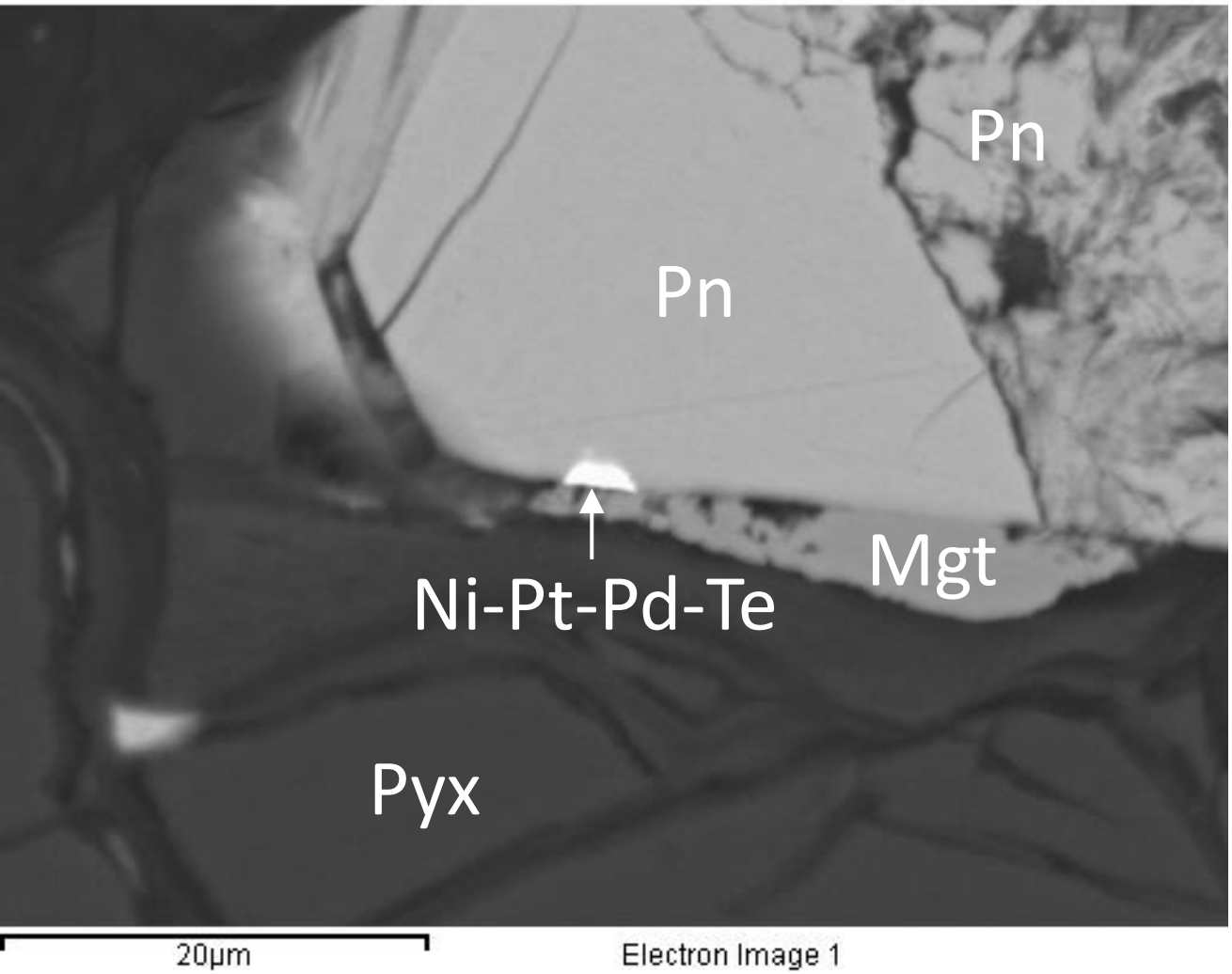
PTSR-43 H 2



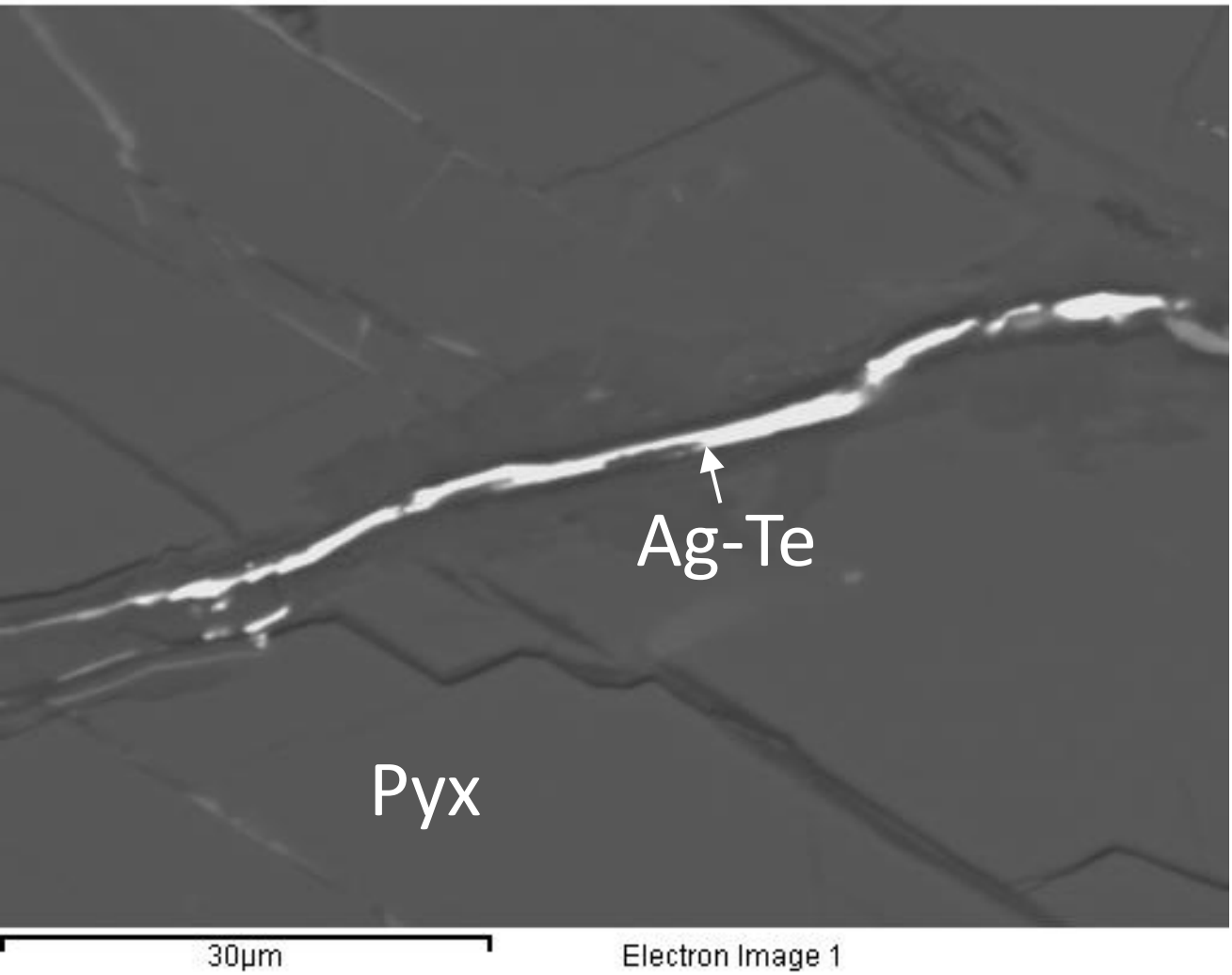
PTSR-43 I 1



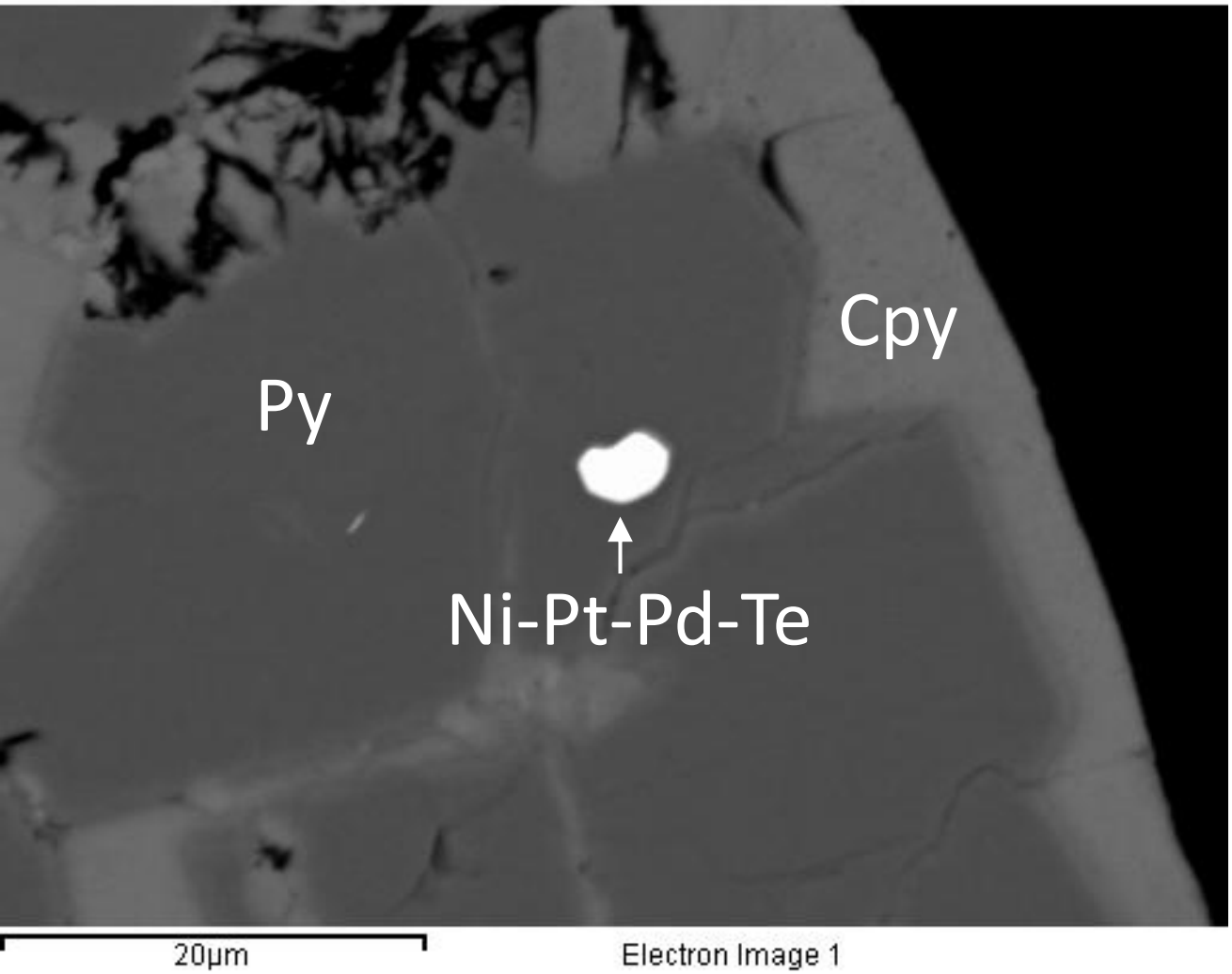
PTSR-43 J 1



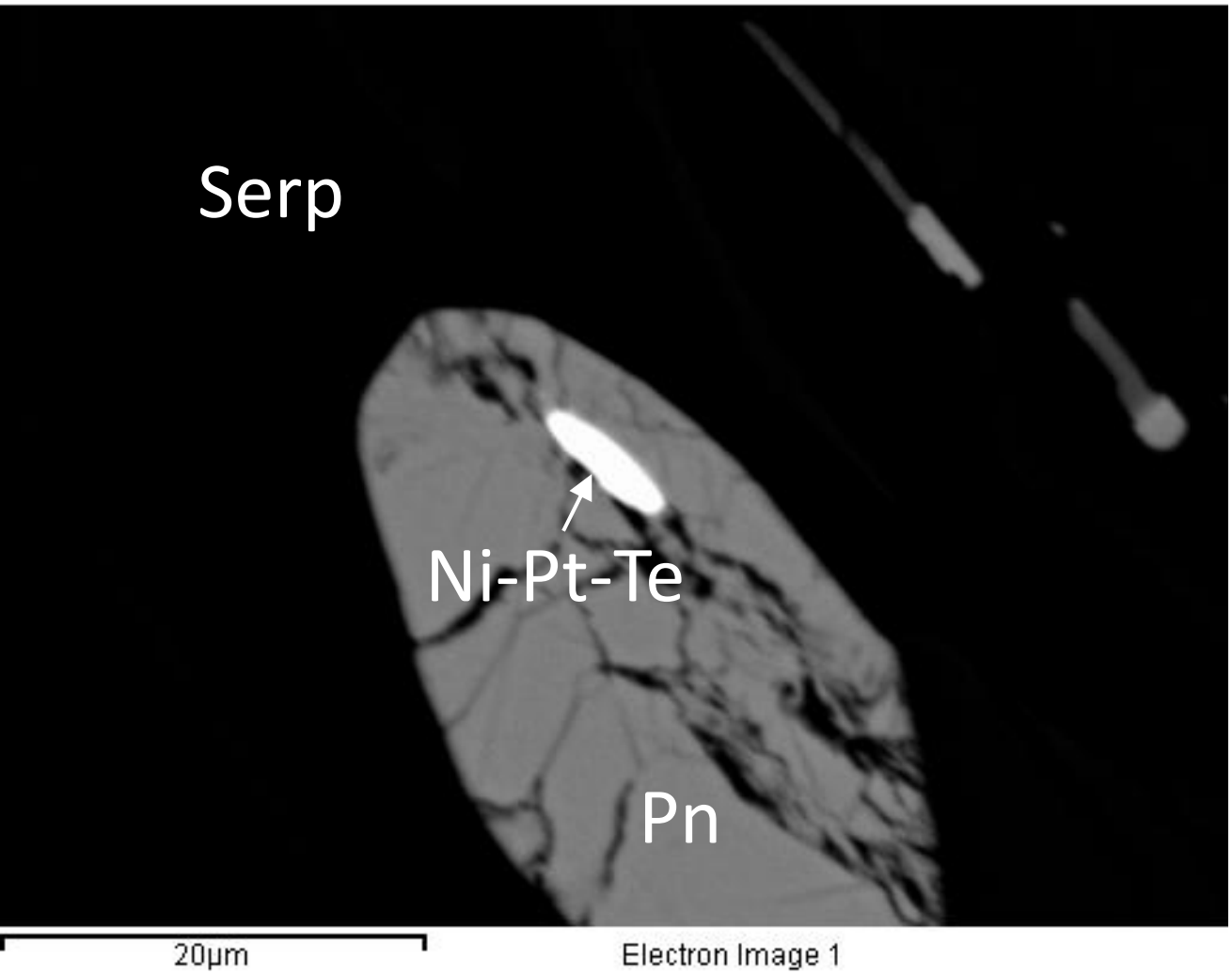
PTSR-43 K 1



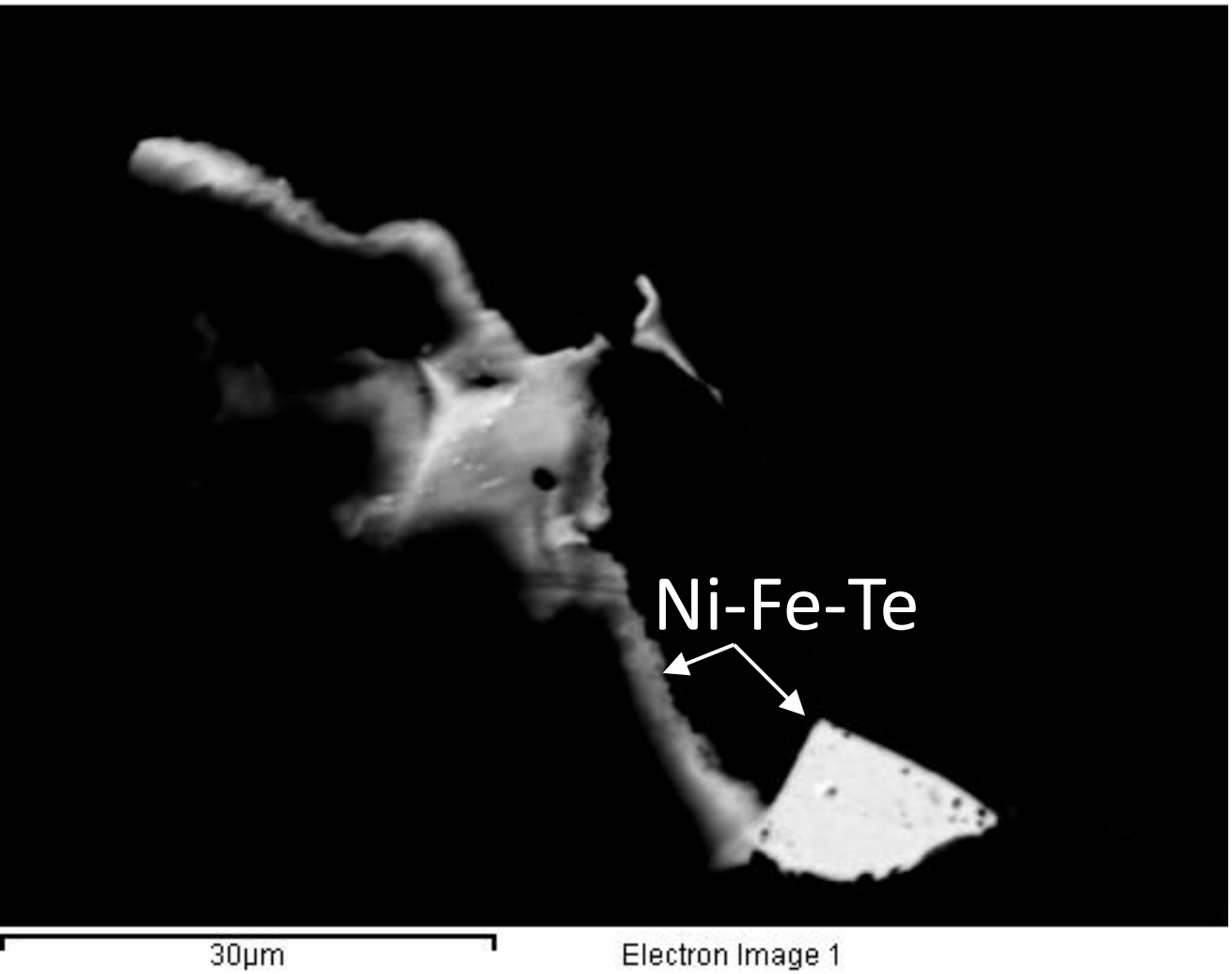
PTSR-43 L 1



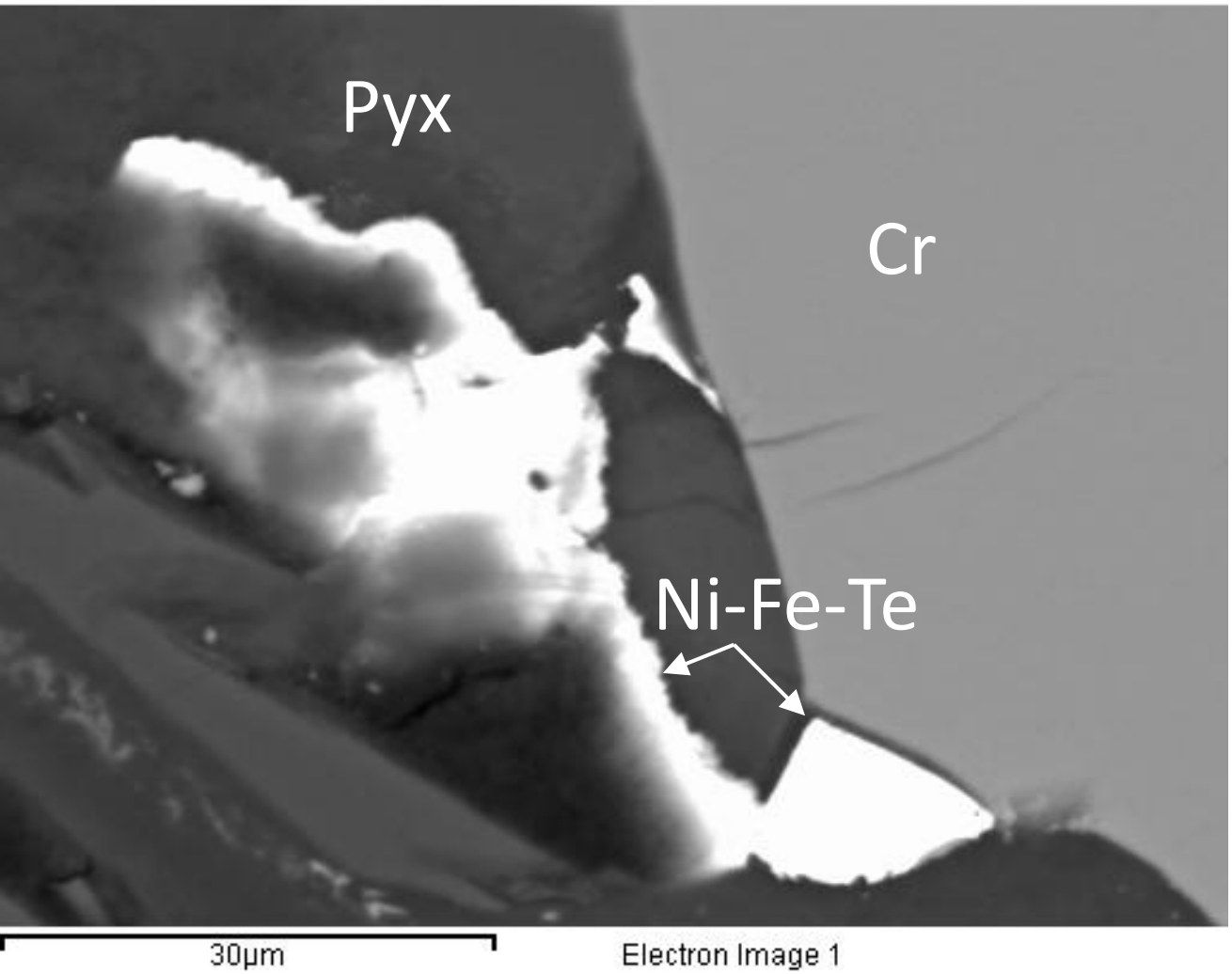
PTSR-43 M 1



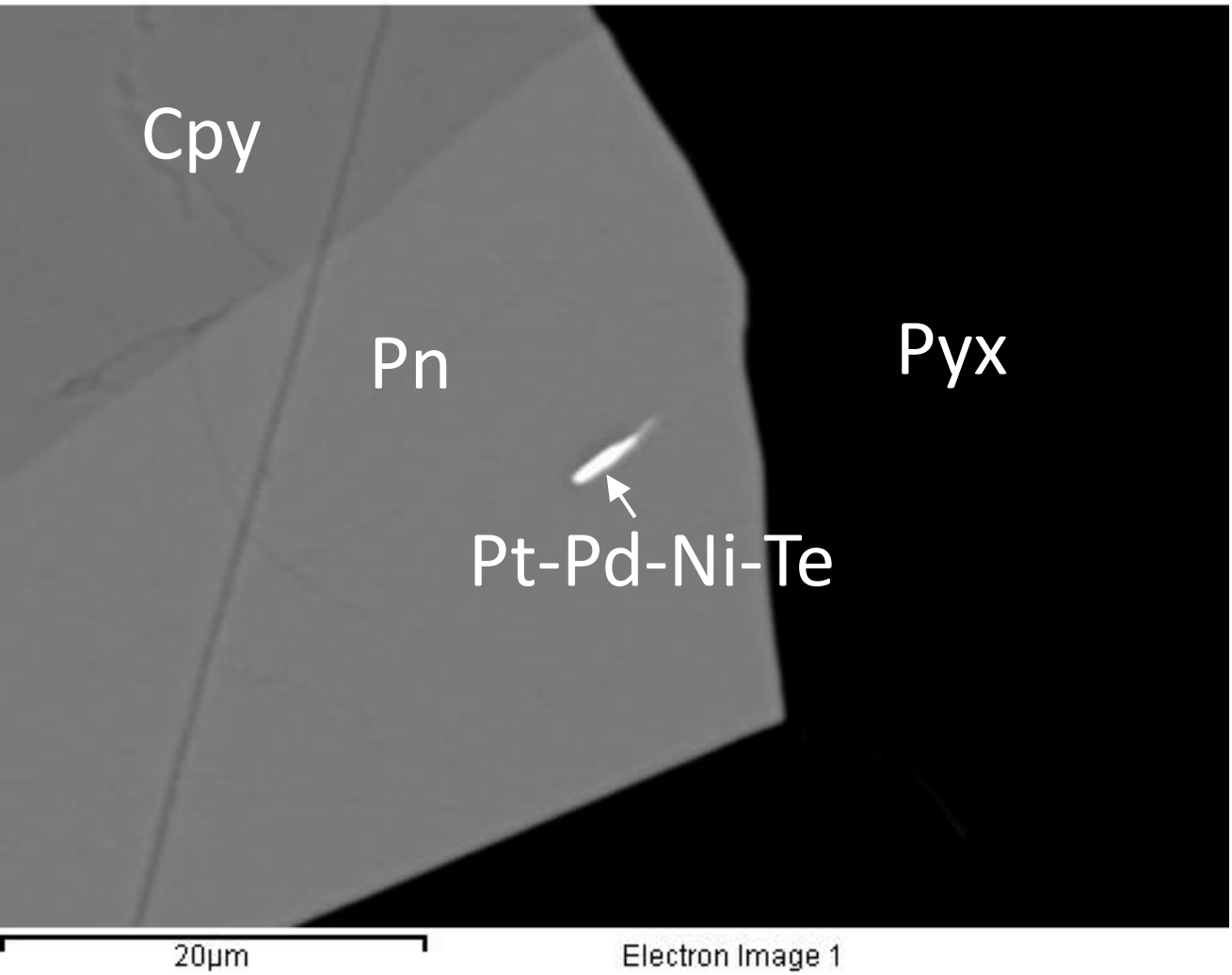
PTSR-43 N 1



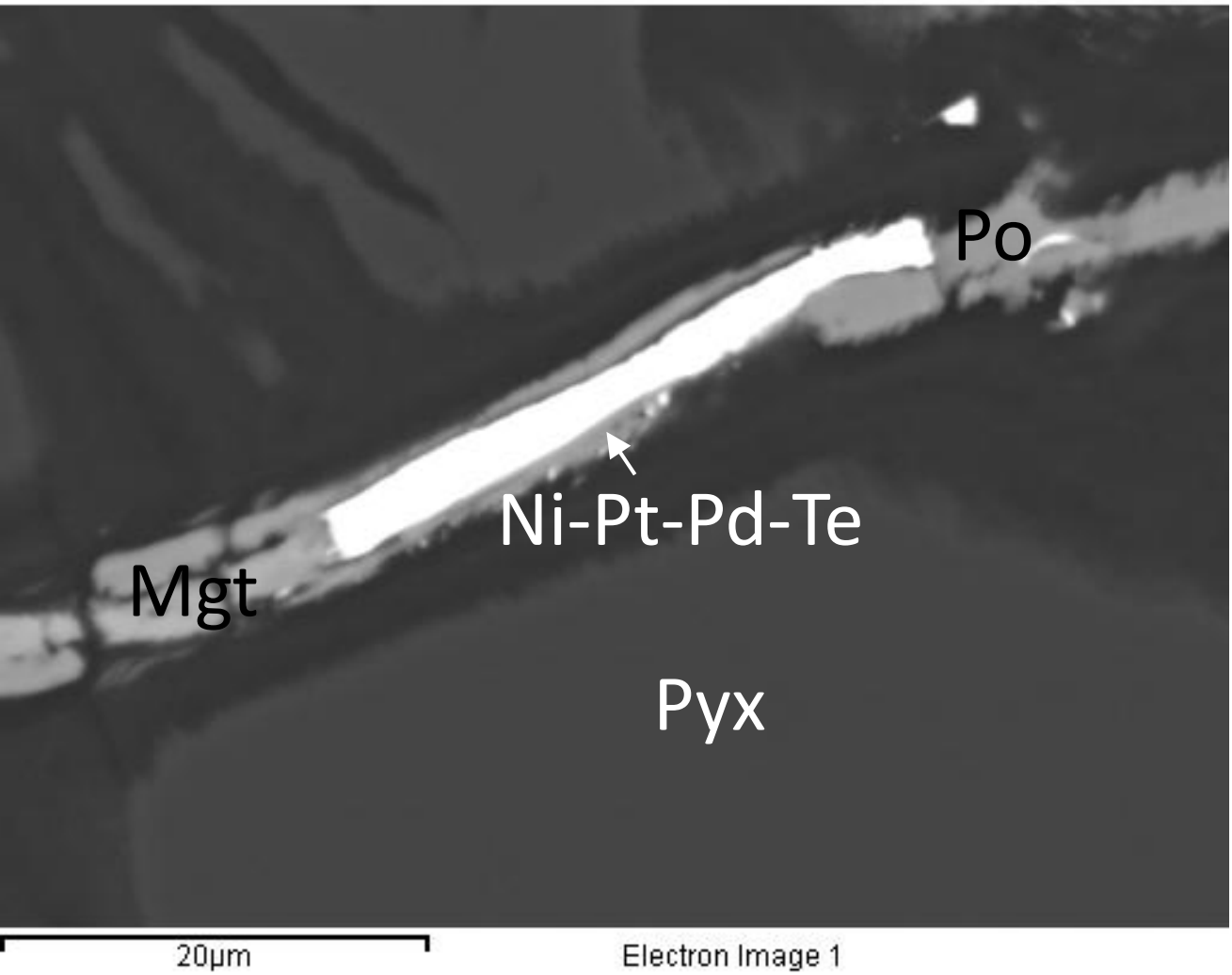
PTSR-43 N 1 Light



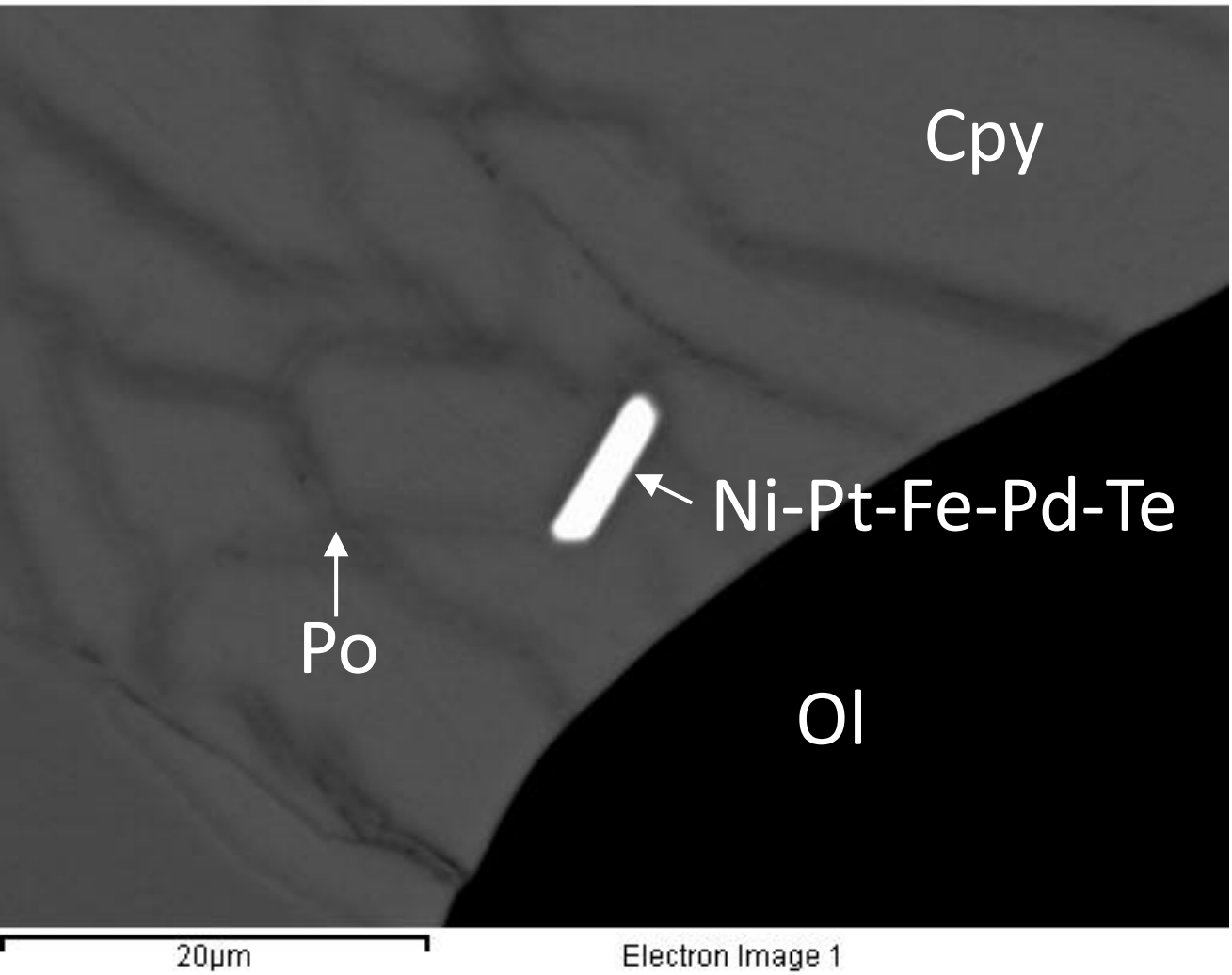
PTSR-43 O 1



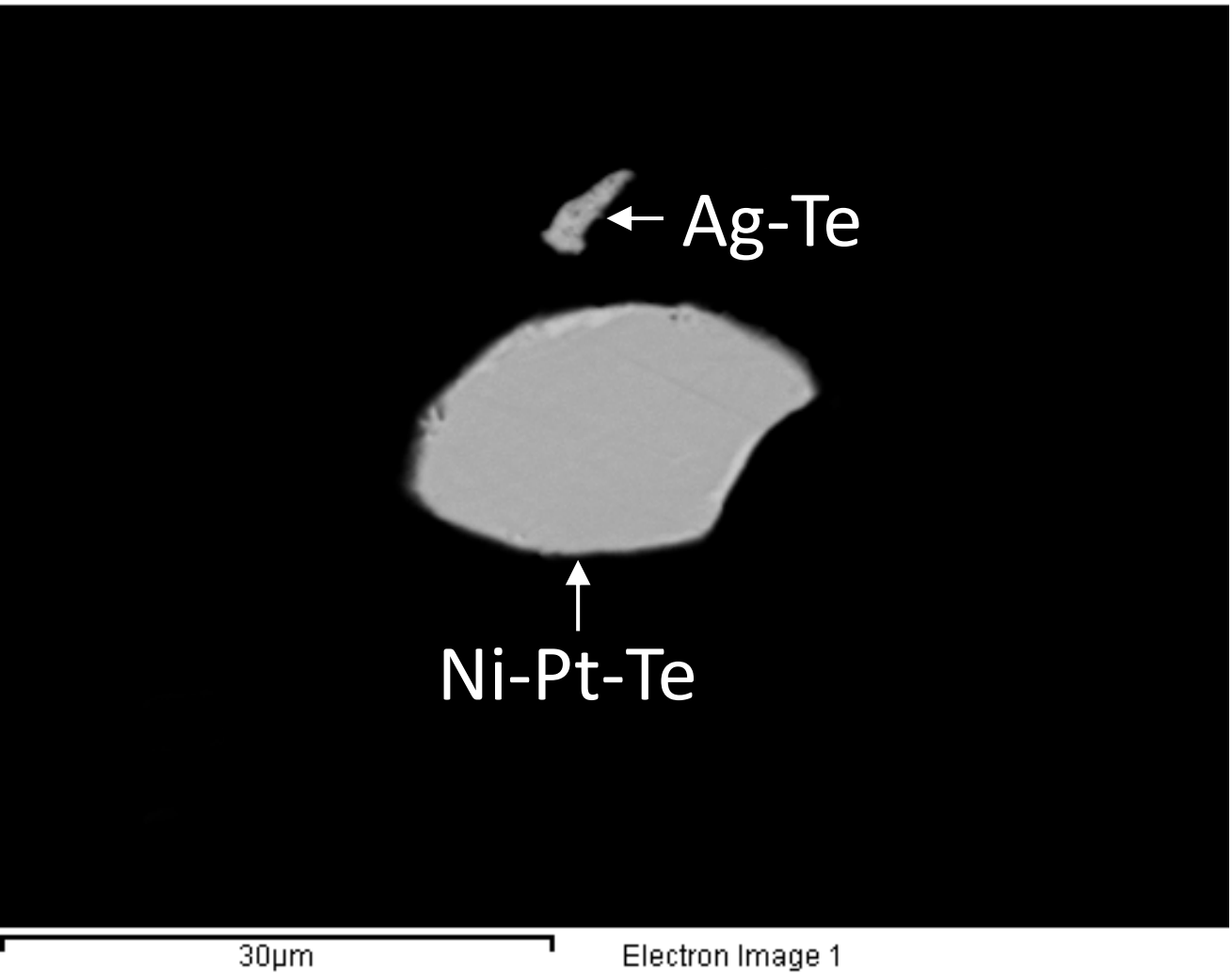
PTSR-43 P 1



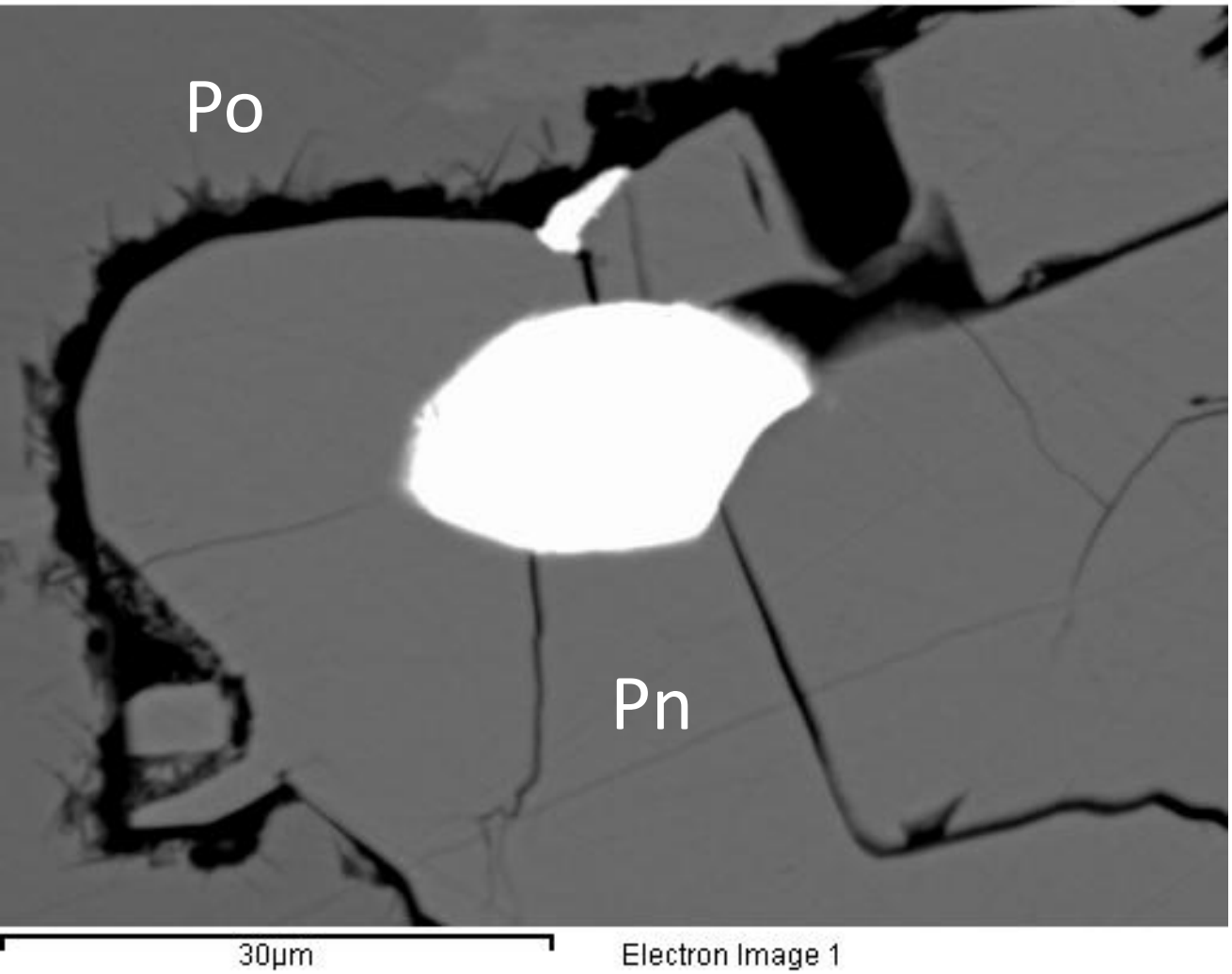
PTSR-43 Q 1



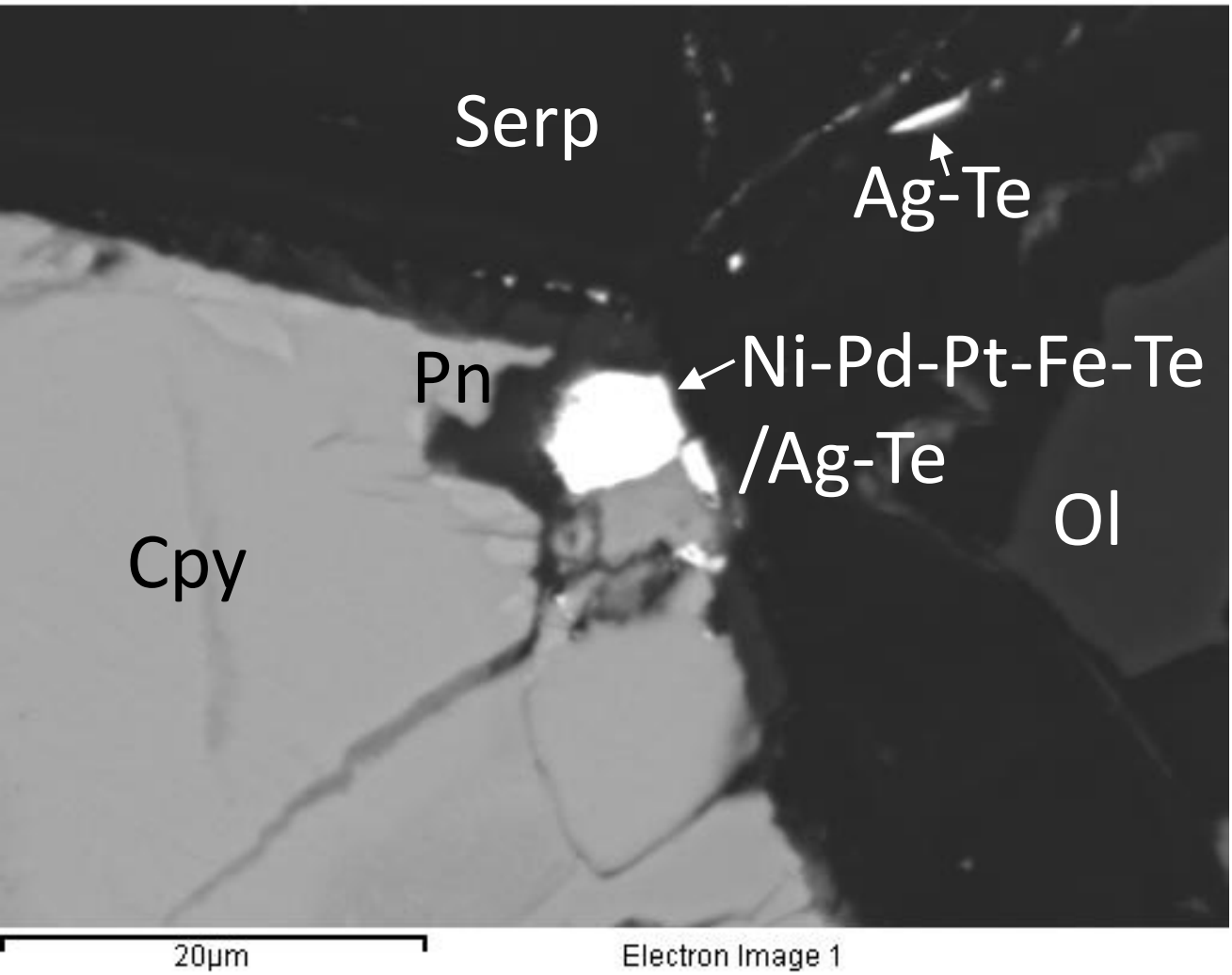
PTSR-43 R 1-2



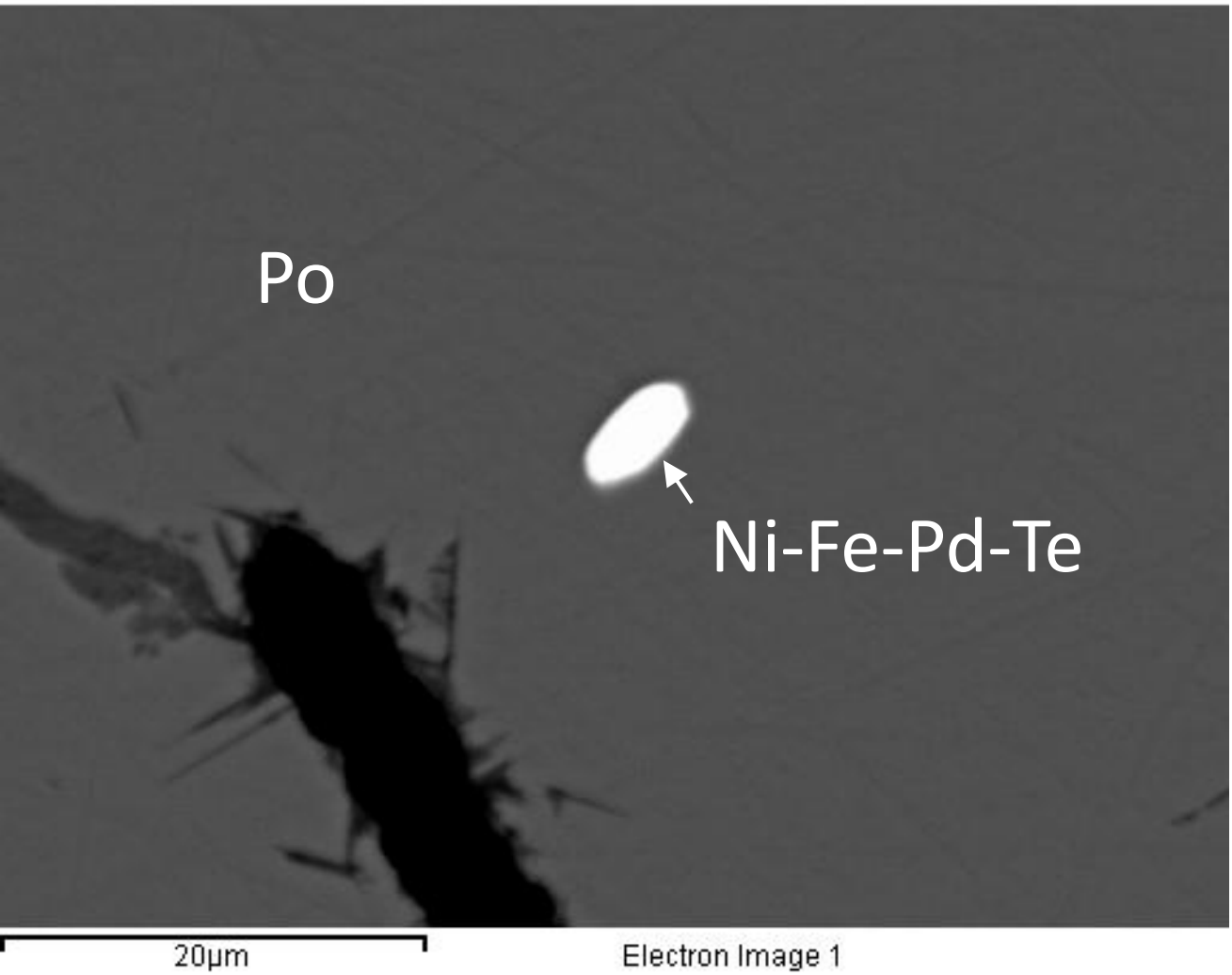
PTSR-43 R 1-2 Light



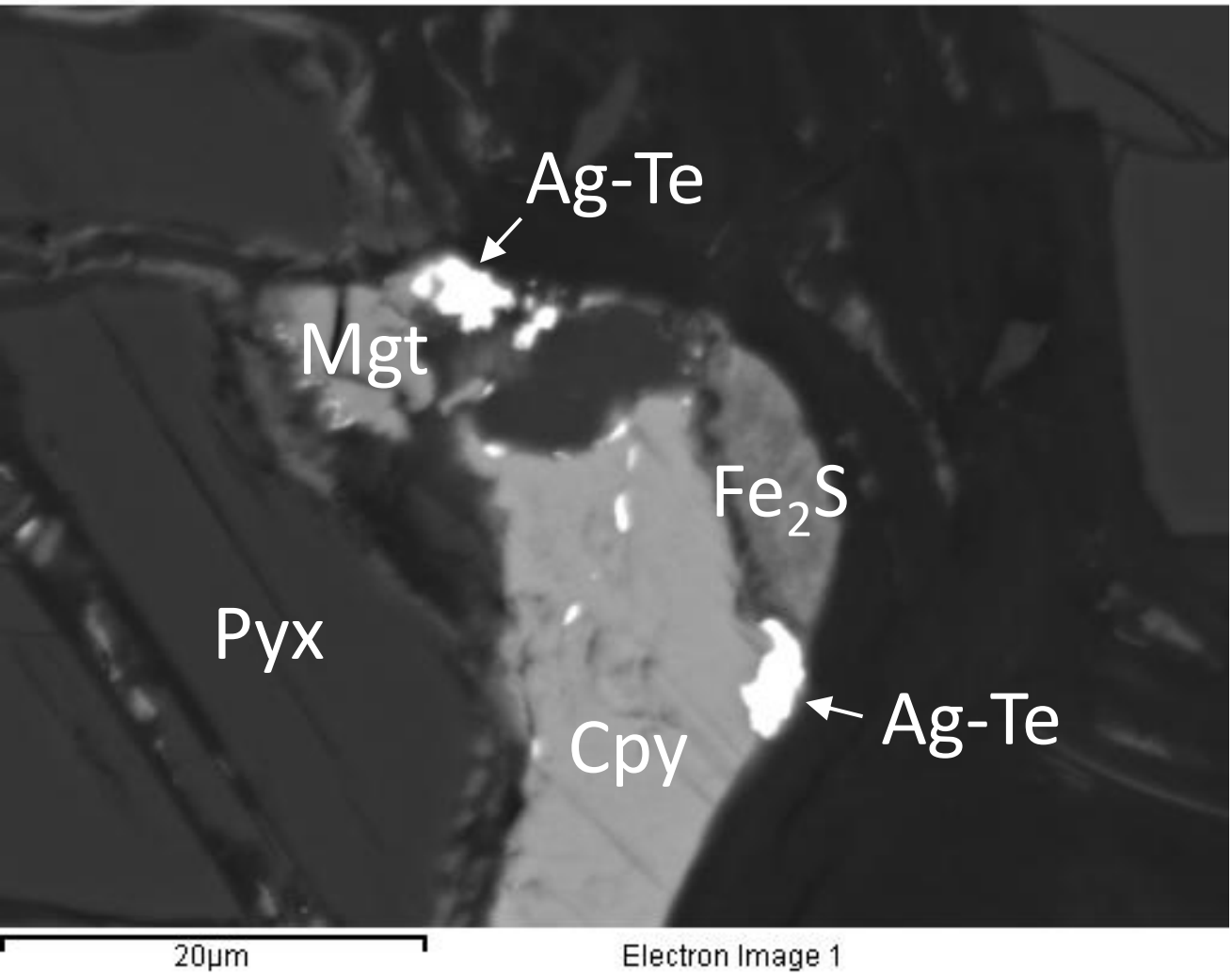
PTSR-43 S 1-2



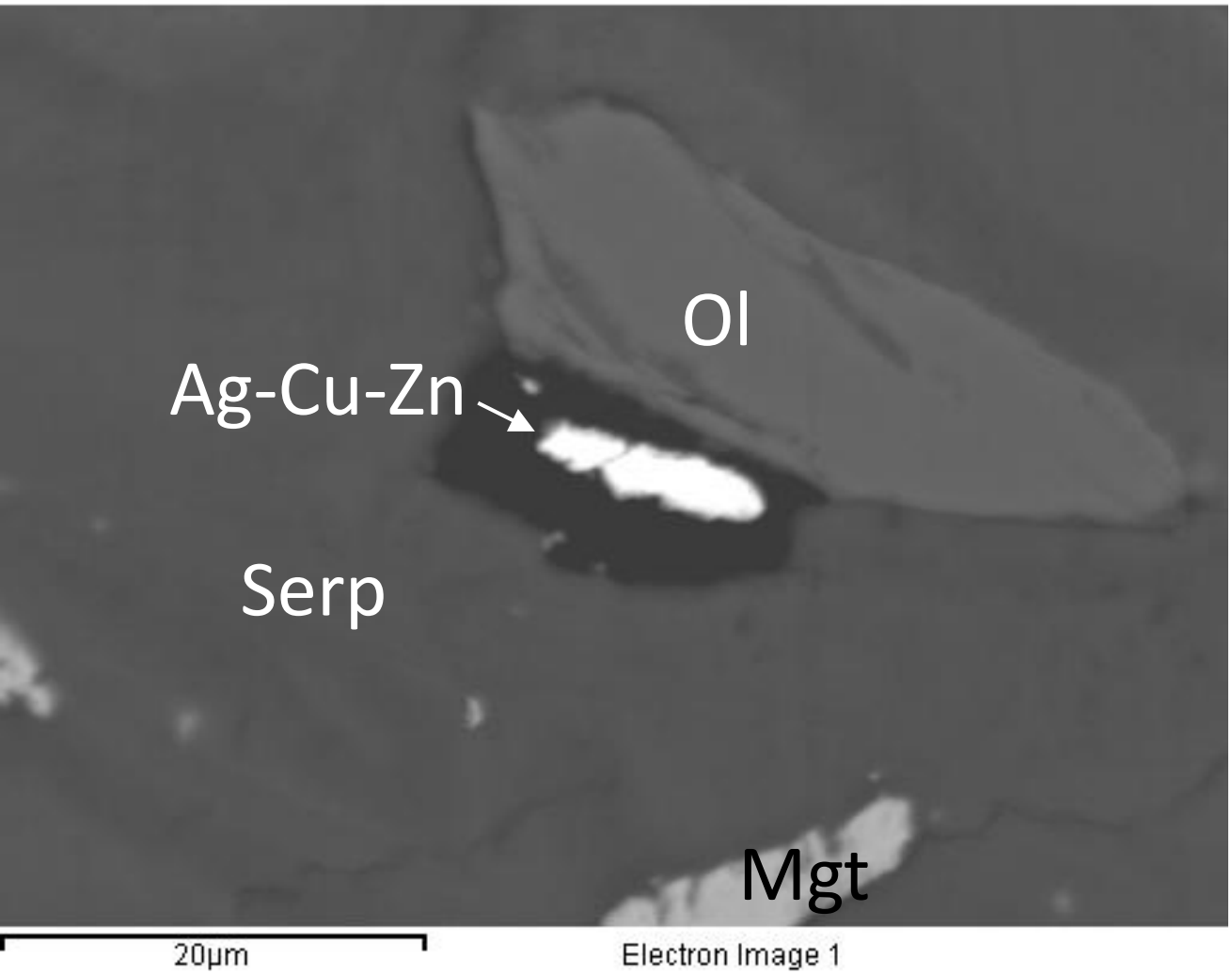
PTSR-43 T 1



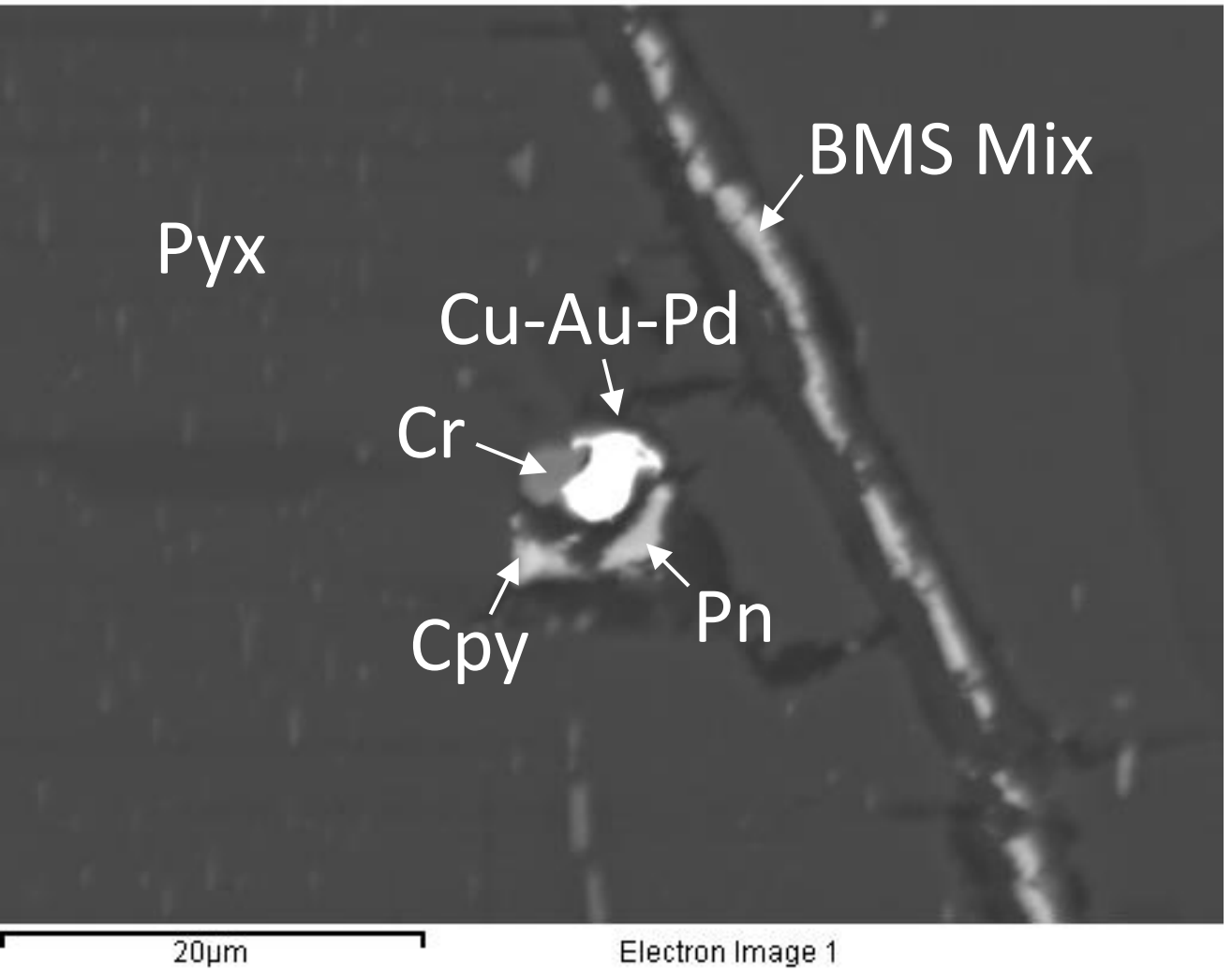
PTSR-43 U 1-2



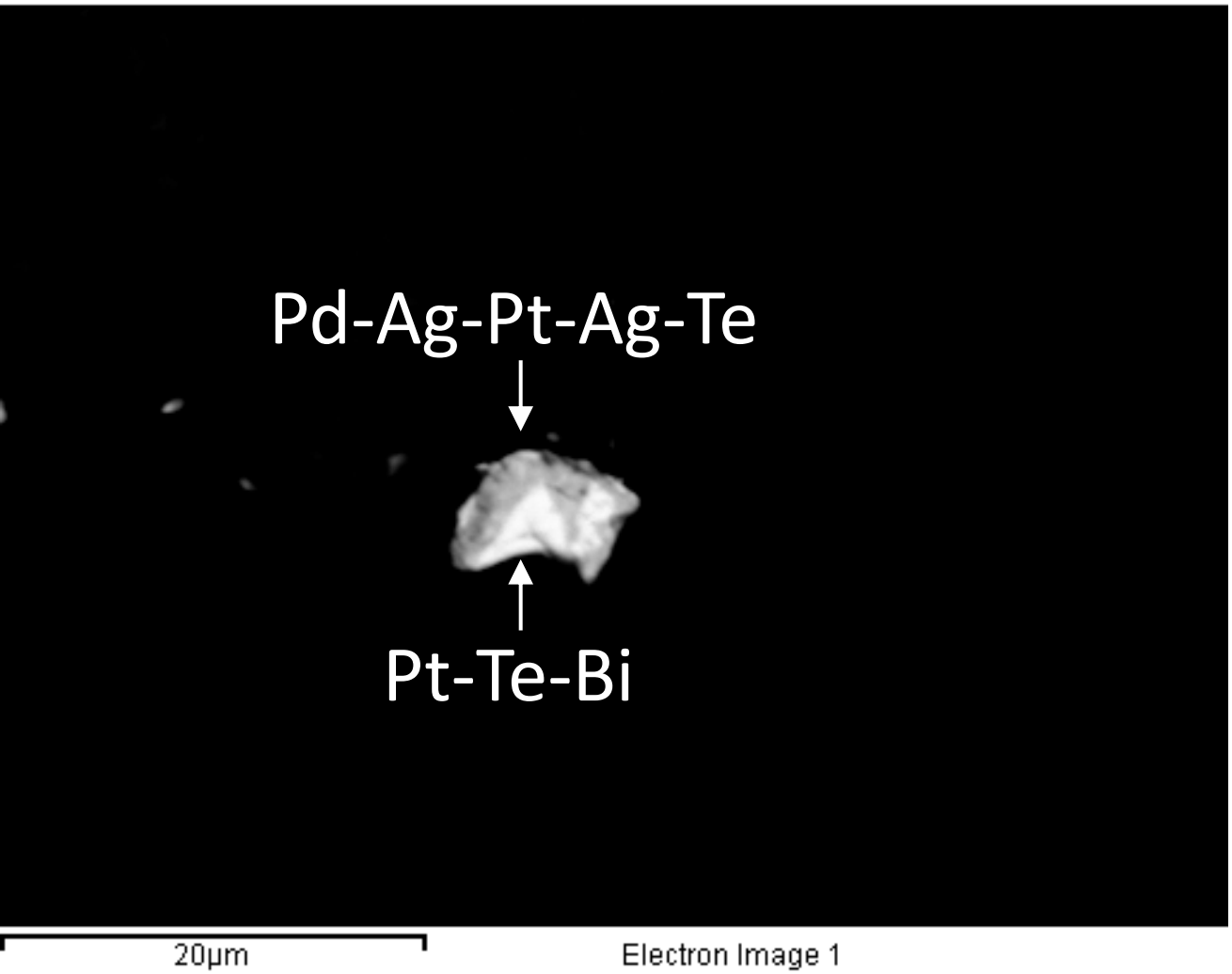
PTSR-44 A 1



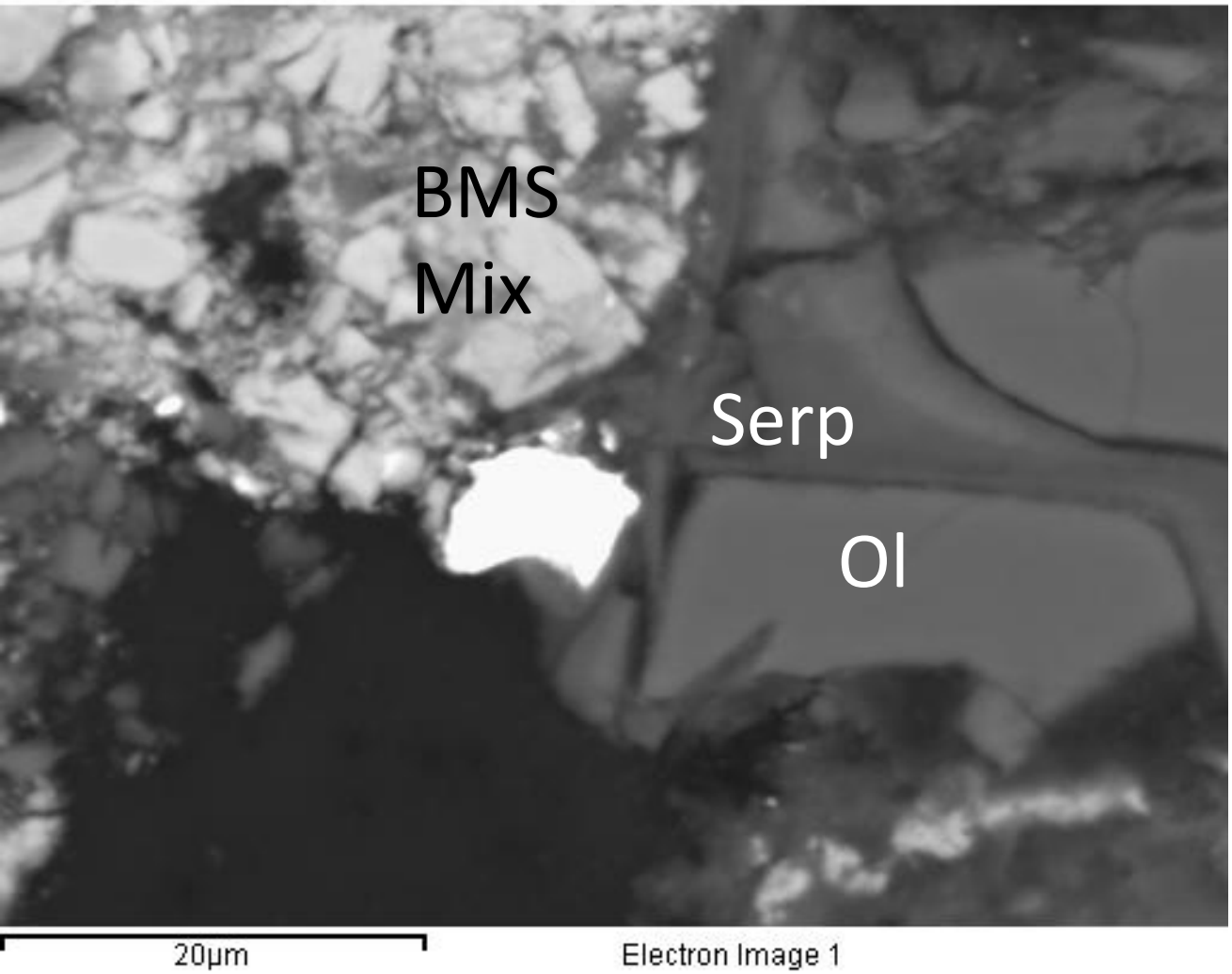
PTSR-44 B 1



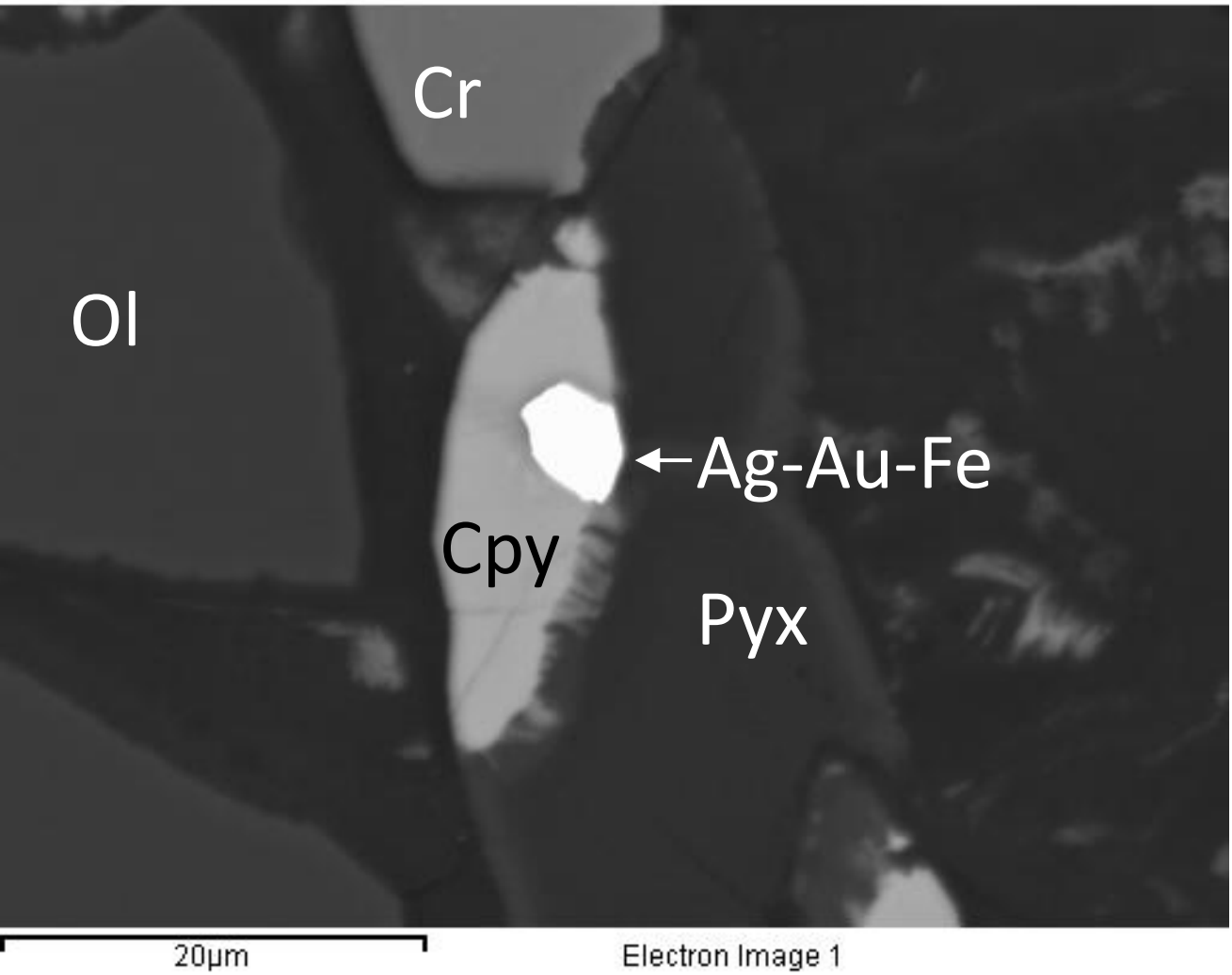
PTSR-44 C 1



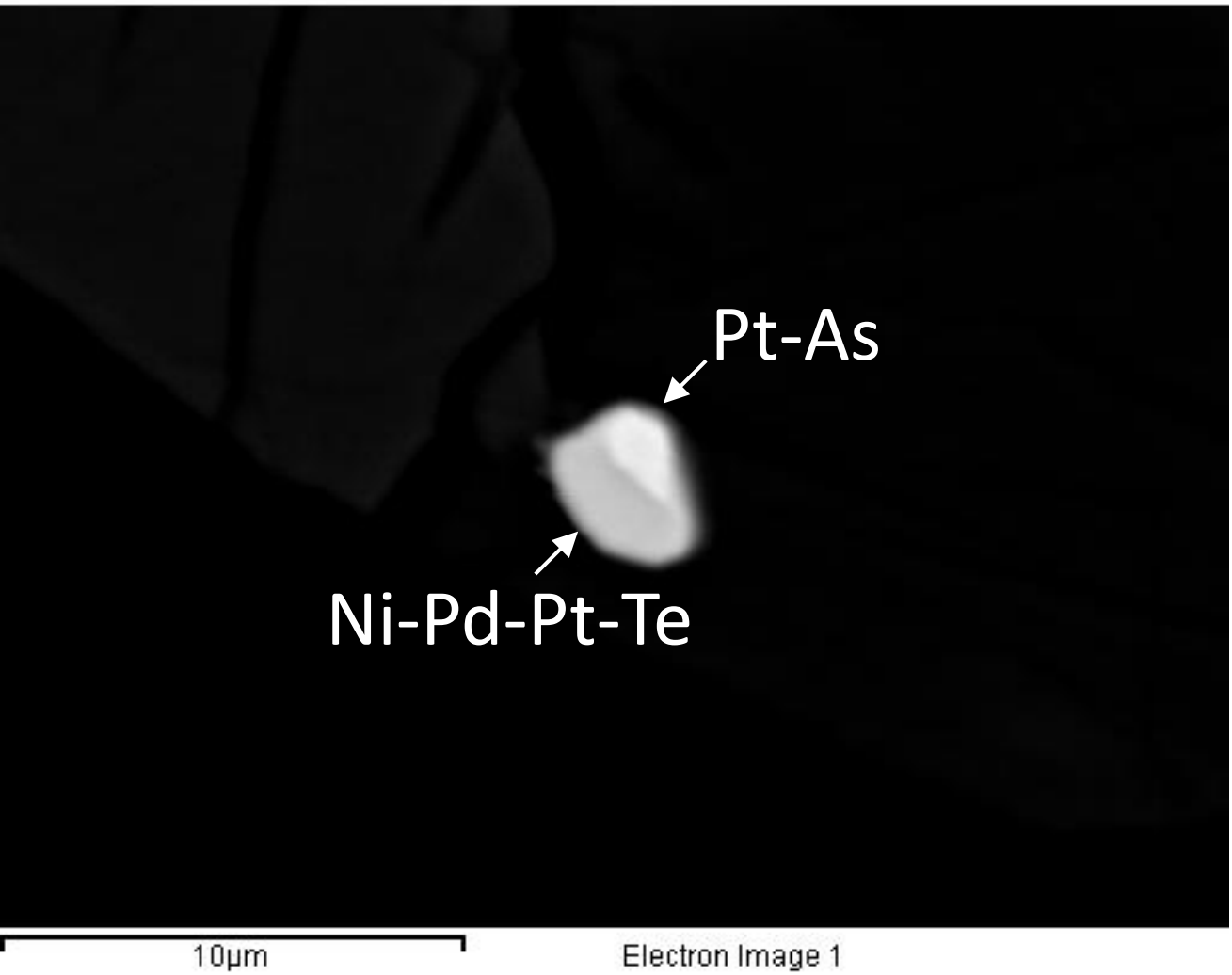
PTSR-44 C 1 Light



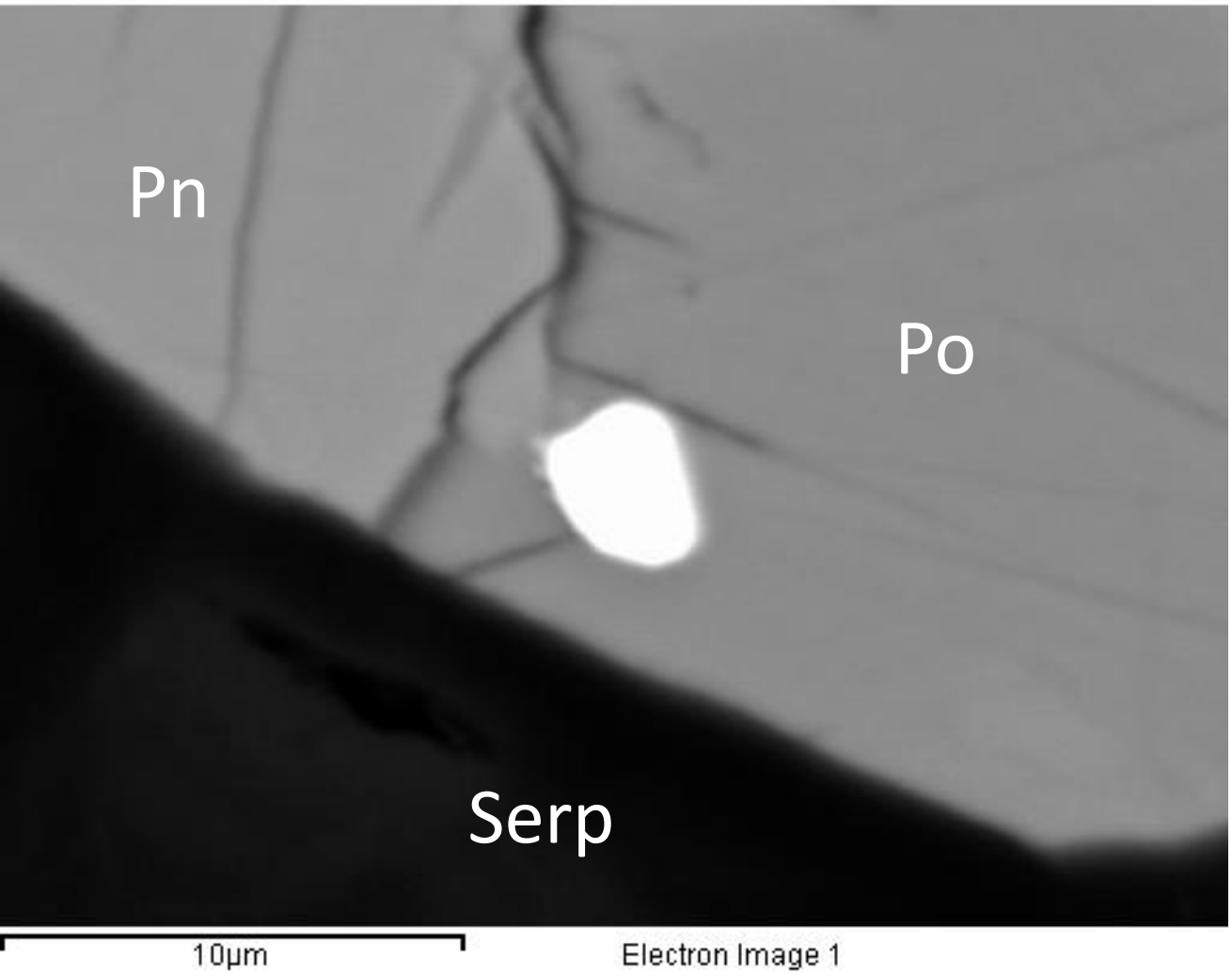
PTSR-45 A 1



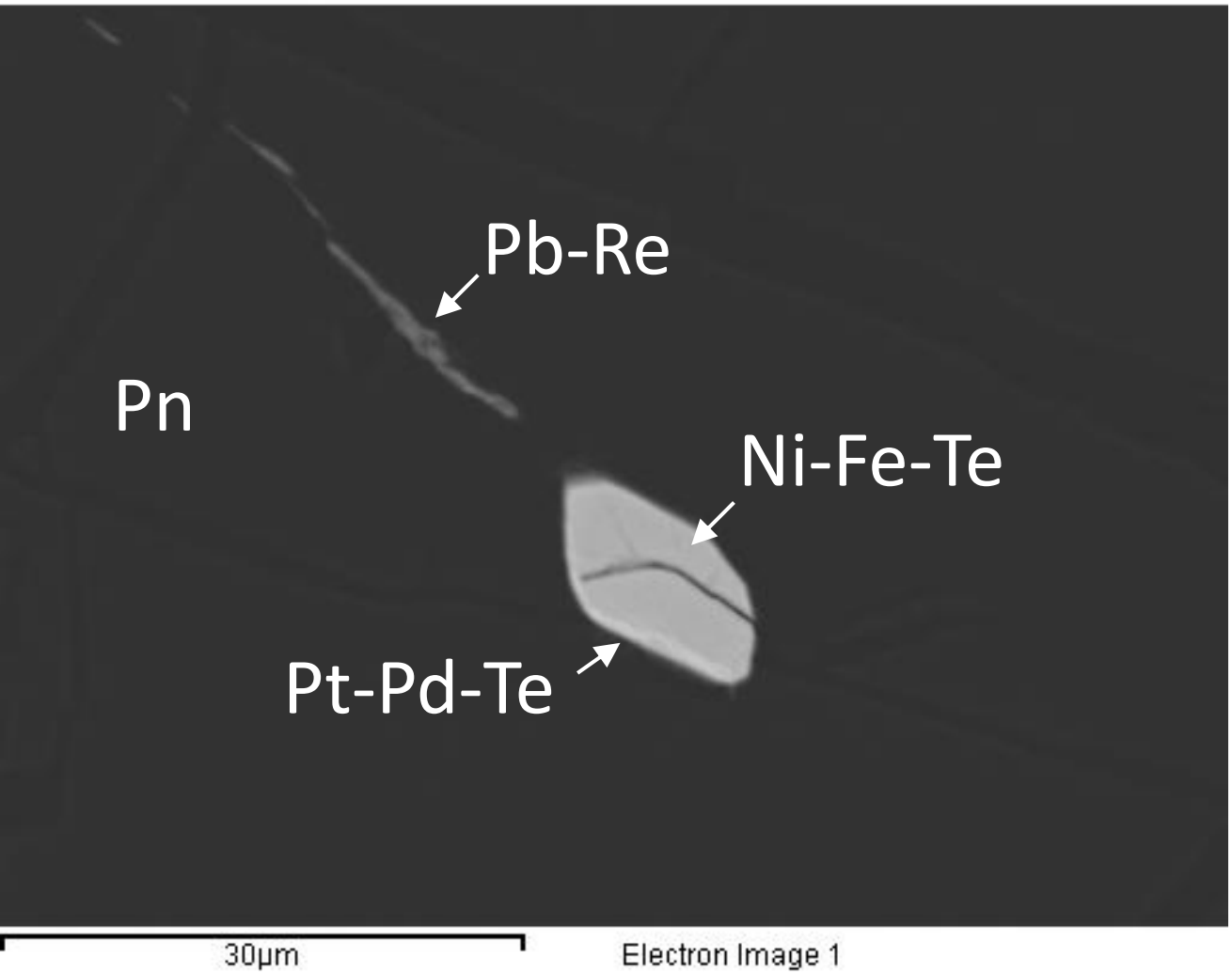
PTSR-45 B 1-2



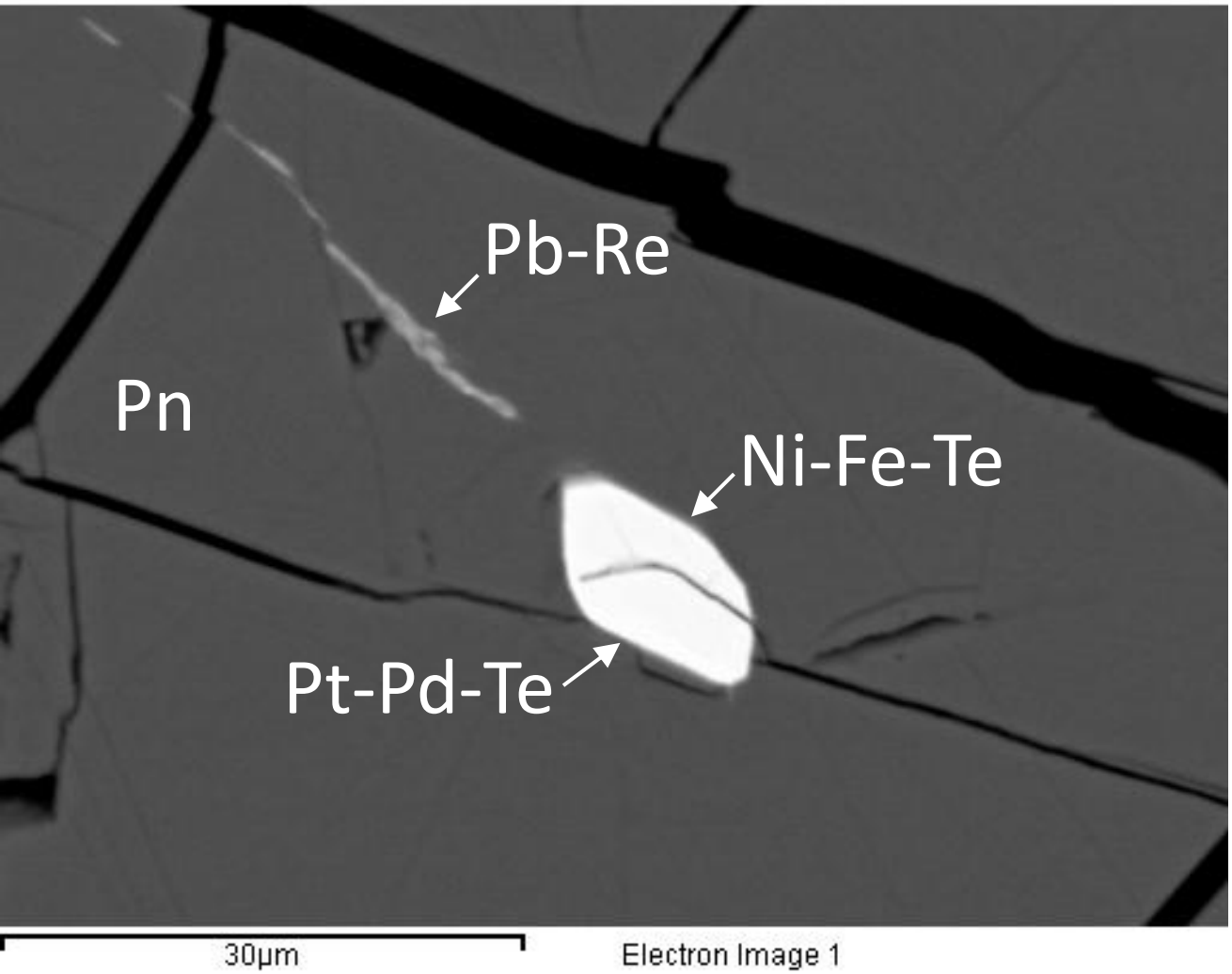
PTSR-45 B 1-2 Light



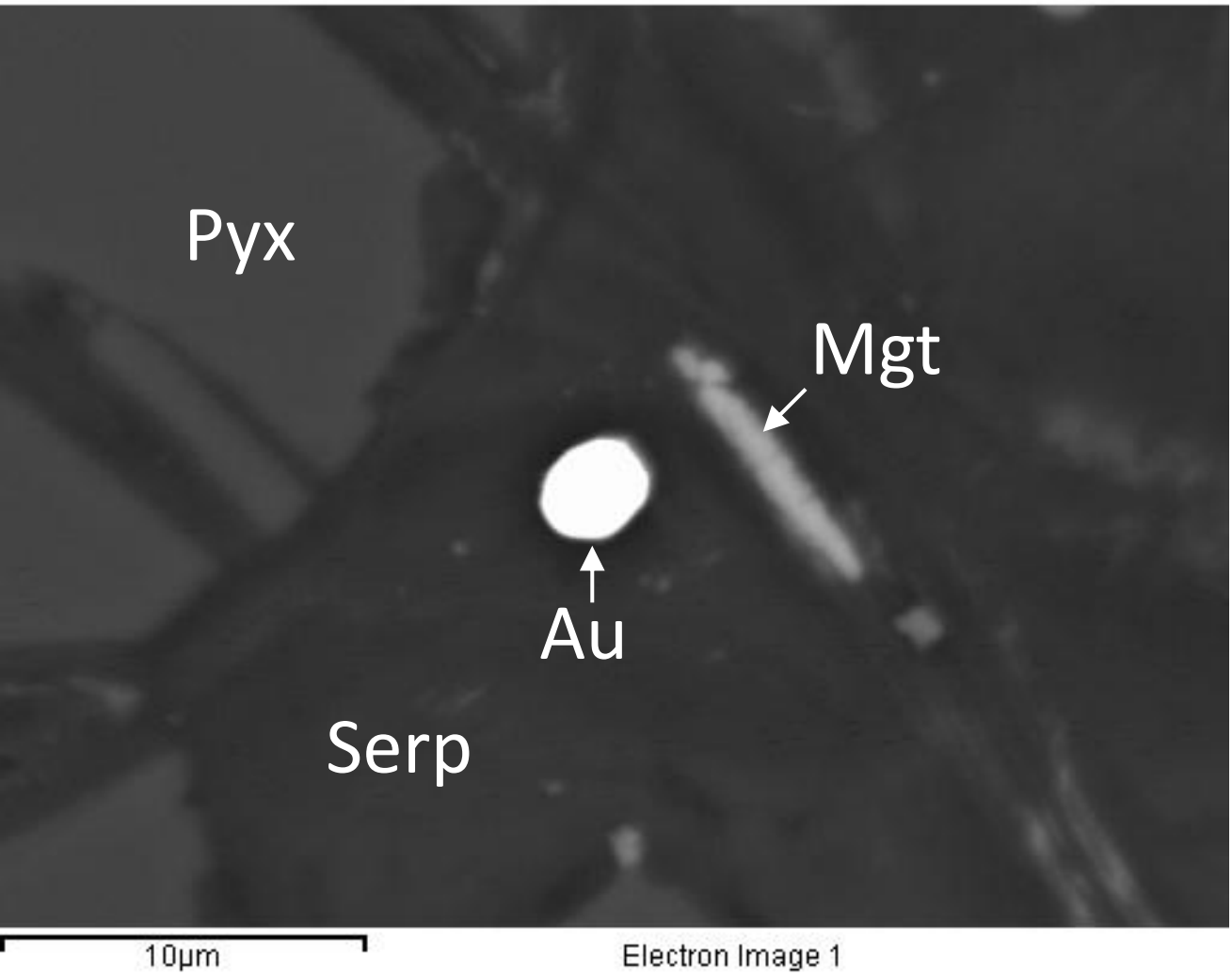
PTSR-45 C 1



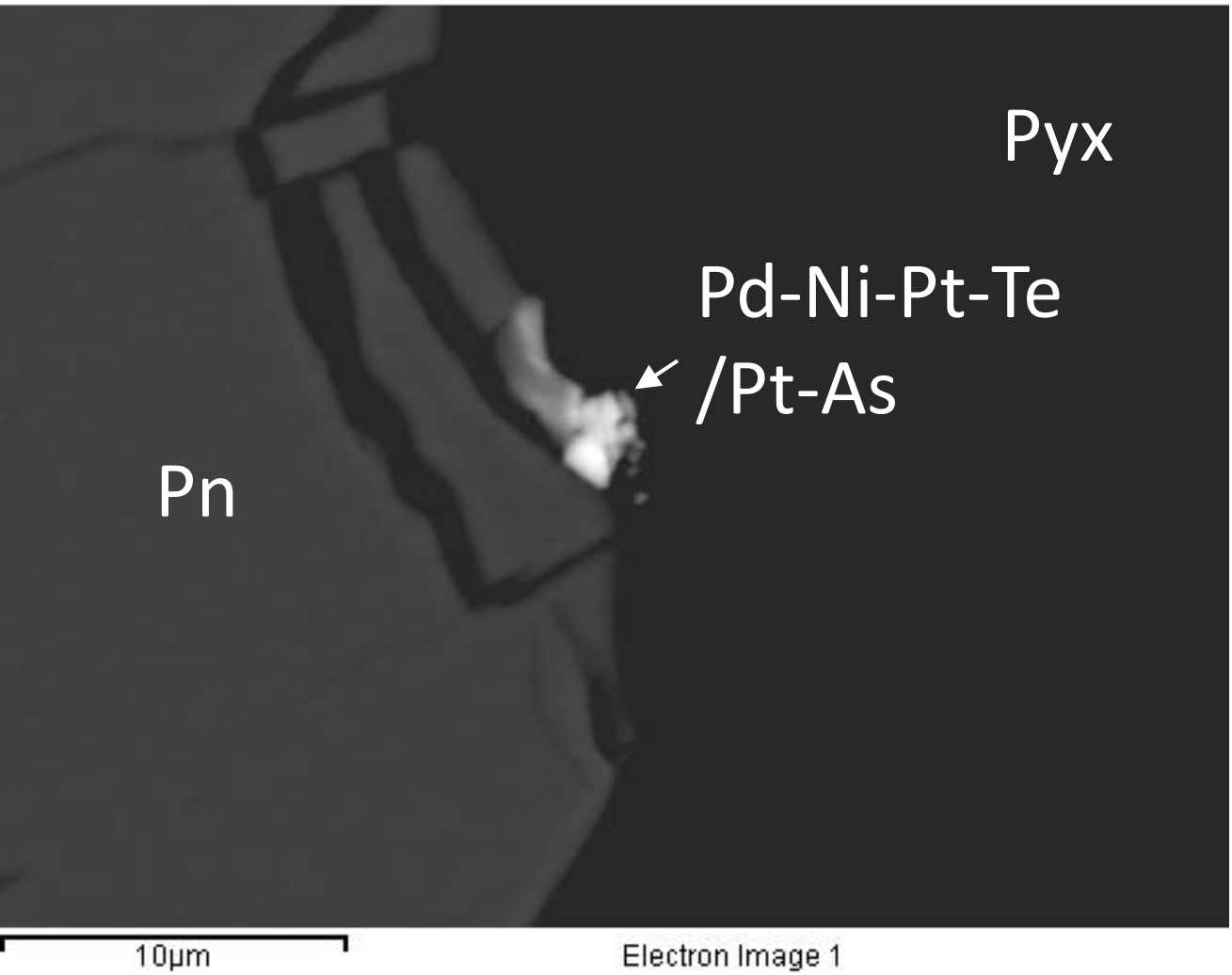
PTSR-45 C 1 Light



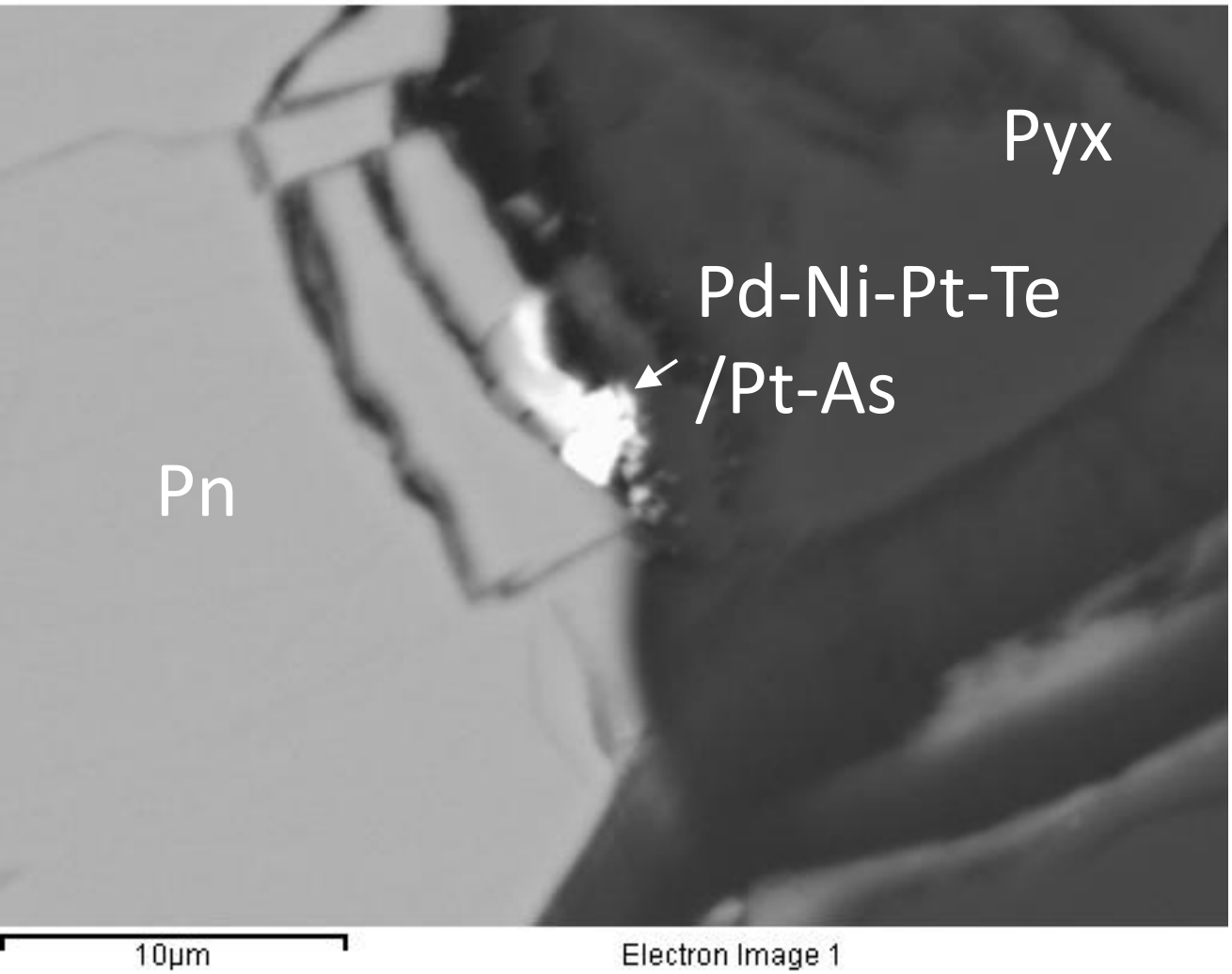
PTSR-45 D 1



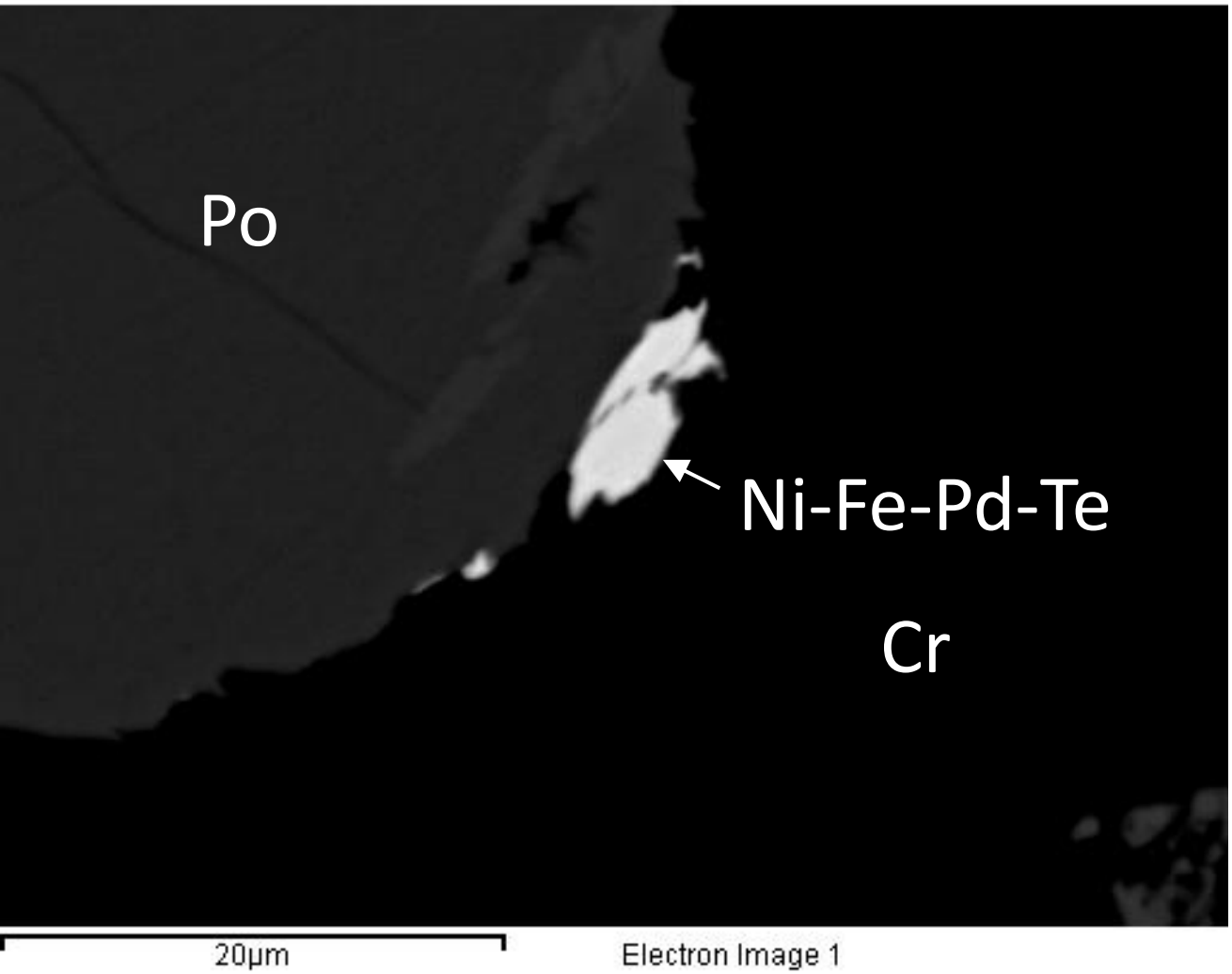
PTSR-45 E 1



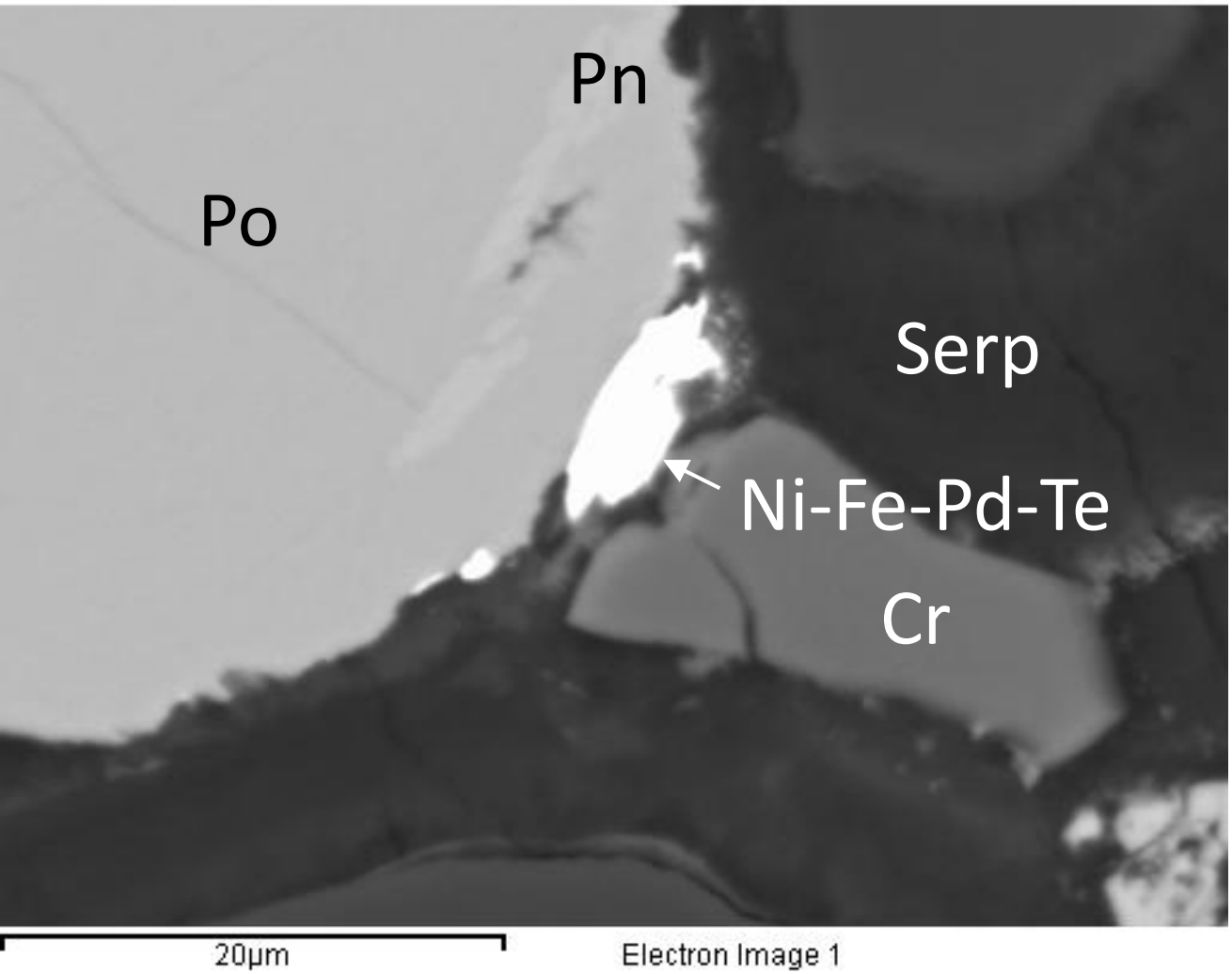
PTSR-45 E 1 Light



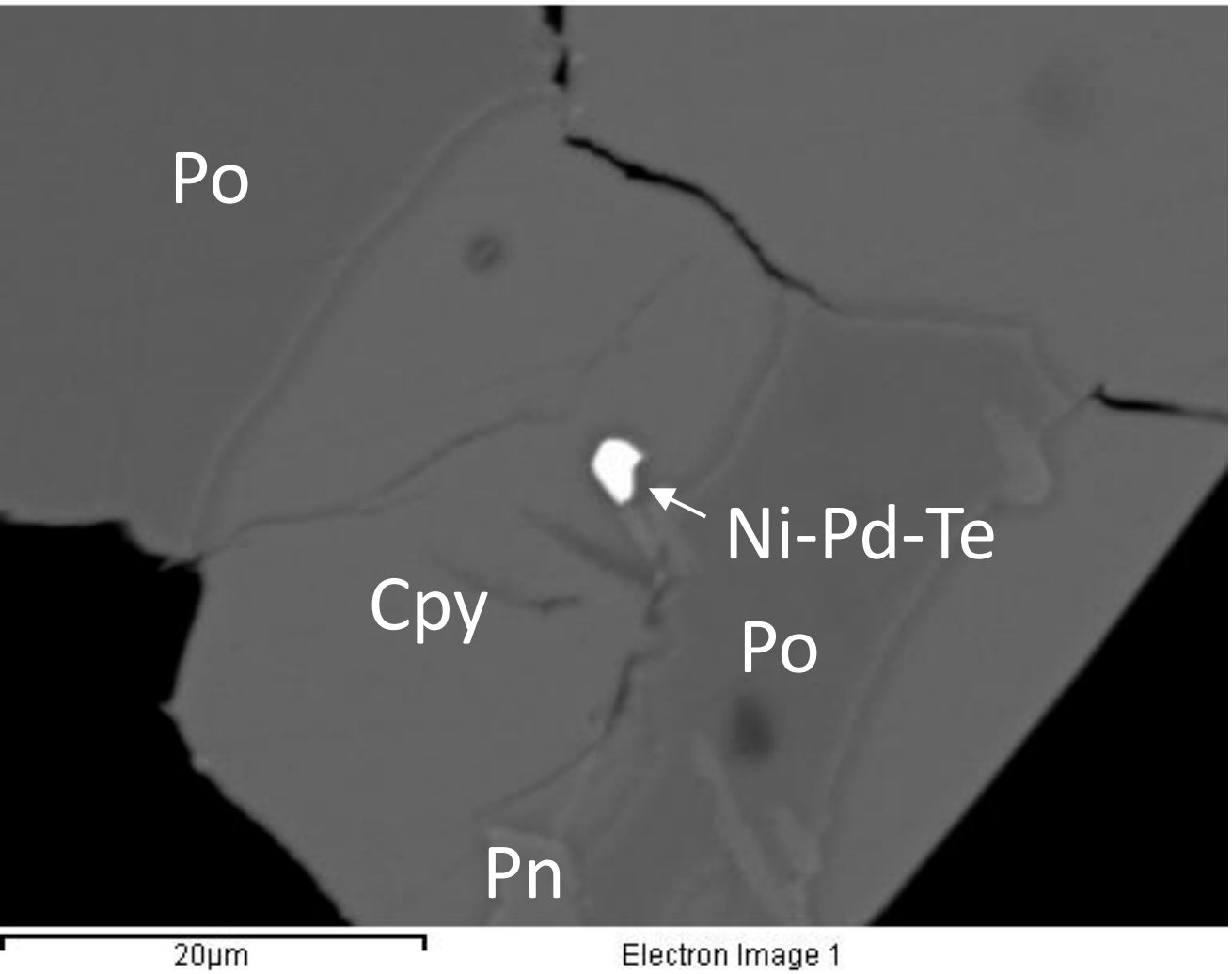
PTSR-45 F 1



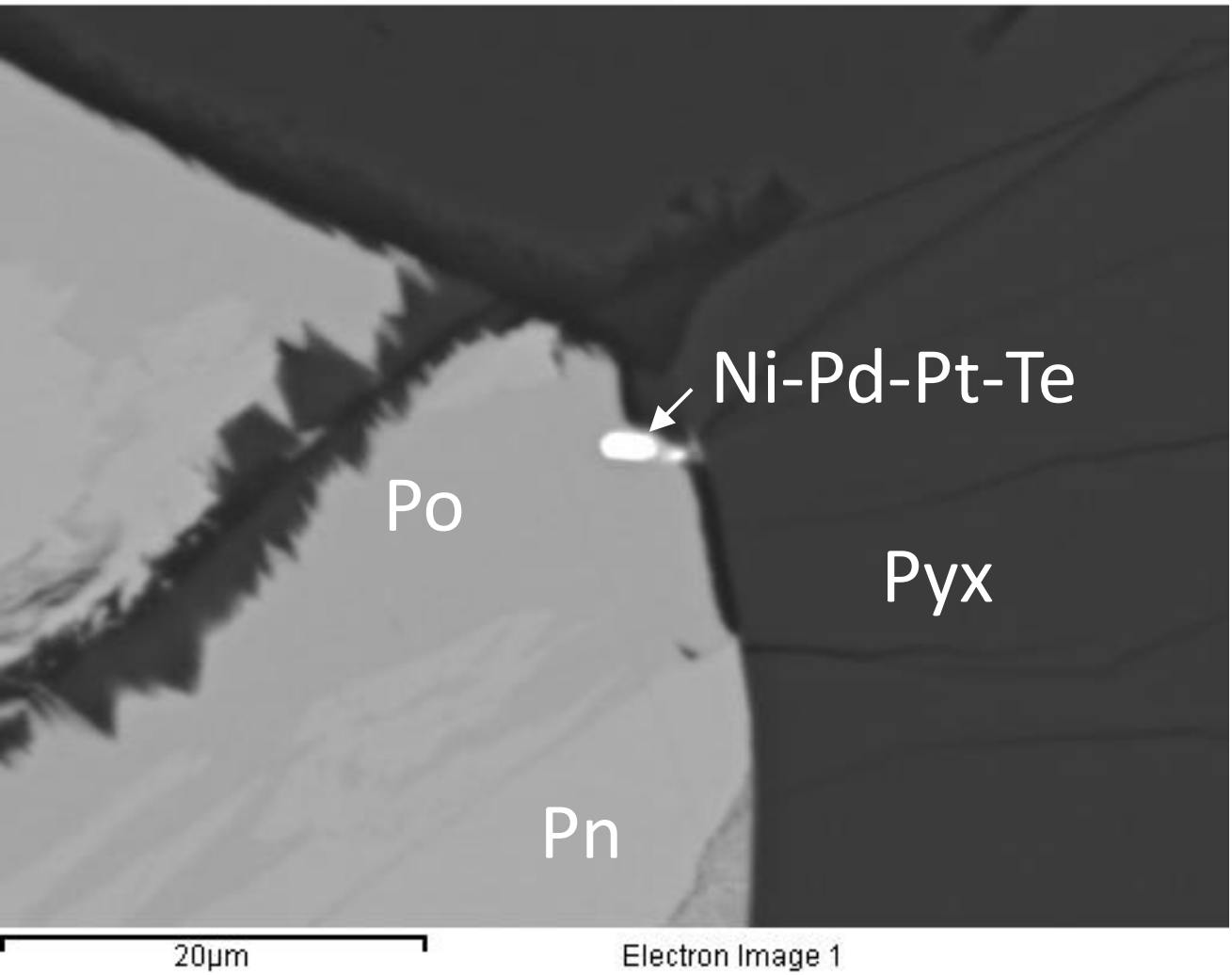
PTSR-45 F 1 Light



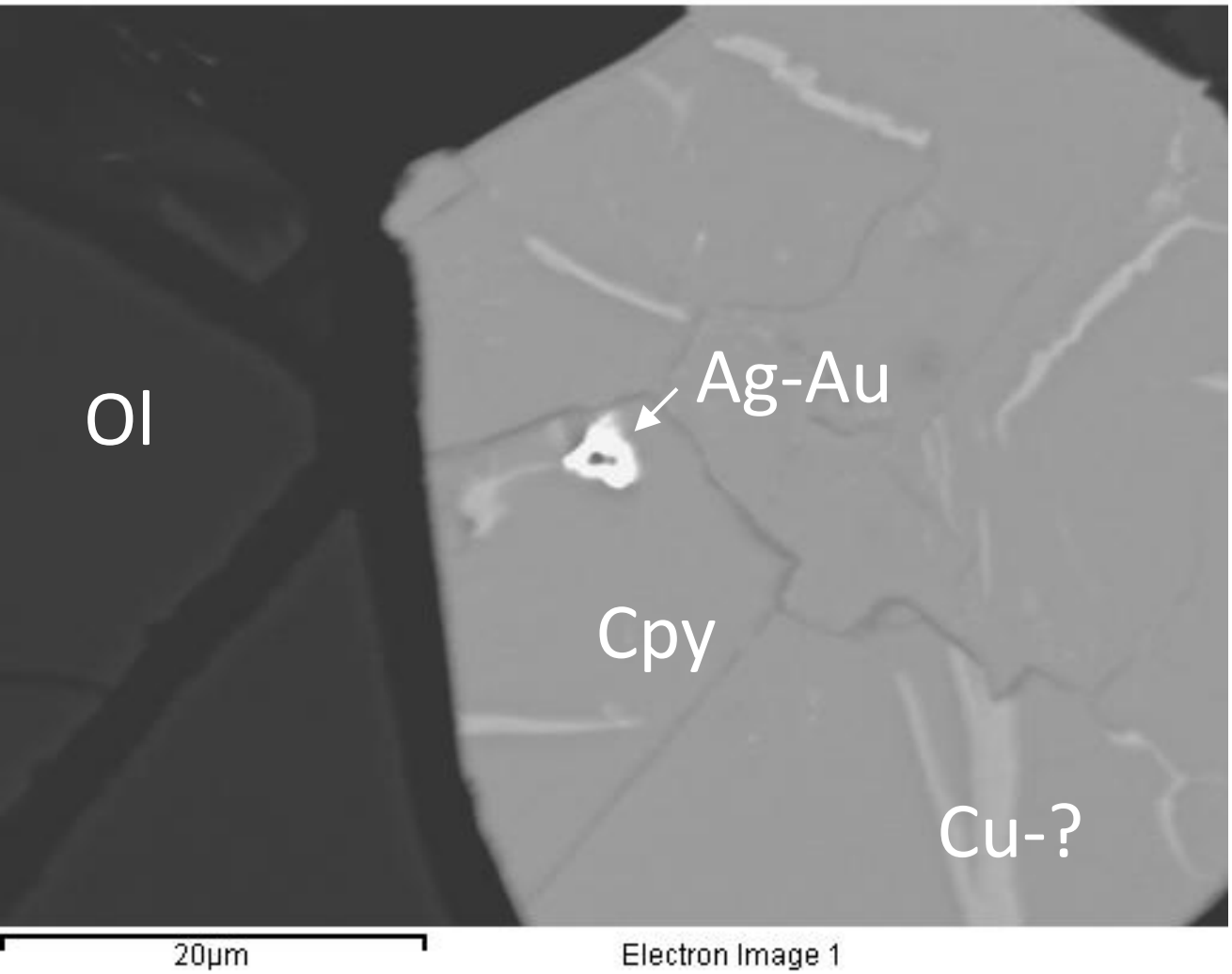
PTSR-45 G 1



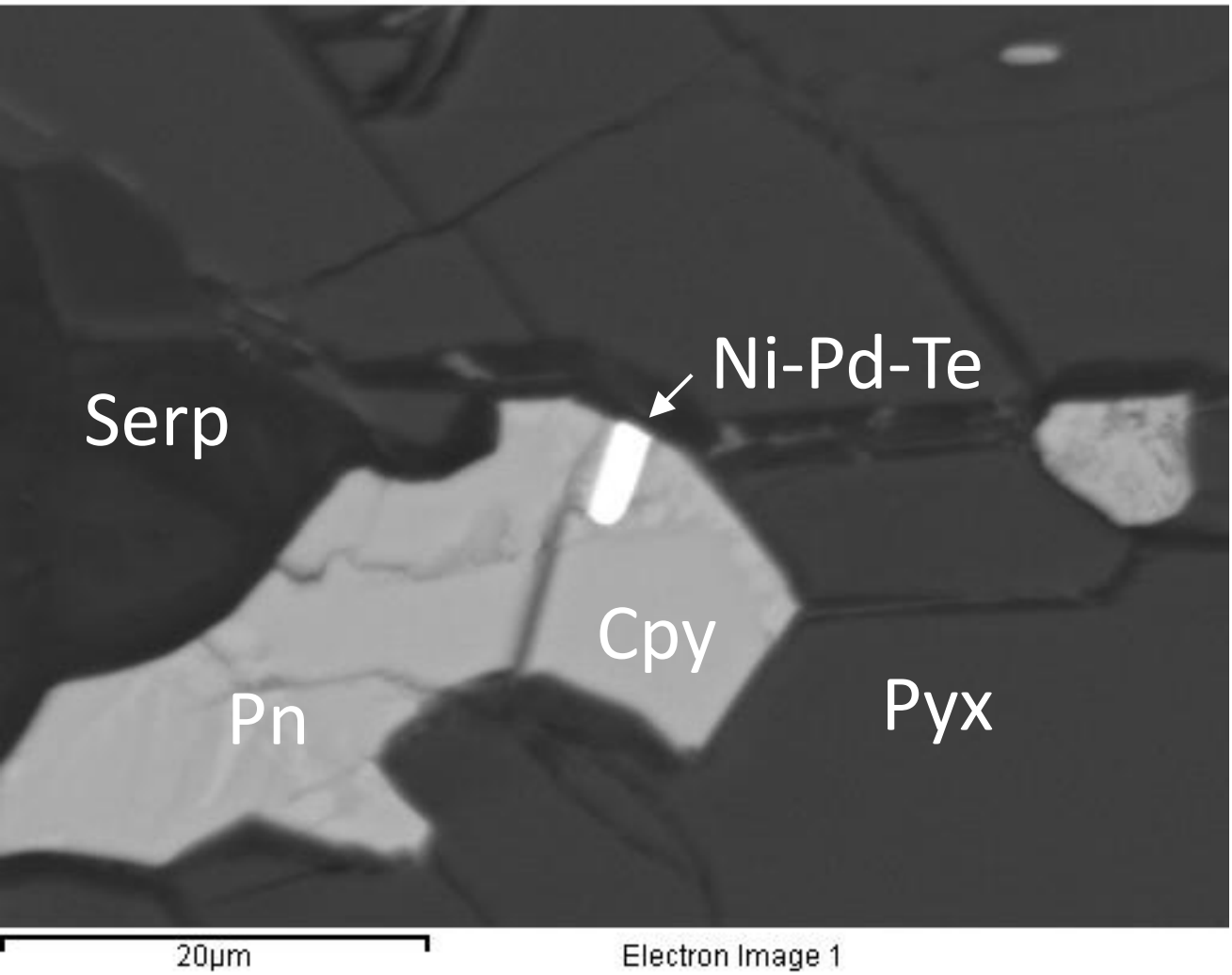
PTSR-45 H 1



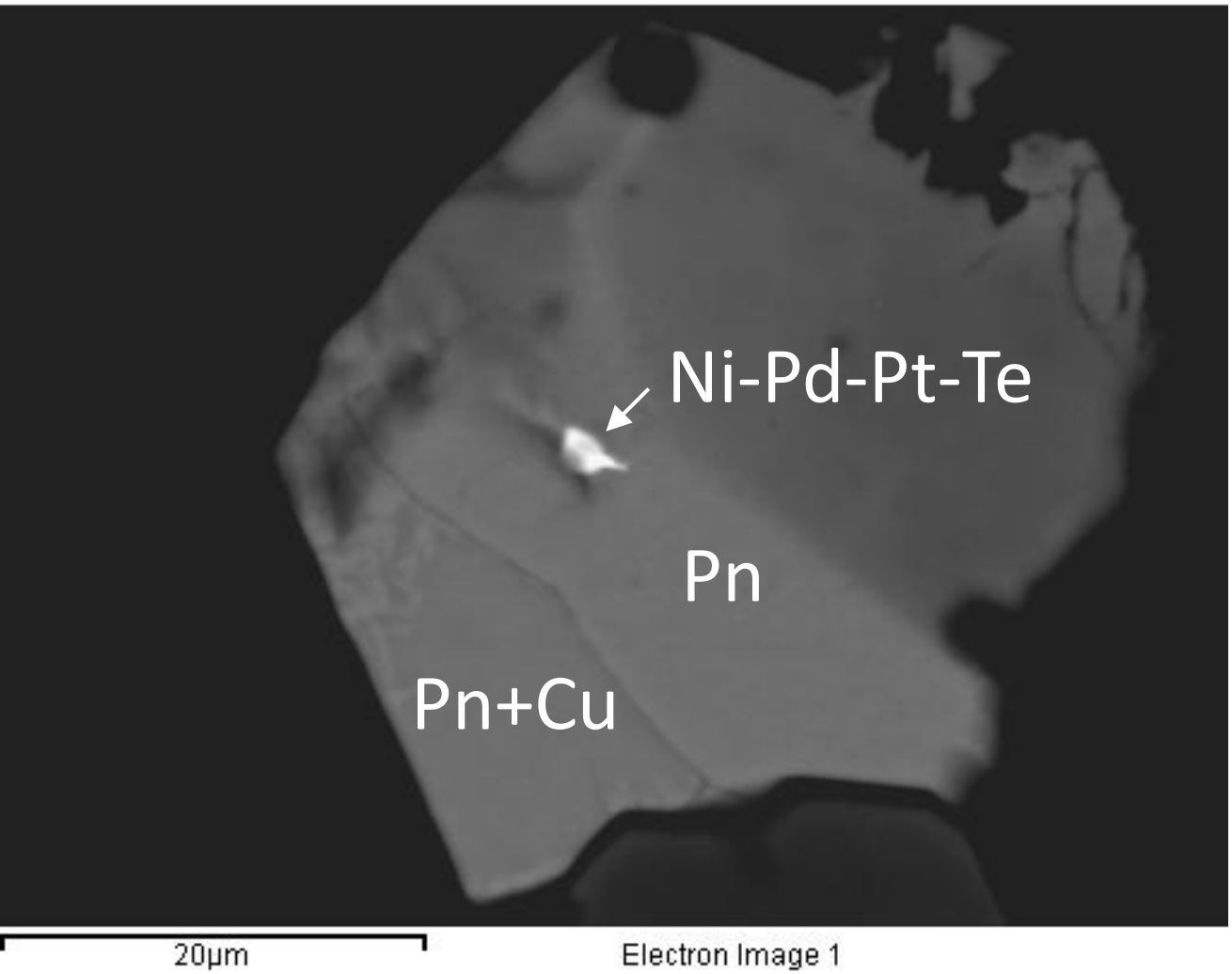
PTSR-45 I 1



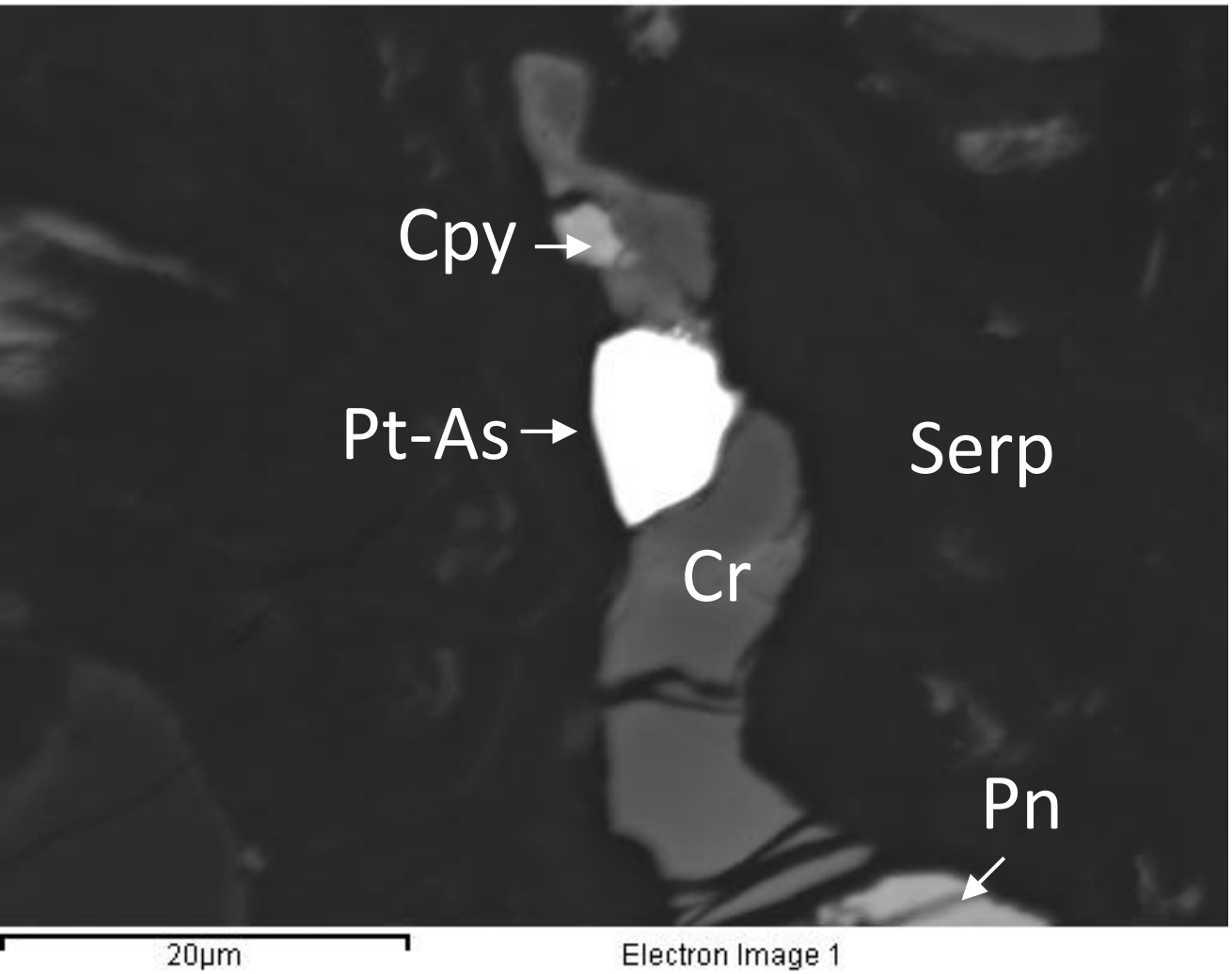
PTSR-45 J 1



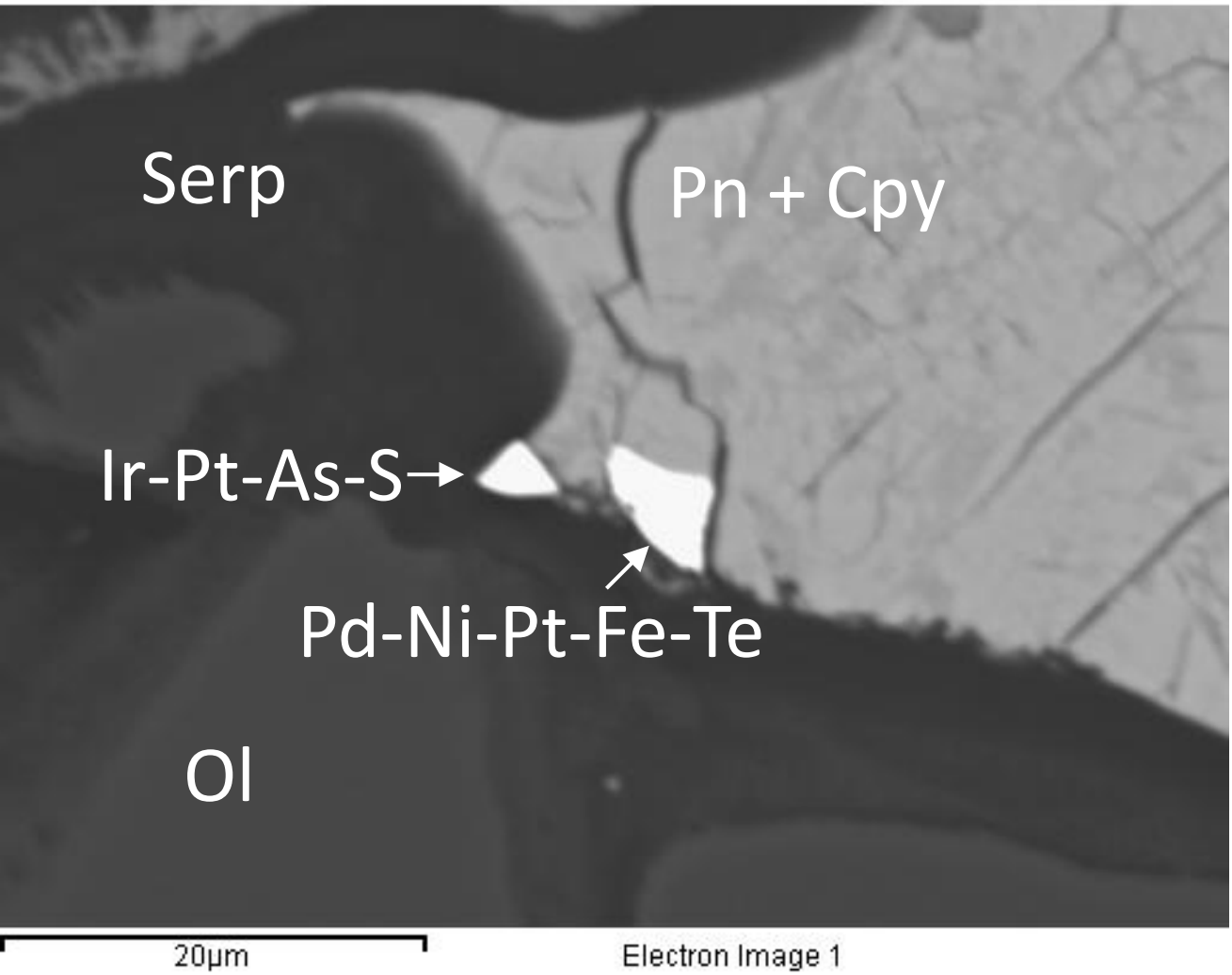
PTSR-45 K 1



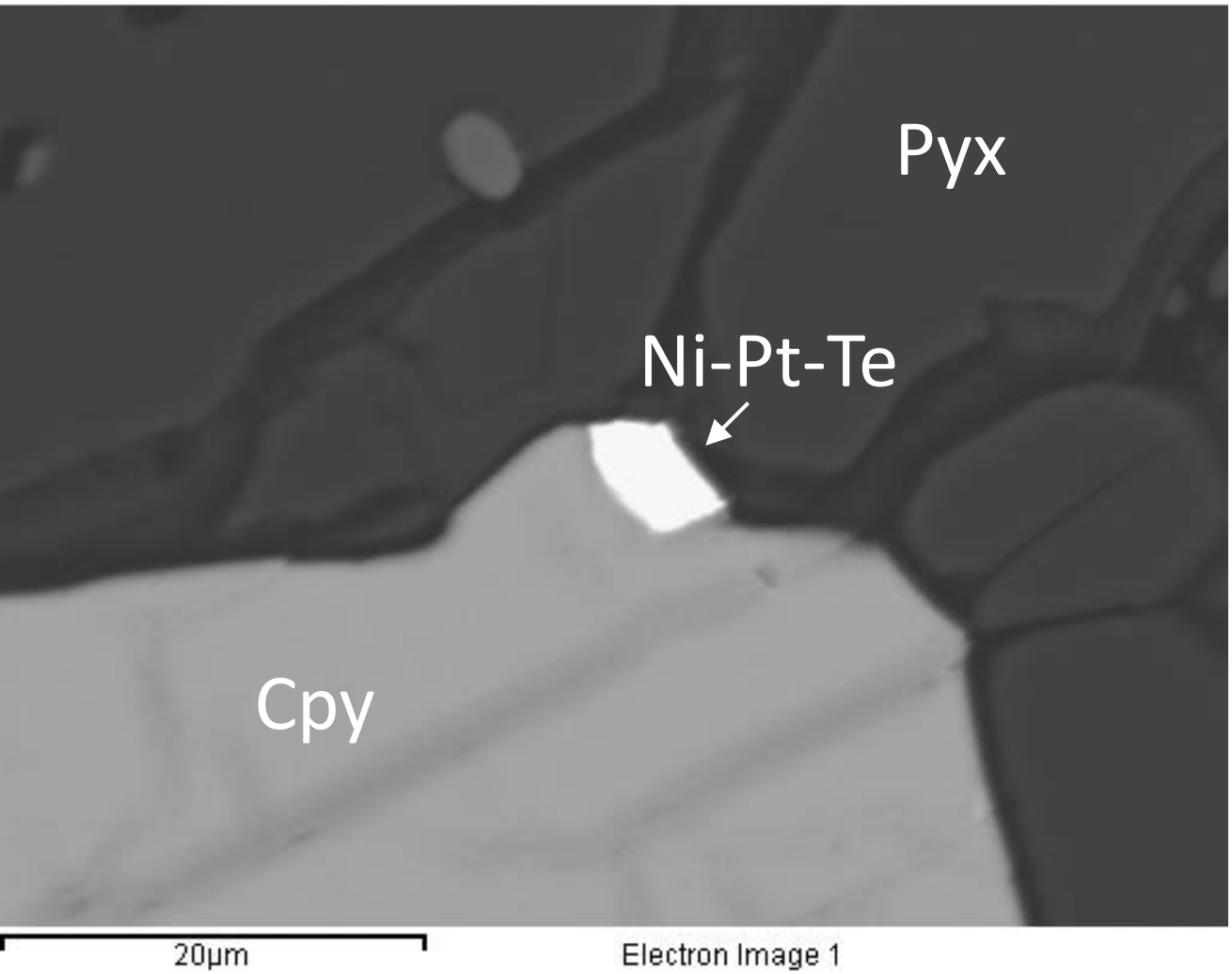
PTSR-45 L 1



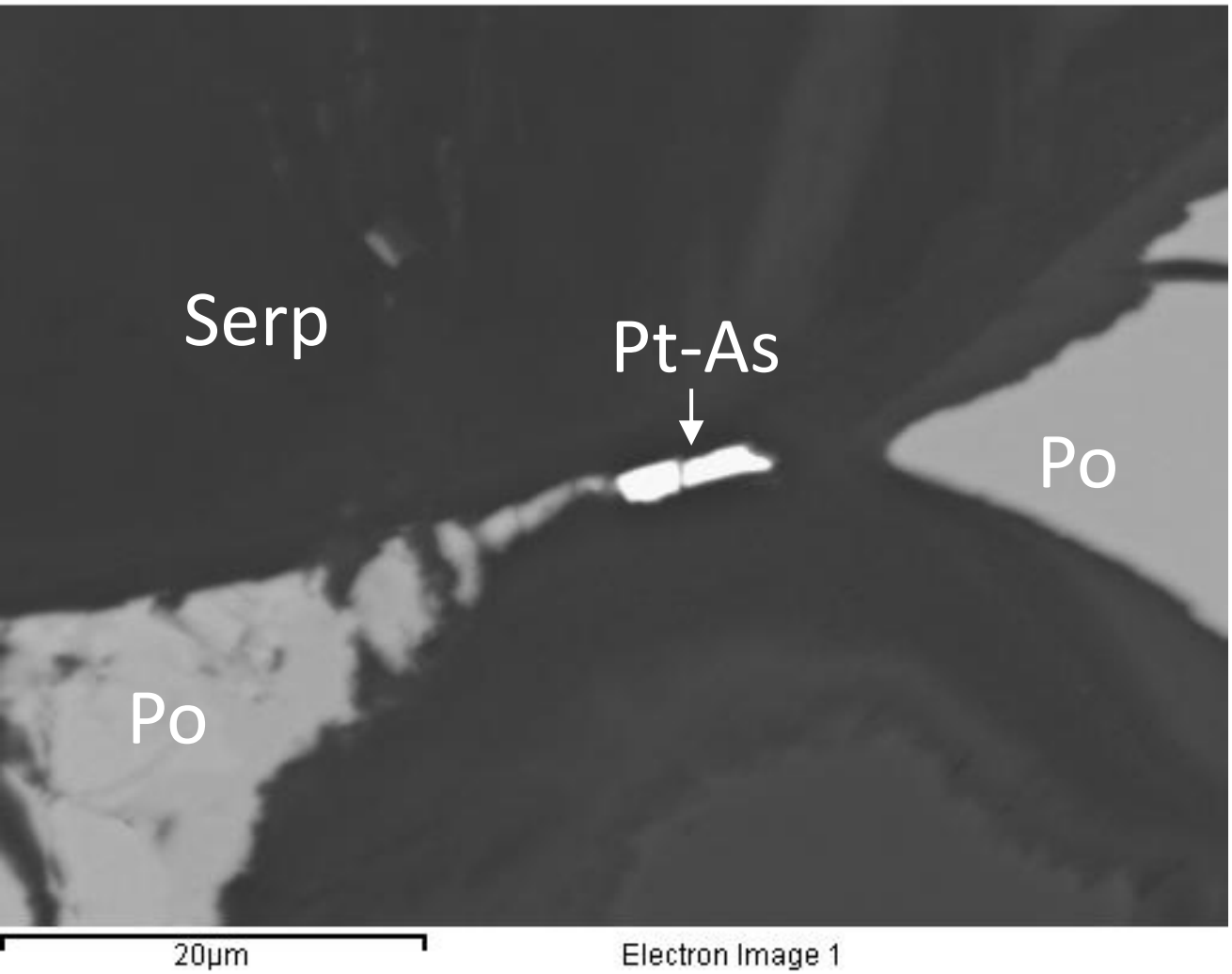
PTSR-45 M 1-2



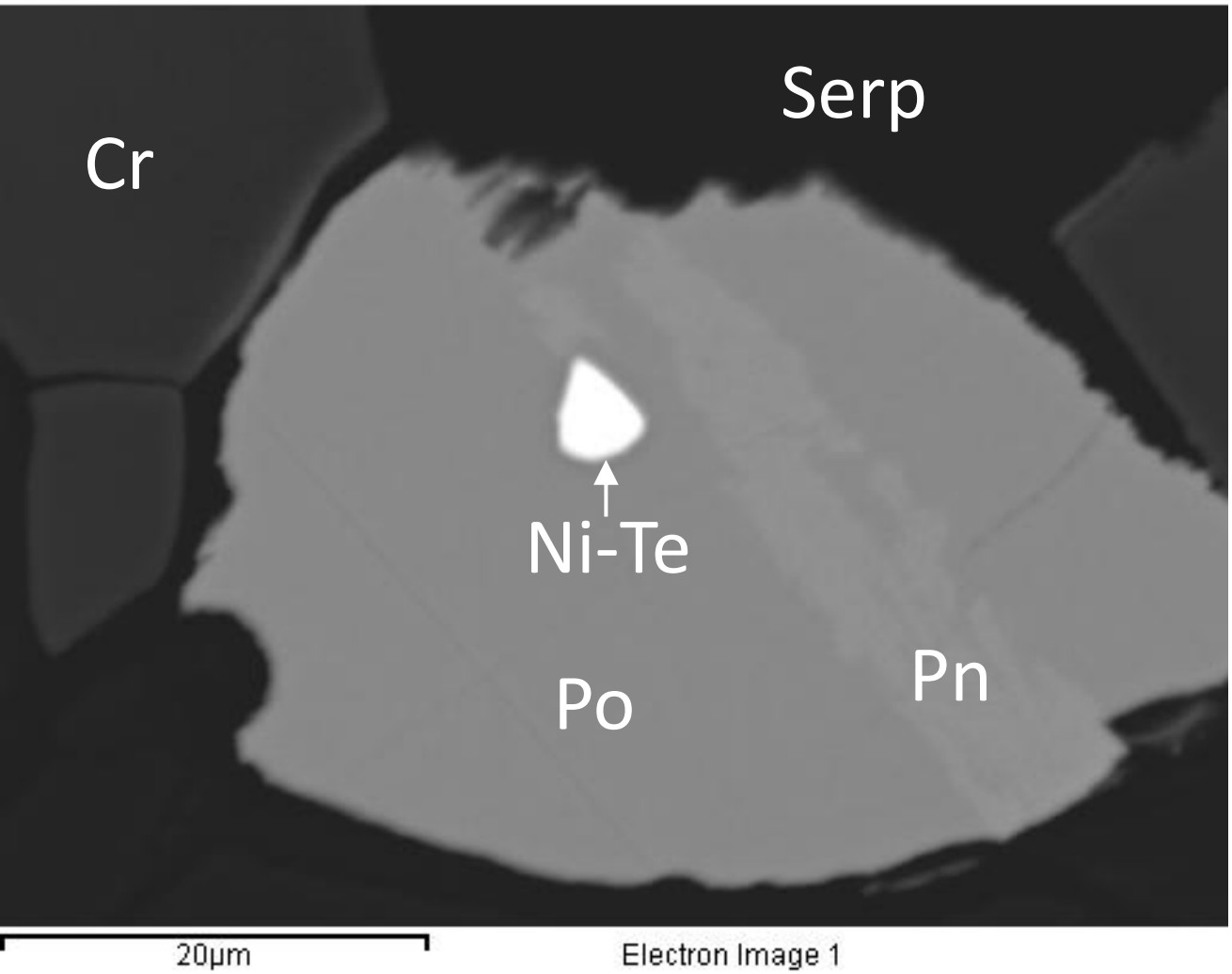
PTSR-45 N 1



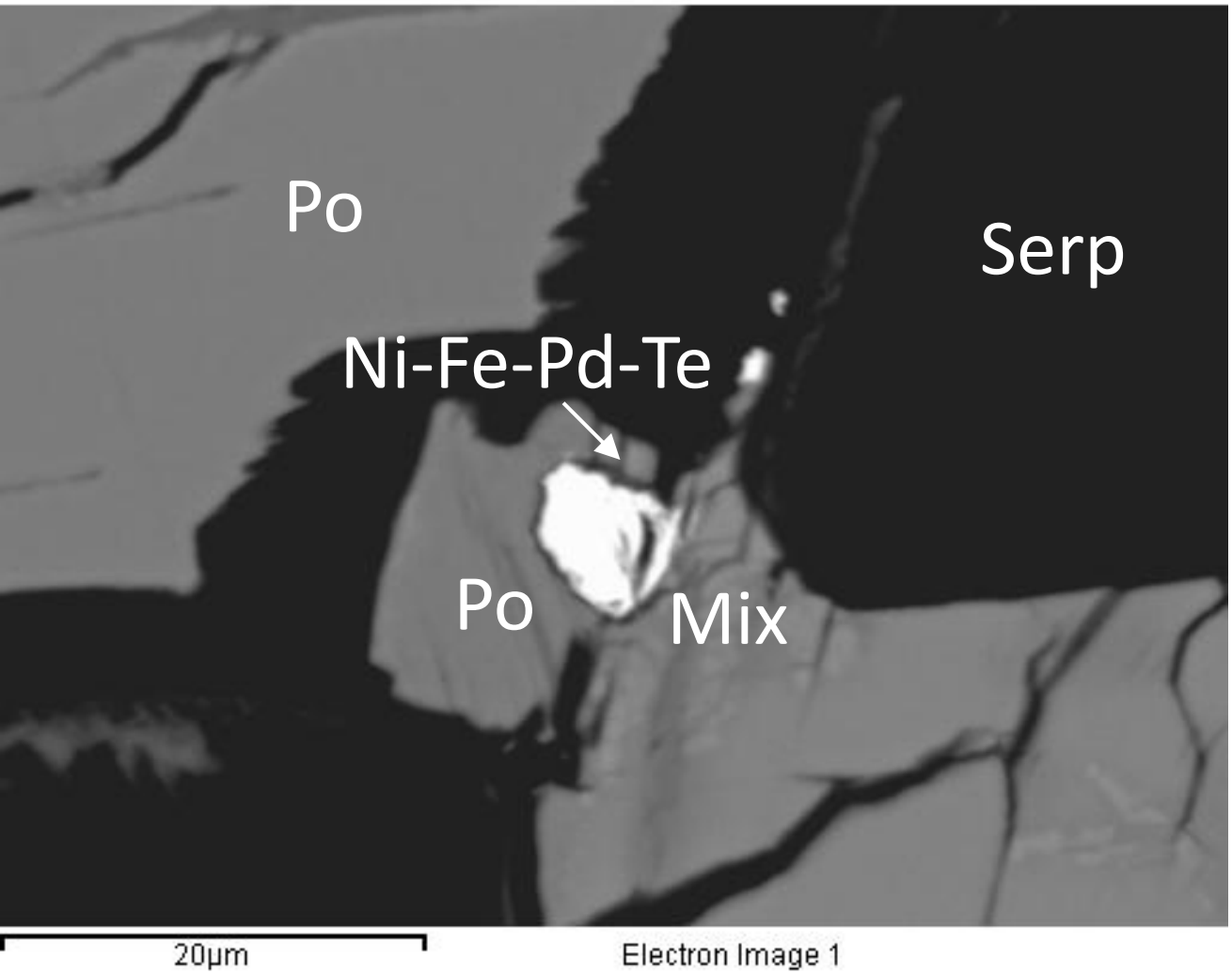
PTSR-45 O 1



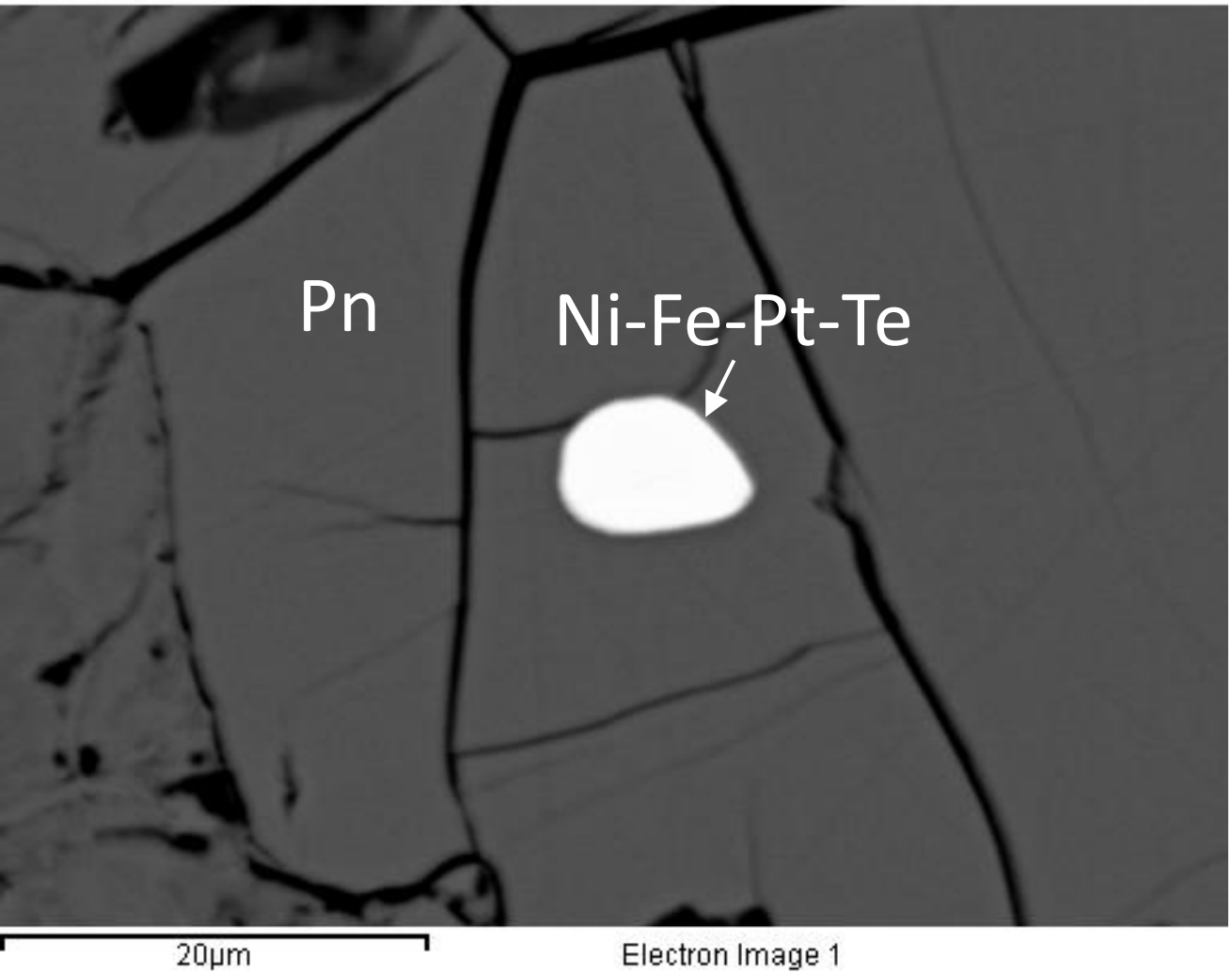
PTSR-45 P 1



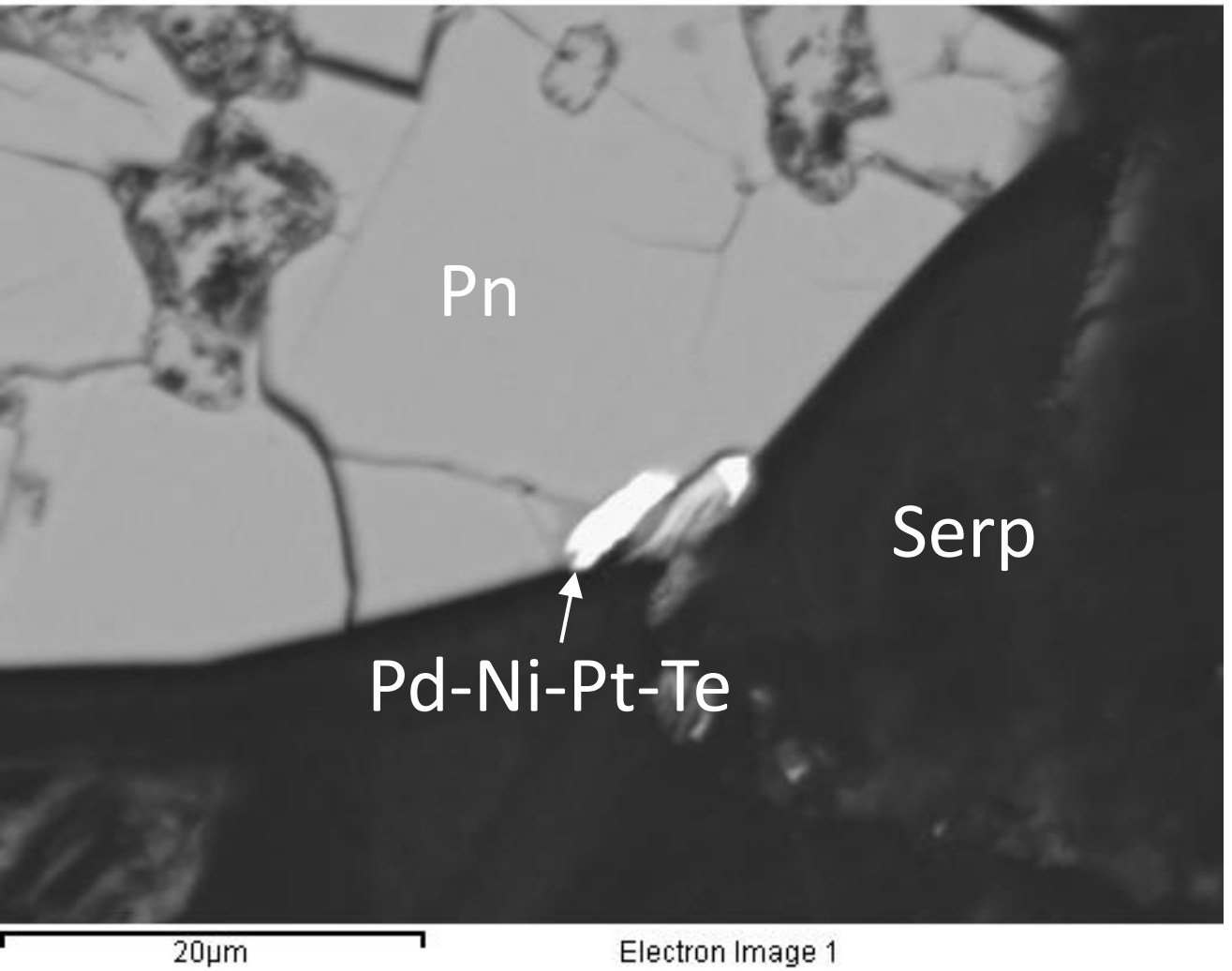
PTSR-45 Q 1



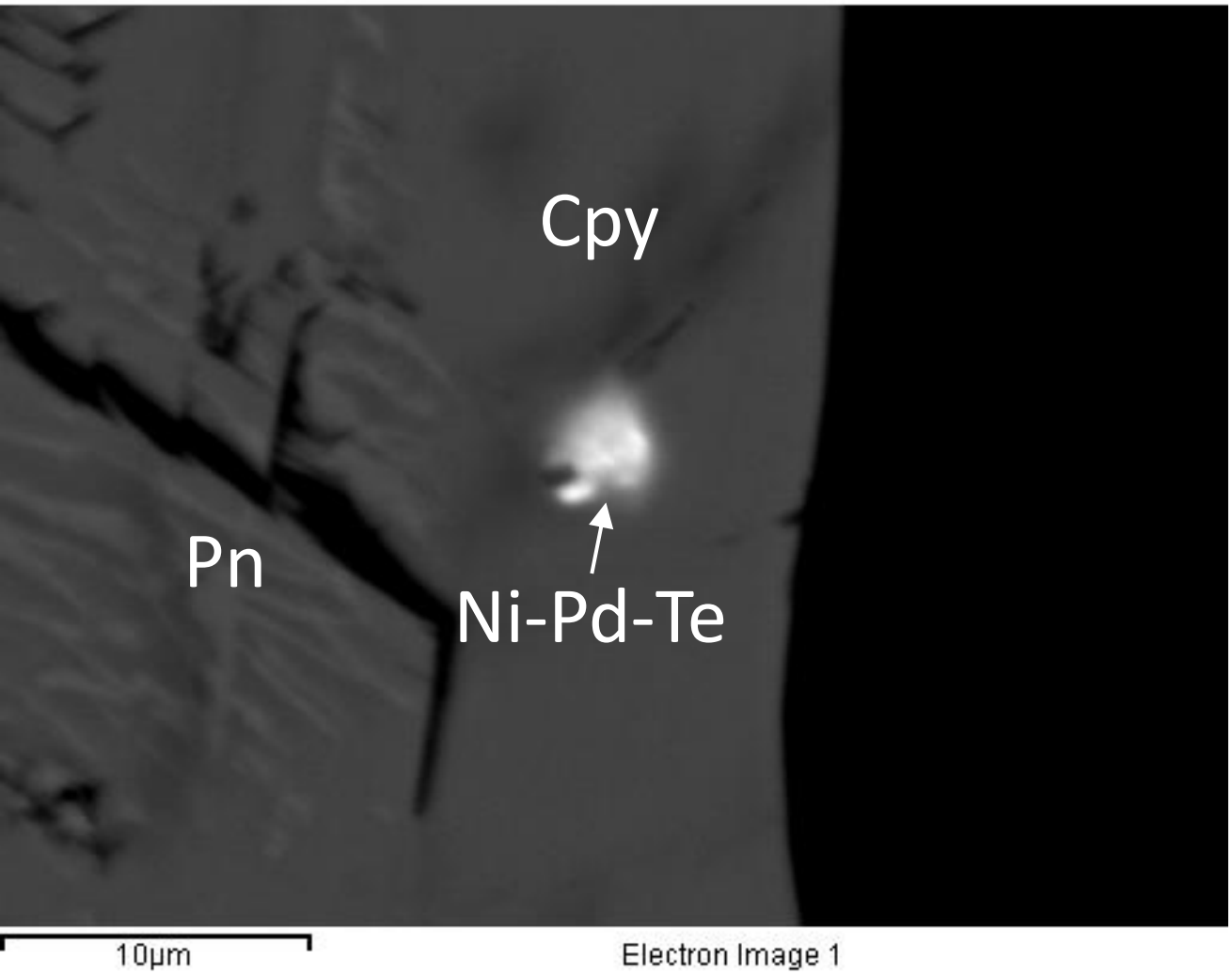
PTSR-45 R 1



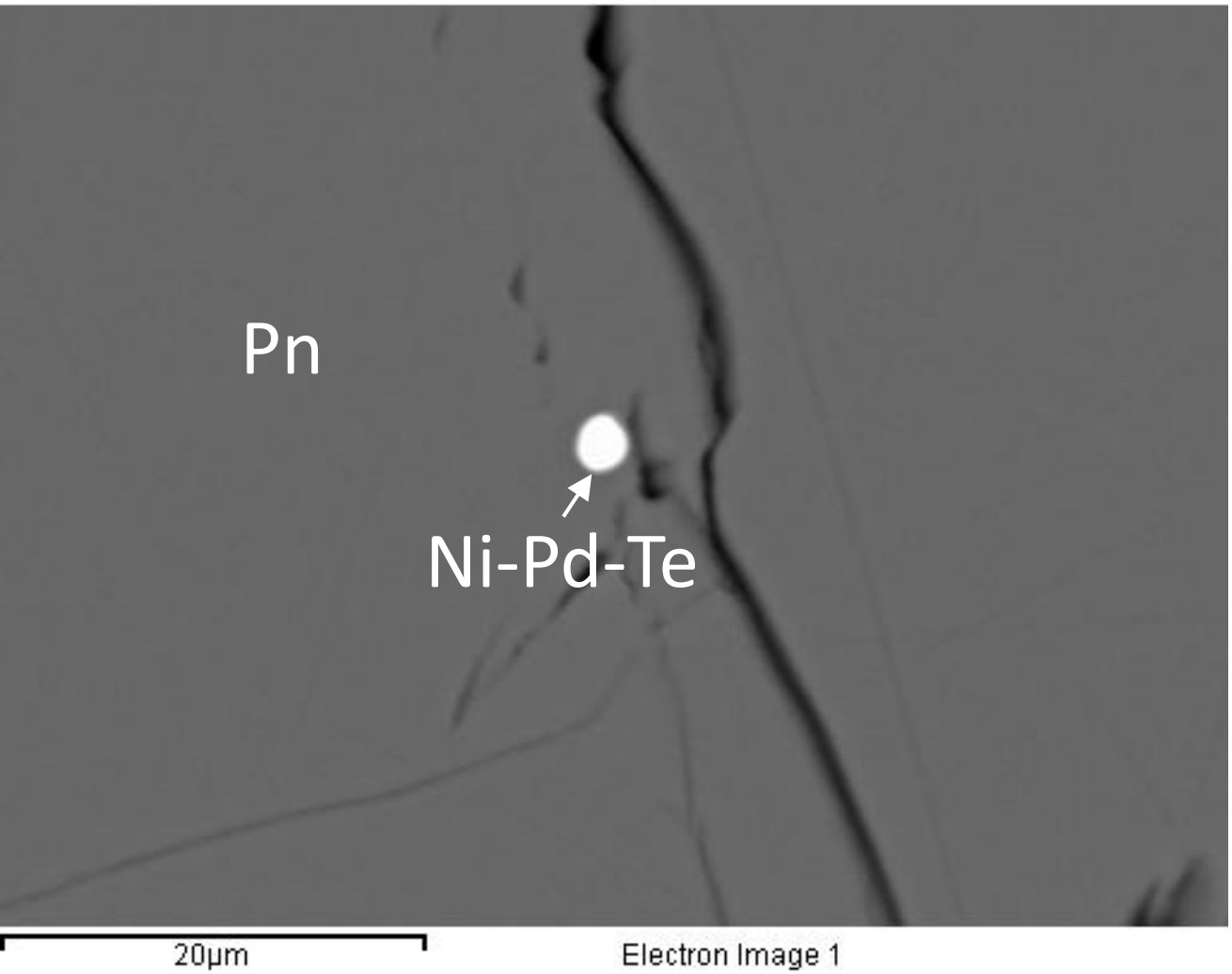
PTSR-45 S 1



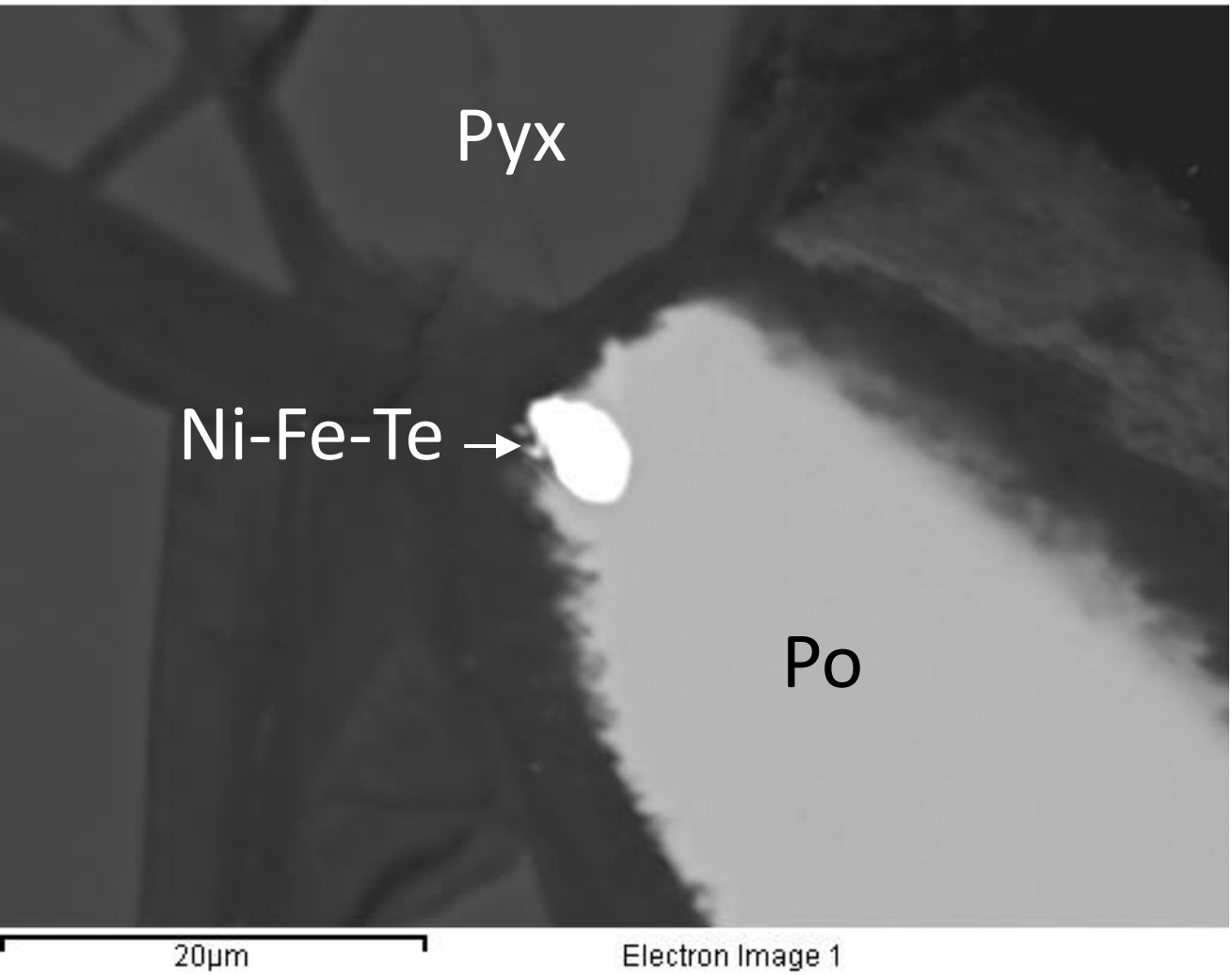
PTSR-45 T 1



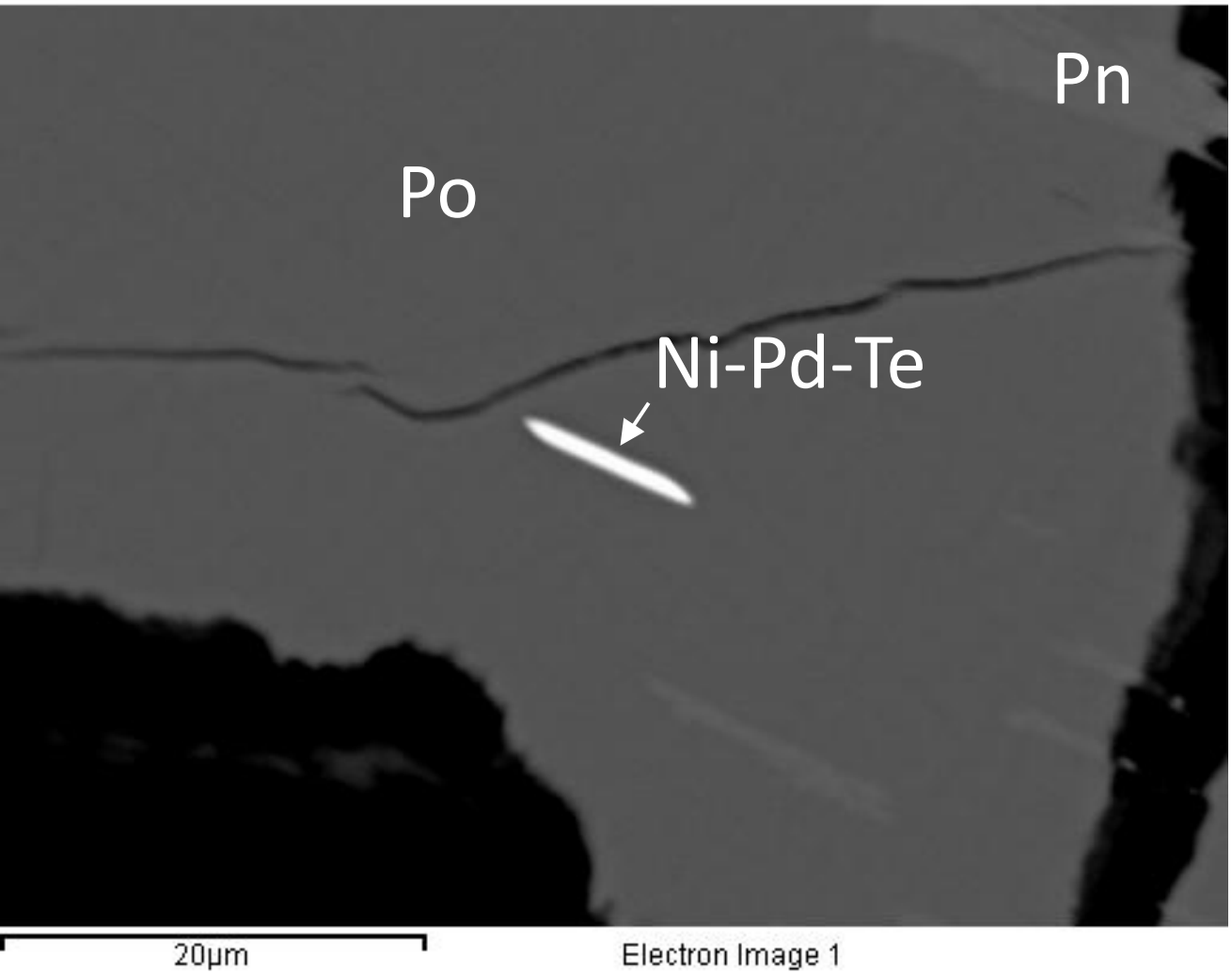
PTSR-45 U 1



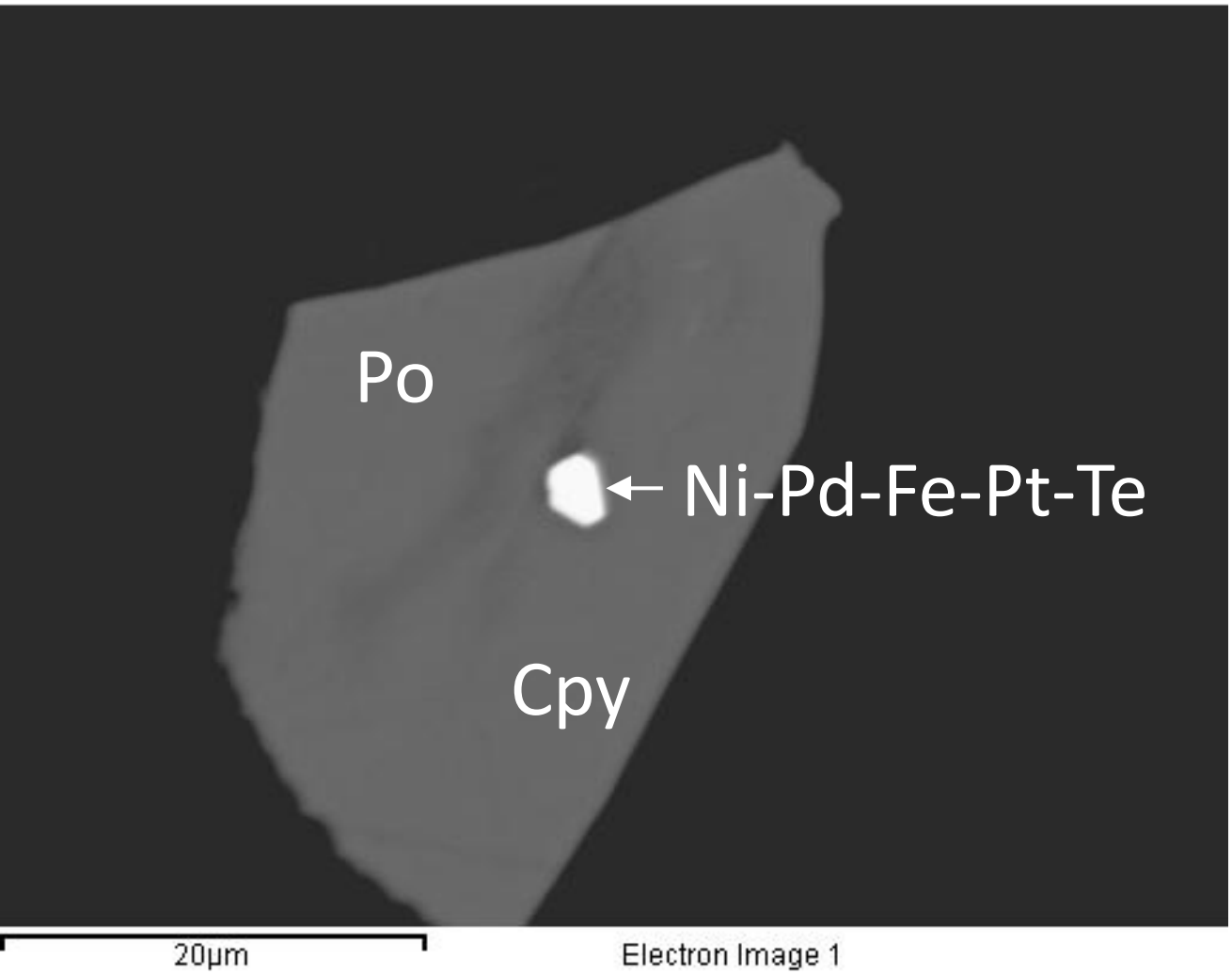
PTSR-45 V 1



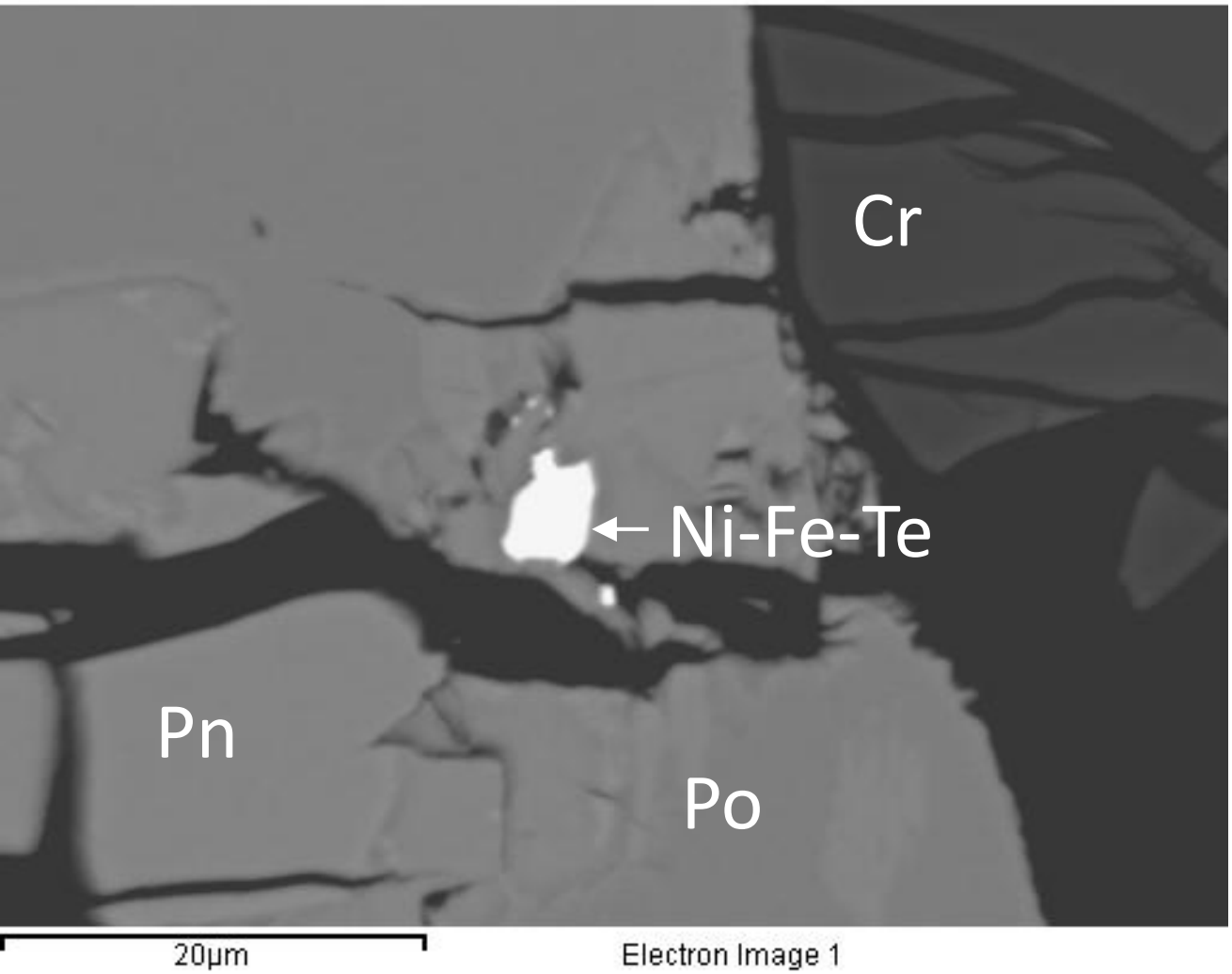
PTSR-45 W 1



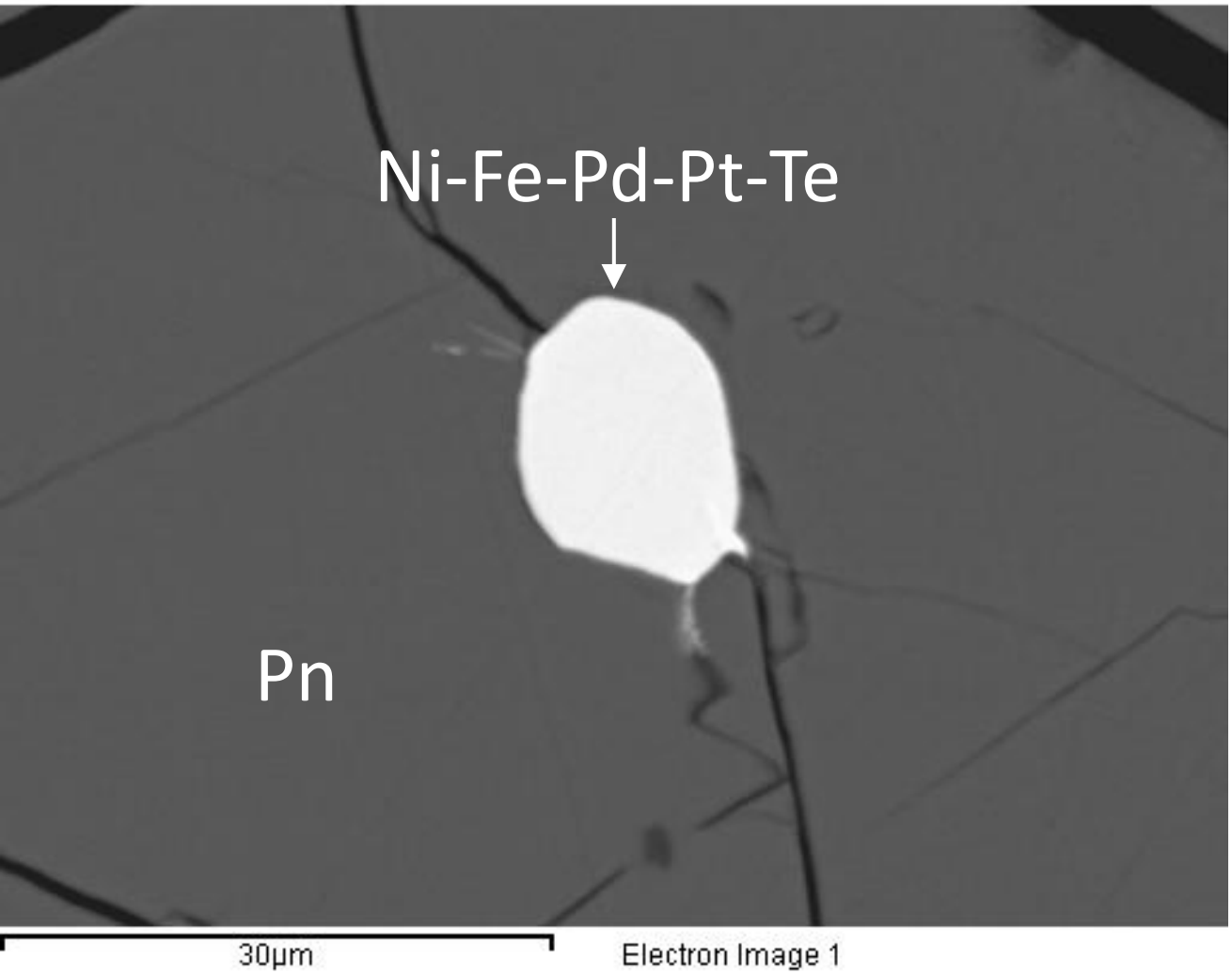
PTSR-45 X 1



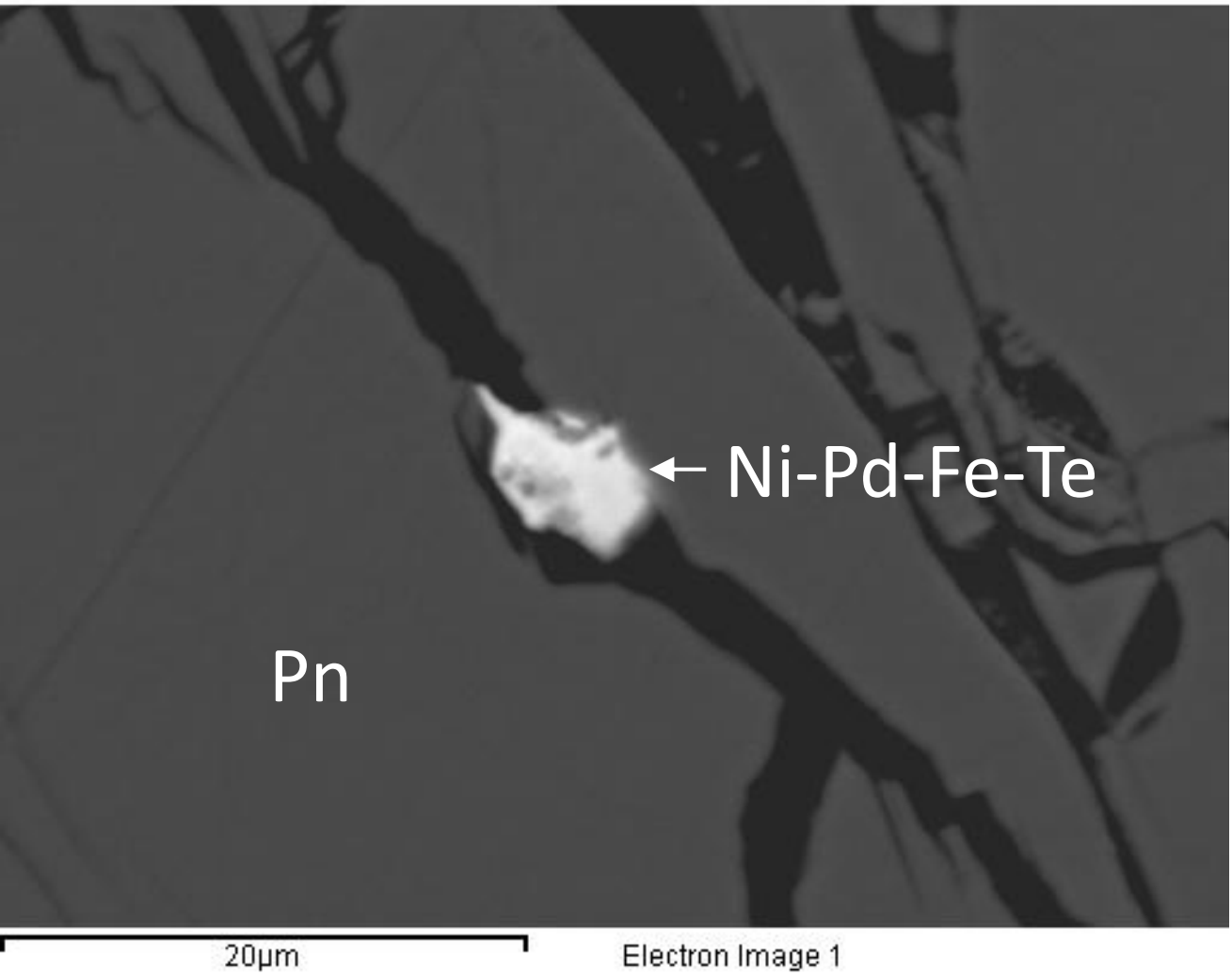
PTSR-45 Y 1



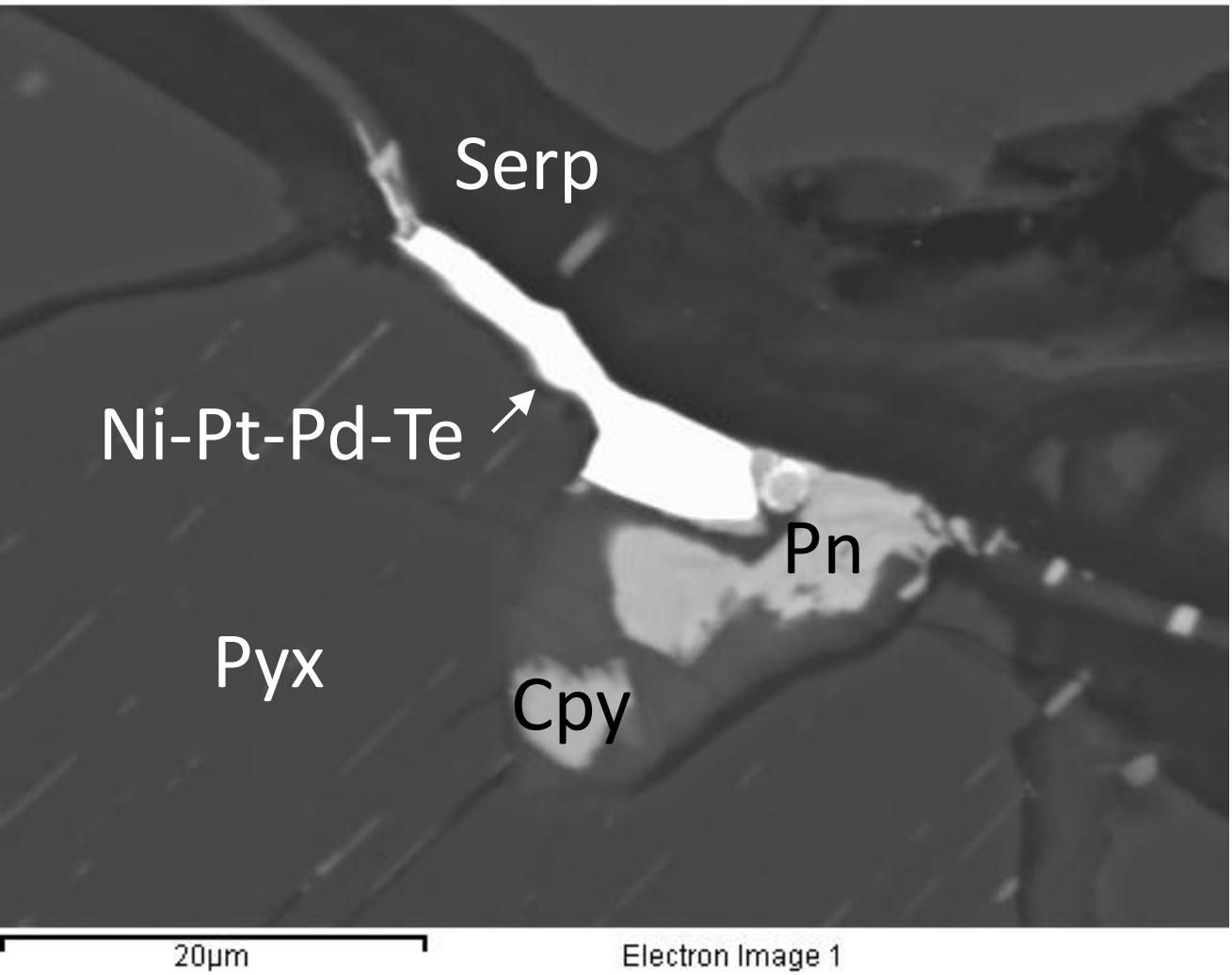
PTSR-45 Z 1



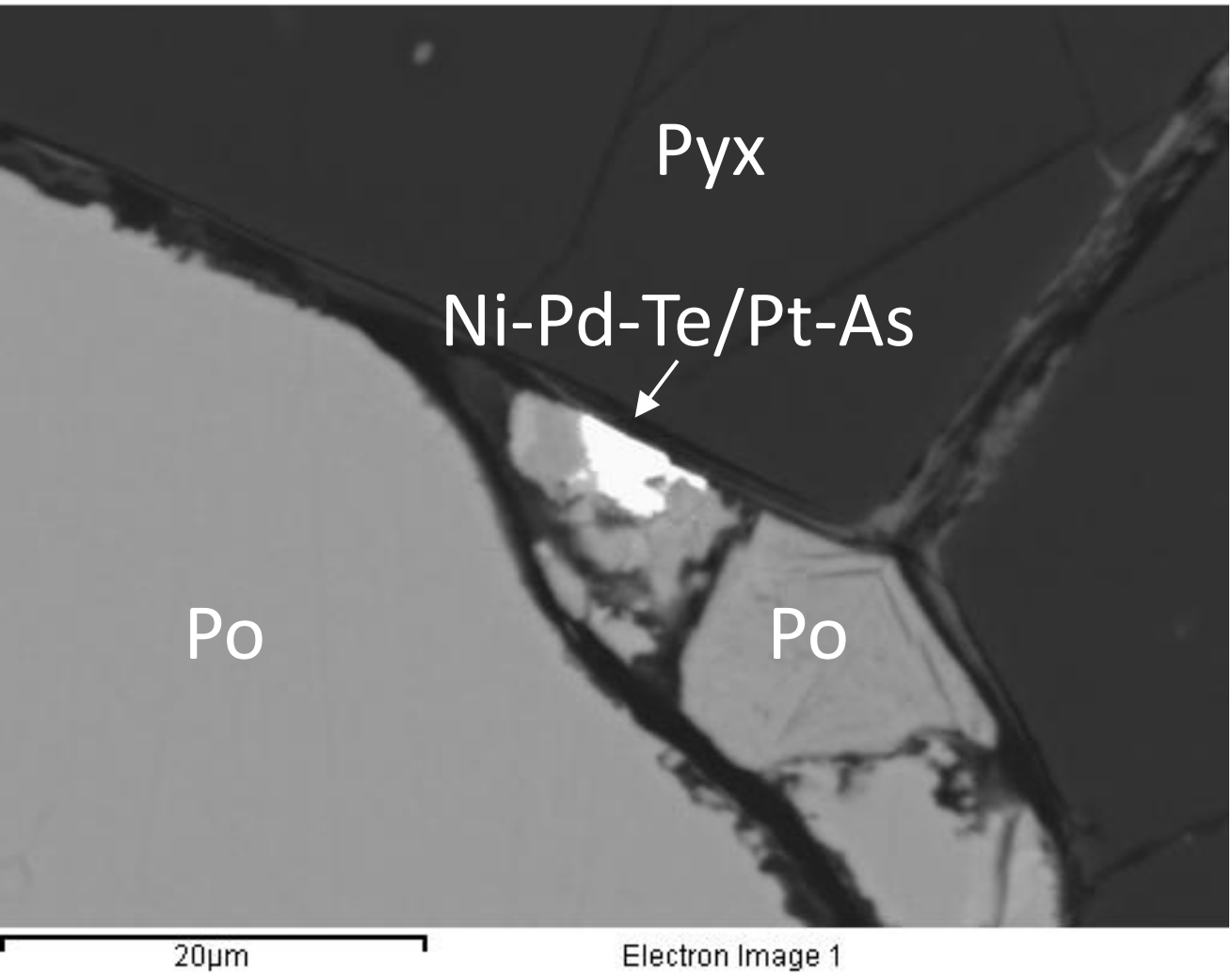
PTSR-45 AA 1



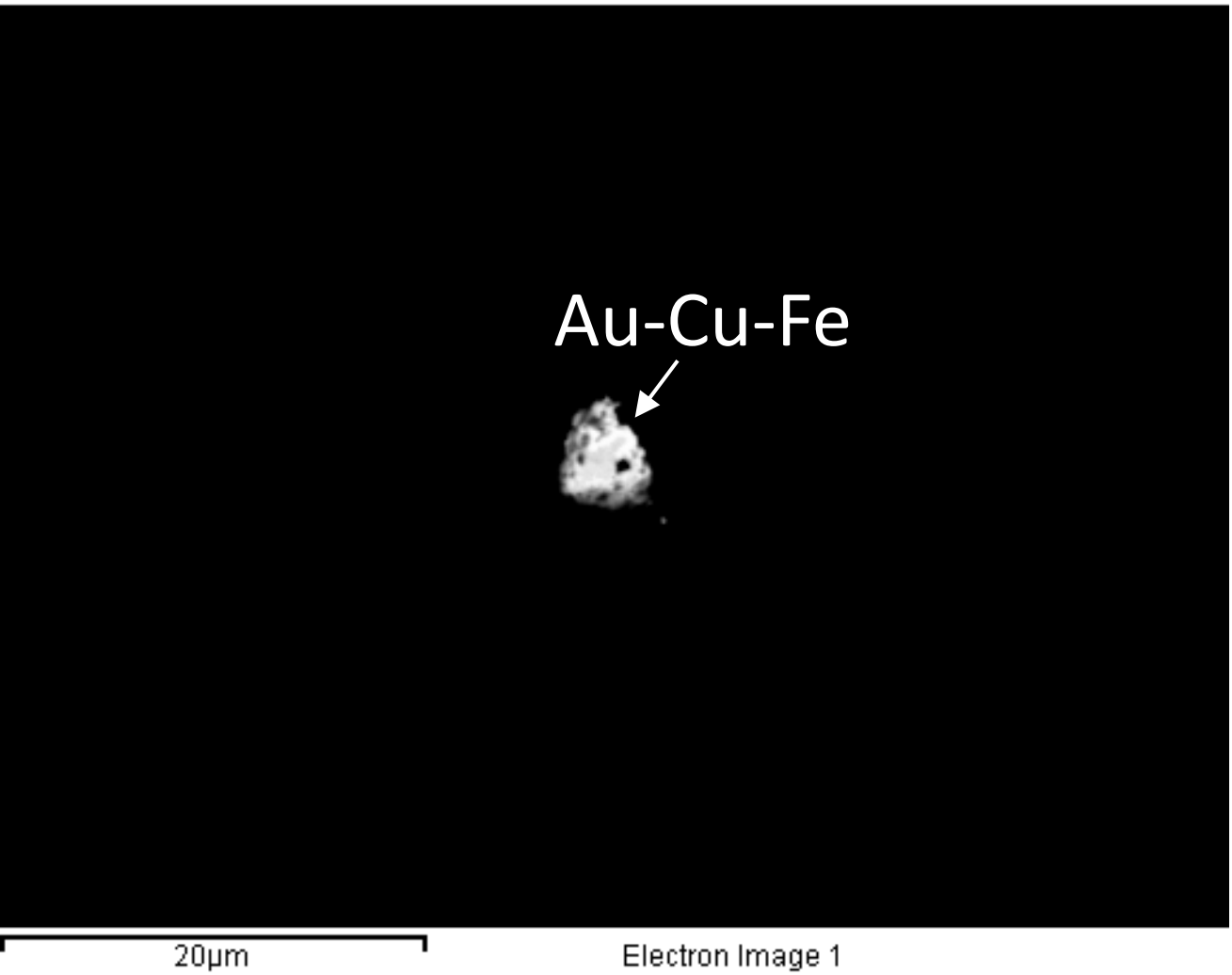
PTSR-46 A 1



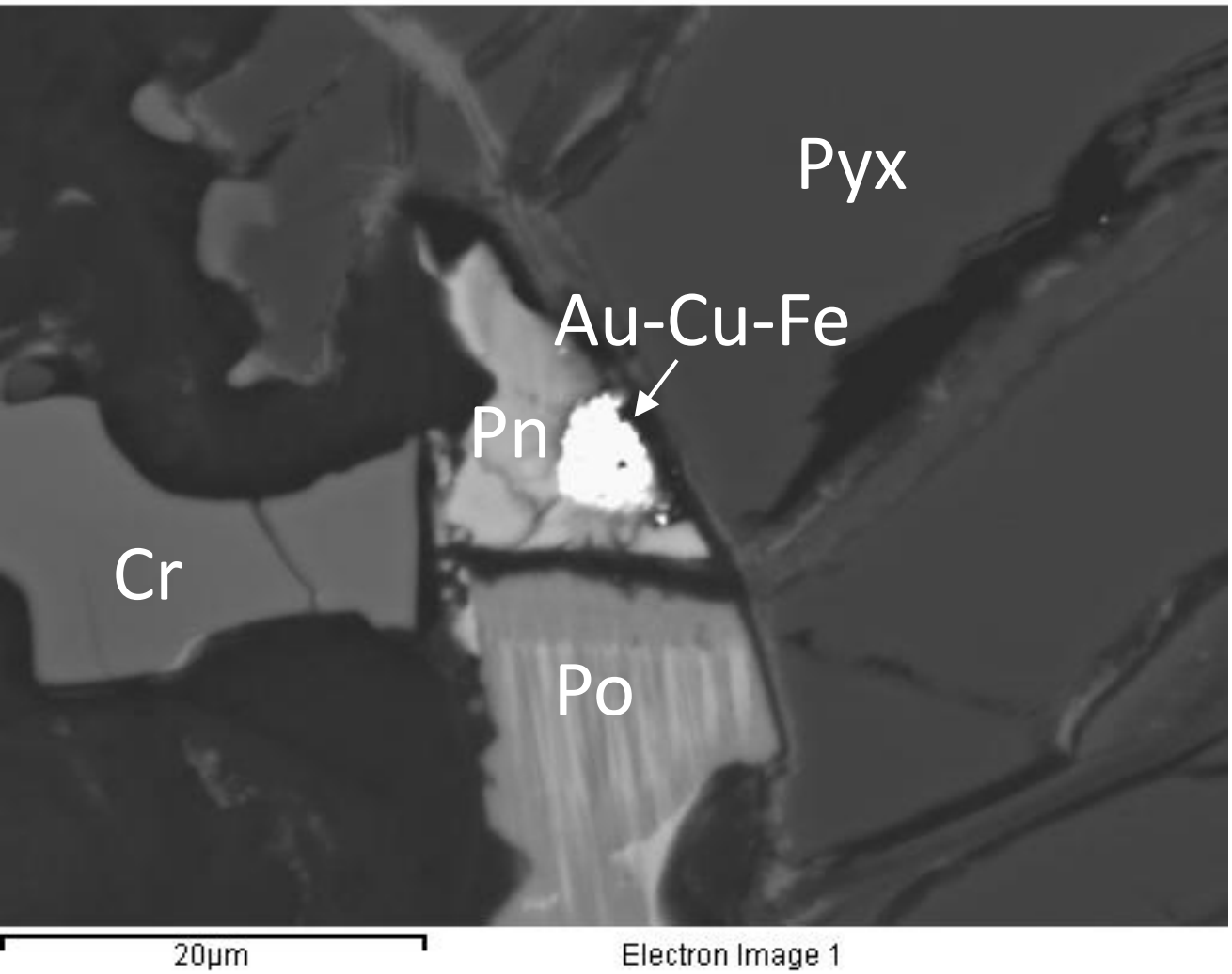
PTSR-46 B 1



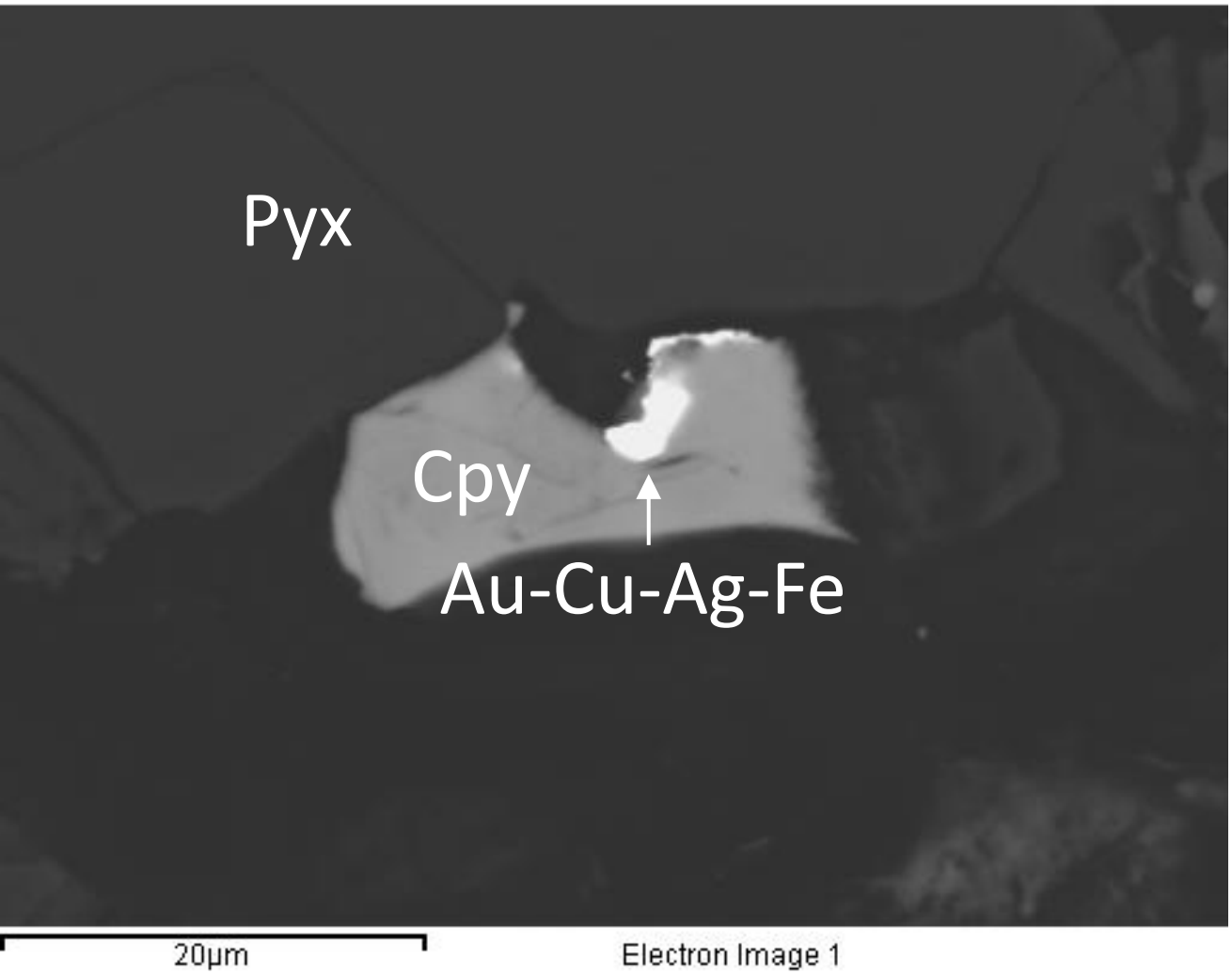
PTSR-46 C 1



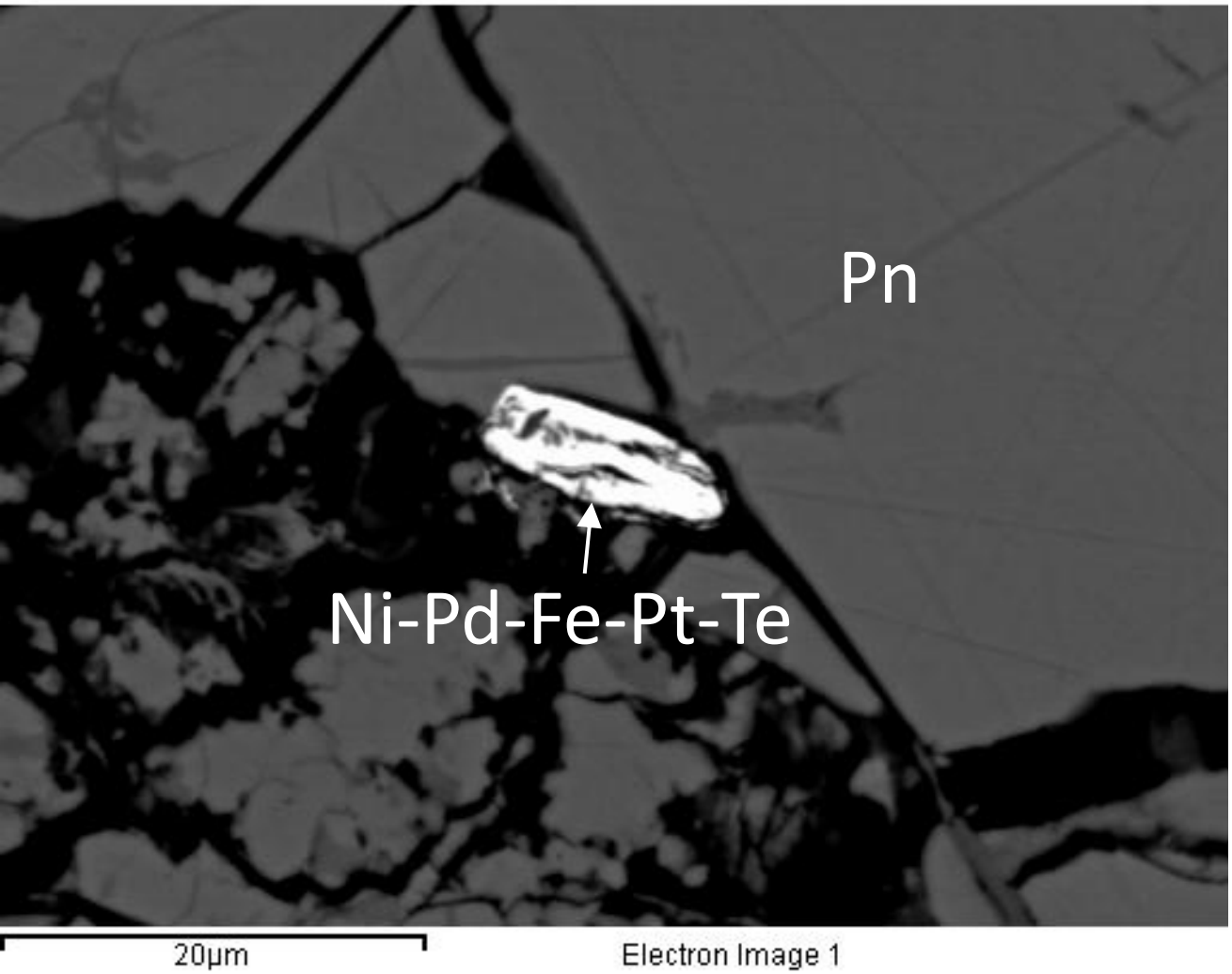
PTSR-46 C 1 Light



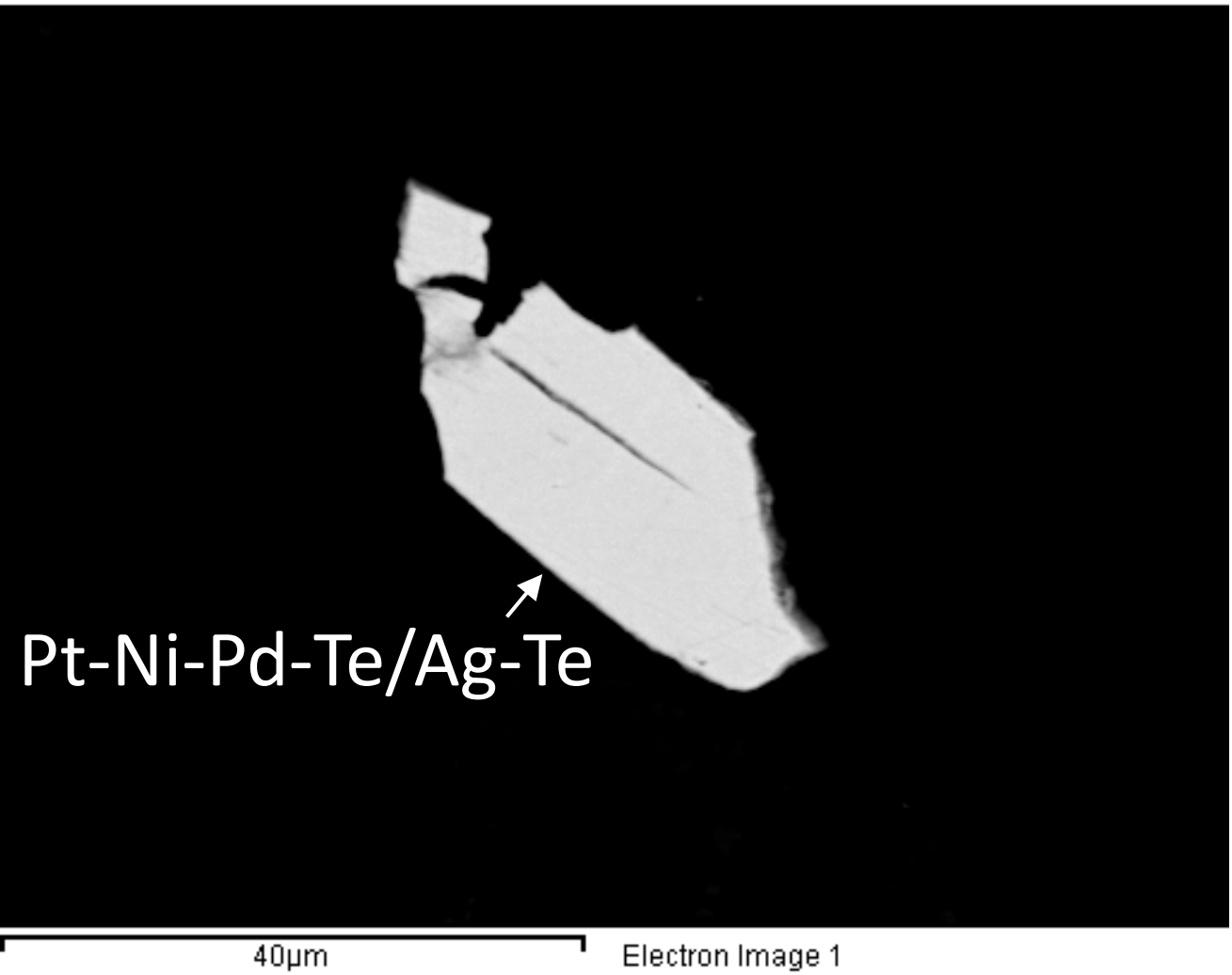
PTSR-46 D 1-2



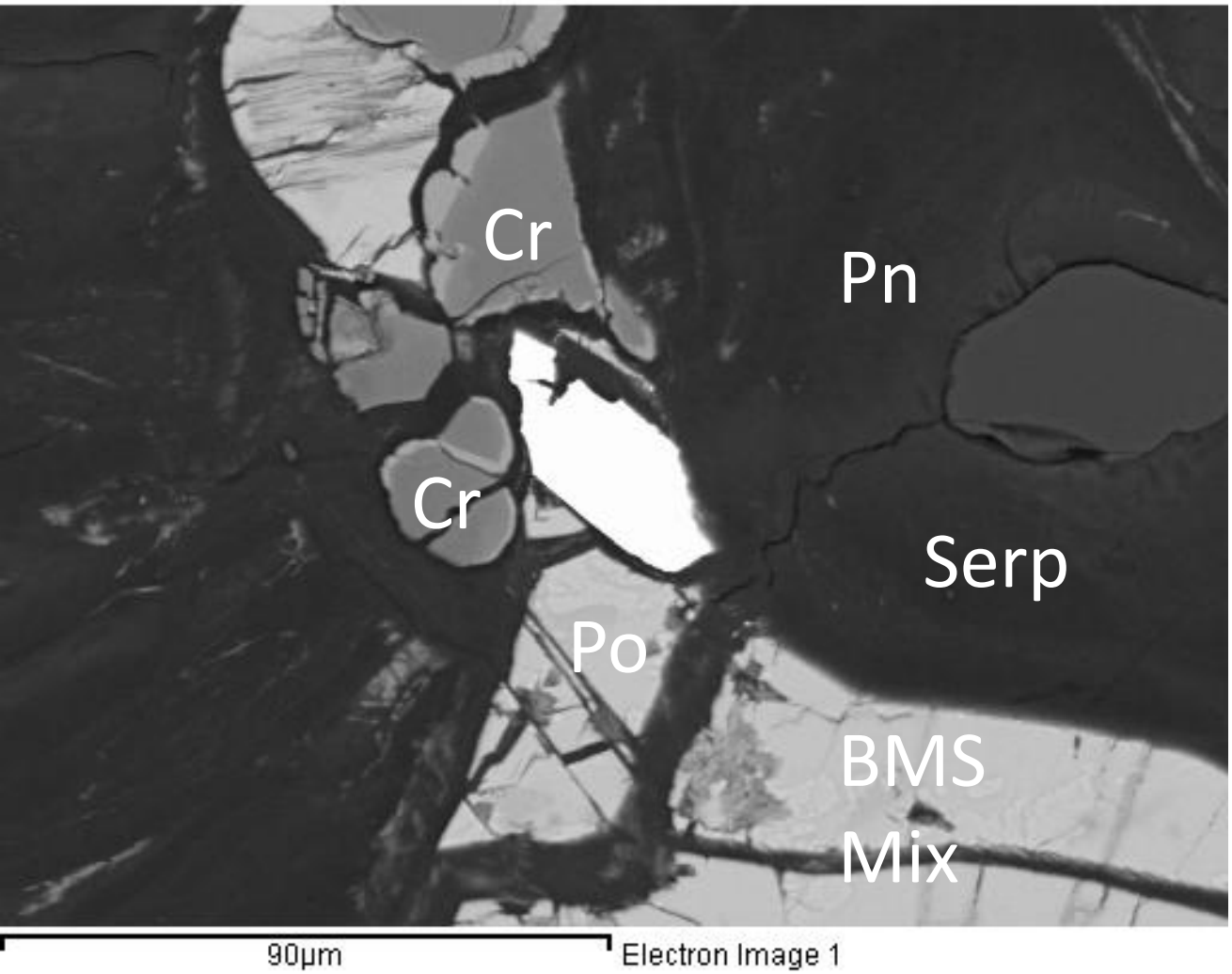
PTSR-46 E 1



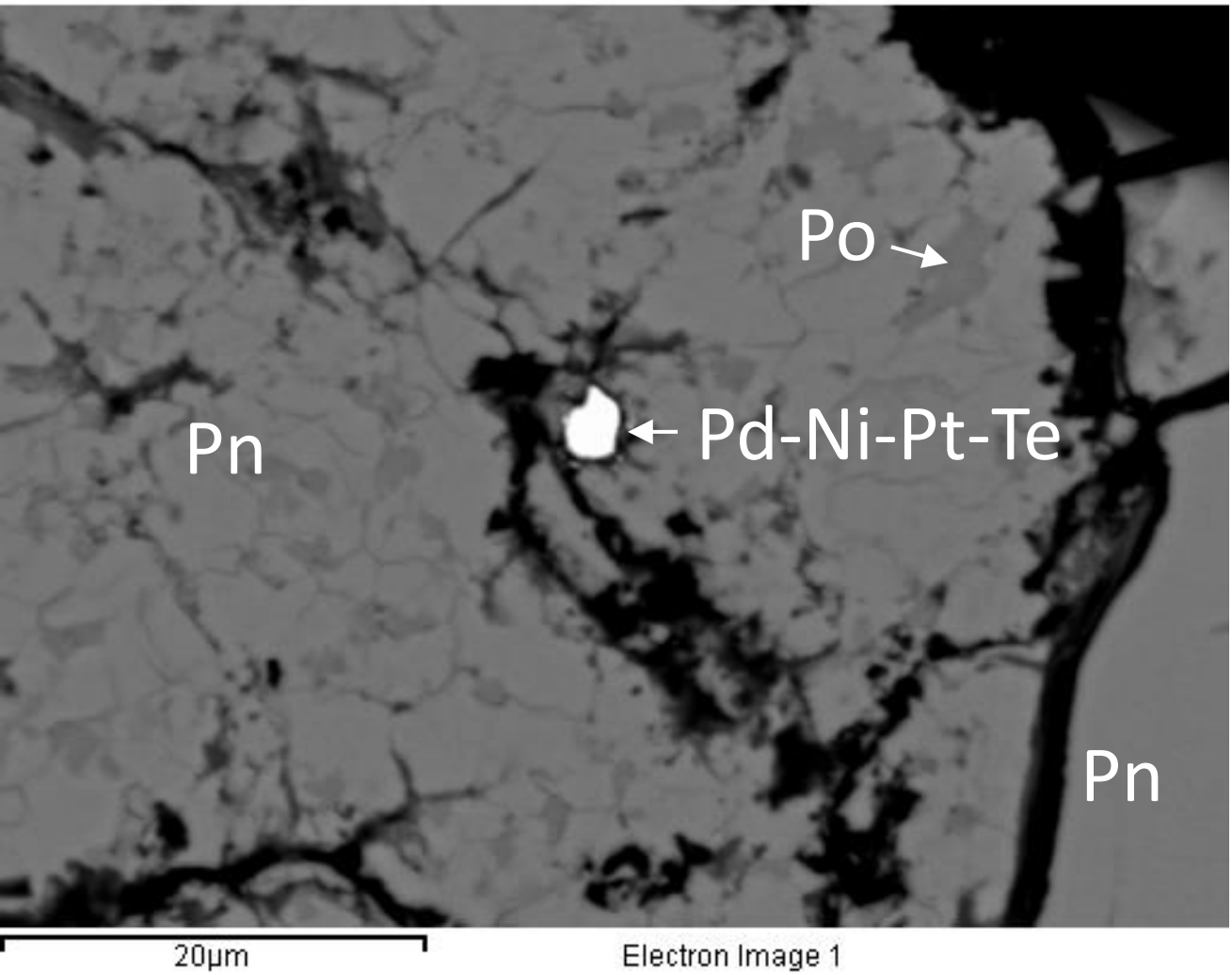
PTSR-46 F 1



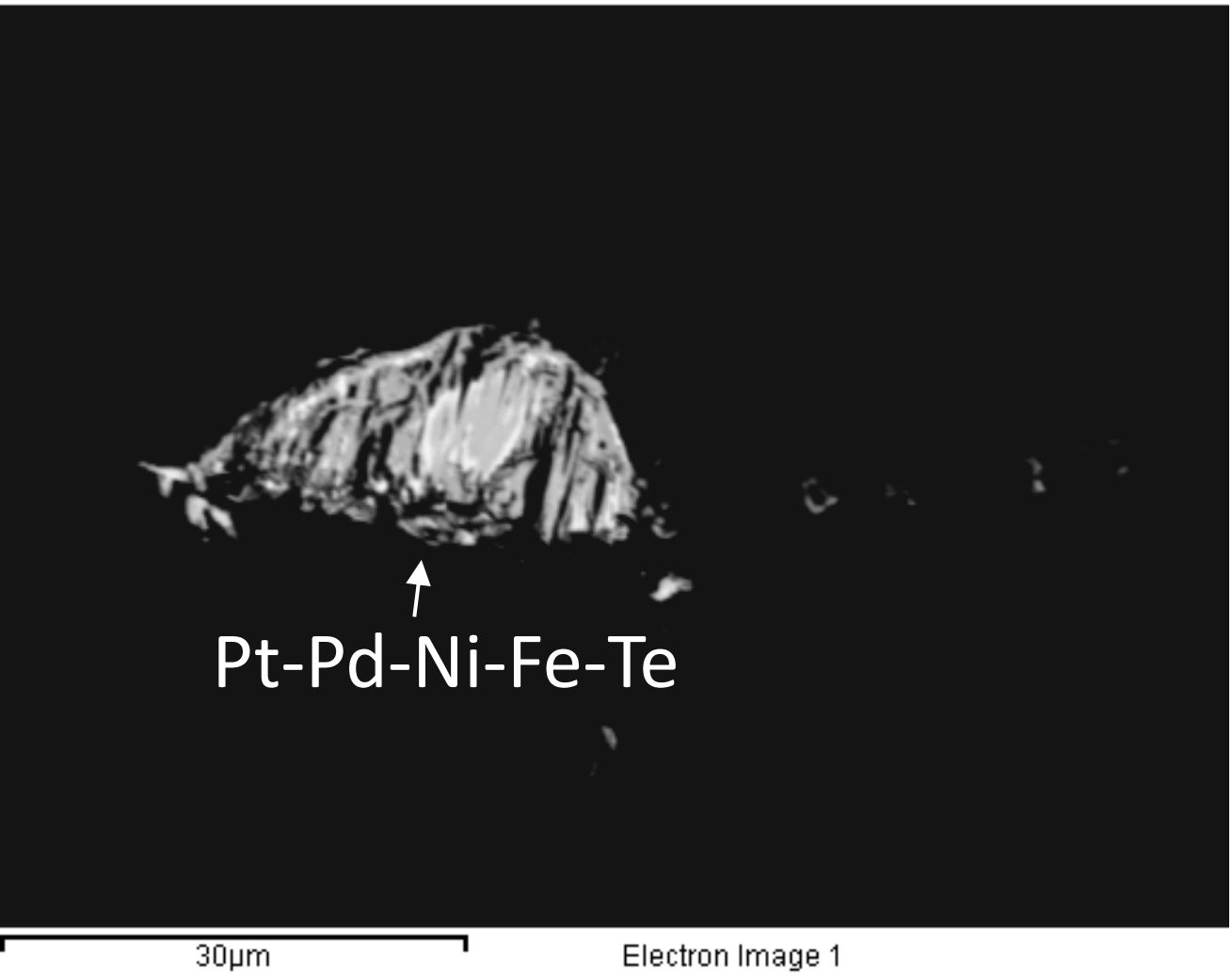
PTSR-46 F 1 Light



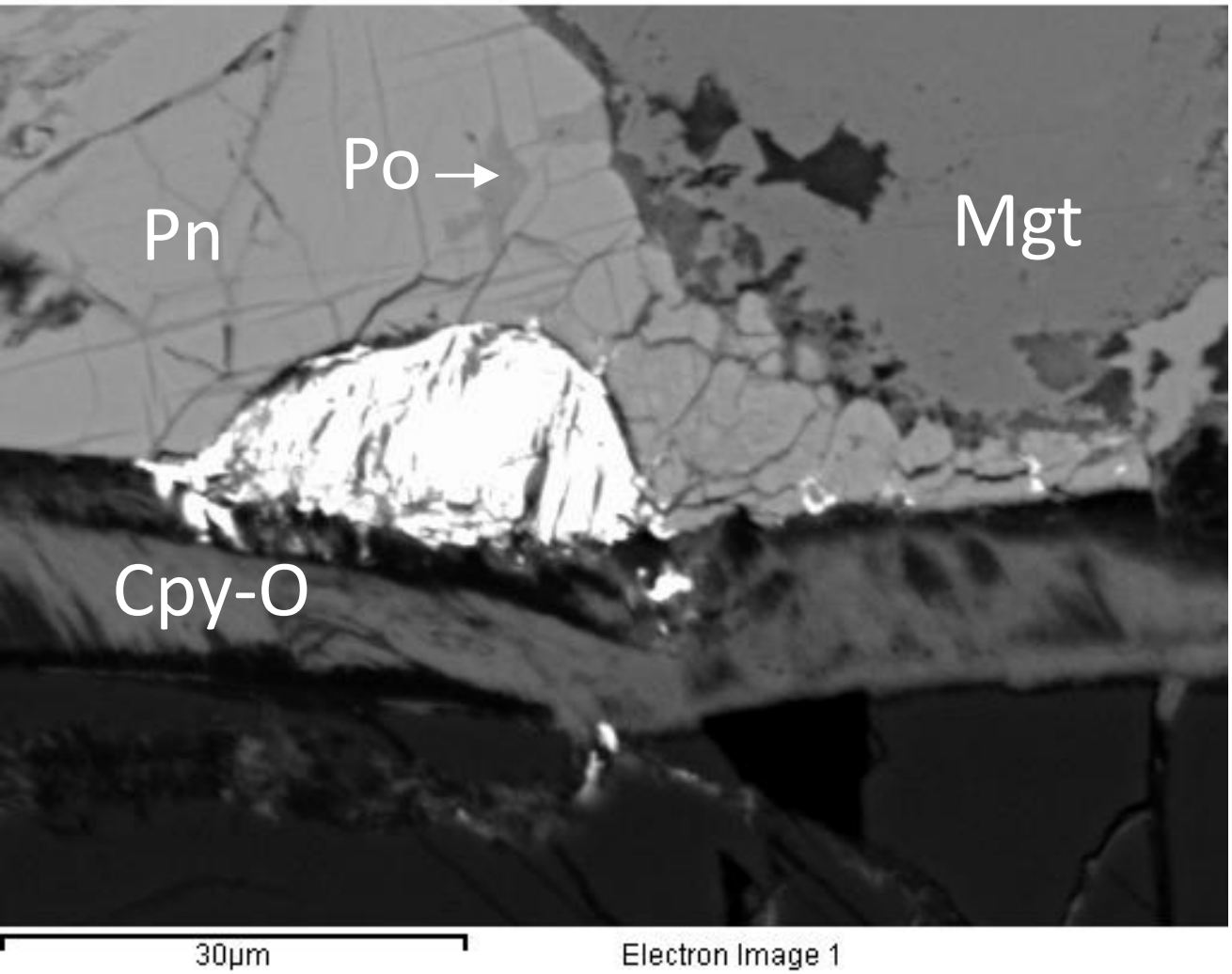
PTSR-46 G 1



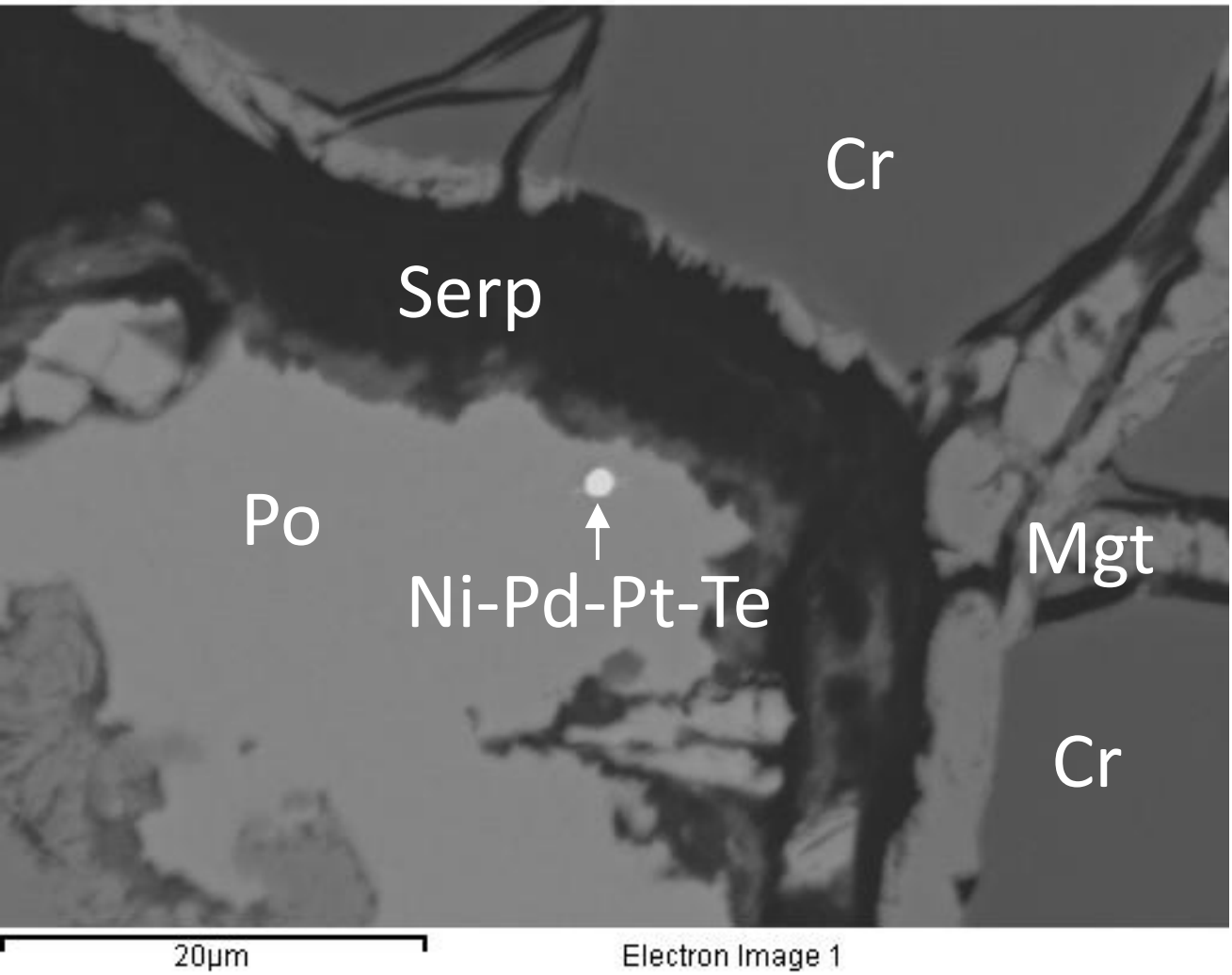
PTSR-46 H 1



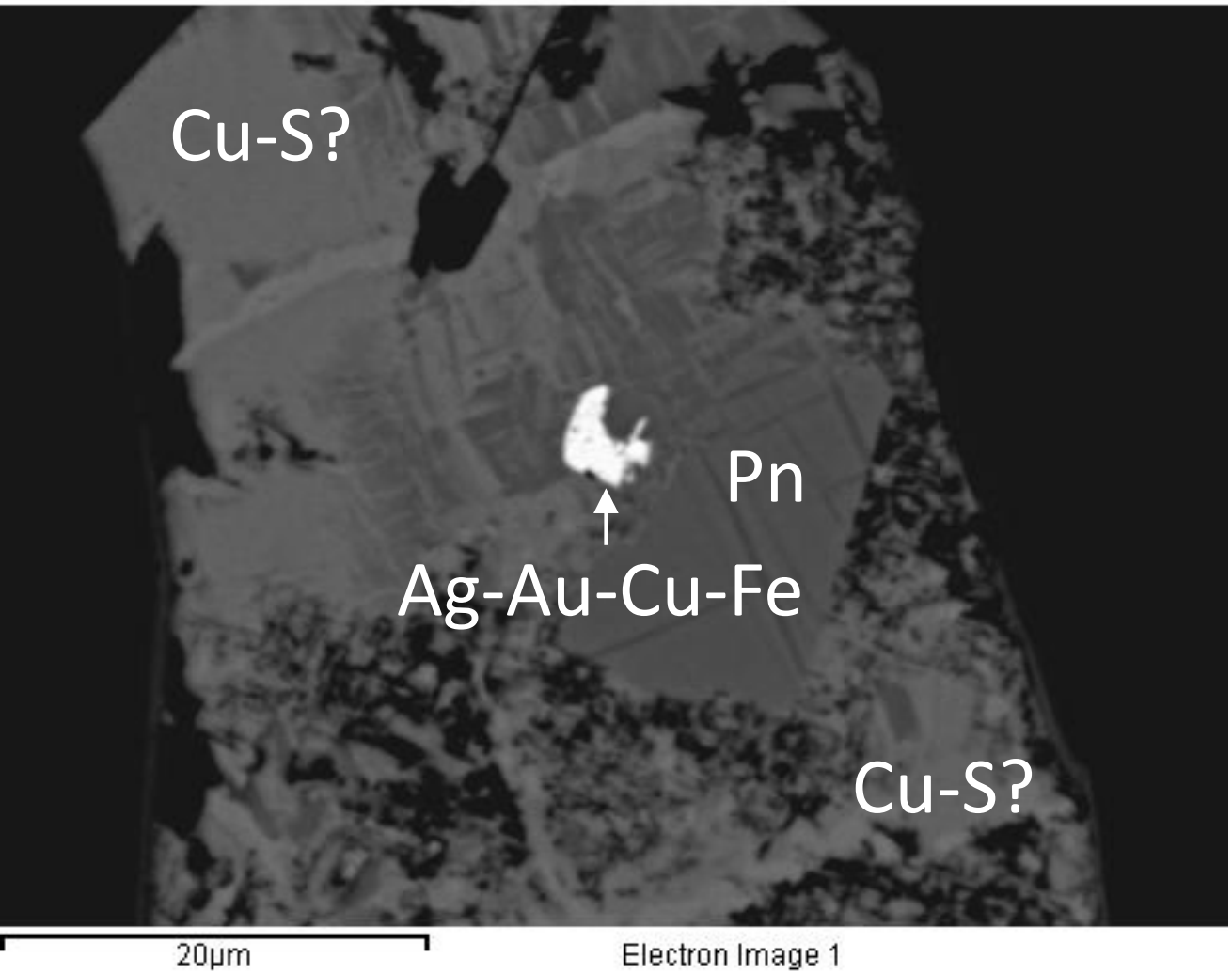
PTSR-46 H 1 Light



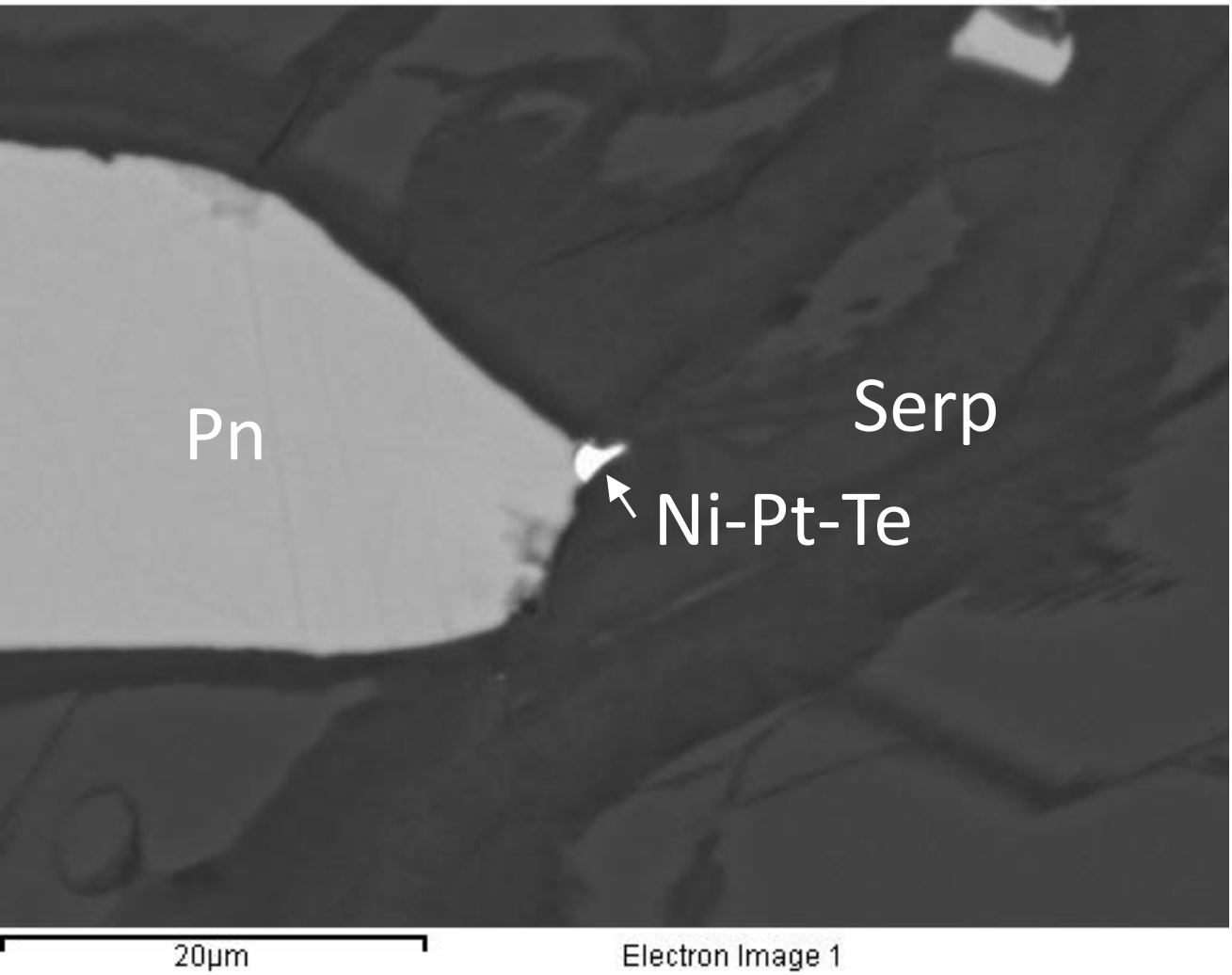
PTSR-46 I 1



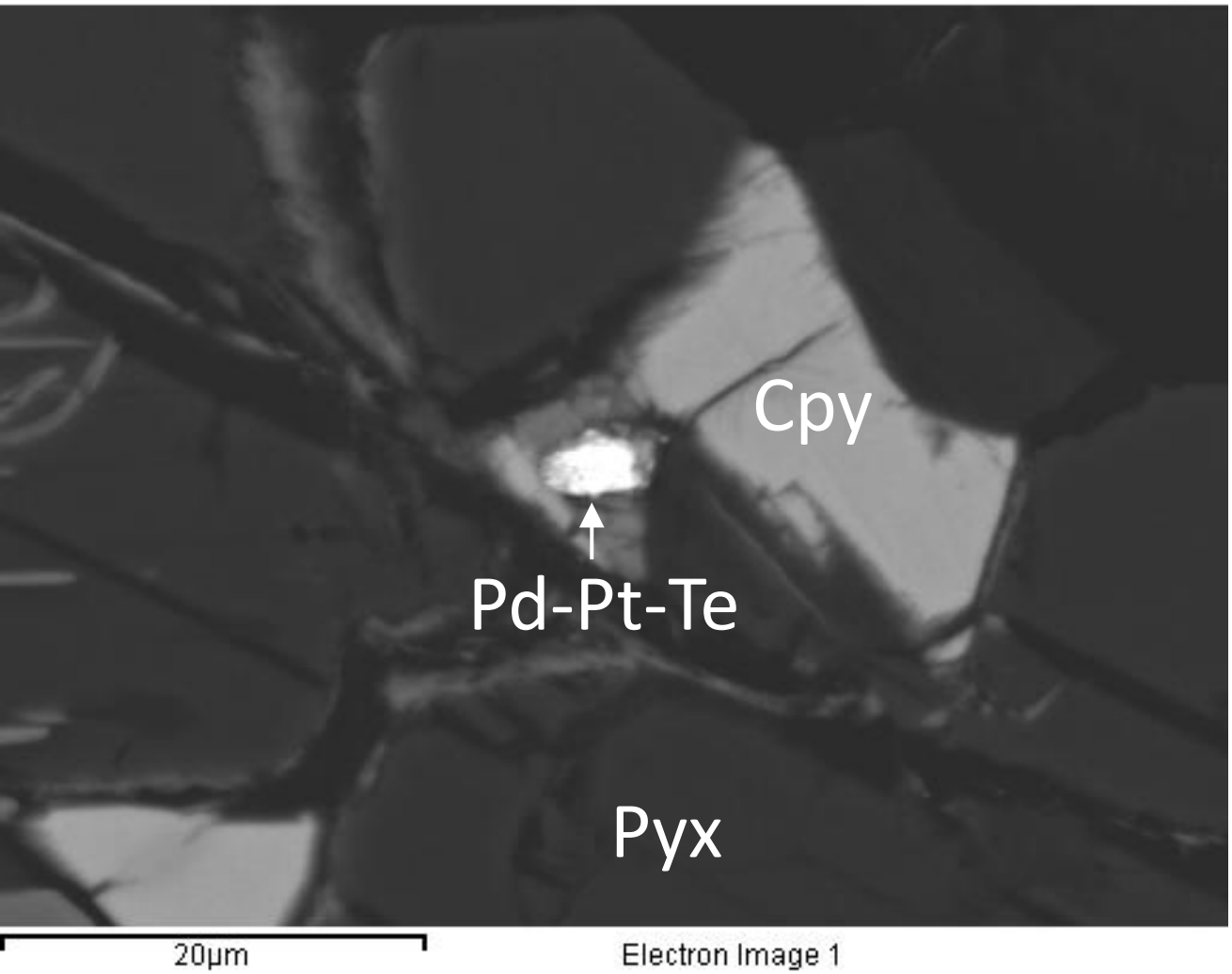
PTSR-46 J 1



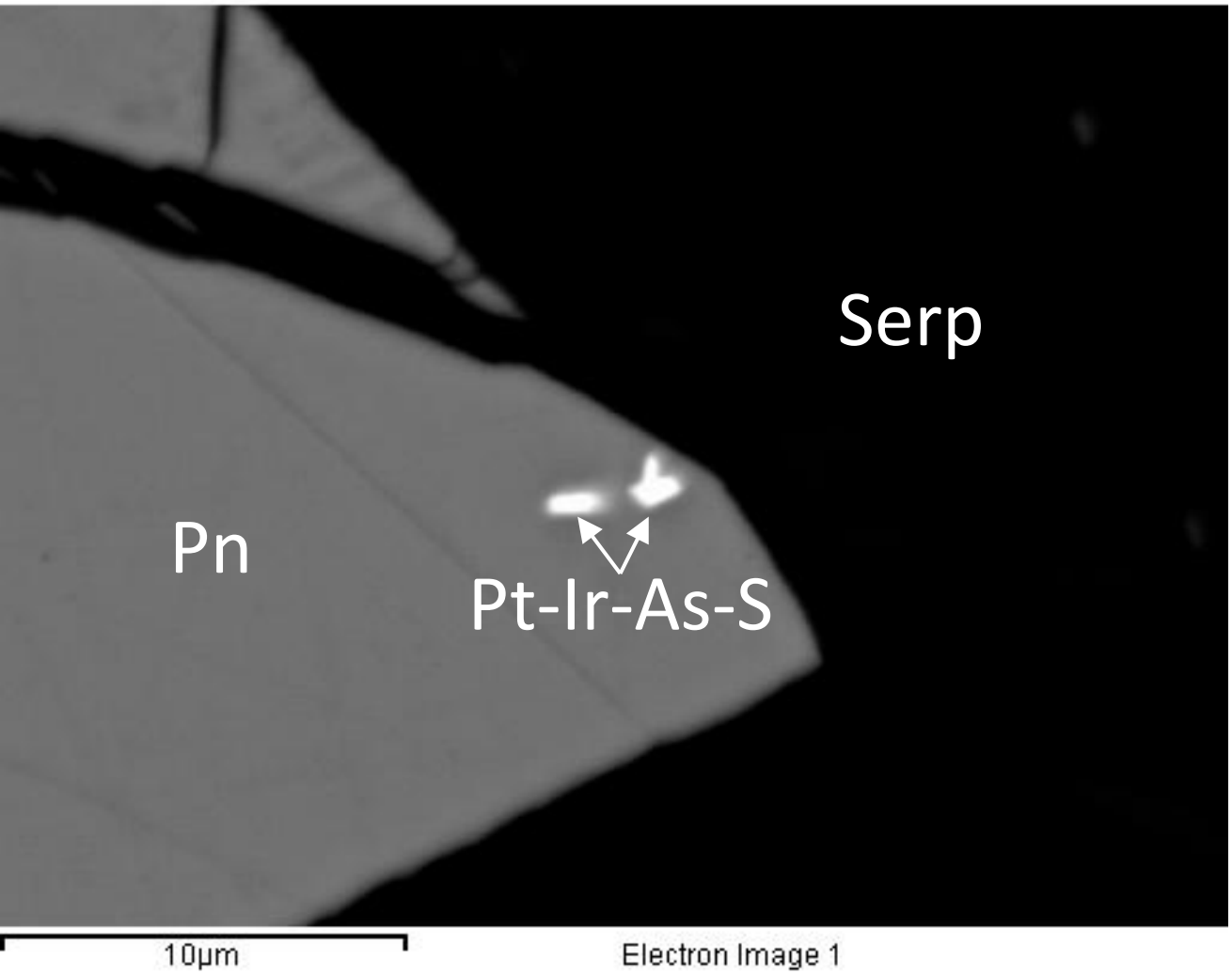
PTSR-46 K 1



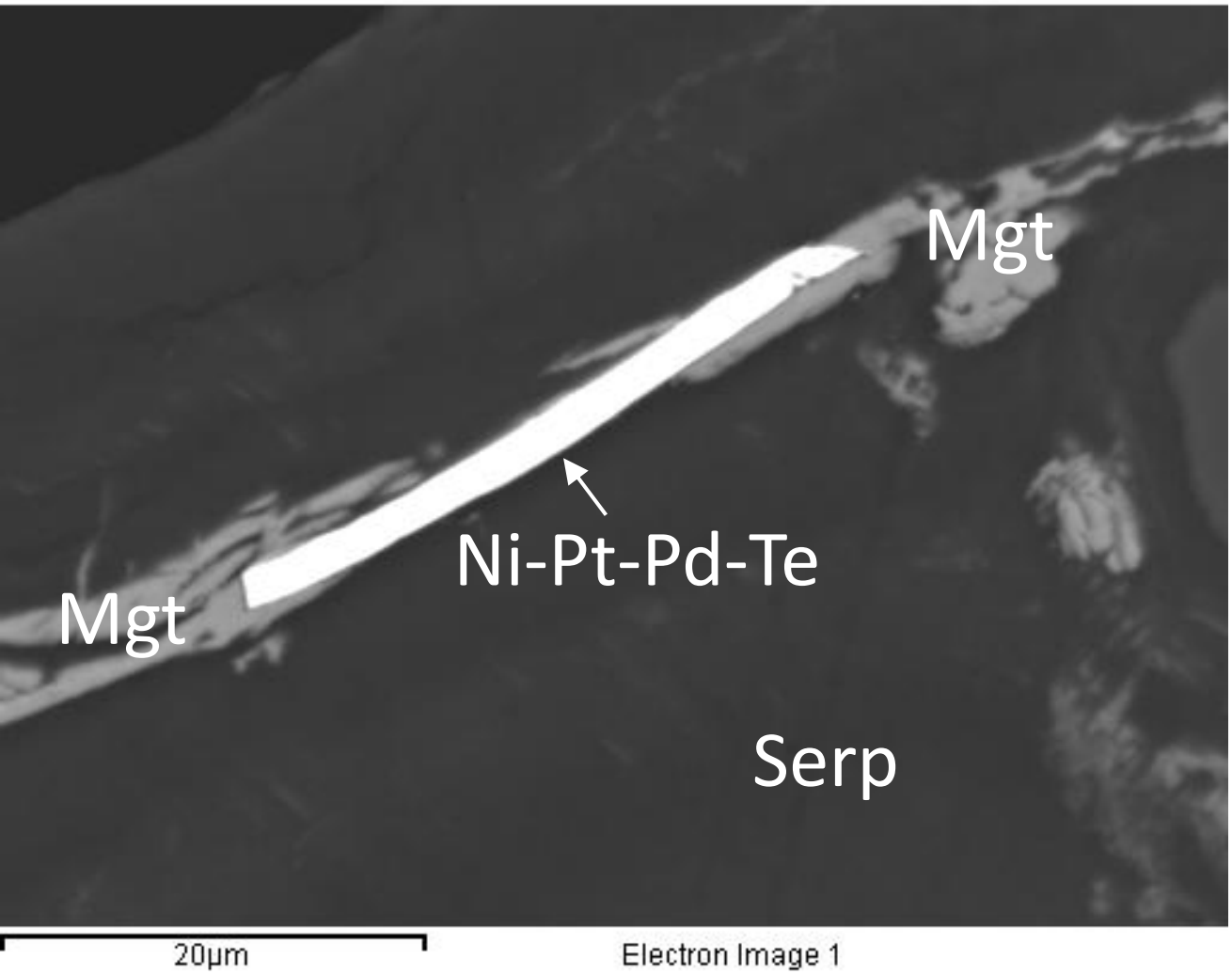
PTSR-46 L 1



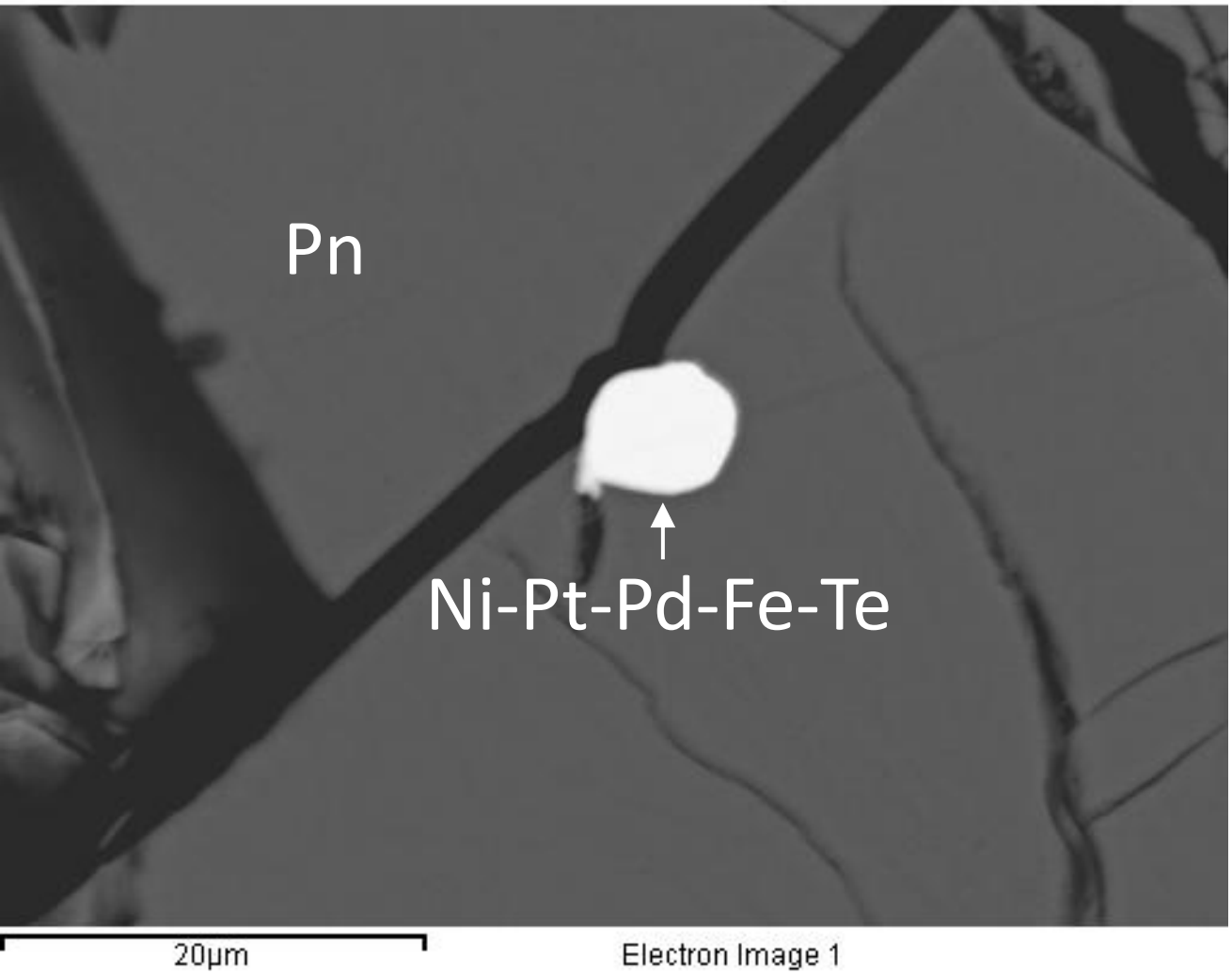
PTSR-46 M 1-2



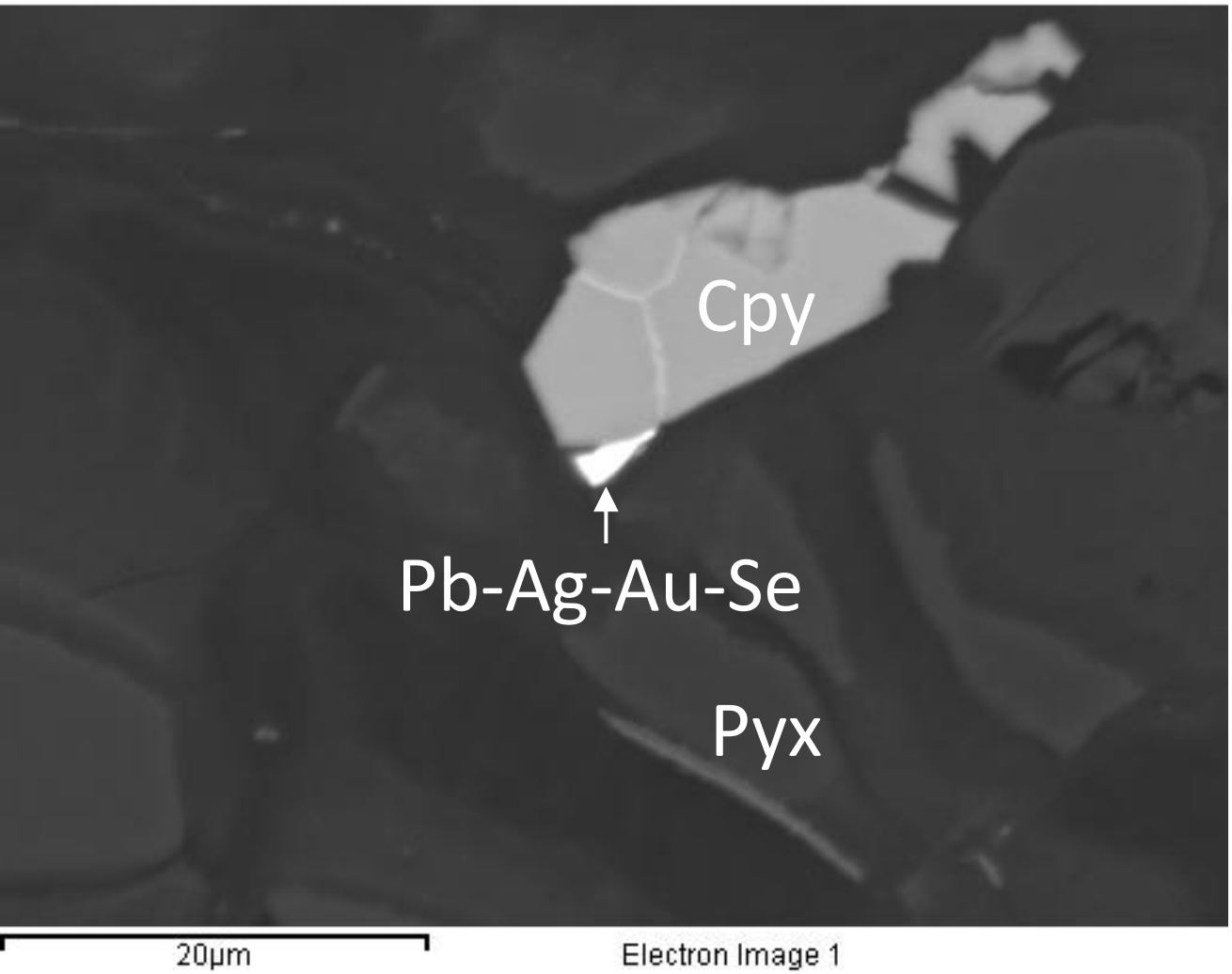
PTSR-47 A 1



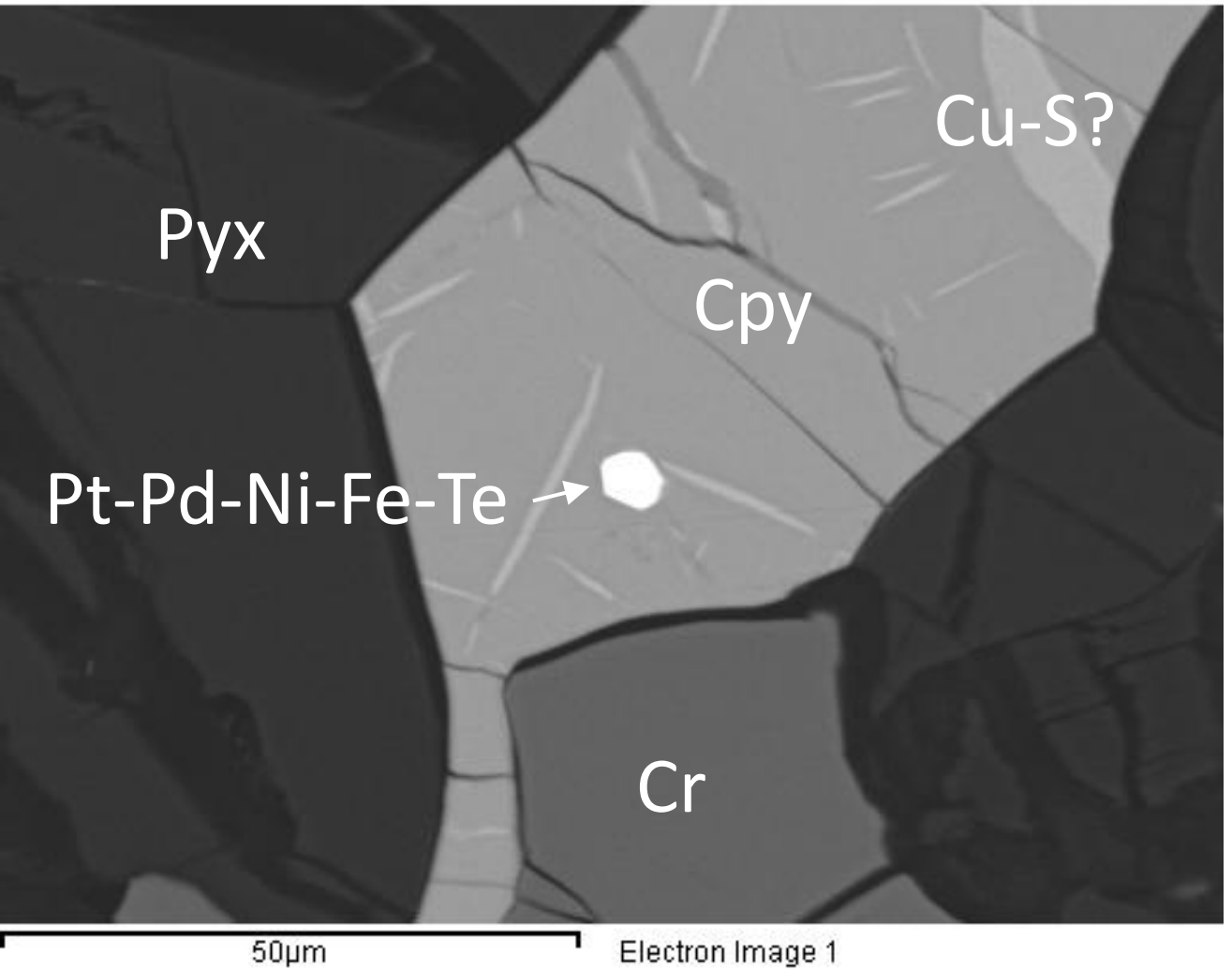
PTSR-47 B 1



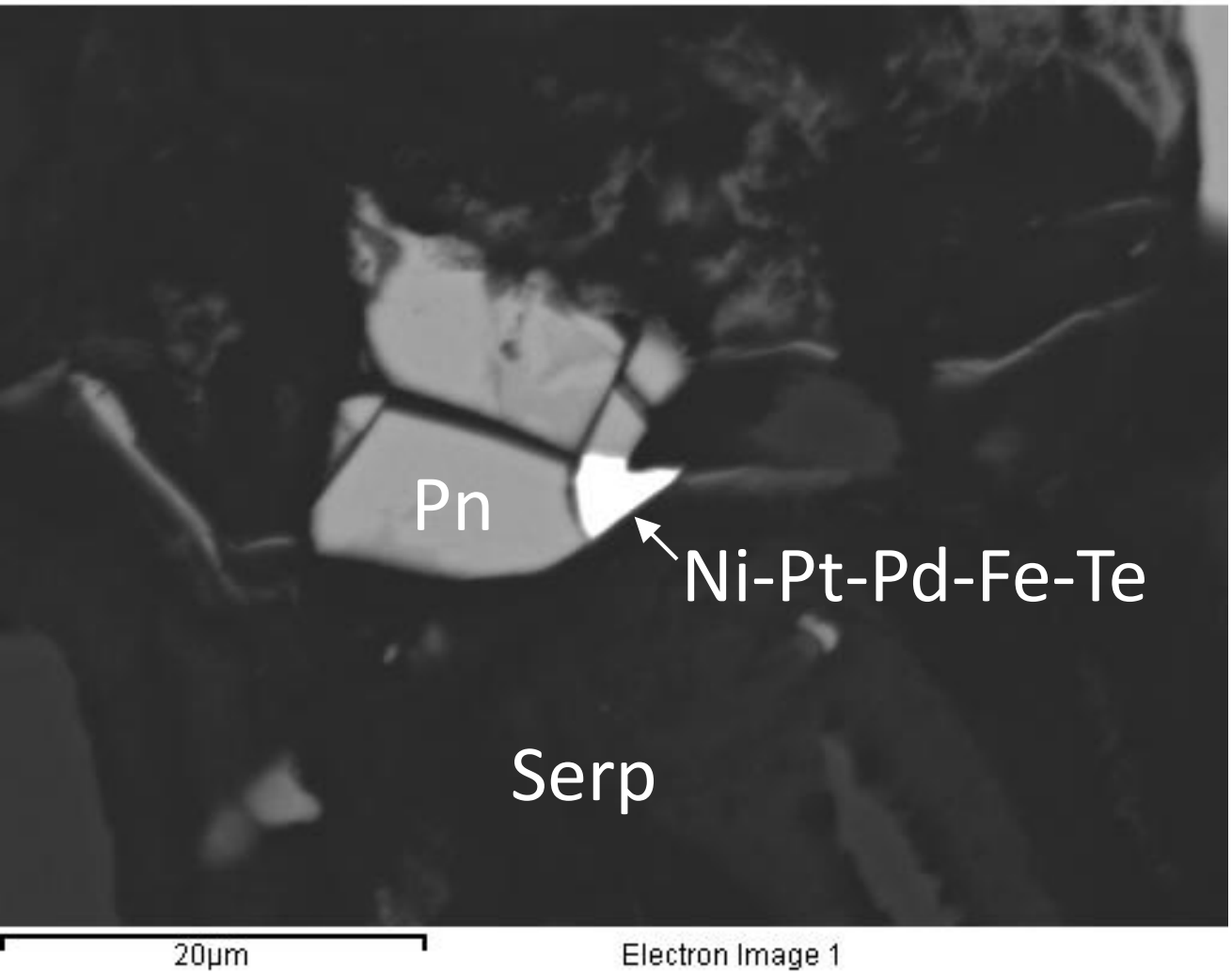
PTSR-47 C 1



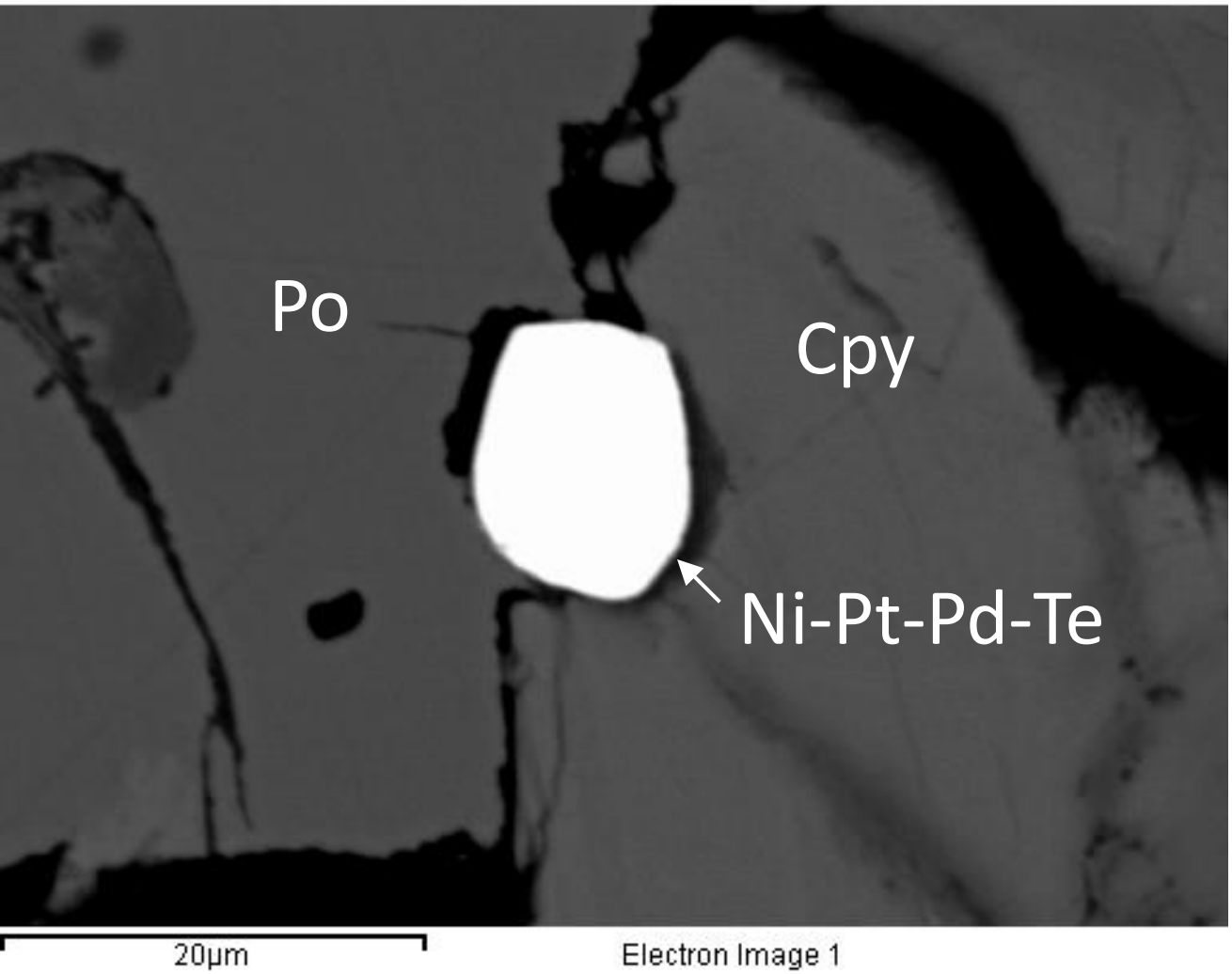
PTSR-47 D 1



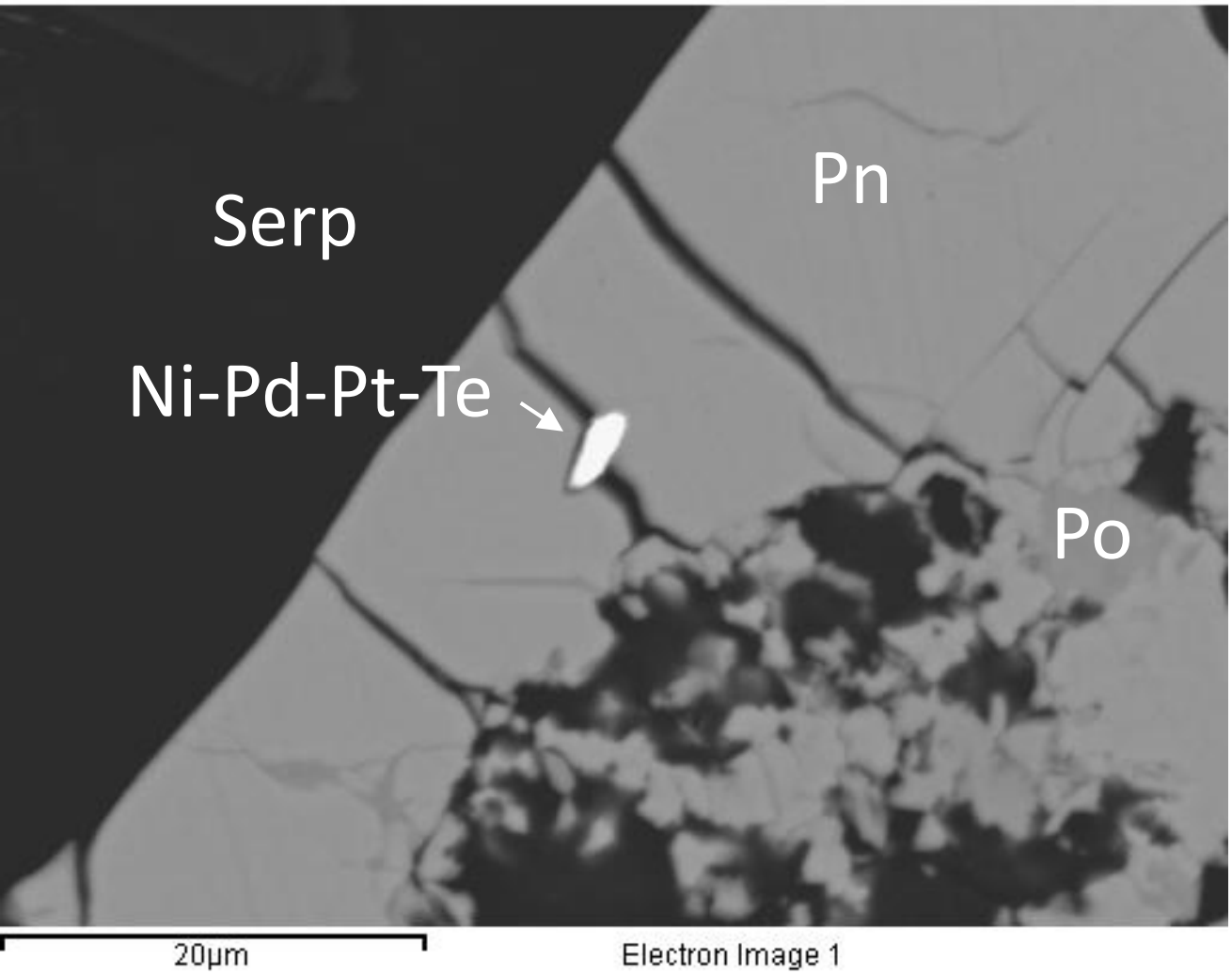
PTSR-47 E 1



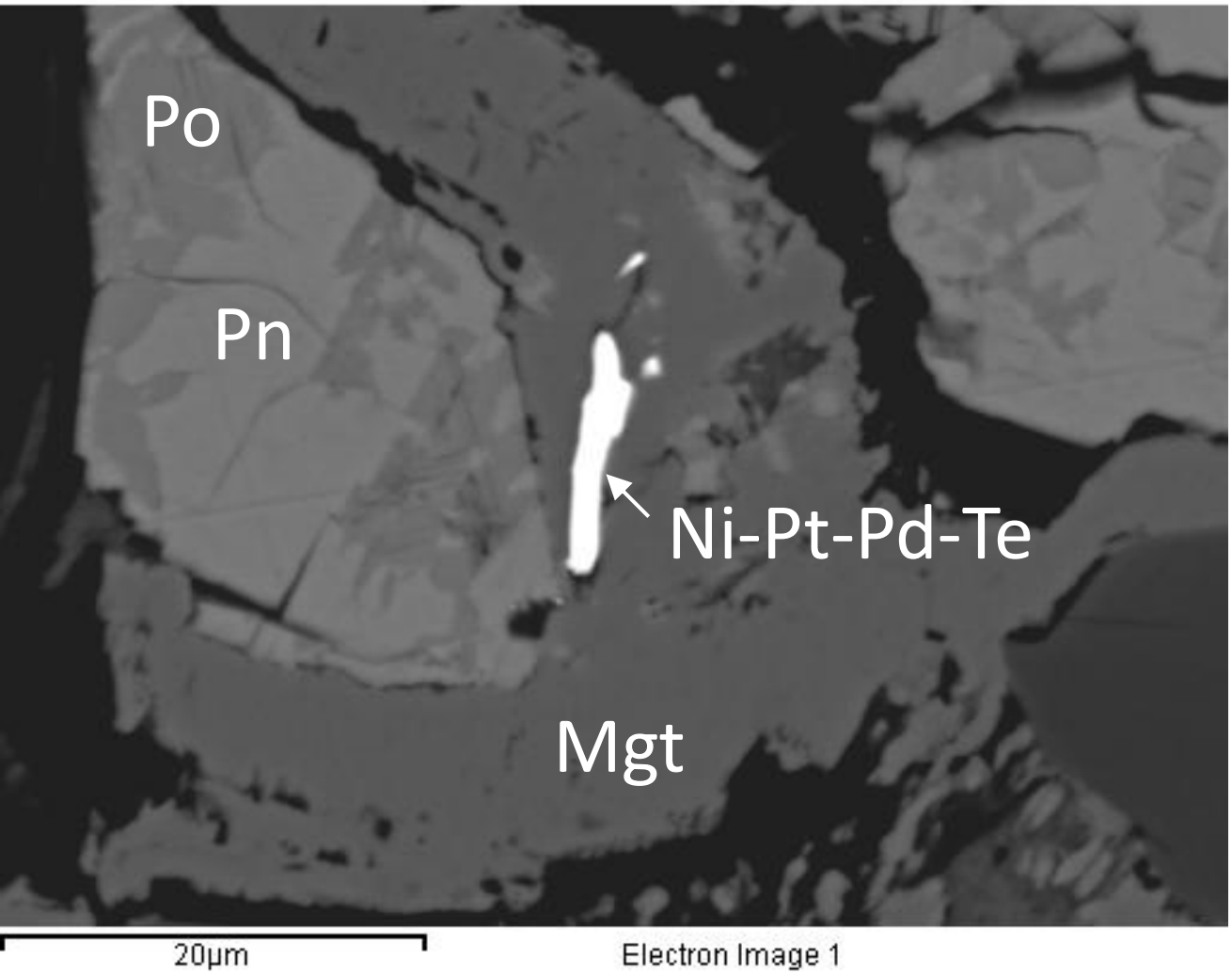
PTSR-47 F 1



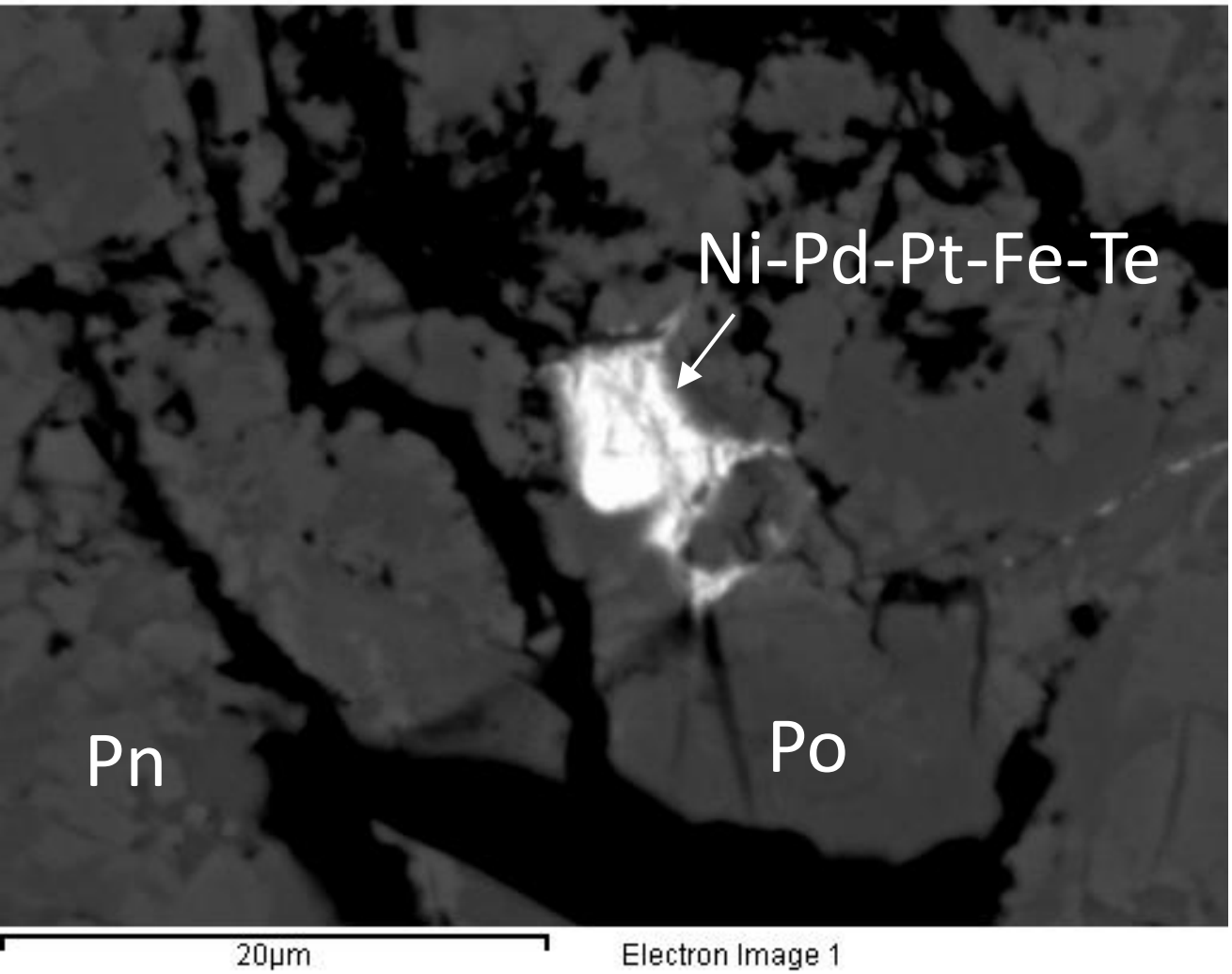
PTSR-47 G 1



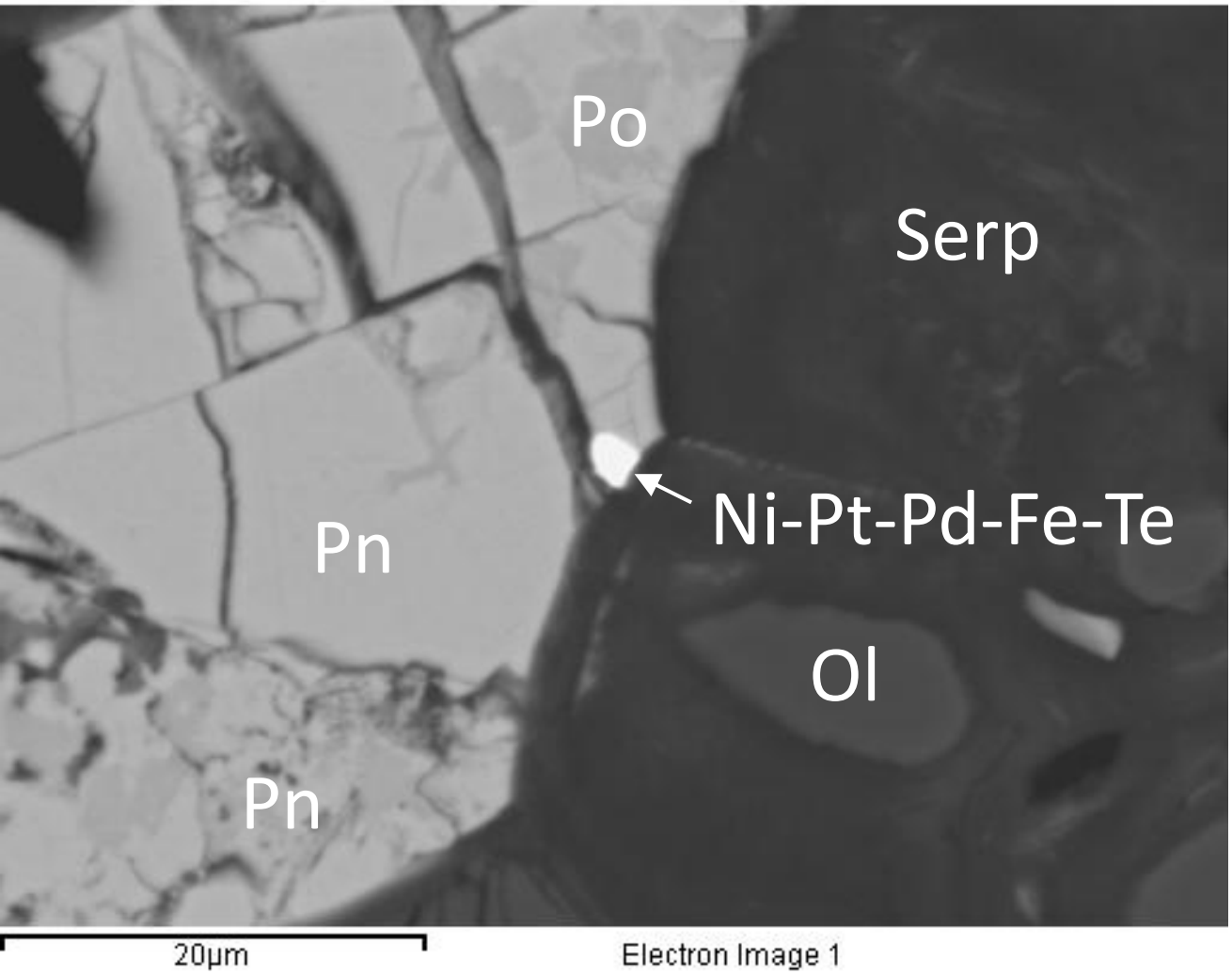
PTSR-47 H 1



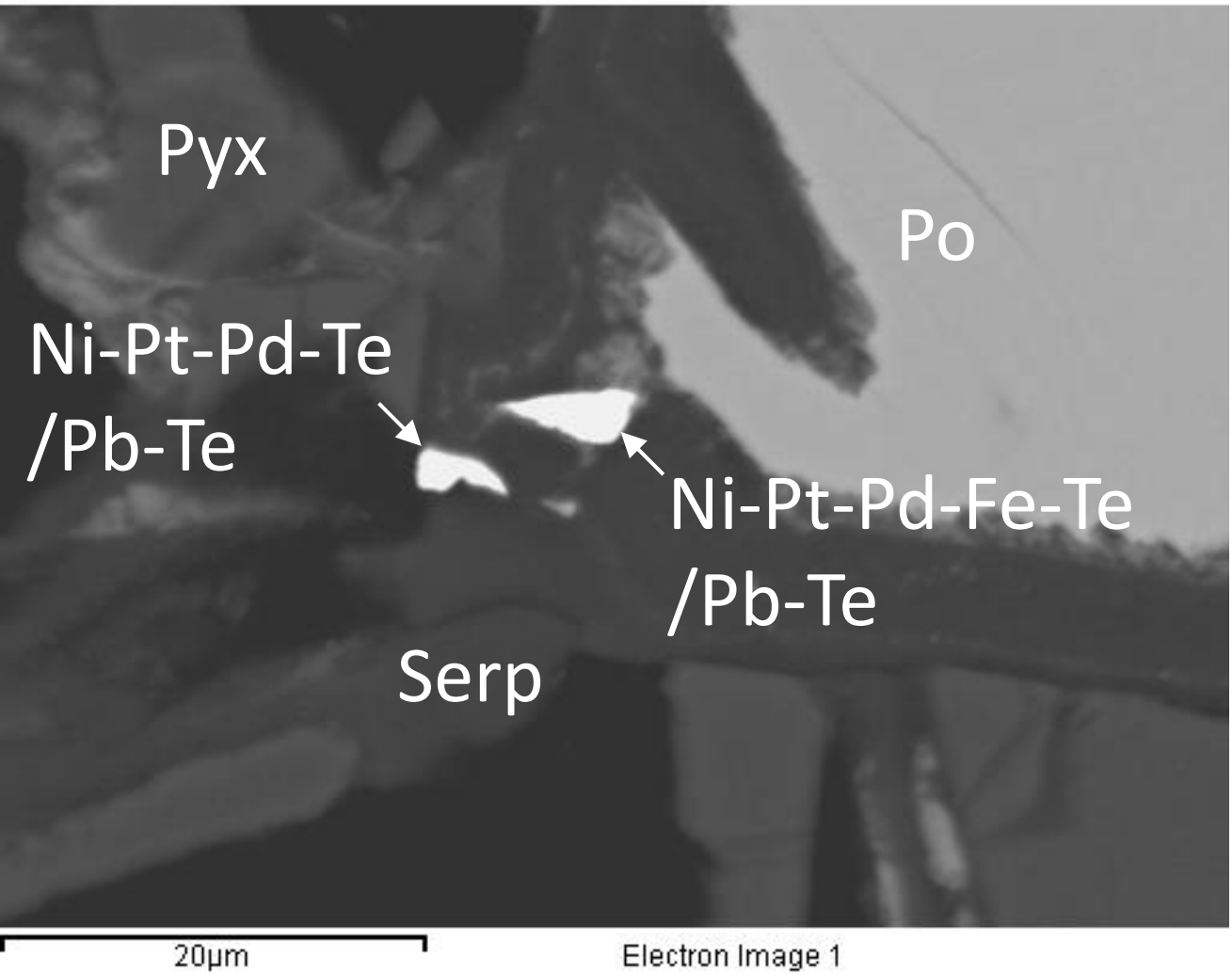
PTSR-47 I 1



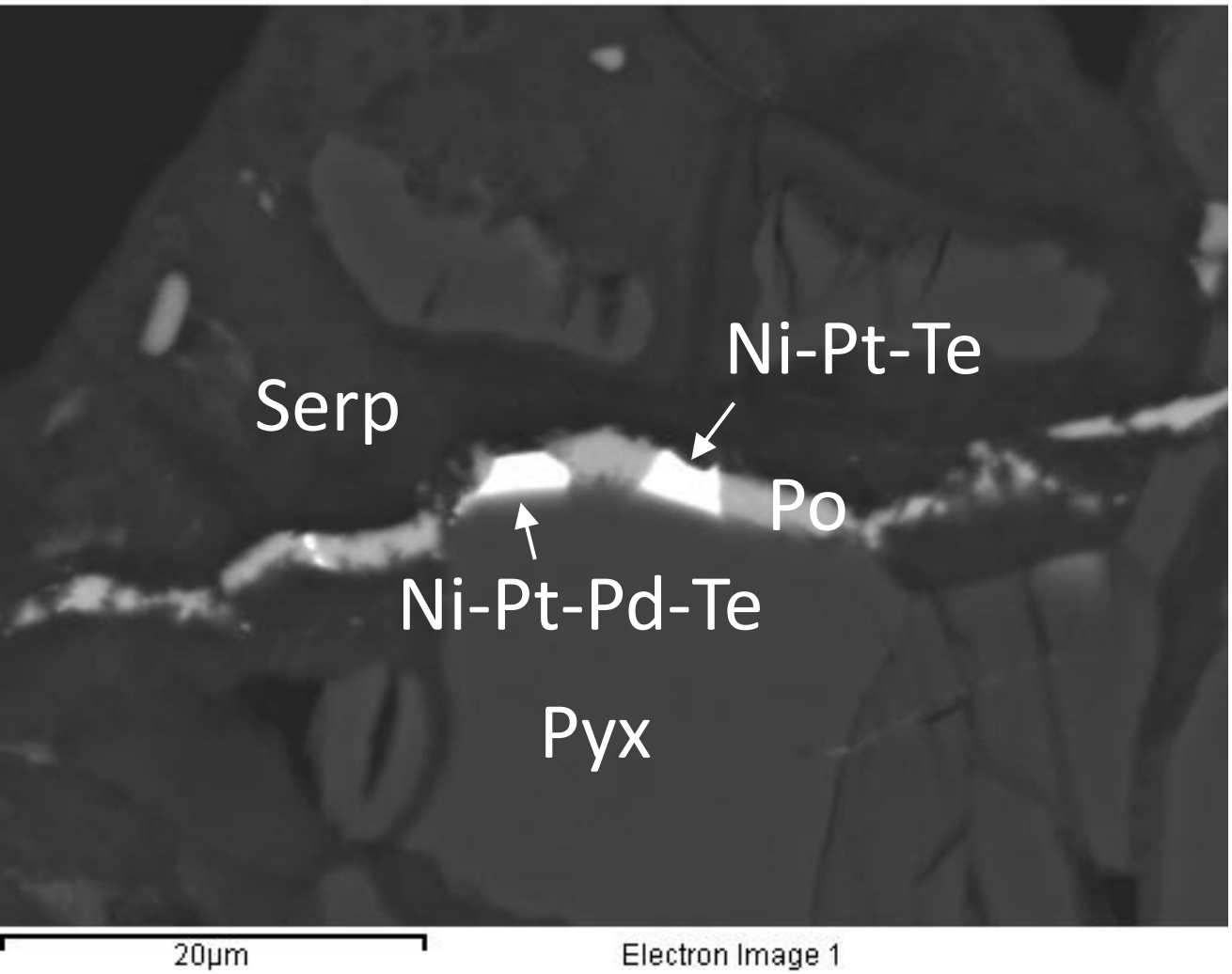
PTSR-47 J 1



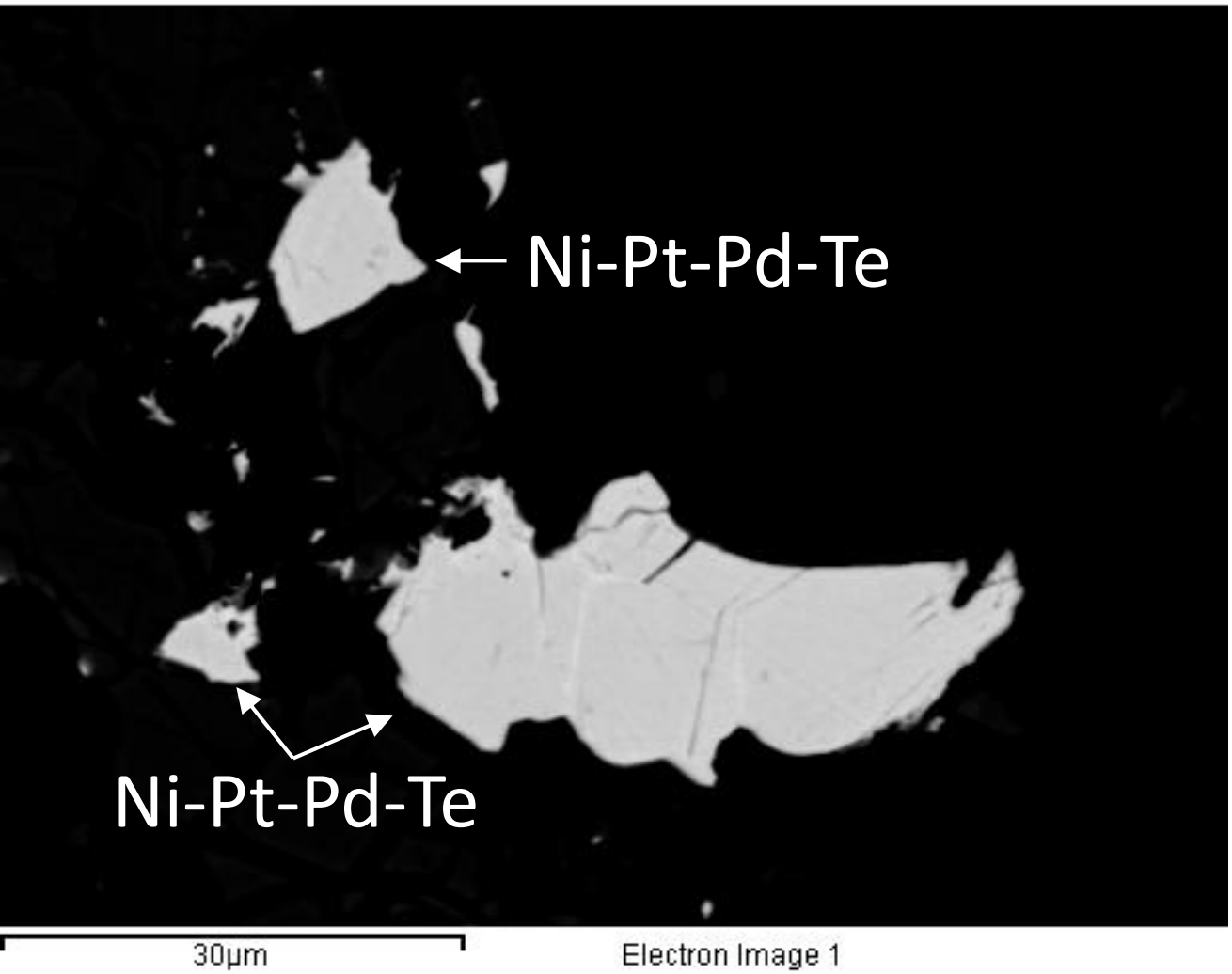
PTSR-47 K 1-2


Pyx
Po
Ni-Pt-Pd-Te
/Pb-Te
Ni-Pt-Pd-Fe-Te
/Pb-Te
Serp
20µm
Electron Image 1

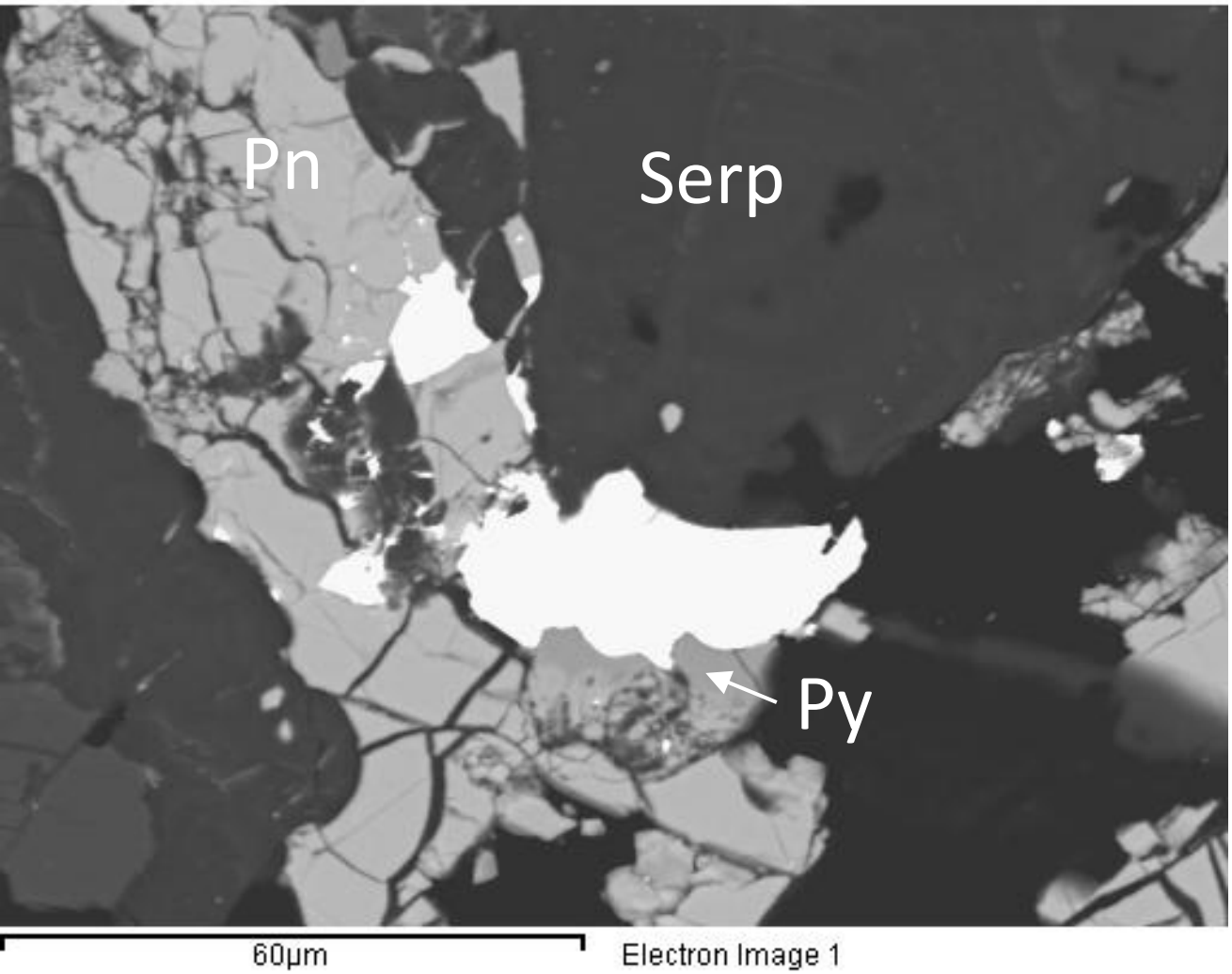
PTSR-47 L 1-2



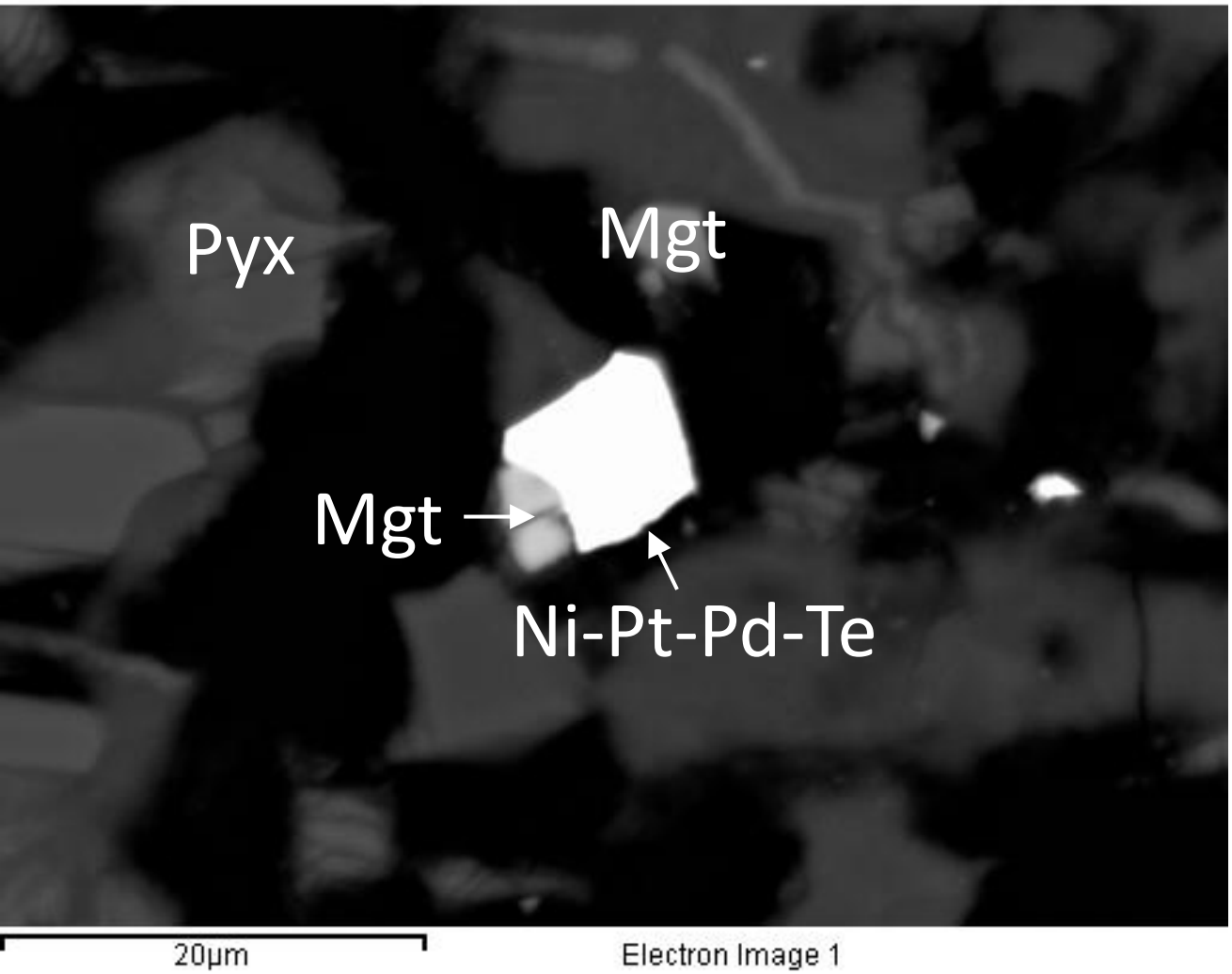
PTSR-47 M 1-3+



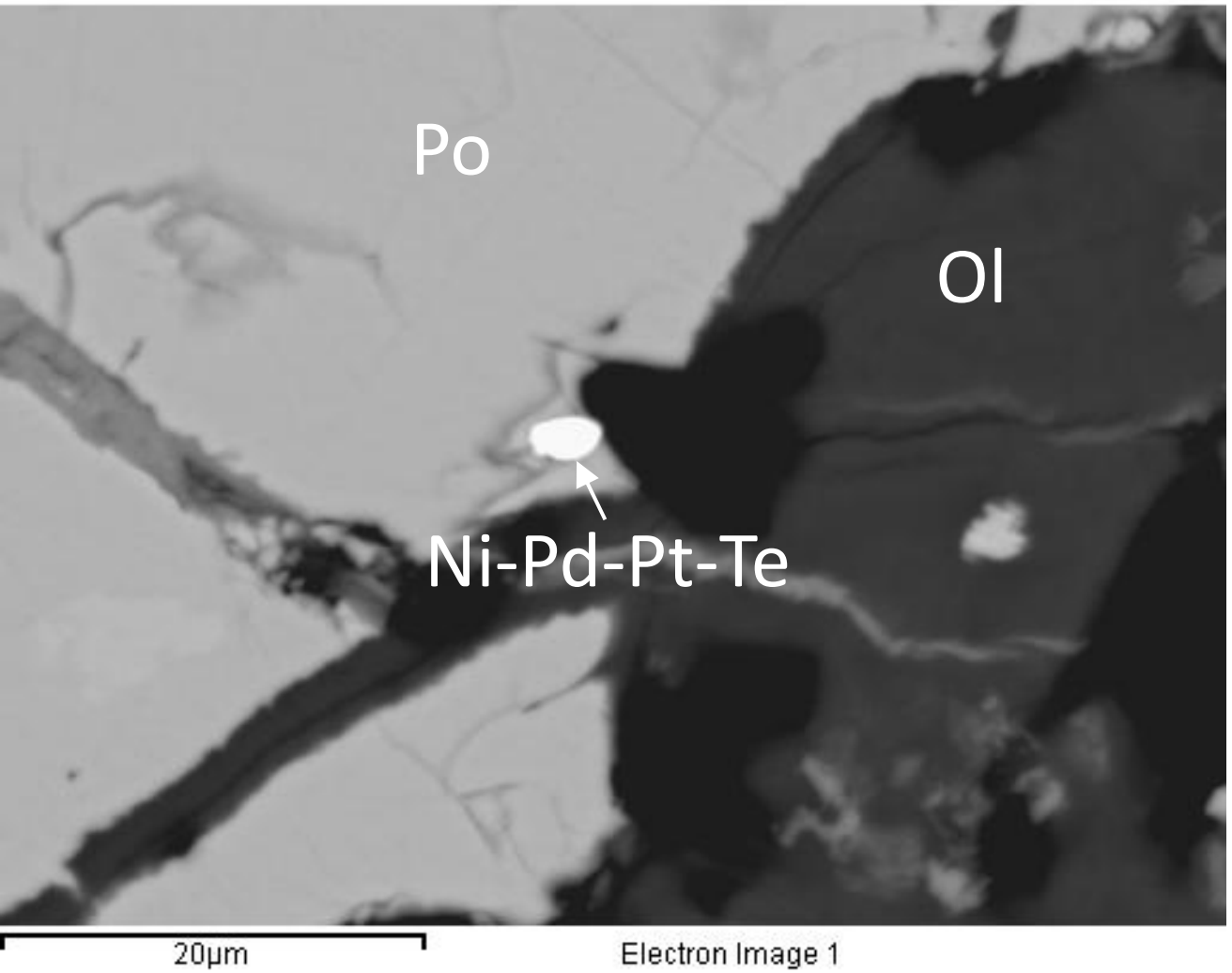
PTSR-47 M 1-3+ Light



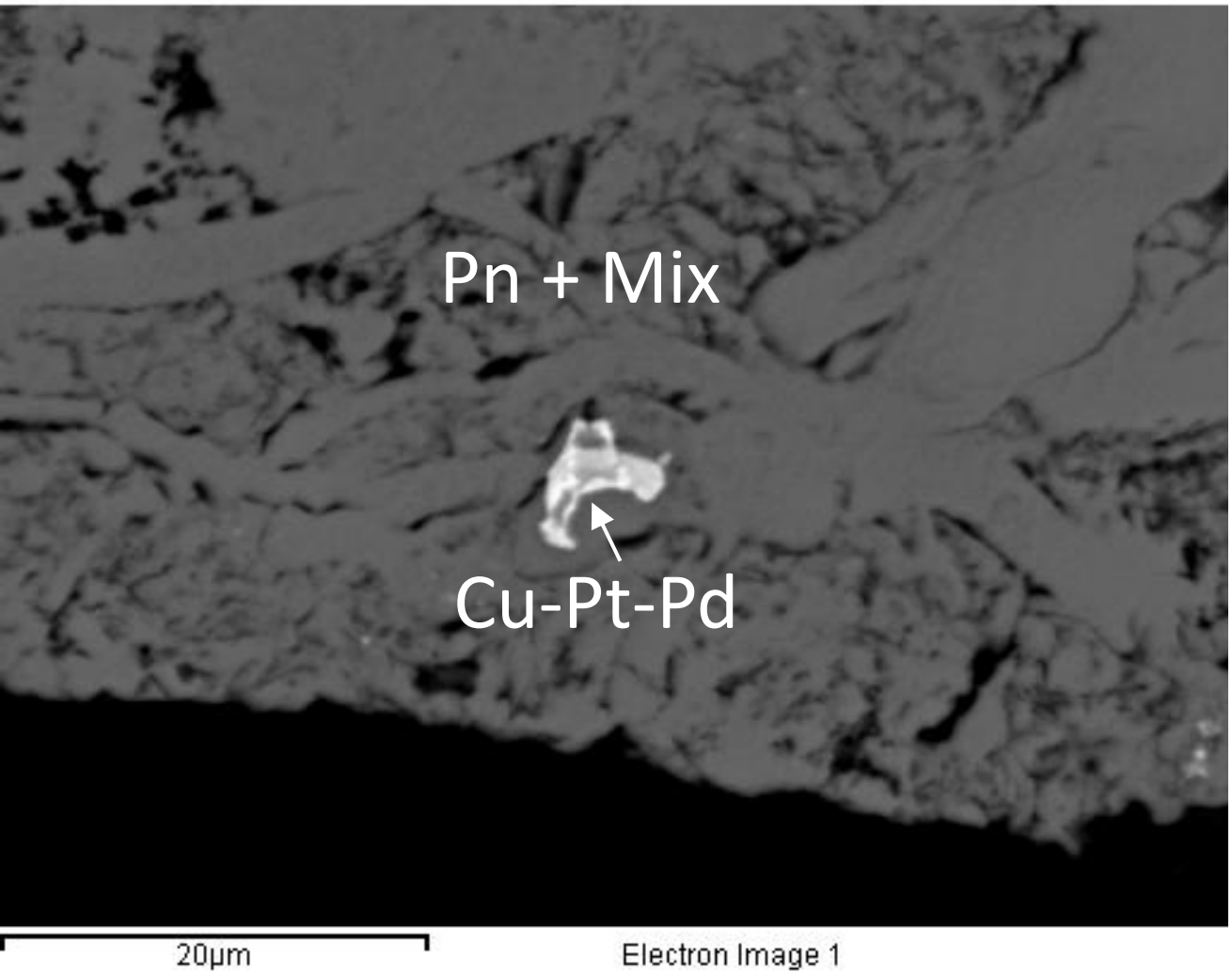
PTSR-47 N 1



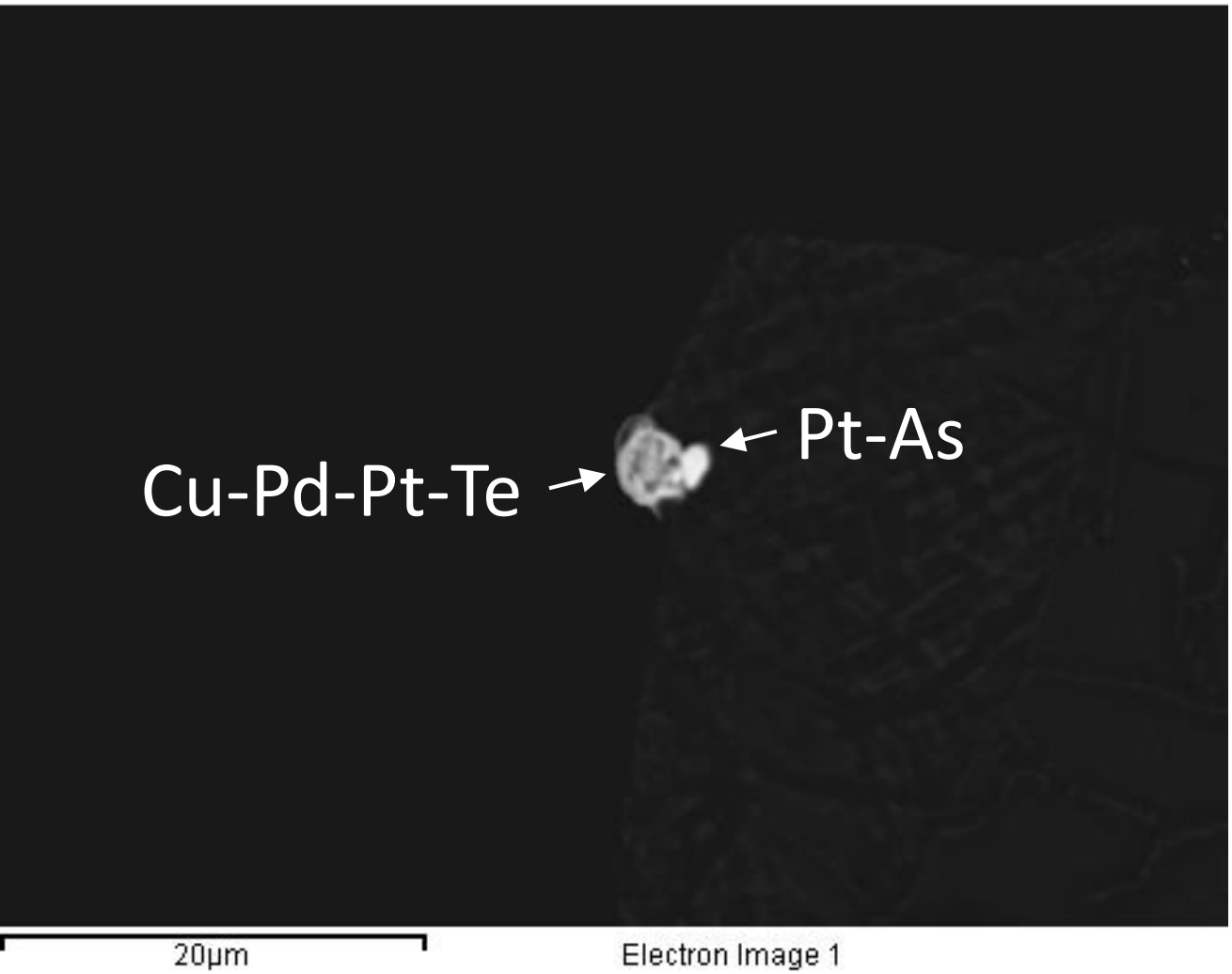
PTSR-47 O 1



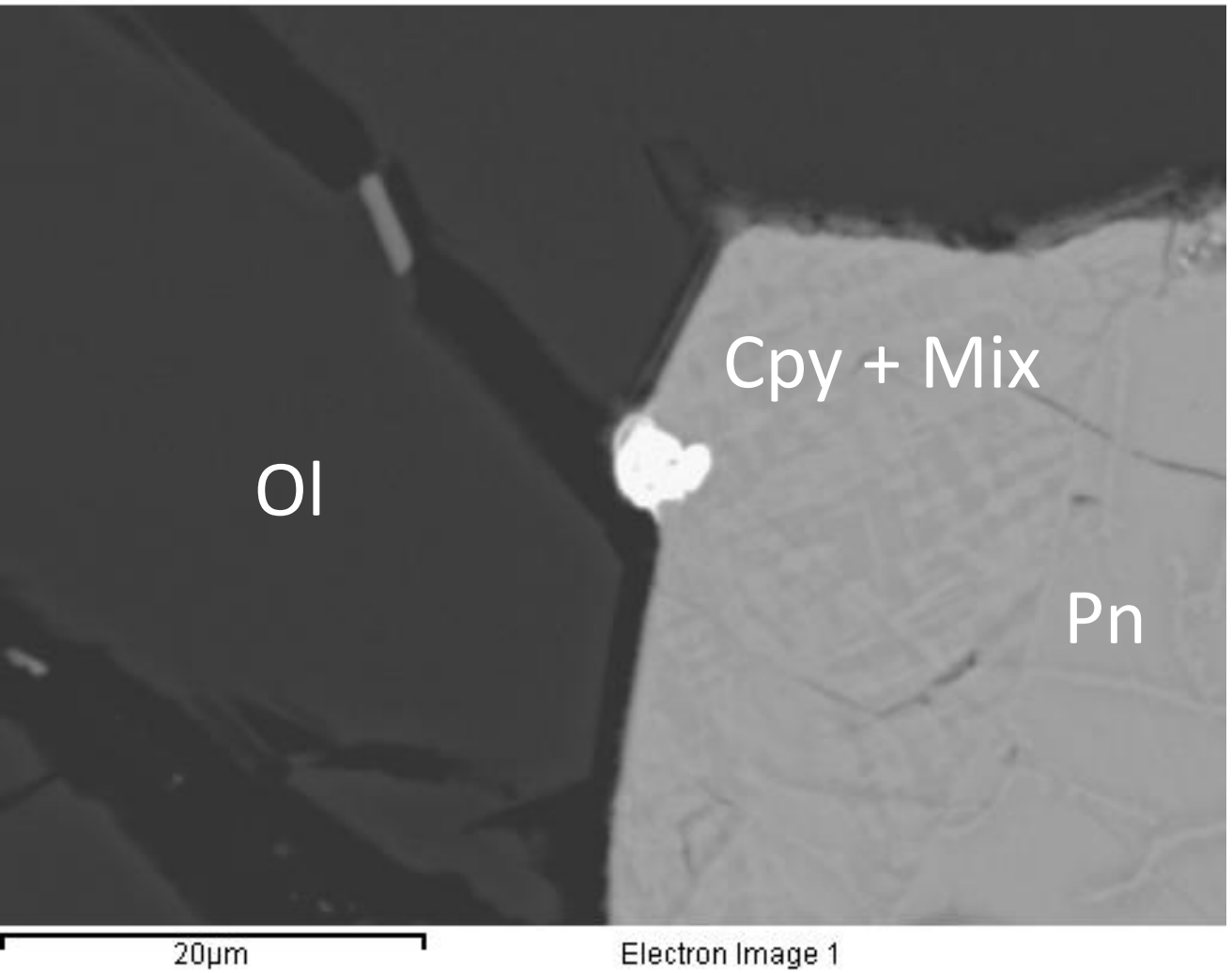
PTSR-48 A 1



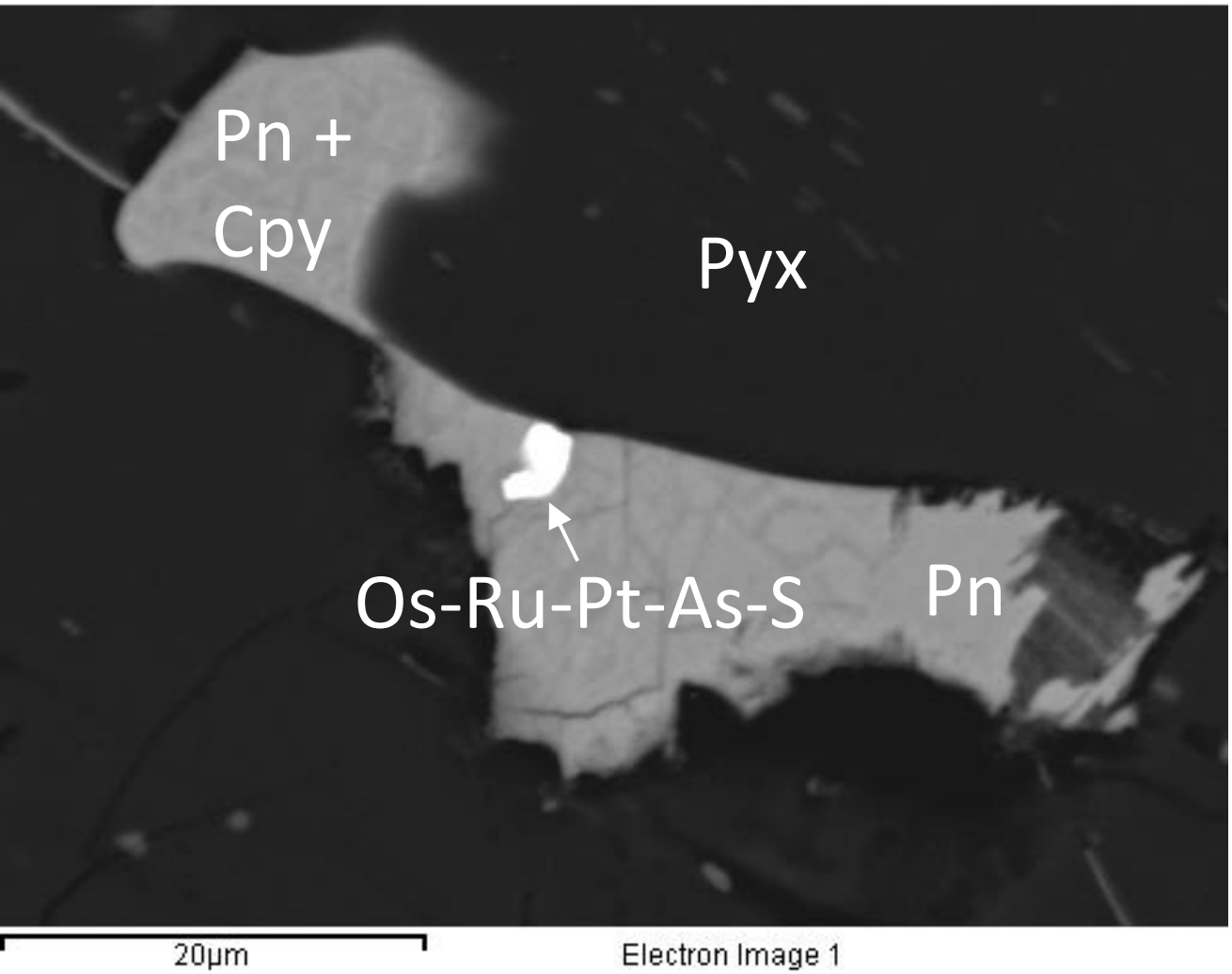
PTSR-48 B 1-2



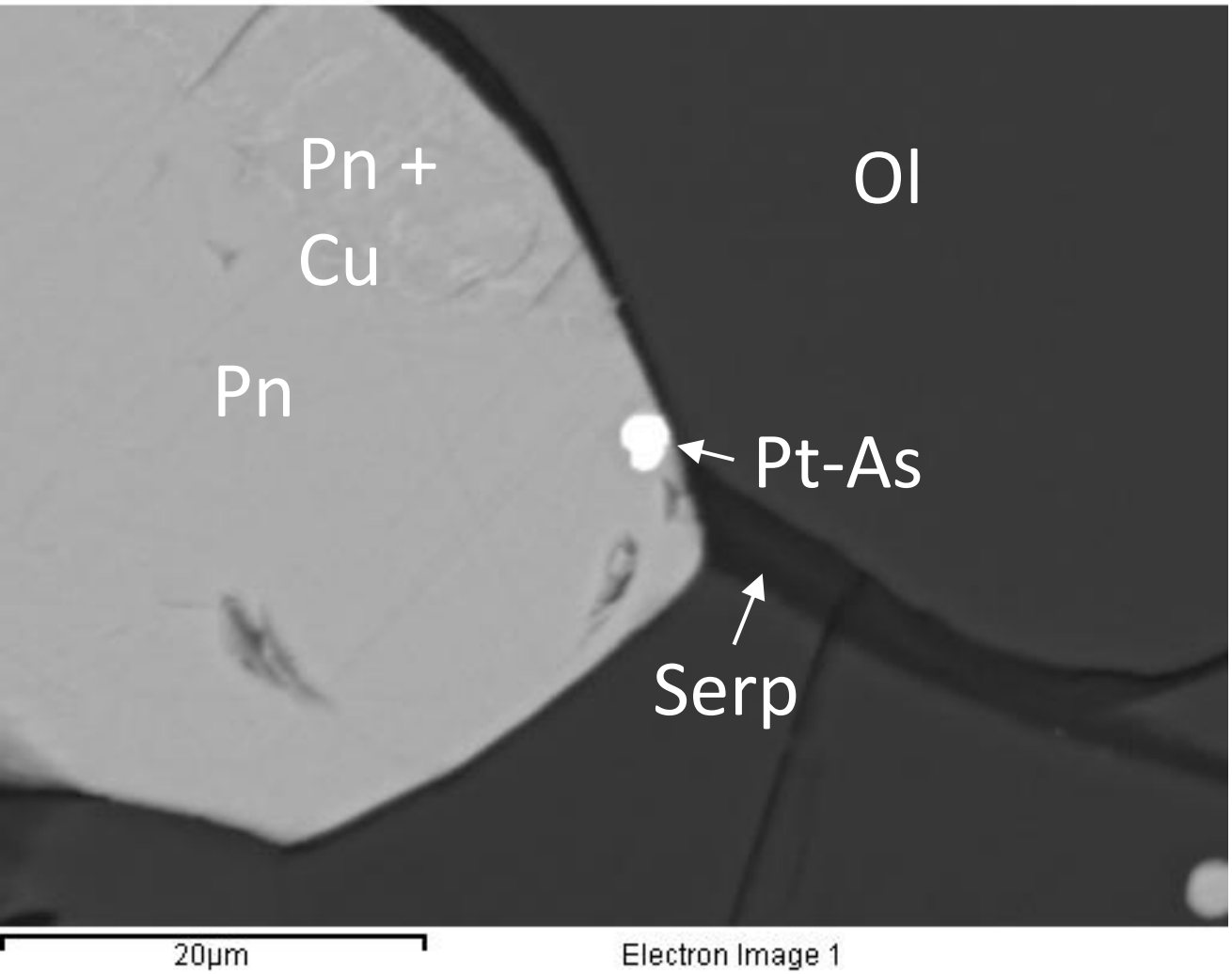
PTSR-48 B 1-2 Light



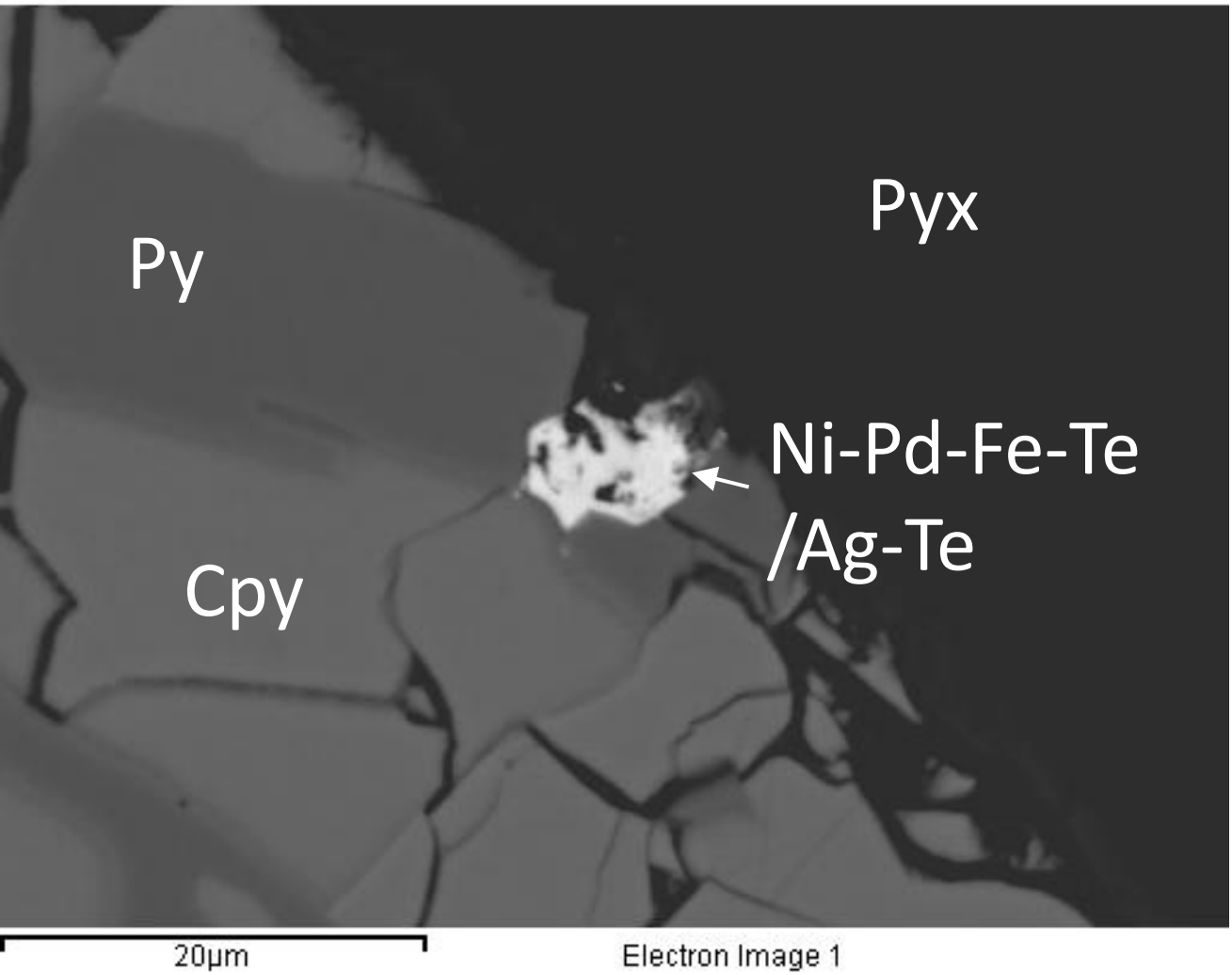
PTSR-48 C 1



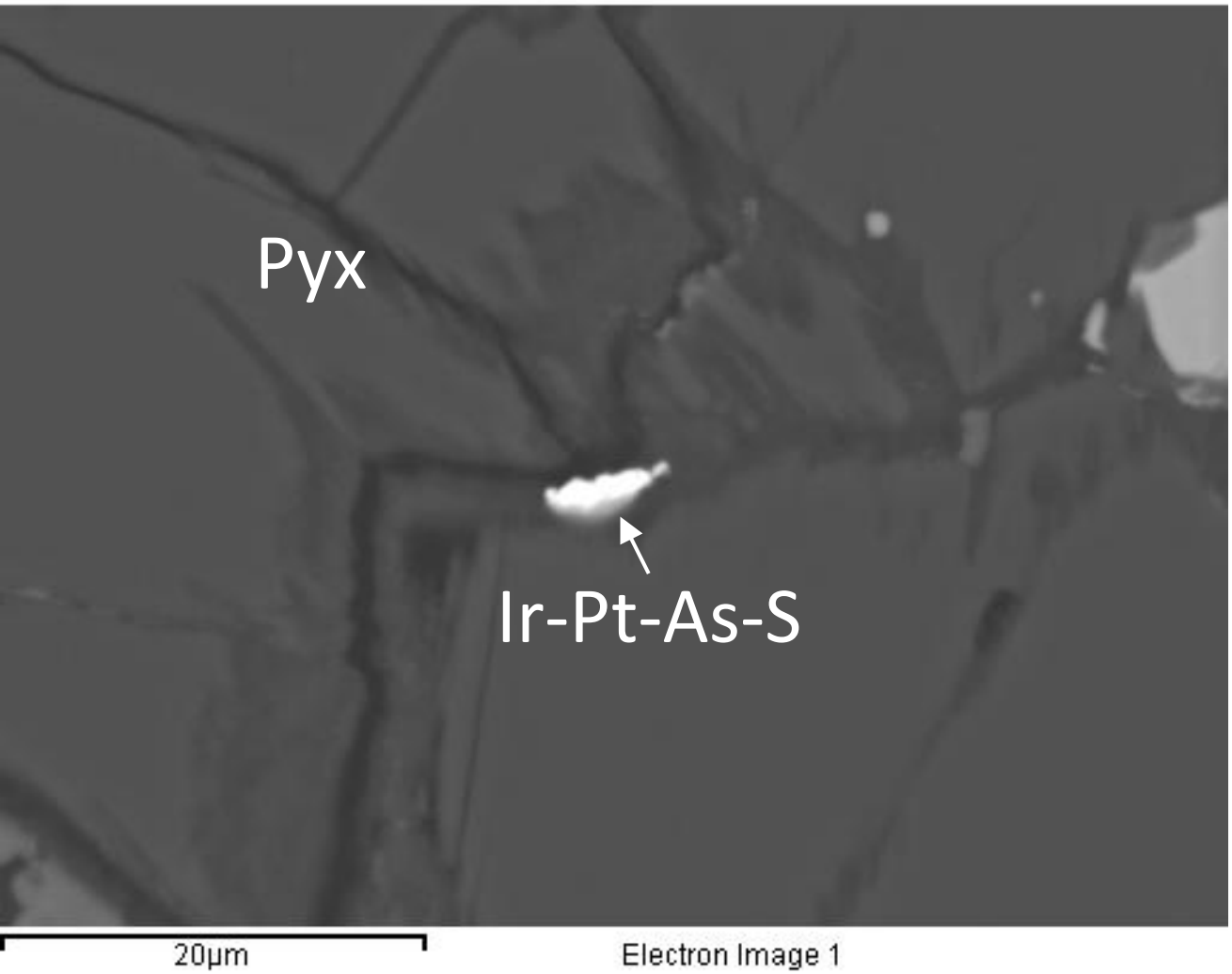
PTSR-48 D 1



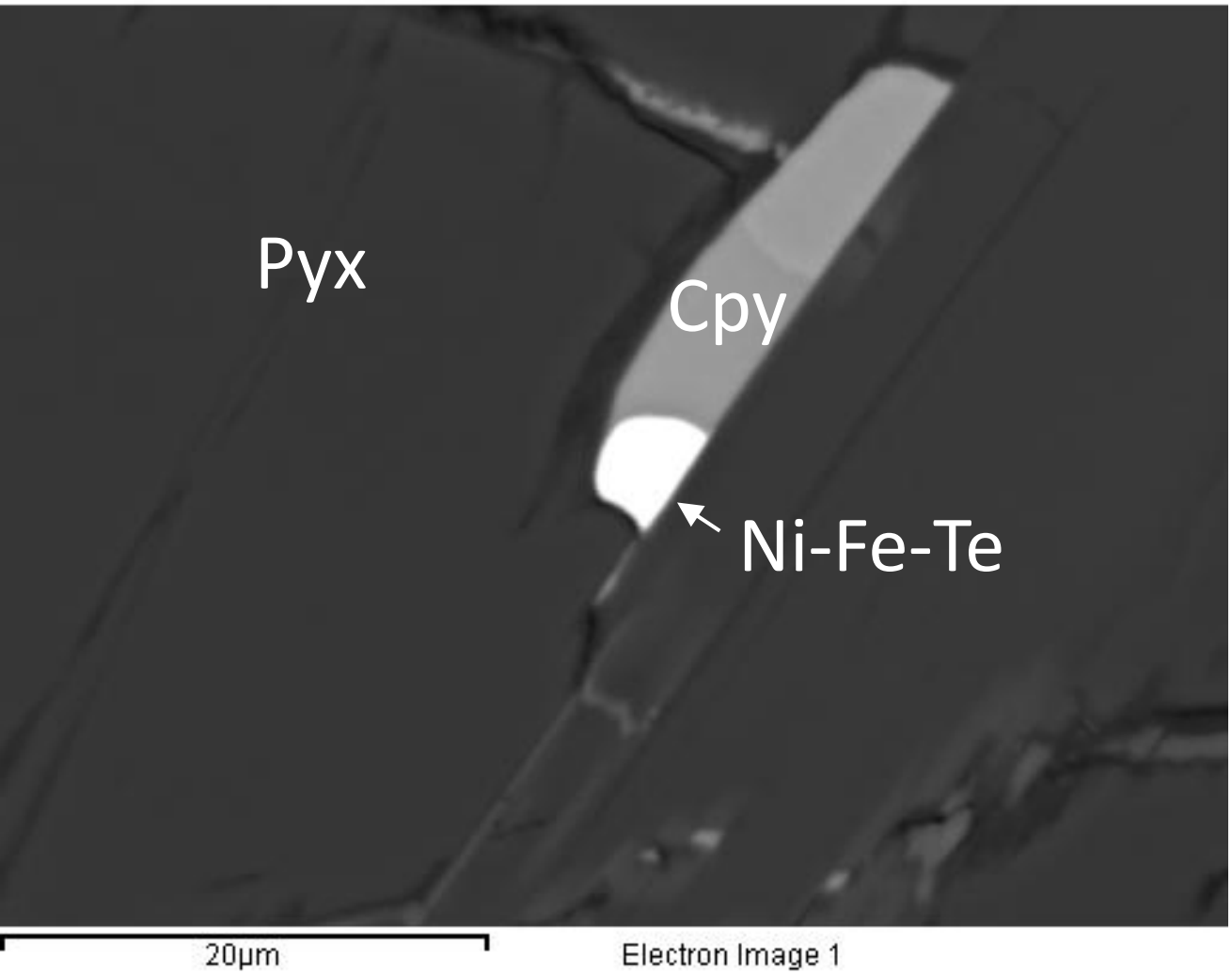
PTSR-51 A 1



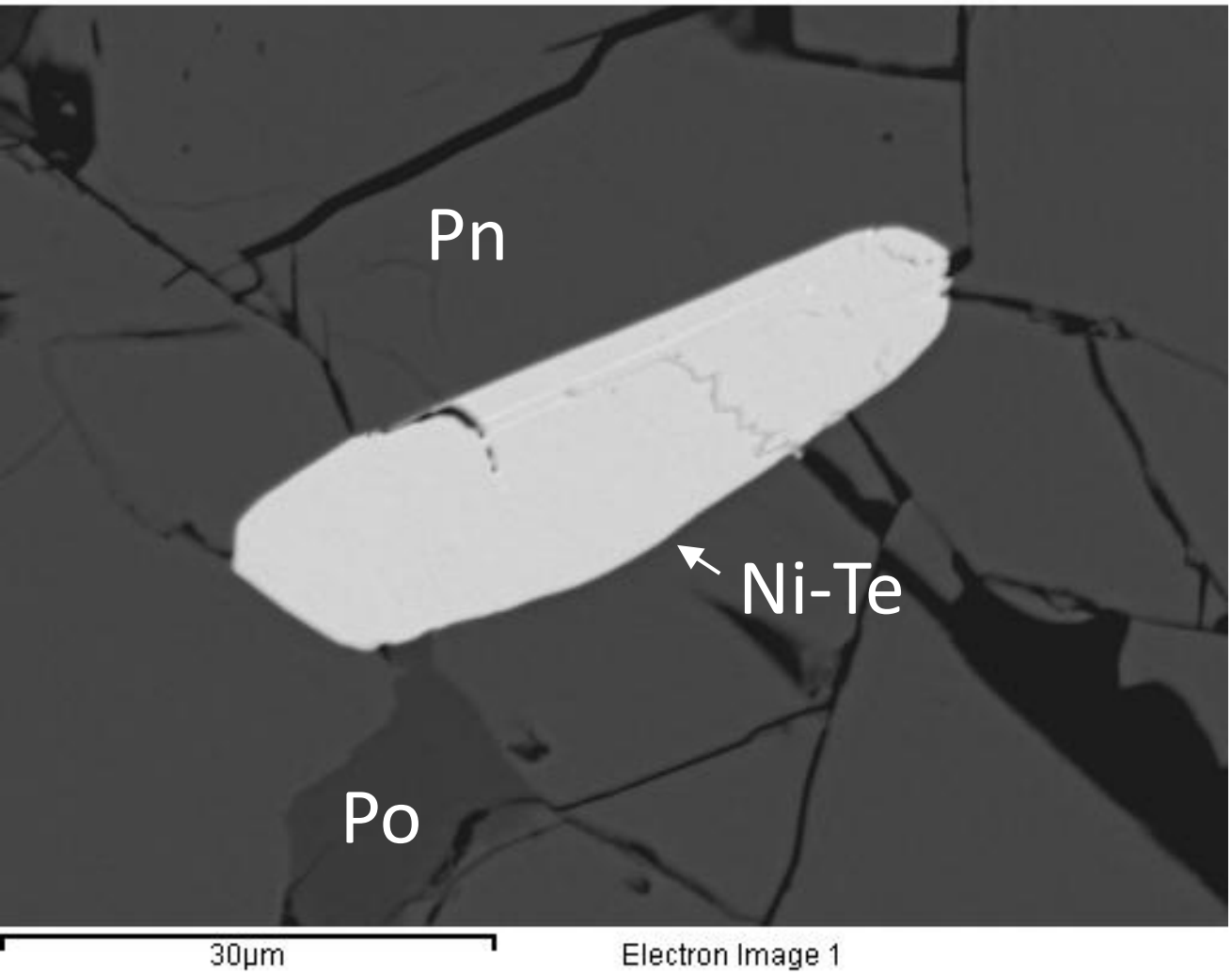
PTSR-51 B 1



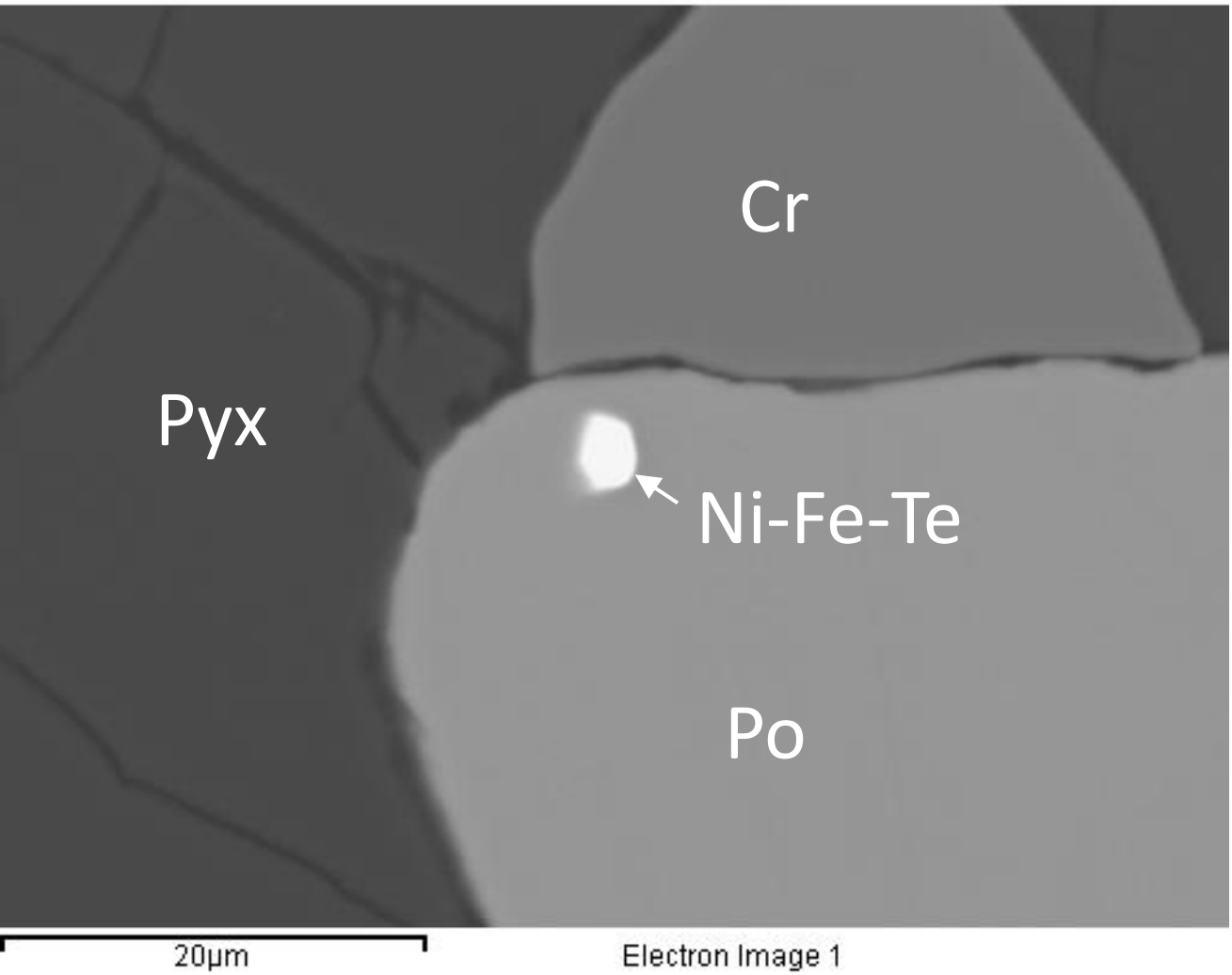
PTSR-51 C 1



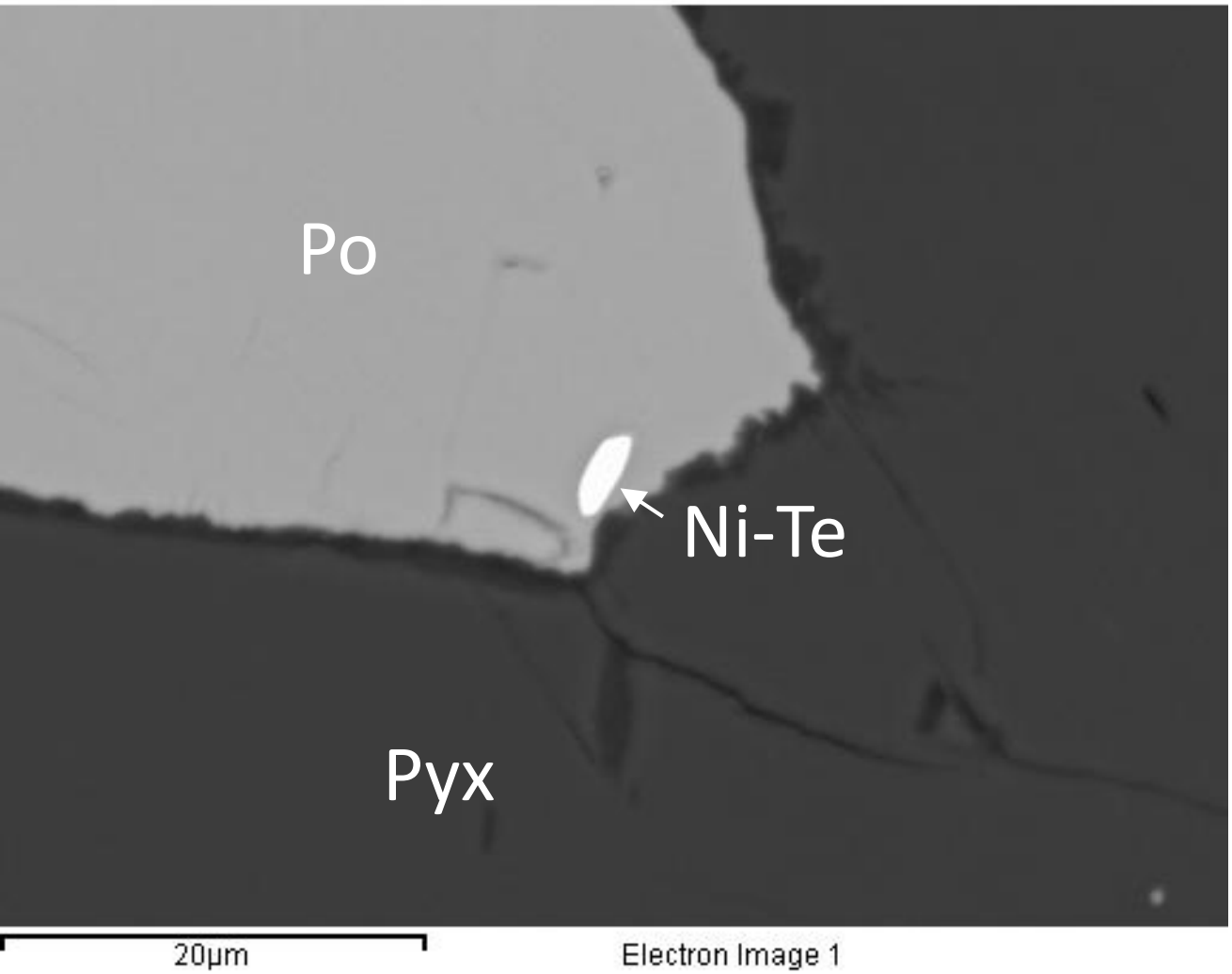
PTSR-51 D 1



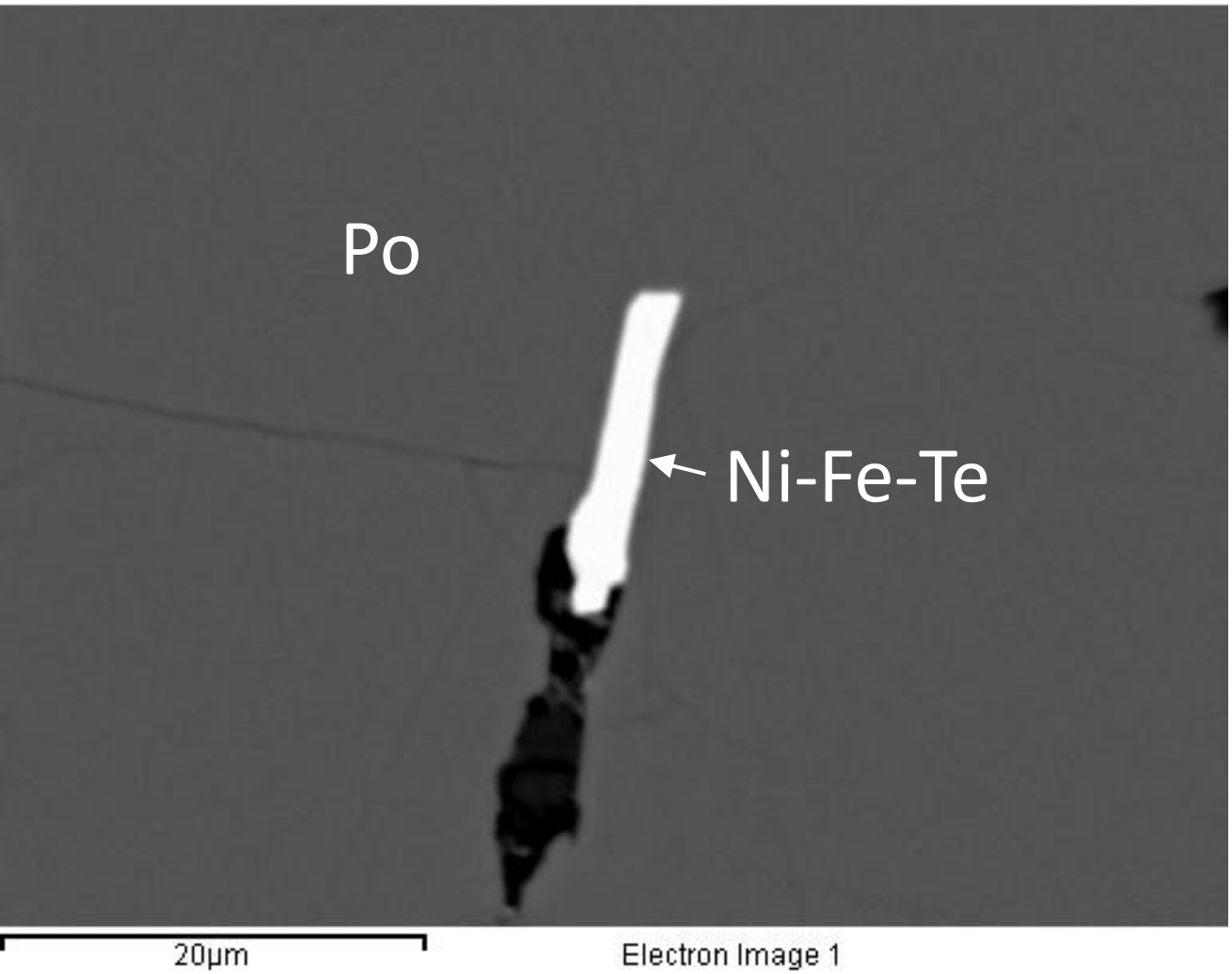
PTSR-51 E 1



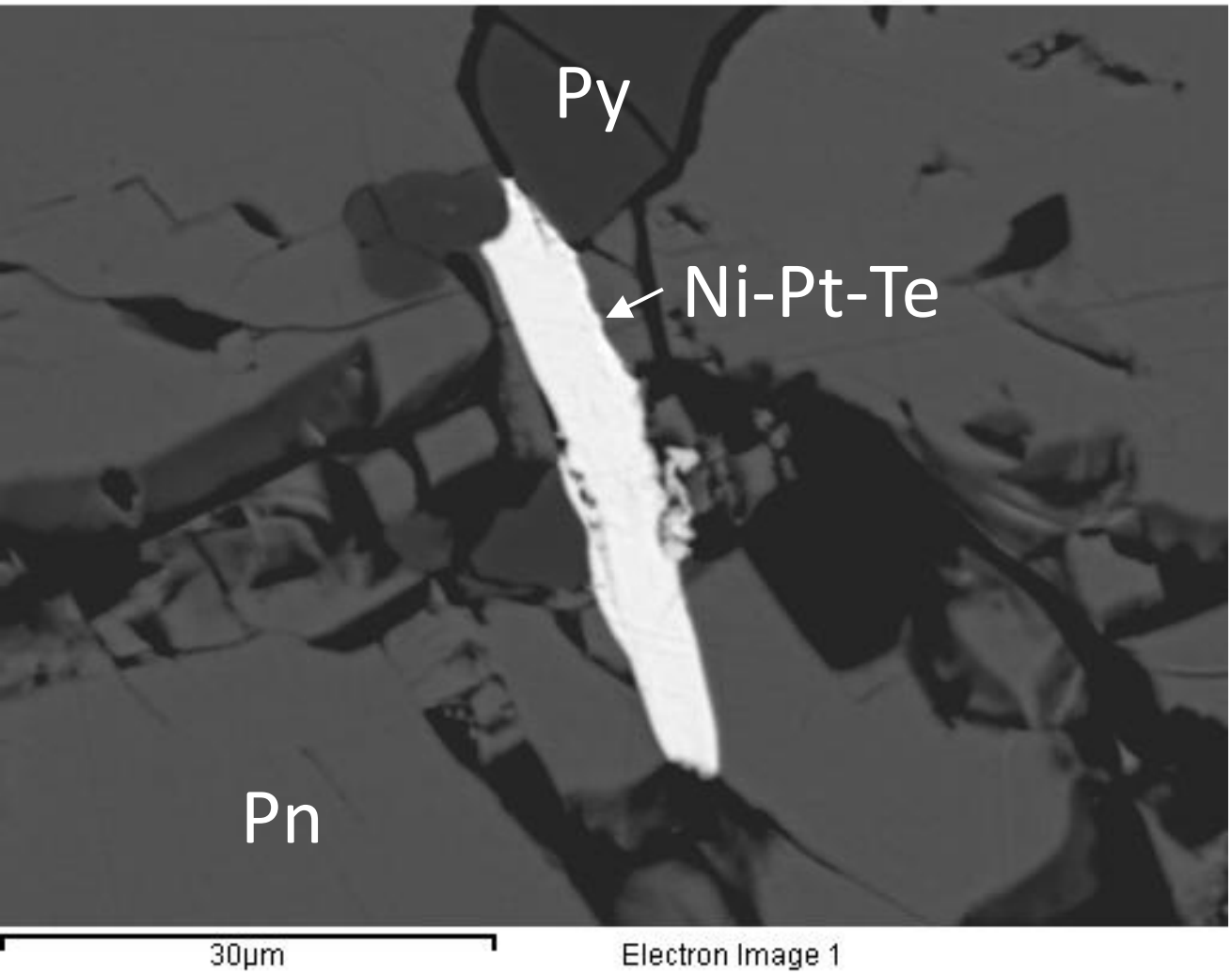
PTSR-51 F 1



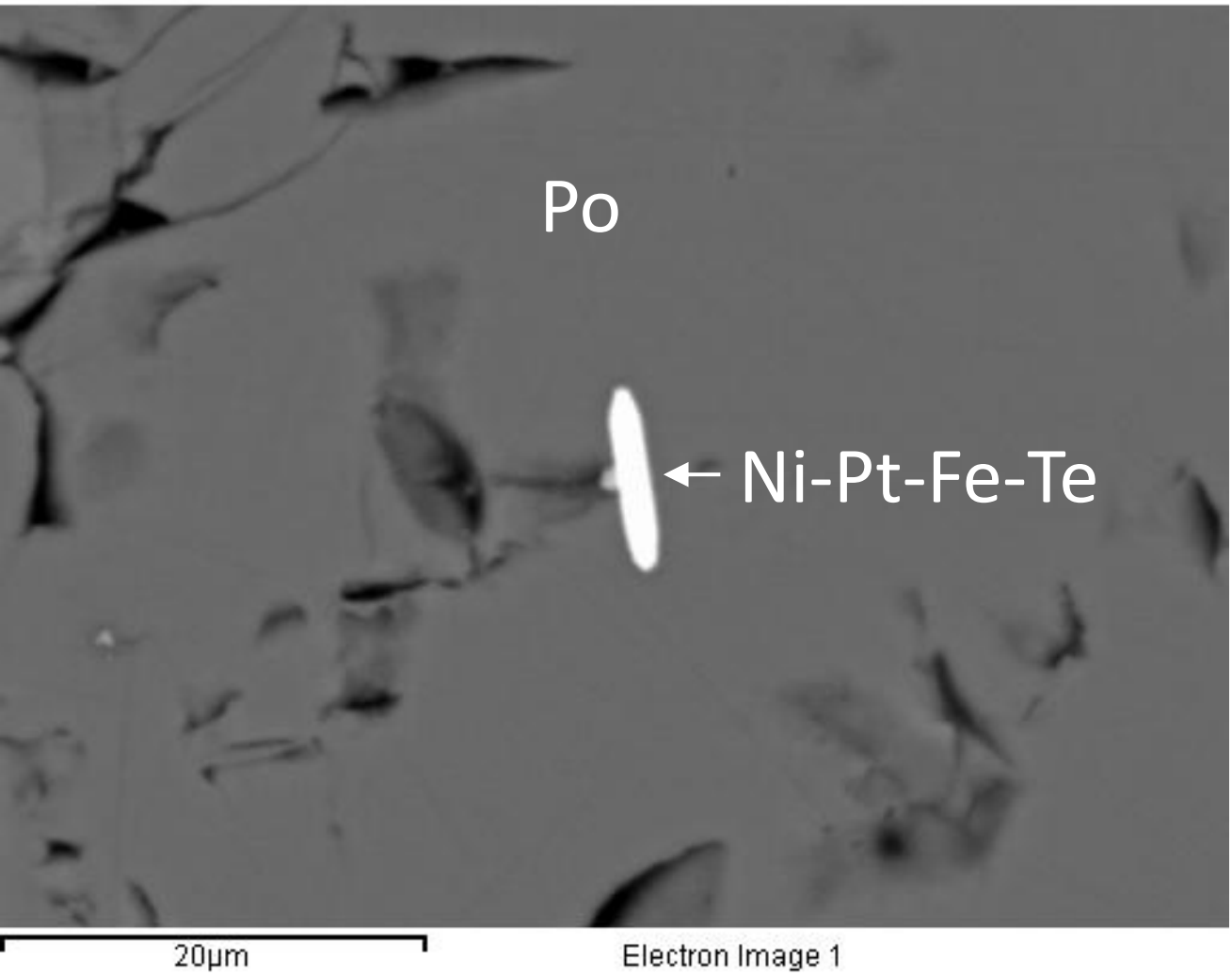
PTSR-51 G 1



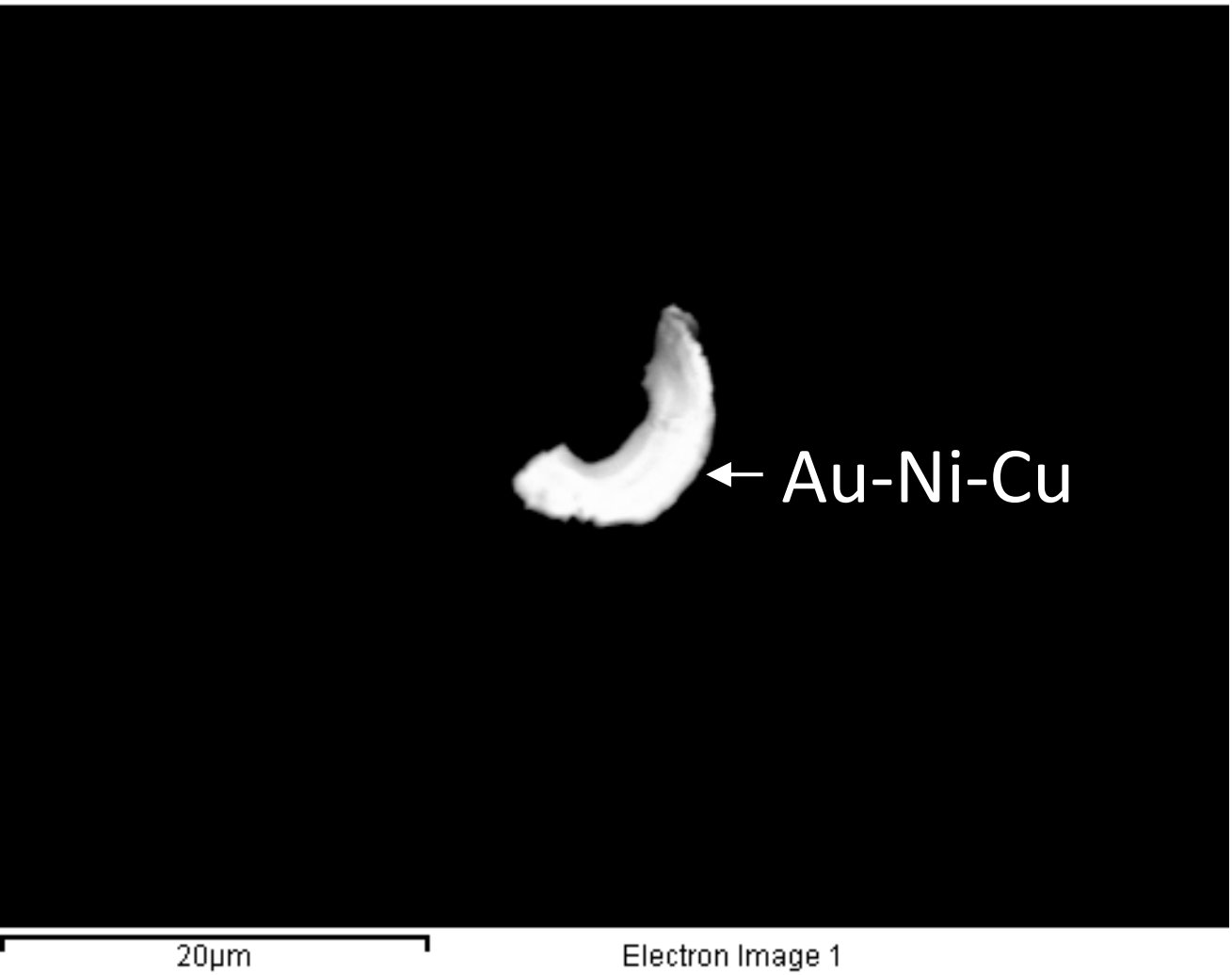
PTSR-51 H 1



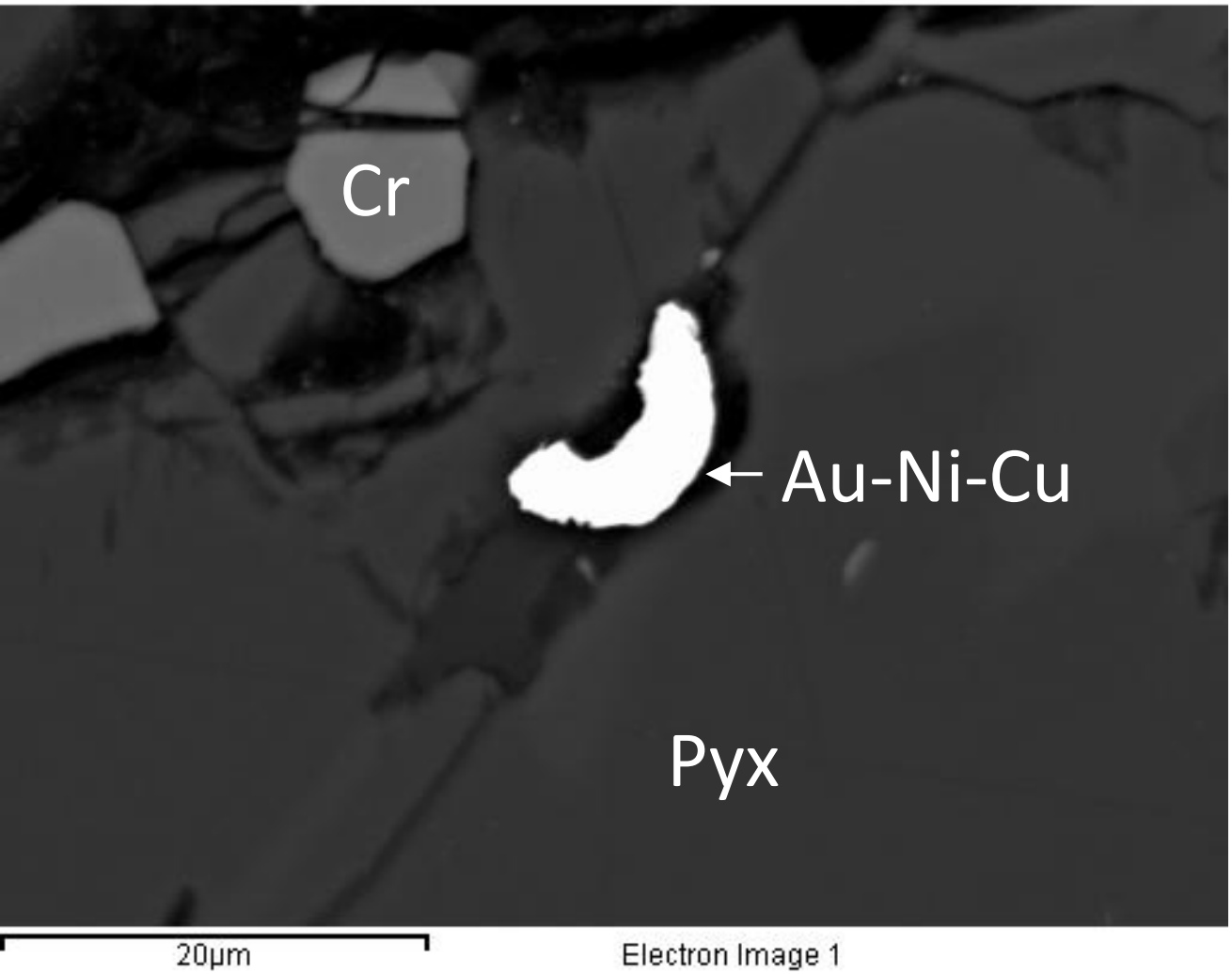
PTSR-51 I 1



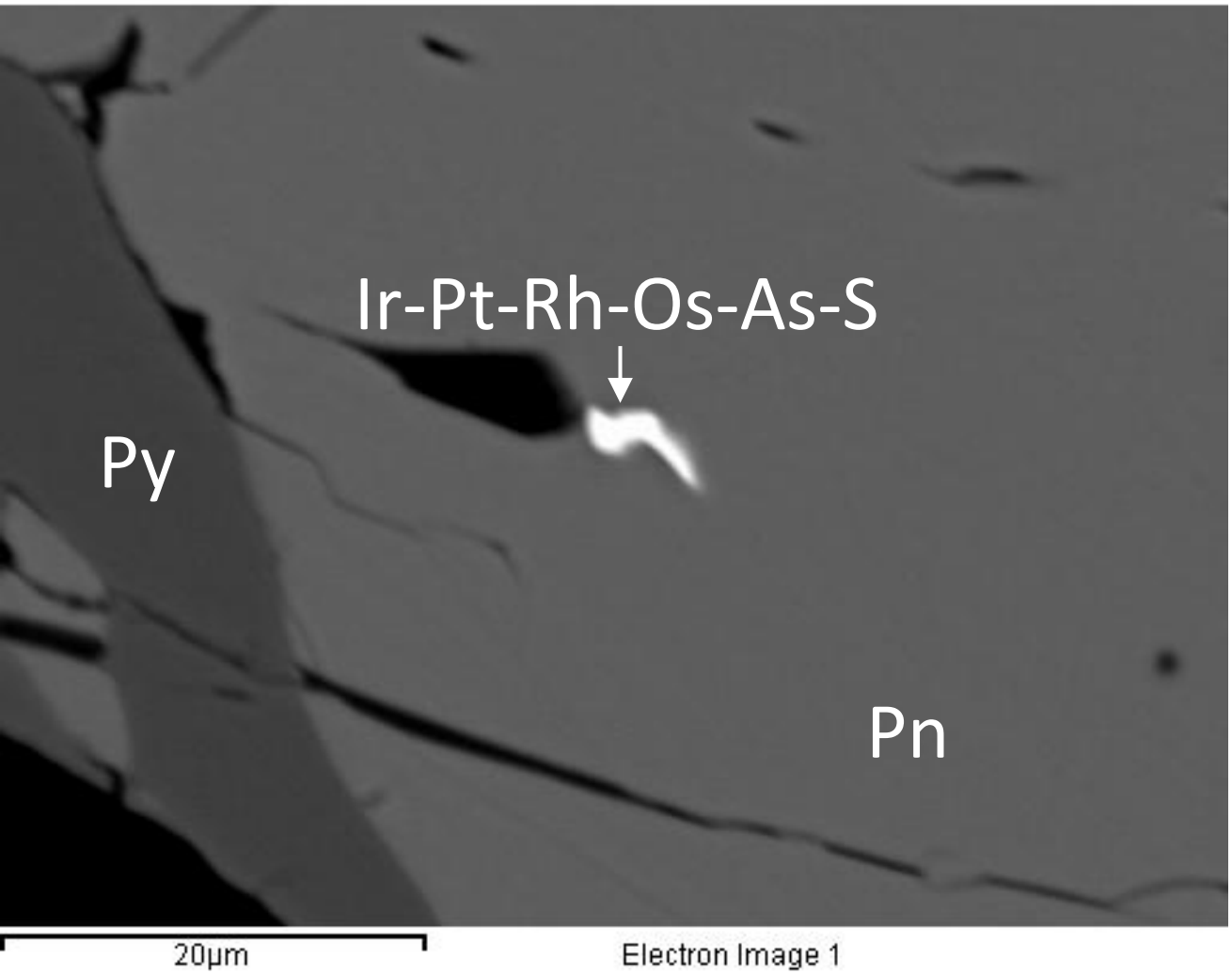
PTSR-51 J 1



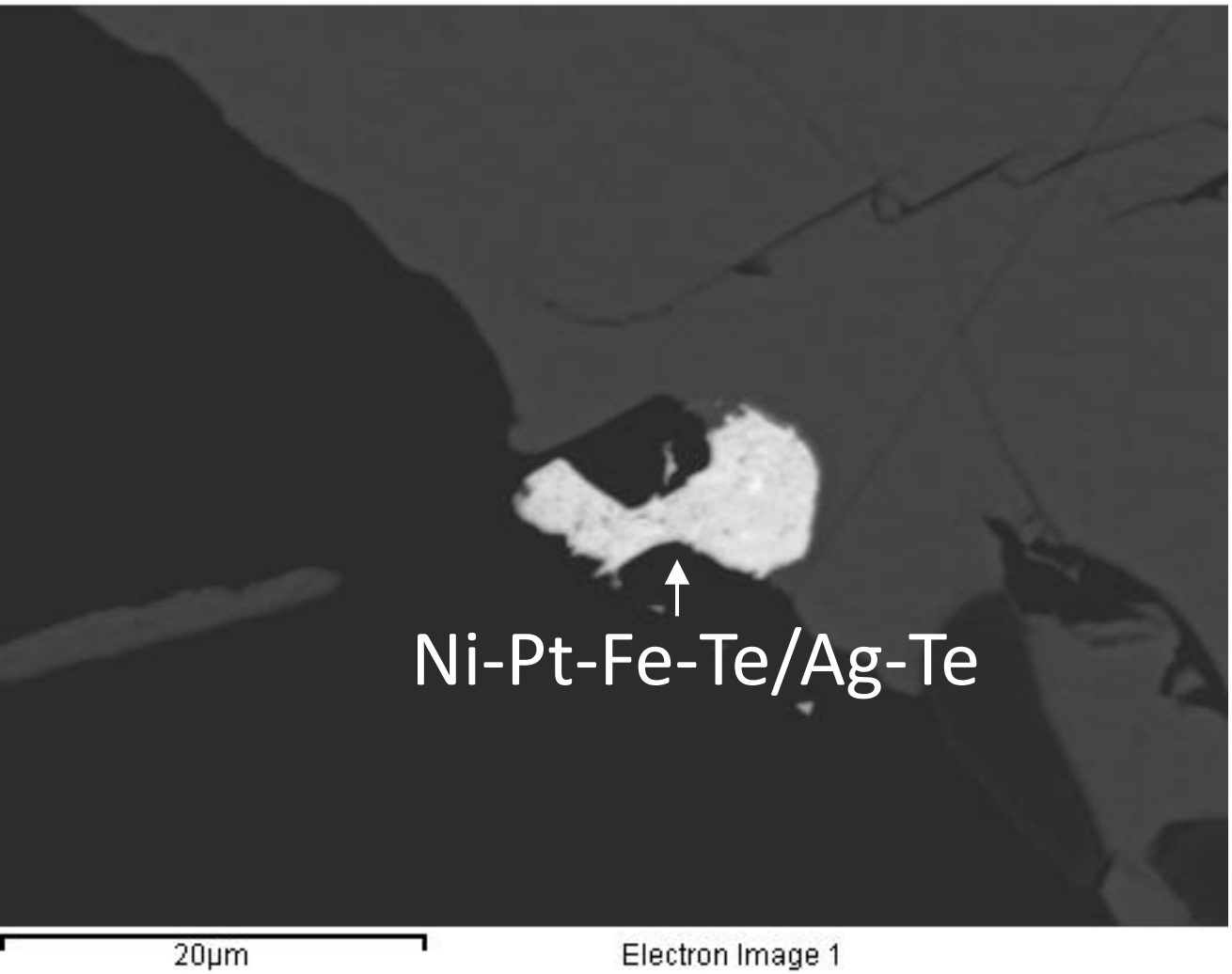
PTSR-51 J 1 Light



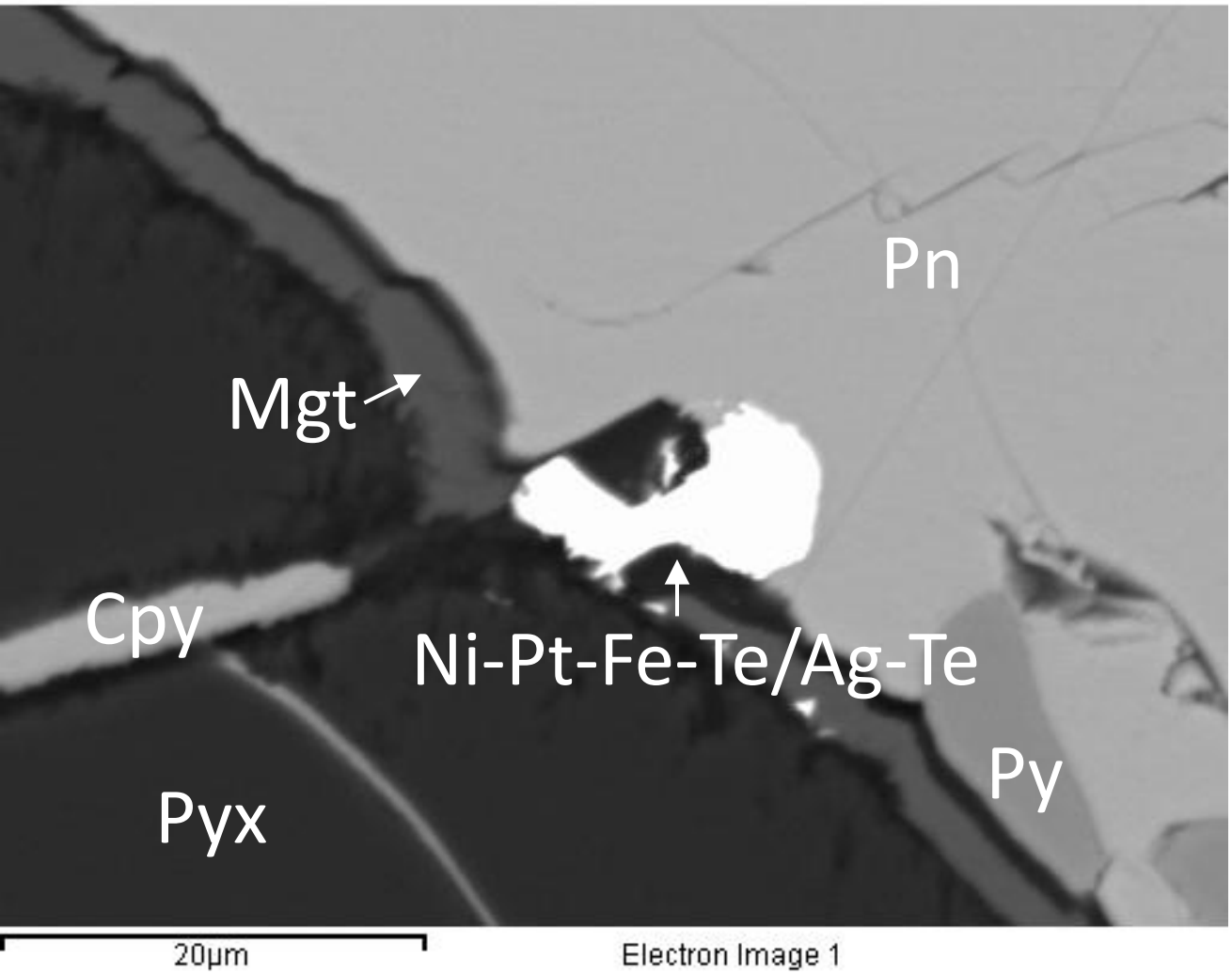
PTSR-52 A 1



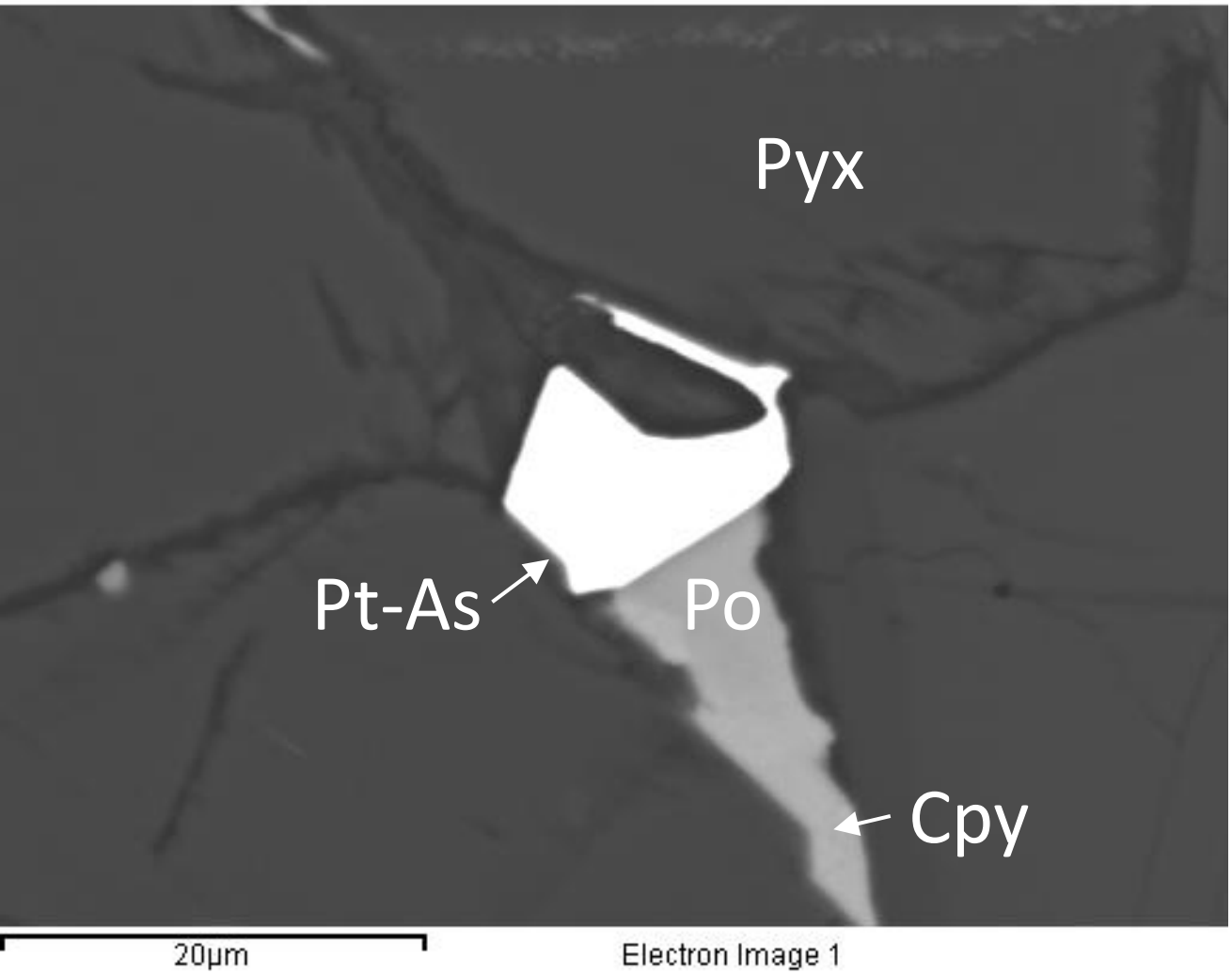
PTSR-52 B 1



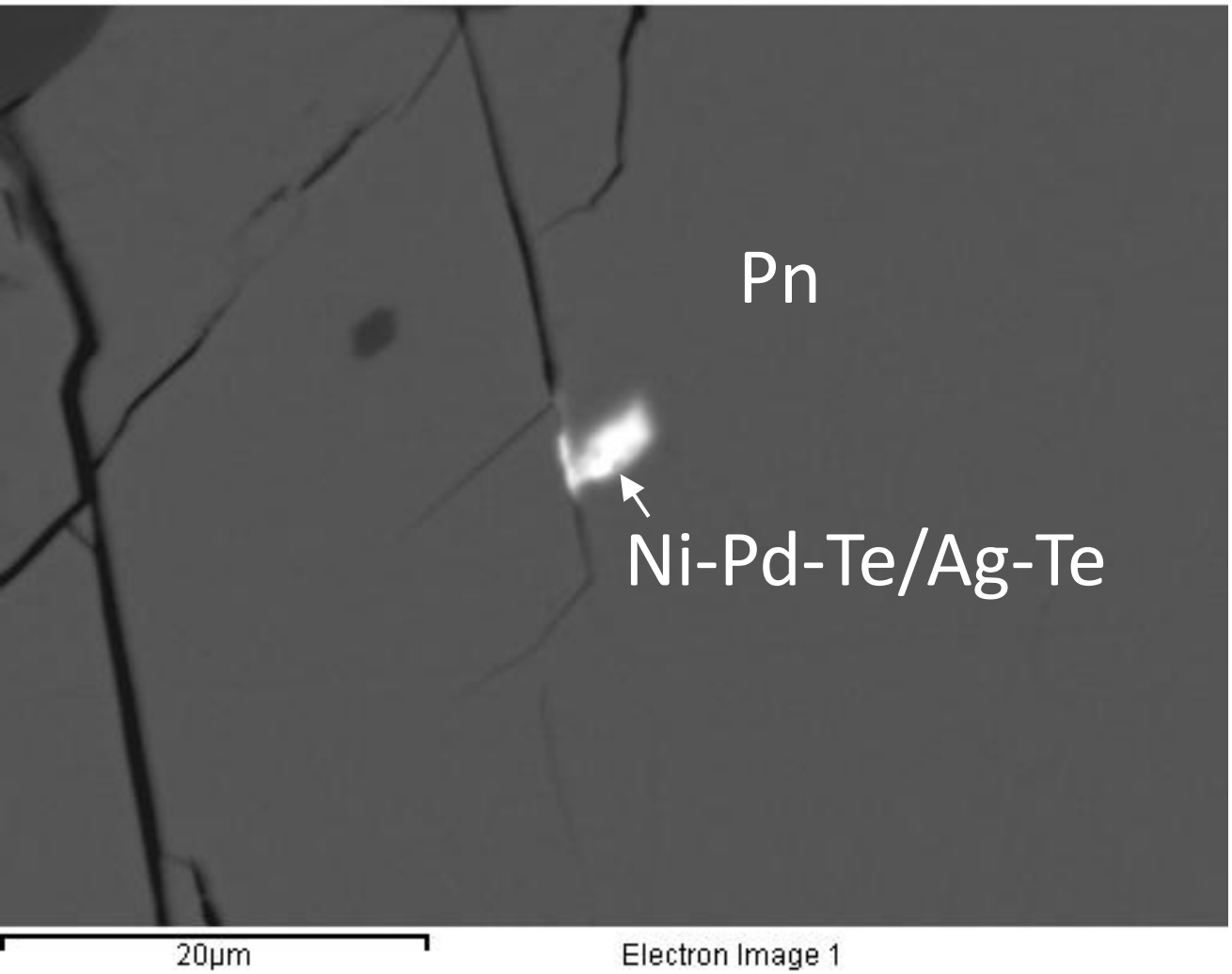
PTSR-52 B 1 Light



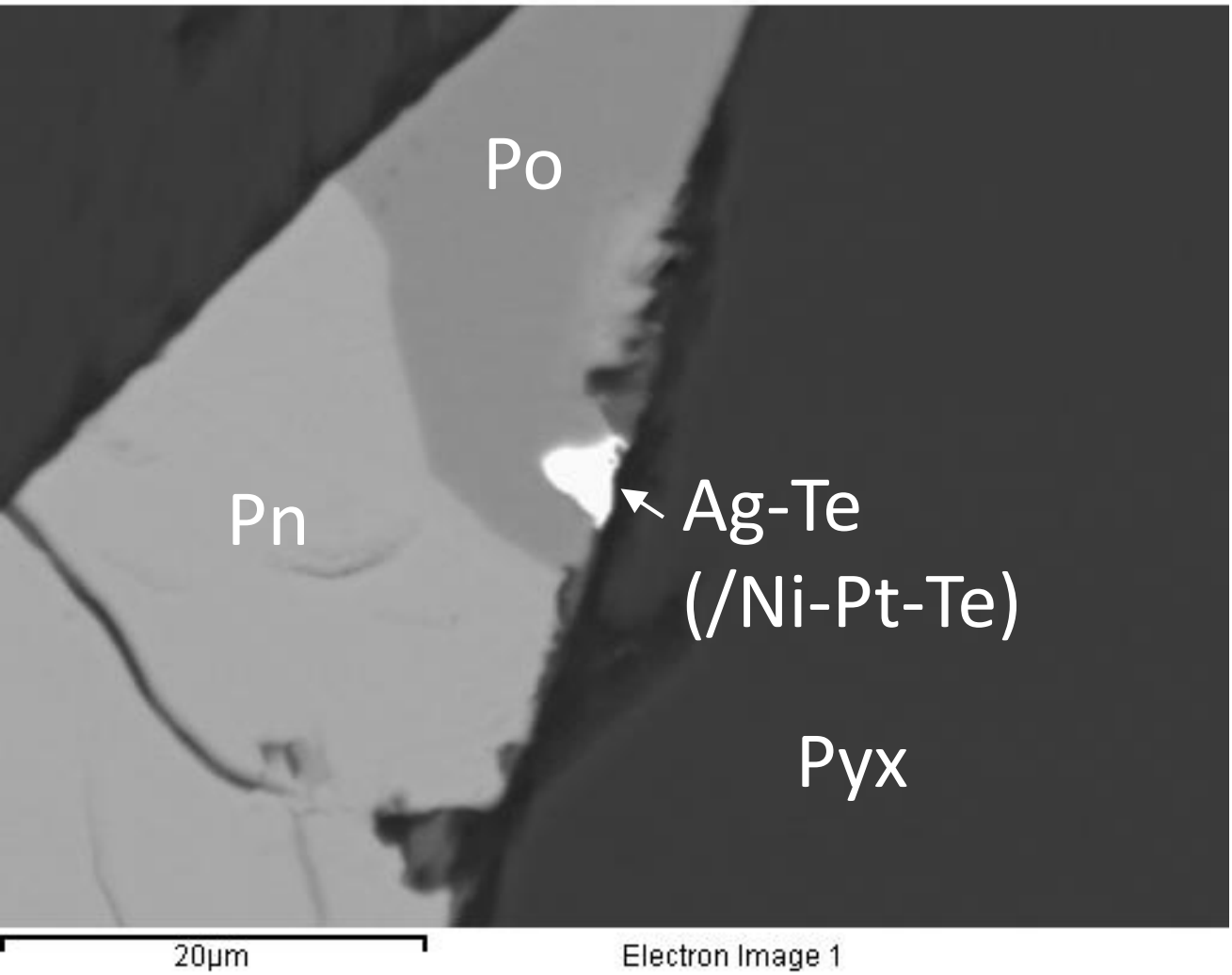
PTSR-52 C 1



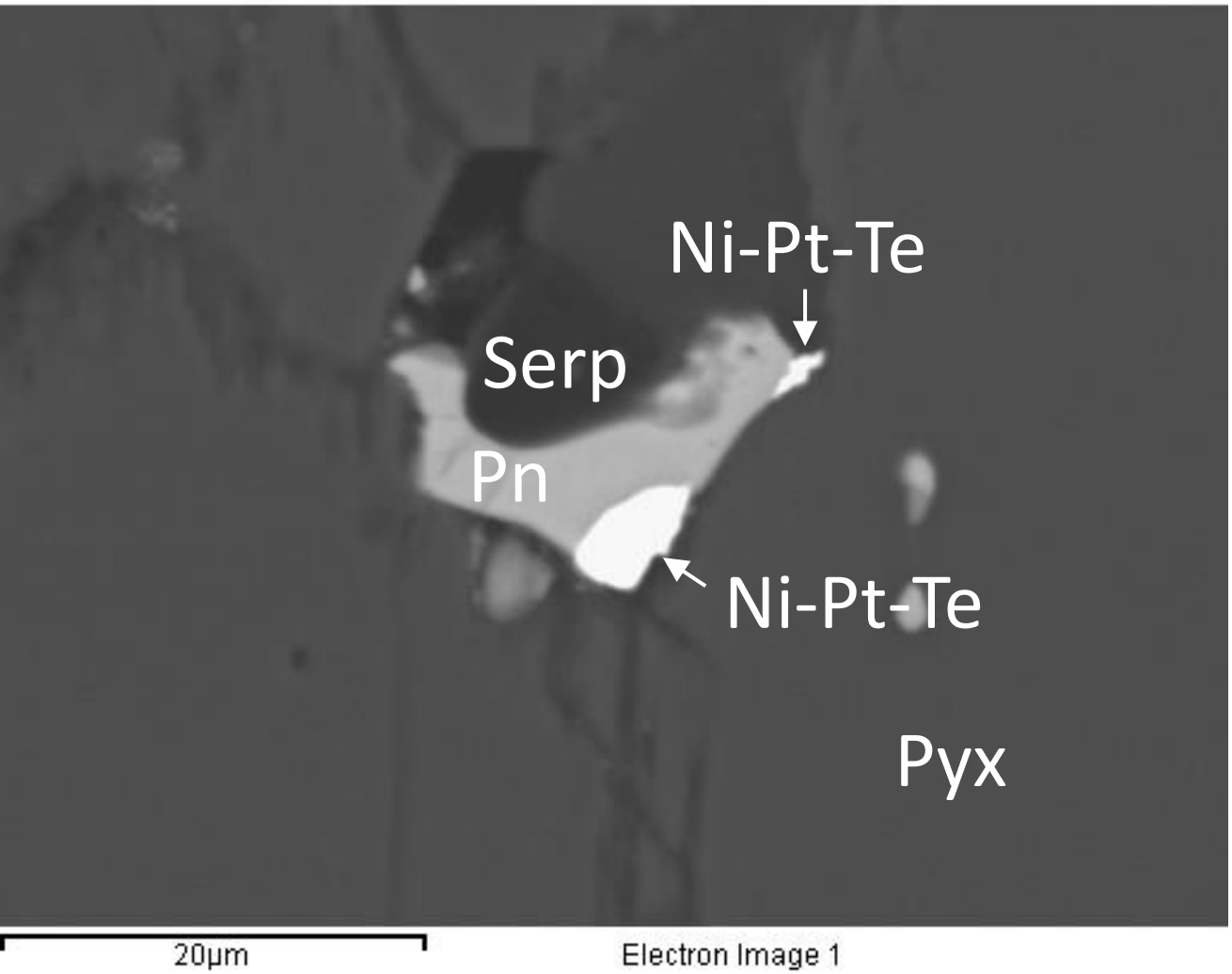
PTSR-52 D 1



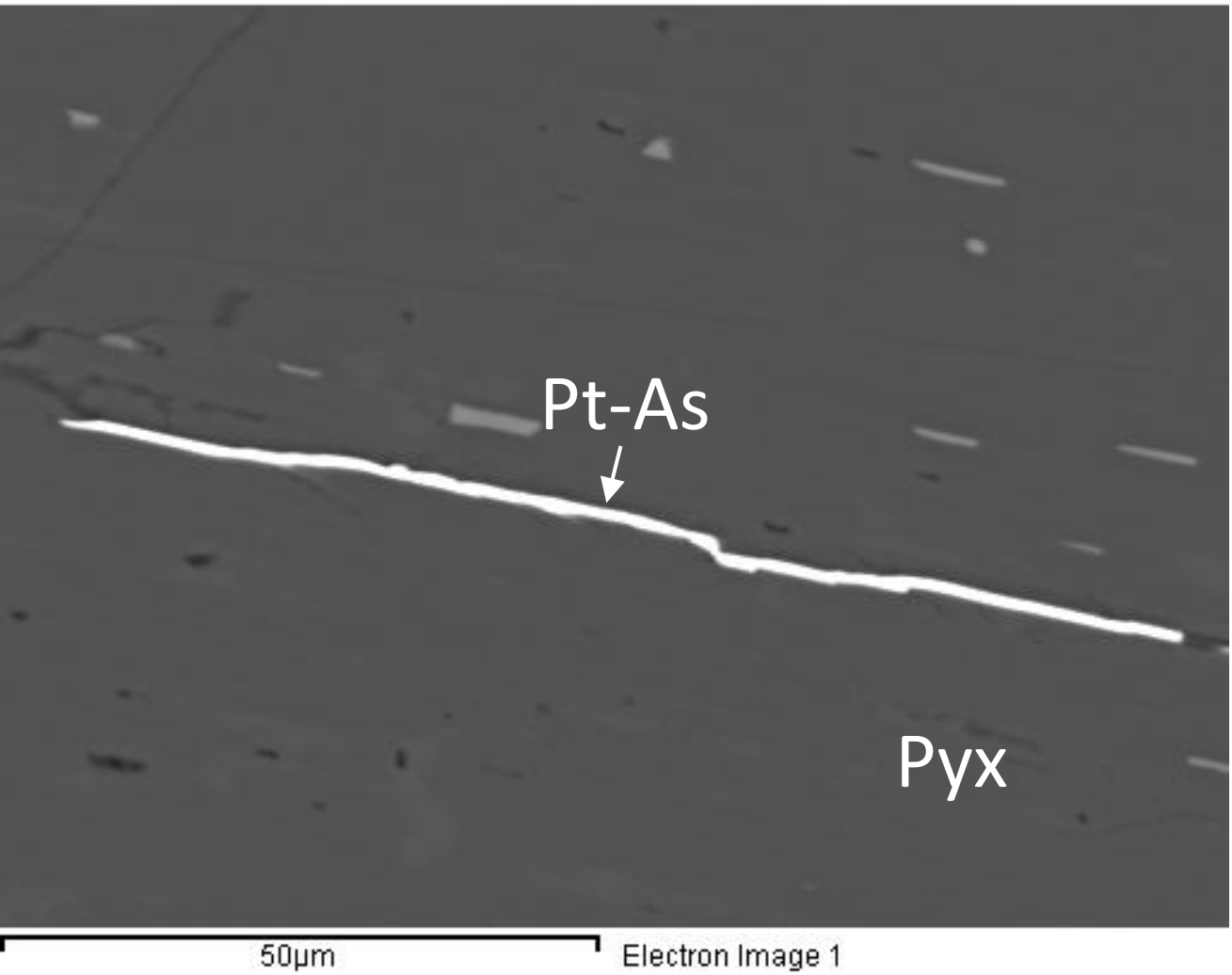
PTSR-52 E 1



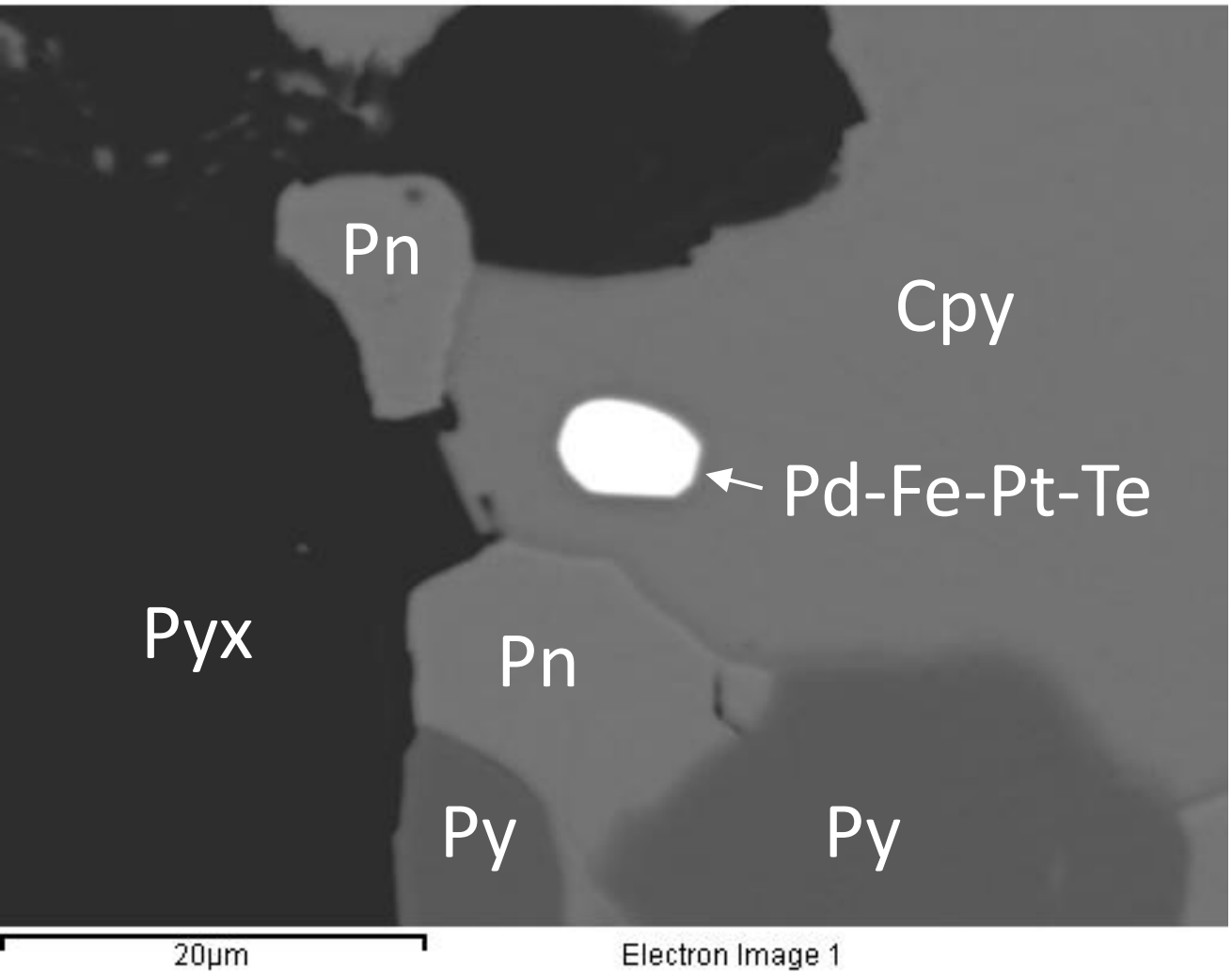
PTSR-52 F 1-2



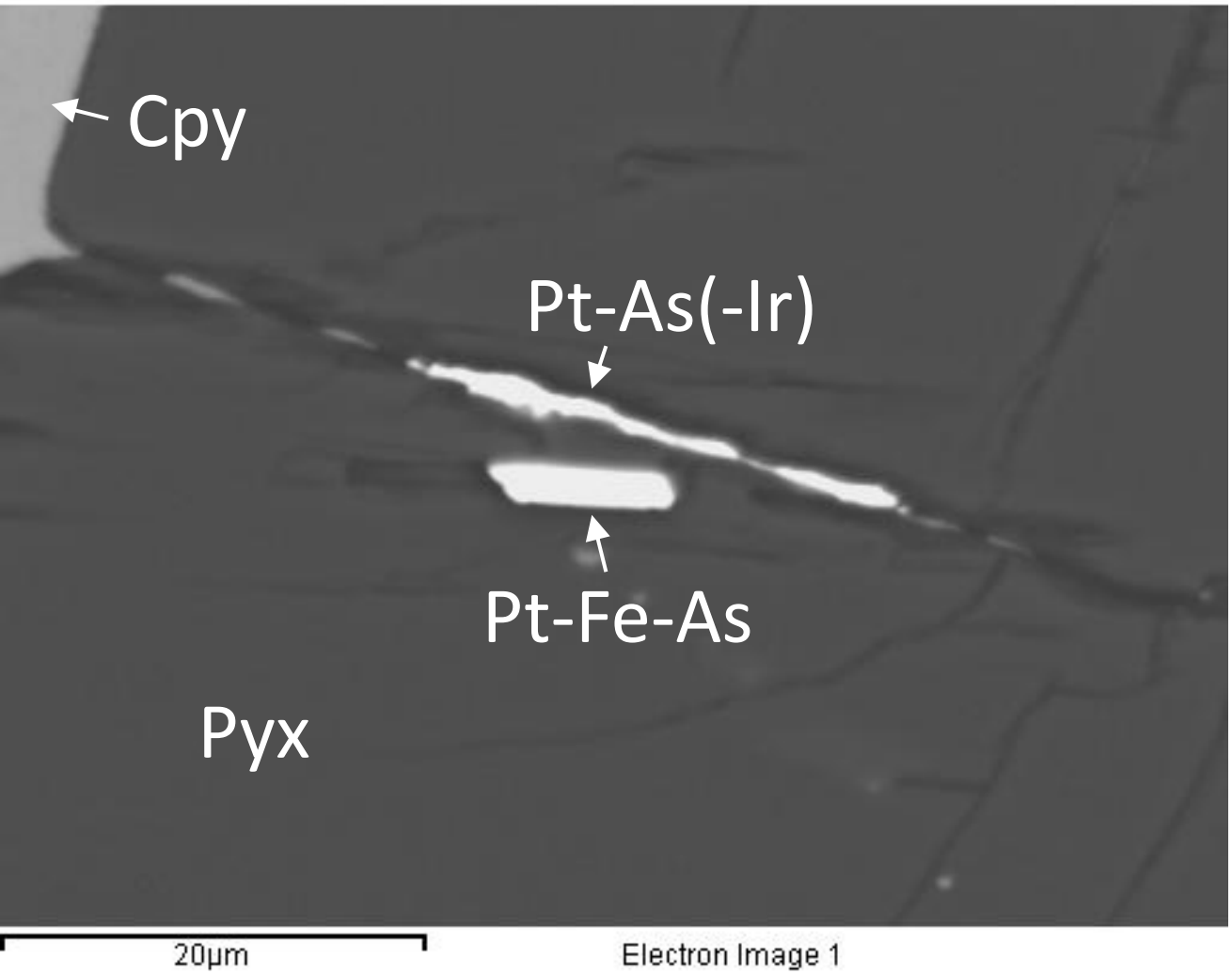
PTSR-52 G 1



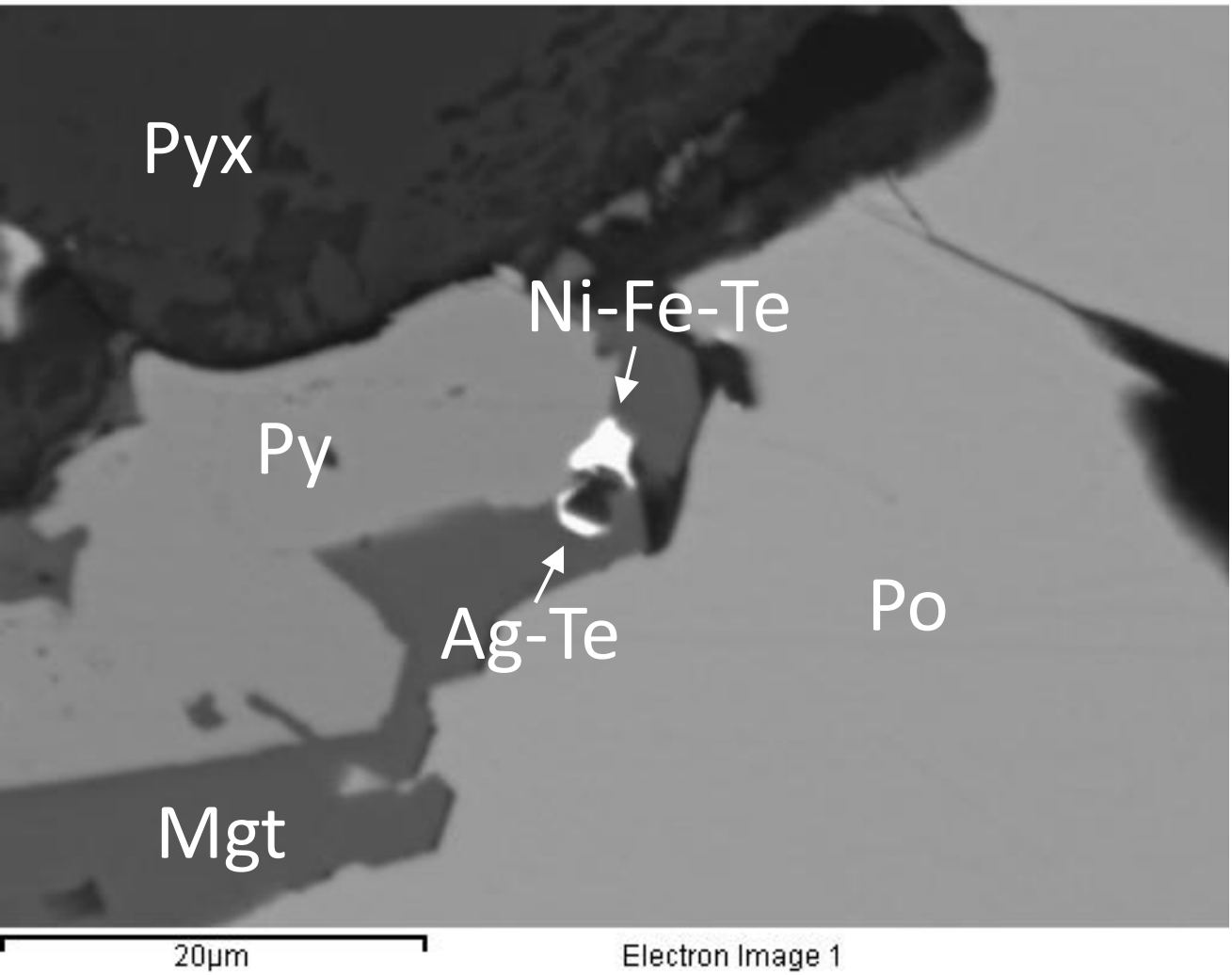
PTSR-52 H 1



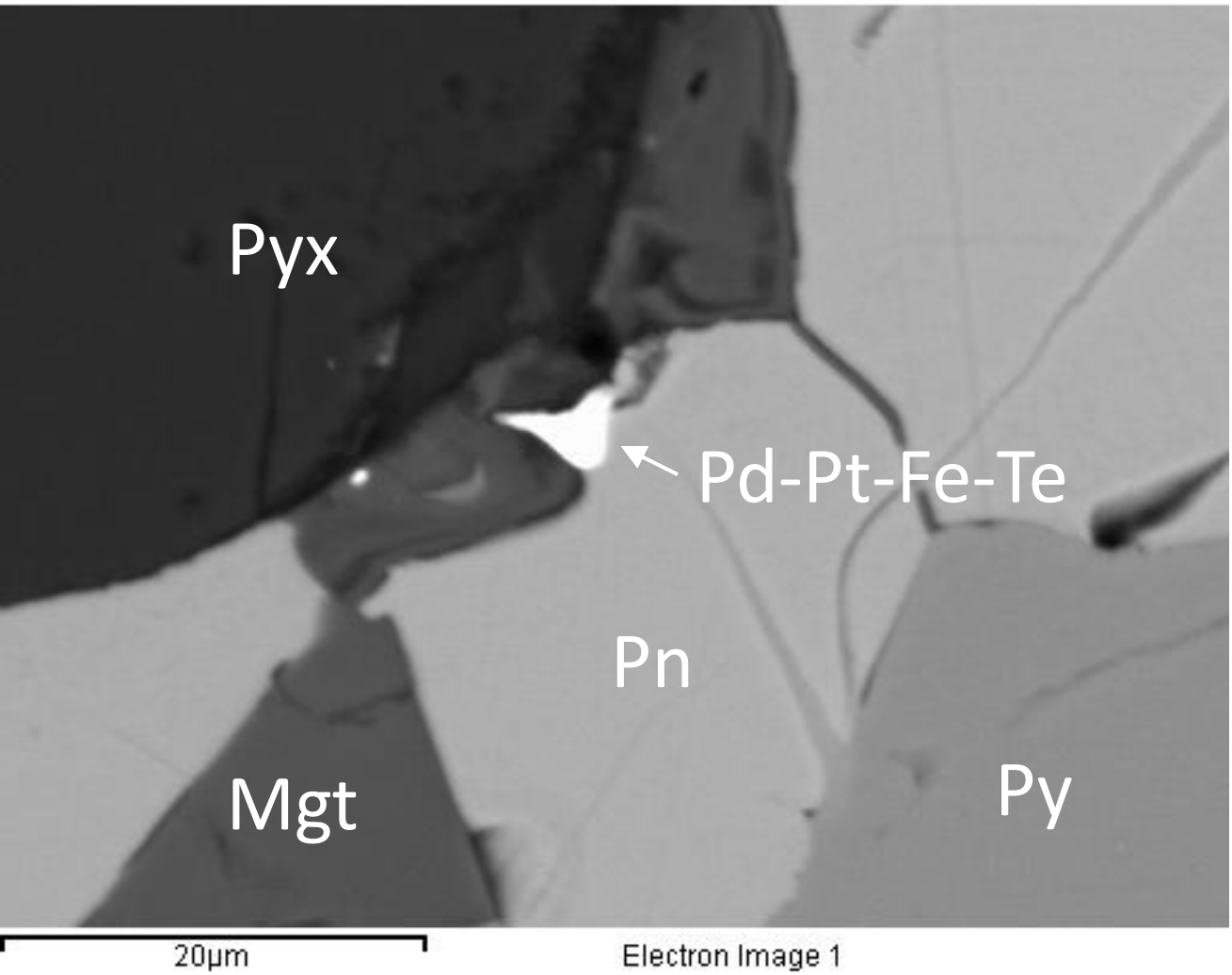
PTSR-52 I 1-2



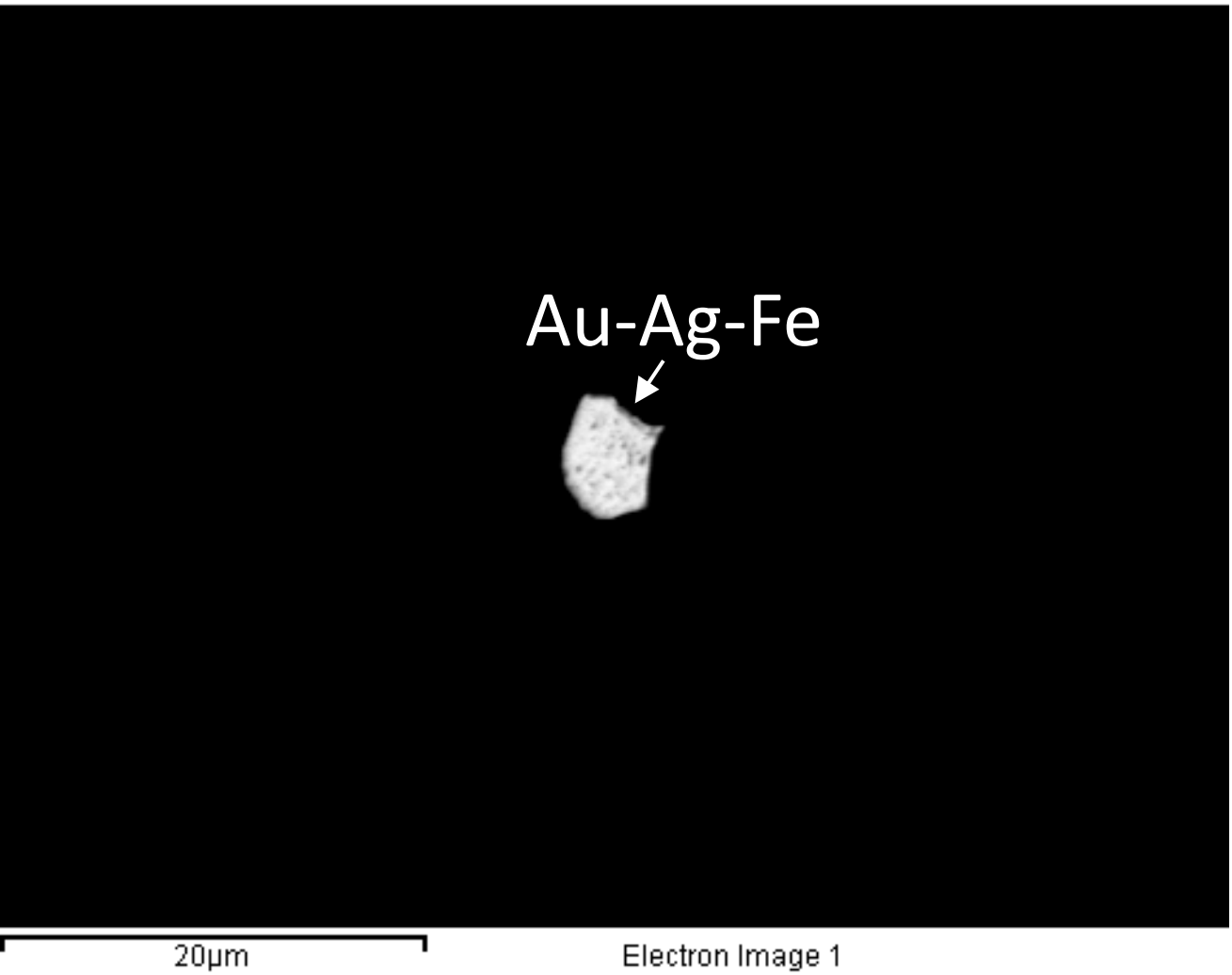
PTSR-52 J 1-2



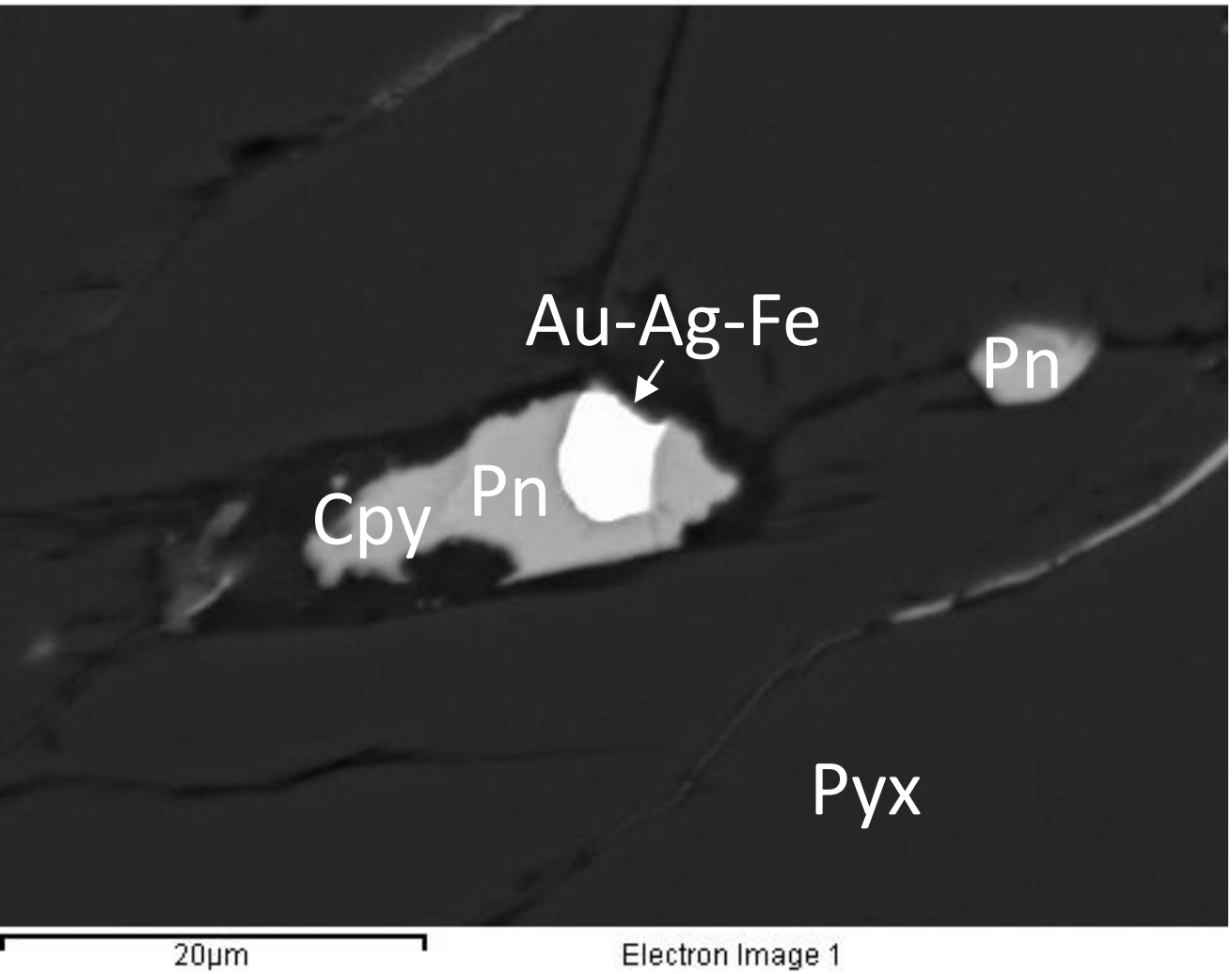
PTSR-52 K 1



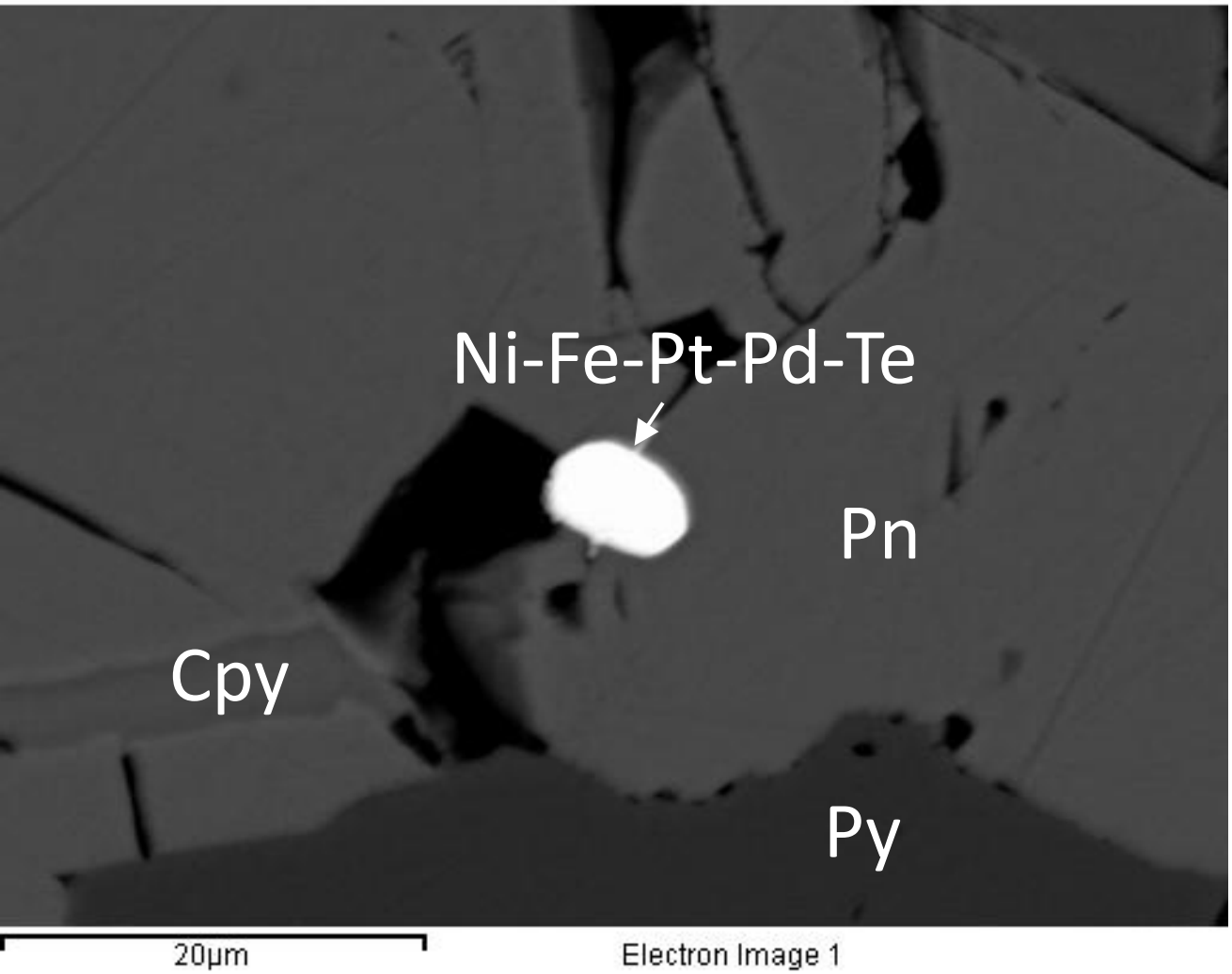
PTSR-52 L 1



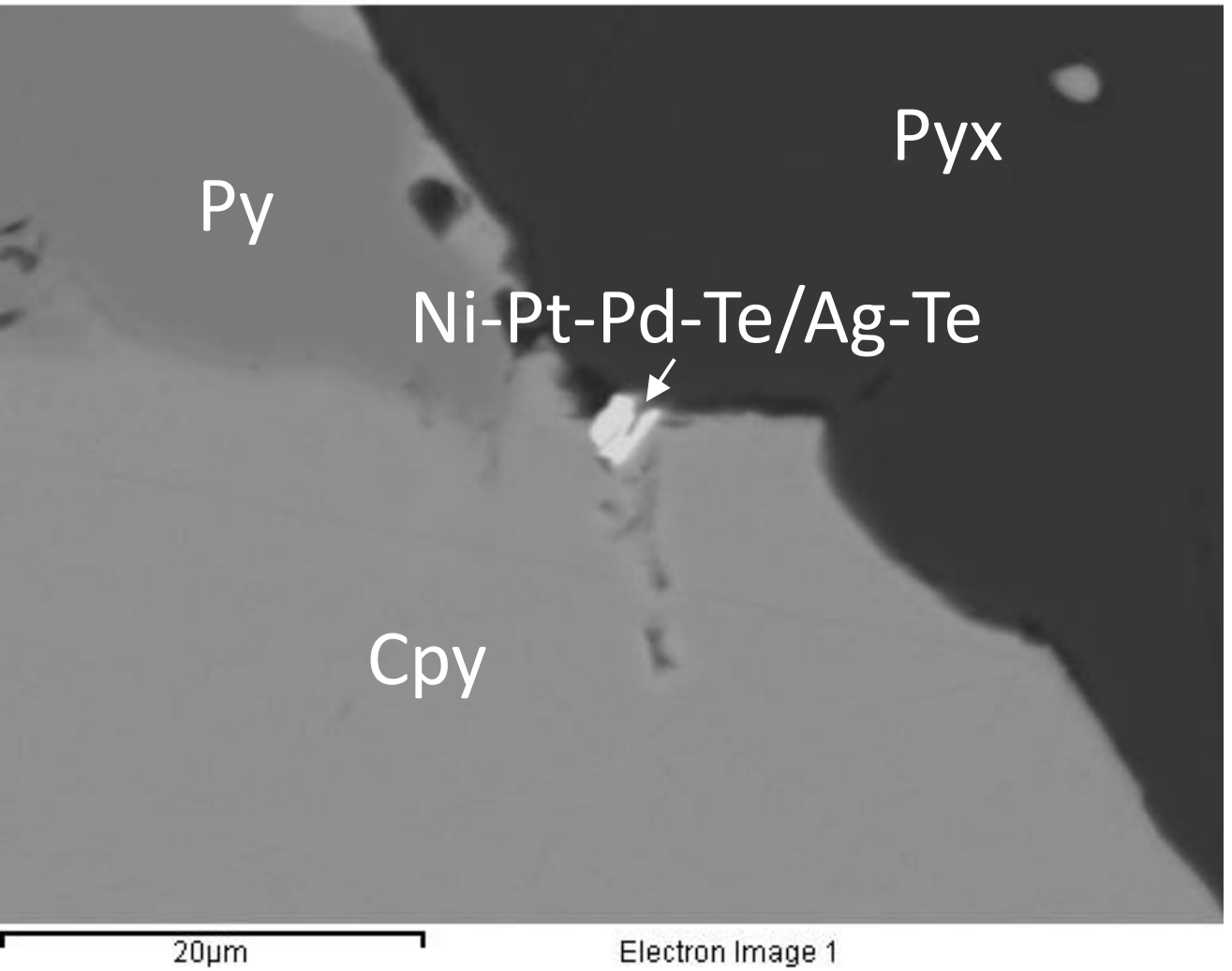
PTSR-52 L 1 Light



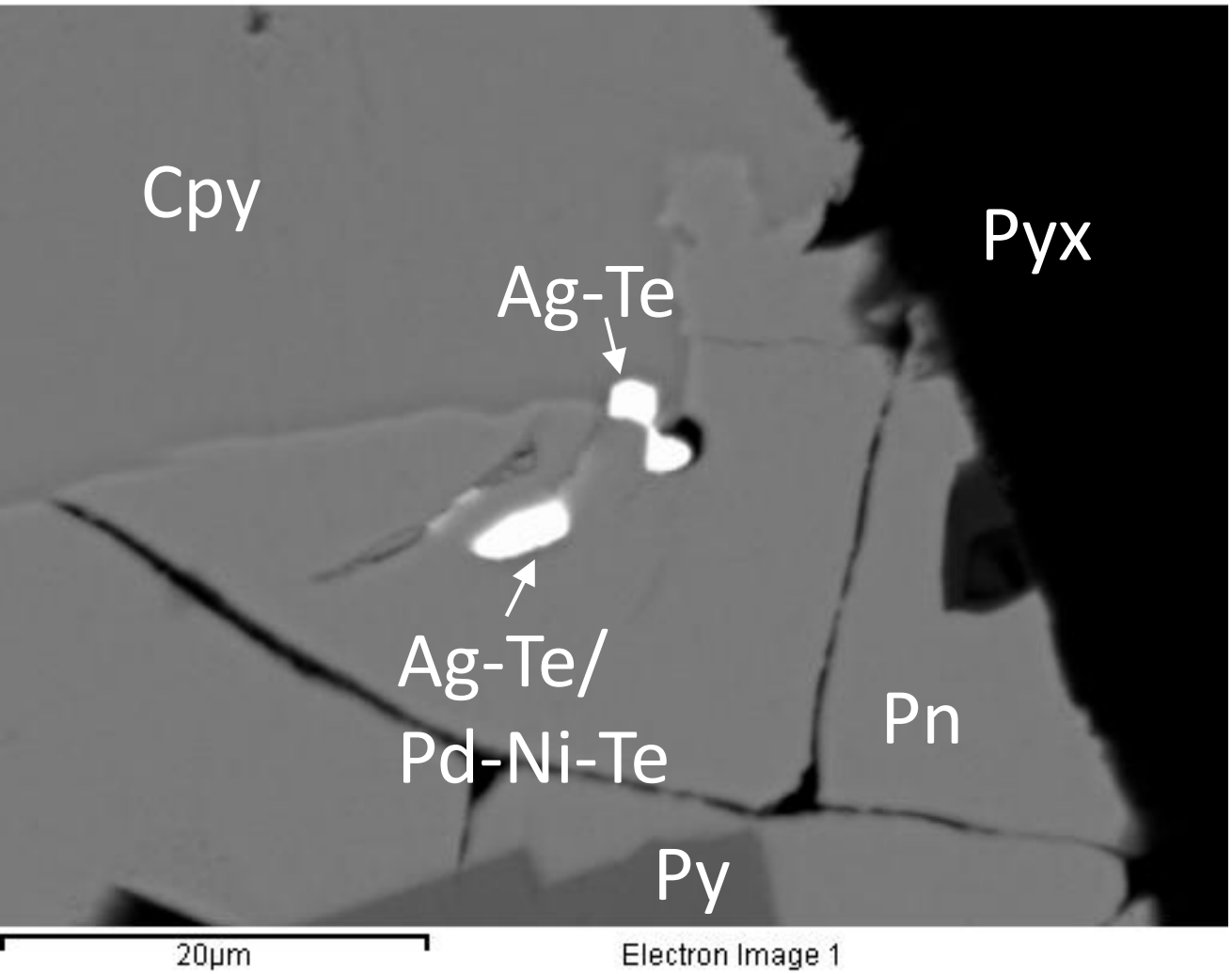
PTSR-52 M 1



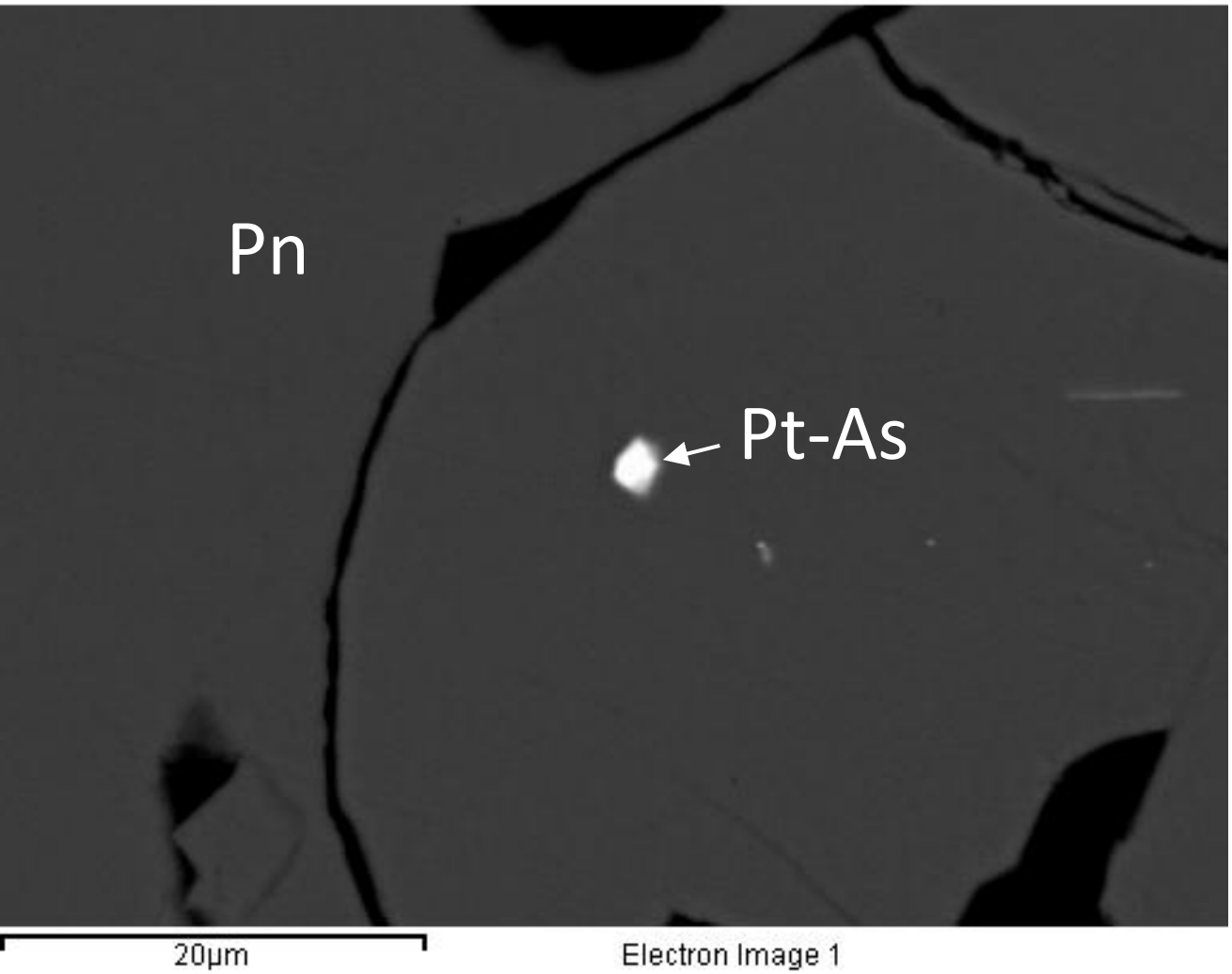
PTSR-52 N 1



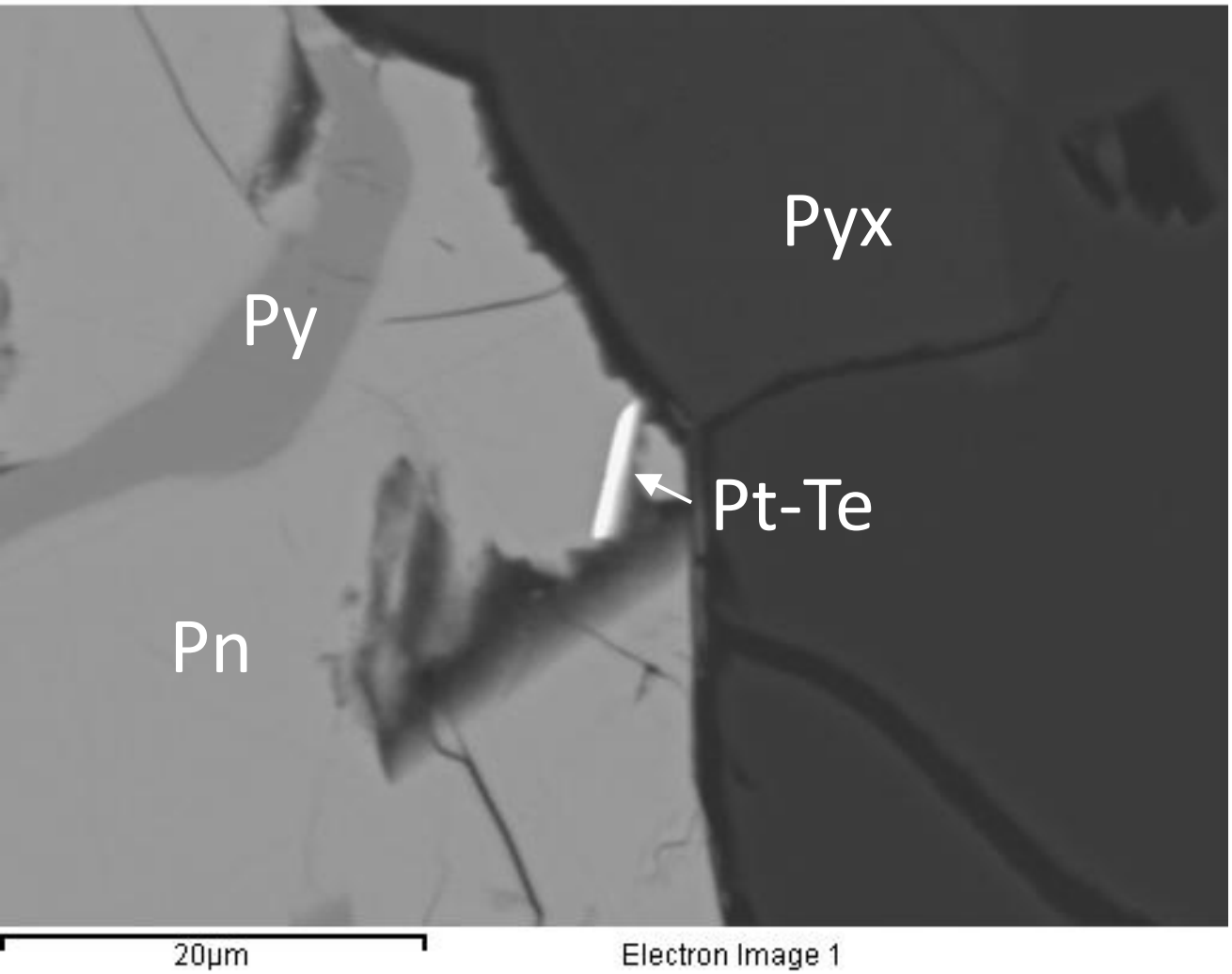
PTSR-52 O 1-2



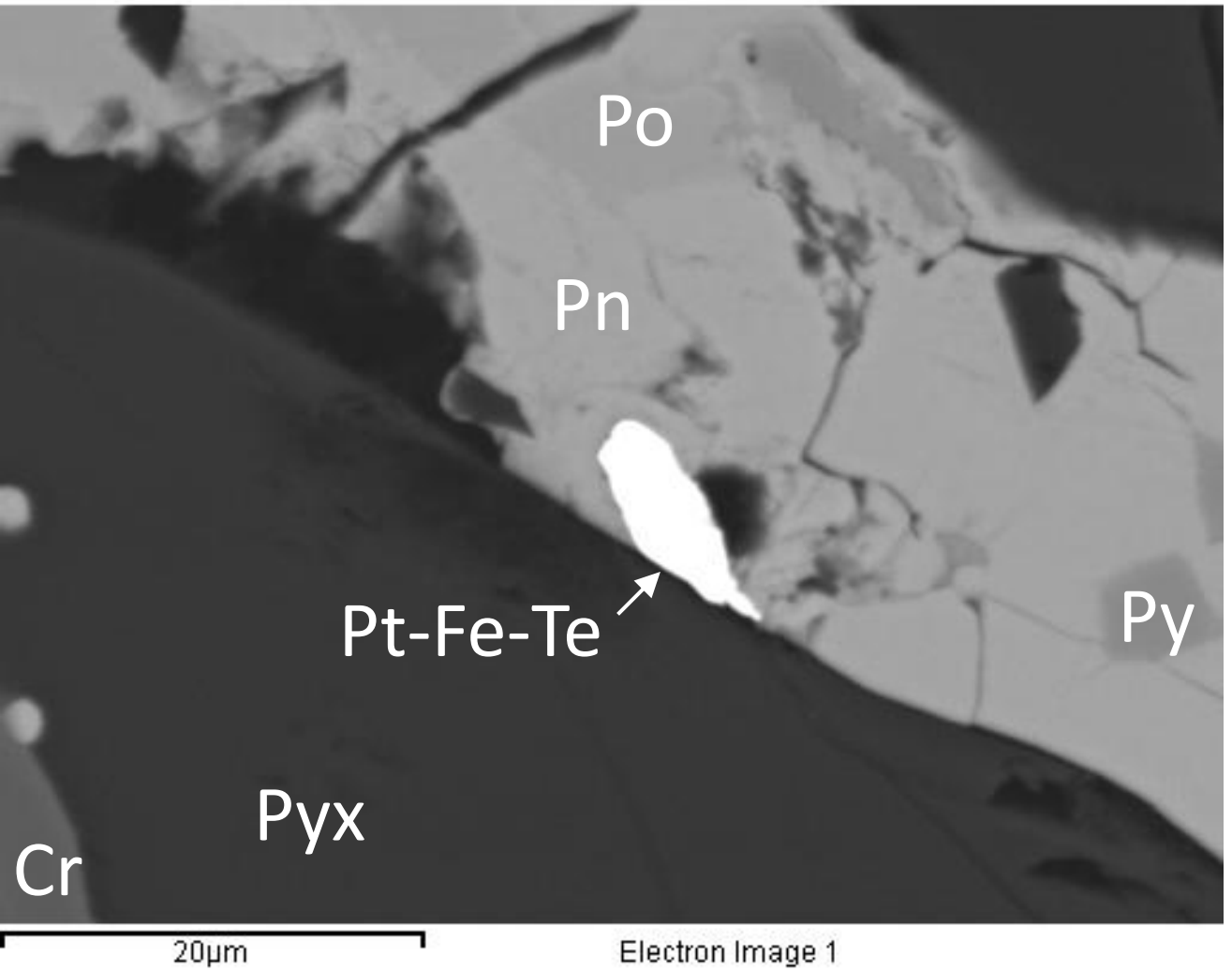
PTSR-53 A 1



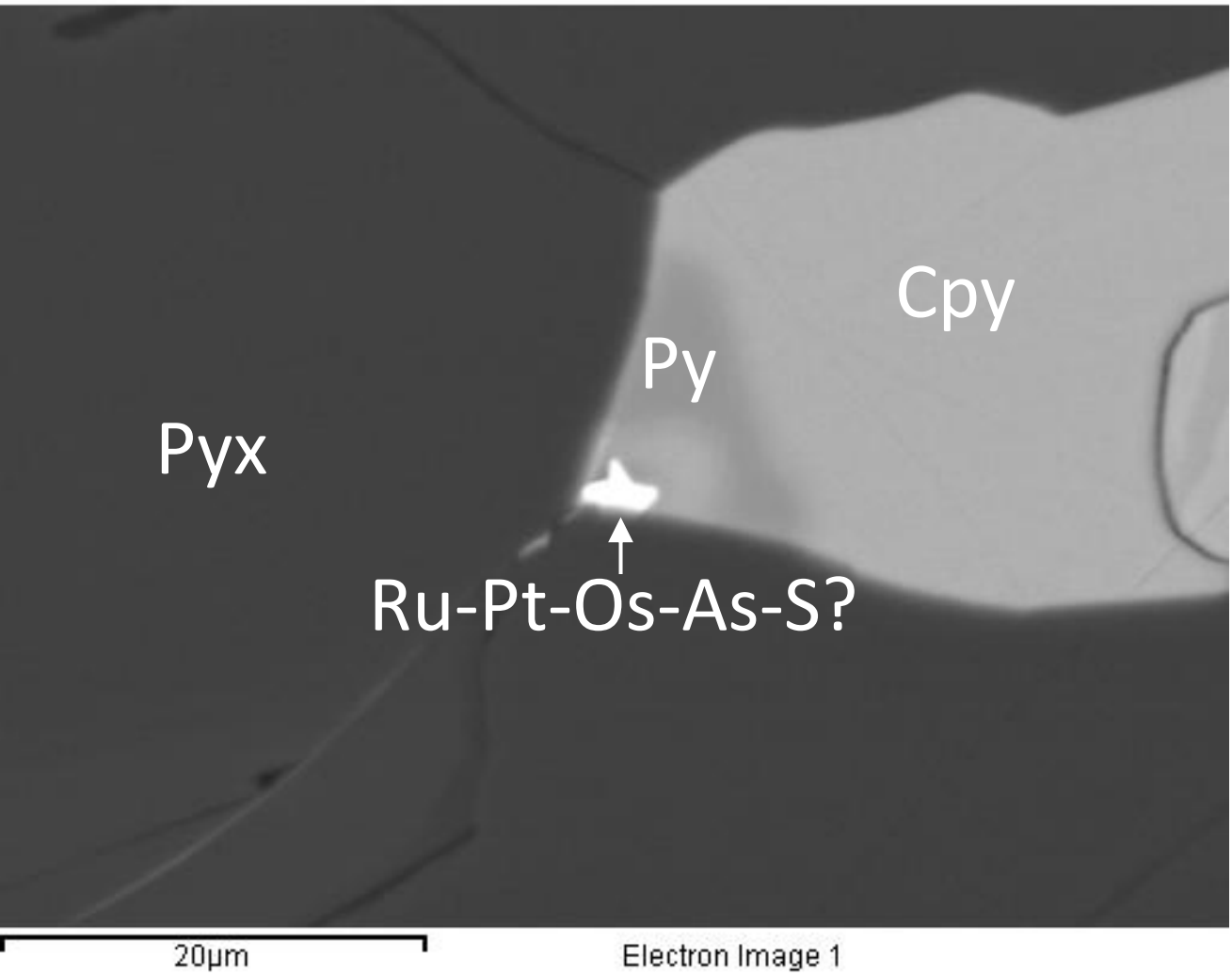
PTSR-53 B 1



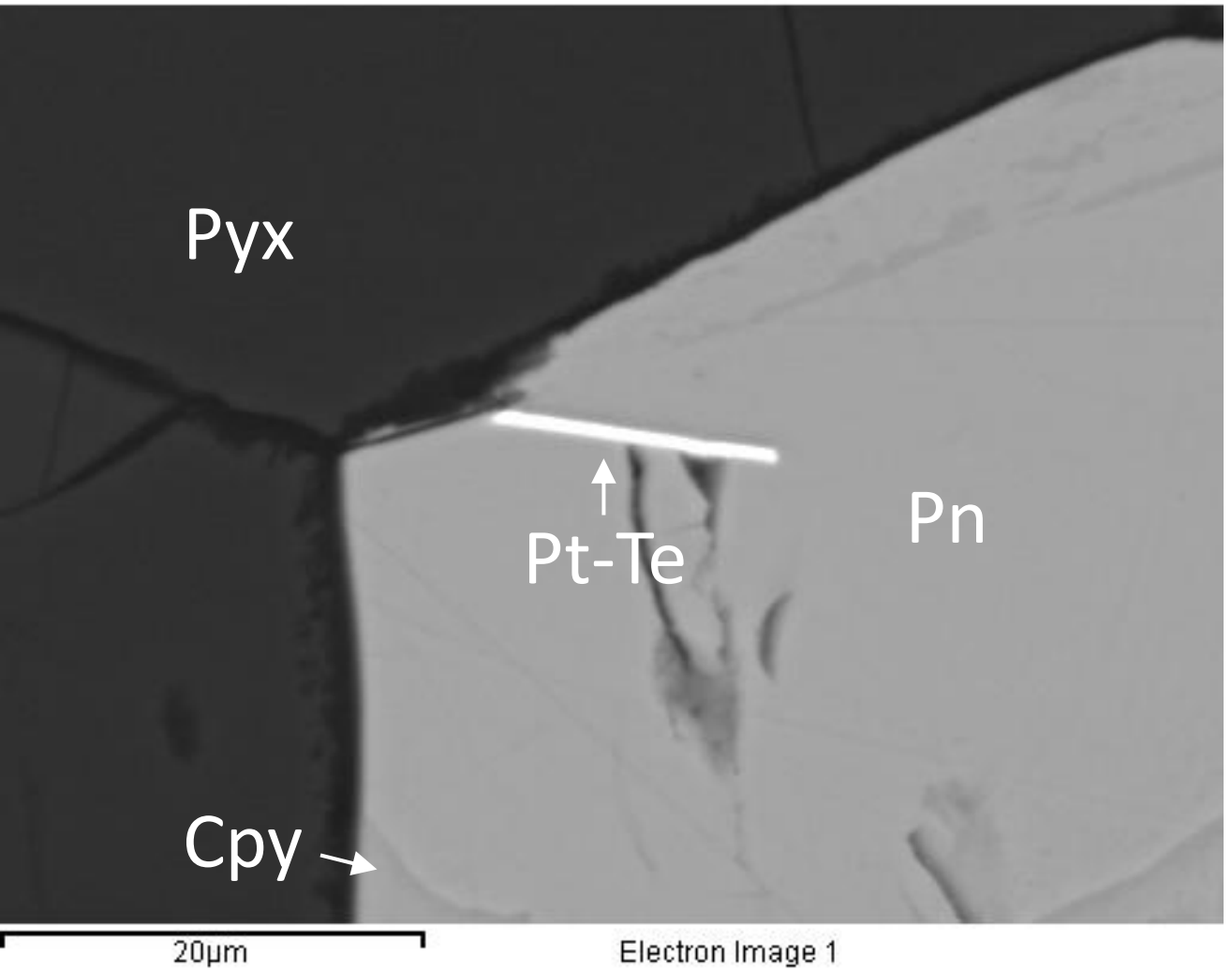
PTSR-53 C 1



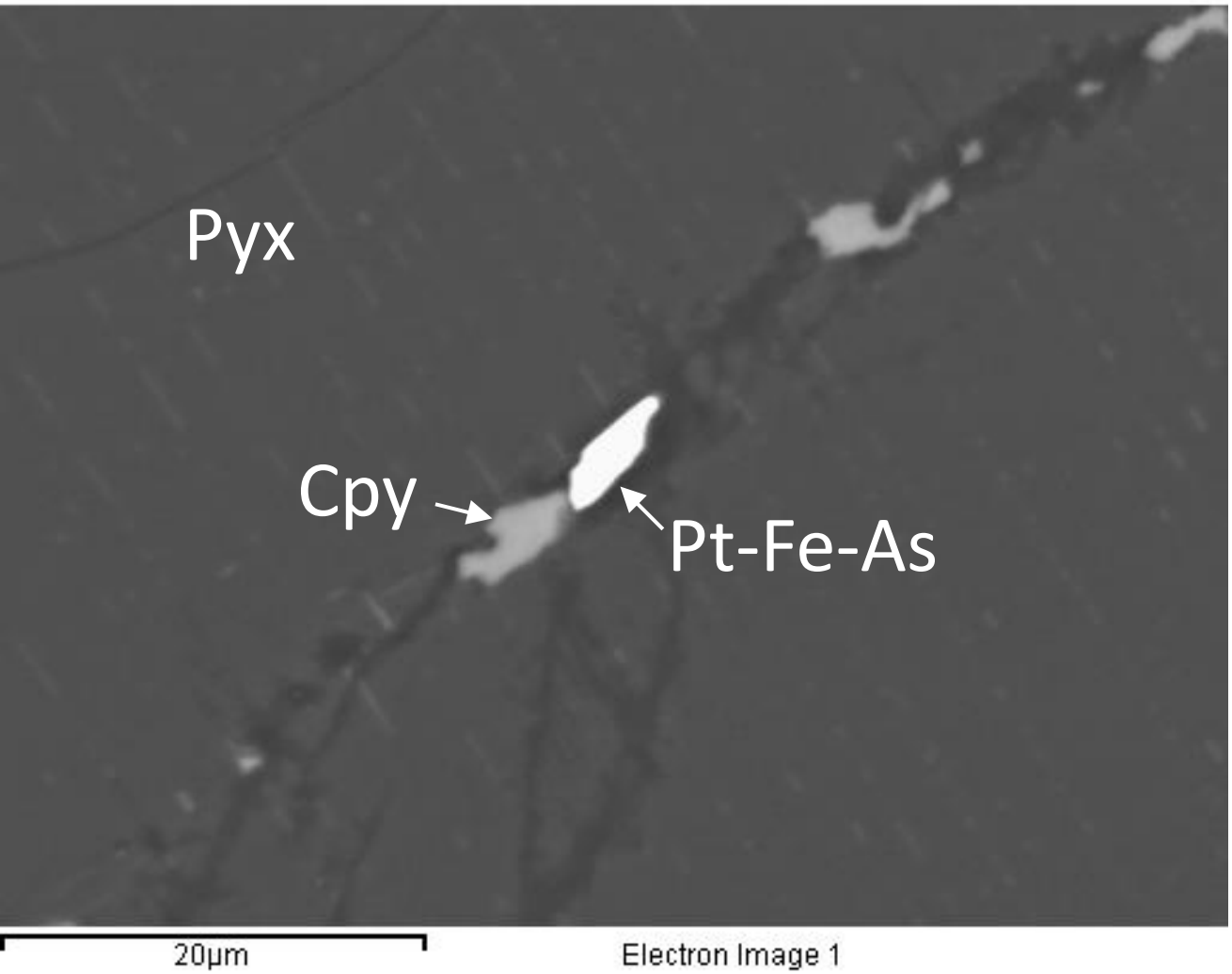
PTSR-53 D 1



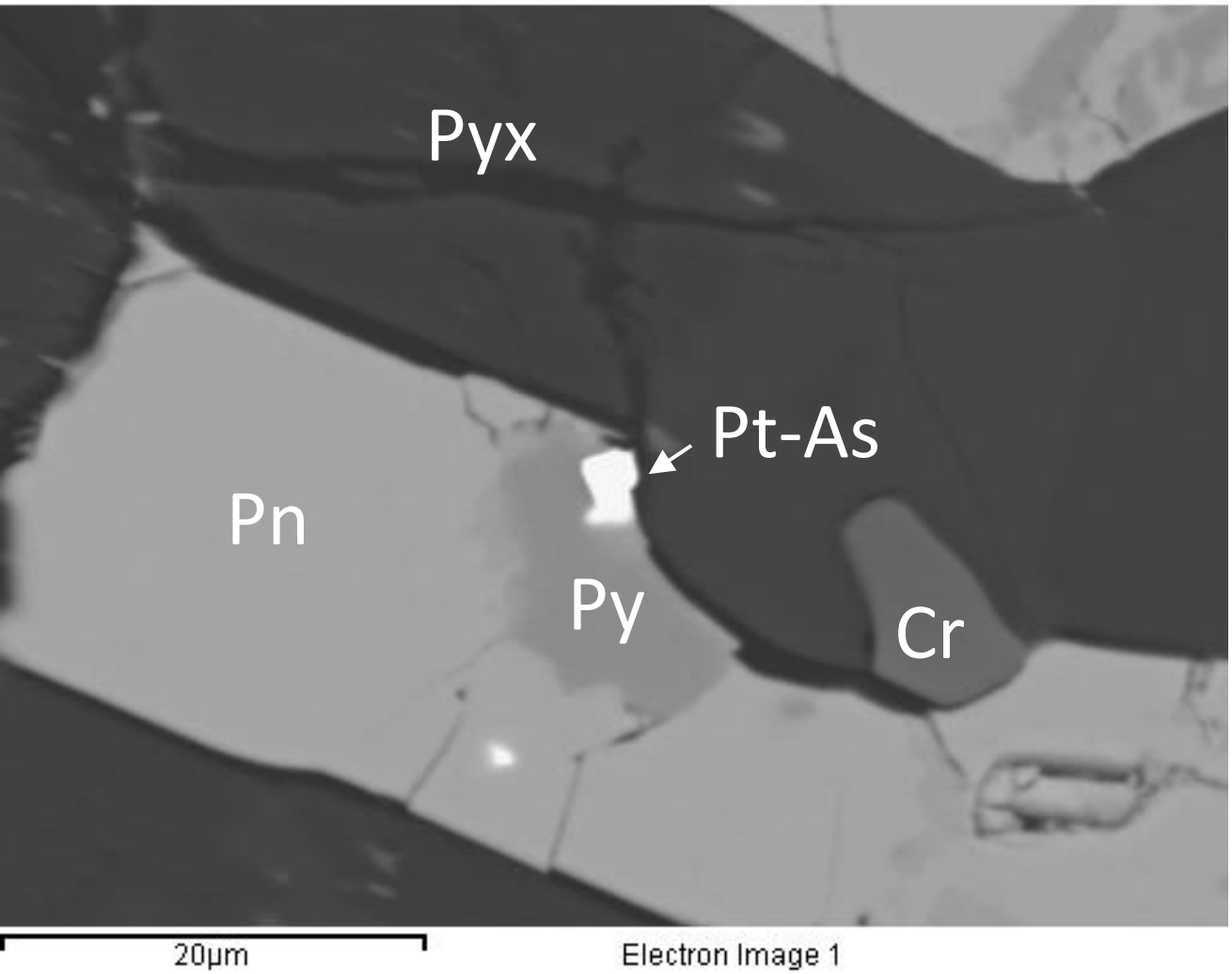
PTSR-53 E 1



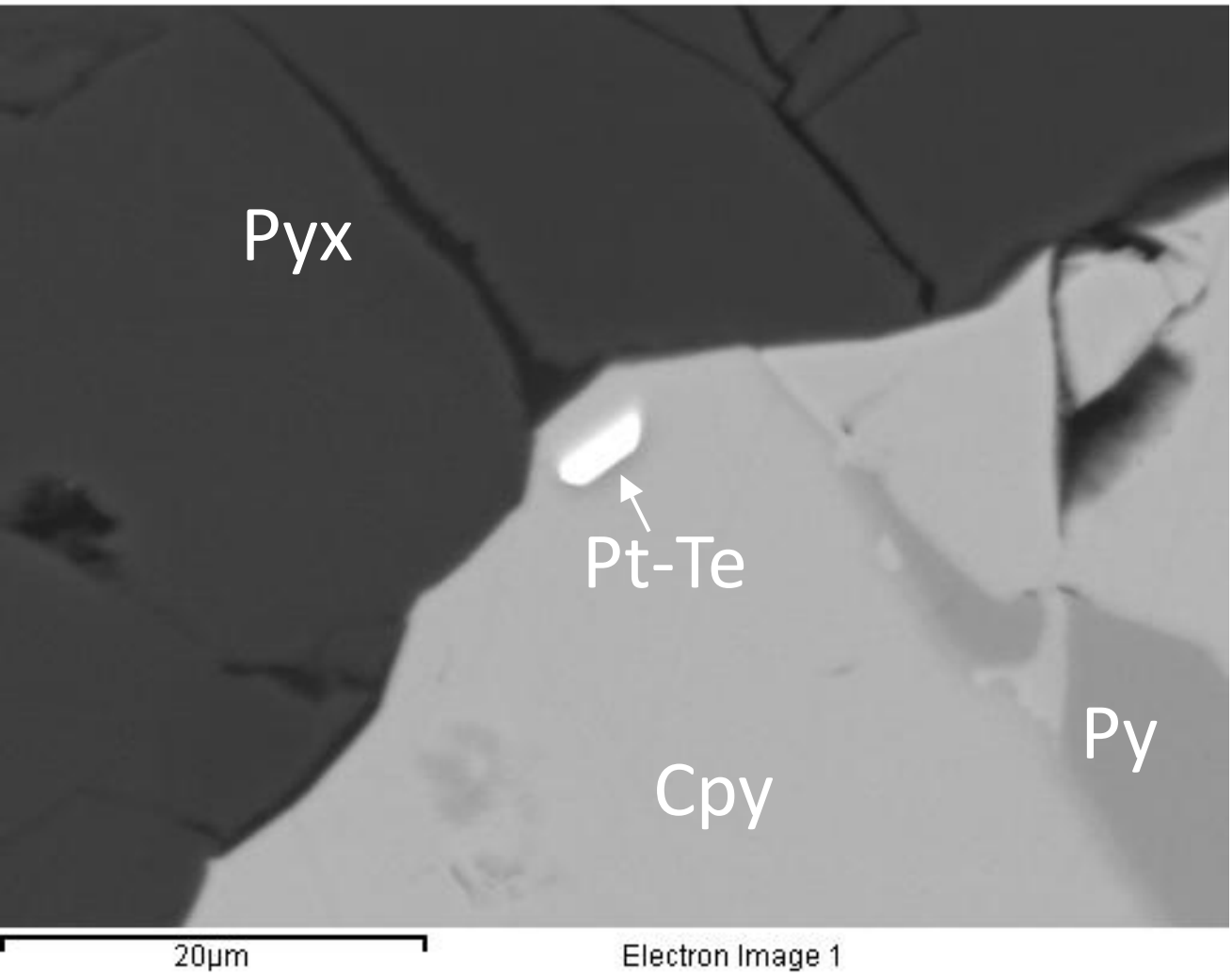
PTSR-53 F 1



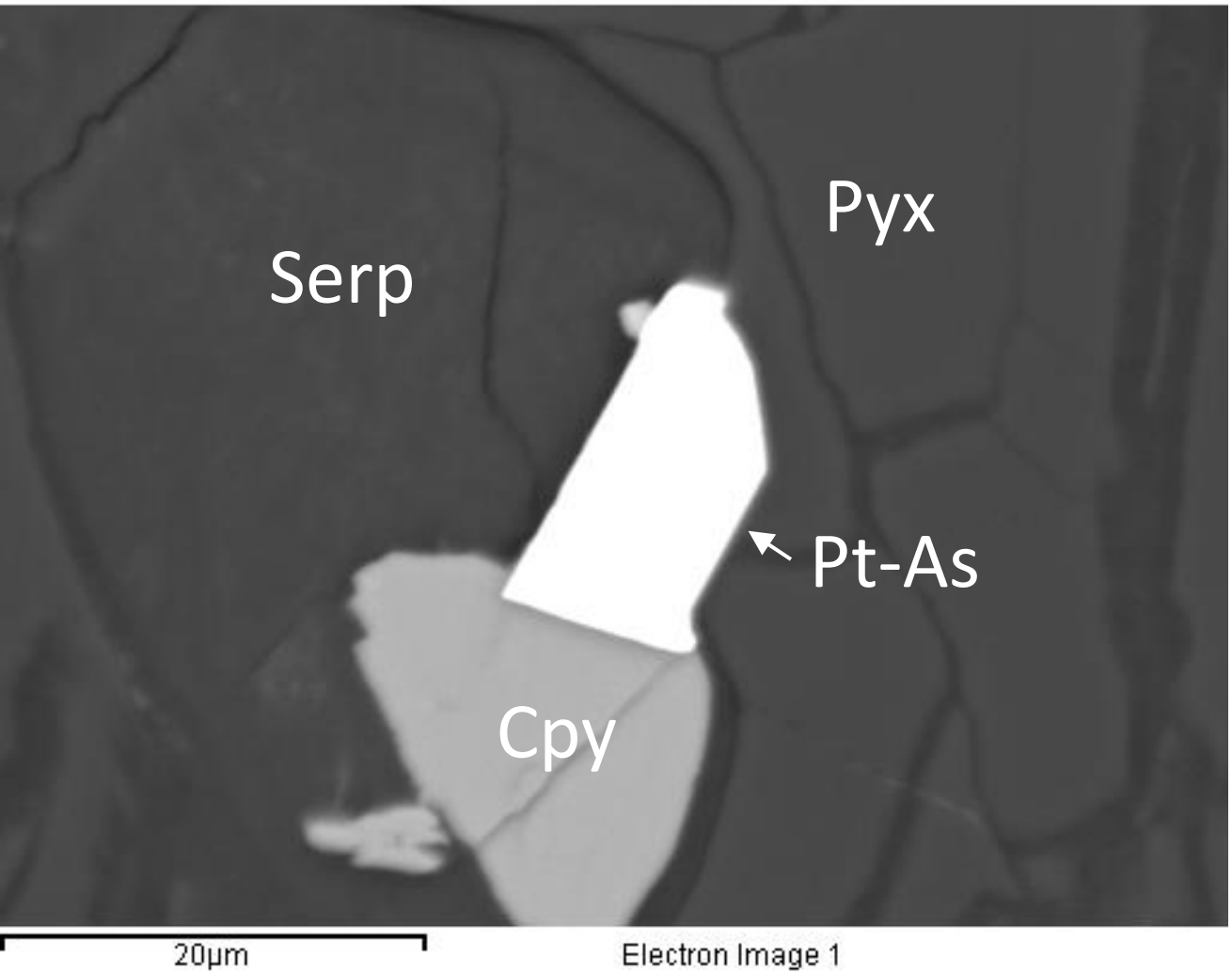
PTSR-53 G 1



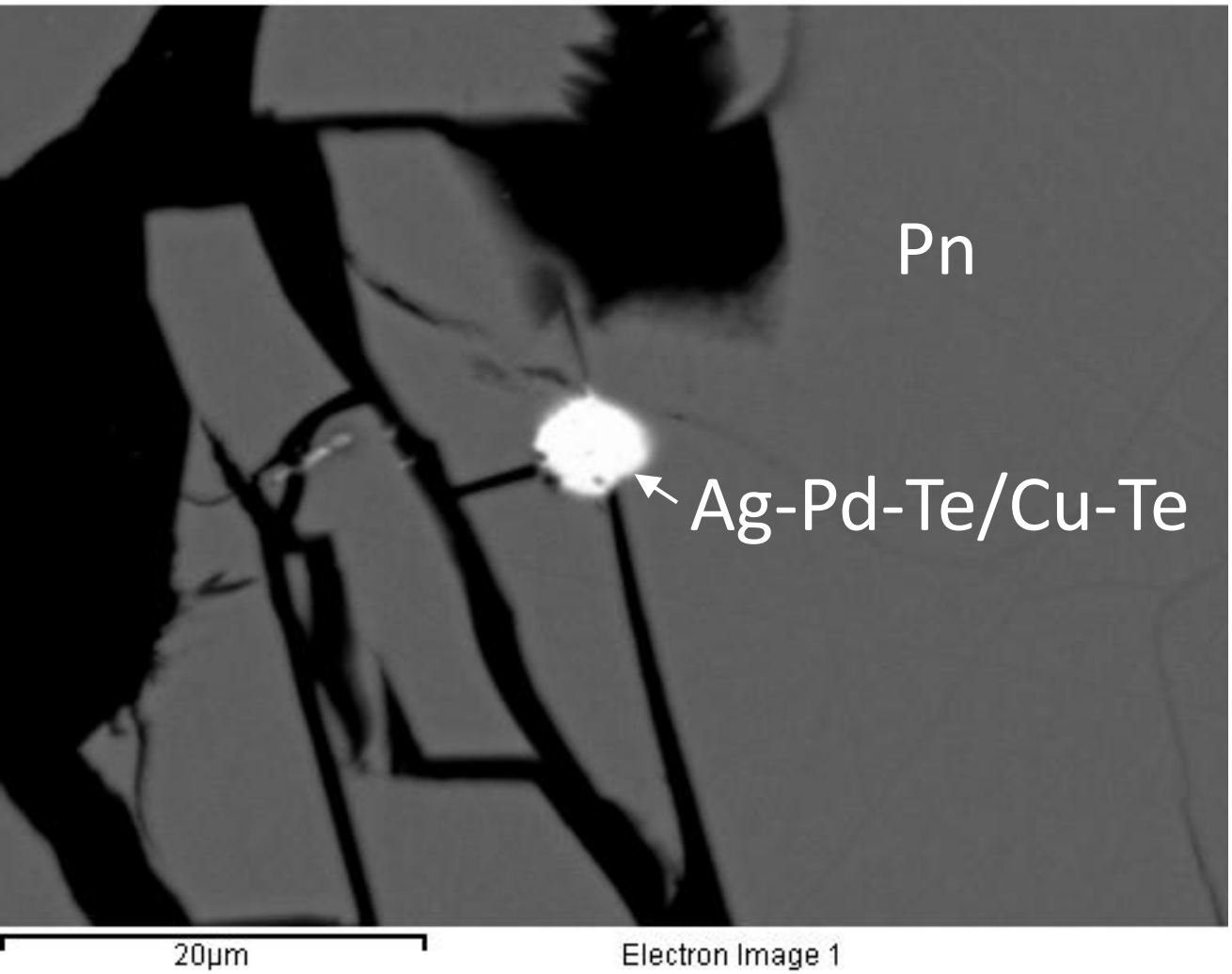
PTSR-53 H 1



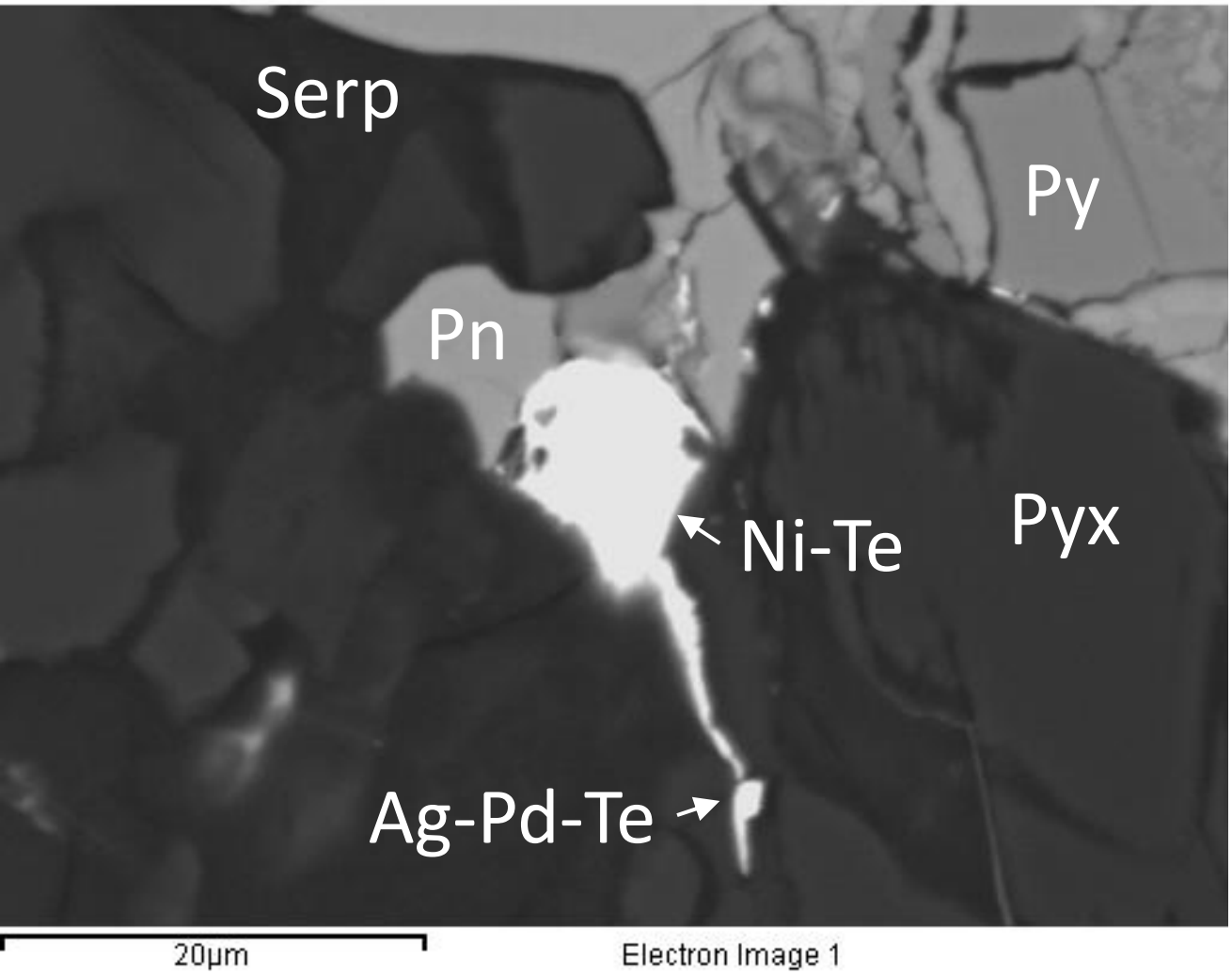
PTSR-54 A 1



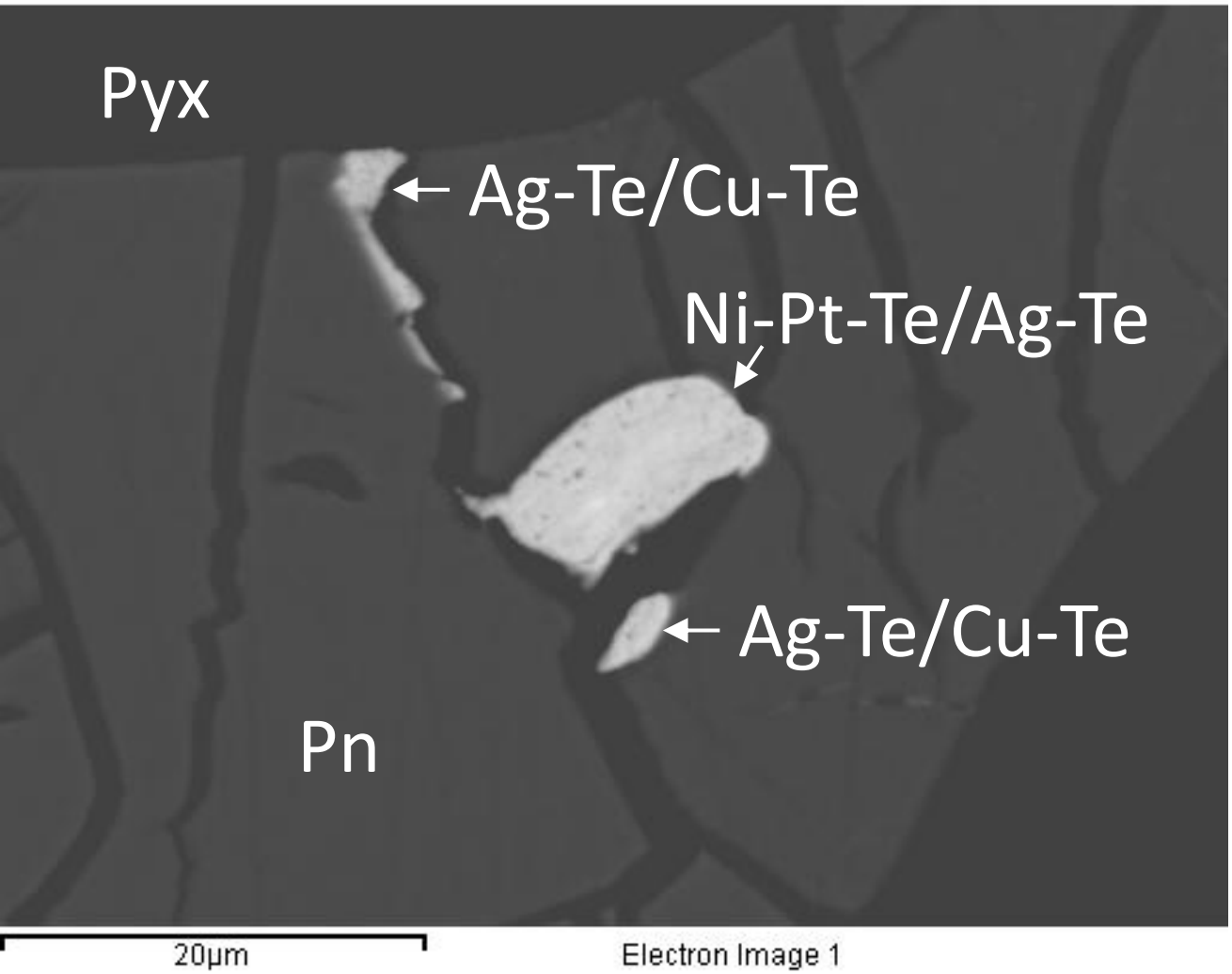
PTSR-54 B 1



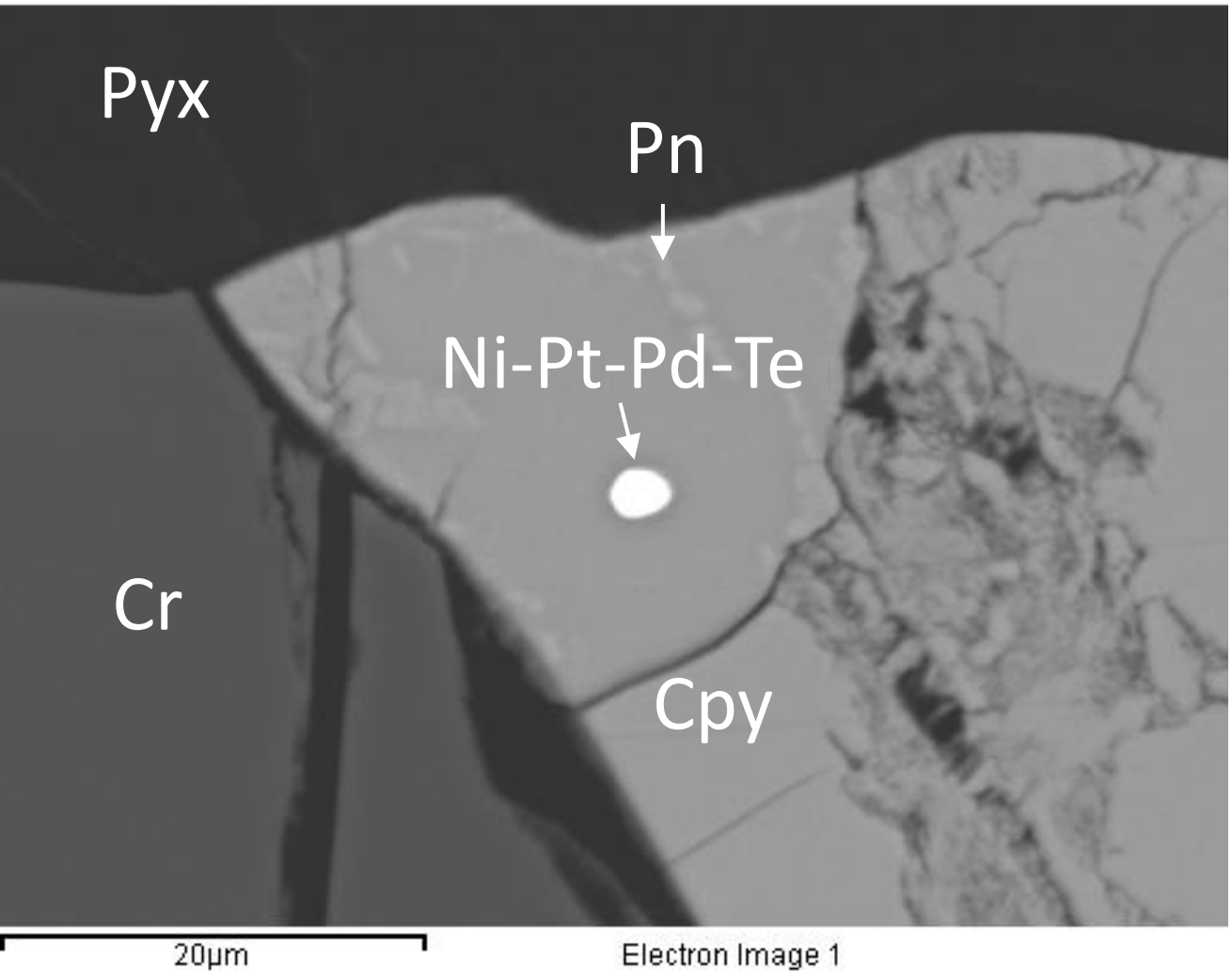
PTSR-54 C 1



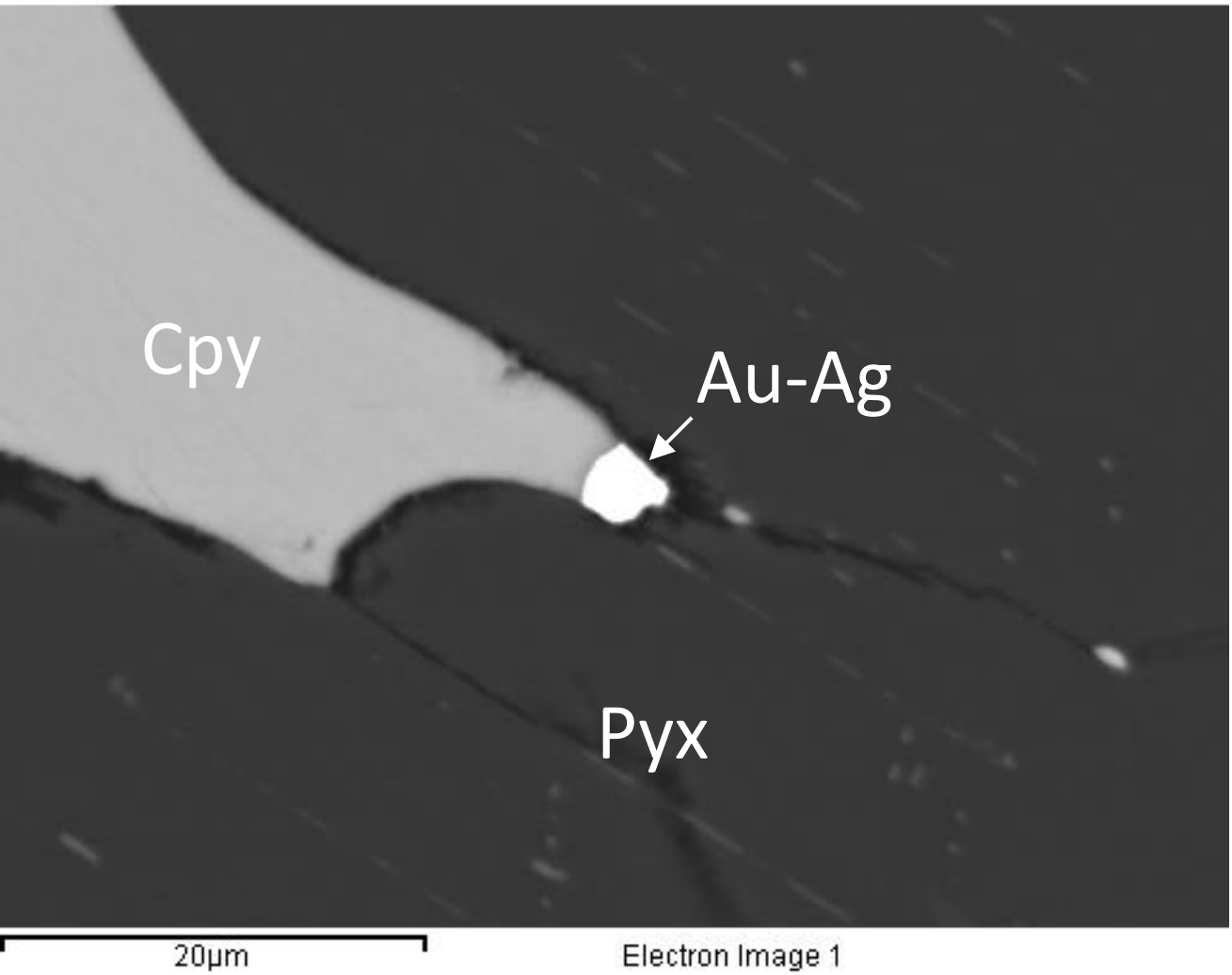
PTSR-54 D 1-3



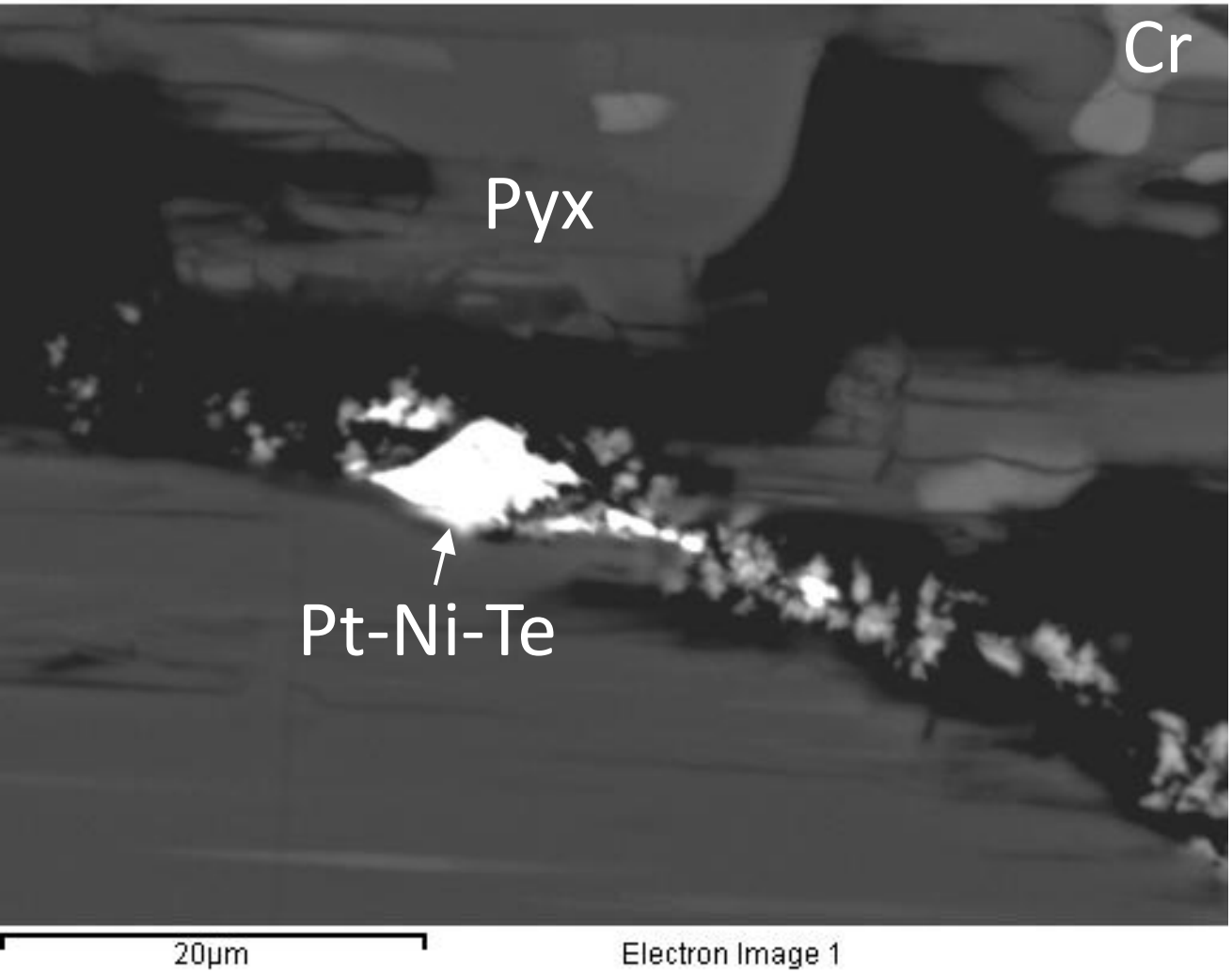
PTSR-54 E 1



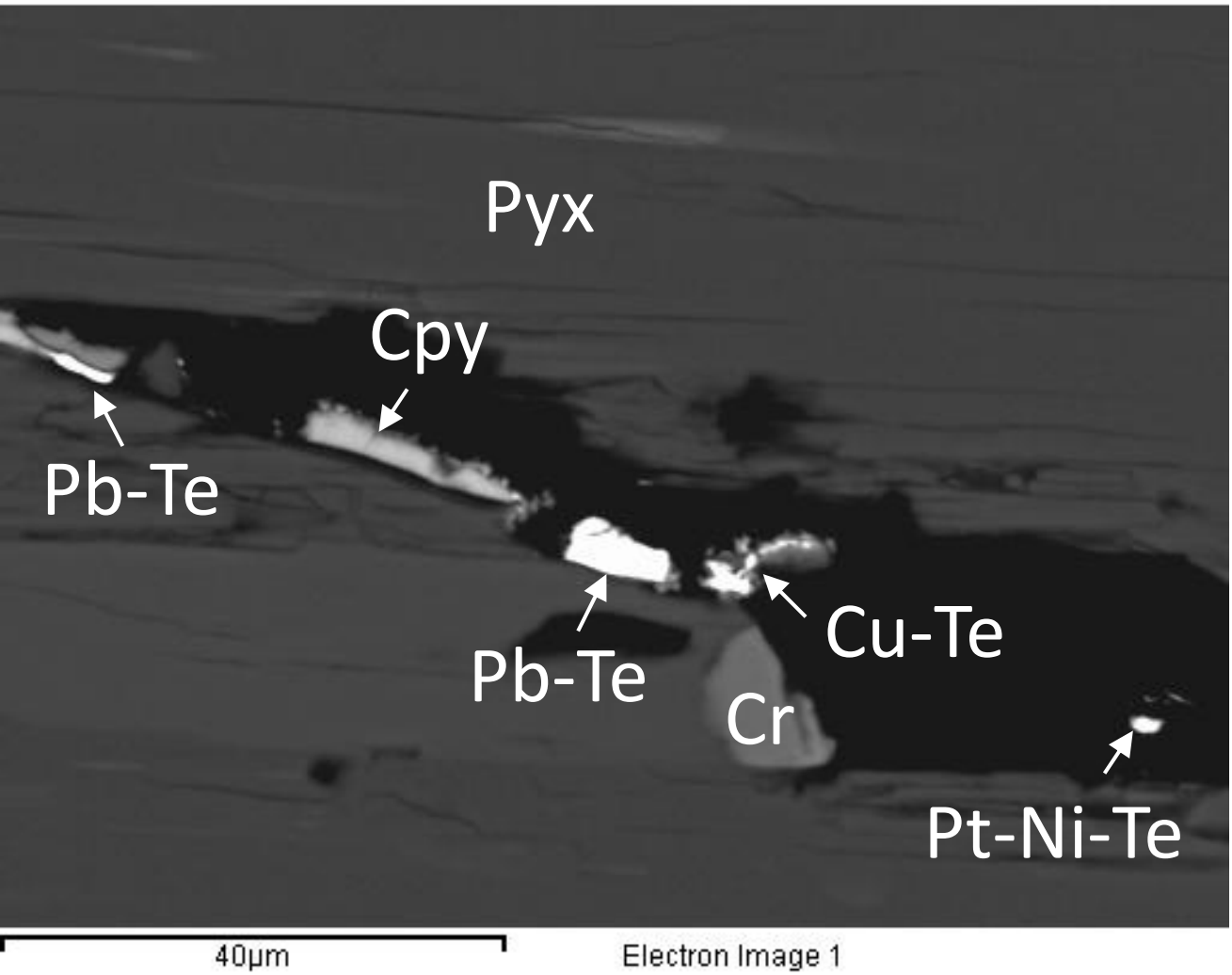
PTSR-55 A 1



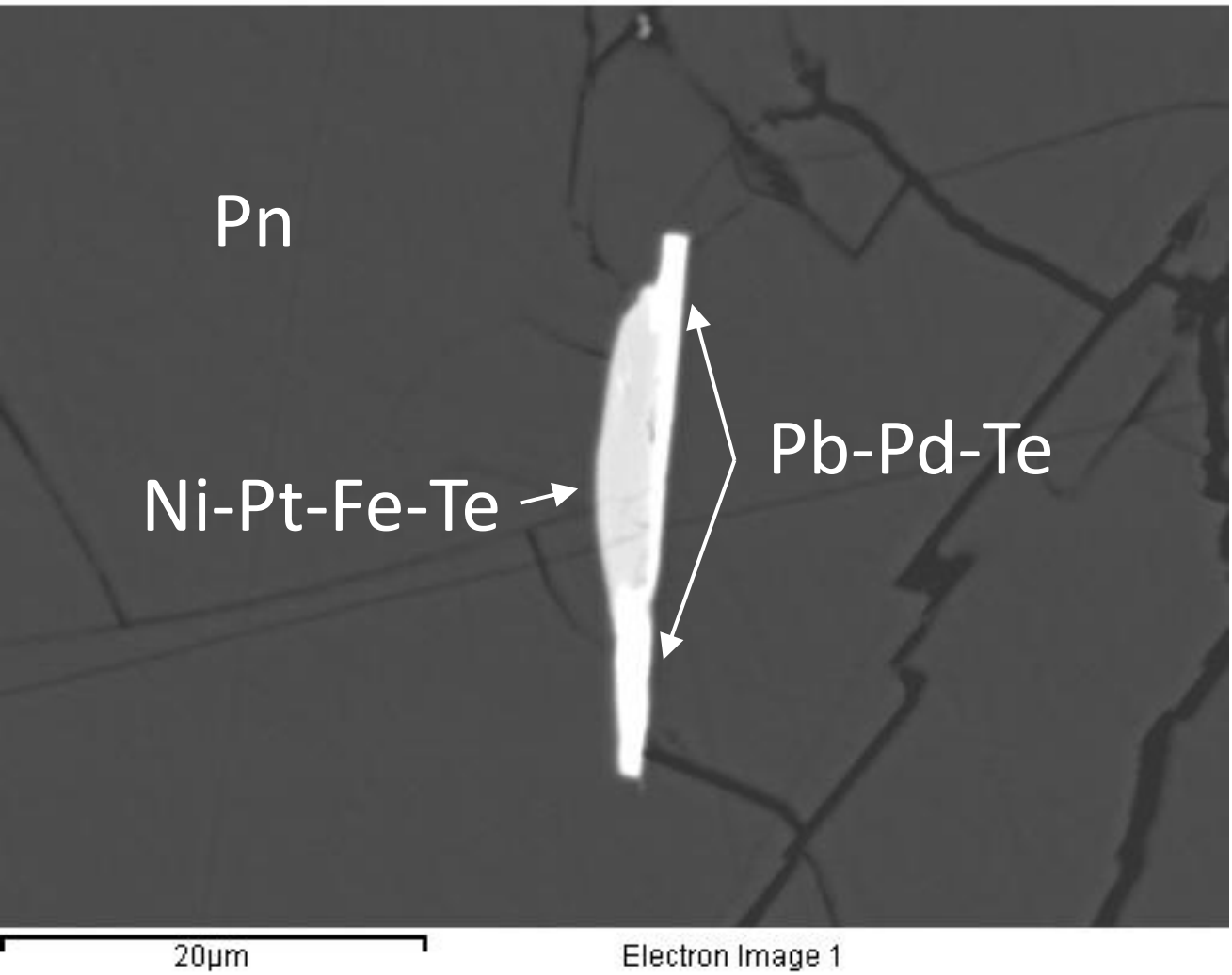
PTSR-55 B 1



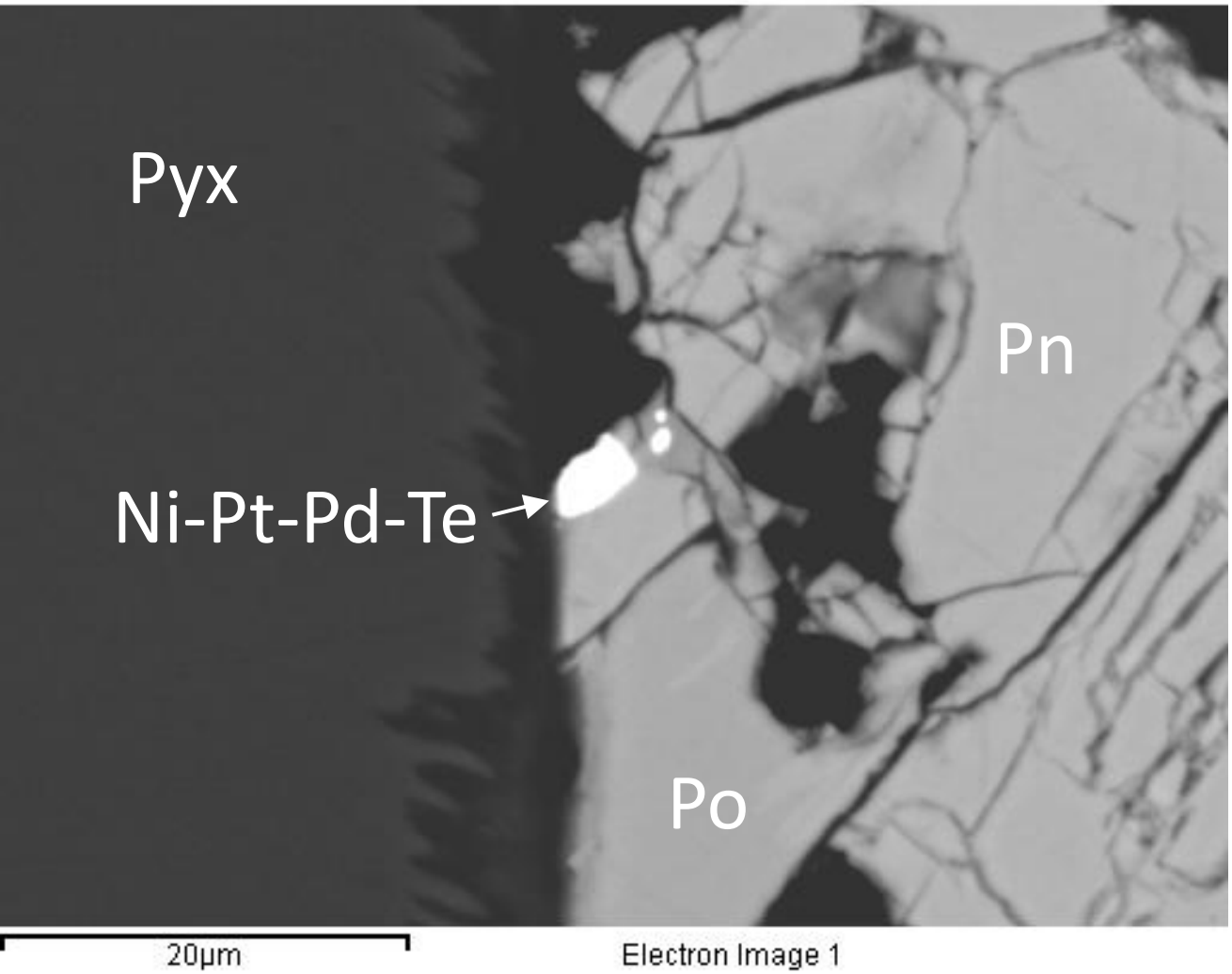
PTSR-55 C 1-4



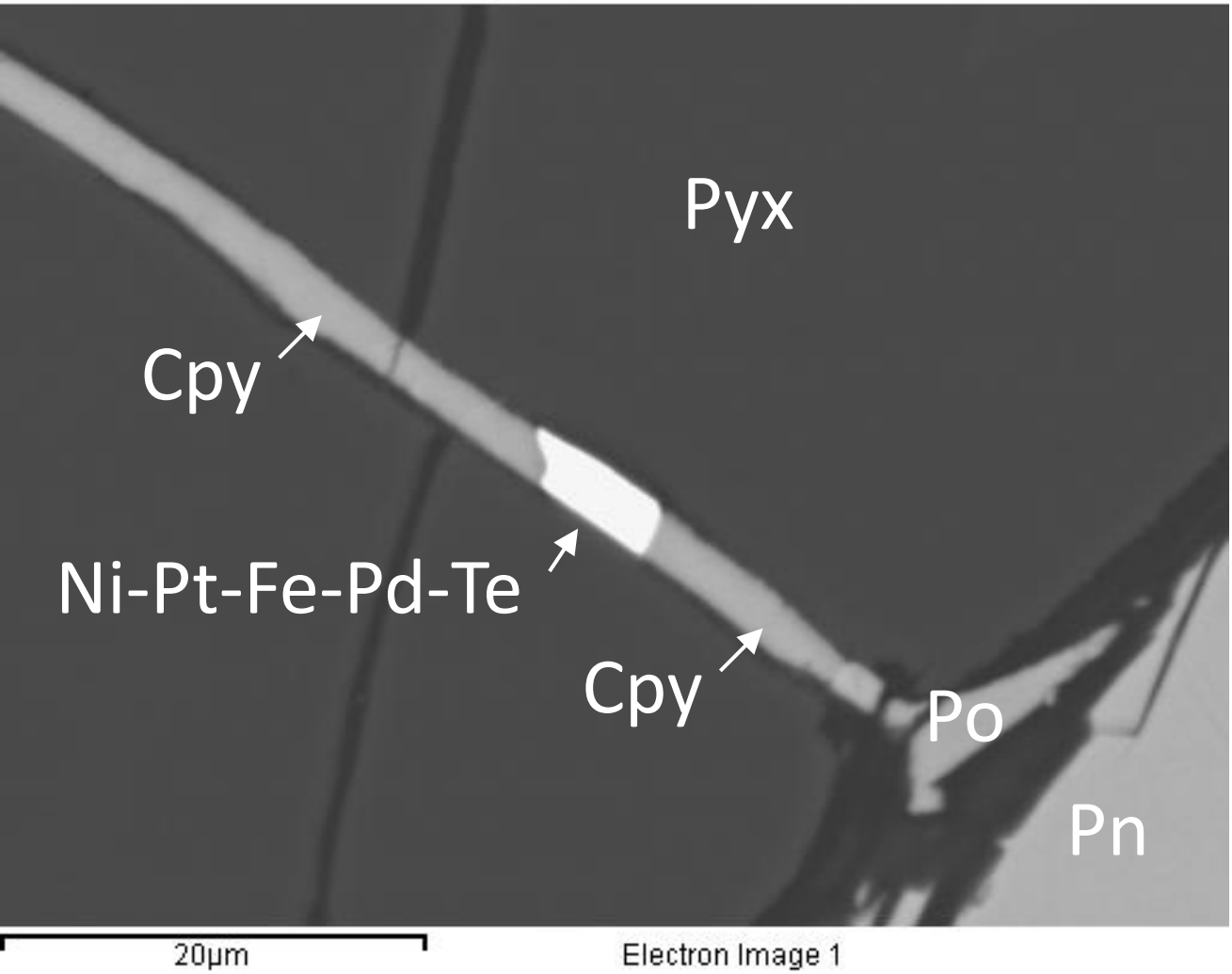
PTSR-55 D 1-2



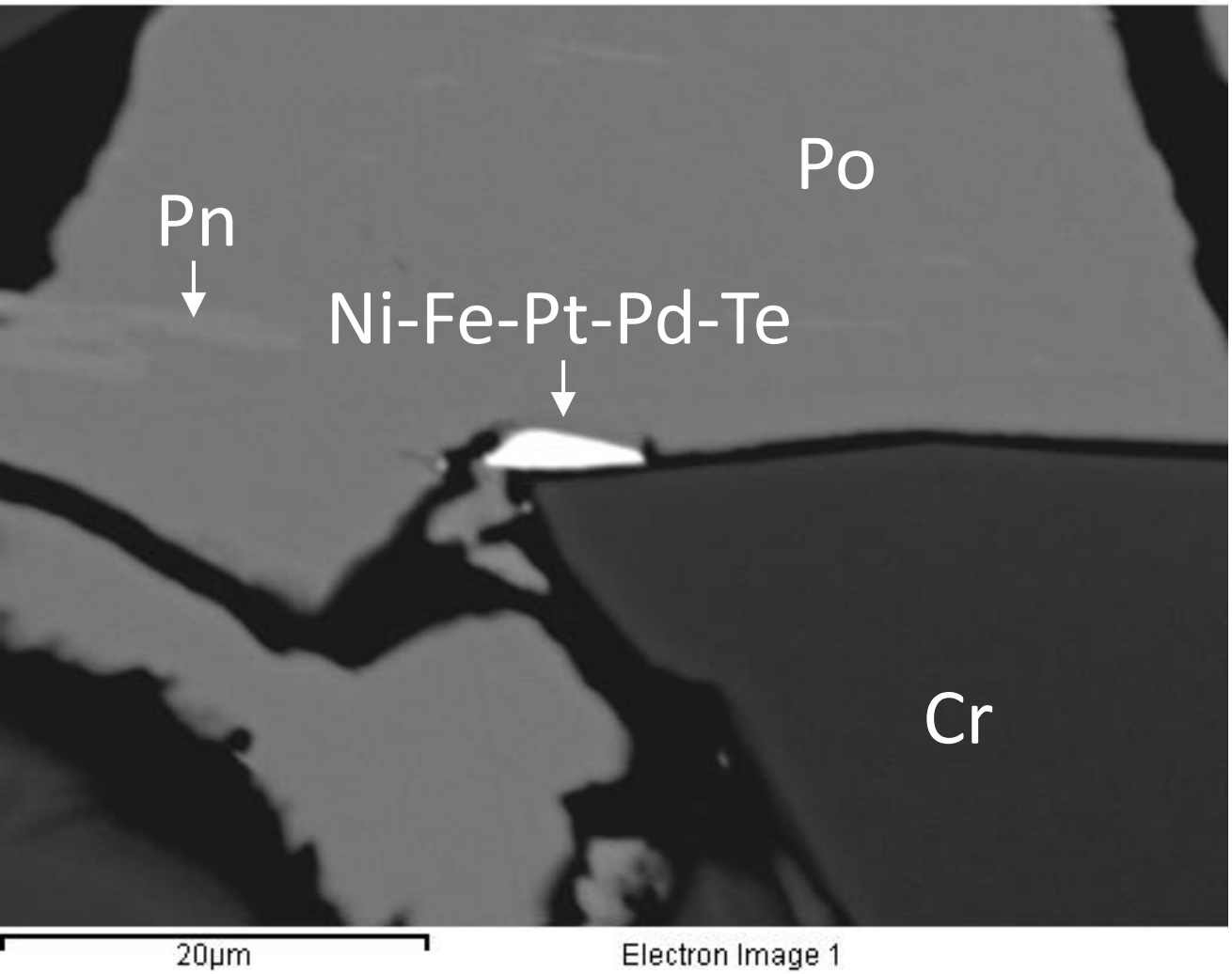
PTSR-55 E 1



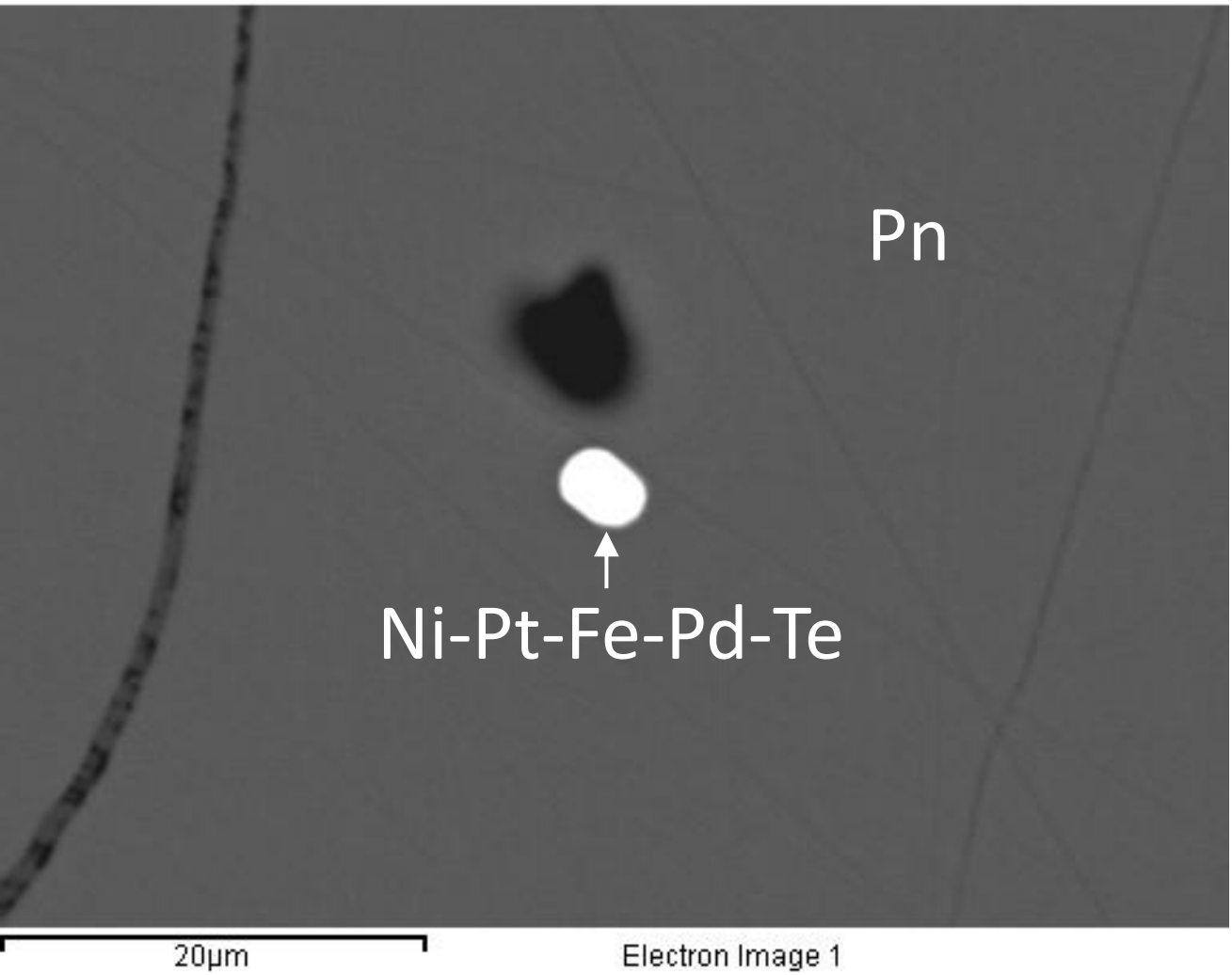
PTSR-55 F 1



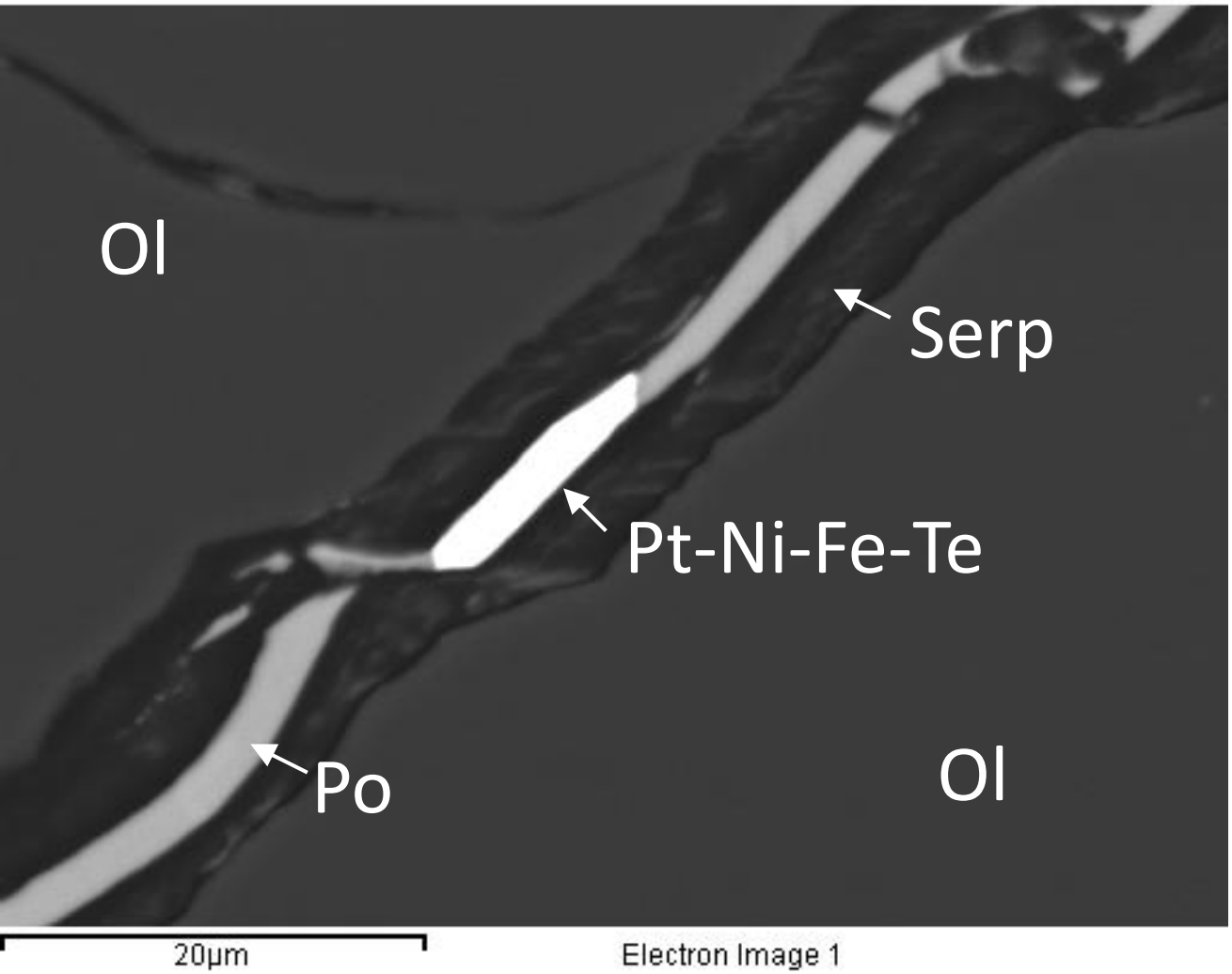
PTSR-55 G 1



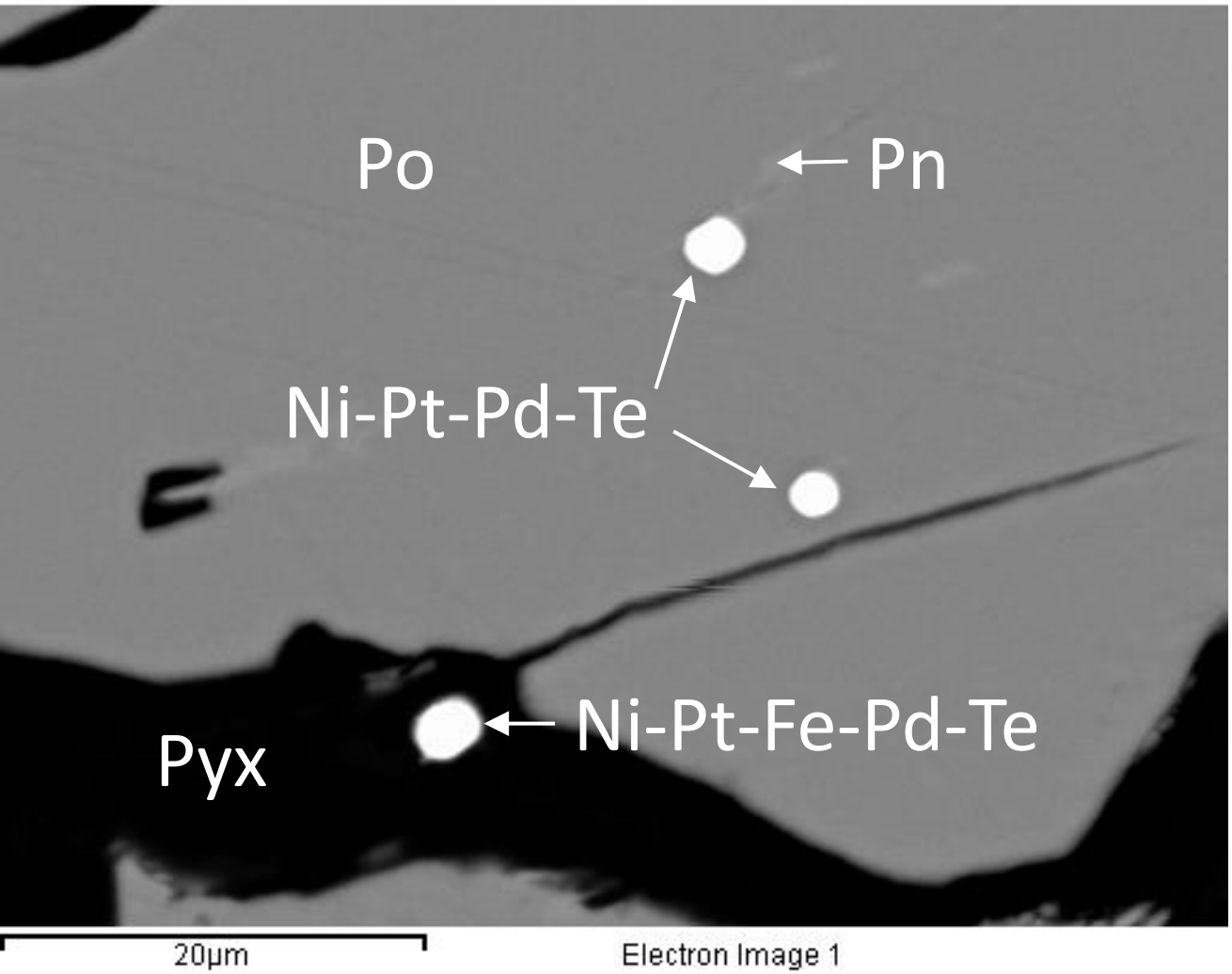
PTSR-55 H 1



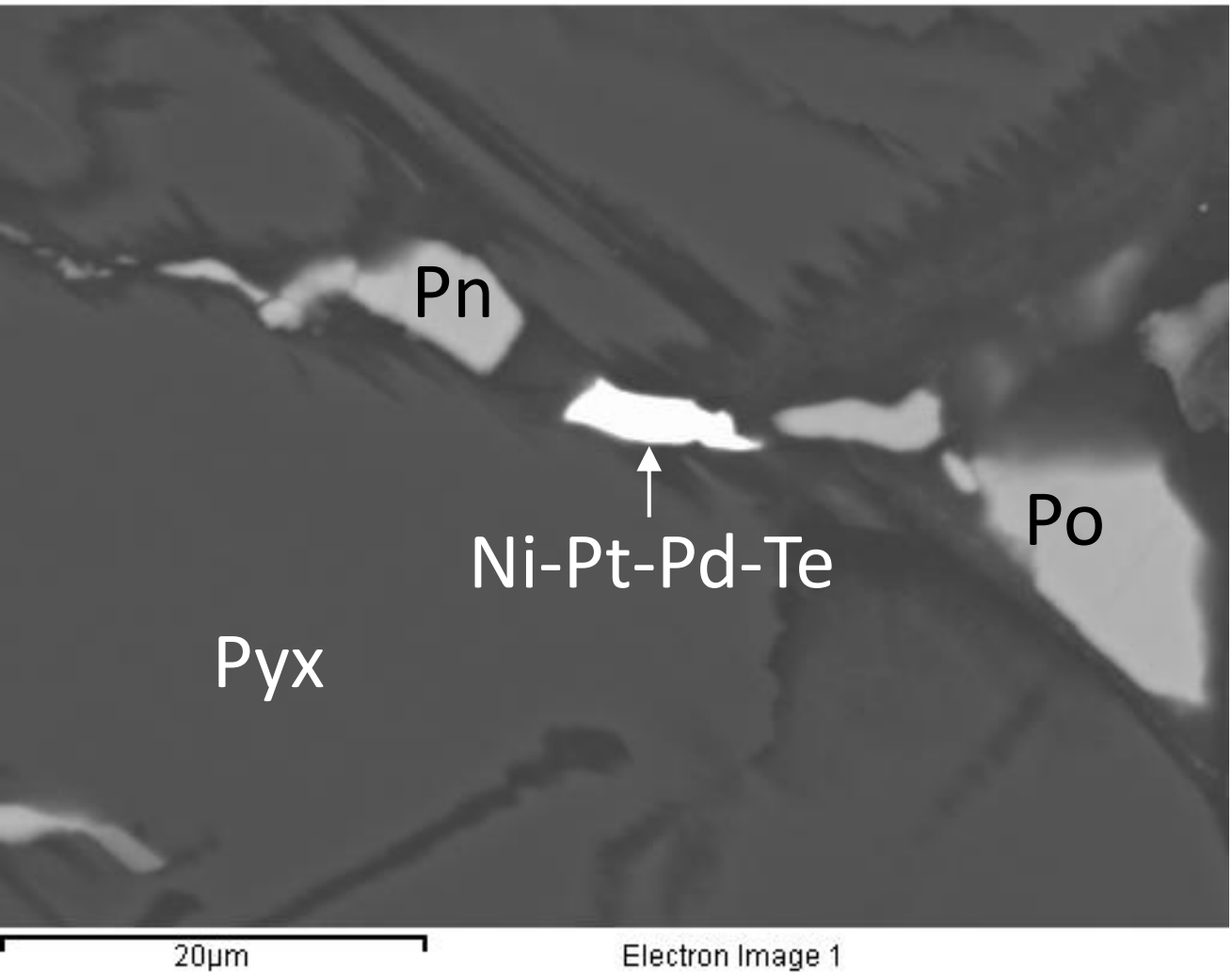
PTSR-55 I 1



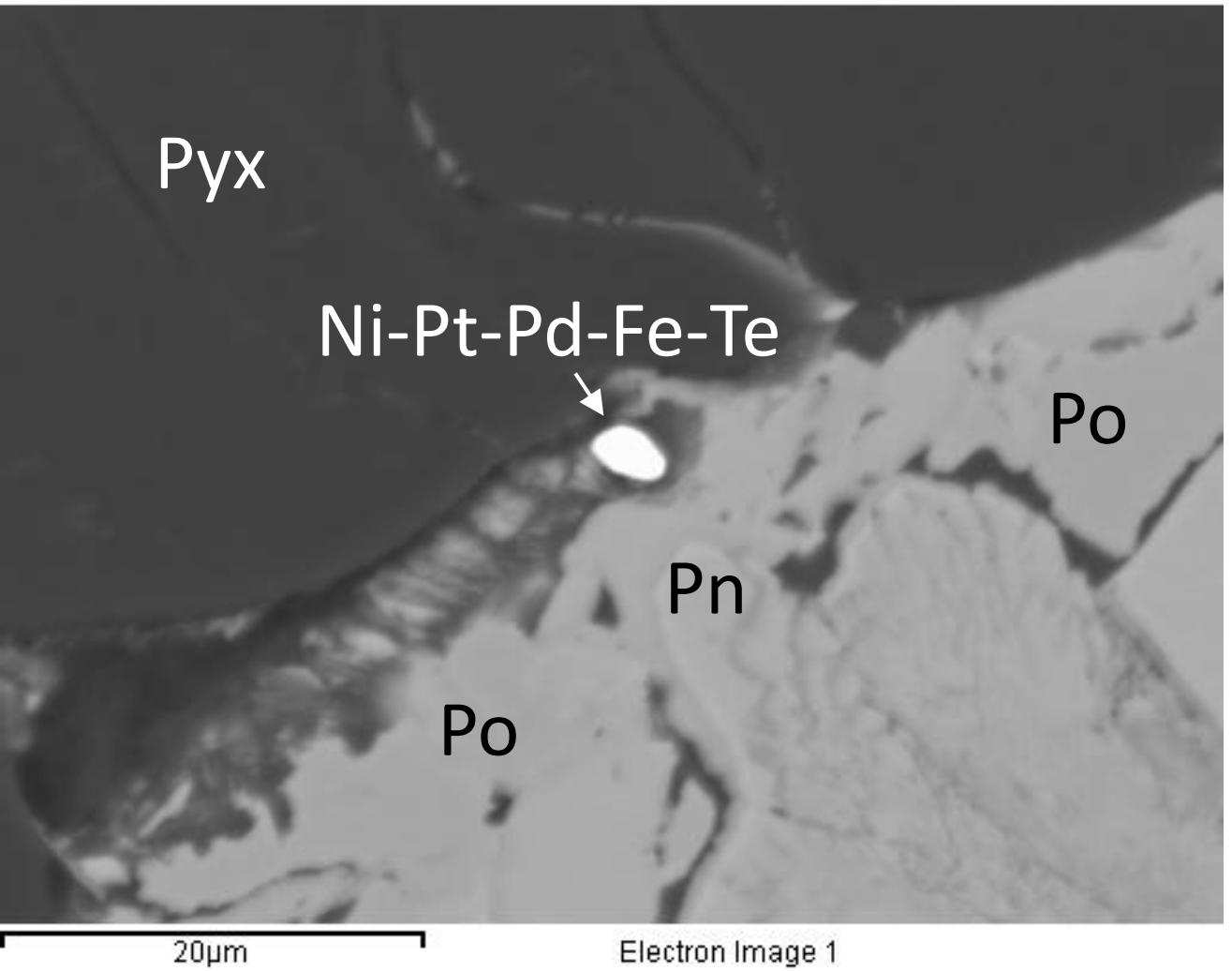
PTSR-55 J 1-3



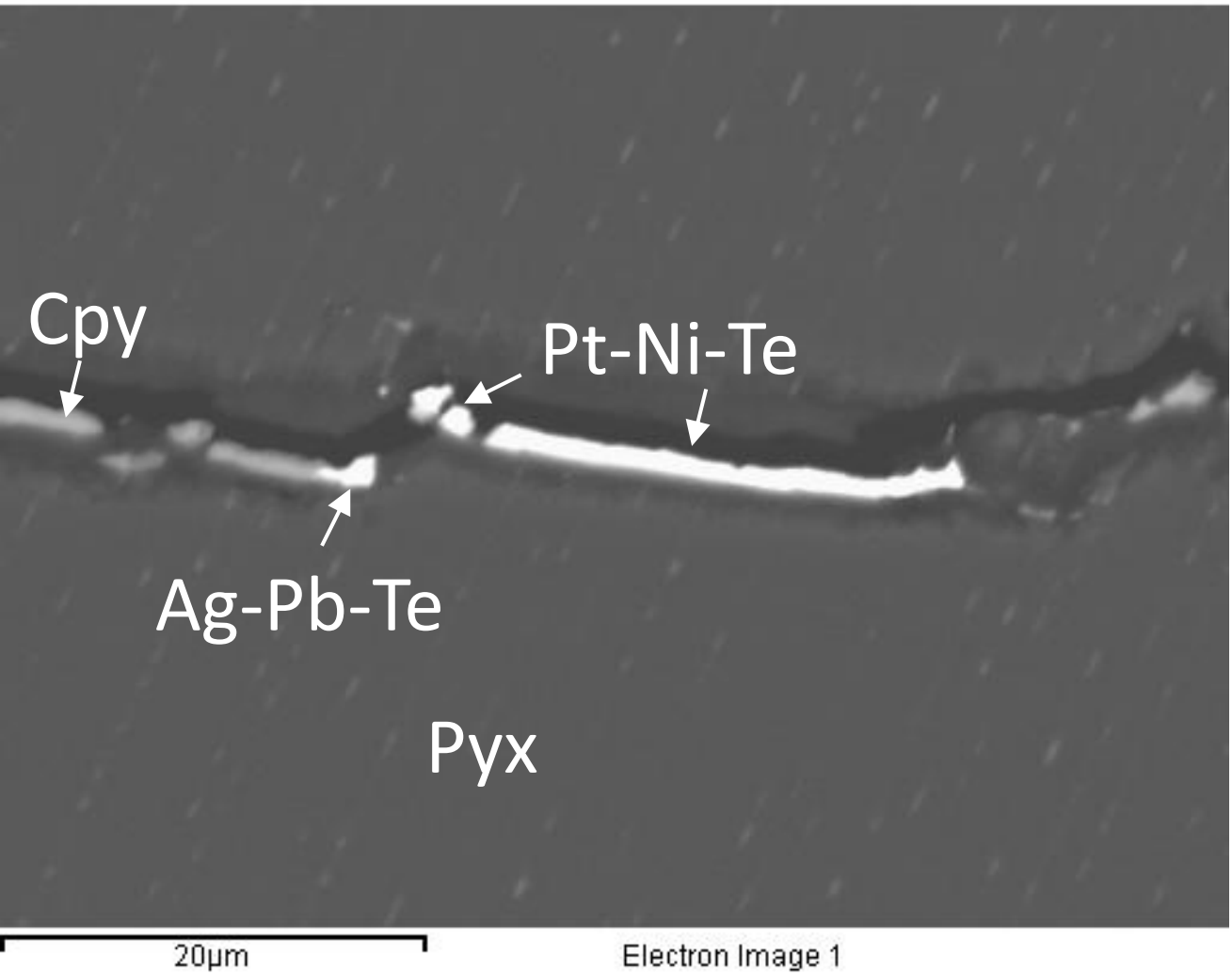
PTSR-55 K 1



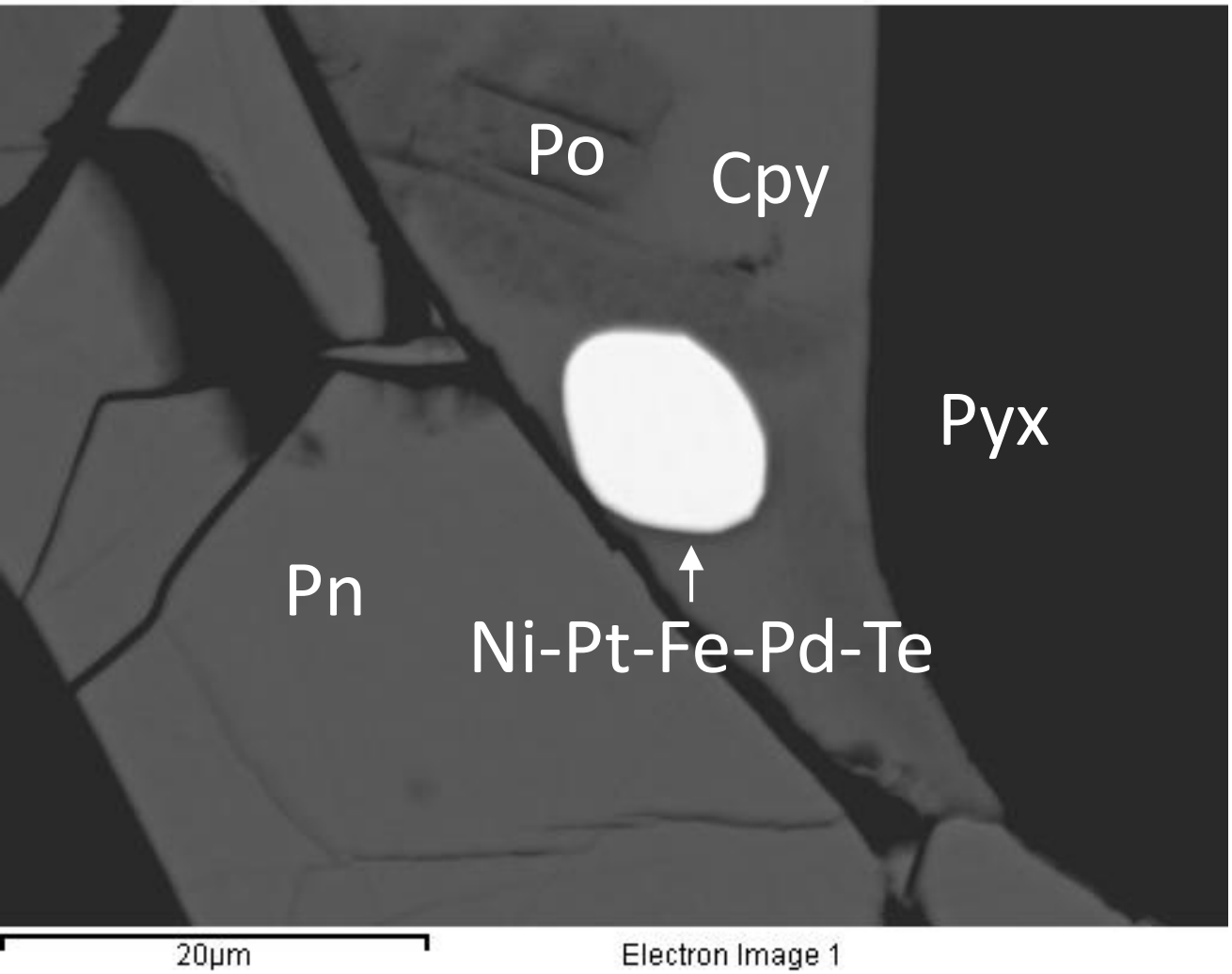
PTSR-55 L 1



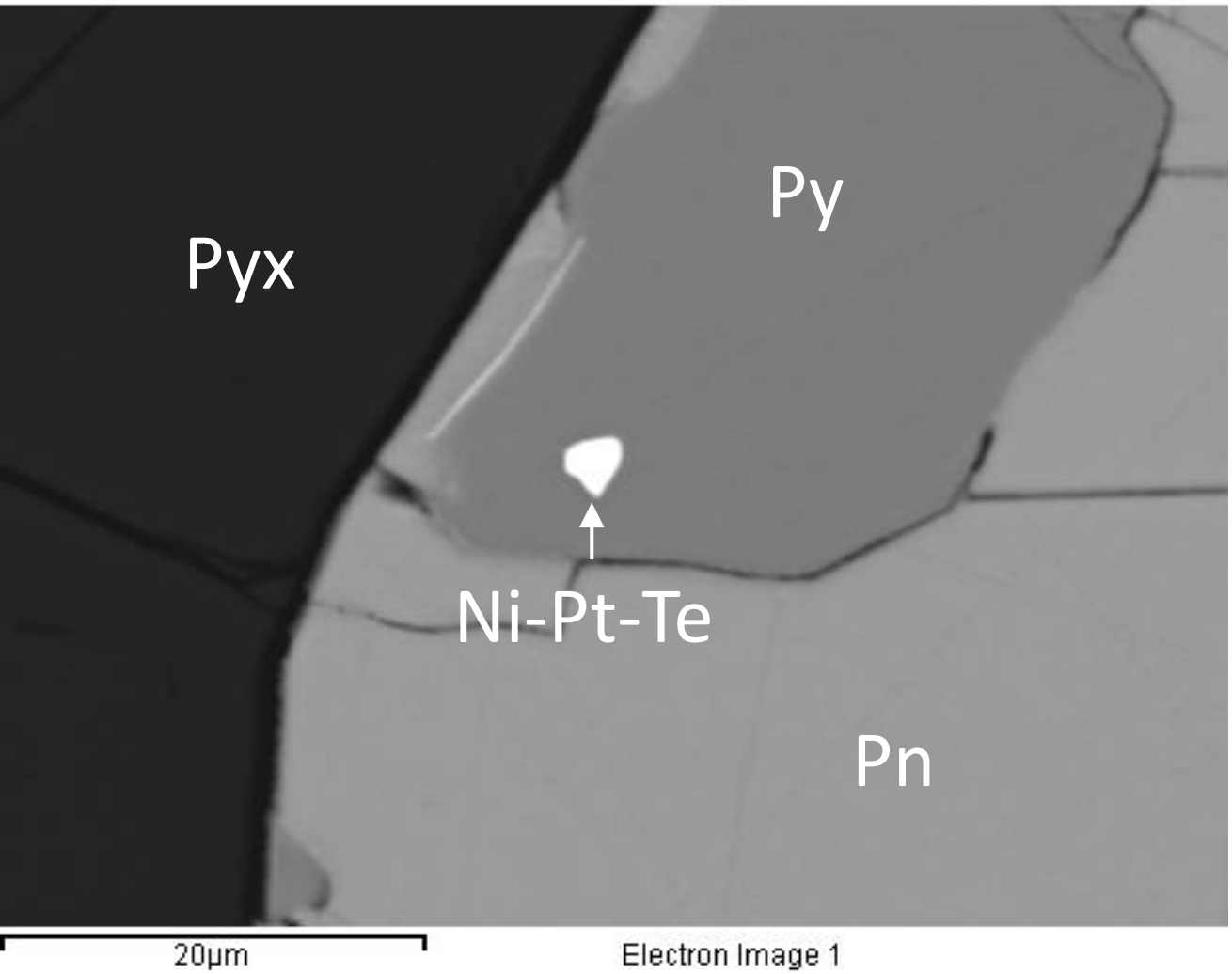
PTSR-55 M 1-2



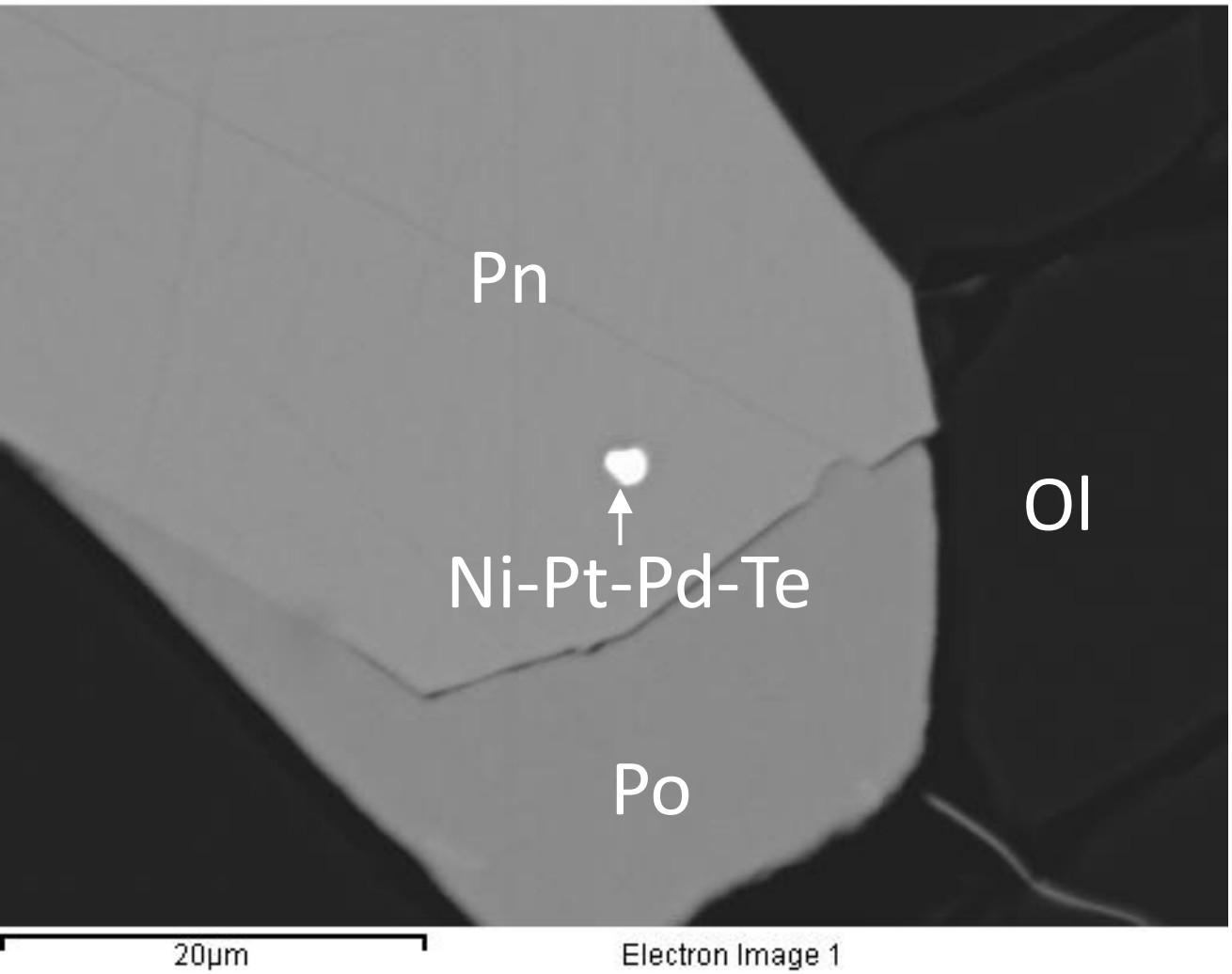
PTSR-55 N 1



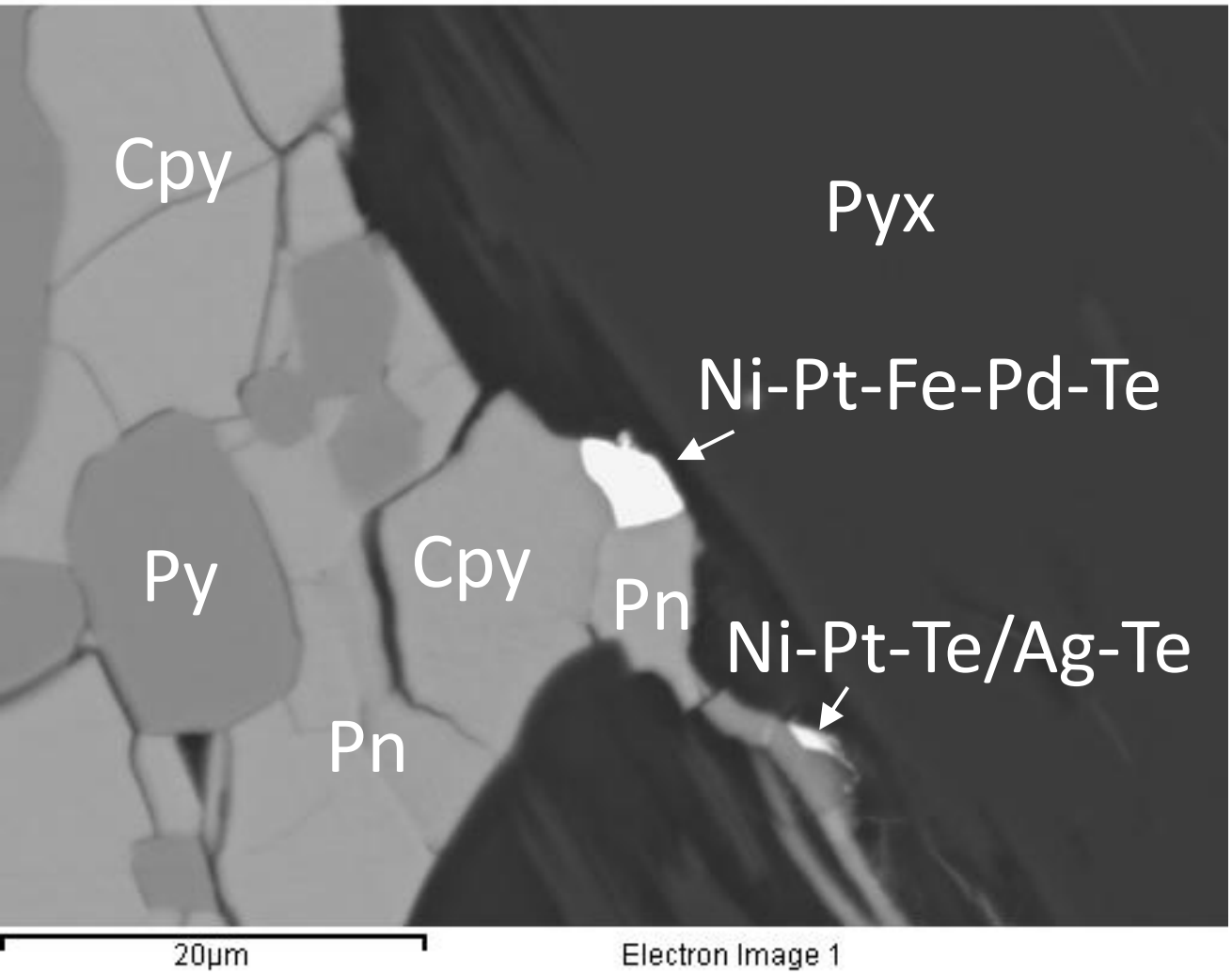
PTSR-55 O 1



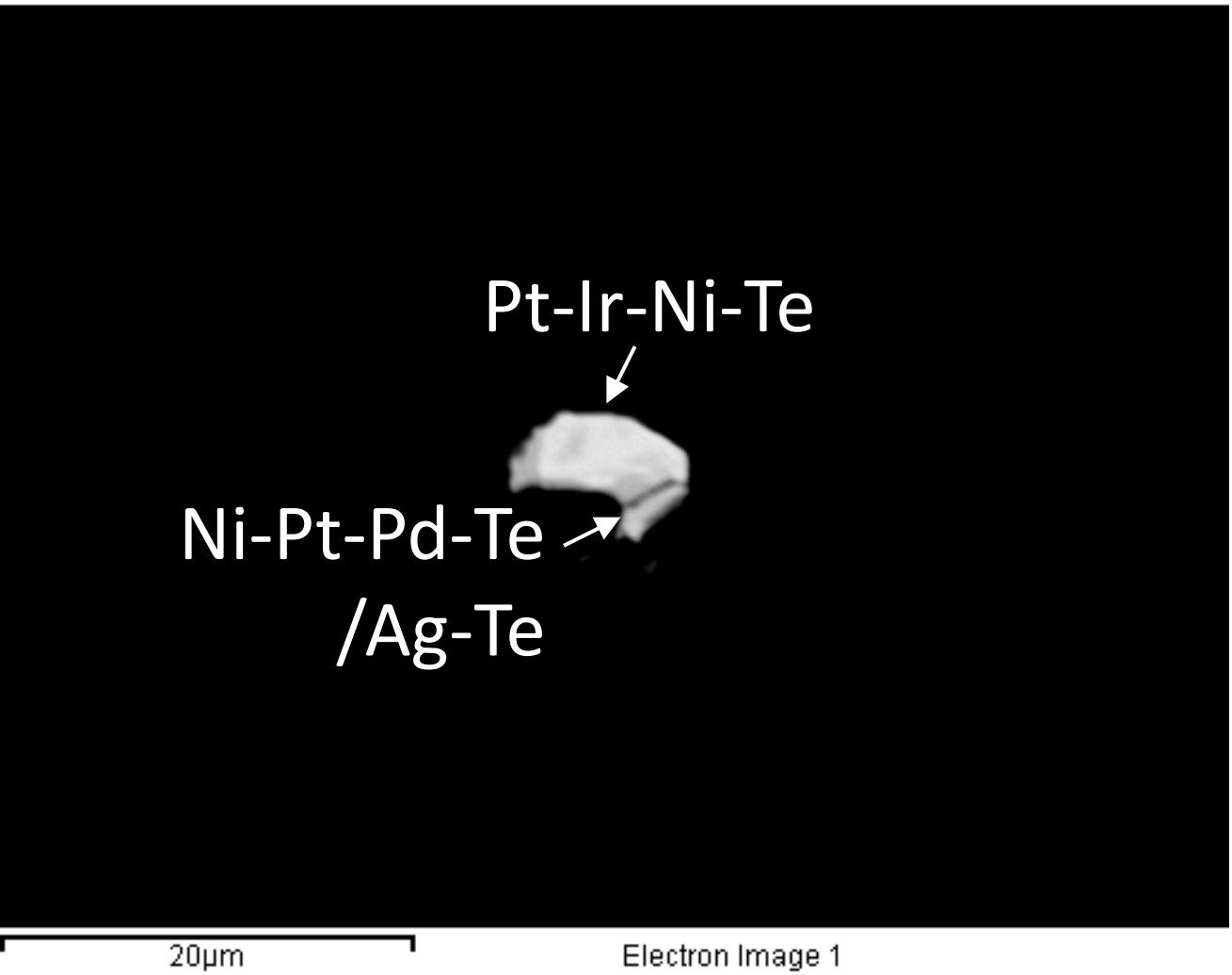
PTSR-55 P 1



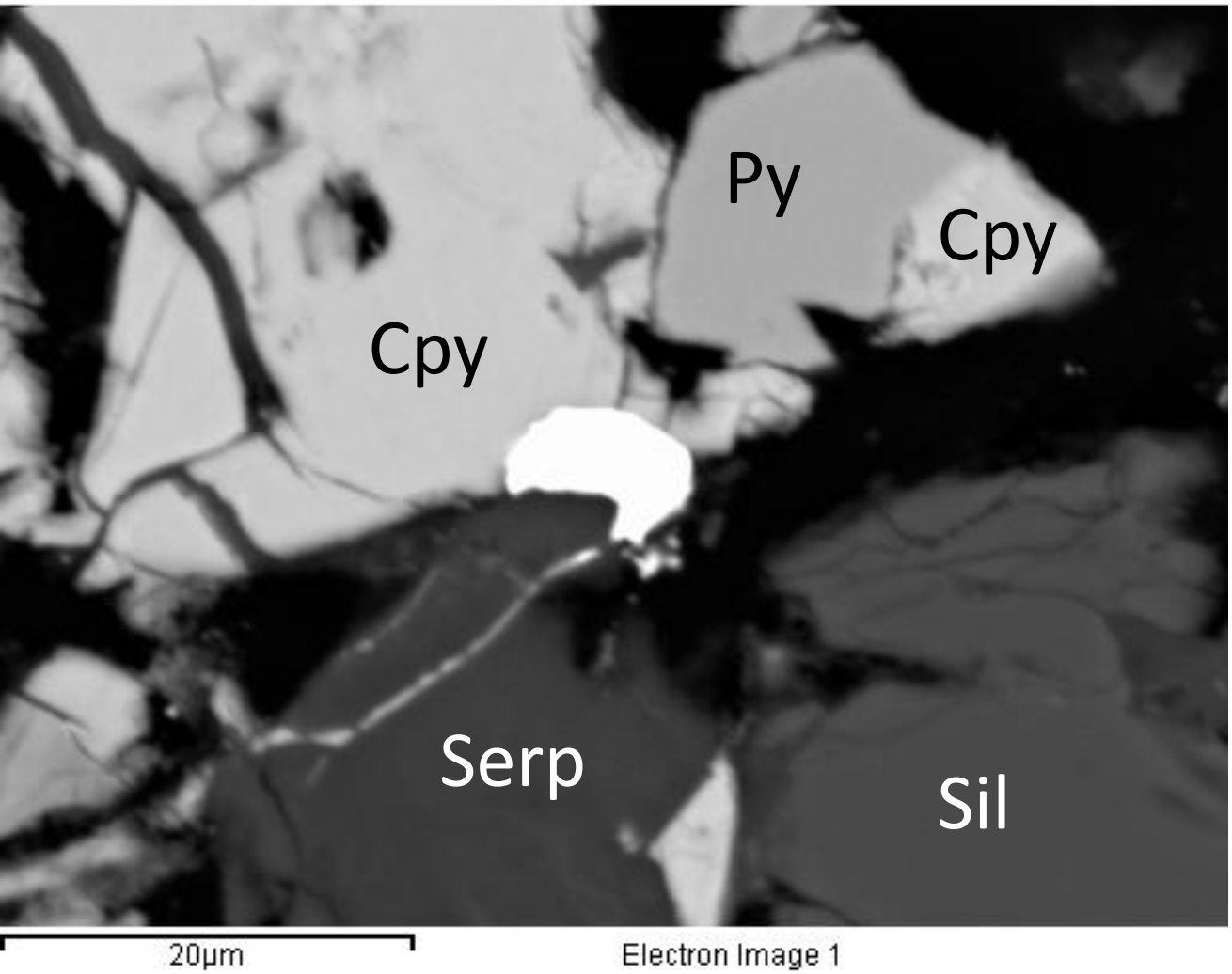
PTSR-55 Q 1-2


Cpy
Pyx
Ni-Pt-Fe-Pd-Te
Py
Cpy
Pn
Ni-Pt-Te/Ag-Te
Pn
20µm
Electron Image 1

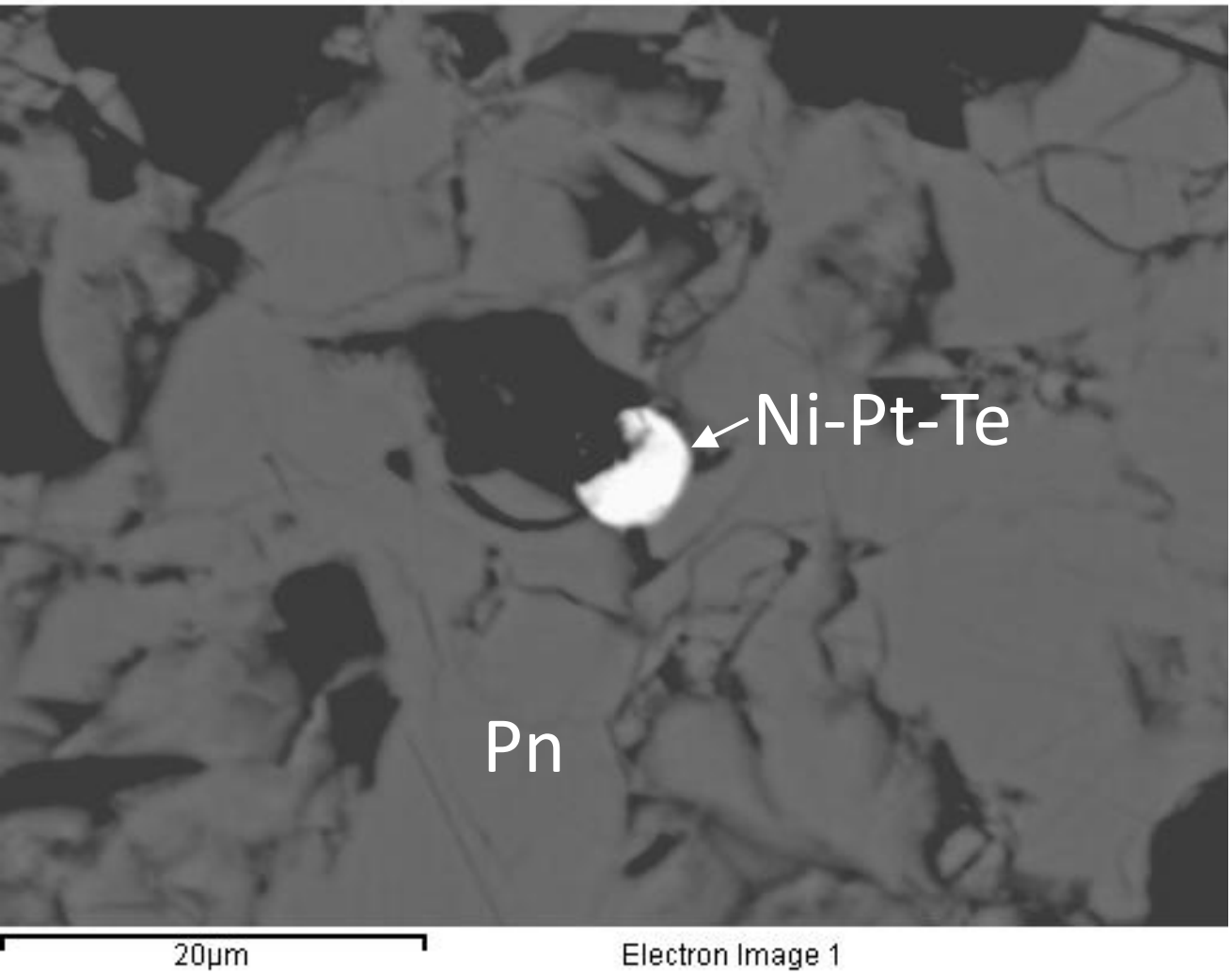
PTSR-55 R 1



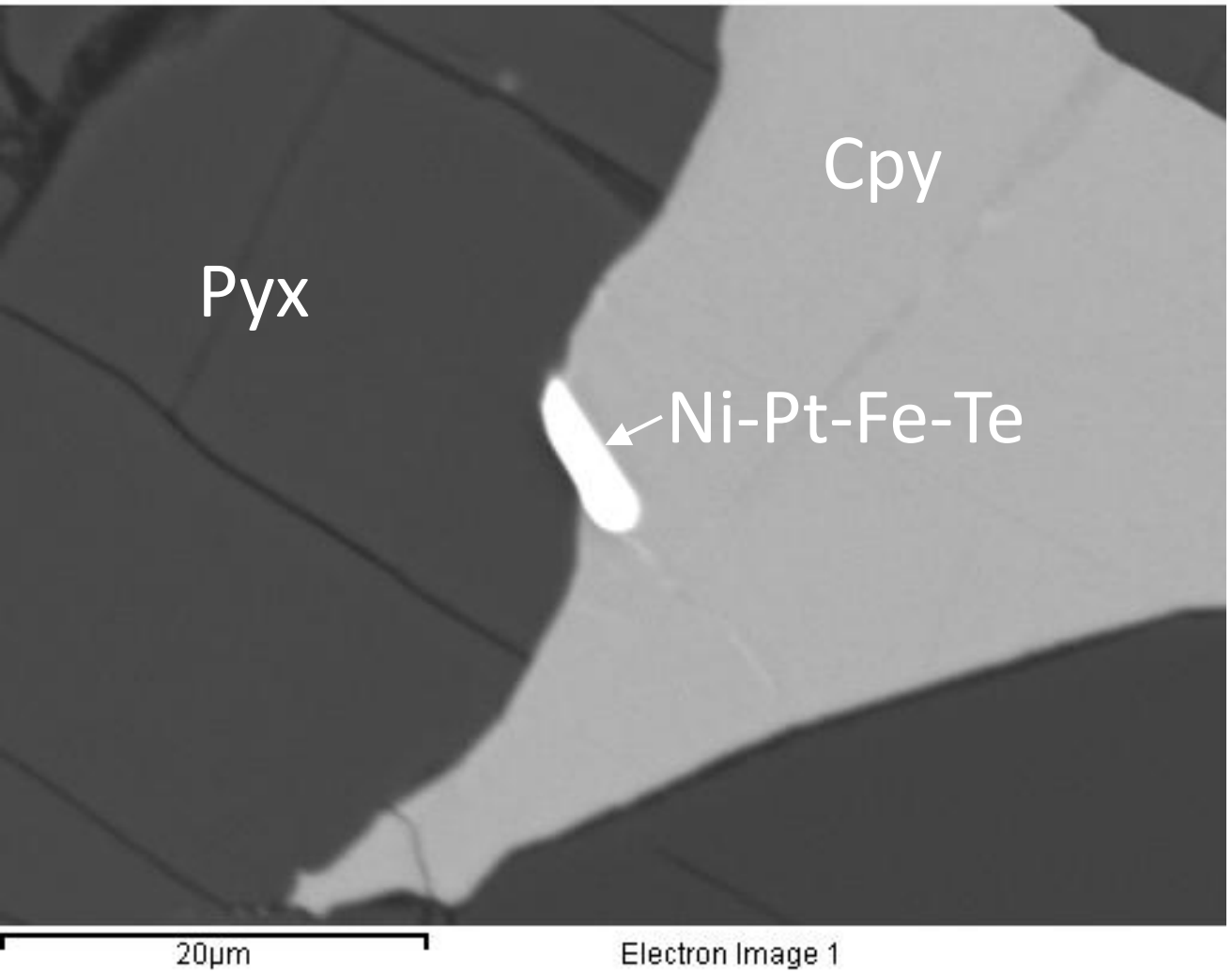
PTSR-55 R 1 Light



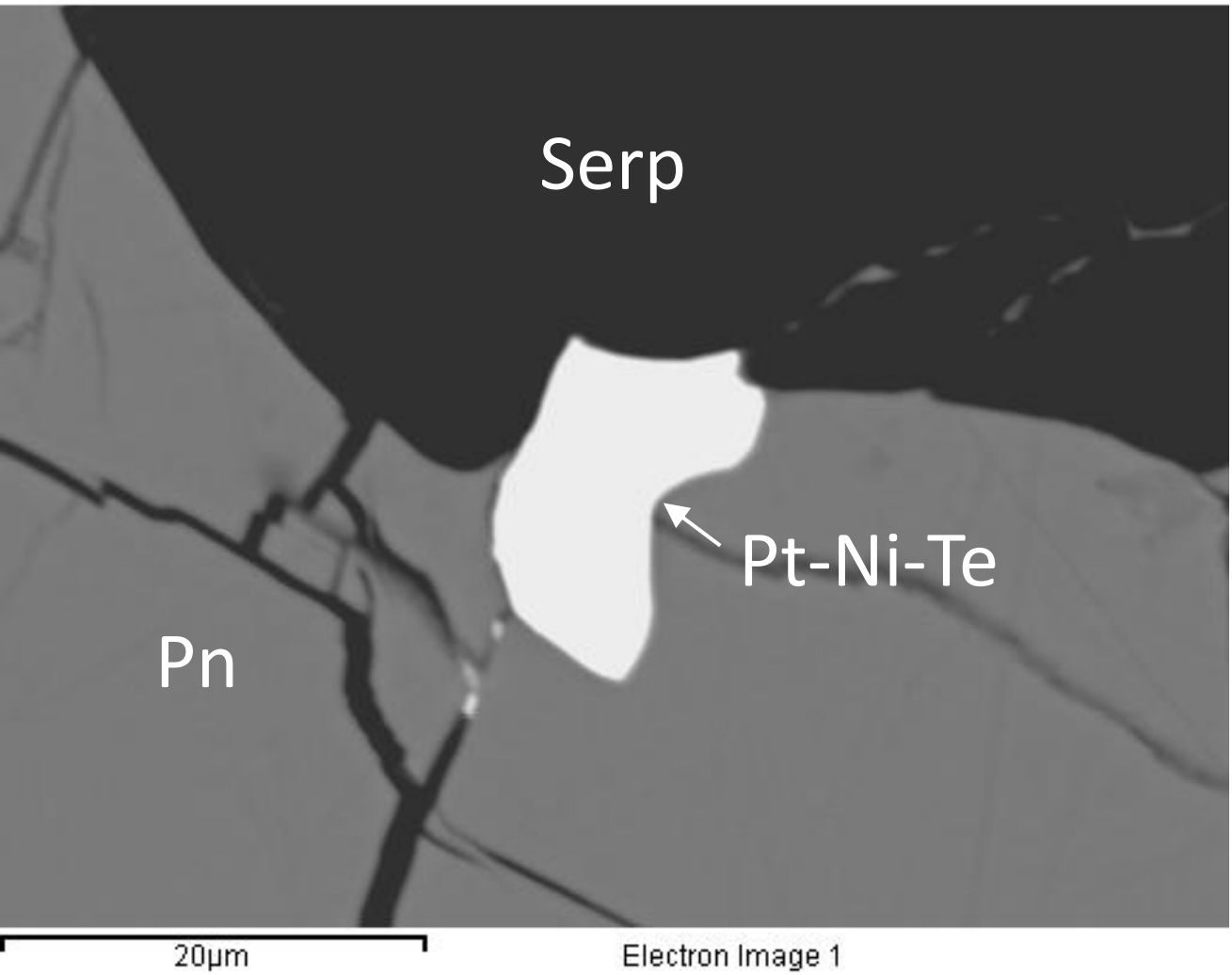
PTSR-55 S 1



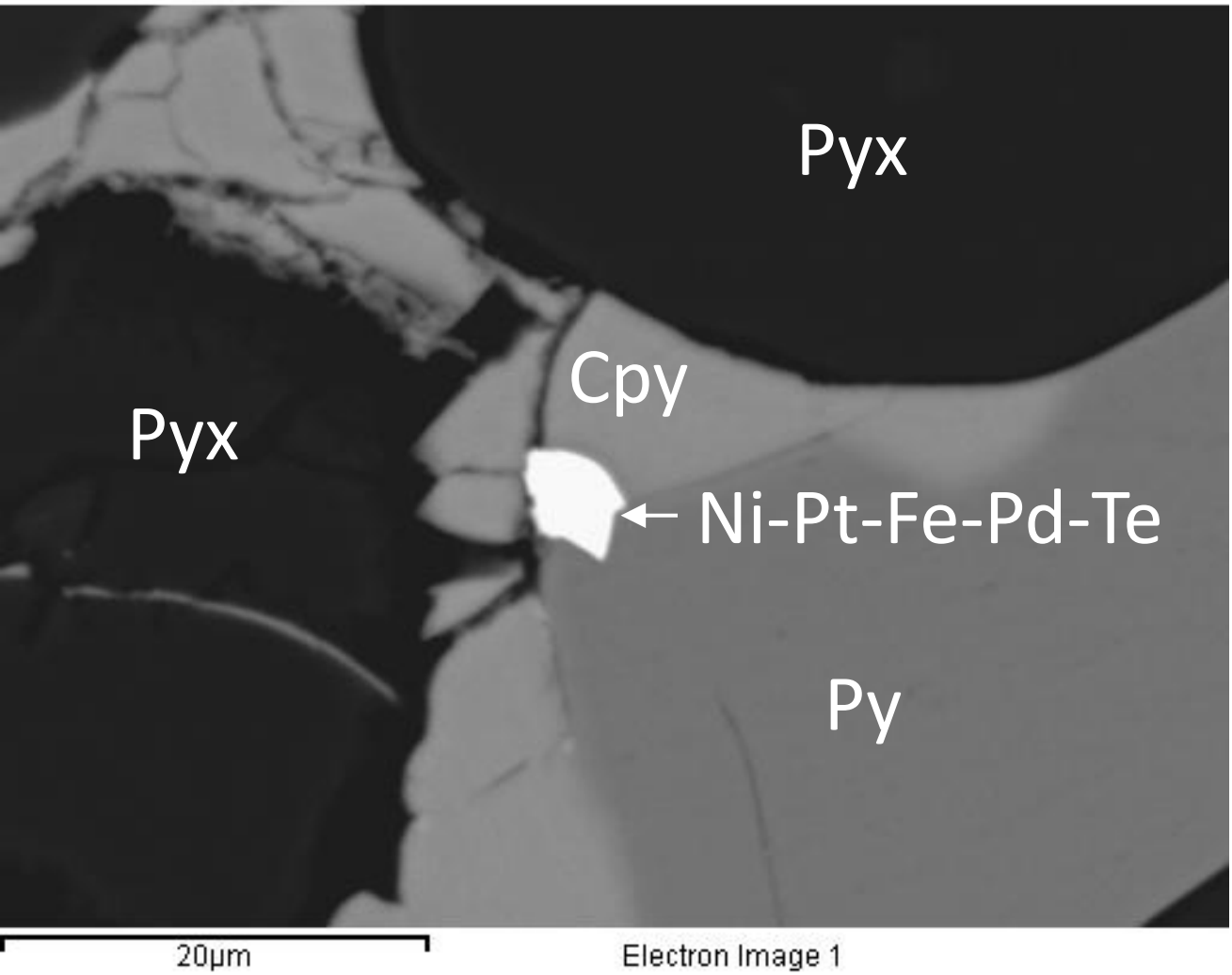
PTSR-55 T 1



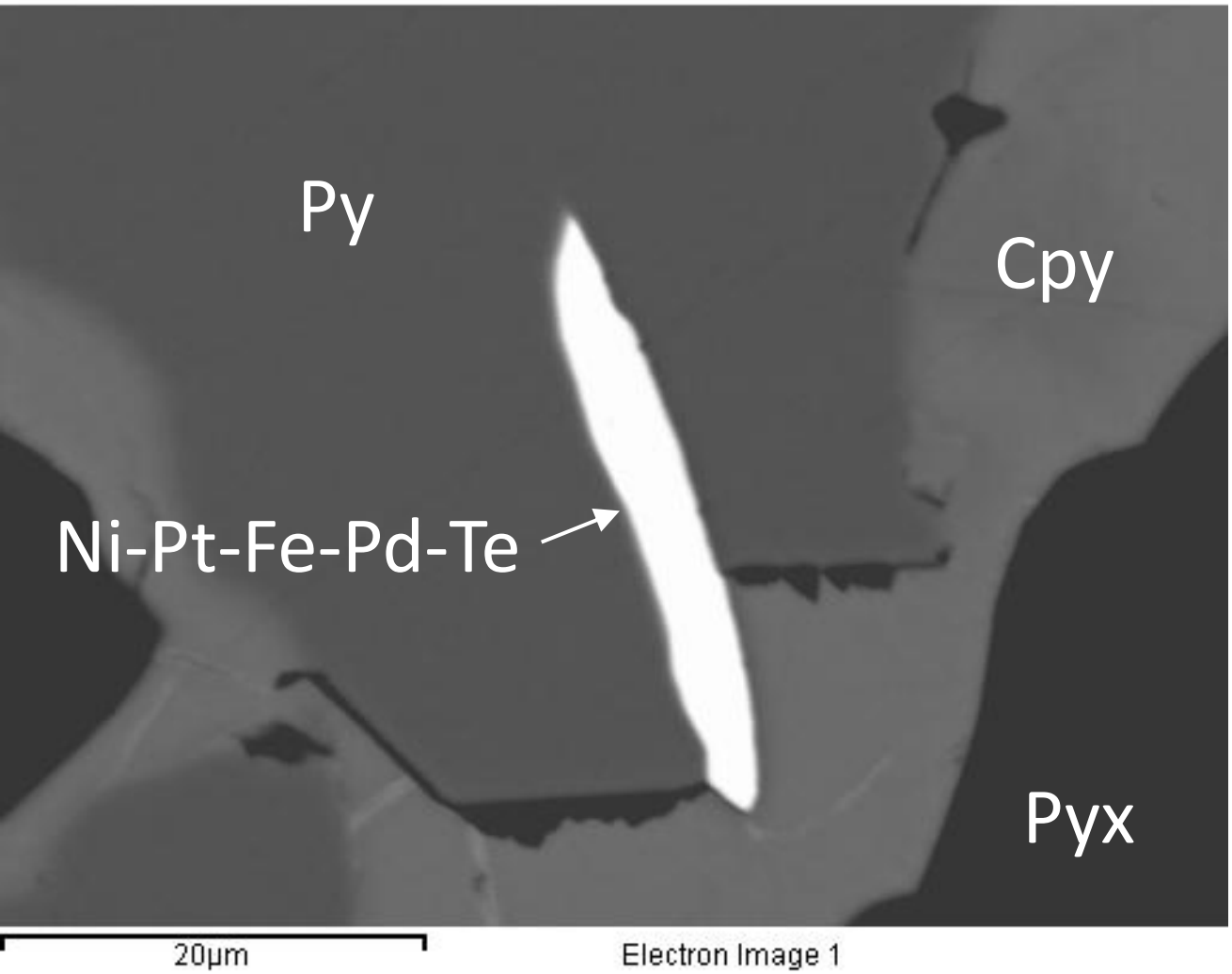
PTSR-55 U 1



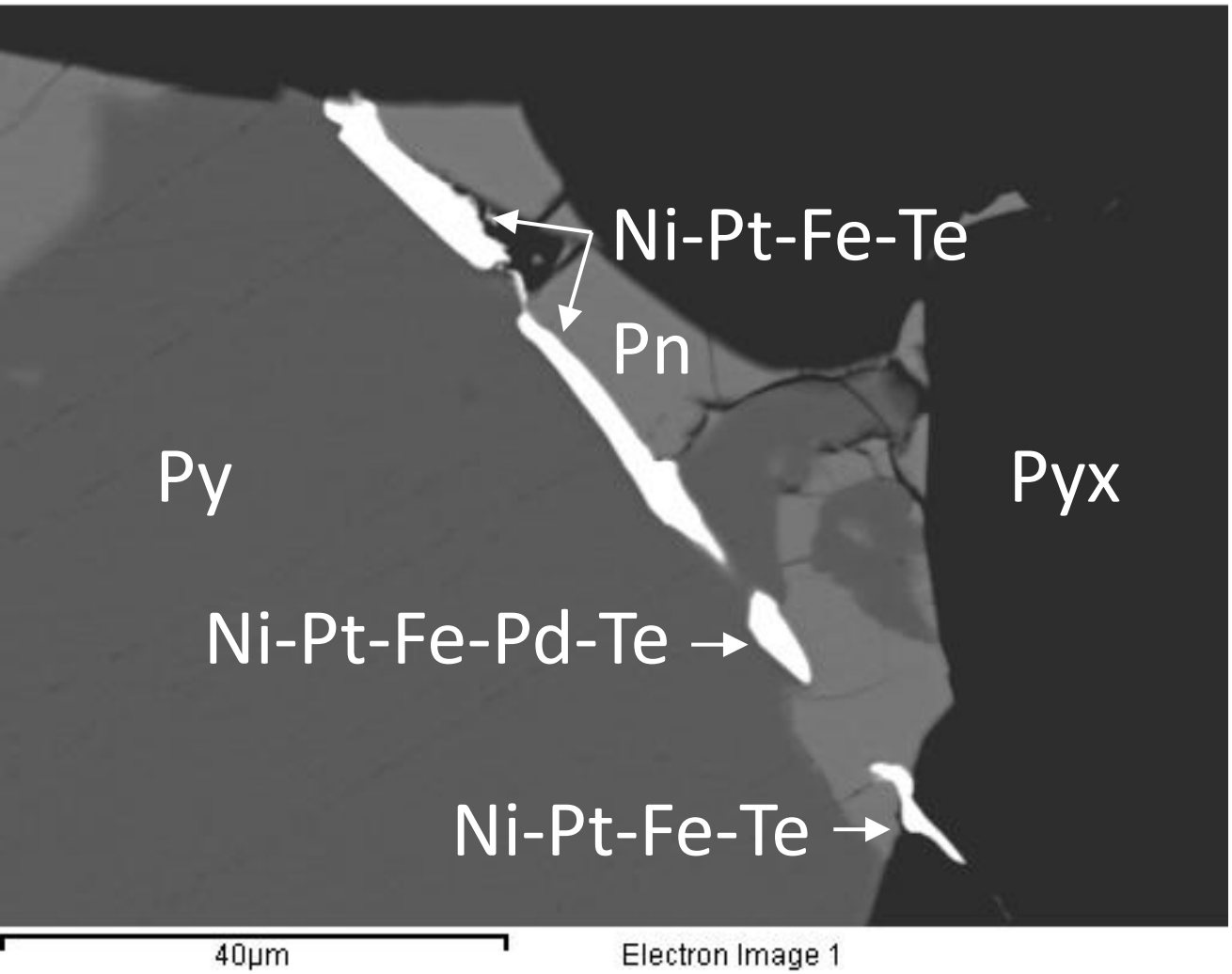
PTSR-55 V 1



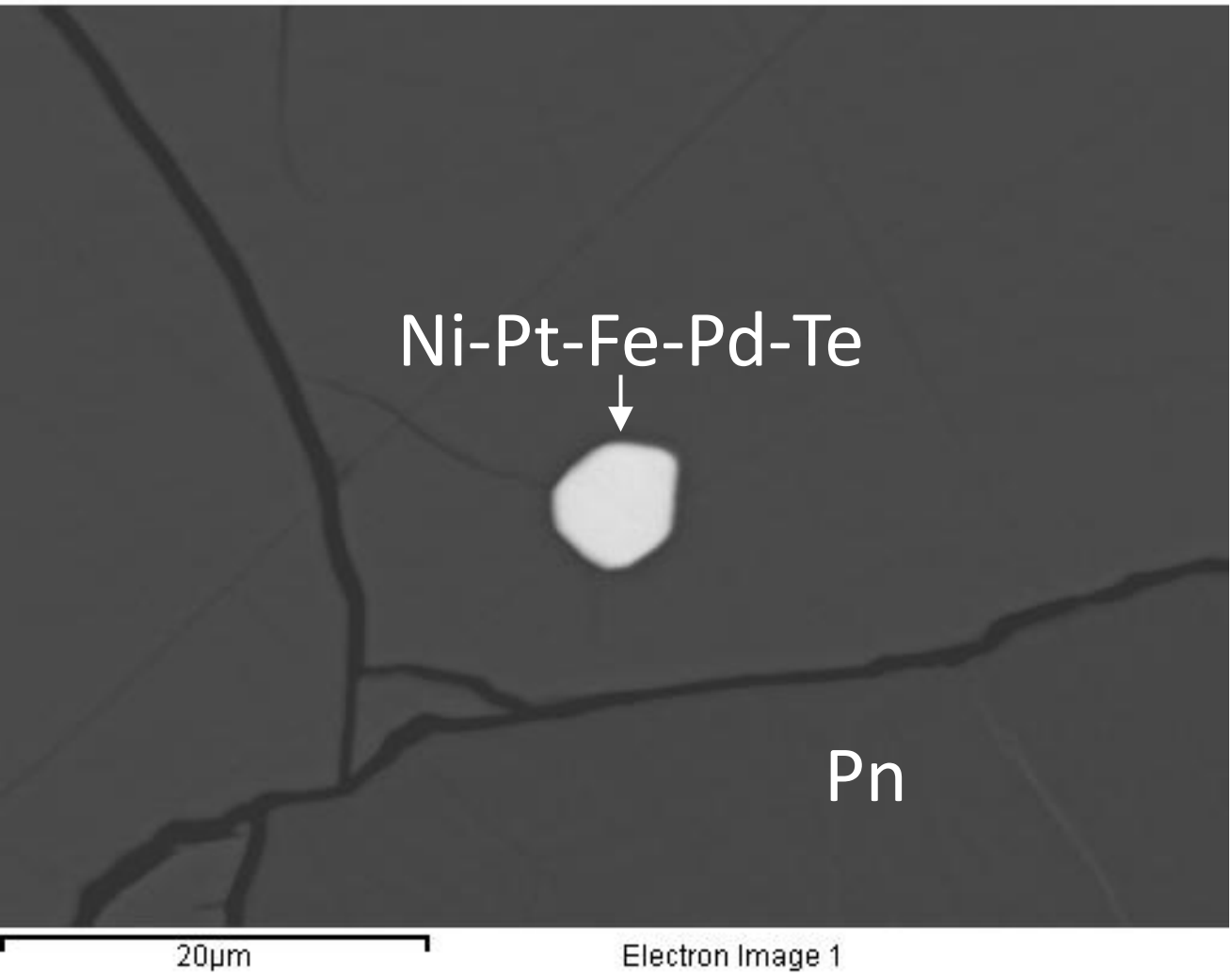
PTSR-55 W 1



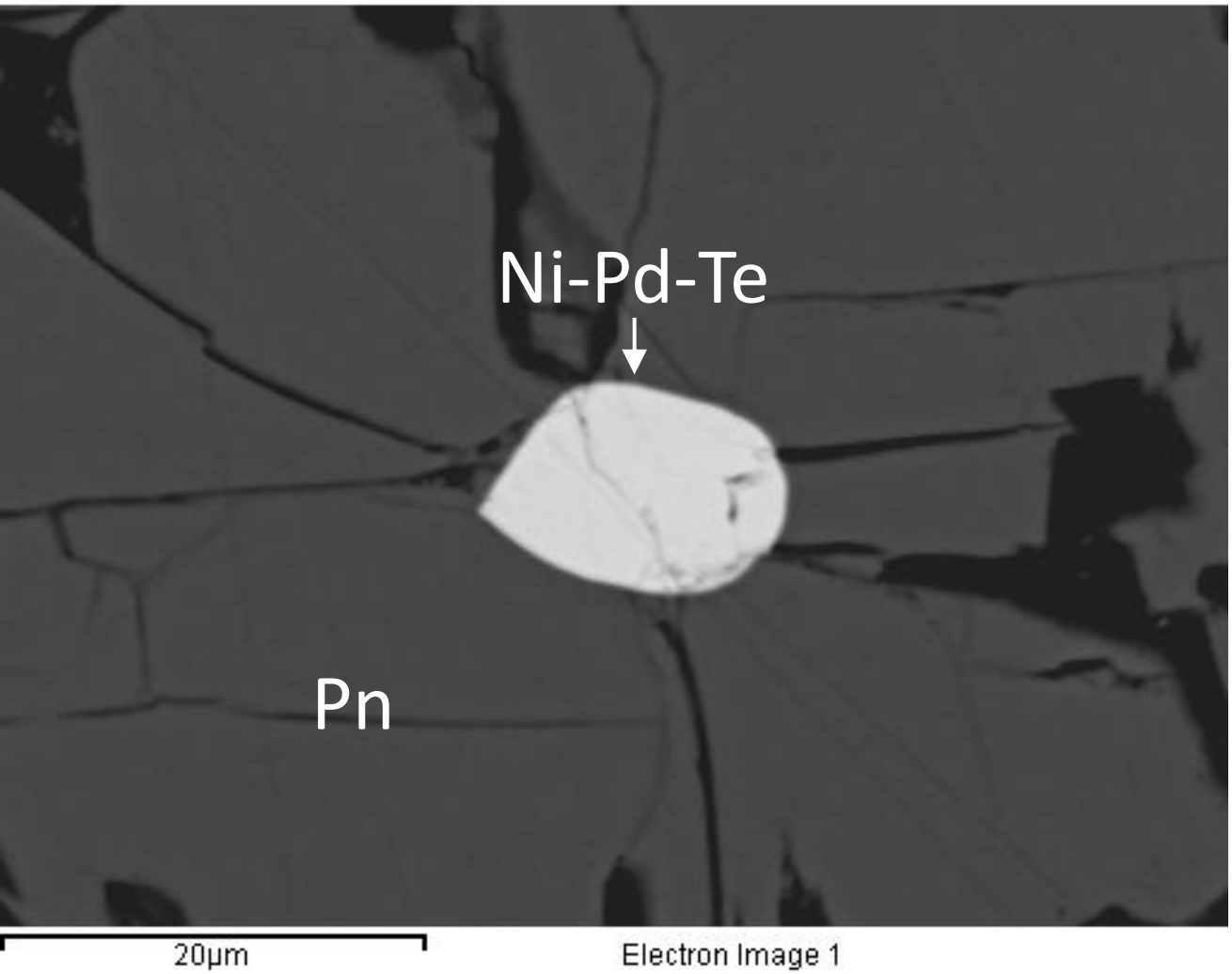
PTSR-55 X 1-4


Ni-Pt-Fe-Te
Pn
Py
Pyx
Ni-Pt-Fe-Pd-Te
Ni-Pt-Fe-Te
40µm
Electron Image 1

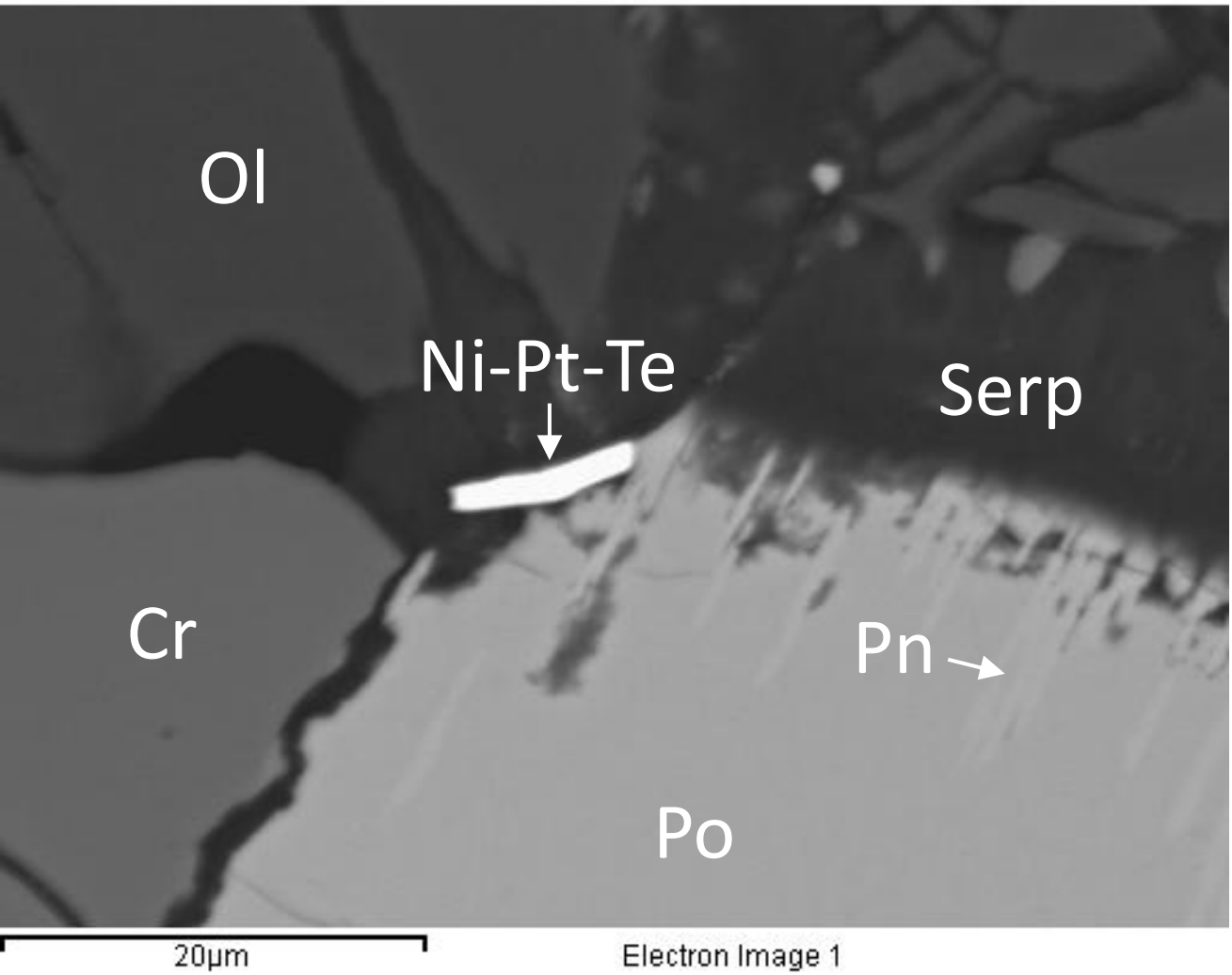
PTSR-55 Y 1



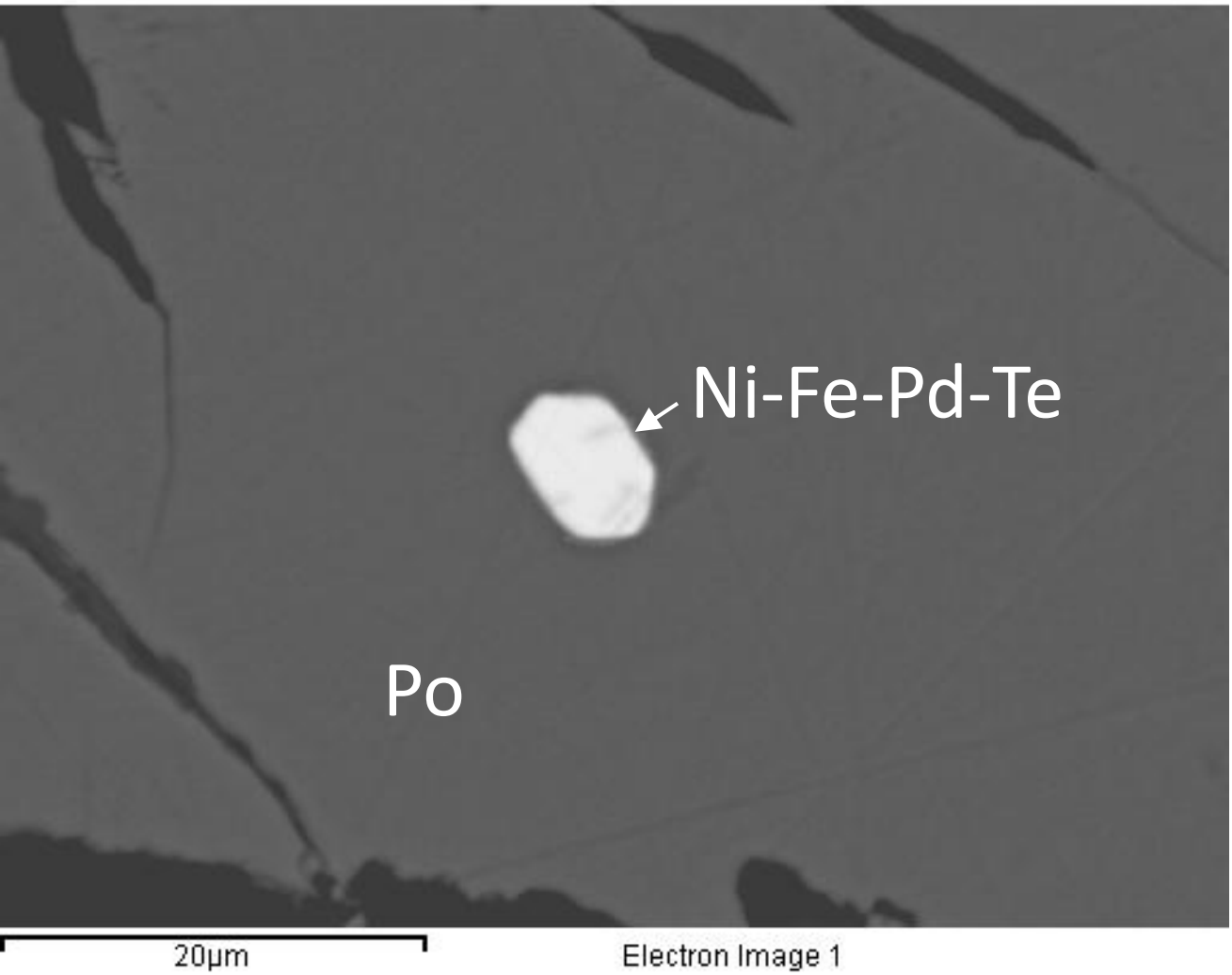
PTSR-56 A 1



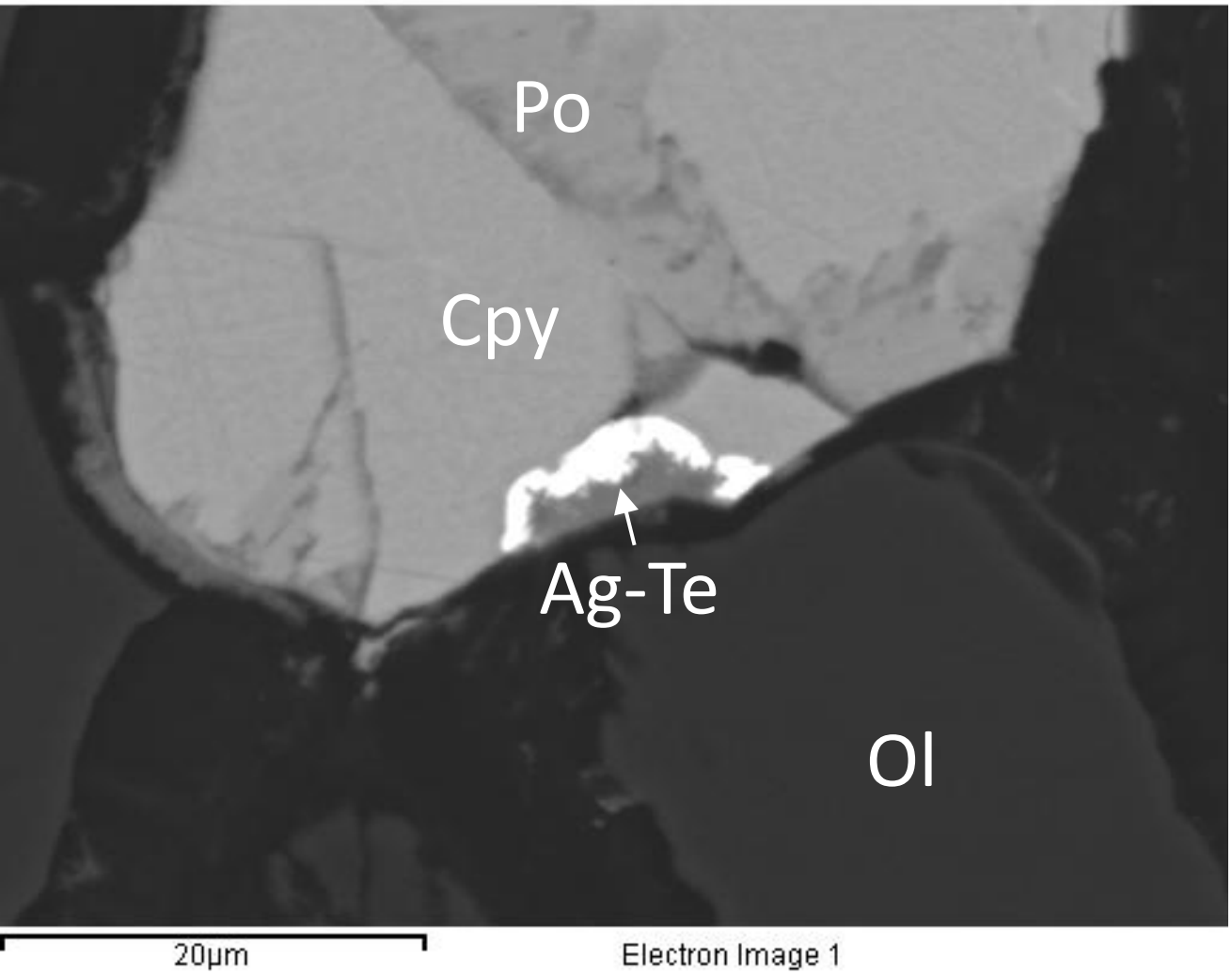
PTSR-56 B 1



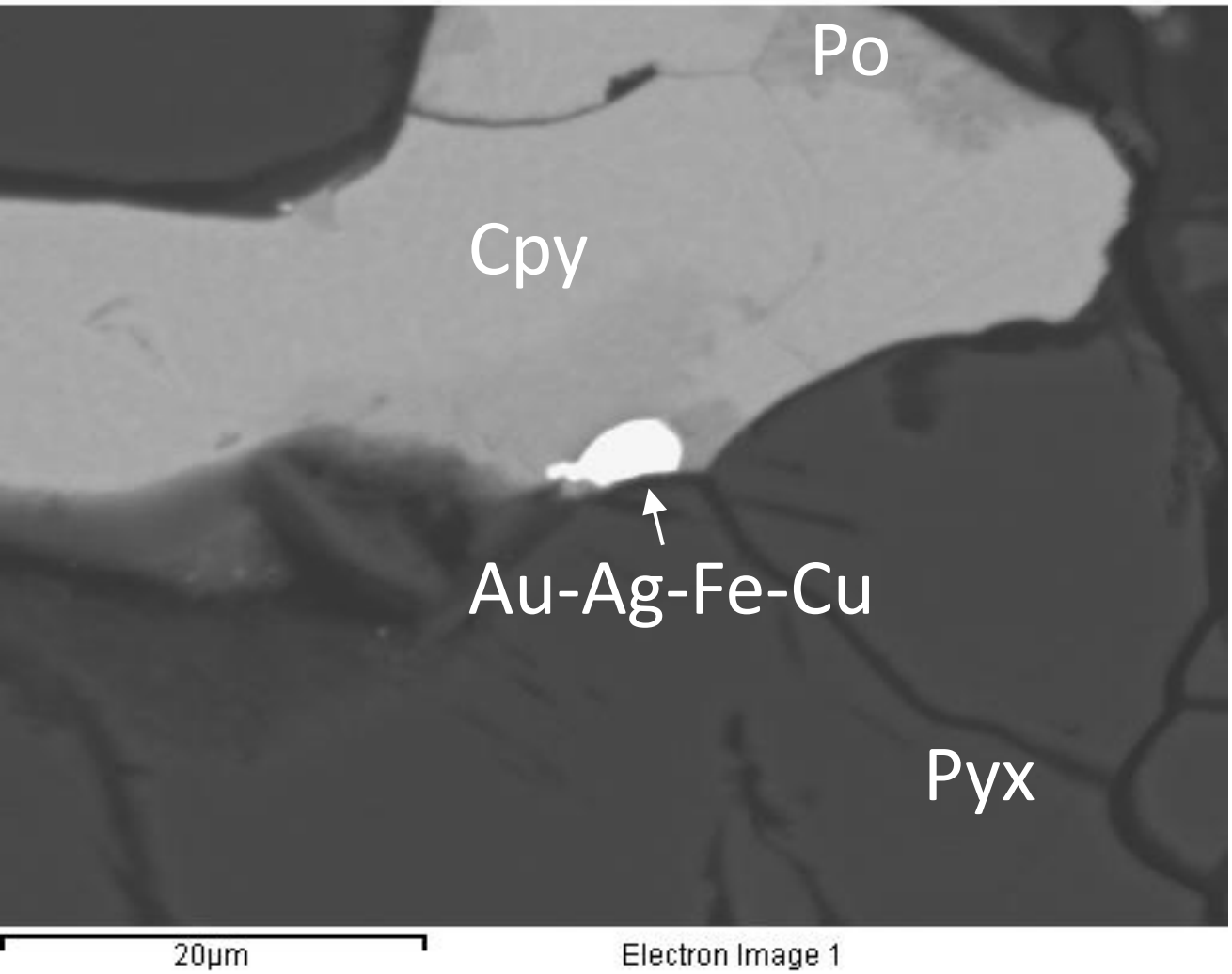
PTSR-56 C 1



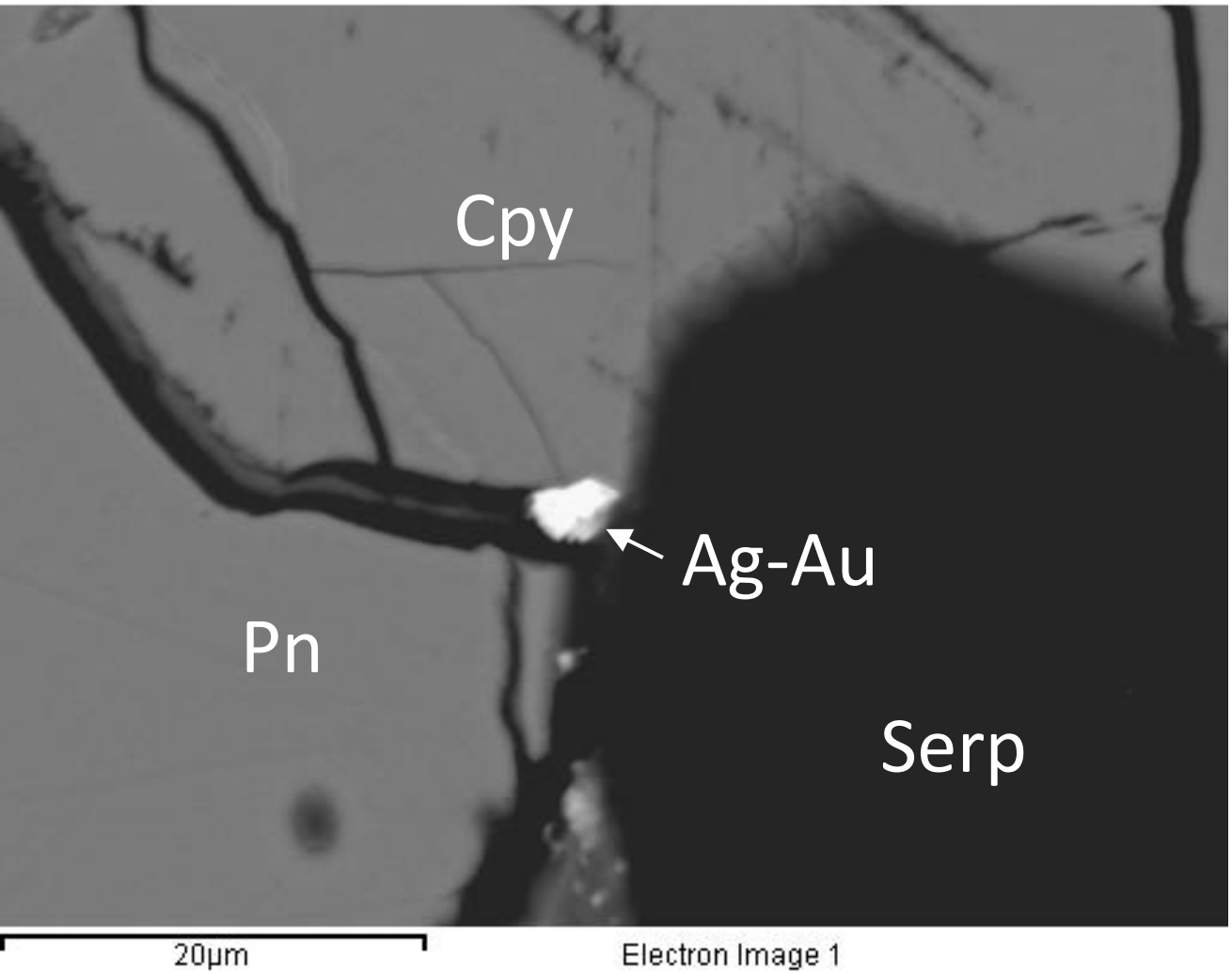
PTSR-56 D 1



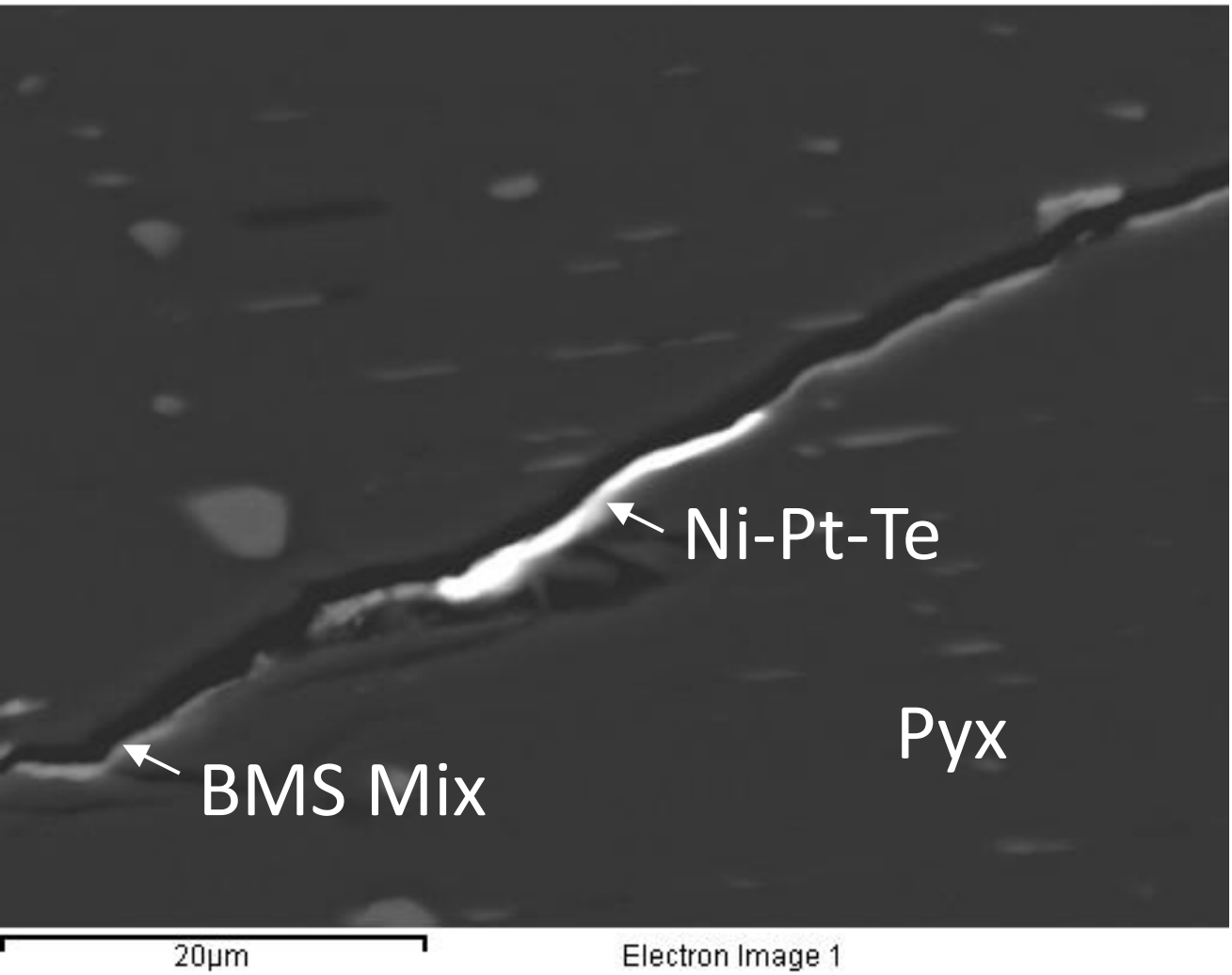
PTSR-56 D 2



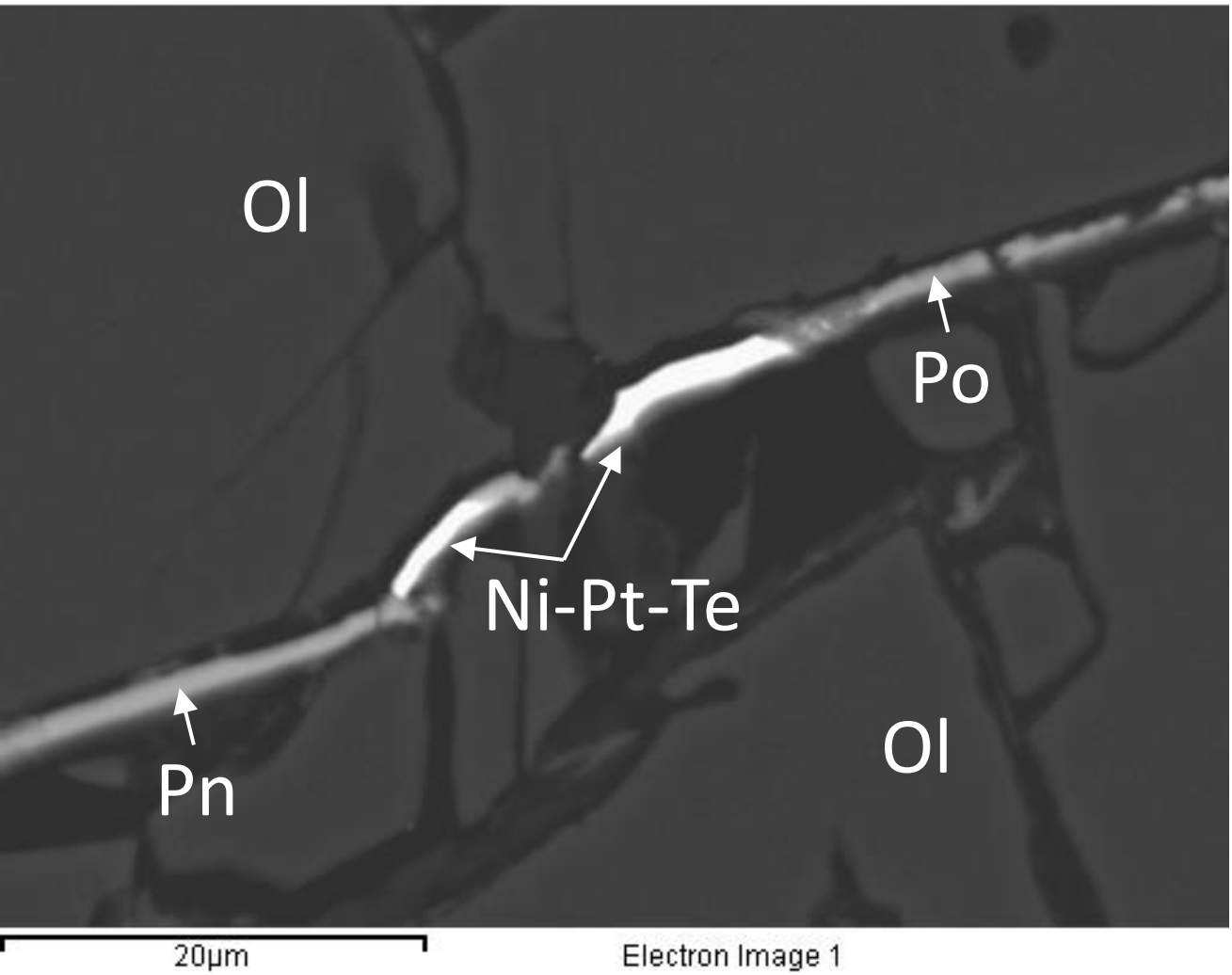
PTSR-56 E 1



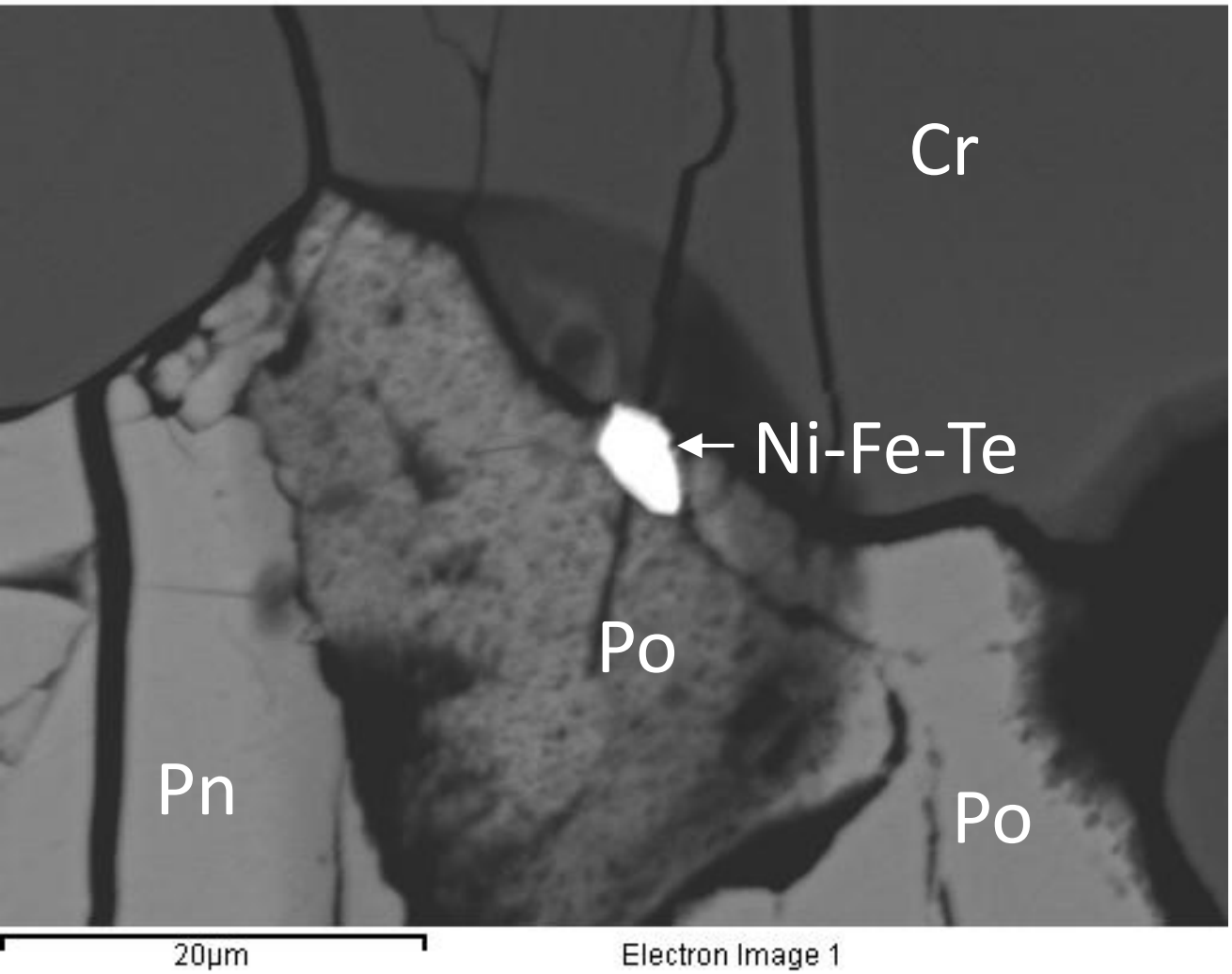
PTSR-56 F 1



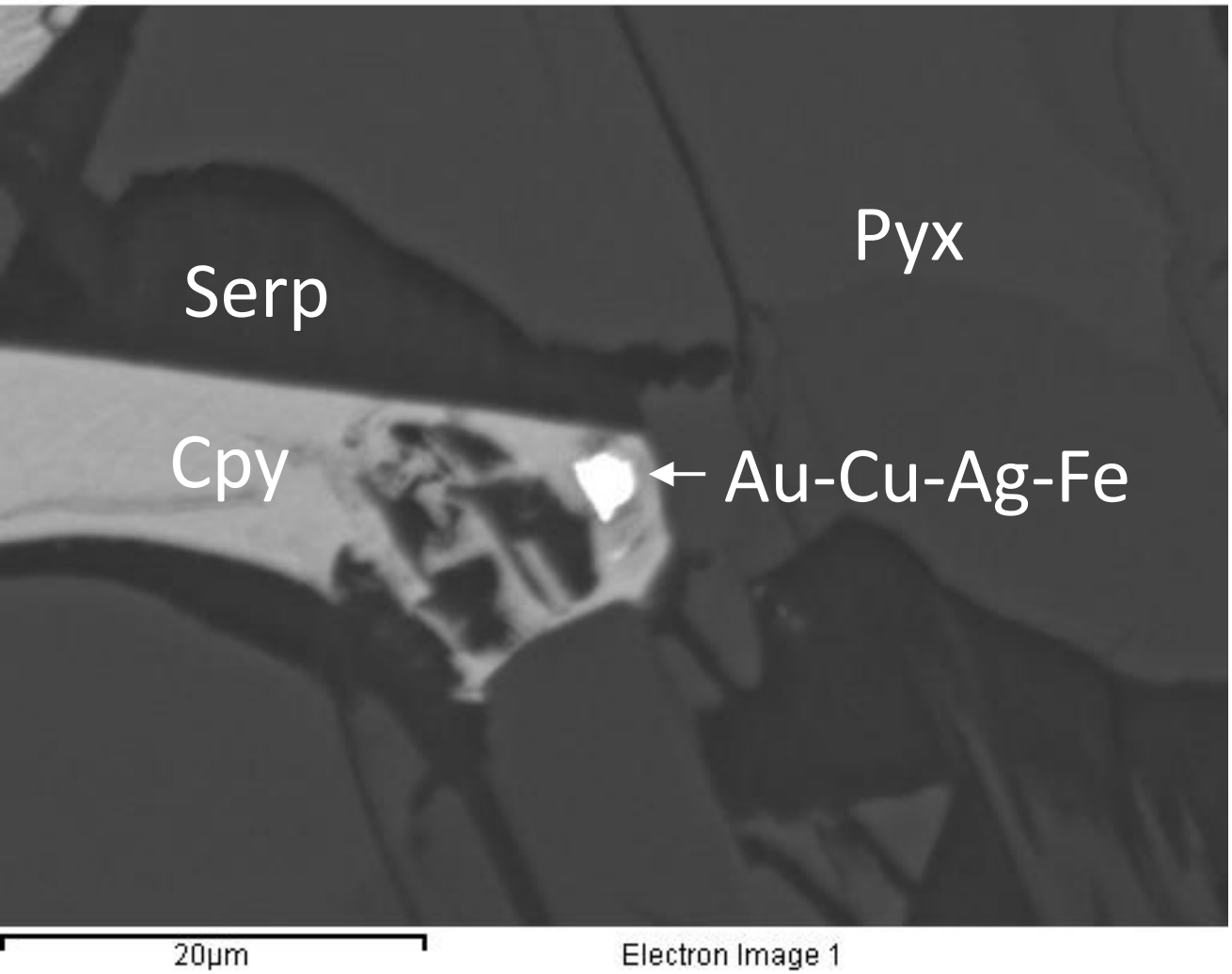
PTSR-56 G 1-2



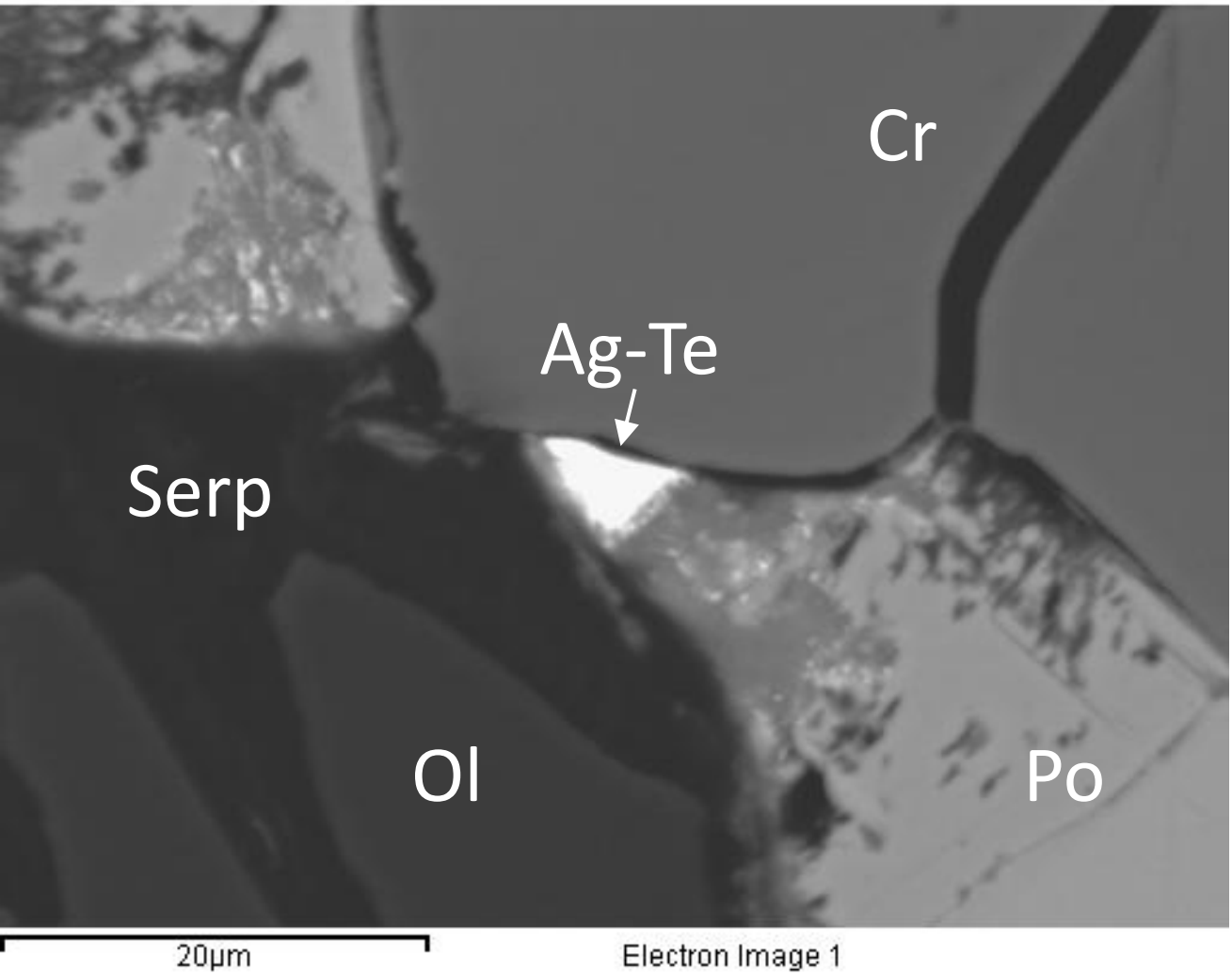
PTSR-56 H 1



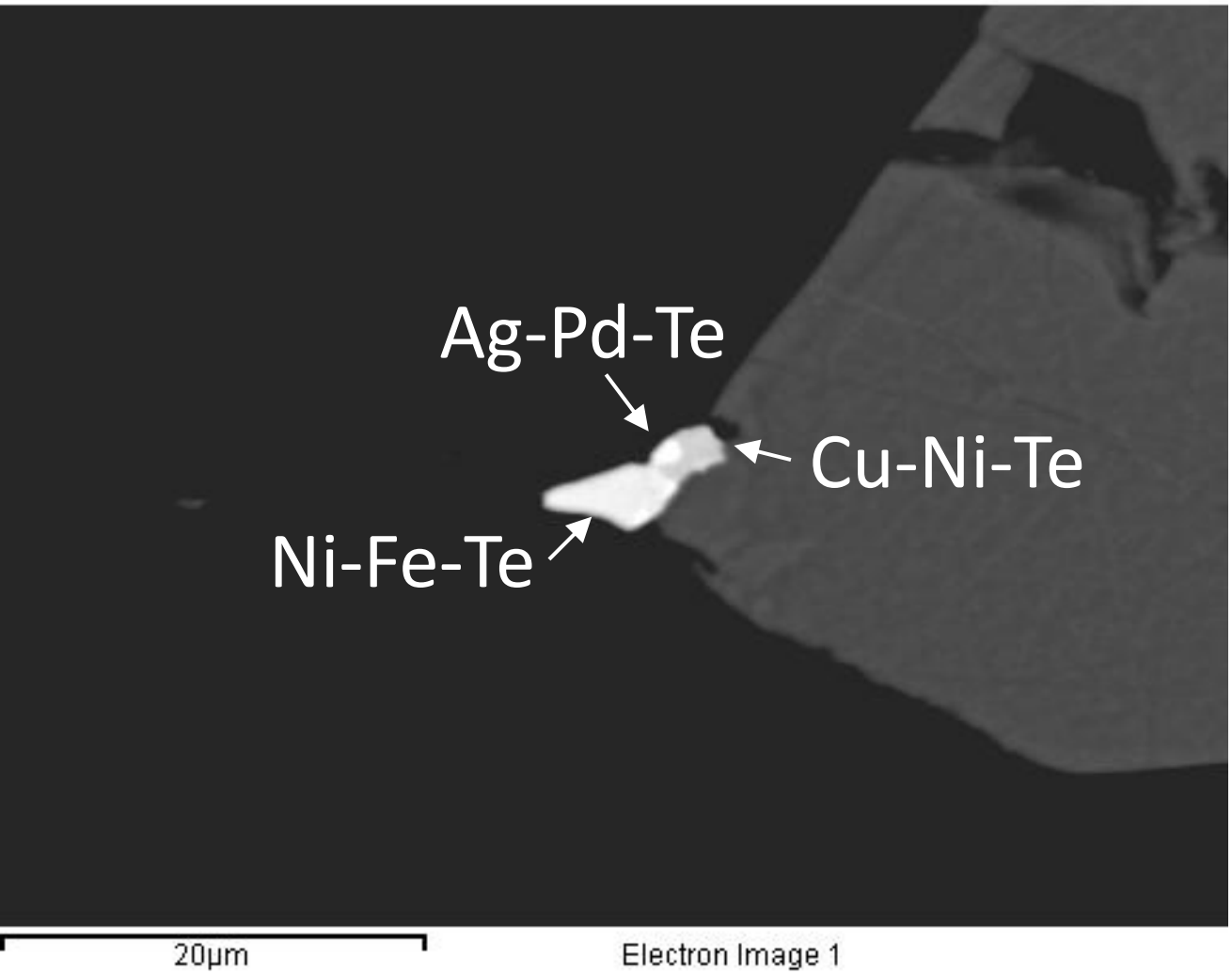
PTSR-56 I 1



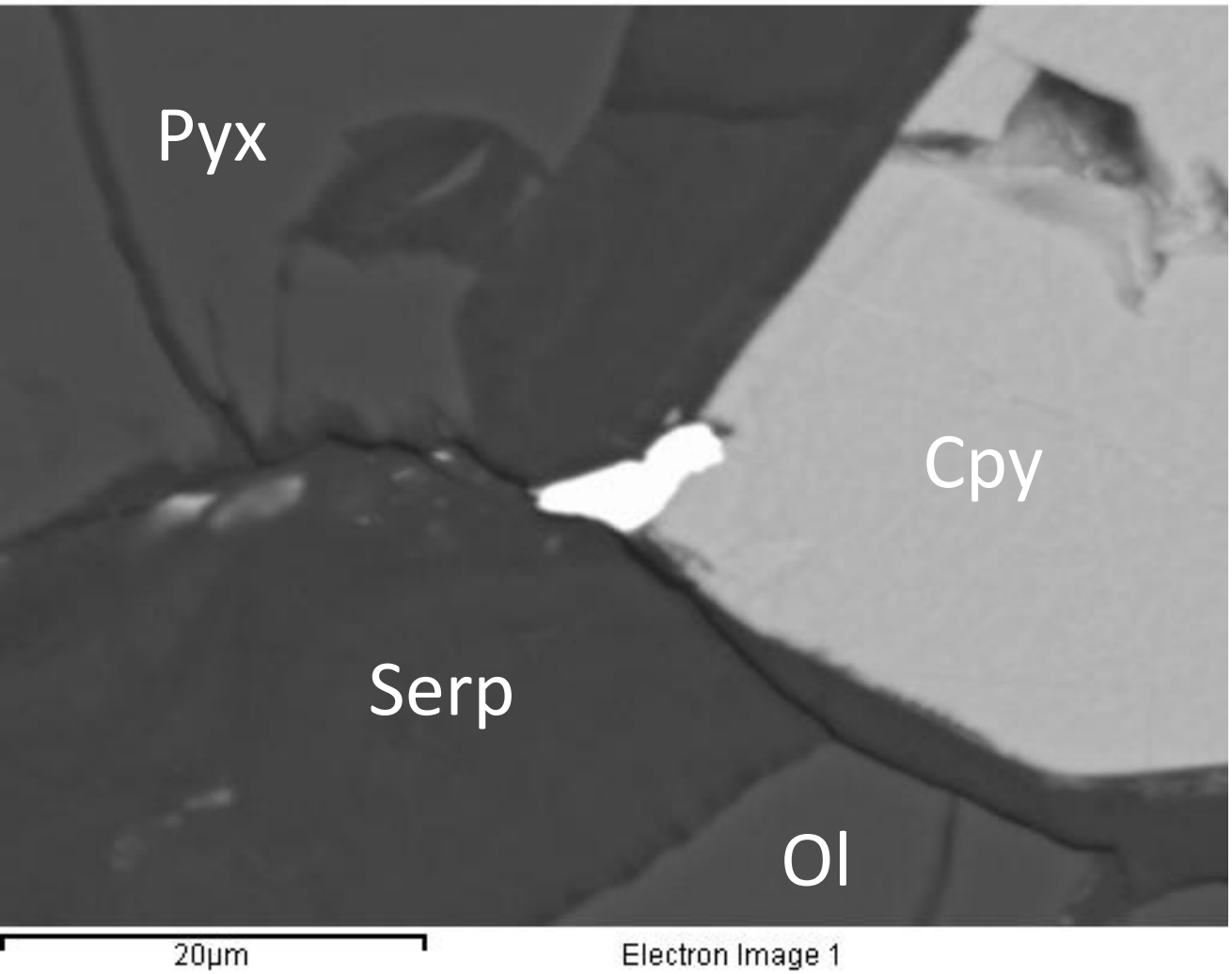
PTSR-56 J 1



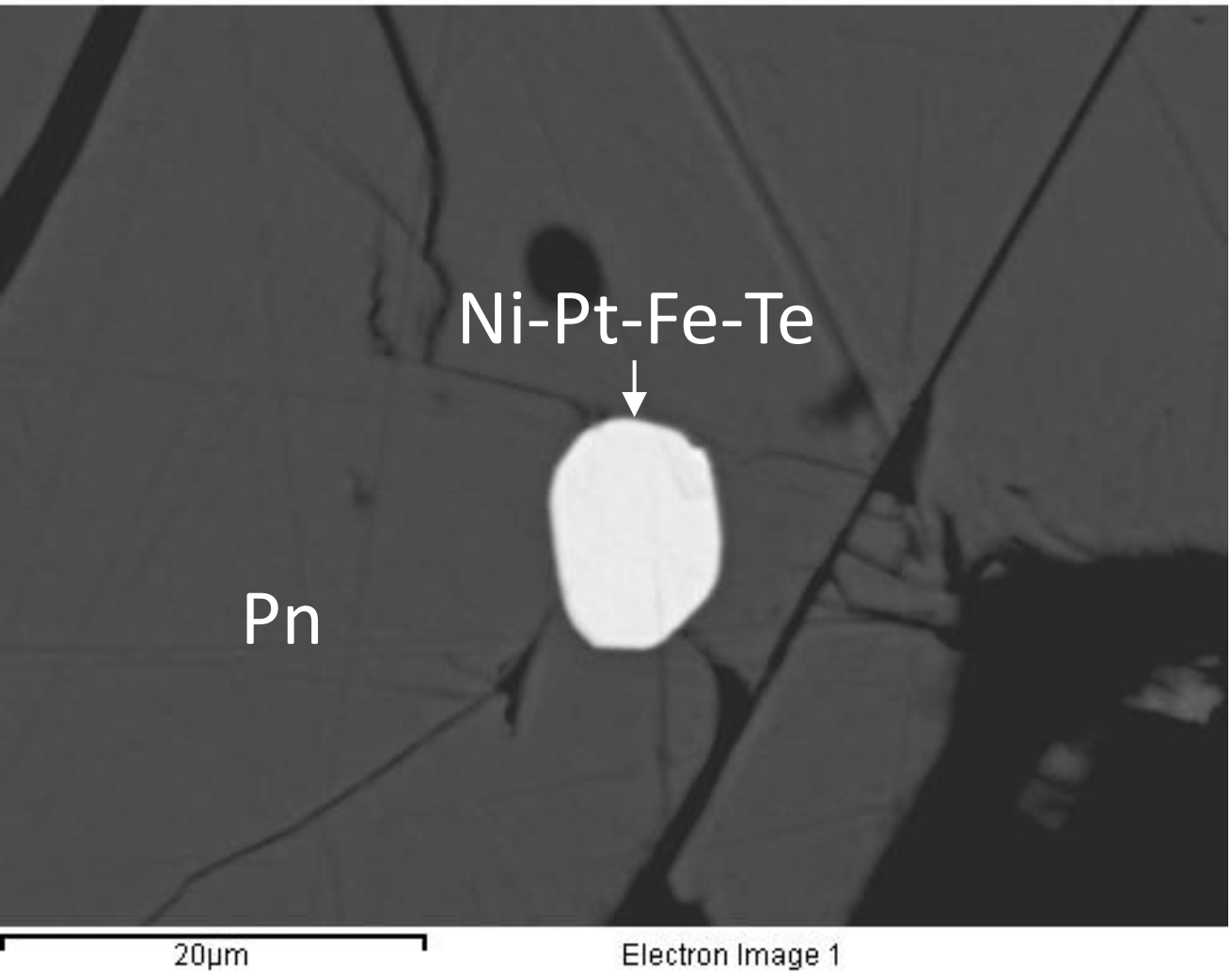
PTSR-56 K 1-3



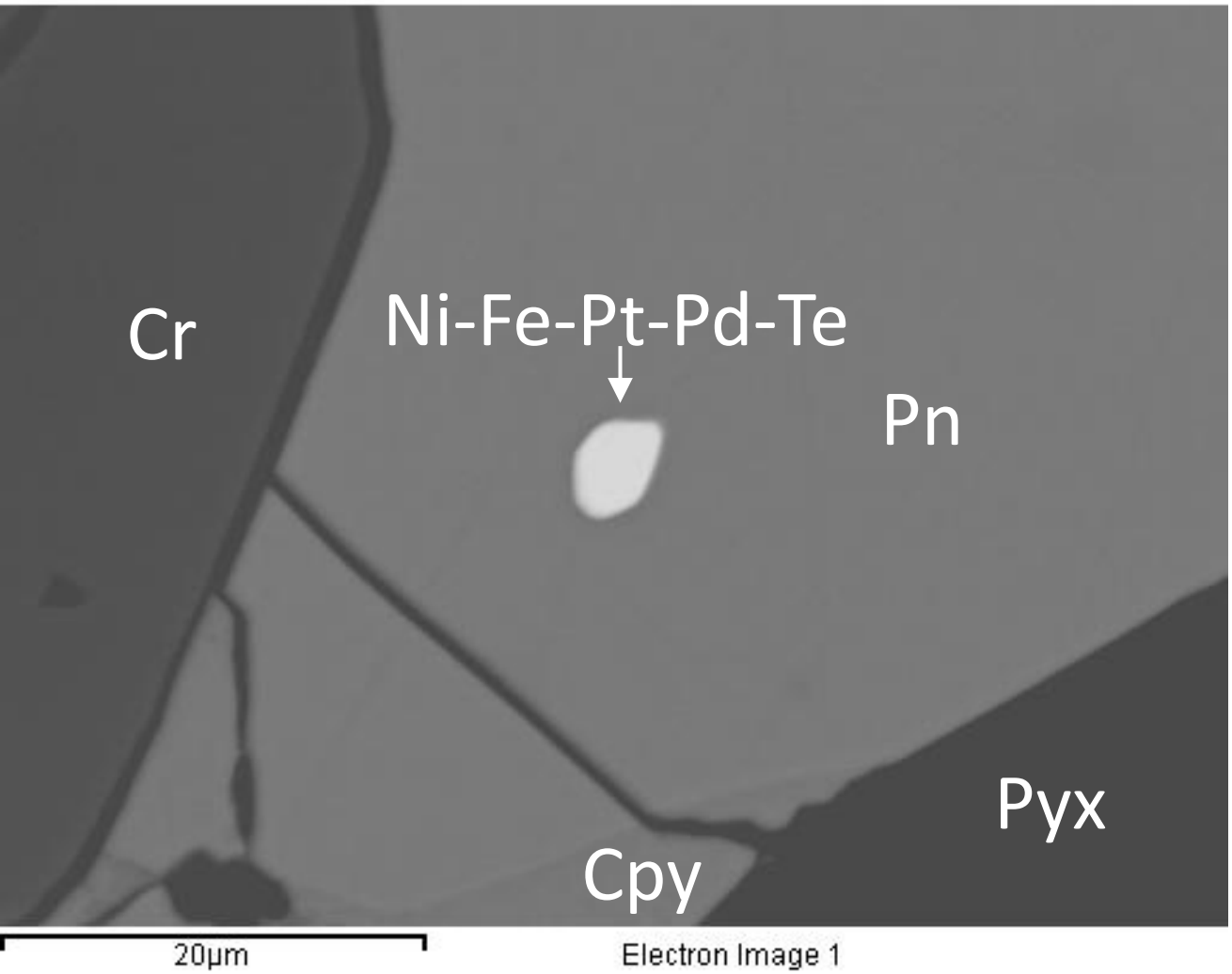
PTSR-56 K 1-3 Light



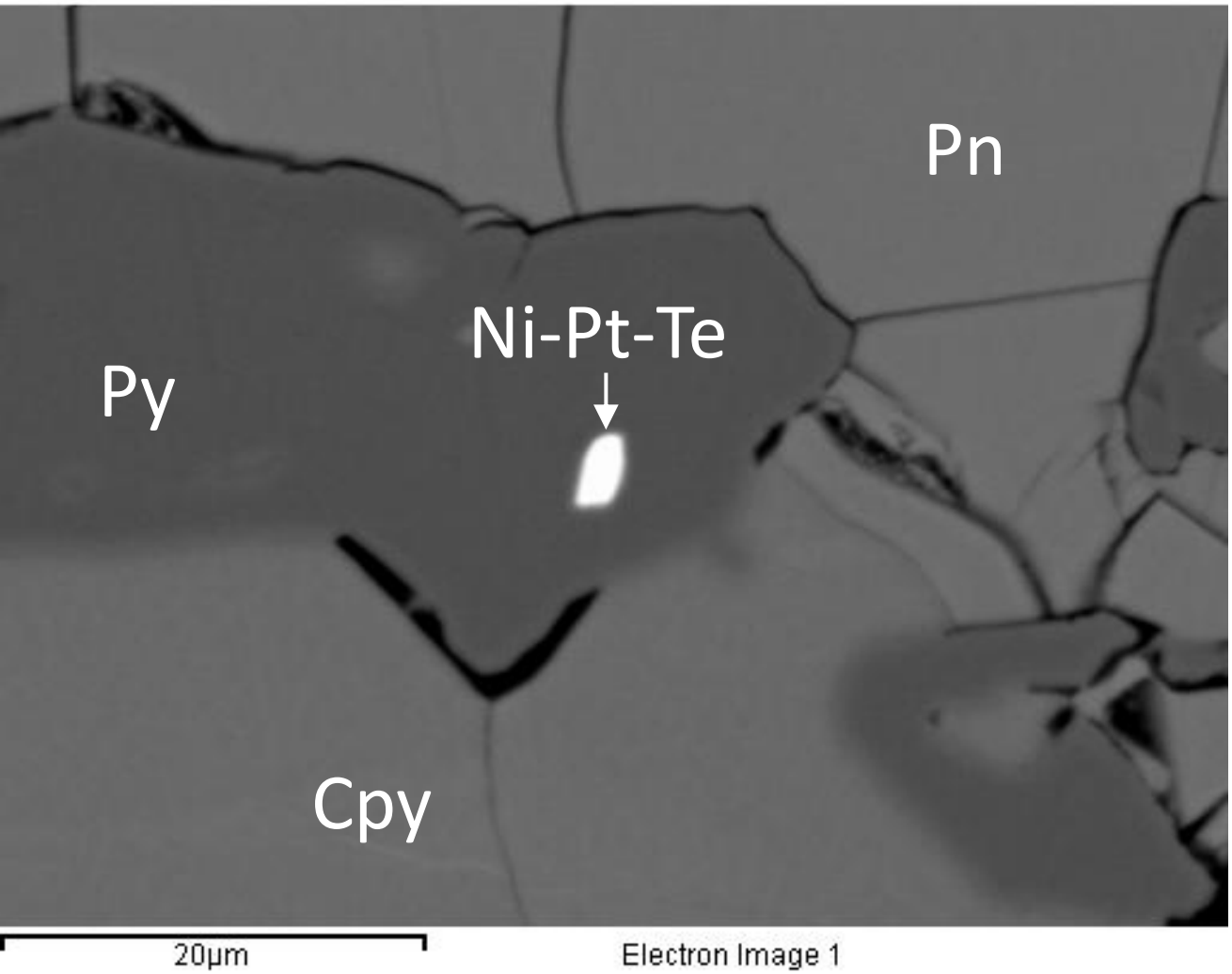
PTSR-56 L 1



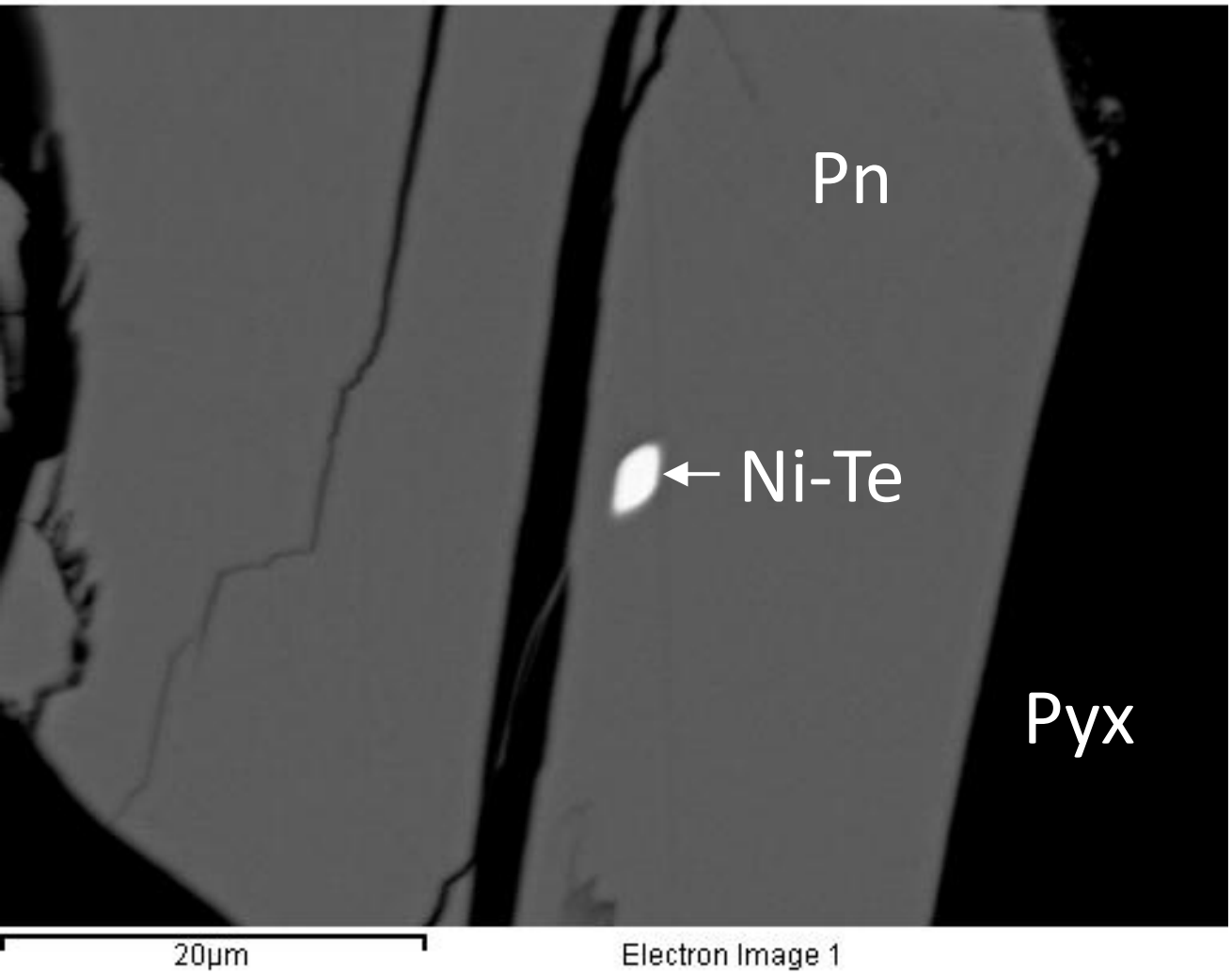
PTSR-56 M 1



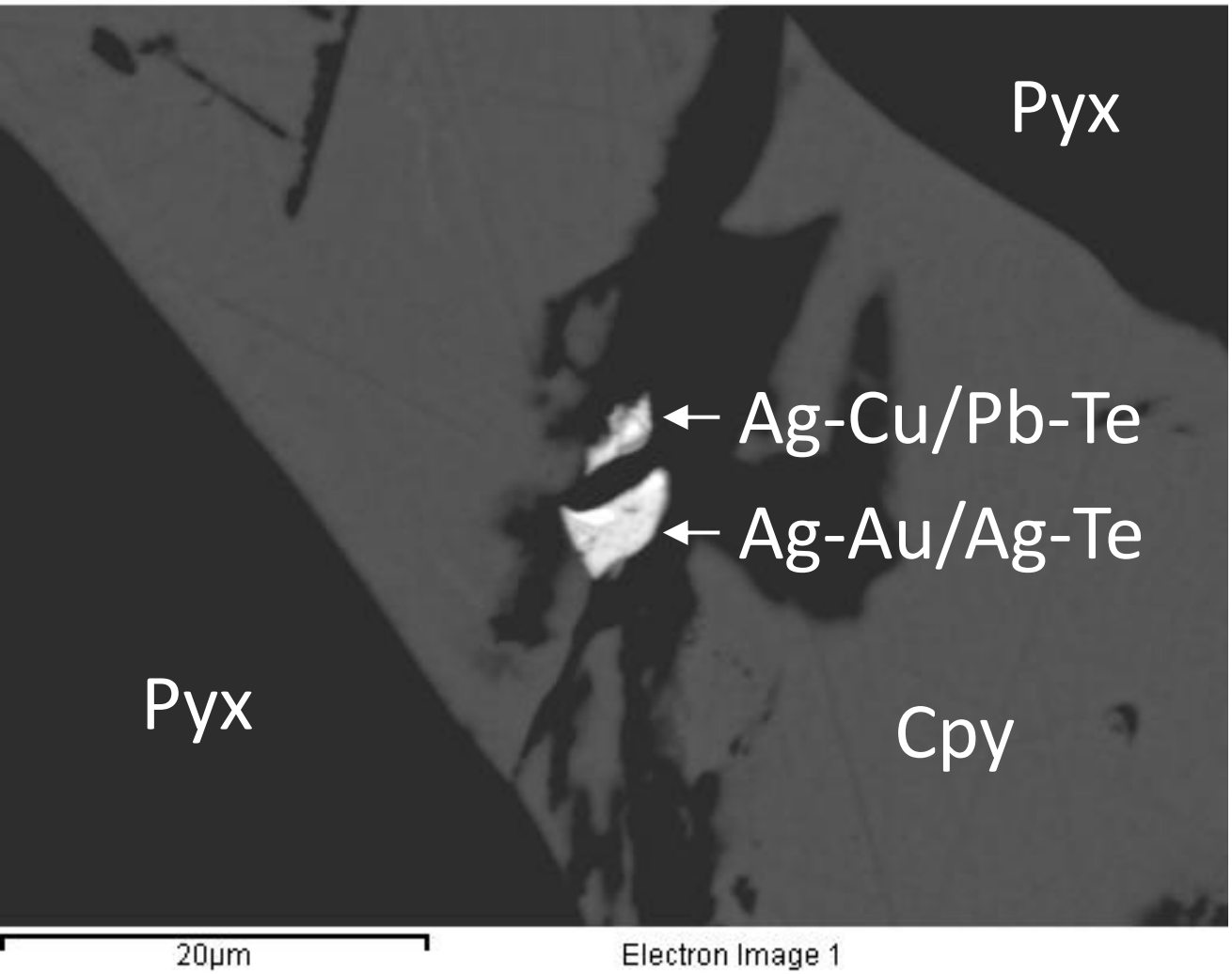
PTSR-56 N 1



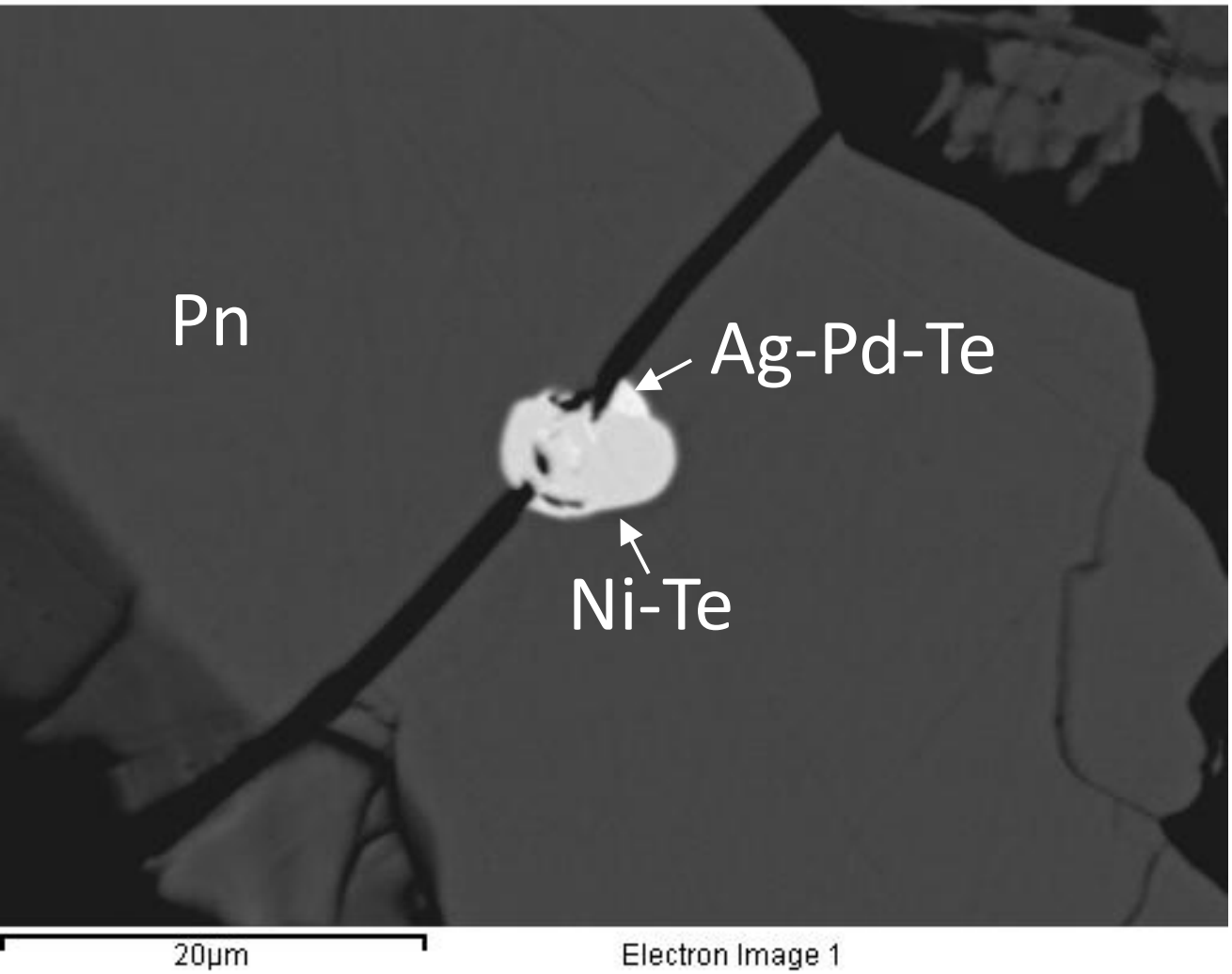
PTSR-56 O 1



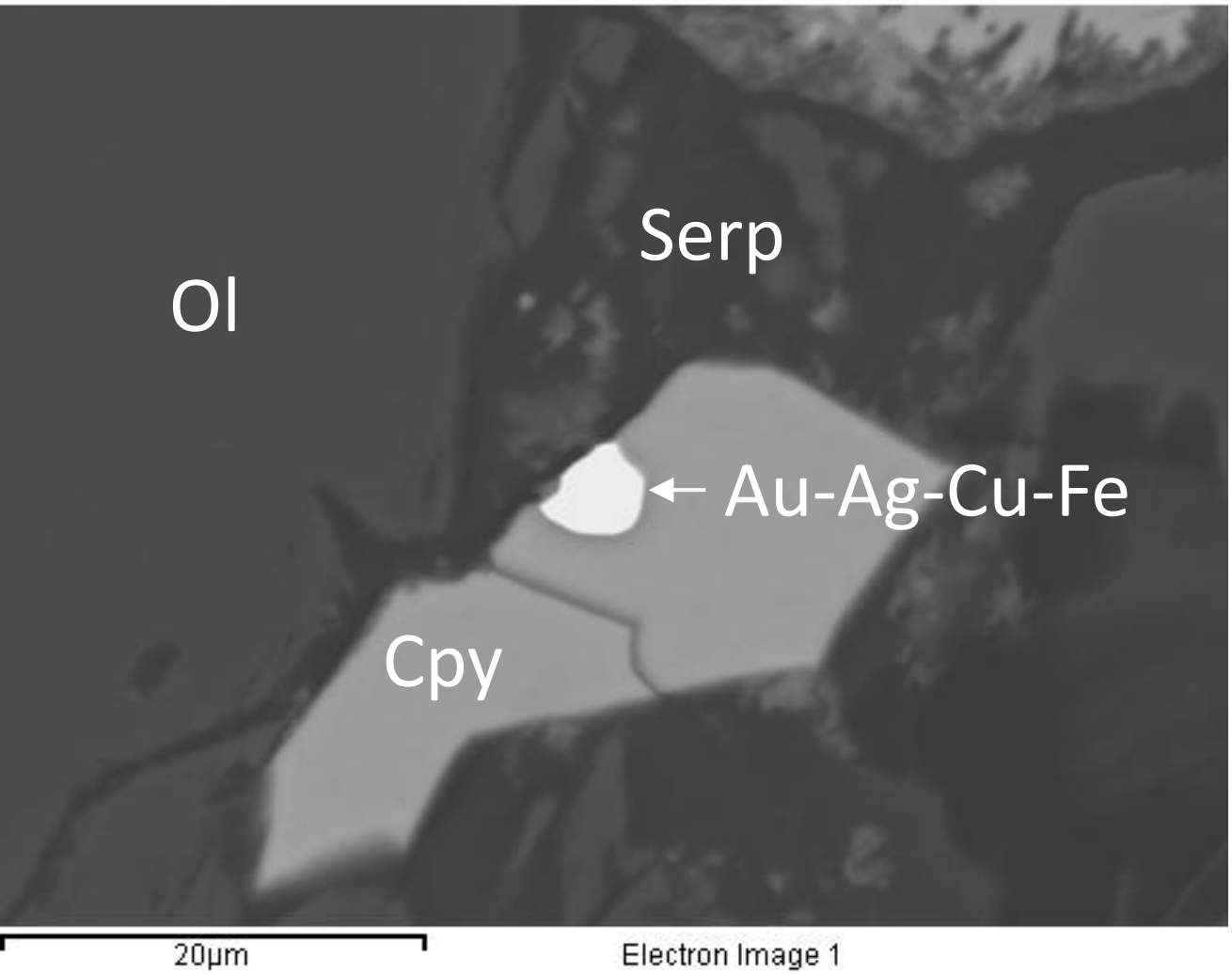
PTSR-56 P 1-2



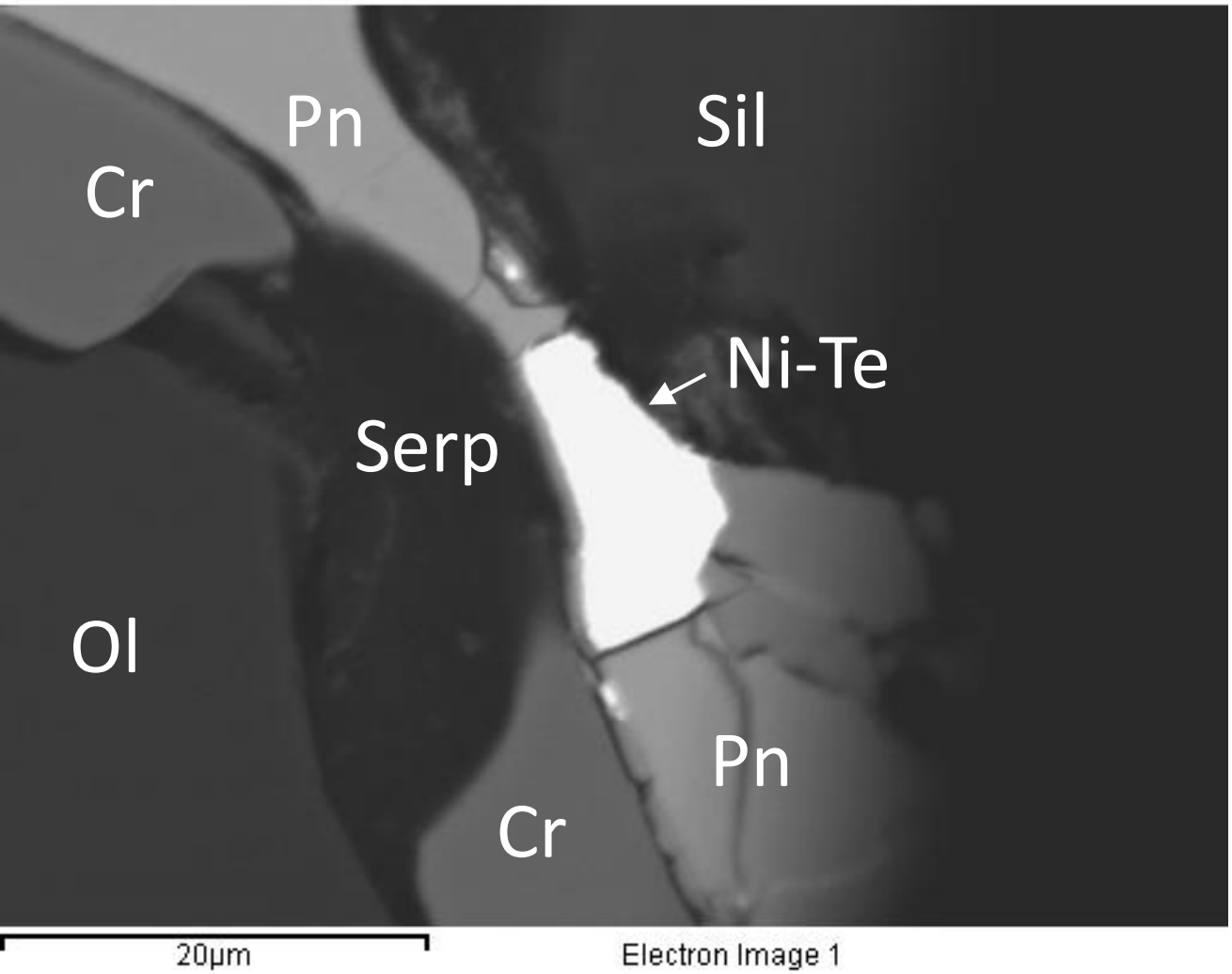
PTSR-56 Q 1-2



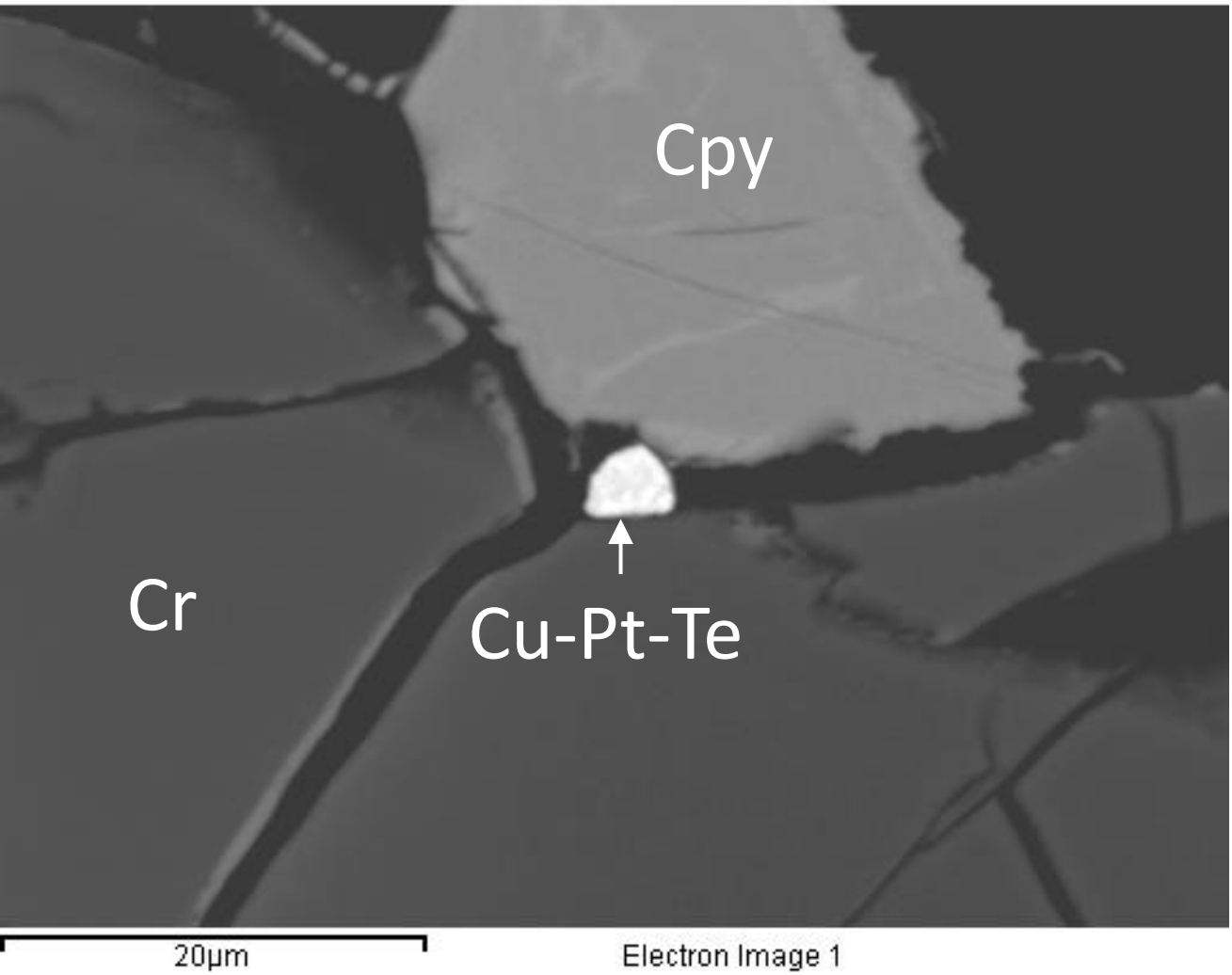
PTSR-56 R 1



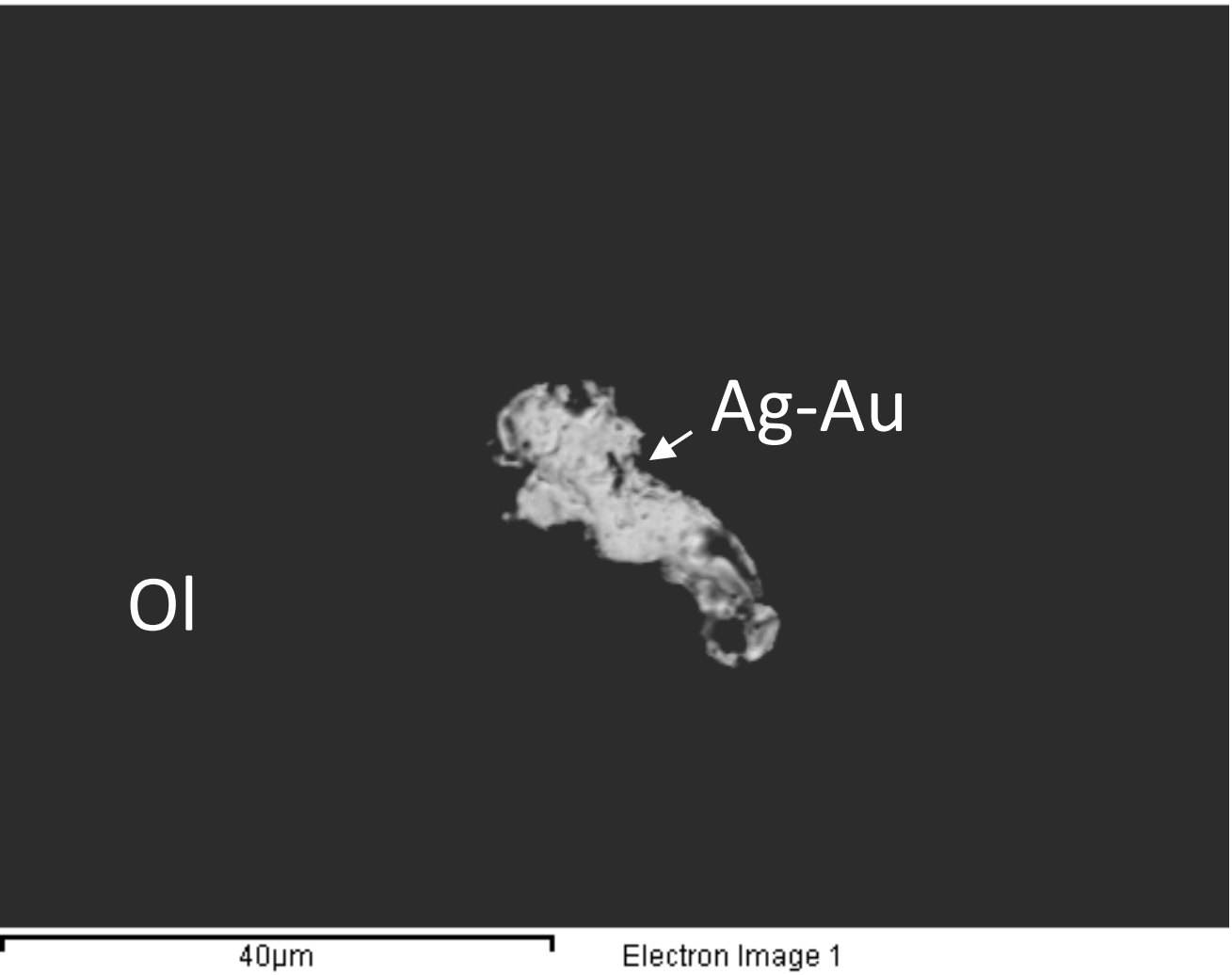
PTSR-56 S 1



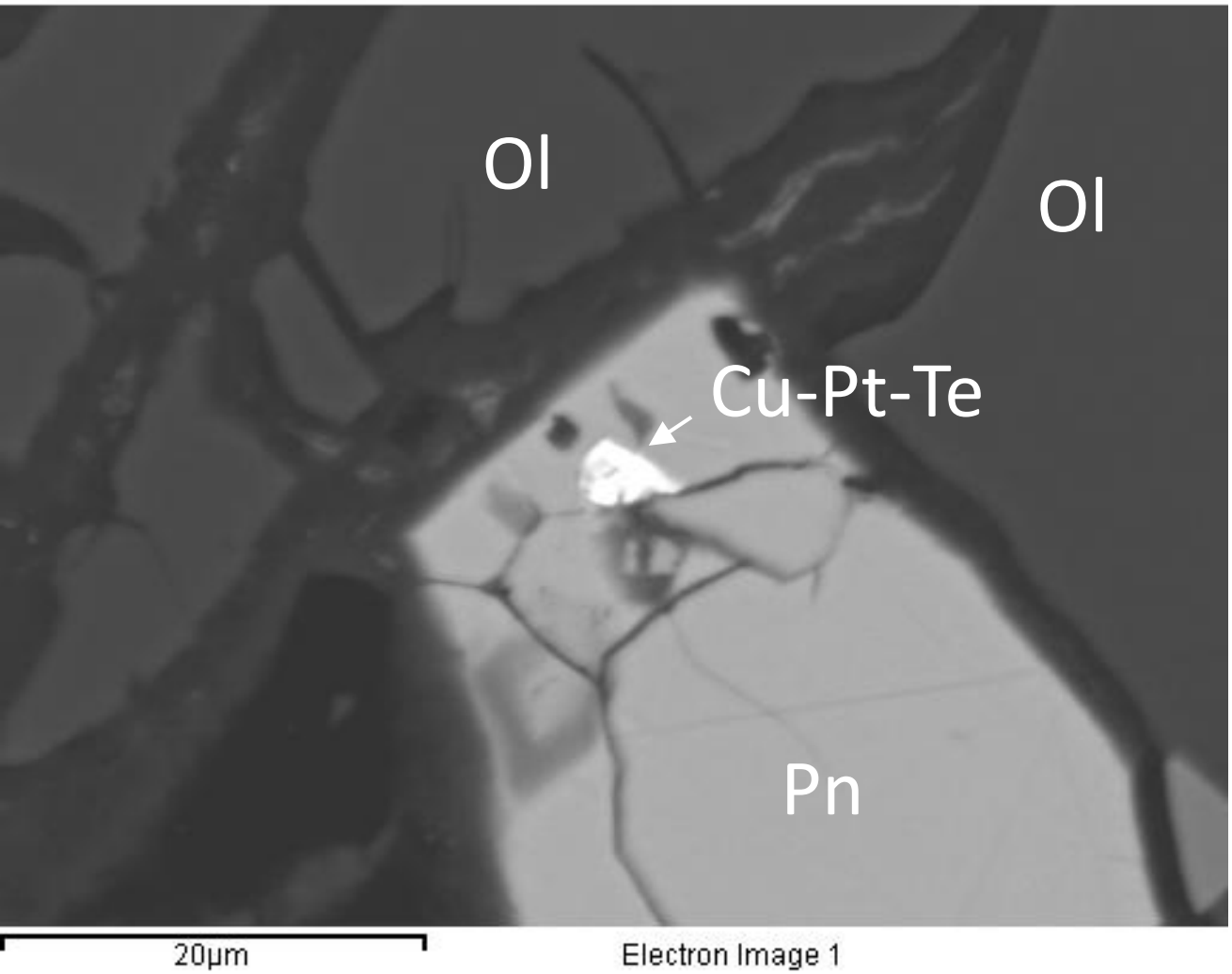
PTSR-57 A 1



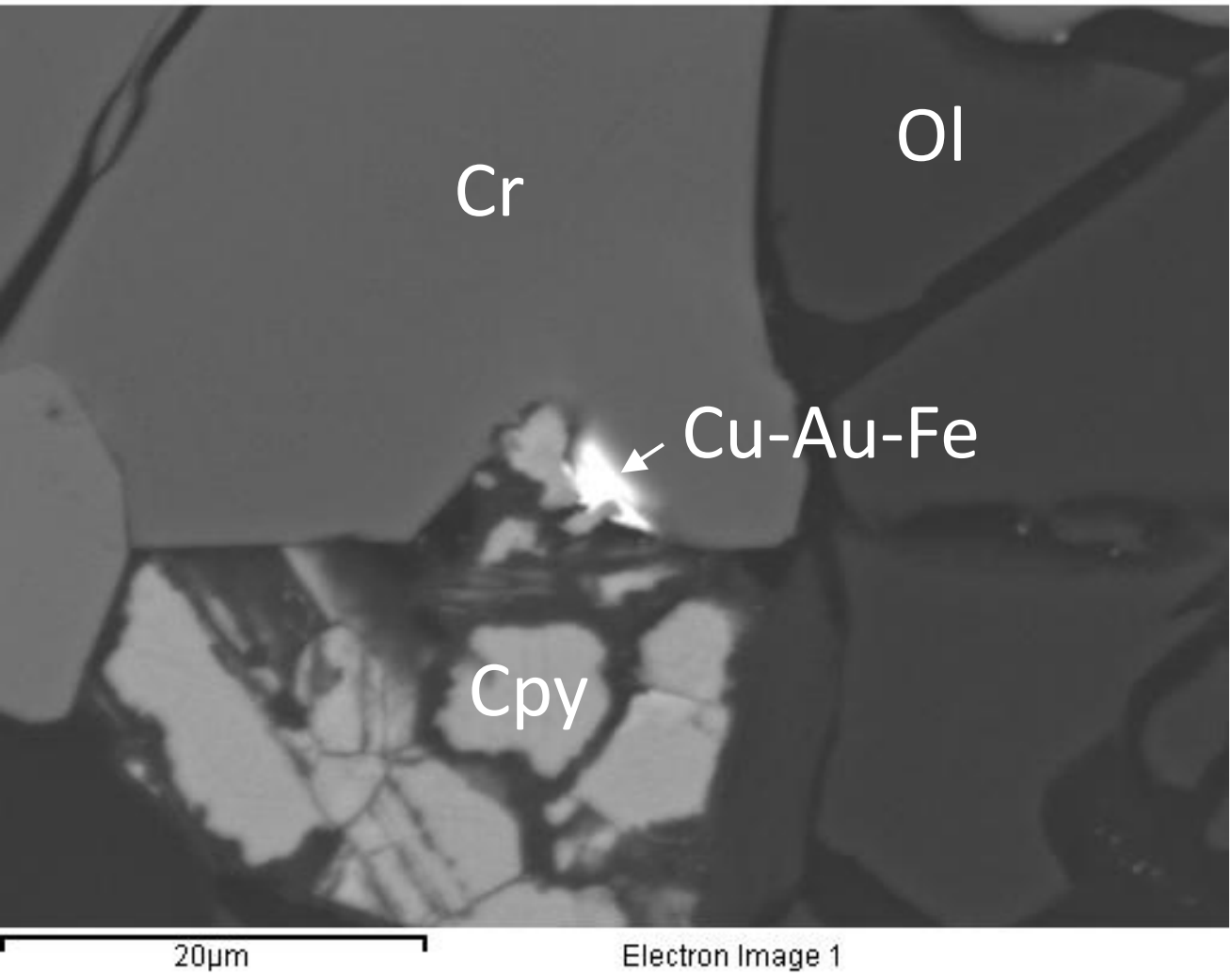
PTSR-57 B 1



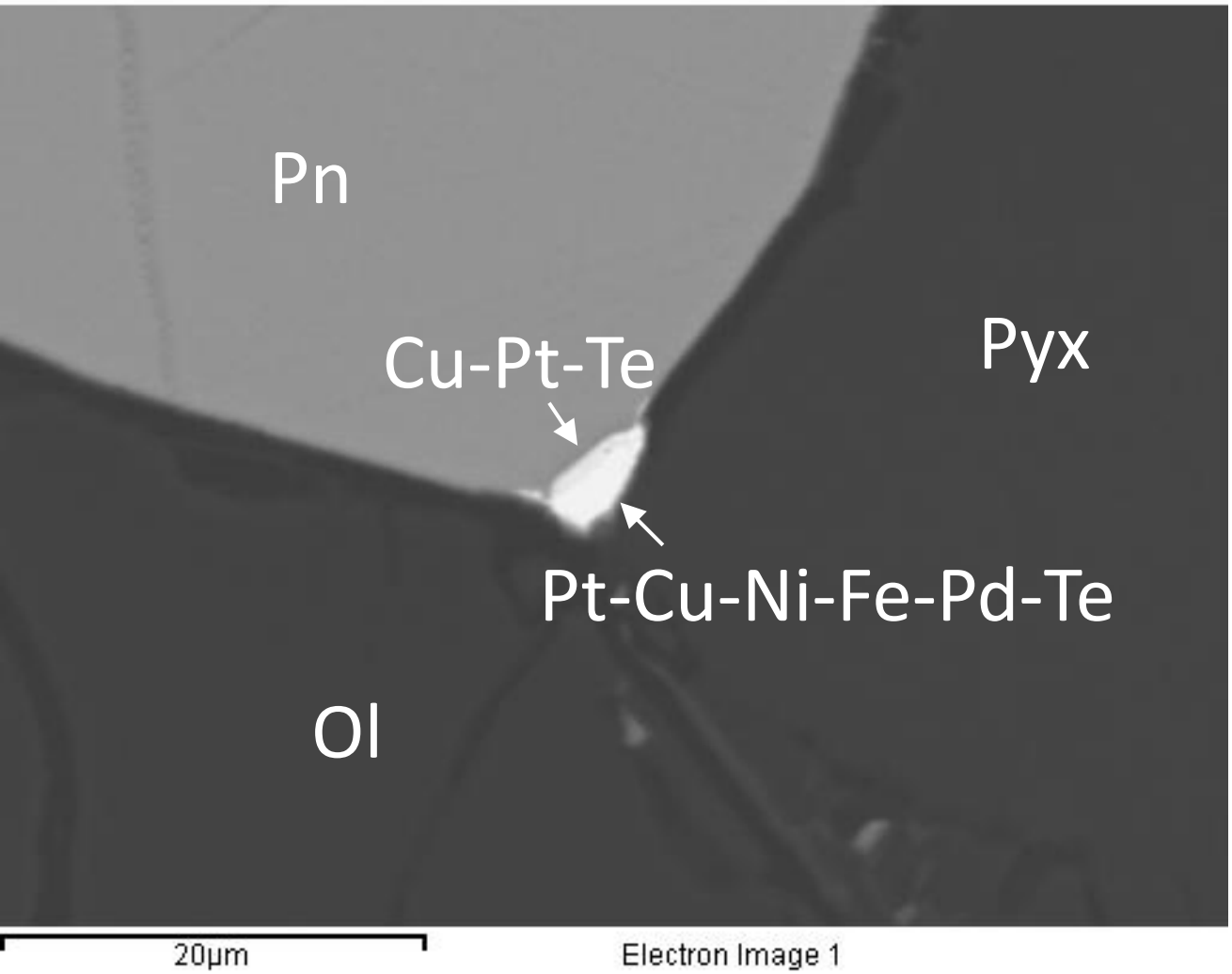
PTSR-57 C 1



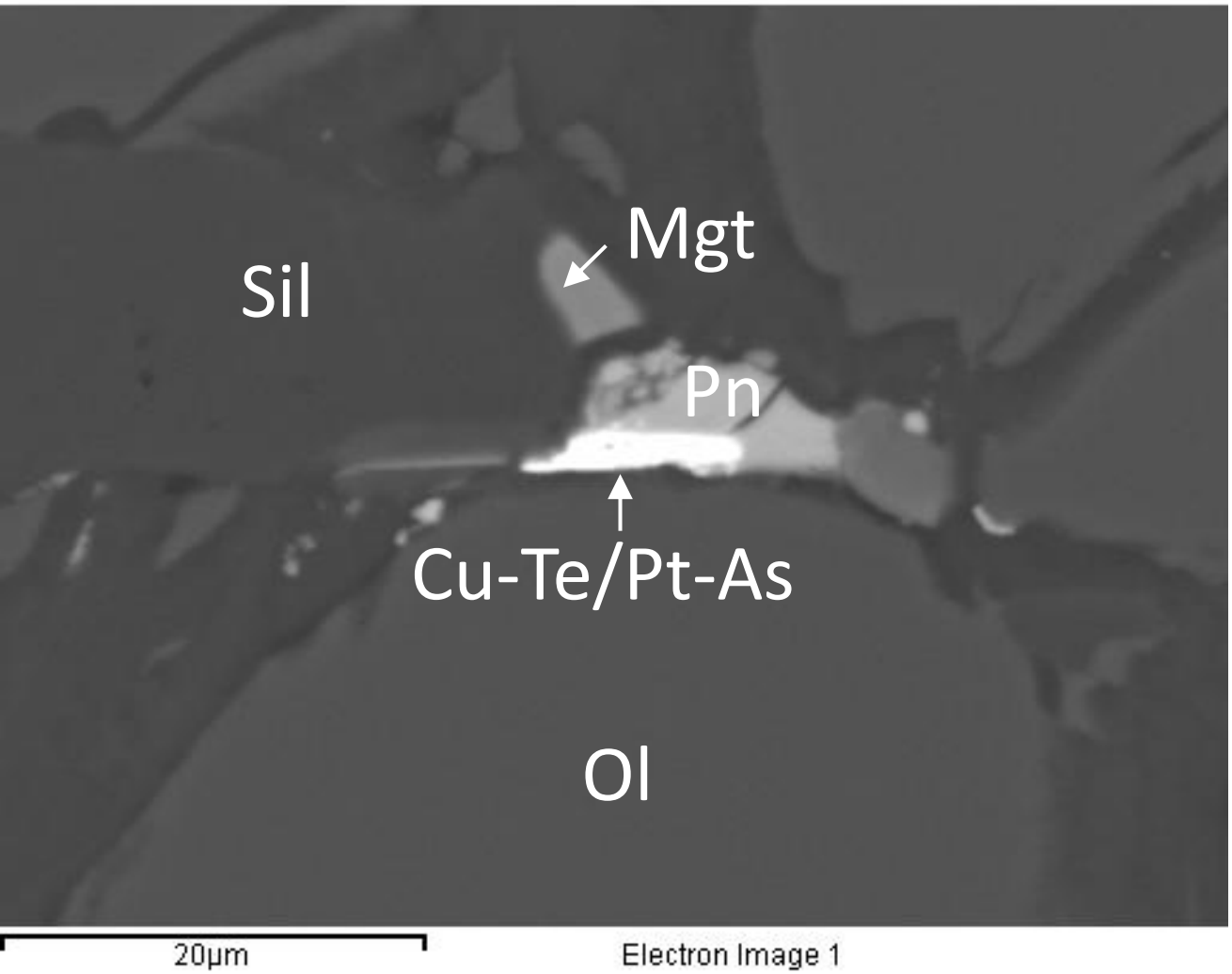
PTSR-57 D 1



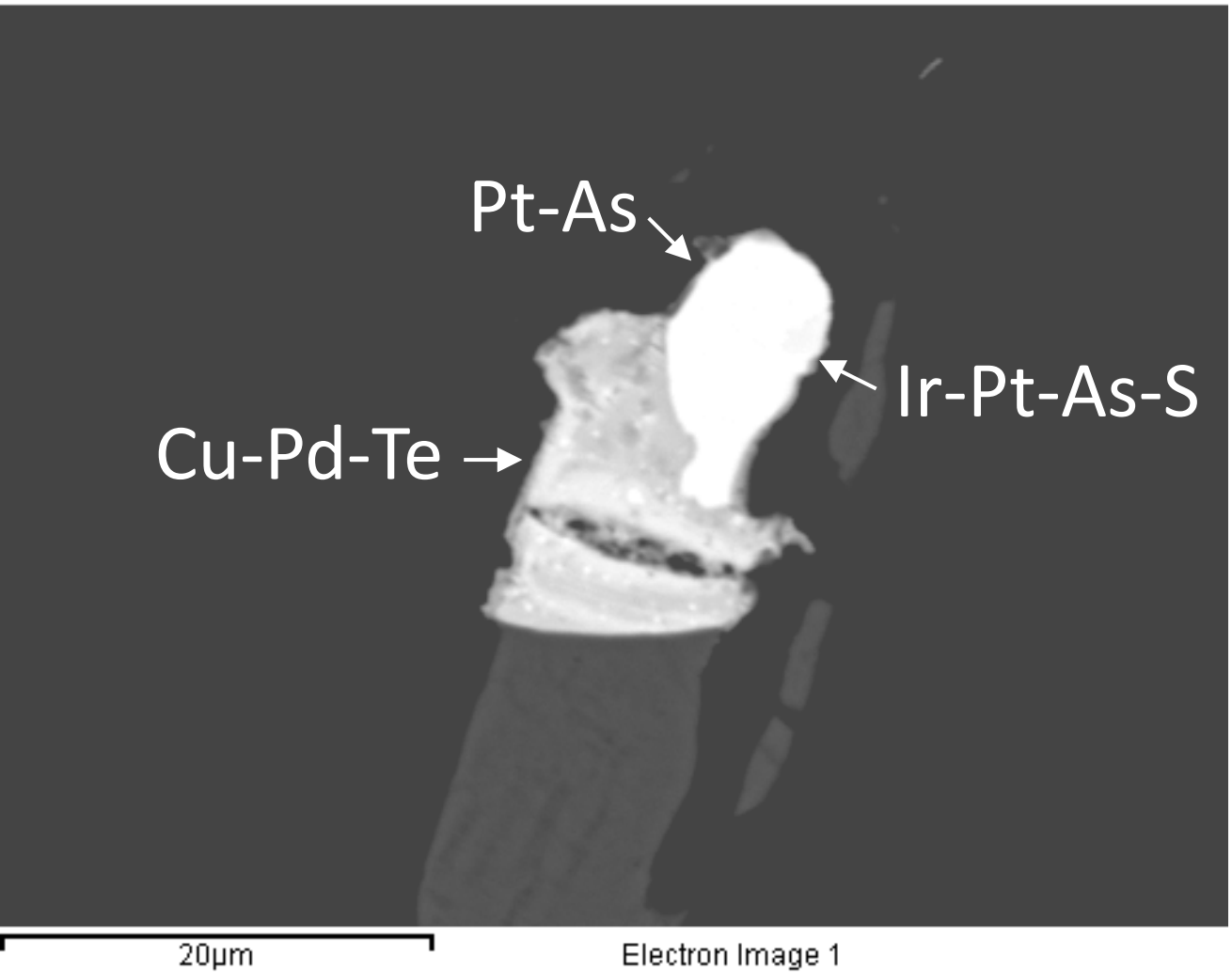
PTSR-57 E 1-2



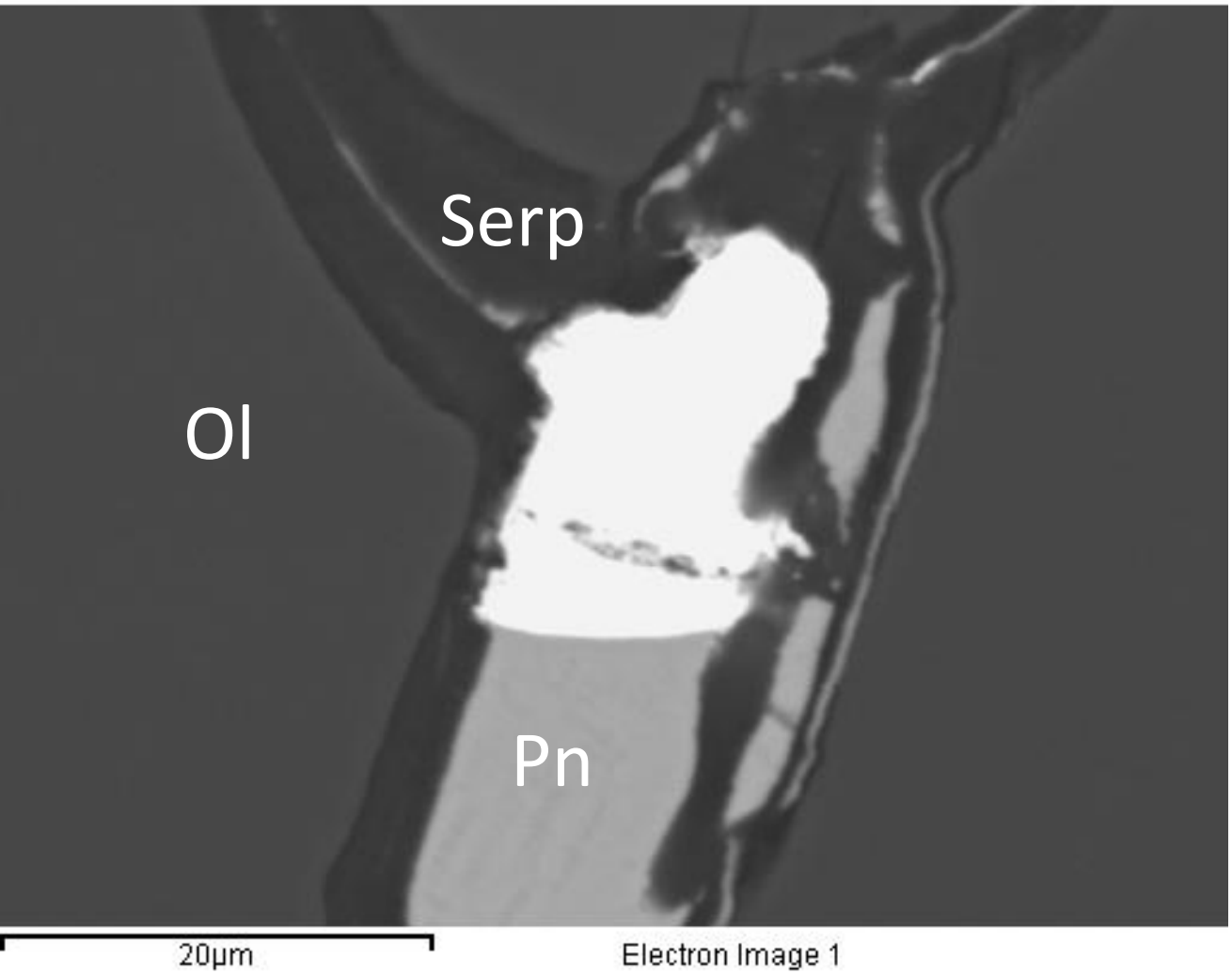
PTSR-57 F 1



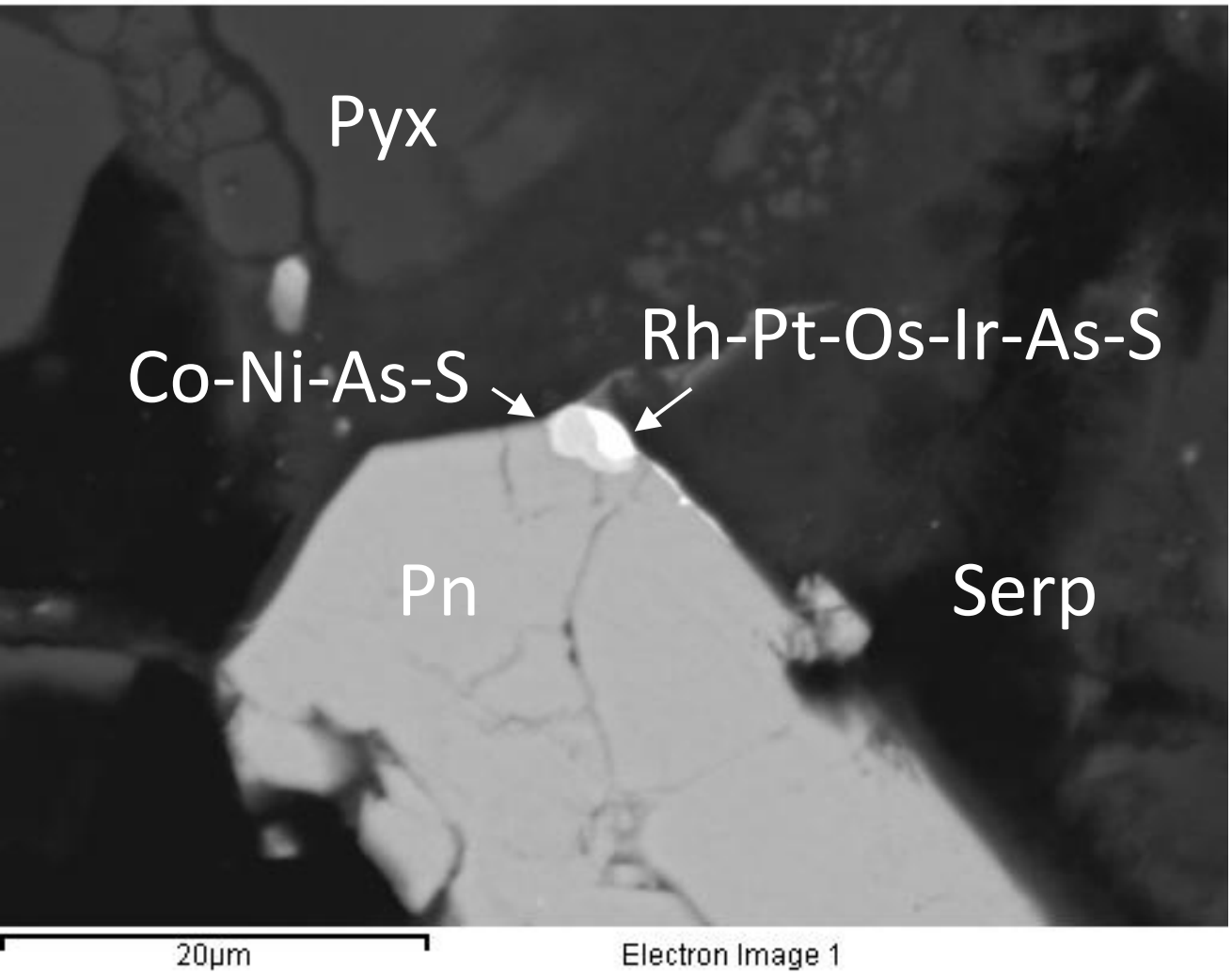
PTSR-58 A 1-3



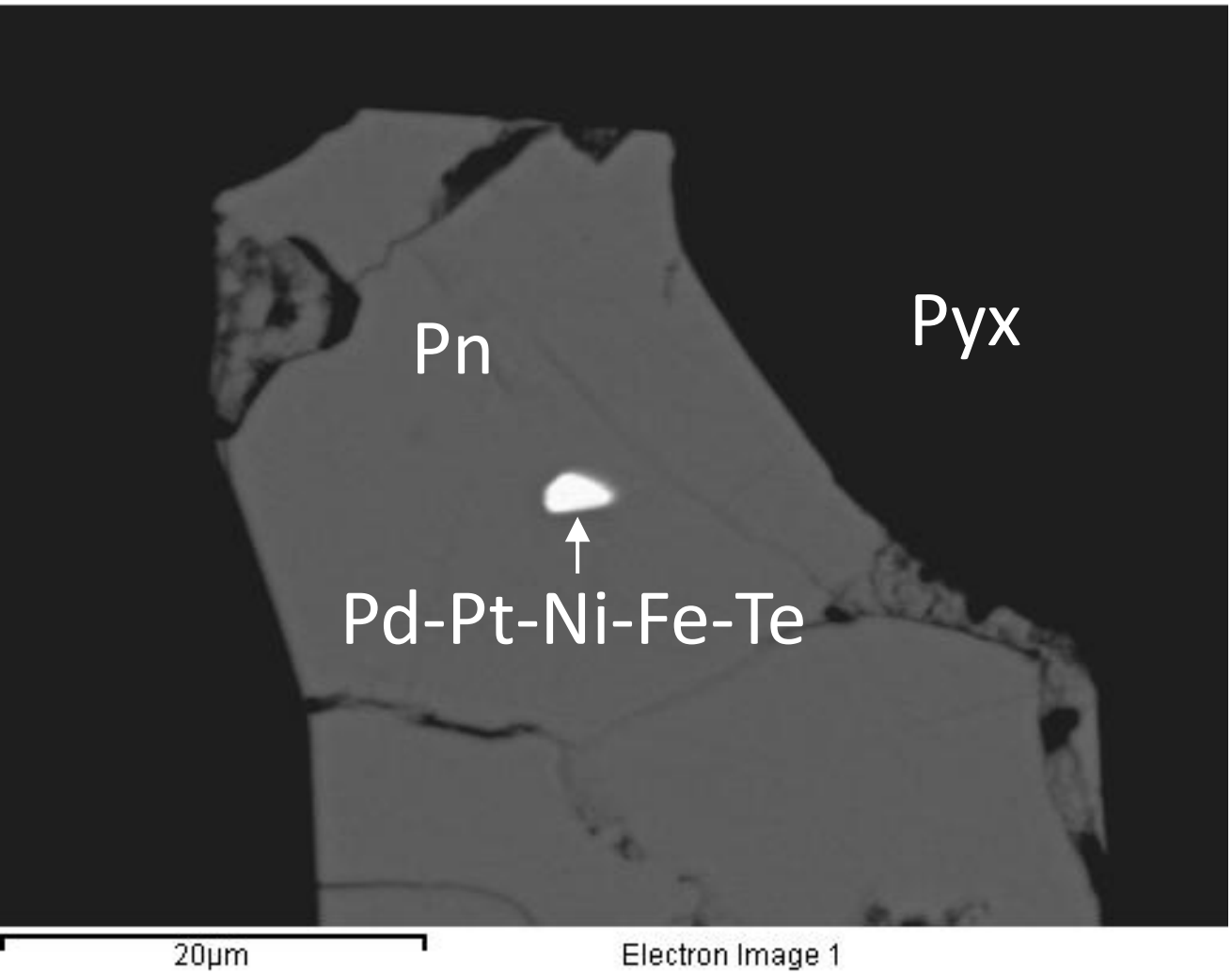
PTSR-58 A 1-3 Light



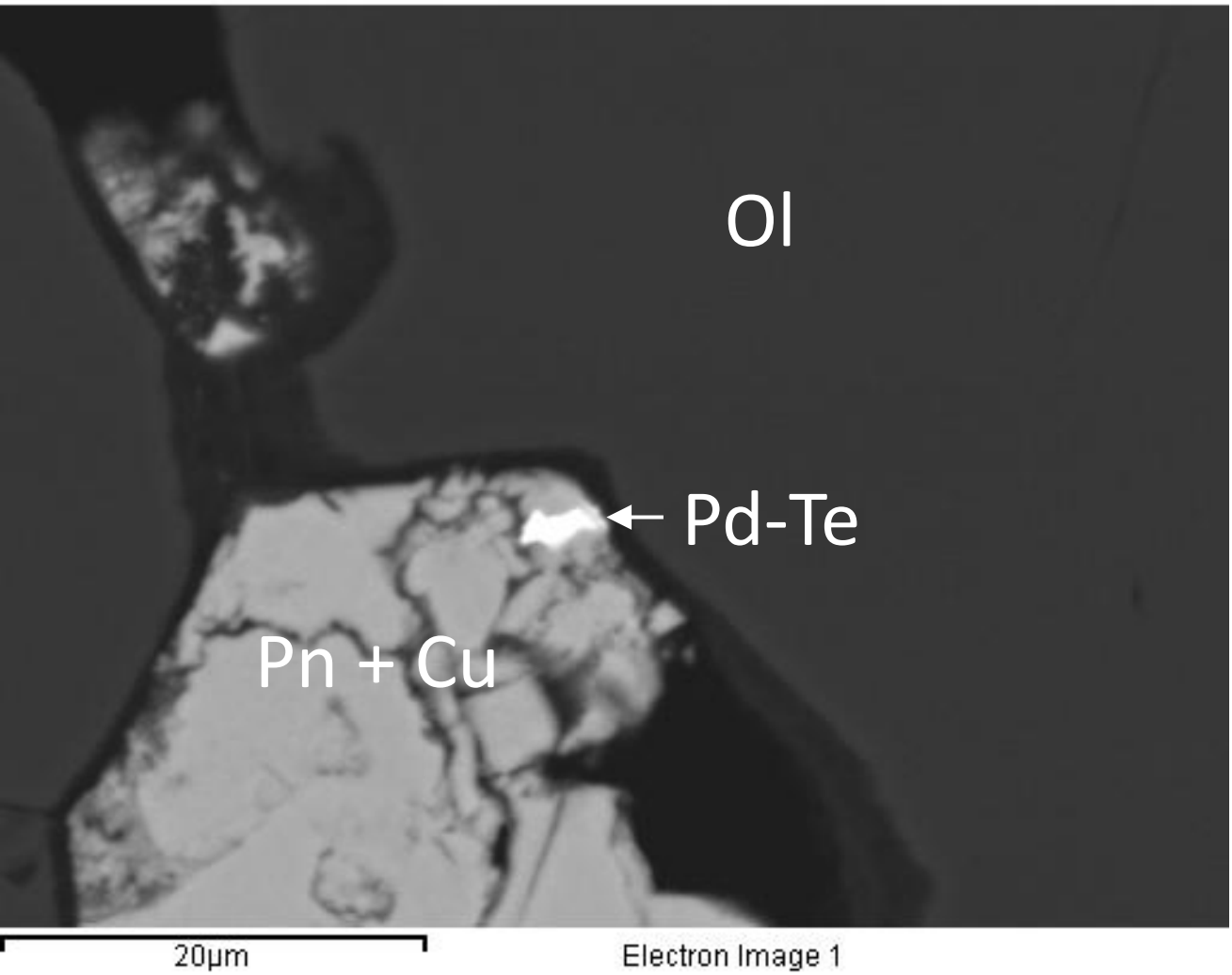
PTSR-58 B 1-2



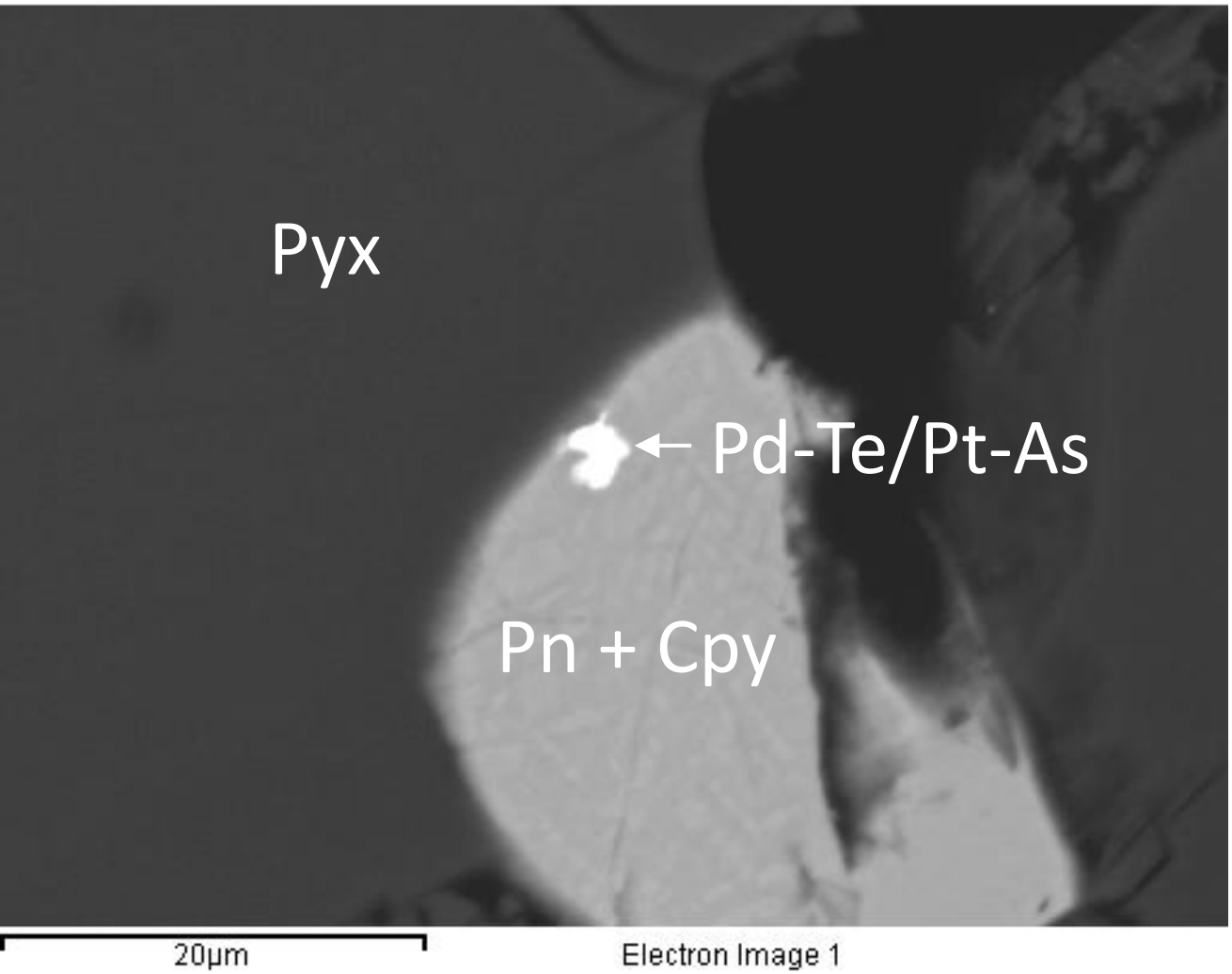
PTSR-58 C 1



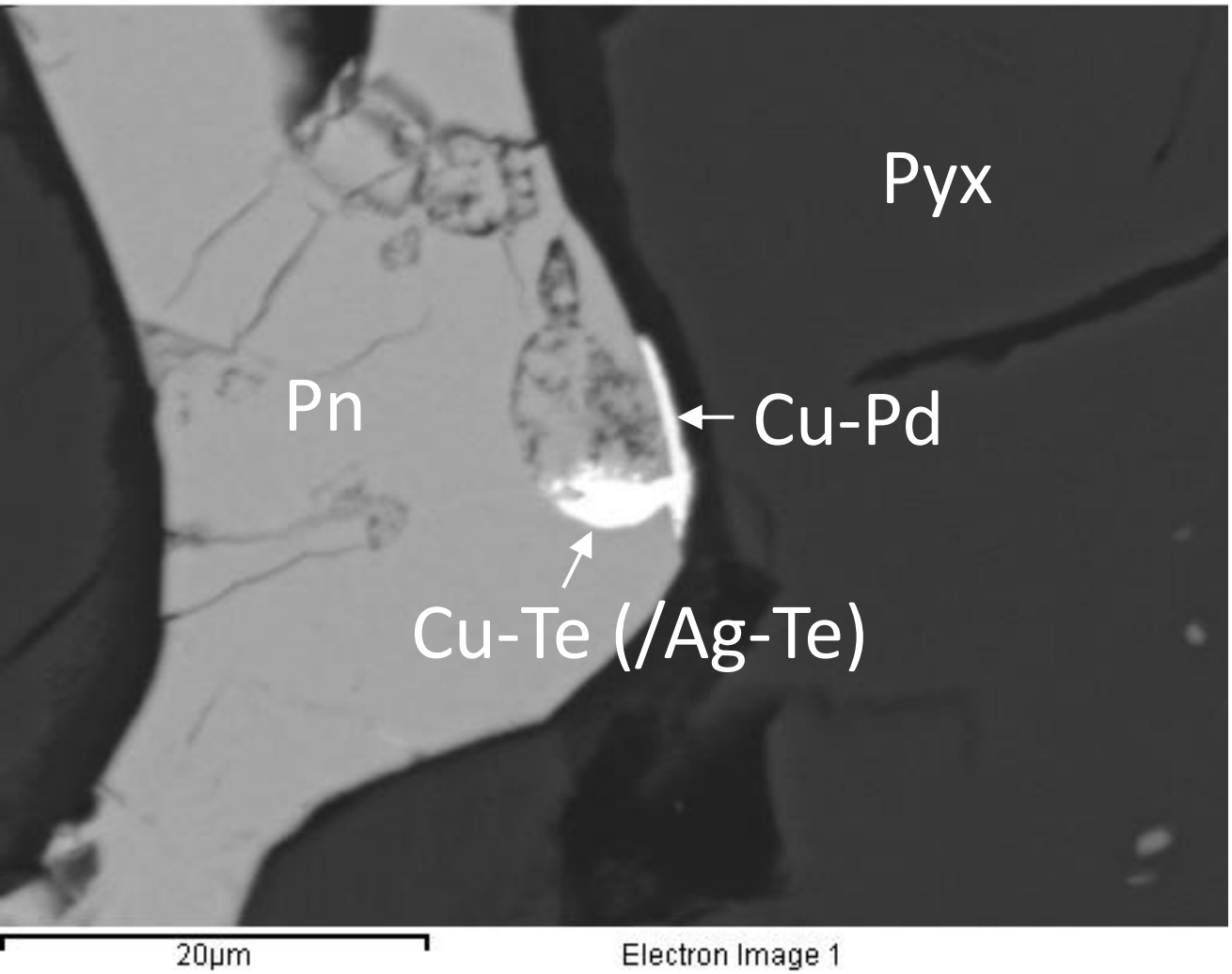
PTSR-58 D 1



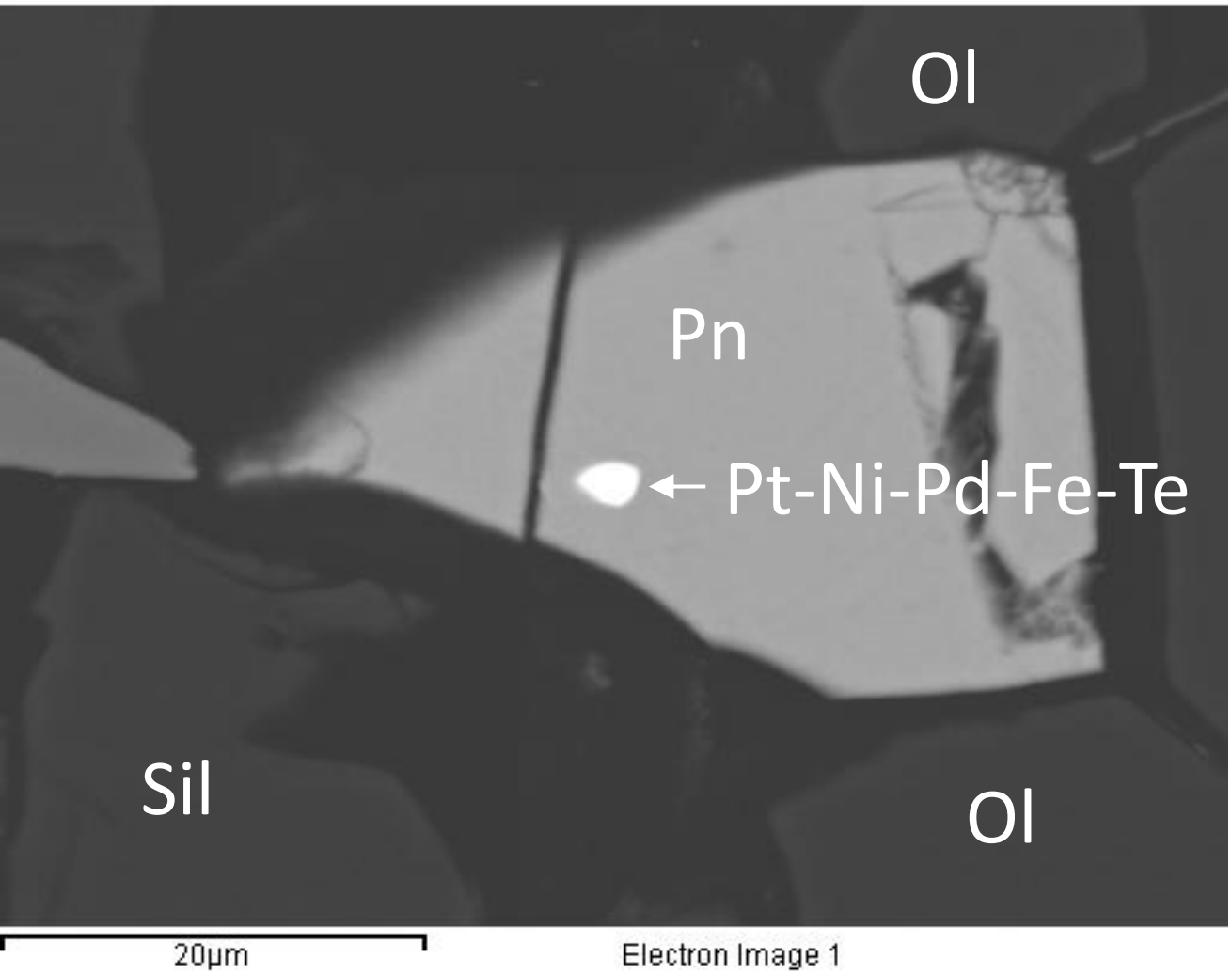
PTSR-58 E 1



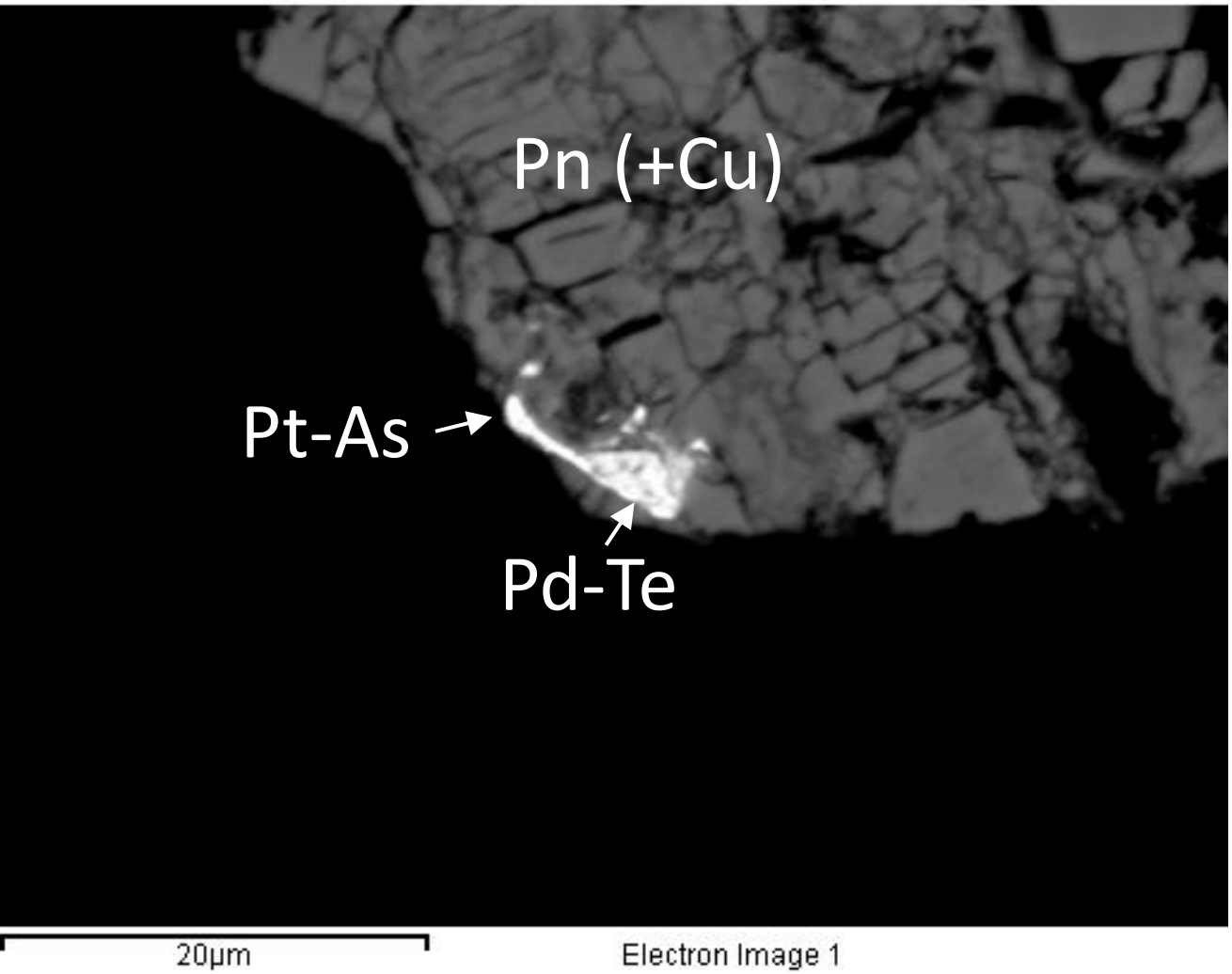
PTSR-58 F 1-2



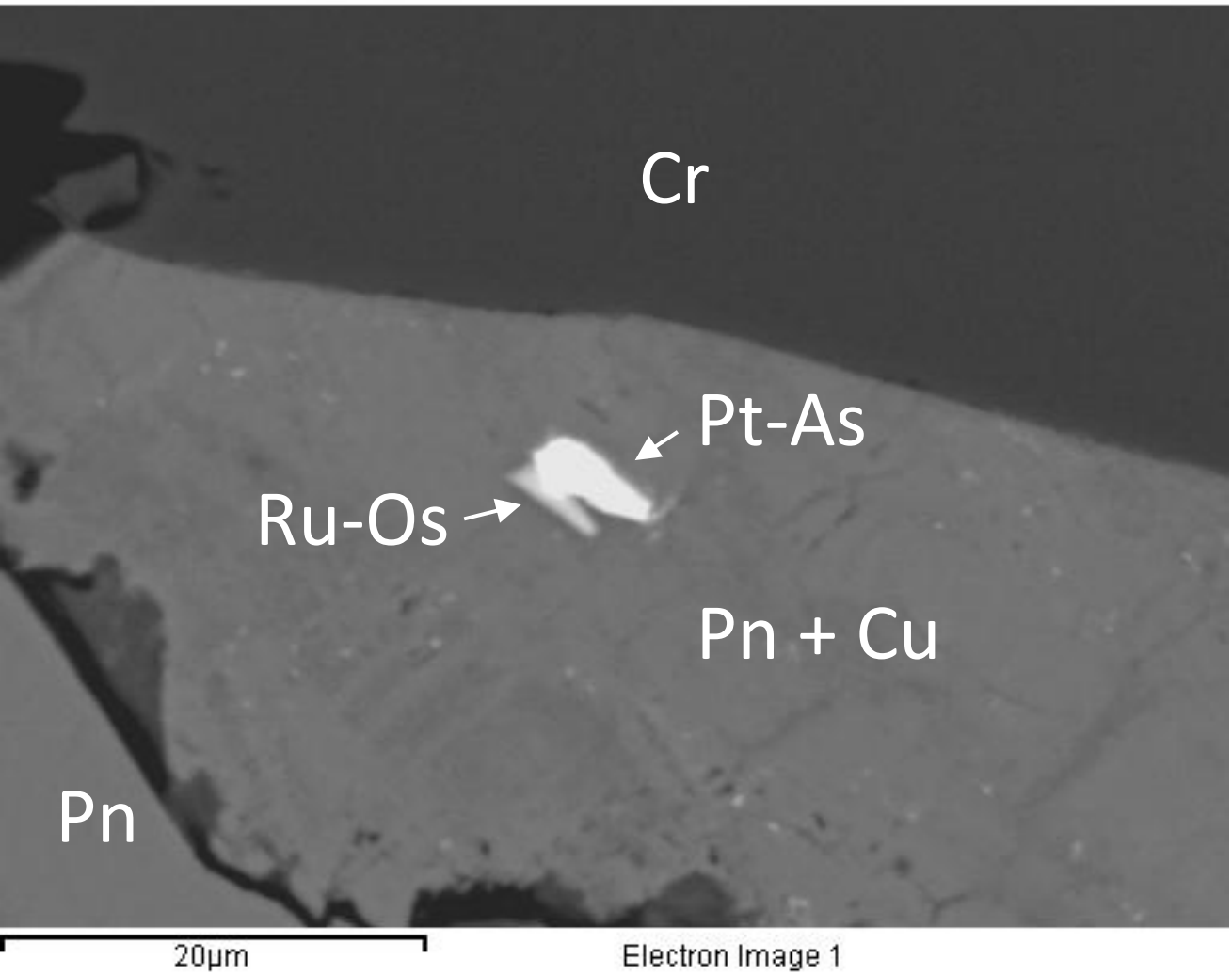
PTSR-58 G 1



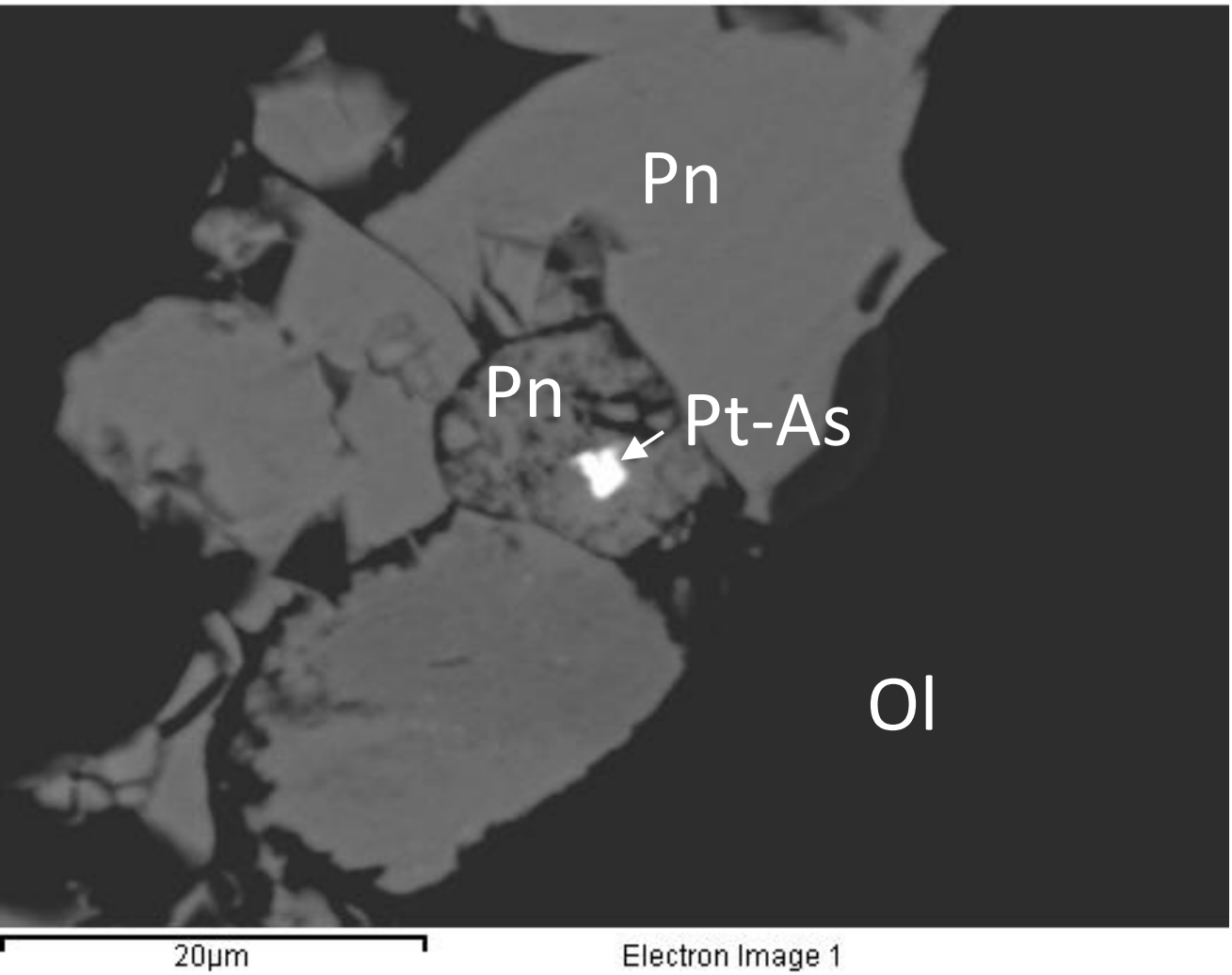
PTSR-58 H 1-2



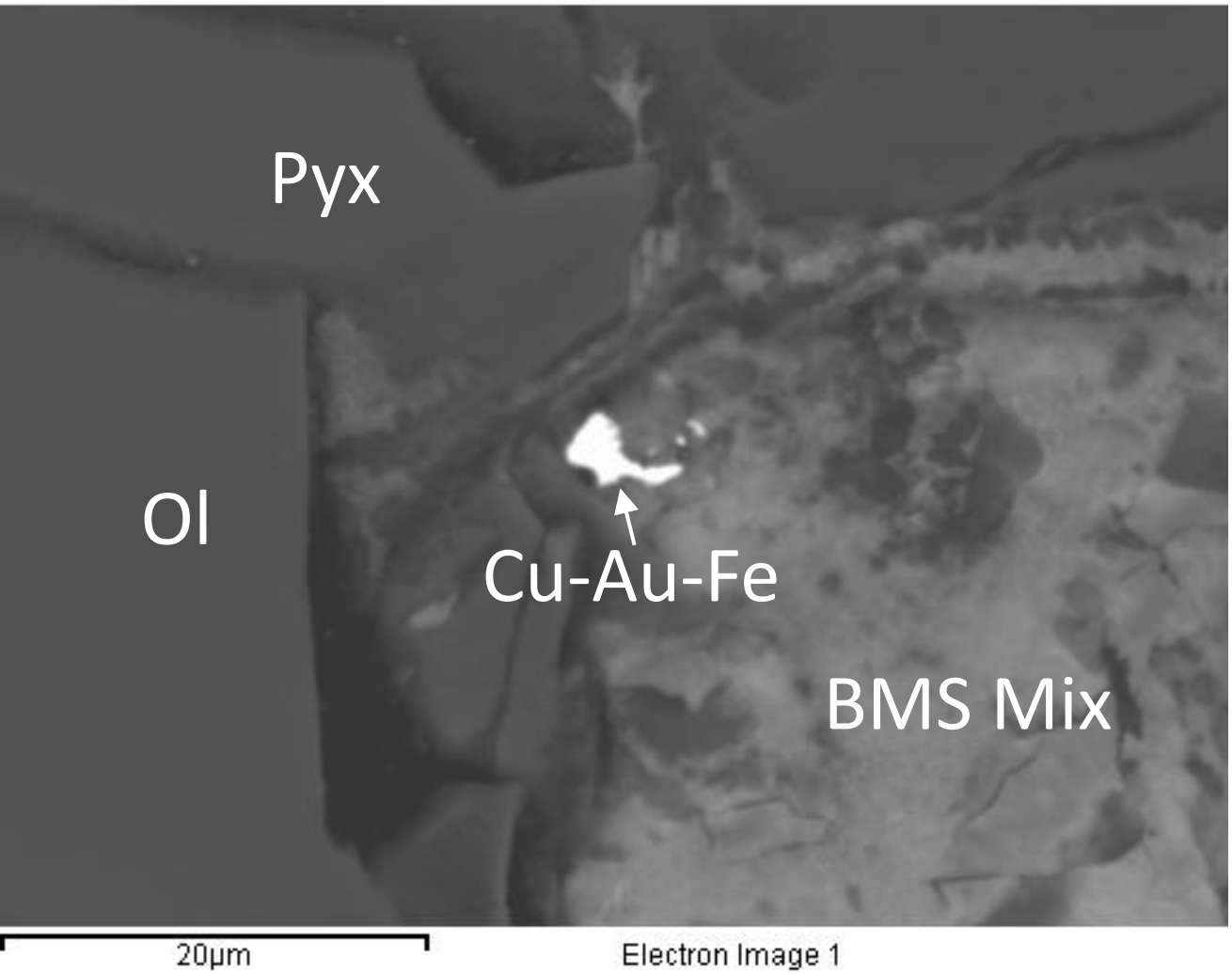
PTSR-58 I 1-2



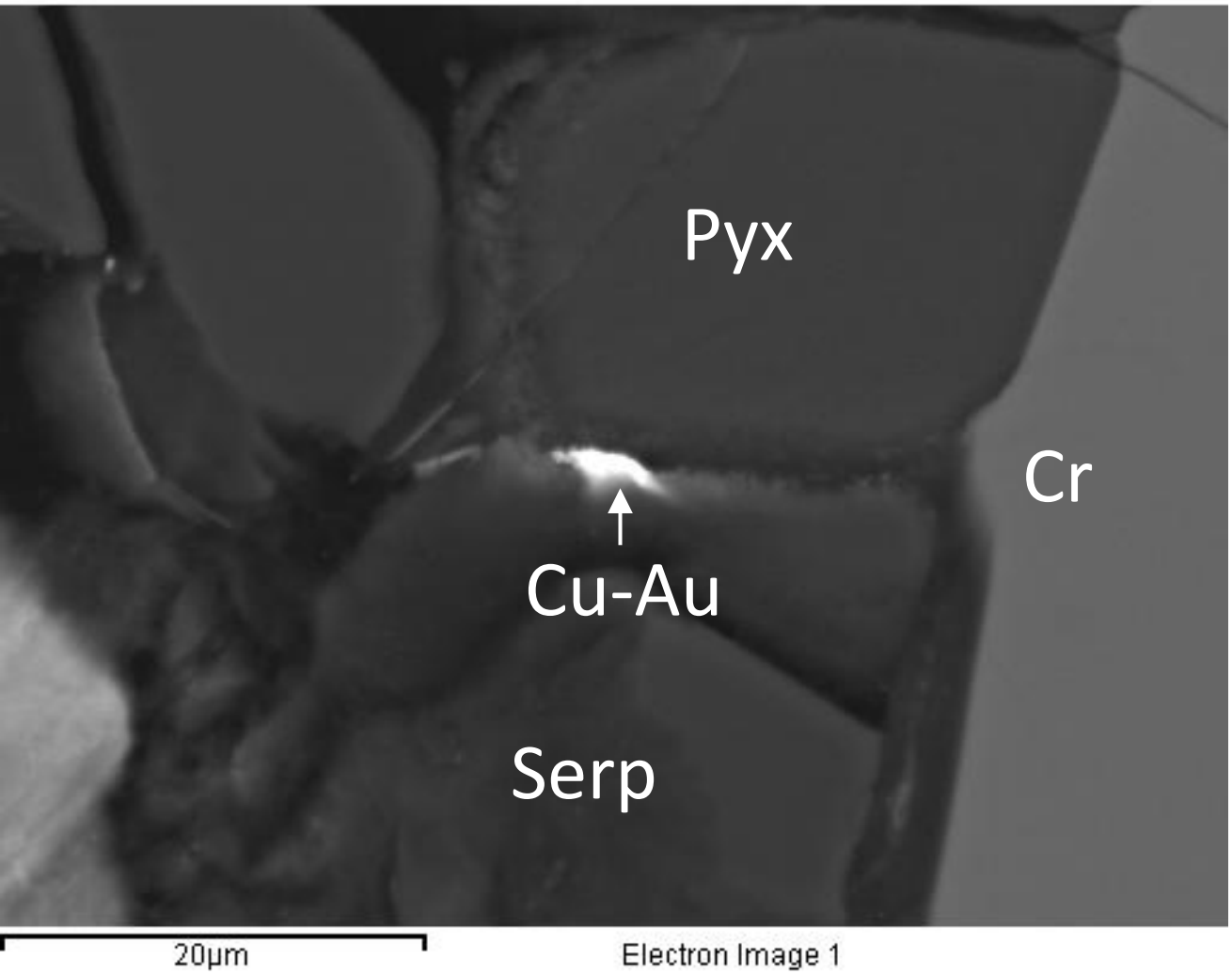
PTSR-58 J 1



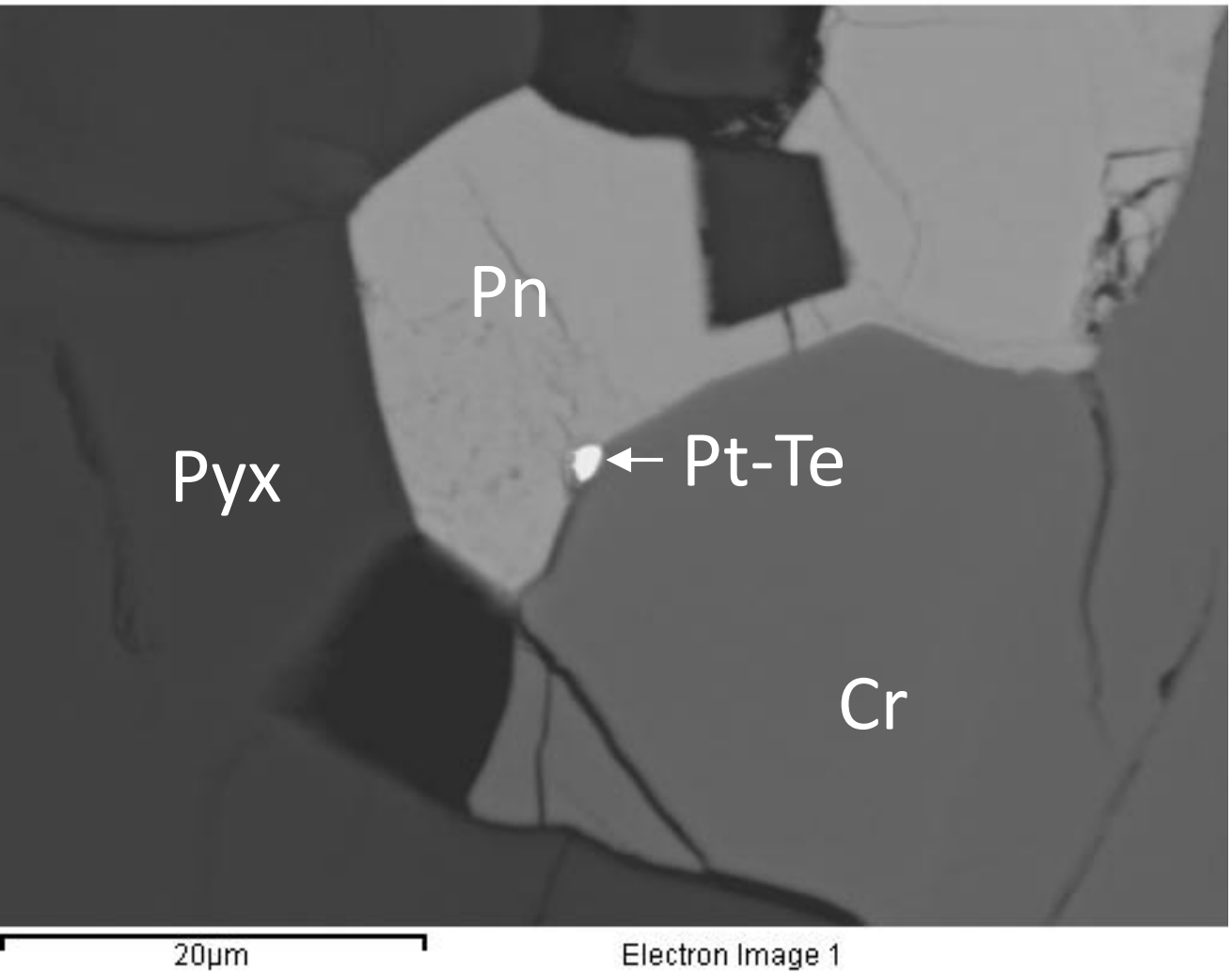
PTSR-59 A 1



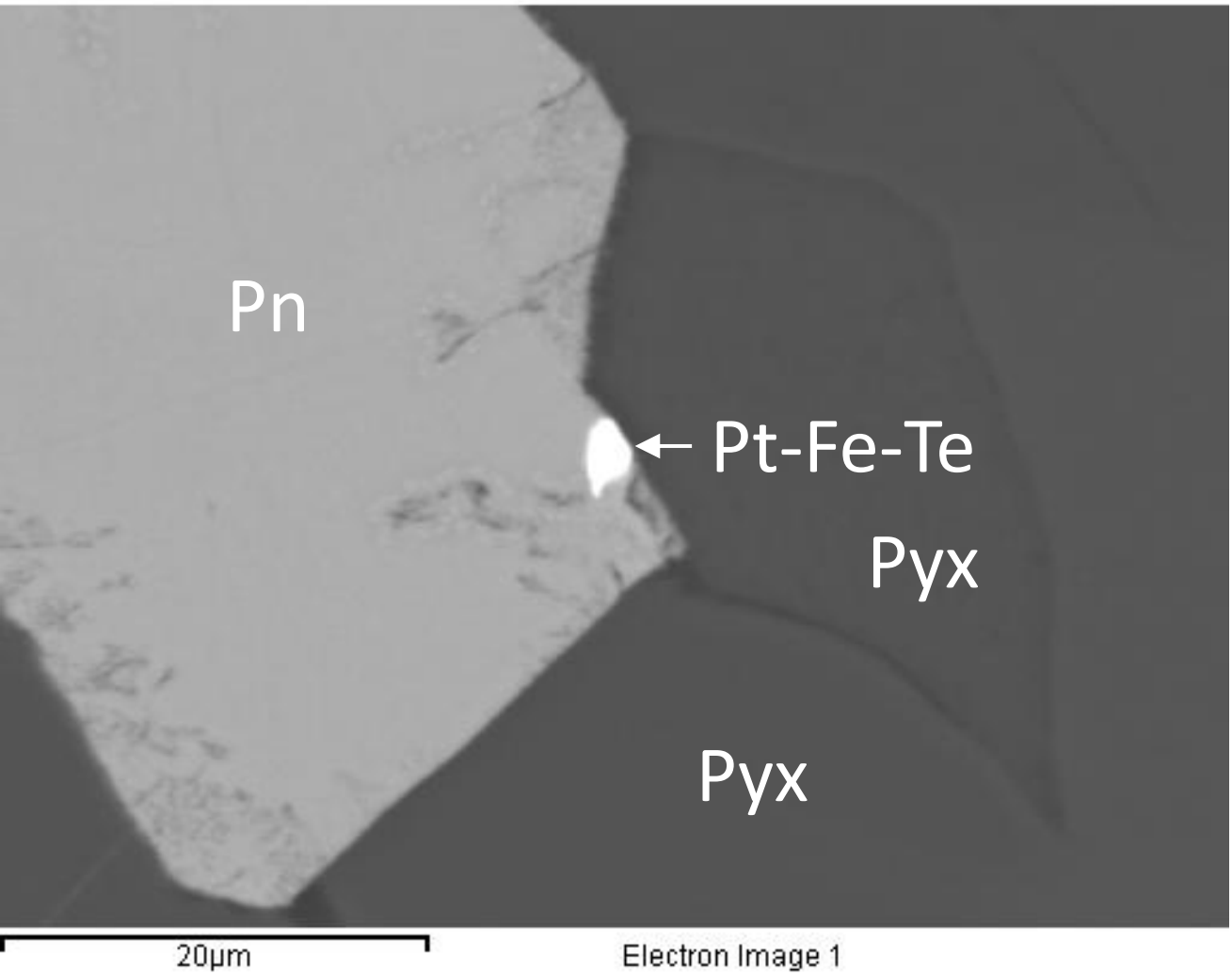
PTSR-59 B 1



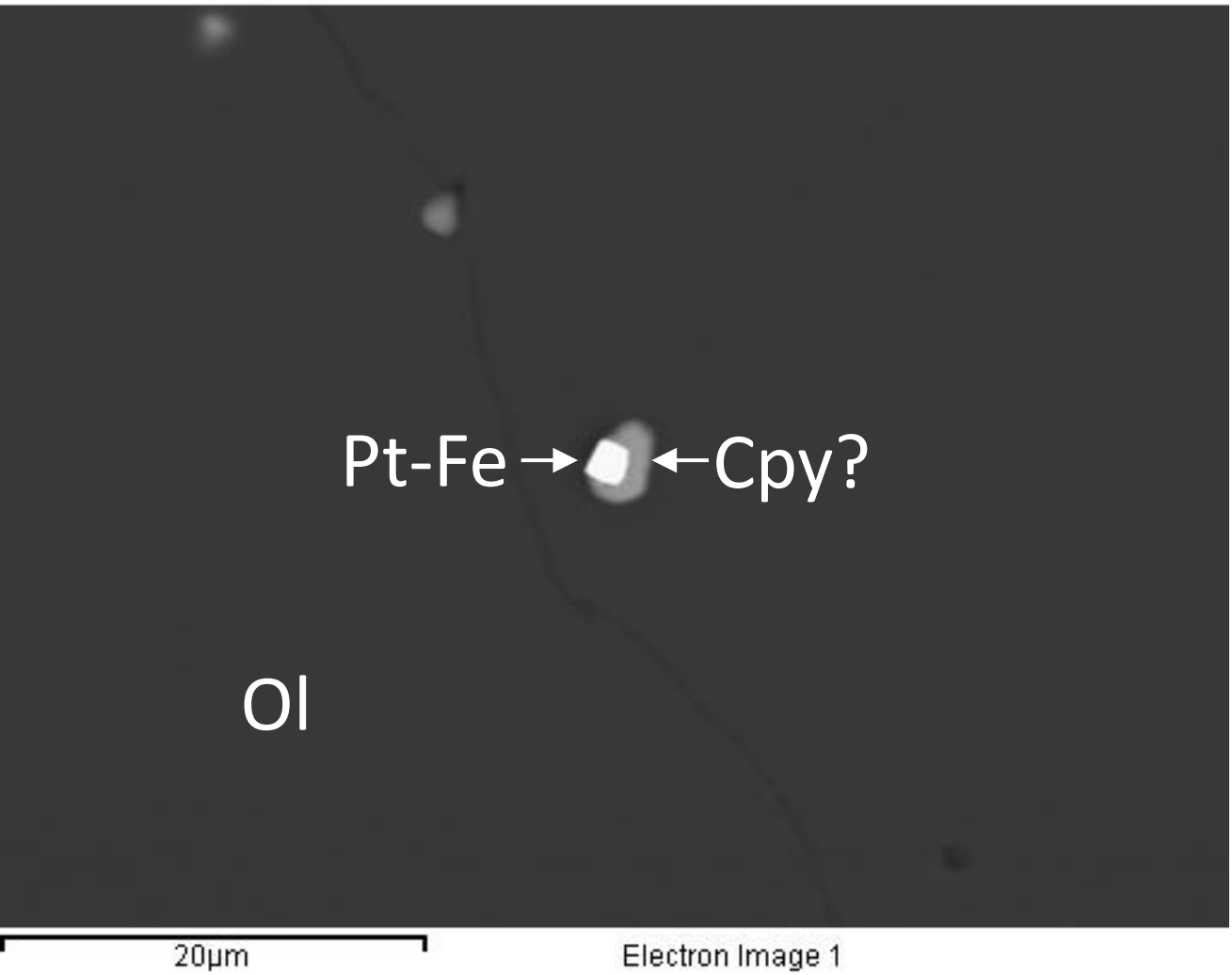
PTSR-59 C 1



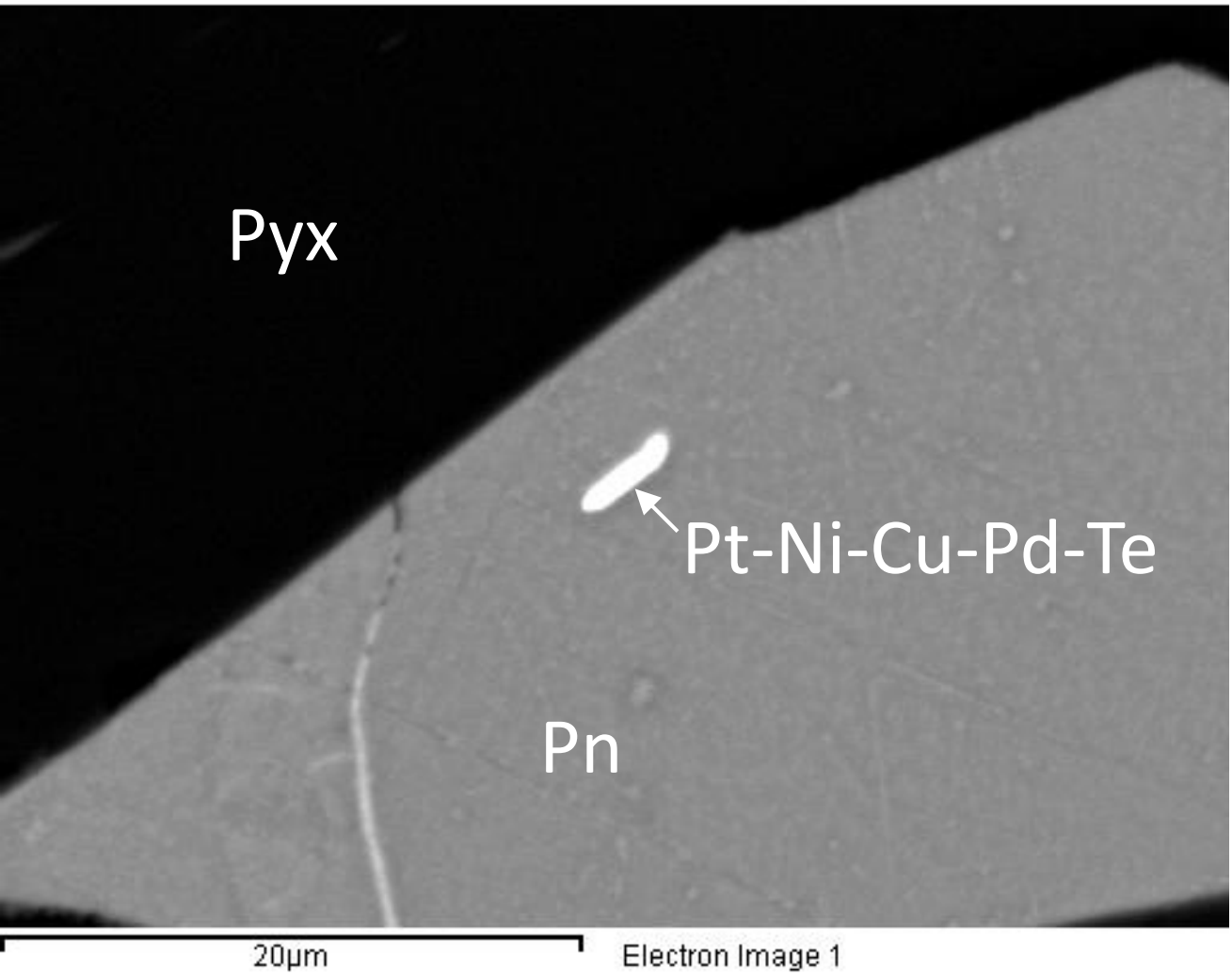
PTSR-59 D 1



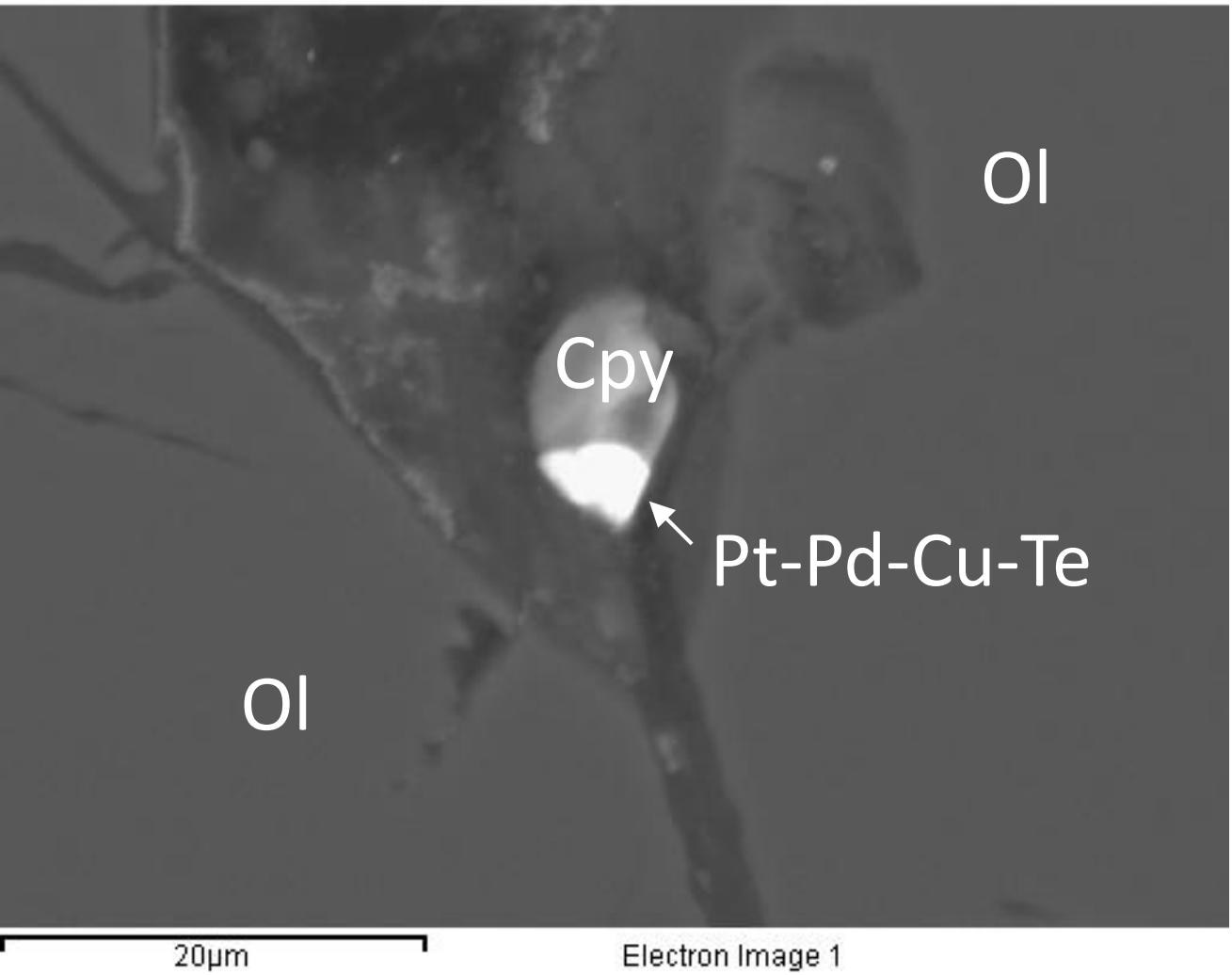
PTSR-59 E 1



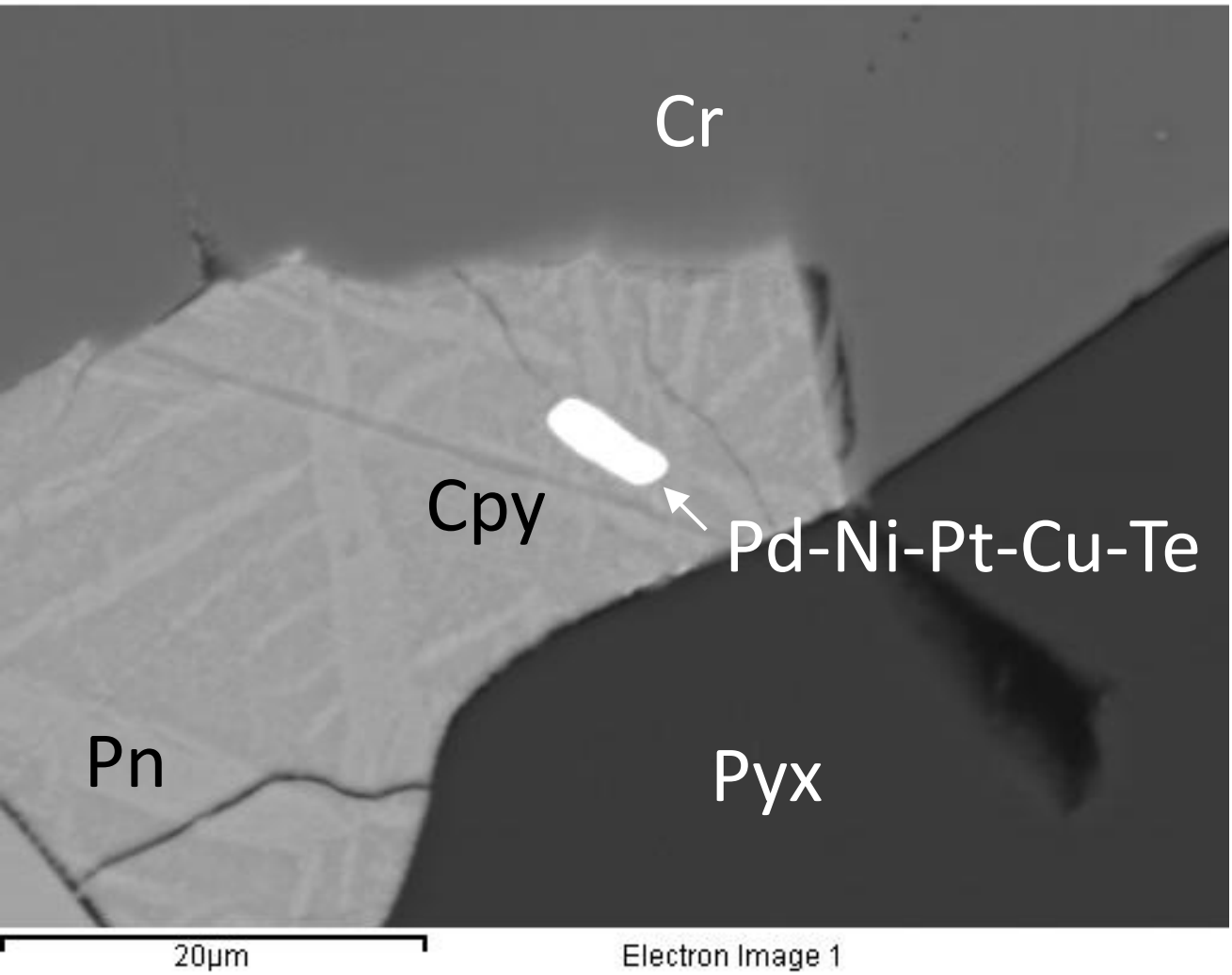
PTSR-60 A 1



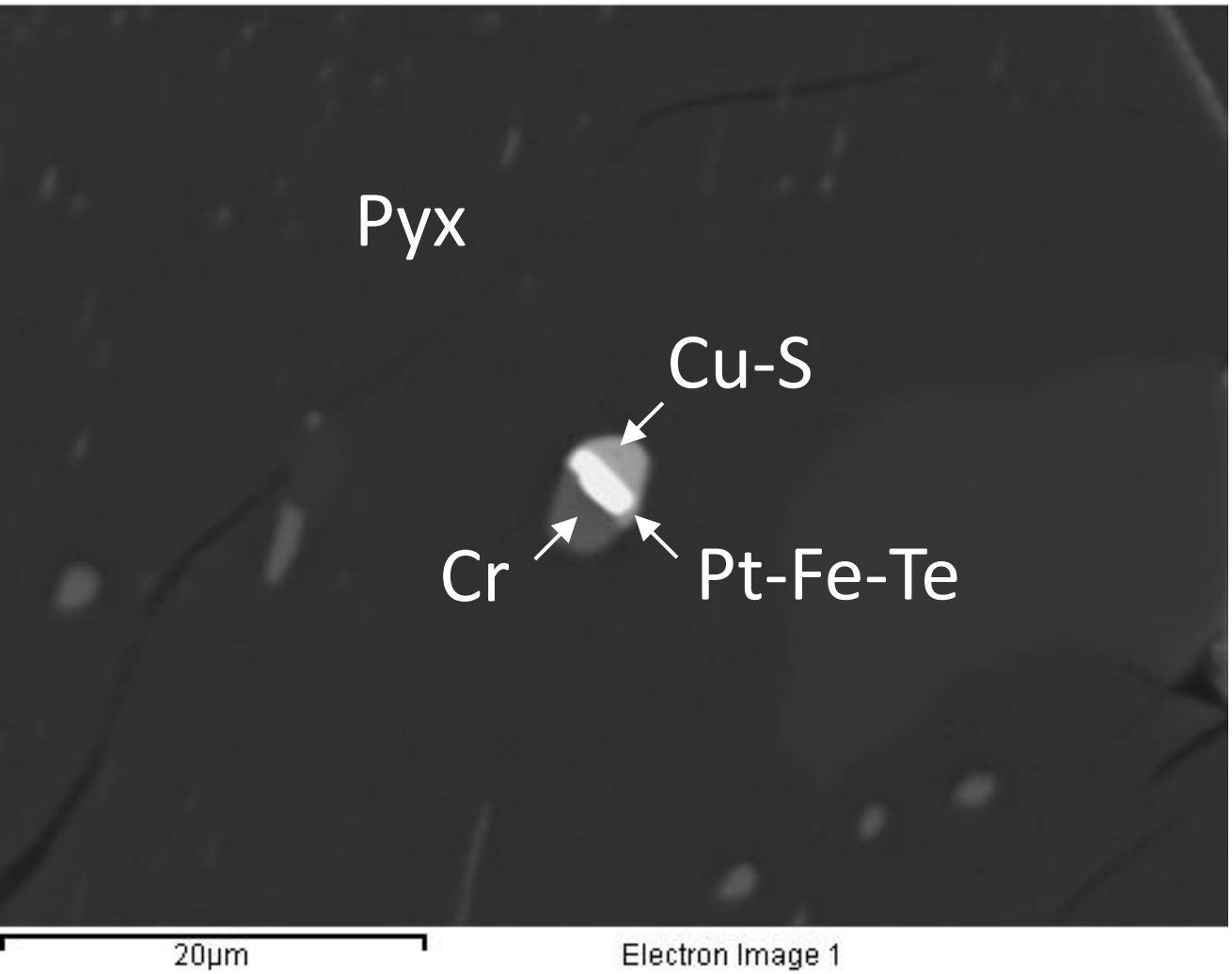
PTSR-60 B 1



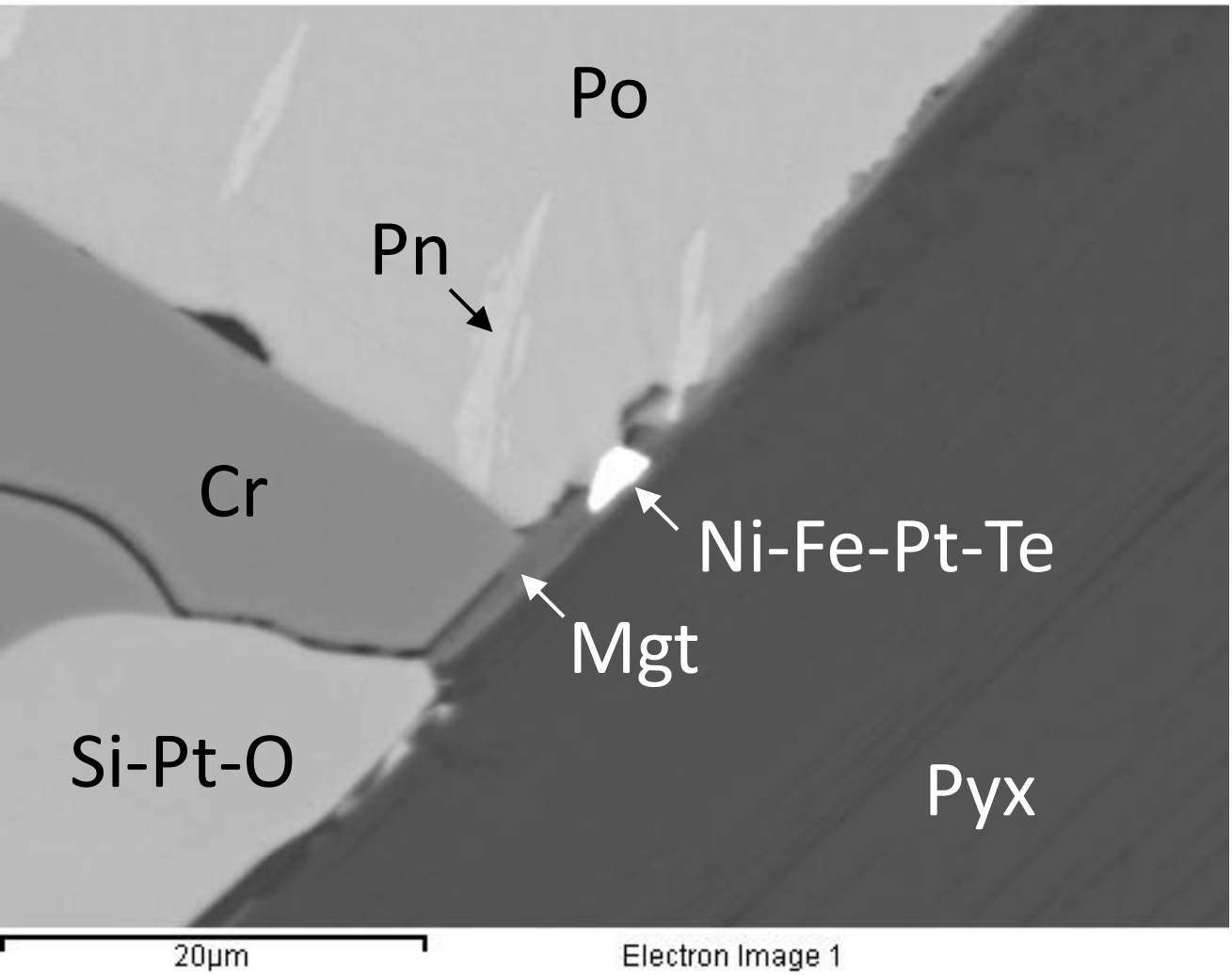
PTSR-60 C 1



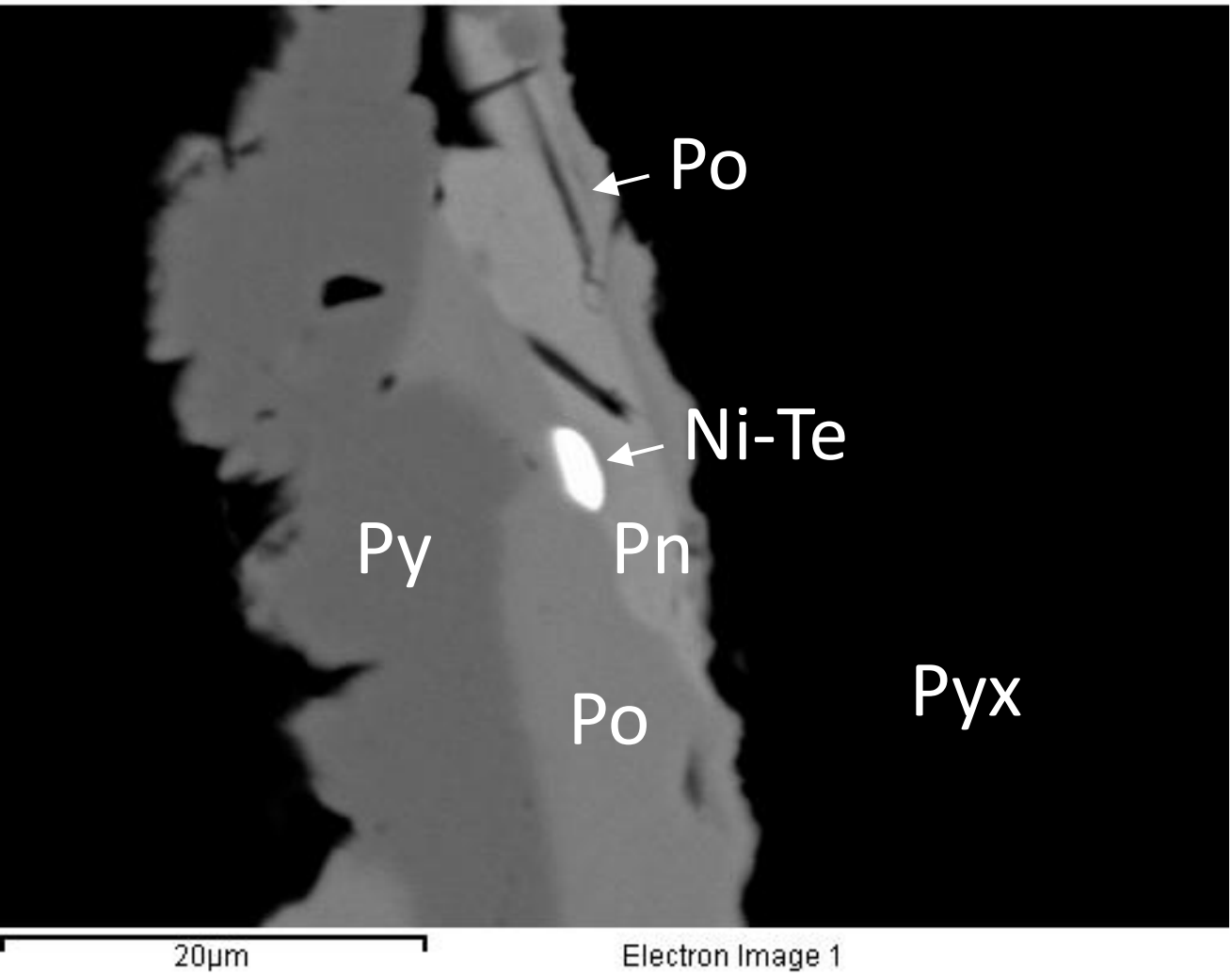
PTSR-60 D 1



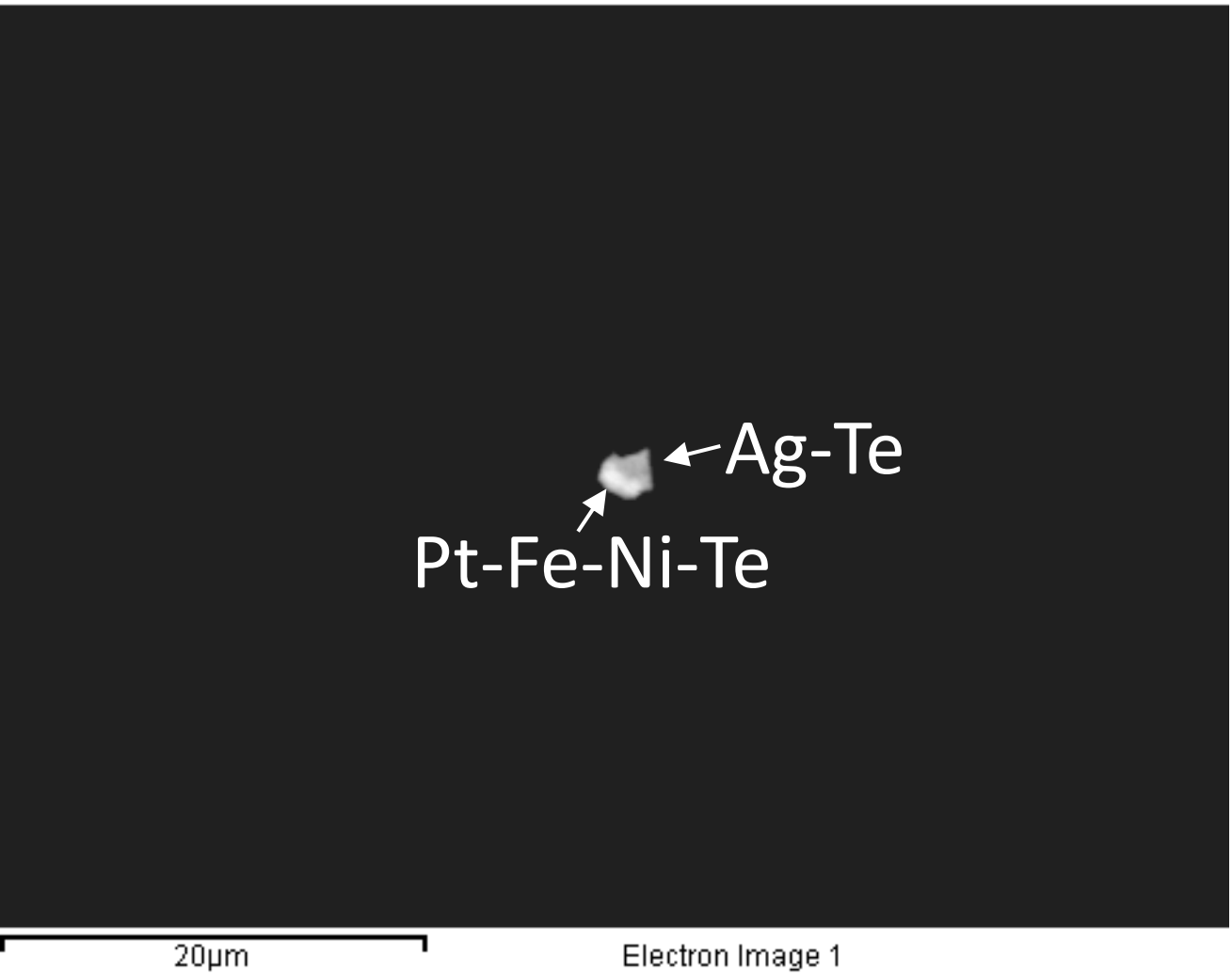
PTSR-63 A 1



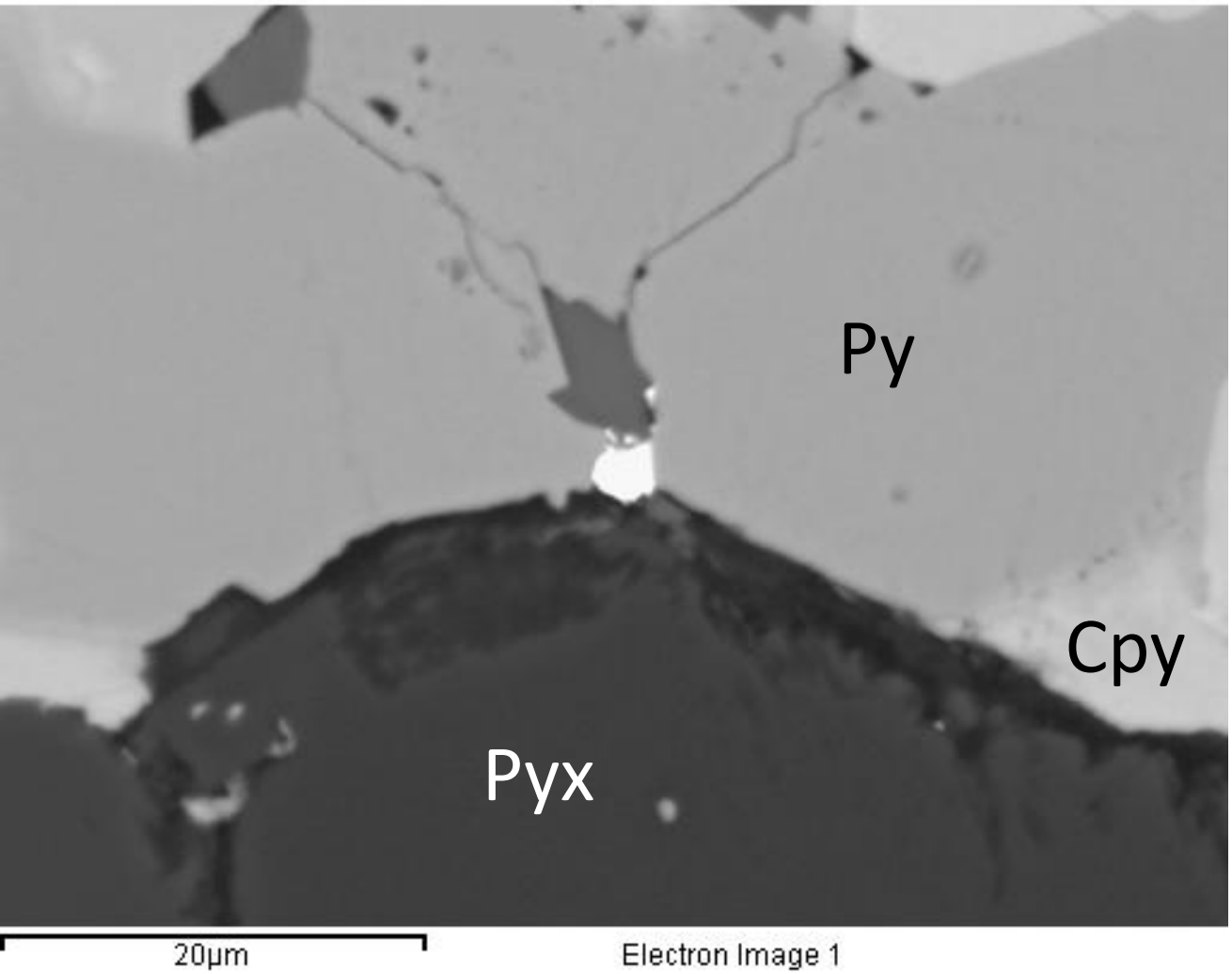
PTSR-63 B 1



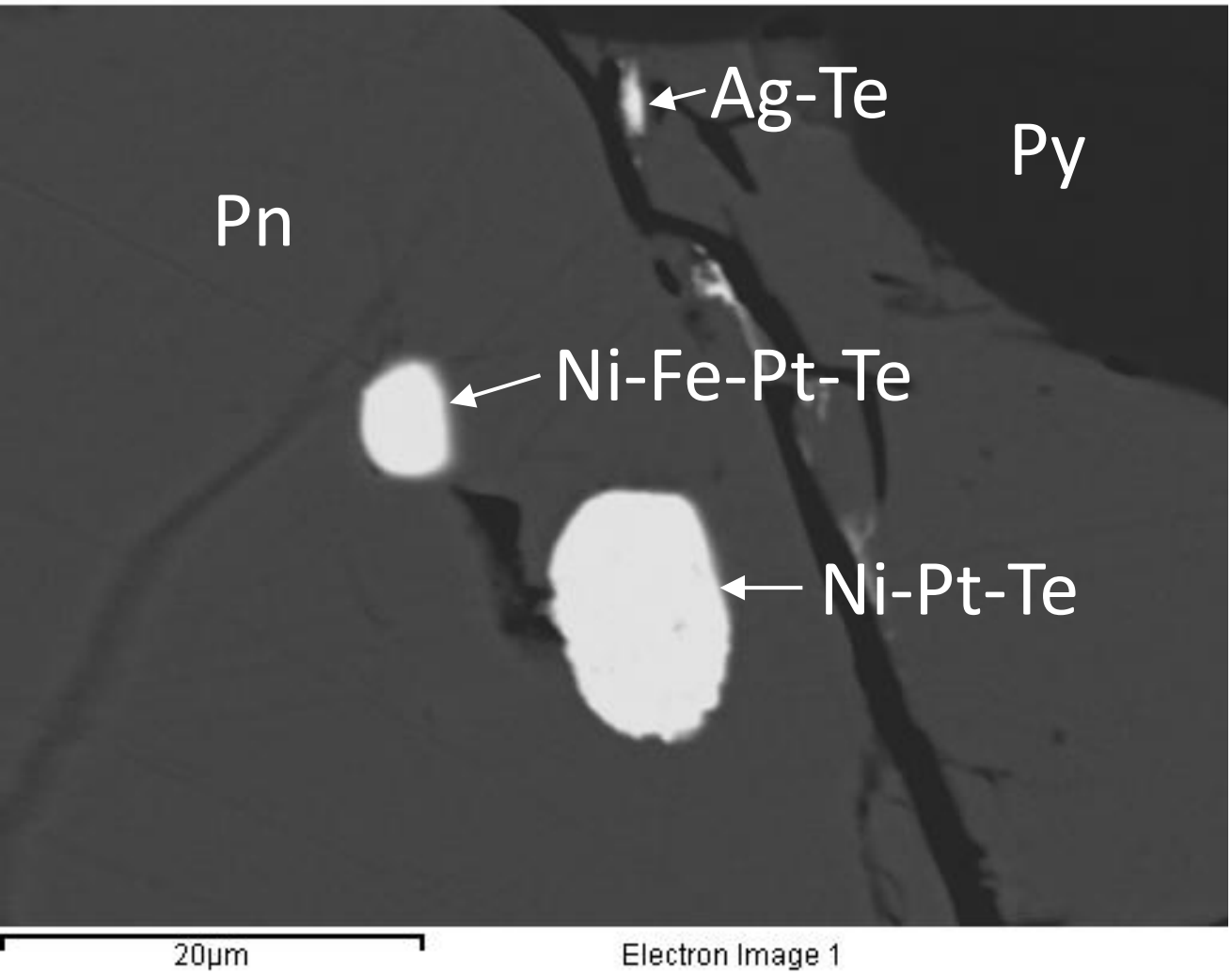
PTSR-63 C 1-2



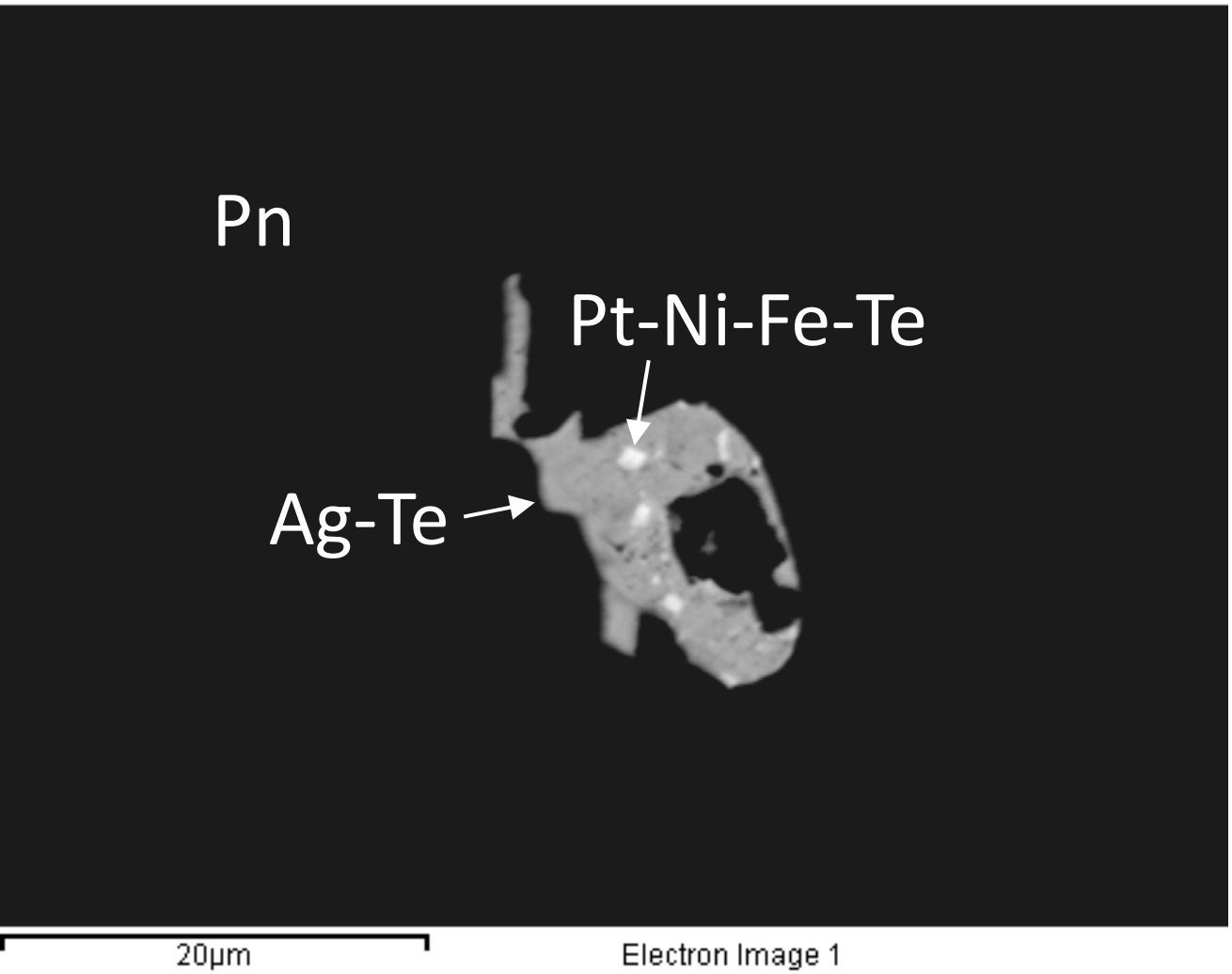
PTSR-63 C 1-2 Light



PTSR-63 D 1-2



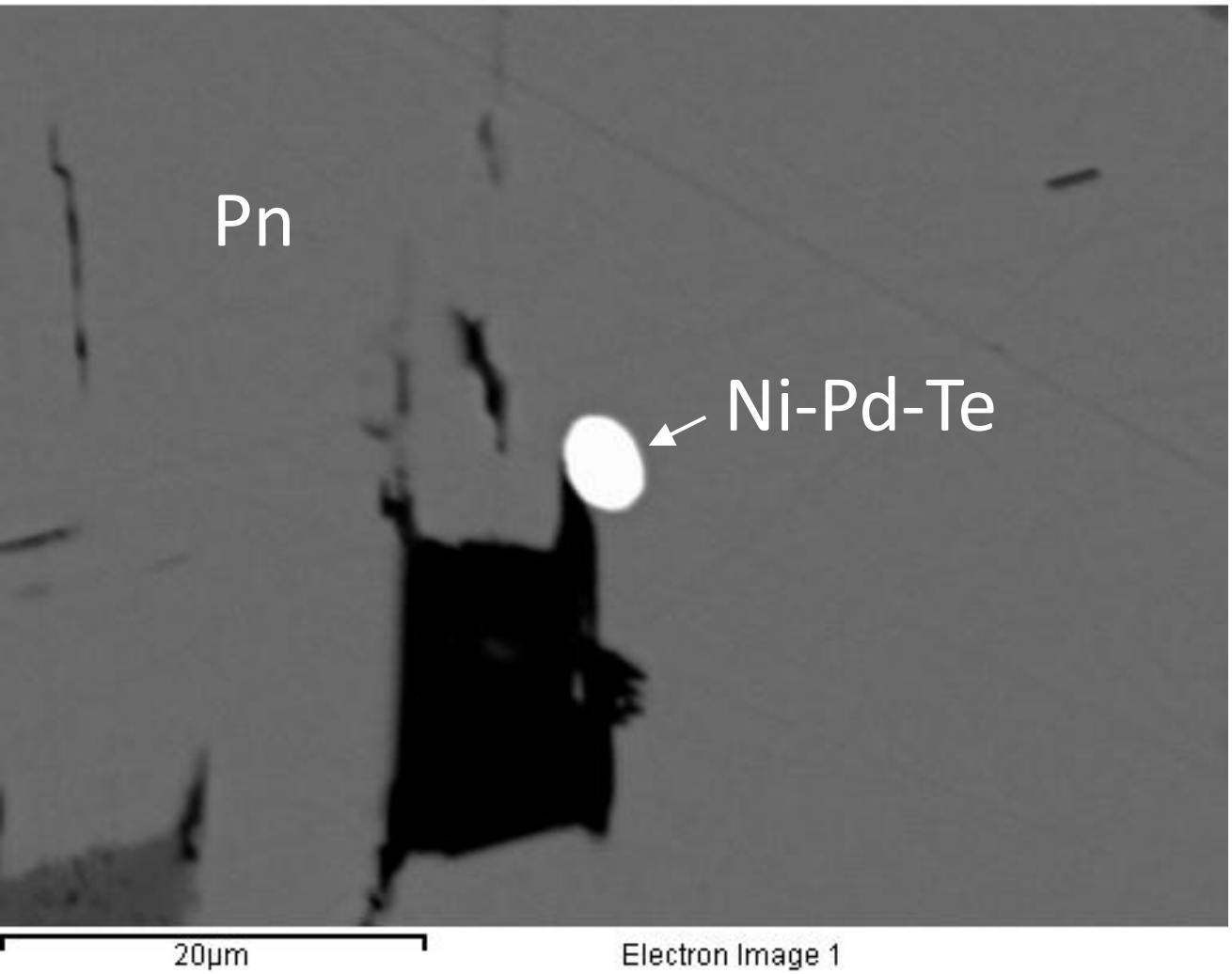
PTSR-63 E 1+



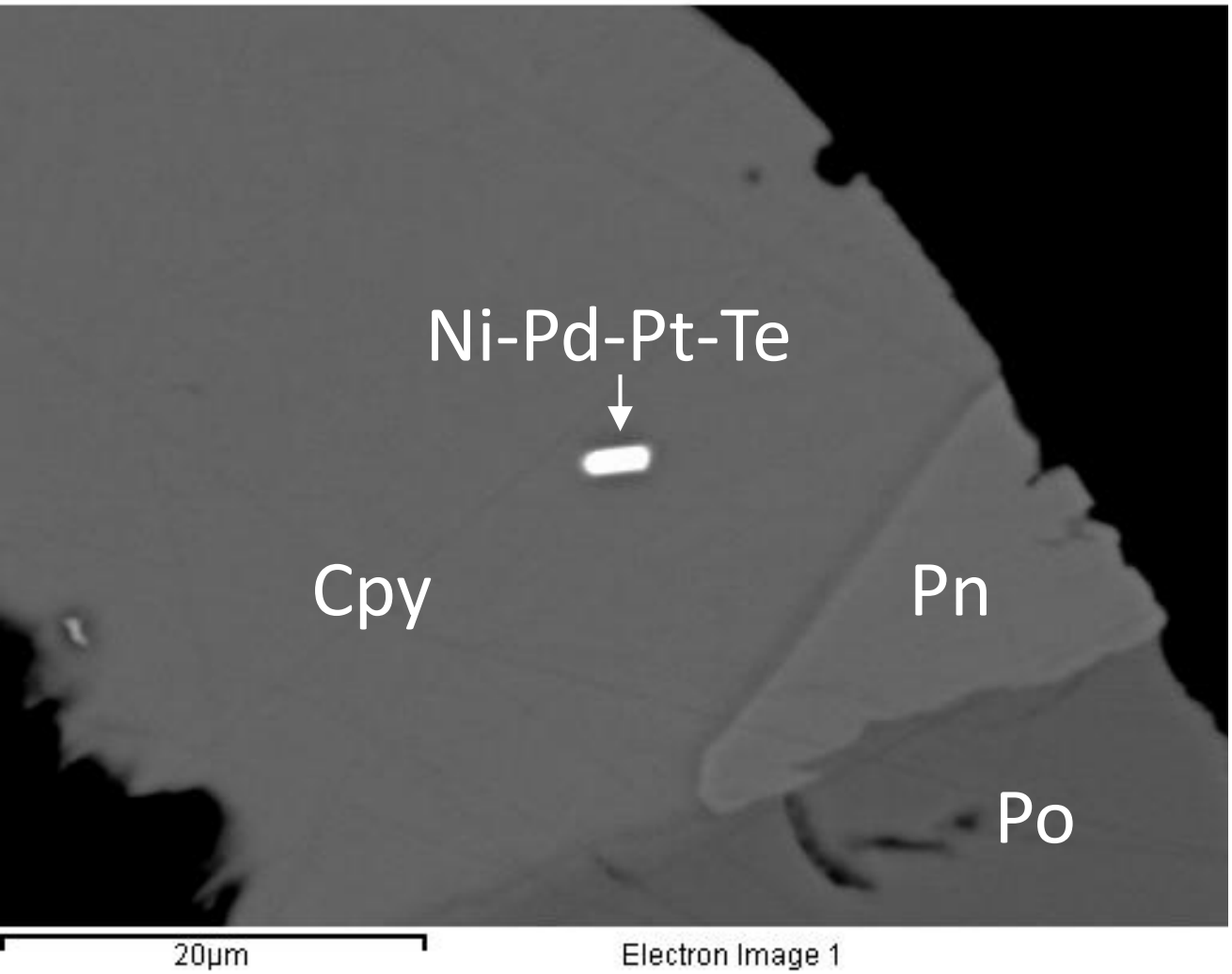
PTSR-63 E 1+ Light



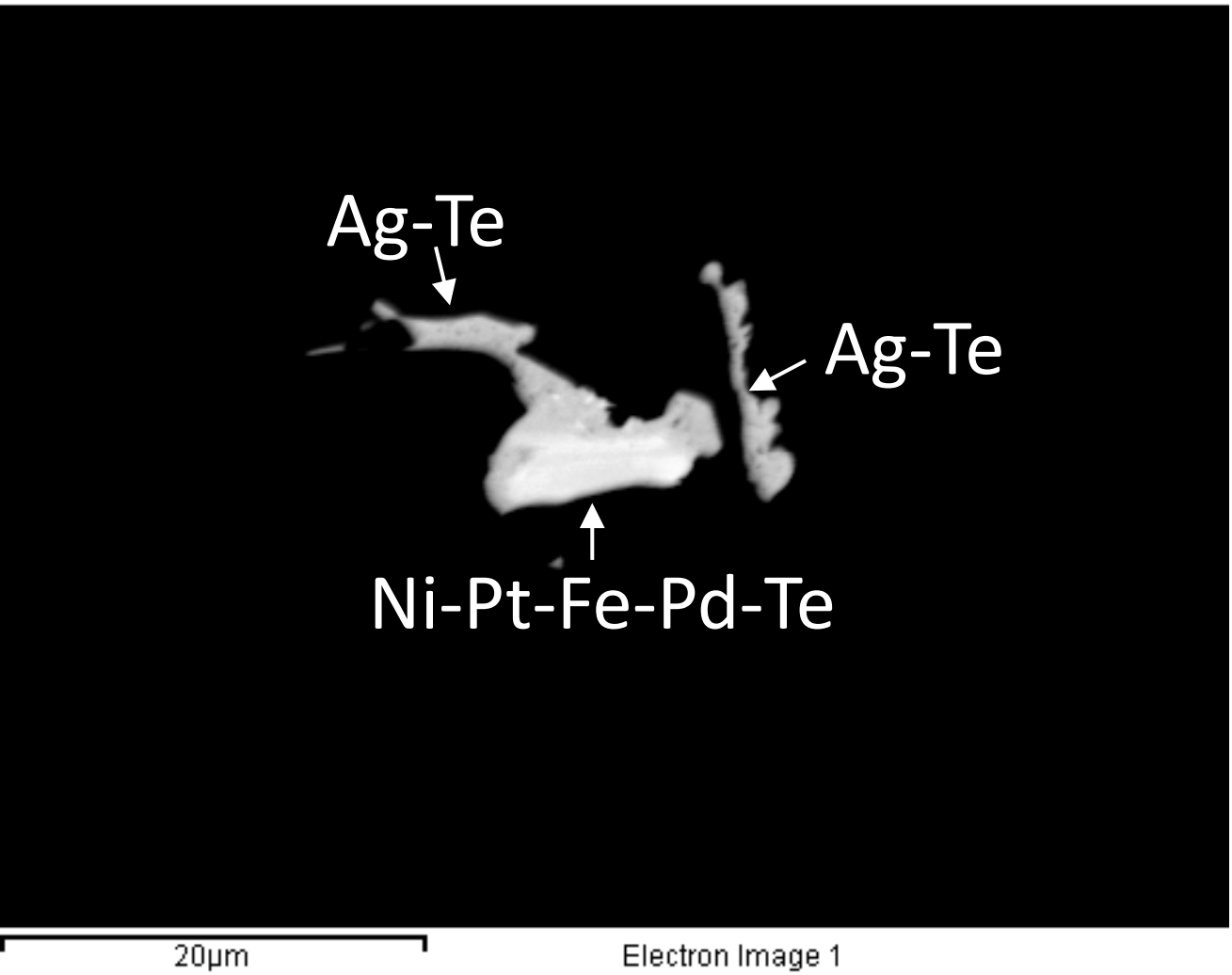
PTSR-63 E 2



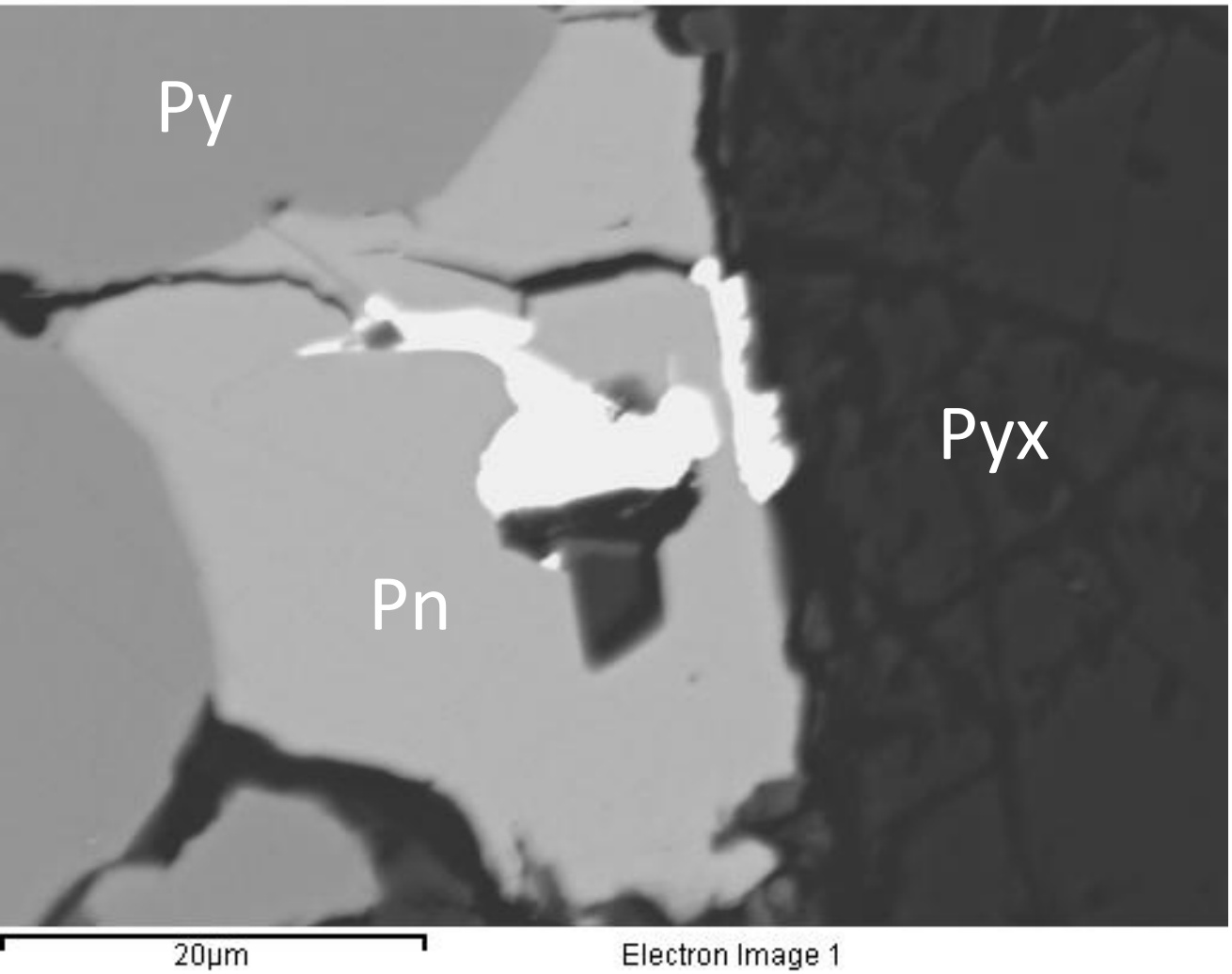
PTSR-63 F 1



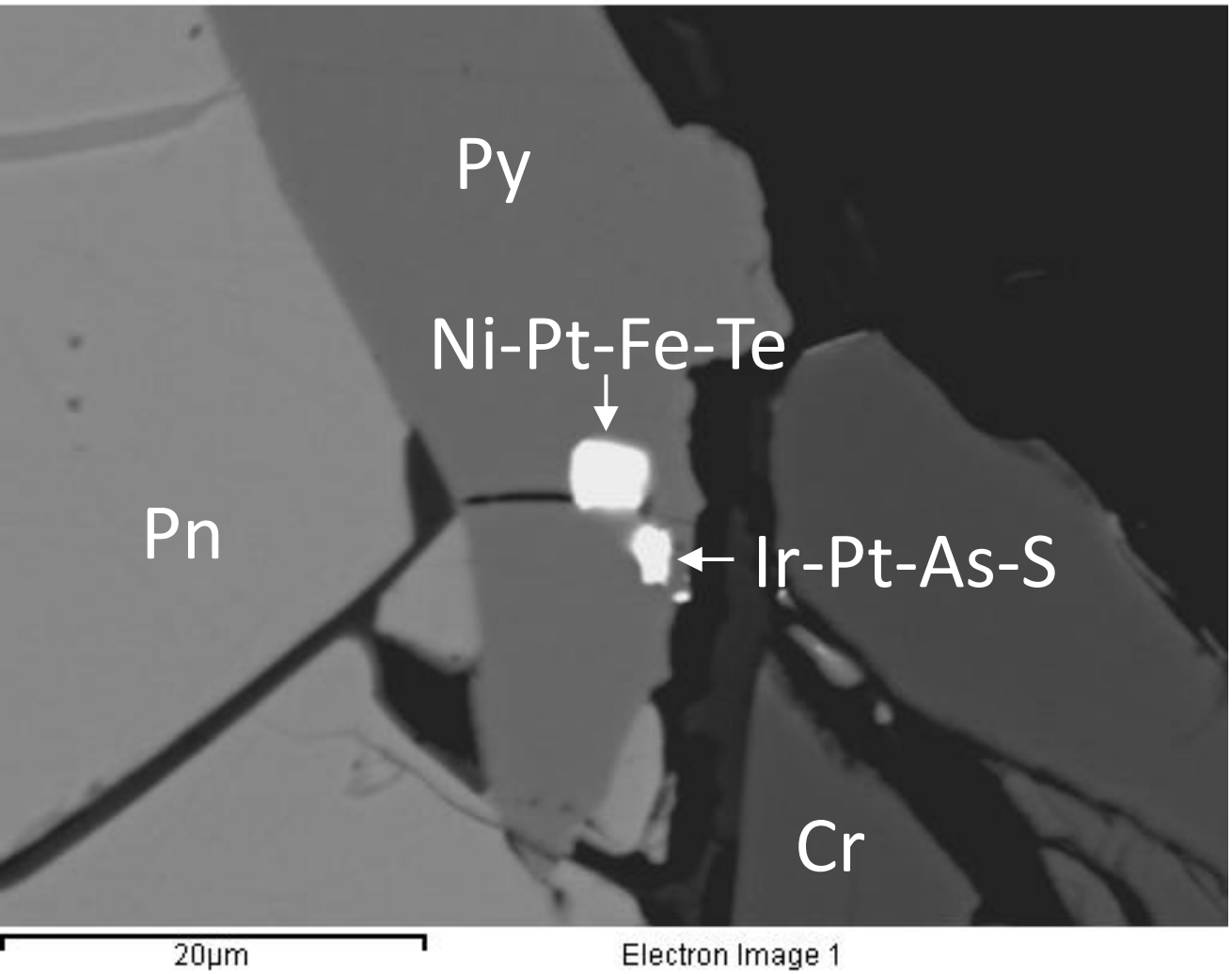
PTSR-63 G 1-3



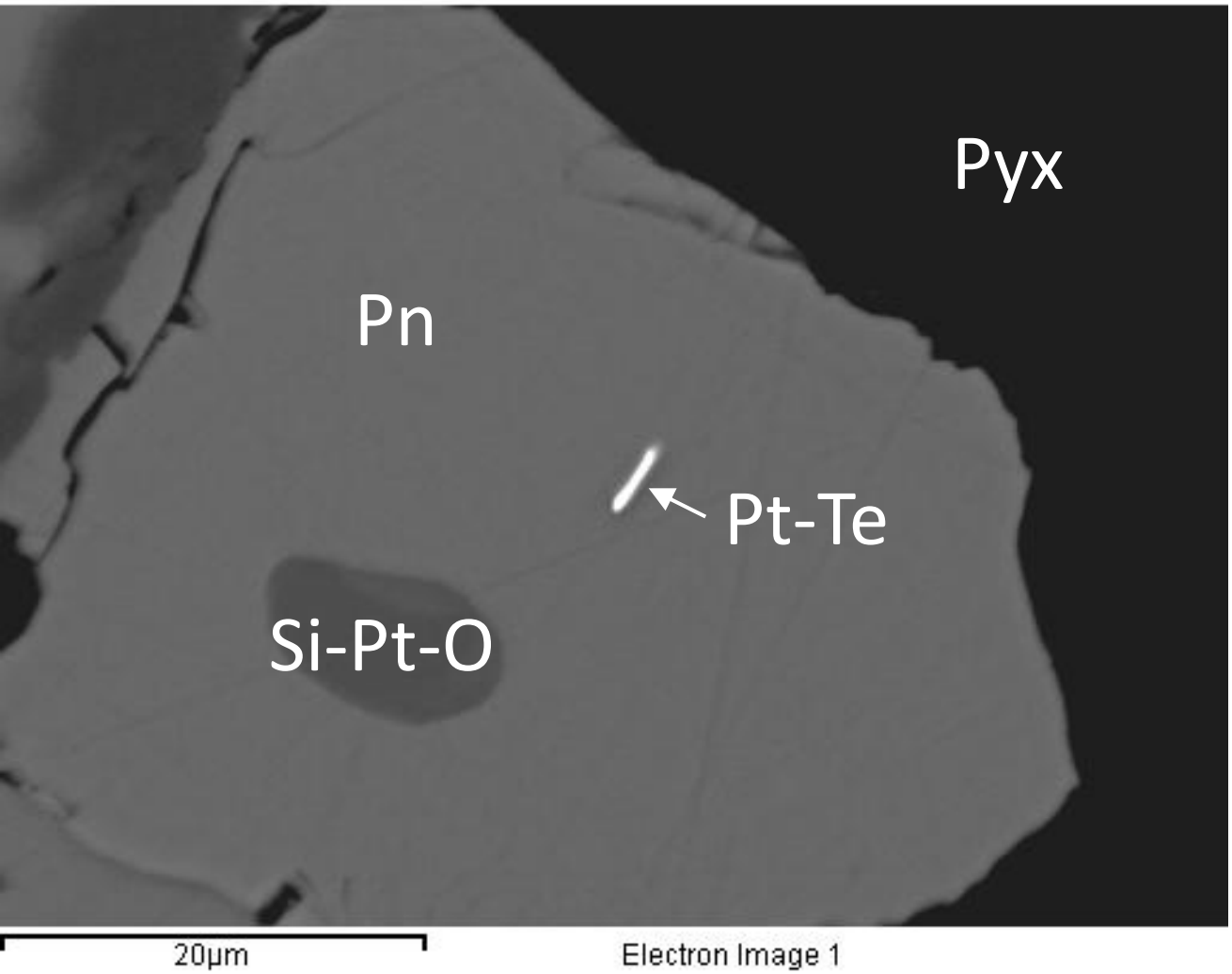
PTSR-63 G 1-3 Light



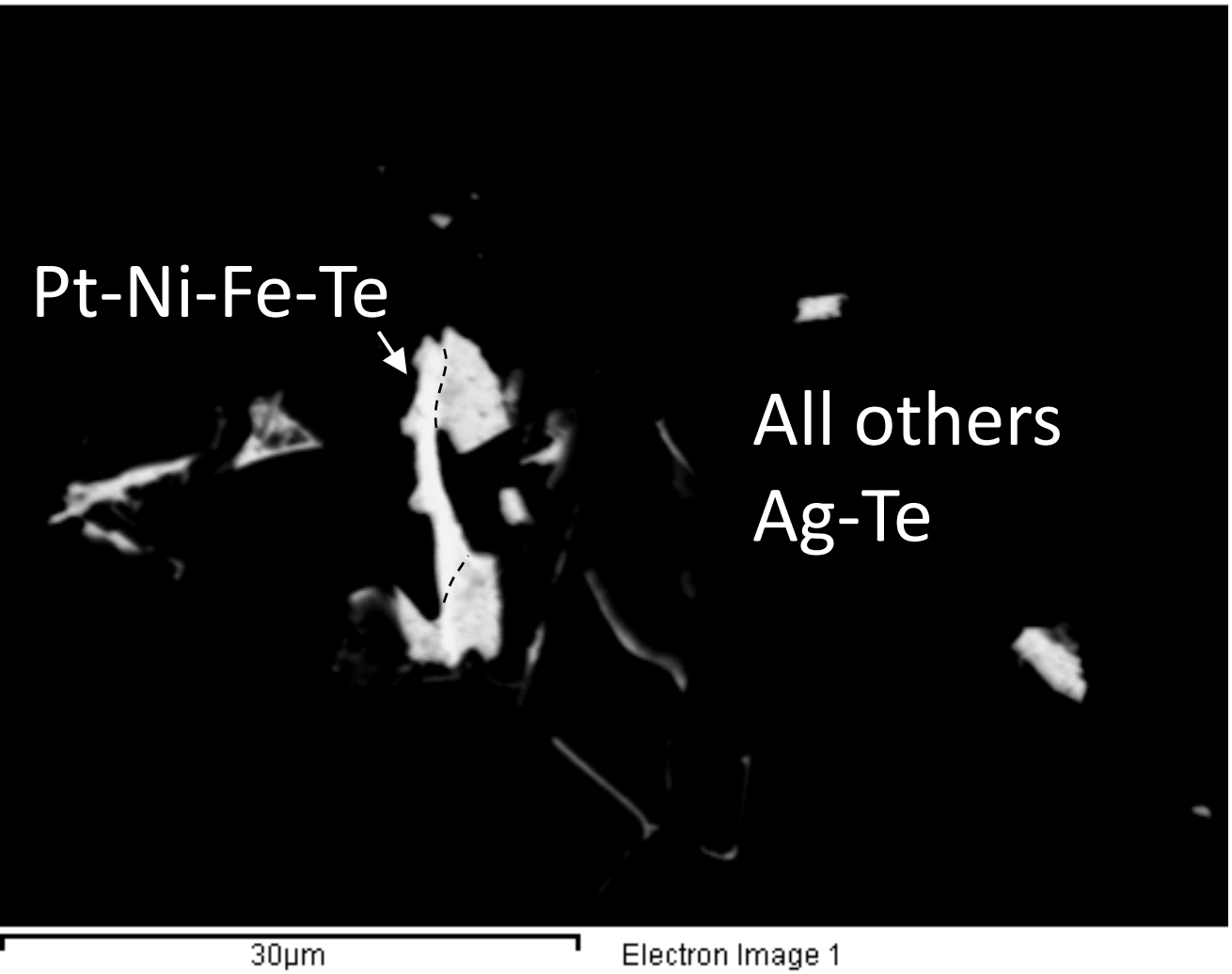
PTSR-63 H 1-3



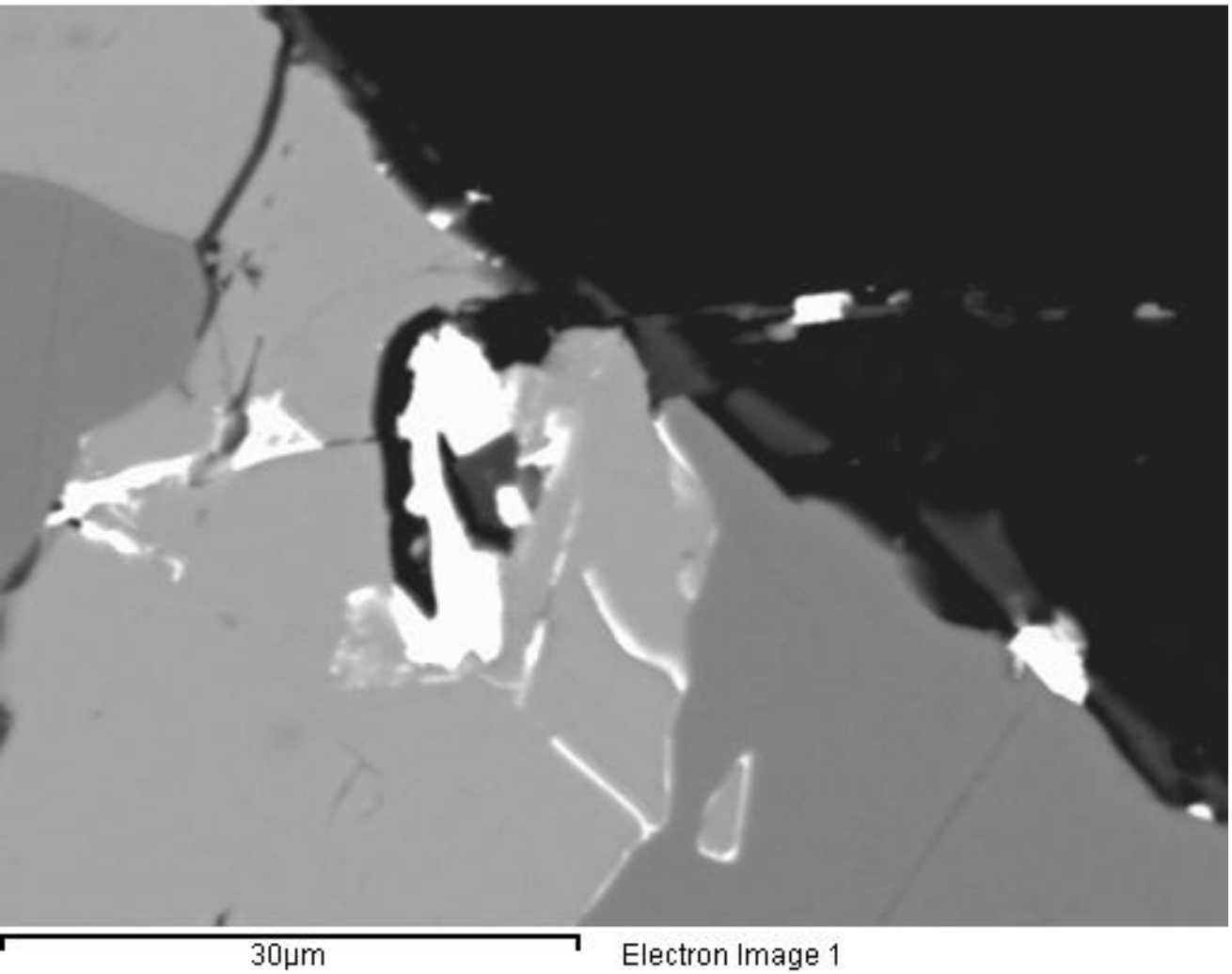
PTSR-63 I 1



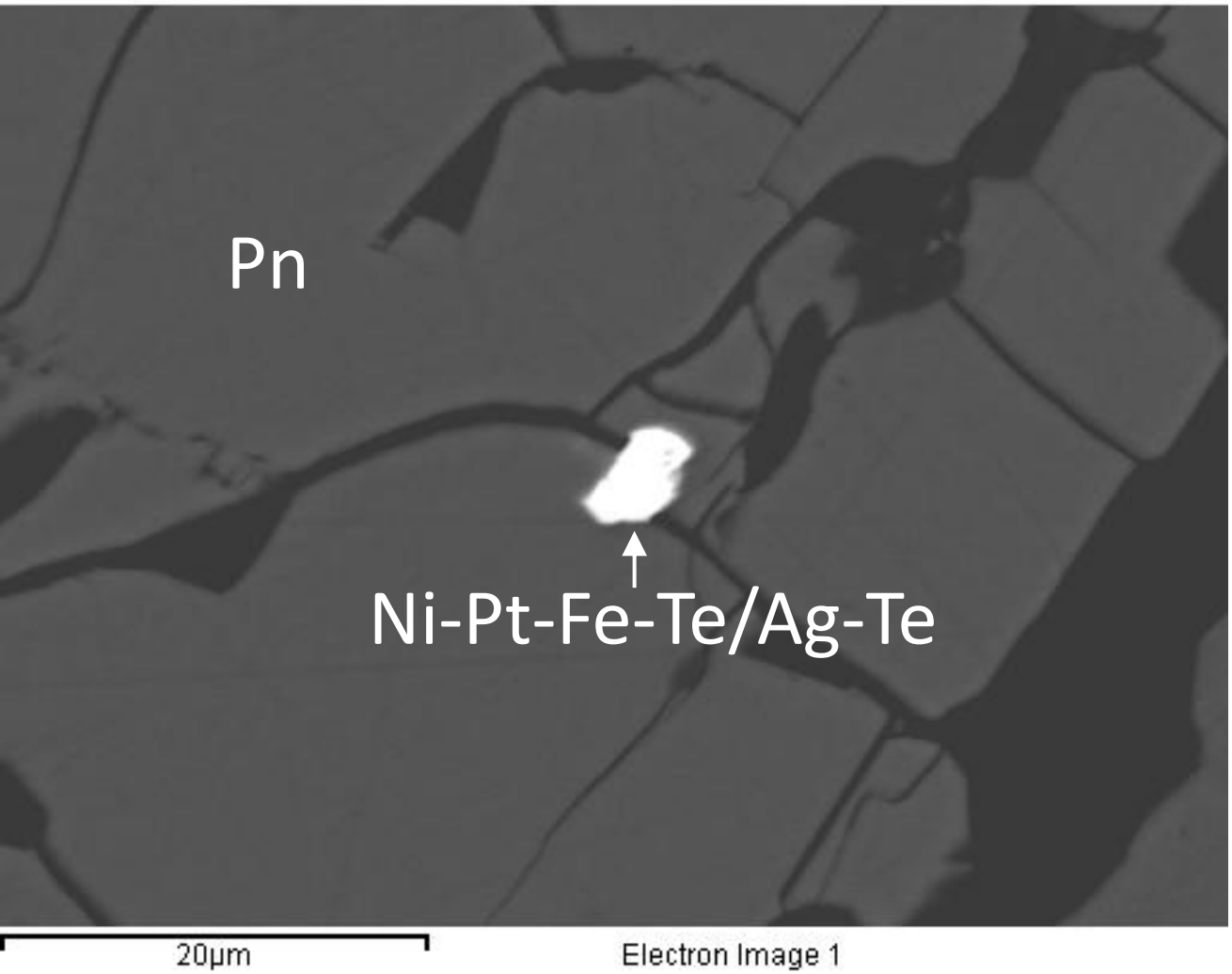
PTSR-63 J 1



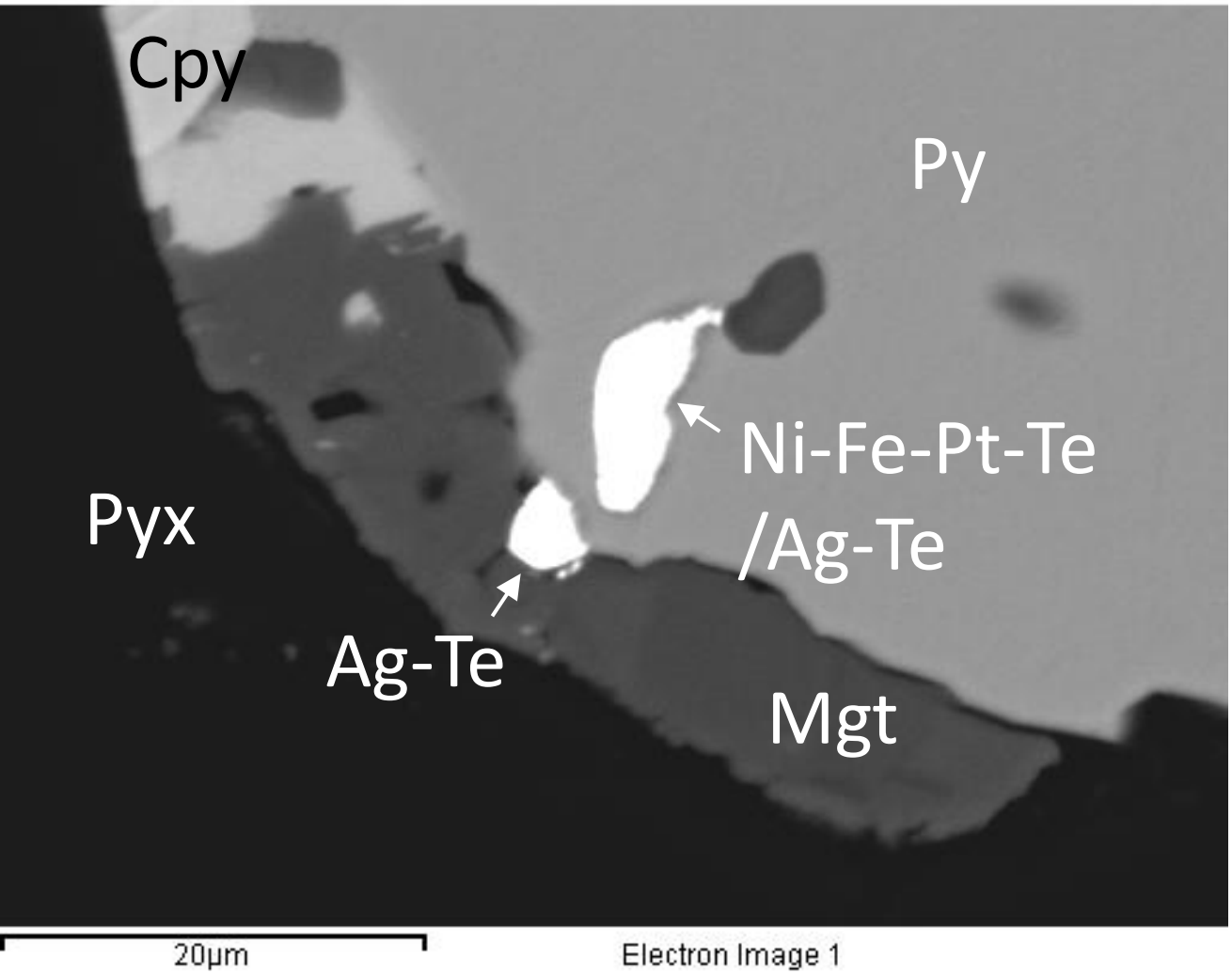
PTSR-63 J 1 Light No Data



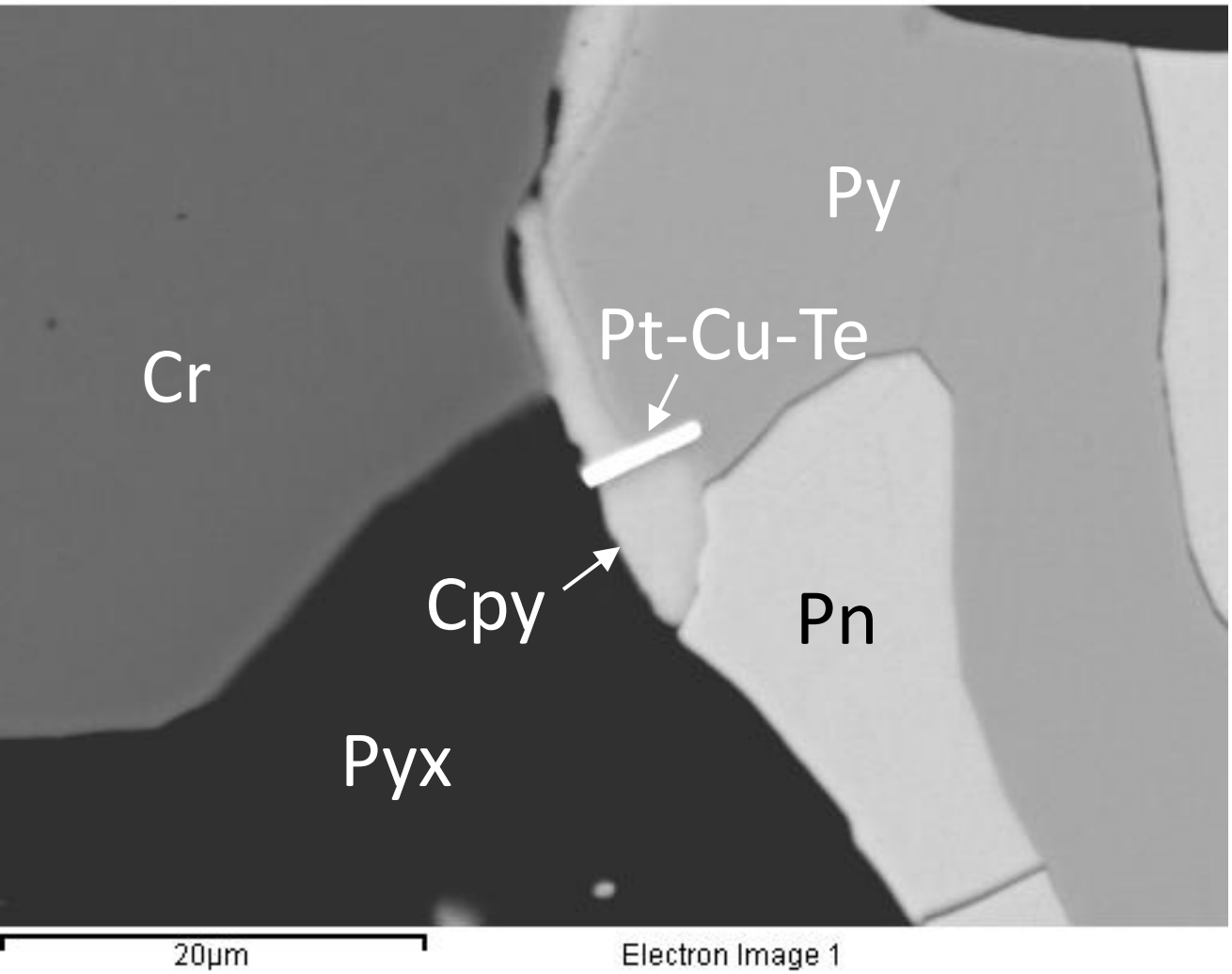
PTSR-63 K 1



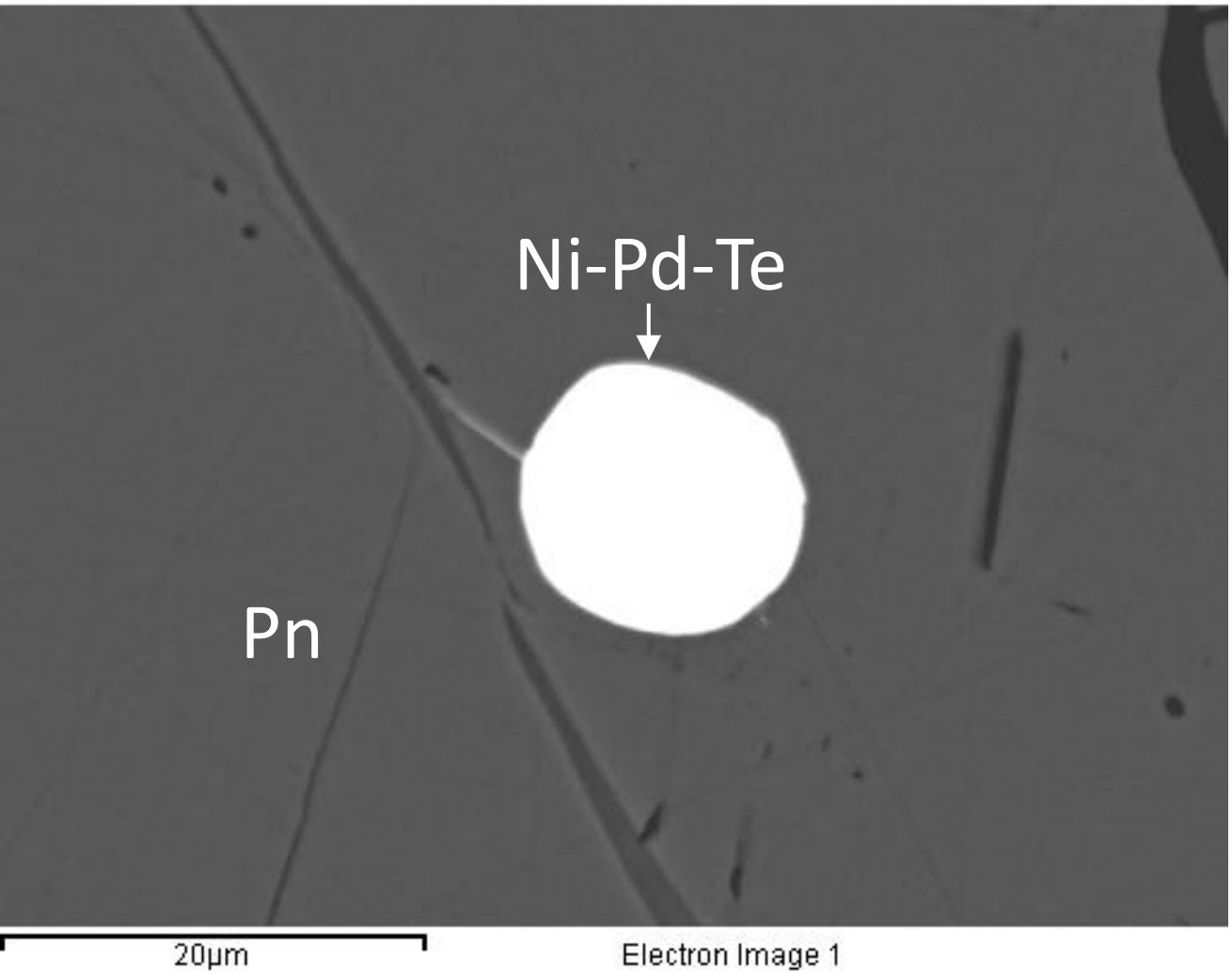
PTSR-63 L 1-2



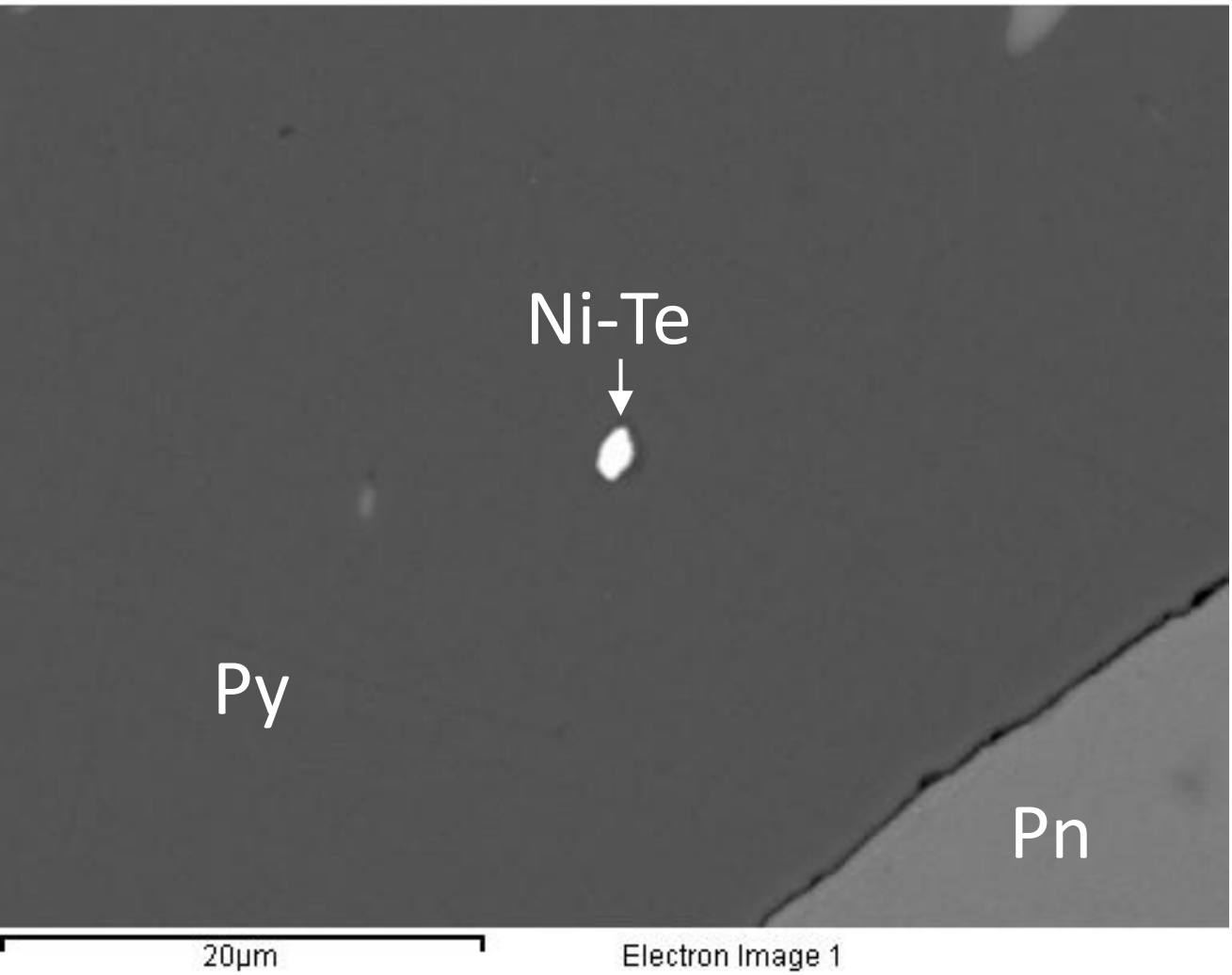
PTSR-64 A 1



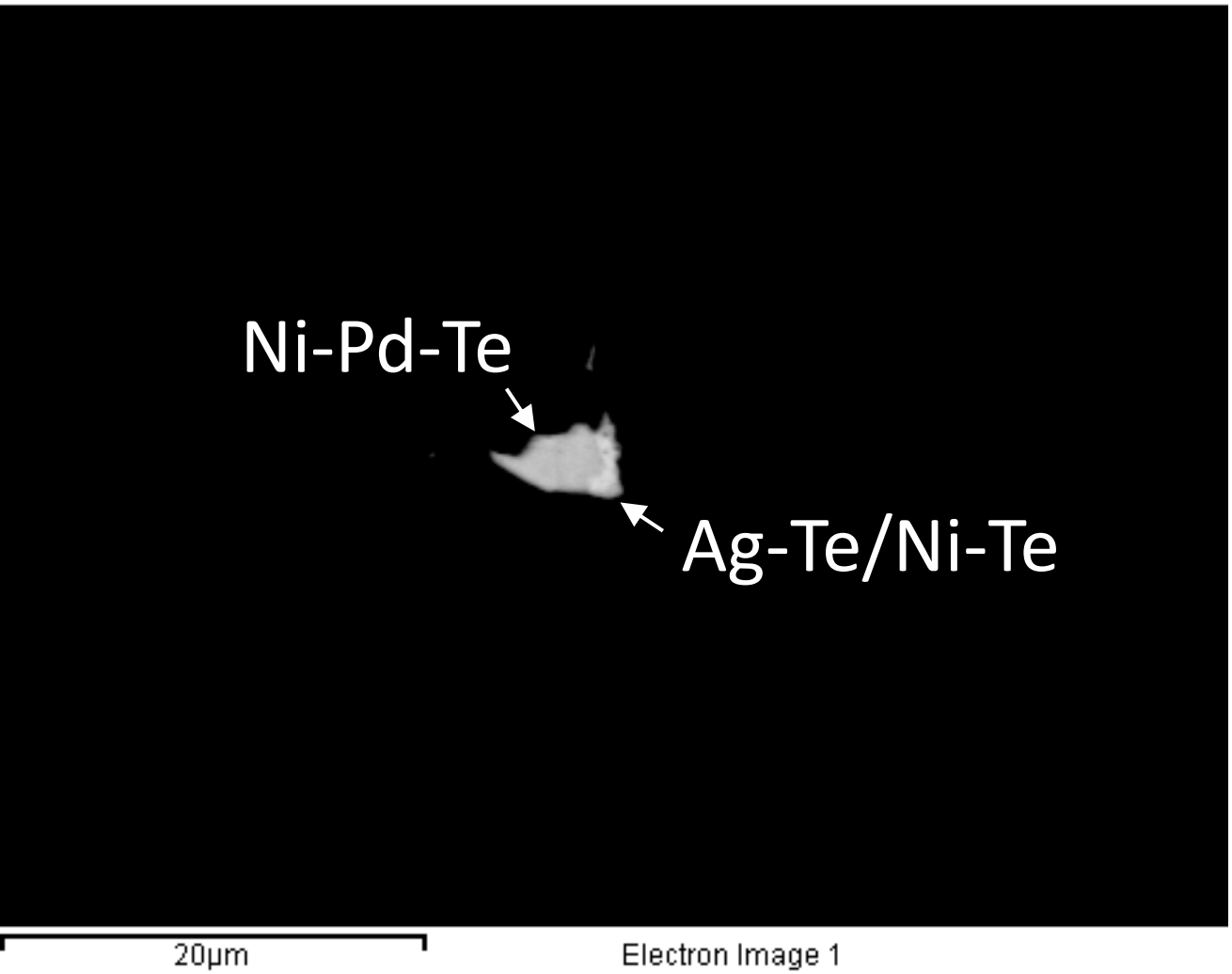
PTSR-64 B 1



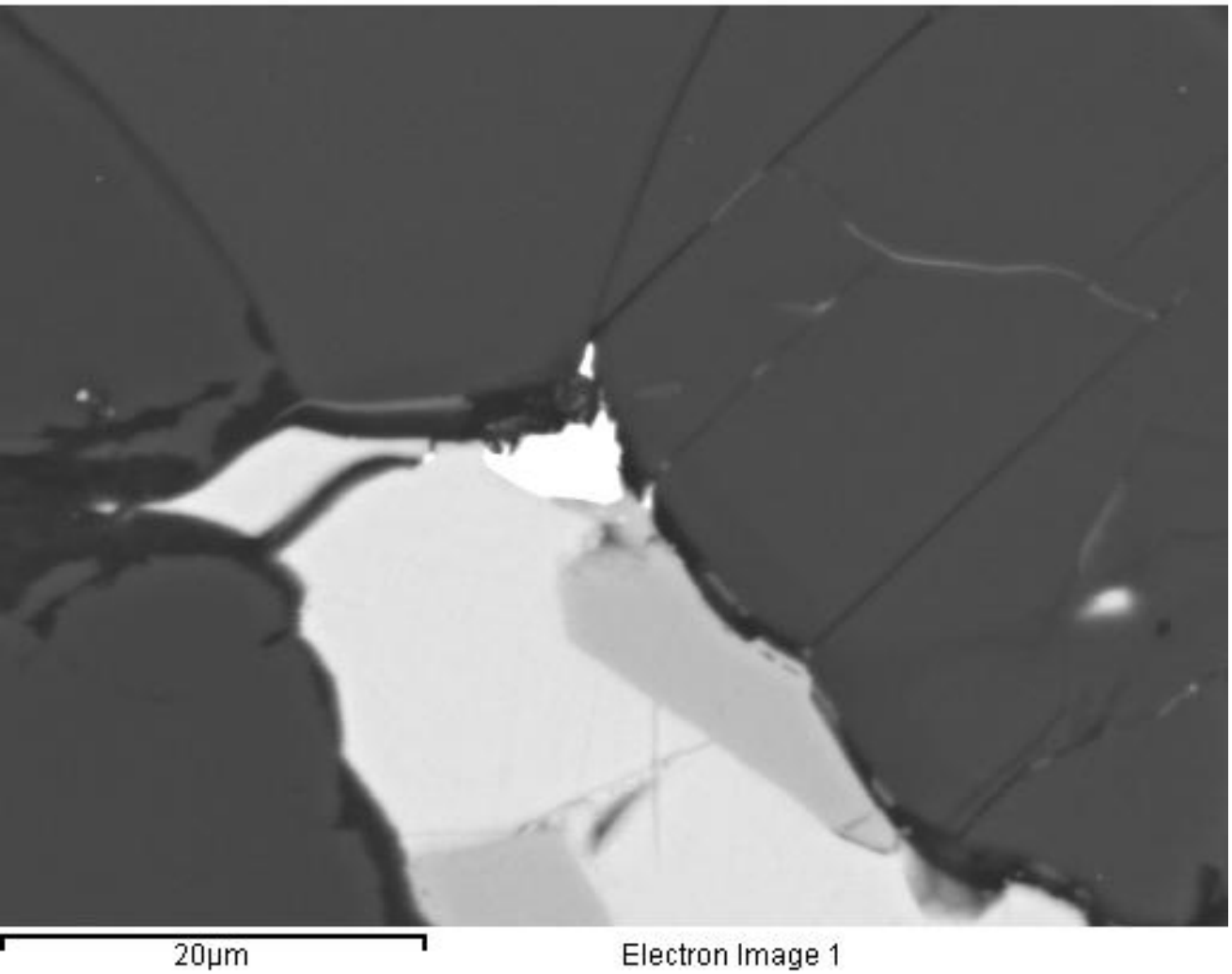
PTSR-64 C 1



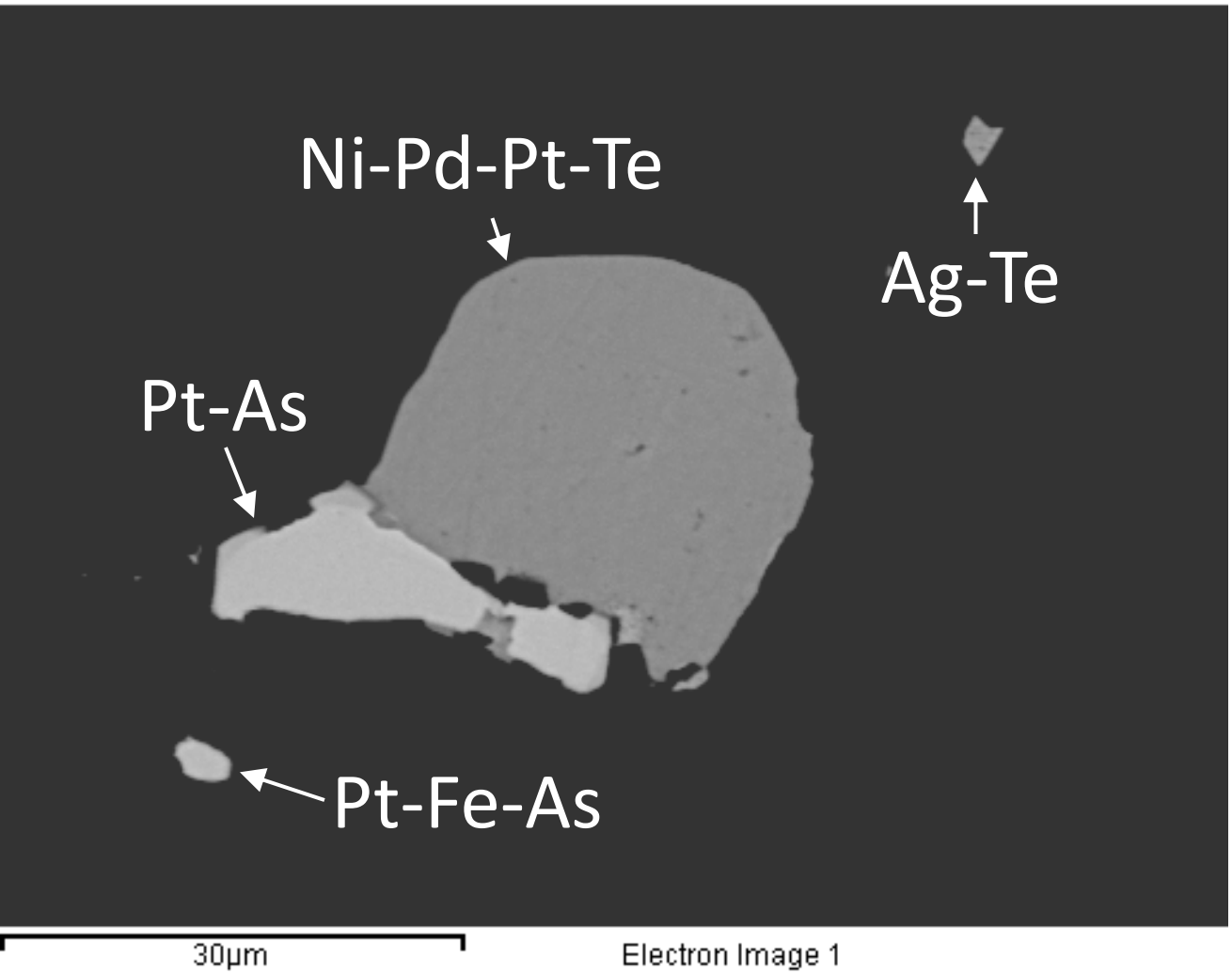
PTSR-64 D 1



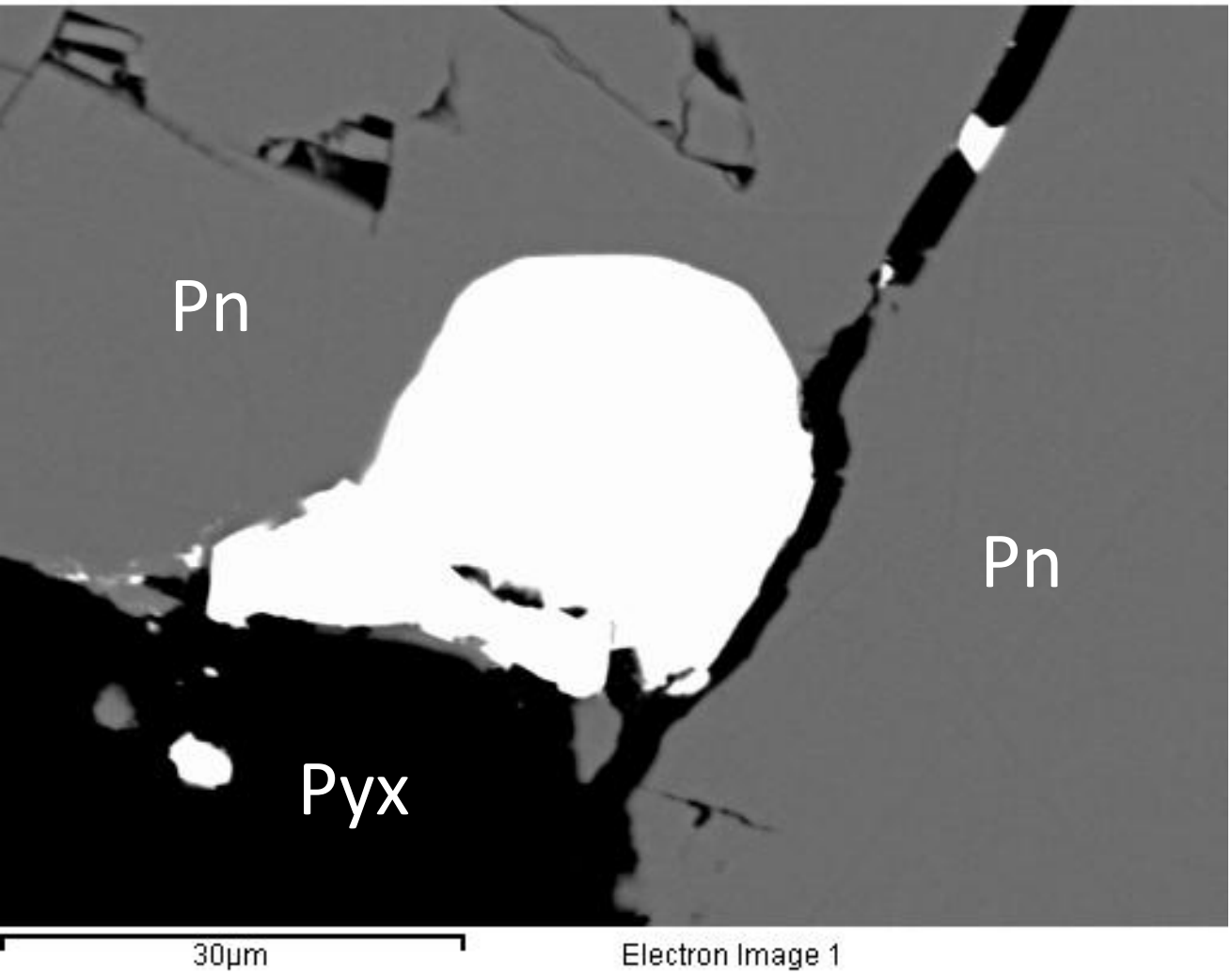
PTSR-64 D 1 Light



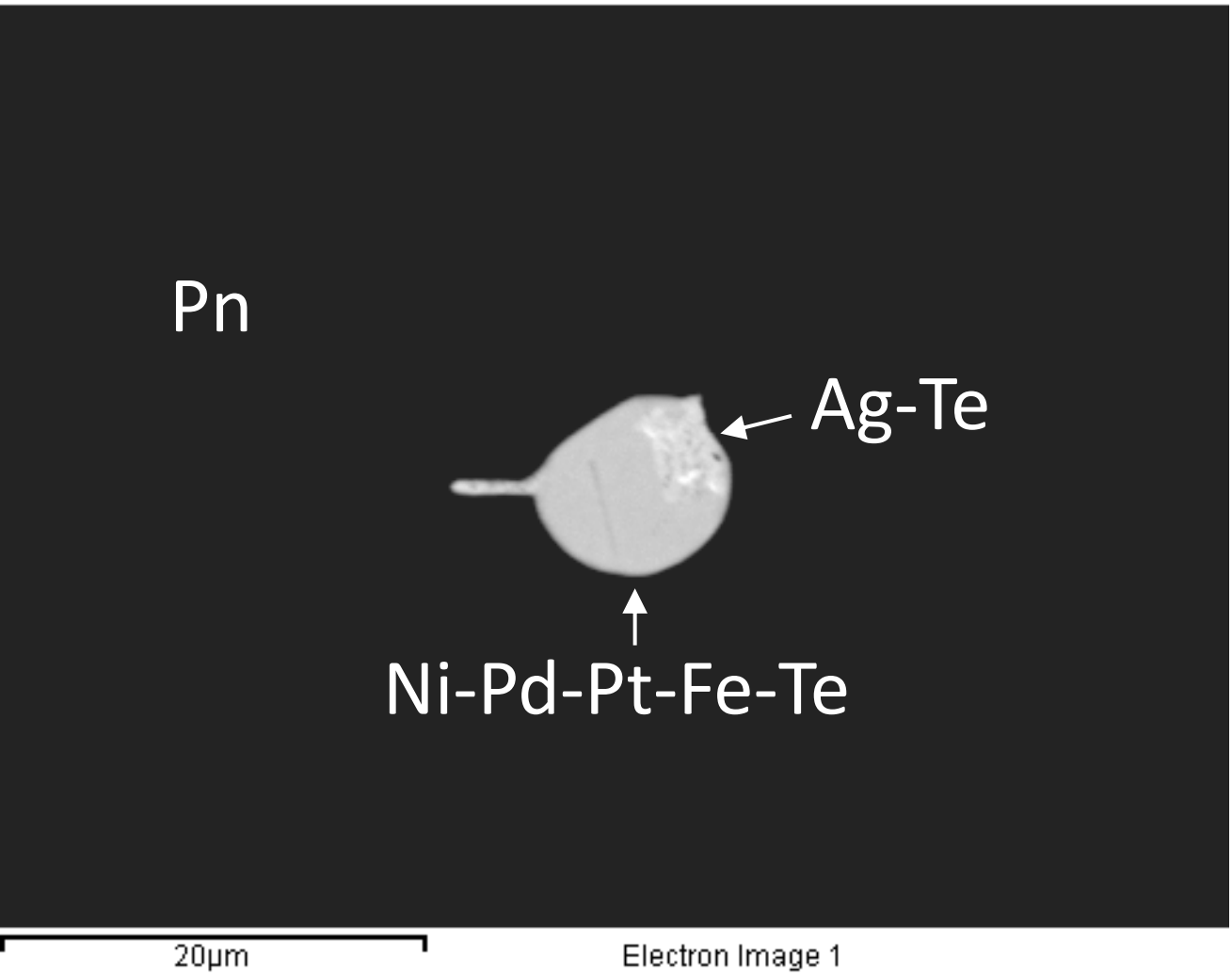
PTSR-64 E 1-4



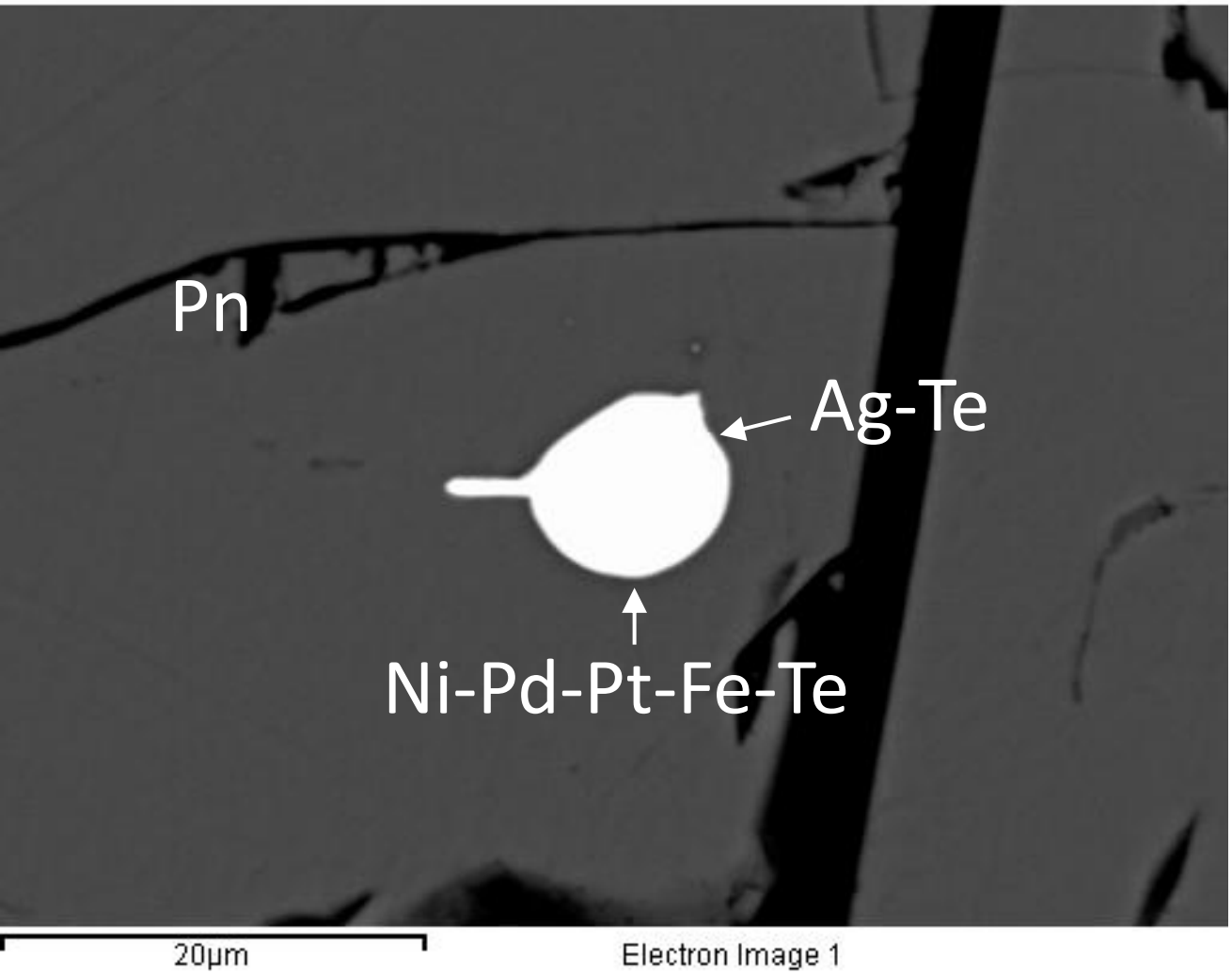
PTSR-64 E 1-4 Light



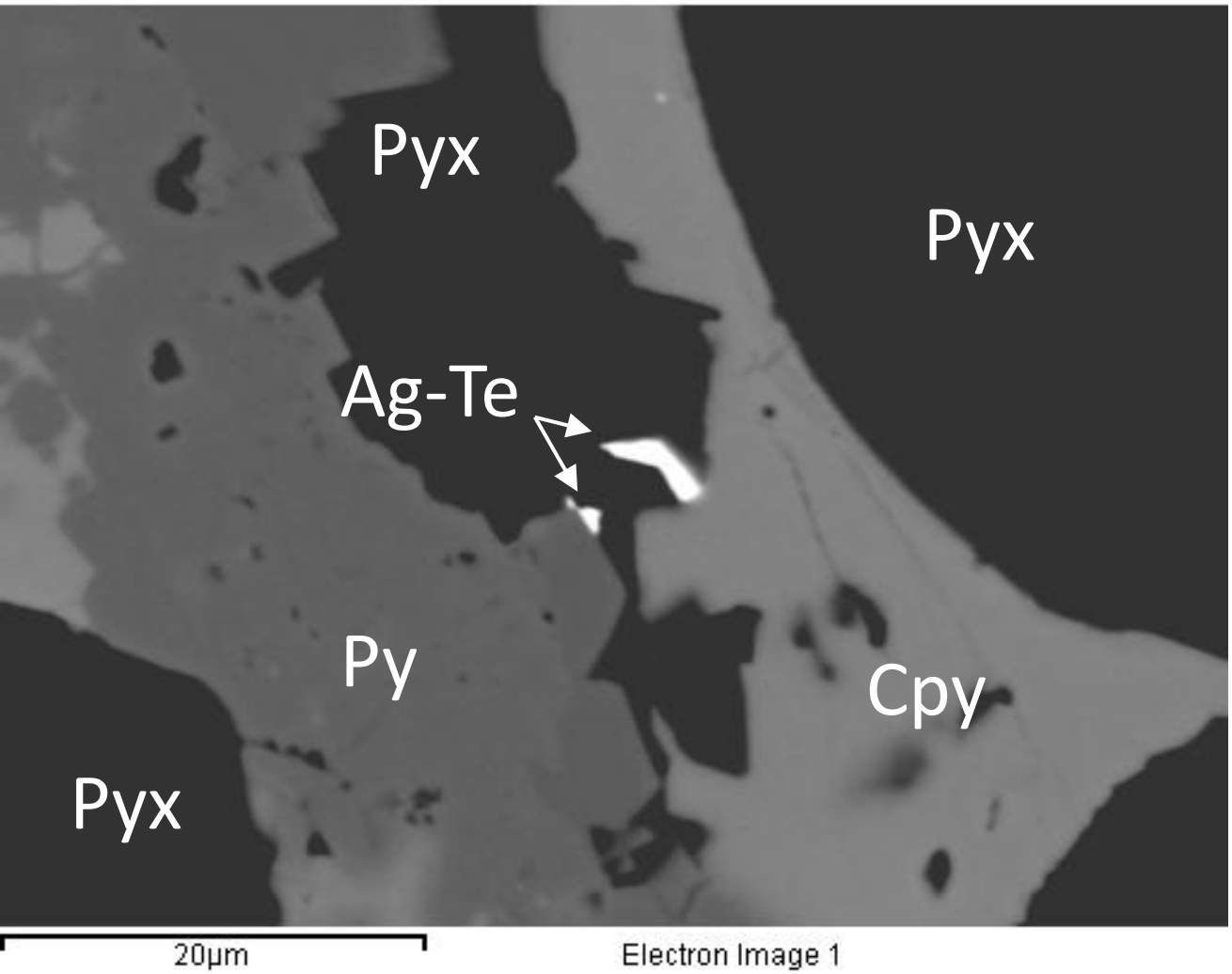
PTSR-64 F 1



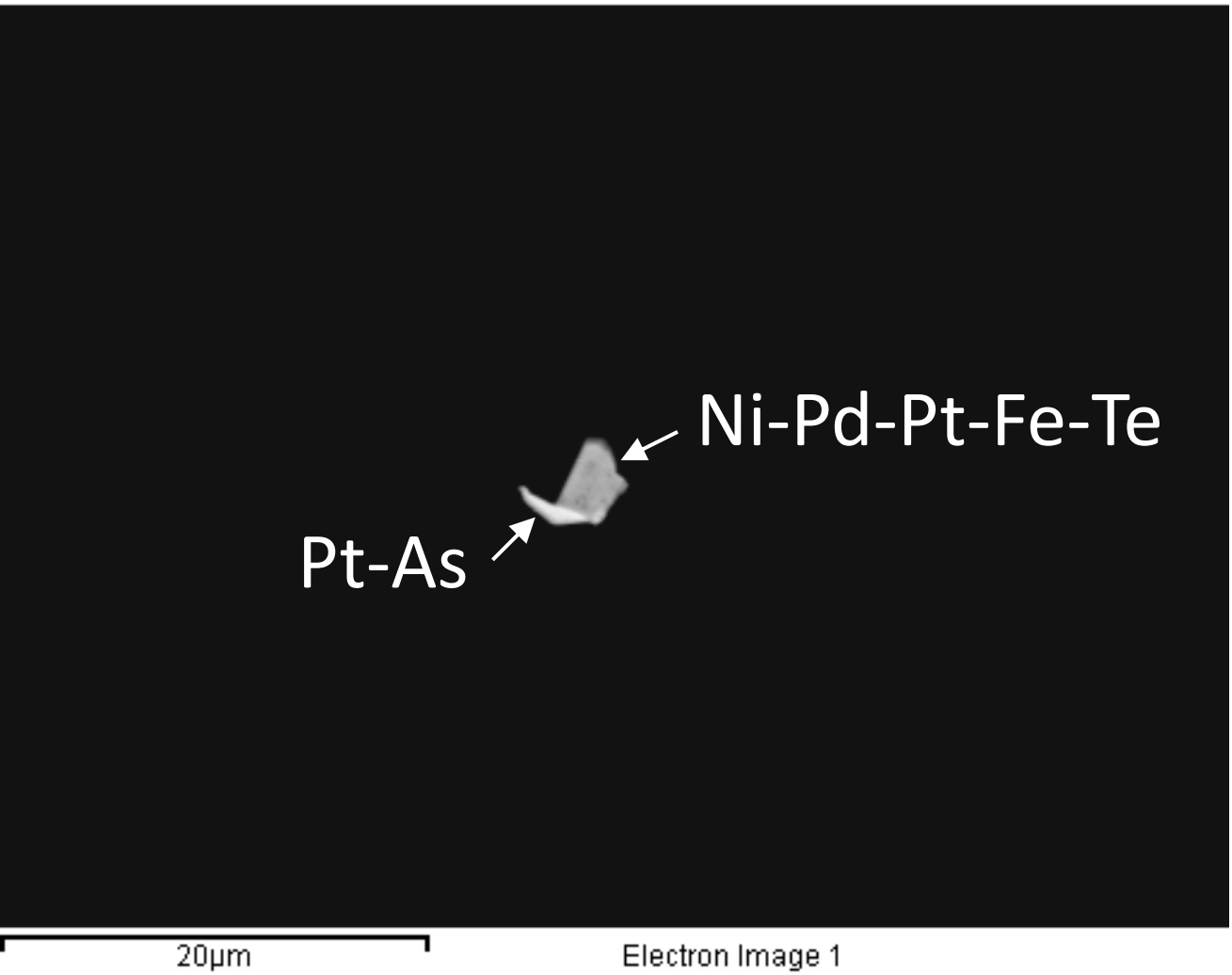
PTSR-64 F 1 Light



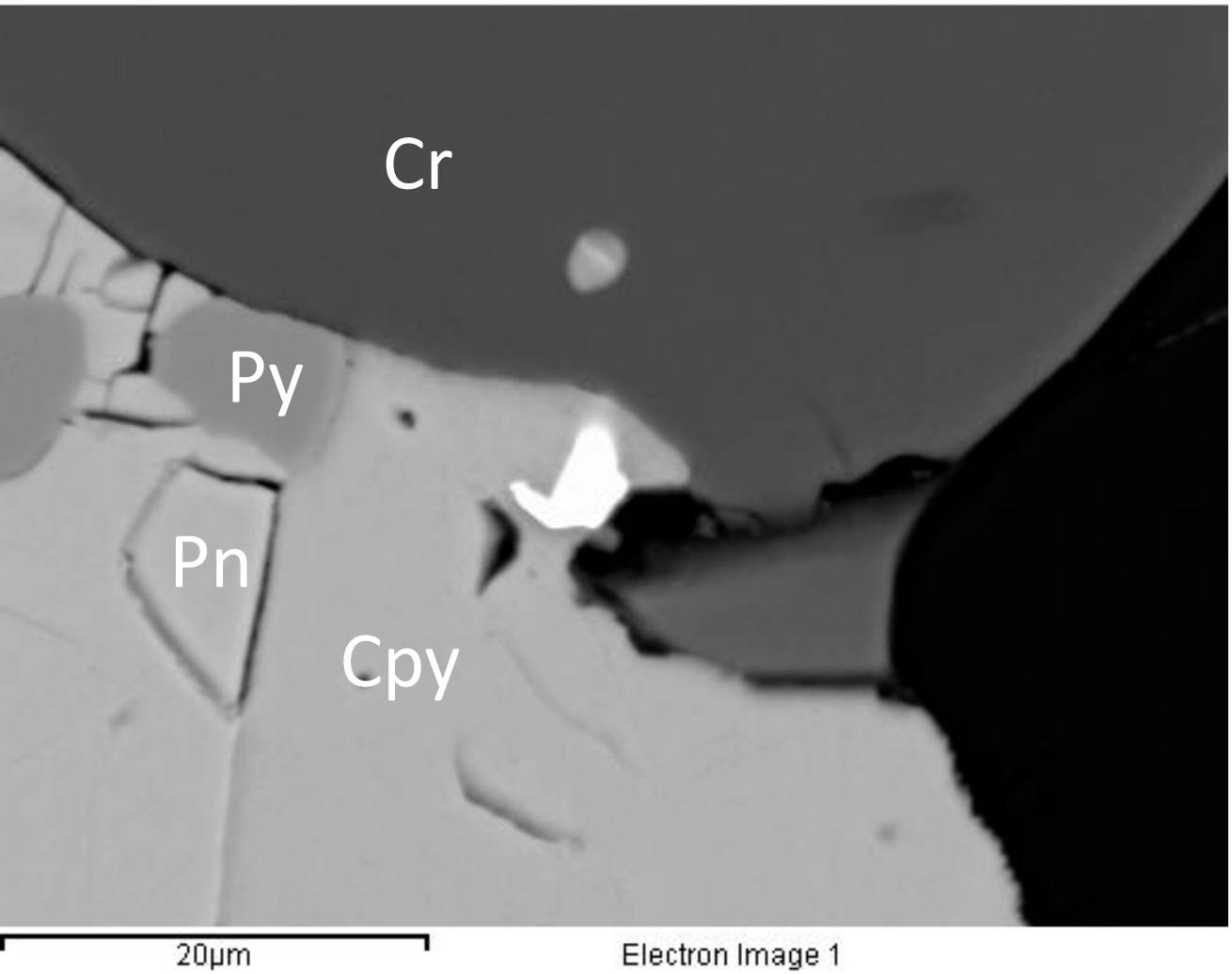
PTSR-64 G 1-2



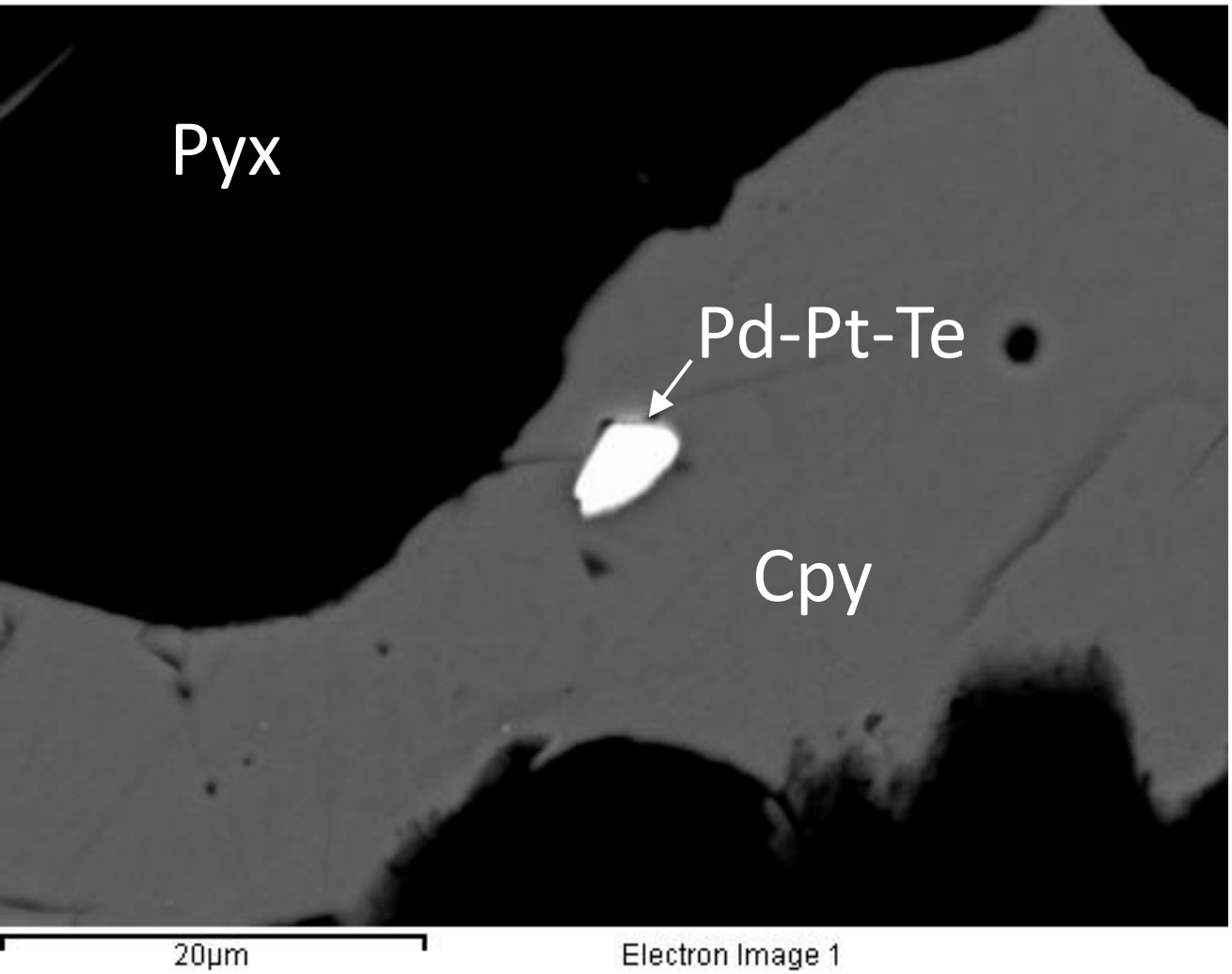
PTSR-64 H 1-2



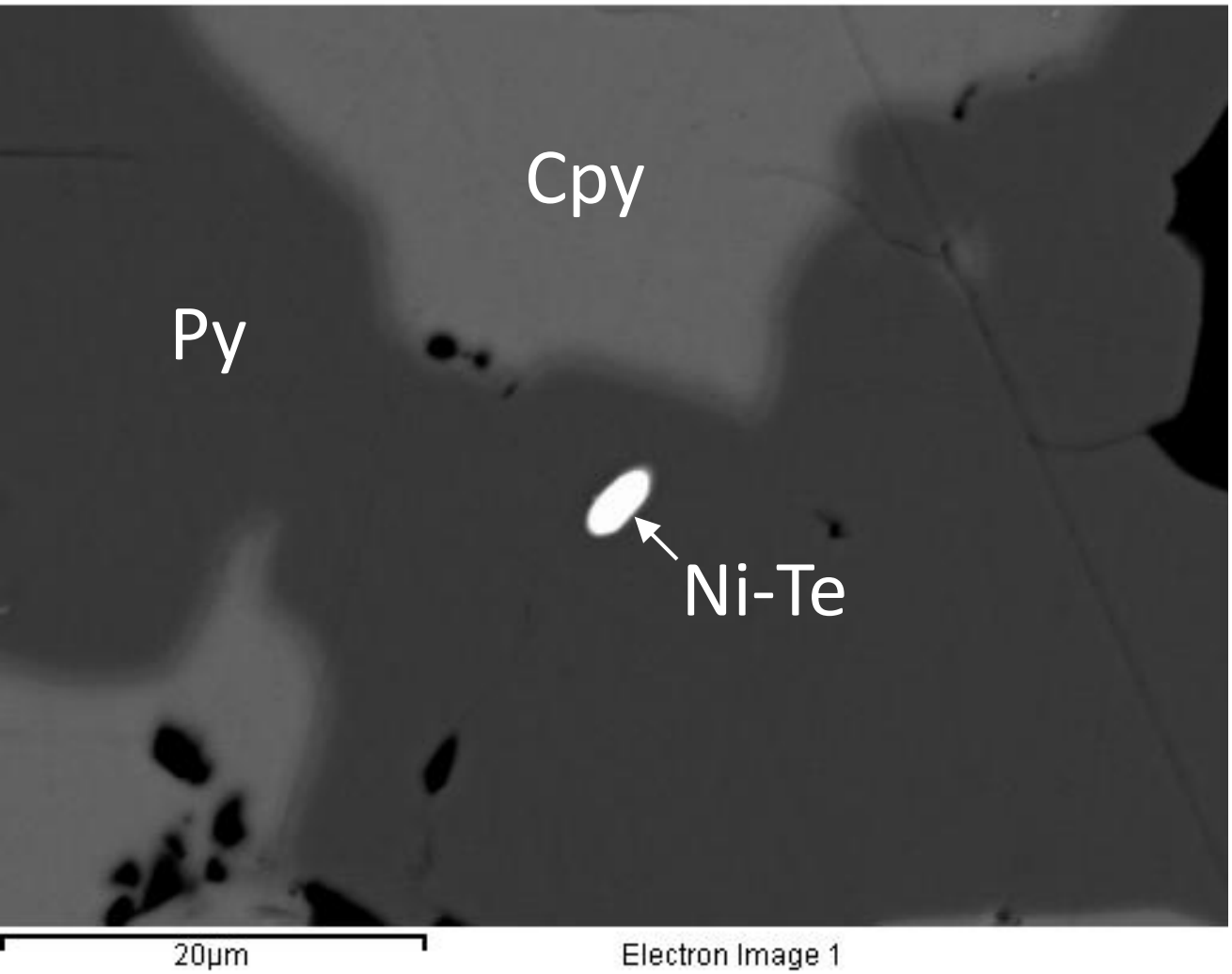
PTSR-64 H 1-2 Light



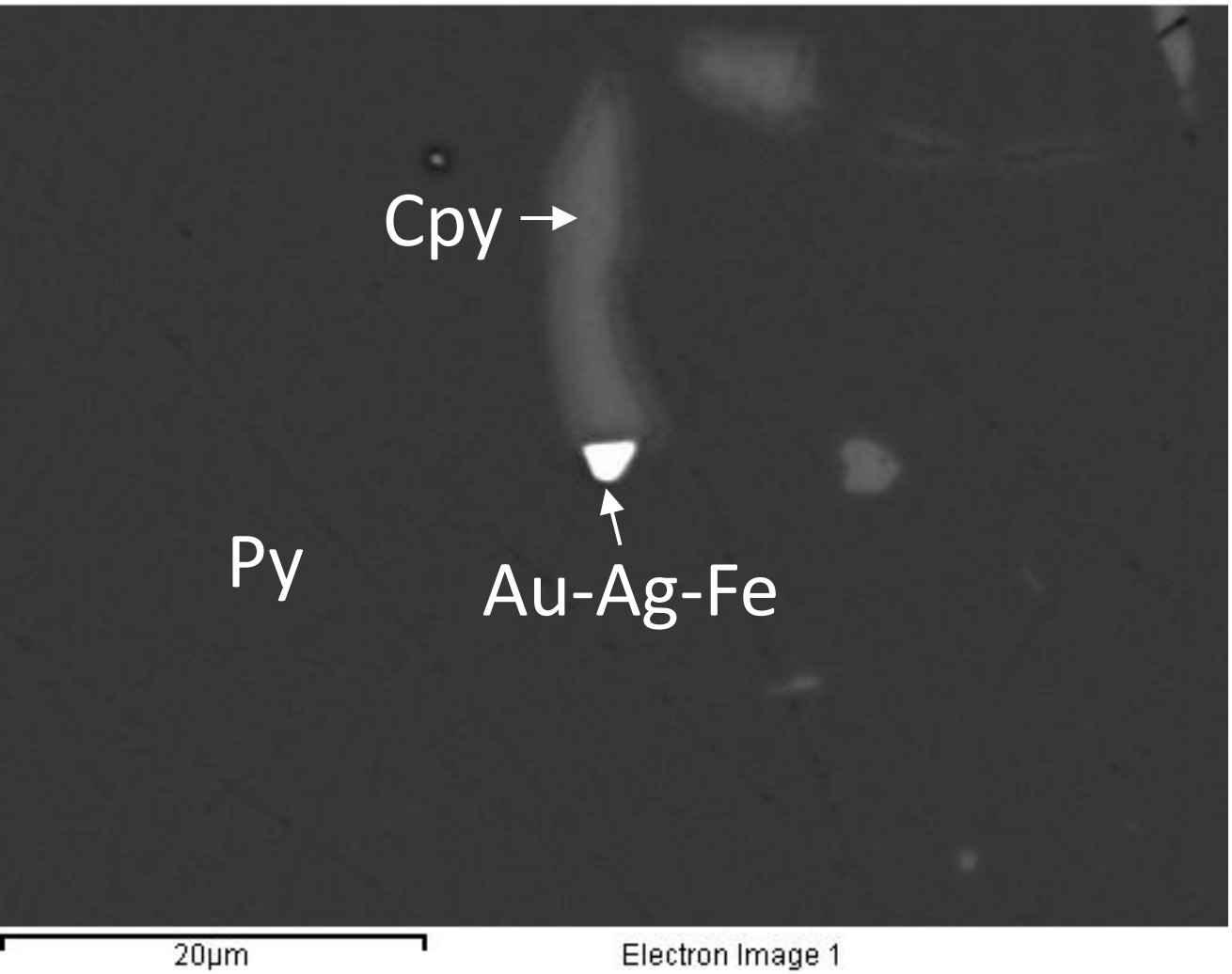
PTSR-64 I 1



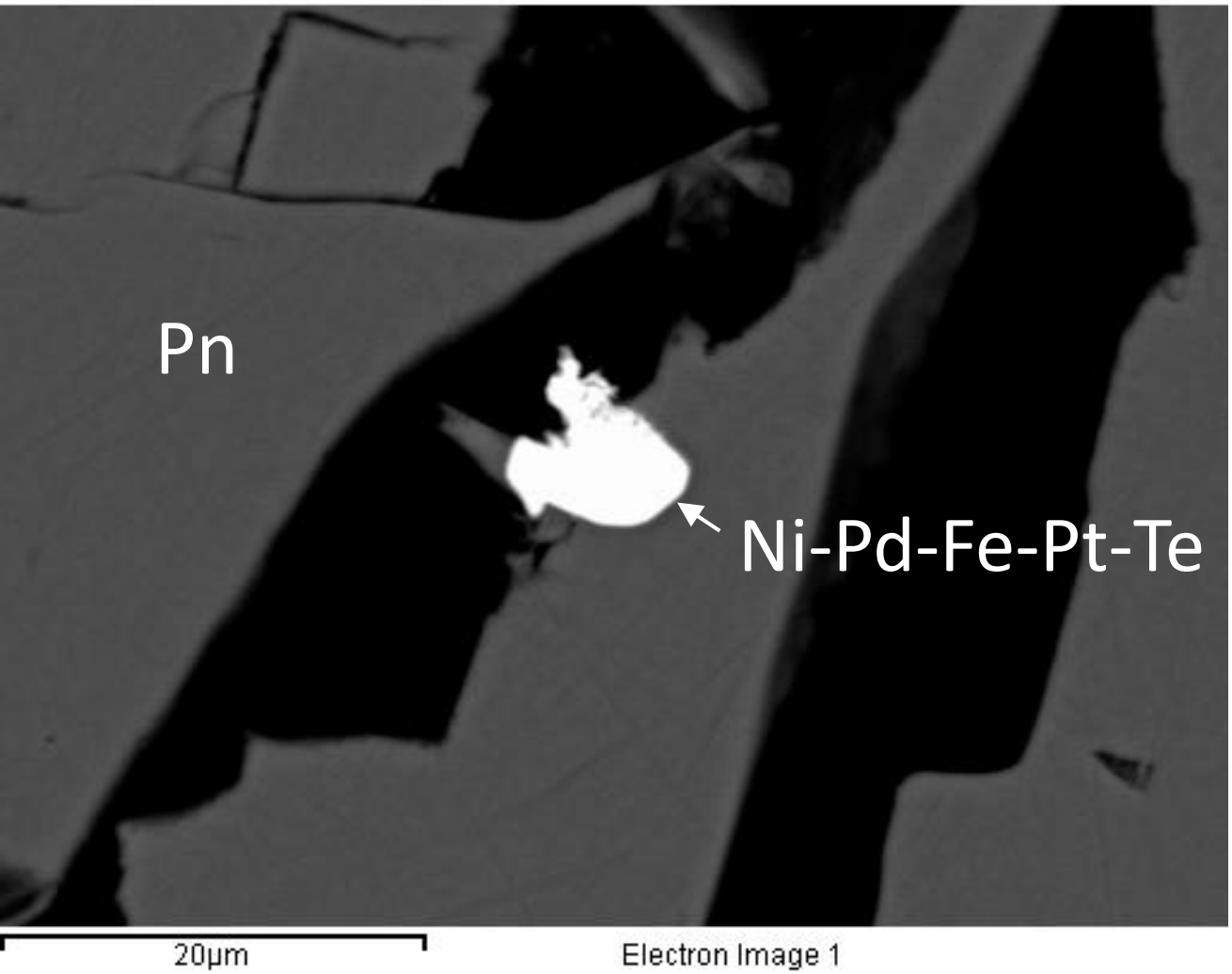
PTSR-64 J 1



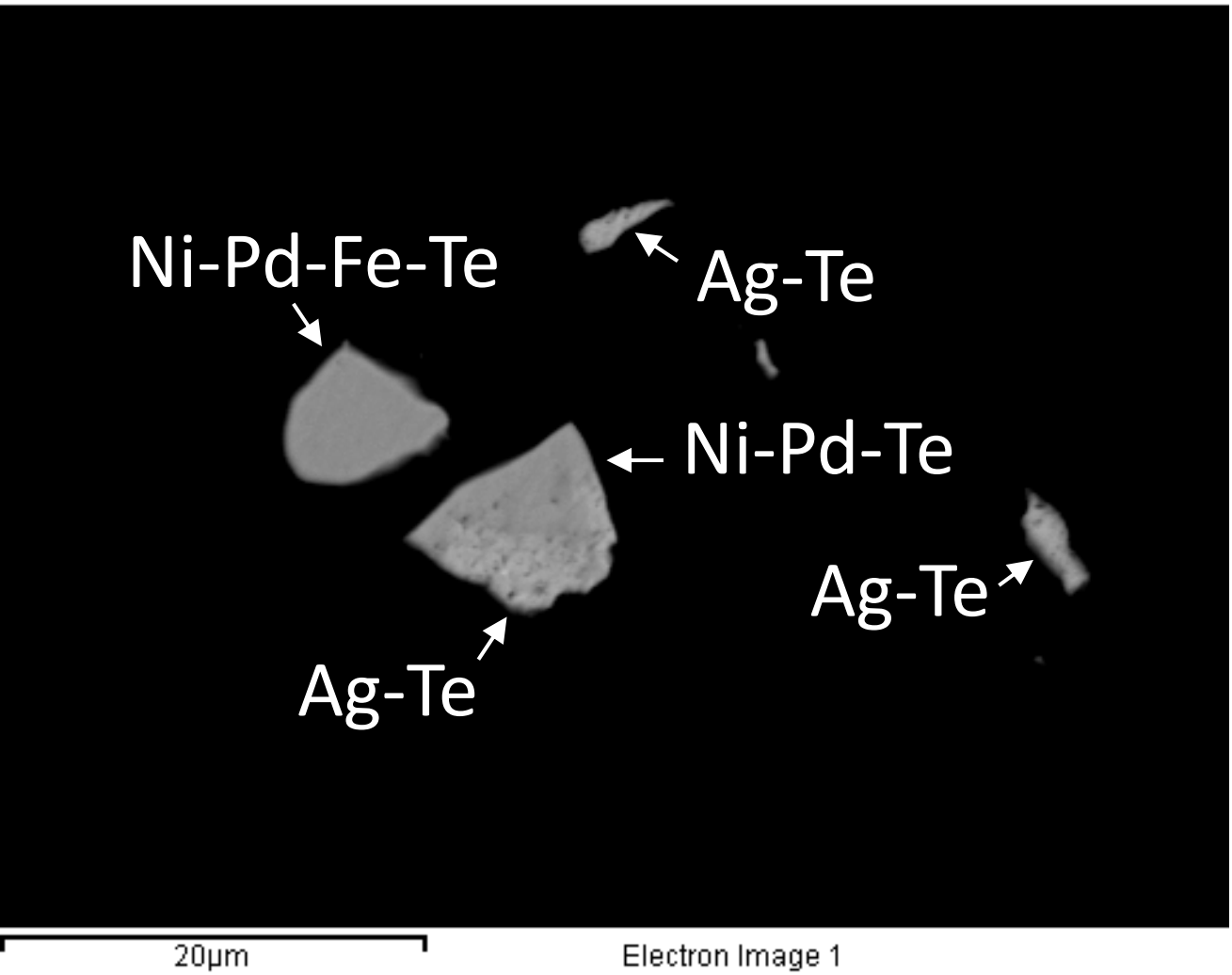
PTSR-64 K 1



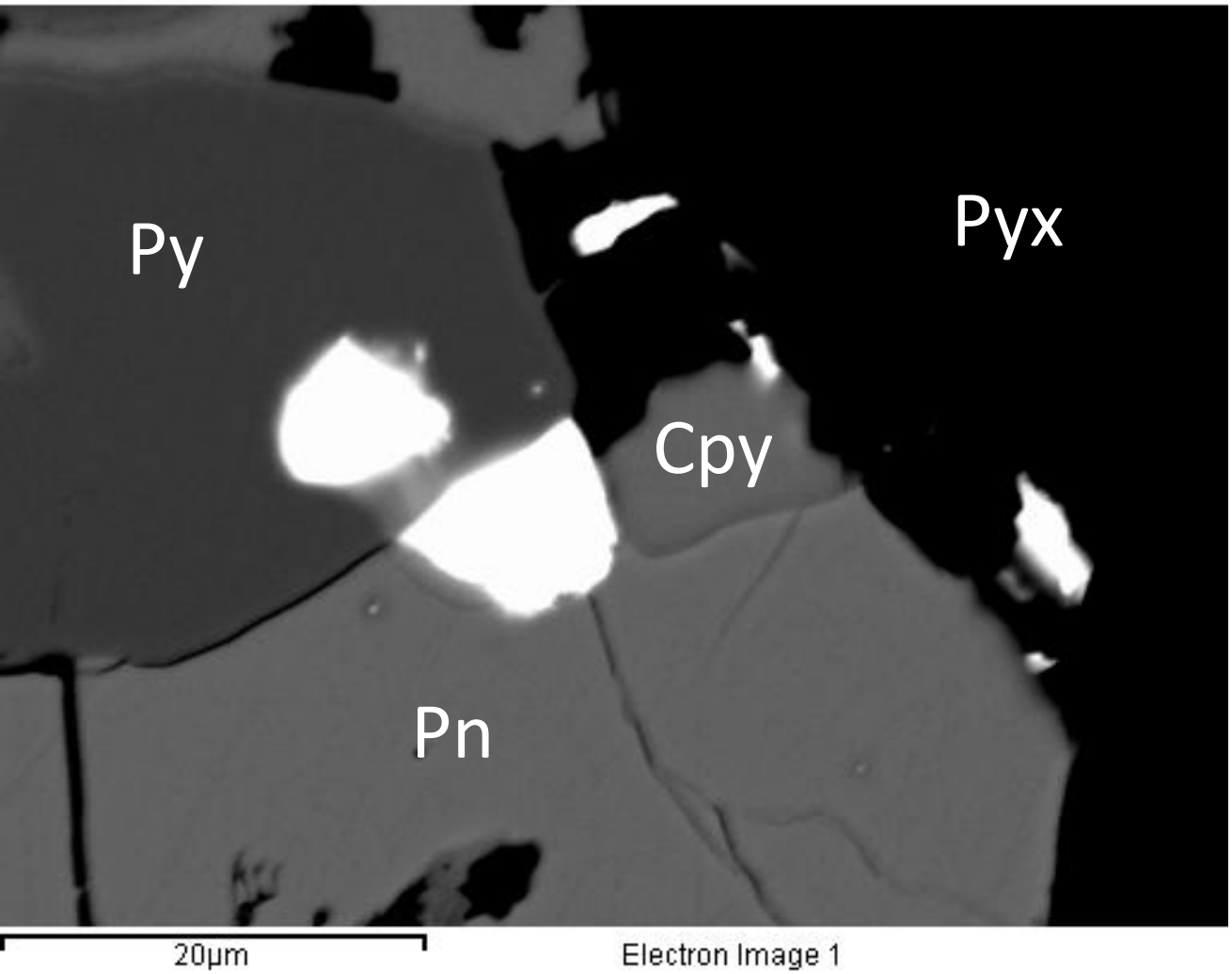
PTSR-64 L 1



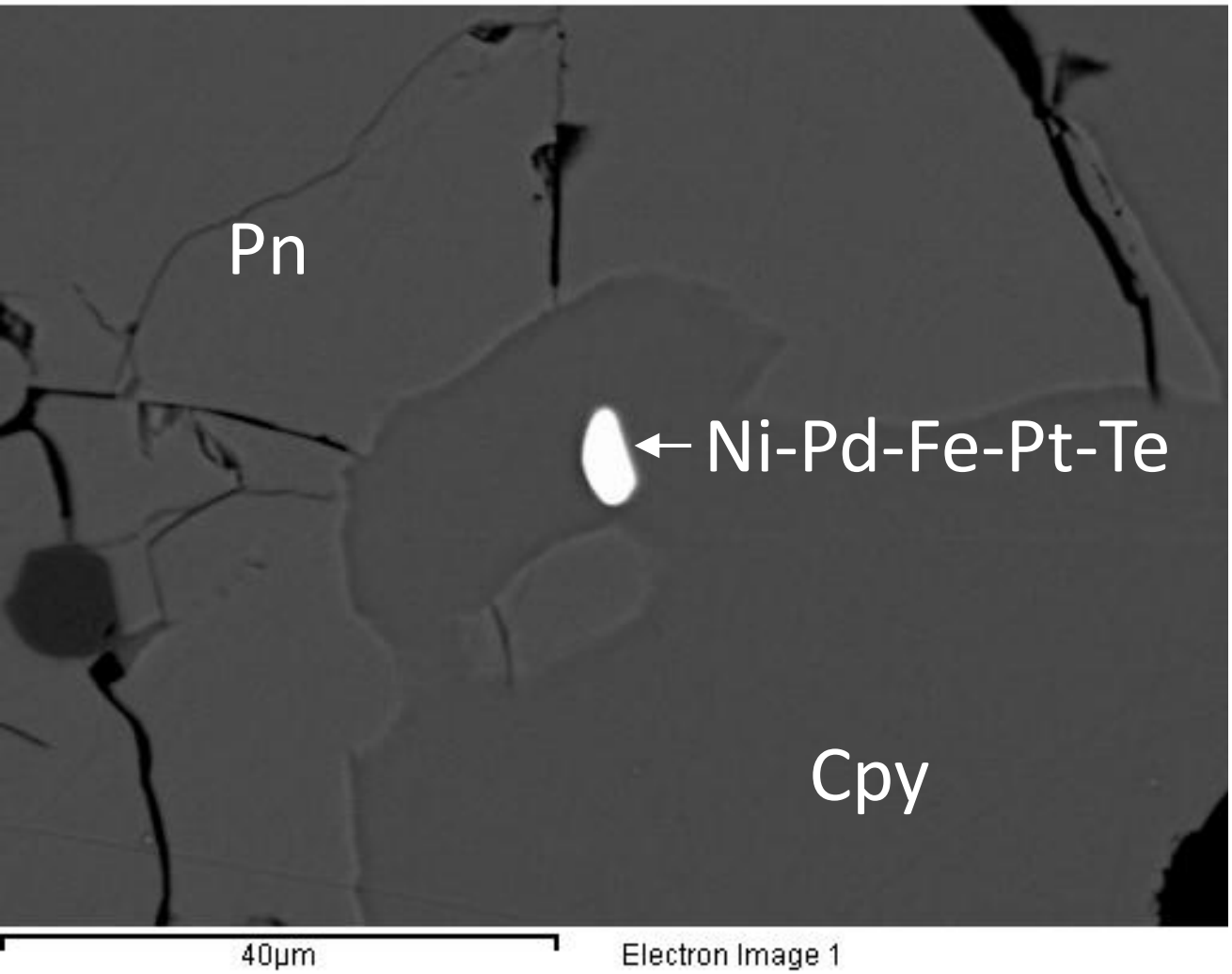
PTSR-64 M 1-4



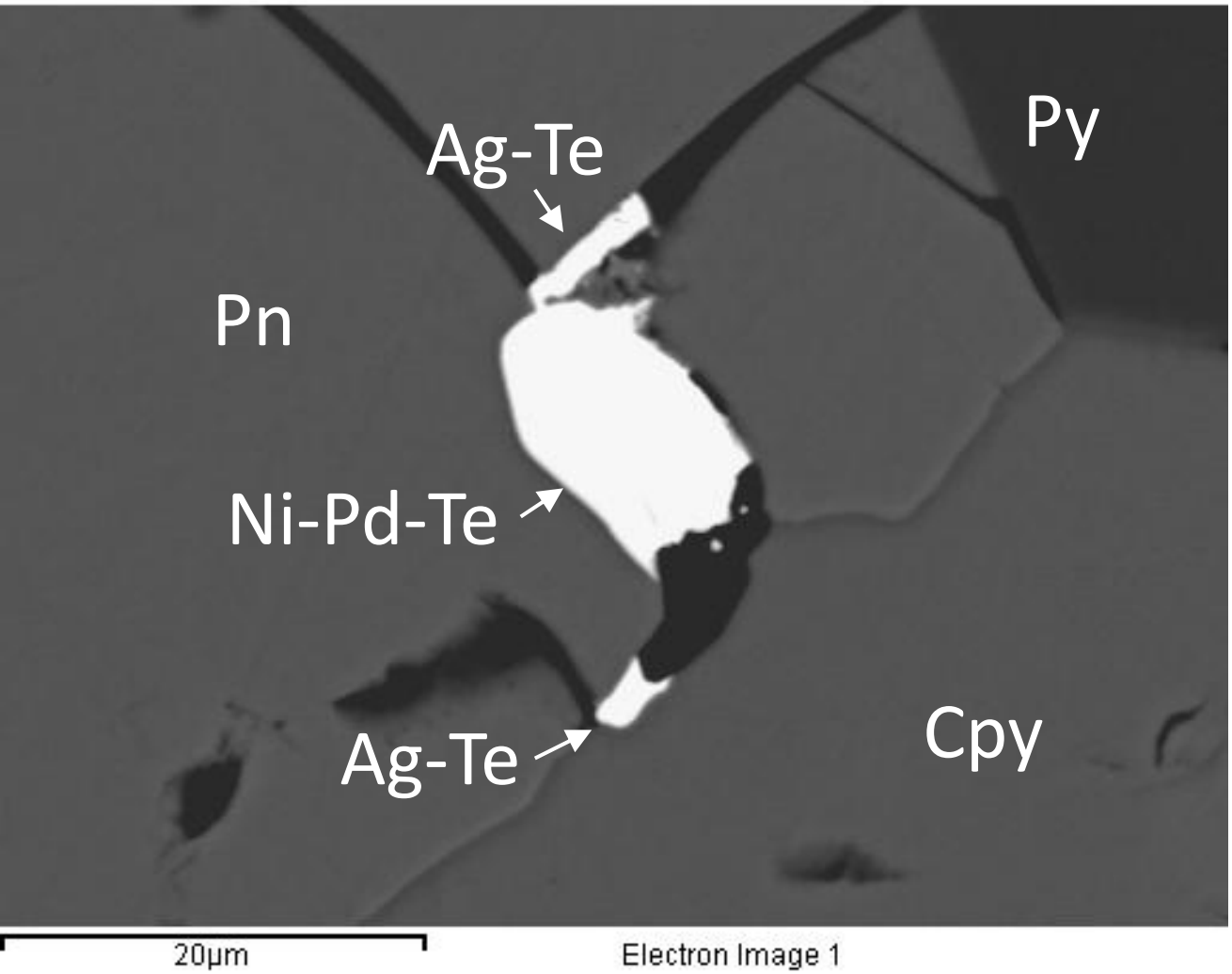
PTSR-64 M 1-4 Light



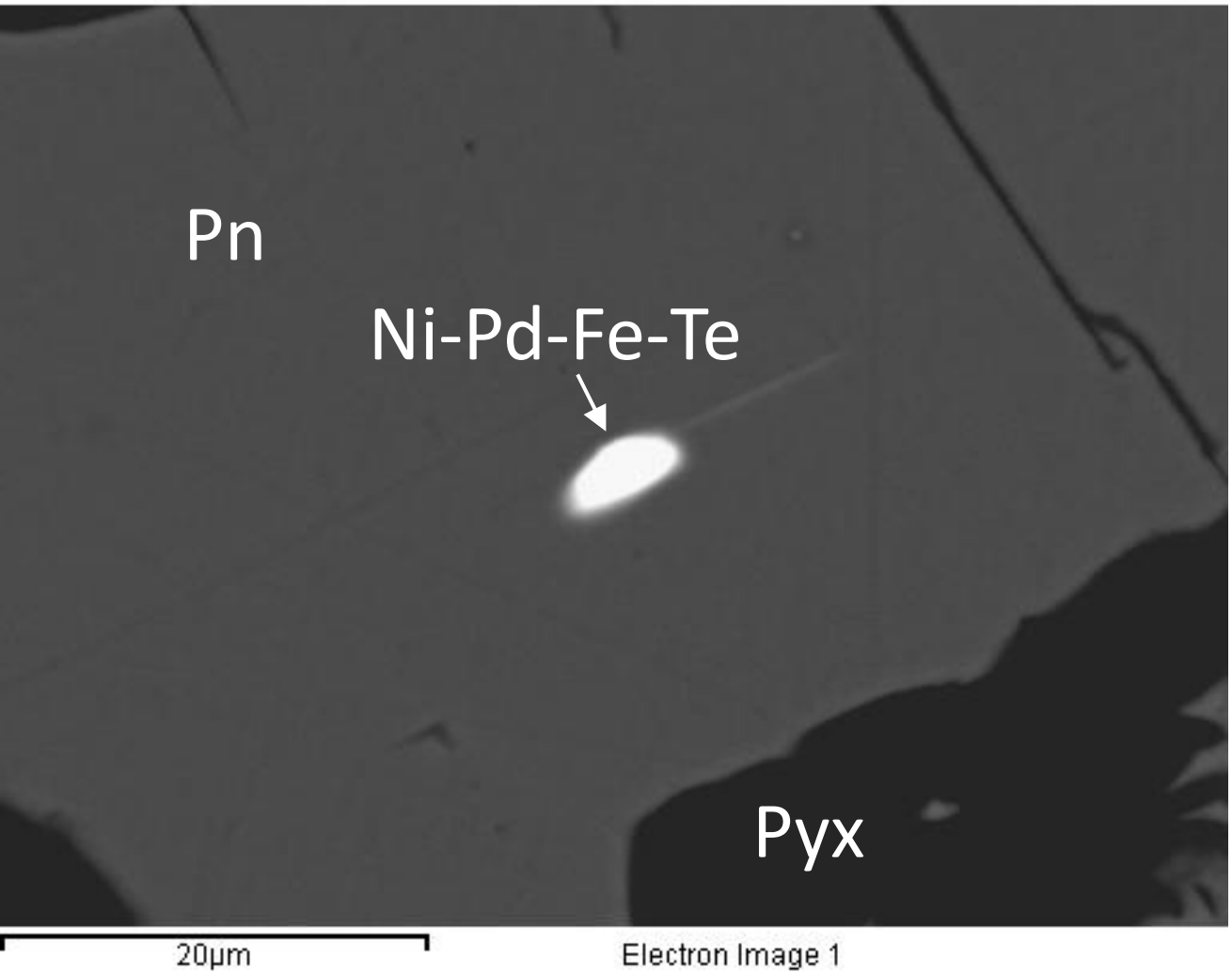
PTSR-64 N 1



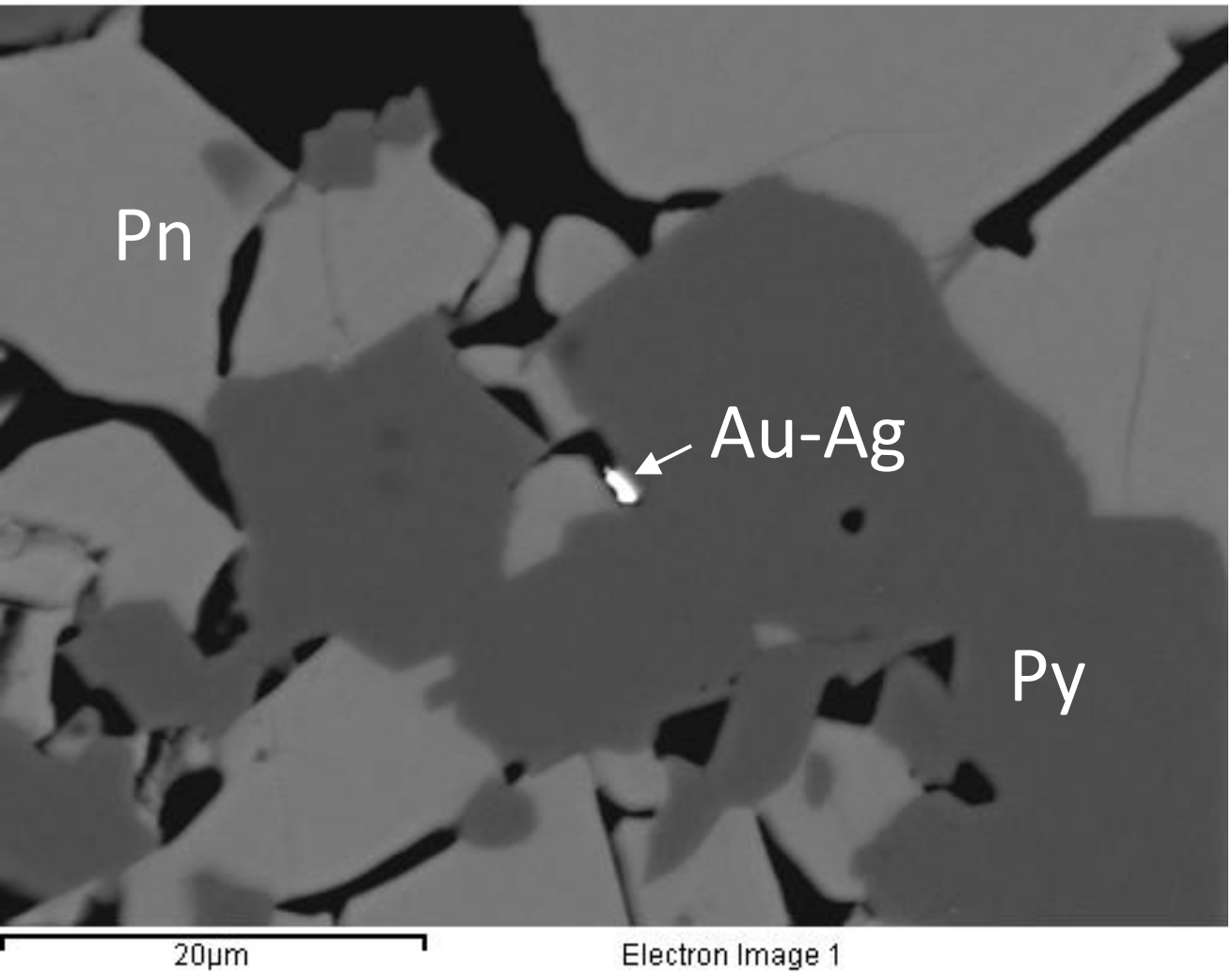
PTSR-64 O 1-3



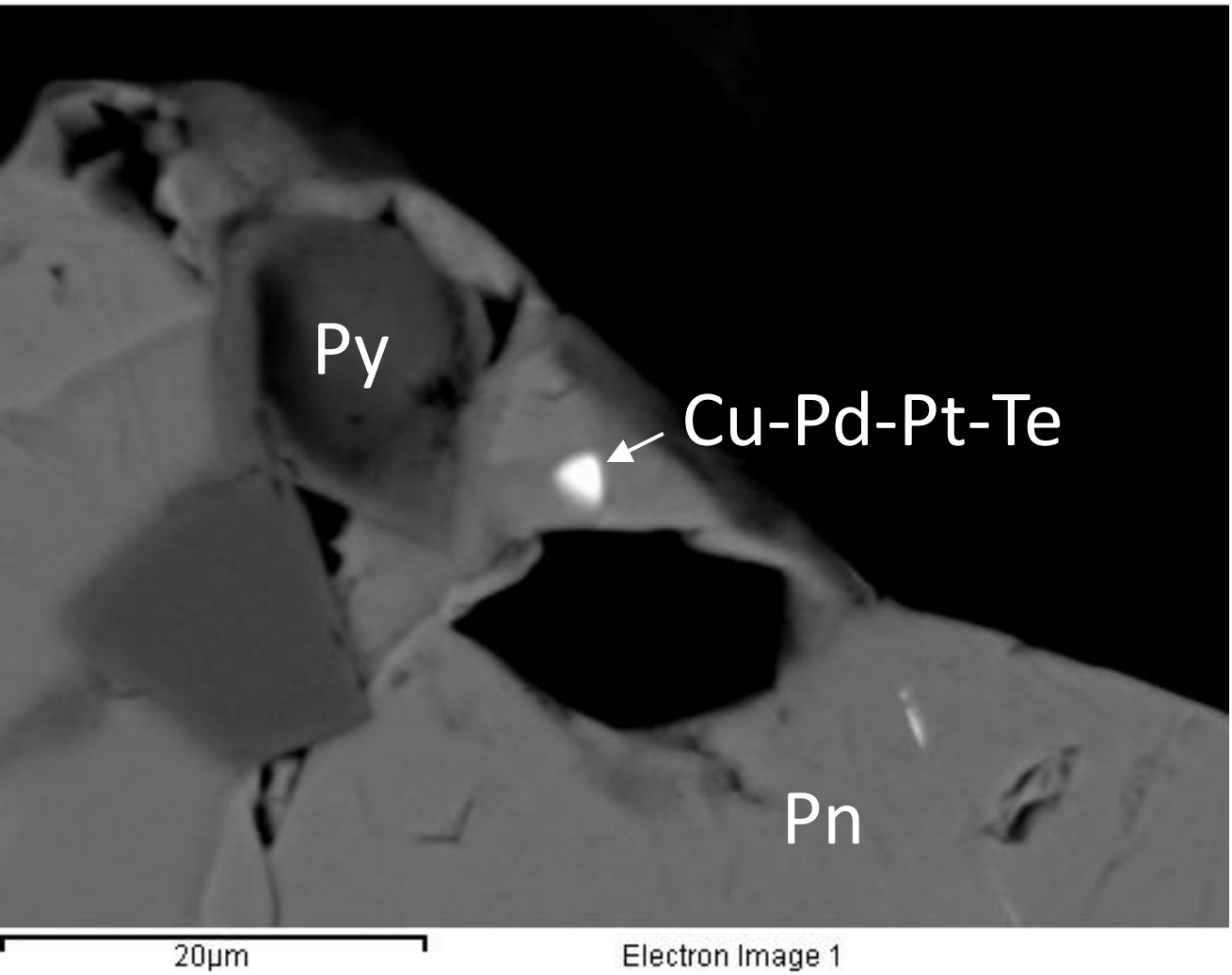
PTSR-64 P 1



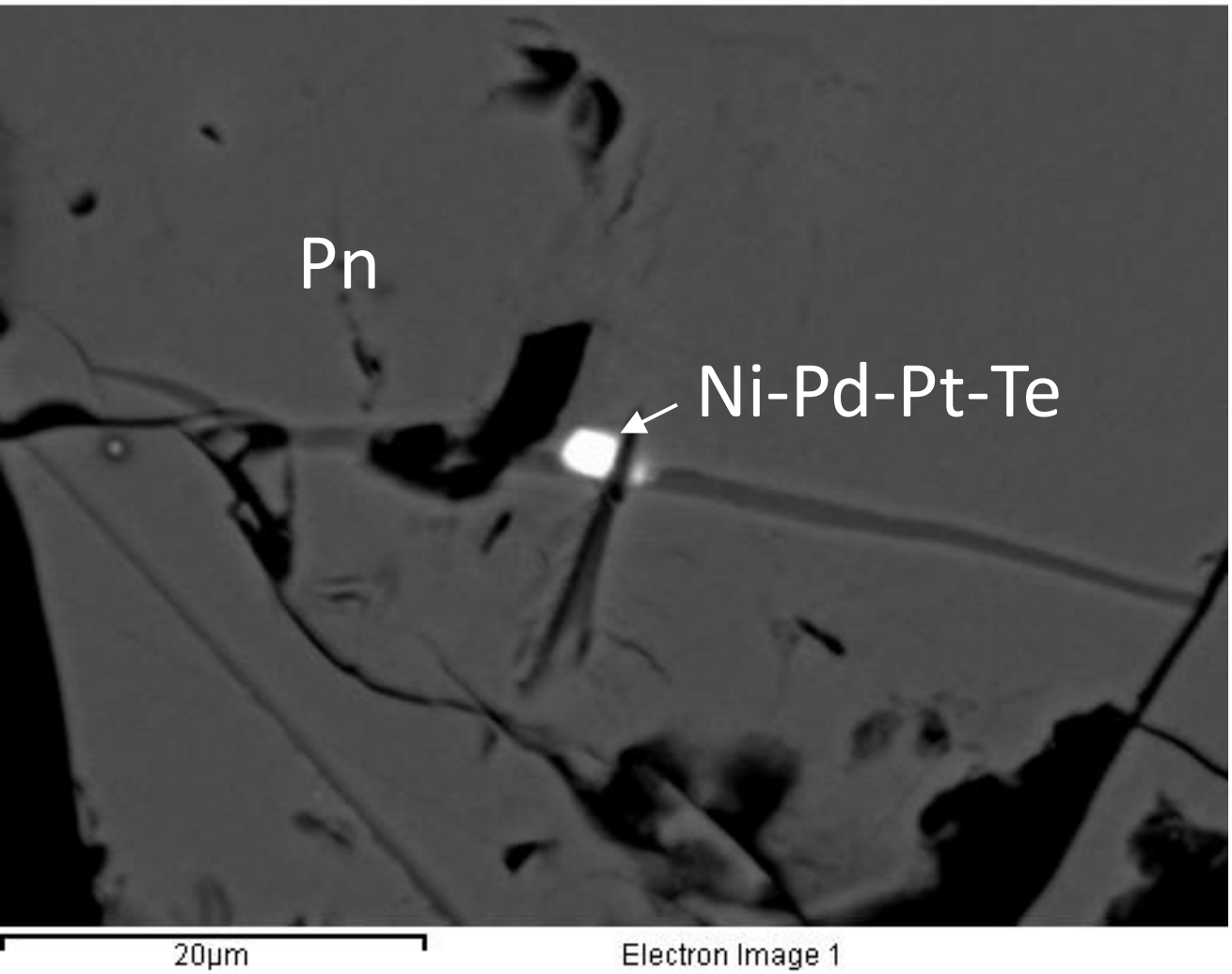
PTSR-64 Q 1



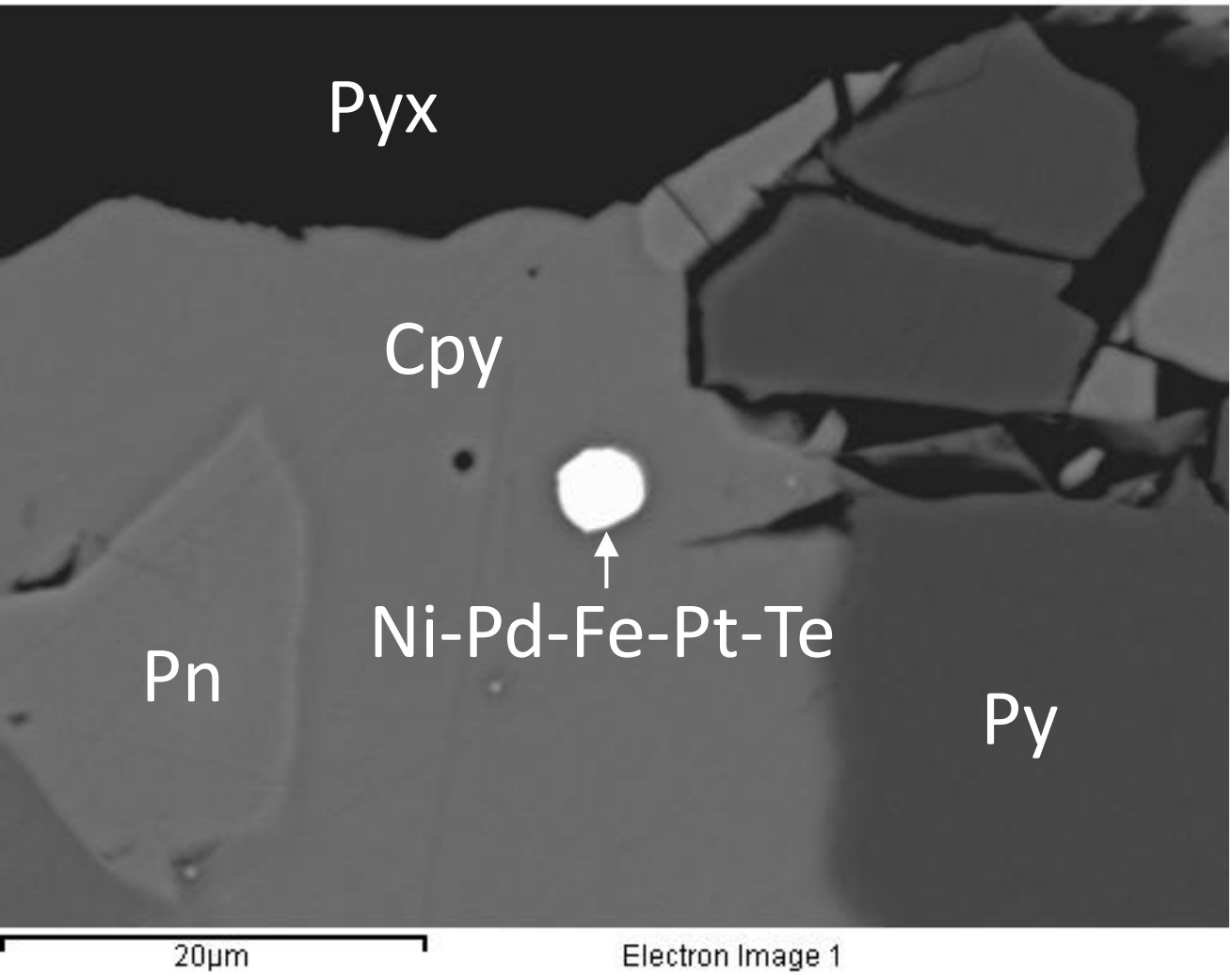
PTSR-64 R 1



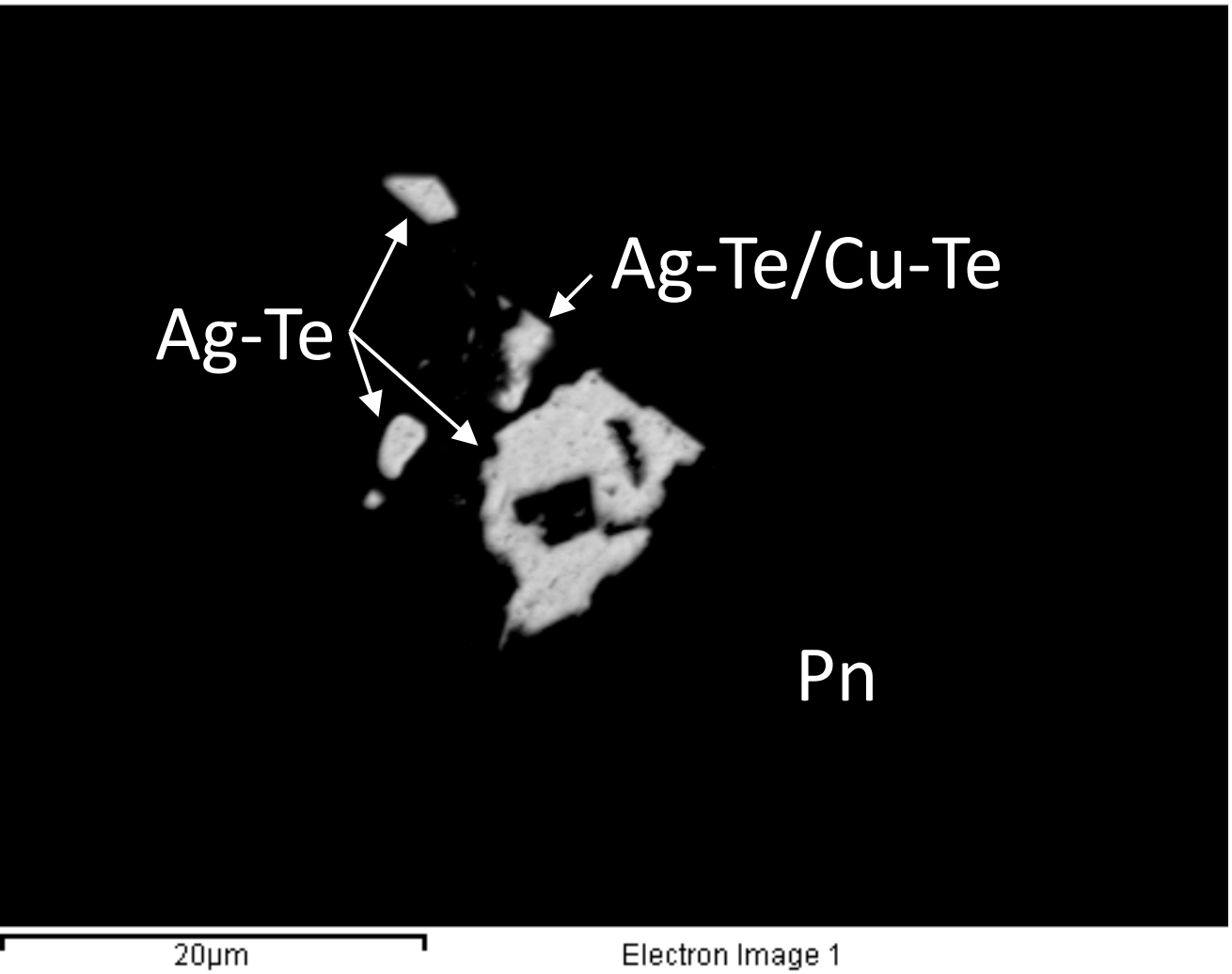
PTSR-64 S 1



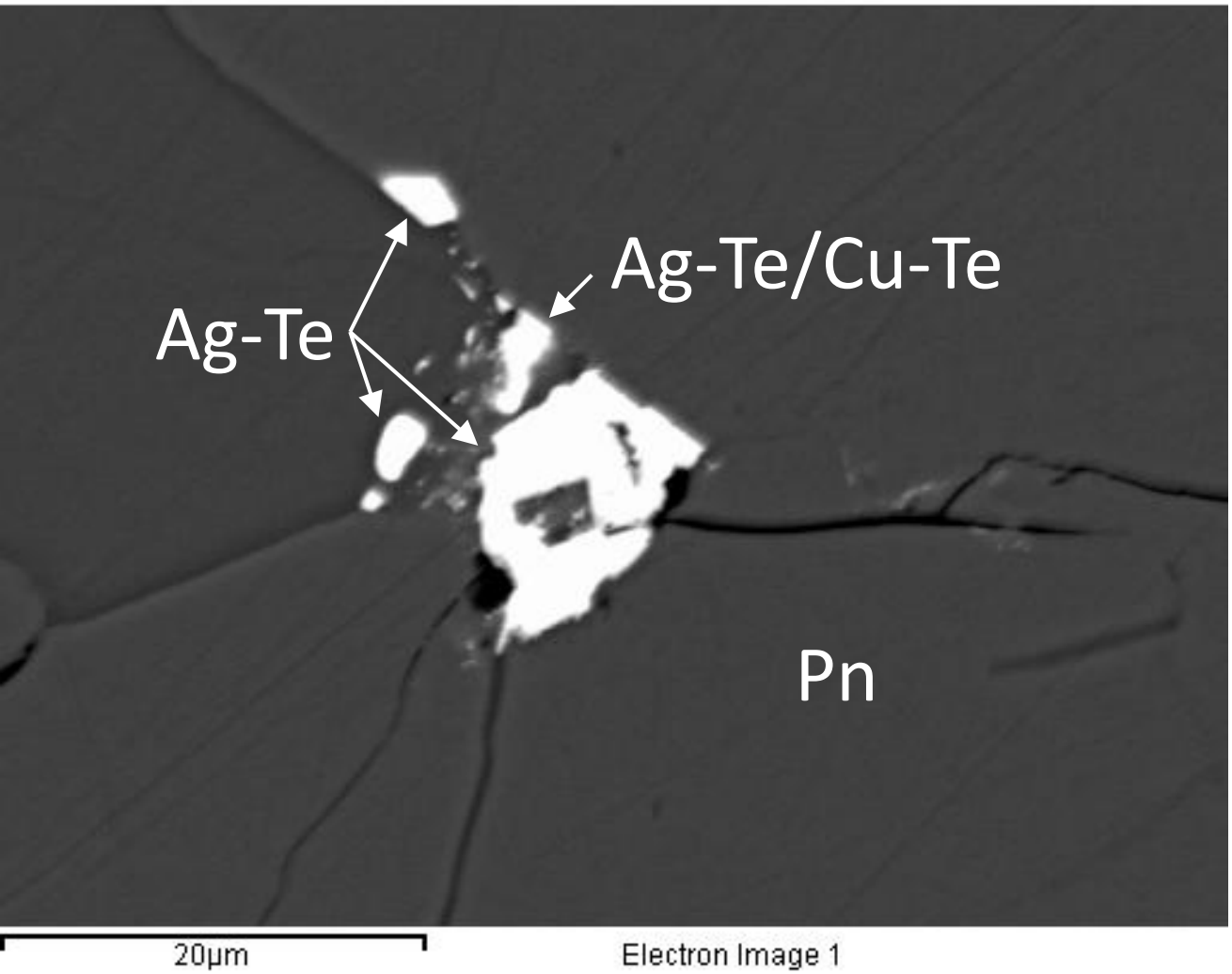
PTSR-64 T 1



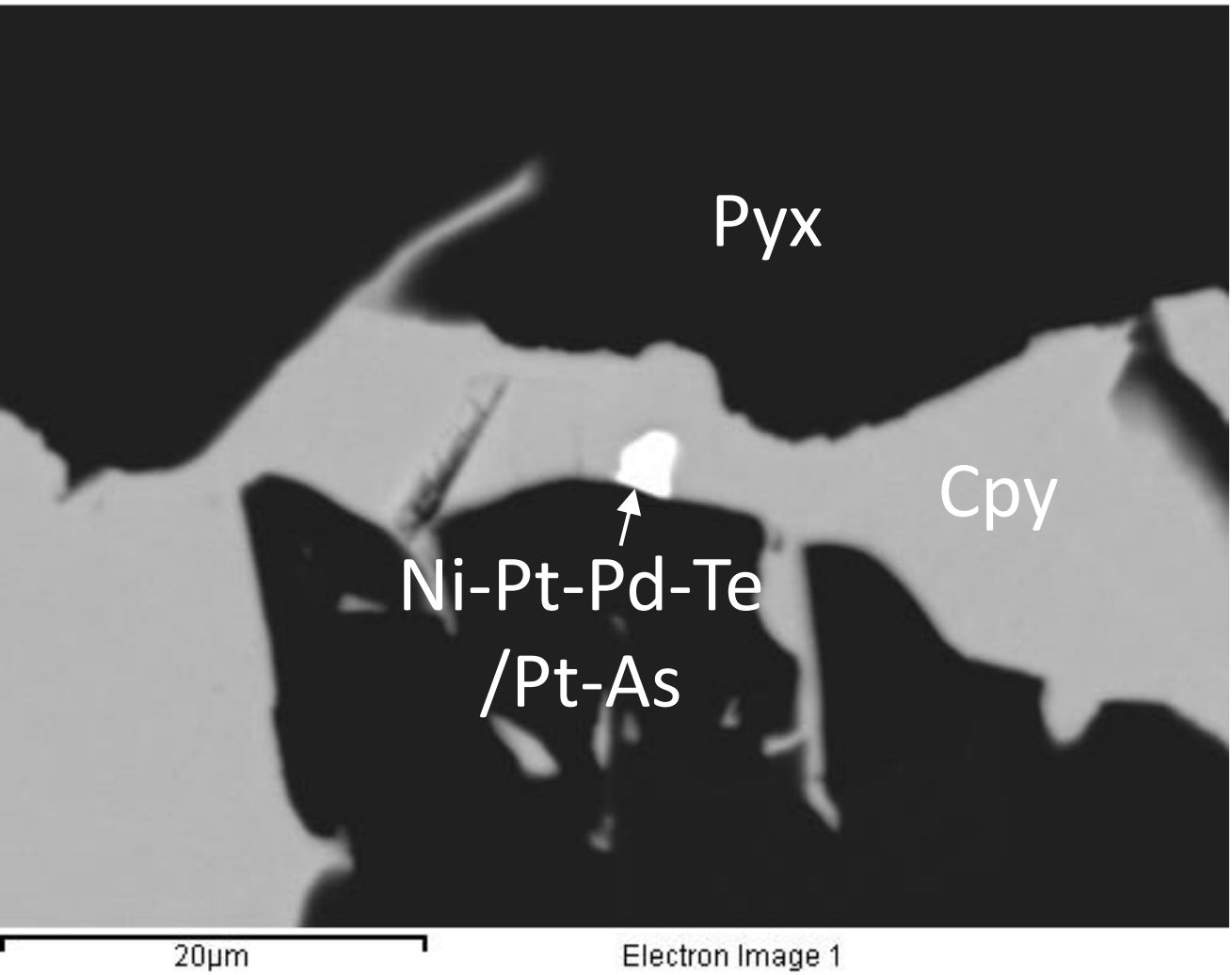
PTSR-64 U 1-4



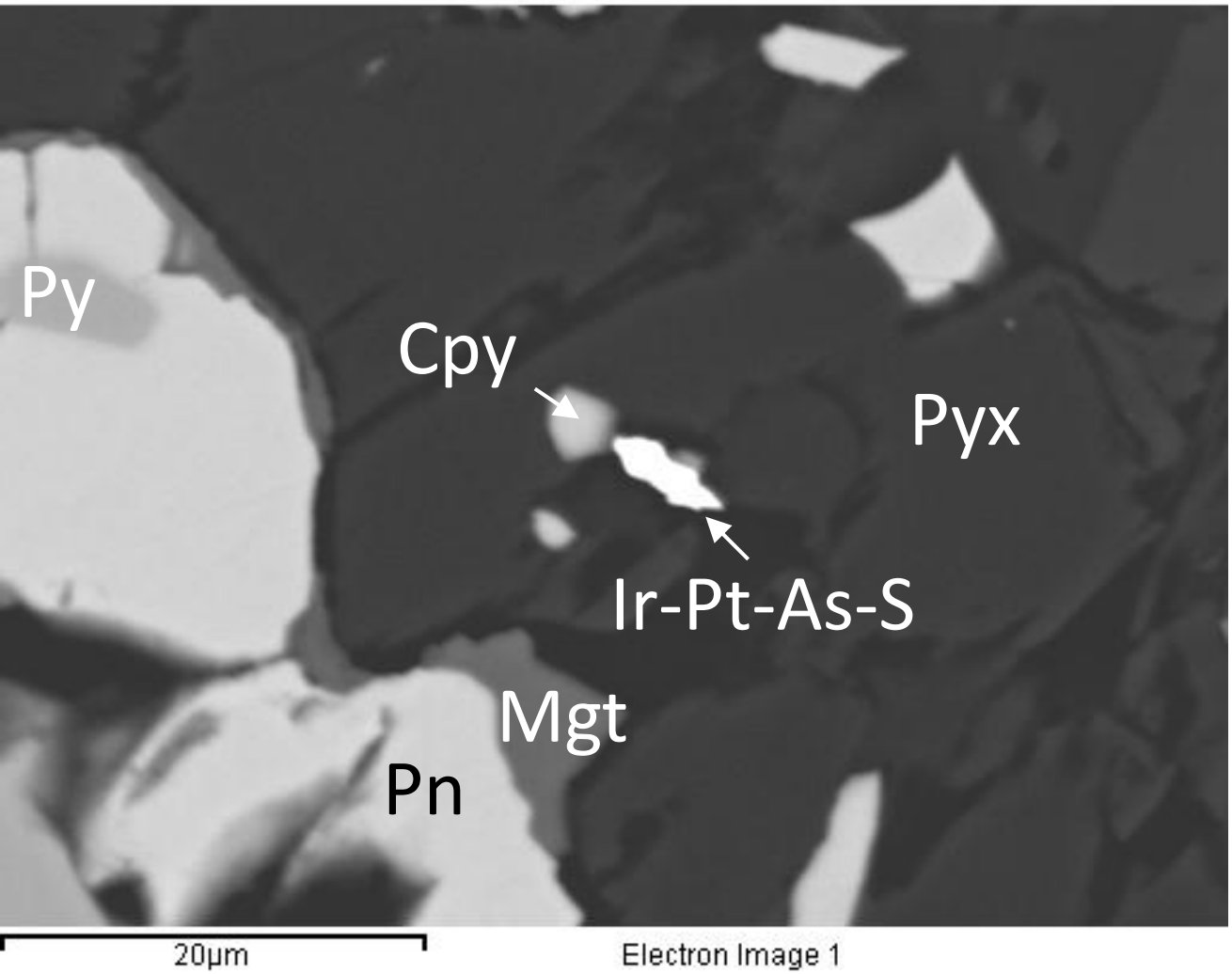
PTSR-64 U 1-4 Light



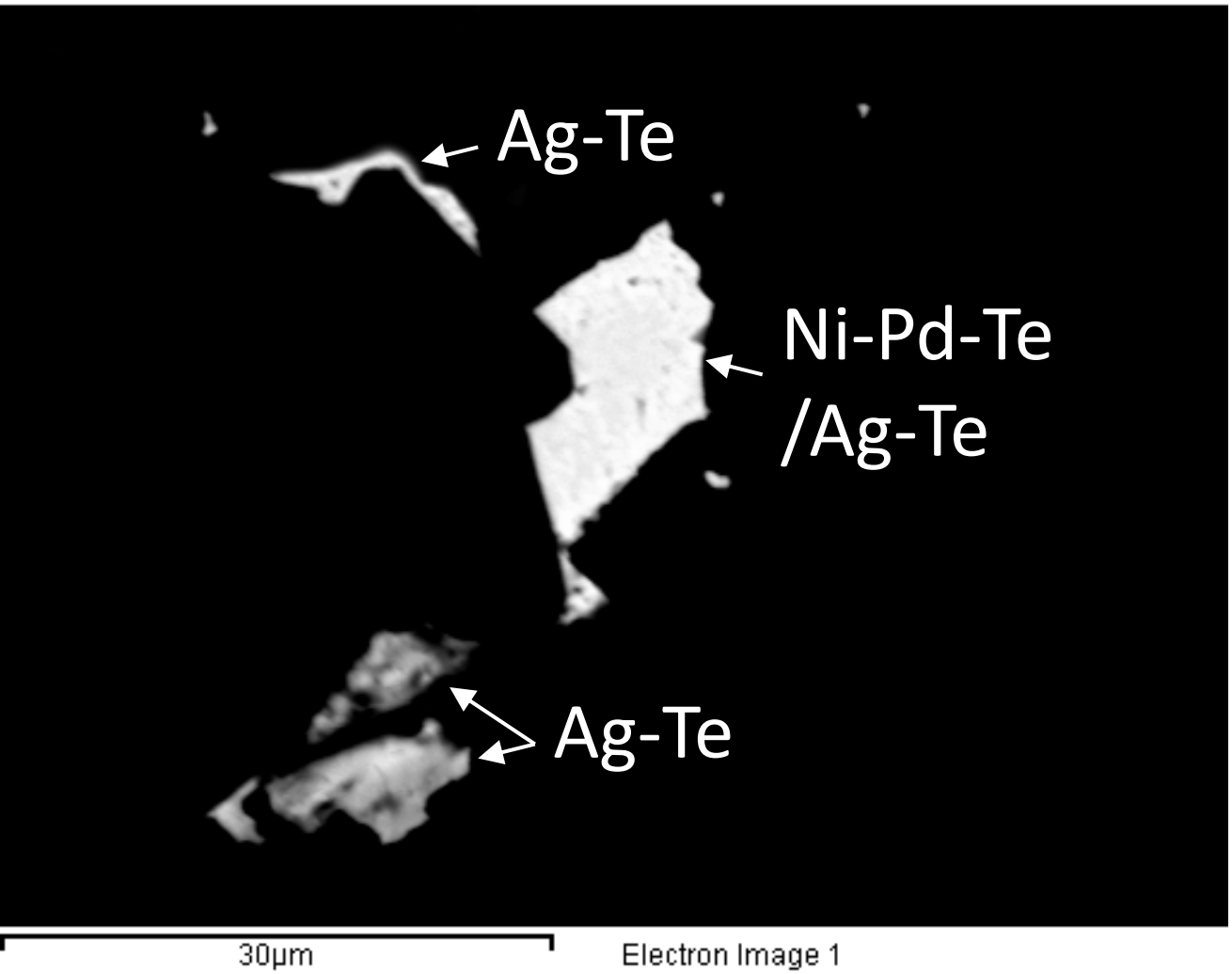
PTSR-64 V 1



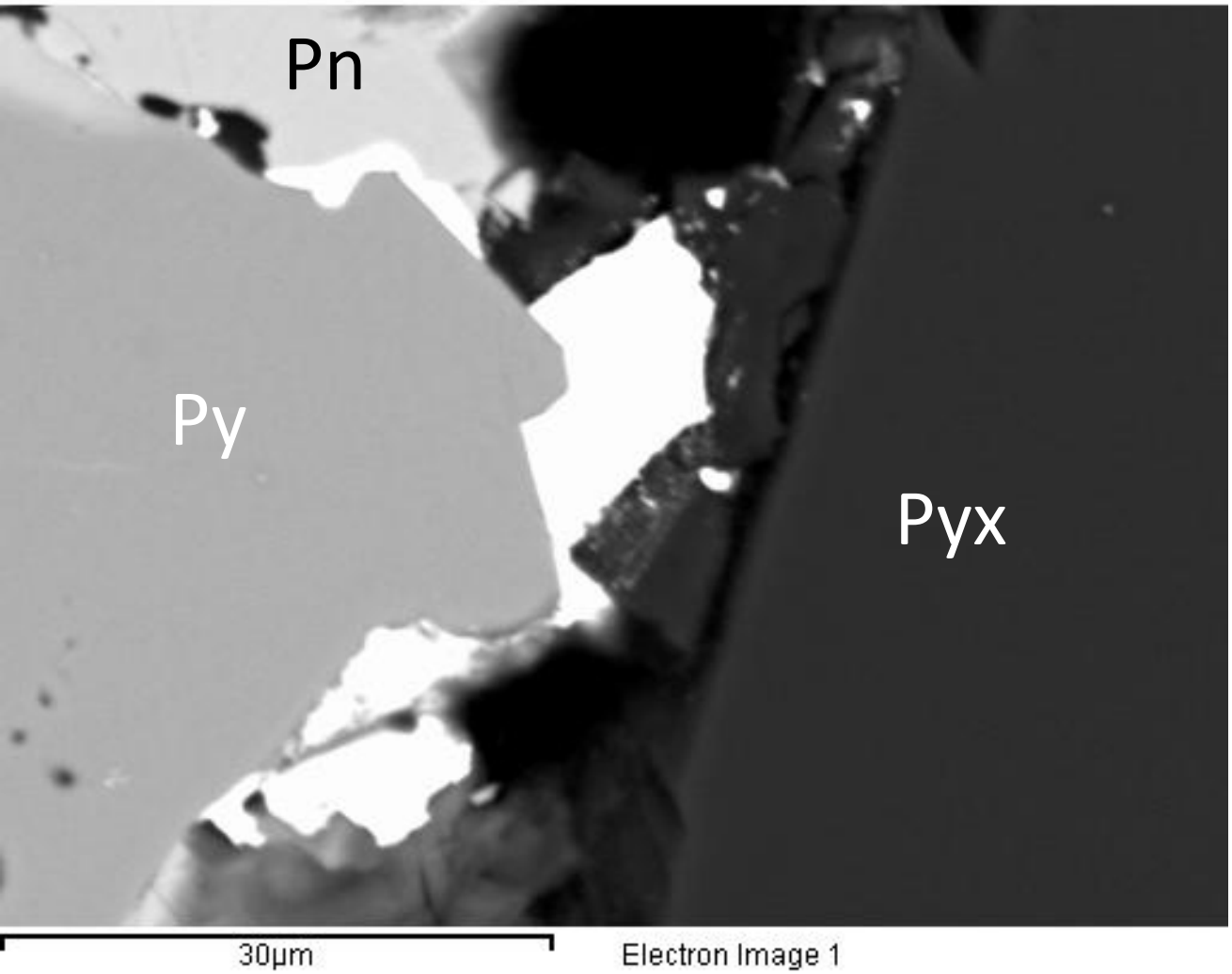
PTSR-64 W 1



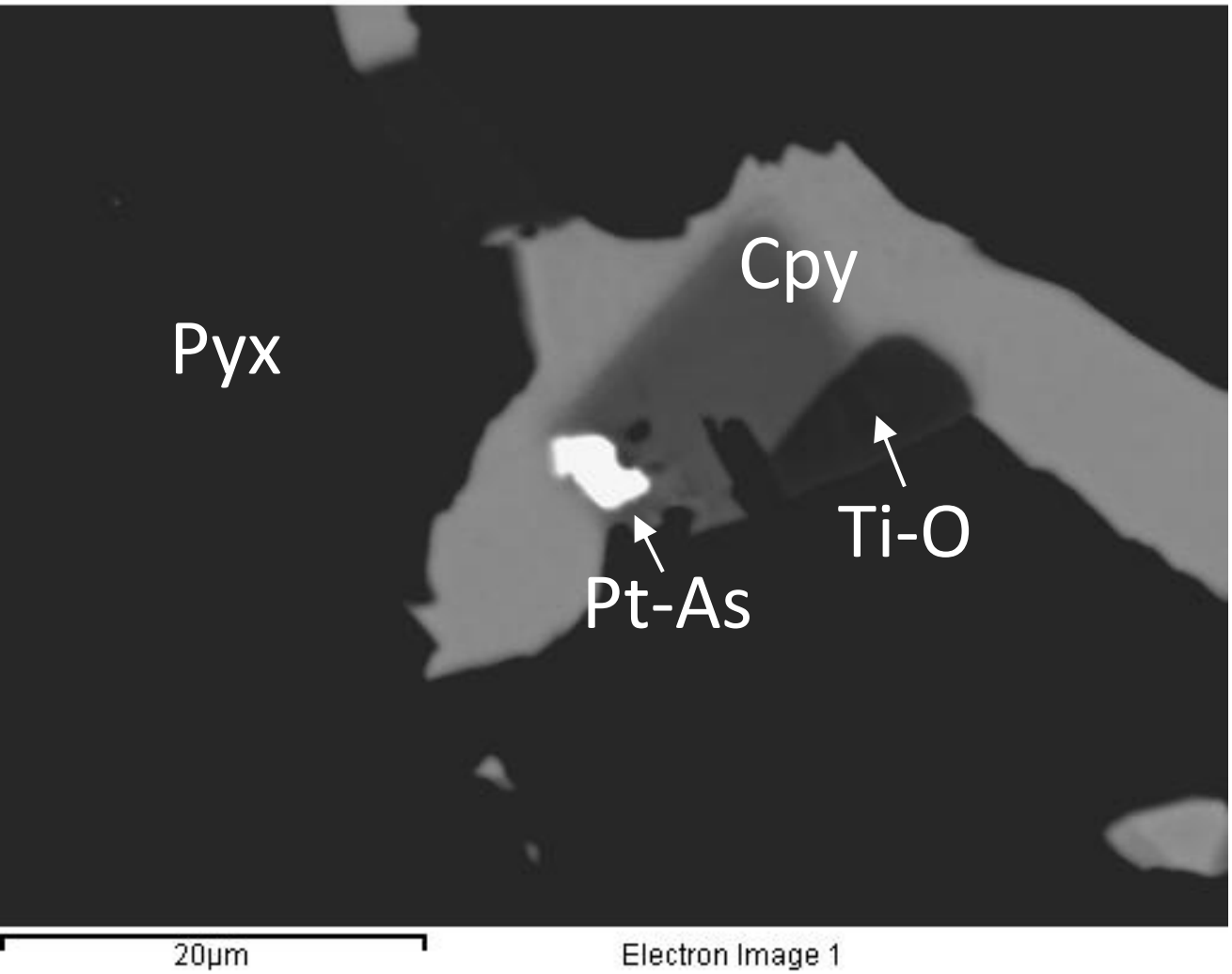
PTSR-64 X 1-4



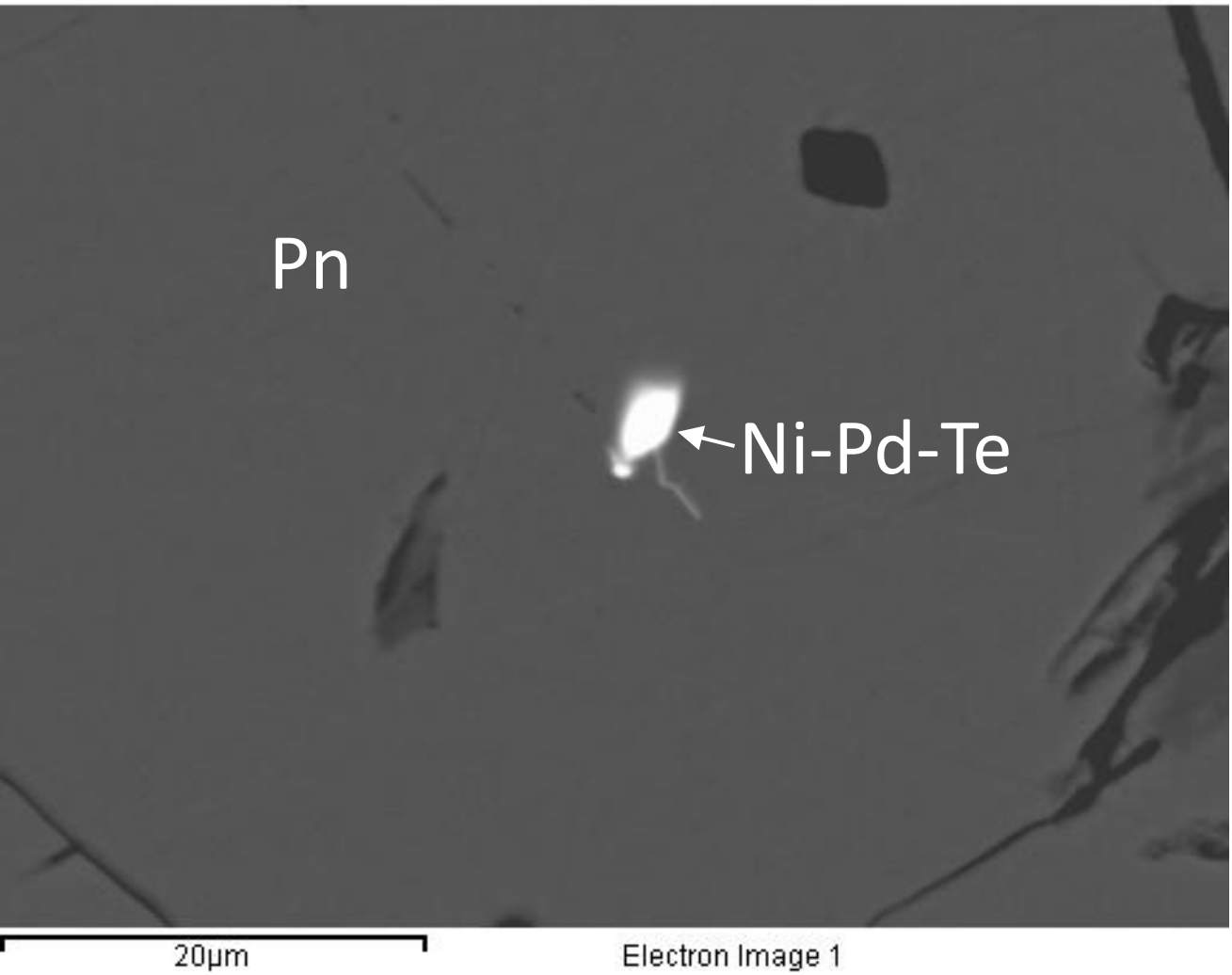
PTSR-64 X 1-4 Light



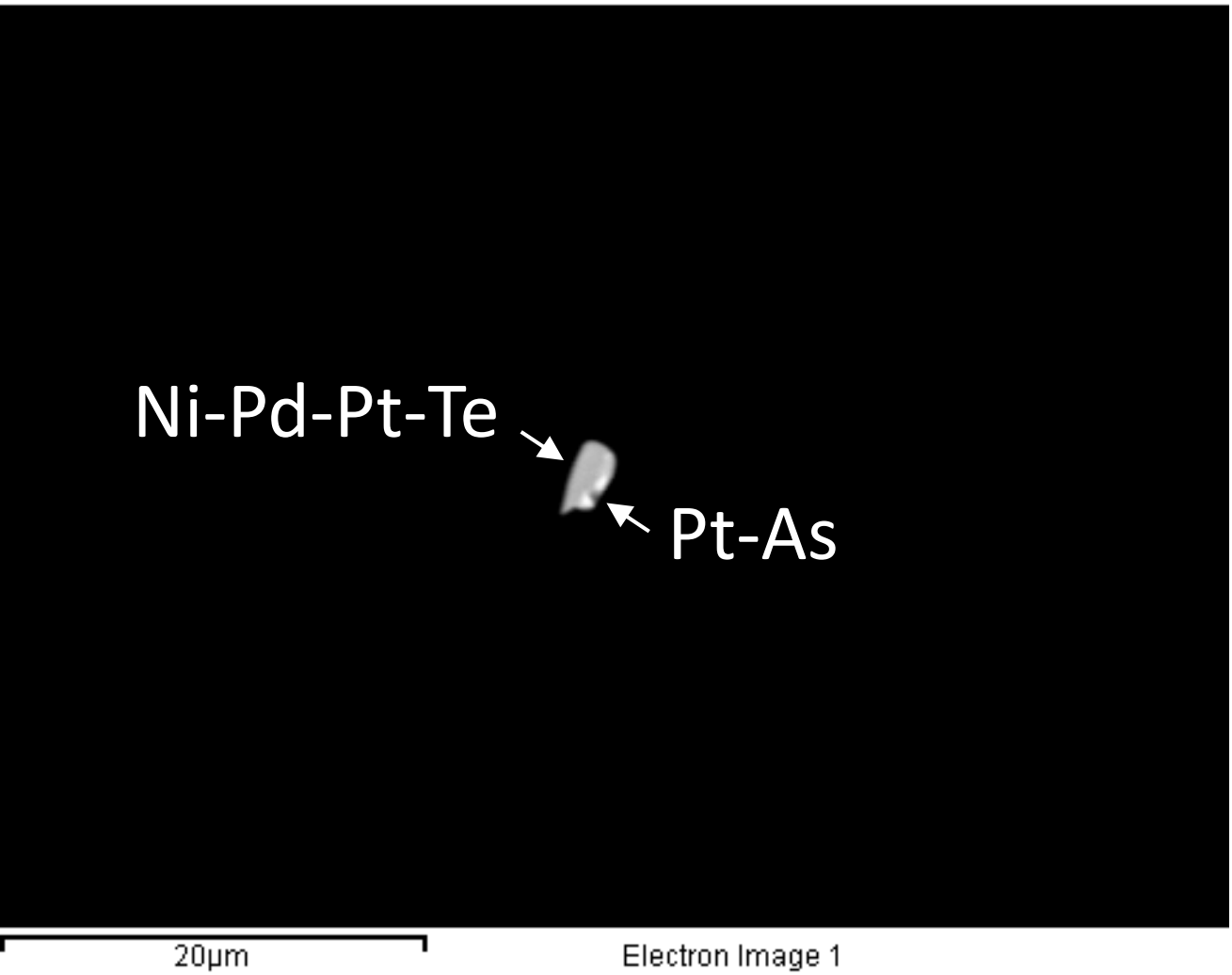
PTSR-64 Y 1



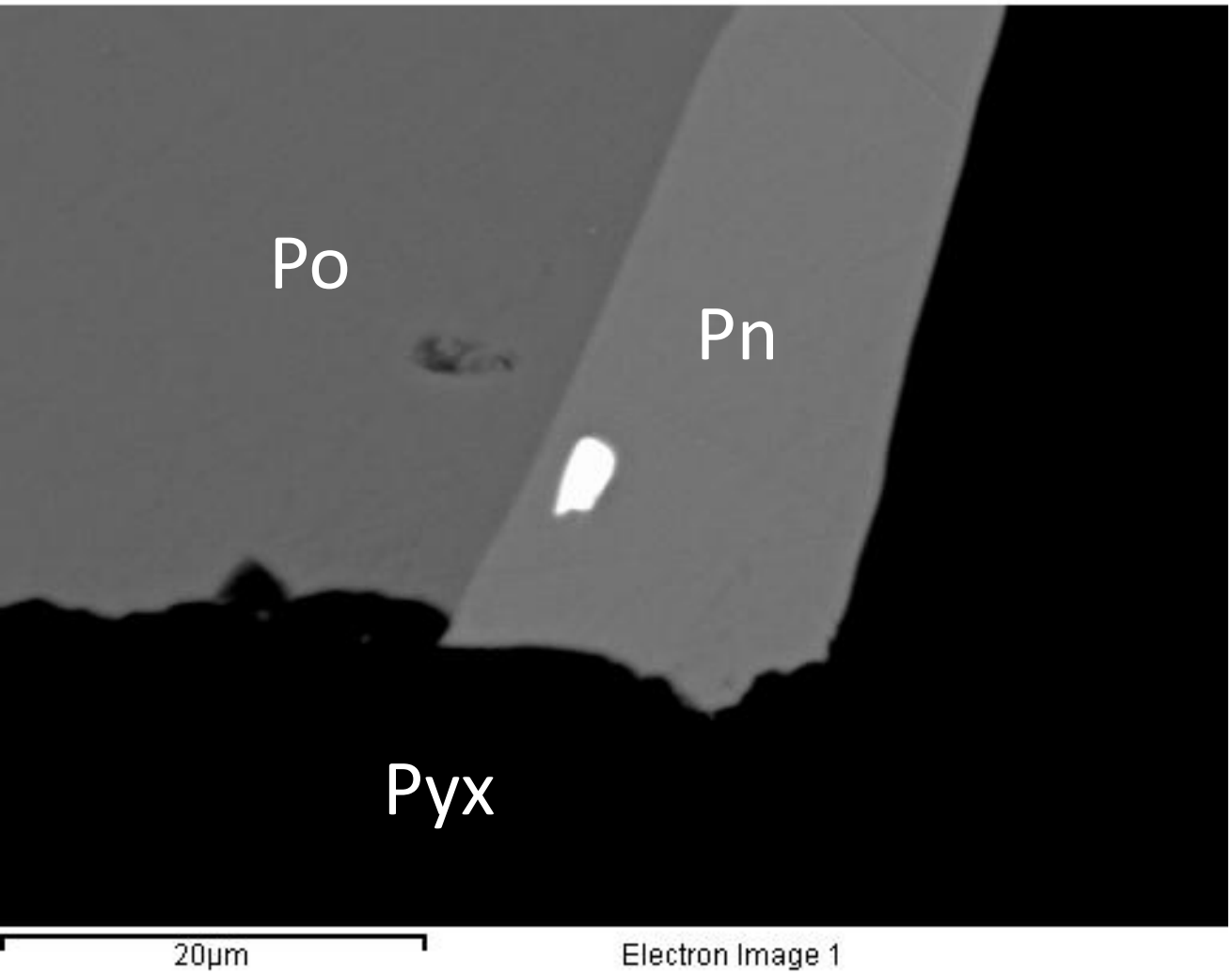
PTSR-64 Z 1



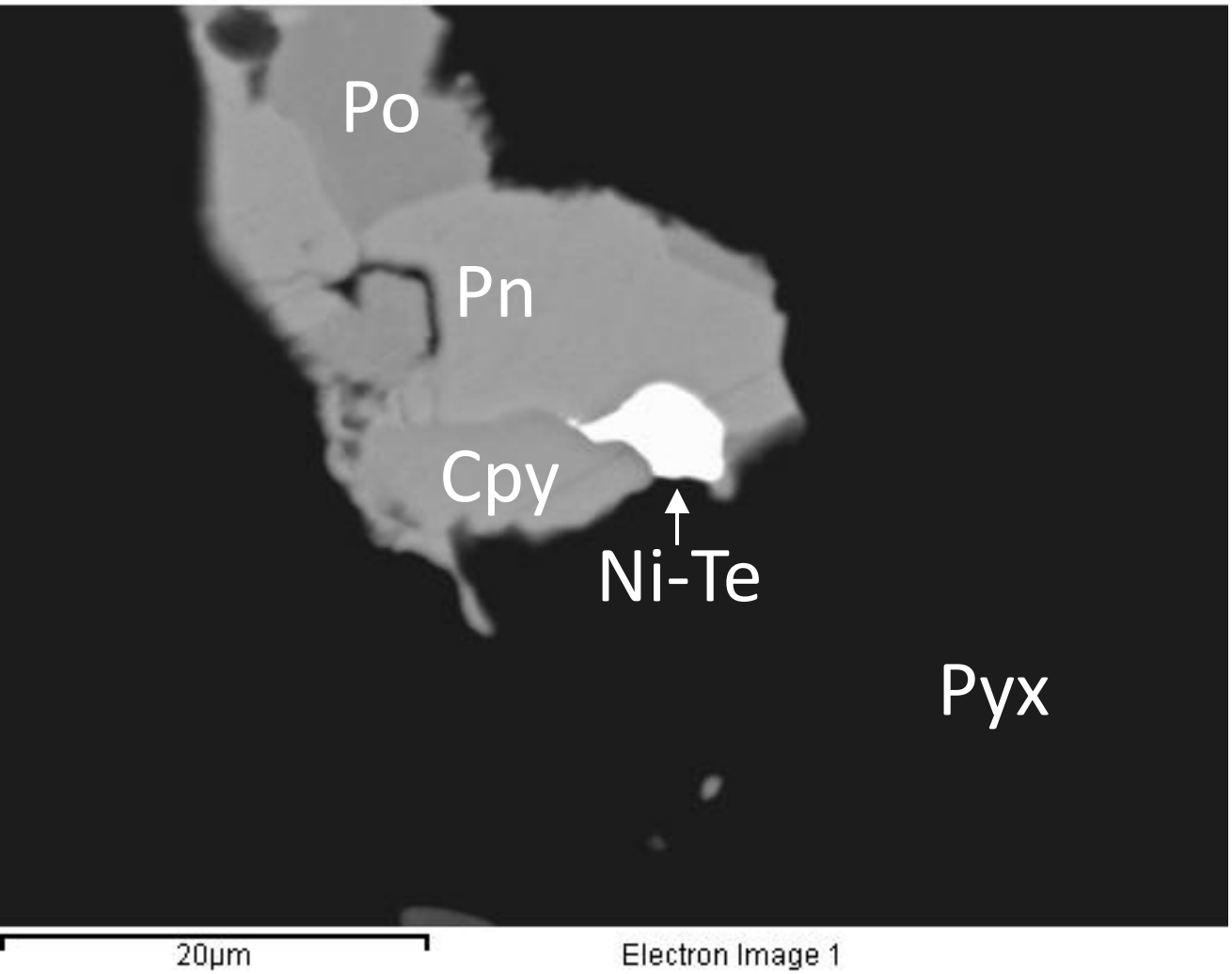
PTSR-64 AA 1



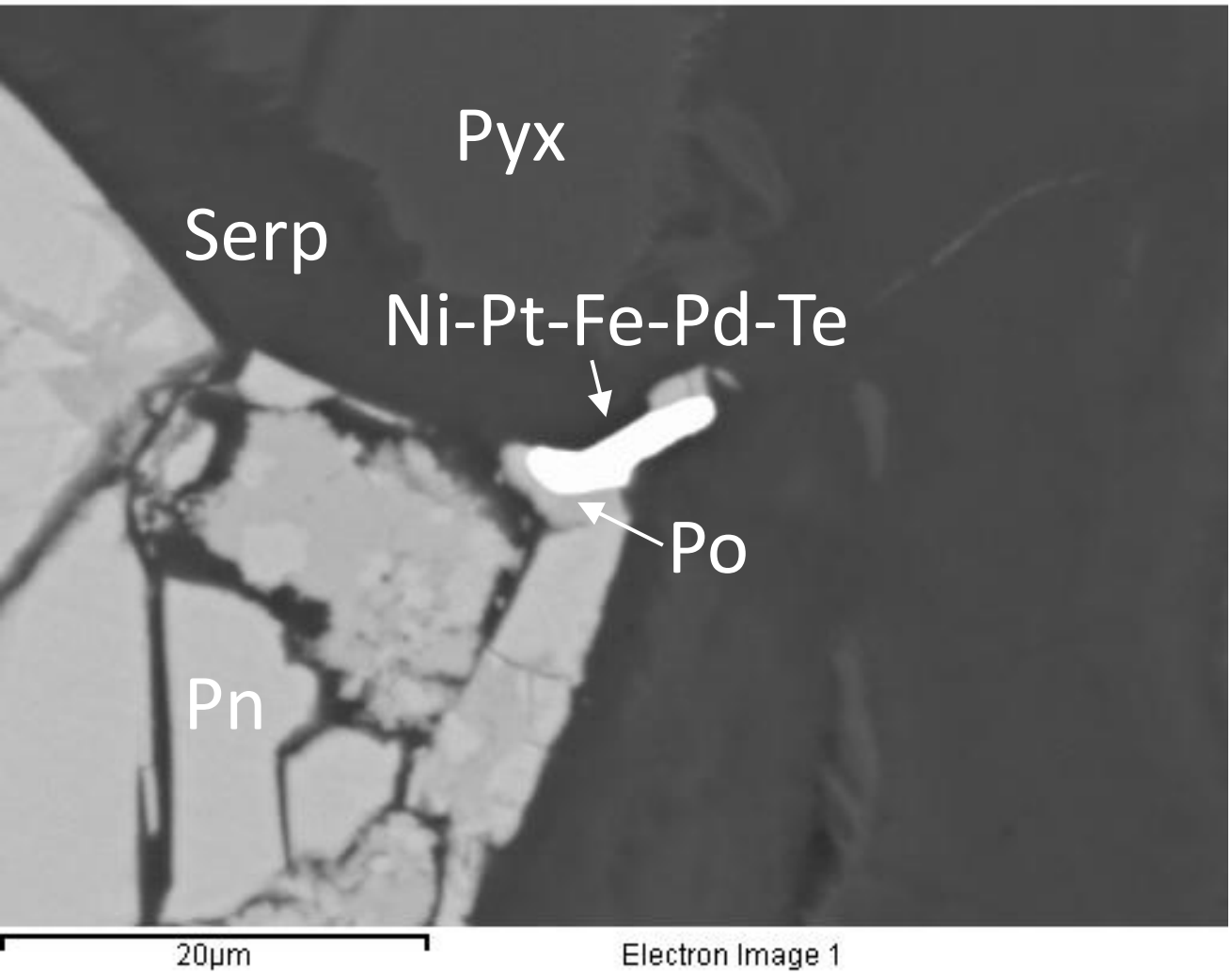
PTSR-64 AA 1 Light



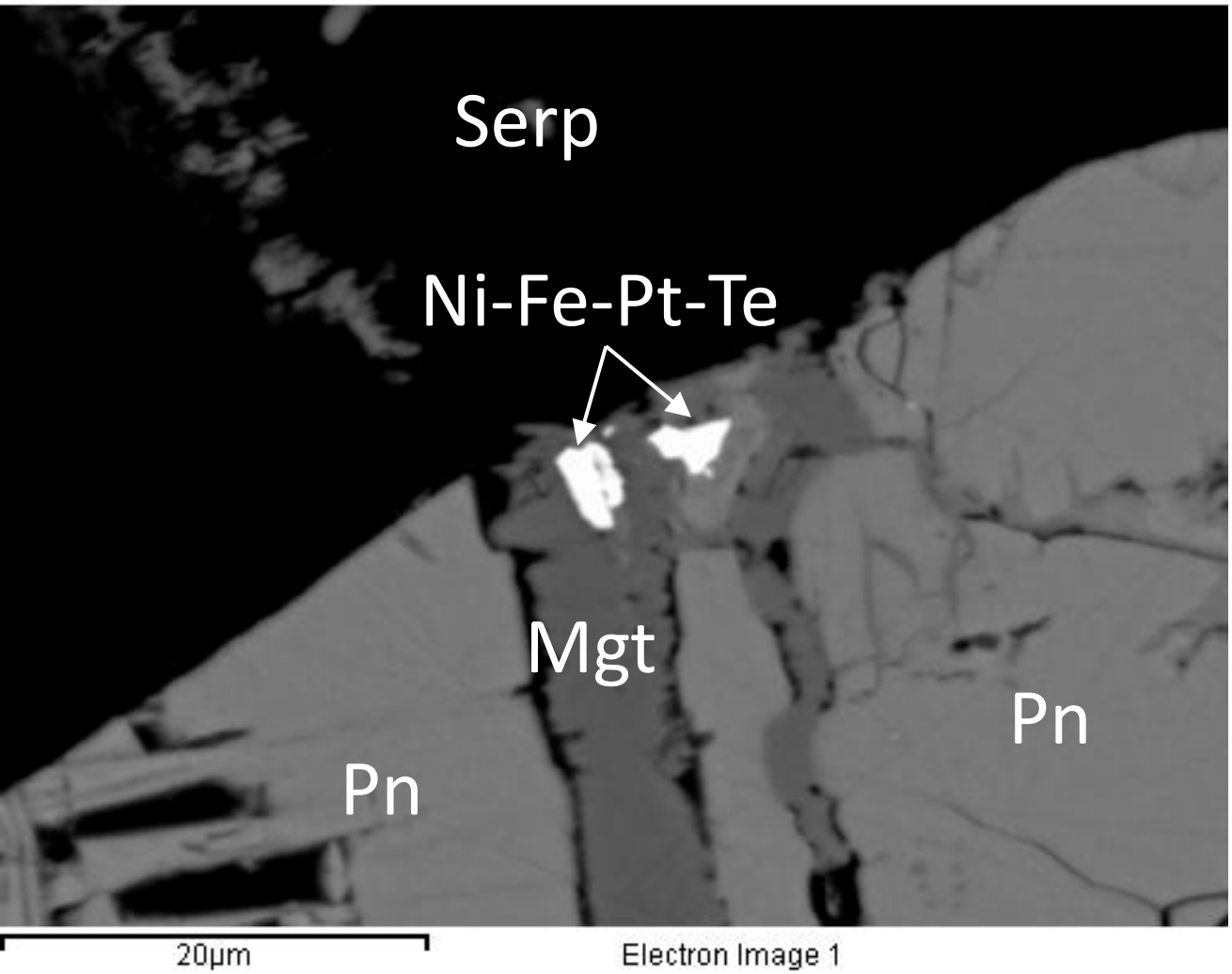
PTSR-64 AB 1



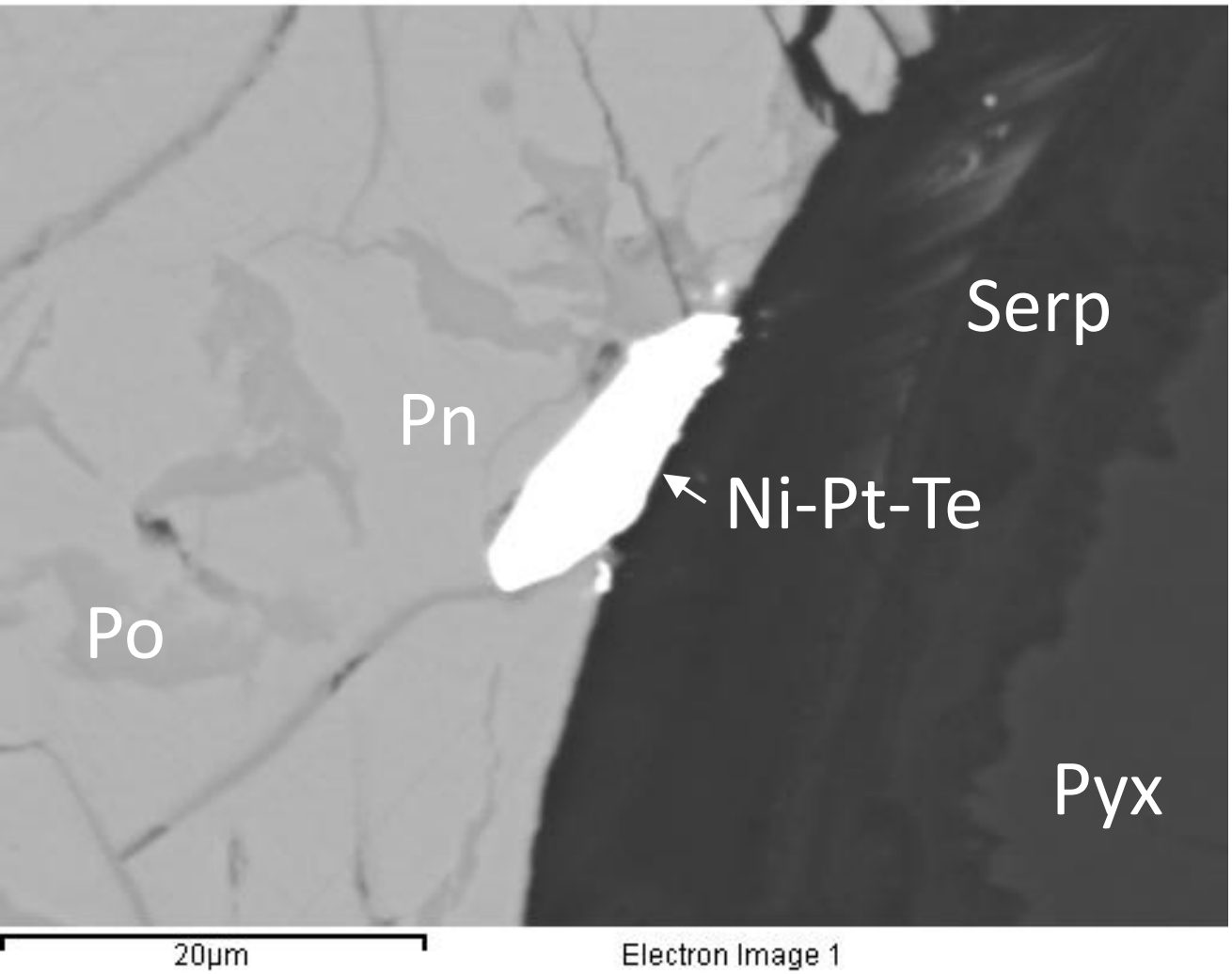
PTSR-65 A 1



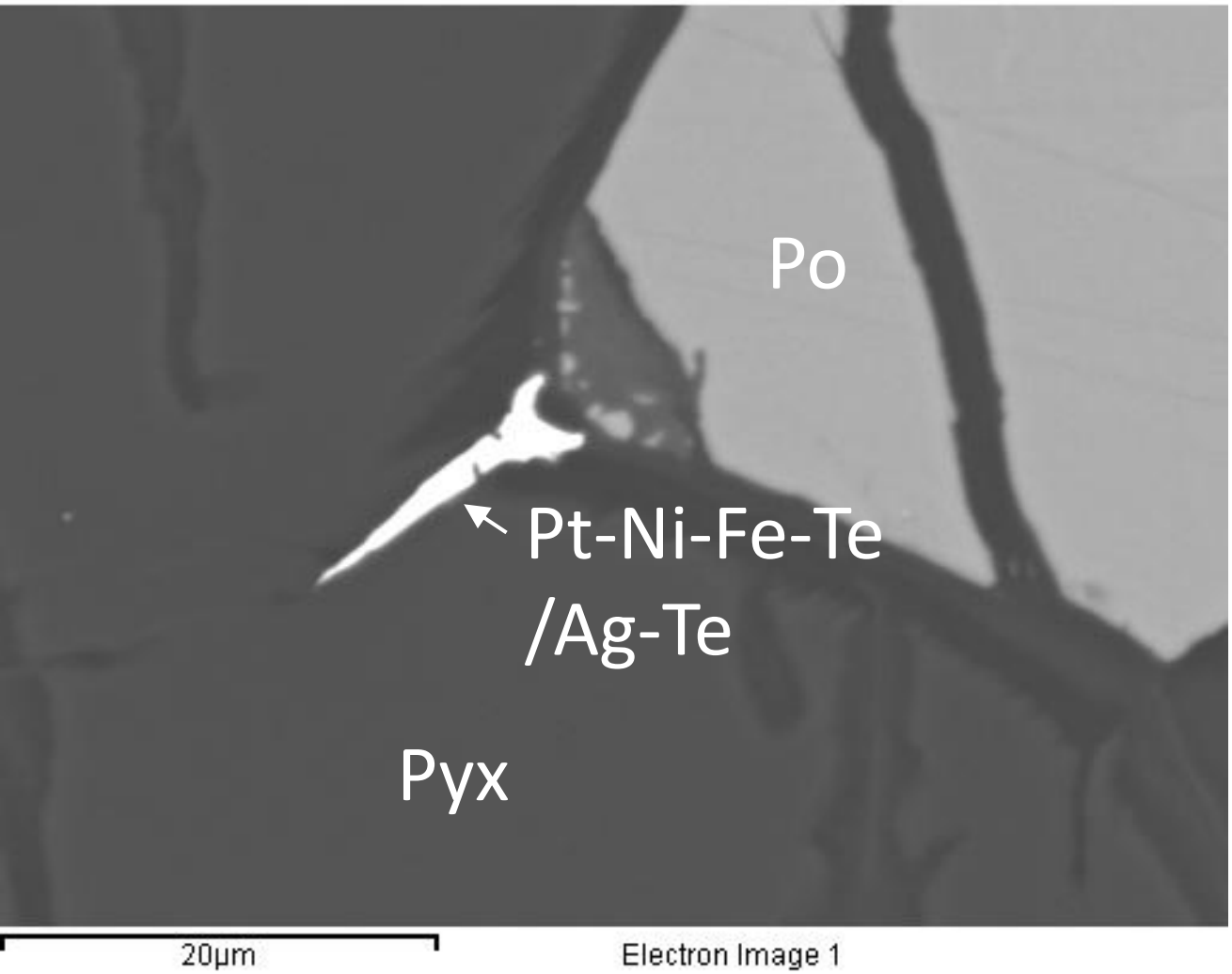
PTSR-65 C 1-2



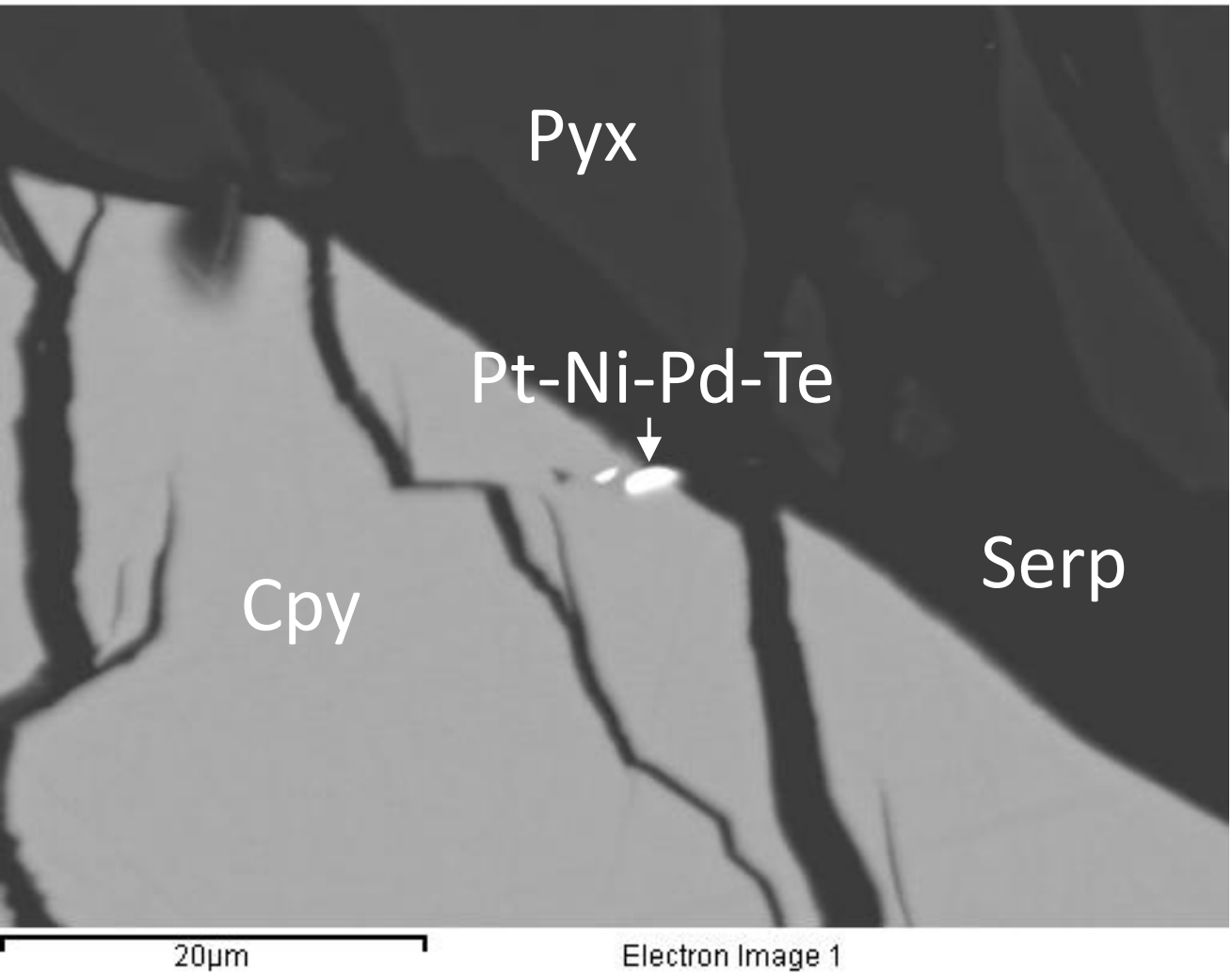
PTSR-65 D 1



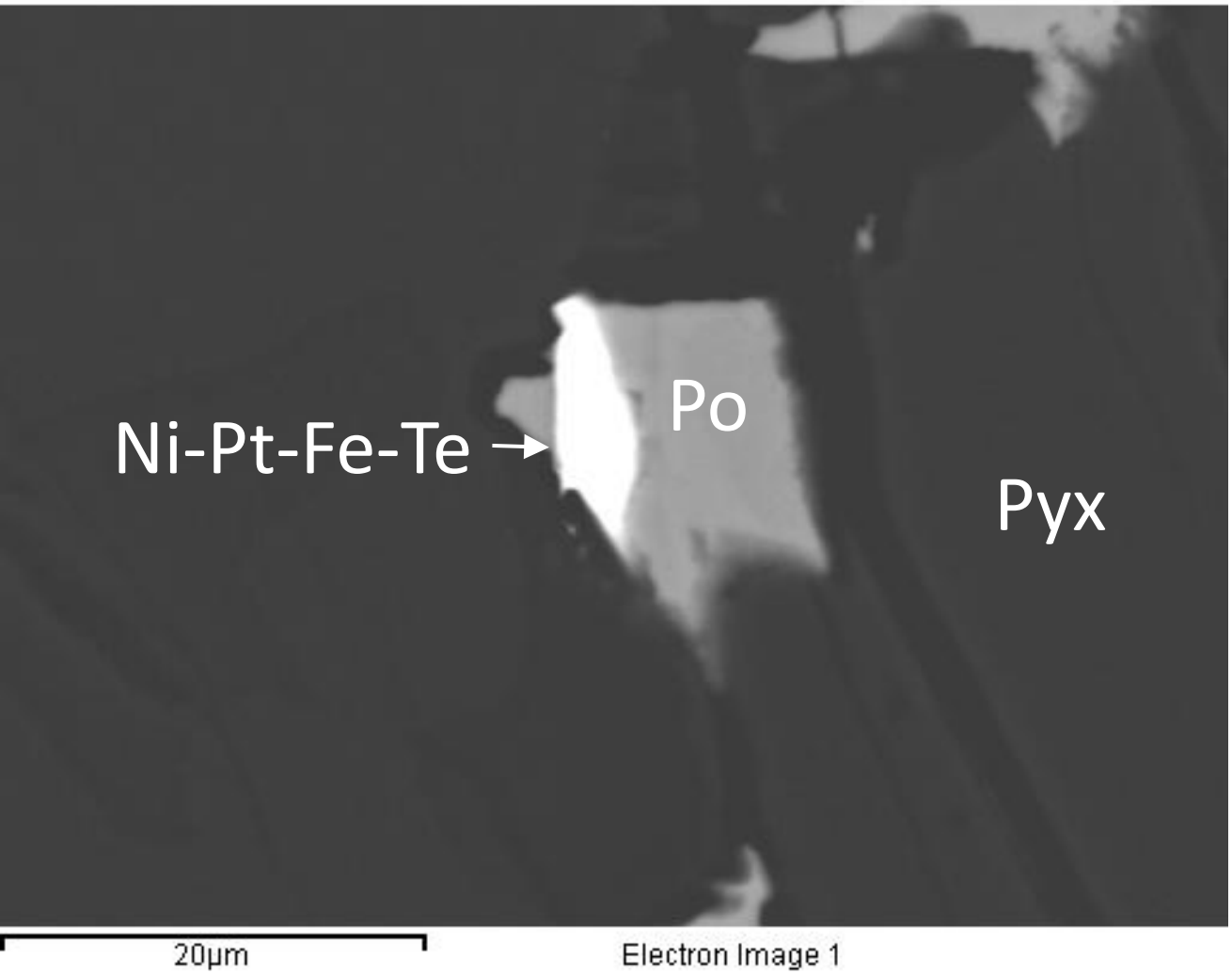
PTSR-65 E 1



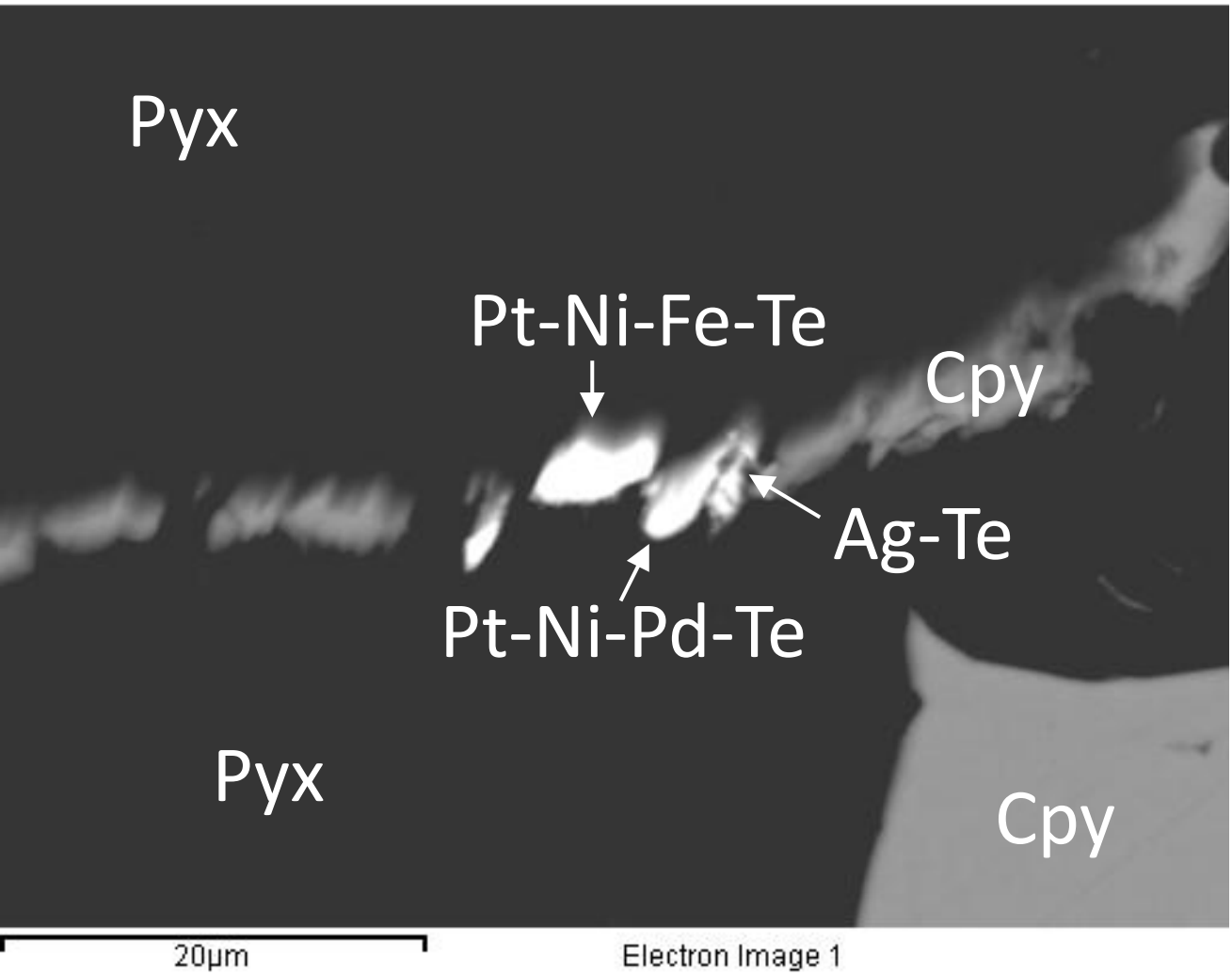
PTSR-65 F 1



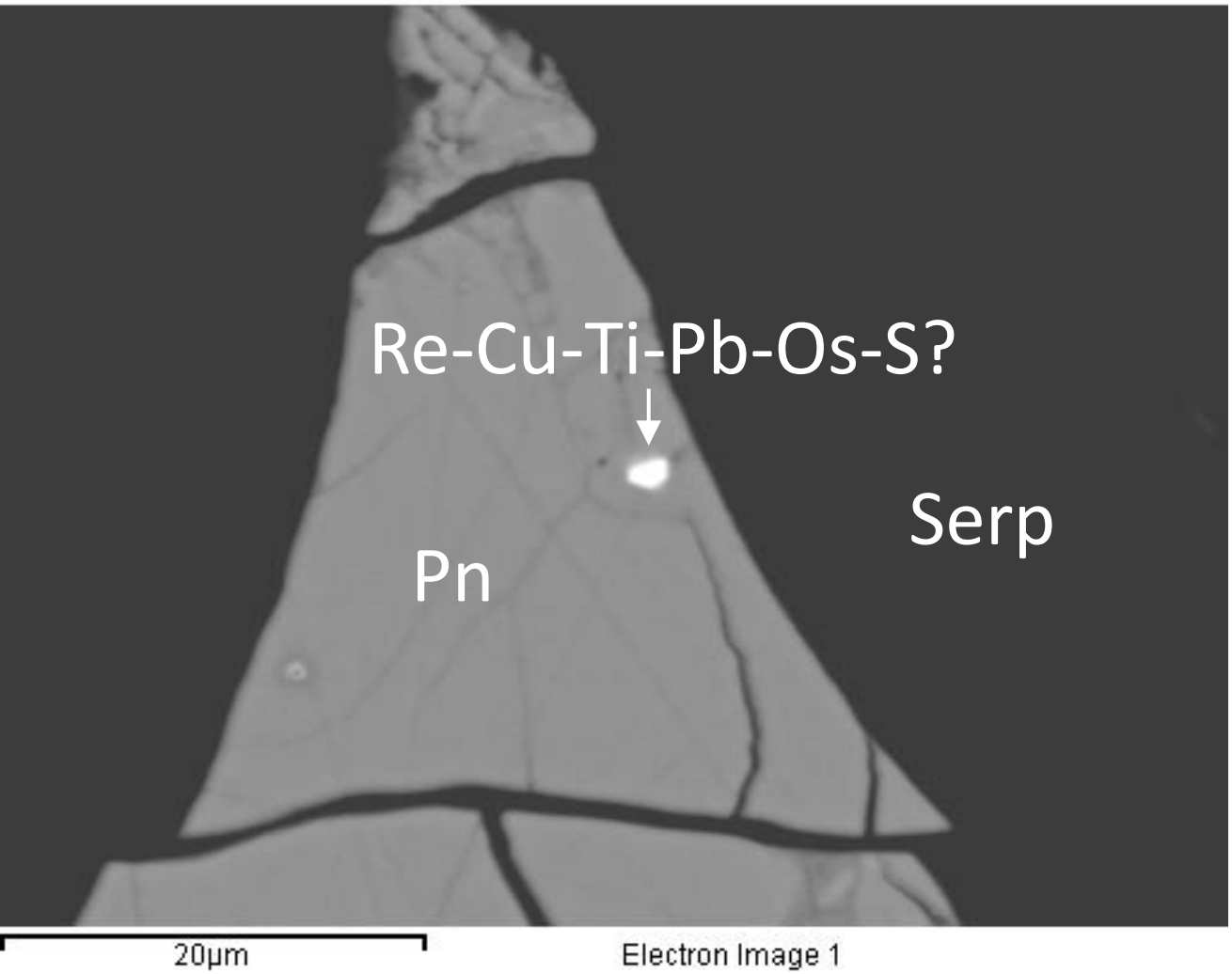
PTSR-65 G 1



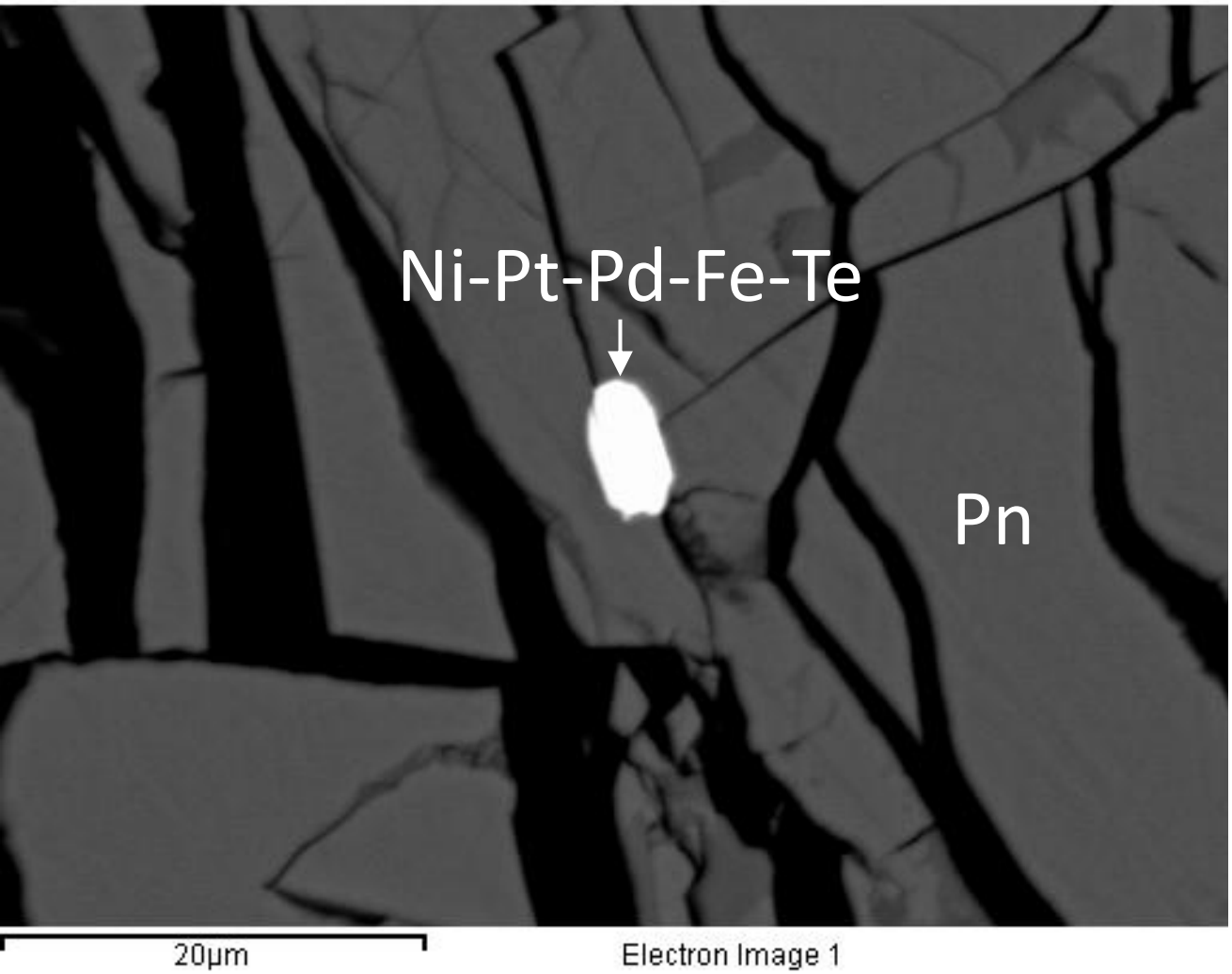
PTSR-65 H 1-2


Pyx
Pt-Ni-Fe-Te
Cpy
Ag-Te
Pt-Ni-Pd-Te
Pyx
Cpy
20µm
Electron Image 1

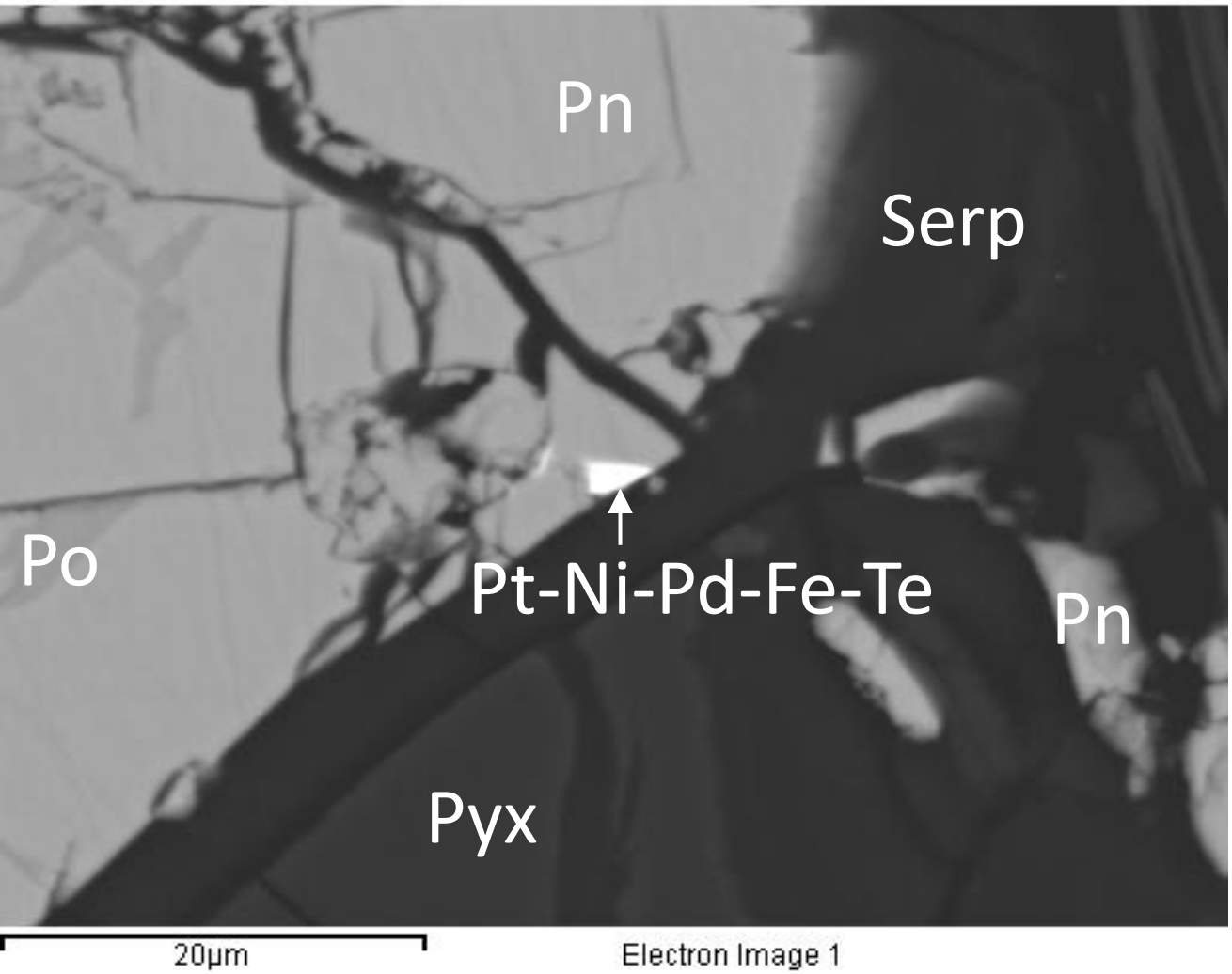
PTSR-65 I 1



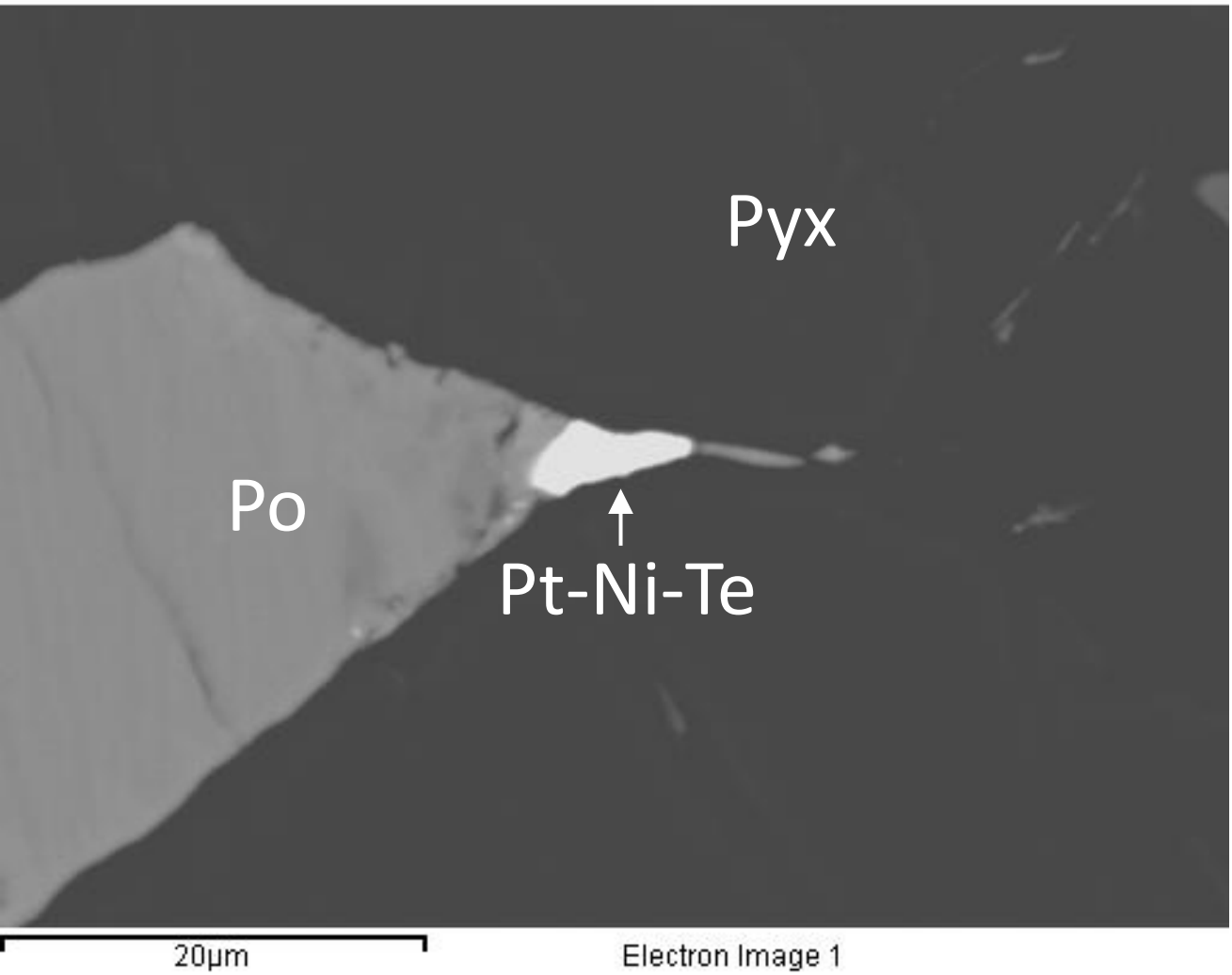
PTSR-65 J 1



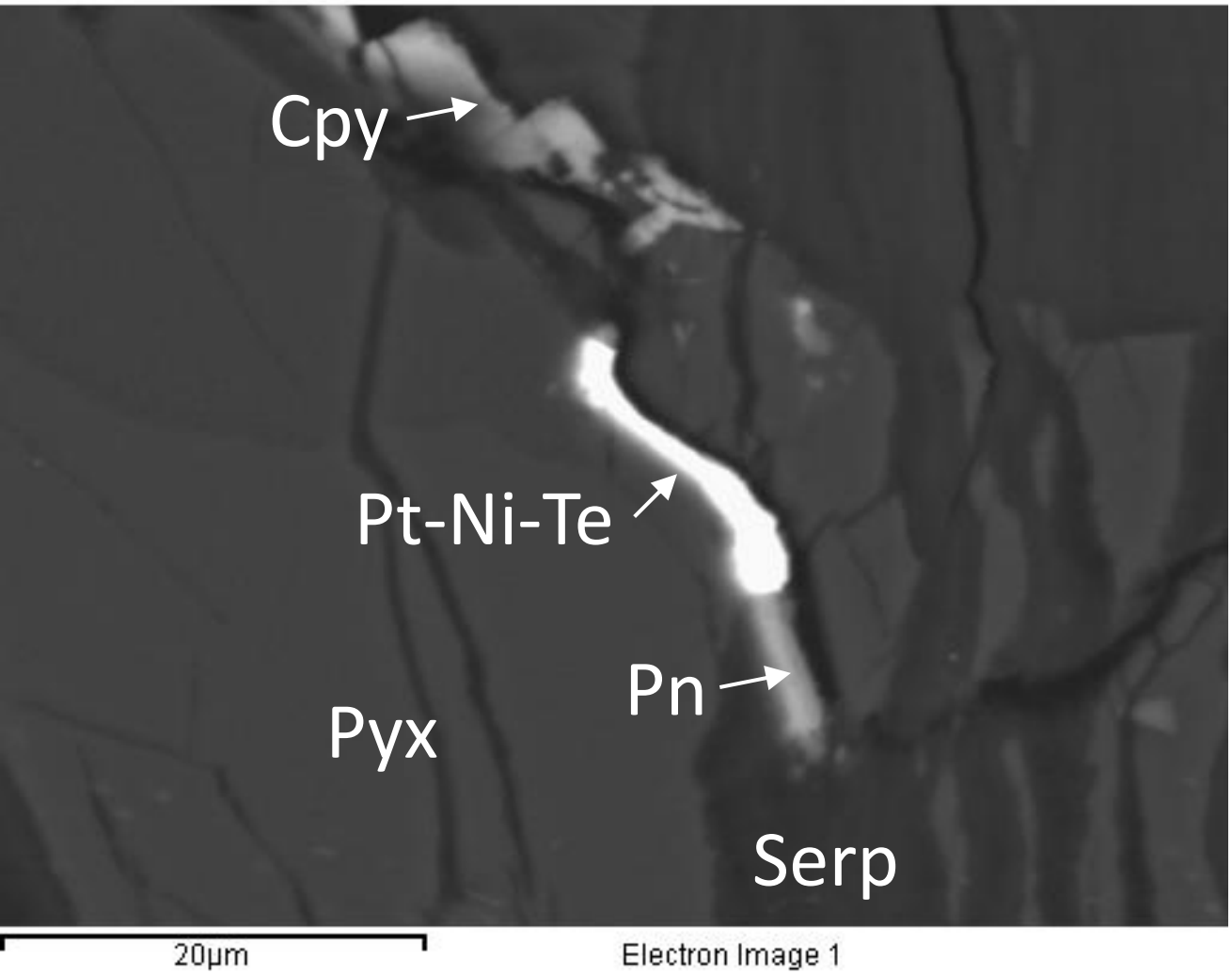
PTSR-65 K 1



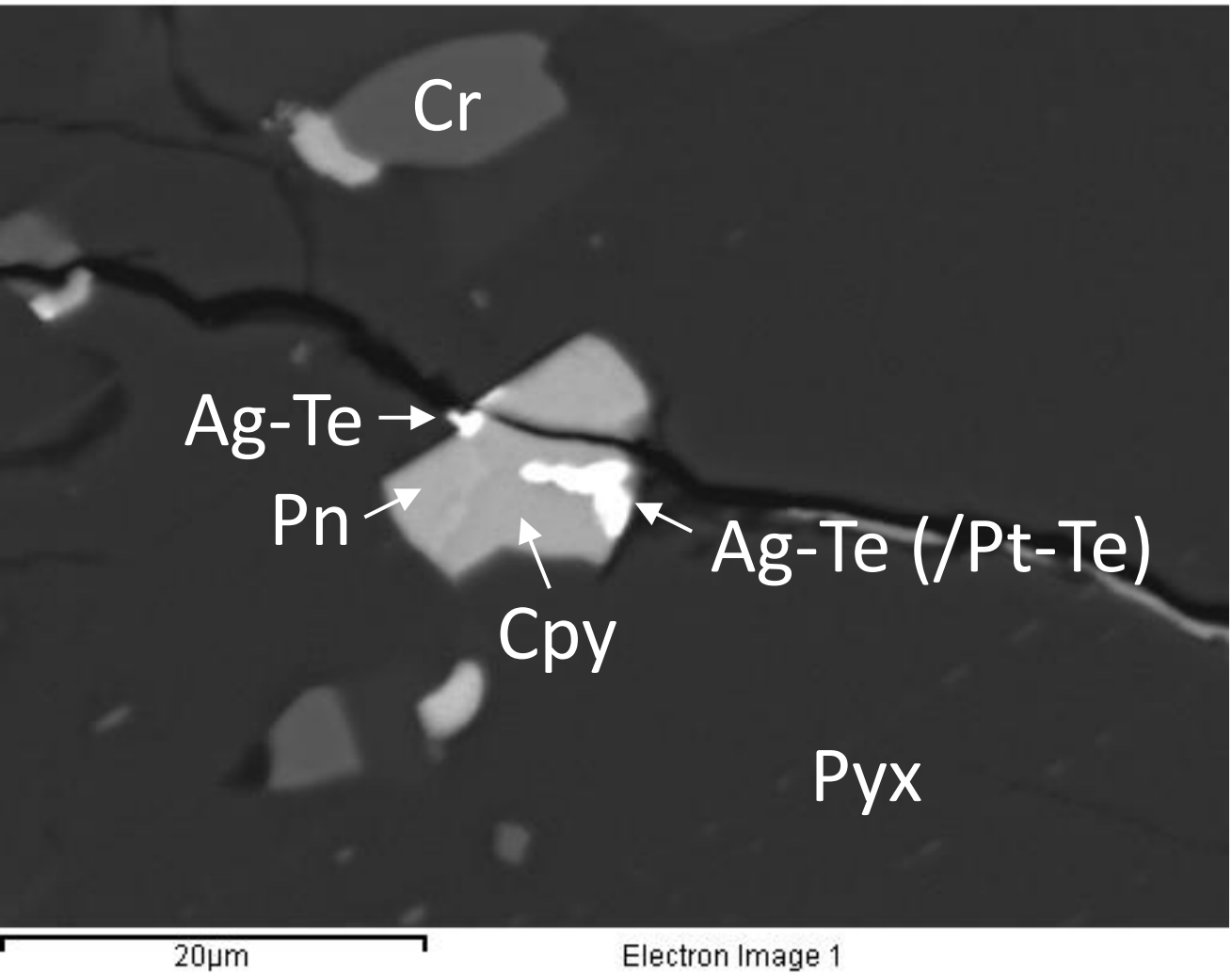
PTSR-65 L 1



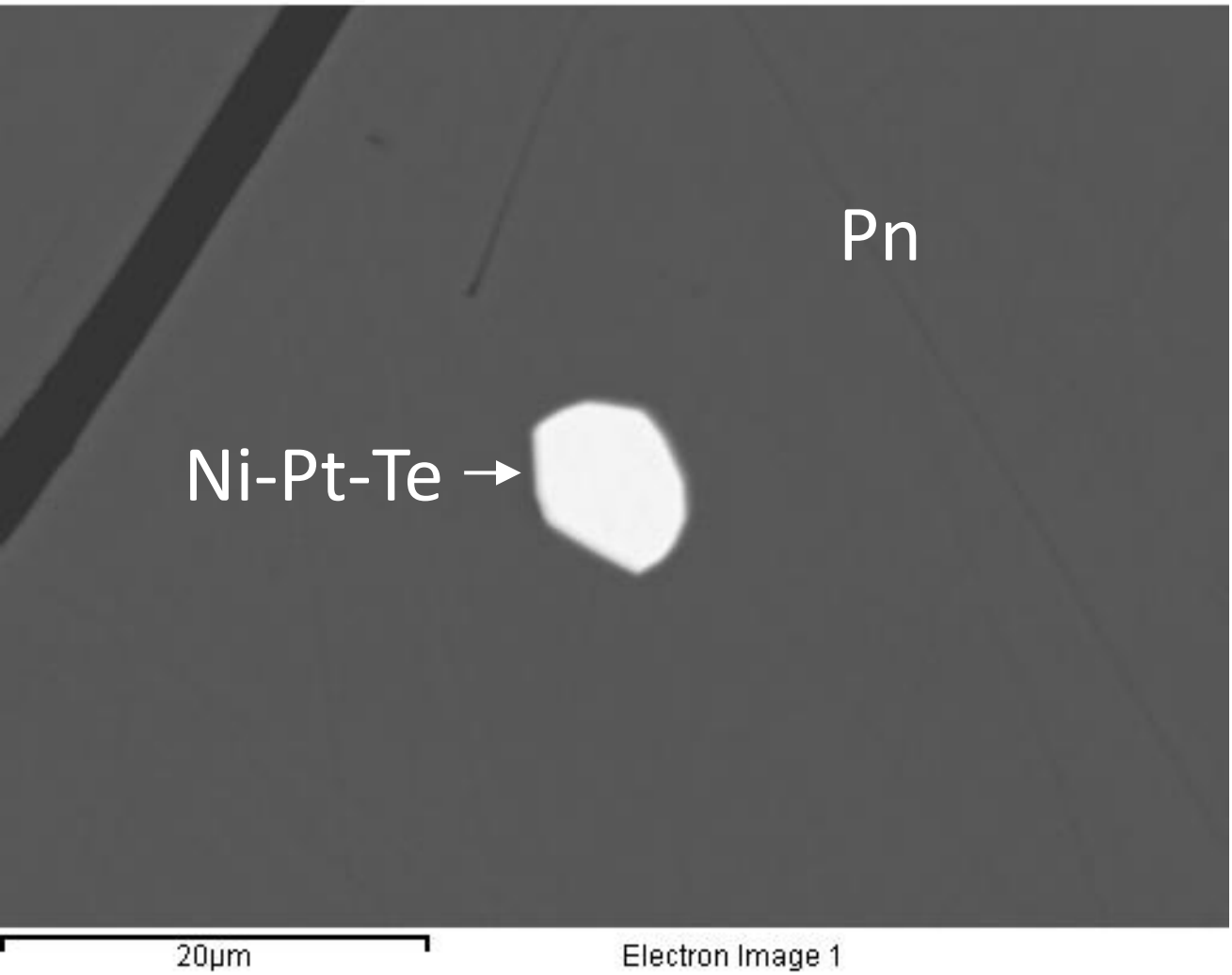
PTSR-65 M 1



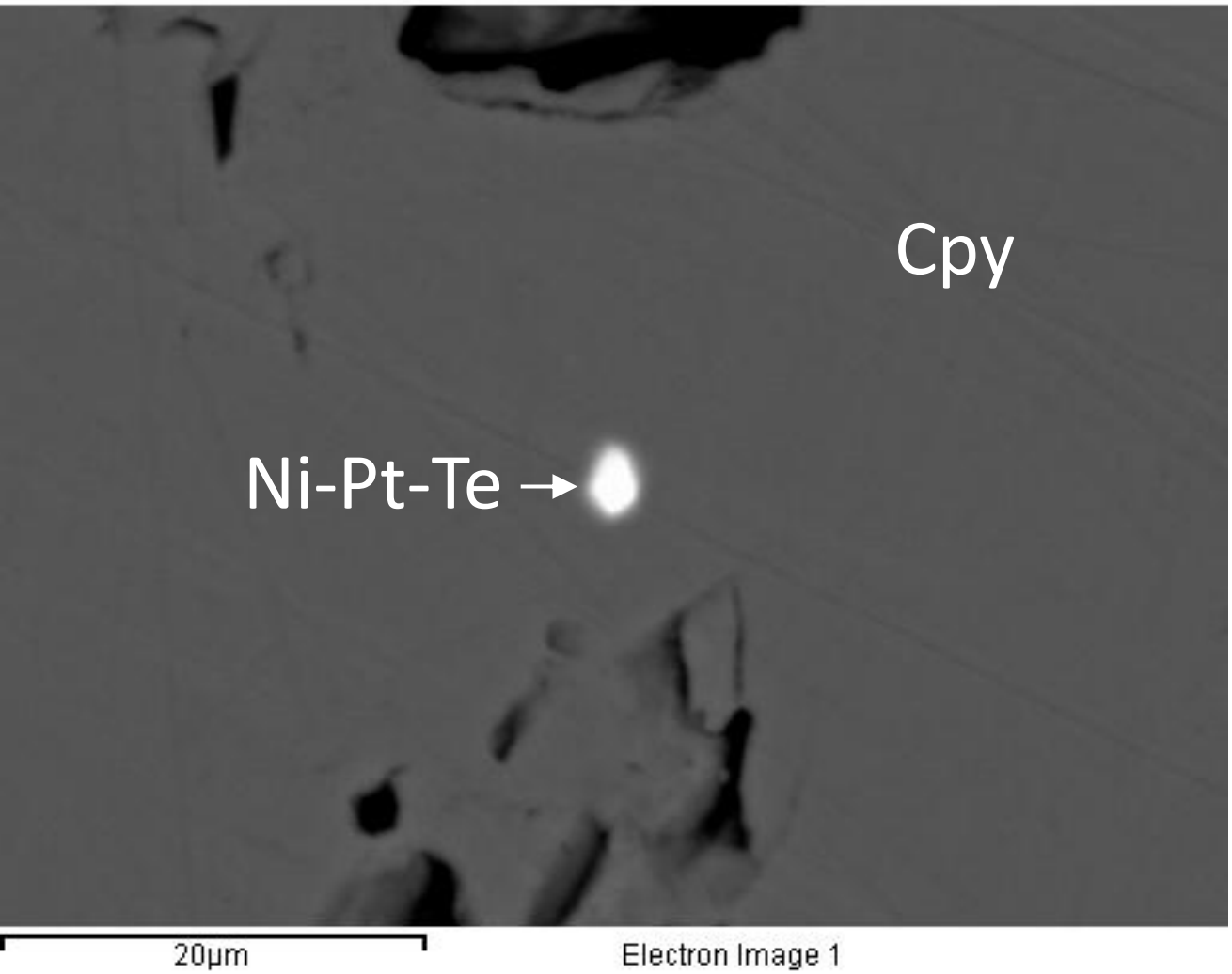
PTSR-66 A 1-2



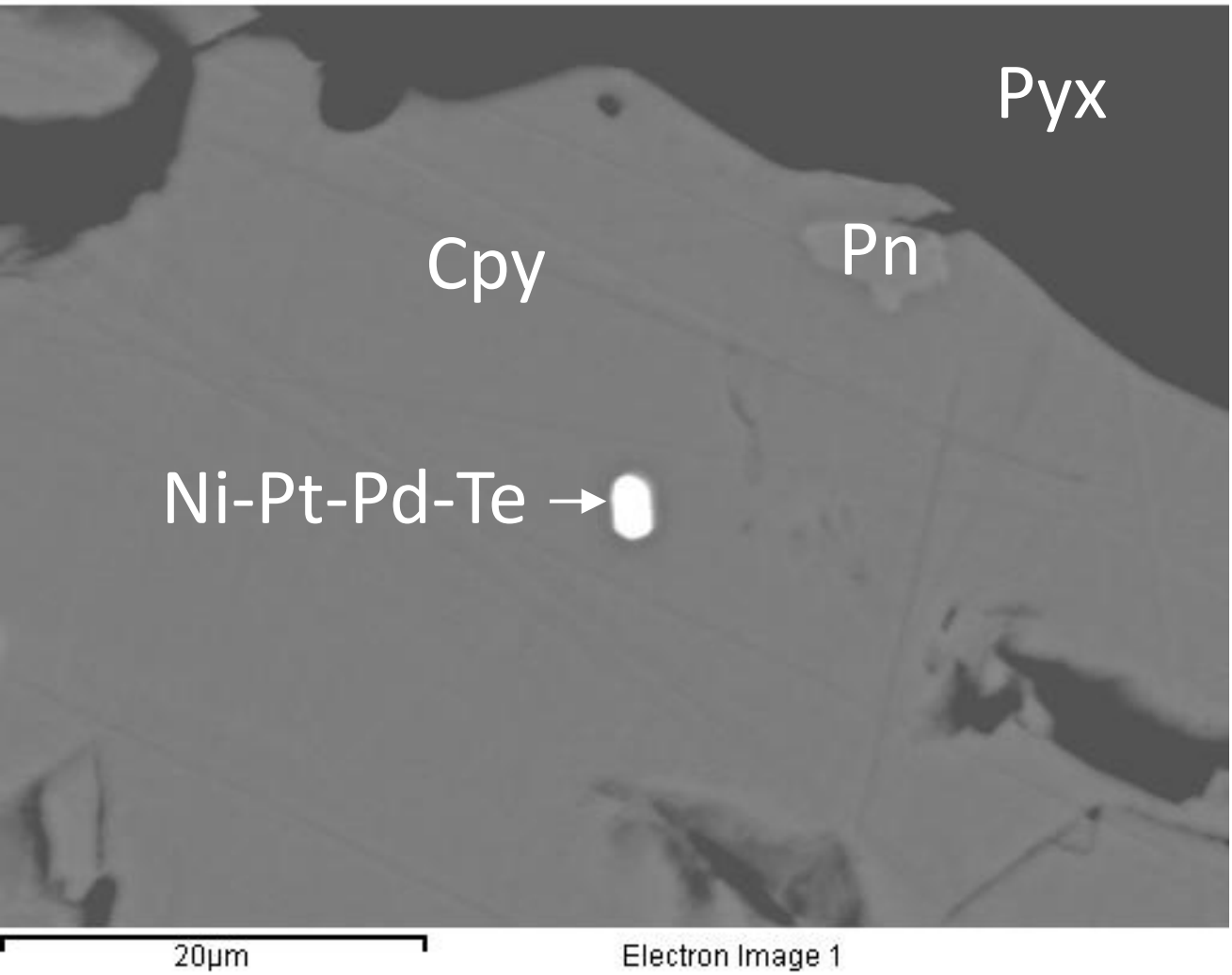
PTSR-66 B 1



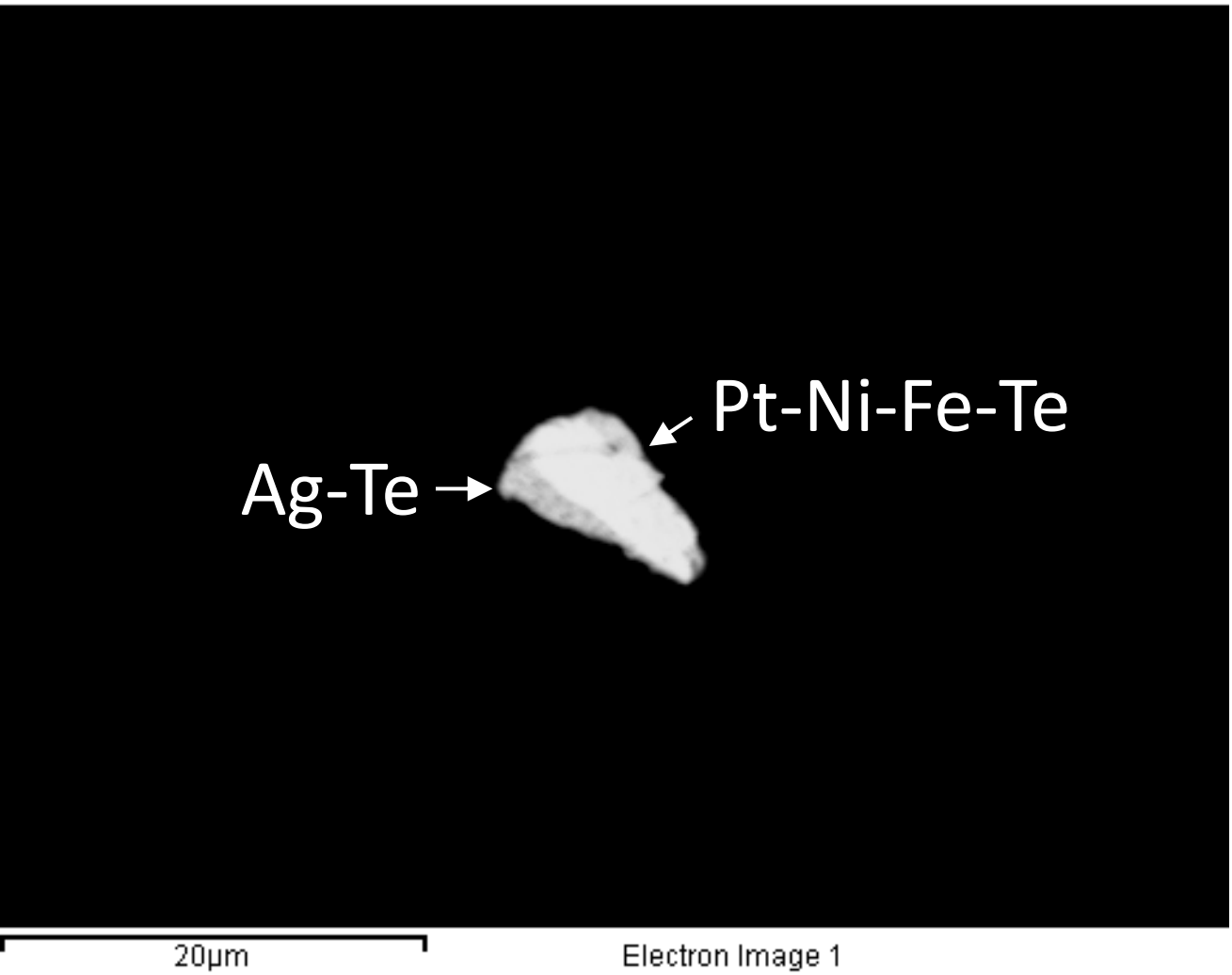
PTSR-66 C 1



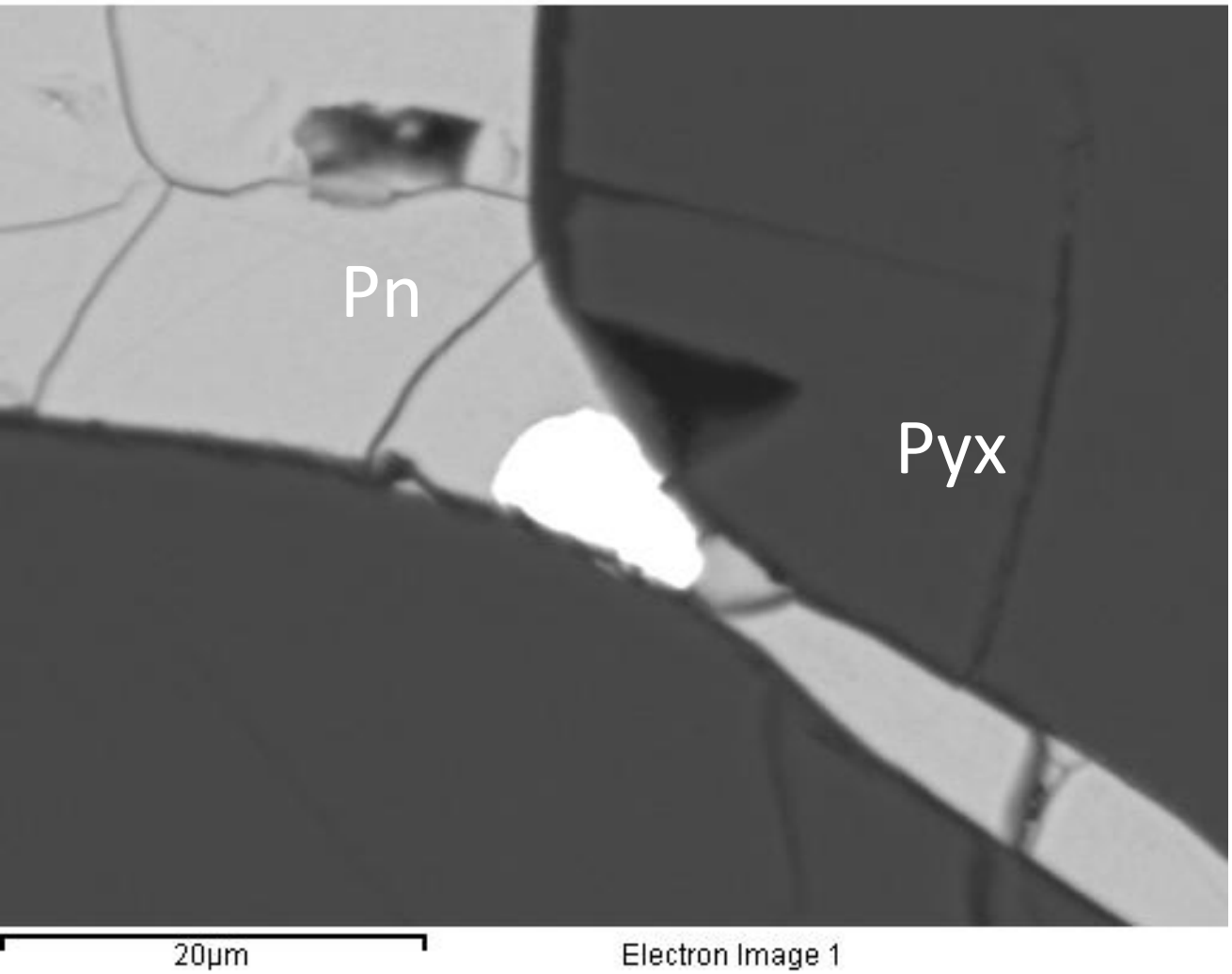
PTSR-66 C 2



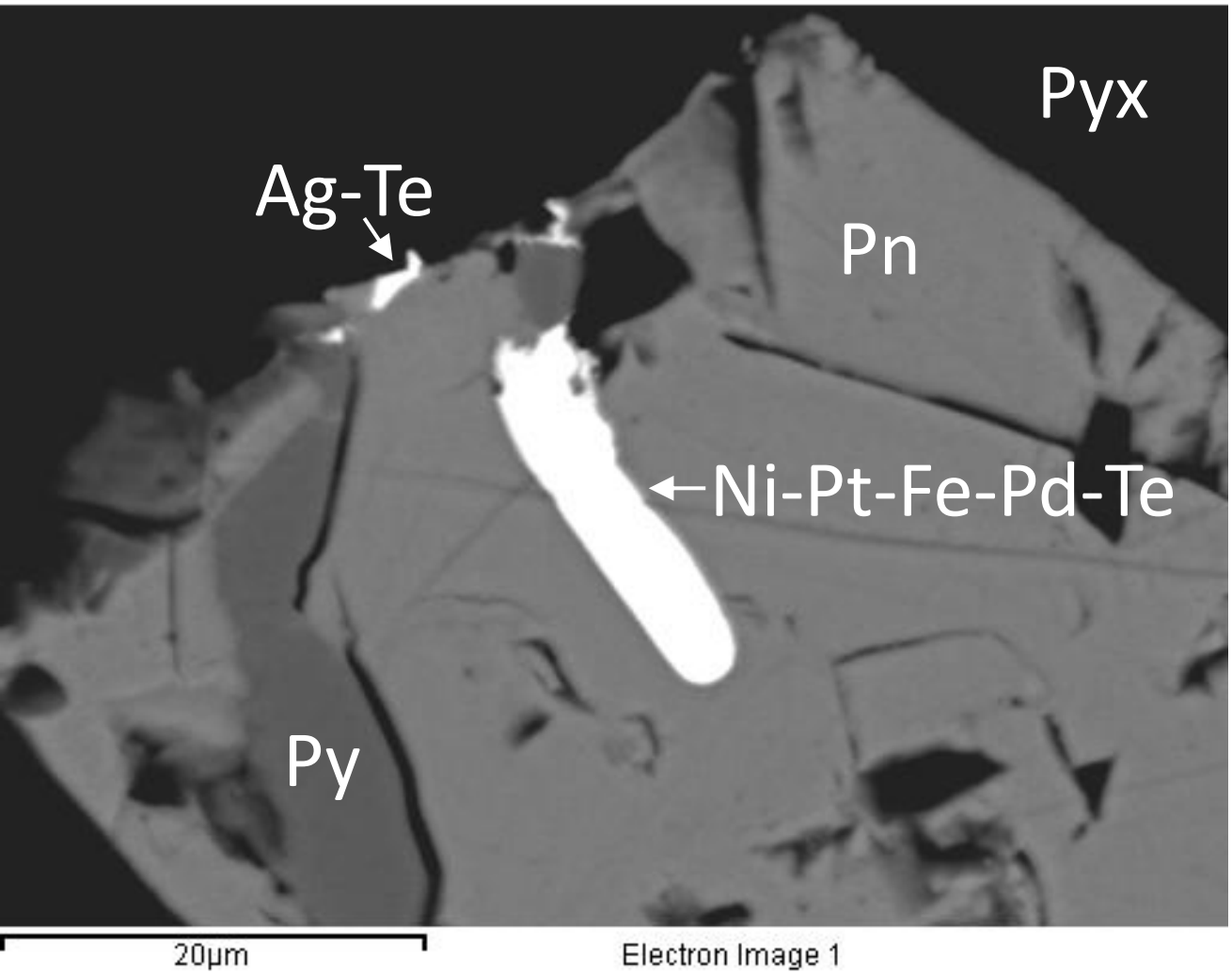
PTSR-66 D 1



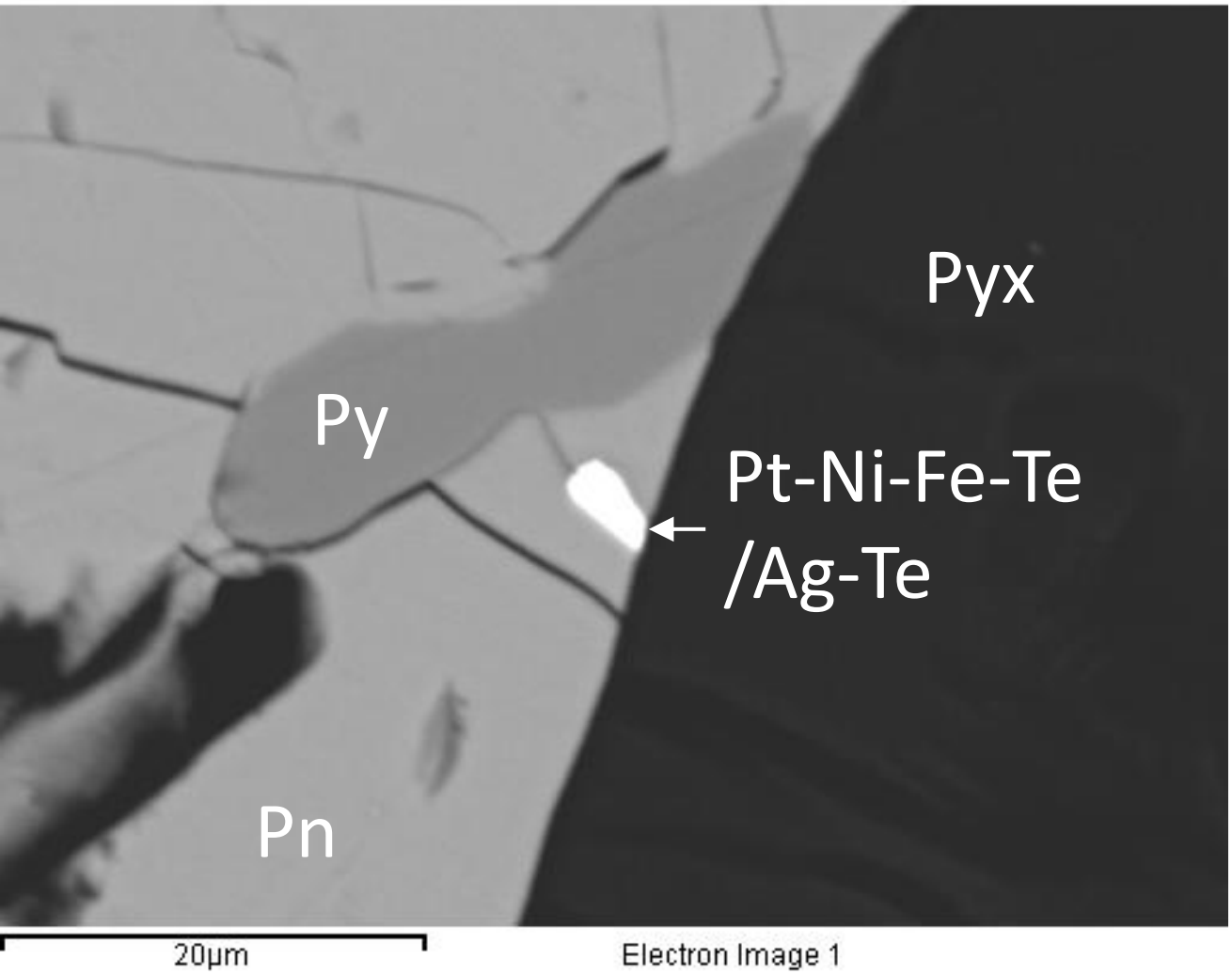
PTSR-66 D 1 Light



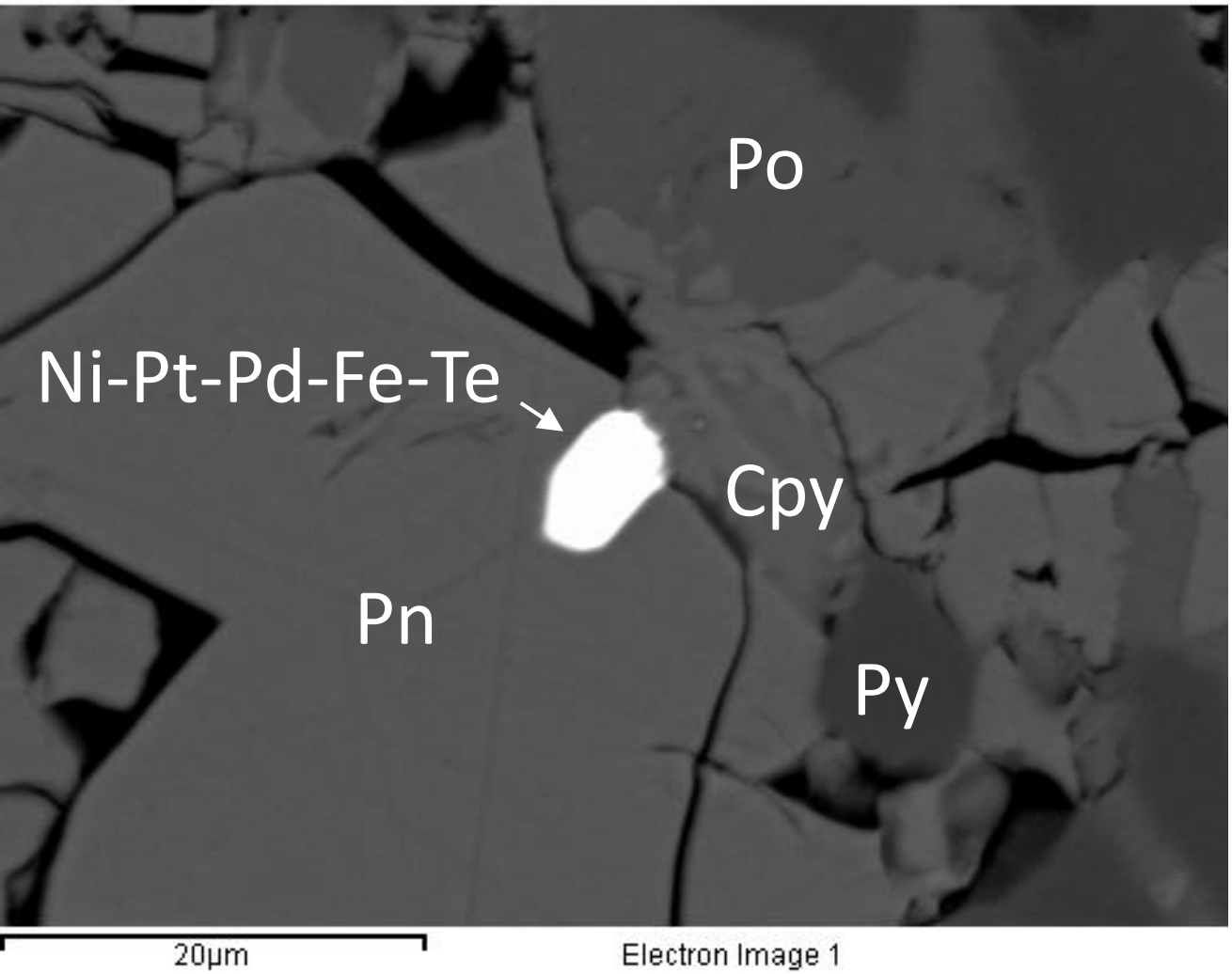
PTSR-66 E 1-2



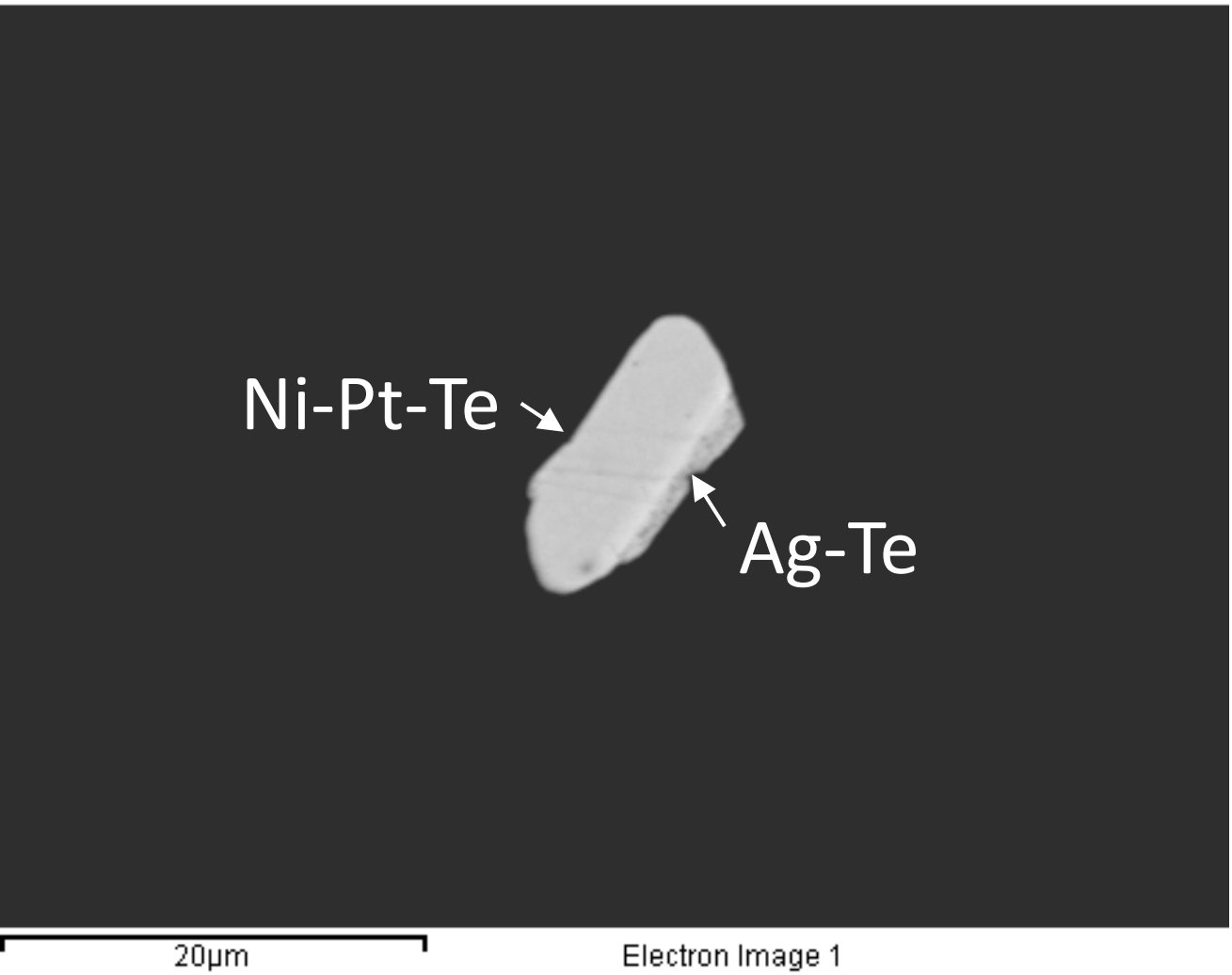
PTSR-66 F 1



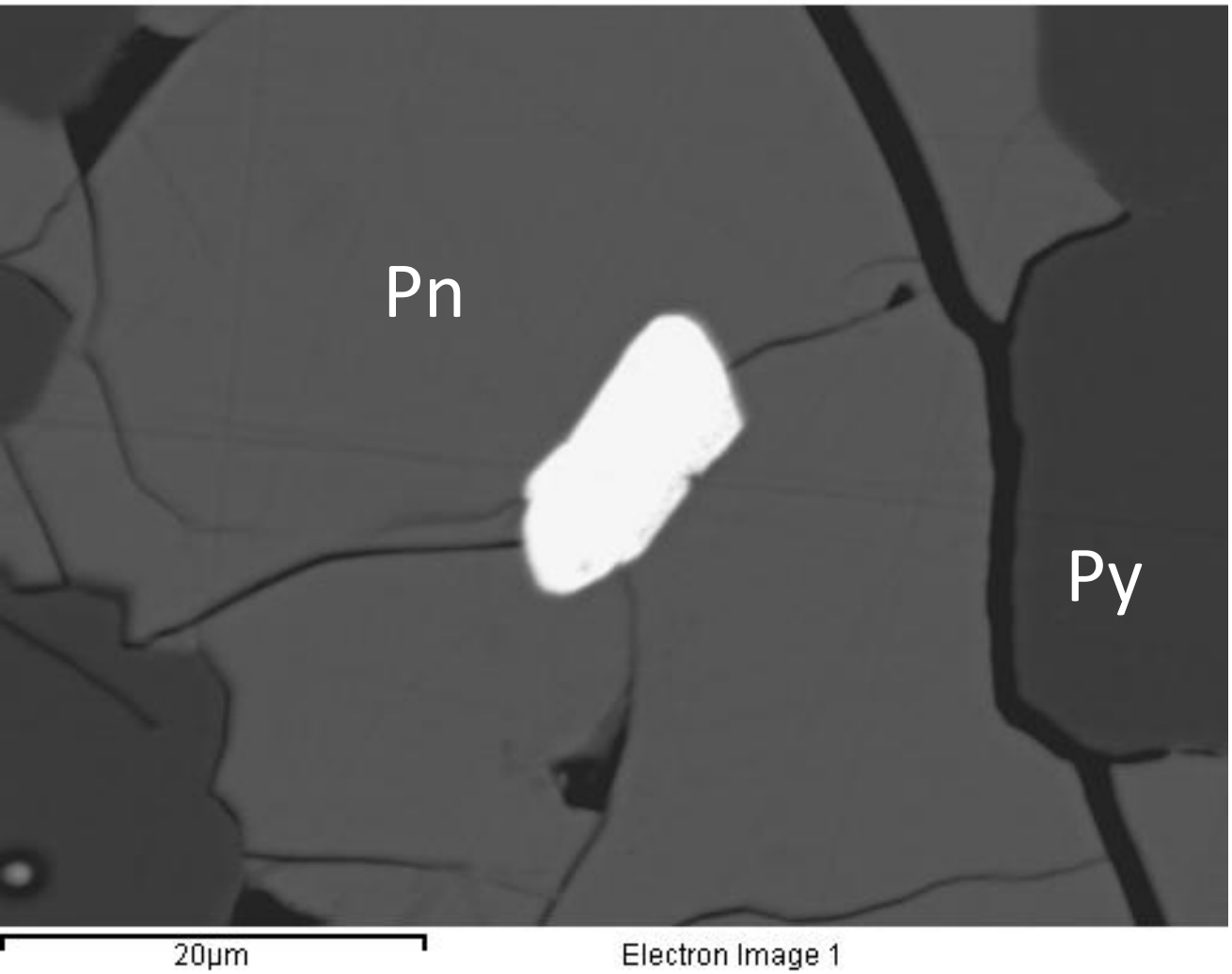
PTSR-66 G 1



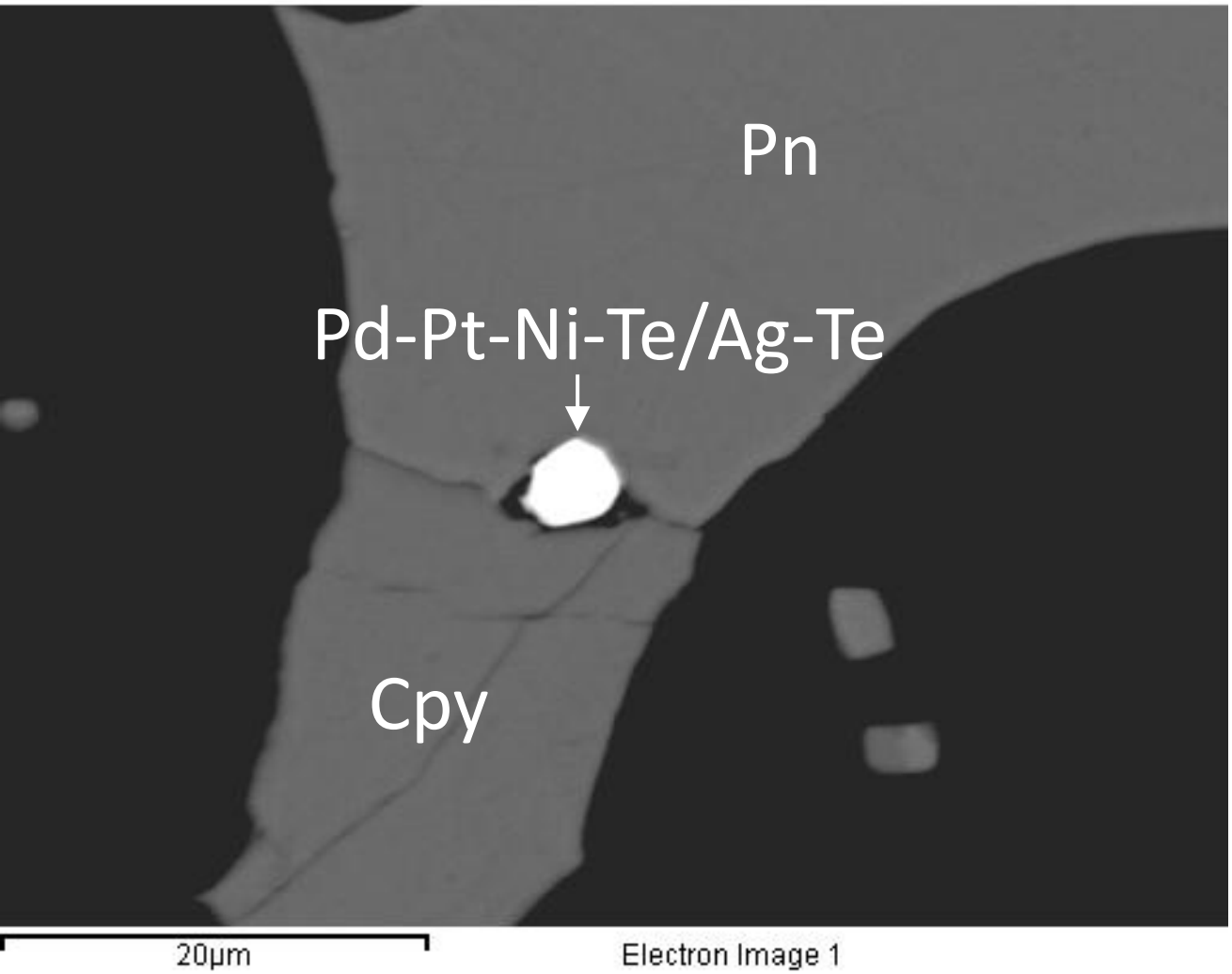
PTSR-66 H 1



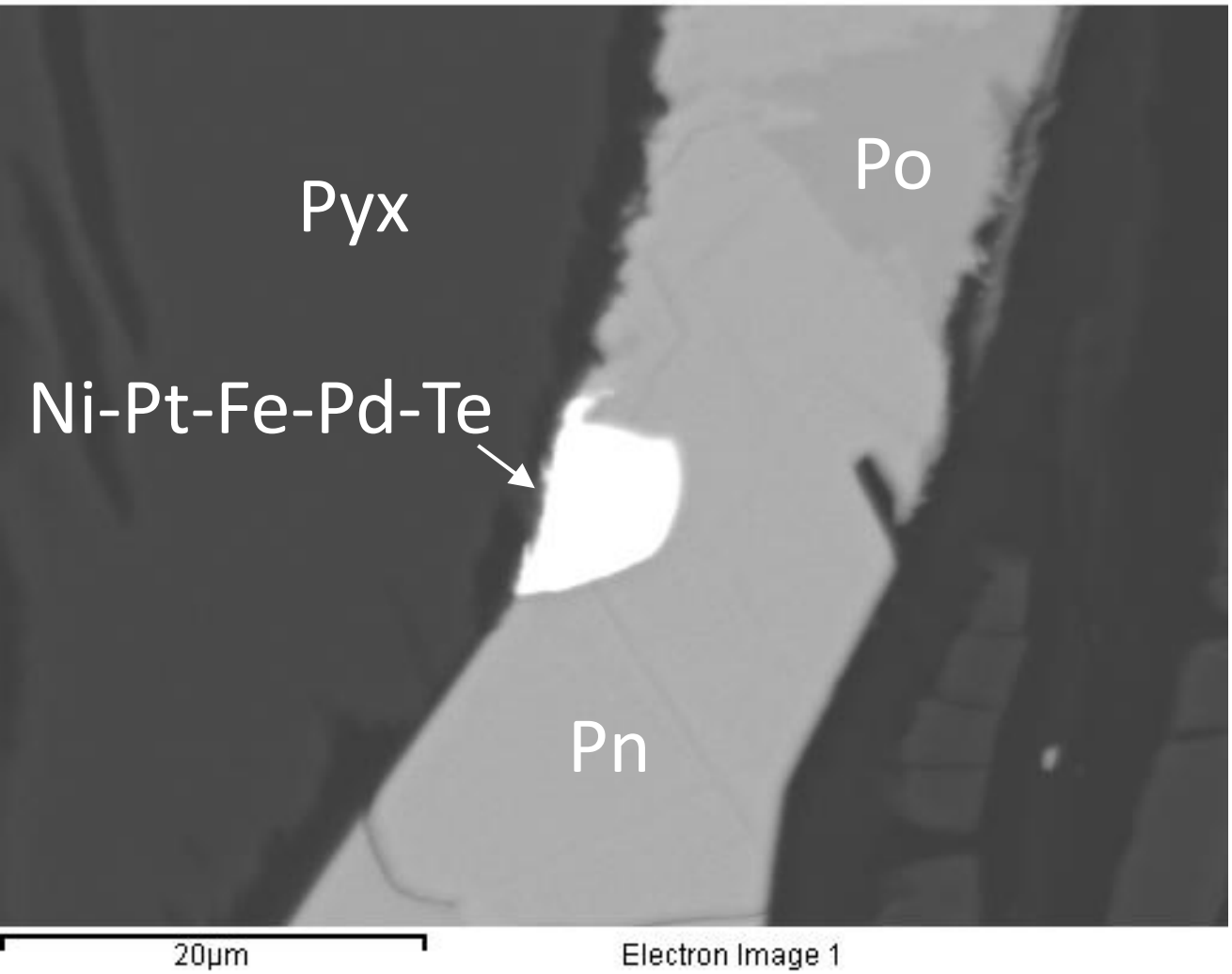
PTSR-66 H 1 Light



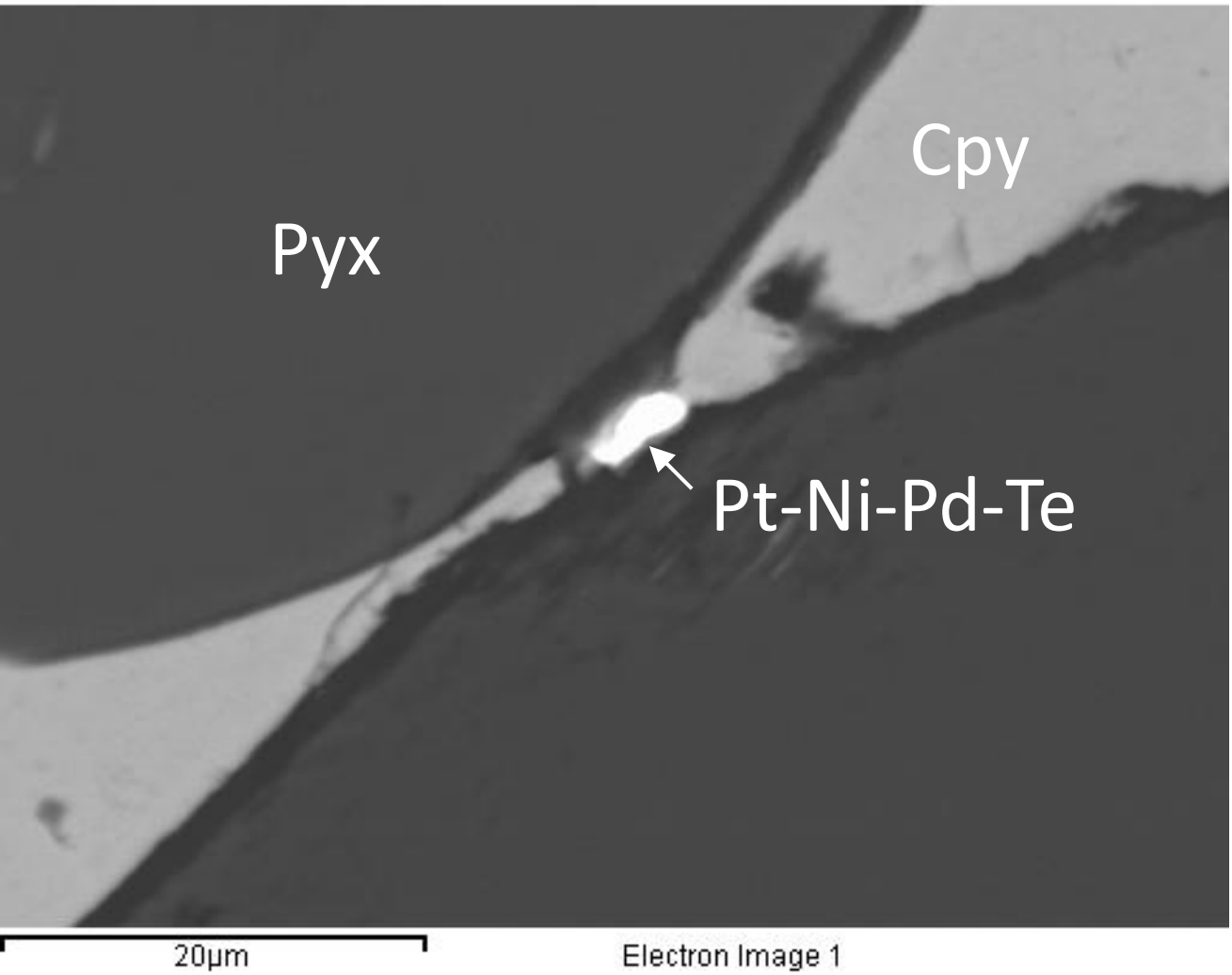
PTSR-66 I 1



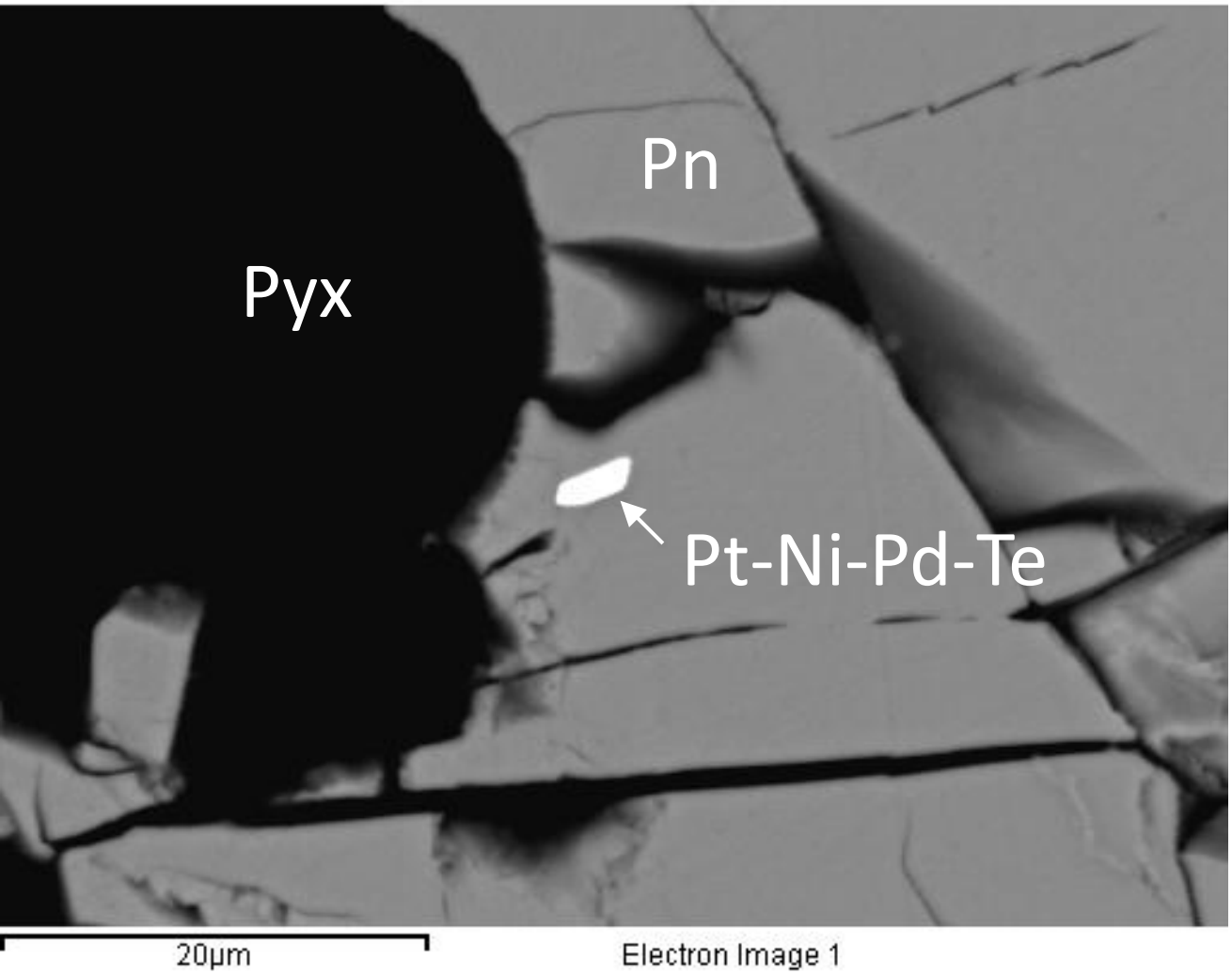
PTSR-66 J 1



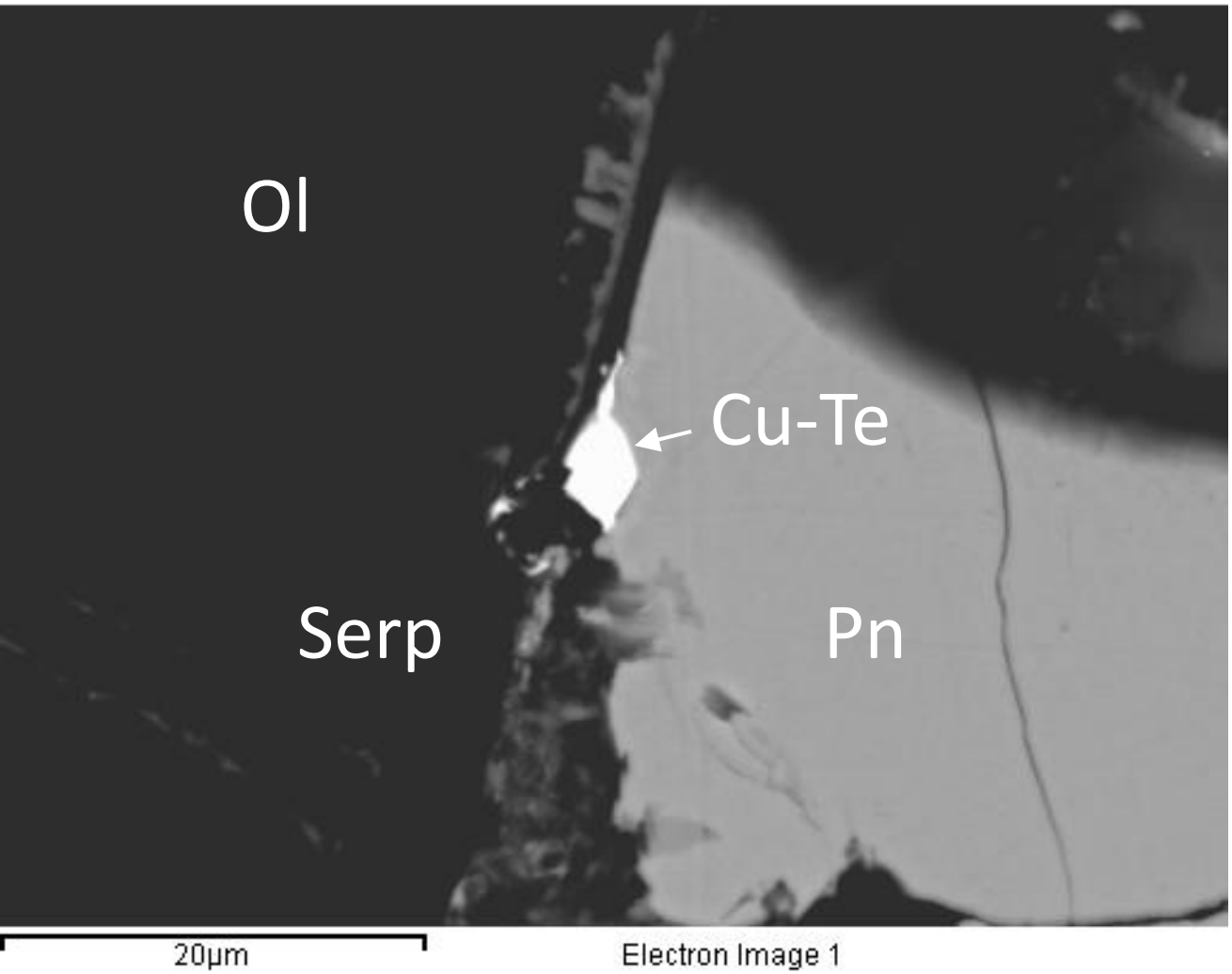
PTSR-66 K 1



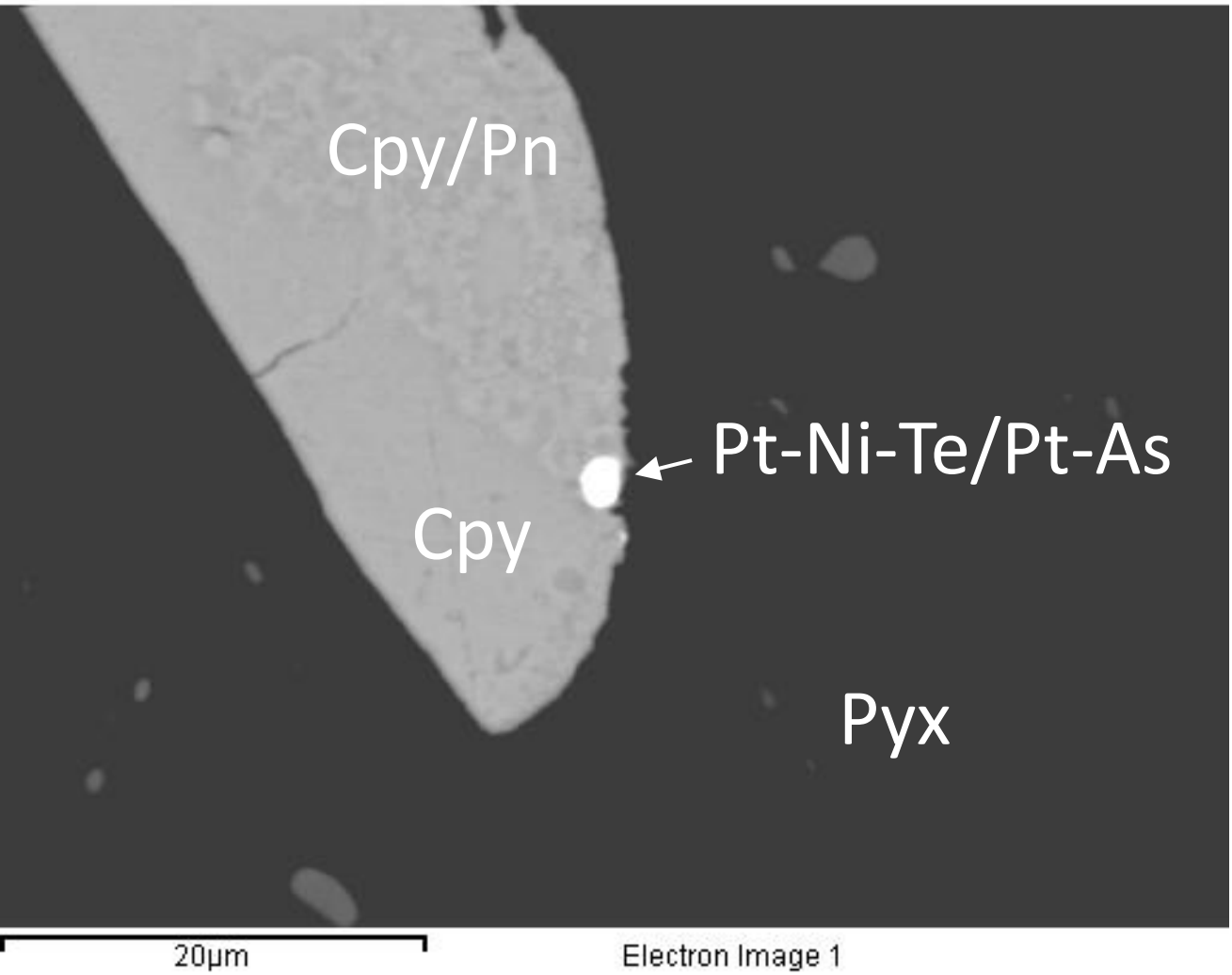
PTSR-67 A 1



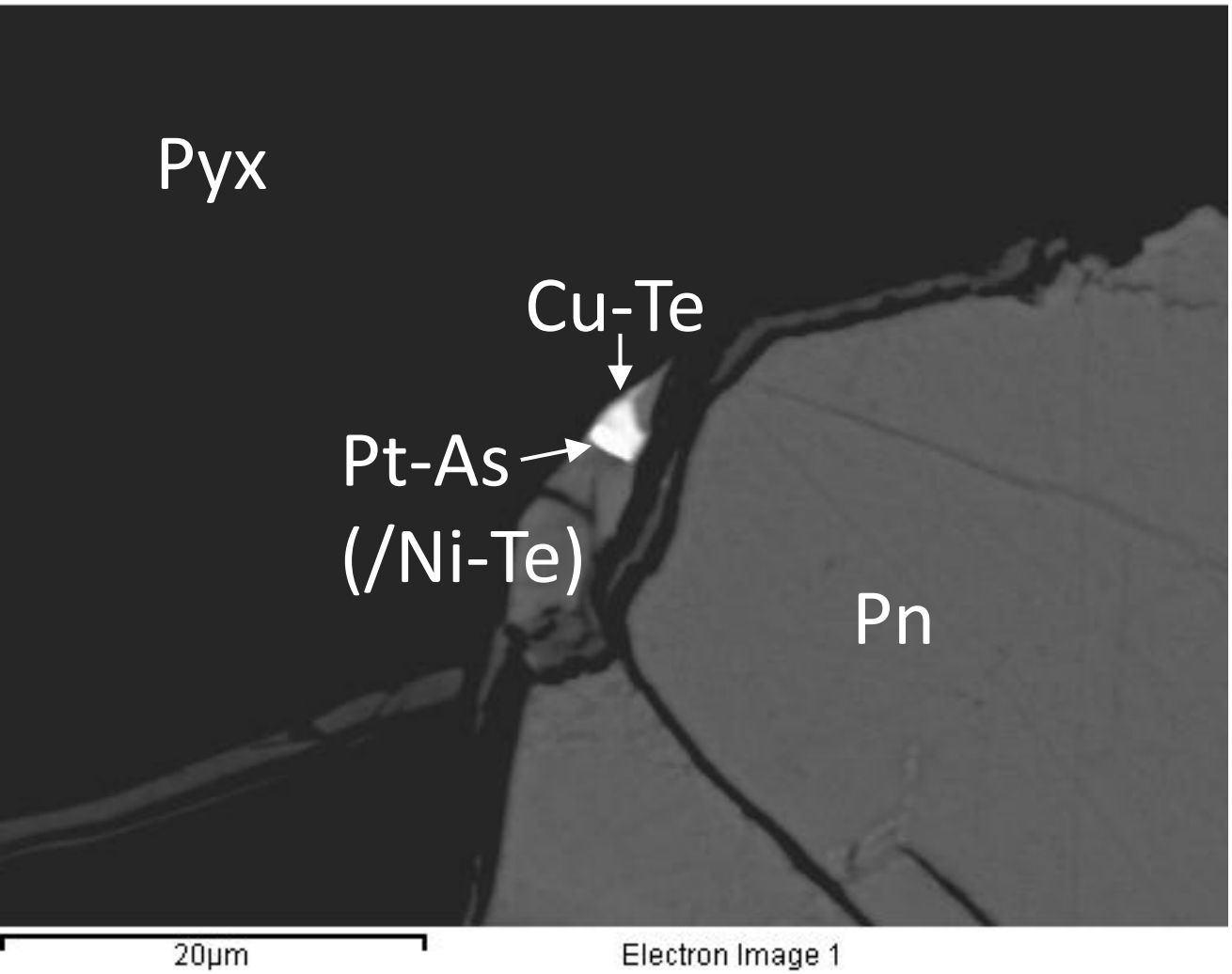
PTSR-67 B 1



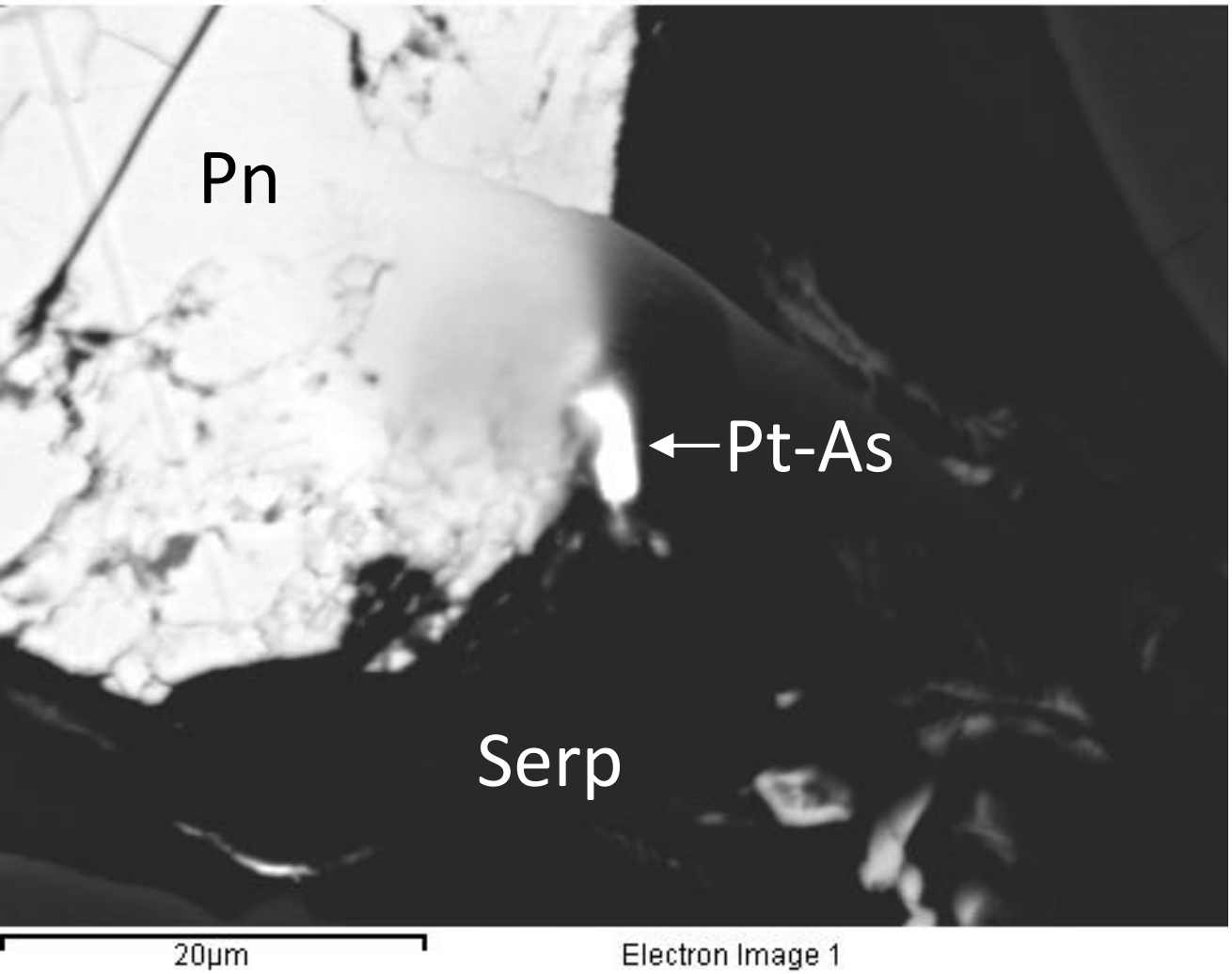
PTSR-68 A 1



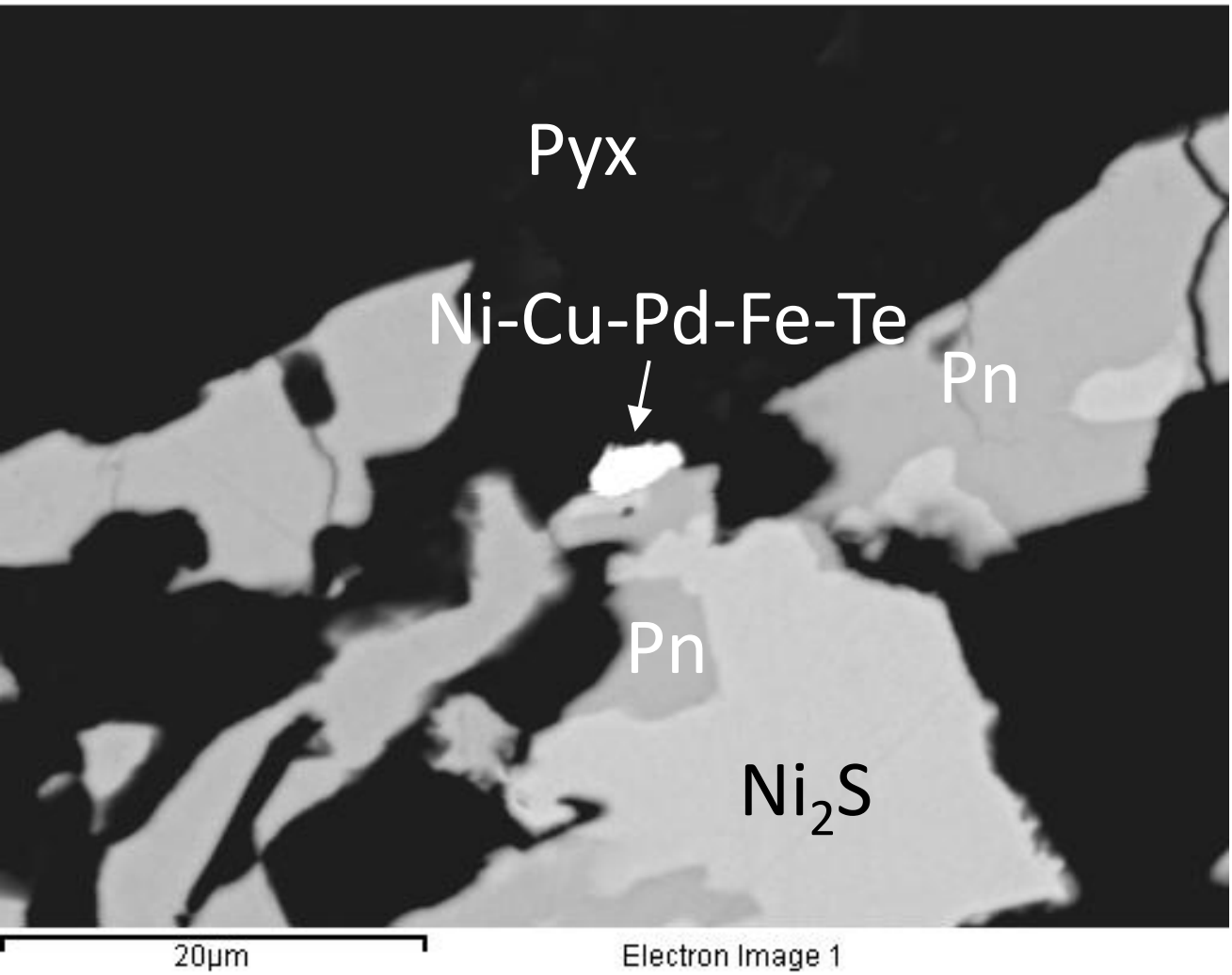
PTSR-68 B 1-2



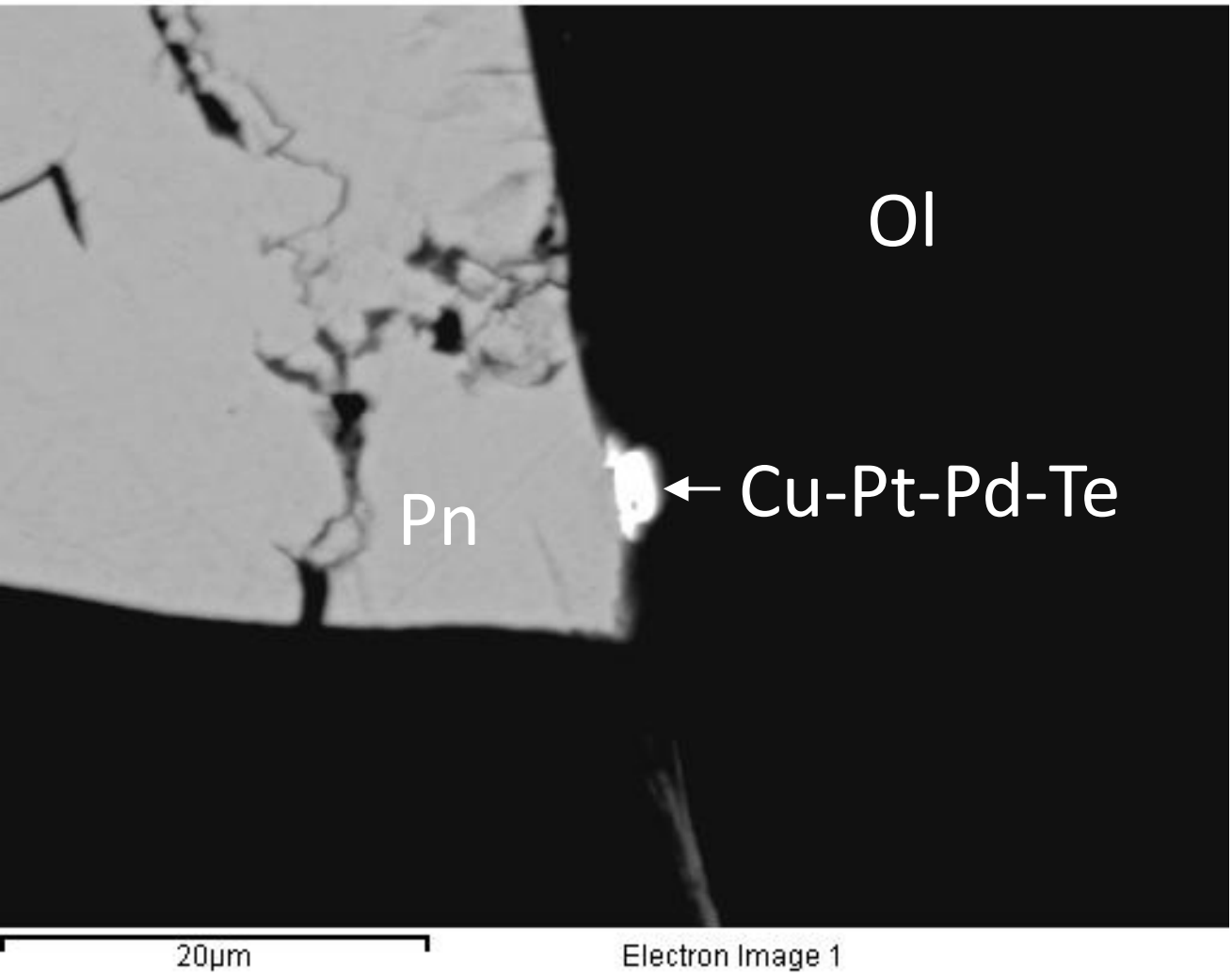
PTSR-68 C 1



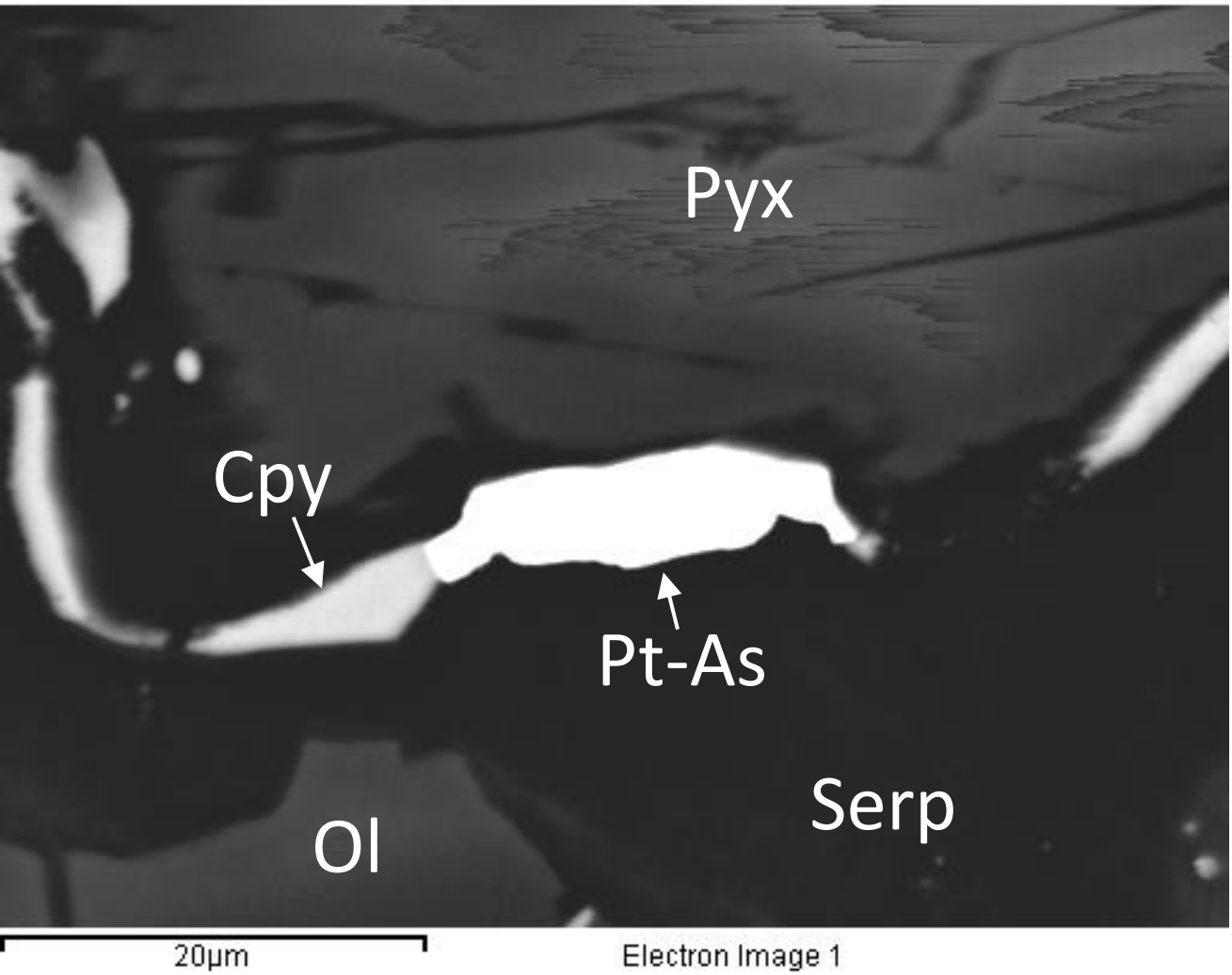
PTSR-68 D 1



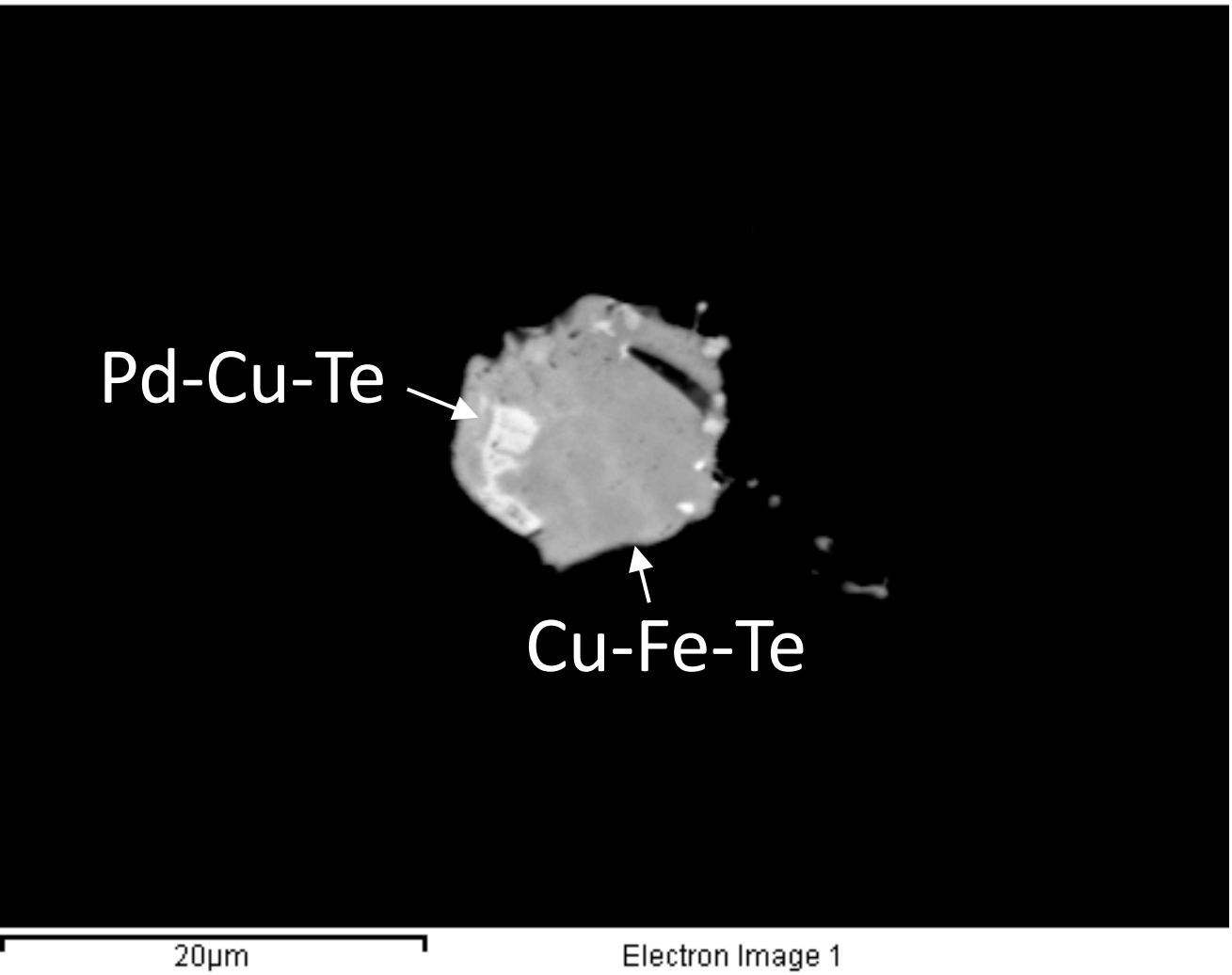
PTSR-68 E 1



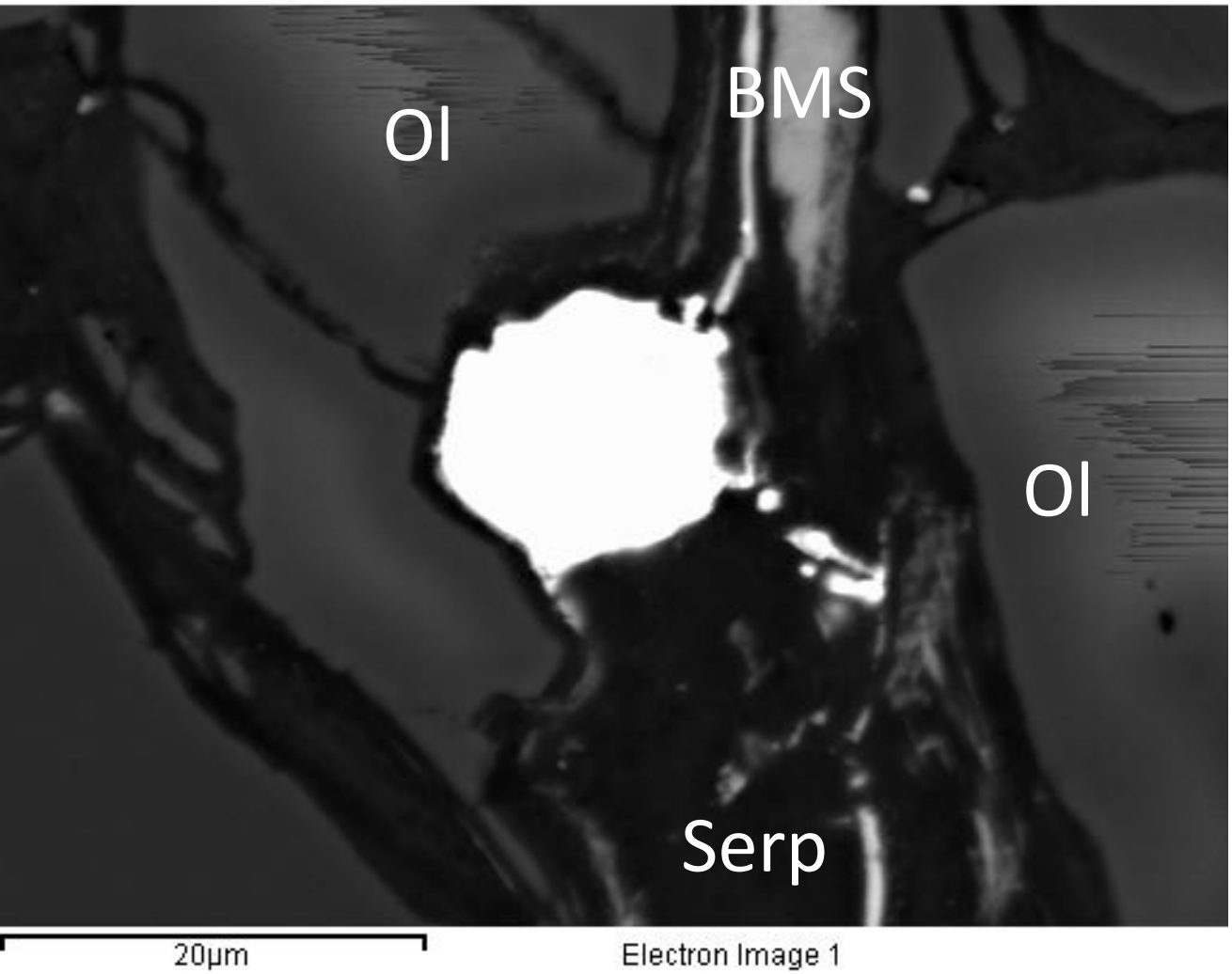
PTSR-68 F 1



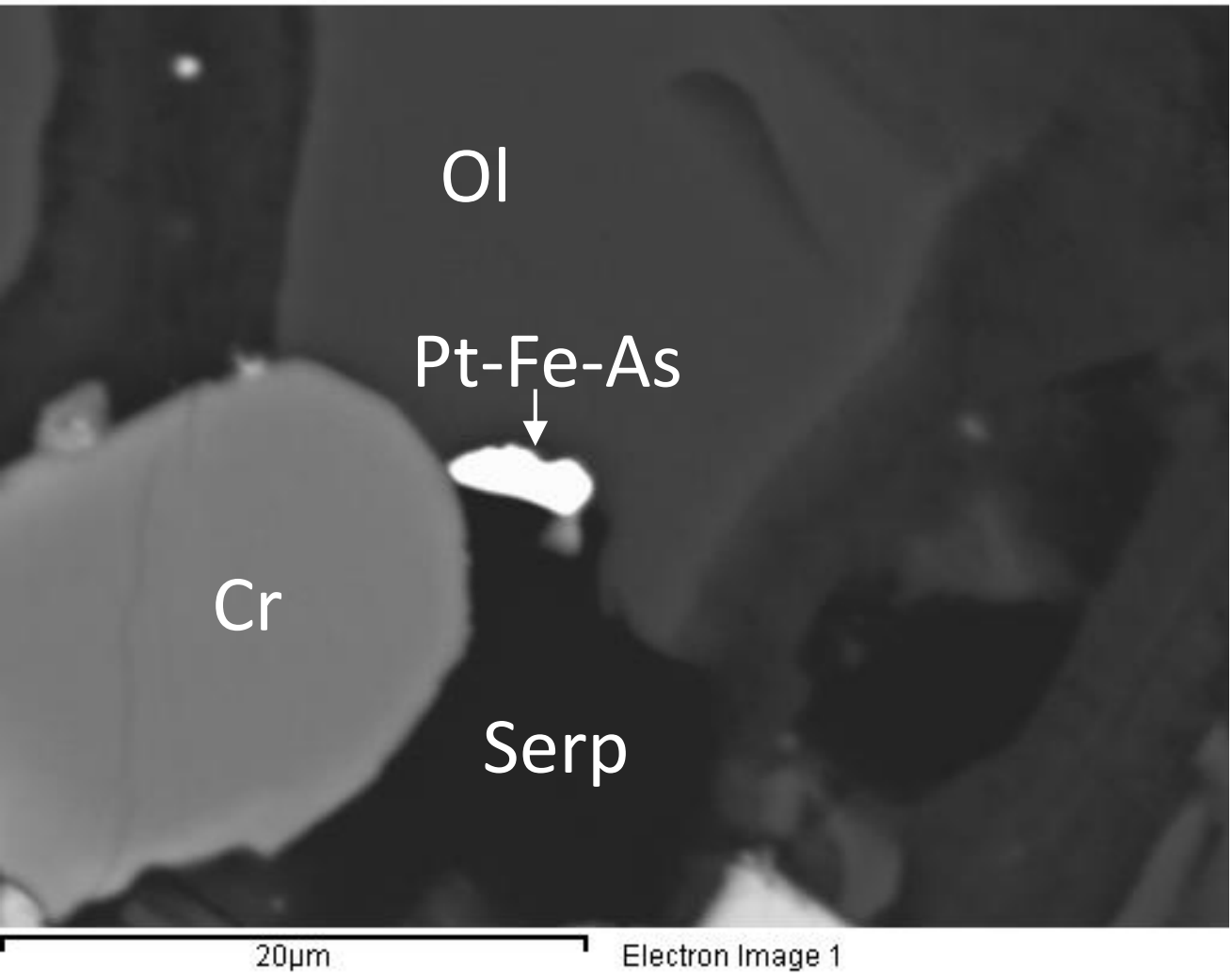
PTSR-68 G 1



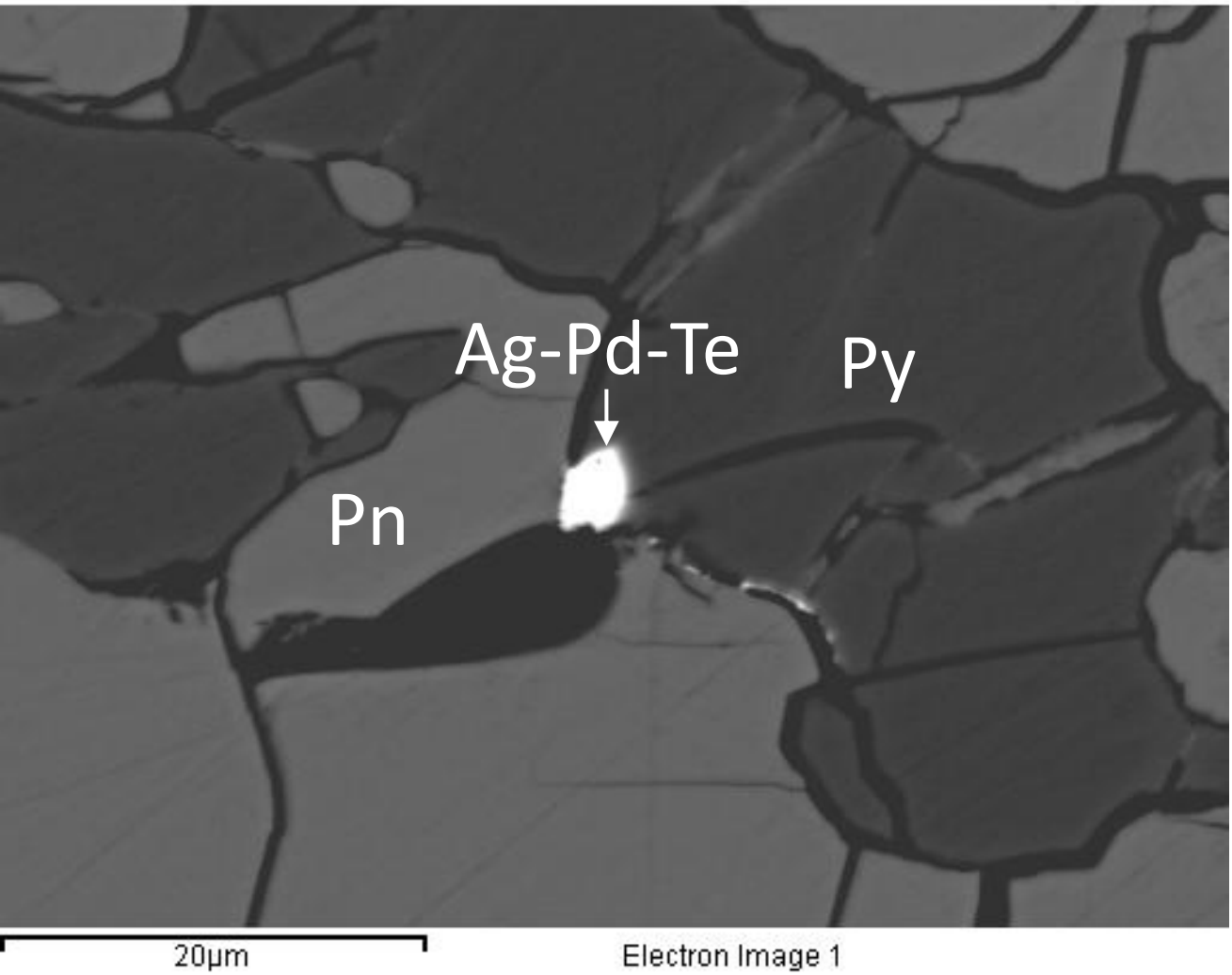
PTSR-68 G 1 Light



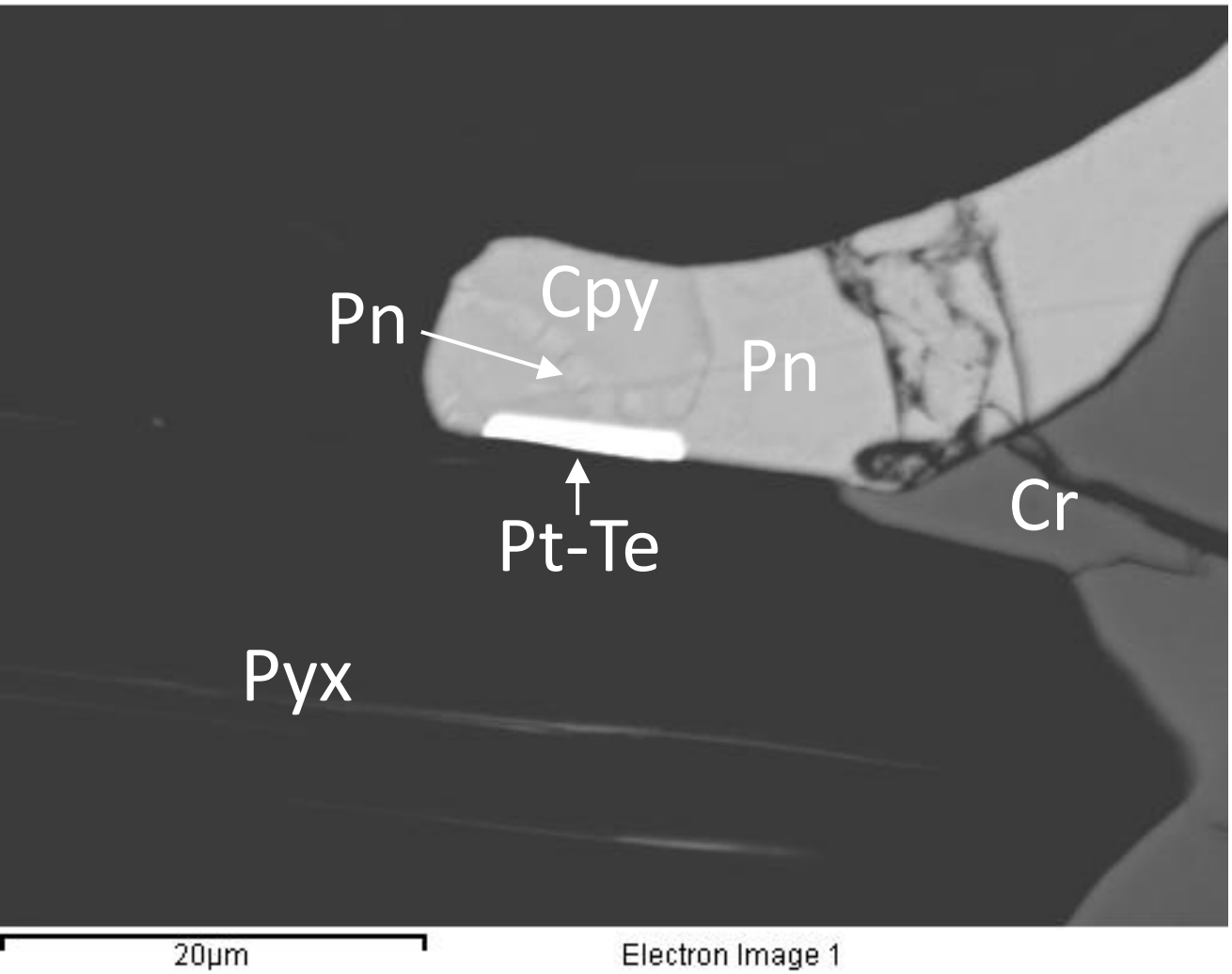
PTSR-68 H 1



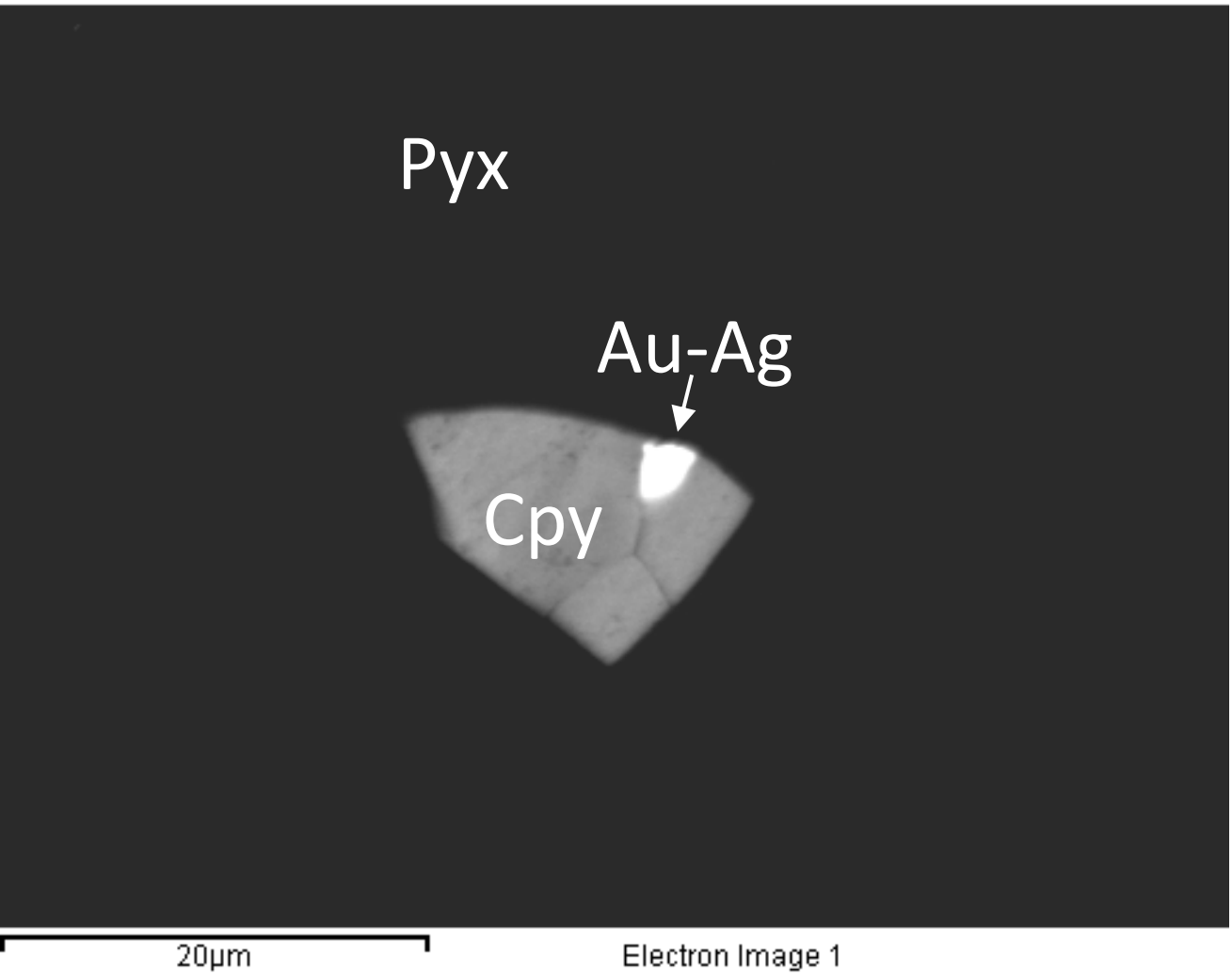
PTSR-69 A 1



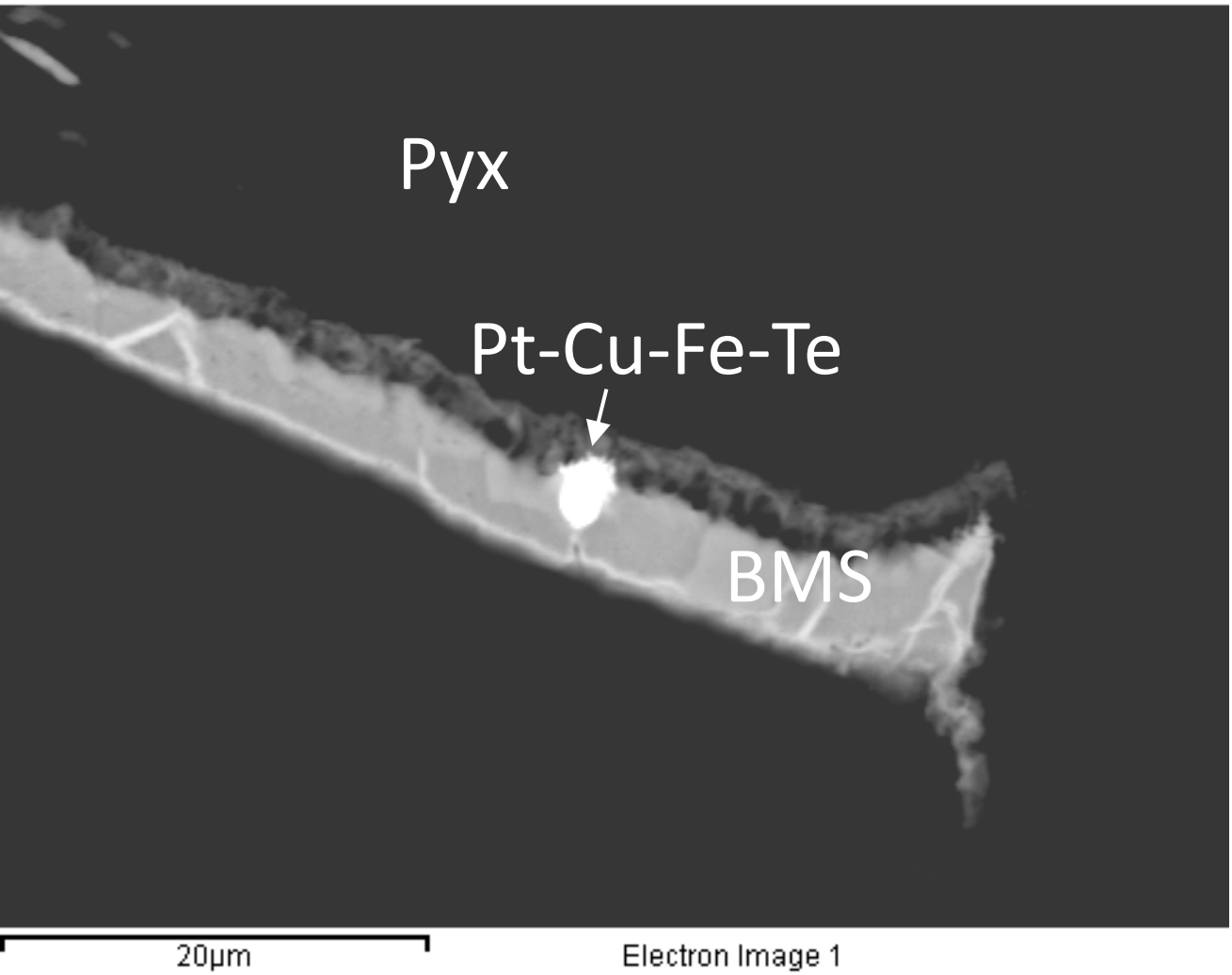
PTSR-69 B 1



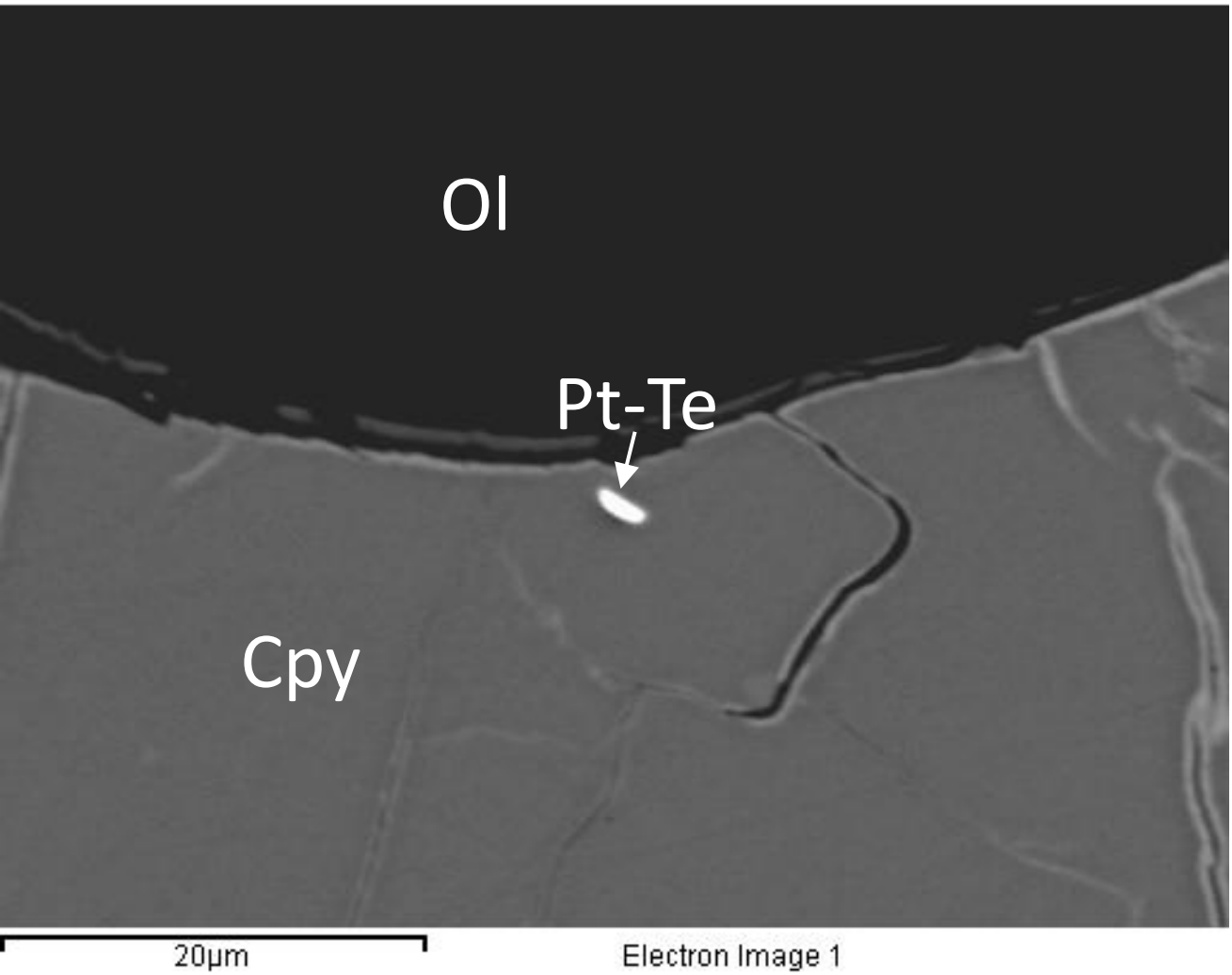
PTSR-69 C 1



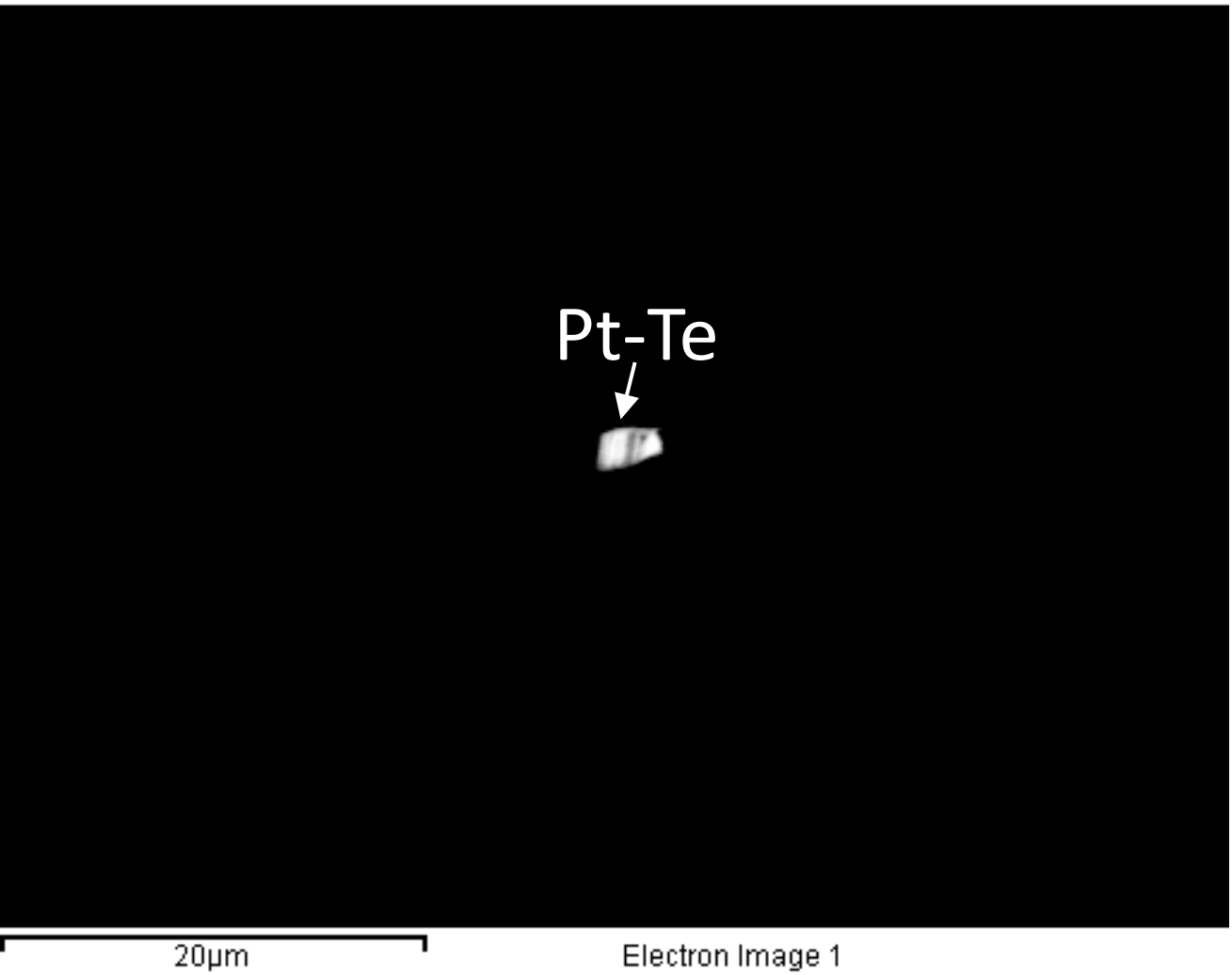
PTSR-70 A 1



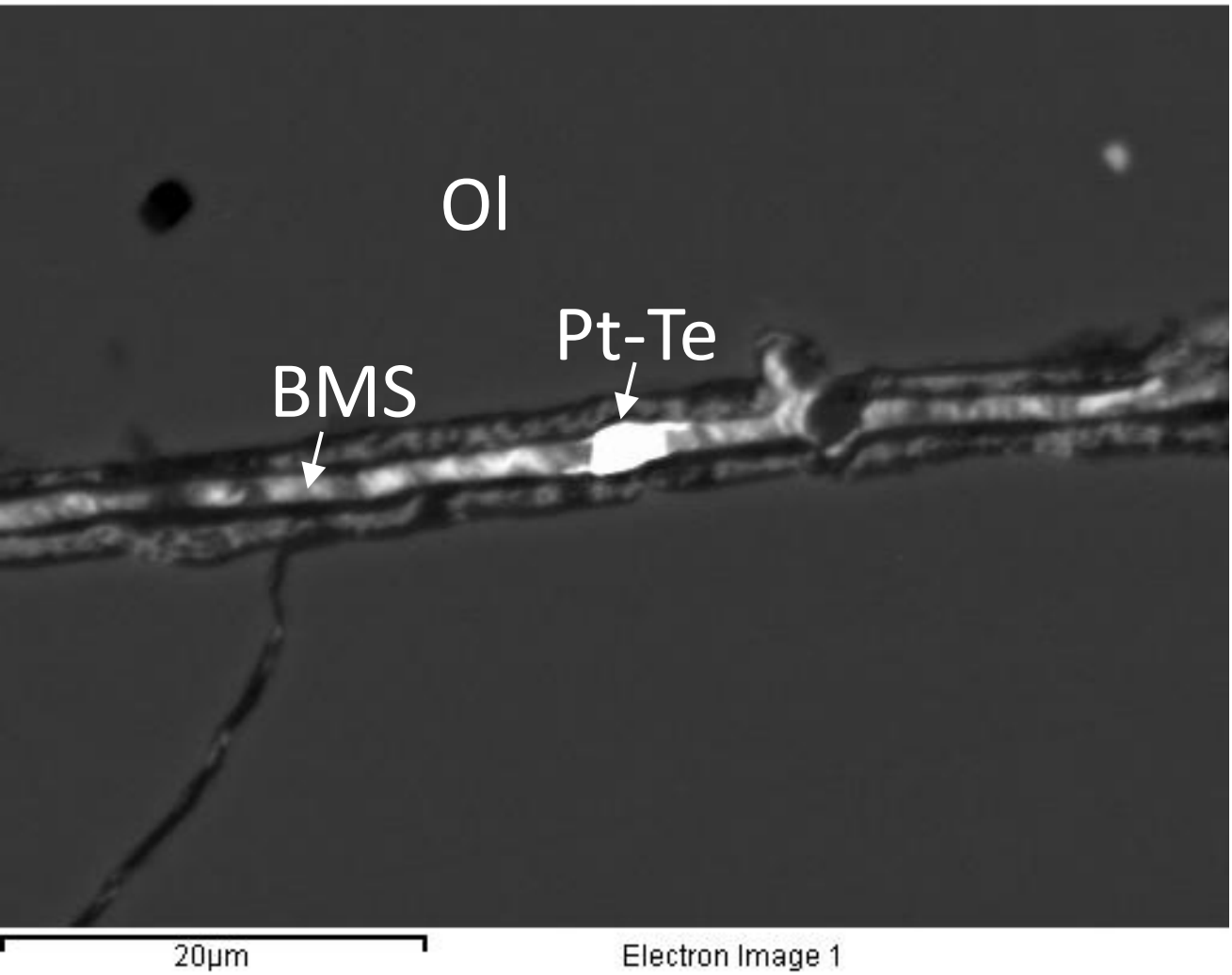
PTSR-70 B 1



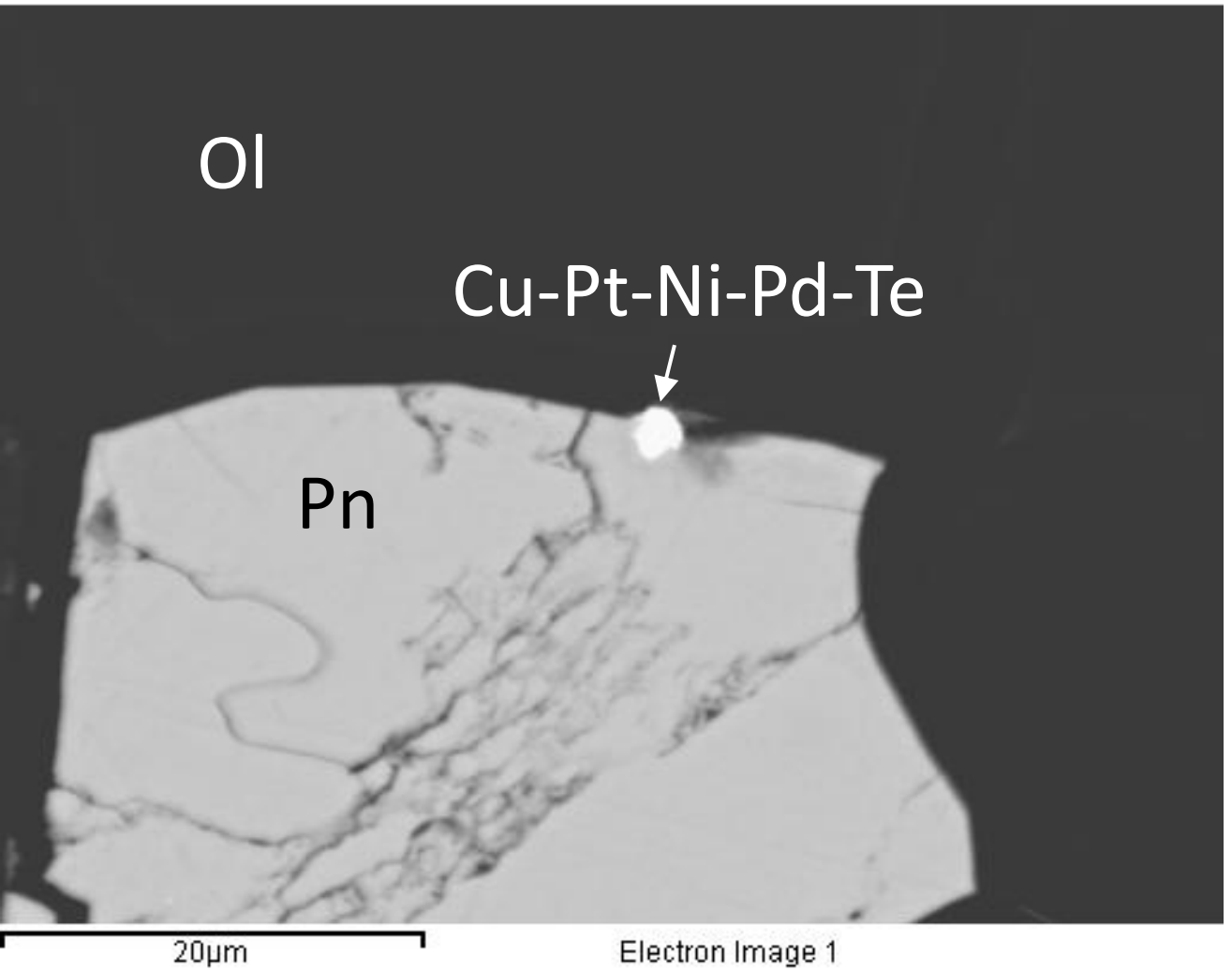
PTSR-70 C 1



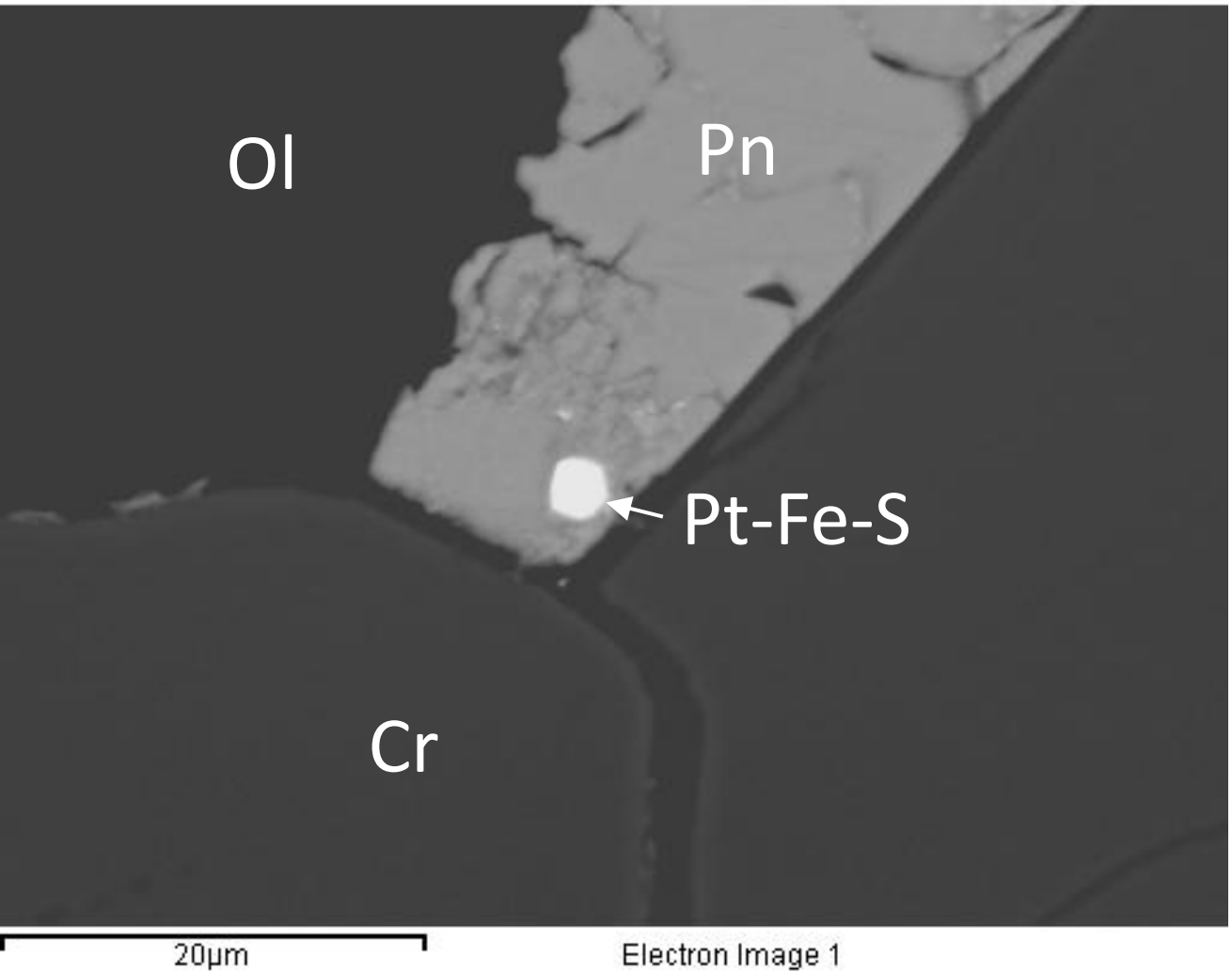
PTSR-70 C 1 Light



PTSR-70 D 1



PTSR-71 A 1



Appendix I: Mirabela Full LA-ICP-MS Data (Cardiff University)
Santa Rita Ore Zone

Zone and Drill Hole	Sample	Mineral Analysed	59Co (ppm)	61Ni (wt. %)	65Cu (wt. %)	189Os (ppm)	193Ir (ppm)	99Ru (ppm)	103Rh (ppm)	195Pt (ppm)	105Pd (ppm)	197Au (ppm)	75As (ppm)	209Bi (ppm)	121Sb (ppm)	125Te (ppm)
Central		Pn 01	865	26.63	0.00	0.04	0.02	0.15	<0.1	<0.02	<0.2	<0.01	29.1	0.10	<0.01	4.23
MBS-604		Pn 02	770	29.53	0.00	<0.02	<0.02	0.21	<0.1	<0.02	0.23	<0.01	24.1	0.28	0.03	9.72
		Pn 03	670	25.76	0.00	0.02	<0.02	0.14	<0.1	<0.02	<0.2	<0.01	28.2	0.22	0.06	8.73
		Pn 04	757	23.11	0.00	0.02	<0.02	0.16	<0.1	<0.02	<0.2	<0.01	35.6	0.24	0.07	4.44
	PTSR-01	Po 01	10	0.59	0.00	0.05	0.03	0.10	<0.1	<0.02	<0.2	<0.01	21.5	0.34	0.07	1.72
		Po 02	11	0.67	0.00	0.05	0.06	0.06	<0.1	<0.02	<0.2	<0.01	24.3	0.26	<0.01	4.49
		Po 03	11	0.65	0.00	0.04	0.03	0.08	<0.1	<0.02	<0.2	<0.01	22.3	0.24	0.05	1.49
		Po 04	16	0.87	0.00	0.03	0.03	0.05	<0.1	<0.02	<0.2	<0.01	25.3	0.55	<0.01	5.21
		Py 01	22990	0.45	0.04	0.03	0.07	0.18	<0.1	<0.02	<0.2	<0.01	7.4	2.75	0.04	1.35
		Py 02	12620	0.12	0.02	0.08	0.06	0.17	<0.1	<0.02	<0.2	0.02	8.5	3.46	0.04	27.16
		Pn 01	1018	25.62	0.00	0.15	0.04	1.03	<0.1	<0.02	2.88	<0.01	17.0	0.26	0.05	12.41
		Pn 02	1222	23.68	0.01	0.75	0.08	1.34	<0.1	<0.02	3.37	<0.01	14.8	0.98	0.07	2.25
		Pn 03	1394	25.94	0.04	1.55	0.06	2.17	0.36	<0.02	5.59	<0.01	23.0	0.04	0.05	7.06
	PTSR-02	Py 01	11140	0.17	0.02	1.77	0.31	0.83	<0.1	<0.02	<0.2	0.17	3.1	18.24	0.07	3.07
		Cpy 01	6	0.01	26.64	<0.02	<0.02	<0.05	<0.1	<0.02	<0.2	<0.01	42.7	0.16	<0.01	0.26
		Cpy 02	2	0.00	23.41	<0.02	<0.02	0.14	<0.1	<0.02	<0.2	<0.01	33.1	0.06	0.05	0.54
		Cpy 03	52	0.94	30.03	<0.02	<0.02	0.08	<0.1	<0.02	0.59	<0.01	42.5	0.01	0.06	<0.02
		Pn 01	878	22.91	0.00	0.04	<0.02	0.78	<0.1	<0.02	4.98	<0.01	19.9	0.21	0.11	1.39
		Pn 02	997	20.56	0.00	0.08	0.10	0.48	0.42	<0.02	4.06	<0.01	23.6	0.23	0.11	9.61
		Pn 03	1270	24.62	0.00	0.45	0.12	3.18	0.73	<0.02	6.25	<0.01	20.8	0.05	0.08	17.66
		Pn 04	998	20.94	0.00	0.27	0.11	0.82	<0.1	<0.02	4.10	<0.01	24.3	0.49	0.08	2.34
	PTSR-03	Po 01	3	0.44	0.00	1.68	0.32	1.74	<0.1	<0.02	<0.2	<0.01	16.3	0.10	0.08	1.29
		Po 02	24	0.70	0.00	3.80	0.90	5.73	0.13	<0.02	<0.2	<0.01	16.4	0.23	0.12	0.79
		Po 03	5	0.26	0.00	1.20	0.50	1.98	<0.1	<0.02	<0.2	<0.01	13.9	0.11	0.04	0.62
		Py 01	8569	5.52	0.00	0.32	0.11	2.67	<0.1	<0.02	1.52	0.03	7.3	10.48	0.10	3.11
		Py 02	12460	0.02	0.00	0.37	0.38	3.68	0.77	<0.02	<0.2	<0.01	20.6	0.09	0.05	0.06
		Cpy 01	3	0.01	31.30	<0.02	<0.02	0.27	<0.1	<0.02	0.41	<0.01	36.6	0.06	0.08	0.39
		Pn 01	1108	23.13	0.09	0.38	0.19	0.68	1.13	<0.02	0.85	<0.01	31.6	0.04	0.08	20.01
		Pn 02	1227	20.09	0.00	0.13	0.12	0.70	<0.1	<0.02	1.23	<0.01	18.8	1.13	0.05	3.32
		Pn 03	1082	20.85	0.00	0.06	0.07	0.55	<0.1	<0.02	0.77	<0.01	24.4	0.10	0.09	2.44
	PTSR-04	Po 01	7	0.34	0.00	0.30	0.04	0.19	<0.1	<0.02	<0.2	<0.01	15.2	0.20	0.05	0.75
		Py 01	16180	0.20	0.10	0.21	0.12	1.26	0.15	<0.02	<0.2	<0.01	5.4	3.62	0.08	0.92
		Py 02	14470	0.06	0.03	0.80	0.49	1.63	0.23	0.14	<0.2	0.03	4.3	6.27	0.05	13.02
		Py 03	13440	0.02	0.07	0.37	0.36	1.59	<0.1	0.04	<0.2	<0.01	3.3	1.40	0.05	0.86
		Cpy 01	1	0.00	20.47	<0.02	<0.02	<0.05	<0.1	<0.02	<0.2	<0.01	45.6	0.05	0.04	<0.02

Zone and Drill Hole	Sample	Mineral Analysed	59Co (ppm)	61Ni (wt. %)	65Cu (wt. %)	189Os (ppm)	193Ir (ppm)	99Ru (ppm)	103Rh (ppm)	195Pt (ppm)	105Pd (ppm)	197Au (ppm)	75As (ppm)	209Bi (ppm)	121Sb (ppm)	125Te (ppm)
		Cpy 02	6	0.11	23.67	0.03	<0.02	0.29	<0.1	<0.02	0.31	0.02	38.3	0.13	0.07	0.23
	PTSR-04	Cpy 03	4	0.01	30.90	<0.02	<0.02	0.10	<0.1	<0.02	<0.2	<0.01	36.6	0.03	0.15	0.60
		Cpy 04	1	0.02	20.72	<0.02	<0.02	0.30	<0.1	<0.02	0.27	0.08	38.8	0.50	<0.01	0.23
		Pn 01	1629	21.19	0.00	0.04	0.04	0.95	<0.1	<0.02	2.60	<0.01	26.4	0.09	0.03	9.69
		Pn 02	1332	21.42	0.37	0.15	0.03	1.35	0.46	<0.02	0.69	<0.01	22.6	0.20	0.19	17.62
		Po 01	3	0.33	0.00	<0.02	<0.02	0.02	<0.1	<0.02	<0.2	<0.01	20.4	0.12	0.04	0.31
		Po 02	6	0.37	0.00	<0.02	<0.02	0.01	<0.1	<0.02	<0.2	<0.01	22.0	0.24	0.03	1.51
	PTSR-05	Py 01	13650	1.47	0.01	0.27	0.44	1.25	<0.1	0.03	<0.2	<0.01	5.8	3.61	0.07	2.73
		Py 02	12530	1.65	0.71	0.73	0.19	1.60	0.77	<0.02	<0.2	0.04	21.6	9.74	0.11	7.06
		Cpy 01	0	0.00	30.74	<0.02	<0.02	0.15	<0.1	<0.02	1.08	<0.01	37.2	0.14	0.02	3.43
		Cpy 02	7	0.03	30.77	<0.02	<0.02	0.17	<0.1	<0.02	0.46	<0.01	40.4	0.10	0.02	0.39
		Cpy 03	2	0.00	30.22	<0.02	<0.02	0.14	<0.1	<0.02	0.28	<0.01	38.7	0.07	0.03	0.42
	PTSR-06	Cpy 01	23	0.17	25.01	<0.02	<0.02	0.12	<0.1	<0.02	0.28	0.08	50.2	0.11	0.05	<0.02
		Cpy 02	0	0.00	26.23	<0.02	<0.02	0.23	<0.1	<0.02	0.23	<0.01	40.8	0.05	0.06	0.56
		Pn 01	1823	26.03	0.00	0.09	<0.02	0.59	<0.1	0.02	2.02	<0.01	30.3	0.40	0.10	8.03
		Pn 02	2206	26.19	0.00	0.03	0.04	0.54	<0.1	<0.02	4.03	<0.01	26.0	0.55	0.05	5.96
		Pn 03	2193	26.14	0.00	0.07	0.15	0.65	0.17	<0.02	1.69	0.02	24.7	0.14	0.13	12.19
		Pn 04	1899	21.64	0.00	<0.02	0.05	0.38	<0.1	<0.02	3.42	0.01	32.1	0.25	0.04	12.30
		Po 01	14	0.44	0.00	0.10	0.04	<0.05	<0.1	<0.02	<0.2	0.01	14.3	0.11	0.04	1.00
	PTSR-07	Po 02	6	0.48	0.00	0.68	0.10	0.34	<0.1	<0.02	<0.2	<0.01	19.3	0.05	0.07	1.18
		Py 01	23640	0.02	0.11	0.29	0.03	0.66	0.14	<0.02	<0.2	0.02	3.8	1.13	0.06	1.83
		Py 02	20640	2.70	0.07	0.46	0.11	0.19	0.10	<0.02	0.42	0.02	15.5	4.36	0.04	1.39
		Py 03	25870	1.87	0.06	0.34	0.09	0.20	<0.1	0.02	0.37	0.03	1.5	4.90	0.09	5.29
		Py 04	22280	0.28	0.00	0.16	0.15	0.13	0.17	0.04	0.30	0.03	5.9	1.83	0.02	3.31
		Cpy 01	113	0.07	28.22	<0.02	0.02	0.12	<0.1	0.04	0.22	0.05	44.0	0.56	0.09	11.62
Central		Pn 01	1855	31.45	1.34	0.03	0.01	0.84	<0.1	0.02	1.88	0.05	25.8	0.03	0.15	6.47
MBS-605		Pn 02	2059	30.07	0.71	0.21	0.03	1.24	<0.1	<0.02	1.40	0.01	19.3	0.44	0.09	4.11
		Pn 03	3158	29.50	0.41	1.63	0.22	2.45	0.32	0.01	3.49	0.07	17.5	0.39	0.17	19.75
		Pn 04	2089	33.19	0.00	0.98	0.64	2.82	<0.1	<0.02	2.67	0.01	15.9	0.04	0.12	21.94
		Po 01	22	0.63	0.00	1.18	0.66	1.66	<0.1	0.04	<0.2	0.05	12.2	0.13	0.07	0.85
	PTSR-17	Po 02	232	0.71	0.03	0.21	0.05	0.41	<0.1	0.06	<0.2	0.18	14.0	0.26	0.15	1.73
		Py 01	14980	0.84	0.08	0.36	0.25	0.69	0.08	0.01	<0.2	0.03	7.4	6.17	0.08	3.42
		Py 02	13320	1.83	0.41	0.53	0.07	0.95	<0.1	<0.02	<0.2	0.02	7.7	2.98	0.06	3.78
		Py 03	15350	0.17	0.20	0.61	0.21	0.82	<0.1	0.01	<0.2	0.02	8.9	2.16	0.10	1.10
		Cpy 01	15	0.11	33.99	<0.02	<0.02	0.07	<0.1	<0.02	0.35	0.06	29.0	0.12	0.11	0.59
		Cpy 02	0	0.00	34.08	<0.02	<0.02	0.06	<0.1	<0.02	0.27	<0.01	24.5	0.04	0.08	0.26
		Cpy 03	225	2.01	31.77	<0.02	<0.02	<0.05	<0.1	<0.02	0.43	0.06	28.7	0.15	0.02	0.48

Zone and Drill Hole	Sample	Mineral Analysed	59Co (ppm)	61Ni (wt. %)	65Cu (wt. %)	189Os (ppm)	193Ir (ppm)	99Ru (ppm)	103Rh (ppm)	195Pt (ppm)	105Pd (ppm)	197Au (ppm)	75As (ppm)	209Bi (ppm)	121Sb (ppm)	125Te (ppm)
		Pn 01	2592	25.03	0.01	0.16	0.08	0.84	<0.1	<0.02	0.96	0.01	22.6	5.52	0.25	6.42
		Pn 02	2824	25.54	0.00	0.05	0.45	0.67	<0.1	0.01	1.15	<0.01	21.8	0.32	0.10	1.78
		Pn 03	2290	25.73	0.00	0.05	0.05	0.75	<0.1	0.01	0.92	0.01	21.3	0.94	0.21	8.07
		Pn 04	1232	19.09	0.00	0.26	0.08	0.82	<0.1	<0.02	0.50	<0.01	22.1	0.13	0.13	0.27
		Pn 05	2411	27.30	1.72	0.07	0.06	0.92	<0.1	<0.02	1.25	0.05	22.7	0.08	0.12	9.67
		Pn 06	1575	22.18	1.10	0.12	0.08	0.67	0.14	<0.02	0.61	0.02	20.4	4.98	0.16	2.20
		Pn 07	1751	25.37	2.42	0.15	0.89	0.98	<0.1	0.08	0.73	<0.01	21.9	0.08	0.07	29.49
	PTSR-18	Po 01	100	1.25	0.00	0.36	0.23	0.36	0.08	0.29	<0.2	0.01	17.6	0.31	0.13	1.55
		Po 02	19	0.44	0.00	0.39	0.41	0.42	<0.1	0.18	<0.2	<0.01	17.4	0.08	0.05	1.57
		Py 01	18220	0.81	0.12	0.22	0.27	0.11	<0.1	0.01	<0.2	0.01	13.2	4.03	0.09	1.07
		Py 02	16830	1.58	0.02	0.33	0.33	0.33	<0.1	0.01	<0.2	0.01	10.8	3.62	0.06	2.08
		Py 03	10960	0.03	2.45	0.20	0.42	0.42	<0.1	<0.02	<0.2	0.05	17.1	6.28	0.14	5.05
		Cpy 01	60	0.65	32.81	<0.02	<0.02	0.06	<0.1	<0.02	<0.2	0.02	29.3	0.01	0.13	0.90
		Cpy 02	45	0.88	30.87	<0.02	<0.02	0.06	<0.1	<0.02	0.44	0.01	29.2	0.18	0.11	0.17
		Cpy 03	322	1.61	26.48	0.02	<0.02	0.12	0.10	0.01	0.29	<0.01	27.9	0.19	0.13	1.62
		Pn 01	1871	25.50	0.24	0.76	0.05	2.00	<0.1	<0.02	0.82	<0.01	20.4	0.29	0.12	39.31
		Pn 02	2751	28.04	0.74	0.37	0.01	1.06	0.15	0.01	1.43	<0.01	15.8	0.08	0.12	32.91
		Pn 03	2239	28.93	0.91	0.43	0.01	1.82	<0.1	<0.02	1.05	<0.01	21.9	0.14	0.12	58.28
		Po 01	134	1.74	0.00	0.04	<0.02	0.10	1.03	<0.02	<0.2	<0.01	12.0	0.66	0.10	1.56
	PTSR-19	Py 01	13940	0.22	0.66	0.40	0.01	0.11	<0.1	0.01	<0.2	0.01	2.4	3.51	0.07	2.14
		Py 02	14980	0.26	0.30	0.86	0.01	0.27	<0.1	0.04	<0.2	0.03	4.0	8.66	0.07	10.42
		Cpy 01	64	0.65	31.11	<0.02	<0.02	0.06	<0.1	0.01	0.24	0.02	26.1	0.08	0.09	0.90
		Cpy 02	522	6.62	23.03	0.07	<0.02	0.53	<0.1	<0.02	0.50	<0.01	27.3	0.24	0.01	9.97
		Cpy 03	762	10.37	21.77	0.06	0.01	0.05	<0.1	<0.02	0.67	0.01	28.9	0.18	0.19	13.79
		Pn 01	3459	18.25	0.34	0.50	0.08	1.05	<0.1	0.01	0.83	<0.01	16.5	3.38	0.10	4.75
		Pn 02	4366	21.48	0.05	0.13	0.09	0.71	<0.1	<0.02	2.41	<0.01	21.8	0.83	0.09	13.87
		Pn 03	1268	21.18	0.32	0.22	0.02	0.64	<0.1	<0.02	0.35	0.02	23.0	0.35	0.10	7.16
		Pn 04	3790	26.13	1.06	0.64	0.07	1.17	0.31	<0.02	3.26	<0.01	23.3	0.03	0.07	30.38
		Pn 05	3977	27.42	0.12	0.32	0.08	1.08	0.27	<0.02	3.17	0.01	16.1	0.05	0.12	55.45
		Pn 06	2935	18.03	0.11	0.06	0.10	0.55	<0.1	0.01	0.95	<0.01	19.4	2.47	0.13	1.73
	PTSR-20	Po 01	44	0.87	0.01	0.52	0.04	0.71	<0.1	0.01	<0.2	0.01	12.8	0.12	0.09	0.56
		Po 02	75	0.50	2.26	0.61	0.02	0.64	<0.1	0.01	<0.2	<0.01	11.8	0.27	0.09	0.71
		Py 01	10570	0.15	1.05	0.62	0.40	0.58	<0.1	0.04	<0.2	0.01	1.1	8.46	0.11	6.31
		Py 02	14850	0.50	0.43	<0.02	0.05	0.02	0.13	0.01	<0.2	0.01	3.4	3.46	0.08	3.31
		Py 03	14740	0.16	0.73	0.17	1.00	<0.05	<0.1	0.04	<0.2	<0.01	4.4	4.43	0.07	2.93
		Cpy 01	349	5.98	23.78	<0.02	<0.02	0.06	<0.1	<0.02	0.39	<0.01	27.8	0.20	0.12	3.17
		Cpy 02	129	0.92	29.96	<0.02	0.01	<0.05	<0.1	<0.02	<0.2	0.01	25.3	0.08	0.05	1.38

Zone and Drill Hole	Sample	Mineral Analysed	59Co (ppm)	61Ni (wt. %)	65Cu (wt. %)	189Os (ppm)	193Ir (ppm)	99Ru (ppm)	103Rh (ppm)	195Pt (ppm)	105Pd (ppm)	197Au (ppm)	75As (ppm)	209Bi (ppm)	121Sb (ppm)	125Te (ppm)
	PTSR-20	Cpy 03	132	0.78	24.59	<0.02	<0.02	<0.05	<0.1	<0.02	0.68	0.04	28.5	0.11	0.11	1.77
		Cpy 04	31	0.07	29.95	0.04	<0.02	0.05	<0.1	<0.02	0.40	0.01	27.5	0.17	0.11	0.79
	PTSR-22	Pn 01	2663	27.47	0.00	0.10	0.05	0.52	<0.1	<0.02	1.54	<0.01	34.4	0.00	0.01	7.74
		Pn 02	2928	25.60	0.01	0.14	<0.02	0.77	<0.1	<0.02	1.37	<0.01	26.6	0.17	0.11	4.83
		Pn 03	2542	18.93	0.05	0.22	0.02	0.74	0.14	<0.02	0.43	0.02	27.8	2.60	0.03	0.70
		Pn 04	2962	23.78	0.06	0.07	0.02	0.68	0.19	<0.02	1.25	<0.01	29.1	0.05	0.09	8.82
		Py 01	26900	1.49	0.88	0.40	0.12	0.28	0.51	<0.02	0.43	0.01	2.5	7.72	0.05	5.30
		Py 02	29470	0.02	0.02	0.28	0.11	0.39	<0.1	0.06	<0.2	<0.01	2.8	0.83	0.03	3.12
		Py 03	32030	0.12	0.07	0.15	0.04	0.15	0.15	<0.02	<0.2	<0.01	2.2	1.19	0.04	2.10
		Cpy 01	3	0.05	27.84	<0.02	<0.02	0.29	<0.1	0.20	0.20	<0.01	40.9	0.17	0.03	1.02
North MBS-209	PTSR-31	Pn 01	6920	27.05	0.40	0.76	0.30	0.81	0.21	0.06	5.74	0.21	8.7	2.60	0.08	30.85
		Pn 02	6457	24.10	0.05	0.03	<0.02	<0.05	0.11	<0.02	6.39	0.10	16.0	4.75	0.27	2.49
		Pn 03	4505	36.43	0.03	1.92	0.07	2.43	0.11	0.05	3.39	0.02	9.9	0.48	0.12	31.46
		Pn 04	4571	41.18	0.11	4.49	0.91	6.36	0.57	0.14	11.48	0.02	15.0	0.29	0.11	24.92
		Pn 05	3244	41.92	0.40	2.02	<0.02	4.87	0.17	0.05	4.07	<0.01	13.9	0.03	0.12	22.34
		Cpy 01	38	0.14	23.70	<0.02	0.03	<0.05	<0.1	0.58	0.24	<0.01	11.1	0.30	0.07	0.54
		Cpy 02	1887	6.77	15.69	0.08	0.03	0.28	<0.1	0.16	1.14	0.07	19.1	1.17	0.05	5.44
	PTSR-33	Pn 01	2662	34.52	0.02	0.92	<0.02	0.59	0.17	0.03	2.73	0.05	15.6	2.90	0.34	7.04
		Pn 02	2913	31.98	0.05	0.03	<0.02	0.22	<0.1	<0.02	2.49	0.08	10.8	1.35	0.17	9.64
		Pn 03	1976	23.32	0.09	<0.02	<0.02	<0.05	<0.1	<0.02	1.31	0.13	20.3	5.99	1.25	1.46
		Pn 04	2699	33.63	2.71	0.28	0.01	0.43	<0.1	0.07	3.41	0.03	10.3	0.27	0.30	13.69
		Pn 05	3354	19.06	0.34	0.25	<0.02	0.20	<0.1	0.05	1.14	0.01	12.7	2.37	0.10	5.45
		Pn 06	2623	34.09	0.00	0.33	<0.02	0.27	0.13	0.06	2.42	0.01	13.4	0.13	0.05	10.07
		Pn 07	2240	27.32	0.10	0.16	<0.02	0.90	0.37	<0.02	2.06	0.02	19.4	0.36	0.12	15.16
		Po 01	65	1.36	0.00	0.01	<0.02	<0.05	<0.1	0.03	<0.2	<0.01	11.2	0.49	0.16	0.85
		Po 02	2	0.40	0.01	0.13	<0.02	0.07	<0.1	0.05	<0.2	0.01	8.5	0.21	0.07	0.19
		Po 03	349	2.89	0.02	0.41	<0.02	0.17	<0.1	0.04	<0.2	<0.01	13.5	0.27	0.10	1.78
		Po 04	11	0.38	0.01	0.32	<0.02	0.09	<0.1	<0.02	<0.2	0.03	14.6	0.08	0.13	0.35
		Py 01	15620	8.38	0.31	1.46	0.03	0.97	0.76	0.06	0.67	0.17	8.1	17.72	0.12	6.79
		Py 02	16240	0.36	0.54	0.77	0.01	1.05	<0.1	0.06	<0.2	0.12	13.6	10.10	0.11	6.21
		Py 03	10500	1.17	1.42	0.94	<0.02	0.59	<0.1	0.05	<0.2	0.08	14.4	10.63	0.12	3.55
		Cpy 01	783	9.87	16.36	<0.02	<0.02	0.63	<0.1	0.13	0.77	<0.01	19.8	0.23	0.03	2.04
		Cpy 02	288	3.94	28.98	0.05	<0.02	0.06	<0.1	<0.02	<0.2	<0.01	14.2	0.18	0.14	1.06
	PTSR-35	Pn 01	5729	26.07	0.73	0.66	<0.02	1.37	<0.1	0.04	8.97	0.08	9.2	3.25	2.20	15.42
		Pn 02	4941	29.38	0.31	1.01	<0.02	0.66	0.09	0.07	12.97	<0.01	11.5	1.10	0.08	5.28
		Pn 03	2723	20.31	0.44	1.01	<0.02	0.07	0.22	0.04	5.75	0.03	15.0	1.99	0.23	3.41
		Po 01	39	0.66	0.11	0.94	<0.02	0.06	<0.1	0.04	<0.2	0.03	13.2	0.05	0.06	1.84

Zone and Drill Hole	Sample	Mineral Analysed	59Co (ppm)	61Ni (wt. %)	65Cu (wt. %)	189Os (ppm)	193Ir (ppm)	99Ru (ppm)	103Rh (ppm)	195Pt (ppm)	105Pd (ppm)	197Au (ppm)	75As (ppm)	209Bi (ppm)	121Sb (ppm)	125Te (ppm)
	PTSR-35	Cpy 01	2	0.01	23.80	<0.02	<0.02	<0.05	<0.1	<0.02	<0.2	<0.01	17.9	0.08	0.21	<0.02
North		Pn 01	4283	24.27	0.00	0.20	<0.02	<0.05	<0.1	0.05	1.84	0.03	8.6	1.12	0.11	8.70
MBS-158		Pn 02	4804	27.44	0.06	0.96	<0.02	0.73	0.20	<0.02	1.82	0.02	15.8	1.52	0.08	9.82
		Pn 03	6058	20.65	0.01	0.59	0.01	2.53	<0.1	<0.02	1.67	0.02	18.2	1.13	0.11	8.66
		Pn 04	2392	22.04	0.00	0.41	<0.02	0.63	<0.1	<0.02	0.88	0.03	12.3	0.20	0.10	5.73
		Pn 05	3497	31.29	1.14	1.30	<0.02	1.58	0.31	0.08	1.95	0.02	11.3	0.11	0.23	28.98
	PTSR-42	Po 01	3	0.02	0.00	0.77	<0.02	0.91	<0.1	0.06	<0.2	0.03	13.0	0.19	0.10	0.50
		Po 02	4	0.25	0.01	0.82	0.01	0.47	<0.1	0.07	<0.2	<0.01	10.5	0.19	0.12	<0.02
		Py 01	14240	3.38	0.22	1.36	0.02	1.41	0.21	0.05	0.33	0.03	15.1	3.64	0.07	3.71
		Py 02	18380	0.06	0.19	2.16	0.03	1.52	0.15	0.06	<0.2	0.03	12.3	3.04	0.11	0.46
		Py 03	20980	3.56	0.47	1.58	0.02	0.73	0.33	0.09	0.23	0.04	12.3	6.58	0.16	9.13
		Cpy 01	17	0.23	25.56	<0.02	<0.02	0.07	<0.1	<0.02	<0.2	<0.01	21.3	0.09	0.12	<0.02
		Cpy 02	309	2.65	21.26	0.22	0.01	0.15	<0.1	<0.02	<0.2	<0.01	19.2	0.14	0.20	1.82
		Pn 01	2732	30.18	1.79	0.62	<0.02	1.06	<0.1	<0.02	3.68	0.01	19.8	0.03	0.12	6.27
		Pn 02	3872	29.84	1.54	0.99	<0.02	1.12	<0.1	0.04	2.93	0.03	15.4	1.22	0.17	18.08
		Pn 03	5995	26.20	1.12	0.74	0.02	1.22	<0.1	<0.02	4.08	0.03	11.7	2.61	0.10	13.24
	PTSR-45	Pn 04	3192	35.06	2.10	0.35	0.01	0.97	0.09	0.02	4.08	0.02	15.3	0.08	0.07	8.09
		Po 01	24	0.16	0.05	0.47	<0.02	0.68	<0.1	0.02	<0.2	0.01	10.3	0.12	0.12	1.35
		Cpy 01	30	0.42	25.42	<0.02	<0.02	0.09	<0.1	<0.02	<0.2	<0.01	19.3	0.06	0.04	<0.02
		Cpy 02	542	4.01	21.38	0.80	<0.02	0.15	<0.1	<0.02	<0.2	<0.01	21.8	1.64	0.15	2.19
		Cpy 03	19	0.16	26.78	<0.02	<0.02	0.12	<0.1	<0.02	<0.2	0.02	22.6	0.06	0.06	1.25
		Pn 01	3220	26.92	2.70	0.17	<0.02	0.46	<0.1	0.09	3.96	0.03	15.8	0.02	0.04	9.29
		Pn 02	3812	32.34	1.31	0.43	<0.02	0.37	0.15	0.04	6.10	0.02	19.3	0.03	0.18	5.56
		Pn 03	1939	21.90	0.17	0.08	0.02	0.17	<0.1	<0.02	0.92	0.26	6.1	0.57	0.18	3.56
		Po 01	17	0.21	0.04	0.52	0.02	0.31	<0.1	0.03	<0.2	0.16	12.9	0.22	0.08	0.62
	PTSR-47	Po 02	23	0.18	0.01	0.72	0.04	0.54	<0.1	1.58	<0.2	<0.01	0.3	0.21	0.03	1.64
		Cpy 01	2	0.02	26.60	<0.02	<0.02	0.14	<0.1	0.07	<0.2	<0.01	25.7	0.03	0.03	1.25
		Cpy 02	70	0.72	25.84	<0.02	0.01	<0.05	<0.1	0.25	<0.2	<0.01	26.5	0.07	0.27	0.24
		Cpy 03	364	5.40	29.08	<0.02	<0.02	0.30	<0.1	0.18	<0.2	0.14	28.6	0.06	0.31	0.05
		Cpy 04	187	4.66	19.96	0.02	<0.02	0.14	<0.1	0.09	<0.2	0.12	24.1	0.45	0.32	0.90
South		Pn 01	4398	32.28	0.00	1.03	0.17	0.83	0.18	<0.02	1.67	<0.01	5.1	0.07	0.08	24.2
MBS-565		Pn 02	3815	30.27	0.04	0.65	0.02	0.37	0.24	<0.02	1.18	<0.01	15.1	0.03	0.08	11.4
		Pn 03	2175	20.96	0.38	0.07	<0.02	<0.05	0.16	0.02	0.41	<0.01	9.9	0.84	0.04	2.56
	PTSR-54	Pn 04	3614	30.64	0.10	0.44	0.02	0.45	<0.1	0.04	1.58	<0.01	4.9	0.04	0.10	19.1
		Po 01	2	0.00	0.02	0.16	<0.02	0.09	<0.1	<0.02	<0.2	<0.01	5.9	0.18	0.06	1.49
		Cpy 01	1070	7.29	27.40	<0.02	<0.02	<0.05	<0.1	<0.02	0.43	0.07	12.0	0.03	0.08	6.30
		Cpy 02	264	1.95	30.23	0.04	<0.02	0.16	<0.1	0.39	1.58	<0.01	21.2	0.23	0.11	18.5

Zone and Drill Hole	Sample	Mineral Analysed	59Co (ppm)	61Ni (wt. %)	65Cu (wt. %)	189Os (ppm)	193Ir (ppm)	99Ru (ppm)	103Rh (ppm)	195Pt (ppm)	105Pd (ppm)	197Au (ppm)	75As (ppm)	209Bi (ppm)	121Sb (ppm)	125Te (ppm)
	PTSR-55	Pn 01	3417	28.48	0.02	0.42	0.27	0.31	<0.1	<0.02	1.10	<0.01	9.4	0.64	0.06	13.4
		Pn 02	2611	32.50	0.73	1.13	0.09	0.76	0.21	<0.02	0.38	<0.01	13.1	0.07	0.05	15.7
		Pn 03	4194	29.76	0.02	0.17	0.36	<0.05	<0.1	<0.02	1.84	<0.01	10.5	0.21	0.03	16.0
		Pn 04	3574	24.46	0.01	0.38	0.04	0.05	<0.1	<0.02	0.73	<0.01	11.9	0.72	0.01	2.73
		Pn 05	3856	30.40	0.04	1.08	0.78	1.37	0.49	0.03	0.82	<0.01	8.4	0.07	0.09	44.7
		Po 01	37	0.63	0.00	0.03	0.04	<0.05	<0.1	<0.02	<0.2	<0.01	12.6	0.13	0.10	1.05
		Po 02	49	0.93	0.01	0.16	0.06	<0.05	<0.1	<0.02	<0.2	<0.01	9.1	0.44	0.07	1.47
		Py 01	15230	0.27	0.00	1.38	0.31	0.92	0.14	<0.02	<0.2	<0.01	5.4	1.04	0.04	0.90
		Py 02	14120	0.06	0.00	0.85	0.11	0.13	<0.1	<0.02	<0.2	<0.01	2.9	0.30	0.05	0.47
		Cpy 01	20	0.37	28.85	<0.02	<0.02	<0.05	<0.1	0.20	<0.2	0.02	16.2	0.08	0.09	2.30
	PTSR-56	Pn 01	4224	29.16	0.17	0.31	0.02	0.32	0.11	<0.02	0.87	<0.01	14.9	0.06	0.46	6.78
		Pn 02	3139	28.46	0.16	2.11	0.04	2.28	0.41	0.01	0.62	<0.01	12.3	0.15	0.04	34.6
		Pn 03	1690	25.81	0.04	0.06	0.03	0.19	0.37	<0.02	0.25	<0.01	8.3	0.02	0.10	8.29
		Pn 04	4576	28.97	0.08	0.50	<0.02	0.25	0.22	0.03	1.19	<0.01	7.8	1.95	0.28	11.1
		Pn 05	4166	29.04	0.06	0.09	<0.02	0.08	<0.1	<0.02	1.33	<0.01	8.1	0.17	0.04	10.1
		Pn 06	4146	29.01	0.02	0.14	<0.02	<0.05	<0.1	0.01	0.95	<0.01	11.4	0.34	0.37	12.0
		Po 01	1	0.28	0.01	<0.02	<0.02	<0.05	<0.1	0.01	<0.2	<0.01	9.3	0.11	0.06	1.25
		Py 01	13990	0.18	0.80	0.55	<0.02	0.40	0.11	0.03	<0.2	<0.01	14.1	2.47	0.05	4.28
		Py 02	16590	0.29	0.07	0.76	0.03	0.63	0.35	0.08	<0.2	<0.01	22.4	1.20	0.90	11.1
		Cpy 01	240	1.51	30.91	<0.02	<0.02	0.05	<0.1	<0.02	<0.2	<0.01	16.6	0.18	0.11	0.03
		Cpy 02	307	2.53	28.87	<0.02	<0.02	0.28	<0.1	0.04	<0.2	0.04	20.9	0.07	0.06	4.94
South MBS-569	PTSR-65	Pn 01	5177	29.35	0.09	1.27	0.29	0.34	<0.1	<0.02	0.69	<0.01	7.9	1.34	0.10	14.0
		Pn 02	3734	31.49	0.07	2.75	<0.02	3.67	<0.1	<0.02	1.07	<0.01	6.5	0.16	0.08	25.7
		Pn 03	2978	33.70	0.09	0.13	0.47	<0.05	<0.1	0.02	0.61	<0.01	15.6	0.11	0.05	1.70
		Pn 04	2990	24.48	1.28	2.03	0.11	1.27	<0.1	<0.02	1.07	0.02	13.6	0.07	0.04	14.8
		Pn 05	3663	26.51	0.98	0.28	<0.02	0.25	<0.1	<0.02	0.95	<0.01	10.9	0.95	0.09	10.2
		Po 01	345	0.49	0.03	0.71	0.05	0.15	<0.1	<0.02	0.52	<0.01	7.1	0.81	0.05	1.16
		Po 02	615	1.36	0.02	2.20	0.17	2.53	0.18	0.02	<0.2	0.32	20.3	1.40	0.06	0.61
		Po 03	29	0.28	0.12	0.21	0.07	0.06	<0.1	0.15	<0.2	<0.01	12.0	0.16	0.05	2.18
		Cpy 01	341	2.91	28.48	0.12	<0.02	0.47	<0.1	<0.02	<0.2	0.01	14.1	1.04	0.09	2.36
	PTSR-67	Pn 01	7313	28.44	0.33	0.86	<0.02	0.50	0.23	0.73	1.96	0.16	27.6	13.10	0.05	40.4
		Pn 02	4677	25.44	0.07	0.69	<0.02	0.16	<0.1	<0.02	1.67	0.08	13.5	0.20	0.60	57.5
		Pn 03	5883	26.84	0.31	0.13	<0.02	<0.05	<0.1	0.06	1.09	0.02	12.3	4.53	0.06	23.0
		Pn 04	7202	26.15	0.08	0.19	<0.02	<0.05	0.05	0.73	4.27	0.18	27.9	25.51	0.08	45.1

Sulphur-Poor Dunite

Zone and Drill Hole	Sample	Mineral Analysed	59Co (ppm)	61Ni (wt. %)	65Cu (wt. %)	189Os (ppm)	193Ir (ppm)	99Ru (ppm)	103Rh (ppm)	195Pt (ppm)	105Pd (ppm)	197Au (ppm)	75As (ppm)	209Bi (ppm)	121Sb (ppm)	125Te (ppm)
Central		Pn 01	9761	15.84	0.02	<0.02	0.65	1.06	1.14	1.37	33.18	<0.01	44.9	1.20	0.13	<0.02
MBS-604	PTSR-11	Pn-Py 01	5750	22.55	0.38	0.30	27.87	1.37	0.68	12.50	570.40	0.05	32.2	2.32	0.04	<0.02
		Pn-Py-Cpy 01	3245	13.70	8.96	0.04	18.68	1.63	<0.1	6.20	371.70	0.20	48.2	0.54	0.04	0.13
Central		Pn 01	3947	20.04	0.31	0.15	0.14	0.55	<0.1	<0.02	12.51	0.01	20.9	0.64	0.12	1.89
MBS-605		Pn 02	3097	23.13	0.01	1.12	0.60	1.39	3.88	<0.02	11.85	<0.01	17.3	0.37	0.09	1.81
		Pn 03	2416	24.76	1.45	2.70	0.82	4.82	4.19	<0.02	16.01	<0.01	21.1	0.07	0.11	2.35
	PTSR-23	Pn 04	2714	24.62	0.02	4.07	0.58	8.72	0.28	<0.02	8.19	0.02	16.3	0.31	0.06	20.90
		Pn 05	2904	20.48	0.01	2.71	0.78	2.03	0.08	<0.02	8.80	<0.01	22.6	1.06	0.06	1.16
		Py 01	11910	0.19	0.92	0.96	0.67	<0.05	<0.1	0.01	0.26	0.01	12.8	2.57	0.08	2.05
		Py 02	9920	0.66	0.39	6.08	2.48	5.61	<0.1	0.01	0.49	<0.01	4.8	1.89	0.09	0.58
		Cpy 01	19	0.28	32.60	<0.02	<0.02	<0.05	<0.1	<0.02	0.52	0.03	25.4	0.02	0.03	0.59
		Pn 01	4567	19.05	1.40	0.14	0.49	0.53	<0.1	4.02	74.14	0.66	21.1	0.04	0.02	0.01
		Pn 02	5623	20.23	1.82	0.03	1.12	0.44	0.17	15.18	49.55	1.61	24.8	0.06	0.15	<0.02
	PTSR-25	Pn 03	5270	18.83	1.35	0.05	1.90	0.47	12.26	0.23	79.28	0.29	16.8	0.49	0.14	0.59
		Pn 04	4520	24.18	2.54	15.01	28.69	29.48	36.15	11.94	254.30	0.05	28.6	1.25	0.21	1.05
		Cpy 01	1346	6.08	19.73	<0.02	0.08	0.12	<0.1	0.24	15.90	0.24	29.0	0.02	0.11	<0.02
		Cpy 02	182	1.19	23.49	<0.02	0.12	0.07	<0.1	0.01	10.02	0.12	31.7	0.01	0.10	0.60
North		Pn 01	7407	25.96	0.23	0.42	0.04	0.68	0.35	0.41	3.88	0.03	12.7	5.10	0.20	11.79
MBS-209		Pn 02	7462	24.83	1.52	3.23	5.21	0.25	3.18	28.89	3.97	0.35	13.1	0.72	0.08	1.15
		Pn 03	7455	24.98	1.01	1.35	0.06	2.84	0.97	<0.02	6.01	0.03	15.5	2.40	0.15	9.63
	PTSR-36	Pn 04	7811	25.42	1.94	1.36	<0.02	2.42	0.81	0.10	6.06	0.19	19.2	2.54	2.77	3.88
		Pn 05	7367	24.54	0.06	7.75	0.08	10.70	1.79	0.24	8.35	0.06	8.0	0.07	0.05	0.05
		Pn-Cpy 01	2321	9.72	15.73	<0.02	0.02	0.47	<0.1	<0.02	0.80	0.10	15.1	0.67	0.18	1.97
		Pn-Cpy 02	7286	26.05	1.19	1.72	2.61	1.12	2.63	0.82	8.39	0.15	11.1	0.65	0.09	0.16
North		Pn 01	6368	28.23	0.42	38.25	0.21	59.13	34.69	9.88	141.90	<0.01	1.8	0.03	0.08	1.62
MBS-158	PTSR-49	Pn 02	6443	25.50	0.41	5.32	0.72	7.81	1.78	13.45	5.99	<0.01	24.3	0.09	0.10	0.03
		Pn 03	7046	31.82	1.69	0.26	0.36	1.24	2.13	5.10	89.08	0.11	18.0	0.21	0.06	1.26
		Pn-Cpy 01	4494	33.95	5.13	5.18	0.04	11.48	8.82	4.52	124.89	0.05	1.3	0.02	0.05	0.34
South		Pn 01	5757	29.67	0.66	6.23	0.04	12.10	4.64	0.01	37.7	0.31	15.8	0.61	0.21	9.53
MBS-565		Pn 02	7680	29.20	0.98	0.06	0.03	<0.05	0.34	4.54	57.0	0.06	16.6	0.20	0.25	0.70
	PTSR-60	Pn-Cpy 01	6448	19.27	8.39	0.78	<0.02	8.76	1.26	0.12	42.1	0.37	24.1	5.83	0.58	11.1
		Pn-Cpy 02	6734	33.26	1.65	0.68	0.05	0.96	2.99	0.11	56.5	0.16	15.8	1.70	0.10	3.61
		Pn-Cpy 03	1367	8.25	18.45	0.18	<0.02	3.70	0.80	<0.02	14.2	0.20	17.6	3.24	0.04	2.80
South		Pn 01	6383	23.22	0.15	0.50	0.15	0.18	0.69	3.37	11.7	<0.01	17.1	0.03	0.05	0.75
MBS-569	PTSR-70	Pn 02	5764	24.96	0.27	10.07	0.44	9.22	0.43	9.57	23.7	<0.01	7.0	0.03	0.16	1.14
		Pn 03	6755	24.95	0.50	1.22	0.50	0.86	0.11	6.89	5.02	<0.01	11.2	0.06	0.11	0.67

Zone and Drill Hole	Sample	Mineral Analysed	59Co (ppm)	61Ni (wt. %)	65Cu (wt. %)	189Os (ppm)	193Ir (ppm)	99Ru (ppm)	103Rh (ppm)	195Pt (ppm)	105Pd (ppm)	197Au (ppm)	75As (ppm)	209Bi (ppm)	121Sb (ppm)	125Te (ppm)
	PTSR-70	Pn 04	5306	21.86	0.46	10.35	3.49	11.96	6.33	1.39	175	<0.01	10.3	0.32	0.66	1.67
		Pn-Cpy 01	6932	23.67	2.66	0.26	1.88	<0.05	1.20	14.70	37.5	<0.01	19.7	0.41	0.08	0.57
	PTSR-71	Pn 01	6020	31.38	0.13	0.28	<0.02	0.27	0.48	0.02	13.3	0.02	13.9	1.12	0.08	5.57
		Pn 02	8099	27.18	0.30	0.82	<0.02	0.28	<0.1	0.22	5.37	<0.01	9.9	0.54	0.09	1.46
		Pn 03	5718	29.47	0.05	0.48	<0.02	0.18	0.17	<0.02	4.50	<0.01	18.3	1.41	0.05	7.48
		Pn-Cpy 01	8910	29.22	2.41	0.49	<0.02	0.15	<0.1	0.26	55.1	0.08	18.9	0.84	0.22	2.38

Appendix J: Jinchuan Sample List (DZK = underground holes all ~1000, below surface but ~850 m above sea level, ZK = surface hole)
Dun = Dunite, Lhz = Lherzolite, Web = Websterite, Carb = Carbonate, Oik = Oikocrysts, Ol =Olivine, Plag = Plagioclase,
Pyx = Pyroxene; LA = Lightly Altered (5-35%), MA = Moderately Altered (35-65%), Heavily Altered (65-95%),
TA = Totally Altered (95-100%)

Name	Segment	Orebody	Borehole	Depth (m)	Ore Description	Lithology	Alteration
RK01	II	#1	DZK12-06 (Central)	26.3	Marble	Marble	N/A
RK02	II	#1	DZK12-06 (Central)	33.0	Disseminated ore	Ol-Web	MA
RK03	II	#1	DZK12-06 (Central)	49.8	Disseminated ore	Ol-Web	MA
RK04	II	#1	DZK12-06 (Central)	71.6	Disseminated ore	Plag-Lhz	LA
RK05	II	#1	DZK12-06 (Central)	86.1	Patchy net textured ore	Lhz, Pyx Oik	MA
RK06	II	#1	DZK12-06 (Central)	98.4	Patchy net textured ore	Lhz, Pyx Oik	LA
RK07	II	#1	DZK12-06 (Central)	109.5	Disseminated ore	Lhz, Pyx Oik	MA
RK08	II	#1	DZK12-06 (Central)	135.3	Patchy net textured, sulphide locally remobilised in veins	Lhz, Pyx Oik	MA
RK09	II	#1	DZK12-06 (Central)	153.0	Patchy net textured, sulphide locally remobilised in veins	Lhz	MA
RK10	II	#1	DZK12-06 (Central)	157.1	Semi-massive ore, predominantly chalcopyrite	Lhz + Minor Carb	TA
RK11	II	#1	DZK12-06 (Central)	158.0	Patchy net textured ore	Lhz + Minor Carb	MA
RK12	II	#1	DZK12-06 (Central)	161.3	Patchy net textured ore with minor BMS remobilisation	Lhz + Minor Carb	TA
RK13	II	#1	DZK12-06 (Central)	167.7	Net textured ore with sulphide vein, minor shear textures	Dun	HA
RK14	II	#1	DZK12-06 (Central)	162.3	BMS enclosed within silicate/carbonate vein	Web	MA
RK15	II	#1	DZK12-06 (Central)	180.8	Marble	Marble	N/A
RK16	II	#1	DZK14-02 (East)	42.5	Disseminated ore, minor BMS vein	Web	MA
RK17	II	#1	DZK14-02 (East)	70.2	Disseminated ore	Web	TA
RK18	II	#1	DZK14-02 (East)	73.3	Disseminated ore	Web	TA
RK19	II	#1	DZK14-02 (East)	85.4	Massive ore with minor carbonate and silicate inclusions	N/A	N/A
RK20	II	#1	DZK14-02 (East)	111.2	Patchy net textured ore	Lhz	LA-MA
RK21	II	#1	DZK14-02 (East)	135.5	Net textured ore with BMS vein	Dun	HA
RK22	II	#1	DZK14-02 (East)	179.5	Net textured/semi-massive ore, minor shear textures	Dun	HA
RK23	II	#1	DZK14-02 (East)	225.3	Net textured ore, minor shear/remobilisation textures	Dun + Minor Carb	TA
RK24	II	#1	DZK14-02 (East)	228.3	Remobilised massive BMS	Lhz + Carb	TA
RK25	II	#1	DZK14-02 (East)	242.4	Patchy net textured ore	Ol-Web	MA
RK26	II	#1	DZK14-02 (East)	252.0	Marble	Marble	N/A
RK27	II	#1	DZK09-01 (West)	78.1	Disseminated ore, BMS remobilised in carbonate veins	Wed + Carb	LA-MA
RK28	II	#1	DZK09-01 (West)	118.8	Net textured ore	Ol-rich Lhz	MA

Name	Segment	Orebody	Borehole	Depth (m)	Ore Description	Lithology	Alteration
RK29	II	#1	DZK09-01 (West)	127.2	Highly altered, remants of net textured ore	Lhz	HA
RK30	II	#1	DZK09-01 (West)	135.9	Net textured ore	Dun	TA
RK31	II	#1	DZK09-01 (West)	146.1	Net textured ore with small sulphide veinlets	Ol-rich Lhz	HA
RK32	II	#1	DZK09-01 (West)	173.6	Net textured ore	Dun	MA
RK33	II	#1	DZK09-01 (West)	194.4	Patchy net textured ore	Ol-Web	MA
RK34	II	#1	DZK09-01 (West)	206.2	Disseminated ore	Web	MA
Cu-rich samples. Drill core started at 1100 m above sea level							
RK39	I	#24	ZKS-09	315.8	Net textured ore (coarse)	Dun	TA
RK40	I	#24	ZKS-09	300.1	Net textured ore (coarse)	Dun	TA
RK41	I	#24	ZKS-09	289.0	Highly altered with partially preserved net textured ore with BMS veins	Highly Carbonatised	TA
RK42	I	#24	ZKS-09	286.4	Highly altered with partially preserved net textured ore with BMS veins	Web	MA
RK43	I	#24	ZKS-09	278.9	Partial net textured ore, BMS enclosed in carbonate/serpentine veins	Lhz Carbonatised	TA
RK44	I	#24	ZKS-09	272.7	Net textured ore (coarse)	Lhz	TA
RK45	I	#24	ZKS-09	267.7	Net textured ore (coarse) with BMS in a carbonate vein	Dun + Carb	TA
RK46	I	#24	ZKS-09	344.2	Disseminated ore with BMS in carbonate veins	Web	HA
RK47	I	#24	ZKS-09	336.0	Altered Net textured ore with small BMS veinlets, minor shear textures	Ol-rich Lhz	TA
RK48	I	#24	ZKS-09	327.6	Net textured ore with BMS in a carbonate vein	Dun + Carb	TA
RK49	I	#24	ZKS-09	322.6	Net textured ore (coarse)	Dun	TA

Appendix K: Jinchuan Major Element Data (Cardiff University)

Name	Segment	Orebody	Borehole	Depth (m)	SiO2 (wt. %)	TiO2 (wt. %)	Al2O3 (wt. %)	Fe2O3 (wt. %)	MnO (wt. %)	MgO (wt. %)	CaO (wt. %)	Na2O (wt. %)	K2O (wt. %)	P2O5 (wt. %)	LOI (wt. %)	Total (wt. %)
RK01	II	#1	DZK12-06 (Central)	26.3	11.79	0.01	0.02	0.33	0.06	14.67	38.19	0.02	0.01	0.00	34.39	99.50
RK02	II	#1	DZK12-06 (Central)	33.0	43.05	0.51	6.39	14.39	0.17	26.75	4.59	0.34	0.21	0.06	4.40	100.85
RK08	II	#1	DZK12-06 (Central)	135.3	39.51	0.31	3.83	15.63	0.17	30.20	2.90	0.39	0.12	0.06	6.21	99.32
RK11	II	#1	DZK12-06 (Central)	158.0	30.39	0.20	1.89	25.77	0.17	27.82	2.05	0.06	0.01	0.00	10.44	98.80
RK13	II	#1	DZK12-06 (Central)	167.7	27.37	0.13	1.04	31.35	0.14	27.71	1.26	0.03	0.01	0.01	10.67	99.72
RK27	II	#1	DZK09-01 (West)	78.1	42.63	0.72	8.83	16.16	0.14	15.06	13.54	1.51	0.87	0.02	-0.35	99.13
RK28	II	#1	DZK09-01 (West)	118.8	28.29	0.08	1.32	26.63	0.15	28.82	0.69	2.68	0.01	0.02	11.94	100.64
RK32	II	#1	DZK09-01 (West)	173.6	22.32	0.05	0.35	34.54	0.14	28.67	0.15	0.55	0.15	0.04	11.88	98.83
RK33	II	#1	DZK09-01 (West)	194.4	32.96	0.31	2.85	24.72	0.17	25.17	3.01	3.95	0.02	0.01	6.92	100.07
RK39	I	#24	ZKS-09	315.8	24.52	0.06	1.17	34.56	0.15	25.61	0.19	0.74	0.07	0.03	12.05	99.16
RK42	I	#24	ZKS-09	286.4	27.10	0.09	1.67	33.15	0.04	25.22	0.92	3.12	0.08	0.02	8.09	99.51
RK43	I	#24	ZKS-09	278.9	24.13	0.05	0.76	32.61	0.21	26.03	3.18	0.86	0.02	0.01	12.45	100.30
RK44	I	#24	ZKS-09	272.7	25.93	0.07	0.77	32.56	0.11	26.83	0.18	0.39	0.01	0.03	12.50	99.38
RK46	I	#24	ZKS-09	344.2	34.80	0.39	3.28	19.81	0.19	23.55	5.68	6.96	0.10	0.02	6.22	101.00
RK47	I	#24	ZKS-09	336.0	26.44	0.17	0.48	33.19	0.22	25.84	0.23	1.17	0.05	0.01	12.24	100.03

Appendix L: Jinchuan PGE Whole-Rock Data (Cardiff University)

Sample No.	Segment	Orebody	Borehole	Os (ppb)	Ir (ppb)	Ru (ppb)	Rh (ppb)	Pt (ppb)	Pd (ppb)	Au (ppb)
RK01	II	#1	DZK12-06 (Central)	0.06	0.10	0.14	0.07	0.79	0.51	1.21
RK02	II	#1	DZK12-06 (Central)	2.08	2.14	4.49	1.48	16.83	15.00	24.34
RK03	II	#1	DZK12-06 (Central)	7.68	6.74	14.04	5.67	38.63	33.78	67.54
RK04	II	#1	DZK12-06 (Central)	2.76	3.96	6.86	4.94	38.34	30.05	30.89
RK05	II	#1	DZK12-06 (Central)	3.99	3.45	7.85	3.02	45.41	37.39	56.71
RK06	II	#1	DZK12-06 (Central)	0.91	1.12	2.19	0.86	7.81	11.65	20.43
RK07	II	#1	DZK12-06 (Central)	0.72	0.50	1.41	0.58	12.46	5.45	84.44
RK08	II	#1	DZK12-06 (Central)	1.06	1.25	3.08	1.00	13.13	22.10	16.87
RK08D	II	#1	DZK12-06 (Central)	0.83	1.37	3.21	1.03	15.70	22.34	15.98
RK09	II	#1	DZK12-06 (Central)	9.73	8.44	18.04	8.71	48.90	51.57	69.33
RK10	II	#1	DZK12-06 (Central)	1.88	9.47	5.86	1.24	182.04	19.88	12.80
RK11	II	#1	DZK12-06 (Central)	30.60	21.99	21.12	10.19	388.58	63.55	15.17
RK12	II	#1	DZK12-06 (Central)	15.26	16.32	31.23	10.78	171.76	108.87	55.40
RK13	II	#1	DZK12-06 (Central)	41.97	36.67	79.61	16.25	64.08	145.56	17.61
RK16	II	#1	DZK14-02 (East)	0.16	0.11	0.27	0.14	3.89	3.29	1.74
RK17	II	#1	DZK14-02 (East)	0.08	0.09	0.11	0.04	1.29	0.98	0.99
RK18	II	#1	DZK14-02 (East)	0.27	0.31	0.95	0.21	2.46	6.10	12.66
RK18D	II	#1	DZK14-02 (East)	0.45	0.50	1.02	1.67	67.07	6.33	31.71
RK19	II	#1	DZK14-02 (East)	97.71	70.74	148.71	28.12	53.22	47.83	6.97
RK20	II	#1	DZK14-02 (East)	2.26	2.51	4.79	2.37	31.06	43.75	12.73
RK20D	II	#1	DZK14-02 (East)	2.64	2.93	5.79	2.51	70.28	49.48	17.46
RK21	II	#1	DZK14-02 (East)	4.71	10.41	8.14	2.70	13.05	62.79	101.12
RK22	II	#1	DZK14-02 (East)	9.52	10.16	13.82	31.12	28.63	433.74	72.19
RK23	II	#1	DZK14-02 (East)	0.89	4.80	2.93	5.64	488.37	224.86	340.60
RK24	II	#1	DZK14-02 (East)	2.79	6.17	5.01	6.69	208.64	126.25	30.65
RK25	II	#1	DZK14-02 (East)	0.99	1.28	1.59	0.78	15.37	120.36	282.02
RK27	II	#1	DZK09-01 (West)	20.24	49.68	76.62	18.17	48.07	67.17	39.82
RK28	II	#1	DZK09-01 (West)	20.14	66.72	62.43	31.84	109.86	216.20	160.12
RK29	II	#1	DZK09-01 (West)	30.14	32.40	47.84	40.13	2,228.32	214.44	42.99
RK30	II	#1	DZK09-01 (West)	4.41	6.02	5.32	36.94	64.92	262.52	334.22

Sample No.	Segment	Orebody	Borehole	Os (ppb)	Ir (ppb)	Ru (ppb)	Rh (ppb)	Pt (ppb)	Pd (ppb)	Au (ppb)
RK31	II	#1	DZK09-01 (West)	3.70	3.89	4.53	10.46	830.12	194.14	42.64
RK32	II	#1	DZK09-01 (West)	17.80	21.52	22.86	15.04	119.33	471.80	29.73
RK32D	II	#1	DZK09-01 (West)	18.75	22.48	23.72	16.67	49.71	487.54	84.57
RK33	II	#1	DZK09-01 (West)	9.16	7.91	16.33	4.96	129.88	111.26	75.08
RK34	II	#1	DZK09-01 (West)	0.49	0.53	0.76	0.43	108.02	33.20	41.14
RK39	I	#24	ZKS-09	48.06	46.34	63.42	49.88	11.66	110.75	210.76
RK40	I	#24	ZKS-09	26.49	26.51	25.86	59.63	9.27	286.91	195.57
RK41	I	#24	ZKS-09	6.86	9.34	5.88	11.17	182.93	163.91	185.09
RK42	I	#24	ZKS-09	7.56	12.47	9.19	11.50	21.29	153.83	338.76
RK43	I	#24	ZKS-09	47.31	52.42	55.95	40.43	53.62	273.86	23.30
RK44	I	#24	ZKS-09	75.71	79.77	90.30	56.40	39.60	131.52	47.20
RK45	I	#24	ZKS-09	41.50	51.56	60.82	55.54	191.10	416.78	123.26
RK46	I	#24	ZKS-09	8.55	9.99	19.15	7.81	269.33	108.00	361.04
RK47	I	#24	ZKS-09	149.78	151.23	247.98	74.42	32.55	210.83	1,716.93
RK48	I	#24	ZKS-09	60.09	54.49	65.05	33.91	48.54	447.08	208.01
RK49	I	#24	ZKS-09	36.41	30.58	28.44	27.46	14.82	249.12	140.23

Appendix M: Jinchuan Full PGM Mineralogical Data (BMS = Base metal sulphides, Chl - Chlorite, Cob = Cobaltite, Cpy = Chalcopyrite, Cr = Chromite, Gers = Gersdorffite, Mgt = Magnetite,Nic = Niccolite, Ol = Olivine, Pn = Pentlandite, Po = Pyrrhotite, Py = Pyrite, Pyx = Pyroxene, Serp = Serpentine, Sil = Unknown Silicate, Wurtz = Wurtzite)

Drill Hole	Sample	No.	Composition	Size (μm)	Area (μm^2)	Association
DZK12-06	RK01		No PGM Observed			No PGM Observed
DZK12-06	RK02	D1	Pd-Bi	0.9 x 2.4	2.2	Within BMS, within Pn
		E1	Pd-Bi	1.3 x 2.6	3.4	Within BMS, within/edge Pn/Po
		F1	Pt-As	4.1 x 13.7	56.2	Within Pyx, spatially associated Po blebs
		G1	Ag-Au-Fe	2.2 x 2.7	5.9	Within/edge BMS, within/edge Cpy vein and in contact with Ti-Mgt
DZK12-06	RK03	A1	Pd-Bi	2.6 x 3.6	9.4	Within BMS, within Cpy (Cpy associated with Pn)
		A2	Pd-Ag-Se-Te	0.5 x 1.2	0.6	Within BMS, within Cpy (Cpy associated with Pn and Wurtz)
		A3	Pd-Te/Pb-Pd-Te	0.6 x 3.4	2.0	Within BMS, within Cpy (Cpy associated with Pn and Wurtz)
		A4	Pd-Bi	1.0 x 1.2	1.2	Within BMS, within Pn/Cpy (Pn/Cpy associated with Wurtz)
		A5	Pb-Bi-Te	1.7 x 1.9	3.2	Within BMS, within Pn (Pn associated with Po)
		B1	Bi	0.8 x 1.3	1.0	Within BMS, within Pn associated with silicate vein (Pn associated with Cpy)
		C1	Ag-Te	1.0 x 2.0	2.0	Within BMS, within Po/Cpy
DZK12-06	RK04	A1	Pb-Te	3.1 x 4.9	15.2	Associated with Cpy veining in silicate
		A2	Pb-Te	0.9 x 3.8	3.4	Associated with Cpy veining in silicate
		A3	Pt-Te-Bi	1.0 x 2.3	2.3	Associated with Cpy veining in silicate
		A4	Pb-Te	1.1 x 4.5	5.0	Associated with Cpy veining in silicate
		A5	Pb-Te	0.7 x 0.9	0.6	Associated with Cpy veining in silicate
		A6	Pb-Te	0.9 x 0.9	0.8	Associated with Cpy veining in silicate
		A7	Pt-Pd-Te-Bi	0.7 x 0.7	0.5	Associated with Cpy veining in silicate
		B1	Pd-Sn-Cu	0.8 x 4.6	3.7	Within/edge Cpy/Mgt (Cpy/Mgt associated with Pn)
		C1	Pt-Te-Bi	2.5 x 3.1	7.8	Within BMS, within Cpy (Cpy associated with Pn and Po)
DZK12-06	RK05	A1	Bi-Te	2.2 x 3.0	6.6	Within/edge BMS, within/edge Pn/Cpy and silicate
		A2	Ag-Te	1.2 x 1.7	2.0	Partially envelopes A1
		B1	Ag-Te	1.0 x 1.9	1.9	Within Mgt (Mgt as vein with silicate cutting Po)
		C1	Ag-Te (Bi in bright spot)	1.4 x 5.0	7.0	Within/edge BMS, within/edge Pn and cross cutting Mgt veins
		C2	Ag-Te	0.5 x 1.6	0.8	Within/edge BMS, within/edge Pn and cross cutting Mgt veins
		C3	Ag-Te	0.8 x 2.1	1.7	Within/edge BMS, within/edge Pn and cross cutting Mgt veins
		D1	Ir-Pt-As-S	1.2 x 1.4	1.7	Within BMS, within Gers-Cob (Gers-Cob within Po)
		D3	D1 rimmed by Ag-Te		NA	Partially rims D1
		E1	Ni-Ag-Te-Bi	1.9 x 2.5	4.8	Within BMS, within Pn
DZK12-06	RK06	A1	Pb-Te	3.0 x 4.6	13.8	Within BMS, within Cpy
		A2	Ag-Te	1.5 x 2.1	3.2	Within BMS, within Cpy
DZK12-06	RK07	A1	Pd-Bi	1.8 x 3.7	6.7	Within BMS, within/edge Cpy/Nic
		A2	Pb-Te	0.4 x 2.7	1.1	Within BMS, within/edge Cpy/Nic
		A3	Bi	1.4 x 5.4	7.6	Within BMS, within/edge Cpy/Nic
DZK12-06	RK08		No PGM Observed			No PGM Observed

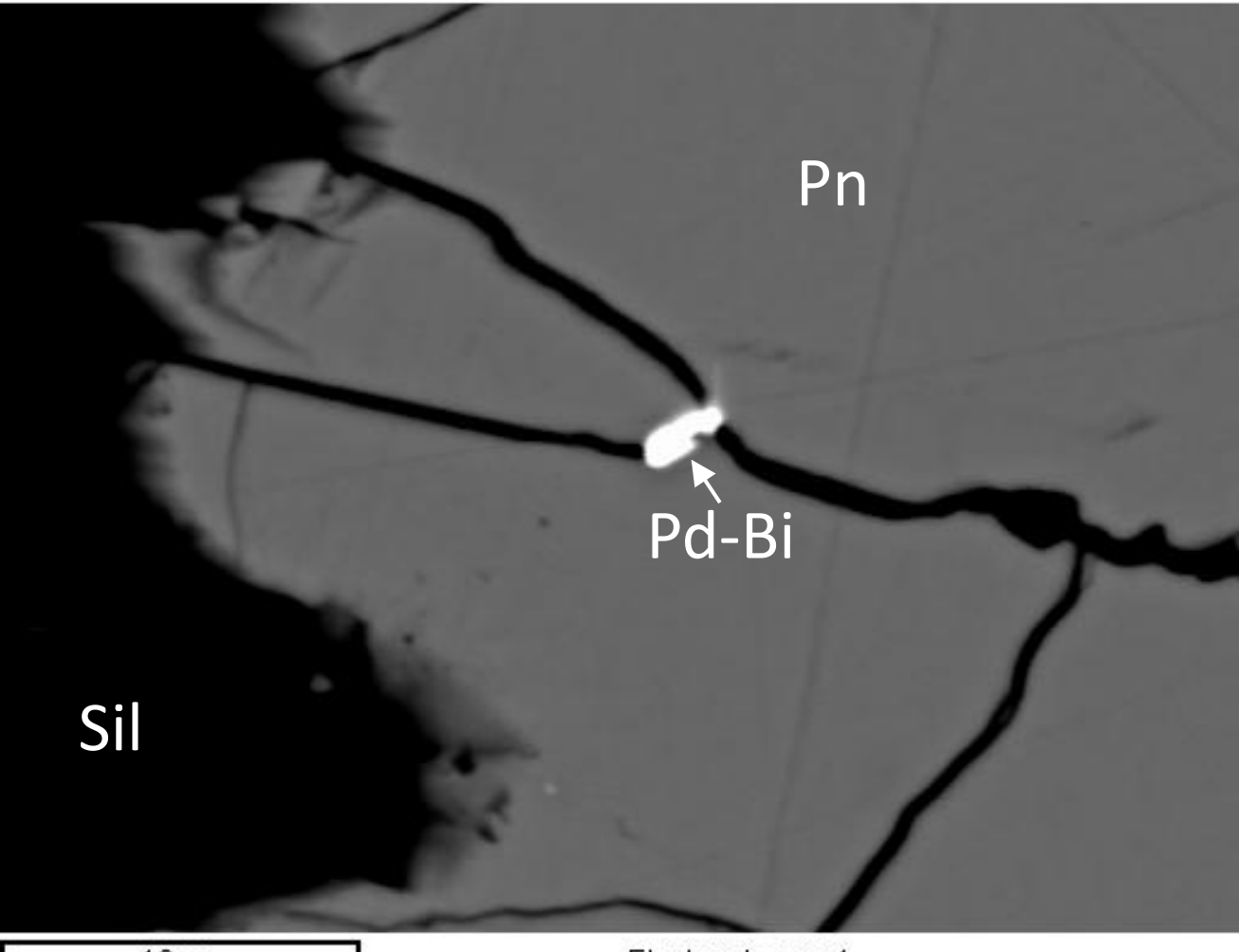
Drill Hole	Sample	No.	Composition	Size (µm)	Area (µm^2)	Association
DZK12-06	RK09	A1	Ir-Pt-As-S	2.2 x 2.9	6.4	Within BMS, within Gers-Cob (Gers-Cob within Po)
DZK12-06	RK10	A1	Ag-Te	1.8 x 5.0	9.0	Within BMS, within Cpy (Cpy associated with Po and Pn)
		B1	Ag-Au	4.2 x 6.5	27.3	Within/edge BMS, within/edge Cpy and in contact with silicate vein (Cpy associated with Mgt)
		C1	Ag-Te	3.8 x 5.9	22.4	Within BMS, within Cpy
		C2	Ag-Te	0.8 x 3.0	2.4	Within BMS, within Cpy
		C3	Ag-Te	0.4 x 1.0	0.4	Within BMS, within Cpy
		C4	Ag-Te	1.0 x 3.1	3.1	Within BMS, within Cpy (Cpy associated with Po)
		D1	Ag-Te	3.4 x 5.8	19.7	Within BMS, within Cpy
		E1	Ag-Te	5.6 x 7.1	39.8	Within BMS, within Cpy
		F1	Ir-Pt-Ni-Fe-Co-As-S	3.8 x 4.0	15.2	Within Serp
		G1	Pt-As	11.5 x 15.0	172.5	Within Serp (close to Ti-Mgt and Cpy)
DZK12-06	RK11		No PGM Observed			No PGM Observed
DZK12-06	RK12	A1	Ir-Pt-As-S	2.4 x 3.6	8.6	Within Chl (close to Po and Mgt bleb)
DZK12-06	RK13	A1	Ir-As-S	1.8 x 3.2	5.8	Within BMS, within Gers-Cob (Gers-Cob associated with Pn/Po/Mgt mix)
DZK12-06	RK14	A1	Ir-As-S	1.8 x 4.1	7.4	Within/edge BMS, within/edge Gers-Cob and in contact with Serp (Gers-Cob associated with Po)
		A2	Ir-Pt-As-S	1.3 x 4.6	6.0	Within/edge BMS, within/edge Gers-Cob and in contact with Serp (Gers-Cob associated with Po)
		A3	Pb-Pt-Te	1.0 x 1.4	1.4	Within BMS, within Gers-Cob (Gers-Cob associated with Po)
DZK14-02	RK16		No PGM Observed			No PGM Observed
DZK14-02	RK17		No PGM Observed			No PGM Observed
DZK14-02	RK18		No PGM Observed			No PGM Observed
DZK14-02	RK19	A1	Ir-Pt-As-S	3.2 x 6.5	20.8	Within BMS, within Gers-Cob (Gers-Cob associated with Po and Cpy)
		B1	Ir-Pt-As-S	3.3 x 5.0	16.5	Within Sil and associated with Cpy
		C1	Ir-Pt-As-S	2.2 x 3.4	7.5	Within Sil (close to Po bleb)
DZK14-02	RK20	A1	Ag-Te	1.5 x 2.5	3.8	Within BMS, within Po
		B1	Ir-As-Co-S	1.1 x 1.2	1.3	Within BMS, within Pn
		C1	Pd-Fe-Bi	1.0 x 1.7	1.7	Within BMS, within partially oxidised Po (Po associated with Pn)
		D1	Fe-Pd-Bi	0.6 x 0.9	0.5	Within/edge Ti-Mgt and spinel (associated with BMS)
		E1	Pd-Fe-Pb-Bi	1.0 x 1.5	1.5	Within BMS, within Po
DZK14-02	RK21	A1	Pd-Fe-Pb-Bi	1.0 x 1.7	1.7	Within BMS, within Cpy (Cpy associated with Pn)
		B1	Gers + Rh in ss	1.6 x 5.0	8.0	Within BMS, within Po
		C1	Gers + Rh in ss	4.8 x 5.0	24.0	Within BMS, within Po
		D1	Rh-Ir in Gers exsolved	0.5 x 0.5	0.3	Within BMS, within/edge Po/Pn/Cpy
DZK14-02	RK23		No PGM Observed			No PGM Observed
DZK14-02	RK24A	A1	Au-Ag	4.8 x 5.1	24.5	Within/edge BMS, within/edge Cpy laths and incontact with Carb
		B1	Pt-As	6.4 x 7.3	46.7	Within BMS, within Cpy (Cpy associated with Serp alteration) (largest PGM fragment measured)
				6.3 x 25.5	159.4	Whole area of PGM which is fragmented

Drill Hole	Sample	No.	Composition	Size (µm)			Area (µm^2)	Association
DZK14-02	RK24B	A1	Ni-Te-Bi		x		NA	Within Serp
		A2	Ni-Pd-Te-Bi	1.6	x	5.9	9.4	Within Serp
		A3	Ag-Te-Bi	1.0	x	1.6	1.6	Within Serp
		A4	Pb-Te-Bi	1.0	x	1.3	1.3	Within Serp
		A5	Bi-Te	1.6	x	1.9	3.0	Within Serp
		A6	Bi-Te	1.0	x	3.9	3.9	Within Serp
		C1	Au-Ag	1.6	x	3.4	5.4	Within/edge BMS, within/edge Pn bleb and in contact with Serp
		D1	Pd-Te-Bi	1.8	x	1.9	3.4	Within/edge BMS, within/edge Pn and in contact with Serp
		D2	Pd-Te-Bi/Ag-Te	0.7	x	1.6	1.1	Within/edge BMS, within/edge Pn and in contact with Serp
		D3	Ag-Te	0.9	x	1.6	1.4	Within/edge BMS, within/edge Po and in contact with Serp
		D4	Ag-Te	0.7	x	0.8	0.6	Within/edge BMS, within/edge Pn and in contact with Serp
		D5	Ag-Te	0.9	x	1.4	1.3	Within/edge BMS, within/edge Pn and in contact with Serp
		D6	Ag-Te	0.8	x	1.1	0.9	Within/edge BMS, within/edge Pn and in contact with Serp
		E1	Pd-Ni-Te-Bi	4.5	x	13.1	59.0	Within/edge BMS/Mgt/Serp/Carb, association unclear
DZK14-02	RK25	A1	Au-Ag-Fe	1.9	x	4.0	7.6	Within/edge BMS, within/edge Po and Mgt + Cr
		A2	Au-Ag-Fe	1.6	x	2.1	3.4	Within/edge BMS, within/edge Cpy and Mgt + Cr
		A4	Au-Ag-Fe	1.5	x	2.3	3.5	Within/edge BMS, within/edge Cpy and Mgt + Cr
		A4	Au-Ag	0.4	x	1.7	0.7	Within BMS, within Cpy bleb within Mgt + Cr
		A5	Bi-Te	0.4	x	0.9	0.4	Within BMS, within Cpy bleb within Mgt + Cr
DZK09-01	RK27	A1	Ru-Os-S	4.5	x	7.2	32.4	Within Carbonate
		A2	Os-Ru-S	0.9	x	8.1	7.3	Within Carbonate
		A3	Ru-Os-S	2.7	x	4.1	11.1	Within Carbonate
		A4	Ru-Os-S	1.8	x	4.5	8.1	Within Carbonate
		A5	Ru-Pt-Rh-Os-As-S	1.8	x	2.0	3.6	Within Carbonate
		A6	Ir-Pt-As-S	3.2	x	3.4	10.9	Within Carbonate
DZK09-01	RK29	A1	Ir-Rh-Pt-As-S	0.8	x	2.5	2.0	Within BMS, within Gers-Cob (with Rh in ss) (Gers-Cob within Po)
		A2	Pb-Te	0.4	x	0.4	0.2	Within BMS, within Gers-Cob (with Rh in ss) (Gers-Cob within Po)
DZK09-01	RK30	A1	Au-Ag	1.0	x	2.7	2.7	Within Mgt
		A2	Pd-Bi/Au	0.5	x	0.5	0.3	Within in silicate
		B1	Pd-Bi	1.8	x	4.3	7.7	Within/edge Mgt and Serp vein
		B2	Pd-Bi	0.5	x	0.7	0.4	Within/edge Mgt and Serp vein
DZK09-01	RK31	A1	Pt-As	3.1	x	8.3	25.7	Within Serp (Serp associated with Mgt and Ol)
DZK09-01	RK33	A1	Pd-Fe-Te-Bi	1.2	x	1.6	1.9	Within BMS, within Po
		A2	Ag-Te	1.2	x	1.2	1.4	Within BMS, within Po
		B1	Pd-Fe-Te-Bi	1.6	x	2.0	3.2	Within BMS, within Po
		B2	Ag-Te	1.1	x	1.9	2.1	Within BMS, within Po
		B3	Pd-Fe-Te-Bi	1.5	x	2.7	4.1	Within BMS, within Po
		C1	Pd-Fe-Te-Bi	1.0	x	2.3	2.3	Within BMS, within Po (Po associated with Pn)
		C2	Ag-Te	1.2	x	4.6	5.5	Within BMS, within Po (Po associated with Pn)
		C3	Pb-Te	0.5	x	0.9	0.5	Within BMS, within Po (Po associated with Pn)

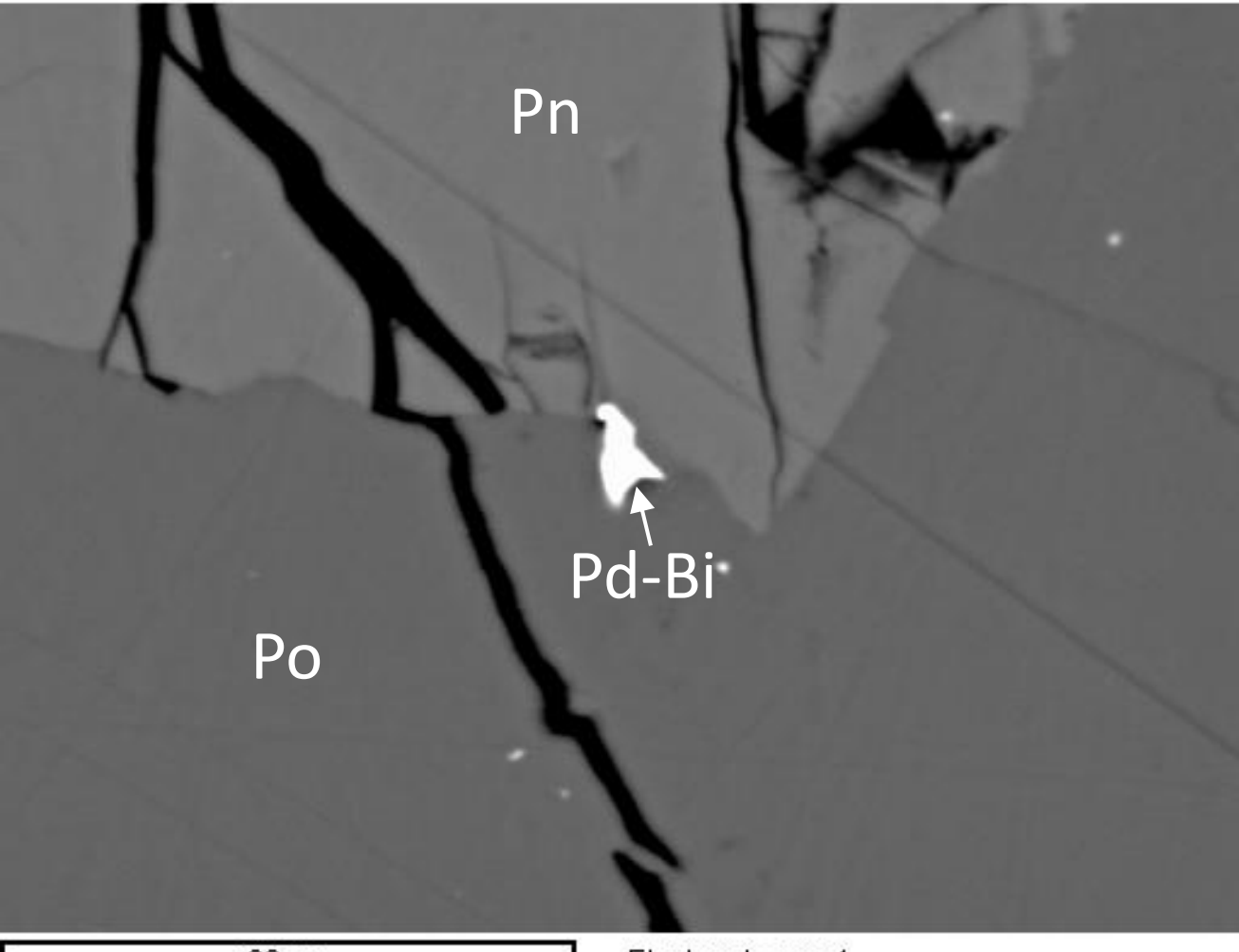
Drill Hole	Sample	No.	Composition	Size (µm)	Area (µm^2)	Association
		D1	Pt-As-Fe	2.7 x 3.8	10.3	Within Sil
DZK09-01	RK33	E1	Au-Ag-Fe	1.8 x 3.9	7.0	Within Sil
		F1	Pd-Fe-Te-Bi/Pb-Ag-Te	2.1 x 3.5	7.4	Within BMS, within Po
		F2	Ni-Pb-Te-Bi	1.1 x 4.3	4.7	Within BMS, within Po
DZK09-01	RK34	A1	Au-Ag	1.8 x 5.0	9.0	Within/edge BMS, within/edge Cpy and in contact with Serp
		A2	Au-Ag	1.9 x 4.8	9.1	Within/edge BMS, within/edge Cpy and in contact with Serp
ZKS-09	RK39	A1	Pd-Bi	1.1 x 1.2	1.3	Within BMS, within/edge Pn/Oxidised Pn
		A2	Pd-Pb-Bi	0.4 x 1.1	0.4	Within BMS, within/edge Pn/Oxidised Pn
ZKS-09	RK40	A1	Pd-Bi	1.2 x 1.6	1.9	Within Pn/Mgt mix
		A2	Pd-Bi	0.9 x 0.5	0.5	Within Pn/Mgt mix
		B1	Pd-Bi	0.7 x 2.3	1.6	Within BMS, within/edge Po/Pn
		C1	Pd-Bi	1.3 x 1.7	2.2	Within BMS, within/edge Po/Pn
		C2	Pd-Fe-Pb-Bi	0.5 x 1.3	0.7	Within BMS, within/edge Po/Pn
		D1	Pd-Fe-Te-Bi	1.6 x 4.1	6.6	Within BMS, within/edge Po/Pn/Cpy mix
		E1	Pd-Bi	1.1 x 1.2	1.3	Within Mgt (Mgt associated with Pn)
		F1	Pd-Bi	3.0 x 5.3	15.9	Within Sil and associated with Pb-S and Mgt
		F2	Pd-Te-Bi	2.5 x 6.3	15.8	Within Sil and associated with Pb-S and Mgt
		F3	Se-Bi-Te	4.1 x 4.5	18.5	Within Sil and associated with Pb-S and Mgt
		F4	Pb-Te	2.0 x 6.8	13.6	Within Sil and associated with Pb-S and Mgt
		F5	Pb-Te	2.3 x 3.4	7.8	Within Sil and associated with Pb-S and Mgt
		F6	Se-Pb-Te-Bi	0.9 x 4.5	4.1	Within Sil and associated with Pb-S and Mgt
ZKS-09	RK41		No PGM Observed			No PGM Observed
ZKS-09	RK42	A1	Ag-Au	2.3 x 3.0	6.9	Within BMS, within Cpy
		B1	Ag-Au-Fe	2.0 x 5.0	10.0	Within Mgt
		B2	Ag-Au	1.0 x 1.0	1.0	Within Mgt
		B3	Au-Ag	0.5 x 1.3	0.7	Within/edge Wurtz/Mgt and associated with carbonate vein
		B4	Au-Ag	1.2 x 2.3	2.8	Within/edge Wurtz/Mgt and associated with carbonate vein
		B5	Au-Ag	0.4 x 1.0	0.4	Within/edge Wurtz/Mgt and associated with carbonate vein
		E1	Ag-Au	6.7 x 37.3	249.9	Within BMS, within Cpy
		E2	Ag-Au	5.0 x 8.0	40.0	Within/edge BMS, within/edge Cpy and in contact with silicate
		F1	Ir-Pt-Os-As-S	6.5 x 16.3	106.0	Within/edge BMS, within/edge Po and in contact with Serp
		F2	Rh-As-S	x	NA	Partially rims F1 (0.7 micron thickness where present)
ZKS-09	RK43	A1	Pd-Fe-Ni-Te-Bi	1.9 x 2.1	4.0	Within BMS, within Po
		A2	Ag-Te	1.1 x 1.2	1.3	Within BMS, within Po
		B1	Pd-Bi-Te	3.5 x 4.3	15.1	Within/edge BMS, within Pn veined by silicate
		C1	Ir-Rh-As-S/Gers-Cob	1.4 x 1.4	2.0	Within/edge BMS, within/edge Pn and in contact with Serp
ZKS-09	RK44	A1	Pd-Bi	1.3 x 2.1	2.7	Within/edge BMS, within/edge Mgt/Po (Mgt/Po associated with Pn)
ZKS-09	RK45	A1	Pd-Te-Bi	1.6 x 1.8	2.9	Within BMS, within Pn (Pn associated with Mgt)
		B1	Pd-Bi	1.5 x 3.3	5.0	Within/edge BMS, within/edge Po and in contact with Mgt
		C1	Pd-Bi-Te	1.6 x 2.2	3.5	Within/edge BMS, within/edge Pn/Mgt

Drill Hole	Sample	No.	Composition	Size (µm)	Area (µm^2)	Association
		C2	Pd-Bi-Te	0.8 x 1.8	1.4	Within/edge BMS, within/edge Pn/Mgt
		D1	Pd-Te-Bi	3.1 x 5.1	15.8	Within/edge BMS, within Pn veined by Mgt
ZKS-09	RK45	E1	Pd-Bi-Te	4.6 x 5.3	24.4	Within Serp (tentative association with minor BMS)
		E2	Pd-Pb-Bi-Te	0.8 x 0.8	0.6	Within Serp (tentative association with minor BMS)
		F1	Pt-Bi-Te	6.4 x 7.4	47.4	Within Serp (tentative association with minor BMS)
		G1	Pd-Fe-Bi	1.6 x 2.0	3.2	Within BMS, within Po
		H1	Pd-Bi	2.0 x 2.6	5.2	Within Pn partially altered to Mgt
		I1	Pd-Pb-Bi	1.7 x 2.7	4.6	Within BMS, within Po
ZKS-09	RK46		No PGM Observed			No PGM Observed
ZKS-09	RK48	A1	Pd-Te-Bi	3.5 x 3.6	12.6	Within/edge BMS, within/edge Cpy/Mgt and in contact with Serp
		B1	Pb-Bi-Te	2.6 x 5.8	15.1	Within BMS, within Po
		C1	Pd-Te-Bi	1.7 x 2.7	4.6	Within BMS, within Cu-Fe-S
		D1	Pd-Pb-Bi-Te	2.5 x 3.5	8.8	Within/edge Mgt/Cpy (Mgt rims Cpy)
		E1	Pd-Bi	2.2 x 2.5	5.5	Within BMS, within Cpy
		F1	Pd-Bi	3.4 x 4.0	13.6	Within BMS, within Cpy
		G1	Pd-Te-Bi	4.5 x 4.7	21.2	Within BMS, within Cu-Fe-S
		G2	Pd-Bi-Te/Pb-Te	1.4 x 3.0	4.2	Within BMS, within Po
		H1	Pd-Bi	1.9 x 2.6	4.9	Within BMS, within Cu-Fe-S
ZKS-09	RK49		No PGM Observed			No PGM Observed

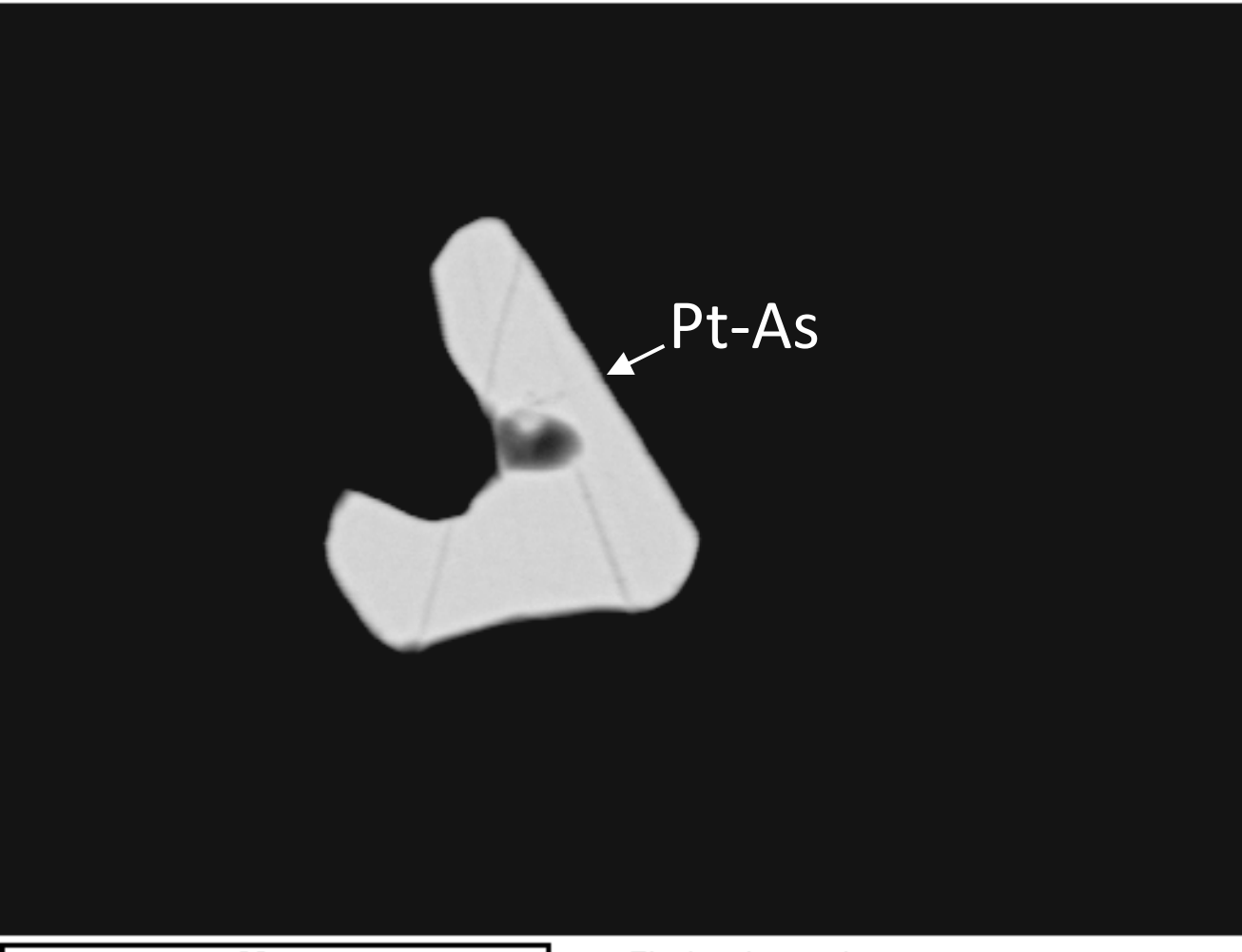
RK02 D1



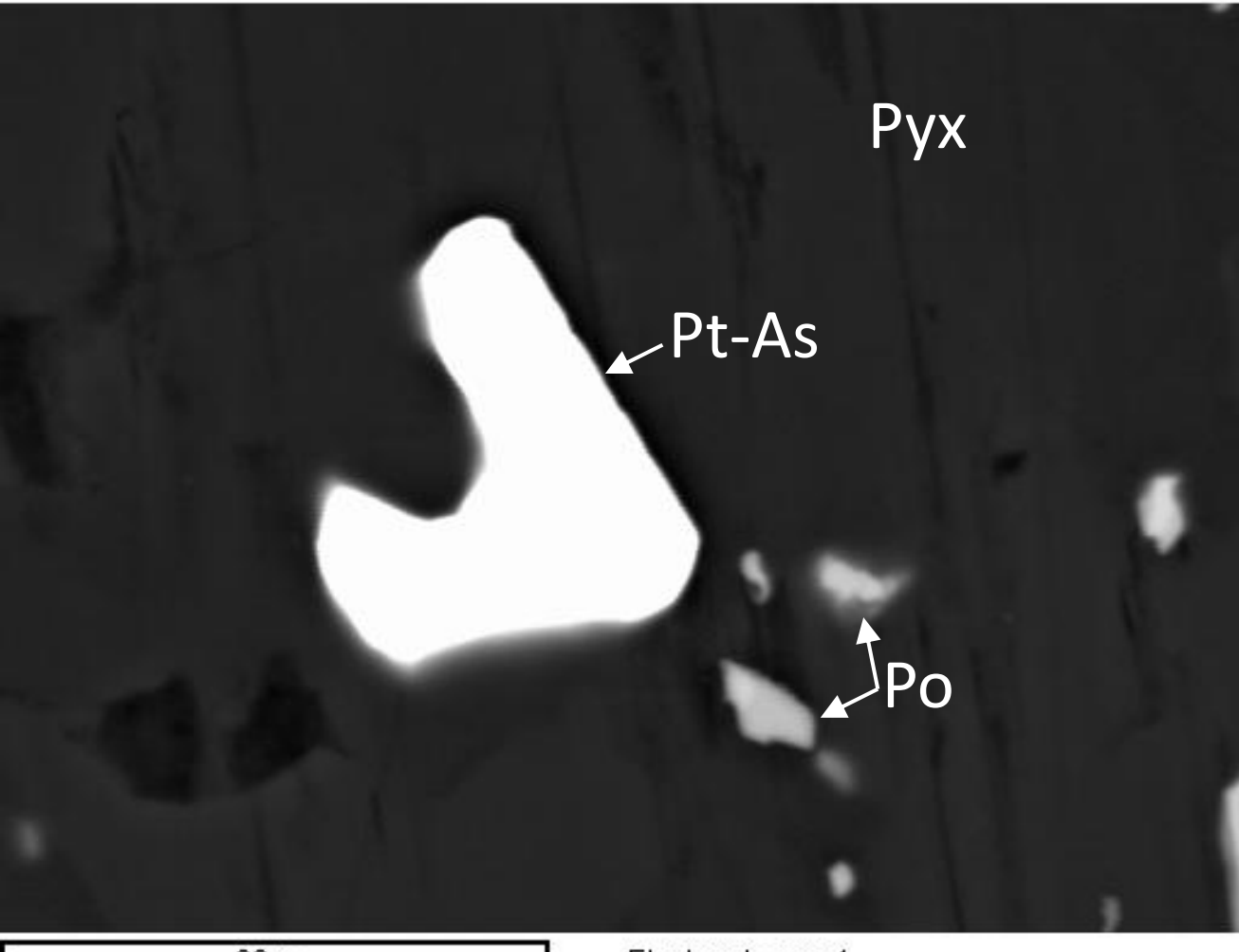
RK02 E1



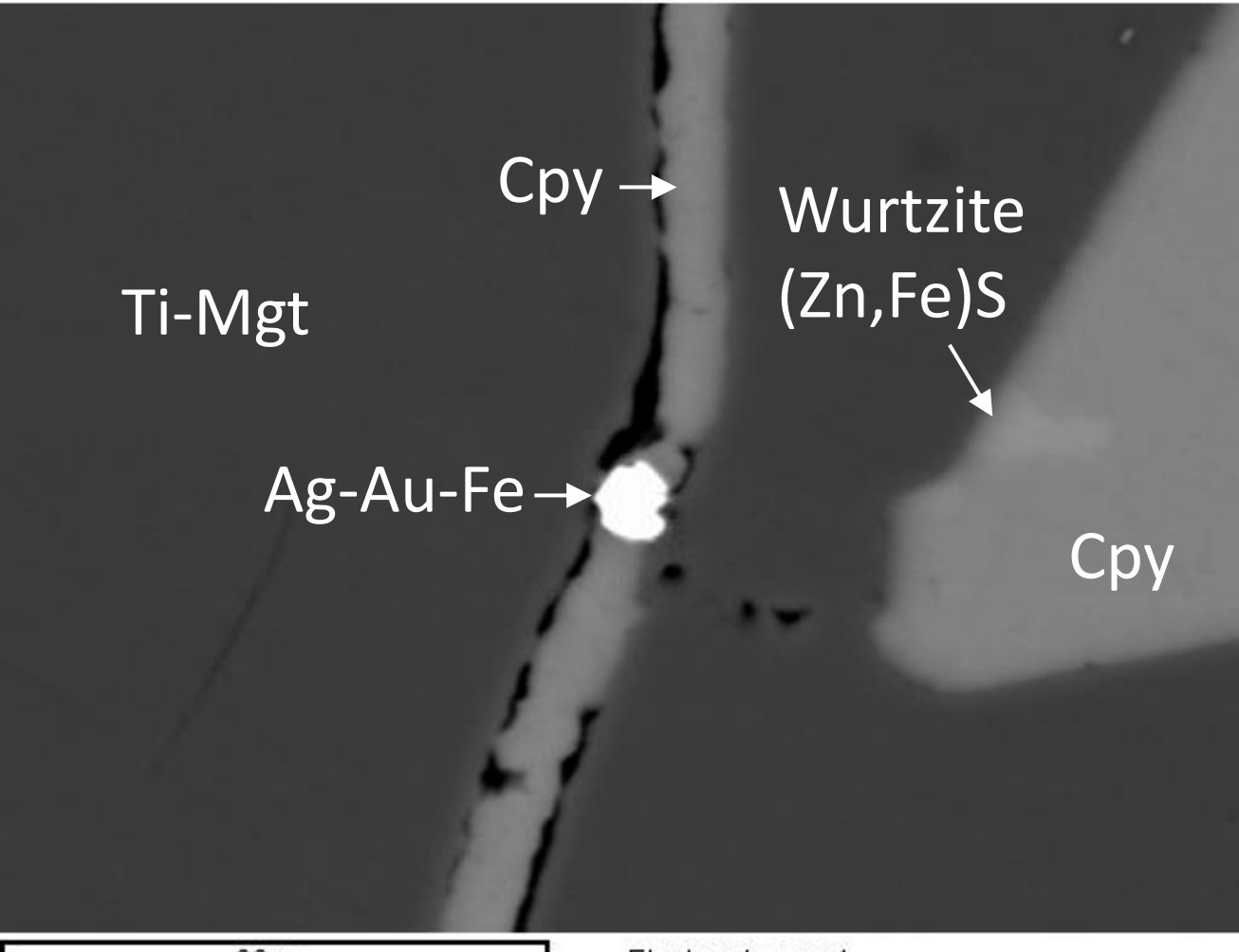
RK02 F1



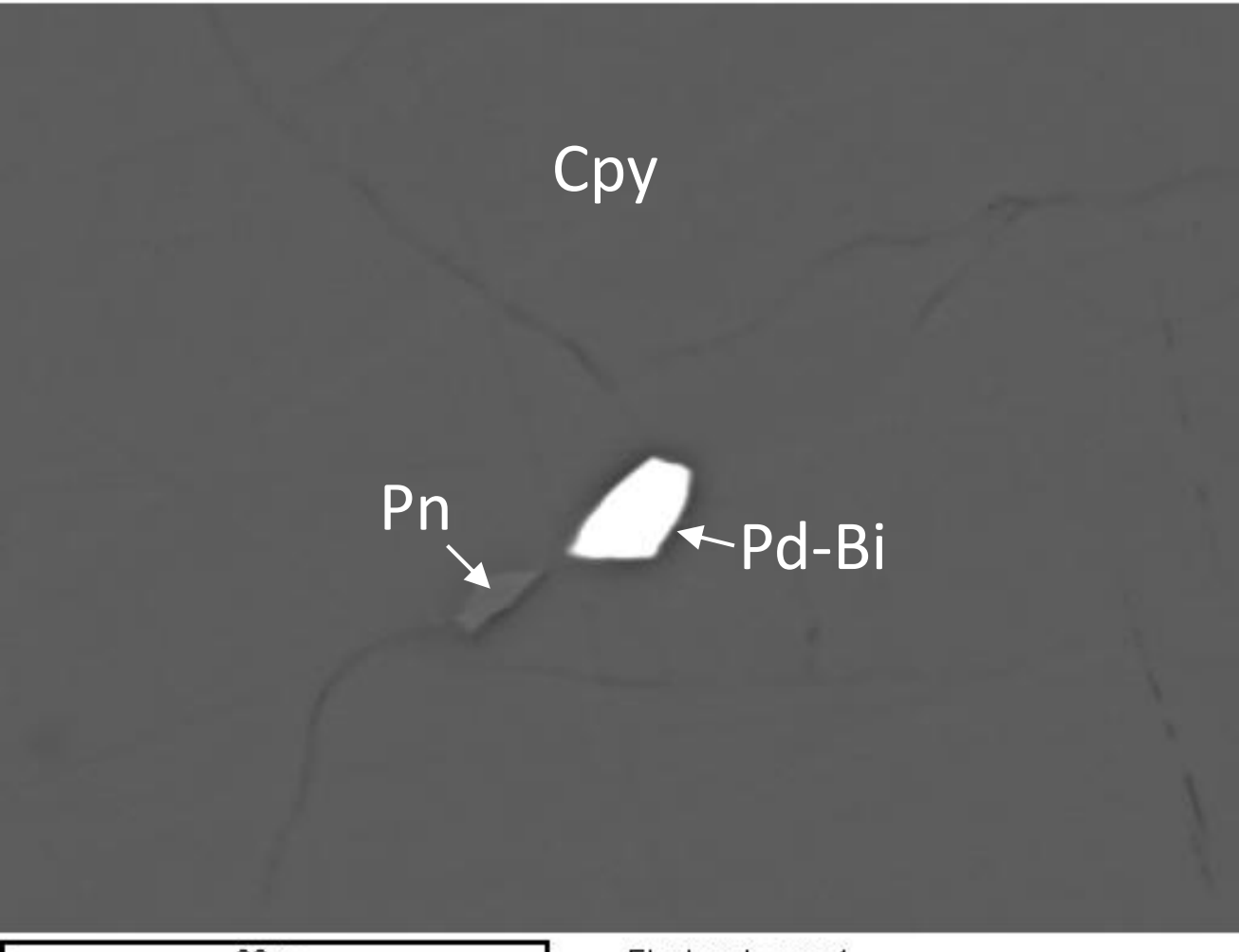
RK02 F1 Light



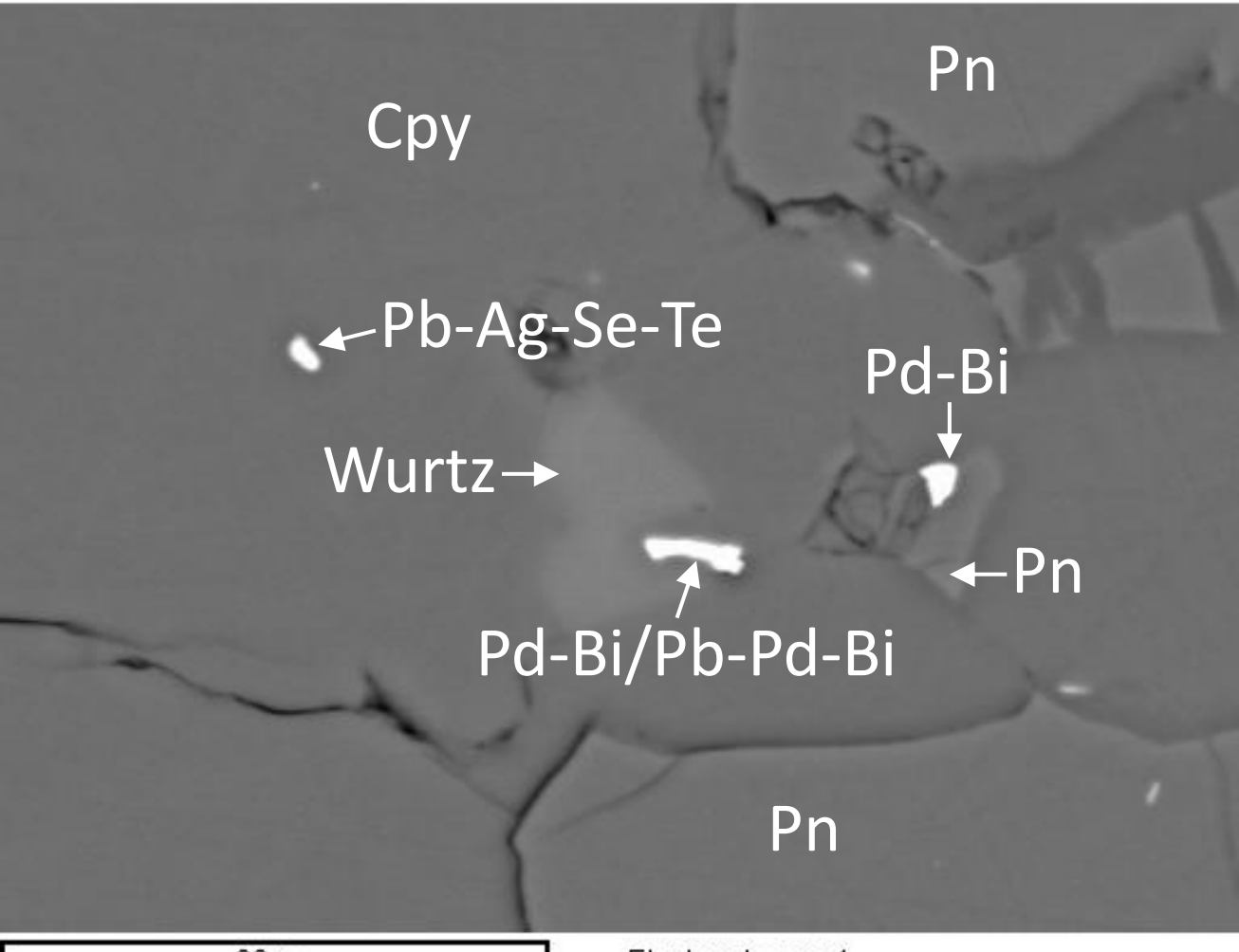
RK02 G1



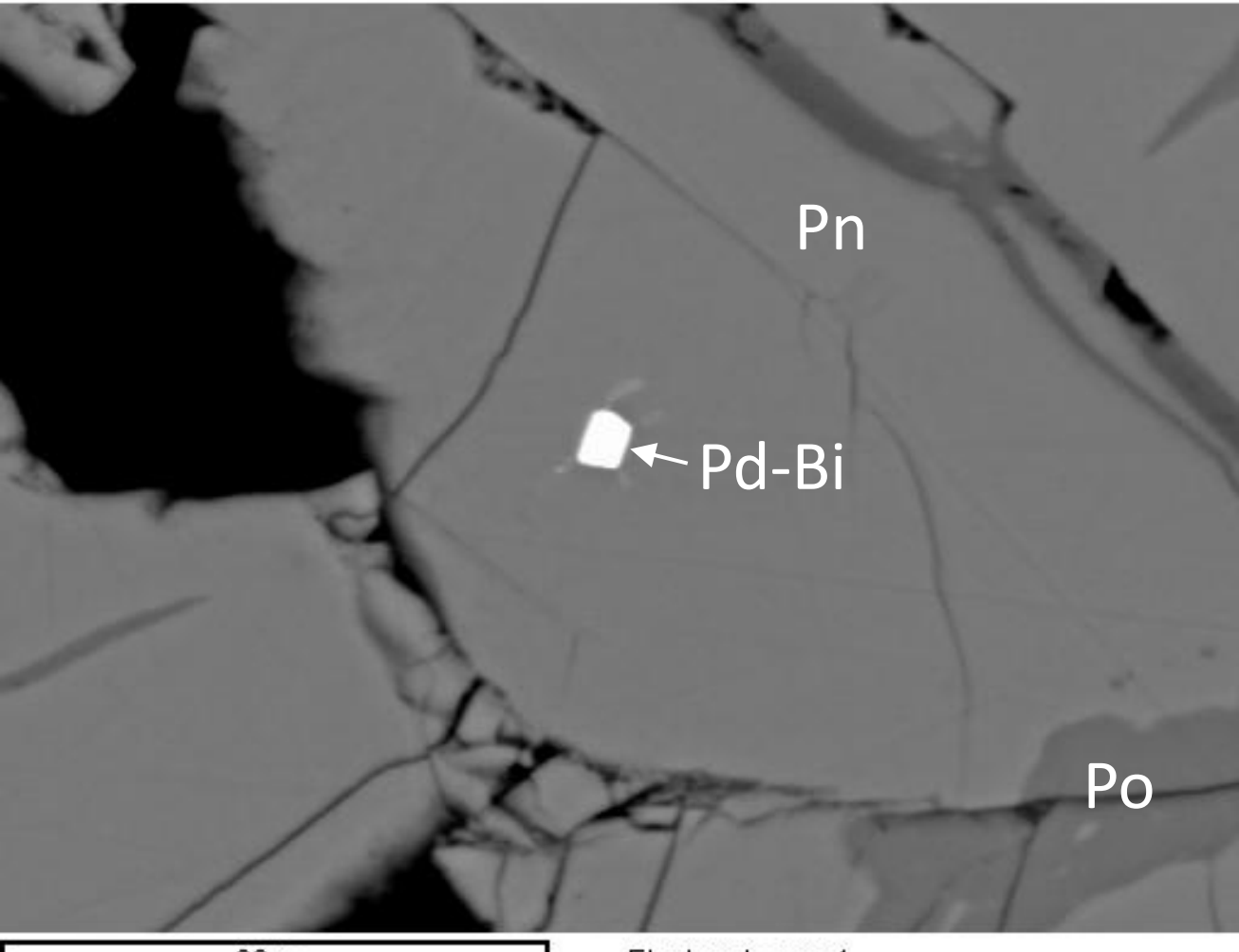
RK03 A1



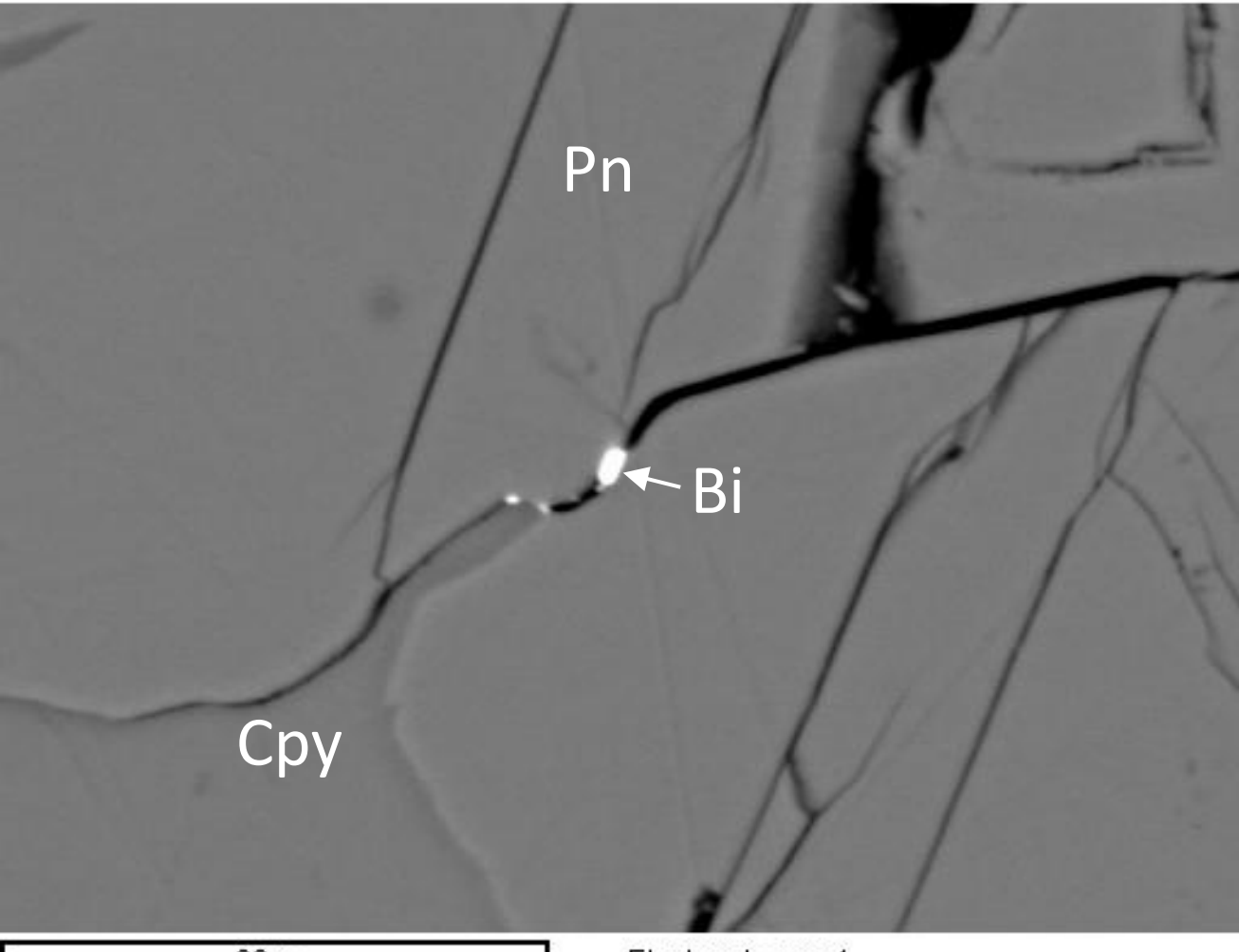
RK03 A2-4


Pn
Cpy
Pb-Ag-Se-Te
Pd-Bi
Wurtz
Pn
Pd-Bi/Pb-Pd-Bi
Pn
20µm
Electron Image 1

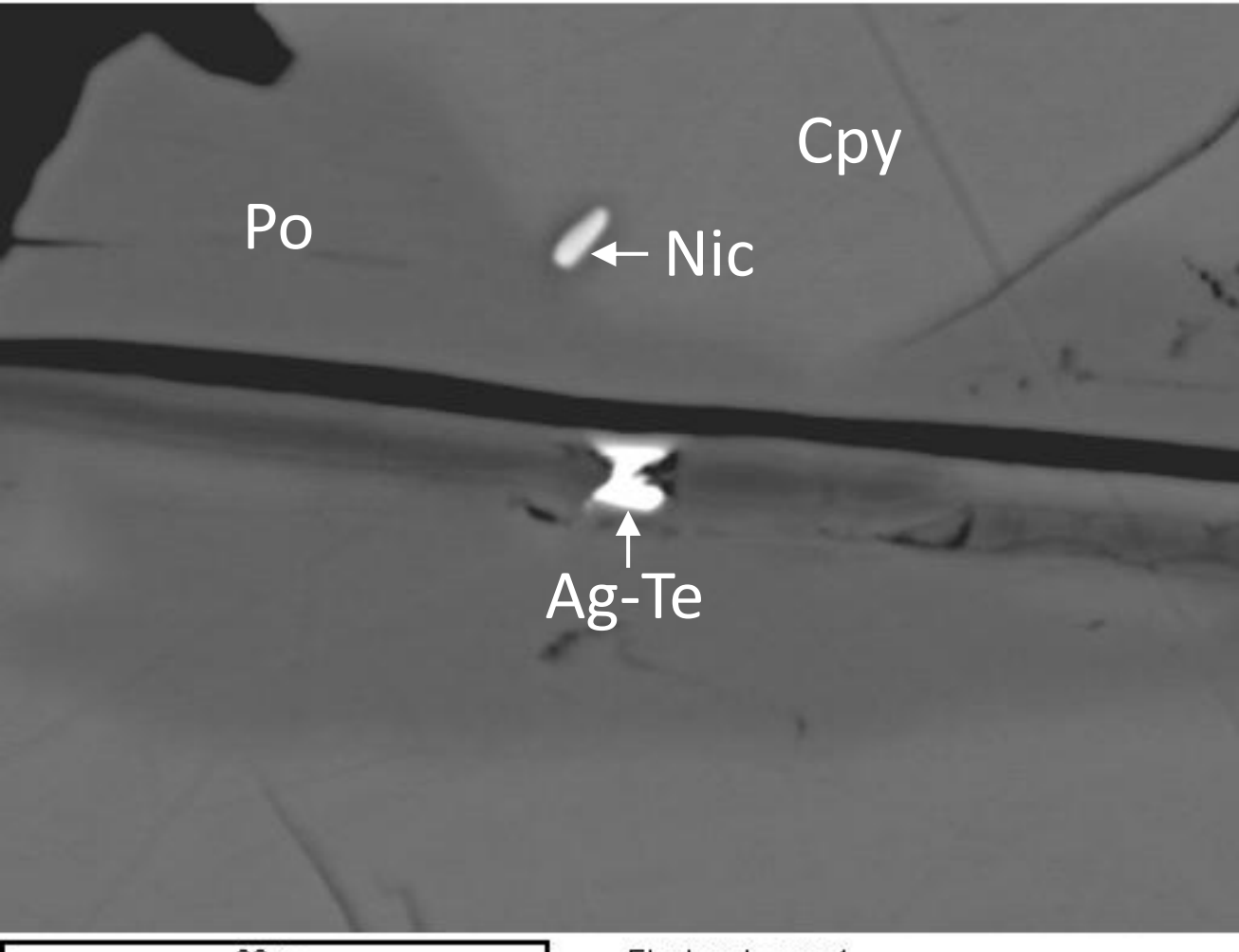
RK03 A5



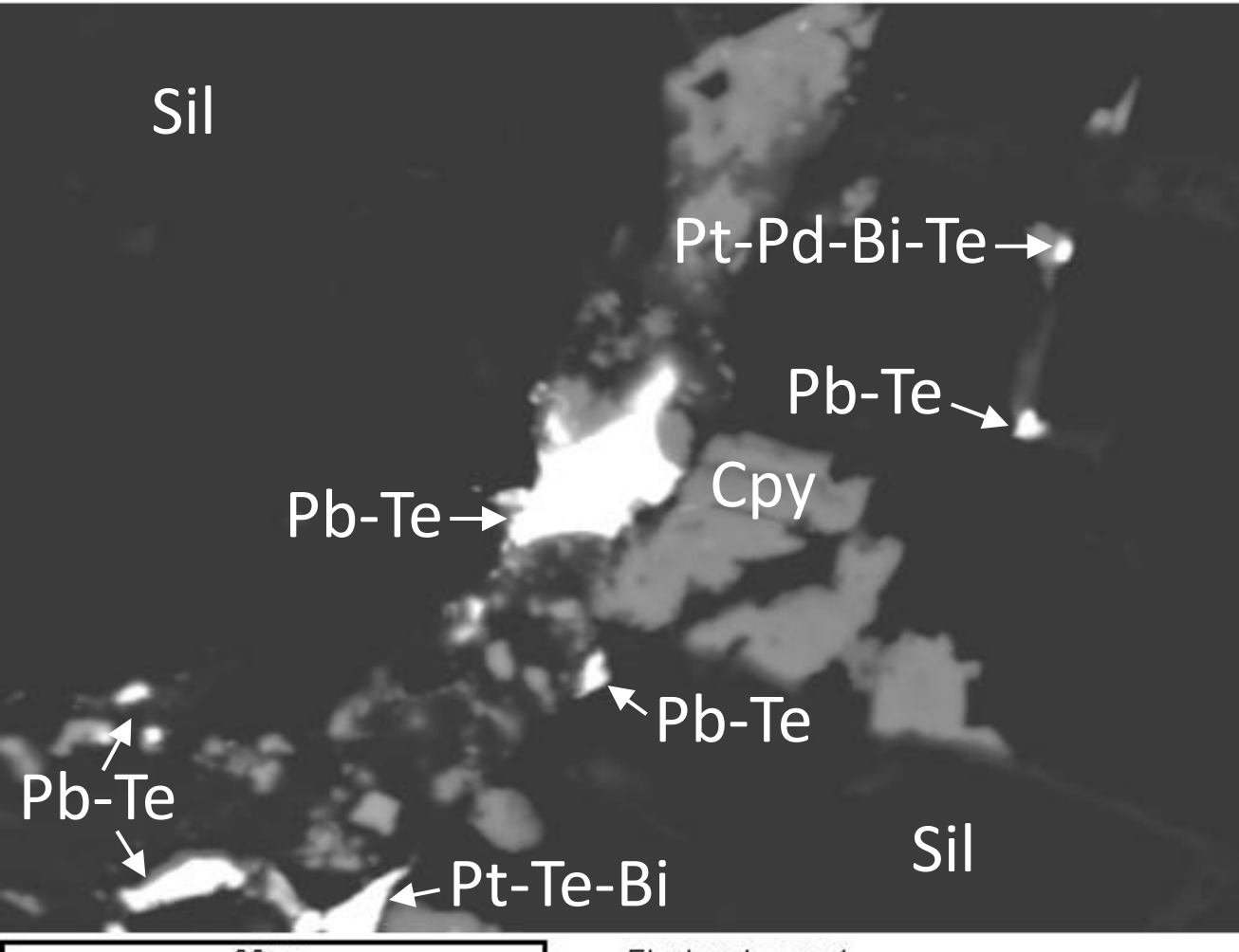
RK03 B1



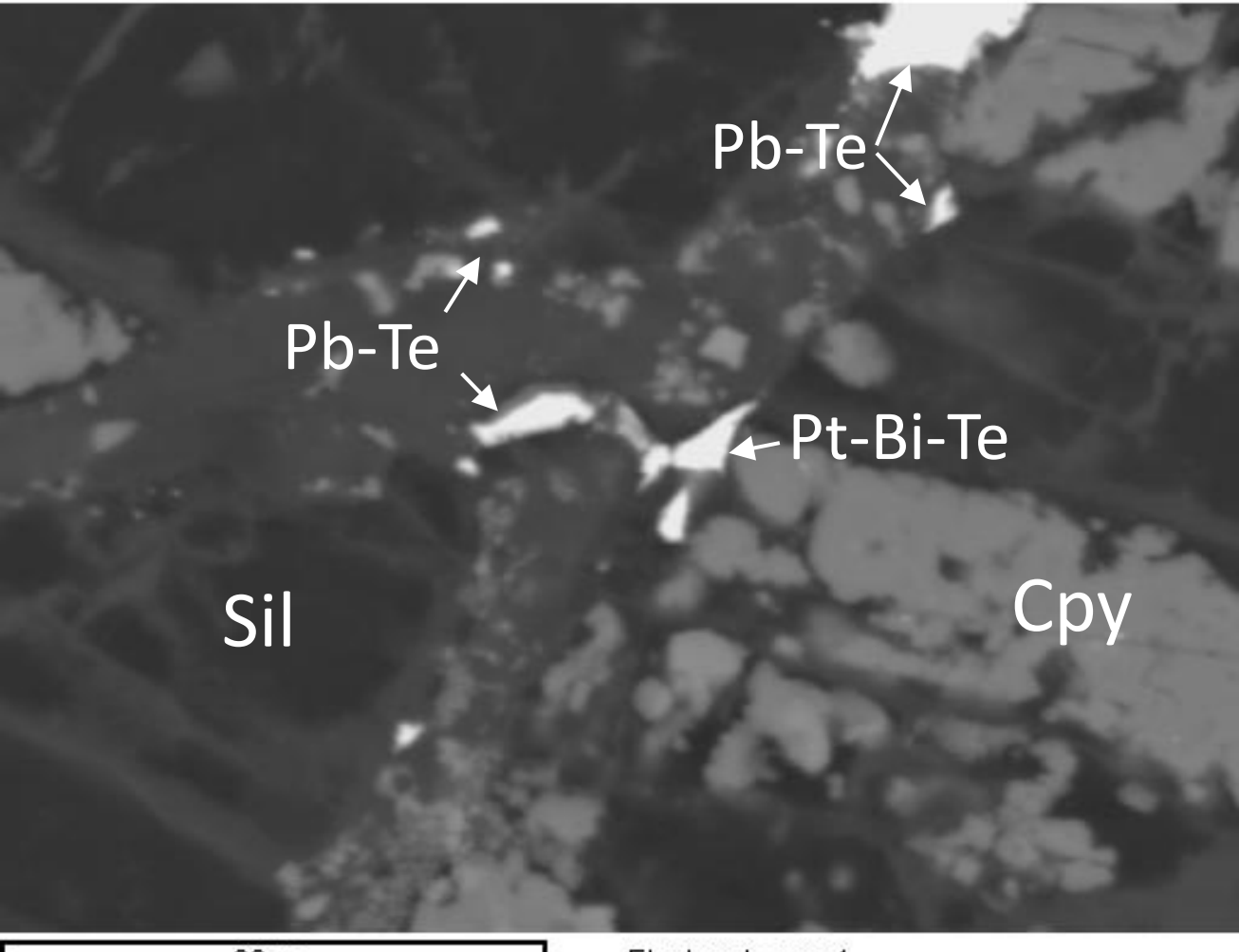
RK03 C1



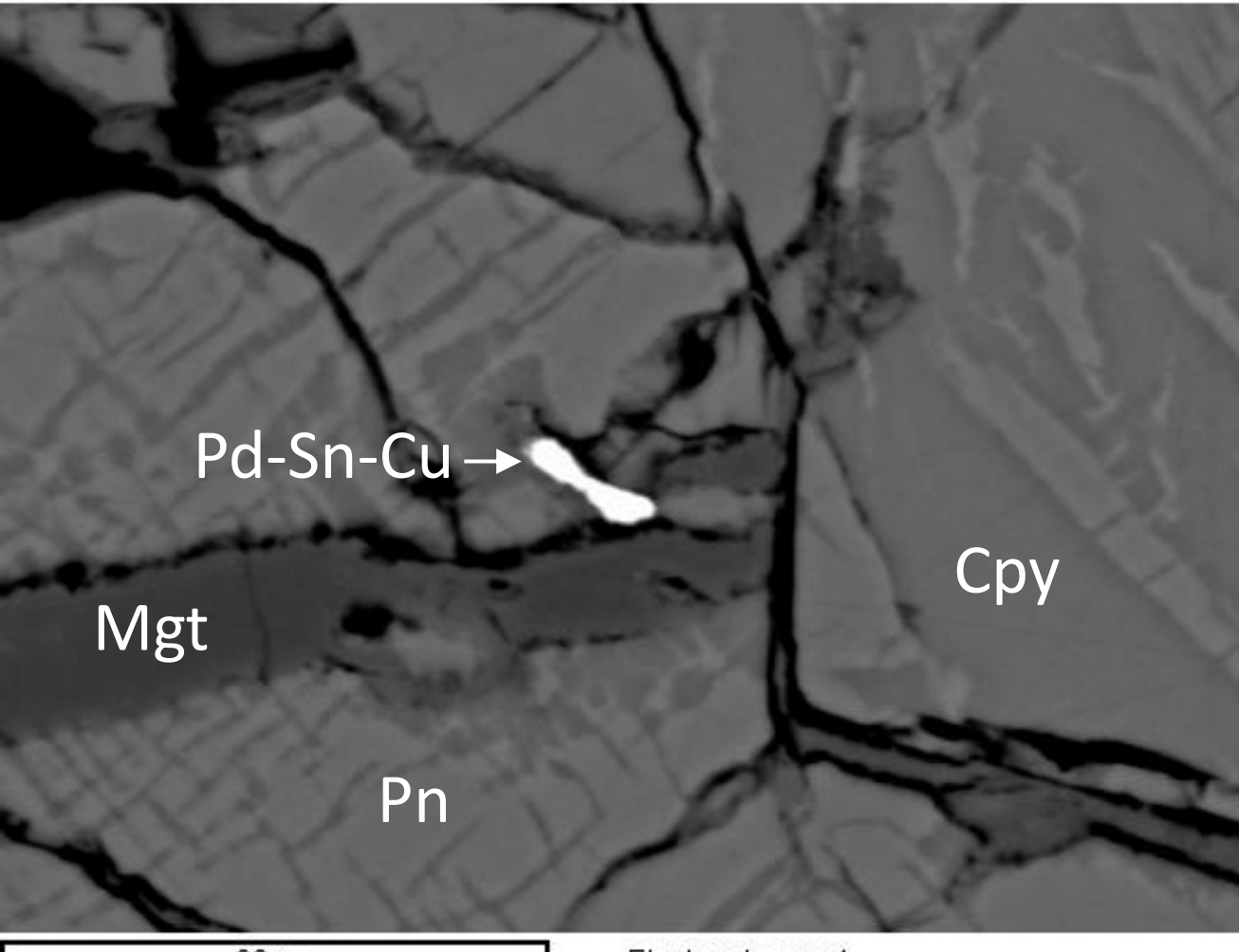
RK04 A1-7


Sil
Pt-Pd-Bi-Te
Pb-Te
Pb-Te
Cpy
Pb-Te
Pb-Te
Sil
Pt-Te-Bi
20µm
Electron Image 1

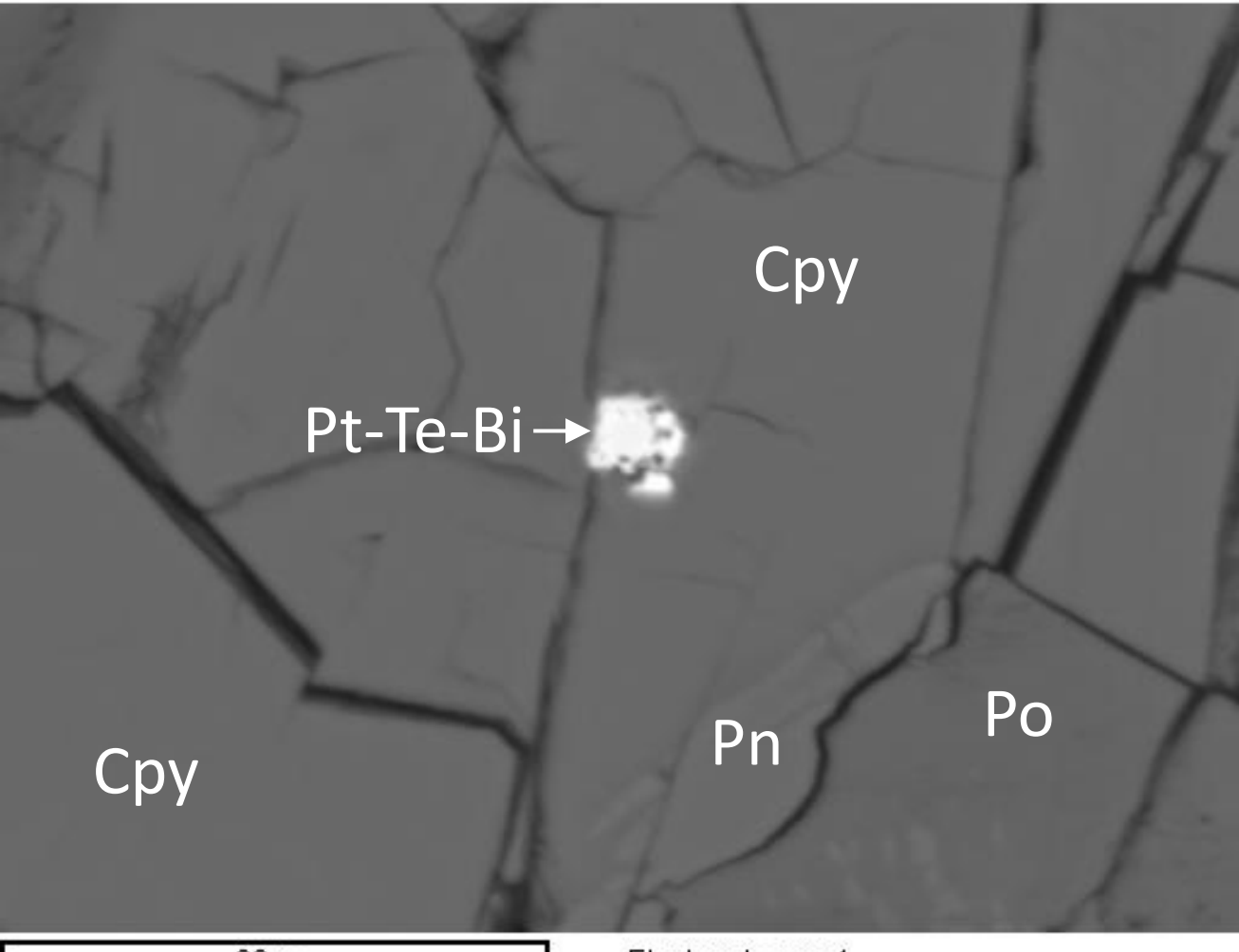
RK04 A1-5



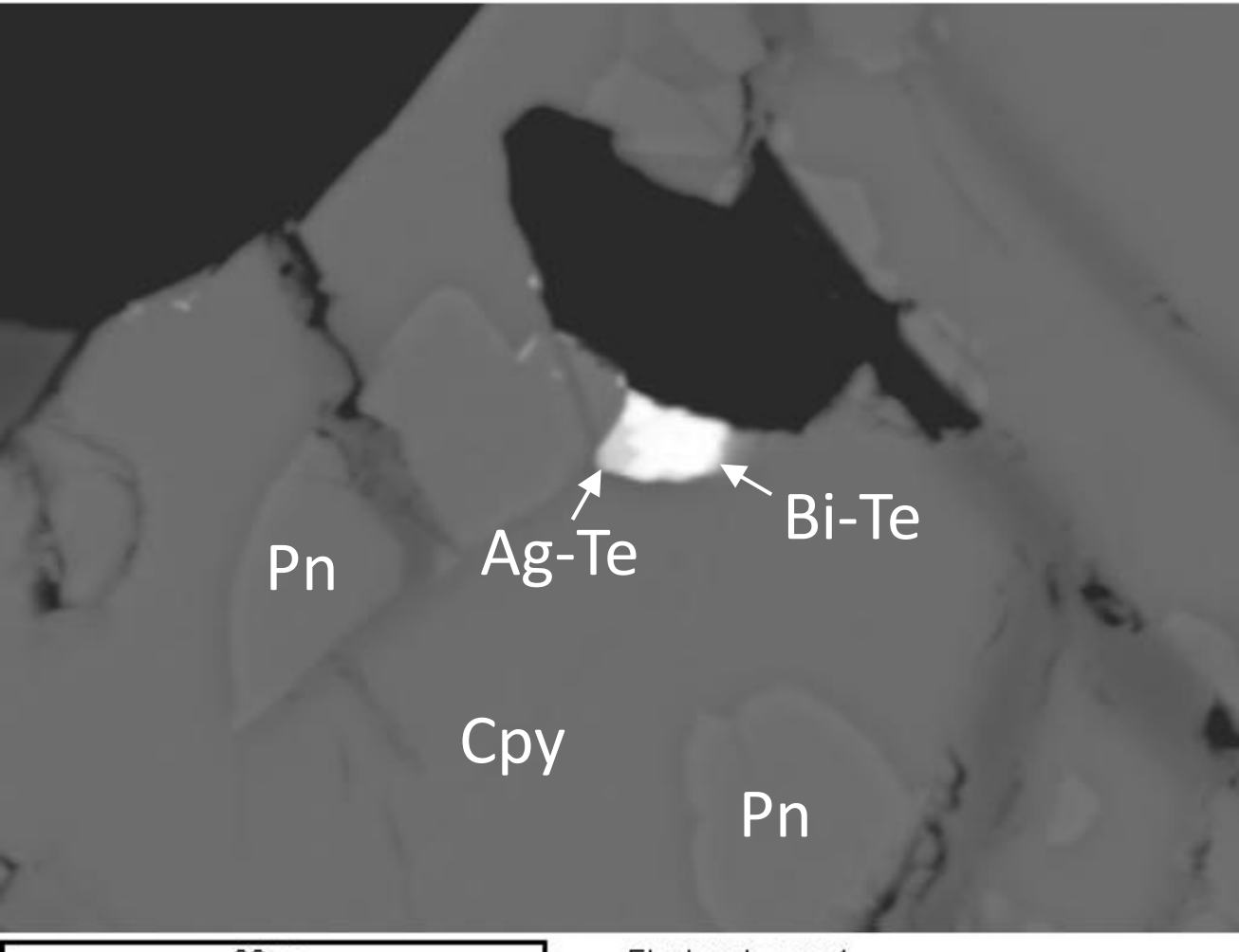
RK04 B1



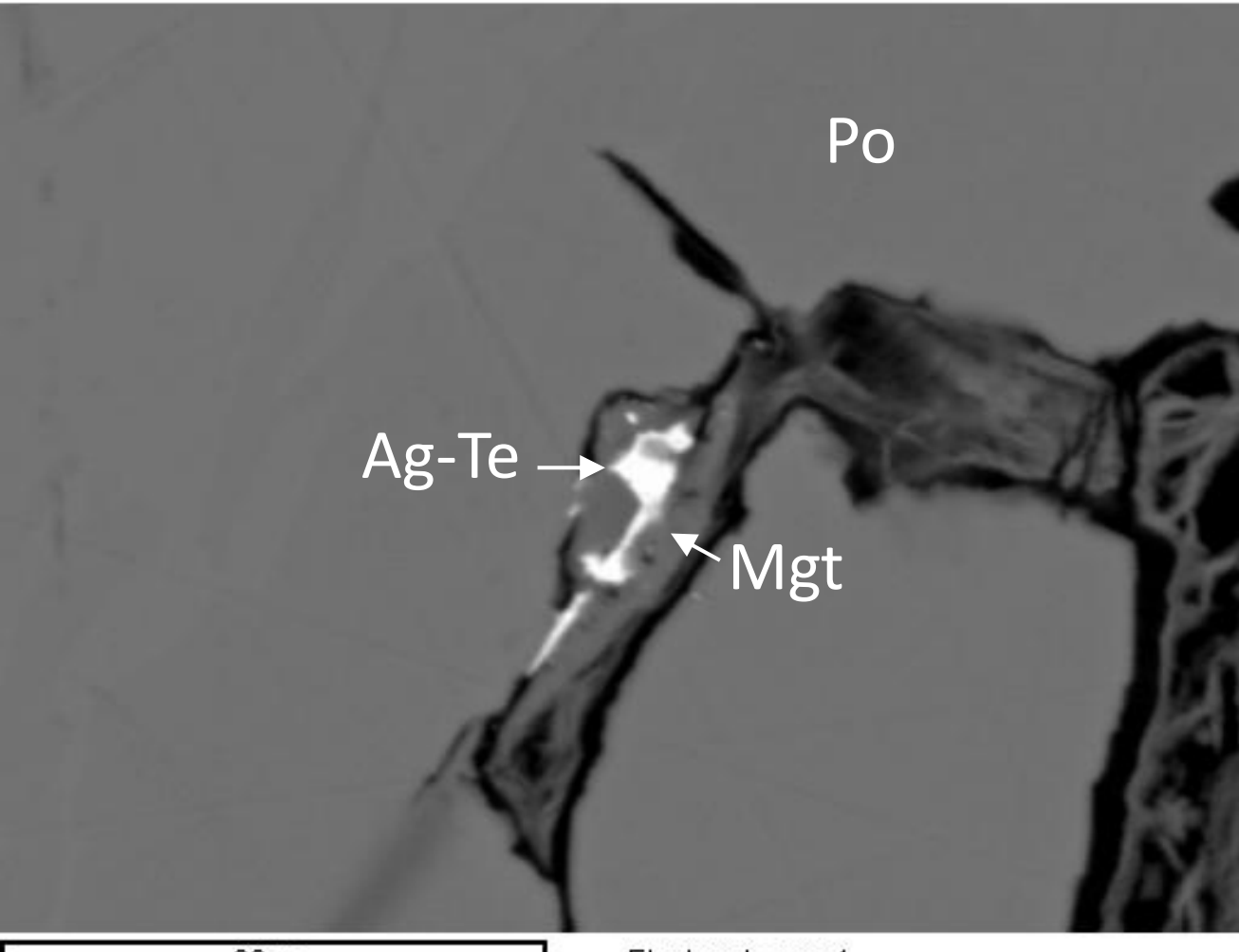
RK04 C1



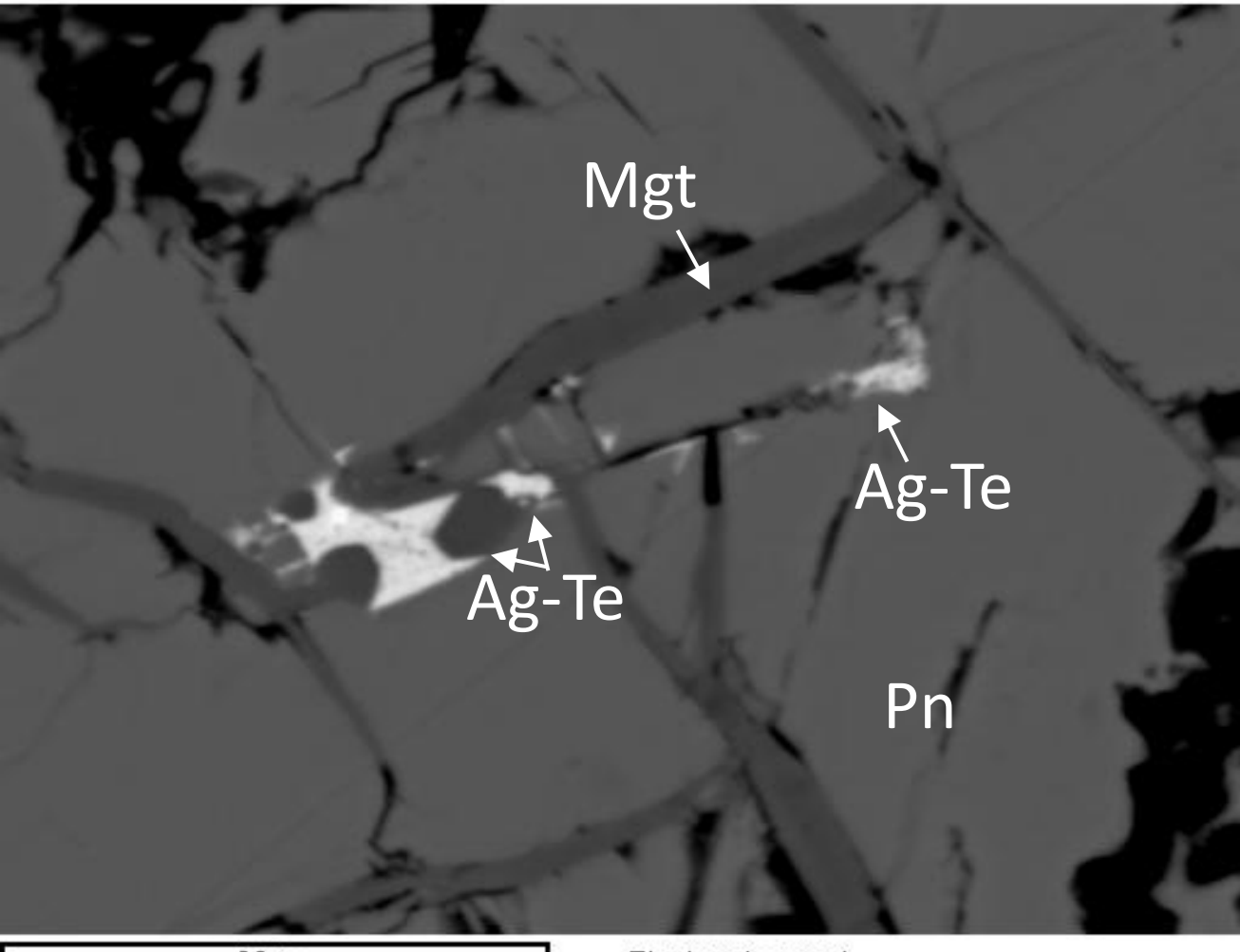
RK05 A1



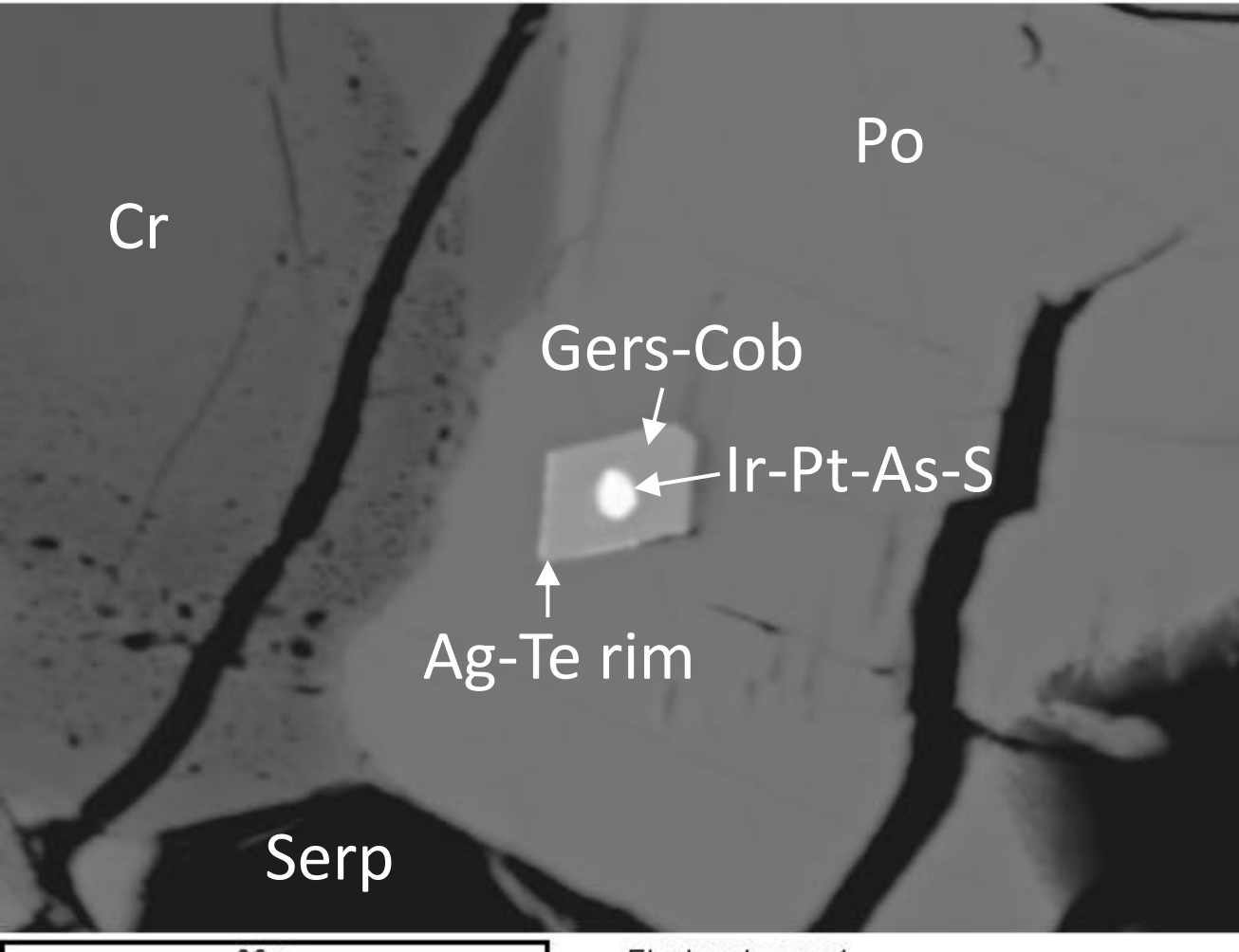
RK05 B1



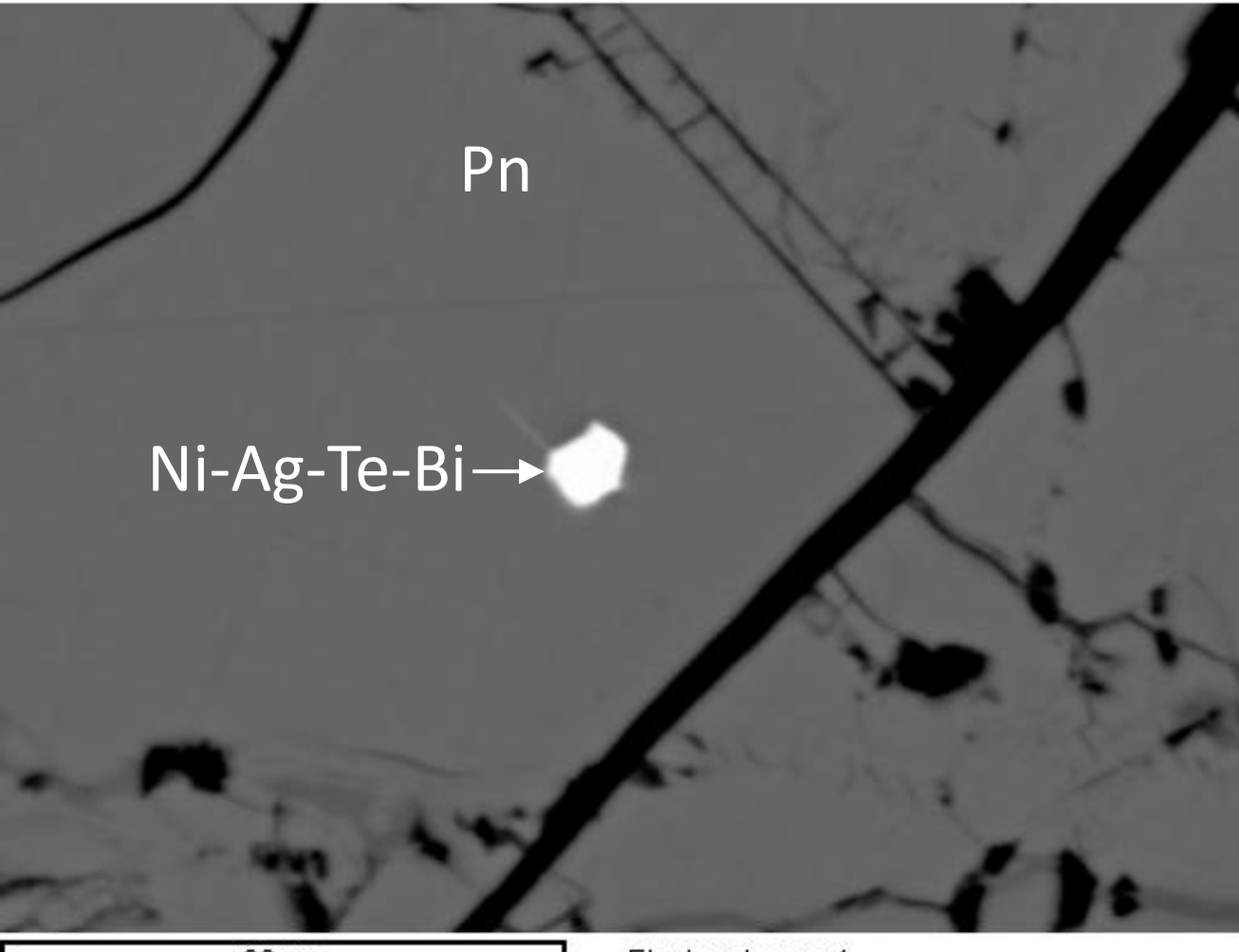
RK05 C1-3



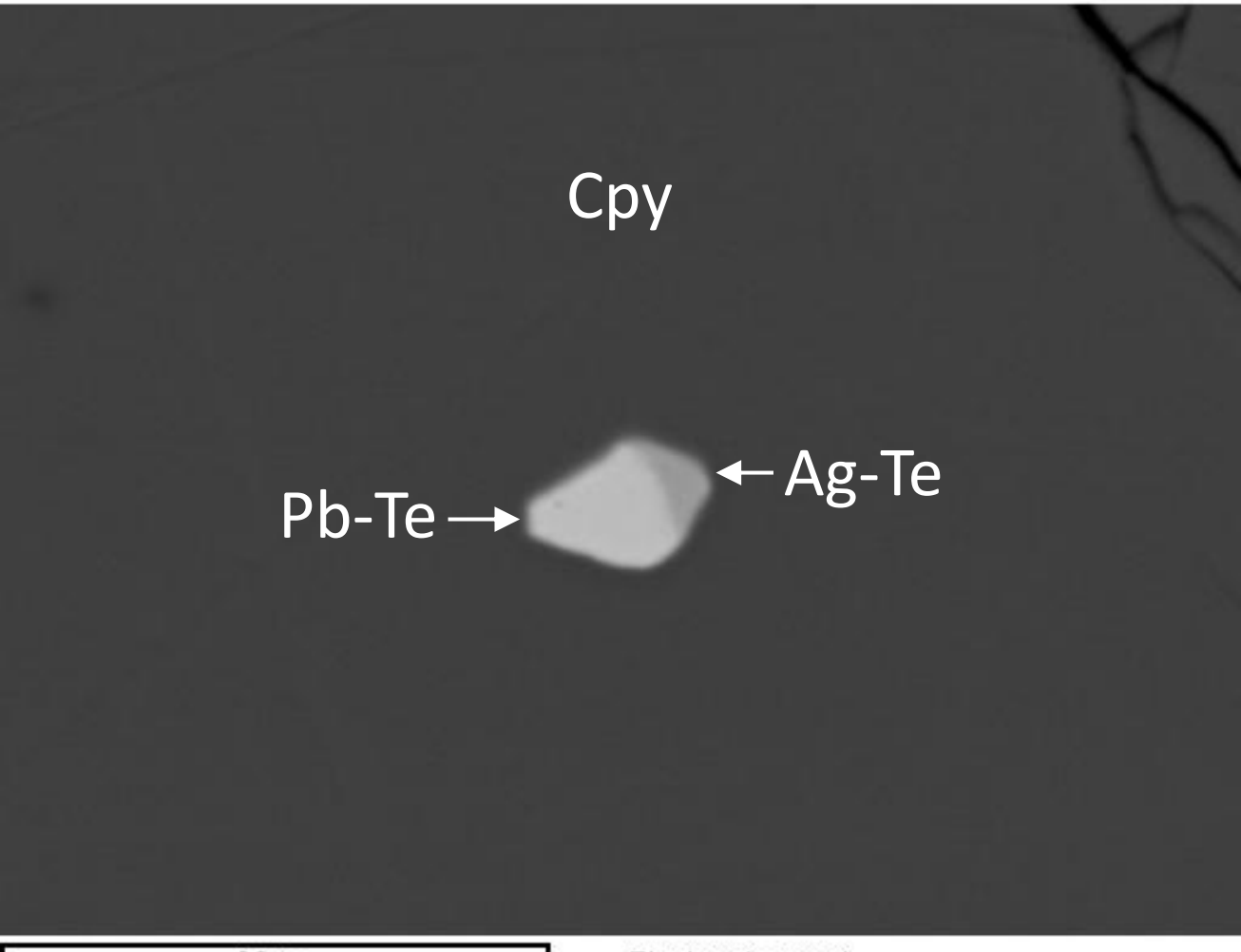
RK05 D1



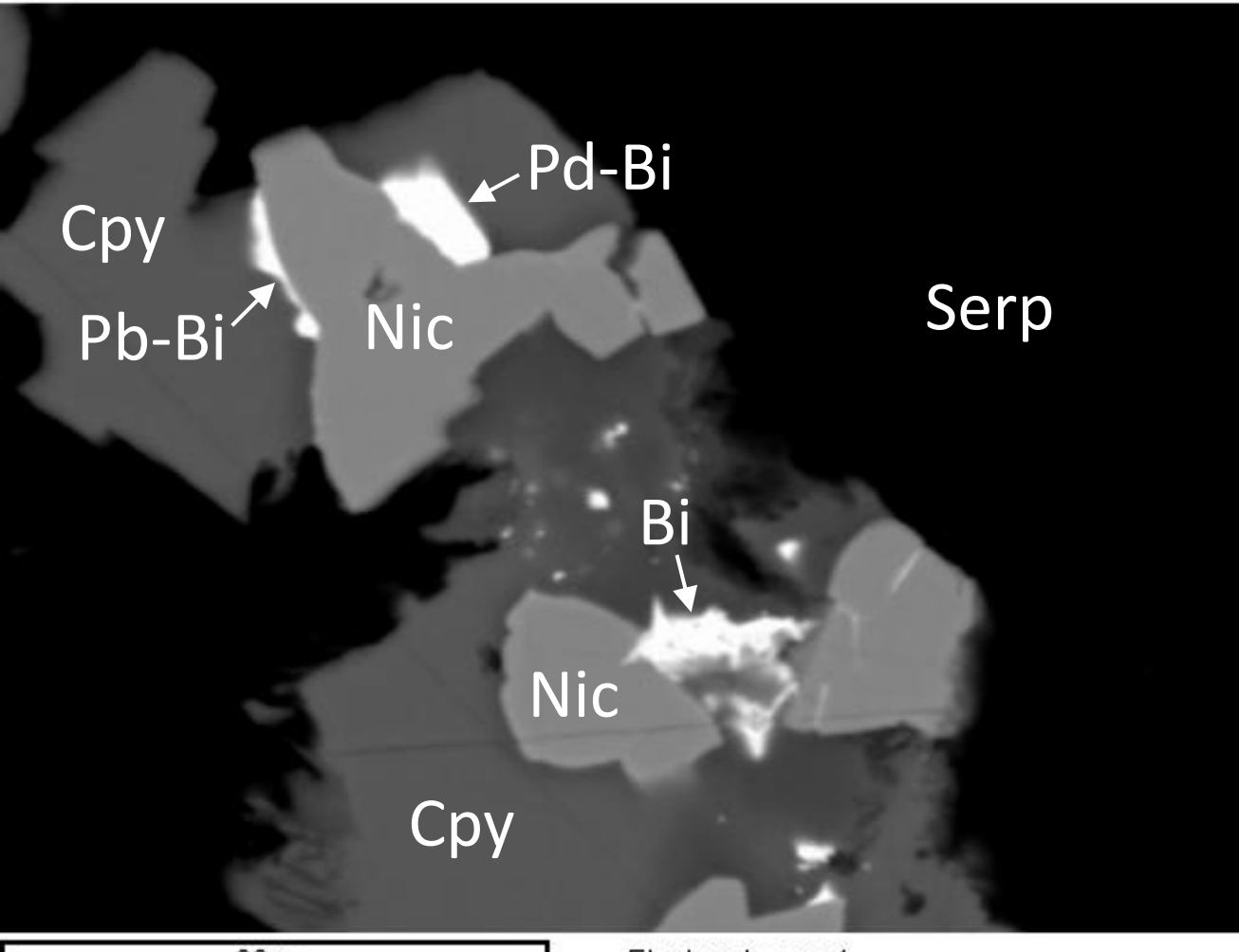
RK05 E1



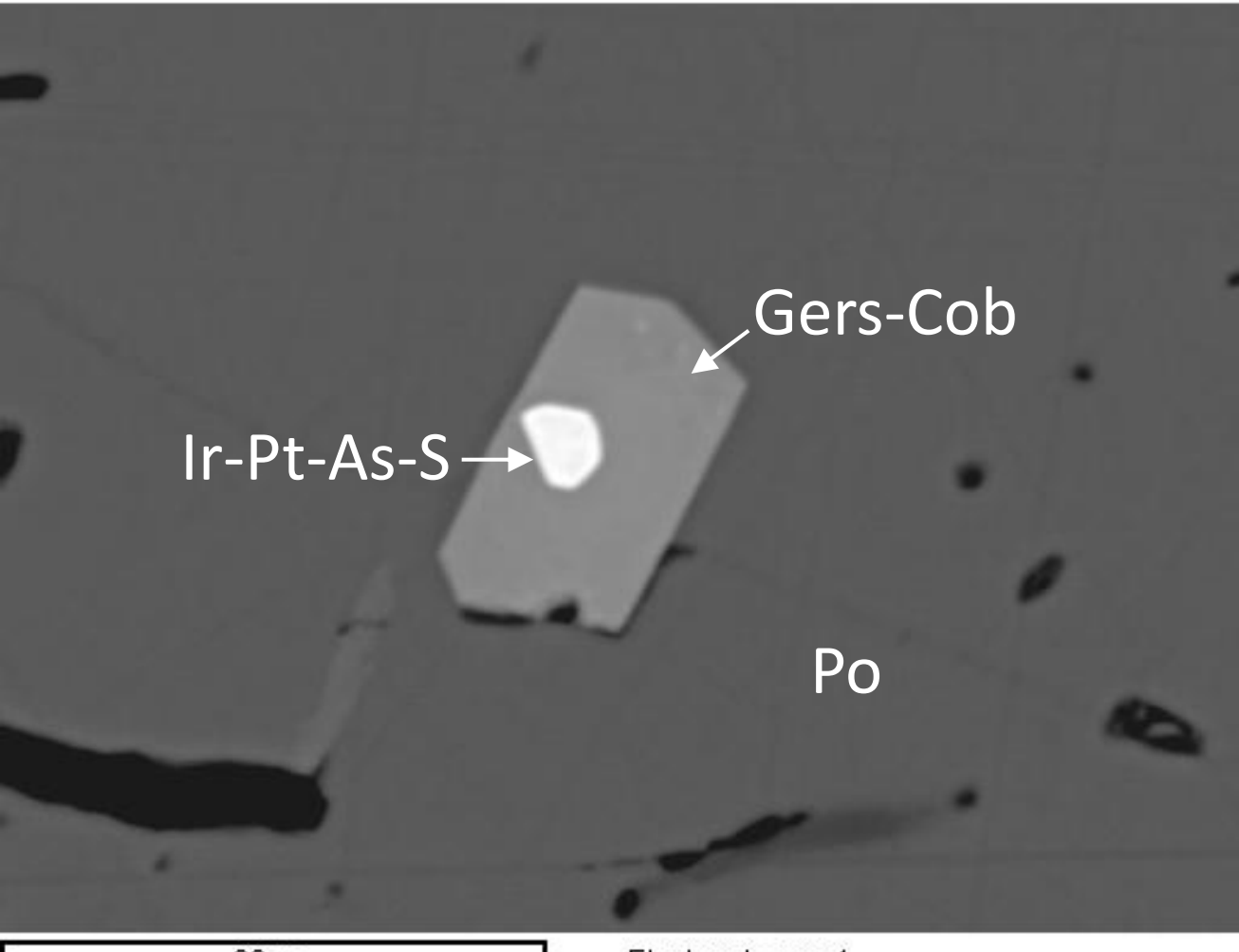
RK06 A1-2



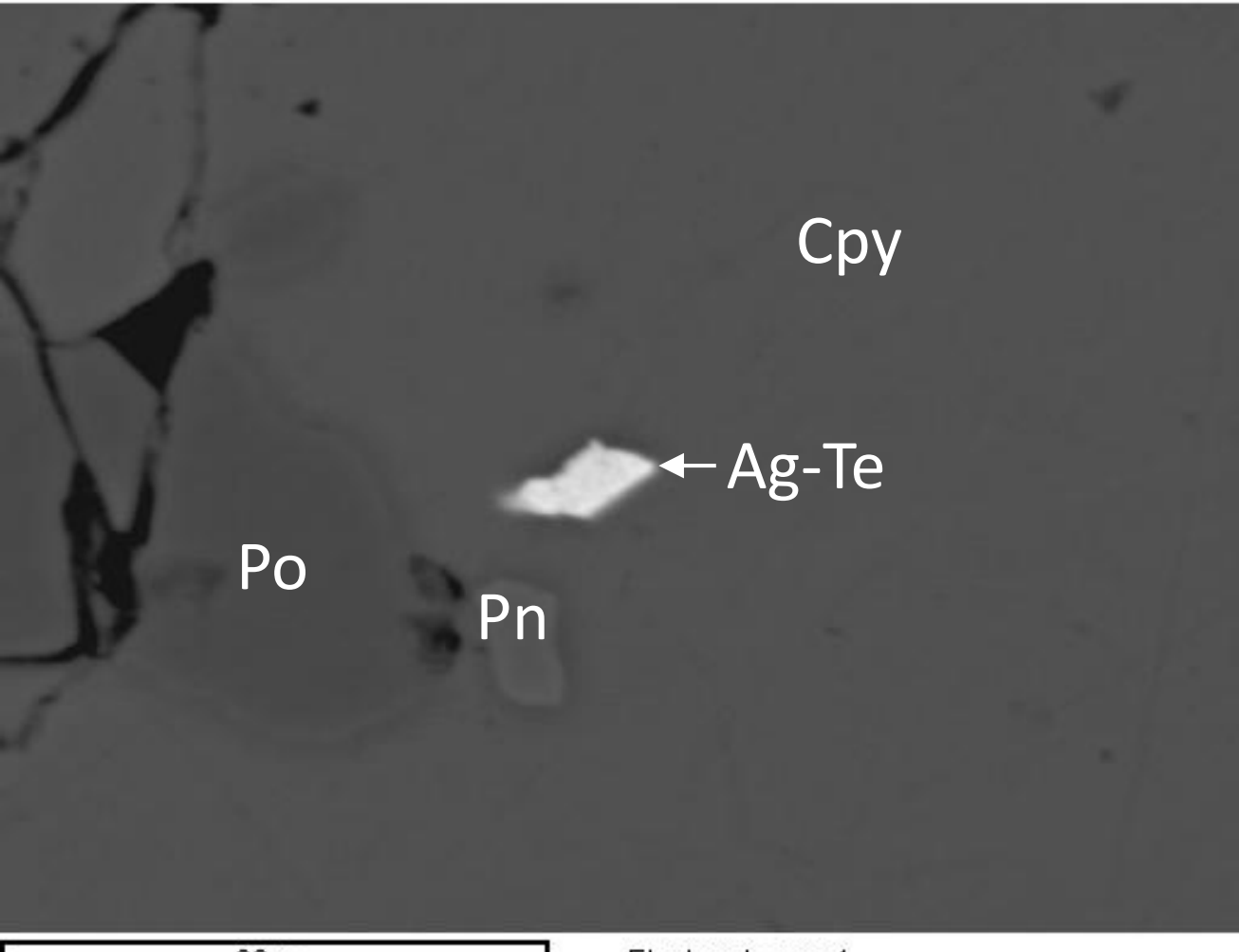
RK07 A1-3



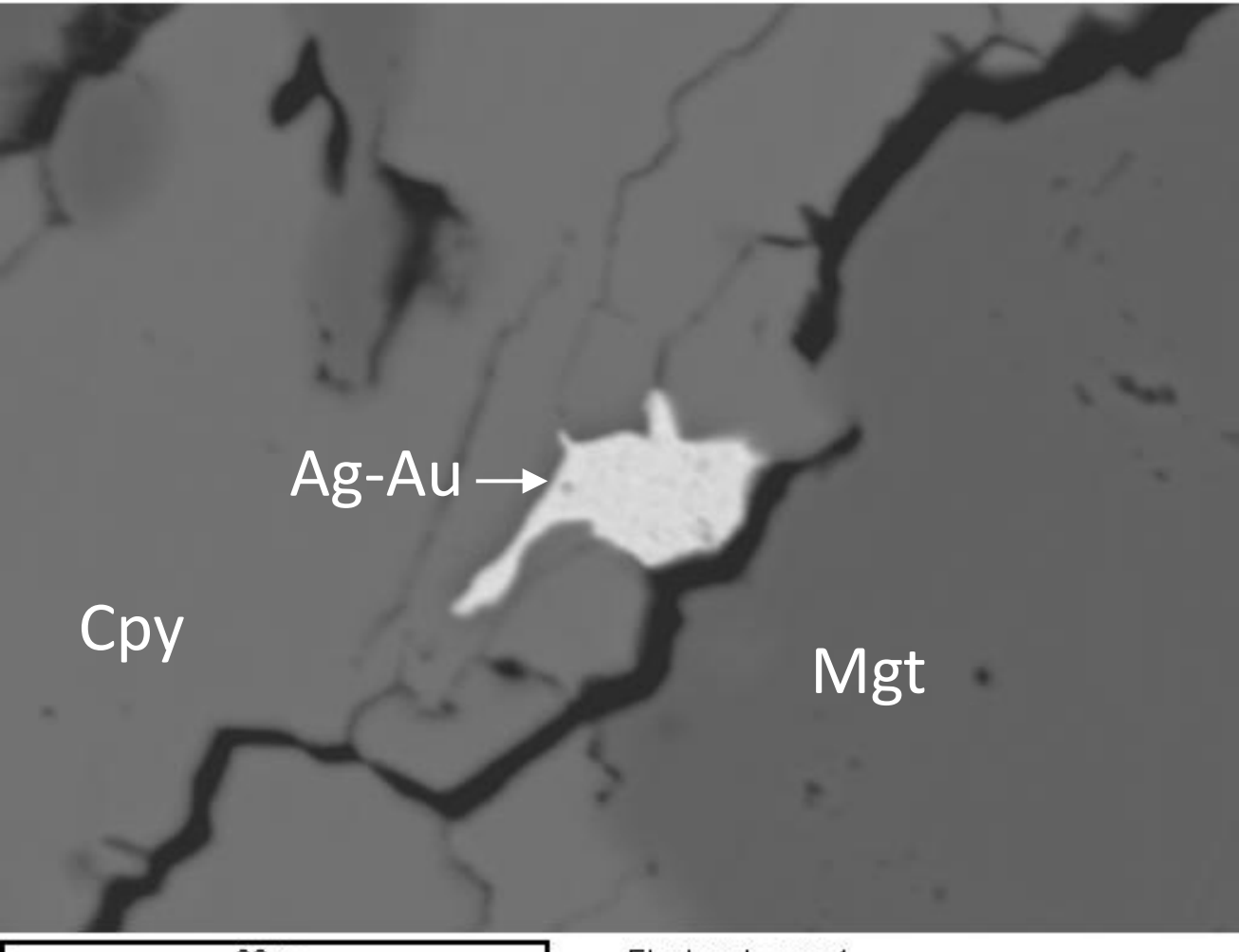
RK09 A1



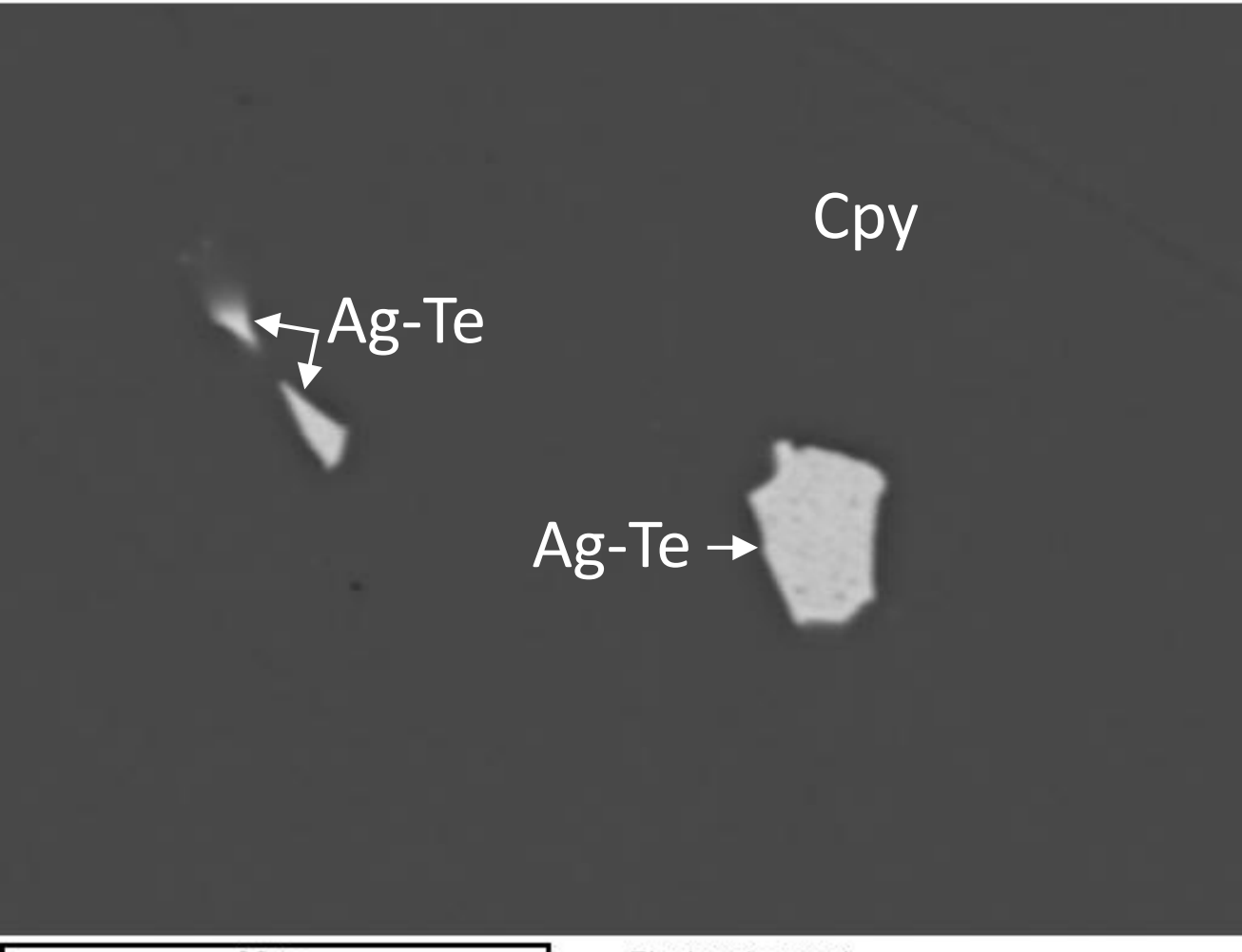
RK10 A1



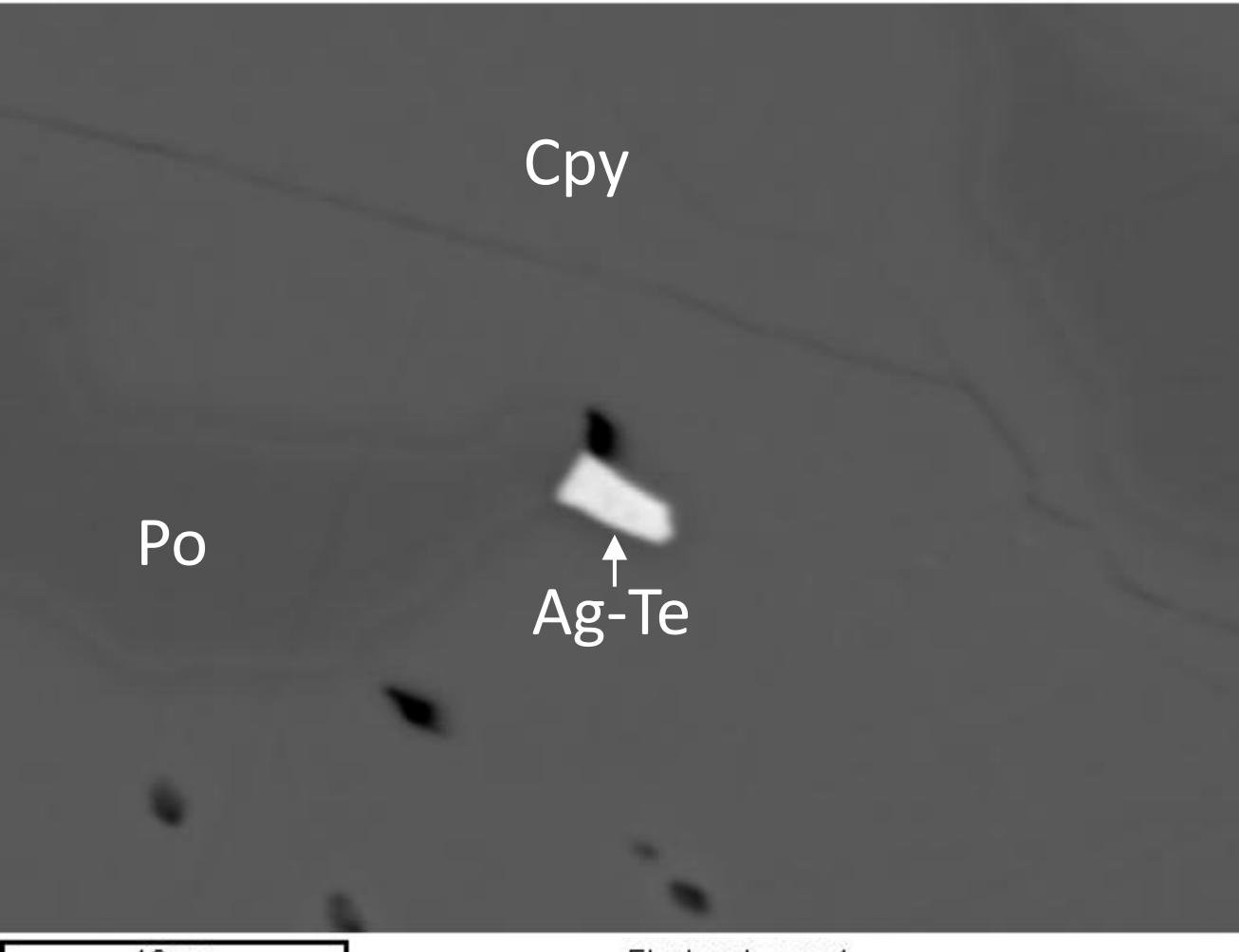
RK10 B1



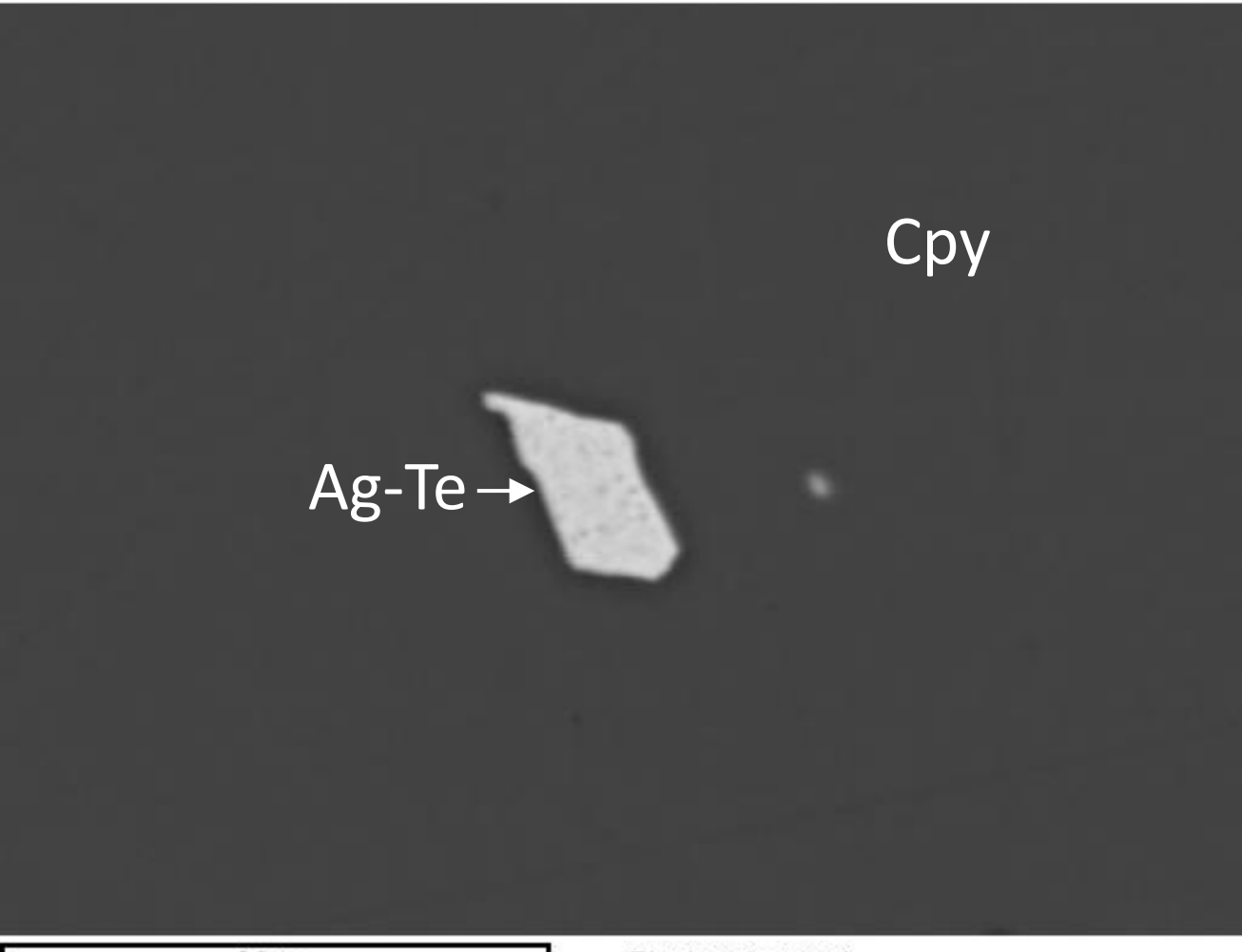
RK10 C1-3



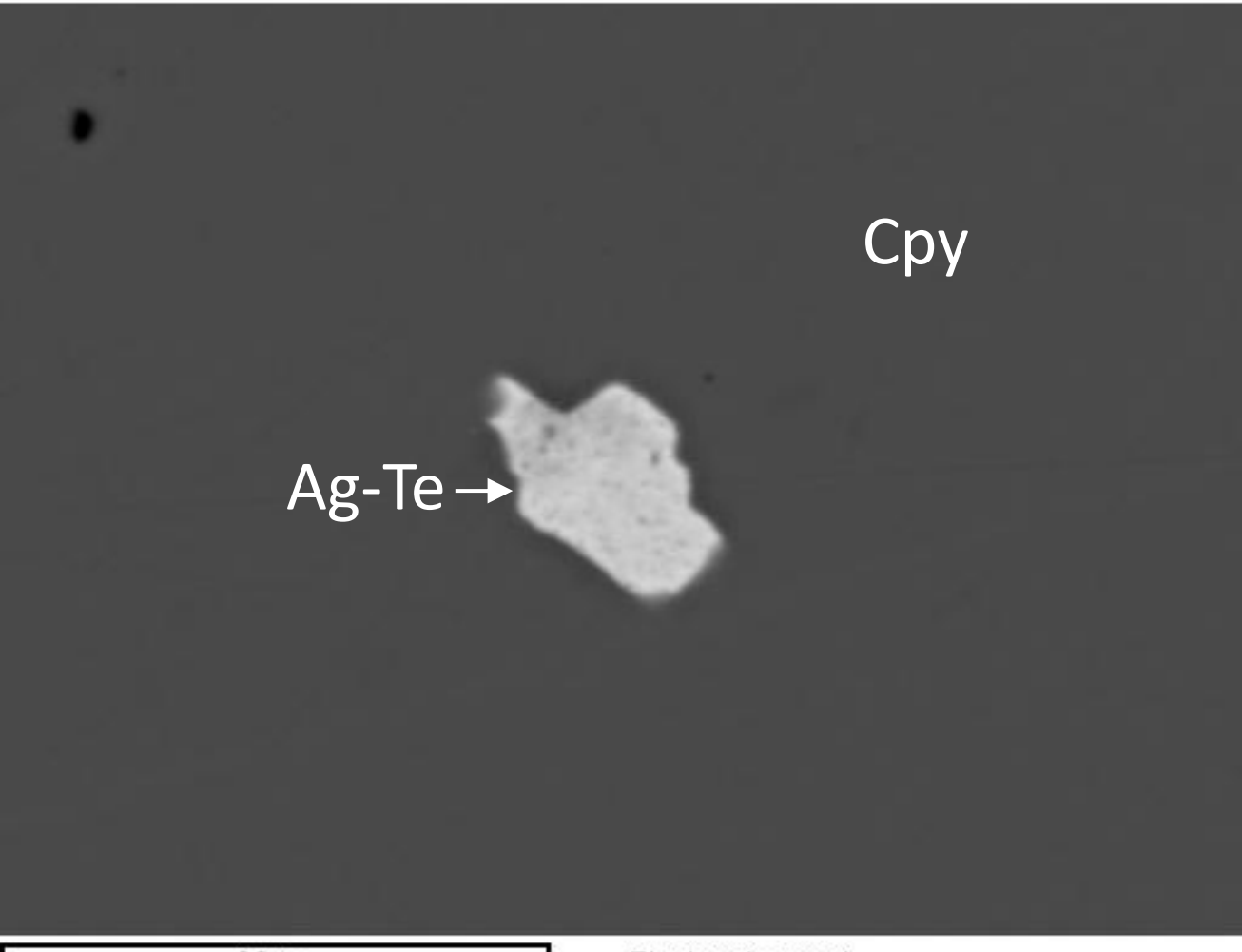
RK10 C4



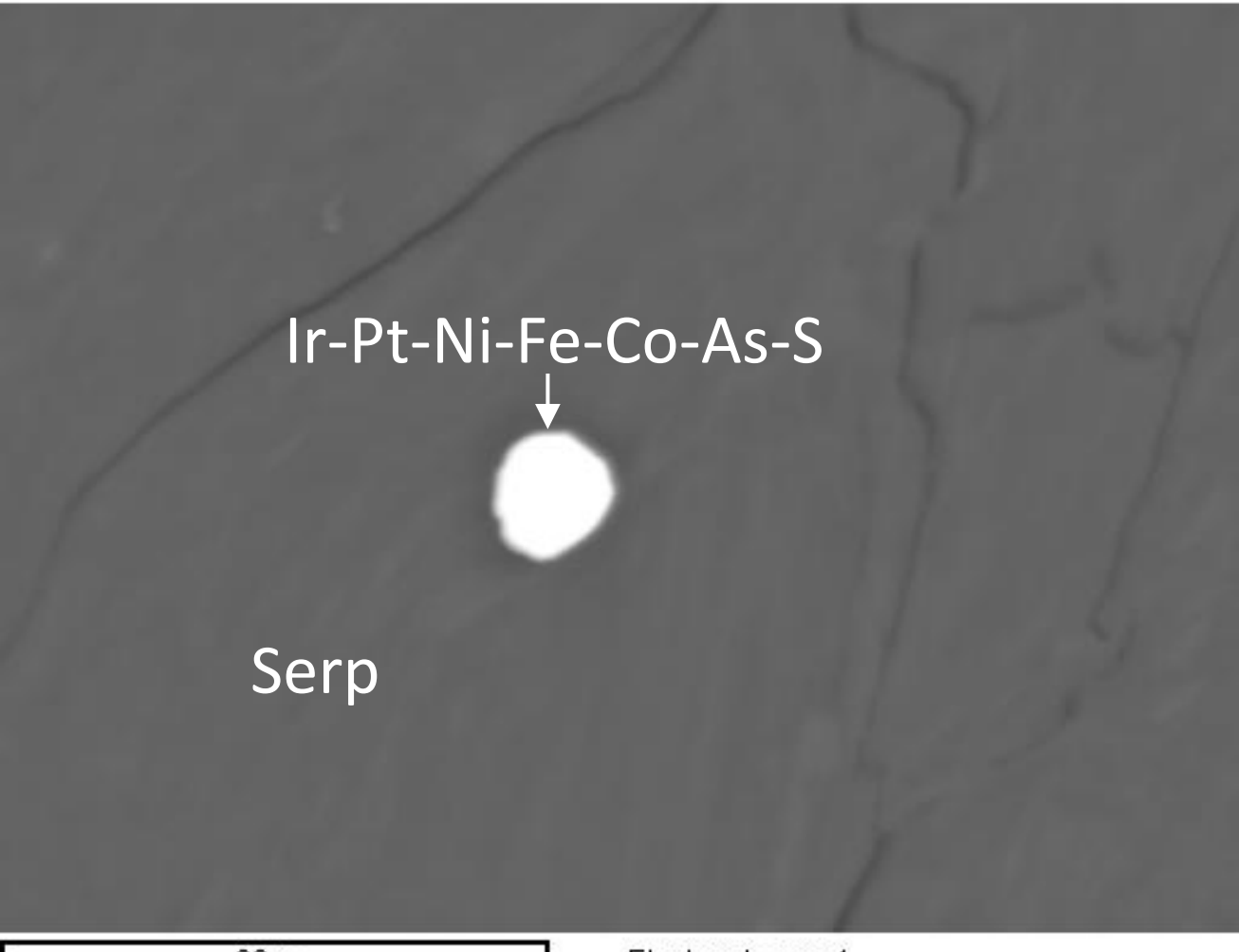
RK10 D1



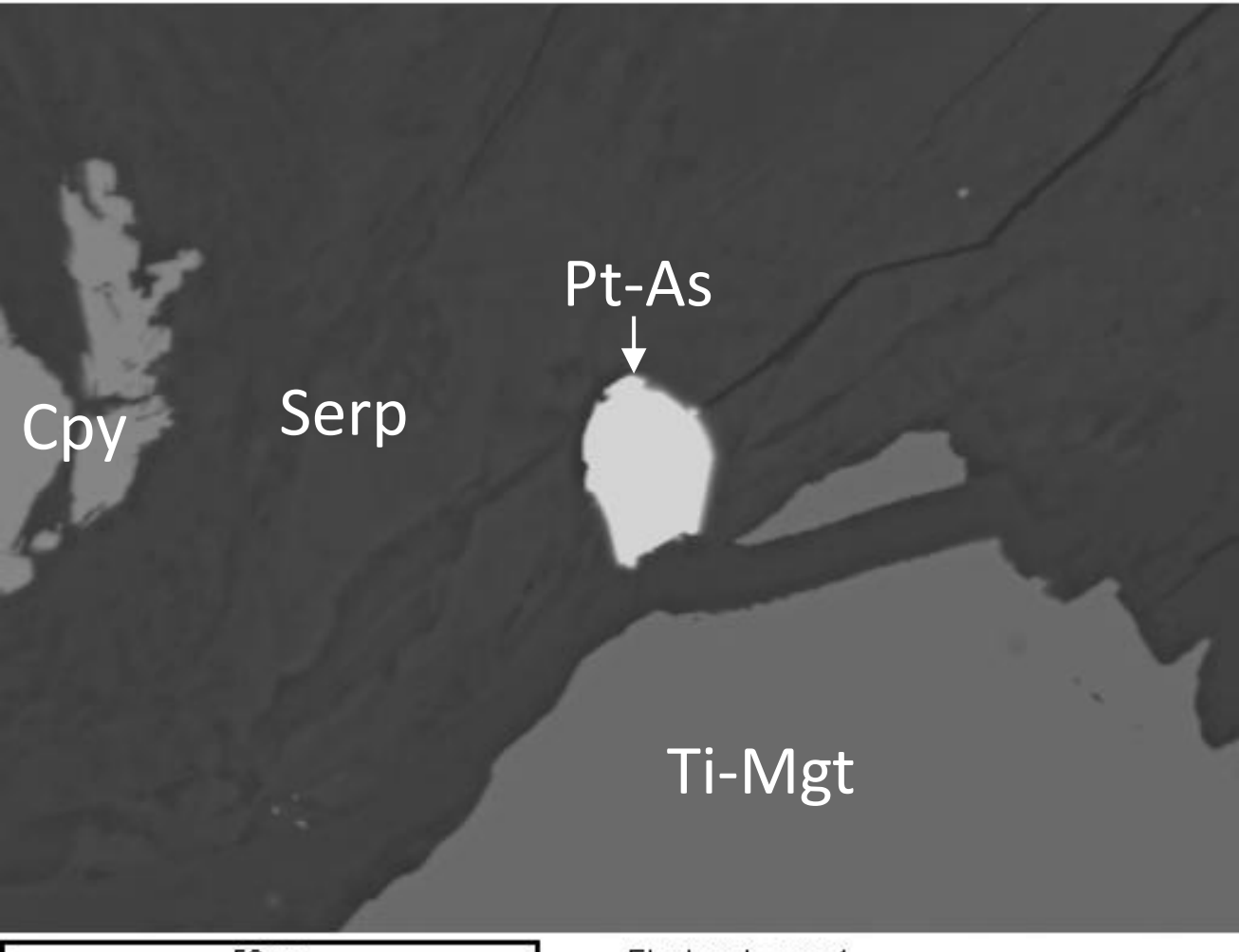
RK10 E1



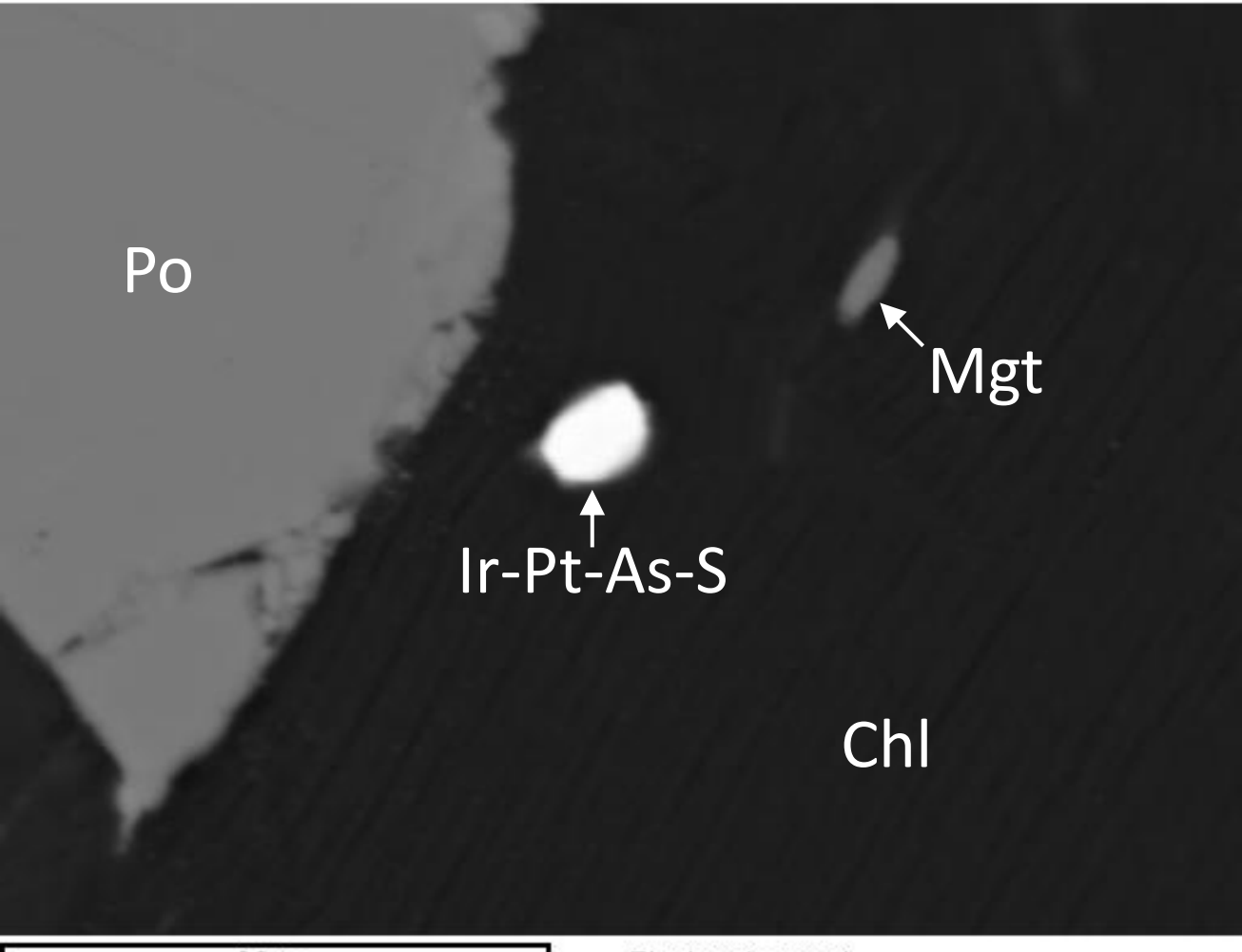
RK10 F1



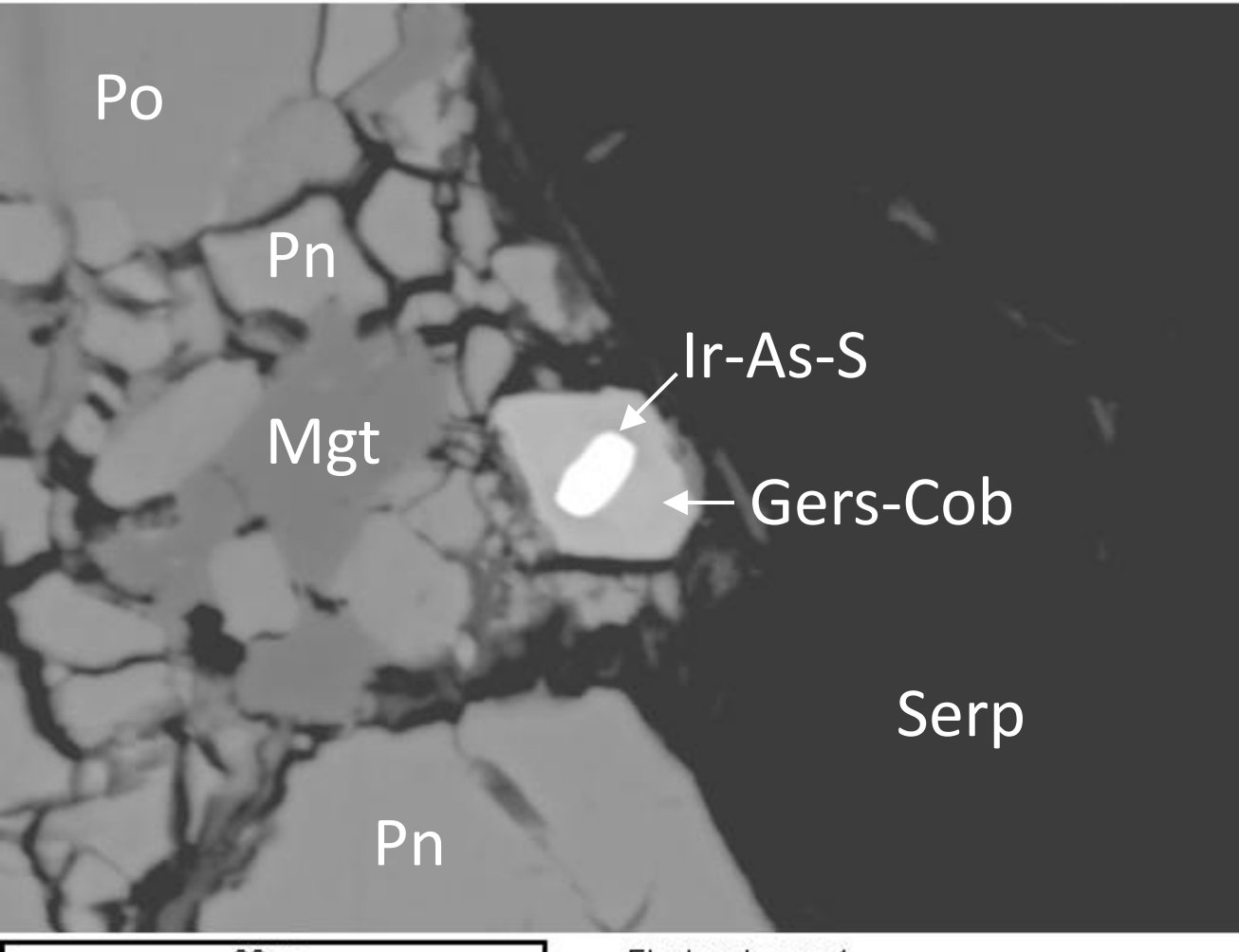
RK10 G1



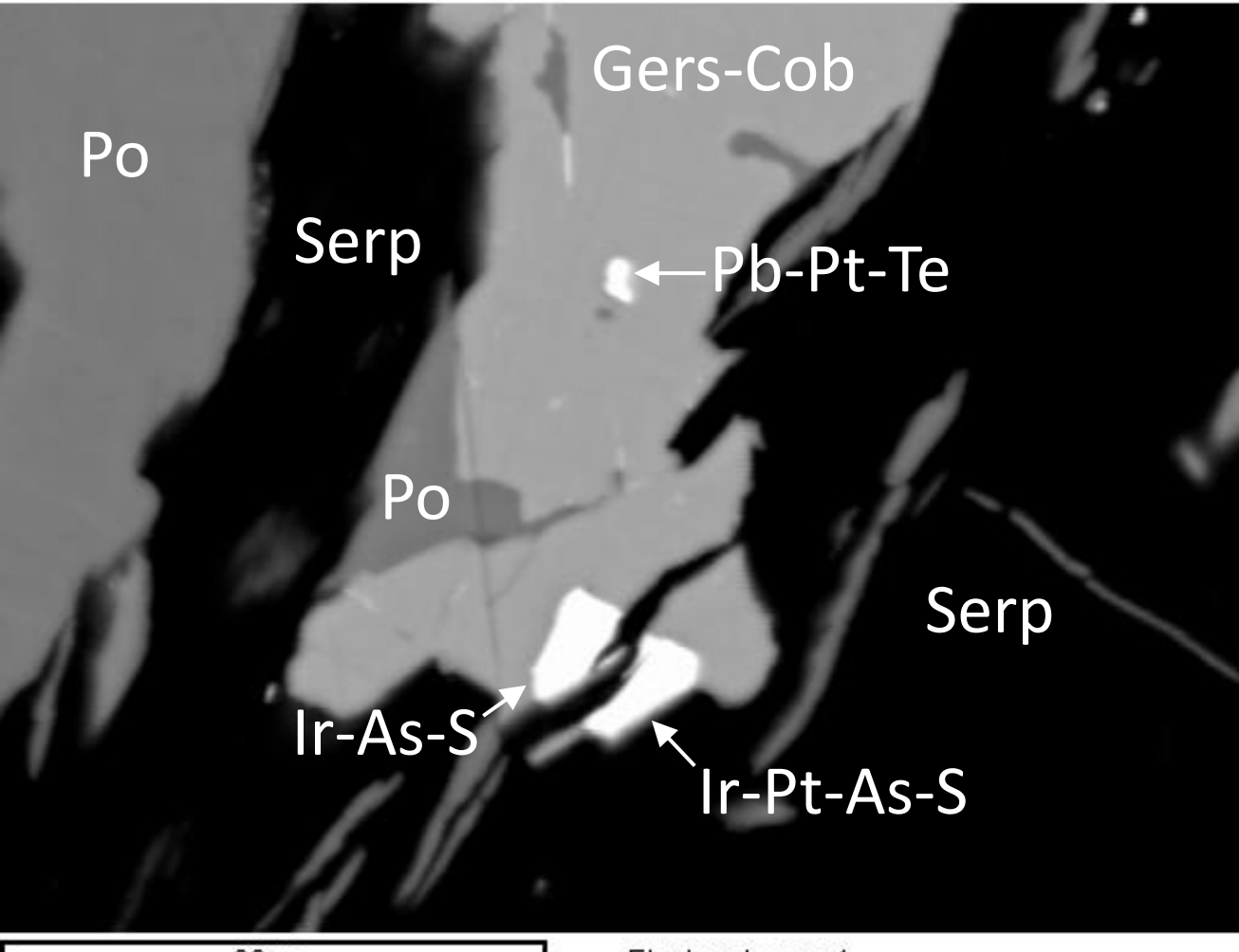
RK12 A1



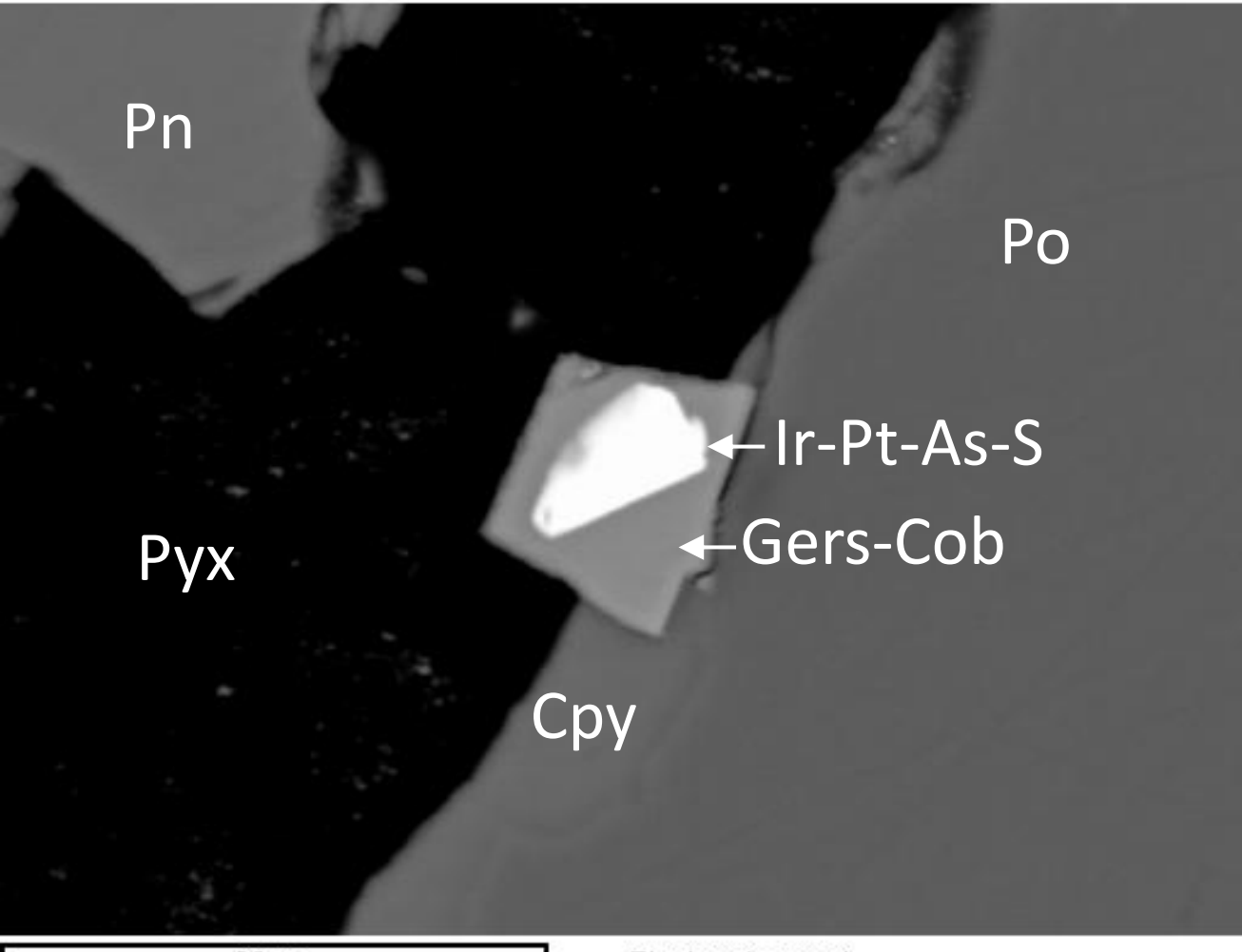
RK13 A1



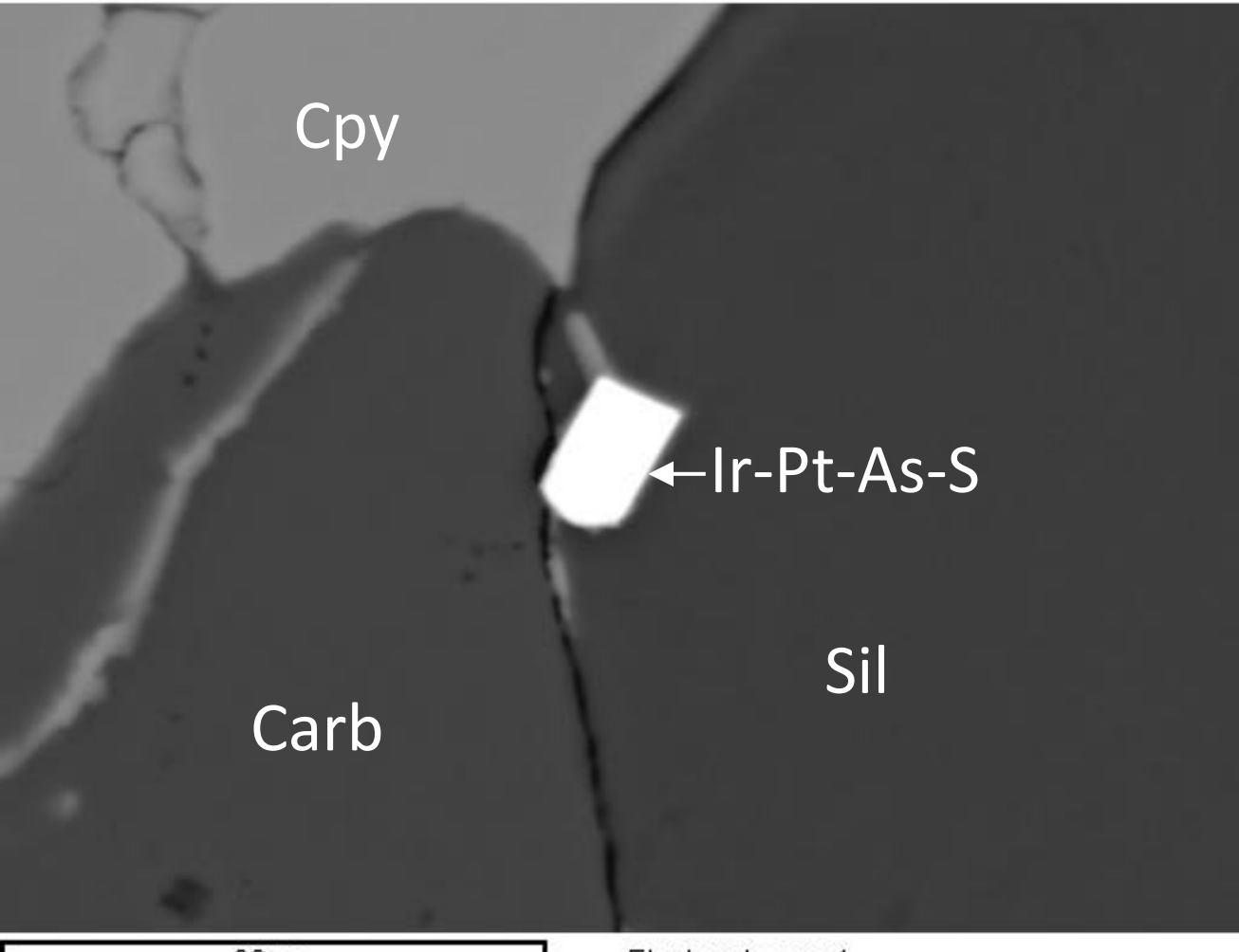
RK14 A1-3


Gers-Cob
Po
Serp
Pb-Pt-Te
Po
Serp
Ir-As-S
Ir-Pt-As-S
20µm
Electron Image 1

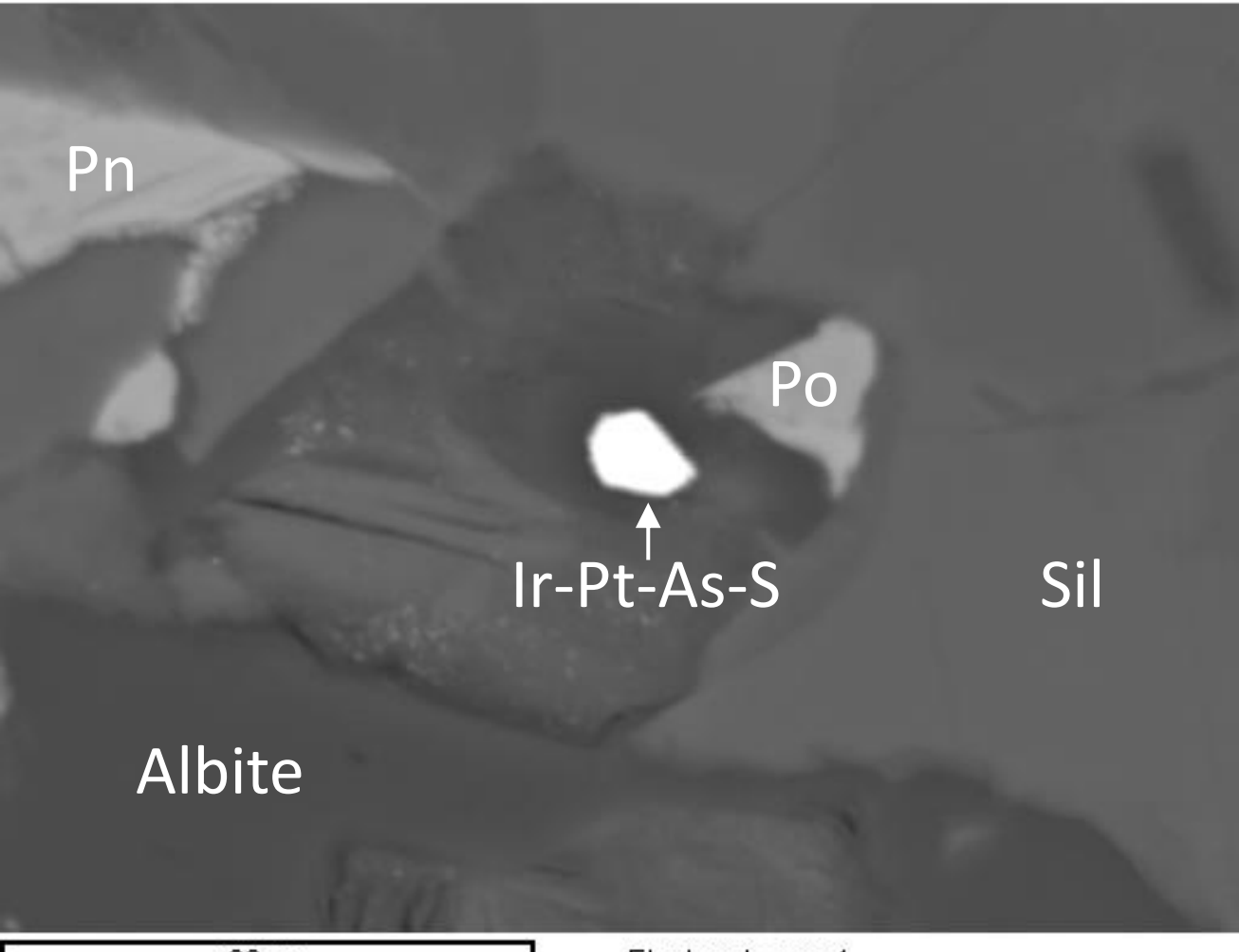
RK19 A1



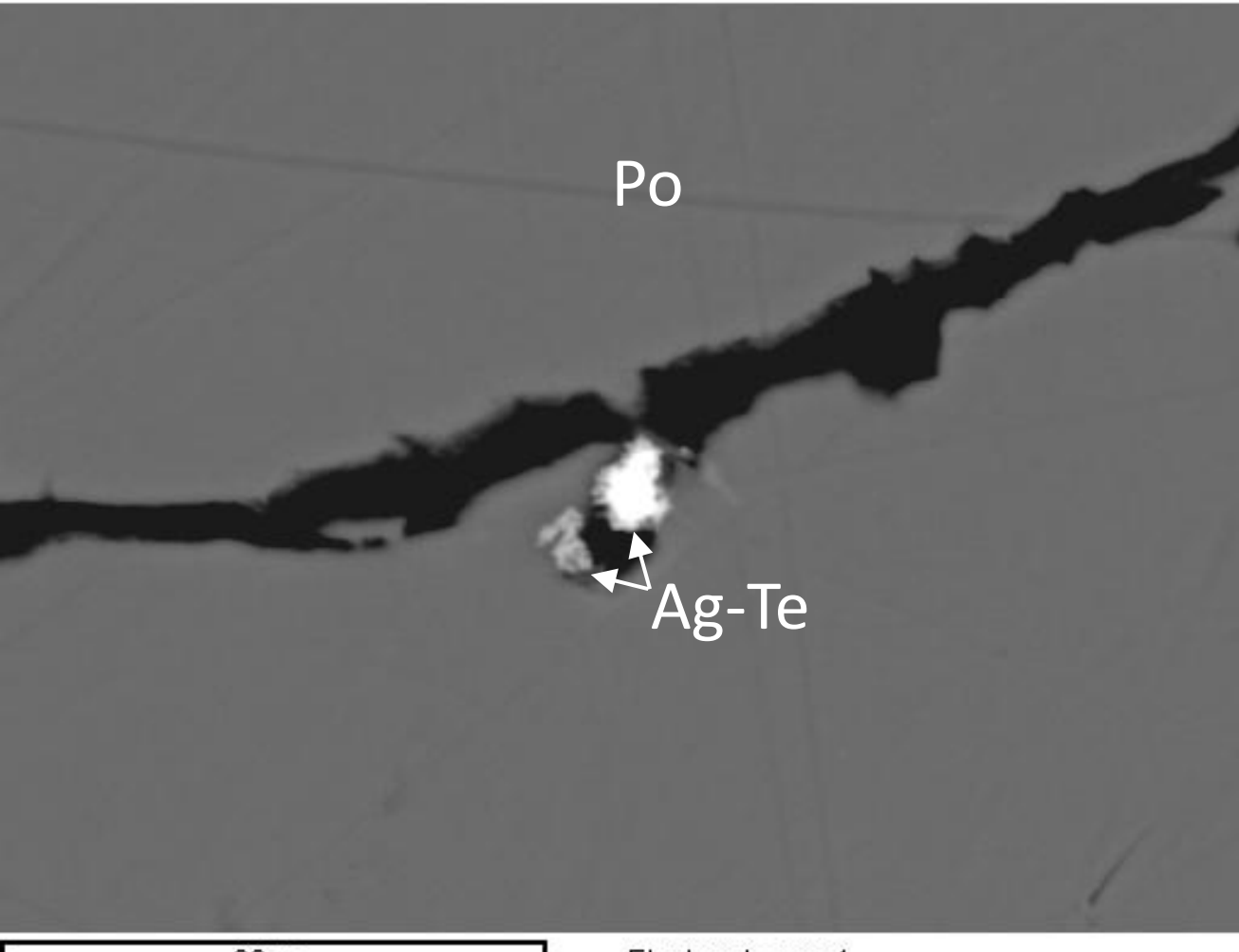
RK19 B1



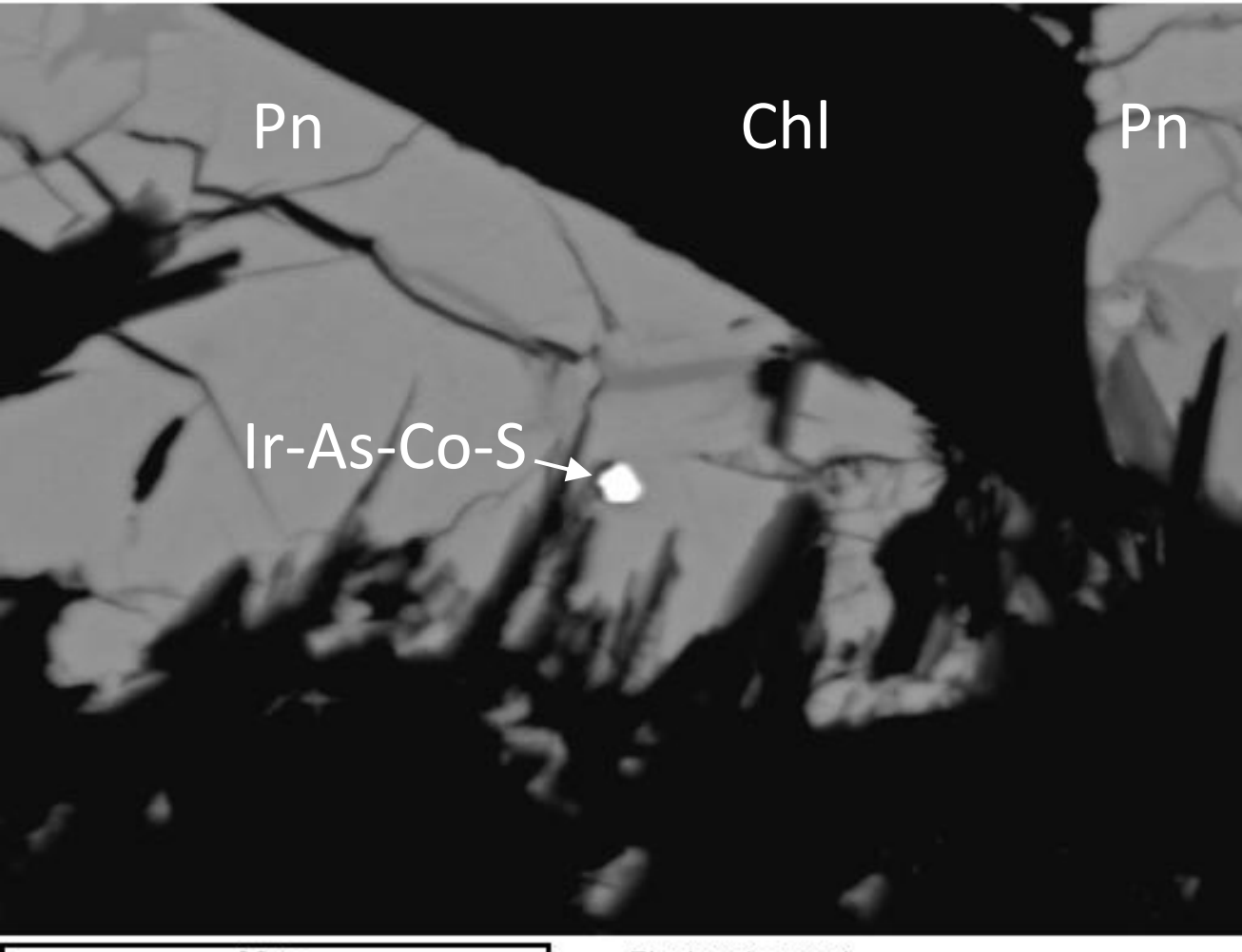
RK19 C1



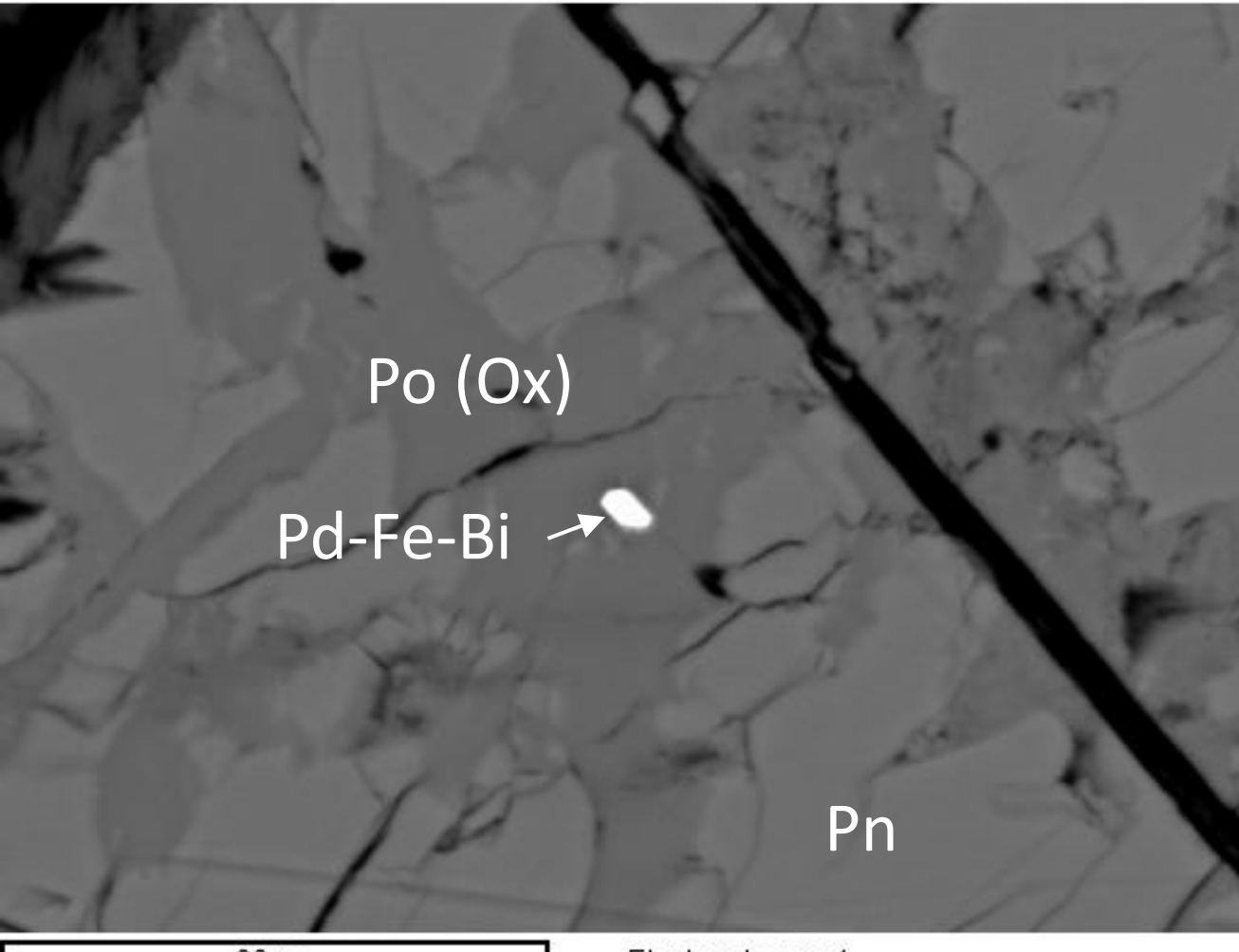
RK20 A1



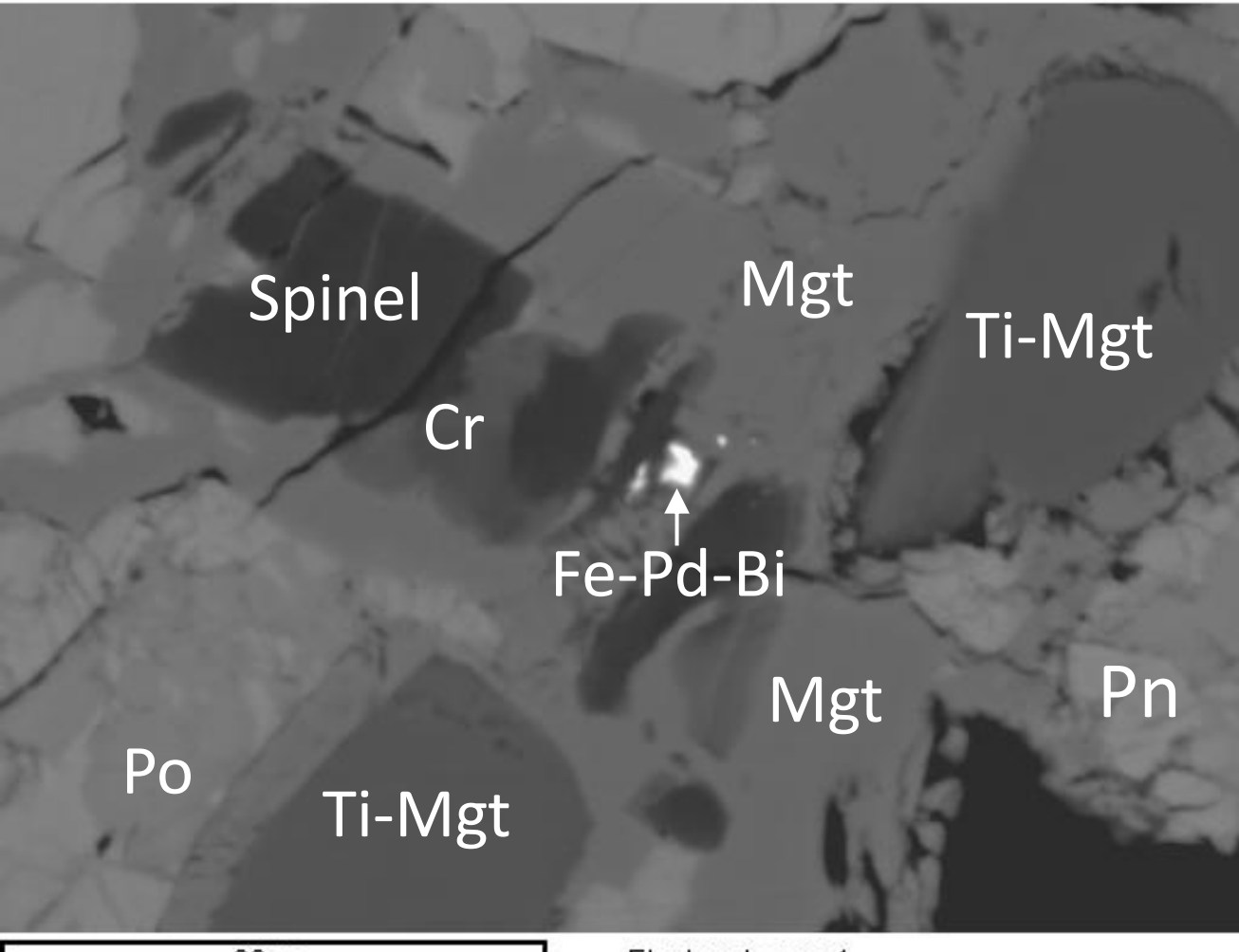
RK20 B1



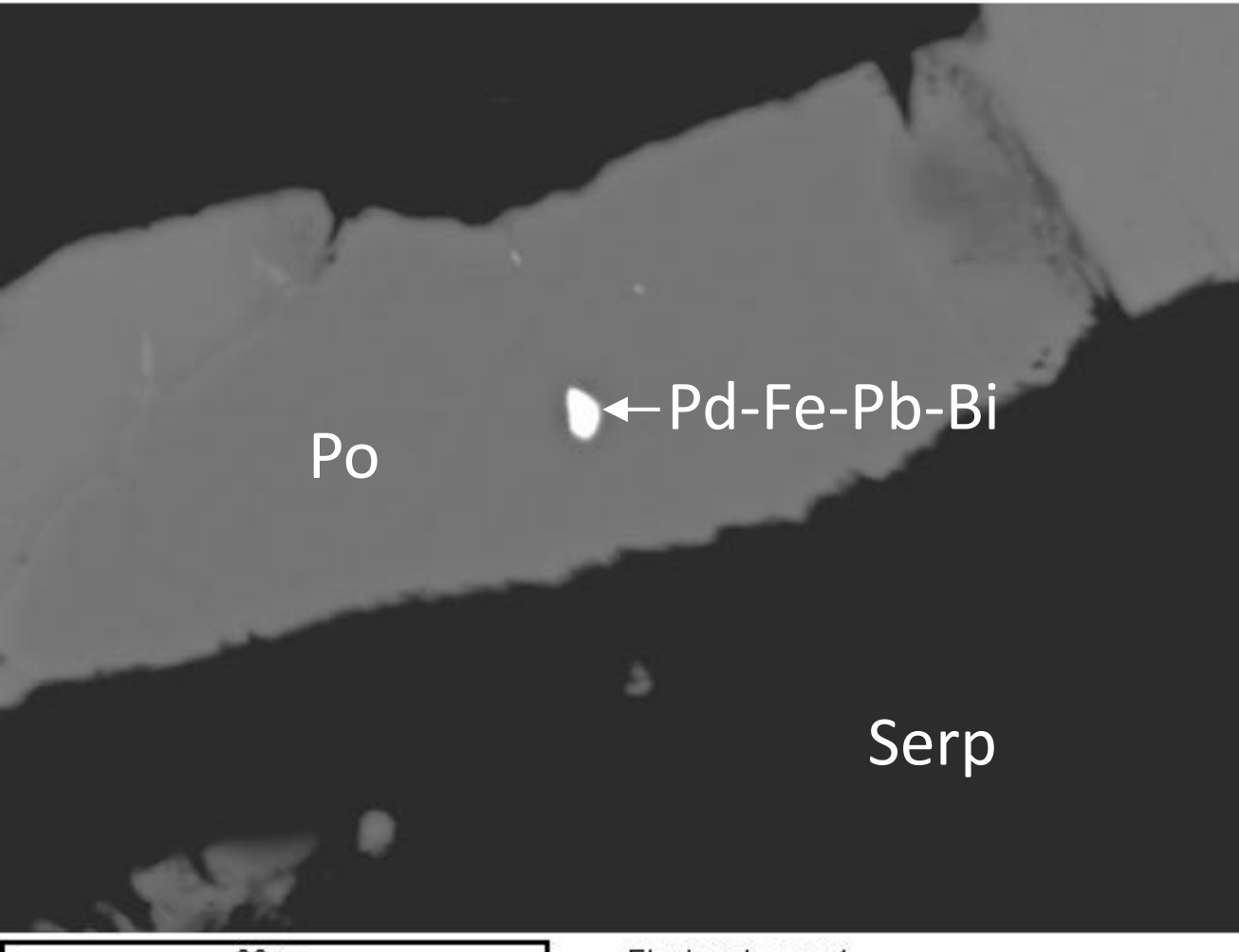
RK20 C1



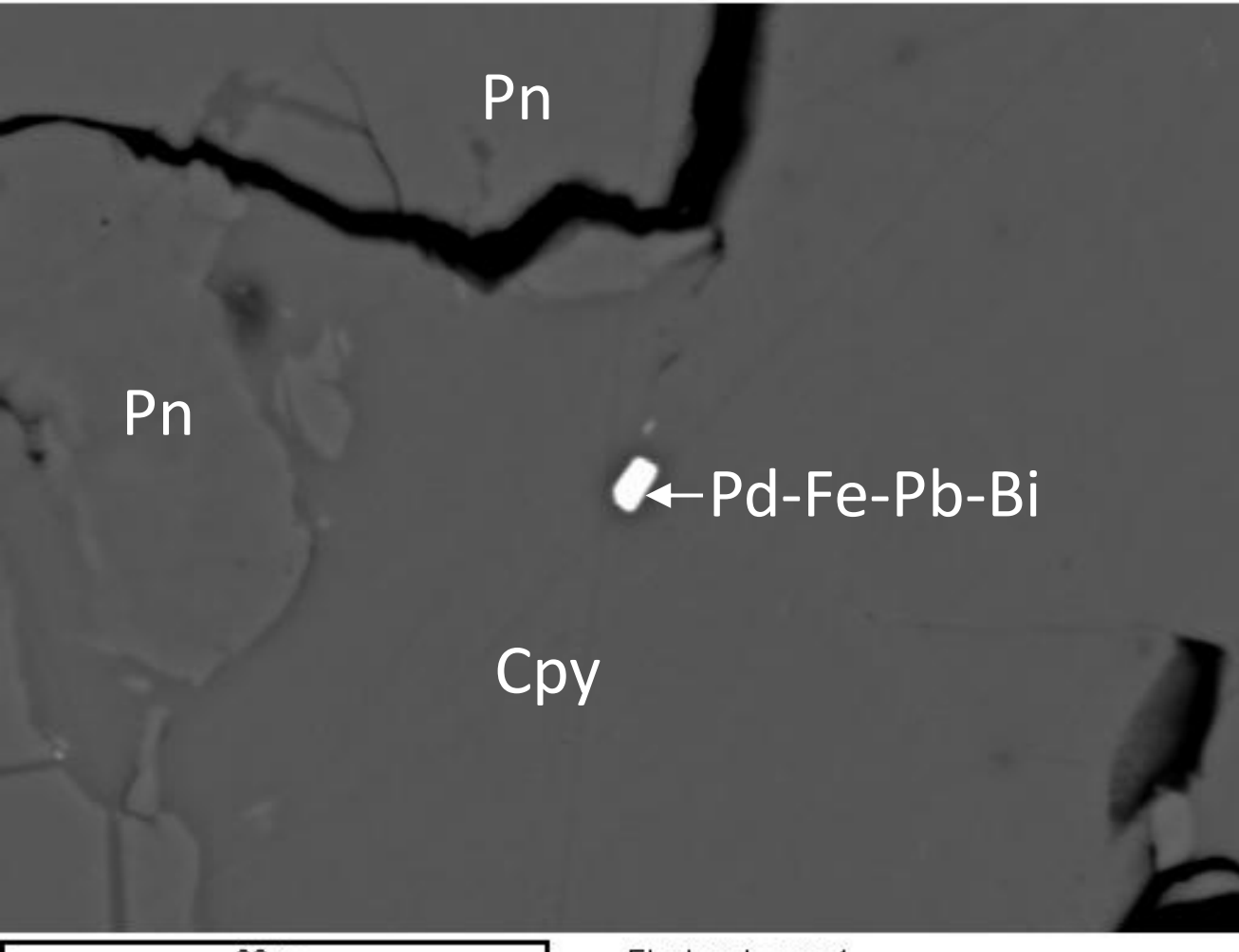
RK20 D1


Spinel
Mgt
Ti-Mgt
Cr
Fe-Pd-Bi
Mgt
Pn
Po
Ti-Mgt
20µm
Electron Image 1

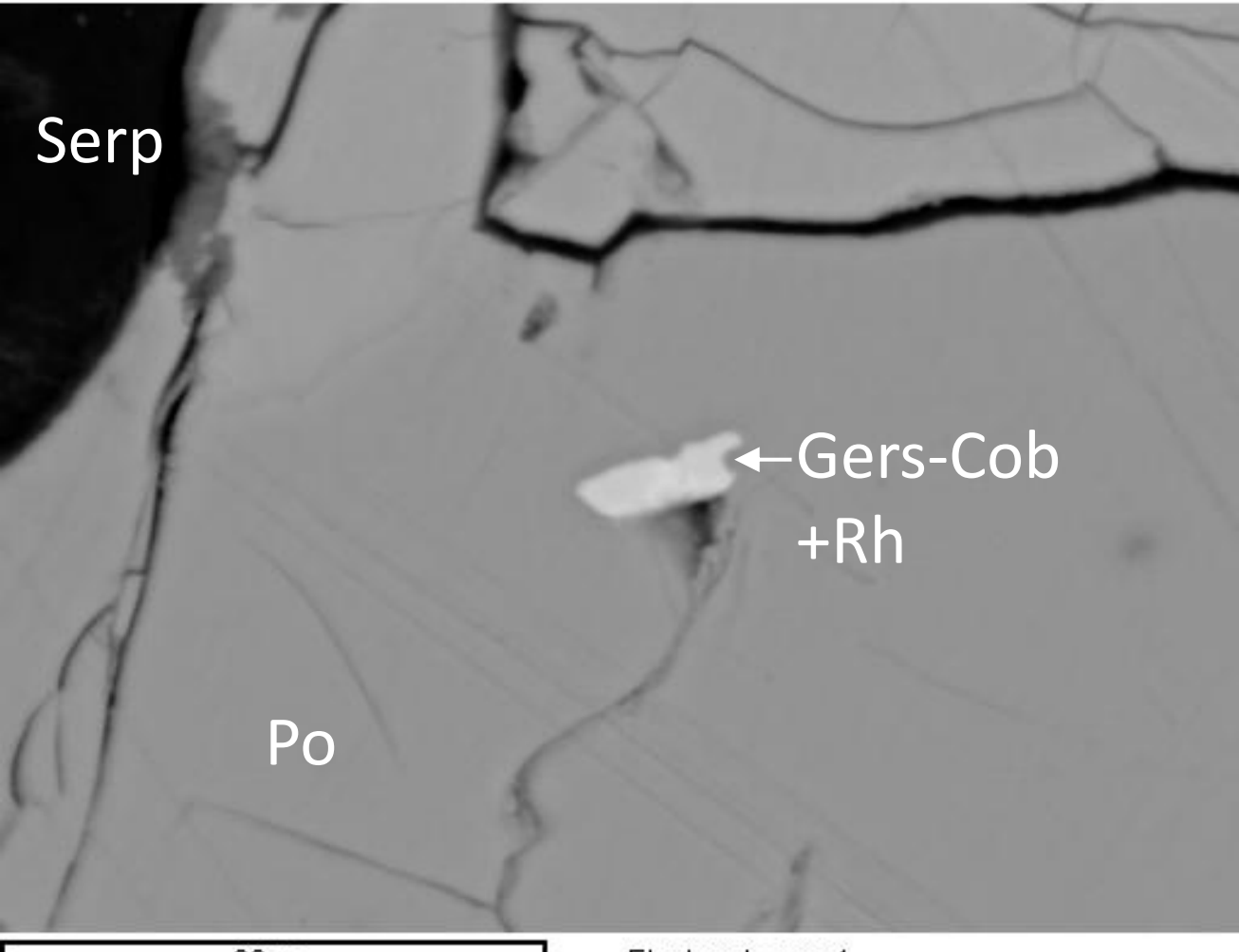
RK20 E1



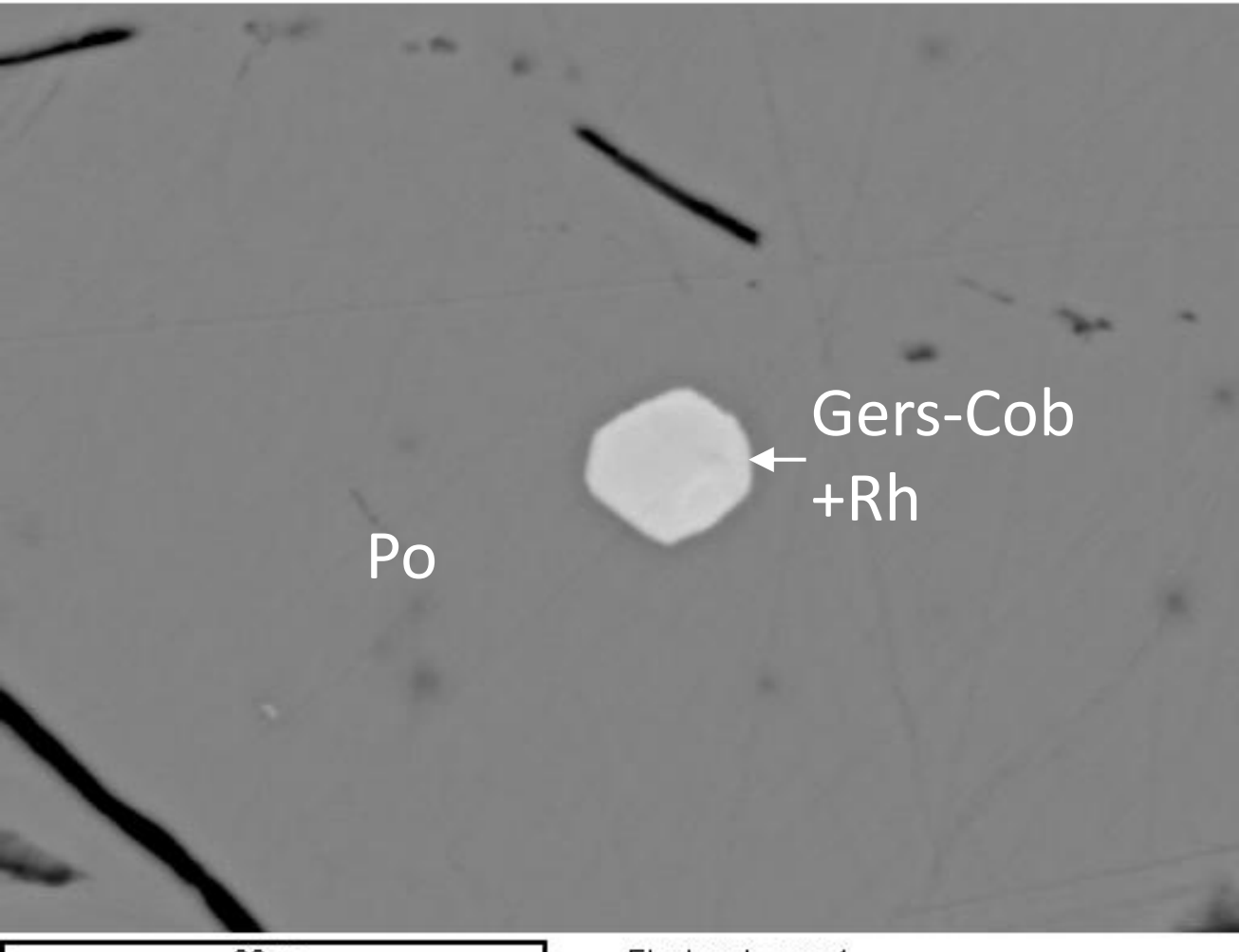
RK21 A1



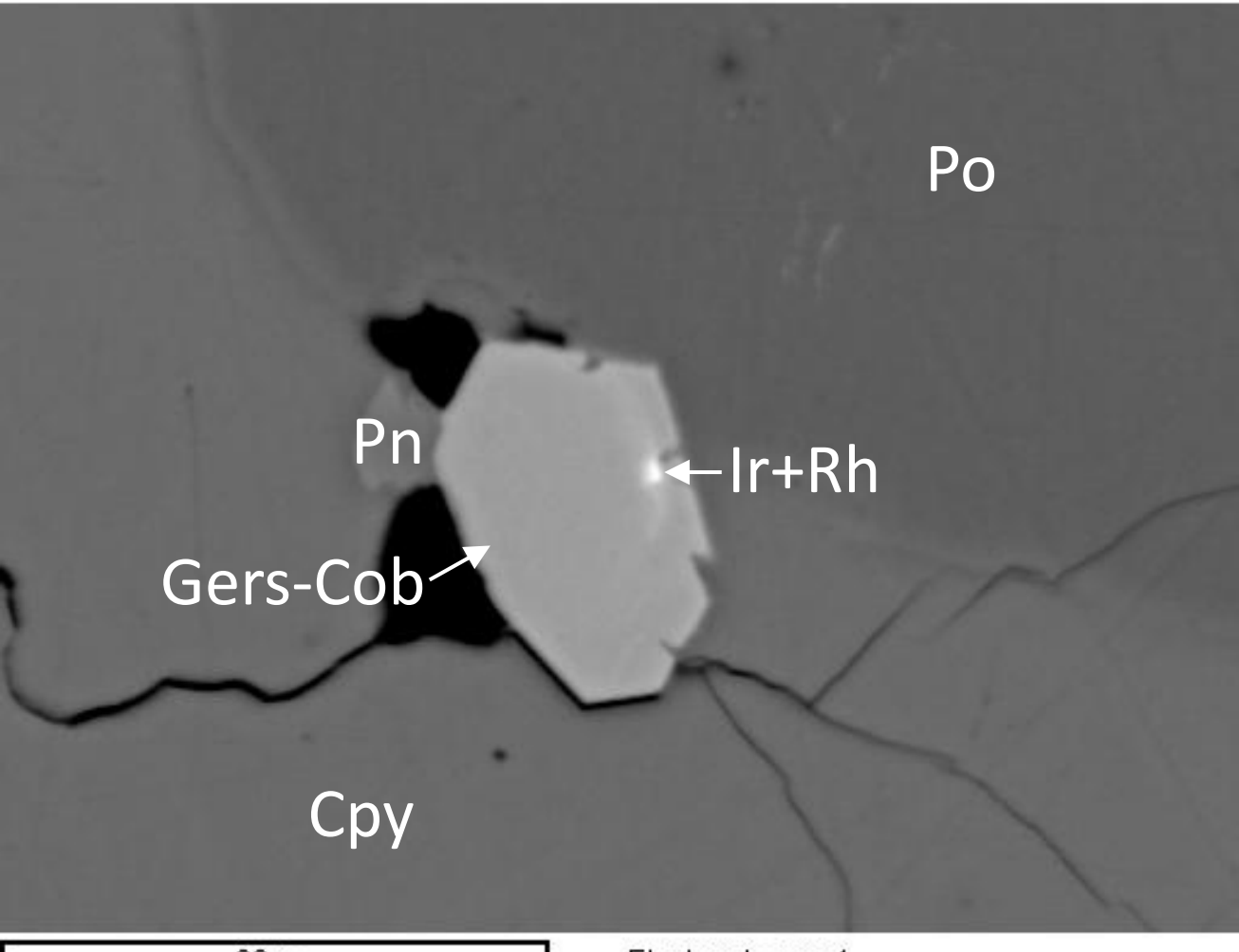
RK21 B1



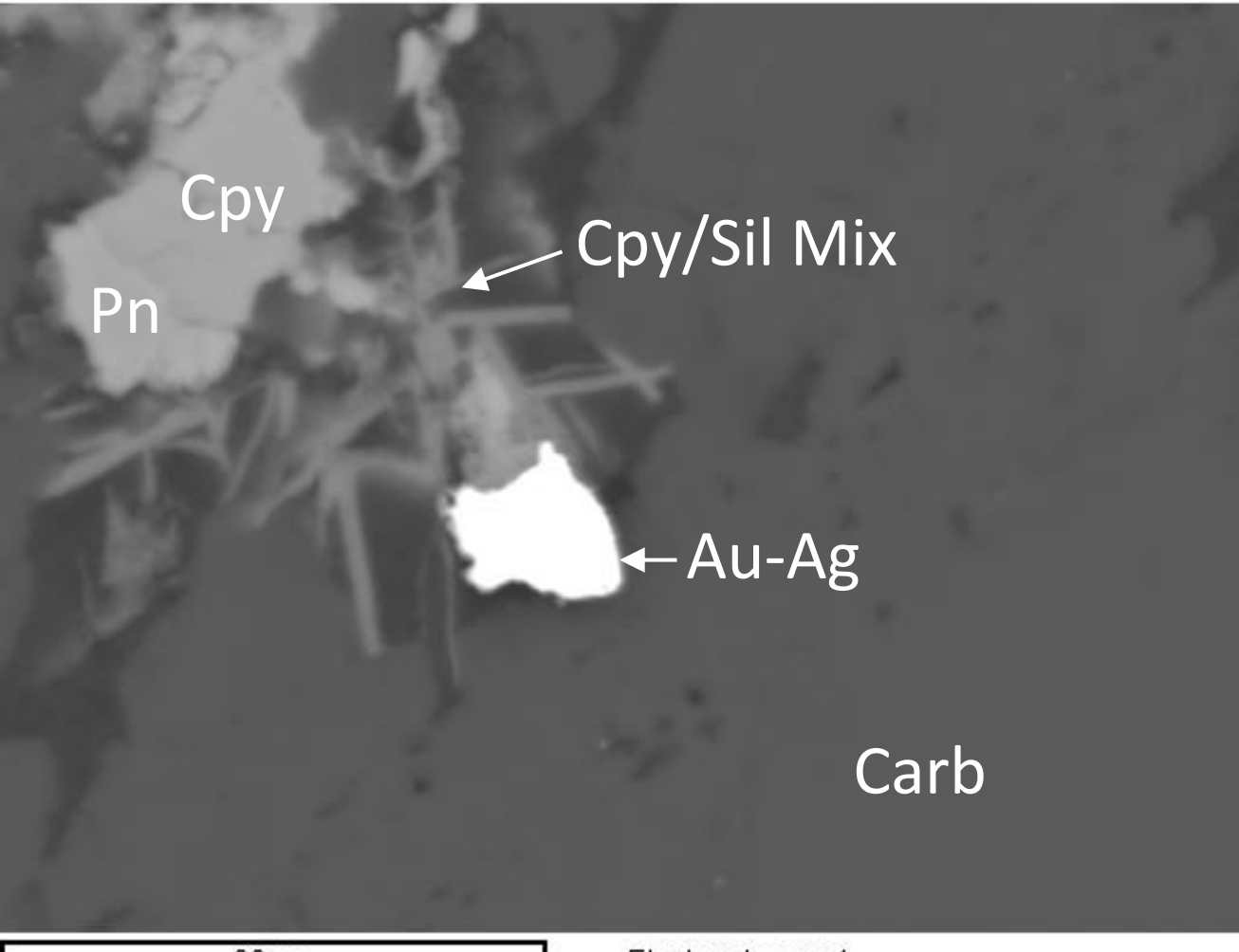
RK21 C1



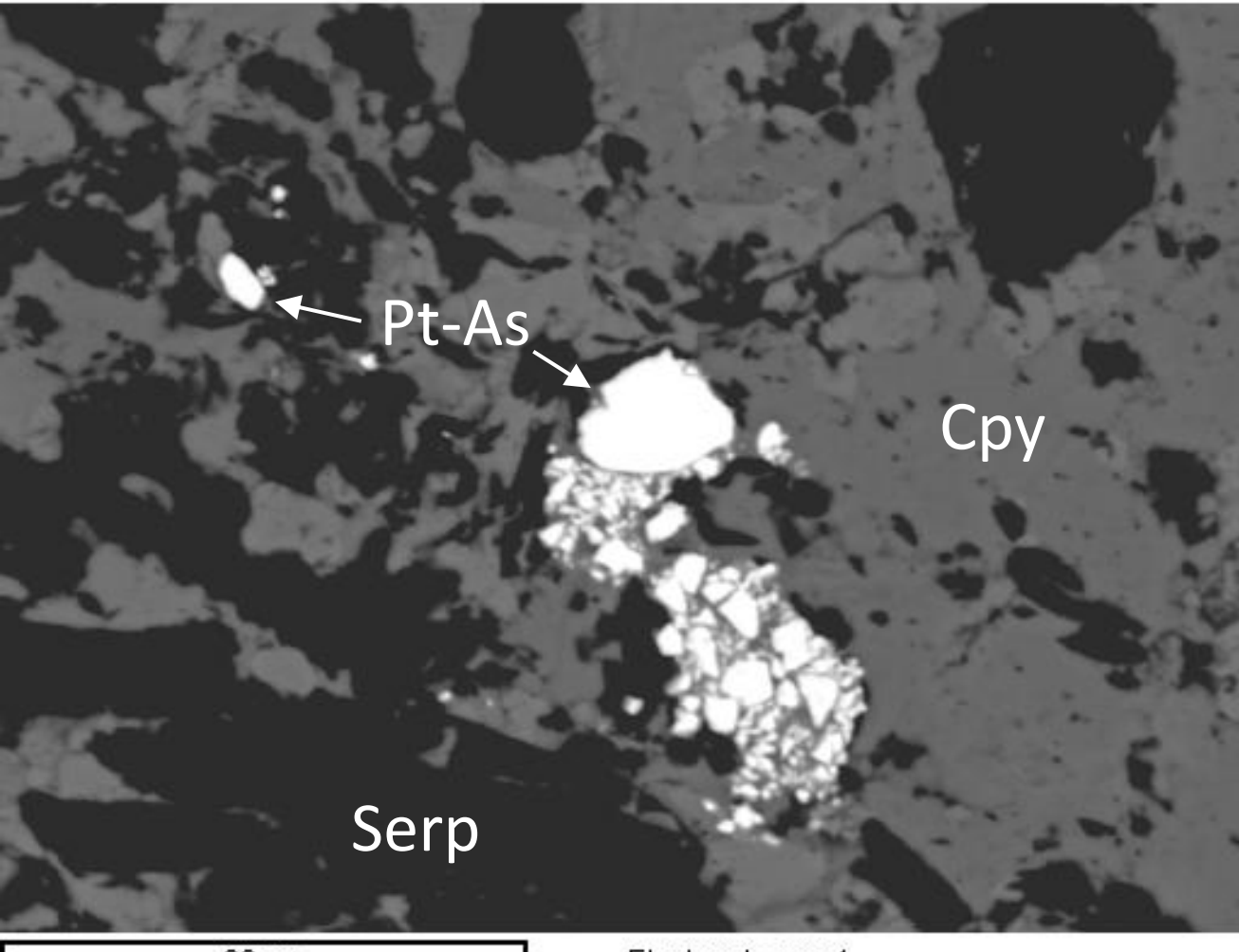
RK21 D1



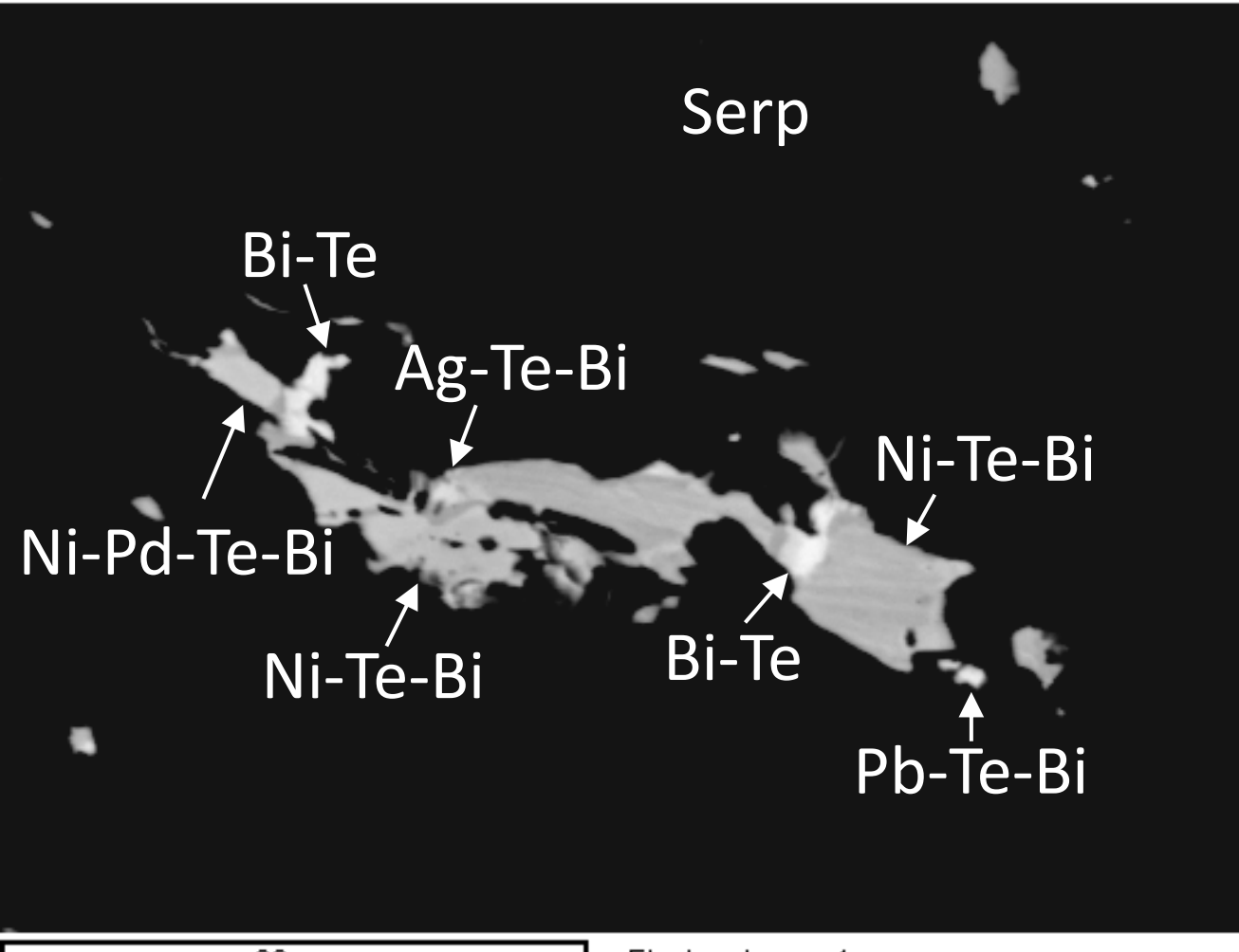
RK24A A1



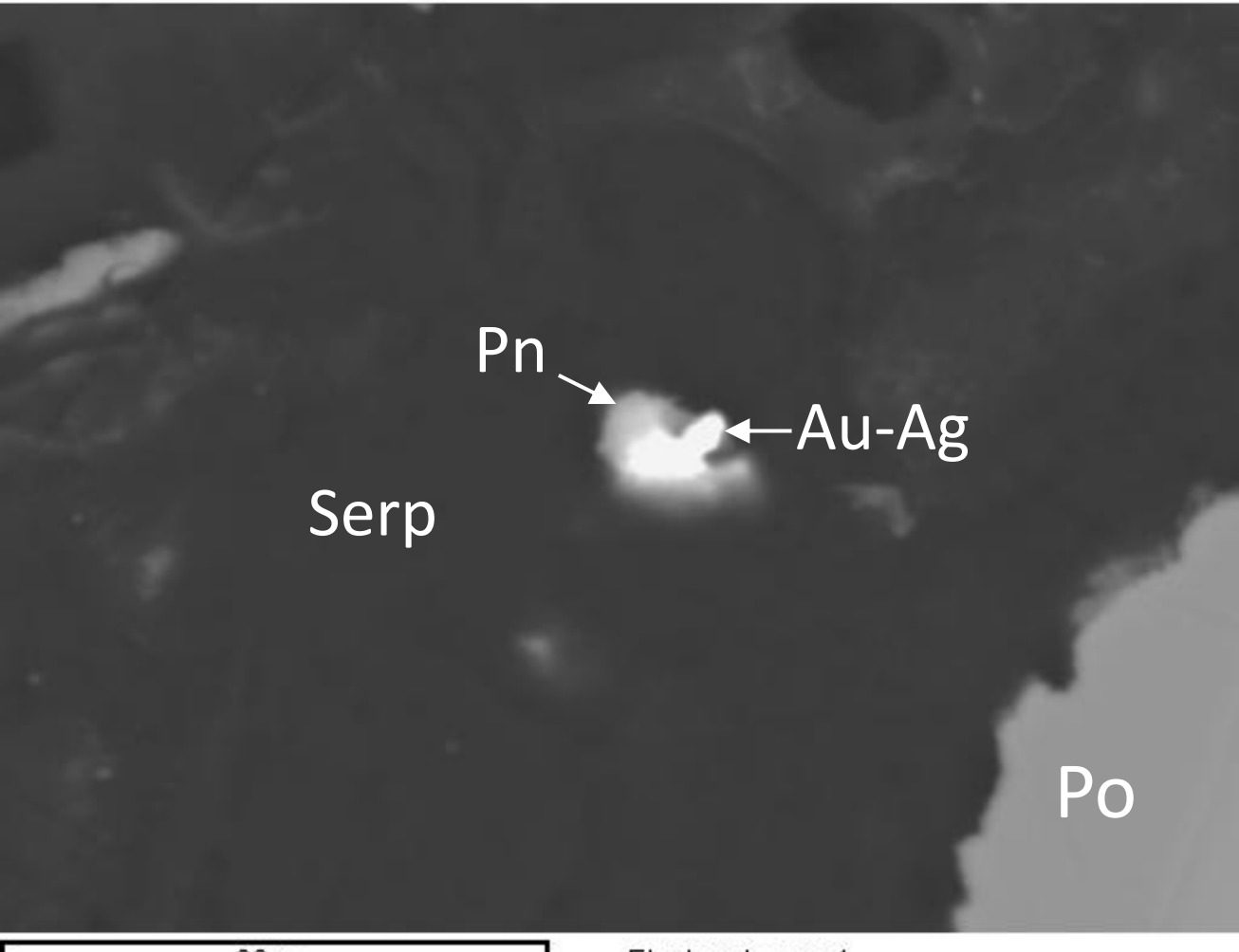
RK24A B1



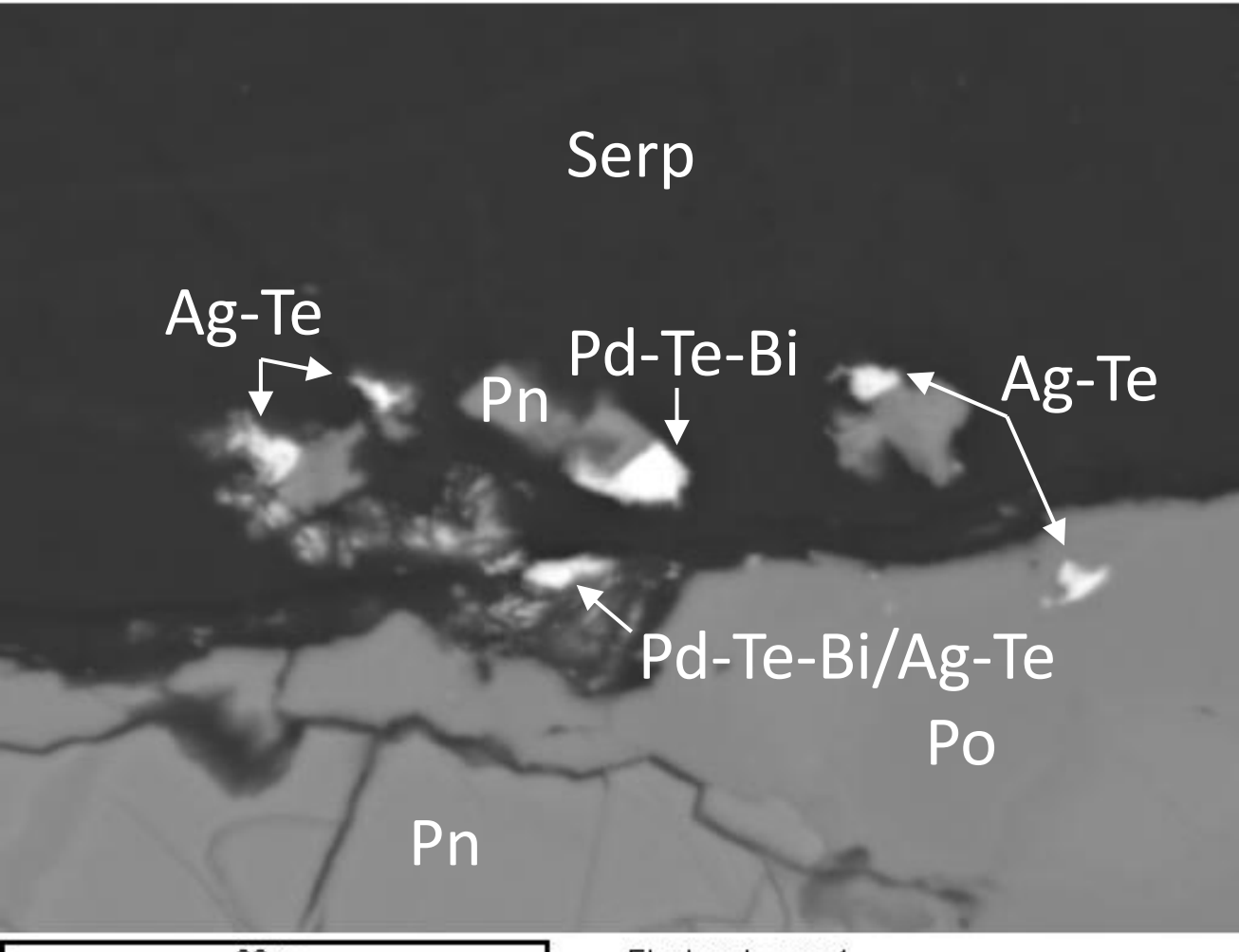
RK24B A1


Serp
Bi-Te
Ag-Te-Bi
Ni-Te-Bi
Ni-Pd-Te-Bi
Ni-Te-Bi
Bi-Te
Pb-Te-Bi
30µm
Electron Image 1

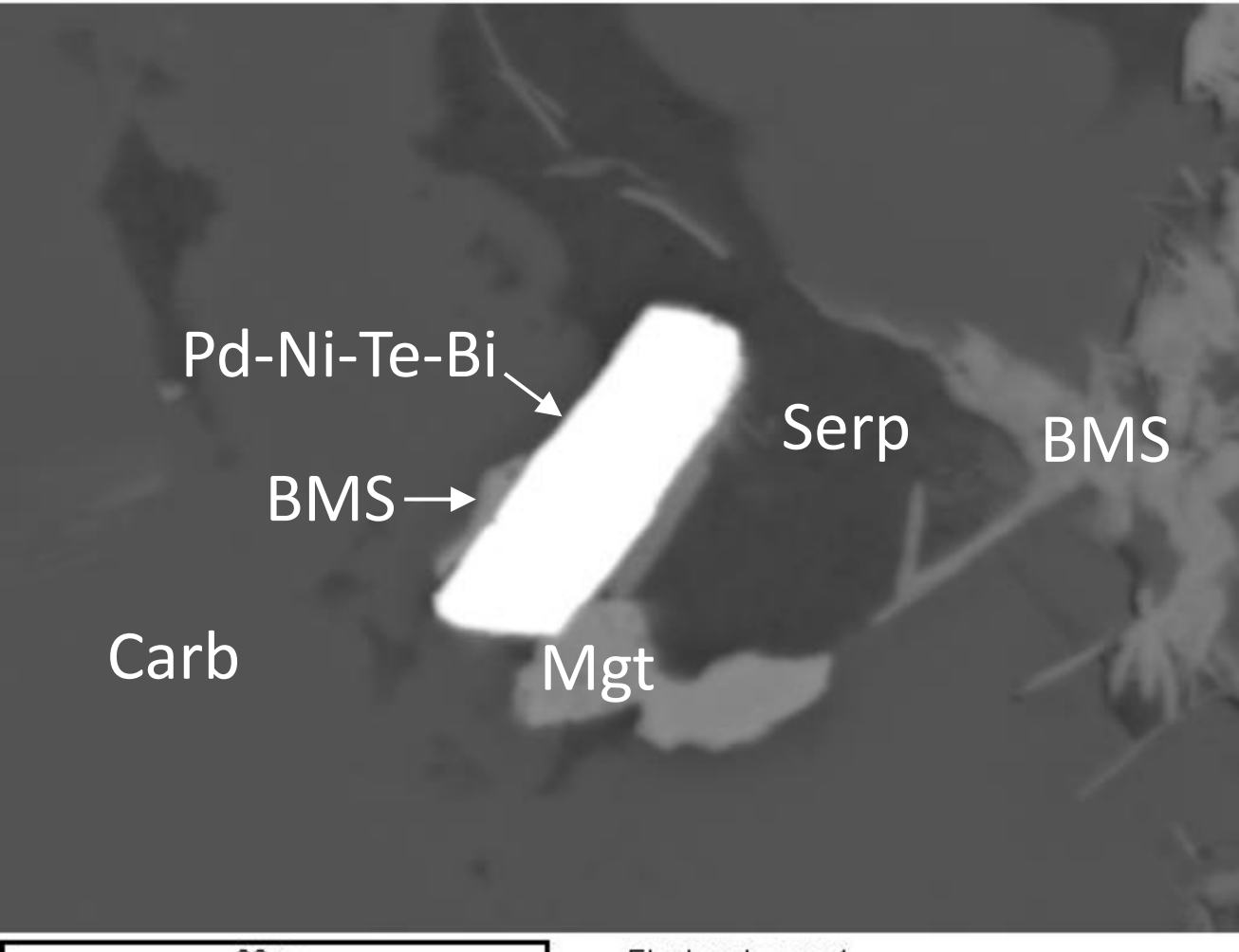
RK24B C1



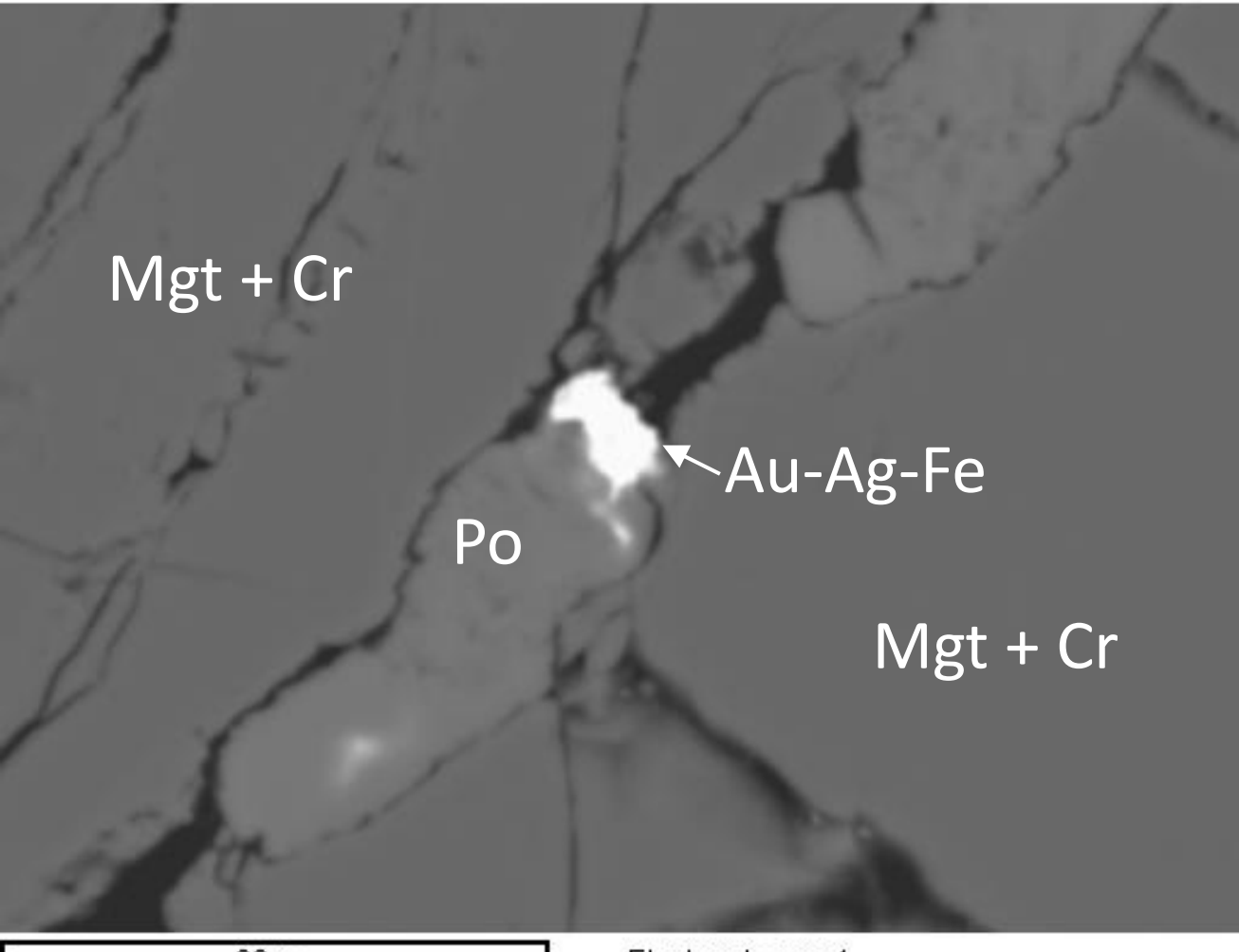
RK24B D1


Serp
Ag-Te
Pn
Pd-Te-Bi
Ag-Te
Pd-Te-Bi/Ag-Te
Po
Pn
20µm
Electron Image 1

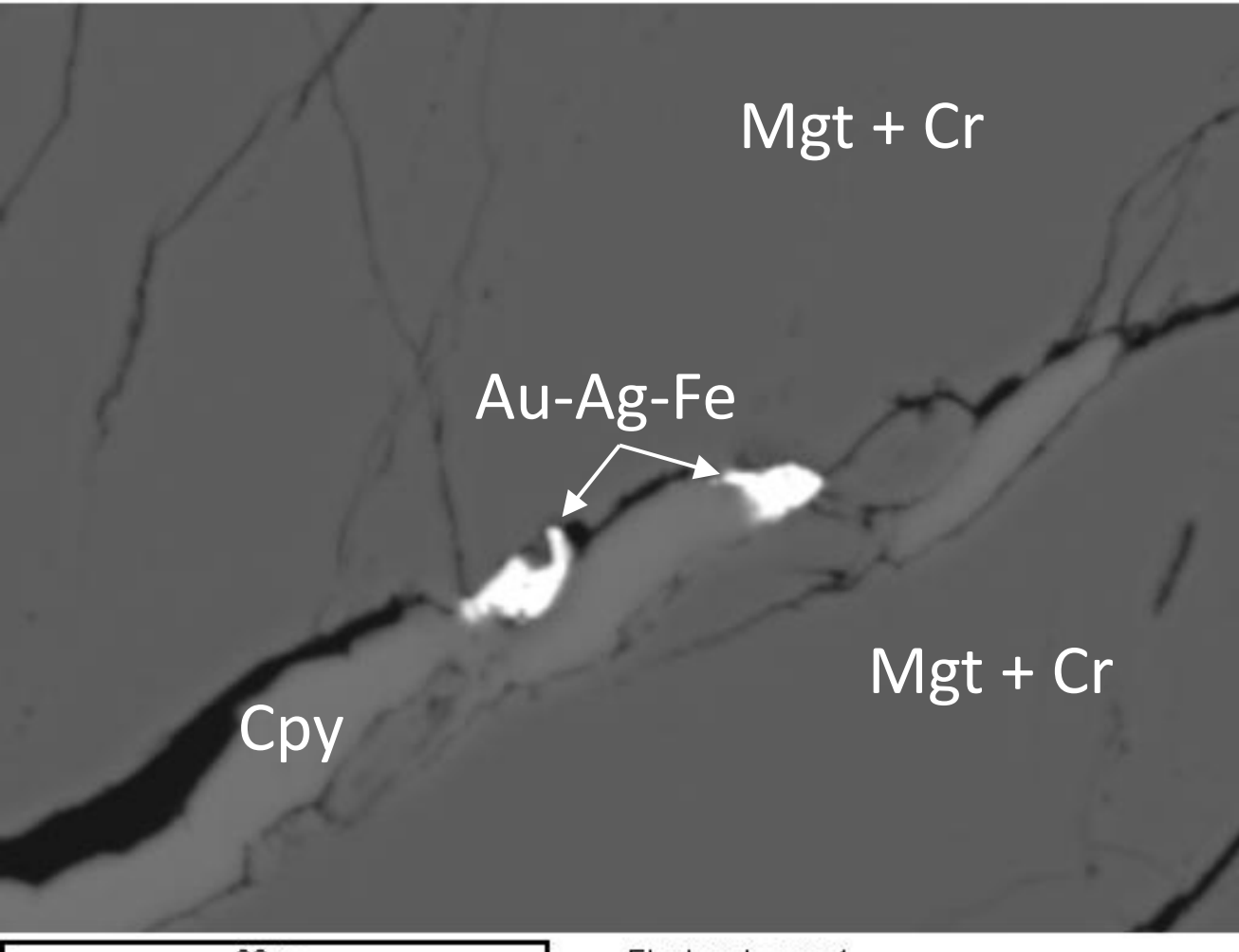
RK24B E1



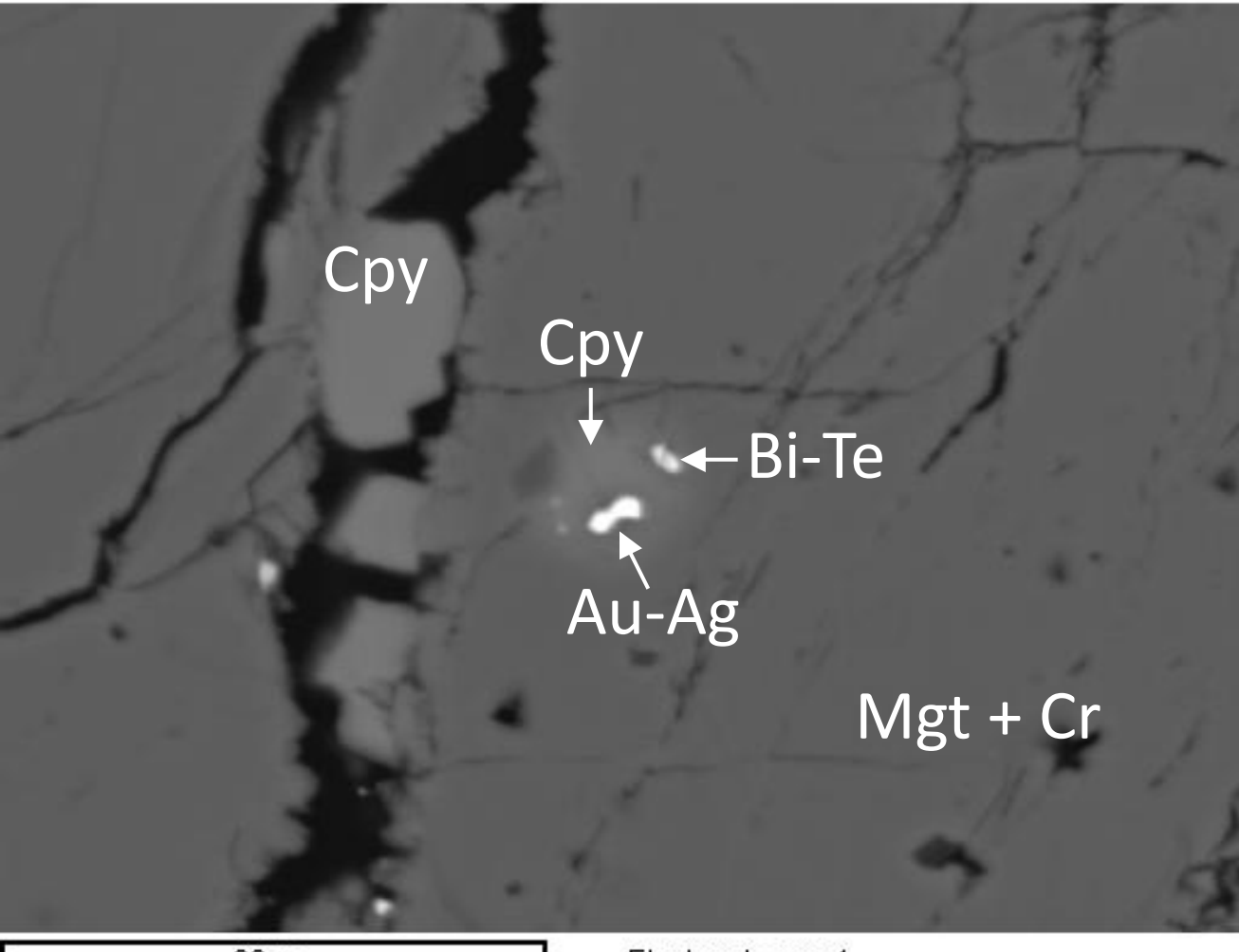
RK25 A1



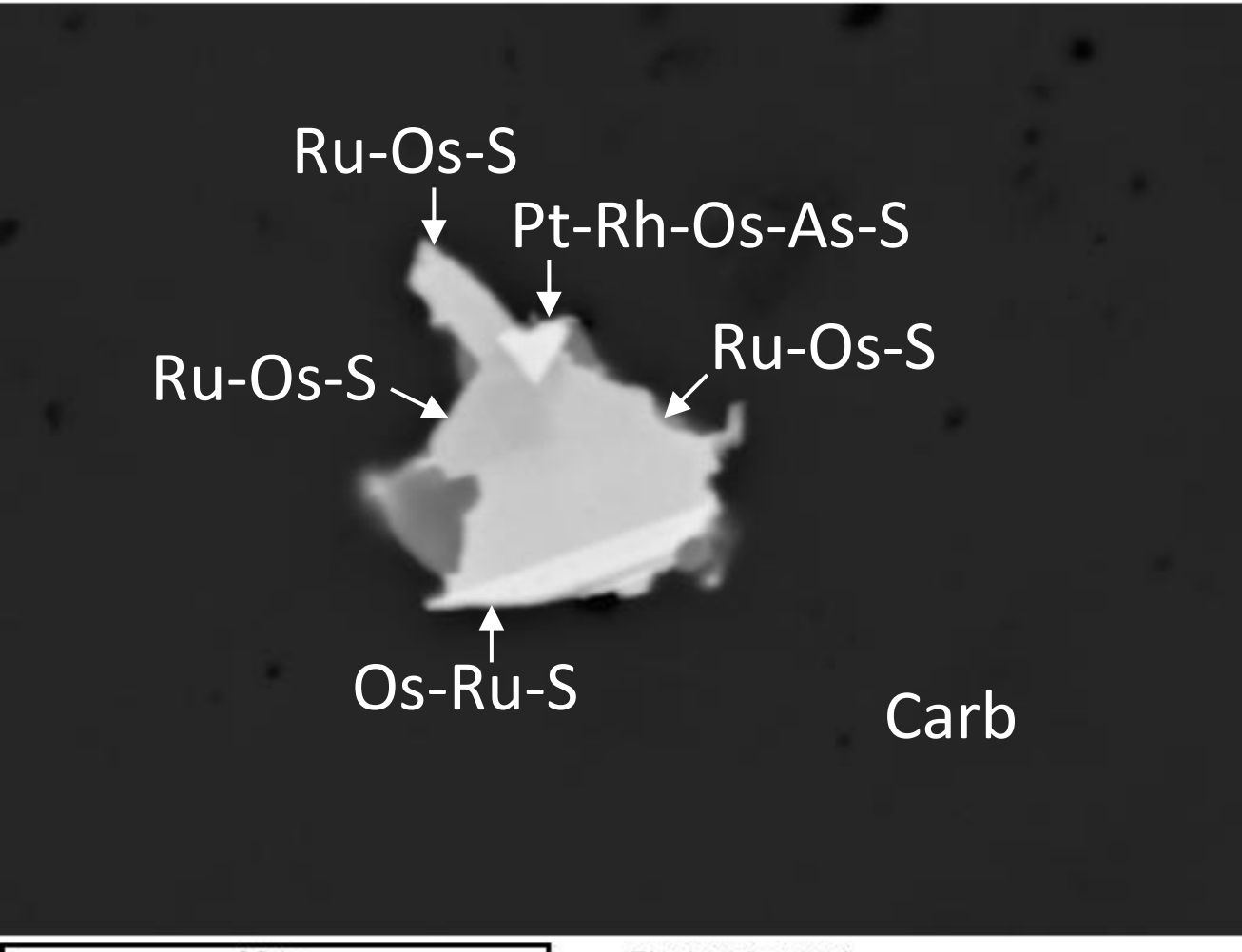
RK25 A2-3



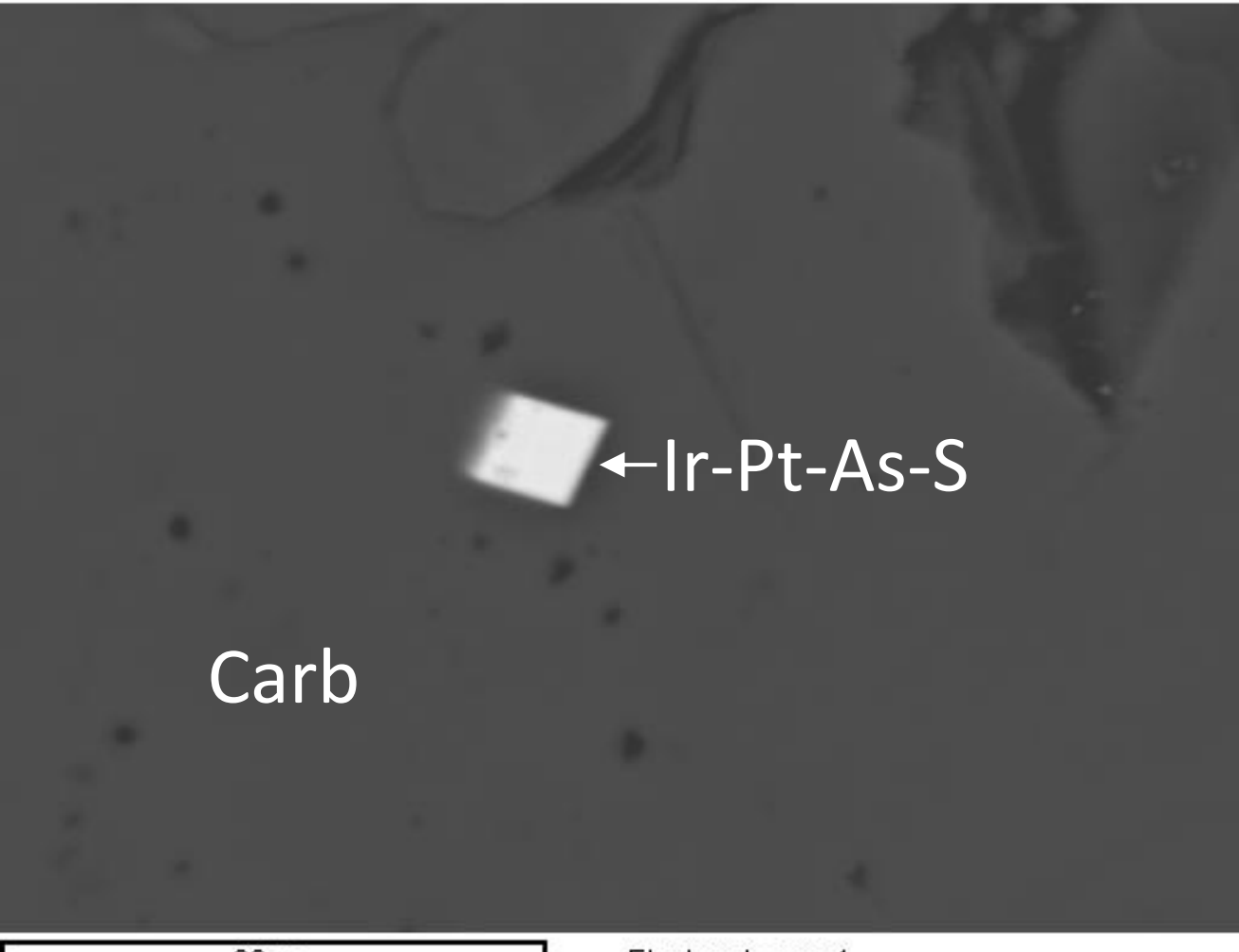
RK25 A4-5



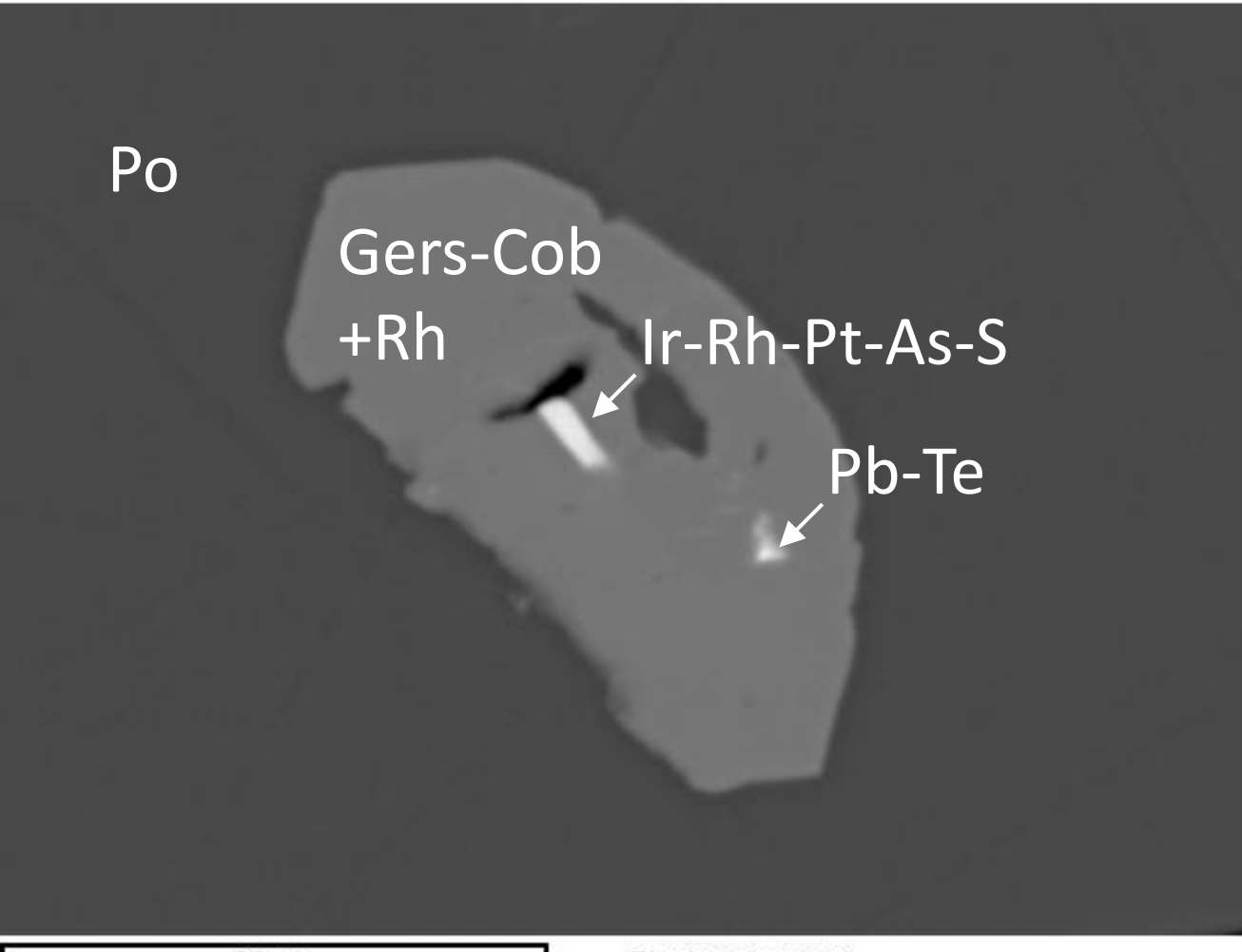
RK27 A1-5


Ru-Os-S
Pt-Rh-Os-As-S
Ru-Os-S
Ru-Os-S
Os-Ru-S
Carb
20µm
Electron Image 1

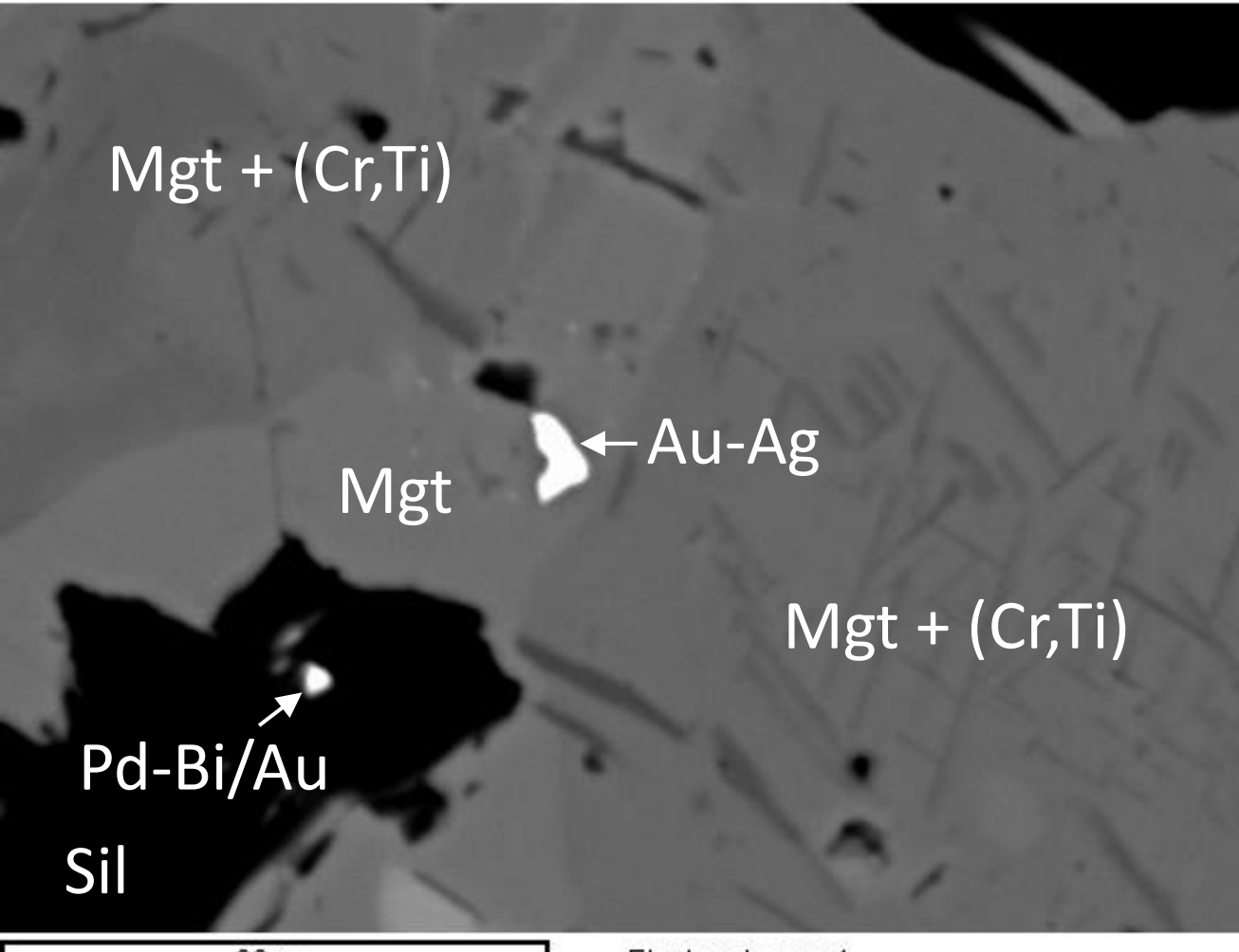
RK27 A6



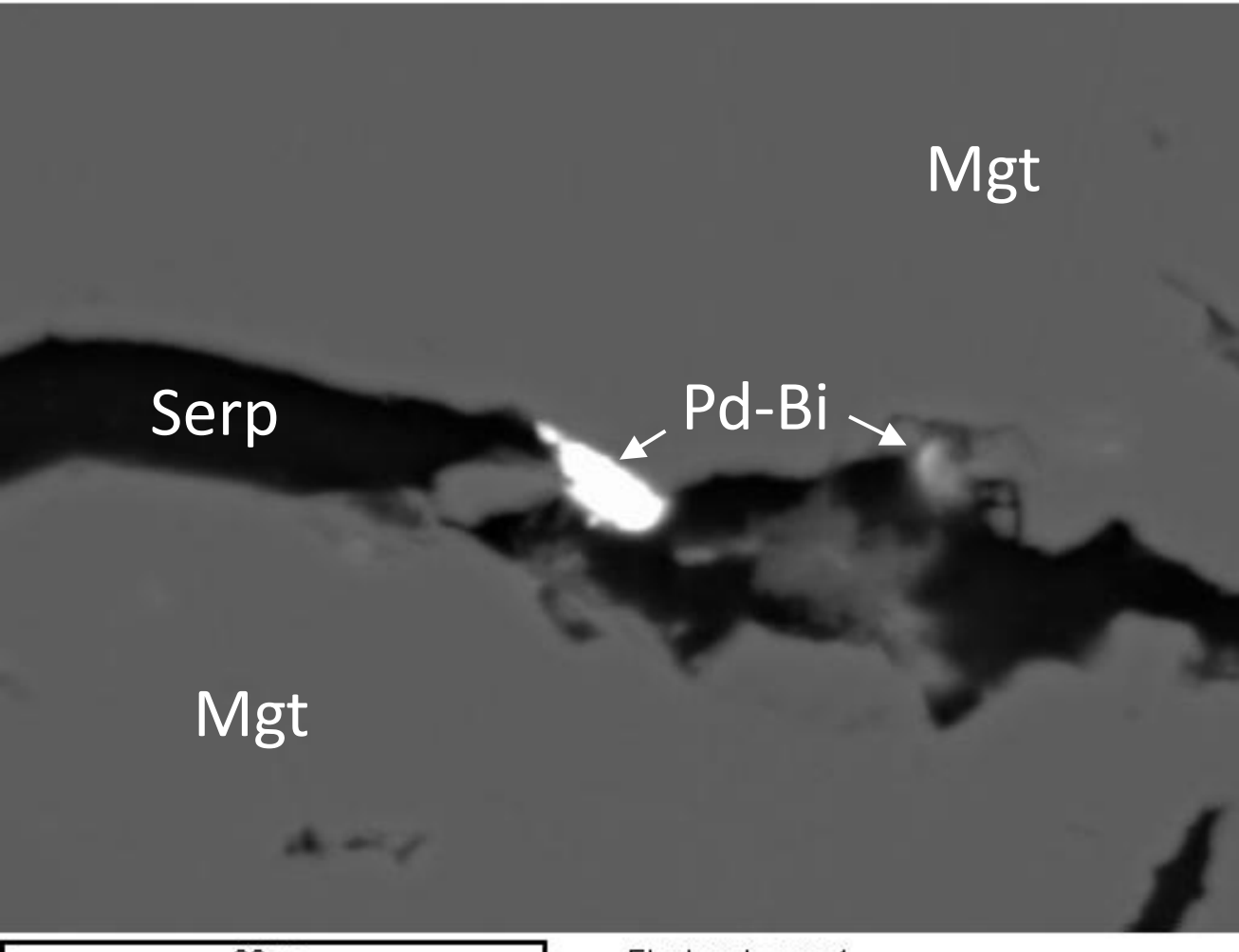
RK29 A1-2



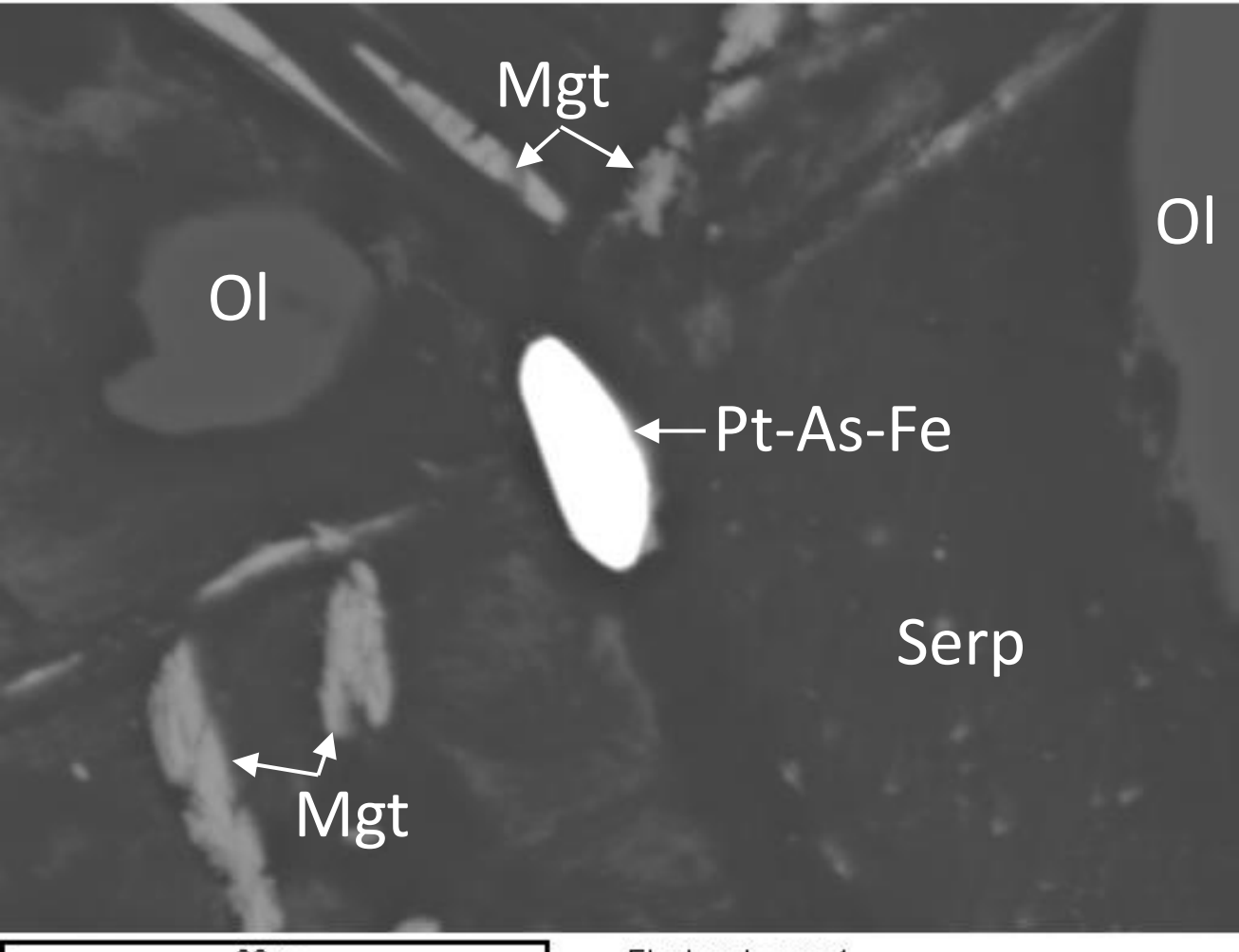
RK30 A1-2



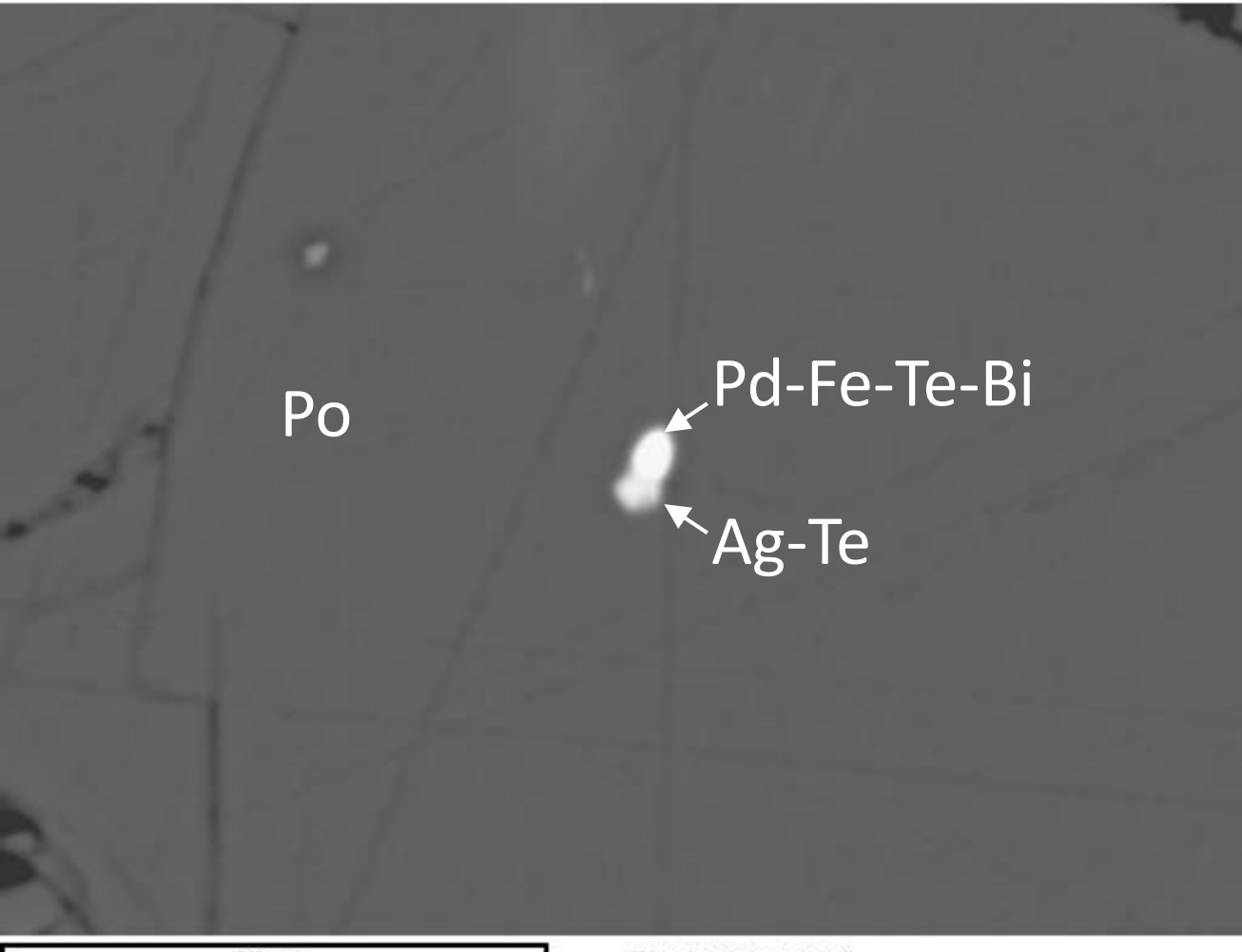
RK30 B1-2



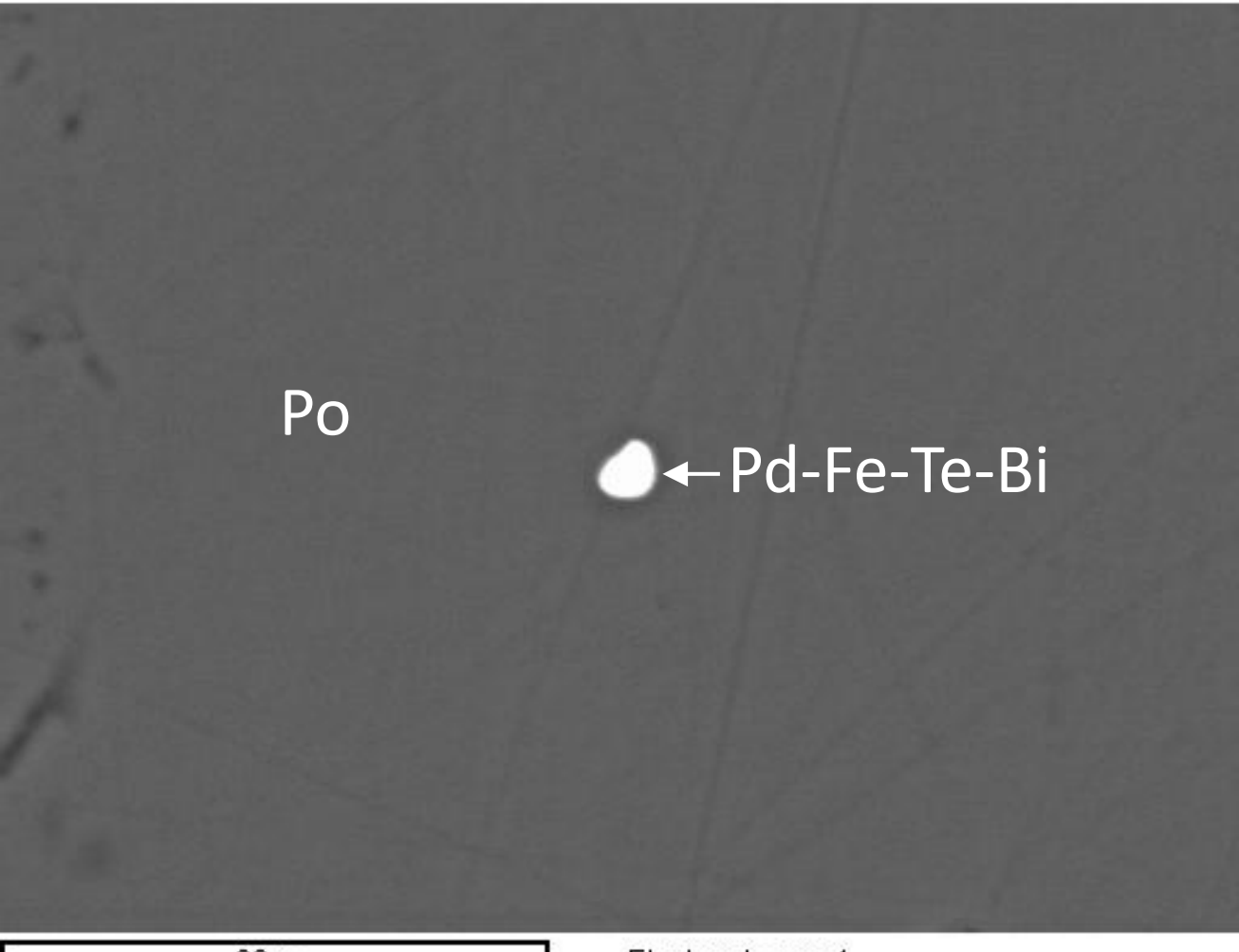
RK31 A1



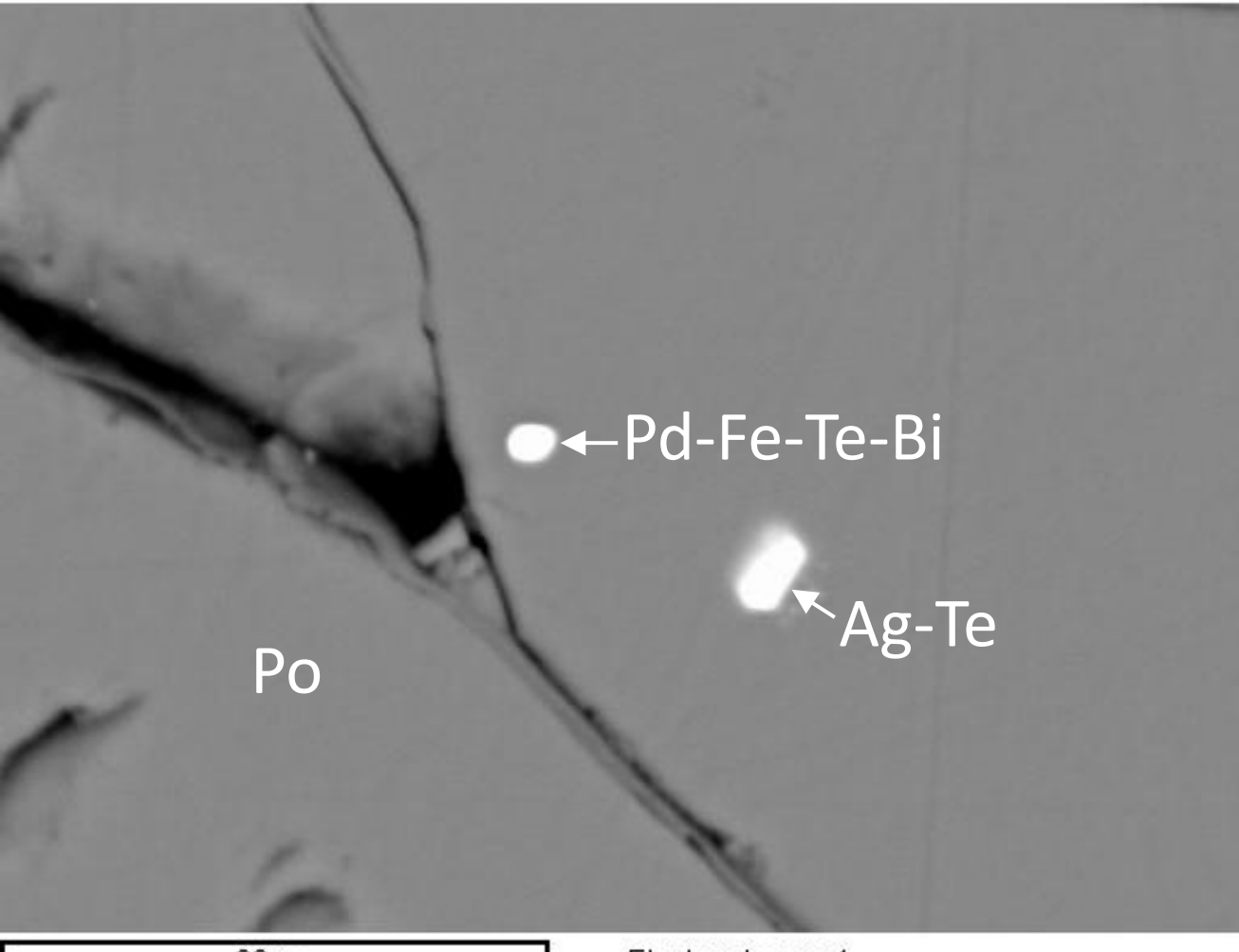
RK33 A1-2



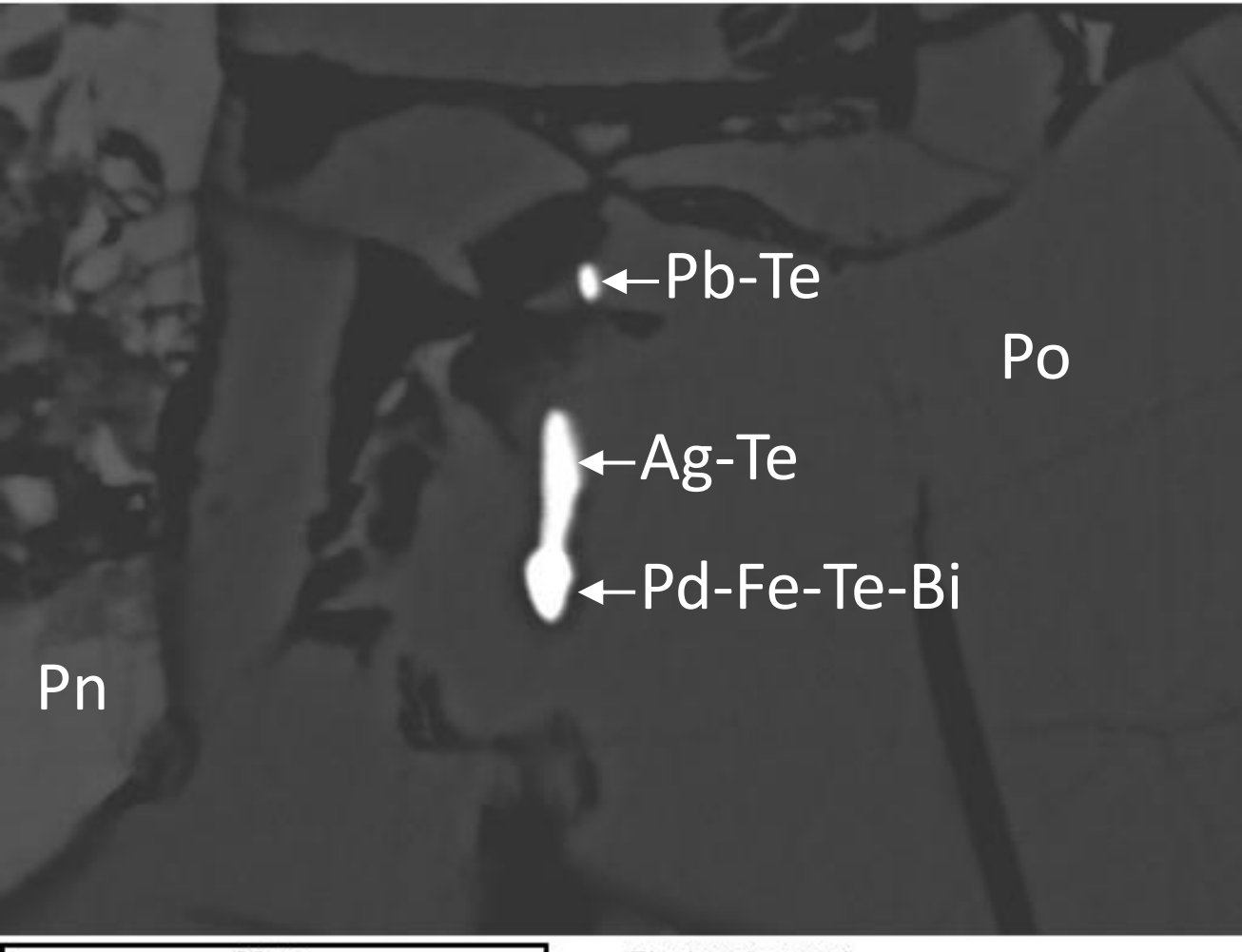
RK33 B1



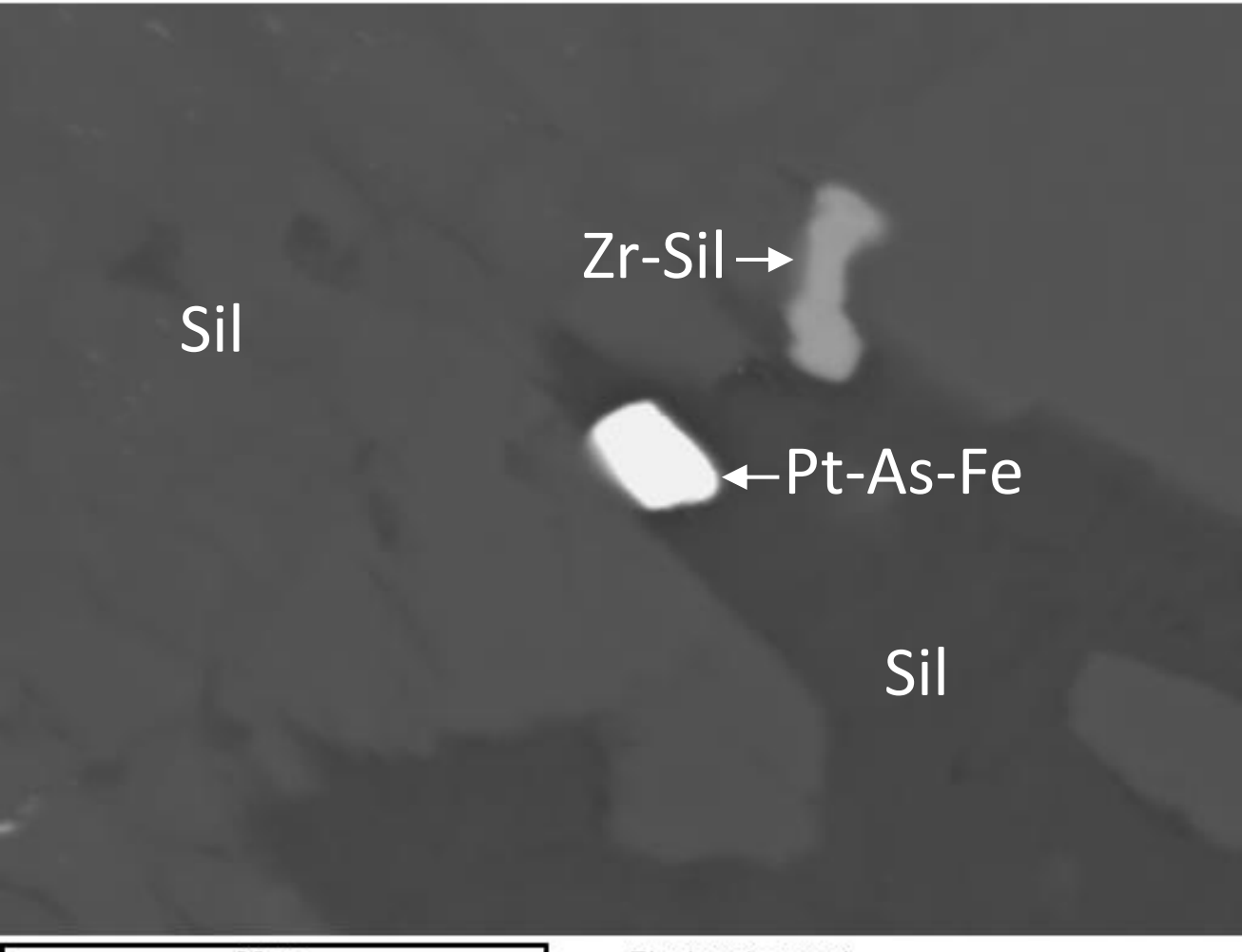
RK33 B2-3



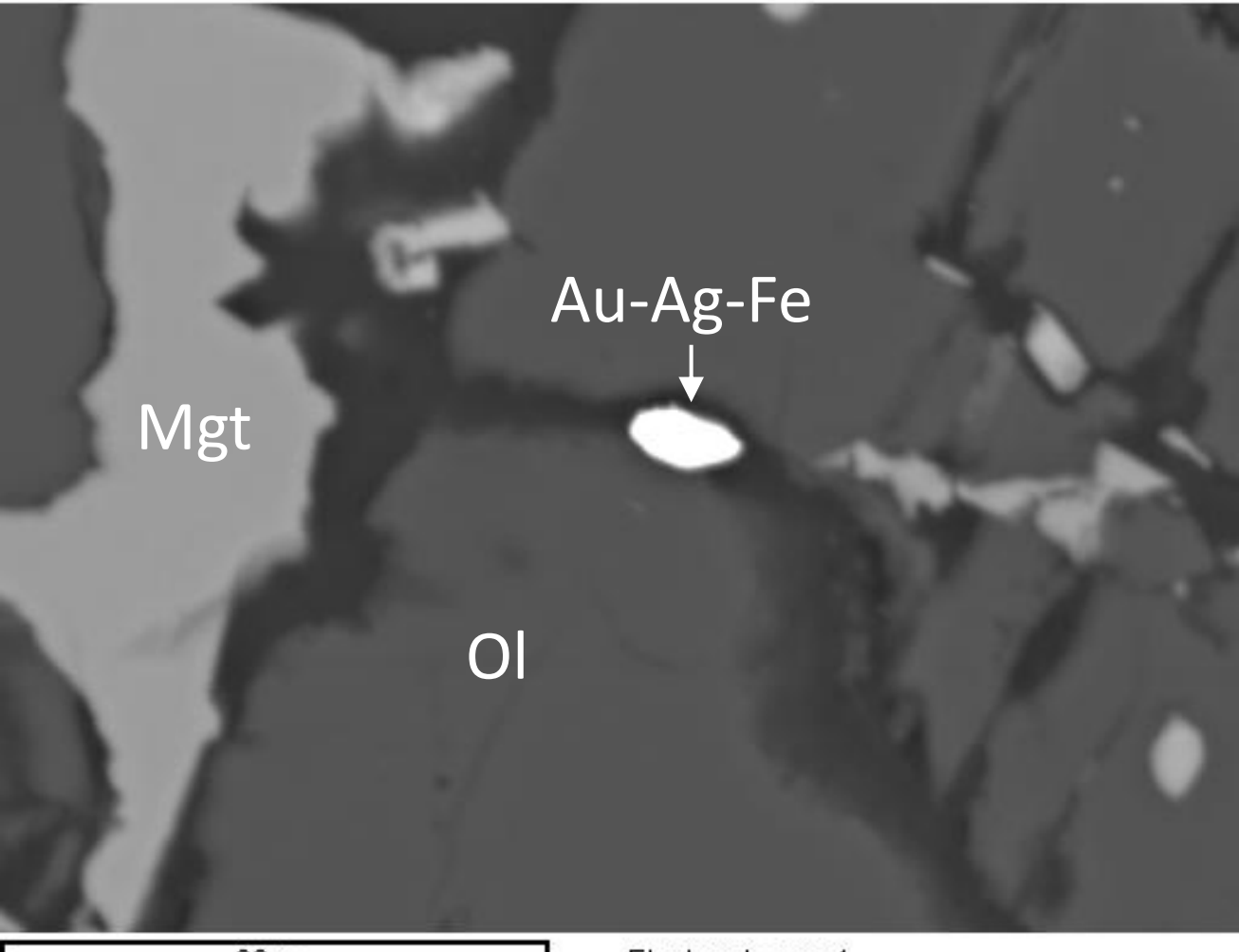
RK33 C1-3



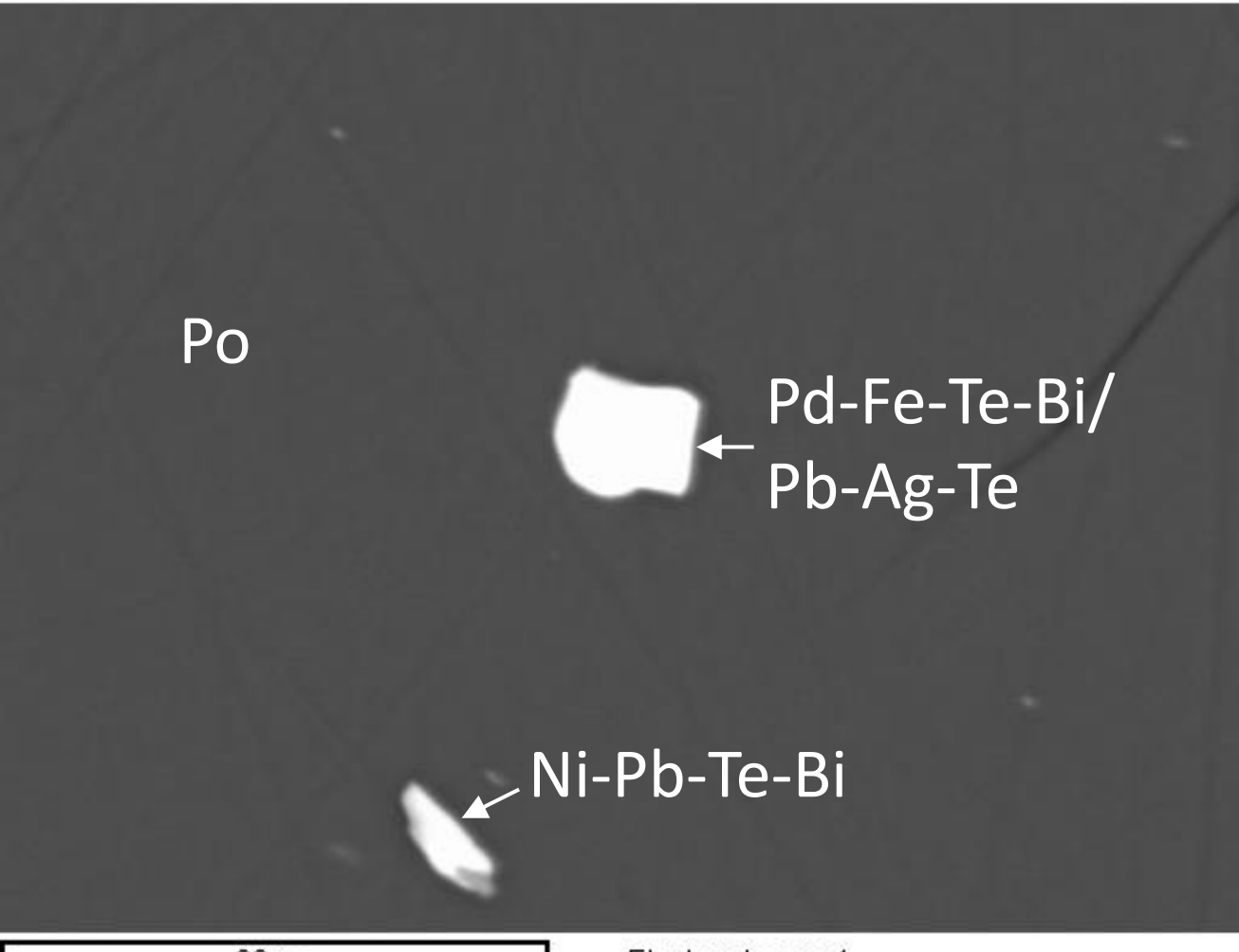
RK33 D1



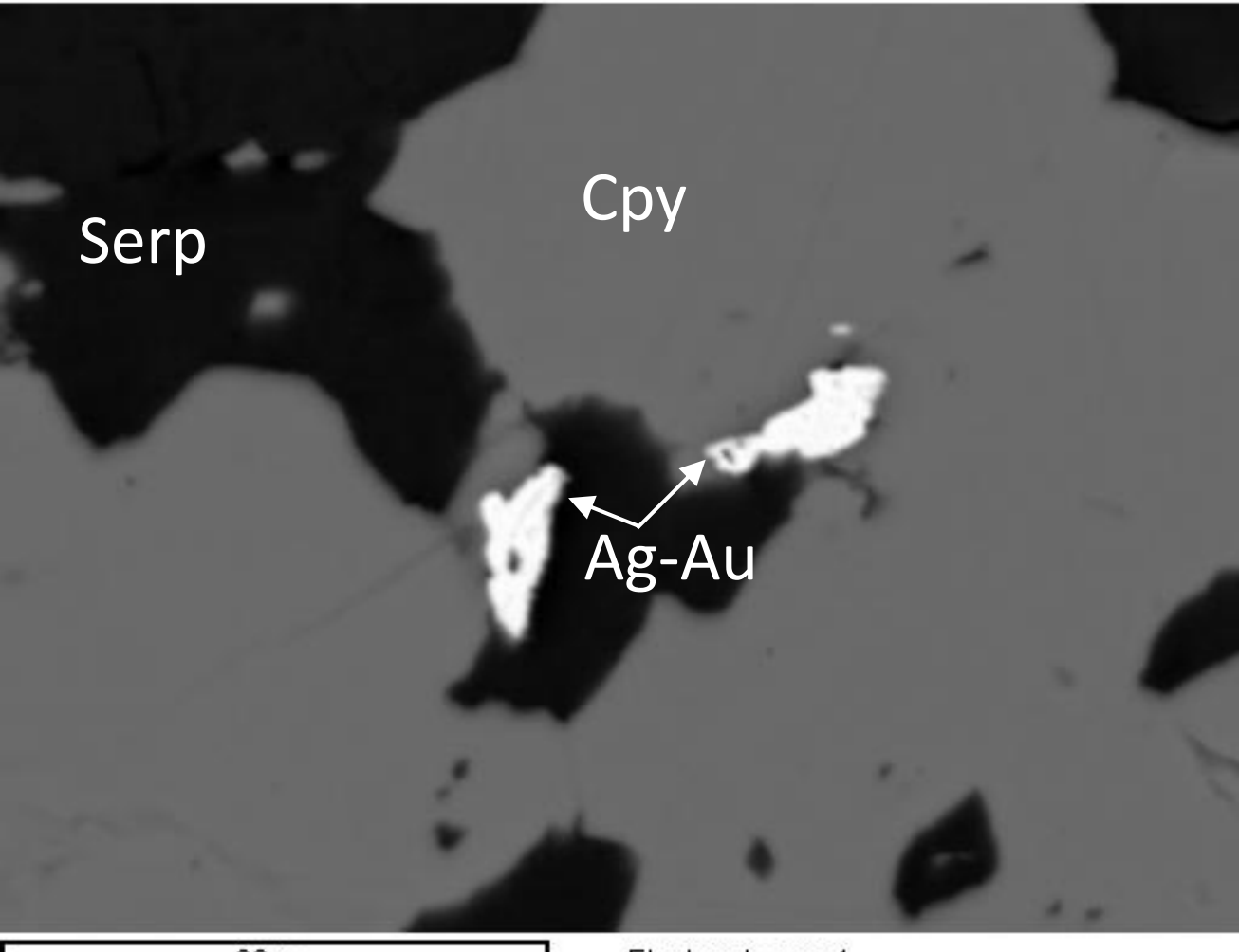
RK33 E1



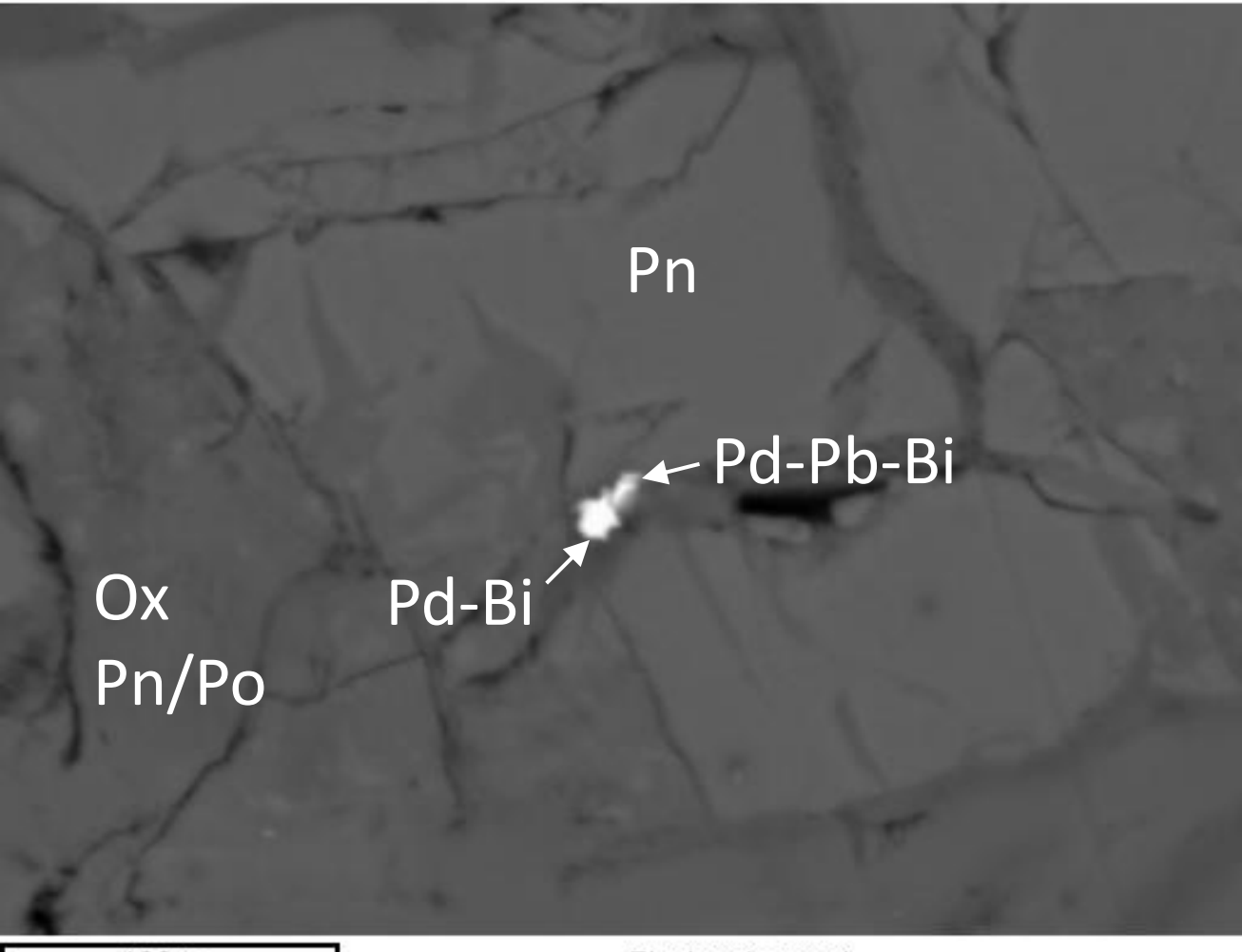
RK33 F1



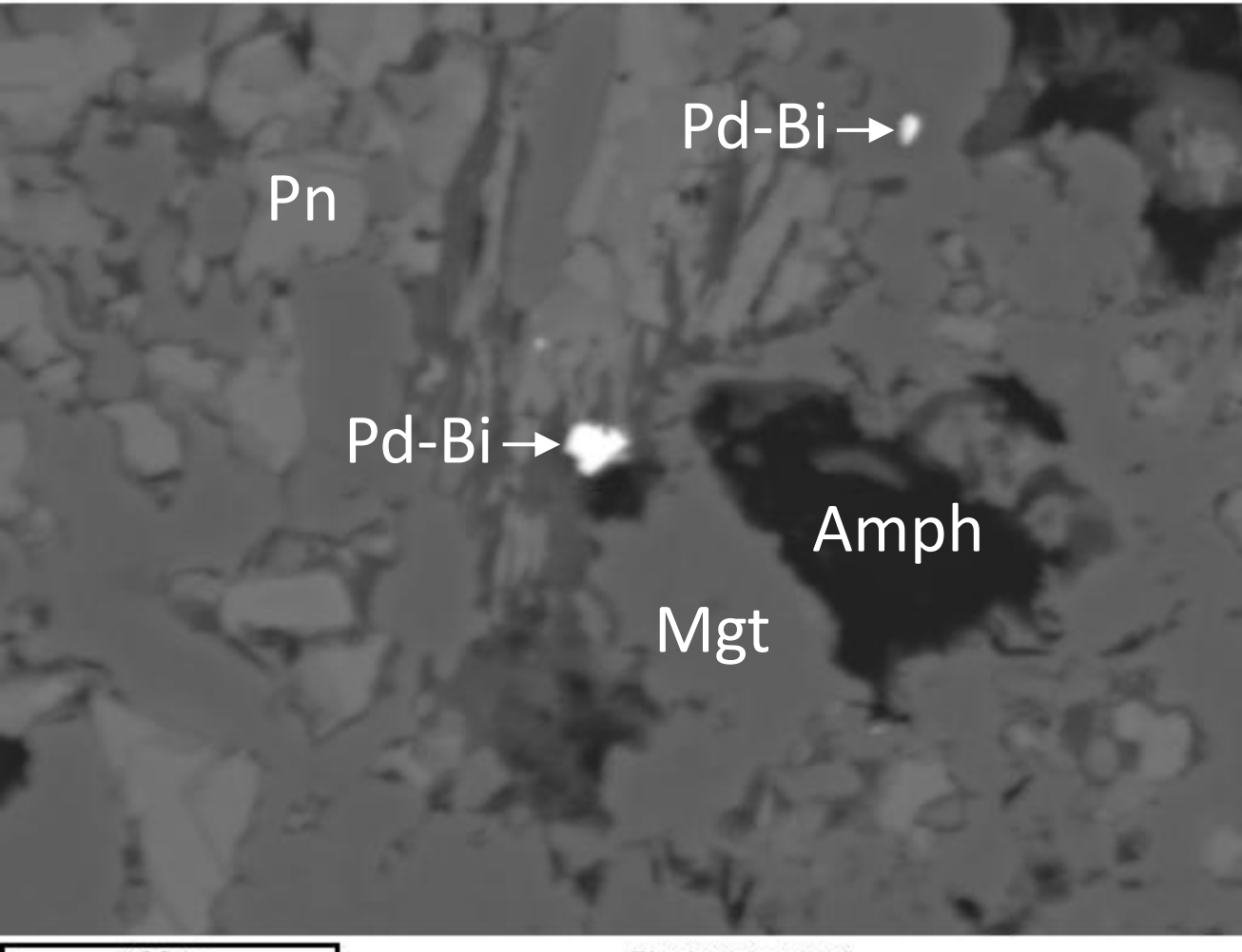
RK34 A1-2



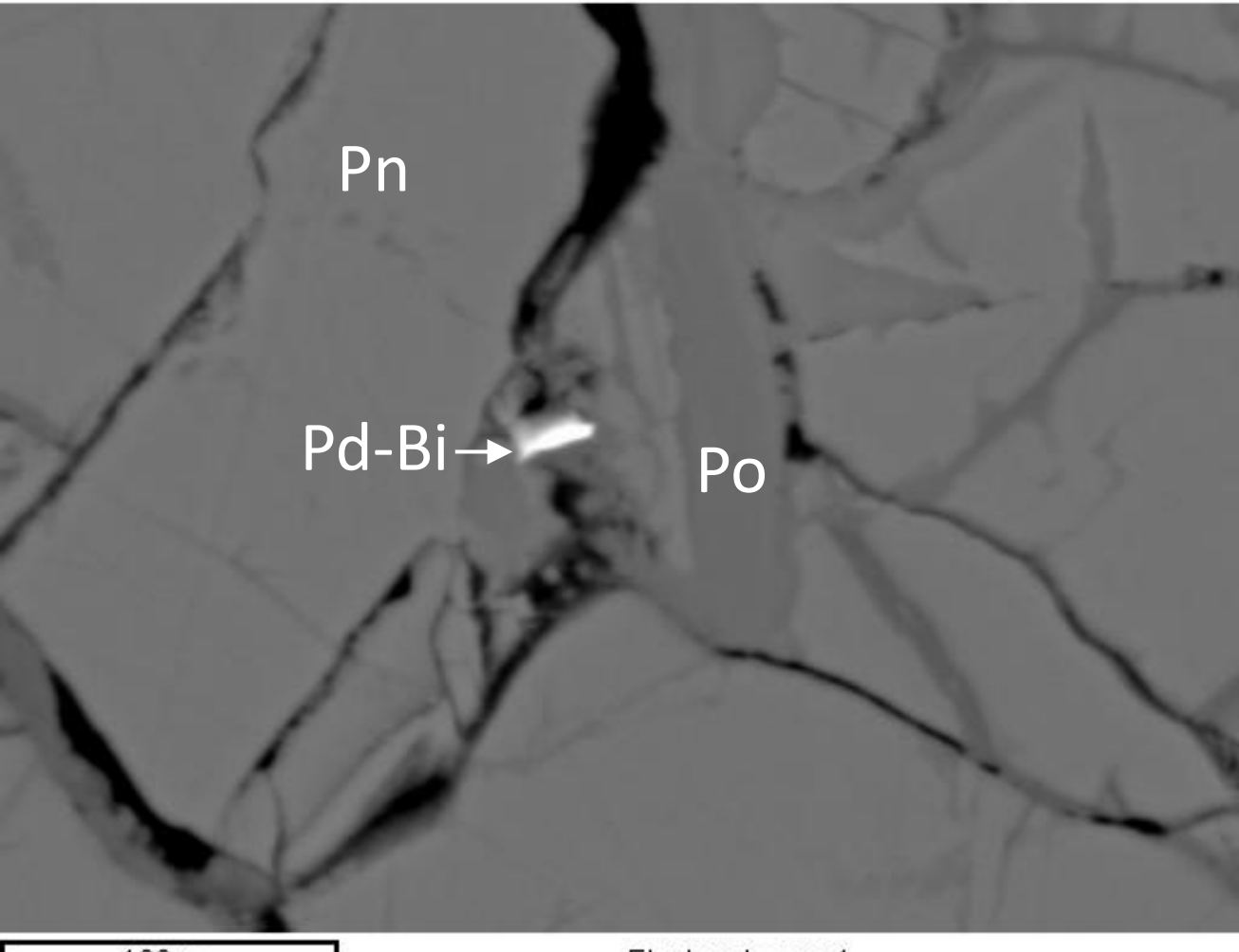
RK39 A1-2



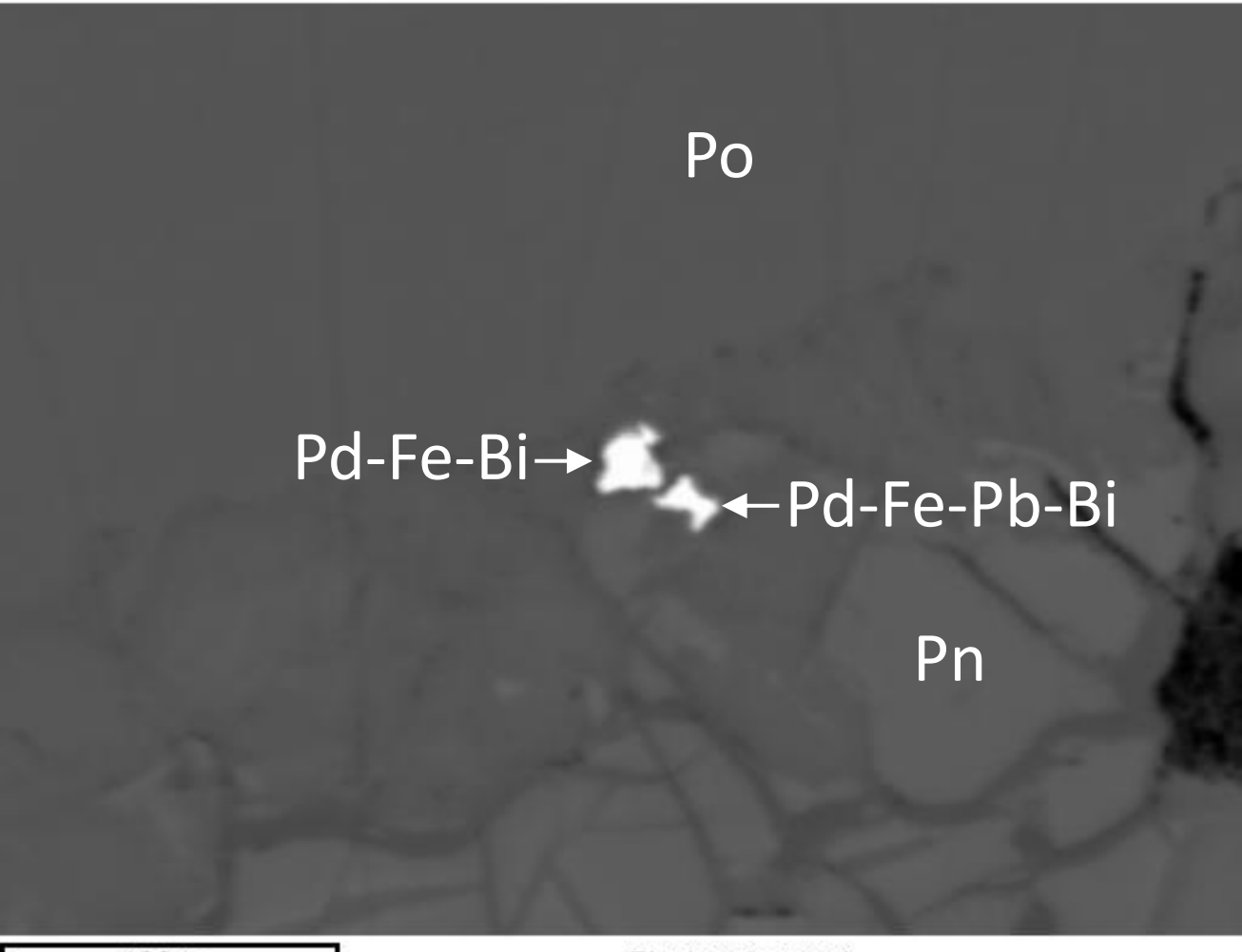
RK40 A1-2



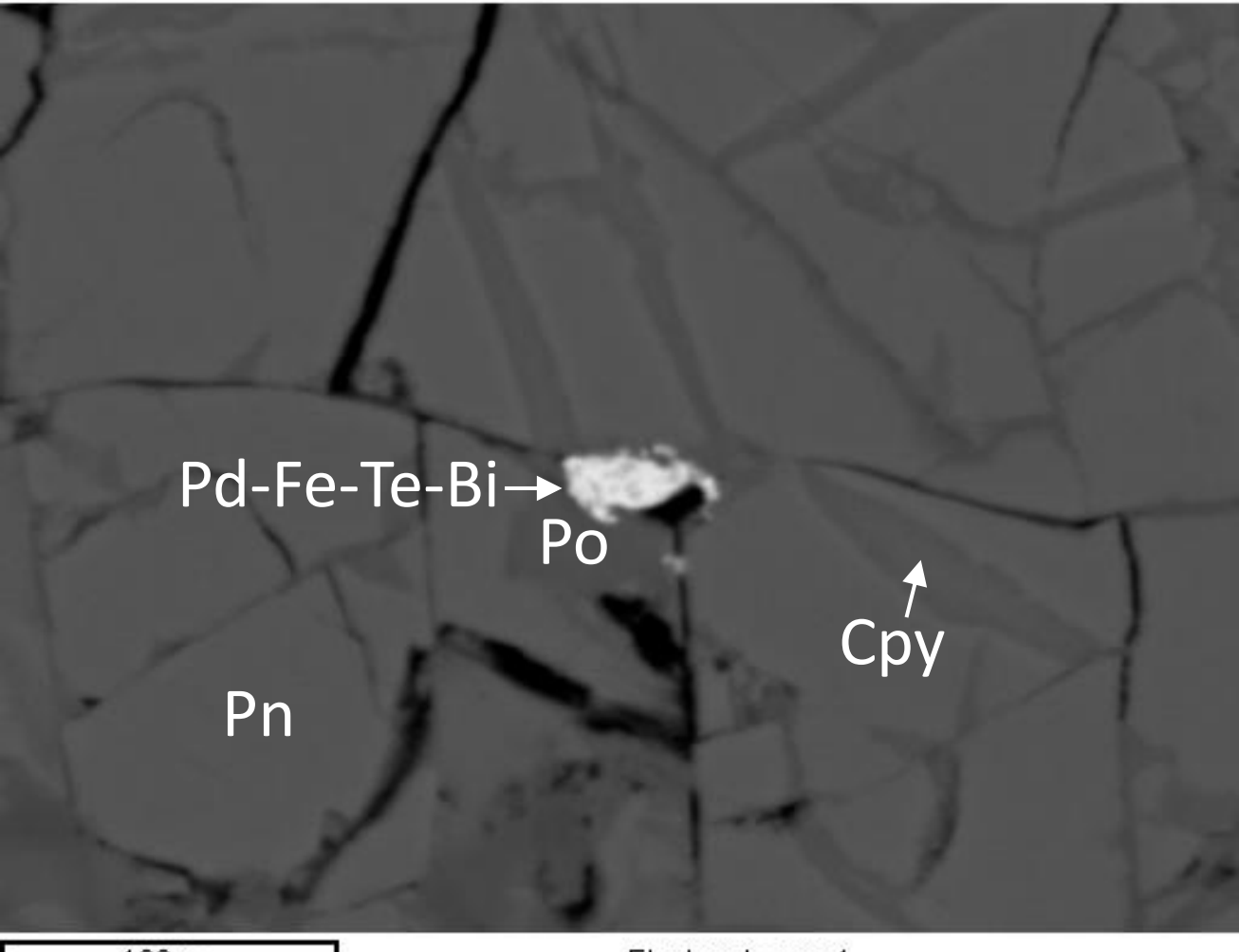
RK40 B1



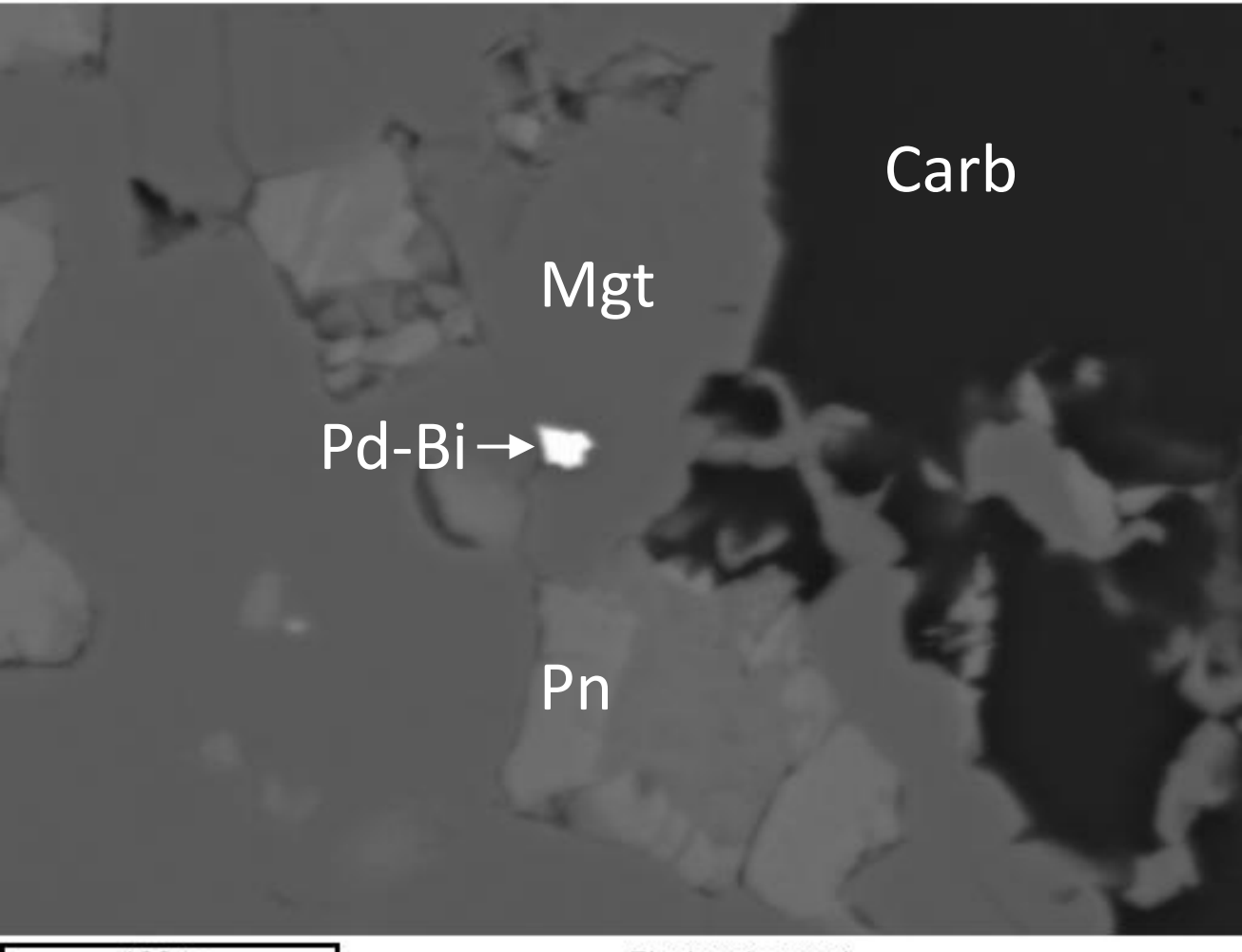
RK40 C1-2



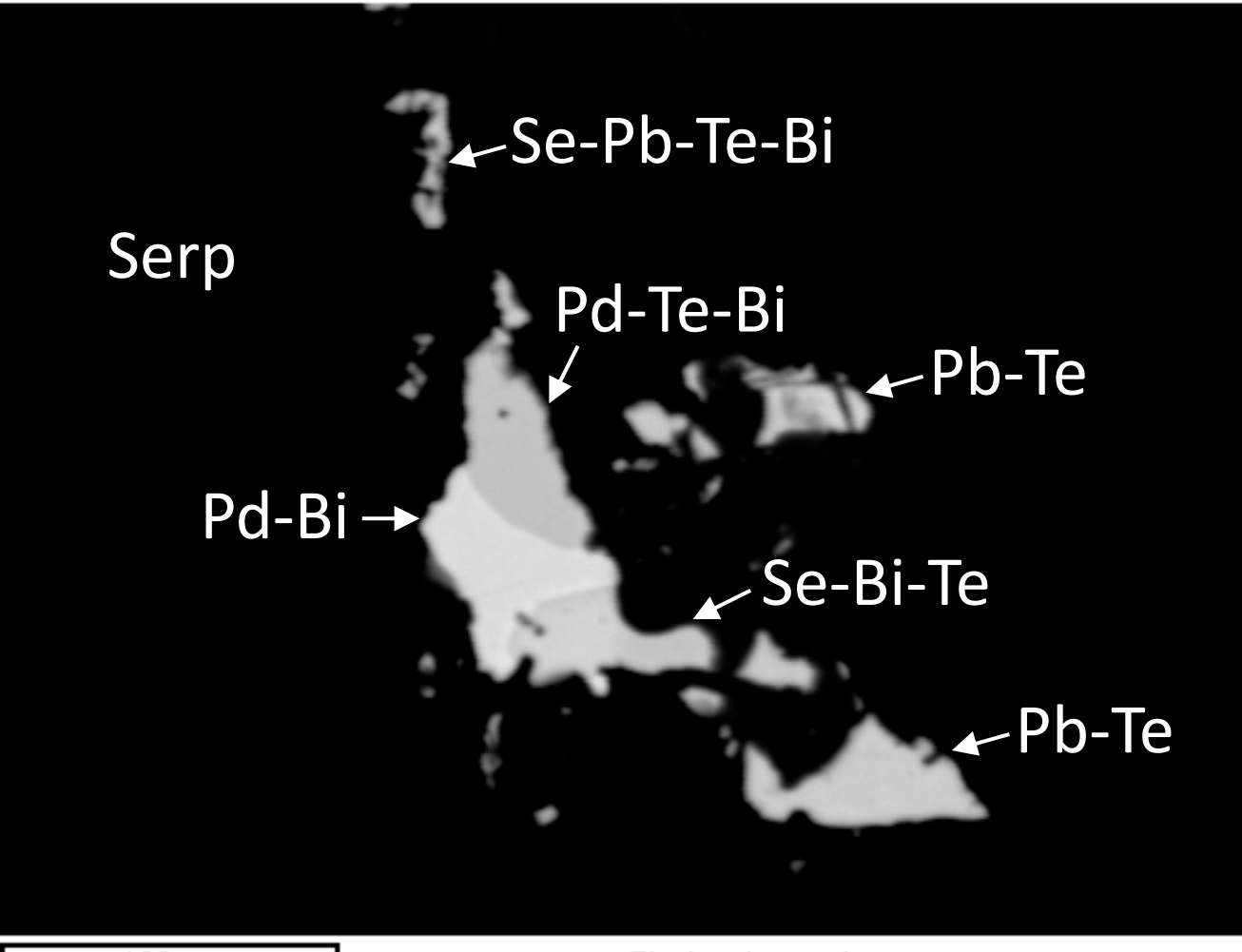
RK40 D1



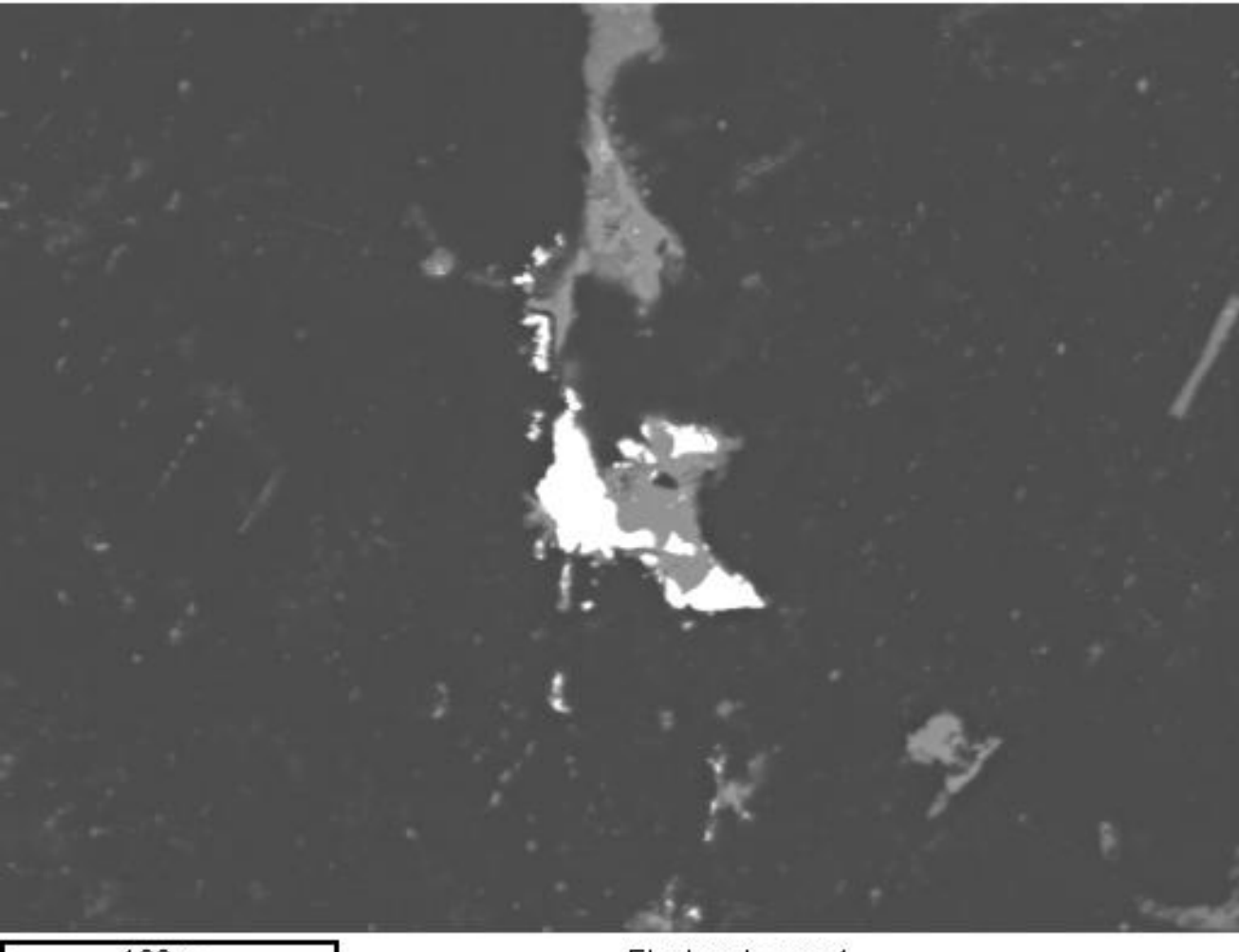
RK40 E1



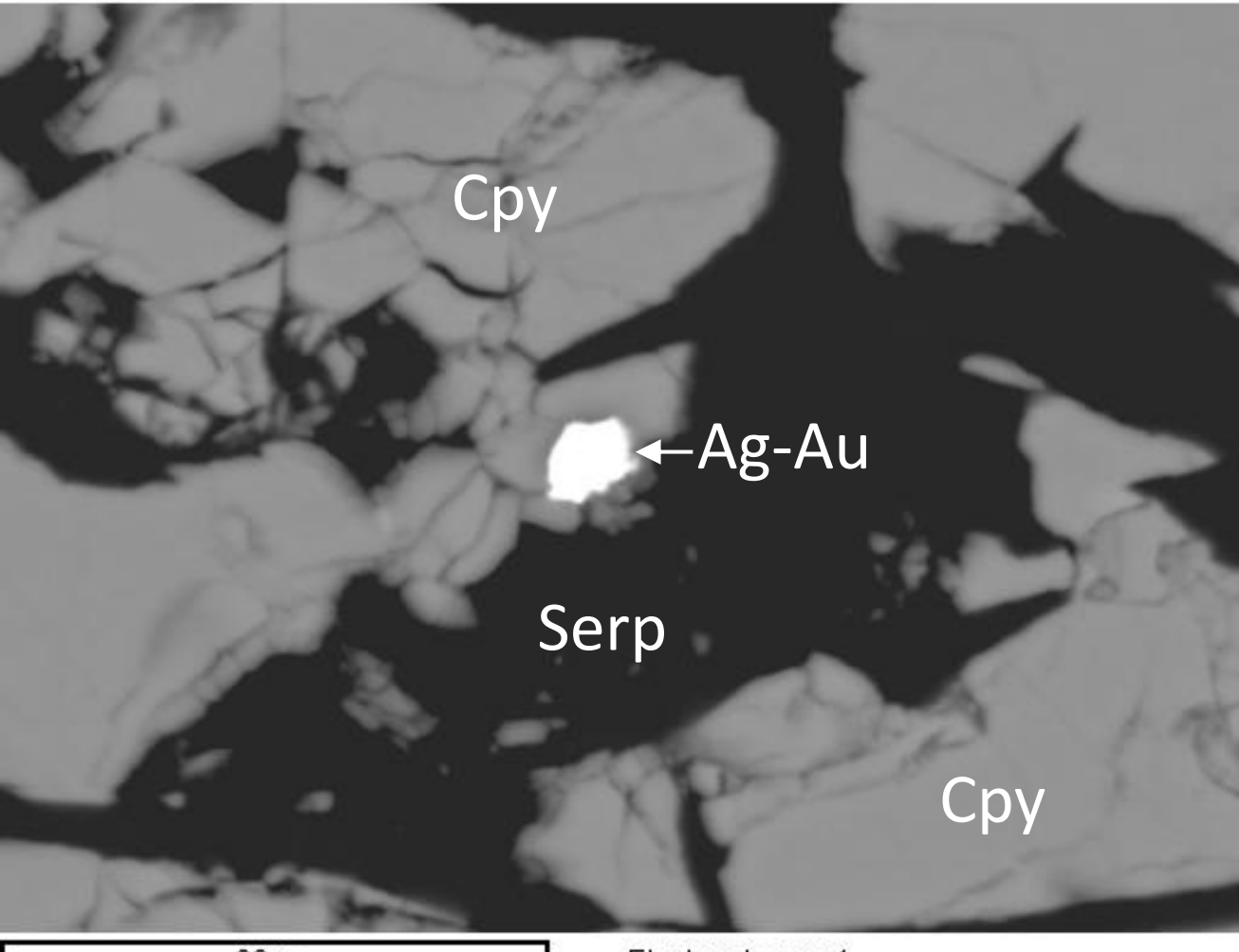
RK40 F1-6


Se-Pb-Te-Bi
Serp
Pd-Te-Bi
Pb-Te
Pd-Bi
Se-Bi-Te
Pb-Te
100µm
Electron Image 1

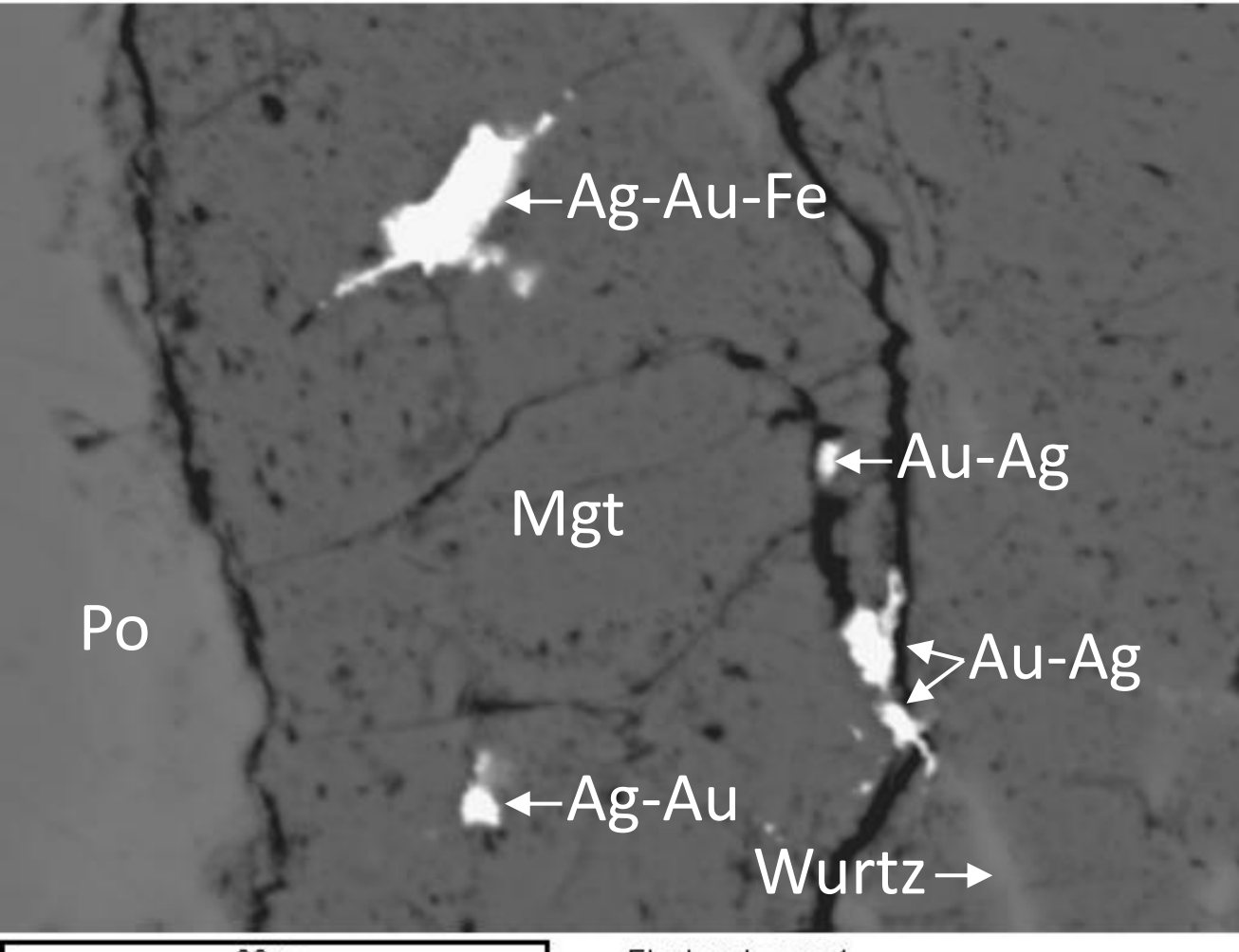
RK42 F1-6 Detail



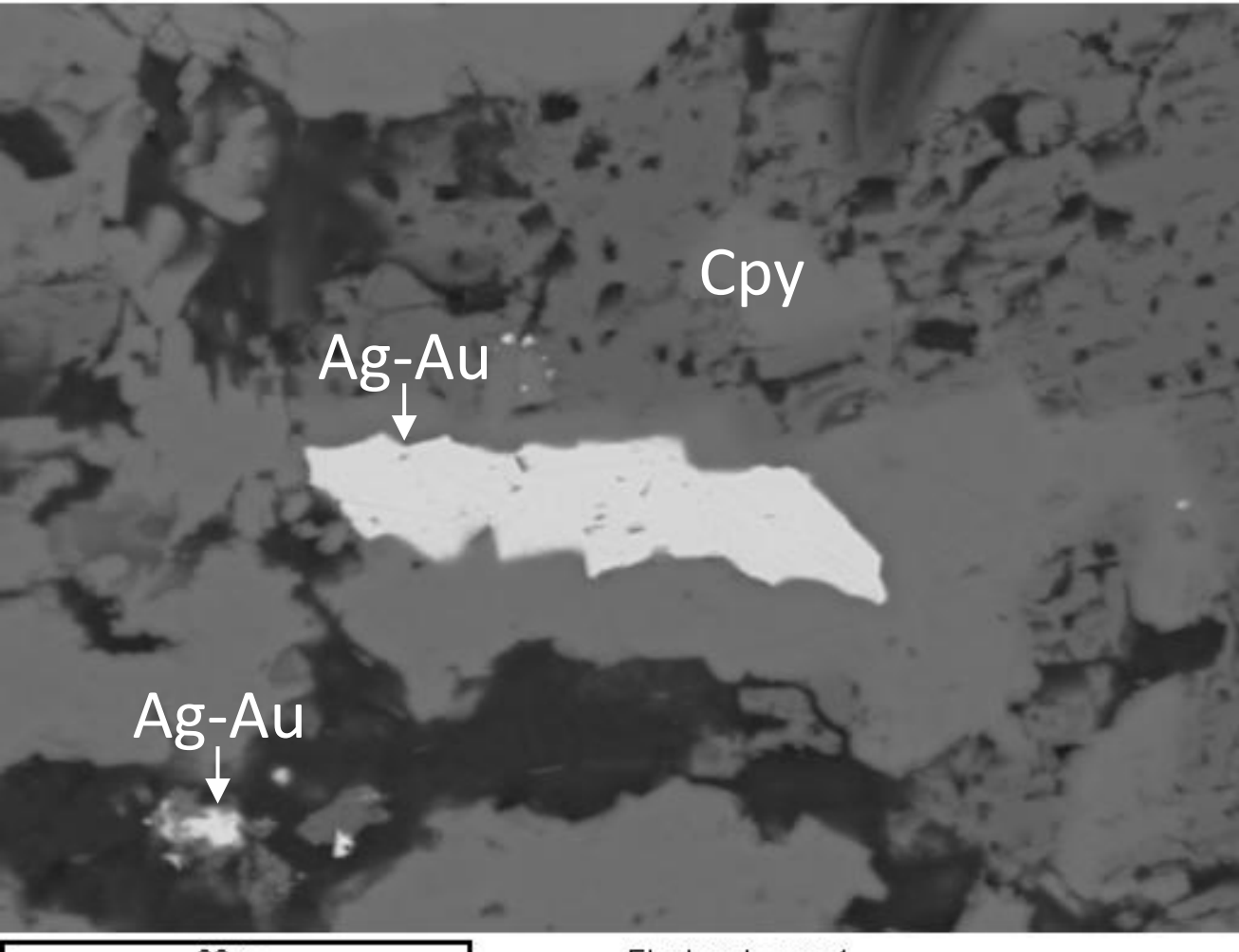
RK42 A1



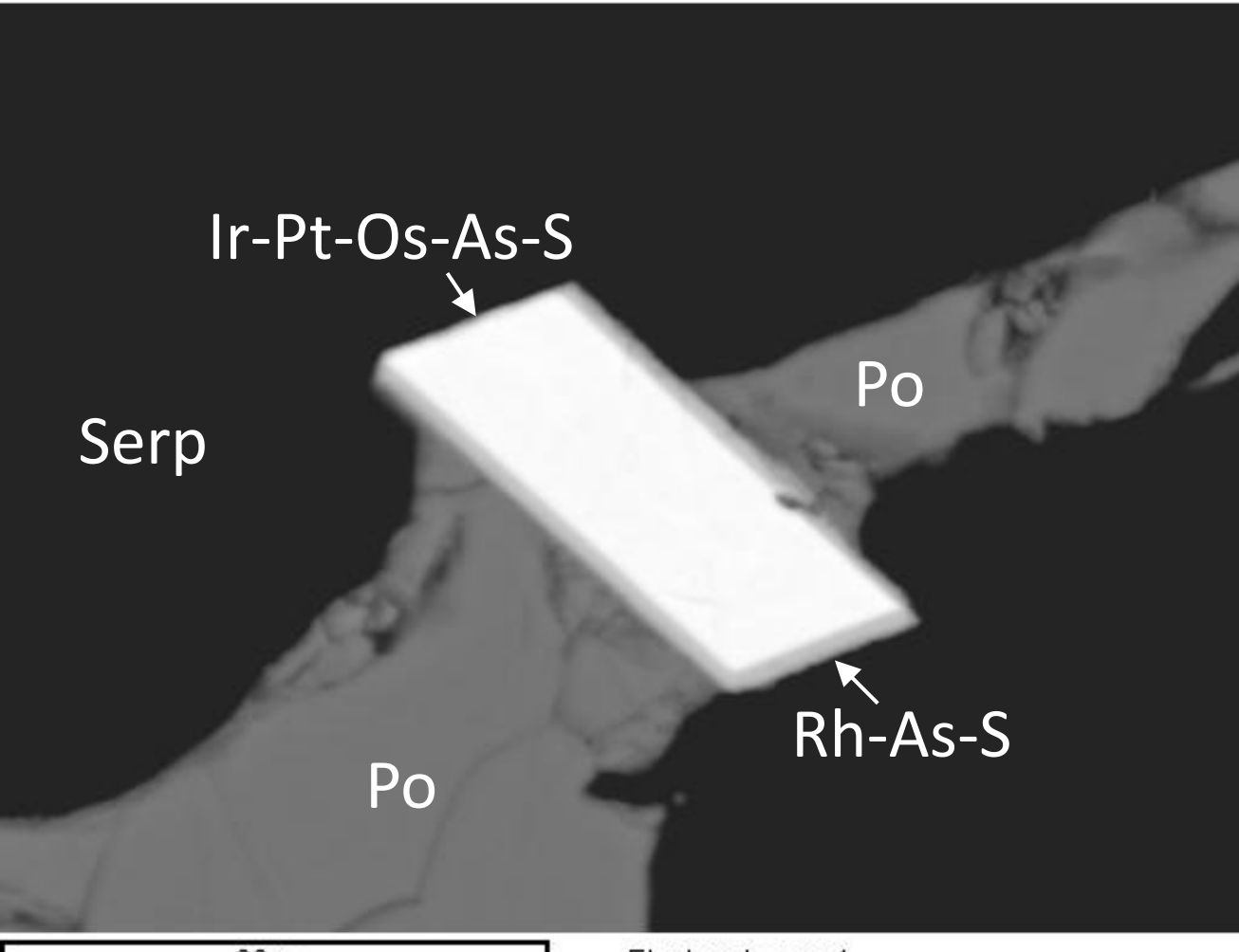
RK42 B1-5



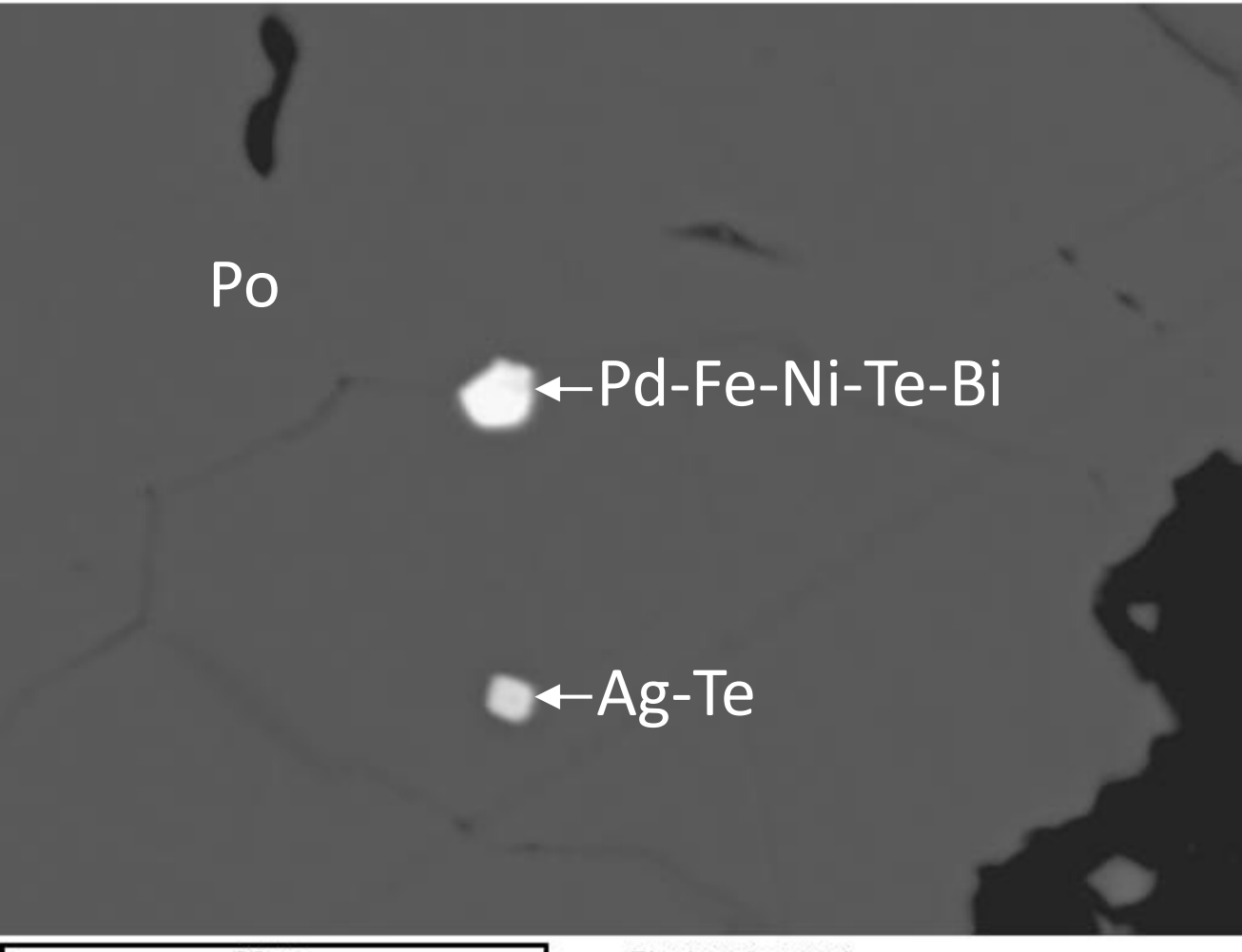
RK42 E1-2



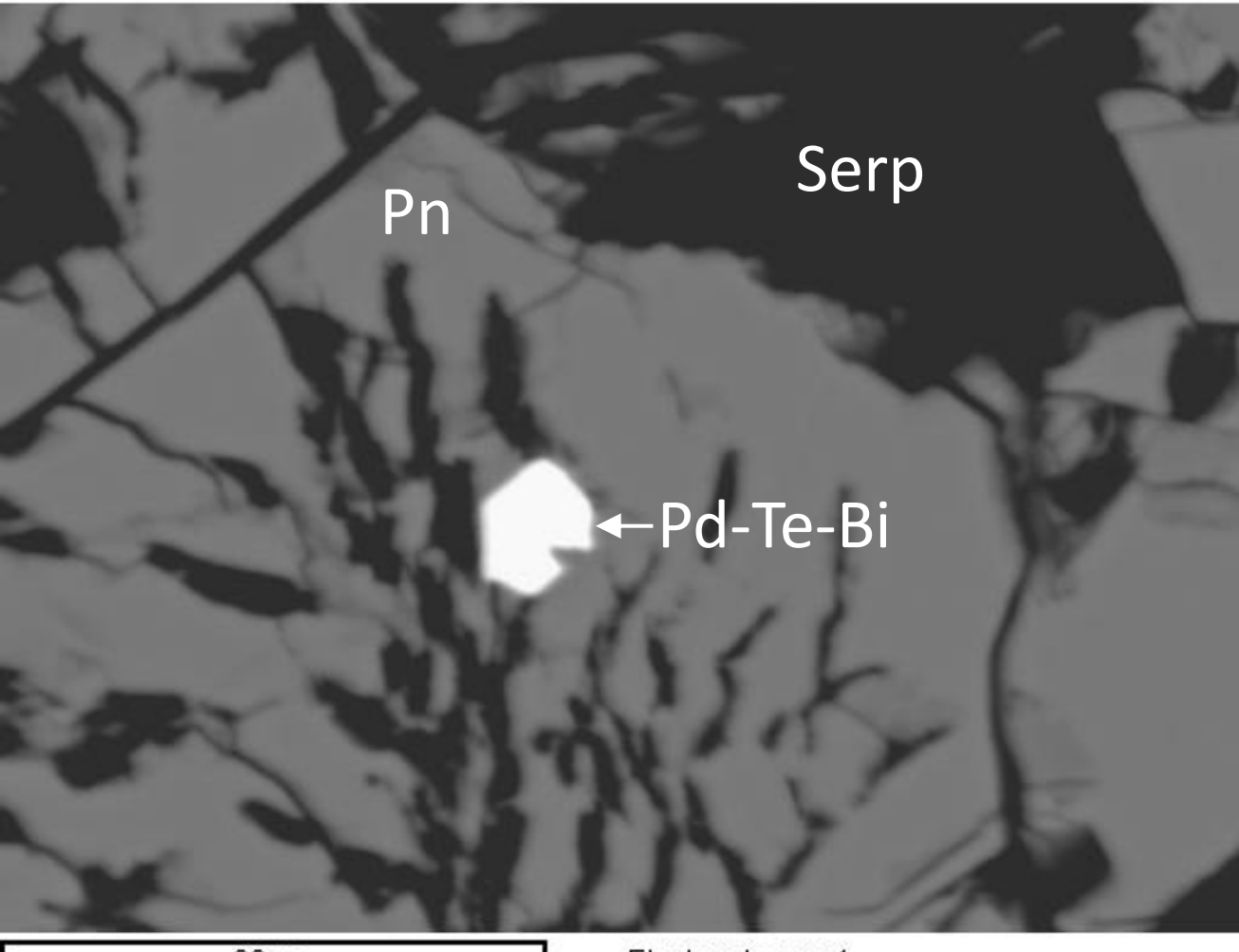
RK42 F1-2



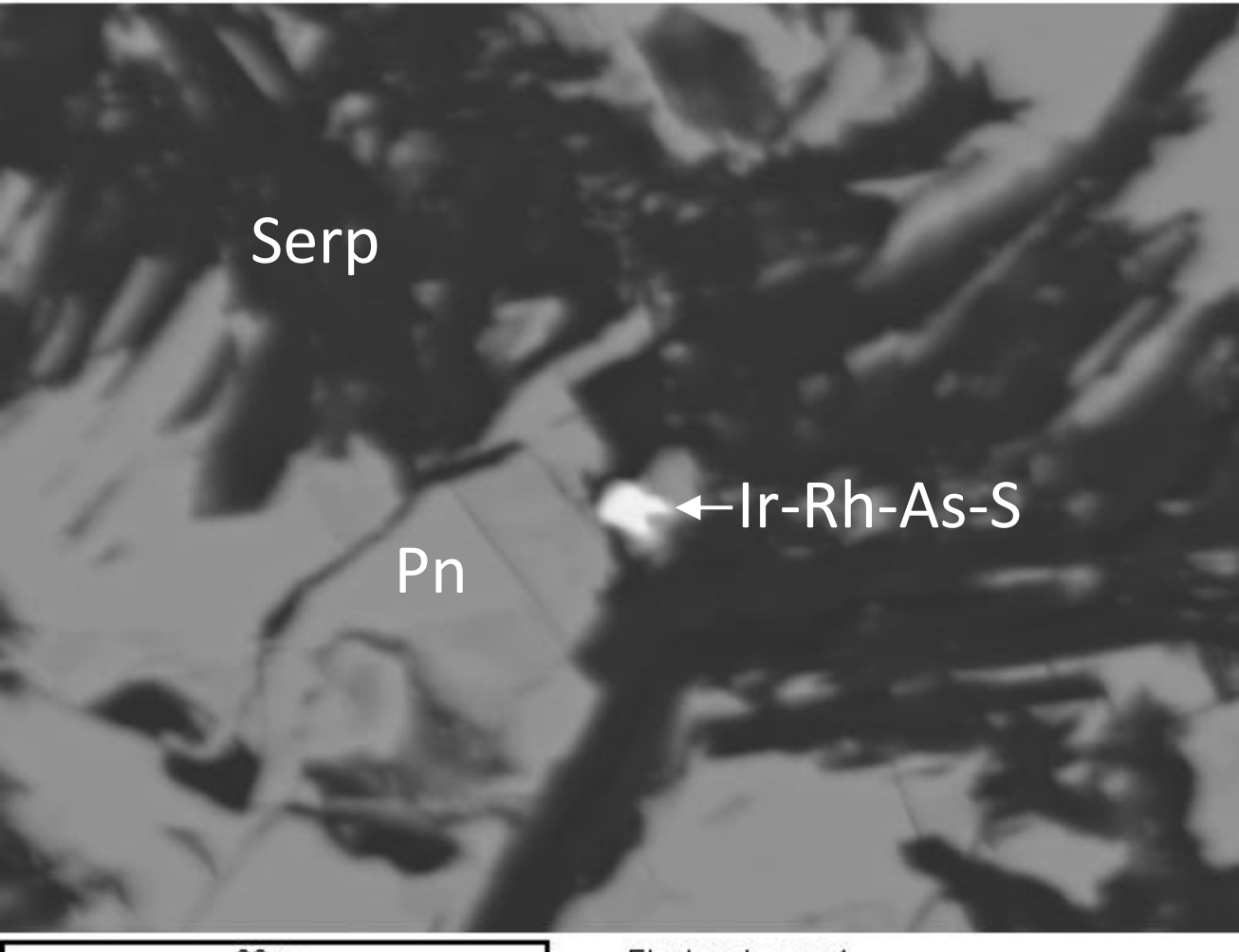
RK43 A1-2



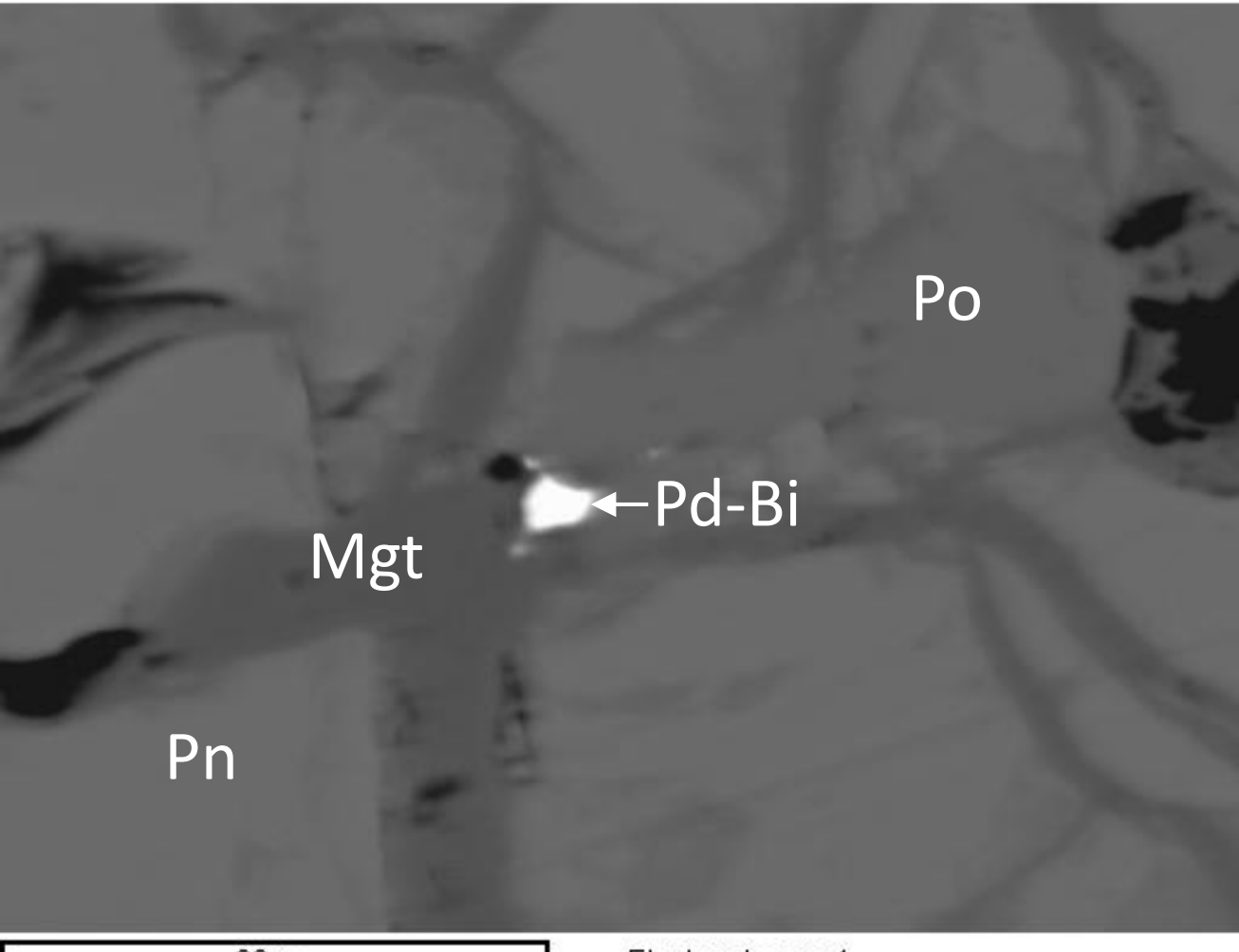
RK43 B1



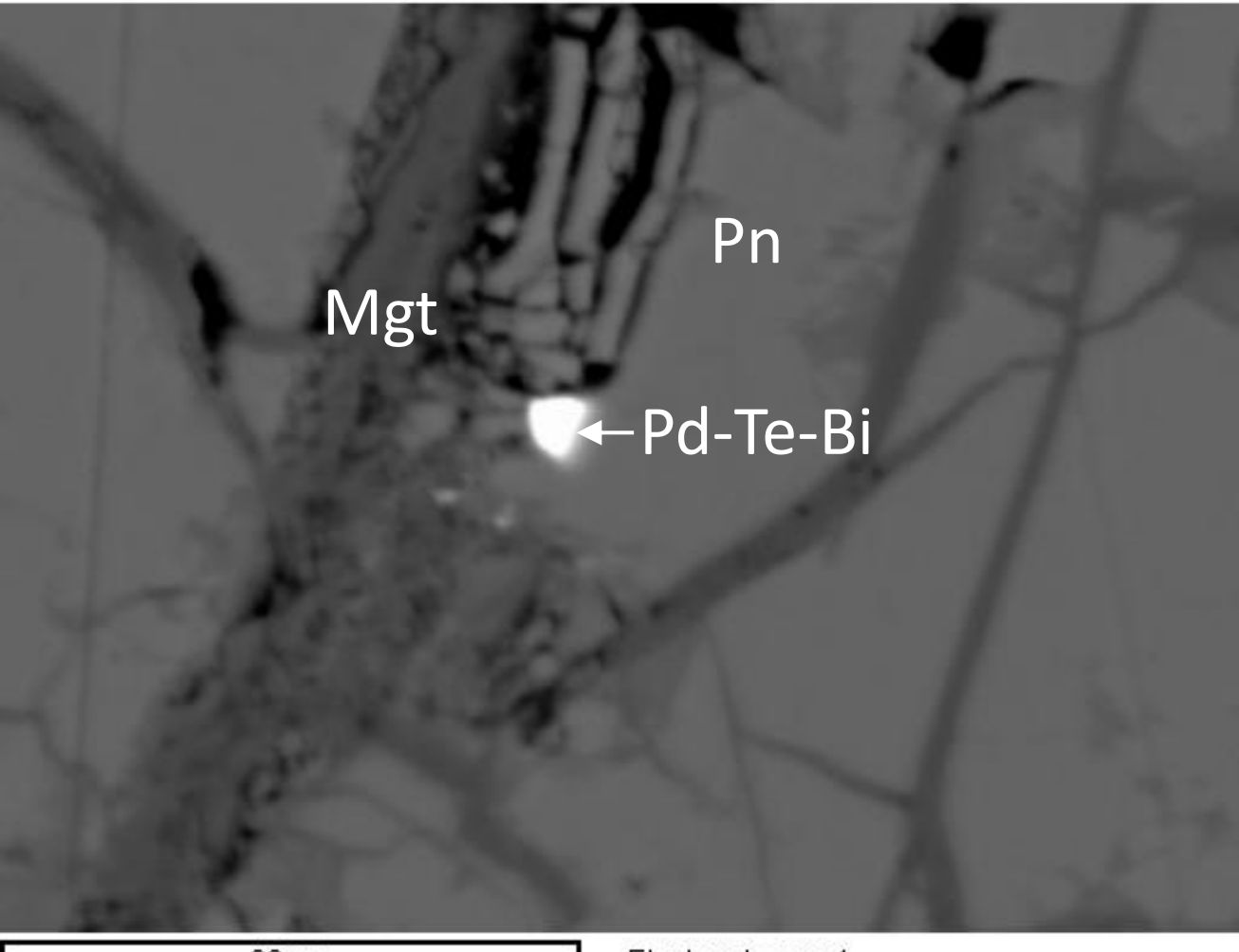
RK43 C1



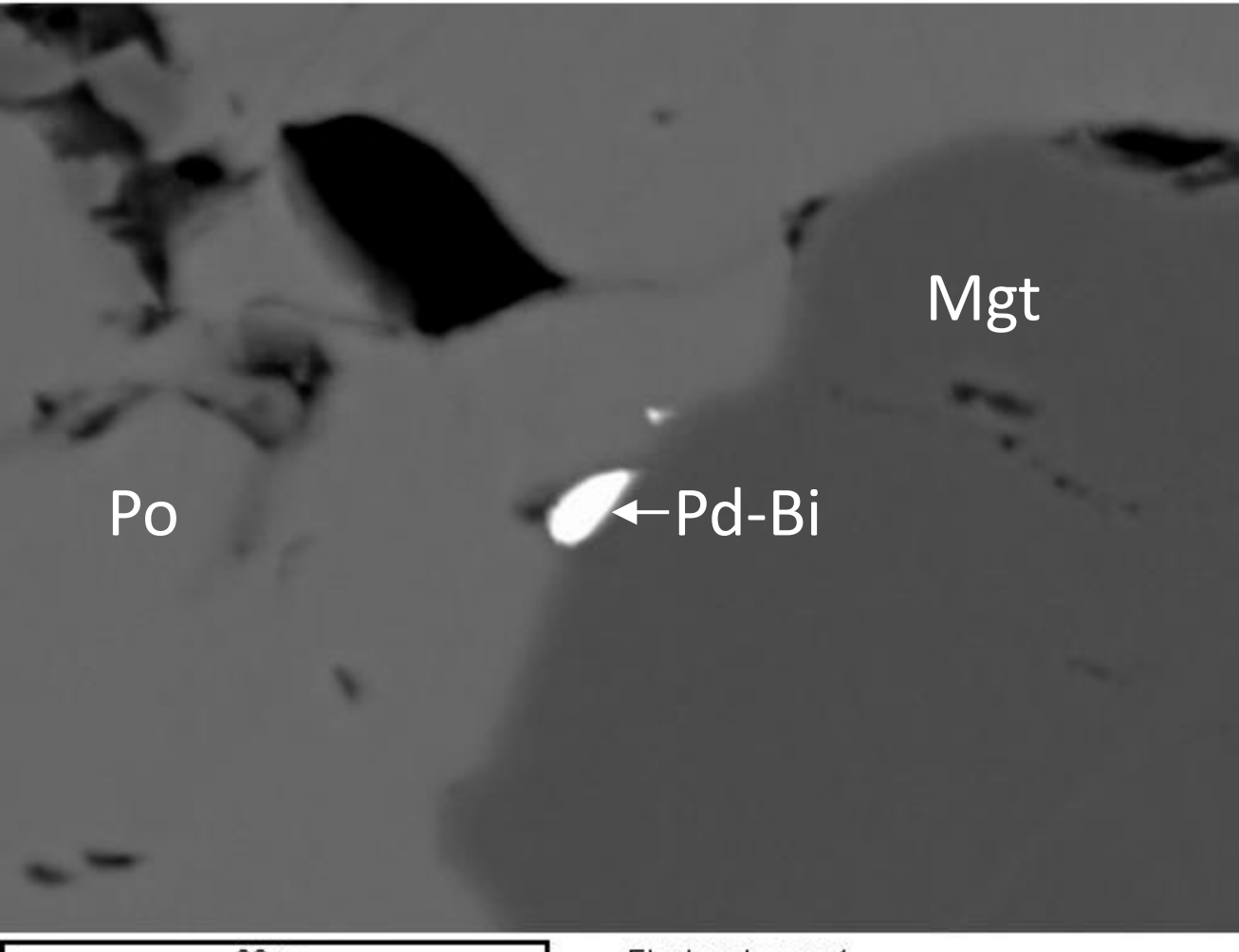
RK44 A1



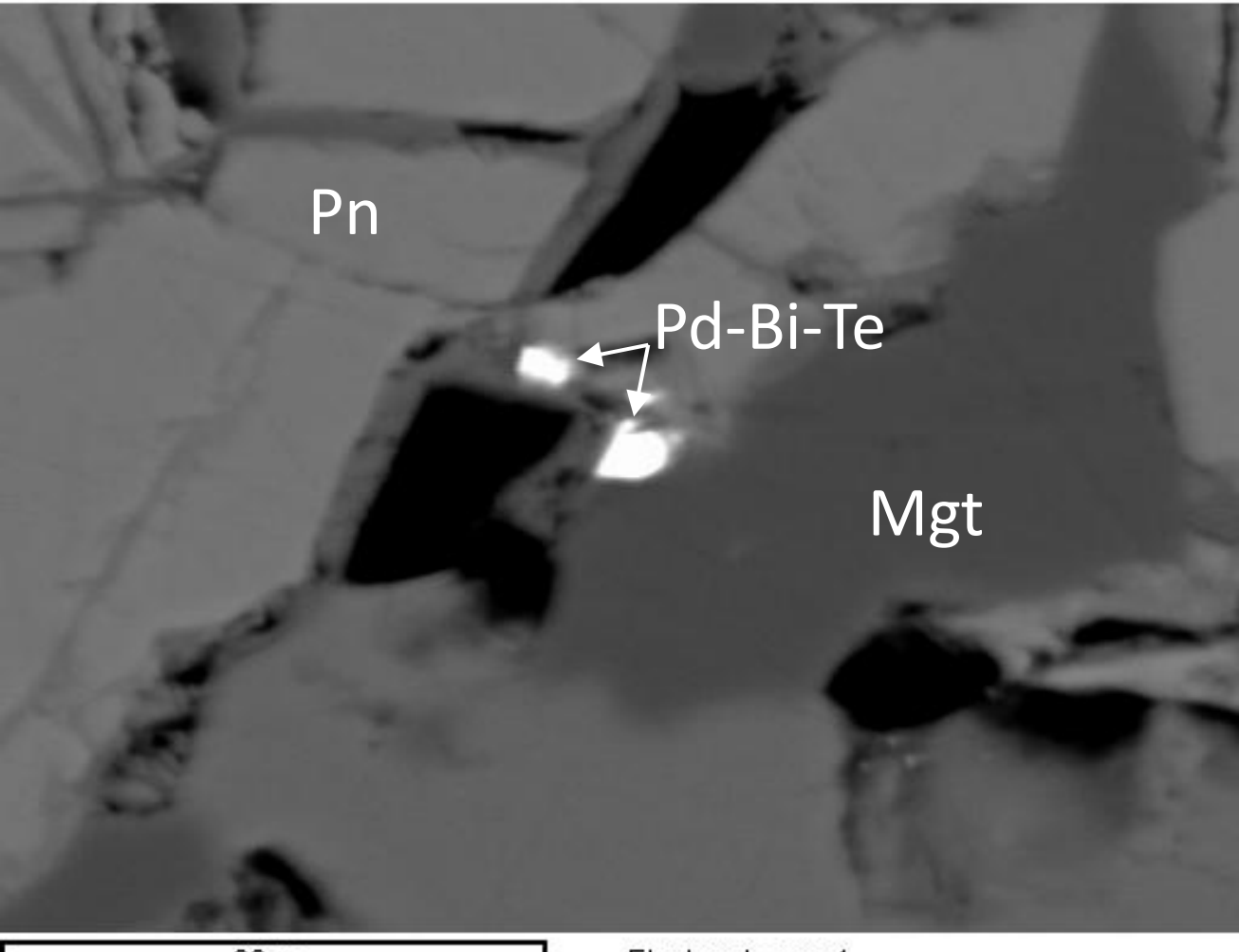
RK45 A1



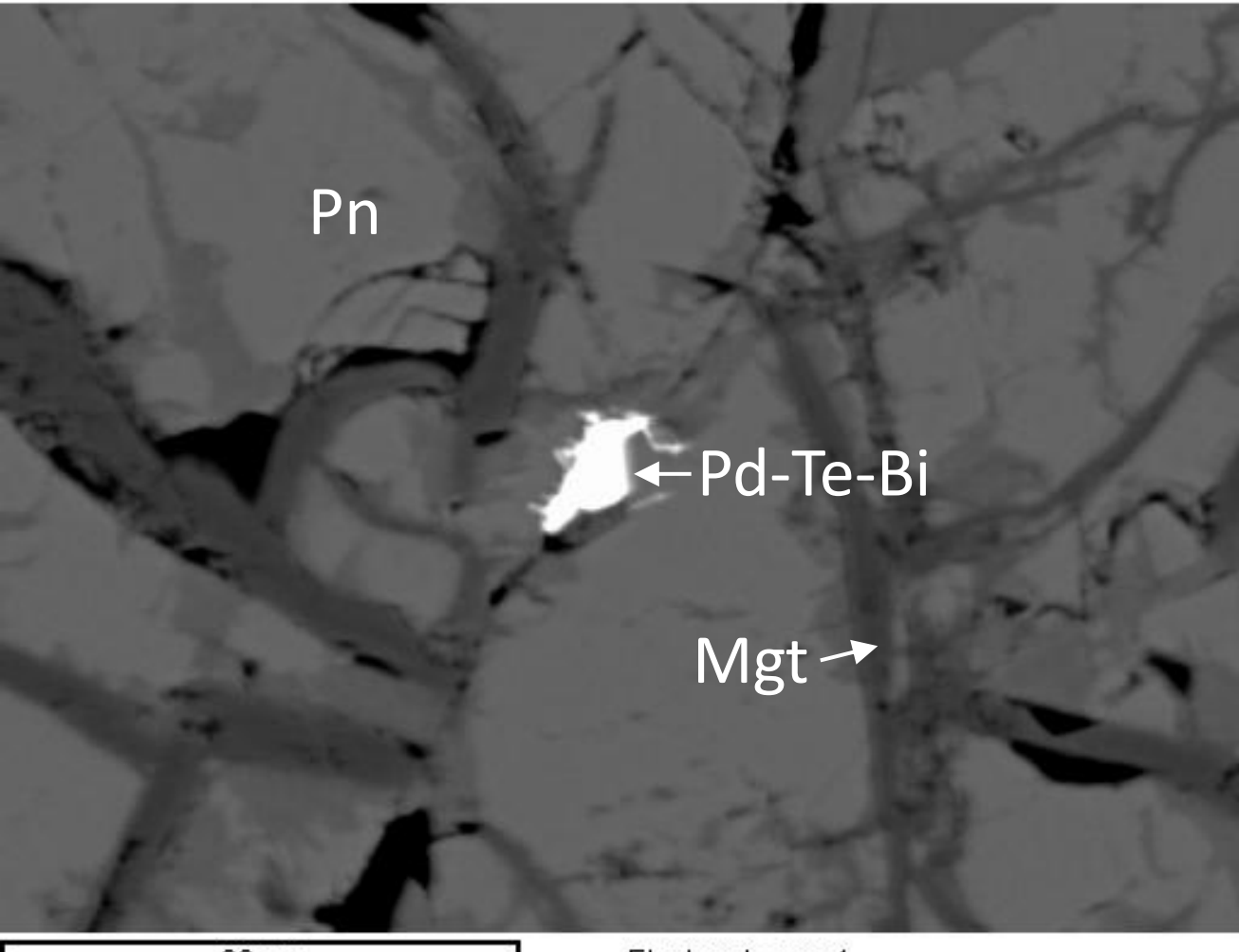
RK45 B1



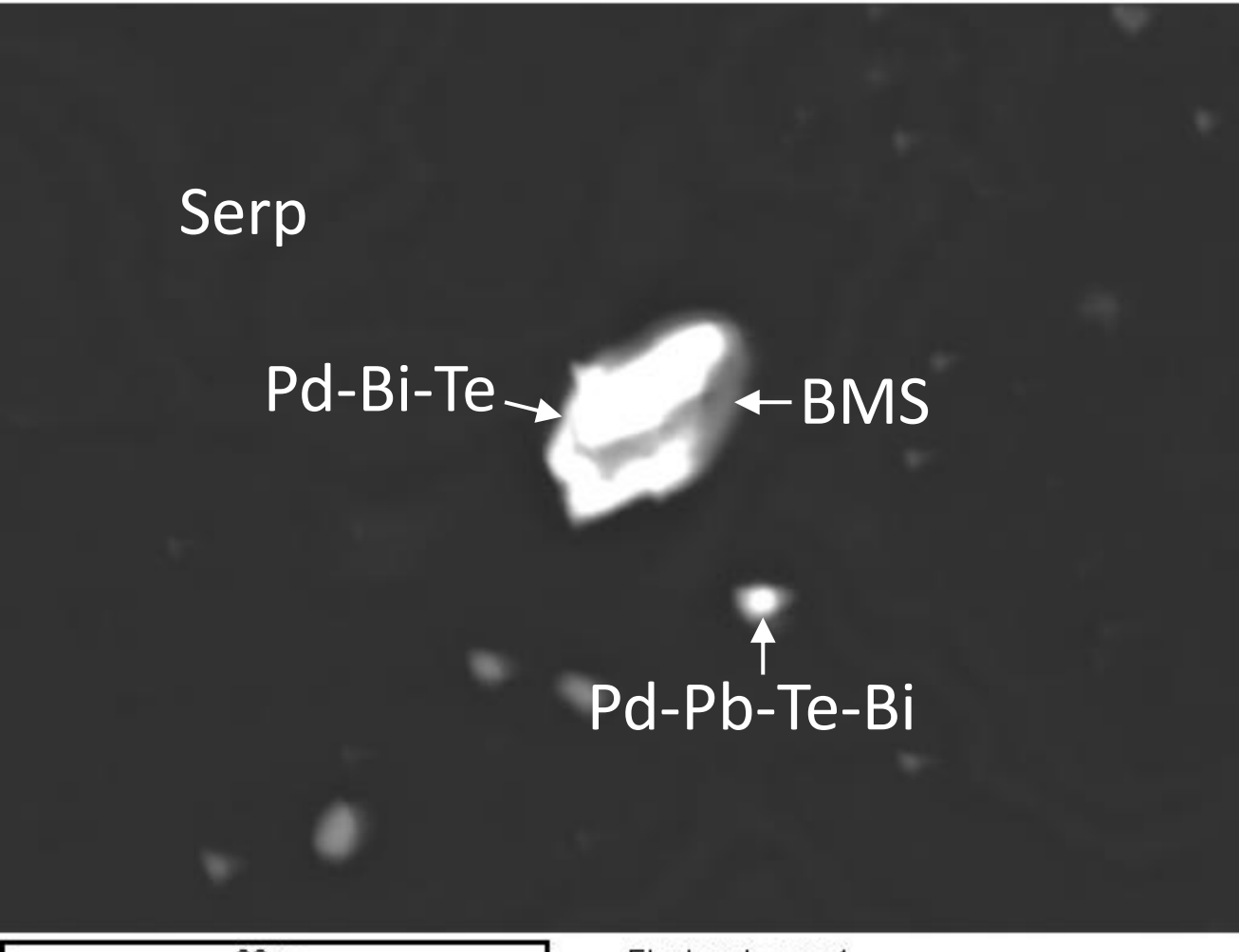
RK45 C1-2



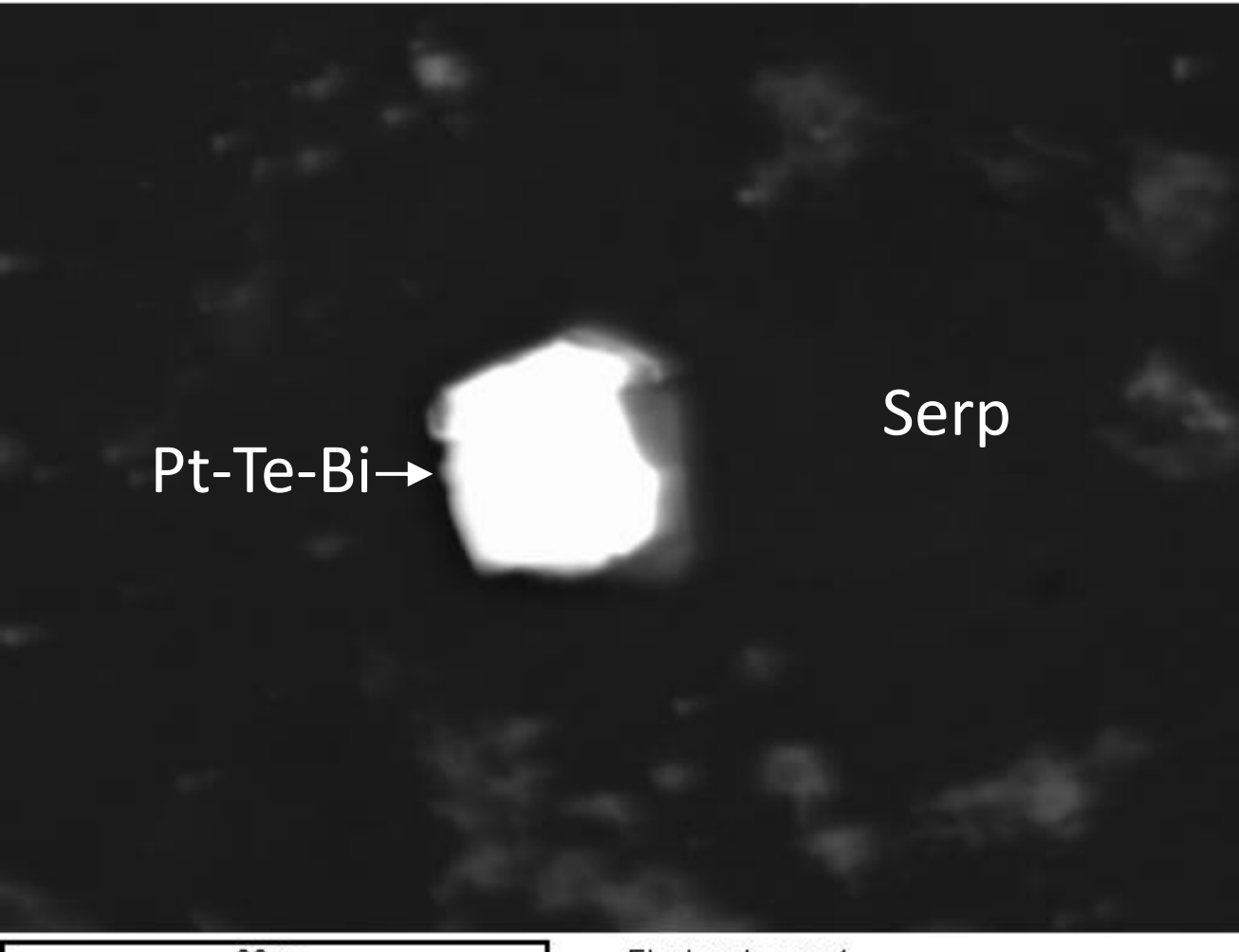
RK45 D1



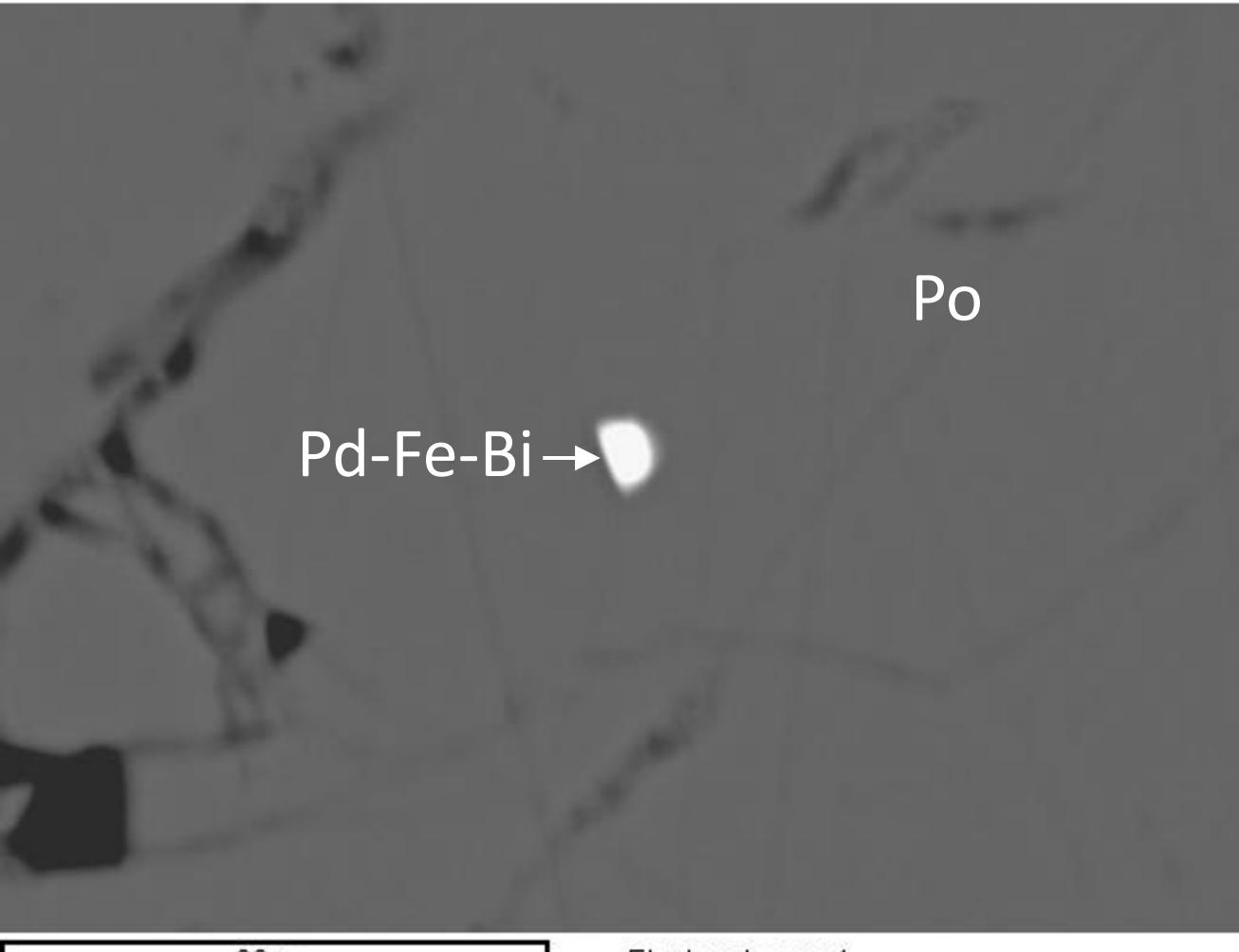
RK45 E1-2



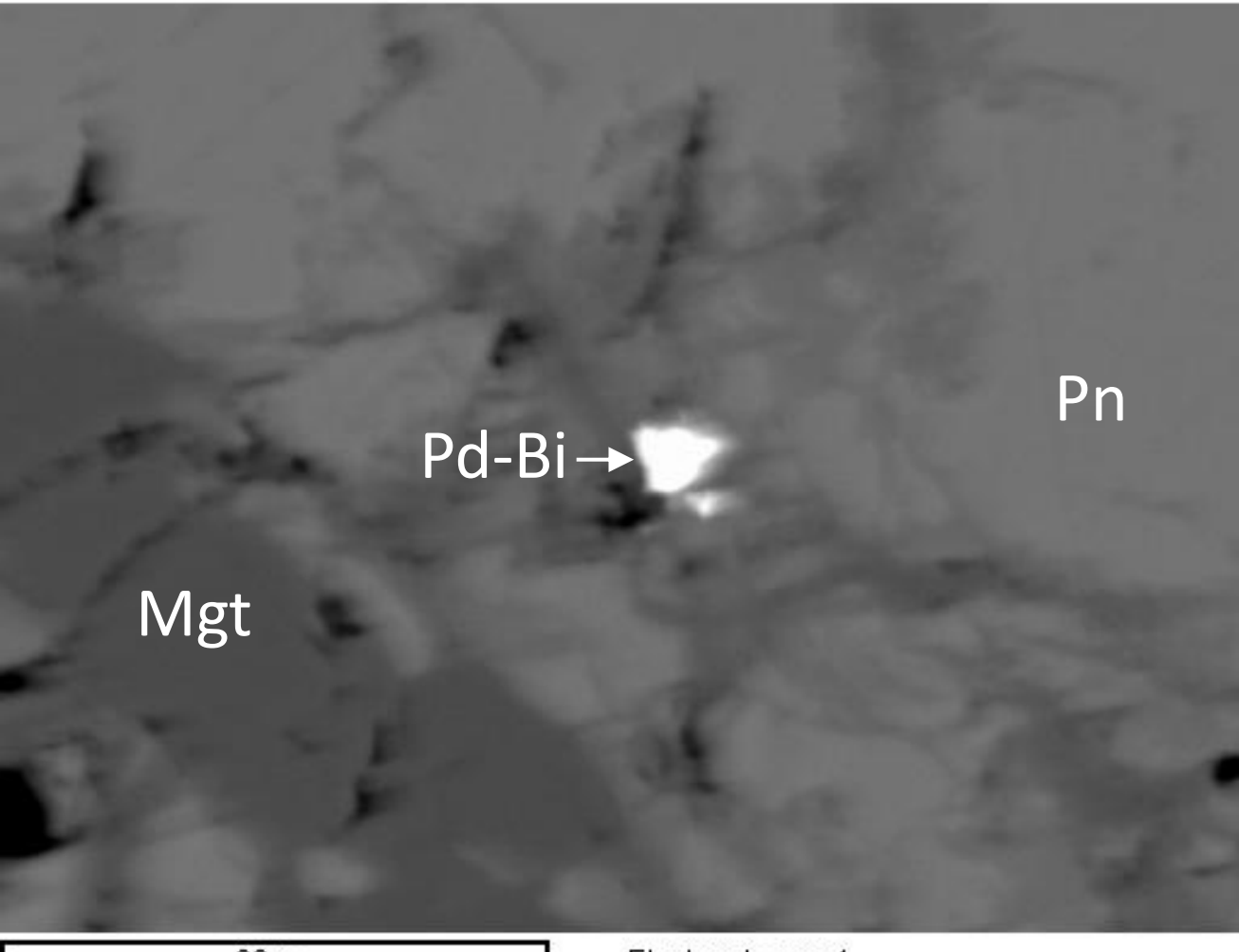
RK45 F1



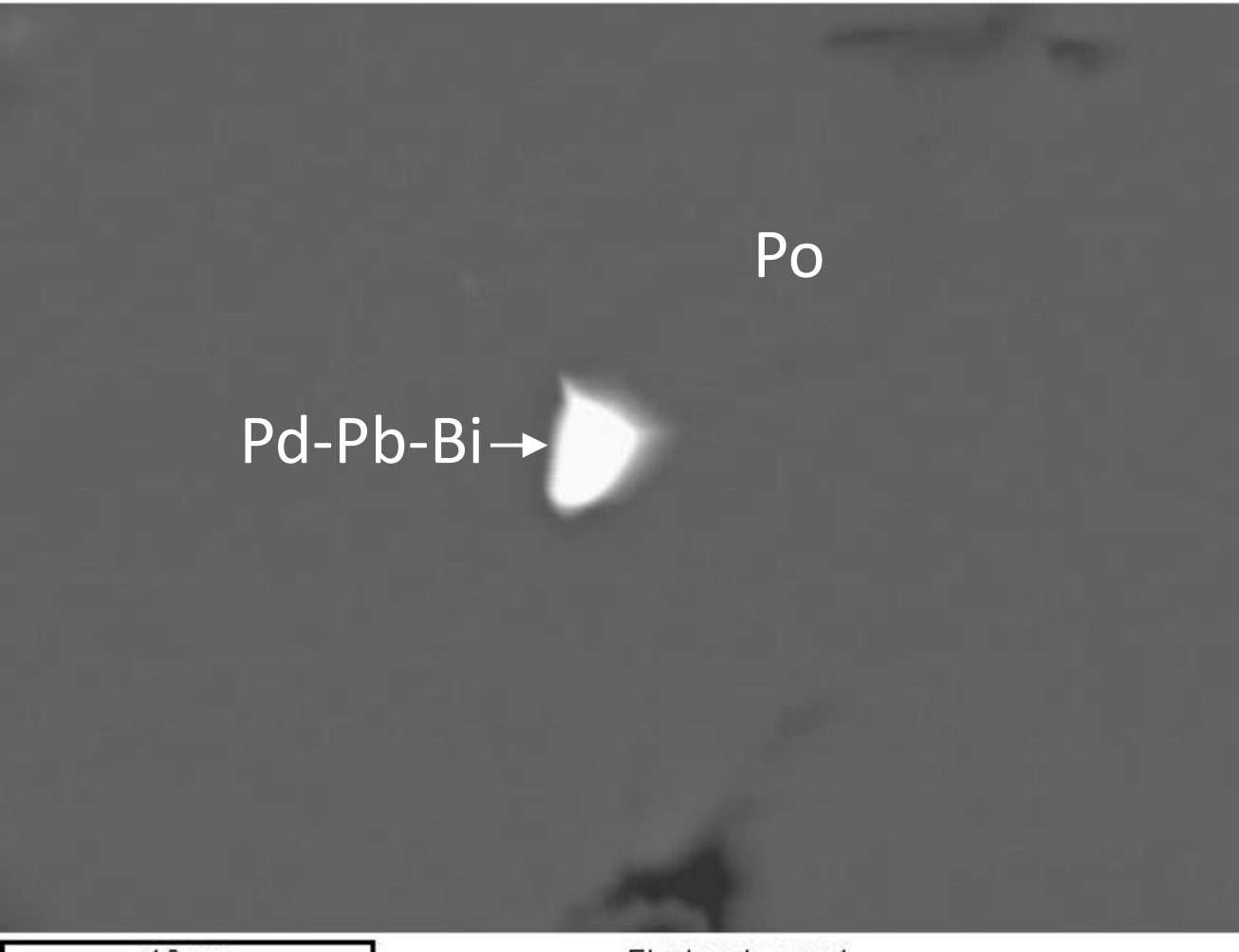
RK45 G1



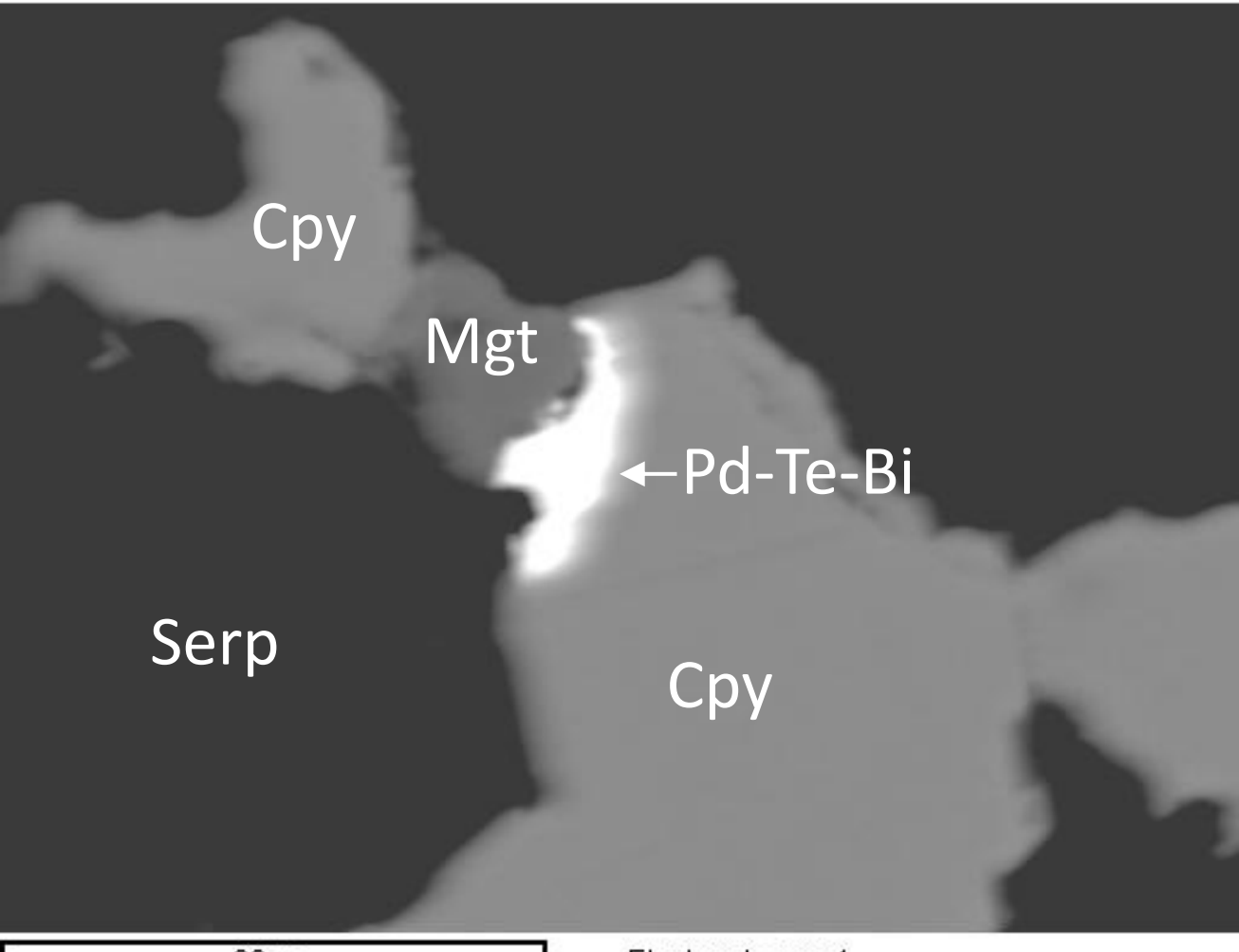
RK45 H1



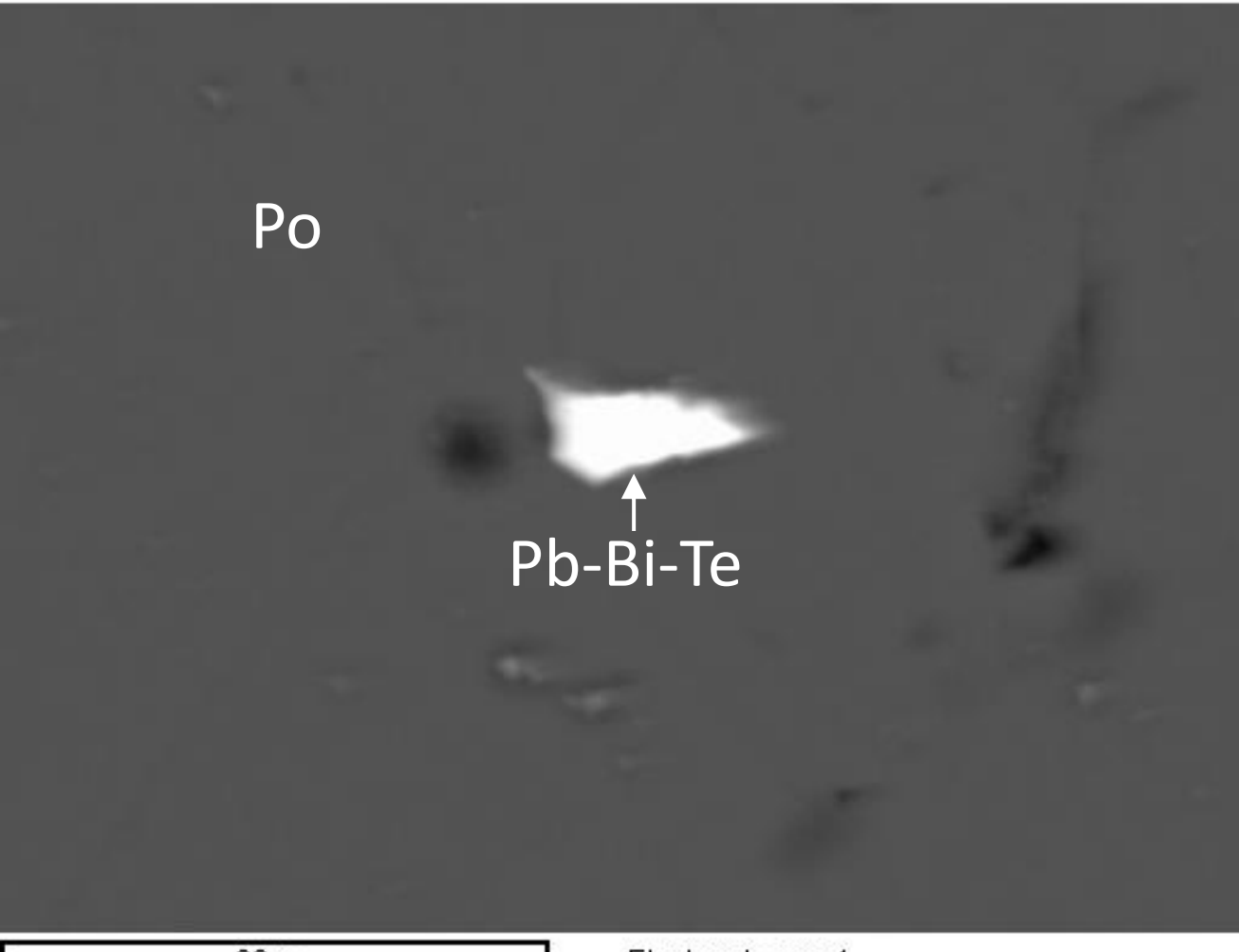
RK45 I1



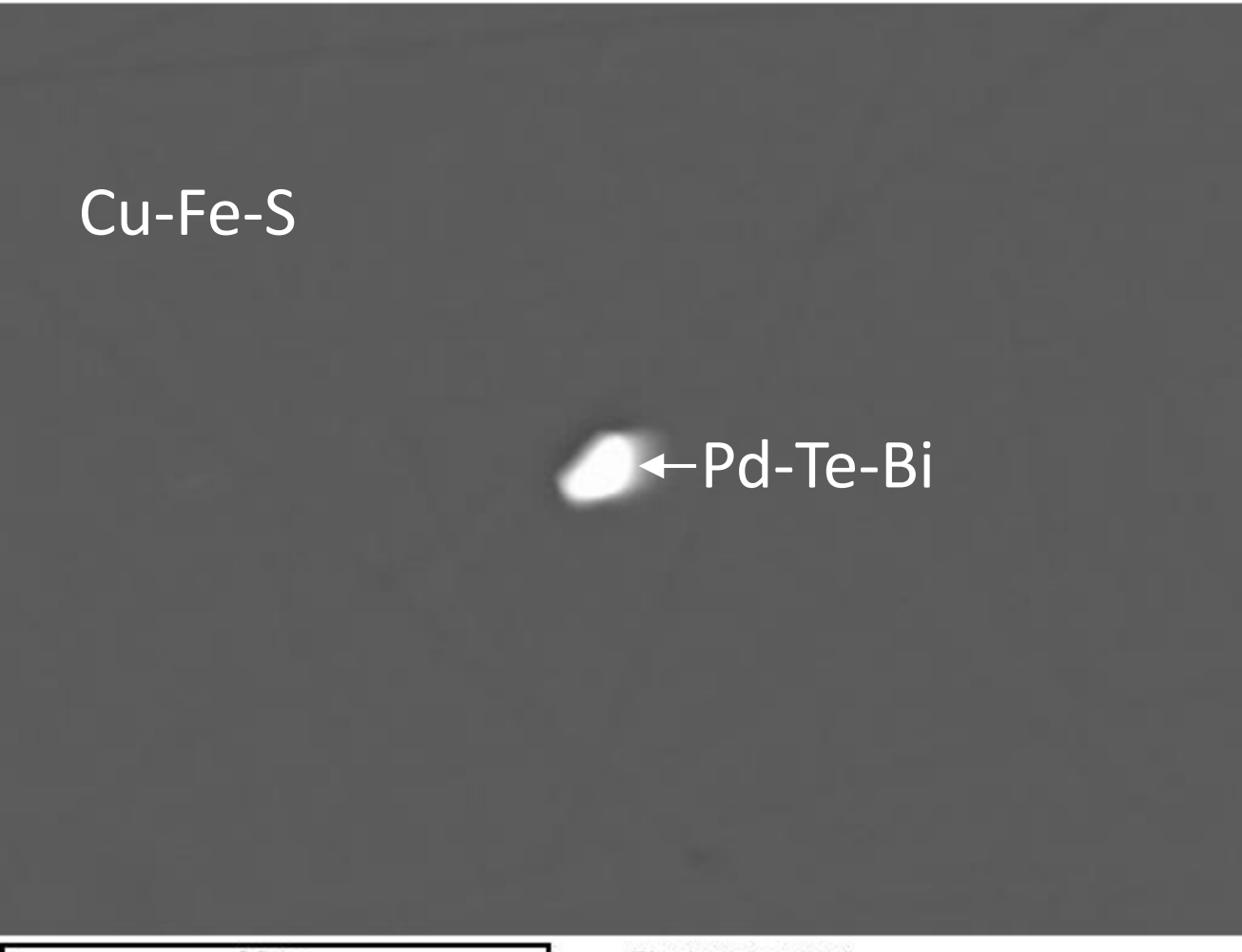
RK48 A1



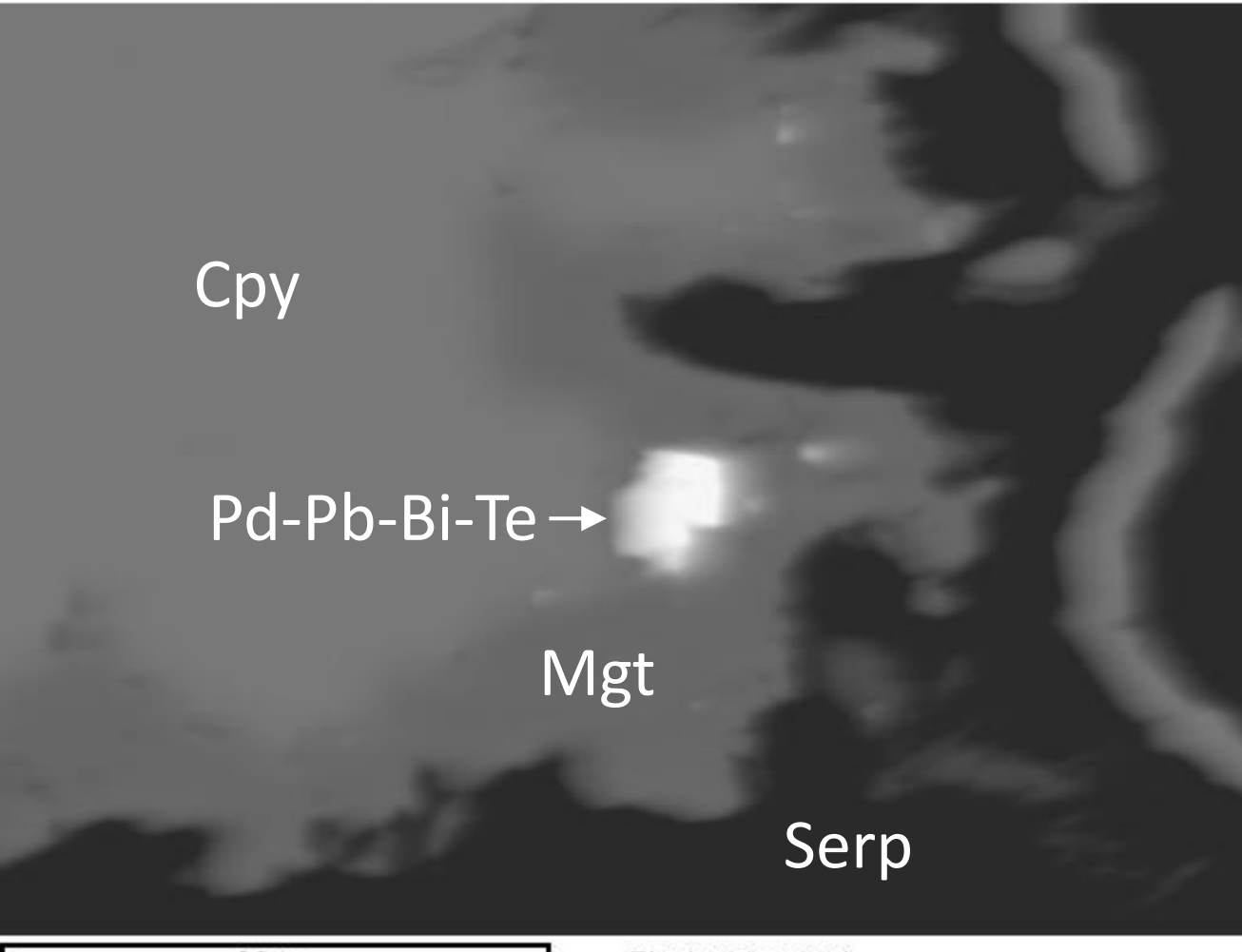
RK48 B1



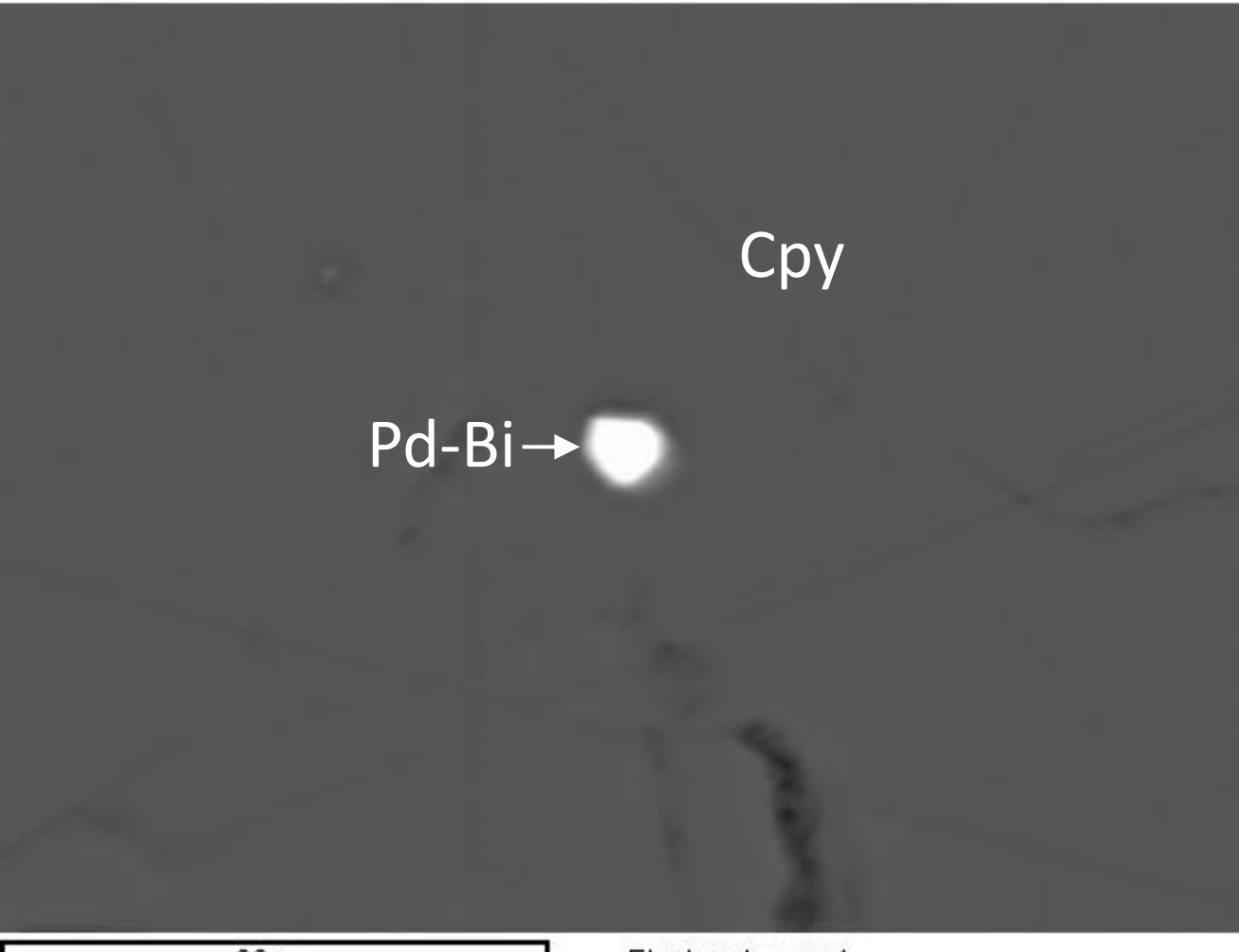
RK48 C1



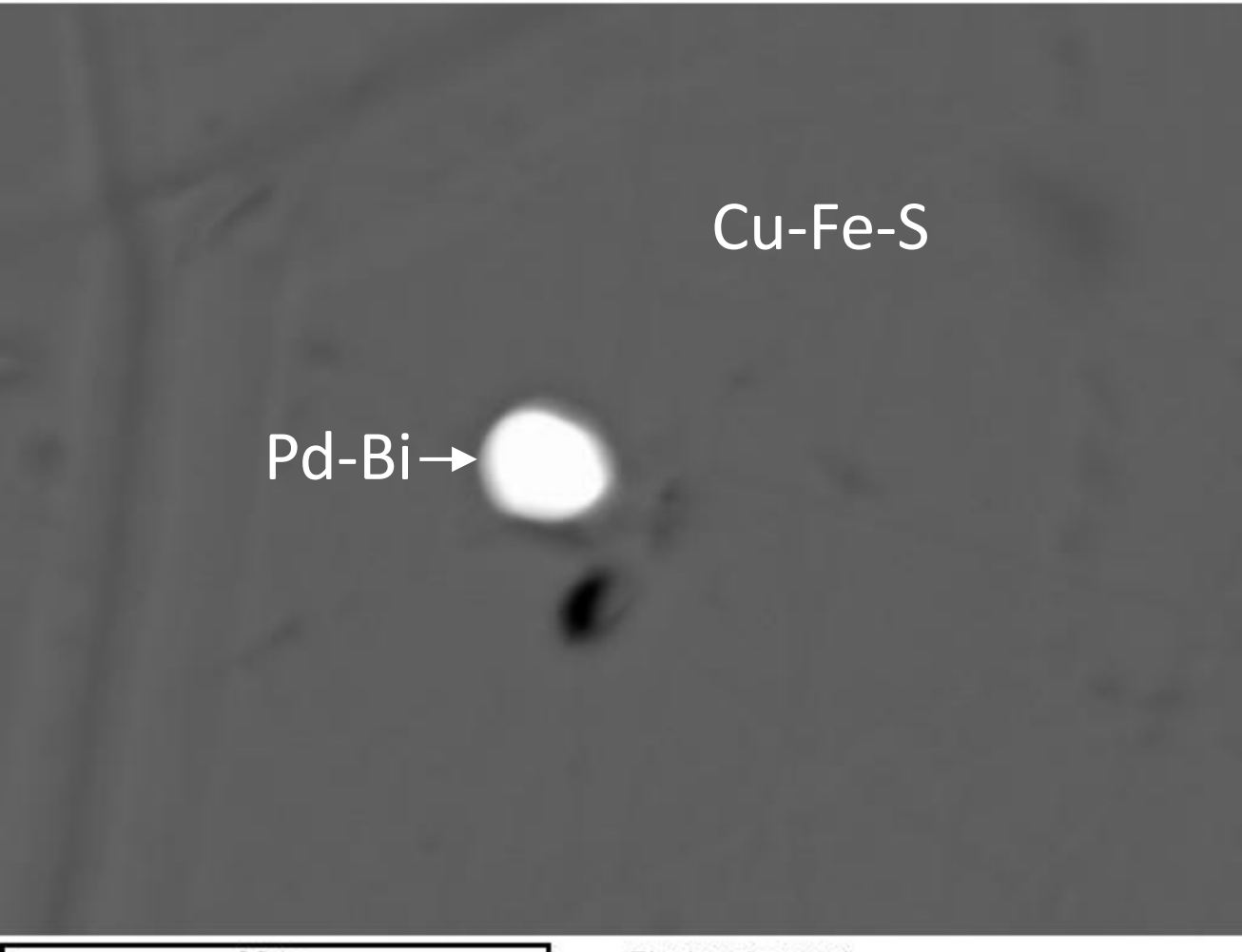
RK48 D1



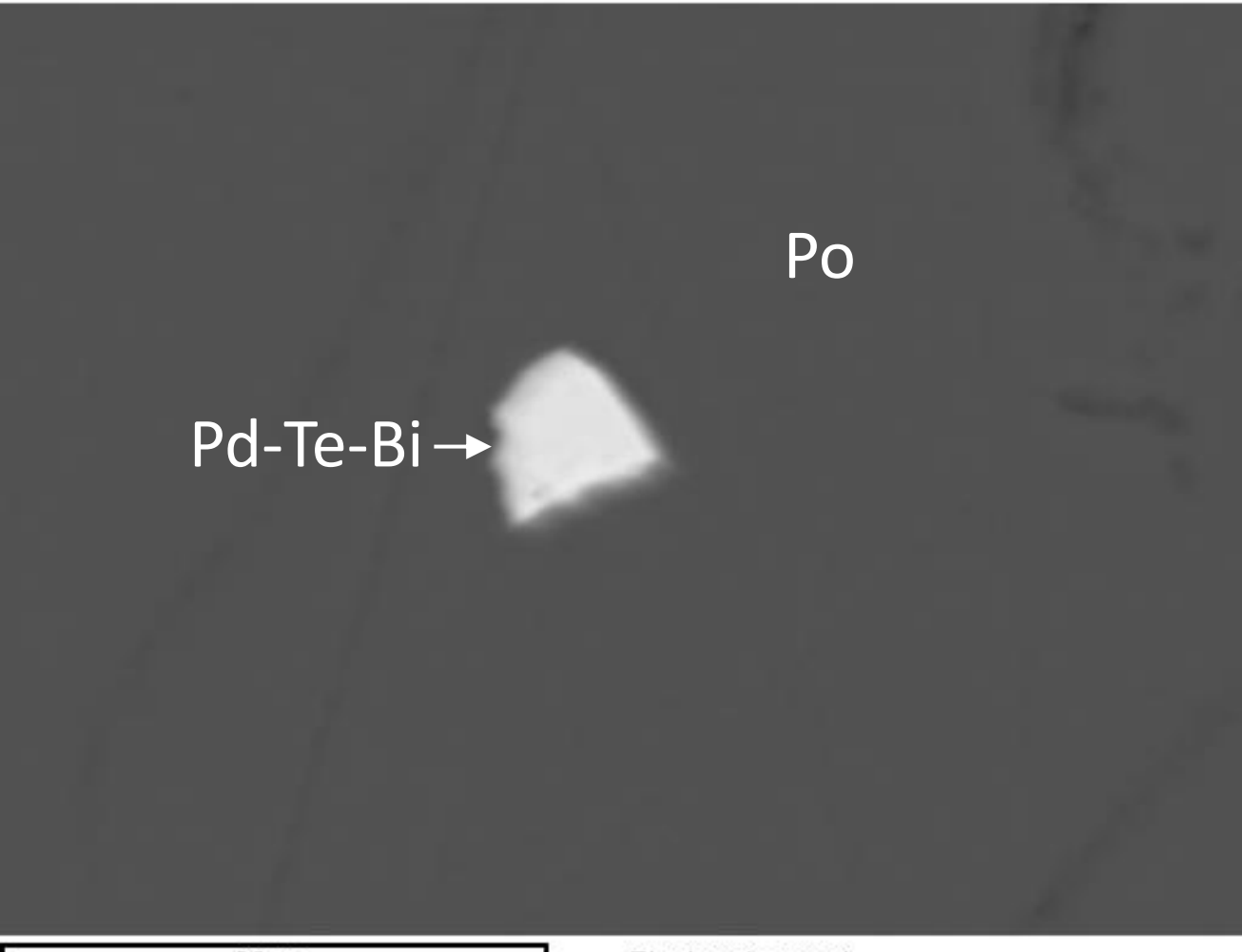
RK48 E1



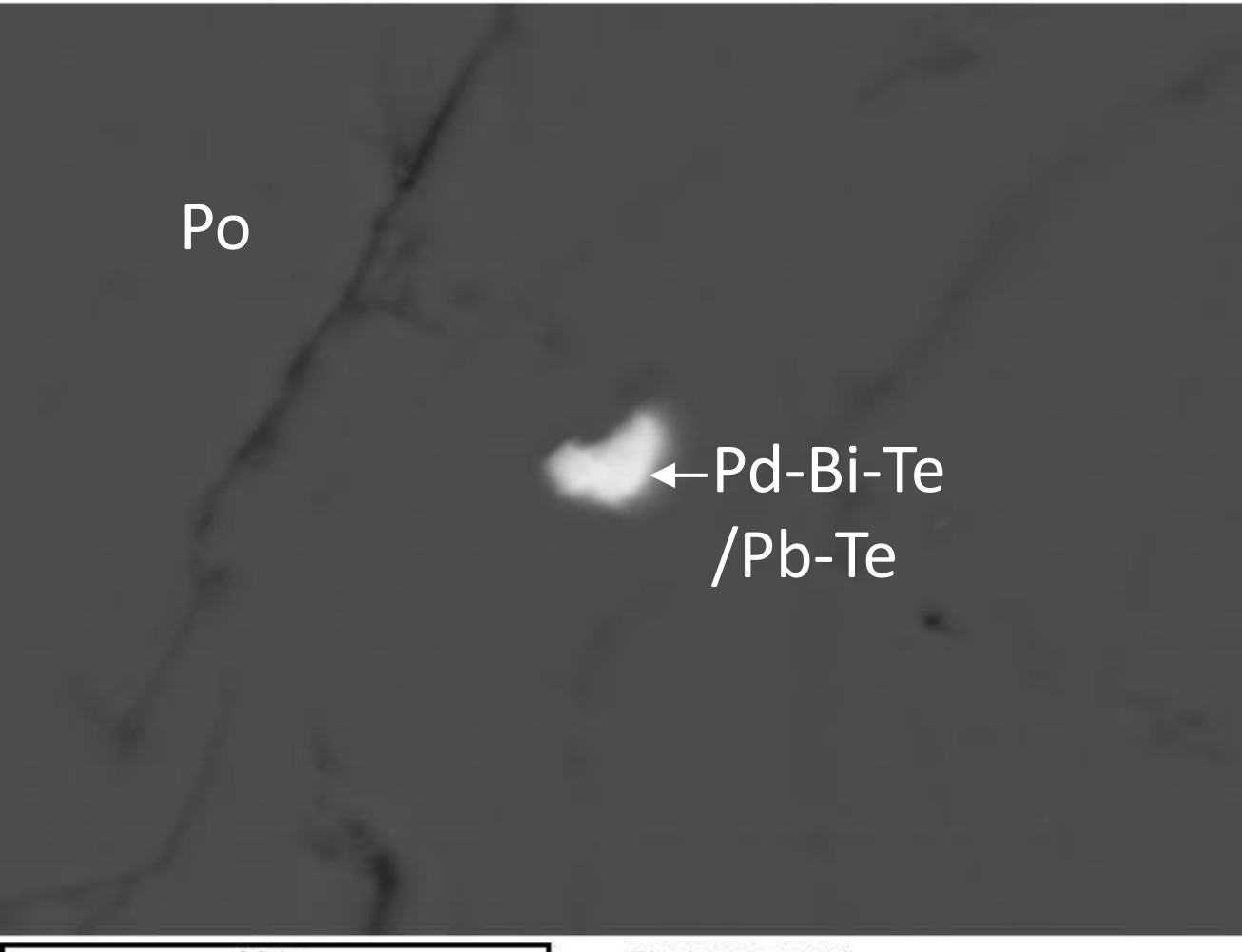
RK48 F1



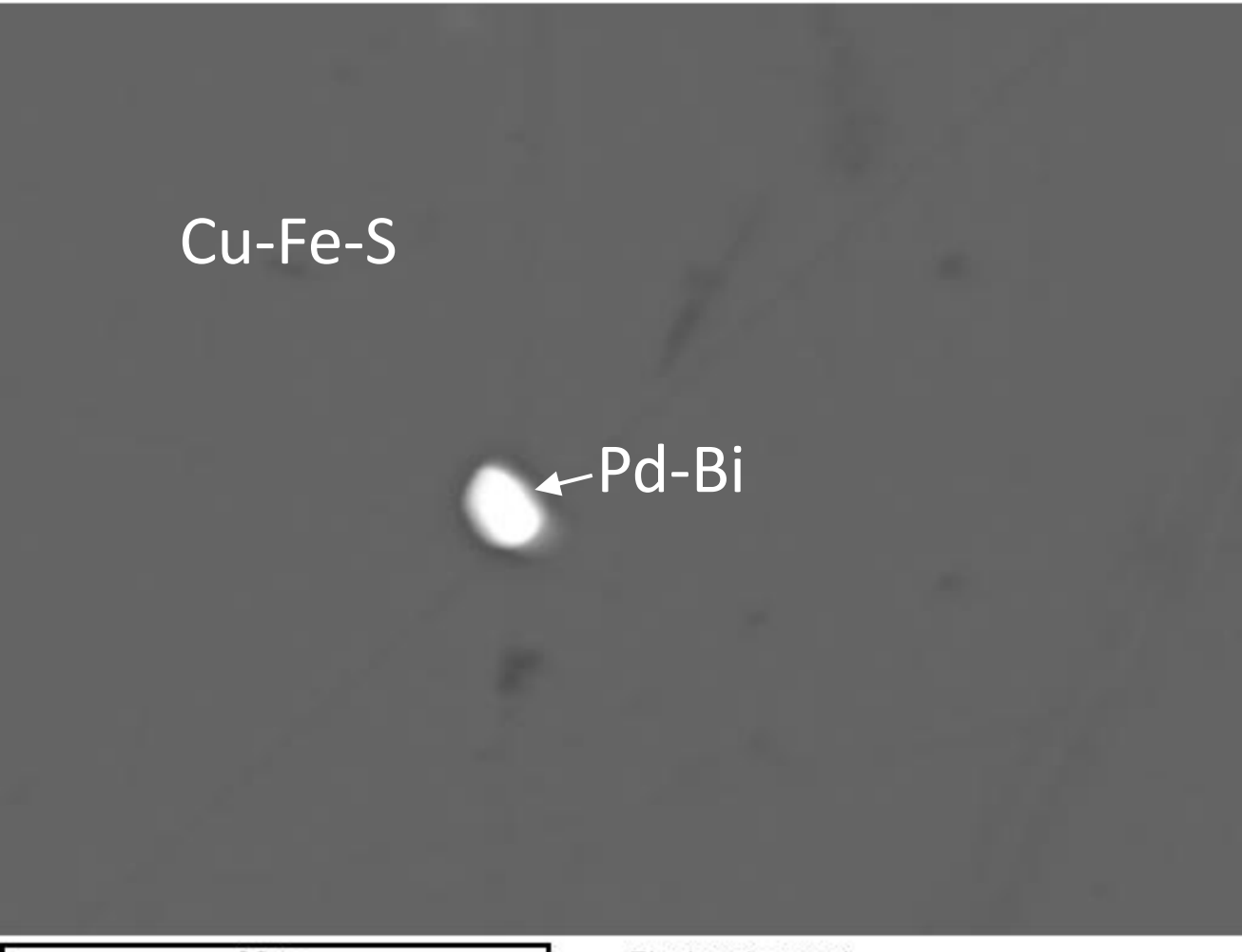
RK48 G1



RK48 G2



RK48 H1



Appendix O: Jincuan Full LA-ICP-MS Data (Cardiff University)

Zone and Drill Hole	Sample No.	Mineral Analysed	57Fe (wt. %)	59Co (ppm)	61Ni (wt. %)	65Cu (wt. %)	189Os (ppm)	193Ir (ppm)	101Ru* (ppm)	103Rh* (ppm)	195Pt (ppm)	106Pd* (ppm)	108Pd* (ppm)	197Au (ppm)	75As (ppm)	209Bi (ppm)	121Sb (ppm)	82Se (ppm)	125Te (ppm)
DZK12-06		Pn1	36.95	5342	31.56	0.84	0.20	<0.02	<0.06	<0.09	<0.02	0.48	0.56	0.01	41	4.87	<0.75	185	34.09
Orebody #1		Pn2	39.88	4775	28.83	0.07	0.15	<0.02	0.24	<0.09	<0.02	0.19	0.16	<0.01	<5	0.12	<0.75	157	<0.8
		Pn3	36.11	4970	29.27	0.05	0.18	<0.02	<0.06	<0.09	<0.02	0.56	0.50	0.02	<5	0.83	<0.75	146	<0.8
		Pn4	43.01	5372	31.89	0.05	<0.02	<0.02	<0.06	<0.09	<0.02	0.48	0.46	0.02	<5	0.22	<0.75	164	8.75
	RK03	Po1	65.90	113	0.61	0.05	0.20	<0.02	0.24	<0.09	<0.02	<0.11	<0.15	<0.01	<5	0.74	<0.75	153	<0.8
		Po2	60.40	128	0.71	0.05	0.22	<0.02	0.14	<0.09	<0.02	<0.11	<0.15	<0.01	<5	0.26	<0.75	168	<0.8
		Po3	68.20	232	1.51	0.05	0.18	<0.02	0.07	<0.09	<0.02	<0.11	<0.15	<0.01	<5	0.19	<0.75	157	<0.8
		Cpy1	31.47	76	0.40	31.60	<0.02	<0.02	<0.06	<0.09	<0.02	0.28	0.27	0.18	<5	2.62	<0.75	171	<0.8
		Cpy2	31.56	<5	<0.05	32.61	<0.02	<0.02	0.07	<0.09	<0.02	0.20	0.21	0.07	<5	1.09	<0.75	119	1.35
		Pn1	38.92	5286	28.68	0.10	<0.02	<0.02	<0.06	<0.09	<0.02	1.16	1.36	0.03	16	4.34	<0.75	133	18.14
		Pn2	42.88	5177	33.78	0.16	<0.02	<0.02	<0.06	<0.09	<0.02	2.63	2.34	0.02	9	0.43	<0.75	139	6.86
		Pn3	39.05	4808	29.13	0.16	0.04	<0.02	<0.06	<0.09	<0.02	1.81	1.87	0.03	<5	1.76	<0.75	128	2.17
	RK12	Pn4	38.71	4033	23.17	5.06	0.09	<0.02	<0.06	<0.09	<0.02	1.27	1.12	<0.01	<5	1.19	<0.75	125	<0.8
		Po1	65.06	7	0.10	0.05	0.06	<0.02	0.10	<0.09	<0.02	<0.11	<0.15	<0.01	<5	0.39	<0.75	134	<0.8
		Po2	63.99	235	1.19	0.05	0.09	<0.02	<0.06	<0.09	<0.02	<0.11	<0.15	<0.01	<5	0.58	<0.75	129	<0.8
		Po3	67.98	100	0.61	0.07	0.06	<0.02	0.15	<0.09	<0.02	<0.11	<0.15	<0.01	<5	1.54	<0.75	124	<0.8
		Pn1	36.96	6006	29.75	0.14	0.16	<0.02	<0.06	<0.09	<0.02	1.03	0.98	<0.01	<5	1.90	<0.75	90	1.57
		Pn2	38.37	6604	29.71	0.09	0.21	<0.02	<0.06	<0.09	<0.02	1.44	1.69	<0.01	14	0.15	<0.75	107	6.90
		Po1	63.94	168	0.95	0.11	0.31	<0.02	0.59	<0.09	<0.02	<0.11	<0.11	<0.01	<5	1.25	<0.75	99	<0.8
		Po2	62.61	127	0.62	0.05	0.19	<0.02	0.19	<0.09	<0.02	<0.11	<0.15	<0.01	<5	0.85	<0.75	87	<0.8
	RK13	Po3	55.31	<5	0.06	1.31	0.14	<0.02	0.25	<0.09	<0.02	<0.11	<0.15	<0.01	<5	1.51	<0.75	80	<0.8
		Cpy1	32.05	234	1.33	28.90	<0.02	<0.02	0.06	<0.09	<0.02	<0.11	<0.11	0.11	<5	1.99	<0.75	98	<0.8
		Cpy2	35.22	<5	<0.05	25.23	<0.02	<0.02	<0.06	<0.09	<0.02	<0.11	<0.11	0.05	<5	2.03	<0.75	95	<0.8
		Cpy3	30.46	130	1.00	28.68	<0.02	<0.02	0.11	<0.09	<0.02	<0.11	0.21	0.04	<5	1.82	<0.75	109	<0.8
		Cpy4	41.96	13	0.07	24.61	<0.02	<0.02	0.09	<0.09	<0.02	<0.11	<0.15	<0.01	<5	2.70	<0.75	87	1.09
DZK14-02		Pn1	31.78	5011	33.16	0.05	0.59	<0.02	0.24	<0.09	<0.02	0.25	0.39	<0.01	<5	3.33	<0.75	107	<0.8
Orebody #1		Pn2	29.46	4882	30.35	0.14	0.25	<0.02	<0.06	<0.09	<0.02	0.77	0.70	0.05	<5	6.44	<0.75	109	5.60
	RK19	Pn3	30.27	4424	29.79	0.71	0.16	<0.02	<0.06	<0.09	<0.02	0.82	0.78	<0.01	<5	4.36	<0.75	101	2.50
		Pn4	30.54	5229	30.70	0.54	0.57	<0.02	0.28	<0.09	<0.02	0.64	0.70	<0.01	<5	0.39	<0.75	115	<0.8
		Po1	60.56	107	1.14	0.05	0.48	<0.02	0.33	<0.09	<0.02	<0.11	<0.15	<0.01	<5	7.26	<0.75	120	1.91

Zone and Drill Hole	Sample No.	Mineral Analysed	57Fe (wt. %)	59Co (ppm)	61Ni (wt. %)	65Cu (wt. %)	189Os (ppm)	193Ir (ppm)	101Ru* (ppm)	103Rh* (ppm)	195Pt (ppm)	106Pd* (ppm)	108Pd* (ppm)	197Au (ppm)	75As (ppm)	209Bi (ppm)	121Sb (ppm)	82Se (ppm)	125Te (ppm)
		Po2	56.19	8	0.24	0.88	0.20	<0.02	<0.06	<0.09	<0.02	<0.11	<0.15	<0.01	<5	3.76	<0.75	112	<0.8
		Po3	59.54	106	0.95	<0.03	0.35	0.06	<0.06	0.14	<0.02	<0.11	<0.15	<0.01	<5	5.19	<0.75	114	<0.8
	RK19	Cpy1	27.97	<5	<0.05	25.93	<0.02	<0.02	0.07	<0.09	<0.02	<0.11	<0.15	0.06	<5	13.18	<0.75	111	<0.8
		Cpy2	29.50	118	0.72	27.59	0.11	<0.02	0.49	<0.09	<0.02	<0.11	<0.15	<0.01	<5	16.84	<0.75	107	4.12
		Cpy3	28.11	86	0.39	27.07	1.25	0.09	0.33	<0.09	<0.02	<0.11	<0.15	0.06	<5	12.96	<0.75	95	<0.8
		Pn1	63.59	4067	23.59	0.14	0.03	<0.02	<0.06	<0.09	<0.02	1.15	1.03	<0.01	25	4.06	<0.75	124	14.61
		Pn2	35.84	4218	27.27	0.08	<0.02	<0.02	<0.06	<0.09	<0.02	1.34	1.29	<0.01	<5	1.13	<0.75	105	<0.8
		Pn3	40.95	4016	21.57	0.08	0.05	<0.02	<0.06	<0.09	<0.02	1.01	0.94	<0.01	42	2.56	<0.75	149	28.86
		Pn4	27.06	3800	22.69	0.05	0.05	<0.02	<0.06	<0.09	<0.02	0.98	1.15	<0.01	34	1.77	<0.75	138	31.02
	RK23	Po1	57.04	<5	0.09	<0.03	<0.02	<0.02	<0.06	<0.09	<0.02	<0.11	<0.15	<0.01	<5	0.73	<0.75	120	1.12
		Po2	57.66	309	1.93	0.08	0.11	<0.02	<0.06	<0.09	<0.02	0.18	0.21	<0.01	<5	1.98	<0.75	112	<0.8
		Po3	60.92	233	1.34	0.12	<0.02	<0.02	<0.06	<0.09	<0.02	0.28	0.29	0.05	<5	2.36	<0.75	109	4.96
		Po4	58.18	<5	0.06	<0.03	<0.02	<0.02	<0.06	<0.09	<0.02	<0.11	<0.15	<0.01	<5	1.09	<0.75	115	<0.8
		Pn1	39.00	4265	22.68	1.99	<0.02	<0.02	<0.06	<0.09	<0.02	1.38	1.96	<0.01	<5	0.49	<0.75	130	<0.8
		Pn2	43.39	4920	22.35	0.24	<0.02	<0.02	<0.06	<0.09	<0.02	3.45	3.14	<0.01	11	2.04	<0.75	139	24.23
	RK24	Po1	63.02	82	0.50	0.06	<0.02	<0.02	<0.06	<0.09	<0.02	<0.11	<0.15	0.02	<5	1.11	<0.75	157	<0.8
		Po2	55.53	110	0.72	0.49	<0.02	<0.02	<0.06	<0.09	<0.02	2.43	2.19	<0.01	<5	9.14	<0.75	143	10.18
		Po3	58.49	31	0.25	0.06	<0.02	<0.02	<0.06	<0.09	<0.02	0.13	<0.15	<0.01	<5	1.04	<0.75	154	<0.8
DZK09-01		Pn1	29.70	5884	32.99	0.05	<0.02	<0.02	2.59	<0.09	<0.02	0.71	0.65	<0.01	<5	0.56	<0.75	119	<0.8
Orebody #1		Pn2	27.08	5851	28.45	0.59	<0.02	<0.02	<0.06	<0.09	<0.02	0.76	0.76	0.02	12	1.97	<0.75	98	<0.8
		Pn3	29.33	4916	31.34	0.05	<0.02	<0.02	<0.06	<0.09	<0.02	0.58	0.69	<0.01	<5	0.18	<0.75	108	3.79
		Pn4	29.65	4522	28.33	0.05	<0.02	<0.02	<0.06	<0.09	<0.02	0.82	0.78	0.01	<5	10.26	0.86	101	<0.8
	RK27	Po1	63.24	29	0.33	0.38	<0.02	<0.02	<0.06	<0.09	<0.02	<0.11	<0.15	<0.01	<5	4.20	<0.75	118	<0.8
		Po2	54.97	89	0.43	0.22	<0.02	<0.02	<0.06	<0.09	0.03	<0.11	<0.15	<0.01	<5	2.87	<0.75	108	<0.8
		Po3	55.72	52	0.56	0.15	<0.02	<0.02	<0.06	<0.09	<0.02	<0.11	<0.15	0.01	<5	4.94	<0.75	109	<0.8
		Cpy1	30.82	<5	<0.05	27.72	<0.02	<0.02	0.10	<0.09	<0.02	<0.11	<0.15	0.27	<5	2.90	<0.75	89	<0.8
		Cpy2	28.25	25	0.09	23.86	<0.02	<0.02	<0.06	<0.09	<0.02	<0.11	0.17	0.05	<5	4.31	<0.75	99	<0.8
		Cpy3	26.83	138	0.71	25.19	<0.02	<0.02	<0.06	<0.09	<0.02	<0.11	<0.15	0.17	<5	4.90	<0.75	101	<0.8
		Pn1	39.09	5697	34.03	<0.03	<0.02	<0.02	<0.06	<0.09	<0.02	0.32	0.33	<0.01	<5	0.50	<0.75	114	20.81
	RK29	Pn2	36.58	5838	34.25	<0.03	0.41	<0.02	1.17	0.12	<0.02	0.49	0.52	0.03	6	0.13	<0.75	138	11.10
		Pn3	34.22	5639	33.03	<0.03	0.06	<0.02	0.27	0.17	<0.02	0.83	1.42	<0.01	<5	0.29	<0.75	106	1.00

Zone and Drill Hole	Sample No.	Mineral Analysed	57Fe (wt. %)	59Co (ppm)	61Ni (wt. %)	65Cu (wt. %)	189Os (ppm)	193Ir (ppm)	101Ru* (ppm)	103Rh* (ppm)	195Pt (ppm)	106Pd* (ppm)	108Pd* (ppm)	197Au (ppm)	75As (ppm)	209Bi (ppm)	121Sb (ppm)	82Se (ppm)	125Te (ppm)
	RK29	Pn4	35.79	6967	34.80	<0.03	0.06	<0.02	0.53	0.18	<0.02	1.28	1.36	0.05	<5	0.11	<0.75	141	4.73
		Po1	69.56	139	1.56	<0.03	0.03	<0.02	<0.06	<0.09	<0.02	<0.11	<0.14	<0.01	<5	0.96	<0.75	114	1.88
		Po2	61.44	206	1.36	<0.03	0.02	<0.02	0.08	<0.09	<0.02	<0.11	<0.14	0.03	<5	0.84	<0.75	105	<0.8
		Po3	66.37	176	1.02	<0.03	0.03	<0.02	<0.06	<0.09	<0.02	<0.11	<0.14	<0.01	<5	2.79	<0.75	115	<0.8
		Po4	68.66	301	2.09	<0.03	<0.02	<0.02	0.13	<0.09	<0.02	<0.11	0.16	0.04	<5	1.19	<0.75	119	<0.8
	RK30	Pn1	38.05	7416	33.59	<0.03	<0.02	<0.02	0.16	<0.09	<0.02	4.71	5.13	<0.01	<5	0.42	<0.75	181	23.77
		Pn2	39.36	6931	31.54	0.52	<0.02	<0.02	<0.06	<0.09	0.03	4.51	4.29	0.02	<5	0.71	<0.75	150	16.60
		Pn3	40.85	7194	32.24	0.06	<0.02	<0.02	0.19	0.14	<0.02	3.96	3.91	<0.01	10	0.55	<0.75	180	23.50
		Pn4	37.30	6369	31.03	0.82	<0.02	<0.02	<0.06	<0.09	<0.02	5.17	5.27	<0.01	<5	0.17	<0.75	163	6.64
		Po1	71.78	178	1.11	0.04	<0.02	<0.02	<0.06	<0.09	<0.02	0.45	0.39	<0.01	<5	2.72	<0.75	134	270.00
		Po2	69.10	136	0.66	0.07	<0.02	<0.02	<0.06	<0.09	<0.02	<0.11	<0.14	0.02	<5	0.43	<0.75	134	<0.8
		Po3	72.75	24	0.24	<0.03	<0.02	<0.02	<0.06	<0.09	<0.02	<0.11	<0.14	<0.01	<5	0.44	<0.75	112	<0.8
		Cpy1	30.81	<5	<0.05	28.74	<0.02	<0.02	<0.06	<0.09	<0.02	0.44	0.47	<0.01	<5	1.96	<0.75	136	4.68
		Cpy2	33.26	246	1.12	30.06	<0.02	<0.02	<0.06	<0.09	<0.02	0.18	0.18	0.01	<5	0.59	<0.75	146	4.03
		Cpy3	32.94	163	0.70	28.83	<0.02	<0.02	<0.06	<0.09	<0.02	0.30	0.29	<0.01	<5	0.24	<0.75	152	4.20
	RK33	Pn1	37.80	7512	29.54	<0.03	0.36	<0.02	<0.06	<0.09	<0.02	0.95	0.82	0.04	<5	1.13	<0.75	130	6.04
		Pn2	41.79	7457	27.76	<0.03	0.09	<0.02	0.22	<0.09	<0.02	1.40	1.32	<0.01	<5	0.72	<0.75	89	1.03
		Pn3	34.27	6954	29.34	0.49	0.80	<0.02	0.43	<0.09	<0.02	1.17	1.27	0.17	5	1.60	<0.75	134	21.39
		Po1	63.65	396	1.56	<0.03	0.10	<0.02	<0.06	<0.09	<0.02	<0.11	<0.14	0.02	<5	1.05	<0.75	109	1.04
		Po2	65.67	23	0.15	<0.03	0.00	<0.02	0.07	<0.09	<0.02	<0.11	<0.14	<0.01	<5	0.85	<0.75	133	0.86
		Po3	66.14	258	1.11	<0.03	0.16	<0.02	0.07	<0.09	<0.02	<0.11	<0.14	<0.01	<5	0.37	<0.75	127	<0.8
		Cpy1	33.50	<5	<0.05	31.44	<0.02	<0.02	0.07	<0.09	<0.02	<0.11	<0.14	<0.01	<5	1.29	<0.75	137	10.28
		Cpy2	31.43	180	0.81	27.27	<0.02	<0.02	<0.06	<0.09	<0.02	<0.11	<0.14	0.04	<5	1.12	<0.75	94	11.51
ZKS-09 Orebody #24	RK41	Pn1	47.77	4758	25.88	0.03	0.14	0.07	<0.06	<0.09	<0.02	0.47	0.48	0.10	<5	0.49	<0.75	116	3.41
		Pn2	43.81	4941	27.02	<0.03	0.38	0.19	<0.06	<0.09	<0.02	1.29	1.21	0.19	<5	1.11	<0.75	115	4.74
		Pn3	54.83	84	0.48	<0.03	0.05	<0.02	0.08	<0.09	<0.02	1.89	1.87	0.07	<5	7.15	<0.75	99	<0.8
		Po1	64.99	110	0.67	0.03	0.08	0.07	<0.06	<0.09	<0.02	<0.11	<0.14	<0.01	<5	0.81	<0.75	117	<0.8
		Po2	56.64	243	1.15	<0.03	0.12	0.04	<0.06	<0.09	<0.02	0.33	<0.14	0.04	<5	1.71	<0.75	135	8.26
		Po3	42.40	5932	29.31	<0.03	0.04	0.12	0.14	0.20	<0.02	1.33	1.30	0.15	<5	2.35	<0.75	161	17.59
		Py1	49.93	<5	<0.05	<0.03	<0.02	<0.02	<0.06	<0.09	<0.02	<0.11	<0.14	0.16	21	0.01	0.85	141	1.41
		Py2	53.77	<5	<0.05	<0.03	<0.02	<0.02	<0.06	<0.09	<0.02	<0.11	<0.14	0.37	<5	0.08	<0.75	120	1.99

Zone and Drill Hole	Sample No.	Mineral Analysed	57Fe (wt. %)	59Co (ppm)	61Ni (wt. %)	65Cu (wt. %)	189Os (ppm)	193Ir (ppm)	101Ru* (ppm)	103Rh* (ppm)	195Pt (ppm)	106Pd* (ppm)	108Pd* (ppm)	197Au (ppm)	75As (ppm)	209Bi (ppm)	121Sb (ppm)	82Se (ppm)	125Te (ppm)
	RK45	Pn1	41.51	6501	27.53	<0.03	0.22	<0.02	<0.06	<0.09	<0.02	1.87	2.04	0.13	<5	0.09	<0.75	138	6.32
		Pn2	43.37	5968	26.16	0.12	0.32	0.21	<0.06	0.22	<0.02	1.97	1.95	0.06	<5	0.18	<0.75	148	13.16
		Pn3	42.31	5903	26.79	<0.03	0.50	0.08	0.11	<0.09	<0.02	1.40	1.35	0.15	<5	0.35	<0.75	122	3.73
		Po1	61.82	379	1.66	<0.03	0.18	0.04	0.14	<0.09	<0.02	<0.11	<0.14	<0.01	<5	0.52	<0.75	143	<0.8
		Po2	60.95	205	1.11	<0.03	0.29	0.06	0.14	<0.09	0.03	<0.11	<0.14	<0.01	<5	0.22	<0.75	130	<0.8
		Po3	58.35	126	0.89	-0.08	0.22	0.03	0.08	<0.09	<0.02	<0.11	<0.14	<0.01	<5	0.21	<0.75	119	<0.8
		Py1	53.20	<5	<0.05	<0.03	<0.02	<0.02	<0.06	<0.09	<0.02	<0.11	<0.14	0.07	<5	<0.05	<0.75	352	2.40
	RK48	Pn1	26.68	4905	23.59	4.36	<0.02	<0.02	0.22	<0.09	<0.02	0.64	0.62	0.21	<5	9.79	<0.75	129	53.63
		Po1	57.73	17	0.09	0.07	0.13	<0.02	<0.06	<0.09	<0.02	<0.11	<0.14	<0.01	<5	0.16	<0.75	126	<0.8
		Po2	56.98	<5	0.27	0.22	<0.02	<0.02	0.14	<0.09	<0.02	<0.11	<0.14	<0.01	<5	0.25	<0.75	95	<0.8
		Cpy1	27.67	95	0.40	28.31	<0.02	<0.02	<0.06	<0.09	<0.02	<0.11	<0.14	0.13	<5	3.67	<0.75	96	7.16
		Cpy2	24.81	61	0.50	22.28	<0.02	<0.02	0.10	<0.09	<0.02	<0.11	<0.14	0.06	<5	0.26	<0.75	108	8.48
		Cpy3	28.93	<5	<0.05	21.90	0.04	<0.02	<0.06	<0.09	<0.02	<0.11	<0.14	0.02	<5	0.23	<0.75	87	3.26
	RK49	Pn1	47.54	6897	28.16	<0.03	0.43	<0.02	0.13	<0.09	<0.02	2.65	2.73	0.04	<5	0.21	<0.75	98	<0.8
		Pn2	39.80	6436	28.65	<0.03	0.58	0.04	0.10	0.28	<0.02	2.92	2.90	0.06	<5	0.13	<0.75	134	10.18
		Pn3	39.15	6718	27.86	<0.03	0.16	<0.02	0.22	<0.09	<0.02	1.36	1.39	0.06	<5	0.42	<0.75	125	4.81
		Pn4	37.60	6654	25.37	0.32	<0.02	<0.02	<0.06	0.78	<0.02	0.57	0.61	0.16	<5	2.01	<0.75	169	33.74
		Po1	61.30	147	0.65	<0.03	0.56	<0.02	0.19	<0.09	<0.02	<0.11	<0.14	<0.01	<5	0.07	<0.75	122	<0.8
		Po2	64.40	232	0.77	<0.03	0.74	<0.02	0.59	<0.09	<0.02	<0.11	<0.14	0.02	<5	0.16	<0.75	137	<0.8
		Po3	59.60	199	0.90	<0.03	<0.02	<0.02	<0.06	<0.09	<0.02	0.19	0.20	0.02	<5	0.58	<0.75	106	1.21